OHBM 2024
JUNE 23~27, SEOUL, KOREA

ABSTRACTS

Sunday, June 23 – Thursday, June 27
COEX CONVENTION & EXHIBITION CENTER | SEOUL

30TH ANNUAL MEETING OF THE
ORGANIZATION FOR HUMAN BRAIN MAPPING

Poster No 1

Acute and longitudinal fMRI brain response to deep brain stimulation in Parkinson's disease

Skyler Deutsch[1], Katelyn Vu[1], Andrea Fuentes[2], Sarah Wang[3], Alastair Martin[1], Jill Ostrem[3], Philip Starr[4], Doris Wang[4], Ian Bledsoe[3], Melanie Morrison[1]

[1]Radiology and Biomedical Imaging, University of California San Francisco, San Francisco, CA, [2]Department of Neurology and Neurological Sciences, Stanford University, Stanford, CA, [3]Neurology, University of California San Francisco, San Francisco, CA, [4]Neurological Surgery, University of California San Francisco, San Francisco, CA

Introduction: Deep brain stimulation (DBS) is an effective second-line therapy for Parkinson's disease symptom management, though there is still significant, unexplained variability in patient outcomes. With recent advances in DBS hardware enabling patients to undergo MRI with stimulation, researchers have been leveraging functional MRI (fMRI) to better understand this variability in response to DBS. (Loh et al. 2022) It has been repeatedly shown that DBS modulates activity in the cerebellum and cortico-basal ganglia-thalamo-cortical network. (Kahan et al. 2012) (Mueller et al. 2018) The direction however in which DBS alters brain activity differs across studies and the time course and relationship of these alterations with symptom response is limitedly understood. (Loh et al. 2022) (Shen et al. 2020) The globus pallidus interna (GPi) target has also been less represented in studies than the subthalamic nucleus (STN). (Boutet et al. 2021) (Zhang et al. 2021) (Hwang et al. 2023) To address the gaps in knowledge, we present our early findings of acute and longitudinal brain patterns underlying STN and GPi DBS, leveraging a prospective imaging dataset where motor response is evaluated immediately prior to imaging under identical stimulation conditions.

Methods: Sixteen patients with PD (mean age 64.88; 19% F) implanted with a Medtronic Percept PC DBS system 4.77-66.48 months prior (STN=7, GPi=9; Fig 1A), consented to postoperative resting-state (rs)-fMRI simultaneous to brain stimulation. Imaging was performed on a 3T GE system in low-SAR mode for a total of 24-min: 12 with stimulation in an alternate bipolar setting programmed to mimic the clinical monopolar settings, and 12 with DBS turned off (Fig 1B). Immediately before scanning, motor testing was performed in the bipolar research configuration with stimulation turned on, then off, to measure degree of acute symptom improvement. Three patients returned for repeat imaging and motor testing 2.33-6.35 months later. All patients had preoperative motor testing done as part of their clinical work up for DBS; five patients had preoperative rs-fMRI available. Time-series data were preprocessed in CONN. (Whitfield-Gabrieli and Nieto-Castanon 2012) The variability (standard deviation) of fMRI signal in brain areas comprising the motor network was calculated, representing neural adaptability. (Garrett et al. 2010) We investigated target-specific patterns of acute and longitudinal fMRI response to DBS in relation to degree of symptom improvement.

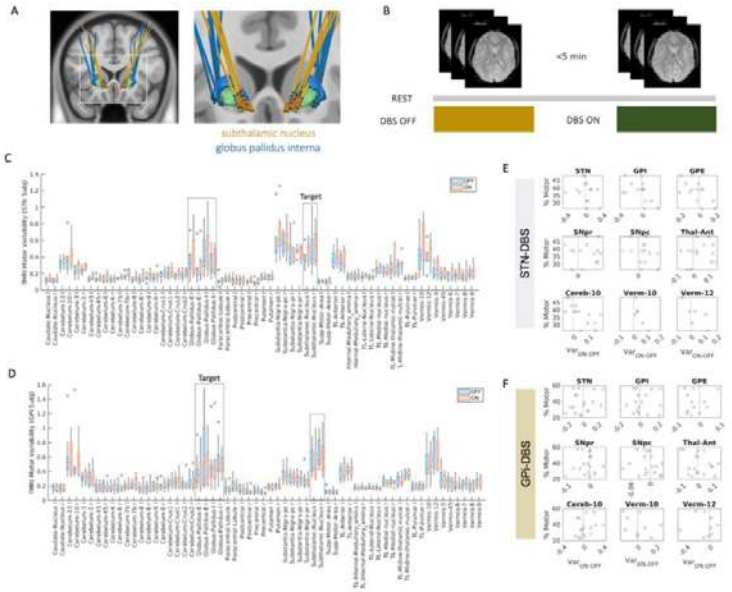

Figure 1: A. Coronal view of reconstructed electrodes for all subjects (N=16) using the Lead-DBS. **B.** Schematic of the test-retest fMRI protocol. **C-D.** Box and whisker plots comparing regional fMRI variability within motor areas across the DBS-ON (red) versus -OFF (blue) condition in STN (C; N=7) and GPi (D; N=9) implanted patients. **E-F.** Scatterplots showing for a subset of motor areas with elevated variability, the correlation between target-specific, acute clinical motor improvement and the degree of change in variability across the DBS-ON versus OFF condition.

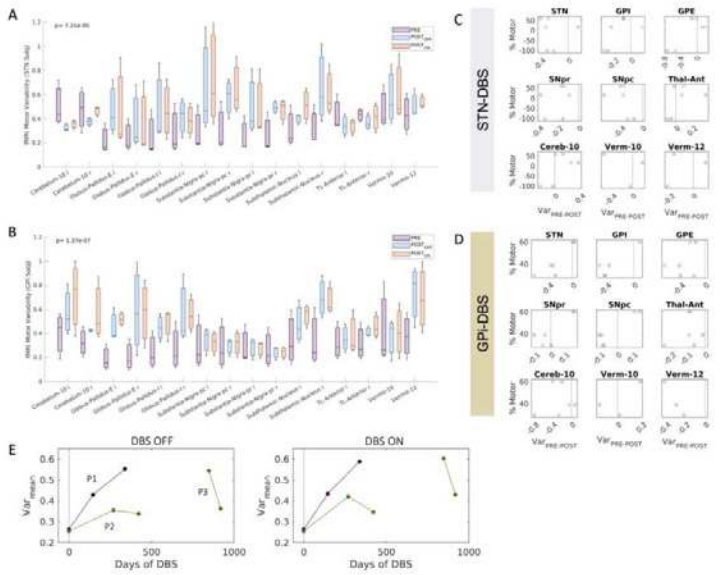

Figure 2: A-B. Box and whisker plots comparing regional fMRI variability within key motor areas across the preop (purple), postop DBS-ON (red), and postop DBS-OFF (blue) conditions in 3 STN (A) and 3 GPi (B) implanted patients. **C-D.** Scatterplots showing a subset of motor areas with elevated variability, target-specific, pre-to-post clinical motor improvement and the degree of change in variability across the preop versus postop DBS-ON condition. **E.** Line plots for three patients tracking the average variability of all key motor areas over multiple visits. Zero line corresponds to the day of or before surgery when preoperative fMRI was performed.

Results: Brain variability was significantly elevated in a subset of basal ganglia and cerebellar areas, both in the DBS-ON and OFF conditions (Fig 1CD). Stimulation altered network variability; the direction and degree of modulation correlated with degree of acute motor improvement, interestingly, with some opposing trends for patients implanted in the STN versus GPi that could reflect target-specific inhibitory and excitatory influence on the network (Fig 1EF). On average, preoperative variability was significantly reduced in multiple brain areas, suggestive of a neuroplastic effect (Fig 2AB). Again, degree and direction of modulation frequently correlated with longitudinal (pre-to-post) motor symptom improvement (Fig CD). In two patients, variability averaged over the subset of key motor areas was mostly consistent across multiple postoperative timepoints and did not approach preoperative values, further supporting the neuroplasticity hypothesis (Fig 2E).

Conclusions: Preliminary results from this study show that in Parkinson's disease, DBS acutely and longitudinally modulates the moment-to-moment variability of brain areas within the motor network. The direction of modulation of specific motor areas is related to patients' degree of clinical motor improvement. With the largest differences in fMRI variability metrics detected across the pre- vs post-DBS imaging conditions, longitudinal findings likely reflect neuroplastic effects and warrant further investigation.

References

1. Boutet, A. (2021), 'Predicting Optimal Deep Brain Stimulation Parameters for Parkinson's Disease Using Functional MRI and Machine Learning', Nature Communications, vol. 12, no.1, pp. 3043
2. Garrett, D.D. (2010), 'Blood Oxygen Level-Dependent Signal Variability Is More than Just Noise', The Journal of Neuroscience, vol. 30, no. 14, pp. 4914–21
3. Hwang, Y.S. (2023), 'Long-Term Motor Outcomes of Deep Brain Stimulation of the Globus Pallidus Interna in Parkinson's Disease Patients: Five-Year Follow-Up', Journal of the Neurological Sciences, vol. 444, pp. 120484
4. Kahan, J. (2014), 'Resting State Functional MRI in Parkinson's Disease: The Impact of Deep Brain Stimulation on 'Effective' Connectivity', Brain, vol. 137, no. 4, pp. 1130–44
5. Loh, A. (2022), 'Probing Responses to Deep Brain Stimulation with Functional Magnetic Resonance Imaging', Brain Stimulation, vol. 15, no. 3, pp. 683–94
6. Mueller, K. (2018), 'Brain Connectivity Changes When Comparing Effects of Subthalamic Deep Brain Stimulation with Levodopa Treatment in Parkinson's Disease', NeuroImage Clinical, vol. 19, pp. 1025–35
7. Shen, L. (2020), 'Subthalamic Nucleus Deep Brain Stimulation Modulates 2 Distinct Neurocircuits', Annals of Neurology, vol. 88, no. 6, pp. 1178–93
8. Whitfield-Gabrieli, S. (2012), 'Conn: A Functional Connectivity Toolbox for Correlated and Anticorrelated Brain Networks', Brain Connectivity, vol. 2, no. 3, pp. 125–41
9. Zhang, C. (2021), 'Subthalamic and Pallidal Stimulations in Patients with Parkinson's Disease: Common and Dissociable Connections', Annals of Neurology, vol. 90, no. 4, pp.670–82

Poster No 2

Neurocircuitry of apathy in Parkinson's patients with subthalamic nucleus deep brain stimulation

Jip de Bruin[1], Ki Sueng Choi[1], Helen Mayberg[1], Joohi Jimenez-Shahed[1], Christina Palmese[1], Juna Khang[1], Ha Neul Song[1], Brian Kopell[1], Martijn Figee[1]

[1]Icahn School of Medicine at Mount Sinai, New York, NY

Introduction: Subthalamic nucleus deep brain stimulation (STN DBS) improves motor symptoms of Parkinson's disease (PD), but its effect on motivation is controversial. Apathy, characterized by lack of motivation and energy, commonly occurs in PD, and is often exacerbated after STN DBS and post-surgical levodopa withdrawal. Apathy is linked to dopaminergic denervation in limbic and associative pathways which are not typically targeted with STN DBS. Similar to motor symptoms, apathy can be a levodopa-responsive PD symptom. The routine withdrawal of levodopa after surgery could therefore reveal apathy when these non-motor pathways are not stimulated with STN DBS. Here, we examined the moderating role of levodopa withdrawal on the relationship between postoperative apathy and the structural connectivity of stimulation volumes to limbic and associative networks.

Methods: Apathy scores and medication information were collected in 28 PD patients before and six months after STN DBS. We modeled stimulation volumes and structural connectivity patterns using patient-specific diffusion-weighted magnetic resonance images and probabilistic tractography. First, we explored the interaction between medication reduction and stimulation of limbic, associative, and motor pathways on apathy change. Second, we investigated the modulatory role of medication withdrawal by testing the relationship between apathy change score and stimulation-related connectivity separately in patients with high (N = 17) and low (N = 11) medication withdrawal.

Results: Apathy increased after STN DBS in 13 of the 28 patients. There was a significant interaction between medication withdrawal and left ventromedial prefrontal cortex (vmPFC) involvement on change in apathy. In patients with high medication withdrawal, DBS-related apathy was associated with lower connectivity of the stimulation volume to the left ventromedial prefrontal cortex and orbital frontal cortex. The change in apathy was unrelated to motor pathway connectivity, or motor symptoms. These findings were additionally used for a tractography guided change in stimulation parameters for a case example with apathy post DBS. Which resulted in a significant apathy decrease.

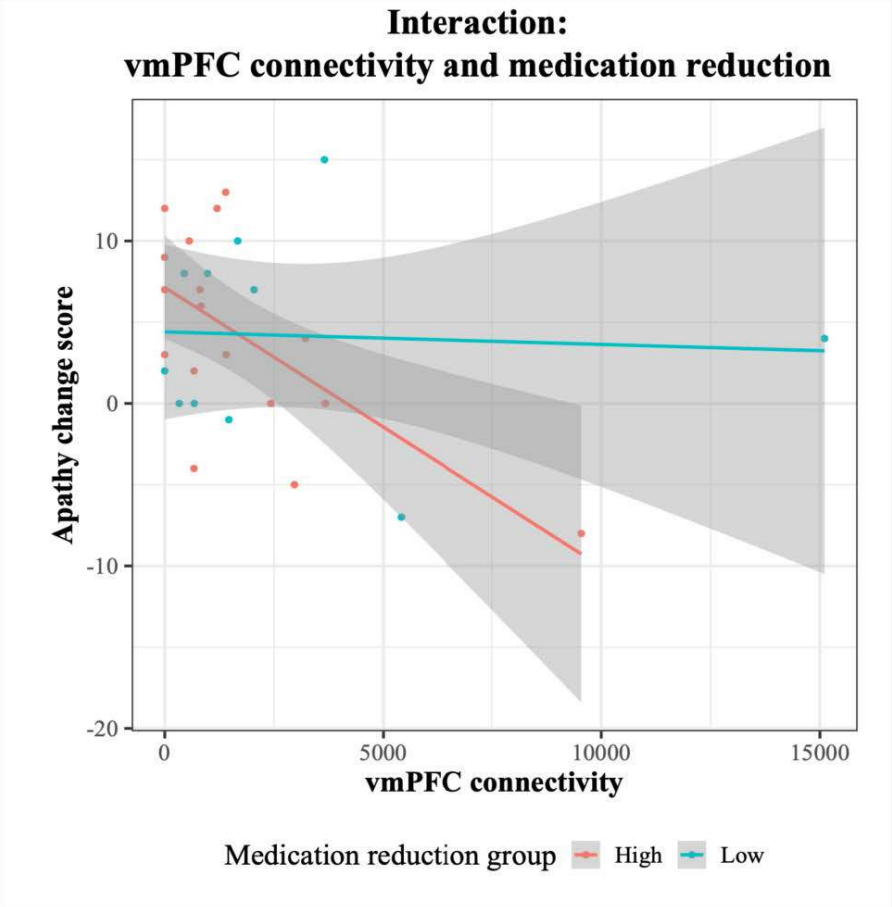

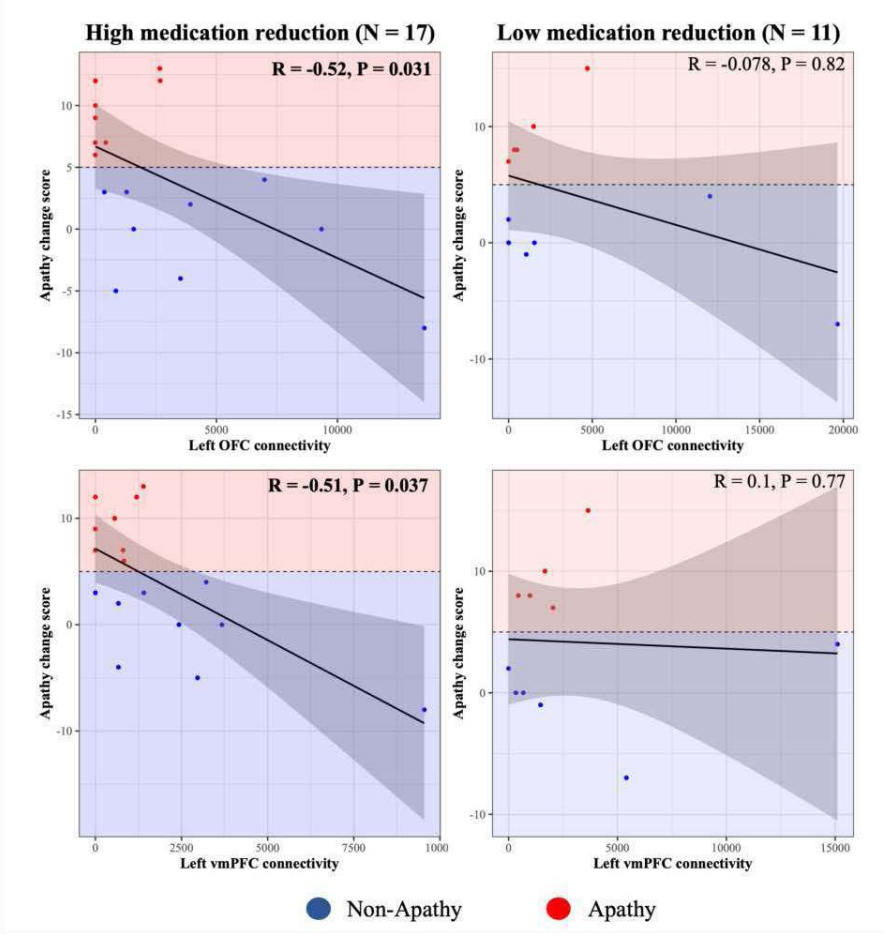

Conclusions: Our study suggests that insufficient stimulation of limbic fronto-subthalamic network connections combined with high levodopa withdrawal contributes to STN DBS-related apathy in PD, which may inspire novel personalized non-motor targeting strategies.

References

1. Boon, L.I. (2021), 'Structural and functional correlates of subthalamic deep brain stimulation-induced apathy in Parkinson's disease'. Brain Stimulation, vol. 14, no. 1, pp. 192-201.
2. Boon, L.I. (2022), 'Structural and functional correlates of deep brain stimulation-induced apathy in Parkinson's disease'. Brain Stimulation, vol. 15, no. 5, pp. 1305-1307.
3. Le Jeune, F. (2009), 'Subthalamic nucleus stimulation in Parkinson disease induces apathy: a PET study'. Neurology, vol. 73, no. 21, pp. 1746-1751.
4. Petry-Schmelzer, J.N. (2019), 'Non-motor outcomes depend on location of neurostimulation in Parkinson's disease'. Brain, vol. 142, no. 11, pp. 3592-3604.
5. Pluck, G.C. (2002), 'Apathy in Parkinson's disease'. Journal of Neurology, Neurosurgery & Psychiatry, vol. 73, no. 6, pp. 636-642.
6. Prange, S. (2019), 'Early limbic microstructural alterations in apathy and depression in de novo Parkinson's disease'. Movement Disorders, vol. 34, no. 11, pp. 1644-1654.
7. Thobois, S. (2010), 'Non-motor dopamine withdrawal syndrome after surgery for Parkinson's disease: predictors and underlying mesolimbic denervation'. Brain, vol. 133, no. 4, pp. 1111-1127.
8. Zoon, T.J.C. (2021), 'Apathy Induced by Subthalamic Nucleus Deep Brain Stimulation in Parkinson's Disease: A Meta-Analysis'. Movement Disorders, vol. 36, no. 2, pp. 317-326.

Poster No 3

Neural circuitry underlying DBS treatment for self-injurious behaviours in Autism Spectrum Disorder

Kristina Zhang[1,2], Rafi Matin[1,2], Mark Ebden[1], Carolina Gorodetsky[3], Jacob Ellegood[4], Jason Lerch[5,4], Flavia Venetucci Gouveia[1], George Ibrahim[1,6,2]

[1]Neurosciences & Mental Health, Hospital for Sick Children, Toronto, Canada, [2]Institute of Medical Science, University of Toronto, Toronto, Canada, [3]Division of Neurology, Hospital for Sick Children, Toronto, Canada, [4]Mouse Imaging Centre (MICe), Hospital for Sick Children, Toronto, Canada, [5]Wellcome Centre for Integrative Neuroimaging, University of Oxford, Oxford, United Kingdom, [6]Division of Neurosurgery, Hospital for Sick Children, Toronto, Canada

Introduction: Children with Autism Spectrum Disorder (ASD) often manifest self-injurious behaviours (SIB) that may become severe and refractory with limited treatment options (Arron et al. 2011). These SIBs may lead to disability or death and deprive children and their families of quality of life. Deep brain stimulation (DBS) has recently been developed in a world-first phase I clinical trial at the Hospital for Sick Children as a potential treatment for affected children (NCT03982888; Yan et al. 2022). The nucleus accumbens (NAcc) is thought to be a relevant target because of its key role in the neurocircuitry regulating SIB. However, the neural underpinnings of NAcc stimulation for SIBs are poorly understood, and multi-disciplinary translational studies using both pre-clinical animal models and clinical data are necessary to explore the mechanisms of disease and treatment. Here, we evaluated the behavioural and neuroanatomical changes induced by NAcc-DBS in a mouse model of SIB and ASD to provide insights into the pathophysiology underlying the treatment being offered in the phase I clinical trial at the Hospital for Sick Children.

Methods: BTBR T+ Itpr3tf/J (BTBR) mouse models of SIB and ASD received chronic DBS or sham stimulation to the bilateral NAcc (100 µA, 100 Hz, 60 µs). Treatment was followed with a series of behavioural tests evaluating ASD-related phenotypes (self-injurious, repetitive, anxiety-like, and social behaviours) and structural MRI. Deformation-based morphometry (Lerch, Sled, and Henkelman 2011) and MAGeTbrain (Multiple Automatically Generated Templates Brain Segmentation Algorithm; Chakravarty et al. 2013) pipelines were applied to identify distinct volumetric changes along the NAcc neurocircuitry and correlated with SIB improvement in BTBR mice.

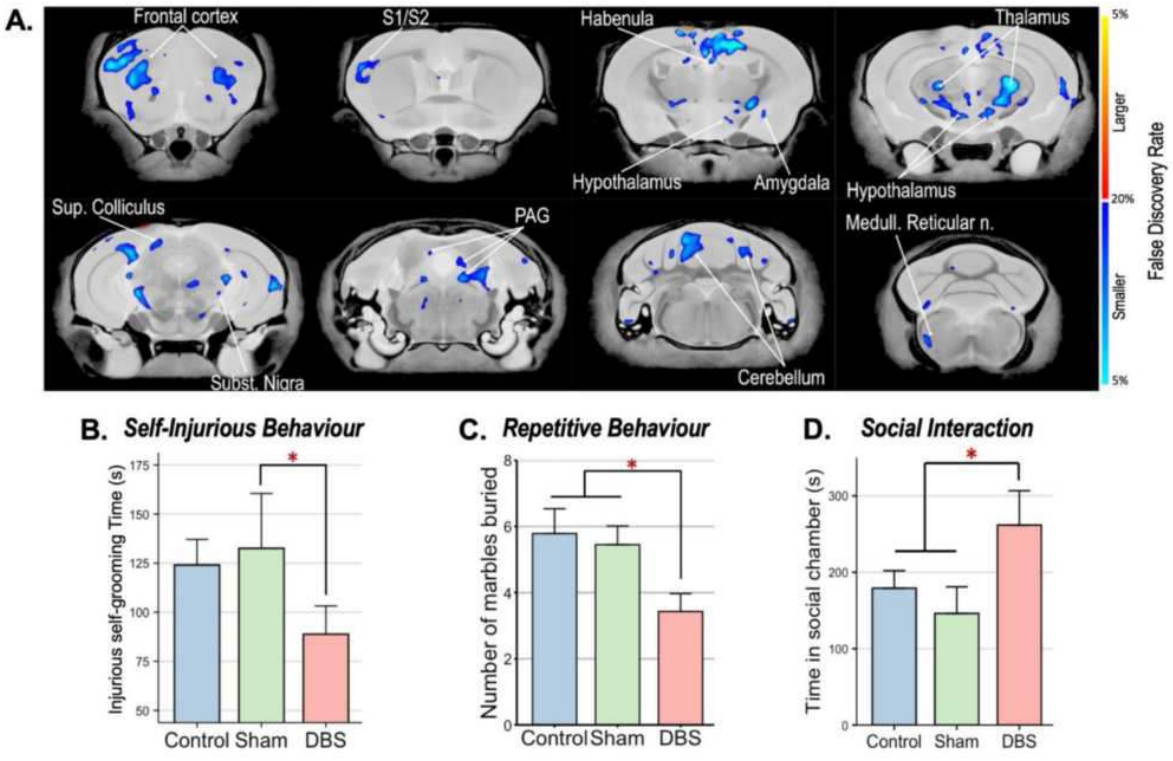

Figure 1. Neuroanatomical and behavioural changes induced by NAcc-DBS in BTBR mice. **(A)** Fly-through of coronal slices in the brain highlighting the volume changes exhibited by BTBR mice treated with NAcc-DBS. Animals treated with NAcc-DBS exhibited reduced **(B)** self-injurious behaviour (as evaluated by a 10-minute grooming assay), **(C)** repetitive behaviour (as evaluated by the marble burying test), and **(D)** improved social interaction (as evaluated by the three-chamber social approach test) relative to animals that did not receive active stimulation. Abbreviations: PAG, periaqueductal gray; S1/S2, primary and secondary somatosensory cortices.

Results: Chronic, high-frequency NAcc-DBS reduced repetitive and SIBs, as well as improved sociability among BTBR mice. These behavioural improvements were correlated with reduced volume in several brain areas thought to be critical for the regulation of SIB, such as the frontal cortex, habenula, amygdala, and hypothalamus (Figure 1).

Conclusions: We demonstrate that NAcc-DBS improves SIB outcomes in BTBR mice through induction of volumetric changes to diverse brain structures involved in SIB regulation. These findings will provide mechanistic insight to the world-first pilot trial of NAcc-DBS in children with severe SIB and ASD. Results from this study will advance our understanding of the neural circuitry subserving SIB, mechanisms underlying symptom improvement following treatment, and provide foundational evidence to establish NAcc-DBS as a therapy for affected children.

References

1. Arron, K. (2011), The prevalence and phenomenology of self-injurious and aggressive behaviour in genetic syndromes. Journal of Intellectual Disability Research: JIDR, vol. 55, no. 2, pp. 109–120
2. Chakravarty, M. (2013). Performing label-fusion-based segmentation using multiple automatically generated templates. Human Brain Mapping, vol. 34, no. 10, pp. 2635–2654
3. Lerch, J. P. (2011). MRI phenotyping of genetically altered mice. Methods in Molecular Biology, vol. 711, pp. 349–361
4. Yan, H. (2022). An open-label prospective pilot trial of nucleus accumbens deep brain stimulation for children with autism spectrum disorder and severe, refractory self-injurious behavior: study protocol. Pilot and Feasibility Studies, vol. 8, no. 1, pp. 24

Poster No 4

Habenula neurostimulation improves neuropsychiatric symptoms in a Fragile X-ASD transgenic model

Flavia Venetucci Gouveia[1], Kristina Zhang[1], Rafi Matin[1], Carolina Gorodetsky[1], George Ibrahim[1]

[1]Hospital for Sick Children, Toronto, Ontario

Introduction: Fragile X syndrome (FX) is the most frequent genetic cause of intellectual disabilities and autism spectrum disorder (ASD) and is caused by mutations in the Fmr1 gene, resulting in changes in the neurocircuitry regulating emotions, cognition, somatosensation and neurotransmitter release[1]. The habenula (Hb) is particularly interesting as it is a key component of the neurocircuitry responsible for modulating the reward value of social interactions, the circadian cycle, and the sensory integration necessary for flexible behavioural adjustments[2,3]. The Hb is a candidate for deep brain stimulation (DBS) in humans[4], a therapy that modulates dysfunctional neural circuitry by delivering intracranial electrical stimulation[5]. Translational studies are necessary to understand DBS's effects and mechanisms of action and facilitate the development of clinical treatments. The Fmr1 knockout (Fmr1-KO) mice are a well-established model of FXS showing comparable behavioural deficits and brain structural and functional differences, as seen in patients with this syndrome[6]. This study aimed to investigate DBS of the Hb (Hb-DBS) as a potential neurostimulation therapy for improving the behavioural deficits observed in the Fmr1-KO mouse model of FX-ASD.

Methods: Adult male and female Fmr1-KO mice (RRID: IMSR_JAX:004624) were randomly assigned to receive Hb-DBS treatment or control. Background strain wild-type (WT) mice (RRID: IMSR_JAX:004828) were used as behavioural control to determine if the Hb-DBS treatment would reduce the behavioural differences between transgenic and healthy animals, thus reflecting a positive effect of treatment on the neuropsychiatric symptoms observed at baseline. All procedures were performed after approval from the Animal Care Committee in accordance with the Canadian Council on Animal Care (AUP #25-0355H). Animals were group-housed in the Digital Ventilated Cages system (DVC®, Tecniplast) with free access to food, water and environmental enrichments. Following the acclimatization period, Fmr1-KO mice were randomly selected to receive surgery for the implantation of electrodes targeting the Hb (AP: -2mm, ML: 0.3mm, DV: -2.5mm)[7] or control surgery. Animals were allowed to recover from surgery for one week. Thereafter, mice in the Hb-DBS group were connected to an external pulse generator and received daily stimulation sessions (3h/session, six sessions total. Stimulation parameters: 0.3V, 100Hz, 60us). Control animals were not connected to the external pulse generator but were kept under the same conditions and for as long as the other group. The circadian cycle pattern, sociability, anxiety-like behaviour, and somatomotor behaviours were evaluated in all mice. Linear mixed effect models were used for statistical analysis (R studio), and the significance level was set as $p<0.05$.

Results: Baseline differences between genotypes were found in all behavioural measures (Figure 1), with Fmr1-KO showing an inconsistent pattern of the circadian cycle ($\beta=6.90$; $SE=2.24$; $df=24$; $p<0.01$), with periods of resting during the active time (i.e., dark time) and periods of activity during the resting time (i.e., light time), increased anxiety-like behaviour ($\beta=71.49$; $SE=20.44$; $df=24$; $p<0.01$), reduced sociability ($\beta=128.84$; $SE=17.284$; $df=24$; $p>0.001$) and impaired thermic sensitivity ($\beta=6.90$; $SE=2.24$; $df=24$; $p<0.01$). Treatment with Hb-DBS was effective in reducing anxiety-like behaviour ($\beta=71.49$; $SE=25.30$; $df=46$; $p<0.01$),

increasing sociability (β=136.58; SE=21.87; df=24; p>0.001) and improving thermic sensitivity (β=1.12; SE=0.32; df=46; p<0.01), however it did not affect the circadian cycle (β=0.87; SE=0.38; df=15; p>0.05).

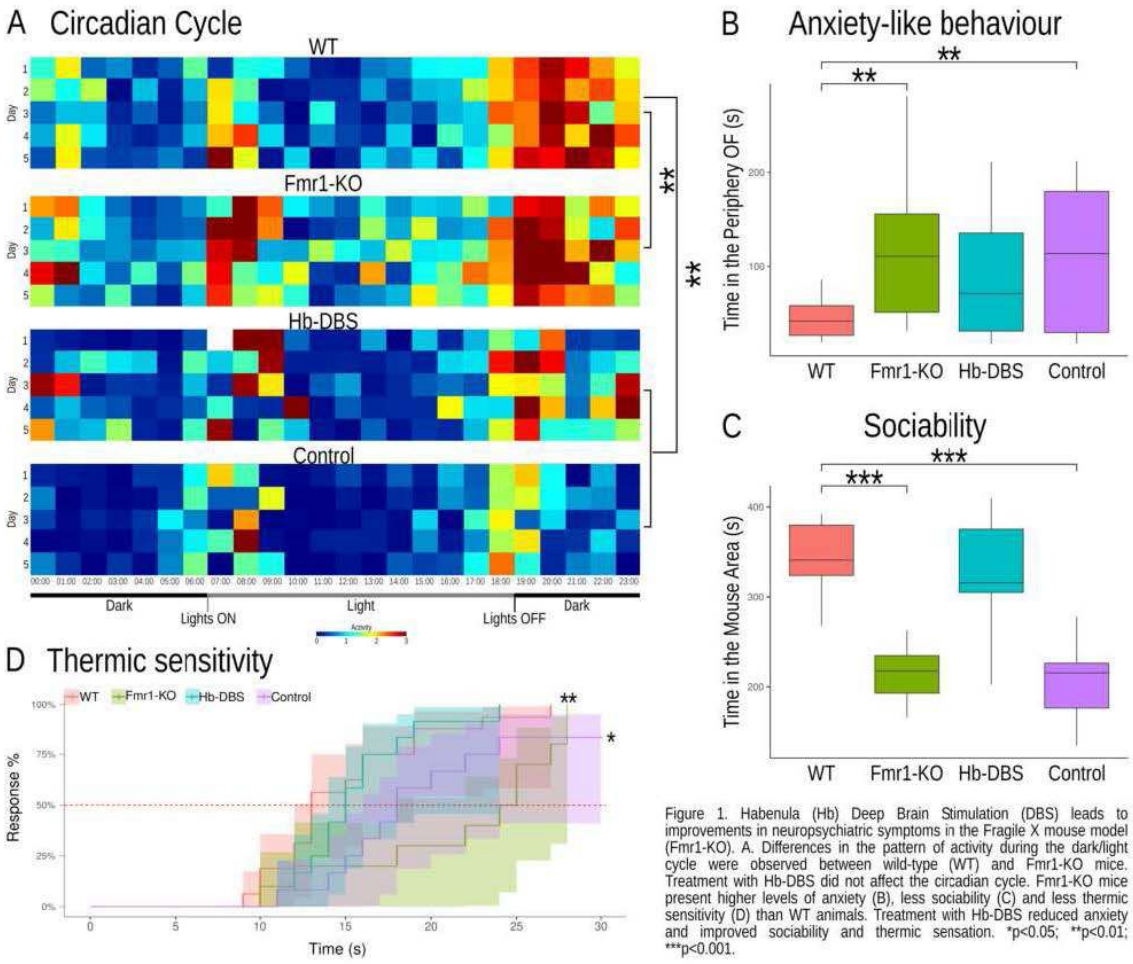

Figure 1. Habenula (Hb) Deep Brain Stimulation (DBS) leads to improvements in neuropsychiatric symptoms in the Fragile X mouse model (Fmr1-KO). A. Differences in the pattern of activity during the dark/light cycle were observed between wild-type (WT) and Fmr1-KO mice. Treatment with Hb-DBS did not affect the circadian cycle. Fmr1-KO mice present higher levels of anxiety (B), less sociability (C) and less thermic sensitivity (D) than WT animals. Treatment with Hb-DBS reduced anxiety and improved sociability and thermic sensation. *p<0.05; **p<0.01; ***p<0.001.

Conclusions: Treatment with Hb-DBS improved the neuropsychiatric symptoms observed in the Fmr1-KO mouse model of FX-ASD, with treated animals showing reduced anxiety-like behaviour, increased sociability and enhanced sensory perception. Further studies are necessary to investigate the neurobiological mechanisms associated with behavioural changes.

References

1. Franklin KBJ & Paxinos G (2019). Paxinos and Franklin's the Mouse Brain in Stereotaxic Coordinates, Compact: The Coronal Plates and Diagrams. Academic Press. (7)
2. Germann J et al. (2021). "Deep Brain Stimulation of the Habenula: Systematic Review of the
3. Literature and Clinical Trial Registries." Frontiers in Psychiatry, 12: 730931. (4)
4. Hagerman RJ et al. (2017). "Fragile X Syndrome." Nature Reviews. Disease Primers 3: 17065. (1)
5. Hikosaka O. (2010). "The Habenula: From Stress Evasion to Value-Based Decision-Making." Nature Reviews. Neuroscience 11 (7): 503–13. (2)
6. Lozano AM & Lipsman N. (2013). "Probing and Regulating Dysfunctional Circuits Using Deep Brain Stimulation." Neuron 77 (3): 406–24. (5)
7. Mizumori SJY & Baker PM. (2017). "The Lateral Habenula and Adaptive Behaviors." Trends in Neurosciences 40 (8): 481–93. (3)
8. The Dutch Belgian Fragile X Consor. (1994). "Fmr1 Knockout Mice: A Model to Study Fragile X Mental Retardation." Cell 78 (1).(6)

Poster No 5

Modulation of Human Spatial-temporal Memory by Deep Brain Stimulation

Yan Li[1], Tao Yu[2], Tong Li[1], Xiaojing Peng[1], Ying Gao[2], Nikolai Axmacher[3], Gui Xue[1]

[1]State Key Laboratory of Cognitive Neuroscience and Learning, Beijing Normal University, Beijing, Beijing, [2]Beijing Institute of Functional Neurosurgery, Xuanwu Hospital, Capital Medical University, Beijing, Beijing, [3]Department of Neuropsychology, Institute of Cognitive Neuroscience, Faculty of Psychology, Ruhr Univ, Bochum, North Rhine-Westphalia

Introduction: As a neuromodulation technique, deep brain stimulation is often used for ameliorating cognitive disabilities, such as improving memory impairment. Existing evidence showed that direct stimulation resulted in different effects in memory performance. Some reported that stimulation impaired memory performance (e.g., Jacobs et al., 2016), while others reported that stimulation improved memory (e.g., Suthana et al., 2012). Therefore, in the present study, we intend to find out different memory performance induced by selective stimulation site and stimulation frequency.

Methods: Participants Twenty-eight medically refractory frontal or temporal epilepsy patients (mean age = 24.03y, sd = 8.36y, 10 female) who were implanted with SEEG depth electrodes were collected in Xuanwu hospital. Experimental procedure & Stimulation protocol A white square moved in the 4*4 grid, and the participants were instructed to learn the sequence and the location of the moving square (Fig1A). All participants learned 3 locations in each color background and they were self-adapted to memorize (1) two to three color backgrounds and (2) repeat four to six times based on their practice performance. After the 10s distractor task, participants were asked to replicate the sequence in each color grid. There were three blocks of spatial temporal sequences in each session. During the encoding period, participants either received stimulation in the hippocampus or no stimulation (Stim-off condition). Stimulation was delivered in the continuous biphasic rectangular pulse at 0.5 mA with 90μs pulse width at 5 Hz or 50 Hz, using RISHENA stimulator (RISHENA, China). Intracranial EEG data was recorded using amplifiers from Brain Products for the whole task periods, with the sampling rate of 2500 Hz. Electrode localization Location for each contact was identified by co-registering the post-implanted CT scans and the pre-implanted MRI image, and we segmented individual's structural T1 image using FreeSurfer and obtained the anatomical label for each contact. White matter categorization All stimulation sites were re-categorized as either located in the gray matter or near white matter, following the procedure from Mohan et al (2020). We calculated the midpoints of the anode and cathode electrodes, and a sphere with a radius of 4 mm was constructed centered on this midpoint. Then, we estimated the number of white matter vertices located in the sphere. Finally, we grouped the stimulation sites as gray matter or near white matter by taking the median of the white matter vertices' number. Here, the median number of white matter vertices located inside the sphere is 165.

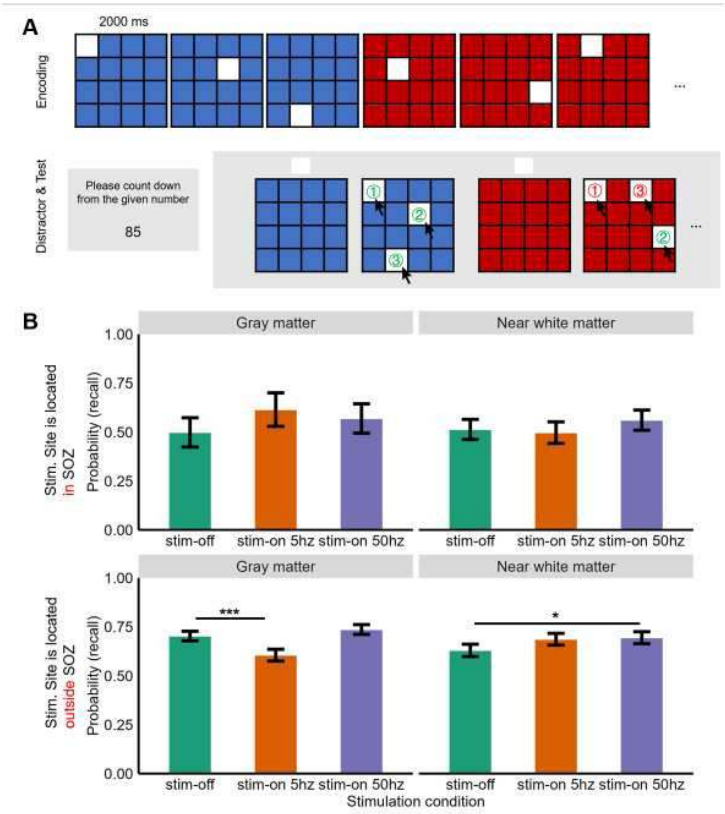

Results: We implemented the generalized linear mixed-effects model in order to investigate whether characteristics of stimulation site and frequency would affect stimulation effect (Fig1B). We defined independent variables as (1) the corresponding location of the stimulation site and seizure onset zone (SOZ), (2) white matter proximity and (3) stimulation frequency. Here, we found a marginal significant three-way interactive effect ($\chi 2=5.59$, $p=.061$). We conducted the simple effect analysis and found that if the stimulation site is located in the SOZ, stimulation would not significantly change memory performance. However, if the stimulation site was located outside the SOZ, 5 Hz stimulation in gray matter would reduce

the probability of recall (z=-3.72, p<.001), whereas stimulation near white matter would improve memory performance (z=2.36, p=.037).

Conclusions: In the present study, we found that the selection of stimulation site and frequency contributed to the stimulation effect. If we stimulate in the SOZ, the stimulation shows no effect on the memory performance. Yet, if we stimulate outside the SOZ, low frequency stimulation in gray matter will impair memory performance, while high frequency stimulation near white matter enhances memory performance.

References

1. Jacobs et al. (2016). Direct Electrical Stimulation of the Human Entorhinal Region and Hippocampus Impairs Memory. Neuron. Vol. 92, no. 5. pp. 983-990.
2. Mohan, et al. (2020). The effects of direct brain stimulation in humans depend on frequency, amplitude, and white-matter proximity. Brain Stimulation. Vol. 3, no. 5, pp. 1183-1195.
3. Suthana, et al. (2012). Memory enhancement and deep-brain stimulation of the entorhinal area. The New England Journal of Medicine, Vol. 366, no. 6, pp. 502-510.

Poster No 6

Bridging brain coordinates and machine learning for surgical targeting and morphometric mapping

Alaa Taha[1], Greydon Gilmore[2], Mohamad Abbass[2], Violet Liu[3], Chris Zajner[2], Brendan Santyr[1], Abrar Ahmed[2], Ali Hadi[2], Sandy Wong[4], Ali Khan[5], Jonathan Lau[4]

[1]University of Western Ontario, London, Ontario, [2]Department of Clinical Neurological Sciences, Division of Neurosurgery, London, Ontario, [3]Imaging Research Laboratories, Robarts Research Institute, London, Ontario, [4]Department of Clinical Neurological Sciences, Division of Neurosurgery, London, ON, [5]Department of Medical Biophysics, Schulich School of Medicine and Dentistry, Western University, London, Ontario

Introduction: A deviation of 2 millimeters (mm) in deep brain stimulation (DBS) electrode positioning can result in variability of upwards of 60% in therapeutic benefit[1]. Suboptimal targeting may require reimplantation, which can pose additional risks. Localizing DBS targets is not always possible because of their small size, lack of contrast, and patient motion. Tools which involve non-linear alignment of an atlas to patient images, considered 'gold standard' for automatic localization, yield errors on the order of 2-3 mm^2 and highly depend on image quality (Figure 1A). Gadolinium enhanced T1w MRI (MRI-gad) is employed during DBS planning, as it helps with avoiding blood vessels. However, MRI-gad presents challenges during non-linear alignment[3]. Automatic localization of brain structures via machine learning (ML) offers faster and generalizable alternatives to registration approaches. However, limited studies cater ML to DBS targets while demonstrating generalizability in clinic (e.g. on MRI-gad)[4]. We validate an ML model (Figure 1) to localize surgical targets from the coordinates of salient brain landmarks[5] in patient space. Our approach is agnostic to field strength, generalizable to other brain regions, and enables more nuanced understanding of brain morphology that can be expressed in millimeters (Figure 2).

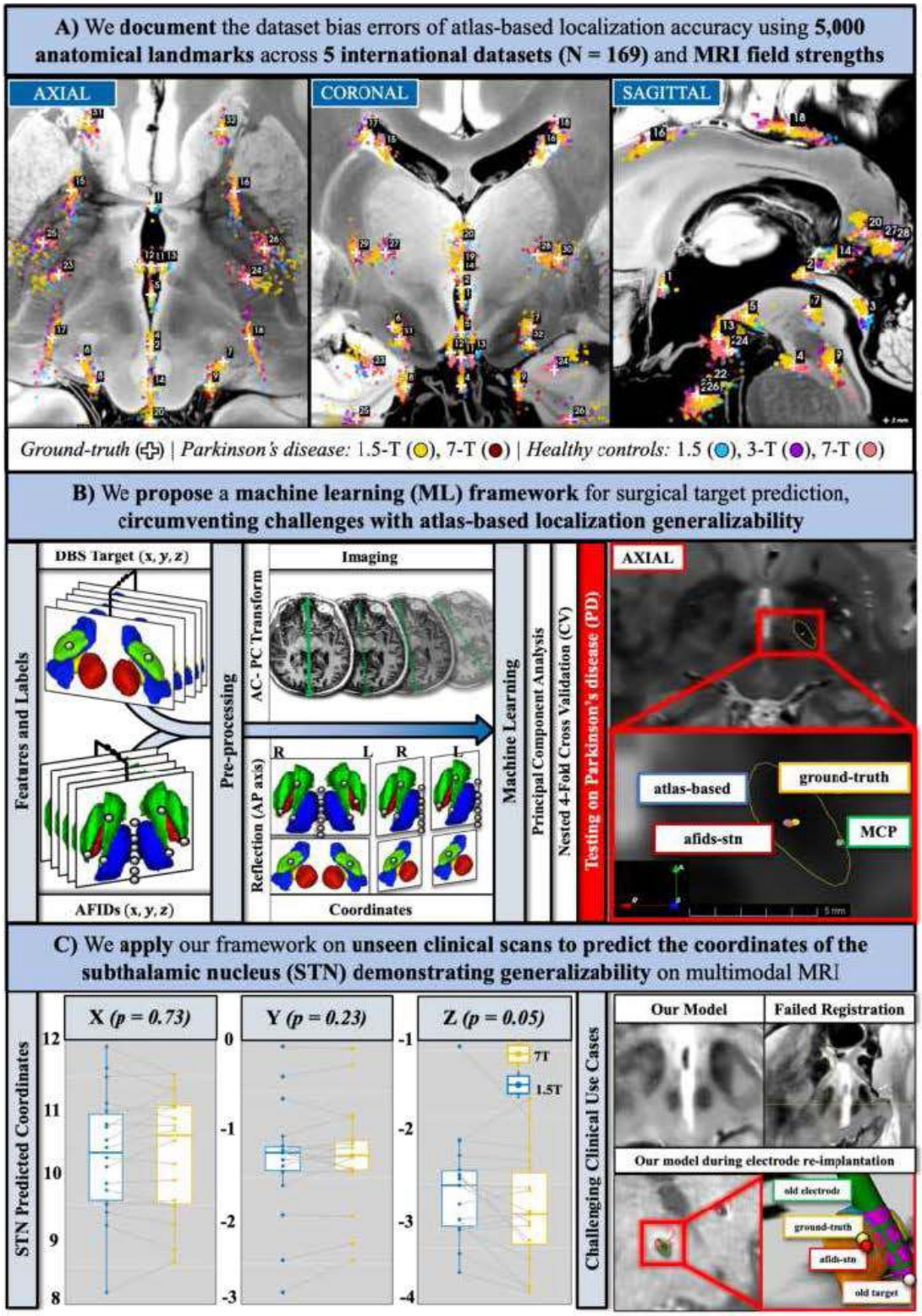

Methods: We curated and openly released[6] three imaging datasets: The SNSX dataset, 64 healthy and DBS patients imaged at 7-T; the LHSCPD dataset, same DBS participants as in SNSX, but imaged at 1.5-T MRI-gad; and the AFIDs dataset, multi-center, multi-resolution MRI data with curated anatomical landmarks across a diverse population (N = 169), including healthy, abnormal ventricular size, and neurodegenerative disease. We leveraged coordinates of 32 anatomical landmarks (called AFIDs) from aforementioned datasets. AFIDs feature an inter-rater localization error of ~1 mm, validated across MRI field strengths and disease via 50,000+ Euclidean distances (ED) from 20 expert and novice human raters[5,6]. We computed the subthalamic nucleus center (STN) from segmentations on T2w 7-T MRI scans curated by 3 expert neurosurgeons and the lead author. Coordinates of AFIDs were used as features to predict the STN center. Principal component analysis and correlations were used to evaluate relationships between AFIDs, subsequently a linear regression model was trained via nested 4-fold

cross validation. We employed an unseen paired dataset of 22 DBS patients imaged at both 7-T and 1.5-T to demonstrate our model's robustness across MRI field strength. We then applied a validated registration framework[7] to predict the STN, and statistically compared that to our model. To simulate the upper limit of mis-localization errors by trained raters, we augmented AFID locations anisotropically by 2 mm and evaluated prediction error. Finally, to evaluate the generalizability of our model to other brain regions we perform a leave-one-AFID out analysis where the excluded AFID was predicted from all other AFIDs.

Results: STN prediction error on our test set is 1.01 ± 0.56 mm, outperforming non-linear alignment which failed for 6 patients (produced irregular wrap fields). Additionally, our model exhibited no statistical difference when predicting STN coordinates from 7T or 1.5T MRI-gad imaging. We leveraged our model to predict the STN on an MRI-gad scan from a DBS electrode re-implantation case, leading to more accurate targeting (Figure 1C). STN predictions from augmented AFID placements (2 mm) featured an error of 0.34 ± 0.12 mm. Finally, our brain target generalizability yielded an error of 1.1 ± 0.36 mm on 7 midbrain AFIDs.

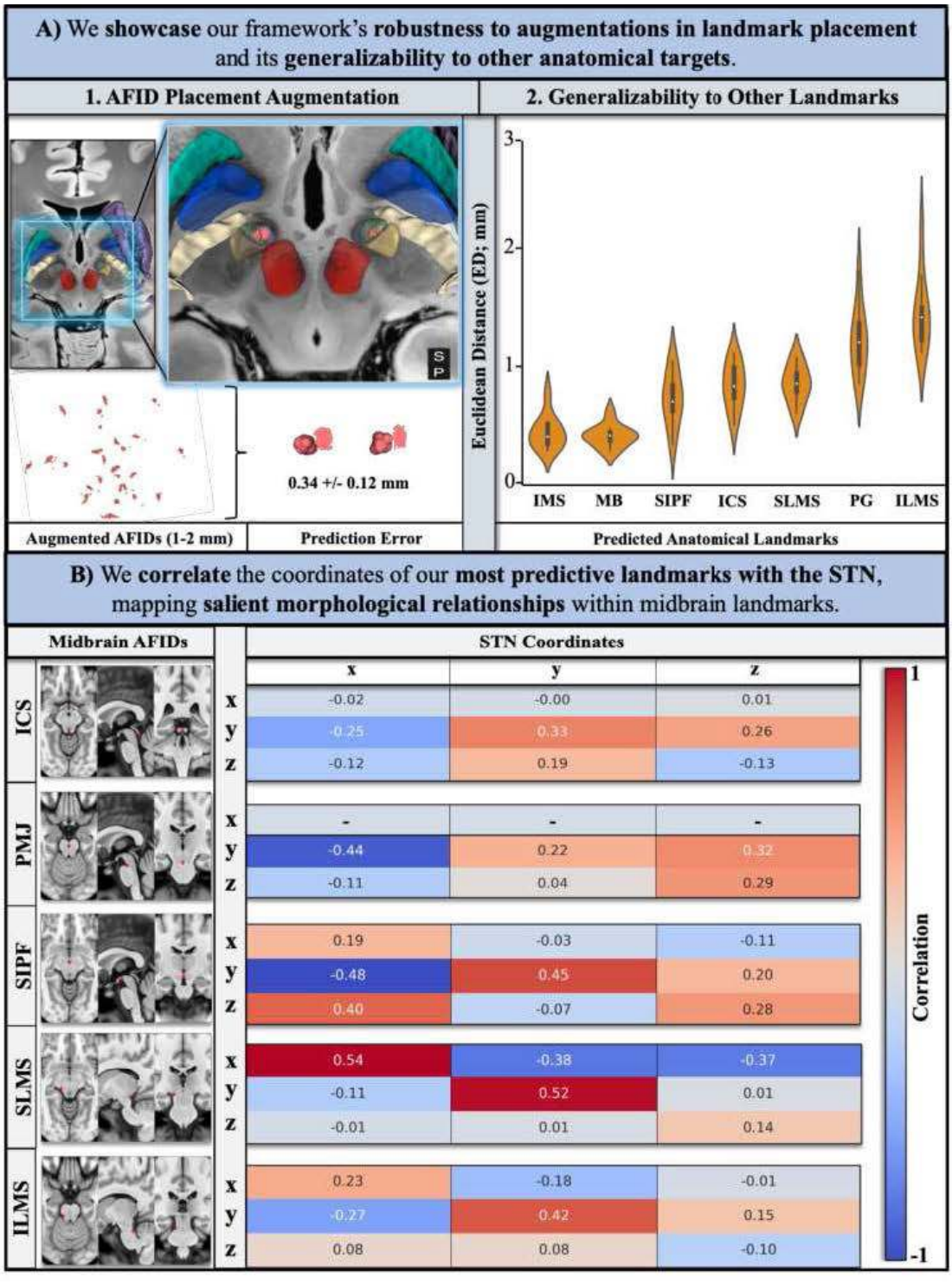

Conclusions: We demonstrate a novel surgical targeting framework that accommodates for inter-patient variability and is agnostic to MRI field strength. We integrate this approach within the clinical workflow and showcase its utility in predicting surgical targets and informing DBS electrode re-implantation where conventional imaging is suboptimal.

References

1. Horn, A. et al. Lead-DBS v2: Towards a comprehensive pipeline for deep brain stimulation imaging. Neuroimage 184, 293–316 (2019)
2. Miller, C. P. K. et al. Automatic Segmentation of Parkinson Disease Therapeutic Targets Using Nonlinear Registration and Clinical MR Imaging: Comparison of Methodology, Presence of Disease, and Quality Control. Stereotact. Funct. Neurosurg. 1–12 (2023)
3. Abbass, M. et al. Application of the anatomical fiducials framework to a clinical dataset of patients with Parkinson's disease. Brain Struct. Funct. 227, 393–405 (2022)
4. Baniasadi, M. et al. DBSegment: Fast and robust segmentation of deep brain structures considering domain generalization. Hum. Brain Mapp. 44, 762–778 (2023)
5. Lau, J. C. et al. A framework for evaluating correspondence between brain images using anatomical fiducials. Hum. Brain Mapp. 40, 4163–4179 (2019)
6. Taha, A. et al. Magnetic resonance imaging datasets with anatomical fiducials for quality control and registration. Sci Data 10, 449 (2023)
7. Ewert, S. et al. Optimization and comparative evaluation of nonlinear deformation algorithms for atlas-based segmentation of DBS target nuclei. Neuroimage 184, 586–598 (2019)

Poster No 7

Structural connectivity changes in severe Anorexia Nervosa following Deep Brain Stimulation

Kilian Abellaneda-Pérez[1], Ignacio Delgado-Martínez[2], Purificación Salgado[3], José María Gines[3], Rocío Guardiola[3], Alba Roca-Ventura[1], Rosa María Manero[3], Víctor Pérez-Sola[3], Gloria Villalba-Martínez[3]

[1]Institut Guttmann, Barcelona, Spain, [2]Universitat Autònoma de Barcelona, Bellaterra, Spain, [3]Hospital del Mar, Barcelona, Spain

Introduction: Anorexia nervosa (AN) is a complex mental health disorder characterized by significant weight loss and associated medical and psychological comorbidities. The relapsing nature of AN relates to high levels of disability and mortality, positioning AN as the psychiatric condition with the greatest risk of death (Zipfel et al., 2015). Due to the limited effectiveness of current treatments for severe AN, new strategies, including deep brain stimulation (DBS) are being explored (Villalba-Martínez et al., 2020). However, the neural mechanisms potentially driving DBS interventions in AN are still not completely elucidated. In this vein, the main goal of this investigation was to explore changes in structural connectivity, as examined through diffusion tensor imaging (DTI), in patients with severe AN before and after DBS.

Methods: In this study, 16 participants (8 AN patients and 8 matched controls) underwent a baseline DTI acquisition. AN patients received DBS targeting either the subcallosal cingulate (DBS-SCC, N=4) or the nucleus accumbens (DBS-NAcc, N=4), based on the presence of anxious-affective comorbidities and AN subtype. Additionally, four AN patients (two from each DBS group) participated in a post-DBS DTI evaluation. We compared fractional anisotropy (FA) values derived from DTI between AN patients and controls and assessed structural connectivity changes pre- vs. post DBS. The analyses were conducted using the TRACULA (TRActs Constrained by UnderLying Anatomy) tool, part of FreeSurfer (Yendiki et al., 2011), and the TBSS (Tract-Based Spatial Statistics) from the FSL (Smith et al., 2006).

Results: We observed statistically significant differences in numerous white matter tracts between patients with severe AN and controls at baseline, as illustrated in Fig. 1A ($p < 0.05$; matched controls > AN patients). Moreover, in AN patients two specific white matter tracts proven significant changes pre vs. post DBS at the group level: the anterior thalamic radiation (ATR; $p = 0.0204$; Fig. 1B) and the superior longitudinal fasciculus – parietal bundle (SLFP; $p = 0.0272$; Fig. 1B). Remarkably, at the individual level, each subject exhibited an increase in at least one of these two white matter tracts following the DBS intervention.

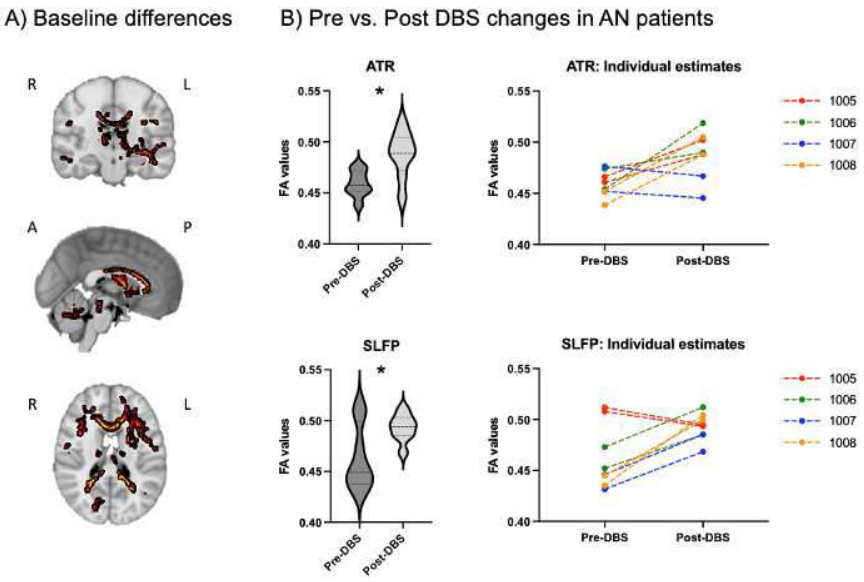

Fig. 1. A) Baseline differences between patients with severe AN and matched controls. Results showing significant differences ($p < 0.05$) are illustrated on a standard MNI brain map. B) Changes in structural connectivity in patients with severe AN following DBS intervention, depicted at both group and individual levels. The top panel shows DBS-related changes in the anterior thalamic radiation (ATR), and the bottom panel in the superior longitudinal fasciculus - parietal bundle (SLFP). Asterisk (*) denotes significant differences ($p < 0.05$). *Abbreviations*: AN, anorexia nervosa; DBS, deep brain stimulation; FA, fractional anisotropy.

Conclusions: Our research provides further support to the notion that white matter integrity is significantly compromised in distinct brain regions in patients with severe AN. Moreover, in AN patients treated with DBS, we originally observed an increase in structural connectivity in two white matter pathways, namely ATR and SLFP, independent of the stimulation target. This change in structural integrity due to DBS may be attributed to the triggering of microstructural neuroplasticity mechanisms following brain stimulation (Antonenko et al., 2023). Altogether, our findings suggest that DTI metrics may serve as a helpful tool for both guiding and tracking brain changes following DBS treatment in psychiatric populations.

References

1. Antonenko, D. (2023). Microstructural and functional plasticity following repeated brain stimulation during cognitive training in older adults', Nature Communications vol. 14,1 3184.
2. Smith, S. (2006). 'Tract-based spatial statistics: voxelwise analysis of multi-subject diffusion data', NeuroImage vol. 31,4.
3. Villalba-Martínez, G. (2020). 'A Randomized Trial of Deep Brain Stimulation to the Subcallosal Cingulate and Nucleus Accumbens in Patients with Treatment-Refractory, Chronic, and Severe Anorexia Nervosa: Initial Results at 6 Months of Follow Up', Journal of Clinical Medicine vol. 9,6 1946.
4. Yendiki, A. (2011). 'Automated probabilistic reconstruction of white-matter pathways in health and disease using an atlas of the underlying anatomy', Frontiers in Neuroinformatics vol. 5 23.
5. Zipfel, S. (2015). 'Anorexia nervosa: aetiology, assessment, and treatment', The Lancet Psychiatry vol. 2,12, pp. 1099-111.

Poster No 8

Cortical Evoked Responses to Enhance Targeting and Personalize DBS Intervention for OCD

Davide Momi[1], Andrew Smith[2], Elisa Xu[3], Sonya Olson[3], Zarghona Imtiaz[3], Samantha Pitts[3], Jip de Bruin[3], Helen Mayberg[3], Brian Kopell[3], Ki Sueng Choi[3], Martijn Figee[3], Allison Waters[3]

[1]CAMH, Toronto, Ontario, [2]Icahn School of Medicine At Mount Sinai, New York, NY, [3]Icahn School of Medicine at Mount Sinai, New York, NY

Introduction: Obsessive-compulsive disorder (OCD) is a debilitating condition, affecting approximately 2.3% of individuals throughout their lifetime (Ruscio et al., 2010). The US FDA allows treatment of severe cases using deep brain stimulation (DBS) to the anterior limb of the internal capsule (ALIC) under an Humanitarian Device Exemption (Anderson and Ahmed, 2003). DBS has demonstrated efficacy in providing relief from symptoms. However, the journey to stable recovery remains unpredictable, often necessitating trial-and-error adjustments in stimulation. This variability is attributed to individual differences in the neural

response to stimulation and uncertainty about surgical target engagement. Subjective symptom reporting is not sufficient for rapid parameter optimization, necessitating the development of objective, brain-based biomarkers to confirm optimal DBS target engagement.

Methods: We recorded high density electroencephalography (hd-EEG, 256-array) in nine OCD patients during 2 Hz stimulation to the anterior limb of the internal capsule (ALIC). Cortical evoked responses, time-locked to the DBS pulse, were captured for each electrode contact within the target region, amounting to eight total conditions (four per hemisphere). The clinically optimal contact in each hemisphere was identified prior to surgery using diffusion weighted MRI tractography. The reliability of the stimulus evoked propagation patterns was examined for every individual and for every stimulation condition. Global Mean Field Power (GMFP) was extracted from every condition, and used to calculate the Area Under the Curve (AUC). We hypothesized that stimulation delivered to the tractography-defined optimal target would result in greater AUC activation.

Results: Results showed that stimulation in the ALIC generates stable and reproducible cortical responses within individuals, with some elements of the cortical response also being consistent between individuals. Moreover we found a significantly stronger propagation pattern when the stimulation was delivered to the tractographically defined target, both for early (0-80ms) and late (130-150ms) responses.

Conclusions: Overall, these novel discoveries pinpoint the potential usage of the cortical evoked potential as a brain-based biomarker of DBS target engagement. These findings have implications for understanding brain function, and potential applications for personalizing therapeutic interventions.

References

1. Anderson, D., Ahmed, A., 2003. Treatment of patients with intractable obsessive-compulsive disorder with anterior capsular stimulation. Case report. J Neurosurg 98, 1104–1108. https://doi.org/10.3171/jns.2003.98.5.1104
2. Ruscio, A.M., Stein, D.J., Chiu, W.T., Kessler, R.C., 2010. The Epidemiology of Obsessive-Compulsive Disorder in the National Comorbidity Survey Replication. Molecular psychiatry 15, 53. https://doi.org/10.1038/mp.2008.94

Poster No 9

Mapping lesion-related human aggression to a common brain network

shaoling peng[1], Frederic Schaper[2], Shira Cohen-Zimerman[3], Gillian Miller[4], Jing Jiang[5], Rob Rouhl[6], Yasin Temel[6], Shan Siddiqi[7], Jordan Grafman[3], Michael Fox[2], Alexander Cohen[2]

[1]Harvard Medical School/Boston Children's Hospital, Brookline, MA, [2]Brigham and Women's Hospital, Harvard Medical School, Boston, MA, [3]Northwestern University, Chicago, IL, [4]Boston Children's Hospital, Brookline, MA, [5]University of Iowa, Iowa, IA, [6]Maastricht University Medical Center, Maastricht, Maastricht, [7]Harvard Medical School/Brigham and Women's Hospital, boston, MA

Introduction: Aggression exacts a significant toll on human societies and is highly prevalent among neuropsychiatric patients, yet treatment options are limited. While the neural mechanisms leading to aggression are unclear, it can occur following focal brain damage. Such cases provide unique insight into brain regions causally responsible for aggression symptoms and may identify therapeutic targets. The most famous case of lesion-induced aggression comes from Phineas Gage, which provides the first clinical evidence showing the causal role of the PFC in regulating aggression. However, later studies have demonstrated that lesions causing aggression are located in different parts of the brain, not just PFC, thus leaving the localization of aggression unclear. Recently, it has become possible to map complex behavior to human brain circuits based on locations of brain damage that modulate the behavior by leveraging a wiring diagram of the human brain termed the human connectome[1,2]. This technique, termed lesion network mapping, is particularly helpful when lesions causing similar symptoms occur in multiple different brain locations.

Methods: We analyzed 182 patients who had suffered penetrating head injuries during their service in the Vietnam War [3]. Aggression was assessed with the aggression/agitation subscale of the Neurobehavioral Rating Scale (NBR-A). Lesion locations were mapped to a common brain atlas. The network of brain regions connected to each lesion location was identified utilizing resting state functional connectivity from healthy participants (n = 1000). Lesion-connections associated with increased aggression were then identified. To validate whether our lesion-derived aggression regions and network are relevant to neuropsychiatric symptoms associated with aggression, we utilized three independent datasets. The first dataset is the lesion location of the historic case of Phineas Gage extracted from Damasio's study[4]. The second dataset is a cohort of 25 patients who received anterior thalamic deep brain stimulation (DBS) as a treatment for drug-resistant focal epilepsy, in which irritability and aggression are frequently shown as side effects[5]. The third dataset is the Harvard Lesion Repository, which contains 928 symptom-causing lesions spanning 25 independent lesion datasets.

Results: We found that lesions associated with aggression occurred in many different brain locations but were characterized by a specific pattern of brain connectivity to a hub region (termed LNM node) in the right prefrontal cortex. This identified hub partially overlaps Gage's lesion (Fig. 1a). Functional connectivity between Gage's lesion (Fig. 1b) and lesions in our VHIS cohort can significantly predict the patients' aggression scores (r = 0.15, p = 0.041; Fig. 1c). Connectivity with our identified hub also predicted improvement in irritability in the independent DBS dataset, suggesting potential therapeutic relevance. This predictive ability was most specific to irritability, as functional connectivity between DBS stimulation sites and our LNM node was significantly distinct between irritability and the remaining 20 symptoms measured (t19 = -10.44, p = 2.59 × 10-9; Fig. 2a). Similar to prior studies[2,5], We derived an "aggression network" based on functional connectivity to our hub region and validated it using the Harvard Lesion Repository. We showed that lesions associated with criminal behavior demonstrated the most alignment with our aggression network amongst these 25 symptoms (Fig. 2b). Not only is the intersection of criminality significantly higher than zero (t16 = 2.20, p = 0.043), but it also exhibited the highest intersection with our lesion-derived aggression network.

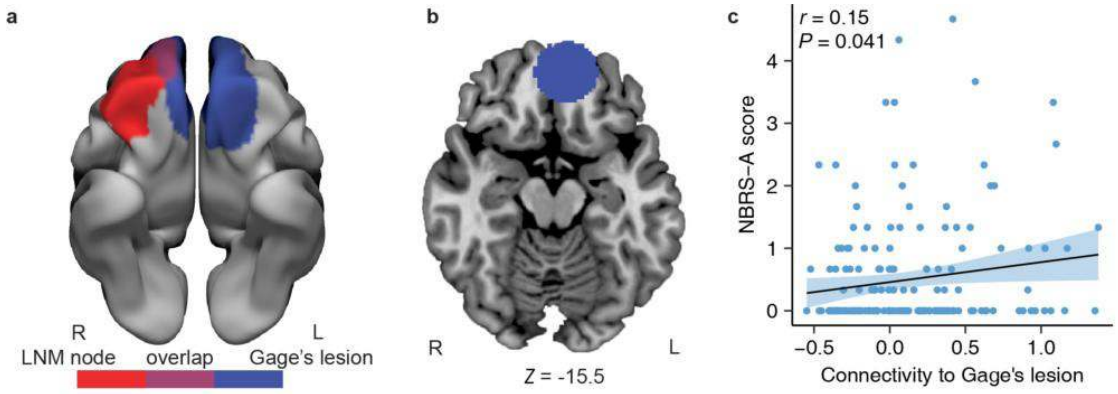

Fig. 1 Relevance to the notable case of Phineas Gage. a, The aggression-associated node we identified using LNM overlapped the location of brain injury that led to Gage's transformation into an irritable, hostile, and verbally aggressive individual. b,c, Functional connectivity between the location of patients' lesion and Gage's lesion (b) significantly predicted the patients' aggression score (c).

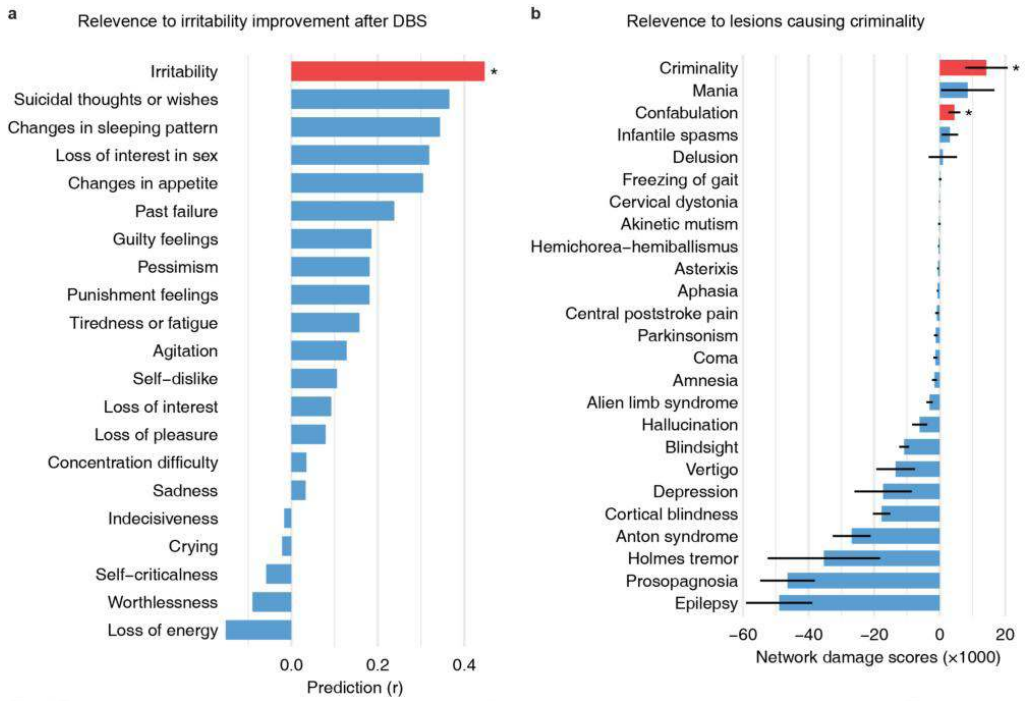

Fig. 2 Relevance to deep brain stimulations improving irritability and lesion locations causing criminal behavior. a, Functional connectivity between DBS stimulation sites and the LNM node in right PFC significantly predicts the improvements in irritability before and after DBS treatment. Notably, this prediction was specific to irritability as the same functional connectivity failed to predict any of the remaining 20 symptoms assessed in BDI-II. Red bar represents significant prediction, whereas blue bars represent non-significant prediction. BDI-II, Beck Depression Inventory - Second Edition. b, Network damage scores, which represent intersection of each lesion with the aggression network based on functional connectivity to our LNM node, was significantly higher for participants with criminality than with the remaining 24 neuropsychiatric symptoms (t23 = -7.26, p = 2.19 × 10-7). Furthermore, not only is the intersection of criminality significantly higher than zero (t16 = 2.20, p = 0.043), but it also exhibited the highest intersection with our lesion-derived aggression network among all the 25 symptoms. Red bars represent significant positive intersections, whereas blue bars represent negative or non-significant positive intersections. Error bars

Conclusions: We conclude that brain lesions associated with aggression map to a specific human brain circuit, and that the hub of this circuit provides a testable target for therapeutic neuromodulation.

References

1. Boes, A. D., S. Prasad, H. Liu, Q. Liu, A. Pascual-Leone, V. S. Caviness, Jr. and M. D. Fox (2015). "Network localization of neurological symptoms from focal brain lesions." Brain 138(Pt 10): 3061-3075.
2. Damasio, H., T. Grabowski, R. Frank, A. M. Galaburda and A. R. Damasio (1994). "The return of Phineas Gage: clues about the brain from the skull of a famous patient." Science 264(5162): 1102-1105.
3. Fox, M. D. (2018). "Mapping Symptoms to Brain Networks with the Human Connectome." N Engl J Med 379(23): 2237-2245.
4. Raymont, V., A. M. Salazar, F. Krueger and J. Grafman (2011). ""Studying injured minds" - the Vietnam head injury study and 40 years of brain injury research." Front Neurol 2: 15.
5. Schaper, F., J. Nordberg, A. L. Cohen, C. Lin, J. Hsu, A. Horn, M. A. Ferguson, S. H. Siddiqi, W. Drew, L. Soussand, A. M. Winkler, M. Simo, J. Bruna, S. Rheims, M. Guenot, M. Bucci, L. Nummenmaa, J. Staals, A. J. Colon, L. Ackermans, E. J. Bubrick, J. M. Peters, O. Wu, N. S. Rost, J.
6. Grafman, H. Blumenfeld, Y. Temel, R. P. W. Rouhl, J. Joutsa and M. D. Fox (2023). "Mapping Lesion-Related Epilepsy to a Human Brain Network." JAMA Neurol 80(9): 891-902.

Poster No 10

Utility of Imaging Predictors in Deep Brain Stimulation

Patricia Zvarova[1], Ningfei Li[1], Ilkem Sahin[1], Barbara Hollunder[1], Martin Reich[2], Jens Volkmann[2], Vincent Odekeren[3], Rob de Bie[3], Xin Xu[4], Zhipei Ling[5], Chen Yao[6], Andrea Kühn[1], Nanditha Rajamani[1], Andreas Horn[7]

[1]Department of Neurology, Charité – Universitätsmedizin Berlin, Berlin, Germany, [2]Department of Neurology, Universitätsklinikum Würzburg, Würzburg, Germany, [3]Department of Neurology, Academisch Medisch Centrum Universiteit van Amsterdam, Amsterdam, Netherlands, [4]Department of Neurosurgery, Chinese PLA General Hospital, Beijing, Beijing, China, [5]Department of Neurosurgery, Hainan Hospital of Chinese PLA General Hospital, Hainan, China, [6]Department of Neurosurgery, Shenzhen Key Laboratory of Neurosurgery, Shenzhen, China, [7]Brigham and Women's Hospital, Harvard Medical School, Boston, MA

Introduction: The clinical efficacy of deep brain stimulation (DBS) is significantly influenced by the accuracy of electrode placement (Okun et al., 2005, 2008; Bot et al., 2018; Neudorfer et al., 2023). Computerized models that reconstruct the electrode in silico have been used to investigate the relationship between electrode placements and clinical improvements. These models may be studied on a local (coordinates and stimulation volumes) and global network level (activated fiber tracts and associated functional networks). If accurate, models may be used to predict clinical outcomes in patients that were not used to create them (Horn et al., 2017; Boutet et al., 2021; Roediger et al., 2022). If successful, this leads to clinical utility of the models to potentially guide both DBS surgery and programming. Given promise, a recent trend in the emergence of computerized DBS models could be seen in the literature. However, a guide for best practices and parameter choices is lacking. Here, our aim was to compare a multitude of models and parameter choices based on a large multi-centre DBS cohort of patients who underwent the subthalamic nucleus DBS (STN-DBS) surgery for Parkinson's disease (PD).

Methods: We base analyses on retrospective data from a large cohort of N = 170 PD patients who underwent bilateral DBS targeting to the STN at five international centres. We used Lead-DBS v3 to localize electrodes and model stimulation volumes in each patient (Neudorfer et al., 2023). Relative motor improvements before and after surgery were measured via the Unified Parkinson's Disease Scale III (UPDRS-III). We then created predictive models on four levels: The first model was solely based on active coordinates of stimulation sites. Euclidean distance of active electrode contacts from an a priori optimal target coordinate (Caire et al., 2013) was calculated. The second model included an estimated stimulation volume based on programming parameters and was based on overlaps between these volumes and a sweet spot that was calculated following the approach by Horn et al., (2022). Third and fourth, DBS Fiber Filtering (Irmen et al., 2020) and DBS Network Mapping (Horn et al., 2017) approaches were carried out to identify the streamlines and functional networks associated with beneficial clinical effects (Figure 1). Sweet spots, optimal streamlines and optimal networks were validated using leave-nothing-out and 10-fold cross-validation to avoid circularity of the models. Results from all four models were fed into a multiple linear regression analysis.

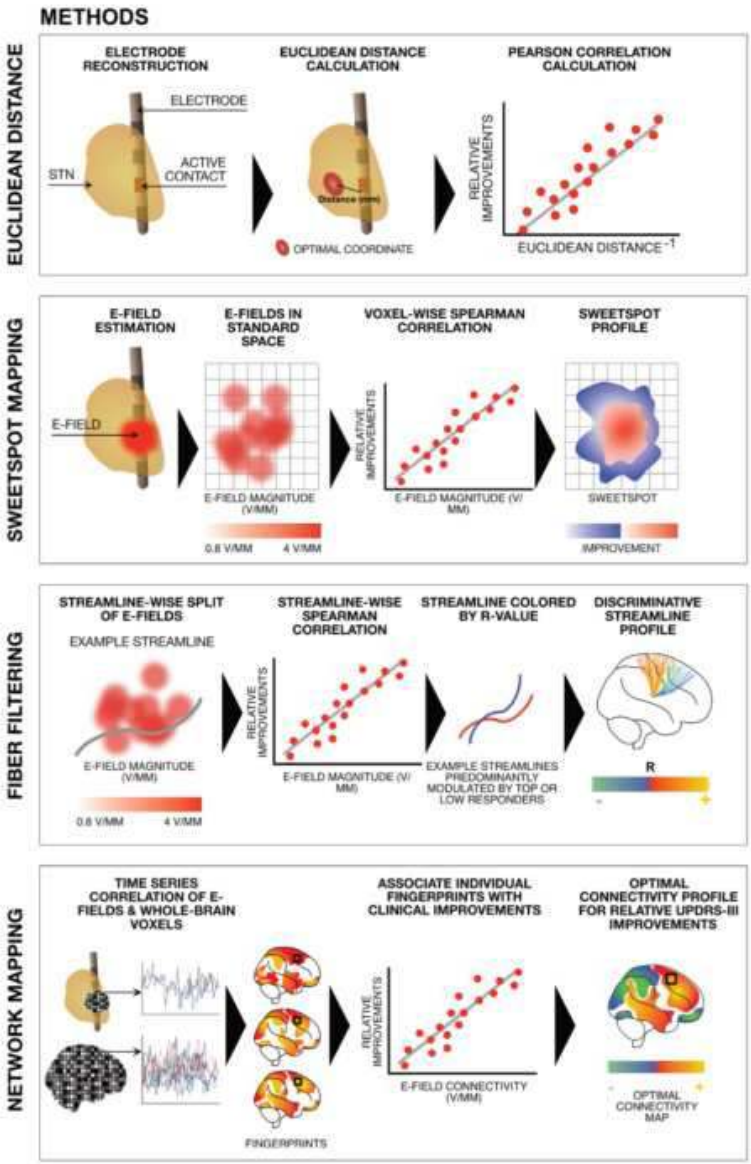

Figure 1. Methods pipeline for studying the impact of electrode placement on clinical outcomes. *Parkinson's disease patients (N=170) received bilateral deep brain stimulation (DBS) into their subthalamic nucleus (STN). First, we calculated the Euclidean distance of patient's active contact from a previously published optimal stimulation coordinate* (Caire *et al.*, 2013) *and correlated it with the patient-specific relative UPDRS-III improvements. Second, we determined an optimal sweetspot by correlating electrical field (E-field) magnitudes with clinical improvements (DBS Sweetspot Mapping). Third, we identified beneficial streamlines from a normative group connectome associated with clinical improvements and color-coded them by their correlation value (DBS Fiber Filtering). The results consisted of bundles of streamlines associated with clinical improvements. Fourth, we correlated the functional MRI time-series (BOLD signal) between E-Fields and other voxels in the brain using a normative functional connectome. We subsequently correlated these functional connections with the relative UPDRS-III improvement (DBS Network Mapping). The result was a map of connections associated with optimal UPDRS-III improvements.*

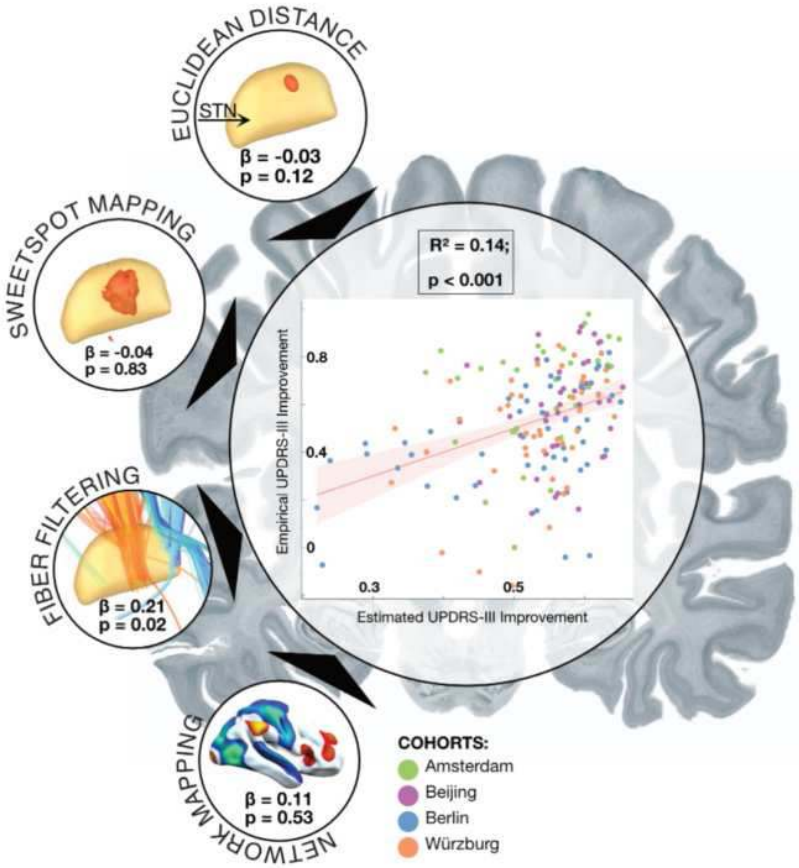

Figure 2. Variance in clinical improvements explained by the combination of four methods analysing the imaging data. *Parkinson's disease patients (N=170) received bilateral deep brain stimulation (DBS) into the subthalamic nucleus (STN). We then created predictive models of clinical improvements based on the electrode position on four levels. Estimates of these four models were calculated and fed into a multiple linear regression analysis. The predicted variable was relative UPDRS-III improvement. Total variance in clinical improvement explained by a combination of four methods was R2 = 0.14, p < 0.001. Each method's contribution is expressed as a regression coefficient (ß) and associated p-value.*

Results: As expected, Euclidean distances between active contacts and the a priori optimal coordinate correlated negatively with clinical improvements (R = -0.30, p < 0.001). Similarly, sweet spot, optimal tract and optimal network models were able to explain significant amounts of variance in clinical improvements (R = 0.19, p = 0.015; R = 0.29, p < 0.001 and R = 0.34, p < 0.001, respectively). In a combined model, 14% of the variance in empirical clinical improvements could be explained (F-statistic = 6.8, p < 0.001). In this model, only the Fiber Filtering scores contributed significantly (ß = 0.21, p = 0.018) (Figure 2).

Conclusions: Our findings confirm a robust relationship between electrode placements and clinical improvements following STN-DBS for PD. When combining results of models from local and global measures, models can still only account for a fraction of the overall variance.

References

1. Bot, M. et al. (2018) 'Deep brain stimulation for Parkinson's disease: defining the optimal location within the subthalamic nucleus', Journal of Neurology, Neurosurgery & Psychiatry, 89(5), pp. 493–498. Available at: https://doi.org/10.1136/jnnp-2017-316907.
2. Boutet, A. et al. (2021) 'Predicting optimal deep brain stimulation parameters for Parkinson's disease using functional MRI and machine learning', Nature Communications, 12(1), p. 3043. Available at: https://doi.org/10.1038/s41467-021-23311-9.
3. Caire, F. et al. (2013) 'A systematic review of studies on anatomical position of electrode contacts used for chronic subthalamic stimulation in Parkinson's disease', Acta Neurochirurgica, 155(9), pp. 1647–1654. Available at: https://doi.org/10.1007/s00701-013-1782-1.
4. Horn, A. et al. (2017) 'Connectivity Predicts deep brain stimulation outcome in Parkinson disease: DBS Outcome in PD', Annals of Neurology, 82(1), pp. 67–78. Available at: https://doi.org/10.1002/ana.24974.
5. Horn, A. et al. (2022) 'Optimal deep brain stimulation sites and networks for cervical vs. generalized dystonia', Proceedings of the National Academy of Sciences, 119(14), p. e2114985119. Available at: https://doi.org/10.1073/pnas.2114985119.

6. Irmen, F. et al. (2020) 'Left Prefrontal Connectivity Links Subthalamic Stimulation with Depressive Symptoms', Annals of Neurology, 87(6), pp. 962–975. Available at: https://doi.org/10.1002/ana.25734.
7. Neudorfer, C. et al. (2023) 'Lead-DBS v3.0: Mapping deep brain stimulation effects to local anatomy and global networks', NeuroImage, 268, p. 119862. Available at: https://doi.org/10.1016/j.neuroimage.2023.119862.
8. Okun, M.S. et al. (2005) 'Management of Referred Deep Brain Stimulation Failures: A Retrospective Analysis From 2 Movement Disorders Centers', Archives of Neurology, 62(8), pp. 1250–1255. Available at: https://doi.org/10.1001/archneur.62.8.noc40425.
9. Okun, M.S. et al. (2008) 'A case-based review of troubleshooting deep brain stimulator issues in movement and neuropsychiatric disorders', Parkinsonism & Related Disorders, 14(7), pp. 532–538. Available at: https://doi.org/10.1016/j.parkreldis.2008.01.001.
10. Roediger, J. et al. (2022) 'StimFit—A Data-Driven Algorithm for Automated Deep Brain Stimulation Programming', Movement Disorders, 37(3), pp. 574–584. Available at: https://doi.org/10.1002/mds.28878.

Poster No 11

Evaluation of Effectiveness of DBS based on the Thalamic Atlases and Shape Analysis in Epilepsy

Yejin Ann[1], Young-Min Sohn[2], Seok-Jun Hong[1]

[1]Center for Neuroscience Imaging Research, Institute for Basic Science, Suwon, South Korea, [2]Samsung Medical Center, Seoul, South Korea

Introduction: The anterior and centromedian thalamic nuclei (ATN/CM) are the two commonly target structures in deep brain stimulation (DBS) for epilepsy. To optimize this surgical planning, several MRI-based thalamic atlases have been introduced, but they were often unsuccessful for precise stimulation targeting[1]. While the efficacy of DBS has been assessed in many previous studies, a comprehensive investigation based on fully quantitative approaches is still lacking, especially in elucidating the relationship between varying rates of seizure reduction (SR) and DBS patterns or relating their pathological effects to an underlying anatomy. Here, we addressed these issues by 1) validating existing MRI thalamic atlases based on comparisons with histological data (to select the best reference atlas), 2) mapping the volume of DBS-activated tissue (VTA) on the thalamic nuclei of selected atlases (to assess how important precisely stimulating the targeted nucleus is to achieve SR), and 3) comparing the morphology of the thalamus between the control and patient groups.

Methods: Through the literature survey, we have found 5 publicly released thalamic atlases (Allen[2], Freesurfer[3], Ilinsky[4], Distal[1] and Thomas[5]). We quantitatively validated these atlases by comparing to the thalamic nuclei from postmortem brain data6. For this, we manually segmented ATN and CM in histology (Fig1A) and calculated a dice index (DI) between our segmentations and the borders of nuclei in MRI atlases to choose the best reference atlas. Analysis 1: We analyzed structural MRI of in-total 50 patients (31 focal [ATN] and 19 generalized epilepsy [CM]). We computed DI between the thalamic nucleus of the selected atlas and VTA at each subject. A receiver operating characteristic (ROC) curve was then plotted to evaluate the accuracy of classifying responder and non-responder groups (RG/NRG) across multiple DI values. Analysis 2: Next, we conducted a shape analysis to investigate the pathological effect on the thalamic morphology across the two patient groups (ATN/CM) compared to the control using a SPHARM-MAT algorithm[7]. After modeling the thalamic structure's surface, two sample t-test was employed to quantify their morphological differences. False discovery rate (FDR) corrected for the Type-I error.

Results: Our atlas validation demonstrated that ATN and CM boundaries in histology match to different MRI atlases, respectively. Indeed, the ATN showed the largest overlap with Thomas5, while in CM, the Freesurfer3 showed the best fit (Fig1B). The ROC (based on the DI between the nucleus atlas and VTA) for the accuracy of distinguishing RG and NRG revealed 0.75 of AUC for ATN and 0.489 for CM (Fig1C). It showed that the higher the overlap is with the atlas, the better seizure outcome is, in only ATN. Similarly, the thalamic shape analysis also showed the significant group changes only in the ATN-targeted patients compared to controls (Fig2) but not in CM patients. In the ATN group, overall trends of findings showed an inward deformation across multiple nuclei (Fig2). Notably, this atrophy was specifically noted in the right ATN. In the CM-targeted group, however, there were no group differences between patients and controls.

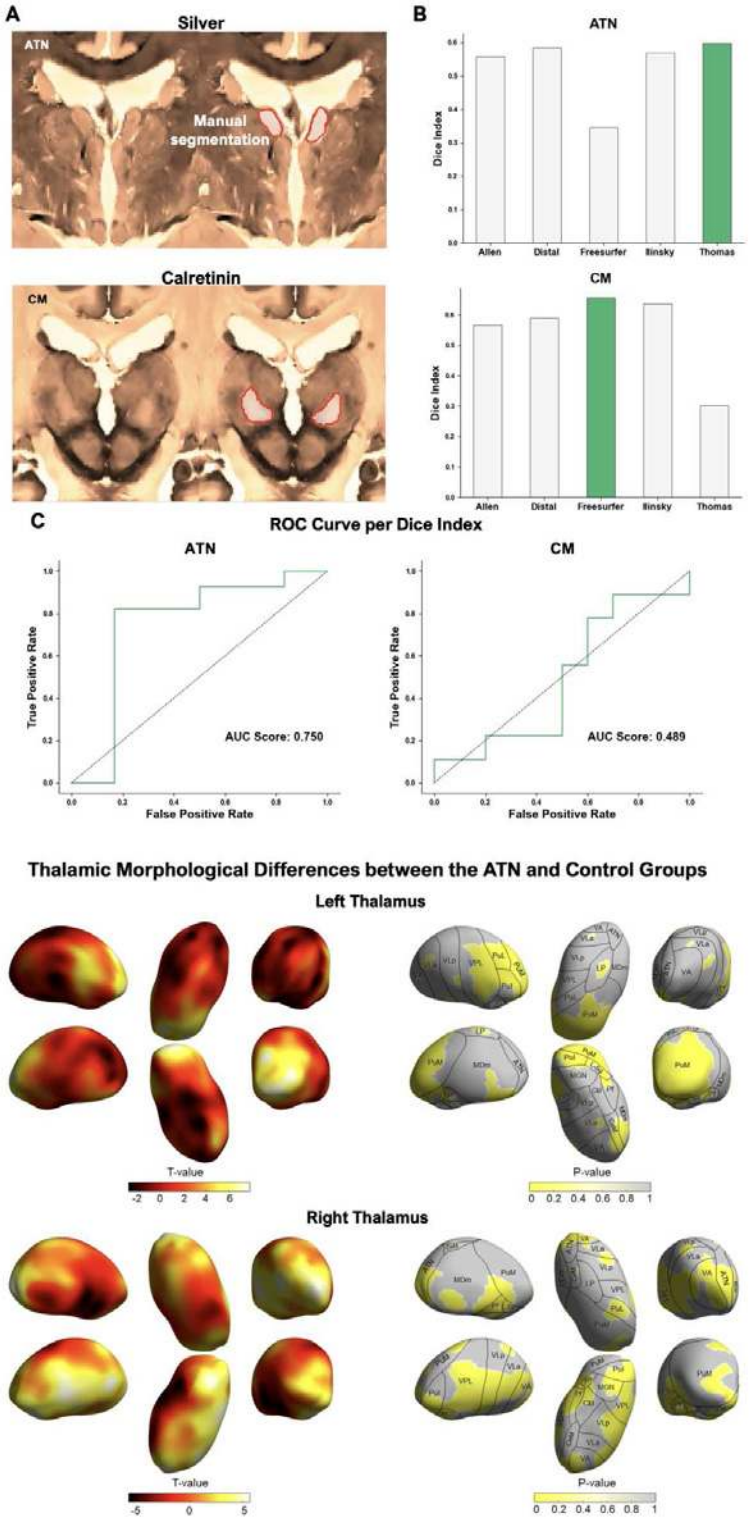

Conclusions: Our study validated the existing MRI-based thalamic atlases based on postmortem histology. The series of analyses demonstrated that the efficacy of DBS may be different, depending on the targeted thalamic nucleus. Indeed, while the DBS targeting ATN seems moderately efficacious in terms of seizure reduction, the CM-DBS cases failed to show comparable therapeutic effects. In the shape analysis, the individual heterogeneity in the CM group may influence the observed negative finding. Further research is required for the individual-level phenotyping and also the whole-brain analysis that targets beyond the thalamic nuclei (e.g., whole-brain connectivity) to comprehensively investigate potential factors of brain substrates that can affect the DBS outcome.

References
1. Ewert, S., Plettig, P., Li, N., Chakravarty, M. M., Collins, D. L., Herrington, T. M., ... & Horn, A. (2018). Toward defining deep brain stimulation targets in MNI space: a subcortical atlas based on multimodal MRI, histology and structural connectivity. Neuroimage, 170, 271-282.
2. Ding, S. L., Royall, J. J., Sunkin, S. M., Ng, L., Facer, B. A., Lesnar, P., ... & Lein, E. S. (2016). Comprehensive cellular-resolution atlas of the adult human brain. Journal of comparative neurology, 524(16), 3127-3481.
3. Iglesias, J. E., Insausti, R., Lerma-Usabiaga, G., Bocchetta, M., Van Leemput, K., Greve, D. N., ... & Alzheimer's Disease Neuroimaging Initiative. (2018). A probabilistic atlas of the human thalamic nuclei combining ex vivo MRI and histology. Neuroimage, 183, 314-326.
4. Ilinsky, I., Horn, A., Paul-Gilloteaux, P., Gressens, P., Verney, C., & Kultas-Ilinsky, K. (2018). Human motor thalamus reconstructed in 3D from continuous sagittal sections with identified subcortical afferent territories. eneuro, 5(3).
5. Su, J. H., Thomas, F. T., Kasoff, W. S., Tourdias, T., Choi, E. Y., Rutt, B. K., & Saranathan, M. (2019). Thalamus Optimized Multi Atlas Segmentation (THOMAS): fast, fully automated segmentation of thalamic nuclei from structural MRI. Neuroimage, 194, 272-282.
6. Alkemade, A., Bazin, P. L., Balesar, R., Pine, K., Kirilina, E., Möller, H. E., ... & Forstmann, B. U. (2022). A unified 3D map of microscopic architecture and MRI of the human brain. Science advances, 8(17), eabj7892.
7. Shen, L. (2010). SPHARM-MAT v1. 0.0 documentation.

Poster No 12

DystoniaDBSNet: A novel deep learning biomarker of predictive treatment outcomes in dystonia

Dongren Yao[1], Harith Akram[2], Kailash Bhatia[3], Thomas Foltynie[2], Patricia Limousin[2], Eoin Mulroy[2], Nutan Sharma[4], Joshua Wong[5], Jun Yu[6], Ludvic Zrinzo[2], Kristina Simonyan[7]

[1]Mass Eye and Ear, Harvard Medical School, Boston, MA, [2]UCL Queen Square Institute of Neurology, London, UK, [3]UCL Queen Square Institute of Neurology, Longon, UK, [4]Harvard Medical School, Boston, MA, [5]University of Florida, Gainesville, FL, [6]Univeresity of Florida, Gainesville, FL, [7]Mass Eye and Ear, Mass General Hospital, Harvard Medical School, Boston, MA

Introduction: Dystonia is a debilitating neurological disorder characterized by involuntary sustained or intermittent muscle contractions causing abnormal movements, postures, or both. Among the established therapeutic options is invasive circuit-based neuromodulation with deep brain stimulation (DBS) of bilateral globus pallidus (GPi), which yields an average of 30%-60% clinical improvement in different forms of dystonia. Yet, only about 5% of dystonia patients undergo DBS surgery and, among those treated, around 25% of patients have poor response. A limiting factor in patient selection for successful DBS treatment is the absence of a pathophysiologically relevant biomarker to inform treatment outcomes prior to neurosurgical intervention.

Methods: We developed and tested a deep learning algorithm, DystoniaDBSNet, which uses a structural brain MRI of patients who underwent DBS-GPi to automatically identify the neural biomarker of predictive treatment efficacy. Whole-brain T1-weighted MRIs from 130 patients with focal, multifocal, segmental, or generalized dystonia (64 M/66 F, age 45.78±18.62 years) treated at Massachusetts General Hospital, University College London, and the University of Florida were included in this study. Clinical improvement was defined as at least a 30% reduction of symptom severity based on the standardized Burke-Fahn-Marsden Dystonia Rating Scale. The DystoniaDBSNet model was trained and validated using phenotype-, sex-, age-, and surgical site-matched patient cohorts, allocating 80% of patients for training and 20% for testing.

Results: The training model of DystoniaDBSNet achieved the area under the receiver operating characteristic curve (AUC) of 100% in discriminating DBS benefiting from non-benefiting patients. DystoniaDBSNet automatically identified a neural biomarker of DBS treatment outcome, which included clusters in the bilateral precentral and middle frontal gyri, left superior frontal gyrus, anterior cingulate cortex, thalamus, and right postcentral gyrus. In the testing set of patients with different clinical phenotypes of dystonia, DystoniaDBSNet achieved an overall accuracy of 96.0%, with 100% sensitivity, 85.7% specificity, and a 3.87% referral rate in predicting the DBS treatment outcome.

Conclusions: DystoniaDBSNet yielded a fully automated, objective, and highly accurate predictive outcome of DBS treatment in patients with different forms of dystonia from a single structural MRI that was collected prior to neurosurgical intervention. The components of the DystoniaDBSNet biomarker included brain regions known for their contribution to dystonia pathophysiology. The translational significance of DystoniaDBSNet is in its potential to enhance clinical decision-making in DBS candidate selection and ultimately to deliver improved clinical care to patients with dystonia.

References
1. Kupsch A et al. (2006); Deep-Brain Stimulation for Dystonia Study Group, Pallidal deep-brain stimulation in primary generalized or segmental dystonia. N. Engl. J. Med. 355, 1978–1990.
2. Volkmann J et al. (2012); DBS study group for dystonia, Pallidal deep brain stimulation in patients with primary generalised or segmental dystonia: 5-year follow-up of a randomised trial. Lancet Neurol. 11, 1029–1038.
3. Moro E et al. (2017), Efficacy of pallidal stimulation in isolated dystonia: A systematic review and meta- analysis. Eur. J. Neurol. 24, 552–560.

4. Lozano A. M. et al. (2019), Deep brain stimulation: Current challenges and future directions. Nat. Rev. Neurol. 15, 148–160.

Poster No 13

Noninvasive Stimulation of the Nucleus Accumbens using Transcranial Focused Ultrasound

Xiaolong Peng[1], Dillon Connolly[1], Falon Sutton[1], John Robinson[1], Brenna Baker-Vogel[1], Edward Short[1], Bashar Badran[1]

[1]Medical University of South Carolina, Charleston, SC

Introduction: Transcranial focused ultrasound (tFUS) is an emerging noninvasive neuromodulation technique that can stimulate deep brain regions with a high spatial resolution[1,2]. Previous clinical trials have demonstrated that tFUS can attenuate sensory processing[3], pain[4], and modulate self-reported mood and mental vigor[5] by stimulating specific brain targets, including the thalamus and lateral frontal gyrus. The penetrative depth and spatial resolution of tFUS expand the scope of traditional noninvasive neuromodulation approaches to previously inaccessible regions, such as the nucleus accumbens (NAc). NAc is a key node of the brain reward circuit[6], and dysregulation of this region has been demonstrated to contribute to pathological markers of addiction such as cue reactivity and drug-seeking behavior in substance use disorder (SUD) making it a potential therapeutic target for tFUS[7]. In this pilot study, we investigated whether tFUS on NAc can modulate the reward network.

Methods: Ten healthy individuals (7 females, mean age ± SD: 31 ± 8.39 years) were recruited for this single-blind, sham-controlled, pilot study. All participants were randomly assigned to either the active tFUS group (N=5) or the sham group (N=5). Participants attended a single experimental visit, and all research methods were conducted within a Siemens 3T Prisma MRI scanner. First, a structural T1 MRI scan was acquired, followed by pre-tFUS resting-state functional MRI (fMRI; four, 6-minute scans). Then, 20 minutes of either active or sham tFUS was administered targeting the left NAc during concurrent fMRI acquisition (two, 10-minute scans). Lastly, a post-tFUS resting-state fMRI was acquired (four, 6-minute scans). This study was approved by the MUSC IRB, registered on ClinicalTrials.gov (NCT05986019), and all participants signed the informed consent before enrollment. The real-time tFUS targeting was conducted within the bore of the MRI prior to ensuring the tFUS transducer was in the correct position to deliver ultrasound to the NAc target as described in our previous study (Figure 1a & b)[4]. After tFUS targeting, the concurrent tFUS-fMRI scan was performed. Each tFUS-fMRI run consisted of a 30s tFUS “ON” block, followed by a 30s “OFF” block, and repeated ten times. During the tFUS “ON” block, ultrasound stimulations were generated using the BrainSonix BXPulsar 1002 tFUS System with sonication parameters as follows: Fundamental frequency = 650 kHz, Pulse repetition frequency = 10 Hz, Pulse width = 5 ms, Duty cycle = 5%, Sonication duration = 30 s, ISPTA.0 = 995 mW/cm2, ISPTA.3 = 719 mW/cm2, Peak rarefactional pressure = 0.72 MPa. For the sham group, the tFUS system was set up identically to the active tFUS group, including targeting, however, tFUS was not turned on during the tFUS-fMRI scan. Both tFUS/fMRI and resting fMRI data were preprocessed using the same procedures as described in our previous study[8,9].

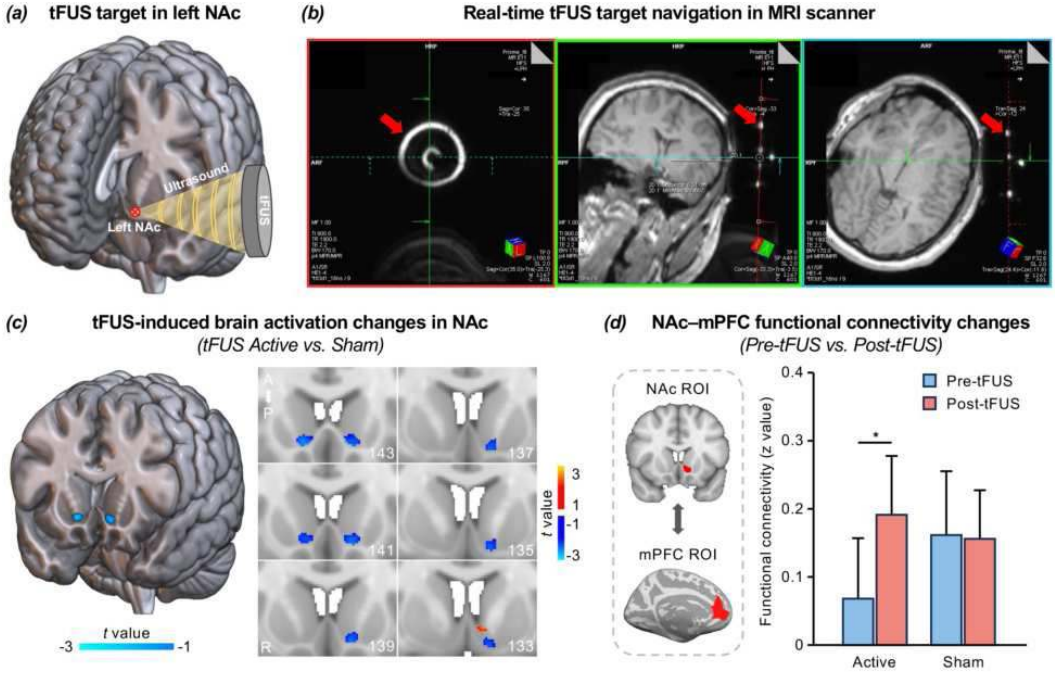

Figure 1. (a) Schematic of delivering ultrasound to the left NAc using tFUS. The red circled cross shows the location of the planned tFUS target – left NAc. (b) An example of the real-time tFUS target navigation procedure in the MRI scanner. These images were acquired from a rapid structure MRI sequence that captured the brain anatomy and the tFUS transducer. The bright circles and dots pointed by the red arrows show the location of the tFUS transducer. Digitized lines were created that intersect the fixed fiducials that are incorporated into the tFUS transducer. Specifically, the red line aligned with the back of the transducer. The blue line and the green line are orthogonal to the center of the transducer and extend into the left NAc target. (c) Decreased brain activities were observed in the anterior part of the bilateral NAc and most regions of the left posterior NAc (two-sample t-test, $p < 0.05$) in the tFUS active group compared to the sham group, indicating that tFUS inhibited NAc activities. (d) A significantly increased functional connectivity between the NAc and mPFC was obtained after stimulating the left NAc in the active group (paired t-test, $t = 2.850$, $p = 0.046$), however, no significant changes were observed in the sham group ($t = 0.041$, $p = 0.969$), indicate that tFUS can modulate NAc functional connections to the mPFC within the reward network.

Results: The brain activation maps demonstrated that tFUS on the left NAc reduced the brain activities in the anterior part of the bilateral NAc and most regions of the left posterior NAc (Figure 1c; two-sample t-test, $p < 0.05$), indicating that tFUS can directly inhibit NAc activities. Additionally, we also demonstrated a significantly increased functional connectivity between the NAc and mPFC after tFUS on the left NAc in the active group (Figure 1d; paired t-test, $t = 2.850$, $p = 0.046$), however, no significant changes were observed in the sham group ($t = 0.041$, $p = 0.969$).

Conclusions: This study demonstrates the feasibility and safety of this novel technique for deep brain stimulation. Furthermore, these preliminary findings suggest that tFUS could be potentially a promising neuromodulation tool for the direct and noninvasive management of the NAc and shed new light on the treatment for SUD and other brain diseases that involve reward processing.

References

1. Rezayat E. (2016), 'A Review on Brain Stimulation Using Low Intensity Focused Ultrasound', Basic Clin Neurosci, 7(3):187-94.
2. Badran B.W. (2023), 'Transcranial focused ultrasound (tFUS): a promising noninvasive deep brain stimulation approach for pain', Neuropsychopharmacology: Official Publication of the American College of Neuropsychopharmacology.
3. Legon W. (2014), 'Transcranial focused ultrasound modulates the activity of primary somatosensory cortex in humans', Nat Neurosci,17(2):322-9.
4. Badran B.W. (2020), 'Sonication of the anterior thalamus with MRI-Guided transcranial focused ultrasound (tFUS) alters pain thresholds in healthy adults: A double-blind, sham-controlled study', Brain Stimul,13(6):1805-12.
5. Sanguinetti J.L. (2020), 'Transcranial Focused Ultrasound to the Right Prefrontal Cortex Improves Mood and Alters Functional Connectivity in Humans', Front Hum Neurosci, 14:52.
6. Haber S.N. (2010), 'The reward circuit: linking primate anatomy and human imaging', Neuropsychopharmacology, 35(1):4-26.
7. Cooper S. (2017), 'Reward Circuitry in Addiction', Neurotherapeutics, 14(3):687-97.
8. Peng X. (2023), 'Robust dynamic brain coactivation states estimated in individuals', Science Advances, 9(3):eabq8566.
9. Peng X. (2023), 'Left or right ear? A neuroimaging study using combined taVNS/fMRI to understand the interaction between ear stimulation target and lesion location in chronic stroke', Brain Stimulation, 16(4):1144-53.

Poster No 14

Deep brain stimulation impacts functional brain connectivity in Parkinson's disease

Robert Jech[1,2], Andrej Lasica[1], Dimitra Kiakou[1,3], Filip Růžička[1], Pavel Filip[1,4], Dušan Urgošík[2], Karsten Mueller[1,3]

[1]Department of Neurology, Charles University, [1]st Faculty of Medicine and General University Hospital, Prague, Czech Republic, [2]Na Homolce Hospital, Prague, Czech Republic, [3]Max Planck Institute for Human Cognitive and Brain Sciences, Leipzig, Germany, [4]Center for Magnetic Resonance Research (CMRR), University of Minnesota, Minneapolis, MN

Introduction: Deep-brain stimulation (DBS) became a successful method to treat Parkinson's disease (PD), particularly with stimulating the subthalamic nucleus (STN-DBS), although the precise mechanisms mediating its efficacy remain elusive. Recent work is investigating the target location of STN-DBS (sweet spot) as a biomarker of the motor outcome of STN-DBS in PD (Dembek 2019) with higher beta-band activity with posterior and dorsal STN lead positions (Horn 2017) which is in-line with increased motor performance. In order to find an impact of STN-DBS target location on functional brain connectivity, we investigated brain network centrality differences using functional MRI in subgroups of PD patients showing a more dorsal and a more ventral position of STN-DBS.

Methods: The study included 99 patients with advanced type of PD (33 fem, age 59.5±7.9 years, disease duration 15.1±6.3 years). Clinical assessment and functional MRI was performed in two sessions in the STN-DBS ON and OFF state. Imaging was performed in resting state using a 1.5T MAGNETOM scanner (Siemens Healthineers, Erlangen, Germany) with a birdcage head coil and a gradient-echo EPI sequence (flip angle 90°; repetition time 3 s; echo time 51 ms). A set of 31 axial slices (thickness 3 mm; 1 mm gap; in-plane resolution 3×3 mm2) were acquired with interleaved slice order covering the whole brain. For each participant and each session, 203 functional volumes were acquired resulting in a total scanning duration of 10 min. Volumes of activated tissue (VTA) were calculated with the Lead-DBS software using T1-weighted structural images (Horn 2019). Data preprocessing and analysis was performed with SPM12 and the CONN toolbox (Whitfield-Gabrieli, 2012) including realignment for motion correction, unwarping to correct for image distortions, slice-time correction, normalization, and spatial filtering using a Gaussian kernel with 10 mm. To correct for nuisance signal fluctuations, a regression analysis was computed using the signal from white matter and cerebrospinal fluid, as well as the parameters from head movements (Friston-24 model). Preprocessing was finalized using a high-pass filter with a cutoff frequency of 0.01 Hz. Thereafter, for each patient, STN-DBS brain network centrality difference was computed using the OFF-ON difference of global correlation (GCOR). All GCOR difference maps were fed into a second-level analysis using a one-sample t-test including the VTA's volume and the coordinates of the center-of-gravity (VTA-CoG) as additional covariates. The same analysis was performed for the 30 patients with the most dorsal and the most ventral VTA-CoG in the left and right hemisphere, respectively. Significant results were obtained using family-wise error (FWE) correction with $P<0.05$ (Flandin 2019, Friston 1994).

Results: We found an STN-DBS-related brain connectivity decrease showing a significant GCOR difference across the whole group of 99 PD patients in the left and right temporal lobe (Fig 1). The same pattern of GCOR decrease was obtained with the subgroup of 30 patients with the most dorsal VTA-CoG in the left hemisphere, however, no significant result was obtained with the subgroup of 30 patients with the most ventral VTA-CoG (Fig 2). A similar result was obtained when investigating subgroups of patients with the most dorsal/ventral VTA-CoG in the right hemisphere.

Conclusions: Our study demonstrated an impact of STN-DBS target location onto functional brain connectivity while significant brain connectivity changes were obtained with a dorsal position of STN-DBS. Thus, our result is in-line with recent findings suggesting the sweet spot of STN-DBS in more dorsal regions of STN (Horn 2017, Dembek 2019), however, the observed temporal lobe connectivity alterations in relationship to the STN-DBS target location remain unclear. Further work is necessary to investigate the causal relationship of STN-DBS motor improvement and functional brain connectivity alterations related to the STN-DBS target location.

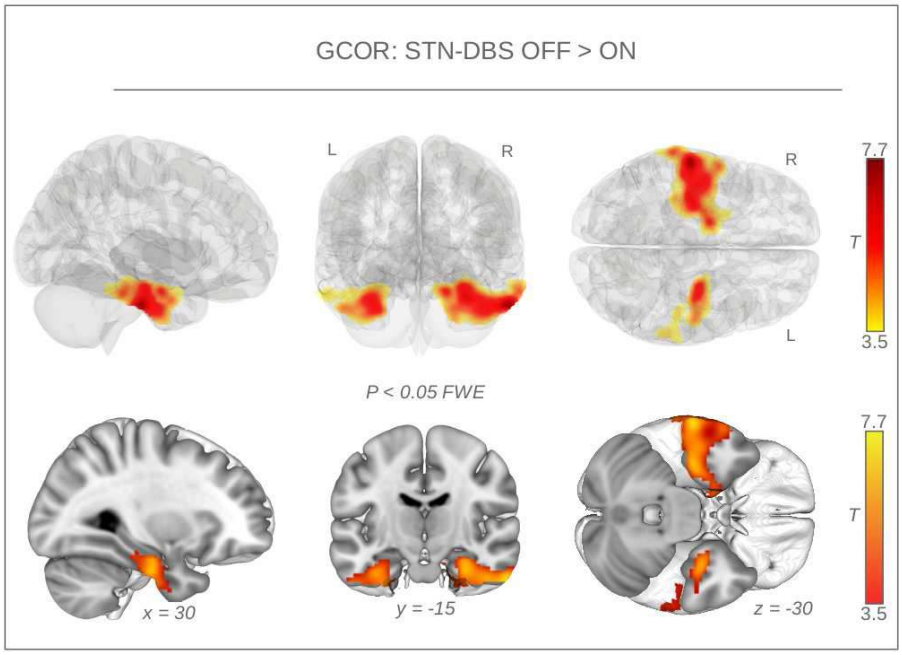

Figure 1. Functional brain connectivity decrease with STN-DBS in a group of 99 PD patients. Color-coded regions show a reduced global correlation (GCOR) with STN-DBS.

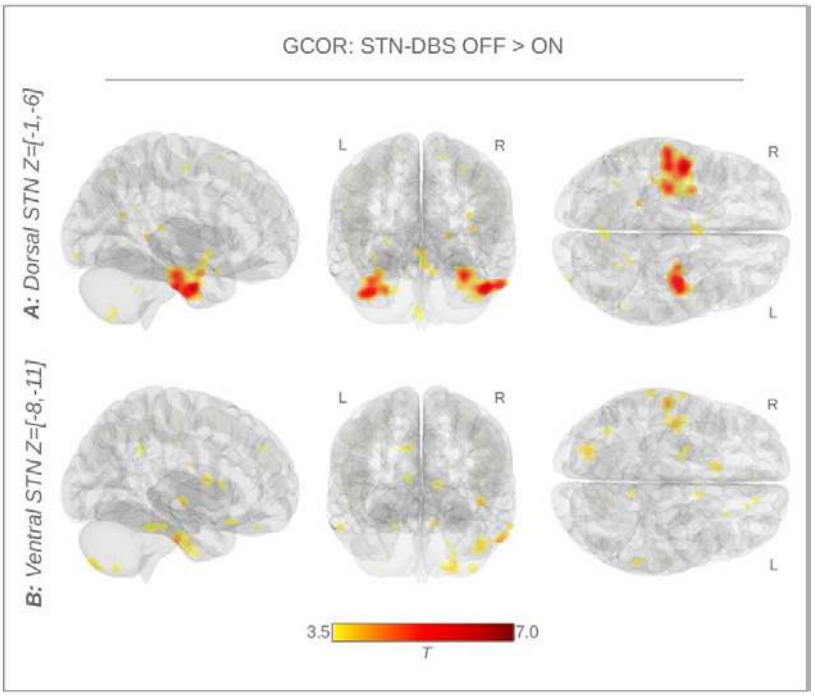

Figure 2. Functional brain connectivity differences with STN-DBS including (A:) 30 PD patients with a dorsal target location of STN-DBS, and (B:) 30 patients with a ventral target location of STN-DBS.

References

1. Dembek, T.A., Roediger, J., Horn, A., Reker, P., Oehrn, C., Dafsari, H.S., Li, N., Kühn, A.A., Fink, G.R., Visser-Vandewalle, V., Barbe, M.T., Timmermann, L. (2019), 'Probabilistic sweet spots predict motor outcome for deep brain stimulation in Parkinson disease', Annals Neurology, vol. 86, no. 4, pp. 527-538, doi: 10.1002/ana.25567
2. Flandin, G., Friston, K.J. (2019), 'Analysis of family-wise error rates in statistical parametric mapping using random field theory', Human Brain Mapping, vol. 40, no. 7, pp. 2052-2054, doi: 10.1002/hbm.23839
3. Friston, K.J., Worsley, K.J., Frackowiak, R.S., Mazziotta, J.C., Evans, A.C. (1994), 'Assessing the significance of focal activations using their spatial extent', Human Brain Mapping, vol. 1, no. 3, pp. 210-220, doi: 10.1002/hbm.460010306
4. Horn, A., Neumann, W.J., Degen, K., Schneider, G.H., Kühn, A.A. (2017), 'Toward an electrophysiological "sweet spot" for deep brain stimulation in the subthalamic nucleus', Human Brain Mapping, vol. 38, no. 7, pp. 3377-3390. doi: 10.1002/hbm.23594

5. Horn, A., Li N., Dembek, T.A., Kappel, A., Boulay, C., Ewert, S., Tietze, A., Husch, A., Perera, T., Neumann, W.J., Reisert, M., Si, H., Oostenveld, R., Rorden, C., Yeh, F.C., Fang, Q., Herrington, T.M., Vorwerk, J., Kühn, A.A. (2019), 'Lead-DBS v2: Towards a comprehensive pipeline for deep brain stimulation imaging', Neuroimage, vol. 184, pp. 293-316. doi: 10.1016/j.neuroimage.2018.08.068
6. Whitfield-Gabrieli, S., Nieto-Castanon, A. (2012), 'Conn: a functional connectivity toolbox for correlated and anticorrelated brain networks', Brain Connectivity, vol. 2, no. 3, pp. 125-141. doi: 10.1089/brain.2012.0073

Acknowledgements
Supported by a grant of the National Institute for Neurological Research, Czech Republic, Programme EXCELES (ID project No. LX22NPO5107) and the Charles University: Cooperatio Program in Neuroscience.

Poster No 15

Symptom Network Modulation by Deep Brain Stimulation in Obsessive-Compulsive Disorder

Barbara Hollunder[1], Garance Meyer[2], Ningfei Li[1], Clemens Neudorfer[2], Nanditha Rajamani[1], Cristina Nombela[3], Philip Mosley[4], Harith Akram[5], Nicola Acevedo[6], Benjamin Borron[7], Tina Chou[7], Jurgen Germann[8], Juan Pablo Castaño Montoya[9], Bryan Strange[10], Juan Barcia[9], Himanshu Tyagi[5], David Castle[11], Susan Rossell[6], Peter Bosanac[12], Carsten Finke[1], Andrea Kühn[1], Jens Kuhn[13], Veerle Visser-Vandewalle[13], Stephan Chabardes[14], Martijn Figee[15], R. Mark Richardson[7], G. Rees Cosgrove[2], Darin Dougherty[7], Shan Siddiqi[2], Andres Lozano[16], Ludvic Zrinzo[5], Eileen Joyce[5], Mircea Polosan[14], Juan Carlos Baldermann[13], Michael Fox[2], Andreas Horn[2]

[1]Charité - University Medicine Berlin, Berlin, Berlin, [2]Brigham and Women's Hospital, Harvard Medical School, Boston, MA, [3]Universidad Autónoma de Madrid, Madrid, Madrid, [4]University of Queensland, St Lucia, Queensland, [5]UCL Queen Square Institute of Neurology, London, London, [6]Swinburne University of Technology, Melbourne, VIC, [7]Massachusetts General Hospital, Harvard Medical School, Boston, MA, [8]Krembil Research Institute, Toronto, Ontario, [9]Universidad Complutense de Madrid, Madrid, Madrid, [10]Universidad Politécnica de Madrid, Madrid, Madrid, [11]University of Tasmania and Centre for Mental Health Service Innovation, Sandy Bay, TAS, [12]University of Melbourne, Melbourne, VIC, [13]Faculty of Medicine and University Hospital Cologne, Cologne, NRW, [14]Université Grenoble Alpes, Grenoble, Rhône-Alpes, [15]Icahn School of Medicine at Mount Sinai, New York, NY, [16]University Health Network, University of Toronto, Toronto, Ontario, Toronto, Ontario

Introduction: Symptom diversity among patients with obsessive-compulsive disorder (OCD) significantly contributes to outcome variability after deep brain stimulation (DBS) (Figee & Mayberg, 2021). Indeed, the same anatomical site is often targeted, without tailoring the surgical strategy to the symptoms dominating a patient's clinical profile. This approach has proven effective for the "average" OCD patient's cardinal symptomatology by activating a specific fiber bundle in the internal capsule (Baldermann et al., 2021; Li et al., 2020). Nonetheless, encompassing a wider range of dysfunctional circuits may require modulating a combination of symptom tracts (Figee & Mayberg, 2021; Hollunder et al., 2022). Here, we segregate the connectome into a set of therapeutic sub-circuits related to enhancements in obsessions, compulsions, depression, anxiety, cognitive flexibility, and cognitive control.

Methods: This study relied on retrospective data from a multi-institutional cohort of OCD patients (N=99), all of whom underwent bilateral DBS at one of six stereotactic sites: anterior limb of the internal capsule (ALIC) (N=51), nucleus accumbens (N=15), inferior thalamic peduncle (N=5), bed nucleus of the stria terminalis (N=9), subthalamic nucleus (N=13), or combined stimulation of subthalamic nucleus and ALIC (N=6, four electrodes per patient) (Figure 1). Using a Lead-DBS based preprocessing pipeline (Neudorfer et al., 2023), electrode reconstructions affirmed positioning within the intended target regions for the majority of patients. Combining 3D reconstructions of electrodes and adjacent anatomy, the localized effect of DBS on tracts was estimated via finite element modeling. Symptom improvement was expressed as percent change from preoperative baseline on established rating scales and neuropsychological tests: obsessions vs. compulsions (Yale-Brown Obsessive Compulsive Scale), depression (Beck Depression Inventory / Montgomery Åsperg Depression Rating Scale / Hamilton Depression Inventory), anxiety (Hamilton and Beck Anxiety Inventories / State-Trait Anxiety Inventory, state section), cognitive flexibility (Intra-Extra Dimensional Set Shift Task / Trail Making Test, part B), and cognitive control (Stroop). The generalized DBS Fiber Filtering method (Irmen et al., 2020) was carried out to identify which streamlines of a normative group connectome were discriminative for beneficial effects per symptom domain. Tract models were confirmed using five-fold cross-validation (CV).

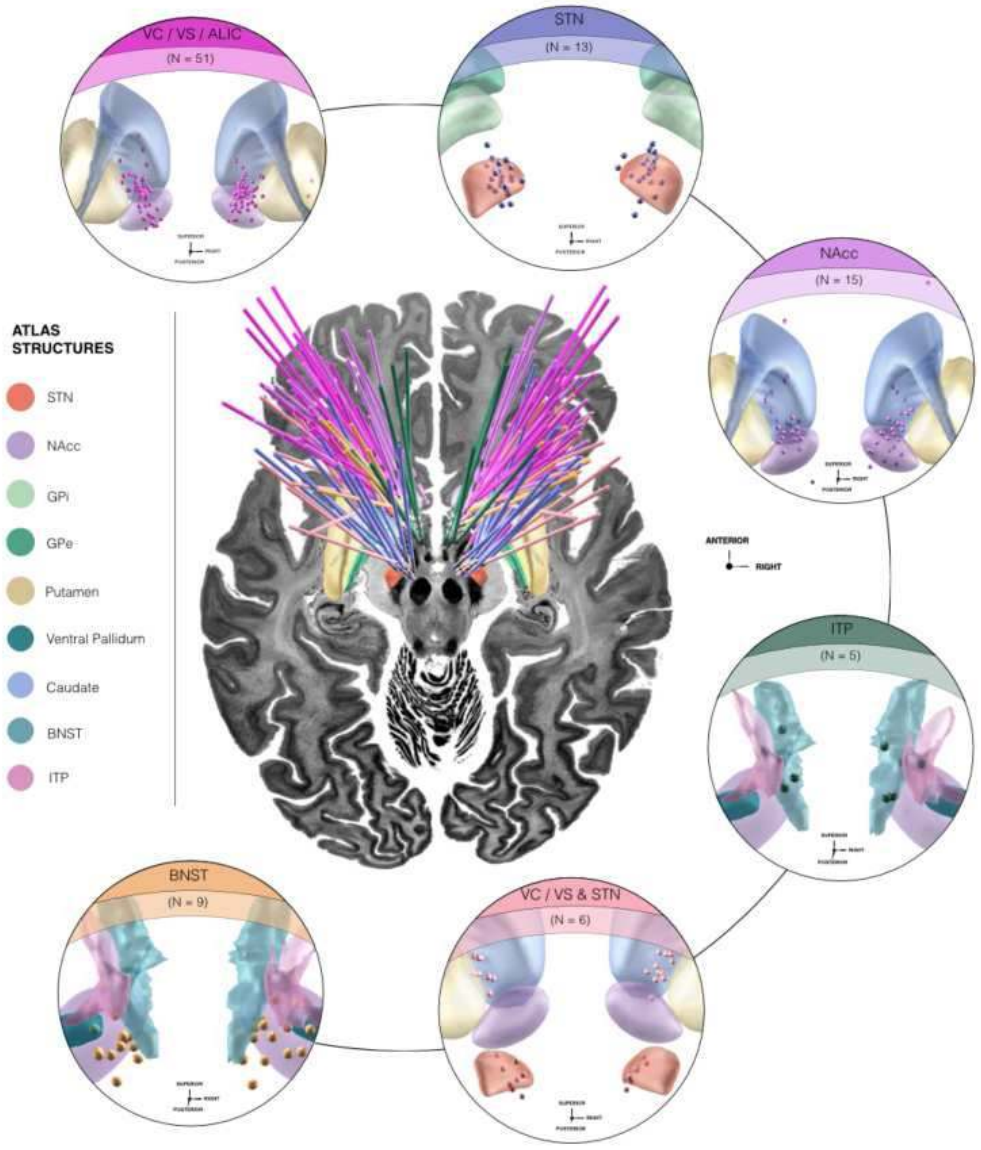

Fig. 1. Overview of electrode placement across obsessive-compulsive disorder (OCD) patients. *Center:* Axial view of deep brain stimulation (DBS) electrode trajectories and anatomical relationship of their placement across cohorts, superimposed on top of an axial plane (z = -10 mm) of the BigBrain template in 100 µm resolution (Amunts et al., 2013). *Circles with close-up views:* Target-wise grouping of active electrode contacts across included cohorts is shown in relation to adjacent anatomical structures. Subthalamic nucleus (STN), globus pallidus internus (GPi) and externus (GPe) as defined by the DBS intrinsic template atlas (DISTAL) atlas (Ewert et al., 2018); nucleus accumbens (NAcc), putamen, ventral pallidum, and caudate by the California Institute of Technology reinforcement learning atlas (CIT-168) (Pauli et al., 2018); bed nucleus of the stria terminalis (BNST) and inferior thalamic peduncle (ITP) by the atlas of the human hypothalamus (Neudorfer et al., 2020).

Results: Despite differences in electrode placement across institutions and surgeons (Figure 1), the therapeutic impact on overall obsessive-compulsive symptomatology consistently implicated a common prefronto-cortical pathway traversing the ALIC. This model showed positive in-sample associations (R=.39, p<1e-3) and was robust to five-fold CV (R=.30, p<.01). Plain electrode connections (Figure 2A) could further be segregated into symptom-wise bundles (Figure 2B), with those beneficial for obsessions (in-sample R=.41, p<1e-3) located most dorsally (dorsolateral prefrontal areas), in dorso-ventral direction followed by those for depression (in-sample R=.40, p<1e-3), compulsions (in-sample R=.40, p<1e-3), cognitive control (in-sample R=.54, p<0.01), cognitive flexibility (in-sample R=.49, p=.042), and anxiety (ventromedial prefrontal areas; in-sample R=.66, p<1e-3). Five-fold CVs confirmed generalizability of results for obsession (R=.31, p=.01), compulsion (R=.26, p=.037), and anxiety models (R=.63, p<1e-3), but not significantly for depression (R=.15, p=.227), cognitive control (R=.22, p=.315), and cognitive flexibility (R=.10, p=.679).

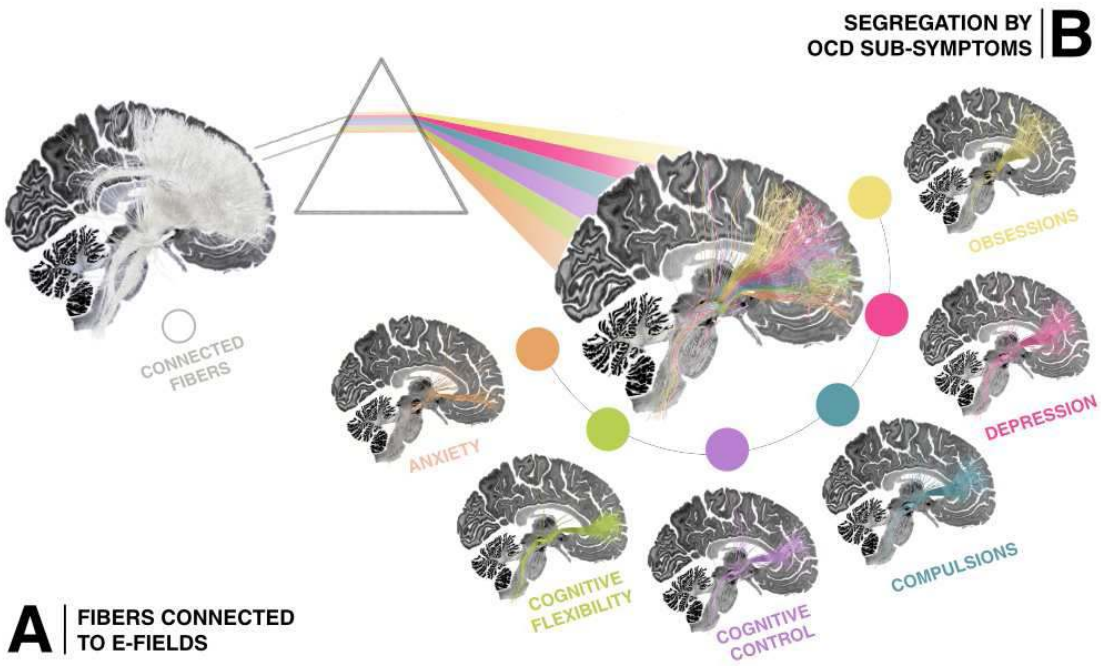

Fig. 2. Multi-symptom taxonomy of therapeutic tracts for deep brain stimulation (DBS) in obsessive-compulsive disorder (OCD). The set of plain connections seeding from bilateral electric fields (E-fields) of patients across the sample is segregated into symptom-wise bundles by association with therapeutic stimulation effects in multiple OCD sub-symptoms: obsessions, compulsions, depression, anxiety, cognitive control, as well as cognitive flexibility. DBS Fiber Filtering results were derived from a high-resolution normative group connectome calculated based on data of 985 participants from the Human Connectome Project and superimposed on a sagittal slice (x = -5 mm) of the 100 µm BigBrain template (Amunts et al., 2013).

Conclusions: Fundamentally, our results may enhance our comprehension of the pathophysiological underpinnings and operative mechanisms of DBS relevant to various OCD symptoms. These insights could be instrumental for addressing symptoms transcending different diagnoses, or for customizing treatments to unique symptom clusters exhibited by individual patients.

References

1. Amunts, K., et al. (2013), 'BigBrain: An ultrahigh-resolution 3D human brain model', Science, vol. 340, no. 6139, pp. 1472–1475
2. Baldermann, J. C., et al. (2021), 'Connectomic deep brain stimulation for obsessive-compulsive disorder', Biological Psychiatry, vol. 90, no. 10, pp. 678–688
3. Ewert, S., et al. (2018), 'Toward defining deep brain stimulation targets in MNI space: A subcortical atlas based on multimodal MRI, histology and structural connectivity', NeuroImage, vol. 170, pp. 271–282
4. Figee, M., et al. (2021), 'The future of personalized brain stimulation', Nature Medicine, vol. 27, pp. 196–197
5. Hollunder, B., et al. (2022), 'Toward personalized medicine in connectomic deep brain stimulation', Progress in Neurobiology, vol. 210, p. 102211
6. Irmen, F., et al. (2020), 'Left prefrontal connectivity links subthalamic stimulation with depressive symptoms', Annals of Neurology, vol. 87, no. 6, pp. 962–975
7. Li, N., et al. (2020), 'A unified connectomic target for deep brain stimulation in obsessive-compulsive disorder', Nature Communications, vol. 11, p. 3364
8. Neudorfer, C., et al. (2023), 'Lead-DBS v3.0: Mapping deep brain stimulation effects to local anatomy and global networks', NeuroImage, vol. 268, p. 119862
9. Neudorfer, C., et al. (2020), 'A high-resolution in vivo magnetic resonance imaging atlas of the human hypothalamic region', Scientific Data, vol. 7 no. 1, 1–14
10. Pauli, W. M., et al. (2018), 'A high-resolution probabilistic in vivo atlas of human subcortical brain nuclei', Scientific Data, vol. 5, p. 180063

Poster No 16

Brain-wide anatomical and functional effects of subcallosal cingulate white matter DBS

Satoka Fujimoto[1], Atsushi Fujimoto[2], Catherine Elorette[1], Davide Folloni[1], Lazar Fleysher[1], Ki Sueng Choi[1], Brian Russ[3], Helen Mayberg[1], Peter Rudebeck[1]

[1]Icahn School of Medicine at Mount Sinai, New York, NY, [2]Icahn School of Medicine at Mount Sinai, New york, NY, [3]Nathan Kline Institute, Orangeburg, NY

Introduction: Deep brain stimulation targeting subcallosal anterior cingulate cortex (SCC-DBS) and adjacent white matter (WM) is a promising therapy for treatment resistant depression (TRD)[1,2]. The neural mechanisms through which SCC-DBS

facilitates recovery from TRD are, however, not fully characterized, making it difficult to optimize treatment for all patients. While white matter abnormality is reported to relevant with depression severity[3], it remains unclear how DBS stimulation of white matter alters brain-wide circuits even in healthy brains, an essential first step in determining the therapeutic mechanisms of SCC-DBS. The aim of the current study was to establish how SCC-DBS works in the healthy brain, focusing on determining the brain-wide network-level functional and anatomical effects of white matter stimulation.

Methods: To model the approach used to successfully treat TRD patients, we implanted SCC-DBS electrodes in two male rhesus macaques. The organization and differentiation of gray matter and the white matter in the macaque brain, especially the frontal and temporal cortex, are highly similar to humans making them the best available animal model[4]. Diffusion-weighted imaging (DWI) (Siemens Skyra 3T, human head 32ch coil, b=1000 s/mm2, 1.5mm isotropic resolution, 8 b0s per scan, two opposite phase encoding = AP/PA) and whole brain resting-state functional MRIs (rs-fMRIs, echo planar image, custom-built 4-channel monkey coil, 1.5mm isotropic) were acquired before electrode implantation. Using probabilistic diffusion tractography analysis (FSL, FMRIB), we identified the confluence of the cingulum bundle (CB), forceps minor (FM), and uncinate fasciculus (UF)[5]. We then unilaterally implanted a single miniaturized DBS lead in this location in one hemisphere. The other hemisphere serves as a control. One month after electrode implantation, stimulation (5mA, 130Hz, 90µsec) began and was maintained for 6 weeks. Following 6 weeks of SCC-DBS stimulation and explantation of the electrode, we acquired functional and diffusion scans to match the pre-electrode scans to investigate the functional and anatomical changes induced by SCC-DBS. Fractional anisotropy (FA), calculated from the DWI, was used to investigate anatomical changes in WM, and rs-fMRI data were analyzed using a seed-based comparative-connectome approach to determine where SCC-DBS stimulation induced changes in functional connectivity (FC), using AFNI, FSL, and MRtrix3. Seed ROI was set in the stimulated area 25 where the artifact was minimized by the absence of the DBS lead. Multiple comparison analyses were conducted to confirm the statistical differences.

Results: Diffusion tractography reconstruction of the CB, FM, and UF revealed a close homology between humans and monkeys. The confluence of the 3 WM tracts was located in the WM adjacent to area 25, and the location was highly similar to humans. Thus, we were able to accurately model the anatomical target that is used in human TRD patients. After 6 weeks of SCC-DBS stimulation, FA was significantly increased in the CB in the stimulated hemisphere. The midcingulate portion of CB carries fibers connecting the anterior and posterior cingulate cortex (PCC), and this specific part showed a significant increase in FA. FC between the stimulated ROI (Area 25) and DMN hubs (medial prefrontal cortex and PCC) and limbic system hubs (cingulate cortex, hippocampus, amygdala) were significantly decreased following 6-weeks of stimulation.

Conclusions: Chronic SCC-DBS changes brain-wide structures and functional networks connected to the SCC. Specifically, WM changes were prominent in the stimulated CB, especially MCC portion, and functional changes were predominant in the DMN. Our data reveal the specific effects of SCC-DBS on brain-wide anatomical and functional connectivity, information essential for establishing the neural mechanisms of DBS for TRD, as well as the biological bases of pathologically depressed mood.

References

1. Mayberg, HS et al. (2005). 'Deep brain stimulation for treatment-resistant depression.' Neuron, 45(5), 651–660.
2. Crowell, AL et al. (2019). 'Long-Term Outcomes of Subcallosal Cingulate Deep Brain Stimulation for Treatment-Resistant Depression.' The American journal of psychiatry, 176(11), 949–956.
3. Alagapan S et al. (2023). 'Cingulate dynamics track depression recovery with deep brain stimulation.' Nature, 622(7981), 130–138.
4. Rudebeck PH et al. (2019). 'From bed to bench side: Reverse translation to optimize neuromodulation for mood disorders.' Proceedings of the National Academy of Sciences of the United States of America, 116(52), 26288–26296.
5. Riva-Posse P et al. (2018). 'A connectomic approach for subcallosal cingulate deep brain stimulation surgery: prospective targeting in treatment-resistant depression.' Molecular psychiatry, 23(4), 843–849.

Poster No 17

White Matter Integrity Predicts Recovery Response Time of Deep Brain Stimulation for Depression

Ha Neul Song[1], Helen Mayberg[1], Ki Sueng Choi[1]

[1]Icahn School of Medicine at Mount Sinai, New York, NY

Introduction: Deep brain stimulation (DBS) targeting the subcallosal cingulate cortex (SCC) has proven effective for treatment-resistant depression (TRD), across a set of consecutive cohorts. SCC is structurally connected with other brain regions via white matter (WM) bundles, and stimulation of all connections is crucial for DBS clinical outcomes. Despite consistent SCC targeting, which aims to maximize the activation of critical WM bundles, variability persists in the recovery response time

across patients, potentially linked to baseline variations in brain abnormalities. This study explores the status of WM integrity (approximated using diffusion MRI) and their longitudinal changes in the critical WM activation pathways.

Methods: We assessed the time to reach a stable response (TSR, more than 50% improvement of HDRS17 in two consecutive weeks) in 33 TRD patients receiving SCC-DBS. Preoperative and longitudinal MRI data were acquired on a 3T scanner with 2 mm isotropic resolution and 60 directions, including five b0 and two opposite phase encoding directions for distortion correction. The study examined the relationship between TSR and baseline fractional anisotropy (FA) of targeted WM bundles (cingulum bundle, forceps minor, subcortical junction, and uncinate fasciculus). Pearson correlation between TSR and FA along each WM bundle's trajectory was conducted, selecting the area with the maximum r value. Selected FA values in WM bundles served as features for linear regression predicting TSR. In the same areas, longitudinal FA changes at 1, 3, and 6 months post-operation were analyzed to compare fast and slow responders (each n = 1).

Results: Our findings reveal a significant negative correlation between TSR and FA in bilateral midcingulate cortex (left: r = -0.64, p < 0.01; right: r = -0.52, p < 0.01), bilateral forceps minor (left: r = -0.40, p = 0.02; right: r = -0.42, p = 0.02), and left uncinate fasciculus adjacent to left hippocampus (r = -0.46, p < 0.01) and left insula (r = -0.42, p = 0.01). A linear model of FA successfully predicted TSR (leave-one-out cross-validation; r= 0.68, r2 = 0.46, p < 0.001), with the left midcingulate cortex emerging as the strongest predictor among critical WM bundles. Moreover, post-hoc analysis found that the magnitude of FA increases in these regions over 6 months was associated with a faster response. Slow response was associated with FA values in cingulum bundles and forceps minor that did not change or decreased over the same period.

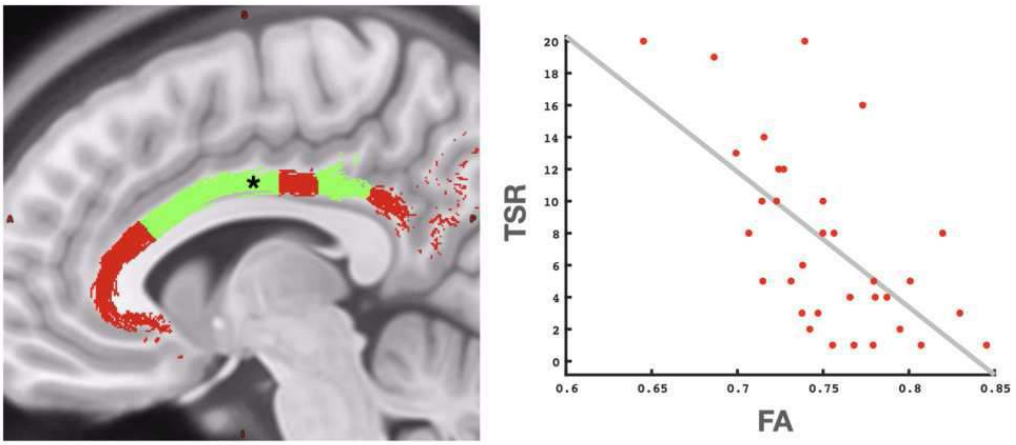

Figure 1. The relationship between TSR and FA in the left cingulum bundle (red in left). Green regions indicate significant correlation between them (the highest r value on a black asterisk). Right scatter plots show individual values of TSR and FA (r = -0.64, p < 0.001).

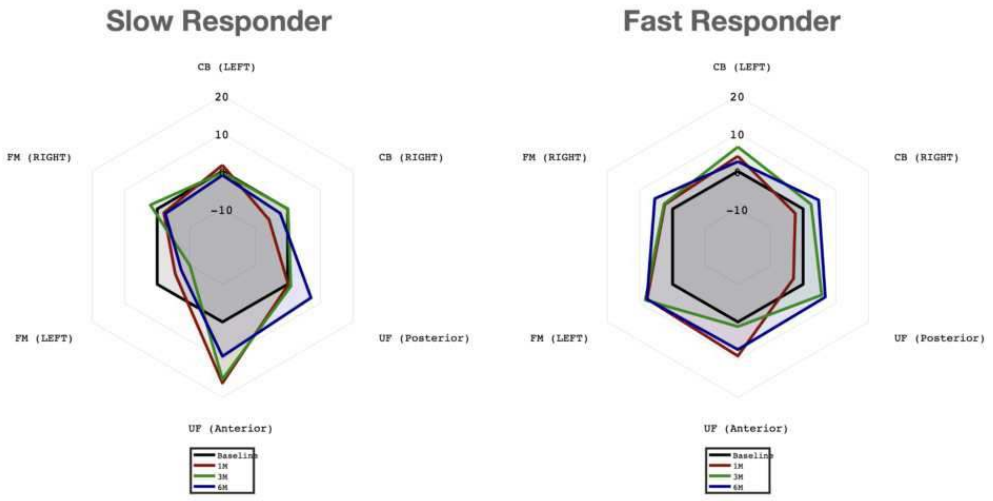

Figure 2. Longitudinal FA change [%] in each critical WM bundle at 1, 3, 6 months post-operation based on pre-operation. Left: Slow responder; Right: Fast responder; CB: Cingulum bundle; FM: Forceps minor; UF: Uncinate fasciculus.

Conclusions: These findings suggest that WM abnormalities in critical WM bundles undergo repair with chronic SCC-DBS suggesting that DBS may facilitate neuroplasticity changes in selective activated WM pathways. This study sheds light on both sources of individual variability in SCC-DBS response time, as well as a potential mechanism mediating DBS antidepressant response.

References

1. Mayberg, H.S., et al (2005). 'Deep brain stimulation for treatment-resistant depression', Neuron 45.5: 651-660.
2. Riva-Posse, Patricio, et al. (2014), 'Defining critical white matter pathways mediating successful subcallosal cingulate deep brain stimulation for treatment-resistant depression.' Biological psychiatry 76.12: 963-969.
3. Riva-Posse, Patricio, et al. (2018), 'A connectomic approach for subcallosal cingulate deep brain stimulation surgery: prospective targeting in treatment-resistant depression.' Molecular psychiatry 23.4: 843-849.
4. Alagapan, Sankaraleengam, et al. (2023), 'Cingulate dynamics track depression recovery with deep brain stimulation.' Nature: 1-9.

Poster No 18

Inter- and Intra-Subject Variability of White Matter Activation Pathways in SCC DBS for Depression

Ha Neul Song[1], Helen Mayberg[1], Ki Sueng Choi[1]

[1]Icahn School of Medicine at Mount Sinai, New York, NY

Introduction: Deep brain stimulation (DBS) of the subcallosal cingulate cortex (SCC) has shown efficacy in treating treatment-resistant depression (TRD). Recent advancements in targeting have shifted the focus from a focal target to a multi-node network target within the SCC. The SCC's interconnectedness with other brain regions through white matter (WM) bundles underscores the necessity of stimulating all connections for a clinical response. Surgical targeting relies on individual structural connectivity analysis to maximize the activation of critical WM bundles including the cingulum bundle, forceps minor, and subcortical junction. Due to the limitations of many clinics to collect high spatial and angular diffusion-weighted data, use of normative connectome data might be a suitable substitute to identify patient-specific targets for SCC DBS surgery because of its high signal-to-noise ratio and test-retest reliability. Applying normative data to define an SCC target, predefined by connectome data, is also more convenient than a personalized SCC target, which necessitates individual diffusion data for each case. We explored inter- and intra-subject variabilities of WM activation pathways in known SCC targets using available human connectome data to investigate connectome-based targeting accuracy.

Methods: We approximated bilateral volumes of tissue activated (VTAs) in 143 TRD patients based on their known DBS stimulation settings (amplitude and contact configuration) using Lead DBS software. For each hemisphere, a probabilistic stimulation map (PSM) was derived using VTAs, and one SCC target was defined by maximum value of PSM (x = ±7, y = 24, z = -8). Whole brain tractography was performed on the Human Connectome Database (HCP; n = 1,000) using this target as the identical center of seed (radius = 3 mm). The inter-subject similarity in each critical WM bundle was measured using correlation coefficient values. Moreover, intra-subject similarity (spatial similarity) was measured in each critical WM bundle while the seed was moved 3 mm in (1) superior-inferior, (2) anterior-posterior, and (3) medial-lateral directions.

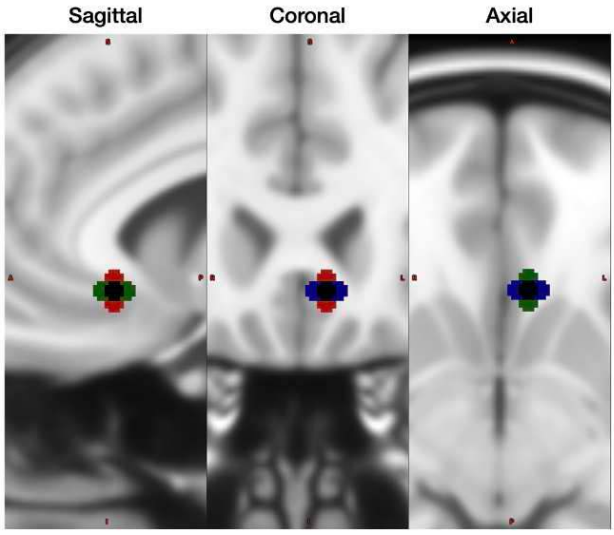

Figure 1. Left SCC targets on conventional T1-weighted images for whole brain tractography. Black: SCC target where the seed center is defined by the maximum value of PSM (x = -7, y = 24, z = -8, radius = 3 mm). The seed is moved 3 mm in superior-inferior (red), anterior-posterior (green), and medial-lateral (blue) directions.

Results: The findings revealed low inter-subject similarity in general (0.53 ± 0.07 out of 1.00), with distinct dissimilarity patterns within the left and right hemispheres. Notably, the cingulum bundle and subcortical junction exhibited significantly lower inter-subject similarity on the left side than right ($p < 0.001$). Intra-subject similarity analysis demonstrated a low similarity in the left hemisphere when the seed was moved in the superior-inferior or medial-lateral axis (0.56 ± 0.14), whereas high similarity was observed with movement in the anterior-posterior axis (0.84 ± 0.11; $p < 0.001$).

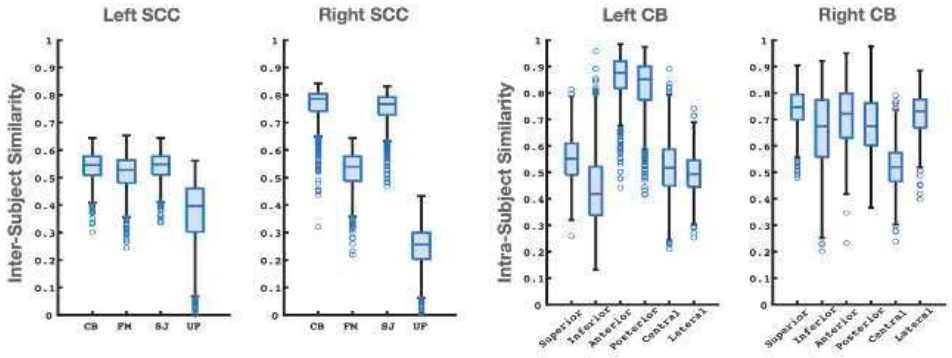

Figure 2. Inter-subject (left) and intra-subject (right) similarity. CB: Cingulum bundle; FM: Forceps minor; UF: Uncinate fasciculus.

Conclusions: The predefined SCC targets, which can be optimal for SCC-DBS in normative data, induced high variability of WM activation in individual subjects. Our findings suggest that identifying SCC targets using normative data may compromise treatment efficacy due to low inter-subject similarity. Moreover, spatial similarity results emphasize the necessity of delivering a precise target identification due to the large variability of WM activation pathways in inferior-superior and medial-lateral directions. This study further validates the importance of patient-specific targeting using individual connectivity profiles.

References

1. Mayberg, Helen S., et al. "Deep brain stimulation for treatment-resistant depression." Neuron 45.5 (2005): 651-660.
2. Van Essen, David C., et al. "The WU-Minn human connectome project: an overview." Neuroimage 80 (2013): 62-79.
3. Elias, Gavin JB, et al. "Normative connectomes and their use in DBS." Connectomic deep brain stimulation. Academic Press, 2022. 245-274.
4. Horn Andreas, et al. Lead-DBS v2: Towards a comprehensive pipeline for deep brain stimulation imaging. Neuroimage 184 (2019): 293-316.

Poster No 19

Can White Matter Tract Measures Predict Post-DBS Recovery in Patients with Parkinson's Disease

Ivan Campbell[1], Brad Caron[2], Harrison Walker[3], Benjamin Hill[1], Virendra Mishra[4]

[1]University of South Alabama, Mobile, AL, [2]Department of Psychology, University of Texas at Austin, Austin, TX, [3]University of Alabama at Birmingham, Birmingham, AL, [4]The University of Alabama at Birmingham, Birmingham, AL

Introduction: Deep Brain Stimulation (DBS) is a neurosurgical procedure typically used in the treatment of Parkinson's disease (PD) and its related motoric dysfunction. While it is highly efficacious, (Bratsos, 2018) there is variability in response to implantation, with some patients improving more than others. Previous research has shown that stimulation of white matter (WM) tracts surrounding the targeted structure (specifically the subthalamic nucleus) may be implicated in the therapeutic effect of DBS. (Abdulbaki, 2021) Therefore, we hypothesize that variability in outcome post-DBS could be explained by the WM measures.

Methods: We selected 8 random patients with PD who underwent DBS surgery at The University of Alabama at Birmingham (UAB). We collected Unified Parkinson's Disease Rating Scale (UPDRS)-III, both before DBS and 12-month post DBS in every patient. Additionally, we collected conventional 30 directions diffusion weighted MRI (dMRI) data on a 3T MRI at a b-value of 1000s/mm2 before the surgery. All MRI processing was performed using the cloud-platform for reproducible neuroimaging analyses known as brainlife.io (Hayashi & Caron et al, 2023). Structural MRI images were segmented into tissue-types (gray-matter, white-matter) for tracking using the brainlife.io app.239, and cortical parcellations were generated using Freesurfer implemented as brainlife.io app.664. Diffusion MRI data was preprocessed using QSIPrep (Cieslak et al, 2021) implemented as brainlife.io app.246. Anatomically constrained tractography (Smith et al, 2012) implemented as brainlife app.297 was used to simulate white matter fiber pathways. Resulting tractograms were then segmented into 3 bi-hemisphere tracts (motor thalamic,

spino-thalamic, and thalamico-cerebellar tracts) using a custom version of the white matter query language (Bullock et al, 2019) implemented as brainlife.io app.188. Measures of macrostructure (streamline count, midpoint density) were estimated using custom MatLAB code implemented as brainlife.io app.189. The diffusion tensor model (DTI) was used to estimate measures of microstructure along each tract using brainlife.io app.297 and app.361 for model fitting and tract profilometry (Yeatman et al, 2012) respectively. Along-the-tract measures such as fractional anisotropy, axial diffusivity, radial diffusivity, mean diffusivity, fiber count, fiber density, and number of streamlines were extracted for each patient and used in linear regression via Jamovi to predict change in UPDRS-III from before and after DBS implantation.

Results: Due to limited sample size (n=8), no significant results at a level of pcorr<.05 were obtained. However, multiple results trended toward significance. The midpoint density of the left motor thalamic tract (r=.694, p=.056), and the axial diffusivity of the right motor thalamic tract (r=.652, p=.08) showed the strongest effect size of correlation for improvement in UPDRS-III.

Conclusions: While evidence is limited due to the small sample size available at the time of the analysis, these results point to a potential link between white matter tract measurements and response to DBS implantation, and warrant further investigation.

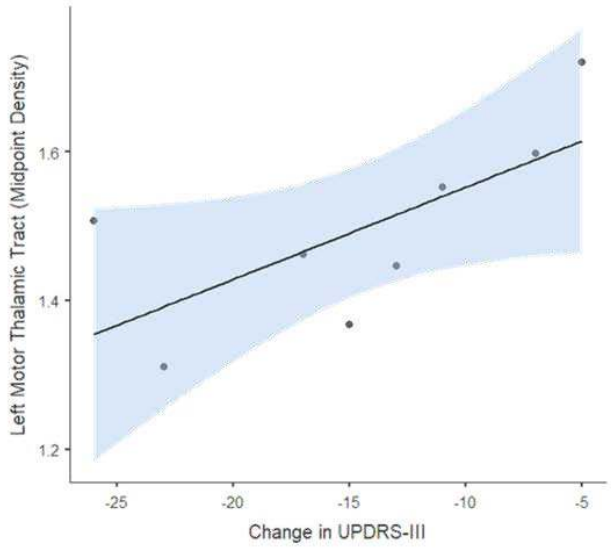

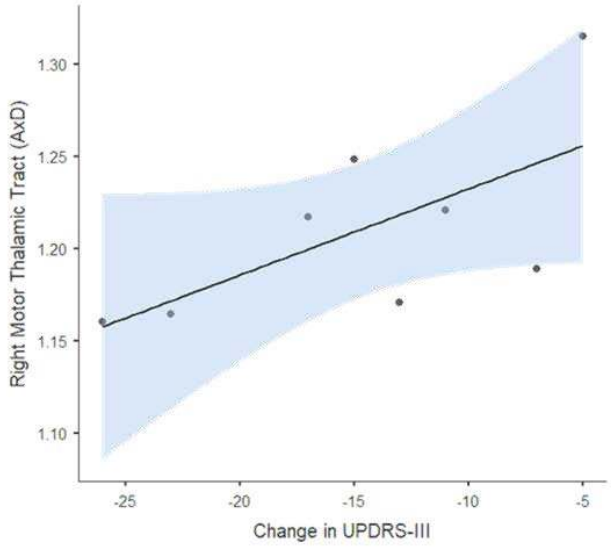

References

1. Abdulbaki A, Kaufmann J, Galazky I, Buentjen L, Voges J. Neuromodulation of the subthalamic nucleus in Parkinson's disease: the effect of fiber tract stimulation on tremor control. Acta Neurochir (Wien). 2021 Jan;163(1):185-195. doi: 10.1007/s00701-020-04495-3. Epub 2020 Nov 10. PMID: 33174115; PMCID: PMC7778622.
2. Bratsos S, Karponis D, Saleh SN. Efficacy and Safety of Deep Brain Stimulation in the Treatment of Parkinson's Disease: A Systematic Review and Meta-analysis of Randomized Controlled Trials. Cureus. 2018 Oct 22;10(10):e3474. doi: 10.7759/cureus.3474. PMID: 30648026; PMCID: PMC6318091.

3. Bullock D, Takemura H, Caiafa CF, Kitchell L, McPherson B, Caron B, Pestilli F. Associative white matter connecting the dorsal and ventral posterior human cortex. Brain Struct Funct. 2019 Nov;224(8):2631-2660. doi: 10.1007/s00429-019-01907-8. Epub 2019 Jul 24. PMID: 31342157.
4. Cieslak, M., Cook, P.A., He, X. et al. QSIPrep: an integrative platform for preprocessing and reconstructing diffusion MRI data. Nat Methods 18, 775–778 (2021). https://doi.org/10.1038/s41592-021-01185-5
5. Hayashi, S., Caron, B. A., Heinsfeld, A. S., Vinci-Booher, S., McPherson, B., Bullock, D. N., Bertò, G., Niso, G., Hanekamp, S., Levitas, D., Ray, K., MacKenzie, A., Kitchell, L., Leong, J. K., Nascimento-Silva, F., Koudoro, S., Willis, H., Jolly, J. K., Pisner, D., ... Pestilli, F. (2023). brainlife.io: A decentralized and open source cloud platform to support neuroscience research.
6. R Core Team (2022). R: A Language and environment for statistical computing. (Version 4.1) [Computer software]. Retrieved from https://cran.r-project.org. (R packages retrieved from CRAN snapshot 2023-04-07).
7. Smith RE, Tournier JD, Calamante F, Connelly A. Anatomically-constrained tractography: improved diffusion MRI streamlines tractography through effective use of anatomical information. Neuroimage. 2012 Sep;62(3):1924-38. doi: 10.1016/j.neuroimage.2012.06.005. Epub 2012 Jun 13. PMID: 22705374.
8. Yeatman JD, Dougherty RF, Myall NJ, Wandell BA, Feldman HM. Tract profiles of white matter properties: automating fiber-tract quantification. PLoS One. 2012;7(11):e49790. doi: 10.1371/journal.pone.0049790. Epub 2012 Nov 14. PMID: 23166771; PMCID: PMC3498174.
9. The jamovi project (2023). jamovi. (Version 2.4) [Computer Software]. Retrieved from https://www.jamovi.org.

Poster No 20

Deep Brain Stimulation for Obsessive-Compulsive Disorder: evolution of tractography-based targeting

Alba Segura-Amil[1], Ki Sueng Choi[2], Sonya Olson[2], Jip de Bruin[2], T. A. Khoa Nguyen[1], Andrew Smith[3], Brian Kopell[2], Helen Mayberg[2], Martijn Figee[2]

[1]University Hospital Bern, Bern, Swaziland, [2]Icahn School of Medicine at Mount Sinai, New York, NY, [3]Icahn School of Medicine At Mount Sinai, New York, NY

Introduction: Deep brain stimulation (DBS) in the anterior limb of the internal capsule (ALIC) for obsessive-compulsive disorder (OCD) can result in large improvements in symptoms and quality of life. However, without a clear stimulation target within the anatomically variable ALIC region, clinical benefits require long trial-and-error periods of parameter optimization. We report an evolution toward precision ALIC DBS targeting for OCD based on patient-specific tractography. Our aim was to develop a targeting method that would result in a more uniform target location and symptom response pattern. We generated a responder common map of ALIC connectivity and used it to target a new cohort of patients prospectively. To validate our targeting method, we generated a tractography-based stimulation model to predict clinical outcomes.

Methods: We included 13 OCD patients implanted with bilateral DBS leads in the ALIC. In the preliminary cohort (n=3), tractography-based DBS targeting was informed by the reconstruction of the lateral ALIC connected to the brainstem and the medial ALIC connected to the dorsomedial thalamus. In cohort A (n=7), we refined our tractography-based target by including additional cortical ALIC projections[1]. Data from patients in the preliminary cohort and cohort A was used to generate a responder common map as in[2]. For each patient, the stimulation volumes were generated with the therapeutic stimulation settings. Probabilistic tractography was performed with FSL bedpostx from the stimulation volumes (seed regions) to the rest of the brain. 5000 streamlines were generated per seed voxel, and a cerebrospinal fluid avoidance mask was used. To obtain the responder common map, individual white matter tracts were warped into MNI space, thresholded at 1% to remove false positives, binarized, and averaged. This map was used to prospectively target patients in cohort B (n=7). A tractography-based stimulation model was generated with data from cohorts A and B (n=10). For each patient, we generated a whole-brain tractogram of 10 million streamlines in MRtrix3 as in[3]. We segregated the ALIC streamlines into different pathways according to their connectivity to the PFC[1] and the medial and lateral midbrain regions highlighted by the common map. Then, we estimated the activation of these ALIC pathways for each stimulation setting and related it to symptom improvement. We fitted a linear regression model to predict Y-BOCS improvement based on the individual pathway activation.

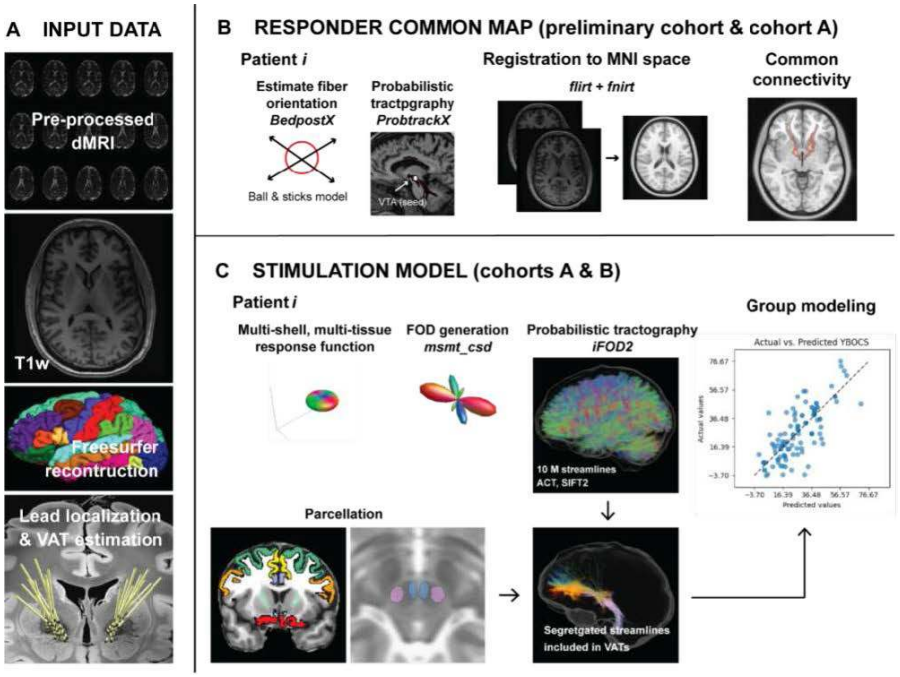

Results: Tractography-based ALIC DBS improved OCD symptoms in cohorts A and B by 41.2% over 6 months with an overall 80% response rate. OCD improvement was faster and larger in cohort B using the common map target versus cohort A, targeted without these data (Month 1, median Y-BOCS improvement 7.7% in cohort A and 19.4% in cohort B; Month 6, 38.9% in cohort A and 45.6% in cohort B). Targeting based on the common map also required fewer trial-and-error parameter adjustments. At the cortical level, the responder common map highlighted connectivity to the vmPFC and vlPFC. At the midbrain level, we observed two tracts: 1) lateral to the red nucleus and medial to the subthalamic nucleus, 2) medial to the red nucleus. A linear model with L2 regularization was implemented and evaluated with 10-fold cross-validation. The model predicted Y-BOCS improvement (R2 = 0.53, mean squared error (MSE)=167). The empirical Y-BOCS scores and model-predicted Y-BOCS scores were also significantly correlated (Pearson's r=0.77, p=8.4e-32).

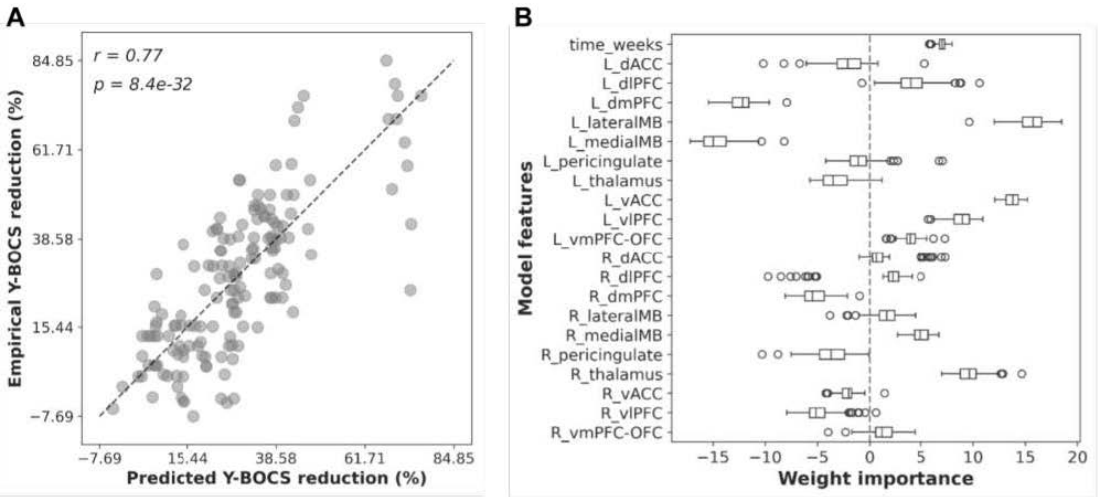

Conclusions: This study demonstrates that patient-specific tractography can help precisely select targets for ALIC DBS. This approach leads to a consistent and selective reduction of OCD symptoms with minimal parameter adjustments. Our therapeutic map of ALIC connections represents progress in overcoming the limitations of ALIC DBS, potentially contributing to a more widespread clinical use of DBS for OCD.

References

1.] S. N. Haber, A. Yendiki, and S. Jbabdi, "Four Deep Brain Stimulation Targets for Obsessive-Compulsive Disorder: Are They Different?," Biol. Psychiatry, vol. 90, no. 10, pp. 667–677, 2021.
2. P. Riva-Posse et al., "Defining critical white matter pathways mediating successful subcallosal cingulate deep brain stimulation for treatment-resistant depression," Biol. Psychiatry, vol. 76, no. 12, pp. 963–969, Dec. 2014.
3. A. Segura-Amil et al., "Programming of subthalamic nucleus deep brain stimulation with hyperdirect pathway and corticospinal tract-guided parameter suggestions," Hum. Brain Mapp., Aug. 2023.

Poster No 21

Longitudinal Functional Changes in Treatment-Resistant Depression with SCC Deep Brain Stimulation

Jungho Cha[1], Ki Sueng Choi[1], Martijn Figee[1], Patricio Riva-Posse[2], Brian Kopell[1], Helen Mayberg[1]

[1]Icahn School of Medicine at Mount Sinai, New York, NY, [2]Department of Psychiatry and Behavioral Sciences, Emory University School of Medicine, Atlanta, GA

Introduction: In recent years, advancements in understanding the safety of MRI in deep brain stimulation (DBS) implanted patients have led to more studies exploring the potential of measuring functional and structural changes with chronic stimulation. While previous studies showed that the subcallosal cingulate cortex (SCC) DBS induces long-term metabolic changes in corticolimbic circuits[1-3], but longitudinal alterations in function using resting-state functional MRI (rs-fMRI) remain unknown. This study rigorously investigates longitudinal resting-state functional changes within intrinsic connectivity networks (ICNs) during a 6-month period of SCC DBS for TRD. Emphasizing its significance, the research aims to replicate key findings observed in a previous positron emission tomography (PET) study[3], specifically highlighting alterations in the default mode network (DMN) and salience network (SN).

Methods: Four TRD patients with fully implanted DBS devices targeting the SCC area underwent 3.0T rs-fMRI at three-time points: baseline, 1-month, and 3-months of chronic stimulation. Additionally, two patients underwent an extra time point at 6 months of chronic stimulation. Image analysis was conducted using the Analysis of Functional NeuroImages (AFNI)[4]. To assess regional neural activity, the Amplitude of Low-Frequency Fluctuations (ALFF) and Regional Homogeneity (ReHo) approaches within individual gray matter regions were applied. We utilized 17 standard ICNs derived from a published resting-state functional connectivity study in healthy adults[5]. ALFF and ReHo values for each ICN were calculated by averaging all gray matter voxels within each ICN, excluding artifact voxels affected by DBS lead and cable. Linear mixed models, accounting for individual variability as random intercepts, were employed to examine longitudinal functional changes and their correlation with the Hamilton Depression Rating Scale 17 (HAMD) scores.

Results: Significant longitudinal alterations in local activity were identified within the Salience B and Default A networks. Particularly, the local activity, encompassing ALFF and ReHo, exhibited substantial increments at the 1-month mark of chronic stimulation. In the Salience B network, significant time effects were observed for both ReHo (p=0.014) and ALFF (p=0.002). Similarly, within the Default A network, both ReHo (p=0.002) and ALFF (p=0.003) showed significant time effects. These functional alterations also showed significant negative correlations with HAMD scores. Specifically, in the Salience B network, both ReHo (p=0.028) and ALFF (p=0.003) demonstrated negative correlations with HAMD scores. In the Default A network, significant negative correlations were also observed for both ReHo (p=0.003) and ALFF (p=0.003) with HAMD scores.

Figure 1. Longitudinal changes in local activity within the Salience B and Default A networks. (A) Regional Homogeneity (ReHo) in Salience B, (B) Amplitude of Low-Frequency Fluctuations (ALFF) in Salience B, (C) ReHo in Default A, (D) ALFF in Default A. Each subpanel includes graphs illustrating the correlation of these local activity changes with HAMD (Hamilton Depression Rating Scale) scores.

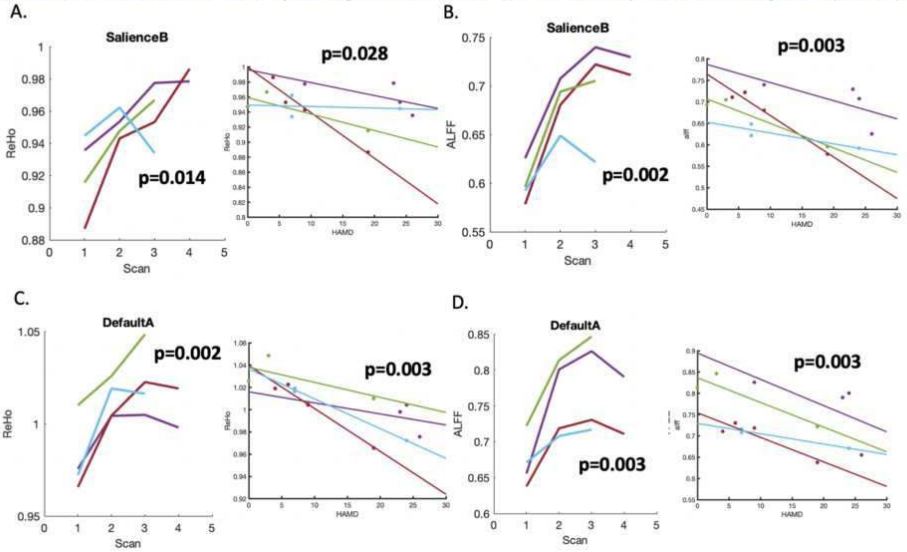

Conclusions: We observed significant longitudinal changes in local activity within the Salience B and Default A networks following SCC DBS. Notably, there was a marked increase in ReHo and ALFF at the 1-month chronic stimulation. While the direction of these changes opposes a previous PET study[3], the observed pattern underscores that both the SN and DMN

undergo significant alterations. This replication of distinct network changes underscores the complexity and meaningful neural shifts induced by SCC DBS in these networks. The dynamic changes in network activity were negatively associated with HAMD scores, indicating a potential link between the observed neural activity changes and symptomatic improvements in TRD. The local brain activity changes in SN and DMN with chronic stimulation highlights the complexity of the neural mechanisms involved in the therapeutic effects of DBS.

References

1. Mayberg HS, Lozano AM, Voon V, McNeely HE, Seminowicz D, Hamani C, et al. Deep brain stimulation for treatment-resistant depression. Neuron. 2005;45(5):651-60.
2. Lozano AM, Mayberg HS, Giacobbe P, Hamani C, Craddock RC, Kennedy SH. Subcallosal cingulate gyrus deep brain stimulation for treatment-resistant depression. Biol Psychiatry. 2008;64(6):461-7.
3. Cha J, Choi KS, Rajendra JK, McGrath CL, Riva-Posse P, Holtzheimer PE, et al. Whole brain network effects of subcallosal cingulate deep brain stimulation for treatment-resistant depression. Mol Psychiatry. 2023.
4. Cox RW. AFNI: software for analysis and visualization of functional magnetic resonance neuroimages. Comput Biomed Res. 1996;29(3):162-73.
5. Yeo BT, Krienen FM, Sepulcre J, Sabuncu MR, Lashkari D, Hollinshead M, et al. The organization of the human cerebral cortex estimated by intrinsic functional connectivity. J Neurophysiol. 2011;106(3):1125-65.

Poster No 22

Characterizing SCC Gray Matter in Depression: Implications for DBS Optimization

Carlos Alcocer[1,2], Helen Mayberg[2], Jungho Cha[2], Ha Neul Song[2], Martijn Figee[2], Brian Kopell[2], Ki Sueng Choi[2]

[1]Weill Cornell Medical College, New York, NY, [2]Nash Family Center for Advanced Circuit Therapeutics, Icahn School of Medicine at Mount Sinai, New York, NY

Introduction: Anatomical changes of the subcallosal cingulate cortex (SCC) have been observed in structural imaging studies demonstrating a volume reduction in depressed patients vs healthy controls (HC). The significance of this is unclear. Likewise, the left SCC volume reduction has been reported in deep brain stimulation (DBS) non-responders versus responders. Therefore, variation of neuroanatomy in the SCC, including structural asymmetry, may moderate differences in response to SCC DBS in patients with treatment-resistant depression (TRD). We aim to characterize pathological structural abnormality of SCC in TRD subjects versus HC, explore the effects of structural asymmetry on the lateralized behavioral response to DBS, and explore whether SCC gray matter (GM) modulates DBS response.

Methods: Participants included 47 subjects with TRD who underwent bilateral SCC DBS along with 16 healthy controls. Segmentation of SCC was performed with FreeSurfer (version 7.1.0, http://surfer.nmr.mgh.harvard.edu/) and further refined with a semi-automated correction. Volume, thickness, and laterality were extracted for all subjects. The volume of tissue activated (VTA) was generated with patient-specific stimulation parameters at 6 months. The volume of overlap between VTA and SCC GM (including overlap volumes of upper and lower banks) and the distance between VTA center of mass (COM) and SCC GM was also calculated for TRD subjects. ANCOVA was conducted to compare the structural asymmetry of the above variables between TRD subjects and HC and between DBS responders (> 50% decrease of HDRS-17 at 2 years) and non-responders. Lastly, multivariate linear regression was performed using these extract features and the following clinical measures: HDRS-17 baseline, HDRS-17 changes at 2 years, and time to stable response (TSR2, more than 50% HDRS-17 decrease for two consecutive weeks).

Results: There was no significant GM volume reduction of left, right, or mean SCC volumes of TRD subjects versus HC nor between DBS non-responders and responders. Left SCC volume was significantly greater than right across TRD subjects [$t(46) = 7.56$, $p < 0.0001$] and HC [$t(15) = 3.55$, $p = 0.003$] with no difference in laterality between HC and TRD and responders and non-responders. There was no difference between responders and non-responders in VTA and SCC overlap volumes. There were also no between-group differences in overlap volumes of the SCC upper and lower banks. There were no differences in upper and lower bank volume of overlap laterality between responders and non-responders. However, an increased overlap, particularly of the right [$t(27) = 2.36$, $p = 0.026$], mean lower bank [$t(27) = 2.27$, $p = 0.031$] and lower right bank of SCC [$t(27) = 2.62$, $p = 0.014$], predicted an increase in TSR2. Finally, non-responders demonstrated a greater Euclidian [$F(1, 44) = 9.52$, $p = 0.004$] and horizontal distance [$F(1, 40) = 5.33$, $p = 0.028$] between the right VTA COM and SCC and increased right-sided Euclidian distance of VTA COM laterality index [$F(1, 44) = 8.76$, $p = 0.005$] than responders.

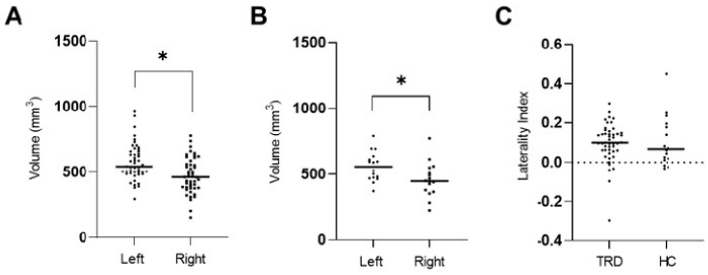

Figure 1. SCC volume laterality of TRD and HC. (A) Left versus right SCC volume in TRD subjects. (B) Left versus right SCC volume in HC. (C) LI in TRD subjects vs HC. *p < 0.05, ANCOVA.

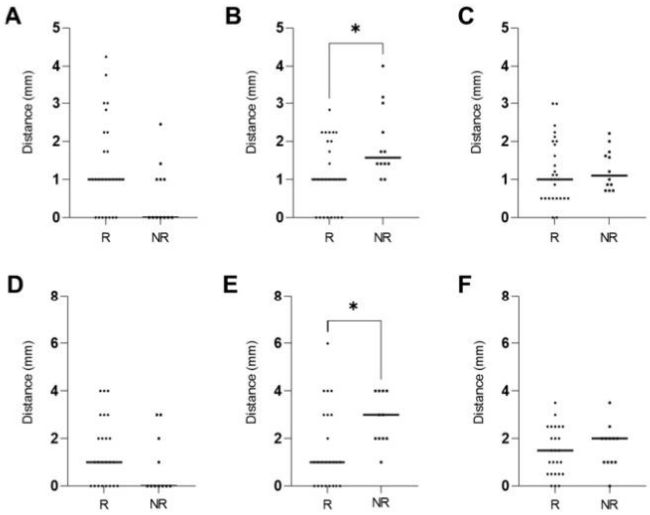

Figure 2. VTA COM distance from SCC. (A-C) VTA COM Euclidian distance from SCC. (A) Left VTA distance from SCC. (B) Right VTA distance from SCC. (C) Mean VTA cistance from SCC. (D-F) VTA COM distance from SCC in x-direction. (D) Left VTA horizontal distance from SCC. (E) Right VTA horizontal distance from SCC. (F) Mean VTA horizontal distance from SCC. *p < 0.05, Mann-Whitney test.

Conclusions: SCC volume and laterality may not serve as biomarkers to predict depression, depression severity, DBS response, or time to response. Left-sided SCC laterality likely represents normal anatomical asymmetry. While the volume of SCC gray matter included in the VTA does not differentiate DBS responders from non-responders, an increase in the volume of overlap of the right and lower banks of SCC predicts an increased time to respond. This suggests the importance of precise anatomical targeting in SCC DBS since placing the DBS lead too medial and inferior may slow the DBS response, and positioning the lead too lateral can prevent DBS response, likely due to missing critical white matter tracts. Therefore, optimal DBS response requires not only consideration of targeting WM tracts but also of the location of SCC GM in relation to the DBS leads.

References

1. Choi, K.S. et al. (2015), 'Mapping the "depression switch" during intraoperative testing of subcallosal cingulate deep brain stimulation', JAMA Neurology, vol. 72, no. 11, pp. 1252-1260.
2. Conroy, S.K. et al. (2021), 'Left versus right subcallosal cingulate deep brain stimulation for treatment-resistant depression', Personalized Medicine in Psychiatry, vol. 25-26.
3. Hajek, T. et al. (2008), 'Reduced subgenual cingulate volumes in mood disorders: a meta-analysis', Journal of Psychiatry and Neuroscience, vol. 33, no. 2, pp. 91-99.
4. Sankar, T. et al. (2020), 'Neuroanatomical predictors of response to subcallosal cingulate deep brain stimulation for treatment-resistant depression', Journal of Psychiatry and Neuroscience, vol. 45, no. 1, pp. 45-54.

Poster No 23

Impact of White Matter Abnormalities in Therapeutic DBS Pathways for Treatment-Resistant Depression

Carlos Alcocer[1,2], Helen Mayberg[2], Jungho Cha[2], Ha Neul Song[2], Martijn Figee[2], Brian Kopell[2], Ki Sueng Choi[2]

[1]Weill Cornell Medical College, New York, NY, [2]Nash Family Center for Advanced Circuit Therapeutics, Icahn School of Medicine at Mount Sinai, New York, NY

Introduction: Whole-brain diffusion tractography analysis has demonstrated that deep brain stimulation (DBS) responders share unique bilateral pathways from their SCC stimulation volumes to 1) the medial prefrontal cortex via forceps minor (FMi) and uncinate fasciculus (UF); 2) rostral and dorsal cingulate cortex via the cingulum bundle (CB); and 3) the subcortical regions via the subcortical junction (SJ) tract. DBS non-responders do not activate these pathways due to suboptimal implantation of leads. We aim to characterize white matter (WM) abnormalities in these SCC DBS-activated brain networks, understand the effects of WM damages on the clinical response, and explore the effects of WM integrity asymmetry on lateralized behavioral response in subjects with treatment resistant depression (TRD).

Methods: Participants included 46 subjects with TRD who underwent bilateral SCC DBS and 40 healthy controls. Diffusion-weighted imaging (DWI) preprocessing was performed using FSL (FMRIB Software Library, http://www.fmrib.ox.ac.uk/fsl). First, a voxel-wise, permutation-based analysis was carried out using tract-based spatial statistics (TBSS) to detect significant differences in fractional anisotropy (FA) and FA laterality index (LI = [L-R]/[L+R]) between TRD subjects and HC and between DBS responders (> 50% decrease of HDRS-17 at 6 months) and non-responders. Voxel-wise correlations were performed between FA and clinical measures, including HDRS-17 baseline, HDRS-17 percent change at 6 months and 2 years, and time to stable response (TSR2, more than 50% HDRS-17 decrease for two consecutive weeks). Second, mean FA was extracted from pre-determined WM regions of interest (ROI), including the FMi, UF, CB, and SJ tracts. Differences in FA and laterality between groups were analyzed using a student's t-test. The mean FA of these tracts was correlated to the above clinical measures using Spearman correlation.

Results: Voxel-wise TBSS analysis demonstrated significant decreases in FA in TRD subjects versus HC in various WM tracts including pathways critical for DBS response such as CB, FMi and UF (corrected $p < 0.05$). There were no significant differences in FA between DBS responders and non-responders. TSR2 was significantly negatively correlated to FA of various tracts, again including those involved in DBS response, particularly CB, FMi, and UF (corrected $p < 0.05$). ROI analysis confirmed these findings as mean FA was significantly decreased in CB [$t(84) = 2.36$, $p = 0.020$], UF [$t(84) = 2.08$, $p = 0.041$], FMi [$t(84) = 3.63$, $p = 0.0005$], and SJ tracts [$t(84) = 2.59$, $p = 0.012$] in TRD subjects versus HC. Both HC and TRD subjects demonstrated significant right-sided FA laterality of CB [HC, $t(39) = 2.97$, $p = 0.005$; TRD, $t(45) = 3.39$, $p = 0.002$] and UF tracts [HC, $t(39) = 3.17$, $p = 0.003$; TRD, $t(45) = 5.08$, $p < 0.0001$] while SJ tract was left-lateralized [HC, $t(39) = 28.6$, $p < 0.0001$; TRD, $t(45) = 20.9$, $p < 0.0001$). There were no differences in LI between groups. Lastly, SJ FA LI was negatively correlated with HDRS-17 percent change at 2 years ($rs = -0.327$, $p = 0.042$), while right UF mean FA ($rs = -0.308$, $p = 0.037$) was negatively correlated with HDRS-17 baseline.

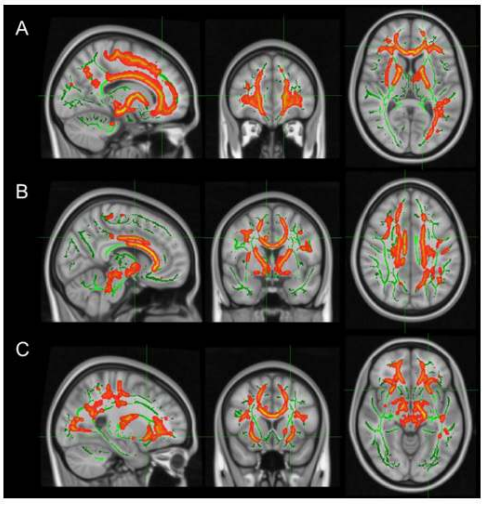

Figure 1. Red-yellow: regions where FA is significantly decreased in TRD patients versus HC. Green: mean FA skeleton projected onto standard MNI template. (A) Forceps minor (B) Cingulum bundle (C) Uncinate fasciculus.

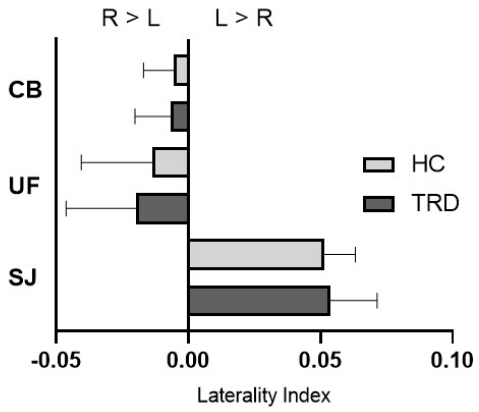

Figure 2. Mean FA LI of CB, UF, and SJ ROI tracts in HC vs TRD. Error bars indicate standard deviation.

Conclusions: Compared to HC, TRD patients have decreased WM integrity in critical WM tracts necessary for DBS response, including CB, UF, SJ, and FMi. Notably, more damaged WM in therapeutic pathways took longer for a stable response. Right-sided FA laterality of CB and UF and left-sided laterality of SJ tracts likely represent normal anatomical asymmetry. However, increased left-sided SJ FA laterality may be a biomarker for reduced clinical response. It remains to be determined to what extent changes in FA in these tracts can serve as a biomarker to differentiate DBS responders and non-responders.

References

1. Alagapan, S. et al. (2023), 'Cingulate dynamics track depression recovery with deep brain stimulation', Nature, vol. 622, pp.130-138.
2. Choi, K.S. et al. (2015), 'Mapping the "depression switch" during intraoperative testing of subcallosal cingulate deep brain stimulation', JAMA Neurology, vol. 72, no. 11, pp. 1252-1260.
3. Conroy, S.K. et al. (2021), 'Left versus right subcallosal cingulate deep brain stimulation for treatment-resistant depression', Personalized Medicine in Psychiatry, vol. 25-26.
4. Riva-Posse, P. et al. (2014), 'Defining critical white matter pathways mediating successful subcallosal cingulate deep brain stimulation for treatment-resistant depression', Biological Psychiatry, vol. 76, no. 12, pp. 963-969.

Poster No 24

Personalized Connectomic Targeting for Ventral Intermediate Nucleus DBS in Essential Tremor

Ha Neul Song[1], Sohae Chung[2], Sema Akkus[1], Brian Kopell[1], Ki Sueng Choi[1]

[1]Icahn School of Medicine at Mount Sinai, New York, NY, [2]New York University, New York, NY

Introduction: Millions of individuals suffer from tremor disorders, such as essential tremor and tremor-dominant Parkinson's disease. Deep brain stimulation (DBS) of the ventral intermediate nucleus (VIM) has proven effective for treatment-resistant essential tremor. However, the clinical outcome of DBS highly depends on precise targeting, which has been challenging due to imaging limitations and inter-individual variability. Moreover, previous studies using diffusion-tractography suggest that the efficacy of VIM DBS may be associated with the dentate-rubro-thalamic tract (DRTT), but no straightforward approach exists to extract DRTT associated with a therapeutic benefit. This study aimed to define therapeutic pathway maps based on anatomical or tractography data and validate them using clinical measures. Additionally, the study evaluated the therapeutic pathway maps by measuring inter-subject similarity using human connectome project (HCP) data.

Methods: We studied 10 patients with severe tremors who underwent VIM DBS surgery (age range, 70 - 82 years). Patients were divided into two groups based on their TETRAS scores measured before and within 1 year post-surgery: responders (n = 8, improvement < 50%) and non-responders (n = 2, improvement < 50%). Individual leads were reconstructed, and volumes of tissue activated (VTAs) were estimated using Lead DBS software with given stimulation settings (amplitude and contact configuration). First, therapeutic anatomical maps were defined by averaging VTAs weighted by clinical improvement. Therapeutic pathway maps were also defined by estimating VTA-based structural connectivity shared by responders. Next, overlapping voxels of anatomical and pathway maps with individual VTAs and connectivity were calculated. Lastly, the inter-subject similarity (reliability) of the therapeutic pathway was evaluated using the Human Connectome Project dataset (n = 100).

Results: Results showed a slight difference in anatomical overlap with VTAs between responders and non-responders ($p = 0.07$; RES = 44.3; NON = 3.0). On the other hand, there was a significant difference in connectomic overlap between responders and non-responders ($p = 0.02$; RES = 161.3; NON = 64.5). This trend and significance were observed explicitly in

the left brain hemisphere. Lastly, high similarity in connectivity toward therapeutic pathways was found among HCP subjects (0.7 out of 1.0).

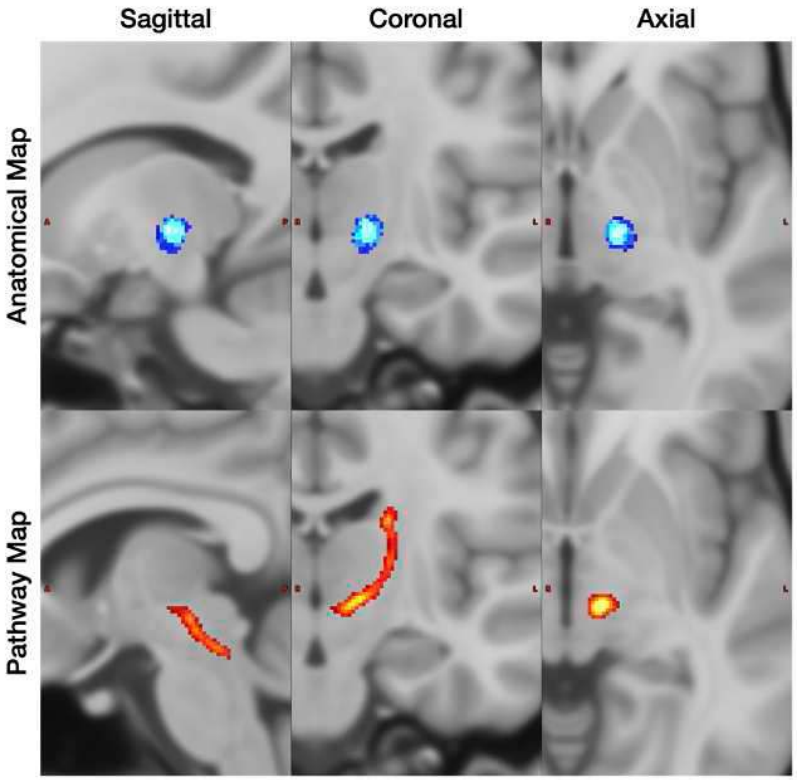

Figure 1. Anatomical map (blue in top row) and pathway map (red in bottom row) on conventional T1-weighted images. Left to right: sagittal, coronal, and axial views.

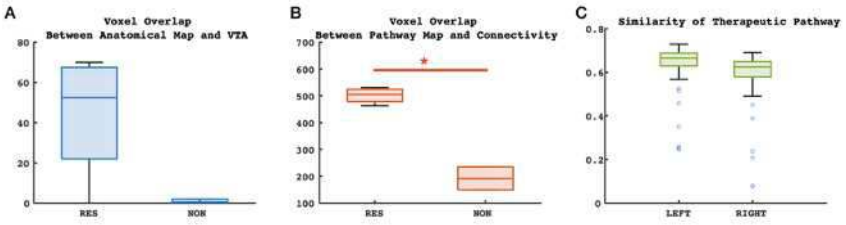

Figure 2. Boxplots show (A) a trend toward difference in voxel overlap of the anatomical map with individual VTAs (p = 0.07; RES = 44.3; NON = 3.0), (B) a significant difference in voxel overlap of pathway map with binary connectivity (p = 0.02; RES = 161.3; NON = 64.5), and (C) inter-subject similarity of therapeutic pathways (range: 0 - 1). Red asterisk indicates p < 0.05.

Conclusions: This study defined the therapeutic pathways for VIM DBS, surpassing anatomical maps in differentiating clinical improvement and demonstrating high similarity among individuals. The results imply the importance of connectomic targeting for VIM DBS and its potential practical applications. Minor variability (0.3 out of 1.0) indicates the need for individual data in personalized DBS targeting. These findings offer valuable insights into accurate and personalized neurosurgical guidance.

References

1. Louis ED, Ferreira JJ. (2010), How common is the most common adult movement disorder? Update on the worldwide prevalence of essential tremor. Mov Disord 25:534-541
2. Louis ED, Machado DG. (2015), Tremor-related quality of life: A comparison of essential tremor vs. Parkinson's disease patients. Parkinsonism Relat Disord 21:729-735
3. Benabid AL, et al. (1991), Long-term suppression of tremor by chronic stimulation of the ventral intermediate thalamic nucleus. Lancet 337:403-406
4. Chung S, et al. (2020), MR susceptibility imaging with a short TE (MR-SISET): A clinically feasible technique to resolve thalamic nuclei. AJNR 41:1629-1631
5. Horn Andreas, et al. (2019), Lead-DBS v2: Towards a comprehensive pipeline for deep brain stimulation imaging. Neuroimage 184: 293-316.

Poster No 25

High-Level features from Deep Language Models predict Subthalamic theta power during sentence proces

Linyang He[1], Alan Bush[1], Latane Bullock[1], Yanming Zhu[1], Yuanning Li[2], Robert Richardson[1]

[1]Massachusetts General Hospital, Boston, MA, [2]ShanghaiTech University, Shanghai, Shanghai

Introduction: The basal ganglia (BG), long associated with motor control, has been less emphasized in language processing compared to cortical regions. However, research has established links between the BG and language-related cortical areas such as the inferior frontal gyrus and other prefrontal regions (Ullman, 2006), indicating its potential involvement in language functions. This has spurred interest in the role of the BG, particularly the subthalamic nucleus (STN), in language processing. While recent studies have identified the STN's participation in motor aspects of speech production and lexical semantics (Chrabaszcz et al., 2021; Lipski et al., 2018), its extent in high-level language aspects like syntax and contextual semantics remains an area of exploration. On another front, deep language models (DLMs), emerging as a new tool in computational neuroscience, have become a powerful lens for exploring brain functions related to language processing (Goldstein et al., 2022; Li et al., 2023). The current project aims to leverage DLMs to investigate the role of the STN in language processing.

Methods: We used local field potential (LFP) recordings during deep brain stimulation (DBS) surgery targeting the left STN in two Parkinson's Disease patients. Patients engaged in a sentence repetition task: repeating 10 sentences from the Harvard Psychoacoustic Sentences set. We analyzed theta, beta, and high gamma frequency bands of the STN-LFP data when patients were articulating sentences, correlating LFP with linguistic features derived from GPT-2 large (Brown et al., 2020). Four types of embeddings from GPT-2 were used: full, lexical, syntactic, and residual contextual. An L2-regularized linear regression model reconstructed the LFP signals from linguistic features, with the correlation coefficient (R score) quantifying the degree of STN's potential involvement in corresponding language aspects. 5-fold cross-validation was applied to obtain reliable R scores.

Results: Our analysis revealed significant correlations across all linguistic features in theta and beta bands for all patients compared to permutation baseline ($p < 1e\text{-}5$). For patient one, the theta band showed the most robust correlation ($R=0.39\pm0.04$, mean±std) and the beta and high gamma bands showed average R scores of 0.22 ± 0.04 and 0.28 ± 0.02, respectively. The second patient, despite a dominant theta band in language processing, showed a lower high-gamma R score of 0.07 ± 0.02, possibly due to speech impairment. Linguistic feature analysis indicated that lexical embedding had lower R scores (0.272 across frequency bands), while syntactic, residual contextual, and full embeddings exhibited similar higher R scores (0.299, 0.301, and 0.299, respectively). Paired-samples t-test indicated a difference between the lexical and three other features ($p = 0.0025$). Different from cortical studies, we found all Transformer layers of DLM encoded STN features similarly. Temporal dynamics analysis, extending word onset to 100~600ms pre-onset, showed that lexical features' R scores remained relatively stable, whereas the scores for other higher-level linguistic features exhibited a strong downward trend. This may suggest that the STN's role in lexicon processing is persistent throughout speech production, whereas its involvement in higher-level language processing is more immediate and transient, differing from cortical processing patterns.

Conclusions: Through the lens of DLM, we found STN theta power can be predicted from both lexical-level and high-level language features. Interestingly, these features predict theta band power better than either beta or gamma power. Our results also suggest that the STN exhibits distinct temporal dynamics and correlations with DLM features compared to the cortex. This study is the first to apply DLMs in dissecting the neural substrates of language within the BG, offering a novel methodological approach that could broaden our understanding of subcortical structures' role in language processing.

References

1. Brown, T.B., et al. (2020). Language Models are Few-Shot Learners. arXiv.
2. Caucheteux, C., et al. (2021). "Disentangling syntax and semantics in the brain with deep networks." In Proceedings of the 38th International Conference on Machine Learning, PMLR, 1336–1348.
3. Chrabaszcz, A., et al. (2021). "Simultaneously recorded subthalamic and cortical LFPs reveal different lexicality effects during reading aloud." Journal of Neurolinguistics, 60, 101019.
4. Goldstein, A., et al. (2022). "Shared computational principles for language processing in humans and deep language models." Nature Neuroscience, 25, 369–380.
5. Li, Y., et al. (2023). "Dissecting neural computations in the human auditory pathway using deep neural networks for speech." Nature Neuroscience.
6. Lipski, W.J., et al. (2018). "Subthalamic Nucleus Neurons Differentially Encode Early and Late Aspects of Speech Production." Journal of Neuroscience, 38, 5620–5631.
7. Tankus, A., et al. (2019). "Degradation of Neuronal Encoding of Speech in the Subthalamic Nucleus in Parkinson's Disease." Neurosurgery, 84, 378–387.

Poster No 26

Therapeutic DBS for OCD Suppresses Default Mode Network and Associated Subcortical Circuits

Natalya Slepneva[1], Genevieve Basich-Pease[1], Adam Frank[2], Tenzin Norbu[1], Leo Sugrue[3,1], Paul Larson[4], Philip Starr[5,6], Melanie Morrison[3], A Moses Lee[1,6]

[1]Department of Psychiatry and Behavioral Sciences, University of California San Francisco, San Francisco, CA, [2]Keck School of Medicine of USC, Los Angeles, CA, [3]Department of Radiology and Biomedical Imaging, University of California San Francisco, San Francisco, CA, [4]Department of Neurological Surgery, University of Arizona, Tuscon, AZ, [5]Neurological Surgery, University of California San Francisco, San Francisco, CA, [6]Weill Institute for Neurosciences, University of California San Francisco, San Francisco, CA

Introduction: Deep brain stimulation (DBS) is a treatment for severe, refractory obsessive-compulsive disorder (OCD) that applies direct electrical stimulation to the anterior limb of the internal capsule (ALIC). To examine the difference between therapeutic and nontherapeutic DBS, we compared BOLD response when DBS was cycled ON and off in different DBS electrode contact configurations.

Methods: Subjects: 5 subjects with severe, refractory OCD were implanted with an MR-compatible Medtronic Percept DBS stimulator as part of clinical care. Quadripolar leads were implanted bilaterally within the ALIC region. Three subjects were classified as treatment responders based on clinical response to DBS. Among responders, contact configurations were classified as therapeutic and nontherapeutic based on long-term clinical response. MRI: MR scans were acquired on a GE Discovery MR750 3T scanner. We collected T1-weighted structural scans and DWI pre- and post-implantation (55 direction HARDI, b=2000). Gradient-echo fMRI was acquired in low-SAR mode with a 32-channel head coil. For each 6-minute fMRI scan, we selected one of 12 bipolar contact configurations to deliver stimulation that was cycled ON/OFF for 1-minute blocks. fMRI Processing: T1 and fMRI were preprocessed with fMRIprep, a standardized pipeline that combines tools from AFNI, ANTs, FreeSurfer, FSL, and Nipype. BOLD runs were corrected for slice-timing and head motion, and resampled to an MNI space template. ICA-AROMA was performed after removal of non-steady state volumes and spatial smoothing with an isotropic, Gaussian kernel of 6mm FWHM. Components were manually reviewed by two expert raters, and those classified as noise by both raters were removed. Using AFNI, motion outliers (FD>0.2) and additional polynomial drift terms were removed and ON-off contrasts and group comparisons were generated. Electrode reconstruction and DWI processing: DWI scans were preprocessed using QSIprep and MRtrix3. MP-PCA denoising and Gibb unringing was performed, and FSL's eddy was used for head motion and Eddy current correction. The DWI images were resampled to ACPC. Using Lead-DBS, a MATLAB toolbox for DBS electrode reconstruction and simulation of DBS stimulation, CT, T1 and DWI scans were co-registered and normalized using ANTs and SPM, after which DBS electrodes were reconstructed and manually localized. White matter tracts were reconstructed from diffusion imaging data using generalized q-sampling. The volume of activated tissue (VAT) was modeled for bipolar contact pairs, and the VATs were used as seeds to generate connectivity to parcels from Schaefer cortical atlas.

Results: We compared stimulation ON and off across subjects for contact pairs that had therapeutic (n=6 runs, 3 subjects) vs nontherapeutic (n=11 runs, 3 subjects) stimulation. In therapeutic compared to nontherapeutic configurations, stimulation correlated with significant BOLD suppression ($p<0.05$) in areas related to OCD, including the right orbitofrontal cortex, bilateral dorsomedial prefrontal cortex, and right thalamus, distant from the sites of the active electrode contacts. We also examined the relationship between DBS and canonical resting-state fMRI networks. Comparing stimulation ON vs off, we found a significant ($p<0.05$) difference in BOLD signal change between therapeutic and nontherapeutic contacts bilaterally in the default mode network. In the diffusion data, a significant percentage of streamlines seeded from therapeutic electrode VAT ROIs connected to areas of the default mode and limbic networks.

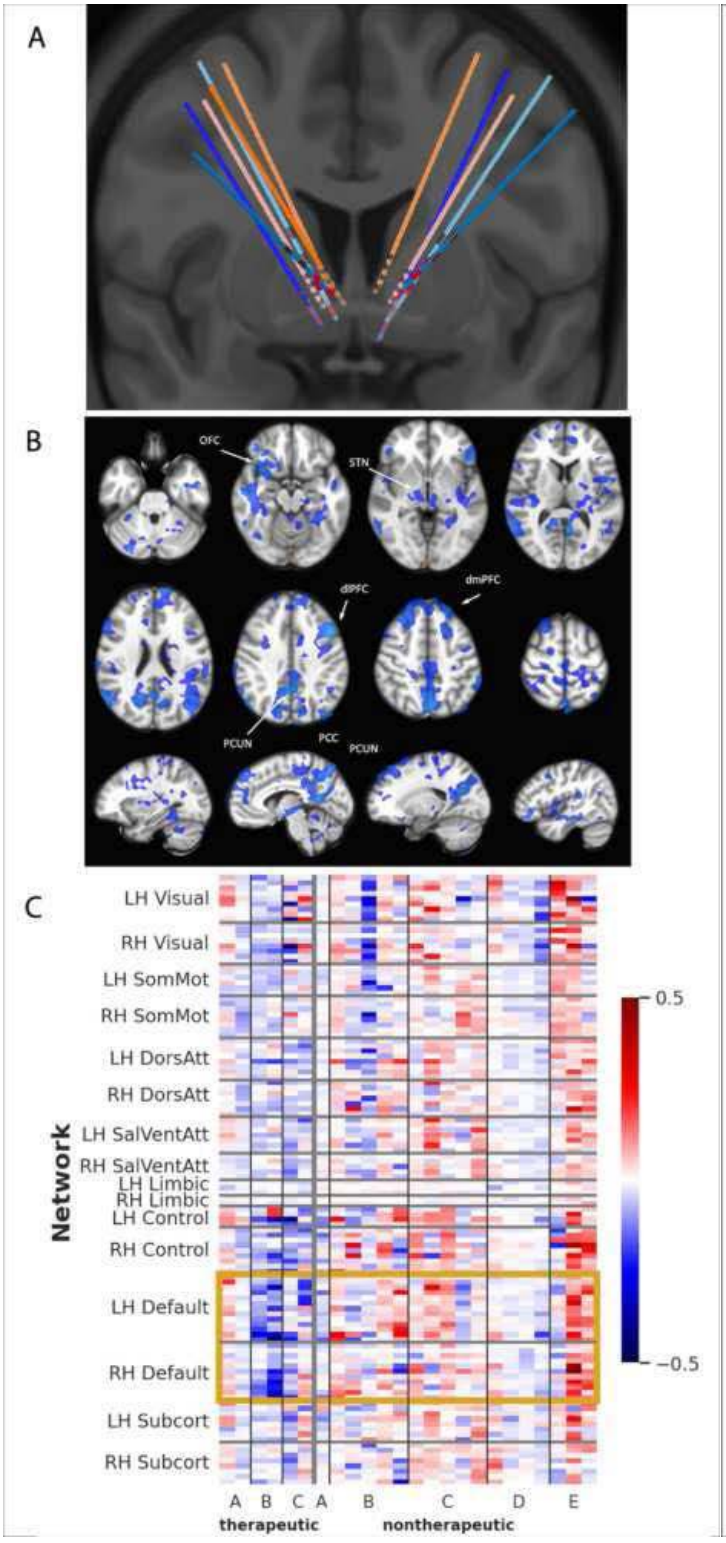

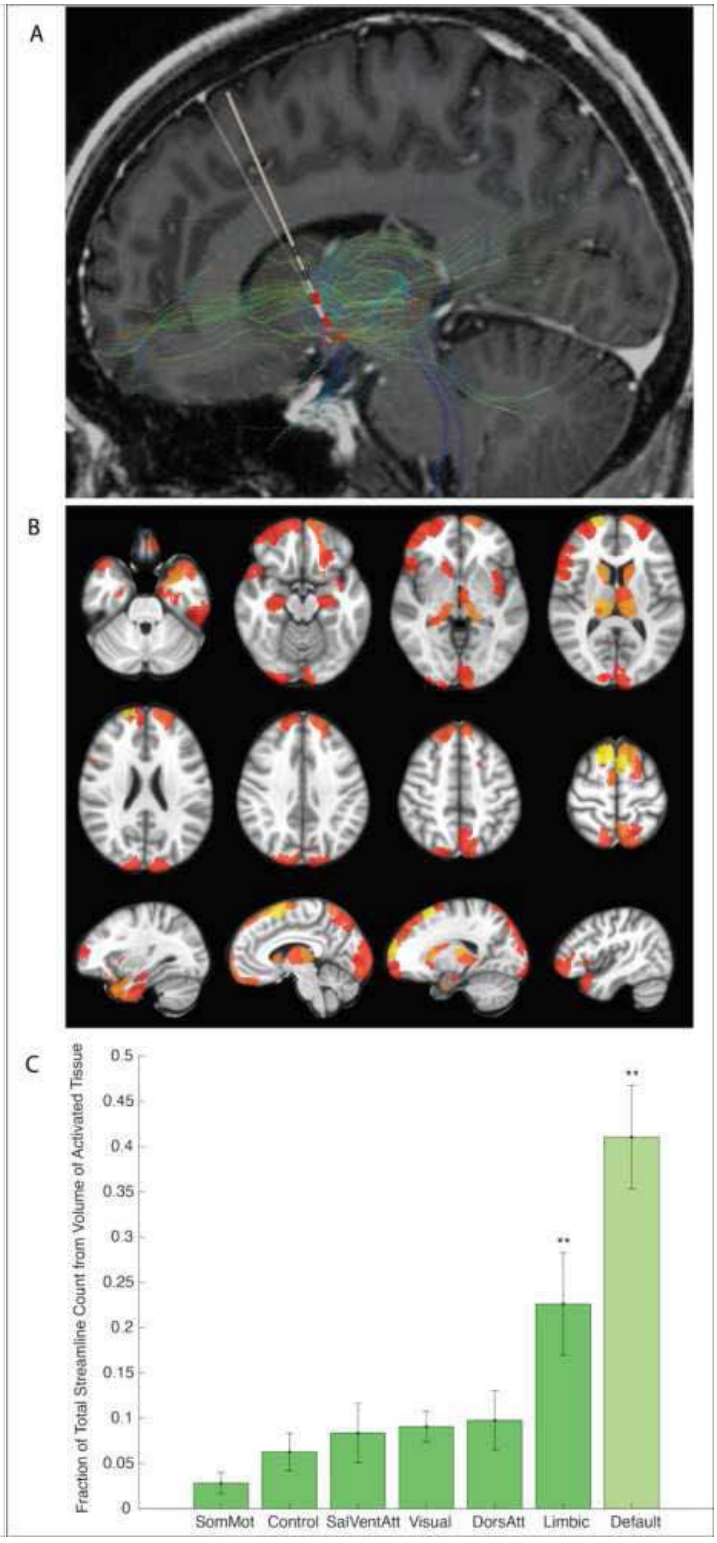

Conclusions: Our findings suggest that relief of OCD symptoms by DBS may be mediated by suppression within the OCD network, as well as in the default mode network via structural connections to the network. This combination of stimulation-based fMRI and diffusion imaging approach to characterizing the impact of DBS on networks may provide a novel method for optimizing contact locations and parameters to treat severe OCD.

References

1. Cox, R.W. (1996). 'AFNI: software for analysis and visualization of functional magnetic resonance neuroimages. Comput Biomed Res', vol. 29, no. 3, pp. 162-173.
2. Cox, R.W. (1997). 'Software tools for analysis and visualization of FMRI Data.' NMR in Biomedicine, vol. 10, pp. 171-178.
3. Denys, D. (2020). 'Efficacy of Deep Brain Stimulation of the Ventral Anterior Limb of the Internal Capsule for Refractory Obsessive-Compulsive Disorder: A Clinical Cohort of 70 Patients.' Am. J. Psychiatry, vol. 177, no. 3, pp. 265–271.

4. Dougherty. D.D. (2018). 'Neuroscientifically Informed Formulation and Treatment Planning for Patients With Obsessive-Compulsive Disorder.' JAMA Psychiatry, vol. 75, no. 10, pp. 1081-1087.
5. Esteban, O. (2019). 'fMRIPrep: A Robust Preprocessing Pipeline for Functional MRI.' Nature Methods, vol. 16, no. 1, pp. 111-116.
6. Horn, A. (2019). 'Lead-DBS v2: Towards a comprehensive pipeline for deep brain stimulation imaging.' Neuroimage, 184, 293-316.
7. Cieslak, M. (2021) QSIPrep: an integrative platform for preprocessing and reconstructing diffusion MRI data. Nat Methods 18 (775–778)
8. Pruim, R.H.R. (2015). 'ICA-AROMA: A robust ICA-based strategy for removing motion artifacts from fMRI data. Neuroimage,' vol. 112, pp. 267-277.
9. Yeh, F.-C., Wedeen, V. J., & Tseng, W.-Y. I. (2010). Generalized q-sampling imaging. IEEE Transactions on Medical Imaging, 29(9), 1626?1635.

Poster No 27

Modeling between DBS signals and brain white matter integrity based Dystonia patients

Sumiko Abe[1], Maral Kasiri[2], Alireza Mousavi[2], Estefania Hernandez-Martin[3], Terence Sanger[2]

[1]CHOC Children's Hospital, City of Orange, CA, [2]University of California, Irvine, Irvine, CA, [3]Universidad de La Laguna, La Laguna, Santa Cruz de Tenerife

Introduction: Dystonia is a disorder of motor programmes controlling semiautomatic movements or postures, with clinical features such as sensory trick, which suggests sensorimotor mismatch as the basis. Dystonia was originally classified as a basal ganglia disease. it is now regarded as a 'network' disorder[1]. Dystonia is a form of dyskinetic cerebral palsy(CP), and CP is associated with white matter injury[3]. We propose that DBS signals travel through white matter tracts to affect both local and distant brain sites. Deep brain stimulation (DBS) has been an important treatment for movement disorders, such as dystonia or Parkinson's disease[2-3]. we hypothesize that the signal of DBS transfer is related with the white matter injury such as demyelination, axonal degeneration etc. DTI is one of the most important method for quantifying these damages of white matter. In this study, we built a general linear modelGML) to descripe the relationships between the DBS signal and DTI coefficients. The result shows the DBS signal peak-to-peak amplitude (P2P) and time-to-(first-) peak delay (T2P) are related with fiber length, fiber diameter and fractional Anisotropy.

Methods: Neuroimages of 6 children with dystonia are used in this study. Our clinical procedure for determining DBS targets includes the implantation of 10 temporary AdTech MM16C depth electrodes (Adtech Medical Instrument Corp., Oak Creek, WI, USA) at potential DBS targets (including basal ganglia and thalamic subnuclei), as identified based on clinical criteria in each patient. Electrophysiology recordings were performed during the first 24 to 48 hours after clinical implantation of the temporary stereo-electroencephalography (sEEG) depth electrodes. Diffusion images were processed using the TOP-UP for motion artifacts were corrected through Eddy-current corrections. After correcting the distortions, both post-surgery CT and DWI volumes were aligned to the same plane using the FLIRT tool in FSL. The voxel size of the T1-weighted images was re-sliced to 1mm3 and used as the source image to warp the CT and DTI images. As a result, the pre-surgery DWI and post-surgery CT volumes were aligned to the structuralMRI volume (T1-weighted) for each subject. The DTI coefficients, such as tract length, tract diameter, and fractional anisotropy (FA), can be used to quantify the characteristics of each fiber tract. On the other hand, the evoked potentials (EPs) can be characterized by their peak-to-peak amplitude (P2P) and time-to-(first-) peak delay (T2P). In this study, our goal was to explore the relationship between these EP characteristics and DTI coefficients. We hypothesize that the fiber length will be correlated with the delay (T2P) while fiber diameter will be inversely correlated with delay and positively correlated with the amplitude (P2P).In order to test our hypotheses at group level we used generalized linear model (GLM). The linear model was defined as: $T\,2P = a \cdot F\,A + b \cdot L + c \cdot R + d \cdot D + p1$ $P\,2P = e \cdot F\,A + f \cdot L + g \cdot R + h \cdot D + p2$

Results: As expected, the multimodal analysis shows a significant correlation between the DTI coefficients and electrophysiological characteristics. The EP amplitude (P2P) is positively correlated with FA and tract volume, while EP delay (T2P) exhibits a negative correlation with both measures. Interestingly, EP amplitude shows a negative correlation with tract length, while EP delay do not show a significant relation to tract length.

Conclusions: Our study has successfully demonstrated the quantification of the relationship between 22-2 electrophysiological signals and white matter integrity using techniques such as DTI and sEEG recordings during DBS. By comparing tractography with ground truth electrophysiology, we have identified significant correlations between neural tract characteristics and neural responses to electrical stimulation in deep brain structures.

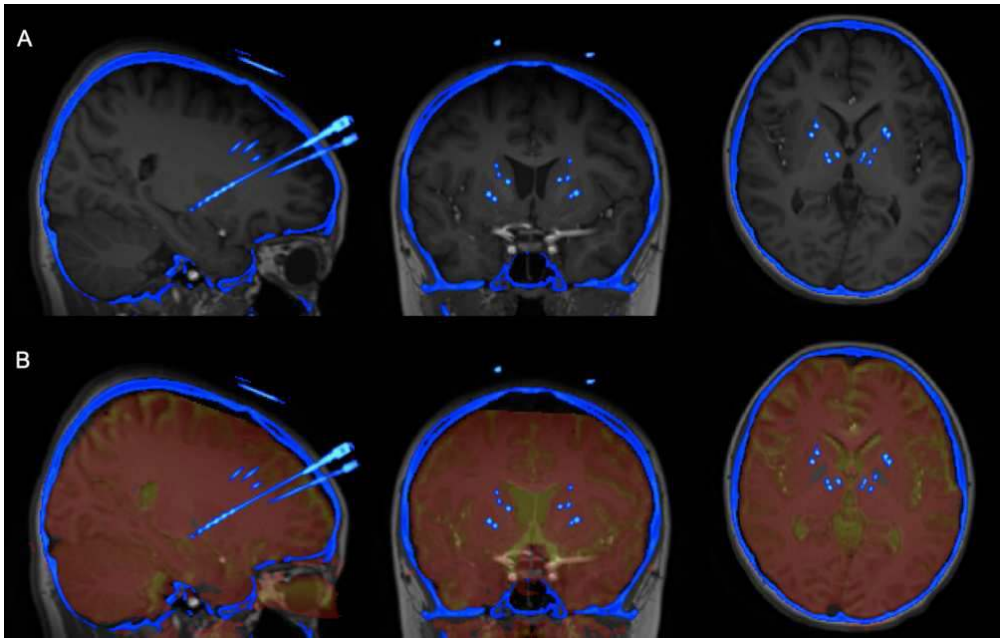

References

1. Kaji R, Bhatia K, Graybiel AM. Pathogenesis of dystonia: is it of cerebellar or basal ganglia origin? J Neurol Neurosurg Psychiatry. 2018 May;89(5):488-492. doi: 10.1136/jnnp-2017-316250. Epub 2017 Oct 31. PMID: 29089396; PMCID: PMC5909758.
2. Sanger TD, Delgado MR, Gaebler-Spira D, Hallett M, Mink JW; Task Force on Childhood Motor Disorders Classification and definition of disorders causing hypertonia in childhood. Pediatrics 2003; 111(1): e89-e97.
3. T. D. Sanger and S. N. Kukke, "Abnormalities of tactile sensory function in children with dystonic and diplegic cerebral palsy," J. Child Neurol., vol. 22, no. 3, pp. 289–293, 2007.

Poster No 28

Rearrangement of the posterior language area with lesion progression

Riho Nakajima[1], Takahiro Osada[2], Masashi Kinoshita[3], Akitoshi Ogawa[2], Hirokazu Okita[4], Seiki Konishi[2], Mitsutoshi Nakada[5]

[1]Department of Occupational therapy, Kanazawa University, Kanazawa, Japan, [2]Department of Neurophysiology, Juntendo University School of Medicine, Tokyo, Japan, [3]Department of Neurosurgery,Kanazawa University, Kanazawa, Japan, [4]Department of Physical Medicine and Rehabilitation, Kanazawa University Hospital, Kanazawa, Japan, [5]Department of Neurosurgery, Kanazawa University, Kanazawa, Japan

Introduction: Damaged functional areas are compensated by other cortical regions to maintain brain function. Although cortical rearrangement can occur in either hemisphere when the tumor grows to the posterior language area (PLA), the rearrangement of Wernicke's area has rarely been reported.[1,2] This study investigated the characteristics of cortical rearrangement of the PLA within the ipsilateral hemisphere using direct electrical stimulation (DES) during awake brain surgery and resting-state functional connectivity.

Methods: Sixty-two patients with left hemispheric glioma who underwent awake brain surgery were included in the study. All the patients underwent structural magnetic resonance imaging (MRI) and resting state functional MRI (rsfMRI) preoperatively. Each structural MRI was spatially normalized to the Montreal Neurological Institute (MNI) template via the segmentation routine using SPM12. Patients were divided into PLA and non-PLA groups based on lesion extension to the PLA. Cortical brain mapping was performed using DES. During intraoperative language assessment, patients were asked to name the pictures presented on the screen. When incorrect (impaired) responses were elicited in the naming task during DES, the point was considered an area with a language function (positive points). The region was considered an area with a non-language function (normal points) if the response was correct (unimpaired). We defined incorrect responses as "positive responses" and correct responses as "normal responses." Spatial locations of the positive and normal responses were retrospectively plotted on the corresponding original 3D T1 images for each patient using operative reports and intraoperative video records with the iPlan software. Each positive point on the original T1 images was transferred to the corresponding point on the normalized T1 images. The positive points were then mapped onto the corresponding lattice cells on the lateral view of the brain. The frequency of the positive responses was calculated as the ratio of the number of patients with positive responses to the

number of stimulated patients. RsfMRI analysis was conducted using SPM12, FSL, and the Human Connectome Project (HCP) pipelines. We calculated the betweenness centrality (BC) among the 360 cerebrocortical parcels,3) which were averaged across the vertices in each parcel from HCP.4) The frequencies of positive responses were compared between the groups using the chi-square test. One- and two-way analysis of variance (ANOVA) was performed to examine the BC characteristics. This study was approved by the Medical Ethics Committee of Kanazawa University (approval numbers: 1797 and 3322).

Results: In awake language mapping, 48 positive and 488 normal points were identified. In the non-PLA group, areas with a high proportion of positive responses were detected in the posterior part of the superior temporal gyrus (pSTG) and middle temporal gyrus, while no positive responses were detected in the supramarginal gyrus (SMG). In the PLA group, a high proportion of positive responses were distributed widely in the cortical area, including the pSTG and temporoparietal junction. The proportion of positive responses in the posterior SMG (pSMG) was significantly higher in the PLA group (47%) than in the non-PLA group (0%) ($P=0.0091$). RsfMRI revealed that BC in the pSMG was significantly higher than that in the surrounding areas in both the non-PLA and PLA groups ($t(41)=4.95$, $P=8.73 \times 10\text{-}6$; $t(19)=3.09$, $P=0.0047$, respectively). Finally, we performed a mixed ANOVA with the areas (pSTG/pSMG) and patient groups (non-PLA/PLA groups) as the main effects. A significant interaction was observed between the areas and the patient groups ($F(1,38)=6.50$, $P=0.013$).

Conclusions: This study suggests that the posterior language area can be rearranged from pSTG to pSMG, which is a hub region in the brain, with lesion progression to the posterior superior temporal gyrus.

References

1. Stockert A, Wawrzyniak M, Klingbeil J, et al. Dynamics of language reorganization after left temporo-parietal and frontal stroke. Brain. 2020;143(3):844-861.
2. Mbwana J, Berl MM, Ritzl EK, et al. Limitations to plasticity of language network reorganization in localization related epilepsy. Brain. 2009;132:347-356.
3. Glasser MF, Coalson TS, Robinson EC, et al. A multi-modal parcellation of human cerebral cortex. Nature. 2016;536:171-178.
4. Fujimoto U, Ogawa A, Osada T, et al. Network Centrality Reveals Dissociable Brain Activity during Response Inhibition in Human Right Ventral Part of Inferior Frontal Cortex. Neuroscience. 2020;433:163-173.

Poster No 29

ECoG high-gamma activity peak during speech production increases the ECS effect

Christoph Kapeller[1], Kyousuke Kamada[2], Mostafa Mohammadpour[1], Christoph Guger[1]

[1]g.tec medical engineering GmbH, Schiedlberg, Austria, [2]Megumino Hospital, Eniwa, Hokkaido

Introduction: Electrical cortical stimulation (ECS) has the capability to induce behavioral and cognitive changes through precise modulation of targeted brain regions. This phenomenon manifests in effects such as involuntary motor movements, visual distortions, and transient language impairments, particularly when specific brain areas related to motor control, vision, or language processing are targeted. Notably, the surgical removal of these regions often results in postoperative functional deficits, underscoring the importance of ECS as a preoperative and perioperative tool for functional mapping. In the context of language mapping, ECS serves as a benchmark for preserving speech function[1]. While established ECS protocols for language tasks exist, they are primarily based on empirical observations and adapted to individual patient variations. Therefore, it is crucial to have a comprehensive understanding of the causal relationship between stimulation parameters and resulting behavioral outcomes. Broadband high-gamma activity (HGA), detected through electrocorticography (ECoG), serves as an additional biomarker with superior spatial resolution, reflecting neural activity related to language[2,3]. This study aimed to investigate whether the timing of ECS initiation during a naming task influences symptom frequency and how this timing aligns with the trajectory of HGA.

Methods: Two epilepsy patients from Megumino Hospital, Japan, provided informed consent for the clinical ECS language mapping extension before brain surgery. Prior to ECS, a picture naming task was used to capture task-related HGA. Subsequent ECS identified stimulation sites inducing transient language impairments through 5-7mA stimulation. The site with the most pronounced HGA was selected for ECS with variable onsets (0.35 to 1 second post-picture onset). ECS, administered at 50Hz for 1 second, resulted in trial classifications as ‘no symptom’ or ‘symptom’ based on speech anomalies.

Results: HGA peaked at 5.44 and 4.72 z-scores at 684 and 454 milliseconds for the first and second patients, respectively, with corresponding intervals of 383-955 and 333-764 milliseconds. Figure 1 shows the HGA together with the time-frequency maps of the the stimulation target area (ROI). The symptom occurrence in Figure 2 was 92% and 47% before the HGA peak for the first and second patients, decreasing to 37% and 13% post-peak

Conclusions: Stimulation before the HGA peaks significantly reduced the response speed compared sham stimulation. This underscores the crucial interplay between speech production, HGA, and ECS efficacy. Moreover, faster-responding patients require earlier ECS, suggesting tailored protocols for efficient functional mapping, particularly in time-sensitive procedures like awake craniotomies.

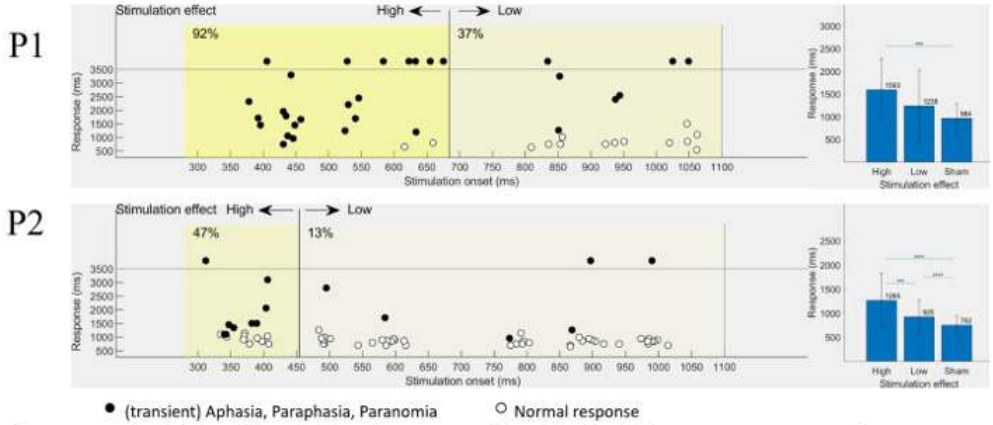

Figure 2: Stimulation effect (left) and response time (right) with respect to HGA peak.

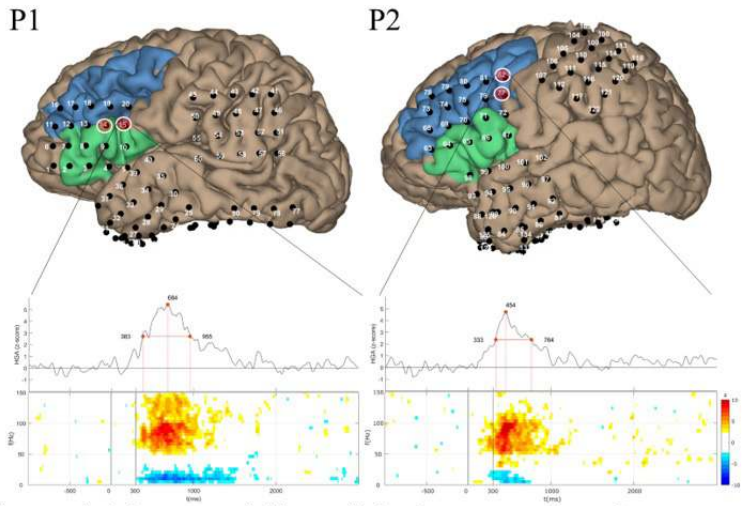

Figure 1: Stimulation target area inside ROI with time-frequency map and HGA time course.

References

1. Hamer, P. D. W., et al. (2012). Impact of intraoperative stimulation brain mapping on glioma surgery outcome: a meta-analysis. J Clin Oncol, 30(20), 2559-2565.
2. Wang, P., et al. (2021). Clinical applications of neurolinguistics in neurosurgery. Frontiers of medicine, 15(4), 562-574.
3. Sonoda, M. et al. (2022). Naming-related spectral responses predict neuropsychological outcome after epilepsy surgery, Brain, Volume 145, Issue 2, Pages 517–530.

Poster No 30

Cortical localization and positive detection rate of bilateral cerebral functions in awake surgery

Masashi Kinoshita[1], Riho Nakajima[2], Mitsutoshi Nakada[1]

[1]Department of Neurosurgery, Kanazawa University, Kanazawa, Ishikawa, Japan, [2]Pharmaceutical and Health Sciences, Kanazawa University, Kanazawa, Ishikawa, Japan

Introduction: In recent years, awake surgery has become the treatment strategy for gliomas, with the aim of preserving cerebral function in both the left and right hemispheres. Cortical localization of various functions has been reported; however, the left-right characteristics related to the frequency of their detection are not known. In this study, we report on functional mapping of the bilateral cerebrum in awake glioma surgery, assuming cortical functional localization and frequency of positive detection.

Methods: We performed intraoperative assessment tasks for motor, sensory, language (picture naming, semantic comprehension, and reading), social cognition (low-level and high-level mentalizing), and visual cognition (visuospatial recognition) in 135 glioma patients (WHO grades 1-4; 56 right, 79 left) who underwent awake surgery to preserve cognitive functions in the bilateral cerebrum at our hospital from 2014 to 2021. Cortical mapping points (MPs) where positive findings were obtained by direct electrical stimulation, and cortical areas where positive and negative findings were obtained were recorded. All MPs were extracted by MNI152 standard brain space analysis using SPM and MRIcron, classified into Brodmann areas (BA), and then each BA positivity rate in all cases was calculated, and brain functions and cortical areas per each positive detection rate were reflected in the standard brain atlas.

Results: The BA 4, 6, and 1-3 areas exhibited positive detection rates >70%, with almost no difference between left and right sides of the brain. The left and right BA22, left BA37 and 44, and right BA7 and 43 areas showed 50-70% positivity, with language on the left and social cognition and visual cognition on the right. In contrast, all areas with positive detection rates >10% were widely located ventral to the temporal lobe on the left and dorsal to the frontal to parietal lobes on the right. In other words, the functional localization and high frequency of detection were consistent in the Roland's area and the peri-Sylvian area. Although the latter showed a left-right difference in positive function and detection area, intraoperative selective functional mapping ensured a nearly symmetrical high positive detection rate.

Conclusions: It should be noted that although the cerebrum has functional anatomical differences between the left and right hemispheres, it is an organ with symmetrical features, as evidenced by similar positive detection frequencies on the left and right hemispheres during awake functional mapping.

Poster No 31

Advanced Mapping Techniques with ECoG in Awake Craniotomies and Consciousness State Assessment

Priscella Asman[1], Mathew Hall[1], Israt Tasnim[2], Giuseppe Pellizzer[3], Shreyas Bhavsar[1], Sudhakar Tummala[1], Firat Ince[2], Sujit Prabhu[4]

[1]Md Anderson, Houston, TX, [2]University of Houston, Houston, TX, [3]University of Minnesota, Minneapolis, MN, [4]MD Anderson, Houston, TX

Introduction: In the treatment of gliomas located in the peri Rolandic areas of the brain, accurately mapping the sensorimotor regions is crucial to preserve both motor and sensory functions. Typically, techniques like electrical cortical stimulation (ECS) and the median nerve somatosensory evoked potential (SSEPs) phase reversal technique (MSSEP-PRT) are employed[1-2]. However, ECS can be time-consuming and carries the risk of inducing seizures, while MSSEP-PRT may be challenging to interpret[3-6]. This study aims to investigate the use of high-density electrocorticography (ECoG) for passive functional mapping, with the spatial-temporal, and spectral features of SSEPs in real time. Additionally, we demonstrate that besides central sulcus (CS) delineation, the spectral patterns of the SSEPs can differentiate between different consciousness states.

Methods: During surgery, SSEPs were recorded using high-density ECoG grids placed on the sensorimotor cortex of fourteen patients, both in an anesthetized and awake state. Neural data from 0.6Hz median nerve stimulation were captured at 2.4kHz and processed in real-time using MATLAB Simulink. The system displays SSEPs' peak activations as a 2D heat map on a screen, particularly around the 20ms time point (N20), and generates the spectral power in the gamma range using Stockwell transform. This was then projected on the 3D rendering of each patient's brain generated from Magnetic Resonance Imaging (MRI). We used the area under the curve (AUC) of the receiver operating characteristic (ROC) curve to determine the accuracy in distinguishing the anterior and posterior channels based on the peak amplitude at N20 and gamma power. We also applied paired t-tests to compare the gamma oscillations in each state.

Results: Consistently across patients, the 20ms time point showed a clear discrimination between anterior (motor) and posterior (sensory) channels with a high separation accuracy of 93.6±14.9%. The color contrast revealed the delineated CS correlating with the sulcus in the 3D rendering, Figure 1A. We also observed late gamma (60–250 Hz) modulation in all subjects approximately 50 ms after stimulation onset, extending up to 250 ms in each state in the primary somatosensory area (S1), Figure 1B. The late gamma activity was suppressed in the anesthetized state (independent t-test $t(13) = -3.2519$, $p = 0.0140$) and increased significantly relative to baseline in the awake state (independent t-test $t(13) = 6.0072$, $p < 0.01$; Figure 3A). The late gamma had a delineation accuracy of 81±10.3% in the anesthetized and 91±13.4% in the awake state.

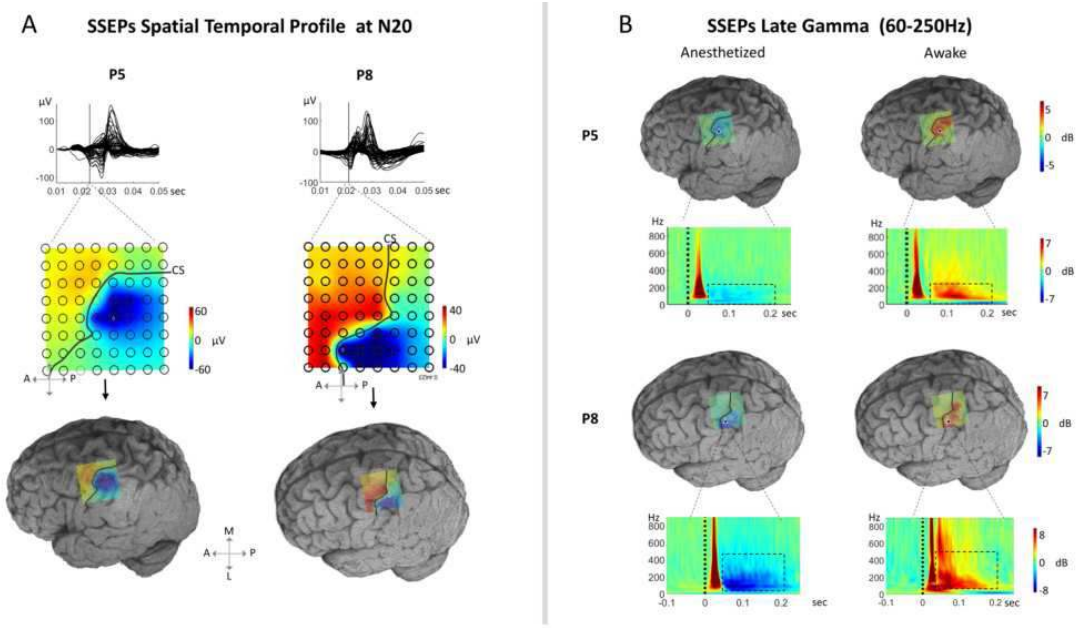

Figure 1: A: Real time mapping with the spatial temporal features of SSEPs shown delineating the central sulcus for Patient 5 and Patient 8 at around 20ms on the 2D grid and 3D rendering. The blue regions represent the posterior (sensory) area and the red regions the anterior (motor) area. The gray line is the central sulcus. A: Anterior P: Posterior M: Medial L: Lateral. B: Late gamma activities shown for both patients suppressed in the anesthetized state and enhanced in the awake state defining the primary somatosensory area. The stockwell transform is shown for the peak area with the triangular dot.

Conclusions: These results show that both spatial-temporal mapping from SSEPs and long-latency gamma modulations can individually delineate sensorimotor areas and the spectral profile can assess consciousness during neurosurgery. These findings have significant implications for operative planning in neurosurgical procedures

References

1. Pondal-Sordo M, Diosy D, Téllez-Zenteno J F, Girvin J P and Wiebe S 2006 Epilepsy surgery involving the sensory-motor cortex Brain 129 3307–14
2. Lavrador J P, Gioti I, Hoppe S, Jung J, Patel S, Gullan R and Vergani F 2021 Altered motor excitability in patients with diffuse gliomas involving motor eloquent areas: the impact of tumor grading Neurosurgery 88 183–92
3. Lesser R P, Koehle R and Lueders H 1979 Effect of stimulus intensity on short latency somatosensory evoked potentials Electroencephalogr. Clin. Neurophysiol. 47 377–82
4. Woolsey C N, Erickson T C and Gilson W E 1979 Localization in somatic sensory and motor areas of human cerebral cortex as determined by direct recording of evoked potentials and electrical stimulation J. Neurosurg. 51 476–506
5. Hamberger, M.J., 2007. Cortical language mapping in epilepsy: a critical review. Neuropsychology review, 17, pp.477-489.
6. Ritaccio, A.L., Brunner, P. and Schalk, G., 2018. Electrical stimulation mapping of the brain: basic principles and emerging alternatives. Journal of clinical neurophysiology: official publication of the American Electroencephalographic Society, 35(2), p.86.

Poster No 33

Thalamo-centric causal connectivity mapping in human brain with intracranial electrical stimulation

Dian Lyu[1], Josef Parvizi[1]

[1]*Stanford University, Palo Alto, CA*

Introduction: The brain's spatiotemporal architecture, marked by functional connectivity motifs, is key to brain health and consciousness. Emerging theories highlight the thalamus' neuromodulatory role in shaping cortical connectivity motifs (Shine et al., 2023). However, testing these theories is challenging due to the small size, deep location and functional complexity of subcortical areas, where non-invasive neuroimaging techniques face limitations. In Stanford, we pioneered multi-site stimulation and recording in the thalamus using deep intracranial electrodes for mapping thalamic-centric causal connectivity. Thalamic stimulations are shown to evoke distinct EEG profiles than cortical stimulations from a recent mice study (Claar et al., 2023). Meanwhile, we have limited knowledge from direct human thalamic measurements. Therefore, our goal is to extract meaningful neural features from stimulation evoked potentials (SEP), then infer whole-brain causal connectivity.

Methods: In this study, we recruited 27 participants with focal epilepsy with implanted electrodes for clinical purpose. Employing our standard single pulse electrical stimulation protocol, we investigated causal connectivity by stimulating a bipolar electrode pair while recording from all others. We utilized UMAP algorithm to encode neural signals (McInnes et al.,

2020), with the input of time-variant power and inter-trial phase coherence spectrograms of SEPs. We derived activation labelling by employing semi-supervised learning, after partially labelling activations manually based on preset criteria. Then, we employed group-level supervised UMAP to map the activated spectrograms to the anatomical labels: THAL-ipsi, THAL-contr, COR-ipsi, and COR-contr (stimulating from THAL/COR in the ipsi/contralateral hemisphere). Category-specific spectral features were determined with cluster-based permutation significance testing. To decode individual evoked signals using these features, we used the spectral information from each significant cluster as a template and apply sliding-window cross-correlation to track dynamic changes in feature proximity for all trials.

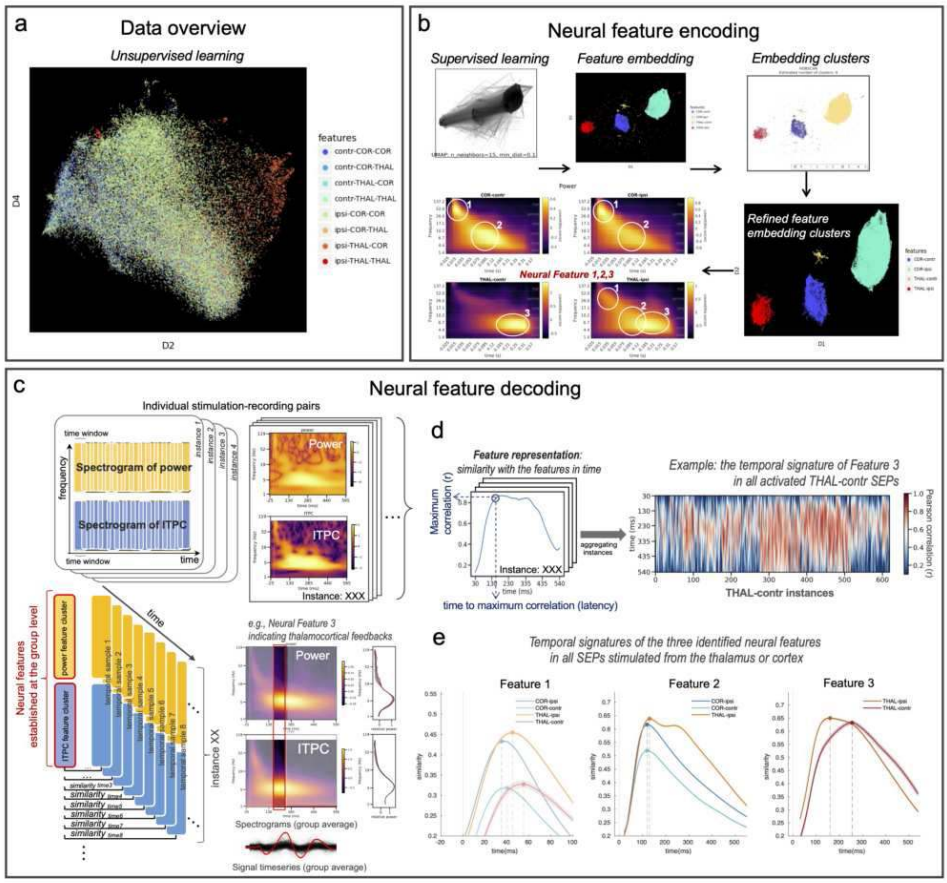

Results: Neural features 1 and 2, corresponding to gamma (~40ms) and high theta (75-165ms), respectively, were distinguished in ipsilateral vs. contralateral recordings of cortical stimulations (COR-ipsi vs. COR-contr). These clusters align with documented N1 and N2 components in brain stimulation literature (Keller et al., 2014). Notably, a third cluster (Feature3) in thalamus stimulations, peaking late (>165ms) and lasting ~250ms in the theta band, is distinct from the N2 component. Examining whole-brain causal connectivity matrices based on feature presentation, we observe: (1) modularity within adjacent anatomical areas in the Feature-1 matrix, suggesting direct connectivity (Fig. 3b); (2) widespread Feature-2 representations across regions and hemispheres, maintaining first-order modularity, indicating indirect connectivity building on the initial connectivity; (3) Feature-3 matrix showing whole-brain connectivity from thalamus without first-order modularity, suggesting persisting thalamocortical feedback. Comparing thalamic subdivisions, anterior thalamus (antTH) exhibits stronger Feature 1 and 3 representations with frontal areas, indicating recurrent connectivity, while posterior thalamus (pstTH) has more connections with parietal and occipital areas than antTH.

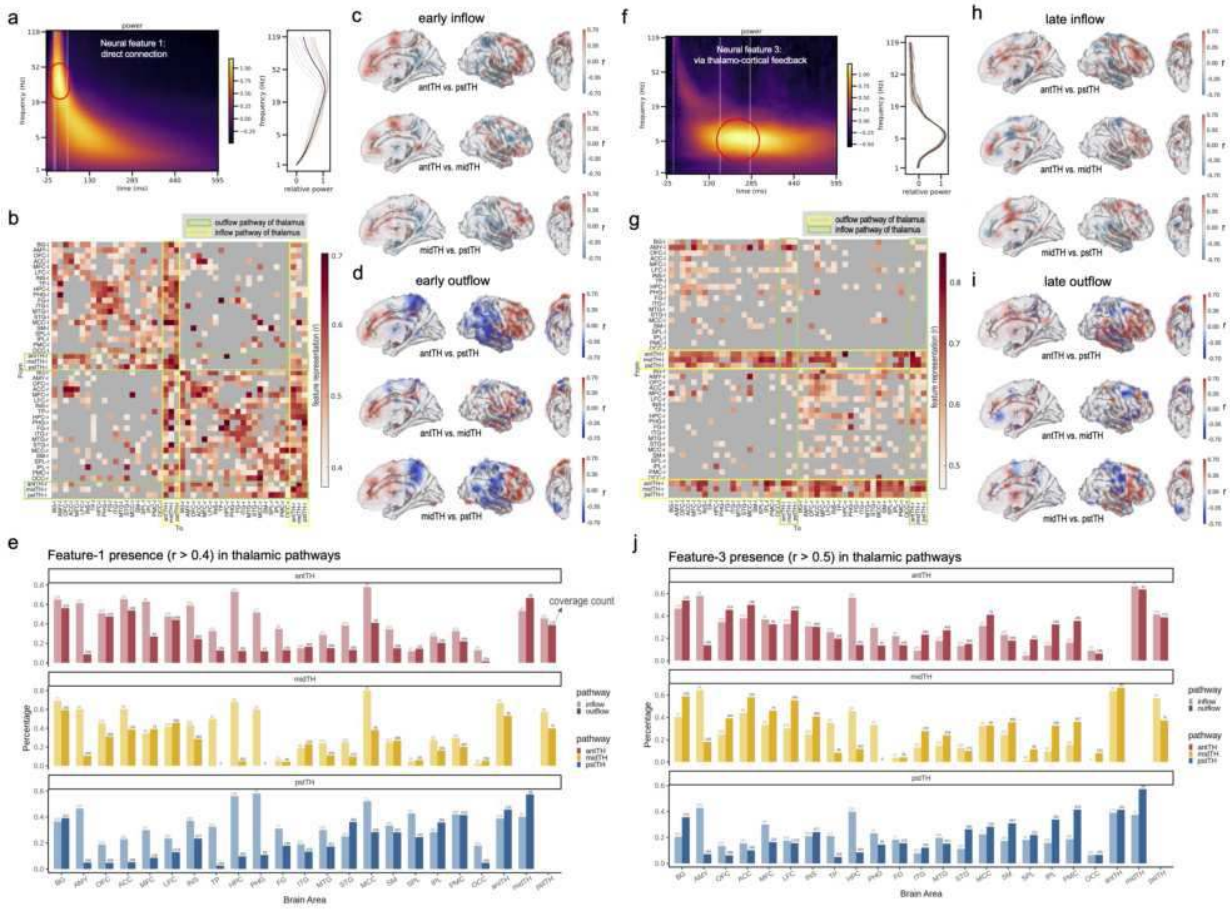

Conclusions: We encoded whole-brain stimulation-evoked potentials into 3 neural features, representing direct connectivity, indirect connectivity via cortex, and indirect connectivity via thalamocortical feedback. Decoding revealed that the thalamus receives direct connectivity from the whole brain, while its direct cortical projection is limited to the same hemisphere. In contrast, the indirect thalamocortical late feedback spans the entire brain, acting as a propagator of theta oscillations persisting in cortical signals for approximately 200 ms post-thalamic excitation.

References

1. Claar, L. D., Rembado, I., Kuyat, J. R., Russo, S., Marks, L. C., Olsen, S. R., & Koch, C. (2023). Cortico-thalamo-cortical interactions modulate electrically evoked EEG responses in mice. eLife, 12, RP84630. https://doi.org/10.7554/eLife.84630
2. Keller, C. J., Honey, C. J., Mégevand, P., Entz, L., Ulbert, I., & Mehta, A. D. (2014). Mapping human brain networks with cortico-cortical evoked potentials. Philosophical Transactions of the Royal Society B: Biological Sciences, 369(1653), 20130528. https://doi.org/10.1098/rstb.2013.0528
3. McInnes, L., Healy, J., & Melville, J. (2020). UMAP: Uniform Manifold Approximation and Projection for Dimension Reduction (arXiv:1802.03426). arXiv. https://doi.org/10.48550/arXiv.1802.03426
4. Shine, J. M., Lewis, L. D., Garrett, D. D., & Hwang, K. (2023). The impact of the human thalamus on brain-wide information processing. Nature Reviews Neuroscience, 1–15. https://doi.org/10.1038/s41583-023-00701-0

Poster No 34

Impaired action recognition in brain tumor patients induced by direct electrical stimulation

Laura de Frutos-Sagastuy[1,2], Ileana Quinones[3,4,5], Santiago Gil-Robles[6], Iñigo Pomposo[7], Garazi Bermudez[7], Manuel Carreiras[3,4], Lucía Amoruso[3,8,4]

[1]Basque Center on Cognition, Brain and Language, Donostia - San Sebastian, Gipuzkoa, [2]University of the Basque Country, Bilbao, Spain, [3]Basque Center on Cognition, Brain and Language, Donostia - San Sebastián, Gipuzkoa, [4]Ikerbasque, Basque Foundation for Science, Bilbao, Spain, [5]Biogipuzkoa Health Research Institute, San Sebastian, Spain, [6]Universitary Hospital Quironsalud Madrid, Madrid, Madrid, [7]BioCruces Research Institute, Bilbao, Bilbao, [8]Cognitive Neuroscience Center, Buenos Aires, Argentina

Introduction: Intraoperative functional mapping during awake brain surgery is the first therapeutic option for tumor resection. Indeed, ~80% of these tumors involve eloquent areas, that is, regions of high functional expressivity that need to be spared from resection. This underscores the need for intraoperative sensitive tasks to map and preserve these regions, avoiding postoperative sequelae. Classically, functional mapping has focused on overt functions in the dominant hemisphere, namely, motricity and language in the left hemisphere. However, there are other distributed functions crucial for daily life that are challenging to map but need preservation[1]. One example is action comprehension, a vital social ability supported by the Action Observation Network (AON). Neuroanatomically, the AON involves dorsal bilateral fronto-parietal regions, including the inferior frontal cortex, premotor cortex, inferior parietal lobe, and superior temporal sulcus[2]. These regions are interconnected subcortically, primarily through the superior longitudinal fasciculus (SLF) and anterior thalamic radiations[3].

Methods: The AON mapping task comprises a series of images depicting a model engaged in incomplete, ongoing actions. Participants must infer the overarching motor goal behind the observed movement by selecting between two alternatives (e.g., to drink or to clean). Actions are observed in naturalistic contexts that can either facilitate or hinder action recognition[4,5]. Four patients diagnosed with brain tumors in the right hemisphere underwent awake surgery for tumor resection along with intraoperative functional mapping of the AON. Patient A had a parietal cavernoma, patient B had a glioma in the insula, patient C had an insular astrocytoma and patient D had a insular glioma. Cortical and subcortical mapping were performed by combining direct electrical stimulation (DES) with a bipolar stimulation electrode, while the patient performed the AON task. If the patient produces an error in at least 2 out of 3 non-consecutive stimulation trials, it indicates that the stimulated region has a functional role and should be preserved from resection. A trial is considered erroneous if, due to stimulation, the patient misinterprets the intentionality of the action or if the response is delayed or absent. It is also considered an error when the patient rectifies the answer only after the stimulation has ended. This task was video recorded during the course of the awake craniotomy for posterior behavioural analysis.

Results: In patient A, both horizontal (SLF) and vertical (thalamocortical fibers) connectivity were consistently disrupted, leading to slowed response times and semantic errors. In patient C, cortical positive stimulation sites were identified in the insula and the roof of the ventricle of the temporal horn, resulting in delayed or incorrect responses.

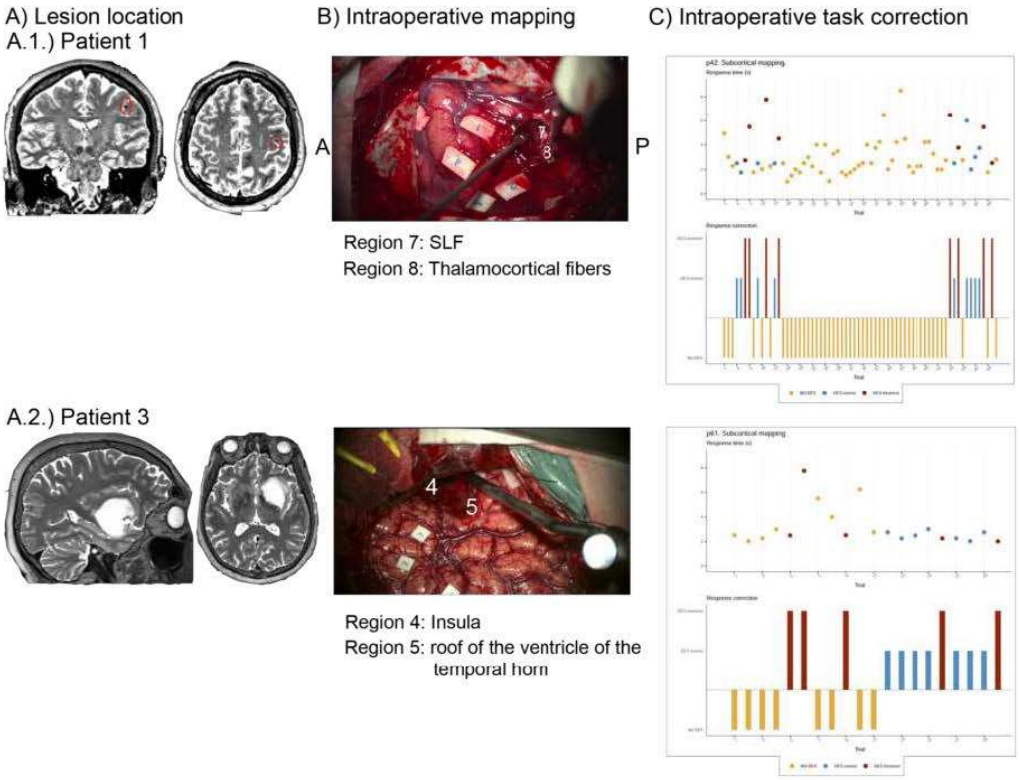

Conclusions: Overall, our findings provide causal evidence for the role of cortical (e.g., IFG) and subcortical (e.g., SLF) AON nodes in facilitating action recognition. At the clinical level, these results validate the effectiveness of the AON task as a valuable tool for mapping social abilities in the right hemisphere, a key element that is currently missing in the surgical management of eloquent areas in the non-dominant hemisphere.

References
1. Herbet, G. (2021). Should Complex Cognitive Functions Be Mapped With Direct Electrostimulation in Wide-Awake Surgery? A Network Perspective. Front in Neur 12, 635439.
2. Caspers, S. (2010). ALE meta-analysis of action observation and imitation in the human brain. NeuroImage 50, 1148-1167
3. Wang, et al. 2018. White matter pathways and social cognition. Neuroscience and biobehavioral reviews 90, 350-370
4. Amoruso, L. (2016). Tracking the Time Course of Top-Down Contextual Effects on Motor Responses during Action Comprehension. Journal of Neuroscience. 36-46, pp.11590-11600.
5. Amoruso, L. (2020). Spatial frequency tuning of motor responses reveals differential contribution of dorsal and ventral systems to action comprehension. Proceedings of the National Academy of Sciences (PNAS), 117 (23), 13151-13161.

Poster No 35

Modeling and predicting neural responses to multisite direct electrical brain stimulation in humans

Uma Mohan[1], John Wittig[2], Oceane Fruchet[2], Sara Inati[2], Kareem Zaghloul[2]

[1]NIH, Bethesda, MD, [2]NIH, NINDS, Bethesda, MD

Introduction: Direct electrical brain stimulation combined with intracranial electrophysiological recordings hold the potential to modulate and test the functional role of neural activity in the awake human brain. While clinicians have used direct electrical brain stimulation for functional mapping and treatment of neurological and psychiatric disorders, the effects of stimulation on neural activity are poorly understood. Changes in neural activity from stimulation in local and remote areas are often highly complex and variable. Stimulation has most often been delivered at locations individually, however, simultaneous or patterned stimulation at multiple locations holds the potential to modulate distributed networks more precisely.

Methods: To better understand and precisely control the responses to stimulation in individual patients, we first took the approach of modelling the effects of stimulation on neural dynamics across the brain. We collected human electrocorticographic recordings from 8 neurosurgical epilepsy patients while systematically delivering cortical stimulation at different frequencies, amplitudes, durations, and locations while patients were at rest. Using a dynamic linear state-space model framework, we fit input-output models to timecourses of neural activity, represented by high frequency activity, while patients received stimulation.

Results: We first show that dynamic responses in brainwide neural activity following stimulation at individual locations across brain regions can be accurately predicted using latent state space models. We further show patient-specific models build can be used to predict responses to novel stimulation locations. Lastly, we analyzed changes in large-scale neural activity in response to multisite stimulation and compare these responses to those predicted from patient-specific state-space models built while patients were stimulated at individual locations. We found that we able to reliably predict the timecourse of responses to stimulation delivered at novel combinations of multiple locations.

Conclusions: The ability to characterize and model neural responses to novel locations as well as patterns of multisite stimulation could allow clinicians and researchers to design stimulation protocols for precise modulation of neural activity. Stimulation parameters and patterns may be selected to elicit specific changes to ongoing behaviorally relevant neural signals in the human brain to modulate higher-order cognitive functions and to more effectively probe functional brain networks and treat neurological disorders.

References
1. Yang, Y. (2021). “Modelling and prediction of the dynamic responses of large-scale brain networks during direct electrical stimulation.” Nature biomedical engineering, 5(4), 324-345.

Poster No 36

Cerebello-Thalamo-Cortical Tract Reorganization After MRgFUS Thalamotomy in Essential Tremor

Neeraj Upadhyay[1,2], Veronika Purrer[2,3], Angelika Maurer[1], Marcel Daamen[1,2], Valeri Borger[4], Alexander Radbruch[5], Ulrike Attenberger[6], Ullrich Wuellner[3], Henning Boecker[1,2]

[1]Clinical Functional Imaging Group, Department of Diagnostic and Interventional Radiology, University Hospital Bonn, Bonn, NRW, Germany, [2]Deutsches Zentrum für Neurodegenerative Erkrankungen e. V. (DZNE), Bonn, NRW, Germany, [3]Department of Neurology, University Hospital Bonn, Bonn, NRW, Germany, [4]Department of Neurosurgery, University Hospital Bonn, Bonn, NRW, Germany, [5]Department of Neuroradiology, University Hospital Bonn, Bonn, NRW, Germany, [6]Department of Diagnostic and Interventional Radiology, University Hospital Bonn, Bonn, NRW, Germany

Introduction: The cerebello-thalamo-cortical tract (CTCT) exhibits pathophysiological disturbances in individuals with essential tremor (ET) when compared to healthy subjects (Gallay et al., 2008). Existing research suggests that both Deep Brain Stimulation and Magnetic Resonance-guided Focused Ultrasound (MRgFUS) (Zesiewicz et al., 2005) are effective interventions for managing tremor activity in drug-resistant ET patients (Giordano et al., 2020; Agrawal et al., 2021; Miller et al., 2022). MRgFUS achieves this by creating a permanent focal brain lesion in the ventral intermediate nucleus (VIM) via ultrasound-induced thermal ablation (Chazen et al., 2018). In response to localized tissue damage, microstructural reorganization of white matter tracts (Pineda-Pardo et al., 2019; Sammartino et al., 2019) may occur in terms of Wallerian degeneration (Rotshenker, 2011) or compensatory rewiring of neural connections . Therefore, it is crucial to comprehend the microstructural changes within the CTCT associated with MRgFUS thalamotomy in longitudinal studies.

Methods: Twenty-seven ET patients (68.7±10.25 years; 19 males and 8 females) underwent VIM MRgFUS, including 24 right-hand dominant and three left-hand dominant tremor patients. Before, 1 month and 6 months after MRgFUS treatment, clinical as well as T1-weighted and Diffusion Tensor Imaging (DTI) data were acquired at 3T (Philips Achieva scanner with 8-channel head coil). We included part B and subscores of the upper extremity tremor rating of part A of the Clinical Rating Scale for Tremor to create a modified outcome measure ("CRST-AB subscale") consisting of 7 items resulting in a maximum of 28 points. Scores were calculated for the treated and non-treated side separately. Probabilistic tractography was performed to map the CTCT (Pohl et al., 2022) taking the ipsilateral dentate nucleus as seed and contralateral precentral gyrus as target to assess probabilistic fiber density (FD). Furthermore, weighted least square tensor fitting was performed to obtain fractional anisotropy (FA), axial diffusivity (AD) and radial diffusivity (RD) measures of microstructural integrity using the FDT pipeline within the FSL toolbox (https://fsl.fmrib.ox.ac.uk/fsl/fslwiki/FDT). The various maps of fiber density and white matter integrity from left dominant tremor subjects were swapped from left to right. Finally, the measures were compared by implementing pairwise comparisons between different time points using FSL's randomise approach (https://fsl.fmrib.ox.ac.uk/fsl/fslwiki/Randomise). Significant results were reported at $p<0.05$ corrected for multiple comparisons using the threshold-free cluster enhancement (TFCE) method.

Results: Significant tremor reduction was observed 1 month (M±SD: 5.02 ± 4.27; $t(26) = -13.8$, $p < 0.001$, Cohen's $d = -2.65$) and remained reduced 6 months after MRgFUS (M±SD = 5.85 ± 4.56; $t(26) = -13.4$, $p < 0.001$, Cohen's $d = -2.58$), relative to before MRgFUS treatment (M±SD = 18.78 ± 4.27) . We observed decreased CTCT fiber density at 1 as well as 6 months after, as compared to before MRgFUS (Figure 1a). Microstructural integrity in terms of FA was reduced 1 month and, though with smaller cluster size, 6 months after MRgFUS (Figure 1b). Similarly, a reduction was observed in AD 1 month after MRgFUS (Figure 1c). Conversely, both AD (Figure 1c) and RD (Figure 1d) were increased at 6 months at the distal part of the CTCT tract (between thalamus and precentral gyrus).

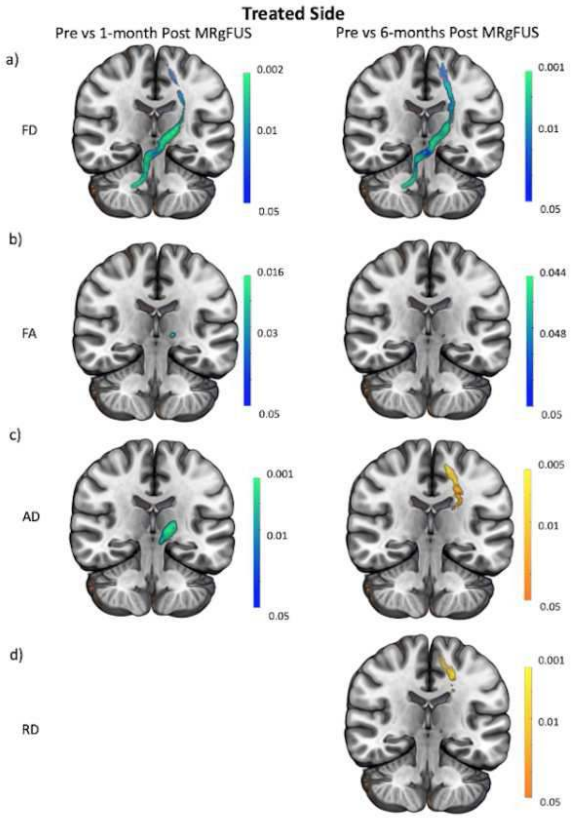

Figure 1. Representation of fiber density and microstructural white matter comparisons between before versus post 1 month and before versus post 6 months of MRgFUS within the CTCT tract of the treated side: a) fiber density (FD), b) fractional anisotropy (FA), c) axial diffusivity (AD), and d) radial diffusivity (RD). The color bar represent the p-value.

Conclusions: In line with a previous report (Mazerolle et al., 2021), this study reports reduced fiber density and microstructural white matter integrity (FA) longitudinally in the CTCT of the treated side. Moreover, increases in AD and RD at 6 months after MRgFUS were found in distal parts of the CTCT of the treated side, suggesting a chronic degeneration leading to axonal damage (Song et al., 2003) or demyelination (Song et al., 2002), respectively.

References

1. Agrawal, M. et al., (2021). Outcome and Complications of MR Guided Focused Ultrasound for Essential Tremor: A Systematic Review and Meta-Analysis. Frontiers in Neurology, 12, 654711.
2. Chazen, J. L. et al., (2018). Clinical improvement associated with targeted interruption of the cerebellothalamic tract following MR-guided focused ultrasound for essential tremor. Journal of Neurosurgery, 129(2), 315–323.
3. Gallay, M. N. et al., (2008). Human pallidothalamic and cerebellothalamic tracts: Anatomical basis for functional stereotactic neurosurgery. Brain Structure & Function, 212(6), 443–463.
4. Giordano, M. et al., (2020). Comparison between deep brain stimulation and magnetic resonance-guided focused ultrasound in the treatment of essential tremor: A systematic review and pooled analysis of functional outcomes. Journal of Neurology, Neurosurgery, and Psychiatry, 91(12), 1270–1278.
5. Mazerolle, E. L. et al., (2021). Diffusion imaging changes in the treated tract following focused ultrasound thalamotomy for tremor. Neuroimage: Reports, 1(1), 100010.
6. Miller, W. K. et al., (2022). Magnetic resonance-guided focused ultrasound treatment for essential tremor shows sustained efficacy: A meta-analysis. Neurosurgical Review, 45(1), 533–544.
7. Pineda-Pardo, J. A. et al., (2019). Microstructural changes of the dentato-rubro-thalamic tract after transcranial MR guided focused ultrasound ablation of the posteroventral VIM in essential tremor. Human Brain Mapping, 40(10), 2933–2942.
8. Pohl, E. D. R. et al., (2022). Coherent Structural and Functional Network Changes after Thalamic Lesions in Essential Tremor. Movement Disorders: Official Journal of the Movement Disorder Society, 37(9), 1924–1929.
9. Rotshenker, S. (2011). Wallerian degeneration: The innate-immune response to traumatic nerve injury. Journal of Neuroinflammation, 8, 109. Sammartino, F. et al., (2019). Longitudinal analysis of structural changes following unilateral focused ultrasound thalamotomy. NeuroImage. Clinical, 22, 101754.
10. Song, S.-K. et al., (2003). Diffusion tensor imaging detects and differentiates axon and myelin degeneration in mouse optic nerve after retinal ischemia. NeuroImage, 20(3), 1714–1722.
11. Song, S.-K. et al., (2002). Dysmyelination revealed through MRI as increased radial (but unchanged axial) diffusion of water. NeuroImage, 17(3), 1429–1436.
12. Zesiewicz, T. A. et al., (2005). Practice parameter: Therapies for essential tremor: report of the Quality Standards. Neurology, 64(12), 08–20

Poster No 37

Multi-channel infrared stimulation on mesoscale cortical units with ultra-high field 7T MRI

Yipeng Liu[1], Feiyan Tian[1,2], Meixuan Chen[1], Anna Roe[1,2,3,4]

[1]Department of Neurosurgery of the Second Affiliated Hospital, Interdisciplinary Institute of Neurosc, Hangzhou, China, [2]College of Biomedical Engineering and Instrument Science, Zhejiang University, Hangzhou, China, [3]MOE Frontier Science Center for Brain Science and Brain-Machine Integration, School of Brain Science and Brain Medicine, Zhejiang University, Hangzhou, China, [4]Key Laboratory for Biomedical Engineering of Ministry of Education, Zhejiang University, Hangzhou, China

Introduction: The cortex of primate is organized by submillimeter functional domains. But little is known about how these coordinated units form a highly organized network on a brain-wide scale. Recently, the use of holographic optogenetics to target multiple brain areas opens up the possibility to modulate cortical information flow with diverse spatiotemporal patterns. Here we develop another patterned illumination method by infrared neural stimulation (INS), which is capable of producing a spatially focal stimulation via heat transients. This effective field is smaller than the column width in cat (~700µm). Combined with BOLD functional MRI in ultrahigh field, coordinated connectivity of the whole-brain can be mapped and further manipulated with patterns.

Methods: Animal preparation Three adult cats were anesthetized with sufentanil and vecutonium bromide and the brain state was examined by a grating visual stimulus. After localized the visual area by structural imaging with reference tubes, a cranial window fitting the size of bundle was opened. Then the bundle tip was attached to the cortical surface. Agar was applied to reduce the artifacts caused by air bubbles. Infrared stimulation Infrared laser was delivered by a solid-state laser generator (CW-1875±10nm) and a pulse modulator (Master-9). Each pulse train consisted of 250µs pulses at 200Hz for 0.5 seconds. Each channel block consisted of 9s stimulation with 3 pulse trains and 9s blank. One piezoelectric switch (Piezosystem) was customized by an Arduino (Mega-2560) to control channel switching. Radiant exposures were calibrated before every experiment (SD within one channel:4.51×10^(-6) J/cm^2; SD between channels: 0.082J/cm^2) and ranged from 0.2 to 0.7J/cm^2 per pulse train. Data acquisition A single-shot echo planar imaging (EPI) sequence (TR=2000ms, TE=17ms, resolution=1×1 mm2, 0.5-mm slice thickness, FA=78°) was acquired in a 7T MR scanner (Siemens Healthcare) with customized 2mm and 3mm surface coils (Suzhou, China). After canonical preprocessing, Fourier coherence analysis and general linear model (GLM) were applied to extract significant activations.

Results: The spatiotemporal feature of local responses depends on the channel distance After validated the tip location (area 18/19) by anatomical registration, we examined the local spatiotemporal feature by alternating pair channels with three distances (0.2, 2, and 3mm). Different components of the hemodynamic response can be distinguished by adjusting the frequency of interest and extracting phase values. Both 2mm- and 3mm- pairs evoked separable channel-specific clusters, whereas 0.2mm-pair had mostly responses of both channels. The channel-specific tuning curves showed alternative negative BOLD dips, indicating the possible surround modulation process. The global activations of pair channels show integration and segregation patterns in diverse areas Significant clusters were extracted by GLM and further categorized by PCA and KNN. The overall network distribution (PMLS, AMLS, 21a, 20a, SVA, 5) was similar to previous anatomical evidences but had variations between patterns. Most ipsilateral area 19 responded to both channels, while only distal areas (area 7a and 5) had separated activations. It might indicate different integrative properties of receptive field along the cortical hierarchy.

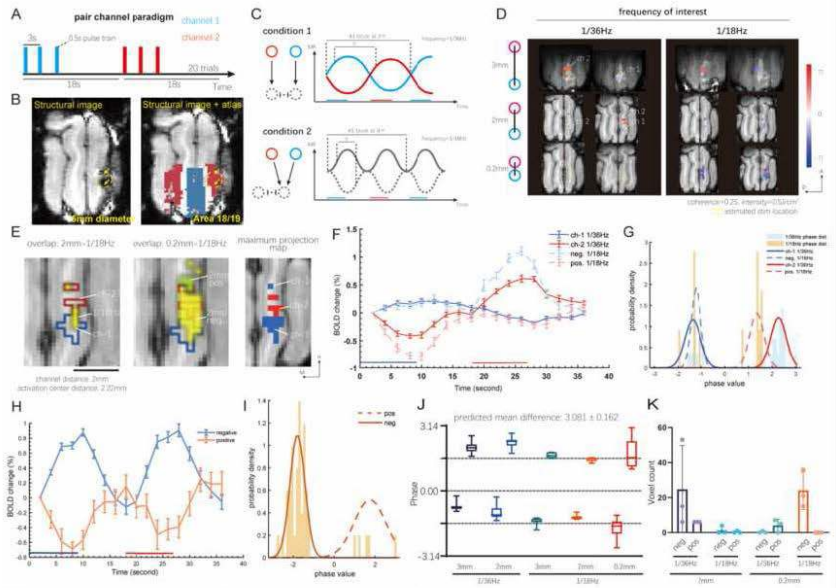

(A) Schematic representation of pair channel stimulation paradigm. Each short line perpendicular to the time axis indicates one 500ms pulse train. Train-to-train interval is 2.5s. Each trail has 2 channel blocks and each channel block contains 9s activation and 9s blank. All activation maps below were calculated based on 3-run average (60 trails). **(B)** Check the tip location by registering atlas to the anatomical image. A small surface defect on the structural image can be used to identify the tip. **(C)** Two possible conditions of local responses. It illustrates that two far channels evoke independent or channel-specific responses; while two close channels have co-activated and co-inhibited responses. Those two conditions are not exclusive for each channel placement but primarily influenced by the effect field of infrared light. **(D)** The overall local activation maps of 3 distances in 2 frequencies of interest under the hypothesis in **(C)**. Both 2mm- and 3mm- pairs evoke channel-specific clusters and also relatively weaker co-influenced responses. However, the 0.2mm-pair has mostly co-influenced response (mostly co-activated). Statistical comparison of the count of significant voxels is in **(K)**. **(E)** In the 2mm-pair case, the co-activation cluster is right at the intersection part of two channel-specific clusters, indicating the overlapping of infrared effect field. **(F-G)** The tuning curves and phase distribution of the 2mm-pair case in 1× and 2× stimuli frequency (1/36Hz and 1/18Hz). **(H-I)** The tuning curves and phase distribution of the 0.2mm-pair case in 2× stimuli frequency (1/18Hz) **(J)** Statistical comparison of the phase values in different distances and frequencies of interest. The phase difference of 1× frequency between channel-specific responses matches the hypothesis in **(C)**, but has a little shift, suggesting the possible lag of BOLD response.

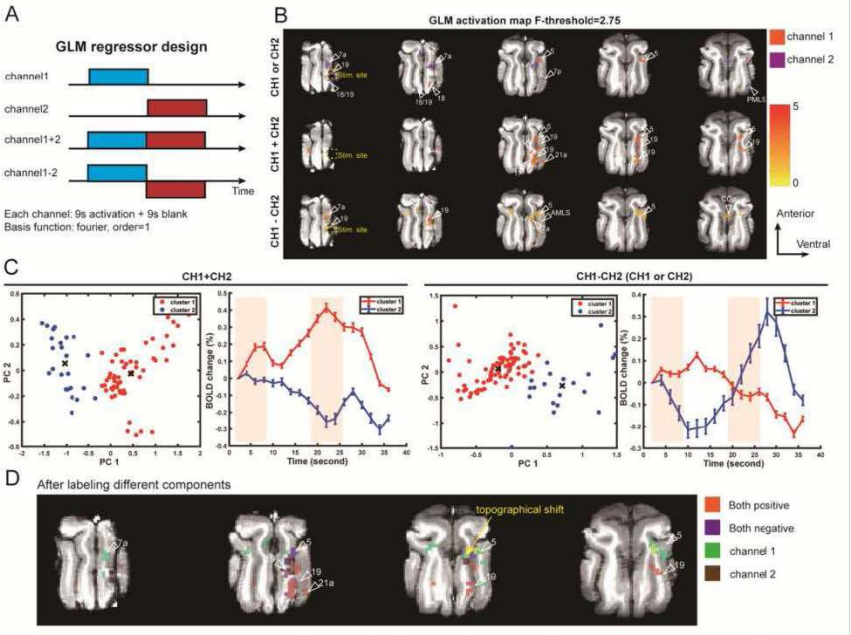

(A) Four regressor designs of the general linear model. The basis function is Fourier at the first order. The channel-1, channel-2 and channel1-2 regressors can all be considered as channel-specific, while the channel1+2 regressor is integrative. Therefore, those 4 regressors can be simplified into 2 main groups for the following distinguishment **(B)** The overall activation maps of 4 regressors. **(C)** Principal component analysis (PCA) is applied to the time series of channel-specific and integrative groups for dimension reduction. K-nearest neighbor (KNN) clustering then is applied to the first four main components. As the tuning curves show, channel-specific and integrated voxels are identified. **(D)** By further observing the distribution of different groups, we found most integrated responses in the ipsilateral area 19. And more channel-specific responses in intra-areal connections including 7a and area 5. Topographical shifting is found in area 19 and neighboring areas (7a).

Conclusions: We developed a multi-channel infrared-fMRI system and demonstrated its feasibility of producing mesoscale stimulus with varying channel spacing and mapping static networks of two separated points. The overall network with separable channel-specific clusters suggests the possible coordinated columnar structure across the whole brain. And the network variability across the hierarchy indicates that, similar to the structural architecture, a regularity of functional connectivity at the mesoscale might exist.

References

1. Alessandra Angelucci (2017),"Circuits and Mechanisms for Surround Modulation in Visual Cortex," Annual Review of Neuroscience
2. Augix Guohua Xu (2019), "Focal Infrared Neural Stimulation with High-Field Functional MRI: A Rapid Way to Map Mesoscale Brain Connectomes,"Science Advances
3. David Eriksson (2022), "Multichannel Optogenetics Combined with Laminar Recordings for Ultra-Controlled Neuronal Interrogation," Nature Communications
4. Giulia Faini (2023), "Ultrafast Light Targeting for High-Throughput Precise Control of Neuronal Networks," Nature Communications
5. Jin Hyung Lee (2010), "Global and Local fMRI Signals Driven by Neurons Defined Optogenetically by Type and Wiring," Nature
6. Joseph M. Stujenske (2015), "Modeling the Spatiotemporal Dynamics of Light and Heat Propagation for In Vivo Optogenetics," Cell Reports
7. Jw Scannell (1995), "Analysis of Connectivity in the Cat Cerebral Cortex," The Journal of Neuroscience
8. Jonathon D. Wells (2005), "Application of Infrared Light for in Vivo Neural Stimulation," Journal of Biomedical Optics
9. Kaushik Ghose (2012), "A Strong Constraint to the Joint Processing of Pairs of Cortical Signals," Journal of Neuroscience
10. Lingyan Shi (2016), "Transmission in Near-Infrared Optical Windows for Deep Brain Imaging," Journal of Biophotonics
11. Mykyta Mikhailovich Chernov (2014), "Histological Assessment of Thermal Damage in the Brain Following Infrared Neural Stimulation," Brain Stimulation
12. Mykyta M. Chernov (2021), "Fiberoptic Array for Multiple Channel Infrared Neural Stimulation of the Brain," Neurophotonics
13. Nikola T. Markov (2013), "The Role of Long-Range Connections on the Specificity of the Macaque Interareal Cortical Network," Proceedings of the National Academy of Sciences
14. Ricardo Gattass (2005), "Cortical Visual Areas in Monkeys: Location, Topography, Connections, Columns, Plasticity and Cortical Dynamics," Philosophical Transactions of the Royal Society of London. Series B, Biological Sciences
15. S. Chenchal Rao (1997), "Optically Imaged Maps of Orientation Preference in Primary Visual Cortex of Cats and Ferrets," Journal of Comparative Neurology
16. Younghoon Shin (2016), "Mesh-Based Monte Carlo Method for Fibre-Optic Optogenetic Neural Stimulation with Direct Photon Flux Recording Strategy," Physics in Medicine and Biology

Poster No 38

Subthreshold Depression Affects EEG Network Patterns in Spatial Cognition Process

Kai Yang[1], Yidong Hu[1], Ying Zeng[1], Li Tong[1], Bin Yan[1]

[1]Strategic Support Force Information Engineering University, Zheng Zhou, He Nan, China

Introduction: Subthreshold depression (StD) refers to clinically relevant depressive symptoms that do not meet the criteria for depression (Hwang et al. 2016). Many studies have reported cognitive impairments in individuals with StD. Especially, spatial cognition impairment can have a severe impact on the StD individuals' ability to judge distance and orientation in daily life (Volz et al. 2022). However, the patterns of neural activity during spatial cognition processes in individuals with StD remain unclear. To explore the impact patterns of StD on spatial cognition, our study designed a spatial cognition experiment that mimics a natural scene and analyzed the EEG networks during both resting and task states.

Methods: According to the definition of StD in previous studies (Volz et al. 2022), this work screened 15 StD and 15 healthy control (HC) subjects each through interviews, the Center for Epidemiological Studies Depression Scale (CES-D, Chinese version) and Beck Depression Inventory-II (BDI-II) scale. The experiment included a 2 minutes eyes-closed resting state (RS) stage and 16 simulated robotic arm docking tasks. The docking tasks were close to natural scenes to induce the spatial cognition of subjects. The EEG data were recorded by 62 channels G.HIamp system and the operation details were recorded through screen recording software. Then each docking process was divided into four stages: observation stage, large-scale movement (LM) stage, fine operation (FO) stage and docking stage, the operation time of each stage were got by offline analysis of screen recording videos. The main steps of EEG preprocessing include: data segmentation, average reference, 1-60Hz filtering, artifact removal, baseline correction, trial rejection (>100μv). Then the preprocessed EEG data were filtered into five frequency bands: delta (1-4Hz), theta (4-8Hz), alpha (8-13Hz), beta (13-30Hz), and gamma (30-50Hz). In each frequency band, the phase locking values of every two EEG channels were calculated, and there were five 62*62 network matrixes. At the end, networks of StD group and HC group were compared by t-test.

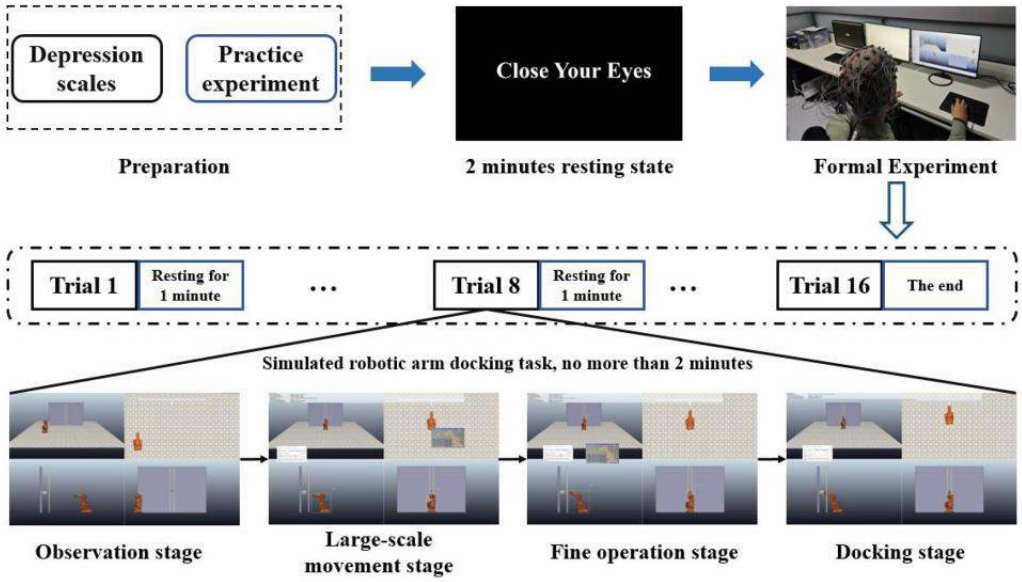

Results: The results of operation time showed that StD group spent significantly more time than HC group ($P<0.05$) in LM stage and FO stage while completing the docking task. The longer operation time of the StD group validated the spatial cognition impairment of StD subjects in previous studies. Then, this study focused on analyzing brain networks of RS stage, LM stage and FO stage. For the RS stage, in the theta and alpha bands, the HC group had stronger connections with the channels in parietal lobe as hub nodes compared to the StD group. Parietal lobe was related to spatial attention, the differential connections in RS stage may indicate that the StD caused spatial attention decline (Aleksandra et al. 2023). For LM and FO task stages, in the delta, beta and gamma bands, the frontoparietal connections of StD group were stronger than those of HC group. These enhanced frontoparietal connections may be neural compensation made by the StD group to complete spatial cognition task (Vallesi et al. 2011; Caldinelli et al. 2022). In the whole, network patterns of RS stage indicated the spatial cognition decline of StD group, and the enhanced frontoparietal connections in LM and FO task stages, possibly indicated the neural compensation mechanism of StD group to ensure spatial cognition task completion.

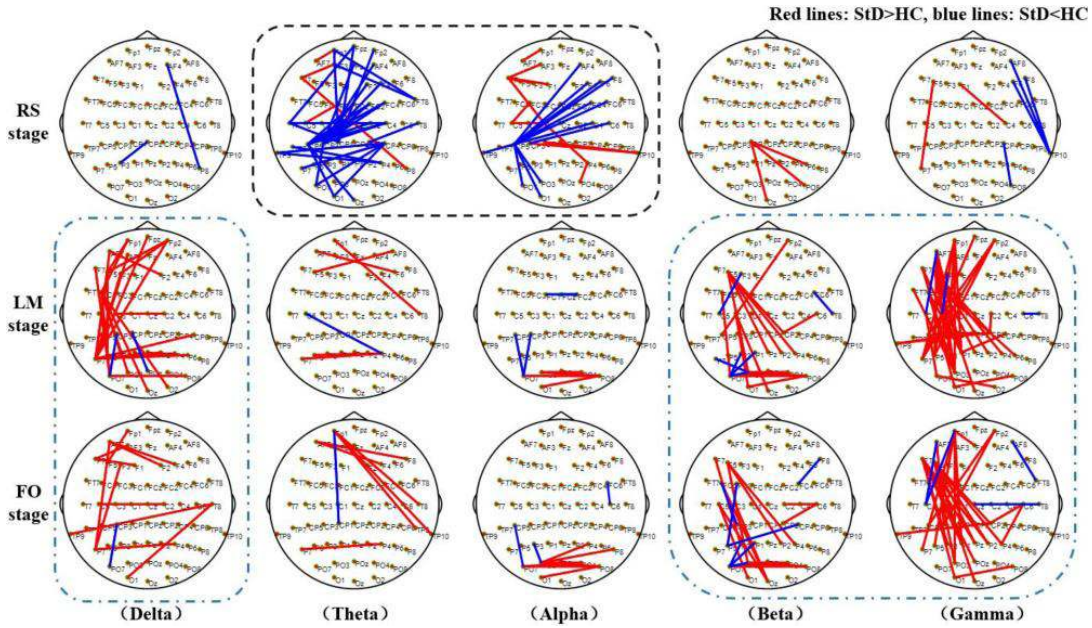

Conclusions: This study analyzed the impacts of StD on spatial cognition based on resting and task state EEG networks. Consistent with previous studies, behavioral results and RS network patterns indicated that StD can lead to spatial cognition decline. At the same time, there was neural compensation mechanism of StD group by enhancing frontoparietal connections to ensure the completion of spatial cognition tasks. This study provides new insights into the impact of StD on spatial cognition.

References
1. J.W. Hwang.(2016),'Enhanced default mode network connectivity with ventral striatum in subthreshold depression individuals',Journal of Psychiatric Research,vol. 76, no. 2, pp. 111-120.
2. Volz, Hans Peter. (2022), 'Subthreshold depression - concept, operationalisation and epidemiological data A scoping review', International Journal of Psychiatry in Clinical Practice, vol. 27, no. 1, pp. 92-106.
3. Aleksandra Miljevic. (2023). 'Perera Alterations in EEG Functional Connectivity in Individuals with Depression: A Systematic Review', Journal of Affective Disorders, vol.328, no. 1, pp. 287-302.
4. Vallesi, Antonino(2011). 'Right fronto-parietal involvement in monitoring spatial trajectories', Neuroimage, vol.57vol.2,pp.558-564.
5. Caldinelli C (2022).'The fronto-parietal network is not a flexible hub during naturalistic cognition'. Human Brain Mapping, vol.43 vol.2,pp.750-759.

Poster No 39

Non-invasive Electrical Brain Stimulation with a Phase lag: a fMRI Study

Jeehye Seo[1], Jehyeop Lee[1], Yukyung Kim[1], Je-Choon Park[1], Jeongwook Kwon[1], Byoung-Kyong Min[1]

[1]Korea University, Seoul, NA

Introduction: Working memory is a cognitive function crucial for a wide range of everyday tasks, including problem-solving, decision-making, and learning. Recent advances in non-invasive brain stimulation techniques have offered a promising avenue for investigating the neural mechanisms underlying working memory and its modulation. Specifically, transcranial alternating current stimulation (tACS) is one of the efficient neuromodulation techniques to improve cognitive abilities non-invasively. This study aimed to examine the effects of non-invasive electrical brain stimulation using tACS, coupled with phase modulation between the central executive network (CEN) and default mode network (DMN), on working-memory performance using functional magnetic resonance imaging (fMRI).

Methods: Twenty-six healthy adult participants were recruited for this study. We conducted an fMRI experiment to investigate whether a cross-frequency coupled tACS protocol with a phase lag (45 and 180 degree) between CEN and DMN modulated working-memory performance. Participants performed the Sternberg working-memory task with tACS during the entire 9-s retention period of every trial. High-resolution structural and functional MRI scans were obtained to measure the blood-oxygen-level-dependent (BOLD) response during task performance. BOLD signal changes were analyzed to assess functional connectivity within the CEN and DMN and their interaction with task-related activation.

Results: We found that the phase lag between the CEN and DMN during tACS modulates working-memory performance. We observed that the 180-phase-lag tACS condition in the fast group showed a significant increase in reaction times. Additionally, the right hippocampus was significantly more activated in the 180-phase-lag tACS condition. Functional connectivity analyses revealed altered network interactions under these two different phase lags between the CEN and DMN.

Conclusions: Our findings suggest that non-invasive electrical brain stimulation, with phase modulation between the CEN and DMN, can effectively enhance working-memory performance. These results shed light on the potential for targeted neuromodulation techniques to optimize cognitive function and may have implications for the development of interventions aimed at improving working-memory abilities. Further investigations are warranted to elucidate the precise neural mechanisms underlying these effects.

Poster No 40

Optimizing Multi-Channel tES to Improve Robustness to Electrode Displacement: A Simulation Study

Sangwoo Lee[1], Jaehoon Jeong[1], Chang-Hwan Im[1]

[1]Hanyang University, Seoul, Seoul

Introduction: In the conventional transcranial electrical stimulation (tES) with a pair of electrodes, small drift of electrode locations could alter the pattern of electric field inside the brain[1]. In this paper, we hypothesized that the similar problem might arise when a commercialized tES system with multiple electrodes mounted on an elastic cap is used. Therefore, the influence of the electrode displacement on the electric field was investigated. In addition, a new optimization method considering the possible displacements of the electrodes was proposed to improve the robustness to the electrode displacement during the repeated use of the tES system.

Methods: A digitizer is used to estimate the average displacement of electrodes during repeated self-wearing of the electrode cap. Ten participants tried on a cap by themselves a total of 25 times. We generated five models for finite element method

(FEM) based on the electrode locations of the international 10-10 EEG system: the original location, forward shift, backward shift, rightward shift, and leftward shift. Left hand motor cortex (HM), right intraparietal sulcus (IPS), left dorsolateral prefrontal cortex (DLPFC), and visual cortex (VC) were set as the regions of interest (ROIs). We optimized the input current distributions for each of the five electrode locations using the FEM-based field simulation and the least squares algorithm to best modulate the designated ROIs. We then generated a new current distribution by averaging the five optimization results. We compared how the intensity of electric field (from the mean value within the ROI) and the focality of electric field (from the maximum value outside the ROI divided by the minimum value within the ROI) decreased when the electrode locations were shifted.

Results: The average displacement of electrodes was 1.08 cm, based on which the electrode locations were shifted. Our method showed higher intensity and focality in all ROIs, exhibiting the superiority of the proposed method.

Table: Performance comparison between conventional and new optimization methods

	Ratio of intensity to original location of the channels (%)		Ratio of focality to original location of the channels (%)	
	Conventional optimization	New optimization	Conventional optimization	New optimization
Left HM	80.41	83.45	72.26	77.81
Right IPS	79.90	82.62	54.10	57.60
Left DLPFC	90.52	91.88	74.53	80.13
VC	87.45	87.90	81.96	88.51
Average	84.57	**86.46**	70.71	**76.01**

HM: hand motor cortex / IPS: intraparietal sulcus / DLPFC: dorsolateral prefrontal cortex / VC: visual cortex

Conclusions: In this study, we improved the robustness of tES to the electrode shift by employing a new optimization method that averages optimization results for five FEM models with different electrode displacements. It is expected that the proposed optimization method can be a useful tool to improve the robustness and reliability of tES in practical scenarios.

References

1. Woods, A. J. (2015), 'Effects of electrode drift in transcranial direct current stimulation.' Brain stimulation, 8(3), 515-519.

Poster No 41

Electroconvulsive therapy regulates brain connectome dynamics in major depressive disorder

Yuanyuan Guo[1], Mingrui Xia[2], Rong Ye[3], Tongjian Bai[1], Yue Wu[4], Yang Ji[1], Yue Yu[1], Gongjun Ji[3], Kai Wang[1], Yong He[2], Yanghua Tian[4]

[1]The First Affiliated Hospital of Anhui Medical University, Hefei, Anhui, [2]Beijing Key Laboratory of Brain Imaging and Connectomics, Beijing Normal University, Beijing, [3]School of Mental Health and Psychological Sciences, Anhui Medical University, Hefei, Anhui, [4]The Second Affiliated Hospital of Anhui Medical University, Hefei, Anhui

Introduction: Major depressive disorder (MDD) is a common and severe affective disorder characterized by negative mood and high risk of suicide. Electroconvulsive therapy (ECT) is an effective treatment for MDD patients, but its underlying neural mechanisms remain largely unknown. The aim of this study was to identify changes in brain connectome dynamics after ECT in MDD and to explore their associations with treatment outcome.

Methods: We collected longitudinal resting-state fMRI data from 80 MDD patients (50 with suicidal ideation and 30 without; SI and NSI, respectively) before and after ECT and 37 age- and sex-matched healthy controls. A multilayer network model was used to assess modular switching over time in functional connectomes. Repeated measures analysis of variance was applied to assess differences in dependent variables (network dynamics) with group (MDD vs. healthy controls and MDD-SI vs. MDD-NSI) and time (before vs. after ECT) served as the independent variables. Post-hoc analyses were also performed using a two-sample t-test between groups and paired t-test between times. Support vector regression was used to assess whether pre-ECT network dynamics could predict treatment response in terms of symptom severity.

Results: Analysis of global modularity ($F = 7.25$, $p = 0.008$, $\eta p2 = 0.06$) and modular variability ($F = 8.80$, $p = 0.004$, $\eta p2 = 0.07$) both revealed significant group-by-time interaction effects. Post-hoc analysis showed that MDD patients had lower global modularity ($t = -4.33$, $p < 0.001$, Cohen's $d = -0.86$) and higher modular variability ($t = 1.99$, $p = 0.049$, Cohen's $d = 0.45$) in functional connectomes compared to controls at baseline. ECT enhanced global modularity ($t = 2.94$, $p = 0.004$, Cohen's $d = 0.47$) and reduced variability ($t = -4.18$, $p < 0.001$, Cohen's $d = -0.61$) in MDD patients. Analysis of regional modular variability

revealed a significant group-by-time interaction effect predominantly located in the default mode and somatomotor networks (all F > 7.76, p < 0.006, FDR corrected). Post-hoc analysis showed that modular variability was significantly lower after ECT in those regions in MDD patients (all t < -2.60, p < 0.011, FDR corrected). Support vector regression analysis showed pre-ECT modular variability could accurately predict symptom improvement in MDD patients (r = 0.315, p = 0.004, 1,000 permutation tests). In suicidal ideation subgroup analysis, ECT was associated with decreased modular variability in the left dorsal anterior cingulate cortex of MDD-SI (t = -4.33, p < 0.001, Cohen's d = -0.38), but not MDD-NSI (t = 0.975, p =0.338, Cohen's d = 0.21) patients, and pre-ECT modular variability could accurately predict symptom improvement in the MDD-SI group (r = 0.295, p = 0.039, 1,000 permutation tests), but not in the MDD-NSI group.

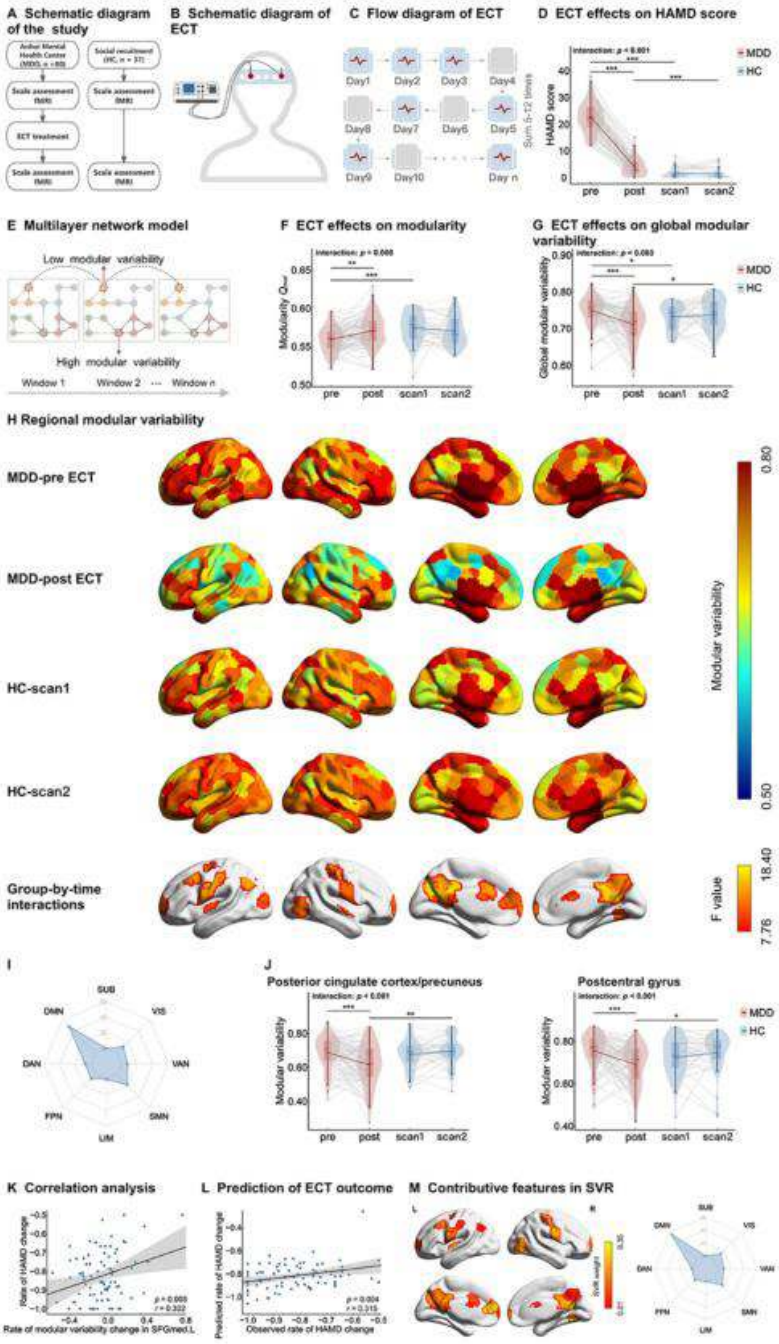

Figure 1. ECT effects on clinical symptom and brain dynamics in MDD patients. A. Schematic illustration of the study. **B.** Schematic illustration of ECT. **C.** Flow illustration of ECT. **D.** Comparison of HAMD score between MDD and HC group at two scans. **E.** Schematic illustration of the multilayer network model and nodal modular variability. **F.** Comparison of global modularity between MDD and HC group at two scans. **G.** Comparison of global modular variability between MDD and HC group at two scans. **H.** Comparison of regional modular variability between MDD and HC group at two scans. The first two panels show the group-level modular variability maps for MDD before and after ECT. The third and fourth panels show the group-level modular variability maps for HC at scan1 and scan2. The lower panel shows regions with significant interaction effects in modular variability between MDD and HC group based on ECT (p < 0.05, FDR corrected). **I.** Proportion of regions with significantly interaction effects in modular variability in each functional system. **J.** Plot of post-hoc results of two typical regions. **K.** Significant positive correlation between decreased rate of HAMD change and modular variability change in SFGmed.L in MDD patients after ECT. **L.** The correlation between the observed rate of HAMD change after ECT and the predicted rate of HAMD change in MDD patients derived from the SVR analysis. **M.** Left: The absolute summed weights in five-fold cross-validation were mapped onto the brain surface. Right: The distribution of predictive power in different systems (MDD group). (*, p < 0.05; **, p < 0.01; ***, p < 0.001).

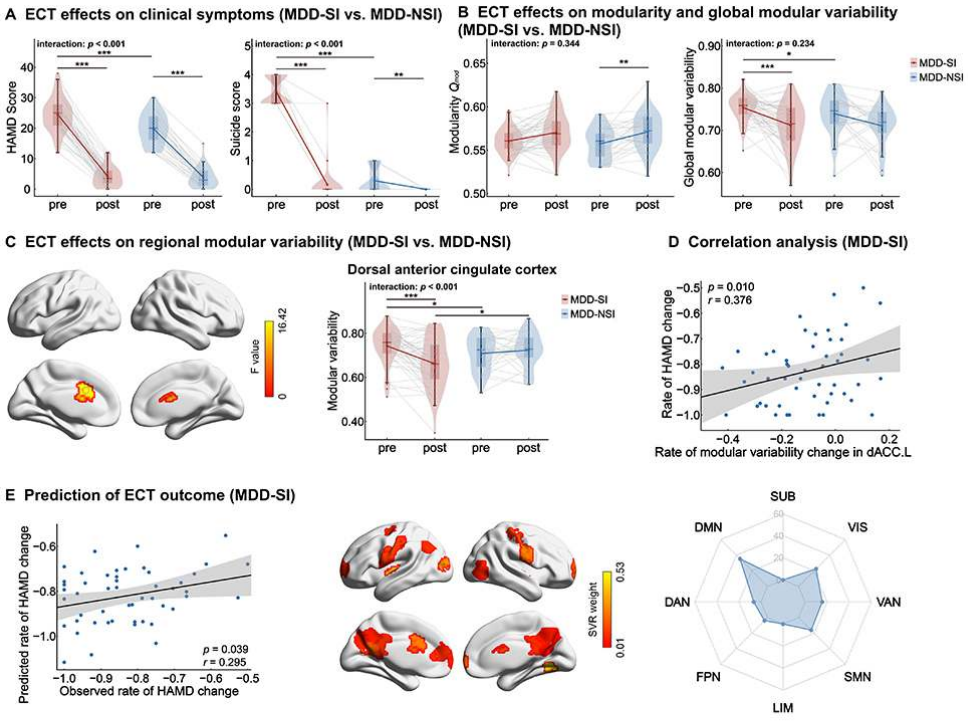

Figure 2. Suicidal ideation subgroup analysis. A. left: Comparison of HAMD score between MDD-SI and MDD-NSI group based on ECT; right: Comparison of suicide score between MDD-SI and MDD-NSI group based on ECT. **B.** left: Comparison of global modularity between MDD-SI and MDD-NSI group based on ECT; right: Comparison of global modular variability between MDD-SI and MDD-NSI group based on ECT. **C.** Spatial distribution of region showing significant interaction effects in modular variability between MDD-SI and MDD-NSI based on ECT. The post-hoc result was showed on the right side of the brain map ($p < 0.05$, FDR corrected). **D.** Significant positive correlation between decreased rate of HAMD change and modular variability change in dACC.L in MDD-SI patients after ECT. **E.** Left: The correlation between the observed rate of HAMD change after ECT and the predicted rate of HAMD change in MDD-SI patients derived from the SVR analysis. Middle: The absolute summed weights in five-fold cross-validation were mapped onto the brain surface. Right: The distribution of predictive power in different systems (MDD-SI group). (*, $p < 0.05$; **, $p < 0.01$; ***, $p < 0.001$).

Conclusions: We highlight ECT-induced changes in MDD brain network dynamics and their predictive value for treatment outcome, particularly in patients with suicidal ideation. This study advances our understanding of the neural mechanisms of ECT from a dynamic brain network perspective and suggests potential prognostic biomarkers for predicting ECT efficacy in patients with MDD.

References

1. A. Takamiya. (2021), 'Neuronal network mechanisms associated with depressive symptom improvement following electroconvulsive therapy', Psychological Medicine, vol. 51, no. 16, pp. 2856–2863.
2. C. Kraus. (2019), 'Prognosis and improved outcomes in major depression: a review', Translational Psychiatry, vol. 9, no. 1, p. 127.
3. J. Li. (2019), 'More than just statics: Temporal dynamics of intrinsic brain activity predicts the suicidal ideation in depressed patients', Psychological Medicine, vol. 49, no. 5, pp. 852–860.
4. J. P. Hamilton. (2011), 'Default-Mode and Task-Positive Network Activity in Major Depressive Disorder: Implications for Adaptive and Maladaptive Rumination', Biological Psychiatry, vol. 70, no. 4, pp. 327–333.
5. P. J. Mucha. (2010), 'Community structure in time-dependent, multiscale, and multiplex networks', Science, vol. 328, no. 5980, pp. 876–878.
6. S. Moussavi. (2007), 'Depression, chronic diseases, and decrements in health: results from the World Health Surveys', Lancet, vol. 370, no. 9590, pp. 851–858.
7. T. Reisch. (2010), 'An fMRI study on mental pain and suicidal behavior', Journal of Affective Disorders, vol. 126, no. 1–2, pp. 321–325.
8. X. Liao. (2017), 'Individual differences and time-varying features of modular brain architecture', Neuroimage, vol. 152, no. February, pp. 94–107.
9. X. Liu. (2021), 'Disrupted rich-club network organization and individualized identification of patients with major depressive disorder,' Progress in Neuro-Psychopharmacology and Biological Psychiatry, vol. 108, no. 338, p. 110074.

Poster No 42

Differences in tDCS-induced E-fields according to Alzheimer's disease and gender: An in-silico study

Chae-Bin Song[1], Cheolki Lim[2], Jongseung Lee[1], Donghyeon Kim[1], Hyeon Seo[3]

[1]NEUROPHET Inc, Seoul, Republic of Korea, [2]Gwangju Institute of Science and Technology, Gwangju, Republic of Korea, [3]Gyeongsang National University, Gyeongsangnam-do, Republic of Korea

Introduction: Alzheimer's disease is considered the most common cause of dementia[1]. Several studies reported that transcranial direct current stimulation (tDCS) could help improve cognition for patients with Alzheimer's disease (AD)[2]. Previous studies used the same montage for AD and cognitively normal individuals (CN). However, anatomical differences for individuals due to brain atrophy affect the flow of tDCS-induced current[3]. Therefore, conventional montages might not sufficiently stimulate the target area of AD. In this study, we investigated tDCS effect for both AD and CN focused on the electric field intensities within each brain region when using the same montages through simulation.

Methods: We used 180 T1-weighted magnetic resonance images (MRIs) from Alzheimer Disease Neuroimaging Initiative (ADNI) dataset[4] for four groups (AD-females, AD-males, CN-females, CN-males). We made no statistical differences in age distribution across groups. An anatomical head model was constructed based on each MRI. We segmented the models into gray matter (GM), white matter (WM), scalp, skull, CSF, and ventricles through our deep learning-based brain segmentation models[5,6]. We divided GM into 68 regions based on the function of each brain region. The mesh generation was performed using CGAL version 4.0[7]. CGAL generated segmented MRI data into 3D tetrahedral mesh based on the Delaunay triangulation method. The electrical potential induced by tDCS was determined according to the transformed Maxwell equation in static conditions and boundary conditions[8]. We used the Eigen library as a solver to calculate the tDCS-induced electric field. We assigned electrical conductivities of each region in units of S/m (GM 0.276; WM 0.126; scalp 0.465; skull 0.01; CSF 1.65; ventricles 1.65). We located electrodes in F3-Fp2 to stimulate the left rostral middle frontal gyrus (RMF) associated with cognitions. The maximum current was analyzed through the 90th percentile to minimize errors. We analyzed statistical differences in the tDCS-induced electric field between AD and CN for each brain region. For statistical analysis, we used the parametric unpaired t-test. A p-value of less than 0.05 was considered statistically significant.

Results: In all regions, the male group showed significantly lower electric field intensities than the female group regardless of disease. The electric field intensity within the ventricle was significantly higher in CN-males than in AD-males. Among the 68 subdivided regions of GM, we focused on the electric field intensities within 14 brain regions associated with cognitions (both sides of RMF, the superior temporal gyrus, the middle temporal gyrus, the inferior temporal gyrus, the insula, the parahippocampal cortex, and the entorhinal cortex) as shown in fig. 1. In females, there were no significant differences between AD and CN. AD-males showed significantly smaller intensities within the left/right superior temporal gyrus, the left/right middle temporal gyrus, and the left insula than CN-males.

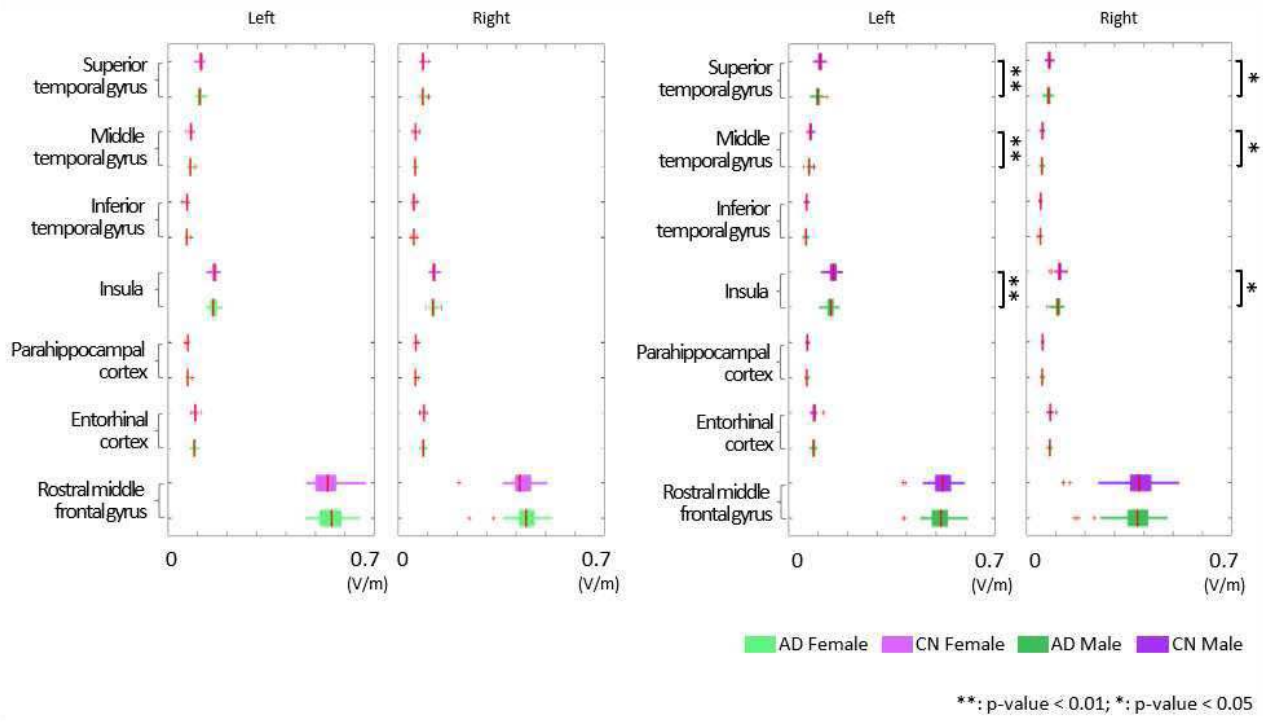

Conclusions: We could not observe significant differences in the target area between AD and CN. However, it is well known by previous studies that not only one specific brain region but also other all anatomical characteristics affect current flows[9]. Our results showed that some regions were significantly different in the electric field intensities between AD and CN while others did not. It might be necessary to consider all brain regions that affect the electric field distribution for improving the stimulation effect. Also, the AD showed lower electric field intensities in subdivided GM regions than the CN even if not at a

statistically significant level . It might be interpreted that stimulating the target area for AD when using the same montages for CN is difficult due to complex factors such as brain atrophy. We propose that montage optimization that considers anatomical variations and brain atrophy might lead to improvement of tDCS effects.

References

1. Coupé, P., Fonov, V. S., Bernard, C., Zandifar, A., Eskildsen, S. F., Helmer, C., Manjon, J. V., Ameiva, H., Dartiques, J.-F., Allard, M., Catheline, G., Collins, D. L. and The Alzheimer's Disease Neuroimaging Initiative. (2015), "Detection of Alzheimer's disease signature in MR images seven years before conversion to dementia: Towards an early individual prognosis,' Human Brain Mapping, vol. 36, pp. 4758-4770.
2. Cammisuli, D. M., Cignoni, F., Ceravolo, R., Bonuccelli, U., and Castelnuovo, G. (2022). 'Transcranial direct current stimulation (tDCS) as a useful rehabilitation strategy to improve cognition in patients with Alzheimer's disease and Parkinson's disease: An updated systematic review of randomized controlled trials', Frontiers in Neurology, vol. 12.
3. Rasmussen, I. D., Mittner, M., Boayue, N. M., Csifcsák, G., and Aslaksen, P. M. (2023), 'Tracking the current in the Alzheimer's brain – Systematic differences between patients and healthy controls in the electric field induced by tDCS', Neuroimage: Reports, vol. 3.
4. Mueller, S.G., Weiner, M.W., Thal, L.J., Petersen, R.C., Jack, C., Jagust, W., Trojanowski, J.Q., Toga, A.W., Beckett, L. (2005), 'The Alzheimer's Disease Neuroimaging Initiative', Neuroimaging Clinics of North America, vol. 15, no. 4, pp. 869–877.
5. Lee, M., Kim, J., Kim, R. E. Y., Kim, H. G., Oh, S. W., Lee, M. K., Wang, S.-M., Kim, N.-Y., Kang, D. W., Rieu, Z., Yong, J. H., Kim, D., and Lim, H. K. (2020), 'Split-attention u-net: A fully convolutional network for robust multi-label segmentation from brain mri', Brain Sciences, vol. 10, no. 12, pp. 1–22.
6. Kim, R. E. Y., Lee, M., Kang, D. W., Wang, S.-M., Kim, N.-Y., Lee, M. K., Lim, H. K., and Kim, D. (2021), 'Deep learning-based segmentation to establish east asian normative volumes using multisite structural MRI," Diagnostics, vol. 11, no. 1, pp. 13.
7. Alliez, P., Rineau, L., Tayeb, S., (2017), '3D Mesh Generation: CGAL User and Reference Manual', CGAL Editorial Board.
8. Plonsey, R., Heppner, DB. (1967), 'Considerations of quasi-stationarity in electrophysiological systems', The Bulletin of mathematical biophysics, vol. 29, pp. 657-64.
9. Unal, G., Ficek, B., Webster, K., Shahabuddin, S., Truong, D., Hampstead, B., Bikson, M., and Tsapkini, K. (2020), 'Impact of brain atrophy on tDCS and HD-tDCS current flow: a modeling study in three variations of primary progressive aphasia', Neurological Sciences, vol. 41, pp. 1781-1789.

Poster No 43

HD-tDCS effects on response inhibition in chronic tobacco users – Electric field simulations

Dario Müller[1], Ute Habel[2], Carmen Weidler[1]

[1]University Hospital Aachen, Aachen, NRW, [2]Department of Psychiatry, Psychotherapy and Psychosomatics, RWTH Aachen University Hospital, Aachen, North Rhine-Westphalia

Introduction: High impulsivity significantly contributes to the likelihood of substance use, relapse rates, and risky behavior. Consequently, interventions to improve impulsivity are highly warranted. High-definition transcranial direct current stimulation (HD-tDCS), a non-invasive brain stimulation technique altering cortical excitability, stands as a powerful tool to modulate brain activation associated with impulsivity. However, previous research has produced inconclusive results regarding stimulation effects on impulsivity. Findings suggest that inter-individual differences in the electric field created by HD-tDCS can partially explain variance in behavioral outcomes[1], as well as functional brain connectivity[2]. Due to the heightened sensitivity of HD-tDCS to individual brain architecture[3], these differences may exert more pronounced influences on outcomes compared to conventional tDCS. Furthermore, literature suggests that nicotine interacts with the effects of tDCS because both affect calcium channel signaling[4]. This study investigates the effects of HD-tDCS on response inhibition in smokers and non-smokers, aiming to understand the underlying mechanisms better and delineate factors influencing responsiveness to (HD-)tDCS.

Methods: In a double-blind, placebo-controlled, between-subjects study employing simultaneous HD-tDCS and functional magnetic resonance imaging (fMRI), we recruited forty-five male chronic tobacco users and forty-five non-smoking male participants. Participants performed the Stop Signal Task before and after receiving either sham tDCS or 20 minutes of 1.5mA anodal HD-tDCS over the right inferior frontal gyrus during resting state fMRI. Carbon monoxide (CO) levels were assessed in chronic tobacco users as a measure of nicotine intake. Using T1 and T2 weighted anatomical images, individual head meshes were created with CHARM[5]. Electric field simulations were computed using SimNIBS[6]. Within the right inferior frontal gyrus, the mean electric field magnitude within a 5mm radius sphere was computed for each participant.

Results: Behavioral data revealed significant improvements in Stop Signal Reaction Times (SSRTs) following active and sham stimulation in non-smoking participants. Chronic tobacco users showed improved SSRTs following sham but not active stimulation. While CO levels did not influence tDCS effects, lower CO levels were associated with shorter SSRTs. Results also highlighted significant variability in HD-tDCS-induced electric fields. Seed-to-voxel analysis indicated increased resting-state functional connectivity (rsFC) under the anode, particularly to the left prefrontal cortex, in active compared to sham stimulation during initial stimulation periods and post-stimulation. These effects were driven by rsFC fluctuations in the sham group, while

the active group remained stable. Additionally, an effect of e-field magnitude was found, with a higher magnitude correlating with increased rsFC during the first part of the stimulation.

Conclusions: Collectively, our findings suggest that enhanced SSRTs are primarily attributed to a training effect rather than being influenced by HD-tDCS. This contradicts many studies using conventional tDCS setups reporting improved response inhibition following anodal prefrontal tDCS. In chronic tobacco users, anodal HD-tDCS even seems to suppress the training effect. Additionally, considering the high variability of electric fields, our study highlights the importance of taking individual differences into account when assessing the impact of HD-tDCS, urging further investigation in this domain.

References

1. Albizu, A., Fang, R., Indahlastari, A., O'Shea, A., Stolte, S. E., See, K. B., ... & Woods, A. J. (2020). Machine learning and individual variability in electric field characteristics predict tDCS treatment response. Brain stimulation, 13(6), 1753-1764.
2. Abellaneda-Pérez, K., Vaqué-Alcázar, L., Perellón-Alfonso, R., Solé-Padullés, C., Bargalló, N., Salvador, R., ... & Bartrés-Faz, D. (2020). Multifocal tDCS modulates resting-state functional connectivity in older adults depending on induced electric field and baseline connectivity. bioRxiv.
3. Mikkonen M, Laakso I, Tanaka S, Hirata A. Cost of focality in TDCS: Interindividual variability in electric fields. Brain Stimul. 2020;13(1):117-124. doi:10.1016/j.brs.2019.09.017
4. Grundey, J., Barlay, J., Batsikadze, G., Kuo, M. F., Paulus, W., & Nitsche, M. (2018). Nicotine modulates human brain plasticity via calcium-dependent mechanisms. The Journal of physiology, 596(22), 5429-5441.
5. Puonti, O., Van Leemput, K., Saturnino, G. B., Siebner, H. R., Madsen, K. H., & Thielscher, A. (2020). Accurate and robust whole-head segmentation from magnetic resonance images for individualized head modeling. Neuroimage, 219, 117044.
6. Thielscher, A., Antunes, A., & Saturnino, G. B. (2015, August). Field modeling for transcranial magnetic stimulation: A useful tool to understand the physiological effects of TMS?. In 2015 37th annual

Poster No 44

TDCS over VLPFC increases reward sensitivity in a two-armed bandit task

Ashley Yttredahl[1], David Smith[2], Bart Krekelberg[1]

[1]Rutgers University - Newark, Newark, NJ, [2]Temple University, Philadelphia, PA

Introduction: Dysfunctional reward processing is a transdiagnostic characteristic of several psychiatric disorders. For example, patients with depression (Vrieze et al., 2013) and schizophrenia (Weiler et al., 2009) can present with impaired probabilistic reward learning, and increased sensitivity to reward has been observed in patients with substance use disorders (Myers et al., 2016) and during manic episodes in patients with bipolar disorder (Pizzagalli et al., 2008). There is growing clinical interest in the use of noninvasive neuromodulation, such as transcranial direct current stimulation (tDCS) for targeting symptoms such as anhedonia. The right ventrolateral prefrontal cortex plays a critical role in probabilistic reward learning (Rudebeck et al., 2017). We hypothesized that anodal tDCS over right ventrolateral prefrontal cortex would result in increased reward sensitivity during a probabilistic reward learning task – the two-armed bandit.

Methods: Thirty healthy participants underwent anodal, cathodal, and sham tDCS in a counterbalanced, block design over two sessions using a four-electrode center-surround montage over right ventrolateral prefrontal cortex. During stimulation, electrical current at the center electrode was ramped up to 2mA (anodal tDCS) or down to -2mA (cathodal tDCS) over 30 seconds, and sustained for 5 minutes. Sham blocks consisted of a 30 second ramp up/down followed by 5 minutes of no stimulation. A two-armed bandit task administered during stimulation (or sham) was used to assess reward learning sensitivity.

Results: Win-stay lose-shift behavior during the task was assessed using linear mixed effects models. Interaction effects indicated that both anodal and cathodal stimulation resulted in increased likelihood of "staying" with a symbol after a winning trial, and increased chance of "shifting" to another symbol after a loss. When post-stimulation sham blocks were divided into early and late phases, the effect of stimulation on win-stay/lose-shift behavior persisted during the early but not late sham blocks, suggesting the presence of an offline carryover effect of both anodal and cathodal stimulation.

Conclusions: As hypothesized, anodal tDCS over right ventrolateral prefrontal cortex increased sensitivity to probabilistic reward learning by increasing both the chances of staying with a stimulus after winning and switching stimulus choice after a loss. Interestingly, cathodal stimulation also increased reward sensitivity. The changes to reward sensitivity persisted after stimulation offset and slowly decayed back to baseline, suggesting a carryover effect of stimulation. Future studies should characterize the magnitude and duration of this carryover effect to better inform both experimental design and protocols using tDCS in the treatment of psychiatric disorders with dysfunctional reward processing.

References

1. Myers, C. E. et al (2016). Probabilistic reward- and punishment-based learning in opioid addiction: Experimental and computational data. Behavioural Brain Research, 296, 240–248. https://doi.org/10.1016/J.BBR.2015.09.018

2. Pizzagalli, D. A. et al. (2008). Euthymic Patients with Bipolar Disorder Show Decreased Reward Learning in a Probabilistic Reward Task. Biological Psychiatry, 64(2), 162–168. https://doi.org/10.1016/J.BIOPSYCH.2007.12.001
3. Rudebeck, P. H. et al. (2017). Specialized Representations of Value in the Orbital and Ventrolateral Prefrontal Cortex: Desirability versus Availability of Outcomes. Neuron, 95. https://doi.org/10.1016/j.neuron.2017.07.042
4. Vrieze, E., et al.(2013). Reduced Reward Learning Predicts Outcome in Major Depressive Disorder. Biological Psychiatry, 73(7), 639–645. https://doi.org/10.1016/J.BIOPSYCH.2012.10.014
5. Weiler, J. A., et al. (2009). Impairment of Probabilistic Reward-Based Learning in Schizophrenia. Neuropsychology, 23(5), 571–580. https://doi.org/10.1037/A0016166

Poster No 45

MRI-based models of electric-field distribution for the modulation of primary progressive aphasia

Antoni Valero-Cabre[1], Xavier Corominas-Teruel[2], Jeanne Salle[3], Nicole Macias[4], Souad Keichiri[5], Maxime Janbon[5], Michel Khachaturyan[6], Clara Sanches[7], Marc Teichmann[8]

[1]CNRS UMR 7225, Paris Brain Institute, Paris, Ile de France, [2]Paris Brain Institute, Paris, Ile de France, [3]COGMASTER program, University of Paris, Paris, Ile-de-France, [4]Universitat Rovira i Virigili, Tarragona, Tarragona, [5]Master BIP Université Sorbonne, Paris, Ile-de-France, [6]Master iMind, Sorbonne Université, Paris, Ile-de-France, [7]CNRS UMR 7225, Paris Brain Institute, Paris, Ile-de-France, [8]Im2a, Hôpital de la Pitié-Salpetrière, Paris, Ile-de-France

Introduction: Transcranial direct current stimulation (tDCS) is a non-invasive technology used to modulate cortical activity in clinical settings[1]. Preliminary evidence suggests its outcomes are dramatically impacted by interindividual differences in head/brain structural features[2]. The optimization of tDCS parameters on the basis of personalized biophysical electric field (E-field) models could boost clinical efficacy. Unfortunately, under-performing tissue-segmentation algorithms limit their reliability, which remains controversial when applied to populations with cortical damage[3]. Additionally, the influence of specific tissue layers modified by pathological conditions, such as neurodegeneration, on tDCS current remains uncertain[4]. We here aimed to: (1) compare the accuracy of E-field distribution models based on automatic vs. manually MRI-segmentation approaches, (2) gauge the influence of head tissue layers on electrical current strength; and (3) assess their ability to predict cognitive modulation in patients with dementia.

Methods: A cohort of n=16 patients diagnosed with semantic variant of primary progressive aphasia (sv-PPA) was stimulated with a single session of anodal tDCS (1.57mA, 0.06 mA/cm2, for 20 min) to the left Anterior Temporal Lobe (ATL). Guided with an MRI-based neuronavigation system, an anode was placed on a scalp site showing the shortest path to relevant ATL MNI coordinates [x=-53; y=4; z=-32] and a cathode over the right supraorbital region (AF8)[5]. language performance was assessed prior and following the tDCS session with a Semantic Association task[6]. A Finite Element Model (FEM) of the patient's head/brain tissue layers was built with the SimNIBS3.2.6 headreco pipeline[5]. In parallel, we manually segmented the layers of the model (White Matter, Gray Matter, CSF, Bone, Air, Eyes and Skin) and used this same tool to build a structural model for comparison. E-field simulations were conducted in both types of models and assessed with metrics assessing local and global E-field impact. Measures regarding the volume of the different tissue layers crossed by the E-Field were also estimated. Non-parametric statistics tested differences on tissue volumes and predicted E-field estimated on manually vs automatically segmented FEM models. Spearman correlations explored associations between structural measures, E-field values and changes in semantic abilities induced by anodal ATL tDCS.

Results: We compared manually vs. automatically segmented head-models' E- total and normal (~tangential) E-field strength throughout the left temporal lobe or in a smaller ROI (10 mm radius sphere on ATL MNI coordinates) (Fig.1A&B). Significantly higher values in total E-field strength were found for manually, compared to automatically segmented FEM models (p=0.0131, Fig.2A). White matter (p=0.0062), CSF (p=0.0443) and skin (p=0.0003) volumes differed statistically between both types of models;) (Fig.2B). Moreover, cortical thickness (r=0.768; p=0.0374), CSF volume (r=-0.520; p=0.0386) for the whole temporal lobe significantly predicted total E-field strength, estimated with manual segmentation (Fig.2C). Unfortunately, no significant correlations between patient's semantic performance gains and E-field estimates were found for any of the two FEM structural models tested (Fig.2D).

Figure 1

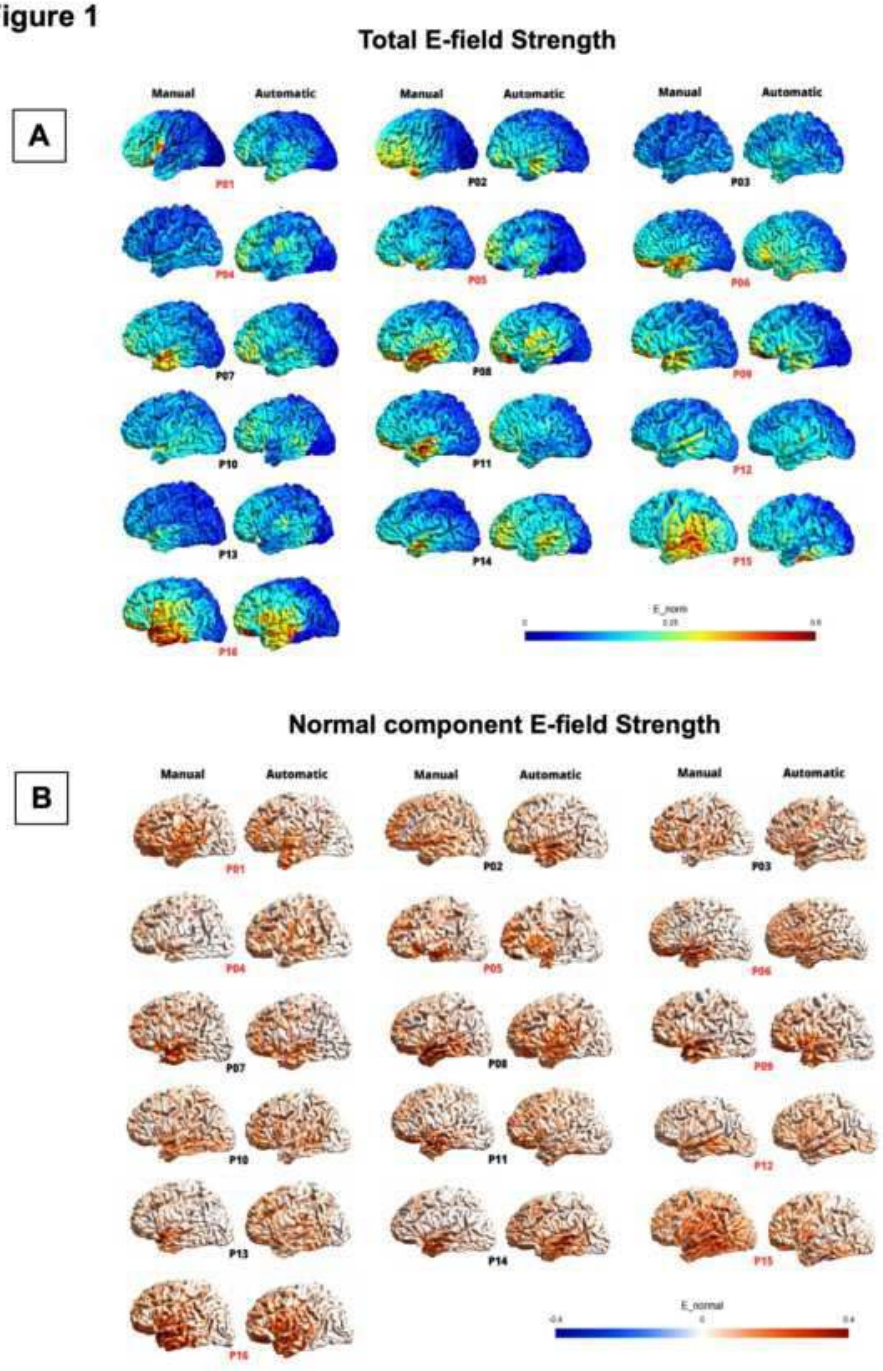

Figure 1. Distribution of **(A)** Total Field Strength and **(B)** Normal (tangential) component of Field Strength on a lateral view of the Left Hemisphere from Individual MRI based FEM/biophysical models of n=16 sv PPA patients for anodal tDCS simulation targeting the left ATL (MNI coordinates [x=53; y=4; z=32]). Tags in black identify the patients (number) showing language improvement (patients P02, P03, P07, P08, P10, P11, P13 and P14, Panel B) in the semantic association task following stimulation. Red tags label patients showing null or negative language modulatory outcomes (patients P01, P04, P05, P06, P09, P12, P15 and P16). Higher levels of field strength characterize models generated on the basis of manual segmentation approach, performed by us, compared to automatic segmentation method implemented by SimNIBS. Note the high interindividual variability of the predicted peak-field strength in the left ATL across patients stimulated with identical anodal tDCS montages and parameters, and the poor relation between the former and semantic association improvements.

Figure 2

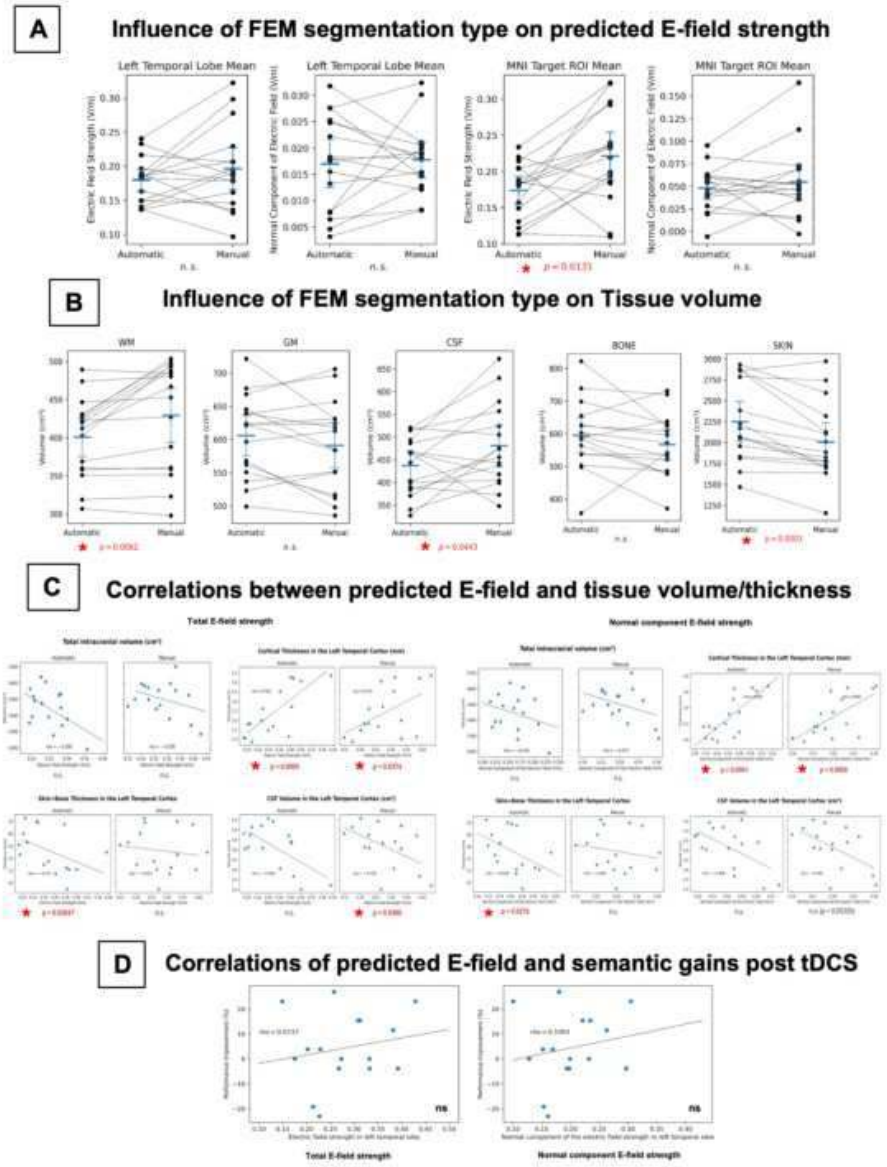

Figure 2. **(A)** Mean ± Standard Deviation and median of the 1% highest values for Total and Normal Component of E-Field strength for each individual patient of our cohort (n=16) and for the group cohort on the whole Left temporal Lobe (from left to right, panels 1 & 2) or from a spheric ROI (10 mm radius around the MNI tDCS target) (panels 3 & 4) on the left ATL. Data were extracted from manually and automatically segmented FEM/biophysical models of tDCS current. Note higher values for E-field measures for manually segmented models compared to automatic, which reached significance only for Total E-Field Strength at the MNI target. Large blue color line refers to the mean value and the two small color signal standard deviation. **(B)** Tissue layer volume (in cm^3) for white matter (WM), gray Matter (GM), cerebro-spinal fluid (CSF), scalp bone, and skin (from left to right) for the Left temporal Lobe ROI comparing automatic and manual segmentation FEM models. Note automatic MRI segmentation procedures significantly underestimated WM and CSF values and overestimated skin thickness, compared to the manual approach. **(C)** Correlation between four selected anatomical head/brain features and individual median values (1% highest) of *Total (left 4x4 panel)* and *Normal component (right, 4x4 panel) Electric Field Strength* estimated for the whole left temporal lobe, from manual and automatic segmented FEM/biophysical models. The regression line, the Spearman's correlation coefficient (rho) and the p-value are displayed on each graph. Note for *Total Electric Field Strength* statistically significant correlations with CSF volume (only for manual segmentation), Cortical Thickness (for both automatic & manual) and with skin-bone-thickness (only automatic segmentation). Significant positive correlation of *Normal component of Electric Field Strength* and skin-bone-thickness (automatic segmentation), with cortical thickness (manual & automatic) and trend towards significance for CSF (manual segmentation) were also found. **(D)** Correlation outcomes between performance improvement in the semantic association language (% change post vs pre tDCS) with the predicted total (Left panel) and Normal component E-field (Right panel) for the whole left temporal lobe ROI, according to manually segmented FEM/biophysical models. Note the lack of statistically significant correlation between language performance following tDCS for *Total Electric* and *Normal component of E-field Strength*. n.s: non-significant results.

Conclusions: We conclude that MRI-based current distribution models built with automatic tissue segmentation algorithms remain suboptimal estimating E-field currents in atrophied brains. Additionally, we identified tissue layers (gray matter and CSF) modified by the pathology that impact the most E-field estimates predicted on the tDCS target. Unfortunately, E-field models failed to correlate with language performance gains. Our results highlight the need for individually customized stimulation strategies to achieve more efficient tDCS clinical interventions via MRI-based biophysically inspired computational models.

References

1. Sanches C, Godard J, Merz J, Stengel C, Teichmann M, Migliaccio R, Valero-Cabré A. Past, present and future of non-invasive brain stimulation approaches to treat cognitive impairment in neurodegenerative diseases: time for a comprehensive critical review? Front Aging Neurosci. 2021; 12:578339.
2. Liu A, Vöröslakos M, Kronberg G, Henin S, Krause MR, Huang Y, et al. immediate neuro-physiological effects of transcranial electrical stimulation. Nat Commun 2018;9.
3. Unal G, Ficek B, Webster K, Shahabuddin S, Truong D, Hampstead B, et al. Impact of brain atrophy on tDCS and HD-tDCS current flow: a modeling study in three variants of primary progressive aphasia. Neurological Sciences 2020; 41:1781–9.
4. Saturnino GB, Thielscher A, Madsen KH, Knösche TR, Weise K. A principled approach to conductivity uncertainty analysis in electric field calculations. Neuroimage 2019;188:821-34.
5. Teichmann M, Lesoil C, Godard J, Vernet M, Bertrand A, Levy R, Dubois B, Lemoine L, Truong DQ, Bikson M, Kas A, Valero-Cabré A. Direct current stimulation of temporal poles boosts semantic processing in primary progressive aphasia. Annals of Neurology 2016, 80(5): 693-707
6. Sanches C, Levy R, Benisty S, Volpe-Gillot L, Habert MO, Kas A, Ströer S, Dubois S, Kaglik A, Bourbon A, Migliaccio R, Valero-Cabré A, Teichmann A. Testing the therapeutic effects of transcranial direct current stimulation (tDCS) semantic dementia: A double blind, sham controlled, randomized clinical trial. Trials 2019 20(1):632.
7. Nielsen JD, Madsen KH, Puonti O, Siebner HR, Bauer C, Madsen CG, et al. Automatic skull segmentation from MR images for realistic volume conductor models of the head: Assessment of the state-of-the-art. Neuroimage 2018;174:587–98.

Poster No 46

Modulating Cerebral Metabolic Rate: Investigating tDCS Effects in Patients with Multiple Sclerosis

Yulin Ge[1], Marco Muccio[1], Giuseppina Pilloni[1], Leigh Charvet[1]

[1]NYU Langone Health, New York, NY

Introduction: Transcranial direct current stimulation (tDCS) is a safe and well-tolerated method which uses weak electrical currents to modulate cortical excitability. TDCS studies of multiple sclerosis (MS) have shown clinical improvements in fatigue[2], motor function[3] and cognitive performance[4]. Although extensive research has been done focusing on the clinical outcomes of tDCS, there remains a notable gap in the exploration of neuronal metabolic responses to this stimulation, a crucial metric for gauging tDCS-induced changes in neuronal activity particularly in a real-time setting. In this study, we investigated cerebral metabolic rate of oxygen (CMRO2) response to tDCS in MS to gain more in-depth understanding of both concurrent (during tDCS) and post-tDCS (immediately after tDCS) effects on the neuronal metabolic response.

Methods: 20 patients (age=45±13 years, 13 females) with MS diagnosis were recruited to participate in this simultaneous tDCS-MRI study. Stimulation was given via an MRI-compatible tDCS device (Soterix Medical) and consisted in a 15 minutes left anodal dorsolateral prefrontal cortex (DLPFC, F3) direct current stimulation at 2.0mA as used in the previous study[4]. The tDCS-MRI protocol used in this study included three timepoints: pre-, during- and post-tDCS (Figure 1). Imaging data was acquired in a 3T scanner fitted with a 64 channels head coil and comprised of the following sequences: phase contrast MRI (PC-MRI) to measure total blood influx through bilateral carotid and vertebral arteries, subsequently normalized for subject-specific brain volumes, from a 3D-T1-MPRAGE, to obtain a global measure of cerebral blood flow (CBF); T2-Relaxation-Under-Spin-Tagging (TRUST)[5] was used to measure venous oxygenation (Yv) in the superior sagittal sinus, just above the venous confluence.
To investigate the tDCS-induced neuronal changes we calculated CMRO2 combining CBF and Yv measures, as reported previously[6]. Paired t-test was used to compare measurements of each imaging parameter amongst combination of the three time points as well as baseline vs follow up.

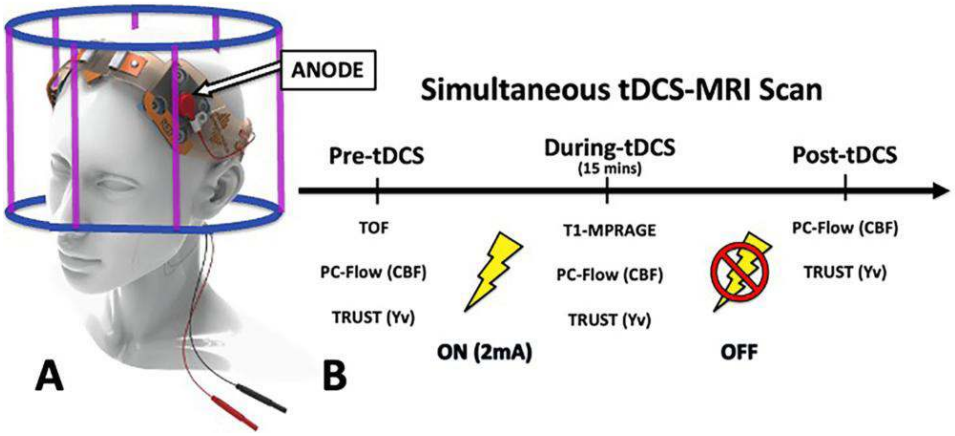

Results: As shown in Figure 2, global CBF increased from pre-tDCS (39.80±5.75 mL/100g/min) to during-tDCS (43.92±5.74 mL/100g/min; p<0.0001). Yv exhibited a slight increase from pre-tDCS (58.83±3.39%) to during-tDCS (59.93±3.34%; p=0.006). CMRO2 showed a notable 7.9% increase from pre-tDCS (128.30±14.00 µmol/100g/min) to during-tDCS (137.77±14.17 µmol/100g/min; p=0.002). Across all parameters, post-tDCS results remained elevated immediately after tDCS, although they didn't reach statistical significance. This implies that a lingering effect may occur, necessitating repeated tDCS sessions to effectively achieve the desired treatment outcome.

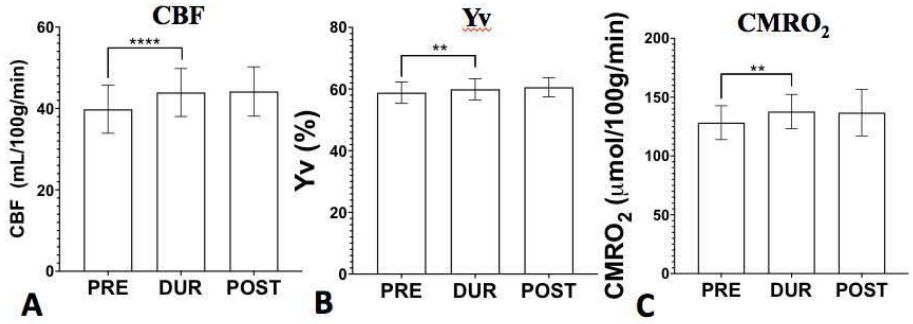

Conclusions: In MS patients, we observed a real-time significant increase in CBF during tDCS stimulation, which notably exceeded the increase observed in Yv (11.0% CBF vs 1.9% Yv). This suggests that the stimulated neurons quickly utilized most of the surplus oxygen, leading to the observed increase in CMRO2 (7.6%) measured with advanced MRI. This aligns with the current understanding that anodal tDCS enhances neuronal firing by further depolarization of the neuronal membrane[7]. Notably, these effects do not rapidly dissipate after stimulation cessation but instead tend to persist or linger. The CMRO2 response to tDCS (the CMRO2 difference between during- and pre-tDCS) measured with concurrent tDCS-MRI may have important implication in predicting future treatment outcome in individual patient and differentiating responders from non-responders before tDCS intervention.

References

1. Charvet, L.E. et al (2018). Remotely supervised transcranial direct current stimulation for the treatment of fatigue in multiple sclerosis: results from a randomized, sham-controlled trial. Multiple Sclerosis Journal, 24(13), pp.1760-1769.
2. Pilloni, G. et al (2020). Walking in multiple sclerosis improves with tDCS: a randomized, double-blind, sham-controlled study. Annals of Clinical and Translational Neurology, 7(11), pp.2310-2319.
3. Simani, L. et al (2022). The effectiveness of anodal tDCS and cognitive training on cognitive functions in multiple sclerosis; a randomized, double-blind, parallel-group study. Multiple Sclerosis and Related Disorders, 68, p.104392
4. Muccio, M. et al (2022). Cerebral metabolic rate of oxygen (CMRO2) changes measured with simultaneous tDCS-MRI in healthy adults. Brain Research, 10.1016/j.brainres.2022.148097.
5. Lu, H. and Ge, Y. (2008). Quantitative evaluation of oxygenation in venous vessels using T2-relaxation-under-spin-tagging MRI. Magnetic Resonance in Medicine 60(2), pp.357-363.
6. Xu, F. et al (2009). Noninvasive quantification of whole-brain cerebral metabolic rate of oxygen (CMRO2) by MRI. Magnetic Resonance in Medicine 62(1), pp.141-148.
7. Nitsche, M.A. and Paulus, W. (2000). Excitability changes induced in the human motor cortex by weak transcranial direct current stimulation. The Journal of physiology, 527(Pt 3), p.633.

Poster No 47

Effects of tACS on electrophysiological signals are task-dependent

Abhijit Chinchani[1], Rafal Skiba[2], Todd Woodward[2]

[1]The University of British Columbia (UBC), Vancouver, British Columbia (BC), [2]University of British Columbia, Vancouver, British Columbia

Introduction: Transcranial alternating current stimulation (tACS) is a non-invasive technique that delivers low-intensity alternating currents intending to affect neural activity and behavior (Liu et al., 2018). Recent research has shown that the effects of tACS are often inconsistent and not replicable (Kasten et al., 2019; B. Krause & Kadosh, 2014). In this study, we investigated the effects of 10Hz alpha (vs 41Hz gamma) stimulation on alpha oscillations during a vigilance-oddball paradigm. Similar tasks involving sustained attention are used to study the effects of tACS on electrophysiology and behavior (Zaehle et al., 2010, Vossen et al., 2015). Here, we aimed to test whether electrophysiology is reliably modulated by neurostimulation.

Methods: In this study, participants (n=38) underwent occipital (Fig. 2A) alpha (10Hz) and gamma (41Hz) stimulation, on separate days. During each session, participants performed three blocks of a vigilance-oddball task: the first without

stimulation (PRE), the second with either alpha or gamma stimulation (STIM), and the third without stimulation (POST). In each block, participants performed a vigilance-oddball task (Fig. 1A); where they were instructed to fixate on a white cross in the center of the screen and respond to color changes to the fixation cross using a button press on a keyboard. The color of the cross changed from white to either red or green, one of which occurred 80% of the time (DEFAULT color change) and the other 20% of the time (ODDBALL color change). Half the participants were instructed to use their left index finger for the DEFAULT color change (Left-hand dominant group, see Fig. 1B) and the other half their right index finger (Right-hand dominant group, see Fig. 1B). Simultaneous EEG was recorded from 256 electrodes during all the blocks.

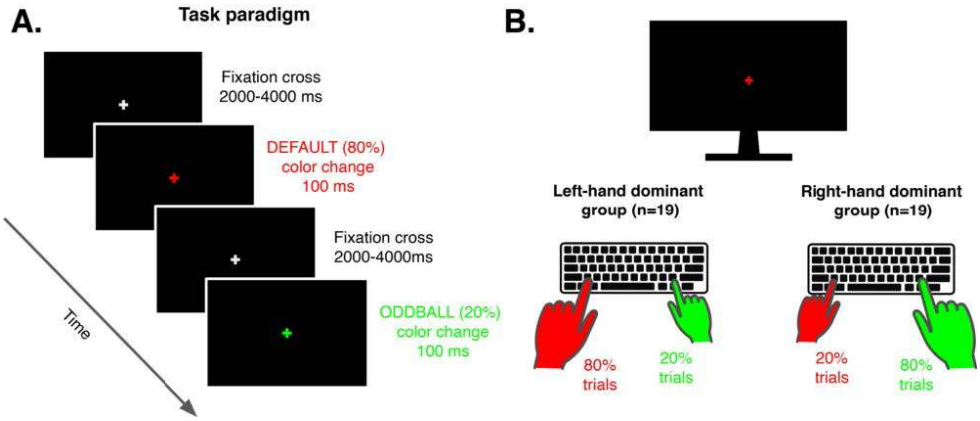

Results: Due to the lateralized nature of the responses, we checked whether tACS affected alpha power in a lateralized manner. We observed that enhancement in alpha power (Δ = POST - PRE) was greater for alpha stimulation than gamma stimulation but only for the contralateral electrodes (Fig. 2C, right; t(37)=-2.55, p=0.015) to the dominant response hand (response hand for DEFAULT color change) and not for the ipsilateral electrodes (Fig. 2C, left; t(37)=1.45, p=0.156). Moreover, the difference in the enhancement of alpha power between alpha and gamma stimulation (ΔΔ = alpha stim - gamma stim) was significantly higher for the contralateral electrodes as compared to the ipsilateral ones (Fig. 2D; t(37)=-3.68, p<0.001).

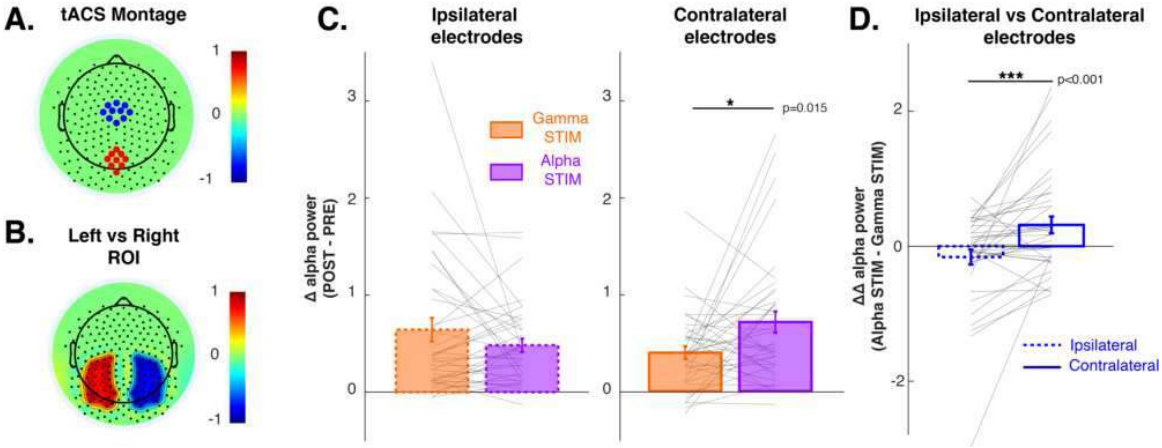

Conclusions: Our findings reveal that alpha tACS enhances alpha power but this enhancement is more pronounced in the electrodes contralateral to the dominant hand involved in the task. It is noteworthy that this lateralized effect is observed even though our tACS electrode montage (Fig. 2A) wasn't lateralized. This implies that the effect is likely driven by the motor planning aspects involved during the task paradigm. Thus suggesting that the effects of tACS on electrophysiological signals depend on the nature of the task being performed.

References

1. Kasten, F. H., Duecker, K., Maack, M. C., Meiser, A., & Herrmann, C. S. (2019). Integrating electric field modeling and neuroimaging to explain inter-individual variability of tACS effects. Nature Communications, 10(1), Article 1. https://doi.org/10.1038/s41467-019-13417-6
2. Krause, B., & Kadosh, R. C. (2014). Not all brains are created equal: The relevance of individual differences in responsiveness to transcranial electrical stimulation. Frontiers in Systems Neuroscience, 8. https://doi.org/10.3389/fnsys.2014.00025
3. Liu, A., Vöröslakos, M., Kronberg, G., Henin, S., Krause, M. R., Huang, Y., Opitz, A., Mehta, A., Pack, C. C., Krekelberg, B., Berényi, A., Parra, L. C., Melloni, L., Devinsky, O., & Buzsáki, G. (2018). Immediate neurophysiological effects of transcranial electrical stimulation. Nature Communications, 9(1), Article 1. https://doi.org/10.1038/s41467-018-07233-7
4. Vossen, A., Gross, J., & Thut, G. (2015). Alpha power increase after transcranial alternating current stimulation at alpha frequency (α-tACS) reflects plastic changes rather than entrainment. Brain stimulation, 8(3), 499-508.
5. Zaehle, T., Rach, S., & Herrmann, C. S. (2010). Transcranial alternating current stimulation enhances individual alpha activity in human EEG. PloS one, 5(11), e13766.

Poster No 48

The impact of accelerated iTBS and cTBS on white matter microstructure in OCD - a pilot study

Bora Kim[1,2], Andrew Geoly[1], Azzezat Azeez[1], Igor Bandeira[1], Flint Espil[1], Jennifer Lissemore[1], Wiebke Struckmann[1], Nolan Williams[1]

[1]Stanford University, Palo Alto, CA, [2]VA Palo Alto Health Care System, Palo Alto, CA

Introduction: Theta burst stimulation (TBS) is a novel repetitive Transcranial Magnetic Stimulation paradigm that employs theta burst stimulation to enhance or dampen cortical excitability by mimicking cortical theta rhythms, allowing for accelerated stimulation in short periods. Despite its potent clinical effects, the mechanisms of TBS, particularly its impact on microstructural integrity, remain largely unknown. This pilot study utilized diffusion tensor imaging (DTI) to examine the relationship between accelerated continuous TBS (acTBS) and intermittent TBS (aiTBS) and white matter microstructure, aiming to further understand the neural mechanisms of action of TBS.

Methods: DTI data were acquired from 21 individuals with Obsessive-Compulsive Disorder (OCD) who participated in an ongoing open-label accelerated TBS study for this pilot analysis [NCT04286126]. The diagnosis of OCD was determined by a structured clinical interview for DSM disorders, and symptom severity was measured using the Yale-Brown Obsessive-Compulsive Scale (YBOCS). All participants received either 18,000 pulses per day of aiTBS to the dorsomedial prefrontal cortex (DMPFC) or acTBS to the right orbitofrontal cortex (rOFC) over 5-10 days at 100% or 110% of the resting motor threshold, respectively. MRI data were acquired at baseline (1 week before treatment) and post-treatment. Multishell diffusion images (1.5mm isotropic, TR/TE = 5650/65 ms, b = 1500, 3000s/mm2, 65 directions) and Anatomical images (3D, T1-weighted, FOV = 256x256mm, 0.9mm isotropic, TR/TE = 6.39/2.62ms) were acquired using a 3T GE Discovery MR750 scanner with a 32-channel head-neck imaging coil at the Center for Cognitive and Neurobiological Imaging at Stanford University. Participants were screened for MRI safety before scanning procedures. We chose to examine fractional anisotropy (FA) changes in five regions of interest (ROI) from a recent ENIGMA paper on OCD. Tract-based spatial statistics (TBSS) were employed to analyze skeletonized microstructural estimates for each ROI. Repeated-measures ANOVA was performed with covariates, including stimulation targets of DMPFC and rOFC, follow-up time between visits (days), sex, age, and baseline OCD symptom severity as measured by the YBOCS.

Results: Demographics included an age range of 18-57 years old (mean 37.3 years old), with 45% male. The mean (SD) baseline YBOCS score was 30.62 (3.92). Thirteen individuals received aiTBS over DMPFC, and eight individuals received cTBS over rOFC. Post-treatment follow-up time ranged from 20 days to 524 days (median 42 days). A repeated-measures ANOVA showed a main effect of study visit on FA in the Uncinate fasciculus after including covariates of age, sex, treatment duration, and follow-up time ($F=4.736$, $p = 0.049$, $\eta^2p = 0.267$), but post-hoc testing comparing FA between Pre- and Post-treatment did not substantiate the main effect ($p > 0.05$). No significant differences were detected for radial diffusivity (RD), axial diffusivity (AD), or mean diffusivity (MD) in any ROI. ROI-based TBSS analysis did not demonstrate significant white-matter microstructural changes from baseline to post-treatment in specific brain regions.

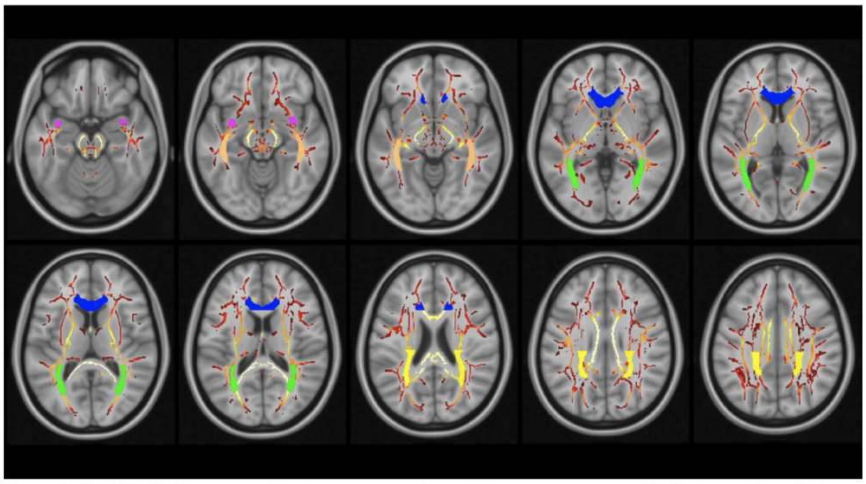

Figure 1. ENIGMA ROIs examined in the present study overlaid on group average FA Skeleton. *Note:* Pink = Uncinate Fasciculus (UNC), Copper = Sagittal Striatum (SS), Blue = Genu of Corpus Callosum (GCC), Green = Posterior Thalamic Radiation (PTR), Yellow = Posterior Corona Radiata (PCR)

Conclusions: Our pilot data (N = 21) analysis suggests the need for a larger sample to thoroughly investigate the effects of acTBS and aiTBS on white matter microstructure with adequate statistical power.

Poster No 49

Transcranial magnetic stimulation simulation reveals electric-field differences between DLPFC and M1

Larissa Behnke[1,2], Yuki Mizutani-Tiebel[2], Kai-Yen Chang[2], Frank Padberg[2], Daniel Keeser[2]

[1]University of Zurich, Department of Psychology, Zürich, Switzerland, [2]Department of Psychiatry and Psychotherapy, University Hospital LMU, Munich, Germany

Introduction: The treatment of psychiatric disorders is challenging and not all patients respond well to primary indicated medications and/or psychotherapy. One promising method investigated for treatment-resistant psychiatric patients is non-invasive neuromodulation. Therefore, repetitive transcranial magnetic stimulation (rTMS) offers a treatment alternative for psychiatric disorders (Kan et al., 2023). Many rTMS treatment protocols target the left dorsolateral prefrontal cortex (lDLPFC) and stimulation intensity is determined by the participants individual resting motor threshold (rMT) of the left primary motor cortex (lM1). Using the rMT is a reliable measure of cortical excitability with a peripheral response, but it is unknown if the stimulation intensity determined by the individual's lM1 results in comparable cortical activation when stimulation is applied at the lDLPFC. Therefore, we investigated the intensity and spread of an electric-field simulation targeting lDLPFC and lM1 using the simulation software SimNIBS 4.0.

Methods: We simulated electric-field distributions (n=17, 8 female, age: M=26.29, SD =3,39, range: 21-36 years) from T1 and T2 structural MRI scans of healthy participants recorded as part of a simultaneous TMS-fMRI setup (Mizutani-Tiebel et al., 2022). The baseline scans we used for this simulation were aquired with a 64-channel coil in a 3T Siemens Prisma Magnetom scanner. Coordinates for each lDLPFC target were located by conducting a reverse co-registration from MNI152 stereotaxic coordinates x=–38, y=+44, z=+26 to the subject space of each scan. The initially recorded stimulation marker (pulse) was used as the stimulation target for each simulation. The coil handle direction was manually adjusted to a 45° angle with the line between hemispheres and stimulation points were projected onto the scalp. Stimulation targets for lM1 and rMT were defined by using electromyography on the right abductor pollicis brevis. The rMT was defined with the di/dt value which induced motor evoked potentials (MEPs) greater than 50µV in 5 out of 10 pulses. For the simulation of DLPFC/M1, we specified the MRi-B91 TMS coil file and set the stimulation intensity to the di/dt value recorded from the TMS stimulator during the actual rTMS protocol. The stimulation intensity was defined as 80% of each participants rMT.

Results: Surprisingly, the 99th percentile electric-field strength was higher for lDLPFC than for lM1 targets. However, at higher (99.9th) and lower (50th, 75th and 90th) percentiles, electric-fields intensity did not show significant difference between lDLPFC and lM1. The field-focality, a measure of gray matter area with a field 75 and 50% of the 99.9th percentile electric-field intensity, significantly differed between stimulation locations. Calculated field-focality at lDLPFC was higher than at lM1, indicating a higher spread of the stimulation at prefrontal areas.

Conclusions: Here we show that TMS stimulation with the same intensity, but different targets do not result in the same activation in the underlying structures. Our simulation shows that electric-field strength and field-focality can differ between stimulation sites. The primary motor cortex (M1) is more specialized for motor control and has less functional diversity than the frontal brain regions. Frontal brain areas are involved in higher-order cognitive functions such as decision making, working memory and executive functions, which require a more complex and variable cytoarchitecture. Stimulation of these diverse and interconnected regions may lead to a wider range of effects, contributing to greater variability (Mueller et al., 2013). Future investigations should delve into these factors and treatment protocols should consider variations in TMS effects across different stimulation targets.

References

1. Kan, R. L. D. et al. (2023), "Effects of repetitive transcranial magnetic stimulation of the left dorsolateral prefrontal cortex on symptom domains in neuropsychiatric disorders: a systematic review and cross-diagnostic meta-analysis", The Lancet, Psychiatry, 10(4), 252–259. https://doi.org/10.1016/S2215-0366(23)00026-3
2. Mizutani-Tiebel, Y. et al. (2022), "Concurrent TMS-fMRI: Technical Challenges, Developments, and Overview of Previous Studies. Frontiers in psychiatry", 13, 825205, https://doi.org/10.3389/fpsyt.2022.825205
3. Mueller, S. et al. (2013), "Individual variability in functional connectivity architecture of the human brain", Neuron, 77(3), 586–595. https://doi.org/10.1016/j.neuron.2012.12.028

Poster No 50

Application of HARDI to assess optimal coil orientation in neuronavigated TMS of the motor cortex

Constanze Ramschütz[1], Andrey Zhylka[2], Silas Preis[3], Sandro Krieg[4], Haosu Zhang[4], Claus Zimmer[3], Bernhard Meyer[5], Nico Sollmann[6], Severin Schramm[7]

[1]Department of Diagnostic an Internventional Neuroradiology, Technical University of Munich, Munich, Germany, [2]Surgical Department, Eindhoven University of Technology, Eindhoven, Netherlands, [3]Department of Neuroradiology, Klinikum Rechts der Isar, Technical University of Munich, Munich, Germany, [4]Department of Neurosurgery, Universitätsklinikum Heidelberg, Heidelberg, Germany, [5]Department of Neurosurgery, Klinikum rechts der Isar, Technical University of Munich, Munich, Germany, [6]Dep. of Diagnostic and Interventional Radiology, University Hospital Ulm, Munich, Germany, [7]Department of Diagnostic and Interventional Neuroradiology, Technical University of Munich, Munich, Germany

Introduction: Transcranial magnetic stimulation (TMS) is a modality for noninvasive brain stimulation with rapidly growing diagnostic[1] and therapeutic[2] applications. While used in the treatment of conditions such as depression or neuropathic pain, results of neuromodulation protocols are known to be heterogeneous between individuals and centers[3]. Additionally, the neurophysiological processes underlying TMS effects are still insufficiently understood (3). One factor that might contribute to optimized results of TMS is the orientation of the stimulating coil in relation to cortical and subcortical anatomy. We present preliminary results from healthy participants in whom we investigated the role of intragyral fiber orientations in terms of TMS effects on the motor cortex.

Methods: 20 healthy participants (average age: 27 years, 10 females) underwent high angular resolution diffusion imaging (HARDI; 60 gradient directions modeled on a sphere [b-value=1500 s/mm2] and 6 interleaved b0 volumes) and T1-weighted (T1w) imaging at 3 Tesla. The T1w images were used for neuronavigated TMS (nTMS). Up to three nTMS sessions separated by at least 14 days were conducted per subject to assess the robustness of the optimal coil orientation. In each nTMS session, we elicited 140 motor-evoked potentials (MEPs) from the abductor pollicis brevis muscle hotspot using 7 different coil orientations (30° - 150° relative to the longitudinal axis of the precentral gyrus, in 20° steps) on the dominant hemisphere. The MEPs were analyzed regarding the influence of coil orientation on MEP amplitudes. Additionally, HARDI data were corrected for signal drift, motion, echo planar imaging /EPI), and eddy current (EC) distortions and coregistered to the T1w imaging used in the navigation of TMS via ExploreDTI[4]. Herein, constrained spherical deconvolution (CSD) truncated at maximum harmonic order L-max=8 was used to model fiber orientation distributions (FODs). These were visualized in relation to the observed optimal stimulation direction (Figure 1).

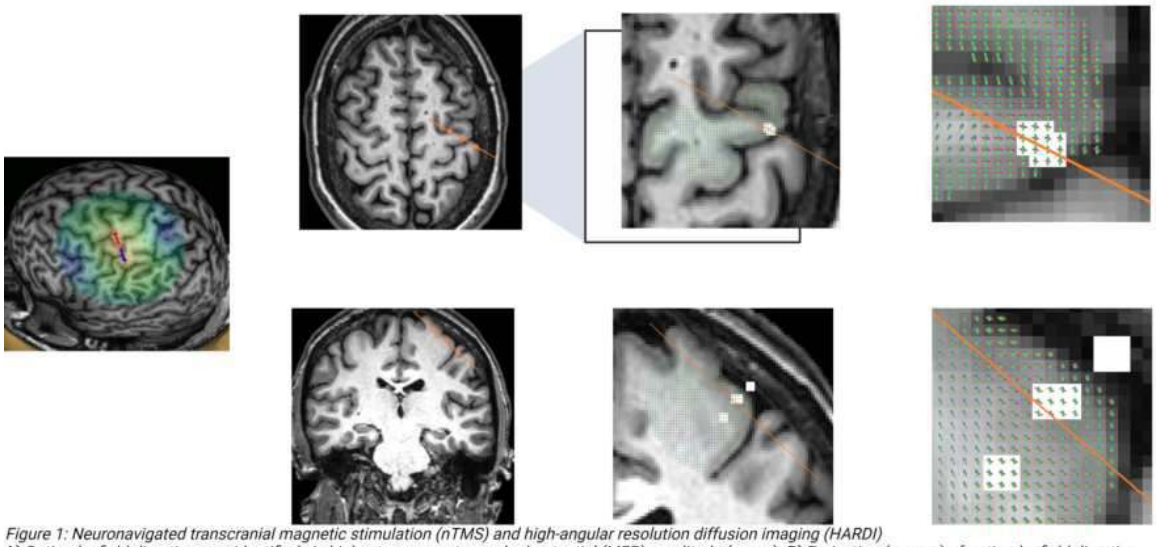

Figure 1: Neuronavigated transcranial magnetic stimulation (nTMS) and high-angular resolution diffusion imaging (HARDI)
A) Optimal e-field direction was identified via highest mean motor evoked potential (MEP) amplitude (arrow). **B)** Projection (orange) of optimal e-field direction in axial and coronal planes. **C)** HARDI was coregistered to the T1-weighted (T1w) imaging data (white dots indicate maximum e-field at different depths within the brain). Fiber orientation distributions (FODs) were modeled for each voxel, representing main diffusion directions along axonal orientations. **D)** The optimal e-field appears to run parallel to one of the dominant FODs. This was interpreted as reflecting maximal excitability when the e-field is oriented parallel to axonal structures.

Results: In total, 6720 individual MEPs were analyzed. The MEP amplitude correlated significantly with coil orientation (rho = -0.39, p << 0.0001; Figure 2). A random effects regression model predicted a deviation from the optimal orientation (defined by highest mean MEP amplitude) by 20 degrees to lead to MEP decreases of -168 µV (β=-168, t=-28.97). On a qualitative level, when comparing the optimal stimulation direction to HARDI-derived fiber orientations, we noticed a notable parallel alignment of FODs to the e-field direction yielding maximal MEPs (Figure 1).

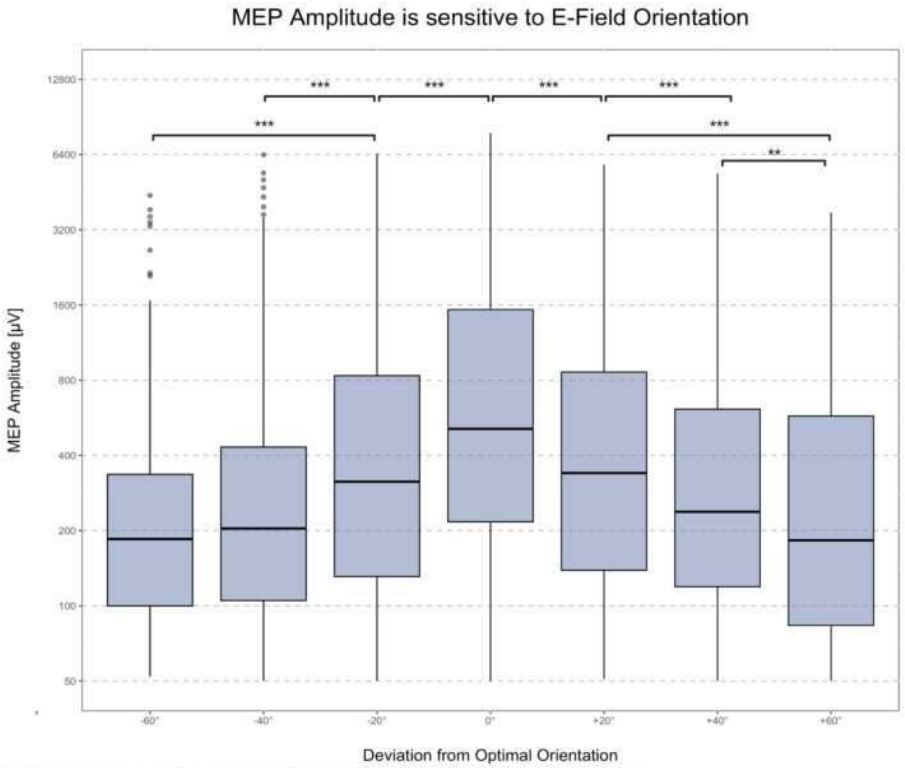

Figure 2: Motor evoked potential (MEP) amplitude is sensitive to e-field orientation
Figure 2 demonstrates MEP amplitude changes dependent on e-field orientation in relation to the optimal direction (0°, middle plot), which was defined as eliciting the maximum mean MEP amplitude out of the tested coil directions. The MEP amplitude was lowered significantly by deviations as little as 20° from the optimum. P-values were adjusted for a family-wise error rate. Line in box: Median; Boxes: 2nd and 3rd quartiles; Whiskers: 1st and 4th quartiles; Dots: Outliers; ***: $p < 0.001$; **: $p < 0.01$.

Conclusions: Coil orientation during TMS in relation to gyral anatomy significantly modulates motor responses. HARDI-derived fiber orientation imaging could aid in predicting optimal coil orientation in non-motor areas, e.g. for therapeutic TMS applications.

References

1. Krieg, S. M. (Ed.). (2017). Navigated transcranial magnetic stimulation in Neurosurgery (Vol. 299). New York, NY: Springer International Publishing.
2. Lefaucheur, J. P., Aleman, A., Baeken, C., Benninger, et al. (2020). Evidence-based guidelines on the therapeutic use of repetitive transcranial magnetic stimulation (rTMS): An update (2014–2018). Clinical neurophysiology, 131(2), 474-528.
3. Goldsworthy, M. R., Hordacre, B., Rothwell, J. C., & Ridding, M. C. (2021). Effects of rTMS on the brain: is there value in variability?. Cortex, 139, 43-59.
4. Leemans, A. J. B. S. J. J. D. K., Jeurissen, B., Sijbers, J., & Jones, D. K. (2009, April). ExploreDTI: a graphical toolbox for processing, analyzing, and visualizing diffusion MR data. In Proc Intl Soc Mag Reson Med (Vol. 17, No. 1, p. 3537).

Poster No 51

Assessing the effects of TMS coil size on quantitative mapping of human motor cortex

Evgenii Kim[1,2], Mohammad Daneshzand[1,2], Sergey Makarov[3], Konstantin Weise[4,5], Ole Numssen[4], Thomas Knösche[4], Dylan Edwards[6,7], Tommy Raij[1,2], Aapo Nummenmaa[1,2]

[1]Massachusetts General Hospital, Boston, MA, [2]Harvard Medical School, Boston, MA, [3]Worcester Polytechnic Institute, Boston, MA, [4]Max Planck Institute for Human Cognitive and Brain Sciences, Leipzig, Saxony, [5]Leipzig University of Applied Sciences, Leipzig, Germany, [6]Thomas Jefferson University, Philadelphia, PA, [7]Moss Rehabilitation Research Institute, Philadelphia, PA

Introduction: Transcranial Magnetic Stimulation (TMS) is a powerful non-invasive neurostimulation method that is established in preoperative functional mapping for neurosurgical interventions[1]. The geometry of the coil plays a crucial role in shaping the induced electric field (E-field), thus influencing the spatial specificity and efficacy of TMS pulses (larger coils provide enhanced depth penetration but with a trade-off of decreased focality)[2]. The spatial extent of the E-field determined by the coil type has been a crucial consideration for improved quantitative TMS protocols, where the goal is to isolate a cortical “hotspot” for a

target muscle[3]. Yet, it is not well-characterized how invariant the mapping results are with respect to the size of the TMS coil, and/or if using different coils would provide complementary information.

Methods: Data were acquired from a single healthy, right-handed male subject who provided written informed consent. The workflow is illustrated in Fig. 1. Before TMS session, T1- and T2-weighted MR images were obtained using a Siemens 3 Tesla scanner. The head model was created from MRI using the SimNIBS headreco[4]. TMS pulses were delivered using a MagPro X100 stimulator (MagVenture, Denmark). Two figure-of-eight coils, B60 and B35 (MagVenture; with coil diameter 2x75 mm and 2x46 mm, respectively) were used in separate runs during the same session. Each run involved 250 TMS single biphasic pulses at 5-second intervals. The stimulation intensity for B60 was set at 150% of the resting motor threshold (rMT), which corresponds to 68% of the maximum stimulator output (MSO). Meanwhile, B35 was operated at 133% of the rMT (limited by 100% MSO). For each stimulation, each coil was randomly positioned around the motor cortex. Coil locations were recorded using a neuronavigation system (TMS Navigator, Localite, Germany). Motor evoked potentials (MEPs) were recorded from three finger muscles - first dorsal interosseous (FDI), abductor digiti minimi (ADM), and abductor pollicis brevis (APB). MEPs were sampled at 5 kHz and post-processed with a bandpass filter (100-1000 Hz). Coil positions and the head model were utilized to compute the E-fields using an LU-based BEM-FMM[5]. The identification of the "hotspot" for each muscle was determined by maximum R2 scores derived from logarithmic sigmoid regression, establishing the correspondence between induced magnitude E-field distribution and MEPs[6].

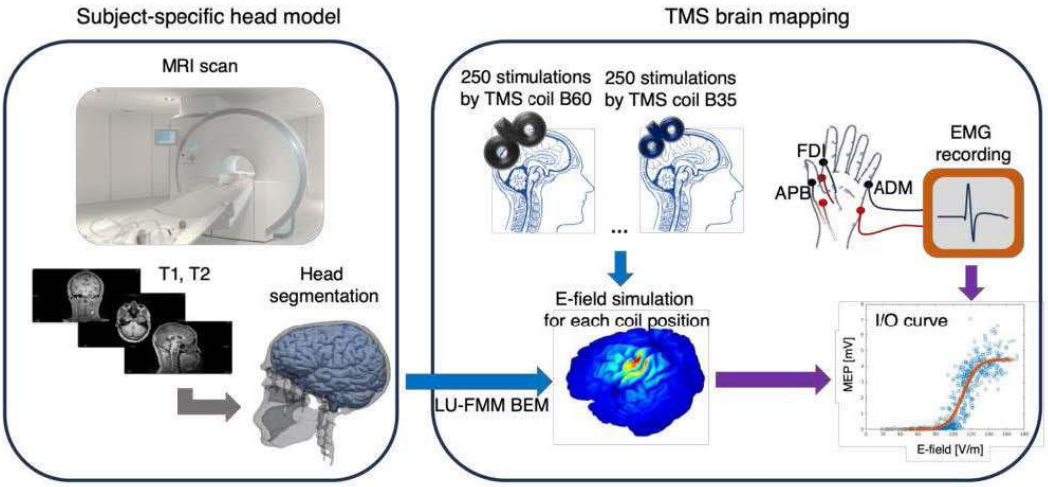

Figure 1. Schematic illustration of the TMS brain mapping procedure. Prior to the TMS session, MRI acquisition was performed, and T1- and T2-weighted images were utilized for head segmentation. The TMS session involved two runs, with the B60 coil in the first run and the B35 coil in the second. Each run consisted of 250 TMS pulses. For each stimulation, coil position and MEPs from three muscles were recorded. The head model and coil position were used to simulate the E-field distribution inside the brain. Subsequently, MEP values and E-field were employed to calculate R^2 for the I/O curve.

Results: A goodness-of-fit map illustrating the functional cortical representation of the fingers under two coils is presented in Fig. 2. The functional map was further derived by combining B60 and B35 datasets. To ensure an equivalent number of data points, 125 random trials were selected from the B60 coil and 125 from the B35 coil. The identified "hotspots" were consistently within a 3 mm range across three coil configurations (B60, B35, combined) for each muscle. As expected, the B35 coil with higher focality of E-field exhibited an improved localization in the goodness-of-fit map. Specifically, the B60 mapping showed a "spread" of the hot spot neighboring gyri (Fig. 2, red arrows) that is likely associated with the limitations of the TMS coil focality, rather than the actual extent of the cortical motor representation. The results from the combination of two coil types produced a functional map that captures the "best of both worlds" – the spatial spread to the neighboring gyri of the B60 coil is reduced, while the R2 scores of the B35 are enhanced.

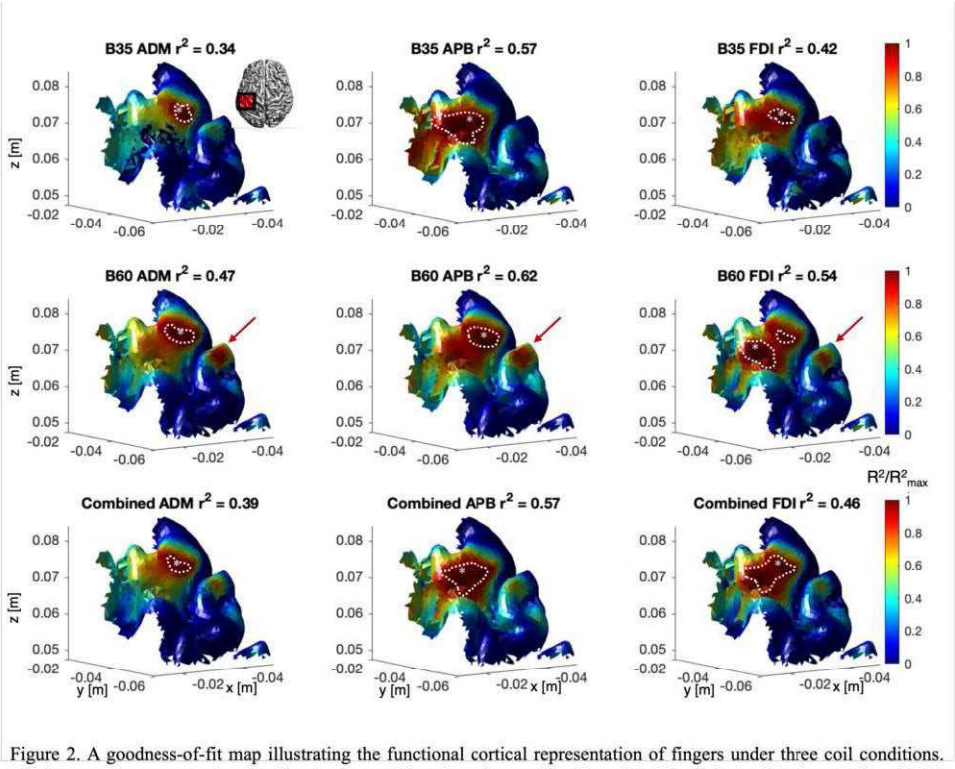

Figure 2. A goodness-of-fit map illustrating the functional cortical representation of fingers under three coil conditions. The bottom row presents the functional map resulting from the combination of 2×125 random trials from B60 and B35 runs. Dashed white contours delineate areas with >90% of the maximum R^2 score, with '*' marking 'hotspot' associated with corresponding muscles. The red arrow highlights the 'spread' of the 'hot area' to neighboring gyri. The inset in the top left corner indicates the location of the Region of Interest (ROI). The x-axis corresponds to the anteroposterior (AP) direction, and the y-axis corresponds to the superoinferior (SI) direction.

Conclusions: Our study showed that TMS mapping results across two coils of different sizes produced qualitatively similar outcomes, indicating the overall robustness of the approach. Combining both coil types produced a balanced mixture of both features in terms of sensitivity and specificity. In the future, by utilizing multichannel TMS coil arrays[7], we may generate a wider range of E-field patterns and further reduce the ambiguity in the localization maps.

References

1. Raffa, G. (2019), "The role of navigated transcranial magnetic stimulation for surgery of motor-eloquent brain tumors: a systematic review and meta-analysis," Clinical Neurology Neurosurgery, 180, 7-17.
2. Drakaki, M. (2022), "Database of 25 validated coil models for electric field simulations for TMS," Brain Stimulation, 15(3), 697-706.
3. Numssen, O. (2021), "Efficient high-resolution TMS mapping of the human motor cortex by nonlinear regression," Neuroimage, 245, 118654.
4. Saturnino, G.B. (2019), "SimNIBS 2.1: A Comprehensive Pipeline for Individualized Electric Field Modelling for Transcranial Brain Stimulation," Brain and Human Body Modeling: Computational Human Modeling at EMBC 2018, Chapter 1.
5. Makaroff, S.N. (2023), "A fast direct solver for surface-based whole-head modeling of transcranial magnetic stimulation," Scientific Reports, 13(1), 18657.
6. Weise, K. (2023), "Precise motor mapping with transcranial magnetic stimulation," Nature Protocol, 18(2), 293-318.
7. Navarro de Lara, L.I. (2021), "A 3-axis coil design for multichannel TMS arrays," Neuroimage, 224, 117355.

Poster No 52

Function-Specific Targeted rTMS Synergy with Motor Imagery Enhances the Learning of Sports Skills

Hong Li[1], Chun Luo[1], Kang-Jia Chen[2], Jia-Hui Liu[1], Zu-Juan Ye[1], Jue Wang[1]

[1]Institute of Sports Medicine and Health, Chengdu Sport University, Chengdu, Sichuan, [2]University of Electronic Science and Technology of China, Chengdu, Sichuan

Introduction: The primary motor cortex stands out as the most commonly targeted region for Transcranial Magnetic Stimulation (TMS) (Stinear et al., 2009), modulating motor function and engaging in activities (Hamano et al., 2021). It currently represents a vital target region for inducing plasticity in motor skill learning (Saisanen et al., 2021). The conventional target hand motor hotspot is determined by Motor Evoked Potentials (MEP), reflecting the conduction of corticospinal tract. Cortical excitability, as assessed by MEP measurements, serves as an indicator of neural architecture in the brain. Studies have shown

that despite no differences in cortical excitability and behavioral test between groups, facilitatory TMS still enhances cortical plasticity in the experimental group (Kolbasi et al., 2023). Pointing function-specific target may yield better modulatory effects than hotspot (Wang et al., 2020). During the early stages of training, instructing participants on errors and correct techniques could enhance sport performance, especially in mastering more challenging skills (Tzetzis and Votsis, 2006). Motor imagery training involves repetitively mentally rehearsing the correct technique, enhancing muscle control through cognitive brain areas associated with motor function. The goal is to improve complex sports skills and prevent injuries during physical activity (Ladda et al., 2021). One study found overlapping voxel activation in the brain when participants imagined wrist flexion and extension movements compared to the actual execution of these movements (Szameitat et al., 2012). In our study, we utilized the back gliding shot-putting as a motor imagery task, identified function-specific targets through fMRI, and applied 10 Hz repetitive TMS in conjunction with motor imagery to enhance participants' motor performance.

Methods: We recruited 45 healthy, right-handed Physical Education students who were randomly assigned to three groups: the function-specific target, hotspot, and without rTMS groups. All three groups underwent 7 consecutive days of motor imagery training and physical practice of the back gliding shot-putting technique. Subsequently, all participants underwent two behavioral assessments and magnetic resonance imaging scans (including task and resting state) both before and after rTMS. The activation peak voxel of the motor imagery task was defined as the function-specific target. The function-specific target and hotspot groups received 7 days of 10 Hz rTMS, with a stimulation intensity set at 100% of the resting motor threshold (RMT), totaling 1800 pulses per day. A spherical region of interest (ROI) with a radius of 4 mm was computed for whole-brain functional connectivity (FC) using the coordinates of the stimulation targets (task activation peak voxel for the without rTMS group).

Results: Significant alterations in thigh angle during the gliding phase, torso angle at left foot landing during the transition phase, and torso angle at right foot landing were observed with the function-specific target group > hotspot group > without rTMS group. Figure 1 illustrates substantial differences in the spatial distribution of function-specific targets and hotspots. ANOVA conducted on FC maps revealed a significant modulatory effect in the supplementary motor area (GRF correction, voxel level $p < 0.001$, cluster level $p < 0.05$) (Figure 2a). Post-hoc comparisons indicated a significantly larger alteration in FC for both rTMS groups compared to the group without rTMS (Figure 2b). All three groups exhibited significant alterations in FC, with a marked decrease in the two rTMS groups and a significant increase in the group without rTMS (Figure 2c).

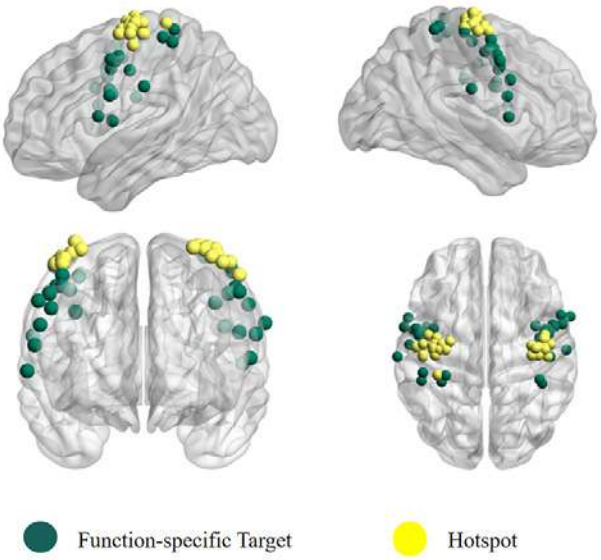

Figure 1. The spatial distribution of function-specific targets and hotspots.

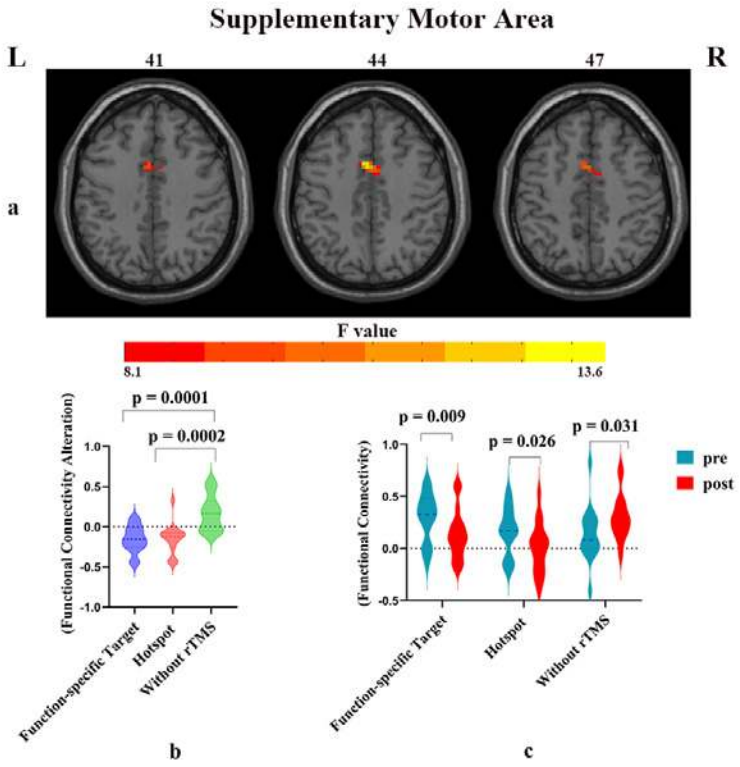

Figure 2. The intervention effect across all three groups.

Conclusions: The application of rTMS, particularly when administered to function-specific targets, has demonstrated a noteworthy synergy with motor imagery training. This synergy significantly contributes to enhancing the learning outcomes of participants involved in acquiring complex sports skills.

References

1. Hamano, Y. (2021), 'The integrative role of the M1 in motor sequence learning', Neuroscience letters, vol. 760, no. 136081
2. Kolbasi, E.N. (2023), 'Enhancement of motor skill acquisition by intermittent theta burst stimulation: a pilot study', Acta Neurologica Belgica, vol. 123, no. 3, pp. 971-977
3. Ladda, A. M. (2021), 'Using motor imagery practice for improving motor performance - A review', Brain and cognition, vol. 150, no. 10570
4. Säisänen, L. (2021), 'Primary hand motor representation areas in healthy children, preadolescents, adolescents, and adults', NeuroImage, vol. 228, no. 117702
5. Stinear, C. M. (2009), 'Repetitive stimulation of premotor cortex affects primary motor cortex excitability and movement preparation', Brain stimulation, vol. 2, no. 1, pp. 152–162
6. Szameitat, A. J. (2012), 'Cortical activation during executed, imagined, observed, and passive wrist movements in healthy volunteers and stroke patients', NeuroImage, vol. 62, no. 1, pp. 266–280.
7. Tzetzis, G. (2006), 'Three feedback methods in acquisition and retention of badminton skills', Perceptual and Motor Skills, vol. 102, no. 1, pp. 275-284
8. Wang, J. (2020), 'High-Frequency rTMS of the Motor Cortex Modulates Cerebellar and Widespread Activity as Revealed by SVM', Frontiers in neuroscience, vol. 14, no. 186

Poster No 53

TMS on the dorsolateral prefrontal cortex induces striatal dopamine release. A 18F-DMFP PET study

Usman Jawed Shaikh[1], Antonello Pellicano[2], Andre Schüppen[1], Alexander Heinzel[3,4], Oliver Winz[3], Hans Herzog[4], Felix Mottaghy[3,5], Ferdinand Binkofski[1,4]

[1]Section Clinical Cognitive Sciences, Department of Neurology, RWTH Uniklinik Aachen, Aachen, Germany, [2]Department of Educational Sciences, University of Catania, Catania, Catania, [3]Department of Nuclear Medicine, RWTH Uniklinik Aachen, Aachen, Germany, [4]Research Centre Juelich, Institute of Neuroscience and Medicine (INM-4), Jülich, Germany, [5]Department of Radiology and Nuclear Medicine, Maastricht University Medical Center (MUMC+), Maastricht, Netherlands

Introduction: Transcranial Magnetic Stimulation (TMS) is a non-invasive brain stimulation technique which can modulate connectivity in the human brain. It is commonly used for depression treatments with long stimulation protocols to the Pre Frontal Cortex (PFC). In this multi-modal study, We combined Positron Emission Tomography (PET) and TMS technique to

investigate the fronto-striatal connectivity in the human brain. Fronto-striatal networks are responsible for a wide range of motor and cognitive functions that includes emotion regulation, movement and attention. In PET sessions, we measured the release of endogenous dopamine in the striatum in response to repeated blocks of excitatory, intermittent theta burst stimulation (iTBS) of the Left-Dorsolateral Prefrontal Cortex (L-DLPFC). The 18F-DesmethoxyFallypride (DMFP) radioligand was utilzed, as it is a high affinity Dopamine receptor-antagonist which binds to the D2,D3 receptors in striatum region.. The radioligand has benefits, including longer physical half-life and its transportation through off-site cyclotron unit, thus accomplishing the demand of pharmacologic challenging studies.The main objective of the current study was to test the dose dependent effects of iTBS over the left DLPFC on the dopamine release in the striatum.

Methods: 23 healthy subjects participated in the study, who underwent iTBS sham (control) and verum (active) stimulations on separate days.The stimulation intensity was set at 90% of resting motor threshold (rMT) for the verum (active) condition. In both stimulation session, the total duration of the PET scan was 120 mins (28 time frames), consisting of 4 excitatory iTBS delivered to the left-DLPFC at 30 mins interval. Excitatory iTBS protocol was comprised of 600 pulses, delivered in a sequence of 20 trains and 10 theta-bursts in a total duration of 190 secs. Each 2 secs long train consisted of a burst of 3 stimuli at 50 Hz, repeated in 5 Hz frequency and having inter-train interval of 8 secs The repeated TMS inside the PET scanner were performed using neuro-navigation. 18F-DMFP was used as the radiotracer, which allowed us to perform measurements lasting 120 minutes. PET dynamic data was analysed using reference method in which cerebellum was used as the reference region (due to lack of D2-D3receptors). Ratio of the striatal and cerebellar activities were calculated at different time points for sham and verum conditions and termed as indices to the receptor binding. Receptor Binding ratios were the main outcome measure representing the ligand binding which is inversely proportional to the Dopamine (DA) levels. Mean Binding ratios in the sub-regions of the striatum (Nucleus Caudate and Putamen) were compared between the two conditions using repeated measures of analysis of variance (ANOVA).

Results: Mean receptor Binding ratios showed a significant difference between sham and verum stimulations. We observed lower Binding ratios in the verum stimulation compared to sham stimulation. Verum iTBS increased the dopamine release in both striatal sub-regions, relative to sham iTBS. Dopamine levels in the verum stimulation session increased progressively across the time frames within about 75 minutes (after three doses of iTBS stimulation) and then essentially remained unchanged until the end of the session.

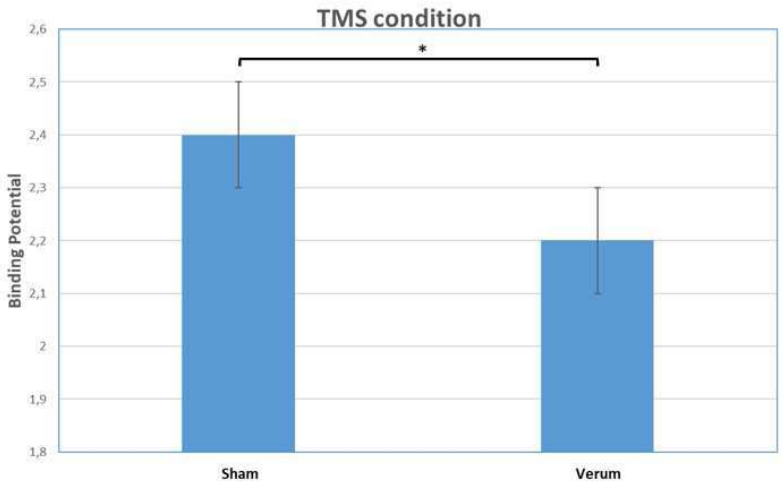

Figure 2: The main effect of TMS on Binding Potential (BP) in the striatum. The verum stimulation showed a reduction of 8.6% [18F]DMFP BP as compared to the sham stimulation.

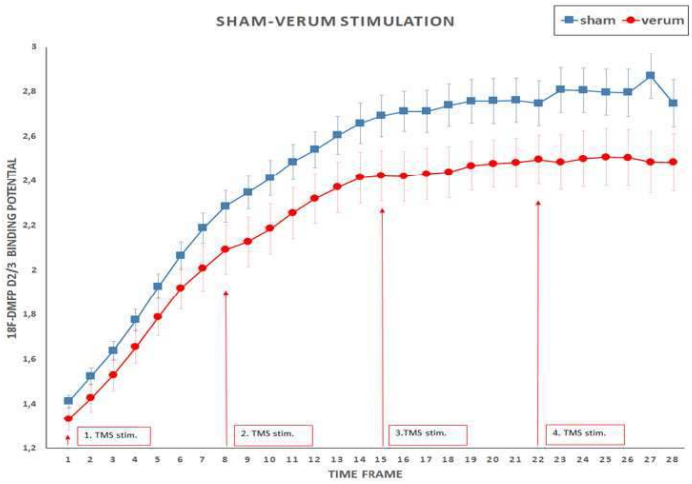

Figure 3: Mean Binding Potentials (BPs) at sham and verum TMSs across 28 time frames. BPs in the verum condition showed a progressive decrease from time frame 1 to time frame 19 (about 75 mins) and then essentially stabilized until the end of the session, frame 28.

Conclusions: Results suggest that the short-timed iTBS protocol performed in time-spaced blocks can effectively induce a dynamic dose dependent increase dopaminergic fronto-striatal connectivity. This scheme could represent a valuable alternative to painful, long stimulation protocols in experimental and therapeutic settings. Specifically, our results demonstrate that three repeated iTBS, spaced by a short time period, achieve larger effects than one single stimulation. This finding has implications for the planning of therapeutic interventions, for example, for the treatment of major depression.

References

1. Alkhasli I., (2019) 'Modulation of Fronto-Striatal Functional Connectivity Using Transcranial Magnetic Stimulation'. Front Hum Neurosci. 2019 Jun 13;13:190.
2. Huang, Y. Z., (2005).'Theta burst stimulation of the human motor cortex'. Neuron 45, 201–206.
3. Ji H. Ko., (2008).'Theta burst stimulation-induced inhibition of dorsolateral prefrontal cortex reveals hemispheric asymmetry in striatal dopamine release during a set-shifting task – a TMS–[11C]raclopride PET study'. Eur J Neurosci.; 28(10): 2147–2155.
4. Strafella, A. P., (2001). 'Repetitive transcranial magnetic stimulation of the human prefrontal cortex induces dopamine release in the caudate nucleus'. J. Neurosci. 21, RC157–RC157.
5. Strafella, A. P.,(2003). 'Striatal dopamine release induced by repetitive transcranial magnetic stimulation of the Human motor cortex'. Brain 126, 2609–2615.
6. Paus, T., (2004). Transcranial magnetic stimulation (TMS) of the human frontal cortex: implications for repetitive TMS treatment of depression. J Psychiatry Neurosci 29, 268–79.
7. Paus, T., (2001). Cortico-cortical connectivity of the human mid-dorsolateral frontal cortex and its modulation by repetitive transcranial magnetic stimulation. Eur J Neurosci 14, 1405–11.
8. Paus, T.,(1997). Transcranial magnetic stimulation during positron emission tomography: a new method for studying connectivity of the human cerebral cortex. J Neurosci 17, 3178–84.

Poster No 54

Preliminary investigation of BOLD dependence on EEG–TMS using a closed-loop TMS–EEG–fMRI

Joonas Laurinoja[1], Umair Hassan[2], Christoph Zrenner[3], Matilda Makkonen[4], Mikko Nyrhinen[4], Pantelis Lioumis[4], Fa-Hsuan Lin[3], Risto Ilmoniemi[4], Dogu Baran Aydogan[1]

[1]University of Eastern Finland, Kuopio, Finland, [2]Stanford University, Stanford, United States, [3]University of Toronto, Toronto, Canada, [4]Aalto University, Espoo, Finland

Introduction: Transcranial magnetic stimulation (TMS) is a powerful tool for non-invasive brain stimulation, with versatile applications in research, diagnostics, and the treatment of psychiatric and neurological disorders. Currently, TMS is administered the same way to all individuals, resulting in inconsistent treatment outcomes. To increase its effectiveness, one approach involves personalizing the treatment by incorporating concurrent neuroimaging methods to guide the procedure. By integrating TMS with real-time neuroimaging modalities such as functional magnetic resonance imaging (fMRI) and electroencephalography (EEG), our objective is to tailor TMS treatment by optimizing stimulation timing, targeting, and dosing on an individualized basis. This abstract outlines our experimental configuration for closed-loop TMS–EEG–fMRI, and shares

our preliminary findings on investigating brain state-dependent TMS–EEG responses and their correlation with concurrently measured BOLD activity in fMRI.

Methods: The experimental setup consists of MRI-compatible EEG amplifiers (NeurOne Tesla, Bittium Ltd.), TMS stimulator (MagPro R30, MagVenture Inc.) and TMS coil (MagVenture MRi-B91). The EEG amplifiers and TMS coil are positioned within the MRI scanner (3T Siemens Skyra) bore. The TMS coil is attached to a custom-made coil holder arm[2] and is integrated with a slightly curved custom-made 8-channel MRI surface head coil array[3]. The subject is equipped with a 64-channel EEG cap (Easycap GmbH) that features seven custom-made carbon-wire-loops (CWLs) leveraged in EEG artifact suppression[6]. EEG is streamed to a real-time processing unit[4] operating on a modified firmware capable of suppressing MRI-induced artifacts and timing TMS to a predefined oscillatory brain state of EEG[5]. 150 single TMS pulses were delivered to the left primary motor cortex (M1) of a right-handed healthy volunteer while the TMS-elicited network activity was monitored with interleaved fMRI acquisition. Functional images were acquired with a gradient-echo echo-planar-imaging (GE-EPI) sequence (TR = 2000 ms; TE = 26.0 ms; voxel resolution 2×2×2 mm3; flip angle 90°). Each TMS–fMRI run consisted of five 30-second "TMS" and "REST" blocks. Each TR included a silent 1-second gap during which a TMS pulse was delivered. 64-channel EEG was recorded at 20 kHz throughout the experiment. The spatially filtered (surface Laplacian) phase of the signal in the C3 electrode at each TMS onset was extracted and divided into four parts: peak, trough, falling, and rising. fMRI images were slice-time and motion corrected, spatially smoothed, coregistrated with anatomical T1 images, and analyzed with SPM12[7]. The design matrix included four regressors, each corresponding to a different EEG phase condition. Additionally, realignment parameters were included in the model as nuisance regressors.

Results: During TMS, a significantly increased ($p < 0.05$ FWE) fMRI signal was detected in M1 and the supplementary motor area (SMA) under the trough, falling, and rising phase conditions. However, the activation varied in strength and morphology across the conditions: TMS applied on the trough of EEG signal elicited broader network activity in SMA and M1 compared to other conditions. TMS applied during the EEG peak condition did not elicit significant activation ($p < 0.05$ FWE) in M1 nor SMA, which has been reported as a low-excitability state in earlier TMS–EEG studies with motor-evoked potentials (MEPs)[4]. The activated regions of M1 and SMA matched the activated sensorimotor network during a voluntary finger-tapping experiment.

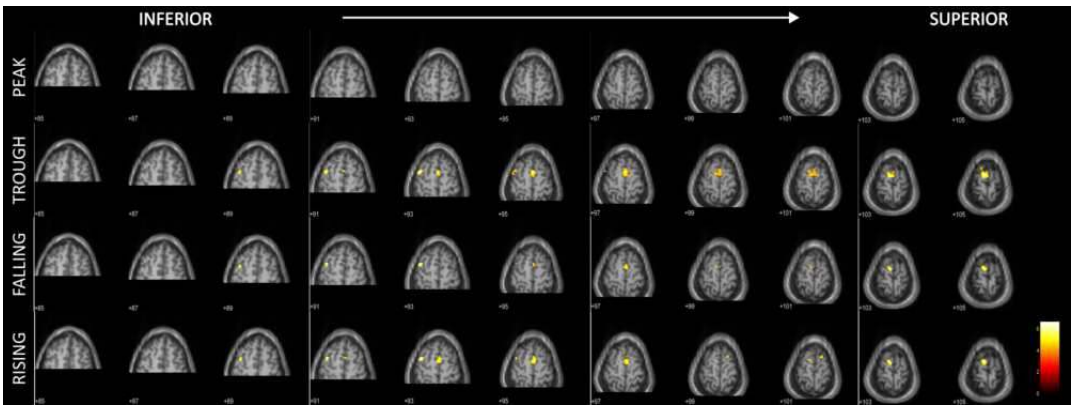

Conclusions: Here we present the preliminary results from our multimodal TMS–EEG–fMRI system. In the future, we aim for full real-time integration including acquisition and data processing of fMRI and EEG as well as TMS delivery. This technical

endeavor could open new avenues of subject-specific research and development of novel diagnostic methods and treatment strategies for a variety of brain disorders.

References
1. Loo, C. K., & Mitchell, P. B. (2005). "A review of the efficacy of transcranial magnetic stimulation (TMS) treatment for depression, and current and future strategies to optimize efficacy". Journal of Affective Disorders, 88(3), 255–267.
2. Lee, H. J. et al. (2023). "Design of coil holder for the improved maneuvering in concurrent TMS-MRI". Brain Stimulation.
3. Wu P.-Y. et al. (2015). "A 10-channel TMS-compatible planar RF coil array for human brain MRI at 3T". Intl. Soc. Mag. Reson. Med., 625.
4. https://sync2brain.com/
5. Zrenner, C. et al. (2018). "Real-time EEG-defined excitability states determine efficacy of TMS-induced plasticity in human motor cortex". Brain Stimulation, 11(2), 374–389.
6. Laurinoja, J. et al, (2023). "Accuracy of EEG-phase estimation for closed-loop brain stimulation inside the MRI device". Brain Stimulation, 16(1), 302–303.
7. http://fil.ion.ucl.ac.uk/spm/

Poster No 55

Neural Correlates of Anosognosia in Neurocognitive Disorders

Serap Özlü[1]

[1]Max Planck Institute for Human Cognitive and Brain Sciences, Leipzig, Germany

Introduction: Dementia, also known as major neurocognitive disorder, is a comprehensive term used to describe the loss of cognitive abilities, changes in memory, language functions and alterations in behavior.[1] Major neurocognitive disorders have significant repercussions on patients, their families, the economy, and healthcare systems.[2] Anosognosia is a word of Ancient Greek origin that translates to "without knowledge of disease". Anosognosia represents a multifaceted neurological phenomenon that exists along a spectrum. It pertains to situations, where individuals are unable to recognize or accurately assess the deficits caused by their disease. Anosognosia has substantial implications for individuals with dementia and the caregivers who support them.[3] The primary objective of this study was to explore the neural underpinnings of anosognosia in individuals with neurodegenerative diseases. Given the complexity of anosognosia research, our approach was characterized by an unbiased, systematic investigation, and a meta-analysis conducted without any predefined hypotheses.

Methods: The systematic review was conducted in accordance with PRISMA guidelines. The protocol for the systematic review and meta-analysis was registered on the database PROSPERO. The comprehensive search is conducted by using the electronic database MEDLINE (PubMed). Anosognosia-related keywords were included following an extensive literature search, while the classification of neurodegenerative diseases was based on the DSM-5 criteria. The search strategy consists of three main categories: neurodegenerative diseases, lack of awareness and neuroimaging methods. Two independent reviewers conducted a thorough screening of article titles and abstracts, and where necessary, they examined full texts in accordance with a predefined search strategy. Studies failing to meet the eligibility criteria were systematically excluded from the analysis. Data are extracted from papers according to a predesigned data collection form. For meta-analysis Brainmap GingerALE (v3.0.2) software is used. GingerALE is designed for conducting meta-analyses of neuroimaging studies via the activation likelihood estimation (ALE) method.[4] For the quality assessment of studies, we used the Newcastle-Ottawa Scale adapted version of cross-sectional studies. Lastly, we conducted Jackknife sensitivity analysis to test the reliability of the results.

Results: During the initial screening phase, we identified a total of 1,904 studies. Following eligibility criteria, we arrived at a final selection of 16 studies that met the criteria for inclusion in the systematic review. All studies used appropriate measurements, and diagnostic criteria, and included representative groups of relative dementia subtypes. In the ALE analysis, the results revealed two clusters and three peak coordinates. Gray matter correlations of dementia across all groups showed that medial frontal gyrus and cingulate gyrus were mainly affected areas by anosognosia. The outcomes of the jackknife sensitivity analysis revealed the stability of specific brain regions. The medial frontal gyrus demonstrated robust stability in 12 out of 16 iterations, while the cingulate gyrus exhibited stability in 14 out of 16 iterations.

Conclusions: Awareness of a disease has significant impacts on both patient and caregiver in terms of having the correct diagnosis and following an appropriate treatment. Patients with anosognosia struggle with self-evaluation of disease-related symptoms and decline. Therefore, it is necessary to understand the underlying mechanisms of this phenomenon and its correlates in the brain. To our knowledge this is the first coordinate based meta-analysis on anosognosia in several types of dementia. Our results,aligning with previous research findings (5) (6), revealed that reduced gray matter volumes and diminished metabolic activity within the medial frontal gyrus and cingulate gyrus are inversely correlated with the severity of anosognosia.

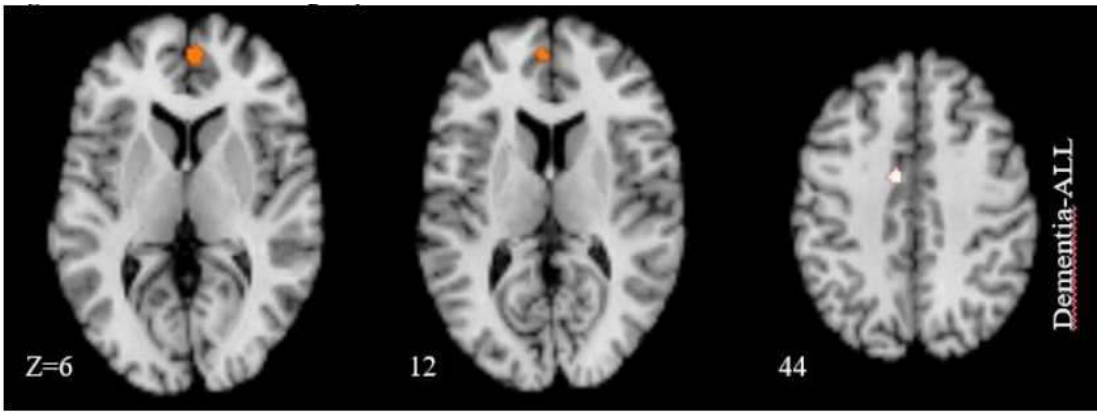

References

1. American Psychiatric Association: Diagnostic and Statistical Manual of Mental Disorders, Fifth Edition, Text Revision. Washington, DC, American Psychiatric Association, 2013.
2. Hugo, J., & Ganguli, M. (2014). Dementia and cognitive impairment: epidemiology, diagnosis, and treatment. Clinics in geriatric medicine, 30(3), 421–442. https://doi.org/10.1016/j.cger.2014.04.001
3. Howard J. Rosen (2011) Anosognosia in neurodegenerative disease, Neurocase: The Neural Basis of Cognition, 17:3, 231-241
4. Eickhoff, S. B., Laird, A. R., Grefkes, C., Wang, L. E., Zilles, K., & Fox, P. T. (2009). Coordinate-based activation likelihood estimation meta-analysis of neuroimaging data: a random-effects approach based on empirical estimates of spatial uncertainty. Human brain mapping, 30(9), 2907–2926. https://doi.org/10.1002/hbm.20718
5. Jobson, D. D., Hase, Y., Clarkson, A. N., & Kalaria, R. N. (2021). The role of the medial prefrontal cortex in cognition, ageing and dementia. Brain communications, 3(3), fcab125. https://doi.org/10.1093/braincomms/fcab125
6. Tan, R. H., Pok, K., Wong, S., Brooks, D., Halliday, G. M., & Kril, J. J. (2013). The pathogenesis of cingulate atrophy in behavioral variant frontotemporal dementia and Alzheimer's disease. Acta neuropathologica communications, 1, 30. https://doi.org/10.1186/2051-5960-1-30

Poster No 56

Improving Coil Setup and Data Processing Strategies for Concurrent MRI and Brain-Stimulation Studies

Michael Burke[1], Yiwu Xiong[1], Lorena de Melo[1], Kuri Takahashi[1], Maximilian Lueckel[2], Emilio Chiappini[1], Til Ole Bergmann[3], Erhan Genc[1]

[1]Leibniz Research Centre for Working Environment and Human Factors, Dortmund, Germany, [2]Neuroimaging Center (NIC), Focus Program Translational Neuroscience, Johannes Gutenberg University, Mainz, Germany, [3]Johannes-Gutenberg University Medical Center, Mainz, Rhineland-Palatinate

Introduction: Transcranial magnetic stimulation (TMS) is an established non-invasive method for stimulating the human brain. However, its neurophysiological and behavioral effects remain poorly understood. The concurrent application of TMS and fmri provides a robust research approach that merges TMS's causal capabilities with fMRI's high spatial resolution. Here, we conduct a comparative assessment of two different TMS-fMRI setups and preprocessing methods, all of which will be compared to data acquired using a standard 64ch head coil without stimulation. Our primary objective is to elucidate the constraints inherent in current procedures and thereby define optimal strategies for probing the impact of brain stimulation on both behavior and neural activity. This investigation holds significant promise for advancing future research employing this sophisticated technique.

Methods: 1. Acquisition a) Testing 3 MRI head coils: 64-Channel coil (Fig1), Custom-made coil setup with two 18ch body array coils wrapped around the head using a home-made holder for maximum accessibility and space for TMS stimulation equipment, commercially available MRI-TMS coil (Navarro et al. MRM 74:1492-1501) consisting of two 7ch coils, one of the two 7ch coils has a MR compatible TMS coil attached, for MR acquisition. b) MRI sessions included resting-state fMRI (rsfMRI) and anatomical MRI at our 3T Prisma scanner. For rsfMRI (10 min), participants were asked to keep their eyes closed. Multiband-multiecho (MBME) EPI sequence: TR=1250 ms, multiband factor=3, and 3 TE times (13, 35, 56 ms). 2. Preprocessing a) Homogenization: Spatial signal intensity homogenization was done by applying a signal intensity correction profile obtained from two images acquired with the respective receive coil and with the scanners integrated body coil. b) Multi echo fMRI data were used to calculate T2*-maps by fitting an exponential decay curve. S0 maps were calculated for each EPI image and time courses with increased SNR were extracted from these S0 maps for further analysis. 3. Postprocessing a) Independent component analysis (ICA) was performed to obtain brain networks from rsfMRI data using FSL's MELODIC. b) Motor and visual ICA networks were identified based on cross-correlation analyses with a set of major brain networks as described by Smith et

al. PNAS 106, 13040-13045 (2009) c) Spatial similarities of visual and motor ICAs were compared using the Dice coefficient (0: no similarity, 1: identical spatial overlap of components).

Three different coil setups used: A) standard 64ch head-neck coil, B) two 18ch body array coils wrapped around the head using a home-built coil holder, C) commercially available MRI-TMS coil consisting of two 7ch coils combined with a MRI compatible TMS brain stimulation coil

Results: Correlation of ICA components with visual component as identified by Smith et al. increased with data preprocessing (from r=0.48 to r=0.59, 64ch,r=0.59 to r=0.61 for body array and r=0.33 to r=0.42 MRI-TMS-coil) and slightly increased for motor components (r=0.33 to r=0.37 for 64ch, r=0.26 to r=0.32 for body array, and remained unchanged for the MRI-TMS coil). Dice coefficient showed higher similarity of components obtained with 64-channel coil and body array coil setup. However, the spatial similarity of components obtained with MRI-TMS coil vs. 64-channel coil or body array coil was lower for visual and motor networks identified by ICA.

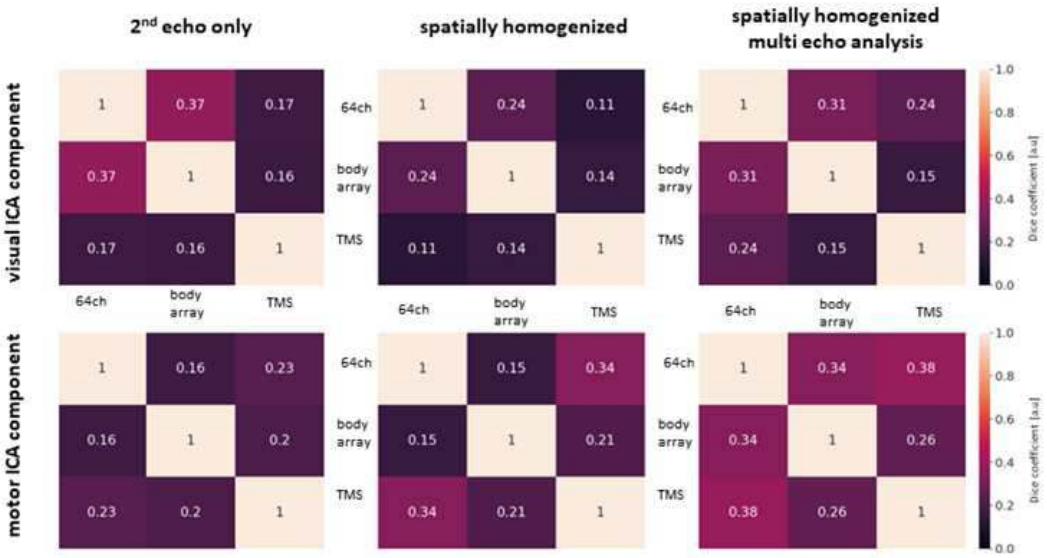

Dice coeffients calculated for the three coils used. Displayed are the Dice spatial-similarity index of activation patterns obtained from the three coils and after the data-preprocessing steps under investigation. Higher Dice coefficients reflect better spatial similarity across coils. Notably we found less similarity between gold standard 64-channel head-neck array and TMS as well as body array ICA components and improved similarity after data preprocessing steps had been applied.

Conclusions: Brain networks identified from rs-fMRI spatially varied depending on the coil setup and data preprocessing strategy used. Results obtained from wrapped around body array coil setup closer resembled the findings obtained with the 64-channel coil. The optimal coil configuration differs depending on whether brain networks or only local cortical activity in proximity to the coil are under investigation. On the other hand, the MRI-TMS coil provides best accessibility for brain stimulation whereas no brain TMS brain stimulation can be performed using the 64ch coil, the best compromise with respect to access and with improved data preprocessing strategies is the body array setup for deep brain and brains network studies. With the enhanced coil setup we will be able to improve concurrent brain networks studies during brain stimulation.

References

1. Navarro de Lara, L. I. et al. A Novel Coil Array for Combined TMS/fMRI Experiments at 3 T, Magnetic Resonance in Medicine 74:1492-1501 (2015)
2. Ahmed, Z. et al. ME-ICA/tedana: 23.0.1. (2023) doi:10.5281/ZENODO.1250561
3. Smith, S. M. et al. Correspondence of the brain's functional architecture during activation and rest. Proc. Natl. Acad. Sci. U.S.A. 106, 13040-13045 (2009).

Poster No 57

Sexing the parental brain in shopping: a 3T fMRI study

Tsai-Jing Yang[1], ChengHsiang Tsai[1], Chun-Chia Kung[2], Ding-Ruey Yeh[3]

[1]National Cheng Kung University, Tainan, Tainan, [2]National Cheng Kung University, Tainan, Taiwan, [3]National Central University, Taichung, Taichung

Introduction: Parental love knows no bounds. This love manifests in various behavioral aspects, such as parents watching animations or playing puzzle games together with their children. Bartels and Zeki (2004) proposed that the activation of the periaqueductal gray (PAG) is more pronounced in mothers when they see their own children compared to unfamiliar ones. This study emphasizes the pivotal role of PAG in the context of parental love, yet there is little exploration of parental love in the context of shopping. Knutson et al. (2007) used functional Magnetic Resonance Imaging (fMRI) to measure neural activation in participants during the shopping process. They found that the nucleus accumbens (NAcc), medial prefrontal cortex (MPFC), and insula could predict human shopping decisions. In this study, we utilize fMRI to investigate the differences in the brain neural circuits of novice parents during shopping decisions.

Methods: In this study, 45 subjects were recruited, of which 21 were fathers and 24 were mothers, aged between 25-40 years, all having children aged 2 to 5 years at the time of the scan. The shopping task involved a set of 400 pictures, including 200 items for children (equally split between boys and girls), 100 items for mothers, and 100 items for fathers. The father and mother subjects are tested separately (e.g., fathers were scanned in Tainan, whereas mothers were scanned in Taichung). The participants only saw pictures related to their own sex (e.g., fathers saw father-related items) and the sex of their child (e.g., fathers saw girl-related items), randomly appearing in the slow event-related fashion. In each 16-second trial, there were 8 seconds to decide whether to buy the presented item (with the picture and the price underneath). The data analysis involved both univariate (i.e., the General Linear Model) and multivariate (i.e., MVPA searchlight) analyses, applied to the SPM-preprocessed data. Additionally, logistic regression was employed to predict their shopping decisions.

Results: The behavioral results showed that, as expected, both mothers and fathers exhibited a higher propensity to purchase items for their children and a lower inclination to buy for themselves: out of the 30% purchase rate, an average of 60-70% were for the children. When examining gender differences, parental love manifests differently in the male and female brain. GLM contrasts indicated that, while both parents activated similar brain regions when contrasting purchases for their children versus themselves, mothers exhibited a more extensive activation of cerebral areas compared to fathers. In contrast, the PAG was more activated in fathers, and was equally salient using both univariate and multivariate analyses (see Fig. 1). Logistic regression analysis further emphasized the predictive role of behavioral indicators, such as reaction time, product price, and product category (parent or children items), in purchasing decisions, as well as the significantly predictive roles of NAcc, MPFC, and PAG activities (Fig. 2). Lastly, parametric analysis with reaction times also showed significant modulation effects in MPFC (i.e., the longer the decision time, the stronger the MPFC activity), the core site of value computation, only when parents shopped for themselves, but not when parents shopped for their children.

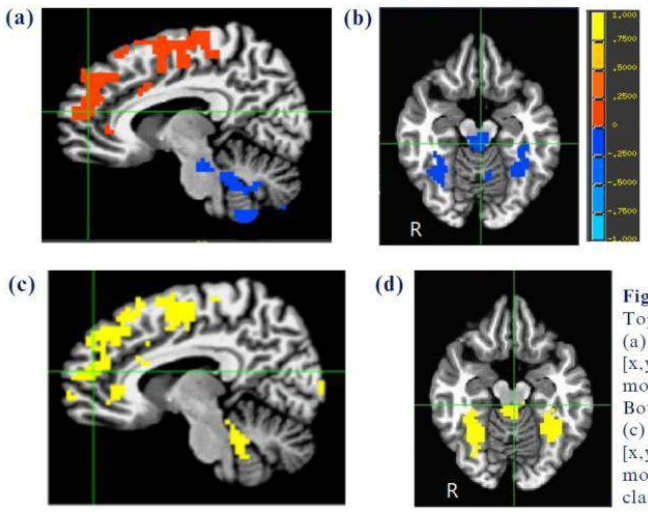

Fig1.
Top: GLM result.
(a) Cortical view (b) Sagittal view
[x,y,z]=[-2,-30,-18](MNI)
mother vs. father buy for child FDR, p = .05.
Bottom: MVPA result.
(c) Cortical view (d) Sagittal view
[x,y,z]=[-2,-30,-18](MNI)
mother vs. father buy for child
classification accuracy > .75.

	Behavioral data	Brain activation	Combined
Constant	**0.341*** [a]**	-0.085	**0.466*** **
Reaction time	**0.076*** **		**0.074*** **
Price	**-0.000*** **		**-0.000*** **
Item category (child)	**0.341*** **		**0.357*** **
Item category (self)	**-0.591*** **		**-0.579*** **
NAcc (bilateral)		0.006	**0.006***
MPFC (bilateral)		**0.013****	**0.012***
Anterior Insula (left)		-0.000	-0.000
Anterior Insula (right)		-0.002	-0.001
PAG		**-0.007***	**-0.007***
Number of observations	8913	8913	8913
AIC[b]	11696.7	12262.4	11683.5

[a] Significance: ***p < 0.001; **p < 0.01; *p < 0.05.
[b] AIC, Akaike Information Criterion (lower score indicates better fit to the data).

Table 1. Logistic Regression Models Predicting Decisions to Purchase or Not

Conclusions: In summary, our results revealed that (a) both mothers and fathers share a comparable dedication to expressing love, as evidenced by a willingness to invest more in their offspring and less in personal purchases; (b) via differential brain mechanisms, mothers exhibiting greater cerebral involvement and fathers showing relatively higher subcortical activities and higher subcortical-cortical connectivities, in purchasing behavior; (c) The PAG, NAcc, and MPFC effectively predicted parental shopping decisions; and (d) when buying for their children, parents are unconditional buyers; when buying for themselves, parents are rational shoppers.

References

1. Bartels A. (2004) The neural correlates of maternal and romantic love. Neuroimge 21,1155-1166
2. Knutson, B. (2007). 44 Neural predictors of purchases. Neuron, 53, 147-156.

Poster No 58

E-field Orientation in Theta Burst Stimulation Modulates Changes in Motor Evoked Potential Amplitude

Silas Preis[1], Constanze Ramschütz[2], Sandro Krieg[3], Claus Zimmer[4], Bernhard Meyer[5], Nico Sollmann[6], Severin Schramm[7]

[1]Technical University of Munich, Munich, Bavaria, [2]Technical University of Munich, München, Germany, [3]Department of Neurosurgery, Universitätsklinikum Heidelberg, Heidelberg, Germany, [4]Dep. of Neuroradiology, School of Medicine, Klinikum Rechts der Isar, Technical University of Munich, Munich, Bavaria, [5]Dep. of Neurosurgery, School of Medicine, Klinikum rechts der Isar, Technical University of Munich, Munich, Bavaria, [6]Dep. of Diagnostic and Interventional Radiology, University Hospital Ulm, Munich, Bavaria, [7]Department of Diagnostic and Interventional Neuroradiology, School of Medicine, Munich, Bavaria

Introduction: Transcranial magnetic stimulation (TMS) is a noninvasive method for brain stimulation employed in an increasing range of diagnostic and therapeutic settings (Krieg, 2017; Lefaucheur et al., 2020). Although TMS-based neuromodulation (NM) protocols are utilized in the treatment of neuropsychiatric and other conditions, the underlying neurophysiological processes remain insufficiently understood (Goldsworthy, Hordacre et al. 2021). One thus far unexamined factor to optimize TMS NM outcomes is the orientation of the stimulating coil relative to individual cortical anatomy, which has been recognized as a relevant factor in single-pulse stimulation (Raffin, Pellegrino et al. 2015). We present preliminary findings from healthy participants in whom we investigated the impact of e-field orientation during continuous theta burst stimulation (cTBS) on NM regarding motor evoked potentials (MEPs).

Methods: 8 healthy participants (average age: 23 ± 3 years, 4 females) underwent T1-weighted (T1w) imaging at 3 Tesla to obtain images for neuronavigated TMS (nTMS). Three nTMS sessions separated by at least 14 days were conducted per subject to assess the impact of the e-field orientation during cTBS on the MEP amplitude. After identification of the abductor pollicis brevis muscle hotspot and the coil orientation for maximum MEP generation within the dominant hemisphere, the resting motor threshold (rMT) was determined and 30 MEPs were elicited at 150% rMT (M. Goldsworthy, Hordacre, & Ridding, 2016; Hordacre et al., 2017). Afterwards, cTBS with conventional parameters (40 s, 600 stimuli, 3 stimuli with 50 Hz every 200 ms) (Huang, Edwards et al. 2005) was performed at 70 % rMT (M. Goldsworthy et al., 2016; Hordacre et al., 2017) at the same site using one out of three protocols (OPT: stimulation with optimal coil direction; 90°: anterior coil end rotated 90° upwards from OPT; SHAM: stimulation with a 7.3-cm spacer). Subsequently, we elicited 3 sets of 30 MEPs at increasing intervals

after cTBS (0-5 min, 5-10 min, 10-15 min). The MEPs were analyzed to evaluate the influence of the e-field orientation on MEP amplitudes.

Results: After adjusting for a family-wise error rate, MEP amplitudes pre- and post-TBS differed significantly between the measured time points, with the observed differences varying by e-field orientation of cTBS (Figure 1A-C). On a group level, cTBS in both OPT and SHAM conditions demonstrated heightened MEPs compared to baseline (OPT: post-cTBS 3553±1999 µV vs. pre-cTBS 2923±2460 µV, $p<0.05$; Figure 1A; SHAM: post-cTBS 3174±2160 µV vs. pre-cTBS 2235±1703 µV, $p<0.0001$; Figure 1C). Here, SHAM demonstrated significantly higher increases of MEP amplitudes compared to the other two conditions (SHAM-cTBS 698±1249 µV vs. OPT-cTBS 321±1293 µV vs. 90°-cTBS 293±1240 µV, $p<0.05$; Figure 1E). Results on the group level did not reflect pronounced and heterogenous NM effects as observed on the single-subject level (Figure 1G-J).

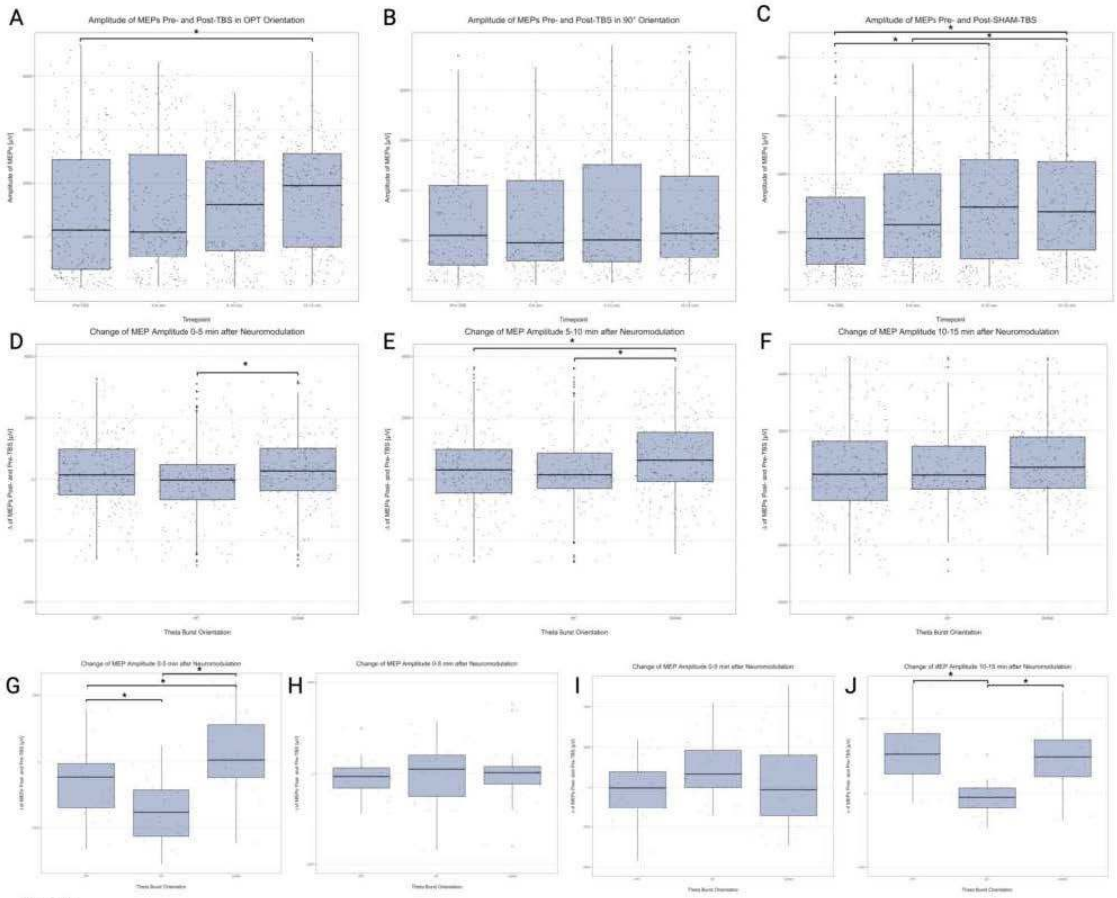

Figure 1:
A-C: Change of motor evoked potential (MEP) amplitudes (y-axis) pre- and post-continuous theta burst stimulation (cTBS) across three short-term intervals (x-axis; 0-5 min, 5-10 min, 10-15 min) for all three conditions (OPT [A]: stimulation with previously determined optimal direction; 90° [B]: stimulation with anterior coil end rotated 90° upwards from OPT; SHAM [C]: stimulation with a 7.3 cm spacer) on group level. OPT (A) and SHAM (C) cTBS led to significantly heightened MEPs compared to baseline.
D-F: Change of MEP amplitude compared to baseline (y-axis) 0-5 minutes (D), 5-10 minutes (E,) and 10-15 minutes (F) after neuromodulation (NM) comparing all three conditions (x-axis: OPT, 90°, SHAM) on group level. MEP facilitation after SHAM was significantly higher both in the first short-term interval (D) compared to 90° and in the second short-term interval (E) compared to both OPT and 90°.
G-J: Investigations in single subjects for 4 exemplary participants (P1-4) showed heterogenous responses to different protocol administrations in the first short-term interval (0-5 minutes). Regarding the change of MEP amplitudes from the 30 trials pre-cTBS (baseline) to the first 30 trials post-cTBS, the differences between OPT, 90°, and SHAM for P2 and P3 were moderate. On the other hand, P1 (G) showed significantly lower MEP changes after OPT and 90° condition compared to SHAM, while P4 (J) showed significantly higher MEP changes after OPT and SHAM compared to 90°. Figure created with Biorender.com.

Conclusions: On a group level, counter to the classical assumption of MEP suppression, we observed MEP facilitation following cTBS in both OPT and SHAM conditions, potentially highlighting the need to further elucidate sham-derived effects in TMS NM (Boucher et al., 2021). These findings add to research questioning the consistency of TMS NM (M. R. Goldsworthy, Hordacre, Rothwell, & Ridding, 2021). Changes in NM response based on e-field orientation were more pronounced for some subjects compared to others (Figure 1G-J), stressing the inter-individual variability in NM responses (M. R. Goldsworthy et al., 2021). Our results may underscore the complexity and variability of cTBS effects on cortical excitability. Additionally, we provide first evidence implying e-field orientation during TMS NM as a factor influencing NM outcome. Individual optimization of e-field orientation could improve NM outcomes in other settings, e.g. therapeutic applications.

References

1. Boucher, P. (2021). Sham-derived effects and the minimal reliability of theta burst stimulation. Scientific Reports, 11(1), 1-12.
2. Goldsworthy, M. (2016). Minimum number of trials required for within-and between-session reliability of TMS measures of corticospinal excitability. Neuroscience, 320, 205-209.
3. Goldsworthy, M. (2021). Effects of rTMS on the brain: is there value in variability? Cortex, 139, 43-59.

4. Hordacre, B. (2017). Variability in neural excitability and plasticity induction in the human cortex: a brain stimulation study. Brain Stimulation, 10(3), 588-595.
5. Krieg, S. M. (2017). Navigated transcranial magnetic stimulation in Neurosurgery (Vol. 299): Springer.
6. Lefaucheur, J.-P. (2020). Evidence-based guidelines on the therapeutic use of repetitive transcranial magnetic stimulation (rTMS): an update (2014–2018). Clinical Neurophysiology, 131(2), 474-528.

Poster No 59

Precise motor mapping with robotic TMS versus finger tapping fMRI activation locations

Zijian Feng[1], Benjamin Kalloch[1], Ole Numssen[1], Gesa Hartwigsen[2], Jens Haueisen[3], Yufeng Zang[4], Thomas Knösche[1], Konstantin Weise[1]

[1]Max Planck Institute for Human Cognitive and Brain Sciences, Leipzig, Saxony, [2]Leipzig University, Leipzig, Saxony, [3]Technische Universität Ilmenau, Institute of Biomedical Engineering and Informatics, Ilmenau, Thuringia, [4]Center for Cognition and Brain Disorders, The Affiliated Hospital of Hangzhou Normal University, Han, Hangzhou, Zhejiang

Introduction: Transcranial Magnetic Stimulation (TMS) offers a non-invasive method to stimulate cortical neurons, allowing to map causal structure-function relationships. Traditional TMS mapping methods, using fixed coil orientations and target grids, often struggle with accurately pinpointing neural structures responsible for effects like motor evoked potentials (MEPs) due to the spatial unfocality of the TMS-induced electric field (e-field) (Weise et al., 2023, Numssen et al., 2023). To address this, we recently proposed and validated a novel TMS-mapping approach that increases the precision of TMS mapping by considering the variance of the e-field across multiple coil positions and orientations (Weise et al., 2023, Numssen et al., 2021, Weise et al., 2020). Additionally, robotic TMS approaches have been reported to facilitate improved efficiency, tolerability, and precision in deriving high-fidelity motor maps (Grab et al., 2018). This study compares TMS-based and functional magnetic resonance imaging (fMRI) based cortical localizations of finger muscle representations in the primary motor. Previous study observed that the fMRI-based activation for a thumb tapping task was positioned more laterally and anteriorly compared to TMS abductor pollicis brevis hotspot (Wang et al., 2020). Here, our objective is to compare the identified cortical position of the first dorsal interosseous (FDI) muscle hotspot, as determined through robotic TMS using our precise localization approach, with the peak activation of index finger tapping in fMRI.

Methods: In our robotic TMS study, fifteen right-handed participants (10 females, average age 24.7 ± 1.7 years) were examined. For an overview of the experimental design and the general workflow, refer to Figure 1A from Weise et al. (2023). Before TMS, they underwent T1-weighted, T2-weighted, DWI, and finger tapping fMRI scans. Participants performed an event-related finger tapping task, responding to visual cues with right index finger movements. The TMS-induced electric field (E-field) was computed using a finite element model (FEM) using SimNIBS (Saturnino et al., 2019). Administering 200 single TMS pulses at 170% MT with varied coil positions and orientations yielded robust cortical maps. To identify the cortical origin of the MEPs we utilized nonlinear regression of a log-transformed sigmoidal function of fit the local E-field to the MEP amplitude (Numssen et al., 2021). Optimal parameters for cortical elements were identified using the Levenberg-Marquardt algorithm, with R^2 values indicating the goodness of fit, illustrated on cortical congruence maps. Figure 1B is an illustrative representation of an example result from an individual participant.

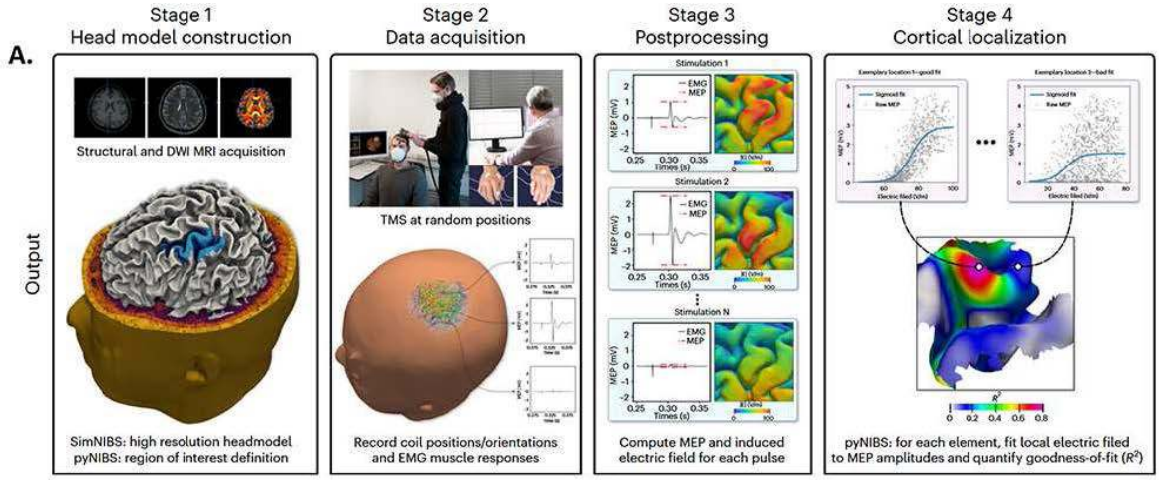

A. Overview of the experimental design and general workflow, as adapted from Weise et al., 2023. B. Illustrative representation of individual participant results. The underlay features an R^2 map computed utilizing the Precise TMS mapping methodology. Green spheres denote areas with the highest R^2 values, signifying the hotspots; red denotes fMRI activations. C. Comparative visualization of TMS hotspots and fMRI activations for finger tapping in Montreal Neurological Institute (MNI) space. The green spheres represent individual TMS hotspots; the red spheres indicate individual fMRI activations. The blue lines connect hotspots and activations originating from the same participant. The large yellow sphere denotes the group-level mean coordinate for TMS hotspots, while the large blue sphere represents the group-level mean coordinate for fMRI activations.

Results: Our findings revealed a notable discrepancy relationship between the fMRI activation and the TMS hotspot in the brain (Figure 1C). A statistically significant difference was noted along the x-axis ($t = -2.48$, $p = 0.026$), indicating that the fMRI activation was more laterally positioned relative to the TMS hotspot. No significant differences were noted along the y and z axes. The mean Euclidean distance between the fMRI activation and TMS hotspot was approximately 8.47 millimeters.

Conclusions: Our precise localization revealed that peak fMRI activation during index finger tapping tasks is typically more lateral compared to the FDI hotspot identified by robotic TMS. This highlights the distinction between neural networks activated by passive cortical stimulation and active movement. TMS evokes direct neural activity, while fMRI detects subsequent hemodynamic changes, which might not coincide spatially with the initial activation site. This discrepancy could be attributed to the intricate dynamics of cortical activation, neurovascular coupling, or activation spread in adjacent areas during task performance.

References

1. GRAB, J. G., ZEWDIE, E., CARLSON, H. L., KUO, H. C., CIECHANSKI, P., HODGE, J., GIUFFRE, A. & KIRTON, A. 2018. Robotic TMS mapping of motor cortex in the developing brain. J Neurosci Methods, 309, 41-54.
2. NUMSSEN, O., VAN DER BURGHT, C. L. & HARTWIGSEN, G. 2023. Revisiting the focality of non-invasive brain stimulation - Implications for studies of human cognition. Neurosci Biobehav Rev, 149, 105154.
3. NUMSSEN, O., ZIER, A. L., THIELSCHER, A., HARTWIGSEN, G., KNOSCHE, T. R. & WEISE, K. 2021. Efficient high-resolution TMS mapping of the human motor cortex by nonlinear regression. Neuroimage, 245, 118654.
4. SATURNINO, G. B., PUONTI, O., NIELSEN, J. D., ANTONENKO, D., MADSEN, K. H. & THIELSCHER, A. 2019. SimNIBS 2.1: A Comprehensive Pipeline for Individualized Electric Field Modelling for Transcranial Brain Stimulation. In: MAKAROV, S., HORNER, M. & NOETSCHER, G. (eds.) Brain and Human Body Modeling: Computational Human Modeling at EMBC 2018. Cham (CH).
5. WANG, J., MENG, H. J., JI, G. J., JING, Y., WANG, H. X., DENG, X. P., FENG, Z. J., ZHAO, N., ZANG, Y. F. & ZHANG, J. 2020. Finger Tapping Task Activation vs. TMS Hotspot: Different Locations and Networks. Brain Topogr, 33, 123-134.
6. WEISE, K., NUMSSEN, O., KALLOCH, B., ZIER, A. L., THIELSCHER, A., HAUEISEN, J., HARTWIGSEN, G. & KNOSCHE, T. R. 2023. Precise motor mapping with transcranial magnetic stimulation. Nat Protoc, 18, 293-318.
7. WEISE, K., NUMSSEN, O., THIELSCHER, A., HARTWIGSEN, G. & KNOSCHE, T. R. 2020. A novel approach to localize cortical TMS effects. Neuroimage, 209, 116486.

Poster No 60

Lateral Prefrontal Cortex rTMS May Affect Functional Controllability in Mild Cognitive Impairment

Simone Papallo[1], Fabrizio Esposito[2], Federica Di Nardo[3], Sabrina Esposito[4], Mario Cirillo[2], Giovanni Cirillo[2], Mattia Siciliano[4], Francesca Trojsi[4], Ilaria Gigi[4]

[1]University of Campania, "Luigi Vanvitelli", Napoli, NA, [2]University of Campania "Luigi Vanvitelli", Naples, Italy, [3]University of Campania "Luigi Vanvitelli", Napoli, Napoli, [4]University of Campania, "Luigi Vanvitelli", Naples, Italy

Introduction: Mild cognitive impairment (MCI) can be viewed as the prodromal stage of Alzheimer's disease[1]. It refers to a condition of cognitive decline greater than expected in relation to a patient's age and education and can affect all brain domains[2]. Non-invasive brain stimulation might play an important role in slowing down or preventing the transition from MCI to dementia as it is relatively free of adverse effects[3]. Particularly, repetitive transcranial magnetic stimulation (rTMS) has provided therapeutic effects, modifying cognitive performances and brain functional connectivity (FC) in many neurological and psychiatric diseases[4]. Varying the frequency of the stimulation protocol, it can induce an excitatory (high frequency, 5–20 Hz) or inhibitory effect (low frequency, ≤1 Hz) on cortical excitability[5] and previous studies have shown FC increases across different brain regions[6]. Here, by leveraging network control theory (NCT) modelling applied to the human connectome, we investigated the effects of high-frequency (10 Hz) rTMS stimulations applied to the dorso-lateral prefrontal cortex on the average (AC) and modal (MC) controllability[78] of functional connectome nodes encompassing the stimulation site.

Methods: All details about subject and procedures, including MRI data acquisition and pre-processing and rTMS stimulation protocol can be found in[6]. We extracted FC matrices from n=11 (age: 64.82 ± 10.03, 5 males) and n=12 (age: 68.33 ± 8.56, 4 males) MCI patients who underwent respectively active and sham rTMS sessions and MRI scans at baseline, 4 weeks and 6 months. We applied a 200-region parcellation[9] whose cortical nodes are pre-labelled to seven large-scale functional networks. Based on the NCT formulation for time-invariant systems, we estimated the AC and MC and regressed out age and gender covariates, separately for each group and time point. Resulting AC and MC were converted to percentile ranks and statistically analysed by fitting a 2-way mixed-effects ANOVA model with one between-subject factor (active vs. sham) and one within-subject factor (baseline vs. 4 weeks vs. 6 months). One- and two-sample T-tests were performed for pairwise post-hoc comparisons. ANOVA F-maps for the interaction were projected on a brain template to descriptively display nodes with significant effects.

Results: The group-by-time interaction was statistically significant in the node closest to the stimulation site (RH_Cont_PFCl_2), within the fronto-parietal control network (FPCN), both for AC (p = 0.033, Figure 1) and MC (p = 0.008, Figure 2). The post-hoc t-test showed a significant difference between groups after 4 weeks from the treatment (p=0.047) for MC, while no effects on AC. However, similar effects were observed in other nodes.

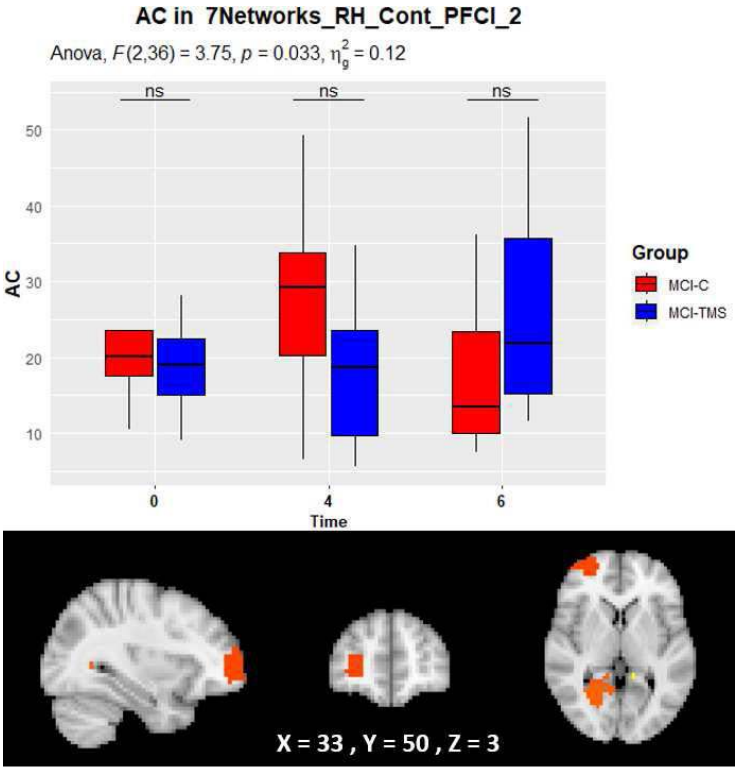

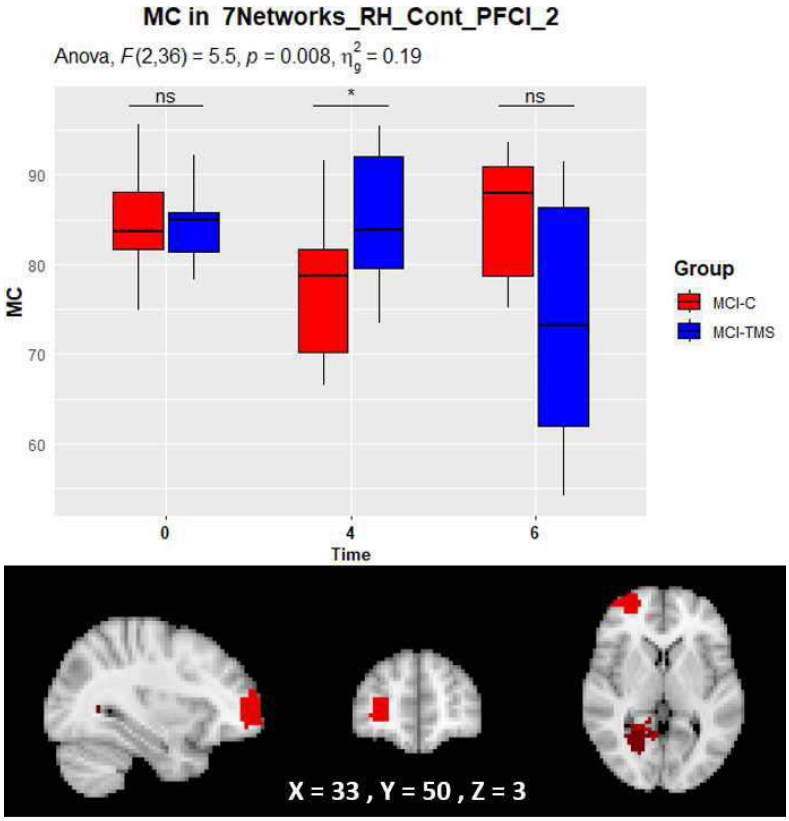

Conclusions: Because the DLPFC was the stimulation site, we focused on lateral pre-frontal cortex (PFCl) nodes to investigate whether and how the treatment had affected their estimated levels of functional controllability. Indeed, DLPFC has a crucial role in cognitive functions early impaired in AD, such as attention, executive functions, and working memory[10] and PFCl nodes are part of the FPCN. Particularly, we expected MC alterations within the FPCN as this NCT metric is supposedly related to the ability of the brain (seen as one networked system) to efficiently transit towards more difficult-to-reach FC states, as required by the performance of cognitively demanding tasks[10]. Albeit only initials, the presented results suggest that DLPFC-rTMS might have affected especially MC changes over the first six months from the treatment.

References

1. A. J. Mitchell e M. Shiri-Feshki, «Rate of progression of mild cognitive impairment to dementia--meta-analysis of 41 robust inception cohort studies», Acta Psychiatr Scand, vol. 119, fasc. 4, pp. 252–265, apr. 2009, doi: 10.1111/j.1600-0447.2008.01326.x.
2. M. S. Albert et al., «The diagnosis of mild cognitive impairment due to Alzheimer's disease: recommendations from the National Institute on Aging-Alzheimer's Association workgroups on diagnostic guidelines for Alzheimer's disease», Alzheimers Dement, vol. 7, fasc. 3, pp. 270–279, mag. 2011, doi: 10.1016/j.jalz.2011.03.008.
3. V. Lissek e B. Suchan, «Preventing dementia? Interventional approaches in mild cognitive impairment», Neuroscience & Biobehavioral Reviews, vol. 122, pp. 143–164, mar. 2021, doi: 10.1016/j.neubiorev.2020.12.022.
4. G. S. Dichter, D. Gibbs, e M. J. Smoski, «A systematic review of relations between resting-state functional-MRI and treatment response in major depressive disorder», Journal of Affective Disorders, vol. 172, pp. 8–17, feb. 2015, doi: 10.1016/j.jad.2014.09.028.
5. M. Hallett, «Transcranial Magnetic Stimulation: A Primer», Neuron, vol. 55, fasc. 2, pp. 187–199, lug. 2007, doi: 10.1016/j.neuron.2007.06.026.
6. S. Esposito et al., «Repetitive Transcranial Magnetic Stimulation (rTMS) of Dorsolateral Prefrontal Cortex May Influence Semantic Fluency and Functional Connectivity in Fronto-Parietal Network in Mild Cognitive Impairment (MCI)», Biomedicines, vol. 10, fasc. 5, p. 994, apr. 2022, doi: 10.3390/biomedicines10050994.
7. T. M. Karrer et al., «A practical guide to methodological considerations in the controllability of structural brain networks», J. Neural Eng., vol. 17, fasc. 2, p. 026031, apr. 2020, doi: 10.1088/1741-2552/ab6e8b.
8. R. Tang et al., «Longitudinal association of executive function and structural network controllability in the aging brain», GeroScience, vol. 45, fasc. 2, pp. 837–849, apr. 2023, doi: 10.1007/s11357-022-00676-3.
9. A. Schaefer et al., «Local-Global Parcellation of the Human Cerebral Cortex from Intrinsic Functional Connectivity MRI», Cereb Cortex, vol. 28, fasc. 9, pp. 3095–3114, set. 2018, doi: 10.1093/cercor/bhx179.
10. A. H. Lara e J. D. Wallis, «The Role of Prefrontal Cortex in Working Memory: A Mini Review», Frontiers in Systems Neuroscience, vol. 9, 2015, Consultato: 28 novembre 2023. [Online]. Disponibile su: https://www.frontiersin.org/articles/10.3389/fnsys.2015.00173

Poster No 61

MRI-guided cTBS Alleviated Auditory Hallucinations: A Randomized Double-blind Sham-controlled Trial

Qiang Hua[1], Gong-Jun Ji[1], Kai Wang[1]

[1]Anhui Medical University, Hefei, Anhui

Introduction: The clinical efficacy of repetitive transcranial magnetic stimulation (rTMS) for treatment-resistant auditory verbal hallucinations (AVH) are undetermined. To address this issue, we develop an optimized continuous theta-burst stimulation (cTBS) protocol and test its efficacy in a randomized, double-blind, sham-controlled trial (NCT02863094).

Methods: We randomly allocated schizophrenia patients with AVH to receive 14 days active or sham cTBS treatment, and collected structural and resting-state functional MRI data for each patient before treatment. Structural MRI was used to guide stimulations over the left temporoparietal junction area (TPJ, [-51, -31, 23] in MNI space). The primary outcome was the auditory hallucinations rating scale (AHRS) changes at post-treatment. The secondary outcomes were the AHRS score change at follow-up, the Positive and Negative Syndrome Scale (PANSS) score change and the number of responders at post-treatment and follow-up. Treatment responders were defined as 25% improvement or greater in AVH symptom alleviation. The efficacy of cTBS treatment was analyzed using linear mixed-effects models and Chi-squared test. We try to explain the outcome variability between patients using the personalized electric field (E-field) and AVH network. E-field was simulated using SimNIBS toolbox and each patient's T1-/T2-weighted images. Personalized AVH network was defined as the connectivity map of AVH hub regions (Kim et al., 2021, Molecular Psychiatry) on each patient's functional MRI data. We tested whether that the effective E-field affecting AVH network can predict the AHRS alleviation for patients in the active group.

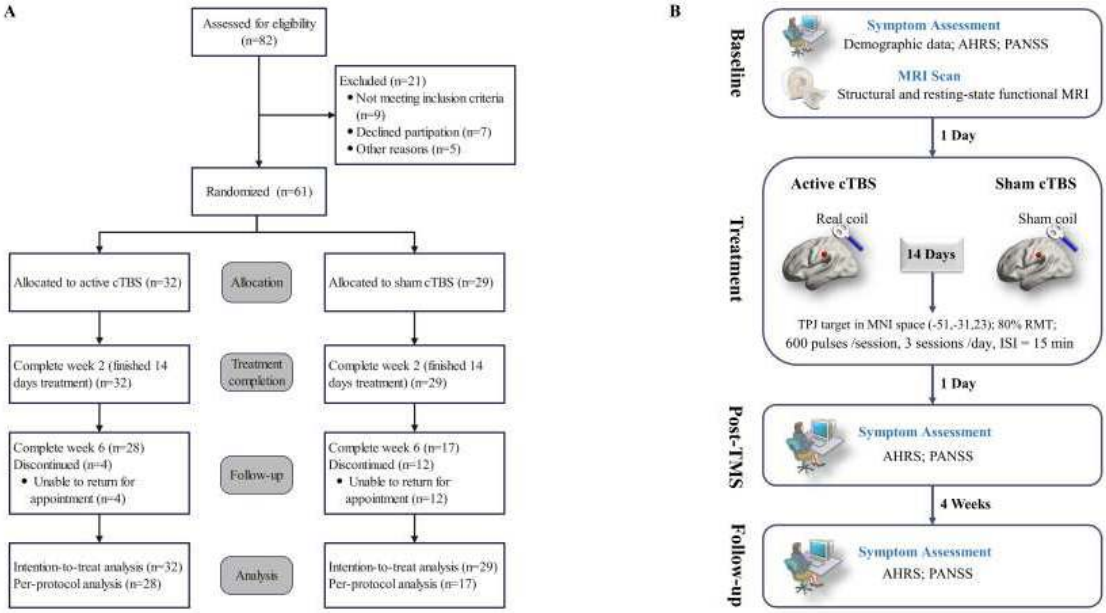

Figure 1. Flow diagram of participant selection and schematic of the trail. (A) A total of 82 patients screened, 61 schizophrenia patients with AVH were included and completed the treatment. **(B)** In active cTBS group, patient received cTBS at 80% of the resting motor threshold for 14 consecutive days (600 pulses per session, 3 session per day, inter-session interval (ISI) = 15 min). The stimulation target was defined as the left temporo-parietal junction (TPJ) (MNI coordinates: −53, −31, 23). The entire stimulation process was monitored by MRI navigation. Patients in the sham group complete the same treatment protocol, but with a sham TMS coil. Baseline assessment was 1 day prior to the first cTBS session. The post-treatment and follow-up assessments were 1 day and 4 weeks after the final cTBS session, respectively. AHRS = auditory hallucinations rating scale; PANSS = Positive and Negative Syndrome Scale.

Results: Sixty-one schizophrenia patients with AVH completed treatment (33 women [54.1%]; mean [SD] age, 27.52 [9.22] years). In the intention-to-treat analysis, patients in active group showed a significantly greater improvement in the AHRS score (difference, 6.10; 95% CI, 3.48 - 8.72; F = 18.60, P < .0001; Figure 2A) and the PANSS score (difference, 11.97; 95% CI, 6.70 - 17.25; F = 17.34, P < .0001; Figure 2B) at post-treatment. The responder rates were higher in the active group (15 of 32 [46.88%]) vs the sham group (4 of 29 [13.80%]) (2=7.76, P = 0.005; Figure 2C). These effects persisted at follow-up. The cTBS was well tolerated, and no adverse event occurs in both groups. The AHRS improvement predicted by the strength of TMS-induced E-field within the personalized AVH-network was positively correlated with the real improvement at post-treatment (r = 0.46, P = 0.009; Figure 2D).

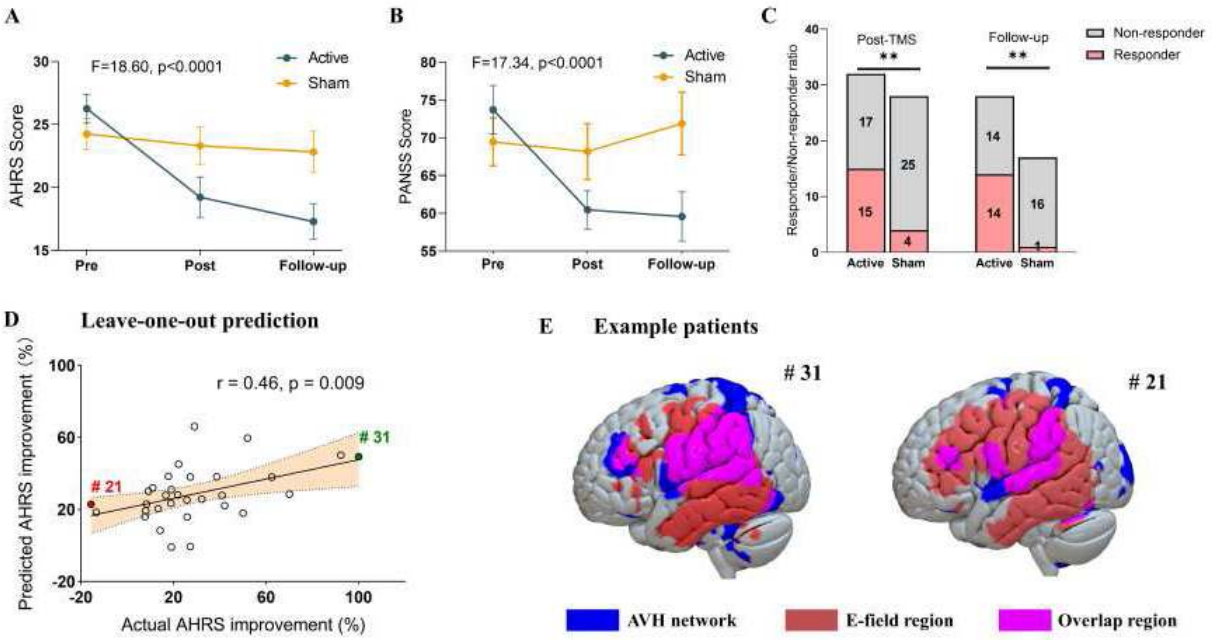

Figure 2. Clinical outcomes of cTBS and its underlying neural mechanism. The mean (SEM) score of AHRS **(A)** and PANSS **(B)** were presented. Patients in the active group showed significantly greater improvement in the AHRS and PANSS score compared with sham group at post-treatment and follow-up. **(C)** The responder/nonresponder ratio was higher in the real group at post-treatment and follow-up. **(D)** The AHRS improvement predicted by the strength of TMS-induced E-field within the personalized AVH-network was positively correlated with the real improvement at post-treatment. **(E)** The brain map shows distributions of AVH network, E-field and overlap regions. The patient #31 and #21 respectively represent two situations of good and poor efficacy of cTBS. The overlap region in patient #31 is larger than patient #21.

Conclusions: MRI-guided cTBS effectively relieve AVH symptom in schizophrenia patients by modulating the personalized AVH network.

References

1. Kim NY. (2021), 'Lesions causing hallucinations localize to one common brain network', Molecular Psychiatry, vol. 26, no. 4, pp. 1299-1309

Poster No 62

Estimating the Primary Activation in TMS-Evoked EEG recordings through Source-Based Filtering

Xavier Corominas-Teruel[1], Tuomas Mutanen[2], Carlo Leto[1], Cécile Gallea[1], Martina Bracco[1], Antoni Valero-Cabré[1]

[1]Sorbonne Université, Paris Brain Institute, Inserm, CNRS, APHP, Hôpital de la Pitié Salpêtrière, Paris, France, [2]Department of Neuroscience and Biomedical Engineering, Aalto University School of Science, Espoo, Finland

Introduction: Transcranial Magnetic Stimulation (TMS) is a well-established non-invasive technology used both for mapping human cognitive processes and therapeutic neuromodulation. Concurrent electroencephalography (EEG) enables to assess the neural impact of TMS[1]. However, due to the limited spatial resolution of EEG, TMS-evoked EEG activity remains spatially unspecific as it represents the sum of mixed spatial sources directly or indirectly activated by TMS[2]. The integration of magnetic resonance imaging (MRI)-based neuronavigation into TMS procedures offers precise information on the TMS coil position during the recordings, enabling individualized modelling of the distribution of TMS-delivered currents (E-fields, Fig. 1A)[3]. Here, we present and test a novel analysis pipeline for TMS-EEG datasets. This approach combines the distribution of TMS-generated E-fields with head and brain structural features extracted from individual MRIs. The aim is to utilize the E-field as prior information to extract the local cortical TMS-evoked activity at the stimulated site more accurately from the recorded EEG.

Methods: The analysis pipeline (Fig.1B) is based upon previous frameworks for the design of spatial filters for EEG/MEG data based on cross-talk functions (DeFleCT)[4]. We first reconstructed individual finite element head models (FEM) in a cohort of n=18 participants with Simnibs4.0[3] and ISO2MESH[5] and computed the lead field matrix through the Helsinki BEM framework[6]. We then estimated the E-field distribution induced by a TMS pulse in this same forward model using Simnibs4.3 and outlined the cortical region most impacted by it (>70% of the maximal TMS-induced E-field strength). Finally, a spatial filter with 2 minimization constraints (one for noise and another for distributed sources decreasing cross-talk leakage within the ROI) was applied[4] to the EEG data to obtain activity in the cortical area directly impacted by TMS. To characterize the pipeline's

performance, we processed EEG datasets from this same cohort, stimulated with 80 TMS pulses (Magstim Rapid2) delivered at 60% of the maximal stimulator output (MSO) to the left primary motor cortex (M1). Non-parametric cluster-based statistics (dependent t-test;[7]) were used to compare TMS-evoked potentials (TEP, from -100 to 600 ms – with respect to the TMS pulse) obtained with our spatial filter, and the same data but at sensor-level from a set of pre-defined electrodes (C1, C3, CP1, CP3).

Results: Our analyses revealed important corrections for spatially filtered compared to non-spatially-filtered data operating in the temporal and spatial domains. More specifically spatially-filtered data were characterized by a consistent lower power amplitude (μV) particularly from ~100 ms with respect to the TMS pulse (t=2.5 p=0.04, t=4.1 p=0.003, Fig.1C). The sensor-level topographies of our TEP (from ~100 ms onwards) suggest signs of possible multisensory activation (Fig.1C.1)[8]. Our pipeline suppresses the contribution of those responses in the filtered signal (Fig.1C.2), originating from the targeted cortical ROI, revealing a damping wave pattern at the directly simulated region.

Conclusions: The spatial resolution of EEG remains a major challenge for combined TMS-EEG experiments. We here present a framework and a pipeline, which provides the community with a tool to estimate more accurately the focal EEG-evoked signals in the cortical region of interest, e.g. at the area experiencing the largest E-fields. Importantly, this can be adapted to varying research goals and integrate multimodal datasets (fMRI, DTI, fNIRS etc.) by projecting its readouts into compatible forward models or by using them in real-time close-loop implementations[9]. Our outcomes set the stage to disentangle complex patterns of TMS-evoked/induced brain dynamics previously inaccessible and foster their implementation in multiple experimental and clinically applied scenarios in which non-invasive brain stimulation shows promise.

FIGURE 1

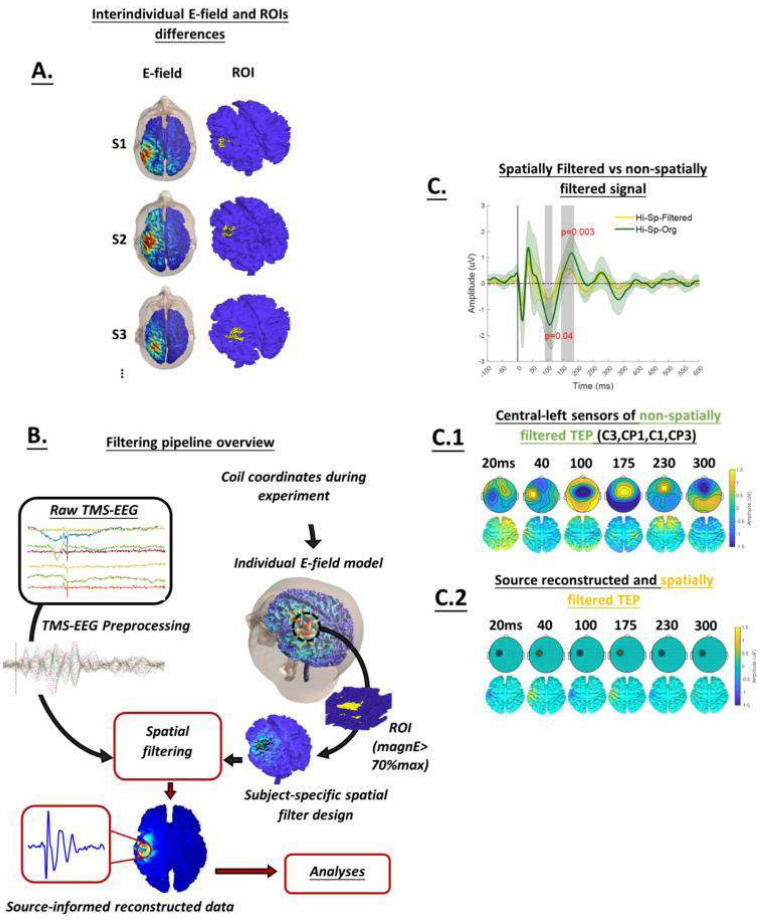

References

1. Hernandez-Pavon JC, Veniero D, Bergmann TO, Belardinelli P, Bortoletto M, Casarotto S, et al. TMS combined with EEG: Recommendations and open issues for data collection and analysis. Brain Stimul 2023;16:567–93. https://doi.org/https://doi.org/10.1016/j.brs.2023.02.009.
2. Rogasch NC, Sullivan C, Thomson RH, Rose NS, Bailey NW, Fitzgerald PB, et al. Analysing concurrent transcranial magnetic stimulation and electroencephalographic data: A review and introduction to the open-source TESA software. Neuroimage 2017;147:934–51. https://doi.org/https://doi.org/10.1016/j.neuroimage.2016.10.031.

3. Thielscher A, Antunes A, Saturnino GB. Field modeling for transcranial magnetic stimulation: A useful tool to understand the physiological effects of TMS? 2015 37th Annual International Conference of the IEEE Engineering in Medicine and Biology Society (EMBC), 2015, p. 222–5. https://doi.org/10.1109/EMBC.2015.7318340.
4. Hauk O, Stenroos M. A framework for the design of flexible cross-talk functions for spatial filtering of EEG/MEG data: DeFleCT. Hum Brain Mapp 2014;35:1642–53. https://doi.org/https://doi.org/10.1002/hbm.22279.
5. Tran AP, Yan S, Fang Q. Improving model-based functional near-infrared spectroscopy analysis using mesh-based anatomical and light-transport models. Neurophotonics 2020;7:1. https://doi.org/10.1117/1.nph.7.1.015008.
6. Stenroos M, Hunold A, Haueisen J. Comparison of three-shell and simplified volume conductor models in magnetoencephalography. Neuroimage 2014;94:337–48. https://doi.org/https://doi.org/10.1016/j.neuroimage.2014.01.006.
7. Maris E, Oostenveld R. Nonparametric statistical testing of EEG- and MEG-data. J Neurosci Methods 2007;164:177–90. https://doi.org/https://doi.org/10.1016/j.jneumeth.2007.03.024.
8. Niessen E, Bracco M, Mutanen TP, Robertson EM. An analytical approach to identify indirect multisensory cortical activations elicited by TMS? Brain Stimulation: Basic, Translational, and Clinical Research in Neuromodulation 2021;14:376–8. https://doi.org/10.1016/j.brs.2021.02.003.
9. Bergmann TO, Karabanov A, Hartwigsen G, Thielscher A, Siebner HR. Combining non-invasive transcranial brain stimulation with neuroimaging and electrophysiology: Current approaches and future perspectives. Neuroimage 2016;140:4–19. https://doi.org/10.1016/j.neuroimage.2016.02.012.

Poster No 63

Theta Burst Stimulation Effects on the Right Ventrolateral Prefrontal Cortex and Emotion Regulation

Joseph Kim[1], Vincent Koppelmans[2], Brian Mickey[2], Somi Lee[3]

[1]Brigham and Women's Hospital / Harvard Medical School, Boston, MA, [2]University of Utah, Salt Lake City, UT, [3]University of Utah, Salt Lake City, UT

Introduction: The study aims to understand the impact of neuromodulation, particularly repetitive transcranial magnetic stimulation (rTMS), on the ventrolateral prefrontal cortex (vlPFC) and its role in emotion regulation, especially in older adults. Dysregulated emotions, prevalent in various neuropsychiatric and neurological disorders, are exacerbated by aging-related brain changes. While functional neuroimaging links vlPFC activity to emotion regulation in younger adults, the causal role and the effects of aging on this process remain unclear. The research characterizes the behavioral effects of non-invasive transcranial stimulation to the right vlPFC in emotion regulation, comparing healthy older and younger adults. The study also investigates the impact of this intervention on intrinsic connectivity within emotion regulation-relevant functional networks using resting functional MRI. The current report focuses on key behavioral data analysis results related to the first aim of the study.

Methods: Participants included 23 healthy individuals (11 older adults, 12 younger adults) recruited from the Greater Salt Lake area and the University of Utah. Exclusion criteria covered neurological disorders, epilepsy in 1st-degree relatives, intellectual/developmental disability, visual/sensory deficits, estimated IQ < 90, history of major psychiatric disorders, current psychotropic medications, contraindications to rTMS, contraindications to MRI, and pregnancy. rTMS parameters targeted the vlPFC based on its consistent involvement in emotion regulation. Coordinates were derived from Wager and colleagues' fMRI study, focusing on the right vlPFC [MNI coordinates: x = 52; y = 31; z = -9]. Subjects received 600 pulses of cTBS, iTBS, or Sham stimulation before the emotion regulation task, each in three separate sessions, using a MagVentureTM TMS Cool-B65 Butterfly Coil at 80% of the resting motor threshold. For the Emotion Regulation Task post-TMS, subjects attended to pictures ("LOOK" condition) or engaged in reappraisal ("DECREASE" condition). Instruction cues ("Neutral Look," "Negative Look," or "Negative Decrease") preceded each picture. Subjects underwent three stimulation sessions, viewing a total of 108 pictures (72 negative, 36 neutral). In the "Look" condition, they attended to the picture without altering feelings; in the "Decrease" condition, they reinterpreted the picture to reduce negative response. After each trial, a visual analog rating scale recorded affect intensity ratings, a key measure of negative affect intensity.

Results: The investigation into Transcranial Magnetic Stimulation (TMS) and emotion regulation yielded key findings. No significant reappraisal differences were found across TMS conditions (cTBS, iTBS, sham), suggesting TMS lacked a distinct impact, potentially influenced by baseline variability. Demographic factors (age, income, education) did not predict emotion regulation, indicating their limited role in TMS impact. While no significant difference in sham stimulation response was noted between Older Adults (OA) and Younger Adults (YA), a contrast emerged with iTBS. YA showed a greater increase in reappraisal effectiveness, aligning with TMS studies favoring younger individuals. Within YA, increasing age correlated positively with baseline reappraisal effectiveness, possibly linked to frontal lobe development. Surprisingly, in OA, older age was positively associated with a greater cTBS-induced emotion regulation increase, aligning with TMS studies reporting unexpected inhibitory effects with age. These nuanced findings illuminate the intricate interplay between TMS, age, and emotion regulation.

Conclusions: Age-related contrast emerged within iTBS. YAs displayed greater increase in reappraisal effectiveness compared to OAs. Notably, in OA, older age was unexpectedly parametrically associated with a greater cTBS-induced emotion regulation effectiveness increase, which warrants further investigation in future studies.

References

1. Ochsner KN. Functional imaging studies of emotion regulation: a synthetic review and evolving model of the cognitive control of emotion. Annals of the New York Academy of Sciences. 2012;1251(1):E1-E24.
2. Ghashghaei HT. Pathways for emotion: interactions of prefrontal and anterior temporal pathways in the amygdala of the rhesus monkey. Neuroscience. 2002;115(4):1261-1279.
3. Allard ES, Age-related differences in neural recruitment during the use of cognitive reappraisal and selective attention as emotion regulation strategies. Front Psychol. 2014;5:296.
4. Opitz PC. Prefrontal mediation of age differences in cognitive reappraisal. Neurobiol Aging. 2012;33(4):645-655.
5. Winecoff A. Cognitive and neural contributors to emotion regulation in aging. Soc Cogn Affect Neurosci. 2011;6(2):165-176.
6. Wager TD. Prefrontal-Subcortical Pathways Mediating Successful Emotion Regulation. Neuron. 2008;59(6):1037-1050.
7. Ziemann U. Consensus: Motor cortex plasticity protocols. Brain Stimulation. 2008;1(3):164- 182.
8. Fettes P. Neural Correlates of Successful Inhibitory OFC- rTMS in Major Depressive Disorder. Biological Psychiatry. 2017;81(10):S402-S403.
9. Nauczyciel C. Repetitive transcranial magnetic stimulation over the orbitofrontal cortex for obsessive- compulsive disorder: a double-blind, crossover study. Translational Psychiatry. 2014;4(9):e436-e436.

Poster No 64

The Information Flow of TMS-evoked Brain Network Dynamics

Xiao Jinming[1], Li Lei[2], Yating Ming[1], Xujun Duan[3]

[1]University of Electronic Science and Technology of China, Chengdu, Sichuan, [2]University of Electronic Science and Technology of China, Chnegdu, China, [3]UESTC, Chengdu, Sichuan

Introduction: Understanding how local perturbation in neural activity influence brain dynamics is a compelling way to inference the information flow of large-scale brain network. The concurrent transcranial magnetic stimulation (TMS) and electroencephalography (EEG) is the best technology to support this non-invasive perturbation-based analysis for inferencing the cortico-cortical directed connectivity in human brain (Biabani, Fornito, Mutanen, Morrow, & Rogasch, 2019; Gollo, Roberts, & Cocchi, 2017; Rogasch & Fitzgerald, 2013). By conducting TMS-EEG, we can track the TMS-evoked activity originating from a target brain region to propagate throughout the whole brain(Momi et al., 2021; Thut & Miniussi, 2009). By using source-localized TMS-EEG analysis and whole-brain connectome-based computational modelling, Moni et al indicated that the initial EEG signal changes was caused by local dynamics in stimulation regions, while later EEG signal changes were influenced by activity within a wider connected network(Momi, Wang, & Griffiths, 2023). However, the information flow of TMS-evoked activity was unclear.

Methods: In this study, we used concurrent TMS-EEG dataset which was collected and provided to community by the Rogasch group (https://figshare.com/articles/dataset/TEPs-_SEPs/7440713). The dataset consisted of a total 20 healthy individuals (24.50±4.86 years; 14 females), all of whom received single-pulse TMS stimulation on primary motor cortex (M1) while brain activity was recorded by density EEG. The detailed description of the dataset and steps for preprocessing can be found at(Biabani et al., 2019). We performed source reconstruction by using MNE software library. Finally, the brain activity was extracted through Schaefer 200 parcellations atlas(Schaefer et al., 2018). The analysis pipeline was as follow: (1) By conducting sparse non-negative matrix factorization (sNMF) model, the TMS-EEG activity was decomposed into co-activation modules and time-varying weights. (2) By calculating phase slope index (PSI) for the time-varying weights, we can inference the directional information flow among co- activation modules. The PSI measures the asymmetry in phase differences between signals, providing insights into the directed interactions among brain regions(Basti et al., 2018).

Results: Our results indicated that TMS-evoked brain activity can be decomposed into 10 co-activation modules (Fig 1). We summarize these 10 modules into 3 modes – 'Left hemisphere dominant module', 'Right hemisphere dominant module', and 'Bilateral modules'. (1) Left hemisphere dominant module include module 1, 2, 3, 4. Module 1 and 2 mainly involves left Somatomotor network (SMN) which can be regarded as stimulation regions. Module 3 mainly involves left Default network (DMN) and Visual network (VN). Module 4 mainly involves left DMN. (2) Right hemisphere dominant module include module 5, 6, 7, 8.3 Bilateral modules include module 9,10. By conducting PSI analysis (Fig 2), our results indicated that (1) TMS-evoked brain activity propagates from the left hemisphere dominant module to the right hemisphere dominant module. This outcome suggests that TMS stimulation extends beyond the stimulated region, transmitting across the network to the contralateral brain areas. (2) Although Module 2 serves as the stimulated region, it concurrently acts as a recipient in the information flow (high in-degree), which validate previews research demonstrating the recurrent, re-entrant activity of stimulation region.

Additionally, we observed the pathway from Modules 3 and 4 on the ipsilateral hemisphere transmitting to Module 2, instead of the transmission originating from modules on the contralateral hemisphere to Module 2.

Conclusions: This finding is instrumental in enhancing our understanding of how signals propagate in the brain, providing a novel connectome perspective to the clinical application of TMS.

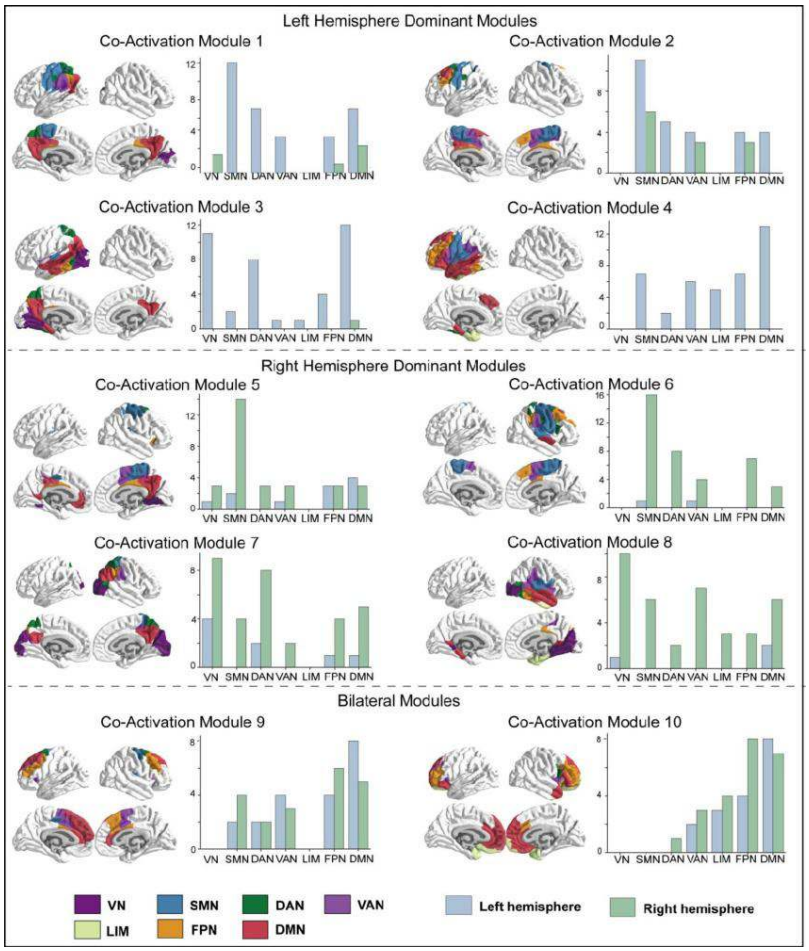

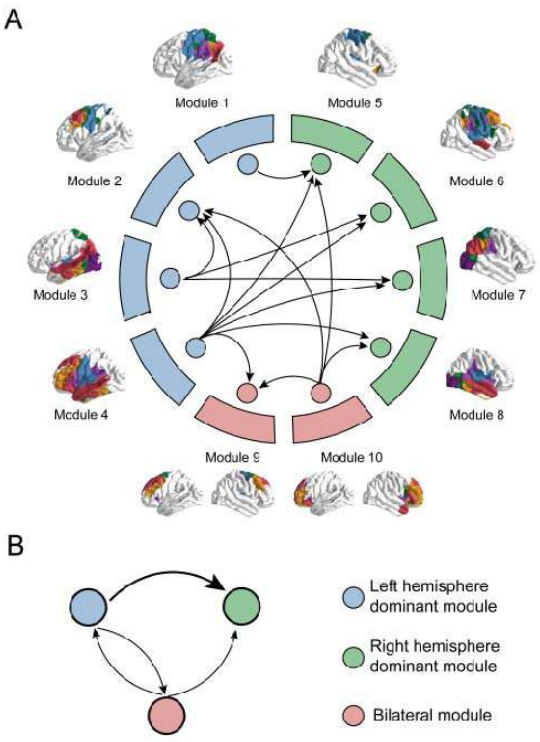

References

1. Basti, A., Pizzella, V., Chella, F., Romani, G. L., Nolte, G., & Marzetti, L. (2018). Disclosing large-scale directed functional connections in MEG with the multivariate phase slope index. Neuroimage, 175, 161-175. doi:10.1016/j.neuroimage.2018.03.004
2. Biabani, M., Fornito, A., Mutanen, T. P., Morrow, J., & Rogasch, N. C. (2019). Characterizing and minimizing the contribution of sensory inputs to TMS-evoked potentials. Brain Stimulation, 12(6), 1537-1552. doi:10.1016/j.brs.2019.07.009
3. Gollo, L. L., Roberts, J. A., & Cocchi, L. (2017). Mapping how local perturbations influence systems-level brain dynamics. Neuroimage, 160, 97-112. doi:10.1016/j.neuroimage.2017.01.057
4. Momi, D., Ozdemir, R. A., Tadayon, E., Boucher, P., Di Domenico, A., Fasolo, M., . . . Santarnecchi, E. (2021). Perturbation of resting-state network nodes preferentially propagates to structurally rather than functionally connected regions. Scientific Reports, 11(1). doi:10.1038/s41598-021-90663-z
5. Momi, D., Wang, Z., & Griffiths, J. D. (2023). TMS-evoked responses are driven by recurrent large-scale network dynamics. Elife, 12. doi:10.7554/eLife.83232
6. Rogasch, N. C., & Fitzgerald, P. B. (2013). Assessing cortical network properties using TMS-EEG. Human Brain Mapping, 34(7), 1652-1669. doi:10.1002/hbm.22016
7. Schaefer, A., Kong, R., Gordon, E. M., Laumann, T. O., Zuo, X. N., Holmes, A. J., . . . Yeo, B. T. T. (2018). Local-Global Parcellation of the Human Cerebral Cortex from Intrinsic Functional Connectivity MRI. Cerebral Cortex, 28(9), 3095-3114. doi:10.1093/cercor/bhx179
8. Thut, G., & Miniussi, C. (2009). New insights into rhythmic brain activity from TMS-EEG studies. Trends in Cognitive Sciences, 13(4), 182-189. doi:10.1016/j.tics.2009.01.004

Poster No 65

Evaluating personalized rTMS impact on network functional connectivity via precision methods

Anne Billot[1], Randy Buckner[1], Stephanie McMains[2], Mark Eldaief[1]

[1]Harvard University, Cambridge, MA, [2]Boston University, Boston, MA

Introduction: Repetitive transcranial magnetic stimulation (rTMS) is used as a treatment for neuropsychiatric disorders, such as depression (O'Reardon et al., 2007). Clinically, rTMS targets are typically identified using anatomical landmarks (Cash et al., 2020). However, multiple studies have shown that the efficacy of rTMS treatments depends on its ability to modulate specific functional networks (Liston et al., 2014). Limited evidence exists regarding the impacts that targeting specific networks has on the functional connectivity of different circuits. Moreover, evidence has focused on network estimates that are based on group data. Recent work in our lab and others (Braga & Buckner 2017) have used precision functional connectivity MRI (fcMRI) estimates to delineate functional network topography in the individual. This study evaluates the specificity of personalized rTMS upon network-level connectivity, defined with precision fcMRI methods, at the individual level.

Methods: Two healthy adults (S1 and S2) underwent a baseline scan (3T MRI) to collect individualized functional data in order to perform fcMRI analyses to delineate the location of their salience (SAL) network. After the baseline session, each individual completed 30 rTMS sessions, at least 4 days apart from each other. Ten sessions targeted a representation of the SAL network in the left dorsolateral prefrontal cortex (LDLPFC), ten sessions targeted the SAL in the right DLPFC (RDLPFC), and 10 sessions targeted the same LDLPFC site but with sham rTMS, administered in a counterbalanced order. RTMS sessions were directly followed by a resting-state MRI scan that included at least two BOLD runs of fixation. After quality control, 59 and 53 runs were used for each subject, respectively. BOLD fMRI data were acquired using a multiband gradient-echo echo-planar pulse sequence. A T1 scan was acquired using an MPRAGE sequence (see acquisition parameters in Braga et al., 2019). MRI data were analyzed using FSL, Freesurfer, SPM, and custom, in-house software. The SAL target was derived using a seed map encompassing the entire SAL network, defined by Yeo et al., 2011, but excluding a DLPFC mask in each hemisphere. The specific target was chosen as the region exhibiting the maximal functional connectivity with the SAL seed map. RTMS was administered with a Magventure Cool B65 A/P liquid-cooled coil, capable of active and sham stimulation, with the following parameters: 20Hz stimulation, at 110% of the subject's resting motor threshold over 45 trains (2s and 40 pulses per train), with an intertrain interval of 28s for a total of 1800 pulses (22.5 min) (Eldaief et al., 2023). During stimulation, a neuronavigation system was used to stimulate the predefined targets precisely and reproducibly across sessions by loading the subject's fcMRI data, overlaid on the subject's native-space structural MRI. To measure differences in post-TMS correlation strengths across conditions, we first used all 31 fMRI runs to estimate 15 functional networks using precision MRI estimates through a Multi-Session Hierarchical Bayesian Model (MS-HBM) (Braga and Buckner 2017), and to determine the network identity of the stimulated targets in each subject. Then, for each rTMS condition, we used the first runs of the ten MRI sessions to compute correlation strength between the target ROI and each functional network using the mean Fisher-transformed Pearson's correlation coefficient between the time course of all vertices within each target ROI (left and right) and the vertices within each predefined network (excluding the target region).

Results: Precision mapping of fcMRI showed that the main network targeted was CG-OP on both sides in S1, and SAL/PMN on the left and DN-A on the right in S2 (Fig1). Connectivity results showed opposite rTMS effects within the targeted left CG-OP in S1 and right DN-A in S2 (Fig2).

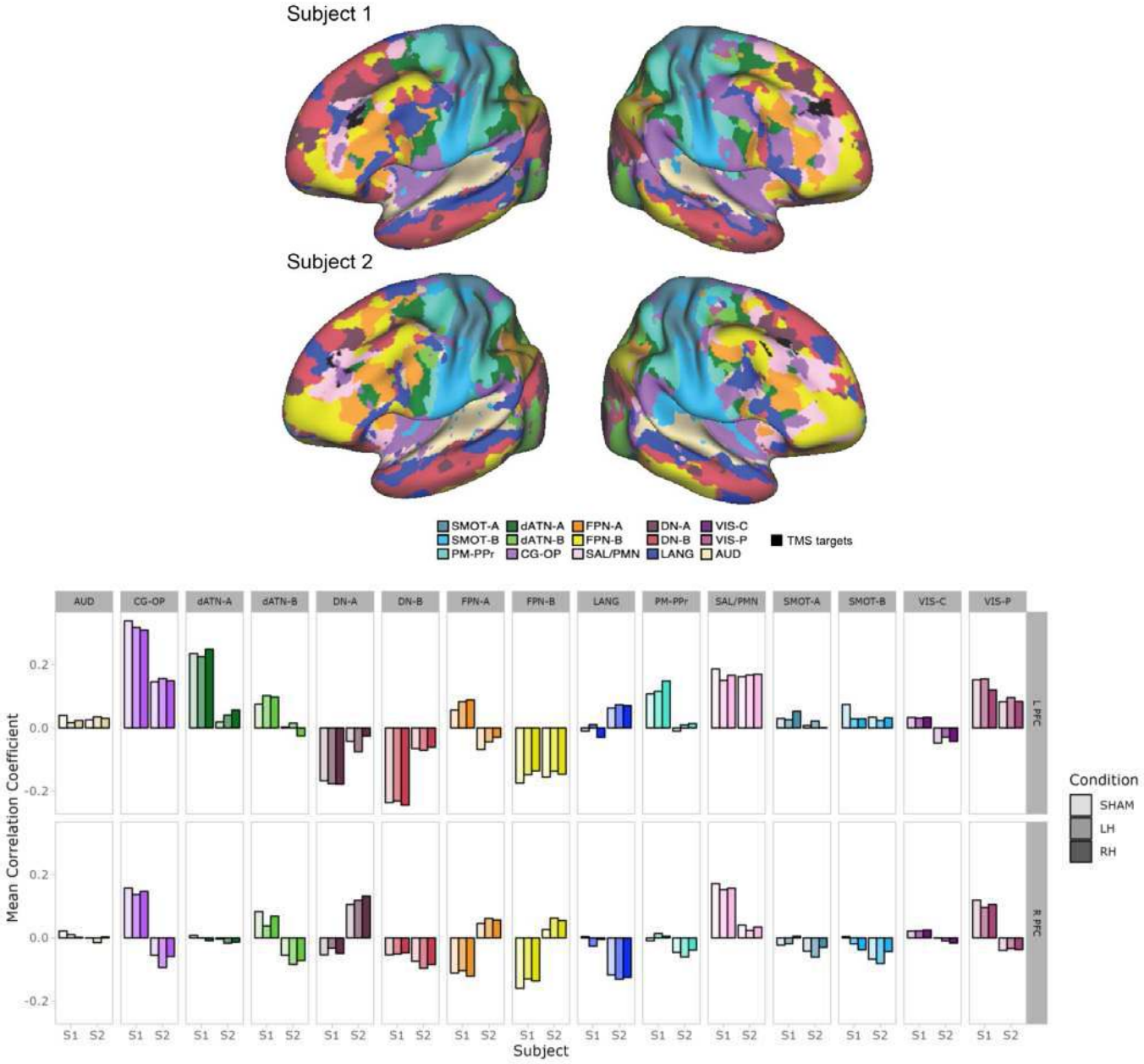

Conclusions: Future research will prospectively use precision fcMRI mapping to investigate individual rTMS effects on distinct circuits.

References

1. O'Reardon, J.P., (2007) Efficacy and safety of transcranial magnetic stimulation in the acute treatment of major depression: a multisite randomized controlled trial. Biol Psychiatry
2. Cash, R.F.H., (2020) Using Brain Imaging to Improve Spatial Targeting of Transcranial Magnetic Stimulation for Depression. Biol Psychiatry
3. Liston, C., (2014) Default mode network mechanisms of transcranial magnetic stimulation in depression. Biol Psychiatry
4. Braga R.M., (2017) Parallel interdigitated distributed networks within the individual estimated by intrinsic connectivity. Neuron.
5. Braga, R.M.,(2019) Parallel distributed networks resolved at high resolution reveal close juxtaposition of distinct regions. J Neurophysiol
6. Yeo B.T., (2011) The organization of the human cerebral cortex estimated by intrinsic functional connectivity. J Neurophysiol
7. Eldaief, M. C., (2023). Network-specific metabolic and haemodynamic effects elicited by non-invasive brain stimulation. Nature Mental Health

Poster No 66

Phase-targeted sleep EEG neurofeedback inside the MR scanner drives cerebrospinal fluid flow

Joshua Levitt[1], Leandro Jacob[2], Laura Lewis[3]

[1]Boston University, Boston, MA, [2]Massachusetts Institute of Technology, Cambridge, MA, [3]Massacusetts Institute of Technology, Cambridge, MA

Introduction: Closed-loop neurofeedback methods hold great promise for enhancing the precision and performance of neurostimulation techniques. However, how closed-loop EEG interventions affect brain function is not well understood, due to the challenges of performing MRI imaging during closed-loop EEG interventions. Recent advances in low latency denoising of EEG have made EEG-fMRI neurofeedback more feasible[1,2]. Here we developed an algorithm that enables low-latency EEG-fMRI neurofeedback and use it to gain insight into the neurobiological effects of closed-loop acoustic stimulation (CLAS). Previous experimentation with CLAS has shown that delivering auditory stimuli in-phase with sleep slow waves (fig. 1a) improves performance on memory tasks, and increases slow wave duration and amplitude[3,4]. By performing a CLAS experiment inside the scanner, we collected high resolution spatial data to examine the neural basis of this intriguing finding. We focused in particular on cerebrospinal fluid (CSF) and slow waves, which have been shown to be temporally correlated[5]. Sleep contains pulsatile waves of CSF flow linked to waste clearance[5,6].

Methods: 8 adults were recruited to participate in an EEG-fMRI nap study, and each completed two 25-minute sleep runs. During each run, they were instructed to press a button with each breath until they fell asleep. A neural network was used to predict upcoming slow wave phase of channel FpZ. When the phase was predicted to fall within a desired range corresponding to the slow-wave peak, the subject randomly received either an audio stimulus (50ms of pink noise; 50% chance) or a sham stimulus (no stimulus; 50% chance). EEG data was collected and preprocessed in real time using LLAMAS[1] to remove scanner artifacts (acquisition code shared at github.com/jalevitt/EEG-LLAMAS/). MR data was collected with a 3T scanner and a TR of 378ms, calling upon recent advances in fast fMRI[7]. Volumes were positioned with the bottom slice at the entrance to the 4th ventricle, and CSF flow was measured as in Williams et al.[5,8]. Stimuli delivered while the subject was awake were excluded from analysis, as were stimuli for which the delta power in the previous 10 seconds was below 3uV^2, to remove those not delivered during a slow wave.

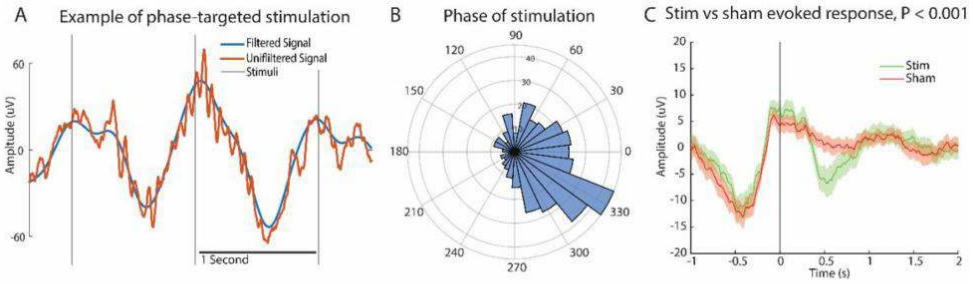

Figure 1. Closed-loop stimulation successfully targets to the correct phase. A) Example of Phase-targeted stimulation. Stimuli (gray lines) are delivered to coincide with the peaks of EEG slow waves. B) Slow wave phase at time of stimulation. (N = 397 stimuli); 0 degrees corresponds with the slow wave peaks. C) EEG response in channel Fpz to the stimulus (green, N = 397) and sham (orange, N = 379) events. Shaded area shows the bootstrap 95% confidence interval. A significant difference was found between stim and sham (p < 0.001, bootstrap shuffle).

Results: We calculated the slow-wave phase at the time of the stimulus and found successful phase-targeting of slow waves (fig. 1 b) and found a significant difference between the stim and sham ERPs (fig. 1c). To assess the effect of the stimulus on oscillatory dynamics, we calculated the mean event-locked power in the spindle band (13-16Hz) and slow wave band (0.4-3Hz) in the time range 0.5-1s . We found that stimulation caused a significant increase in slow wave power and spindle power (fig. 2a-c). We calculated the stimulus-evoked response of the CSF signal and found a significant increase in CSF flow after stimulation in the stim condition compared to the sham condition (fig. 2d).

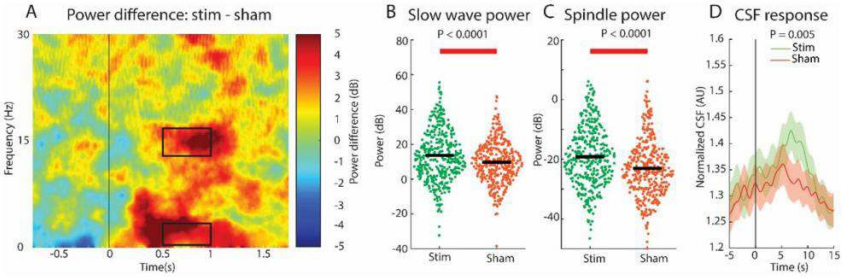

Figure 2. Closed-loop stimulation increases EEG slow wave power and CSF flow. A) Difference between the EEG spectral content in the stimulus and sham conditions. Black boxes indicate the regions used to assess changes in slow wave and spindle power. B) slow wave power following stim (green, N = 397) and sham events (orange, N = 379). Black bars show group means. Red bar indicates significance. C) Same as B, but for spindle power. D) Evoked response of the normalized CSF signal to stimulus (green) and sham events (orange). Shaded areas show bootstrap 95% confidence intervals, and vertical line shows stimulus timing. CSF flow is significantly increased after stimulation (p=0.005; bootstrap shuffle).

Conclusions: We successfully performed EEG-fMRI neurofeedback, enabling us to image the neural consequences of EEG-targeted sensory stimulation in sleep. Furthermore, we show that were able to deliver stimuli in-phase with slow waves using a neural network, which is a novel approach. Our results replicate prior studies that an evoked response and enhanced slow-wave power with CLAS. We also found an increase in spindle power, which supports the hypothesis that spindles act as a 'sensory gate'[9]. We found that phase-targeted stimulation increased CSF flow into the 4th ventricle. Previous research found an increase in CSF flow following slow waves[5], and our results demonstrate this effect can be causally increased using an audio stimulus to enhance slow waves. This study establishes the feasibility of EEG-fMRI neurofeedback, enabling a wide range of studies to image the effects of EEG-based neuromodulation. Furthermore, our results demonstrate that CLAS can provide a noninvasive way to enhance CSF flow in the human brain.

References

1. Levitt J, Yang Z, Williams SD, Espinosa SEL, Garcia-Casal A, Lewis LD (2023) EEG-LLAMAS: a low-latency neurofeedback platform for artifact reduction in EEG-fMRI. NeuroImage, :120092.
2. Bullock M, Jackson GD, Abbott DF (2021) Artifact Reduction in Simultaneous EEG-fMRI: A Systematic Review of Methods and Contemporary Usage. Frontiers in Neurology, 12:193.
3. Ngo H-VV, Martinetz T, Born J, Mölle M (2013) Auditory Closed-Loop Stimulation of the Sleep Slow Oscillation Enhances Memory. Neuron, 78(3):545–553.
4. Ngo H-VV, Antony JW, Rasch B (2022) Real-time stimulation during sleep: prior findings, novel developments, and future perspectives. Journal of Sleep Research, 31(6):e13735.
5. Fultz NE, Bonmassar G, Setsompop K, Stickgold RA, Rosen BR, Polimeni JR, Lewis LD (2019) Coupled electrophysiological, hemodynamic, and cerebrospinal fluid oscillations in human sleep. Science, 366(6465):628–631.
6. Xie L, Kang H, Xu Q, Chen MJ, Liao Y, Thiyagarajan M, O'Donnell J, Christensen DJ, Nicholson C, Iliff JJ, Takano T, Deane R, Nedergaard M (2013) Sleep Drives Metabolite Clearance from the Adult Brain. Science (New York, N.Y.), 342(6156)
7. Lewis LD, Setsompop K, Rosen BR, Polimeni JR (2016) Fast fMRI can detect oscillatory neural activity in humans. Proceedings of the National Academy of Sciences of the United States of America, 113(43):E6679–E6685.
8. Williams SD, Setzer B, Fultz NE, Valdiviezo Z, Tacugue N, Diamandis Z, Lewis LD (2023) Neural activity induced by sensory stimulation can drive large-scale cerebrospinal fluid flow during wakefulness in humans. PLOS Biology, 21(3):e3002035.
9. Elton M, Winter O, Heslenfeld D, Loewy D, Campbell K, Kok A (1997) Event-related potentials to tones in the absence and presence of sleep spindles. Journal of Sleep Research, 6(2):78–83.

Poster No 67

The effect of transcranial photobiomodulation on EEG power: variation with light pulsation frequency

Hannah Van Lankveld[1,2], Alicia Mathew[2], Sophie Niculescu[2], Reza Zomorrodi[3], Lew Lim[4], Nazanin Hosseinkhah[4], J. Jean Chen[1,2]

[1]University of Toronto, Toronto, Ontario, [2]Rotman Research Institute, Baycrest, Toronto, Ontario, [3]Centre for Addiction and Mental Health, Toronto, Ontario, [4]Vielight Inc., Toronto, Ontario

Introduction: Transcranial photobiomodulation (tPBM) involves the delivery of near-infrared (NIR) light through the cranium to stimulate neural tissues[1]. Evidence of the interaction between NIR light and neuronal processes in the human brain will not only help establish PBM as a brain-stimulation tool on par with such established methods as transcranial magnetic stimulation but will also lead to a deeper understanding of biophotonics and their role in brain function. In PBM research, EEG has been used to show an increase in alpha (α), beta (β) and gamma (γ) power as well as a decrease in gamma (γ) power post PBM in comparison to the sham condition[2,3,4,5]. However, the real-time EEG response to tPBM in humans is currently unknown. In this study, we use pulsed tPBM at two frequencies to demonstrate the real-time in vivo human EEG response in the γ band.

Methods: EEG data from five healthy subjects (4F/1M, age 19-25) were recorded during transcranial photobiomodulation stimulation using the Magstim geodesic EEG system (256 channels). tPBM was applied using a 1064nm pulsed NIR laser with an optical power density of 150 mW/cm2. The frequency of the pulsation was alternated between 10Hz and 40Hz. The stimulation paradigm was [4-min off; 6-min on; 4-min off]. The target area was the left forehead, with the irradiated surface area and application technique remaining the same for all subjects and recordings. EEGlab toolbox was used for data resampling, artifact removal, independent component analysis and channel rejection. A custom MATLAB script was used to divide the EEG signal into the five main frequency bands (δ, θ, α, β, γ) and to compute epoch-specific band-specific power spectra using a sliding window of 4.5 seconds. The tPBM response in these power spectra time courses for each band were assessed using a general linear model. We focused on the γ band specifically, and used cluster-based permutation thresholding to determine electrodes that responded to the stimulus.

Results: Figure 1 shows both positive and negative γ power responses to tPBM at both 10Hz pulsation frequency and 40Hz. Most subjects displayed a localized frontal-lobe positive EEG response, in accordance with the site of stimulation. However, while subjects 2, 3 and 4 also showed spatially extensive negative responses, subjects 1 and 5 did not. The responses to 10Hz and 40Hz stimulation are largely spatially similar. Figure 2 shows the average percent change in γ power, across all subjects at all significantly responding electrodes, which are also summarized as bar graphs. The 40Hz pulsation frequency elicits a larger positive response across all positively significant electrodes, and the 10Hz pulsation frequency elicits a larger negative response across all negatively significant electrodes. In both cases, a time lag of approximately 90 seconds after the onset of photobiomodulation is observed (Fig. 2a).

Conclusions: This study demonstrates, for the first time in humans, a real-time lagged EEG-power response to tPBM. Our work further shows an important relationship between light pulsation frequency and the neuronal current response. We demonstrate localized positive γ response in contrast to an extensive negative γ response for both 10 Hz and 40 Hz pulsation. The 40 Hz stimulation elicits a greater positive response than 10 Hz. Given the lack of such data in the literature, this work is an important first step towards accelerating PBM research to the level of other brain stimulation modalities.

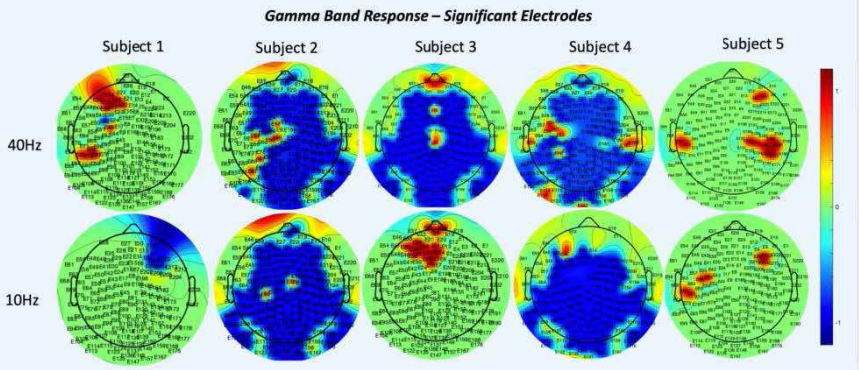

Figure 1: Significant gamma band positive (red) and negative (blue) electrodes based on general linear modelling mapped per subject and per pulsation frequency. The colour bar shows a binary representation of the positive and negative electrodes, blue (-1) representing the negative electrodes and red (+1) representing the positive electrodes.

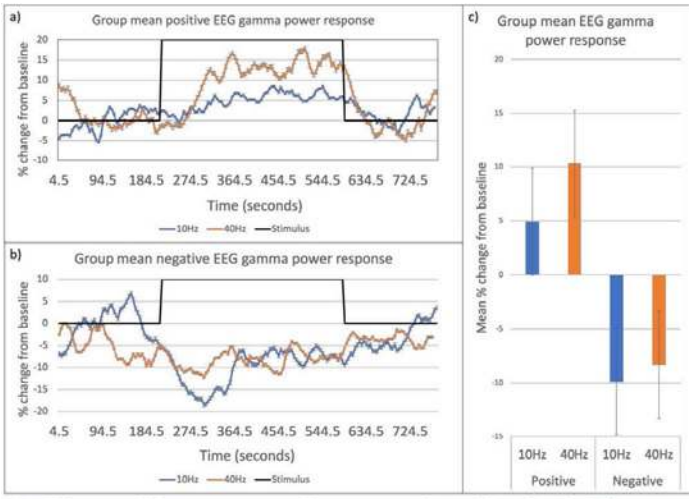

Figure 2: Group mean EEG gamma power response time course, averaged across all five subjects, for significant electrodes that have a positive (a) response to the stimulus as well as a negative (b) response to the stimulus. The mean percent change during the stimulus block is noted in (c), showing that the 40Hz pulsation frequency had a significantly larger positive response than the 10Hz.

References
1. Q. Zhang, H. Ma, S. Nioka and B. Chance. (2000), "Study of near infrared technology for intracranial hematoma detection," Journal of Biomedical Optics, pp. 206-213.
2. X. Wang. (2019), "Transcranial photobiomodulation with 1064-nm laser modulates brain electroencephalogram rhythms," Neurophotonics, pp. 6(2), 025013
3. R. Zomorrodi, G. Loheswaran, A. Pushparaj and L. Lim. (2019), "Pulsed Near Infrared Transcranial and Intranasal Photobiomodulation Significantly Modulates Neural Oscillations: a pilot exploratory study," Scientific Reports 9, p. Article 6309
4. S. Shahdadian. (2022), "Neuromodulation of brain power topography and network topology by prefrontal transcranial photobiomodulation," Neural Eng, p. 19 066013
5. X. Wang, H. Wanniarachchi, A. Wu and H. Liu. (2022), "Combination of Group Singular Value Decomposition and eLORETA Identifies Human EEG Networks and Responses to Transcranial Photobiomodulation," Front. Hum. Neurosci

Poster No 68

Enhancing Cognitive Performance by Rhythmic Auditory Stimulation at Individual EEG Theta Frequency

Andre Gómez-Lombardi[1,2,3,4], Begoña Góngora[3,4], Pavel Prado-Gutiérrez[5], Pablo Muñoz[6], Wael El-Deredy[1,7,8]

[1]Brain Dynamics Laboratory, Universidad de Valparaíso, Valparaíso, Chile, [2]Doctorado en Ciencias e Ingeniería para la Salud, Universidad de Valparaíso, Valparaíso, Chile, [3]Escuela de Fonoaudiología, Universidad de Valparaíso, Valparaíso, Chile, [4]Centro de Investigación en Cognición y Lenguaje, Universidad de Valparaíso, Valparaíso, Chile, [5]Escuela de Fonoaudiología, Universidad San Sebastián, Santiago, Chile, [6]Departamento de Patología y Fisiología, Universidad de Valparaíso, Valparaíso, Chile, [7]Department of Electronic Engineeing, School of Enginnering, University of Valencia, Valencia, Spain, [8]ValgrAI, Valencian Graduate School & Research Network of Artificial Intelligence, Valencia, Spain

Introduction: Rhythmic sensory stimulation is a safe and effective method of non-invasive brain stimulation that has been shown to improve different cognitive functions in a variety of health conditions, including normal aging and Alzheimer's disease (Manippa et al., 2022; Sahu & Tseng, 2023; Traikapi & Konstantinou, 2021). Significant results have been obtained in the auditory, somatosensory, and visual rhythmic stimulation modalities (Henry & Obleser, 2012; Lea-Carnall et al., 2017; Ronconi et al., 2018) inducing resonant brain responses at the presentation frequencies. However, there is no consensus about the best method for setting the frequency parameter. We propose that the individual EEG-induced frequency observed during the execution of an inhibitory control task is related to performance, and using this parameter in rhythmic auditory stimulation could potentially enhance cognitive performance.

Methods: Older adults between 60 and 75 years old (n =38, 19 female) were recruited for this study. All participants were right-handed, had more than 12 years of schooling, and did not have neurological impairment or hearing disorders that impacted their communication. Participants realized the auditory version of the Simon task (Simon & Rudell, 1967) before and after receiving rhythmic auditory stimulation. Their brain activity was registered through EEG using Biosemi 64 channels. Following the preprocessing of the EEG data from the pre-stimulation phase and the implementation of a time-frequency analysis of induced response, we identify the frequency of each participant (individual frequency) as the one with the highest amplitude within the theta band. To contrast the results of using different stimulation conditions through clicks, we included individual frequency, lower frequency (2Hz), higher frequency (33% upper than individual frequency), and irregular stimulation (non-periodical). Finally, the reaction time (RT) change of the Simon task before and after stimulation was compared between the different conditions.

Results: The individual frequency of older adults was in the range of theta band (M = 3.64 Hz, SD = 0.82), revealing a significant negative correlation with RTs in both conditions of the Simon task (congruent, r = -.59, p < .001; incongruent: r = -.54, p < .001). We conducted a repeated measures ANOVA to investigate the effect of stimulation and congruency on the change in the reaction times pre-post stimulation in the Simon task. The results showed a main effect of stimulation type (p < .001, ηp2 = 0.48) and congruency [p = .023, ηp2 = 0.13]. Furthermore, an interaction effect between stimulation and congruency was observed [p = .015, ηp2 = 0.09] (Figure 1). Based on post hoc analyses, it was found that the two stimulation conditions that yielded the best results were the individual frequency (M = 28.28 ms, SD = 35.72) and the higher frequency (M = 30.26 ms, SD = 37.08), with no significant difference between them. The irregular stimulation obtained the worst result (M = 2.88 ms, SD = 34.37). The lower frequency produced a moderate result (M = 17.57 ms, SD = 36.93), which was significantly better than the irregular stimulation (mean difference = 14.68 ms, t = 4.85, p < .001), but worse than the results obtained with the individual frequency (mean difference = 10.71 ms, t = 3.54, p = 0.001) and the higher frequency (mean difference = 12.68 ms, t = 4.19, p < .001).

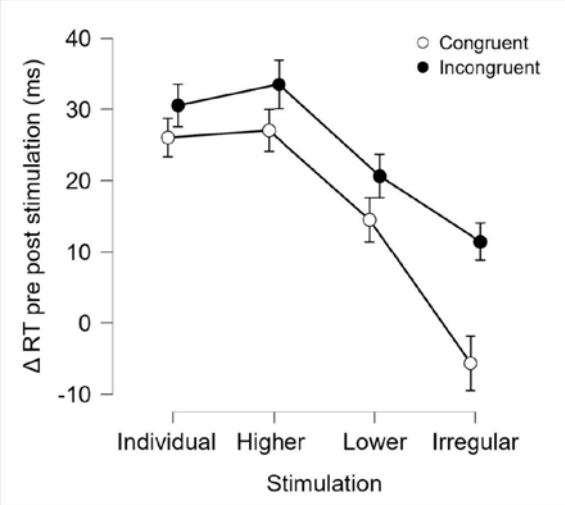

Conclusions: Our findings suggest that rhythmic auditory stimulation can enhance performance on the Simon task compared to non-periodical stimulation. Notably, the greatest improvements were observed when the stimulation was customized to the individual EEG-induced frequency, even if it was higher. Considering individual oscillatory activity related to specific cognitive tasks could improve the outcomes of neurorehabilitation programs using rhythmic auditory stimulation.

References

1. Henry, M. J. (2012). 'Frequency modulation entrains slow neural oscillations and optimizes human listening behavior', Proceedings of the National Academy of Sciences, 109(49), 20095-20100.
2. Lea-Carnall, C. A. (2017). 'Evidence for frequency-dependent cortical plasticity in the human brain', Proceedings of the National Academy of Sciences, 114(33), 8871-8876.
3. Manippa, V. (2022). 'An update on the use of gamma (multi)sensory stimulation for Alzheimer's disease treatment', Frontiers in Aging Neuroscience, 14.
4. Ronconi, L. (2018). 'Alpha-band sensory entrainment alters the duration of temporal windows in visual perception', Scientific Reports, 8(1), Article 1.
5. Sahu, P. (2023). 'Gamma sensory entrainment for cognitive improvement in neurodegenerative diseases: Opportunities and challenges ahead', Frontiers in Integrative Neuroscience, 17, 1146687.
6. Simon, J. R. (1967). 'Auditory S-R compatibility: The effect of an irrelevant cue on information processing', Journal of Applied Psychology, 51(3), 300-304.
7. Traikapi, A. (2021). 'Gamma Oscillations in Alzheimer's Disease and Their Potential Therapeutic Role', Frontiers in Systems Neuroscience, 15, 782399.

Poster No 69

Effect of the Stimulus Timing in the fNIRS-based BCI using a RSVP paradigm

Seongyeon Lim[1], Suh-Yeon Dong[1]

[1]Sookmyung Women's University, Seoul, Korea, Republic of

Introduction: Functional near-infrared spectroscopy (fNIRS) has recently gained prominence in advancing brain-computer interfaces (BCIs) but faces limitations in rapid serial visual presentation (RSVP) tasks due to its temporal resolution issues[1,2]. Despite delays in hemodynamic responses, we observed notable differences in hemodynamic responses between target and non-target groups. These finding suggests the potential of fNIRS-BCI with quick stimuli.

Methods: From the STL-10 dataset[3], we used vehicle images with 288×288 pixels such as airplanes, cars, ships, and trucks. A single airplane image was the target, while non-target images were randomly chosen from other vehicles. The background of each image was blurred to minimize its interference with object recognition. In total, we made 40 image sequences. Each image sequence comprised 20 randomly selected images, with target image sequence containing one target image along with 19 non-target images. Thirty healthy adult females (22.34 ± 2.48 years) participated. Participants completed 40 sets, each with 20 target and 20 non-target image sequences in a random order. Figure 1 shows the timeline of the experiment. The onset and offset of each set were signaled by 'Start' and 'End' messages for 1-second, respectively. Participants viewed a burst of 20 images for 2 seconds, presented at a rate of 10 Hz They were required to identify the presence of the target image by key press. A 30-second resting period accounted for response delays. The fNIRS were recorded using a 15-channel NIRSIT Lite device (OBELAB Inc., Seoul, Republic of Korea. Approval for this study was granted by the Institutional Review Board of Sookmyung Women's University (IRB No. SMWU- 2209-HR-083-01). The target groups were categorized into early, middle,

and last groups based on image presentation order. The 20 target image sequences were distributed into 7 for early group, 7 for middle group, and 6 for last group. We extracted ΔHbO mean values and normalized the data by scaling the range from 0 to 1. We performed normality and homoscedasticity of the data using Shapiro-Wilk and Levene tests, respectively. Games-Howell and Bonferroni post-hoc tests were applied to compare each group after conducting One-way ANOVA, Welch's ANOVA, and Kruskal-Wallis tests. If the data exhibit characteristics of normality and homogeneity of variance, we performed One-way ANOVA, and Bonferroni post-hoc tests. For non-parameter data, we conducted Kruskal-Wallis and Bonferroni post-hoc tests. We conducted Welch's ANOVA and the Games-Howell test on parametric data with non-homogeneity of variance. Significance was determined based on Bonferroni and Games-Howell adjusted p-values <0.05.

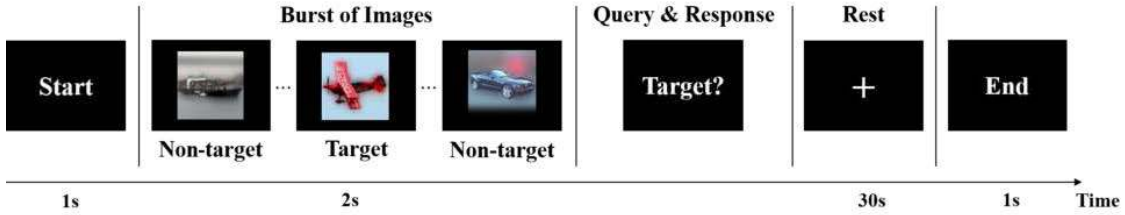

Figure 1. Timeline of the experiment

Results: After excluding poor-quality data, we analyzed 28 data. We examined the concentration changes of oxygenated hemoglobin (ΔHbO) variations in the prefrontal cortex (PFC) across four groups using mean values. Across all PFC channels, significant distinctions were observed between the target and non-target groups($p<0.001$), as shown in Figure 2. Specially, Channel 3 showed noticeable differences among all groups ($p<0.001$). Channel 7 exhibited significant differences within target groups($p<0.001$). Differences between early and middle groups were observed in Channels 4($p=0.002$), 8($p=0.025$), 1, 5, 9, and 11($p<0.001$). Among the early and last groups, there were distinctions in Channels 4($p=0.006$), 6($p=0.014$), 1, 9, 10, 12 and 15($p<0.001$). Channels 10, 11, 12, and 15 significantly differed between middle and last groups ($p<0.001$), with lower significance in Channel 8($p=0.046$). However, there was no significant difference in Channel 13 among all groups.

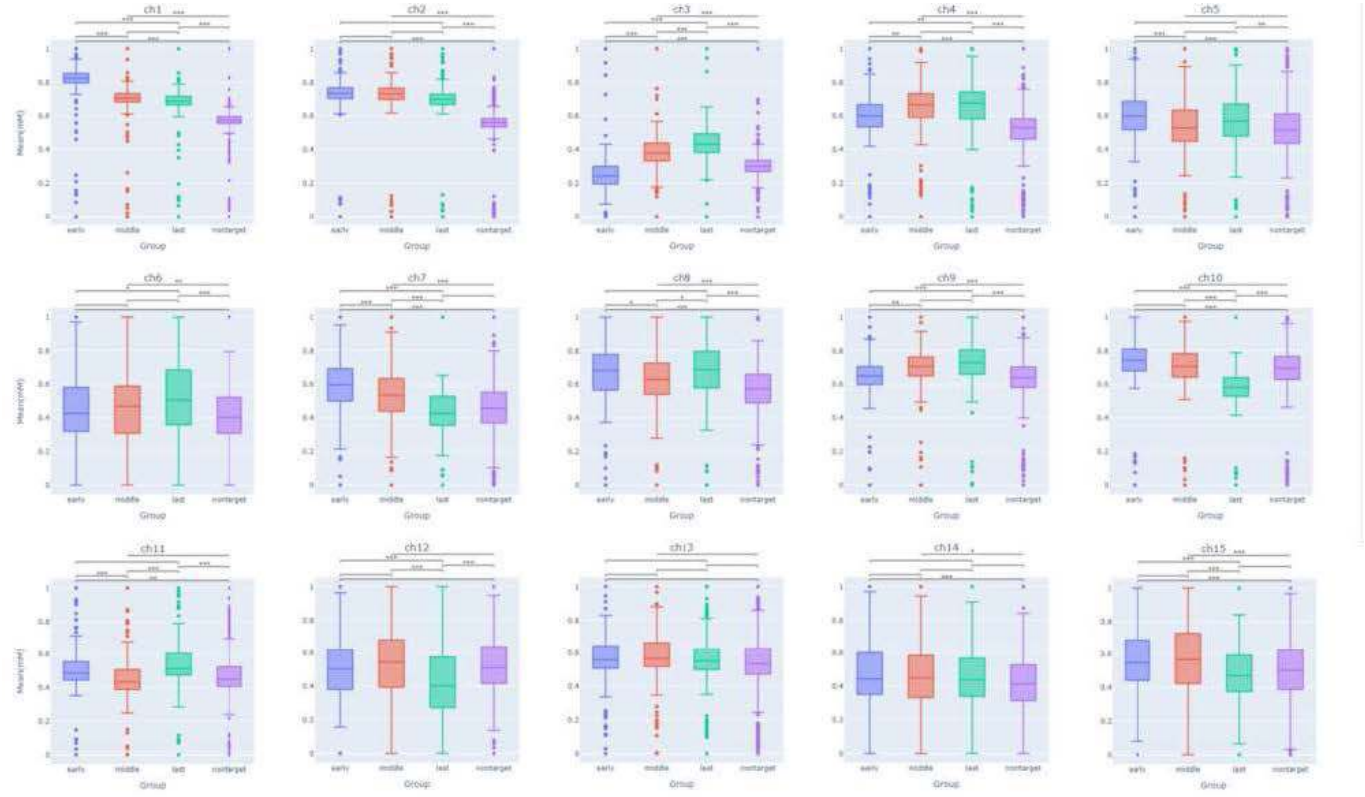

Figure 2. Boxplots of ΔHbO mean values in 15 channels

Conclusions: Our findings back the use of fNIRS-BCI in RSVP tasks, showing discernible differences in hemodynamic responses between target and non-target groups. These differences varied with the timing of the target image presentation. Our future work aims to develop a dependable and robust BCI system using fNIRS.

References
1. Khan, M.A. (2020), 'Task-specific stimulation duration for fNIRS brain-computer interface', IEEE Access, vol. 8, pp. 89093-89105.
2. Ahn, S. (2017), 'Multi-modal integration of EEG-fNIRS for brain-computer interfaces–current limitations and future directions', Frontiers in human neuroscience, vol. 11, pp. 503.
3. Coates, N.A. (2011), 'An analysis of single-layer networks in unsupervised feature learning', In Proceedings of the Fourteenth International Conference on Artificial Intelligence and Statistics, pp. 215-223.
4. This work was supported by the Agency For Defense Development Grant Funded by the Korean Government(UI233005TD).

Poster No 70

Learning to control the visual cortex and enhancing visual attention via fMRI-based Neurofeedback

Riccardo Galli[1], Lucas Peek[1], Soraya Brosset[1], Frédéric Grouiller[1], Patrik Vuilleumier[1]

[1]University of Geneva, Geneva, Switzerland

Introduction: Attention is a crucial cognitive function allowing us to select pertinent sensory information while ignoring irrelevant stimuli in the environment[1]. This capacity emerges from top-down mechanisms involving bilateral fronto-parietal networks that interact with early visual areas[7]. Following frontal or parietal brain lesions and therefore disruption in this system, peculiar conditions may emerge, such as unilateral spatial neglect (USN): a syndrome denoted by impaired awareness of stimuli presented in the visual field contralateral to the lesion site, in absence of pure sensorial or motor losses. One functional explanation of this condition might rely on abnormal biases in top-down regulation of sensory pathways from higher-level attentional networks towards early visual areas[8]. Neuromodulation and up-regulation of such preserved sensory areas have proved to account for partial restoration of this balance[3,4,6] and improvement in clinical symptoms[5]. In particular, functional MRI (fMRI) based real-time neurofeedback (NFB)[3,4,5,6] represents a promising and effective neuromodulation tool. However, specific mechanisms underlying successful modulation of visual areas via fMRI NFB are still unclear. For this reason, we couple the spatial precision of fMRI with the temporal resolution of EEG in EEG-MRI multimodal imaging fashion during NFB training to unravel structural and functional correlates of such learning process in the brain. Results from this study will further help develop an informed EEG-NFB based protocol to apply in clinical context for USN rehabilitation.

Methods: Following a double-blind randomized clinical trial routine, we train 30 participants to upregulate either left (N = 15) or right visual cortex (VC) over the course of 2 NFB training sessions, while a control group (N = 30) receives a sham feedback (i.e. a feedback sampled from another participant's brain activity). We then investigate the effects of NFB on behavior using several computerized tasks for visual attention as well as multiple neural (MRI, EEG) measures. Furthermore, we address the question of how successful NFB modulation of the visual cortex takes place in the brain at high spatial and temporal resolution thanks to multimodal EEG-MRI imaging applied during the second session of NFB. Finally, baseline EEG-MRI measures (resting-state fMRI, EEG, Diffusion Tensor Imaging) allow us to investigate possible predictive biomarkers of a successful NFB intervention at single subject level. NFB is performed using an open-source Python/Matlab based software (OpenNFT[2]) in combination with an in-house-developed Matlab based software for NFB sessions preparation (prepNFB[9]).

Results: Results show significant training effects in real-time estimated brain activity across NFB sessions in the experimental group training right VC (Fig.1, * denotes cluster at $p < .05$). Concomitant EEG time-frequency topographies during the second session of NFB show how such learning could be explained by beta and alpha band neuronal oscillations modulation. Furthermore, whole-brain analysis shows recruitment of higher-level brain areas generally involved in attentional processes (Fig.2, $p < .001$ unc), such as the Middle Frontal Gyrus (MFG), during neurofeedback regulation. Finally, such neural changes seem to differentially affect behavioral responses, biasing accuracy towards the contralateral visual field (compared to trained visual cortex) during a visual search task.

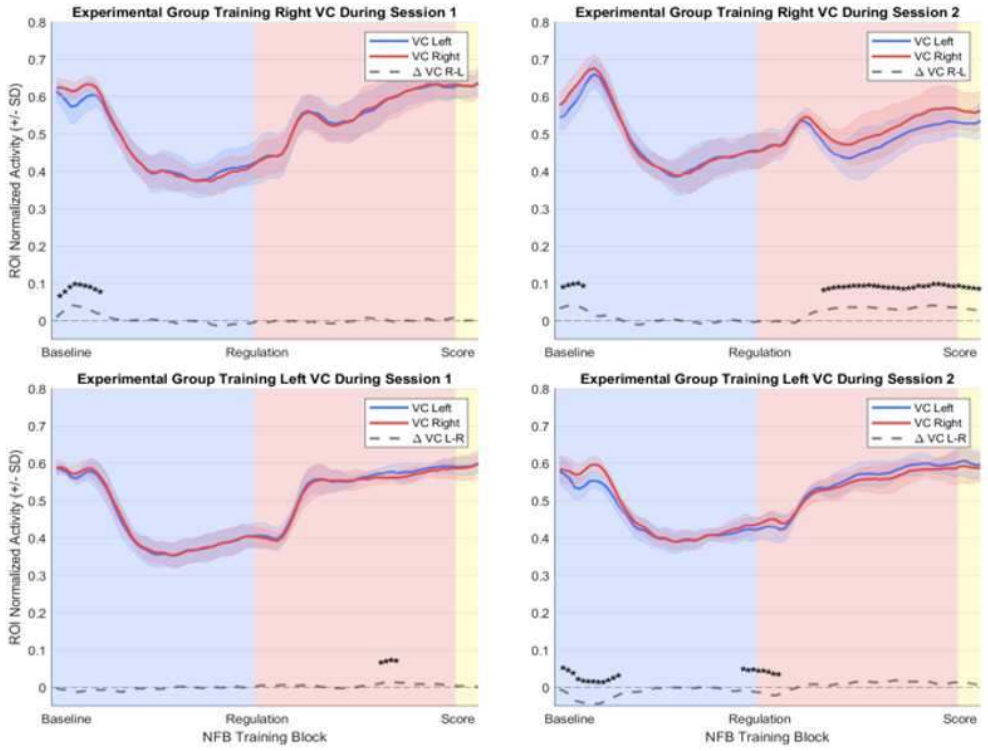

Figure 1

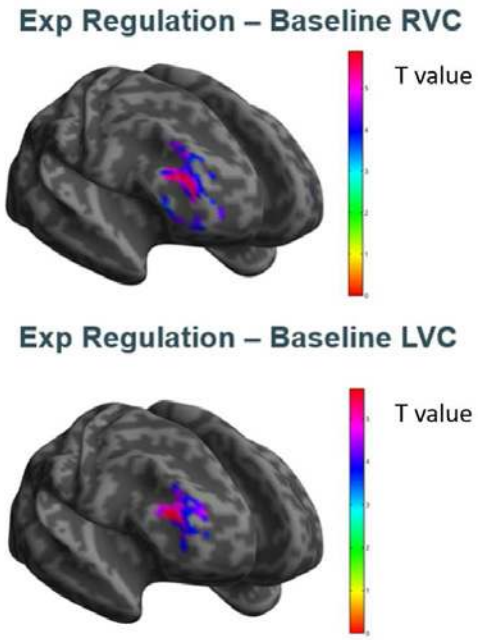

Figure 2

Conclusions: Participants appear able to learn how to regulate their occipital cortex activity thanks to real-time NFB and improve, according to training direction, behavioral performances in visual attention task(s). At the same time, such learning process might be reflected in modulation of alpha/beta brain frequencies and recruitment of higher-level attentional hubs.

References

1. Carrasco, M. (2011). Visual attention: The past 25 years. Vision research, 51(13), 1484-1525.
2. Koush, Y., Ashburner, J., Prilepin, E., Sladky, R., Zeidman, P., Bibikov, S., ... & Van De Ville, D. (2017). OpenNFT: An open-source Python/Matlab framework for real-time fMRI neurofeedback training based on activity, connectivity and multivariate pattern analysis. NeuroImage, 156, 489-503.

3. Robineau, F., Meskaldji, D. E., Koush, Y., Rieger, S. W., Mermoud, C., Morgenthaler, S., Van De Ville, D., Vuilleumier, P., & Scharnowski, F. (2017). Maintenance of Voluntary Self-regulation Learned through Real-Time fMRI Neurofeedback. Frontiers in Human Neuroscience, 11.
4. Robineau, F., Rieger, S. W., Mermoud, C., Pichon, S., Koush, Y., Van De Ville, D., Vuilleumier, P., & Scharnowski, F. (2014). Self-regulation of inter-hemispheric visual cortex balance through real-time fMRI neurofeedback training. NeuroImage, 100, 1–14.
5. Robineau, F., Saj, A., Neveu, R., Van De Ville, D., Scharnowski, F., & Vuilleumier, P. (2019). Using real-time fMRI neurofeedback to restore right occipital cortex activity in patients with left visuo-spatial neglect: Proof-of-principle and preliminary results. Neuropsychological Rehabilitation, 29(3), 339–360.
6. Scharnowski, F., Hutton, C., Josephs, O., Weiskopf, N., & Rees, G. (2012). Improving Visual Perception through Neurofeedback. Journal of Neuroscience, 32(49), 17830–17841.
7. Vossel, S., Geng, J. J., & Fink, G. R. (2014). Dorsal and ventral attention systems: distinct neural circuits but collaborative roles. The Neuroscientist, 20(2), 150-159.
8. Vuilleumier, P., Schwartz, S., Verdon, V., Maravita, A., Hutton, C., Husain, M., & Driver, J. (2008). Abnormal attentional modulation of retinotopic cortex in parietal patients with spatial neglect. Current Biology, 18(19), 1525-1529.
9. https://github.com/lucp88/prepNFB

Poster No 71

Effects of personalized near-infrared LED therapy based on brain networks from EEG

Boeun Choi[1], Ukeob Park[1], DeaKeun Kim[1], Seung Wan Kang[1]

[1]iMediSync, Inc., Seoul

Introduction: Mild cognitive impairment (MCI) is a preliminary stage of dementia characterized by a decline in cognitive function compared to the same age group, yet with retained abilities to perform activities of daily living. Early diagnosis and treatment during this stage can slow down the progression of dementia. Near-infrared (NIR) LED therapy is being researched for its potential to improve brain nerve function through light stimulation. NIR therapy targeting the brain is known to promote the activation of mitochondria in brain cells within the cerebral cortex, facilitating increased blood flow and simultaneously enhancing neurological activity. This study conducted LED therapy on participants diagnosed with MCI at the community level and investigated any changes in the EEG signal-based brain network. As previous studies have indicated, particularly about brain network, small-worldness is identified as an indicator that can differentiate between dementia, MCI, and the normal control group. Among the frequency bands, the small-worldness value in the theta band has been shown to be higher in MCI patients compared to dementia patients, and higher in healthy group compared to MCI patients. These findings demonstrate the potential utility of the small-worldness in distinguishing between these cognitive states.

Methods: A total of 48 participants, consisting of 11 males and 37 females, with an average age of 74.26, took part in the experiment. The experiment spanned 8 weeks, and to assess the effects of the experiment, brain networks were calculated based on EEG measurements at both baseline and the conclusion of the 8-week period. The equipment used in this experiment was the dry type, 10-20 system EEG measurement device (iSyncWave) developed by iMediSync, the organization conducting this study. This device is equipped with near-infrared LED diodes with a wavelength of 850nm on each electrode, allowing for the provision of individualized therapy protocols tailored to the participant's EEG patterns. The calculated features were based on a network with 68 regions of interest (ROIs) using the Desikan–Killiany atlas. Features were calculated for different frequency bands of EEG signals, including Theta (4~8Hz), Alpha1 (8~10Hz), Alpha2 (10~12Hz), and Beta1 (12~15Hz). The brain network features examined included characteristic path length and small-worldness. Characteristic path length is an indicator of the efficiency of information integration in the network. Small-worldness is a feature describing the efficiency of network structure.

Results: After the therapy, there was a noteworthy reduction in characteristic path lengths across all frequency bands (Theta: $0.001<p\leq0.01$, Alpha1: $0.01<p\leq0.05$, Alpha2: $0.001<p\leq0.01$, Beta1: $0.0001<p\leq0.001$). Moreover, small-worldness significantly increased after treatment in all frequency bands (Theta: $0.0001<p\leq0.001$, Alpha1: $0.01<p\leq0.05$, Alpha2: $0.0001<p\leq0.001$, Beta1: $0.001<p\leq0.01$).

Conclusions: Through personalized LED therapy, we examined brain network features, including characteristic path length and small-worldness. Characteristic path length is known to increase when connections between brain regions are disrupted. Therefore, the observed decrease in characteristic path length after therapy can be considered a result of improved overall brain network integration. Furthermore, small-worldness significantly increased after therapy, with a trend towards values closer to 1. This tendency suggests an enhancement in the structural efficiency of the network. In particular, the increase in small-worldness in the theta band can be viewed as a positive change, considering previous research indicating that normal individuals exhibit greater small-worldness in the theta band compared to MCI patients. This is a pilot study of the impact of LED therapy. Future research will delve into quantitative EEG(QEEG) changes based on different types of LED therapy protocols and explore indicators of brain network across various frequency bands.

References
1. F. Vecchio et al. (2014), "Human Brain Networks in Cognitive Decline: A Graph Theoretical Analysis of Cortical Connectivity from EEG Data," Journal of Alzheimer's Disease, vol. 41, no. 1, pp. 113–127
2. F. Vecchio et al. (2021), "Contribution of Graph Theory Applied to EEG Data Analysis for Alzheimer's Disease Versus Vascular Dementia Diagnosis," Journal of Alzheimer's Disease, vol. 82, no. 2, pp. 871–879
3. Y. He, Z. Chen, and A. Evans (2008), "Structural Insights into Aberrant Topological Patterns of Large-Scale Cortical Networks in Alzheimer's Disease," The Journal of Neuroscience, vol. 28, no. 18, pp. 4756–4766
4. J. Tsai, J. Grutzendler, K. Duff, and W.-B. Gan (2004), "Fibrillar amyloid deposition leads to local synaptic abnormalities and breakage of neuronal branches," Nature Neuroscience, vol. 7, no. 11, pp. 1181–1183

Poster No 72

Combination of Real-Time fMRI Neurofeedback and Mindfulness Instructions in Problematic Alcohol Use

Jingying Zhang[1], Falk Kiefer[2], Martin Gerchen[1,3], Peter Kirsch[1,3]

[1]Department of Clinical Psychology, Central Institute of Mental Health, Mannheim, Germany, [2]Department of Addictive Behaviour and Addiction Medicine, Central Institute of Mental Health, Mannheim, Germany, [3]Institute of Psychology, University of Heidelberg, Heidelberg, Germany

Introduction: Hyperreactivity towards alcoholic cues is a key aspect in understanding and treating alcohol use disorders, particularly in the ventral striatum (VS) (Heinz et al. 2009). Real-time fMRI neurofeedback (rtfMRI NF) is a newly emerging non-invasive method to reduce ventral striatal alcohol-cue reactivity. Existing studies have found its capacity on decreasing cue-induced craving and empowering participants modulating their brain processes (Karch et al., 2015; Kirsch et al., 2016; Pindi et al., 2022). However, the efficacy of rtfMRI NF might be subject to effective strategies that participants can employ to regulate the brain process (Oblak et al., 2017). Mindfulness, which aims at building insight and non-reactive acceptance of one's own experience, might provide promising strategies to regulate brain activity elicited by alcohol triggers. In our randomized, double-blind, sham-controlled study, we investigated the hypothesis that mindfulness-based instructions will increase the rtfMRI NF training efficiency in reducing VS alcohol-cue reactivity for participants with problematic alcohol use. The study was approved by the Ethics Committee of the Medical Faculty Mannheim at Heidelberg University (2020-632N) and pre-registered at the Open Science Foundation (OSF, NeuMinds https://osf.io/7bmqw/).

Methods: Participants with problematic alcohol use, as in our previous study (Kirsch et al., 2016) identified with the online version of the alcohol use disorder identification test (AUDIT), were enrolled and randomly assigned to one of three groups: group 1: NF with mindfulness-based instruction, group 2: NF without mindfulness-based instruction, and group 3: sham NF without mindfulness-based instruction. Participants received a 2-session rtfMRI NF at a 3T Scanner (Biograph, Siemens Healthineers, Erlangen, Germany) at the Central Institute of Mental Health (CIMH). Before NF, participants received either a mindfulness-based instruction or a length-matched neutral message (an introduction to CIMH) for 5 min. During NF, an alcohol picture and a thermometer display reflecting the brain activation induced by alcohol pictures were presented on the screen. Participants were instructed to down-regulate the thermometer. Both real NF groups (groups 1 and 2) were presented with NF signals from VS, while the sham NF group (group 3) received signals from the auditory cortex (A1) which is not involved in cue reactivity or cognitive control. (see rtfMRI NF setup in Figure 1a, and training process in Figure 1b).

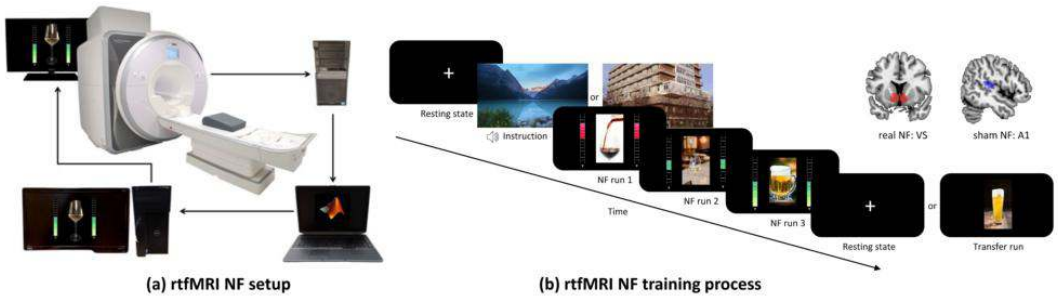

Figure 1. (a) rtfMRI NF setup. Acquired brain images are sent to a laptop running in-house MATLAB scripts for pre-processing and extraction of the NF signal. The value was calculated as the percentage change of the activation at a time compared with the mean activation during the preceding baseline phase and was continuously updated with every acquired fMRI volume (every 1s). Then the value is forwarded to a computer running Presentation software and is displayed to the participant in the scanner as the thermometer value. See setup parameters in our previous proposal (Weiss et al., 2020). **(b) rtfMRI NF training process.** The rtfMRI NF training has two sessions (T1 and T2), each session consists of an anatomical MPRAGE scan, a resting state scan, an instruction phase (either mindfulness-based instruction or a length-matched neutral message), and three NF runs. An additional resting run and a transfer run, which tests the transfer effects of the learned strategy in the absence of feedback, were conducted at the end of the two sessions respectively. The real NF signals were extracted from VS, while the sham NF signals were from the auditory cortex (A1).

Results: A total of 66 participants have been enrolled (age: 23.82±7.52, 37/29 male/female), group1: n=25, group2: n=19, group3: n=22. The randomized groups did not differ in gender, age, alcohol consume associated measures, or trait mindfulness. Craving was assessed before and after each session using a visual analog scale to track NF-related dynamics (Figure 2a). Group1 (real NF with mindfulness instruction) showed a decreasing tendency of craving after NF at the first NF session. The VS activity to alcohol cues is shown in Figure 2b, and group1 decreased VS activity from the 2nd run to the transfer run. To test whether mindfulness instruction has an impact on real NF, group1 and group2 (real NF with control instruction) were compared (Figure 2d). The negative effects across all NF runs reflect that VS activity of group1 was lower than that of group2 during all NF runs, but the differences were not significant. The negative effect size in the transfer run, although not significant, indicates a possible larger learning effect in group1.

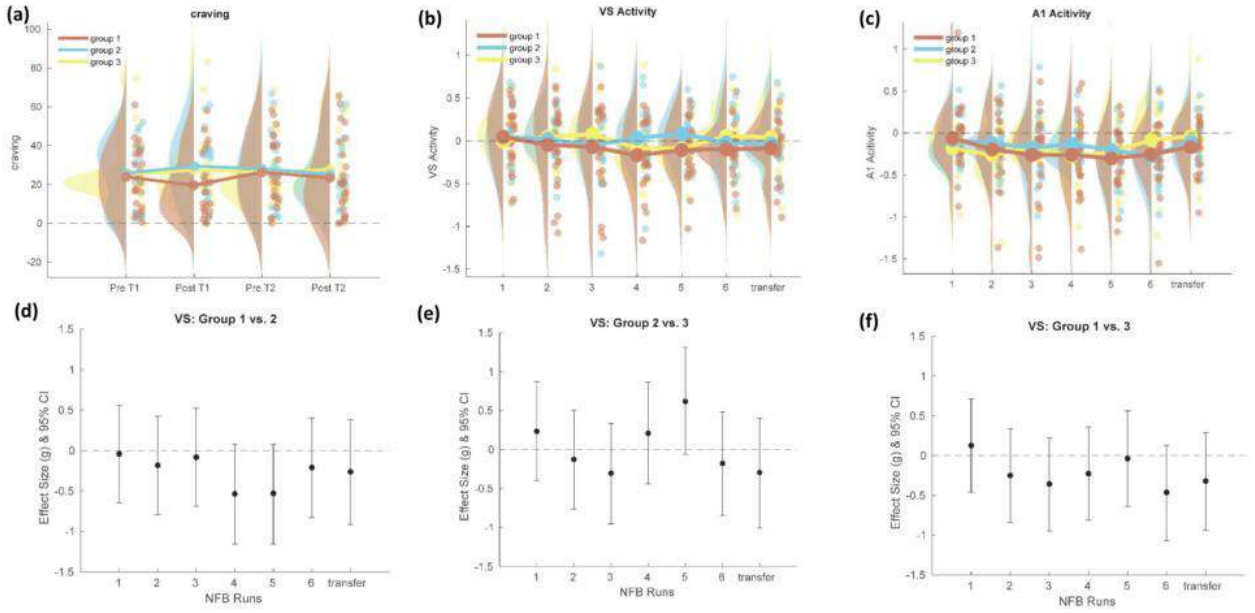

Figure 2. (a), (b), and (c) are "raincloud" figures plotting raw data (rain dot), probability density (cloud), mean (dot in the cloud), and the change of mean (solid line) between time points (T1: session1, T2: session2, pre: before, post: after) of the craving, VS activity, and A1 activity respectively. (a) and (b) shows the craving and VS activity of group 1 (in red) decreased after the NF training at both sessions. (d), (e) and (f) depict group comparisons of VS activity during NF runs, the dots present the effect size (Hedge's g, calculated based on t value) and the error bar represents 95% confidence interval. A negative effect size reflects a lower VS activity of group 1, 2, and 1 respectively.

Conclusions: These preliminary results suggest a possible supportive effect of mindfulness-based instruction on rtfMRI NF training on both clinical outcomes (reduction in self-reported cravings) and neurobiological outcomes (reduction in alcohol cue-induced VS activity) for people with problematic alcohol use. We will continue recruiting participants to reach our recruitment goals (N=111) and make solid conclusions with sufficient statistical power.

References

1. Heinz, A., Beck, A., Grüsser, S. M., Grace, A. A., & Wrase, J. (2009). Identifying the neural circuitry of alcohol craving and relapse vulnerability. Addiction biology, 14(1), 108-118.
2. Karch, S., Keeser, D., Hümmer, S., Paolini, M., Kirsch, V., Karali, T., Kupka, M., Rauchmann, B. S., Chrobok, A., Blautzik, J., Koller, G., Ertl-Wagner, B., & Pogarell, O. (2015). Modulation of Craving Related Brain Responses Using Real-Time fMRI in Patients with Alcohol Use Disorder. PloS one, 10(7), e0133034.
3. Kirsch, M., Gruber, I., Ruf, M., Kiefer, F., & Kirsch, P. (2016). Real-time functional magnetic resonance imaging neurofeedback can reduce striatal cue-reactivity to alcohol stimuli. Addiction Biology, 21(4), 982-992.
4. Pindi, P., Houenou, J., Piguet, C., & Favre, P. (2022). Real-time fMRI neurofeedback as a new treatment for psychiatric disorders: A meta-analysis. Progress in neuro-psychopharmacology & biological psychiatry, 119, 110605.
5. Oblak, E. F., Lewis-Peacock, J. A., & Sulzer, J. S. (2017). Self-regulation strategy, feedback timing and hemodynamic properties modulate learning in a simulated fMRI neurofeedback environment. PLoS computational biology, 13(7), e1005681.
6. Weiss, F., Aslan, A., Zhang, J., Gerchen, M. F., Kiefer, F., & Kirsch, P. (2020). Using mind control to modify cue-reactivity in AUD: the impact of mindfulness-based relapse prevention on real-time fMRI neurofeedback to modify cue-reactivity in alcohol use disorder: a randomized controlled trial. BMC psychiatry, 20(1), 309.

Poster No 73

An fMRI Study of Instant Brain Effects of taVNS on Parkinson's Disease

Shanshan Gao[1], Chunlei Guo[1], Yi Luo[1], Yue Ma[1], Qingyan Chen[1], Xiaojuan Dan[2], Yongtao Zhou[2], Xiaojing Ma[1], Biao Chen[2], Jiliang Fang[1]

[1]Guang'anmen Hospital, China Academy of Chinese Medical Sciences, Beijing, China, [2]Department of Neurology, Xuanwu Hospital of Capital Medical University, Beijing, China

Introduction: The incidence of Parkinson's disease (PD) among individuals over the age of 60 in China is approximately 1.37%[1]. It is predicted that by 2030, there will be 5 million Parkinson's disease patients in China, accounting for approximately half of the world's Parkinson's disease patients. In addition to the typical motor symptoms such as resting tremor, bradykinesia, muscle rigidity, and postural gait disorders, Parkinson's disease is accompanied by nonmotor symptoms such as constipation, fatigue, mood disorders, and sleep disturbances, and is slowly progressive[2]. Currently, the primary treatment for Parkinson's disease is dopamine substitution therapy[3]. The patient population is primarily elderly, and this elderly group has many underlying health conditions and takes multiple medications. Therefore, it is necessary to identify a convenient non-pharmaceutical therapy for patients with Parkinson's disease. Currently, non-drug therapies available for Parkinson's disease include repetitive transcranial magnetic stimulation, transcranial direct current stimulation, surgery, and the like, which are often complex and invasive. In contrast, taVNS offers a non-invasive, portable therapy that holds significant advantages. Previous clinical studies have demonstrated that transcutaneous auricular vagus nerve stimulation-taVNS-significantly improves gait freezing[4] and other motor disorders[5] in patients with Parkinson's disease and can regulate other non-motor symptoms such as insomnia[6], depression[7], mild cognitive impairment[8], and more. Therefore, this study aims to utilize resting-state fMRI to investigate the brain mechanism of the immediate adjunctive treatment of mild to moderate Parkinson's disease with taVNS.

Methods: 17 patients with Parkinson's disease in the early to middle stage who were taking medication regularly were recruited, and 17 healthy people matched by gender, age and education level were collected as a control group. The PD group was treated with taVNS for 30 min during the "off " state, and resting fMRI scans were performed before and after the taVNS, while the HC group obbtained the same fMRI scan. Observations were made to compare the differences in whole-brain-wide amplitude of low-frequency fluctuation (ALFF), fractional amplitude of low-frequency fluctuation (fALFF), and Regional Homogeneity (ReHo) between the 2 groups of subjects, as well as the changes in whole-brain-wide ALFF values of patients before and after taVNS treatment.

Results: Compared with the HC group, the bilateral cerebellar ALFF values were reduced; the fALFF values of the right cuneate lobe/right superior occipital gyrus and the left precentral gyrus/left postcentral gyrus were reduced; and the ReHo values of the right cerebellum-and right cuneate lobe/Calcarine fissure /right lingual gyrus were reduced in PD group. After immediate treatment with taVNS, ALFF values were elevated in bilateral supplementary motor areas/bilateral medial superior frontal gyrus/left anterior cingulate and paracingulate gyrus in the PD group compared with pre-treatment.

Table 1 General information

Group	Number	Age (years)	Sex (M/F)	Years of education
PD	17	61.24±12.54	10/7	12.24±2.02
HC	17	62.35±12.17	10/7	12.65±2.27
Statistical value	-	t=-0.26	χ^2=0	t=-0.54
P value	-	0.87	1	0.60

Table 2 Comparison of Differential Brain Areas between PD and HC Groups in Resting State

	Difference brain area	BA partition	MNI peak			Cluster size	T value
			x	y	z		
ALFF	bilateral cerebellum	-	21	-75	-57	322	-4.1503
fALFF	right cuneate lobe/ right superior occipital gyrus	18/19	12	-87	18	95	-5.3664
	left precentral gyrus/ left postcentral gyrus	4/6	-54	-6	36	58	-5.1356
ReHo	right cerebellum	-	24	-75	-60	158	-3.9146
	right cuneate lobe/Calcarine fissure /right lingual gyrus	17/18/19	12	-84	18	124	-4.6129

Table 3 Comparison of differential brain regions before and after immediate treatment in the PD group

	Difference brain area	BA partition	MNI peak			Cluster size	T value
			x	y	z		
ALFF	bilateral supplementary motor areas/bilateral medial superior frontal gyrus/left anterior cingulate and paracingulate gyrus	6/8/32	-9	51	18	168	6.6444

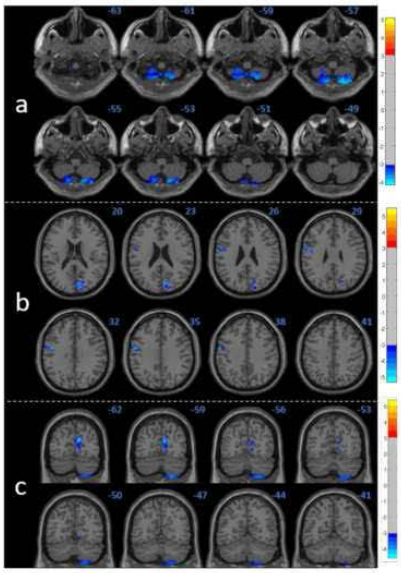

Fig.1 Differential brain regions between the PD/HC using two-sample t-tests

Note: a: Amplitude of low-frequency fluctuation (ALFF) discrepant brain regions: bilateral cerebellum (21, -75, -57); b: fractional amplitude of low-frequency fluctuation (fALFF) discrepant brain regions: right cuneate lobe/right superior occipital gyrus (12, -87, 18), left precentral gyrus/left postcentral gyrus (-54, -6, 36); c: Regional Homogeneity (ReHo) discrepant brain regions: right cerebellum (24, -75, -60), right cuneate lobe/Calcarine fissure /right lingual gyrus (12, -84, 18). Colour from blue to yellow indicates the degree of low to high ALFF values (threshold voxel level $P < 0.005$; cluster level $P < 0.05$).

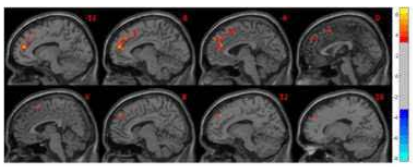

Figure 2 Differences in ALFF values before and after immediate treatment in the PD group Brain regions: bilateral supplementary motor areas/bilateral medial superior frontal gyrus/left anterior cingulate and paracingulate gyrus (-9, 51, 18), with colours ranging from blue to yellow denoting the degree of low to high ALFF values (threshold voxel level $P < 0.005$; cluster level $P < 0.05$).

Conclusions: Brain function abnormalities in cerebellar, sensory, and motor-related cortical brain regions still exist in early and middle stage Parkinson's disease patients who take medication regularly. The immediate modulating effect of taVNS mainly focuses on bilateral auxiliary motor area and prefrontal lobe, which may be the brain mechanism for its adjuvant treatment of mild-to-moderate Parkinson's disease patients.

References

1. QI S. Prevalence of Parkinson's Disease: A Community-Based Study in China[J]. Mov Disord, 2021,36(12): 2940-2944.
2. POSTUMA R B. MDS clinical diagnostic criteria for Parkinson's disease[J]. Mov Disord, 2015,30(12): 1591-1601.
3. BLOEM B R. Parkinson's disease[J]. Lancet, 2021,397(10291): 2284-2303.
4. Zhang H. Transcutaneous auricular vagus nerve stimulation improves gait and cortical activity in Parkinson's disease: A pilot randomized study. CNS Neurosci Ther. 2023;29(12):3889-3900.
5. Zaehle. "The LC-NE system as a potential target for neuromodulation to ameliorate non-motor symptoms in Parkinson's disease." Autonomic neuroscience : basic & clinical vol. 236 (2021): 102901.
6. Lench DH. Multi-session transcutaneous auricular vagus nerve stimulation for Parkinson's disease: evaluating feasibility, safety, and preliminary efficacy. Front Neurol. 2023;14:1210103. Published 2023 Jul 18.
7. Zhao B. Altered functional connectivity of the thalamus in patients with insomnia disorder after transcutaneous auricular vagus nerve stimulation therapy. Front Neurol. 2023;14:1164869. Published 2023 Jul 6.
8. Fang J. Transcutaneous Vagus Nerve Stimulation Modulates Default Mode Network in Major Depressive Disorder. Biol Psychiatry. 2016;79(4):266-273.
9. Wang L. The efficacy and safety of transcutaneous auricular vagus nerve stimulation in patients with mild cognitive impairment: A double blinded randomized clinical trial. Brain Stimul. 2022;15(6):1405-1414.

Poster No 74

An Endogenic Attentional Visuomotor Regulator

Yiqing Hu[1], Hao Zhang[2], Xiaoli Li[3], Yan Song[3], Zaixu Cui[1], Chenguang Zhao[4]

[1]Chinese Institute for Brain Research, Beijing, China, [2]School of Systems Science, Beijing Normal University, Beijing, China, [3]State Key Laboratory of Cognitive Neuroscience and Learning, Beijing Normal University, Beijing, China, [4]Chinese Institute for Brain Research, Beijing, Beijing

Introduction: Attention is not constant but fluctuates from moment to moment(Esterman & Rothlein, 2019). Although a lot of studies have found alpha (8-12 Hz) synchrony appears to influence sensory processing during visual attention tasks(Esterman & Rothlein, 2019; Foxe et al., 1998; Fu et al., 2001; Herrmann & Knight, 2001), most of them only show correlation but not causality(Peylo et al., 2021). Here, we established a cognitive brain-machine interface (cBMI)(Chinchani et al., 2022), which was designed to monitor real-time alpha oscillations and was proved to regulate endogenous attention in visuomotor tasks successfully.

Methods: 2 electroencephalograph (EEG) experiments with 75 young adults aged 18-28 years old were included in our study. A cartoon visual search paradigm with 5 green planes (non-target) and one yellow plane (target) distributed in a clockwise manner (Fig. 1A). Participants were asked to use the computer joystick, an efficient and cost-effective response device for recording continuous movements(Szul et al., 2020), to maneuver to the target position while maintaining their gaze on the central fixation. In this case, we can precisely measure participants' response time and belief time (Fig. 1B). Experiment 1 (N = 50) was designed to find the neural biomarker related to different attention levels in which the target search array appeared in 10 Hz frequency between 2-10 s intertrial interval after response end (Fig. 1C). Importantly, in experiment 2 (N = 25), we monitored the positive or negative biomarker contained from experiment 1 every second to determine the target appeared time which demonstrated our system can casually regulate the endogenic attentional visuomotor in real-time (Fig. 1D). The EEG recording, preprocessing processes, and EEG analyses methods, including N2pc (time-locked to target onset), alpha power, and channel tuning functions (CTFs) were based on the former attention studies(Jensen & Mazaheri, 2010; Zhao et al., 2023).

Figure 1

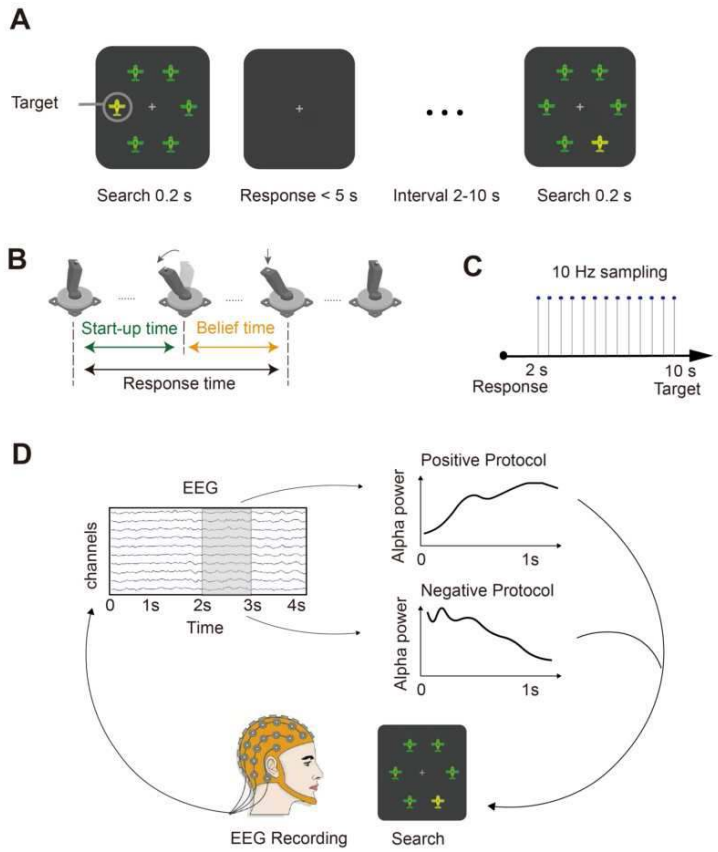

Results: In experiment 1, we found different cognitive protocols connected to attention fluctuates that the alpha power decreased in good performance trials but increased in bad performance trials (Fig. 2A). In experiment 2, the belief time became shorter ($t = -2.378$, $p < 0.05$) when using the positive protocol (when alpha power decreased in the test segment, the target search array will appear) than using the negative protocol (target search array only appeared while alpha power increased) (Fig. 2B). N2pc component which appears to reflect target selection(Eimer, 1996) was larger in the negative protocol condition than in the positive protocol condition ($t = -2.248$, $p < 0.05$), which indicated that in the positive attention condition, benefit in the spatial representation for target selection during the search array is no longer needed (Fig. 2C). CTFs which reflect the spatial distribution of alpha power measured by scalp after the target search array for positive and negative protocol condition (Fig. 2D). The time-resolved slope of CTFs results suggest that alpha power tracked the target location earlier in positive condition ($T = 175$ ms) than in the negative protocol condition ($T = 412$ ms) (Fig. 2E).

Figure 2

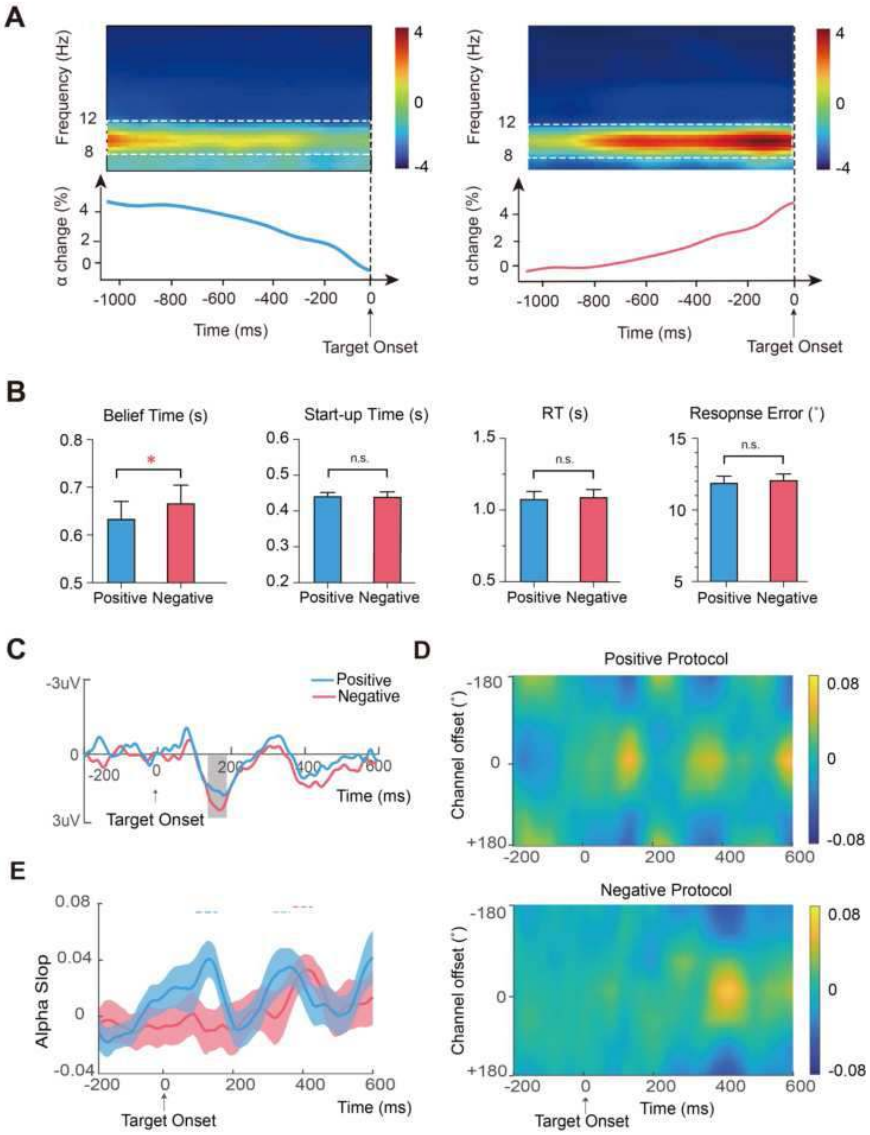

Conclusions: Taken together, we monitored real-time alpha oscillations attached to attention fluctuations and successfully regulated endogenous attention to motivate better behavior performance. This work may be helpful in understanding the mechanism of attention and can be applied to improve cognition in diverse psychiatric disorders, including ADHD and schizophrenia.

References

1. Chinchani, A. M. (2022). Tracking momentary fluctuations in human attention with a cognitive brain-machine interface. Communications Biology, 5(1), 1346.
2. Eimer, M. (1996). The N2pc component as an indicator of attentional selectivity. Electroencephalography and Clinical Neurophysiology, 99(3), 225–234.
3. Esterman, M. (2019). Models of sustained attention. Current Opinion in Psychology, 29, 174–180.
4. Foxe, J. J. (1998). Parieto-occipital approximately 10 Hz activity reflects anticipatory state of visual attention mechanisms. Neuroreport, 9(17), 3929–3933.
5. Fu, K.-M. G.m(2001). Attention-dependent suppression of distracter visual input can be cross-modally cued as indexed by anticipatory parieto–occipital alpha-band oscillations. Cognitive Brain Research, 12(1), 145–152.
6. Herrmann, C. S. (2001). Mechanisms of human attention: event-related potentials and oscillations. Neuroscience & Biobehavioral Reviews, 25(6), 465–476.
7. Jensen, O. (2010). Shaping Functional Architecture by Oscillatory Alpha Activity: Gating by Inhibition. Frontiers in Human Neuroscience, 4, 186.
8. Peylo, C.m(2021). Cause or consequence? Alpha oscillations in visuospatial attention. Trends in Neurosciences, 44(9), 705–713.
9. Szul, M. J.m(2020). The validity and consistency of continuous joystick response in perceptual decision-making. Behavior Research Methods, 52(2), 681–693.
10. Zhao, C. (2023). Suppression of distracting inputs by visual-spatial cues is driven by anticipatory alpha activity. PLOS Biology, 21(3), e3002014.

Poster No 75

NIR-LED Photobiomodulation(PBM) on elderly improves cognitive functions and EEG patterns

Namheon Kim[1], Ukeob Park[2], DeaKeun Kim[3], Seung Wan Kang[3]

[1]iMediSync Inc., Gangnam-gu, Seoul, [2]iMediSync, Inc., Seoul, Seoul, [3]iMediSync, Seoul, Seoul

Introduction: In recent years, photobiomodulation (PBM), known as low-level light therapy (LLLT), has become popular to treat various neurodegenerative diseases . The positive effects, such as increased blood circulation and ATP production, resulting from the stimulation of mitochondria by PBM have been confirmed in in vitro and in vivo experiments . In some experiments conducted on humans, it has been confirmed that LED light penetrating the skull produces similar effects on nerve cells . In some experiments conducted on humans, it has been confirmed that LED light penetrating the skull produces similar effects on nerve cells. Zomorrodi et al. investigated the results of 17 weeks of PBM therapy in AD patients, assessing cognitive function, quality of life, and EEG dimensions. However there is a notable absence of large-scale human studies applying PBM to a substantial number of elderly individuals with cognitive impairment to discern the specific improvements in cognitive function and changes in EEG features. This study focused on assessing actual cognitive function and monitoring changes in diverse EEG features, including both EC and EO power, as well as Dominant Frequency Variability (DFV), a parameter known to be associated with cognitive function.

Methods: Before the PBM Intervention, eye-closed and eye-open resting-state QEEG data were collected from 70 Subject, each of which is longer than 2 minutes. 48 subjects are diagnosed as MCI, and 22 as early dementia. We measured 19ch EEG based on international 10-20 system. They were pre-processed by bad epoch rejection and ICA method using iSyncBrain®, and spectrum power were calculated. On the other hand, with the cleaned data, which underwent a Band Pass Filter (6.5 to 12 Hz), peak points exceeding the threshold were selected. Then, the distance between peaks was calculated, determining the intervals between each peak. DFV was calculated from the standard deviation of the distribution. Additionally, CDR was obtained by experienced neurologists. Each participant received PBM three times a week for 10 minutes over 8 week period. Near-infrared light emission was conducted using iSyncWave, with a wavelength of 850 nm and a frequency of approximately 10 Hz (proportional to the Dominant Frequency identified in EEG measurements for each participant). Following the intervention, EEG measurements and CDR calculations were performed in the same manner to the pre-intervention assessments.

Results: In the Eye-closed EEG power spectrum, a trend of decreased theta and increased alpha was observed in most regions after PBM. In the Eye-open EEG power spectrum, a tendency of decreased alpha peaks power was observed after the intervention. DFV showed significant increase.

Conclusions: According to previous studies, in healthy individuals, alpha peaks in eye-closed are suppressed in eye-open, but in patients with cognitive impairment, the suppression does not occur normally, leading to a reduced difference between EC and EO . In the cognitive impairment group participating in this experiment, it was confirmed that the suppression was impaired, and after PBM, improvement in this aspect was observed. Additionally, it is generally known that as cognitive function declines, DFV decreases . In this study, a tendency of recovery in DFV was observed after PBM, suggesting a positive impact on cognitive function.

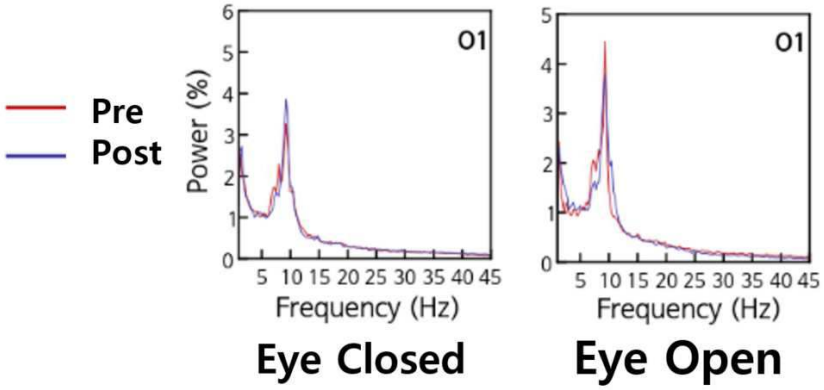

References

1. Mitrofanis, J., Henderson, L. A. (2020). How and why does photobiomodulation change brain activity? Neural Regen. Res. 15, 2243–2244.
2. Purushothuman, Sivaraman, et al. (2014) Photobiomodulation with near infrared light mitigates Alzheimer's disease-related pathology in cerebral cortex–evidence from two transgenic mouse models. Alzheimers Res Ther. 6: 1-13.

3. Stepanov YV, et al (2022). Near-infrared light reduces β-amyloid-stimulated microglial toxicity and enhances survival of neurons: mechanisms of light therapy for Alzheimer's disease. Alzheimers Res Ther. 18;14(1):84.
4. Zomorrodi, Reza, et al. (2017) Complementary EEG evidence for a significantly improved Alzheimer's disease case after photobiomodulation treatment. 26th Annual Scientific Conference, Canadian Academy of Geriatric Psychiatry Toronto.
5. Jennings, J.L., Peraza, L.R., Baker, M. et al. (2022) Investigating the power of eyes open resting state EEG for assisting in dementia diagnosis. Alz Res Therapy 14, 109
6. Myrto Stylianou, et al. (2018) Quantitative electroencephalography as a marker of cognitive fluctuations in dementia with Lewy bodies and an aid to differential diagnosis. Clinical Neurophysiology, 129, 6,1209-1220,

Poster No 76

Asymmetrical Impacts of Motion Vibrational Stimulations on Resting-State Brain Connectivity

Yueh-Hsun Lu[1], Chih-Hsueh Wang[2], Changwei Wu[3]

[1]Taipei Medical University - Shuang-Ho Hospital, New Taipei ity, Zhonghe Dist., [2]Taipei Medical University - Shuang-Ho Hospital, New Taipei City, Jhonghe, [3]Taipei Medical University, Zhonghe, New Taipei

Introduction: Previous research has substantiated and elucidated the existence of brain asymmetry between hemispheres[1]. Functional asymmetry primarily manifests as left-right disparities in brain activation, and from a network perspective, the laterality of functional networks provides avenues for investigating the brain plasticity following intervention[2]. The asymmetrical brain organization not only influences motor control but extends its impact to high-order cognitive processes, including language, spatial perception, and emotional processing.[3] A previous study identified an association between handedness and differences in effective connectivity within the human motor network, emphasizing the significant role of the left supplementary motor area (SMA) in individuals with right-handed dominance[4]. Vibration stimulation had been used in improvement of muscle power, decreasing spasticity, and enhancement of exercise effect[5,6]. The different effect of vibration stimulation from bilateral hands was not tested yet. In this context, we investigate the functional connectivity following vibration stimulations applied to both the left and right hands.

Methods: In this study, 15 healthy participants (4 females, all exhibiting right-handedness) were subjected to distinct vibrational stimulations applied to their right and left hands. Resting-stat data were acquired during an 8-minute scan under eyes-closed conditions using a 3T MR scanner (GE750). Each participant underwent two MRI sessions, with baseline image acquisition occurring prior to the application of vibrations. Following the initial imaging session, participants dismounted the MRI table for intervention while seated in a chair with a backrest. Subsequently, they underwent a second fMRI resting-state scan. During vibrational stimulation, participants were seated with their hand's elbow flexed at 90 degrees and a slight separation from the trunk. Participants were instructed not to touch their trunk and to securely grip the device. Vibrational muscle force stimulation was sequentially administered at four frequencies: 15, 30, 45, and 60Hz, each lasting 1 minute, with a 1-minute rest interval between frequency switches. Data underwent preprocessing and analysis using CONN toolbox version 19.c. Large-scale network analysis encompassed a priori selected regions of interest within the default mode network (DMN), sensorimotor, visual, salience, dorsal attention, fronto-parietal, language, and cerebellar networks. Two-way ANOVA test was used to check the significance. A statistical significance threshold of uncorrected $p < 0.001$ was applied.

Results: When seeding at the post-central gyrus (post-CGr), we found the connectivity was enhanced in both left and right hand. Increasing connectivity between post-CGr and the same side lateral occipital cortex was observed in both sides ($p < 0.001$). Decreasing connectivity between post-CGr and supramarginal/angular gyrus was observed ($p < 0.001$). Weaker connectivity change of right-hand vibrations was noticed as compared to that of left-hand vibrations. Additional negative connectivity was noticed between post-CGr and dorsomedial prefrontal cortex (DMPFC).

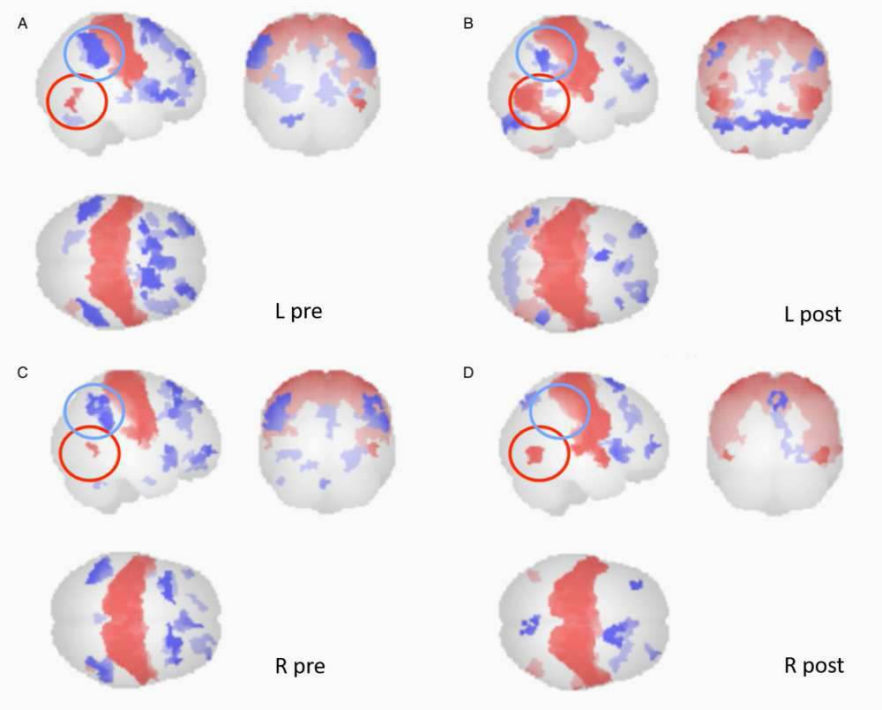

A (pre) & B (post): Stimulation was from left hand. C (pre) & D (post): Stimulation was from right hand. Red circle: Lateral occipital lobe. Blue circle: Supramarginal and angular gyrus.

Conclusions: After vibration muscle force stimulations, brain connectivity in the posterior brain area surpassed that in the anterior area and left-sided connections to right-sided motor areas increased. The effect of increasing connectivity between bilateral motor areas was more pronounced in left-hand vibrations than right-hand vibrations. Our results underscored the asymmetric effects resulting from stimulations applied to different hands. Further exploration involving left-handed volunteers is warranted.

References

1. Wang B, Yang L, Yan W, An W, Xiang J, Li D. Brain asymmetry: a novel perspective on hemispheric network. Brain Science Advances. 2023;9(2):56-77.
2. Hoch MM, Doucet GE, Moser DA, et al. Initial Evidence for Brain Plasticity Following a Digital Therapeutic Intervention for Depression. Chronic Stress. 2019;3.
3. turria-Medina Y, Pérez Fernández A, Morris DM, et al. Brain hemispheric structural efficiency and interconnectivity rightward asymmetry in human and nonhuman Primates. Cereb Cortex 2011, 21(1): 56–67.
4. Li ML, Chen H, Wang JP, et al. Handedness- and hemisphere-related differences in small-world brain networks: a diffusion tensor imaging tractography study. Brain Connect 2014, 4(2): 145–156.
5. Desrosiers, J., Hebert, R., Bravo, G., and Dutil, E. (1995). Upper extremity performance test for the elderly (TEMPA): normative data and correlates with sensorimotor parameters. Arch. Phys. Med. Rehabil. 76, 1125–1129.
6. Hu, J., Du, J., Xu, Q., Yang, F., Zeng, F., Dai, X.-J., et al. (2017). Altered coupling between motion-related activation and resting-state brain activity in the ipsilesional sensorimotor cortex after cerebral stroke. Front. Neurol. 8:339.

Poster No 77

Transcranial photobiomodulation increases functional connectivity and cortical excitability

Zhilin Li[1], Yiqing Hu[1], Yang Li[1], Chenguang Zhao[1], Zaixu Cui[1]

[1]Chinese Institute for Brain Research, Beijing, China

Introduction: Transcranial photobiomodulation (tPBM), a promising noninvasive intervention, has been shown promising for modulating brain activity(Dmochowski et al. 2020; Song et al. 2020; Zhao et al. 2022). However, the mechanism underlying how tPBM modulates brain activity has not been systematically discussed(Dole et al. 2023). In the current study, we utilized the latest Transcranial Magnetic Stimulation(TMS) evoked potentials (TEP) and electroencephalogram(EEG) functional connectivity to shed light on this problem(Conde et al. 2019; Schoffelen and Gross 2009).

Methods: The study consisted of two experiments. In experiment I, data was collected from 75 subjects who were divided into three groups based on the frontoparietal(FP1/2) stimulation sites and wavelengths: 1) 1064 nm tPBM applied to the FP2,

2) 1064 nm tPBM applied to the FP1, 3) 852 nm applied to the FP2. To investigate the effect of tPBM on the brain network, all participants received a 12-minute non-invasive laser tPBM session, followed by an 8-minute EEG data acquisition to construct functional connectivity. In experiment II, data were collected from 60 subjects divided into two groups based on wavelengths (1064 nm / 852nm). All participants received 12 minutes of laser tPBM at FP2 followed by 8 minutes of EEG acquisition with pulsed TMS at 0.2 Hz to calculate TEP, some of the 1064 nm group underwent the same protocol again after 24 hours. Both experiments mentioned above were double-blind and included a sham control group. The diode-pumped solid-state laser utilized in this study had a linewidth of ±1 nm. The laser beam was uniformly distributed and covered an area of 13.57 cm2 (4 cm in diameter), producing a continuous power output of 2271 mW. This resulted in a power density or irradiance of 167 mW/cm2(Zhao et al. 2022). The stimulation site in our experiment(FP1/2)was based on the 10-20 system used for EEG electrode placement.

Results: The results of Experiment I indicate that the effects of tPBM on brain network modulation are site and wavelength-specific, with delayed effects observed(Fig 1). Specifically, when the stimulation site was FP2, only the wavelength of 1064 nm led to significant enhancement of functional connectivity. Although the number of functional connectivity enhancements in the 0-2 min period after the stimulation was low, it increased significantly in the 6-8 min period, becoming ten times more than in the 0-2 min period. Most of these enhancements were observed in the occipital-parietal and parietal-frontal lobes. The findings from Experiment II indicate that tPBM has wavelength-specific and sustained effects on the modulation of neural activity(Fig 2). When a wavelength of 1064 nm was applied to FP2, a significant difference was found between the pre and post-stimulation TEP within the 0-100ms and 200-250ms after TMS pulse, and the significant difference at 200-250ms even lasted for up to 24 hours.

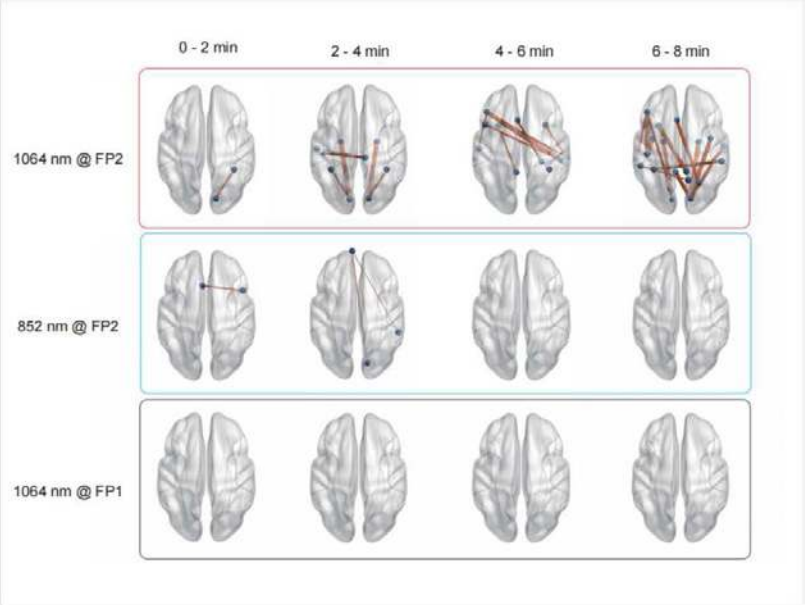

Figure 1. Brain network patterns in 3 conditions. 1064 nm tPBM applied to FP2 led to a significant enhancement of functional connectivity.

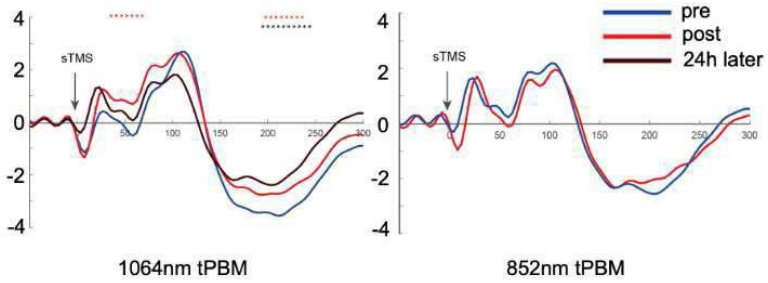

Figure 2. TMS evoked potentials at 2 wavelengths.

Conclusions: This study presents two experiments demonstrating that tPBM at 1064 nm on FP2 can modify brain activity and network patterns, with effects lasting up to 24 hours. By providing a systematic investigation of the modulation effect the tPBM applies to the brain, this study may be important in paving the way for developing and applying this promising neuromodulation technology.

References
1. Conde, V (2019), 'The non-transcranial TMS-evoked potential is an inherent source of ambiguity in TMS-EEG studies', NeuroImage, 185, 300–312
2. Dmochowski, GM (2020), 'Near-infrared light increases functional connectivity with a non-thermal mechanism', Cerebral Cortex Communications, 1(1), tgaa004
3. Dole, M (2023), 'A systematic review of the effects of transcranial photobiomodulation on brain activity in humans', Reviews in the Neurosciences, 34(6), 671–693
4. Schoffelen, J (2009), 'Source connectivity analysis with MEG and EEG', Human Brain Mapping, 30(6), 1857–1865.
5. Song, P (2020), 'Transcranial near-infrared stimulation may increase cortical excitability recorded in humans', Brain Research Bulletin, 155, 155–158
6. Zhao, C (2022), 'Transcranial photobiomodulation enhances visual working memory capacity in humans', Science Advances, 8(48), eabq3211

Poster No 78

An fMRI study on various a auricular neurostimulation parameters to optimize anti-pain effects

Bashar Badran[1], Xiaolong Peng[2], John Robinson[2], Falon Sutton[2], Marion Wood[3], Dillon Connolly[2], Andrew Manett[2], Ethan Ashley[2], Baron Short[2], Viswanathan Ramakrishnan[2], Jeffrey Borckardt[2]

[1]Medical University of South Carolina, Charleston, SC, [2]MUSC, Charleston, SC, [3]College of Charleston, Charleston, SC

Introduction: Recently, a form of noninvasive neuromodulation known transcutaneous auricular neurostimulation (tAN) has emerged as a promising form of brain stimulation. Although preliminary findings suggest tAN is safe and effective in reducing opioid withdrawal symptoms, the mechanism at which it achieves this is unknown. Furthermore, the optimal stimulation parameters (frequency, ear stimulation target) are still unclear. In this prospective neuroimaging study, we use a novel concurrent tAN/fMRI paradigm to administer tAN within the MRI scanner in various settings and targets to activate auricular cranial nerves both independently and concurrently. We aim to understand whether combining stimulation at multiple ear sites produces greater neurophysiologic effects than stimulating solely the auricular branch of the vagus nerve (ABVN) or the auricular trigeminal nerve (ATN) alone.

Methods: Up to 96 healthy adult participants will attend a single experimental visit during which they will receive ear stimulation at one of three active conditions (ATN, ABVN, COMBO) and at two sham conditions (earlobe 15Hz, earlobe 100Hz). Enrolled participants will first have a baseline stimulation calibration conducted after which participants will be placed in the MRI scanner and electrodes will be connected to the MRI-compatible stimulation system. 8 minutes of stimulation will be delivered to the various ear targets in a 30s ON/OFF block design while acquiring high-resolution functional imaging. The fMRI data was processed to obtain the first-level task activation maps for each participant at each stimulation frequency. A one-sample t-test was then performed to generate the mean task activation maps.

Results: To date, we have enrolled n=39 (mean age +/-SD = 37.1 +/-13.2 years, n=28 female), and in this analysis, we present blinded data from the first 20 participants. All three active tAN conditions showed positive brain activations in the supramarginal gyrus, while ABVN and combo tAN have higher brain activity in the anterior insular compared to tragus tAN (one sample t-test, $p < 0.05$). Moreover, combo tAN also revealed strong deactivation in the primary sensorimotor area. In contrast, sham conditions (both 15Hz and 100Hz) induced brain activities have a similar spatial pattern, including positive brain activation in the temporoparietal junction (TPJ), insular, ventral lateral prefrontal cortex, and posterior temporal lobe. However, stimulation at 100Hz resulted in an overall higher intensity of activation compared to 15Hz.

Conclusions: This NIH Heal Initiative study is part of a five-year mission to understand how to create non-opioid treatments for pain and reduce opioid dependence. Using functional MRI acquired concurrently during neurostimulation allows us to map the specific auricular dermatomes that may have biologic impacts, and determine whether specific parameters may optimally recruit brain areas in the pain network. Although still early with a small sample size to date, there are likely identifiable differences between ear stimulation targets and understanding these differences will allow us to optimize tAN for pain disorders.

References
1. Jenkins DD, Khodaparast N, O'Leary GH, Washburn SN, Covalin A, Badran BW. Transcutaneous auricular neurostimulation (tAN): a novel adjuvant treatment in neonatal opioid withdrawal syndrome. Frontiers in Human Neuroscience. 2021 Mar 8;15:648556.

Poster No 79

Resting-state fMRI Study of Neurofeedback Emotion Regulation in DLPFC

Hui Gao[1], Chi Zhang[1], Li Tong[1], Zhonglin Li[2], Tianyuan Liu[1], Bao Li[1], Panpan Chen[1], Kai Yang[1]

[1]PLA Strategic Support Force Information Engineering University, Zhengzhou, China, [2]Henan Provincial People's Hospital, People's Hospital of Zhengzhou University, Zhengzhou, China

Introduction: Real-time functional MRI neurofeedback (rtfMRI-NF) is a safe non-pharmacological intervention (Weiskopf, N. 2012). This technique has been successfully applied to enhance the ability for autonomous emotion regulation. Although the dorsolateral prefrontal cortex (DLPFC) is associated with both emotion and cognition. the mechanism of emotional regulation through stimulating DLPFC remains incompletely understood. Our purpose is to investigate alterations in resting-state function before and after DLPFC regulation through neurofeedback training, so as to get a better understanding of the brain's mechanisms of emotional regulation and cognitive control, and provide new methods for future neurofeedback therapy.

Methods: All fMRI data were collected on a 3T Siemens Prisma of Henan Key Laboratory of Imaging and Intelligent Processing using the 64-channel head coil. Real time online data processing was performed on the OpenNFT system (Koush, Y., et al. 2017). We designed a rt-fMRI neurofeedback experiment based on regulation of left DLPFC activity in Healthy Human. Twenty-seven healthy young people participated in the experiment. The subjects completed two visits with an interval of 5-10 days (Figure 1A). The rtfMRI-NF experiment paradigm consisted of two sessions. First NF session included a resting state run (Rest1, 6 min 40 s) before training, a pre-training run (6 min 2 s) during which the person could adapt to NF training and then the three NF runs (each 6min 2s). Second NF session included the three NF runs (each 6 min 2 s), a transfer run (6 min 2 s) to observe whether the patient had mastered the regulation strategy, and then a resting state run (Rest2, 6 min 40 s) after training. Each NF run consisted of 12s for experiment preparation and alternating 18 s negative emotion stimulus block, 40 s feedback block, 12 s rest with cycle for 5 times. At stimulus blocks, subjects saw three negative emotion pictures (Lu Bai, et al. 2005), each lasting for 6 seconds. At rest blocks, subjects were asked to calm the mind and during feedback blocks, subjects were instructed to regulate feedback score in the screen as high as possible (Figure 1B). feedback blocks were designed to provide feedback of left DLPFC activity in real time and instructed subjects to voluntarily control the feedback signal by recalling a positive autobiographical memory. The resting-state fMRI data were performed using SPM12 (www.fil.ion.ucl.ac.uk/spm) and DPABI (Chaogan Yan, et al. 2010). ReHo and ALFF (YuFeng Zang, et al. 2004, 2007) were analyzed using a paired-sample t-test before and after NF training.

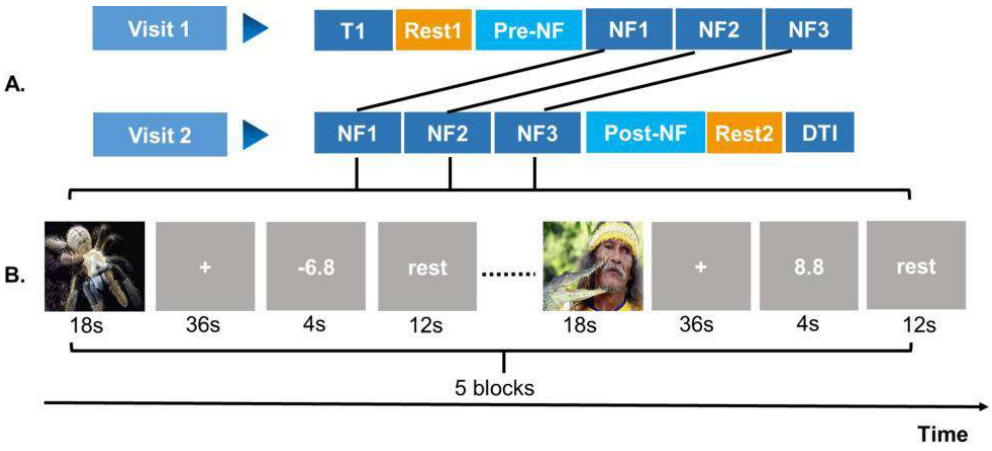

Fig. 1. (A) rt-fMRI NF experimental procedure of two visits and procedure of two NF sessions. (B) Design of NF training runs.

Results: In this paper, we explored alterations in resting-state before and after NF training in subjects (Figure 2A, 2B). We observed an increase in the ReHo map score following the training in the right middle temporal gyrus, and a decrease in the ReHo map score in the left lingual, left cuneus, bilateral calcarine, and insula. Additionally, we identified significantly increased ALFF in the left inferior occipital gyrus and right middle temporal gyrus, and reduced ALFF in the left Rolandic operculum. Furthermore, we found a significant reduction in rumination, state anxiety, and Beck Depression Scale scores following neurofeedback training (Figure 2C).

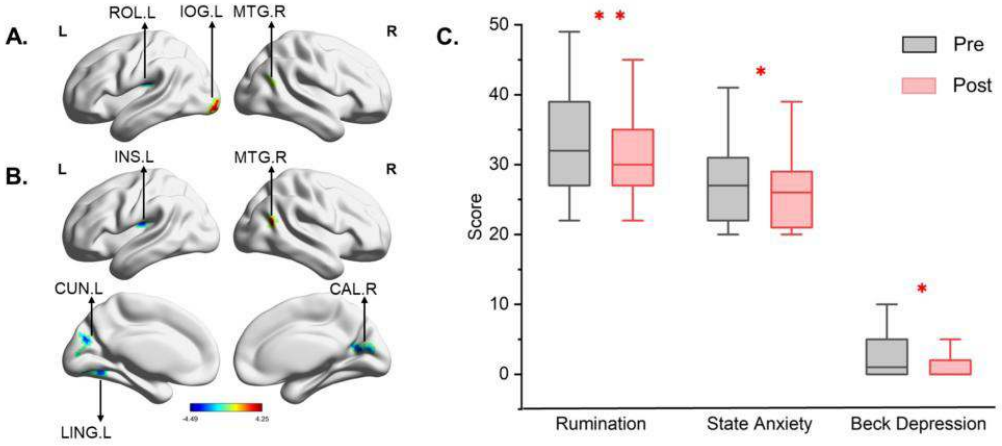

Fig. 2. A) Regions with altered ALFF score after rtfMRI-NF training (B) Regions with altered ReHo score after rtfMRINF training (GRF corrected voxel p<0.005). (C) Significantly different scale scores.

Conclusions: Through rt-fMRI NF training based on the left DLPFC, alterations in resting-state ReHo and ALFF in emotional and cognitive brain regions may be related to enhanced cognitive function and improved emotional regulation abilities. Furthermore, rt-fMRI NF has demonstrated effectiveness in modulating negative effects and is anticipated to serve as a potential adjunct for clinical treatment in the future.

References

1. Weiskopf, N. (2012), 'Real-time fMRI and its application to neurofeedback', Neuroimage, 62(2): p. 682-692.
2. Koush, Y., et al. (2017), 'OpenNFT: An open-source Python/Matlab framework for real-time fMRI neurofeedback training based on activity, connectivity and multivariate pattern analysis', Neuroimage, vol. 156, p. 489-503.
3. Lu Bai, et al. (2005), 'Development of the Chinese Affective Picture System: A Pilot Study in 46 Chinese College Students', Chinese Mental Health Journal, 19(11), p. 719-722.
4. Chaogan Yan, et al. (2010), 'DPARSF: A MATLAB Toolbox for "Pipeline" Data Analysis of Resting-State fMRI', Frontiers in Systems Neuroscience, 4(13), p. 13.
5. YuFeng Zang, et al. (2004), 'Regional Homogeneity Approach to fMRI Data Analysis', NeuroImage, vol. 22, p. 394-400.
6. YuFeng Zang, et al. (2007), 'Altered baseline brain activity in children with ADHD revealed by resting-state functional MRI', Brain Dev. vol. 29, p. 83–91.

Poster No 80

Monte Carlo Dosimetry Simulation of Transcranial and Intranasal Photobiomodulation

Hannah Van Lankveld[1], Anh Que Mai[2], Lew Lim[3], Nazanin Hosseinkhah[3], Paolo Cassano[4], J. Jean Chen[2]

[1]University of Toronto, Toronto, Ontario, [2]Baycrest Health Sciences, Toronto, Ontario, [3]Vielight Inc., Toronto, Ontario, [4]Massachusetts General Hospital, Boston, MA

Introduction: Photobiomodulation (PBM) is defined as the application of low levels of red or near-infrared light to stimulate neural tissue[1,2]. Wavelength, optical power density, pulsation frequency, skin colour and light source are commonly known parameters that impact the overall energy delivered to the tissue. Previous in vitro research suggests that the peak PBM response happens when the deposited energy reaches 3 Joules/cm3, but it is unclear how this relates to different stimulation parameters. Despite the many in vivo studies, the PBM stimulation protocols vary amongst studies, and there has yet to be a full characterization of light energy deposition based on the physics, likely leading to the large variabilities in responses[3]. This study will model the extent that local transcranial and intranasal photobiomodulation (tPBM & iPBM) can penetrate through neural tissue using Monte Carlo simulations[4,5].

Methods: The Monte Carlo Extreme (MCX) package was utilized to simulate the near-infrared light propagation through the multi-layer tissues of the human head, using the colin27 brain atlas, in which light propagation through different tissue types is mainly governed by coefficients of (1) absorption, (2) scattering (dispersion), and (3) transmission. We simulated a single optode laser source positioned for transcranial (tPBM) and intranasal (iPBM) simulation (as shown in Figure 1), with 8e9 incidental photons. Wavelengths simulated: 670nm, 810nm and 1064nm; power densities: 100mW/cm2 200mW/cm2 and 300mW/cm2. These are typical values from the literature. Moreover, we incorporated attenuation and scattering coefficients associated with Caucasian (white), African and Asian skin colours[6]. Matlab was used to compute the energy deposition in the brain regions closest to the optodes, as summarized in Fig. 1.

Results: Simulations show that the rostral dorsal prefrontal cortex for tPBM and the ventromedial prefrontal cortex for iPBM accumulate the highest energy (Figure 2). As shown in Figure 2.a, the 810 nm wavelength for tPBM and (Fig 2.e) 1064 nm wavelength for iPBM produced the highest energy accumulation. As shown in Fig. 2.b,e, optical power density is linearly correlated with energy. Moreover, in Fig. 2.c, we show that Caucasian (white) skin accumulates higher energy than other modelled skin colours. A maximum of 15% of the incidental energy for tPBM and 1% for iPBM reach the cortex (Fig 2.a). These correspond to a minimum of 100 and 40,000 minutes to reach the 3 J/cm3 target for tPBM (810nm and 100 mW/cm2) and iPBM (1064nm and 5 mW/cm2), respectively.

Conclusions: We found that the optimal wavelength depends on the penetrated tissue types. Thus, 810 nm and 1064 nm are optimal in tPBM and iPBM, respectively. The simulation also illustrated energy deposition being a linear function of power density. Moreover, melanin produces skin pigmentation and is the main variable in characterizing skin colour[8]. This study is the first to account for skin colour as a PBM consideration, demonstrating light skin being most conducive to light propagation. Moreover, we predict a maximum of 15% of the incidental energy is deposited into brain tissue, higher than previously reported using cadaver heads and skull fragments[9]. Even then, we show that at 300 mW/cm2 and 810 nm, at least 40 min of irradiation is required to reach the currently assumed optimal energy of 3J/cm3 (Fig 2.b). However, clinical research has shown increases in brain rhythms[10], and cognitive improvements with much lower energy dosages. This highlights the need to further understand the dynamic physiological processes impacting the PBM response in vivo.

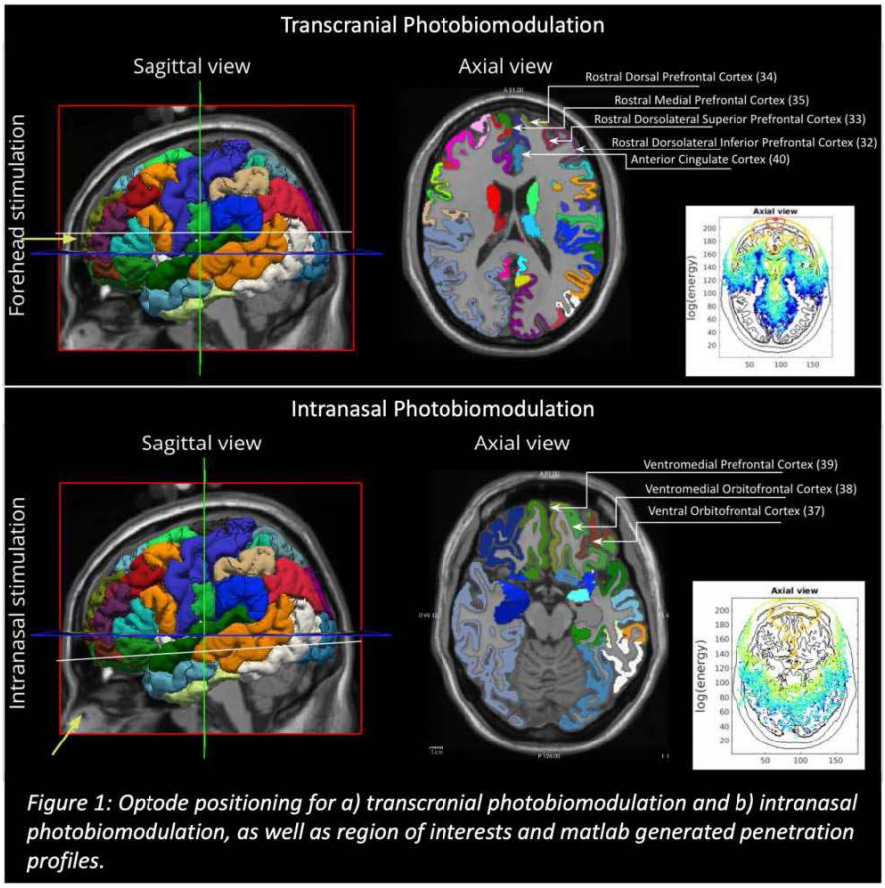

Figure 1: Optode positioning for a) transcranial photobiomodulation and b) intranasal photobiomodulation, as well as region of interests and matlab generated penetration profiles.

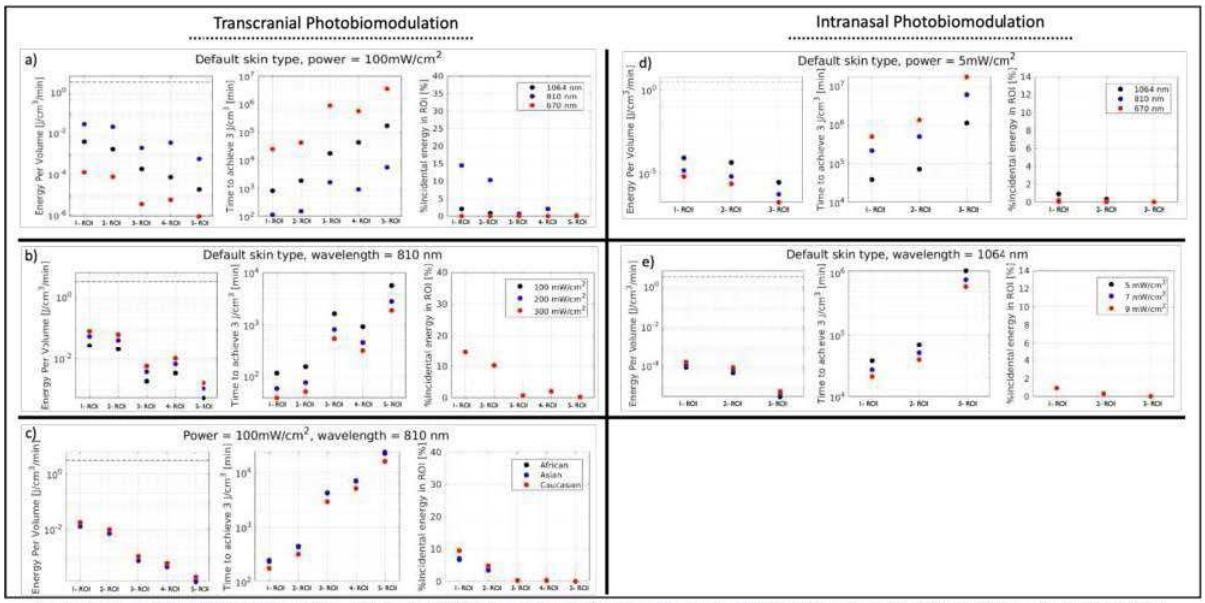

Figure 2: Transcranial and Intranasal Photobiomodulation (tPBM/iPBM) energy deposition simulation results. a) tPBM skin colour analysis. b) tPBM wavelength analysis c) tPBM optical power density analysis. d) iPBM wavelength analysis. e) iPBM optical power density analysis. tPBM: ROI1: Rostral Dorsal Prefrontal; ROI2: Rostromedial Prefrontal, ROI3: Rostral Dorsolateral Superior Prefrontal, ROI4: Anterior cingulate, ROI5: 'Rostral Dorsolateral Inferior Prefrontal. iPBM: ROI1: Ventromedial Prefrontal ROI2: Ventromedial Orbitofrontal ROI3: Ventral Orbitofrontal.

References

1. Q. Zhang, H. Ma, S. Nioka and B. Chance. (2000), "Study of near infrared technology for intracranial hematoma detection," Journal of Biomedical Optics, pp. 5(2), 206-213.
2. M. Hamblin. (2016), "Shining light on the head: Photobiomodulation for brain disorders," BBA Clin, p. 113–124.
3. F. Salehpour, J. Mahmoudi, F. Kamari, S. Sadigh-Eteghad, S. Rasta and M. Hamblin. (2018), "Brain Photobiomodulation Therapy: A Narrative Review," Mol Neurobiol, vol. 55, no. 8, pp. 6601-6636.
4. P. Cassano, A. Tran, H. Katnani, B. Bleier, M. Hamblin, Y. Yuan and Q. Fang. (2019), "Selective photobiomodulation for emotion regulation: model-based dosimetry study," Neurophotonics, Vol. 6, Issue 1.
5. Q. Fang and S. Yan. (2022), "MCX Cloud—a modern, scalable, high-performance and in-browser Monte Carlo simulation platform with cloud computing," Journal of Biomedical Optics, Vol. 27, Issue 8.
6. S. Tseng, A. Grant and A. Durkin. (2008), "In vivo determination of skin near-infrared optical properties using diffuse optical spectroscopy," J Biomed Opt., vol. 13, no. 1.
7. Y. Huang and M. Hamblin. (2019), "Chapter 4 - Photobiomodulation on cultured cortical neurons," in Photobiomodulation in the Brain, pp. 35-47.
8. A. Young. (1997), "Chromophores in human skin," Physics in Medicine and Biology, pp. Volume 42, Issue 5, Pages 789-802.
9. J. Jagdeo, L. Adams, N. Brody and D. Siegel. (2012), "Transcranial Red and Near Infrared Light Transmission in a Cadaveric Model," PLOS ONE, vol. 7, no. 10.
10. R. Zomorrodi, G. Loheswaran, A. Pushparaj and L. Lim. (2019), "Pulsed Near Infrared Transcranial and Intranasal Photobiomodulation Significantly Modulates Neural Oscillations: a pilot exploratory study," Scientific Reports 9, p. Article 6309.

Poster No 81

Acute effects of auricular vagus nerve stimulation on the gut-brain axis in functional dyspepsia

Roberta Sclocco[1], Harrison Fisher[2], Andrew Bolender[2], Junhwan Lee[3], Braden Kuo[2], Vitaly Napadow[4]

[1]Spaulding Rehabilitation, Harvard Medical School, Charlestown, MA, [2]Massachusetts General Hospital, Boston, MA, [3]Korea Institute of Oriental Medicine, Daejeon, Korea, Republic of, [4]Massachusetts General Hospital, Harvard Medical School, Charlestown, MA

Introduction: Functional dyspepsia (FD) is a disorder of gut-brain interactions associated with upper gastrointestinal (GI) pain and discomfort, but lacking effective therapies. FD has been linked with dysregulation of the gut-brain axis, mediated by abnormal vagal afference and brainstem neurocircuitry. In fact, the vagus nerve is intimately involved in autonomic control of the upper GI tract, with afferent projections to medullary brainstem nuclei, mainly to the nucleus tractus solitarii (NTS). Our own functional Magnetic Resonance Imaging (MRI) data found altered NTS-cortical connectivity in FD patients compared to controls in a post-meal state, associated with slower propagation of gastric peristaltic waves (Sclocco et al., 2022), as measured by our recently developed abdominal cine-MRI whole-stomach dynamic imaging approach (Sclocco et al., 2021). We propose that such maladaptive plasticity across different aspects of gut-brain communication can be targeted by transcutaneous auricular vagal nerve stimulation (taVNS), which interacts with brainstem vagal circuitry.

Methods: 15 FD patients (13F, 29.1±13.2y/o) and 15 healthy controls (HC; 10F, 32.1±7.7y/o) consumed their maximum tolerable amount of a 470ml high-calorie food-based contrast meal (pineapple-based for enhanced gastric MRI contrast). Post-meal, subjects were scanned with stomach MRI (+15, +45, +70min) and brain fMRI (+25, +55, +80min) at 3T, while experiencing active ("A", 1.5s stimulation trains delivered at 100Hz in left cymba concha during exhalation) or sham ("S", no current) taVNS on two separate visits (Fig.1A). During stomach scans, 4D cine-MRI were collected continuously for 5min (temporal resolution 7s). After gastric segmentation, peristaltic propagation velocity in the antrum was calculated by comparing cross-sectional area time series from two sections 10 antral slices apart to track the duration of time for a peristalsis contractile wave peak to propagate from one location to the next. Velocities were compared between conditions using a mixed effects model with fixed effects of Scan and Ingested Volume. During brain fMRI, resting-state data were acquired using an accelerated multiband sequence (2mm isotropic voxels, 1.27s TR, 288 volumes). Following preprocessing (FMRIPREP, AFNI), average BOLD timeseries extracted from a region previously localized as NTS were used to generate seed-to-voxel whole-brain functional connectivity maps. These maps were combined across scans for each subject in a fixed effects model, and then contrasted between conditions ($z>2.3$, $pFWE<0.05$).

Results: taVNS did not modulate gastric function in HC. In FD, peristaltic propagation velocity was on average 0.7mm/s faster during active taVNS compared to sham (β =0.67, SE=0.28, t=2.39; Fig.1B). Since there was no significant effect of time, data were averaged across post-meal time points, and follow-up comparison confirmed significantly higher velocity during active taVNS (A: 5.1±0.3mm/s (mean±SEM); S: 3.7±0.4mm/s; p=0.017). Relative to HC, FD patients demonstrated a significant reduction in NTS connectivity to anterior cingulate cortex (ACC) and medial and ventrolateral prefrontal cortices (m/vlPFC; Fig.1C) during active taVNS compared to sham. Interestingly, we had previously reported higher NTS connectivity in FD compared to HC in a similar set of brain regions.

Conclusions: Our analysis found that taVNS acutely modulates gut-brain communication in FD patients, potentially restoring impaired gastric motility by reversing altered cognitive processing of interoceptive (gastric) signaling. Further, our MRI approach allowed for a fully non-invasive evaluation of gut-brain interaction in a post-meal state. Future work focusing on longitudinal effects of taVNS will inform therapeutic applicability in disorders of gut-brain interaction such as FD.

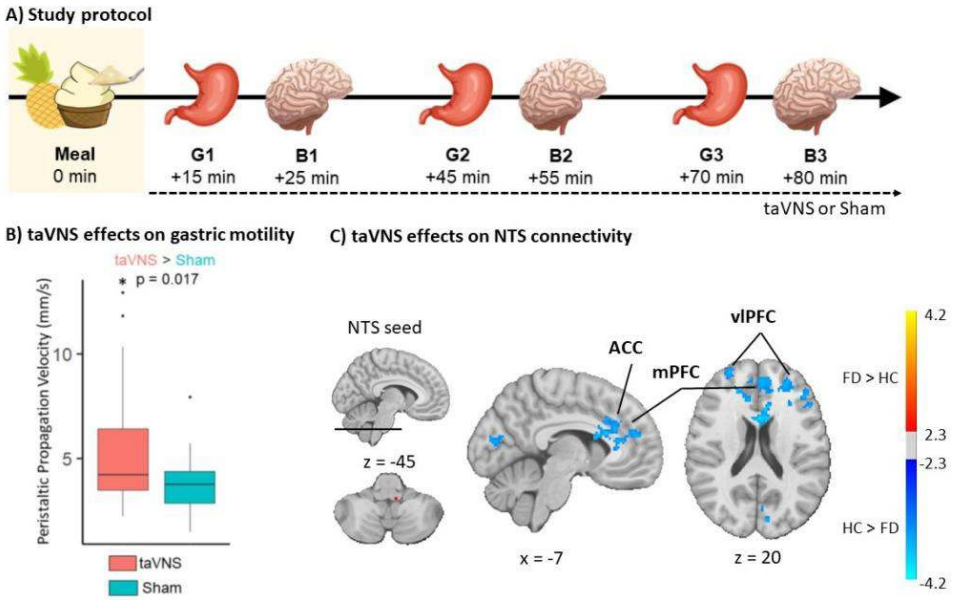

References

1. Sclocco R. (2021), 'Non-uniform gastric wall kinematics revealed by 4D Cine magnetic resonance imaging in humans', Neurogastroenterology and Motility, 33(8):e14146
2. Sclocco R. (2022), 'Cine gastric MRI reveals altered Gut-Brain Axis in Functional Dyspepsia: gastric motility is linked with brainstem-cortical fMRI connectivity', Neurogastroenterology and Motility, 34(10):e14396

Poster No 82

Functional connectivity changes in low back pain patients after α-wave neurofeedback training

Camille Grande[1], Manal Ikram[2], Joel Greffier[3], Jean Paul Beregi[3], Alexis Hom[3], Arnaud Dupeyron[3], Fabricio Pereira[4]

[1]Aix-Marseille University, Marseille, Provence-Alpes-Côte d'Azur, [2]University of Montpellier, Montpellier, Occitanie, [3]University Hospital Center of Nimes, Nimes, Occitanie, [4]University of Nimes, Nimes, Occitanie

Introduction: Low-back pain (LBP) is a prevalent condition, impacting around 23% of the population and ranking as a primary musculoskeletal disorder with an 84% prevalence rate. It is characterized by discomfort spanning from the T12 to S1 vertebrae, lacking a specific identifiable pathological cause. LBP manifests in three distinct phases: the acute phase, a brief flare-up lasting less than 6 weeks; the sub-acute phase extending from 6 to 12 weeks; and the chronic stage. The chronic low back pain (cLBP) is defined by persistent pain persisting for more than three months, significantly affecting daily life and work commitments[1]. Despite constituting only 20% of LBP cases, cLBP incurs a substantial 80% of France's total annual expenditure on LBP, amounting to 2.7 billion euros. Pain perception extends beyond a simple stimulus-response pattern, involving activation in motor, sensory, and emotional regions, displaying substantial variability among individuals and within the same person. The literature frequently illustrates a "pain matrix," depicting consistent activation of cortical and subcortical networks during the acute pain experience in healthy individuals[2]. This includes primary (S1) and secondary sensory cortices (S2) and the posterior insula, processing sensory details (pain location, duration). Furthermore, it encompasses regions like the anterior cingulate cortex (ACC), anterior insula, prefrontal cortical areas (PFC), and subcortical areas (basal ganglia and thalamus), contributing to the motivational and emotional facets of pain and its modulation. In this longitudinal study, fMRI was utilized to evaluate alterations in fronto-striatal functional connectivity in patients with cLBP who underwent a 20-day neurofeedback program centered on alpha-synchrony. While these brain oscillations are believed to significantly influence individual pain perception, the specific mechanisms remain to be fully elucidated

Methods: We conducted a pilot study on a neurofeedback alpha-synchronization training in cLBP patients. Participants underwent a first meeting with an fMRI, a questionnaire set and a neurofeedback session. Then, they practiced neurofeedback in alpha-synchronization training for 20 days and came back to the hospital for the same monitoring under a rsfMRI acquisition. The first objective of this study was to describe the observed functional connectivity alterations between the medial prefrontal cortex and the nucleus accumbens on fMRI acquisitions in "resting state" and "alpha-synchronization", before and after a neurofeedback protocol. The second objective was to search for correlations between the functional connectivity alterations, and the changes in clinical scores (pain, disability, and quality of life) following the neurofeedback protocol

Results: Wilcoxon test showed no significant medial prefrontal cortex - nucleus accumbens functional connectivity. We then we correlated the connectivity maps with pain scales and found 6 significantly functionally connected regions to the medial prefrontal cortex: the right middle occipital gyrus, primary visual cortex, precuneus and caudate nucleus at two distinct locations, and the left putamen. Spearman's correlation displayed significant results ($p<.05$) between the resting state "before" and the "worst mental pain in the past 7 days" as assessed with the psychological and physical pain visual analogue scale (PPP-VAS)[3]

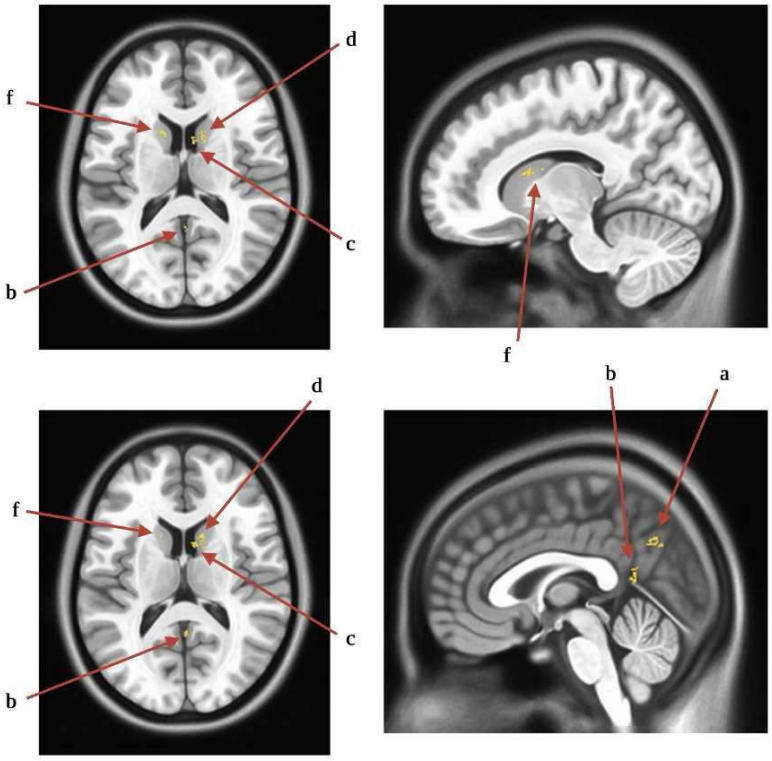

Fig. 1. Cortical and subcortical regions showing enhanced rsfcMRI following the protocol. Right Middle Occipital Gyrus [a], Right Primary Visual Cortex [b], Right Caudate Nucleus [c-e], Left Putamen [f]

Conclusions: This study brings clinical evidence of functional connectivity alterations between the medial prefrontal cortex and cortical and subcortical regions in chronic low back pain patients. We also showed that clinical scores could perhaps be correlated with changes in functional connectivity. Clinical studies with a higher number of participants are needed in order to highlight clear chronic pain cortical processes.

References

1. Balagué, F. (2012), 'Non-specific low back pain', The Lancet, 379(9814), 482–491
2. Apkarian, A. V. (2011), 'Pain and the brain: Specificity and plasticity of the brain in clinical chronic pain', Pain, 152(3), S49–S64
3. Jollant, F. (2020), 'A Visual Analog Scale to measure Psychological and Physical Pain: A preliminary validation of the PPP-VAS in two independent samples of depressed patients', Prog Neuropsychopharmacol Biol Psychiatry, vol 90,55-61

Poster No 83

Transcranial photobiomodulation modulates brain signal variability in older adults

Hong LI[1], Ying Han[2], Haijing Niu[1]

[1]Beijing Normal University, Beijing, Beijing, [2]Xuanwu Hospital of Capital Medical University, Beijing, Beijing

Introduction: Transcranial photobiomodulation (tPBM), as a a safe and noninvasive neuromodulation technique, plays a critical role in preventing normal brain aging and maintaining or improving cognition in older adults. Recently, Hu et al. conducted a study to investigate the effect of tPBM on brain activation during a working memory (WM) task in healthy older adults and found that tPBM resulted in a decrease in brain activation mainly in the right hemisphere. Brain signal variability is the fluctuation of functional brain activity within an individual at different temporal and spatial levels, which allows for adaptation and adjustment to changing internal and external demands. There is a growing body of evidence suggesting that moment-to-moment brain signal variability could be considered an important neuro marker in characterizing healthy aging. However, it is still unknown whether tPBM can modulate brain signal variability and thereby enhance working memory ability in older adults.

Methods: In this study, 84 healthy adults aged 49-79 (mean ± SD, 64.19 ± 6.22, 60 females) participated in a single-blind, counterbalanced design. Participants first received either a 12-minute active or sham tPBM stimulation targeted on the left dorsolateral prefrontal cortex, followed by a digit n-back working memory task with three loads (n = 1, 2, 3). Functional near-infrared spectroscopy (fNIRS) was used to record the hemodynamic changes of the whole head during the task. The sham

session followed the same procedure as the active tPBM session, except that the laser device was turned off after 5 seconds. The active tPBM and sham-controlled sessions were separated by one month. After preprocessing the fNIRS data, the brain signal variability (operationalized as the SD HbO) was estimated by averaging the variability within each block for each WM load. The n-back task performance was evaluated by accuracy (ACC) and mean response time (RT). To extract spatial patterns of brain signal variability associated with task conditions or behavior performance, we used a multivariate Partial Least Squares (PLS) analysis. The task PLS analysis was used to examine the effect of tPBM stimulation on SD HbO for each memory load. Next, we utilized a behavioral PLS analysis to examine the relationship between tPBM-related changes in SD HbO and tPBM-related changes in WM performance.

Results: A task-PLS model revealed one significant latent variable (LV) (permuted $p < 0.001$) indicating a decrease in brain signal variability after tPBM compared to the sham-controlled condition, regardless of 1-, 2-, or 3-back condition (Figure 1). This was observed in several regions typical of WM studies, including the bilateral dorsolateral prefrontal cortex (DLPFC), pre-motor cortex and supplementary motor area (PMA), supramarginal gyrus (SMG), visual cortex 3 (V3), frontal eye fields (FEF), and left angular gyrus (AG). No regions showed an increase in variability on tPBM compared to the sham-controlled condition. Additionally, a behavioral PLS analysis was conducted to examine whether the reduction of tPBM-related fNIRS signal variability could predict improved WM performance. Results revealed that the decreased tPBM-related fNIRS signal variability was associated with improved accuracy, as indicated by a single significant LV (permuted $p = 0.005$, Figure 2). This negative relationship was mainly significant in several regions, including bilateral DLPFC, SMG, AG, V3, left primary somatosensory cortex (PSS), somatosensory association cortex (SAC), right V2, and PMA. However, no significant LV (permuted $p = 0.289$) was found for the mean RT model.

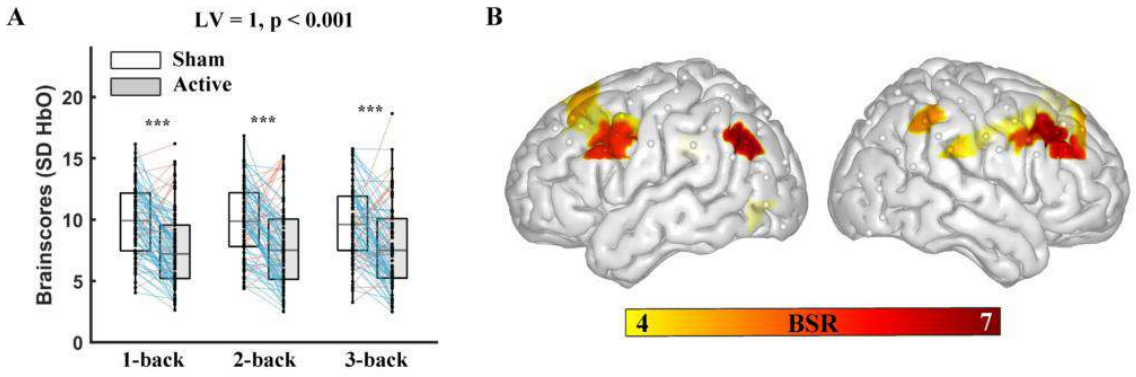

Figure 1. Effect of tPBM stimulation and memory load on SD HbO. (A) SD HbO was significantly decreased in active stimulation regardless of n-back level. (B) Spatial patterns expressing the effect of tPBM stimulation. Higher brain scores reflect higher HbO signal variability in yellow/red regions. Bootstrap ratios increase from red to yellow are thresholded at a value of > 4.00. BSR, bootstrap ratio. ***, $p < 0.001$.

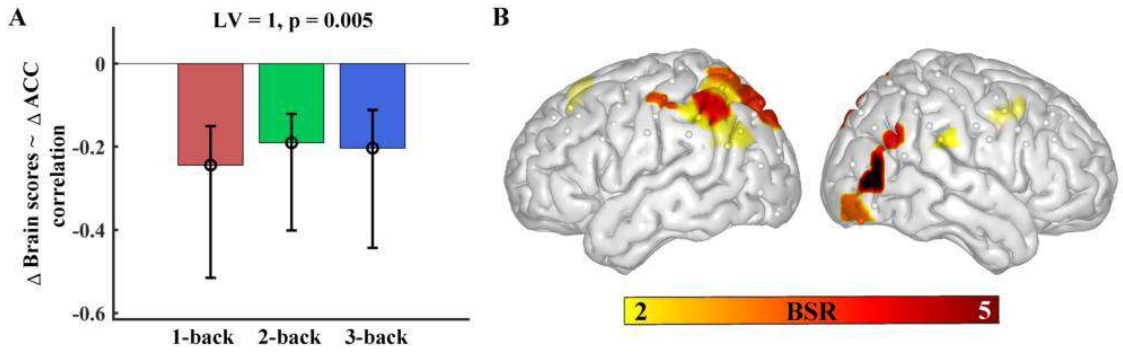

Figure 2. (A) Relation between tPBM-related changes in fNIRS signal variability and tPBM-related changes in working memory performance. Decreased tPBM-related SD HbO was associated with improved accuracy regardless of n-back level. Error bars represent bootstrapped 95% confidence intervals. If the confidence interval does not overlap with zero, the correlation is regarded as significant. (B) Spatial patterns expressing the relationship in (A). Yellow/red regions exhibited a reliable negative relationship. Bootstrap ratios (increase from yellow to red) are thresholded at a value of > 2.00. BSR, bootstrap ratio.

Conclusions: In summary, tPBM has been shown to reduce task-related fNIRS signal variability in older adults, and this reduction has been linked to improved WM performance. This suggests that tPBM may reduce the cognitive effort required to complete WM tasks, offering a potential avenue for inducing long-term cognitive improvements in normal aging or age-related conditions.

References

1. Alavash, M., Lim, S. J., Thiel, C., Sehm, B., Deserno, L., & Obleser, J. (2018). Dopaminergic modulation of hemodynamic signal variability and the functional connectome during cognitive performance. Neuroimage, 172, 341-356
2. Chan, A. S., Lee, T. L., Hamblin, M. R., & Cheung, M. C. (2021). Photoneuromodulation makes a difficult cognitive task less arduous. Scientific Reports, 11(1), 13688.
3. Hu, Z., Qu, X., Li, L., Zhou, X., Yang, Q., Dong, Q., ... & Niu, H. (2023). Repeated Photobiomodulation Induced Reduction of Bilateral Cortical Hemodynamic Activation during a Working Memory Task in Healthy Older Adults. IEEE Journal of Biomedical and Health Informatics.
4. Qu, X., Li, L., Zhou, X., Dong, Q., Liu, H., Liu, H., ... & Niu, H. (2022). Repeated transcranial photobiomodulation improves working memory of healthy older adults: behavioral outcomes of poststimulation including a three-week follow-up. Neurophotonics, 9(3), 035005-035005.
5. Shafiei, G., Zeighami, Y., Clark, C. A., Coull, J. T., Nagano-Saito, A., Leyton, M., ... & Mišić, B. (2019). Dopamine signaling modulates the stability and integration of intrinsic brain networks. Cerebral Cortex, 29(1), 397-409.
6. Waschke, L., Kloosterman, N. A., Obleser, J., & Garrett, D. D. (2021). Behavior needs neural variability. Neuron, 109(5), 751-766.
7. Zhao, C., Li, D., Kong, Y., Liu, H., Hu, Y., Niu, H., ... & Song, Y. (2022). Transcranial photobiomodulation enhances visual working memory capacity in humans. Science Advances, 8(48), eabq3211.

Poster No 84

Electroconvulsive therapy alters connectivity in treatment-resistant depressive disorders

Noora Tuovinen[1], Laurin Mauracher[1], Nataliia Maronchuk[1], Timo Schurr[1], Ruth Steiger[1], Christian Siedentopf[1], Elke Gizewski[1], Alex Hofer[1]

[1]Medical University of Innsbruck, Innsbruck, Austria

Introduction: Electroconvulsive therapy (ECT) is an established, safe and highly effective treatment for treatment-resistant depression. There are cognitive deficits in episodic memory and executive function following ECT, although these are mostly transient and moderate. While changes in brain morphometry following ECT are robust findings, functional connectivity findings are inconsistent. However, changes specifically in limbic connectivity have been suggested, a finding consistent with known structural modulations. One of the specific aims of our ECT-MRI project is to understand whether changes in functional connectivity occur after treatment.

Methods: Included participants were diagnosed according to DSM-V with major depressive disorder (MDD) without psychotic features or bipolar disorder (BD) currently in a major depressive episode without psychotic features, scored ≥25 on the Montgomery-Åsberg Depression Rating Scale (MADRS), and were aged between 18 and 75 years. Neurocognitive data were assessed using the Montreal Cognitive Assessment (MoCA) and the Brief Assessment of Cognition in Schizophrenia (BACS). MRI data were acquired pre-ECT and immediately post-ECT using a Siemens Magnetom Skyra 3T whole-body scanner. T1-weighted sequence parameters were set to: repetition time (TR)=2.5s, echo time (TE)=2.18ms, inversion time=1040ms, slice thickness=0.8mm, acquisition matrix (AM)=256×256, flip angle=8°, and field of view (FOV)=256mm. Resting-state functional MRI sequence parameters were set to: TR=0.8s, TE=30ms, flip angle=52°, multiband=6, FOV=216mm, AM=90×90, slice thickness=2.4mm, and acquisition time=10 minutes. Participants were instructed to fixate to a cross shown on the screen. Functional and anatomical images were preprocessed using the standard preprocessing pipeline in CONN functional connectivity toolbox 22.a in Statistical Parametric Mapping 12. Region of interest (ROI)-to-ROI and ROI-to-voxels analyses were performed with bivariate (hrf weighting, GLM) correlation with the 32 network regions predefined in the CONN toolbox. A standard combination of an uncorrected $p<0.001$ height threshold (to initially define clusters of interest) and a FDR-correction of $\alpha<0.05$ were used.

Results: Twelve depressed patients (age=51.3±9.9 years, female/male=5/7, MDD/BD=10/2) were assessed before (MADRS_pre=35.5±6.8, MoCA_pre=25.9±3.4, BACS_pre=-1.3±1.1) and after ECT (MADRS_post=10.3±9.6, MoCA_post=27.0±3.0, BACS_post=-1.0±1.3, number of ECTs=8.9±2.7). ROI-to-voxels analyses revealed significant ($p<0.05$, FDR corrected) changes in functional connectivity induced by ECT from eight seed ROIs originating from five networks (Figure 1).

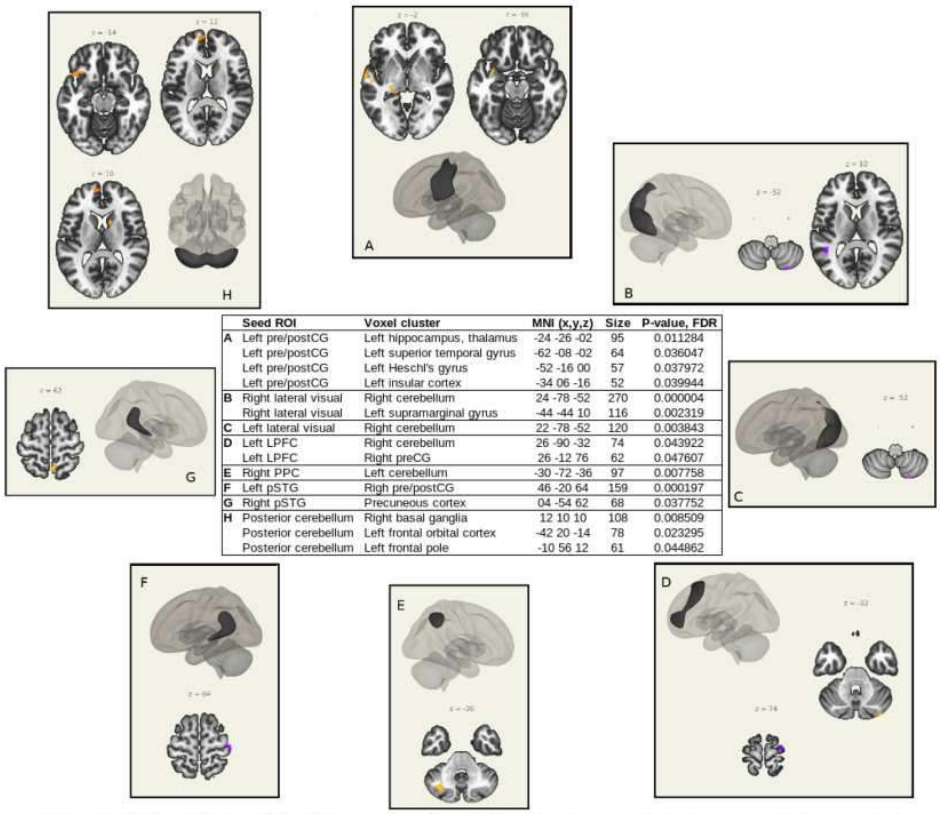

	Seed ROI	Voxel cluster	MNI (x,y,z)	Size	P-value, FDR
A	Left pre/postCG	Left hippocampus, thalamus	-24 -26 -02	95	0.011284
	Left pre/postCG	Left superior temporal gyrus	-62 -08 -02	64	0.036047
	Left pre/postCG	Left Heschl's gyrus	-52 -16 00	57	0.037972
	Left pre/postCG	Left insular cortex	-34 06 -16	52	0.039944
B	Right lateral visual	Right cerebellum	24 -78 -52	270	0.000004
	Right lateral visual	Left supramarginal gyrus	-44 -44 10	116	0.002319
C	Left lateral visual	Right cerebellum	22 -78 -52	120	0.003843
D	Left LPFC	Right cerebellum	26 -90 -32	74	0.043922
	Left LPFC	Right preCG	26 -12 76	62	0.047607
E	Right PPC	Left cerebellum	-30 -72 -36	97	0.007758
F	Left pSTG	Righ pre/postCG	46 -20 64	159	0.000197
G	Right pSTG	Precuneous cortex	04 -54 62	68	0.037752
H	Posterior cerebellum	Right basal ganglia	12 10 10	108	0.008509
	Posterior cerebellum	Left frontal orbital cortex	-42 20 -14	78	0.023295
	Posterior cerebellum	Left frontal pole	-10 56 12	61	0.044862

Figure 1. Region of interest (ROI)-to-voxel analyses of functional connectivity following electroconvulsive therapy (ECT). Post-ECT connectivity from eight seed ROIs (in black) revealed significant increases (in violet) and decreases (in orange) to several regions: A) SensoriMotor network: from left lateral (pre/postCG) ROI to left hippocampus/thalamus, superior temporal gyrus, Heschl's gyrus and insular cortex, B) Visual network: from right lateral visual ROI to righ cerebellum and left supramarginal gyrus, C) Visual network: from left lateral visual ROI to right cerebellum, D) FrontoParietal network: from left lateral prefrontal cortex (LPFC) ROI to right cerebellum and precentral gyrus (preCG), E) FrontoParietal network: from right posterior parietal cortex (PPC) ROI to left cerebellum, F) Language network: from left posterior superior temporal gyri (pSTG) ROI to right post/preCG, G) Language network: from right pSTG ROI to precuneus cortex, and H) Cerebellar network: from posterior cerebellum ROI to right basal ganglia, left frontal orbital cortex and frontal pole.

Conclusions: Our preliminary results show ECT induced changes in functional connectivity, particularly in regions related to memory, emotional and motor functions. Consistent with previous studies (Fu et al., 2023; Porta-Casteràs et al., 2021; Wei et al., 2021), the results suggest an involvement of the cerebellar and limbic regions that may be related to treatment response as well as to transient cognitive deficits following ECT. More rigorous evaluation in relation to cognitive symptoms is needed.

References

1. Fu Z, Abbott CC, Miller J, Deng ZD, McClintock SM, Sendi MSE, Sui J, Calhoun VD. (2023), 'Cerebro-cerebellar functional neuroplasticity mediates the effect of electric field on electroconvulsive therapy outcomes', Transl Psychiatry, vol. 13, no. 1, pp. 43.
2. Porta-Casteràs D, Cano M, Camprodon JA, Loo C, Palao D, Soriano-Mas C, Cardoner N. (2021), 'A multimetric systematic review of fMRI findings in patients with MDD receiving ECT', Prog Neuropsychopharmacol Biol Psychiatry, vol. 108, pp. 110178.
3. Wei Q, Ji Y, Bai T, Zu M, Guo Y, Mo Y, Ji G, Wang K, Tian Y. (2021), 'Enhanced cerebro-cerebellar functional connectivity reverses cognitive impairment following electroconvulsive therapy in major depressive disorder', Brain Imaging Behav, vol. 15, no. 2, pp. 798-806.

Poster No 85

Brain Function Changes of taVNS treatment for MDD Based on resting-state BOLD fMRI

Chunlei Guo[1], Jifei Sun[2], Yue Ma[3], Shanshan Gao[4], Yi Luo[5], Qingyan Chen[6], Jiliang Fang[6]

[1]Guanganmen Hospital, China Academy of Chinese Medical Sciences, Beijing, BeiJing, [2]BeiJing Hospital Traditional Chinese Medicine, BeiJing, BeiJing, [3]Guanganmen Hospital, China Academy of Chinese Medi, Beijing, China, [4]Guanganmen Hospital, China Academy of Chinese Medical Sciences, Beijing, Beijing, [5]Guang'anmen Hospital of Chinese Academy of Traditional Chinese Medicine, Beijing, Beijing, [6]Guanganmen Hospital, China Academy of Chinese Medical Sciences, Beijing, China

Introduction: Major depressive disorder(MDD) is a condition with high recurrence rate and high disability rate[1]. Unfortunately, the effect of antidepressants are poor currently[2]. It is necessary to find a new treatment for MDD. Transcutaneous aurucular vagus nerve stimulation(taVNS) is confirmed to be effective for MDD[3], but it's mechanism is unclear. Therefore, this study employed resting-state BLOD-fMRI to explore the brain mechanism of taVNS in the treatment of MDD.

Methods: Including 63 MDD patients and 68 healthy controls (HCs) matching sex, age and education, MDD patients were treated with taVNS for 8 weeks, and 17 items of Hamilton Depression Scale (17-HAMD) and Hamilton Anxiety Scale (HAMA) were evaluated before and after treatment, and resting-state BOLD-fMRI data were collected at the same time. HCs were not treated, only evaluate 17-HAMD and HAMA and scan resting-state BOLD-fMRI once when entering the group. DPABI was used to preprocess the resting-state BOLD-fMRI data, calculating the low frequency amplitude (ALFF), and then use the ALFF result of the baseline as the seed point to calculate function connectivity (FC). The results before and after treatment of taVNS were analyzed in a partial correlation with the clinical scale.

Results: After 8 weeks of taVNS treatment, the depression and anxiety symptoms of MDD patients improved. Compared with HCs, the ALFF values of the right Frontal_Med_Orb (MOFC) of MDD patients were increased, and the FC values of right MOFC and left MOFC were increased. Compared with before treatment, the ALFF value of the right putamen was reduced, and the FC value of the right MOFC and the right Frontal_Inf_Oper, the right superior temporal gyrus, the left middle temporal gyrus and the right supp;ementary motor area (SMA) were reduced. Among them, the FC difference between the right MOFC and the right SMA before and after treatment is significantly negatively correlated with the 17-HAMD score difference before and after treatment.

Conclusions: taVNS may play an antidepressant role by reducing the FC values of right MOFC and right SMA in MDD patients.

References

1. Schechter LE. Major depressive disorder. Curr Pharm Des. 2005;11(2):143-4.
2. Vöhringer PA, Ghaemi SN. Solving the antidepressant efficacy question: effect sizes in major depressive disorder. Clin Ther. 2011 Dec;33(12):B49-61.
3. Wang L, Wang Y, Wang Y, Wang F, Zhang J, Li S, Wu M, Li L, Rong P. Transcutaneous auricular vagus nerve stimulators: a review of past, present, and future devices. Expert Rev Med Devices. 2022 Jan;19(1):43-61.

Poster No 86

Non-invasive modulation of post-stroke hemianopia: Influence of gray and white matter integrity

Monica Toba[1,2], Nicole Macias[3], Xavier Corominas-Teruel[4], Corentin Gobatto[5], Thomas Guenin[4], Krishna Priya Radhakrishnan[4], Alexia Potet[4], Antoni Valero-Cabre[6]

[1]Paris Brain Institute, Paris, France, [2]LNFP University of Picardy Jules Verne, Amiens, France, [3]Universitat Rovira i Virigili, Tarragona, Tarragona, [4]Paris Brain Institute, Paris, Ile de France, [5]Pitie Salpetriere Hospital, Paris, Ile de France, [6]CNRS UMR 7225, Paris Brain Institute, Paris, Ile de France

Introduction: Homonymous lateral hemianopia (HLH) is a visual deficit following retro-chiasmal lesions in which conventional visual rehabilitation has shown poor effectiveness. We present interim analysis of visual perimetry and neuroimaging datasets from a pre-therapeutic, randomized cross-over, double-blind trial in HLH patients after a unilateral stroke. It assesses the ability of Transcranial Alternating Current Stimulation (tACS) to improve visual perception via the synchronization of dorsal attentional orienting systems[1,2,3]. We hypothesized a high degree of variability in visual outcomes and a strong influence of gray matter regions and white matter tracts (either spared or impacted by the stroke) subtending perceptual and attentional orienting abilities[4,5], following active tACS.

Methods: A cohort of n=9 HLH patients (8 male & 1 female, age: 59±12 years old) without pre-existing severe ophthalmological disorders or contraindication to tACS and/or MRI, was recruited at least 3 months after a stroke, for this study. A group of matched controls (4 male & 1 female, 49±14 years old) was studied for comparison. All participants underwent an MRI battery including T1-3D (TE=3.2ms, 1x1x1 mm3) and Diffusion (60 dir., b=1500 s/mm2, RT=14s, TE=88ms, 2 mm thickness) sequences. In 3 independent sessions set a week apart, we assessed the short-term modulation of the following tACS conditions: (A) Right hemisphere frontal 30 Hz tACS to the Frontal Eye Field (FEF); (B) Contralesional occipito-parietal 10Hz tACS to the intraparietal sulcus (IPS) and (C) Sham tACS. Effects were estimated by changes in the surface of the 'seen' visual field in kinetic (binocular) and static (monocular) visual field perimetry (Octopus 900, Haag-Streit), prior vs. immediately following 20 minutes of tACS. Stroke lesions of each patient were delineated on the original 3DT1 sequences with MRIcron[6] then normalized to the MNI template using SPM[7]. For lesion mapping, the AAL[8] and Natbrainlab[9] templates were used respectively, to estimate the % of damaged grey/white matter structures. Additionally, white matter tractography (DSI studio) was used to assess disconnections

of key white matter notably, the optic radiations (OR) and the superior longitudinal fasciculus (SLF) by estimating their Fractional anisotropy (FA).

Results: Visual field perimetry at baseline showed higher accuracy for kinetic (~56%) compared with static (~41%) visual field assessments, suggesting the presence of blindsight phenomena in these patients. Group analyses failed at this stage of recruitment to reveal significant effects or differences between the tACS conditions on the surface of the 'seen' visual field surface (all comparisons $p>0.05$, Wilcoxon Rank). Regardless, detailed examination of response patterns suggested improvements to different degrees in individual patients (particularly for those following occipito-parietal tACS) compared to sham. Most importantly, gray matter MRI assessments showed lesion patterns encompassing mainly the superior, middle and inferior occipital gyri, the lingual gyrus and the calcarine fissure (Fig.1) Tractography analyses of the OR and SLF revealed partial disconnections and lower FA in HLH patients for the OR ($p<0.02$) but not the SLF ($p>0.05$) compared to healthy controls (Fig. 2).

Figure 1. Individual and group HLH lesion patterns

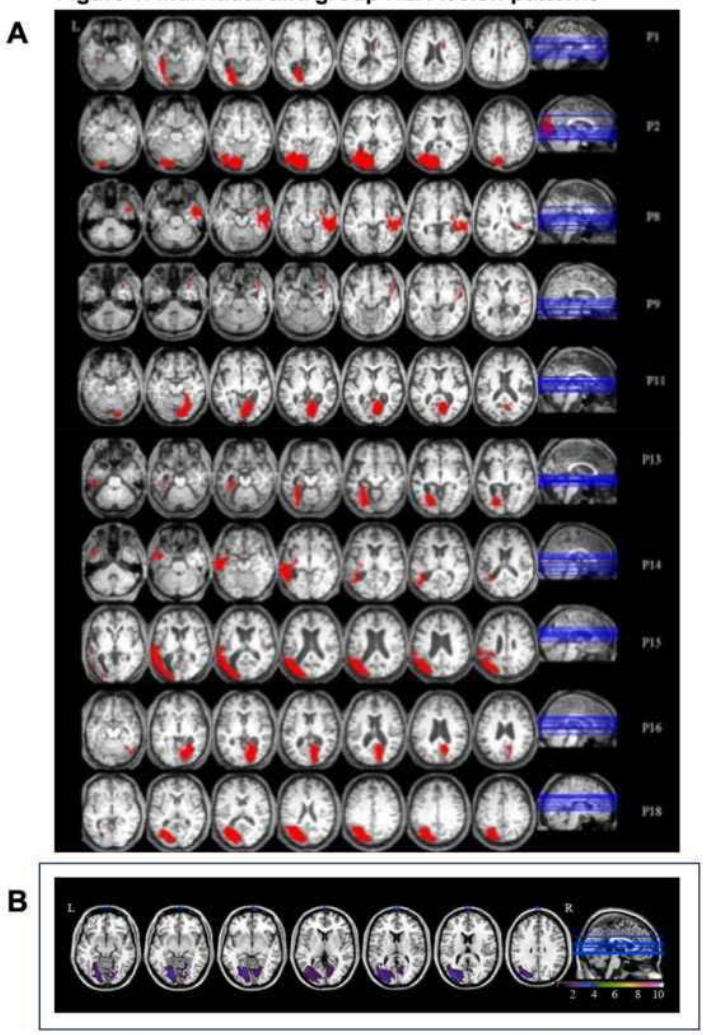

(A) Location and extent of brain damage in each individual patient of our cohort (n=10) note the large variability of cortical and subcortical lesions that generate right or left hemianopia in our population. (B) Overlap of brain lesions for all patients (Z-coordinates from -11 to 31 in MNI [Montreal Neurological Institute] space). Color range indicates the proportion of overlap between patients (from 0 to 10). The levels of the axial slices are marked by blue lines on the sagittal view of the brain. (Z- coordinates from -41 to 33 in MNI (Montreal Neurological Institute) space. Note that the highest overlap of lesions in the right hemisphere is found in the lingual gyrus, the calcarine fissure, the optic radiations and the ILF. In the left hemisphere, the highest overlap of lesions was found in the occipital lobe, the temporal and parietal regions, the IFOF and the optic radiations

Figure 2. Tracking of Optic Radiations

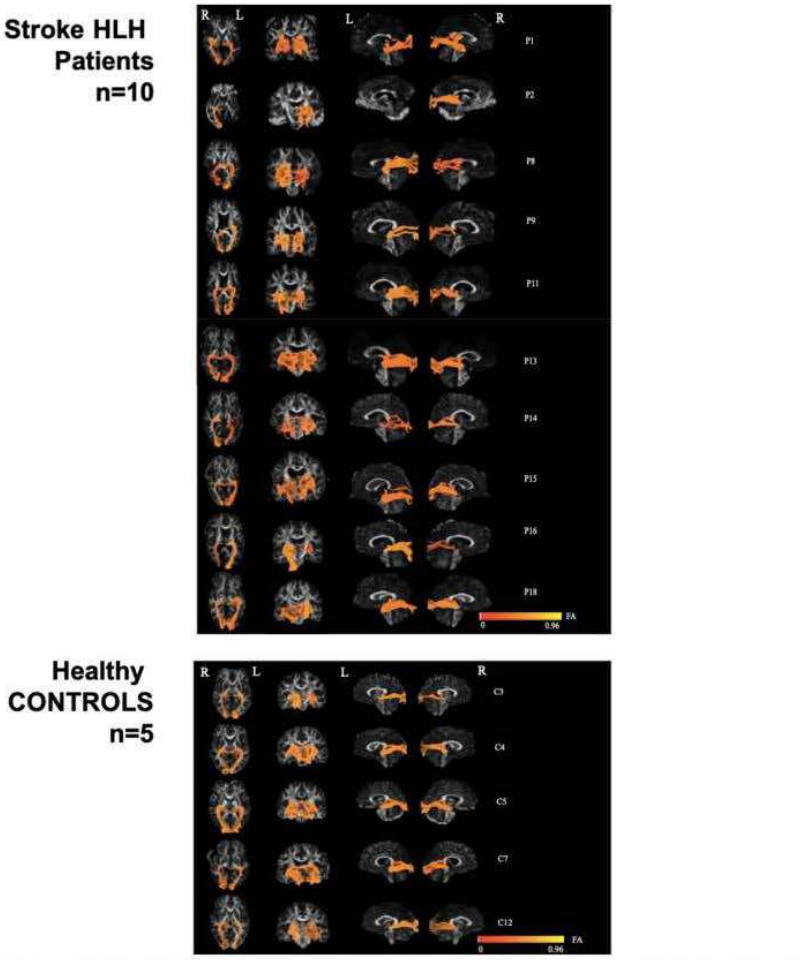

Diffusion imaging tractography reconstruction of the optic radiation (OR) in our cohort of n=10 post-stroke homonymous lateral hemianopsia (HLH) patients and in our population of n=5 matched-healthy controls. This tract was chosen for being the only one which showed statistically significant differences between HLH patients and controls. The color bars represent the Fractional Anisotropy (FA) values of the OR tract. Abbreviations: FA: Fractional Anisotropy, L: Left; R: Right.

Conclusions: At the current stage of recruitment, our analysis attests of the large heterogeneity of lesion patterns, spared visual field surface, predicted E-fields and the tACS outcomes. The recruitment of further patients is compulsory to allow reliable assessments of lesion patterns and modulatory effects. Recovery patterns shown by individual patients argue in favor of an influence of the status of key white matter tracts, and particularly the optic radiations (OR). Heterogeneity suggests a need for treatment customization based on the presence or absence of blindsight phenomena as guided by MRI-based biophysically tACS current distribution models.

References

1. Vernet, M. (2019), 'Entrainment of local synchrony reveals a causal role of frontal oscillations in visual consciousness', Scientific Reports 9(1):14510
2. Stengel, C. (2021), 'Causal modulation of right hemisphere fronto-parietal phase synchrony with Transcranial Magnetic Stimulation during a conscious visual detection task', Scientific Reports, 11(1):3807
3. Lin, Y.J. (2021), 'Transcranial magnetic stimulation entrains alpha oscillatory activity in occipital cortex', Scientific Reports; 11: 18562
4. Toba, M.N. (2017), 'Game theoretical mapping of causal interactions underlying visuo-spatial attention in the human brain based on stroke lesions', Hum Brain Mapp., 38(7):3454-3471
5. Toba, M.N. (2020), Game theoretical mapping of white matter contributions to visuo-spatial attention in stroke patients with hemineglect. Human Brain Mapping, Apr 3. doi: 10.1002/hbm
6. Rorden, C. (2000), 'Stereotaxic display of brain lesions', Behavioural Neurology, 12(4): 191–200
7. Toba, M.N. (2018) 'Component deficits of visual neglect: "Magnetic" attraction of attention vs. impaired spatial working memory' Neuropsychologia, 109: 52–62
8. Tzourio-Mazoyer, N. (2002), 'Automated anatomical labeling of activations in SPM using a macroscopic anatomical parcellation of the MNI MRI single-subject brain'. NeuroImage, 15(1):273–289
9. Catani, M. (2008), 'A diffusion tensor imaging tractography atlas for virtual in vivo dissections'. Cortex; a Journal Devoted to the Study of the Nervous System and Behavior, 44(8): 1105–1132.

Poster No 87

Virtual brain twin for diagnosis of epileptogenic networks using temporal interference stimulation

Chloe Duprat[1], Borana Dollomaja[2], Jan Paul Triebkorn[3], Jean-Didier Lemaréchal[4], Fariba Karimi[5], Maxime Guye[6], Fabrice Bartolomei[7], Huifang Wang[3], Viktor Jirsa[8]

[1]AMU, Marseille, Bouches-Du-Rhone, [2]Institut de Neurosciences des Systemes UMR1106, Marseille, Marseille, [3]AMU, INS, INSERM U1106, Marseille, PACA, [4]AMU INS, Marseille, Bouches-Du-Rhone, [5]ETH, Zurich, Zurich, [6]Aix Marseille Université, Marseille, PACA, [7]AMU, INS, INSERMU1106, Marseille, PACA, [8]nstitut de Neurosciences des Systèmes, Marseille, N/A

Introduction: The exploration of brain activity in the context of refractory epilepsy has been attempted through modeling and simulation to provide patient-specific diagnosis. The efficacy of whole-brain models, such as the Virtual Epileptic Patient (VEP), has been demonstrated in simulating seizure-patterned brain activity, specifically induced by intra-cortical stimulation[1]. Recent studies have introduced the innovative technique of temporal interference (TI) to stimulate the brain non-invasively that effectively targets deep brain tissue with focal precision, avoiding overlying brain tissue[2]. Diagnosing epilepsy is challenging, especially in complex focal cases where specific brain areas, known as epileptogenic zones (EZ), are responsible for seizure onsets. Inducing seizures through brain stimulation, such as stereo-electroencephalography (SEEG) implantation based on the EZ hypothesis, is a current diagnosis approach[3]. However, this method has limitations: not every area can be implanted due to cognitive considerations, the location scheme established before induced-ictal recording cannot be modified between stimulations, the stimulated area is sensitively dependent to electrode contacts location inside the brain region and implantations can involves complications. The temporal interference method offers the same advantages i.e. depth and focality, without the aforementioned invasiveness-related challenges. Thus, combining temporal interference with scalp EEG allows simultaneous non-invasive monitoring of the whole brain activity. This study aims to assess the diagnosis performance of temporal interference stimulation in identifying epileptogenic networks.

Methods: A high-resolution virtual brain, built from a patient's magnetic resonance and diffusion images (MRI and dMRI), incorporates the anatomical specifics and structural connectivity of the individual. The whole brain was discretized as a Neural Mass Model (NMM) for the subcortical regions and as a Neural Field Model (NFM) for the pial surface of the cortical regions[4]. Temporal interference fields are calculated and linearly summed to derive the modulation envelope of interfering electric fields. This resulting field, directly responsible for stimulation, is interpolated onto the virtual brain. The effective neural response is computed through the Epileptor-Stimulation model[5]. Simulations are conducted considering EEG, SEEG, and simultaneous EEG-SEEG recording methods. The results are fitted to the real time-series, and the model is inferred[6] to extract corresponding region parameters. These parameters are crucial, as they are intricately linked to properties of the brain, such as excitability associated with seizure onsets (Fig. 1). The parameters inferred from TI-induced ictal recordings are validated using ground truth parameters obtained from spontaneous seizure recordings. To assess the efficiency of EEG recording, we compare parameters inferred from TI-EEG with those from TI-SEEG and identify any additional information contributed by EEG during concurrent SEEG-EEG co-recording (Fig. 2).

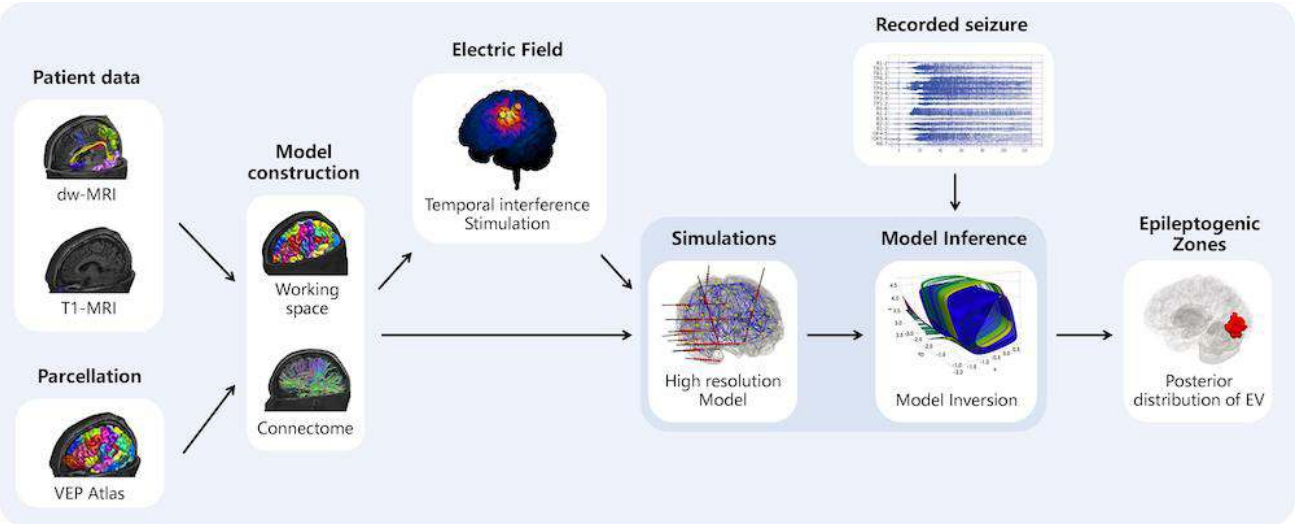

Figure 1: Workflow of the VEP-TIS. From raw data (T1-MRI, dw-MRI) of the patient, we constructed the personalized high-resolution virtual twin. Based on this patient-specific interconnected anatomical space, we computed the electrical field resulting from the interference of the two alternative currents introduced by Temporal Interference Stimulation (TIS). After interpolating both the virtual brain and the TIS field, we simulated the brain activity with the Epileptor-Stimulation model using optimized stimulation parameters to target specific areas. Then, we performed model inversion to fit the simulated activity to the recorded activity and infer the model parameters. Epileptogenic values (EV) are derived from the inferred parameters. When these values surpass certain thresholds, the corresponding brain areas are designated as epileptogenic zones.

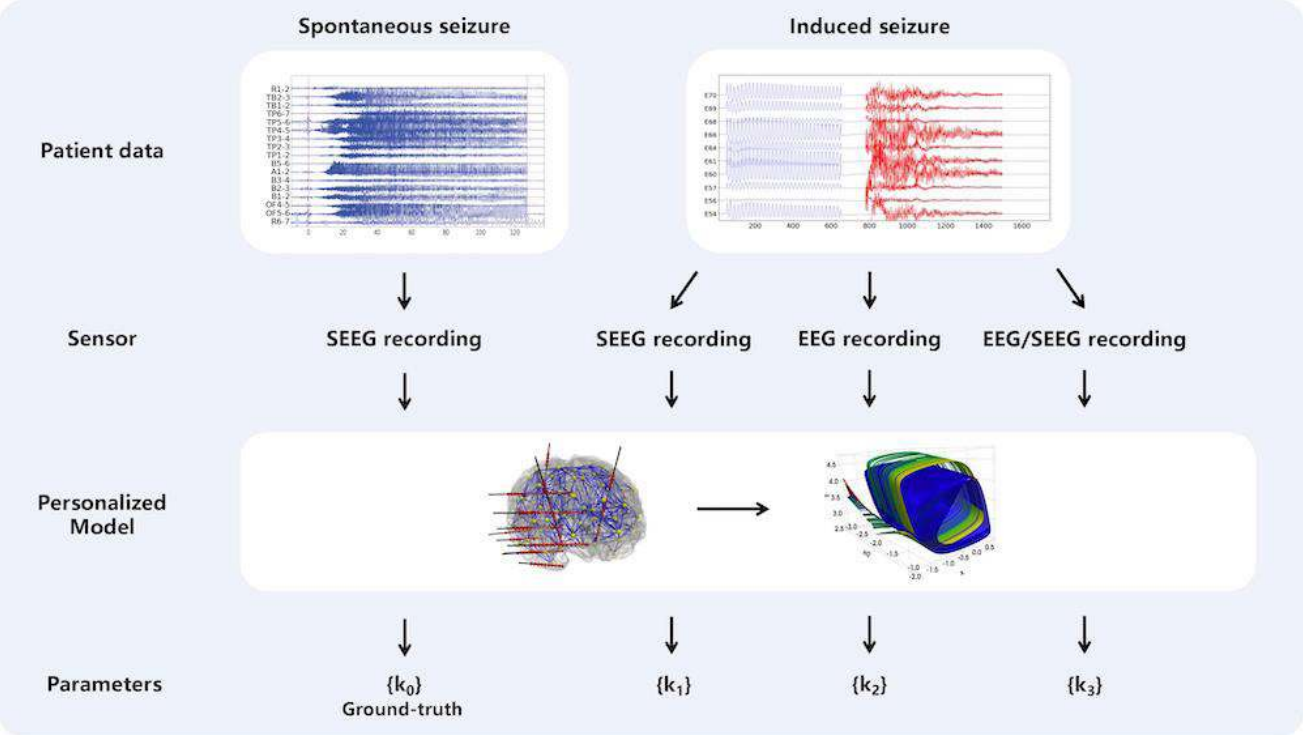

Figure 2: Parameter inference for temporal interference in diagnosing focal epilepsy validation. Parameters $\{k_0\}$ inferred from SEEG recordings of spontaneous seizures are considered the ground truth. Parameters inferred from SEEG signals $\{k_1\}$, EEG signals $\{k_2\}$, and co-recording SEEG-EEG $\{k_3\}$ are compared to this ground truth $\{k_0\}$. A comparison between the three sets of parameters $\{k_1\}$, $\{k_2\}$ and $\{k_3\}$ from stimulated seizures is conducted to identify the added value of the EEG from SEEG method.

Results: The workflow was performed on a cohort of 20 patients from La Timone Hospital in Marseille. All patients experienced spontaneous and SEEG-induced seizures, all recorded by SEEG. The recorded ictal activity is then mapped at the source-level by the inverse solution and mapped again at the EEG-level by the forward solution on the virtual brain. We compared the performance of model inversion using SEEG, EEG and SEEG-EEG simultaneously. Results show that their performance depends on the different locations of EZNs and the seizure types.

Conclusions: The efficacy of the TI stimulation modeling approach attests to its potential as a valuable tool for inducing seizure for drug-resistant epilepsy diagnosis. This study can contribute to the development of effective, targeted, low-volume, and cost-effective treatment options for refractory-epilepsy patients, providing a safer non-invasive therapeutic option.

References

1. Wang, H. E., Woodman, M., Triebkorn, P., Lemarechal, J.-D., Jha, J., Dollomaja, B., Vattikonda, A. N., Sip, V., Medina Villalon, S., Hashemi, M., Guye, M., Makhalova, J., Bartolomei, F., & Jirsa, V. (2023). 'Delineating epileptogenic networks using brain imaging data and personalized modeling in drug-resistant epilepsy'. Science Translational Medicine, 15(680). https://doi.org/10.1126/scitranslmed.abp8982
2. Grossman, N., Bono, D., Dedic, N., Kodandaramaiah, S. B., Rudenko, A., Suk, H. J., Cassara, A. M., Neufeld, E., Kuster, N., Tsai, L. H., Pascual-Leone, A., & Boyden, E. S. (2017). 'Noninvasive Deep Brain Stimulation via Temporally Interfering Electric Fields'. Cell, 169(6), 1029–1041.e16. https://doi.org/10.1016/j.cell.2017.05.024
3. Bartolomei, F., Lagarde, S., Wendling, F., McGonigal, A., Jirsa, V., Guye, M., et al. (2017). 'Defining epileptogenic networks: Contribution of seeg and signal analysis'. Epilepsia 58, 1131–1147. doi:10. 1111/epi.13791
4. Proix, T., Jirsa, V., Bartolomei, F., Guye, M., Truccolo, W. (2018). 'Predicting the spatiotemporal diversity of seizure propagation and termination in human focal epilepsy'. Nature communications, 9(1), 1088. https://doi.org/10.1038/s41467-018-02973-y
5. Wang, H. E., Dollomaja, B., Duma, G. M., Lemarechal, J-D., Williamson, A., Makhalova, J., Triebkorn, P., Bartolomei, F., Jirsa, V. (2023). 'Personalized high-resolution virtual brain modeling for stimulation in epilepsy'. Frontiers. Submitted
6. Jha, J., Hashemi, M., Vattikonda, A., Wang, H., Jirsa, V. (2022). 'Fully Bayesian estimation of virtual brain parameters with self-tuning Hamiltonian Monte Carlo'. Machine Learning: Science and Technology. 3. 10.1088/2632-2153/ac9037

Poster No 88

Volumetric changes after convulsive therapies in treatment-resistant depressive patients

Pedro da Silva[1], Helena Bellini[1], Eric Cretaz[1], Adriana Carneiro[1], Leonardo dos Santos[1], José Gallucci-Neto[1], Andre Brunoni[1]

[1]Service of Interdisciplinary Neuromodulation, Laboratory of Neurosciences, Universidade de São Paulo, São Paulo, Brazil

Introduction: Electroconvulsive Therapy (ECT) is the most effective treatment for depression. However, self-limiting physical side effects and serious cognitive dysfunctions limits the application of ECT. In Magnetic Seizure Therapy (MST), as there is no direct electrical stimulation of structures such as the hippocampus, implicated in ECT-related memory impairment, memory dysfunctions are not expected. However, MST-related studies are limited by small sample sizes and open label designs. Then, it was proposed the "Electro-Magnetic Convulsive Therapies for Depression (EMCODE): a double blind, randomized, non-inferiority study", comparing 100Hz MST with bitemporal ECT. The primary objective involves assessing changes in depressive symptoms and cognitive measures in treatment-resistant depression (TRD) patients undergoing MST as compared to ECT treatment. A secondary objective involves the investigation of structural MRI changes and associations with clinical and cognitive outcomes.

Methods: Details of the study protocol can be found in[1]. The co-primary outcome scales were the Hamilton Rating Scale for Depression (HAMD-17) and the Autobiographical Memory Task (AMT). Longitudinal volumetric weighted 3D T1 MRI images were acquired using a 3.0 T device (Achieva, Phillips, Amsterdam, The Netherlands). Processing was performed using the Longitudinal pipeline provided by the Computational Anatomy Toolbox 12 (CAT12), a toolbox of the Statistical Parametric Mapping software (SPM12). Voxel-Based (VBM) and Region-Based Morphometry (RBM) were performed. We used the Neuromorphometrics atlas for RBM analysis. A statistical model was built with the flexible factorial design. The following contrasts were used: post-treatment > baseline in ECT and MST, post-treatment > baseline in ECT & MST and post-treatment > baseline & ECT > MST (interaction). Associations between MRI findings with outcomes were performed using R Version 4.1.2. We used linear mixed models with a three-way interaction between the fixed predictors volume, time, and treatment. HAMD-17 and ATM sub scores were the outcomes. Participants were included as random intercept. To each three-way significant interaction, we performed two-way interaction between brain volume and time separately to each group.

Results: Forty-one patients were included. There was a progressive reduction of HDRS-17 scores for both groups (Fig. 1a). The MST group presented a better profile for the AMT sub scores (Fig. 1b-c). In VBM analysis, no significant structural changes were observed for any contrast. In RBM analysis, the following structures present significant changes in patients who received ECT: left and right hippocampus (t = 8.23, p = .00008; t = 8.23, p = .0004), left and right entorhinal area (t = 4.73, p = .025; t = 4.71, p = .035), left posterior insula (t = 3.15, p = .014), right amygdala (t = 5.01, p = .023), and right temporal pole (t = 4.46, p = .03) (Fig. 2a). No significant structural changes were observed in patients who received MST. The following structures present significant changes when considering patients who received ECT or MST: left and hippocampus (t = 6.36, p = .003; t = 4.88, p = .008), left entorhinal area (t = 3.54, p = .019), and right amygdala (t = 3.79, p = .009) (Fig. 2b). Only the left hippocampus (t = 5.73, p = .006) presented significant change after treatment when comparing both interventions (Fig 2c). For the contrast post-treatment > baseline in ECT & MST in RBM analysis, significant interactions with HAMD-17 as outcome were found for the right hippocampus (t = -7.12, p = 0.04) and amygdala (t = -7.12, p = 0.04). For both interventions, the higher the volume increase, the bigger the antidepressant effect. However, only the MST group showed significant two-way interactions.

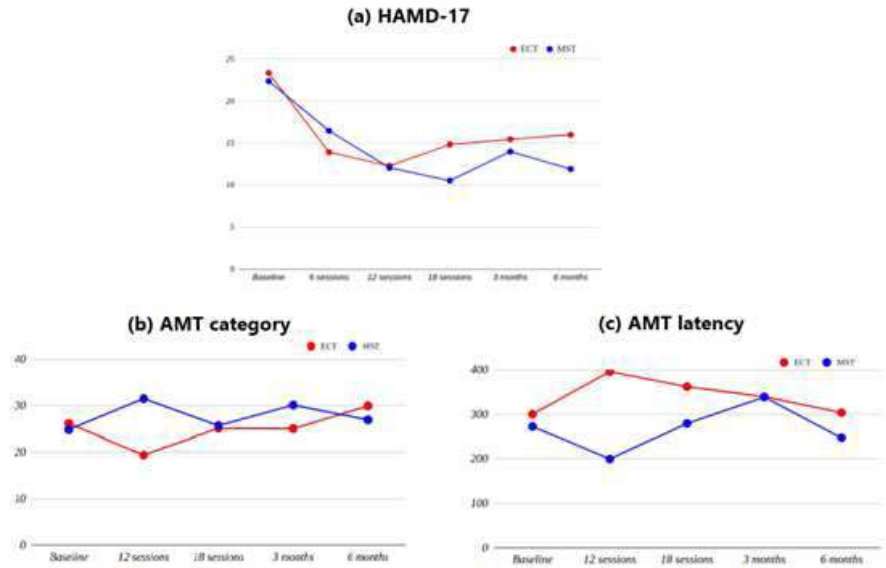

Figure 1: (a) Hamilton Depression Rating Scale (HDRS-17) through treatment time and follow-up for both electroconvulsive (ECT, in red) and magnetic seizure (MST, in blue) therapies. (b) Autobiographical Memory Test (AMT) sub score Category through treatment time and follow-up for both ECT (in red) and MS (in blue) therapies. (c) Autobiographical Memory Test (AMT) sub score Latency through treatment time and follow-up for both ECT (in red) and MST (in blue) therapies.

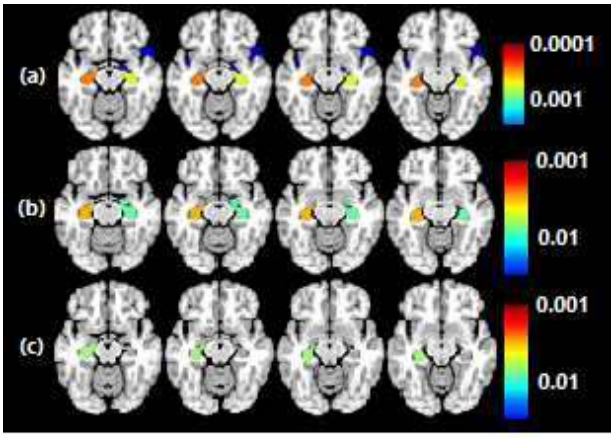

Figure 2: Region-based morphometry (RBM) results. Structures with significant volumetric changes (p-Holm Bonferroni < .05) when using the contrast (a) post-treatment > baseline in ECT, (b) post-treatment > baseline in ECT & MST and (c) post-treatment > baseline & ECT > MST (interaction). Color bars represent p-values. ECT = electroconvulsive thehrapy. MST = magnetic seizure therapy.

Conclusions: Regional-based, and not voxel-based, volumetric changes after MST in TRD patients were associated with depressive symptoms.

References

1. Bellini H, et al. 'Magnetic Waves vs. Electric Shocks: A Non-Inferiority Study of Magnetic Seizure Therapy and Electroconvulsive Therapy in Treatment-Resistant Depression', Biomedicines 2023, vol. 11. https://doi.org/10.3390/biomedicines11082150.

Poster No 89

Effects of Theta-Burst-Like Transcranial Focused Ultrasound Stimulation on M1 Cerebral Blood Flow

Daniel Keeser[1,2], Max Hasslberger[3], Theresa Fäßler[1], Maximilian Lueckel[4], Kai-Yen Chang[1,2], Lukas Roell[1,2], Lucia Bulubas[1,2], Julian Melcher[1], Frank Padberg[1], Til Ole Bergmann[5], Boris-Stephan Rauchmann[6]

[1]Department of Psychiatry and Psychotherapy, University Hospital LMU, Munich, Germany, [2]NeuroImaging Core Unit Munich (NICUM), University Hospital LMU, Munich, Germany, [3]Technical University Munich (TUM), Munich, Germany, [4]Neuroimaging Center (NIC), Focus Program Translational Neuroscience, Johannes Gutenberg University, Mainz, Germany, [5]Johannes-Gutenberg University Medical Center, Mainz, Rhineland-Palatinate, [6]Department of Neuroradiology, University Hospital LMU, München, Deutschland

Introduction: The aim of this study was to investigate the direct effects of transcranial focused ultrasound stimulation (FUS) on cerebral blood flow in the primary motor cortex using a double-blind, theta-burst-like protocol (1). Given the limited efficacy of current treatments for severe psychiatric disorders, the investigation of FUS as a potential neuromodulatory tool in psychiatry is of relevance. The technique is still being established - this study is the first FUS study to investigate the effects on arterial spin labeling (pcASL).

Methods: Seventeen healthy volunteers (mean age=26.31, SD=3.34; 9 women) participated in a rigorous experimental design in which they underwent FUS stimulation guided by precise neuronavigation targeting motor regions that utilized the maximum of the individual finger tapping BOLD signal from the baseline MRI measurement. The study spanned three days and included a baseline and randomized active/shame stimulation conditions. Arterial spin labeling (ASL) was performed both before and after the two stimulations, resulting in 5 measurements per subject and a total of 85 ASL measurements for the complete sample. The evaluation was performed with Oxford ASL (2) and used the regions of the Glasser atlas (3) for the primary motor cortex: 6cdl, 6cvl, 6dl, 6m, and 6vl and 8dl, 8m, and 8vl for both hemispheres.

Results: Contrary to expectations, the study found no significant changes in cerebral blood flow in the primary motor cortex after FUS stimulation.

Conclusions: These initial findings suggest that the current intensity parameters may not be robust enough to produce noticeable effects (we followed the current internationally recommended safety regulations). However, this finding forms the basis for future investigations, including secondary analyses using resting-state functional MRI (rsfMRI), magnetic resonance spectroscopy (MRS), and finger tapping paradigm, which have also been recorded but not yet analyzed. Given the limited treatment options and the promising results from animal studies, research into FUS as a neuromodulatory approach for psychiatric patients remains important. Although no significant changes in cerebral blood flow in the primary motor cortex were achieved in this study, the translational aspect is of great importance, which probably needs to apply higher but safe intensities. This first pilot study underlines the need for further optimization of the stimulation parameters. The results of the study contribute to the ongoing discourse on innovative therapeutic modalities in psychiatry.

References

1. Samuel et al. Brain Stimulation 2022
2. Chappell et al., IEEE Transactions on Signal Processing 2009
3. Glasser et al., Nature 2015

Poster No 90

Facilitating Meditation with Focused Ultrasound Neuromodulation in Both Experts and Novices

Joshua Cain[1], Tracy Brandmeyer[1], Ninette Simonian[1], Jay Sanguinetti[2], Shinzen Young[2], Matthew Sacchet[3], Nicco Reggente[1]

[1]Institute for Advanced Consciousness Studies, Santa Monica, CA, [2]University of Arizona, Tuscon, AZ, [3]Meditation Research Program, Department of Psychiatry, Massachusetts General Hospital, Harvard Medic, Boston, MA

Introduction: Here, we first investigate if focused ultrasound (FUS) neuromodulation-which is uniquely capable of producing spatially precise[1] brain stimulation, non-invasively, anywhere in the brain[2]-may be leveraged to assist in the development of a fruitful meditation practice. Growing empirical evidence supports meditation's benefits wellbeing, protecting both psychological[3] and physical health[4–7]. However, even with extant meditation-assistance (e.g., mobile applications, neurofeedback[8]), many struggle to regularly practice[9]. FUS now offers the ability to directly alter the activity of known neural correlates of meditation[10–12], avoiding many limitations of EEG (spatial resolution, questionable efficacy[13] and MRI[14] (cost)-based neurofeedback. Here, we directly inhibit[2] three candidate regions derived from prior findings[10–12]-the posterior cingulate cortex (PCC), bilateral caudate (CAUD), or bilateral ventral anterior insula during meditation in 36 expert and 36 novice Vipassana meditators while multimodal data streams record effects on phenomenology and physiology during and after meditation/FUS.

Methods: 36 Expert Vipassana practitioners (>5y consistent practice, >20m, 5d/w), 36 Novice practitioners (no meditation experience or spiritual practice). Novices are trained over 1w, 4 sessions, 3h guided meditation, and assessed for skill. All subjects participate in 5 sessions (Fig. 1c). S1:Baseline trait questionnaire and MRI scanning (T1 for targeting, DTI, fMRI). S2-5:Subjects report expectations, mood, and sleep quality. Subjects are seated and comfortably secured in place while FUS-emitting transducers target one region. For 1 session/subject, a FUS-blocking gel pad provides a sham control (Fig 1d; detection n.s.). 1-hour vipassana meditation. Beginning at minute 12, 12m of FUS inhibition[2] begins. Every ~4m(+-30s) subjects report meditative depth and "intensity" (any altered phenomenology) from 1-5, while heart rate (HR), HR variability (HRV), respiration rate, and galvanic skin response are measured. Post-questionnaires record phenomenology during meditation-e.g., quality of meditation via Meditation Depth Index[15] and broader metrics (e.g., Profile of Mood States[16]). All online measures (during meditation, e.g., depth, HRV) are assessed for a main effect of condition (CAUD/PCC/SHAM/INSU) within each 4m segment of meditation. Each (Offline) battery within the post-questionnaire is independently assessed for a main effect of condition with appropriate follow-ups. Sig. findings are regressed on trait data (e.g., meditation experience, connectivity measures). MRI measures include functional and structural connectivity between targets and the whole brain. A completely novel innovation, new methods[17] allow us to relate expected[18], [19] variation in FUS energy deposition to behavioral/physiological effects for each brain voxel, producing fMRI-esc spatial maps of what tissue drives our effects.

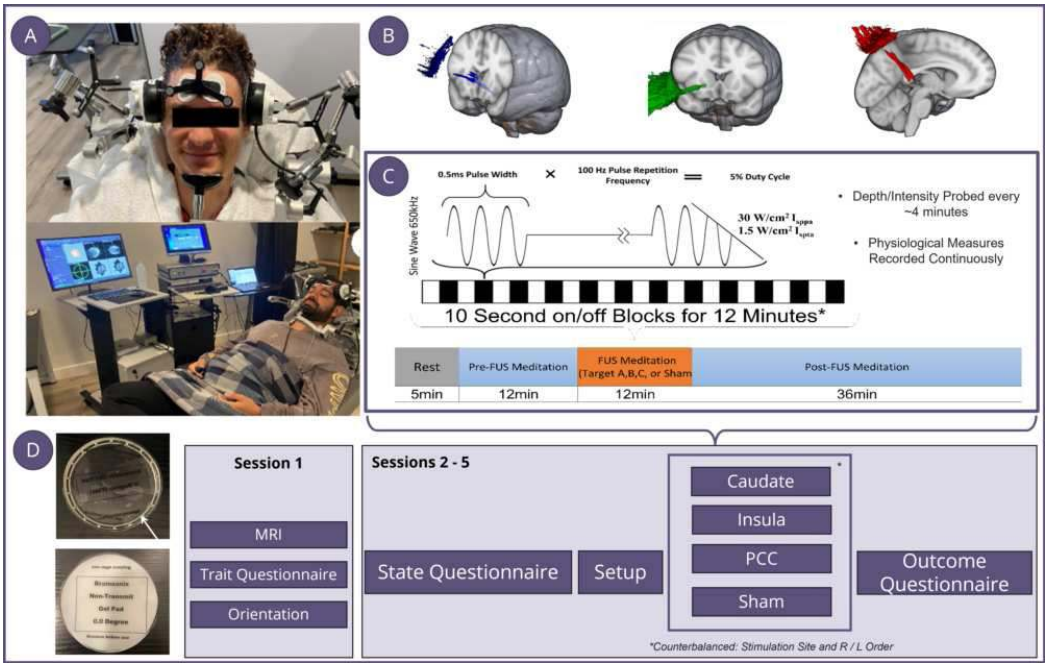

Figure 1. A: Subject and equipment prior to meditation. B: Simulations of FUS foci for each target. C: Study design, FUS parameters. D. Gel pad for transducer-head coupling, FUS permeable (clear).

Results: Preliminary data in experts (n=14; full 36 by OHBM) suggests a substantial improvement in meditative depth during/after caudate FUS (vs. Sham), both in online probes and offline questionnaires (Fig. 2a,b,d). Caudate FUS also reduced HR and increased HRV and induced a high correlation between each measure and depth ($p<0.0001$). FUS simulations predict increased depth in sessions where more FUS pressure was found in caudate tissue (Fig. 2e). Similar, weaker effects of PCC FUS were found. More limited data in novices(n=6; 36 by OHBM)reveals no clear trends.

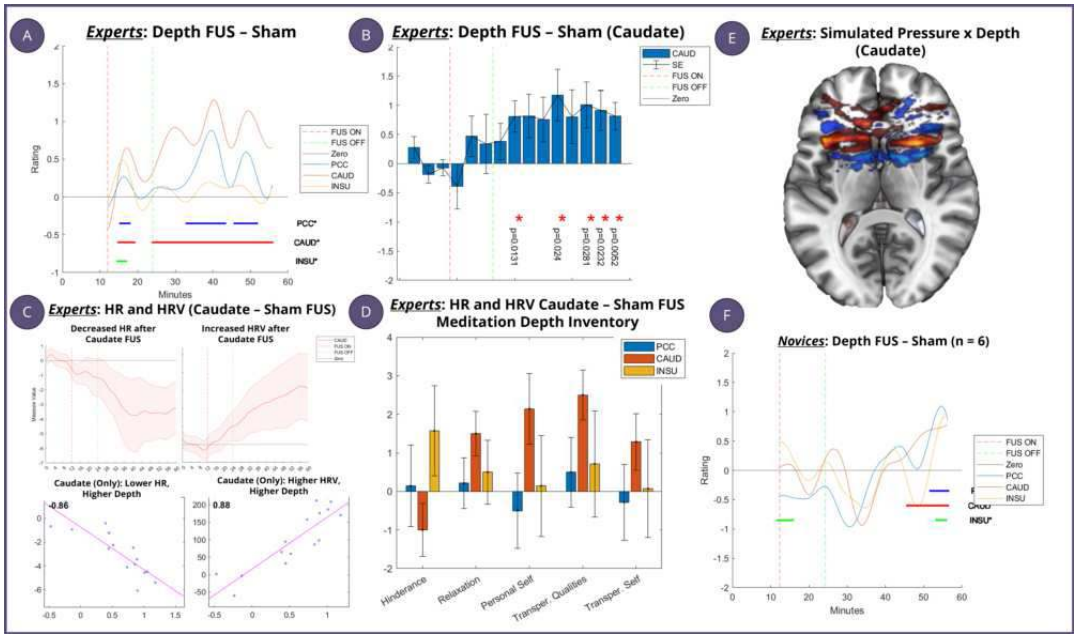

Figure 2. A: Online depth in experts (smoothed), active FUS conditions vs. sham, solid lines depict significant portions. B: CAUD depth (vs. Sham) in in experts, 4m blocks, p values. C: HR, HRV in CAU.

Conclusions: Highly convergent multimodal data supports the notion that caudate FUS increases meditative depth, which strongly correlates with adaptive physiological changes. No such correlation during Sham FUS suggests a mechanistic relationship between physiological changes and successful meditation induced by caudate FUS. Our ambitious first look at FUS-based meditative aids has produced extremely hopeful preliminary results.

References

1. Afonso, R. F., Kraft, I., Aratanha, M. A., & Kozasa, E. H. (2020). Neural correlates of meditation: A review of structural and functional MRI studies. Frontiers in Bioscience (Scholar Edition), 12(1), 92–115. https://doi.org/10.2741/S542
2. Blackmore, J., Shrivastava, S., Sallet, J., Butler, C. R., & Cleveland, R. O. (2019). Ultrasound Neuromodulation: A Review of Results, Mechanisms and Safety. Ultrasound in Medicine & Biology, 45(7), 1509–1536. https://doi.org/10.1016/j.ultrasmedbio.2018.12.015
3. Cain, J. A., Visagan, S., Johnson, M. A., Crone, J., Blades, R., Spivak, N. M., Shattuck, D. W., & Monti, M. M. (2021). Real time and delayed effects of subcortical low intensity focused ultrasound. Scientific Reports, 11(1), Art. 1. https://doi.org/10.1038/s41598-021-85504-y
4. Cain, J. A., Visagan, S., & Monti, M. M. (2022). S.M.A.R.T. F.U.S: Surrogate Model of Attenuation and Refraction in Transcranial Focused Ultrasound. PLOS ONE, 17(10), e0264101. https://doi.org/10.1371/journal.pone.0264101
5. Creswell, J. D., Irwin, M. R., Burklund, L. J., Lieberman, M. D., Arevalo, J. M. G., Ma, J., Breen, E. C., & Cole, S. W. (2012). Mindfulness-Based Stress Reduction training reduces loneliness and pro-inflammatory gene expression in older adults: A small randomized controlled trial. Brain, Behavior, and Immunity, 26(7), 1095–1101. https://doi.org/10.1016/j.bbi.2012.07.006
6. Garrison, K. A., Zeffiro, T. A., Scheinost, D., Constable, R. T., & Brewer, J. A. (2015). Meditation leads to reduced default mode network activity beyond an active task. Cognitive, Affective & Behavioral Neuroscience, 15(3), 712–720. https://doi.org/10.3758/s13415-015-0358-3
7. Garrison, K., Santoyo, J., Davis, J., Thornhill, T., Kerr, C., & Brewer, J. (2013). Effortless awareness: Using real time neurofeedback to investigate correlates of posterior cingulate cortex activity in meditators' self-report. Frontiers in Human Neuroscience, 7. https://www.frontiersin.org/articles/10.3389/fnhum.2013.00440
8. Gasquoine, P. G. (2014). Contributions of the Insula to Cognition and Emotion. Neuropsychology Review, 24(2), 77–87. https://doi.org/10.1007/s11065-014-9246-9
9. Huberty, J., Green, J., Glissmann, C., Larkey, L., Puzia, M., & Lee, C. (2019). Efficacy of the Mindfulness Meditation Mobile App "Calm" to Reduce Stress Among College Students: Randomized Controlled Trial. JMIR MHealth and UHealth, 7(6), e14273. https://doi.org/10.2196/14273
10. Kang, D.-H., Jo, H. J., Jung, W. H., Kim, S. H., Jung, Y.-H., Choi, C.-H., Lee,

Poster No 91

DTI Indices and Tractography in Evaluating Treatment Efficacy in FUS on Essential Tremor

Yan-Hua Su[1,2], Shin Tai Chong[3], Cheng-Chia Lee[4], Ching-Po Lin[5,6]

[1]National yang ming chiao tung university, Taipei City, Beitou Dist., [2]Division of Neurosurgery, Department of Surgery, Fu Jen Catholic University Hospital, New Taipei City, Taiwan, [3]Institute of Neuroscience, National Yang Ming Chiao Tung University, Taiepi, Taiwan, [4]Taipei Veteran General Hospital, Taipei, Taiwan, [5]Institute of Neuroscience, National Yang Ming Chiao Tung University, Taipei, Taiwan, [6]Department of Education and Research, Taipei City Hospital, Taipei, Taiwan

Introduction: Essential Tremor (ET) is a prevalent movement disorder characterized by involuntary rhythmic tremors.[1] The Dentate tract (DRTT) plays a crucial role in modulating movement[2]. The DRTT consists of two portions: the decussating DRTT (dDRTT), the more prominent one, crosses the midline to the contralateral red nucleus and thalamus[3]; the less prevalent non-decussating DRT (ndDRTT) proceeds ipsilaterally from the dentate nucleus to the red nucleus and thalamus. Focused Ultrasound (FUS) is a non-invasive method gaining popularity for treating movement disorders, including ET, by precisely targeting the DRT to alleviate symptoms. Currently, there is still no radiological parameter to predict the outcome after MRgFUS. We plan to apply MRI techniques, including Diffusion Tensor Imaging (DTI), to reconstruct the corticospinal tract (CST), dDRTT and ndDRTT and investigate changes in the tract after FUS treatment in ET patients. We aim to correlate the changes in the DRT with the treatment outcome

Methods: Seven patients diagnosed with ET were enrolled in the study. Pre-treatment, post-treatment, and 3 months post-treatment TETRAS scores (The Essential Tremor Rating Assessment Scale) were measured. All patients underwent 3T magnetic resonance imaging for high resolution T1-weighted image (T1w) and diffusion-weighted images (DWI). All images were pre-processed with iDIO package[5]. We used generalized q-sampling imaging inDSI-Studio for fiber tracking. Whole brain deterministic fiber tracking with 100,000 seeds were used, the CST, nd-DRTT, and dDRTT were reconstructed with the following related region of interest: primary motor area, red nucleus, dentate nucleus, and spinal cord. (Figure 1) All images were registered to the pre-treatment images for extracting all diffusion indices along each fiber tracts (only target on treatment field of view). Finally, we then used the paired T-tests to compare Fractional Anisotropy (FA), Radial Diffusivity (RD), Mean Diffusivity (MD), and Axial Diffusivity (AD) before treatment, immediately after treatment, and 3 months later at the lesion site.[5]

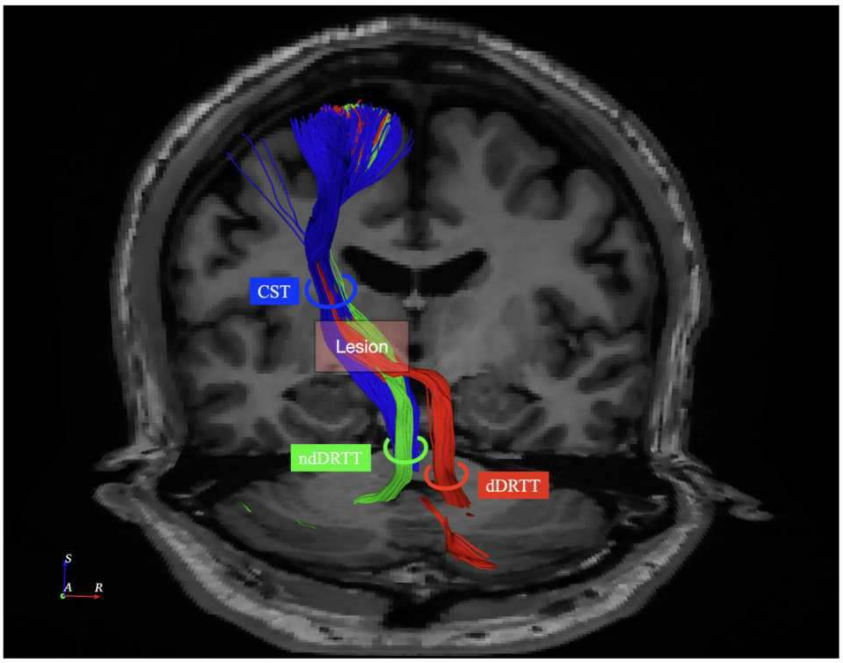

Figure 1. Demonstration of CST, dDRTT and ndDRTT. The indice was measure over the lesion site where focus ultrasound produce lesion.

Results: The average TETRAS score was 23.6 points preoperatively, 17.8 points immediately after MRgFUS, and 12.8 points 3 months after MRgFUS. No significant side effects were noted after MRgFUS. In the treatment side DTI analysis, we performed three groups of paired T-tests (Group 1: pre-treatment vs post-treatment, Group 2: pre-treatment vs 3 months follow-up, Group 3: post-treatment vs 3 months follow-up). We found a decrease in FA of the corticospinal tract (CST), a decrease in FA, and an increase in RD in dDRT, and a decrease in FA in ndDRT in Group 1. In Group 2, we found a decrease in FA in CST, a decrease in AD in dDRT, and ndDRT. In Group 3, we discovered an increase in FA in CST, an increase in FA, and a decrease in RD and MD in dDRT; an increase in FA and a decrease in MD in ndDRT. Figure 2 showed the change of dDRTT in pre-treatment, post treatment and 3 months follow up.

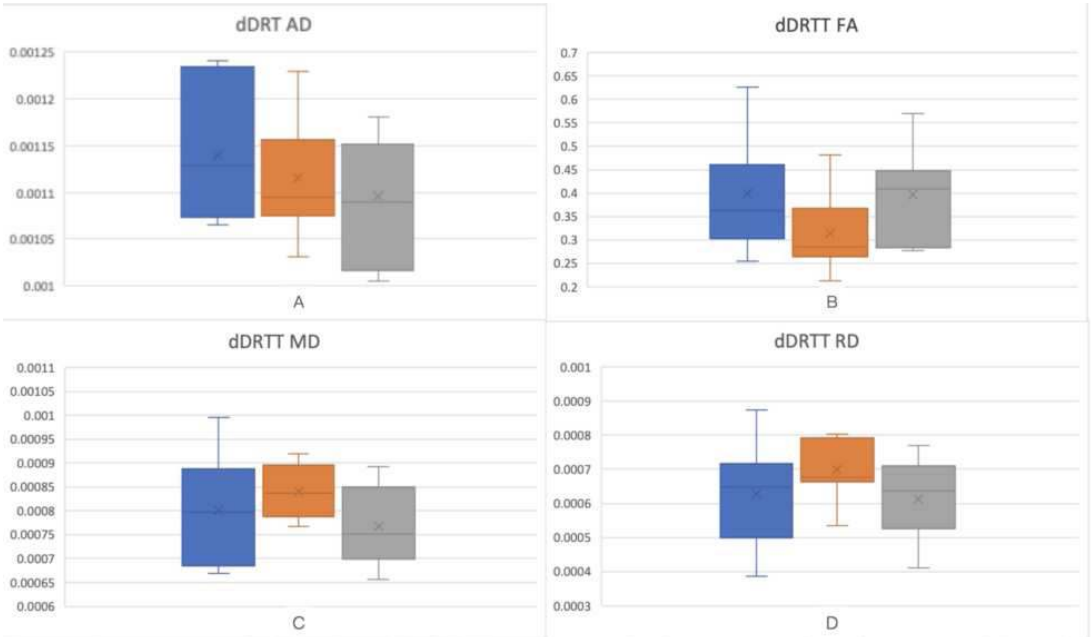

Figure 2.A-D shows changes of AD, FA, MD and RD of dDRTT in pre-treatment (blue), post-treatment (orange) and 3 months follow up (grey). Figure 2A showed significance decrease of AD in 3 months follow up, Figure 2B showed decrease of FA in post-treatment, but then increase in 3 months follow up. Figure 2C MD was increase in post treatment, but then decrease in 3 months follow up. Figure 2D showed RD increase in post treatment and then return to pre-treatment level in 3 months follow up.

Conclusions: There is a significant improvement in TETRAS after MRgFUS treatment, with further tremor improvement observed 3 months later. The changes in FA could indicate microstructural changes after FUS, observable in CST, dDRT, and

ndDRT. However, the changes in RD and AD observed in dDRT and ndDRT could serve as MRI evidence of tract destruction after MRgFUS, suggesting that RD and AD in dDRT and ndDRT could serve as MRI markers for ET patients.

References
1. Ferreira JJ et al. 2010: How common is the most common adult movement disorder? Update on the worldwide prevalence of essential tremor. Movement Disorders 2010, 25(5):534-541.
2. Reinacher PC et al. 2020: The dentato-rubro-thalamic tract as the potential common deep brain stimulation target for tremor of various origin: an observational case series. Acta Neurochirurgica 2020, 162:1053-1066.
3. Fernandez-Miranda JC et al. 2016: The nondecussating pathway of the dentatorubrothalamic tract in humans: human connectome-based tractographic study and microdissection validation. Journal of neurosurgery 2016, 124(5):1406-1412
4. Heinsen H et al. 2021: Use of computational fluid dynamics for 3D fiber tract visualization on human high thickness histological slices: histological mesh tractography. Brain Structure and Function 2021, 226:323-333.
5. Lin CP et al. 2023: Integrated diffusion image operator (iDIO): A pipeline for automated configuration and processing of diffusion MRI data. In.: Wiley Online Library; 2023.

Poster No 92

Individualized Neuroimaging-based Prediction Model for tFUS in Insomnia Patients

Seo Young Lee[1], Sora An[2], Chang-hyun Park[1], Song E Kim[3], Seong Eun Hwang[4], Young Goo Kim[5], Hyang Woon Lee[6]

[1]Artificial Intelligence Convergence Program, Ewha Womans University, Seoul, Korea, Republic of, [2]Department of Communication Disorders, Ewha Womans University, Seoul, Korea, Republic of, [3]Departments of Neurology and Medical Science, Ewha Womans University School of Medicine, Seoul, Korea, Republic of, [4]Department of Neurology, Ewha Womans University Mogdong Hospital, Seoul, Seoul, [5]Department of NeuroSurgery, Ewha Womans University Mogdong Hospital, Seoul, Seoul, [6]Graduate School of Ewha Womans University, Seoul, Korea, Republic of

Introduction: Insomnia is a prevalent sleep disorder that profoundly impacts individuals' quality of life. Transcranial focused ultrasound stimulation (tFUS) is a non-invasive brain stimulation technique that has shown promise in neuromodulation. The medial prefrontal cortex (mPFC) is a region of the brain that plays a crucial role in regulating sleep and wakefulness. In this study, we aimed to investigate the therapeutic potential of tFUS on functional connectivity (FC) in the medial prefrontal cortex (mPFC) of insomnia patients.

Methods: We conducted a randomized controlled trial with 45 participants, including 24 insomnia patients and 21 healthy controls. Participants were randomly assigned to either the tFUS group or the sham group. The tFUS group received excitatory stimulation (70% duty cycle with 5 sec sonication interval) for 20 minutes per session. The sham group received a similar procedure but without actual stimulation. We used resting-state functional magnetic resonance imaging (fMRI) to measure FC between the mPFC and other sites of the brain before and after tFUS. We also collected data on sleep quality, sleep duration, and other sleep-related parameters. The neuroimaging-based prediction model was built based on brain structures and connectome, reconstructed from individual structural brain images, and neural mass models that describe the local dynamics of each brain region. We analyzed changes in simulated FC through resting-state simulations before and after tFUS, and further investigated the correlation between the results and clinical indices (i.e., improvement in Insomnia Severity Index (ISI)).

Results: tFUS significantly increased FC in the mPFC of insomnia patients compared to the sham group. We also observed noticeable improvement in insomnia-related symptoms in the patient group after tFUS. The long-term effects of tFUS on sleep quality will be further investigated in our research. The correlation between the predictive model and the actual improvement degree of the ISI was also investigated.

Conclusions: Our findings suggest that tFUS could modulate the brain functional network of insomniac patients, potentially providing an effective therapeutic approach to insomnia. Individualized prediction model may enhance the clinical application potential and the realization of personalized precision medicine. However, further studies are needed to confirm these results and to optimize the sonication protocol for clinical application.

References
1. Kim, Y. G., Kim, S. E., Lee, J., Hwang, S., Yoo, S. S., & Lee, H. W. (2022), 'Neuromodulation Using Transcranial Focused Ultrasound on the Bilateral Medial Prefrontal Cortex', Journal of clinical medicine, 11(13), 3809.

Acknowledgements
Supported by the National Research Foundation of Korea (NRF) (No.2020R1A2C2013216, 2019M3C1B8090803, 2019M3C1B8090802, and RS-2023-00265524), Institute of Information & Communication Technology Planning & Evaluation (IITP) grant (No. RS-2022-00155966) by the Korea government (MSIT), and BK21-plus FOUR and Artificial Intelligence Convergence Innovation Human Resources Development programs of Ewha Womans University.

Poster No 93

Uncertainty-Aware Deep Learning for 3D Fetal Brain Pose Prediction from Freehand 2D Ultrasound

Jayroop Ramesh[1], Pak Hei Yeung[2], Ana Namburete[1]

[1]University of Oxford, Oxford, Oxfordshire, [2]University of Oxford, OXFORD, Oxfordshire

Introduction: Two-dimensional (2D) ultrasound (US) is the preferred tool for routine monitoring and assessment of fetal growth and anatomy[1]. By capitalizing on the availability and flexibility of low-cost freehand 2D US scanners, it is possible to provide routine prenatal monitoring in resource-constrained settings. However, scanning is heavily operator-dependent, and scarcity of skilled sonographers limits its use. Deep Neural Networks (DNNs) can assist with automated US analysis[2], but their robustness is affected by variability in quality of US images collected by different operators with subjective acquisition protocols. We, therefore, propose an uncertainty-aware deep learning model for 3D pose prediction of 2D fetal brain images, to be used for scanning guidance. Specifically, we train a multi-head network to jointly regress 3D plane poses from 2D images in terms of different geometric transformations and their respective data-dependent uncertainties. Leveraging the output uncertainties can result in a model that is more robust to noise effects observed in freehand US scanning.

Methods: Our data consisted of 3D US volumes acquired at 19 gestational weeks as part of the INTERGROWTH-21st study[3] and aligned to a reference 3D atlas space[4]. We selected 24, 2, and 7 3D volumes for training, validation, and testing respectively. The proposed network took as input 2D slices sampled from arbitrary cross-sectional planes of the 3D volumes. The corresponding plane poses are parameterized by xyz coordinates of 3 reference points and defined as 3D pose P Rheight×width×9. We adapt existing work[2] which predicts the 3D pose P¬ of 2D US fetal brain images by incorporating components to account for uncertainty. We refer to our proposed model as QAERTS, which predicts the pose represented by various parameterizations of rotation (i.e., Quaternions, Axis-angles, Euler angles, Rotation matrices) in addition to shared Translation and Scaling using a multi-head DNN (Fig 1). We hypothesize that confidence of predictions with inputs of variable quality can be quantified by measuring variance between different parameterizations of predicted poses. As the original loss function of MSE in[2] does not capture predictive uncertainty and assumes uniform variance across all inputs, we utilize the outputs to predict a multivariate normal distribution parameterized by the ensemble mean (P¬avg) of poses and the learned variances (σ2avg) after each geometrical transformation. Then, Gaussian Negative Likelihood Loss (GNLL) is minimized with respect to ground-truth reference poses. Accounting for heteroscedasticity during training allows higher weight to be assigned to inputs with lower variance, and improves learning by focusing on lower-noise regions in feature space[6]. The evaluation metrics used are Euclidean distance (ED), plane angle (PA), normalized cross-correlation (NCC) and structural similarity (SSIM)[2].

Results: As shown in Fig 1(b-e) and 2, our proposed model, QAERTS, with ablation studies, were compared to Base[2], and its modification to predict mean and variance (MVE) from separate heads[6], as well as current uncertainty-based deep learning baselines, namely Monte-Carlo Dropout (MCD)[7], Deep ensembles (DE)[8] and Deep Evidential Regression (EDL)[9]. QAERTS reports improved performances across each metric compared to base, MVE, MCD and EDL, but is not as capable as DE (Fig 1b-e)[10]. Nevertheless, QAERTS mitigates computational overhead in terms of time and parameters compared to DE, while maintaining competitive performance on pose prediction quality compared to other baselines (Fig 2).

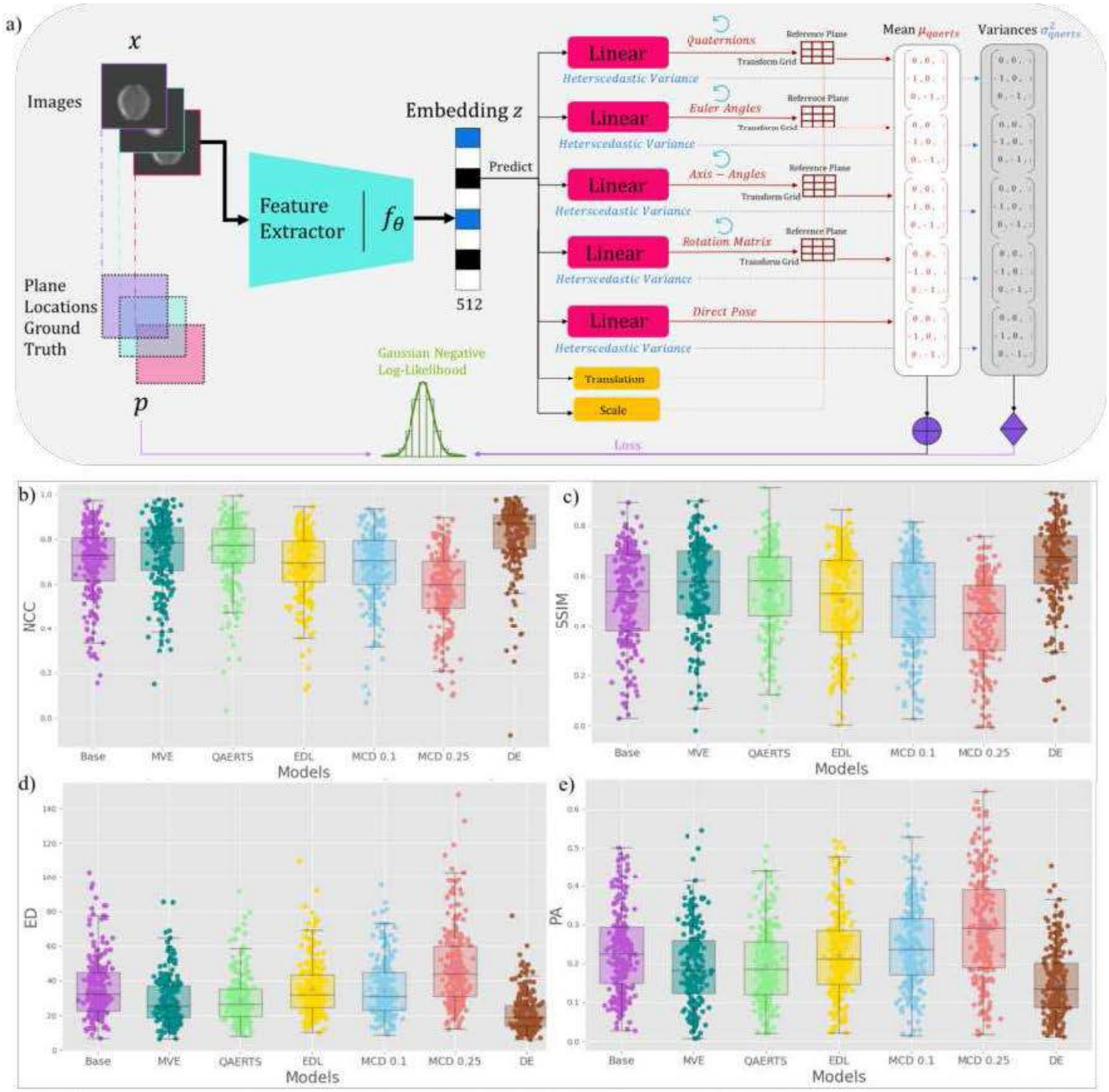

Fig. 1: Pipeline of our proposed work and quantitative results. a) During training, 2D slices sampled from aligned 3D volumes are augmented and used to train our proposed uncertainty-aware multi-head model with diverse parameterizations. A Gaussian Negative Log-Likelihood is minimized under the assumption that the distribution of mean, and variances follow a normal distribution. The trained network can be used to predict the averaged 3D poses obtained from five different geometric transformations for an arbitrary number of 2D images and obtain both measures of aleatoric and epistemic uncertainty in a single forward pass. b) Among all models DE and QAERTS respectively shows the most consistent NCC performance, c) Among all models DE and QAERTS respectively shows the most consistent SSIM performance, d) Among all models DE and QAERTS respectively shows the most consistent ED performance and e) DE and QAERTS shows the most consistent PA performance respectively.

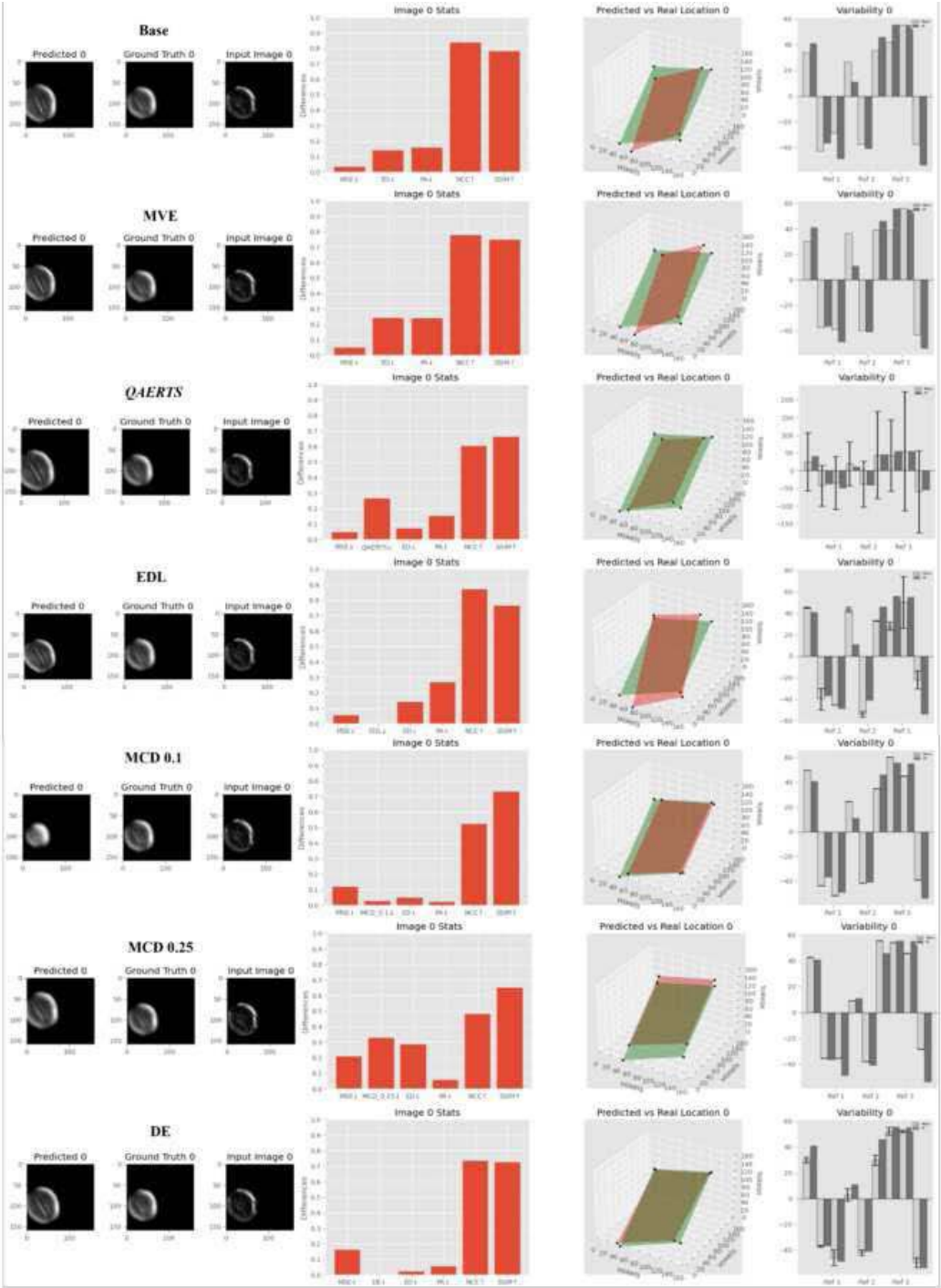

Fig 2: The predictions for gestational age at 19 weeks for a "high quality" prediction: i) Images are extracted from the associated 3D volumes using the predicted plane location, ii) Images are extracted from the associated 3D volumes using the ground-truth plane location, iii) The model relies on an augmented input image to make its prediction. iv) Various metrics, such as normalized mean squared error (MSE), variance with the model-predicted mean, error distance (ED), pixel accuracy (PA), normalized cross-correlation (NCC), and structural similarity (SSIM) are used for evaluation. v) The prediction plane location is represented in red, while the ground truth plane location is in green for each 2D input video frame within the 3D space vi) The mean value of predictions is shown in gray, accompanied by error bars representing the standard deviation of inter-pose variance. These are plotted against the ground truth values (GT) for the xyz coordinates of the first (centre), second (bottom right), and third (bottom-left) reference coordinates, respectively.

Conclusions: We observe overall performance of all techniques improves through uncertainty-aware learning and our proposed model, QAERTS, was second only in predictive performance to DE but with ~5x fewer parameters. This suggests QAERTS can reduce model ambiguity with respect to input quality while being computationally efficient.

References

1. N. K. Dinsdale, E. Bluemke, V. Sundaresan, M. Jenkinson, S. M. Smith, and A. I. L. Namburete, 'Challenges for machine learning in clinical translation of big data imaging studies', Neuron, vol. 110, no. 23, pp. 3866–3881, Dec. 2022, doi: 10.1016/j.neuron.2022.09.012.
2. P.-H. Yeung, M. Aliasi, A. T. Papageorghiou, M. Haak, W. Xie, and A. I. L. Namburete, 'Learning to map 2D ultrasound images into 3D space with minimal human annotation', Med. Image Anal., vol. 70, p. 101998, May 2021, doi: 10.1016/j.media.2021.101998.

3. A. T. Papageorghiou et al., 'The INTERGROWTH-21st fetal growth standards: toward the global integration of pregnancy and pediatric care', Am. J. Obstet. Gynecol., vol. 218, no. 2S, pp. S630–S640, Feb. 2018, doi: 10.1016/j.ajog.2018.01.011.
4. A. I. L. Namburete et al., 'Normative spatiotemporal fetal brain maturation with satisfactory development at 2 years', Nature, pp. 1–9, Oct. 2023, doi: 10.1038/s41586-023-06630-3.
5. A. Kendall and R. Cipolla, 'Geometric Loss Functions for Camera Pose Regression with Deep Learning'. arXiv, May 23, 2017. doi: 10.48550/arXiv.1704.00390.
6. D. A. Nix and A. S. Weigend, 'Estimating the mean and variance of the target probability distribution', in Proceedings of 1994 IEEE International Conference on Neural Networks (ICNN'94), Jun. 1994, pp. 55–60 vol.1. doi: 10.1109/ICNN.1994.374138.
7. Y. Gal and Z. Ghahramani, 'Dropout as a Bayesian Approximation: Representing Model Uncertainty in Deep Learning'. arXiv, Oct. 04, 2016. Accessed: May 15, 2023. [Online]. Available: http://arxiv.org/abs/1506.02142
8. B. Lakshminarayanan, A. Pritzel, and C. Blundell, 'Simple and Scalable Predictive Uncertainty Estimation using Deep Ensembles'.arXiv, Dec. 05, 2016. doi: https://arxiv.org/abs/1612.01474.
9. A. Amini, W. Schwarting, A. Soleimany, and D. Rus, 'Deep Evidential Regression'. arXiv, Nov. 24, 2020. doi: 10.48550/arXiv.1910.02600.
10. M. Havasi et al., 'Training independent subnetworks for robust prediction'. arXiv, Aug. 04, 2021. doi: 10.48550/arXiv.2010.06610.

Poster No 94

Enhancement of glymphatic activity in early Alzheimer's disease using low-intensity ultrasound

Sang Won Jo[1], Jaeho Kim[1], Bo-yong Park[2]

[1]Dongtan Sacred Heart Hospital, Hallym University College of Medicine, Hwaseong, Gyeonggi-do, [2]Inha University, Incheon, Incheon

Introduction: Alzheimer's disease (AD) is marked by the accumulation of metabolic waste in the brain, with glymphatic dysfunction implicated in its progression. Low-intensity ultrasound (LIUS) has emerged as a potential non-invasive modality to facilitate glymphatic clearance. This study was aimed to evaluate the efficacy and safety of LIUS in improving glymphatic system activity and cognitive function in early AD patients.

Methods: In this prospective pilot study, conducted from September to November 2022, ten participants (mean age 69 years; 5 men) with positive amyloid positron emission tomography (PET) imaging underwent LIUS. The LIUS treatment involved thrice-weekly sessions over four weeks. Magnetic resonance imaging (MRI) and amyloid PET scans were used for quantitative analysis of glymphatic activity, blood-brain barrier (BBB) integrity, microbleeds occurrence and amyloid deposition changes, respectively. The study also employed neuropsychological tests to assess cognitive changes. To analyze the quantitative values of different MRI sequences and neuropsychological test results before and after LIUS treatment, the paired sample t-test (or Wilcoxon signed-rank test) was used.

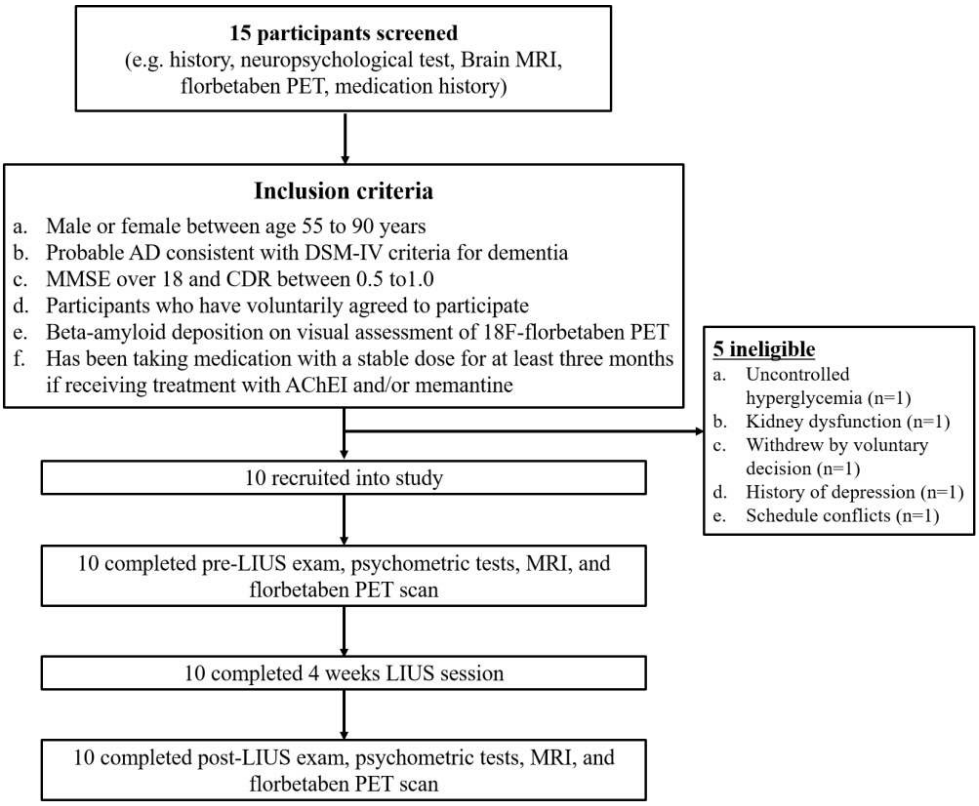

Results: All participants completed the treatment without significant adverse events. Post-treatment, the cerebral cortex showed increased glymphatic activity (slope mean ratio on T1 value-time graph [slope (post-treatment)/slope (pre-treatment)]: 1.14, p=0.048). Neuropsychological testing demonstrated improvements in cognitive function (the Trail Making Test Black & White Part A and B, p=0.017 and p=0.044, respectively; the Korean version of Quality of Life, p=0.046; Attention Questionnaire Scale, p=0.036). No significant changes were observed in blood-brain barrier integrity, microbleed, or brain volumetry.

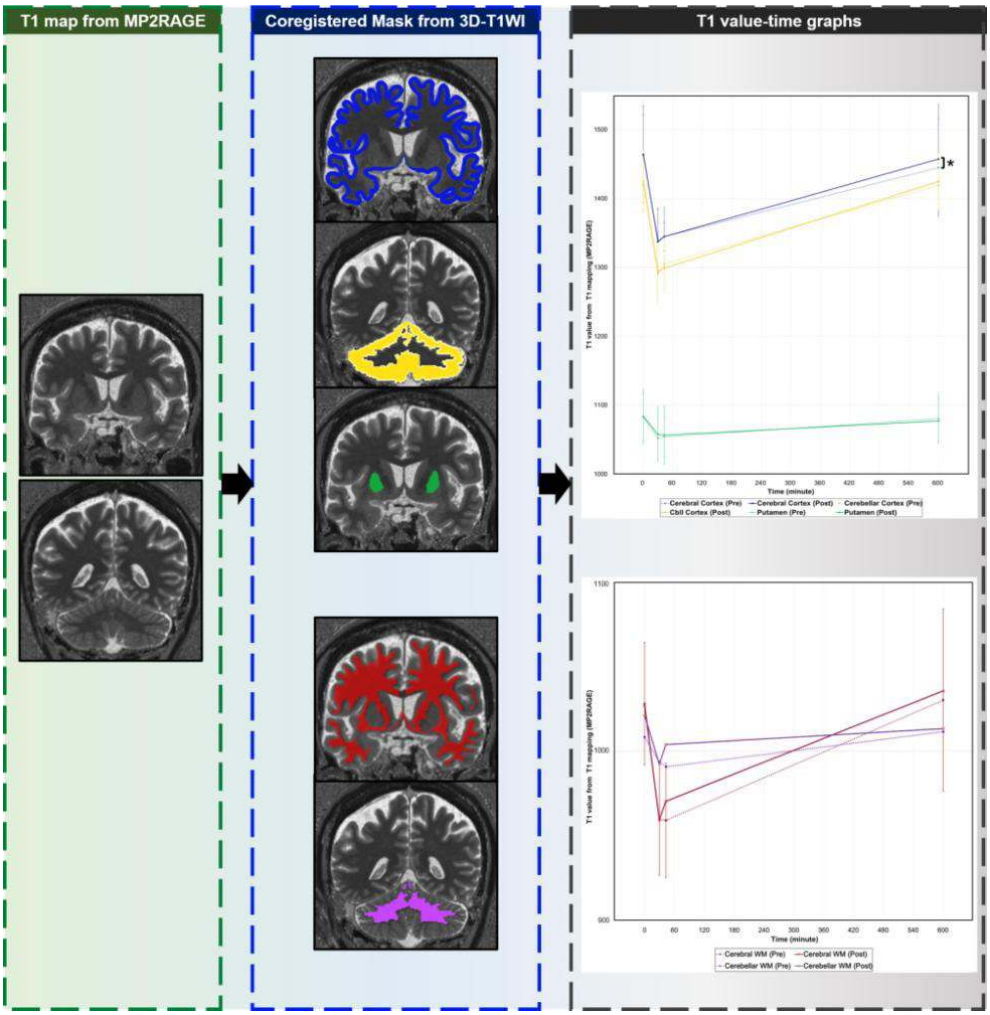

Conclusions: LIUS appears to be a safe method for enhancing glymphatic clearance and cognitive function in early AD patients. These results highlight LIUS's potential as an effective therapeutic option for AD, warranting further investigation with a larger cohort and a control group for more definitive conclusions.

References

1. Jeong H, (2021). 'A pilot clinical study of low-intensity transcranial focused ultrasound in Alzheimer's disease', Ultrasonography 2021;40(4):512-519.
2. Lee S, Yoo RE (co-first authors), (2021), 'Contrast-enhanced MRI T1 Mapping for Quantitative Evaluation of Putative Dynamic Glymphatic Activity in the Human Brain in Sleep-Wake States', Radiology 2021;300(3):661-668.
3. Popescu T, (2021), 'Transcranial ultrasound pulse stimulation reduces cortical atrophy in Alzheimer's patients: A follow-up study' Alzheimers Dement (N Y) 2021;7(1):e12121.
4. Yoo SS, (2022) 'Enhancement of cerebrospinal fluid tracer movement by the application of pulsed transcranial focused ultrasound', Sci Rep 2022;12(1):12940.
5. Yoo SS, (2023), 'Non-invasive enhancement of intracortical solute clearance using transcranial focused ultrasound' Sci Rep 2023;13(1):12339.

Poster No 95

Steerable transcranial ultrasound stimulation (TUS) validated by acoustic radiation force imaging

Bernardo Campilho[1], Holger Hewener[2], Aidin Arbabi[3], Sarah Grosshagauer[1], Christoph Risser[2], Dann Heuvel[3], Jose Marques[4], Christian Degel[2], Steffen Tretbar[2], David Norris[4], Christian Windischberger[5]

[1]Medical University of Vienna, Vienna, Vienna, [2]Department Ultrasound, Fraunhofer Institute for Biomedical Engineering IBMT, Sankt Ingbert, Saarland, [3]Donders Institute, Radboud University, Nijmegen, Gelderland, [4]Donders Institute for Brain, Cognition and Behaviour, Radboud University, Nijmegen, Gelderland, [5]Medical University of Vienna, Vienna, Austria

Introduction: Transcranial Ultrasound Stimulation (TUS) is a non-invasive technique that has considerable potential in the field of neuromodulation, given its spatial precision in the millimetre range and ability to reach deep targets in the human brain (Yaakub et al., 2023). Combining TUS with Magnetic Resonance Acoustic Radiation Force Imaging (MR-ARFI; Darmani et al., 2022) potentially enables the assessment of stimulation focus and intensity, both of which are extremely important for stimulation validation. Different to monitoring approaches based on temperature rises as used in high-intensity focussed ultrasound (HIFU), MR-ARFI assesses TUS effects via MR signal phase changes from subtle tissue displacements (Pauly, 2015). Due to the correlation between tissue displacement (quantified by phase difference maps) at a given position and the acoustic intensity of the beam there, MR-ARFI offers an opportunity for real-time target validation. This is essential not only for safety reasons, but also to validate the acoustic simulations and make sure the desired stimulation outcomes are reached. We extend our previous work on MR-ARFI (van den Heuvel et al., 2023) by showing how a novel using 256-element transducers allows for well-defined steering of the TUS focus by changing stimulation parameters without any change in the setup.

Methods: Our method uses a novel setup consisting of a custom-made MR-compatible, 256-element TUS system for precise beam steering, as well as a developed framework for TUS stimulation control, from which the desired acoustic intensity can be controlled. The focus localization is done using an MR-ARFI sequence (van den Heuvel, 2023) as the imaging method. Images (1.5x1.5x5mm3 voxel size, TE/TR=80/1000, 32 averages) are acquired with and without TUS sonication, in an interleaved scheme. A soft tofu phantom (e.g., McGarry et al., 2013) is used to simulate brain tissue, given their similar density and acoustic properties. Sonication was performed at 283kHz with a duration of 19ms. This study involves two separate experiments, designed to address the current challenges encountered in TUS implementation. Beam steering capabilities of the system are verified by varying the specified focus coordinates to the corners of a 10mm by 10mm square. Intensity effects were tested by varying voltages from 20V to 80V (Figure 2).

Results: Our beam steering experiment validates the ability of the developed system to precisely control the location of the ultrasound focus (Figure 1), as well as its intensity (Figure 2). From Figure 1, we can see that the focus shifts to the desired position with a high degree of accuracy. Moreover, despite the presence of slight artefacts arising from the fragile structure of the used tofu phantom, it is clear that the focus intensity is quadrant-independent, which suggests consistent results regardless of the chosen steering direction. Regarding the voltage experiment (Figure 2), the gradual transition of the intensity of the focus is in agreement with the linear relationship found in previous studies (e.g., Li et al., 2022). This predictability is important for acoustic dose planning, particularly in clinical applications, where precise knowledge of the acoustic intensity is critical.

Conclusions: Here we have shown that MR-ARFI can be used to measure TUS effects with high spatial resolution. As expected, phase changes at the focus were increasing with the voltage used. Beam steering capabilities were successfully demonstrated by shifting focus location around the initial central target. Our proposed TUS-MRI setup shows that multi-element TUS transducers enable precise steering of the TUS focus without any change in the mechanical setup. This enables online adjustments to not only compensate for discrepancies between simulation results and accrual sonication effects, but also to switch stimulation targets on-the-fly, i.e. during an TUS/MR experiment.

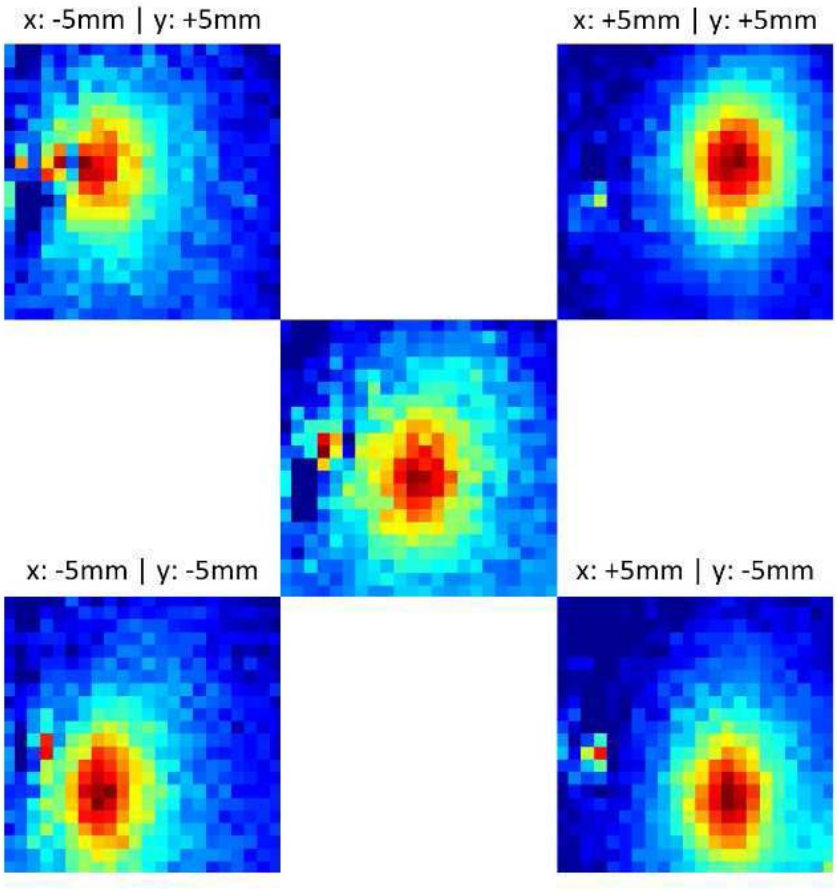

Figure 1: Phase shift maps resulting from ultrasound beam focus steering experiment. Each image corresponds to a separate imaging sequence, consisting of 32 averages, where the ultrasound focus was set to a different position, as illustrated by the phase map positions. Phase maps after sonication were subtracted from the baseline image, obtained without sonication.

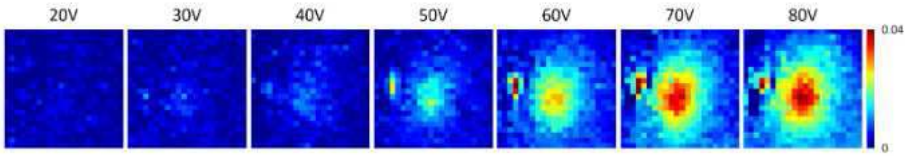

Figure 2: Phase shift maps showing increased changes with increasing stimulation power (values refer to stimulation output voltage).

References

1. Darmani, G., et al. (2022), "Non-invasive transcranial ultrasound stimulation for neuromodulation", Clinical Neurophysiology 135, 51-73.
2. Li, N., Gaur, P., Quah, K., & Butts Pauly, K. (2022), "Improving in situ acoustic intensity estimates using MR acoustic radiation force imaging in combination with multifrequency MR elastography", Magnetic Resonance in Medicine, 88(4), 1673-1689.
3. McGarry, Matthew, et al. (2013), "Including spatial information in nonlinear inversion MR elastography using soft prior regularization", IEEE transactions on medical imaging, 32.10: 1901-1909.
4. Pauly, K. B. (2015), "Magnetic resonance acoustic radiation force (impulse) imaging (MR-ARFI)", Journal of Therapeutic Ultrasound, 3(1), 1-1.
5. van den Heuvel, D., et al (2023), Proc. of the ESMRMB, P204
6. Yaakub, Siti N., et al. (2023), "Transcranial focused ultrasound-mediated neurochemical and functional connectivity changes in deep cortical regions in humans.", Nature Communications: 5318.

Poster No 96

Quantitative Susceptibility Mapping in Cerebral Cavernous Malformations: Phantom vs Human lesions

Ogechukwu Ngwu-Hyacinth[1], Williams Willoughby[1], Mark Bolding[1]

[1]*The University of Alabama at Birmingham, Birmingham, AL*

Introduction: Cerebral cavernous malformation (CCM) is a vascular anomaly affecting over 0.5% of the population, with a heightened risk of stroke and epilepsy due to recurring lesional hemorrhages. Currently, surgery is the only definitive treatment[1], but this poses a significant risk of morbidity and mortality. We propose magnetic resonance image-guided focused ultrasound (MRgFUS) treatment of CCM lesions, a technique combining magnetic resonance imaging (MRI) and focused ultrasound (fUS) for visualizing, targeting, and monitoring lesions. Studies have shown that the thermal energy released at the focus of the ultrasound can induce ablation of vascular lesions. Furthermore, MRI, particularly utilizing gradient echo T2 star-weighted and susceptibility-weighted imaging, is recommended for CCM detection[1]. Additionally, MRI has been shown to produce real-time temperature maps and estimates of tissue coagulation during the ablation process[2]. However, susceptibility artifacts from hemorrhagic residues in vascular lesions hinder accurate temperature monitoring during MRgFUS treatment[3]. The study aims to address this knowledge gap by using quantitative susceptibility mapping (QSM), an MRI technique, to estimate iron content in CCM phantoms. Objectives: - To compare the susceptibility of CCM phantoms with the susceptibility of CCM lesions in humans.

Methods: To make the CCM phantom, jelly beads were made from a mixture of red-colored liquid containing 2g of Iron (III) citrate (0.1g Fe2+) and sodium alginate spherified in a Calcium lactate solution and frozen to achieve a solid consistency. To mimic CCM lesions, three gelatin brain molds were embedded with the frozen jelly beads and the mold was allowed to form at room temperature. MRI images were acquired at 3.0T using TE = 10ms, TR = 100 ms, 30cm field of view and 128*128 matrix. MRI data were analyzed using FSL (www.fmrib.ox.ac.uk/fsl). QSM maps were reconstructed from data acquired with a 3-dimensional T2*-weighted gradient echo sequence. To validate our QSM estimates, the mean susceptibility values of the CCM phantoms were correlated with the QSM-derived iron measurements in human patients[4].

Results: The iron-embedded jelly beads appeared hyperintense on the QSM maps compared to the nearby gelatin mold. The susceptibility of iron in these phantoms, as demonstrated by QSM, averages about 2ppm, similar to the iron content of human CCM lesions, as shown in this paper[4].

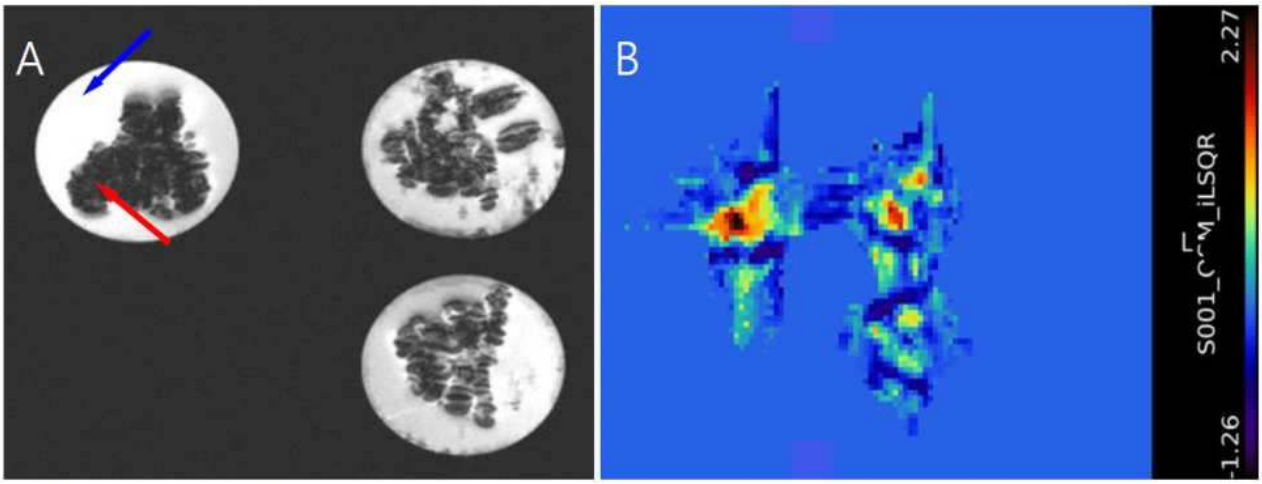

Figure 1. A: *Conventional MRI T2* maps of our CCM phantom. The red arrow depicts the iron-embedded beads, which appeared hypointense on the conventional T2*-weighted MRI relative to the surrounding gelatin mold (blue arrow).* ***B****: Reconstructed QSM images. While the CCM mimic lesions appear hypointense on GRE T2*, they are hyperintense on QSM. The hypointensity on the GRE T2* is a qualitative measurement and cannot be used to assess lesional iron content. On the other hand, QSM is a quantitative measurement, and the total susceptibility is directly proportional to the lesional iron content. The susceptibility distribution within a single phantom is displayed on the top right. The scale unit is ppm.*

Conclusions: This preliminary experiment developed a phantom with similar magnetic, spin relaxation and susceptibility properties as a human CCM to enable testing various MRI pulse sequences and monitoring temperature feedback during fUS treatment on phantom models. While acknowledging iron as the assumed predominant susceptibility source in the phantom, the study concludes that high-field MRI techniques, particularly QSM, offer new avenues for CCM lesion monitoring. Future investigations will explore correlations between susceptibility and physical properties of CCM phantoms, informing the transition to in-vivo animal models and, eventually, clinical trials.

References
1. Mouchtouris, N. (2015). Management of Cerebral Cavernous Malformations: From Diagnosis to Treatment. The Scientific World Journal, 2015, e808314.
2. Nosova, K. (2023). History of Ablation Therapies in Neurosurgery. Neurosurgery Clinics of North America, 34(2), 193–198.
3. Tan, H. (2016). Quantitative Susceptibility Mapping in Cerebral Cavernous Malformations: Clinical Correlations. AJNR. American journal of neuroradiology, 37(7), 1209–1215.
4. Tan, H. (2014). Evaluation of iron content in human cerebral cavernous malformation using quantitative susceptibility mapping. Investigative radiology, 49(7), 498–504.

Poster No 97

Transcranial Ultrasound (TUS) applied to Corpus Callous Diminishes EEG Alpha Power

PK Douglas[1], Pardis Azarmi-por[2], Joshua Cain[3]

[1]IACS, Los Angeles, CA, [2]UCLA, Los Angeles, CA, [3]Institute for Advanced Consciousness Studies, Los Angeles, CA

Introduction: The alpha rhythm is perhaps the most prominent feature in EEG recordings, yet its spatial origins and functional significance have been debated since its was first observed in 1929. In Berger's pioneering work, he noted prominent "alpha waves" that were abolished with the eyes open in the first recorded human EEG (Berger 1929). Combined cortical surface, intracortical depth electrode, and intra-thalamic recordings provided additional evidence that alpha may be generated by the pulvinar nucleus and other nuclei of the thalamus influence cortical alpha activity (Lopes da Silva 2023). At birth and throughout infancy, there is no distinguishable EEG alpha rhythm (Trujillo, Gao et al. 2019). Given that the emergence of the alpha rhythm appears to parallel the development of myelin and the formation of white matter fiber bundles, we hypothesized that white matter signaling may also play a role in generating or carrying the alpha rhythm. To explore this theory, we applied transcranial ultrasound (TUS) sonication to healthy adult subjects in the following brain regions: corpus callosum, medial dorsal thalamus, and the pulvinar nucleus and measured changes in EEG alpha power.

Methods: All study protocols were approved by the CCN IRB prior to commencing studies. A total of 24 subjects were enrolled in the study. A subset of subjects (N=8) returned on a different day to receive sonication at a different brain target. Thus, there were a total of 30 data collection sessions across the study cohort (mean age = 19 +/- 6 y.o., 33% female). EEG data was collected at baseline, following a sham condition, and after TUS sonication. EEG was recorded while subjects performed an "eyes open/eyes closed" task consisting of 3 blocks of each task for 30 seconds each to permit time for changes in alpha power. T1 MRI scans were used for neuronavigation purposes. Subjects received sonication to one of the three brain targets or 30 seconds on, and 30 seconds off for a total of 10 minute.

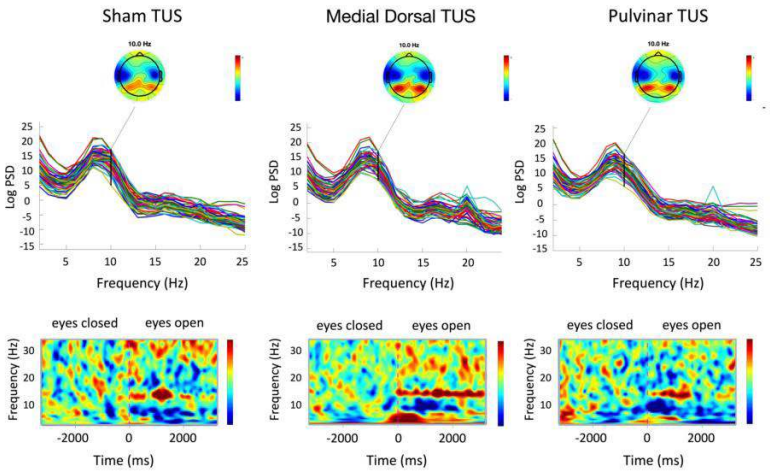

Figure 1: (Top) Spectral decompositions calculated for 2 seconds of eyes closed data for sham-TUS (left), medial dorsal nucleus (middle), and pulvinar nucleus (right) from the occipital EEG channel. Suppressive TUS at 650kHz, was applied using a 10Hz envelope for 10 minutes prior to the eyes open/eyes closed task. In the case of the sham condition, the stand-off pad was placed between the transducer and the scalp to block ultrasound waves, while permitting instrumentation noise to alter brain activity. (Lower) Wavelet decompositions from occipital channels for sham, medial dorsal, and pulvinar nucleus show clear diminution in the alpha power during the eyes open condition.

Results: During both baseline and "sham-TUS" EEG recordings, we observed a prominent alpha peak in spectral decompositions across participants during the eyes closed. We found no significant alpha power changes following TUS to thalamus or pulvinar (Figure 1). In contrast, we observed a significant diminution in alpha power following sonication of the corpus callosum (Figure 2).

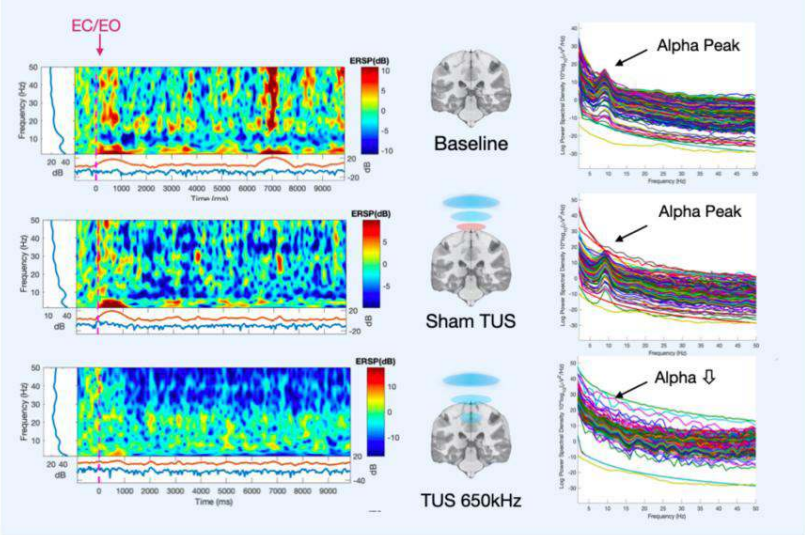

Figure 2: Alpha Power Desynchronization following Suppressive TUS to Corpus Callosum midline crossings in a representative subject. (Left) Time-frequency decompositions for 1 second before and 10 sec after the subject transitioned from eyes closed to eyes open for baseline (top), sham-TUS (middle), and TUS sonication (lower). (Right) Special decompositions calculated from 2 seconds of eyes closed EEG data for baseline, sham, and TUS (top, middle, lower panels, respectively). At baseline, a prominent alpha peak is observed during the eyes closed condition. This peak is also evident during sonication with a sham stand-off pad, controlling for signal noise. TUS at 650kHz, was applied with a 10Hz envelope, using the same sonication parameters as Figure 1.

Conclusions: TUS applied to the medial dorsal thalamus and pulvinar nuclei, did not significantly alter alpha power during the eyes closed state, when the alpha peak is conspicuous. The frequency position of the alpha peak also remained unchanged when TUS was applied to gray matter targets. In contrast, TUS applied to corpus callosum caused a prominent desynchronization in alpha power during the idle eyes closed state, as evident across both frequency and time-frequency decompositions. Our results provide exciting new evidence that the corpus callosum is either responsible for, or is an integral component requisite for the generation of the alpha rhythm in human EEG recordings.

References

1. Berger, H. (1929). "Über das Elektrenkephalogramm des Menschen." Archiv für Psychiatrie und Nervenkrankheiten 87(1): 527-570.
2. Lopes da Silva, F. H. (2023). EEG: Origin and Measurement. EEG-fMRI: Physioological Basis, Technique, aan Applications. Switzerland, Springer Nature: 23-48.
3. Trujillo, C. A., R. Gao, P. D. Negraes, J. Gu, J. Buchanan, S. Preissl, A. Wang, W. Wu, G. G. Haddad, I. A. Chaim, A. Domissy, M. Vandenberghe, A. Devor, G. W. Yeo, B. Voytek and A. R. Muotri (2019). "Complex Oscillatory Waves Emerging from Cortical Organoids Model Early Human Brain Network Development." Cell Stem Cell 25(4): 558-569.e557.

Poster No 98

The effect of tDCS targeting the left inferior frontal gyrus on fear extinction

Yuanbo Ma[1,2], Fatemeh Yavari[1], Fujia Jiao[1,3], Michael Nitsche[1,4]

[1]Psychology and neurosciences, Leibniz Research Centre for working environment and human factors, Dortmund, Germany, [2]Neuropsychology, Institute of Cognitive Neuroscience, Faculty of Psychology, Ruhr University Bochum, Bochum, Germany, [3]Key Laboratory of Exercise and Health Sciences of Ministry of Education, Shanghai University of Sport, Shanghai, China, [4]Bielefeld University, University Hospital OWL, Protestant Hospital of Bethel Foundation, University Clinic of Psychiatry and Psychotherapy, and University Clinic of Child and Adolescent Psychiatry and Psychotherapy, Bielefeld, Germany

Introduction: Impaired fear extinction is an essential factor contributing into several anxiety disorders, such as post-traumatic stress disorder (PTSD) and phobias[1]. Based on the fear extinction model, exposure therapy is considered as an effective treatment method for anxiety disorders. However, some patients experience reappearance of fear in real-life contexts after

treatment, indicating the crucial role of contextual factors in the efficiency of fear extinction (renewal effect). A recent fMRI study has shown activation of the left inferior frontal gyrus (LiFG) during the extinction phase of a predictive learning task, implying the correlational involvement of LiFG in context processing during extinction learning[2]. In this study, we aimed to investigate the suggested causal role of LiFG in the context-dependency of fear extinction learning via non-invasive transcranial direct current stimulation (tDCS), which alters cortical excitability, to target this area.

Methods: 180 healthy subjects (92 females) were recruited and randomly assigned to 9 groups (3 tDCS types (anodal, cathodal, and sham) × 3 context combinations (AAA, ABA, and ABB)). The fear conditioning task was conducted over three consecutive days: acquisition, the first extinction, and the second extinction phases. tDCS (2 mA, 10 min) was administered during the first extinction phase to the LiFG using a 4-electrode montage. Skin conductance response (SCR) data was collected and analyzed using a mixed-model ANOVA, Bonferroni comparisons were performed when results appeared significant.

Results: During the extinction phase, subjects who received anodal tDCS showed a significantly higher fear response compared to the cathodal and sham conditions, and this effect was stable till the 2nd extinction phase. Cathodal tDCS caused a significant decrease in the difference of the response to the threat and safety cues during the 2nd extinction phase compared to anodal and sham conditions. An interaction between tDCS and context was only observed during the extinction phase.

Conclusions: Our results do not support the causal role of LiFG in the context-dependency of fear extinction learning, though anodal tDCS led to augmented fear responses independent of the context. It has been previously indicated that in fear conditioning, a positive prediction error (PPE) can update and increase fear responses to the threat cues, and increased activation of the LiFG has been observed to be associated with PPE[3]. This is in line with our results, as hyperactivation of LiFG by anodal tDCS could have evoked a positive prediction error which increases fear responses. Furthermore, previous fMRI data have shown that the LiFG is activated when participants are asked to increase their negative emotions in response to aversive images[4]. Increasing the activity of the LiFG by tDCS in our study might therefore elevate the negative interpretation of the fear stimulus (CS+), leading to increased fear responses and deteriorate fear extinction learning.

References

1. Craske, M.G. (2018), 'State-of-the-art and future directions for extinction as a translational model for fear and anxiety'. Philosophical transactions of the Royal Society of London. Series B, Biological sciences, 373(1742), 20170025.
2. Lissek, S. (2019), 'Effects of Noradrenergic Stimulation Upon Context-Related Extinction Learning Performance and BOLD Activation in Hippocampus and Prefrontal Cortex Differ Between Participants Showing and Not Showing Renewal'. Frontiers in behavioral neuroscience, 13, 78.
3. Spoormaker, V.I. (2011). 'The neural correlates of negative prediction error signaling in human fear conditioning'. NeuroImage, 54(3), 2250–2256.
4. Urry, H.L. (2006). Amygdala and ventromedial prefrontal cortex are inversely coupled during regulation of negative affect and predict the diurnal pattern of cortisol secretion among older adults. The Journal of neuroscience: the official journal of the Society for Neuroscience, 26(16), 4415–4425.

Poster No 99

Exploring effects of prefrontal tDCS on Metabolite Levels in MDD, SCZ, and healthy subjects

Gizem Vural[1,2], Antonia Šušnjar[3], Lucia Bulubas[4], Eva Mezger[5], Andre Brunoni[6], Birgit Ertl-Wagner[7], Sophia Stoecklein[5], Stephan Goerigk[8,9], Aldo Soldini[5], Joanna Moussiopoulou[10], Frank Padberg[4], Daniel Keeser[4]

[1]LMU Klinikum, Munich, Other, [2]General and Experimental Psychology Ludwig-Maximilians-University, Munich, Germany, [3]Purdue University, West Lafayette, IN, [4]Department of Psychiatry and Psychotherapy, University Hospital LMU, Munich, Germany, [5]LMU Klinikum, Munich, Bavaria, [6]Department of Psychiatry and Laboratory of Neurosciences Institute of Psychiatry, São Paulo, Estado de Sao Paulo, [7]Department of Diagnostic Imaging, The Hospital for Sick Children, Ontario, Ontario, [8]Ludwig-Maximilians-University of Munich, Munich, Bavaria, [9] LMU · Department of Psychology, N/A, [10]LMU Klinikum, München, Germany

Introduction: Transcranial Direct Current Stimulation (tDCS) is a non-invasive brain stimulation technique that is gaining attention for its potential to modulate cortical brain activity, with applications in cognition and potential treatment options in various psychiatric conditions including major depressive disorder (MDD) and schizophrenia (SCZ). This study aimed to investigate how bifrontal tDCS might influence brain metabolite concentrations within the medial prefrontal cortex (mPFC). To achieve this, we employed a concurrent tDCS-magnetic resonance spectroscopy (MRS) setup, allowing us to observe potential changes in brain chemistry associated with the application of tDCS in real-time.

Methods: A total of 30 subjects with MDD (20 men, mean age 30.4±11), and 23 subjects with SCZ (17 men, mean age 35.78±11) and 36 healthy control subjects (26 men, mean age 31±10), matched for age and gender with the MDD and SCZ samples participated. A 3 Tesla Siemens Skyra MRI scanner in conjunction with a neuroConn DC-Stimulator MR device was used for the study. In vivo MRS was obtained utilizing a MEGA-PRESS sequence to monitor neurometabolic shifts before, during, and after 20 min of 2 mA tDCS administration with 5 x 7 cm electrodes. The anode was positioned over F3 (left DLPFC) and the cathode over F4 (right DLPFC). Stimulation sessions were performed in a randomized and counterbalanced order in a cross-over design.

Results: Before the application of tDCS, a baseline comparison between the groups was performed to evaluate inherent differences in metabolite concentrations under both active and sham conditions. Accordingly, the MDD group exhibited higher Glu and Glx concentrations compared to the healthy group. To evaluate the tDCS effect, baseline corrected metabolite concentrations were quantified as separate analyses for each group comparing active and sham conditions. The notable finding emerged in the SCZ group, where active tDCS initially had a significant impact on NAA concentrations compared to sham in the beginning of the stimulation. However, this effect did not persist throughout the stimulation period. Comprehensive group comparisons further revealed pronounced differences in NAA concentrations, with SCZ group having significantly lower values compared to the healthy group. Furthermore, in both active and sham conditions, the healthy group exhibited significantly higher NAA, Glu, and Glx levels compared to the MDD group during the study period.

Conclusions: The findings shed light on the neurochemical underlying prefrontal tDCS for our study subjects at the two specific measurement times, highlighting possible cross-sectional utility for two major psychiatric diseases. MDD patients exhibited inherently higher concentrations of Glu and Glx compared to healthy controls, suggesting a potential neurochemical distinction associated with major depressive disorder. Contrastingly, when examining the metabolite levels over time, our results indicated a consistent decrease in all three metabolite concentrations in the MDD group compared to healthy controls. However, the absence of a significant three-way interaction (group by stimulation by time) suggests that these observed reductions are not dependent on the type of stimulation-active or sham. Interestingly, while tDCS influenced metabolite levels in the SCZ group, the effects were transient, indicating a temporary neurochemical response to tDCS in schizophrenia. Nevertheless, the absence of certain findings does not rule out possible effects on NAA, Glu, and Glx levels in lateral prefrontal regions or under varying tDCS conditions, such as different montages, intensities, and durations. Future research employing multi-voxel MRS might address these gaps and allow for a more comprehensive localization of the effects of tDCS on neurotransmitter levels, including network effects over predefined regions of interest.

References

1. Mezger, E. (2021). Effects ofbifrontal transcranial direct current stimulation on brain glutamate levels and resting state connectivity: multimodal MRI data for the cathodal stimulation site. European archives of psychiatry and clinical neuroscience, 271(1), 111-122.

Poster No 100

TDCS Modulates Baseline fMRI Activity and Population Receptive Fields in the Human Visual Cortex

Jeongyeol Ahn[1], Juhyoung Ryu[1], Sangjun Lee[2], Chany Lee[3], Chang-Hwan Im[4], Sang-Hun Lee[1]

[1]Seoul National University, Seoul, Seoul, [2]University of Minnesota, Minneapolis, MN, [3]Korea Brain Research Institute, Daegu, North Gyeongsang, [4]Hanyang University, Seoul, Seoul

Introduction: Transcranial direct current stimulation (tDCS) is a widely employed method for modulating various kinds of human cognition. Despite its widespread application, recent neuroimaging studies investigating the impact of tDCS on cortical excitability have yielded highly inconsistent results. This inconsistency underscores the need for a comprehensive understanding of how tDCS affects system-level neural activity, an essential prerequisite for the informed application of tDCS in the field of human cognition. In this study, our objective is to elucidate this understanding by examining the spatial and temporal functional magnetic neuroimaging (fMRI) activity within the human early visual cortex, assessed through diverse parameters, all while carefully controlling the polarity and presence of tDCS. The selection of the early visual cortex as our target allows us to leverage its well-established anatomical and functional architecture, readily accessible through non-invasive quantitative neuroimaging methods.

Methods: To precisely and effectively create an electric field in the early visual cortex, we tailored high-definition stimulation montages for 15 individuals (25.7 ± 4.17 years, five females) by conducting electric field simulations based on individual head models (Fig. 1). Subsequently, we implemented an fMRI-tDCS experiment on each brain with a sham-controlled crossover design over multiple days. To investigate the impact of tDCS on the temporal and spatial dynamics of cortical activity, we measured fMRI responses to both brief (3 s) whole-field stimuli and traveling-wave stimuli (Fig. 2a-b). The temporal dynamics

were characterized by estimating baseline, response amplitude, and sustained response parameters, while the spatial tuning was quantified using a population receptive field (pRF) model. We assessed the significance of these parameters using mixed ANOVA and further validated their robustness against across-voxel and across-subject variability.

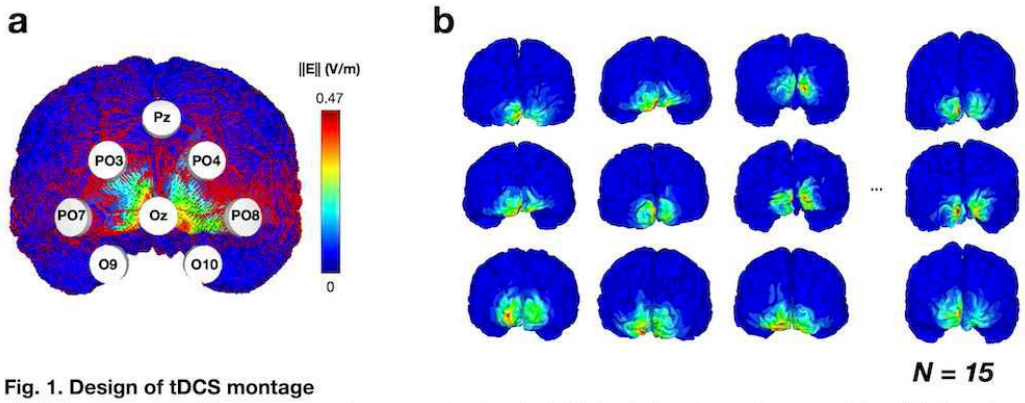

Fig. 1. Design of tDCS montage
(a) Eight-channel tDCS montage and an example electric field simulation shown for one subject. (b) Electric field simulation for individual subjects based on their own head model

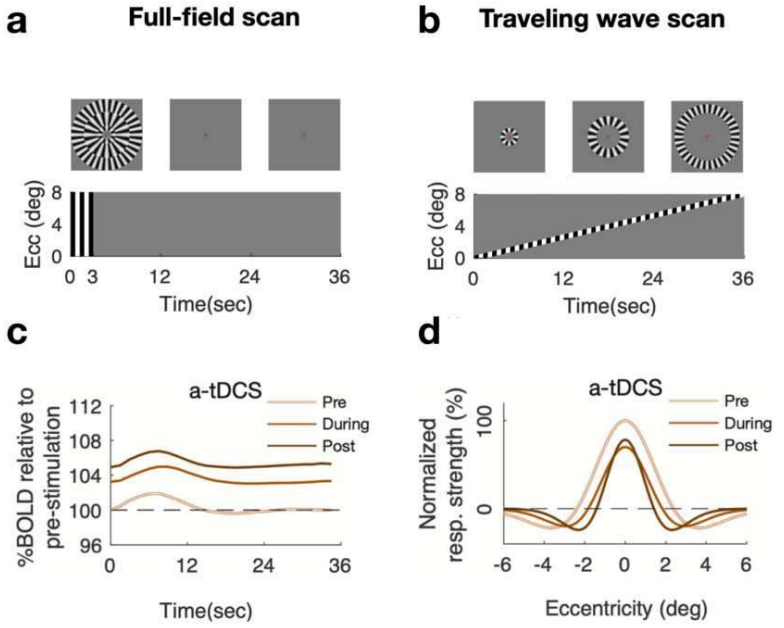

Fig. 2. Illustrative summary of the principal tDCS effects on fMRI response to visual stimuli
(a-b) Stimuli and paradigm for characterizing the fMRI responses to transient full-field (a) and traveling-wave (b) input. (c-d) Illustrative summary of tDCS effects on fMRI responses to the transient full-field input (c) and pRF shapes (d).

Results: We observed significant impacts of tDCS on the baseline measure and the pRF after anodal tDCS. The offline anodal tDCS resulted in an increase in the baseline of the fMRI time course (z = 7.38, FDR-adjusted p = 3.E-13 across voxels), a decrease in spatial tuning width (z = -5.19, FDR-adjusted p = 4.E-07 across voxels), and an augmentation of surround suppression (z = 4.47, FDR-adjusted p = 1.E-05 across voxels) (Fig. 2c-d).

Conclusions: Comparisons between our findings and previous studies indicate fundamental differences in the effects of transcranial direct current stimulation (tDCS) on the visual and motor cortices. Our results suggest a prevalence of inhibitory effects in the visual cortex, contrasting with the excitatory effects predominant in the motor cortex. These observations underscore the importance of considering variations in the excitatory-inhibitory recurrent network across different brain regions when predicting or interpreting the effects of tDCS.

References

1. Ahn, J. (2023). Transcranial direct current stimulation elevates the baseline activity while sharpening the spatial tuning of the human visual cortex. Brain Stimulation, 16(4), 1154–1164.

Poster No 101

Impact of tDCS on brain metabolites in the left DLPFC in healthy subjects

Aldo Soldini[1], Gizem Vural[2], Frank Padberg[3], Eva Mezger[1], Julian Melcher[1], Sophia Stoecklein[1], Lucia Bulubas[3], Antonia Šušnjar[4], Daniel Keeser[3]

[1]LMU Klinikum, Munich, Bavaria, [2]LMU Klinikum, Munich, Other, [3]Department of Psychiatry and Psychotherapy, University Hospital LMU, Munich, Germany, [4]Purdue University, West Lafayette, IN

Introduction: Transcranial Direct Current Stimulation (tDCS) is emerging as a non-invasive brain stimulation (NIBS) technique for modulating cortical brain activity, with potential implications in cognitive enhancement and treatment in psychiatry. Current knowledge on tDCS primarily pertains to its neurophysiological effects, encompassing motor-eveoked potentials, cognitive studies, EEG investigations, and fMRI research; however, there is limited understanding regarding its impact on brain metabolites in the dorsolateral prefrontal cortex (DLPFC), a target region for NIBS in mental disorder. The aim of this double-blind, placebo-controlled investigation was to explore the impacts of prefrontal tDCS on neurotransmitter levels, specifically glutamine/glutamate (Glx), N-Acetylaspartate (NAA), and gamma-aminobutyric acid (GABA) in the left dorsolateral prefrontal cortex (DLPFC), utilizing a combined tDCS/MRS approach in a sample of healthy volunteers.

Methods: A total of 41 healthy individuals (19 females; mean age: 25) underwent bifrontal active (2 mA for 20 min) or sham tDCS targeting the left (anode: F3) and right (cathode: F4) DLPFC within a 3 Tesla Siemens Prisma MRI scanner, utilizing a neuroConn DC-Stimulator MR device. In vivo magnetic resonance spectroscopy (MRS) was employed to monitor neurometabolic changes before, during, and after tDCS administration. A Siemens vendor and MEGA-PRESS sequence specific basis set was used for linear-combination modeling deployed in LC Model software. A single voxel, positioned underneath F3, was utilized to quantify metabolite levels at four 10-minute measurement time points at baseline, during the first and second 10 minutes of stimulation and after the stimulation. LCModel (Linear Combination Model, Version 6.3-1R), a reliable and model-free method for analyzing brain metabolites, was employed. For in vivo data, eddy current correction and water scaling were applied. Furthermore, we utilized Osprey (version 2.5.0) for voxel registration and tissue segmentation. Statistical analyses were conducted using the R programming language (version 4.2.2) in R Studio (version 2022.12.0.353: R Development Core Team, 2008).

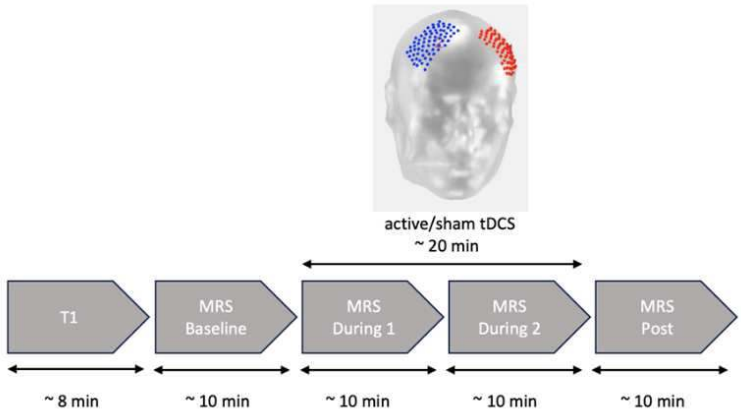

Assessment of 20-minute, 2mA active or sham prefrontal tDCS at four timepoints using an edited MRS sequence in between the resting state measurements.

Results: There was a significant increase in Glx levels during active tDCS compared to sham tDCS. This effect was still detectable during the 10 min post- stimulation period. Three-way interaction was not ssignificant for GABA and NAA between stimulation conditions and, time points, however, sex and sex-specific variations were observed in GABA and NAA metabolites.

Conclusions: This concurrent tDCS-MRS study demonstrates that a single session of anodal tDCS of the left DLPFC has acute effects on Glx levels at the target site, whereas effects on GABA and NAA were not detected. Further studies should investigate sex effects in larger samples and compare the acute effects in health and disease.

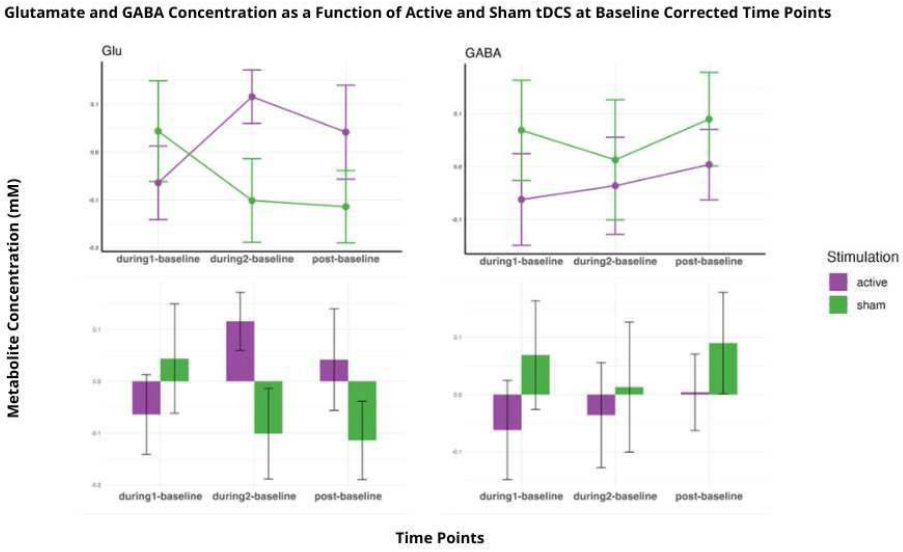

References

1. Hone-Blanchet, (2016). Online effects of transcranial direct current stimulation in real time on human prefrontal and striatal metabolites. Biological psychiatry, 80(6), 432-438.
2. Dickler, M. (2018). Online effects of transcranial direct current stimulation on prefrontal metabolites in gambling disorder. Neuropharmacology, 131, 51-57.
3. Mezger, E. (2021). Effects ofbifrontal transcranial direct current stimulation on brain glutamate levels and resting state connectivity: multimodal MRI data for the cathodal stimulation site. European archives of psychiatry and clinical neuroscience, 271(1), 111-122.
4. Friston, K. J. (1994). Statistical parametric maps in functional imaging: a general linear approach. Human brain mapping, 2(4), 189-210.

Poster No 102

Effect of left DLPFC electric field magnitude on tDCS-induced resting brain connectivity changes

Eunkyung Kim[1], Seo Jung Yun[1], Byung-Mo Oh[1], Han Gil Seo[1]

[1]Seoul National University Hospital, Seoul, Korea, Republic of

Introduction: Although transcranial direct current stimulation (tDCS) is known to be effective for modulating cortical activity, there is considerable variability in response and lack of understanding how resting state functional connectivity (rsFC) changes. The aim of this study was to investigate how variations in electrical field magnitude (E-field) applied to the target area of tDCS, which was the left dorsolateral prefrontal cortex (L-DLPFC), affect L-DLPFC-based rsFC changes in healthy adults.

Methods: A double-blind, sham-controlled, counterbalanced cross-over design was applied on 21 healthy individuals (37.6±8.6y). Participants received either constant 2 mA anodal or sham tDCS targeting the L-DLPFC during 10 min (wash-out period; at least 3 d, Mindd Stim, Ybrain, Inc, South Korea). The resting-state fMRI (3-T) was acquired before and after stimulation. The L-DLPFC was localized in each individual (Mylius et al., 2013) and E-field (V/m) was estimated. A spherical region of interest (ROI) surrounding individual peak of the L-DLPFC (radius 10 mm) was generated to construct seed-based rsFC. The subject-level regression coefficients (COPEs), representing rsFC strength, fed into a higher-level group analysis. To examine alterations in overall L-DLPFC rsFC after active and sham tDCS, average beta-estimates for both positive and negative L-DLPFC rsFC were extracted from the subject-level COPEs images within each condition. These estimates were obtained after masking the COPEs images by the thresholded connectivity map derived from all pre-stimulation conditions. Repeated measure of analysis of variance (RM-ANOVA) and paired-sample t-tests was conducted to test the significance of difference using MATLAB. To assess locally distributed L-DLPFC rsFC changes, mixed-effect analysis was conducted using FSL FLAME1, treating participants as random effects. Pairwise post-hoc comparison was also performed. The relationship between the E-field delivered to the L-DLPFC and changes in L-DLPFC rsFC was investigated. The positive connectivity map of active tDCST0 (cluster-extent based thresholding $|z| > 3.1$, FWE $p < 0.05$) revealed 9 clusters, while the negative connectivity map revealed 14 clusters. Average beta-estimates of 23 clusters were extracted from the subject-level COPEs images of both active tDCST0 and tDCST1.The difference in beta-estimates between active tDCST0 and tDCST1 was correlated with the

E-field while controlling for age, sex, and instances where subject incorrectly identified active tDCS as sham using a partial correlation analysis.

Results: There was a significant main effect of time on overall L-DLPFC positive and negative connectivity (F(1,20)=12.397, p=0.002, and F (1,20)=8.469, p=0.009, respectively) while the main effect of condition was not significant (F (1,20)=1.255, p=0.276 and F (1,20)=1.244, p=0.278, respectively). Post-hoc paired t-tests revealed that there was a significant decrease in rsFC after sham whereas the change was modest and not significant after active tDCS (Fig 1). No brain area was observed showing a significant main effect of condition but the left precuneus (x=-14, y=-48, z=58) exhibited an interaction effect, demonstrating that (active tDCST0 + sham tDCST1) > (active tDCST1 + sham tDCST0). A pairwise comparison revealed no significant difference between and within conditions. Among the 23 clusters showing significant connectivity with the L-DLPFC, changes in connectivity of the left DLPFC, left inferior parietal area, and bilateral lateral visual areas exhibited moderate and strong correlations with the E-field (Fig 2).

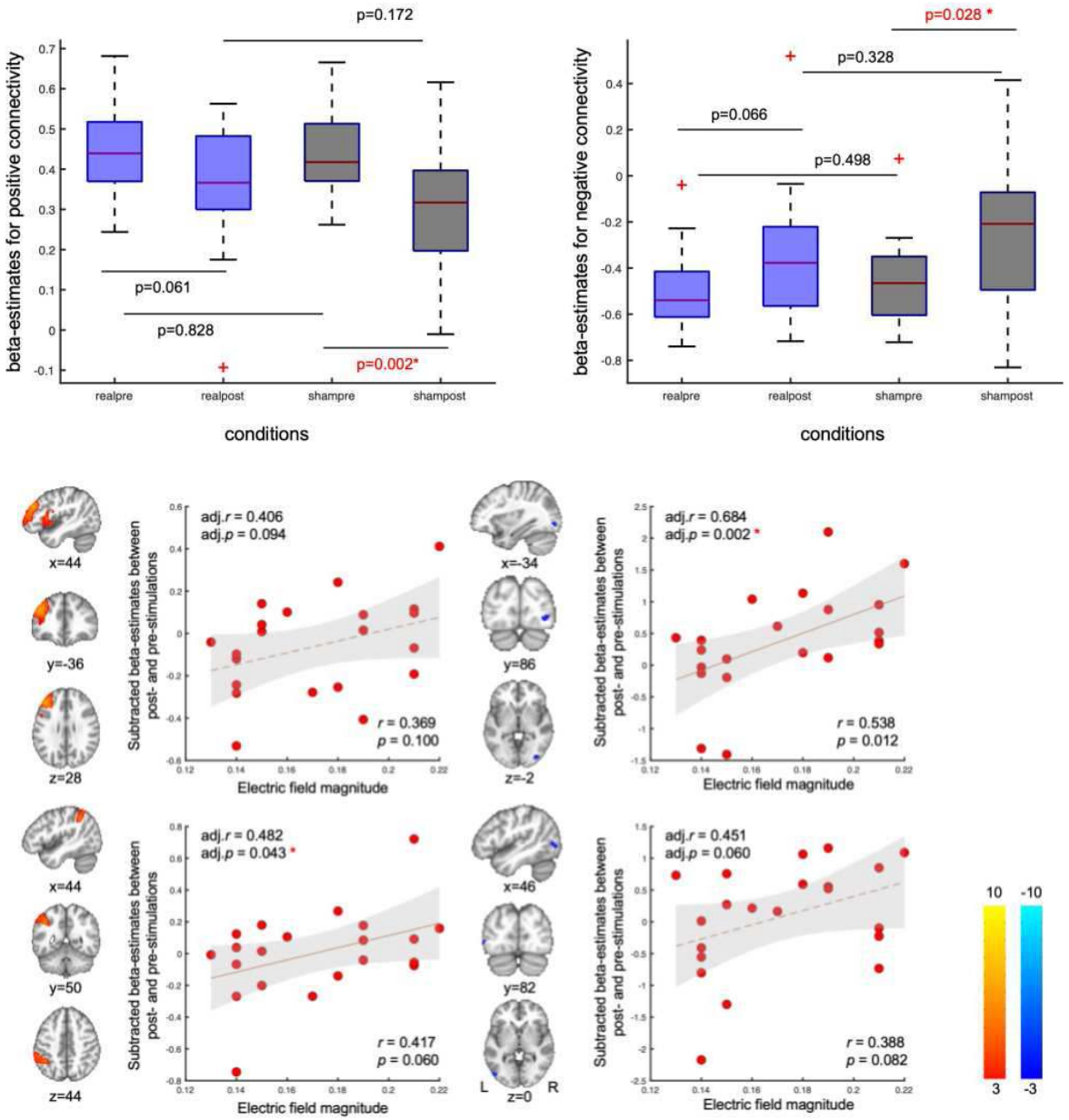

Conclusions: TDCS may help to maintain overall rsFC while sham induced reduced rsFC. The impact of single-session active tDCS was subtle to change local connectivity of L-DLPFC. Nevertheless, E-field applied on the target area is associated with changes in rsFC, observed in both proximal and distally connected brain regions with L-DLPFC. Funding: NRF-2020R1C1C1012785

References

1. Mylius, V., Ayache, S. S., Ahdab, R., Farhat, W. H., Zouari, H. G., Belke, M., Brugières, P., Wehrmann, E., Krakow, K., Timmesfeld, N., Schmidt, S., Oertel, W. H., Knake, S., & Lefaucheur, J. P. (2013). Definition of DLPFC and M1 according to anatomical landmarks for navigated brain stimulation: inter-rater reliability, accuracy, and influence of gender and age. NeuroImage, 78, 224–232.

Poster No 103

Effects of transcranial electrical stimulation on primary visual cortex using resting-state fMRI

Yangling Zhou[1], Rui Qian[1], Chengjiaao Liao[1], Huaijin Gao[1], Zhiyong Zhao[1], Minmin Wang[1], Dan Wu[1], Shaomin Zhang[2]

Zhejiang University, Hangzhou, China, [2]Qiushi Academy for Advanced Studies, Zhejiang University, Hangzhou, China

Introduction: Transcranial direct current stimulation (tDCS) has been demonstrated to be effective in the treatment of neurological and psychiatric diseases by regulating neural activities[1]. Recent evidence shows that human primary visual cortex (V1) plays a vital role in neurocognitive function[2,3], however, the impact of tDCS on the V1 remains unclear. Therefore, this study aims to investigate the effect of tDCS on V1 using resting-state functional magnetic resonance imaging (rs-fMRI).

Methods: The study included 10 healthy adults (6 males, age 22.8±1.9 years) and received approval from the IRB. Participants underwent 15 days of stimulation and a two-week follow-up. In the stimulation period, each participant received 2mA anodal tDCS for 20 minutes, targeting V1 (stimulation montage: PO3, 2 mA; FT7, -0.6 mA; CZ, -0.5 mA; Iz, -0.9 mA) with Molecular Neurological Institute coordinates (x, y, z) = (6, -63, 15) (Figure 1a), who experienced three sessions in which each one of them included MRI scanning before, during and after stimulation, respectively. In the follow-up, MRI data were collected on the 8th and 15th day respectively. The pipeline of the entire experiment is shown in Figure 1b. All MRI data were acquired on a 3.0T Siemens Prisma scanner .The rs-fMRI data were preprocessed using DPABI[4], including slice timing correction, realignment, normalization, smoothing, and filtering (0.01–0.1 Hz), and then fractional amplitude of low-frequency fluctuation[5] (fALFF) and functional connectivity[6] (FC) were calculated for each participant. Paired t-tests were conducted on fALFF and FC before and after each stimulation to explore the short-term effect of tDCS, and between the 8th, 15th, 22nd as well as 29th day and the baseline (the 1st day) to explore the long-term effects of tDCS (Figure 1b). Gaussian Random Field (GRF) theory was used to perform multiple comparison corrections on the results of the paired t-tests, with a voxel threshold of $p < 0.01$ and a cluster threshold of $p < 0.05$.

Results: The tDCS on V1 increased fALFF values in the bilateral superior frontal gyrus, middle frontal gyrus, and posterior cerebellar lobes during three short-term stimulations (Figure 1c). Long-term stimulation showed increased activity in the frontal regions on the 8th day and decreased activity in the superior parietal lobe and precuneus on the 8th and 15th day, while the occipital lobe and posterior cerebellum exhibited increased activity on the 22nd and 29th day after stimulation (Figure 1d). FC analysis revealed two recurring brain states, in which State 1 exhibited strong connectivity between the medial frontal lobe as well as posterior cingulate gyrus (default mode network, DMN) and the V1, and State 2 showed a common strong connectivity in widespread regions with the V1(Figure 2a). During 20-mintue stimulation, State 1 occurred more frequently than State 2(Figure 2b-c), and transitions from State 2 to State 1 were predominant (Figure 2d).

Conclusions: This study explored the effects of tDCS targeting V1 on resting-state brain activity. The increased fALFF in the frontal and cerebellar regions after short- and long-term stimulations suggests that electrical stimulation may exert a regulatory influence on cognitive functions[7]. The FC-based state analysis found that the brain preferred to stay in the state with strong connectivity between DMN and V1 during the stimulation. This suggests that tDCS may regulate emotional and cognitive functions[8] by modulating the DMN. Additionally, the cerebellum was significantly activated by tDCS, which was implicated in cognitive and psychological activity[9,10]. In summary, these findings contribute to the understanding of the mechanisms of tDCS on V1 and its potential for non-invasive interventions in neurological disorders and cognitive enhancement.

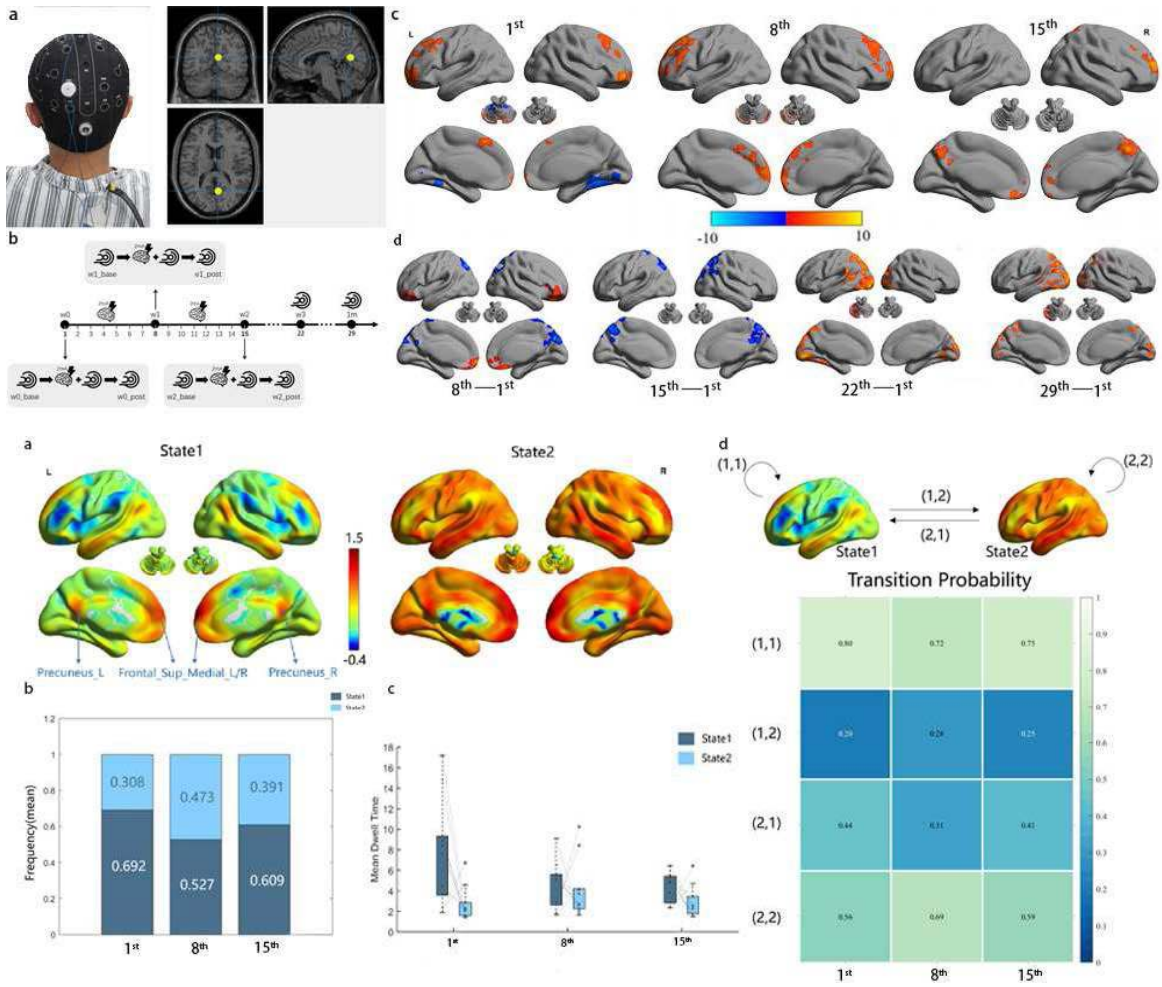

References

1. Nitsche, M.A. & Paulus, W. 2000, 'Excitability changes induced in the human motor cortex by weak transcranial direct current stimulation', The Journal of Physiology, vol. 527, no. 3, pp. 633-639, doi: 10.1111/j.1469-7793.2000.t01-1-00633.x
2. Wang, D., Tang, L., Xi, C., et al. 2023, 'Targeted visual cortex stimulation (TVCS): a novel neuro-navigated repetitive transcranial magnetic stimulation mode for improving cognitive function in bipolar disorder', Translational Psychiatry, vol. 13, no. 1, pp. 193, doi: 10.1038/s41398-023-02498-z
3. Olkoniemi, H., Hurme, M. & Railo, H. 2023, 'Neurologically Healthy Humans' Ability to Make Saccades Toward Unseen Targets', Neuroscience, vol. 513, pp. 111-125, doi: 10.1016/j.neuroscience.2023.01.014
4. Yan, C.G., Wang, X.D., Zuo, X.N. & Zang, Y.F. 2016, 'DPABI: Data Processing & Analysis for (Resting-State) Brain Imaging', Neuroinformatics, vol. 14, pp. 339-351, doi: 10.1007/s12021-016-9299-9
5. Zang, Y.F., Yong, H., Chao-Zhe, Z., et al. 2007, 'Altered baseline brain activity in children with ADHD revealed by resting-state functional MRI', Brain and Development -International Edition-, vol. 29, no. 2, pp. 83-91, doi: 10.1016/j.braindev.2006.07.002
6. Friston, K.J., Frith, C.D., Liddle, P.F., et al. 1993, 'Functional connectivity: the principal-component analysis of large (PET) data sets', Journal of Cerebral Blood Flow & Metabolism, vol. 13, no. 1, pp. 5-14, doi: 10.1038/jcbfm.1993.4
7. Chang M, Womer F Y, Gong X, et al. 2021, 'Identifying and validating subtypes within major psychiatric disorders based on frontal–posterior functional imbalance via deep learning', Molecular Psychiatry, vol. 26, no. 7, pp. 2991-3002, doi: 10.1038/s41380-020-00998-4
8. Cabral-Calderin Y, Williams K A, Opitz A, et al. 2016, 'Transcranial alternating current stimulation modulates spontaneous low frequency fluctuations as measured with fMRI', Neuroimage, vol. 141, pp. 88-107, doi: 10.1016/j.neuroimage.2016.07.013
9. Bugalho P, Correa B, Viana-Baptista M. 2006, 'Role of the cerebellum in cognitive and behavioural control: scientific basis and investigation models', Acta medica portuguesa, vol. 19, no. 3, pp. 257-267.
10. Van Overwalle F, Ma Q, Heleven E. 2020, 'The posterior crus II cerebellum is specialized for social mentalizing and emotional self-experiences: a meta-analysis', Social Cognitive and Affective Neuroscience, vol. 15, no. 9, pp. 905-928, doi: 10.1093/scan/nsaa114

Poster No 104

Effects of anodal tDCS over primary motor cortex on motor learning and brain activity

Tatsuya Miyazaki[1], Masaya Hirashima[2], Daichi Nozaki[3], Hiroshi Kadota[1]

[1]Graduate School of Engineering, Kochi University of Technology, Kami, Kochi, [2]CiNet, Advanced ICT Research Institute, NICT, Suita, Osaka, [3]Graduate School of Education, University of Tokyo, Bunkyo-ku, Tokyo

Introduction: Humans learn and improve various motor skills through repeated training in daily life. Transcranial direct current electrical stimulation (tDCS) during motor learning is a useful tool to promote and consolidate motor learning[1]. A previous study using tDCS during reaching tasks in a force field environment suggested that anodal stimulation of the primary motor cortex (M1) is involved in the acquisition of internal models[2]. However, changes in brain activity following brain stimulation have not yet been fully elucidated. Therefore, we investigated the effects of tDCS on task performance and brain activity using a reaching task in a force field environment and functional MRI (fMRI).

Methods: Thirty-two healthy right-handed adults (18–27 years old, 10 women) participated in this study. Four participants were excluded from the analysis because of poor image quality. This study was approved by the Ethics Committee of Kochi University of Technology. The participants manipulated the robotic device using right-wrist movements to move a cursor and perform a reaching task. Each set consisted of 60 trials and 10 sets were conducted. This experiment was divided into four segments: base segment (1 set), learning segment (3 sets), washout segment (3 sets), and recall segment (3 sets). Participants were trained in a velocity-dependent clockwise force field in the learning and recall segments. We acquired fMRI data for all segments. The tDCS was applied three times for each set in the learning segment (tDCS group, 14 participants) or not applied (sham group, 14 participants). The center of the anode was placed over the left M1, and the center of the reference electrode was placed over the right supraorbital area. The reaching error as task performance was analyzed by calculating the vertical distance from the line connecting the start and target at the cursor's maximum speed. We averaged the reaching error as a block of 10 trials and compared it between the tDCS and sham groups. Analyses of fMRI data were performed using SPM12. Brain activity was assessed by comparing the tDCS and sham groups in each segment.

Results: The reaching error was significantly smaller in the late learning segment (block 13–18) and late recall segments (block 13), and significantly larger in the early washout segment (block 2–5) in the tDCS group than in the sham group. In a group comparison of brain activity, the caudate nucleus was activated during learning, washout and recall segments in the tDCS group than in the sham group after small-volume correction.

Conclusions: Using anodal tDCS on the M1 during force field adaptation facilitates and retains adaptation, with the involvement of the caudate nucleus being crucial for this outcome.

References

1. Ethan R. Buch et al. (2017), 'Effects of tDCS on motor learning and memory formation: A consensus and critical position paper', Clinical Neurophysiology, vol. 128, no. 4, pp. 589-603.
2. Timothy Hunter et al. (2009), 'Modulation of internal model formation during force field-induced motor learning by anodal transcranial direct current stimulation of primary motor cortex', The Journal of Physiology, vol. 587, no. 12, pp. 2949-2961.

Poster No 105

Comparison of Personalised Dosage Between HD-tDCS and Conventional tDCS

Irtisha Chakraborty[1], Rajan Kashyap[2], S. Sreeraj[3], Faheem Arshad[4], B.K. Yamini[5], Rose Bharath[2], P. T. Sivakumar[3], Suvarna Alladi[4], Ganesan Venkatsubramanian[3], T N Sathyaprabha[1], Kaviraja Udupa[1], Sagarika Bhattacharjee[1]

[1]Department of Neurophysiology, NIMHANS, Bengaluru, Karnataka, [2]Department of Neuroimaging and Interventional Radiology, NIMHANS, Bengaluru, Karnataka, [3]Department of Psychiatry, NIMHANS, Bengaluru, Karnataka, [4]Department of Neurology, NIMHANS, Bengaluru, Karnataka, [5]Speech Pathology and Audiology Department, NIMHANS, Bengaluru, Karnataka

Introduction: The variability in the effects of transcranial Direct Current Stimulation (tDCS) is seen due to the inter-individual differences in brain anatomy causing variability in the current intensity reaching the Region of Interest (ROI). Evans et al. showed that variability in current intensity within the ROI can be reduced by varying the dose (amount of current applied to the scalp) from outside the brain[3]. It is known that current intensity at target ROI also depends on montage configurations like conventional (1x1) and high-definition (HD) tDCS (4x1) as HD-tDCS is thought to be more focal[1]. The present study investigates the variability in the personalised dose needed to obtain a constant intensity at the target ROI across individuals for both HD-tDCS and Conventional tDCS. This will be investigated in dementia patients, known to have severely atrophied brains, compared against a control major depressive disorder group expected to have relatively lesser brain atrophy.

Methods: T1 weighted MRI images of 125 subjects (78 Dementia and 47 Depression), were used to simulate 2 language pathway montages (dorsal CP5_Cz and ventral TP7_Nape of the neck)[2] using 2 montage configurations (Conventional and HD electrode) and 2mA input current through ROAST software. ROAST final output gives electric field distribution for both montages[4]. ROAST output i-SATA (MNI) software[5] estimates Average Current Density (ACD) across individual cortical lobes and gyri in two ROIs for each dorsal [Inferior parietal lobule (IPL) and angular gyrus (AG)] and ventral [middle temporal gyrus

(MTG) and inferior temporal gyrus (ITG)] pathways of language (Figure 1). Using ACD data, we calculate the required dose (RD) for conventional and HD-tDCS by following formulae.[3,5] Required Dose= 2/(simulated current at ROI)× Desired intensity at ROI The desired intensity at the target ROI was determined as the intensity obtained at the same ROI after simulating MNI brain with 2 mA as the current dose. DTDI (Dose-target determination index) measured the probability of target ROI receiving the maximum current, was calculated by following formulae[5] DTDI=(ACD at the target ROI)/(Maximum value of ACD formed at any ROI) A DTDI value of 1 show that the maximum stimulation intensity (ACD) is generated at the target ROI. However, the peak intensity may be received at non-targeted ROI, resulting in a DTDI value <1. A DTDI value of 0 will indicate no stimulation of the target ROI. Three separate Linear regression analysis was performed to understand the relationship between the dose, ACD at ROIs and DTDI index as dependent variable and montage configuration (conventional vs HD) as the independent variable while controlling for age and sex.

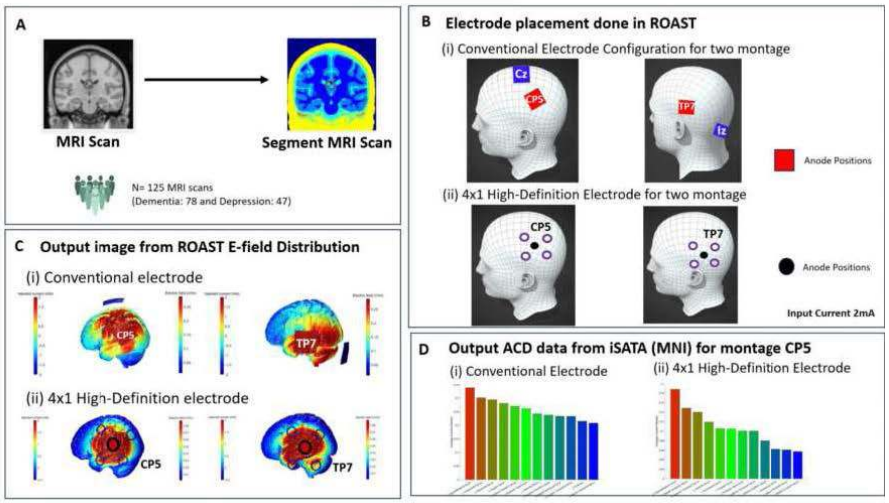

Fig 1: Modelling pipeline for dose estimation using E-field distribution and ACD. Steps A-C are automated in ROASTv3.0 to generate E-filed Distribution. Step D is automated in iSATA (MNI) to generate ACD: (A) Using structural MRI scan segmentations done in SPM12 run by ROAST. (B) Anodal electrodes for Conventional (RED) and HD-tDCS (BLACK) are placed at CP5 and TP7. (C) ROAST solves E-field distribution. (D) iSATA (MNI) use E-field output from ROAST to estimate ACD at individual cortical lobes and gyri.

Results: For all 4 target ROIs in both the groups (dementia and depression), the ACD at ROI was significantly higher for conventional tDCS than HD-tDCS. For the dementia group, the dorsal and ventral pathway ROIs needed significantly lesser doses for conventional tDCS than HD tDCS. However, such a difference in the dosage requirement was seen only for dorsal pathway ROIs in the control depression group. The DTDI values were almost similar between the two montage configurations in both the groups, except IPL(both dementia and depression) and AG (only dementia) ROIs showed a higher probability of reaching peak current for conventional montage (Figure 2).

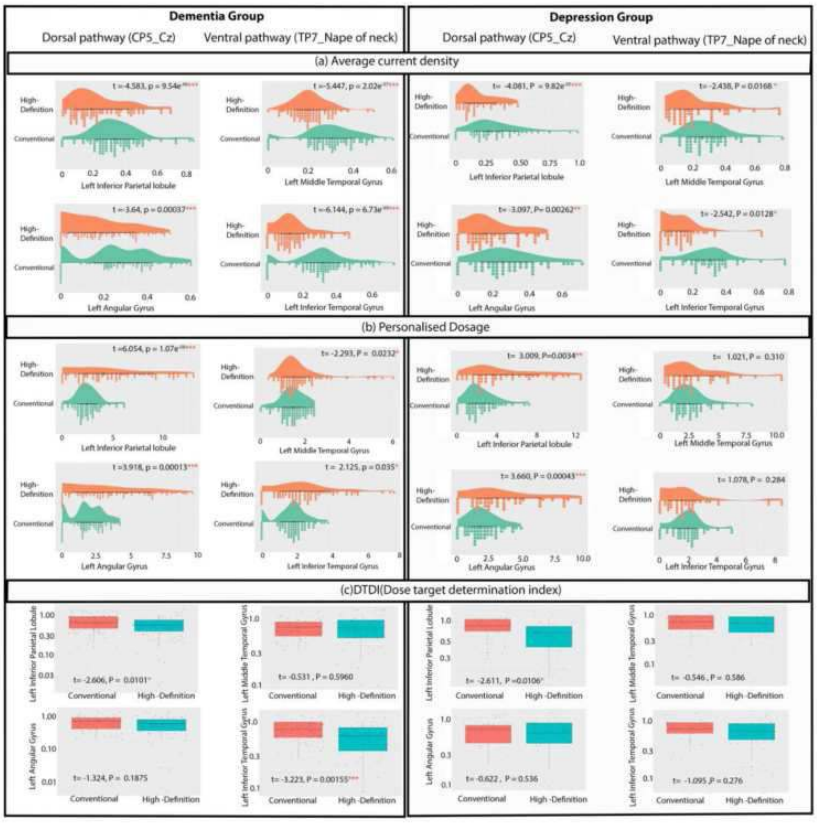

Figure 2: The comparison of (a) average current density, (b) personalised dosage, and (c) DTDI (Dose target determination index) between high definition and conventional montages for two target regions each for dorsal (Left inferior parietal lobule and Left Angular gurus) and ventral (Left middle and inferior temporal lobes) pathways of language.

Conclusions: We found that significantly higher ACD is received at the target ROI for conventional montage than HD-tDCS, consistent across different ROIs and disease groups. However, depending on the disease population (with varying degrees of atrophy), conventional tDCS requires a lower individual current dose (within the maximum tolerable dosage of 4mA) outside the scalp to generate a consistent current intensity at the target ROI across individuals. However, the probability of hitting the target region with peak current remains unchanged, irrespective of the montage configuration.

References

1. Alam, M. (2016). 'Spatial and polarity precision of concentric high-definition transcranial direct current stimulation (HD-tDCS)', Physics in Medicine & Biology, 61(12), 4506.
2. Bhattacharjee, S.(2019). 'Simulation analyses of tDCS montages for the investigation of dorsal and ventral pathways', Scientific reports, 9(1), 12178.
3. Evans, C. (2020). 'Dose-controlled tDCS reduces electric field intensity variability at a cortical target site', Brain stimulation, 13(1), 125-136.4.
4. Huang, Y. (2019). 'Realistic volumetric-approach to simulate transcranial electric stimulation—ROAST—a fully automated open-source pipeline', Journal of neural engineering, 16(5), 056006.
5. Kashyap, R.(2021). 'Focality-oriented selection of current dose for transcranial direct current stimulation', Journal of Personalized Medicine, 11(9), 940.

Poster No 106

Radiomics-informed Brain Age for Predicting Treatment Response of rTMS in Neurocognitive Disorder

Hanna LU[1], Sandra Sau Man Chan[1], Suk Ling Ma[1], Arthur DP Mak[2], Linda Chiu Wa Lam[1]

[1]The Chinese University of Hong Kong, Hong Kong, Hong Kong, [2]University of Cambridge, London, United Kingdom

Introduction: One major clinical challenge of repetitive transcranial magnetic stimulation (rTMS) is that the treatment responses to rTMS exhibited high individual variations. Anatomical factors that may contribute to the heterogeneity in rTMS effects on depression and cognition, and rTMS-induced neuroplastic changes, are less investigated.

Methods: Fifty-five older patients (aged 65 years or over) with co-occurring depression and cognitive impairments were randomly assigned to receive either active or sham rTMS on left dorsolateral prefrontal cortex (DLPFC). Individual's brain age was calculated with morphometric features using support vector machine (SVM). Brain-predicted age difference (brain-PAD) was computed as the difference between estimated brain age and chronological age. The changes of motor threshold (MT) and brain-derived neurotrophic factor (BDNF) were used to evaluate the neuroplasticity.

Results: The rTMS responders and remitters had younger brain age. Every additional year of brain-PAD at baseline decreased the odds of the relief of depressive symptoms by ~25.7% in responders (Odd ratio [OR] = 0.743, Nagelkerke R2 = 0.392, p = 0.045) and by ~39.5% in remitters (OR = 0.605, Nagelkerke R2 = 0.606, p = 0.022) at 3rd week in active rTMS group. Using brain-PAD as feature, responder-nonresponder classification accuracies of 85% (3rd week) and 84% (12th week), respectively were achieved.

Conclusions: Pre-treatment brain age matrices by macro-level morphometric features in patients with neurocognitive disorders, may be relevant to inter-individual variability in treatment responses to rTMS treatment.

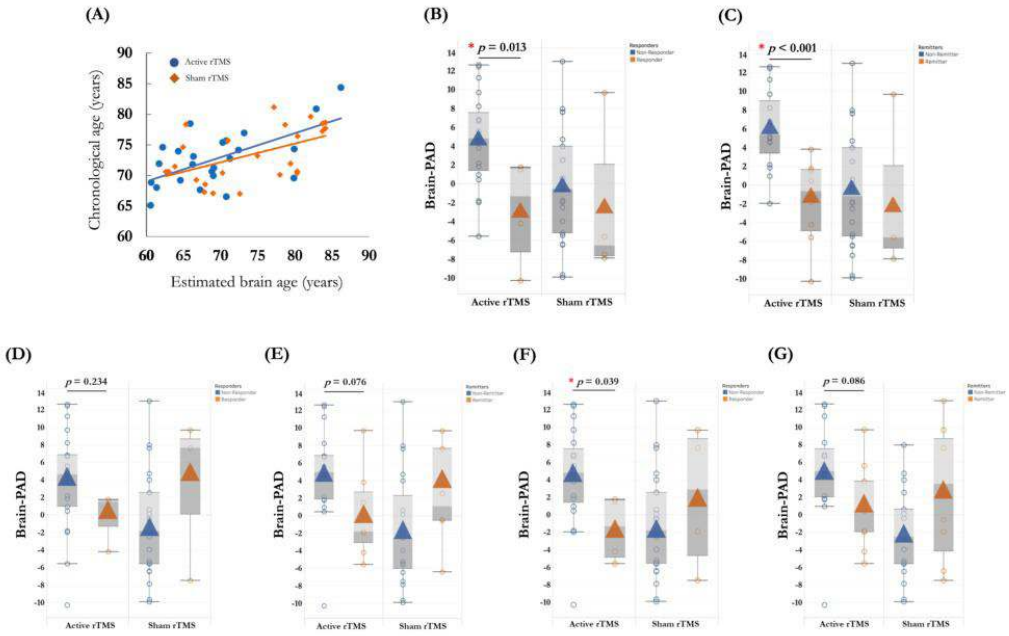

References

1. Polanía, R., Nitsche, M. A., & Ruff, C. C. (2018). Studying and modifying brain function with non-invasive brain stimulation. Nature neuroscience, 21(2), 174-187.
2. Lu, H., Chan, S. S. M., Ma, S., Lin, C., Mok, V. C. T., Shi, L., Wang, D., Mak, A. D. P., & Lam, L. C. W. (2022). Clinical and radiomic features for predicting the treatment response of repetitive transcranial magnetic stimulation in major neurocognitive disorder: Results from a randomized controlled trial. Human Brain Mapping, 43(18), 5579-5592.
3. de Lange, A. M. G., Anatürk, M., Rokicki, J., Han, L. K., Franke, K., Alnæs, D., Ebmeier, K. P.,
4. Draganski, B., Kaufmann, T., Westlye, L. T., Hahn, T., & Cole, J. H. (2022). Mind the gap: Performance metric evaluation in brain-age prediction. Human Brain Mapping, 43(10), 3113-3129.

Poster No 107

TMS Modulation of Sensory-Evoked Neural Activity in Autistic Adults with Sensory Over-Responsivity

Amy Than[1], Melis Cakar[1], Akila Kadambi[1], Elizabeth Matsiyevskiy[1], Sapna Ramappa[2], Megan Banchik[1], Apurva Chaturvedi[1], Urvi Shah[1], Emily Wood[1], Mirella Dapretto[1], Marco Iacoboni[1], Shulamite Green[1]

[1]University of California, Los Angeles, Los Angeles, CA, [2]University of California, San Francisco, San Francisco, CA

Introduction: Autism Spectrum Disorder (ASD) is a neurodevelopmental disorder marked by challenges with social communication, language, and repetitive behaviors as well as sensory processing. Of the sensory symptoms in ASD, sensory over-responsivity (SOR) is highly impairing and affects 50-70% of autistic individuals (Baranek et al., 2006). SOR is characterized by an aversive response to ordinary sensory stimuli and dysregulation in brain regions such as the prefrontal and sensory cortices (Schwarzlose et al., 2023; Green et al., 2017). To date, there are no pharmacological or behavioral treatments for SOR. While repetitive transcranial magnetic stimulation (rTMS) has been a promising treatment for core symptoms of ASD such as repetitive and stereotyped behaviors as well as social impairments (Barahona et.al., 2018; Gomez et.al., 2017), its effect on symptoms within the sensory domain remains unclear. This study utilized functional magnetic resonance imaging (fMRI) to investigate the effects of intermittent theta-burst stimulation (iTBS) to the left dorsolateral prefrontal cortex (dlPFC) on sensory processing in adults with ASD and SOR.

Methods: Participants were young adults, 18-24 years of age, with ASD and SOR (N=12). Task-based fMRI data were collected at two time points. The fMRI task consisted of 15-second blocks of mildly aversive tactile stimuli (scratchy cloth rubbed on participant's left arm) presented simultaneously with alternating auditory or visual stimuli, with 12.5 seconds of fixation between blocks. In the current analysis, we focused on the auditory plus tactile stimulation condition, as this joint condition has previously been shown to elicit the most atypical neural responses in autistic youth (e.g., Green et al., 2015, 2019). Six blocks of each condition were presented, for a total of 6.7 minutes. The order of stimulus conditions was counterbalanced among participants. Immediately before the second MRI session, intermittent Theta-Burst Stimulation (iTBS) was administered to the left dlPFC, which has been shown to produce NMDA receptor dependent long-lasting facilitatory effects on cortical excitability (Huang et al., 2007; Huang et al., 2005). A Figure 8, 700mm coil (Magstim Rapid2) was used with an intensity of 80% active motor threshold. A total of 600 pulses was delivered in 20 two-second on and 8-second off cycles. Statistical analyses were conducted using the general linear model (GLM) implemented in FSL.

Results: During joint auditory and tactile stimulation, excitatory TMS administration elicited greater neural activity in occipital fusiform gyrus and inferior lateral occipital cortex compared to baseline (Figure 1, left). Additionally, excitatory TMS administration diminished neural activity in the postcentral gyrus/supramarginal gyrus/operculum (Figure 1, right), compared to baseline.

Figure 1. Sensory-evoked neural activity

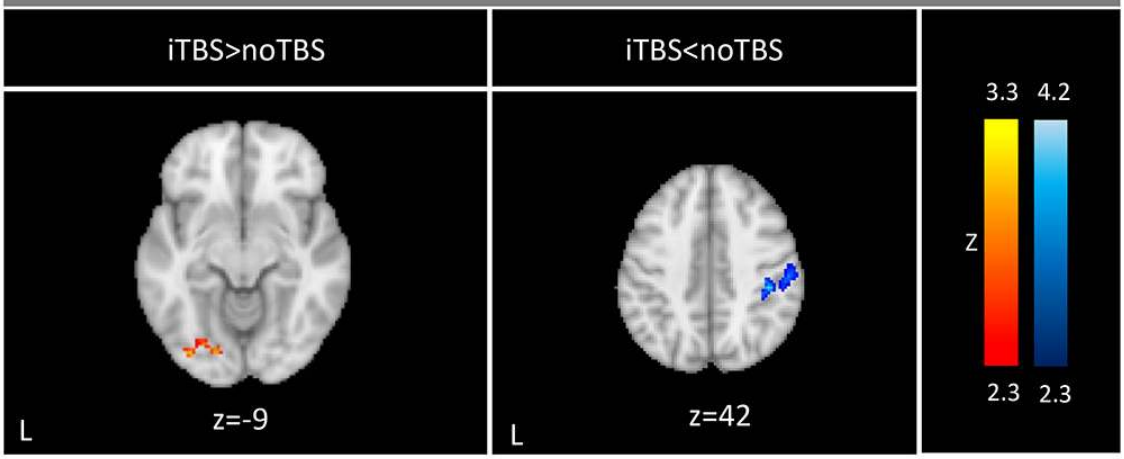

Red represents stronger and blue indicates weaker neural activity after iTBS administration compared to baseline.

Conclusions: Our results show that iTBS to the left dlPFC modulates atypical neural responses to mildly aversive stimuli in autistic adults with SOR. More specifically, iTBS to the left dlPFC downregulated neural responses in primary and higher-order somatosensory processing regions that have previously been shown to be hyperactive in individuals with ASD and SOR (Green et al. 2015, 2019). Results suggest that iTBS to the PFC, a region implicated in sensory regulation in ASD (e.g., Green et al., 2019), facilitated inhibition of sensory responses. Additionally iTBS to the left dlPFC elicited more activity in visual processing regions, indicating recruitment of task-irrelevant information possibly to disengage from aversive task-related sensory experiences. Future directions include replicating results with a larger sample. To the best of our knowledge, this is the first study to examine changes in MRI-based brain responses to aversive sensory stimuli following TMS over the dlPFC in adults with ASD. Our findings may inform future TMS intervention strategies for SOR in autistic individuals.

References

1. Barahona-Corrêa, J.B. (2018), "Repetitive Transcranial Magnetic Stimulation for Treatment of Autism Spectrum Disorder: A Systematic Review and Meta-Analysis." Frontiers in Integrative Neuroscience 12:27

2. Baranek, G.T. (2006), “Sensory Experiences Questionnaire: Discriminating Sensory Features in Young Children with Autism, Developmental Delays, and Typical Development.” J Child Psychol Psychiatry 47(6):591-601
3. Green, S.A. (2013), “Overreactive Brain Responses to Sensory Stimuli in Youth with Autism Spectrum Disorders.” Journal of the American Academy of Child and Adolescent Psychiatry 52(11): 1158–72
4. Green, S.A. (2015), “Neurobiology of Sensory Overresponsivity in Youth with Autism Spectrum Disorders.” JAMA Psychiatry 72(8): 778–86
5. Green, S.A. (2019), “Distinct Patterns of Neural Habituation and Generalization in Children and Adolescents With Autism With Low and High Sensory Overresponsivity.” Am J Psychiatry 176: 1010–20
6. Huang, Y.Z. (2005), “Theta Burst Stimulation of the Human Motor Cortex.” Neuron 45(2): 201–6.
7. Huang, Y.Z. (2007), “The After-Effect of Human Theta Burst Stimulation Is NMDA Receptor Dependent.” Clinical Neurophysiology 118(5): 1028–32.
8. Schwarzlose, R.F. (2023), “Sensory Over-Responsivity: A Feature of Childhood Psychiatric Illness Associated With Altered Functional Connectivity of Sensory Networks.” Biological Psychiatry 93(1): 92–101

Poster No 108

Non-Invasive Mapping Predicts Language Outcomes after Eloquent Tumor Resection

Matthew Muir[1], Kyle Noll[1], Hayley Michener[1], Sarah Prinsloo[1], Sujit Prabhu[1]

[1]MD Anderson Cancer Center, Houston, TX

Introduction: Glioma patients undergoing surgery in eloquent regions consistently sustain permanent postoperative language deficits that decrease both quality of life and survival. The origins of these poor outcomes remain unknown. Despite the advent of intraoperative mapping techniques, subjective judgements frequently determine important surgical decisions. Transcranial magnetic stimulation (TMS) has recently emerged as a promising non-invasive, preoperative language mapping technique. We aim to elucidate the determinants of aphasic surgical deficits by building an individualized predictive model based on TMS, routinely acquired preoperative imaging data, and the resection volume. The results shed light on the structure and function of large-scale language networks in glioma patients and lead to a clinical imaging approach for predicting and avoiding postoperative aphasic decline.

Methods: This retrospective study included 79 consecutive patients who underwent preoperative TMS language mapping and subsequent awake craniotomy for the resection of language eloquent gliomas. We used a deformable registration algorithm to co-register the postoperative MRI with the preoperative MRI containing functional and structural imaging features. We correlated the resection versus preservation of regions identified by preoperative reconstructions with pre to postoperative changes in the Western Aphasia Battery. We used TMS points as a collective seed for fiber tracking. We used a fractional anisotropic threshold selection approach standardized to the individual profile of each patient (25%, 50%, 75%, and 85%). We normalized the resected portion of the tracts to MNI space and analyzed their relationship with normative white matter tracts (7 language associated tracts: AF, SLF, IFOF, ILF, MdLF, FAT, UF) from the Human Connectome Project. We used binary logistic regression and confusion matrix elements to evaluate the predictive value of each model. We determined 1 versus 0 predictions if the region identified by the cortical or subcortical reconstruction was resected or not. We determined 1 versus 0 outcomes based on the language status of the patient at 1-2 months postoperatively (aphasia was counted as a 1).

Results: While the resection of TMS points alone did not significantly predict postoperative outcome (OR=2.8, p=.15), the resection of TMS points with robust subcortical connectivity with different fractional anisotropic profiles significantly predicted aphasic deficits at every threshold (Figure 1B: 25%-OR=6.1, p=.011; 50%- OR=5.1, p=.017; 75%- OR=8.6, p=.004; 85%- OR=5.9, p=.019). An ROC curve based on the FA threshold for different connectivity groups of TMS points showed an AUC of .72 (Figure 1A). The same ROC curve for the subcortical TMS seeded tracts showed an AUC of .89 (Figure 1C). Multivariate analysis revealed that the resection of subcortical tracts independently predicts aphasic deficits while cortical resections do not (Figure 1D). We found that true positive tract-resection volumes significantly associated with normative HCP tracts compared to false positive tract-resection volumes (Figure 2). We used these measures to preoperatively predict the functional subdomains of TMS tracts based on their interaction with HCP volumes. This improved the positive predictive value (PPV) of the resulting composite model (TMS + tracts + HCP classification) from 50% (TMS + tracts) to 89%. This final model showed an odds ratio of 155 (p<.001), PPV of 89%, negative predictive value of 95%, sensitivity of 84%, a specificity of 97%, and an accuracy of 94%.

Figure 1: Non-compensable language function localizes at the subcortical level

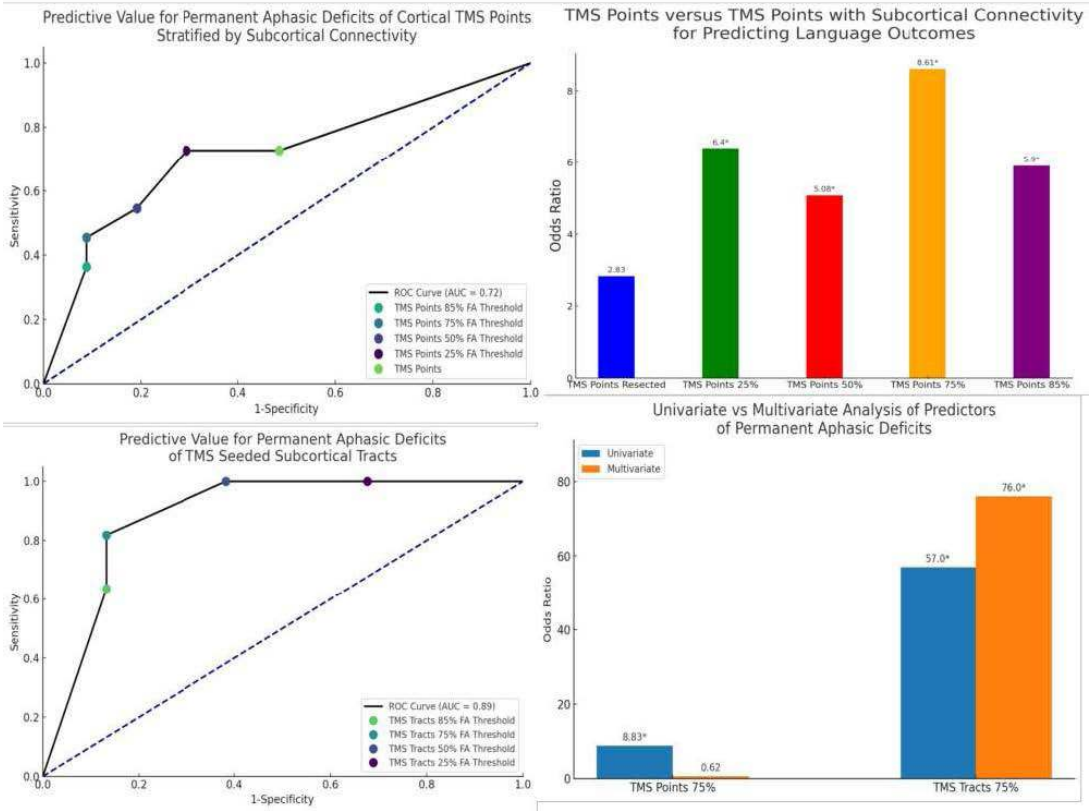

Figure 2: True positive tract resections are significantly associated with normative HCP tracts compared to false positive tract resections using three different measures: percentage overlap, volume overlap, and number of HCP tracts overlapped

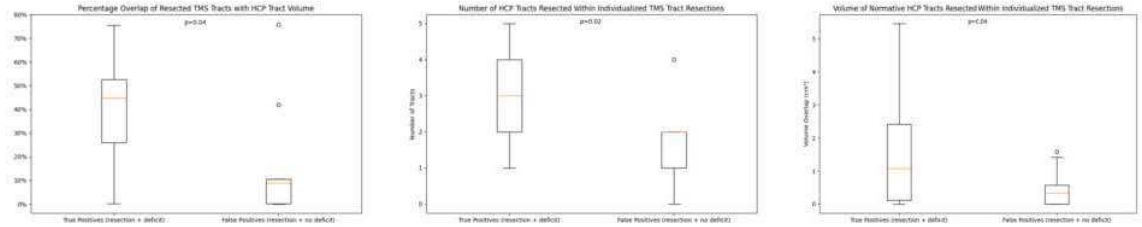

Conclusions: These results show that non-compensable language function in glioma patients localizes at the subcortical level to individualized subdomains within the normative structure of canonical white matter tracts. We integrate the findings into an actionable preoperative predictive model for permanent aphasic surgical deficits based on the resection versus preservation of regions identified by non-invasive imaging data.

References

1. Lus, T (2012) Low-grade glioma surgery in eloquent areas: volumetric analysis of extent of resection and its impact on overall survival. A single-institution experience in 190 patients: clinical article. J Neurosurg. 117(6):1039-1052.
2. Marko, NF (2014) Extent of resection of glioblastoma revisited: personalized survival modeling facilitates more accurate survival prediction and supports a maximum-safe-resection approach to surgery. J Clin Oncol. 32(8):774-782.
3. Haddad, AF (2021) Preoperative Applications of Navigated Transcranial Magnetic Stimulation. Front Neurol. 11:628903. doi: 10.3389/fneur.2020.628903. PMID: 33551983; PMCID: PMC7862711.

Poster No 109

Prefrontal rTMS Modulates Emotion Processing Circuitry

Maria Vasileiadi[1], Anna-Lisa Schuler[2], Michael Woletz[1], Sarah Grosshagauer[1], Christian Windischberger[1], Nolan Williams[3], Martin Tik[1,3]

[1]Medical University of Vienna, Vienna, Austria, [2]Max Planck Institute for Human Cognitive and Brain Sciences, Leipzig, Germany, [3]Stanford University, California, United States

Introduction: Major depressive disorder (MDD) is characterized by significant changes in brain activity during emotional processing, particularly in the left dorsolateral prefrontal cortex (DLPFC), anterior cingulate cortex (ACC), and amygdala (Jaworska et al., 2015; Simon et al., 2022). Transcranial magnetic stimulation (TMS) targeting the left DLPFC has been validated as an effective therapy for treatment-resistant MDD (Chen et al., 2023). The current study aims to explore the impact of left DLPFC-targeted TMS on emotion-processing circuits. We employ an emotion discrimination task (EDT), previously established to engage areas critical for face recognition and emotion processing (Geissberger et al., 2020; Hariri et al., 2002), within a sham-controlled experimental design.

Methods: 10 healthy volunteers (age M = 26.6, SD = 4.8) participated in the current study. The study consisted of two sessions including left DLPFC stimulation and vertex (sham) stimulation. In each session, participants first completed a run of the EDT. In each EDT trial, subjects were presented with three emotional faces, one on top and two on the bottom and were instructed to either match the PERSON or the EMOTION of the top face to one of the bottom faces. In the control condition, the object discrimination task (ODT), patients were instructed to match OBJECTS presented in the same position as the faces in the test condition on backgrounds of similar color distribution. Images were acquired on a SIEMENS Magnetom 7T whole-body MR scanner, using a 32-channel head coil with the CMRR multiband (Moeller et al., 2010) EPI sequence (TR = 1.4s, TE = 23ms, 78 slices, voxel size = 1.5x1.5x1mm3). After completion of the first EDT run, subjects were transported out of the scanner room on a MR compatible stretcher. Subsequently, stimulation was performed using a MRi-B91 TMS coil and a MagProX100 stimulator (MagVenture, Denmark). In one session, neuronavigated 10 Hz TMS was applied to a predefined left DLPFC target based on the individual functional connectivity (Fox et al., 2012) and in another session the vertex (sham) was targeted. The order of sham and real stimulation was counterbalanced across subjects. An overview of the experimental procedure can be seen in Figure 1.

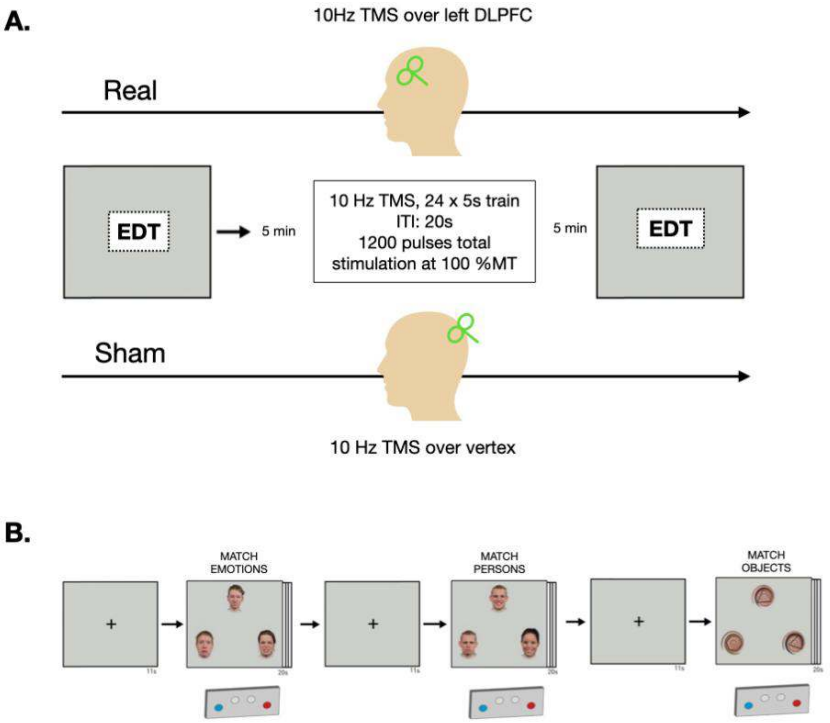

Figure 1. Experimental procedure overview. **A.** Emotion processing related brain activity was assessed with the EDT at 7T fMRI before and after TMS stimulation. Subjects underwent two sessions, receiving stimulation over the left DLPFC and over vertex (sham) in each. **B.** Flowchart depicting emotions, persons, and objects matching trials. Participants matched one of two bottom images to the top target image. Each task block lasted 20s and was followed by 11s of rest.

Results: The behavioral results indicated no significant differences in accuracy for all conditions before (M = 0.93, SD = 0.05) and after stimulation (M = 0.93, SD = 0.03). No differences in response times were observed when comparing averages before (M =1.23s, SD = 0.17) and after stimulation (M = 1.26s, SD = 0.21). The EDT revealed brain activity patterns (Figure 2A) in accordance with those described in literature (Spies et al., 2017). In the contrast of EDT and ODT, a deactivation in the anterior cingulate cortex (ACC) was observed following TMS over the left DLPFC (Figure 2B, t = 4.59, p < 0.001, FWE-corrected cluster-level). Notably, there were no observed differences in brain activity before and after sham stimulation in the comparison between EDT and ODT. Importantly, the observed effect can not be ascribed to a mere task repetition effect as we have previously established the high reliability of task activation over sessions and runs (Geissberger et al., 2020).

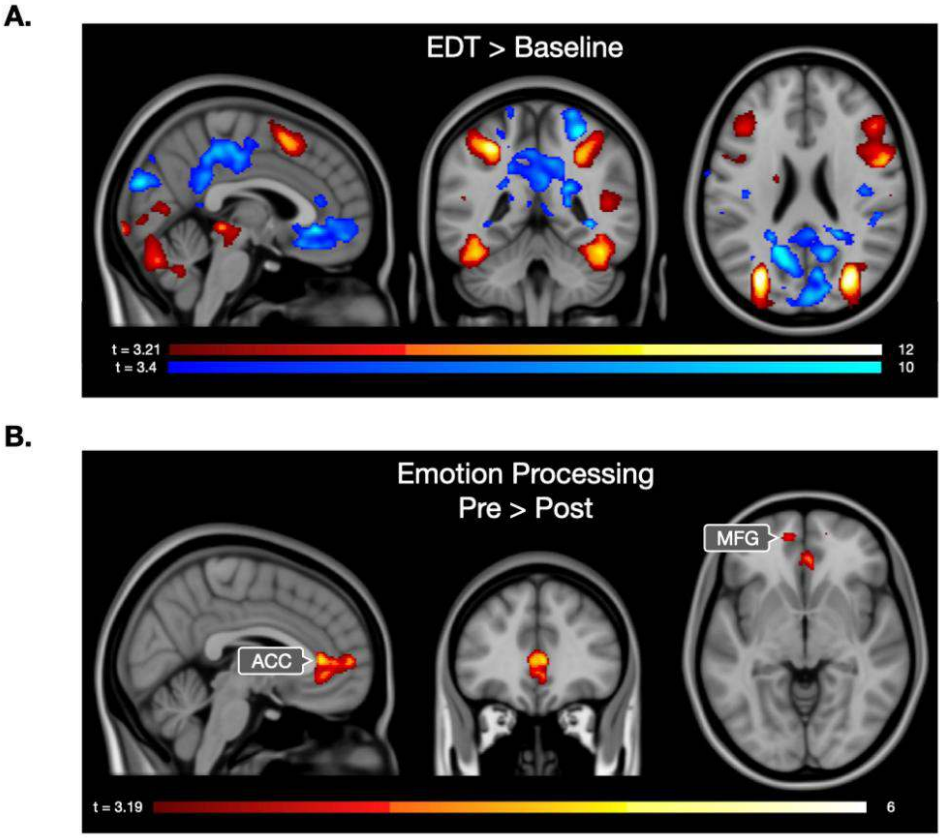

Figure 2. Emotion-processing-related brain activity assessed with the EDT and 7T fMRI. **A.** Performance of EDT resulted in activation of emotion- and face-processing regions such as the amygdala, DLPFC, fusiform gyrus and the parietal cortex and deactivation of regions involved in the DMN (Fox et al., 2005) **B.** Emotion-processing related regions are down-regulated after stimulation with TMS over the left DLPFC.

Conclusions: Here, we find evidence that stimulation over prefrontal areas modulates emotion-processing related activity in a key region of the default mode network (DMN). This aligns with the broader literature that emphasizes the significance of the subgenual anterior cingulate cortex (sgACC), a component of the DMN, in depression (Cash et al., 2019). Previous research has revealed that down-regulation of the DMN correlates with reduced depressive symptoms (Spies et al., 2017). The current observation, in a healthy subject sample, provides mechanistic evidence that more pronounced inhibition of the DMN might be a key factor in mitigating depressive states through TMS.

References

1. Cash, R. (2019). Subgenual Functional Connectivity Predicts Antidepressant Treatment Response to Transcranial Magnetic Stimulation: Independent Validation and Evaluation of Personalization. Biological Psychiatry, 86. https://doi.org/10.1016/j.biopsych.2018.12.002
2. Chen, L. (2023). Accelerated Repetitive Transcranial Magnetic Stimulation to Treat Major Depression: The Past, Present, and Future. Harvard Review of Psychiatry, 31(3), 142. https://doi.org/10.1097/HRP.0000000000000364
3. Fox, M. D. (2005). The human brain is intrinsically organized into dynamic, anticorrelated functional networks. Proceedings of the National Academy of Sciences, 102(27), 9673-9678.
4. Fox, M. D. (2012). Efficacy of Transcranial Magnetic Stimulation Targets for Depression Is Related to Intrinsic Functional Connectivity with the Subgenual Cingulate. Biological Psychiatry, 72(7), 595–603. https://doi.org/10.1016/j.biopsych.2012.04.028
5. Geissberger, N. (2020). Reproducibility of amygdala activation in facial emotion processing at 7T. NeuroImage, 211, 116585. https://doi.org/10.1016/j.neuroimage.2020.116585
6. Jaworska, N. (2015). A review of fMRI studies during visual emotive processing in major depressive disorder. The World Journal of Biological Psychiatry, 16(7), 448–471.

7. Moeller, S. (2010). Multiband multislice GE-EPI at 7 tesla, with 16-fold acceleration using partial parallel imaging with application to high spatial and temporal whole-brain fMRI. Magnetic Resonance in Medicine, 63(5), 1144–1153. https://doi.org/10.1002/mrm.22361
8. Simon, M. (2022). MDD patients with early life stress deactivate the frontostriatal network during facial emotion recognition paradigm: A functional MRI study. European Psychiatry, 65(S1), S78–S79.
9. Spies, M. (2017). Default mode network deactivation during emotion processing predicts early antidepressant response. Translational Psychiatry, 7(1), e1008–e1008.

Poster No 110

E-field Modelling Explains Variability in Behavioural Response to Chronometric TMS During N-back

Sarah Grosshagauer[1], Maria Vasileiadi[1], Anna-Lisa Schuler[2], Michael Woletz[1], Christian Windischberger[3], Martin Tik[4]

[1]Medical University of Vienna, Vienna, Vienna, [2]Max Planck Institute for Human Cognitive and Brain Sciences, Leipzig, Saxony, [3]Medical University of Vienna, Vienna, Austria, [4]High Field MR Center, Center for Medical Physics and Biomedical Engineering, Medical University of V, Vienna, Austria

Introduction: Transcranial Magnetic Stimulation (TMS) allows for non-invasive, transient modulation of human brain activity, affecting cognitive functions. Chronometric TMS offers a time-sensitive window into studying how brain regions contribute to behaviour during different phases of task processing. However, TMS effects are associated with high inter-individual variation (Hartwigsen et al. 2022). We performed chronometric TMS-fMRI by stimulating an individualised left dorsolateral prefrontal cortex (DLPFC) target during precisely defined timepoints of N-back task processing. While the primary focus of this study was on modulation of clinically relevant network nodes, high subject-to-subject variability in behavioural changes was identified. Thus, we aimed to evaluate whether variation in induced electric field (E-field) could explain differences in behavioural response.

Methods: We performed chronometric TMS during an N-back task[2] in 14 healthy participants (9 female/5 male, age mean±std 24±5.8 y). TMS was applied to the portion of left DLPFC most anti-correlated to subgenual anterior cingulate cortex (sgACC)[3]. Participants received 10 Hz triplets of TMS at 100% of resting motor threshold at two precisely defined timepoints (pre or post letter onset) of the task paradigm (figure 1a). For both cognitive loads (0- and 2–back), stimulation was performed on target letters as well as randomly selected non-target letters. Target letters were defined as the second letter of the 2-back pair (decoding). Additionally, participants were invited for a second measurement, where the chronometric stimulation protocol was modified: during 2-back TMS was exclusively applied during random letters and first letters of the 2-back pairs (encoding). Based on individual T1 scans and the recorded TMS coil position and orientation, E-field models were created for each participant using SimNIBS 4.0.0[4]. E-fields were transformed to MNI space and smoothed (FWHM=6 mm) to reduce effects of individual gyrification. To assess behaviour, we evaluated reaction time (RT) for two task difficulties and each timing condition separately. To account for individual variability in subject-specific reaction time, RT in TMS-blocks was divided by the average RT of the same task difficulty without TMS, resulting in a reaction time ratio (RTR). RTRs of each task/timing combination were used for voxel-wise correlation between electric fields and the behavioural covariates using SPM12. Correlation was performed within areas with mean E-field ≥ 30 V/m. Thresholds for statistical significance were defined at p<0.05.

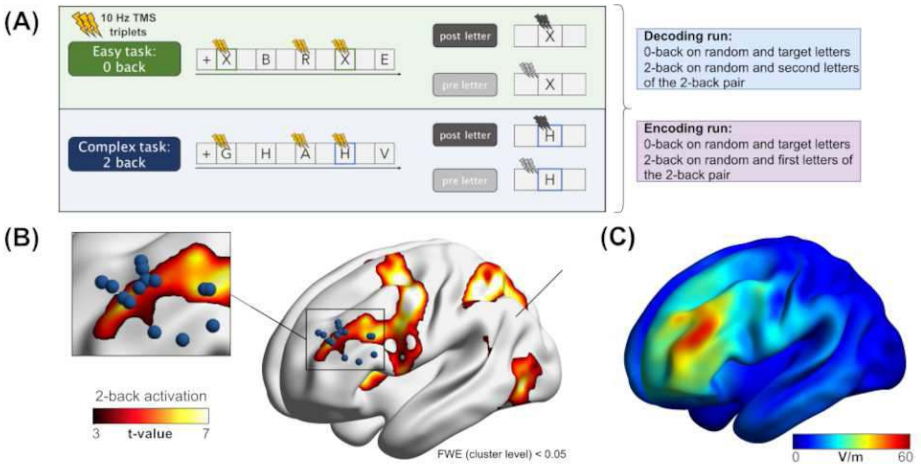

Figure 1: Assessing correlation between behavioural changes and electric fields in chronometric TMS. **(A)** shows the experimental design, TMS was performed for an easy task (0-back) and during a working memory task (2-back) with two disting timings (pre letter onset, post letter onset). **(B)** shows the individual target positions overlayed on a group level 2-back activation (p<0.05, FWEc). Based on the individual targets and electric fields, the average induced electric field is displayed in **(C)**.

Results: RTRs were statistically significantly different to one on a group level for 0-back stimulation prior to letters, i.e. TMS induced a statistically significant ($p<0.001$) group level decrease in reaction time compared to baseline (RTR<1, figure 2a). In addition, 0-back TMS post letter ($p=0.025$) and 2-back stimulation prior to letter appearance (encoding) were statistically significant at $p<0.05$. Maps showing correlation coefficients between E-field and RTR are depicted in figure 2. For the 0-back task both timings resulted in similar patterns, however, significantly different correlated clusters were identified. Interestingly, high E-fields close to the 2-back activation hotspot (peak: -40, 26, 36 [MNI]; $R=0.76$; $p<0.001$) showed positive correlation with RTR if stimulation was performed at the pre-timepoint, especially if stimulation occurred on target letters.

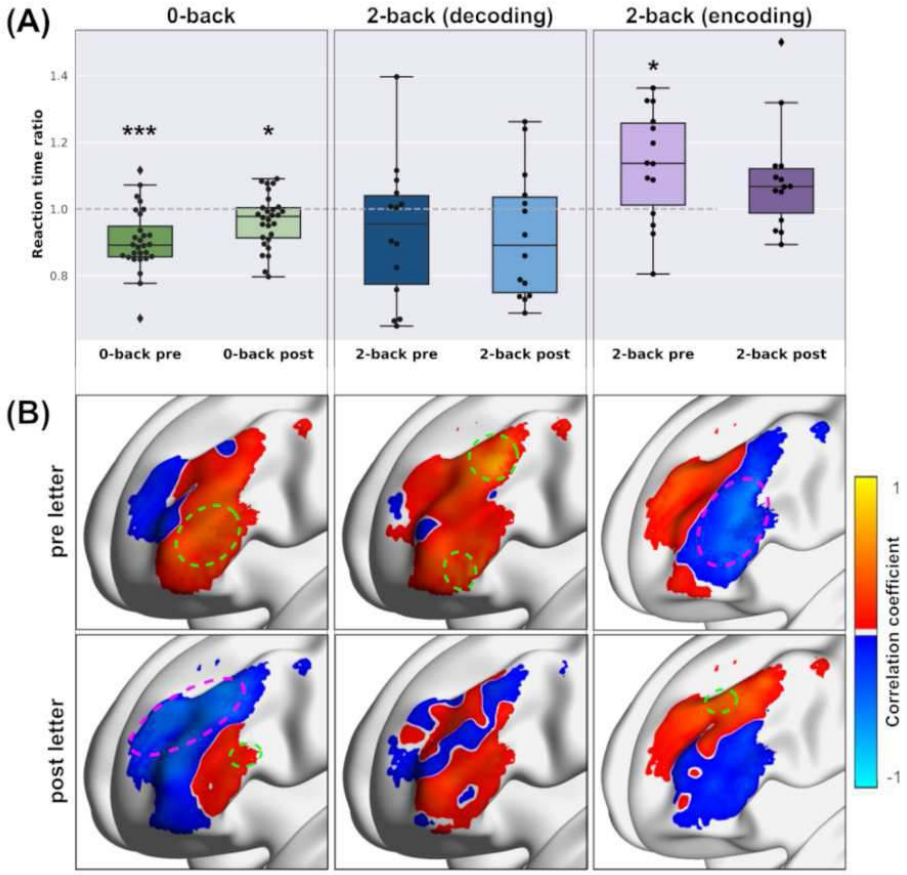

Figure 2: Changes in behaviour in terms of reaction time ratios (A) and correlation with induced electric field magnitude (B) for six different task-timing combinations of TMS. Positive correlation indicates an increase in RTR with increasing E-field, whereas negative correlation shows areas where high E-field correlates with faster responses. Pink and green outlines highlight areas which show statistically significant correlation ($p<0.05$). No significant cluster could be identified for 2-back post-letter stimulation in the decoding TMS run.

Conclusions: Correlation analysis between RTR and E-fields shows that induced E-fields contribute to inter-individual variability in behaviour. Specific timings of the same task condition resulted in different correlation maps. This indicates that TMS at different timepoints result in either enhancements or disruptions of the ongoing and subsequent neural processing. In conclusion, these results indicate distinct prefrontal subregions contributing to early vs. late phases of N-back task processing.

References

1. Fox, Michael D. (2012). "Efficacy of Transcranial Magnetic Stimulation Targets for Depression Is Related to Intrinsic Functional Connectivity with the Subgenual Cingulate." Biological Psychiatry 72 (7): 595–603. https://doi.org/10.1016/j.biopsych.2012.04.028.
2. Hartwigsen, Gesa (2022). "Noninvasive Brain Stimulation: Multiple Effects on Cognition." The Neuroscientist, July, 10738584221113806. https://doi.org/10.1177/10738584221113806.
3. Owen, Adrian M. (2005). "N-back Working Memory Paradigm: A Meta-analysis of Normative Functional Neuroimaging Studies." Human Brain Mapping 25 (1): 46–59. https://doi.org/10.1002/hbm.20131.
4. Thielscher, Axel (2015). "Field Modeling for Transcranial Magnetic Stimulation: A Useful Tool to Understand the Physiological Effects of TMS?" In 2015 37th Annual International Conference of the IEEE Engineering in Medicine and Biology Society (EMBC), 222–25. https://doi.org/10.1109/EMBC.2015.7318340.

Poster No 111

Distinct TMS-EEG profiles reflect motor homunculus variability

Negar Namdar[1], Jukka Saari[2], Sara Määttä[2], Laura Säisänen[3], Jelena Hyppönen[2], Päivi Koskenkorva[2], Elisa Kallioniemi[1]

[1]New Jersey Institute of Technology, Newark, NJ, [2]Kuopio University Hospital, Kuopio, Northern Savonia, [3]Kuopio University Hospital, University of Eastern Finland, Kuopio, Northern Savonia

Introduction: Transcranial magnetic stimulation (TMS) is a non-invasive brain stimulation technique. When electroencephalography (EEG) is used concurrently with TMS, the resulting TMS-evoked EEG potentials (TEPs) offer a means to assess the excitability, connectivity, and oscillatory patterns within the targeted cortical region (Ilmoniemi et al., 1997). So far, most motor cortex studies have focused on the hand area for two main reasons: Its low stimulation intensity, which results from its proximity to the scalp, and its easily detectable hand knob structure (Yousry et al., 1997). The reason for the limited research on other motor areas, such as the leg, arises from its deeper location in the homunculus, the challenge of targeting individual muscles, and the differences in the corticospinal tract of the upper and lower limbs (Kesar et al., 2018). On the other hand, the challenges in evaluating the cortical face and tongue representations arise from directly stimulating peripheral facial nerve fibers due to the spread of the TMS-induced electric field (Dubach et al., 2004). Consequently, TEPs have been mainly studied in the hand area, with no research available evaluating the TEPs across the homunculus. In this study, we recorded and assessed TEPs in the hand, leg, and face areas to characterize them.

Methods: Eighteen healthy volunteers (11 females, 7 males, age 46.5±17.3 years) participated in the study. First, the cortical representation areas for the right leg (tibialis anterior), hand (first dorsal interosseous), and face (mentalis) were mapped, and the resting motor threshold (rMT) of these areas was measured as the percentage of maximum stimulator output (%MSO). After that, 150 TEPs from each region were measured using single TMS pulses with a stimulation intensity of 90% rMT. TEPs were recorded with a 60-channel electrode system. The TEPs were averaged over subjects in each stimulated area in three different ROIs: left M1 (9 electrodes), right M1 (9 electrodes), and Cz (1 electrode). Artifacts in the data were removed with independent component analysis. Differences between the TEPs between different muscle groups were evaluated with a two-sample t-test ($p < 0.05$, uncorrected) calculated every 1ms.

Results: In the TEPs of the right motor area there were peaks at 16, 27, 34, 54, 80, 100, 102, 112, 117, 155, 164, 168, 180, and 182ms after the TMS for the face area; at 19, 35, 51, 64, 76, 80, 88, 98, 109, 137, 147, 162, 171, and 196ms for the leg; and at 21, 31, 53, 86, 117, 126, 132, 178, 190, and 195ms for the hand area. The TEPs differed between face and leg in the time windows 15-22ms, 178-201ms, between face and hand in windows 15-23ms, 137-156ms, and between leg and hand in windows 33-41ms, 73-99ms, 179-182ms. In the TEPs of the left motor area, there were peaks at 21, 35, 142, 145, 154, and 199ms after TMS for the face area; at 17, 31, 47, 82, 90, 107, 114, 138, 158, 162, 169, 178, and 182ms for the leg and at 34, 84, 129, and 170ms, for the hand area. The TEPs differed between face and leg in the time windows 36-53ms, 192-206ms, between face and hand in the windows 73-83ms, 198-233ms, and between leg and hand in the window 37-55ms. Lastly, the TEP results from the Cz electrode show peaks at 31, 56, 78, 92, and 182ms for the face area; at 32, 50, 57, 76, 137, and 181ms for the leg, and at 30, 50, 63, 72, 157, and 165ms for the hand area. The TEPs differed between face and leg in the time windows 73-79ms, 115-143ms, 164-195ms, and between leg and hand in the windows 29-36ms, 67-94ms, 120-150ms.

Conclusions: TEPs of the hand, face, and leg areas are different.

References

1. Amassian, V. E., Stewart, M., Quirk, G. J., & Rosenthal, J. L. (1987), 'Physiological basis of motor effects of a transient stimulus to cerebral cortex', Neurosurgery, vol. 20, no.1, pp. 74–93
2. Ilmoniemi, R. J., Virtanen, J., Ruohonen, J., Karhu, J., Aronen, H. J., Näätänen, R., & Katila, T. (1997), 'Neuronal responses to magnetic stimulation reveal cortical reactivity and connectivity', Neuroreport, vol. 8, no.16, pp. 3537–3540
3. Ilmoniemi, R. J., Ruohonen, J., & Karhu, J. (1999), 'Transcranial magnetic stimulation—A new tool for functional imaging of the brain', Critical Reviews in Biomedical Engineering, vol. 27, no. 3–5, pp. 241–284
4. Kesar, T. M., Stinear, J. W., & Wolf, S. L. (2018), 'The use of transcranial magnetic stimulation to evaluate cortical excitability of lower limb musculature: Challenges and opportunities', Restorative neurology and neuroscience, vol. 36, no. 3, pp. 333–348
5. Yousry, T. A., Schmid, U. D., Alkadhi, H., Schmidt, D., Peraud, A., Buettner, A., & Winkler, P. (1997), 'Localization of the motor hand area to a knob on the precentral gyrus. A new landmark', Brain: a journal of neurology, vol. 120, pp. 141–157

Poster No 112

Electric field optimization to improve multichannel TMS-based functional localization

Ole Numssen[1], Thomas Knösche[2], Evgenii Kim[3], Mohammad Daneshzand[4], Sergey Makarov[5], Tommy Raij[4], Aapo Nummenmaa[4], Konstantin Weise[1,6]

[1]Max Planck Institute for Human Cognitive and Brain Sciences, Leipzig, Saxony, [2]Max Planck Institute, Leipzig, Saxony, [3]Harvard University, Boston, MA, [4]Massachusetts General Hospital, Boston, MA, [5]Worcester Polytechnic Institute, Boston, MA, [6]Leipzig University of Applied Sciences, Leizig, Germany

Introduction: Transcranial magnetic stimulation (TMS) is a powerful tool for non-invasive modulation of cortical activity. In our previous work, we employed a regression approach[1] relating the local electric field strength across stimuli with motor evoked potentials (MEPs) to pinpoint muscle representations in the primary motor cortex (M1)[2]. This method relies on differences in the cortical stimulation patterns across pulses to functionally differentiate cortical areas from one another and, thus, is limited by the significant spatial autocorrelation of induced e-fields from standard TMS coils. Here, we present a strategy to utilize multi-channel TMS techniques (Fig. 1a) for TMS mapping. Specifically, we aim to minimise the cross-correlation of electric fields across TMS pulses (Fig. 1b) by optimizing the channel currents to improve the mapping resolution and shorten the experimental duration by reducing the number of TMS pulses needed.

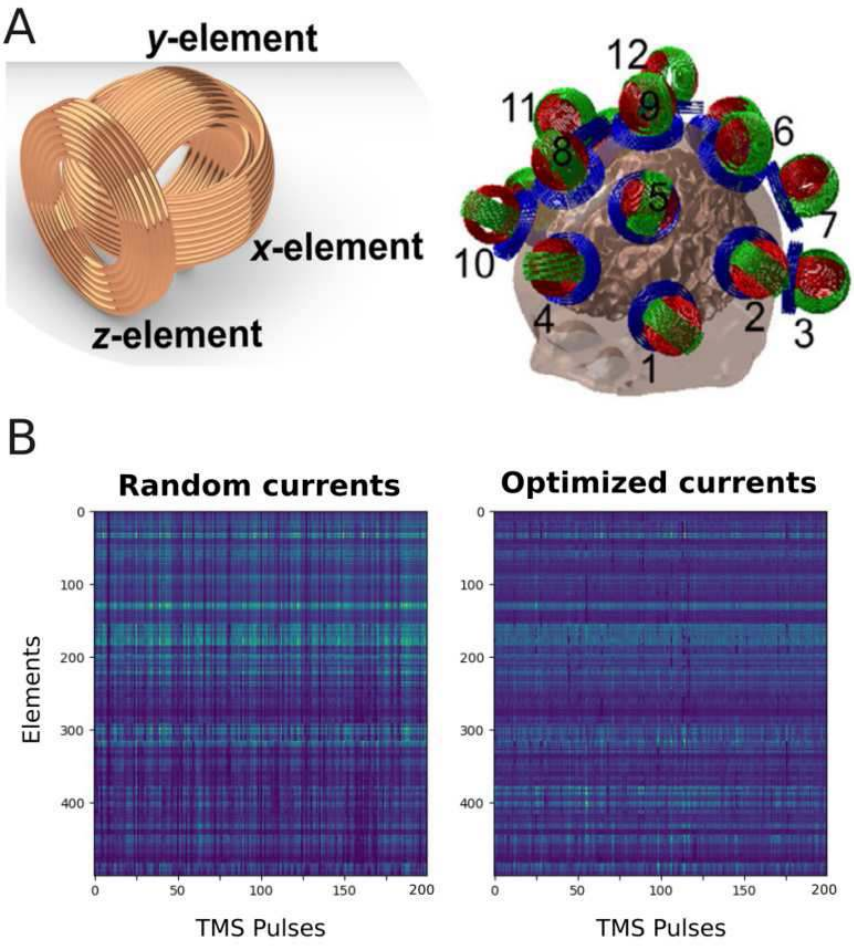

Multichannel TMS uses the combination of multiple, independent coils to yield one combined e-field. A) Exemplary 3-channel TMS coil (Figure taken from [3]). B) Realized cortical fields for 200 pulses in a region of interest with 500 elements from random intensities (left) and after current optimization (right).

Methods: For a multichannel TMS array with nc channels (e.g. Nc = 6) the induced e-field etotal is the superposition of the Nc individual e-fields[3,4]. To take the individual head and brain anatomy into account, an initial e-field computation has to be computed for all Nc channels individually at the (to be) realized coil placements with an arbitrary stimulation intensity (e.g. 1A/µS)[5,6]. Due to the computational cost of the optimization procedure, etotal (Ncomp * Nelm; Ncomp = 3 spatial components: x, y, z) is optimized only within pre-defined region of interest (ROI) with Nroi (e.g. Nroi = 10,000) elements. We employ the SLSQP

solver to determine the currents (Nchan * Npulse) for each channel that minimize the average correlation across Npulse TMS pulses. Two complementing optimization schemes solve the two major practical requirements: Pre-experimental optimization of a fixed number of pulses (1) and pulse-by-pulse optimization that includes previously realized currents (2). The optimization routine is implemented in our pyNIBS[1] Python package.

Results: Downsampling of the region of interest from Nroi elements to a spatially equidistant subset of elements Nelm (Nelm = 100 to 1000) yields a considerable speed up of the optimization procedure without significantly impeding the results (Fig. 2a - 2c). Restraining the number of optimization iterations (Niter) does impact optimization duration as well as the optimization result (Fig. 2b & 2c), as the SLSQP solver does not yield the global optimum. As expected, optimization duration strongly depends on Niter and Nelm, ranging from < 1 min for Nelm = 100 and Niter = 100 to > 1 hr for Nelm = 1000 and Niter = 500 (Fig. 2a). The optimization score only marginally improves from 200 to 500 iterations for Nelm ≥ 500 (Fig. 2c). Across all tested combinations of Nelms and Niter the optimization routine significantly decreases the correlation of the induced e-fields compared to randomly chosen currents (Fig. 2d). The computation time to optimize a fixed number of pulses ('pre-experimental optimization') grows exponentially with the number of pulses, with computation times exceeding 20 min for Nelm = 1000 for 150 TMS pulses. In contrast, pulse-by-pulse optimization yields fast current results for subsequent stimuli without reaching the levels of decorrelation from the pre-experimental optimization (Fig. 2e).

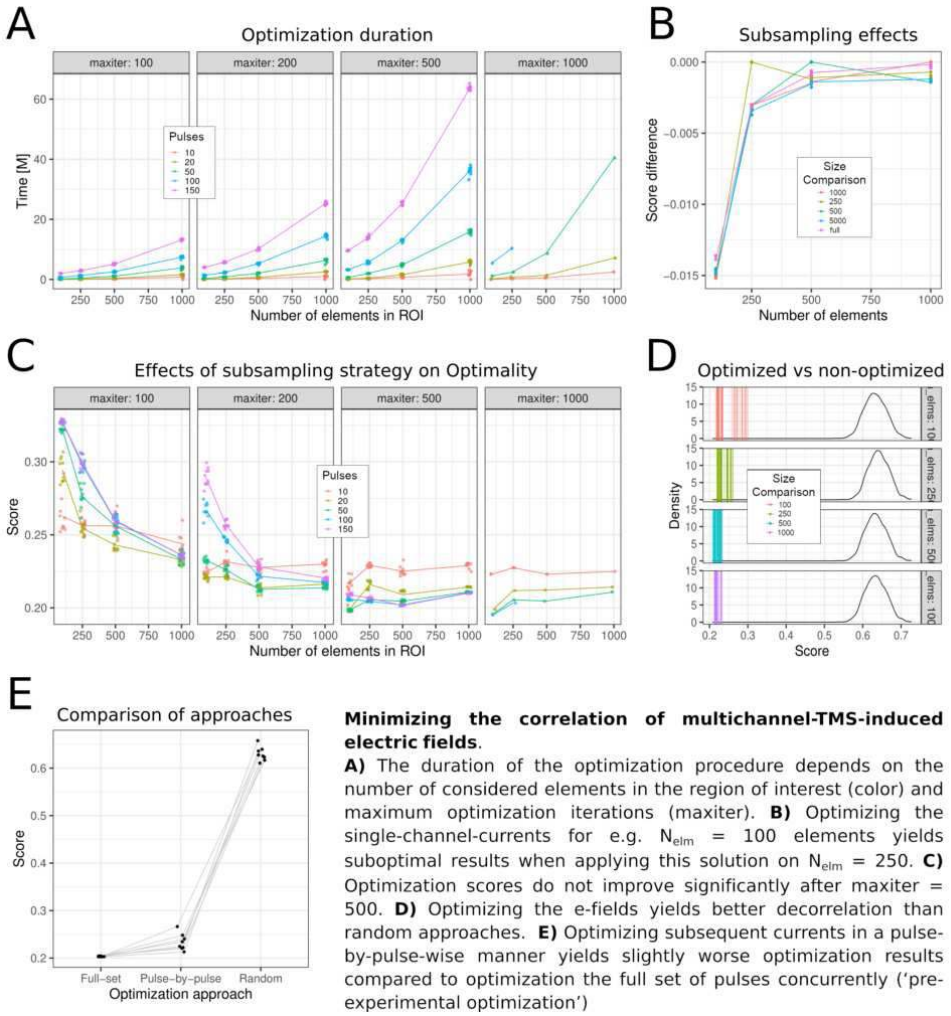

Minimizing the correlation of multichannel-TMS-induced electric fields.
A) The duration of the optimization procedure depends on the number of considered elements in the region of interest (color) and maximum optimization iterations (maxiter). **B)** Optimizing the single-channel-currents for e.g. N_{elm} = 100 elements yields suboptimal results when applying this solution on N_{elm} = 250. **C)** Optimization scores do not improve significantly after maxiter = 500. **D)** Optimizing the e-fields yields better decorrelation than random approaches. **E)** Optimizing subsequent currents in a pulse-by-pulse-wise manner yields slightly worse optimization results compared to optimization the full set of pulses concurrently ('pre-experimental optimization')

Conclusions: In summary, our routine successfully decreases the spatial autocorrelation of induced e-fields from multichannel TMS arrays across pulses by optimizing the channel currents. Reducing the computational load, by restricting the optimizer and by subsampling the cortical region of interest, allows to complete optimizations in reasonable time. Importantly, tuning these hyperparameters does not significantly impede the overall optimization goal. Increasing the across-pulse variance is a strong lever to reduce the number of TMS pulses needed to perform structure-function mappings.

References

1. Numssen O, Zier AL, Thielscher A, Hartwigsen G, Knösche TR, Weise K. Efficient high-resolution TMS mapping of the human motor cortex by nonlinear regression. Neuroimage. 2021 Dec 15;245:118654. doi: 10.1016/j.neuroimage.2021.118654. Epub 2021 Oct 12. PMID: 34653612.

2. Weise K, Numssen O, Kalloch B, Zier AL, Thielscher A, Haueisen J, Hartwigsen G, Knösche TR. Precise motor mapping with transcranial magnetic stimulation. Nat Protoc. 2023 Feb;18(2):293-318. doi: 10.1038/s41596-022-00776-6. Epub 2022 Dec 2. PMID: 36460808.
3. Navarro de Lara LI, Daneshzand M, Mascarenas A, Paulson D, Pratt K, Okada Y, Raij T, Makarov SN, Nummenmaa A. A 3-axis coil design for multichannel TMS arrays. Neuroimage. 2021 Jan 1;224:117355. doi: 10.1016/j.neuroimage.2020.117355. Epub 2020 Sep 9. PMID: 32916290; PMCID: PMC7837414.
4. Koponen, L. M., Nieminen, J. O., & Ilmoniemi, R. J. (2018). Multi-locus transcranial magnetic stimulation—theory and implementation. Brain Stimulation, 11(4), 849-855.
5. Saturnino GB, Puonti O, Nielsen JD, Antonenko D, Madsen KH, Thielscher A. SimNIBS 2.1: A Comprehensive Pipeline for Individualized Electric Field Modelling for Transcranial Brain Stimulation. 2019 Aug 28. In: Makarov S, Horner M, Noetscher G, editors. Brain and Human Body Modeling: Computational Human Modeling at EMBC 2018 [Internet]. Cham (CH): Springer; 2019. Chapter 1. PMID: 31725247.
6. Makaroff SN, Qi Z, Rachh M, Wartman WA, Weise K, Noetscher GM, Daneshzand M, Deng ZD, Greengard L, Nummenmaa AR. A fast direct solver for surface-based whole-head modeling of transcranial magnetic stimulation. Sci Rep. 2023 Oct 31;13(1):18657. doi: 10.1038/s41598-023-45602-5. PMID: 37907689; PMCID: PMC10618282.

Poster No 113

Leveraging brain network plasticity before neurosurgery: An fMRI-based prehabilitation case study

Kilian Abellaneda-Pérez[1], Leonardo Boccuni[1], Alba Roca-Ventura[1], Edgar Buloz-Osorio[1], David Leno-Colorado[1], Jesús Martín-Fernández[2], María Cabello-Toscano[3], Rubén Perellón-Alfonso[3], José Carlos Pariente[4], Carlos Laredo[4], César Garrido[4], Emma Muñoz-Moreno[4], Núria Bargalló[4], Gloria Villalba-Martínez[5], Francisco Martínez-Ricarte[6], Carlo Trompetto[7], Lucio Marinelli[7], David Bartrés-Faz[3], Alvaro Pascual-Leone[8], Jose M. Tormos[9]

[1]Institut Guttmann, Barcelona, Spain, [2]Hôpital Gui de Chauliac, Montpellier, France, [3]University of Barcelona, Barcelona, Spain, [4]Institut d'Investigacions Biomèdiques August Pi i Sunyer (IDIBAPS), Barcelona, Spain, [5]Hospital del Mar, Barcelona, Spain, [6]Vall d'Hebron Hospital, Barcelona, Spain, [7]University of Genova, Genova, Italy, [8]Harvard Medical School, Boston, MA, [9]Universidad Católica de Valencia, Valencia, Spain

Introduction: Brain tumor surgery aims to achieve maximal tumor resection while minimizing damage to healthy brain tissue to reduce post-operative functional sequelae. Invasive prehabilitation strategies before surgery have been used but pose an increased risk of complications. Recent research has highlighted the potential of brain plasticity to non-invasively establish new brain connections and transfer functional activity from one area of the brain to another. However, the neural mechanisms underlying these plastic processes are, not yet fully understood, especially in the context of space-occupying lesions.
The objective of this fMRI-based case report was twofold: first, to investigate whether brain functional patterns at risk, as evidenced by task-based fMRI, can be modified through a non-invasive prehabilitation protocol; and second, to examine the role of functional connectivity, assessed during resting-state fMRI, as a putative mechanism underlying the observed changes in brain network topography.

Methods: A 48-year-old male with a large tumor affecting multiple brain regions, particularly entailing the left frontal lobe and the frontotemporal opercular region was admitted for non-invasive prehabilitation (Fig.1A). A functional magnetic resonance imaging (fMRI) was conducted before prehabilitation to define the therapeutic plan, which involved inhibitory non-invasive brain stimulation over the language fMRI task accompanied with intensive language and cognitive training. fMRI data was also collected after prehabilitation and after surgery. Neuroimaging data was analyzed using the SPM12 and CONN Toolbox software tools.

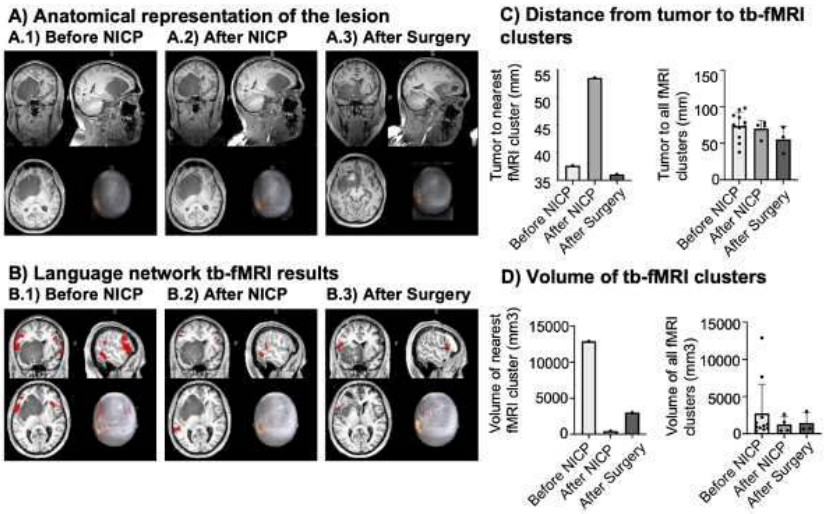

Fig. 1. Illustration of brain tumor lesion and language network tb-fMRI results. A) Anatomical representation of the tumor lesion at the three different time-points, with the center of the figure positioned around the center of masses. B) Language network tb-fMRI results at the three different time-points, with the center of the figure placed over the stimulation site. C) Distance from the tumor to tb-fMRI clusters, presenting all tb-fMRI clusters and the nearest fMRI cluster. D) Volume of tb-fMRI clusters, displaying the nearest one from the tumor and all of them.

Results: Prehabilitation resulted in an increment of the distance between the tumor and the nearest fMRI cluster during the language task by 15.9mm, returning to a similar distance as baseline after surgery (Fig.1B-C). Further, the volume of the closest activation fMRI cluster decreased after prehabilitation in 12,432 mm3 and normalized after surgery (Fig.1B-D). Besides, there was an increase in the resting-state functional connectivity between the left inferior frontal gyrus, which overlapped with the transcranial magnetic stimulation target, and the other regions of the language network (Fig.2). This pattern, which was maintained after surgery, was not observed in a control visual network.

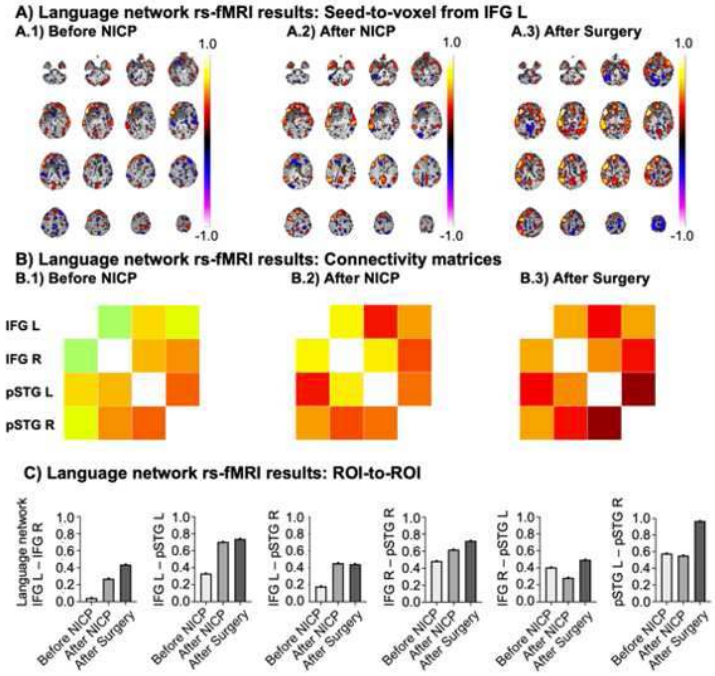

Fig. 2. Representation of the language network rs-fMRI results. A) Seed-to-voxel results displayed from the IFG L at three different time-points. The color-map represents the connectivity strength, ranging from 1 to -1. The slices are ordered along the Z-axis, ranging from -46 to 74 in increments of 8 units. B) Connectivity matrices considering the four network ROIs at the three time-points. The color-map also represents the connectivity strength, ranging from 1 to -1. ROI-to-ROI results encompassing all the network couplings at the three time-points.

Conclusions: This study investigated non-invasive prehabilitation in a brain tumor patient, revealing how externally-guided neuroplasticity can reorganize the topography of the language network before surgery, while also shedding light on its potential neural underpinnings. This fMRI-based case study exposes two key findings: firstly, prehabilitation may establish a plasticity window, thereby hypothetically optimizing surgical outcomes. Second, functional connectivity emanating from the stimulation site may amplify to other regions of the network, potentially strengthening network-specific functional pathways. While these outcomes are auspicious, prudence dictates the need for more comprehensive cohorts to authenticate and broaden these insights.

References

1. Barcia, J. (2012a). 'High-frequency cortical subdural stimulation enhanced plasticity in surgery of a tumor in Broca's area', Neuroreport vol. 23,5, pp. 304-309.
2. Barcia, J. (2012b). 'rTMS stimulation to induce plastic changes at the language motor area in a patient with a left recidivant brain tumor affecting Broca's area', Neurocase vol. 18,2, pp. 132-138.
3. Boccuni, L. (2023). 'Neuromodulation-induced prehabilitation to leverage neuroplasticity before brain tumor surgery: a single-cohort feasibility trial protocol', Frontiers in neurology vol. 14 1243857.
4. Miller, D. (2021). 'Brain and other central nervous system tumor statistics, 2021', CA: a cancer journal for clinicians vol. 71,5, pp. 381-406.
5. Rivera-Rivera, P. (2017). 'Cortical plasticity catalyzed by prehabilitation enables extensive resection of brain tumors in eloquent areas', Journal of neurosurgery vol. 126,4, pp. 1323-1333.
6. Serrano-Castro, P. (2020). 'Neuroplasticity and Epilepsy Surgery in Brain Eloquent Areas: Case Report', Frontiers in neurology vol. 11 698.
7. Whitfield-Gabrieli, S. (2012). 'Conn: a functional connectivity toolbox for correlated and anticorrelated brain networks', Brain connectivity vol. 2,3, pp. 125-141.

Poster No 114

Network meta-analysis on non-invasive brain stimulation for acute major depressive episode treatment

Ping Wang[1], Yingxue Gao[1], Shuangwei Chai[1], Jiawen Tian[1], Zilin Zhou[1], Hailong Li[1], Lianqing Zhang[1], Weijie Bao[1], Xinyue Hu[1], Yidan Wang[1], Xiaoqi Huang[1]

[1]Huaxi MR Research Center (HMRRC), Department of Radiology, West China Hospital of Sichuan University, Chengdu, China

Introduction: Major depressive disorder (MDD) is a highly prevalent illness worldwide, with more than 264 million people affected. Its clinical course is often recurrent and can become chronic, with relapse rates of up to 80% within one year of remission. Although there are effective pharmacological and psychological therapies for MDD, even with a full course of treatment, at least one third of patients fail to achieve remission. Non-invasive brain stimulation (NIBS) therapies, such as transcranial magnetic stimulation (TMS) and transcranial direct current stimulation (tDCS), offer a potential alternative or add-on treatment strategy. Previous meta-analyses provide limited insights into the overall treatment hierarchy because treatment effects are estimated from, and presented for, a subset of relevant treatment comparisons only. We sought to perform a systematic review and meta-analysis of the antidepressant efficacy and tolerability of non-invasive neuromodulation in treating current depressive episode in major depressive disorder from randomized sham-controlled trials (RCTs), to estimate the comparative clinical efficacy and acceptability of NIBS for the acute treatment of major depressive episodes in adults.

Methods: The databases PubMed, Embase, and Web of Science were searched for randomized controlled trials (RCTs) reporting on the therapeutic efficacy of transcranial magnetic stimulation (repetitive (rTMS), accelerated, priming, deep, and synchronised), theta burst stimulation (bilateral, intermittent, continuous), transcranial direct current stimulation (tDCS) for MDD compared to sham, published until October 2023. Study and sample demographic characteristics as well as all of the above non-invasive brain stimulation parameters and outcome variables were extracted. Effect sizes were calculated for change in depression score and risk ratios for response and discontinuation.

Fig 1| PRISMA flow diagram:

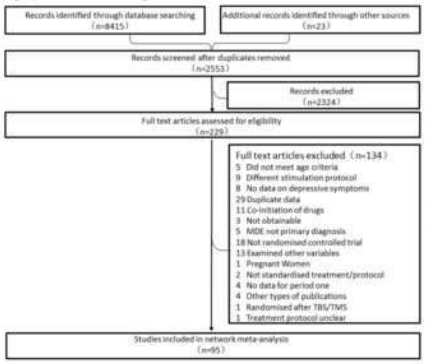

Table 1 Characteristics of Randomized Clinical Trials Included in the Network Meta-Analysis

Characteristic	Studies,No.(%)
Number of studies	95
Number of patients	5385
Sex,female% of patients	54.10%
Age,mean,y	45.6
Year of publication	
1991-2000	8(8.4)
2001-2010	35(36.8)
2011-2018	36(37.9)
2019-2023	16(16.8)
Study duration,wk	
1-6	88(94.6)
7-12	5(5.4)
Number of sessions	
5-10	44(50.6)
11-20	36(41.4)
21-30	7(8.0)

therapy			Systematic review
TMS Transcranial magnetic stimulation	Low frequency repetitive (left)	LFL rTMS	5
	High frequency repetitive (right)	HFR rTMS	1
	Deep	dTMS	3
	Accelerated	aTMS	2
	Synchronised	sTMS	2
	High frequency repetitive (left)	HFL rTMS	48
	Low frequency repetitive (right)	LFR rTMS	7
	Bilateral repetitive	BL rTMS	12
	Priming	pTMS	2
TBS Theta burst stimulation	Continuous	cTBS	1
	Intermittent	iTBS	8
	Bilateral	bITBS	4
tDCS	Transcranial direct current stimulation	tDCS	17
total			95

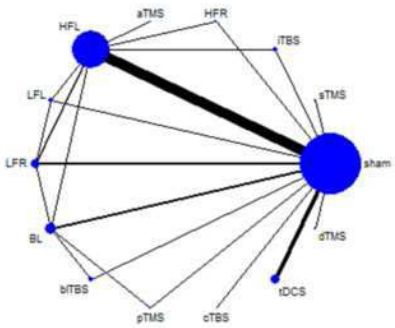

Response rate

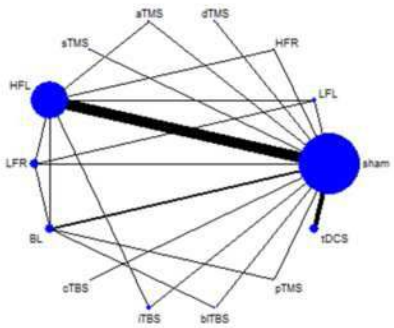

Discontinuation

Fig 2| Network plot of available treatment comparisons for response rates and discontinuation. Size of node is proportional to number of patients randomised to each treatment. Line width is proportional to number of randomised controlled trials comparing each pair of treatments. aTMS=accelerated transcranial magnetic stimulation; BL rTMS=bilateral repetitive transcranial magnetic stimulation; bITBS=bilateral theta burst stimulation; cTBS=continuous theta burst stimulation; dTMS=deep transcranial magnetic stimulation; HFL rTMS=high frequency left repetitive transcranial magnetic stimulation; HFR rTMS=high frequency right repetitive transcranial magnetic stimulation; iTBS=intermittent theta burst stimulation; LFL rTMS=low frequency left repetitive transcranial magnetic stimulation; LFR rTMS=low frequency right repetitive transcranial magnetic stimulation; pTMS=priming transcranial magnetic stimulation; SHM=sham therapy; sTMS=synchronised transcranial magnetic stimulation; tDCS=transcranial direct current stimulation

Results: 95 RCTs (202 treatment arms) that randomised 5385 patients (mean age 45.6 years; 54.1% women) with major depressive disorder met the inclusion criteria and were included in this meta-analysis. We analyzed effects on response, all-cause discontinuation rates and continuous depression severity measures. The most studied treatment comparisons were high frequency left rTMS and tDCS versus sham therapy, whereas recent studies have gradually turned to focus on cognitive function in the past five years. In network meta-analysis, 12 out of 13 treatment strategies were associated with higher response compared with sham therapy: priming transcranial magnetic stimulation (summary odds ratio 3.67, 95% confidence interval 1.19 to 11.36), bilateral theta burst stimulation (3.67, 1.43 to 9.49), low frequency right repetitive TMS (3.10, 1.73 to 5.53), bilateral TMS (3.03, 1.73 to 5.37), high frequency right repetitive TMS (2.61, 0.66 to 10.28), high frequency left repetitive TMS (2.51, 1.92 to 3.29), and synchronized TMS (2.27, 0.79 to 6.49). It's worth noting that one of the most efficacious treatment bilateral theta burst stimulation also accompanied the highest all-cause discontinuation rates, meanwhile most other treatment strategies were at least as tolerable as sham therapy.

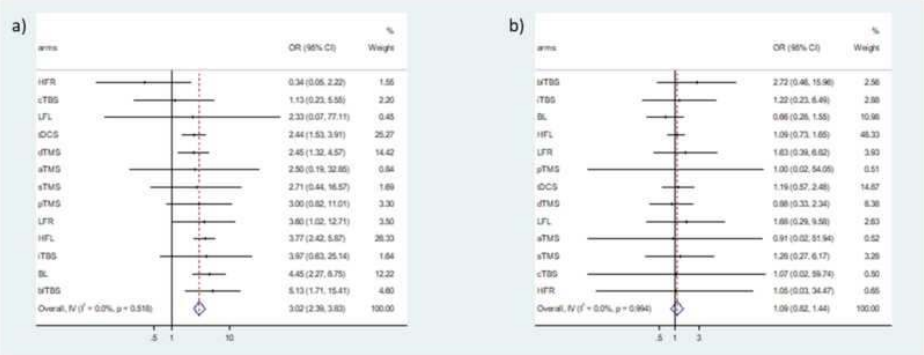

Fig 3| a) Forest plot of active versus sham treatment comparisons for response rate. b) Forest plot of active versus sham treatment comparisons for discontinuation. Effect sizes represent summary odds ratios with 95% confidence intervals and 95% prediction intervals estimates from network meta-analysis.

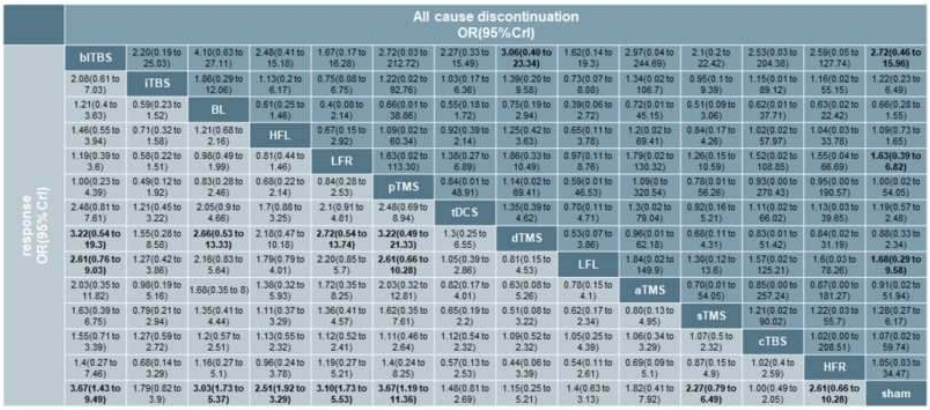

Fig 4 | Network meta-analysis of response and all cause discontinuation rates. Effect sizes represent summary odds ratios and 95% confidence intervals. For the lower triangle (response rates) and upper triangle (all cause discontinuation rates), values less than 1 favour the treatment in the corresponding row, whereas values greater than 1 favour the treatment in the corresponding column. aTMS=accelerated transcranial magnetic stimulation; BL rTMS=bilateral repetitive transcranial magnetic stimulation; bITBS=bilateral theta burst stimulation; cTBS=continuous theta burst stimulation; dTMS=deep transcranial magnetic stimulation; HFL rTMS=high frequency left repetitive transcranial magnetic stimulation; HFR rTMS=high frequency right repetitive transcranial magnetic stimulation; iTBS=intermittent theta burst stimulation; LFL rTMS=low frequency left repetitive transcranial magnetic stimulation; LFR rTMS=low frequency right repetitive transcranial magnetic stimulation; pTMS=priming transcranial magnetic stimulation; SHM=sham therapy; sTMS=synchronised transcranial magnetic stimulation; tDCS=transcranial direct current stimulation

Conclusions: As far as we know, our study is the largest and most comprehensive network meta-analysis of NIBS for MDD so far. We found that there is strong evidence for the application of non-invasive brain stimulation techniques as alternative or add-on treatments for adults with major depressive episodes. Our findings also highlight important research priorities in the specialty of brain stimulation, such as the need to conduct further randomized controlled trials for novel treatment protocols such as tDCS or pTMS, to warrant more direct comparisons between different treatment modalities, and to examine what biomarkers are available to predict cognitive response in MDD patients.

References

1. Fekadu A, Wooderson SC, Markopoulo K, et al,(2009).'What happens to patients with treatment resistant depression? A systematic review of medium to long term outcome studies'. J Affect Disord,vol.116,pp.4-11.
2. GBD 2017 Disease and Injury Incidence and Prevalence Collaborators,(2018),'Global, regional, and national incidence, prevalence, and years lived with disability for 354 diseases and injuries for 195 countries and territories, 1990–2017: a systematic analysis for the Global Burden of Disease Study 2017'. Lancet.vol.392(10159),pp.1789–858.
3. Rush AJ, Trivedi MH, Wisniewski SR, et al,(2006).'Acute and longer-term outcomes in depressed outpatients requiring one or several treatment steps: a STAR*D report'. Am J Psychiatry. Vol.163(11),pp.1905-17.
4. WHO. (2020),'Depression [Internet]. 2020. Available from: https://www.who.int/ news-room/fact-sheets/detail/depression'.

Poster No 115

TMS promotes emotional regulation in adults with high-level perceived stress

Youze He[1], Jingsong Wu[1], Xiujuan Geng[2]

[1]Fujian University of Traditional Chinese Medicine, Fuzhou, NA, [2]The Chinese University of Hong Kong, Hong Kong, NA

Introduction: The prevalence of high-level stress has been reported to be over 30% in young adults (Ramón-Arbués et al., 2021). Individuals with high-level perceived stress exhibit abhnormal activities of the dorsolateral prefrontal cortex (DLPFC), associated with low mood and anxiety symptoms (Scult et al., 2017). Repetitive transcranial magnetic resonance stimulation (rTMS) has been evidenced to be effective on modulating DLPFC functions in stress-related psychiatric disorders, such as major depression and anxiety. However, whether the modulation of DLPFC with rTMS benefits to the recovery of negative feelings in adults with high-level perceived stress remain unclear. This study aimed to explore the effect of rTMS on the recovery of stress-related symptoms and its potential neural effect on DLPFC functions.

Methods: This was a randomized controlled trial that enrolled 50 young adults aged 18-24 years old with high-level perceived stress to verify the rTMS effect on their emotional trait: depression, anxiety, and stress. Subjects were randomly assigned to the experimental group (12-session active rTMS in four weeks, thrice per week) and control group (sham rTMS with the same dose). Outcome measurements included the negative symptoms using the Depression Anxiety Stress scale (DASS) and DLPFC functional connectivity. Both the DASS and MRI data were collected before and after the intervention. We conducted the rTMS stimulation on the bilateral DLPFC using the Magstim Rapid 2 stimulator. The intermittent theta burst stimulation (TBS) model and continuous TBS model with both 600 pulses were used on the left and right sides, respectively (Wu et al., 2021). Both T1-weighted structural and resting-state functional MRI images were acquired under Siemens Prisma 3.0 Tesla scanner. The resting state fMRI data were preprocessed using DPABI version 6.0 and SPM12. The ROI-wise functional connectivity (FC) analysis was performed using the MNI coordinate of left (-27, 43, 31) and right DLPFC (30, 37, 36) with 6mm radius according to the Brainnetome atlas. The changes between baseline and post-intervention of DLPFC FC were calculated and compared using the SPM12 with the threshold: voxel P<0.005 uncorrected, cluster P<0.05 FDR corrected. Statistical analyses were conducted by an independent statistical analyst. The analysis of covariances was conducted to compare the between-group difference of outcome changes. The models included dependent variables (changes of measured outcomes), fixed factors (i.e., treatment arms), and covariance as predictors (i.e., age, gender, and years of education). Then, to examine the within-group difference of each group between baseline and end of the intervention, the paired t-test or Wilcoxon test was conducted according to data normality.

Results: Forty-eight subjects (24 in each group) were finally included after excluding two data due to over-threshold head-motion. The comparison of demographics and baseline assessments showed there was no significant group difference in age, sex, years of education, smoking, alcohol, TONI3 scores, total intracranial volume, and baseline scores of perceived stress scale and DASS (ps>0.05). There were significant decreases in DASS total scores (p<0.001), anxiety (p=0.008), and stress (p=0.002) scores in experimental groups, while only stress scores decreased in the control group (p=0.006) (see Fig. 1). There was significant between-group difference in DASS total scores (p=0.016) after controlling age, gender, and years of education. The FC between left DLPFC and left Supplementary motor area and between right DLPFC and right frontal superior medial cortex were significantly decreased after active rTMS (Voxel p<0.005 uncorrected, Cluster p<0.05 FDR corrected) (See Fig. 2).

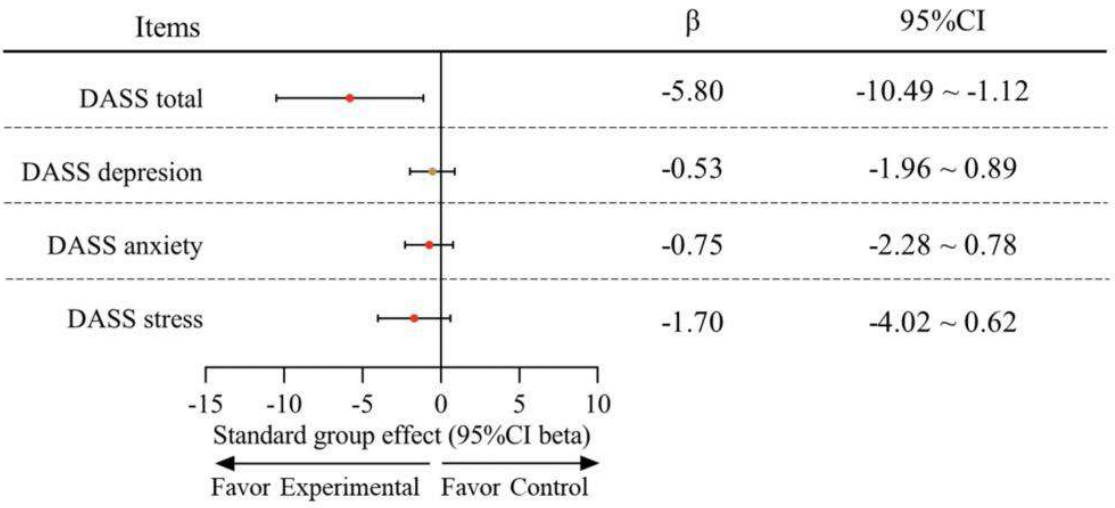

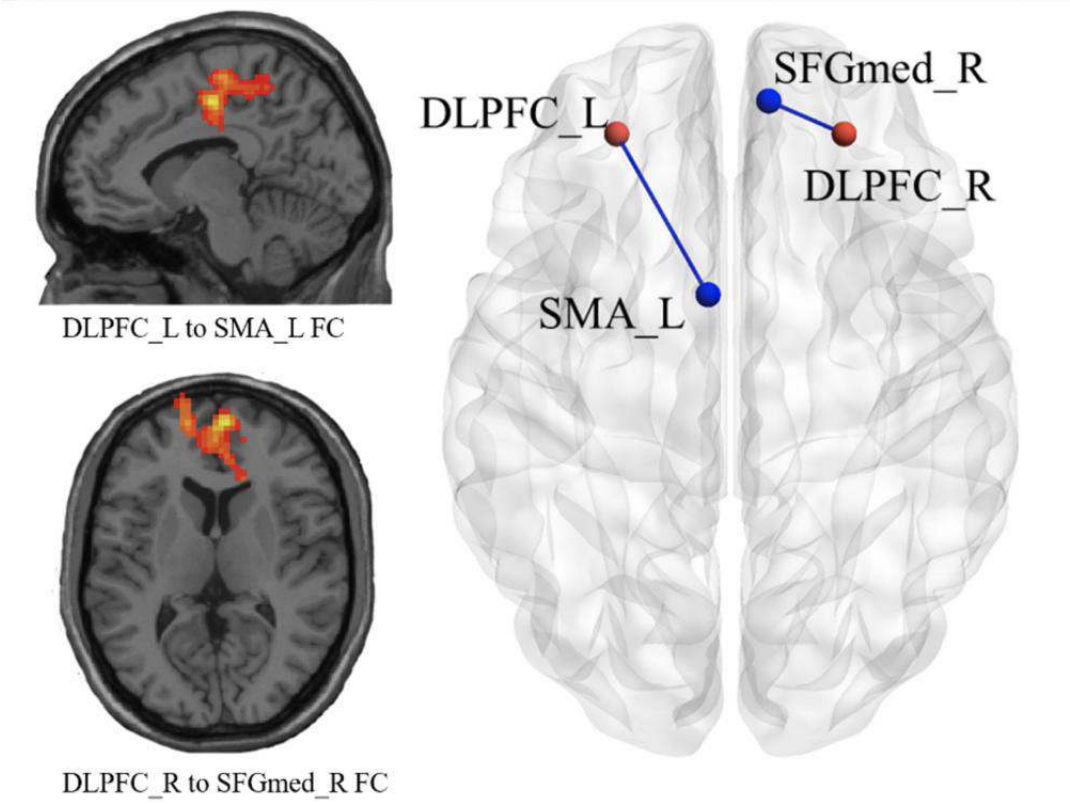

Fig.2. Results of significant changes in seed-based functional connectivity between Experimental and Control groups. FC: functional connectivity; L: left; R: Right; SMA: supplementary motor area; SFGmed: frontal superior medial gyrus.

Conclusions: The twelve-session rTMS effectively improved the stress and anxiety level of young adults with high-level perceived stress; meanwhile it also modulated the DLPFC functions.

References

1. Cirillo, P., et al. (2019), 'Transcranial magnetic stimulation in anxiety and trauma-related disorders: A systematic review and meta-analysis', Brain Behav 9, e1284.
2. De Risio, L., et al. (2020), 'Recovering from depression with repetitive transcranial magnetic stimulation (rTMS): a systematic review and meta-analysis of preclinical studies', Transl Psychiat 10, 393.
3. Ramón-Arbués, E. et al. (2020), 'The Prevalence of Depression, Anxiety and Stress and Their Associated Factors in College Students', Int J Env Res Pub He 17.
4. Scult, M.A., et al., (2017), 'Thinking and Feeling: Individual Differences in Habitual Emotion Regulation and Stress-Related Mood are Associated with Prefrontal Executive Control', Clin Psychol Sci 5, 150-157.
5. Wu, J., et al., (2021), 'The efficacy of repetitive transcranial magnetic stimulation (rTMS) for young individuals with high-level perceived stress: study protocol for a randomized sham-controlled trial', Trials 22, 365.

Poster No 116

The Spatial Distributions of Neuroimaging-guided Personalized Targets for TMS in Depression

Gai Kong[1], Lijiang Wei[2], Sirui Wang[1], Jijun Wang[1], Chaozhe Zhu[2], Yingying Tang[1]

[1]Shanghai Mental Health Center, Shanghai Jiaotong University School of Medicine, Shanghai, China, [2]Beijing Normal University, State Key Laboratory of Cognitive Neuroscience and Learning, Beijing, China

Introduction: Repetitive transcranial magnetic stimulation (rTMS) over the left dorsolateral prefrontal cortex (DLPFC) has been an effective treatment for major depressive disorder (MDD)[1]. Recent studies have further developed a precision rTMS strategy with personalized targets guided by personalized functional connectivity (FC) between the DLPFC and the subgenual cingulate cortex (sgACC) to improve the antidepressant effects in MDD[2]. As depression is a disorder with distinct symptom domains, whether the spatial distribution of personalized DLPFC targets are related to these symptom domains remains

uncertain. We thus explore whether the personalized DLPFC targets can be clustered into distinct subtypes and exam their association with clinical characteristics.

Methods: We recruited a total of 133 MDD patients from two centers (Shanghai Mental Health Center (SMHC) and Suzhou Guangji Hospital (SZGJ) with a diagnosis of MDD using the Diagnostic and Statistical Manual of Mental Disorders (DSM-4) criteria. All MDD patients completed the 17-item Hamilton Depression Scale (HAMD-17), Hamilton Anxiety Scale (HAMA), and Montgomery-Asberg Depression Rating Scale (MADRS) assessments. Resting-state functional MRI (fMRI) data were acquired and preprocessed. After the quality control of fMRI images, 120 MDD were included in the following analysis. We calculated FC between each voxel within the left DLPFC and a sgACC-based seed, as described in detail in our previous study[3], and determined a personalized DLPFC target with a maximum negative DLPFC-sgACC FC. Then, the k-means clustering method was applied to cluster MDD subgroups based on the spatial distributions of their personalized targets. Between-subgroup comparisons were performed for the demographic and clinical characteristics.

Results: We obtained two distinct clusters of personalized targets in MDD patients, as shown in Fig 1. One subgroup had personalized targets over the anterior part of the left DLPFC (in red in Fig.1A, termed as the anterior subgroup), and the other subgroup had personalized targets over the posterior part (in blue in Fig.1A, termed as the posterior subgroup). The anterior subgroup, constituting the majority (73.3%), were closer to the group-average DLPFC target with a median distance of 12.5mm. In comparison, those in the posterior subgroup (26.7%) had a median distance of 50.5mm. There were no significant differences in gender, education, or illness duration between these two subgroups ($p>0.05$). However, we observed significant between-subgroup differences in various anxiety indicators. The posterior subgroup showed higher HAMD-17 total scores ($p=0.034$) and HAMA total scores ($p=0.008$) than the anterior subgroup. Factor scores of anxiety/somatization ($p=0.001$) in HAMD-17 and factor scores of somatic ($p=0.030$) and psychic anxiety ($p=0.020$) in HAMA were higher in the posterior subgroup than the anterior subgroup, whereas all other factors did not differ between two subgroups.

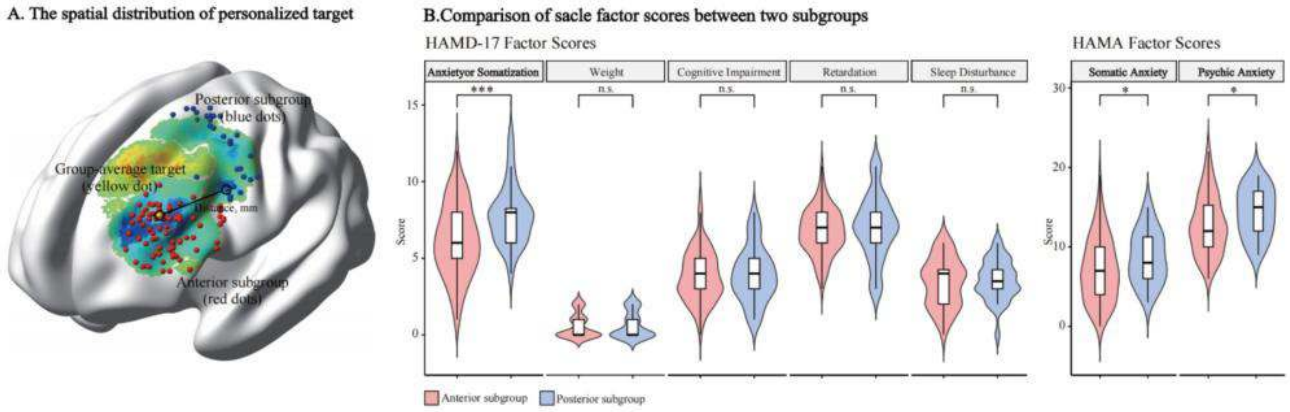

Fig. 1 A.The spatial distributions of personalized transcranial magnetic stimulation targets within the left dorsolateral prefrontal cortex in patients with major depressive disorder, which clustered into two subgroups (the anterior subgroup in red, the posterior subgroup in blue, and the group-average target (MNI, -42,44,30) referenced in Weigand et al.'s study in yellow). B. Comparisons of factor scores of the 17-item Hamilton Depression Scale (HAMD-17) and Hamilton Anxiety Scale (HAMA).

Conclusions: In the present study, we identified two MDD subgroups with distinct spatial distributions of their personalized DLPFC targets based on the DLPFC-sgACC FC. Most MDD patients had anterior DLPFC targets close to the group-average DLPFC target, consistent with the clinical rTMS efficacy in MDD. More importantly, we identified another posterior MDD subgroup, who had more posterior DLPFC targets and presented severe anxiety symptoms. The heterogeneity of personalized target distributions within the DLPFC highlights the importance of individualized rTMS intervention in MDD.

References

1. Lefaucheur, J.P. (2020), 'Evidence-based guidelines on the therapeutic use of repetitive transcranial magnetic stimulation (rTMS): An update (2014-2018)', Clinical Neurophysiology, vol. 131, no. 3, pp. 474-528
2. Cash, R.F.H. (2021), 'Personalized connectivity-guided DLPFC-TMS for depression: Advancing computational feasibility, precision and reproducibility', Human Brain Mapping, vol. 42, no. 13, pp. 4155-4172
3. Kong, G. (2022), 'The therapeutic potential of personalized connectivity-guided transcranial magnetic stimulation target over group-average target for depression', Brain Stimulation, vol. 15, no. 6, pp. 1063-1064

Poster No 117

A comprehensive approach for TMS targeting identifies better targets than typical approaches

Dylan Nielson[1], Marie Zelenina[2], Safa Rahman[2], Andre Zugman[3], Daniel Pine[4], Francisco Pereira[2]

[1]National Institute of Mental Health, Washington, DC, [2]National Institute of Mental Health, Bethesda, MD, [3]NIMH, Bethesda, MD, [4]National Institute of Mental Health (NIMH), National Institutes of Health (NIH), Bethesda, MD

Introduction: Functional connectivity is being used clinically to target TMS treatment for depression[1,2]. Most targeting approaches restrict their search space by first identifying a cortical target based on functional connectivity, then optimize the stimulator position to reach that target without consideration of any additional cortical regions that might be stimulated[2,3]. In fact, stimulator positions found this way sometimes deliver stimulation to a broad swath of the cortex that is at least as strong as that delivered to the cortical target (Fig. 1A). The dispersed patterns of stimulation delivered by TMS are a challenge for delivering stimulation to specific, compact cortical targets. Here we propose a comprehensive approach for TMS targeting of depression in which the stimulated cortical area of all reasonable stimulator orientations are simulated. We then select the stimulator position with the strongest mean anticorrelation with the subgenual cortex (SGC), as opposed to the stimulator position that does the best job at stimulating the single most anticorrelated cluster.

1A

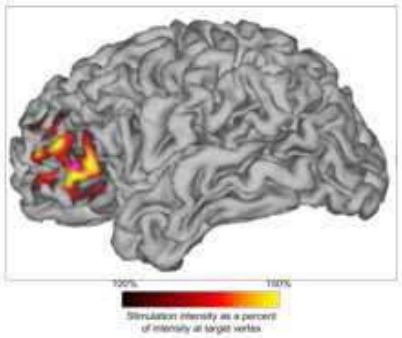

Figure 1A: This simulated E-field illustrates the breadth of cortex that can be stimulated in addition to the target (in pink).

1B

Participant	Age	Sex	Per session rsFMRI Time (minutes)	Intersession Interval	Intersession Connectivity Correlation
24546	25	F	60	7 days	0.95
24563	25	M	20	21 days	0.66
24573	65	F	20	14 days	0.69
24704	29	M	30	11 days	0.76
24718	26	M	20	21 days	0.82
24740	29	F	30	78 minutes	0.86
24742	47	M	30	69 minutes	0.93

1C

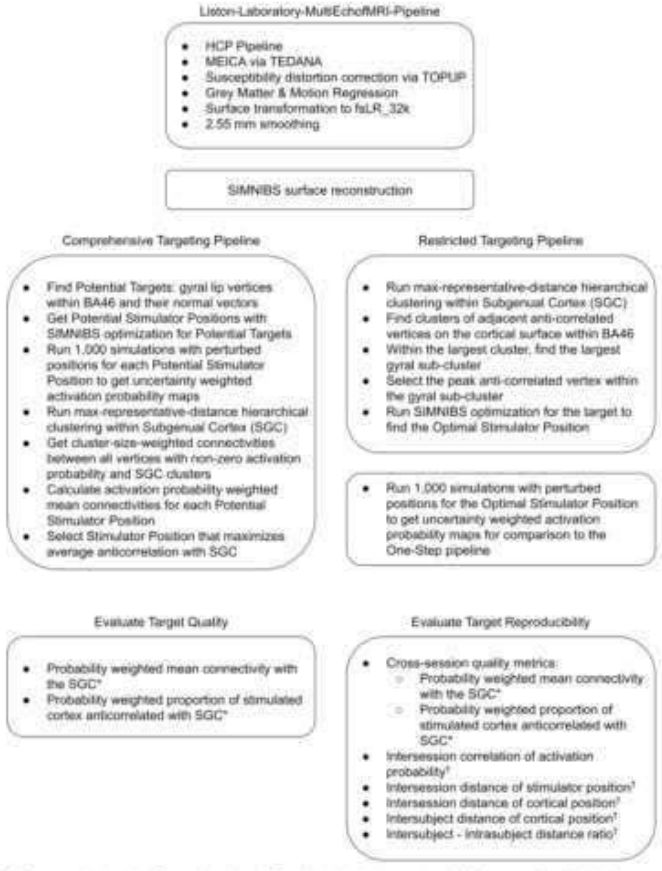

* Differences between the Comprehensive and Restricted methods were tested for these metrics with mixed effects models accounting for grouping of sessions within participants of the form: metric ~ 1 + method + (1 | participant).
† We did not test for differences in these metrics because the distributions for the Comprehensive method were strongly skewed because 4 subjects had the same targets between sessions.

Methods: METER Sample The NIMH Multi-Echo TEst-Retest sample consists of multi-session data from 7 healthy adults collected on a 3-T GE MR-750[4] (Fig. 1B). We collected 0.8 mm isotropic T1- and T2-weighted images and echo planar resting state sequences (2.5mm isotropic, TR=2.5 s; TEs=[12.9 ms, 32.2 ms, 51.6 ms, 70.9 ms]). This data was collected under protocol 01-M-0192 approved by the NIH IRB. Targeting approach Our targeting approach was inspired by Lynch et al.'s[5] approach for stimulating functional networks and makes use of their preprocessing pipeline[6] (detailed in Fig. 1C), Amongst other changes, we have refined the search of stimulator positions to focus on delivery of stimulation to the gyral lip, since modeling indicates neurons here have the lowest activation threshold[7]. Target Quality Evaluation We evaluate target quality based on uncertainty weighted activation probability maps. We expect that stimulation with a higher weighted mean SGC correlation will be more likely to have a clinical effect. It is also possible that the sign of the stimulated cortex is relevant to clinical effects, so we evaluated the weighted proportion of stimulated cortex anticorrelated with the SGC. Target Reliability Evaluation Many studies of targeting reliability have reported intersession distance between cortical targets, but this is a poor metric if there are multiple nearly equivalent stimulation sites. To account for this, we evaluate the quality of the targets from each session with the connectivity data from the other. This cross-session analysis tells us if a target remains a good quality target across sessions, even if it is not necessarily the single best target in all sessions. Code is available at https://github.com/nih-fmrif/contarg.

Results: The Comprehensive approach stimulates cortical areas with a stronger mean anticorrelation with the SGC (p = 7.25x 10-7) and a greater proportion of anticorrelated cortical area (p = 3.39 x 10-7) than the Restricted method (Fig 2A). It was also more reliable that the Restricted approach with stronger mean anticorrelation with the SGC (p = 7.30x 10-5) and a greater proportion of anticorrelated cortical area (p = 3.99 x 10-5) in the crossed-session evaluation (Fig 2B). 4 of 7 participants had the same target in both sessions with the Comprehensive method, but none did with the Restricted method (Fig 2C).

2A

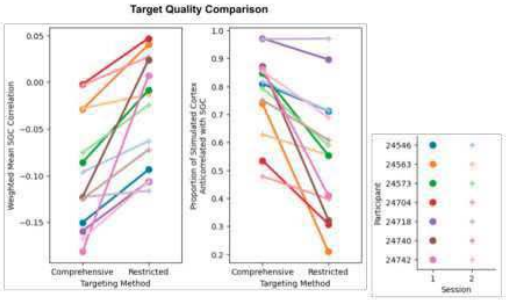

Figure 2A: As shown in the left panel, the Comprehensive targeting method's stimulated area is significantly more anticorrelated with subgenual cortex (SGC) (mean difference = -0.064, z = -4.96, p = 7.25x 10^{-7}). The right panel shows that a greater proportion of the Comprehensive targeting method's stimulated area is anticorrelated with the SGC (mean difference = 0.214, z = 5.10 p = 3.39 x 10^{-7}). Each participant is in their own color, their first session is shown in a darker color circular markers; the second session is shown in lighter colors with + markers.

2B

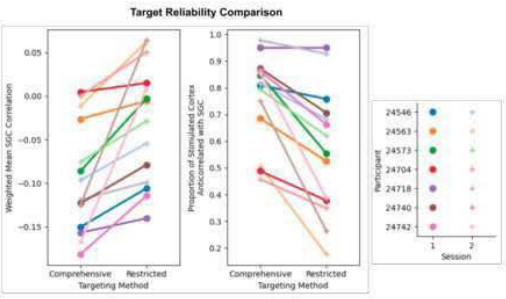

Figure 2B:These are the results from the cross-session evaluation of metrics. Targets from session 1 were evaluated based on the connectivity of session 2 and vice-versa. As shown in the left panel, the Comprehensive targeting method's stimulated area is significantly more anticorrelated with subgenual cortex (SGC) (mean difference = -0.063, z = -3.97, p = 7.30x 10^{-5}). The right panel shows that a greater proportion of the Comprehensive targeting method's stimulated area is anticorrelated with the SGC (mean difference = 0.1.95, z = -4.11 p = 3.99 x 10^{-5}). Each participant is in their own color, their first session is shown in a darker color circular markers; the second session is shown in lighter colors with + markers.

2C

	Comprehensive Targeting Method				Restricted Targeting Method			
Participant	Spatial Correlation of Activation	Scalp Distance (mm)	Cortical Distance (mm)	Intersubject - Intrasubject Ratio	Spatial Correlation of Activation	Scalp Distance (mm)	Cortical Distance (mm)	Intersubject - Intrasubject Ratio
24546	1	0	0	--	0.76	8.78	14.51	1.03
24563	0.48	28.88	25.53	0.77	0.30	22.71	27.66	0.54
24573	1	0	0	--	0.72	18.57	15.95	0.94
24704	0.97	4.96	6.99	2.82	0.67	17.63	16.85	0.89
24718	0.65	13.31	22.52	0.88	0.72	18.38	4.47	3.34
24740	1	0	0	--	0.55	5.35	9.62	2.25
24742	1	0	0	--	0.43	18.62	4.75	3.14

Figure 2C: Target Reproducibility Comparison. 4 of 7 participants had the same target in both sessions with the Comprehensive method. None of the participants had the same target with the Two-Step method. The average intersubject distance was 19.71 mm for the Comprehensive method and 14.92 for the Restricted method.

Conclusions: In this pilot, we showed that taking a comprehensive approach to TMS targeting allows simulation to be delivered to an area of the cortex that is more anticorrelated with the SGC than a restricted targeting approach. The length of resting state sequences we collected allows us to evaluate the quality of the targeting but it may exaggerate measures of target reliability compared to shorter sequences. However, this work does demonstrate the feasibility and promise of a comprehensive TMS targeting approach.

References

1. US Food and Drug Administration C for D and RH (2022, September 1): Equivalence of Magnus Neuromodulation System (MNS) with SAINT Technology, Model Number 1001K. Retrieved December 1, 2023, from https://www.accessdata.fda.gov/cdrh_docs/pdf22/K220177.pdf
2. Cole EJ et al. (2022): Stanford Neuromodulation Therapy (SNT): A Double-Blind Randomized Controlled Trial. American Journal of Psychiatry 179: 132–141.
3. Cash RFH et al. (2021): Personalized connectivity-guided DLPFC-TMS for depression: Advancing computational feasibility, precision and reproducibility. Human Brain Mapping 42: 4155–4172.
4. Nielson DM et al. (2023): NIMH METeR (Multi-Echo Test-Retest). Openneuro. https://doi.org/10.18112/OPENNEURO.DS004787.V1.1.0
5. Lynch CJ et al. (2022): Automated optimization of TMS coil placement for personalized functional network engagement. Neuron 110: 3263-3277.e4.
6. Lynch CJ et al. (2020): Rapid Precision Functional Mapping of Individuals Using Multi-Echo fMRI. Cell Reports 33: 108540.
7. Aberra AS et al. (2020): Simulation of transcranial magnetic stimulation in head model with morphologically-realistic cortical neurons. Brain Stimulation 13: 175–189.

Poster No 118

Causal role of angular gyrus and premotor cortex in human habit formation: A TMS study

xiaoyu Wang[1], Hannes Ruge[1], Katharina Zwosta[1], Franziska Korb[1], Uta Wolfensteller[1]

[1]Technische Universität Dresden, Dresden, Germany

Introduction: Learning novel behaviors involves a complex transition from goal-related to habit-related brain systems which have been investigated and evidenced in animal studies[1]. However, how habits are formed and maintained in the human brain still remains unclear. For instance, Tricomi induced habitual behavior in humans via extensive training and successfully demonstrated a relationship between habit strength and increased activity in the posterior putamen (habitual system)[2]. However, these findings could not be replicated in a recent study using a larger data set[3]. Instead, other recent studies suggested that habit strength might be associated with decreasing engagement of the goal-directed brain system as learning progresses, such as the angular gyrus (AG)[4] or the head of the caudate[3]. The present study therefore aimed to probe the causal role of these two antagonistic brain systems during habit formation to investigate whether it relied on decreasing involvement of the goal-directed or on an increasing involvement of the habitual system. To this end, we used repetitive transcranial magnetic stimulation (rTMS) with AG and premotor cortex (PMC) as separate goal- and habit-directed stimulation targets. We assessed the behavioral and neural effects of rTMS on habit formation during a subsequent fMRI session.

Methods: Fifty-one subjects (16 male, mean age: 24) were randomly divided into two groups (26 PMC and 25 AG). All took part in two separate sessions, receiving both real and sham stimulation. We used a slightly modified goal-habit paradigm which comprises three consecutive phases[4]. First, goal-directed behavior based on explicit stimulus-response-outcome associations was established. Subsequently, subjects received the off-line TMS stimulation (1Hz, 2 trains of 15 min, 1 min break) on either right AG (42 -57 36) or PMC (39 -6 48). After stimulation, participants were required to learn stimulus-response (S-R) associations via trial-and-error for a subset of the stimuli during scanning, for 98 repetitions per stimulus in order to induce strong S-R associations (habit formation). Finally, those habitual and goal-directed action tendencies were put into competition to measure the behavioral impact of habits on goal-directed behavior. ANOVAs were conducted to assess the stimulation effects on error rates and response times during habit formation and the later goal-habit competition. The learning-related changes in neural activity during the habit formation phase were modeled by parametric regressors reflecting the amount of training and examined by ANOVAs on the group level.

Results: Behaviorally, error rates and reaction time decreased significantly during habit formation in general. Interestingly, AG stimulation resulted in an increased error rate specifically early on, though there was no significant interaction with block/time. Replicating previous findings, we found a generally decreasing activation in IPL, IFJ and anterior insula across training. However, TMS did not differentially influence those training induced changes. Most importantly, we found a significant accuracy-based compatibility interaction effect in the goal-habit competition phase (Figure 1b). Following AG stimulation, there was an increased competition between habitual and goal-directed action tendencies as evidenced by an increased compatibility effect compared to the sham stimulation. In contrast, following PMC stimulation, the competition was decreased. A similar pattern emerged for RTs following PMC stimulation (Figure 1c).

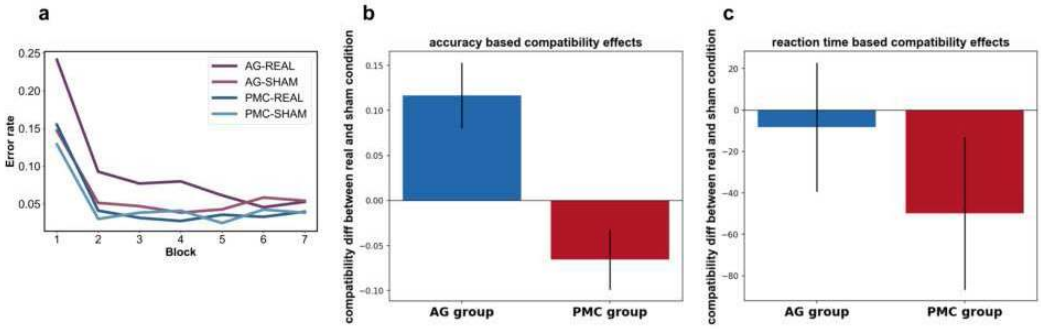

Conclusions: Considering the goal-habit compatibility effect as a proxy for habit strength the current study successfully demonstrated a causal relationship between the involvement of the goal-directed and habit-related brain systems and human habit strength. More specifically, TMS reduced the habit strength when the habit system was disturbed by targeting PMC and increased habit strength when the goal-directed system was disturbed by targeting AG.

References

1. Yin et al., 2006. The role of the basal ganglia in habit formation. Nat. Rev. Neurosci. 7 (6), 464–476.
2. Tricomi et al., 2009. A specific role for posterior dorsolateral striatum in human habit learning. Eur. J. Neurosci. 29 (11), 2225–2232.
3. Gera et al., 2023. Characterizing habit learning in the human brain at the individual and group levels: A multi-modal MRI study. NeuroImage. 272, 120002.
4. Zwosta et al., 2018. Habit strength is predicted by activity dynamics in goal-directed brain systems during training. Neuroimage 165, 125–137.

Poster No 119

Multi-muscle TMS mapping for motor cortex reorganization during finger independence training

Anastasiia Asmolova[1], Anastasiia Sukmanova[2], Milana Makarova[2], Pavel Novikov[2], Vadim Nikulin[3], Arno Villringer[3,4], Maria Nazarova[5,6]

[1]Max Planck School of Cognition, Leipzig, Germany, [2]National Research University Higher School of Economics, Moscow, Russian Federation, [3]Max Planck Institute for Human Cognitive and Brain Sciences, Leipzig, Germany, [4]Leipzig University, Leipzig, Germany, [5]Aalto University, Helsinki, Finland, [6]Harvard Medical School, Boston, MA

Introduction: MRI-navigated transcranial magnetic stimulation (nTMS) is an approach widely used for non-invasively mapping of the motor cortex. In our recent test-retest study we established the absolute and relative reliability of multi-muscle nTMS motor mapping (Nazarova et al., 2021). Given that motor learning is known to alter plasticity in the motor cortex (Raffin & Siebner, 2019), our current objective was to explore the reorganization of the muscle cortical representations (MCRs) following finger-independence training.

Methods: 26 healthy young right-handed male volunteers (18-35 y.o.) underwent two nTMS mapping sessions separated by ten sessions of the finger-independence training using EMG-based biofeedback (TMSphi, Novikov et al., 2020). During nTMS motor mapping MRI surface EMG was recorded from abductor pollicis brevis (APB), abductor digiti minimi (ADM), first dorsal interosseous (FDI), extensor digitorum communis (EDC) and biceps brachii. Within the 10 motor training sessions participants were mastering their motor task consisting of abducting their thumb while keeping their little finger still. As behavioral outcomes we measured: the success of the independent muscle contraction (in % from the maximum muscle contraction), amplitudes of the maximum voluntary contraction (MVC) of the trained muscles (APB, ADM) and general hand dexterity using 9-hole peg test (9HPT). For nTMS motor mapping, MCRs and their parameters (Figure 1) were evaluated using TMSmap software (Novikov et al., 2018).

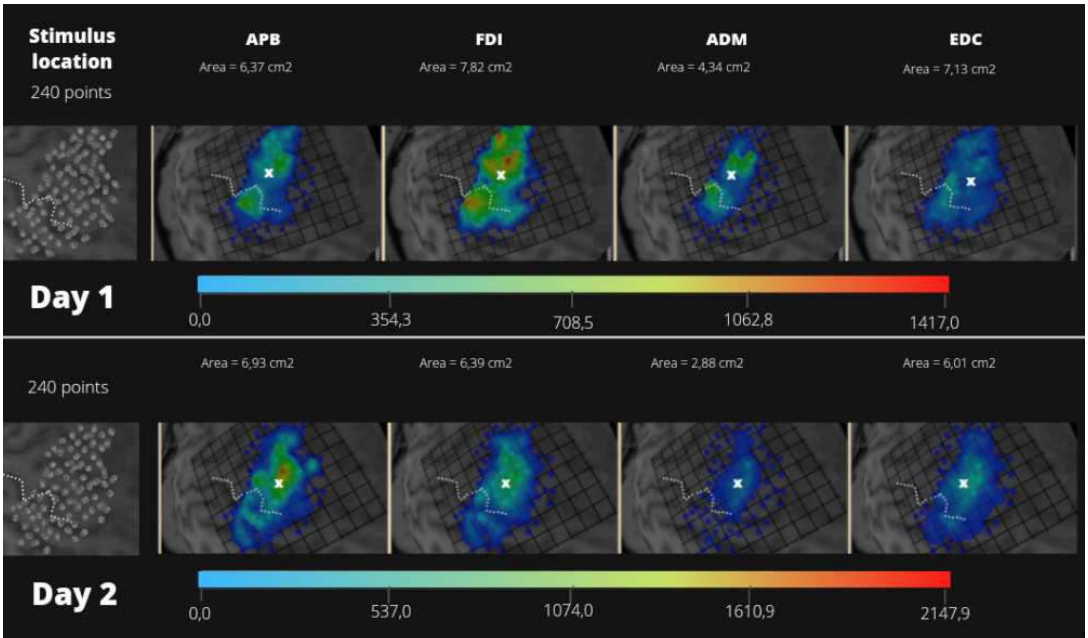

Figure 1. TMS muscle cortical representations (MCRs) of the four investigated hand muscles for both days in a representative subject. MCR visualization in TMSmap based on 240 points per day, points located closer than 2 mm are merged. White dotted line indicates the central sulcus. The areas of the MCR are shown. The scale represents motor evoked potential amplitude in microvolts (μV).

Results: The success of independent contraction increased: for APB from 16% to 29% (p = 0.003, all p-values are FDR-corrected), for ADM – from 16% to 30% (p = 0.004). Time of the 9HPT performance significantly decreased from 19.96 s to 18.42 s (p = 0.005). The amplitudes of APB and ADM MVC did not change significantly. At the group level changes in the MCR parameters were not significant, showing only a trend for increase (APB MCR area increased from 6.17 to 6.81 cm2, ADM MCR - from 5.22 to 5.92 cm2). Comparing to the smallest detectable changes (SDC) from our previous test-retest reliability study (Nazarova et al., 2021) APB MCR area significantly increased in 7 participants and decreased in 4 (>2.01 cm2, CI – 95%); while ADM MCR area increased in 5 and decreased in 4 participants (>2.11 cm2, CI – 95%); the normalized overlap between APB and ADM MCRs increased in 1 - decreased in 2 (>0.34%, CI – 95%).

Conclusions: We showed that the finger-independence training significantly increased hand dexterity, but not hand strength – the finding which is in line with the previous studies showing that hand strength and dexterity are not associated directly (Jing Xu et al., 2017). Our TMS findings do not support the hypothesis that the overlaps between muscles trained to be independent may decrease as it was shown in case of finger immobilization (Raffin & Siebner, 2019). We suppose that it may be explained by the fact that both voluntarily contraction and relaxation of both muscles (APB, ADM) were needed for the motor task performance. TMS maps changes reflecting voluntary muscle relaxation training should be investigated in further studies.

References

1. Nazarova, M., Novikov, P., Ivanina, E., Kozlova, K., Dobrynina, L. & Nikulin, V. V. (2021). Mapping of multiple muscles with transcranial magnetic stimulation : absolute and relative test – retest reliability, (February), 1–21.
2. Novikov, P. A., Nazarova, M. A., & Nikulin, V. V. (2018). TMSmap – Software for Quantitative Analysis of TMS Mapping Results. Frontiers in Human Neuroscience, 12, 239.
3. Novikov P.A., Reshetnikov M.L., Nazarova M.A., Gribov D.A., Nikulin. V. V. (2020). Nejronavigaciya TMSphi. Byul. N°2, Reestr programm dlya EVM.
4. Raffin, E., & Siebner, H. R. (2019). Use-Dependent Plasticity in Human Primary Motor Hand Area: Synergistic Interplay Between Training and Immobilization. Cerebral Cortex (New York, N.Y. : 1991), 29(1), 356–371.
5. Jing Xu, X., Naveed Ejaz, X., Hertler, B., Branscheidt, M., Widmer, M., Faria, A. V, Harran, M. D., Cortes, J. C., Kim, N., Celnik, P. A., Kitago, T., Andreas Luft, X. R., Krakauer, J. W., Diedrichsen, J., Xu, J., & Ejaz, N. (2017). Separable systems for recovery of finger strength and control after stroke Even healthy people show in-voluntary force production (enslaving) on the uninstructed. J Neurophysiol, 118, 1151–1163.

Poster No 120

In-silico analysis of motion-informed dose adjustment strategies for TMS-fMRI

Sarah Grosshagauer[1], Michael Woletz[1], Maria Vasileiadi[1], Martin Tik[2], Christian Windischberger[3]

[1]Medical University of Vienna, Vienna, Vienna, [2]High Field MR Center, Center for Medical Physics and Biomedical Engineering, Medical University of V, Vienna, Austria, [3]Medical University of Vienna, Vienna, Austria

Introduction: Concurrent TMS/fMRI leverages the high temporal resolution of TMS interventions and the spatial resolution of BOLD-fMRI, yet, motion remains a major challenge. Using real-time motion monitoring, we could previously detect that participants moved significantly throughout a concurrent TMS/fMRI session, resulting not only in reduced image quality, but also in changes of the induced electric field (E-field) in the targeted brain region. Thus, we previously developed a framework for real-time adjustment of stimulation intensity based on motion tracking (figure 1a). Within this study we evaluate methodologies for dose-adjustments by performing in-silico comparisons between distance-correction, vector-potential informed corrections and E-field simulation.

Methods: We used SimNIBS 4.0.0 (Thielscher et al. 2015) and the MagVenture MRi-B91 coil model to simulate many different coil orientations and positions. Simulations were targeted to the hand knob on M1 (MNI: -40 -20 42 (Cárdenas-Morales et al. 2014)), mapped to the space of the individual head model. Samples were defined within a cylindrical volume of interest (VOI, r=10 mm, h=10 mm) to simulate the potential range of motion during TMS/fMRI. In addition to coil position, we included coil orientation (rotation/tilt) by applying a uniform deterministic sampling of the 3D-rotation group SO(3) using Hopf fibration (Yershova et al. 2010). All obtained poses were checked for plausibility, e.g. that the TMS coil did not intersect with the headmesh. Using the fast auxiliary dipole technique (Gomez et al. 2021), we obtained the E-field magnitude within the target ROI for all plausible poses. The optimal coil pose and corresponding E-field were defined as reference (figure 1b). Subsequently, we performed an in-silico comparison between different dose adjustment methods: distance-based correction for Euclidean and orthogonal distance between coil and target as proposed by (Stokes et al. 2005; 2007) (change in stimulation intensity of 2.9%/mm) and dose adjustment based on the vector potential of the TMS coil in the target ROI, which was calculated by transforming and interpolating the SimNIBS coilfile (Drakaki et al. 2022) according to the evaluated coil pose. We obtained adjustment factors for the stimulator output (maintaining the reference dose) for all methods and compared them to the change in E-field.

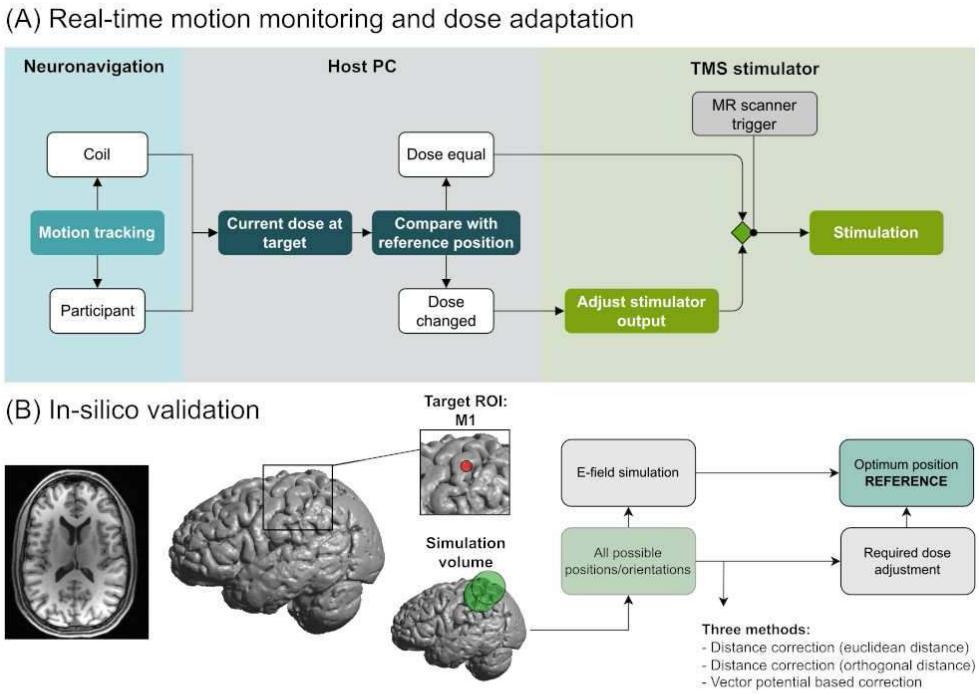

Figure 1: In-silico validation of dose adjustment techniques for the implementation in real-time motion-informed dose adaptation in concurrent TMS/fMRI. (A) shows the developed software for communication between TMS, neuronavigation and MR scanner, while **(B)** depicts the framework for comparing different dose-adaptation techniques in simulation.

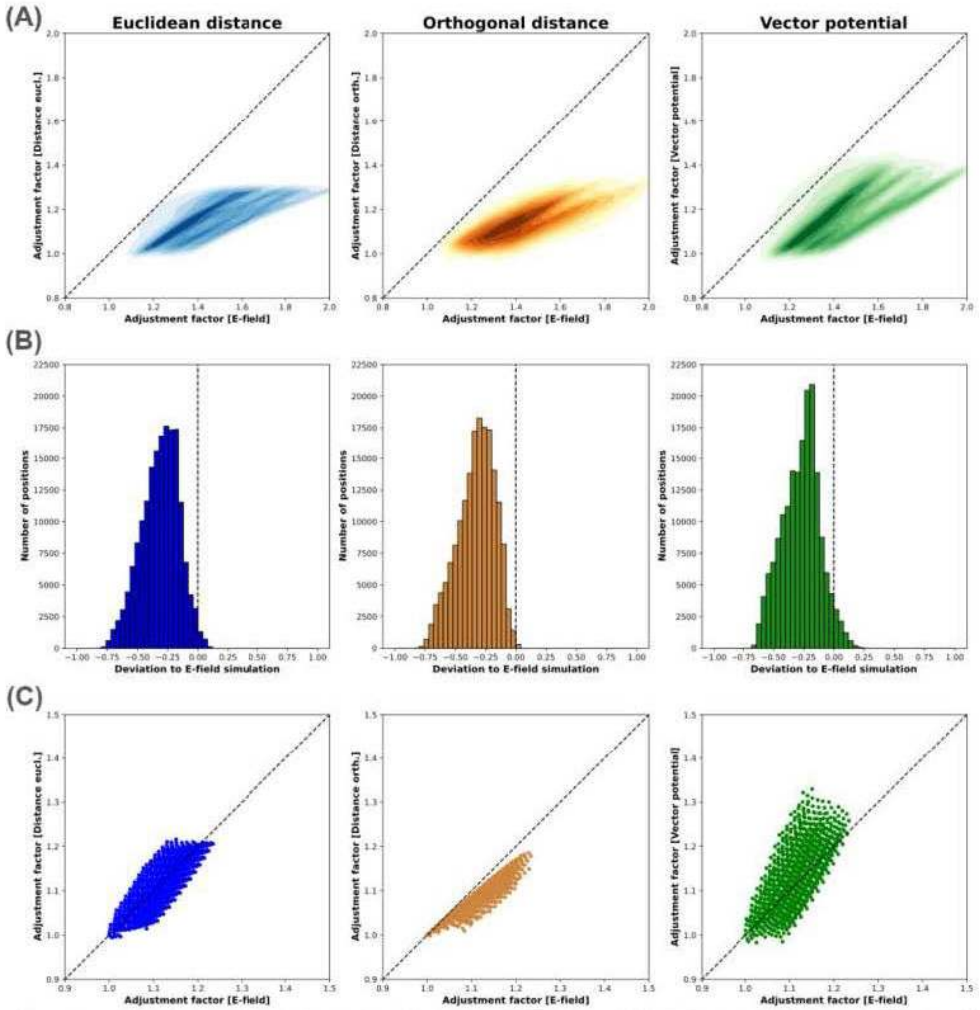

Figure 2: Comparing different dose-adjustment techniques for TMS with changes in simulated E-field for a large number of coil poses. Columns 1 and 2 correspond to distance based corrections [6] using either Euclidean distance or orthogonal distance between coil and target. Column 3 shows the adjustments based on vector potential of the coil in air. **(A)** depicts KDE-plots of the correlation between estimated adjustment and simulated E-field for all samples. Histograms of deviations between dose adjustment factors proposed by one of the assessed methodologies vs. E-field simulation are shown in **(B)**. **(C)** depicts a subsample of coil poses with identical rotation/tilt compared to the reference pose, but different positions within the volume of interest, i.e. considering only the translation of the TMS coil.

Results: Kernel-density estimate plots of the calculated dose adjustments compared to E-field associated changes can be found in figure 2a. All methods underestimated correction factors compared to simulated E-field changes for most samples (figure 2b). Mean squared errors (MSE) compared to E-field guided adjustments were 0.12 (Euclidean) and 0.13 (z-distance) for distance based corrections and 0.09 for corrections based on vector potential. A subsample of poses with identical orientation compared to the reference position, i.e. pure translation of the coil, is plotted in figure 2c. In this case, MSE was 0.001 for distance based corrections but 0.003 if vector potential was used.

Conclusions: We successfully extended available E-field simulation software to allow for simulations in an extended volume including a homogeneous sampling of tilt and orientation of the coil. Comparisons of different dose adjustment methodologies revealed closest agreement with E-field based simulations if adjustment is based on interpolations of the vector potential, if translation as well as rotation/tilt of the coil is considered. For constant orientation, the distance based correction performed best. However, none of the available correction methods could capture the full extent of E-field changes as the tissue-interactions are simply not included. While simplified corrections might be valid if coil motion is small, a-priori E-field simulations and corrections based on these values are of utmost importance to obtain high consistency in target dose.

References

1. Cárdenas-Morales, Lizbeth (2014). “Network Connectivity and Individual Responses to Brain Stimulation in the Human Motor System.” Cerebral Cortex 24 (7): 1697–1707. https://doi.org/10.1093/cercor/bht023.
2. Drakaki, Maria (2022). “Database of 25 Validated Coil Models for Electric Field Simulations for TMS.” Brain Stimulation 15 (3): 697–706. https://doi.org/10.1016/j.brs.2022.04.017

3. Gomez, Luis J., Moritz Dannhauer, and Angel V. Peterchev. 2021. “Fast Computational Optimization of TMS Coil Placement for Individualized Electric Field Targeting.” NeuroImage 228 (March): 117696. https://doi.org/10.1016/j.neuroimage.2020.117696.
4. Stokes, Mark G. (2007). “Distance-Adjusted Motor Threshold for Transcranial Magnetic Stimulation.” Clinical Neurophysiology 118 (7): 1617–25. https://doi.org/10.1016/j.clinph.2007.04.004.
5. Stokes, Mark G. (2005). “Simple Metric for Scaling Motor Threshold Based on Scalp-Cortex Distance: Application to Studies Using Transcranial Magnetic Stimulation.” Journal of Neurophysiology 94 (6): 4520–27. https://doi.org/10.1152/jn.00067.2005.
6. Thielscher, Axel (2015). “Field Modeling for Transcranial Magnetic Stimulation: A Useful Tool to Understand the Physiological Effects of TMS?” In 2015 37th Annual International Conference of the IEEE Engineering in Medicine and Biology Society (EMBC), 222–25. https://doi.org/10.1109/EMBC.2015.7318340.
7. Yershova, Anna (2010). “Generating Uniform Incremental Grids on SO(3) Using the Hopf Fibration.” The International Journal of Robotics Research 29 (7): 801–12. https://doi.org/10.1177/0278364909352700.

Poster No 121

Personalized threshold-free tree-based localization approach for connectome-guided brain stimulation

Ruby Kong[1], Aihuiping Xue[1], Xiaowei Tan[2], Leon Ooi[1], Trevor Wei Kiat Tan[1], Shan Siddiqi[3], Michael Fox[4], Christopher Asplund[5], Bjorn Burgher[6], Luca Cocchi[6], Phern-Chern Tor[2], B. T. Thomas Yeo[1]

[1]National University of Singapore, Singapore, Singapore, [2]Institute of Mental Health, Singapore, Singapore, [3]Harvard Medical School/Brigham and Women’s Hospital, boston, MA, [4]Harvard Medical School/Brigham and Women’s Hospital, Boston, MA, [5]Yale-NUS College, Singapore, Singapore, [6]QIMR Berghofer Medical Research Institute, Brisbane, Queensland

Introduction: Evidence suggests that individualized connectome-guided localization yields better transcranial magnetic stimulation (TMS) efficacy for treatment-resistant depression than anatomical approaches[1–4,6]. Treatment response rates improved when stimulation was delivered at dorsolateral prefrontal cortex (DLPFC) regions with stronger anti-correlation with subgenual anterior cingulate cortex (sACC)[2,4,7]. However, previous work for selecting targets require setting parameters. Here, we develop a personalized threshold-free tree-based localization approach using individual-specific functional networks.

Methods: We use the multi-session hierarchical Bayesian model (MSHBM) to estimate reliable individual networks for each participant using resting fMRI (Fig1A)[5]. Since attention networks are known to be anticorrelated with sACC, we select the salience/ventral attention and dorsal attention network components within DLPFC. As targeting gyri close to the scalp is preferred (Fig1B), the attentional DLPFC components are further refined by only considering gyral regions based on the gyral map (Fig1C). Within the attentional DLPFC components, we select a stimulation location which is close to the scalp and anticorrelated with sACC (Fig1D). We have to set parameters for gyral map and sACC negative correlation. A tree-based approach is used to estimate a consensus location across two sets of parameters (Fig1E, 1F). Within the attentional DLPFC components, we consider a range of gyrus thresholds (0% to 5%). For each gyrus threshold, we gradually vary the sACC correlation thresholds (100% to 5%). A x% sACC threshold represents the top x% of brain locations most anticorrelated with sACC. For given threshold, brain locations that survives are extracted, yielding one or more connected components. The centroid of each component corresponds to a tree node. For a given gyrus threshold, the centroids of the more stringent sACC correlation threshold will be the children of the centroids of the less stringent sACC correlation threshold (Fig1E). For each tree, we select candidate targets corresponding to tree nodes with no children and tree nodes with multiple children. Among all the candidates across all trees, a final target is obtained by finding the candidate that is closest in distance on average to all other candidates (Fig1F). To verify our localization approach, we use 2 healthy datasets. Dataset 1 had 18 local participants with two 10min runs (2 weeks apart) of resting fMRI. Dataset 2 had 32 Human Connectome Project (HCP) participants with 2 sessions of resting fMRI roughly 1 year apart. We use a single run (~15min) from each session. We compare our approach with a group-average location (Fox2012) and connectome-guided individualized locations (Cash2021). We evaluate localizations using test-retest reliability (ratio of inter-subject target distance and intra-subject target distance) and inter-session sACC correlation (connectivity between target of one session and sACC in the other session). As test-retest reliability is ill-defined for Fox2012, the comparison is only made between Cash2021 and our approach. We perform leave-one-out cross-validation which minimizes sACC correlation for Cash2021 because Cash2021 requires setting sACC correlation threshold.

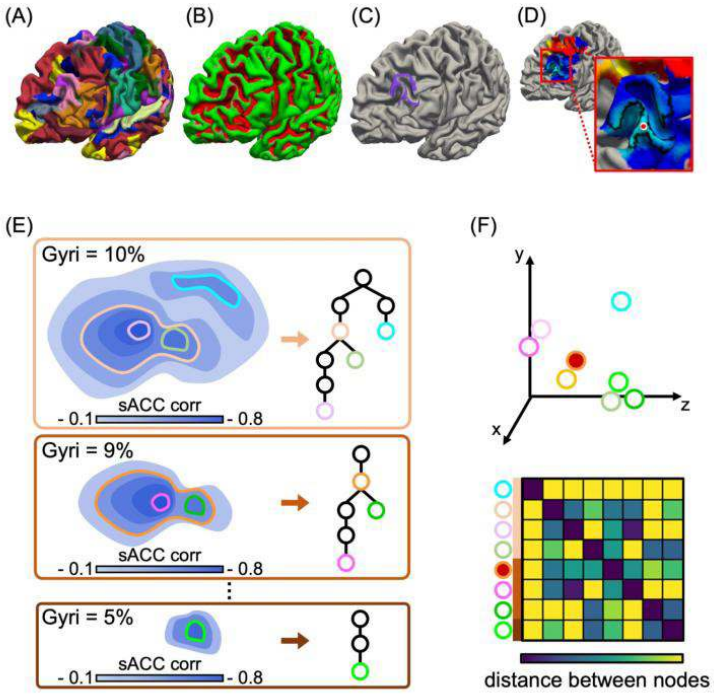

Figure 1. Illustration of individualized threshold-free tree-based localization approach. (A) Individual-specific MSHBM networks. (B) Individual gyral map. The green color represents gyral regions close to the scalp. (C) Gyral portion of the individual's salience/ventral attention and dorsal attention network components within the DLPFC is shown in purple (D) Blue-red color shows functional connectivity (correlation) with sACC. The location which is close to the scalp and negatively correlated with sACC (within the region of interest in panel C) is chosen as the stimulation location using a threshold-free tree-based approach (E and F). White tree nodes with colored boundaries represent candidate targets. Red node indicates the final target.

Results: Fig2 shows the test-retest reliability and sACC correlation for both datasets. Our approach was numerically better (greater) inter/intra-subject distance than Cash2021 in both datasets, with statistical significance achieved in HCP. Our approach exhibited statistically better (more negative) sACC correlation than both Fox2012 and Cash2021.

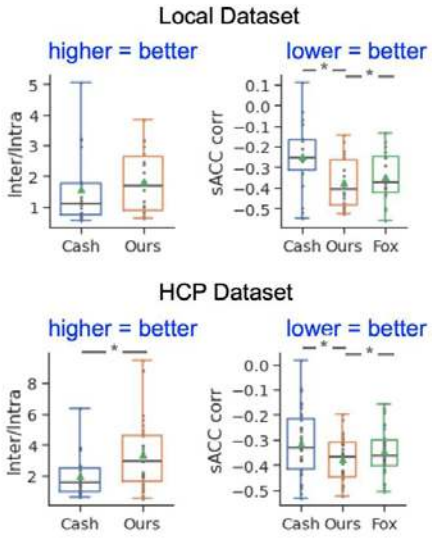

Figure 2. Test-retest reliability (inter/intra-subject distance) and sACC correlation in local and HCP datasets. * indicates statistical significance after multiple comparisons correction with FDR q < 0.05. Inter/intra reliability is ill-defined for the Fox2012, the comparison was only made between Cash2021 and our approach.

Conclusions: Our analyses suggest that our threshold-free tree-based approach is highly robust and led to better performance metrics across datasets compared with other approaches. This is highly desirable because this means that our approach can be easily translated to new clinics/hospitals/MRI scanners without the need to collect pilot data for tuning parameters.

References

1. Cash, R.F.H. et al. (2019) 'Subgenual Functional Connectivity Predicts Antidepressant Treatment Response to Transcranial Magnetic Stimulation: Independent Validation and Evaluation of Personalization', Biological Psychiatry, 86(2), pp. e5–e7. Available at: https://doi.org/10.1016/j.biopsych.2018.12.002.
2. Cash, R.F.H. et al. (2021) 'Personalized connectivity-guided DLPFC-TMS for depression: Advancing computational feasibility, precision and reproducibility', Human Brain Mapping, 42(13), pp. 4155–4172. Available at: https://doi.org/10.1002/hbm.25330.
3. Cole, E.J. et al. (2020) 'Stanford Accelerated Intelligent Neuromodulation Therapy for Treatment-Resistant Depression', American Journal of Psychiatry, 177(8), pp. 716–726. Available at: https://doi.org/10.1176/appi.ajp.2019.19070720.
4. Fox, M.D. et al. (2012) 'Efficacy of Transcranial Magnetic Stimulation Targets for Depression Is Related to Intrinsic Functional Connectivity with the Subgenual Cingulate', Biological Psychiatry, 72(7), pp. 595–603. Available at: https://doi.org/10.1016/j.biopsych.2012.04.028.
5. Kong, R. et al. (2019) 'Spatial Topography of Individual-Specific Cortical Networks Predicts Human Cognition, Personality, and Emotion', Cerebral Cortex (New York, N.Y.: 1991), 29(6), pp. 2533–2551. Available at: https://doi.org/10.1093/cercor/bhy123.
6. Siddiqi, S.H. et al. (2021) 'Identification of Personalized Transcranial Magnetic Stimulation Targets Based on Subgenual Cingulate Connectivity: An Independent Replication', Biological Psychiatry, 90(10), pp. e55–e56. Available at: https://doi.org/10.1016/j.biopsych.2021.02.015.
7. Weigand, A. et al. (2018) 'Prospective Validation That Subgenual Connectivity Predicts Antidepressant Efficacy of Transcranial Magnetic Stimulation Sites', Biological Psychiatry, 84(1), pp. 28–37. Available at: https://doi.org/10.1016/j.biopsych.2017.10.028.

Poster No 122

Single-pulse and paired-pulse TMS reveal spatially distinct corticomotor maps in human motor cortex

Mads Madsen[1], Lasse Christiansen[1], Hartwig Siebner[1]

[1]Danish Research Centre for Magnetic Resonance (DRCMR), Copenhagen, Denmark

Introduction: Transcranial magnetic stimulation (TMS) of the primary motor hand area (M1-HAND) can probe corticomotor physiology by recording motor evoked potentials (MEP) in contralateral hand muscles (Barker, Jalinous et al. 1985). Paired-pulse TMS at peri-threshold intensity induce short-latency intracortical facilitation (SICF) at distinct interstimulus intervals (ISIs). The first two peaks of SICF occur at inter-pulse intervals (IPIs) of around 1.0-1.5 ms (SICF1) and 2.4-2.9 ms (SICF2)(Ziemann, Tergau et al. 1998) mimicking the timing of indirect (I)-waves recorded from the spinal cord (Di Lazzaro, Oliviero et al. 1998). Objective: To test the hypothesis that SICF is generated by intracortical circuits that are spatially distinct from the circuits evoking single-pulse MEPs.

Methods: In 14 healthy subjects we used neuronavigated biphasic TMS over the left sensorimotor hand area to construct sulcus-shaped corticomotor maps following a 7x3 grid (figure 1)(Raffin, Pellegrino et al. 2015). We constructed a total of three motor maps using single-pulse TMS and paired-pulse TMS targeting individual SICF1 and SICF2 peak latencies. Maps were constructed for both the right first-dorsal interosseous (FDI) and abductor digiti minimi (ADM) muscles. We calculated map area, volume, and center of gravity (CoG) for each corticomotor map and for each muscle.

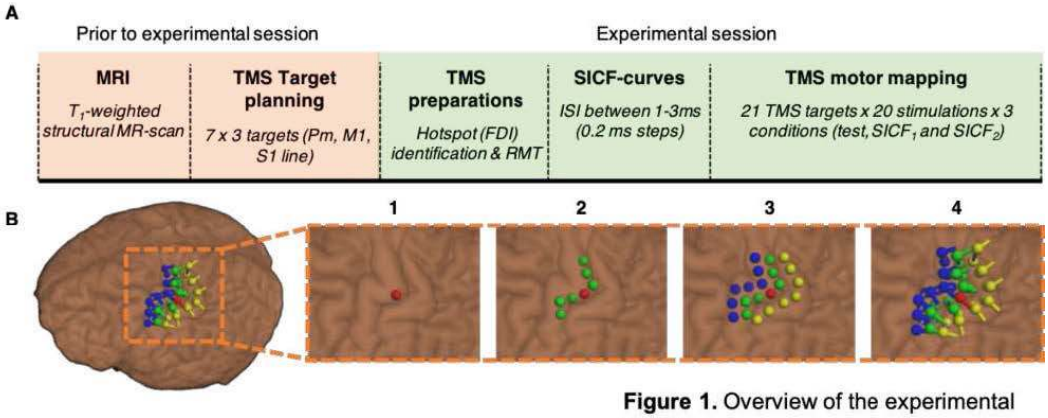

Figure 1. Overview of the experimental setup

Results: Paired-pulse SICF TMS resulted in larger corticomotor maps than single-pulse TMS ($P<0.001$). For both hand muscles, SICF maps consistently showed a posterior shift of CoGs towards the central sulcus relative to the CoG derived from single-

pulse maps (SICF2: 0.62 +/- 0.21, P=0.01, SICF1: 1.28, +/- 0.21, P<0.001). The CoG shift was more pronounced for the SICF1 compared to SICF2 map (0.66 +/- 0.21, P=0.005)(figure 2). ADM and FDI maps consistently displayed a medial-to-lateral segregation in all maps (P<0.001).

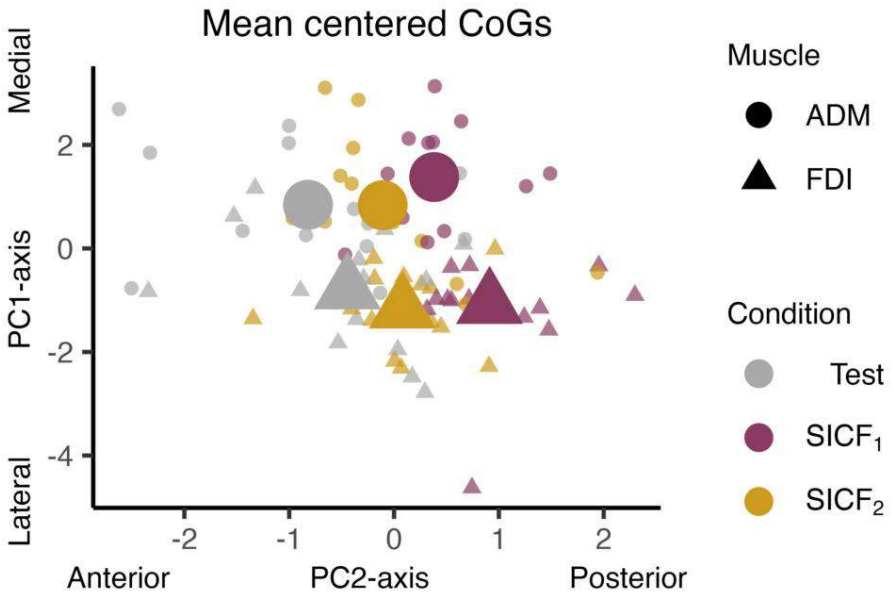

Conclusions: SICF-generating circuits have a more posterior corticomotor representation in the precentral crown than single pulse MEP generating circuits. This finding indicates that spatially distinct cortical circuits are engaged by paired pulse TMS probing SICF compared to single-pulse TMS, at least when using biphasic pulses. The findings also support the notion that spatially distinct circuits are involved in the generation of the first and second SICF peaks.

References

1. Barker, A. T., R. Jalinous and I. L. Freeston (1985). "Non-invasive magnetic stimulation of human motor cortex." Lancet 1(8437): 1106-1107.
2. Di Lazzaro, V., A. Oliviero, P. Profice, E. Saturno, F. Pilato, A. Insola, P. Mazzone, P. Tonali and J. C. Rothwell (1998). "Comparison of descending volleys evoked by transcranial magnetic and electric stimulation in conscious humans." Electroencephalogr Clin Neurophysiol 109(5): 397-401.
3. Raffin, E., G. Pellegrino, V. Di Lazzaro, A. Thielscher and H. R. Siebner (2015). "Bringing transcranial mapping into shape: Sulcus-aligned mapping captures motor somatotopy in human primary motor hand area." Neuroimage 120: 164-175.
4. Ziemann, U., F. Tergau, E. M. Wassermann, S. Wischer, J. Hildebrandt and W. Paulus (1998). "Demonstration of facilitatory I wave interaction in the human motor cortex by paired transcranial magnetic stimulation." J Physiol 511 (Pt 1): 181-190.

Poster No 123

Real-time control software for EEG- and EMG-guided TMS

Olli-Pekka Kahilakoski[1], Kyösti Alkio[1], Kim Valén[1], Matilda Makkonen[1], Tuomas Mutanen[1], Risto Ilmoniemi[1], Timo Roine[1]

[1]Aalto University School of Science, Espoo, Finland

Introduction: Transcranial magnetic stimulation (TMS) is routinely used in functional mapping of the human brain and in treatment of several neurological and psychiatric disorders (Tremblay et al. 2019). TMS can be combined with electroencephalography (EEG) and electromyography (EMG) to measure brain and muscle responses, respectively (Ilmoniemi & Kicić 2010), and to allow adjusting the stimulation online in a closed loop. However, guiding the stimulation based on EEG or EMG has traditionally been performed manually (Casarotto et al. 2022), has taken place in non-real-time scenarios, or has relied on specialized hardware (Zrenner et al. 2018). Moreover, there has been a lack of general frameworks that would allow arbitrary stimulation algorithms to be implemented using high-level programming languages.

Methods: We introduce real-time control software for EEG- and EMG-guided TMS, integrating (i) customizable Python-based preprocessing and stimulation algorithms, (ii) a user-friendly graphical user interface for selecting algorithms and monitoring the system state, and (iii) presentation of sensory stimuli for the subject, synchronized with the EEG and the stimulation pulses. The software runs on a desktop computer with real-time-enabled Ubuntu Linux. The core of the software is written in C++ to achieve the determinism and high performance needed for real-time applications. The communication architecture of the software is Robot Operating System (ROS2), chosen for its flexible communication patterns and suitability for real-time

computing. The customizability of the software allows it to support a variety of existing and novel stimulation protocols, such as timing the stimulation pulses at specific phases of an ongoing EEG rhythm or at a high-excitability connectivity state.

Conclusions: Our software enables controlling closed-loop EEG–TMS experiments in real time on a desktop computer. Employing Python for algorithm implementation has the advantage of a large userbase and strong support in the research community. In addition, its relative ease of use allows for rapid prototyping and facilitates developing novel stimulation and data analysis protocols. Using ROS as the communication architecture has several benefits: (i) it enables a modular design, distributing the state across the services, and (ii) it includes support for recording and playing back experiments. By following many of the best practices in software development, such as continuous integration, version control, and regular code reviews, we aim to ensure the maintainability and extensibility of the software. Future work includes supporting several EEG devices and integrating application programming interfaces (APIs) of various TMS devices with the software, as well as establishing a library of predefined preprocessing and stimulation algorithms.

References

1. Casarotto, S., et al. (2022), 'The rt-TEP tool: real-time visualization of TMS-Evoked Potentials to maximize cortical activation and minimize artifacts', Journal of Neuroscience Methods, vol. 370, 109486. ISSN 0165-0270. https://doi.org/10.1016/j.jneumeth.2022.109486.
2. Ilmoniemi, R.J. and Kičić, D. (2010), 'Methodology for combined TMS and EEG', Brain Topography, vol. 22, no. 4, pp. 233–248. DOI: 10.1007/s10548-009-0123-4.
3. Tremblay, S., et al. (2019), 'Clinical utility and prospective of TMS–EEG', Clinical Neurophysiology, vol. 130, no. 5, pp. 802–844. DOI: 10.1016/j.clinph.2019.01.001
4. Zrenner, C., et al. (2018), 'Real-time EEG-defined excitability states determine efficacy of TMS-induced plasticity in human motor cortex', Brain Stimulation, vol. 11, no. 2, pp. 374–389. DOI: 10.1016/j.brs.2017.11.016.

Poster No 124

A quality metric to assess pulsewise-coil displacements during TMS

Ole Numssen[1], Kathleen Williams[1], Sandra Martin[1], Thomas Knösche[2], Gesa Hartwigsen[3]

[1]Max Planck Institute for Human Cognitive and Brain Sciences, Leipzig, Saxony, [2]Max Planck Institute, Leipzig, Saxony, [3]Leipzig University, Leipzig, Saxony

Introduction: Transcranial Magnetic Stimulation (TMS) has emerged as a powerful non-invasive brain stimulation technique with applications in both clinical and research settings. Recently, the field has seen a surge in methodological rigor[1,2], yet a notable gap persists - the absence of a standardized quality metric to thoroughly assess and report pulse-by-pulse placement accuracy in TMS applications. Especially in manually-guided TMS, where experimenters compensate for movements, coil displacements significantly impact stimulation exposure, potentially hindering therapeutic or scientific outcomes. Despite extensive use of neuronavigation systems, there is currently no straightforward metric to quantify this critical factor. Unlike other neuroscientific modalities, such as functional magnetic resonance imaging (fMRI), where motion quantification is firmly integrated[3], TMS lacks a standardized method to quantify TMS coil displacement during experiments. Here, we introduce a novel metric for TMS coil displacement: pulsewise coil displacement (PCD). PCD combines three positional (x, y, and z) and three rotational parameters (α, β, γ) for each TMS pulse into one compound metric. This metric, PCD, offers a meaningful and straightforward assessment tool for both trial-to-trial stimulation accuracy and the overall quality of a TMS experiment. PCD fills a critical void, providing researchers and clinicians with means to evaluate and report the accuracy of TMS applications, contributing to enhanced methodological rigor and reporting standards in the field.

Methods: TMS coil placements are tracked by neuronavigation systems with six parameters defining its position and orientation [Fig. 1a]. To assess positional displacements in a meaningful manner, a coordinate transformation is applied to differentially quantify orthogonal and tangential coil movements. Rotational displacement of the coil was assessed by transforming roll and pitch displacements into positional displacements using a beam projection method. With this approach, the roll and pitch displacements are transformed into a positional displacement of the stimulation center at a specific skin-cortex distance. Yaw displacements are quantified separately, because effects of yaw displacements critically depend on the coil geometry. To provide one metric, yaw displacements are included in the PCD compound metric by sin(yaw) (Fig. 1b). Validation: (1) For a large set of virtual TMS experiments (50,000 pulses) e-fields[4] at target and off-targets were extracted to analyze PCD's correlation with cortical stimulation exposure. (2) To assess PCD's correlation with online TMS effects we analyzed a dataset on primary motor cortex stimulation and motor evoked potentials (MEPs)[5]. (3) Finally, we used linear mixed models to identify PCD's potential to explain variance in cortical activity modulation after cTBS to the left and right inferior parietal lobe.

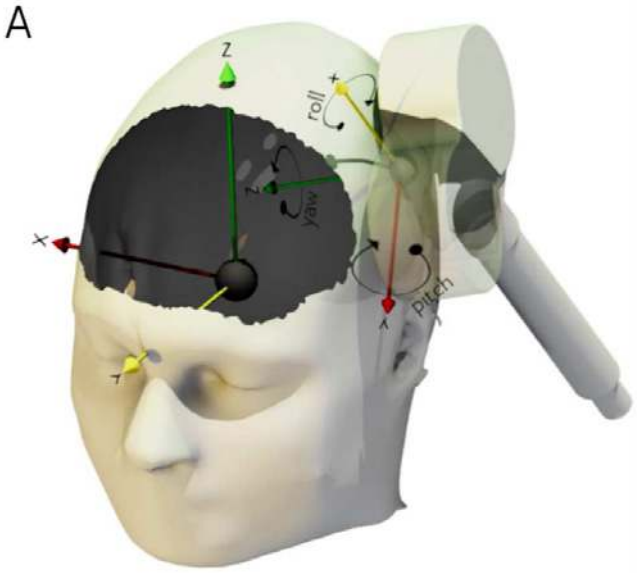

B

$$\sum Pos_n = \sqrt{\Delta x_{cn}^2 + \Delta y_{cn}^2} + \Delta z_{cn}^2 \cdot \text{sign}(\triangle z_{cn})$$

$$\sum Rot_n = SCD \cdot \sin(\Delta roll_n) + SCDprojection(\Delta pitch, \Delta yaw)$$

$$PCD_n = \sum Pos_n + \sum Rot_n$$

Results: (1) PCD, consolidating information from all six displacement parameters (Fig. 2a), exhibited significant correlations with the induced e-fields at target (Fig. 2b) and off-target regions. (2) Validation against motor-evoked potentials (MEPs) demonstrated a similar correlation strength of r(PCD, MEP) and r(e-field, MEP) (Fig. 2c). (3) PCD explained variance in local cortical activity modulation. Specifically, PCD explained fractional amplitude of low frequency fluctuations (fALFF)[6] variance in stimulated regions only (Fig. 2c).

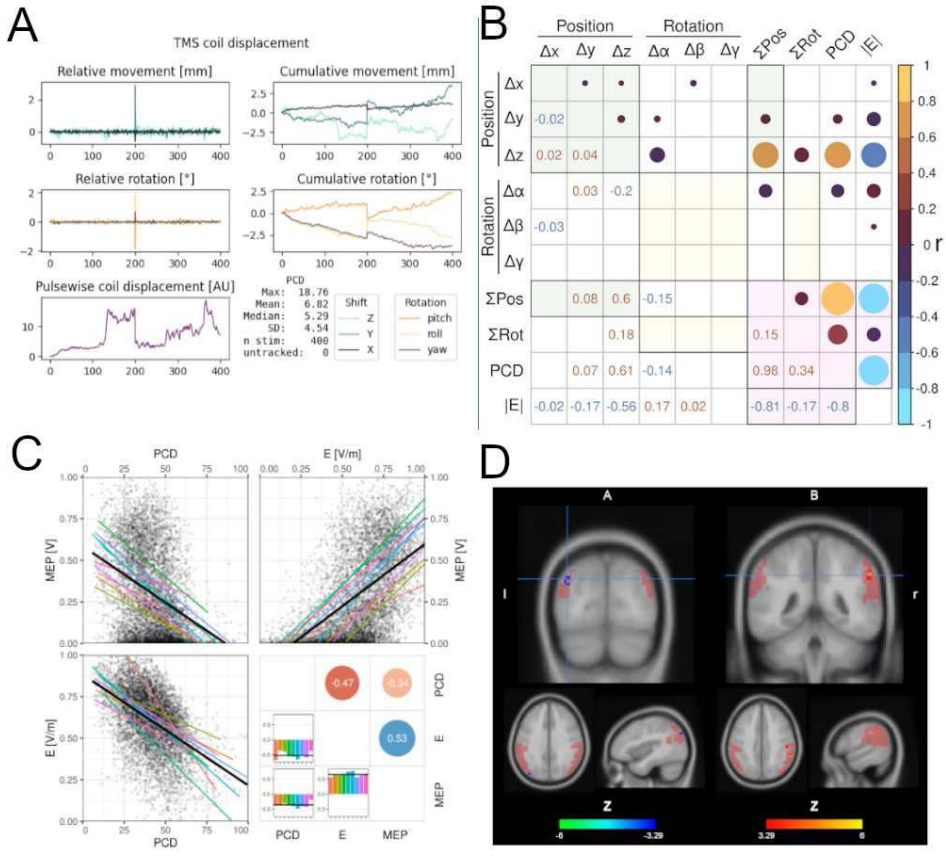

Conclusions: We present a novel metric to quantify subject- or TMS-coil-movement throughout a TMS experiment or therapeutic intervention in a pulse-by-pulse manner. The validation against physical and physiological effects underlines its capabilities to capture relevant variance of TMS effects stemming from experimental imperfections. We provide means for automated PCD quantification within our pyNIBS[5] python package. Potential applications of PCD include quality control, statistical model strengthening, and intervention monitoring.

References

1. Bertazzoli, G. (2022). BIDS Extension Proposal NIBS (BEP37NIBS). https://bids.neuroimaging.io/bep037
2. Anil, S., & D'Souza, J. (2023). Toward Semantic Publishing in Non-Invasive Brain Stimulation: A Comprehensive Analysis of rTMS Studies. arXiv preprint. https://arxiv.org/pdf/2310.06517.pdf
3. Power, J. D., Mitra, A., Laumann, T. O., Snyder, A. Z., Schlaggar, B. L., & Petersen, S. E. (2014). Methods to detect, characterize, and remove motion artifact in resting state fMRI. Neuroimage, 84, 320-341. DOI: 10.1016/j.neuroimage.2013.08.048
4. Puonti, O., Van Leemput, K., Saturnino, G. B., Siebner, H. R., Madsen, K. H., & Thielscher, A. (2020). Accurate and robust whole-head segmentation from magnetic resonance images for individualized head modeling. Neuroimage, 219, 117044.
5. Numssen O, Zier AL, Thielscher A, Hartwigsen G, Knösche TR, Weise K. Efficient high-resolution TMS mapping of the human motor cortex by nonlinear regression. Neuroimage. 2021 Dec 15;245:118654. doi: 10.1016/j.neuroimage.2021.118654. Epub 2021 Oct 12. PMID: 34653612.
6. Zou, Q. H., Zhu, C. Z., Yang, Y., Zuo, X. N., Long, X. Y., Cao, Q. J., Wang, Y. F., & Zang, Y. F. (2008). An improved approach to detection of amplitude of low-frequency fluctuation (ALFF) for resting-state fMRI: fractional ALFF. Journal of neuroscience methods, 172(1), 137–141. DOI: 10.1016/j.jneumeth.2008.04.012

Poster No 125

Electric-field-based TMS-dosing

Ole Numssen[1], Philipp Kuhnke[2], Konstantin Weise[1,3], Gesa Hartwigsen[2]

[1]Max Planck Institute for Human Cognitive and Brain Sciences, Leipzig, Saxony, [2]Leipzig University, Leipzig, Saxony, [3]Leipzig University of Applied Sciences, Leipzig, Germany

Introduction: Non-invasive brain stimulation (NIBS), notably transcranial magnetic stimulation (TMS), has transformed our understanding of brain function and its modulation in health and disease. However, challenges persist, particularly in achieving consistent and reliable outcomes due to high variability in individual responses. One crucial factor influencing the variability of NIBS effects is the stimulation intensity or "dosing". The gold standard for dosing, the motor threshold (MT), faces limitations in accurately calibrating cortical stimulation exposure across diverse brain regions. Here[1], we present an electric field (e-field) based dosing approach, providing a promising avenue to overcome these limitations. This approach utilizes individualized simulations of NIBS-induced e-fields to precisely match cortical stimulation exposure within and across individuals, offering potential improvements in the reliability and efficacy of NIBS.

Methods: Based on high-resolution head models[2] constructed from structural MRI images, we computed the TMS-induced e-fields for several stimulation sites for 18 healthy subjects. By using our previously proposed TMS-mapping procedure[3], we precisely identified finger muscle representations in the primary motor cortex. After measuring the resting motor threshold (rMT) in an experimental session, we calculated the cortical stimulation intensity (|E| in V/m) in the primary motor cortex at rMT to quantify the cortical excitation threshold on an individual and bio-physiologically plausible level. Subsequently, we compared the realized cortical stimulation intensity at four cortical regions (somatomotor cortex, auditory cortex, inferior parietal lobe, dorsolateral prefrontal cortex) in each subject for three different TMS dosing approaches: rMT-based dosing, Stokes-adjusted[4], and e-field based dosing. Specifically, we compared the realized stimulation intensities at these four targets for all three dosing approaches with the individual, cortical excitability threshold quantified in M1.

Results: In comparison to MT-based and Stokes-adjusted dosing, e-field dosing optimally matches the cortical stimulation strength both within (Fig. 1) and across individuals (Fig. 2). Interestingly, the Stokes adjustment does not better match the cortical stimulation strength between targets than simple MT-based dosing. E-field based dosing minimizes the within-subject variance of cortical stimulation exposure, as each cortical target receives the same stimulation strength, addressing a longstanding challenge in NIBS research. Across subjects, the cortical excitation threshold is determined at ~60 V/m, with substantial differences between individuals ranging from ~40 V/m to ~90 V/m, potentially identifying imperfections in the modeling pipeline (such as differences in tissue conductivities). On average, however, e-field dosing matches the cortical stimulation strength between targets also across participants.

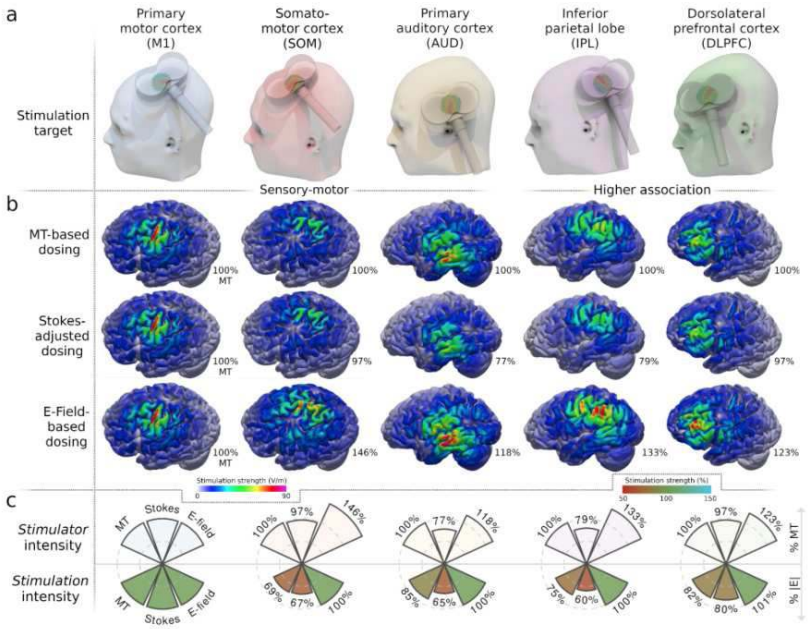

Figure 1. E-field dosing outperforms other dosing strategies on the subject level. (a) All coil placements were selected to maximize the cortical target stimulation. (b) Dosing based on the motor threshold (MT) alone (upper row) applies the same *stimulator* intensity across different cortical target regions (columns), yielding highly variable cortical *stimulation* strengths (quantified in volts per meter; V/m). The "Stokes" method (middle row) linearly adjusts the *stimulator* intensity for coil-to-target distance, but still results in a suboptimal match of cortical *stimulation* across targets. E-field based dosing (bottom row) yields the same cortical *stimulation* strength for all targets. Color: |E|. Percentages: % of MT stimulator intensity. All e-fields are visualized on the gray matter surface for one exemplary subject. (c) The relationship between *stimulator* intensity (upper row) and cortical *stimulation* exposure (bottom row) differs strongly across cortical targets. The *stimulation* exposures were extracted at the cortical targets and related to M1 exposure at MT intensity ('100%').

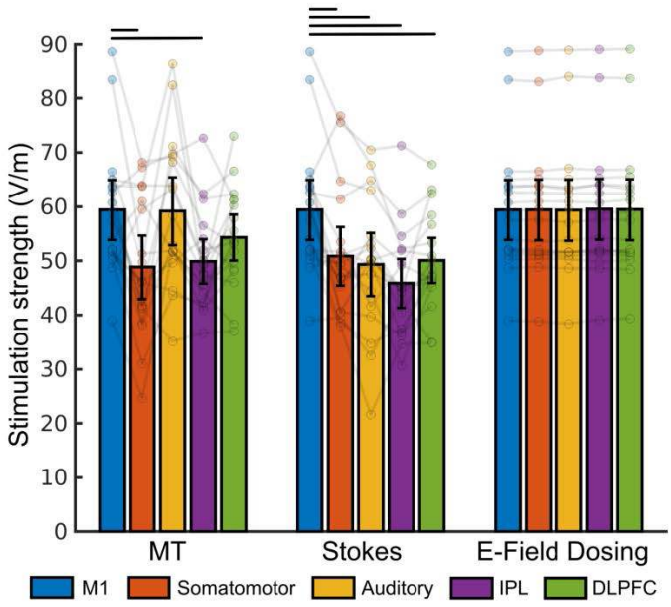

Figure 2. E-field based dosing outperforms other dosing strategies on the group level. The cortical stimulation strength is highly variable for MT-based dosing (left) and Stokes-adjusted dosing (middle), both within and between the 18 participants across the different cortical targets. In contrast, e-field based dosing (right) yields the same stimulation strength for all targets within each participant, which also minimizes the between-subject variability. E-field magnitudes (|E|) were extracted and averaged within spherical ROIs (r = 5 mm) from gray matter volume only. Connected dots show individual subject data; error bars represent the 95% confidence interval. Black bars indicate significant differences ($p < 0.05$; Bonferroni-Holm corrected for multiple comparisons).

Conclusions: In conclusion, e-field based dosing represents a promising advancement in the field of non-invasive brain stimulation, both for neuroscientific research and clinical applications. By moving beyond the limitations of MT-based (and

Stokes-adjusted) dosing, this approach offers a robust and individualized strategy for calibrating cortical stimulation exposure. By better standardizing the cortical stimulation exposure across subjects and within subjects across brain regions, we aim to decrease the variance of NIBS effects that often impede strong group-level effects.

References

1. Numssen, O., Kuhnke, P., Weise, K., & Hartwigsen, G. (2023). Electrical field based dosing improves non-invasive brain stimulation. bioRxiv, 2023-07.
2. Puonti, O., Van Leemput, K., Saturnino, G. B., Siebner, H. R., Madsen, K. H., & Thielscher, A. (2020). Accurate and robust whole-head segmentation from magnetic resonance images for individualized head modeling. Neuroimage, 219, 117044.
3. Numssen O, Zier AL, Thielscher A, Hartwigsen G, Knösche TR, Weise K. Efficient high-resolution TMS mapping of the human motor cortex by nonlinear regression. Neuroimage. 2021 Dec 15;245:118654. doi: 10.1016/j.neuroimage.2021.118654. Epub 2021 Oct 12. PMID: 34653612.
4. Stokes, M. G., Chambers, C. D., Gould, I. C., Henderson, T. R., Janko, N. E., Allen, N. B., & Mattingley, J. B. (2005). Simple Metric For Scaling Motor Threshold Based on Scalp-Cortex Distance: Application to Studies Using Transcranial Magnetic Stimulation. J. Neurophysiol., 94, 4520–4527. DOI: 10.1152/jn.00067.2005

Poster No 127

TMS direct effects of orbitofrontal cortex stimulation: An interleaved TMS-fMRI study

Hyuntaek Oh[1], Julia Myerson[2], Ramiro Salas[1]

[1]Baylor College of Medicine, Houston, TX, [2]The Menninger Clinic, Houston, TX

Introduction: Transcranial magnetic stimulation (TMS) is an FDA-approved non-invasive brain stimulation technique that effectively treats a variety of psychiatric disorders, including major depressive disorder (MDD). TMS over the left dorsolateral prefrontal cortex (dlPFC) has shown promise as a therapeutic tool for treatment-resistant depression (TRD). Recently, TMS has been applied to the orbitofrontal cortex (OFC) as a new possible treatment tool for substance use disorders (SUD). The OFC has been associated with decision-making and goal-directed behavior, and previous studies have found that functional connectivity dysfunction in the OFC is associated with the abuse of various substances. However, the direct effects of OFC stimulation using TMS, which could be a promising brain target for SUD, are largely unknown. Here, we investigated the mechanisms by which TMS induces functional activation in the human brain network by capturing dynamic changes. Specifically, we combined TMS with functional magnetic resonance imaging (fMRI) in an interleaved TMS-fMRI approach to characterize functional and distributed networks through the causal manipulation of human brain activity.

Methods: Healthy participants (N = 15) were recruited locally in Houston, Texas. Depression, substance use, and suicidality were assessed using the PHQ-9, WHO-ASSIST, and SBQ-9, respectively. Urine samples were collected before the fMRI scan to confirm eligibility. Subjects reported no history of neurological or psychiatric disorders, and they signed a written informed consent form to be enrolled in this study. The interleaved TMS-fMRI setup utilized the posterior elements of the 12-channel head matrix coil and the flexible 6-channel body matrix coil, creating sufficient space to accommodate a custom-built coil holder securing the TMS coil to the scanner bed. The TMS coil position on the left OFC was determined using the standardized international 10-20 EEG system (with FP1). Participants were scanned in a 3T Siemens Prisma MR scanner in the Core for Advanced MR Imaging at Baylor College of Medicine. Three runs of interleaved TMS-fMRI were acquired using the Multi-Echo EPI sequence (TR/TE1/TE2/TE3 = 2000/23.4/61.26/99.12 ms, 2.75 mm isotropic voxels, FOV = 210 mm). To generate brief periods of neural activity, single TMS pulses were delivered during a 250ms gap between volumes, and participants received a total of 60 single TMS pulses. Interleaved TMS-fMRI data was preprocessed with a standard pipeline in MNI space using AFNI. AFNI's 3dttest+ function was utilized to test the average estimate in a group level analysis.

Results: Average scores of PHQ-9, SBQ-9, and WHO-ASSIST total were 1.86 (± 2.25), 1.57 (± 2.87), and 10.21 (± 7.66), respectively, which indicate participants had minimal or low severity of psychiatric symptoms. All participants showed negative urine drug tests. Group-wise average resting motor threshold (rMT) was 74% (±10.24) of the maximum stimulator output. Figure 1 shows the group average of brain responses to the TMS effects of OFC stimulation. The results of a whole-brain analysis revealed that single TMS pulses to the left OFC could evoke brain responses in specific brain regions, including the right middle frontal gyrus, anterior and posterior cingulate cortex, bilateral caudate, putamen, and amygdala, and precuneus (FDR-corrected $q < 0.01$).

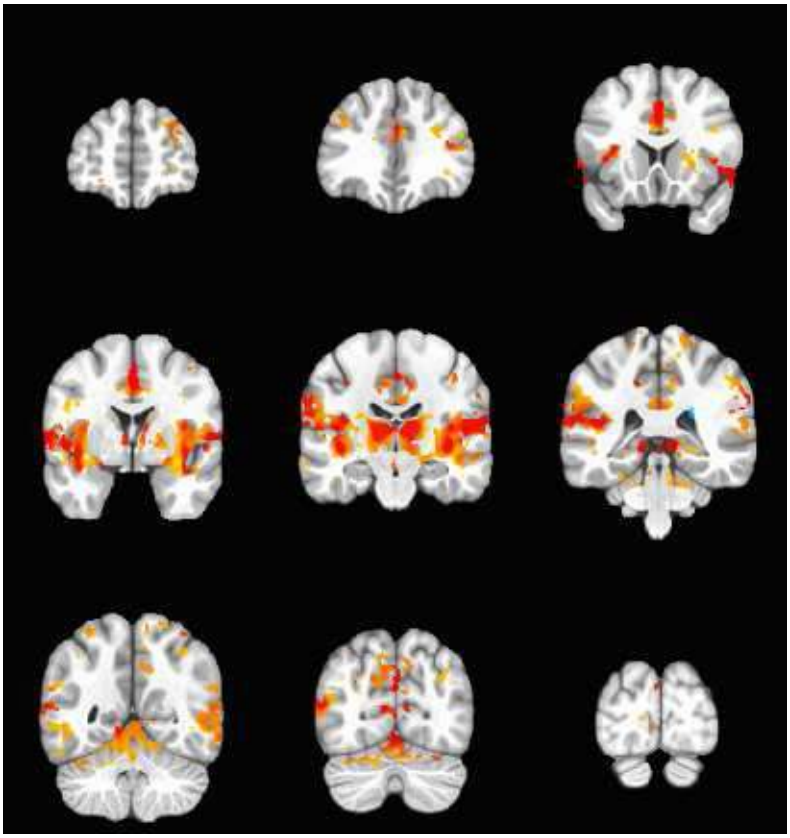

Conclusions: In this study, we administered single TMS pulses to investigate the direct effects of TMS stimulation on the left OFC. Our findings suggest that the left OFC could serve as a potential target for TMS intervention in psychiatric disorders, including SUD and depression. Future studies will explore the clinical application of repetitive TMS (rTMS) for patients with SUD.

References

1. Fox, M. D. (2012). Measuring and manipulating brain connectivity with resting state functional connectivity magnetic resonance imaging (fcMRI) and transcranial magnetic stimulation (TMS). Neuroimage, 62(4), 2232-2243.
2. Hanlon, C. A. (2015). What goes up, can come down: Novel brain stimulation paradigms may attenuate craving and craving-related neural circuitry in substance dependent individuals. Brain research, 1628, 199-209.
3. Oh, H. (2019). EPI distortion correction for concurrent human brain stimulation and imaging at 3T. Journal of neuroscience methods, 327, 108400.
4. Oh, H. (2020). Orbitofrontal, dorsal striatum, and habenula functional connectivity in psychiatric patients with substance use problems. Addictive Behaviors, 108, 106457.
5. Schoenbaum, G. (2008). The role of orbitofrontal cortex in drug addiction: a review of preclinical studies. Biological psychiatry, 63(3), 256-262.
6. Tik, M. (2023). Acute TMS/fMRI response explains offline TMS network effects–An interleaved TMS-fMRI study. NeuroImage, 267, 119833.
7. Vink, J. J. (2018). A novel concurrent TMS-fMRI method to reveal propagation patterns of prefrontal magnetic brain stimulation. Human brain mapping, 39(11), 4580-4592.

Poster No 128

A network meta-analysis for rTMS in the treatment of Obsessive-Compulsive Disorder in Adults

Jiawen Tian[1], Hailong Li[1], Ping Wang[1], Yingxue Gao[1], Xiaoqi Huang[1]

[1]Huaxi MR Research Center (HMRRC), Department of Radiology, West China Hospital of Sichuan University, Chengdu, Sichuan

Introduction: Obsessive-compulsive disorder (OCD) detrimentally affects individuals' personal, social, and professional lives, making it a pressing psychiatric challenge. Although traditional cognitive-behavioral therapy and selective serotonin reuptake inhibitors provide relief, a significant proportion of patients respond inadequately[1-2]. The potential of adjunctive therapies like repetitive transcranial magnetic stimulation (rTMS), which may alleviate symptoms by modulating cortical activity, has gained attention[3]. Nevertheless, determining the optimal strategies for rTMS, including target areas and frequencies, is an ongoing

area of research and debate. Our network meta-analysis aims to evaluate and rank rTMS modalities for OCD treatment, establishing a hierarchy of efficacy and tolerability.

Methods: We focused on randomized controlled trials (RCTs) involving adults with OCD, this systematic review and network meta-analysis adhered to the PRISMA guidelines. The study conducted a comprehensive database search (Cochrane Central, PubMed, Web of Science, Embase) until November 15, 2023. Eligible studies compared various rTMS strategies against sham rTMS. We performed pairwise meta-analyses to assess each direct comparison within a random-effects model, using the "metan" package in STATA14.0. Random-effects network meta-analyses were conducted to assess each direct and indirect comparison within a Bayesian framework using the "gemtc" and "rjags" packages in R4.3.1. Both methods indicated by changes in Y-BOCS scores before and after treatment. On this basis, we also conducted a sensitivity analysis by sequentially removing individual studies from the pooled research in STATA.

Results: The search yielded 1877 references, ultimately including 33 RCTs totalling 1113 patients in the final analysis. (Figure 1a) Regarding the efficacy, pairwise meta-analysis indicated that low-frequency rTMS (LF-rTMS) targeting the right/left dorsolateral prefrontal cortex (DLPFC) were significantly more efficacious than sham rTMS in reducing the Y-BOCS scores. Alternatively, no significant differences were found in the drop-out rates between active and sham rTMS of tolerability. (Figure 1b) Network meta-analysis provided ranking through cumulative probability plots and SUCRA value. In terms of efficacy, high-frequency rTMS (HF-rTMS) applied over the bilateral DLPFC and LF-rTMS over right DLPFC achieved the highest efficacy ranks (SUCRA: 93.7 and 85.3%). Stimulation of the right DLPFC was generally better than the left side, regardless of LF/HF-rTMS, and LF-rTMS was more effective than HF-rTMS. In addition, LF-rTMS to the pre-supplementary motor area (pre-SMA) demonstrated higher efficacy to SMA. cTBS appears to be the least effective. In terms of tolerability, LF-rTMS applied over pre-SMA was the most tolerated. Sensitivity analysis, conducted by systematically excluding each study, confirmed the stability of the results. (Figure 2)

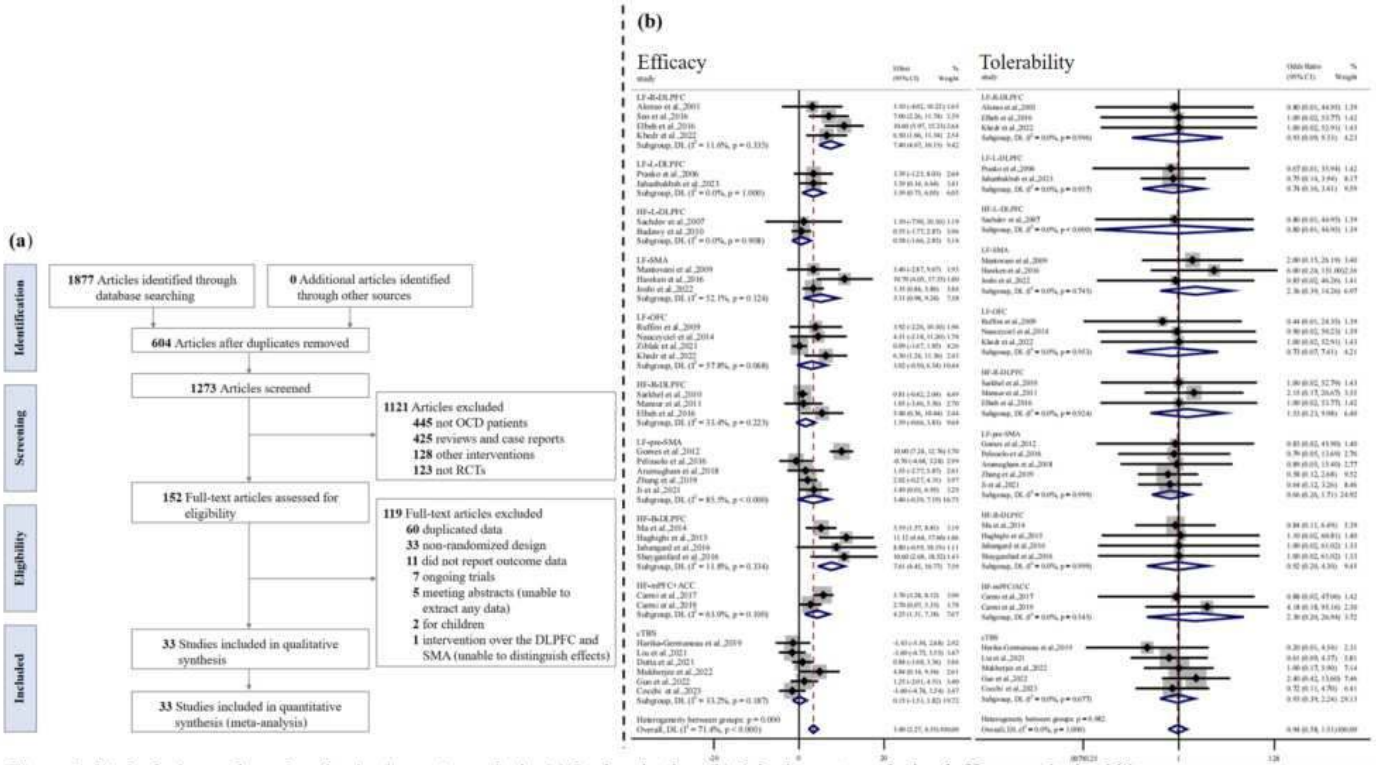

Figure 1. Study design and results of pairwise meta-analysis. (a) Study selection. (b) Pairwise meta-analysis of efficacy and tolerability.

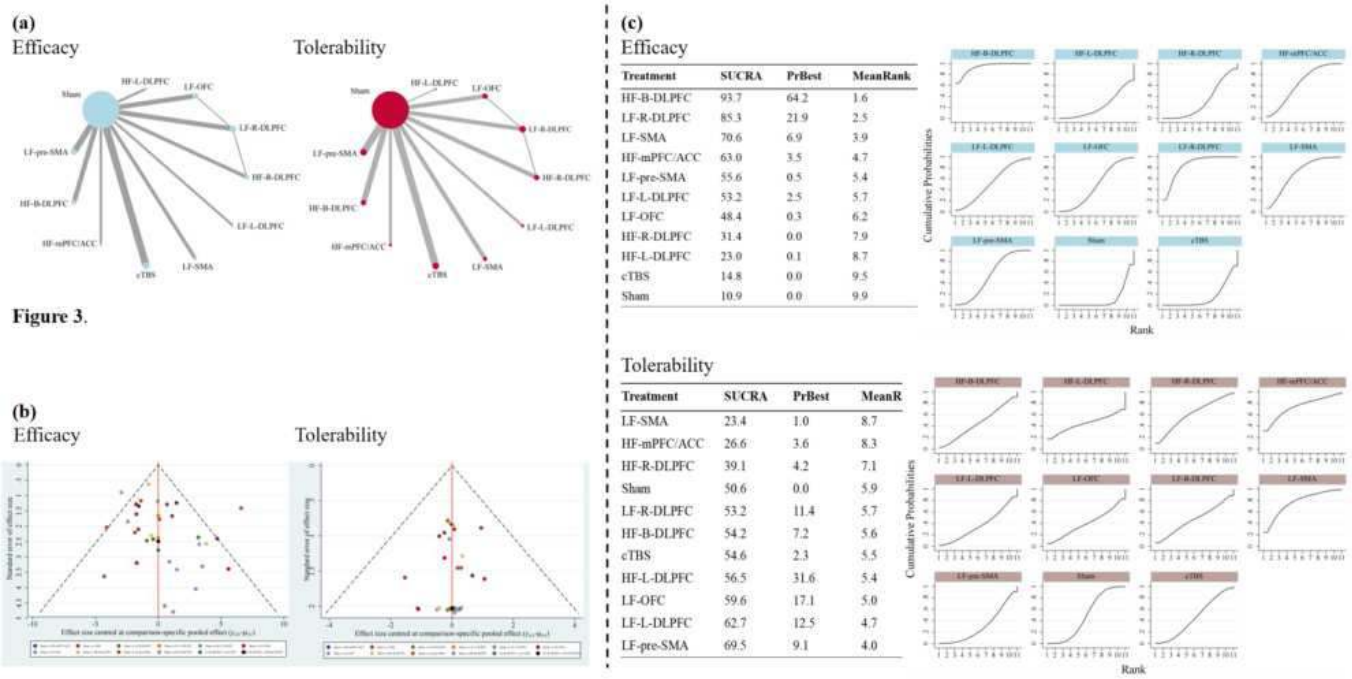

Treatment	SUCRA	PrBest	MeanRank
HF-B-DLPFC	93.7	64.2	1.6
LF-R-DLPFC	85.3	21.9	2.5
LF-SMA	70.6	6.9	3.9
HF-mPFC/ACC	63.0	3.5	4.7
LF-pre-SMA	55.6	0.5	5.4
LF-L-DLPFC	53.2	2.5	5.7
LF-OFC	48.4	0.3	6.2
HF-R-DLPFC	31.4	0.0	7.9
HF-L-DLPFC	23.0	0.1	8.7
cTBS	14.8	0.0	9.5
Sham	10.9	0.0	9.9

Treatment	SUCRA	PrBest	MeanR
LF-SMA	23.4	1.0	8.7
HF-mPFC/ACC	26.6	3.6	8.3
HF-R-DLPFC	39.1	4.2	7.1
Sham	50.6	0.0	5.9
LF-R-DLPFC	53.2	11.4	5.7
HF-B-DLPFC	54.2	7.2	5.6
cTBS	54.6	2.3	5.5
HF-L-DLPFC	56.5	31.6	5.4
LF-OFC	59.6	17.1	5.0
LF-L-DLPFC	62.7	12.5	4.7
LF-pre-SMA	69.5	9.1	4.0

Figure 2. Network meta-analysis (a) Networks of comparisons for efficacy and tolerability. (b) Comparison-adjusted funnel plots for efficacy and tolerability. (c) Ranking regarding efficacy and tolerability are assessed by the surface under the cumulative ranking curve (SUCRA) values.

Conclusions: In current study, we offer a comprehensive comparison of rTMS modalities, which is the largest sample size network meta-analysis of rTMS for adult OCD to date. Differing from previous studies, we further refined the stimulation targets into the right/left DLPFC, SMA/pre-SMA. Both pairwise and network meta-analyses revealed that LF-rTMS applied over the right DLPFC and HF-rTMS applied over the bilateral DLPFC were significantly more efficacious than sham rTMS, which appear to be the most promising rTMS strategy for OCD treatment. Building on previous studies, we further innovatively found that when targeting the DLPFC, the right side was generally better than the left side, and low frequencies were generally better than high frequencies, aligning with the preference for low-frequency stimulation of the right DLPFC in current clinical practice. Moreover, we noted that cTBS appears to be the least effective. Future research investigating the long-term effects of rTMS and more personalized protocols will be needed to advance treatment for OCD.

References

1. Hirschtritt, M. E. (2017), 'Obsessive-compulsive disorder: advances in diagnosis and treatment', JAMA, vol. 317, pp. 1358-1367.
2. Khedr, E. M. (2022), 'A double blind randomized clinical trial of the effectiveness of low frequency rTMS over right DLPFC or OFC for treatment of obsessive-compulsive disorder'. Journal of psychiatric research, vol. 156, pp. 122-131.
3. Carmi L (2019), 'Efficacy and Safety of Deep Transcranial Magnetic Stimulation for Obsessive-Compulsive Disorder: A Prospective Multicenter Randomized Double-Blind Placebo-Controlled Trial', Am J Psychiatry, vol. 176, no. 11, pp. 931-938.

Poster No 129

TMS Intensity and the Brain: A Computational Approach to Understanding and Predicting Responses

Parsa Oveisi[1,2,3], Davide Momi[1], Zheng Wang[1], Sorenza Bastiaens[1,4], Taha Morshedzadeh[1,4], Christoph Zrenner[2,3,5], John Griffiths[1,4,3,5]

[1]Krembil Centre for Neuroinformatics, Centre for Addiction and Mental Health (CAMH), Toronto, Canada, [2]Temerty Centre for Therapeutic Brain Intervention, Centre for Addiction and Mental Health (CAMH), Toronto, Canada, [3]Institute of Biomedical Engineering, University of Toronto, Toronto, Canada, [4]Institute of Medical Science, University of Toronto, Toronto, Canada, [5]Department of Psychiatry, University of Toronto, Toronto, Canada

Introduction: The growing potential of computational brain models in clinical and research applications is increasingly evident. A crucial advantage for these models is their ability to generalize from one scenario to predict other untested conditions. For instance, modeling a patient's data to simulate their response to various treatments can help identify the most effective treatment protocol. Transcranial magnetic stimulation (TMS) therapy is emerging as a promising treatment for neuropsychiatric disorders like depression1. A key factor affecting brain engagement in TMS is stimulation intensity, which engages individual

brains differently2. Our group has developed a framework for whole-brain connectome-based neural mass modeling in PyTorch ('whobpyt'), previously used to investigate TMS propagation patterns across brain networks3. The present study leverages whobpyt to investigate TMS-evoked brain dynamics at different intensities, and the model's predictive and generalization capabilities. This research will enhance our understanding of TMS-brain interactions and facilitate in-silico testing of TMS treatments for better clinical outcomes.

Methods: We collected single-pulse TMS-EEG data (64 channels, stimulating at the dorsolateral prefrontal cortex) from 21 healthy participants. Pulses were randomized at five different intensities in each session based on participants' unique resting motor threshold (%80 to %120). Empirical analyses: We quantify the TMS-induced brain activity, as well as its response profiles to varying stimulation intensities in terms of: a) localized peak latencies and amplitude changes near the site of stimulation (via Pearson correlation and linear regression), and b) broader spatiotemporal activity changes at different stimulation intensities through permutation cluster testing4. Modeling analyses: We train our model at all 5 intensity conditions to assess if any results in better goodness-of-fit (assessed via cosine similarity (CS) with empirical data). We then assess each of the 5 fitted models' overall prediction accuracy, as well as their ability to replicate the intensity scaling patterns quantified in the empirical analyses. Lastly, we examine relationships between various biologically-interpretable model parameters and intensity of TMS stimulation (via Pearson correlation) to infer potential underlying causes leading to the brain's intensity scaling patterns.

Results: The model showed overall high fitting capabilities (mean CS=0.88, SD=0.04), across different intensities, with performance increasing with intensity ($r=0.39$, $p<0.001$). Predictive accuracy, though generally high (mean CS=0.77, SD=0.12), was highest when the difference between fitted and simulated intensities was minimal. For the model's intensity scaling profiles, while the same empirical peak latencies were replicated, similar amplitude scaling was observed primarily for early peaks at around 75ms ($r=-0.27$, $p<0.05$). In spatiotemporal patterns, the models trained on higher intensities partially replicated certain empirical clusters, particularly those observed in frontocentral regions around 200ms. However, these simulated clusters did not reach statistical significance. Finally, we also found significant correlations between TMS stimulation intensity and the following model parameters: pyramidal-to-excitatory interneuron gains ($r=+0.22$, $p<0.05$), pyramidal-to-inhibitory interneuron gains ($r=-0.25$, $p<0.01$), and the inhibitory interneuron time constant ($r=-0.21$, $p<0.05$). Taken together, results suggest a role of cortical excitation-inhibition balance in TMS-related intensity response profiles.

Conclusions: Here, we demonstrated the capability of our model to reliably capture and replicate the dynamics of TMS across various intensities, albeit with potential for further refinement. Furthermore, we illustrated the utility of analyzing model parameters to deduce the underlying biological mechanisms governing TMS engagement.

References

1. Saini, R. et al. (2018) 'Transcranial magnetic stimulation: A review of its evolution and current applications', Industrial Psychiatry Journal, 27(2), p. 172. doi:10.4103/ipj.ipj_88_18.
2. Pellegrini, M., Zoghi, M. and Jaberzadeh, S. (2018) 'The effect of transcranial magnetic stimulation test intensity on the amplitude, variability and reliability of motor evoked potentials', Brain Research, 1700, pp. 190–198. doi:10.1016/j.brainres.2018.09.002.
3. Momi, D., Wang, Z. and Griffiths, J.D. (2023) 'TMS-evoked responses are driven by recurrent large-scale network dynamics', eLife, 12. doi:10.7554/elife.83232.
4. Maris, E. and Oostenveld, R. (2007) 'Nonparametric statistical testing of EEG- and Meg-Data', Journal of Neuroscience Methods, 164(1), pp. 177–190. doi:10.1016/j.jneumeth.2007.03.024.

Poster No 130

Precision TMS Target Guided by the Amygdala: How Effects Propagate to Deep Nuclei via Fiber Bundles

Yating Ming[1], Jinming Xiao[1], Lei Li[1], Xujun Duan[2]

[1]University of Electronic Science and Technology of China, Chengdu, Sichuan, [2]UESTC, Chengdu, Sichuan

Introduction: Transcranial Magnetic Stimulation (TMS), a non-invasive neuromodulation technique, shows promise in alleviating severe core symptoms of Autism Spectrum Disorder (ASD). Conventional TMS interventions, with fixed stimulation targets, overlook the heterogeneity in the ASD community. To address this, we propose an individualized approach based on amygdala functional connectivity for optimized stimulation targets. A clinical double-blind randomized controlled trial revealed significant improvements with 20 sessions of continuous theta-burst stimulation (cTBS) in the Amygdala-Optimized Functional Connectivity (AOFC) group. Previous research suggests electrophysiological effects of TMS reach deep nuclei via bundles, but specifics involved bundles, impacted nuclei, and their correlation with therapeutic outcomes remain unclear.

Methods: Forty-four children with ASD were randomly assigned to AOFC and NO groups. After excluding incomplete sessions or poor T1 and diffusion-weighted image quality, 32 subjects underwent data analysis. Initial diffusion data preprocessing

included head motion denoising, Gibbs artifacts removal, and bias field correction through FSL. Non-diffusion weighted reference images were registered to corresponding T1 weighted images, and the displacement field was applied to other diffusion weighted images. T1 weighted images were segmented using Freesurfer for fiber tracking and constructing a fiber structural network through MRtrix. Graph theory analysis and tract-based morphometry detected changes influenced by TMS in the global and local structural network and specific fiber bundles. Further investigation explored changes in the amygdala-seed structural network pre- and post-intervention.

Results: Global and local efficiency of the structural network and hippocampuslocal efficiency significantly improved in the AOFC group (P_{FDR}<0.05), along with enhanced small-world properties, while these results were not observed in the NO group. Additionally, the AOFC group exhibited increased diameter, volume, and total surface area of the left arcuate fasciculus fiber, as well as the mean length of the superior longitudinal fasciculus fiber (P_{FDR}<0.05). In contrast, the NO group showed increased fractional anisotropy (FA) in several fibers, particularly the posterior corticostriatal tract (P_{FDR}<0.05). Moreover, the mean length of the superior longitudinal fasciculus was significantly correlated with the symptomatic improvement level in the AOFC group (R^2=0.48, P_{FDR}<0.05), with no similar findings in the NO group. Lastly, the investigation of amygdala-seed structural network changes in the AOFC group revealed a significant increase in FA between the anterior transverse temporal gyrus and the amygdala (P_{FDR}<0.05).

Conclusions: Our study introduced personalized precision targeting, revealing distinct effects on deep nuclei compared to traditional TMS. Optimizing the amygdala target enhanced brain-wide influence from the DLPFC, significantly correlating with the superior longitudinal fasciculus length and therapeutic outcomes. This influence extended to the amygdala's connectivity network, particularly in the anterior transverse temporal gyrus region.

References

1. Kleinhans NM, Richards T, Weaver K, Johnson LC, Greenson J, Dawson G, et al. Association between amygdala response to emotional faces and social anxiety in autism spectrum disorders. Neuropsychologia. 2010;48(12):3665-70.
2. Sturm V, Fricke O, Buhrle CP, Lenartz D, Maarouf M, Treuer H, et al. DBS in the basolateral amygdala improves symptoms of autism and related self-injurious behavior: a case report and hypothesis on the pathogenesis of the disorder. Front Hum Neurosci. 2012;6:341.
3. Oberman LM, Enticott PG, Casanova MF, Rotenberg A, Pascual-Leone A, McCracken JT. Transcranial magnetic stimulation (TMS) therapy for autism: an international consensus conference held in conjunction with the international meeting for autism research on May 13th and 14th, 2014. Front Hum Neurosci. 2014;8:1034.
4. Fox MD, Buckner RL, Liu H, Chakravarty MM, Lozano AM, Pascual-Leone A. Resting-state networks link invasive and noninvasive brain stimulation across diverse psychiatric and neurological diseases. Proc Natl Acad Sci U S A. 2014;111(41):E4367-75
5. Valerie J. Sydnor et al.,Cortical-subcortical structural connections support transcranial magnetic stimulation engagement of the amygdala.Sci. Adv.8,eabn5803(2022).

Poster No 131

Causal network localization of brain stimulation targets for trait anxiety

Shan Siddiqi[1], Julian Klingbeil[2], Ian Kratter[3], Daniel Blumberger[4], Mark George[5], Jordan Grafman[6], Alvaro Pascual-Leone[7], R. Mark Richardson[8], Pratik Talati[9], Fidel Vila-Rodriguez[10], Jonathan Downar[4]

[1]Harvard Medical School/Brigham and Women's Hospital, boston, MA, [2]University of Leipzig, Leipzig, Germany, [3]Stanford University, Palo Alto, CA, [4]University of Toronto, Toronto, Ontario, [5]Medical University of South Carolina, Charleston, SC, [6]Northwestern University, Chicago, IL, [7]Harvard Medical School, Boston, MA, [8]Massachusetts General Hospital, Harvard Medical School, Boston, MA, [9]Massachusetts General Hospital, Boston, MA, [10]University of British Columbia, Vancouver, BC

Introduction: Transcranial magnetic stimulation (TMS) and deep brain stimulation (DBS) can treat some neuropsychiatric disorders, this approach has only been used to optimize existing targets, not to identify novel targets. Lesions have been used to map causal circuitry and optimize stimulation targets for various disorders such as depression, Parkinson's, addiction, and epilepsy. However, no clear brain stimulation targets are available for anxiety. Here, we use convergent causal data to derive and validate brain stimulation targets for anxiety.

Methods: Across seven datasets (n=936), we mapped circuitry connected to lesion sites and stimulation sites that selectively modify anxiety, independently of depression. First, we mapped the normative connectivity (using a normative human connectome database) of 111 heterogeneous TMS sites and compared it to TMS-induced change in anxiety, yielding a map of connectivity of stimulation sites that relieve anxiety. Next, we used a similar analysis to map the connectivity of 451 lesions that modify anxiety. Next, in 300 TMS patients who were all navigated to the same coordinate, we mapped individualized connectivity of TMS sites that selectively modified anxiety. We combined this information into a common brain circuit, and used this circuit to predict anxiety changes after DBS for Parkinson's disease in 74 patients with heterogeneous DBS sites.

Results: Lesions (n=451) and TMS sites (n=111) that modify anxiety mapped to a common normative brain circuit (p=0.01). In an independent dataset (n=300), individualized TMS site connectivity to this circuit predicted anxiety change (p=0.02). Subthalamic DBS sites overlapping the circuit caused more anxiety (n=74, p=0.006), thus demonstrating a network-level effect, as the circuit was derived without any subthalamic sites. The circuit was specific to trait versus state anxiety in datasets that measured both (p=0.003). The analyses converged on a target in the right superior frontal gyrus.

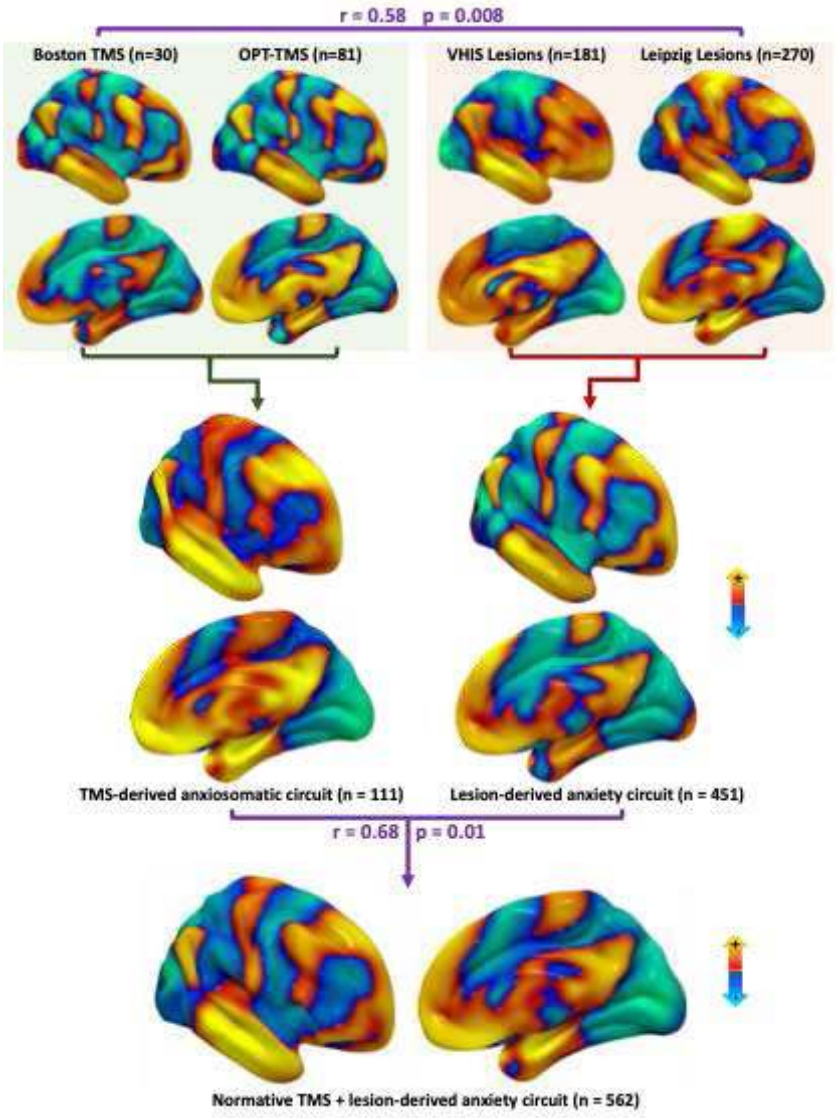

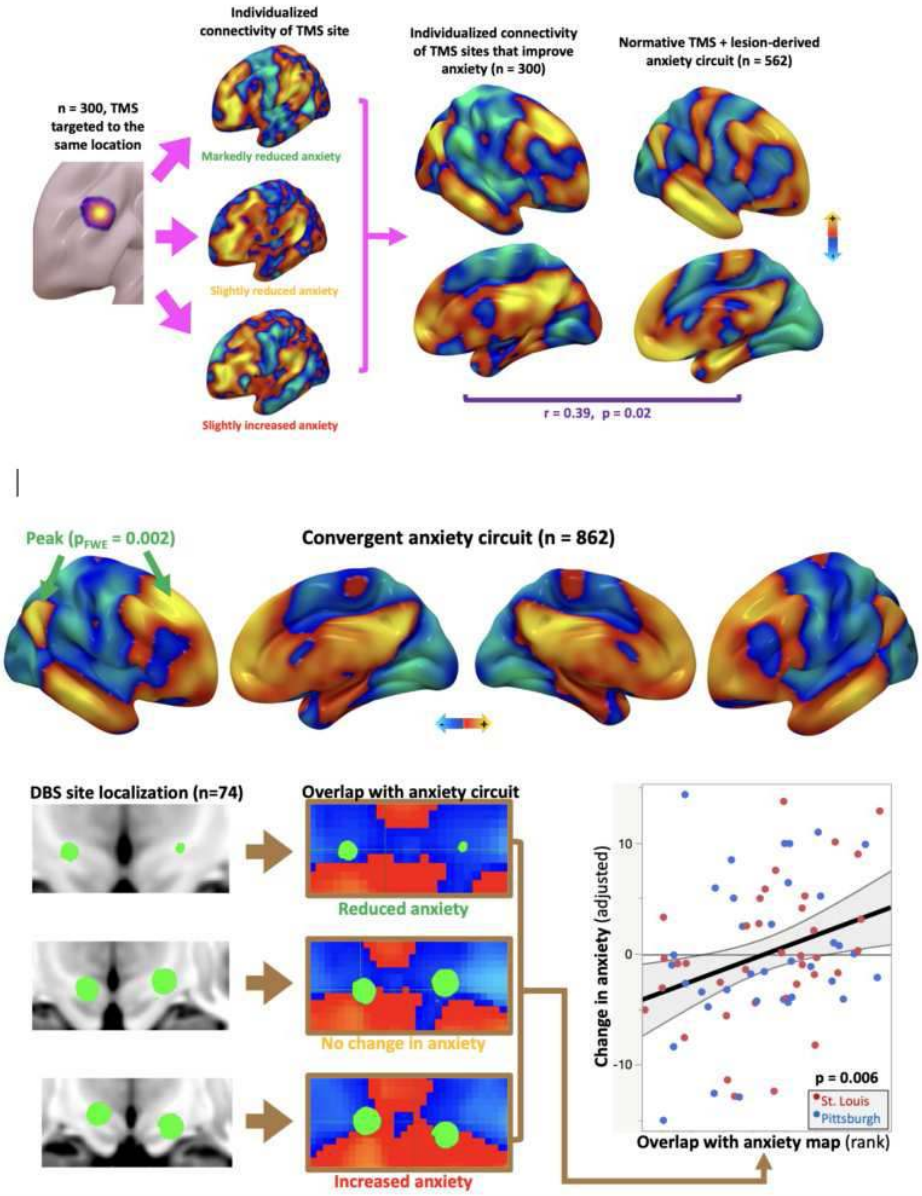

Conclusions: We derived and validated a novel brain stimulation target for trait anxiety. More broadly, this illustrates a pathway for discovering novel circuit-based targets across neuropsychiatric disorders.

References

1. S. H. Siddiqi, K. P. Kording, J. Parvizi, M. D. Fox, Causal mapping of human brain function. Nature reviews. Neuroscience 23, 361-375 (2022).
2. S. H. Siddiqi et al., Brain stimulation and brain lesions converge on common causal circuits in neuropsychiatric disease. Nature human behaviour 5, 1707-1716 (2021).
3. S. H. Siddiqi et al., Distinct Symptom-Specific Treatment Targets for Circuit-Based Neuromodulation. The American journal of psychiatry 177, 435-446 (2020).
4. S. A. Eisenstein et al., Functional anatomy of subthalamic nucleus stimulation in Parkinson disease. Ann Neurol 76, 279-295 (2014).

Poster No 132

Lower brain tissue volume in limbic predominant age-related TDP43 neuropathological change (LATE-NC)

Mahir Tazwar[1], Arnold Evia[2], Abdur Raquib Ridwan[2], David Bennett[2], Julie Schneider[2], Konstantinos Arfanakis[1,2]

[1]Illinois Institute of Technology, Chicago, IL, [2]Rush University Medical Center, Chicago, IL

Introduction: Limbic-predominant age-related TDP-43 encephalopathy neuropathological change (LATE-NC) is common in older adults and is associated with neurodegeneration, cognitive impairment and dementia[9]. However, the association of LATE-NC with brain morphometry has not been thoroughly investigated[3,5,9]. In this work, we examined the voxel-wise association of LATE-NC with brain morphometric anomalies by combining deformation-based morphometry (DBM) on ex-vivo MRI with detailed neuropathology data in a large number of community-based older adults that came to autopsy (N=897).

Methods: Participants, MRI, neuropathology Cerebral hemispheres were acquired from 897 deceased older adults participating in four epidemiological cohort studies of aging: Rush Memory and Aging Project, Religious Orders Study, Minority Aging Research Study, and Clinical Core of Rush Alzheimer's Disease Center[2,4]. Hemispheres were imaged ex-vivo on 3T clinical MRI scanners within approximately 1-month postmortem using 2D multi-echo spin-echo sequence (TE=10–50ms, voxel size=0.6×0.6×1.5mm3) (Fig.1B). The images from the first echo were non-linearly registered to an ex-vivo brain hemisphere template using ANTs[1]. The logarithm of the Jacobian determinant (LogJ) of the deformation fields was calculated in each voxel, and the resulting LogJ maps were smoothed by a 4mm FWHM Gaussian filter (Fig.1A)[6]. Following ex-vivo MRI, hemispheres underwent detailed neuropathologic examination by a board-certified neuropathologist (Fig.1C). Statistical analyses Voxel-wise linear regression was used to test the association between deformations shown in the LogJ maps and LATE-NC stages, controlling for other age-related neuropathologies (Alzheimer's disease, Lewy bodies, arteriolosclerosis, atherosclerosis, cerebral amyloid angiopathy, gross and microscopic infarcts), demographics (age at death, sex, education), postmortem intervals, and scanners. Statistical tests were performed using FSL's PALM tool with 10,000 permutations and threshold-free cluster enhancement[10]. To identify the earliest LATE-NC stage exhibiting morphometric abnormalities, LogJ values were compared between LATE-NC stages 1–5 and stage 0, using voxel-wise linear regression and controlling for the same variables as described above. Statistical significance was set at $p<0.05$ after family-wise error rate (FWER) adjustment to correct for multiple comparisons.

A

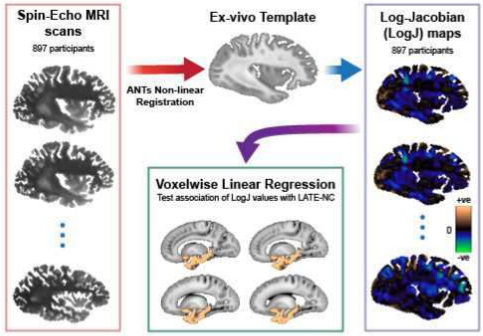

Figure 1A. Deformation-based morphometry (DBM) pipeline. DBM is an image analysis technique that describes localized structural abnormalities at the voxel level from the non-linear deformation fields that align MRI scans to a common anatomical template. Here, the spin-echo images of cerebral hemispheres acquired ex-vivo (left column) were non-linearly registered to an ex-vivo hemisphere template. The log of Jacobian determinant (LogJ) of the deformation fields was calculated for each participant (right column). These LogJ maps were used in a linear regression analysis to test the association between LATE-NC and brain morphometric characteristics.

B

Characteristics	
N	897
Age at death, y (SD)	91 (6)
Male, n (%)	252 (28)
Education, years (SD)	16 (4)
Antemortem clinical diagnosis*	
No cognitive impairment	291 (32)
Mild cognitive impairment	208 (23)
Dementia	398 (45)
Mini-Mental State Examination* (MMSE), mean (SD)	20 (10)
At least one copy of the ε4 allele, n (%)	228 (25)
Left hemisphere, n (%)	486 (54)
Postmortem interval to fixation, hours (SD)	10 (7)
Postmortem interval to imaging, days (SD)	37 (16)
Scanner for ex-vivo MRI, n (%)	
3T GE Signa	75 (8)
3T Siemens Trio	81 (9)
3T Philips Achieva	278 (31)
3T Siemens Verio	463 (52)

*Proximate to death

Figure 1B. Demographic and clinical characteristics of the participants.

C

Characteristics	
N	897
LATE-NC, n (%)	
(Stage 0) no TDP-43 inclusions	**393 (44)**
(Stage 1) TDP-43 inclusions in amygdala	**159 (18)**
(Stage 2) Entorhinal cortex and hippocampus CA1	**100 (11)**
(Stage 3) Anterior temporal cortex	**72 (8)**
(Stage 4) Midtemporal and orbitofrontal cortex	**97 (10)**
(Stage 5) Middle frontal gyrus	**76 (9)**
AD neuropathological change (NIA-AA criteria), n (%)	
No AD	109 (12)
Low	169 (19)
Intermediate	389 (43)
High	230 (26)
Composite score of global AD pathology, mean (SD)	0.8 (0.6)
Lewy bodies, n (%)	257 (29)
Gross infarcts, n (%)	366 (41)
Microscopic infarcts, n (%)	349 (39)
Cerebral amyloid angiopathy, n (%)	
None	183 (20)
Mild	381 (43)
Moderate	222 (25)
Severe	111 (12)
Atherosclerosis, n (%)	
None	193 (22)
Mild	478 (53)
Moderate	183 (20)
Severe	43 (5)
Arteriolosclerosis, n (%)	
None	313 (35)
Mild	338 (37)
Moderate	185 (21)
Severe	61 (7)

NIA-AA, National Institute on Aging and Alzheimer's Association; AD, Alzheimer's disease; LATE-NC, Limbic predominant age-related transactive response DNA binding protein 43 (TDP-43) encephalopathy neuropathological change.

Figure 1C. Neuropathologic characteristics of the participants.

Results: Voxel-wise linear regression revealed an independent association of LATE-NC with significantly lower volume in both gray and white matter regions within the temporal and frontal lobes and basal ganglia ($p<0.05$) (Fig.2A). Significantly lower volume was observed in amygdala, hippocampus, entorhinal, parahippocampal, temporal pole, inferior temporal, middle temporal, fusiform, medial orbitofrontal, lateral orbitofrontal, insula, accumbens, and putamen cortices (Fig.2A). Groupwise comparison of LogJ values revealed significant morphometric anomalies in LATE-NC stages 1–5 compared to stage 0 ($p<0.05$) (Fig.2B). The spatial pattern included small temporal lobe areas in stages 1–2, more temporal lobe tissue as well as basal ganglia tissue in stage 3, and finally also included frontal lobe areas in stages 4–5 (Fig.2B).

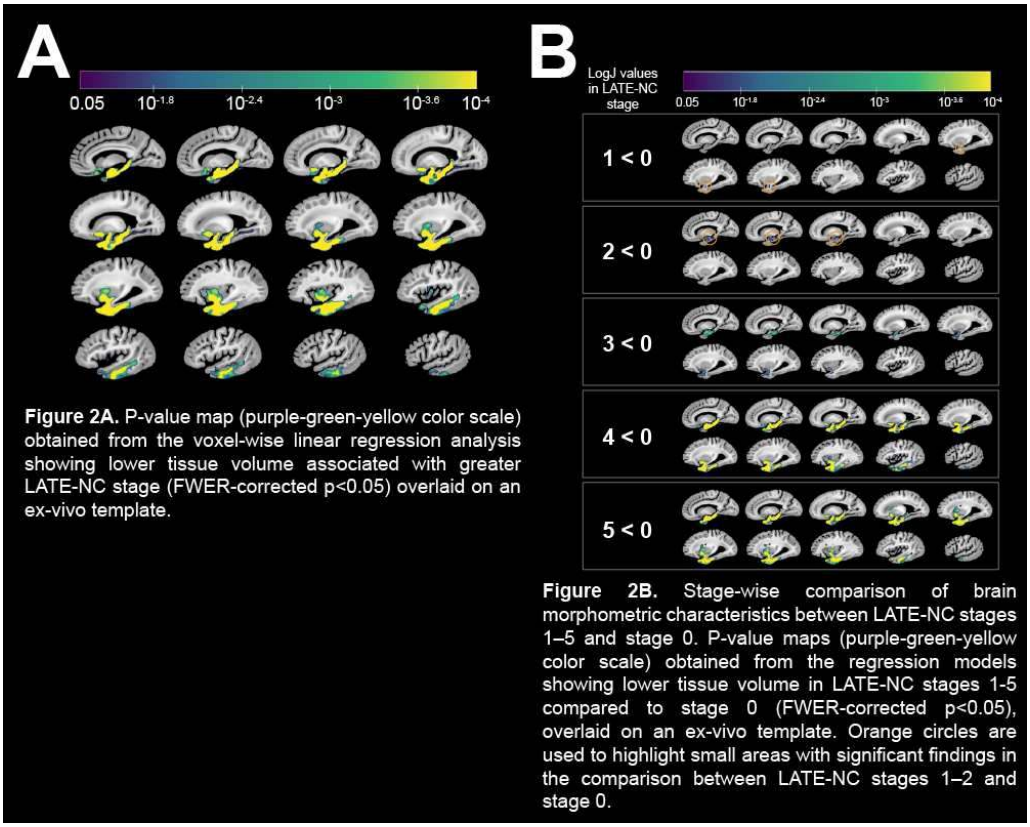

Figure 2A. P-value map (purple-green-yellow color scale) obtained from the voxel-wise linear regression analysis showing lower tissue volume associated with greater LATE-NC stage (FWER-corrected p<0.05) overlaid on an ex-vivo template.

Figure 2B. Stage-wise comparison of brain morphometric characteristics between LATE-NC stages 1–5 and stage 0. P-value maps (purple-green-yellow color scale) obtained from the regression models showing lower tissue volume in LATE-NC stages 1-5 compared to stage 0 (FWER-corrected p<0.05), overlaid on an ex-vivo template. Orange circles are used to highlight small areas with significant findings in the comparison between LATE-NC stages 1–2 and stage 0.

Conclusions: The present study in autopsied brains from a large community-cohort of older adults showed an independent association of LATE-NC with lower volume in both gray and white matter areas of the temporal and frontal lobes and basal ganglia. This pattern is consistent with the known pathological distribution of LATE-NC in the brain[7-9] and may potentially be used in the development of a marker of this devastating neuropathology. Finally, morphometric anomalies were detected as early as LATE-NC stage 1, suggesting that MRI is sensitive to the early stages of the disease.

References

1. Avants, B.B. et al. (2011) 'A reproducible evaluation of ANTs similarity metric performance in brain image registration', NeuroImage, 54(3), pp. 2033–2044.
2. Barnes, L.L. et al. (2012) 'The Minority Aging Research Study: Ongoing Efforts to Obtain Brain Donation in African Americans without Dementia', Current Alzheimer Research, 9(6), pp. 734–745.
3. Bejanin, A. et al. (2019) 'Antemortem volume loss mirrors TDP-43 staging in older adults with non-frontotemporal lobar degeneration', Brain, 142(11), pp. 3621–3635.
4. Bennett, D.A. et al. (2018) 'Religious Orders Study and Rush Memory and Aging Project', Journal of Alzheimer's Disease. Edited by G. Perry et al., 64(s1), pp. S161–S189.
5. Buciuc, M. et al. (2022) 'TDP-43-associated atrophy in brains with and without frontotemporal lobar degeneration', NeuroImage: Clinical, 34, p. 102954.
6. Chung, M.K. et al. (2001) 'A Unified Statistical Approach to Deformation-Based Morphometry', NeuroImage, 14(3), pp. 595–606.
7. Josephs, K.A. et al. (2016) 'Updated TDP-43 in Alzheimer's disease staging scheme', Acta Neuropathologica, 131(4), pp. 571–585.
8. Nag, S. et al. (2018) 'TDP-43 pathology in anterior temporal pole cortex in aging and Alzheimer's disease', Acta Neuropathologica Communications, 6(1), p. 33.
9. Nelson, P.T. et al. (2019) 'Limbic-predominant age-related TDP-43 encephalopathy (LATE): consensus working group report', Brain, 142(6), pp. 1503–1527.
10. Winkler, A.M. et al. (2014) 'Permutation inference for the general linear model', NeuroImage, 92, pp. 381–397.

Poster No 133

Clinical and brain morphological characteristics of LRRK2-associated Parkinson disease

Qin Tao[1], Shady Rahayel[2,3], Christina Tremblay[1], Andrew Vo[1], Alain Dagher[1]

[1]Montreal Neurological Institute and Hospital, McGill University, Montreal, QC, [2]Department of Medicine and Medical Specialities, University de Montreal, Montreal, QC, [3]Center for Advanced Research in Sleep Medicine, Hôpital du Sacré-Coeur de Montréal, Montreal, QC

Introduction: LRRK2 mutation is the most significant genetic risk factor for developing late-onset Parkinson disease (PD), accounting for around 1% of sporadic PD (sPD) and 4-36% of familial PD[1-3]. However, the impact of LRRK2 mutation in PD remains unclear. The preclinical markers of LRRK2 mutation carriers who will develop PD still need to be explored[4,5]. Here we examined the clinical and brain morphological characteristics of non-manifest LRRK2 mutation carriers (LRRK2-NMC) and LRRK2-associated PD (LRRK2-PD).

Methods: We collected samples from the Parkinson's Progression Marker Initiative (PPMI, www.ppmi-info.org/) and analyzed the baseline clinical and T1 MRI data from 331 sPD, 77 LRRK2-PD, 78 LRRK2-NMC, and 162 healthy controls (HC)[6]. The LRRK2 patients do not have known GBA variants associated with PD. The analyzed clinical characteristics include 1) demographic, cognitive, motor, and nonmotor features; 2) dopamine transporter binding ratio of bilateral caudate and putamen (DAT SBR); and 3) four PD-related CSF biomarkers. Brain morphological features include cortical thickness, surface area, and cortical and subcortical volume (using FreeSurfer 7.2). Afterwards, the clinical and brain morphological features were analyzed statistically between the four groups. For clinical data, differences between groups were analyzed using chi-square and t-tests with Bonferroni correction. For brain morphological features, general linear models were used for whole cortical surface vertex-wise statistics, controlling for age, sex, education, and disease duration. In the model, age and sex were included as covariates for cortical thickness and the estimated total intracranial volume was added as an additional covariate for surface area and volume. Differences between groups were corrected for multiple comparisons using the random field theory[7].

Results: HC vs LRRK2-NMC. The LRRK2-NMC group showed a significantly higher MDS-UPDRS score and SCOPA-AUT total score than HC, suggesting that LRRK2-NMC may already present slight motor and autonomic deficits. Specifically, the tremor score was higher in LRRK2-NMC than in HC, while their postural instability and gait disorder scores were similar. No sleep or smell differences were found between the two groups. For brain morphometry, LRRK2-NMC had decreased surface area but thicker cortical thickness in parts of bilateral temporal lobes compared to HC. In addition, regions in the left paracentral lobe showed lower cortical thickness, surface area, and cortical volume in LRRK2-NMC than in HC. Moreover, LRRK2-NMC had a smaller surface area and cortical volume in parts of bilateral medial orbitofrontal lobes. There was no subcortical volume difference between the two groups. LRRK2-PD vs sPD. There were no age, sex, or education differences between LRRK2-PD and sPD and the disease duration was longer in LRRK2-PD than in sPD. Thus, the lower DAT SBR and higher MDS-UPDRS scores in LRRK2-PD may be influenced by disease progression. However, the cognitive scores were almost similar between LRRK2-PD and sPD, suggesting slower cognitive decline in LRRK2-PD. In terms of brain morphometry, after matching for disease duration, LRRK2-PD patients showed thinner cortical thickness in a part of the left lingual gyrus and smaller surface area in parts of the right paracentral and middle temporal lobes compared to sPD. No subcortical volume difference was found between the two groups.

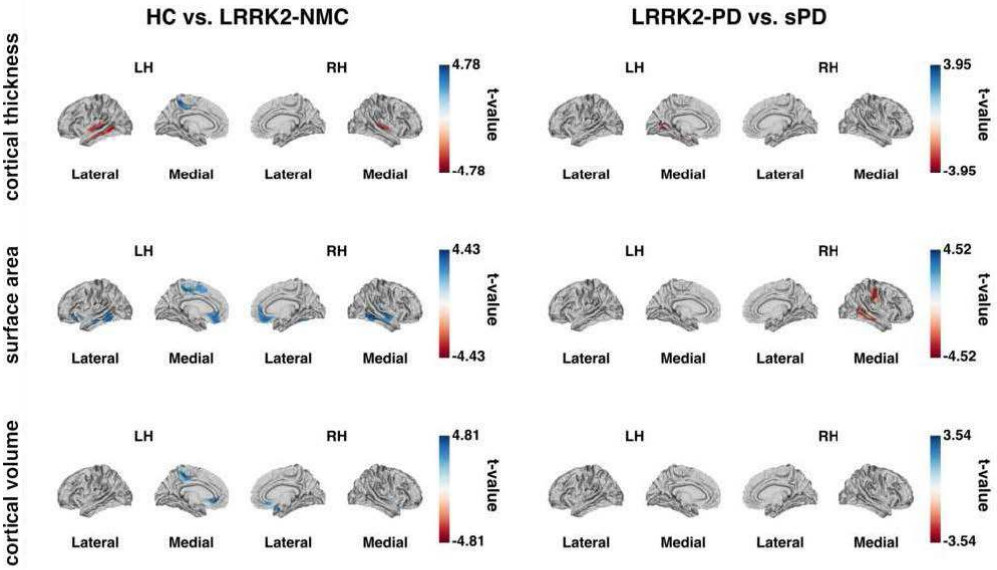

Figure 1. Brain morphometry differences between HC and LRRK2-NMC and between LRRK2-PD and sPD. The groups were matched for age, sex, education, and disease duration. Significant areas with P-value < 0.05 are shown. RH: Right Hemisphere; LH: Left Hemisphere. Blue color: HC > LRRK2-NMC or LRRK2-PD > sPD; Red color: HC < LRRK2-NMC or LRRK2-PD < sPD.

Conclusions: This study investigated the clinical and brain morphological characteristics of LRRK2 mutation carriers with and without PD. Our findings show that early LRRK2-NMC presents different clinical and brain structural patterns compared

to HC. This research may deepen our understanding of LRRK2-related PD mechanisms and contribute to disease prediction and diagnosis.

References
1. Healy, D. G. (2008). "Phenotype, genotype, and worldwide genetic penetrance of LRRK2-associated Parkinson's disease: a case-control study." The Lancet Neurology 7(7): 583-590.
2. Marek, K. (2011). "The Parkinson progression marker initiative (PPMI)." Progress in neurobiology 95(4): 629-635.
3. Menozzi, E. (2023). "Who is at Risk of Parkinson Disease? Refining the Preclinical Phase of GBA1 and LRRK2 Variant Carriers: a Clinical, Biochemical, and Imaging Approach." Current Neurology and Neuroscience Reports.
4. Sosero, Y. L. (2023). "LRRK2 and Parkinson's disease: from genetics to targeted therapy." Annals of Clinical and Translational Neurology.
5. Taymans, J.-M. (2023). "Perspective on the current state of the LRRK2 field." npj Parkinson's Disease 9(1).
6. Tolosa, E. (2020). "LRRK2 in Parkinson disease: challenges of clinical trials." Nature Reviews Neurology 16(2): 97-107.
7. Worsley, K. J. (1996). "A unified statistical approach for determining significant signals in images of cerebral activation." Human Brain Mapping 4(1): 58-73.

Poster No 134

Decoding MRI-informed Brain-predicted Age Using Mutual Information

Jing Li[1], Chiu Wa Lam[1], Hanna Lu[1]

[1]*The Chinese University of Hong Kong, Hong Kong, China*

Introduction: In the ever-evolving realms of neuroscience and cognitive health, the concept of 'brain-predicted age' has merged as a fascinating and enlightening paradigm. 'Brain-predicted age' harnesses advanced computational algorithms to analyse a wide range of neuroimaging data, facilitating early detection and prediction of dementia and cognitive disorders(Franke and Gaser 2019). However, in contrast to conventional statistical models, computational models often lack the capacity to offer neuroanatomical interpretability and specificity. In other words, most machine learning approaches typically fail to reveal ageing-related regional alterations in brain structure or their contributions to 'brain-predicted age'. This dearth of transparency presents significant limitations within the domain of 'brain-predicted age', particularly in clinical applications. To address this challenge, we have pioneered the implementation of mutual information (MI) to quantitatively assess, rank, and elucidate the distinct contributions and relevance of various cortical structures to 'brain-predicted age'.

Methods: We developed a brain age prediction model utilizing the support vector regression (SVR) machine. For the training set, we employed T1-weighted MRI scans of 609 healthy participants (18-88 years of age), sourced from the Cam-CAN dataset. The testing set was comprised of 547 healthy subjects, aged 19.98-86.32 years, selected from the Brain-development (IXI) dataset. All T1-weighted MRIs underwent pre-processing and quantification using BrainSuite software into four distinct regional brain feature types: mean cortical thickness (GMT), gray matter volume (GMV), white matter volume (WMV), and cerebrospinal fluid (CSF) volume. The Kraskov (KSG) method was applied to calculate the MI score between each regional brain feature and 'brain-predicted age' within the testing set. In addition to calculating MI scores for the four individual brain feature types, we also computed MI scores for two unique combinations of these feature types. These included the assessment of regional brain parenchymal volume, which was a combination of GMV and WMV, as well as regional intracranial total volume, derived from the combination of GMV, WMV, and CSF volume.

Results: After age-bias correction, the trained brain age prediction model exhibited the following performance metrics within the training set: MAE=5.15 years, RMSE=6.27 years, and R^2=0.88. In the testing set, where the model's performance was evaluated, the following results were observed: MAE=6.65 years, RMSE=8.53 years, and R^2=0.74. Among the four individual cortical features, GMV exhibited the most substantial total MI value (8.705), with the pre-central gyrus recording the highest MI score (0.694). The second-highest total MI value was associated with CSF volume (7.760), with the cingulate gyrus displaying the highest MI score (0.872). The third-highest total MI value corresponded to mean GMT (6.222), with the superior temporal gyrus achieving the highest MI value (0.526). Conversely, WMV demonstrated the lowest total MI value (4.594), with the highest MI value observed in the insula (0.349). In terms of brain parenchymal volume, the superior frontal gyrus exhibited the highest total MI value (0.804). In the context of intracranial total volume, the cingulate gyrus displayed the highest total MI value (1.181).

Conclusions: We identified GMV emerged as the paramount influence in the determination of 'brain-predicted age', underscoring its pivotal role within the four distinct brain feature types in the context of age-related considerations. Moreover, the superior frontal gyrus and the cingulate gyrus displayed significant importance within the construct of 'brain-predicted age'

References
1. Franke, K. and C. Gaser (2019). "Ten years of BrainAGE as a neuroimaging biomarker of brain aging: what insights have we gained?" Frontiers in neurology: 789.

Poster No 135

Cortical reorganization manifested as reduced thickness in patients with peripheral neuropathic pain

Chien-Ho Lin[1], Tsai-Jou Su[1], Chung-Wei Lee[1], Sung-Tsang Hsieh[2], Chi-Chao Chao[3], Ming-Chang Chiang[1]

[1]National Yang Ming Chiao Tung University, Taipei, Taiwan, [2]National Taiwan University College of Medicine, Taipei, Taiwan, [3]National Taiwan University Hospital, Taipei, Taiwan

Introduction: Peripheral neuropathic pain is a consequence of enhanced nociceptive sensitivity due to lesions or diseases of peripheral nerves. Although such pain originates from peripheral nerve injury, its effects are far beyond the peripheral nervous system. Previous research documented that long-term abnormal sensory input associated with chronic neuropathic pain may induce maladaptive neural plasticity, causing structural and functional alterations of the brain. The current study aimed to investigate changes in cortical thickness in patients with neuropathic pain due to peripheral neuropathy, to identify neuroimaging biomarkers for brain structural disruptions following peripheral neuropathic pain.

Methods: We recruited 92 patients with neuropathic pain due to peripheral neuropathy (46 women, age = 53.5 9.8 years), and 97 age- and sex-matched healthy adults (44 women, age = 50.8 13.4 years) for controls. All participants received MRI scanning on a Siemens-Trio 3T scanner (Erlangen, Germany) for acquisition of the T1-weighted image under the magnetization-prepared rapid gradient-echo (MP-RAGE) sequence (TR/TI/TE = 2530/1100/2.27 ms; flip angle = 9°; FoV = 251 × 220 mm; acquisition matrix = 256 × 224 × 176; voxel dimensions = 0.98 × 0.98 × 1 mm). The thickness of the cerebral cortex was estimated from the T1-weighted MR image using the CAT12 toolbox (http://www.neuro.uni-jena.de/cat/, (Dahnke, Yotter et al. 2013)) implemented in SPM12. Cortical thickness was defined as the distance between the pial and the gray-white matter boundary surfaces, and estimated using the projection-based thickness method (Dahnke, Yotter et al. 2013). The surface map of cortical thickness was mapped to the MNI space, followed by Gaussian smoothing at 15-mm FWHM. Differences in cortical thickness between the patients and controls were compared using a two-sample t-test. Multiple comparisons across the cortical surface were corrected using the 'threshold free cluster enhancement' (TFCE) algorithm (Smith and Nichols 2009) to control the cluster-level family-wise error (FWE) at a level of 0.05 after 5000 permutations.

Results: Figure 1 shows a significant reduction in cortical thickness in patients (Pt) with neuropathic pain compared with controls (Ctrl), particularly in pain-related cortical areas including bilateral anterior cingulate cortices, prefrontal cortices, supramarginal gyri, and precentral gyri.

Conclusions: The current study demonstrates widespread cortical thinning in patients with peripheral neuropathic pain, showing that cortical reorganization is a manifestation of maladaptive plasticity following chronic neuropathic pain. Our findings also show that cortical thickness may serve as a biomarker that facilitates future assessments of pharmacological or non-pharmacological interventions for the treatment of neuropathic pain.

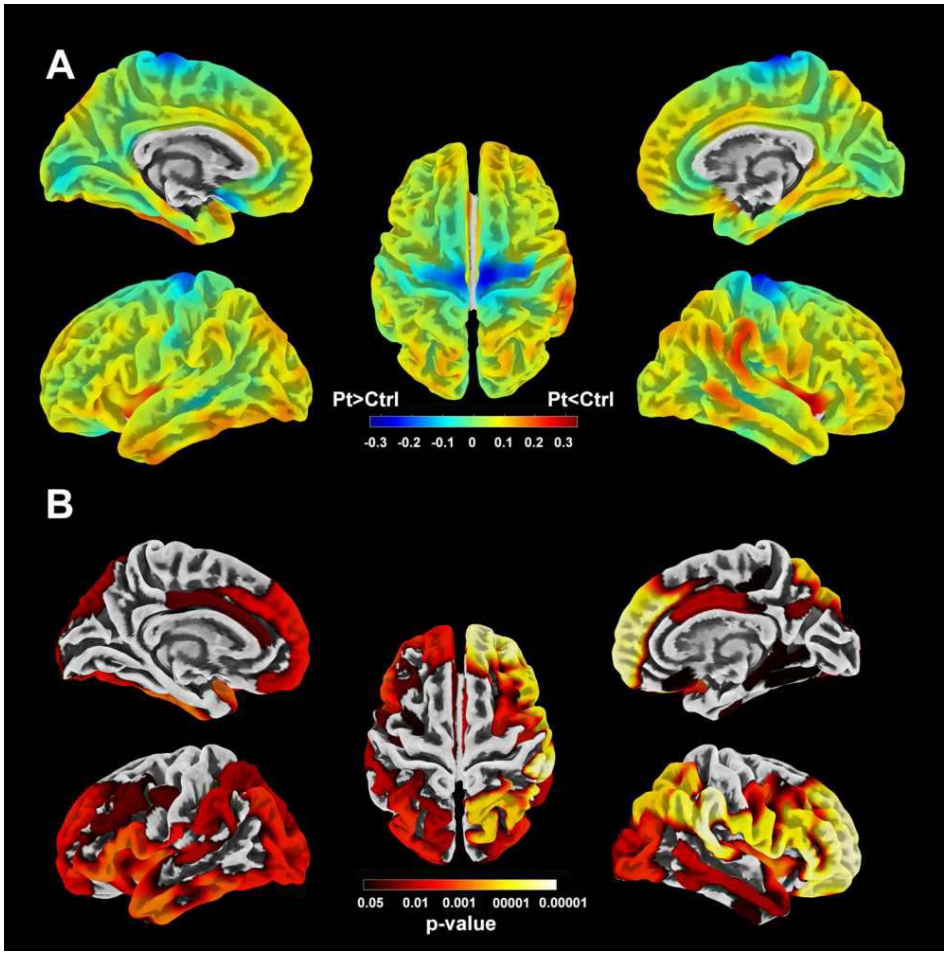

References
1. Dahnke, R., R. A. Yotter and C. Gaser (2013). "Cortical thickness and central surface estimation." Neuroimage 65: 336-348.
2. Smith, S. M. and T. E. Nichols (2009). "Threshold-free cluster enhancement: addressing problems of smoothing, threshold dependence and localisation in cluster inference." Neuroimage 44(1): 83-98.

Poster No 136

Cerebellar changes in Alzheimer's disease: Subregional atrophy, Functional connectivity, and Myelin

Soyun Kim[1], Jennna Adams[1], Lea Stith[1], Lisa Taylor[1], Alyssa Harris[1], Marielena Mendoza[1], Liv McMillan[1], Niels Janssen[2], Michael Yassa[1]

[1]University of California Irvine, Irvine, CA, [2]Universidad de La Laguna, Tenerife, Tenerife

Introduction: The cerebellum has long been recognized for its integral role in motor learning and control. However, recent findings suggest its involvement extends beyond motor functions, potentially impacting non-motor domains (i.e., cognition) and contributing to cognitive decline in Alzheimer's disease (AD). Despite its relative resilience to AD-related pathology, such as beta amyloid (Aβ) accumulation, previous studies indicate a decline in cerebellar volume over progression of AD. A few neuroimaging studies in AD have also demonstrated disrupted cerebellar-cortical functional networks that likely support cognitive functions. Nevertheless, our understanding of other changes in the cerebellum, such as subregional volume alterations, changes in cerebellar functional connectivity with various cortical networks, and variations in myelin content during aging and in AD, remains to be investigated.

Methods: We analyzed cross-sectional as well as longitudinal neuroimaging data from the Alzheimer's Disease Neuroimaging Initiative (ADNI 3, N Sessions = 325, N Subjects = 109, 62 females). Structural and resting-state fMRI data were first processed with the Human Connectome Project pipeline (v4.7.0). Cerebellar subregional volumes were derived using an automated cerebellar parcellation method (Han et al., 2020). Functional connectivity between the cerebellum and cortical networks (Yeo et al., 2011) was computed by group independent component analysis and dual regression approaches. Aβ measures were obtained from [18F]-Florbetapir or [18F]-Florbetaben PET, and standardized uptake value ratio values were transformed to

the Centiloid scale. Myelin content was estimated using the T1- and T2-weighted (T1W/T2W) ratio mapping (Glasser M. F. and Van Essen D. C., 2011). Linear mixed-effects models were used to investigate the effects of age or Aβ on cerebellar regional volume, cerebello-cerebral functional connectivity, and estimated cerebellar myelin content.

Results: Cerebellar volume reduction was significantly associated with older age in areas Crus I, Crus II, or VI. Aβ was also significantly associated with atrophy in regions Crus I, Crus II, VIII A, and VIII B. Functional connectivity between the regions Crus II and vermis X and the cortical default mode network changed with age. Functional connectivity between the region VII B and cortical somatomotor network changed with Aβ. Estimated cerebellar myelin content was negatively related with age in regions Crus I and Crus II, but positively associated in the vermis. Estimated cerebellar myelin content was negatively associated with Aβ in regions Crus I, Crus II, VIII A and VIII B.

Conclusions: Our findings underscore the intricate relationship between age-related changes, Aβ pathology, subregional atrophy, functional connectivity, and estimated myelin content in the cerebellum. Further understanding of these associations could potentially offer valuable insights into the role of the cerebellum in both aging and Alzheimer's disease.

References

1. Glasser, M.F., Van Essen, D.C. (2011), 'Mapping human cortical areas in vivo based on myelin content as revealed by T1- and T2-weighted MRI', Journal of Neuroscience, vol. 31, no. 32, pp. 11597-616.
2. Han, S., Carass, A., He, Y., Prince, J.L. (2020), 'Automatic cerebellum anatomical parcellation using U-Net with locally constrained optimization', NeuroImage, vol. 218, pp. 116819.
3. Yeo, B.T., Krienen, F.M., Sepulcre, J., Sabuncu, M.R., Lashkari, D., Hollinshead, M., Roffman, J.L., Smoller, J.W., Zöllei, L., Polimeni, J.R., Fischl, B., Liu, H., Buckner, R.L. (2011), 'The organization of the human cerebral cortex estimated by intrinsic functional connectivity', Journal of Neurophysiology, vol. 106, no. 3, pp. 1125-65.

Poster No 137

Regional brain free water and gene expression provide new insights into Parkinson's disease

Junye Yao[1,2], Dongling Zhang[3,4,5,6], Lingyu Li[1,7], Tao Wu[3,4,5], Hongjian He[1,6,8]

[1]Center for Brain Imaging Science and Technology, Zhejiang University, Hangzhou, China, [2]College of Biomedical Engineering and Instrument Science, Zhejiang University, Hangzhou, China, [3]Center for Movement Disorders, Beijing Tiantan Hospital, Capital Medical University, Beijing, China, [4]China National Clinical Research Center for Neurological Diseases, Beijing, China, [5]Parkinson's Disease Center, Beijing Institute for Brain Disorders, Capital Medical University, Beijing, China, [6]School of Physics, Zhejiang University, Hangzhou, China, [7]Polytechnic Institute, Zhejiang University, Hangzhou, China, [8]State Key Laboratory of Brain-Machine Intelligence, Zhejiang University, Hangzhou, China

Introduction: Parkinson's disease (PD) is a neurodegenerative disorder characterized by the progressive loss of the dopaminergic neurons in the substantia nigra, and the appearance of intraneuronal a-synuclein inclusions (Lewy bodies) (Bloem et al. 2021). Free-water (FW) imaging has emerged as a promising tool for detecting microstructural alterations in brain in vivo. Increased FW values have been suggested as an early diagnostic marker of PD. However, the underlying mechanisms of the increased FW in PD remain unclear despite its association with neuroinflammation, edema, and demyelination (Zhang et al. 2023). In this study, we used brain FW values and regional gene expression profiles obtained from the Allen Institute for Brain Science (AIBS) to elucidate potential genetic mechanisms for regional microstructural alterations in PD. Characterizing the genetic factors associated with regional FW changes may provide valuable insights into the biological processes driving increased FW in PD. Moreover, identifying promising genetic pathways through this investigation is vital for the development of effective therapeutic interventions.

Methods: In this study, we measured FW values in 207 cortical and subcortical regions of 157 PD patients and 56 healthy controls with diffusion-weighted images. Data included in this study were acquired from the Parkinson's Progression Markers Initiative dataset. The protocols are available at www.ppmi-info.org/study-design. The diffusion weighted images were processed with FSL as detailed in a previous study (Zhang et al. 2023), FW mappings were fitted based on a bi-tensor model (Pasternak et al. 2009). A total of 180 cortical regions from the Glasser atlas, 14 subcortical regions from the CIT168 atlas, 11 thalamic subregions and 2 amygdala subregions from the left hemisphere were selected as regions of interest (ROI). Mean FW values in each ROI were extracted from all participants. PD patients' age- and sex-adjusted regional means were normalized to the control mean for that region by a z-score transformation. The association between FW z-score and gene expression was investigated using Partial Least Squares (PLS) regression. Gene expression data was obtained from the AIBS using abagen toolbox. Gene ontological (GO) enrichment analysis was performed on the significantly positively weighted genes identified by PLS2 using gProfiler.

Results: In occipital, orbitofrontal and para-hippocampal cortex, amygdala and thalamus, significant increases of FW values in PD patients were detected (Fig. 1a). The FW z-score map had a significant correlation with the regional linearly weighted sum of gene expression scores defined by the PLS2 (Fig. 1b, c, R=0.465, P=4.34×10-13), suggesting that genes positively weighted on PLS2 were also more highly expressed in brain regions with higher FW values. Using GO analyses, we found genes more highly expressed in regions with higher FW values in PD were enriched for biological processes relating to synaptic and cellular functions (Fig. 2a). There is evidence that Lewy bodies are initially deposit in pre-synaptic terminals (Tagliaferro and Burke 2016), and gradually spread toward neuronal soma, leading to neuronal loss (Uchihara et al. 2016). Then, a-synuclein can be transmitted from cell to cell in a prion-like manner (Luk et al. 2012). Neuroinflammation is associated with synaptic and cellular dysfunction induced by aggregation of Lewy bodies, which in turn may lead to accumulation of free water molecules in the extracellular space.

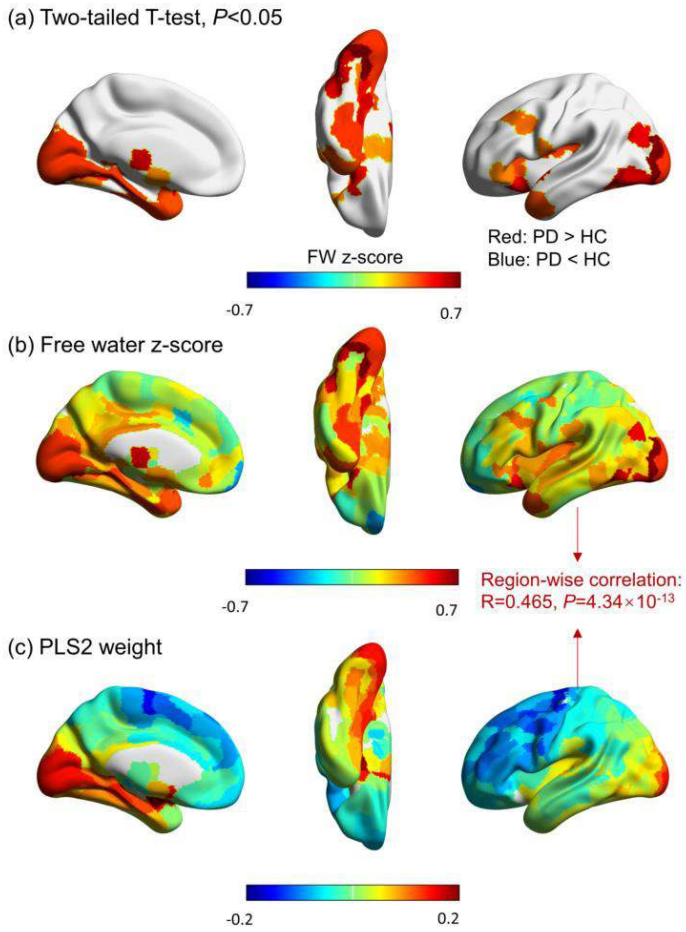

Fig 1. Regional cortical differences in free water between Parkinson's disease and controls.

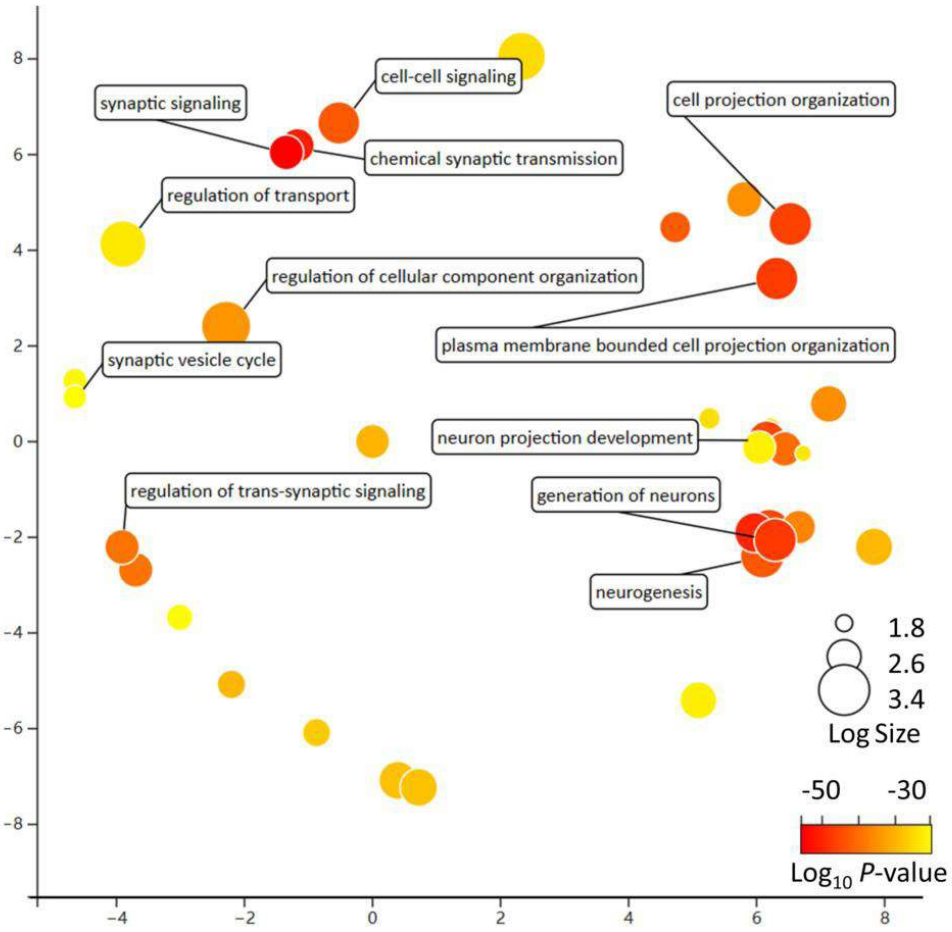

Fig 2. Enrichment analyses for genes associated with cortical free-water in Parkinson's disease visualized by REViGO. The terms are plotted in semantic space with more similar terms clustered together

Conclusions: In this study, regional increases in FW values in PD were explored. Moreover, we found that increased FW values are associated with higher intrinsic levels of gene expression relating to disturbances in synaptic and cellular functions, indicating that these damages might be responsible for the increased free water. These findings provide valuable insights into the underlying neurodegeneration in PD and the specific vulnerabilities of affected brain regions.

References

1. Bloem Bastiaan R (2021), "Parkinson's disease." Lancet, vol. 397, no. 10291 pp. 2284-2303.
2. Hawrylycz MJ (2012), 'An anatomically comprehensive atlas of the adult human brain transcriptome', Nature, vol. 489, no. 7416, pp. 391-399
3. Luk K (2012), "Pathological a-synuclein transmission initiates parkinson-like neurodegeneration in nontrans-genic mice" Science, vol. 338, no.6109, pp.949-954
4. Pasternak O (2009), 'Free water elimination and mapping from diffusion MRI', Magnetic Resonance Medicine, vol.62, no. 3, pp. 717-730
5. Tagliaferro P (2016), "Retrograde Axonal Degeneration in Parkinson Disease", Journal of Parkinson's Disease, vol.6, no.1, pp.1-15
6. Thomas GEC (2021), 'Regional brain iron and gene expression provide insights into neurodegeneration in Parkinson's disease', Brain, vol. 144, no. 6, pp. 1787-1798
7. Uchihara T (2016), "Propagation of alpha-synuclein pathology: Hypotheses, discoveries, and yet unresolved questions from experimental and human brain studies", Acta Neuropathologica, vol. 131, no.1, pp.49-73
8. Zhang Dongling (2023), 'Free-Water Imaging of the Substantia Nigra in GBA Pathogenic Variant Carriers', Movement Disorders, vol. 38, no.6, pp.764-773

Poster No 139

Absence of fMRI adaptation in patients with chronic fatigue syndrome

Zack Shan[1], Laura Schönberg[2], Abdalla Mohamed[1], Richard Kwiatek[1], Peter Del Fante[1], Vince Calhoun[3]

[1]Thompson Institute, University of the Sunshine Coast, Birtinya, QLD, [2]Department of Health Sciences and Technology, ETH Zurich, Zurich, Zurich, [3]Georgia State University, Atlanta, GA

Introduction: Myalgic Encephalomyelitis/Chronic Fatigue Syndrome (ME/CFS) is a debilitating disease of unknown etiology. The hallmark feature of ME/CFS is severe and persistent fatigue that does not improve following rest. Many factors can cause fatigue. However, fatigue is essentially a feeling generated by the brain. Thus, task fMRI (tfMRI) may provide valuable insights into neural mechanisms associated with fatigue in ME/CFS. A systematic review of tfMRI studies in ME/CFS identified a consistent observation of larger recruitment of brain regions during cognitive tasks in ME/CFS patients compared to healthy controls (HCs)[3]. Patients with other neuropathologies with diffuse damage, such as traumatic brain injury, have similarly shown augmented functional recruitment[4]. Moreover, Kohl et al. observed that traumatic brain injury patients showed progressively increased fMRI signals over time, while HCs' fMRI activities decreased after multiple trial repetitions during a prolonged cognitive task[5]. This study investigates how fMRI signal changes during cognitive tasks in patients with ME/CFS. We hypothesise that sustained cognitive function induces cognitive fatigue, i.e., an increase in cerebral activity over time as indexed by BOLD response, in ME/CFS but not in HCs. In contrast, we hypothesise that HCs will show decreased cerebral activity over time because of an adaptation to the task.

Methods: This prospective study uses data collected for the ongoing study of ME/CFS (6), approved by the University of the Sunshine Coast Ethic Committee (A191288) and registered with The Australian New Zealand Clinical Trials Registry (ACTRN12622001095752). Sixty-eight participants, 34 ME/CFS participants (mean age, 38 ± 10 [standard deviation]; 27 women) and 34 HCs (mean age, 38 ± 10 [standard deviation]; 27 women), were included. The fMRI paradigm consisted of two task blocks where participants performed a symbol digit modalities test (SDMT) alternating with resting conditions. Details of the structural and tfMRI data collection parameters were reported previously (6). Standard pre-processing of fMRI was conducted and then analysed using the two-level general linear model approach of SPM12. The subject-specific activation maps were built on correctly answered trials only with realignment parameters as nuisance regressors. Four first-level contrasts were determined for task vs rest, block 1 vs block 2, block 1 – 1st set vs block 1 – 2nd set and block 2 – 1st set vs block 2 – 2nd set. At the second level, first-level contrasts were entered into random-effect one-sample t-tests for within-group analyses and two-sample t-tests for between-group analyses. Sex, age, and BMI were included as nuisance covariates in all analyses. The significance was determined at the cluster level $P_{FWE} < .05$ with cluster-forming of uncorrected $P < .001$ at the voxel level and number of voxels ≥ 25.

Results: Within-group analyses of BOLD responses associated with the SDMT showed patients with ME/CFS recruited broader brain areas in the right dorsolateral prefrontal and left somatosensory cortex than HCs (Fig 1). In the second block, within-group analyses investigating the changes between its first and second set showed an increase in brain activity in the ME/CFS group, whereas HCs showed a decrease in brain activity. Between-group analysis showed significantly higher brain activity in the bilateral pre- and post-central gyrus, inferior parietal lobule, and the right superior temporal gyrus in ME/CFS compared to HCs (block 2 - second set vs block 2 -first set) (Fig. 2).

Conclusions: Neurophysiologic and hemodynamic adaptation in HCs may improve the energy economy. Conversely, this adaptation was absent in our ME/CFS group, which may provide an underlying neurophysiological process for neurological symptoms in ME/CFS.

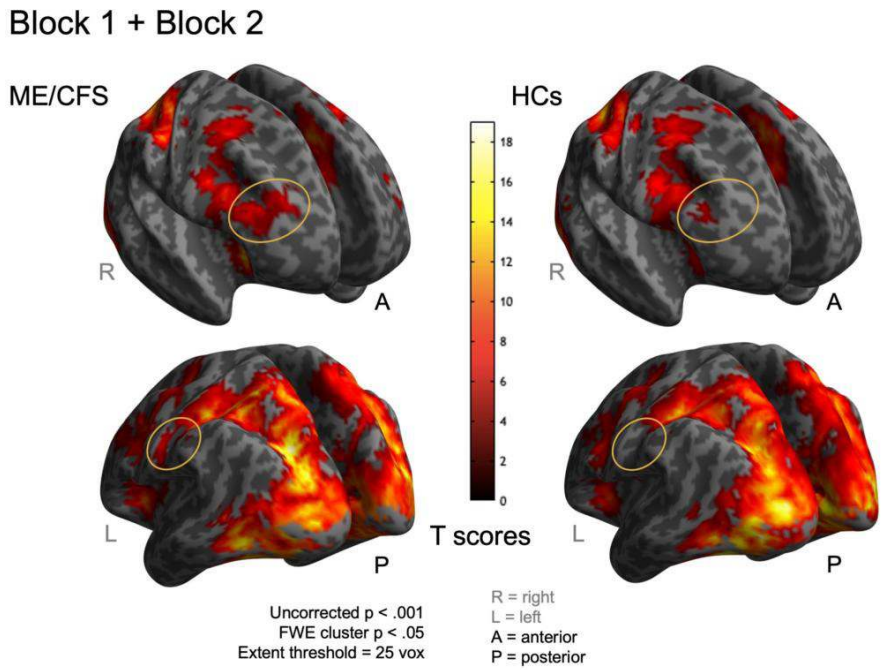

Fig. 1 Neural correlates of symbol digit modalities test task.

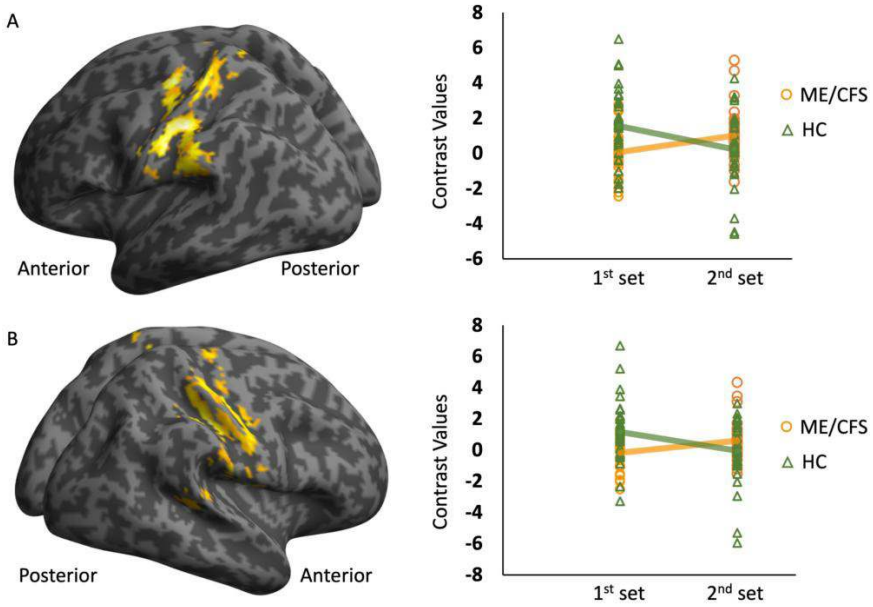

Fig. 2 Differences in fMRI changes comparing the first and second half trials in the second block between patients and health controls (HC).

References

1. de Lange F, Kalkman J, Bleijenberg G, Hagoort P, Sieberen P, van der Werf S, Van der Meer J, Toni I. Neural correlates of the chronic fatigue syndrome - an fMRI study. Brain 2004;127:1948-1957.
2. Holgate S, Komaroff A, Mangan D, Wessely S. Chronic fatigue syndrome: understanding a complex illness. Nat Rev Neurosci 2011;12:539-544.
3. Shan ZY, Barnden LR, Kwiatek RA, Bhuta S, Hermens DF, Lagopoulos J. Neuroimaging characteristics of myalgic encephalomyelitis/chronic fatigue syndrome (ME/CFS): a systematic review. J Transl Med 2020;18(1):335. doi: 10.1186/s12967-020-02506-6
4. Turner GR, Levine B. Augmented neural activity during executive control processing following diffuse axonal injury. Neurology 2008;71(11):812-818. doi: 10.1212/01.wnl.0000325640.18235.1c
5. Kohl AD, Wylie GR, Genova HM, Hillary FG, Deluca J. The neural correlates of cognitive fatigue in traumatic brain injury using functional MRI. Brain Inj 2009;23(5):420-432. doi: 10.1080/02699050902788519
6. Shan ZY, Mohamed AZ, Andersen T, Rendall S, Kwiatek RA, Fante PD, Calhoun VD, Bhuta S, Lagopoulos J. Multimodal MRI of myalgic encephalomyelitis/chronic fatigue syndrome: A cross-sectional neuroimaging study toward its neuropathophysiology and diagnosis. Front Neurol 2022;13:954142. doi: 10.3389/fneur.2022.954142

Poster No 140

Atrophy trajectories in Alzheimer's disease: how sex matters

Anna Inguanzo[1], Konstantinos Poulakis[1], Javier Oltra[2], Silvia Maioli[3], Anna Marseglia[1], Daniel Ferreira[1], Rosaleena Mohanty[1], Eric Westman[1]

[1]Division of Clinical Geriatrics, Centre for Alzheimer Research, NVS, Karolinska Institutet, Stockholm, Sweden, [2]Aging Research Center (ARC), Centre for Alzheimer Research, NVS, Stockholm, Sweden, [3]Division of Neurogeriatrics, Centre for Alzheimer Research, NVS, Stockholm, Sweden

Introduction: Longitudinal subtypes in Alzheimer's disease (AD) have been recently identified based on their distinct brain atrophy trajectories (Poulakis et al., 2022), which follow either a mediotemporal or a cortical atrophy pathway. The most prevalent, the mediotemporal, included three longitudinal subtypes: the limbic predominant (LPA), the limbic predominant plus (LPA+), and the minimal atrophy (MA). LPA+ is characterised by the fastest rate of atrophy, beginning in the entorhinal cortex, later involving the temporal lobe and the rest of the cortex, while LPA is confined to atrophy in temporal regions. In contrast, the MA subtype is characterised by minimal atrophy in mediotemporal areas. Within the cortical pathway, there are two less common subtypes, the hippocampal sparing (HS) subtype, characterised by parietal atrophy but preserved medial-temporal cortex at AD diagnosis, and the diffuse atrophy (DA) subtype with temporal and frontal atrophy already at AD diagnosis, as well as a rapid progression. Although the discovery of distinct brain atrophy trajectories in AD represents a significant contribution to advancing precision medicine, the impact of sex – a major risk factor for AD – on these trajectories has yet to be explored. This study aims to investigate sex-specific effects within these trajectories.

Methods: We analysed MRI from three international AD cohorts (ADNI, J-ADNI and AIBL; N=320). All participants with AD were amyloid-β positive and were classified into one of the following longitudinal subtypes using a longitudinal clustering approach (Poulakis et al., 2022): LPA+, LPA, MA, HS or DA. Clustering was based on W-scores of atrophy measures over 8 years, including grey matter volumes from seven subcortical regions and thickness from 34 cortical regions, which were adjusted for cohort and normal brain ageing relative to an amyloid-β negative cognitively normal control group (N=305). The W-scores were also adjusted for field strength, and additionally, in the case of volumetric measures, for intracranial volume. The W-scores represented standard deviations of atrophy below the control group. To address the main goal of our study, we subsequently stratified each atrophy trajectory by sex to delineate atrophy trajectories for women and men within each longitudinal subtype. We compared women and men within each subtype in relation to socio-demographic information and changes in global cognition (assessed with the Mini Mental State Examination test, MMSE) using linear mixed-effects models.

Results: The frequency of women in each subtype was as follows: LPA+ (N=23, 61% women), LPA (N=93, 48% women), MA subtype (N=189, 48% women), HS subtype (N=10, 40% women) and DA subtype (N=5, 60% women). For all AD subtypes, women consistently exhibited hippocampal atrophy at earlier disease stages than men (Figure 1). Regarding the mediotemporal pathway, LPA+ women showed greater atrophy over time compared to LPA+ men in frontal regions, while LPA+ men experienced precentral atrophy sooner. LPA+ men had an older age of onset (U=20.5, p=0.008), and showed a faster cognitive decline compared to women ($\chi2(1)=5.19$, p=0.023). In contrast, in the LPA subtype, women presented with precentral atrophy earlier than men. MA women showed lateral temporal atrophy earlier compared to MA men. In the cortical pathway, HS women showed frontal atrophy earlier compared to men. Within the DA subtype, both men and women exhibited a widespread pattern of atrophy over time.

Figure 1. Brain atrophy trajectories for women and men in each AD subtype

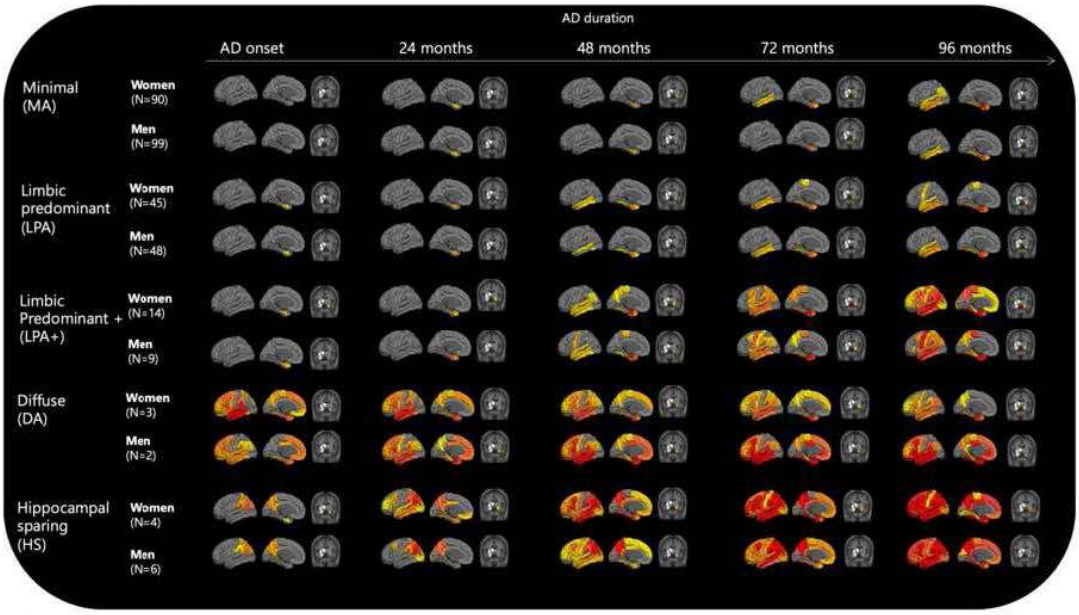

The data are W-scores based on atrophy measures adjusted for field strength, cohort and ageing. Additionally volumetric measures were adjusted for intracranial volume. Warmer colours indicate increasing cortical thinning and subcortical volume loss in the AD participants compared to the control group.

Conclusions: Our findings revealed unique atrophy trajectories in women and men within longitudinal AD subtypes, emphasizing the importance of investigating sex-related differences in AD heterogeneity. This highlights the need for future research to consider sex differences in order to develop tailored monitoring and treatment approaches in both sexes.

References

1. Poulakis, K. (2022), 'Multi-cohort and longitudinal Bayesian clustering study of stage and subtype in Alzheimer's disease', Nature Communications, 13(1):4566.

Poster No 141

Proteomics analysis unveils proteins underpinning diabetes-driven white matter hyperintensity growth

Noah Schweitzer[1], Sang Joon Son[2], Nicholas Fitz[3], Chang-Le Chen[1], Chang Hyung Hong[2], Hyun Woong Roh[2], Yong Hyuk Cho[2], Bumhee Park[4], Na-Rae Kim[4], Jin Wook Choi[5], Jaeyoun Cheong[6], Sangwon Seo[7], Young-Sil An[8], So Young Moon[9], Seung Jin Han[10], Bistra Iordanova[1], Shaolin Yang[11], Howard Aizenstein[11], Minjie Wu[11]

[1]Department of Bioengineering, University of Pittsburgh, Pittsburgh, PA, [2]Department of Psychiatry, Ajou University School of Medicine, Suwon, Korea, Republic of, [3]Department of Environmental and Occupational Health, University of Pittsburgh, Pittsburgh, PA, [4]Department of Biomedical Informatics, Ajou University School of Medicine, Suwon, Korea, Republic of, [5]Department of Radiology, Ajou University School of Medicine, Suwon, Korea, Republic of, [6]Department of Gastroenterology, Ajou University School of Medicine, Suwon, Korea, Republic of, [7]Samsung medical center, Seoul, Korea, Republic of, [8]Department of Nuclear Medicine and Molecular Imaging, Ajou University School of Medicine, Suwon, Korea, Republic of, [9]Department of Neurology, Ajou University School of Medicine, Suwon, Korea, Republic of, [10]Department of Endocrinology and Metabolism, Ajou University School of Medicine, Suwon, Korea, Republic of, [11]Department of Psychiatry, University of Pittsburgh, Pittsburgh, PA

Introduction: White matter hyperintensities (WMH) are surrogate markers of cerebral small vessel disease. There is a need to understand its pathophysiology to prevent cognitive decline and a potential contributing factor is diabetes as it is a chronic macrovascular risk factor[1]. Blood biomarkers might be a useful tool to elucidate the role of diabetes in WMH. There is limited research on blood biomarkers' association with WMH. We aimed to investigate differentially expressed proteins (DEP) in diabetes as detected in blood plasma that have a significant interaction effect with diabetes on WMH.

Methods: This study was a part of the Biobank Innovations for Chronic Cerebrovascular Disease With ALZheimer's Disease Study (BICWALZS). Blood samples were collected to test for HbA1c. Protein levels were measured with Olink's Cytokine and Neurology panel (https://olink.com/) and transformed into log base-2 values. Participants completed baseline 3T MRI scans

which included T1w and T2w-FLAIR sequences. 348 subjects had a baseline MRI (N=245 female, 79 diabetic, mean age 72.0+-7.2). 64 subjects (N=39 female, 11 diabetic, 72.1+-7.5 years) completed a follow-up scan two-years after baseline and held out for a separate longitudinal analysis. WMH on T2w FLAIR images were automatically segmented based on previous method[2]. WMH volume (WMHV) was normalized by intracranial volume and log-transformed. WMHV change was calculated as WMHV at time point 2 minus time point 1. Proteins were tested for differential expression based on diabetes status for each Olink panel. DEP analysis was conducted using the linear model implemented in "limma"[3]. Functional annotation clustering was performed using the DAVID database. A multivariate linear regression model was tested on DEP for interaction between the protein and diabetes on WMHV controlling for age, sex, and scanner site. Proteins with significant interaction effect were tested on the held-out longitudinal sample. Two linear regression models were tested on WMHV change controlling for age at baseline, sex and scanner site: the interaction between diabetes, protein expression and HbA1c levels, protein expression, respectively. We applied the Johnson–Neyman technique to probe and visualize the conditional effect of HbA1c on WMHV change based on protein expression[4]. Throughout the study, multiple comparison was adjusted using Benjamini-Hochberg method.

Results: We observed 42 and 11 DEP based on diabetes status for Neurology and Cytokine panel, respectively (Fig1A,B). KEGG pathways such as cytokine-cytokine receptor interaction and gene ontology terms such as axon guidance were significantly enriched (Fig1C). The only DEP that had significant interaction effect with diabetes on WMHV were Nerve Growth Factor (NGF)-β (p=5.8E-4, Fig2A) and Carboxypeptidase A2 (CPA2) (p=1.1E-3, Fig2B). WMHV increased with higher NGF-β expression for diabetic subjects and decreased expression in non-diabetic subjects. In the held-out sample, significant interaction effects on WMHV change were observed between NGF-β, diabetes and NGF-, HbA1c, respectively (Fig 2C, p=0.03, 0.019), but not CPA2 (p=0.26, 0.69). Johnson–Neyman analysis indicated the association between WMHV change and NGF-β had a significant negative correlation at HbA1c levels less than 5.59%, and a significant positive correlation at HbA1 levels higher than 7.8% (Fig2D).

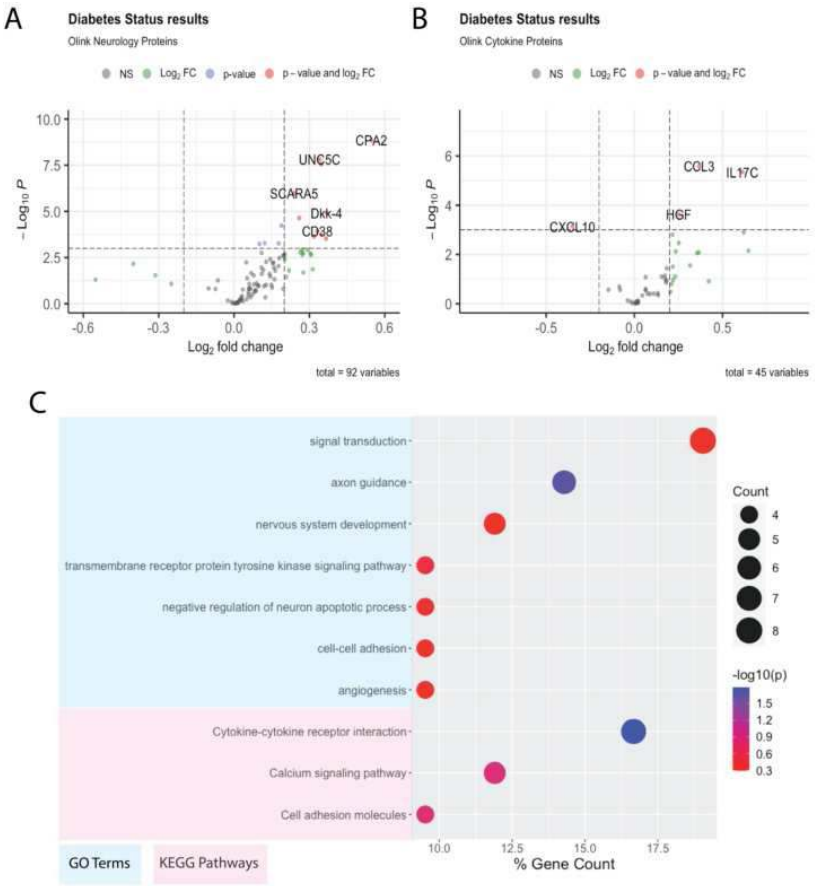

Figure 1: A.) The Olink Neurology panel tested 92 proteins for differential expression based on Diabetes status. We observed 41 proteins to be significantly upregulated, and 1 protein to be significantly downregulated. Of note, Nerve Growth Factor was significantly upregulated in Diabetes. B.) For the Olink Cytokine panel, we observed 10 proteins to be upregulated and 1 protein to be downregulated out of the 42 proteins tested. C.) Bubble plots depicting GO terms and KEGG pathways associated with the Oink Neurology panel proteins disregulated in Diabetes. X axis indicates % gene count, circle size is positively correlated with gene number, and circle color denotes statistical significance.

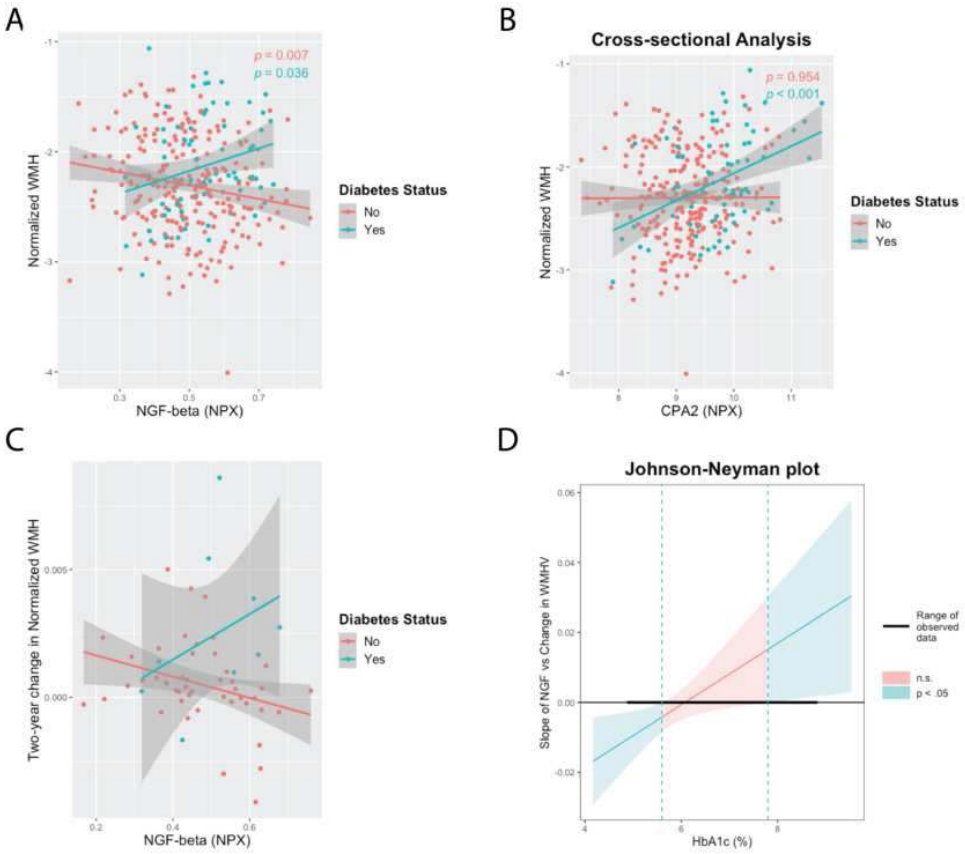

Figure 2: The interaction effect between NGF-beta and Diabetes is significant in WMHV prevalence and progression. A.) In cross-sectional sample, WMHV increased with higher NGF-beta levels for subjects with diabetes and decreased for non-diabetic subjects. B.) In cross-sectional sample, WMHV increased with higher CPA2 levels for diabetic subjects but had no significant association for non-diabetic subjects. C.) In a held-out sample with follow-up MRI scans two-years after baseline, there was a significant interaciton effect betweenNGF-beta and diabetes on WMHV change. D.) Johnson–Neyman technique indicated that the association between WMHV change and NGF-beta had a significant negative correlation ($p<0.05$) at HbA1c levels less than 5.59%, and then a significant positive correlation at HbA1 levels higher than 7.8%. Of note, the prediabetes level for HbA1c is >= 5.7% and diabetes level is 6.5%.

Conclusions: Our proteomic analysis reveals a potential independent pathway through which diabetes contributes to WMH progression. To the best of our knowledge, we are the first to report about an association between NGF, CPA2 with WMH. NGF plays a significant role in neuronal integrity and angiogenesis. Elevated NGF and CPA2, observed in diabetes[5,6], may indicate a worsened diabetic state leading to cerebrovascular complications. Our study emphasizes the importance of managing diabetic health to improve brain health outcomes. Finally, targeting NGF may have potential diagnostic and therapeutic benefits in preventing WMH progression.

References

1. Sanahuja, J. et al. Increased Burden of Cerebral Small Vessel Disease in Patients With Type 2 Diabetes and Retinopathy. Diabetes Care 39, 1614-1620 (2016).
2. Wu, M. et al. A fully automated method for quantifying and localizing white matter hyperintensities on MR images. Psychiatry Res 148, 133-142 (2006).
3. Ritchie, M.E. et al. limma powers differential expression analyses for RNA-sequencing and microarray studies. Nucleic Acids Res 43, e47 (2015).
4. D'Alonzo, K.T. The Johnson-Neyman Procedure as an Alternative to ANCOVA. Western Journal of Nursing Research 26, 804-812 (2004).
5. Ding, X.-W., Li, R., Geetha, T., Tao, Y.-X. & Babu, J.R. Nerve growth factor in metabolic complications and Alzheimer's disease: Physiology and therapeutic potential. Biochimica et Biophysica Acta (BBA) - Molecular Basis of Disease 1866, 165858 (2020).
6. Lu, Y., Li, Y., Li, G. & Lu, H. Identification of potential markers for type 2 diabetes mellitus via bioinformatics analysis. Mol Med Rep 22, 1868-1882 (2020).

Poster No 142

Cognitive training reorganize functional lateralization in vascular cognitive impairment no dementia

Xinhu Jin[1], Yi Xing[2], Xiuyi Wang[1], Yi Tang[2], Yi Du[1]

[1]Chinese Academy of Sciences, Beijing, Beijing, [2]Capital Medical University, Beijing, Beijing

Introduction: Vascular cognitive impairment no dementia (VCIND) refers to cognitive deficits associated with an underlying vascular cause but is not sufficient for diagnosing dementia[1]. Early intervention of VCIND holds the potential to delay or even reverse cognitive impairment[2]. Cognitive training refers to a structured intervention where individuals engage in practice activities that target specific cognitive functions, such as executive function and memory. However, the impacts of subcortical VCIND and cognitive training on functional lateralization, an intrinsic organizational principle of human brain, remain unclear.

Methods: In a randomized, active controlled design, 30 patients with VCIND underwent a 7-week computerized, adaptive, multidomain training while the other 30 patients received fixed processing speed and attention tasks set to a primary difficulty level. Based on resting-state functional connectivity (FC) processed by fMRIPrep and XCP-D[3,4], we first defined two different types of FC among the whole brain, named interhemispheric heterotopic FC and intrahemispheric FC. For a specific parcel in multimodal parcellation[5], the heterotopic (he) was defined as the sum of heterotopic FCs between this parcel and all the others in the opposite hemisphere except the homotopic one, whereas the intrahemispheric (intra) was defined as the sum of intrahemispheric FCs between this parcel and all the others within the same hemisphere. The resting-state functional lateralization between each homotopic pair of parcels was quantified by a commonly used laterality index (LI) calculated as: LI = (L-R)/|(L+R)|. According to Cole-Anticevic Brain-wide Network Partition version 1.0 (CAB-NP v1.0)[6], all cortical parcels were mapped into 12 networks. Since executive dysfunction is the characteristic impairment in subcortical vascular cognitive impairment[7,8], brain areas within the fronto-parietal network (FPN) may play a crucial role in cognitive training for subcortical VCIND. In order to calculate the LI of FPN, we only chose the homotopic pair of parcels both belonging to FPN in CAB-NP v1.0. After averaging the LIs across these pairs of FPN parcels, we acquired the LI_he/LI_intra of FPN for each participant. Larger positive values of LI_he and LI_intra imply stronger bilateral across-hemisphere interactions or ipsilateral within-hemisphere interactions in left-hemispheric FPN nodes, whereas larger negative values indicate stronger interactions in right-hemispheric FPN nodes. Thus, LIs of FPN, along with neuropsychological assessments (Trail Making Test (TMT) to measure executive function[9] and the WHO-UCLA Auditory Verbal Learning Test (AVLT) to measure episodic memory function[10]), were acquired at three different time points: baseline 0, end of intervention (7-week), and 6-month follow-up. A healthy older group with 30 participants only provided data at baseline 0.

Results: At baseline 0, the two VCIND groups showed a similar lateralization pattern in FPN to healthy older adults (Figure 1A). However, a stronger right-lateralized LI_he correlated with better memory performance only in the healthy older group (Figure 1B). At the end of the 7-week intervention, only the VCIND training group, but not the control group, exhibited reduced lateralization with a bilateralized LI_he in FPN (Figure 2A), where stronger leftward changes were correlated with better executive and memory functions (Figure 2B). Notably, all these changes disappeared at the 6-month follow-up.

Conclusions: Subcortical VCIND impaired the cognitive benefit of right-lateralized FPN typically observed in healthy older adults. Instead of restoring the cognitive reserve with right-lateralizated FPN, the 7-week cognitive training facilitated executive and memory functions through functional compensation by reorganizing and balancing the hemispherical symmetry of FPN. These findings have important implications for understanding and intervening cognitive impairment.

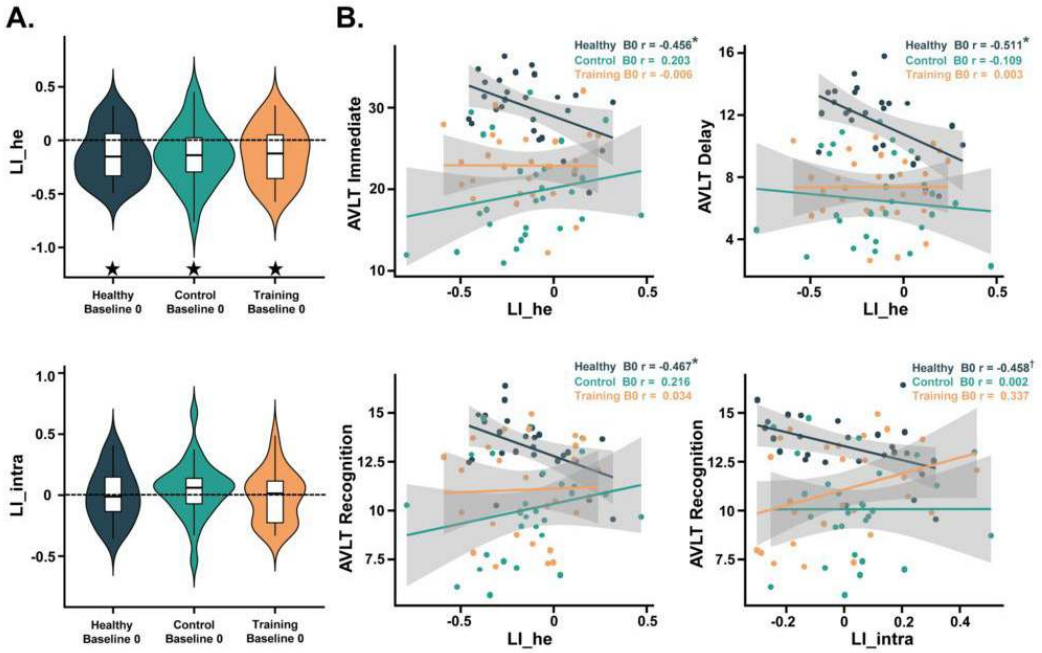

FPN lateralization patterns and their relationships with behaviors in three groups at baseline.

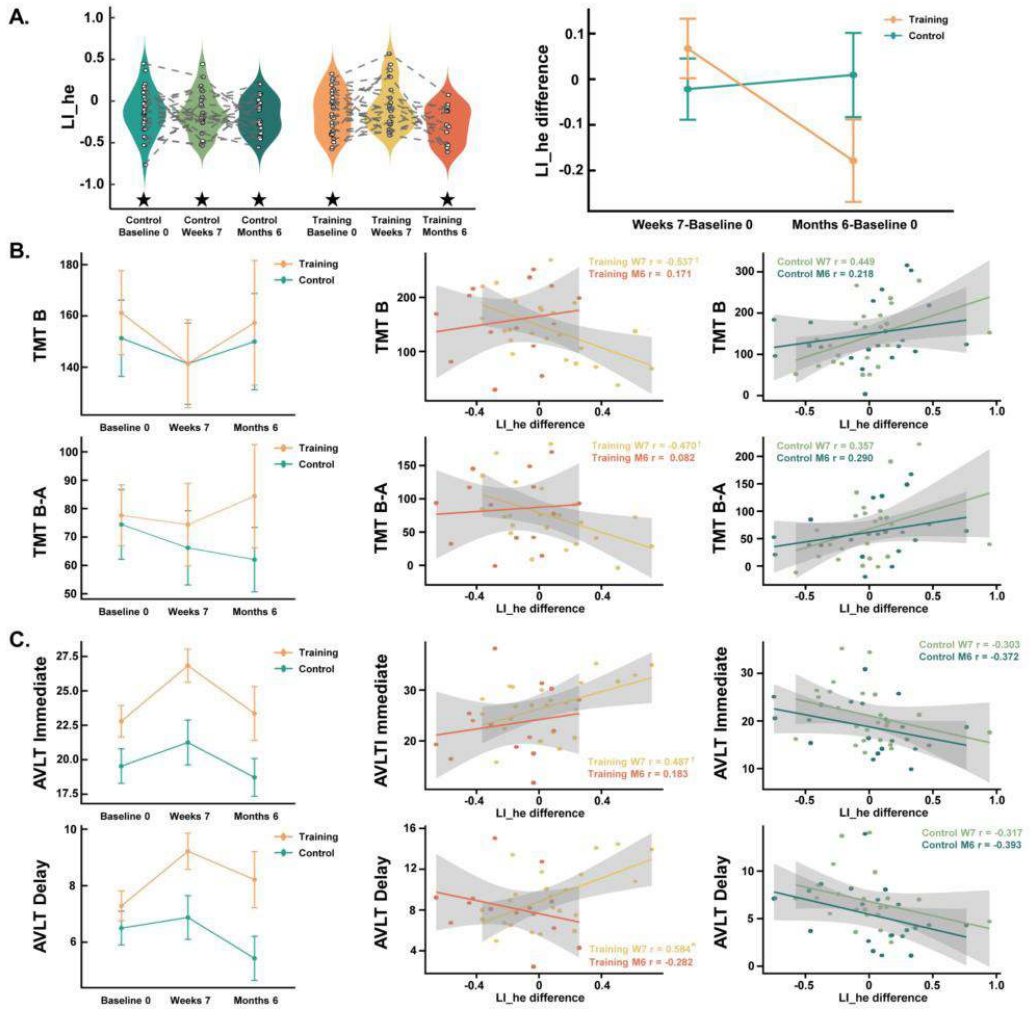

LI_he and LI_he difference of FPN and their correlations with behavioral performances in subcortical VCIND patients.

References

1. Wentzel C, Rockwood K, MacKnight C, Hachinski V, Hogan D, Feldman H, et al. (2001), Progression of impairment in patients with vascular cognitive impairment without dementia. Neurology,57:714–6.
2. Tang Y, Zhu Z, Liu Q, Li F, Yang J, Li F, et al. (2016), The efficacy of Cognitive training in patients with VAsCular Cognitive Impairment, No dEmentia (the Cog-VACCINE study): study protocol for a randomized controlled trial. Trials, 17:392. https://doi.org/10.1186/s13063-016-1523-x.
3. Esteban O, Markiewicz CJ, Blair RW, Moodie CA, Isik AI, Erramuzpe A, et al. (2019), fMRIPrep: a robust preprocessing pipeline for functional MRI. Nature Methods, 16:111–6.
4. Ciric R, Rosen AF, Erus G, Cieslak M, Adebimpe A, Cook PA, et al. (2018), Mitigating head motion artifact in functional connectivity MRI. Nature Protocols, 13:2801–26.
5. Glasser MF, Coalson TS, Robinson EC, Hacker CD, Harwell J, Yacoub E, et al. (2016), A multi-modal parcellation of human cerebral cortex. Nature, 536:171–8. https://doi.org/10.1038/nature18933.
6. Ji JL, Spronk M, Kulkarni K, Repovš G, Anticevic A, Cole MW. (2019), Mapping the human brain's cortical-subcortical functional network organization. NeuroImage, 185:35–57. https://doi.org/10.1016/j.neuroimage.2018.10.006.
7. Jokinen H, Kalska H, Mäntylä R, Pohjasvaara T, Ylikoski R, Hietanen M, et al. (2006), Cognitive profile of subcortical ischaemic vascular disease. Journal of Neurology, Neurosurgery & Psychiatry, 77:28–33.
8. Kramer J, Reed B, Mungas D, Weiner M, Chui H. (2002), Executive dysfunction in subcortical ischaemic vascular disease. Journal of Neurology, Neurosurgery & Psychiatry, 72:217–20.
9. Bowie CR, Harvey PD. (2006), Administration and interpretation of the Trail Making Test. Nature Protocols, 1:2277–81.
10. Jia J, Zhao T, Liu Z, Liang Y, Li F, Li Y, et al. (2023), Association between healthy lifestyle and memory decline in older adults: 10 year, population based, prospective cohort study. BMJ, e072691. https://doi.org/10.1136/bmj-2022-072691.

Poster No 143

Altered intrinsic neural timescales in mild cognitive impairment and Alzheimer's disease

Aiying Zhang[1,2], Seonjoo Lee[2], Xi Zhu[2], Kenneth Wengler[2], Guillermo Horga[2], Terry Goldberg[3]

[1]University of Virginia, Charlottesville, VA, [2]New York State Psychiatric Institute, New York, NY, [3]Columbia University Medical Center, New York, NY

Introduction: Alzheimer's disease (AD) is a devastating neurodegenerative disease that affects millions of older adults in the US and worldwide. Resting-state functional magnetic resonance imaging (rs-fMRI) has become a widely used neuroimaging tool to study neurophysiology in AD and its prodromal condition, mild cognitive impairment (MCI). The intrinsic neural timescale (INT), which can be estimated through the magnitude of the autocorrelation of intrinsic neural signals using rs-fMRI, is thought to quantify the duration that neural information is stored in a local cortical circuit. The heterogeneity of the timescales is considered to be a basis of the functional hierarchy in the brain. In addition, INT captures an aspect of circuit dynamics relevant to excitation/inhibition (E/I) balance, which is thought to be broadly relevant for cognitive functions. Here we examined its relevance to AD.

Methods: We used rs-fMRI data of 904 individuals from the Alzheimer's Disease Neuroimaging Initiative (ADNI) database. The subjects were divided into 4 groups based on their baseline and end-visit clinical status, which were cognitively normal (CN), stable MCI, Converter, and AD groups. The rs-fMRI preprocessing was implemented through fMRIprep. Voxel-wise INT was estimated as the area under the curve of the autocorrelation function from the fMRI time-series during the initial positive period. ROI-specific INT were calculated as the mean of the voxel INTs within the ROI, where the Desikan-Killiany (DK) Atlas was used. Linear Mixed Effect (LME) Model to Detect Altered Hierarchical Gradient Effects on INT: LME model was applied to predict the INT value in our ADNI sample using hierarchical level (HL) in the cerebral cortex, assuming different intercepts and slopes by diagnosis group. The HL of the ROIs is determined using the rs-fMRI of 100 unrelated young and healthy subjects from the Human Connectome Project WU-Minn Consortium. We considered age, sex, motion, and cortical thickness (CT) extracted from the T1 MRI as covariates (fixed effects), and allowed for variations of intercept and slope at the subject level (random effects). Pairwise Comparison for Significant INT Differences among Groups: We averaged the INT values of the same ROIs on the left and right hemisphere, t-tests were conducted to compare the differences between each pair of the 4 groups. Multiple comparison correction was performed using the Tukey method for comparing a family of 4 estimates.

Results: Hierarchical Gradient Effect on INTs among Various Groups: The parameters of fitted lines of INT as a function of HL of the 4 diagnosis groups are shown in Figure 1A. In terms of group differences (see Figure 1B), the MCI had a less pronounced hierarchical-gradient effect (i.e., slope) when compared to the CN; the AD showed longer INT values in lower HL areas than CN (i.e., the contrast of intercept); the AD and Converter had longer INT across all cortical areas compared to the MCI. Significant ROIs in which AD and Converter Had Longer INT Values than CN and MCI: In Figure 2, 4 ROIs (entorhinal, fusiform, inferior temporal and temporal pole areas) were identified having higher INT in the AD than the CN. The pairwise comparison results indicate that INT alterations of these areas in the Converter are very similar to the AD at baseline, suggesting similar pathological changes prior to clinical presentation of AD.

Conclusions: We used rs-fMRI data to investigate INTs in CN, MCI, including those who convert to AD, and AD populations. Using established INTs as a functional index of hierarchy, we found that compared to CN, 1) AD and Converter are similar, as they both had longer INTs in low HL areas; and 2) stable MCI is distinct from AD and Converter, which had a less pronounced hierarchical-gradient effect with shorter INTs in high HL areas, suggesting distinct pathophysiological changes in the stable MCI and AD/Converter.

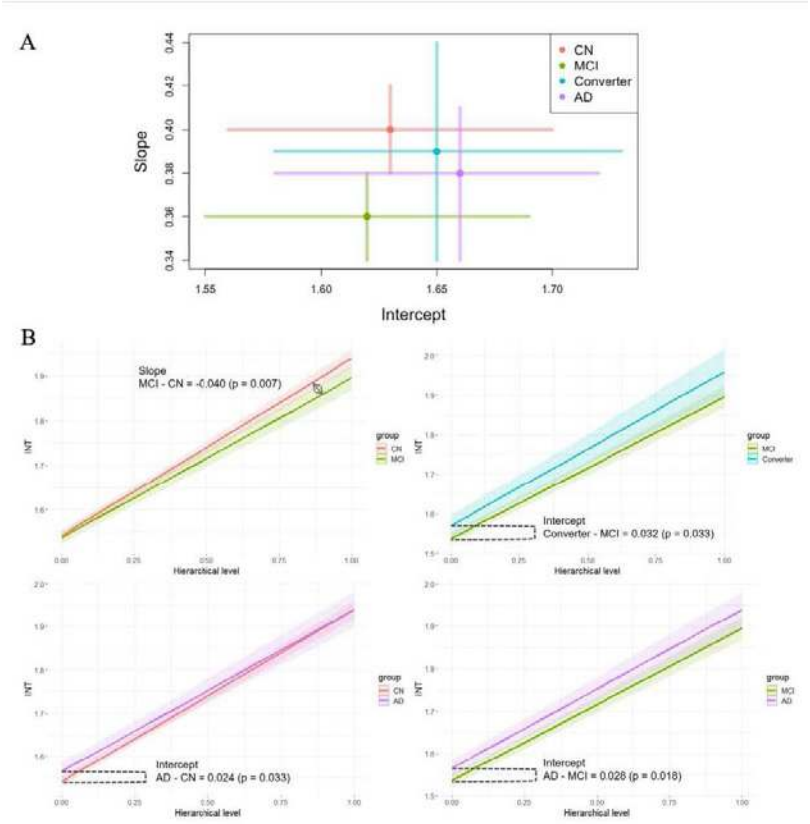

Figure 1: The results of the LME fitting. A) The estimated intercept and slope of the hierarchical gradient effects by diagnosis groups. B) Pairwise comparisons.

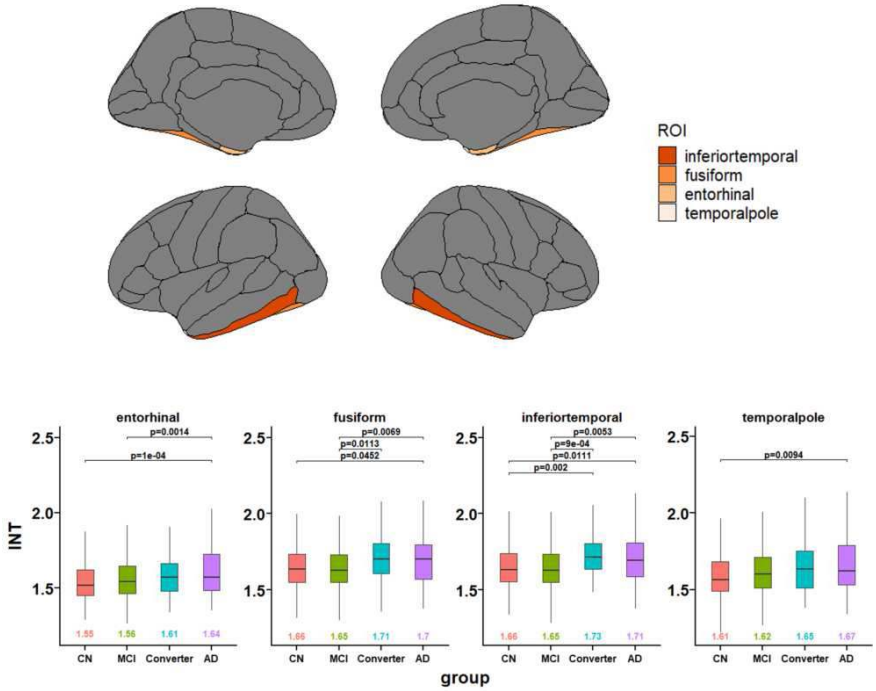

Figure 2: Cortical ROIs in which the INT values in AD group (and Converter group) are significantly longer than those in CN and MCI groups.

References
1. Desikan RS, Ségonne F, Fischl B, et al. An automated labeling system for subdividing the human cerebral cortex on MRI scans into gyral based regions of interest. Neuroimage. 2006;31:968–980.
2. Van Essen DC, Smith SM, Barch DM, et al. The WU-Minn human connectome project: an overview. Neuroimage. 2013;80:62–79
3. Wengler K, Goldberg AT, Chahine G, Horga G. Distinct hierarchical alterations of intrinsic neural timescales account for different manifestations of psychosis. Elife. 2020;9:e56151.

Poster No 144

Common and specific effects in oscillations and motor symptoms of tDCS and tACS in Parkinson disease

Junjie Bu[1], Ying Zhu[1], Qiujian Meng[1], Jiafang Liu[1]

[1]*Anhui Medical University, Hefei, Anhui*

Introduction: Parkinson's disease (PD) is a prototypical oscillation-related neurodegenerative disorder, and these aberrant neural oscillations lead to the pathophysiology of various motor phenotypes specific to patients[1]. Recently, transcranial direct/alternating current stimulation (tDCS/tACS) are widely utilized for non-invasive modulation and restoration of brain neural oscillations, and have been demonstrated to have potential to ameliorate motor symptoms in PD patients. However, it is unclear whether tDCS and tACS improve motor symptoms in PD patients through a consistent oscillatory modulation mechanism. Here, we conducted the first randomized controlled trial (RCT) to compare the modulation in PD patients by tDCS and tACS.

Methods: To observe abnormal baseline brain oscillations in PD patients, we first analyzed 41 PD patients and 41 healthy controls (HC) from two external open-source datasets. Then, we conducted a double-blind RCT (NCT05678725) with 60 idiopathic PD patients randomly assigned to the tDCS, beta tACS (20Hz), or sham stimulation groups, applying stimulation to left primary motor cortex. Participants completed a 15-minute simple reaction task (sRT) during and after stimulation to assess changes in motor function. Before and after stimulation, we collected 5-minute eyes-open resting-state electroencephalogram (EEG), the unified Parkinson's disease rating scale part III (UPDRS III), and the Montreal cognitive assessment (MoCA) to assess changes in brain oscillations, motor functions, and global cognitive function respectively.

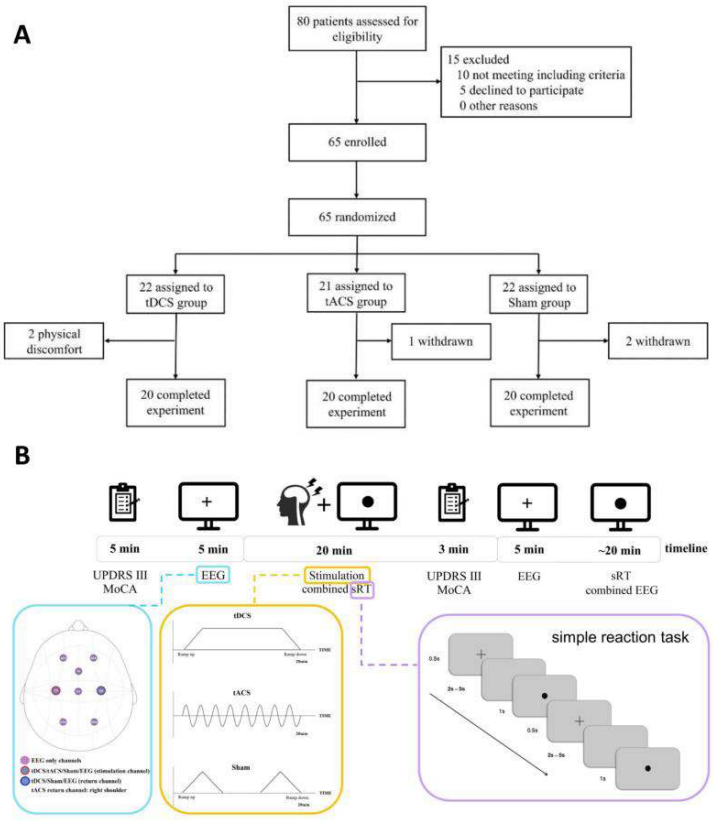

Figure 1. Trail profile (A) and experimental protocol (B) in the double-blind randomized controlled trial.

Results: In external datasets, PD patients displayed abnormal cortical oscillations compared to HC, marked by significantly increased cortical theta power and decreased cortical beta power. In the RCT, for brain oscillations, both tDCS and tACS induced a common and significant increase in beta power compared to the sham. However, reduced theta power was specific to the tDCS group. The alterations in theta and beta power induced by tDCS or tACS were moving toward a more 'normal' level. Furthermore, for motor symptoms, both tDCS and tACS significantly ameliorated rigidity-bradykinesia symptoms, which were associated with changes in beta power induced by tDCS and tACS. Interestingly, tDCS exhibited specific improvements in tremor and cognition, with tremor improvement being linked to tDCS-induced specific reduction in theta power. Exploratory analyses uncovered that tDCS significantly also decreased theta/beta ratio, and that tDCS-induced tremor-specific change could be more effectively fully mediated and predicted by theta/beta ratio than theta alone, supporting the theta and beta independently together roles in tremor.

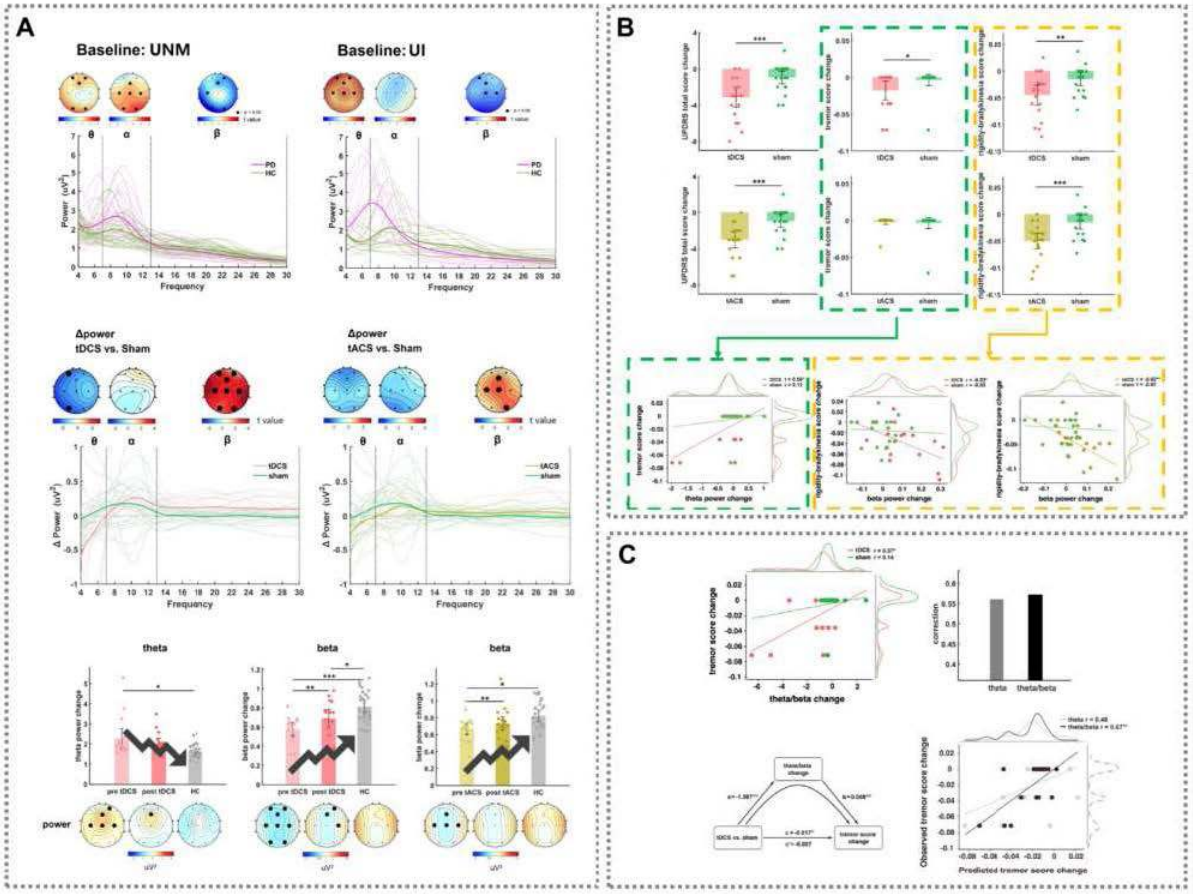

Figure 2. Common and specific effects in brain oscillations and motor symptoms of tDCS and tACS. (A) Top panel: PD pathophysiological brain oscillations in external open-source baseline resting-state EEG datasets. Middle panel: Both tDCS and tACS induced a common and significant increase in beta power compared to the sham. However, reduced theta power was specific to the tDCS group. Bottom panel: The alterations in theta and beta power induced by tDCS or tACS were moving toward a more 'normal' level. (B) Both tDCS and tACS significantly ameliorated rigidity-bradykinesia symptoms, which were associated with changes in beta power induced by tDCS and tACS. Interestingly, tDCS exhibited specific improvements in tremor, with tremor improvement being linked to tDCS-induced specific reduction in theta power. (C) Exploratory analyses uncovered that tDCS significantly also decreased theta/beta ratio, and that tDCS-induced tremor-specific change could be more effectively fully mediated and predicted by theta/beta ratio than theta alone, supporting the theta and beta independently together roles in tremor.

Conclusions: This RCT represents the first attempt to compare changes in cortical oscillations and symptom improvements following tDCS or tACS modulation in PD patients, thereby highlighting both their common and specific effects. tDCS exerts a broad-spectrum modulatory effect on oscillations, resulting in the improvement of multiple symptoms in PD patients, while tACS provides specific modulation by targeting single oscillation to impact specific symptom. These findings elucidate the different oscillatory mechanisms underlying symptom improvements in PD, underscoring the pivotal role of aberrant oscillations in the pathophysiology of PD tremor and rigidity-bradykinesia.

References

1. Arun S et al. (2023), 'Evoked mid-frontal activity predicts cognitive dysfunction in Parkinson's disease', Journal of Neurology, Neurosurgery & Psychiatry, vol. 94, no. 11, pp. 945-953.

Poster No 145

Quantitative MRI microstructural features of medial temporal lobe subfields relates to tauopathy

Alfie Wearn[1], Christine Tardif[2], Ilana Leppert[2], Giulia Baracchini[3], Colleen Hughes[1], Elisabeth Sylvain[4], Jennifer Tremblay-Mercier[4], Judes Poirier[4], Sylvia Villeneuve[5], Gary Turner[6], Nathan Spreng[3]

[1]McGill University, Montreal, Québec, [2]McConnell Brain Imaging Centre, Montreal Neurological Institute and Hospital, Montreal, Quebec, [3]Montreal Neurological Institute and Hospital, Montreal, Quebec, [4]Douglas Mental Health University Institute, Montreal, Québec, [5]Brain Imaging Centre, Douglas Institute Research Centre, Montreal, Qc, [6]York University, Toronto, Ontario

Introduction: Characterizing early brain changes in Alzheimer's disease (AD) is essential to develop effective therapies. The medial temporal lobe (MTL) is one of the earliest affected brain areas in AD, however, macroscale atrophy is a relatively late-stage change[1]. Brain microstructure and composition can be assessed with quantitative MRI (qMRI) and may reveal signs of pathology earlier than volumetry[2]. qMRI measures are sensitive to features like myelin and iron but tend to be non-specific. By assessing multiple MR properties we can gain a more complete picture of underlying biological tissue composition. We describe associations between qMRI measures of microstructure and macrostructure (volume) for different MTL subfields. We also test the hypothesis that these measures are sensitive to pathology in prodromal AD.

Methods: 197 participants with family history of AD were included from the PResymptomatic EValuation of Experimental or Novel Treatments for AD (PREVENT-AD) cohort[3] (mean age 68.4y, 74% female). 3T MRI sequences: - Anatomical scans: o T1w MPRAGE: 1mm isotropic, TR/TE/TI=2300/2.96/900ms, FA=9° o T2w SPACE: 0.6mm isotropic, TR/TE=2500/198ms - Multiparametric Mapping: 3 multi-echo gradient-echo sequences (1mm isotropic, TA=17:30) with weighting for: o T1: TR=18ms, 6 echoes, TE=2.16-14.81ms, FA 20° o Magnetization transfer (MT): TR=27ms, 6 echoes, TE=2.04-14.89ms, FA 6°, MT pulse FA 540°, 2.2kHz off-resonance, 12.8ms o Proton density (PD): TR=27ms, 8 echoes, TE=2.04-22.20ms, FA 6° - B1+ field maps: 2 spin-echo echo-planar sequences: 2x2x4mm, TR/TE=4010/46 ms, FA [60,120]° Image Processing: Microstructure maps (R1, MT saturation (MTsat), R2* and PD) were computed using hMRI toolbox v0.5.0[4]. MTL subfields were segmented using the Automatic Segmentation of Hippocampal Subfields (ASHS) software, using the T1w and T2w anatomical scans[5]. Brain tau was assessed using PET (18-F Flortaucipir) in the 'meta ROI', a collection of brain regions known to be affected by tau early in AD, primary in middle and inferior temporal lobe[6]. Tau positivity was defined as a standardized uptake value ratio >1.3. Statistical Analysis: Interparameter correlations were calculated within each subfield using Product-moment correlations. We tested the relationship between Tau PET and MTL subfield structure using a linear regression model for each structural measure containing all five subfields: Tau Load ~ Subfield : (Structure : Tau status) + Tau status + age + sex + education

Results: Across all ROIs R1 and MTsat correlated positively with each other and negatively with PD (Fig 1). R1 and MTsat correlated positively with R2* in hippocampal subfields (CA1, dentate gyrus, subiculum), but negatively with R2* in MTL cortices. Greater volume was associated with greater R1 and MTsat in CA1 and subiculum. In Tau+ individuals, greater tau load was associated with smaller volume of CA1, dentate gyrus and entorhinal cortex (Fig 2). Greater tau load was also associated with lower R1, MTsat and R2* and greater PD throughout the hippocampus. In contrast, greater tau load positively correlated with R1 and MTsat in MTL cortices.

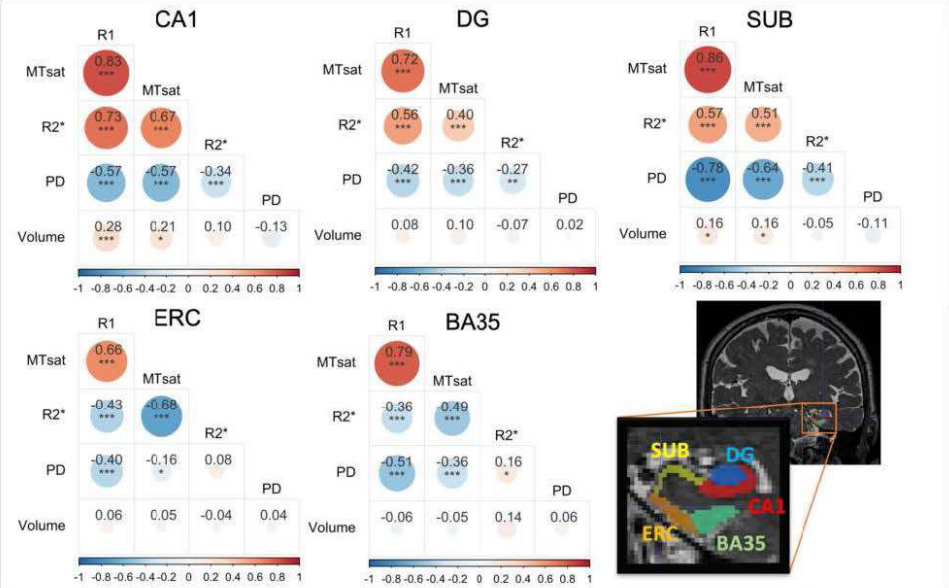

Figure 1 | Product-moment correlation matrices between structural and microstructural measures, for each medial temporal lobe subfield. A coronal view of the automated segmentation of hippocampal subfields masks is also shown in the bottom right with labels. DG = Dentate Gyrus, SUB = subiculum, EC = Entorhinal Cortex, BA35 = Brodmann Area 35 / Transentorhinal Cortex. *p<0.05, **p<0.01, ***p<0.001.

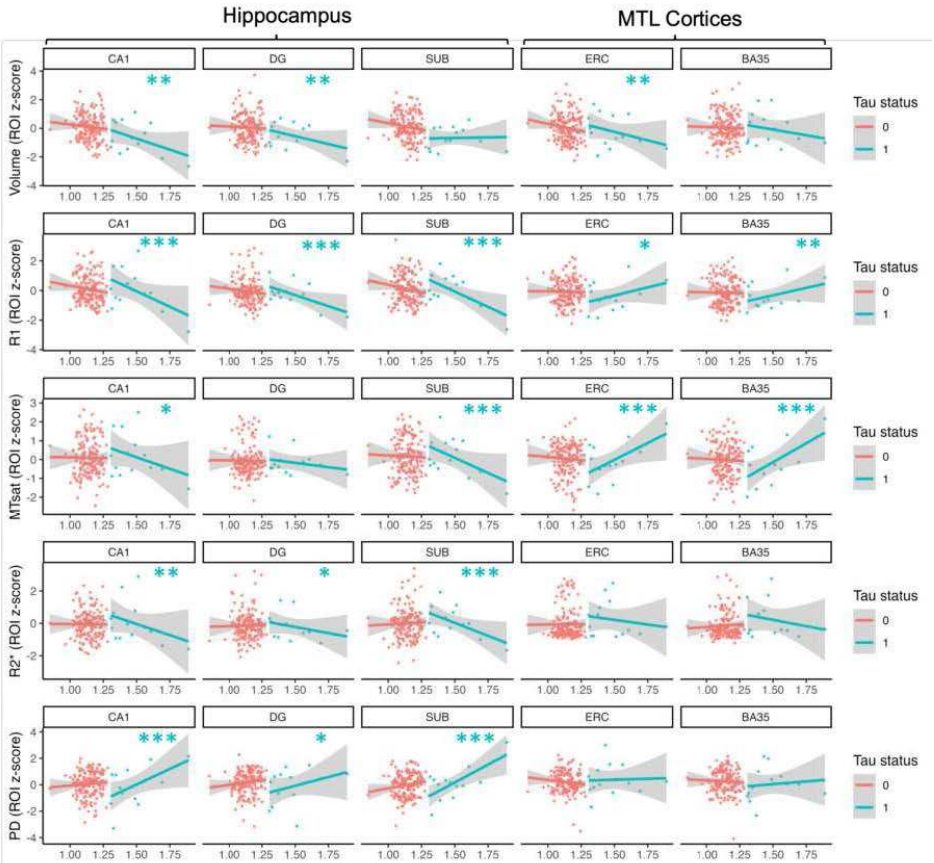

Figure 2 | Scatter plots of brain tau load and structural and microstructural measures in each medial temporal lobe subfield. Regression lines with standard error are shown in different colors for tau+ (1, blue) and tau- (0, red) individuals. *p<0.05, **p<0.01, ***p<0.001.

Conclusions: In hippocampal subfields we identify a pattern of covariance between qMRI measures of microstructure that reflects myelination (R1, MTsat and R2* covarying negatively with PD). Consistent with a model of AD-related demyelination, we see that in tau+ individuals (likely prodromal AD), greater tau load was associated with lower R1, MTsat and R2* and greater PD, as well as smaller volume. Negative covariance between MTsat and R2* in the MTL cortices indicates driving factors other than myelin. Here, greater tau load associated with higher MTsat in the tau+ group. MTsat may be directly sensitive to the presence of neurofibrillary tangles. We highlight regional differences in qMRI measures of microstructure. This study takes steps toward a more complete understanding of the biological driving factors of these measures.

References

1. Jack, C.R. et al. (2013). Tracking pathophysiological processes in Alzheimer's disease: an updated hypothetical model of dynamic biomarkers. The Lancet. Neurology. DOI: 10.1016/S1474-4422(12)70291-0.
2. Weiskopf, N. et al. (2015). Advances in MRI-based computational neuroanatomy: from morphometry to in-vivo histology. Current Opinion in Neurology. DOI: 10.1097/WCO.0000000000000222.
3. Tremblay-Mercier, J. et al. (2021). Open science datasets from PREVENT-AD, a longitudinal cohort of pre-symptomatic Alzheimer's disease. NeuroImage: Clinical. DOI: 10.1016/j.nicl.2021.102733.
4. Tabelow, K. et al. (2019). hMRI - A toolbox for quantitative MRI in neuroscience and clinical research. NeuroImage. DOI: 10.1016/j.neuroimage.2019.01.029.
5. Yushkevich, P.A. et al. (2015). Automated volumetry and regional thickness analysis of hippocampal subfields and medial temporal cortical structures in mild cognitive impairment. Human Brain Mapping. DOI: 10.1002/hbm.22627.
6. Jack, C.R. et al. (2017). Defining imaging biomarker cut-points for brain aging and Alzheimer's disease. Alzheimer's & dementia : the journal of the Alzheimer's Association. DOI: 10.1016/j.jalz.2016.08.005.

Poster No 146

Unravelling the heterogeneity of Mild Cognitive Impairment using Subtype and Stage Inference

Rodolfo Chiari-Correia[1], Carlos Ernesto Garrido Salmon[1], Neil Oxtoby[2], Alexandra Young[2], Francesca Biondo[2], James Cole[2]

[1]University of Sao Paulo, Ribeirao Preto, Sao Paulo, [2]University College London, London, London

Introduction: Individuals diagnosed with mild cognitive impairment (MCI) typically experience initial signs of an abnormal cognitive decline without losing the ability to independently perform basic activities of daily living. This stage is commonly considered to be a prodromal stage of dementia-causing diseases such as Alzheimer's disease (AD). Nonetheless, the most commonly used diagnostic criteria, MCI due to Alzheimer's Disease (AD)[1], have several limitations, resulting in a complex diagnostic process, low accuracy, and a high heterogeneous group of patients[2,3]. One possible way to address this issue, is to classify MCI patients into more biologically specific subgroups - an approach that can be aided by quantitative biomarkers and unsupervised machine learning algorithms. However, clustering algorithms may incorrectly identify subtypes that are merely temporally distinct, that is, essentially only in different stages of a disease progression rather than phenotypically different. In this context, this study aimed to identify MCI subtypes using two different sets of biomarkers and a machine-learning technique named "Subtype and Stage Inference" (SuStaIn)[4]. The Sustain can uncover data-driven disease subtypes but also infer disease progression stages with entirely cross-sectional data.

Methods: Participants We analyzed data from 558 MCI subjects (mean age 73.5, 234 Female) and 215 amyloid-negative cognitively normal controls (mean age 72.4, 111 Female) obtained from the Alzheimer's Disease Neuroimaging Initiative (ADNI) database[5]. Biomarker Sets Neuropsychological: Animals Category Fluency (CATANIMSC), Boston Naming Test (BNTTOTAL), Trail Making Test B (TRABSCOR), Rey Auditory Verbal Learning Test Trail 1 (AVTOT1), RAVLT Immediate (AVTOTAL)[6], RAVLT Learning[6], RAVLT Forgetting[6], Mini Mental State Exam (MMSCORE), and Geriatric Depression Scale (GDTOTAL). Brain MRI and CSF-derived biomarkers: Volumes of Hippocampus, Cortical, Subcortical, Ventricles, and White Matter Hypointensities. CSF Amyloid-β 42 and Phosphorylated TAU concentration levels. Biomarkers were selected based on data quality, sample size, variability, and correlation with variables within the same domain. The volume of each brain region was acquired using FastSurfer software[7] and normalized by intracranial volume. Z-score Sustain The z-score Sustain version characterizes the progression of a disease through a series of stages, in which each stage is associated with an increase in a biomarker to a new z-score relative to a control population[4].

Results: Two subtypes were identified by running SuStaIn on neuropsychological data. Subtype 1 was characterized mainly by changes in z-score in RAVLT forgetting and GDSCORE, while Subtype 2 in the TRABSCOR, as seen in figure 1A. Subtype 2 individuals exhibited worse performance in most neuropsychological tests, as well as lower cortical and hippocampal volumes, and higher ventricular and WM hyperintensities volumes. Additionally, they had a higher conversion rate to AD after 1 and 2 years (figure 2). Using the MRI and CSF data, the SuStaIn also identified 2 subtypes. Subtype 1 characterization was led by z-score changes in PTAU, while subtype 2 was by changes in ventricular volume and WM hypointensities (figure 1B).

Subtype 1 also had a higher percentage of individuals with the ε3ε4 and ε4ε4 APOE allele pair, as well as a higher rate of individuals who converted to AD. In both analyses, MCI patients in stage 0 were reclassified as subtype 0, where biomarkers abnormalities were sub-threshold (z < 1).

Conclusions: The SuStaIn can identify MCI subtypes based on different biomarkers, each with distinct disease progression patterns and neurobiological characteristics. Additionally, it enables the detection of individuals with a higher risk of conversion to AD. (i.e., Neuropsychological subtype 2 and MRI/CSF subtype 1). In our future research, we plan to investigate the ability of the SuStaIn stage to predict conversion to AD using ML models.

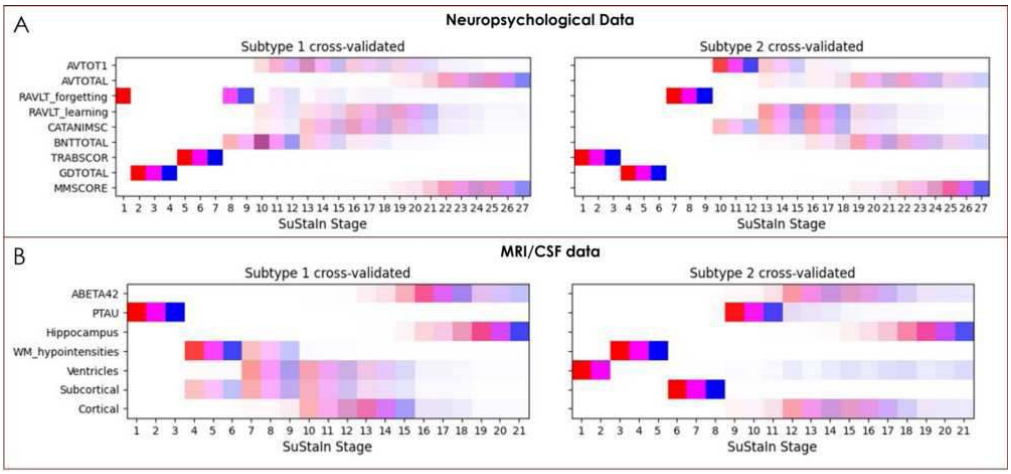

Figure 1: Positional variance diagrams showing the probability of a particular z-score event occurs at that particular stage: red = 1, magenta = 2, and blue = 3. **A** Using Neuropsychological data. **B** Using MRI/CSF data

Sustain Biomarkers	Neuropsychological				MRI/CSF			
Subtype	0	1	2		0	1	2	
Subjects N°	275	140	143		242	173	143	
	Mean (std)	Mean (std)	Mean (std)	F	Mean (std)	Mean (std)	Mean (std)	F
AVTOT1	4.62 (1.5)	4.81 (1.4)	3.78 (1.4)	20.17	4.75 (1.5)	4.18 (1.4)	4.27 (1.5)	8.49
AVTOTAL	35.56 (10.9)	38.74 (9.6)	29.43 (8.7)	31.88	37.67 (11.0)	32.09 (9.2)	33.16 (10.2)	17.19
RAVLT_forgetting	4.10 (2.0)	6.01 (2.7)	4.56 (2.1)	33.22	4.25 (2.4)	5.21 (2.3)	4.83 (2.2)	8.6
RAVLT_learning	4.11 (2.6)	5.15 (2.4)	3.56 (2.4)	14.46	4.71 (2.6)	3.77 (2.6)	3.97 (2.4)	7.76
CATANIMSC	18.01 (5.1)	18.74 (4.6)	14.97 (4.8)	24.69	18.73 (5.1)	16.34 (4.2)	16.49 (5.5)	14.8
BNTTOTAL	26.73 (3.5)	27.67 (2.2)	24.92 (4.3)	23.23	27.12 (3.1)	26.22 (3.4)	25.80 (4.3)	6.82
TRABSCOR	80.99 (22.5)	87.29 (27.4)	200.62 (61.8)	518.39	95.14 (50.8)	118.64 (64.7)	137.29 (72.6)	22.15
GDTOTAL	1.04 (0.8)	3.21 (1.3)	1.55 (1.2)	180.7	1.76 (1.4)	1.69 (1.4)	1.66 (1.3)	0.23
MMSCORE	27.76 (1.8)	28.41 (1.5)	27.09 (1.8)	20.39	28.12 (1.7)	27.37 (1.8)	27.59 (1.8)	9.94
ABETA42	1102.90 (624.9)	1086.59 (520.7)	784.23 (350.5)	17.89	1203.49 (589.0)	871.10 (525.0)	878.47 (433.9)	26.1
PTAU	26.70 (12.9)	26.36 (13.8)	31.59 (16.3)	6.7	20.65 (6.0)	43.85 (13.2)	20.74 (8.6)	360.95
Hippocampus (10^3 mm^3)	3.25 (0.9)	3.34 (0.9)	2.99 (0.9)	5.26	3.44 (0.9)	3.15 (0.9)	2.88 (0.9)	16.29
WM_hypointensities (10^3 mm^3)	5.14 (8.8)	5.65 (8.0)	9.64 (13.3)	9.98	2.89 (4.4)	5.81 (10.1)	13.14 (13.5)	54.56
Ventricles (10^3 mm^3)	26.67 (18.0)	27.65 (19.3)	39.19 (22.4)	20.79	20.68 (10.0)	22.33 (12.2)	55.54 (19.3)	333.09
Subcortical (10^3 mm^3)	21.96 (3.1)	21.81 (3.0)	21.21 (3.2)	2.75	21.92 (2.9)	21.70 (3.0)	21.45 (3.6)	1.02
Cortical (10^3 mm^3)	196.53 (28.7)	195.90 (28.0)	179.43 (30.4)	18.01	199.23 (28.0)	188.70 (29.1)	183.72 (31.1)	14.23
	APOE Allele				APOE Allele			
ε3ε4	98 (35%)	48 (34%)	62 (43%)	-	69 (28%)	90 (52%)	49 (34%)	-
ε4ε4	32 (11%)	18 (12%)	13 (9%)	-	21 (8%)	30 (17%)	12 (8%)	-
	Conversion to AD				Conversion to AD			
1 year after baseline	29 (10%)	12 (8%)	35 (24%)	-	21(8%)	32 (18%)	23 (16%)	-
2 year after baseline	N=251	N=124	N=112	-	N=218	N=148	N=121	-
	44 (17%)	27 (21%)	48 (42%)	-	31 (14%)	58 (39%)	30 (24%)	-

Figure 2: Descriptive statistics table separated by Sustain subtype. In green, data referring to the experiment with neuropsychological data and in blue, MRI/CSF data.

References

1. Albert, M. S. et al. (2011) 'The diagnosis of mild cognitive impairment due to Alzheimer's disease: recommendations from the National Institute on Aging-Alzheimer's Association workgroups on diagnostic guidelines for Alzheimer's disease', Alzheimer's & dementia : the journal of the Alzheimer's Association. 2011/04/21, 7(3), pp. 270–279. doi: 10.1016/j.jalz.2011.03.008.
2. Beach, T. G. et al. (2012) 'Accuracy of the clinical diagnosis of Alzheimer disease at National Institute on Aging Alzheimer Disease Centers, 2005-2010.', Journal of neuropathology and experimental neurology, 71(4), pp. 266–273. doi: 10.1097/NEN.0b013e31824b211b.
3. Estévez-González, A. et al. (2003) 'Rey verbal learning test is a useful tool for differential diagnosis in the preclinical phase of Alzheimer's disease: comparison with mild cognitive impairment and normal aging.', International journal of geriatric psychiatry, 18(11), pp. 1021–1028. doi: 10.1002/gps.1010.
4. Henschel, L. et al. (2020) 'FastSurfer - A fast and accurate deep learning based neuroimaging pipeline', NeuroImage, 219, p. 117012. doi: https://doi.org/10.1016/j.neuroimage.2020.117012.
5. Petersen, R. C. et al. (2010) 'Alzheimer's Disease Neuroimaging Initiative (ADNI): clinical characterization.', Neurology, 74(3), pp. 201–209. doi: 10.1212/WNL.0b013e3181cb3e25.
6. Rabinovici, G. D. et al. (2019) 'Association of Amyloid Positron Emission Tomography With Subsequent Change in Clinical Management Among Medicare Beneficiaries With Mild Cognitive Impairment or Dementia', JAMA, 321(13), pp. 1286–1294. doi: 10.1001/jama.2019.2000.
7. Young, A. L. et al. (2018) 'Uncovering the heterogeneity and temporal complexity of neurodegenerative diseases with Subtype and Stage Inference', Nature Communications, 9(1), p. 4273. doi: 10.1038/s41467-018-05892-0.

Poster No 147

Arterial Territories Mediate White Matter Hyperintensities association to Processing Speed in MCI/AD

Ikrame Housni[1,2,3,4], Natalie Phillips[5], Ali Filali-Mouhim[4], Simon Duchesne[6,7], Sridar Narayanan[8,9], AmanPreet Badhwar[1,2,3,4]

[1]Multiomics investigation of neurodegenerative diseases (MIND) Laboratory, Montreal, Canada, [2]Département de pharmacologie et physiologie, Faculté de médecine, Université de Montréal, Montreal, Canada, [3]Institut de génie biomédical, Université de Montréal, Montreal, Canada, [4]Centre de Recherche de l'Institut Universitaire de Gériatrie de Montréal (CRIUGM), Montreal, Canada, [5]Department of Psychology, Concordia University, Montreal, Canada, [6]Département de radiologie et médecine nucléaire, Université Laval, Quebec, Canada, [7]Quebec Heart and Lung Institute, Quebec, Canada, [8]McConnell Brain Imaging Centre, Montreal Neurological Institute, Montreal, Canada, [9]Department of Neurology and Neurosurgery, McGill University, Montreal, Canada

Introduction: MRI-detected white matter hyperintensities (WMHs) are widely recognized as markers of cerebrovascular abnormalities and can serve as an index of vascular brain injury (Wardlaw et al., 2013). The literature (i) strongly establishes a link between an increase in WMH volume (WMHv) and cognitive decline (Guo and Shi, 2022), and (ii) suggests that the anatomical distribution of WMHs exerts a mediating effect on cognitive dysfunction (Garnier-Crussard et al., 2022). It has also been reported that pathological remodeling of the major cerebral arteries (anterior, ACA; middle, MCA; posterior, PCA) potentially increases WMHv in an arterial territory (AT)-specific manner (Gutierrez et al., 2018). Recently, we characterized the anatomical distribution of WMH within ATs in age-related neurodegenerative diseases (NDDs), and demonstrated NDD-specific signatures of WMHv distribution across ATs (Housni et al., 2023). However, the relationship between AT-specific WMHv and cognitive performance remains largely unexplored, and our current study addresses this gap in knowledge.

Methods: We selected participants from six clinical groups (cognitively unimpaired, subjective cognitive decline, mild cognitive impairment (MCI), Alzheimer's disease (AD), and MCI and AD with high vascular brain injury (Fig. 1a)) from the CCNA COMPASS-ND cohort (N=756;7th-release)(Chertkow et al., 2019). WMHs were segmented from FLAIR MRI (Dadar et al., 2017) and mapped onto an arterial atlas (Schirmer et al., 2019). The cognitive performance of participants was measured using four psychometric tests: Simple Reaction Time (SRT), Choice Reaction Time (CRT), Digit Symbol Substitution Test (DSST), and Montreal Cognitive Assessment (MoCA) (Fig. 1b). Statistical analyses consisted of a series of linear regression models, with cognitive performance as the dependent variable and region-size-normalized AT-WMHv as the independent variable, controlling for age and sex. We investigated the interaction between cognition and AT-specific WMHv both (i) adjusting for diagnosis, and (ii) within each clinical category, to identify disease-specific effects. A 5% False Discovery Rate threshold was applied to correct for multiple comparisons.

Results: Adjusting for clinical diagnosis: (i) SRT scores were associated with ACA WMHv ($p=0.002;t=2.44$); (ii) CRT and MoCA scores were associated with PCA WMHv (CRT: $p=0.002;t=2.40$ | MoCA: $p=0.001;t=-3.21$); and (iii) DSST scores were associated with WMHv across all ATs (PCA: $p<0.001;t=-3.96$ | MCA: $p=0.004;t=-2.83$ | ACA: $p=0.02;t=-2.26$). NDD-specific analyses showed that MCI and AD were the only categories to show AT-specific WMHv associations with cognitive performance (Fig. 1c). In MCI, lower DSST scores were associated with higher PCA WMHv ($p=0.02;t=-2.78$) (Fig. 1d). In AD, a lower % of correct answers in CRT tasks was associated with higher ACA ($p=0.006;t=-3.32$) and MCA ($p=0.02;t=-2.59$) WMHv (Fig. 1e).

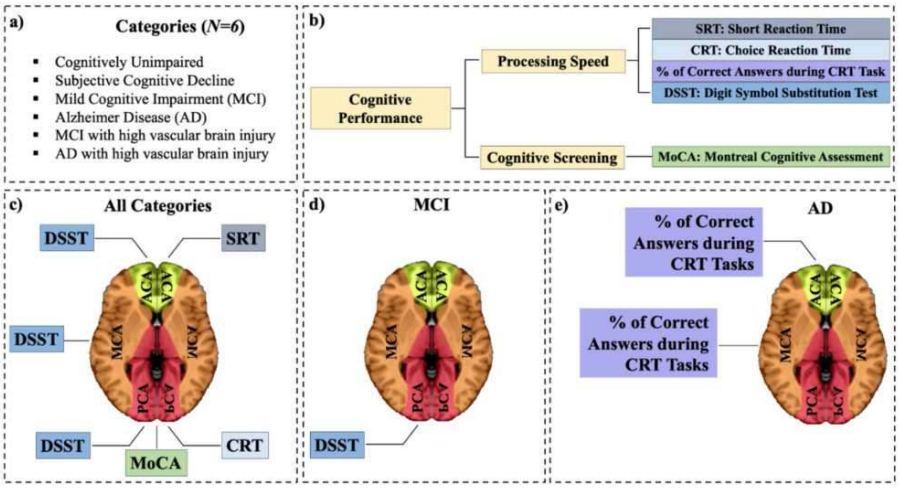

Fig. 1: Associations between AT-specific WMHv and Cognitive Performance

a) Clinical categories analyzed; b) Tasks used for cognitive assessment; c) Across categories analysis: AT-specific WMHv associations with cognitive scores from different cognitive assessments; d) NDD-specific analysis: PCA WMHv was associated with DSST scores in MCI; e) NDD-specific analysis: ACA and MCA WMHv were significantly associated with the percentage of Correct Answers in CRT Tasks in AD. *Note: All presented results maintain significance ($p < 0.05$) after correcting for multiple comparisons.*

Conclusions: Overall, greater WMHv was associated with poorer cognitive performance (i.e., higher SRT, CRT | lower MoCA, DSST, % of correct answers in CRT tasks). Mounting evidence suggests that WMHs exert an independent effect on cognition in AD, which is additive to that exerted by the core proteinopathies (i.e., beta-amyloid, tau) (Ng et al., 2023). A study found that WMHv in PCA sub-regions contributes to lower cognition, independent of amyloid deposition or atrophy in early AD (Garnier-Crussard et al., 2022). Adding strength to this finding, we observed an association between PCA WMHv and processing speed at the MCI stage. This association however evolved to the ACA and MCA at the AD stage. As AD is characterized by increased amyloid deposits in areas perfused by the ACA and MCA (Adlard et al., 2014), further investigation is warranted to determine whether the observed associations are driven by WMH or other AD pathologies.

References

1. Adlard, P.A. (2014) 'A review of β-amyloid neuroimaging in Alzheimer's disease', Frontiers in neuroscience, 8, p. 327.
2. Chertkow, H. (2019) 'The Comprehensive Assessment of Neurodegeneration and Dementia: Canadian Cohort Study', The Canadian journal of neurological sciences. Le journal canadien des sciences neurologiques, 46(5), pp. 499–511.
3. Dadar, M. (2017) 'Performance comparison of 10 different classification techniques in segmenting white matter hyperintensities in aging', NeuroImage, 157, pp. 233–249.
4. Garnier-Crussard, A. (2022) 'White matter hyperintensity topography in Alzheimer's disease and links to cognition', Alzheimer's & dementia: the journal of the Alzheimer's Association, 18(3), pp. 422–433.
5. Guo, W. (2022) 'White matter hyperintensities volume and cognition: A meta-analysis', Frontiers in aging neuroscience, 14, p. 949763
6. Gutierrez, J. (2018) 'Relationship between brain large artery characteristics and their downstream arterioles', Journal of neurovirology, 24(1), pp. 106–112.
7. Housni, I. (2023) 'Associations of white matter hyperintensities with cerebrovascular architecture in Alzheimer's disease and related dementias', in Alzheimer's Association International Conference. ALZ. Available at: https://alz.confex.com/alz/2023/meetingapp.cgi/Paper/73694 (Accessed: 30 November 2023)
8. Ng, K.P. (2023) 'White Matter Hyperintensity as a Vascular Contribution to the AT(N) Framework', The journal of prevention of Alzheimer's disease, 10(3), pp. 387–400.
9. Schirmer, M.D. (2019) 'Spatial Signature of White Matter Hyperintensities in Stroke Patients', Frontiers in neurology, 10, p. 208
10. Wardlaw, J.M. (2013) 'Neuroimaging standards for research into small vessel disease and its contribution to ageing and neurodegeneration', Lancet neurology, 12(8), pp. 822–838.

Poster No 148

A Summary Statistics Approach to providing Imaging Results for the Cleveland ADRC Neuroimaging Core

Jian Lin[1], Ken Sakaie[1], Wanyong Shin[1], Katherine Koenig[1], Dan Ma[2], Sehong Oh[1], Sally Durgerian[1], Ajay Nemani[1], Pillai Jagan[1], Brian Appleby[2], Alan Lerner[2], James Leverenz[1], Mark Lowe[1]

[1]The Cleveland Clinic, Cleveland, OH, [2]Case Western Reserve University, Cleveland, OH

Introduction: The NIH/NIA supports a network of 33 Alzheimer's Disease Research Centers (ADRC) to promote translation of research to improved patient care. The neuroimaging core in Cleveland (CADRC-NIC) has developed a panel of advanced MRI methods to explore their use in the context of AD and related dementia. We provide an overview of the methods and the overall framework for analysis and distillation of the imaging data into a summary statistics report of regional measures of the brain.

Methods: Subjects are recruited from the community for annual evaluation. All imaging is performed on a Siemens Prisma 3T MRI with a standard 32 channel head coil (Siemens Healthineers, Erlangen, Germany). Imaging included anatomical, resting state functional MRI (rs-fMRI)[1] and diffusion MRI (dMRI) scans based on the ADNI3 advanced protocol (https://adni.loni.usc.edu/). Additional scans including quantitative arterial spin labeling (ASL)[2,3], multiecho gradient echo (MGE), myelin-weighted image (MWI)4 using ViSTa[5], dynamic contrast enhancement (DCE)[6] and magnetic resonance fingerprinting (MRF)[7]. MGE is used to generate susceptibility-weighted images (SWI) and quantitative susceptibility maps (QSM)[8]. dMRI is used to calculate both diffusion tensor imaging (DTI)[9] and neurite orientation dispersion and density imaging (NODDI)[10] maps. Due to concerns related to patient comfort and compliance, scans are acquired in two separate scan sessions, allowing subjects to take a break between sessions. Further details about the imaging and purpose of each scan are provided in Table 1. Histograms of tissue properties of each scan are generated from each scan session as a quality assurance step. Outcome measures consist of average values from within brain parcels defined by FreeSurfer[11] that have been coregistered to native space using AFNI[12], FSL[13], and ANTs[14].

Results: To date, eighty six subjects (36 female) have been scanned. Age was 68±11 years (mean±std). Years of education was 16±3 years. Thirty-seven were cognitively normal, 33 had mild cognitive impairment related to typical AD/atypical AD/DLB/Other etiologies, while 13 had dementia related to typical AD/atypical AD/Down's syndrome/Other etiologies, and 3 were awaiting consensus diagnosis. Figure 1 shows an example of histograms used as part of the quality assurance. Figure 2 depicts an example of outcome measures. Tables 2 and 3 show examples of outcome measures from one subject in regions commonly affected in AD.

Conclusions: We present a brief overview of the imaging acquired by the CADRC-NIC. While measures of neurodegeneration from structural imaging are well-established for AD, imaging data from other modalities need to be acquired from a large population of subjects in order to evaluate their utility for patient management. Providing a quantitative summary of regional brain measures from an advanced imaging protocol can help to facilitate analyses by the regional and national network of AD and ADRD researchers. These data are made readily available and are intended to help in furthering the development of these advanced measures as biomarkers for AD diagnosis and progression.

Table1	FOV (mm^3)	TR (ms)	TE (ms)	Flip Angle (°)	Voxel Size (mm^3)	Purpose
3D Sagittal MPRAGE	208x240x256	2300	2.98	9	1x1x1	freesurfer parcellation
3D Sagittal FLAIR	160x256x256	4800	441	120	1.2x1x1	Radiological identification of pathology
2D Coronal High Resolution Hippocampus	448x30x448	8020	50	122	0.391x2.0x0.391	Segmentation of subfields of the hippocampus
2D Axial Multiecho Gradient Echo	256x256x44	650	15/20	20	0.859x0.859x4.0	Radiological identification of vascular pathology
2D Axial Gradient Echo Echo Planar Imaging (EPI)	88x88x64	607	32	50	2.5x2.5x2.5 (976 volumes)	Resting-state functional connectivity
2D Axial Diffusion MRI	116x116x78	3300	71	90	2x2x2 (127 vols)	DTI, NODDI measures of tissue integrity
2D Axial Pulsed ASL	128x128x32	4000	20.26	180	1.875x1.875x4.5	Perfusion
3D Axial Multiecho Gradient Echo	192x256x176	27	16/22	20	1x1x1	SWI, QSM
3D Axial Myelin Water imaging	96x96x80	1160	8.4	90	2x2x2	White Matter Integrity
3D Axial DCE	128x128x16	6120	1.36	15	1.875x1.875x5.0	Blood brain barrier integrity
MRF	300x300x144	10	2.2	1.5-30	1x1x1	Quantitative T1, T2

Table 1. Summary of MRI acquisitions

Table2	DTI-FA	DTI-TD	MRF-T1	MRF-T2	pASL-CBF	ViSTa-MWI	MGE-QSM
Right							
Hippocampus	0.1774	0.8471	1263.63	68.85	55.15	1.251	0.0002
Mid. temporal gyrus	0.1361	0.8057	1296.56	46.95	60.92	0.830	-0.0009
Posterior cingulate							
Mid	0.1522	0.8181	1170.95	54.38	69.86	1.177	0.0009
Dorsal	0.1522	0.7940	1053.93	51.49	74.43	0.967	-0.0025
ventral	0.1854	0.7855	1134.18	68.69	61.49	1.004	-0.0037
Left							
Hippocampus	0.1800	0.8436	1110.76	63.75	53.75	1.231	-0.0013
Mid. temporal gyrus	0.1282	0.7810	1343.04	59.58	64.21	1.084	0.0032
Posterior cingulate							
Mid	0.1469	0.7644	1190.64	54.26	61.03	1.128	0
Dorsal	0.1522	0.7896	1050.58	51.42	59.89	0.975	0.0003
ventral	0.1769	0.9309	1178.94	69.07	67.80	1.136	-0.0017

Table 2. Mean MRI values for a single subject measured in brain areas typically affected in AD.

Table3	Right	Left
ASHS		
CA1	1243.59	1289.98
CA2	17.09	11.90
DG	835.57	886.23
CA3	56.76	28.69
Subiculum	400.70	332.64
ERC	540.77	462.65
BA35	395.51	341.80
BA36	1234.44	1541.44
CS	124.82	191.96
FreeSurfer		
Lateral Ventricle	8070	7421

Table 3. Volume measures in a single subject. Hippocampal subfield volumes were generated by ASHS, and lateral ventricle volumes by FreeSurfer.

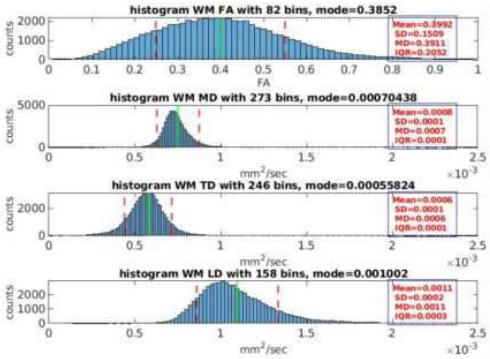

Figure 1. Quality assurance example. Histograms of DTI parameters in white matter are shown. For each subject and outcome, histograms are generated to quickly assess if values fall in expected ranges.

Figure 2. Example of outcome measures. Median T1 values, derived from MRF, from each region defined by freesurfer are depicted. Note that only a subset of regions and subjects' data are shown.

	A	B	C	D	E	F	G	H	I	J
1	PID	Left-Cerebral-White-Matter	Left-Lateral-Ventricle	Left-Inf-Lat-Vent	Left-Cerebellum-White-Matter	Left-Cerebellum-Cortex	Left-Thalamus	Left-Caudate	Left-Putamen	Left-Pallidum
2	0	890	1830	1630	870	1150	1030	1210	1110	930
3	1	850	1770	1630	870	1190	930	1110	1030	890
4	2	810	1470	1610	810	1170	850	1090	970	790
5	3	830	1770	1590	890	1190	930	1170	1070	850
6	4	950	1950	1730	910	1210	1070	1290	1190	990
7	5	850	1850	1610	950	1270	1010	1150	1070	930
8	6	890	1750	1930	850	1190	1010	1250	1010	870
9	7	930	1850	1570	930	1170	990	1190	1070	930
10	8	890	1870	1770	870	1210	970	1190	1010	890
11	9	990	2100	1730	950	1270	1130	1610	1130	970
12	10	890	1630	1610	890	1150	930	1230	1070	970
13	11	910	1770	1530	950	1190	970	1170	1070	970
14	12	950	1810	1710	890	1110	1010	1290	1190	990
15	13	870	1750	1550	890	1170	930	1250	1090	930
16	14	930	1590	1910	990	1570	1230	1710	1090	990
17	15	870	1750	1450	890	1250	990	1250	1050	890
18	16	910	1730	1650	930	1250	1010	1270	1170	990
19	17	910	1690	1530	990	1230	1050	1170	1070	990
20	18	930	1970	1670	910	1170	1230	1470	1190	1090
21	19	890	1610	1470	910	1170	930	1230	1110	990
22	20	930	1950	1850	870	1150	890	970	1090	930
23	21	810	1790	1410	770	1050	910	1090	1010	850
24	22	950	1670	1670	870	1050	910	1210	1070	870
25	23	870	1610	1430	890	1170	990	1150	1070	910
26	24	930	1670	1650	990	1410	1030	1450	1070	1030
27	25	970	2100	1910	910	1230	1110	1590	1070	1010
28	26	890	1670	1590	870	1230	950	1250	1110	930
29	27	930	1930	2000	930	1230	990	1270	1110	990
30	28	850	1530	1790	910	1230	950	1250	1150	910
31	29	930	1810	1870	950	1230	1030	1310	1150	1050
32	30	890	1710	1590	950	1230	1030	1410	1150	990
33	31	950	1850	1630	950	1370	970	1150	1170	970
34	32	890	1650	1670	910	1250	1010	1270	1110	870
35	33	910	1810	1450	950	1230	990	1250	1110	990
36	34	930	1710	1450	870	1210	930	1130	1070	950
37	35	850	1990	1370	910	1210	970	1230	1030	910
38	36	910	1830	1890	1030	1250	990	1150	1090	990
39	37	930	1670	1650	970	1310	950	1250	1110	970
40	38	1050	1990	1790	1030	1230	950	1370	1330	990
41	39	870	1570	1310	850	1190	910	1150	1030	890
42	40	910	1730	1810	950	1230	1030	1270	1170	1010
43	41	930	1510	1370	870	1170	1010	1210	1110	970
44	42	890	1610	1670	890	1190	950	1190	1090	970
45	43	890	1770	1630	910	1210	990	1170	1070	930
46	44	910	1810	1810	950	1390	1090	1230	1110	970

References

1. Biswal, B. (1995) 'Functional connectivity in the motor cortex of resting human brain using echo-planar MRI'. Magn Reson Med 1995; 34:537-541.
2. Williams, D. S. (1992) 'Magnetic resonance imaging of perfusion using spin inversion of arterial water'. Proc Natl Acad Sci U S A 1992; 89:212-216.
3. Gunther, M. (2005) Single-shot 3D imaging techniques improve arterial spin labeling perfusion measurements.
4. MacKay, A. (1994) 'In vivo visualization of myelin water in brain by magnetic resonance'. Magn Reson Med 1994; 31:673-677.
5. Oh, S. H. (2013) Direct visualization of short transverse relaxation time component (ViSTa). Neuroimage 2013; 83:485-492.
6. Tofts, P. S. (1997) Modeling tracer kinetics in dynamic Gd-DTPA MR imaging. J Magn Reson Imaging 1997; 7:91-101.
7. Ma, D. (2019) 'Development of high-resolution 3D MR fingerprinting for detection and characterization of epileptic lesions'. J Magn Reson Imaging 2019; 49:1333-1346.
8. Li, L (2001) 'Magnetic susceptibility quantification for arbitrarily shaped objects in inhomogeneous fields'. Magn Reson Med 2001; 46:907-916.
9. Basser, P. J. (1994) 'MR diffusion tensor spectroscopy and imaging. Biophys' J 1994; 66:259-267.
10. Zhang, H. (2012) 'NODDI: practical in vivo neurite orientation dispersion and density imaging of the human brain'. Neuroimage 2012; 61:1000-1016.
11. Fischl, B. (2002) 'Whole brain segmentation: automated labeling of neuroanatomical structures in the human brain'. Neuron 2002; 33:341-355.
12. Cox, R. W. (1996) 'AFNI: software for analysis and visualization of functional magnetic resonance neuroimages'. Comput Biomed Res 1996; 29:162-173.
13. Jenkinson, M. (2012) 'FSL'. Neuroimage 2012; 62:782-790.
14. Avants, B. B. (2011) 'reproducible evaluation of ANTs similarity metric performance in brain image registration'. Neuroimage 2011; 54:2033-2044.

Poster No 149

RegionFormer: A Simple Region Transformer for Alzheimer's Disease Diagnosis

Yanling Fu[1], Qi Zhu[1], Wei Shao[1], Wan Peng[2], Jiashuang Huang[3], Daoqiang Zhang[1], Liang Sun[1]

[1]Nanjing University of Aeronautics and Astronautics, Nanjing, Jiangsu, [2]Nanjing University of Aeronautics and Astronautics, Nanjing, China, [3]Nantong University, Nantong, Jiangsu

Introduction: The anatomical structure changes in the regions of the brain are key for understanding brain diseases. However, it is difficult to find slight anatomical structural changes from whole brain images by voxel-level/patch-level deep learning methods. Meanwhile, the recent region-level deep learning methods usually employ multiple sub-networks to learn feature map in each brain region, which are difficult to implement. To address these issues, we propose an effective region-based transformer method for Alzheimer's disease (AD) diagnosis, named RegionFormer. RegionFormer consists of two components:1) a very simple region feature learning network to extract the feature map for each brain region from whole structure magnetic resonance imaging (sMRI), and 2) a transformer-based classifier to capture the dependencies of each brain region for Alzheimer's disease diagnosis.

Methods: Region Feature Learning Network. Region feature learning network has two parts-i.e., an image feature learning module and a region-level feature learning module. We first employ the image feature learning module to learn the high-level contextual feature maps of input sMRI image. It's an encoder-decoder architecture, containing six 3D convolutional layers, two max-pooling layers and two 3D deconvolutional layers. Simultaneously, in the region-level feature learning module, the input sMRI image is segmented by a trained segmentation model to obtain 95 brain regions, denoted as L_I. Meanwhile, the output of image feature learning module is fed into a 1×1×1 convolutional layer with 95 channels (i.e., the number of brain regions), denoted as F_BR. Then, we extract region-level feature learning representation based on the label map L_I. Specifically, we first obtain a region-enhanced feature map A_r=(α-one_hot(L_I)+β)-F_BR, where one_hot(•) is one-hot coding and - is element-wise multiplication. α and β are hyperparameters to adjust the features within and outside the corresponding brain region. Then, the feature map A_r is fed into two group convolutional layers to obtain region-level feature vectors. Finally, the sequence of region-level tokens is used as the input of a transformer-based classifier for Alzheimer's disease diagnosis. Transformer-based Classifier. In the transformer-based classifier, we stack four transformer encoders to process the region-level features. Similar to ViT, the transformer encoder consists of a multi-head attention (MSA) block and an MLP block. Finally, a softmax function is applied to normalize the outputs.

Results: Our RegionFormer has been evaluated on the baseline sMRI scans of 1193 subjects on the ADNI dataset. The dataset contains 389 AD, 172 pMCI, 232 sMCI, and 400 NC subjects. The accuracy achieved by our RegionFormer in AD vs. NC, pMCI vs. sMCI, pMCI vs. NC, and sMCI vs. NC tasks are 0.983, 0.901, 0.956, and 0.932, which is superior to the state-of-the-art methods. Meanwhile, our RegionFormer finds the AD-related brain regions, which suggests RegionFormer has good pathology interpretability.

Conclusions: The experimental results on ADNI datasets demonstrate that our RegionFormer achieves much better classification performance than several state-of-the-art methods, especially in the relatively challenging task of MCI conversion prediction and early AD diagnosis. Besides, our RegionFormer is easily implemented and extended with the state-of-the-art deep learning framework, segmentation methods, or different brain atlases.

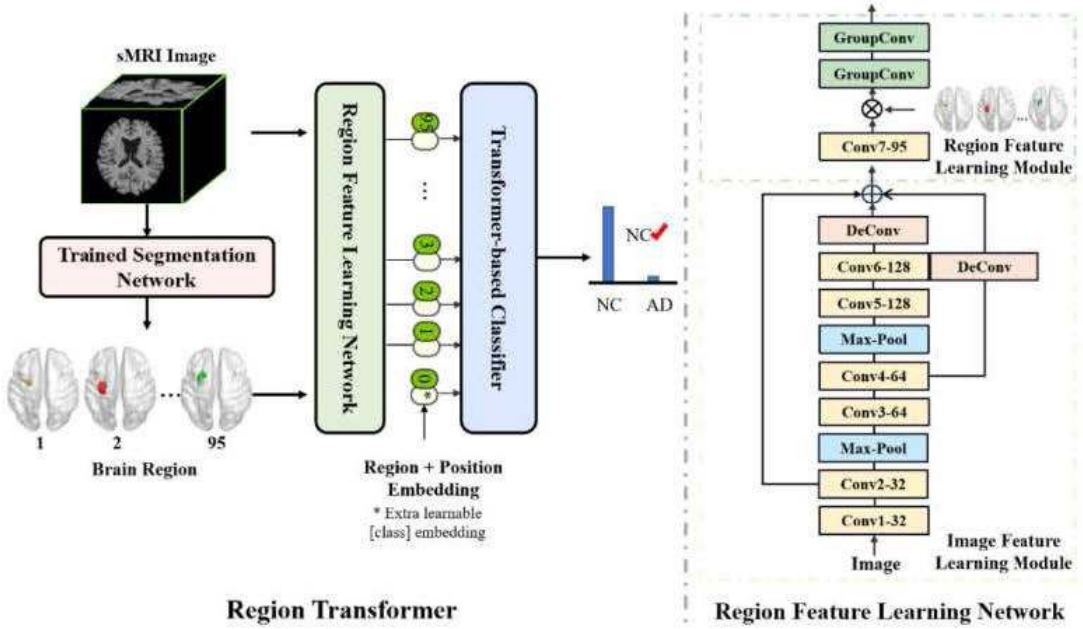

Figure 1. Illustration of our proposed RegionFormer, which consists of region feature learning network and transformer-based classifier. Specifically, the region feature learning network extracts the feature map for each brain region from the whole sMRI scan with the segmented label map. Then, the region-level features are fed into the transformer-based classifier to further learn the subtle structural changes and grasp the long dependencies of each region. More specifically, the region feature learning network contains an image feature learning module and a region feature learning module. The image feature learning module is used to learn the high-level contextual feature of input sMRI image. The region feature learning module is used to generate region tokens based on the segmented label map.

Method	AD *vs.* NC				pMCI *vs.* sMCI			
	ACC	SEN	SPE	AUC	ACC	SEN	SPE	AUC
VLM	0.816	0.756	0.875	0.883	0.679	0.629	0.717	0.709
PLM	0.848	0.846	0.850	0.905	0.716	0.657	0.761	0.732
RLM	0.804	0.718	0.888	0.852	0.667	0.571	0.739	0.692
DMIL	0.892	0.859	0.925	0.950	0.765	0.714	0.804	0.790
H-FCN	0.905	0.897	0.913	0.942	0.778	0.686	0.848	0.812
DA-MIDL	0.924	0.910	0.938	0.965	0.802	0.771	0.826	0.851
Ours	**0.983**	**0.978**	**0.988**	**0.995**	**0.901**	**0.899**	**0.903**	**0.967**

Table 1. Results for AD classification (AD *vs.* NC) and MCI conversion prediction (pMCI *vs.* sMCI) on the ADNI dataset.

Method	pMCI *vs.* NC				sMCI *vs.* NC			
	ACC	SEN	SPE	AUC	ACC	SEN	SPE	AUC
VLM	0.816	0.647	0.888	0.853	0.698	0.674	0.713	0.742
PLM	0.825	0.765	0.850	0.876	0.738	0.652	0.788	0.756
RLM	0.789	0.618	0.862	0.846	0.675	0.652	0.688	0.698
DMIL	0.868	0.735	0.925	0.908	0.794	0.783	0.800	0.808
H-FCN	0.877	0.795	0.913	0.910	0.802	0.717	0.850	0.832
DA-MIDL	0.895	0.824	0.925	0.917	0.825	0.804	0.838	0.860
Ours	**0.956**	**0.941**	**0.963**	**0.991**	**0.932**	**0.928**	**0.935**	**0.976**

Table 2. Results for MCI classification task (pMCI *vs.* NC and sMCI *vs.* NC) on the ADNI dataset.

References

1. Ashish Vaswani (2017), 'Attention is all you need', In Neural Information Processing Systems.
2. Alexey Dosovitskiy (2021), 'An image is worth 16x16 words: Transformers for image recognition at scale', In International Conference on Learning Representations.
3. Chunfeng Lian (2020), 'Hierarchical fully convolutional network for joint atrophy localization and Alzheimer's disease diagnosis using structural MRI', IEEE Transactions on Pattern Analysis and Machine Intelligence, vol.42, no.4, pp.880–893.
4. Liang Sun (2020), 'Anatomical attention guided deep networks for ROI segmentation of brain MR images', IEEE Transactions on Medical Imaging, vol.39, no.6, pp.2000–2012.
5. Trygve B. Leergaard (2022), 'Atlas-based data integration for mapping the connections and architecture of the brain', Science, vol.378, no.6619, pp.488–492.
6. Wenyong Zhu (2021), 'Dual attention multi-instance deep learning for Alzheimer's disease diagnosis with structural MRI', IEEE Transactions on Medical Imaging, vol.40, no.9, pp.2354–2366.

Poster No 150

Brain Iron in Prodromal and Early Parkinson's Disease: A 4-year Longitudinal QSM and R2* Study

Rahul Gaurav[1], François-Xavier Lejeune[1], Mathieu Santin[1], romain valabregue[1], Jean-Baptiste Pérot[1], Nadya Pyatigorskaya[1,2], Graziella Mangone[1,2], Smaranda Leu-Semenescu[2], Isabelle Arnulf[2,1], Marie Vidailhet[2,1], Jean-Christophe Corvol[2,1], Stéphane Lehéricy[2,1]

[1]Sorbonne Université, Paris Brain Institute (ICM), Paris, France, [2]Pitié-Salpêtrière Hospital, AP-HP, Paris, France

Introduction: Parkinson's disease (PD) demonstrates a progressive depletion of neuromelanin (NM)-containing dopaminergic neurons in the substantia nigra pars compacta (SNc)[1] and a high nigral iron concentration that can be quantified using quantitative susceptibility mapping (QSM) or R2*maps[2,3]. Rapid eye movement (REM) Sleep Behavior Disorder (RBD) is characterized by abnormal behaviors during REM sleep[4]. Isolated RBD (iRBD) is considered a prodromal parkinsonian condition as most patients convert to α-synucleinopathies[5]. Regional brain iron progression in prodromal and early PD is partially understood[6].

Methods: Participants: We included polysomnography-confirmed early PD with (PDRBD+) and without RBD (PDRBD-), iRBD, and healthy volunteers (HVs) scanned at 3T and evaluated at baseline (V1), 2-(V2) and 4-year (V3) follow-ups. Image Analysis: QSM images were computed using MEDI toolbox[7]. The reconstructed images were used to construct a QSM template using Advanced Normalization Tools (ANTs)[8]. R2* maps were obtained using a nonlinear fit over echo times. NM-sensitive images were acquired using a T1-weighted (T1w) 2D axial turbo spin echo protocol. The subthalamic nucleus, entire SN and its subdivisions (anterior and posterior territories of dorsal and ventral SN) were manually segmented on the template by experienced raters[9]. Subject-wise regions were obtained using inverse transformation. We automatically segmented

the caudate nucleus, putamen, globus pallidus and thalamus on the 3D T1w images and coregistered to the QSM images using NiftyReg[10]. Statistical Analyses: Baseline between-group differences were tested using multivariate linear regression models with age and sex as covariates. Longitudinal analyses were performed on subjects with at least two visits using linear mixed-effects models (LMM). Each LMM took the groups and the visit intervals with interaction as fixed effects, and the subject identifiers as a random (intercept) effect. Significance effects of the main or interaction effects were tested by Type II Wald Chi-square tests. Evolution was tracked with respect to the age of the non-PD subjects. PD was added by aligning all individual ages at onset to the baseline mean age of the HVs. During the study, 7 iRBDs converted to PD. Correlations were studied with clinical variables and nigral NM normalized signal intensity (NSI) computed using a template.

Results: At V1/V2/V3, 47/31/13 HV, 36/19/7 iRBD, 25/11/6 PDRBD+ and 80/40/12 PDRBD- were included. Baseline: QSM was increased in the posteroventral SN only and not in any other regions. PDRBD- had +17.8% elevated iron in the posteroventral SN (p= 0.03) vs. HV, while iron changes did not reach significance in PDRBD+ (+15.9%) and iRBD (+10.3%). No differences were found in the other regions. Results were similar for R2*. Longitudinal: Overall group and time effects were observed only in the posteroventral SN iron for both QSM and R2* along with an interaction in R2* but not in QSM. Posteroventral SN iron in PDRBD- showed 26.2% significantly higher rate of increase at V3 compared to HV. Progression model: Our modeling suggested that the iron increase at age of onset (60.6 years) would be approximately +10.7% compared to the mean HV level. Among the iRBD converters, the prediction suggested a greater increase in this group at age of onset (66.4 years) reaching +27.6%. Correlations: Posteroventral nigral iron showed positive correlations (r=0.31; p adjusted=0.025) with disease duration for PDRBD-. Negative correlations were found with NSI for HV and PDRBD-, and a trend for PDRBD+.

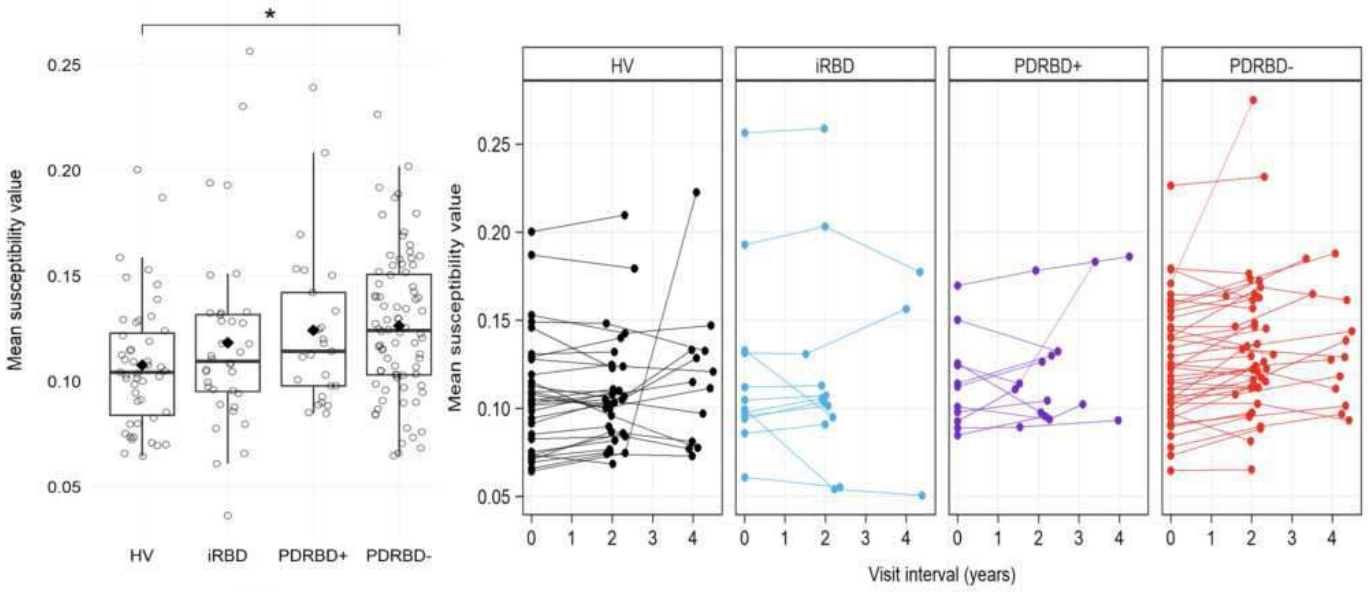

Box plot of baseline posteroventral nigral iron changes using the quantitative susceptibility mapping (QSM).

Group comparisons were based on a multivariate linear model adjusted for baseline age and sex. The asterisk depicts significant difference.

Line plots showing longitudinal posteroventral nigral iron changes using quantitative susceptibility mapping (QSM) over the years

Conclusions: PDRBD- had increased iron only in the posteroventral nigral region, which was related to disease duration and decreased NM signal. Iron deposition also increased in iRBD and PDRBD- although not significantly probably because of the lower number of subjects in these groups.

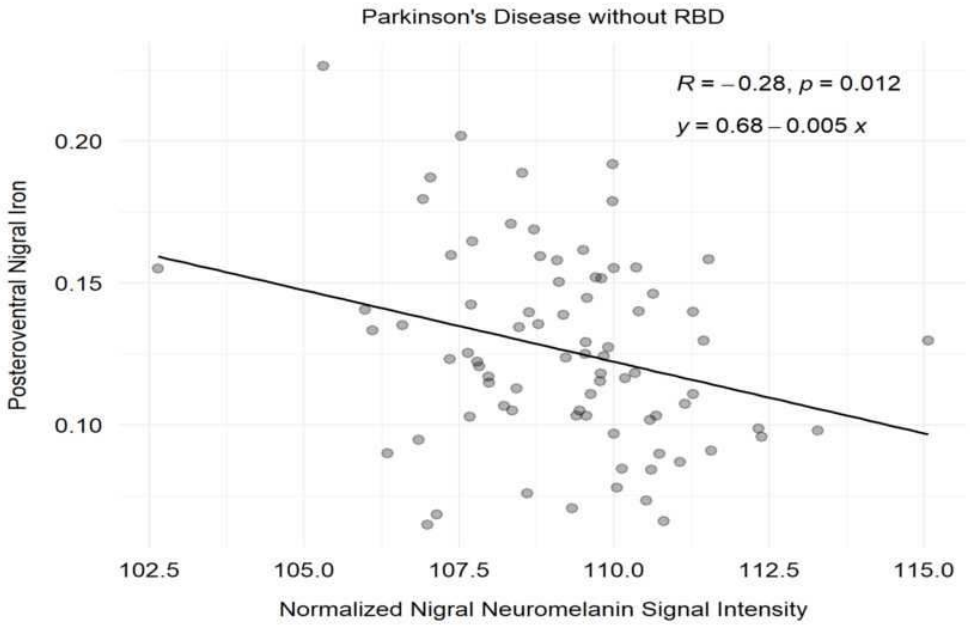

Scatter plot showing significant negative correlations between posteroventral nigral iron using the quantitative susceptibility mapping (QSM) and nigral neuromelanin normalized signal intensity (NSI).

References

1. Poewe W, Seppi K, Tanner CM, et al. (2017), 'Parkinson disease'. Nat Rev Dis Primers, Mar 23;3:17013.
2. Barbosa, J. H. O., Santos, A. C., Tumas, V., et al. (2015), 'Quantifying brain iron deposition in patients with Parkinson's disease using quantitative susceptibility mapping, R2 and R2', Magnetic resonance imaging, 33(5), 559-565.
3. Langkammer, C., Pirpamer, L., Seiler, et al. (2016), 'Quantitative susceptibility mapping in Parkinson's disease', PLoS One, 11(9), e0162460.
4. Ehrminger M, Latimier A, Pyatigorskaya N, et al. (2016), 'The coeruleus/subcoeruleus complex in idiopathic rapid eye movement sleep behaviour disorder', Brain,139(4):1180-1188. doi:10.1093/brain/aww006.
5. Iranzo A, Fernandez-Arcos A, Tolosa E, et al. (2014), 'Neurodegenerative disorder risk in idiopathic REM sleep behavior disorder: study in 174 patients, PLoS One, 9(2): e89741.
6. Sun J, Lai Z, Ma J, et al. (2020), 'Quantitative evaluation of iron content in idiopathic rapid eye movement sleep behavior disorder'. Mov. Disord, 35(3):478–485.
7. Zhou, D., Liu, T., Spincemaille, P., & Wang, Y. (2014), 'Background field removal by solving the Laplacian boundary value problem'. NMR in Biomedicine, 27(3), 312-319.
8. Liu, J., Liu, T., de Rochefort, L., et al. (2012), 'Morphology enabled dipole inversion for quantitative susceptibility mapping using structural consistency between the magnitude image and the susceptibility map'. Neuroimage, 59(3), 2560-2568.
9. Bergsland N, Zivadinov R, Schweser F, et al. (2019), 'Ventral posterior substantia nigra iron increases over 3 years in Parkinson's disease'. Mov. Disord, 34(7):1006–1013.
10. Ourselin, S., Roche, A., Subsol, G., Pennec, X., & Ayache, N. (2001). 'Reconstructing a 3D structure from serial histological sections'. Image and vision computing, 19(1-2), 25-31.

Poster No 151

Progressive Neurodegeneration of Noradrenergic Locus Coeruleus in REM Sleep Behavior Disorder

Rahul Gaurav[1], François-Xavier Lejeune[1], Pauline Dodet[1,2], Romain Valabrègue[1], Graziella Mangone[1,2], Smaranda Leu-Semenescu[2], Jean-Christophe Corvol[1,2], Marie Vidailhet[1,2], Isabelle Arnulf[1,2], Stéphane Lehéricy[1,2]

[1]Paris Brain Institute (ICM), Paris, France, [2]Pitié-Salpêtrière Hospital, AP-HP, Paris, France

Introduction: The locus coeruleus (LC) and the locus subcoeruleus (LsC) are brainstem nuclei that are affected in neurodegenerative parkinsonism[1]. The LC is the main source of noradrenergic innervation in the human brain[2]. The LsC contains neurons driving muscle atonia during REM sleep[3]. The LsC damage is known to be associated with rapid eye movement (REM) sleep behavior disorder (RBD), that is characterized by abnormal violent behaviors during REM sleep[3,4,5]. The LC/LsC complex contain catecholaminergic neurons that exhibit high neuromelanin (NM) concentrations, and can be visualized using NM-MRI[6]. Parkinson's disease (PD) and isolated RBD (iRBD), a prodromal parkinsonism stage[7,8], demonstrate LC/LsC neurodegeneration[9]. Longitudinal changes over years in the LC/LsC complex in these conditions remain unclear.

Methods: Participants: Polysomnography-confirmed early PD with (PDRBD+) and without RBD (PDRBD-), iRBD and healthy volunteers (HVs) were scanned using 3T MRI and assessed three times (V1/V2/V3) with an interval of 2.0 ± 0.2 years between the visits. Image analysis: LC/LsC was automatically analyzed blindly to the clinical status of the participants. Firstly, for signal intensity standardization, we defined three anatomical regions of interest (ROIs) in a brain template comprising left and right LC/LsC and a background region. Secondly, we resampled these ROIs onto NM-MRI using rigid and nonlinear transformations. Thirdly, we obtained the 10 connected voxels with the brightest intensities in both left and right LC/LsC. Lastly, we computed the ratio between the average signal intensities inside LC/LsC and the background ROI. Statistical analyses: Baseline between-group differences were tested using multivariate linear regression models including age and sex as covariates. Longitudinal analyses were performed in subjects with at least two visits using linear mixed-effects models (LMMs). In each LMM, the group, the visit interval and their interaction term were considered as fixed effects, while a random (intercept) effect was applied on subject identifiers. Significance effects of the main or interaction effects was tested by Type II Wald Chi-square tests. Pearson's correlations corrected for multiple testing were performed to test baseline LC/LsC signal with clinical variables, REM without atonia, nigral NM contrast to noise ratio (CNR)[10], ventral nigral iron using QSM, and striatal DaT specific binding ratios (SBR).

Results: Clinical characteristics: At V1/V2/V3, 55/45/32 HVs, 46/31/21 iRBD, 32/30/20 PDRBD+ and 99/64/29 PDRBD- were included respectively. Age, sex, MDS-UPDRS-OFF and HY scores were different between groups. Baseline: Groups were different with highest LC/LsC signal in the HVs, lowest in PDRBD+ (p=0.01), a trend in iRBD (p=0.06) and no change in PDRBD- (p=0.31). The right values were significantly lower than the left for all groups. Longitudinal: Overall, we observed group, visit and group X visit interaction effects (p<0.01 for right and p=0.09 for bilateral LC/LsC). All groups showed progressive decrease over time with PDRBD- demonstrating most significant decrease as compared to HVs (p=0.03). An annual decrease of 0.22% for HVs, 0.36% for iRBD, 0.32% for PDRBD+, and 0.58% for PDRBD- was observed. Correlations: LC/LsC signal decreased with the increase in age (r=-0.44, p<0.01) for HVs and PDRBD- (r=-0.40, p<0.001). It also decreased with the increase in MDS-UPDRS-ON score for PDRBD+ (r=-0.48, p=0.03). Further, it decreased with the increase in REM without atonia in iRBD (r=-0.37, p=0.02), nigral CNR in PDRBD- (r=-0.28, p<0.01) and ventral nigral iron in PDRBD- (r=-0.23, p=0.04). No group showed correlations with the SBR.

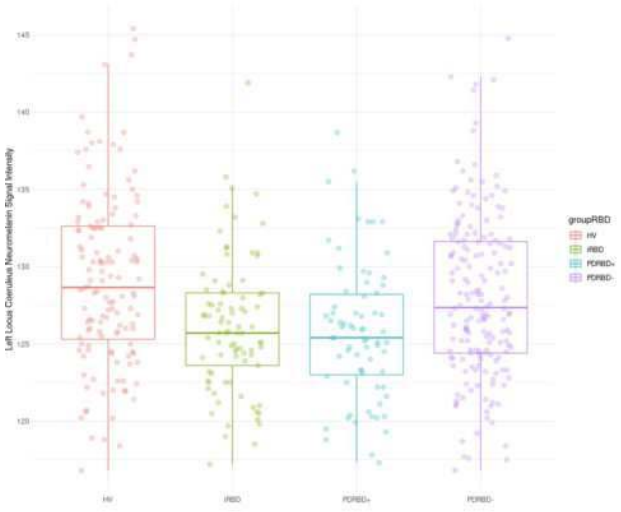

(A) Baseline left side LC/LsC signal changes in groups

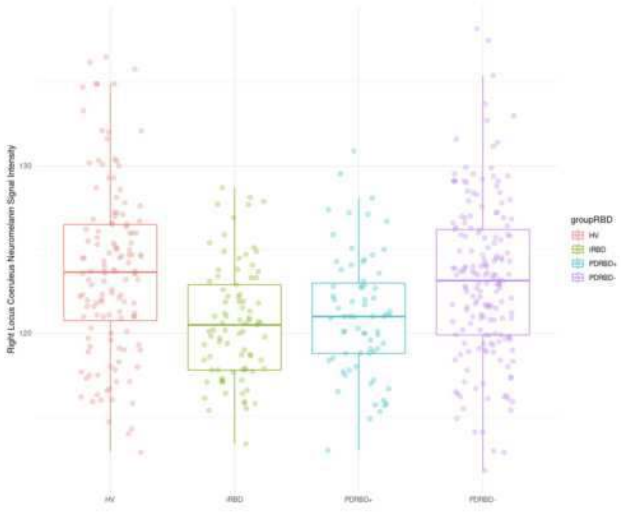

(B) Baseline right side LC/LsC signal changes in groups

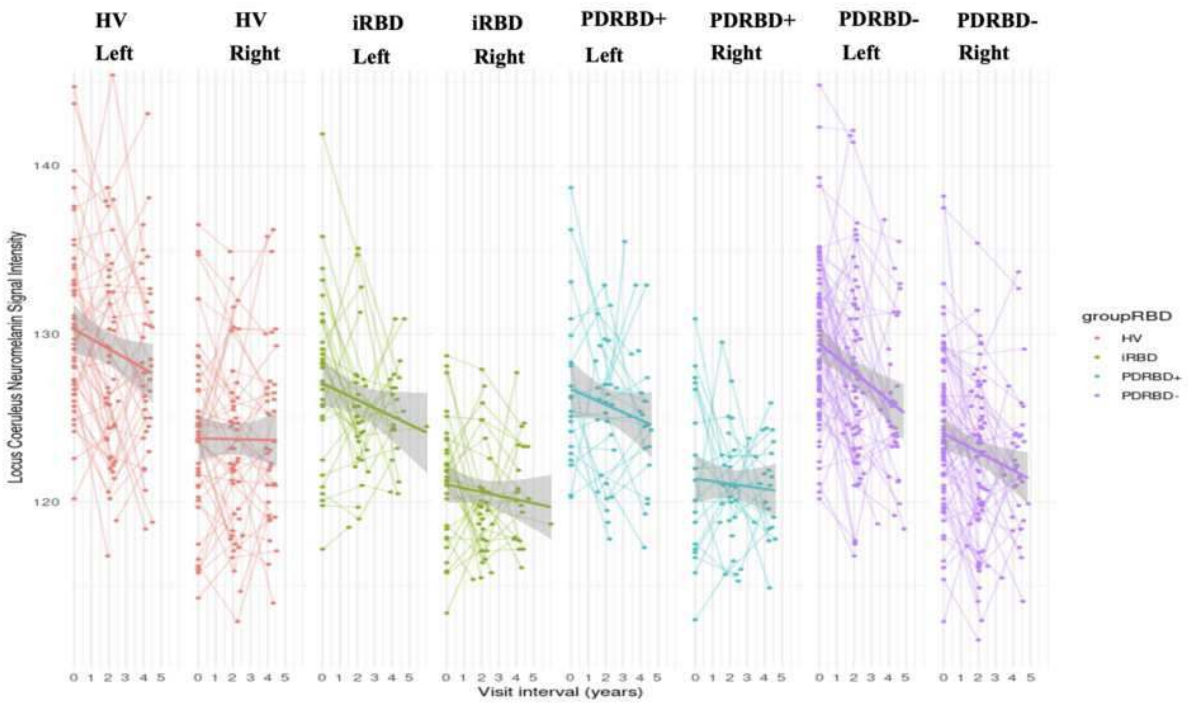

Longitudinal left and right side LC/LsC signal changes in groups

Conclusions: Taken together, we demonstrated an age-related progressive LC/LsC degeneration in all groups. PDRBD+ had the lowest baseline signal, but PDRBD- decreased more rapidly over time.

References

1. German DC, Manaye KF, White CL, Woodward DJ, McIntire DD, Smith WK, et al. Disease-specific patterns of locus coeruleus cell loss. Ann Neurol 1992; 32: 667–76.
2. Baker KG, Törk I, Hornung JP, Halasz P. The human locus coeruleus complex: an immunohistochemical and three dimensional reconstruction study. Exp Brain Res 1989; 77(2):257–270. https://doi.org/10.1007/BF00274983.
3. García-Lorenzo D, Longo-Dos Santos C, Ewenczyk C, et al. The coeruleus/subcoeruleus complex in rapid eye movement sleep behaviour disorders in Parkinson's disease. Brain. 2013;136(7):2120-2129. doi:10.1093/brain/awt152
4. Nobileau A, Gaurav R, Chougar L, et al. Neuromelanin-Sensitive Magnetic Resonance Imaging Changes in the Locus Coeruleus/Subcoeruleus Complex in Patients with Typical and Atypical Parkinsonism. Mov Disord. 2023;38(3):479-484. doi:10.1002/mds.29309
5. Ehrminger M, Latimier A, Pyatigorskaya N, et al. The coeruleus/subcoeruleus complex in idiopathic rapid eye movement sleep behaviour disorder. Brain 2016;139(4):1180–1188. https://doi.org/10.1093/brain/aww006
6. Sasaki M, Shibata E, Tohyama K, et al. Neuromelanin magnetic resonance imaging of locus ceruleus and substantia nigra in Parkinson's disease. Neuroreport 2006;17(11):1215–1218. https://doi.org/10.1097/01.wnr.0000227984.84927.a7
7. Galbiati A, Verga L, Giora E, Zucconi M, Ferini-Strambi L. The risk of neurodegeneration in REM sleep behavior disorder: A systematic review and meta-analysis of longitudinal studies. Sleep Med Rev. 2019;43:37-46. doi:10.1016/j.smrv.2018.09.008
8. Gaurav, Rahul, et al. "Deep learning-based neuromelanin MRI changes of isolated REM sleep behavior disorder." Movement Disorders 37.5 (2022): 1064-1069.
9. Betts MJ, Kirilina E, Otaduy MCG, et al. Locus coeruleus imaging as a biomarker for noradrenergic dysfunction in neurodegenerative diseases. Brain 2019;142(9):2558–2571.
10. Biondetti, E., Gaurav, R., Yahia-Cherif, L., Mangone, G., Pyatigorskaya, N., Valabrègue, R., ... & Lehéricy, S. (2020). Spatiotemporal changes in substantia nigra neuromelanin content in Parkinson's disease. Brain, 143(9), 2757-2770.

Poster No 152

Improving Diagnosis of Dementia through Longitudinal analysis of structural Brain Data

Samuel Maddox[1], Jacob Newman[1], Michal Mackiewicz[1], Saber Sami[1]

[1]*University of East Anglia, Norwich, Norfolk*

Introduction: Early identification of cognitive biomarkers could play a key role in formulating effective treatment strategies for individuals affected by mild cognitive impairment. The challenge lies in discerning and quantifying these early changes, a task complicated by their subtle nature and the diverse manifestations unique to each patient. Recent findings leveraging the structural connectomes extracted from T1-weighted Magnetic Resonance Imaging (MRI) and Diffusion Tensor Imaging (DTI) can identify subtle regional changes from neurodegeneration. In this study, we employ robust structural and diffusion tensor

processing algorithms on longitudinal data from participants exhibiting initial signs of cognitive decline. Our objective is to elucidate the earliest brain structural changes in these individuals.

Methods: Longitudinal data was accessed from the Alzheimer's Disease Neuroimaging Initiative (ADNI) dataset (ADNI2), and age matched participants were identified from their test scores acquired as part of the original study[1]. 20 participants showing a decline in cognitive impairment over one year were considered as Early Mild Cognitive Impairment (EMCI). A control group of 20 Cognitive Normal (CN) participants was also included, with test scores showing no change over the same time period. T1-weighted Magnetic Resonance Imaging (MRI) structural data was pre-processed for structural segmentations with FreeSurfer[2]. To create a connectome from the structural MRI data, we adopted the Morphometric INverse Divergence (MIND) approach[3]. This enabled the estimation of similarities between cortical areas by utilising multiple MRI features extracted from Freesurfer. DTI data, with 41 gradient directions, was collected from the EMCI participants at the same timepoints. This data was processed with Mrtrix3 using standard pre and post processing steps[4]. 70 million streamlines were computed for each EMCI participant using Anatomically constrained Multi Shell Multi Tissue-Spherical Deconvolution (MSMT-CSD) Tractography. Spherical-deconvolution Informed Filtering of Tractograms (SIFT2) was applied before producing the connectome[4]. This allowed us to further investigate the structural differences shown in EMCI participants and visualise regions that exhibit significant changes, utilising the Desikan-Killiany Atlas for this analysis[5]. GraphVar was used to perform statistical analysis on the differences in the raw matrix values produced between longitudinal MRI sessions[6]. Permutation testing was performed on MIND data at 5000 repetitions, with Bonferroni corrections applied, and a p-value of 0.001 was set for the tractography data.

Results: Using MIND, three sets of connected nodes exposed significant reduction in connectivity between sessions. These reductions occurred between the cuneus and lingual, the banks of the superior temporal sulcus and supramarginal, and the isthmus cingulate and lateral orbitofrontal. The two most significant sets of connections exposed with reduction in connectivity from EMCI tractography were the lateral occipital and banks of the superior temporal sulcus, and the cuneus and supramarginal.

Conclusions: By applying techniques developed from MIND, we have been able to identify a selection of regions that are affected in the earliest stages of potential progression to AD, and further supported by tractography analysis. These regions are also known to be affected in the later stages of AD with the early signs of regional Aβ burden[7,8]. Future research employing these techniques has the potential to facilitate cortical genetic mapping, effectively identifying individual variations in connectomes.

References

1. Mueller, S. G., Weiner, M. W., Thal, L. J., Petersen, R. C., Jack, C. R., Jagust, W., ... & Beckett, L. (2005). Ways toward an early diagnosis in Alzheimer's disease: the Alzheimer's Disease Neuroimaging Initiative (ADNI). Alzheimer's & Dementia, 1(1), 55-66.
2. Fischl, B. (2012). FreeSurfer. Neuroimage, 62(2), 774-781.
3. Sebenius, I., Seidlitz, J., Warrier, V., Bethlehem, R. A., Alexander-Bloch, A., Mallard, T. T., ... & Morgan, S. E. (2023). Robust estimation of cortical similarity networks from brain MRI. Nature Neuroscience, 26(8), 1461-1471.
4. Tournier, J. D., Smith, R., Raffelt, D., Tabbara, R., Dhollander, T., Pietsch, M., ... & Connelly, A. (2019). MRtrix3: A fast, flexible and open software framework for medical image processing and visualisation. Neuroimage, 202, 116137.
5. Desikan, R. S., Ségonne, F., Fischl, B., Quinn, B. T., Dickerson, B. C., Blacker, D., ... & Killiany, R. J. (2006). An automated labeling system for subdividing the human cerebral cortex on MRI scans into gyral based regions of interest. Neuroimage, 31(3), 968-980.
6. Kruschwitz, J. D., List, D., Waller, L., Rubinov, M., & Walter, H. (2015). GraphVar: a user-friendly toolbox for comprehensive graph analyses of functional brain connectivity. Journal of neuroscience methods, 245, 107-115.
7. Mak, E., Zhang, L., Tan, C. H., Reilhac, A., Shim, H. Y., Wen, M. O. Q., ... & Chen, C. L. H. (2023). Longitudinal associations between β-amyloid and cortical thickness in mild cognitive impairment. Brain Communications, 5(4), fcad192.
8. Tosun, D., Schuff, N., Mathis, C. A., Jagust, W., Weiner, M. W., & Alzheimer's Disease NeuroImaging Initiative. (2011). Spatial patterns of brain amyloid-β burden and atrophy rate associations in mild cognitive impairment. Brain, 134(4), 1077-1088.

Poster No 153

Distinct grey matter patterns and their determinants in a Swedish birth cohort of septuagenarians

Giulia Lorenzon[1], Anna Marseglia[1], Konstantinos Poulakis[1], Sebastian Muehlboeck[1], Daniel Ferreira[1], Miia Kivipelto[1], Lina Ryden[2], Silke Kern[2], Sara Shams[1], Anna Zettergren[2], Ingmar Skoog[2], Eric Westman[1]

[1]Karolinska Institutet, Stockholm, Sweden, [2]University of Gothenburg, Gothenburg, Sweden

Introduction: Dementia is a growing burden on global healthcare (Gauthier et al., 2022). Detecting individuals at risk in the early preclinical stage is crucial to implement prevention strategies. However, this is challenged by the high inter-individual neuropathological heterogeneity long before the clinical manifestation of dementia (Jack et al., 2013)(Jack et al., 2013). Distinct patterns of cortical and subcortical atrophy have been previously identified in neurodegenerative disorders including Alzheimer's Disease (AD) (Ferreira et al., 2020; Mohanty et al., 2022; Poulakis et al., 2022). However, knowledge of brain

heterogeneity in the general population is still lacking, yet crucial to inform early detection and intervention. Furthermore, it is important to understand the factors contributing to such heterogeneity. The aim of this study is therefore to identify specific patterns of grey matter atrophy and their lifelong determinants among relatively cognitively intact older individuals.

Methods: This cross-sectional study included 792 individuals from the Gothenburg H70-1944 Birth cohort identified through the Swedish Tax Agency's population register and living in Gothenburg (Sweden) who underwent clinical examinations and MRI between January 2014 and December 2016. We selected 746 septuagenarians without dementia or neuropsychiatric disorders, and with good quality MRI. Patterns (subtypes) of grey matter patterns were identified using unsupervised Random Forest applied to 34 regions assessing cortical thickness and 7 subcortical regions assessing volume (Poulakis et al., 2018). Next, we characterized the subtypes in relation to the following features: sociodemographic factors, cardiometabolic risk factors, cognitive function, risk gene (apolipoprotein e4 allele), and biomarkers of cerebrovascular pathology, neurodegeneration, inflammation, and lipid alterations. Linear and multinomial logistic regression models were used to compare the clusters pairwise (cluster 1 vs. remaining) and estimate their associations with the abovementioned features.

Results: We identified 5 different grey matter clusters. Cluster 1 was the most prevalent (n=278, 37.3%). Cluster 2 (n=142, 19%) exhibited diffused but primarily frontal atrophy. Cluster 3 (n=121, 16.2%) and Cluster 4 (n=157, 21%) showed thicker frontotemporal and temporal thickness. Cluster 5 (n=48, 6.4%) mostly showed posterior atrophy. Small vessel disease, heart disease, alcohol consumption, smoking history, cardiometabolic disorders, lipid alterations, and depression were key determinants of the clusters. Cluster 2 showed a higher prevalence of diabetes, alcohol consumption and elevated C-reactive protein; Cluster 4 had less odds of elevated triglycerides, brain lacunes, smoking and depression history; Cluster 5 was associated with more heart disease, alcohol consumption, elevated homocysteine and t-tau, but less white matter lesions compared to the reference cluster.

Conclusions: Our study uncovered GM heterogeneity in cognitively intact older adults and their associations with cardiometabolic and lifestyle factors. Our findings revealed the presence of distinct patterns of atrophy in elderly individuals otherwise cognitively healthy. Small vessel disease, cardiovascular and cardiometabolic risk factors, as well as inflammatory and neuropathological biomarkers may contribute to these patterns. These findings help understanding the potential mechanisms driving different atrophy patterns and highlight the importance of cardio- and cerebrovascular health to preserve cognitive function and brain structure in old age, with potential implications for early detection and prevention of cognitive decline.

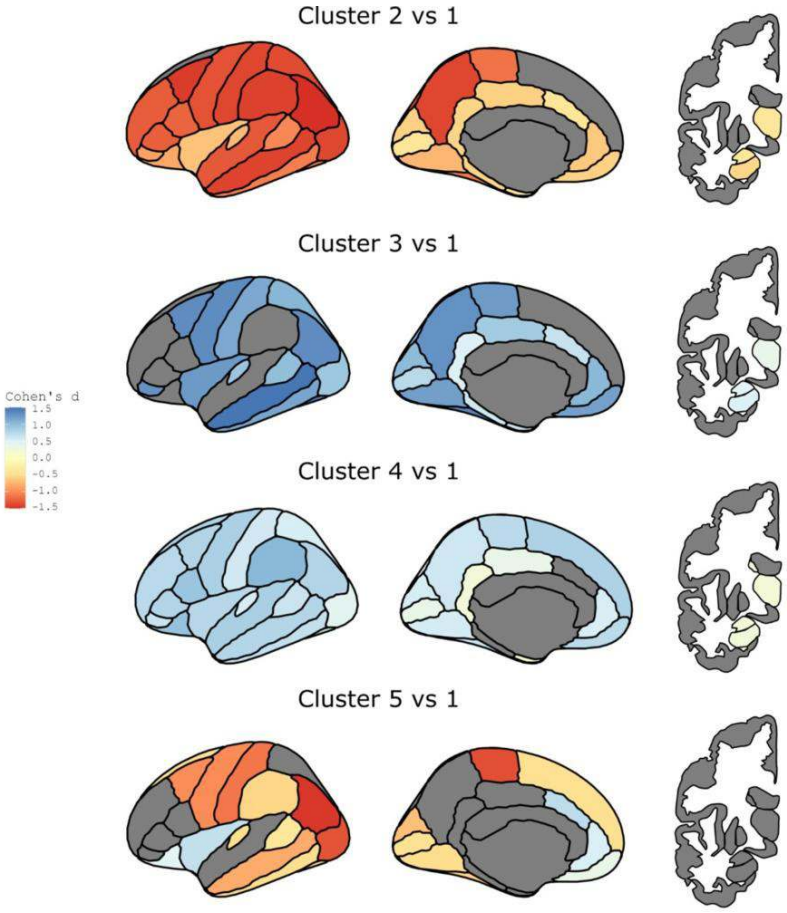

References

1. Ferreira, D., Nordberg, A., & Westman, E. (2020). Biological subtypes of Alzheimer disease: A systematic review and meta-analysis. Neurology, 94(10), 436–448. https://doi.org/10.1212/WNL.0000000000009058
2. Gauthier, S., Webster, C., Servaes, S., Morais, J., & Pedro, R. (2022). World Alzheimer Report 2022: Life after diagnosis: Navigating treatment, care and support. Alzheimer's Disease International, 1–414.
3. Jack, C. R., Barrio, J. R., & Kepe, V. (2013). Cerebral amyloid PET imaging in Alzheimer's disease. Acta Neuropathologica, 126(5), 643–657. https://doi.org/10.1007/S00401-013-1185-7
4. Mohanty, R., Ferreira, D., Frerich, S., Muehlboeck, J.-S., Grothe, M. J., Westman, E., & Initiative, on behalf of the A. D. N. (2022). Neuropathologic Features of Antemortem Atrophy-Based Subtypes of Alzheimer Disease. Neurology, 99(4), e323–e333. https://doi.org/10.1212/WNL.0000000000200573
5. Poulakis, K., Pereira, J. B., Mecocci, P., Vellas, B., Tsolaki, M., Kłoszewska, I., Soininen, H., Lovestone, S., Simmons, A., Wahlund, L. O., & Westman, E. (2018). Heterogeneous patterns of brain atrophy in Alzheimer's disease. Neurobiology of Aging, 65, 98–108. https://doi.org/10.1016/J.NEUROBIOLAGING.2018.01.009
6. Poulakis, K., Pereira, J. B., Muehlboeck, J.-S., Wahlund, L.-O., Smedby, Ö., Volpe, G., Masters, C. L., Ames, D., Niimi, Y., Iwatsubo, T., Ferreira, D., & Westman, E. (2022). Multi-cohort and longitudinal Bayesian clustering study of stage and subtype in Alzheimer's disease. Nature Communications 2022 13:1, 13(1), 1–15. https://doi.org/10.1038/s41467-022-32202-6

Poster No 154

Transformer-based unified tissue and white matter hyperintensity segmentation

James Ruffle[1], Guilherme Pombo[1], Chris Foulon[2], Robert Gray[1], Samia Mohinta[1], Holger Engleitner[1], Harpreet Hyare[1], Geraint Rees[1], Parashkev Nachev[1]

[1]UCL Queen Square Institute of Neurology, London, London, [2]UCL Brain Sciences, London, London

Introduction: The causes and consequences of white matter hyperintensities (WMH), amongst the commonest findings in neuroradiology, remain a subject of intense study. UK Biobank provides the largest research cohort of MRI studies with accompanying WMH labels, with great potential to cast light on this important condition. Unfortunately, many of the lesion labels are spurious, misidentifying healthy choroid plexus, normal ependymal lining, or imaging artefact, leading to reduced accuracy and potential confounding of downstream analytic tasks. Here we derive a substantially improved set of WMH labels through the combination of classical and vision-transformer based segmentation methods.

Methods: In a cohort of 33241 UK Biobank participants, we develop a pipeline employing classical multi-channel volumetric (T1 and FLAIR) tissue segmentation, brain extraction, and WMH segmentation based on a vision transformer model with a custom tissue-leveraging loss. We quantify segmentation fidelity out-of-sample with conventional metrics, intra-subject stability over time, and a downstream predictive task.

Results: We obtained out-of-sample Dice scores for brain extraction (>0.999), gray matter (0.98), white matter (0.99), cerebrospinal fluid (0.96), and WMH (0.87). At 8 seconds per participant, processing time was significantly faster than conventional tissue segmentation with SPM (218 seconds, $p<0.0001$). No differences in model performance were observed between young or old, and male or female ($p>0.05$), indicating good demographic calibration. WMH segmentation showed significantly greater temporal stability compared with current UK Biobank WMH labels ($p<0.0001$) for a subset of the cohort imaged twice. Age regression based on WMH count was superior compared with the original labels ($R2=0.18$ vs 0.14) (Figure 1).

Conclusions: We provide a tissue and WMH segmentation model optimized for UK Biobank data with evidence of fidelity superior to existing labels. We make our model and segmentations available through UK Biobank to assist in the study of this important disorder.

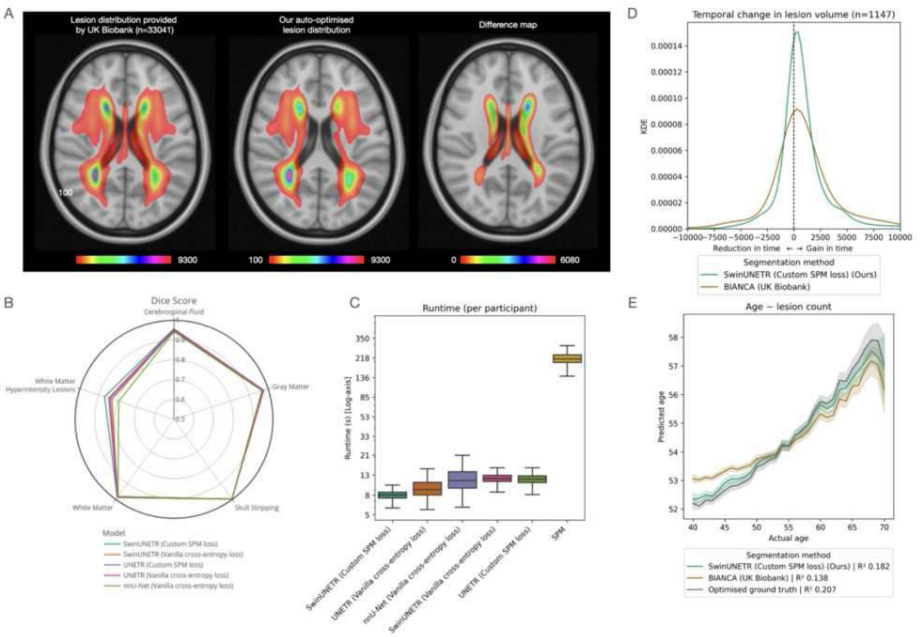

A) UK Biobank original WMH label distribution map (left), map of our optimised labels (middle), and the difference between the two (right). The colourmap indicates the number of lesioned voxels. B) Radar plot showing out-of-sample Dice coefficients between all models trained, for all compartments. C) Box and whisker plot showing runtime per participant for trained models and compared with conventional tissue segmentation (SPM). D) KDE plot showing greater temporal stability of lesions with our model, compared to original UK Biobank labels. E) Multiple linear regression shows superior performance using our model-segmented WMH lesions, compared to original UK Biobank labels.

References
1. MONAI - https://monai.io
2. PyTorch - https://pytorch.org

Poster No 155

Alzheimer's Disease Psychosis-related Brain Network: A Deep Learning and Explainable AI Framework

Nha Nguyen[1], Jesus Gomar[2], Jack Truong[3], János Barbero[4], Patrick Do[5], Andrea Rommal[6], David Eidelberg[2], Jeremy Koppel[2], An Vo[2]

[1]Albert Einstein College of Medicine, Bronx, NY, [2]The Feinstein Institutes for Medical Research, Manhasset, NY, [3]Adelphi University, Garden City, NY, [4]Donald and Barbara Zucker School of Medicine at Hofstra/Northwell, Hempstead, NY, [5]University of Massachusetts Amherst, Amherst, MA, [6]Donald and Barbara Zucker School of Medicine at Hofstra/Northwell, Hempstead, NY

Introduction: Brain network analysis has been used successfully to identify and characterize network patterns in Alzheimer's disease (AD), Parkinson's disease (PD), and most recently, Dementia with Lewy Bodies (DLB)[6]. Deep learning has shown efficacy in assessing AD dementia[7,8]. Evidence suggests that the emergence of psychosis in AD, manifested by delusional beliefs and/or hallucinatory experiences, represents a distinct pathophysiologic subtype with a unique clinical course distinguishable from non-psychotic AD[1,5]. In this study, we aimed to determine the existence of an AD psychosis network (ADPN), distinguishing those who develop psychosis during the course of AD from those who do not.

Methods: We studied 88 AD patients (n=174 scans) who developed psychosis during the study (AD+P, 75.0 ± 7.5 years), 174 AD patients without psychosis (AD−P, 74.5 ± 8.6 years) and 174 cognitively normal (NC, 74.4 ± 5.8 years) participants with no signs of depression, mild cognitive impairment, or dementia. FDG PET scans were retrieved from the ADNI (https://adni.loni.usc.edu). To assess psychotic symptoms, the first 2 items (delusions and hallucinations) of the 12-item Neuropsychiatric Inventory were used, following consensus criteria for psychosis in dementia[1]. FDG PET scans were registered to a standard Montreal Neurological Institute (MNI)-based PET template, smoothed with an isotropic Gaussian kernel (8 mm), and intensity normalized to the mean of the cerebellum using the FMRIB (http://www.fmrib.ox.ac.uk/fsl/). Initially, we employed a 3D deep residual neural network[3] to identify and validate the ADPN using Deep Learning Toolbox in Matlab 2023a. The classifier was trained using 142 AD+P and 142 NC scans and subsequently tested on a dataset consisting of 32 AD+P and 32 NC scans. We

utilized an explainable deep learning technique[9] to compute expression scores used to construct an ADPN-based classifier for predicting psychosis in AD, incorporating a support vector machine (SVM). Classifier performance metrics of classifiers were compared to a conventional classifier, achieved through 95 FDG PET regions of interest based on the AAL atlas[10] and SVM. Significant difference between two groups was computed using Student's t test with Bonferroni correction.

Results: The ADPN classifier exhibited higher accuracy (96.9%) compared to the conventional approach (92.2%) (Fig. 1). The ADPN was characterized by significant differences in activation maps between NC and AD+P in the frontal cortex, insula, amygdala, hippocampus, parahippocampal gyrus, cingulate cortex, parietal and temporal cortices. The ADPN exhibited significant differences in expression scores between AD+P and NC ($P<0.05$). Notably, the AD+P demonstrated regions (Fig. 1) with significantly elevated expression scores compared to the NC. In additional, the ADPN-based classifer achieved superior accuracy (77%) and sensitivity (86.2%) compared to the conventional classifier (68.4% and 67.8%) (Fig. 2) in distinguishing between AD+P and AD−P. When compared with the AD−P subjects, the AD+P exhibited key regions with significantly higher expression score ($P<0.05$) (Fig. 2). The regions specific to the difference between the two groups included the frontal cortex (superior and middle), the cingulate cortex (anterior and middle), the primary auditory cortex (Hesch's and superior temporal), the inferior parietal cortex, and the sensorimotor cortex (precentral, postcentral and SMA).

Figure 1. Alzheimer's Disease psychosis network

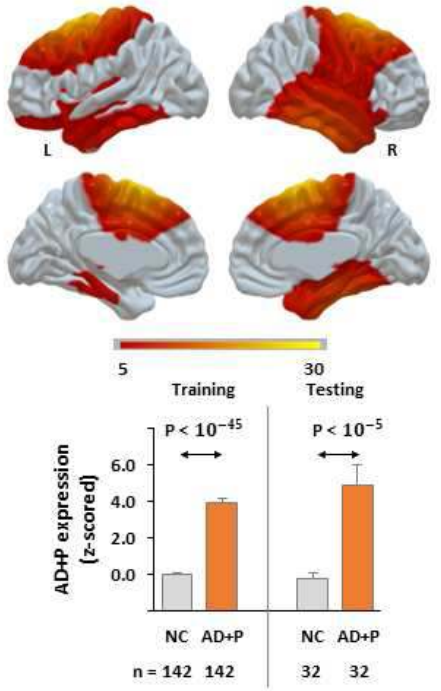

Classifier	ADPN	Conventional
Accuracy (%)	96.9	92.2
Sensitivity (%)	96.9	90.6
Specificity (%)	96.9	93.4
Precision (%)	96.9	93.6
F1 score	0.97	0.92

Figure 2. Difference of activation maps between AD with and without psychosis

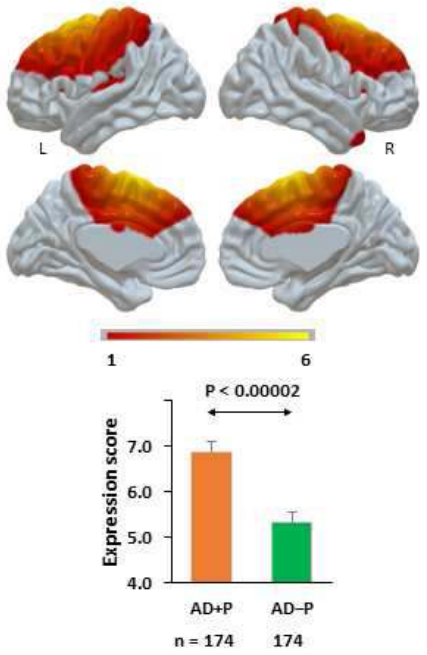

Classifier	ADPN-based	Conventional
Accuracy (%)	77.0	68.4
Sensitivity (%)	86.2	67.8
Specificity (%)	67.8	69.0
Precision (%)	72.8	68.6
F1 score	0.79	0.68

Conclusions: The ADPN, identified by the 3D ResNet101, revealed significant differences in activation maps between the AD+P and both NC and AD−P. The findings are consistent with previous PET studies (2, 4) conducted in this disorder. Leveraging explainable AI enhanced our understanding and trust in the results generated by deep learning.

References

1. Cummings, J (2020), 'Criteria for Psychosis in Major and Mild Neurocognitive Disorders: International Psychogeriatric Association (IPA) Consensus Clinical and Research Definition', American Journal of Geriatric Psychiatry, vol. 28, no. 12, pp. 1256-1269.
2. Gomar, JJ (2022), 'Increased retention of tau PET ligand [(18)F]-AV1451 in Alzheimer's Disease Psychosis', Translational Psychiatry, vol. 12, no. 1, pp. 82.
3. He, K (2016), 'Deep residual learning for image recognition', Proceedings of the IEEE conference on computer vision and pattern recognition, pp. 770-778.
4. Koppel, J (2014), 'Alzheimer's Disease Neuroimaging I. Psychosis in Alzheimer's disease is associated with frontal metabolic impairment and accelerated decline in working memory: findings from the Alzheimer's Disease Neuroimaging Initiative', American Journal of Geriatric Psychiatry, vol. 22, no. 7, pp. 698-707.
5. Koppel, J (2014), 'Optimal treatment of Alzheimer's disease psychosis: challenges and solutions', Neuropsychiatric Disease and Treatment, vol. 10, no., pp. 2253-62.
6. Perovnik, M (2023), 'Functional brain networks in the evaluation of patients with neurodegenerative disorders', Nature Reviews Neurology, vol. 19, no. 2, pp. 73-90.
7. Puente-Castro, A (2020), 'Automatic assessment of Alzheimer's disease diagnosis based on deep learning techniques', Computers in Biology and Medicine, vol. 120, pp. 103764.
8. Qiu, S (2022), 'Multimodal deep learning for Alzheimer's disease dementia assessment', Nature Communications, vol. 13, no. 1, pp. 3404.
9. Selvaraju, R.R., (2020), 'Grad-CAM: Visual Explanations from Deep Networks via Gradient-Based Localization', International Journal of Computer Vision, vol. 128, pp. 336–359.
10. Tzourio-Mazoyer, N. (2002), 'Automated anatomical labeling of activations in SPM using a macroscopic anatomical parcellation of the MNI MRI single-subject brain', NeuroImage, vol. 15, no. 1, pp. 273-289.

Poster No 156

A comprehensive exploration of longitudinal white matter microstructure and cognitive trajectories

Derek Archer[1], Chris Peter[2], Aditi Sathe[2], Yisu Yang[2], Alaina Durant[2], Niranjana Shashikumar[3], Kimberly Pechman[2], Katherine Gifford[2], Shubhabrata Mukherjee[4], Brandon Klinedinst[5], Michael Lee[4], Seo-Eun Choi[4], Phoebe Scollard[6], Emily Trittschuh[4], Shannon Risacher[7], Lori Beason-Held[8], Yang An[9], Kurt Schilling[1], Bennett Landman[1], Lisa Barnes[10], Julie Schneider[10], David Bennett[10], Paul Crane[11], Walter Kukull[4], Sterling Johnson[12], Marilyn Albert[13], Angela Jefferson[2], Susan Resnick[8], Andrew Saykin[7], Timothy Hohman[2]

[1]Vanderbilt University Medical Center, Nashville, TN, [2]Vanderbilt Memory & Alzheimer's Center, Nashville, TN, [3]Vanderbilt memo, Nashville, TN, [4]University of Washington School of Medicine, Seattle, WA, [5]Unive, Seattle, WA, [6]Uni, Seattle, WA, [7]Indiana University School of Medicine, Indianapolis, IN, [8]National Institute on Aging, Baltimore, MD, [9]Nation, Baltimore, MD, [10]Rush University Medical Center, Chicago, IL, [11]Univer, Seatt, WA, [12]University of Wisconsin, Madison, WI, [13]Johns Hopkins University School of Medicine, Baltimore, MD

Introduction: The primary clinical manifestation of Alzheimer's disease (AD) is cognitive impairment and longitudinal cognitive decline, and several prior diffusion MRI studies have investigated the association between white matter microstructure and cognitive decline in normal aging and AD[1–7]. Recent work from our group explored the free-water (FW)-corrected associations with longitudinal scores of memory and executive function and found that medial temporal lobe tracts were significantly associated with both domains[8]. One interesting finding from this prior study is that the FW component, which is a separate 3D map which is created in the FW-correction pipeline, is particularly sensitive to cognitive impairment and decline. This is in line with several prior studies which have demonstrated similar findings in other neurodegenerative diseases. While these studies have been foundational to our understanding of white matter contributions to cognitive impairment and decline, large-scale studies using harmonized scores of cognitive function would drastically enhance our understanding by elucidating which white matter tracts are most vulnerable in individuals with cognitive decline.

Methods: The dataset used in this study was collated from seven longitudinal cohorts of aging (ADNI, BIOCARD, BLSA, NACC, ROS/MAP/MARS, VMAP, WRAP). In total, this dataset included 2,220 participants aged 50+ who had both diffusion MRI and harmonized composites of memory performance and executive function. This dataset included a total of 4,918 imaging sessions with corresponding cognitive data (mean number of visits per participant: 1.69 ± 1.67, interval range: 1-10 years). Diffusion MRI data was preprocessed using the PreQual pipeline and free-water (FW) correction was conducted to obtain FW and FW-corrected fractional anisotropy (FAFWcorr) maps. Conventional diffusion MRI (FAconv, MDconv, AxDconv, RDconv and FW-corrected (FW, FAfwcorr, MDfwcorr, AxDfwcorr, RDfwcorr) measures were quantified within 48 white matter tracts consistent with prior publications9,10, which were subsequently harmonized using the Longitudinal ComBat package. Linear mixed effects regression was used for longitudinal analysis, in which we covaried for age, age squared, education, sex, race/ethnicity, diagnosis at baseline, APOE-ε4 status, and APOE-ε2 status. We also controlled for age x diagnosis converter and age squared x diagnosis converter interactions. Separate models were conducted to determine the association with longitudinal memory performance and executive function performance. All models were corrected for multiple comparisons using the FDR approach.

Results: For longitudinal memory performance, we found global associations with conventional diffusion MRI metrics, in which lower FAconv was associated with lower memory performance. In contrast, higher ADconv, RDconv, and MDconv were associated with lower memory performance. Following FW correction, we found that the FW metric itself was strongly associated with memory performance, in which higher FW was associated with lower memory performance and decline. Interestingly, following FW-correction the intracellular contributions were largely mitigated. As illustrated in Figure 1A, the most significant effects were found in the limbic tracts, with the most significant associations found for cingulum bundle FW ($p=5.80x10-45$). Figure 1B illustrates the association between cingulum FW and longitudinal memory performance. Findings for longitudinal executive function performance are shown in Figure 2.

Conclusions: To date, this is the largest study combining FW corrected diffusion MRI data and harmonized cognitive composites to understand cognitive trajectories in aging. Future studies evaluating how white matter microstructure may be incorporated into models of AD may further our knowledge into the neurodegenerative cascade of AD.

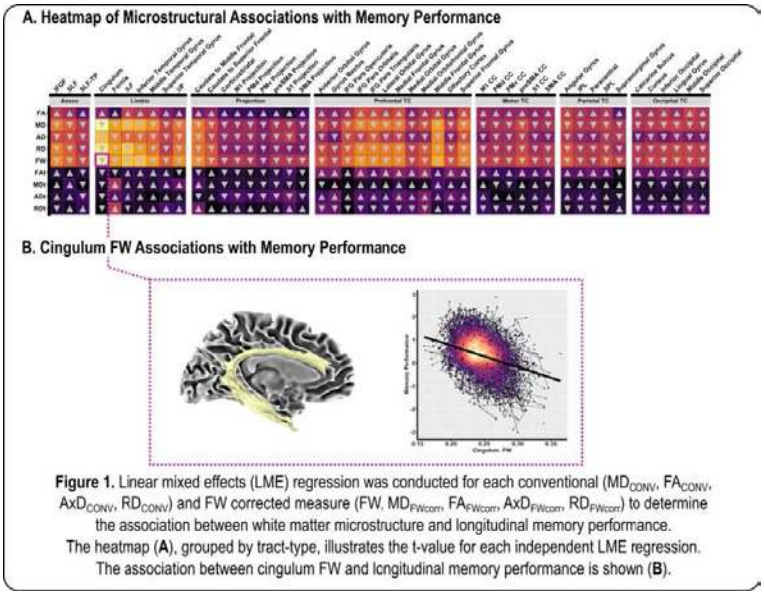

Figure 1. Linear mixed effects (LME) regression was conducted for each conventional (MD_{CONV}, FA_{CONV}, AxD_{CONV}, RD_{CONV}) and FW corrected measure (FW, MD_{FWcorr}, FA_{FWcorr}, AxD_{FWcorr}, RD_{FWcorr}) to determine the association between white matter microstructure and longitudinal memory performance. The heatmap (**A**), grouped by tract-type, illustrates the t-value for each independent LME regression. The association between cingulum FW and lcngitudinal memory performance is shown (**B**).

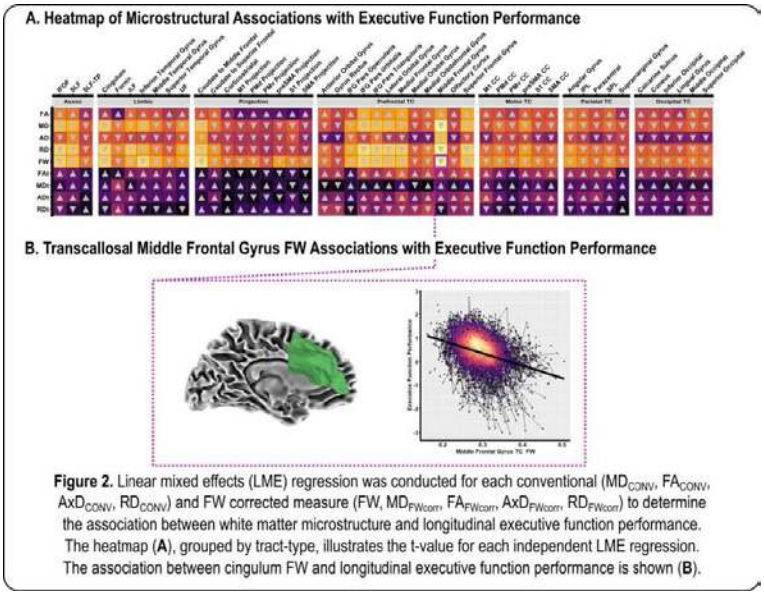

Figure 2. Linear mixed effects (LME) regression was conducted for each conventional (MD_{CONV}, FA_{CONV}, AxD_{CONV}, RD_{CONV}) and FW corrected measure (FW, MD_{FWcorr}, FA_{FWcorr}, AxD_{FWcorr}, RD_{FWcorr}) to determine the association between white matter microstructure and longitudinal executive function performance. The heatmap (**A**), grouped by tract-type, illustrates the t-value for each independent LME regression. The association between cingulum FW and longitudinal executive function performance is shown (**B**).

References

1. Bozzali, M. et al. Damage to the cingulum contributes to Alzheimer's disease pathophysiology by deafferentation mechanism. Hum Brain Mapp 33, 1295–308 (2012).
2. Mielke, M. M. et al. Fornix integrity and hippocampal volume predict memory decline and progression to Alzheimer's disease. Alzheimers Dement 8, 105–13 (2012).
3. Walsh, R., Bergamino, M. & Stokes, A. Free-Water Diffusion Tensor Imaging (DTI) Improves the Accuracy and Sensitivity of White Matter Analysis in Alzheimer's Disease (4979). Neurology 94, (2020).
4. Dumont, M. et al. Free Water in White Matter Differentiates MCI and AD From Control Subjects. Frontiers in Aging Neuroscience 11, (2019).
5. Dalboni da Rocha, J. L., Bramati, I., Coutinho, G., Tovar Moll, F. & Sitaram, R. Fractional Anisotropy changes in Parahippocampal Cingulum due to Alzheimer's Disease. Sci Rep 10, 2660 (2020).
6. Cremers, L. G. et al. Altered tract-specific white matter microstructure is related to poorer cognitive performance: The Rotterdam Study. Neurobiol Aging 39, 108–17 (2016).
7. Kennedy, K. M. & Raz, N. Aging white matter and cognition: differential effects of regional variations in diffusion properties on memory, executive functions, and speed. Neuropsychologia 47, 916–27 (2009).
8. Archer, D. B. et al. Free-water metrics in medial temporal lobe white matter tract projections relate to longitudinal cognitive decline. Neurobiol Aging 94, 15–23 (2020).
9. Archer, D. B. et al. Leveraging longitudinal diffusion MRI data to quantify differences in white matter microstructural decline in normal and abnormal aging. Alzheimer's & Dementia: Diagnosis, Assessment & Disease Monitoring 15, e12468 (2023).
10. Yang, Y. et al. White matter microstructural metrics are sensitively associated with clinical staging in Alzheimer's disease. Alzheimer's & Dementia: Diagnosis, Assessment & Disease Monitoring 15, e12425 (2023).

Poster No 157

Consistent genes associated with structural changes in clinical Alzheimer's disease spectrum

Yingqi Lu[1], Shangjie Chen[2], Jinping Xu[1]

[1]Shenzhen Institutes of Advanced Technology, Chinese Academy of Sciences, Shenzhen, Guangzhou, [2]The People's Hospital of Baoan Shenzhen, Shenzhen, Guangzhou

Introduction: Alzheimer's disease (AD) is considered a late-onset disease caused by a complex combination of genetic, epigenetic, and environmental factors. Previous studies have demonstrated that one of the major pathological changes in AD is widespread brain neurodegeneration, represented by irreversible gray matter volume (GMV) atrophy (Tondelli, Wilcock et al. 2012). However, the neurobiological and pathogenic substrates underlying this structural atrophy across AD spectrum remain largely understood. At present, gene-by-brain structure interactions of AD are widely studied (Nho, Corneveaux et al. 2013, Luis, Ortega-Cubero et al. 2014). Considering these, studying whether structural changes in the AD spectrum are driven by similar gene variants is important for fully understanding disease mechanisms and developing personalized therapeutics. The aim of the current study was to investigate structural atrophy across the full clinical AD spectrum and its genetic mechanism using gene expression data from the Allen Human Brain Atlas (AHBA) (Arnatkeviciute, Fulcher et al. 2019).

Methods: In this research, we obtained structural MRI imaging from the Alzheimer's Disease Neuroimaging Initiative (ADNI) datasets, including 83 early-stage mild cognitive impairments (EMCI), 83 late-stage mild cognitive impairments (LMCI), 83 AD, and 83 normal controls (NC), and gene expression data from the AHBA. Firstly, DPABI was used to obtain voxel-wise GMV differences map between EMCI, LMCI, and AD patients compared to NC. Secondly, 41 interesting genes were screened for AD risk genes intersected with background genes. Then, cross-sample non-parametric Spearman rank was performed to determine relationship between gene expression and regional GMV alterations. Lastly, functional enrichment analyses were used to understand the biological mechanism of related genes.

Results: The results indicated that significant volume atrophy in left thalamus, left cerebellum, and bilateral middle frontal gyrus across AD spectrum (Figure 1). These structural changes were positively associated with gene expression levels of ABCA7, SORCS1, SORL1, PILRA, PFDN1, PLXNA4, TRIP4, and CD2AP, whereas were negatively associated with gene expression levels of CD33, PLCG2, APOE, and ECHDC3 across clinical AD spectrum (Figure 2). Further gene enrichment analyses revealed that these positively associated genes were mainly involved in positive regulation of cellular protein localization and negative regulation of cellular component organization, whereas the negatively associated genes were mainly involved in positive regulation of iron transport.

Conclusions: This exploratory study linked the structural changes to gene expression levels by assessing similarity of spatial distribution patterns. These genes were mostly involved in cellular protein localization, cellular component organization, and regulation of iron transport. Overall, these results offered a better understanding of biological mechanisms underlying structural changes in prodromal and clinical AD.

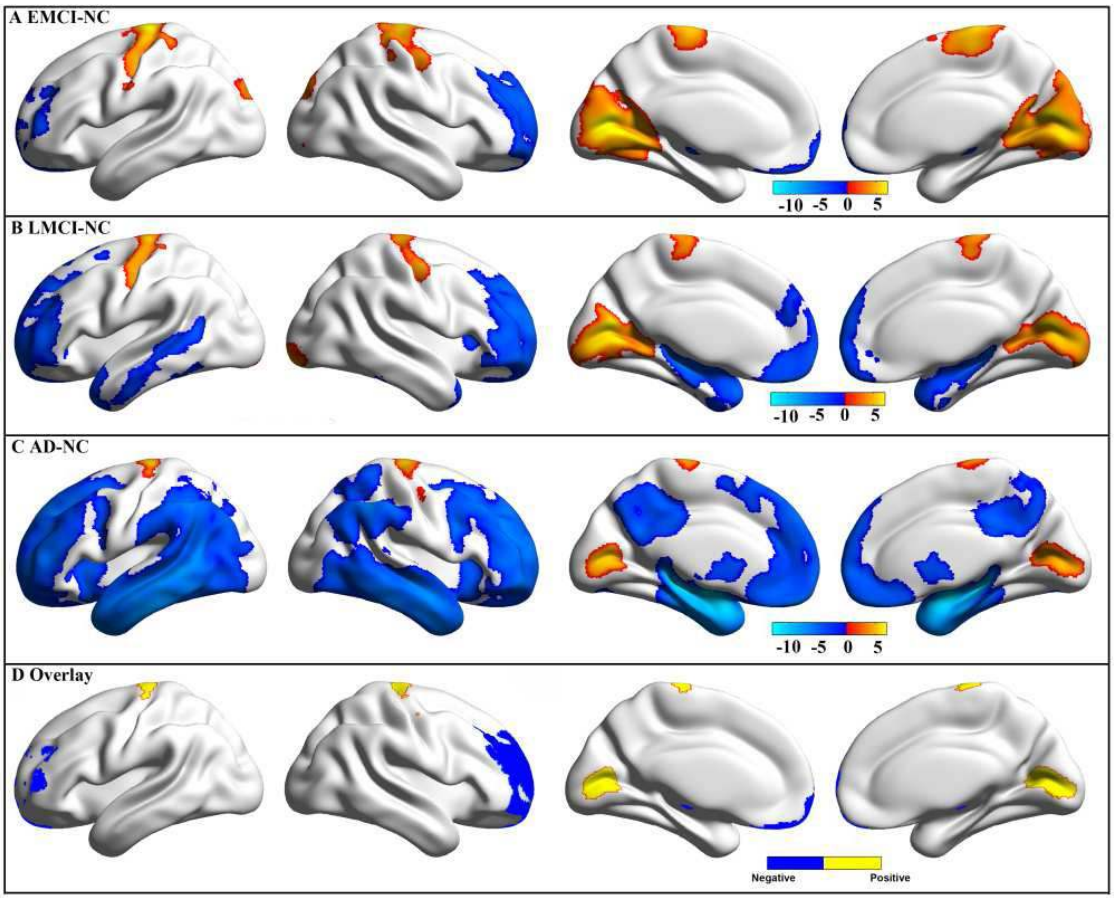

Figure 1. GMV difference for EMCI (A), LMCI (B), and AD (C) patients as compared to NC. The results were obtained using two sample t tests and were corrected using Gaussian random field (GRF, a cluster level of $p < 0.05$ and a voxel level of $p < 0.001$). The color bar represents t -values and a positive t -value (warm color) indicates increased GMV in this group as compared to NC. Negative and positive (D) overlap among three groups.

R values

Genes	EMCI-NC	LMCI-NC	AD-NC
ABCA7	0.280	0.304	0.259
SORCS1	0.295	0.300	0.153
SORL1	0.313	0.339	0.311
PILRA	0.228	0.219	0.168
PFDN1	0.268	0.304	0.287
PLXNA4	0.235	0.225	0.143
TRIP4	0.215	0.242	0.192
CD2AP	0.164	0.203	0.210
CD33	-0.190	-0.164	-0.103
PLCG2	-0.139	-0.159	-0.147
APOE	-0.235	-0.296	-0.285
ECHDC3	-0.425	-0.499	-0.403

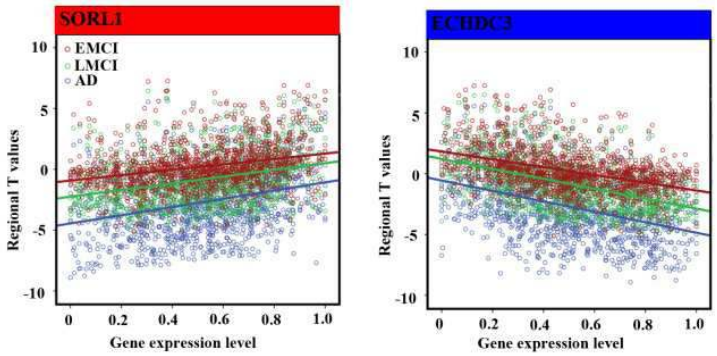

Figure 2. Spearman correlations between gene expression levels of overlap genes and regional GMV difference of EMCI, LMCI, and AD patients compared to NC. Blue font represents for negative association and red for positive association.

References

1. Arnatkeviciute, A. (2019), 'A practical guide to linking brain-wide gene expression and neuroimaging data', Neuroimage, vol. 189, pp. 353-367.
2. Luis, E. O. (2014), 'Frontobasal gray matter loss is associated with the TREM2 p.R47H variant', Neurobiol Aging, vol. 35, no. 12, pp.2681-2690.
3. Nho, K., J. J. (2013), 'Identification of functional variants from whole-exome sequencing, combined with neuroimaging genetics', Mol Psychiatry, vol. 18, no. 7, pp.739.
4. Tondelli, M. (2012), 'Structural MRI changes detectable up to ten years before clinical Alzheimer's disease', Neurobiol Aging, vol. 33, no. 4, pp. 825.e825-836.

Poster No 158

ENIGMA-HIV: White matter microstructural abnormalities in a global sample of people living with HIV

Talia Nir[1], Elizabeth Haddad[1], Catherine Wedderburn[2,3], Aliaa Ibnidris[2], Jasmina Boban[4], Linda Chang[5,6], Lucette Cysique[7], Thomas Ernst[5], Jaroslaw Harezlak[8], Jonathan Ipser[2], John Joska[2], Kalpana Kallianpur[9,10], Joel Kramer[11], Taylor Kuhn[12], Hei Lam[1], Andrew Levine[12], Beau Nakamoto[9], Bradford Navia[13], Eric Porges[14], Cecilia Shikuma[9], April Thames[12], Victor Valcour[11], Sophia Thomopoulos[1], Ronald Cohen[14], Paul Thompson[1], Robert Paul[15], Dan Stein[2], Neda Jahanshad[1]

[1]University of Southern California Keck School of Medicine, Marina del Rey, CA, [2]University of Cape Town, Cape Town, South Africa, [3]London School of Hygiene & Tropical Medicine, London, United Kingdom, [4]University of Novi Sad, Novi Sad, Serbia, [5]University of Maryland School of Medicine, Baltimore, MD, [6]Johns Hopkins School of Medicine, Baltimore, MD, [7]University of New South Wales, Sydney, New South Wales, [8]Indiana University School of Public Health, Bloomington, IN, [9]University of Hawaii, Honolulu, HI, [10]Kamehameha Schools - Kapālama, Honolulu, HI, [11]University of California San Francisco, San Francisco, CA, [12]University of California Los Angeles, Los Angeles, CA, [13]Tufts University Medical School, Boston, MA, [14]University of Florida, Gainesville, FL, [15]University of Missouri St. Louis, St. Louis, MO

Introduction: HIV remains a global public health challenge with an estimated 39 million people living with HIV[1]. Despite widespread access to antiretroviral therapy (ART), neurocognitive impairment is a persistent issue in people living with chronic HIV infection[2]. Persistent HIV viral reservoir instigates an inflammatory cascade that leads to neural dysfunction, often accompanied by white matter (WM) damage. However, clinical and demographic heterogeneity in people with HIV (PwH) worldwide, and variations in MRI acquisition, processing, and analysis methods yielded inconsistencies in reported HIV-related WM differences detected across studies. Here, we pooled diffusion MRI (dMRI) data from ten independent worldwide neuroHIV studies as part of the ENIGMA-HIV consortium[3]; we aimed to identify generalizable WM microstructural associations with infection using standardized data analysis pipelines.

Methods: The ENIGMA-HIV DTI working group is currently made up of ten neuroHIV studies from the United States, South Africa, Australia, and Serbia (Table 1). In total, dMRI data from 840 PwH (all studies; aged 20.5-80 yrs; 71.8% male; 78.1% on ART) and 280 HIV-negative controls were analyzed (6 studies; aged 17-29 yrs; 66.8% male). dMRI were preprocessed and DTI FA, MD, RD, and AD maps were computed, in addition to a more advanced dMRI model FA, TDF FA[4]. Using the standardized ENIGMA-DTI protocols[5], each subject's dMRI maps were warped to the ENIGMA-DTI template and dMRI indices projected onto the template skeleton with TBSS[6]. Mean skeletonized dMRI measures were extracted from 24 JHU WM atlas regions of interest (ROIs) and the full WM skeleton (FullWM). Random effects linear regressions were performed to evaluate associations between regional dMRI measures and 1) HIV-diagnosis when compared to controls (Dx; 6 studies); or 2) blood plasma markers in PwH (all studies): current CD4+ T-cell count (cells/mm3) and a detectable or undetectable viral load (VL). We also tested for Dx- or plasma marker-by-age interactions, as HIV may accelerate age-related effects on WM microstructure. Study was used as the random-effects grouping variable; fixed-effects covariates included age, sex, and their interaction. Statistical models testing for HIV plasma marker associations within PwH also included ART status at the time of scan (ART+ or ART-) as a covariate. The false discovery rate was used to correct for multiple comparisons (q=0.05).

Table 1. ENIGMA-HIV demographic, clinical information, and dMRI protocol by study. Only 6 of 10 studies contributed data from both PwH (HIV+) and HIV-negative controls (HIV-).

Site name	DX	Total, N	Male, N (%)	Age, *yrs*, Mean (SD), Range	On ART, N (%)	Detectable Viral Load, N (%)	CD4+ Count, *cells/mm*^{3}, Mean (SD)	dMRI Protocol
University of California, Los Angeles, USA	HIV+	60	52 (86.7)	51.0 (12.5) 24-76	60 (100)	25 (45.5) N=55	603.9 (308.7) N=50	3T Siemens Vox: 2x2x2 mm^3 7 b_0/ 64 DWI b=1000 s/mm^2
	HIV-	32	15 (46.9)	49.7 (13.9) 23-66	--	--	--	
Brown University, USA	HIV+	78	51 (65.4)	46.1 (9.9) 24-65	78 (66.0)	23 (30.3) N=76	507.5 (274.9) N=76	3T Siemens Vox: 1.8x1.8x1.8 mm^3 11 b_0/ 64 DWI b=1000 s/mm^2
	HIV-	50	29 (58)	45.5 (13.5) 25-79	--	--	--	
Brown University's Alcohol Research Center on HIV (ARCH), USA	HIV+	72	51 (70.8)	48.3 (9.6) 27-69	65 (95.6) N=68	18 (25.4) N-71	573/8 (282.0) N=68	3T Siemens Vox: 2x2x2 mm^3 11 b_0/ 64 DWI b=1000 s/mm^2
	HIV-	54	24 (44.4)	39.7 (11.8) 21-69	--	--	--	
University of California, San Francisco, USA	HIV+	57	55 (96.5)	64.1 (3.9) 60-80	53 (96.4) N=55	19 (37.3) N=51	518.6 (212.6) N=50	3T Siemens Vox: 2x2x2 mm^3 1 b_0/64 DWI b=2000 s/mm^2
	HIV-	29	26 (89.7)	65.5 (2.2) 61-69	--	--	--	
University of New South Wales, Australia	HIV+	80	80 (100)	55.2 (6.7) 44-69	80 (100)	1 (1.3)	556.5 (278.2)	3T Philips Vox: 1x1x2.5 mm^3 2 b_0/32 DWI b=1000 s/mm^2
	HIV-	40	40 (100)	54.6 (6.4) 45-67	--	--	--	
University of Novi Sad, Serbia	HIV+	74	69 (93.2)	43.2 (10.7) 25-66	66 (100) N=66	20 (27.0)	582.3 (330.5) N=72	3T Siemens Vox: 2x2x2 mm^3 3 b_0/ 64 DWI b=1500 s/mm^2
	HIV-	75	53 (70.7)	37.4 (11.8) 17-76	--	--	--	
HIVNC Rochester, USA	HIV+	50	32 (64)	48.0 (7.6) 25-62	43 (86)	13 (26)	361.3 (202.1)	3T GE Vox: 1x1x5 mm^3 1 b_0/ 21 DWI b=1000 s/mm^2
University of Hawaii, USA (Chang/Ernst)	HIV+	171	155 (90.6)	47.8 (10.7) 20.5-73.7	159 (93.0)	50 (31.4) N=159	473.4 (284.7) N=170	3T Siemens Vox: 1.7x1.7x5 mm^3 1 b_0/ 12 DWI b=1000 s/mm^2
University of Hawaii, USA (Shikuma)	HIV+	53	45 (84.9)	50.9 (8.0) 40-71	53 (100)	6 (11.3)	491.1 (208.5)	3T Siemens Vox: 1.8x1.8x2 mm^3 1 b_0/ 15 DWI b=1000 s/mm^2
University of Cape Town, South Africa	HIV+	145	18 (12.4)	32.3 (4.8) 22-45	0 (0)	112 (96.6) N=116	224.5 (138.1)	3T Siemens Vox: 1.7x1.7x1.7 mm^3 3 b_0/ 30 DWI (x2) b=1000 s/mm^2

Results: Lower anisotropy and higher diffusivity measures were associated with (1) HIV-Dx when compared to controls (Fig 2a,b) and (2) lower CD4+ counts in PwH (Fig 2d); no associations with detectable VL were found. Widespread regional associations were detected across all dMRI measures except DTI FA. Significant FullWM CD4+ and Dx associations were also found suggesting global WM effects. The largest effect sizes in case-control analyses were found in regions of the CC, CR, UNC, and Fx; these effects remained significant when also covarying for FullWM dMRI values. The largest CD4+ dMRI associations were found in the TAP, CR, EC, FX, and FX/ST. Only AD FX and TAP effects were significant beyond the FullWM effect (Fig 2a). Widespread Dx-by-age interactions revealed steeper negative anisotropy and positive diffusivity slopes with respect to age in PwH compared to controls (Fig 2c). No plasma marker-by-age interactions were found.

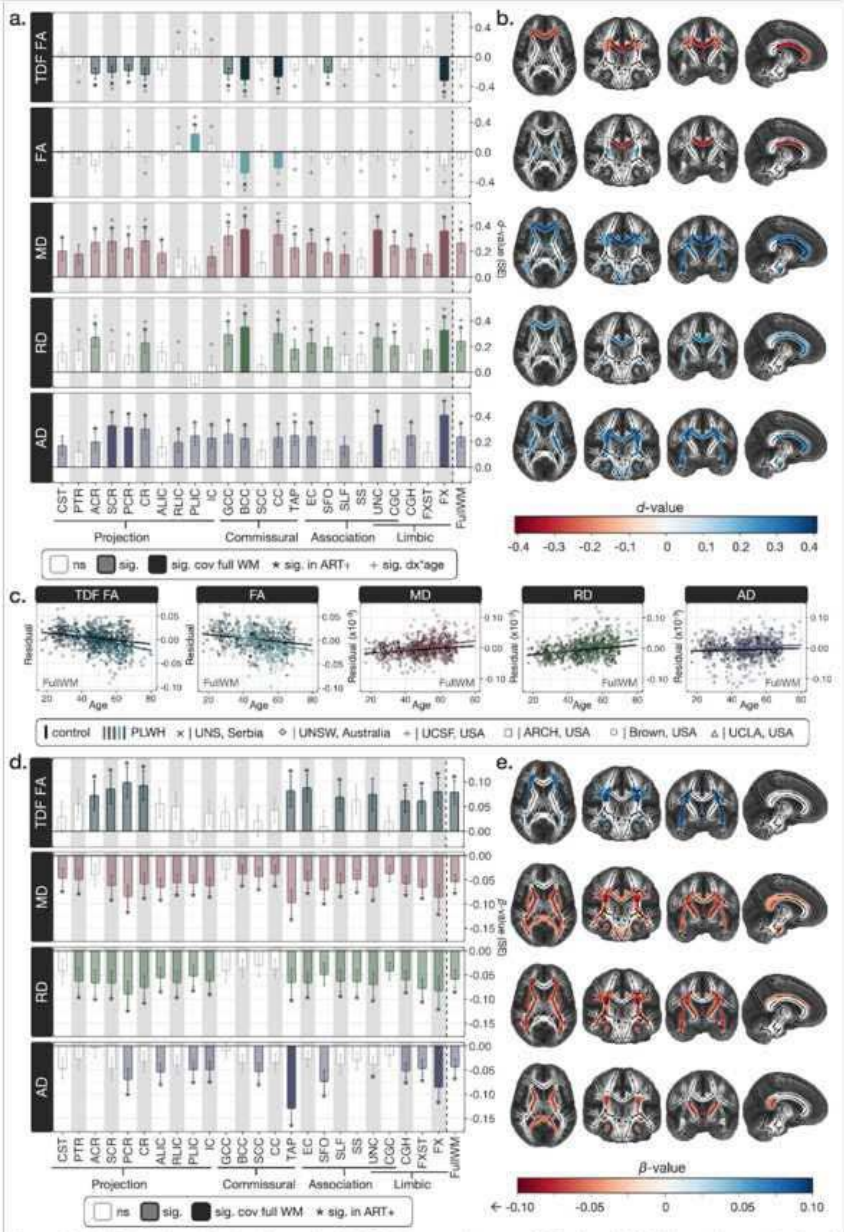

Figure 2. (a, b) Effect sizes (*d*-values) for regional dMRI differences between 421 PwH and 280 HIV-negative controls from 6 studies (P_{FDR}<0.05). **(a)** In the subset of significant ROIs (N=64), ROIs that remain significant when additionally covarying for the Full WM are denoted by darker opaque color bars; our findings suggest corpus callosum (CC), corona radiata (CR), uncinate (UNC), and fornix (Fx) dMRI effects beyond the global WM effect. Stars denote significant effects when the PwH group was limited to those on ART (96% of HIV+ participants). ROIs with significant Dx-by-age interactions are marked with a plus sign. **(c)** Residualized Full WM dMRI measure scatter plots show steeper negative anisotropy and positive diffusivity slopes with age in PwH compared to HIV-negative controls. Full WM dMRI measures were adjusted for sex and study before plotting. **(d, e)** Effect sizes (*β*-values) for dMRI associations with CD4+ counts in 801 PwH from 10 studies; no associations were found with DTI FA. In the subset of significant ROIs (N=66), only AD Fx and tapetum (TAP) effects were significant beyond the global WM effect. Stars denote significant effects from sensitivity analyses within the subset of ART+ PwH (N=621; 77.5% of participants). No significant associations were detected in ART- PwH (N=180). ART status was not a significant covariate in any analysis.

Conclusions: In a large-scale international population of PwH, widespread WM microstructural abnormalities were consistently associated with HIV infection. While effects were often global, the largest effects were detected in limbic and temporal lobe tracts often implicated in aging and neurodegenerative conditions such as Alzheimer's disease. Coupled with significant HIV diagnosis-by-age interactions, our results support evidence that common age and HIV-related pathological processes, such as inflammation and blood brain barrier impairment, may accelerate age-related neurodegenerative processes[7].

References

1. https://aidsinfo.unaids.org/
2. Keng LD, et al. (2023), 'The global burden of cognitive impairment in people with HIV', AIDS, 37(1):61-70.
3. Nir TM, et al. (2021), 'Association of Immunosuppression and Viral Load With Subcortical Brain Volume in an International Sample of People Living With HIV', JAMA Network Open, 4(1):e2031190.
4. Nir TM, et al. (2017), 'Fractional anisotropy derived from the diffusion tensor distribution function boosts power to detect Alzheimer's disease deficits', Magn Reson Med, 78(6):2322-2333.

5. Jahanshad N et al. (2013), 'Multi-site genetic analysis of diffusion images and voxelwise heritability analysis: a pilot project of the ENIGMA-DTI working group', Neuroimage, 1(8)1:455-469.
6. Smith SM et al. (2006), 'Tract-based spatial statistics: Voxelwise analysis of multi-subject diffusion data', NeuroImage, 31:1487-1505.
7. Cysique LA, Brew BJ (2014), 'The effects of HIV and aging on brain functions: proposing a research framework and update on last 3 years' findings', Current opinion in HIV and AIDS, 9(4):355-364.

Poster No 159

A Brain Age Prediction Method Using Multi-Scale Attention Mechanism and Fully Convolutional Network

Zhewei Zhang[1], Jinping Xu[1], Fan Xinxin[1]

[1]Shenzhen Institute of Advanced Technology, Shenzhen, Guangdong

Introduction: Currently, deep learning has made significant progress in the field of biomedical image processing[6], and there are some structural MRI-based methods in the field of brain age prediction, but most of the methods used use 2D slices or use 3D convolution for feature extraction followed by age regression[1], but there are some problems as follows: 1) the methods using 2D slices do not focus on the information in 3D voxel space, and 2) the methods using 3D methods do not focus on both global and local information. Therefore, we provide a 3D network that takes into account both local and global information, we use SFCN[3] as the backbone network for feature extraction, and then use 3D cross attention mechanism[2] to fuse global and local features (Figure 1).We collected a total of 2559 cases of data from 4 datasets (ADNI[7], OASIS[8], IXI, CORR[9]), and the results show that our network is able to predict age with high accuracy on different datasets, achieving better results compared to some existing networks. The improved accuracy of our results in predicting brain age may help clinicians in diagnosing diseases and making treatment recommendations.

Methods: In this paper, to solve the problem of considering both global contextual information and local structural information in 3DMRI, we first used SFCN for feature extraction, then we provide a 3D cross-attention mechanism, which extracts features from the whole 3DMRI image through a global path to obtain global contextual information, and extracts local features through multiple segmentation of local patches to obtain local detailed features, and uses attention to fuse global and local features using the attention mechanism. The study shows that by using the attention module, irrelevant information in contextual features can be ignored by global features and important information can be better extracted from the feature space[5]. At the same time, this cross-attention mechanism, unlike the normal transformer[4], does not use concat to fuse local and global features and does not require spatial alignment.

Results: In our recent experiments, we compared the age prediction results of six methods on four datasets as well as the combined dataset, and the results show that we achieved the best results on the ADNI, OASIS, and combined datasets. Since the ADNI and OASIS datasets are more focused on older adults, the results show that our network can better predict the age of the brain in older adults. The results also show that our network can better predict the age of the brain in the elderly, and can be used in clinical applications to assist physicians in making targeted diagnoses for the elderly.

Conclusions: In this work, we proposed a 3D cross-attentional mechanisms with SFCN for brain age prediction from whole-brain sMRI image information, and validated on 4 datasets. Moreover, our methods were superior to several existing methods.

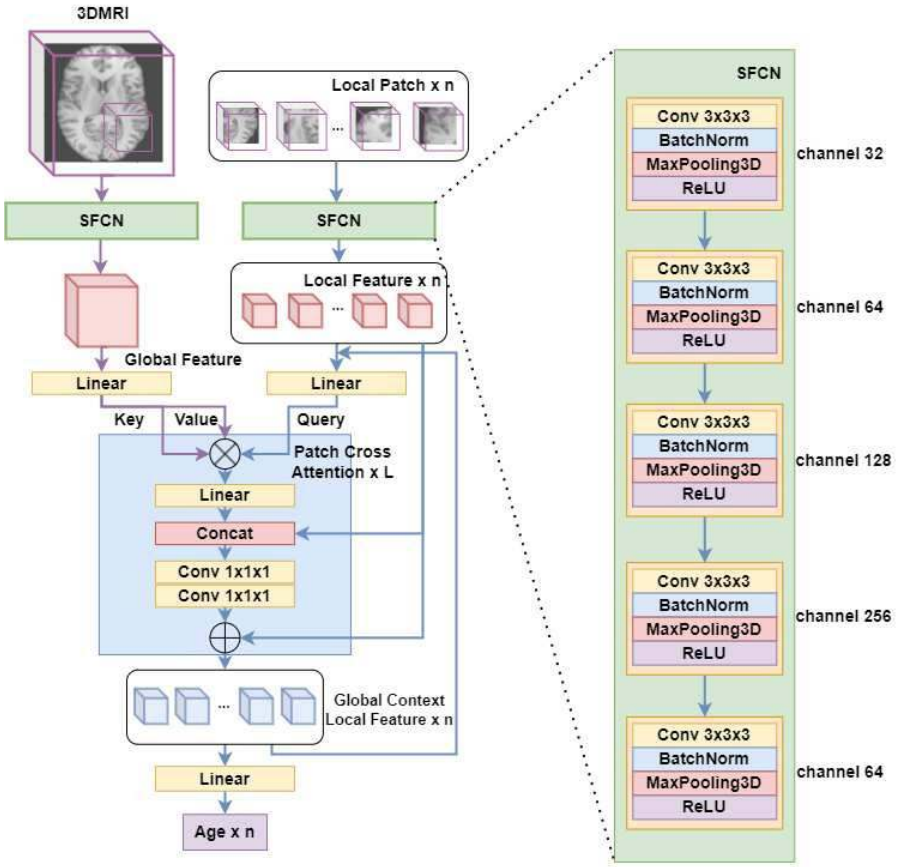

Figure 1 SFCN with cross-attention mechanism

Models $N_{samples}$	ADNI 300	OASIS 314	IXI 588	CORR 1357	Merged 2559
ResNet50	6.4962	7.0552	6.3915	4.2518	5.4944
SEResNet50	7.4434	6.8672	7.7523	3.9839	5.7622
DenseNet	6.7436	5.8528	4.7717	**2.7425**	4.2893
SFCN	6.6056	4.8408	**4.0488**	3.1300	4.1417
VGG	6.2478	5.6213	5.8882	3.5896	4.8049
Global-Local-Transformer	5.7907	4.3264	4.3387	2.8932	3.8328
ours	**5.0263**	**4.3687**	4.2904	2.8781	**3.7452**

Figure 2 Result

References

1. Tanveer, M., et al. “Deep learning for brain age estimation: A systematic review.” Information Fusion (2023).
2. He, Sheng, P. Ellen Grant, and Yangming Ou. “Global-local transformer for brain age estimation.” IEEE transactions on medical imaging 41.1 (2021): 213-224.
3. Peng, Han, et al. “Accurate brain age prediction with lightweight deep neural networks.” Medical image analysis 68 (2021): 101871.
4. Dosovitskiy, Alexey, et al. “An image is worth 16x16 words: Transformers for image recognition at scale.” arXiv preprint arXiv:2010.11929 (2020).
5. He S, Feng Y, Grant P E, et al. Deep relation learning for regression and its application to brain age estimation[J]. IEEE transactions on medical imaging, 2022, 41(9): 2304-2317
6. Baecker L, Garcia-Dias R, Vieira S, et al. Machine learning for brain age prediction: Introduction to methods and clinical applications[J]. EBioMedicine, 2021, 72: 103600.
7. Jack Jr C R, Bernstein M A, Fox N C, et al. The Alzheimer’s disease neuroimaging initiative (ADNI): MRI methods[J]. Journal of Magnetic Resonance Imaging: An Official Journal of the International Society for Magnetic Resonance in Medicine, 2008, 27(4): 685-691
8. LaMontagne, Pamela J., et al. “OASIS-3: longitudinal neuroimaging, clinical, and cognitive dataset for normal aging and Alzheimer disease.” MedRxiv (2019): 2019-12.
9. Zuo X N, Anderson J S, Bellec P, et al. An open science resource for establishing reliability and reproducibility in functional connectomics[J]. Scientific data, 2014, 1(1): 1-13.

Poster No 160

Symptom-specific brain networks identified in rsfMRI data of Parkinson's disease patients

Jurgen Germann[1], Gavin Elias[1], Andrew Yang[1], Alexandre Boutet[1], Andres Lozano[1]

[1]*University Health Network, University of Toronto, Toronto, Ontario*

Introduction: Parkinson's disease (PD) is a neurodegenerative disorder; patients with PD exhibit motor symptoms such as tremor rigidity, bradykinesia, and axial impairment. (Poewe et al., 2017) Treatments for PD include pharmacological and surgical therapies such as deep brain stimulation (DBS). DBS is an invasive neuromodulation technique that can deliver immense therapeutic benefits in PD through the modulation of local and distal brain networks. (Lozano & Lipsman, 2013) Treatment response in DBS depends on the precise location of stimulation, and previous work has demonstrated that symptom-specific clinical improvement is associated with the stimulation of different diencephalic brain regions. (Boutet et al., 2021) The goal of this work was to identify symptom-specific brain networks using patient-specific pre-operative rsfMRI data. The presence of such networks would open an avenue for therapies to be tailored to individual patients. Furthermore, the work may identify symptom-specific target regions that would allow for the use of non-invasive neuromodulation techniques such as transcranial magnetic stimulation (TMS) or focused ultrasound (FUS).

Methods: Following ethics approval (University Health Network Research Ethics Board #15–9777), rsfMRI scans were prospectively acquired in 133 PD patients (47 female; average age: 62.3 years (Stdev 10.6); average disease duration: 10.5 years (Stdev 5.1)) as part of their pre-operative planning MRI session (field strength: 1.5-3T, TR: 1880-2200 ms, TE: 30-35 ms, flip angle: 50-85°, slice thickness: 2.5-4.5 mm, matrix: 64-88×64-88 voxels). Pre-operative baseline (Med-OFF) motor item scores of the Unified Parkinson's Disease Rating Scale (UPDRS-III) were also collected for each patient, and symptom-specific scores calculated. The rsfMRI data were processed using the BRANT toolbox (http://brant.brainnetome.org/). (Xu et al., 2018) Following preprocessing (removal of first 10 volumes; motion correction; normalization; resampling; denoising for nuisance variables; filtering with a temporal bandpass filter [0.01–0.08 Hz]; smoothing with a Gaussian kernel [6mm fwhm]), the functional connectivity of the motor network of each individual was assessed using the motor region of the thalamus as the seed region. The Pearson correlations between the time courses of the ROI and all other voxels in the brain were calculated and Fisher z-transformed. Additional maps were calculated using the supplementary motor area and the motor/premotor cortex as seeds. Using R (version 4.0.2) and RMINC, symptom-specific patterns of connectivity were calculated using a linear regression between individual rsfMRI connectivity and symptom scores.

Results: Independent of seed region, each symptom was associated with distinct functional connectivity across various motor regions (Figure 1). Each symptom network involves distinct regions of the motor/premotor region (Figure 1). These are in close proximity to the 'hand knob,' a standard reference target for TMS, and could readily be targeted using non-invasive neuromodulation such as TMS or FUS toameliorate specific symptoms. Furthermore, each symptom-specific connectivity network showed unique connectivity in the diencephalic region that is targeted in DBS (Figure 2). The pattern of peak locations is highly similar to the optimal symptom-specific DBS stimulation locations derived from sweet-spot mapping previously reported. (Boutet et al., 2021)

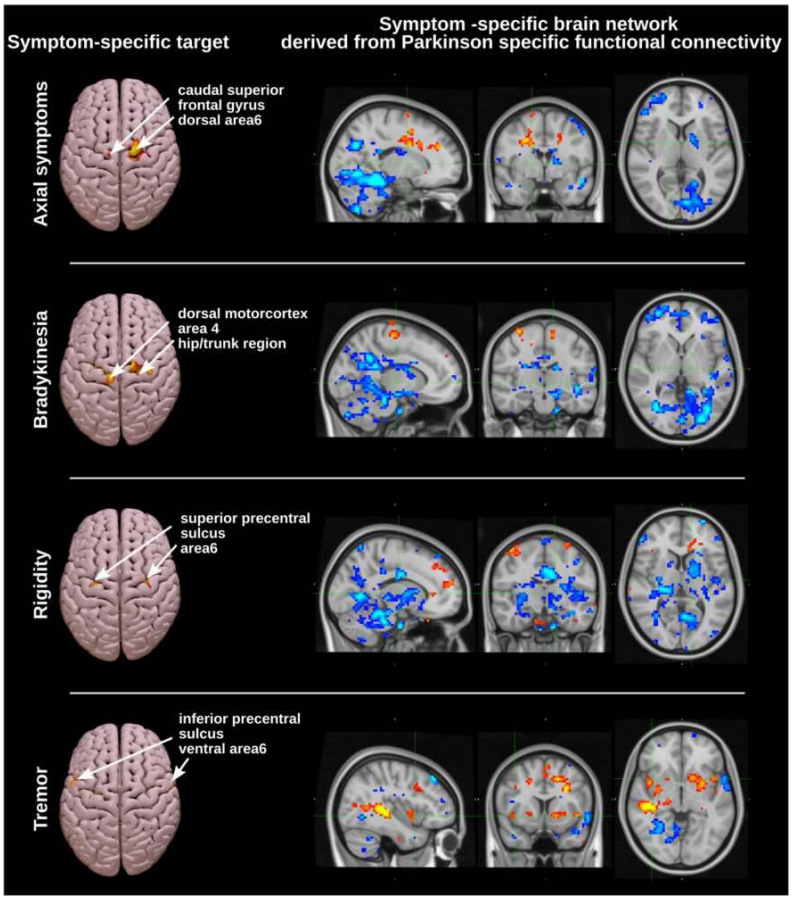
Symptom-specific target
Symptom -specific brain network
derived from Parkinson specific functional connectivity
Axial symptoms
caudal superior
frontal gyrus
dorsal area6
Bradykinesia
dorsal motorcortex
area 4
hip/trunk region
Rigidity
superior precentral
sulcus
area6
Tremor
inferior precentral
sulcus
ventral area6

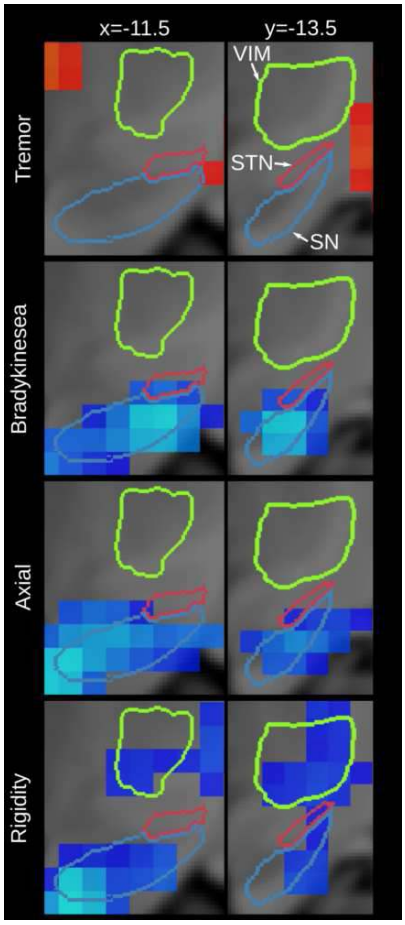
x=-11.5
y=-13.5
VIM
STN
SN
Tremor
Bradykinesea
Axial
Rigidity

Conclusions: This work demonstrates that individual preoperative rsfMRI shows distinct patterns associated with individual symptom severity. The symptom-specific brain networks identified may be used for individual treatment planning and provide potential brain targets for non-invasive neuromodulation techniques such as FUS or TMS. The availability of non-invasive techniques could allow more PD patients to benefit from neuromodulation therapies to alleviate motor symptoms.

References

1. Boutet, A., Germann, J., Gwun, D., Loh, A., Elias, G. J. B., Neudorfer, C., Paff, M., Horn, A., Kuhn, A. A., Munhoz, R. P., Kalia, S. K., Hodaie, M., Kucharczyk, W., Fasano, A., & Lozano, A. M. (2021). Sign-specific stimulation "hot" and "cold" spots in Parkinson's disease validated with machine learning. Brain Communications, 3(2), fcab027. https://doi.org/10.1093/braincomms/fcab027
2. Lozano, A. M., & Lipsman, N. (2013). Probing and regulating dysfunctional circuits using deep brain stimulation. Neuron, 77(3), 406–424. https://doi.org/10.1016/j.neuron.2013.01.020
3. Poewe, W., Seppi, K., Tanner, C. M., Halliday, G. M., Brundin, P., Volkmann, J., Schrag, A.-E., & Lang, A. E. (2017). Parkinson disease. Nature Reviews Disease Primers, 3(1), 1–21. https://doi.org/10.1038/nrdp.2017.13
4. Xu, K., Liu, Y., Zhan, Y., Ren, J., & Jiang, T. (2018). BRANT: A Versatile and Extendable Resting-State fMRI Toolkit. Frontiers in Neuroinformatics, 12, 52. https://doi.org/10.3389/fninf.2018.00052

Poster No 161

Striatal and thalamic automatic segmentation, morphology, and clinical correlates in Parkinsonism

May Erlinger[1], Jeffrey Looi[2], Rosa Molina-Ruiz[3], Eva Lopes Valdes[3]

[1]Australian National University, Canberra, Australia, [2]Research Centre for the Neurosciences of Ageing, Academic Unit of Psychiatry and Addiction Medicine, Canberra, ACT, [3]Hospital Clinico San Carlos, Madrid, Spain

Introduction: Parkinson's disease (PD), multisystem atrophy (MSA), and progressive supranuclear palsy (PSP) are each considered progressively degenerative neurological movement disorders, characterised by variable, but similar, presentations of movement impairment and accompanying cognitive and behavioural neuropsychiatric symptoms such as sleep disturbances, depression, and autonomic dysfunction[1]. MSA-parkinsonian type is most significantly clinically differentiated from Parkinson's disease through its widespread impacts on autonomic functions[2]. PSP can be clinically differentiated from PD through its supranuclear gaze palsy and postural instability[3] which can also occasionally present in MSA. However, these diseases do not always classically present with their characteristic symptom, and instead have significant overlap in their clinical features of bradykinesia, rigidity, tremors, rendering them difficult to discriminate and diagnose in-vivo. The thalamus and striatum have been previously identified as having potential as biomarkers for neurodegenerative disorders, especially as related to disease onset[4,5], progression[6,7] and severity[8] and therefore may serve as potent and reliable disease-specific biomarkers for differentiating atypical parkinsonism. This poster investigates striatal and thalamic volume and morphology as distinguishing biomarkers, and their relationship to neuropsychiatric symptoms.

Methods: Automatic segmentation to calculate volume and shape analysis of the caudate nucleus, putamen, and thalamus were performed in 18 PD patients, 12 MSA, 15 PSP, and 21 healthy controls. T1-weighted MRI data were acquired for patients and healthy controls by a 3.0T Phillips MR scanner, with pre-processing of the images conducted through FSL, and automatic bilateral subcortical structure segmentations of the relevant regions of interest (ROI) (bilateral caudate nucleus, putamen, and thalamus) created using FSL-FIRST. The segmentations created were included in a shape analysis using the SPHARM-PDM module in 3D Slicer[9]. Multivariate analysis of covariance was conducted to determine significant differences between PD, MSA, PSP, and controls in the ROI volumes. The covariates included in analysis were age, sex, and total ICV to account for head size. For shape analyses, we used the Covariate Significance Testing module of SlicerSALT, with a family-wise error correction for multiple comparisons, with age and sex included as covariates, to compare PD, MSA, PSP and controls. Volume and shape of ROIs were then correlated clinical measures of parkinsonism and neuropsychiatric function.

Results: The volumetric analyses determined there was a significant difference in all the ROIs between groups, with the bilateral thalami (L: $p=0.017$, R: $p=0.011$) and right putamen ($p=0.032$) of PSP patients found to be significantly smaller than controls. The left caudate ($p=0.025$) and left putamen ($p=0.025$) significantly correlated with the Neuropsychiatric Inventory total score. Bilateral thalamus, caudate, and left putamen had significantly different morphology between groups. The antero-ventral medial portion of the bilateral caudate head varied significantly (L: $p=0.004$, R: $p=0.012$) between groups, driven by differences between PSP and healthy controls ($p=0.004$). The ventro-posterior aspect of the left putamen differed significantly ($p=0.028$), and was driven by PSP ($p<0.001$) and PD ($p<0.001$) compared to controls. The left antero-ventral thalamus ($p=0.004$), and the right dorsolateral thalamus ($p=0.012$) were significantly different between groups, which was bilaterally driven by differences in PSP patients compared to controls (L: $p=0.002$, R: $p<0.001$).

Conclusions: This study demonstrated that PSP striatal and thalamic volumes and shapes are significantly different when compared with controls. Parkinsonian disorders could not be differentiated on volumetry or morphology, however there are trends for volumetric and morphological changes associated with PD, MSA, and PSP.

References

1. Chaudhuri, K. R. (2006). Non-motor symptoms of Parkinson's disease: diagnosis and management. Lancet Neurol, 5(3), 235-245.
2. Wenning, G. K. (2000). What clinical features are most useful to distinguish definite multiple system atrophy from Parkinson's disease? Journal of Neurology, Neurosurgery & Psychiatry, 68, 434-440.
3. Liscic, R.M. (2013). Differentiation of progressive supranuclear palsy: clinical, imaging and laboratory tools. Acta Neurol Scand, 127(5), 362-370.
4. Halliday, G. M. (2009). Thalamic changes in Parkinson's disease. Parkinsonism & Related Disorders, 15, S152-S155.
5. Power, B. D. (2015). The thalamus as a putative biomarker in neurodegenerative disorders. Australian & New Zealand Journal of Psychiatry, 49(6), 502-518.
6. Lee, S. H. (2011). Regional Volume Analysis of the Parkinson Disease Brain in Early Disease Stage: Gray Matter, White Matter, Striatum, and Thalamus. American Journal of Neuroradiology, 32(4), 682-687.
7. Looi, J. C. L.(2013). Striatal morphology as a biomarker in neurodegenerative disease. Molecular Psychiatry, 18(4), 417-424.
8. Bohnen, N. I. (2011). The cholinergic system and Parkinson disease. Behavioural Brain Research, 221(2), 564-573.
9. Vicory, J.(2018). SlicerSALT: Shape AnaLysis Toolbox. In (pp. 65-72): Springer International Publishing.

Poster No 162

Stability of MEG and EEG Spectral Features in Mild Cognitive Impairment (MCI)

Shrikanth Kulashekhar[1,2], Antti Kinnunen[1], Timo Saarinen[1], Ville Mäntynen[1], Jaakko Hotta[3], Anne Koivisto[3], Mia Liljeström[1,2], Hanna Renvall[1,2]

[1]BioMag Laboratory, HUS Diagnostic Center, Helsinki University Hospital (HUS), Helsinki, Finland, [2]Department of Neuroscience and Biomedical Engineering, Aalto University, Helsinki, Finland, [3]Department of Clinical Neurosciences, Neurology, Helsinki University Hospital (HUS), Helsinki, Helsinki

Introduction: In mild cognitive impairment (MCI), the first neurodegenerative changes may occur years be-fore they can be effectively detected with current clinical tools. Early pathology has been linked to synaptic dysfunction causing brain network disturbances that may be observed with electroencephalography (EEG) and magnetoencephalography (MEG) (Pusil S, 2019; Miraglia F, 2020). However, current clinical practice lacks critical tools for early identification of those at greatest risk of developing into clinical dementia, and in need of preventive actions. In a 5-year EU Horizon2020 project 'AI-Mind', we collect EEG and MEG data from 1000 participants with MCI in Europe (Finland, Italy, Norway, and Spain), to be compiled with cognitive, genetic and plasma biomarker measures and techniques based on artificial intelligence (AI) for predicting the overall dementia risk. We aim at earlier and more accurate interception of those MCI individuals in a 'prodromal' stage of dementia, to allow timely intervention for known modifiable risk factors (Figure 1). Various features of the MEG and EEG signals have been compared between MCI patients and healthy controls, including the peak frequency, peak and average power, at different frequency bands. The occipital alpha (8-13 Hz) rhythm has been shown to reduce in power, slow down in its peak frequency, and change in its cortical distribution in MCI (Kowalski JW, 2001). However, the stability and reliability of these measures have not been addressed in large subject cohorts nor in MCI. A good biomarker should be stable within a measurement in all subjects, and, in case of MCI, show differences between measurements separated in time, but only in subjects who are in risk of disease progression.

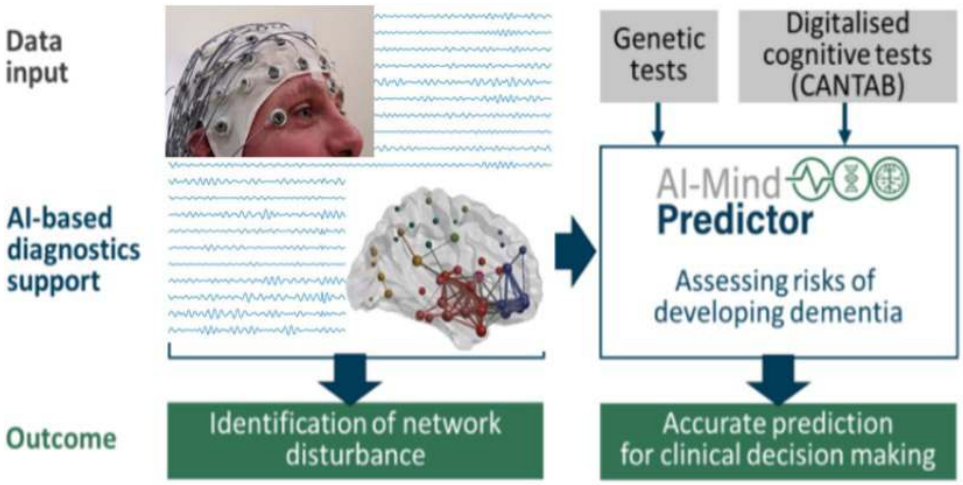

Methods: Here, data from 41 Finnish MCI subjects (20 females, age 68 ± 5; mean ± SD) were used. These subjects were recruited via HUS neurology departments and general advertisements to participate in the AI-Mind study and were initially screened by a neurologist in reference to the inclusion and exclusion criteria of the study. The subjects underwent a combined MEG and EEG resting-state measurement consisting of two sessions of 5 min of eyes open and two sessions of 5 min with their eyes closed. MEG recordings were conducted at the BioMag Laboratory in Helsinki University Hospital (HUS) with a 306-channel neuromagnetometer (Triux, MEGIN); the EEG recordings were conducted simultaneously with the MEG with 128-channel system (eegoTM, eemagine Medical Imaging Solutions GmbH). The data analysis was performed using custom Python software developed in BioMag Laboratory and external software such as Maxfilter, Freesurfer, FOOOF, and MNE python. We determined the within-session test-retest reliability for spectral peak frequencies and relative peak power (Figure 2A). The peak frequency and power were computed for the alpha-band (8-13 Hz) over the occipital brain regions and for the beta-band (14-30 Hz) over the fronto-central brain regions. For each subject the peak frequency and power were automatically identified and visually verified. Finally, the test-retest stability of the spectral features was accessed using intraclass correlation (ICC) method.

Results: The results indicate good (ICC>0.6) test-retest reliability across runs for EEG (peak frequency: 0.72 (EC); relative power: 0.86 (EC) and 0.66 (EO); p<0.001) and excellent test-retest reliability (ICC>0.75) for MEG (peak frequency: 0.83 (EC); relative power: 0.96 (EC) and 0.85 (EO); p<0.001). Consistency across EEG and MEG was excellent (peak frequency: 0.86 (EC); relative power 0.89 (EC) and 0.84 (EO); p<0.001).

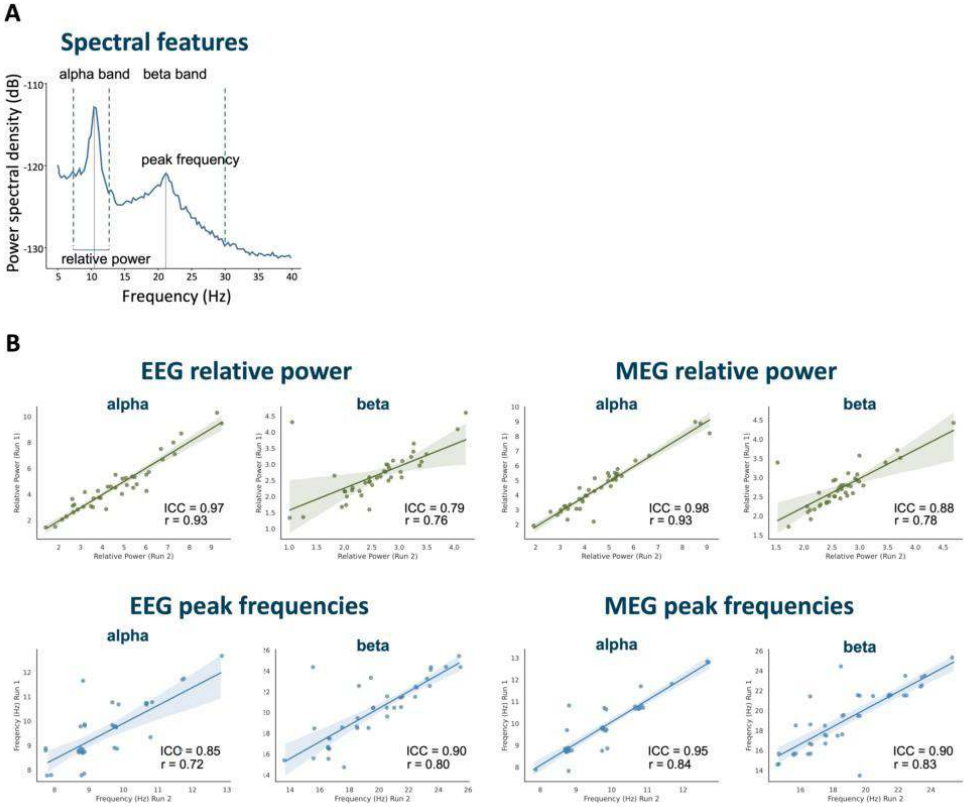

Conclusions: Electrophysiological recordings of brain networks are emerging as a diagnostic tool for early detection of dementia. Good stability of the measured signal features is a prerequisite for diagnosis. Here, we demonstrate good or excellent stability for prominent spectral features both within and across EEG and MEG recordings.

References

1. Kowalski J.W. (2001), 'The diagnostic value of EEG in Alzheimer disease: correlation with the severity of mental impairment', Journal of Clinical Neurophysiology, 18(6):570-5.
2. Miraglia F. (2020), 'Small World Index in Default Mode Network Predicts Progression from Mild Cognitive Impairment to Dementia', International Journal of Neural Systems, 30: 2050004.
3. Pusil S. (2019), 'Aberrant MEG multi-frequency phase temporal synchronization predicts conversion from mild cognitive impairment-to-Alzheimer's disease', Neuroimage Clin 24:101972.

Poster No 163

Evaluating Deep Learning Hippocampal Segmentation Pipelines for Alzheimer's Disease

Jiongqi Qu[1,2], Sophie Martin[1,2], James Cole[1,2]

[1]Centre for Medical Image Computing, Department of Computer Science, University College London, London, United Kingdom, [2]Dementia Research Centre, Queen Square Institute of Neurology, University College London, London, United Kingdom

Introduction: Deep learning has recently shown considerable promise at hippocampal segmentation from structural MRI. However, most studies focus primarily on segmentation accuracy, and overlook generalisability which is key for the clinical deployment of automated methods. Here, we aimed to evaluate 1) sensitivity to Alzheimer's disease (AD): by assessing group differences in hippocampal volume between patients with AD and cognitively normal (CN) people, and 2) reliability: by assessing intra-patient agreement of hippocampal volumes. We evaluated three "off-the-shelf" deep learning approaches (FastSurfer [Henschel et al. 2020], SynthSeg [Billot et al. 2023], nnUNet [Isensee et al. 2021)], as well as an nnUNet trained from scratch and benchmarked these models against an atlas-based method (FreeSurfer [Fischl 2012]).

Methods: To assess sensitivity, 816 scans from the Alzheimer's Disease Neuroimaging Initiative (ADNI) [Jack Jr et al. 2008] and 1276 scans from the National Alzheimer's Coordinating Center (NACC) [Beekly et al. 2007] were used, with age- and sex-matched groups. To assess reliability, we used BNU1, HNU1 and IPCAS1 from the Consortium for Reliability and Reproducibility (CoRR) [Zuo et al. 2014] database, which contains 2 repeat scans (n=48), 10 repeat scans (n=28) and 2 repeat scans (n=29) correspondingly. Among the pipelines, the original nnUNet required sub-sectioned brain data, which had unclear pre-processing steps and involved human fine-tuning. It was also trained using a mixture of healthy and non-affective psychotic disorder patients' data. To avoid under-evaluating the pipeline's performance due to these issues, an nnUNet was retrained using 366 scans from the Open Access Series of Imaging Studies (OASIS) [LaMontagne et al. 2019] data.

Results: For sensitivity to Alzheimer's, all pipelines achieved large effect sizes (Cohen's d [Cohen 2013] > 0.5; Figure 1a). The effect sizes of the original nnUNet were substantially lower than the other pipelines. After retraining, nnUNet reached comparable performance with FreeSurfer. Generally, group-different effects were lower in NACC participants compared to ADNI, though the Cohen's d values shared a similar ordering across the two datasets. FastSurfer returned absolute volumes that were most similar to FreeSurfer (see Figure 1b for the hippocampal volume distributions in the AD and CN groups). The original nnUNet often returned lower hippocampal volumes, while SynthSeg and the retrained nnUNet tended to overestimate the volumes. For test-retest reliability (Figure 2), the BNU1 results indicated that the four deep learning pipelines had better segmentation stability than FreeSurfer with higher median values and narrower and less overlapped confidence intervals. However, there were no significant differences between them. For the HNU1 data, both nnUNets produced unstable results for left and right hippocampal segmentation. However, their intra-class correlation coefficient (ICC(3,1)) [Weir 2005] values were still much higher than FreeSurfer (>0.94). In the IPCAS1 data, the original nnUNet was less stable and its confidence intervals overlapped with FreeSurfer by >60%.

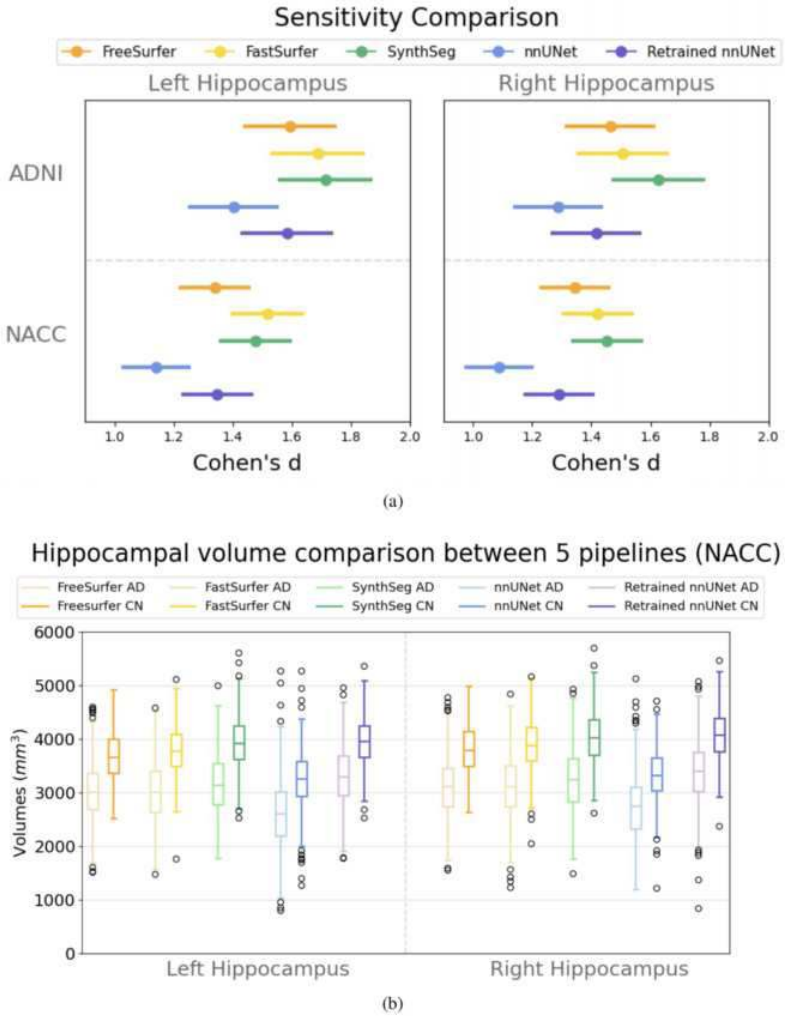

Figure 1: Sensitivity Experiment: (a) The Cohen's d values [Cohen 2013] between the Alzheimer's disease (AD) and the cognitively normal (CN) groups of all five pipelines on ADNI and NACC datasets. (b) The volume distribution of AD and CN groups using five pipelines on the NACC dataset. All pipelines had p-values between AD and CN groups <0.01.

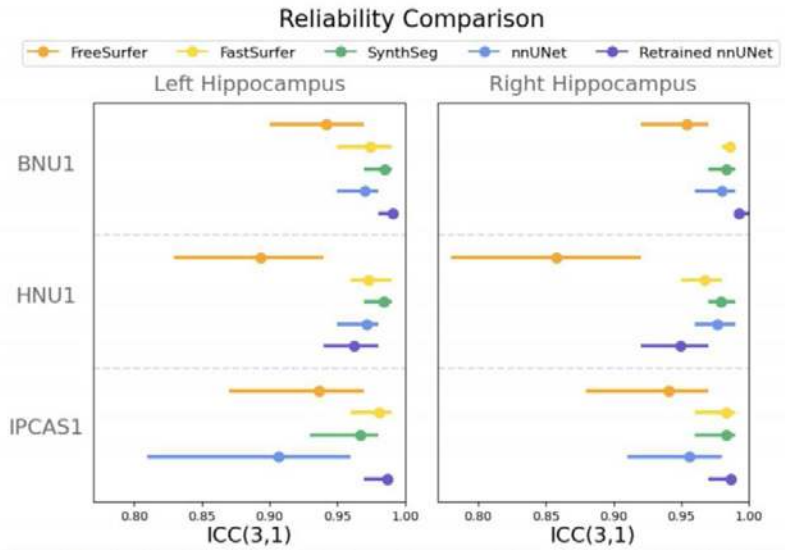

Figure 2: Reliability Experiment: The intra-class correlation coefficient (ICC(3,1)) [Weir 2005] values between the repetitive sessions of all five pipelines on BNU1, HNU1 and IPCAS1 datasets.

Conclusions: We found that deep learning hippocampal segmentation methods can achieve comparable or better results than FreeSurfer, in terms of sensitivity to AD and test-retest reliability. These findings could help guide study design considerations or sample size calculations for research into the hippocampus in AD. Future research could evaluate reducing similarity constraints and allow more freedom in variation during training (especially as a ground truth hippocampal segmentation does not exist), data augmentation, increasing the proportion of AD data and minimising the amount of preprocessing require.

References

1. Beekly, Duane L et al. (2007). "The National Alzheimer's Coordinating Center (NACC) database: the uniform data set". In: Alzheimer Disease & Associated Disorders 21.3, pp. 249–258.
2. Billot, Benjamin et al. (2023). "SynthSeg: Segmentation of brain MRI scans of any contrast and resolution without retraining". In: Medical image analysis 86, p. 102789.
3. Cohen, Jacob (2013). Statistical power analysis for the behavioral sciences. Academic press.
4. Fischl, Bruce (2012). "FreeSurfer". In: Neuroimage 62.2, pp. 774–781.
5. Henschel, Leonie et al. (2020). "Fastsurfer-a fast and accurate deep learning based neuroimaging pipeline". In: NeuroImage 219, p. 117012.
6. Isensee, Fabian et al. (2021). "nnU-Net: a self-configuring method for deep learning-based biomedical image segmentation". In: Nature methods 18.2, pp. 203–211.
7. Jack Jr, Clifford R et al. (2008). "The Alzheimer's disease neuroimaging initiative (ADNI): MRI methods". In: Journal of Magnetic Resonance Imaging: An Official Journal of the International Society for Magnetic Resonance in Medicine 27.4, pp. 685–691.
8. LaMontagne, Pamela J et al. (2019). "OASIS-3: longitudinal neuroimaging, clinical, and cognitive dataset for normal aging and Alzheimer disease". In: MedRxiv, pp. 2019–12.
9. Weir, Joseph P (2005). "Quantifying test-retest reliability using the intraclass correlation coefficient and the SEM". In: The Journal of Strength & Conditioning Research 19.1, pp. 231–240.
10. Zuo, Xi-Nian et al. (2014). "An open science resource for establishing reliability and reproducibility in functional connectomics". In: Scientific data 1.1, pp. 1–13.

Poster No 164

Identifying healthy individuals with Alzheimer's disease neuroimaging phenotypes

Tiago Azevedo[1], Richard Bethlehem[2], David Whiteside[3], Nol Swaddiwudhipong[3], James Rowe[3], Pietro Lio[4], Timothy Rittman[3]

[1]Department of Computer Science and Technology, University of Cambridge, Cambridge, United Kingdom, [2]Autism Research Centre, Department of Psychiatry, University of Cambridge, Cambridge, United Kingdom, [3]Department of Clinical Neurosciences and Cambridge University Hospitals NHS Trust, Cambridge, United Kingdom, [4]Department of Computer Science and Technology, University of Cambridge, Cambridge, United Kingdom, Cambridge, United Kingdom

Introduction: Challenges in timely and accurate Alzheimer's disease (AD) diagnosis have an impact on patients and impede clinical trial success. Noteworthy findings in previous cohorts suggest changes in structural neuroimaging decades before symptoms. Deep learning has been proved to be effective in addressing diverse neuroscientific challenges; however, despite some recent success in AD's classification, few studies have validated results in completely independent datasets. In this work, we identify a group of people at high risk of developing dementia in the healthy UK Biobank dataset, using Bayesian deep learning modelling techniques. We demonstrate that our approach can be applied to identify people at high risk of developing dementia.

Methods: We preprocessed structural MRI (MPRAGE) scans across three cohorts. Firstly, from ADNI, we used baseline scan sessions with a diagnosis of AD (n=331) and Controls (n=405). Secondly, we used the NACC dataset for validation of which we used a total of 1706 scans from patients with an AD diagnosis, as well as controls (n=2824), and other disorders (n=679). Finally, we used 37104 scans from the UK Biobank. We extracted regional cortical thicknesses and cortical volumes from 68 surface-based regions, as well as brainstem volume, and 9 other volume features per hemisphere, totalling 155 features per brain scan. To avoid data leakage, 155 deconfounding regression models (using age, estimated intracranial volume, and sex) were fitted only on the ADNI training set, and the corresponding learned statistics were later employed to deconfound all the other datasets. As illustrated in Figure 1, we implemented a neural network with two hidden layers with empirically found hyperparameters giving stable learning curves. We used Monte Carlo dropout to approximate Bayesian inference by activating the dropout layers at inference time. Gal and Ghahramani showed that, after training, each forward pass in the network corresponds to a good approximation to sampling from the true posterior distribution, with very little added computational cost.

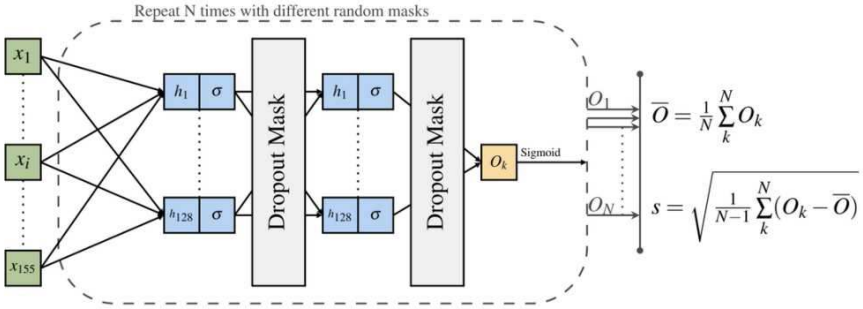

Figure 1: The neural network consists of two hidden layers of 128 dimensions and non-linear activation function σ = tanh(). For each set of 155 inputs, N = 50 forward passes are run, each time with a different dropout mask sampled from a Bernoulli distribution. An AD likelihood score is generated as the mean, and model uncertainty as the standard deviation calculated from the 50 forward passes.

Results: Table 1 shows the performance of our model. We compared our model with a simple hippocampal volume measure, other machine learning models as well as to TPOT, a tool which tries to find the best possible pipeline for a specific dataset. The highest performance was found in the ADNI test set, which is expected; however, performance in NACC was still comparable to previous literature. The NPV performance of our model was the best; this is important given our application in the UK Biobank, where the rate of AD is substantially lower than either ADNI or NACC and we want to avoid the risk of misclassifying healthy people. Our model was able to give a better balance of sensitivity/specificity; other models had higher specificity, but with low sensitivity. We applied Bayesian regression models with age as a covariate to assess the clinical validity of the AD score. For the UK Biobank, there were 3.4% of people with a positive AD score and the group with a positive AD score was only slightly older than the AD score negative group (1.79 years). There was strong evidence of worse fluid intelligence in the AD score positive group (−0.35), and strong evidence that people in the AD group were more likely to report their overall health as 'poor' or 'fair' rather than 'good' or 'excellent'. There was some evidence of a difference in both diastolic blood pressure (1.12) and systolic blood pressure (2.29).

Table 1: Performance metrics across datasets with a model trained on the ADNI training set, using a cut-off of an Alzheimer's disease (AD) score of 0.5. For the NACC, we evaluated AD prediction against two groups: (1) controls alone, and (2) controls and non-AD diagnoses. (AUC: area under the ROC curve, PPV: positive predictive value, NPV: negative predictive value.)

Model	Accuracy	AUC	Sensitivity	Specificity	PPV	NPV
ADNI Test Set						
Ours	0.92	0.97	0.90	0.93	0.90	0.93
SVM RBF	0.88	0.96	0.90	0.86	0.82	0.93
SVM Poly	0.92	0.97	0.87	0.95	0.93	0.91
XGBoost	0.88	0.95	0.87	0.89	0.84	0.91
ElasticNet	0.92	0.96	0.87	0.95	0.93	0.91
TPOT	0.91	0.97	0.90	0.91	0.87	0.93
NACC AD vs Controls						
Ours	0.74	0.79	0.68	0.78	0.65	0.80
SVM RBF	0.75	0.78	0.55	0.87	0.72	0.76
SVM Poly	0.75	0.76	0.60	0.84	0.69	0.78
XGBoost	0.74	0.78	0.58	0.84	0.68	0.77
ElasticNet	0.76	0.79	0.55	0.89	0.76	0.77
TPOT	0.76	0.79	0.65	0.84	0.70	0.80
NACC AD vs Controls and non-AD diagnoses						
Ours	0.72	0.76	0.68	0.73	0.56	0.83
SVM RBF	0.74	0.75	0.55	0.83	0.61	0.79
SVM Poly	0.73	0.73	0.60	0.79	0.59	0.80
XGBoost	0.72	0.75	0.58	0.79	0.57	0.79
ElasticNet	0.75	0.76	0.55	0.85	0.64	0.80
TPOT	0.74	0.76	0.65	0.78	0.59	0.82

Conclusions: By using a Bayesian deep learning network, we have identified an AD-like cohort in the UK Biobank, with a diagnosis of dementia or reported symptoms. For disease prevention, our results highlight smoking history, greater pack-year exposure, and hypertension as potentially modifiable risk factors. Bayesian statistics for group comparisons and regression

models offered advantages in our work as they ultimately allow us to distinguish a small effect size from an incorrect parameter estimate.

References
1. Pedregosa, F. et al. Scikit-learn: machine learning in Python. Journal of Machine Learning Research 12, 2825–2830 (2011).
2. Gal, Y. & Ghahramani, Z. Dropout as a Bayesian approximation: Representing model uncertainty in deep learning. In Balcan, M. F. & Weinberger, K. Q. (eds) Proc. 33rd International Conference on Machine Learning Research (PMLR, 2016), Vol. 48, 1050–1059. (ML Research Press, 2016).
3. Kinnunen, K. M. et al. Presymptomatic atrophy in autosomal dominant Alzheimer's disease: a serial magnetic resonance imaging study. Alzheimer's & Dementia 14, 43–53 (2018).
4. Abrol, A. et al. Deep learning encodes robust discriminative neuroimaging representations to outperform standard machine learning. Nature Communications 12, 353–380 (2021).

Poster No 165

Distinct graded pattern of hippocampal atrophy and its association with memory deficits in dementia

Fang Lan[1], Daniel Roquet[2], Marshall Dalton[1], Olivier Piguet[1], Muireann Irish[1]

[1]Brain and Mind Centre, The University of Sydney, Sydney, Australia, [2]GIP Cyceron, Caen, France

Introduction: Semantic dementia is a younger-onset dementia characterized by progressive loss of conceptual knowledge with atrophy in anterior temporal lobe, commonly lateralised to the left hemisphere. Recent studies have found that hippocampal atrophy is also presented in semantic dementia, especially the anterior hippocampus, if no greater, than that observed in Alzheimer's disease. A paradox arises that although both diseases present with marked hippocampal atrophy, episodic memory is compromised in Alzheimer's disease yet remains relatively intact in semantic dementia. It is now clear that hippocampus is not a unitary structure and instead should be viewed with distinct functional properties along its anterior-posterior axis. However, no study to our knowledge has comprehensively quantify how the spatial distribution of hippocampal atrophy varies in a graded manner along the long-axis of the hippocampus in these syndromes. Therefore, this study aimed to quantify hippocampal volumetric differences in Alzheimer's disease and semantic dementia. Further, we aimed to explore the relationship between hippocampal atrophy profiles and episodic memory performances in these two diseases.

Methods: 21 left-lateralised semantic dementia patients, 24 Alzheimer's disease patients, and 27 healthy older control participants were recruited from Frontotemporal Dementia Clinic in Sydney, Australia. All participants underwent whole-brain 3T structural MRI. T1 images were preprocessed using SPM12 on MATLAB. We adapted the parcellation masks developed by Plachti et al (2019), which employed multimodal connectivity-based parcellation to reveal an anterior-posterior functional organization. Grey matter volumes were subsequently assessed into four subregions: anterior, intermediate rostral, intermediate caudal, and posterior. Furthermore, participants completed validated neuropsychological tests to index overall cognitive performance along with integrity of episodic (Addenbrooke's Cognitive Examination-III Memory subscale, Rey Complex Figure three-min recall) and semantic (Sydney Language Battery Naming subscale) memory function.

Results: Relative to controls, all hippocampal subregions showed significant volume loss in Alzheimer's disease, whereas semantic dementia patients showed relatively preserved volume of right posterior hippocampus, while the remaining subregions exhibited significant atrophy. Within patient groups, Alzheimer's disease showed a relatively flat profile of atrophy with no pattern of gradation or lateralisation. In semantic dementia, however, two patterns of hippocampal atrophy were evident. First, there was a graded pattern of atrophy running from anterior to posterior direction on both hippocampi, with anterior subregions disproportionately affected relative to posterior subregions. Secondly, all left hippocampal subregions were more atrophied when compared to their contralateral counterparts, indicating a left-lateralised hippocampal atrophy. Correlational analysis revealed evident associations between verbal episodic memory performance and left mid-posterior hippocampal atrophy in semantic dementia and left posterior hippocampus in Alzheimer's disease. Semantic processing, on the other hand, was associated with more left anterior subregions in both patient groups. These results mesh well with previous whole-brain structural analyses on associations between hippocampal degeneration and memory deficits in these syndromes.

Conclusions: This study provides novel evidence for distinct atrophy profiles of hippocampal long axis in dementia and offers preliminary insights into its contributions to the memory impairments experienced by these clinical groups. These findings resonate with a growing body of work highlighting the functional complexity of the hippocampus, providing important implication for understanding how differential vulnerability along the anterior-posterior axis of the hippocampus relates to canonical clinical features.

References
1. Plachti, A, (2019), "Multimodal parcellations and extensive behavioral profiling tackling the hippocampus gradient." Cerebral cortex 29.11 (2019): 4595-4612.

Poster No 166

Intracranial atherosclerosis is linked to lower volume in hippocampal posterior body and tail

Gulam Mahfuz Chowdhury[1], Mahir Tazwar[1], Arnold Evia[2], Alifiya Kapasi[2], Sonal Agrawal[2], David Bennett[2], Julie Schneider[2], Konstantinos Arfanakis[1,2]

[1]Illinois Institute of Technology, Chicago, IL, [2]Rush University Medical Center, Chicago, IL

Introduction: Intracranial atherosclerosis is a common age-related neuropathology that has been linked to cognitive decline and dementia[1–3]. Intracranial atherosclerosis is often mixed with Alzheimer's and other neuropathologies increasing the odds of dementia[4]. Despite its prevalence, its negative impact on cognitive function and its role in aging and dementia, the association of atherosclerosis with brain morphometric abnormalities has not been explored. Deformation-based morphometry (DBM) is an approach that allows investigation of brain morphometry at the voxel level[5]. Here, we combined DBM on ex-vivo MRI with detailed neuropathological examination in a large number of community-based older adults to investigate the association of intracranial atherosclerosis with brain morphometric anomalies.

Methods: Participants, MRI, neuropathologic examination: This work included 891 community-based older adults participating in four cohort studies of aging: the Rush Memory and Aging Project, Religious Orders Study[6], Minority Aging Research Study, and African American Clinical Core of the Rush Alzheimer's Disease Research Center[7]. All participants came to autopsy. Hemispheres from all participants were submerged in 4% formaldehyde solution and imaged approximately one month postmortem on 3T clinical MRI scanners using a multi-echo spin-echo sequence with a voxel size=0.6×0.6×1.5 mm3. All images were non-linearly registered to an ex vivo brain hemisphere template using ANTs[8]. The logarithm of the Jacobian determinant of the deformation fields was calculated in each voxel and the resulting maps(LogJ) were smoothed using a Gaussian filter with a FWHM=4mm. Following ex-vivo MRI, all hemispheres underwent detailed neuropathologic examination. The assessed pathologies included atherosclerosis, arteriolosclerosis, cerebral amyloid angiopathy, gross and microscopic infarcts, Alzheimer's pathology, Lewy bodies, limbic-predominant age-related TDP-43 encephalopathy neuropathological change(LATE-NC), and hippocampal sclerosis. Statistical Analyses: Voxel wise linear regression was used to test the association of atherosclerosis with deformations shown in the smoothed LogJ maps, controlling for other age-related neuropathologies(Alzheimer's pathology, Lewy bodies, limbic-predominant age-related TDP-43 encephalopathy(LATE), hippocampal sclerosis, arteriolosclerosis, cerebral amyloid angiopathy, gross infarcts, microscopic infarcts), demographics(age at death, sex, years of education), postmortem interval to fixation, postmortem interval to imaging, and scanner(Fig.1). The FSL PALM tool with 1000 permutations, threshold-free cluster enhancement, and tail acceleration was used for the statistical analysis[9]. Associations were considered significant at $p<0.05$ after family-wise error rate(FWER) correction for multiple comparisons.

Fig. 1a

Characteristics	
N	891
Age at death, y (SD)	90.6 (6.4)
Male, n (%)	251 (28.1)
Education, y (SD)	15.75 (3.5)
Antemortem clinical diagnosis[a]	
No cognitive impairment	290 (32.5)
Mild cognitive impairment	205 (23.0)
Dementia	396 (44.4)
Mini-Mental State Examination[a] (MMSE), mean (SD)	19.89 (9.6)
At least one copy of the ε4 allele, n (%)	225 (25.3)
Left hemisphere, n (%)	482 (54.1)
Postmortem interval to fixation, h (SD)	9.59 (6.9)
Postmortem interval to imaging, d (SD)	36.63 (16.4)
Scanner for ex vivo MRI, n (%)	
3T GE Signa	75 (8.4)
3T Siemens Trio	81 (9.1)
3T Philips Achieva	278 (31.2)
3T Siemens Verio	457 (51.3)

[a]Proximate to death

Fig. 1b

Characteristics	
N	891
Atherosclerosis, n (%)	
None	192 (21.6)
Mild	474 (53.2)
Moderate	182 (20.4)
Severe	43 (4.8)
LATE-NC, n (%)	
(stage 0) no TDP-43 inclusion	391 (43.9)
(stage 1) TDP-43 inclusions in amygdala only	158 (17.7)
(stage 2) TDP-43 inclusions in amygdala and entorhinal cortex or hippocampus	100 (11.2)
(stage 3) TDP-43 inclusions in amygdala, entorhinal cortex or hippocampus, and neocortex	242 (27.2)
AD-NC (NIA-AA criteria), n (%)	
None	109 (12.2)
Low	169 (18.9)
Intermediate	385 (43.2)
High	228 (25.6)
Lewy bodies, n (%)	256 (28.7)
Gross infarcts, n (%)	364 (40.9)
Microscopic infarcts, n (%)	345 (38.7)
Cerebral amyloid angiopathy, n (%)	
None	185 (20.8)
Mild	378 (42.4)
Moderate	221 (24.8)
Severe	109 (12.2)
Arteriolosclerosis, n (%)	
None	192 (21.6)
Mild	474 (53.2)
Moderate	182 (20.4)
Severe	128 (14.4)

AD-NC, Alzheimer's Disease neuropathological change; LATE-NC, Limbic predominant age-related transactive response DNA binding protein 43 (TDP-43) encephalopathy neuropathological change; NIA-AA, National Institute on Aging-Alzheimer's Association.

Fig.1a: Demographic and clinical characteristics of the participants; 1b: Neuropathologic characteristics of the participants

Results: Voxel-wise linear regression showed that intracranial atherosclerosis was significantly associated with lower volume in the posterior body and tail of the hippocampus($p<0.05$), independently of the effects of other age-related neurodegenerative and vascular pathologies(Fig.2). No part of the brain showed significantly higher volume with atherosclerosis. This suggests that intracranial atherosclerosis is associated with focal neurodegeneration of the posterior portion of the hippocampus, sparing other brain tissues.

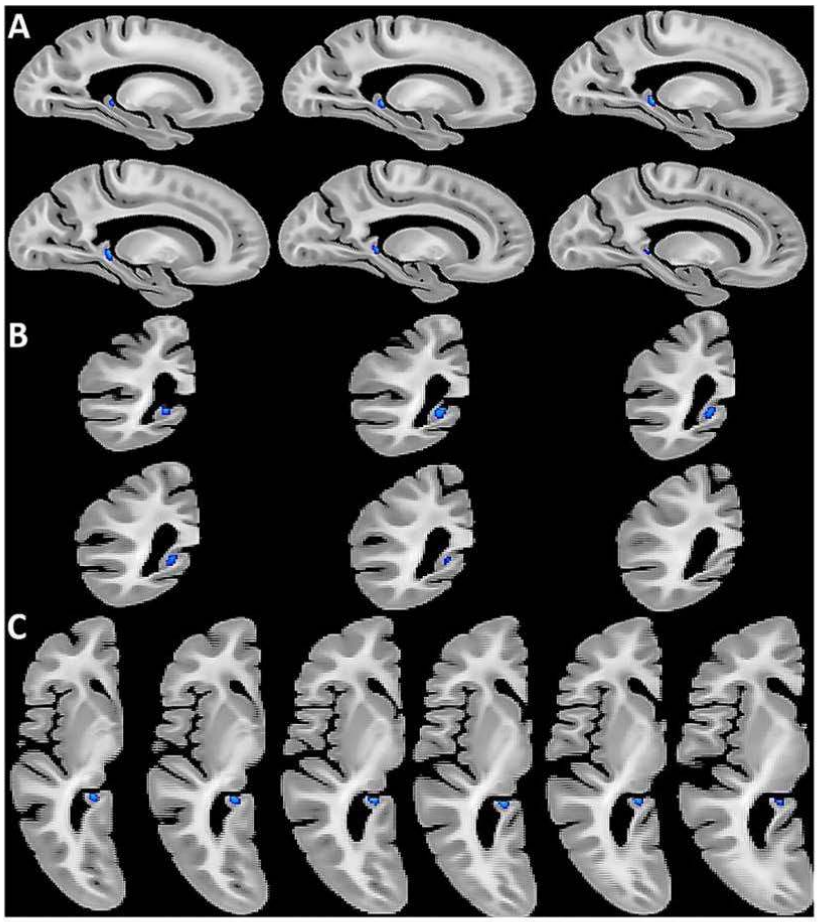

Fig. 2: Maps of p-values (blue color scale) showing a region in the posterior body and tail of the hippocampus exhibiting lower volume for higher intracranial atherosclerosis severity. A - Sagittal Plane, B – Coronal Plane, C – Axial Plane

Conclusions: This work combined DBM on ex-vivo MRI with detailed neuropathologic examination in a large number of community-based older adults and demonstrated that intracranial atherosclerosis is associated with lower volume of the posterior body and tail of the hippocampus. Atherosclerosis is often mixed with Alzheimer's pathology and/or LATE neuropathological change, which have previously shown independent associations with lower hippocampal volume. Hippocampal volume by itself cannot serve as a reliable marker of any of the three pathologies, but more localized metrics of hippocampal atrophy may potentially provide higher specificity.

References

1. Arvanitakis, Zoe, Ana W. Capuano, Sue E. Leurgans, David A. Bennett, and Julie A. Schneider. 2016. "Relation of Cerebral Vessel Disease to Alzheimer's Disease Dementia and Cognitive Function in Older Persons: A Cross-Sectional Study." The Lancet. Neurology 15 (9): 934–43.
2. Avants, Brian B., Nicholas J. Tustison, Gang Song, Philip A. Cook, Arno Klein, and James C. Gee. 2011. "A Reproducible Evaluation of ANTs Similarity Metric Performance in Brain Image Registration." NeuroImage 54 (3): 2033–44.
3. Barnes, Lisa L., Raj C. Shah, Neelum T. Aggarwal, David A. Bennett, and Julie A. Schneider. 2012. "The Minority Aging Research Study: Ongoing Efforts to Obtain Brain Donation in African Americans without Dementia." Current Alzheimer Research 9 (6): 734–45.
4. Bennett, David A., Aron S. Buchman, Patricia A. Boyle, Lisa L. Barnes, Robert S. Wilson, and Julie A. Schneider. 2018. "Religious Orders Study and Rush Memory and Aging Project." Journal of Alzheimer's Disease: JAD 64 (s1): S161–89.
5. Dearborn, Jennifer L., Yiyi Zhang, Ye Qiao, Muhammad Fareed K. Suri, Li Liu, Rebecca F. Gottesman, Andreea M. Rawlings, et al. 2017. "Intracranial Atherosclerosis and Dementia: The Atherosclerosis Risk in Communities (ARIC) Study." Neurology 88 (16): 1556–63.
6. Gaser, C., I. Nenadic, B. R. Buchsbaum, E. A. Hazlett, and M. S. Buchsbaum. 2001. "Deformation-Based Morphometry and Its Relation to Conventional Volumetry of Brain Lateral Ventricles in MRI." NeuroImage 13 (6 Pt 1): 1140–45.
7. Gorelick, Philip B., Angelo Scuteri, Sandra E. Black, Charles Decarli, Steven M. Greenberg, Costantino Iadecola, Lenore J. Launer, et al. 2011. "Vascular Contributions to Cognitive Impairment and Dementia: A Statement for Healthcare Professionals from the American Heart Association/American Stroke Association." Stroke 42 (9): 2672–2713.
8. Kapasi, Alifiya, Charles DeCarli, and Julie A. Schneider. 2017. "Impact of Multiple Pathologies on the Threshold for Clinically Overt Dementia." Acta Neuropathologica 134 (2): 171–86.
9. Winkler, Anderson M., Gerard R. Ridgway, Matthew A. Webster, Stephen M. Smith, and Thomas E. Nichols. 2014. "Permutation Inference for the General Linear Model." NeuroImage 92 (100): 381–97.

Poster No 167

Prediction of Motor Symptom Progression in Parkinson's Disease Using Diffusion Tensor Imaging

Yi-Ching Chen[1], Albert Yang[1,2,3,4]

[1]Institute of Brain Science, National Yang Ming Chiao Tung University, Taipei City, Taiwan, [2]Digital Medicine and Smart Healthcare Research Center, National Yang Ming Chiao Tung University, Taipei CIty, Taiwan, [3]Department of Medical Research, Taipei Veterans General Hospital, Taipei CIty, Taiwan, [4]Brain Research Center, National Yang Ming Chiao Tung University, Taipei CIty, Taiwan

Introduction: Parkinson's disease (PD) is a common neurodegenerative disease primarily characterized by motor symptoms. Previous studies have shown that individuals with early-stage PD exhibited white matter microstructural abnormalities in specific brain regions compared to healthy controls (HCs). Diffusion tensor imaging (DTI) enables the quantification of the integrity of white matter tracts by calculating parameters such as fractional anisotropy (FA) and mean diffusivity (MD). Notably, alterations in FA and MD have been demonstrated to correlate with the progression of PD. However, the progression of motor symptoms in PD is typically assessed using clinical assessments, and brain biomarkers for predicting motor symptom progression remain unidentified. Using a machine learning approach to predict the progression of motor symptoms in PD could lead to more precise and personalized clinical treatment strategies. Therefore, this study aimed to integrate a machine learning approach with DTI to construct the predictive model that identified the brain biomarkers linking white matter microstructural with the progression of motor symptoms in PD.

Methods: We sourced the DTI data from the Parkinson's Progression Markers Initiative database, including 127 individuals with PD with an average disease duration of 8.46 months (average age of 60.86 years; 66.14% in males) and 60 HCs (average age of 60.32 years; 61.67% in males). We segmented the DTI data using the JHU-ICBM-labels-1mm atlas into 48 fiber tracts and calculated voxel-based FA and MD for all participants. We performed a general linear regression (GLM) to find the white matter tracts that exhibited significantly lower FA and higher MD in the PD group than those of the HC group. Next, individuals with PD were divided into worsening and improving groups based on changes in their total scores from Part III of the MDS-Unified Parkinson's Disease Rating Scale (MDS-UPDRS-III) over a two-year period. Furthermore, we constructed a total of 96 CatBoost classification models using voxel-based FA and MD maps of white matter tracts. These models were constructed separately for each FA and MD map. Concurrently, we incorporated demographic and clinical features such as sex, age, total score from MDS-UPDRS-III, and medication history into these models. Finally, the model performance was assessed based on accuracy and F1 score.

Results: We observed lower FA in the middle cerebellar peduncle and bilateral corticospinal tract, while higher MD in the middle cerebellar peduncle and bilateral inferior cerebellar peduncle in the PD group compared to the HC group. We subsequently constructed 96 models to classify the worsening and improving of motor symptoms progression. Among these models, those achieving an accuracy exceeding 70% were characterized by the FA in various white matter tracts, including the right corticospinal tract, right anterior corona radiata, left superior corona radiata, right cingulum, right fornix, and right superior longitudinal fasciculus. Models incorporating MD in the right anterior corona radiata, right superior longitudinal fasciculus, and bilateral tapetum also exhibited accuracy above 70%. Notably, The FA of the right corticospinal tract not only had a significant difference between PD and HC groups by GLM but also demonstrated effectiveness in predicting the progression of motor symptoms in PD with an accuracy of 70.26% and an F1 score of 82.11%.

Conclusions: This study focused on investigating the progression of motor symptoms in PD with DTI characteristics. We constructed classification models to effectively differentiate between worsening and improving motor symptoms in individuals with PD. Importantly, the fiber tracts identified with higher accuracy might be associated with motor symptoms in PD. In conclusion, our study revealed specific DTI indices associated with the progression of motor symptoms in PD. These findings may potentially enhance clinical diagnosis and the assessment of disease progression.

References

1. Abbasi, N. (2020), 'Predicting severity and prognosis in Parkinson's disease from brain microstructure and connectivity', NeuroImage Clinical, vol. 25, pp. 102111
2. Kim, J. Y. (2022), 'White Matter Microstructural Alterations in Newly Diagnosed Parkinson's Disease: A Whole-Brain Analysis Using dMRI', Brain sciences, vol. 12, no. 2, pp. 22
3. Xia, R. (2012), 'Progression of motor symptoms in Parkinson's disease', Neuroscience bulletin, vol. 28, no. 1, pp. 39–48
4. Zhang, Y. (2020), 'Diffusion Tensor Imaging in Parkinson's Disease and Parkinsonian Syndrome: A Systematic Review', Frontiers in neurology, vol. 11, pp. 531993

Poster No 168

Sleep quality and Brain glucose uptake in Middle-aged Healthy subjects

Kyoungjune Pak[1], Seunghyeon Shin[2], Hyun Yeol Nam[3]

[1]179 Gudeok-ro, Seo-gu, Busan 49241, Republic of Korea, Busan, Busan, [2]Samsung Changwon Hospital, Changwon, Changwon, [3]Samsung Changwon Hospital, Changwon, [3]Department of Nuclear Medicin

Introduction: Short sleep duration and poor sleep quality is associated with greater amyloid beta burden and an increased risk of dementia. Also, even one night of sleep deprivation increases amyloid beta accumulation. In this study, we investigate the association of sleep quality with brain glucose uptake (BGU) measured by F18-Fluorodeoxyglucose positron emission tomography (PET) in middle-aged healthy subjects.

Methods: We retrospectively analyzed data from 378 healthy males who underwent health check-up: 1) 18F-FDG PET, 2) Pittsburgh Sleep Quality Index Korean version (PSQI-K). PET scans were acquired 60 mins after injection of 18F-FDG (3.7 MBq/kg). PET scans were spatially normalized to MNI space using PET templates from SPM5. Automated Anatomical Label 2 atlas was used to define region-of-interests (ROIs). The mean uptake of each ROI was scaled to the mean of global cortical uptake of each individual, and defined as standardized uptake value ratio (SUVR). For a full-volume analysis, the statistical threshold was set at a cluster level and corrected with false discovery rate with $p < 0.05$ in a regression model (correction with age) after smoothing SUVR images with a Gaussian kernel of FWHM 8mm (SPM 12). All subjects completed PSQI-K to assess subjective quality and sleep pattern. Each of the questionnaire's 19 self-reported items belongs to one of seven subcategories: subjective sleep quality, sleep latency, sleep duration, habitual sleep efficiency, sleep disturbances, use of sleeping medication, and daytime dysfunction. Scores for each question range from 0 to 3, with higher scores indicating more acute sleep disturbances, ranging from 0 to 21. The effects of sleep quality on regional SUVR were investigated using Bayesian hierarchical modelling that applies the Markov-Chain Monte Carlo sampling. We set up a model with regional SUVR as a dependent variable and PSQI-K as predictors. These fixed effects (PSQI-K and age) were calculated individually and subject and ROI were added as random intercepts to allow SUVR to vary between subjects and ROIs. Bayesian models were estimated using four Markov chains, each of which had 4,000 iterations including 1,000 warm-ups, thus totaling 12,000 post-warmup samples. The sampling parameters were slightly modified to facilitate convergence (max treedepth = 20).

Results: 378 subjects were included in this study (mean age 42.8, range 38-50 years). The average of total PSQI-K score was 4.0, ranging from 0 to 12. The average 9 sleep duration PSQI-K scores for each category were 1.0 (subjective sleep quality), 0.8 (sleep latency), 0.9 (sleep duration), 0.2 (habitual sleep efficiency), 0.6 (sleep disturbances), 0 (use of sleeping medication), 0.6 (daytime dysfunction). From a Bayesian regression model, BGU of posterior cingulate, precuneus, thalamus was negatively associated with total PSQI-K score (Figure 1). In a subgroup model with each category of PSQI-K, BGU of precuneus and posterior cingulate was negatively associated with all categories of PSQI-K except for sleep disturbances. Full-volume analysis revealed the consistent finding that shows negative association of BGU of posterior cingulate, precuneus, thalamus, postcentral gyrus in middle-aged healthy males (Figure 2).

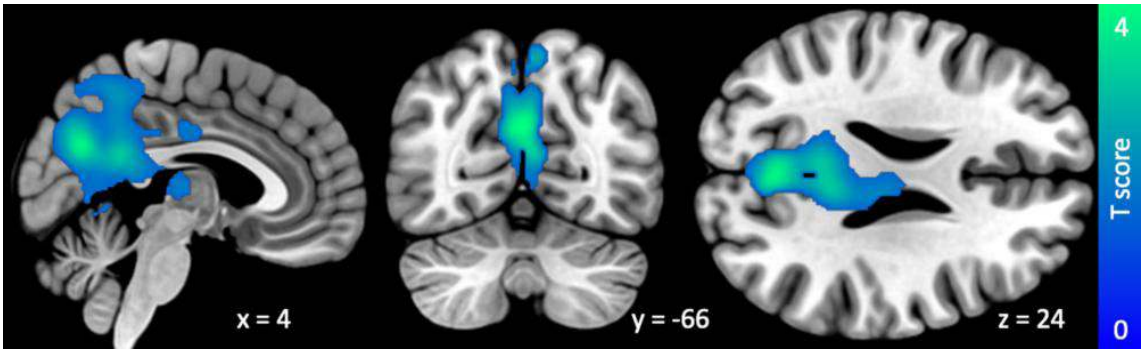

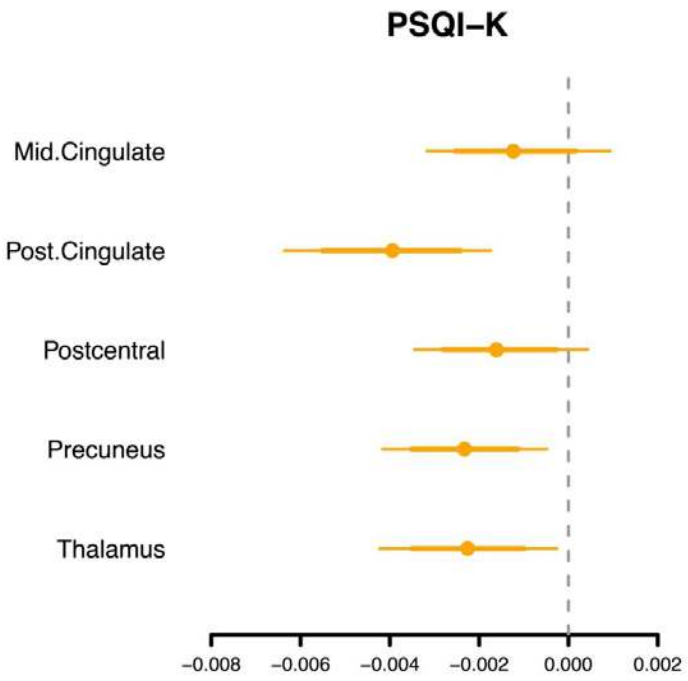

Conclusions: The poor sleep quality is associated with lower BGU of precuneus and posterior cingulate in middle-aged healthy males, which are main findings of dementia. Therefore, sleep might be one of the key components of pathophysiology of dementia. In addition, even in healthy subjects, the importance of sleep quality should not be ignored.

References

1. Association of sleep duration in middle and old age with incidence of dementia.
2. Sabia S, Fayosse A, Dumurgier J, van Hees VT, Paquet C, Sommerlad A, Kivimäki M, Dugravot A, Singh-Manoux A.Nat Commun. 2021 Apr 20;12(1):2289
3. β-Amyloid accumulation in the human brain after one night of sleep deprivation.
4. Shokri-Kojori E, Wang GJ, Wiers CE, Demiral SB, Guo M, Kim SW, Lindgren E, Ramirez V, Zehra A, Freeman C, Miller G, Manza P, Srivastava T, De Santi S, Tomasi D, Benveniste H, Volkow ND.Proc Natl Acad Sci U S A. 2018 Apr 24;115(17):4483-4488
5. Sleep and Neuroimaging.
6. Pak K, Kim J, Kim K, Kim SJ, Kim IJ.Nucl Med Mol Imaging. 2020 Apr;54(2):98-104

Poster No 169

Time-series analysis of processing speed indicates multiple cortical atrophy in multiple sclerosis

Shu Umezawa[1], Yuki Matsumoto[2], Yasuko Tatewaki[3], Naohiro Sakamoto[2], Naoki Yamamoto[2], Naoya Yamazaki[2], Chihiro Namatame[2], Hirohiko Ono[2], Kimihiko Kaneko[2], Yoshiki Takai[2], Hiroshi Kuroda[4], Kazuo Fujihara[4], Tatsuro Misu[2], Yasuyuki Taki[3], Masashi Aoki[2]

[1]Department of Neurology, Graduate School of Medicine, Tohoku University, Sendai, Miyagi, [2]Department of Neurology, Tohoku University Hospital, Sendai, Miyagi, [3]Department of Aging Research and Geriatric Medicine, Tohoku University Hospital, Sendai, Miyagi, [4]Department of Multiple Sclerosis Therapeutics, Fukushima Medical University, Fukushima, Fukushima

Introduction: The information processing speed (IPS) test, such as the Symbol-Digit Modalities Test (SDMT), is a brief cognitive test widely used to assess IPS. It is also included in the Brief International Cognitive Assessment for Multiple Sclerosis (BICAMS), one of the major cognitive batteries for patients with multiple sclerosis (MS). These assessments often aid neurologists in selecting treatment strategies for MS patients. Many psychological and functional magnetic resonance imaging studies previously suggested that the task involves various cognitive functions, including working memory (WM) and decision-making (DM). Consequently, the conventional IPS test scores are considered to reflect the composites of these cognitive functions, and they cannot separately evaluate multiple functions related to the test. Here, we examined our patients using the conventional IPS test and an electrically-presented IPS test program we developed (information processing acceleration test, or IPAT). IPAT is designed to measure IPS for each single symbol presented in a trial. We compared IPAT performance with the

conventional IPS test to validate its effectiveness. From the time-series IPS data collected, we estimated coefficients reflecting WM and DM and their associations with cerebral cortical atrophy.

Methods: In this preliminary study, ten patients with relapsing-remitting MS participated. Each patient was assessed using both the conventional IPS test and IPAT. Structural brain MRI data were acquired within a month of the cognitive assessment. We compared the accomplishment scores of IPAT with those of the conventional IPS tests to ensure IPAT validity. Subsequently, we calculated IPS, which is the inverse of each reaction time for every single trial that the patients took for the stimulus presented. A nonlinear regression model was applied to these time-series IPS data, and we estimated two coefficients: one indicative of corrected IPS in the plateau phase (p) and another representing IPS acceleration rate (a). The patients' T1-weighted brain images underwent preprocessing with the sMRIPrep pipeline before analyzed with FreeSurfer (6.0.0) for surface-based morphometry. The association between the coefficients and cortical atrophy was examined using a multiple regression model.

Results: The conventional IPS accomplishment score correlated linearly with those obtained from IPAT. Analysis of the time-series IPS data from IPAT revealed an initial adaptive phase with increased IPS, followed by a plateau phase where IPS stayed at the level. The nonlinear regression analysis estimated curves that closely fit with the observed IPS patterns. Notably, the coefficients p for the corrected IPS in the plateau were significantly correlated with cortical thickness in the right suborbital sulci. Moreover, the coefficients a for IPS acceleration rate showed significant correlations with regions in the left parahippocampal gyrus and the right superior parietal gyrus ($p<0.05$).

Conclusions: The conventional IPS test serves as a helpful tool for roughly grasping the declined IPS of patients with MS, but the score is composed of multiple functions. In our preliminary study, the IPAT program, developed by our team, effectively assesses IPS comparably to the conventional test. Furthermore, we were able to decompose the observed time-series IPS into two distinctive phases: an adaptive phase marked by accelerating IPS and a subsequent plateau phase. We extracted coefficients representing these phases linked with WM and DM functions, respectively. These two coefficients were associated with cortical atrophy in the regions known to play roles in these cognitive functions. After accumulating data from MS patients at various stages longitudinally, we hope to use the IPAT for a more detailed evaluation of cognitive functions to support clinical decision-making for treatment.

References

1. Benedict, R. H. B. (2020). 'Cognitive impairment in multiple sclerosis: clinical management, MRI, and therapeutic avenues', The Lancet. Neurology, 19(10), 860–871

Poster No 170

FMRI exposes visual deficits in a progressive stage of a Parkinson's Disease mouse model

Ruxanda Baiao[1], Francisca Fernandes[1], Sara Monteiro[1,2], Patricia Figueiredo[2], Tiago Outeiro[3], Noam Shemesh[1]

[1]Champalimaud Research, Champalimaud Foundation, Lisbon, Portugal, [2]Instituto Superior Técnico, Universidade de Lisboa, Lisboa, Portugal, [3]Department of Experimental Neurodegeneration, University of Göttingen, Göttingen, Göttingen

Introduction: Parkinson's disease (PD) is marked by α-synuclein aggregates, brain volume reduction, and declines in motor and cognitive functions1. With 70% of PD patients exhibiting diminished visual acuity2,3, there's evidence of involvement in sensory systems. While the αSYN mouse model has been extensively studied at molecular5,6,7 and behavioral8 levels, its functional deficits remain ambiguous. Our investigation utilizes fMRI to delve into potential impairments in the visual pathway. Through validation via C-FOS expression9 and pCASL mapping10, our study aims to deepen our understanding of the functional implications within PD pathology.

Methods: All animal experimentation procedures received prior approval from both institutional and national authorities in adherence to European Directive 2010/63. Animal subjects included the transgenic αSYN mouse model11 (C57BL/6-DBA/2Thy1-αSYN) and their corresponding wildtype littermates, aged 39±3 weeks and weighing approximately 42g±15g. Visual fMRI experiments were performed under medetomidine sedation on a 9.4T Bruker BioSpec scanner; Binocular stimulation was executed12 in mice (N=12/13 PD/WT) using two blue LEDs (λ=470nm) placed above the eyes, alternating between rest (40 seconds) and stimulation (20 seconds) at a frequency of 1Hz during the fMRI design. fMRI acquisitions used GE-EPI with TR/TE=1250/12ms, FOV=15x12mm^2, resolution=150×150µm^2, slice thickness=0.45mm (10slices). Data preprocessing, GLM activation mapping, and ROI analysis13 were performed using SPM12. C-FOS expression was quantified through immunohistochemistry9 from other N=6/6 PD/WT animals. In a separate cohort (N=3/3 PD/WT) a pCASL sequence10 was used for high-resolution (100x100µm^2) CBF mapping under isoflurane sedation.

Results: Following visual stimulation, healthy controls exhibited strong activation in the visual pathway (Fig.1A). In contrast, PD mice showed lower t-statistics and reduced activation compared to controls. Anatomically placed ROIs in key visual pathway structures (Fig.1B) supported these findings, displaying significant reductions in fMRI signals across most areas in PD mice, with a control area showing no notable differences. C-FOS protein expression analysis revealed marked reductions in protein expression across all visual areas compared to WT controls (Fig.2A). However, in a control ROI (entorhinal cortex), no significant differences were observed between groups (Fig.2A-iv). Preliminary CBF measurements aimed at detecting vascular differences showed no significant distinctions (Fig.2B). It's important to note that our scanning protocol involved only 3 animals per group, potentially limiting the detection of small effect sizes.

Conclusions: This extensive study unveiled deficiencies in fMRI signals across the entire visual pathway, validated by neuronal origins through C-FOS experiments and pCASL. Initial CBF measurements eliminated potential vascular differences14, indicating that observed functional map variances predominantly arise from other factors. This suggests reduced neuronal activity within the visual regions in 9-month PD mice, potentially linked to αSyn aggregation and ensuing impairments. The study conducted fMRI at a late PD stage; future research aims to explore the evolution of these deficits longitudinally. Correlation with C-FOS and CBF mapping bolstered the understanding of our BOLD-fMRI results, encouraging further investigation into sensory deficits and early PD biomarkers.

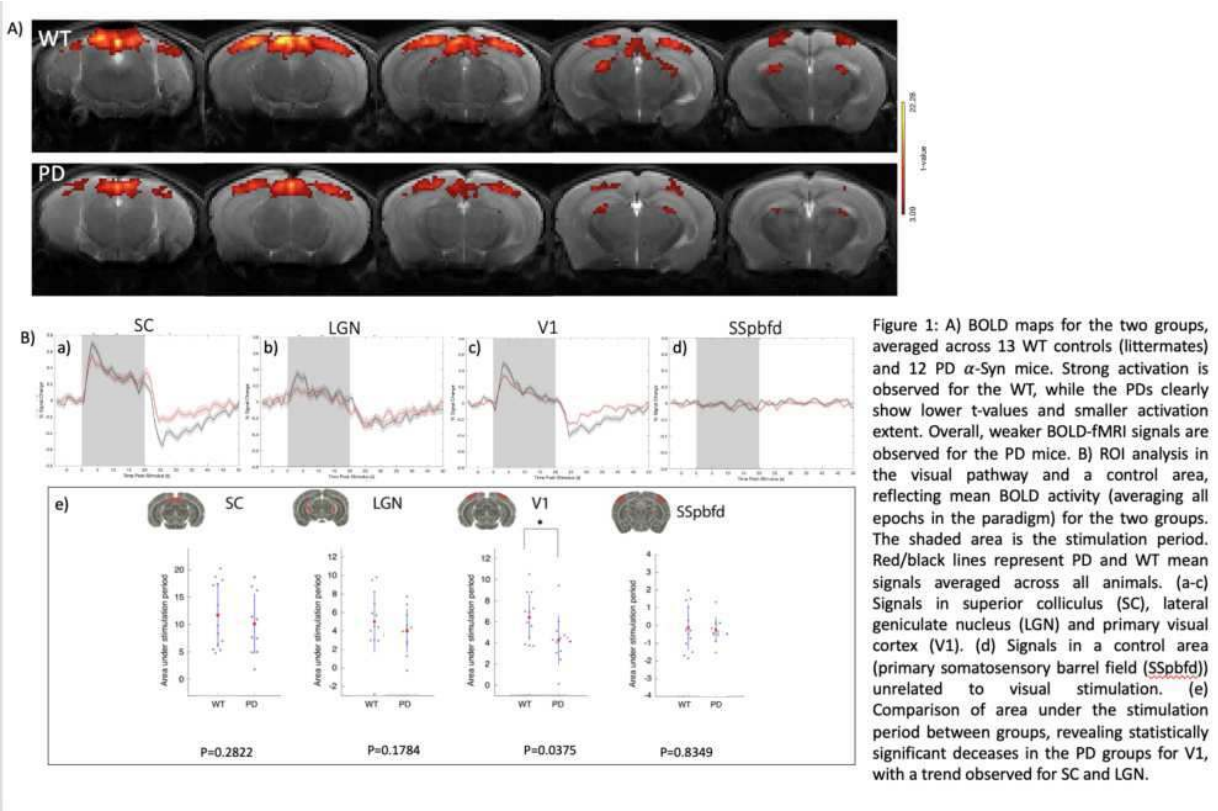

Figure 1: A) BOLD maps for the two groups, averaged across 13 WT controls (littermates) and 12 PD α-Syn mice. Strong activation is observed for the WT, while the PDs clearly show lower t-values and smaller activation extent. Overall, weaker BOLD-fMRI signals are observed for the PD mice. B) ROI analysis in the visual pathway and a control area, reflecting mean BOLD activity (averaging all epochs in the paradigm) for the two groups. The shaded area is the stimulation period. Red/black lines represent PD and WT mean signals averaged across all animals. (a-c) Signals in superior colliculus (SC), lateral geniculate nucleus (LGN) and primary visual cortex (V1). (d) Signals in a control area (primary somatosensory barrel field (SSpbfd)) unrelated to visual stimulation. (e) Comparison of area under the stimulation period between groups, revealing statistically significant deceases in the PD groups for V1, with a trend observed for SC and LGN.

References

1. Calabresi P, Di Filippo M. The changing tree in Parkinson's disease. Nat Neurosci. Published online 2015. doi:10.1038/nn.4092
2. Haehner A, Hummel T, Reichmann H. Olfactory loss in parkinson's disease. Park Dis. Published online 2011. doi:10.4061/2011/450939
3. Urwyler P, Nef T, Killen A, et al. Visual complaints and visual hallucinations in Parkinson's disease. Parkinsonism Relat Disord. 2014;20(3):318-322. doi:10.1016/j.parkreldis.2013.12.009
4. Armstrong RA. Visual Symptoms in Parkinson's Disease. Park Dis. 2011;2011:1-9. doi:10.4061/2011/908306
5. Cong L, Muir ER, Chen C, et al. Multimodal MRI evaluation of the mitopark mouse model of Parkinson's disease. PLoS ONE. Published online 2016. doi:10.1371/journal.pone.0151884
6. Yao L, Wu J, Koc S, Lu G. Genetic Imaging of Neuroinflammation in Parkinson's Disease: Recent Advancements. Front Cell Dev Biol. 2021;9. doi:10.3389/fcell.2021.655819
7. Hisahara S, Shimohama S. Toxin-Induced and Genetic Animal Models of Parkinson's Disease. Park Dis. 2011;2011. doi:10.4061/2011/951709
8. Campos FL, Carvalho MM, Cristovão AC, et al. Rodent models of Parkinson's disease: beyond the motor symptomatology. Front Behav Neurosci. 2013;7. doi:10.3389/fnbeh.2013.00175
9. Perrin-Terrin AS, Jeton F, Pichon A, et al. The c-FOS Protein Immunohistological Detection: A Useful Tool As a Marker of Central Pathways Involved in Specific Physiological Responses In Vivo and Ex Vivo. J Vis Exp. 2016;(110):53613. doi:10.3791/53613
10. Hirschler L, Debacker CS, Voiron J, Köhler S, Warnking JM, Barbier EL. Interpulse phase corrections for unbalanced pseudo-continuous arterial spin labeling at high magnetic field. Magn Reson Med. 2018;79(3):1314-1324. doi:10.1002/mrm.26767

11. Hansen C, Angot E, Bergström AL, et al. α-Synuclein propagates from mouse brain to grafted dopaminergic neurons and seeds aggregation in cultured human cells. J Clin Invest. 2011;121(2):715-725. doi:10.1172/JCI43366
12. Gil R, Fernandes FF, Shemesh N. Neuroplasticity-driven timing modulations revealed by ultrafast functional magnetic resonance imaging. NeuroImage. Published online 2021. doi:10.1016/j.neuroimage.2020.117446
13. 'Keith F, 'George P. Atlas of the Developing Mouse Brain. Vol 1. (Academic Press, ed.). Academic Press; 2019.
14. Biju K, Shen Q, Hernandez ET, Mader MJ, Clark RA. Reduced cerebral blood flow in an α -synuclein transgenic mouse model of Parkinson's disease. J Cereb Blood Flow Metab. 2020;40(12). doi:10.1177/0271678X19895432

Poster No 171

In Vivo Neurological Signatures of Chronic Traumatic Encephalopathy: An MRI study of QSM and MRS

Pamela González Méndez[1,2], Elías Alfaro Nasta[1,2], Aline Xavier[3], Marisleydis García-Saborit[3,4,5], Carlos Juri Clavería[1], Juan Tichauer[6], Carlos Milovic[7], Marcelo Andía Kohnenkampf[1,2,5], Maximiliano Rovegno Echavarría[1,6], Waldo Cerpa Nebott[8]

[1]School of Medicine, Pontificia Universidad Catolica de Chile, Santiago, Chile, [2]Millennium Institute for Intelligent Healthcare Engineering - iHEALTH, Santiago, Chile, [3]Faculty of Engineering, Universidad de Santiago de Chile, Santiago, Chile, [4]Department of Electrical Engineering, Pontificia Universidad Catolica de Chile, Santiago, Chile, [5]Biomedical Imaging Center, Pontificia Universidad Catolica de Chile, Santiago, Chile, [6]Department of Intensive Care Medicine, Pontificia Universidad Catolica de Chile, Santiago, Chile, [7]School of Electrical Engineering, Pontificia Universidad Catolica de Valparaiso, Valparaiso, Chile, [8]Faculty of Biological Sciences, Pontificia Universidad Catolica de Chile, Santiago, Chile

Introduction: Chronic Traumatic Encephalopathy (CTE) is a neurodegenerative condition associated with repeated brain trauma, often seen in former players of contact sports including soccer. It presents a range of symptoms, such as cognitive impairments and behavioral changes. The diagnosing of CTE is challenging due to the absence of definitive in vivo biomarkers, relying on postmortem confirmation (McKee A.C., Acta Neuropathol. 2023). This limitation has hindered the comprehension of CTE's progression and the development of proactive intervention strategies. Advanced Magnetic Resonance Imaging (MRI) techniques, such as Quantitative Susceptibility Mapping (QSM) and Magnetic Resonance Spectroscopy (MRS) have the potential to address this challenge. QSM is used to quantify iron deposition in the brain, which may indicate oxidative stress, a crucial element in neurodegenerative diseases (Ward R.J., Lancet Neurol. 2014). MRS assesses metabolic alterations, offering insights into cellular pathophysiology, particularly in the diffuse brain injury common in CTE. We aim to enhance our understanding of CTE's in vivo pathology and contribute to the development of non-invasive diagnostic approaches. This research carries significant implications for early detection and management of CTE in populations at high risk.

Methods: Using a cross-sectional design, we analyzed 10 former professional soccer players under 65 yrs, retired for +8 yrs, with a history of repeated head trauma. We reconstructed QSM and R2* maps from a 3D Gradient Recalled Echo sequence. QSM pipeline: ROMEO (Dymerska B., Magn Res Med. 2021) unwrapping, PDF background field removal (Liu T., NMR Biomed. 2011), and FANSI dipole inversion (Milovic C., Magn Res Med. 2018). Both, QSM and R2* are used to confirm iron deposition (Yan F., JMRI 2018). For registration and segmentation, we used SPM 12 (WCHN, UCL) and FSL (FMRIB, Oxford), respectively. Single Voxel Spectroscopy (PRESS, TE = 35 ms, voxel size 3x3x3 cm) was acquired at the posterior cingulate gyrus (PCG) and used for metabolite quantification using LCModel (Provencher). We also included the Up and Go motor test and the telephonic Montreal Cognitive Assessment (MOCA). We examined QSM maps in 15 subcortical areas and metabolite concentrations at the PCG, a region key for cognition and part of the default mode network (Leech and Sharp, BRAIN 2014). We used Spearman's correlations to associate MRI findings with cognitive and motor function, and descriptive statistics to identify patterns. Using data from QSM and MRS, we performed a dimensionality reduction analysis with the Robust-PCA methodology through the rpca library of the R statistical package (RStudio 2023) and analyzed the data separated into two groups (high and low risk by position on the playing field). Funding: ANID-ICN2021_004.

Results: We found a correlation between higher QSM values at the left pallidum and reduced cognitive function (Spearman's r = -0.67). Also, a positive correlation between QSM and R2* values (Spearman's r = 0.78) was observed. We described a metabolic pattern; particularly, low NAA+NAAG was linked to poor motor performance (Spearman's r = -0.75). Notably, the data are distributed into 2 clusters, the first of them only with high-risk individuals, and the second with a predominance of lower-risk individuals. High risk: central defense. (Fig.1-2)

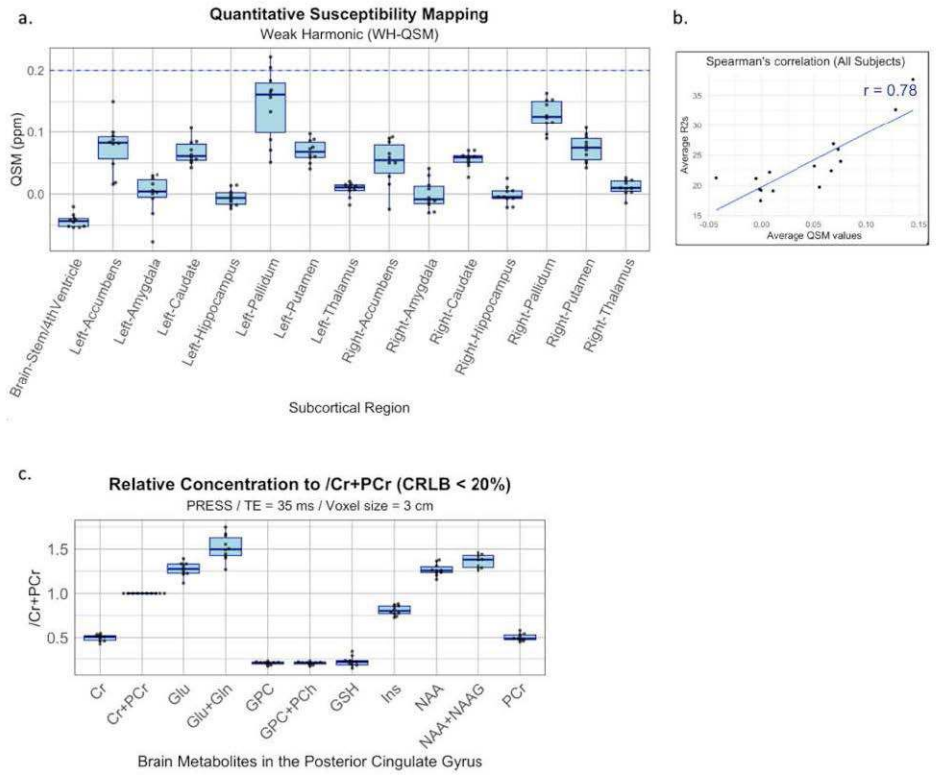

Figure 1. In vivo MRI in Former Soccer Players. a. Tissue susceptibility (QSM), ≥0.2 ppm high QSM values. b. QSM vs R2*(all regions). c. MRS, metabolites concentration /tCr (NAA, NAA+NAAG <1.5). n=10.

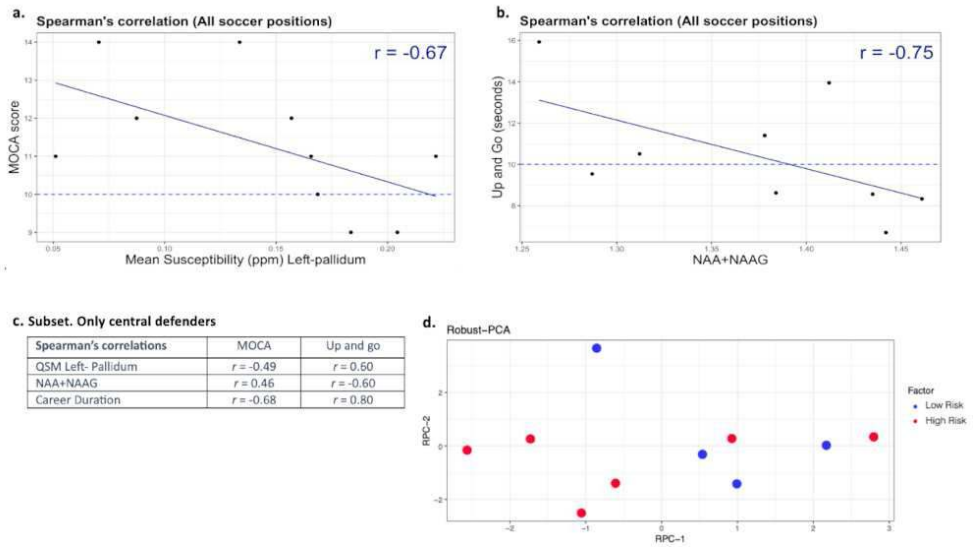

Spearman's correlations	MOCA	Up and go
QSM Left- Pallidum	r = -0.49	r = 0.60
NAA+NAAG	r = 0.46	r = -0.60
Career Duration	r = -0.68	r = 0.80

Figure 2. a. NAA+NAAG vs Up and Go (<10s normal). b. QSM vs MOCA (≤ 10 mild cognitive impairment). n=10. c. Corr. only central defenders. d. High risk: position on the playing field: central defense.

Conclusions: We explored CTE signatures in vivo using MRI. QSM values at the left pallidum were higher than the ones found in control brains and similar to those seen in Parkinson's disease (Shahmaei V., Eur. J. Radiol. 2019). Lower NAA/tCr and NAA+NAAG/tCr at the PCG suggested neuronal damage compared with healthy subjects (Wijtenburg S.A., NMR Biomed. 2019). We found signatures correlated with motor and cognitive changes. The R-PCA analysis suggests that our in-vivo methodology would be able to differentiate high and lower-risk groups. Our study aims to advance a better understanding of CTE and the development of early detection methods.

References

1. Dymerska B. (2021), 'Phase unwrapping with a rapid opensource minimum spanning tree algorithm (ROMEO) '. Magnetic Resonance in Medicine. Apr;85(4):2294–308.

2. Leech R. and Sharp D.J. (2014), 'The role of the posterior cingulate cortex in cognition and disease'. Brain. Jan;137(Pt 1):12–32.
3. Liu T. (2011), 'A novel background field removal method for MRI using projection onto dipole fields (PDF)'. NMR in Biomedicine. Nov;24(9):1129–36.
4. McKee A.C. (2023), 'Chronic traumatic encephalopathy (CTE): criteria for neuropathological diagnosis and relationship to repetitive head impacts', Acta Neuropathology. Apr;145(4):371–94.
5. Milovic C. (2018), 'Fast nonlinear susceptibility inversion with variational regularization'. Magnetic Resonance in Medicine. Aug;80(2):814–21.
6. Shahmaei V. (2019), 'Evaluation of iron deposition in brain basal ganglia of patients with Parkinson's disease using quantitative susceptibility mapping'. European Journal of Radiology Open. 6:169–74.
7. Ward R.J. (2014), 'The role of iron in brain ageing and neurodegenerative disorders'. Lancet Neurology. Oct;13(10):1045–60.
8. Wijtenburg S.A. (2019), 'Reproducibility of brain MRS in older healthy adults at 7T'. NMR in Biomedicine. Feb;32(2):e4040.
9. Yan F. (2018), 'Iron deposition quantification: Applications in the brain and liver'. Journal of Magnetic Resonance Imaging. Aug;48(2):301–17.

Poster No 172

Absence Frontal-parietal EEG Network in Theta Band in MCI Patients During High-recall Movie-watching

Ao Xie[1,2], Wei Jian[1,2], Yulin He[1,2], Haiyang Sun[1,2], Yulan Zhou[1,2], Hua Ren[1,2], Zihao Zheng[1,3], Ziqi Wang[1,2], Li Dong*[1,2], Dezhong Yao[1,2]

[1]The Clinical Hospital of Chengdu Brain Science Institute, MOE Key Lab for Neuroinformation, University of Electronic Science and Technology of China, Chengdu, China, [2]School of Life Science and Technology, Center for information in medicine, University of Electronic Science and Technology of China, Chengdu, China, [3]School of Life Science and Technology, Center for information in medicine, University of Electronic, Chengdu, China

Introduction: Alzheimer's disease (AD) is a neurodegenerative disease that is prevalent in aging people and is characterized by abnormalities in cognition and memory. Mild cognitive impairment (MCI) is a precursor to the progression of AD (Dubois, Feldman et al. 2007). And, cognitive and memory performance has been found to be related to functional connectivity during resting state (Eyler, Sherzai et al. 2011, Grady 2012, Sala-Llonch, Bartres-Faz et al. 2015). However, little is known about how cognitive impairment disease such as MCI affects the brain memory functions during high-recall movie-watching which may offer rich and complex stimulation closely relative to memory function. The purpose of the current work was to investigate potential changes in functional connectivity relative to memory function in MCI patients using electroencephalogram (EEG) during high-recall movie-watching state.

Methods: In this study, EEG data of 41 normal control (NC) individuals and 31 patients with MCI were recorded during the movie-watching state. Each EEG recording consisted of 2 conditions (high-recall vs low-recall movie-watching), and each condition lasted 5 minutes. The high-recall movie is a black and white film containing everyday life in the 1970s-80s, while the low-recall movie is a scenery film. Both movies were assessed by recruited normal elders who were not recorded. Preprocessing of raw EEG data (including identifying and removing segments of EEG contaminating excessive noise, a band-pass filtering at 1-40 Hz, inspecting for artifacts automatically and removing eye blinks and muscle movements using Independent Component Analysis (ICA), interpolating bad channels using reference electrode standardization interpolation technique (RESIT) and re-referencing to REST) was conducted using the WeBrain Platform (http://webrain.uestc.edu.cn). The functional connectivity coefficients between each pair of EEG channels were estimated with the phase synchronization index (PSI). Each analysis was performed separately in typical EEG frequency bands (delta: 1-4 Hz, theta: 4-8 Hz, alpha: 8-12.5 Hz, beta: 12.5-30 Hz, gamma: 30-40 Hz). Next, a two-way mixed (2 groups×2 conditions) analysis of variance (ANOVA), and a post-hoc t-test were used to investigate potential changes of the interaction factor. At last Pearson correlations between connectivities and neuropsychological measures were also calculated across all subjects.

Results: Results of ANOVA and the post-hoc t-test showed significant differences between conditions for the NC group but not the MCI group, especially in the theta rhythm (Fig. 1 B, $p<0.05$, FDR corrected). Those differences were mainly located in the frontal-parietal network of NC group, indicating that connectivity is stronger in the presence of high-recall movie-watching than in the low-recall conditions (Fig. 1 A). Fig. 1 C showed that changes of PSI measures between high-recall and low-recall movies were significantly positively correlated to neuropsychological measures including Montreal Cognitive AssessmentMoCA, $r=0.4206$, $p=0.0002$, Boston Naming Test (BNT, $r=0.3093$, $p=0.0082$) and Minimum Mental State Examination (MMSE, $r=0.2804$, $p=0.0170$).

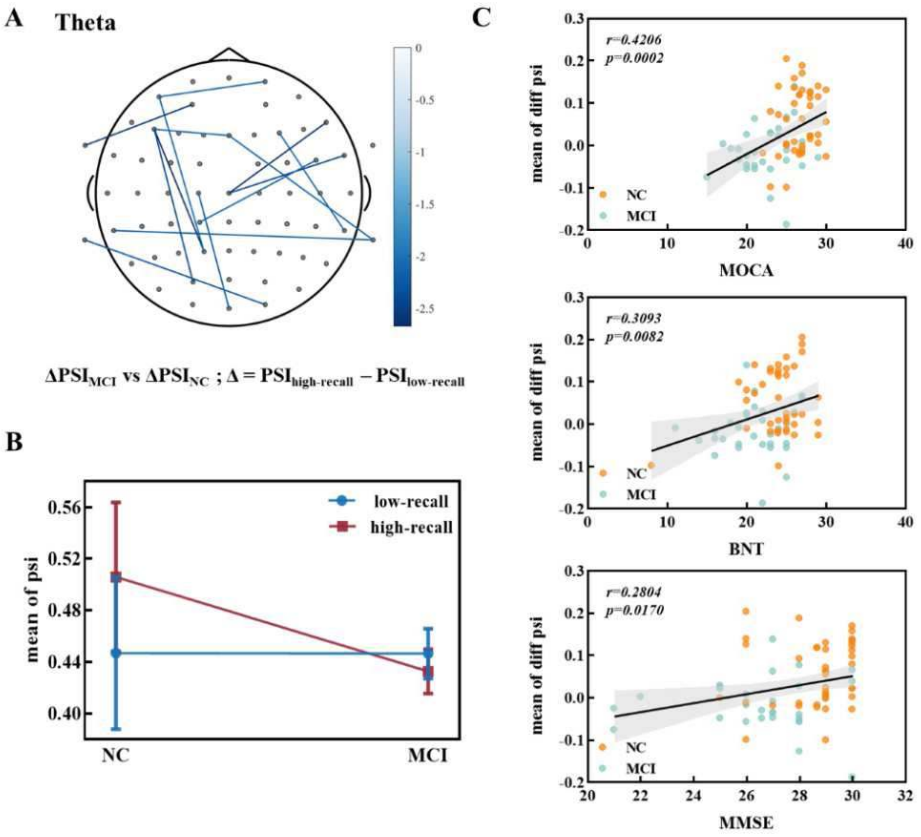

Fig. 1 ANOVA and correlation analysis during two states in theta band. **A:** Post-hoc test on significant lines (ΔPSI_{MCI} vs ΔPSI_{NC}; $\Delta = PSI_{high\text{-}recall} - PSI_{low\text{-}recall}$, $p<0.05$). **B:** Change on the mean PSI of the significant lines in the two groups during two movie-watching conditions. **C:** Correlation between the mean PSI differences and neuropsychological measures. r: correlation coefficient; *p*: *p*-value; psi: phase synchronization index; NC: normal control; MCI: mild cognitive impairment.

Conclusions: The results of the current study demonstrated that absence frontal-parietal EEG network in theta band in MCI patients during high-recall movie-watching state, compared with NC group. Moreover, the correlations with neuropsychological measures suggested that worse cognitive performance might be related to the lower frontal-parietal network in the theta band in MCI patients. Our findings may imply that there was a potential mechanism relative to the absence of key 'memory circuits' in MCI, and may provide new insight towards cognitive rehabilitation during the aging process.

References

1. Dubois, B., H. H. Feldman, C. Jacova, S. T. Dekosky, P. Barberger-Gateau, J. Cummings, A. Delocourte, D. Galasko, S. Gauthier, G. Jicha, K. Meguro, J. O'Brien, F. Pasquier, P. Robert, M. Rossor, S. Solloway, Y. Stern, P. J. Visser and P. Scheltens (2007), 'Research criteria for the diagnosis of Alzheimer"s disease: revising the NINCDS-ADRDA criteria', LANCET NEUROLOGY, vol. 6, no. 8, pp. 734-746.
2. Eyler, L. T., A. Sherzai, A. R. Kaup and D. V. Jeste (2011), 'A Review of Functional Brain Imaging Correlates of Successful Cognitive Aging', BIOLOGICAL PSYCHIATRY, vol. 70, no. 2, pp. 115-122
3. Grady, C. (2012), 'BRAIN AGEING The cognitive neuroscience of ageing', NATURE REVIEWS NEUROSCIENCE, vol. 13, no. 7, pp. 491-505.
4. Sala-Llonch, R., D. Bartres-Faz and C. Junque (2015), 'Reorganization of brain networks in aging: a review of functional connectivity studies', FRONTIERS IN PSYCHOLOGY, vol. 6.

Poster No 173

ParkCore: Harmonized analysis of neuroimaging datasets from NorthAmerican & Indian Parkinson studies

Nikhil Bhagwat[1], Shweta Prasad[2], Michelle Wang[1], Brent McPherson[1], Sebastian Urchs[1], Jitender Saini[2], Pramod Pal[2], Ravi Yadav[2], Edward Fon[1], Madeleine Sharp[1], Alain Dagher[1], Jean-Baptiste Poline[1]

[1]McGill University, Montreal, Quebec, [2]NIMHANS, Bangalore, Karnataka

Introduction: Parkinson's disease (PD) is a neurodegenerative movement disorder with increasing global prevalence and societal burden. The significant heterogeneity in symptom and neurological presentations has hindered the development of reliable diagnostic and progression biomarkers. Further, despite growing availability of large-scale PD studies across

the globe, data aggregation and analytic comparisons have been limited due to lack of standardization across acquisition protocols, image processing, and statistical analysis. In the ParkCore project (Fig.1), we compare neuroanatomical phenotypes across multiple PD cohorts from the US, Canada, and India by 1) harmonizing imaging and clinical variables and 2) standardizing MRI processing. We highlight the commonalities and differences in brain morphometry in PD patients resultant of acquisition and biological factors.

Methods: We harmonize and process age-matched samples from PPMI (n=294) (Marek et al., 2018), QPN (n=162) (Gan-Or et al., 2020), and three NIMHANS (n=132, 91, 295) cohorts (Prasad et al., 2022). Harmonization of demographic and clinical variables is performed using Neurobagel (https://neurobagel.org/) tools. The MRI data are acquired on different scanners but scans are processed identically using Nipoppy workflows. We quantify 1) cortical thickness (CTh) and subcortical volumes using FreeSurfer-7 (Fischl, 2012), 2) cerebellar lobular volumes using the MAGeT Brain pipeline (Pipitone et al., 2014), 3) structural connectomes based on white-matter tracts using TractoFlow (Theaud et al., no date), and 4) functional networks using fMRIPrep (Esteban et al., 2019) and Nilearn pipelines. We calculate regional CTh and subcortical volumes using DKT parcellation (Klein and Tourville, 2012). To control for site effects, we assess CTh and volumetric differences of PD-vs-control separately for the three cohorts using GLM. We control for age and sex in all models and additionally for total-intracranial-volume in regional and total-cerebellar-volume in cerebellar volumetric analyses.

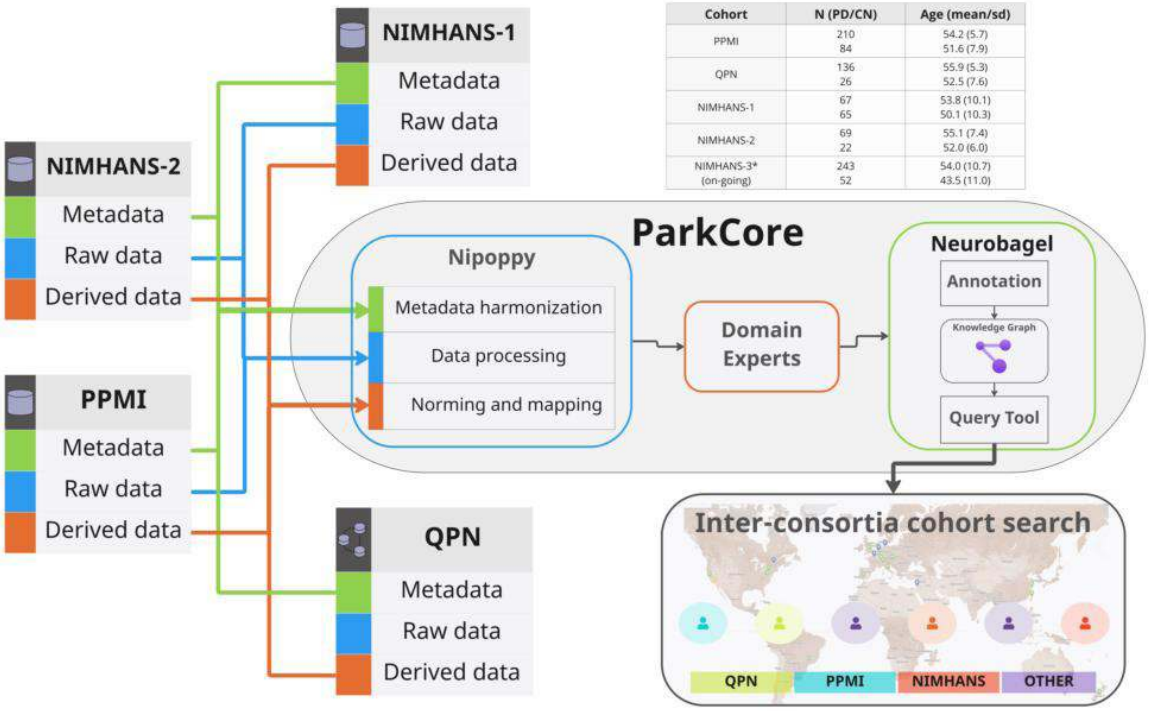

Cohort	N (PD/CN)	Age (mean/sd)
PPMI	210 84	54.2 (5.7) 51.6 (7.9)
QPN	136 26	55.9 (5.3) 52.5 (7.6)
NIMHANS-1	67 65	53.8 (10.1) 50.1 (10.3)
NIMHANS-2	69 22	55.1 (7.4) 52.0 (6.0)
NIMHANS-3* (on-going)	243 52	54.0 (10.7) 43.5 (11.0)

Figure 1: ParkCore hub comprising Neurobagel and Nipoppy tools for harmonization and standardized processing of multiple Parkinson's datasets. The processing workflow begins with harmonization of demographic and clinical variables, followed by BIDS data organization and containerized image processing of MRI data. Finally the entire annotated datasets is made discoverable through Neurobagel inter-consortia cohort search tool.

Results: Fig.2 shows distributions for several image derived phenotypes (IDPs) for the various cohorts. NIMHANS-1 shows scanner related bias with higher CTh values on average. The PD-vs-control comparisons show significant differences in CTh of posterior-cingulate (right) in both QPN and NIMHANS cohorts. Significant differences in Thalamic (bilateral) volume are seen in PPMI, but not in QPN or NIMHANS. PD cohorts consistently show higher CSF volumes but are not statistically significant.

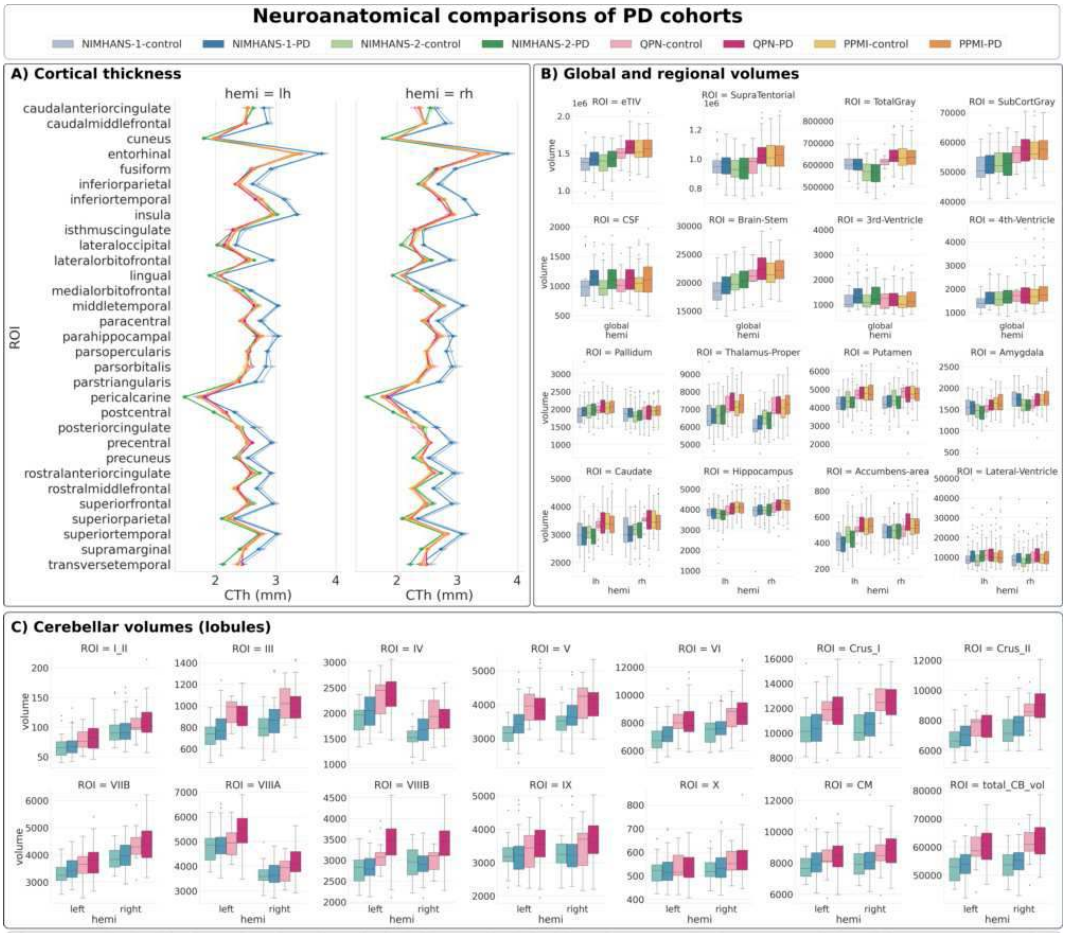

Figure 2: A) Distribution of regional cortical thickness (CTh) values from FreeSurfer output defined by DKT parcellation B) Distribution of global and regional subcortical volumes from FreeSurfer output C) Distribution of cerebellar lobular volumes from MAGeT Brain pipelines (Shown only for two cohorts).

Conclusions: Data harmonization and standardized processing is essential to minimize methodologically induced phenotypic variations in cross-cohort comparisons. Image acquisition - scanners and protocols - seem to play a stronger role in cortical thickness quantification compared to the regional volumetry. Scanner specific image normalization of MRI data and analysis of clinical phenotypes are needed (ongoing) to address cohort-specific feature shifts and isolate reliable PD-specific neurological signatures across datasets. In the future we will work to make these distributed results searchable with the Neurobagel project.

References

1. Esteban, O. et al. (2019) 'fMRIPrep: a robust preprocessing pipeline for functional MRI', Nature methods, 16(1), pp. 111–116.
2. Fischl, B. (2012) 'FreeSurfer', NeuroImage, 62(2), pp. 774–781.
3. Gan-Or, Z. et al. (2020) 'The Quebec Parkinson Network: A Researcher-Patient Matching Platform and Multimodal Biorepository', Journal of Parkinson's disease, 10(1), pp. 301–313.
4. Klein, A. and Tourville, J. (2012) '101 labeled brain images and a consistent human cortical labeling protocol', Frontiers in neuroscience, 6, p. 171.
5. Marek, K. et al. (2018) 'The Parkinson's progression markers initiative (PPMI) - establishing a PD biomarker cohort', Annals of clinical and translational neurology, 5(12), pp. 1460–1477.
6. Pipitone, J. et al. (2014) 'Multi-atlas segmentation of the whole hippocampus and subfields using multiple automatically generated templates', NeuroImage, 101, pp. 494–512.
7. Prasad, S. et al. (2022) 'Early onset of Parkinson's disease in India: Complicating the conundrum', Parkinsonism & related disorders, 105, pp. 111–113.
8. Theaud, G. et al. (no date) 'TractoFlow: A robust, efficient and reproducible diffusion MRI pipeline leveraging Nextflow & Singularity'. Available at: https://doi.org/10.1101/631952.

Poster No 174

Prediction of amyloid and tau status in nondemented older adults using tree-based ensemble models

Hwamee Oh[1], Younghoon Seo[2]

[1]Brown University, Providence, RI, [2]Bowdoin College, Brunswick, ME

Introduction: Current gold standards for monitoring brain amyloidosis and tauopathy, the prominent pathological features of Alzheimer's disease (AD), are based on positron emission tomography (PET) scans. Given the expensive and invasive nature of amyloid and tau PET scans, predicting amyloid and tau status in pre-dementia older adults with AD pathologies using more affordable and accessible measures can facilitate early intervention and clinical trials by reducing the screen failure rate. The goal of the present study was to develop interpretable tree-based ensemble models to predict PET-based amyloid and tau burden using non-invasive and widely available variables.

Methods: The amyloid (Aβ; n = 1062) and tau (n = 410) PET datasets consisted of individuals with normal cognition and mild cognitive impairment from the Alzheimer's Disease Neuroimaging Initiative (ADNI) database. Amyloid PET with the [18F] Florbetapir tracer was used as the gold-standard measure for binary amyloid status classification with established positivity cutoffs (< 1.11), while tau PET with the [18F]Flortaucipir tracer was used for the three-stage (low, intermediate, and high) tau status determination using cut-off values found based on pre-established protocols (lower cut-off: < 1.27; upper cut-off: < 1.44). For each subject, we obtained the demographic data, neuropsychological data, apolipoprotein (APOE) ε4 genotype, and volumetric MRI measures, as well as plasma Aβ 42/40 ratio for a subset of the amyloid sample (n = 285). We trained random forest (RF), extreme gradient boosting machine (XGBoost), and light gradient boosting machine (lightGBM) models using different combinations of the features, and measured the model performance using area under the receiver operating curve (AUROC). Shapley Additive exPlanations (SHAP) values were used to rank feature importance.

Results: The performance of baseline non-imaging model showed modest performance for Aβ (RF = 0.665, XGB = 0.650, LGBM = 0.659). Subsequent additions of features improved the predictive performance, with the model using demographic data, cognitive data, and volumetric MRI measures demonstrating the highest performance (RF = 0.762, XGB = 0.763, LGBM = 0.761). Meanwhile, the baseline model achieved modest performance for the three-stage tau classification (RF = 0.643, XGB = 0.654, LGBM = 0.643), and the further addition of features improved the performance, with the feature combination of demographic data, cognitive, volumetric MRI measures, and continuous Aβ PET standardized uptake value ratios (SUVRs) achieving very good performance (RF = 0.799, XGB = 0.801, LGBM = 0.800). SHAP summary plots for Aβ classification revealed the most important features being age, entorhinal cortex volume, and several neuropsychological and functional measures. For tau groups, the low tau group was characterized by low Aβ load, high global cognition scores, and higher hippocampal and middle temporal gyrus volume, intermediate group by higher age, intermediate global cognition, and higher memory scores, and high group by higher Aβ load, more impaired functional scores, lower age, and lower memory scores.

Conclusions: Tree-based ensemble machine learning models achieved modest to very good performance in predicting amyloid and tau status among nondemented older adults. These results suggest that using noninvasive and widely available measures are promising to be used as pre-screening filter for AD clinical trials.

References

1. Jack, C. R., Wiste, H. J., Algeciras-Schimnich, A., et al. (2023). Predicting amyloid PET and tau PET stages with plasma biomarkers. Brain : a journal of neurology, 146(5), 2029–2044. https://doi.org/10.1093/brain/awad042
2. Landau, S. M., Lu, M., Joshi, A. D., et al. (2013). Comparing positron emission tomography imaging and cerebrospinal fluid measurements of β-amyloid. Annals of neurology, 74(6), 826–836. https://doi.org/10.1002/ana.23908
3. Landau, S. M., Mintun, M. A., Joshi, A. D., et al. (2012). Amyloid deposition, hypometabolism, and longitudinal cognitive decline. Annals of neurology, 72(4), 578–586. https://doi.org/10.1002/ana.23650
4. Ossenkoppele, R., Rabinovici, G. D., Smith, R., et al. (2018). Discriminative Accuracy of [18F]flortaucipir Positron Emission Tomography for Alzheimer Disease vs Other Neurodegenerative Disorders. JAMA, 320(11), 1151–1162. https://doi.org/10.1001/jama.2018.12917
5. Sonni, I., Lesman Segev, O. H., Baker, S. L., et al. (2020). Evaluation of a visual interpretation method for tau-PET with 18F-flortaucipir. Alzheimer's & dementia (Amsterdam, Netherlands), 12(1), e12133. https://doi.org/10.1002/dad2.12133

Poster No 175

Transdiagnostic brain module dysfunctions across sub-types of frontotemporal dementia

Zeng Xinglin[1], Kaixi Zhang[1], Zhen Yuan[1]

[1]University of Macau, Macau, Macau

Introduction: Background: Frontotemporal dementia (FTD) is a complex neurodegenerative disorder encompassing heterogeneous subtypes, including behavioral variant frontotemporal dementia (BV-FTD), semantic variant frontotemporal dementia (SV-FTD), and progressive non-fluent aphasia frontotemporal dementia (PNFA-FTD). Unraveling the shared and distinctive brain module organizations among these subtypes is critical for unraveling the underlying neural basis of the disease. This study aims to explore brain module organization in FTD subtypes, seeking potential biomarkers and insights into their pathophysiology.

Methods: Methods: Resting-state functional magnetic resonance imaging data were obtained from the Frontotemporal Lobar Degeneration Neuroimaging Initiative, comprising 41 BV-FTD, 32 SV-FTD, 28 PNFA-FTD, and 94 healthy controls, following exclusion of participants with excessive head motion. Individual functional brain networks were constructed at the voxel level of gray matter and binarized with a 1% density threshold. Using predefined brain modules, we computed the modular segregation index (MSI) for each module, analyzed intermodular and intramodular connections to identify driving modular connections, and calculated the participation coefficient (PC) to detect regions with altered nodal properties associated with module integrity. A machine learning algorithm was employed for FTD subtype classification based on these matrices. Correlations between modular measures and clinical scores in each FTD subtype were examined.

Results: Results: Distinct brain module organizations were observed across FTD subtypes, with lower MSI in the subcortical module (SUB), default mode network (DMN), and ventral attention network (VAN) in both BV-FTD and SV-FTD. Specifically, only BV-FTD exhibited disruption in the frontoparietal network (FPN). Notably, the bilateral fusional gyrus, left orbitofrontal cortex, left precuneus, and right insular thalamus showed significant group effects on PC, indicating altered nodal properties associated with module integrity. Our machine learning achieved a multiple classification accuracy of 85%. Correlations between specific network alterations and clinical variables in each FTD subtype were also identified.

Conclusions: Conclusions: These findings illuminate the diverse brain module organization in different FTD subtypes, offering insights into potential neurobiological differences that underlie the clinical heterogeneity of the disease. Regions with altered modular properties may serve as valuable biomarkers for early diagnosis and disease monitoring. Furthermore, understanding disruptions in modular connectivity provides valuable insights into the neuropathological mechanisms of FTD subtypes, paving the way for targeted therapeutic interventions.

References

1. This study drew its participant pool from the Frontotemporal Lobar Degeneration Neuroimaging Initiative (FTLDNI) databases.

Poster No 176

Longitudinal Iron and Neuromelanin in Restless Legs Syndrome associated with Parkinson's Disease

Rahul Gaurav[1], Pauline Dodet[1,2], François-Xavier Lejeune[1], Mathieu Santin[1], Smaranda Leu-Semenescu[2], Romain Valabrègue[1], Nadya Pyatigorskaya[1,2], Graziella Mangone[1,2], Jean-Christophe Corvol[1,2], Marie Vidailhet[1,2], Stéphane Lehéricy[1,2], Isabelle Arnulf[1,2]

[1]Paris Brain Institute (ICM), Paris, France, [2]Pitié-Salpêtrière Hospital, AP-HP, Paris, France

Introduction: Restless legs syndrome (RLS) is a sensorimotor disorder demonstrated by an urge to move the legs with an unpleasant sensation during rest1. RLS can be idiopathic or manifest with Parkinson disease (PD)[1,2]. PD is characterized by neuromelanin (NM) loss and elevated iron in the substantia nigra (SN)[3]. Isolated REM sleep behavior disorder (iRBD), a prodromal parkinsonism stage, is characterized by abnormal violent behaviors during REM sleep[4]. Unlike PD, RLS patients often demonstrate nigral iron deficiency[5,6,7]. Neuropathological studies suggested that the iron scarcity might come from the damage in iron acquisition by the nigral neuromelanin cells[6,7]. Some patients with idiopathic RLS also demonstrate dopaminergic abnormality[8]. Nonetheless, the longitudinal regional iron changes in RLS associated with PD are still debated.

Methods: Participants: Early PD with (PDRLS+) and without RLS (PDRLS-), iRBD and HVs were scanned using 3T MRI and assessed thrice (V1/V2/V3) with a 2-year interval between the visits. Image analysis: QSM images were computed using MEDI toolbox[9] and were used to construct a QSM template using Advanced Normalization Tools (ANTs). R2* maps were obtained using a nonlinear fit over echo times. The subthalamic nucleus, entire SN and its subdivisions (anterior and posterior territories of dorsal and ventral SN) were manually segmented on the template by experienced raters. Subject wise regions were obtained automatically using inverse transformation. NM images were aligned to an average brain template. Contrast to noise ratio (CNR) was computed using an SN mask partitioned into sensorimotor, associative and limbic territories and a background region[10]. Statistical analyses: Baseline between-group differences were tested using multivariate linear regression models including age and sex as covariates. Longitudinal analyses were performed on subjects with at least two visits using

linear mixed-effects models (LMMs). In each LMM, the group, the visit interval and their interaction term were considered as fixed effects, while a random (intercept) effect was applied on subject identifiers. Significance effects of the main or interaction effects were tested by Type II Wald Chi-square tests. Pearson's correlations corrected for multiple tests were performed to test iron with clinical variables, REM without atonia (RWA), periodic limb movements (PLM) and CNR.

Results: Clinical characteristics: At V1/V2/V3, 60/52/41 HVs, 58/43/33 iRBD, 148/145/96 PD were included respectively. Age, sex, MDS-UPDRS-OFF score and RWA differed between groups and there was a trend for PLM. IRBD had the highest rate of RWA and PLM. PDRLS+ were older and had longer disease duration (2.4 ± 1.0 years) compared to PDRLS- (1.3 ± 0.9 years). Baseline: Groups were different in QSM and R2* (p=0.04). QSM and R2* increased in the posteroventral SN only and not in any other regions. We found that PDRBD- had +17.8% elevated posteroventral SN iron (p= 0.03) vs. HV, but there was no evidence for a difference of PDRLS- with PDRRLS+ or with iRBD. Regional SN CNRs were also different. Longitudinal: We observed group and visit effects for posteroventral SN iron for QSM, R2* and CNRs in all regional SN territories (p<0.001). Only CNR in the sensorimotor region showed group X visit interaction effect (p=0.02). Correlations: In PDRLS-, posteroventral SN iron increased with the decrease in CNR in the sensorimotor region (r=-0.21, p=0.04) and with the increase in disease duration (r=0.27, p =0.04) and PLM (r=0.36, p=0.002).

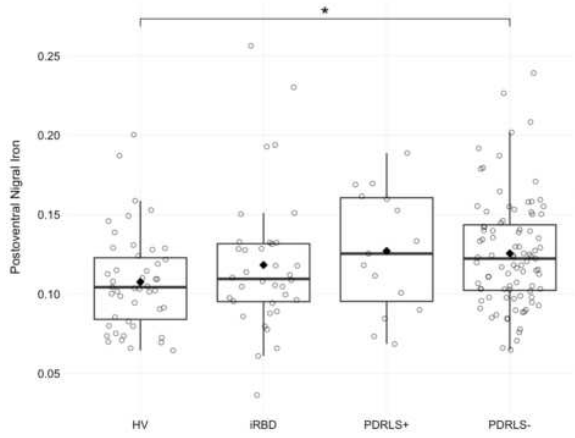

(A)

Box plot of baseline posteroventral nigral iron changes using the quantitative susceptibility mapping (QSM).

Group comparisons were based on a multivariate linear model adjusted for baseline age and sex. The asterisk depicts significant difference.

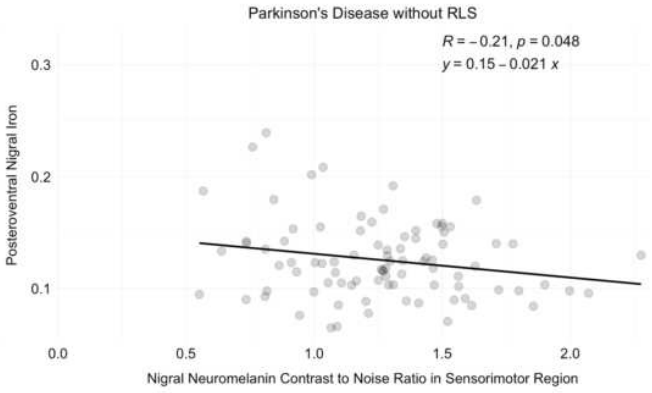

(B)

Scatter plot showing significant negative correlations between posteroventral nigral iron using the quantitative susceptibility mapping (QSM) and nigral neuromelanin contrast to noise ratio (CNR) in sensorimotor region.

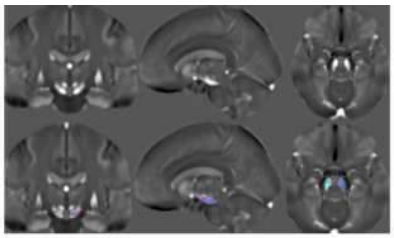

(A) Ventral substantia nigra in a representative healthy volunteer using a quantitative susceptibility mapping (QSM) image. Color-coding indicating anterior and posterior territories.

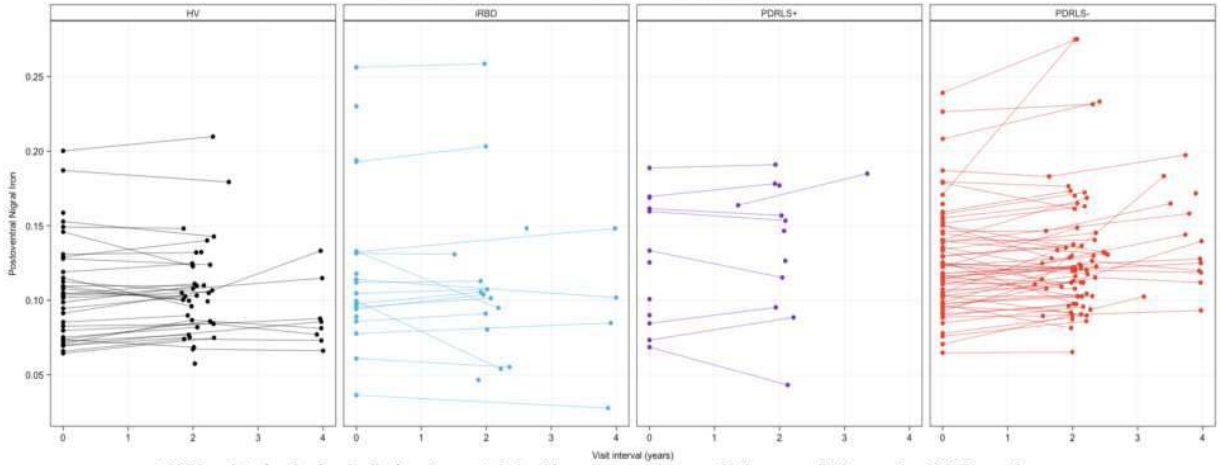

(B) Line plots showing longitudinal posteroventral nigral iron changes using quantitative susceptibility mapping (QSM) over the years.

Conclusions: PD patients without RLS had a greater longitudinal iron increase in the posteroventral SN region and CNR decrease in the sensorimotor SN region. These iron changes were related to the disease duration and the decreased in NM signal. Nonetheless, further studies including patients with idiopathic RLS are warranted.

References

1. Allen RP, Picchietti D, Hening WA, Trenkwalder C, Walters AS, Montplaisir J. (2003), 'Restless legs syndrome: diagnostic criteria, special considerations, and epidemiology: a report from the restless legs syndrome diagnosis and epidemiology workshop at the National Institutes of Health', Sleep Med:101–119
2. Lee JE, Shin HW, Kim KS, Sohn YH. (2009), 'Factors contributing to the development of restless legs syndrome in patients with Parkinson disease', Movement Disorder ;24: 579 –582
3. Barbosa, J. H. O., Santos, A. C., Tumas, V., et al. (2015), 'Quantifying brain iron deposition in patients with Parkinson's disease using quantitative susceptibility mapping, R2 and R2', Magnetic resonance imaging, 33(5), 559-565
4. Sun J, Lai Z, Ma J, et al. (2020), 'Quantitative evaluation of iron content in idiopathic rapid eye movement sleep behavior disorder', Movement Disorder, 35(3):478–485
5. Allen, R.P.R.P., Barker, P.B.B., Wehrl, F., Song, H.K.K., Earley, C.J.J., . (2001), 'MRI measurement of brain iron in patients with restless legs syndrome', Neurology 56 (2), 263–265
6. Connor JR, Boyer PJ, Menzies SL, et al. (2003), 'Neuropathological examination suggests impaired brain iron acquisition in restless legs syndrome', Neurology ;61(3):304–309
7. Connor, J.R., Wang, X.S., Patton, S.M., et al., (2004), 'Decreased transferrin receptor expression by neuromelanin cells in restless legs syndrome', Neurology 62 (9), 1563–1567
8. Allen R., 'Dopamine and iron in the pathophysiology of restless legs syndrome (RLS)', Sleep Medicine. (2004) ;5(4):385–391
9. Liu, J., Liu, T., de Rochefort, L., et al. (2012), 'Morphology enabled dipole inversion for quantitative susceptibility mapping using structural consistency between the magnitude image and the susceptibility map', Neuroimage, 59(3), 2560-2568.
10. Biondetti E, Santin MD, Valabrègue R, et al. (2021), 'The spatiotemporal changes in dopamine, neuromelanin and iron characterizing Parkinson's disease', Brain, 144(10):3114–3125

Poster No 177

Interactions between subcortical structure, fMRI vigilance signals, and cognition in aging

Kate Wang[1], Sarah Goodale[1], Derek Doss[1], Deepak Gupta[2], Katherine Gifford[2,3], Kimberly Pechman[2,3], Timothy Hohman[2,3], Dario Englot[1,2], Angela Jefferson[2,3], Catie Chang[1]

[1]Vanderbilt University, Nashville, TN, [2]Vanderbilt University Medical Center, Nashville, TN, [3]Vanderbilt Memory & Alzheimer's Center, Nashville, TN

Introduction: Daytime sleepiness and changes in sleep patterns are commonly reported among patients with Alzheimer's Disease (AD)[1]. In fact, some of the earliest brain regions to degrade in AD include subcortical regions, such as the basal forebrain (BF) and its constituent Nucleus Basalis of Meynert (NBM), which play an important role in maintaining wakefulness or alertness (also known as vigilance)[2]. We hypothesize that alterations in vigilance-related brain activity are related to cognitive decline through the disruption of subcortical structures. Here, we propose a novel investigation to characterize fMRI-linked vigilance patterns in an aging population and determine how these patterns relate to subcortical atrophy and cognition.

Methods: We used the Vanderbilt Memory and Aging Project (VMAP) fMRI dataset[3], consisting of 46 MCI patients and 75 healthy controls (HCs). Since vigilance measures are not collected with the fMRI data, we used a data-driven technique for extracting vigilance information directly from fMRI data[4]. We then derived subject-specific spatial maps reflecting a whole-brain activity pattern that is correlated with vigilance. We first investigated the relationships between structural measures (BF and NBM volumes obtained using subject-specific segmentation methods[5,6]) and cognitive measures (subject memory composite and executive function scores) using Pearson correlations. To investigate how our cognitive covariates relate to fMRI vigilance patterns, we then conducted a voxel-wise regression analysis, controlling for sex, age, ethnicity, education, total intracranial volume, and APOE4 status. Using FSL Randomise, group differences were investigated with 2-sample unpaired t-tests, and significant clusters were identified with threshold-free cluster enhancement (TFCE). Finally, we performed a mediation analysis to evaluate how NBM volume may mediate fMRI-derived vigilance effects on memory composite in MCI subjects[7]. Significance was assessed in resulting path coefficient maps using FDR correction for multiple comparisons ($q = 0.05$).

Results: BF volume was significantly correlated with executive function in MCI subjects ($r = 0.295$, $p = 0.047$) and HCs ($r = 0.249$, $p = 0.037$). Further, NBM volume was also significantly correlated with executive function in HCs ($r = 0.426$, $p = 2.103e-04$). BF volume was significantly correlated with memory composite in MCI subjects ($r = 0.437$, $p = 0.0024$), and NBM volume was significantly correlated with memory composite in both MCI subjects ($r = 0.364$, $p = 0.013$) and HCs ($r = 0.3004$, $p = 0.011$). Voxel-wise regression analysis revealed significant differences in the association of fMRI vigilance activity and memory in the thalamus and hippocampus (HC < MCI). We also observed significant differences in the association of fMRI vigilance activity

and executive function in the thalamus, hippocampus, and insula (HC < MCI). Mediation analysis revealed significant clusters involved in the association between fMRI vigilance patterns and NBM volume in the anterior cingulate cortex, hippocampus, and caudate in MCI patients. In the MCI group, fMRI vigilance activity and memory composite were significantly associated in the hippocampus, anterior cingulate cortex, and thalamus.

Conclusions: These results indicate that BF and NBM volumes are significantly correlated with memory composite scores in MCI subjects and with executive function in HCs. In addition, our cognitive measures have region-specific correlations with fMRI vigilance fluctuations. Thus, both subcortical structural changes and fMRI vigilance patterns may play a role in cognitive decline in AD. Overall, this work sheds light onto the role of fMRI vigilance patterns in pathological and healthy aging and establishes potential avenues for integrating brain state changes, structure, and cognition to derive biomarkers of early-stage AD.

References

1. References
2. Bubu, O.M. (2017), 'Sleep, Cognitive impairment, and Alzheimer's disease: A Systematic Review and Meta-Analysis', Sleep, vol. 40, no. 1.
3. Schmitz, T.W. (2016), 'Basal forebrain degeneration precedes and predicts the cortical spread of Alzheimer's pathology', Nature Communications, vol. 7, no. 13249.
4. Jefferson, A. L. (2016), 'The Vanderbilt Memory & Aging Project: study design and baseline cohort overview', Journal of Alzheimer's disease, vol. 52, no. 2, pp. 539-559.
5. Goodale, S. E. (2021), 'fMRI-based detection of alertness predicts behavioral response variability', Elife, vol. 10.
6. Huo, Y. (2016), "Consistent cortical reconstruction and multi-atlas brain segmentation," NeuroImage, vol. 138, pp. 197–210.
7. Doss, D.J. (2023), "Deep Learning Segmentation of the Nucleus Basalis of Meynert on 3T MRI," AJNR Am J Neuroradiol, vol. 44, pp. 1020-1025.
8. Wager, T. D. (2008), "Prefrontal-subcortical pathways mediating successful emotion regulation," Neuron, vol. 59, pp. 1037–1050.

Poster No 178

EEG Beta Spectrum Changes in MCI Patients During High-recall Movie-watching

Hua Ren[1], Yulin He[2], Yuxi Zhou[2], Ao Xie[2], Wei Jian[1], Ziqi Wang[1], Jianfu Li[2], Tiejun Liu[2], Li Dong*[2]

[1]The Clinical Hospital of Chengdu Brain Science Institute, MOE Key Lab for Neuroinformation, Chengdu, China, [2]University of Electronic Science and Technology of China, Chengdu, China

Introduction: Electroencephalogram (EEG) is a quantified electrophysiological technology which has good sensitivity in judging cognitive function and can reflect the cognitive status of the elderly (Abazid, et al., 2022). Previous resting-state studies reported a decreased alpha and beta band functional connectivity in Mild cognitive impairment (MCI) patients and the memory load-related modulation of global functional connectivity will be less prominent since their reduced available cognitive capacity (Fodor, et al., 2021). However, little is known about how cognitive impairment disease such MCI affects the brain memory functions during high-recall movie-watching which may allow human perception and cognition to be studied in more complex and more real-life-like situations (Espenhahn, et al., 2020; Finn and Bandettini, 2021; Wang, et al., 2023). The purpose of this study was to evaluate the differences of EEG spectral changes in MCI and normal controls (NC) during high -recall movie-watching and to explore potential biomarkers that distinguish MCI from normal controls.

Methods: We recorded the EEG of 41 normal controls individuals and 31 patients with MCI using a 62-channel Brain Product System when they were watching film clips which consisted of the low recall movie for 5 minutes and the high recall movie for 5 minutes. Age, gender and education level were carefully matched across the two groups. The high or low recall of the movie was defined by assessing recall with a pre-experimental measure. Preprocessing of raw EEG data was done using the WeBrain platform(Dong L, et al.,2021) (http://webrain.uestc.edu.cn). A band-pass filter at 1-40 Hz was applied to identify and remove segments of EEG contaminating excessive noise. Next, data were inspected for artifacts automatically and Independent Component Analysis (ICA) was carried out in order to remove eye blinks and muscle movements. And then, bad channels were interpolated by using reference electrode standardization interpolation technique (RESIT) and all channels were re-referenced to REST. The relative power indices were calculated by time–frequency analysis with fast-Fourier transform (FFT), and each analysis was performed separately in typical EEG frequency bands (delta: 1-4 Hz, theta: 4-8 Hz, alpha1: 8-10.5 Hz, alpha2 10.5-12.5 beta1: 12.5 -18.5 Hz, beta2: 18.5-21Hz, gamma1: 30-40 Hz). At last, two-way mixed (2 groups×2 conditions) analysis of variance (ANOVA), and a post-hoc t-test were used to investigate potential changes of the interaction factor. Pearson correlations between power indices and neuropsychological measures were also calculated across all subjects.

Results: In the present study, significant difference of EEG spectrum changes between MCI and NC during the high and low recall movie-watching states were found ($F > 4.05$, $p < 0.05$). In beta1 (12.5 -18.5 Hz) and beta2 (18.5-21 Hz) rhythm, decreased relative beta power indices were found in frontal and parietal regions ($p<0.05$, FDR adjusted) under recall state in MCI group

(Fig. 1A). As shown in Fig. 1B, the differences of EEG beta spectrum between high and low recall movie watching conditions were significant correlated with neuropsychological measures including Montreal Cognitive Assessment (MoCA) (r=0.2870, p=0.0145) and Animal Fluency Test (AFT) (r=0.2556, p=0.0302).

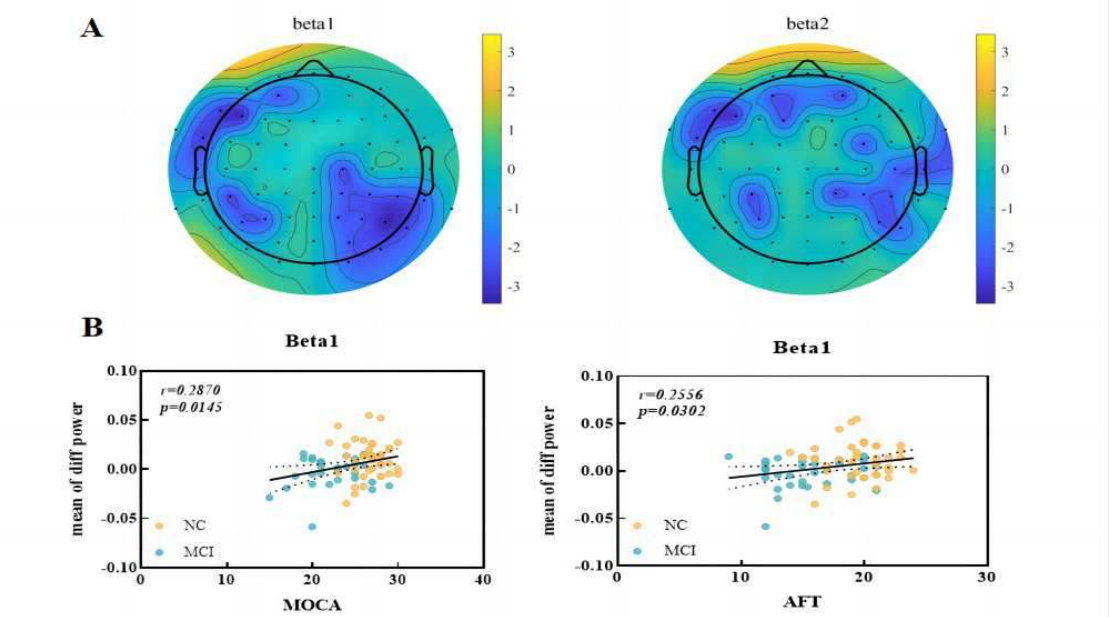

Fig.1 Results of ANOVA and post-hoc t-test. **A**: The reduction of beta spectrum activation in frontal and parietal regions in MCI group (ΔPowerMCI vs ΔPowerNC, Δ means Powerhigh recall - Powerlow recall). **B**: Pearson correlations between power indices and neuropsychological measures. r: correaltions; p: p-value; NC: normal control; MCI: mild cognitive impairment.

Conclusions: These findings indicated that functional changes of EEG beta spectrum during recall background may account for the potential cognitive impairment. These results have implications for our basic understanding of state-dependent roles in relationship between EEG spectral changes and cognition, and for the future efforts aimed at the early identification and intervention of cognitive impairment.

References

1. Abazid M, Houmani N, Dorizzi B, Boudy J, Mariani J, Kinugawa K. Weighted Brain Network Analysis on Different Stages of Clinical Cognitive Decline. Bioengineering (Basel). 2022. 9(2): 62.
2. Dong L, Li J, Zou Q, et al. 2021. WeBrain: A web-based brainformatics platform of computational ecosystem for EEG big data analysis. Neuroimage. 245: 118713.
3. Espenhahn S, Yan T, Beltrano W, et al. The effect of movie-watching on electroencephalographic responses to tactile stimulation. Neuroimage. 2020. 220: 117130.
4. Finn ES, Bandettini PA. Movie-watching outperforms rest for functional connectivity-based prediction of behavior. Neuroimage. 2021. 235: 117963.
5. Fodor Z, Horváth A, Hidasi Z, Gouw AA, Stam CJ, Csukly G. EEG Alpha and Beta Band Functional Connectivity and Network Structure Mark Hub Overload in Mild Cognitive Impairment During Memory Maintenance. Front Aging Neurosci. 2021. 13: 680200.
6. Wang Z, Yang J, Zheng Z, et al. Trait- and State-Dependent Changes in Cortical-Subcortical Functional Networks Across the Adult Lifespan. J Magn Reson Imaging. 2023. 58(3): 720-731.

Poster No 179

Effects of Parkinson's Disease on Viscoelastic Properties of the Brain

Christoffer Olsson[1], Mikael Skorpil[2], Per Svenningsson[2], Rodrigo Moreno[1]

[1]KTH, Stockholm, Sweden, [2]Karolinska Institutet, Stockholm, Sweden

Introduction: Magnetic resonance elastography (MRE) is a relatively new method for imaging the brain. By vibrating the head while inside of an MR scanner MRE detects minute displacements that can be used to measure the viscoelastic properties of the brain. This information can be used to, for example, assess how the microscopical environment of the tissue is affected by neurological pathologies. In this study, we use MRE to explore the effects of Parkinson's disease (PD) on the microstructural properties of the brain by comparing data from healthy controls (HC) and PD patients. To improve the analysis of the microstructural properties, we also included multidimensional diffusion imaging (MUDI), which can also be used for this purpose by detecting diffusion properties within the tissue.

Methods: The 12 HC and 12 PD subjects were on average 58 (σ=6) and 63 (σ=9) years old respectively, and both groups had a gender ratio of 1:3 (F:M). Disease severity of the PD subjects were evaluated by a clinician using the Unified Parkinson's Disease Rating Scale motor score (UPDRS-III)(Goetz et al. 2008), and had an average score of 19 (σ=11), where the scale ranges from 0-132 (where 12 and below is considered mild effect). All MR images were acquired on a Philips Ingenia CX 3T scanner. MRE images were taken with an EPI sequence and driver pillow (vibrating at 60Hz) provided by Mayo clinic (see e.g. (Kruse et al. 2008)). The resulting displacement images (3x3x3mm3 resolution) were then inverted to viscoelastic parameters(Oliphant et al. 2001),given by the complex shear modulus, G*=G'+iG''. Stiffness is defined as|G*|, and the viscosity-related phase angle φ=arctan(G''/G'). MUDI images were acquired as explained in (Topgaard 2017) with a resolution of 2.5x2.5x2.5 mm3, using spherical and linear b-tensors with 5 b-values spaced between 0 and 2000s/mm2. The images were post-processed using an open-source MD-dMRI software (Nilsson et al. 2018) to estimate microscopic fractional anisotropy (μFA), mean diffusivity (MD), and variance of MD (Var(MD)). All images were registered to subject-specific T1 images (1x1x1mm3), which had been parcellated into the Desikan-Killiany atlas(Desikan et al. 2006) with the use of FreeSurfer v7.2.

Results: Total brain stiffness is shown in Fig. 1a & 2a to decrease with age for both HC and PD. However, the effect is stronger for PD subjects, showing that PD softens the brain. For different specific regions, the most significant correlations with a PD diagnosis are located in the occipital and temporal lobes (Fig. 2b). Likewise, MD and μFA is shown to increase and decrease respectively with age for these structures, consistent with neural atrophy (Kamiya et al. 2020; Westin et al. 2016). However, these effects are in general much less significantly correlated with PD (compare Fig. 2a and 2b). For PD subjects, the severity of the disease is most significantly correlated with a decrease of φ in the lentiform nucleus (fig 1b).

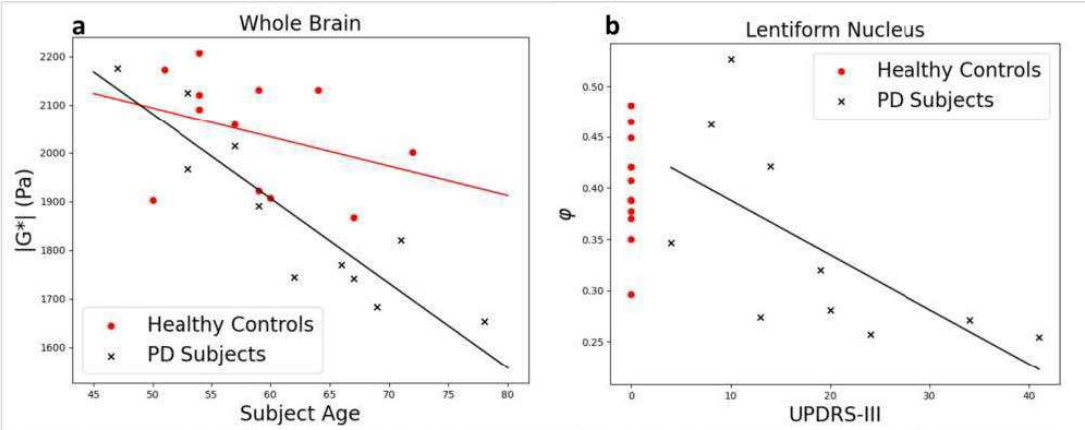

Figure 1. a) Average stiffness of the whole brain (|G*|) versus age of the subject. b) Phase angle φ of the Lentiform Nucleus vs UPDRS-III score of the PD subjects (HC shown with UPDRS-III score of 0).

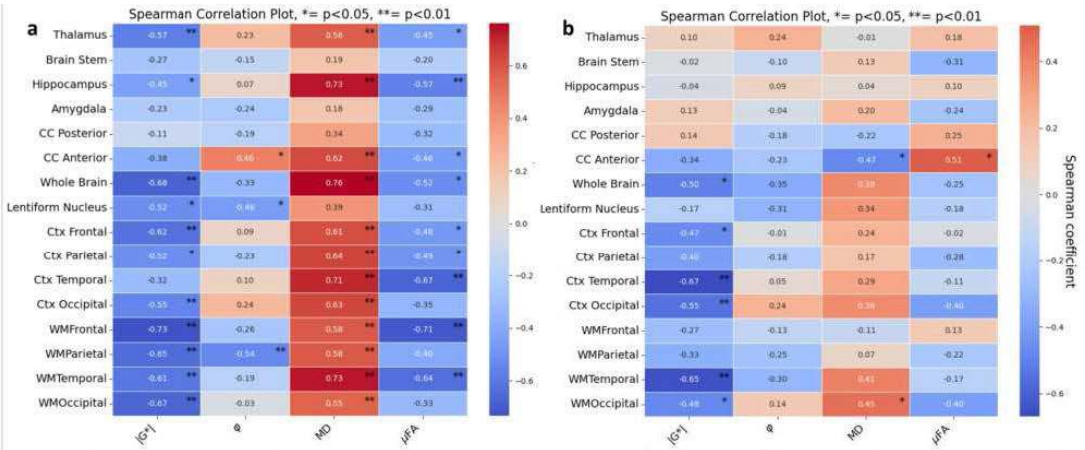

Figure 2. a) Spearman correlation plot for measured values in various regions with age for all subjects. b) Correlations between these values with a PD diagnosis, for all subjects after age correction. CC=Corpus Callosum. Ctx=Cortex. WM=White Matter

Conclusions: The softening effect due to age has been previously shown (see e.g. (Hiscox et al., 2021)), and softening of the brain due to PD has also been previously shown by (Lipp et al., 2013, 2018), however here we specifically show that this is most pronounced in the occipital and temporal lobes (in line with the atrophy findings by (Pieperhoff et al., 2022)). We also measured MUDI which indicated neural atrophy in the softened regions due to aging (Fig 2a), however for PD, the MUDI quantities indicate that more mechanisms than atrophy is responsible for the softening. In line with (Lipp et al. 2013) we also showed that the lentiform nucleus (a region known to be particularly affected by PD) becomes more elastic (lower φ) with

higher UPDRS-III score (Fig. 1b), which we here show not to be significantly correlated with neural atrophy (minor increase in MD, unchanged μFA). A limitation of this study at this stage is the relatively low number of subjects. We are currently collecting more data to increase the study's statistical power.

References

1. Desikan, Rahul S et al. (2006). "An Automated Labeling System for Subdividing the Human Cerebral Cortex on MRI Scans into Gyral Based Regions of Interest." NeuroImage, 31, 968–80.
2. Goetz, C. G. et al. (2008), "Movement Disorder Society-sponsored revision of the Unified Parkinson's Disease Rating Scale (MDS-UPDRS): Scale presentation and clinimetric testing results". Movement Disorder. 23, 2129–2170.
3. Hiscox, L. V. et al. (2021) Aging brain mechanics: Progress and promise of magnetic resonance elastography. Neuroimage 232.
4. Kamiya, K. et al. (2020), "Brain White-Matter Degeneration Due to Aging and Parkinson Disease as Revealed by Double Diffusion Encoding.", Frontiers in Neuroscience, 14, 1091.
5. Kruse, S. A. et al (2008), "Magnetic resonance elastography of the brain." Neuroimage 39, 231–237.
6. Lipp, A. et al. (2013) Cerebral magnetic resonance elastography in supranuclear palsy and idiopathic Parkinson's disease. NeuroImage Clinical, 3, 381–387.
7. Lipp, A. et al. (2018), Progressive supranuclear palsy and idiopathic Parkinson's disease are associated with local reduction of in vivo brain viscoelasticity. European Radiology, 28, 3347–3354.
8. Nilsson, M., et al. (2018). "An open-source framework for analysis of multidimensional diffusion MRI data implemented in MATLAB". Proceedings of the International Society for Magnetic Resonance in Medicine, 26, 5355.
9. Oliphant, T. E., et al. (2001) "Complex-valued stiffness reconstruction for magnetic resonance elastography by algebraic inversion of the differential equation." Magnetic Resonance in Medicine, 45, 299–310
10. Topgaard, D. (2017), "Multidimensional diffusion MRI", Journal of Magnetic Resonance, 275, 98–113 .
11. Westin, C.-F. et al. (2016), "Q-space trajectory imaging for multidimensional diffusion MRI of the human brain." Neuroimage 135, 345–362.

Poster No 180

Structural brain alterations in patients with criminal behavior in frontotemporal dementia

Karsten Mueller[1,2], Timo Grimmer[3], Lina Riedel[3], Janine Diehl-Schmid[3], Adrian Danek[4], Johannes Levin[4], Jens Wiltfang[5], Sarah Anderl-Straub[6], Markus Otto[7], Matthias Schroeter[1,8]

[1]Max Planck Institute for Human Cognitive and Brain Sciences, Leipzig, Germany, [2]Department of Neurology, Charles University, First Faculty of Medicine and General University Hospital in Prague, Prague, Czech Republic, [3]Department of Psychiatry and Psychotherapy, Technical University of Munich, Munich, Germany, [4]Department of Neurology, LMU University Hospital, LMU Munich, Munich, Germany, [5]Department of Psychiatry and Psychotherapy, Medical University Göttingen, Göttingen, Germany, [6]Department of Neurology, University of Ulm, Ulm, Germany, [7]University Hospital Halle/Saale, Halle/Saale, Germany, [8]Clinic for Cognitive Neurology, University Hospital Leipzig, Leipzig, Germany

Introduction: The behavioral variant of the frontotemporal dementia (bvFTD) is related to a variety of social misbehavior including criminal behavior (CB), aggression, loss of job, alienation from family/friends, financial recklessness, sexually deviant behavior, and abnormal response to spousal crisis (Mychack 2001). Recent work suggests that impairment in emotional processing of others, along with disinhibition, constitute the necessary elements for CB in bvFTD (Mendez 2022), however, the underlying neurobiological mechanisms are still unclear. Therefore, we aim at investigating structural brain changes related to CB in bvFTD using magnetic resonance (MR) imaging data of the German Consortium for Frontotemporal Lobar Degeneration (FTLD).

Methods: The study comprised 87 bvFTD patients (39 fem, age 62.9±9.8 y) and 26 healthy controls (HC, 13 fem, age 64.5±11.8 y) recruited within different locations (Göttingen, Leipzig, Munich, Ulm) of the FTLD Consortium. For each centre, clinical evaluation and neuropsychological assessments were performed according to standard operating procedures. A subset of 21 bvFTD patients (7 fem, age 64.2±11.2 y) showed CB including theft, physical violence, sexual assault, drug abuse, and violations against traffic law. High-resolution T1-weighted images were obtained using 3T Siemens MR scanners (Siemens Healthineers, Erlangen, Germany) with an MP-RAGE sequence. Data analysis was performed using SPM12 rev7771 with the CAT toolbox 12.8.2 rev2170 (Gaser 2022). For all participants, voxel-based morphometry was performed generating gray matter density (GMD) images using image segmentation and modulation by scaling with the amount of volume changes due to spatial registration (Ashburner 2005). Finally, GMD images were smoothed using a spatial Gaussian filter of 8 mm FWHM. In addition, surface-based morphometry was performed by reconstruction of cortical thickness using a projection-based thickness approach (Dahnke 2012). Both GMD and cortical thickness were further analyzed in order to detect group differences between bvFTD patients with and without CB, and between bvFTD patients with CB and HC. Group comparison was performed using a general linear model (GLM) with a full-factorial design using the factors 'group' (CB vs no-CB) and 'subgroup of bvFTD' (possible vs probable/definite). Analyses also included age and sex as nuisance covariates. Further, GMD

analyses included the total intracranial volume as an additional regressor. Group differences were computed using an initial voxel/vertex-threshold of P<0.001, and significant clusters were obtained using family-wise error (FWE) correction at cluster- and peak-level with P<0.01 (Flandin 2019, Friston 1994).

Results: Comparing bvFTD patients with and without CB, we obtained reduced GMD with CB in the left temporal lobe including the left amygdala (Fig 1A) and reduced cortical thickness in the left temporal lobe (Fig 2A). Comparing patients with CB in bvFTD with HC, we obtained a much larger pattern of CB-related reduced GMD and cortical thickness in larger regions of the left and right temporal lobe and also regions of the frontal lobe (Fig 1B and 2B, respectively).

Conclusions: Our study revealed structural brain differences between bvFTD patients with and without CB showing CB-related reduced GMD and cortical thickness in the left amygdala and the left temporal lobe. Interestingly, the same regions are discussed with CB in bvFTD in the current literature, however, dominantly affected in the right hemisphere (Mendez 2022). The involvement of the temporal lobe was also reported in criminal psychopaths (Müller 2008) in both left and right temporal lobe, but with higher sensitivity in the right hemisphere. In contrast, a recent study with homicide offenders showed the most prominent structural finding in the left temporal lobe (Sajous-Turner 2020) which is in line with our work. Further work is necessary to shed more light onto the role of the left and the right temporal lobe in bvFTD patients with CB.

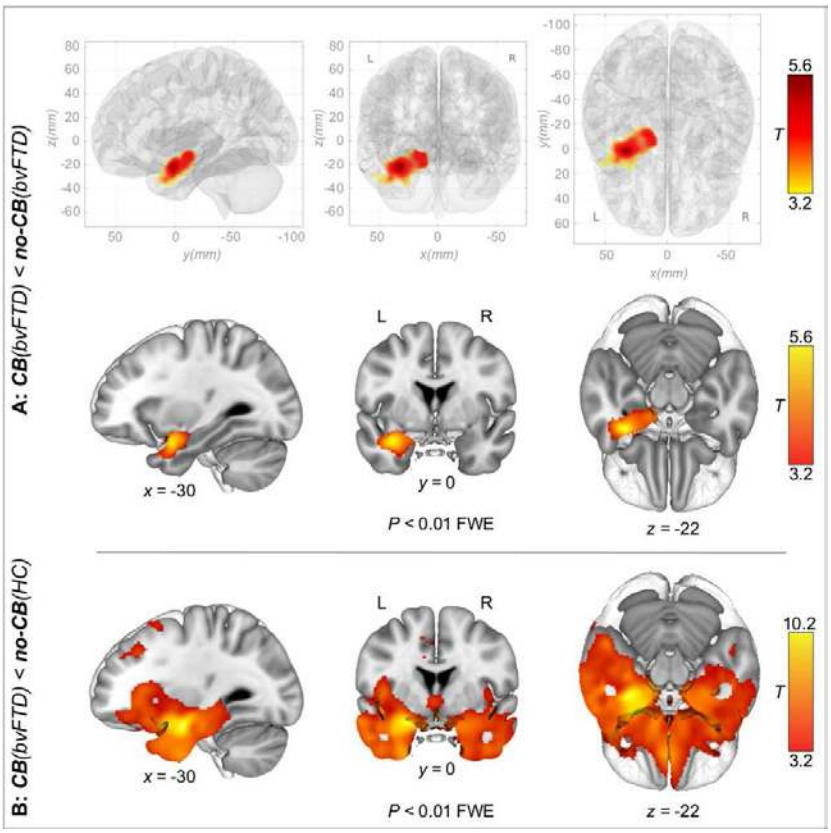

Figure 1. Reduced gray matter density in bvFTD patients with criminal behavior (CB) when comparing (A) bvFTD patients with and without CB, and (B) CB-bvFTD patients with healthy controls (HC).

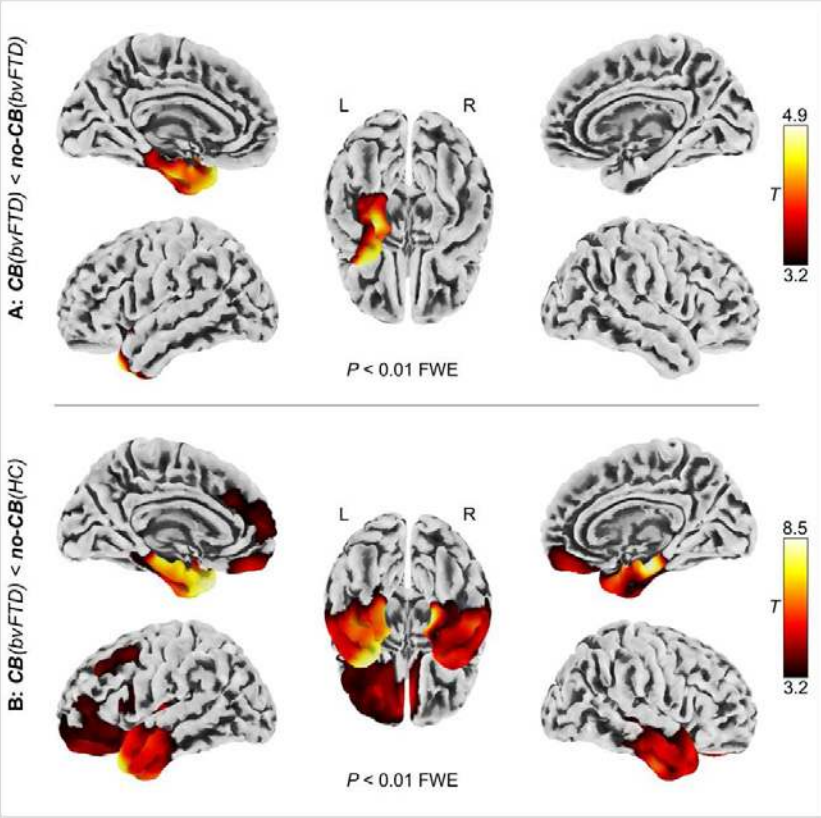

Figure 2. Reduced cortical thickness in bvFTD patients with criminal behavior (CB) when comparing (A) bvFTD patients with and without CB, and (B) CB-bvFTD patients with healthy controls (HC).

References

1. Ashburner, J., Friston, K.J. (2005), 'Unified segmentation', Neuroimage, vol. 26, no. 3, pp. 839-851, doi: 10.1016/j.neuroimage.2005.02.018
2. Dahnke, R., Yotter, R.A., Gaser, C. (2013), 'Cortical thickness and central surface estimation', Neuroimage, vol 65, pp. 336-348, doi: 10.1016/j.neuroimage.2012.09.050
3. Flandin, G., Friston, K.J. (2019), 'Analysis of family-wise error rates in statistical parametric mapping using random field theory', Human Brain Mapping, vol. 40, no. 7, pp. 2052-2054, doi: 10.1002/hbm.23839
4. Friston, K.J., Worsley, K.J., Frackowiak, R.S., Mazziotta, J.C., Evans, A.C. (1994), 'Assessing the significance of focal activations using their spatial extent', Human Brain Mapping, vol. 1, No. 3, pp. 210-220, doi: 10.1002/hbm.460010306
5. Gaser, C., Dahnke, R., Kurth, K., Luders, E. (2022), 'Alzheimer's Disease Neuroimaging Initiative. A Computational Anatomy Toolbox for the Analysis of Structural MRI Data', BioRxiv, doi: 10.1101/2022.06.11.495736
6. Mendez, M.F. (2022), 'Behavioral Variant Frontotemporal Dementia and Social and Criminal Transgressions', Journal Neuropsychiatry and Clinical Neurosciences, vol. 34, no. 4, pp. 328-340, doi: 10.1176/appi.neuropsych.21080224
7. Müller, J.L., Gänssbauer, S., Sommer, M., Döhnel, K., Weber, T., Schmidt-Wilcke, T., Hajak, G. (2008), 'Gray matter changes in right superior temporal gyrus in criminal psychopaths. Evidence from voxel-based morphometry', Psychiatry Research, vol. 163, no. 3, pp. 213-322, doi: 10.1016/j.pscychresns.2007.08.010
8. Mychack, P., Kramer, J.H., Boone, K.B., Miller, B.L. (2001), 'The influence of right frontotemporal dysfunction on social behavior in frontotemporal dementia', Neurology, vol. 56, suppl. 4, pp. 11-15, doi: 10.1212/wnl.56.suppl_4.s11
9. Sajous-Turner, A., Anderson, N.E., Widdows, M., Nyalakanti, P., Harenski, K., Harenski, C., Koenigs, M., Decety, J., Kiehl, K.A. (2020), 'Aberrant brain gray matter in murderers', Brain Imaging and Behavior, vol. 14, pp. 2050-2061, doi: 10.1007/s11682-019-00155-y

Poster No 181

Functional 7T MRI analyses reveal altered cerebellar activity and connectivity in multiple sclerosis

Myrte Strik[1,2,3], Emma Brouwer[1,2], Nikos Priovoulos[1,2,4], Renan Mukerjee[1], Mark Wessels[5], Eva Strijbis[5], Frederik Barkhof[6,7], Menno Schoonheim[3], Wietske van der Zwaag[1,2]

[1]Spinoza Centre for Neuroimaging, Amsterdam, Netherlands, [2]Computational Cognitive Neuroscience and Neuroimaging, Netherlands Institute for Neuroscience, Royal Netherlands Academy for Arts and Sciences (KNAW), Amsterdam, Netherlands, [3]Department of Anatomy and Neurosciences, MS Center Amsterdam, Amsterdam Neuroscience, Amsterdam UMC, Vrije Universiteit Amsterdam, Amsterdam, Netherlands, [4]Department of Biomedical Engineering and Physics, Amsterdam UMC, Amsterdam, Netherlands, [5]Department of Neurology, MS Center Amsterdam, Amsterdam Neuroscience, Amsterdam UMC, Vrije Universiteit Amsterdam, Amsterdam, Netherlands, [6]Department of Radiology and Nuclear Medicine, MS Center Amsterdam, Amsterdam Neuroscience, Amsterdam UMC, Vrije Universiteit Amsterdam, Amsterdam, Netherlands, [7]UCL Institutes of Neurology and Healthcare Engineering, London, United Kingdom

Introduction: The cerebellum is a small but finely organized region, highly connected and integrated in major brain networks involved in cognition and motor control.[1] In multiple sclerosis (MS), these functions are often affected, and the cerebellum is a prevalent injury site.[2] Despite the clinical importance and interest, the cerebellum is often overlooked due to technical challenges in imaging its thin and highly folded cortex. As such, the functional involvement of the cerebellum in MS is currently understudied and likely underestimated. Previous functional MRI studies shown altered network connectivity[3,4] and task-based activation[5] in MS, but primarily focused on the cerebrum, and cerebellar results often lack specificity. To image the cerebellum in greater detail, 7T MRI can be valuable due to the higher signal-to-noise ratio and increased spatial and temporal resolutions compared to clinical field strengths. Using 7T, a somatotopic organization has been mapped in anterior and posterior cerebellar lobules,[6] yet it's unclear whether this is altered in MS. In this preliminary study, we investigated cerebellar motor task responses and resting-state connectivity disturbances in people with MS and controls using 7T fMRI and submillimetre resolution anatomical images.

Methods: Six people with MS with signs of cerebellar damage (2 females, age=54±9 years) and 3 healthy controls (HC) (1 female, age=57±14 years) were scanned using a 7T-Phillips MRI-scanner (8Tx/32Rx whole-head coil). For the flexing motor task (10s-ON, 10s-OFF, 5min) and resting-state scan (fixation on cross, 7min), a 3D-EPI slab covering the cerebellum was used (1mm-isotropic, TR/TE=3288ms/21ms, SENSE=2.6/3.27-AP/RL, FOV=192x60x192mm3, α=20°). Anatomical imaging included: whole-brain 1mm-isotropic MP2RAGE (TR/TE=2.3ms/6.2ms, TI1/TI2=800/2700, TRvolume=5500ms, α=7°/5°, FOV=230x230x185)[7] and a submillimeter whole-cerebellar image (0.4mm isotropic) with prospective motion correction (5.65/1.88; TI1/TI2, 1000ms/2900ms; TI1/TI2, α =7°/5, FOV=210×120×60mm3, sensitivity encoding y/z, 1.5/1) (more details[8]). Motion correction involved real-time FOV updates by realignment of reconstructed fat navigators (3D EPI; 2mm; fat-selective binomial excitation pulse; 5.65/1.88; Tvol=550ms; α=1°; sensitivity encoding y/z, 4/2; Tacq=0.55s, FOV=240×240×120mm3). Functional data was motion/distortion-corrected and 0.4mm cerebellar anatomical images were denoised using a spatially adapted filter.[9] For the motor task, a first level GLM (FSL, flex>rest, Z>3.1, p<0.05) was used. A cerebellar motor function mask[10] was warped into each participant's anatomical space and manually divided to identify four relevant regions of interest (ROIs) (Fig1-A). To investigate cerebellar connectivity, a spherical seed mask (radius=4px) was generated from the highest motor task Z-score voxel (Fig-2-A), from which mean time-courses were extracted and used as first level GLM input (motor-seed>rest, Z>3.1, p<0.05).

Results: Flexing of the hand resulted in significant (Z>3.1, p<0.05) bilateral cerebellar activation in both anterior and posterior ROIs for all HCs, contrary to less than 50% of MS patients (Fig-1B/C). Maximum Z-scores were lower in MS (Right Anterior: MED=4.28±2.07, Posterior: MED=4.22±1.08) compared to HC (Right Anterior: MED=7.85±0.5, Posterior: MED=5.37±0.62). All participants had significant (Z>3.1, p<0.05) RS connectivity within cerebellar parts of the motor network (Fig2-B/C). Compared to HC, MS patients had lower average RS connectivity Z-scores (Fig-2B).

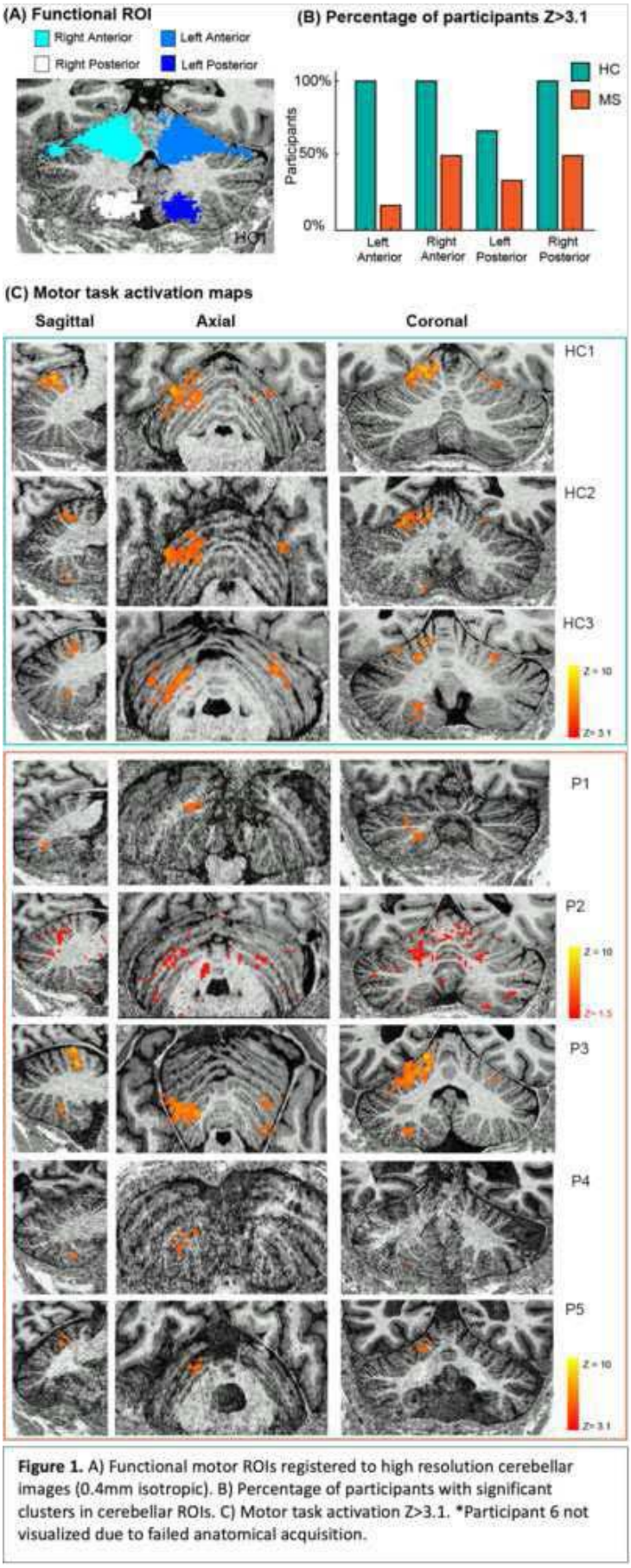

Figure 1. A) Functional motor ROIs registered to high resolution cerebellar images (0.4mm isotropic). B) Percentage of participants with significant clusters in cerebellar ROIs. C) Motor task activation Z>3.1. *Participant 6 not visualized due to failed anatomical acquisition.

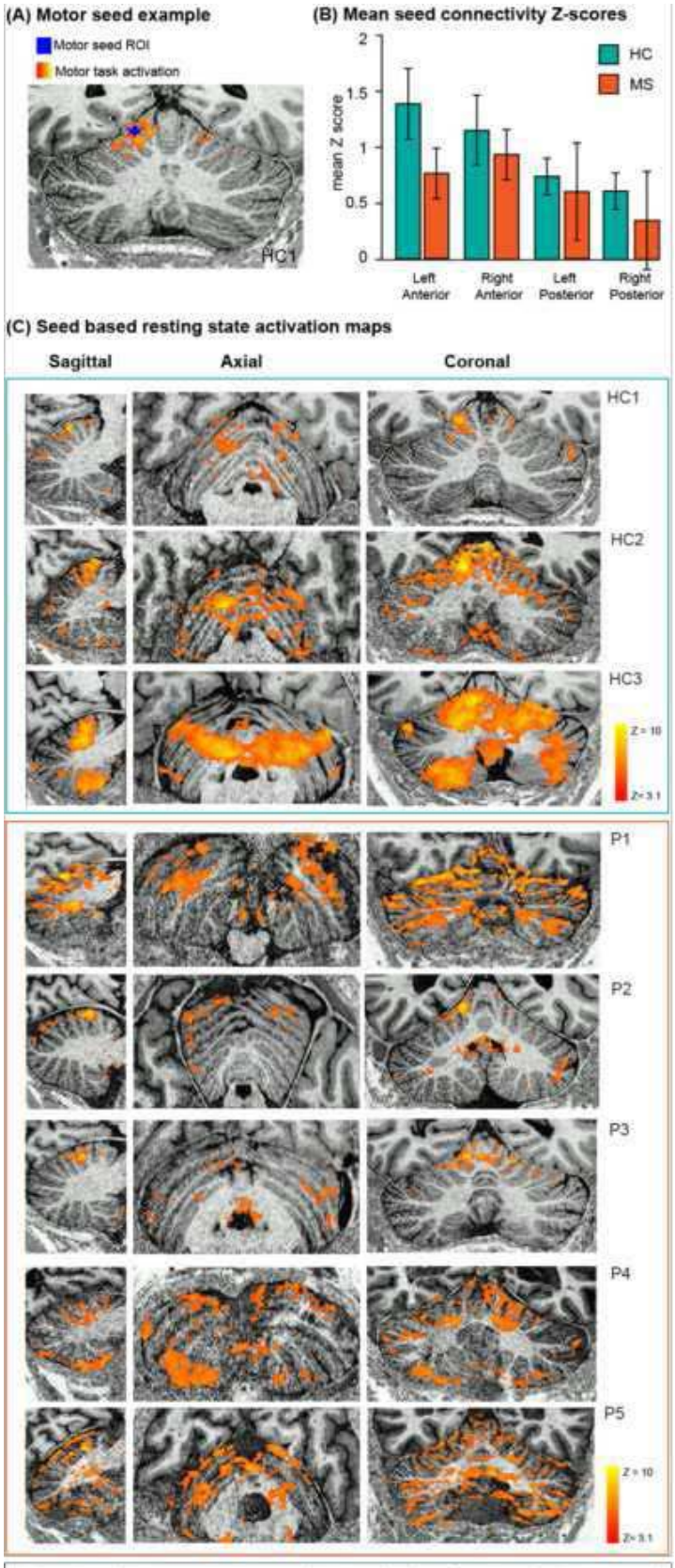

Figure 2. A) Motor activation seed HC1 overlaid on functional activation and anatomical image (0.4mm). Seed-based B) average RS Z-scores and C) RS activation (Z>3.1). *Participant 6 is not visualized due to failed anatomical acquisition.

Conclusions: We studied the communication and mapped regional activation during movements and preliminary results indicate lower and inconsistent cerebellar task-based activation, as well as lower resting-state connectivity in MS. Future

investigations will involve a larger cohort and a more in-depth to confirm findings and identify subject specific differences in cerebellar motor network activity and connectivity.

References

1. Buckner RL, Krienen FM, Castellanos A, Diaz JC, Thomas Yeo BT. The organization of the human cerebellum estimated by intrinsic functional connectivity. J Neurophysiol [Internet]. 2011 Nov [cited 2023 Jul 20];106(5):2322. Available from: /pmc/articles/PMC3214121/
2. Weissert R, Ayache SS, Bauer J, Wilkins A. Cerebellar Dysfunction in Multiple Sclerosis. Cerebellar Dysfunction in Multiple Sclerosis Front Neurol [Internet]. 2017 [cited 2023 Oct 31];8:312. Available from: www.frontiersin.org
3. Meijer KA, Eijlers AJC, Douw L, Uitdehaag BMJ, Barkhof F, Geurts JJG, et al. Increased connectivity of hub networks and cognitive impairment in multiple sclerosis. Neurology. 2017;
4. Strik M, Eijlers AJC, Dekker I, Broeders TAA, Douw L, Killestein J, et al. Sensorimotor network dynamics predict decline in upper and lower limb function in people with multiple sclerosis. Multiple Sclerosis Journal [Internet]. 2023 Jan 1 [cited 2023 Nov 29];29(1):81–91. Available from: https://journals.sagepub.com/doi/full/10.1177/13524585221125372
5. Rocca MA, Colombo B, Falini A, Ghezzi A, Martinelli V, Scotti G, et al. Cortical adaptation in patients with MS: A cross-sectional functional MRI study of disease phenotypes. Lancet Neurology. 2005;4(10):618–26.
6. Boillat Y, Bazin PL, Van Der Zwaag W. Whole-body somatotopic maps in the cerebellum revealed with 7T fMRI. 2020 [cited 2023 Nov 27]; Available from: https://doi.org/10.1016/j.neuroimage.2020.116624
7. Marques JP, Kober T, Krueger G, van der Zwaag W, Van de Moortele PF, Gruetter R. MP2RAGE, a self bias-field corrected sequence for improved segmentation and T1-mapping at high field. Neuroimage. 2010 Jan 15;49(2):1271–81.
8. Priovoulos N, Andersen M, Dumoulin SO, Boer VO, van der Zwaag W. High-Resolution Motion-corrected 7.0-T MRI to Derive Morphologic Measures from the Human Cerebellum in Vivo. Radiology. 2023 Apr 1;307(2).
9. Tustison NJ, Avants BB, Cook PA, Zheng Y, Egan A, Yushkevich PA, et al. N4ITK: Improved N3 Bias Correction. IEEE Trans Med Imaging [Internet]. 2010 Jun [cited 2023 Nov 27];29(6):1310. Available from: /pmc/articles/PMC3071855/
10. King M, Hernandez-Castillo CR, Poldrack RA, Ivry RB, Diedrichsen J. Functional boundaries in the human cerebellum revealed by a multi-domain task battery. Nature Neuroscience 2019 22:8 [Internet]. 2019 Jul 8 [cited 2023 Oct 26];22(8):1371–8. Available from: https://www.nature.com/articles/s41593-019-0436-x

Poster No 182

Revisiting cortical face-to-hand area reorganisation after tetraplegia

Paige Howell[1], Finn Rabe[2], Simon Schading[3], Harshal Sonar[4], Jamie Paik[4], Patrick Freund[5], Nicole Wenderoth[1], Sanne Kikkert[2]

[1]ETH Zürich, Zürich, Zürich, [2]ETH Zürich, Zürich, Switzerland, [3]Spinal Cord Injury Center Balgrist, University of Zürich, Zürich, Switzerland, [4]École Polytechnique Fédérale de Lausanne, Lausanne, Switzerland, [5]Spinal Cord Injury Center Balgrist, University of Zürich, Zürich, Zürich

Introduction: Following tetraplegia (i.e., cervical spinal cord injury; SCI), individuals experience a loss of muscle function and sensation in their limbs and torso. Seminal non-human primate studies demonstrated that this leads to extensive reorganisation in brain areas containing detailed map-like body representations (e.g., the primary somatosensory cortex; S1), such that the cortical area deprived of sensory inputs (e.g., of the hand) becomes responsive to touch on intact body parts (e.g., of the face; Reed et al., 2016)). While animal models of SCI have consistently revealed reorganisation in S1, the degree and pattern of cortical remapping in humans following SCI is less clear (Jutzeler et al., 2015; Makin et al., 2015; Makin & Bensmaia, 2017). There are several potential reasons for the apparent divergence of reorganisation results in non-human primates and humans: Firstly, while work in non-human primates showed chin-to-hand area reorganisation in S1, research in humans has primarily explored lip-to-face area reorganisation. Second, non-human primate research made use of tactile stimulation protocols, while human reorganisation research typically made use of movement paradigms due to the difficulty of providing tactile face stimulation inside an MRI. Lastly, while the S1 face representation is inverted in non-human primates with the chin neighbouring the hand area (Kaas, 1983), we (Kikkert et al., 2023), and others (Root et al., 2022), have shown that in human S1 the forehead is least distance to the hand representation. In this study, we attempt to tackle these methodological differences and uncover the full architecture of S1 face reorganisation in human tetraplegic patients. We used fMRI during tactile stimulation of the forehead, lips, and chin to characterize S1 face-to-hand reorganisation in detail in tetraplegic patients.

Methods: Suprathreshold vibrotactile stimulation was applied to the forehead, lips, cheek, and thumb of 16 chronic tetraplegic patients and 21 healthy control participants while they underwent 3T fMRI. The patient sample was heterogeneous in neurological level of injury (C1-C7), severity of neurological loss (ASIA A-D), and retained hand functioning (GRASSP score 22-188, healthy score = 232). Tactile stimulation was provided in a blocked-design fashion using an in-house build MRI-compatible pneumatic stimulator device that we previously validated for use in somatotopic mapping fMRI experiments (Kikkert et al., 2023; Sonar et al., 2021; Sonar & Paik, 2016). To uncover reorganisation, we first assessed the level of forehead, lips, and chin activity in an anatomical S1 hand area. We further assessed potential cortical shifts by extraction the geodesic distance of the peak S1 forehead, lips, and chin activity from an S1 foot area anchor.

Results: Our results did not show any differences in level of face parts activity in the S1 hand area between control participants and tetraplegic patients ($p > 0.51$; $BF10 < 0.38$), nor any representational shifts of the forehead, lips, or chin ($p > 0.73$; $BF10 < 0.34$). We did not find any significant correlations between our indicators of reorganisation and patients' retained hand functioning, time since injury, or anatomically defined amount of tissue bridges at the level of the spinal injury.

Conclusions: Our results did not show evidence for face-to-hand area reorganisation in S1 of human tetraplegic patients. Given that we aimed to match our approaches to those used in classical non-human primates experiments demonstrating face reorganisation, we suggest that face reorganisation is not apparent in humans. Future experiments that use intracortical recording methods (as in non-human primate studies) are needed.

References

1. Jutzeler, C. R., Freund, P., Huber, E., Curt, A., & Kramer, J. L. K. (2015). Neuropathic pain and functional reorganization in the primary sensorimotor cortex after spinal cord injury. The Journal of Pain, 16(12), 1256–1267. https://doi.org/10.1016/j.jpain.2015.08.008
2. Kaas, J. H. (1983). What, if anything, is SI? Organization of first somatosensory area of cortex. Physiological Reviews, 63(1), 206–231.
3. Kikkert, S., Sonar, H. A., Freund, P., Paik, J., & Wenderoth, N. (2023). Hand and face somatotopy shown using MRI-safe vibrotactile stimulation with a novel soft pneumatic actuator (SPA)-skin interface. NeuroImage, 269. https://doi.org/10.1016/j.neuroimage.2023.119932
4. Makin, T. R., & Bensmaia, S. J. (2017). Stability of Sensory Topographies in Adult Cortex. Trends in Cognitive Sciences, 21(3), 195–204. https://doi.org/10.1016/j.tics.2017.01.002
5. Makin, T. R., Scholz, J., Henderson Slater, D., Johansen-Berg, H., & Tracey, I. (2015). Reassessing cortical reorganization in the primary sensorimotor cortex following arm amputation. Brain, 138(8), 2140–2146. https://doi.org/10.1093/brain/awv161
6. Reed, J. L., Liao, C. C., Qi, H. X., & Kaas, J. H. (2016). Plasticity and recovery after dorsal column spinal cord injury in nonhuman primates. Journal of Experimental Neuroscience, 2016, 11–21. https://doi.org/10.4137/JEN.S40197
7. Root, V., Muret, D., Arribas, M., Amoruso, E., Thornton, J., Tarall-Jozwiak, A., Tracey, I., & Makin, T. R. (2022). Complex pattern of facial remapping in somatosensory cortex following congenital but not acquired hand loss. 11. https://doi.org/10.7554/eLife
8. Sonar, H. A., Huang, J.-L., & Paik, J. (2021). Soft Touch using Soft Pneumatic Actuator–Skin as a Wearable Haptic Feedback Device. Advanced Intelligent Systems, 3(3), 2000168. https://doi.org/10.1002/aisy.202000168
9. Sonar, H. A., & Paik, J. (2016). Soft pneumatic actuator skin with piezoelectric sensors for vibrotactile feedback. Frontiers in Robotics and AI, 2, 38. https://doi.org/10.3389/frobt.2015.00038

Poster No 183

Decoupling between cerebral blood volume and CSF in cognitive impairment is linked to brain volume

Riya Mahajan[1], Adam Wright[1], Qiuting Wen[2], Andrew Saykin[2], Shannon Risacher[2], Yunjie Tong[1]

[1]Purdue University, West Lafayette, IN, [2]Indiana University School of Medicine, Indianapolis, IN

Introduction: Cerebrospinal fluid (CSF) is crucial for eliminating misfolded proteins from the brain[1], but the mechanisms driving CSF dynamics in the human brain remain incompletely understood. Prior research demonstrates a tight coupling between CSF motion and cerebral blood volume (CBV), directly linked to low-frequency (LFO) hemodynamic oscillations[2-4]. In cognitive impairment (CI), there is a reduction in brain volume due to loss of neurons, gray and white matter, and ventricular expansion[5]. A resting-state fMRI (rs-fMRI) study showed reduced coupling between the CBV and CSF dynamics in CI individuals[6]. To build upon this study, we investigate how reduced brain volume in CI may alter the coupling between CBV and CSF dynamics. We hypothesize that a reduced brain volume weakens the driving force of brain pulsations, which may lower the coupling between CBV and CSF dynamics. Neurodegenerative diseases like Alzheimer's disease (AD) accelerate brain atrophy[5], possibly resulting in a more pronounced decoupling.

Methods: This study analyzed 40 participants, with 15 excluded due to poor image quality. The remaining 25 participants (10 female, 15 male, aged 51-87) included 12 cognitively normal (CN) and 14 with CI. MRI data were obtained using a 3T SIEMENS MRI scanner: T1W images (res = 1.2 x 1.1 x 1.1 mm3, TR/TE = 2300/2.98 ms) and rs-fMRI (res = 2.5 × 2.5 × 2.5 mm3, TR/TE = 1200/29 ms). Rs-fMRI were slice time corrected, motion corrected, and spatially smoothed. The global mean signal (GMS) was extracted from the whole brain excluding ventricles. CSF inflow signal was extracted with ROIs manually defined on the first slice (near the cerebellum) of non-motion corrected rs-fMRI. The selected voxel's time series had a maximum skewness > 0.5 to enhance sensitivity to CSF inflow effect. The GMS and CSF signals were linearly detrended, oversampled to 10 Hz sampling frequency, and band-pass filtered (0.01 to 0.1 Hz) using a zero delay, 4th-order Butterworth filter. The GMS signal's time derivative (d(GMS)/dt) can be used to assess the effect of hemodynamic oscillations in the brain, as CSF movement occurs during CBV oscillations3. The d(GMS)/dt was multiplied by -1, and negative values were set to zero to restrict the analysis to inflow. The coupling strength was quantified by calculating the maximal cross-correlation coefficients between the -d(GMS)/dt and CSF signals. Volumetric brain analysis was completed using the vol2Brain 1.0 software analysis7 and brain tissue volume (gray + white matter) was normalized to the total intracranial volume. Spearman correlation quantified the associations between -d(GMS)/dt-CSF coupling and normalized brain volume, with respect to cognition and biological sex.

Group-level comparisons of cognition and biological sex with -d(GMS)/dt-CSF coupling, and normalized brain volumes were performed using a student's t-test. p<0.05 was regarded as significant.

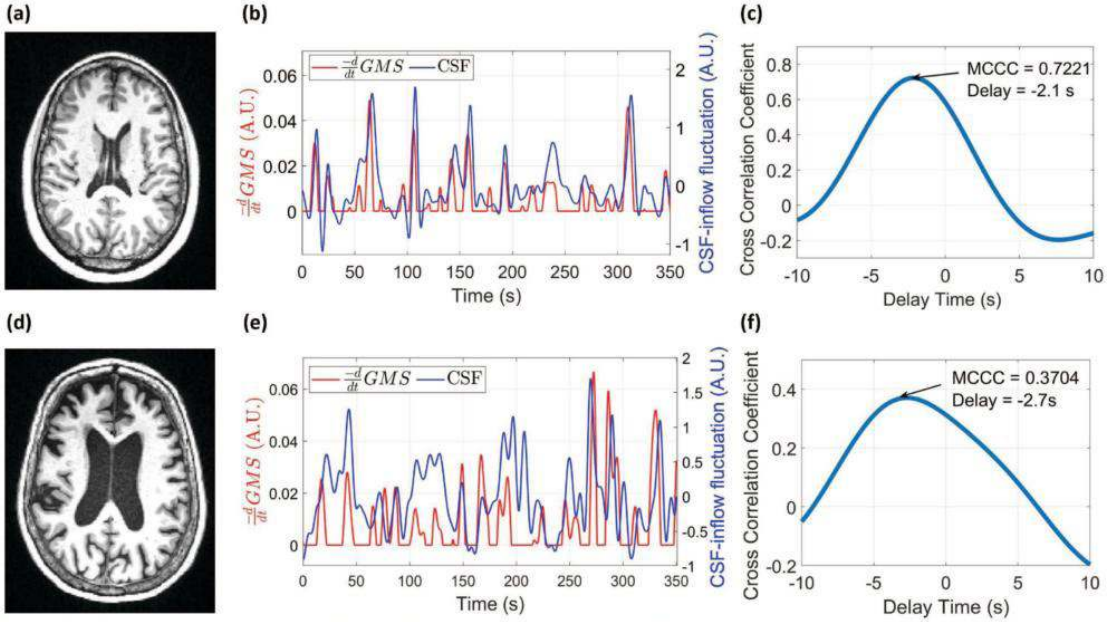

Figure 1: The negative derivative of GMS and CSF inflow fluctuation shows increased coupling between CBV and CSF dynamics in participants with larger brain volumes. (a) Axial slice from T1-weighted image of example participant (58-year-old, Female, CN) with greater brain volume and smaller lateral ventricle (b) Example time series showing greater correlation in participant with greater brain volume (c) Cross-correlation between $-\frac{d}{dt}(GMS)$ and CSF inflow fluctuation. There is a larger $-\frac{d}{dt}(GMS)$ -CSF coupling in participants with greater brain volume (d) Axial slice from T1-weighted image of example participant (67-year-old, Female, CI) with smaller brain volume and larger lateral ventricle (e) Example time series showing smaller correlation in participant with smaller brain volume (f) Cross-correlation between $-\frac{d}{dt}(GMS)$ and CSF inflow fluctuation. There is smaller $-\frac{d}{dt}(GMS)$-CSF coupling in participant with smaller brain volume. A negative delay time indicates that CSF inflow to the brain occurs ~2-3 s after cerebral blood volume decreases. GMS, Global Mean Signal; CSF, cerebrospinal fluid; CN, cognitively normal; CI, cognitive impairment; MCCC, maximum cross-correlation coefficient

Results: The -d/dt(GMS)-CSF coupling showed significant positive association with brain volume across all participants (r = 0.408, p = 0.043). This coupling was significantly positively associated with brain volume in CI patients (r = 0.555, p = 0.049), but not in CN patients (r = 0.252, p = 0.430). There was no significant difference in the coupling between CN and CI groups (t-test, p = 0.462). A significant difference (t-test, p = 0.008) was observed in the brain volumes between CN and CI, where the CI group had smaller brain volumes.

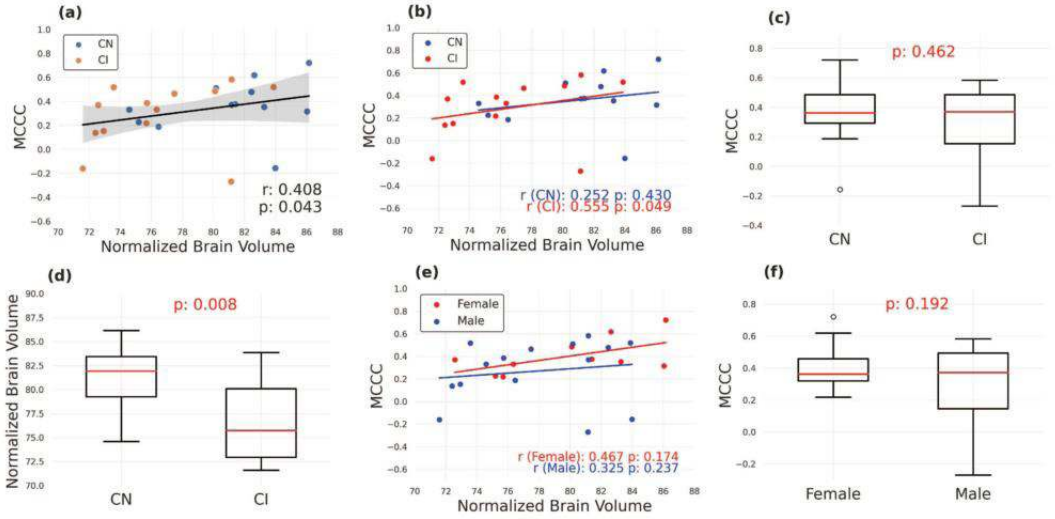

Figure 2: The relationship between cerebral blood volume (CBV) and CSF dynamics in terms of normalized brain volume, sex, and disease condition. (a) The $-\frac{d}{dt}(GMS)$-CSF coupling shows a significant correlation (Spearman's r = 0.408, p = 0.043) with normalized brain volume. The linear regression line was estimated based on the linear least-squares fitting. (b) There is no significant correlation found between the $-\frac{d}{dt}(GMS)$-CSF coupling and normalized brain volume in the CN group (p > 0.05). However, a significant correlation is observed in the CI group (p < 0.05). (c) There is no significant difference in $-\frac{d}{dt}(GMS)$-CSF coupling between the CN and CI groups (p > 0.05) (d) CN participants showed a larger amplitude of atrophy than CI participants (p < 0.05). (e) There is no significant correlation found between the $-\frac{d}{dt}(GMS)$-CSF coupling and normalized brain volume in female and male participants (p > 0.05). (f) There is no significant difference in $-\frac{d}{dt}(GMS)$ -CSF coupling between the female and male participants (p > 0.05). GMS, Global Mean Signal; CSF, cerebrospinal fluid; CN, cognitively normal; CI, cognitive impairment; MCCC, maximum cross-correlation coefficient

Conclusions: Our results suggest a significant positive correlation between the -d(GMS)/dt-CSF and brain volume in CI. This could indicate that a reduced brain volume weakens the interaction between CBV and CSF dynamics and impair a major driving force of CSF movement. This could lead to reduced CSF flow and an accelerated accumulation of toxic proteins, ultimately leading to greater atrophy and accelerating progression of neurodegenerative diseases like AD.

References

1. Benveniste, H. (2018), 'The Glymphatic System and Waste Clearance with Brain Aging: A Review'. Gerontology, 65, 106–119
2. Fultz, N. E. (2019), 'Coupled electrophysiological, hemodynamic, and cerebrospinal fluid oscillations in human sleep'. Science, 366, 628–631
3. Yang, H.-C. (2022), 'Coupling between cerebrovascular oscillations and CSF flow fluctuations during wakefulness: An fMRI study'. Journal of Cerebral Blood Flow and Metabolism, 42, 1091–1103
4. Nair, V.V. (2022), 'Human CSF movement influenced by vascular low frequency oscillations and respiration'. Frontiers in Physiology, 13
5. Blinkouskaya, Y. (2021), 'Brain Shape Changes Associated With Cerebral Atrophy in Healthy Aging and Alzheimer's Disease'. Frontiers in Mechanical Engineering, 7
6. Han, F. (2021), 'Reduced coupling between cerebrospinal fluid flow and global brain activity is linked to Alzheimer disease–related pathology'. PLOS Biology 19, e3001233–e3001233
7. Manjón, J. V. (2022), 'vol2Brain: A New Online Pipeline for Whole Brain MRI Analysis'. Frontiers in Neuroinformatics,16

Poster No 184

ASL blood-brain barrier permeability is associated with amyloid and cognitive impairment

Beatriz Padrela[1], Sandra Tecelão[2], Oliver Geier[3], Markus Sneve[4], David Vallez Garcia[1], Amnah Mahroo[5], Lene Pålhaugen[2], Bjørn-Eivind Kirsebom[6], Klaus Eickel[5], David Thomas[7], Atle Bjørnerud[4], Anders Fjell[4], Kristine Beate Walhovd[4], Frederik Barkhof[1], Per Selnes[2], Matthias Günther[5], Jan Petr[8], Tormod Fladby[2], Henk Mutsaerts[1]

[1]Department of Radiology and Nuclear Medicine, Amsterdam University Medical Center, Location VUmc, Amsterdam, Netherlands, [2]Department of Neurology, Akershus University Hospital, Oslo, Norway, [3]Department of Physics and Computational Radiology, Division of Radiology and Nuclear Medicine, Oslo, Norway, [4]Department of Psychology, Center for Lifespan Changes in Brain and Cognition, University of Oslo, Oslo, Norway, [5]Fraunhofer-Institute for Digital Medicine MEVIS, Bremen, Germany, [6]Institute of Clinical Medicine, Campus Ahus, University of Oslo, Oslo, Norway, [7]Queen Square Institute of Neurology, University College London, London, UK, [8]Helmholtz-Zentrum Dresden-Rossendorf, Institute of Radiopharmaceutical Cancer Research, Dresden, Germany

Introduction: Blood-brain barrier (BBB) dysfunction is potentially one of the earliest microvascular changes in Alzheimer's disease (AD) and related dementias[1]. An emerging technique to image the time of exchange (Tex) of water across the BBB is multi-echo[2,3] arterial spin labeling (ASL) which obviates the need for exogenous contrast, making it a less invasive and less costly alternative to existing contrast-based agents, and may even be more sensitive to subtle BBB changes. Tex has been shown to provide reproducible values of BBB integrity in healthy volunteers[2]. Here, we investigate the associations of Tex values with amyloid positivity and cognitive status. As cerebral blood flow (CBF) can be seen as an established ASL biomarker, we repeated all analyses for CBF for comparison.

Methods: Data from 116 participants older than 50 years were selected from the Center for Lifespan Changes in Brain and Cognition (LCBC) and the Dementia Disease Initiation (DDI) cohorts. LCBC comprises a population-based cohort including only cognitively normal (CN) participants (n=77, CNLCBC), while DDI is a clinical outpatient cohort including CN and subjective cognitive decline patients (n=24, merged here into a single cohort CNDDI) and mild cognitive impairment (n=15, MCIDDI)[4] patients. Amyloid status was defined as positive (A+) or negative (A-) from the CSF amyloid-beta 42/40 ratio (cut-off ≤ 0.077) or amyloid-PET by visual read, when available. All cohorts were scanned on the same 3T Siemens Prisma scanner with a 32-channel head coil. Two recently developed multi-post-labeling delay (PLD) Hadamard-encoded (HAD) 3D GRASE PCASL sequences were used to estimate Tex and CBF: 1) HAD-8 with a labeling duration (LD) 400 ms, PLD [600:400:3400] ms, and single echo time (TE) 12.5 ms; 2) multi-TE HAD-4 with LD 1000 ms, PLD [1500:1000:3500] ms, and 8 TEs [14.4:28.9:217.2] ms. Data were analyzed with ExploreASL 1.11.0 beta[5], and gray matter (GM) CBF and Tex were quantified with FSL-FABBER[6]. Tex and CBF associations with amyloid and cognitive status were assessed using linear regression adjusted for age and sex.

Results: Of the 116 participants, 77 were from the LCBC (64.6±8.4 years, 64% female) and 39 from the DDI (67.7±7.9 years, 51% female) cohorts. DDI included 15 MCIs and 28 A+, of which 12 were both MCI and A+. Across the whole population, GM Tex was negatively correlated with age ($r = -0.38$, $p < 0.001$), whereas for GM CBF, this correlation was not statistically significant ($r = -0.26$, $p = 0.069$). Whole-brain group average Tex (Figure 1A) and CBF (Figure 1B) maps show data from CN A- controls, MCI patients, and A+ subjects, where Tex and CBF appear higher in the NC A- group than in the MCI or A+ groups. Tex was 15% lower in A+ compared to A- ($t=2.75$, $p=0.01$; Figure 2A). CBF was 5% higher in the A+ group than the A- group but did

borderline not reach statistical significance (t=-1.94, p=0.06; Figure 2B)[7,8]. The linear regression analysis showed that amyloid status was associated with BBB water permeability (given by Tex), with higher permeability in A+ compared with A- groups when correcting for age, sex, and CBF (β = -35 s, p < 0.001; Figure 2C). Moreover, cognitive staging was related to Tex, even when correcting for age and sex (βMCI = -31.3 s, p < 0.01). A similar relationship was not found for CBF.

Conclusions: Interestingly, both amyloid positivity and cognitive status were associated with increased BBB water permeability, even when correcting for age and sex. In agreement with previous studies, BBB water permeability was shown to increase with age. These permeability increases might be explained by a normal aging process of increased brain clearance or by BBB dysfunction promoting leakage of toxins to cross from the capillary site to the brain parenchyma. These findings encourage the use of BBB-ASL to non-invasively investigate BBB integrity in the early stages of dementia.

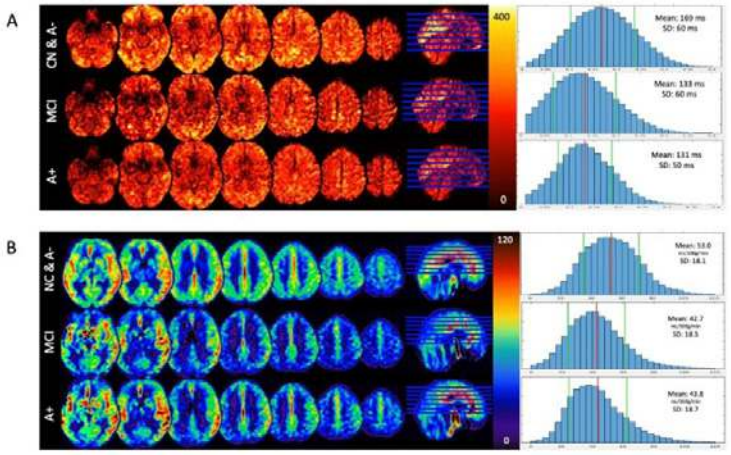

Figure 1. Group-average whole-brain Tex (A) and CBF (B) maps and the respective GM values histograms showing the mean (red vertical line) and standard deviation (green vertical lines) from DDI subjects: cognitively normal group (n=12, top row); mild cognitive impaired group (n=15, middle row); amyloid positive group (n=28, bottom row). All maps have the same color scale. NB: In total, DDI includes 15 MCIs and 28 A+, of which 12 were both MCI and A+.

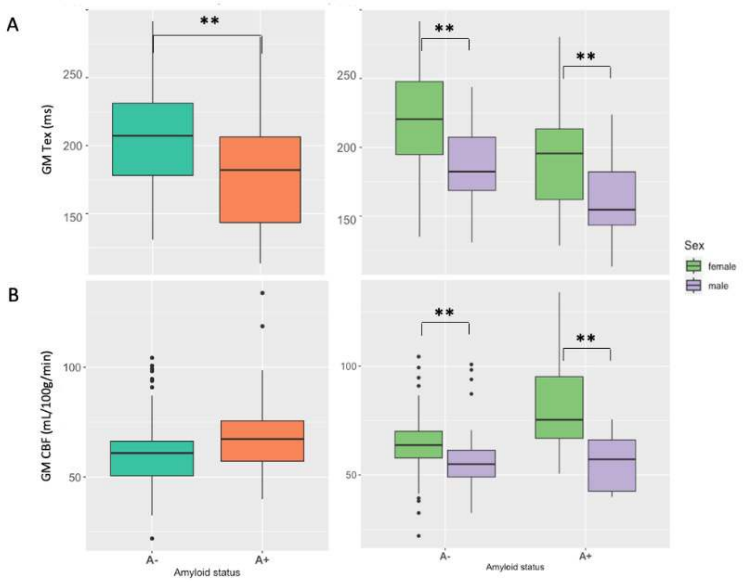

C

	Amyloid status		Amyloid status + age + sex						Amyloid status + age + sex + CBF							
	β	p	β (A+)	p (A+)	β (age)	p (age)	β (male)	p (male)	β (A+)	p (A+)	β (age)	p (age)	β (male)	p (male)	β (CBF)	p (CBF)
GM Tex (ms)	-28.2	**	-22.3	*	-1.6	**	-28.2	***	-35.4	***	-1.1	N.S	-20.3	**	1.3	***
GM CBF (mL/100g/min)	2.9	NS	13.3	**	-0.5	*	-8.4	*	-	-	-	-	-	-	-	-

Figure 2 - Gray matter CBF (A) and Tex (B) values from amyloid negative and positive groups (left) also stratified by sex (right). Linear model parameters (C) comparing differences between the cognitive stage (column) and the reference group CN_{LCBC}, without (left) and with (right) adjustment for age and sex. *p<0.05, **p<0.01, ***p<0.001.

References
1. Montagne, A. et al. (2020) 'APOE4 leads to blood-brain barrier dysfunction predicting cognitive decline'. Nature 581, 71–76
2. Mahroo, A. et al. (2021) 'Robust Multi-TE ASL-Based Blood-Brain Barrier Integrity Measurements'. Front. Neurosci. 15, 719676
3. Gregori, J., Schuff, N., Kern, R. & Günther, M. (2013) 'T2-based arterial spin labeling measurements of blood to tissue water transfer in human brain'. J. Magn. Reson. Imaging 37, 332–342
4. Fladby, T. et al. (2017) 'Detecting At-Risk Alzheimer's Disease Cases. J. Alzheimers'. Dis. 60, 97–105
5. Mutsaerts, H. J. M. M. et al. (2020) 'ExploreASL: an image processing pipeline for multi-center ASL perfusion MRI studies'. Neuroimage 117031
6. Chappell, M. A., Groves, A. R., Whitcher, B. & Woolrich, M. W. (2009) 'Variational Bayesian Inference for a Nonlinear Forward Model. IEEE Trans'. Signal Process. 57, 223–236
7. Fazlollahi, A. et al. (2020) 'Increased cerebral blood flow with increased amyloid burden in the preclinical phase of alzheimer's disease'. J. Magn. Reson. Imaging 51, 505–513
8. Padrela, B. E. et al. (2023) 'Genetic, vascular, and amyloid components of cerebral blood flow in a preclinical population'. J. Cereb. Blood Flow Metab. 271678X231178993

Poster No 185

PET Amyloid Predicts Longitudinal Atrophy in Non-Demented Individuals: Results from the AMYPAD PNHS

Leonard Pieperhoff[1], Luigi Lorenzini[1], Sophie Mastenbroek[1], Mario Tranfa[2], Mahnaz Shekari[3], Alle Meije Wink[1], Robin Wolz[4], Sylke Grootoonk[4], Isadora Lopes Alves[1], Craig Ritchie[5], Mercè Boada[6], Marta Marquié[6], Philip Scheltens[1], Rik Vandenberghe[7], Bernard Hanseeuw[8], Pablo Martinez-Lage[9], Pierre Payoux[10], Pieter Jelle Visser[1], Michael Schöll[11], Giovanni B. Frisoni[12], Andrew Stephens[13], Christopher Buckley[14], Gill Farrar[14], Frank Jessen[15], Oriol Grau-Rivera[3], Juan Domingo Gispert[3], David Vallez Garcia[1], Lyduine Collij[1], Frederik Barkhof[1]

[1]Amsterdam UMC, Amsterdam, Netherlands, [2]University of Naples, Naples, Italy, [3]Barcelonaβeta Brain Research Center, Barcelona, Spain, [4]IXICO, London, United Kingdom, [5]University of Edinburgh, Edinburgh, United Kingdom, [6]Ace Alzheimer Center Barcelona, Barcelona, Spain, [7]UZ Leuven, Leuven, Belgium, [8]UCLouvain, Louvain, Belgium, [9]Fundación CITA-alzhéimer, San Sebastián, Spain, [10]Centre hospitalier universitaire de Toulouse, Toulouse, France, [11]University of Gothenburg, Gothenburg, Sweden, [12]Geneva University Hospital, Geneva, Switzerland, [13]Life Molecular Imaging, Berlin, Germany, [14]GE HealthCare, Chalfont St Giles, United Kingdom, [15]German Center for Neurodegenerative Diseases (DZNE), Bonn, Germany

Introduction: As the field of anti-amyloid therapy is shifting towards early intervention, there is a need to understand the effect of amyloid-beta (Aβ) accumulation on atrophy in preclinical stages of the disease. We investigated the cross-sectional and longitudinal association between cortical amyloid deposition and subsequent neurodegeneration in a large cohort of non-demented individuals.

Methods: We included 1365 participants from the AMYPAD Prognostic & Natural History study (PNHS; v202306, doi:10.5281/zenodo.8017084) with available MRI and amyloid-PET. Among those, 708 had longitudinal MRI and PET, with a mean follow-up time of 3.74 years (SD=1.87). Grey matter thickness and volumes in 40 regions of interest (ROI) were measured using the FreeSurfer 7.1.1 longitudinal pipeline. Global cortical amyloid burden was determined using the Centiloid (CL) method from PET scans. MRI-derived atrophy measures were harmonised across sites with neuroCombat. All PET and MR variables were Z-scored to obtain standardised regression coefficients. Linear mixed-effect models with subject-specific random intercept and slope were used to investigate the effect of amyloid burden at baseline and its interaction with time on longitudinal, regional volume and thickness measurements. Covariates included age, sex, and baseline CDR score. P-values were FDR-adjusted. For the subset of 708 participants, secondary, nested models including longitudinal amyloid PET were compared to the original model using ANOVA based on the Akaike Information Criterion (AIC). Finally, the modulating effect of sex and APOE-ε4 carriership on the interaction of amyloid and time was investigated by adding each covariate to the model in a three-way interaction term.

Figure 1. *Sample Demographics Stratified by Amyloid Stage*

Variable	**Overall**, N = 1,329[1]	**Negative**, N = 757[1]	**Grey-Zone**, N = 268[1]	**Positive**, N = 304[1]	*p*
Age, years	68.18 (8.78)	66.36 (8.31)	67.61 (7.86)	73.21 (8.81)	<0.001[2]
Follow-Up, years	3.74 (1.87)	3.86 (1.97)	3.56 (1.56)	3.45 (1.79)	0.075[2]
(Missing)	585	282	107	196	
Gender					0.085[3]
Female	741 / 1,329 (56%)	442 / 757 (58%)	140 / 268 (52%)	159 / 304 (52%)	
Male	588 / 1,329 (44%)	315 / 757 (42%)	128 / 268 (48%)	145 / 304 (48%)	
Education, years	14.56 (3.97)	14.68 (3.86)	14.82 (4.18)	14.05 (4.01)	0.053[2]
(Missing)	3	2	0	1	
CDR, score					<0.001[3]
0 - Normal	1,070 / 1,329 (81%)	660 / 757 (87%)	231 / 268 (86%)	179 / 304 (59%)	
0.5 - Very mild	259 / 1,329 (19%)	97 / 757 (13%)	37 / 268 (14%)	125 / 304 (41%)	
MMSE, score	28.82 (1.54)	29.05 (1.28)	29.01 (1.35)	28.00 (1.99)	<0.001[2]
(Missing)	108	46	19	43	
APOE ε4 carriership (% carriers)	517 / 1,289 (40%)	223 / 745 (30%)	112 / 261 (43%)	182 / 283 (64%)	<0.001[3]
(Missing)	40	12	7	21	
Amyloid PET, CL	19.51 (32.33)	-0.19 (6.49)	17.16 (5.27)	70.62 (29.28)	<0.001[2]
est. Total Intracranial Volume, cm^3	1.48 (0.18)	1.47 (0.18)	1.50 (0.18)	1.48 (0.17)	0.043[2]

Note. CDR = Clinical Dementia Rating; MMSE = Mini-Mental State Examination; PET = Positron Emission Tomography; CL = Centiloid; Amyloid stages are defined based on a value of under 10 CL for negativity, over 30 CL for positivity and a subsequent grey-zone of 10 to 30 CL.

[1]Mean (SD); n / N (%)
[2]Kruskal-Wallis rank sum test
[3]Pearson's Chi-squared test

Results: Cohort characteristics are shown in Figure 1. At baseline, higher amyloid burden was related to reduced volumes and thickness in multiple temporal and parietal ROIs, as well as hippocampal and amygdala volume. Over time, individuals with higher baseline amyloid burden experienced greater volume- and thickness loss primarily in temporal and parietal regions, as well as cingulate, amygdala and hippocampal volume (Figure 2A). Incorporating longitudinal amyloid PET improved the prediction especially in medial-parietal, cingulate and basal-frontal ROIs (Figure 2B). Sex differences in how predictive cortical amyloid burden was of longitudinal atrophy were only found for caudate volume, while differences between APOE ε4 carriers and non-carriers could be observed in thickness of the medial and lateral orbitofrontal cortex, as well as hippocampal and pallidum volume.

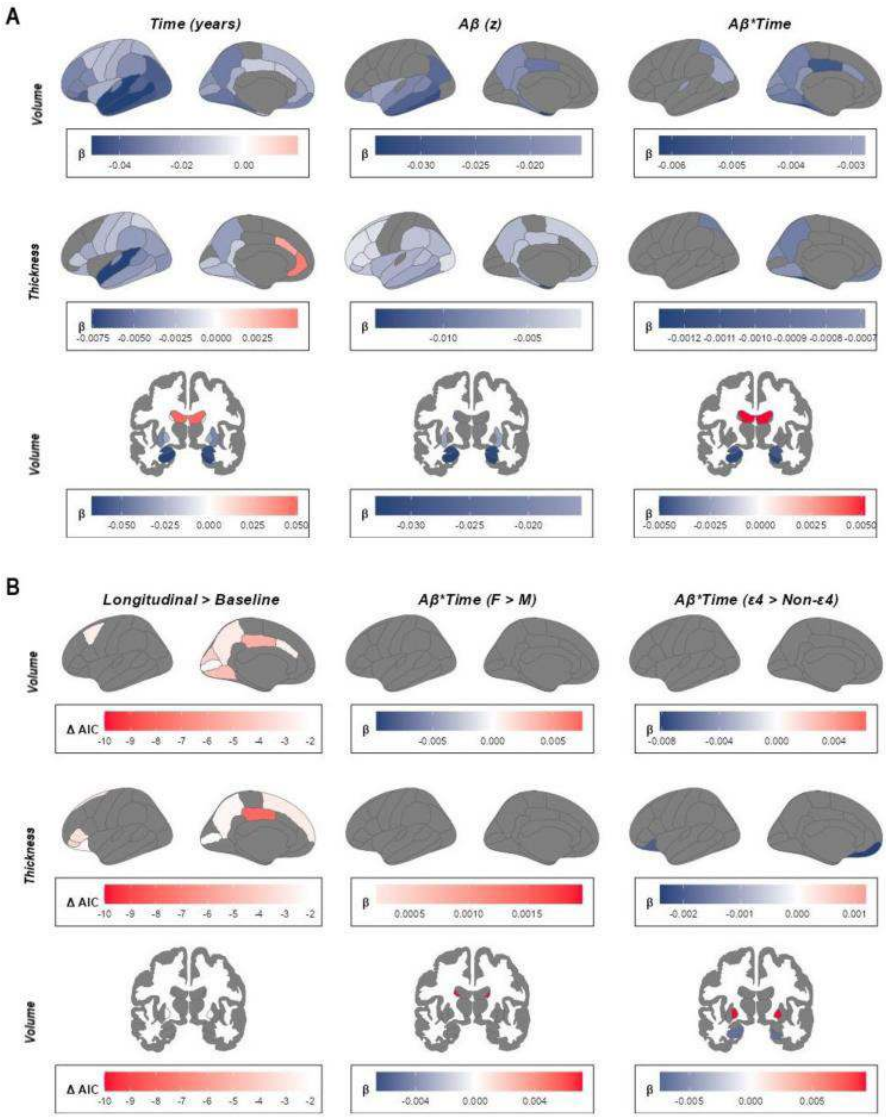

Figure 2. *Regression Coefficients (β) and Differences in Akaike Information Criterion (Δ AIC) of the Analyses.*
(A) Columns 1 and 2 depict the main effects of time and amyloid on each image-derived phenotype, column 3 depicts the effect of their interaction. (B) Column 1 shows the difference in AIC between the "baseline PET only" model and "longitudinal PET" model, columns 2 and 3 the effect of the added threeway interaction terms.

Conclusions: In the largely asymptomatic AMYPAD PNHS cohort, we demonstrate that baseline amyloid burden is predictive of future neurodegeneration, particularly affecting parietal volume and thickness in addition to hippocampal volume, rather than lateral temporal regions. Prediction of future atrophy improved when changes in amyloid burden were included in the model, illustrating the potential of natural history studies to act as trial readiness cohorts for optimal patient selection.

References

1. Collij, L.E. (2023), 'The amyloid imaging for the prevention of Alzheimer's disease consortium: A European collaboration with global impact', Frontiers in Neurology, vol. 13
2. Desikan, R.S. (2006), 'An automated labeling system for subdividing the human cerebral cortex on MRI scans into gyral based regions of interest', NeuroImage, vol. 31, no. 3, pp. 968–980
3. Fortin, J.-P. (2018), 'Harmonization of cortical thickness measurements across scanners and sites', NeuroImage, vol. 167, pp. 104–120
4. Lopes Alves, I. (2020). 'Quantitative amyloid PET in Alzheimer's disease: the AMYPAD prognostic and natural history study' Alzheimer's & Dementia, vol. 16, no. 5, pp. 750–758
5. Pemberton, H.G. (2022), 'Quantification of amyloid PET for future clinical use: a state-of-the-art review', European Journal of Nuclear Medicine and Molecular Imaging, vol. 49, pp. 3508–3528

Poster No 186

Effects of Beta-amyloid on the Temporo-parietal Network across the Alzheimer's Disease Continuum

Yanin Suksangkharn[1,2], Björn Schott[3,4,5,6], Peter Zeidman[7], René Lattmann[2], Renat Yakupov[2], Holger Amthauer[8], Arda Cetindag[9], Nicoleta Cosma[9], Dominik Diesing[9], Marie Ehrlich[9], Silka Freiesleben[9], Manuel Fuentes[9,10], Wenzel Glanz[2], Dietmar Hauser[9], Nicole Hujer[9], Enise Incesoy[9], Christian Kainz[11], Catharina Lange[9], Katja Lindner[9], Herlind Megges[9,10], Oliver Peters[9,10], Lukas Preis[9], Slawek Altenstein[10,12], Andrea Lohse[12], Christiana Franke[12], Josef Priller[10,12], Eike Spruth[12], Klaus Fließbach[13], Doreen Grieger-Klose[2], Deike Hartmann[2], Coraline Metzger[2], Christin Ruß[2], Franziska Schulze[2], Oliver Speck[2], Frank Jessen[13,14], Anne Maass[2], Emrah Düzel[1,2], Gabriel Ziegler[1,2]

[1]Institute of Cognitive Neurology and Dementia Research, Otto-von-Guericke University Magdeburg, Magdeburg, Germany, [2]German Center for Neurodegenerative Diseases (DZNE), Magdeburg, Germany, [3]German Center for Neurodegenerative Diseases (DZNE), Göttingen, Germany, [4]Leibniz Institute for Neurobiology (LIN), Magdeburg, Germany, [5]Center for Behavioral Brain Sciences (CBBS), Magdeburg, Germany, [6]Department of Psychiatry and Psychotherapy, University Medical Center Göttingen, Göttingen, Germany, [7]Wellcome Centre for Human Neuroimaging, London, England, [8]Charité – Universitätsmedizin Berlin - Department of Nuclear Medicine, Berlin, Germany, [9]Charité – Universitätsmedizin Berlin - Institute of Psychiatry and Psychotherapy, Berlin, Germany, [10]German Center for Neurodegenerative Diseases (DZNE), Berlin, Germany, [11]Center for Cognitive Neuroscience Berlin (CCNB), Freie Universität Berlin, Berlin, Germany, [12]Department of Psychiatry and Psychotherapy, Charité, Berlin, Germany, [13]German Center for Neurodegenerative Diseases (DZNE), Bonn, Germany, [14]Department of Psychiatry, University of Cologne, Medical Faculty, Cologne, Germany

Introduction: Beta-amyloid aggregation in Alzheimer's disease (AD) and subsequent accumulation of Tau protein predominantly affect a temporo-parietal network crucial for the memory encoding process (Düzel et al., 2022; Pasquini et al., 2019). Current evidence indicates an inverted U-shape pattern in the activity of the precuneus and a declining pattern in the hippocampus as the disease progresses (Billette et al., 2022). However, the relationship between CSF biomarkers and connectivity remains insufficiently established, hindering insights into pathology within the circuitry. Hence, our investigation focuses on effective connectivity (EC) in the temporo-parietal network during an encoding process across the AD continuum.

Methods: We investigated the three cohorts from different study sites in the DELCODE study (Jessen et al., 2018). The participants (n=158; 36, 38, and 84 in cohorts 1, 2, and 3, respectively) were over 65 years old and were categorized as cognitively normal (CN), subjective cognitive decline (SCD), or mild cognitive impairment with Alzheimer's disease (MCI/AD). The participants were also identified as amyloid positive (A+) or amyloid negative (A-) status based on beta-amyloid 42/40 level (<= 0.08 for A+ status) (Düzel et al., 2022). The task included the presentation of novel and pre-familiarized images during the fMRI session and the post-fMRI self-report confidence score whether the images were seen in the fMRI session. The score was regarded as successfulness of memory encoding. We assessed the EC of the temporo-parietal memory network using dynamic causal modelling (DCM) (Zeidman et al., 2019a), using a previously described model (Schott et al., 2023). We focused on the following regions of interest (ROI): parahippocampal place area (PPA), hippocampus (HC), and precuneus (PCU). ROIs were defined by anatomical constraints using Automated Anatomical Labelling (AAL) as implemented in WFU PickAtlas (Tzourio-Mazoyer et al., 2002), and by functional constraints derived from previous literature and activation maps. The model assumed full connectivity between the ROIs, including self-inhibitory connections. The driving input to the DCM model was defined as novelty-related activation of the PPA. The interregional connectivity was assumed to be modulated by memory encoding success. EC was compared as a function of amyloid status (A+ vs. A-), separately for each diagnostic group (CN, SCD, and MCI/AD). The group-level inference was performed using parametric empirical Bayes (PEB) framework (Zeidman et al., 2019b). The design matrix included regressors representing the effect of group and A+ status on each parameter. We then calculated the posterior probability of each parameter at group-level using Bayesian model reduction. Parameters were considered relevant when exceeded a posterior probability (Pp) >= 0.95 in at least two cohorts, with no contradictory results. Inferece statistics were performed to identify changes in EC between diagnostic groups in A+ and A- status.

Results: While no significant effect of A+ status on connectivity parameters was observed in CN (Figure 1), A+ status was associated with a stronger excitatory input from PCU to PPA in individuals with SCD and with MCI/AD. Individuals with MCI/AD additionally showed an association of A+ status with a weaker self-inhibitory connection of the HC. A significant increase in connection strength from PCU to PPA was observed across the trajectory from CN to SCD in the A+ group ($p = 0.03$), whereas a decrease from CN to SCD was found in the A- group ($p = 0.05$) (Figure 2). A nominal decrease was from SCD to MCI/AD in the A+ group did not reach significance ($p = 0.13$).

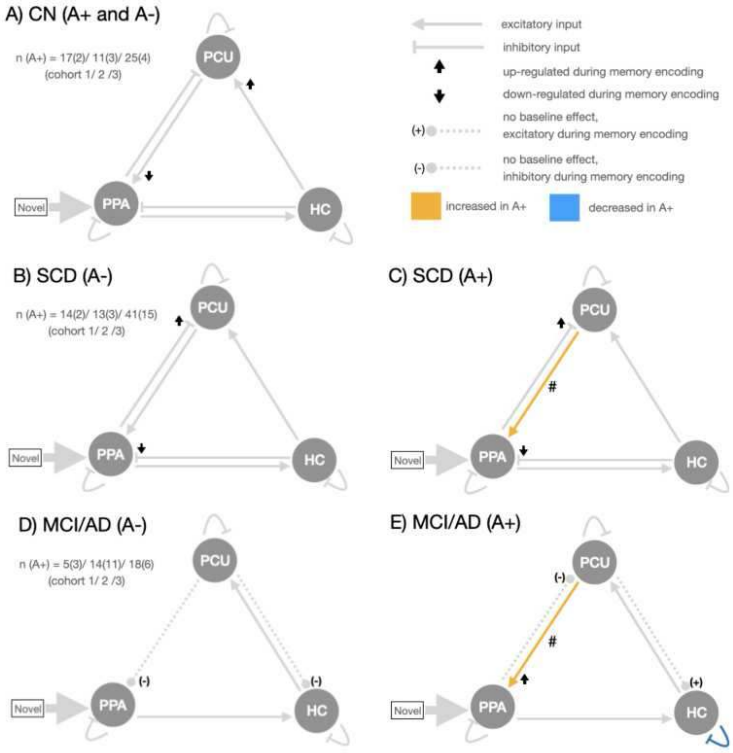

Figure 1. Effective connectivity of temporal-parietal network during novelty processing and memory encoding. A) Effective connectivity in CN in A- and A+ groups. No effect of A+ status is observed. **B)** Effective connectivity in SCD in A- group. **C)** Effective connectivity in SCD in A+ group. A+ status is associated with increased excitatory input from PCU to PPA, as marked in yellow. **D)** Effective connectivity in MCI/AD in A- group. **E)** Effective connectivity in MCI/AD in A+ group. A+ status is associated with increased excitatory input from PCU to PPA with opposite response to memory encoding and decreased self-inhibition in HC, as marked in yellow and blue. # denotes effects of A+ that are strongly evident (Pp>=0.95) across three cohorts.

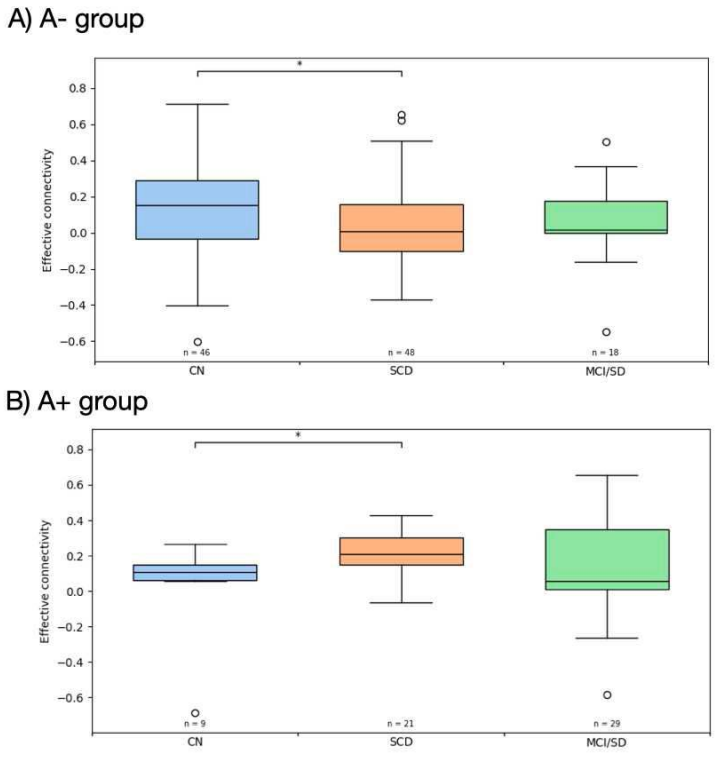

Figure 2. Difference in the connection from PCU to PPA between diagnostic groups in A- and A+ groups. A) Effective connectivity in A- group. **B)** Effective connectivity in A+ group. The connectivity parameters were compared with Mann-Whitney U Test. * p<0.05

Conclusions: Collectively, our results suggest an inverted U-shaped progression of parieto-temporal connectivity across diagnostic groups. Particularly the connection from PCU to PPA appears to be susceptible to beta-amyloid as its increase in connection strength is dependent on A+ versus A- status in individuals with SCD and MCI/AD.

References

1. Billette, O. V. (2022), Novelty-Related fMRI Responses of Precuneus and Medial Temporal Regions in Individuals at Risk for Alzheimer Disease. Neurology, 99(8), e775–e788. https://doi.org/10.1212/wnl.0000000000200667
2. Düzel, E. (2022), Amyloid pathology but not \textitAPOE ε4 status is permissive for tau-related hippocampal dysfunction. Brain, 145(4), 1473–1485. https://doi.org/10.1093/brain/awab405 AB42/AB40
3. Jessen, F. (2018), Design and first baseline data of the DZNE multicenter observational study on predementia Alzheimer's disease (DELCODE). Alzheimer's Research & Therapy, 10(1), 15. https://doi.org/10.1186/s13195-017-0314-2
4. Pasquini, L. (2019), Medial Temporal Lobe Disconnection and Hyperexcitability Across Alzheimer's Disease Stages. Journal of Alzheimer's Disease Reports, 3(1), 103–112. https://doi.org/10.3233/adr-190121
5. Schott, B. H. (2023), Inhibitory temporo-parietal effective connectivity is associated with explicit memory performance in older adults. iScience, 26(10), 107765. https://doi.org/10.1016/j.isci.2023.107765
6. Tzourio-Mazoyer, N. (2002), Automated Anatomical Labeling of Activations in SPM Using a Macroscopic Anatomical Parcellation of the MNI MRI Single-Subject Brain. NeuroImage, 15(1), 273–289. https://doi.org/10.1006/nimg.2001.0978
7. Zeidman, P. (2019a), A guide to group effective connectivity analysis, part 1: First level analysis with DCM for fMRI. NeuroImage, 200, 174–190. https://doi.org/10.1016/j.neuroimage.2019.06.031
8. Zeidman, P. (2019b), A guide to group effective connectivity analysis, part 2: Second level analysis with PEB. NeuroImage, 200, 12–25. https://doi.org/10.1016/j.neuroimage.2019.06.032

Poster No 187

Stepwise connectivity patterns along the gradients of brain organization in Alzheimer's disease

Jazlynn Tan[1], Min Su Kang[2], Yi-Hsuan Yeh[2], Gleb Bezgin[3], Nesrine Rahmouni[4], Firoza Lussier[4], Seok Jun Hong[5], Jean-Paul Soucy[6], Serge Gauthier[4], Boris Bernhardt[7], Sandra Black[2,8], Pedro Rosa-Neto[4,6], Maged Goubran[2,1,9], Julie Ottoy[2]

[1]Department of Medical Biophysics, University of Toronto, Toronto, Ontario, Canada, [2]LC Campbell Cognitive Neurology Unit, Hurvitz Brain Sciences Program, Sunnybrook Research Institute, Toronto, Ontario, Canada, [3]Neuroinformatics for Personalized Medicine lab, Montreal Neurological Institute, McGill University, Montreal, Quebec, Canada, [4]Translational Neuroimaging laboratory, McGill Centre for Studies in Aging, Montreal, Quebec, Canada, [5]Center for Neuroscience Imaging Research, Institute for Basic Science, Suwon, Gyeonggi-do, Republic of Korea, [6]McConnell Brain Imaging Centre, Montreal Neurological Institute and Hospital, McGill University, Montreal, Quebec, Canada, [7]Montreal Neurological Institute and Hospital, Montreal, Quebec, Canada, [8]Department of Medicine (Division of Neurology), University of Toronto, Toronto, Ontario, Canada, [9]Physical Sciences Platform, Sunnybrook Research Institute, University of Toronto, Toronto, Ontario, Canada

Introduction: In Alzheimer's Disease (AD), the entorhinal cortex (EC) is recognized as one of the earliest sites of tau tangle deposition. Existing studies have predominantly focused on tau propagation along direct (seed-to-target) neural connections between brain regions (Sepulcre et al. 2018). Here, we hypothesize that exploring indirect, multi-step connections adds new insights on the spread of AD in the brain. We first employ graph theory-based stepwise connectivity (Sepulcre et al. 2012) to elucidate multi-step functional and structural connections between the EC and the rest of the brain. We then implement a novel integration of stepwise connectivity with low-dimensional gradient space (Margulies et al. 2016) to elucidate connectivity trajectories along the major axes of functional and structural brain organization.

Methods: We acquired resting-state functional MRI (rs-fMRI) and diffusion-weighted MRI (dMRI) in 213 participants from the Translational Biomarkers in Aging and Dementia (TRIAD) cohort, including 103 cognitively normal Aβ-negative controls, 35 cognitively normal Aβ-positive (CN A+) and 75 cognitively impaired Aβ-positive (CI) participants. Subject-specific functional and structural connectomes were estimated using regional time series correlations (Esteban et al. 2019) and probabilistic fiber tractography (Tournier et al. 2019), respectively, with parcellations from a high-resolution atlas adapted from Glasser et al. (2016). We then employed functional or structural stepwise connectivity (SFC or SSC) analyses (Sepulcre et al. 2012) to unveil higher-order indirect connectivity patterns between the EC and the rest of the brain. The SFC or SSC value assigned to a region denotes the number of walks of a particular edge length (1 to 7 edges) to reach the EC from that region (Fig 1A). Groupwise (within-subject normalized) SFC/SSC values were compared via linear regression adjusted for age, sex, and APOE-ε4. Finally, we investigated these stepwise connectivity patterns within a coordinate system spanned by the principal components ('gradients') explaining the most variance in connectivity after non-linear dimensionality reduction (Margulies et al. 2016).

Results: SFC was highest closest to the EC seed (step 1) and propagated to regions of the default-mode network at step 2 before shifting to sensorimotor regions at steps 3-7. SSC from the EC propagated from posterior (step 1-2) to anterior (step

3-7) regions (Fig 1B). Group comparisons revealed hypoconnectivity from the EC to temporal and posterior regions in CI compared to controls. Conversely, hyperconnectivity from the EC to frontoparietal and sensorimotor regions were observed in CI compared to controls (Fig 1C). In functional gradient space, CN A+ showed accelerated SFC propagation from the EC to the rest of the brain (Fig 2A, yellow pixels), which may be compensatory connectivity in preclinical stages. Later-stage CI subjects showed diminished SFC to the default-mode at the transmodal pole of gradient 1 (Fig 2A: green pixels; 2B: blue t-stats), with accelerated propagation to the sensorimotor regions at the unimodal pole of gradient 1 which were not revealed in the standard SFC analysis (Fig 2A: yellow pixels, 2B: red t-stats). Finally, in structural gradient space, propagation was restrained in the temporal-posterior pole of the structural gradient in CI compared to controls (Fig 2C: yellow pixels, 2D: blue t-stats).

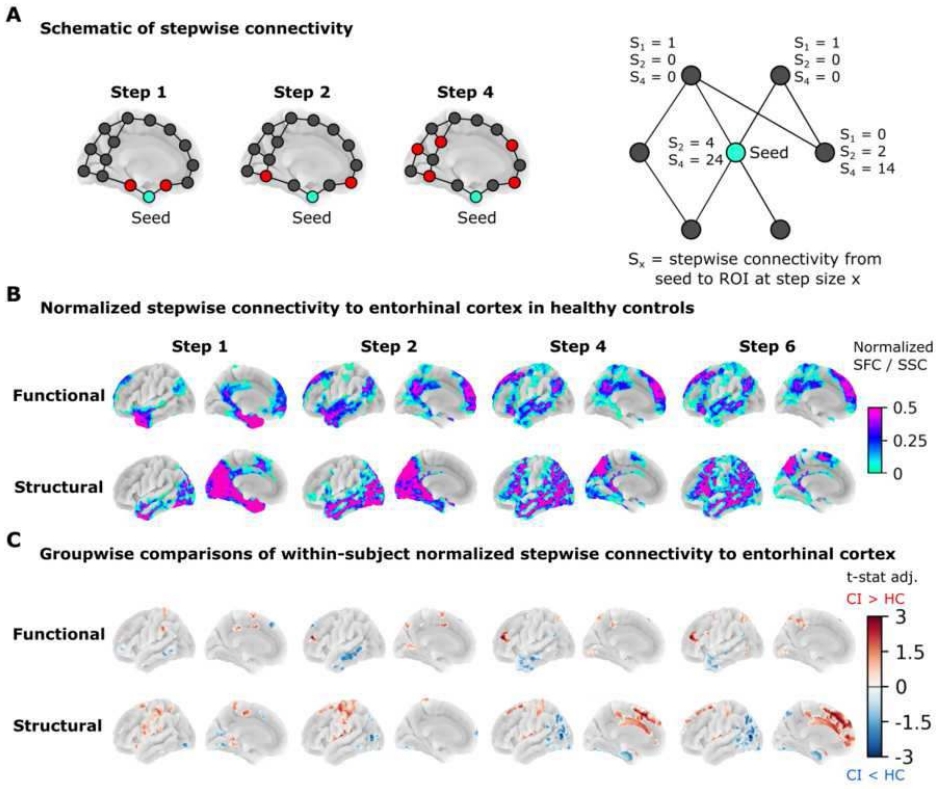

Figure 1. Stepwise functional and structural connectivity patterns. A. The number of walks leading from the seed to the ROI for each step size forms the stepwise connectivity value of that ROI for that step size. **B.** In controls, stepwise functional connectivity propagated from the seed to DMN and medial/anterior temporal lobes while stepwise structural connectivity moved from caudal to rostral cortices. **C.** Normalized stepwise connectivity showed hypo and hyperconnectivity trajectories across step sizes in CI compared to controls.

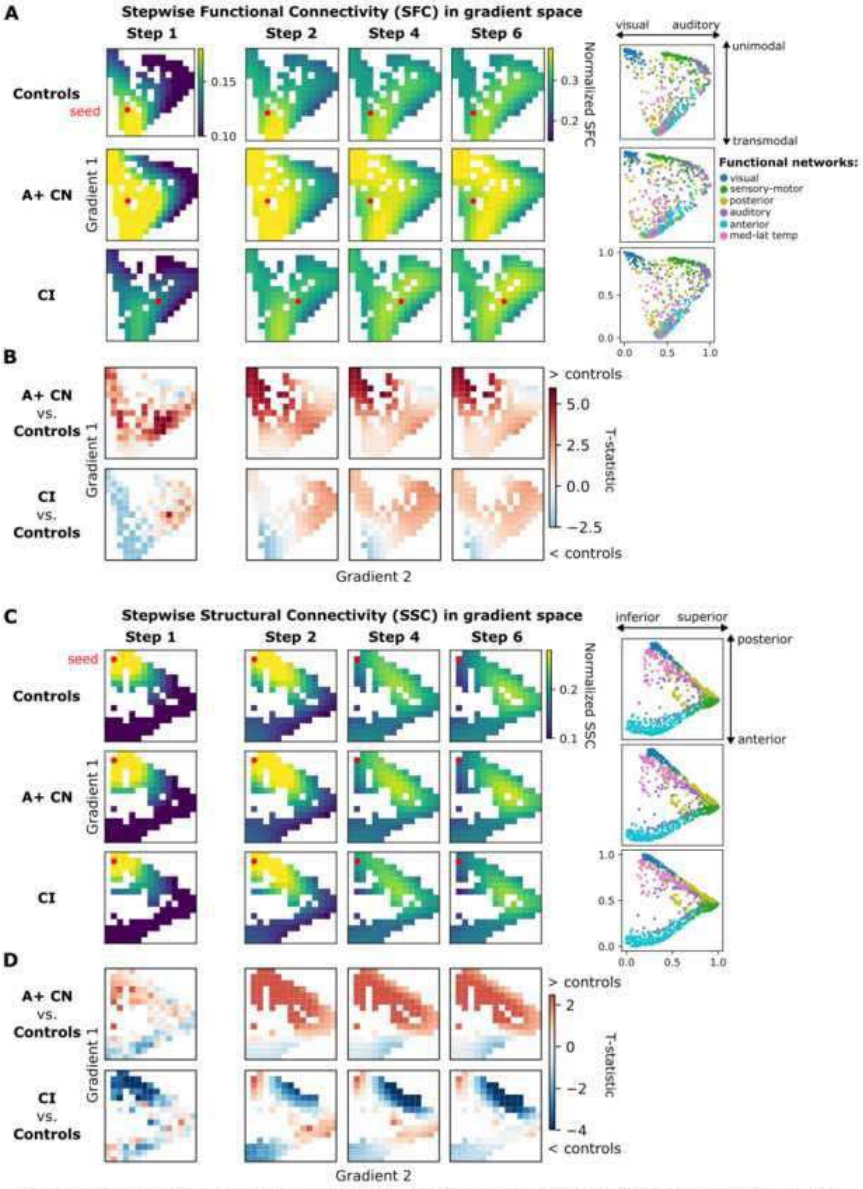

Figure 2. Stepwise connectivity trajectories in gradient space. A. Within-subject normalized stepwise functional connectivity in gradient space projected on a template gradient space for each group (right). **B.** Groupwise comparisons between diagnostic groups reveal hypoconnectivity and hyperconnectivity of the EC with transmodal and unimodal networks, respectively. **C.** Within-subject normalized stepwise structural connectivity in gradient space projected on a template gradient space for each group (right), and **D.** groupwise comparisons between diagnostic groups.

Conclusions: Using a novel integrated stepwise connectivity and gradient approach, we demonstrated widespread network reorganization in AD affecting both short and long connections. Combining the stepwise connectivity and gradient space allows new insight previously inaccessible through conventional analyses in anatomical space. It unveils how AD affects connectivity strength along the major axes of brain organization.

References

1. Esteban O, Markiewicz CJ, Blair RW, et al (2019) fMRIPrep: a robust preprocessing pipeline for functional MRI. Nat Methods 16:111–116
2. Glasser MF, Coalson TS, Robinson EC, et al (2016) A multi-modal parcellation of human cerebral cortex. Nature 536:171–178
3. Margulies DS, Ghosh SS, Goulas A, et al (2016) Situating the default-mode network along a principal gradient of macroscale cortical organization. Proc Natl Acad Sci U S A 113:12574–12579
4. Sepulcre J, Grothe MJ, d'Oleire Uquillas F, et al (2018) Neurogenetic contributions to amyloid beta and tau spreading in the human cortex. Nat Med 24:1910–1918
5. Sepulcre J, Sabuncu MR, Yeo TB, et al (2012) Stepwise connectivity of the modal cortex reveals the multimodal organization of the human brain. J Neurosci 32:10649–10661
6. Tournier J-D, Smith R, Raffelt D, et al (2019) MRtrix3: A fast, flexible and open software framework for medical image processing and visualisation. Neuroimage 202:116137

Poster No 188

Differences in local connectivity strength relate to disease stage in multiple sclerosis

Katherine Koenig[1], Xuemei Huang[1], Daniel Ontaneda[1], Kedar Mahajan[1], Sehong Oh[1], Stephen Jones[1], Mark Lowe[1]

[1]*The Cleveland Clinic, Cleveland, OH*

Introduction: In people diagnosed with multiple sclerosis (MS), disease progression can occur at all disease stages and regardless of disease course. Although MRI is critical to the diagnosis and monitoring of MS, conventional measures such as lesion burden are not strongly related to clinical impairment. A measure that strongly relates to clinical measures of disability and predicts disease progression would be valuable for disease monitoring and as an outcome measure in clinical trials of novel treatments. Here, we use high resolution MRI at 7 tesla to assess the relationship of between MS-related disability and regional homogeneity1 (ReHo) of functional connectivity in cortical grey matter.

Methods: Seventy-one participants with MS (mean age: 52.0 ± 8.2; 16 males; median Expanded Disability Status Scale (EDSS): 3.5, range 1.5-7) were enrolled in an IRB-approved protocol. Six participants were classified as early MS (EMS; time from diagnosis ≤ 5 years, EDSS ≤ 4.5) and 20 were classified as late MS (LMS; time from diagnosis > 5 years, EDSS ≥ 5). Measures of disease severity included the Multiple Sclerosis Functional Composite (MSFC). A whole-brain T1-weighted MP2RAGE sequence (0.75mm3 isotropic voxel size) and a rsfMRI scan were acquired on a Siemens 7T Magnetom with a SC72 gradient (Siemens Medical Solutions, Erlangen) using a 1-Tx and 32-Rx channel head coil (Nova Medical). RsfMRI acquisition parameters were: 132 repetitions of 81 1.5mm thick axial slices acquired with TE/TR=21ms/2800ms, voxel size 0.75×0.75×1.5mm3, matrix 160×160, FOV 210mm×210mm, receive bandwidth = 1562 Hz/pixel. Subjects were instructed to keep their eyes closed during scans. RsfMRI scans were corrected for motion and measured physiologic noise, detrended, and lowpass filtered.2,3 ReHo maps were calculated in all cortical grey matter voxels.1 For each participant, the T1-weighted MP2RAGE and cortical parcellation maps (Freesurfer 7.1; 2009 Destrieux atlas4) were coregistered and warped to rsfMRI space. The median ReHo value (neighborhood size 19) was calculated in each of 75 cortical regions (150 bilateral parcels). Parcels with ReHo values in less than 50 voxels were excluded from further analysis. Unpaired t-tests were used to compare median ReHo values in each parcel between EMS and LMS participants and corrected using the false discovery rate. For each significant parcel, median ReHo values were correlated with MSFC values and associated measures in the full sample.

Results: Figures 1 and 2 report cortical grey matter regions where ReHo was significantly lower in LMS compared to EMS. No regions showed higher ReHo in LMS. In the full sample, MSFC score was significantly related to ReHo in all regions except the left orbitalfrontal gyrus and horizontal ascending ramus of the lateral fissure (HALF). Higher MSFC indicates lower disability. Relationships between MSFC and ReHo measures were driven by the motor function components of the MSFC.

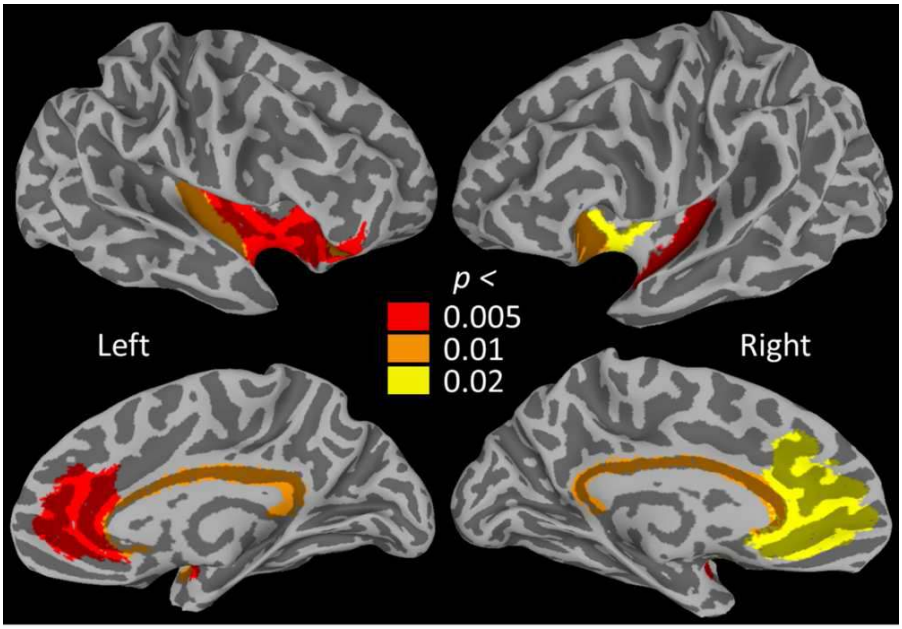

Figure 1. Cortical grey matter regions showing lower ReHo in late MS compared to early MS.

	Left			Right		
	EMS v LMS	MSFC (n=71)		EMS v LMS	MSFC (n=71)	
	p	r	*p*	*p*	r	*p*
Anterior cingulate	**0.005**	0.28	0.020	**0.012**	**0.39**	**0.0009**
Pericallosal sulcus	**0.007**	**0.34**	**0.004**	**0.006**	**0.35**	**0.003**
Orbitofrontal gyrus	**0.002**	0.17	0.162	-	-	-
HALF	**0.005**	0.19	0.117	-	-	-
Insula:						
Circular sulcus, anterior	**0.002**	**0.30**	**0.013**	**0.007**	**0.30**	**0.014**
Circular sulcus, inferior	**0.008**	**0.31**	**0.009**	**0.004**	**0.32**	**0.007**
Short gyri	**0.005**	**0.32**	**0.008**	**0.014**	**0.35**	**0.004**
Long gyrus/central sulcus	**0.002**	**0.33**	**0.005**	-	-	-

Figure 2. Regions that showed significant ReHo differences between early MS (n = 6) and late MS (n = 20) groups and results of correlations between ReHo and MSFC in the full MS sample (n = 71).

Conclusions: ReHo represents the homogeneity of the BOLD time series within a spatially constrained cluster. Our results agree with previous work showing that, in MS, local connectivity strength is weaker in those with higher levels of disability.5,6 The neuropathological basis of these changes is unclear, and could involve local grey matter damage or degeneration of associated white matter. Future work will assess the relationship of ReHo longitudinal clinical measures and specific domains of disability. This work was supported by the Department of Defense (MS150097). We thank Siemens Healthineers Tobias Kober for use of WIP944 and Thomas Benner for use of WIP770B.

References

1. Zang Y, Jiang T, Lu Y et al. (2004) Regional homogeneity approach to fMRI data analysis. NeuroImage. 22(1): 394-400.
2. Beall EB and Lowe MJ. (2014) SimPACE: generating simulated motion corrupted BOLD data with synthetic-navigated acquisition for the development and evaluation of SLOMOCO: a new, highly effective slicewise motion correction. Neuroimage. 101:21-34.
3. Glover et al. (2000) Image-Based Method for Retrospective Correction of Physiological Motion Effects in fMRI: RETROICOR. Magnetic Resonance in Medicine. 44:162-67.
4. Destrieux C, Fischl F, Dale A et al. (2010) Automatic parcellation of human cortical gyri and sulci using standard anatomical nomenclature. NeuroImage. 53(1): 1:15.
5. Zhu Y, Huang M, Zhao Y et al. (2020) Local functional connectivity of patients with acute and remitting multiple sclerosis. Medicine. 99(43):e22860.
6. Dogonowski AM, Andersen KW, Madsen KH et al. (2013) Multiple sclerosis impairs regional functional connectivity in the cerebellum. Neuroimage Clin. 4:130-8.

Poster No 189

Deciphering white-matter changes in Progressive Supranuclear Palsy using free-water diffusion MRI

Amir Fazlollahi[1,2], Lena Oestreich[3,4], Peter Nestor[5,6]

[1]Queensland Brain Institute, The University of Queensland, Brisbane, Australia, [2]Department of Radiology, Royal Melbourne Hospital, The University of Melbourne, Melbourne, Australia, [3]School of Psychology, The University of Queensland, Brisbane, Queensland, Australia, Brisbane, Australia, [4]Australian Institute for Bioengineering and Nanotechnology, The University of Queensland, Brisbane, Australia, [5]Queensland Brain Institute, The University of Queensland, Brisbane, Australia, [6]Mater Hospital, Brisbane, Australia

Introduction: The overlapping motor and non-motor features of progressive supranuclear palsy (PSP) with Lewy body disorders (LBD comprising Parkinson's disease ± dementia, and dementia with Lewy bodies) may lead to misdiagnosis. Previous studies have suggested white-matter changes measured by diffusion-weighted MRI are prominent in PSP in the whole brain (Sajjadi, Acosta-Cabronero et al. 2013, Talai, Sedlacik et al. 2018) and in particular in the corpus callosum (Spotorno, Hall et al. 2019, Nguyen, Cheng et al. 2021) and the internal capsule (Agosta, Pievani et al. 2012, Nguyen, Cheng et al. 2021). We aimed to assess the usefulness of diffusion metrics to reliably discriminate PSP from LBD patients and understand the pathogenesis of the underlying disease. We focused on the corpus callosum as a proof-of-concept because the confounds of partial volume effects, white-matter lesions and crossing fibres can be eliminated in this region.

Methods: Thirty-nine healthy controls, 28 LBD (including 15 with dementia) and 13 PSP patients underwent 3.0T MRI. Multi-shell diffusion-weighted images were acquired using: repetition/echo times= 4100/75ms, FA = 90°, field-of-view 244 × 244 × 136, acquisition matrix 122 × 122 × 68 slices. The acquisition includes 9 non-diffusion weighted images (b = 0 s/mm2) as well as 27 (b = 1000 s/mm2) and 62 (b = 2500 s/mm2) unique directions. A FLAIR image was also acquired to assess global white-matter lesion load using SPM 12. The pre-processing of the diffusion images included head motion correction (using rigid registration), denoising, susceptibility distortions correction and removing intensity inhomogeneities. Free-water imaging was used on the pre-processed DWI data to quantify the amount of extracellular free-water (FW) by separating the diffusion properties of brain tissue, such as white matter tracts, from the surrounding extracellular free water, such as cerebrospinal fluid (Pasternak, Sochen et al. 2009). The DWI metrics of fractional anisotropy (FA), mean diffusivity (MD), axial diffusivity (AD), and radial diffusivity (RD) were estimated using MRtrix3 before and after free-water correction. Two regions of interest were automatically placed using an atlas-based approach on the centre of the genu (GCC), and splenium (SCC), of corpus callosum. Differences between groups were assessed using two-tailed unpaired Wilcoxon-rank sum tests (after correcting for age and sex).

Results: There was no significant difference in global white-matter lesion load between PSP and LBD patients (Figure 1). FA, MD and RD were significantly different in PSP compared with controls in GCC with p=0.001, p=0.022 and p=0.0018, respectively, as well as between PSP and LBD patients (p=0.0047, p=0.05 and p=0.0043, respectively) as shown in Figure 2. None of the diffusion metrics showed a statistically significant change in SCC. When DTI metrics were corrected for free-water, no significant difference was observed between PSP and LBD patients. However, free-water component showed a significant increase in PSP compared to LBD patients (p=0.0047) and control participants (p=0.01).

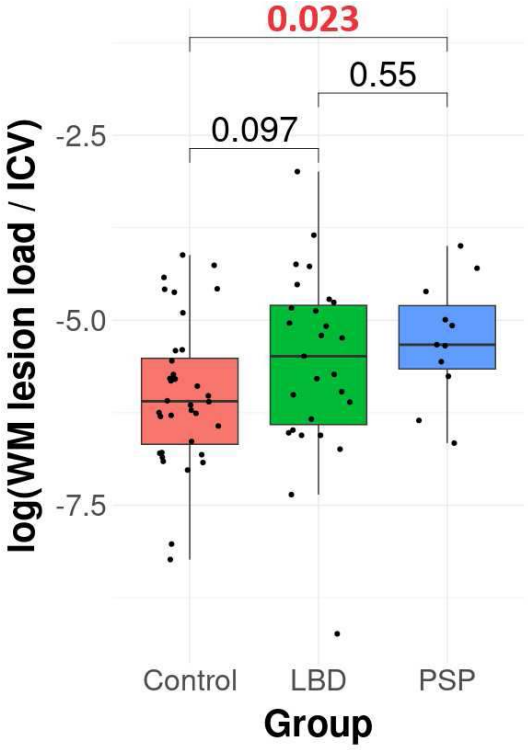

Figure 1. White-matter lesion load calculated from FLAIR image across control, Lewy body disorders (LBD) and progressive supranuclear palsy (PSP).

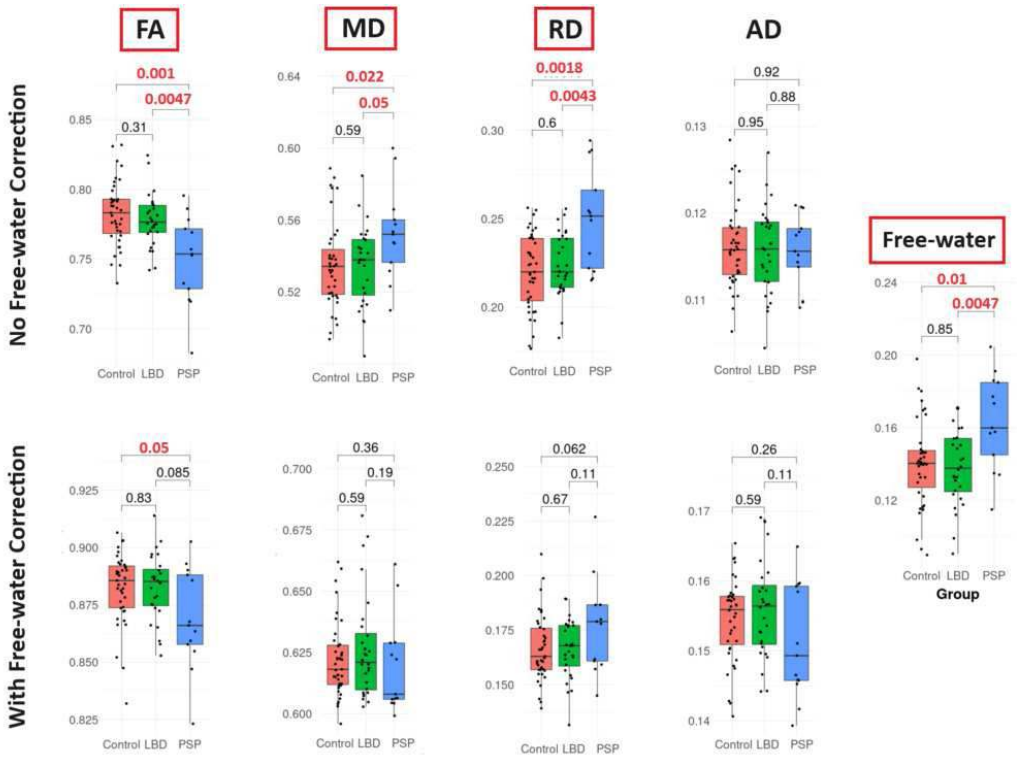

Figure 2. DTI metrics comparison across control, Lewy body disorders (LBD) and progressive supranuclear palsy (PSP) in the genu of corpus callosum (GCC).

Conclusions: White-matter changes in progressive supranuclear palsy patients in the rostral corpus callosum (genu) showed a significant focal decrease in FA and an increase in RD using conventional DTI processing. However, after applying the free-water correction, it became evident that the FA and RD changes in the genu could be attributed to an increase in the extracellular space. Previous pathological studies have noted an abundance of white-matter tau pathology in PSP (Zhukareva, Joyce et al. 2006) and the present results suggest that this tau pathology is associated with an increase in extracellular water. When integrated into a multimodal diagnostic imaging approach, diffusion MRI metrics in the genu of the corpus callosum may hold the potential to aid in distinguishing individuals with progressive supranuclear palsy from those with Lewy body disorders.

References

1. Agosta, F., M. Pievani, M. Svetel, M. Jecmenica Lukic, M. Copetti, A. Tomic, A. Scarale, G. Longoni, G. Comi, V. S. Kostic and M. Filippi (2012). "Diffusion tensor MRI contributes to differentiate Richardson's syndrome from PSP-parkinsonism." Neurobiol Aging 33(12): 2817-2826.
2. Nguyen, T. T., J. S. Cheng, Y. L. Chen, Y. C. Lin, C. C. Tsai, C. S. Lu, Y. H. Weng, Y. M. Wu, N. T. Hoang and J. J. Wang (2021). "Fixel-Based Analysis of White Matter Degeneration in Patients With Progressive Supranuclear Palsy or Multiple System Atrophy, as Compared to Parkinson's Disease." Front Aging Neurosci 13: 625874.
3. Pasternak, O., N. Sochen, Y. Gur, N. Intrator and Y. Assaf (2009). "Free water elimination and mapping from diffusion MRI." Magn Reson Med 62(3): 717-730.
4. Sajjadi, S. A., J. Acosta-Cabronero, K. Patterson, L. Z. Diaz-de-Grenu, G. B. Williams and P. J. Nestor (2013). "Diffusion tensor magnetic resonance imaging for single subject diagnosis in neurodegenerative diseases." Brain 136(Pt 7): 2253-2261.
5. Spotorno, N., S. Hall, D. J. Irwin, T. Rumetshofer, J. Acosta-Cabronero, A. F. Deik, M. A. Spindler, E. B. Lee, J. Q. Trojanowski, D. van Westen, M. Nilsson, M. Grossman, P. J. Nestor, C. T. McMillan and O. Hansson (2019). "Diffusion Tensor MRI to Distinguish Progressive Supranuclear Palsy from alpha-Synucleinopathies." Radiology 293(3): 646-653.
6. Talai, A. S., J. Sedlacik, K. Boelmans and N. D. Forkert (2018). "Widespread diffusion changes differentiate Parkinson's disease and progressive supranuclear palsy." Neuroimage Clin 20: 1037-1043.
7. Zhukareva, V., S. Joyce, T. Schuck, V. Van Deerlin, H. Hurtig, R. Albin, S. Gilman, S. Chin, B. Miller, J. Q. Trojanowski and V. M. Lee (2006). "Unexpected abundance of pathological tau in progressive supranuclear palsy white matter." Ann Neurol 60(3): 335-345.

Poster No 190

Worldwide analysis of brain microstructure across Parkinson's disease stages

Conor Owens-Walton[1], Sarah Al-Bachari[2], Tim Anderson[3,4,5], Fernando Cendes[6,7], John Dalrymple-Alford[4,8], Michiel Dirkx[9], Jason Druzgal[10], Hedley Emsley[11,12], Rick Helmich[9,13], Michele Hu[14], Johannes Klein[14], Christine Lochner[15], Corey McMillan[16], Tracy Melzer[17], Fabrizio Piras[18], Kathleen Poston[19], Reinhold Schmidt[20], Petra Schwingenschuh[20], Gianfranco Spalletta[18], Dan Stein[21], Duygu Tosun[22], Odile van den Heuvel[23,24], Chris Vriend[24,23], Jiun-Jie Wang[25,26,27], Paul Thompson[1], Neda Jahanshad[1], Ysbrand van der Werf[24,28]

[1]Imaging Genetics Center, Keck School of Medicine, University of Southern California, Los Angeles, California, USA, [2]Lancaster Medical School, Lancaster University, Lancaster, UK, [3]Department of Medicine, University of Otago, Christchurch, New Zealand, [4]New Zealand Brain Research Institute, Christchurch, New Zealand, [5]Neurology Department, Te Wahtu Ora - Health New Zealand Waitaha, Christchurch, New Zealand, [6]Department of Neurology, University of Campinas, Campinas, São Paulo, Brazil, [7]Brazilian Institute of Neuroscience and Neurotechnology, Campinas, São Paulo, Brazil, [8]Te Kura Mahi ā-Hirikapo, School of Psychology, Speech and Hearing, University of Canterbury, Christchurch, New Zealand, [9]Department of Neurology and Center of Expertise for Parkinson & Movement Disorders, Nijmegen, Netherlands, [10]Department of Radiology and Medical Imaging, University of Virginia, Charlottesville, Virginia, USA, [11]Lancaster Medical School, Lancaster University, Lancaster, United Kingdom, [12]Department of Neurology, Lancashire Teaching Hospitals NHS Foundation Trust, Preston, United Kingdom, [13]Centre for Cognitive Neuroimaging, Donders Institute for Brain, Cognition and Behaviour, Radboud University, Nijmegen, Netherlands, [14]Oxford Parkinson's Disease Centre, Department of Clinical Neurosciences, Oxford University, Oxford, United Kingdom, [15]SAMRC Unit on Risk & Resilience in Mental Disorders, Department of Psychiatry, Stellenbosch Universi, Stellenbosch, South Africa, [16]University of Pennsylvania, Philadelphia, Pennsylvania, USA, [17]New Zealand Brain Research Institute, Christchurch, Christchurch, [18]Laboratory of Neuropsychiatry, IRCCS Santa Lucia Foundation, Rome, Italy, [19]Department of Neurology & Neurological Sciences, Stanford University, Palo Alto, California, USA, [20]Department of Neurology, Medical University of Graz, Graz, Austria, [21]SA MRC Unit on Risk and Resilience in Mental Disorders, Stellenbosch University, Cape Town, South Africa, [22]Department of Radiology and Biomedical Imaging, University of California San Francisco, San Francisco, California, USA, [23]Amsterdam UMC, Deptartment of Psychiatry, Vrije Universiteit Amsterdam, Amsterdam, Netherlands, [24]Amsterdam UMC, Department of Anatomy and Neurosciences, Vrije Universiteit Amsterdam, Amsterdam, Netherlands, [25]Department of Diagnostic Radiology, Chang Gung Memorial Hospital, Keelung, Taiwan, [26]Healthy Aging Research Center, Chang Gung University, Taoyuan City, Taiwan, [27]Department of Medical Imaging and Radiological Sciences, Chang Gung University, Taoyuan City, Taiwan, [28]Amsterdam Neuroscience, Neurodegeneration, Vrije Universiteit Amsterdam, Amsterdam, Netherlands

Introduction: Diffusion tensor imaging (DTI) can reveal the profile and progression of white matter (WM) microstructural features in Parkinson's disease (PD). Even so, single-site studies and reviews show conflicting changes associated with the disorder[1,2], potentially due to small sample sizes, cohort heterogeneity, and varying analysis methods. To address these issues, we performed a coordinated multisite analysis of data from 17 international cohorts from Africa, Asia, Europe, Oceania, North and South America, providing a large sample sized to detect WM abnormalities across Hoehn and Yahr (HY) stages of PD.

Methods: We analyzed whole brain diffusion MRI data (17 sites; 3T, single b-value shell, 1000 s/mm^2; diffusion encoding gradients: 7-80) from 1,312 participants with PD and 885 controls (age: 20-89 years; 39% female). PD participants were categorized into HY disease progression stages: 1 (n=275), 2 (n=742), 3 (n=220) and 4/5 (n=75). Image processing pipelines followed ENIGMA-DTI protocols[3]. Fractional anisotropy (FA) and mean diffusivity (MD) maps were generated and then skeletonized using tract-based spatial-statistics[4]; mean DTI metrics were extracted for 21 WM regions of interest (ROI)[5]. A mega-analytic approach, modeling site as a random effect, and adjusting for age and sex, was used to evaluate group differences between PD-HY subgroups and controls. We tested for associations between DTI measures and time since diagnosis, Montreal Cognitive Assessment (MoCA) scores, and MDS-UPDRS-III scores across the entire PD cohort.

Results: Relative to controls, HY1 participants showed higher FA across the entire WM skeleton (d=0.30) and in 4 ROIs. HY2 PD participants had lower FA in the fornix (d=-0.26), while HY3 PD participants showed lower FA across the entire WM skeleton (d=-0.24) and 9 ROIs. HY4/5 PD participants had much greater FA decreases across the entire WM skeleton (d=-0.74), and in 20 out of 21 ROIs (Fig. 1). Relative to controls, HY1 PD participants displayed lower MD across the entire WM skeleton (d=-0.19) and in 5 ROIs. HY2 PD participants displayed lower MD at the fornix/stria terminalis (d=-0.22), retrolenticular limb of the internal capsule, fornix and the hippocampal cingulum. No significant MD differences were detected in HY3 PD participants. HY4/5 PD participants displayed higher MD in the fornix (d=0.69), and in 7 ROIs. HY4/5 PD participants also displayed lower MD in the hippocampal cingulum (d=-0.32) (Fig. 2). Time since diagnosis (PD n=1,441) was negatively

correlated with FA across the entire WM skeleton (d=-0.09). We also found positive correlations between time since diagnosis and MD in the genu of the corpus callosum (d=0.08), the anterior corona radiata and external capsule. MoCA scores (PD n=953), were positively correlated with FA across the entire WM skeleton (d=0.12) and negatively correlated with MD across the entire WM skeleton (d=-0.13). MDS-UPDRS-III scores (n=597) were inversely associated with FA across the entire WM skeleton (d=-0.17). MD in the fornix was positively correlated with MDS-UPDRS-III scores (d=0.13).

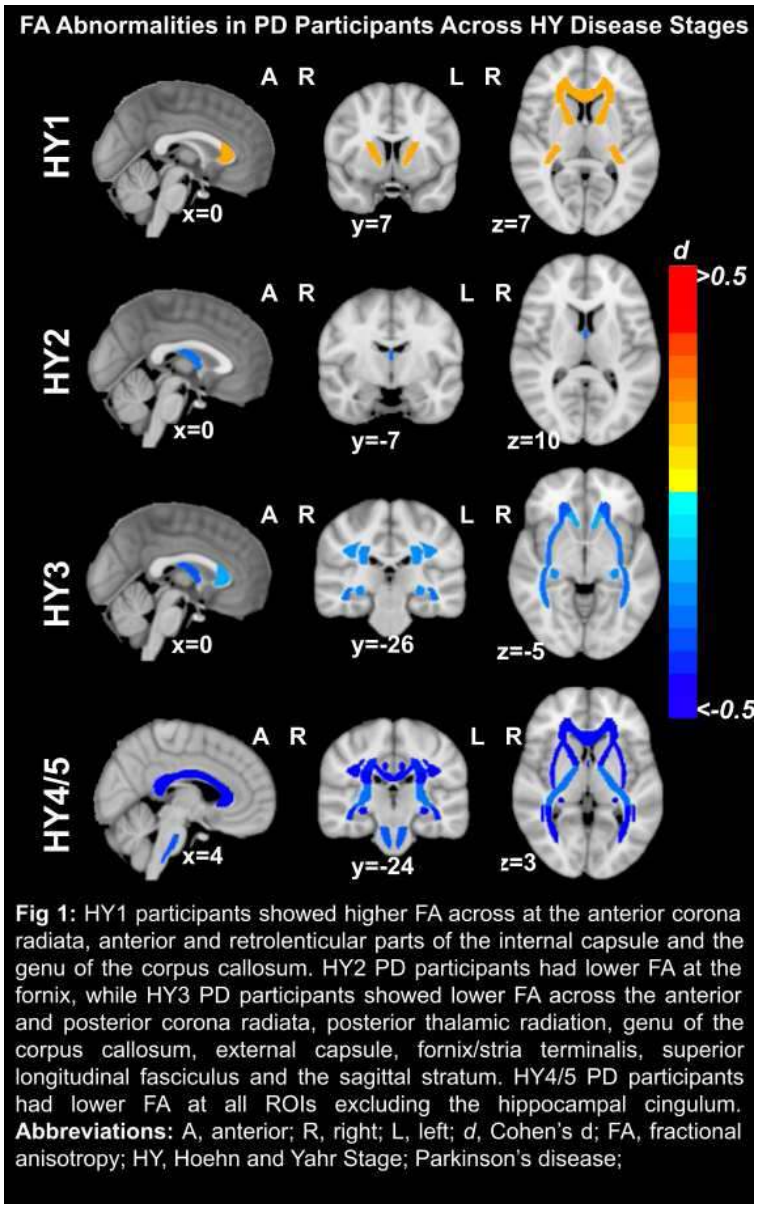

Fig 1: HY1 participants showed higher FA across at the anterior corona radiata, anterior and retrolenticular parts of the internal capsule and the genu of the corpus callosum. HY2 PD participants had lower FA at the fornix, while HY3 PD participants showed lower FA across the anterior and posterior corona radiata, posterior thalamic radiation, genu of the corpus callosum, external capsule, fornix/stria terminalis, superior longitudinal fasciculus and the sagittal stratum. HY4/5 PD participants had lower FA at all ROIs excluding the hippocampal cingulum. **Abbreviations:** A, anterior; R, right; L, left; *d*, Cohen's d; FA, fractional anisotropy; HY, Hoehn and Yahr Stage; Parkinson's disease;

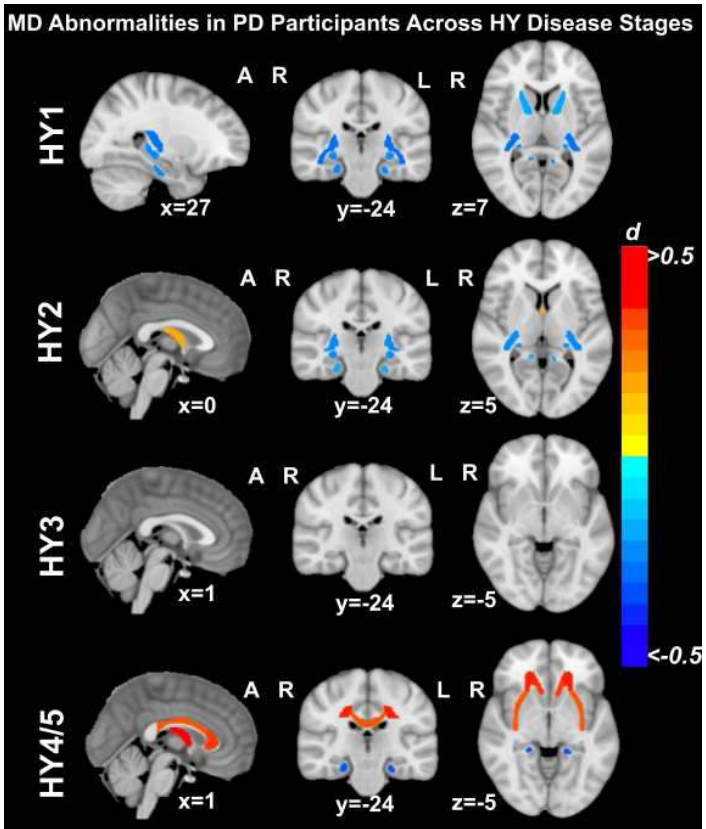

Fig 2: HY1 PD participants showed lower MD at the anterior and retrolenticular limbs of the internal capsule, fornix/stria terminalis, hippocampal cingulum and the sagittal stratum. HY2 PD participants showed lower MD at the fornix/stria terminalis and in the retrolenticular limb of the internal capsule, fornix and the hippocampal cingulum. HY4/5 PD participants showed higher MD in the fornix, anterior and superior corona radiata, external capsule, genu and body of the corpus callosum and the superior fronto-occipital fasciculus. HY4/5 PD participants also displayed lower MD in the hippocampal cingulum. **Abbreviations:** A, anterior; R, right; L, left; *d*, Cohen's d; MD, mean diffusivity; HY, Hoehn and Yahr Stage; PD, Parkinson's disease.

Conclusions: Pronounced patterns of FA differences emerged when stratifying PD participants according to HY stage. Widespread WM microstructural alterations in people with PD appeared as higher FA and lower MD in the initial HY stage. This pattern was reversed at advanced HY stages. Poorer clinical function associated with lower FA and higher MD. Higher FA, early in the disorder, may relate to compensatory reorganization of neural circuits indicative of adaptive neuroplasticity[6], while lower FA and higher MD may reflect neurodegeneration[7]. Prior work on brain morphometry by ENIGMA-PD has also shown greater subcortical volumes at HY stage 1, before shifting to thinner cortical GM and lower subcortical volumes at advanced disease stages[8].

References

1. Bergamino M, Keeling EG, Mishra VR, ... Walsh RR. Assessing White Matter Pathology in Early-Stage Parkinson Disease Using Diffusion MRI: A Systematic Review. Front Neurol [Internet]. 2020 May 14;11.
2. Zhang Y, Burock MA. Diffusion Tensor Imaging in Parkinson's Disease and Parkinsonian Syndrome: A Systematic Review. Front Neurol. 2020; Vol 11, 531993.
3. Jahanshad, N., Kochunov, P. V., Sprooten, E., ... & Glahn, D. C. (2013). Multi-site genetic analysis of diffusion images and voxelwise heritability analysis: A pilot project of the ENIGMA–DTI working group. NeuroImage, 81, 455-469.
4. Smith, S. M., Jenkinson, M., Johansen-Berg, H., ... & Behrens, T. E. (2006). Tract-based spatial statistics: voxelwise analysis of multi-subject diffusion data. NeuroImage, 31(4), 1487-1505.
5. Hua, K., Zhang, J., Wakana, S., ... & Mori, S. (2008). Tract probability maps in stereotaxic spaces: analyses of white matter anatomy and tract-specific quantification. NeuroImage, 39(1), 336-347.
6. Hanganu, A., Houde, J. C., Fonov, ... & Monchi, O. (2018). White matter degeneration profile in the cognitive cortico-subcortical tracts in Parkinson's disease. Movement Disorders, 33(7), 1139-1150.
7. Sykova, E. (2004). Extrasynaptic volume transmission and diffusion parameters of the extracellular space. Neuroscience, 129(4), 861–876
8. Laansma, MA., Bright, JK., Al-Bachari, S., ... & ENIGMA-Parkinson's Study. (2021). International Multicenter Analysis of Brain Structure Across Clinical Stages of Parkinson's Disease. Movement Disorders, 36(11), 2583-2594.

Poster No 191

Pathology-based and functional connectivity of affective symptoms in Alzheimer's disease continuum

Taein Lee[1], Yong Jeong[1]

[1]*Korea Advanced Institute of Science & Technology, Daejeon, Republic of Korea*

Introduction: Neuropsychiatric symptoms (NPS) are prevalent along the Alzheimer's disease continuum and can be one of the important factors related to the patients and their caregivers' quality of life. There have been various studies on NPS with different modalities, however, only a few investigated the NPS in the aspect of combining the molecular level with the whole-brain functional level information. Here, we aimed to explain NPS, mainly focusing on affective symptoms, with the relationship between the different levels of neuronal representation.

Methods: We used preprocessed positron emission tomography (PET) images with AV-1451 and AV-45, resting-state functional magnetic resonance imaging (rsfMRI), T1, and clinical datasets such as neuropsychiatric inventory (NPI) scores of 74 amyloid-positive subjects from Alzheimer's Disease Neuroimaging Initiative (ADNI) site. NPS were measured with NPI and grouped with 4 factors including affective symptoms. The score of affective symptoms was determined as the sum of the product of frequency and severity scores in depression and anxiety. Subjects with over zero scores of affective symptoms were classified into the group with affective symptoms (AS, n =25), and subjects with zero scores were classified into the group without affective symptoms (nAS, n = 49). To minimize the signal distortion from each region-of-interest (ROI) during normalization, all the neuroimages were coregistered to individual structural T1 image which was parcellated and annotated by Freesurfer with Desikan-Killany-Tourville atlas. Amyloid and tau deposition were measured with the standardized uptake value ratio (SUVR) after applying partial volume correction. Resting-state fMRI was preprocessed along realignment, slice timing correction, outlier detection, and smoothing. The ROIs with more burden of both tau and amyloid in AS were found through t-test or Mann-Whitney U test and determined as seeds. Then, functional connectivity (FC) between the pathological seed and voxel from the rest part of the brain was compared between the groups with age, education, the mini-mental state examination (MMSE) score, and sex as covariates. Lastly, a generalized linear model (GLM) for the severity of affective symptoms was conducted with significant FC and SUVR of two pathologies in the seed region.

Results: Twenty-three regions along temporal to part of frontal cortex showed more AD pathological burden in AS than in nAS ($p < 0.05$). Among these regions, the right middle temporal gyrus was negatively connected with parts of the left supramarginal and angular gyrus in AS (voxel threshold, $p < 0.001$ (p-uncorrected, two-sided); cluster threshold, $p < 0.05$ (cluster-size p-FWE corrected)). FC between these regions became more negative as affective symptoms got more severe after considering the interaction between tau and amyloid in the right middle temporal gyrus.

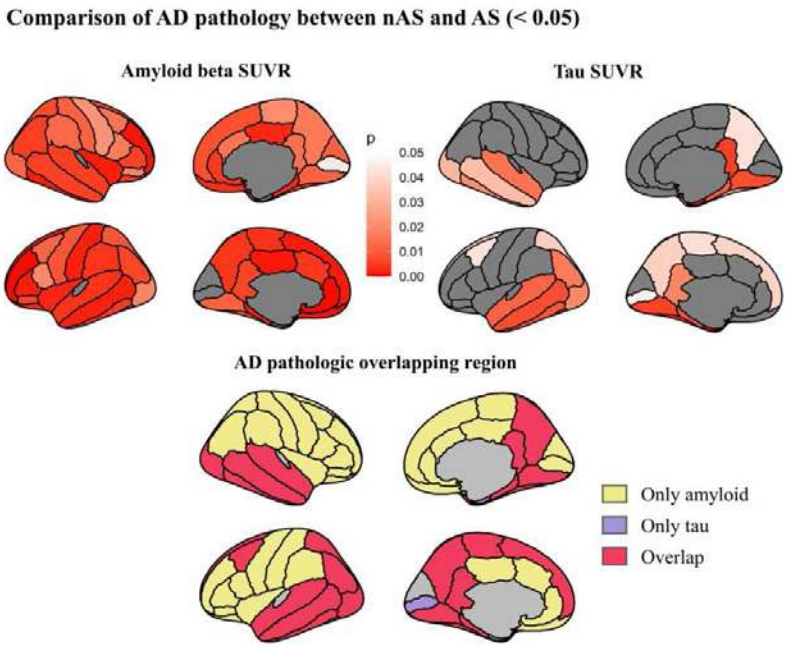

Functional connectivity comparison (nAS > AS)

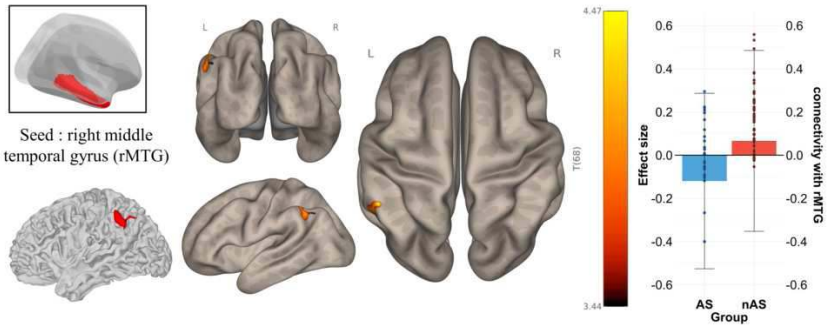

Generalized linear model for the severity of affective symptoms

Variables	β	Standard error	p-Value
Intercept	12.39952	15.28838	0.42924
Age	0.09905	0.09920	0.33293
Sex	2.82998	1.64348	0.10435
Education	0.25140	0.33544	0.46446
MMSE	-0.42227	0.20208	0.05298
Connectivity with rMTG**	-12.01779	3.96349	0.00793
Tau SUVR in rMTG	-9.48998	5.54861	0.10652
Amyloid SUVR in rMTG	-10.13096	8.47529	0.24937
Tau : Amyloid SUVR	7.93248	4.16512	0.07476

Multiple R-squared, 0.579; Adjusterd R-Squared, 0.3685; p-value, 0.04045; right middle temporal gyrus, rMTG

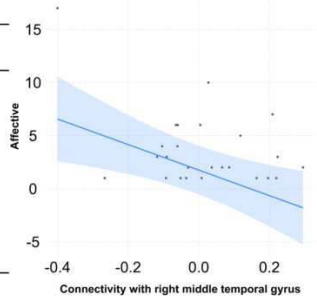

Conclusions: In our study, the NPS of the AS group showed a negative correlation with the FC between the rMTG, heavily affected by amyloid and tau deposition, and the left inferior parietal lobule (lIPL). Considering that rMTG is geometrically close to the suggested hub for tau propagation to the neocortex facilitated by amyloid-tau interactions, the pathological collapse of surrounding regions of the hub can be associated with affective symptoms. In addition, this rMTG is known to react to self-related negative stimuli, and lIPL, the negatively connected region with rMTG associated with affective symptoms, is included in emotion regulation. Therefore, through multi-modal imaging analysis at different levels, our study suggests that the change of FC of the AD pathologically damaged region is associated with affective symptoms in the AD continuum.

References

1. Aalten, P. (2007), Neuropsychiatric syndromes in dementia. Results from the European Alzheimer Disease Consortium: part I. Dementia and Geriatric Cognitive Disorders, 24(6), 457–463
2. Cummings, J. L. (1997), The Neuropsychiatric Inventory: Assessing psychopathology in dementia patients. Neurology, 48(Issue 5, Supplement 6), 10S16S
3. Cummings, J. L. (1994), The Neuropsychiatric Inventory: Comprehensive assessment of psychopathology in dementia. Neurology, 44(12), 2308–2308
4. Eikelboom, W. S. (2021), Neuropsychiatric and Cognitive Symptoms Across the Alzheimer Disease Clinical Spectrum. Neurology, 97(13), e1276–e1287
5. Folstein, M. F.(1975), “Mini-mental state”. A practical method for grading the cognitive state of patients for the clinician. Journal of Psychiatric Research, 12(3), 189–198
6. Fumihiko Y. (2020), Relationship between neuropsychiatric symptoms and Alzheimer’s disease pathology: An in vivo positron emission tomography study. International Journal of Geriatric Psychiatry, 36(4), 598–605
7. Hua, J. P. Y. (2020), Daily-life affective instability in emotional distress disorders is associated with function and structure of posterior parietal cortex. Psychiatry Research: Neuroimaging, 296, 111028
8. Jack, C. R. (2018), NIA-AA Research Framework: Toward a biological definition of Alzheimer’s disease. Alzheimer’s & Dementia : The Journal of the Alzheimer’s Association, 14(4), 535–562
9. Lee, W. J. (2022), Regional Aβ-tau interactions promote onset and acceleration of Alzheimer’s disease tau spreading. Neuron, 110(12), 1932-1943.e5
10. Lima Portugal, L. C. (2020), Interactions between emotion and action in the brain. NeuroImage, 214, 116728
11. Serra, L. (2020), Behavioral psychological symptoms of dementia and functional connectivity changes: a network-based study. Neurobiology of Aging, 94, 196–206
12. Shin, I. S. (2005), Neuropsychiatric Symptoms and Quality of Life in Alzheimer Disease. The American Journal of Geriatric Psychiatry : Official Journal of the American Association for Geriatric Psychiatry, 13(6), 469–474
13. Tissot, C. (2021), Association between regional tau pathology and neuropsychiatric symptoms in aging and dementia due to Alzheimer’s disease. Alzheimer’s & Dementia: Translational Research & Clinical Interventions, 7(1)
14. Tommasi, N. S. (2021), Affective symptoms and regional cerebral tau burden in early-stage Alzheimer’s disease. International Journal of Geriatric Psychiatry, 36(7), 1050–1058

Poster No 192

Cortical neurodegeneration influences annual white matter hyperintensity progression

Jose Bernal[1], Inga Menze[1], Renat Yakupov[1], Oliver Peters[2], Josef Priller[2], Anja Schneider[3], Klaus Fliessbach[3], Jens Wiltfang[4], Frank Jessen[3], Katharina Buerger[5], Robert Perneczky[5], Stefan Teipel[6], Christoph Laske[7], Annika Spottke[3], Michael Heneka[8], Stefanie Schreiber[1], Emrah Düzel[1], Gabriel Ziegler[1]

[1]German Centre for Neurodegenerative Diseases (DZNE), Magdeburg, Germany, [2]German Centre for Neurodegenerative Diseases (DZNE), Berlin, Germany, [3]German Centre for Neurodegenerative Diseases (DZNE), Bonn, Germany, [4]German Centre for Neurodegenerative Diseases (DZNE), Göttingen, Germany, [5]German Centre for Neurodegenerative Diseases (DZNE), Munich, Germany, [6]German Centre for Neurodegenerative Diseases (DZNE), Rostock, Germany, [7]German Centre for Neurodegenerative Diseases (DZNE), Tübingen, Germany, [8]University of Luxembourg, Luxembourg, Luxembourg

Introduction: During late adulthood, the cortical thickness decreases as white matter hyperintensities (WMH) emerge(Shirzadi et al. 2023)-a co-incidence that has prompted consideration of coupled temporal dynamics for over three decades(Garnier-crussard et al. 2023). Longitudinal evidence substantiating such a coupling remains nonetheless scarce(Ter Telgte et al. 2018). We integrated surface-based morphometry and bivariate latent change score modelling (BLCSM) to examine the interrelationships between WMH and cortical thickness over a one-year period in older individuals without objective cognitive impairment and with a low vascular profile.

Methods: We used baseline and 12-month follow-up data from cognitively unimpaired participants enrolled in DELCODE (n=393; median age 70.31 [IQR 66.06, 74.87] years; 52% females; median years of education 15 [IQR 13, 17]; European origins). We segmented WMH using the Lesion Prediction Algorithm and T2w FLAIR data(Schmidt and Wink 2019). We estimated WMH volumes in two regions which we previously found associated with amyloid pathology and cardiovascular risk: a posterior one, comprising both parietal and occipital lobes, and a periventricular one, respectively(Bernal et al. 2023) (Figure 1A). We also obtained cortical thickness using the CAT12 longitudinal pipeline (ageing workflow; default parameters; final resolution 1 mm3; 12-mm Gaussian smoothing; resampling to 32k HCP surface template)(Gaser et al., n.d.) and T1w MPRAGE data. Using BLCSM in a vertex-wise fashion (Figure 1B), we tested two hypotheses: (a) ischemic or hypoxic damage-operationalised as WMH-causes a depletion of oxygen, nutrients, and tropic support, thereby affecting both neighbouring and distant cortical regions and leading to cortical atrophy7; (b) cortical neurodegeneration-especially when in conjunction with amyloid or tau pathologies(Garnier-crussard et al. 2023; Salvadores, Gerónimo-Olvera, and Court 2020)-initiates degenerative axonal loss and contributes to the emergence and progression of WMH(Garnier-crussard et al. 2023). Note that the second association should be more evident when considering the posterior WMH pattern as opposed to the periventricular one. We adjusted the model for age, sex, years of education, total cardiovascular risk factors, and CSF-derived amyloid-β (Aβ) 42/40 ratio. We log-10 transformed WMH volumes and corrected WMH volumes and thickness measurements for TICV via residualisation.

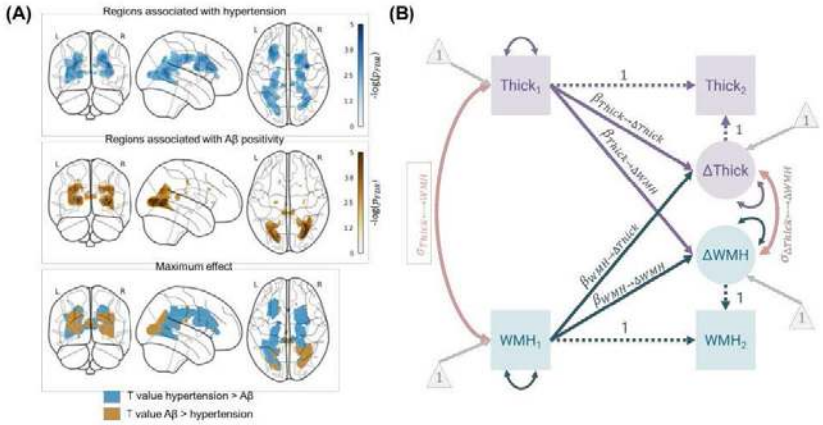

Figure 1. (A) Glass brain projections display regions where we found evidence for a link between WMH probability and hypertension and Aβ positivity (top and middle rows, respectively). In the bottom row, we coloured regions blue if *T* values for hypertension were greater than for Aβ positivity and gold otherwise. (A) BLCSM to probe the coupling of cortical thickness and WMH over the course of a year. We controlled for age, sex, years of education, total cardiovascular risk factors, and CSF-derived amyloid-β (Aβ) 42/40 ratio. We corrected WMH volumes and thickness values for TICV via residualisation. We omitted these paths for visualisation purposes. Note: Employing the conventional notation for structural equation modelling, squared variables indicate observed and measured variables and circular ones unmeasured latent variables. Single-headed solid arrows illustrate a relationship between two variables, with the arrow pointing towards the dependent variable. Single-headed dashed arrows signify a relationship between two variables, where the weight is set at 1. Double-headed arrows represent the correlation between two variables.

Results: The BLCSM converged at all vertices and fitted the data well (χ^2(15)=8.857, p=0.885, RMSEA=0.000 90%-CI[0.000;0.000], CFI=1.000, SRMR=0.034). On average, individuals with thinner cortices at baseline had greater baseline WMH volumes (Figure 2A; σThick-WMH=-0.239, SE=0.048, Z=-4.968, p<0.001) and showed stronger WMH volume increase over the course of a year (Figure 2B; βThick->ΔWMH=-0.168, SE=0.056, Z=-3.001, p=0.003). The annual progression of WMH in posterior regions, as opposed to periventricular ones, was associated with cortical thickness at baseline, especially that spanning posterior cortices (Figure 2B; peak at parieto-occipital sulcus: βThick->ΔWMH=-0.064, SE=0.015, Z=-4.409, p<0.001). Further investigation of this relationship revealed that subjects with a lower Aβ42/40 ratio and thinner baseline cuneal, precuneal, and superior parietal cortices experienced larger annual changes in posterior WMH volumes (Figure 2C; interaction between baseline cortical thickness and the Aβ42/40 ratio on posterior WMH changes: β=0.028, SE=0.010, Z=2.718, p=0.007).

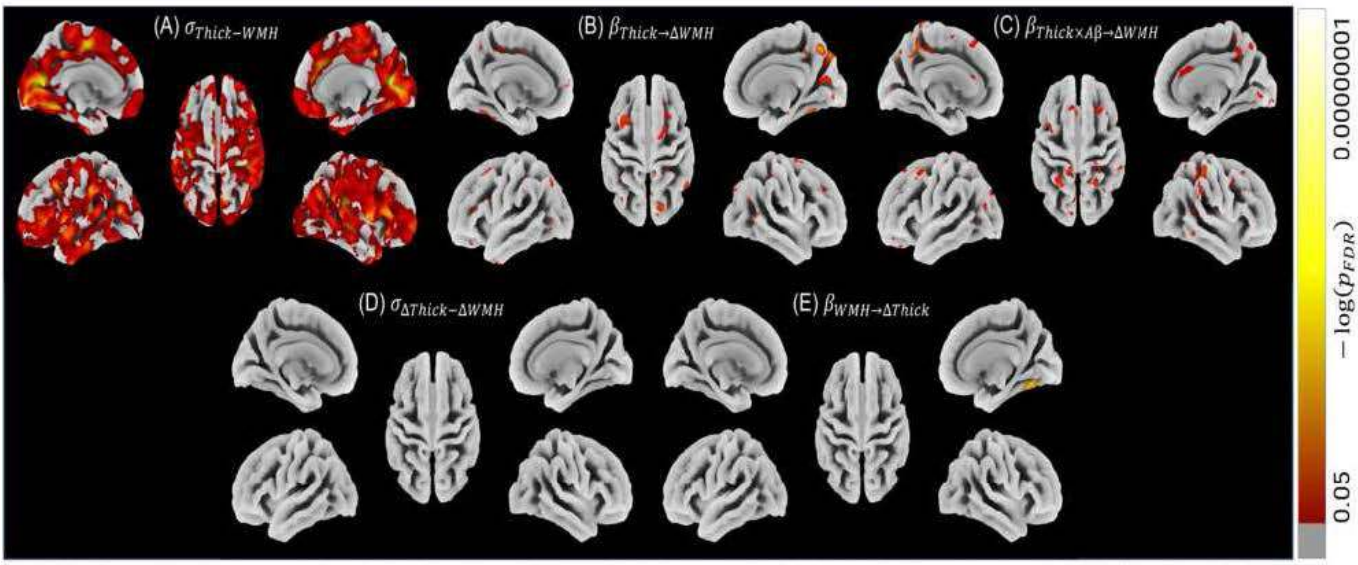

Figure 2. The baseline precuneal, cuneal, and superiorparietal cortex predicts changes in occipital and parietal WMH. (A) Individuals with thinner cortices at baseline had greater baseline WMH volumes (correlation = -0.239, SE = 0.048, Z = -4.968, p-value < 0.001). (B) The annual progression of WMH in parietal and occipital regions, as opposed to periventricular ones, was associated with cortical thickness at baseline, especially that in the same lobes (peak at parieto-occipital sulcus: β = -0.064, SE = 0.015, Z = -4.409, p-value < 0.001). (C) The association between baseline cortical thickness and WMH progression is moderated by the concentration of amyloid in CSF (Aβ42/40 ratio). (D) Changes in cortical thickness and WMH over a year are not strongly correlatec (does not survive FDR-correction). (E) Baseline WMH in parietal and occipital regions predicts cortical thinning of the left fusiform cortex.

Conclusions: The progression of WMH in parietal and occipital regions within a year can in part be explained by the extent of cortical neurodegeneration occurring in those very same regions at baseline; an association that becomes stronger with higher retention of amyloid in the brain. Our work therefore suggests that posterior WMH might be influenced by cortical neurodegeneration and amyloidosis, and these alterations occur prior to the onset of any detectable cognitive deficits.

References

1. Bernal, Jose, Stefanie Schreiber, Inga Menze, Anna Ostendorf, Malte Pfister, Jonas Geisendörfer, Aditya Nemali, et al. 2023. 'Arterial Hypertension and β-Amyloid Accumulation Have Spatially Overlapping Effects on Posterior White Matter Hyperintensity Volume: A Cross-Sectional Study'. Alzheimer's Research and Therapy 15 (1). https://doi.org/10.1186/s13195-023-01243-4.
2. Garnier-crussard, Antoine, Pierre Krolak-salmon, Antoine Garnier-crussard, François Cotton, and Pierre Krolak-salmon. 2023. 'White Matter Hyperintensities in Alzheimer ' s Disease : Beyond Vascular Contribution', no. April. https://doi.org/10.1002/alz.13057.
3. Gaser, Christian, Robert Dahnke, Paul M Thompson, Florian Kurth, Eileen Luders, and Disease Neuroimaging Initiative. n.d. 'CAT - A Computational Anatomy Toolbox for the Analysis of Structural MRI Data'. https://doi.org/10.1101/2022.06.11.495736.
4. Salvadores, Natalia, Cristian Gerónimo-Olvera, and Felipe A. Court. 2020. 'Axonal Degeneration in AD: The Contribution of Aβ and Tau'. Frontiers in Aging Neuroscience. Frontiers Media S.A. https://doi.org/10.3389/fnagi.2020.581767.
5. Schmidt, Paul, and Lucie Wink. 2019. 'LST : A Lesion Segmentation Tool for SPM'.
6. Shirzadi, Zahra, Stephanie A. Schultz, Wai-Ying W. Yau, Nelly Joseph-Mathurin, Colleen D. Fitzpatrick, Raina Levin, Kejal Kantarci, et al. 2023. 'Etiology of White Matter Hyperintensities in Autosomal Dominant and Sporadic Alzheimer Disease'. JAMA Neurology, October. https://doi.org/10.1001/jamaneurol.2023.3618.
7. Telgte, Annemieke Ter, Esther M.C. Van Leijsen, Kim Wiegertjes, Catharina J.M. Klijn, Anil M. Tuladhar, and Frank Erik De Leeuw. 2018. 'Cerebral Small Vessel Disease: From a Focal to a Global Perspective'. Nature Reviews Neurology 14 (7): 387–98. https://doi.org/10.1038/s41582-018-0014-y

Poster No 193

Brain radiomics-based network tracks distinct subtypes in prodromal Parkinson's disease

Lin Hua[1], Canpeng Huang[1], Fei Gao[2], Zhen Yuan[1]

[1]University of Macau, Taipa, Macau, [2]Fudan University, Shanghai, Shanghai

ABSTRACTS

Introduction: Individuals in the prodromal phase of Parkinson's disease (PD) exhibit significant heterogeneity and can be divided into distinct subtypes based on clinical symptoms, pathological mechanisms, and brain network patterns. However, little has been done regarding the valid subtyping of prodromal PD, which hinders the early diagnosis of PD. In this study, we aimed to identify the subtypes of prodromal PD using the brain radiomics-based network and examine the unique patterns linked to the clinical presentations of each subtype.

Methods: Individualized brain radiomics-based network was constructed for normal controls (NC; N=110), prodromal PD patients (N=262), and PD patients (N=108). Data-driven clustering approach using the radiomics-based network was carried out to cluster prodromal PD patients into higher-/lower-risk subtypes. Then, the dissociated patterns of clinical manifestations, anatomical structure alterations, and gene expression between these two subtypes were evaluated. Finally, to ensure the consistency of the prodromal PD subtypes identified through brain radiomics-based network, reproducibility was used to access their robustness across various brain atlases or parcellation schemes.

Results: Compared with NC, widespread radiomics-based connections were statistically significant changes in PD. Furthermore, 50 key connections that contributed to separating NC and PD were mainly involved in the thalamus, precentral gyrus, and inferior temporal gyrus. Clustering findings based on key connections indicated that one prodromal PD subtype closely resembled the pattern of NCs (N-P; N=159), while the other was similar to the pattern of PD (P-P; N=103). Additionally, significant differences ($p<0.05$) were observed between two prodromal PD subtypes in terms of multiple clinical measurements, neuroimaging for morphological changes, and gene enrichment for synaptic transmission. Finally, the prodromal PD subtypes were able to reproduce among 13 brain atlases or parcellation schemes.

Conclusions: The present study confirmed that patients in the prodromal phase of PD manifest heterogeneous clinical presentations, and that variation across individuals cannot be attributed solely to a single impairment. Furthermore, prodromal PD subtypes exhibited unique neuroanatomic patterns and clinical symptoms. Notably, the morphological alterations observed between prodromal PD subtypes are meaningfully associated with gene expression, which provided a more stable alternative to the symptom-based definitions of subtypes. Therefore, our work could significantly advance our understanding into the heterogeneity in the biological mechanisms that underlie prodromal PD and facilitates the accurate prediction of disease profiles for individuals. Ultimately, the findings can further inform precise and personalized intervention in PD during its early stages.

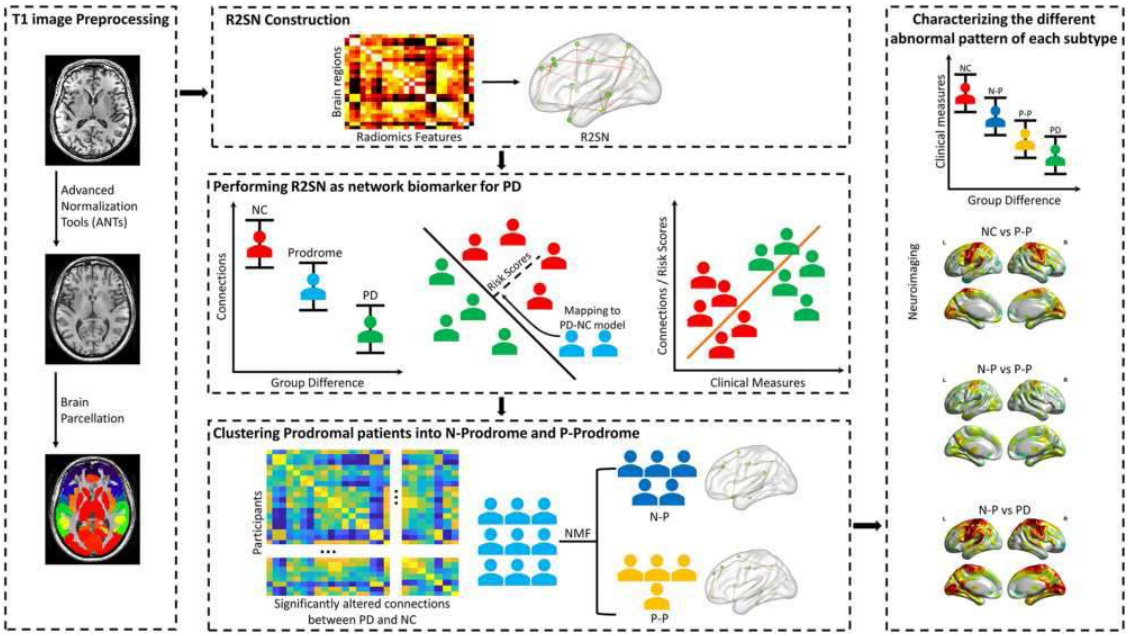

References

1. Tolosa, E. (2021). Challenges in the diagnosis of Parkinson's disease. The Lancet Neurology, 20(5), 385-397.
2. Berg, D. (2021). Prodromal Parkinson disease subtypes—key to understanding heterogeneity. Nature Reviews Neurology, 17(6), 349-361.
3. Postuma, R. B. (2016). Advances in markers of prodromal Parkinson disease. Nature Reviews Neurology, 12(11), 622-634.
4. Marek, K., Jennings, D., Lasch, S., Siderowf, A., Tanner, C., Simuni, T., ... & Parkinson Progression Marker Initiative. (2011). The Parkinson progression marker initiative (PPMI). Progress in neurobiology, 95(4), 629-635.
5. Fan, L. (2016). The human brainnetome atlas: a new brain atlas based on connectional architecture. Cerebral cortex, 26(8), 3508-3526.

Poster No 194

Multimodal neuroimaging and plasma marker evidence of white matter loss in Parkinson's dementia

Angeliki Zarkali[1], Naomi Hannaway[2], Peter McColgan[3], Amanda Heslegrave[3], Elena Veleva[3], Rhiannon Laban[3], Henrik Zetterberg[3], Andrew Lees[3], Nick Fox[3], Rimona Weil[3]

[1]University College London, London, NA, [2]University College London, LONDON, United Kingdom, [3]University College London, London, United Kingdom

Introduction: Parkinson's (PD) is common and debilitating with over half of patients progressing to dementia or death within 10 years[1]. However, onset and rate of progression is highly variable, reflecting heterogeneity in underlying pathology. Biomarker studies to-date have been limited to a single modality or assessed patients with established cognitive impairment.

Methods: We assessed multimodal neuroimaging and plasma markers in 98 PD patients and 28 controls followed-up over 3 years, to identify baseline markers predicting future poor outcomes. Participants underwent clinical and neuropsychological assessments at baseline, after 18- and 36-months. PD patients were classified as PD poor outcomes if they developed death, frailty, dementia[2] or mild cognitive impairment[3] during follow-up. Remaining PD patients were defined as PD good outcome. We assessed: 1) Gray matter imaging: cortical thickness and volume-based analyses 3D MPRAGE images were processed using FreeSurfer v6.0, default cross-sectional parameters. We used a general linear model to compare baseline cortical thickness between PD poor vs PD good outcomes, age, sex and total intracranial volume (TIV) as nuisance covariates, FDR-corrected over both hemispheres. We also performed a volume-based region-of-interest analysis over 360 cortical regions (Glasser parcellation4) and 19 subcortical regions (age, sex, TIV as covariates, FDR-corrected). 2) White matter imaging: fixel-based analysis Diffusion weighted imaging (DWI, b=0-2000) was acquired; after preprocessing, multi-shell 3-tissue constrained spherical deconvolution was performed, each participant's fibre-orientation distribution image registered to a group template[5]. We derived: fibre density (microstructure), fibre cross-section (macrostructure) and combined fibre density and cross-section (FDC). Whole brain connectivity-based fixel enhancement and non-parametric permutation testing was performed to assess whole-brain changes (FWE-corrected, extent-based threshold:10 voxels). We confirmed findings on tract-of-interest analysis across 52 tracts reconstructed using TractSeg[6]. 3) Structural and functional connectivity Structural images were used to parcellate the brain into 360 cortical[4] and 19 subcortical regions (ROIs). For structural connectomes, these were warped in DWI-space and anatomically constrained tractography was performed with 10 million streamlines[7]. For functional connectomes (preprocessed via fmriprep[8]) Pearson correlation coefficient between ROIs was performed. Network-based statistics was used to identify structural and functional connectivity changes in PD poor outcomes (5000 permutations, t=3.0, FWE-correction, age and sex as covariates). 4) Plasma biomarker Neurofilament light chain (NFL), a disease agnostic marker of axonal damage[9] and phosphorylated tau (p-tau) 181, a marker of brain tau and β-amyloid[10] were assessed, corrected for age, sex and batch effect.

Results: We found extensive baseline white matter macrostructural changes in PD who progress to poor outcomes (Figure 1): up to 19% reduction in fibre cross-section and a subnetwork of reduced structural connectivity strength (105 nodes, 215 edges, p=0.017). This subnetwork particularly involved connections between right fronto-parietal and left frontal, right fronto-parietal and left parietal and right temporo-occipital and left parietal modules. In contrast, grey matter and functional connectivity were preserved in PD with poor outcomes at baseline. NFL (β=4.378, p=0.016), but not p-tau181 levels (β=0.461, p=0.106) were increased in PD with poor outcomes and correlated with white matter loss (Figure 2).

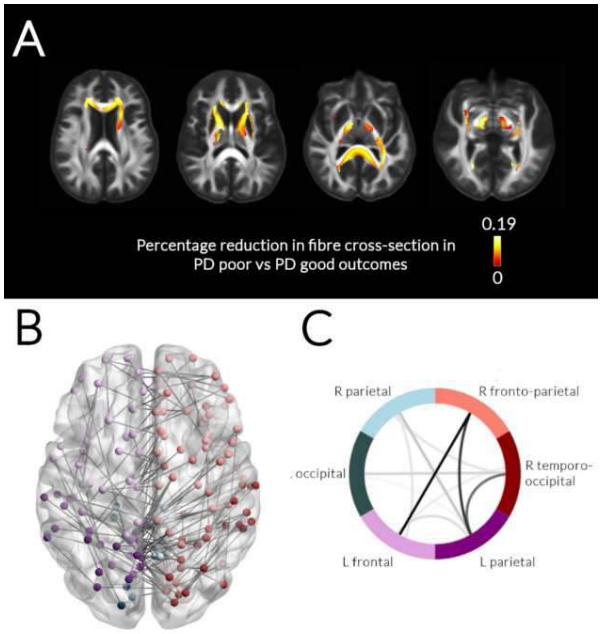

Figure 1.
A. White matter macrostructural changes in PD patients with poor outcomes (percentage reduction in fibre cross-section) compared to PD patients with good outcomes at baseline whole-white matter analysis with age, sex and total intracranial volume as nuisance covariates. Effect size is shown as percentage (0-19% reduction), presented as streamlines, FWE-p<0.05.
B. Network based statistical analysis revealed a network of reduced connectivity strength in PD with poor outcomes (FDR-corrected p<0.05, t=3.0, 5000 permutations, correcting for age and sex), comprised 215 edges and 105 nodes.
C. The subnetwork comprised of 6 modules: R parietal, R fronto-parietal, R temporo-occipital, L parietal, L frontal and L occipital. The sum number of connections between modules showing reduced connectivity strength is visualised with darker colour. Connection within R fronto-parietal and L frontal, R frontoparietal and L parietal and R temporo-occipital and L parietal modules were most affected in PD with poor outcomes.

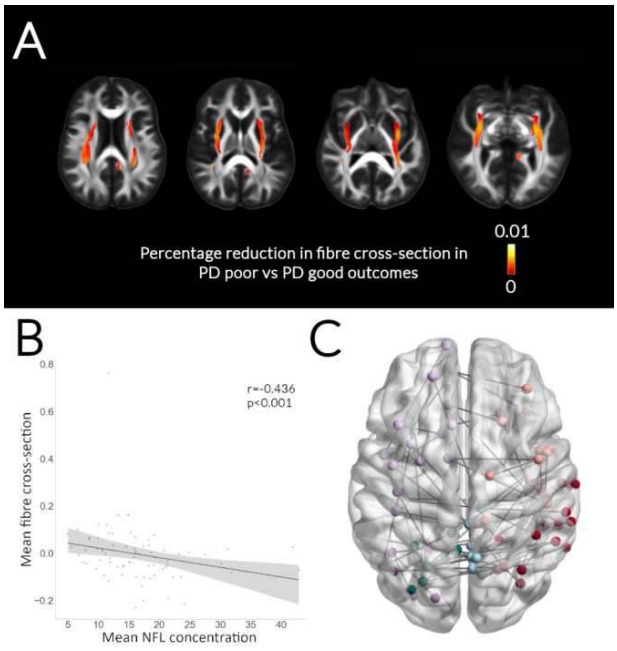

Figure 2.
A. White matter macrostructural changes in PD patients in relation to NFL levels (percentage reduction in fibre cross-section) at baseline whole-white matter analysis with age, sex and total intracranial volume as nuisance covariates. Effect size as percentage (0-1% reduction), presented as streamlines, FWE-p<0.05.
B. Mean fibre cross-section (fibre cross-section) in areas showing significant whole-white-matter reductions in PD with poor outcomes was significantly correlated with plasma NFL concentration within patients with PD.
C. Network based statistical analysis revealed a network of reduced connectivity strength in PD patients in relation to plasma NFL levels (FDR-corrected p<0.05, t=3.0, 5000 permutations, correcting for age and sex), comprised 118 edges and 117 nodes.

Conclusions: Our findings provide convergent evidence of white matter axonal loss in PD patients who progress to poor outcomes. Imaging of white matter macrostructure and plasma NFL may be useful biomarkers in PD. As new targeted treatments emerge, these may aid patient selection for treatments and improve stratification to clinical trials.

References

1. Williams-Gray, C. H. (2013) The CamPaIGN study of Parkinson's disease: 10-year outlook in an incident population-based cohort. J. Neurol. Neurosurg. Psychiatry 84, 1258–1264.
2. Emre, M. (2007). Clinical diagnostic criteria for dementia associated with Parkinson's disease. Mov. Disord. 22, 1689–1707; quiz 1837.
3. Litvan, I. (2012). Diagnostic Criteria for Mild Cognitive Impairment in Parkinson's Disease: Movement Disorder Society Task Force Guidelines. Mov. Disord. 27, 349–356.
4. Glasser, M. F. (2016). A multi-modal parcellation of human cerebral cortex. Nature 536, 171–178.
5. Raffelt, D. (2011) Symmetric diffeomorphic registration of fibre orientation distributions. NeuroImage 56, 1171–1180.
6. Wasserthal, J. (2018) TractSeg - Fast and accurate white matter tract segmentation. NeuroImage 183, 239–253.
7. Smith, R. E. (2012). Anatomically-constrained tractography: improved diffusion MRI streamlines tractography through effective use of anatomical information. NeuroImage 62, 1924–1938.
8. Esteban, O. (2019). fMRIPrep: a robust preprocessing pipeline for functional MRI. Nat. Methods 16, 111–116.
9. Sjögren, M. (2001). Neurofilament protein in cerebrospinal fluid: a marker of white matter changes. J. Neurosci. Res. 66, 510–516.
10. Karikari, T. K. (2020). Blood phosphorylated tau 181 as a biomarker for Alzheimer's disease: a diagnostic performance and prediction modelling study using data from four prospective cohorts. Lancet Neurol. 19, 422–433.

Poster No 195

Understanding of Regional Contributions to Memory Impairment in Progressive Supranuclear Palsy

Iryna Vlasiuk[1], Timothy Rittman[1]

[1]University of Cambridge, Cambridge, United Kingdom

Introduction: Progressive supranuclear palsy is a rare neurodegenerative disorder characterized by motor impairment, executive dysfunction and general cognitive decline (Litvan et al.,1998; Pilon et al., 1995). Patients with PSP report memory impairment, however, the degree and characteristics of memory impairment in PSP are uncertain. It is important to understand the nature of memory impairment and its relationship to other cognitive domains to provide explanations to patients and caregivers regarding memory complaints, and to identify potential targets for therapeutic interventions to improve their quality of life. Additionally, gaining insights into the changes in memory function in PSP can enhance our understanding of the underlying mechanisms of memory impairment and shed light on their neural origins. Our hypothesis was that memory impairments in PSP would be predominantly driven by impaired executive function, which would be reflected in the brain regions associated with memory impairment.

Methods: A total of 324 patients with PSP and 244 controls underwent standard clinical and neuropsychological assessments, including the Addenbrooke's Cognitive Examination Revised (ACE-R), Frontal Assessment Battery (FAB), and the INECO Frontal Screening Assessment. Cumulative frequency distribution and The Kolmogorov-Smirnov test were used for group comparison of total memory, and composite measures of encoding, storage and retrieval. To investigate how closely memory was related to other cognitive variables we applied hierarchical cluster analysis to the components of memory, other cognitive domains from the ACE-R (Language, Attention, Visuospatial abilities and Verbal fluency), and executive measures of FAB and INECO total scores. Neuroimaging was carried out using 3T MRI scanning. To assess brain structure, a Magnetization Prepared Rapid Gradient Echo sequence was acquired (TR 2s, TE 2.93ms, flip angle 8Åã, voxel size 1.1mm isotropic). Regional brain volumes were calculated using Freesurfer (version 7.1) applying the Desikan-Killiany atlas, and with additional analysis for subcortical volumes. Spearman rank correlation coefficient was applied to examine the relationship between memory subscore of the ACE-R and regional brain volume. P-values were corrected for multiple comparisons using FDR.

Results: The results revealed that individuals with PSP exhibited impairments in global memory functioning, as well as in the components of memory of encoding, storage, and retrieval. Global memory impairment was associated with executive dysfunction and general cognitive impairment, indicating a complex relationship between memory and other cognitive processes. Hierarchical cluster analysis revealed that the encoding component of memory was most closely related to executive function (see Fig.1), while storage and retrieval components formed separate clusters, suggesting relatively independent processes. Spearmen correlation analysis revealed significant moderate positive correlations between total memory score and several brain regions. These included the posterior cingulate cortex, lateral occipital cortex, rostral middle frontal gyrus, inferior temporal gyrus, fusiform gyrus, caudal anterior cingulate cortex. Additionally, significant positive correlations were found between the encoding memory component and atrophy in the lateral occipital cortex, superior frontal gyrus, inferior temporal gyrus, rostral middle frontal gyrus, middle temporal gyrus.

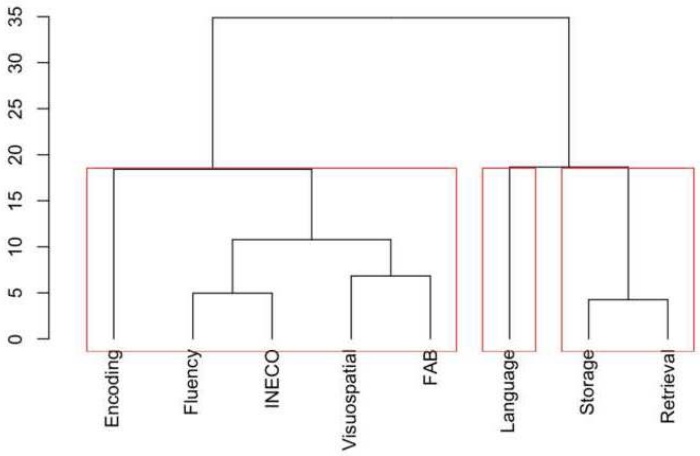

Figure 1. The dendrogram of a Hierarchical clustering that was conducted on the cognitive variables of the ACE-R, including memory components, FAB and INECO total scores. The y-axis represents the measurement of distance between clusters. The X axis of a dendrogram depicts the variables being grouped into clusters.

Conclusions: Overall, the findings from this study provide valuable insights into our understanding of the nature of memory impairment in PSP. It highlights the relationship between memory function and other cognitive variables, as well as regional cortical brain atrophy. These findings provide evidence to guide the development of targeted interventions aimed at addressing memory impairments in PSP, facilitating personalized approaches to diagnosis and clinical interventions.

References

1. Boxer, A. L., Yu, J.-T., Golbe, L. I., Litvan, I., Lang, A. E., & H.glinger, G. U. (2017). Advances in progressive supranuclear palsy: New diagnostic criteria, biomarkers, and therapeutic approaches. The Lancet. Neurology, 16(7), 552–563.
2. Gerstenecker, A., Mast, B., Duff, K., Ferman, T. J., Litvan, I., & for the ENGENE-PSP Study Group. (2013). Executive Dysfunction Is the Primary Cognitive Impairment in Progressive Supranuclear Palsy. Archives of Clinical Neuropsychology, 28(2), 104–113.
3. Hoglinger, G. U., Respondek, G., Stamelou, M., Kurz, C., Josephs, K. A., Lang, A. E., Mollenhauer, B., Müller, U., Nilsson, C., Whitwell, J. L., Arzberger, T., Englund, E., Gelpi, E., Giese, A., Irwin, D. J., Meissner, W. G., Pantelyat, A., Rajput, A., van Swieten, J. C., … Movement Disorder Society-endorsed PSP Study Group. (2017). Clinical diagnosis of progressive supranuclear palsy: The movement disorder society criteria. Movement Disorders: Official Journal of the Movement Disorder Society, 32(6), 853–864.
4. Litvan, I. (1994). Cognitive disturbances in progressive supranuclear palsy. In E. Tolosa, R. Duvoisin, & F. F. Cruz-S.nchez (Eds.), Progressive Supranuclear Palsy: Diagnosis, Pathology, and Therapy (pp. 69–78). Springer Pillon, B., Deweer, B., Michon, A., Malapani, C., Agid, Y., & Dubois, B. (1994). Are explicit memory disorders of progressive supranuclear palsy related to damage to striatofrontal circuits? Comparison with Alzheimer's, Parkinson's, and Huntington's diseases. Neurology, 44(7), 1264–1264
5. Van der Hurk, P. R., & Hodges, J. R. (1995). Episodic and semantic memory in alzheimer's disease and progressive supranuclear palsy: A comparative study. Journal of Clinical and Experimental Neuropsychology, 17(3), 459–471.

Poster No 196

Investigation of common EEG features between PD and MDD

Chia-Yen Yang[1], Fan-Ning Kuo[1]

[1]*Department of Biomedical Engineering, Ming-Chuan University, Taoyuan, Taiwan*

Introduction: Parkinson's disease (PD) is the second most common neurodegenerative disease[1]. While its exact cause remains elusive, it's widely thought to intertwine with genetic, environmental, and neurological factors[2]. Complex clinical profiles of PD patients include motor and non-motor symptoms. Numerous studies have highlighted certain non-motor symptoms (such as depression) that manifest years prior to disease onset [e.g., 3], potentially aiding early diagnosis. Depression, a prevalent mental illness with diverse symptoms, stems from intricate causes like psychology, life stress, genetics, personality traits, physical ailments, and brain abnormalities[4]. Although depression and PD are distinct, many studies have identified some shared physiological mechanisms[5-7], such as mitochondrial dysfunction, the monoamine hypothesis, and the inflammation hypothesis. The identified abnormalities might alter brain activity. Utilizing brainwave analysis, shared traits between the two diseases could be further investigated for assessment applications. Therefore, the aim of this study was to identify distinctive differences in resting-state electroencephalography (EEG) between PD patients and healthy controls (HCs), as well as between patients with major depressive disorder (MDD) and HCs, while also to explore common features between PD and MDD.

Methods: 2.1 Datasets All EEG data used in this study were downloaded from the Patient Repository of EEG Data + Computational Tools (PRED+CT) developed by Cavanagh et al.[8,9]. 27 PD patients, 21 MDD patients and 27 HCs were included. Participants were instructed to minimize movements and to remain thoughtless for 3 or 5 min in the eye closed state. EEG signals were recorded with a sampling rate of 500 Hz. 2.2 EEG Processing There were two steps for pre-processing of EEG signals: detrending and 0.5–50 Hz bandpass filtering. After preprocessing, the signals were decomposed into five frequency bands through discrete wavelet decomposition: delta (0.5–4 Hz), theta (4–8 Hz), alpha (8–12 Hz), beta (12–30 Hz), and gamma (30–50 Hz). Five features were then calculated: mean frequency, frequency power, alpha interhemispheric asymmetry, sample entropy and detrended fluctuation analysis (DFA). 2.3 Statistical analysis The Mann-Whitney U test was used to compare the EEG features between the patients with PD and HCs and between the patients with MDD and HCs ($p < 0.05$ for significance). Furthermore, Pearson correlation coefficient was used to evaluate the similarity of features between PD and MDD patients ($R > 0.8$ and $p < 0.05$ for significance).

Results: We first identified distinct EEG features between PD patients and HCs, and between MDD patients and HCs. Then, we intersected these features, considering those showing consistent trends across groups as candidate of common EEG features between the two diseases. Figure 1 displays the types and quantities of significant features identified. Additionally, we conducted correlations of EEG features between PD and MDD. Figure 2 illustrates three significantly correlated features, i.e., relative power, sample entropy and DFA. The combined results of comparison and correlation analyses suggested potential common EEG features encompassing delta, alpha, beta, and gamma bands in relative power, delta, theta and alpha bands in sample entropy, and delta in DFA. Specifically, delta, alpha, and beta power, along with delta entropy, emerge as pronounced common EEG traits. These findings might aid in understanding the neurophysiological connections between PD and MDD.

Feature	Way	Delta	Theta	Alpha	Beta	Gamma
Relative Power	MDD-HC	23	8	32	22	23
	PD-HC	16	18	26	2	1
	MDD-HC & PD-HC	**14**	**0**	**26**	**2**	**1**
Sample Entropy	MDD-HC	16	15	9	9	1
	PD-HC	5	11	7	1	3
	MDD-HC & PD-HC	**3**	**11**	**3**	**0**	**0**
DFA	MDD-HC	0	4	1	30	0
	PD-HC	3	12	0	0	3
	MDD-HC & PD-HC	**0**	**1**	**0**	**0**	**0**

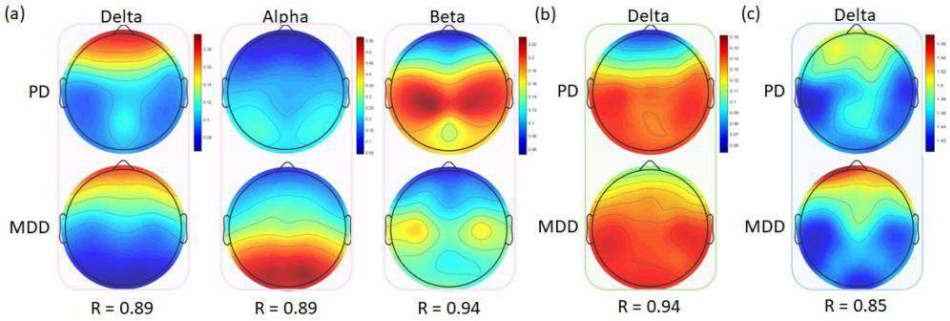

Conclusions: This study demonstrated that there were certain similarities in EEG features between PD and MDD diseases, i.e., traits in delta, alpha, and beta power, alongside delta entropy. The results may facilitate in future applications for transfer learning models between the two diseases, or even in model training for other rare diseases.

References

1. World Health Organization. (2023). Parkinson disease. Retrieved from https://www.who.int/news-room/fact-sheets/detail/parkinson-disease.
2. Lu, J., Wu, M., & Yue, Z. (2020), Autophagy and Parkinson's Disease. Advances in Experimental Medicine and Biology, vol 1207, pp. 21:51.
3. Cheng, Y.C and Su, C.H. (2020), Evidence Supports PA Prescription for Parkinson's Disease: Motor Symptoms and Non-Motor Features: A Scoping Review. International Journal of Environmental Research and Public Health (IJERPH), vol. 17, no. 8, pp. 2894.
4. Pitsilloun, E., Bresnehan, S.M., Kagarakis, E.A., & et al. (2019), The cellular and molecular basis of major depressive disorder: towards a unified model for understanding clinical depression. Molecular Biology Reports, vol. 47, pp. 753–770.
5. Yang, L., Youngblood, H., Wu, C., et al. (2020), Mitochondria as a target for neuroprotection: role of methylene blue and photobiomodulation. Translational Neurodegeneration, vol. 9, pp. 19.
6. Dallé E. and Mabandla M.V. (2018), Early Life Stress, Depression And Parkinson's Disease: A New Approach. Mol Brain, vol. 11, no.1, pp. 18.

7. Lessie E.N. (2021), Neurobiological similarities between depression and parkinson's disease: etiological and therapeutic implications (bachelor's thesis, university of arizona, tucson, usa).
8. Cavanag, J.F.h., Bismark, A.W., Frank, M.J., Allen, J.J.B. (2019), Multiple dissociations between comorbid Depression and anxiety on reward and punishment processing: evidence from computationally informed EEG. Computational Psychiatry, vol. 3, no.1, pp. 1–17.
9. Cavanag, J.F.h., Kumar, P., Mueller, A.A., Richardson, S.P., & et al. (2018), Diminished EEG habituation to novel events effectively classifies Parkinson's patients. Clinical Neurophysiology, vol. 129, no. 2, pp. 409–418.

Poster No 197

Assessing the Sensitivity of Brain-Age to Alzheimer's Disease in different Ethnic Groups

Zeena Shawa[1], Aghogho Onojuvbevbo[2], Sophie Martin[1], Neil Oxtoby[1], James Cole[1]

[1]University College London, London, England, [2]Sheffield Hallam University, Sheffield, England

Introduction: Alzheimer's Disease is the most common neurodegenerative disease and cause of dementia[1,2]. The global burden of dementia is growing, with the number of people living with dementia projected to increase to 152 million by 2050. This growth is estimated to rise particularly in low and middle-income countries[2]. Although there have been advances regarding predicting dementia onset and progression, it is important that the performance of these research outputs are verified in different populations. Additionally, there is a lack of literature examining the potential impact of ethnic and racial factors[3,4]. Brain-age is an index of the brain's biological age derived from structural imaging. It correlates with an increased risk of dementia in memory clinic patients and has the potential to aid in early dementia diagnosis[5]. However, a significant portion of the brain-age literature uses less diverse cohorts[5,2]. Thus, this research aims to investigate the sensitivity and generalizability of brain-age in non-white individuals.

Methods: We analysed data across 23 sites from the National Alzheimer's Coordinating Centre (NACC) database[6]. 389 cognitively normal (CN) individuals (68.7±8.5 years; 278 female) and 189 patients living with Alzheimer's Disease (AD) (73.0±9.9 years; 118 female) were included, after some filtering to age and sex-match the groups (non-White and White for CN and AD each). Fig. 1 contains the demographics across all groups. The brainageR model[7] was used to estimate individuals' brain-age. This model was trained on n=3377 predominantly White healthy individuals from seven public datasets. To assess brainageR's generalisability, we compared the brain-predicted age difference (brain-PAD) between CN and AD groups within the non-White and White populations in the NACC dataset. T-tests and Cohen's d effect sizes were compared between the groups examined.

	Non-White*		White	
	CN	AD	CN	AD
Total Participants (n)	196	93	193	96
Male (n)	54	33	57	38
Female (n)	142	60	136	58
Age, years (SD)	68.2 (9.1)	73.2 (10.7)	69.2 (7.8)	72.7 (9.1)
Sites (n)	18	17	22	18

* The Non-White Group has the following ethnic breakdown: 67.5% are Black or African American, 20.4% are multiracial, 8.0% are Asian, 3.8% are American Indian or Alaska Native, and 0.3% are Native Hawaiian or Other Pacific Islander.

Figure 1. Demographics Table for all groups examined.

Results: Fig. 2(a) shows the brain age against chronological age for individuals in each group and associated R2 values for the line of best fit. Both CN groups have an R2 value above 0.5, indicating that there is a moderate and similar amount of variance explained in these groups. This provides no evidence of ethnic differences in model fit in CN samples. Mean Absolute Error (MAE) and 95% confidence intervals of brain predicted age compared to chronological age for each group was: 6.66 ± 1.37 for Non-White AD, 5.93 ± 0.84 for Non-White CN, 5.86 ± 1.19 for White AD individuals, and 5.36 ± 0.76 for White CN. Consequently, the MAE of individuals with AD for both ethnic groups are within the confidence intervals of the respective

CN groups. A Welch Two Sample t-test showed significant differences in the mean Brain-PAD values between the CN and AD groups (p=0.000 for both White and Non-White, Fig. 2(b)), reflecting the impact of AD on brain structure. The Cohen's d effect sizes when comparing the White AD and White CN subgroups were d=0.83 ± 0.22, while for the Non-White CN and Non-White AD subgroups was d=0.55 ± 0.25. The effect size of AD on brain-PAD is weaker in the Non-White group, though still significantly greater than 0 (based on 95% CIs).

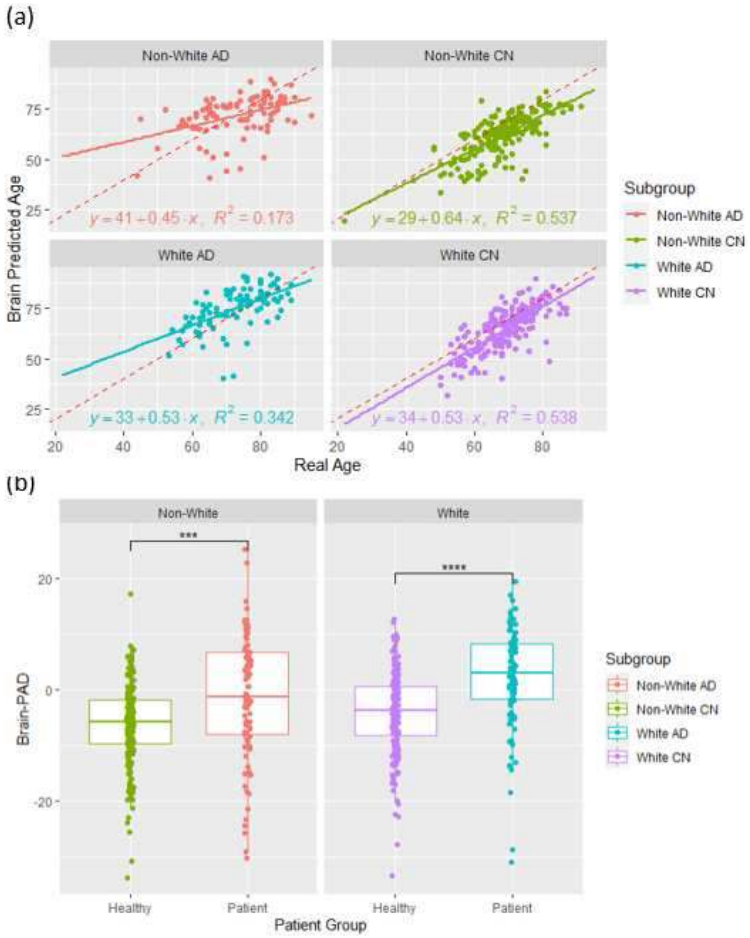

Figure 2. (a) A scatterplot with superimposed linear regression of the Brain Predicted Age against the Real Age of individuals in each group. The equation for the line of best fit, and the corresponding R^2 values are superimposed on each subplot. The dashed red line signifies perfect prediction. **(b)** A box plot comparing the Brain-predicted age difference (Brain-PAD) of AD and CN individuals within each ethnic group, with the Welch's t-test significance value shown. CN = Cognitively Normal. AD = Alzheimer's Disease.

Conclusions: A brain-age model trained on a less diverse dataset generalised similarly to white and non-white CN groups and was partially robust to AD when tested in a sample of different ethnicity. Thus, brain-age could be used in under-represented groups to aid patient prognosis, clinical trial stratification, disease staging, and more[8,9]. However, more work is required to demonstrate and improve generalisability in further demographic groups.

References

1. Hou Y. (2019), 'Ageing as a risk factor for neurodegenerative disease', Nature Reviews Neurology, vol. 15, pp. 565-581.
2. Patterson C. (2018), 'World Alzheimer Report 2018', Alzheimer's Disease International.
3. Babulal G. (2019), 'Perspectives on ethnic and racial disparities in Alzheimer's disease and related dementias: Update and areas of immediate need', Alzheimer's & Dementia, vol. 15, pp. 292-312.
4. Alzheimer's Association (2023), '2023 Alzheimer's disease facts and figures', Alzheimer's & Dementia, vol. 19, no. 4, pp. 1598-1695.
5. Biondo F. (2022), 'Brain-age is associated with progression to dementia in memory clinic patients' NeuroImage: Clinical, vol. 36. pp. 103175.
6. Beekly BL. (2004), 'The National Alzheimer's Coordinating Center (NACC) Database: An Alzheimer Disease Database', Alzheimer Disease & Associated Disorders, vol. 18, no. 4, pp. 270-277.
7. Cole JH. (2019), james-cole/brainageR: brainageR v2.1 (2.1), Zenodo. https://doi.org/10.5281/zenodo.3476365.
8. Franke K. (2019), 'Ten Years of BrainAGE as a Neuroimaging Biomarker of Brain Aging: What Insights Have We Gained?', Frontiers in Neurology, vol. 10.
9. Cole JH. (2019), 'Brain age and other bodily 'ages': implications for neuropsychiatry', Molecular Psychiatry, vol. 24, pp. 266-281.

Poster No 198

Preservation of Neural Activation Along the Somatosensory Processing Stream After Tetraplegia

Paige Howell[1,2,3], Finn Rabe[1], Simon Schading[2,3], Sarah Meissner[1], Patrick Freund[2,3], Nicole Wenderoth[1,3,4], Sanne Kikkert[1,3,2]

[1]Neural Control of Movement Lab, Swiss Federal Institute of Technology (ETH), Zürich, Switzerland, [2]Spinal Cord Injury Center Balgrist, University Hospital Zürich, Zürich, Switzerland, [3]Neuroscience Center Zürich, University of Zürich and ETH Zürich, Zürich, Switzerland, [4]Future Health Technologies, Singapore-ETH Centre, Campus for Research Excellence and Technological Enterprise (CREATE), Singapore, Singapore

Introduction: Following a spinal cord injury (SCI), individuals experience a partial or complete loss of sensorimotor function below the level of injury. This sensory deprivation has long been considered a major driving force for plasticity within the brain (Merzenich et al., 1983). However, in apparent contrast to the notion of deprivation-driven plasticity, we previously found that tetraplegic patients, who lack sensorimotor hand function, could activate somatotopic hand representations in the primary somatosensory cortex (S1) through attempted hand movements (Kikkert et al., 2021). This finding demonstrates that intracortical, i.e., top-down, processes may drive somatotopic activity within S1. While the somatosensory stream primarily relies on bottom-up input, research in cats and primates has indicated that it is also subject to descending cortical modulation through corticothalamic and corticocuneate projections (Liao et al., 2021; Aguilar et al., 2003). It remains unknown to what extent similar top-down processing may activate thalamic and brainstem somatosensory nuclei in humans and whether this processing remains preserved following SCI. Here, we tested the hypothesis that attempted movements in tetraplegic patients, engaging the somatosensory processing stream via a top-down pathway, leads to preserved activation within the ventroposterior lateral (VPL) nuclei of the thalamus and the cuneate nuclei of the brainstem.

Methods: We used 3T fMRI (2mm3 resolution) in sixteen chronic tetraplegic patients (mean age ± s.e.m.=52.4 ± 3.5 years) and twenty age-, sex-, and handedness-matched able-bodied control participants (mean age=50.8 ± 3.5 years). The patient sample was heterogeneous in terms of neurological level of injury (C1-C7), the severity of neurological loss (ASIA A-D), and retained hand functioning (GRASSP score 22-188, normal function = 232). Participants were visually cued to make overt or attempted right- and left-hand movements in a blocked-design fashion. We used a region-of-interest approach to analyse right- and left-hand movement activity within the ipsi- and contralateral somatosensory hand nuclei of the brainstem, thalamus and S1. Additionally, we assessed clinical and behavioural traits to explore how they may correlate with functional activation.

Results: We found a clear laterality of hand activity in controls, with significantly higher activation within the ipsilateral cuneate nucleus, contralateral VPL nucleus and the contralateral S1 hand cortex as compared to the opposing stream. Importantly, this canonical pattern of hand activation was similar in tetraplegic patients, suggesting preserved hand representations along the somatosensory processing stream. Indeed, similar activity was observed even within patients with a complete absence of incoming sensory input, suggesting that top-down processing drives activation across the somatosensory processing stream through corticothalamic and corticocuneate projections. Notably, we did not observe any significant correlations between clinical measures and the amount of activation.

Conclusions: Our results reveal preserved activation of the hand somatosensory relay nuclei of tetraplegic patients despite absent or only partially intact transmission of sensory input. This suggests, for the first time, that mere cortical processing can selectively activate the VPL and cuneate nuclei in humans. This finding goes beyond the literature on preserved cortical representations after a loss of sensorimotor function and demonstrates that sensorimotor processing is also preserved subcortically. The results support recent work in non-human primate SCI models, showing that anatomical corticocuneate projections can be preserved post-SCI. Given the sensory gating function of the cuneate nucleus, these findings are also clinically relevant for rehabilitation treatments that attempt to restore somatosensation through the enhanced transmission of spared or restored sensory inputs post-SCI.

References

1. Aguilar, J., Rivadulla, C., Soto, C., Canedo, A. (2003), 'New corticocuneate cellular mechanisms underlying the modulation of cutaneous ascending transmission in anesthetized cats', Journal of Neurophysiology, vol. 89, no 6, pp. 3328-3339.
2. Kikkert, S., Pfyffer, D., Verling, M., Freund, P., Wenderoth, N. (2021), 'Finger somatotopy is preserved after tetraplegia but deteriorates over time', elife, vol. 10, pp. e67713
3. Liao, C.C., Qi, H.X., Reed, J.L., Jeoung, H.S., Kaas, J.H. (2021), 'Corticocuneate projections are altered after spinal cord dorsal column lesions in New World monkeys', Journal of Comparative Neurology, vol. 529, no. 7, pp. 1669-1702.
4. Merzenich, M.M., Kaas, J.H., Wall, J., Nelson, R.J., Sur, M., Felleman, D. (1983), 'Topographic reorganization of somatosensory cortical areas 3b and 1 in adult monkeys following restricted deafferentation', Neuroscience, vol. 8, no. 1, pp. 33-55.

Poster No 199

Structural desegregation of intrinsic brain networks in behavioral variant frontotemporal dementia

Melanie Matyi[1], Hamsanandini Radhakrishnan[1], Jeffrey Phillips[1], Philip Cook[1], Emma Rhodes[1], David Irwin[1], Corey McMillan[1], Lauren Massimo[1]

[1]*University of Pennsylvania, Philadelphia, PA*

Introduction: Behavioral variant frontotemporal dementia (bvFTD) is a neurodegenerative disease associated with significant changes in behavior and personality (Rascovsky et al., 2011). Prior work suggests that variability in the behavioral features of bvFTD may, in part, result from differences in the organization of intrinsic brain networks, particularly of the salience network (Ferreira et al., 2022). The characteristic of intrinsic network organization that supports functional specialization of cognitive domains is known as modular segregation (Sporns, 2013). In the aging brain, loss of network segregation contributes to cognitive decline, but this has not been investigated in bvFTD (Chan et al., 2014). Examination of network segregation may provide insights into the variability of behavioral symptoms observed in bvFTD. We hypothesized that patterns of structural network desegregation will be associated with distinct behavioral features in bvFTD patients.

Methods: Participants (90 bvFTD and 48 controls) underwent diffusion MRI and a carepartner or participant completed the Neuropsychiatric Inventory (NPI). Structural connectivity was derived from deterministic tracking among 100 regions mapped to 7 intrinsic networks (Yeo et al., 2011) using DSI-Studio (Yeh et al., 2013) as implemented in QSIPrep (Cieslak et al., 2021). The default mode, frontoparietal control, limbic, somatomotor and salience networks were examined. Graph metrics included within network connectivity (mean connections of regions within a network), between network connectivity with the salience network (mean connections of regions from one network to salience network), and segregation ((within – between) / within network connectivity). Integration of salience network was examined as functional integration of this network is disturbed in bvFTD (Ferreira et al., 2022). A series of one-way ANOVAs were conducted, first to establish divergent patterns of network desegregation in bvFTD by comparing bvFTD and control participants, and next, to assess the effect of presence of NPI items characteristic of bvFTD (apathy, elation, motor, disinhibition, irritability, eating) on segregation metrics within bvFTD. All analyses controlled for age, motion, and disease severity.

Results: Compared to controls, bvFTD patients were characterized by network desegregation as exhibited by desegregation of salience and frontoparietal control networks, reduced connectivity between salience and default mode network, and increased connectivity between salience and somatomotor network (see Fig.1). Within bvFTD patients, symptoms characteristic of bvFTD, including presence of apathy, elated mood, motor disturbance and disinhibition were all associated with desegregation of key intrinsic networks (see Fig. 2). Specifically, patients with apathy exhibited desegregation of default mode network, elated mood exhibited desegregation of limbic, default mode, and salience networks, motor disturbance exhibited desegregation of default mode network, and disinhibition exhibited desegregation of limbic network. Additionally, bvFTD patients with irritability exhibited segregation of salience network and increased connectivity between salience and somatomotor network.

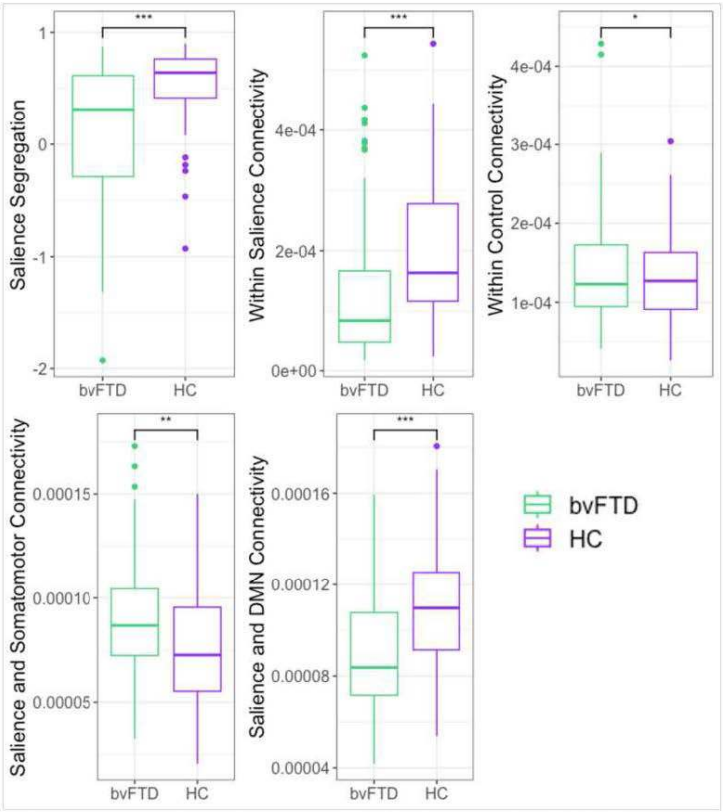

Fig. 1 Segregation of structural intrinsic networks differ between bvFTD patients and healthy control (HC) participants. DMN=default mode network. *=p<.05, **=p<.01, ***= p<.001.

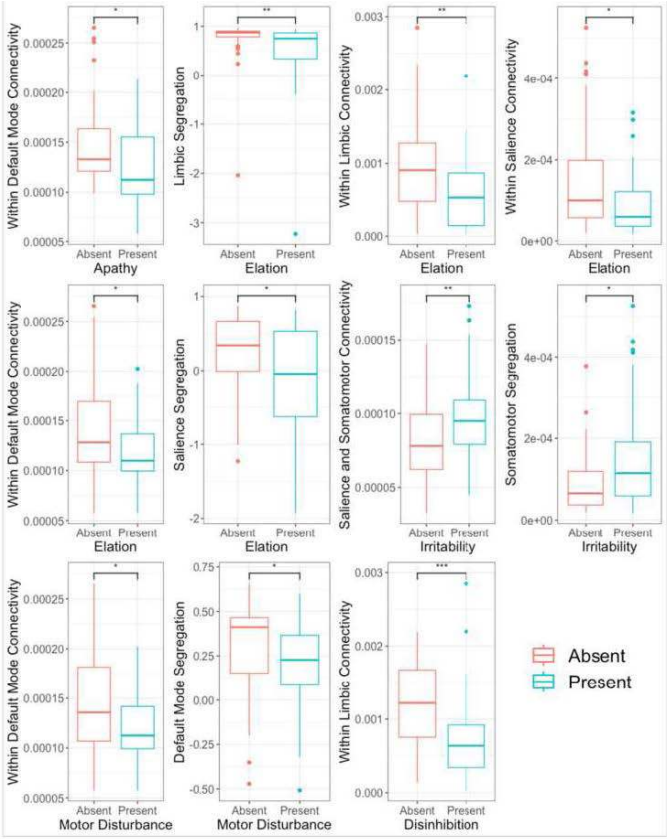

Fig. 2 Desegregation of structural intrinsic networks are associated with presence of bvFTD features. *=p<.05, **=p<.01, ***= p<.001.

Conclusions: Results indicated that greater network desegregation, particularly of salience network, is characteristic of bvFTD. Additionally, presence of features characteristic of bvFTD were associated with desegregation of related networks. Future studies examining network associations longitudinally may provide more nuanced understanding of these relationships. Overall, loss of specialized processing within networks posited to underlie features characteristic of bvFTD (e.g., limbic network and elated mood) were associated with the presence of those features. Results underscore the importance of intrinsic network integrity in bvFTD and suggest that desegregation of intrinsic networks may represent a mechanism of disease progression.

References

1. Chan, M. Y., et al. (2014), 'Decreased Segregation of Brain Systems Across the Healthy Adult Lifespan', Proceedings of the National Academy of Sciences, vol. 111, no. 46.
2. Cieslak, M., et al. (2021), 'QSIPrep: An Integrative Platform for Preprocessing and Reconstructing Diffusion MRI Data', Nature Methods, vol. 18, no. 7.
3. Ferreira, L. K., et al. (2022), 'Functional Connectivity in Behavioral Variant Frontotemporal Dementia', Brain and Behavior, vol. 12, no. 12.
4. Ng, A. S. L., et al. (2021), 'Distinct Network Topology in Alzheimer's Disease and Behavioral Variant Frontotemporal Dementia', Alzheimer's Research & Therapy, vol. 13, no. 1.
5. Rascovsky, K., et al. (2011), 'Sensitivity of Revised Diagnostic Criteria for the Behavioural Variant of Frontotemporal Dementia', Brain, vol. 134, no. 9, pp. 2456–2477.
6. Sporns, O. (2013), 'Network Attributes for Segregation and Integration in the Human Brain', Current Opinion in Neurobiology, vol. 23, no. 2, pp. 162–171.
7. Yeh, F.-C., et al. (2013), 'Deterministic Diffusion Fiber Tracking Improved by Quantitative Anisotropy', PLoS ONE, vol. 8, no. 11, e80713.
8. Yeo, B. T., et al. (2011), 'The Organization of the Human Cerebral Cortex Estimated by Intrinsic Functional Connectivity', Journal of Neurophysiology, vol. 106, no. 3, pp. 1125–1165.

Poster No 200

Towards associative memory in convolutional neural networks for in silico neurodegenerative diseases

Chris Kang[1], Jasmine Moore[1], Matthias Wilms[1], Nils Forkert[1]

[1]University of Calgary, Calgary, Alberta

Introduction: Convolutional neural networks (CNNs) have emerged as a popular choice of deep learning architecture for modeling visual processing, as their hierarchical structure and flow of information processing closely resembles the human ventral stream [LeCun, Y. (1989)]. While CNNs have been used to model healthy visual cognition, there remain limitations in biologically plausible in silico modeling of cognitive decline in neurodegenerative diseases, such as Alzheimer's (AD). Previously, we developed methods to simulate neurodegeneration of the visual system through iterative synaptic injury in CNNs [Tuladhar, A. (2021), Moore, J. (2023)]. However, the limitation of CNNs lies in the lack of biologically meaningful learning mechanisms that are similar to cognitive functions, such as memory. These mechanisms are essential for accurately capturing the neuropathogenesis. For instance, the deposition of beta-amyloid peptide and neurofibrillary tangles of tau polymers in the hippocampus leads to cognitive decline in memory tasks among AD patients. Building on our prior work, in this study, we equipped a CNN with associative memory to enhance biological plausibility, combining two critical cognitive functions of the brain: visual processing of the ventral stream and associative memory of the hippocampus. The model demonstrates intriguing and beneficial properties, including (1) robustness to noisy or occluded image queries and (2) interpretable and sparse representations in network weights. We argue that this model is an improved in silico framework for a healthy brain, as well as the cognitive profiles of AD progression.

Methods: VGG19, a CNN with a high similarity to the human brain as measured by Brain-Score [Schrimpf, M. (2018)], was equipped with a flattened layer of the modern Hopfield network [Krotov, D. (2016), Ramsauer, H. (2020)], replacing the penultimate fully-connected layer (Figure 1a). This VGG-MHN model was independently trained on two commonly used vision datasets, MNIST and CIFAR-10, for image classification. Previously trained CIFAR-10 images and test images were injected with Gaussian noise, according to varying signal-to-signal plus noise ratios, and classification tasks were performed to measure the ability to recall noisy queries, a known ability of the human brain. The result was compared to the baseline performance of VGG19, which has been shown to perform poorly when inputs are even slightly altered [Tang, H. (2018)]. For a more challenging recall task, training and classification with MNIST images was performed on partially occluded test sets featuring images masked by 30% and 50% of the total area, and the network weights were analyzed.

Results: VGG-MHN exhibited significantly improved robustness to noisy queries for previously seen images compared to the baseline VGG19 (Figure 1b). In case of unseen images, both VGG-MHN and VGG19 performed equally in the high SSNR domain. However, VGG-MHN underperformed when the SSNR level was below w=0.8. In the occluded MNIST experiment, VGG-MHN significantly outperformed VGG19 (Figure 1c). Further analysis of the VGG-MHN when tested on the occluded

MNIST dataset revealed that, in the Hopfield layer, the weights preserve feature and prototype representations depending on the model choice of energy function. This phenomenon was first characterized as a “feature-to-prototype” transition (Figure 1d) [Krotov, D. (2018)].

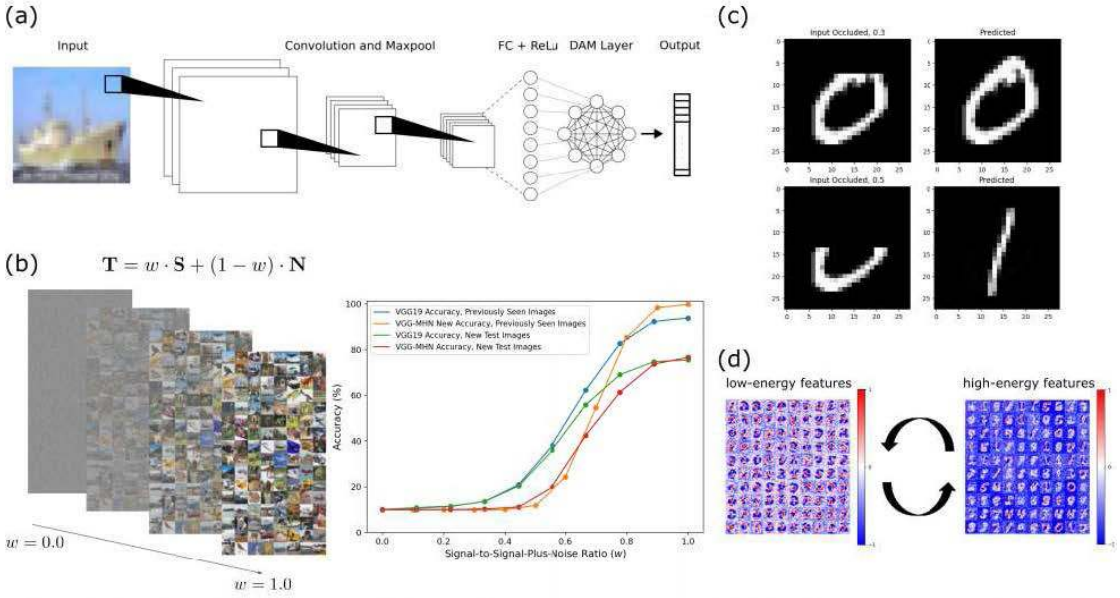

Figure 1: (a) VGG-MHN Architecture. (b) Noisy CIFAR-10 Query Experiment. VGG-MHN showed greater robustness to noisy queries for previously seen images compared to the baseline VGG19. (c) Occluded MNIST Test. VGG-MHN performed better than VGG19. (d) Representations in VGG19-MHN: Feature-to-prototype transition is seen in the modern Hopfield layer between low-energy and high-energy interactions.

Conclusions: The biologically inspired CNN, equipped with associative memory, extends our existing framework for in silico neurodegeneration. VGG-HMN effectively integrates visual processing with memory systems grounded on fundamental cognitive principles (i.e., Hebbian learning) and offers many advantages, simulating a healthy brain. These include enhanced robustness against noisy and occluded queries and the production of interpretable representations. We believe that such an architecture is well suited for in silico analysis of neurodegenerative diseases in the forthcoming work.

References

1. Krotov, D. (2016). ‘Dense associative memory for pattern recognition’, Advances in Neural Information Processing Systems, 29
2. Krotov, D. (2018). ‘Dense associative memory is robust to adversarial inputs’, Neural Computation, 30(12):3151–3167
3. LeCun, Y. (1989). ‘Backpropagation applied to handwritten zip code recognition’, Neural Computation, 1(4):541–551
4. Moore, J. A. (2023a). ‘Dementia in convolutional neural networks: Using deep learning models to simulate neurodegeneration of the visual system’, Neuroinformatics, 21(1):45–55
5. Moore, J. A. (2023b). ‘Simulation of neuroplasticity in a CNN-based in-silico model of neurodegeneration of the visual system’, Frontiers in Computational Neuroscience, 17
6. Ramsauer, H. (2020). ‘Hopfield networks is all you need’, arXiv preprint arXiv:2008.02217
7. Schrimpf, M. (2018). ‘Brain-score: Which artificial neural network for object recognition is most brain-like?’, BioRxiv, page 407007
8. Tang, H. (2018). ‘Recurrent computations for visual pattern completion’, Proceedings of the National Academy of Sciences, 115(35):8835–8840
9. Tuladhar, A. (2021). ‘Modeling neurodegeneration in silico with deep learning’, Frontiers in Neuroinformatics, 15:748370

Poster No 201

Transfer Learning for Optimal Adaptation of Normative Neuroimaging models in Alzheimer’s Disease

Camille Elleaume[1,2], Bruno Hebling Vieira[1], Dorothea Floris[1], Nicolas Langer[1,2]

[1]University of Zurich, Zürich, Switzerland, [2]Neuroscience Center Zürich (ZNZ), Zürich, Switzerland

Introduction: Alzheimer’s Disease (AD) is a neurodegenerative disorder impacting memory and cognition, with associated hippocampal atrophy[1]. Disentangling healthy-aging related shrinkage and AD-related pathological atrophy is crucial for early disease detection and understanding. Building on this research objective, recent advances in neuroimaging methods, such as normative modelling, offer promising avenues. These methods establish normative trajectories using large-scale datasets, allowing the assessment of deviations in clinical populations[2-5]. Despite their growing use and benefits, the application of

normative models to independent clinical populations presents methodological challenges, such as site-specific variations in MRI scanner parameters[4-6]. Our study addresses these challenges by using transfer learning to align pretrained models with new datasets. We explore how sample size and scanner variations impact model adaptation in healthy controls (HC) and examine the influence of sample size on accurately representing AD neuroanatomical deviations, assessed through a classifier's performance in differentiating between HC and AD individuals.

Methods: Utilizing FreeSurfer to extract hippocampal volume from T1-weighted MRI scans, normative models for left and right hippocampal volumes were established in the UK Biobank dataset (N=42,747). These models were transferred to the AIBL dataset (N=462, 12% AD) using 80% of healthy controls (HC) as an adaptation set (N_adj=322). The remaining 20% of HC, along with participants diagnosed with AD (N_test=140, with 42% AD), were used for testing (Fig. 1A-B). Bayesian Linear Regression implemented in the PCN toolkit[7] was employed for normative modeling, incorporating age, sex, and image acquisition site as covariates. Deviation from the normative model was quantified as Z-scores (Fig. 1A). To transfer models to AIBL, we used bootstrapping to sub-sample the adaptation set with sample sizes ranging from 5 to 100 subjects per site. For each sample size bin, model adaptation was evaluated through evaluation parameters (MSLL, SMSE, EV, Rho) on HC in the test set from AIBL (Fig. 2.A). To further evaluate the impact of both sample size and scanner variability in the adaptation set, we calculated Z-score differences between the full adaptation set (N=322) and obtained Z-scores across different sample sizes and scanners. To highlight the improved AD classification achieved with transfer learning of normative models, we compared the Receiver Operating Characteristic Area Under the Curve (ROC-AUC) obtained from each normative model with those derived from raw hippocampal volumes. This comparison was conducted using a Logistic Regression classifier on the complete test set.

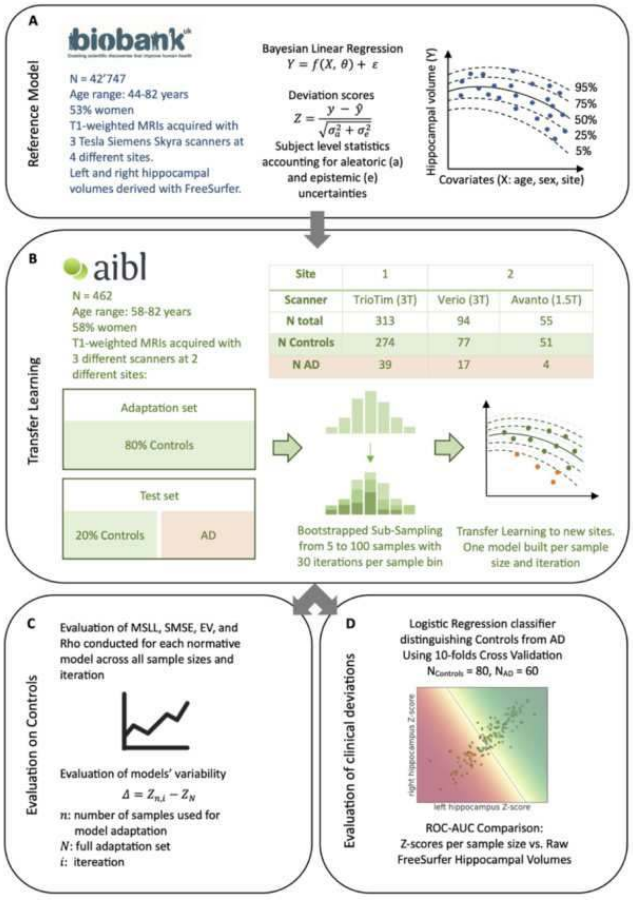

Figure 1. Overview of the methodological approach. A: Left and right hippocampal volumes were derived from T1-weighted MRIs using FreeSurfer for participants of the UK Biobank. Normative models for both hippocampal volumes were fitted to the UK Biobank reference cohort using Bayesian Linear Regression including age, sex, and image acquisition site as covariates. B: Normative models were transferred to the adaptation set of the AIBL dataset including 80% of the healthy control individuals. This adaptation set was sub-sampled from 5 to 100 samples with 30 iterations per sample bin. For each sample bin and iteration, we applied transfer learning to adjust models to the new sites and derived deviation Z-scores on the test set which included the remaining 20% of controls along with individuals diagnosed with Alzheimer's disease. C: The quality of each transferred models was evaluated on controls form adaptation and test set using Mean Standardized Log-Likelihood (MSLL), Standardized Mean Squared Error (SMSE), Explained Variance (EV) and Pearson correlation between true and predicted responses (Rho). We calculated the differences in Z-scores generated by the full model (which employs transfer learning with the complete adaptation data set) and those obtained with models using sub-sampled adaptation sets. This was conducted for each control individual in the test set, aiming to evaluate the variability of the models and scanners. D: For each transferred model, a logistic regression classifier was used on the test set's Z-scores to differentiate control individuals from individuals with Alzheimer's Disease. We assess the clinical classification performance of the deviation scores using ROC-AUC across the different sample sizes used for adjustment and compare it to the classification performance achieved using raw FreeSurfer hippocampal volumes.

Results: The results indicated that transfer learning reached an optimal plateau, as determined by model evaluation parameters, at approximately 20 samples in the adaptation dataset (Fig. 2A). This was further substantiated by the significant decrease in Z-scores differences compared to the full model (Fig. 2B). The scanner with a distinct magnetic field strength (i.e. 1.5T) exhibited a significant differences in Z-score deviations, which indicates a bias in transfer learning across different magnetic field strength for small adaption sets (Fig. 2B). The AD-classification confirms that 20 samples in the adaption set is sufficient to reach the performance asymptote, while 9 samples already surpass the classification performance achieved with raw hippocampal volumes (Fig. 2C).

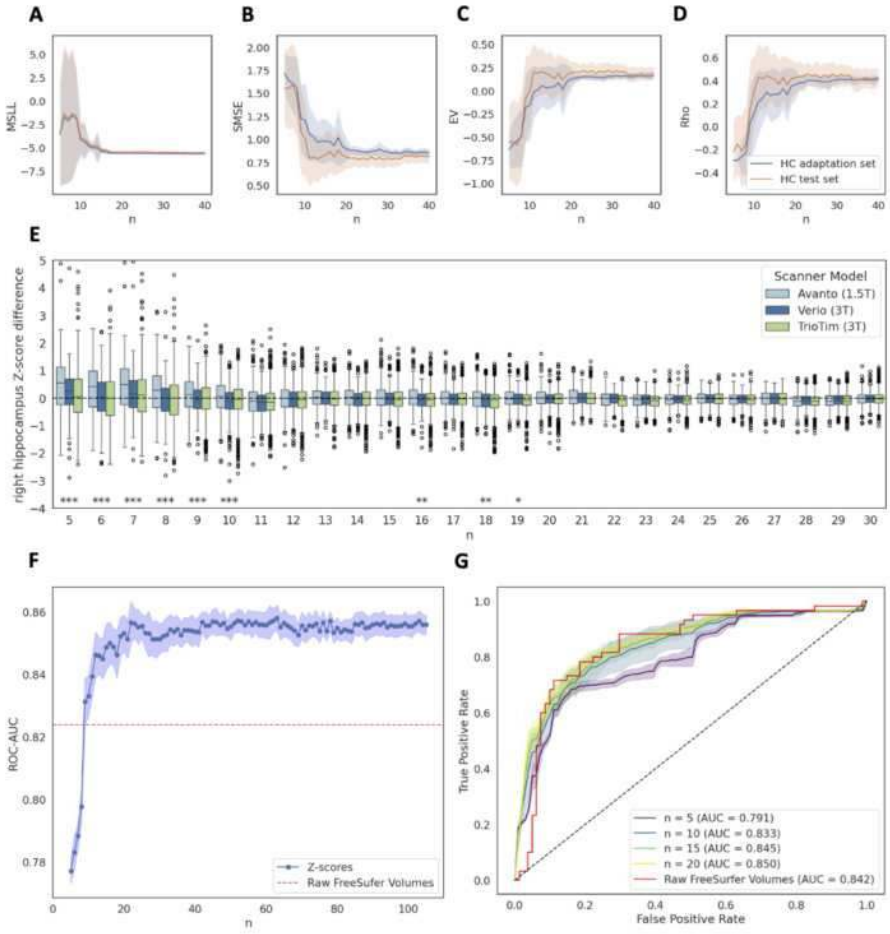

Figure 2. Normative models performance and variability in relation to sample size used in adaptation set for transfer learning. Subplots A-D show improvements in model performance, as a function of number of subjects in the adaptation set (n) indicated by the reduced MSLL (Mean Standardized Log-Likelihood) and SMSE (Standardized Mean Squared Error) and increased EV (Explained Variance) and Rho (Pearson correlation). The results indicate that the transfer learning stabilizes with 20 Healthy Control (HC) individuals used in adaptation set. E: Displayed are the differences in Z-scores for each model compared to the full model per scanner. The variability of deviations stabilizes at n=20. We also note an overestimation in deviation scores for smaller n when comparing to the 0-difference dashed line, particularly for the Avanto scanner using 1.5T magnetic strength. This difference between scanners was found significant using Student t-test with Bonferroni correction for multiple testing up to n=20 (Statistical significance levels are indicated as follows: * $p < 0.05$, ** $p < 0.01$, *** $p < 0.001$). Subplots F and G confirm that a minimum sample of 20 samples is necessary to achieve maximum ROC-AUC. Notably, the ROC-AUC obtained with FreeSurfer's raw hippocampal volumes is exceeded from 9 subjects in the adaption set onwards.

Conclusions: Our study indicates that for the AIBL data, a minimum of 20 samples are necessary to adapt the UK-based normative models to a new site and correctly map clinical deviations in the hippocampus for AD. Going forward, we aim to validate these results using independent datasets to ensure generalizability and extend this work by including a comprehensive study of all brain regions. This work can aid future studies to economically use resources for efficient biomarker development in AD.

References

1. hippocampal atrophy rates in Alzheimer's disease. Neurobiology of Aging. 2009 Nov 1;30(11):1711–23.
2. Marquand AF, Rezek I, Buitelaar J, Beckmann CF. Understanding Heterogeneity in Clinical Cohorts Using Normative Models: Beyond Case-Control Studies. Biol Psychiatry. 2016 Oct 1;80(7):552–61.
3. Marquand AF, Kia SM, Zabihi M, Wolfers T, Buitelaar JK, Beckmann CF. Conceptualizing mental disorders as deviations from normative functioning. Mol Psychiatry. 2019 Oct;24(10):1415–24.
4. Rutherford S, Kia SM, Wolfers T, Fraza C, Zabihi M, Dinga R, et al. The normative modeling framework for computational psychiatry. Nat Protoc. 2022 Jul;17(7):1711–34.
5. Rutherford S, Fraza C, Dinga R, Kia SM, Wolfers T, Zabihi M, et al. Charting brain growth and aging at high spatial precision. Baker CI, Taschler B, Esteban O, Constable T, editors. eLife. 2022 Feb 1;11:e72904.
6. Bozek J, Griffanti L, Lau S, Jenkinson M. Normative models for neuroimaging markers: Impact of model selection, sample size and evaluation criteria. NeuroImage. 2023 Mar 1;268:119864.
7. Fraza CJ, Dinga R, Beckmann CF, Marquand AF. Warped Bayesian linear regression for normative modelling of big data. Neuroimage. 2021 Dec 15;245:118715.

Poster No 202

Fast Imaging of the Substantia Nigra with Zero-Shot Super-Resolution

Vincent Beliveau[1,2], Christoph Birkl[3], Florian Krismer[1], Frank Jagusch[1], Ruth Steiger[3], Christian Kremser[3], Stefan Kiechl[1], Elke Gizewski[3], Klaus Seppi[1], Christoph Scherfler[1]

[1]Department of Neurology, Medical University of Innsbruck, Innsbruck, Austria, [2]Neurobiology Research Unit, Copenhagen University Hospital Rigshospitalet, Copenhagen, Denmark, [3]Department of Radiology, Medical University of Innsbruck, Innsbruck, Austria

Introduction: The assessment of dorsolateral nigral hyperintensities (DNH) has consistently been shown to provide excellent diagnostic accuracy between patients with Parkinson's disease (PD) and healthy controls (Kim et al., 2019). Although research efforts have been expanded to develop fast and accurate MRI sequences, imaging of the substantia nigra remains challenging and further improvement is required to enable nigral imaging into daily clinical practice. To date, the segmented echo-planar imaging (EPISEG) sequence previously proposed by Hernadi et al. (2021) is the fastest MRI sequence for imaging DNH. In this pilot study, we explored the possibility of reducing the acquisition time of the EPISEG sequence by exploiting redundancy in the acquisition and simultaneously improving imaging quality by using a deep learning super-resolution approach.

Methods: The EPISEG sequence was acquired for 7 PD patients (64.4 ± 10.8 years; 3 female) and 8 healthy controls (62.4 ± 4.1 years; 1 female) on a 3T MRI scanner. The original sequence consists of 6 measurements acquired over 2:20 min which were averaged online on the scanner to obtain images with an isotropic resolution of 1 mm^3. Here, we used the same sequence but each of the 6 measurements were saved independently. A 3D zero-shot super-resolution (ZSSR) model (Shocher et al., 2018) was trained to double the resolution of the images. The model is a fully convolutional neural network, with 8 hidden layers, each with 64 channels and rectified linear unit (ReLU) activations. Low-resolution images used for training were created by 1) downsampling the original images by a given scale factor using trilinear interpolation and 2) upsampling them back to their original size. Then, the model was taught to predict the residual between the original and low-resolution images. In this way, the model learns to revert the loss of information caused by the downsampling at specific scale factors, a process that can then directly be applied to upsample images. Figure 1 presents an overview of the training and inference. The model was gradually trained to upsample images at increasing scale factors of 1.25, 1.5, 1.75, and 2. Two approaches were evaluated: 1) the original EPISEG sequence where 6 measurements are upsampled to 0.5 mm^3 using trilinear interpolation and averaged, and 2) the proposed approach where 3 out of 6 measurements are upsampled to 0.5 mm^3 using the 3D ZSSR model and averaged. The presence of DNH was assessed by a neurologist with 10 years of experience in processing brain MRI. The rater was presented with randomized and anonymized images which were flipped left-right between approaches. Images where both DNH were visible were labeled as "healthy".

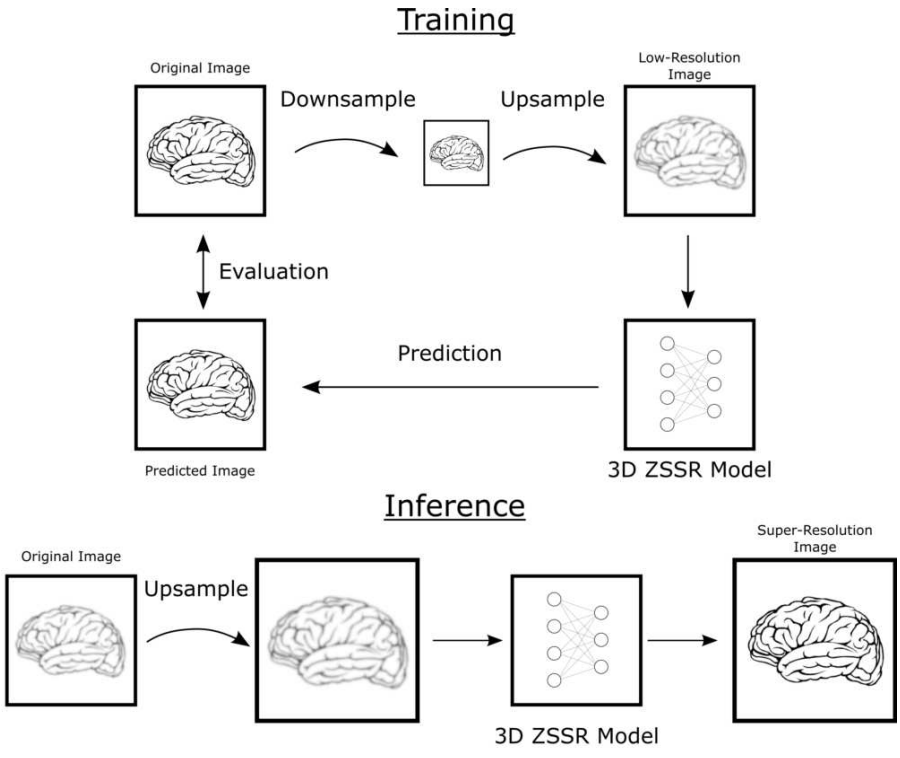

Figure 1. Overview of the training (top) and inference (bottom) for the 3D zero-shot super-resolution (ZSSR) model.

Results: By design, the images upsampled with ZSSR exhibited sharper details; see Figure 1 for examples in a healthy control and a PD patient. For the EPISEG approach, the rater identified PD patients and healthy controls with an accuracy of 67% (10/15) (sensitivity=100%; 7/7 and specificity=38%; 3/8), whereas for the images processed with ZSSR, he obtained an accuracy of 80% (12/15) (sensitivity=86%; 6/7 and specificity=75%; 6/8).

Conclusions: In the original EPISEG sequence, multiple measurements are acquired to average out noise in the images. By acquiring fewer measurements, it is possible to reduce the acquisition time, but, increased noise is correspondingly expected. ZSSR provides an alternative approach to reduce noise and enhance the details of individual measurements. In our evaluation, fewer EPISEG measurements upsampled with ZSSR allowed, in all cases but one, for similar or improved assessment of DNH compared to the original EPISEG sequence. With 3 measurements, the acquisition time for the EPISEG sequence is reduced to a mere 1:10 min, thus making the addition of this sequence to any scanning protocol negligible. More experimentation in larger datasets is required to evaluate this approach thoroughly.

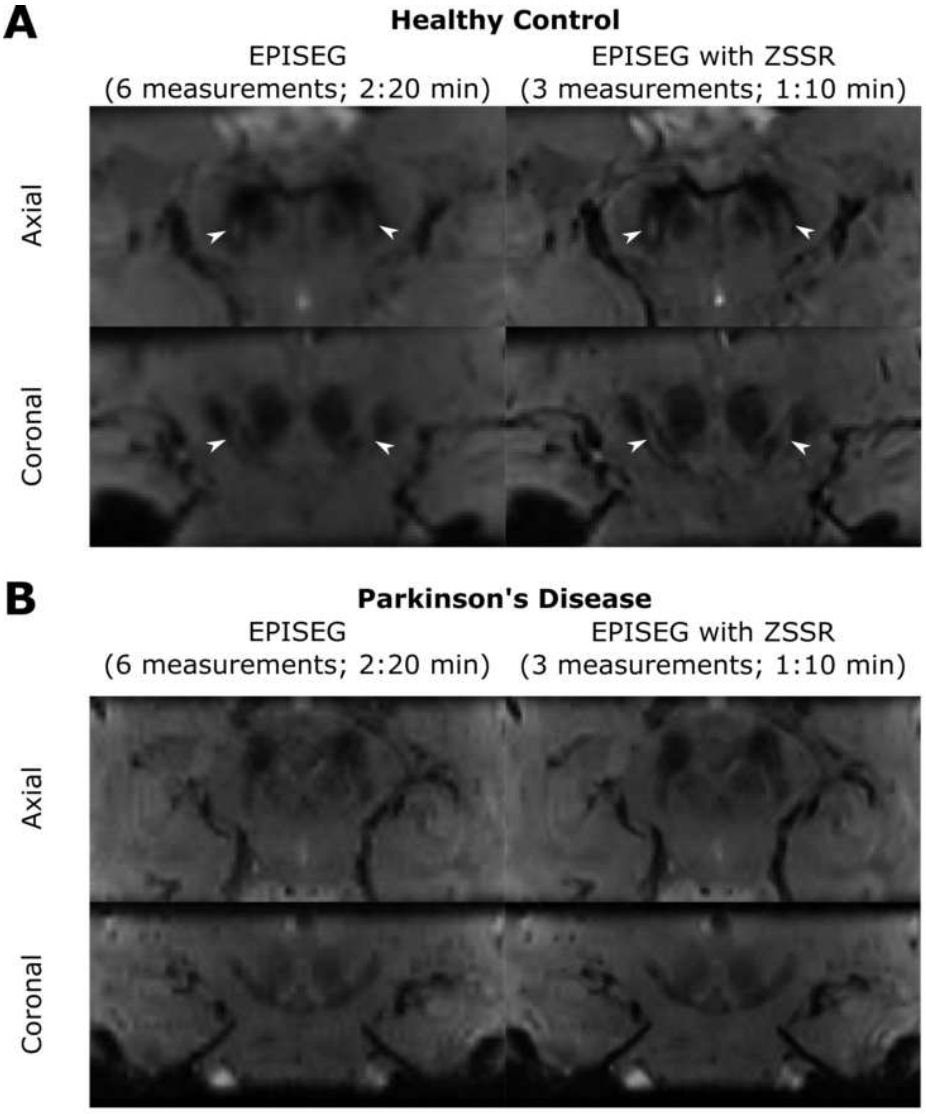

Figure 2. Visualization of the substantia nigra in (A) a healthy control and (B) a Parkinson's disease patient with the segmented echo-planar imaging (EPISEG) sequence without and with 3D zero-shot super-resolution (ZSSR). Dorsolateral nigral hyperintensities are visible for the healthy control (white arrowheads) whereas they are absent bilaterally for the Parkinson's disease patient.

References

1. Hernadi, G., Pinter, D., Nagy, S. A., Orsi, G., Komoly, S., Janszky, J., ... & Perlaki, G. (2021). Fast 3 T nigral hyperintensity magnetic resonance imaging in Parkinson's disease. Scientific Reports, 11(1), 1179.
2. Kim, E. Y., Sung, Y. H., & Lee, J. (2019). Nigrosome 1 imaging: technical considerations and clinical applications. The British Journal of Radiology, 92(1101), 20180842.
3. Shocher, A., Cohen, N., & Irani, M. (2018). "zero-shot" super-resolution using deep internal learning. In Proceedings of the IEEE conference on computer vision and pattern recognition (pp. 3118-3126).

Poster No 203

Sex differences in the relationship of cognition and brain in midlife adults at risk for dementia

Qing Qi[1,2], Feng Deng[1,2], Maria-Eleni Dounavi[3], Graciela Muniz-Terrera[4,5], Ivan Koychev[6], Paresh Malhotra[7,8], Craig Ritchie[4,9], John O'Brien[10], Brian Lawlor[1,2], Lorina Naci[1,2]

[1]Trinity College Institute of Neuroscience, School of Psychology, Trinity College Dublin, Dublin, Ireland, [2]Global Brain Health Institute, Trinity College Dublin, Dublin, Ireland, [3]Department of Psychiatry, School of Clinical Medicine, niversity of Cambridge, Cambridge, United Kingdom, [4]Edinburgh Dementia Prevention, University of Edinburgh, Edinburgh, United Kingdom, [5]Department of Social Medicine, Ohio University, Athens, United States, [6]Department of Psychiatry, Oxford University, Oxford, United Kingdom, [7]Department of Brain Science, Imperial College London, London, United Kingdom, [8]UK Dementia Research Institute Care Research and Technology Centre, Imperial College London and the University of Surrey, London, United Kingdom, [9]Scottish Brain Sciences, Edinburgh, United Kingdom, [10]Department of Psychiatry, School of Clinical Medicine, University of Cambridge, Cambridge, United Kingdom

Introduction: Two-thirds of Alzheimer's Disease (AD) cases occur in women[1]. Compared to men, women exhibit more rapid cognitive decline and brain atrophy in the presence of AD-related neuropathology[2]. It is now acknowledged that AD processes are present decades before the onset of clinical symptoms[3]. However, whether there are sex differences in cognition-brain structure coupling and how AD risk affects their relationships in midlife remain unclear. In this study, we investigated associations between sex, AD risk, brain structure and cognition.

Methods: Participants: 701 cognitively unimpaired middle-aged participants (40–59 years) were recruited in the PREVENT-Dementia study from five study sites: West London, Edinburgh, Cambridge, Oxford and Dublin. In total, 614 participants (233 M/ 381 F) who had completed cognitive, clinical and structural Magnetic Resonance Imaging (sMRI) data were included in this study. Risk factors: The Apolipoprotein E [APOE] Ɛ4 risk is determined by ≥1 APOE Ɛ4 allele. The Cardiovascular Risk Factors Aging and Dementia (CAIDE) score is calculated based on eight variables[4], with higher scores indicating greater risk. MRI data acquisition and processing: sMRI data were acquired using a T1-weighted MPRAGE sequence (TR = 2.3 s, TE = 2.98 ms, 160 slices, flip angle = 9°, voxel size = 1 mm3 isotropic). Freesurfer v7.1.0 was used for data processing[5]. The recon-all pipeline was run with default settings for each participant. The cortical thickness in 68 regions was quantified based on the Desikan-Killiany atlas[6]. The global cortical thickness (CT) was obtained by averaging the values from the bilateral hemispheres for each participant. We chose nine regions of interest (ROIs) relating to AD from previous studies[7-9], and the mean CT within each ROI was calculated by averaging the values from the bilateral hemispheres. Statistical analyses: Linear regression models were used to investigate the association of CAIDE with global CT and episodic and relational memory separately. To investigate the relationships between CT and cognition, and the moderating role of the sex variable, we used the linear regression model for episodic and relational memory, with global CT and nine regional CT as the independent variable (in independent models), sex as the moderator, and age, years of education, ICV and study sites included as covariates. The same moderation regression analysis was repeated in APOE Ɛ4+ and APOE Ɛ4− groups separately to further delineate the sex moderation effect on cognition-CT relationships in participants belonging to different risk groups. Multiple comparisons correction was carried out using the Bonferroni method.

Results: CAIDE was negatively associated with global CT (Fig. 1a), and negatively associated with episodic and relational memory (Fig.1b). We didn't find a significant association between global CT and cognition (Fig. 2a) but found a sex-specific coupling of global CT and episodic and relational memory (Fig. 2b). Males showed a positive association between global CT and cognition, while females showed no relationship between them. Such sex-specific coupling between global CT and cognition was absent in APOE Ɛ4 carriers, and only shown in APOE Ɛ4 non-carriers (Fig. 2c, 2d). Among the nine ROIs, we only found a significant sex-specific coupling of episodic and relational memory and precuneus CT after Bonferroni correction. Furthermore, cognition was decoupled from the precuneus CT in APOE Ɛ4 carriers, and only coupled with CT of precuneus in APOE Ɛ4 non-carriers (Fig. 2e, 2f).

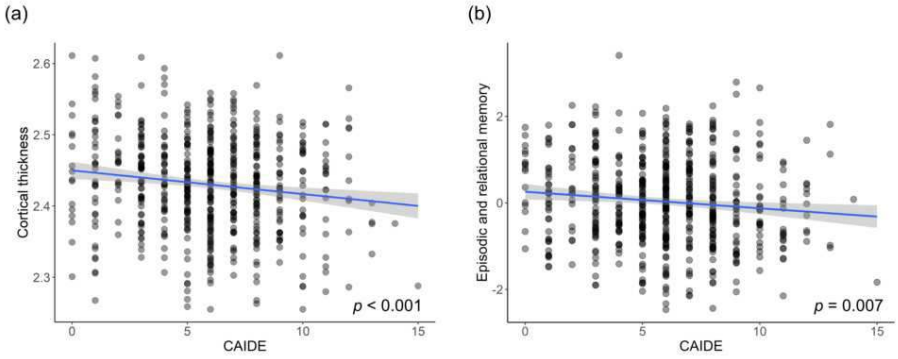

Figure 1. Association of CAIDE score with (a) cortical thickness, and (b) episodic and relational memory performance. On the x axis, higher scores represent higher CAIDE score, and on the y axis, higher scores represent thicker cortical thickness and better episodic and relational memory performance. Scatter plots show unadjusted values. Full regression statistic for cortical thickness, after controlling for head size and study sites: β (SE) = -0.004 (0.001), $p < 0.001$. Full regression statistic for episodic and relational memory: β (SE) = -0.04 (0.01), $p = 0.007$. Abbreviation: CAIDE, Cardiovascular Risk Factors, Aging and Dementia.

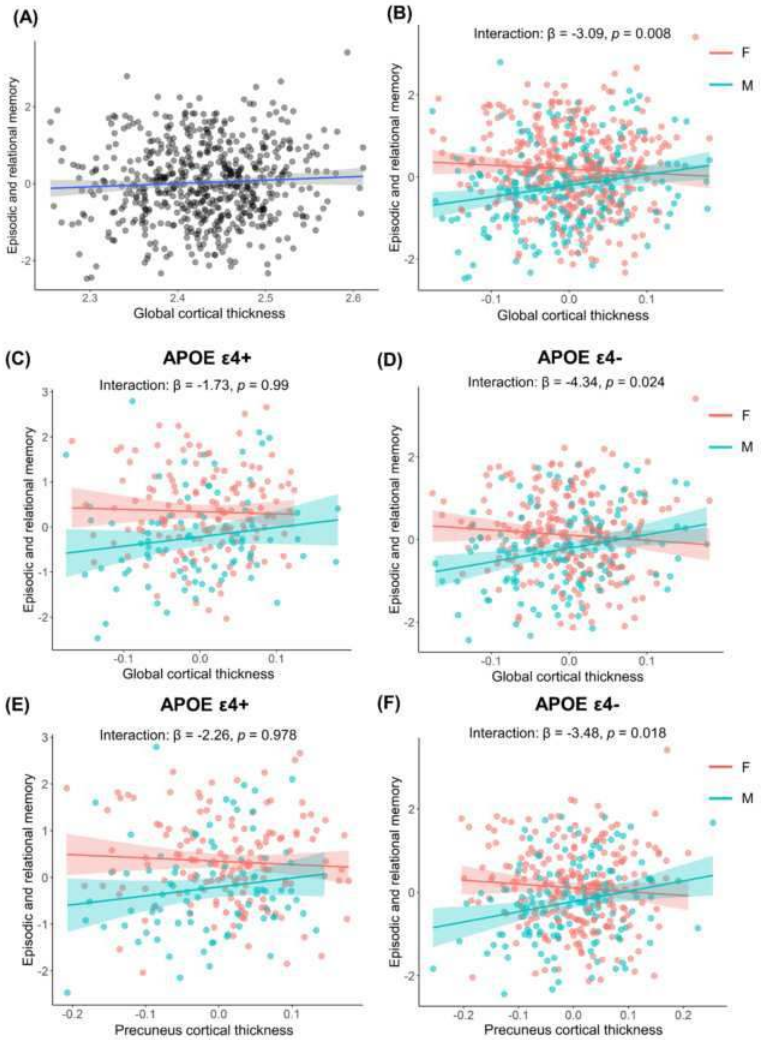

Figure 2. Associations between risk, cortical thickness and cognition in midlife. (a) No significant association between global cortical thickness and cognition. Interactions of sex and global cortical thickness on cognition in (b) the full cohort, (c) the APOE Ɛ4+ group, and (d) the APOE Ɛ4- group. Interactions of sex and precuneus cortical thickness on cognition in (e) the APOE Ɛ4+ group, and (f) the APOE Ɛ4- group. The scatter plot shows unadjusted values, but the statistical significance was based on the regression models where we controlled for covariates. P values for the interaction effects were Bonferroni corrected for multiple comparisons.

Conclusions: We found inherent sex-specific differences in the coupling between brain structure and cognition. Our results suggest that these sex-specific differences are being eroded by APOE Ɛ4 carriership in mid-life. Longitudinal follow-up in this

cohort will shed light on the long-term sex-specific impact of APOE genotype on brain structure and cognition in preclinical populations with risk for AD.

References

1. Alzheimer's Association. 2017 Alzheimer's disease facts and figures. Alzheimer's & Dementia. 2017;13(4):325-373.
2. Gamache, J., Yun, Y., & Chiba-Falek, O. (2020). Sex-dependent effect of APOE on Alzheimer's disease and other age-related neurodegenerative disorders. Disease models & mechanisms, 13(8), dmm045211.
3. Jack CR Jr, Knopman DS, Jagust WJ, et al. Tracking pathophysiological processes in Alzheimer's disease: an updated hypothetical model of dynamic biomarkers. Lancet Neurol. 2013;12(2):207-216.
4. Kivipelto M, Ngandu T, Laatikainen T, Winblad B, Soininen H, Tuomilehto J. Risk score for the prediction of dementia risk in 20 years among middle aged people: a longitudinal, population-based study. Lancet Neurol. 2006;5(9):735-741.
5. Fischl, B. (2012). FreeSurfer. Neuroimage, 62(2), 774-781.
6. Desikan, R. S., Ségonne, F., Fischl, B., Quinn, B. T., Dickerson, B. C., Blacker, D., ... & Killiany, R. J. (2006). An automated labeling system for subdividing the human cerebral cortex on MRI scans into gyral based regions of interest. Neuroimage, 31(3), 968-980.
7. Jack Jr, C. R., Wiste, H. J., Weigand, S. D., Knopman, D. S., Mielke, M. M., Vemuri, P., ... & Petersen, R. C. (2015). Different definitions of neurodegeneration produce similar amyloid/neurodegeneration biomarker group findings. Brain, 138(12), 3747-3759.
8. Cieri, F., Zhuang, X., Cordes, D., Kaplan, N., Cummings, J., Caldwell, J., & Alzheimer's Disease Neuroimaging Initiative (ADNI). (2022). Relationship of sex differences in cortical thickness and memory among cognitively healthy subjects and individuals with mild cognitive impairment and Alzheimer disease. Alzheimer's Research & Therapy, 14(1), 36.
9. Dickerson, B. C., Bakkour, A., Salat, D. H., Feczko, E., Pacheco, J., Greve, D. N., ... & Buckner, R. L. (2009). The cortical signature of Alzheimer's disease: regionally specific cortical thinning relates to symptom severity in very mild to mild AD dementia and is detectable in asymptomatic amyloid-positive individuals. Cerebral cortex, 19(3), 497-510.

Poster No 204

Frontoparietal connectivity strength relates to changes in disability metrics in multiple sclerosis

Katherine Koenig[1], Daniel Ontaneda[1], Kedar Mahajan[1], XUEMEI HUANG[2], Sehong Oh[1], Stephen Jones[1], Stephen Rao[1], Mark Lowe[1]

[1]The Cleveland Clinic, Cleveland, OH, [2]Cleveland Clinic, Cleveland, OH

Introduction: Disease progression is variable in multiple sclerosis (MS). MRI-based measures that track and predict MS disease progression could identify patients who are at risk of decline and serve as outcome measures in clinical trials of novel disease modifying treatments. Here, we focus on within-network resting state functional connectivity (rsfMRI) of the frontoparietal network (FPN), considered critical for coordination of brain function and cognitive control[1]. We assess connectivity of the FPN in people with MS (pwMS) at two time points, hypothesizing that changes in rsfMRI strength will be related to measures of disability, particularly to cognitive function.

Methods: Under an IRB-approved protocol, 47 patients with MS [mean age: 50.2 ± 8.5, 10 males, median EDSS: 3.5, range 1.5-6.5] completed an MRI, clinical evaluation, and cognitive testing at two time points separated by one year. Measures included the Multiple Sclerosis Functional Composite (MSFC) and tests of memory, processing speed, and executive function. A whole-brain T1-weighted MP2RAGE (0.75mm3) and rsfMRI scan were acquired on a Siemens 7T Magnetom with a SC72 gradient (Siemens Medical Solutions, Erlangen) using a 1-Tx and 32-Rx channel head coil (Nova Medical). RsfMRI acquisition parameters were: 132 repetitions of 81 1.5mm thick axial slices acquired with TE/TR=21ms/2800ms, voxel size 0.75×0.75×1.5mm3, matrix 160×160, FOV 210mm×210mm, receive bandwidth = 1562 Hz/pixel, eyes closed. All rsfMRI scans were corrected for motion and physiologic noise, detrended, and lowpass filtered[2,3]. Freesurfer 7.1 was used to generate cortical grey matter parcellations and apply the Yeo 7-network FPN template[4]. The MP2RAGE was coregistered and warped to rsfMRI and rsfMRI volumes from visit 1 (V1) were coregistered to visit 2 (V2) for each participant (AFNI). Using a previously described method[5] and the FPN template, the V1 rsfMRI scan was used to identify 9-voxel in-plane seeds in the bilateral grey matter of the middle frontal gyrus (MFG; BA 9), representing the FPN. Seeds were propagated to V2 for each participant and used to calculate whole-brain normalized[6] connectivity maps at both visits. Individual FPN maps were moved to Talairach space[7]. FPN connectivity was averaged across all participants (Figure 1) and used to create a mask of significant regions. AFNI 3dttest++ was used to perform a voxel-wise t-test of masked rsfMRI between V1 and V2. In regions showing significant V1-V2 differences, mean rsfMRI strength and the change in rsfMRI was correlated with performance on clinical and cognitive measures.

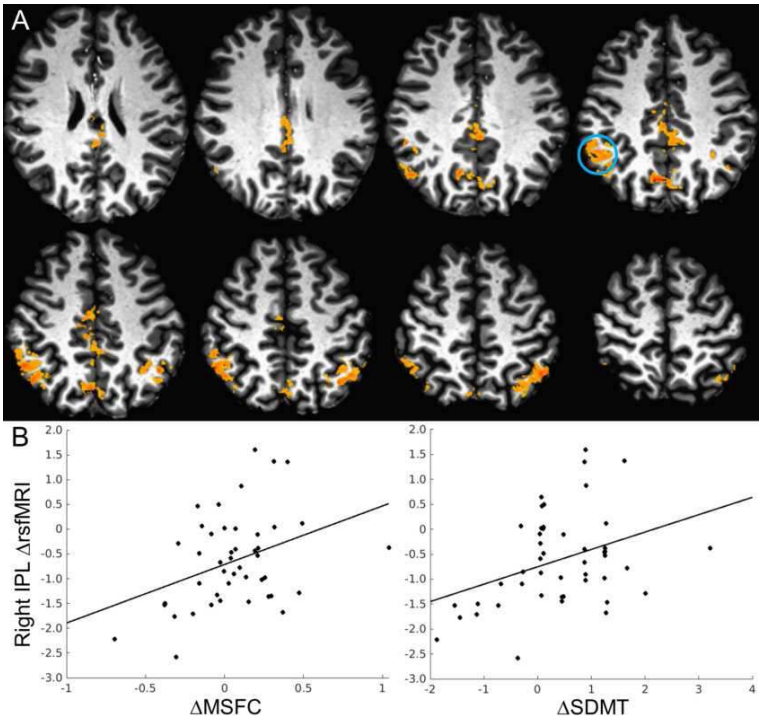

Figure 2. A. V1-V2 differences in FPN rsfMRI ($p < 0.05$, cluster size 1500). All regions show stronger connectivity at V1. B. The V1-V2 change in rsfMRI of the right IPL (circled in blue) is related to the V1-V2 change in MSFC ($r = 0.37$, $p < 0.012$) and SDMT ($r = 0.369$, $p < 0.011$).

Results: All significant V1-V2 differences were the result of a decline in rsfMRI at V2 (Figure 2). V1 rsfMRI was positively related to V1 MSFC, the symbol digit modalities test (SDMT), and memory ($p < 0.05$), but did not survive a correction for multiple comparisons. The V1-V2 change in rsfMRI of the left precuneus and right inferior parietal lobule IPL was positively related to change on the MSFC ($r = 0.45$, $p < 0.002$; $r = 0.37$, $p < 0.012$, respectively) and the SDMT ($r = 0.53$, $p < 1.1\times10\text{-}4$; $r = 0.369$, $p < 0.011$, respectively), so that a decline in functionality was associated with a decline in rsfMRI (Figure 2).

Conclusions: Here, we show that the change in rsfMRI of the FPN is related to the change in MSFC, driven by performance on the SDMT. Although the direction of the relationship between behavior and V1 rsfMRI was in line with our previous findings[8], these relationships did not reach significance. SDMT performance draws on multiple cognitive domains, including speed of processing, attention, and memory. Degradation of the FPN may lead to a breakdown of coordination between networks responsible for these functions. Future work will investigate this possibility by assessing between-network connectivity. This work was supported by the Department of Defense (MS150097). The authors acknowledge technical support by Siemens Medical Solutions.

References

1. Marek S, Dosenbach NUF. (2018) The frontoparietal network: function, electrophysiology, and importance of individual precision mapping. Dialogues Clin Neurosci. 20(2): 133-140.
2. Beall EB and Lowe MJ. (2014) SimPACE: generating simulated motion corrupted BOLD data with synthetic-navigated acquisition for the development and evaluation of SLOMOCO: a new, highly effective slicewise motion correction. Neuroimage. 101: 21-34.
3. Glover GH et al. (2000) Image-Based Method for Retrospective Correction of Physiological Motion Effects in fMRI: RETROICOR. Magnetic Resonance in Medicine. 44: 162-67.
4. Yeo BT et al. The organization of the human cerebral cortex estimated by intrinsic functional connectivity. J Neurophysiol. 106(3): 1125-65, 2011.
5. Lowe MJ et al. (2014) Anatomic connectivity assessed using pathway radial diffusivity is related to functional connectivity in monosynaptic pathways. Brain Connectivity. 4(7): 558-65.
6. Lowe MJ et al. (1998) Functional connectivity in single and multislice echoplanar imaging using resting-state fluctuations. NeuroImage. 7(2): 119-32.
7. Avants, BB et al. (2011). A reproducible evaluation of ANTs similarity metric performance in brain image registration. Neuroimage. 54(3): 2033–2044.
8. Koenig, KA, Beall, EB, Lin, J, Sakaie, K, Stone, L, Rao, SM, Phillips, M, and Lowe, MJ. (2017, April) Functional and structural connectivity of the cingulate bundle related to future cognitive performance in MS. Oral presentation at the meeting of the International Society for Magnetic Resonance in Medicine, Honolulu, Hawaii.

Poster No 205

Training Vision Transformers to Predict Amyloid Positivity from Brain Structural MRI

Tamoghna Chattopadhyay[1], Saket Ozarkar[1], Ketaki Buwa[1], Sophia Thomopoulos[2], Paul Thompson[3]

[1]University of Southern California, Los Angeles, CA, [2]USC, Marina del Rey, CA, [3]USC, Marina Del Rey, CA

Introduction: According to the World Health Organization (WHO), around 55 million individuals worldwide suffer from dementia - of whom 60-70% are diagnosed with Alzheimer's disease (AD). The defining features of AD include abnormal buildup of beta-amyloid (Aβ) plaques and tau protein tangles in the brain[2]. Amyloid positivity (Aβ+) is commonly assessed through positron emission tomography (PET) or sampling of cerebrospinal fluid (CSF) via lumbar puncture, but these procedures are costly and invasive. Although Aβ accumulation slightly precedes atrophy[3] on MRI, there is interest in how well standard anatomical MRI may detect Aβ-related brain changes, which include atrophy and structural alterations. Deep learning methods, like Vision Transformers (ViTs), can capture long-range spatial dependencies in images using self-attention mechanisms, and show great promise in computer vision. We examined the ViT architecture's performance in predicting Aβ+ status from T1-weighted scans and compared it to widely-used 3D DenseNet convolutional neural network (CNN) architecture[6].

Methods: We analyzed 3D T1-weighted (T1w) brain MRI data from the Alzheimer's Disease Neuroimaging Initiative (ADNI) dataset (phases 2/GO and 3) from 1,841 participants (age: 74.04 ± 7.40 years; 860 F/981 M) with distribution of 889 CN (cognitively normal controls)/658 with mild cognitive impairment (MCI), and 294 AD; 946 Aβ+/ 895 Aβ-. All 3D T1w brain MRI volumes were pre-processed using the following steps: nonparametric intensity normalization (N4 bias field correction), 'skull stripping' for brain extraction, 6 degrees of freedom registration to a template and isometric voxel resampling to 2 mm. These images of size 91x109x91 were scaled to take values between 0 and 1 using min-max scaling, and registered to a template created using T1w MRI from the UK Biobank dataset in MNI space[7,8]. They were resized to dimensions of 64x64x64 and 128x128x128 to guarantee direct correspondence with patch sizes used in ViT models and divided into train, validation and test sets in the ratio 80:10:10. The DenseNet architecture includes four dense blocks and three transition layers, and was used as a baseline comparison architecture. In ViT architectures[9], the input image is divided into fixed-sized patch embeddings, which are amalgamated with learnable position embeddings and class tokens. The resulting sequence of vectors is fed into a transformer encoder, which comprises alternating layers of multi-head attention and a multi-layer perceptron (MLP). We used two different ViTs - neuroimage transformer (NiT) and multiple instance NiT (MINiT)[9] - where a learned block embedding was introduced to maintain positional information of the block within the scan containing each patch. Hyperparameters were tuned and model performance was assessed using test accuracy.

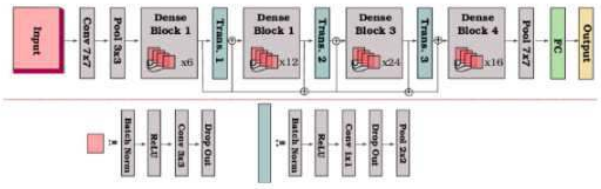

Fig 1. 3D DenseNet Architecture reproduced from [10]

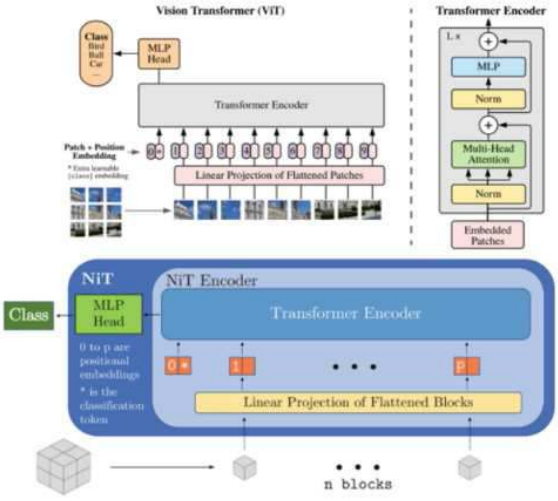

Fig 2. Overview of the Vision Transformer Architecture reproduced from [9]

Results: Results are shown in Table 1. Best performance was achieved by MINiT architecture for image size of 64x64x64; giving test accuracy of 0.791 and test ROC-AUC of 0.857. Thus, MINiT architecture improved upon both 3D DenseNet and NiT architectures. Hyperparameter tuning of attention heads, learning rate, the encoder layer and weight decay helped to improve model performance. In our experiments, performance for 64x64x64 downscaled images was better than that for 128x128x128 upsampled images.

Table 1. Experiment Results for DenseNet, NiT and MINiT models. Here, the columns 3 to 6 are the hyperparameters of the transformer architectures, namely Transformer Layers, No. of Attention Heads, Dimension and MLP Dimension. The experiments are compared using Test ROC-AUC, Accuracy and F1 Score. Bolded numbers indicate the best result.

Architecture	Image Size	Hyperparameters of Transformer Architectures				Test ROC-AUC	Test Accuracy	Test F1 Score
		Transformer Layers	Attention Heads	Dimension	MLP Dimension			
DenseNet 121	$(64)^3$	-	-	-	-	0.826	0.773	0.792
	$(128)^3$	-	-	-	-	0.720	0.678	0.687
NiT	$(64)^3$	512	3	12	175	0.494	0.541	0.614
		256	6	8	64	0.579	0.592	0.609
		256	4	8	234	0.485	0.516	0.221
	$(128)^3$	512	3	12	175	0.569	0.581	0.600
		256	6	8	64	0.692	0.590	0.584
		256	4	8	234	0.692	0.468	0.495
MINiT	$(64)^3$	6	12	256	309	**0.857**	**0.791**	**0.793**
		6	8	256	309	0.755	0.697	0.674
		6	8	128	128	0.585	0.599	0.686
		6	12	258	128	0.794	0.776	0.782
	$(128)^3$	6	12	256	309	0.503	0.534	0.557
		6	8	256	309	0.668	0.649	0.688
		6	8	128	128	0.799	0.747	0.766
		6	12	258	128	0.476	0.527	0.584

Conclusions: We evaluated prediction capabilities of the Vision Transformer architecture for inferring Aβ+ from T1w brain MRI, benchmarked against the DenseNet121 architecture. In initial experiments, MINiT architecture performed better than the other two architectures considered. Our results are promising, in that less invasive scans may be beneficial for screening individuals, prior to more intrusive Aβ+ detection procedures. This study also has some limitations, including the limited testing, for now, on the ADNI dataset. Performance may improve by increasing the size and diversity of the training data, by including multimodal brain MRI, and additional cohorts.

References

1. World Health Organization, "Dementia," 2022. https://www.who.int/news-room/fact-sheets/detail/dementia.
2. Jack, C. R., Jr et al. "NIA-AA Research Framework: Toward a biological definition of Alzheimer's disease." Alzheimer's & Dementia: the Journal of the Alzheimer's Association vol. 14, 4 (2018): 535-562.
3. Jack, C. R., Jr, et. al. (2013). Tracking pathophysiological processes in Alzheimer's disease: an updated hypothetical model of dynamic biomarkers. The Lancet. Neurology, 12(2), 207–216.
4. Chattopadhyay, T., et al., (2023). Predicting Brain Amyloid Positivity from T1 weighted brain MRI and MRI-derived Gray Matter, White Matter and CSF maps using Transfer Learning on 3D CNNs. bioRxiv.
5. Matsoukas, C., et al., "Is it Time to Replace CNNs with Transformers for Medical Images?" 2021, [Online]. Available: http://arxiv.org/abs/2108.09038
6. Huang, G., et. al. "Densely Connected Convolutional Networks," CVPR, 4700–4708 (2017).
7. Zavaliangos-Petropulu, A., et al., "Diffusion MRI Indices and Their Relation to Cognitive Impairment in Brain Aging: The Updated Multi-protocol Approach in ADNI3", Front Neuroinformatics 13:2 (2019).
8. Thomopoulos, S., et al., "Diffusion MRI Metrics and their relation to Dementia Severity: Effect of Harmonization Approaches," medRxiv (2021).
9. Singla, A., et al., "Multiple Instance Neuroimage Transformer," in Predictive Intelligence in Medicine: 5th International Workshop, MICCAI PRIME 2022, vol. 1, pp. 36–48.
10. Radwan, N. (2019). Leveraging sparse and dense features for reliable state estimation in urban environments.

Poster No 207

Longitudinal Changes in Parkinson's Disease-Related Network Organization in REM Sleep Disorder (RBD)

Yoshikazu Nakano[1], Nha Nguyen[2], An Vo[3], Chris Tang[1], David Eidelberg[4]

[1]The Feinstein Instetutes for Medical Research, Manhasset, NY, [2]Albert Einstein College of Medicine, New York, NY, [3]Feinstein Institutes for Medical Research, Manhasset, NY, [4]The Feinstein Institutes for Medical Research, Manhasset, NY

Introduction: Parkinson's disease (PD)-related covariance pattern (PDRP) derived from a network analysis of resting brain images is a feasible imaging biomarker for differential diagnosis and disease progression (Perovnik, Rus, et al. 2023). Moreover, functional connectivity within the network was found to change with disease progression. In particular, assortativity, a connectivity parameter associated with unstable and inefficient flow, increased over time (Vo, Schindlbeck, et al., 2023). Isolated REM sleep behavior disorder (iRBD) is known to be a high-risk feature of prodromal PD. We have reported that the expression of the PD-related covariance pattern (PDRP), an imaging biomarker of PD, is elevated in patients with iRBD before phenoconversion to PD (Holtbernd, Gagnon et al. 2014). However, it remains unclear how the brain connectivity in the PDRP network changes longitudinally.

Methods: Thirteen patients with iRBD (age 63.5 ± 8.4 years, 13 males) and 17 age-matched normal controls (NC) (age 59.8 ± 10.4 years, 15 males and two females) were recruited. They underwent resting metabolic positron emission tomography (PET) with [18F]-fluorodeoxyglucose (FDG), and the iRBD group underwent follow-up scans at two and four years after baseline. We identified 38 anatomical regions of interest (ROIs) as nodes corresponding to the PDRP network previously validated by voxel-wise analysis of FDG PET (Schindlbeck, Vo et al. 2020). They were classified into 20 active nodes and 18 underactive nodes on the basis of the hyper- and hypometabolism. The pairwise correlation in each node of normalized metabolic activity driven from FDG-PET data was computed for NC and each timepoint of iRBD by 100 bootstrapping iterations. The correlation matrices provided an assortativity coefficient and a degree centrality for each group. Assortativity is a correlation between node degrees across a link. In a network, increased assortativity in a subject group is reflected by a significantly higher coefficient. Assortativity is deemed reduced if the coefficient is lower. Degree centrality is the number of connections within a network or subgraph divided by total nodes. From the comparison of correlation coefficients in each time point, the edges that showed a significant increase compared to the NC group were identified as gained connections, while those showing a significant decrease were classified as lost connections. The ratio of gained to lost connections was defined as the Gaind-to-Lost Ratio (GLR). Differences between iRBD at each timepoint and NC were evaluated using ANOVA with the post hoc Bonferroni correction for multiple comparisons.

Results: The assortativity in PDRP network showed no significant differences between NC and iRBD at baseline ($P = 1.00$). However, at the 2-year and 4-year follow-ups in iRBD, it was significantly elevated compared to NC ($P < 0.01$). Degree Centrality within the same space was higher in iRBD compared to the NC group at every timepoint ($P < 0.01$). Although no significant differences were observed between baseline and the 2-year follow-up ($P = 1.00$), a significant increase was noted at the 4-year follow-up when compared to baseline and 2-year ($P < 0.036$). The gained connections between active nodes showed a decrease at the 2-year and 4-year time points compared to the baseline ($P < 0.001$) with no significant changes between 2- and 4-year ($P = 0.052$). Conversely, the lost connections between active regions increased from baseline to the 2-year and 4-year follow-ups ($P < 0.001$). The GLR between active nodes decreased at the 2-year follow-up compared to the baseline and slightly improved at the 4-year follow-up. The GLR between active and inactive regions increased at the 2-year follow-up compared to the baseline and remained elevated at the 4-year follow-up ($P < 0.001$).

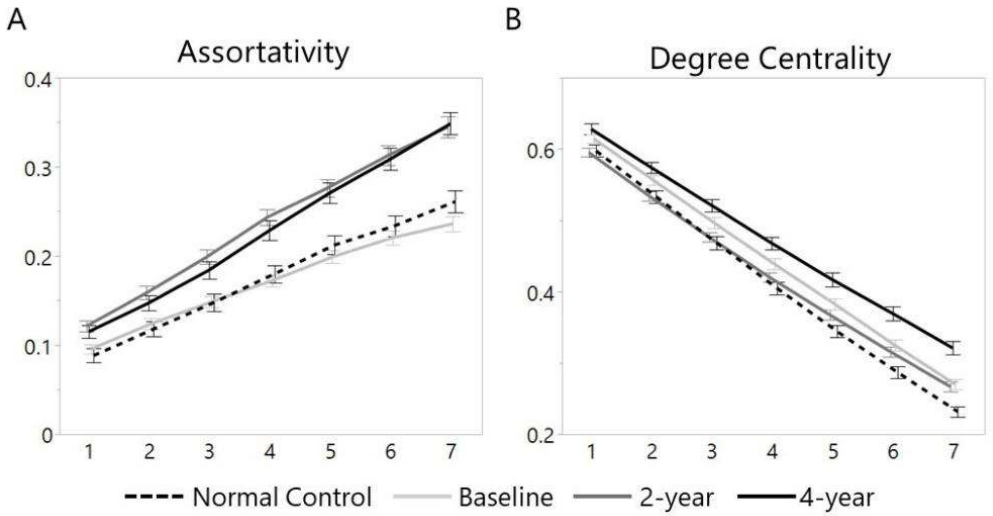

Figure 1. Graphical metrics of Parkinson's disease related-pattern (PDRP) nods in normal controls (dashed line) and patients with isolated REM sleep behavior disorder (iRBD) at baseline (light gray), 2-year (gray), and 4-year (black). (A) Assortativity in iRBD at baseline was at the same level as normal control (NC), but those at 2-year and 4-year were elevated ($P < 0.01$). (B) Degree centrality in iRBD was higher than NC at each time point ($P < 0.001$). In addition, it was higher at 4-year follow-up than at baseline and 2-year follow-up ($P < 0.001$). P values were corrected by the Bonferroni method after repeated measures ANOVA. Error bars represent the standard error.

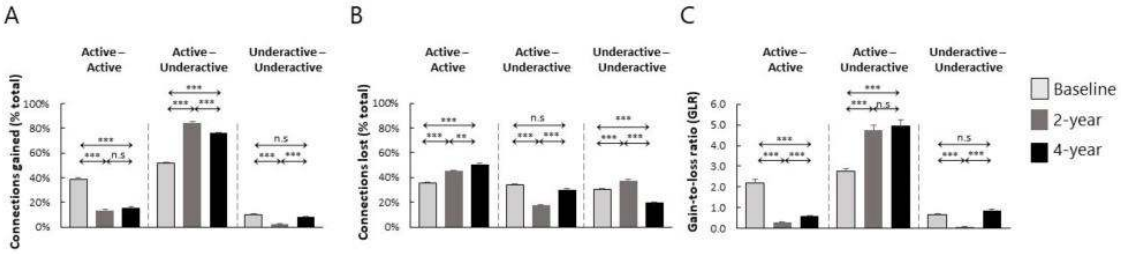

Figure 2. The gain (A) and loss (B) of connection relative to normal controls and the gain/loss ratio (C) of isolated REM sleep behavior disorder (iRBD) at baseline (light gray), 2 years (gray), and 4 years (black) were shown separately for the connection between active nodes of the Parkinson's disease-related pattern (PDRP) (left), between active and underactive nodes (middle), and between underactive nodes (right). *** $P < 0.001$, Bonferroni correction after ANOVA.

Conclusions: In the context of iRBD, the connectivity within the PDRP network is observed from the early stages and gradually converges toward changes reminiscent of those seen in PD over time.

References

1. Holtbernd, F. (2014), "Abnormal metabolic network activity in REM sleep behavior disorder." Neurology 82(7): 620-627.
2. Perovnik, M. (2023), "Functional brain networks in the evaluation of patients with neurodegenerative disorders." Nat Rev Neurol 19(2): 73-90.
3. Schindlbeck, K. (2020), "LRRK2 and GBA Variants Exert Distinct Influences on Parkinson's Disease-Specific Metabolic Networks." Cereb Cortex 30(5): 2867-2878.
4. Vo, A. (2023), "Adaptive and pathological connectivity responses in Parkinson's disease brain networks." Cereb Cortex 33(4): 917-932.

Poster No 208

Progressive thalamic nuclear atrophy in blepharospasm and blepharospasm-oromandibular dystonia

Haoran Zhang[1], Qinxiu Cheng[1], Jinping Xu[1]

[1]*Shenzhen Institutes of Advanced Technology, Chinese Academy of Sciences, Shenzhen, Guangdong*

Introduction: Idiopathic blepharospasm is a focal dystonia characterized by excessive blinking and eyelid spasms, potentially causing functional blindness (Defazio, Hallett et al. 2017). Patients with blepharospasm have a high risk and rapid symptom spread to other body regions, particularly the oromandibular area (Svetel, Marina et al. 2015). It is a multifactorial clinical syndrome, but the neuro-mechanisms specific and/or common to them were largely unexplored. The pathogenesis of idiopathic blepharospasm is a network model involving the combined action of multiple brain regions, with the thalamus responsible for receiving and distributing information among different brain areas (Hwang, Bertolero et al. 2017). In most

previous studies, the potential useful information about distinct thalamic nuclei has been overlooked. They may be associated with different symptoms or disorders (Weeland, Vriend et al. 2022, Lee, Lee et al. 2023). We aimed to investigate: (1) thalamic atrophy in blepharospasm and blepharospasm-oromandibular dystonia; (2) associations between different thalamic nuclei and the clinical manifestation of blepharospasm and blepharospasm-oromandibular dystonia; (3) causal relationships among abnormal thalamic nuclei; and (4) whether these abnormal features can be used as biomarkers.

Methods: We recruited patients from movement disorder clinics who were diagnosed with adult onset blepharospasm or hemifacial spasm based on established criteria. T1-weighted MRI data using a 3T MRI scanner was collected from 56 patients with blepharospasm, 20 patients with blepharospasm-oromandibular dystonia, and 58 healthy controls. There were no significant differences in age or gender among the three groups. T1 images were processed using the standard segmentation pipeline in Freesurfer v7.1.1 with default settings. A statistical model was constructed using age, gender, and estimated intracranial volume as covariates to analyze differences in subcortical gray matter volume and 15 thalamic nuclei between the groups. Pearson correlation analysis was performed to examine the relationship between abnormal thalamic nucleus volume and disease course/JRS scores in patients with blepharospasm, and abnormal thalamic nucleus volume were used to train a support vector machine (SVM) classification model. Furthermore, a region-based Granger causality analysis (GCA) was conducted using the Brain Covariance Junction Toolkit (BCCT_V1.2, available at https://github.com/JLhos-fmri/NeuroimageTools) to explore the causal relationship between abnormal thalamic nuclei.

Results: The lateral geniculate and pulvinar inferior nuclei in patients with blepharospasm, and ventral anterior and ventral lateral anterior nuclei in patients with blepharospasm-oromandibular dystonia were significantly decreased compared with healthy controls (Figure 1). These thalamic nuclear atrophy were negatively correlated with clinical severity and/or disease duration in these patients (Figure 2A). Using gray matter volume of the lateral geniculate, pulvinar inferior, ventral anterior and ventral lateral anterior nuclei as inputs, the SVM resulted accuracy = 0.89 and AUC=0.89 to distinguish blepharospasm from healthy controls, accuracy = 0.82 and AUC=0.86 to distinguish blepharospasm-oromandibular dystonia from healthy controls, as well as accuracy = 0.94 and AUC=0.96 to distinguish blepharospasm from blepharospasm-oromandibular dystonia (Figure 2B).

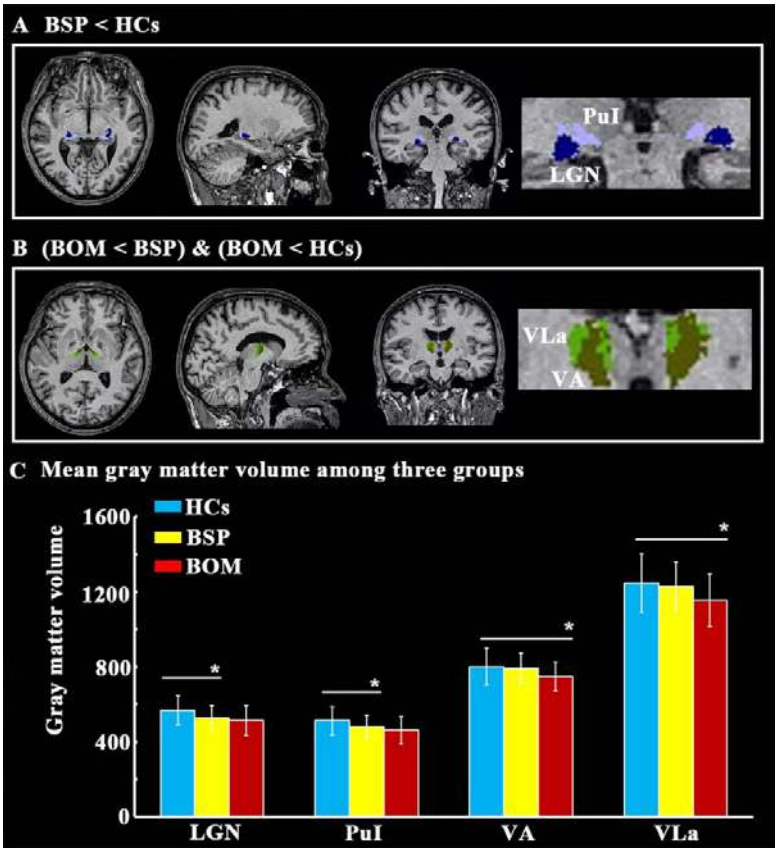

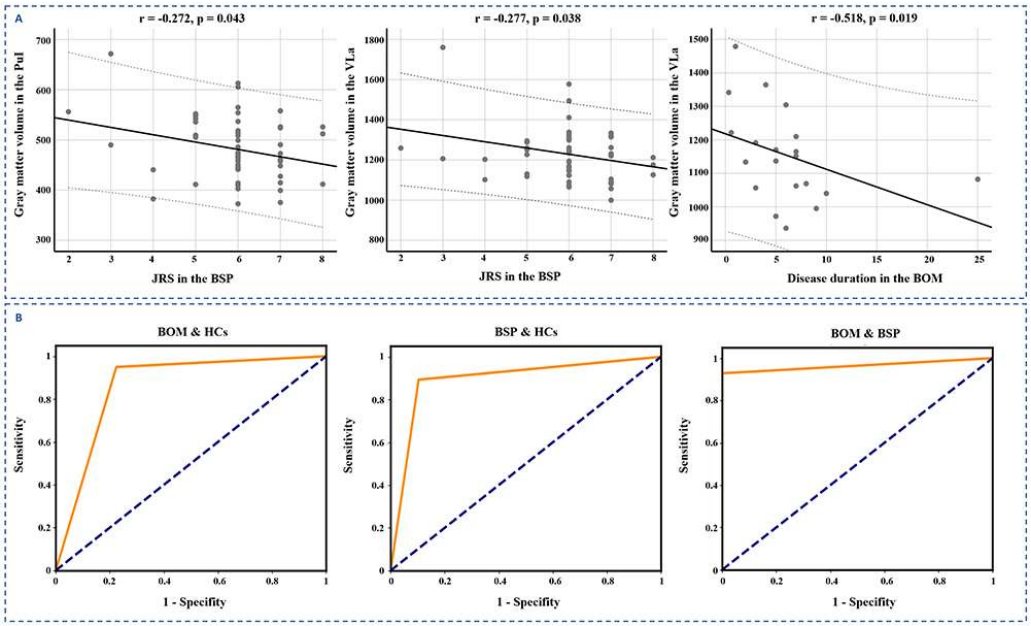

Conclusions: Taken together, these results suggested that the pulvinar inferior nuclear might be the focal origin in the thalamus of blepharospasm, extending to lateral geniculate nuclear atrophy, and subsequently extending to ventral lateral anterior nuclei causing involuntary lower facial and masticatory movements known as blepharospasm-oromandibular dystonia. Moreover, our results also provided potential targets for neuro-modulation especially deep brain stimulation in patients with blepharospasm and blepharospasm-oromandibular dystonia.

References

1. Defazio, Giovanni, Mark Hallett, Hyder A. Jinnah, Antonella Conte, and Alfredo Berardelli. "Blepharospasm 40 years later." Movement Disorders 32, no. 4 (2017): 498-509.
2. Svetel, Marina, Tatjana Pekmezovic, Aleksandra Tomic, Nikola Kresojevic, and Vladimir S. Kostic. "The spread of primary late-onset focal dystonia in a long-term follow up study." Clinical Neurology and Neurosurgery 132 (2015): 41-43.
3. Hwang, Kai, Maxwell A. Bertolero, William B. Liu, and Mark D'Esposito. "The human thalamus is an integrative hub for functional brain networks." Journal of Neuroscience 37, no. 23 (2017): 5594-5607.
4. Weeland, Cees J., Chris Vriend, Ysbrand van der Werf, Chaim Huyser, Manon Hillegers, Henning Tiemeier, Tonya White, and Odile A. van den Heuvel. "Thalamic subregions and obsessive-compulsive symptoms in 2,500 children from the general population." Journal of the American Academy of Child & Adolescent Psychiatry 61, no. 2 (2022): 321-330.
5. Lee, Dong Ah, Ho-Joon Lee, and Kang Min Park. "Thalamic nuclei volumes and intrinsic thalamic network in patients with occipital lobe epilepsy." Brain and Behavior 13, no. 4 (2023): e2968.

Poster No 209

Brain arteriolosclerosis linked to lower gray matter volume in elderly community-cohort

Ana Tomash[1], Mahir Tazwar[1], Md Tahmid Yasar[1], David Bennett[2], Julie Schneider[2], Konstantinos Arfanakis[1,2]

[1]Illinois Institute of Technology, Chicago, IL, [2]Rush University Medical Center, Chicago, IL

Introduction: Brain arteriolosclerosis, characterized by thickening of vessel walls and arteriolar stenosis, is one of the key pathologies of cerebral small vessel disease[4]. It is linked to lower cognitive and motor function[5], and an increased risk of dementia[2]. Despite its prevalence and detrimental effects, the impact of arteriolosclerosis on brain macrostructure remains unexplored. Therefore, this study aimed to investigate the association of brain arteriolosclerosis with regional gray matter volumes in a large number of community-based older adults.

Methods: Participants, MRI, neuropathology A combination of ex-vivo MRI and detailed neuropathological evaluation of 882 older adults participating in four longitudinal, clinical-pathologic cohort studies of aging were included[3,8]: Rush Memory and Aging Project (MAP), Religious Orders Study (ROS), Minority Aging Research Study (MARS), and Clinical Core (CC) of the Rush Alzheimer's Disease Research Center (Fig. 1A). Cerebral hemispheres were obtained at autopsy and imaged ex-vivo with a multi-echo spin-echo (ME-SE) sequence on 3T clinical MRI scanners about one-month postmortem[1]. The acquired voxel size was 0.6mm × 0.6mm × 1.5mm, and the scan time was approximately 30 minutes[1]. Gray and white matter segmentation was performed on the ex-vivo MRI data, and gray matter was subdivided into 42 cortical and subcortical regions using multi-atlas segmentation[7]. The volume of each region was measured and normalized by the participant's cerebral hemisphere volume[6].

Following ex-vivo MRI, all hemispheres underwent detailed neuropathologic examination. The assessed pathologies included arteriolosclerosis[5], atherosclerosis, cerebral amyloid angiopathy, gross and microscopic infarcts, Alzheimer's pathology, Lewy bodies, limbic-predominant age-related TDP-43 encephalopathy neuropathological change (LATE-NC), and hippocampal sclerosis (Fig. 1B). Statistical analysis Linear regression was used to investigate the association of brain arteriolosclerosis with regional gray matter volumes (normalized by cerebral hemisphere volume) controlling for all other neuropathologies (Fig. 1B), demographics (age at death, sex, years of education), postmortem intervals, and scanner (Fig. 1A). Statistical analysis was conducted using FSL's PALM tool, with 10,000 permutations. After false discovery rate (FDR) correction for multiple testing, significance was set at $p<0.05$.

Figure 1: (A) Demographic characteristics

Characteristics	Total	
N	882	
Age at death, years (SD)	90.7	(6.4)
Female, n (%)	641	(73%)
Education, years (SD)	15.7	(3.5)
Postmortem interval to fixation, h (SD)	9.8	(7.5)
Postmortem interval to imaging, d (SD)	36.5	(16.3)
MRI scanner, n (%)		
- 3T GE Signa, n (%)	66	(7%)
- 3T Siemens Trio, n (%)	81	(9%)
- 3T Philips Achieva, n (%)	281	(32%)
- 3T Siemens Verio, n (%)	454	(51%)

(B) Neuropathologic characteristics

Characteristics	Total	
Arteriolosclerosis, n (%)		
- Severe	58	(7%)
- Moderate	180	(20%)
- Mild	329	(37%)
- None	315	(36%)
Composite score of global AD pathology, mean (SD)	0.8	(0.6)
Lewy bodies, n (%)	253	(29%)
Gross infarcts, n (%)	358	(41%)
Microscopic infarcts, n (%)	341	(39%)
Atherosclerosis, n (%)		
- Severe	42	(5%)
- Moderate	176	(20%)
- Mild	471	(53%)
- None	193	(22%)
Cerebral amyloid angiopathy, n (%)		
- Severe	105	(12%)
- Moderate	220	(25%)
- Mild	376	(43%)
- None	181	(21%)
LATE-NC pathology, n (%)		
- Stage 3	239	(27%)
- Stage 2	98	(11%)
- Stage 1	153	(17%)
- Stage 0	392	(44%)
Hippocampal sclerosis, n (%)	101	(11%)

AD - Alzheimer's disease; LATE-NC - Limbic-predominant age-related transactive response DNA binding protein 43 encephalopathy neuropathological change; NIA - National Institute on Aging.

Results: Severe brain arteriolosclerosis was associated with lower gray matter volume in regions like medial orbitofrontal, superior frontal, pericalcarine, cuneus, and lateral occipital areas, independently of the effects of other neuropathologies (Fig. 2). No regions exhibited higher volume with more severe arteriolosclerosis. These findings significantly expand our understanding of arteriolosclerosis-related brain anomalies, challenging its presumed association mainly with white matter

hyperintensities[1]. The present work in a large number of community-based older adults provides strong evidence that arteriolosclerosis is also related to neurodegenerative changes in gray matter. Furthermore, the brain regions involved are distributed in both the anterior and posterior parts of the brain in line with the more widespread distribution of arteriolosclerosis pathology in the brain.

Figure 2: (A) Results of linear regression investigating the association of brain arteriolosclerosis with regional gray matter volumes (normalized with the cerebral hemisphere volume) controlling for all other neuropathologies, demographics, postmortem intervals, and scanner. P values are FDR-corrected.

Regions of interest	Coefficient x10^{-3}	Standard error x10^{-3}	P value
Medial orbitofrontal	-0.3	0. 067	0.0019
Superior frontal	-0.6	0.165	0.0055
Pericalcarine	-0.1	0.048	0.046
Cuneus	-0.2	0.051	0.0055
Lateral occipital	-0.4	0.111	0.0019

(B) Sagittal, coronal, and axial images of gray matter regions that exhibited lower volume with more severe arteriolosclerosis, overlaid on the MIITRA atlas[10]. The color scale represents FDR-corrected p-values.

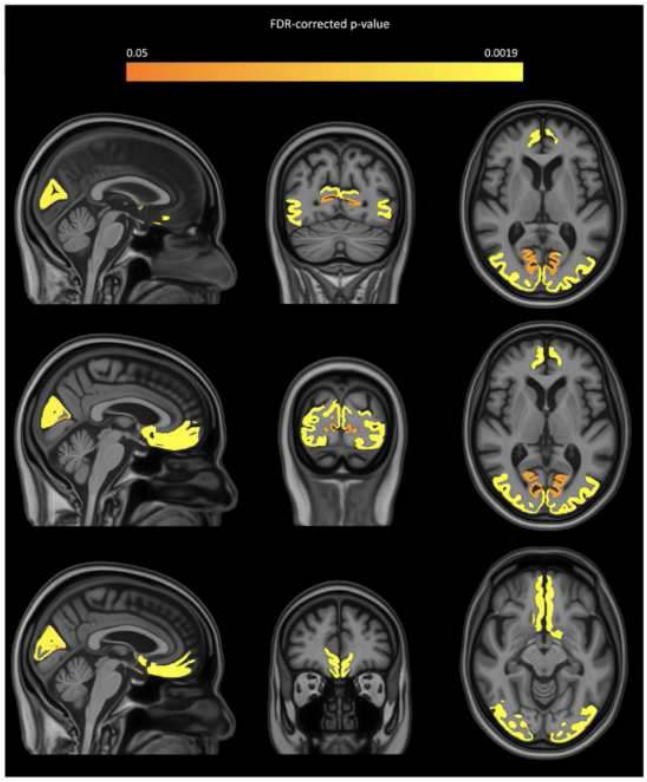

Conclusions: By combining ex-vivo MRI and detailed neuropathological examination in a large number of community-based older adults this study demonstrated that brain arteriolosclerosis is associated with lower volume in several gray matter regions. The findings were independent of the effects of other vascular or neurodegenerative pathologies. Hence, this discovery enhances our understanding of the impact of arteriolosclerosis on the brain.

References

1. Arfanakis, K. et al. 2020. Neuropathologic Correlates of White Matter Hyperintensities in a Community-Based Cohort of Older Adults. Journal of Alzheimer's Disease. 73, 1 (Jan. 2020), 333–345.
2. Arvanitakis, Z. et al. 2016. Relation of cerebral vessel disease to Alzheimer's disease dementia and cognitive function in elderly people: a cross-sectional study. The Lancet Neurology. 15, 9 (Aug. 2016), 934–943.
3. Bennett, D.A. et al. 2018. Religious Orders Study and Rush Memory and Aging Project. Journal of Alzheimer's Disease. 64, s1 (Jun. 2018), S161–S189.
4. Blevins, B.L. et al. 2021. Brain arteriolosclerosis. Acta Neuropathologica. 141, 1 (Jan. 2021), 1–24.
5. Buchman, A.S. et al. 2013. Microvascular brain pathology and late-life motor impairment. Neurology. 80, 8 (Feb. 2013), 712–718.
6. Dawe, R.J. et al. 2011. Neuropathologic Correlates of Hippocampal Atrophy in the Elderly: A Clinical, Pathologic, Postmortem MRI Study. PLoS ONE. 6, 10 (Oct. 2011), e26286.
7. Kotrotsou, A. et al. 2014. Ex vivo MR volumetry of human brain hemispheres. Magnetic Resonance in Medicine. 71, 1 (Jan. 2014), 364–374.
8. L. Barnes, L. et al. 2012. The Minority Aging Research Study: Ongoing Efforts to Obtain Brain Donation in African Americans without Dementia. Current Alzheimer Research. 9, 6 (Jun. 2012), 734–745.
9. Makkinejad, N. et al. 2021. ARTS: A novel In-vivo classifier of arteriolosclerosis for the older adult brain. NeuroImage: Clinical. 31, (2021), 102768.
10. Wu, Y. et al. 2023. High resolution 0.5mm isotropic T1-weighted and diffusion tensor templates of the brain of non-demented older adults in a common space for the MIITRA atlas. NeuroImage. 282, (Nov. 2023), 120387.

Poster No 210

HRV as a Measure of Brain-Heart Connectivity Focus on Symptoms in Alzheimer's and Lewy Body Disease

Gangyoung Lee[1], Ukeob Park[1], Byoung Seok Ye[2], Seung Wan Kang[1,3]

[1]iMediSync, Inc., Seoul, Korea, Republic of, [2]Yonsei University College of Medicine, Seoul, Korea, Republic of, [3]Data Center for Korean EEG, Seoul National University College of Nursing, Seoul, Korea, Republic of

Introduction: In recent research, Electroencephalography (EEG) has been established as a powerful biomarker, already in use for predicting both Alzheimer's Disease (AD) and Lewy Body Disease (LBD)[1]. Expanding beyond EEG, Electrocardiography (ECG) also holds potential as a robust biomarker, particularly considering the concept of Brain-Heart Connectivity[2]. Heart Rate Variability (HRV), derived from ECG measurements, serves as a well-established metric reflecting responses to internal physiological states and external stimuli[34]. The combined EEG and HRV-based multimodal biometric approach have been noted for its contribution to garnering interest across various studies[5] and enhancing performance[67]. Nevertheless, a distinct gap persists in research on Multimodal Biometrics, specifically leveraging the combined potential of EEG and ECG for the classification of AD and LBD. To address this gap, this study aims to explore and compare HRV specifically between pure AD and pure LBD groups. Through this comparison, we seek to uncover potential multimodal biometric indicators. This exploration will allow us to further investigate and expand the understanding of Brain-Heart Connectivity, utilizing insights derived from both EEG and ECG.

Methods: Participant In this study, Electrocardiography (ECG) was measured for individuals in a resting state, including pure Alzheimer's Disease (AD) patients (n=63) and pure Lewy Body Disease (LBD) patients (n=142). Clinical labeling was conducted by experienced specialists at Severance Hospital, Yonsei University, with substantial expertise in the field. Data & pre-Processing ECG signals were preprocessed using a 60Hz notch filter to eliminate power line noise, and measurements were taken for a minimum of 3 minutes at sampling rates of 200Hz or 512Hz. To pinpoint accurate R-peaks, a Butterworth bandpass filter (5–15Hz) was applied for preprocessing, and visual inspections ensured signal integrity post-filtering. The Pan-Tompkins algorithm was then employed to compute RR intervals. Data points outside the normal RR interval range (300ms–2000ms) and those deviating by more than twice the standard deviation was removed. Remaining data was interpolated using the cubic spline method. HRV Using the R-peaks as the foundation, several metrics were derived from the RR intervals. Time domain features, including SDNN and frequency domain features extracted via FFT analysis-absolute (abs) and log(ln) power-were computed based on these intervals. These derived indices comprised TF (total power), UVLF(~0.0033Hz), VLF(0.0033–0.04Hz), LF(0.04–0.15Hz), HF(0.15–0.4Hz), PNS(parasympathetic nervous system activity, HF/HF+LF), and SNS(sympathetic nervous system activity, LF/HF+LF), resulting in a total of 16 indices. Analysis Since both the pure AD and pure LBD groups exceed 30 individuals, it was assumed that they followed a normal distribution. Therefore, an independent samples t-test method was employed to compare each HRV feature between the two groups.

Results: Sympathetic nervous system indicators, including SNS (p=0.0173) and ln_VLF (p=0.0082), revealed higher activity in pure AD compared to pure LBD. Additionally, UVLF (p=0.0347) recognized as a stress recovery metric, was also found among these indicators. Conversely, the parasympathetic nervous system indicator, PNS(p=0.0173), exhibited higher activity in pure LBD when compared to pure AD. However, no significant differences were observed between the two groups concerning autonomic nervous system activity indicators (TF, SDNN).

Conclusions: this study confirmed the potential for HRV, in conjunction with EEG, to be utilized as biomarkers for classifying pure AD and pure LBD. Furthermore, it hints at the advantage of using both biomarkers together in the more accurate classification of pure AD and pure LBD.

References

1. Schumacher, J., Thomas, A. J., Peraza, L. R., Firbank, M., Cromarty, R., Hamilton, C. A., ... & Taylor, J. P. (2020). EEG alpha reactivity and cholinergic system integrity in Lewy body dementia and Alzheimer's disease. Alzheimer's research & therapy, 12(1), 1-12.
2. de la Cruz, F., Schumann, A., Köhler, S., Reichenbach, J. R., Wagner, G., & Bär, K. J. (2019). The relationship between heart rate and functional connectivity of brain regions involved in autonomic control. Neuroimage, 196, 318-328.
3. Ernst, G. (2017). Heart-rate variability—more than heart beats?. Frontiers in public health, 5, 240.
4. Porges, S. W. (2007). The polyvagal perspective. Biological psychology, 74(2), 116-143.
5. Olmi, B., Frassineti, L., Lanata, A., & Manfredi, C. (2021). Automatic Detection of Epileptic Seizures in Neonatal Intensive Care Units Through EEG, ECG and Video Recordings: A Survey. IEEE Access, 9, 138174-138191.
6. Mesbah, M., Balakrishnan, M., Colditz, P. B., & Boashash, B. (2012). Automatic seizure detection based on the combination of newborn multi-channel EEG and HRV information. EURASIP Journal on Advances in Signal Processing, 2012, 1-14.
7. Lyu, J., Shi, W., Zhang, C., & Yeh, C. H. (2023). A Novel Sleep Staging Method based on EEG and ECG Multimodal Features Combination. IEEE Transactions on Neural Systems and Rehabilitation Engineering.

Poster No 211

Exploring White Matter Pattern Variability in Alzheimer's Disease: Associations with Biomarkers

Hyun Woong Roh[1], Nishant Chauhan[2], Youngju Lee[2], Weonjeong Yoo[2], Sang Joon Son[1], Chang Hyung Hong[1], Dongha Lee[2]

[1]Department of Psychiatry, Ajou University School of Medicine, Suwon, Republic of Korea, [2]Cognitive Science Research Group, Korea Brain Research Institute, Daegu Metropolitan City, Republic of Korea

Introduction: Neurodegenerative disorders, marked by the abnormal accumulation of proteins, result in structural and functional impairments in neurons and glial cells, contributing to conditions like Alzheimer's disease (AD) and vascular cognitive impairment. The diagnostic complexity lies in the limitations of initial cognitive screening tests and the challenge of assessing independent daily functioning. Recent advancements in neuroimaging technology have increased the frequency of brain magnetic resonance imaging (MRI) and amyloid positron emission tomography (PET) examinations for patients with neurodegenerative disorders. While conventional focus centered on gray matter, our study highlights the critical role of white matter (WM), a crucial region facilitating both large and small neuronal connections. Significant WM damage manifests diverse clinical symptoms, including Parkinsonism, cognitive decline, and depression

Methods: We analyzed 455 subjects from the BICWALZS database, which were categorized into four groups: subjective cognitive decline (SCD), mild cognitive impairment (MCI), Alzheimer's disease (AD), and vascular dementia (VD). Employing the DARTEL toolbox and the International Consortium for Brain Mapping (ICBM) template, we constructed the WM populational connection label map (pCLM) for each participant. Our investigation focused on the efficacy of inter-subject variability of WM patterns (WM-ISV) across all groups, analyzing its statistical associations with blood-based biomarkers, polygenic risk score (PRS), cognitive function, and disability scores.

Results: Pairwise comparisons unveiled significant differences in WM patterns between SCD and AD individuals, as well as between MCI and AD, and AD and VD groups. The intricate correlations between WM-ISV and blood-based biomarkers indicated variations across diagnostic groups, with elevated WM-ISV in individuals with MCI, AD, and VD compared to SCD. The PRS for AD exhibited significant links with WM-ISV, emphasizing genetic influences on WM variability.

Conclusions: The significant associations between cognitive scores and WM-ISV highlight the complex relationship between WM patterns and cognitive functioning in diverse neurodegenerative disorders, suggesting its potential as a valuable biomarker for diagnosis and prognosis.

References

1. Lee D . A populational connection distribution map for the whole brain white matter reveals ordered cortical wiring in the space of white matter. Neuroimage 2022; 254: 119167.
2. Roh HW, Baseline Clinical and Biomarker Characteristics of Biobank Innovations for Chronic Cerebrovascular Disease With Alzheimer's Disease Study: BICWALZS. Psychiatry Investig 2022; 19(2): 100-109.

Poster No 212

Deep Learning Based Simulation of Amyloid-β accumulation

ByeongChang Jeong[1], Daegyeom Kim[1], Hyun-Ghang Jeong[2], Cheol Han[1]

[1]Korea University, Sejong, Republic of Korea, [2]Korea University College of Medicine, Seoul, Republic of Korea

Introduction: Alzheimer's disease (AD) is a serious neurodegenerative condition marked by progressive brain tissue decline due to the accumulation of the toxic protein such as amyloid-β[1]. Recent studies[2,3] have employed mathematical models to simulate amyloid-β accumulation in the brain, aiming to enhance understanding of AD development and progression. These models involve parameter estimation through observed data and an iterative process for parameter updates, but increased complexity can hinder this optimization. To overcome this, we converted the mathematical model into a deep learning model, combining multi-layer perceptron (MLP) and graph convolutional neural network (GCN)[4].

Methods: We first modeled a mathematical model of amyloid-β accumulation based on the logistic growth equation and translated it into a deep learning model with MLP and GCN. The model accounts for amyloid-β generation, clearance, and spreading dynamics. The logistic growth model for each region is defined in Equation 1. In this equation, δ and γ is the generation and clearance coefficient, respectively. Akij defines the connection weight, capturing both local and transneuronal[5] spreading, where N(i) is the neighboring regions. We translated it into a deep learning model, and the model is defined in Equation 2. Where X̂t+1 is the predicted accumulation level of all regions, Zt, and Gt correspond to clearance rate, and generation, respectively. Ãk represents the Laplacian normalized adjacency matrix of local and transneuronal A, respectively.

We used Alzheimer's Disease Neuroimaging Initiative (ADNI) data with 436 subjects to construct a graph capturing amyloid-β accumulation. In this graph, nodes represented region-of-interests (ROIs) from T1 structural magnetic resonance (MR) images, with node features represented accumulation levels from 18F-Florbetapir positron emission tomography (PET) scans. Edges indicated local and transneuronal connectivity based on structural characteristics and neuronal fibers from diffusion weighted MR images. Longitudinal data with more than two datapoints per subject were used, with 354 subjects for training and 82 subjects for testing.

Equation 1.

$$P_t^i = P_{t-1}^i + \left\{(\delta - \gamma)P_{t-1}^i + \sum_k \sum_{j \in N(i)} \alpha_k A_k^{ij} P_{t-1}^j\right\}\left(1 - \frac{P_{t-1}^i}{K}\right)$$

Equation 2.

$$\widehat{\boldsymbol{X}}_{t+1} = \boldsymbol{X}_t + \boldsymbol{Z}_t\left(\boldsymbol{G}_t + \sum_k \tanh\left(\widetilde{\boldsymbol{A}}_k \boldsymbol{X}_t \boldsymbol{\theta}_k\right) - \boldsymbol{X}_t\right)$$

$$\boldsymbol{Z}_t = \sigma(\boldsymbol{\theta}_c \boldsymbol{X}_t)$$

$$\boldsymbol{G}_t = \tanh(\boldsymbol{\theta}_g \boldsymbol{X}_t)$$

Results: The proposed model predicted accumulation level after 2 years (Figure 1). It demonstrated a strong correlation with the real data (in test dataset, median = 0.8273, IQR = [0.7708, 0.8692]), outperforming the previous model(average 0.58)[3]. For interpretability, we examined the clearance (Zt) and generation (Gt) terms. We averaged each term over subjects and mapped the top 30% ROIs onto the brain (Figure 2). The brain regions with high clearance term were bilateral cuneus, paracentral, postcentral, precentral, supramarginal, frontal pole, insula, right superior frontal, and superior temporal. The regions with high generation term were bilateral entorhinal, fusiform, inferior temporal, lateral orbitofrontal, lingual, medial orbitofrontal, middle temporal, left posterior cingulate, and right parahippocampal. Brain activity may play a crucial role in efficiency of amyloid-β clearance[6,7]. Previous studies reported reduced metabolism in specific regions in early AD[8,9]. The regions with high clearance in our model (Figure 2a) were matched with regions of normal metabolism, which exhibit relatively high brain activity. The regions with early AD amyloid-β accumulation were suspected to be connected with the default mode network and prefrontal network[10]. The identified regions (Figure 2b) also supported this.

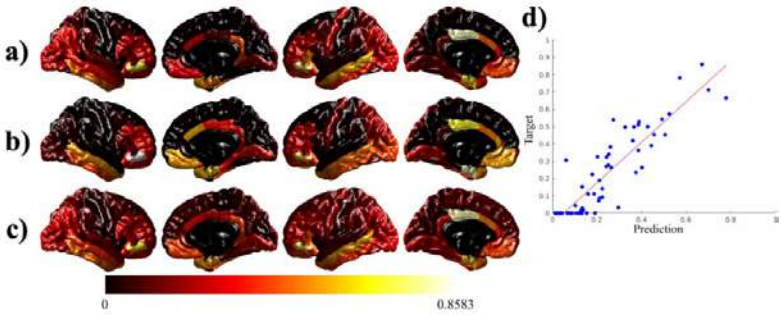

Figure 1. Example result from test dataset. a) input accumulation of amyloid-β, b) actual accumulation of amyloid-β after 24 months, c) model's prediction, and d) scatter plot between b) and c) (correlation coefficient = 0.9041, MSE = 0.0114).

Figure 2. Brain overlay for regions with top 30% of a) clearance term, and b) generation term.

Conclusions: We introduced a deep learning model to simulate amyloid-β accumulation achieving high predictive performance and interpretability. Although further investigation of each term's interpretability is needed, our model may help to understand the role of amyloid-β accumulation in AD progression.

References

1. Murphy, M. P. and H. LeVine III (2010). "Alzheimer's disease and the amyloid-β peptide." Journal of Alzheimer's disease 19(1): 311-323.
2. Peraza, L. R., A. Díaz-Parra, O. Kennion, D. Moratal, J.-P. Taylor, M. Kaiser, R. Bauer and A. s. D. N. Initiative (2019). "Structural connectivity centrality changes mark the path toward Alzheimer's disease." Alzheimer's & Dementia: Diagnosis, Assessment & Disease Monitoring 11: 98-107.
3. Kim, H.-R., P. Lee, S. W. Seo, J. H. Roh, M. Oh, J. S. Oh, S. J. Oh, J. S. Kim and Y. Jeong (2019). "Comparison of Amyloid β and tau spread models in Alzheimer's disease." Cerebral Cortex 29(10): 4291-4302.
4. Kipf, T. N. and M. Welling (2016). "Semi-supervised classification with graph convolutional networks." arXiv preprint arXiv:1609.02907.
5. Nath, S., L. Agholme, F. R. Kurudenkandy, B. Granseth, J. Marcusson and M. Hallbeck (2012). "Spreading of neurodegenerative pathology via neuron-to-neuron transmission of β-amyloid." Journal of Neuroscience 32(26): 8767-8777.
6. Mergenthaler, P., U. Lindauer, G. A. Dienel and A. Meisel (2013). "Sugar for the brain: the role of glucose in physiological and pathological brain function." Trends in neurosciences 36(10): 587-597.
7. Ullah, R. and E. J. Lee (2023). "Advances in Amyloid-β Clearance in the Brain and Periphery: Implications for Neurodegenerative Diseases." Experimental Neurobiology 32(4): 216.
8. Chételat, G., J. Arbizu, H. Barthel, V. Garibotto, I. Law, S. Morbelli, E. van de Giessen, F. Agosta, F. Barkhof and D. J. Brooks (2020). "Amyloid-PET and 18F-FDG-PET in the diagnostic investigation of Alzheimer's disease and other dementias." The Lancet Neurology 19(11): 951-962.
9. Kantarci, K., B. F. Boeve, S. A. Przybelski, T. G. Lesnick, Q. Chen, J. Fields, C. G. Schwarz, M. L. Senjem, J. L. Gunte and C. R. Jack (2021). "FDG PET metabolic signatures distinguishing prodromal DLB and prodromal AD." NeuroImage: Clinical 31: 102754.
10. Palmqvist, S., M. Schöll, O. Strandberg, N. Mattsson, E. Stomrud, H. Zetterberg, K. Blennow, S. Landau, W. Jagust and O. Hansson (2017). "Earliest accumulation of β-amyloid occurs within the default-mode network and concurrently affects brain connectivity." Nature communications 8(1): 1214.

Poster No 213

Brain age prediction in people with Parkinson's disease using minimally processed images

Franziska Albrecht[1], Anna Inguanzo[1], Caroline Dartora[1], Erika Franzén[1], Eric Westman[1]

[1]Karolinska Institutet, Stockholm, Sweden

Introduction: The emerging field of brain age prediction has garnered significant attention in recent years due to its potential to revolutionize healthcare, personalized medicine, and our understanding of aging. Brain age prediction aims to estimate an individual's brain age based on various factors and measurements, e.g., magnetic resonance imaging (MRI). The early detection of misalignment of brain age with the chronological age may allow for timely intervention and treatment, potentially improving patient outcomes and quality of life. Furthermore, brain age prediction could be used to assess the effectiveness of interventions aimed at improving brain health. This knowledge may pave the way for the development of innovative preventive strategies and therapeutic interventions that target the root causes of advanced brain aging.

Methods: Recently, we developed and validated a convolutional neural network for brain age prediction utilizing only minimally processed T1-weighted structural MRI (Dartora et al. 2023). Multi-cohort data of 15289 cognitively healthy participants was included, using only MNI-space registered images. This model predicted brain age in people with Parkinson's disease (PD) in two cohorts: baseline data of 84 people with PD taking part in an intervention (EXPANd trial (Franzén et al. 2019)) and 341 people with de novo PD from the Parkinson's Progression Markers Initiative (PPMI (Marek et al. 2018)). The brain age gap was calculated as predicted brain age - chronological age. Thus, positive values mean an older-looking brain, as the brain looks older than expected, and negative values relate to a younger-looking brain. We aimed to replicate the pattern of the only other PD brain age study that has been published so far (Eickhoff et al. 2021). Spearman correlations between the brain age gap and measures of cognition, disease severity, and other clinical measures were run using RStudio (2022.07.0+548). In exploratory analyses, we corrected the brain age gap for chronological age by dividing the gap by the chronological age.

Results: The EXPANd cohort had a mean age of 70.65 (Standard deviation, SD 5.84) and a predicted brain age of 72.14 (SD 4.98). Predicted brain age correlated significantly with chronological age ($r=0.72$, $p<0.001$). The brain age gap was negatively correlated with disease duration, i.e., the older-looking the brain, the longer the disease duration ($r=-0.27$ $p=0.015$)(Figure 1). There were no further significant correlations with either the brain age gap or the corrected one. The PPMI cohort had a mean chronological age of 61.58 (SD 9.59) and a brain age of 67.17 (SD 7.29). Predicted brain age correlated significantly with chronological age ($r=0.69$, $p<0.001$). We found no other significant correlations with clinical or other demographic data in our PPMI cohort.

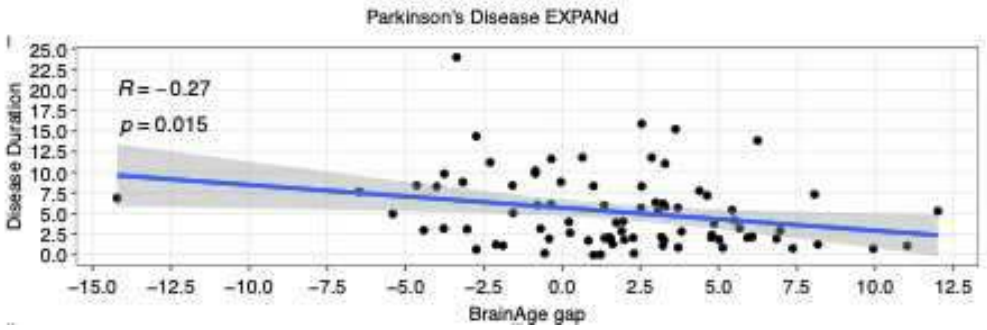

Conclusions: We identified a brain age gap in both cohorts. However, the gap was larger in the de novo PPMI cohort. This might be a bit surprising since one might expect the more severe people with Parkinson's disease (i.e., the EXPANd cohort) to have a larger brain age gap. We can only speculate that medications could reduce the brain age gap and thus lead to the EXPANd cohort having younger-looking brains. Further, we found that only disease duration in the interventional cohort was related to the brain age gap. Nevertheless, our study is an important step toward the assessment of the clinical applicability and usability of brain age prediction in people with Parkinson's disease. Brain age may yield the potential to identify those individuals who might need more intensive treatment. Thus, brain age prediction holds immense promise as a powerful tool in the field of healthcare and individualized treatment. With its ability to assess brain health, guide interventions, and deepen our understanding of aging, it has the potential to revolutionize how we approach brain health and improve patient outcomes.

References

1. Dartora, Caroline, Anna Marseglia, Gustav Mårtensson, Gull Rukh, Junhua Dang, J-Sebastian Muehlboeck, Lars-Olof Wahlund, Rodrigo Moreno, José Barroso, Daniel Ferreira, Helgi B. Schiöth, Eric Westman, Alzheimer's Disease Neuroimaging Initiative, Australian Imaging Biomarkers, Lifestyle flagship study of ageing, Japanese Alzheimer's Disease Neuroimaging Initiative, and AddNeuroMed consortium. 2023. 'A Deep Learning Model for Brain Age Prediction Using Minimally Pre-processed T1w-images as Input', medRxiv: 2022.09.06.22279594.
2. Eickhoff, C. R., F. Hoffstaedter, J. Caspers, K. Reetz, C. Mathys, I. Dogan, K. Amunts, A. Schnitzler, and S. B. Eickhoff. 2021. 'Advanced brain ageing in Parkinson's disease is related to disease duration and individual impairment', Brain Commun, 3: fcab191.
3. Franzén, E., H. Johansson, M. Freidle, U. Ekman, M. B. Wallen, E. Schalling, A. Lebedev, M. Lovden, S. Holmin, P. Svenningsson, and M. Hagstromer. 2019. 'The EXPANd trial: effects of exercise and exploring neuroplastic changes in people with Parkinson's disease: a study protocol for a double-blinded randomized controlled trial', BMC Neurol, 19: 280.
4. Marek, K., S. Chowdhury, A. Siderowf, S. Lasch, C. S. Coffey, C. Caspell-Garcia, T. Simuni, D. Jennings, C. M. Tanner, J. Q. Trojanowski, L. M. Shaw, J. Seibyl, N. Schuff, A. Singleton, K. Kieburtz, A. W. Toga, B. Mollenhauer, D. Galasko, L. M. Chahine, D. Weintraub, T. Foroud, D. Tosun-Turgut, K. Poston, V. Arnedo, M. Frasier, and T. Sherer. 2018. 'The Parkinson's progression markers initiative (PPMI) - establishing a PD biomarker cohort', Ann Clin Transl Neurol, 5: 1460-77.

Poster No 214

Amyloid-induced hyperconnectivity drives connectivity-based tau spreading in Alzheimer's disease

Sebastian Niclas Roemer[1], Fabian Wagner[1], Anna Steward[2], Davina Biel[2], Anna Dewenter[2], Jannis Dennecke[2], Mattes Gross[1], Zeyu Zhu[2], Lukai Zheng[2], Amir Dehsarvi[2], Martin Dichgans[2], Michael Ewers[2], Matthias Brendel[1], Nicolai Franzmeier[2]

[1]University Hospital LMU Munich, Munich, Bavaria, [2]Institute for Stroke and Dementia Research, Munich, Bavaria

Introduction: In Alzheimer's disease, amyloid-beta (Ab) accumulation triggers tau spreading, which drives neurodegeneration and cognitive decline. Thus, understanding how Ab facilitates tau spread is key to identify treatment targets for attenuating tau spreading. We found previously that tau spreads in an activity-dependent manner across functionally connected brain regions in AD and that stronger inter-regional connectivity and less segregated brain networks accelerate tau spreading (Franzmeier, Rubinski et al. 2019, Frontzkowski, Ewers et al. 2022, Steward, Biel et al. 2023). Ab has been shown to induce neuronal hyperexcitability (Busche, Chen et al. 2012) via different mechanisms, such as an increased glutamate release and reduced glutamate re-uptake (Li, Hong et al. 2009), reduced sensitivity to GABA (Wu, Guo et al. 2014) and increased direct postsynaptic Ca2+-influx (Lam, Sarkis et al. 2020, Horvath, Papp et al. 2021). Congruently, patient studies have reported a higher prevalence of subclinical epileptiform brain activity related to Ab deposition (Lam, Sarkis et al. 2020), as well as Ab-related hyperactivity and hyperconnectivity on EEG and resting-state fMRI (Ying, Najm et al. 2014). Together these preclinical and clinical data provide converging evidence that Ab induces a hyperexcitatory shift in neuronal activity. Since synaptic secretion of hyperphosphorylated tau seeds and subsequent spread to connected neurons is activity-dependent, Ab-related increases in neuronal activity may accelerate tau spreading from local epicenters across connected brain regions. The key aim of this project was to better understand the cross-link between Ab deposition and connectivity-associated tau spreading

in AD. Specifically, we aimed to test whether Ab induces neuronal hyperconnectivity resulting in reduced brain network segregation, therefore accelerating inter-regional tau spreading. Specifically, our key aims were to test i) Whether regional PET-assessed Ab deposition is associated with regional resting-state fMRI-assessed connectivity increases and reduced brain network segregation in AD ii) Whether regional Ab-related connectivity increases and reduced brain network segregation are associated with accelerated tau spreading across connected brain regions iii) Whether reduced brain network segregation mediates the association between Ab deposition and PET-assessed tau accumulation.

Methods: We included 116 Ab-positive subjects across the preclinical to clinical AD spectrum plus 52 Ab-negative controls, all with baseline amyloid-PET, 3T resting-state fMRI and longitudinal Flortaucipir tau-PET data. PET data were parceled into 200 cortical ROIs of the Schaefer atlas, longitudinal tau-PET change rates were computed per ROI using linear mixed models. Resting-state fMRI connectivity was computed across the 200 ROIs. Tau epicenters were defined per subject as 5% of brain regions with highest baseline tau-PET SUVRs.

Results: Higher amyloid-PET (i.e. centiloid) is associated with increased connectivity of temporal-lobe tau epicenters to temporo-occipital and parietal regions (Fig.1), i.e. typical tau vulnerable regions. Higher connectivity of the tau epicenters to these brain regions predicted faster tau-PET increase over time. Mediation analysis revealed that Ab-associated connectivity increase to temporal, parietal and occipital brain regions mediated the association between higher amyloid-PET and faster tau-PET increase over time (Fig.2).

Figure 1: ROI-wise association between average centiloid (target-Roi & tau-epicenter) und FC to tau-epicenter

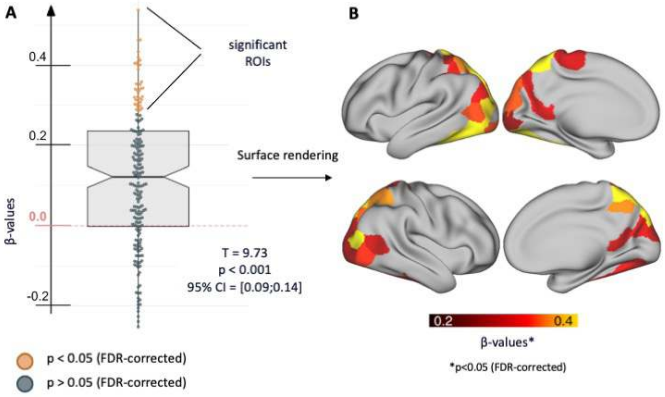

Figure 1: We used linear regression to determine whether regional amyloid-PET levels (i.e. centiloid) predict higher functional connectivity to the tau epicenter. The Boxplot (A) illustrates the distribution of standardized beta coefficients of this regression analysis. The distribution of standardized beta coefficients is significantly greater than zero ($p < 0.001$; 95% CI = [0.09-0.14]), showing that higher centiloid levels are linked to overall higher connectivity to the tau epicenter. Single ROIs with a significant correlation (FDR-corrected p-value < 0.05) are highlighted in yellow in the beeswarm panel (A) and plotted on the brain surface (B). Regression analyses are corrected for age, sex, diagnosis and mean head motion during the resting-state fMRI scan.

Figure 3: ROI-wise mediation analysis

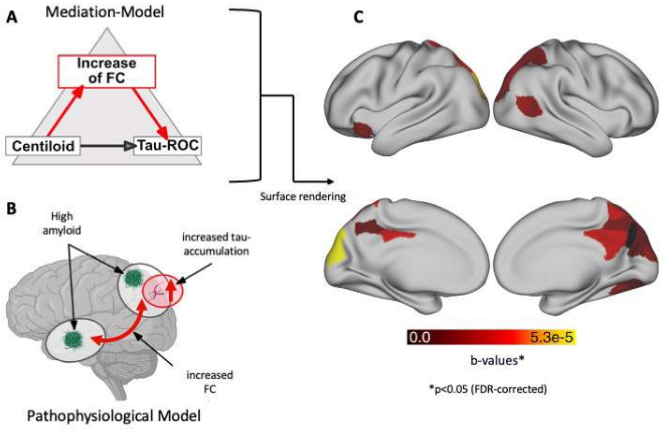

Figure 3: We performed bootstrapped mediation with 1000 iterations per ROI, to test whether the effect of amyloid on faster tau accumulation is explained by an amyloid-associated increase in connectivity (i.e. illustrated in panels A&B). Regions showing a significant mediation effect ($p<0.05$, FDR corrected) are plotted on the brain surface.

Conclusions: We demonstrate a close link between Ab-associated connectivity increases and faster tau spread across connected regions in AD. These findings suggest that Ab promotes tau spreading via increasing neuronal activity and connectivity, hence Ab-associated neuronal hyperexcitability may be a promising target for attenuating tau spreading in AD.

References

1. Bellaver, B. (2023). "Astrocyte reactivity influences amyloid-beta effects on tau pathology in preclinical Alzheimer's disease." Nat Med 29(7): 1775-1781.
2. Biel, D. (2023). "sTREM2 is associated with amyloid-related p-tau increases and glucose hypermetabolism in Alzheimer's disease." EMBO Mol Med 15(2): e16987.
3. Busche, M. A. (2020). "Patient-centered connectivity-based prediction of tau
4. pathology spread in Alzheimer's disease." SCIENCE ADVANCES 6.
5. Franzmeier, N., J. Neitzel, A. Rubinski, R. Smith, O. Strandberg, R. Ossenkoppele, O. Hansson, M. Ewers and I. Alzheimer's Disease Neuroimaging (2020). "Functional brain architecture is associated with the rate of tau accumulation in Alzheimer's disease." Nat Commun 11(1): 347.
6. Franzmeier, N. (2019). "Functional connectivity associated with tau levels in ageing, Alzheimer's, and small vessel disease." Brain 142(4): 1093-1107.
7. Frontzkowski, L. (2022). "Earlier Alzheimer's disease onset is associated with tau pathology in brain hub regions and facilitated tau spreading." Nat Commun 13(1): 4899.
8. Horvath, A. A. (2021). "Subclinical epileptiform activity accelerates the progression of Alzheimer's disease: A long-term EEG study." Clin Neurophysiol 132(8): 1982-1989.
9. Johansson, C., S. Thordardottir, J. Laffita-Mesa, E. Rodriguez-Vieitez, H. Zetterberg, K. Blennow and C. Graff (2023). "Plasma biomarker profiles in autosomal dominant Alzheimer's disease." Brain 146(3): 1132-1140.
10. Lam, A. D., R. A. Sarkis, K. R. Pellerin, J. Jing, B. A. Dworetzky, D. B. Hoch, C. S. Jacobs, J. W. Lee, D. S. Weisholtz, R. Zepeda, M. B. Westover, A. J. Cole and S. S. Cash (2020). "Association of epileptiform abnormalities and seizures in Alzheimer disease." Neurology 95(16): e2259-e2270.
11. Li, S. (2009). "Soluble oligomers of amyloid Beta protein facilitate hippocampal long-term depression by disrupting neuronal glutamate uptake." Neuron 62(6): 788-801.
12. Schmitt, J.(2021). "Dual-Phase beta-Amyloid PET Captures Neuronal Injury and Amyloidosis in Corticobasal Syndrome." Front Aging Neurosci 13: 661284.
13. Steward, A. (2023). "Functional network segregation is associated with attenuated tau spreading in Alzheimer's disease." Alzheimers Dement 19(5)
14. Ying, Z. (2014). Growth-associated protein 43 and progressive epilepsy in cortical dysplasia. Ann Clin Transl Neurol 1, 453-461, doi:10.1002/acn3.69 .

Poster No 215

Association between Blood-Brain Barrier Damage in Alzheimer's Disease and Known Risk Variants

Min Soo Byun[1,2], Dahyun Yi[3], Joon Sik Park[4], Gihwan Byeon[5], Hyejin Ahn[6], Gijung Jung[3], Yen-Ning Huang[7], Yu Kyeong Kim[8,1], Yun-Sang Lee[1], Jun-Young Lee[8,1], Koung Mi Kang[2,1], Chul-Ho Sohn[2,1], Andrew Saykin[7], Kwangsik Nho[7], Jaeseok Park[4], Dong Young Lee[1,2]

[1]Seoul National University College of Medicine, Seoul, Korea, Republic of, [2]Seoul National University Hospital, Seoul, Korea, Republic of, [3]Seoul National University Medical Research Center, Seoul, Korea, Republic of, [4]Sungkyunkwan University, Suwon, Korea, Republic of, [5]Kangwon National University Hospital, Chuncheon, Korea, Republic of, [6]Seoul National University College of Humanities, Seoul, Korea, Republic of, [7]Indiana University School of Medicine, Indianapolis, IN, [8]SMG-SNU Boramae Medical Center, Seoul, Korea, Republic of

Introduction: Previous research has showed that blood-brain barrier (BBB) dysfunction has a role in the pathogenesis of Alzheimer's disease (AD). However, the geographical pattern of BBB degradation in early Alzheimer's disease and its genetic basis are poorly understood. We looked at the relationship between BBB permeability and beta-amyloid (Aβ) deposition, and its connection with known AD-related single nucleotide polymorphisms (SNPs) in older persons using high-resolution 3-dimensional (3D) dynamic contrast-enhanced (DCE) MRI.

Methods: Participants were recruited from the Korean Brain Aging Study of the Early Diagnosis and Prediction of Alzheimer's Disease (KBASE) cohort (1) and dementia clinic of Seoul National University Hospital. Both cognitively normal (CN) and cognitively impaired (CI) older adults consisted of mild cognitive impairment and AD dementia were included in this study. A total 91 participants underwent comprehensive clinical and neuropsychological assessments. In addition, [11C] Pittsburgh Compound B (PiB) PET for measurement of cerebral Aβ deposition, high-resolution DCE- and T1-weighted-MRI scans were obtained from all participants, which were used to classify the participants into Aβ-positive or negative groups. After preprocessing of the high-resolution 3D DCE imaging, we calculated BBB permeability index (Ktrans) for the whole brain, incorporating FreeSurfer-based (v6.0) segmentation of T1 scans in order to exclude non-brain voxels such as that of ventricles. Next, voxel-wise whole brain analyses were conducted to demonstrate regional changes of the Ktrans map

between two groups using SPM12 implemented in MATLAB 2018b. Apolipoprotein E (APOE) genotyping was done for all participants. Additionally, total of 38 AD-related SNPs with genetic evidence compiled by the AD Sequencing Project (ADSP) (minor allele frequency [MAF] > 1%, except APOE) were extracted from TOPMed-based imputed GWAS genotyping data in KBASE in a subset of participants (n=74). Comparison of Ktrans values between carriers and noncarriers of candidate SNPs were performed.

Results: First, we observed greater BBB damage in multiple cerebral regions including the precuneus, posterior cingulate, and temporal regions in the Aβ-positive CN compared to Aβ-negative CN in a voxel-wise analysis of Ktrans map (cluster-wise FDR corrected $p < 0.05$). We then extracted the Ktrans value from the region-of-interests (ROIs) including the abovementioned regions for further analysis. Genetic susceptibility analysis of APOE4 revealed that APOE4 carriers showed increased Ktrans value in this ROI compared to noncarriers after adjusting age and sex ($F(2,72) = 6.49$, $p = 0.013$), indicative of greater breakdown of BBB in the carriers. Furthermore, we found increased Ktrans of the ROI in the carriers of rs7401792, located in Solute Carrier Family 24 Gene Member 4 (SLC24A4) compared to non-carriers after controlling the effect of age and sex ($F(2,72) = 5.08$, $p = 0.027$). This association remained significant after we additively controlled the effect of APOE4 carrier status ($F(2,71) = 4.68$, $p = 0.034$).

Conclusions: We found that BBB breakdown is associated with Aβ accumulation in AD early on, before clinical symptoms appear. Furthermore, in older individuals, regional BBB damage is associated with genetic risks such as APOE4 and rs7401792 in SLC24A4; and, the genetic risk effect of SLC24A4 remains significant even after correcting for the effects of APOE4. More research is needed to explain the intricate interplay between these genes' biochemical pathways in connection to BBB integrity and AD.

References

1. Byun et al. (2017), 'Korean Brain Aging Study for the Early Diagnosis and Prediction of Alzheimer's Disease: Methodology and Baseline Sample Characteristics', Psychiatry Investigation, vol. 14, no. 6, pp. 851-863

Poster No 216

Integrated MRI Analysis and Quality Control Pipeline for Memory Clinic Use of UK Biobank Imaging

Grace Gillis[1,2], Gaurav Bhalerao[1], Jasmine Blane[1,2], Pieter Pretorius[1,3], Lola Martos[1,2], Vanessa Raymont[1,2], Clare Mackay[1], Ludovica Griffanti[1,2]

[1]Department of Psychiatry, University of Oxford, Oxford, Oxfordshire, [2]Oxford Health NHS Foundation Trust, Oxford, United Kingdom, [3]Oxford University Hospitals NHS Foundation Trust, Oxford, United Kingdom

Introduction: Sophisticated imaging protocols and analysis techniques have been developed in research contexts to extract metrics known as imaging-derived phenotypes (IDPs). However, it remains unclear whether these methods can also yield accurate and meaningful measures when applied in a clinical setting. In a clinical context, it is also essential to perform quality control (QC) in parallel with any analyses to inform the interpretation of the generated metrics. Therefore, in this study we aimed to adapt the UK Biobank (UKB) MRI analysis pipeline, assess its performance in a memory clinic setting (the Oxford Brain Health Clinic), and provide an integrated analysis and QC pipeline for use in the memory clinic.

Methods: As part of their memory clinic assessment at the Oxford Brain Health Clinic (O'Donoghue et al., 2023), 213 patients were scanned using an adapted version of the UKB protocol [T1-weighted, T2-FLAIR, susceptibility-weighted (swMRI), quantitative susceptibility mapping (QSM), diffusion-weighted (dMRI), arterial spin labelling (ASL), and resting-state functional MRI (rfMRI)] (Miller et al., 2016; Griffanti et al., 2022). As previously described, the UKB processing pipeline was adapted to include lesion-masking of the SIENAX grey matter segmentations and CSF-masking of the FIRST hippocampal segmentations (Griffanti et al., 2022). Downstream pipeline components reliant on these corrected segmentations were also adapted, and white matter hyperintensities (WMHs) were further classified into periventricular and deep WMHs, in line with neuroradiologist-reported metrics (Figure 1). Quality control (QC) was performed on the raw scans and pipeline outputs to assess the quality of the acquired data and explore whether additional pipeline modifications may be necessary for this clinical application. Although supplemented by visual QC where necessary (SWI, QSM, and ASL), automated tools were used where possible for the first-pass QC: MRIQC (Esteban et al., 2017) for T1-weighted and T2-FLAIR scans, QUAD (Bastiani et al., 2019) for dMRI, and MRIQC and DSE decomposition (Afyouni and Nichols, 2018) for rfMRI. The core outputs from all flagged scans were visually inspected. We investigated the associations of IDPs with diagnoses and cognitive scores (ACE-III) in this unselected memory clinic population.

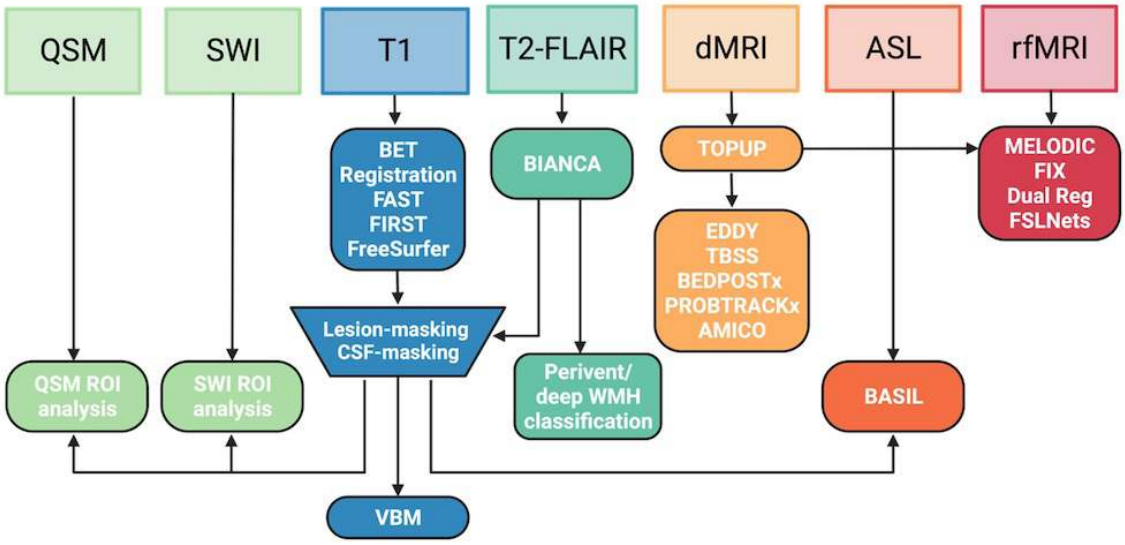

Figure 1: Simplified overview of the UK Biobank image analysis pipeline with adaptations for use in the Oxford Brain Health Clinic. QSM, quantitative susceptibility mapping; SWI, susceptibility-weighted MRI; dMRI, diffusion MRI; ASL, arterial spin labelling; rfMRI, resting-state functional MRI.

Results: QC results are summarised in Table 1. MRIQC was capable of flagging T1-weighted and T2-FLAIR scans for further inspection, but the adapted pipeline still generated mostly high- or medium-quality outputs in these scans (96.8%, 93.5%, and 94.6% for grey matter, hippocampal, and WMH segmentations, respectively). QUAD was able to flag lower quality dMRI scans, but visual inspection revealed that all of the flagged scans had high (66.7%) or medium-quality (33.3%) tractography results. DSE decomposition and MRIQC together could identify challenging rfMRI scans. Over half of the flagged scans still had significant structured noise present in their processed data, highlighting the need for further optimisation of the rfMRI pipeline for this memory clinic use. Compared to the other T2-FLAIR IDPs, periventricular WMH volume associated most strongly with cognition and diagnoses, supporting the use of this additional metric in the memory clinic setting.

Modality	First-pass QC		Detailed visual QC	
	QC method	Flagged - N/total (%)	Output	High or medium quality (%)
T1	MRIQC	31/212 (14.6%)	Corrected SIENAX	96.8%
			Corrected FIRST	93.5%
T2-FLAIR	MRIQC	37/210 (17.6%)	BIANCA	94.6%
dMRI	QUAD with SNR/CNR	24/126 (19.0%)	Tractography	100%
rfMRI	MRIQC & DSE decomposition	34/120 (28.3%)	DSE plot of processed data	47.1%

Table 1: Results of first-pass and detailed visual quality control for T1-weighted, T2-FLAIR, dMRI, and rfMRI scans. QC, quality control; dMRI, diffusion MRI; rfMRI, resting-state functional MRI; SNR, signal-to-noise ratio; CNR, contrast-to-noise ratio.

Conclusions: We adapted research-quality MRI acquisition and processing, aligned with the UK Biobank, into the memory clinic setting at the Oxford Brain Health Clinic. We integrated the analysis and quality control steps into a processing pipeline for clinical use and have explored its value to extend research findings into an unselected clinical population.

References

1. Afyouni, S. and Nichols, T.E. (2018) 'Insight and inference for DVARS', Neuroimage, 172, pp. 291–312.
2. Bastiani, M. et al. (2019) 'Automated quality control for within and between studies diffusion MRI data using a non-parametric framework for movement and distortion correction', Neuroimage, 184, pp. 801–812.
3. Esteban, O. et al. (2017) 'MRIQC: Advancing the automatic prediction of image quality in MRI from unseen sites', PLOS ONE, 12(9), p. e0184661.
4. Griffanti, L. et al. (2022) 'Adapting UK Biobank imaging for use in a routine memory clinic setting: The Oxford Brain Health Clinic', NeuroImage: Clinical, 36, p. 103273.
5. Miller, K.L. et al. (2016) 'Multimodal population brain imaging in the UK Biobank prospective epidemiological study', Nature Neuroscience, 19(11), pp. 1523–1536.
6. O'Donoghue, M.C. et al. (2023) 'Oxford brain health clinic: protocol and research database', BMJ Open, 13(8), p. e067808.

Poster No 217

Reduced myelin contributes to cognitive decline in monogenic small vessel disease

Jannis Denecke[1], Anna Dewenter[1], Jongho Lee[2], Nicolai Franzmeier[1,3,4], Lukas Pirpamer[5], Benno Gesierich[6,1], Marco Duering[6,7,1], Michael Ewers[1,8]

[1]Institute for Stroke and Dementia Research (ISD), LMU University Hospital, Munich, Germany, [2]Laboratory for Imaging Science and Technology, Department of Electrical and Computer Engineering, S, Seoul, Republic of Korea, [3]Department of Psychiatry and Neurochemistry, Institute of Neuroscience and Physiology, The Sahlgrenska Academy, University of Gothenburg, Gothenburg, Sweden, [4]Munich Cluster for Systems Neurology (SyNergy), Munich, Germany, [5]Medical Image Analysis Center (MIAC) and Department of Biomedical Engineering, University of Basel, Basel, Switzerland, [6]Medical Image Analysis Center, University of Basel, Basel, Switzerland, [7]Department of Biomedical Engineering, University of Basel, Basel, Switzerland, [8]German Center for Neurodegenerative Disease (DZNE), Munich, Germany

Introduction: Myelin enwraps axonal connections in the brain and is of critical importance for information transfer between the connected brain regions. Small vessel disease (SVD), a major cause of stroke, is associated with white matter changes such as white matter hyperintensities (WMH). However, myelin alterations in SVD were predominantly characterized in histopathological studies focusing on WMH alterations, with only a few neuroimaging studies having assessed myelin alterations. A major barrier so far in neuroimaging of myelin has been the confounding of the myelin related MR signal by confounding factors such as iron in the case of T2-star weighted images. In order to assess SVD-related myelin alterations in the whole white matter and its association with cognitive decline, we leveraged χ-separation, a newly developed technique, to separate myelin from potentially iron related MRI signal in a pure monogenic caused form of SVD, i.e. CADASIL (which stands for cerebral autosomal dominant arteriopathy with subcortical infarcts and leukoencephalopathy).

Methods: We included 65 patients with confirmed CADASIL (mean age 55.1) and 27 cognitively normal controls (NC, age = 71.5) from an in-house study. All Participants were assessed with a 3D-T2-star-weighted multi-echo gradient-echo sequence on 3T MRI scanner, alongside conventional MRI markers (see Baykara et al., 2016). As a measure of myelin, we employed the χ-separation method (Shin et al. 2021). This technique separates the total susceptibility χ into diamagnetic (|χ-negative|, e.g. myelin) and paramagnetic (χ-positive, e.g. iron) sources which both cause a faster spin dephasing, hence magnitude loss, but opposingly influence the phase. For comparison, we assessed DTI-based mean diffusivity (MD), i.e. a standard measure of microstructural white matter changes unspecific to myelin. For each participant, ROI values of |χ-negative|, χ-positive, and MD were extracted from areas of WMH and normal appearing white matter (NAWM). Difference-scores between CADASIL and group averaged NC scores were computed to derive abnormality scores for each ROI. In addition to those ROI values, all measures were obtained from the left anterior thalamic radiation (ATR) and the genu of the corpus callosum (CCg) which are regarded as strategic fiber tracts for information processing speed (Duering et al., 2011). As a measure of processing speed, the power-transformed average of the TMT A & B test scores, normalized by age and education (Tombaugh, 2004) were computed. Linear regression and ridge regression were used to test our hypotheses.

Results: We found significantly reduced |χ-negative| values in the WMH, NAWM, and fiber tracts including the ATR and CCg in CADASIL compared to the controls, adjusted for age, sex, education, and χ-positive values (Figure 1A). The decrease in |χ-negative| difference scores in CADASIL was stronger in WMH compared to NAWM (Figure 1B), suggesting pronounced myelin damage in WMH areas. In contrast, χ-positive values were reduced in WMH areas but not NAWM or tracts (Figure 1, 2nd row). Consistent with previous findings, MD values were increased in CADASIL WMH areas and negatively correlated to |χ-negative| scores (Fig 1C, standardized $\beta = -0.46$, $t(60) = -4.3$, $p < .001$). For cognition, a decrease in |χ-negative| values in WMH (Figure 2A, $p = .029$, partial-R2 = .08) and CCg (Figure 2B, $p = .016$) but not ATR (Figure 2C, $p = .49$) was associated with slower scores of processing speed, controlled for MD, χ-positive, age, sex, and education.

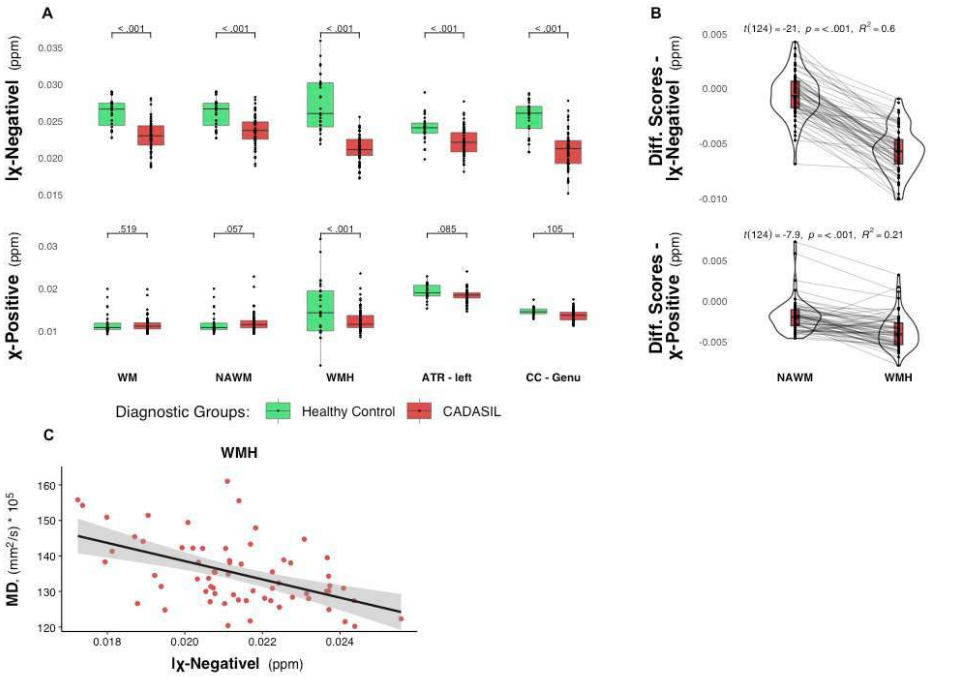

Figure 1. Box plots and violin plots of |χ-negative|, χ-positive showing the group difference and relation to MD in CADASIL and HC. (A) Mean values extracted from WM, WMH, NAWM masks and ATR left and CCg tracts. (B) Difference-Scores have been calculated in CADASIL from each subject specific WMH/NAWM mask. They are the difference between the individual mean value and the mean value of the HC group. For the statistics, a random intercept linear mixed model was used. (C) Correlation of MD and |χ-negative| scores in WMH areas in CADASIL. ATR - anterior thalamic radiation, CCg - corpus callosum - genu, MD - mean diffusivity, NAWM - normal appearing white matter, ppm – parts per million, QSM - quantitative susceptibility mapping, WM - global white matter, WMH - white matter hyperintensity.

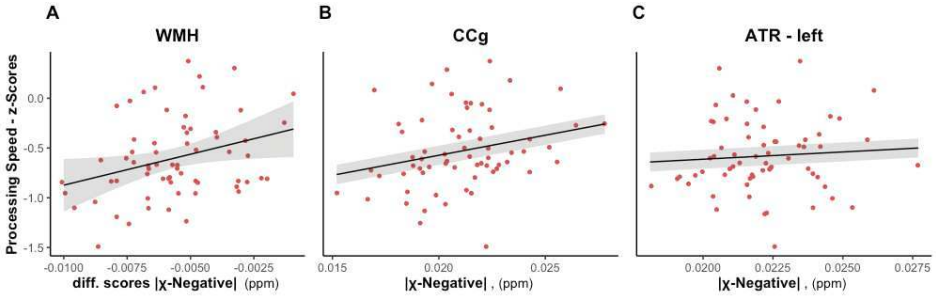

Figure 2. Regression plots of the association between |χ-negative| and processing speed in CADASIL for WMH (A), CCg fiber tract (B) and the left ATR fiber tract (C). All models used χ-positive, mean diffusivity, age, sex, and years of education as covariates. The plots show the covariate-adjusted residuals. Model (B) and (C) are ridge regression models, each with the original linear regression having a condition index > 30. ATR - anterior thalamic radiation, CCg - corpus callosum - genu, ppm – Parts Per Million, WMH - white matter hyperintensity.

Conclusions: We found that |χ-negative| values were reduced in CADASIL independently of MR signal highly sensitive to iron, suggesting that myelin is significantly reduced in monogenic SVD. The contribution of χ-negative to cognitive decline was in addition to that by the increase in MD values, suggesting that MR measures with increased specificity to myelin alterations contribute to explain cognitive decline in monogenic SVD.

References

1. Baykara, Ebru, et al. "A Novel Imaging Marker for Small Vessel Disease Based on Skeletonization of White Matter Tracts and Diffusion Histograms." Annals of Neurology, vol. 80, no. 4, Oct. 2016, pp. 581–92
2. Duering, Marco, et al. "Strategic Role of Frontal White Matter Tracts in Vascular Cognitive Impairment: A Voxel-Based Lesion-Symptom Mapping Study in CADASIL." Brain, vol. 134, no. 8, Aug. 2011, pp. 2366–75
3. Shin, Hyeong-Geol, et al. "χ-Separation: Magnetic Susceptibility Source Separation toward Iron and Myelin Mapping in the Brain." NeuroImage, vol. 240, Oct. 2021, p. 118371
4. Tombaugh, Tom N. "Trail Making Test A and B: Normative Data Stratified by Age and Education." Archives of Clinical Neuropsychology: The Official Journal of the National Academy of Neuropsychologists, vol. 19, no. 2, Mar. 2004, pp. 203–14

Poster No 218

Uncovering the progressive trajectory of GBM invasion & contralesional neuroplasticity synchrony

Hang Cao[1], Penghu Wei[2], Yongzhi Shan[2], Xiaosong He[3], Guoguang Zhao[2]

[1]Xuanwu Hospital, Capital Medical University, BEIJING, Beijing shi, [2]Xuanwu Hospital, Capital Medical University, BEIJING, Beijing Shi, [3]University of Science and Technology of China, Hefei, Anhui

Introduction: Glioblastoma multiforme (GBM) presents significant treatment challenges due to its rapid progression and invasive nature. In vitro studies have demonstrated GBM's capability to propagate excitatory signals through neuron-glioma synapses, facilitating its invasion into adjacent neural networks[2]. However, an in vivo understanding of these tumor-neural interactions is still lacking. Here, we employ virtual brain grafting and the SuStaIn algorithm[3,4] to tackle the complexities posed by tumor heterogeneity, and hypothesize that by examining contralesional hemisphere neuroplasticity, patients with GBM, despite varying clinical profiles, can be mapped onto a unified model of disease progression.

Methods: We enrolled 244 GBM patients, divided into matched left- and right-lesioned subgroups, and 244 matched healthy controls from the UPenn-GBM Project[5] and the Cam-CAN dataset[6]. Pre-operative T1-weighted MRI scans using 3T scanners were conducted. In the GBM groups, lesion segmentation was validated by expert neuro-oncologists and radiologists to exclude cases with bilateral invasion or significant midline shifts. We used FreeSurfer to obtain contralesional DK atlas defined cortical thickness and subcortical volumes. We then quantified contralesional neuroplasticity using Cohen's d map between GBM patients and controls. To assess progressive trajectory, we calculated z-scores for morphometric measures in GBM patients against control norms and used the SuStaIn algorithm's linear z-score model to stage each patient. The primary phases of the trajectory were determined using X-tile's survival cut-off. Last, we conducted phenotype-genotype analyses, starting with phase-correlated gene lists extraction via the GAMBA toolbox, permuting AHBA microarray gene expression data. Gene list annotation utilized Metascape, the cancer single-cell functional state atlas, and oncoEnrichR, focusing on phase-specific pathways and oncological conditions. We also performed pan-tissue cell type annotation using cellKB to examine cell type abundance signature across phases.

Results: In GBM cohort, contralesional neuroplasticity characterized by reduced cortical thickness was observed in both left- and right-lesioned patients. Specifically, trajectories reconstructed with SuStaIn showed progressive cortical thinning starting from the sensorimotor to the limbic system on the cortex, but bidirectional changes in subcortical volumes. No significant correlation was found between the patients' stage with tumor volume, but with age ($r's = 0.66/0.71$; $p's<0.01$). Survival analysis suggested a three-phases division, with Phase I showing the best prognosis and subsequent phases showing poorer outcomes ($p<0.01$). Due to the left-dominance of AHBA data, we performed genetic analysis primarily on the left hemisphere of patients with right GBM. We found that BDNF signaling was the only enriched pathway in Phase I, which was confirmed for influencing neuron-glioma synapse strength and tumor growth[7]. Typical GBM malignancy pathways including WNT signaling, and oxidative phosphorylation pathways were noted across phases, alongside an increase in epithelial-mesenchymal transition activity[8]. Consistently, cell type analysis indicated a shift from astrocytes in Phase I to mesenchymal-type cardiac muscle cells in Phase II. Consistent with Venkataramani et al.'s report that GBM may cause proliferate hyperexcitability through non-synaptic glutamate secretion[9], Phase III showed the highest enrichment for excitatory glutamatergic neurons. Last, compared to other cancers, single cell atlas supported our phase-related genes exhibited GBM-specific functional state changes.

Fig.1 The progressive trajectories of contralesional neuroplasticity in Glioblastoma

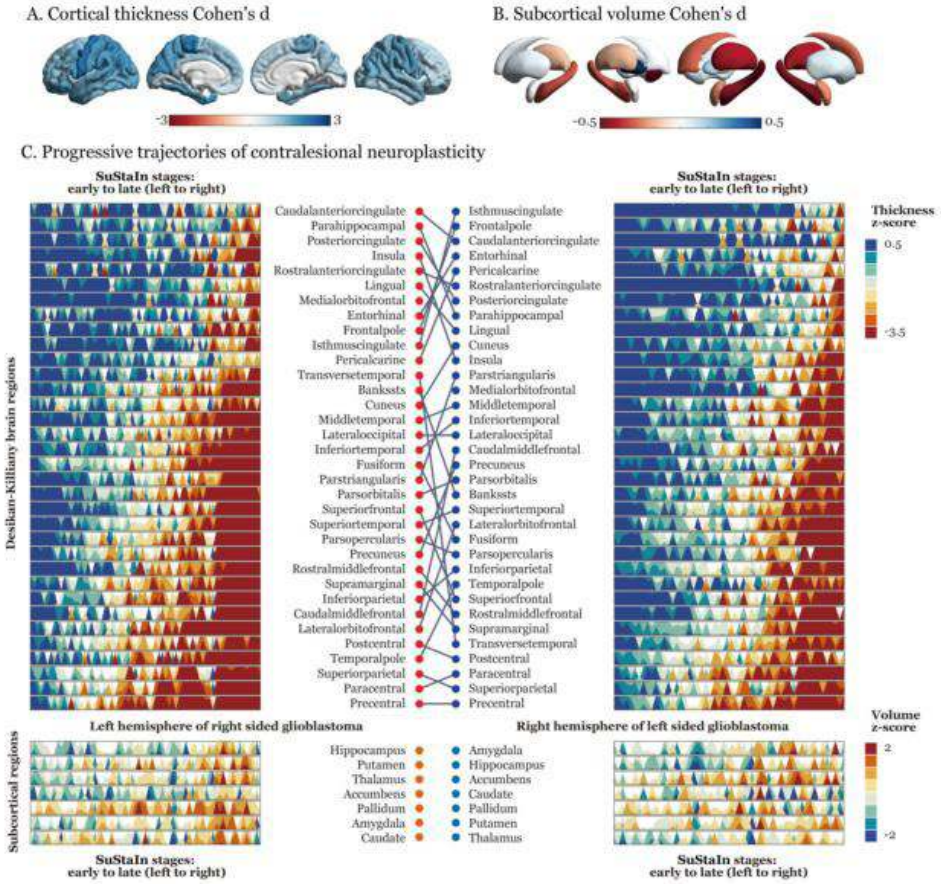

Panels A and B display Cohen's d effect size maps for contralesional cortical and subcortical neuroplasticity, respectively.
Panel C utilizes horizon plots to illustrate the z-score changes in brain regions during the early and late stages of the Sustain phase. The arrangement of brain regions in this panel is ordered from top to bottom based on skewness. Lower-positioned cortical regions exhibit earlier stages of thickness thinning, while lower-positioned subcortical regions demonstrate earlier stages of volume increase. Cortical regions on the left and right hemispheres are interconnected via straight lines.
Panel D presents the average z-maps for each phase established by segmenting continuous stages using a survival cut-off.

*Five-fold CV was used in the SuStaIn stagin for parameter determination.

Fig.2 Genetic analysis revealed glioblastoma invasive mechianisms of phases in neuroplastic progressive trajectories

A. Heatmap of Metascape enriched terms across phases

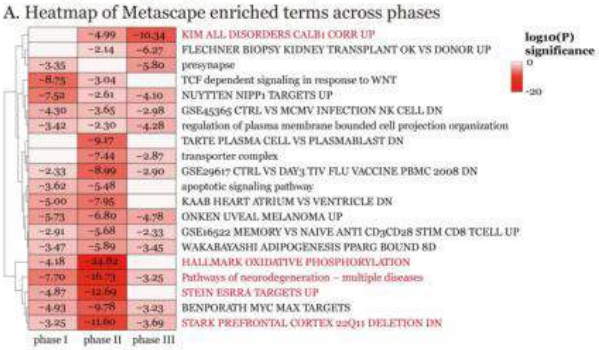

B. Cancer single cell functional state and cell-type enrichment results

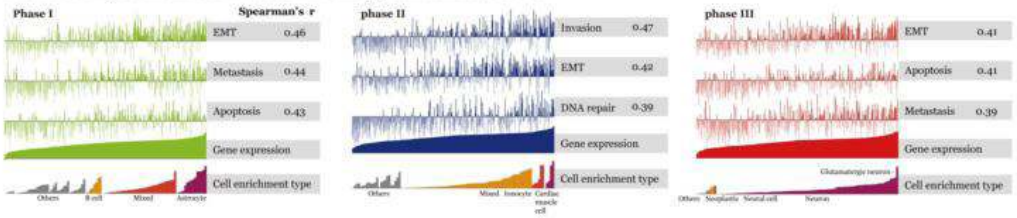

C. Correlation between gene expression of glioblastoma-contralateral hemisphere phases and functional states of other cancer types

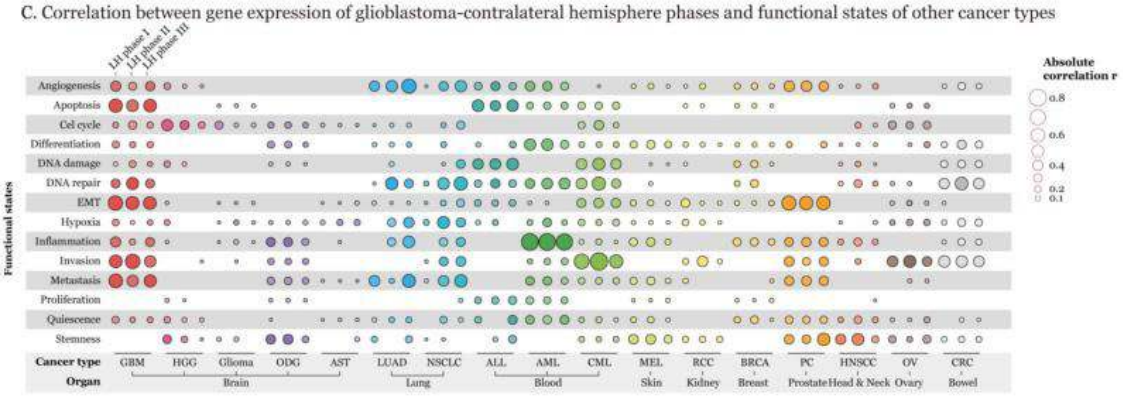

Panel A displays the top 20 terms obtained from enrichment analysis of gene lists corresponding to each phase, conducted through Metascape. The top 5 terms with the lowest hypergeometric distribution P-values are highlighted in red, aligning with the characteristic metabolic abnormalities found in Glioblastoma Multiforme (GBM).
Panel B showcases the cancer cell functional states corresponding to each phase, based on GBM single-cell RNA-seq analysis data from Darmanis et al. (PMID: 29091775), alongside pan-tissue cell-type enrichment results. The cell categories are arranged in ascending order from left to right according to their enrichment scores.
Panel C presents the enrichment of gene lists from GBM progressive phases in the functional states of other cancers. The results indicate that, including lower-grade gliomas, the gene expression correlation strength in other cancer types is lower than in GBM. This supports the specificity of genes derived from the contralesional neuroplasticity map for GBM.
*$p < 0.01$ or $q<0.01$ in multi-test was used as statistical threshold.

Conclusions: By revealing the alignment between progressive trajectory of contralesional neuroplasticity with known invasive mechanisms of GBM, this study offers a novel perspective on the tumor-neural dynamics and may facilitate the identification of new targets for therapeutic interventions.

References

1. Schaff, L. R. and I. K. Mellinghoff (2023). "Glioblastoma and other primary brain malignancies in adults: a review." Jama 329(7): 574-587.
2. Krishna, S., A. Choudhury, M. B. Keough, K. Seo, L. Ni, S. Kakaizada, A. Lee, A. Aabedi, G. Popova and B. Lipkin (2023). "Glioblastoma remodelling of human neural circuits decreases survival." Nature: 1-9.
3. Radwan, A. M., L. Emsell, J. Blommaert, A. Zhylka, S. Kovacs, T. Theys, N. Sollmann, P. Dupont and S. Sunaert (2021). "Virtual brain grafting: Enabling whole brain parcellation in the presence of large lesions." NeuroImage 229: 117731.
4. Young, A. L., R. V. Marinescu, N. P. Oxtoby, M. Bocchetta, K. Yong, N. C. Firth, D. M. Cash, D. L. Thomas, K. M. Dick and J. Cardoso (2018). "Uncovering the heterogeneity and temporal complexity of neurodegenerative diseases with Subtype and Stage Inference." Nature communications 9(1): 4273.
5. Bakas, S., C. Sako, H. Akbari, M. Bilello, A. Sotiras, G. Shukla, J. D. Rudie, N. F. Santamaría, A. F. Kazerooni and S. Pati (2022). "The University of Pennsylvania glioblastoma (UPenn-GBM) cohort: Advanced MRI, clinical, genomics, & radiomics." Scientific data 9(1): 453.

6. Taylor, J. R., N. Williams, R. Cusack, T. Auer, M. A. Shafto, M. Dixon, L. K. Tyler and R. N. Henson (2017). "The Cambridge Centre for Ageing and Neuroscience (Cam-CAN) data repository: Structural and functional MRI, MEG, and cognitive data from a cross-sectional adult lifespan sample." neuroimage 144: 262-269.
7. Taylor, K. R., T. Barron, A. Hui, A. Spitzer, B. Yalçin, A. E. Ivec, A. C. Geraghty, G. G. Hartmann, M. Arzt and S. M. Gillespie (2023). "Glioma synapses recruit mechanisms of adaptive plasticity." Nature: 1-9.
8. Crunkhorn, S. (2019). "Targeting cancer cell metabolism in glioblastoma." Nature Reviews Cancer 19(5): 250-250.
9. Venkataramani, V., D. I. Tanev, C. Strahle, A. Studier-Fischer, L. Fankhauser, T. Kessler, C. Körber, M. Kardorff, M. Ratliff and R. Xie (2019). "Glutamatergic synaptic input to glioma cells drives brain tumour progression." Nature 573(7775): 532-538.

Poster No 219

High-resolution Diffusion MRI for Tissue Microstructure of Multiple Sclerosis

Nian Wang[1], Surendra Maharjan[1]

[1]*Indiana University, Indianapolis, IN*

Introduction: Multiple sclerosis (MS) is a long-lasting chronic inflammatory-demyelinating and neurodegenerative auto-immune neurological disorder[1,2,3,4]. Although the cause of MS is not fully known, the characteristic lesions are focal areas of demyelination and inflammation in the white matter followed by gray matter and cortical lesions[5]. These demyelinated plaques can scatter throughout the brain with a predilection for optic nerves and spinal cord[3]. Although it becomes too late for treatment when the anatomical structures get damaged and focal lesions get appeared, MS could also be present in normal-appearing white matter (NAWM) and normal-appearing gray matter (NAGM)[6]. The early cognitive symptoms might be difficult to diagnose using anatomical images in conventional MRI. It is limited by low pathological specificity and low sensitivity to diffuse damage in NAWM and NAGM. To overcome these limitations, diffusion MRI has proved to be a valuable technique to investigate the disease at microscopic level[7].

Methods: 1) Specimen preparation: All the experiments on an ex-vivo human brain tissue were carried out in compliance with the Indiana University Institutional Animal Care and Use Committee. Five postmortem brain specimens from MS patients were used for MRI scans. 2) MRI Experiment: MRI images of the specimen were carried out on a 30-cm bore 9.4 T magnet with a maximum gradient strength 660 mT/m on each axis. A multi-shot 3D echo planar imaging (EPI) pulse sequence was used for high-resolution MRI. Diffusion encoded volumes at 456 directions with b-values 1, 2, 4, 6 and 8k, 90 volumes for each b-value and 6 b0 images were acquired at 300 µm isotropic resolution. 3) Data Processing: All data will be preprocessed using following pipeline: denoising using Marchenko-Pastur Principal Component Analysis (PCA) method; Gibb's artifact removal using local sub voxel shift method, eddy current-induced distortions and subject movements correction, and bias field correction using N4 algorithm. The diffusion-weighted volumes were fitted calculate diffusion tensor metrics, namely Fractional Anisotropy (FA), Mean Diffusivity (MD), Axial Diffusivity (AD), and Radial Diffusivity (RD). The data was fitted to calculate diffusion kurtosis metrics, i.e., Kurtosis Fractional Anisotropy (KFA), Mean Kurtosis (MK). Neurite Orientation Dispersion and Density Imaging (NODDI) will be performed using AMICO package. The NODDI metrics, namely Neurite Density Index (NDI) and Orientation Dispersion Index (ODI) will be calculated. The fiber orientation distribution (FOD) was calculated directed from the diffusion-weighted volumes using "Tournier" response function. The FODs were segmented to generate fibers within a specific voxel, also known as fixel. Thus, the fiber density (FD) map was created. The mean values of Lesions, NAWM, and WM were calculated, and t-statistics will be conducted to determine statistical significance between two groups. P-value was set at 0.05 level of significance.

Results: Figure 1 showed the vector map in three principal diffusion directions, FOD and fiber density in voxel space. Figure 2 illustrated various dMRI metric, where MS lesion, WM, and GM are depicted by red arrows in NDI map. Different parameters exhibited different sensitivities to different tissue compartments. For instance, FA was lower in NAWM compared to Lesion and WM. Both NAWM and WM showed significant lower MD, AD, and RD values ($p<0.001$) compared to Lesion. Compared to NAWM and WM, significant lower NDI and FD values were observed in Lesion.

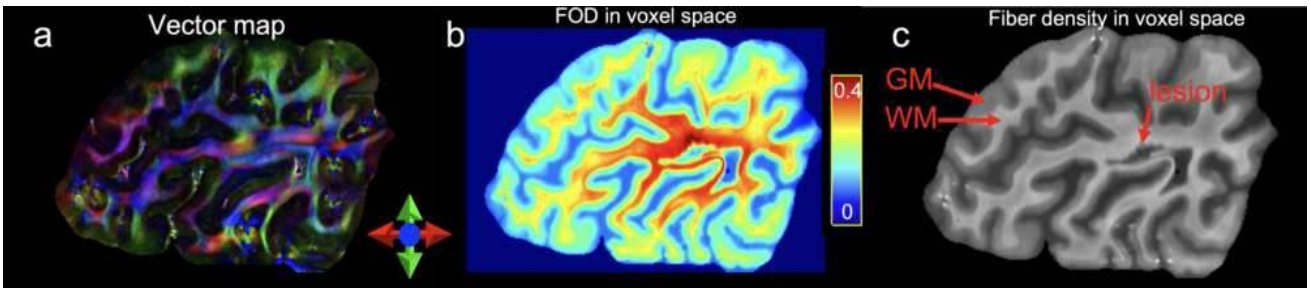

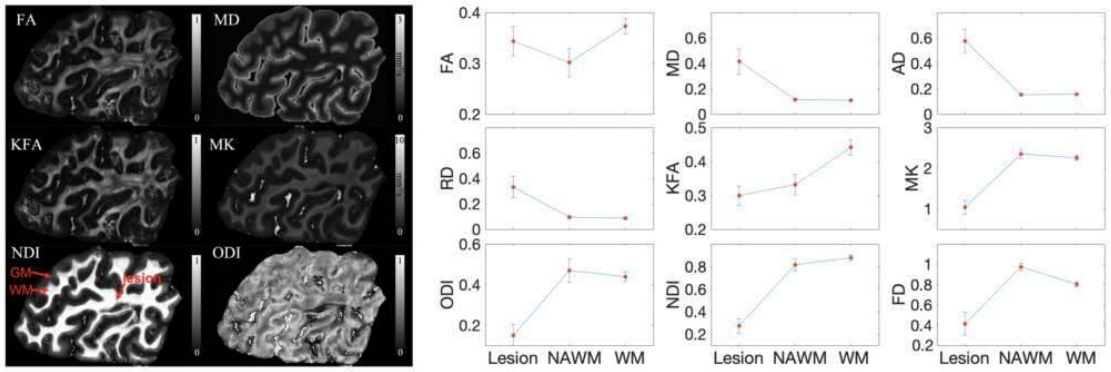

Conclusions: In this project, we demonstrated that high-resolution dMRI with different biophysical models provides a comprehensive understanding of the pathophysiological process at microstructural level. Integrating different quantitative dMRI metrics can better understand the complicated brain microstructure changes in MS.

References

1. References
2. Rovaris M, Gass A, Bammer R, Hickman SJ, Ciccarelli O, Miller DH, et al. Diffusion MRI in multiple sclerosis. Neurology. 2005;65(10):1526-32.
3. ElSayed MEKA, El-Toukhy MMB, Asaad RE, El-Serafy OA. Diffusion tensor imaging for assessment of normally appearing white matter of the brain and spinal cord in cases of multiple sclerosis: a multi-parametric correlation in view of patient's clinical status. Egypt J Radiol Nuc M. 2019;50(1).
4. Inglese M, Bester M. Diffusion imaging in multiple sclerosis: research and clinical implications. NMR Biomed. 2010;23(7):865-72.
5. Lassmann H. Multiple Sclerosis Pathology. Cold Spring Harb Perspect Med. 2018;8(3).
6. McGinley MP, Goldschmidt CH, Rae-Grant AD. Diagnosis and Treatment of Multiple Sclerosis A Review. Jama-J Am Med Assoc. 2021;325(8):765-79.
7. Beaudoin AM, Rheault F, Theaud G, Laberge F, Whittingstall K, Lamontagne A, et al. Modern Technology in Multi-Shell Diffusion MRI Reveals Diffuse White Matter Changes in Young Adults With Relapsing-Remitting Multiple Sclerosis. Front Neurosci-Switz. 2021;15.
8. Kolasa M, Hakulinen U, Brander A, Hagman S, Dastidar P, Elovaara I, et al. Diffusion tensor imaging and disability progression in multiple sclerosis: A 4-year follow-up study. Brain Behav. 2019;9(1):e01194.

Poster No 220

Analysis of Costs for Imaging-Assisted Intervention in Alzheimer's Disease with Lecanemab

Jarrad Perron[1], Carly Scramstad[2], Ji Hyun Ko[2]

[1]University of Manitoba, Winnipeg, MB, [2]University of Manitoba, Winnipeg, Manitoba

Introduction: Alzheimer's disease is the most common neurodegenerative disorder (Cao 2020). Lecanemab is an anti-amyloid drug that recently gained full FDA approval and demonstrated its ability to reduce cognitive decline and amyloid burden (Van Dyck 2023). The ability of physicians to effectively and ethically select candidates for anti-amyloid therapy remains an open question (Beach 2012). Dementia diagnosis is a complex process relying on medical history and neuropsychological exams (Arvanitakis 2019). Identifying prodromal AD in the mild cognitive impairment (MCI) stage is prohibitively difficult with current methods, but represents the most effective and efficient path for treatment, and so accurate discrimination between progressive (pMCI) and stable (sMCI) cases is crucial for early intervention in AD with anti-amyloid drugs. Diagnostic neuroimaging provides insight into AD progression, however clinical adoption of neuroimaging remains limited, with FDG-PET as the primary modality for differential diagnosis (Jack 2016, Minoshima 2021). Current practices lack specificity for the ethical use of anti-AD medications at the MCI stage. We explore neuroimaging's potential to predict forecast cognitive status in those with prodromal AD to cost-effectively and ethically evaluate candidates for anti-AD pharmaceutical therapy.

Methods: We are concerned with a discussion the potential costs of the first 3 years of mass prescription of lecanemab to patients with MCI per 1,000,000 people under a variety of scenarios. We examined the status quo scenario, a prophylactic scenario and multiple scenarios of different neuroimaging modalities at varying levels of sensitivity and specificity, and then compared costs of pharmaceutical intervention under a variety of pricing scenarios. All costs are calculated in 2020 USD. Monthly direct (patient-focused) and indirect (society-focused) costs are estimated for those with MCI and mild AD dementia were computed. Survival throughout the 3-year period and 90% efficacy for lecanemab treatment are assumed. Diagnosis for MCI per-subject cost are assumed to be $697 based on clinical experience. Local imaging program experiences suggest

$2,000 for FDG-PET, $4,000 for amyloid PET, and $500 for MR imaging. Lecanemab's estimated annual cost is $26,500 and we assume moderate and large price adjustments of 20% and 65% in two different pricing scenarios.

Results: With the status quo pricing of lecanemab at $26,500 annually, prophylactic anti-AD therapies is extremely expensive compared to status quo at $509,000 per positive outcome (preventing progression from MCI to dementia) every 3 years. The price anti-AD drugs is much larger than the savings introduced by their successful usage, however this is primarily driven by the cost of providing treatment to patients with prodromal AD who will not develop dementia (sMCI). Since these sMCI subjects represent the majority of those with MCI (77.7%) is it economical to exclude these as candidates for treatment. Total costs may be reduced to as low as $246,000 per positive outcome every 3 years using combined FDG-PET and MR imaging specifically due to its high specificity, however this is still prohibitively expensive compared to status quo of no treatment. In a scenario where cost of lecanemab is reduced by 65%, we see the same imaging modalities reducing the cost of treatment to $177,00, approximately $3,000,000,000 below cost of status quo per million patients.

Direct & Indirect Costs	Cost of Imaging	Cost of Anti-AD Drugs	Cost of MCI Diagnostics	Total Cost
Scenario 0: No treatment, 0% sensitivity, 100% specificity				
$34,994,304,000	$0	$0	$0	$34,994,304,000
Scenario 1: Prophylactic treatment, 100% sensitivity, 0% specificity				
$22,051,526,400	$0	$79,500,000,000	$697,000,000	$102,248,526,400
Scenario 2: amyloid-PET + MR, 95% sensitivity, 80% specificity				
$22,110,547,320	$4,500,000,000	$29,196,375,000	$697,000,000	$56,503,922,320
Scenario 3: amyloid-PET + MR + FDG, 95% sensitivity, 95% specificity				
$22,110,547,320	$6,500,000,000	$19,930,650,000	$697,000,000	$49,238,197,320
Scenario 4: FDG + MR, 90% sensitivity, 95% specificity				
$22,169,568,240	$2,500,000,000	$19,044,225,000	$697,000,000	$44,410,793,240
Scenario 5: FDG, 90% sensitivity, 90% specificity				
$22,169,568,240	$2,000,000,000	$22,132,800,000	$697,000,000	$46,720,682,400

Table 3. Summary of costs for current price scenario (case 1). All costs are in 2020 USD per million people.

Direct & Indirect Costs	Cost of Imaging	Cost of Anti-AD Drugs	Cost of MCI Diagnostics	Total Cost
Scenario 0: No treatment, 0% sensitivity				
$34,994,304,000	$0	$0	$0	$34,994,304,000
Scenario 1: Prophylactic treatment, 100% sensitivity, 0% specificity				
$22,051,526,400	$0	$27,825,000,000	$697,000,000	$50,573,526,640
Scenario 2: amyloid-PET + MR, 95% sensitivity, 80% specificity				
$22,110,547,320	$4,500,000,000	$10,218,731,250	$697,000,000	$37,526,278,570
Scenario 3: amyloid-PET + MR + FDG, 95% sensitivity, 95% specificity				
$22,110,547,320	$6,500,000,000	$6,975,727,500	$697,000,000	$36,283,274,820
Scenario 4: FDG + MR, 90% sensitivity, 95% specificity				
$22,169,568,240	$2,500,000,000	$6,665,478,750	$697,000,000	$32,032,046,990
Scenario 5: FDG, 90% sensitivity, 90% specificity				
$22,169,568,240	$2,000,000,000	$7,746,480,000	$697,000,000	$32,613,048,240

Table 5. Summary of costs for large price adjustment scenario (case 3). All costs are in 2020 USD per million people.

Conclusions: We examined expected costs associated with public availability of lecanemab and how imaging-assisted pharmaceutical intervention can reduce costs in selecting appropriate candidates. The most cost-efficient outcome was determined to be a combination of FDG and MR neuroimaging studies at $177,000 for every positive outcome of preventing progression from MCI to dementia for 3 years, driven by the increase in assumed specificity, the lower cost of FDG-PET compared to amyloid-PET and a reduction in the annual cost of lecanemab to $9,275.

References

1. Arvanitakis, Z. (2019), 'Diagnosis and Management of Dementia: Review', JAMA vol. 322, pp. 1589–1599.
2. Beach, T.G. (2012), 'Accuracy of the Clinical Diagnosis of Alzheimer Disease at National Institute on Aging Alzheimer's Disease Centers, 2005–2010', J Neuropathol Exp Neurol, vol. 71, pp. 266–273.
3. Cao, Q. (2020), 'The Prevalence of Dementia: A Systematic Review and Meta-Analysis', J Alzheimers Dis, vol. 73, pp. 1157–1166.
4. Jack, C.R. (2016), ' A/T/N: An unbiased descriptive classification scheme for Alzheimer disease biomarkers', Neurology vol. 87, pp. 539–547.
5. Perron, J. (2023), 'Analysis of Costs for Imaging-Assisted Pharmaceutical Intervention in Alzheimer's Disease with Lecanemab: Snapshot of the First 3 years', Journal of Alzheimer's Disease, in press.
6. Minoshima, S. (2021), 'Brain [F-18] FDG PET for clinical dementia workup: differential diagnosis of Alzheimer's disease and other types of dementing disorders', Seminars in Nuclear Medicine, vol. 51, no. 3, pp. 230-240
7. Van Dyck, C.H. (2023), 'Lecanemab in Early Alzheimer's Disease', N Engl J Med, vol. 388, pp. 9–21.

Poster No 221

Diffusion MRI-based Deep Learning to detect Alzheimer's Disease in US and Indian Cohorts

Tamoghna Chattopadhyay[1], Neha Joshy[1], Yixue Feng[2], Julio Villalón-Reina[1], Himanshu Joshi[3], Ganesan Venkatasubramanian[4], John John[5], Paul Thompson[6]

[1]University of Southern California, Los Angeles, CA, [2]University of Southern California, Marina Del Rey, CA, [3]Multimodal Brain Image Analysis Laboratory, NIMHANS, Bangalore, Karnataka, [4]National Institute of Mental Health & Neurosciences (NIMHANS), Bangalore, India, [5]National Institute of Mental Health and Neuro Sciences, Bangalore, Karnataka, [6]USC, Marina Del Rey, CA

Introduction: According to the World Health Organization (WHO), around 55 million people worldwide have dementia, and 60-70% of these patients have Alzheimer's disease (AD). The recent advent of new anti-amyloid therapies makes early, accurate AD diagnosis crucial. Automated disease classifiers that analyze vast imaging databases would also help in discovering genetic or environmental factors affecting disease onset and progression. One novel approach to disease classification involves deep learning models, such as convolutional neural networks (CNNs), which can directly analyze raw or minimally processed images, avoiding the lengthy quality control required for traditional, parcellation-based brain morphometry. Here we trained CNNs to detect AD based on diffusion MRI (dMRI), which is sensitive to brain microstructure changes not visible on standard anatomical MRI, based on prior work linking dMRI metrics to age, dementia severity, and brain amyloid levels, a key component of AD pathology[2,3]. Existing CNNs to detect AD mostly use T1-weighted brain MRI data from European or North American cohorts. To address this limitation, we tested our dMRI-based AD classifier in both Indian and North American cohorts.

Methods: We analyzed two datasets: (1) the Alzheimer's Disease Neuroimaging Initiative (ADNI) dataset with 1,195 participants (age: 74.36+/-7.74 years; 600F/595M; 633 healthy controls, CN, 421 with mild cognitive impairment, MCI, and 141 with AD, and (2) the NIMHANS cohort from Bengaluru, India, comprising 301 participants (age: 67.23+/-7.86 years; 169F/132M; 123 CN/88 MCI/90 AD). Preprocessing steps included N4 bias field correction, brain extraction, 6 degree-of-freedom registration to a template with, and resampling to 2 mm isotropic voxels. The T1-weighted (T1w) images were scaled to an intensity range of 0 and 1, aligned to a common template. The DWI were nonlinearly registered to T1w and warped to a common template. The dMRI processing pipeline details may be found in[2,3]. The 3D CNN architecture is shown in Fig. 1. Training was conducted for 100 epochs, with batch size of 8, an exponentially decaying learning rate of 0.96, Adam optimizer, and mean square error loss function. Dropout and early stopping were used to prevent overfitting. Images were split into independent training, validation, and testing sets (in a 70:20:10 ratio). In the architecture (Fig. 2) after flattening, the layers were concatenated and sent through a dense layer with sigmoid activation function. This Y-shaped architecture merged predictive features distilled from T1w MRI and DTI maps for disease classification, while maintaining previous training parameters.

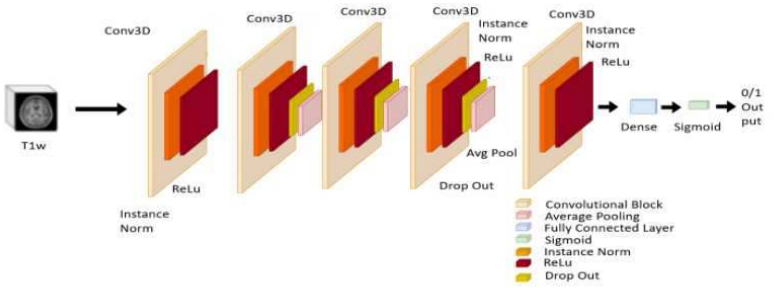

Fig 1. 3D CNN Architecture used for training on data from a single modality (here, anatomical MRI).

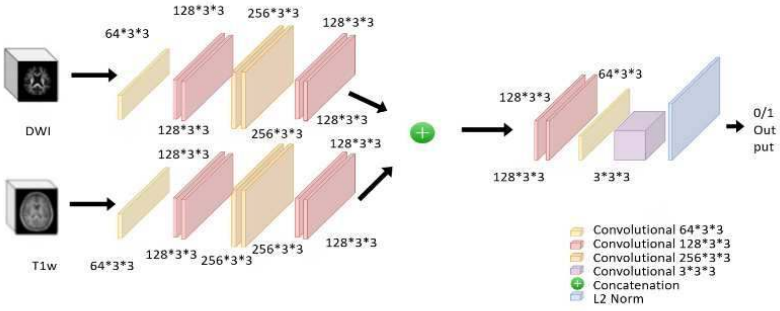

Fig 2. 3D CNN Architecture used for dual modality training

Results: Overall, DTI-derived metrics performed better on the classification task, with higher balanced accuracy and F1 Score, compared to T1w MRIs. The best balanced accuracy was obtained for DTI-RD maps at 0.896, with F1 Score 0.870. Combining T1w and DTI-MD and DTI-AD for the dual modality experiments gave best results compared to the other two combinations. In most cases, balanced accuracy was higher when T1w and dMRI were combined, relative to using T1 alone.

Table 1: Experimental results for both architectures - 3D CNN and Combined Y-shaped Architecture. **Bold** indicates the best result, and *italics* indicate the best result for the combined model architecture.

	T1	DTI-FA	DTI-MD	DTI-RD	DTI-AD	T1 + DTI-FA	T1 + DTI-MD	T1 + DTI-RD	T1 + DTI-AD
Balanced Accuracy	0.595	0.873	0.889	**0.896**	0.874	0.726	0.852	0.845	*0.868*
F1 Score	0.609	0.844	0.857	**0.870**	0.840	0.649	0.824	0.816	*0.840*

Conclusions: We trained 3D CNNs on both diffusion MRI and standard T1w MRI to classify individuals as AD patients vs healthy controls. We tested DTI maps as inputs and found that they outperformed T1w MRI. We evaluated different combinations of maps, but multimodal training did not always work best, because it increases the number of trainable parameters, requiring more data to stabilize the model. Additionally, we evaluated these models on both Indian and North American cohorts, with comparable performance on both. Future work will train methods on larger, more diverse datasets, examining various AD stages and other dementia subtypes. We will also evaluate the added value of quantitative parametric MRI, DAT-SPECT, and resting state fMRI, to enhance AD classification. A robust AD classifier may accelerate the discovery of risk factors for AD in the genome or environment.

References

1. World Health Organization, "Dementia," 2022. https://www.who.int/news-room/fact-sheets/detail/dementia.
2. Zavaliangos A., et al., "Diffusion MRI Indices and Their Relation to Cognitive Impairment in Brain Aging: The Updated Multi-Protocol Approach in ADNI3, "Front Neuroinformatics 13:2 (2019).
3. Thomopoulos S., et al., "Diffusion MRI Metrics and their relation to Dementia Severity: Effect of Harmonization Approaches," medRxiv (2021).
4. Lu, B., et al., (2022). A practical Alzheimer's disease classifier via brain imaging-based deep learning on 85,721 samples. Journal of Big Data, 9(1), Article 101.
5. Wang D., et al., "Application of multimodal MR imaging on studying Alzheimer's disease: a survey," Curr. Alzheimer Res. 877-92 (2013).
6. Knudsen L., et al., "The role of multimodal MRI in mild cognitive impairment and Alzheimer's disease," J Neuroimaging 148-157 (2022).
7. Chattopadhyay, T., et al. (2023, March). Predicting dementia severity by merging anatomical and diffusion MRI with deep 3D convolutional neural networks. In 18th International Symposium on Medical Information Processing and Analysis (SIPAIM; Vol. 12567, pp. 90-99). SPIE.
8. Lam, P., et al., "3-D Grid-Attention Networks for Interpretable Age and Alzheimer's Disease Prediction from Structural MRI," arXiv (2020).
9. Gupta, U., et al. (2023, April). Transferring Models Trained on Natural Images to 3D MRI via Position Encoded Slice Models. In 2023 IEEE 20th International Symposium on Biomedical Imaging (ISBI) (pp. 1-5). IEEE.
10. Nir T., et al., "Fractional anisotropy derived from the diffusion tensor distribution function boosts power to detect Alzheimer's disease deficits, "Magn Reson Med. 78(6):2322-2333 (2017).

Poster No 222

The differing effects of region of interest statistics in exploratory brain morphological analysis

Konstantinos Poulakis[1,2], Rosaleena Mohanty[1], Anna Inguanzo[1], Eric Westman[1,3]

[1]Karolinska Institutet, Stockholm, Sweden, [2]McGill University, Montreal, Quebec, Canada, [3]Kings College London, London, United Kingdom

Introduction: Human brain grey matter atlases, based on sulci and/or gyri hallmarks, are used to parcellate the human brain into regions of interest (ROIs) and thus reduce the information and noise inherent in brain imaging to a few relevant features. Although ROI measures are employed in research to understand neurological diseases, it is unknown whether these parcellations consider potential disease-specific atrophy patterns. Moreover, a single central tendency ROI statistic (mean or median) is often used, ignoring the potentially important within ROI dispersion, e.g. standard deviation (SD) or median absolute deviation.

Methods: Utilizing a multi-view latent factor model for multiple dataset exploration (joint and individual variation explained (Lock et al., 2013)), we investigated the relationship between the mean and SD of 148 grey matter thickness ROI measures (right/left hemisphere) in the context of cognitively unimpaired healthy aging (CU, n = 471), mild cognitive impairment

(MCI, n= 339), Alzheimer's disease (AD, n = 336), and Parkinson's disease (PD, n = 324). We utilized cross-sectional T1 magnetic resonance imaging data from the ADNI (CU, MCI, AD), J-ADNI (CU, AD), AIBL (CU, AD), and PPMI (CU, PD) cohorts. Furthermore, longitudinal global and specific neuropsychological measures of cognitive and motor health (Alzheimer's disease assessment scale-cog, mini mental state examination, clinical dementia rating scale, Montreal cognitive assessment, neuro QoL: cognition function - short form, modified Boston naming test total correct, clock drawing total score, rapid eye movement symptoms, Hoehn and Yahr Stage) were correlated with the discovered ROI-based latent factors.

Results: Mean and SD grey matter thickness at the ROI level exhibited common but also independent patterns of variation, showcasing that each statistic retrieves different disease-related anatomical information. The CU, MCI, and AD datasets exhibited similarities between their grey matter latent factor estimates. The CU, MCI, and AD latent factors increasingly correlated with cognition with the advancement of clinical progression . Interestingly, although the CU, MCI, and AD groups presented both common and individual variation in their mean and SD signals, the PD group showed only individual mean and SD variation signals. Moreover, the patterns of atrophy (latent atrophy factors based on mean and SD cortical thickness) in the MCI, AD, and PD groups were different .

Conclusions: The SD of grey matter thickness shares common features with mean grey matter thickness but also provides unique disease-related information in the healthy and cognitively impaired populations. SD is complementary to mean grey matter thickness in predicting future cognitive decline. AD and PD differ significantly in their mean-SD grey matter thickness dynamics, showcasing the potential of combined atrophy descriptive markers for differentiating and exploring these diseases.

References

1. E. F. Lock, K. A. Hoadley, J. S. Marron, and A. B. Nobel. (2013), "Joint and individual variation explained (JIVE) for integrated analysis of multiple data types," Ann. Appl. Stat., vol. 7, no. 1, doi: 10.1214/12-AOAS597.

Poster No 223

Functional Brain Network Alterations in a Korean Brain Aging Study of Alzheimer's Disease

Evgeny Chumin[1], Lauren Hirschfield[1], Sahith Peddireddy[1], Rachael Deardorff[1], Matt Tharp[1], Dahyun Yi[2], Min Soo Byun[3], Jun-Young Lee[3], Yu Kyeong Kim[4], Koung Mi Kang[5], Chul-Ho Sohn[6], Shannon Risacher[1], Olaf Sporns[7], Kwangsik Nho[1], Andrew Saykin[1], Dong Young Lee[2]

[1]Indiana University School of Medicine, Indianapolis, IN, [2]Seoul National University, Seoul, Korea, Republic of, [3]Seoul National University College of Medicine, Seoul, Korea, Republic of, [4]SMG-SNU Boramae Medical Center, Seoul, Korea, Republic of, [5]Department of Radiology, Seoul National University Hospital, Seoul, Korea, Republic of, [6]Seoul National University Hospital, Seoul, Korea, Republic of, [7]Indiana University, Bloomington, IN

Introduction: MRI studies of Alzheimer's disease (AD) have shown utility in quantifying neurodegeneration and alterations in brain structural (diffusion) and functional (task and resting state) connectivity. However, much of our knowledge comes predominantly from samples of European ancestry. In recent years, the field has begun to address the lack of diversity through initiatives that aim to recruit African American, Hispanic, and Asian participants into large multicenter studies such as the AD Neuroimaging Initiative (Weiner 2023). Here we analyze functional connectivity in 588 participants form the Korean Brain Aging Study for the Early Diagnosis and Prediction of AD (KBASE; Byun 2017) using methods previously applied to samples from the Indiana AD Research Center (Contreras 2019; Chumin 2021). We also apply edge community detection (Chumin 2022) to assess its potential as a metric of interest for AD studies/trials.

Methods: Anatomical and resting state functional MRI from 70 younger and 284 older cognitively normal (yCN, mean age: 38yo and oCN, 69yo), 147 mild cognitive impairment (MCI, 73yo), and 87 AD dementia (72yo) participants were processed using a publicly available pipeline (Chumin 2021). Anatomical data were denoised and skull-stripped, with the Schaefer (2018) 200 node parcellation registered to each subject's T1 and then fMRI scan. FMRI data underwent standard preprocessing, with nuisance and global signal regressed out (ICA-AROMA and aCompCor) and average time series extracted. Network contingency analysis comparison (t-thresholds 2:0.25:6, 10,000 permutations) of oCN vs. AD connectivity among the 7 canonical resting state networks (Yeo 2011) and multiresolution consensus clustering (1000 partitions from group averaged data, from which agreement matrices and consensus partitions at α=.05 were estimated) were done as previously reported (Contreras 2019). Edge community detection (Faskowitz 2020; k-means algorithm k=2-20) was applied as in Chumin (2022), computing a group consensus partition, edge community similarity matrix, and node entropy.

Results: Functional connectivity (Fig1A) showed a qualitative weakening of connectivity in group averaged data. Network contingency analysis showed that AD had lower connectivity within 6/7 networks (excluding limbic; Fig1C shows frontoparietal

connectivity values by group) across multiple t-thresholds (p<0.0018, adjusted for 28 network blocks tested), and for interaction blocks that fell within primary (visual and attention) or heteromodal (frontoparietal and default mode; Fig1D) systems (Fig1B). Greater connectivity in AD was found in interaction blocks that connect the primary and heteromodal systems (Fig1E shows the frontoparietal-visual interaction). Multiresolution community detection derived agreement matrices showed a breakdown of organization across diagnosis (lower agreement) particularly in the higher order systems (frontoparietal and default mode, Fig2A). Similarity of consensus community partitions decreased with greater separation in diagnostic severity (Fig2B, oCN and MCI vs. AD). Edge community structure (Fig2C, lower triangles) supports this view of breakdown in organization, which can be seen in increasing between network similarity (Fig2C, upper triangles) and entropy (Fig2D).

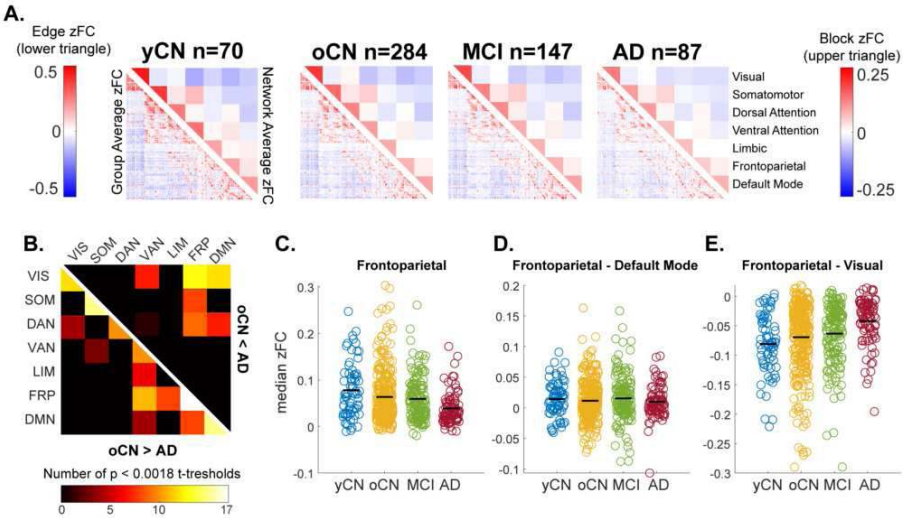

Figure 1. Network Contingency Analysis. (A) Group average Fisher *z*-scored functional connectivity (zFC; lower triangle) and network block average connectivity matrices (upper triangle) for the 4 groups in the Korean Brain Aging Study cohort. (B) Network contingency analysis to assess block-level significance was ran at t-threshold range 2 - 6 in steps of 0.25 (17 total *t*-thresholds). A pairwise comparison was done for older cognitively normal (oCN) versus Alzheimer's disease (AD) groups ($p < 0.0018$; two-tailed permutation testing; 10,000 group label permutations; Bonferroni adjusted for 28 network blocks tested), with number of *t*-thresholds that met significance in each block displayed for oCN greater than AD (lower triangle) and AD greater than oCN (upper triangle). **(C-E)** Median participant zFC values by group for select significant blocks: **(C)** within frontoparietal, **(D)** frontoparietal and default mode interaction, and **(E)** frontoparietal and visual interaction. **Acronyms: zFC** - Fisher z-scored functional connectivity; **yCN** - young cognitively normal; **oCN** - older cognitively normal; **MCI** - mild cognitive impairment; **AD** - Alzheimer's disease. **Resting state network labels: VIS** - visual; **SOM** - somatomotor; **DAN** - dorsal attention; **VAN** - ventral attention; **LIM** - limbic; **FRP** - frontoparietal; **DMN** - default mode.

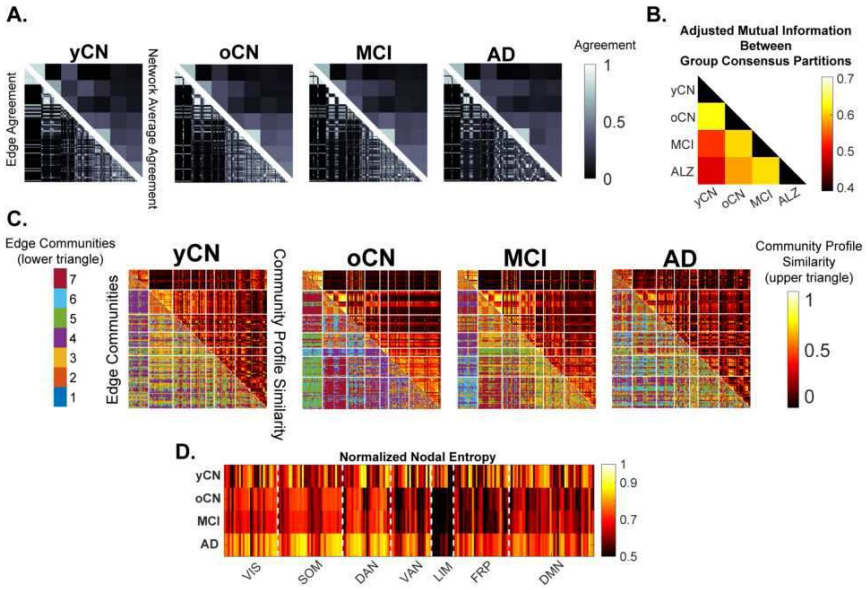

Figure 2. Multiresolution and Edge Community Detection. (A) Node and network block (lower and upper triangle, respectively) averaged agreement matrices (probability that any node pair is assigned to the same community across community scales) for each group. **(B)** Similarity of multiresolution consensus partitions at $\alpha = 0.05$ quantified as adjusted mutual information. **(C)** Edge community assignment matrices (lower triangle) for k = 7 clusters and profile similarity (upper triangle; quantifies how much overlap there is between edge communities of any node pair). **(D)** Normalized entropy of edge community distributions for each node in the network by group and resting state network. **Acronyms: yCN** - young cognitively normal; **oCN** - older cognitively normal; **MCI** - mild cognitive impairment; **AD** - Alzheimer's disease. **Resting state network labels: VIS** - visual; **SOM** - somatomotor; **DAN** - dorsal attention; **VAN** - ventral attention; **LIM** - limbic; **FRP** - frontoparietal; **DMN** - default mode.

Conclusions: These results show overlap with prior research (Contreras 2019), replicating the findings within the frontoparietal system. However, an opposite relationship for frontoparietal/default mode interaction among other differences were

observed, perhaps due to the greater sample size compared to prior work. Findings with edge community detection support its application in future AD research. Our characterization of functional alterations in a Korean participant sample showed both overlap and discrepancy relative to prior literature in samples of European ancestry, reinforcing the need for population diversity when studying aging and prodromal AD.

References

1. Byun MS, Yi D, Lee JH, et al. (2017). Korean Brain Aging Study for the Early Diagnosis and Prediction of Alzheimer's Disease: Methodology and Baseline Sample Characteristics. Psychiatry Investigation, 14(6):851-863.
2. Chumin, EJ, Risacher, SL, West, JD, Apostolova, LG, et al. (2021). Temporal stability of the ventral attention network and general cognition along the Alzheimer's disease spectrum. Neuroimage: Clinical, 31:102726.
3. Chumin EJ, Faskowitz, J, Esfahlani FZ, Jo Y, et al. (2022). Cortico-subcortical interactions in overlapping communities of edge functional connectivity. NeuroImage, 250:118971.
4. Contreras, JA, Avena-Koenigsberger, A, Risacher, SL, West, JD, et al. (2019). Resting state network modularity along the prodromal late onset Alzheimer's disease continuum. Neuroimage: Clinical, 22:101687.
5. Faskowitz, J, Esfahlani, FZ, Jo Y, Sporns, O, & Betzel, RF. (2020) Edge-centric functional network representations of human cerebral cortex reveal overlapping system-level architecture. Nature Neuroscience, 23(12):1644-1654.
6. Schaefer, A, Kong, R, Gordon, EM, Laumann, TO, et al. (2018). Local-global parcellation of the human cerebral cortex from intrinsic functional connectivity MRI. Cerebral cortex, 28(9), 3095-3114.
7. Weiner, MW, Veitch, DP, Miller, MJ, et al. (2023). Increasing participant diversity in AD research: Plans for digital screening, blood testing, and a community-engaged approach in the Alzheimer's Disease Neuroimaging Initiative 4. Alzheimer's Dement. 2023, 19:307–317.
8. Yeo BT, Krienen FM, Sepulcre J, et al. (2011). The organization of the human cerebral cortex estimated by intrinsic functional connectivity. Journal of Neurophysiology, 106(3):1125-1165.

Poster No 224

Inflammation in the white matter relates to core Alzheimer's disease pathophysiological processes

Julie Ottoy[1], Min Su Kang[1], Eric Yin[1], Nesrine Rahmouni[2], Jenna Stevenson[2], Jean-Paul Soucy[3], Andrea Benedet[4], Kaj Blennow[5], Henrik Zetterberg[6,4], Nicolas Ashton[4,7], Serge Gauthier[2], Sandra Black[1], Pedro Rosa-Neto[2,8], Maged Goubran[1,9]

[1]LC Campbell Cognitive Neurology Unit, Sunnybrook Research Institute, University of Toronto, Toronto, Ontario, [2]Translational Neuroimaging laboratory, McGill Centre for Studies in Aging, Montreal, Quebec, [3]McConnell Brain Imaging Centre, Montreal Neurological Institute and Hospital, McGill University, Montreal, Quebec, [4]Department of Psychiatry and Neurochemistry, The Sahlgrenska Academy at the University of Gothenburg, Mölndal, Mölndal Municipality, [5]Clinical Neurochemistry Laboratory, Sahlgrenska University Hospital, Gothenburg, Västergötland, [6]UK Dementia Research Institute at University College London, London, United Kingdom, [7]Institute of Psychiatry, Psychology and Neuroscience, Maurice Wohl Institute Clinical Neuroscience Institute, King's College London, London, United Kingdom, [8]Montreal Neurological Institute-Hospital BIC, Montreal, Quebec, Canada, [9]Department of Medical Biophysics, University of Toronto, Toronto, Ontario, Canada

Introduction: In-vivo PET imaging studies have demonstrated neuroinflammation (microglia reactivity) in the neocortex of patients with Alzheimer's disease (AD)[1]. However, the extent and implication of microglia reactivity in regions of the white matter remains unclear. Here, we explored microglia reactivity in the white matter using PET imaging of the translocator protein (TSPO)[2,3] in relation to core AD biomarkers (amyloid [Aβ], tau, and astrogliosis), microstructural damage (fibre integrity and free water levels), and cognitive decline. We hypothesized that TSPO-PET signal is elevated in posterior white matter regions reflecting ongoing gliosis and tau pathology in AD.

Methods: Ninety-one participants were recruited from the Translational Biomarkers in Aging and Dementia (TRIAD) cohort (45% Aβ-positive, 39% cognitively impaired) with high-affinity binding TSPO genotype. They underwent multi-shell diffusion-weighted MRI, PET imaging of TSPO (11C-PBR28), Aβ (18F-NAV4694), and tau (18F-MK6240), as well as plasma Aβ42/40, ptau181, ptau217, and ptau231. White matter regions were extracted using Freesurfer after masking out the white matter hyperintensities, and were eroded by 2mm3 to account for partial volume effects and lesion borders. For PET, we extracted uptake values using Petsurfer[4] averaged in each of the lobar white matter regions (frontal, temporal, parietal, cingulate, occipital, and insular) and calculated standardized uptake value ratios (SUVR). For diffusion-MRI, we performed two-compartment modeling to differentiate between free water levels and tissue-specific fractional anisotropy (FAt) and mean diffusivity (MDt)[5]. For statistical analysis, we investigated the associations of lobar white matter TSPO-PET with each of the AD biomarkers, diffusion metrics, and cognition, adjusted for age, sex, and global cortical TSPO-PET. Longitudinally, we performed a linear mixed effects model of the interaction between time (up to 2 years) and baseline lobar TSPO-PET on cognitive decline, adjusted for age, sex, education, and cortical Aβ.

Results: Higher white matter TSPO-PET was observed with older age in all lobes and males showed frontal increases compared to females ($p<0.05$). In cognitively impaired individuals, TSPO-PET signals were elevated in occipital ($p=0.01$)

and temporal (p=0.02) white matter regions compared to controls. These occipital increases were associated with reactive astrogliosis quantified by plasma GFAP (p=0.011) and with neocortical higher-Braak tau quantified by PET (p=0.003-0.034 for Braak3-4) or plasma ptau181 (p=0.014) (Fig.1A-B), but not with Aβ, ptau231 or ptau217. In addition, higher occipital TSPO-PET was associated with lower fibre integrity (FAt, p=0.025), but not with free water content. Finally, in relation to cognition, higher occipital and parietal TSPO-PET was significantly associated with impaired memory (both delayed and immediate) and language, respectively, independent of Aβ (Fig.1C). Longitudinally, within the same patient, high white matter TSPO-PET uptake at baseline was significantly associated with favorable clinical outcome over time (Fig.1D).

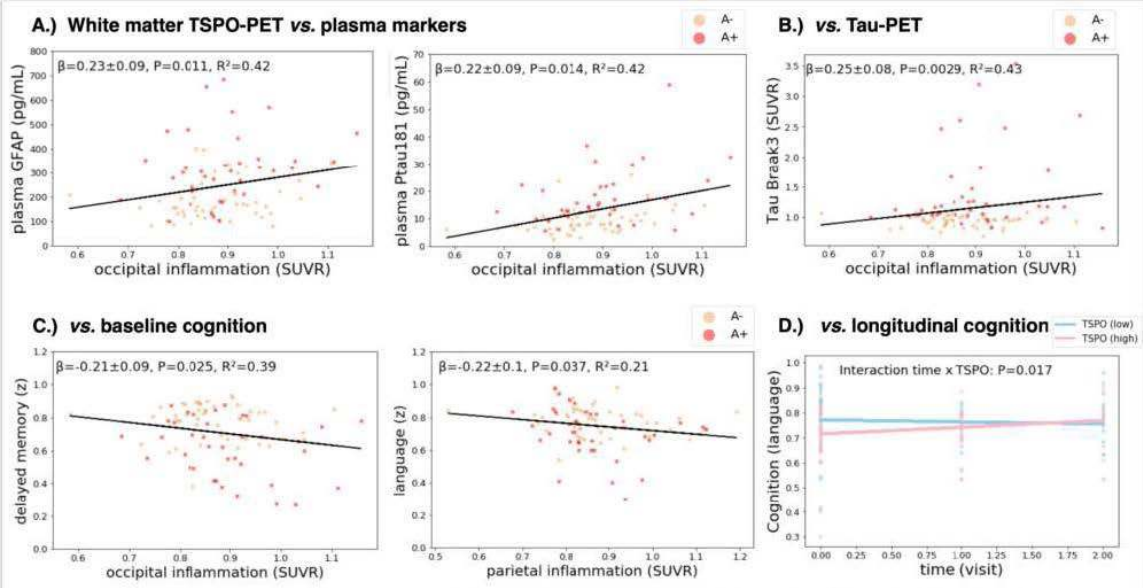

Figure 1. Association of white matter inflammation (quantified with TSPO-PET) with AD biomarkers, including plasma markers (A), Tau-PET (B), cognition (C), and longitudinal cognitive changes.

Conclusions: Increased TSPO-PET uptake in posterior white matter may be a later-stage marker associated with astrogliosis, tau pathology, and cognitive dysfunction of the memory and language domains in AD. Importantly, individuals with the highest initial white matter TSPO-PET profile displayed a better clinical prognosis over time, in line with previous findings for TSPO-PET in the cortex[6]. As such, microglia reactivity in the white matter could be a key mechanism of AD pathophysiological progression, serve as an indicator for assessing target engagement in clinical trials of anti-inflammatory drugs, and be employed in patient subtyping to identify individualized treatment approaches.

References

1. De Picker LJ, Morrens M, Branchi I, et al. TSPO PET brain inflammation imaging: A transdiagnostic systematic review and meta-analysis of 156 case-control studies. Brain Behav Immun 2023;113:415–431.
2. Nutma E, Stephenson JA, Gorter RP, et al. A quantitative neuropathological assessment of translocator protein expression in multiple sclerosis. Brain 2019;142(11):3440–3455.
3. Gulyás B, Makkai B, Kása P, et al. A comparative autoradiography study in post mortem whole hemisphere human brain slices taken from Alzheimer patients and age-matched controls using two radiolabelled DAA1106 analogues with high affinity to the peripheral benzodiazepine receptor (PBR) system. Neurochemistry International 2009;54(1):28–36.
4. Greve DN, Svarer C, Fisher PM, et al. Cortical Surface-based Analysis Reduces Bias and Variance in Kinetic Modeling of Brain PET Data. Neuroimage 2014;92:225–236.
5. Pasternak O, Sochen N, Gur Y, et al. Free water elimination and mapping from diffusion MRI. Magn Reson Med 2009;62(3):717–730.
6. Hamelin L, Lagarde J, Dorothée G, et al. Distinct dynamic profiles of microglial activation are associated with progression of Alzheimer's disease. Brain 2018;141(6):1855–1870.

Poster No 225

Cognitive Profiles and Brain Alterations in Prodromal and Parkinson's Disease Individuals

Edith Gaspar Martínez[1], Sarael Alcauter[1]

[1]*Instituto de Neurobiología, Universidad Nacional Autónoma de México, Querétaro, México*

Introduction: Detecting Mild Cognitive Impairment (MCI) in Parkinson's Disease (PD) has proven valuable in identifying individuals at risk of developing dementia and has been described as an important risk factor for individuals in the prodromal stage of the disease (Hobson & Meara, 2015). Therefore, we aimed at characterizing the cognitive profiles of prodromal and

PD patients, and their brain morphology correlates, in a large sample of participants of the Parkinson's Progression Markers Initiative Program (PPMI; Marek et al., 2011).

Methods: K-means clustering analysis was performed to identify distinct cognitive profiles in 551 PD patients (age: 63 ± 9 years) and 361 prodromals (age: 64 ± 6 years), based on the normalized scores of the 7 cognitive domains assessed by the Montreal Cognitive Assessment at baseline. The optimal cluster structure was determined using validation methods implemented in the NbClust R package (Charrad et al., 2014). Volumetric quantification of cortical, subcortical, cerebellar, and ventricular regions was performed using AssemblyNet pipeline (Coupé et al., 2020) on T13D MRI brain images that survived visual and quantitative quality control (87.6%) using MRIQC (Esteban et al., 2017).

Results: Three distinct cognitive profiles were identified among PD patients: Cognitively intact (n=260), Mildly affected (n=239) characterized by low performance (0.45) in the episodic memory domain, and Mostly affected (n=52), with notably lower performances in the language, abstraction and episodic memory domains (0.66, 0.35 and 0.36, respectively). Similarly, the Prodromal cohort clustered into three comparable profiles: Cognitively intact (n=171), Mildly affected (n=124) with low performance (0.41) in episodic memory, and Mostly affected (n=66), with low performances in language and episodic memory (0.51 and 0.53, respectively). Demographic analysis revealed significant sex proportion differences among the participants with distinctive cognitive profiles in both cohorts. Only Cognitively intact and Mostly affected in the Prodromal cohort showed significant age differences. In the PD cohort, decreased left cerebellar volume in Mildly affected participants ($p<0.05$), and decreased total cerebellar white matter volume in the Mostly affected group ($p=0.015$), were identified when contrasting to Cognitively intact subjects. In the Prodromal cohort, overall decreased brain volume was evident in the Mostly affected group in contrast to the Cognitively intacts, with the right hemisphere being the most affected ($p=0.017$). Total cerebral white matter ($p=0.018$) and right cerebellar white matter ($p<0.01$) were significantly reduced in volume, while lateral ventricular volume was increased ($p=0.012$). Altered structures in the Mostly affected group of Prodromal participants were compared to a Control cohort without MCI (n=144) from the PPMI, also showing a volume reduction ($p<0.01$). Cognitively affected participants of the PD cohort showed no cerebellar volume differences compared to the Control cohort. All p values were FDR-corrected ($q < 0.05$).

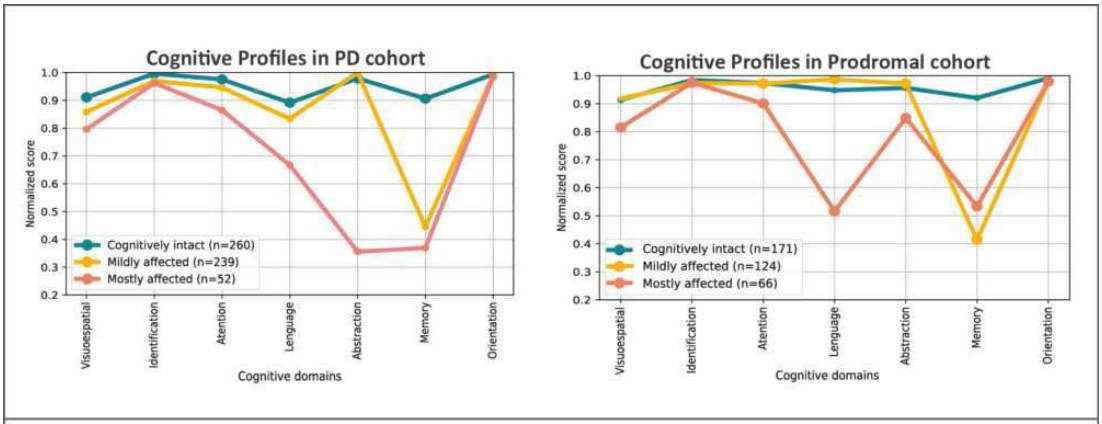

Figure 1. Cognitive Profiles. Our clustering results revealed three distinct cognitive profiles for both Prodromal and PD cohorts: (1) Cognitively intact, (2) Mildly affected and (3) Mostly affected

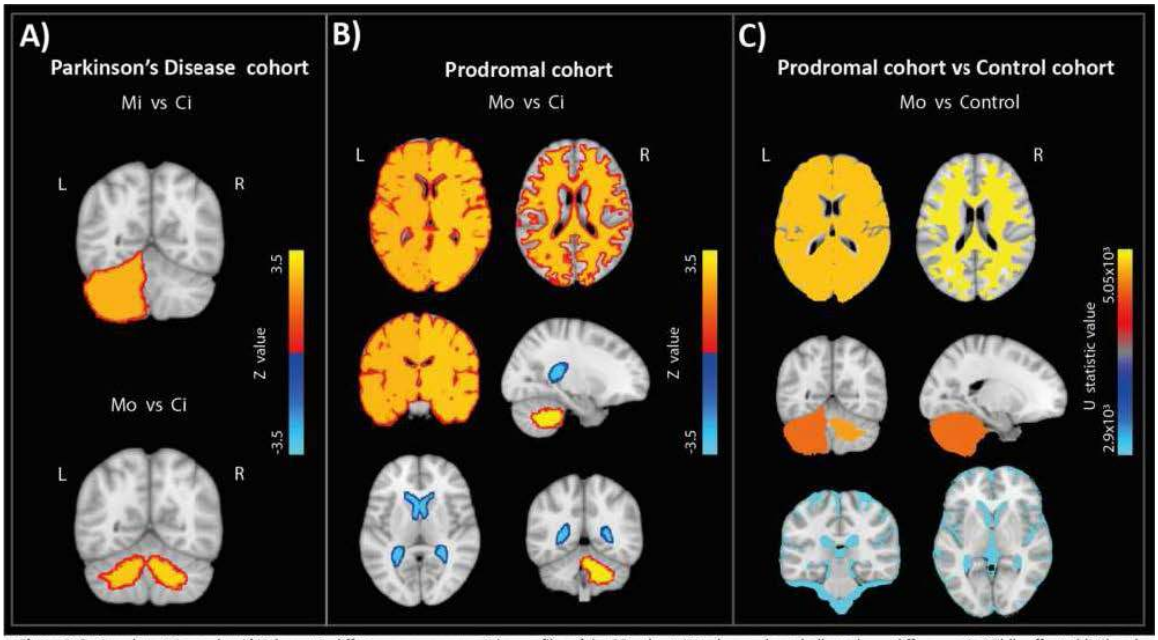

Figure 2. Brain volumetric results. **A)** Volumetric differences among cognitive profiles of the PD cohort. We observed cerebellar volume differences in Mildly affected (Mi) and Mostly affected (Mo) individuals compared to Cognitively intact (Ci). **B)** Volumetric differences among cognitive profiles of the Prodromal cohort. We observed brain and cerebellar volume loss with a higher ventricle volume in Mostly affected (Mo) individuals compared to Cognitively intact (Ci). **C)** Volumetric differences between Mostly affected (Mo) of the Prodromal cohort and individuals of the Control cohort without Mild Cognitive Impairment. We observed a loss of volume in cerebellar and brain regions, and a higher volume in Cerebro Spinal Fluid. Z value and U statistic value of the statistical comparissons are showed.

Conclusions: Similar cognitive profiles observed in both Prodromal and PD cohorts suggest the presence of comparable cognitive deficits in these individuals, being the PD patients and the episodic memory domain the most affected. Specific brain volume alterations were evident, particularly a reduction in cerebral and cerebellar white matter volume in the most cognitively affected participants. Interestingly, the prodromal cohort showed the greatest morphological differences, suggesting that PD involves diverse morphological alterations (volume increments and decrements)(Pieperhoff et al., 2022) that result in less evident differences between cognitive profiles. These results highlight the relevance of correlating clinical features and structural brain properties to better characterize the complex alterations in both prodromal and PD patients, potentially identifying risk factors and early brain changes before the onset of the disease.

References

1. Charrad, M. (2014), "NbClust: An R Package for Determining the Relevant Number of Clusters in a Data Set", Journal of Statistical Software, 61(6), 1–36. https://doi.org/10.18637/JSS.V061.I06
2. Coupé, P. (2020), "AssemblyNet: A large ensemble of CNNs for 3D whole brain MRI segmentation", NeuroImage, 219, 117026. https://doi.org/10.1016/j.neuroimage.2020.117026
3. Esteban, O. (2017), "MRIQC: Advancing the automatic prediction of image quality in MRI from unseen sites", PLOS ONE, 12(9), e0184661. https://doi.org/10.1371/journal.pone.0184661
4. Hobson, P. (2015), "Mild cognitive impairment in Parkinson's disease and its progression onto dementia: a 16-year outcome evaluation of the Denbighshire cohort", International Journal of Geriatric Psychiatry, 30(10), 1048–1055. https://doi.org/10.1002/GPS.4261
5. Marek, K. (2011), "The Parkinson Progression Marker Initiative (PPMI)", Progress in Neurobiology, 95(4), 629–635. https://doi.org/10.1016/j.pneurobio.2011.09.005
6. Pieperhoff, P. (2022), "Regional changes of brain structure during progression of idiopathic Parkinson's disease – A longitudinal study using deformation based morphometry", Cortex, 151, 188–210. https://doi.org/10.1016/J.CORTEX.2022.03.009

Poster No 226

Style transfer GANs for synthesizing controls for case-only studies in multi-study analyses

Shruti Gadewar[1], Alyssa Zhu[1], Iyad Ba Gari[2], Sunanda Somu[3], Sophia Thomopoulos[4], Paul Thompson[5], Talia Nir[6], Neda Jahanshad[7]

[1]USC, Marina Del Rey, CA, [2]University of Southern California, Marina Del Rey, CA, [3]University of Southern California, Los Angeles, CA, [4]USC, Marina del Rey, CA, [5]Imaging Genetics Center, Keck School of Medicine of University of Southern California, Los Angeles, CA, [6]University of Southern California Keck School of Medicine, Marina del Rey, CA, [7]Imaging Genetics Center, Keck School of Medicine of University of Southern California, Los Angeles, California

Introduction: Pooling data from multiple sites in neuroimaging studies enhances sample size, statistical power, and reproducibility[1]. Multi-study analyses require harmonization approaches to adjust for measurement variability in MRI

acquisition protocols across studies. Statistical harmonization is often a first step after pooling subject level imaging features derived from raw scans across data collection sites[2]. This harmonization is often applied with respect to controls, and in studies that also include 'cases', the resulting harmonization parameters are then applied to the cases[3]. Some studies focus exclusively on variations within cases and lack controls, making harmonization challenging. To address this, we propose creating synthetic control T1-weighted (T1w) MRI for a target dataset by harmonizing the "style" of control images to that of target dataset 'cases'. We used ComBat-GAM[4] to statistically harmonize regional brain volumes across multiple Alzheimer's disease (AD) case/control datasets. We compared the effects of using either true or synthetic control T1w MRI brain volumes for statistical harmonization on resulting clinical associations.

Methods: The AD datasets (Fig 1A) analyzed in this study were ADNI1, OASIS3, NACC and AIBL. 272 T1w MRI controls from OASIS1 and UK Biobank were age- and sex-matched to AIBL dementia cases (aged 60-81 years). We then created synthetic T1w control data for AIBL by harmonizing the "style" of OASIS1 and UKB images to AIBL dementia T1w. True AIBL control T1w images were used for validation. All T1w images were bias field corrected, skull-stripped using HD-BET[5], registered to MNI template using FSL's flirt[6] command with 9 degrees of freedom, and then zero-padded to 256x256x256 voxels. After "style" harmonization, images were moved back to subject space. Regional volumes for the thalamus, hippocampus, amygdala, putamen, caudate, accumbens, pallidum and ventricles were extracted from the T1ws for all datasets using FastSurfer[7]. Two ComBat-GAM harmonization models were trained with control volumes from ADNI1, OASIS3, NACC and either true or synthetic control volumes from AIBL. Site was used as the batch effect with age, sex and intracranial volume (ICV) covariates; age was specified as a nonlinear term. Linear mixed models were run to compare AIBL AD subcortical volumes to either 1) true AIBL, 2) synthetic AIBL, or 3) the original unharmonized OASIS and UKB control volumes. Linear regressions were also performed to compare control and AD subcortical volumes across ComBat harmonized studies; again, the use of AIBL true vs synthetic volumes was compared. Finally, we evaluated associations between ApoE4 count (0/1/2) and harmonized subcortical measures within the AD population; AD data was harmonized using either true or synthetic control volumes for comparison. All regressions included age, sex, ICV as fixed effect covariates.

A

Dataset	No. of Sites	Scanner	Field Strength	Age (yrs)	N (Male)	CN/AD count	ApoE4 count 0/1/2
OASIS1	1	Siemens	1.5T	71.40 ± 6.05	62 (16)	62/-	-
UKB	1	Siemens	3T	70.62 ± 6.17	210 (105)	210/-	84/84/42
AIBL (Site 1)	-	Siemens	3T	71.84 ± 4.99	201 (88)	178/23	139/54/8
AIBL (Site 2)	-	Siemens	1.5T, 3T	69.63 ± 5.45	92 (43)	83/9	54/35/3
ADNI1	47	Siemens, GE, Philips	1.5T, 3T	73.9 ± 4.24	299 (145)	187/112	165/103/31
OASIS3	5	Siemens	1.5T, 3T	70.43 ± 5.12	740 (316)	674/66	470/234/36
NACC	3	Siemens, GE, Philips	1.5T, 3T	70.94 ± 5.98	250 (100)	203/47	156/79/15

B

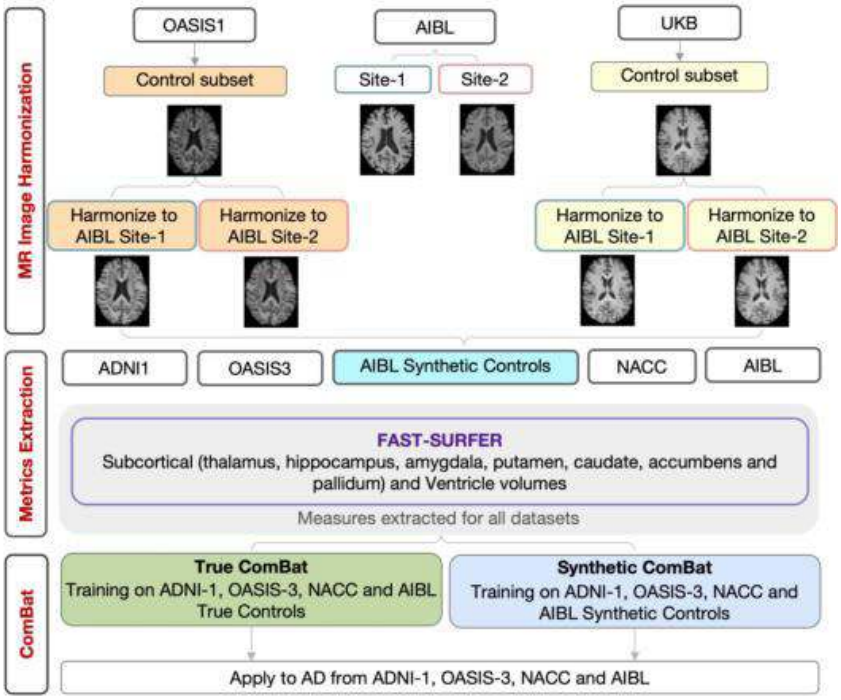

Figure 1. A) Demographics for datasets used in the study. **B) Flowchart for generating cohort-specific controls**: In UKB, for every age between 60 and 81, we randomly selected five males and five females; for each age-sex combination, there were five individuals selected, two of whom had no ApoE4 risk alleles, two of whom had one, and one of whom had two. 139 out of the 210 T1w images from UKB and 41 images from OASIS1 were harmonized to one AD subject in site-1 in AIBL, and 71 from UKB and 21 from OASIS1 were harmonized to site-2 to generate synthetic controls using style harmonization model [8]. Volumes of subcortical structures and ventricles were extracted for all the datasets using Fast-Surfer. Two ComBat-GAM models were trained on these extracted measures: **True ComBat:** training on controls from ADNI1, OASIS3, NACC and AIBL; **Synthetic ComBat:** training on controls from ADNI1, OASIS3, NACC and Synthetic AIBL. Both these models were applied to the AD populations of these cohorts.

Results: Results are shown in Fig 2. In AIBL, AD cases had lower bilateral hippocampal volumes compared to both true and synthetic control participants (p=1.1x10^-13 for true, p=2.6x10^-10 for synthetic). A paired t-test comparing pooled case-control effect sizes across all volumes when using true or synthetic AIBL control data was not significant (p=0.62) showing that both sets of regressions had similar results. Bilateral amygdala volume was found to be significantly associated with ApoE4 count in pooled AD participants, when true AIBL (r=-0.18; p=0.002) and synthetic AIBL control volumes (r=-0.19; p=0.003) were used for ComBat.

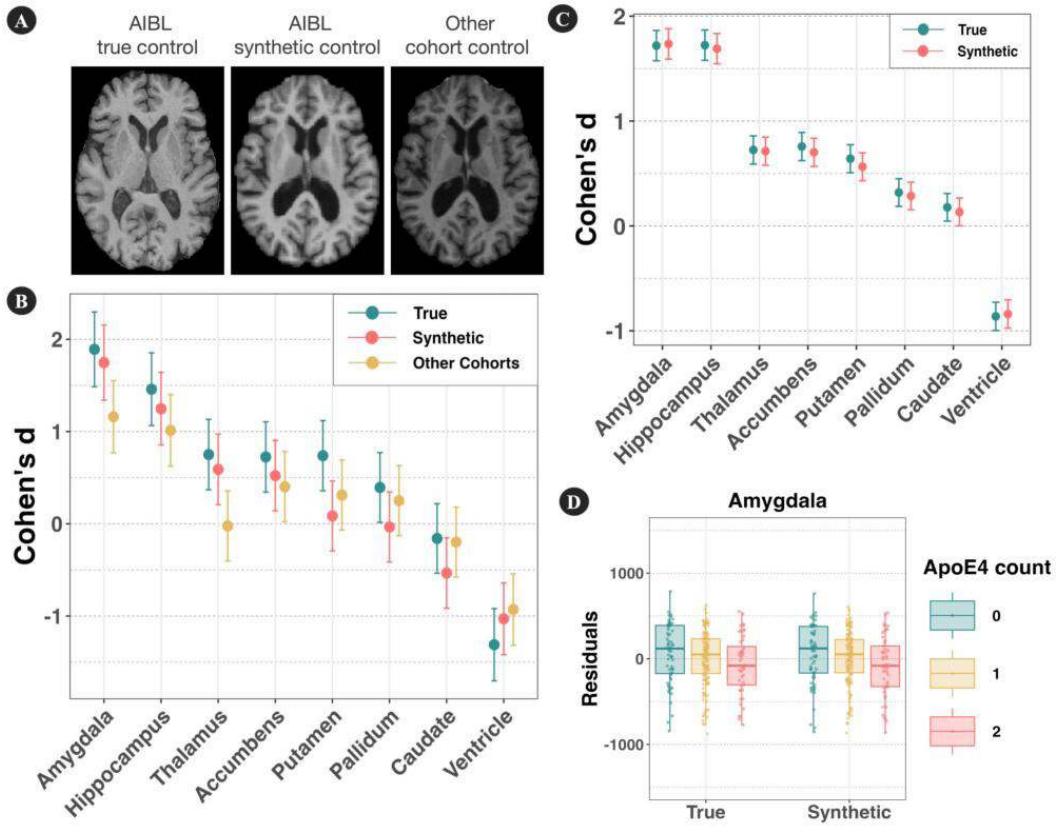

Figure 2. A) T1w images of true AIBL control, synthetic AIBL control (OASIS1 harmonized to a subject from AIBL site 1) and unharmonized control from OASIS1 at age 74. **B)** Case-control effect sizes for differences in subcortical and ventricle volumes when comparing AIBL AD patients to either true or synthetic AIBL controls, or when compared to directly using the T1w images from other cohorts without style harmonization. **C)** Case-control effect sizes with the confidence intervals for all the subcortical and ventricle volumes when comparing ComBat-GAM run across studies using either true or synthetic AIBL controls. **D)** Box plot for comparisons of residualized volumes of amygdala for each ApoE4 count using true and synthetic ComBat.

Conclusions: This work is preliminary and has several limitations. We only evaluated synthetic controls in the case of AD, where the effect of neurodegeneration is more evident than in mood disorders or other psychiatric conditions. We performed a case-control analysis for validation, yet the primary objective of this work is to better allow for statistical harmonization of case-only datasets for case-only statistical analyses and avoid over-correction.

References

1. P. M. Thompson et al. (2014), "The ENIGMA Consortium: large-scale collaborative analyses of neuroimaging and genetic data," Brain Imaging Behav., vol. 8, no. 2, pp. 153–182.
2. J. Radua et al. (2020), "Increased power by harmonizing structural MRI site differences with the ComBat batch adjustment method in ENIGMA," NeuroImage, vol. 218, p. 116956.
3. R. Da-Ano et al. (2020), "Performance comparison of modified ComBat for harmonization of radiomic features for multicenter studies," Sci. Rep., vol. 10, no. 1, p. 10248.
4. R. Pomponio et al. (2020), "Harmonization of large MRI datasets for the analysis of brain imaging patterns throughout the lifespan," NeuroImage, vol. 208, p. 116450.
5. F. Isensee et al. (2019), "Automated brain extraction of multisequence MRI using artificial neural networks," Hum. Brain Mapp., vol. 40, no. 17, pp. 4952–4964.
6. M. Jenkinson et al. (2002), "Improved optimization for the robust and accurate linear registration and motion correction of brain images," NeuroImage, vol. 17, no. 2, pp. 825–841.
7. L. Henschel et al. (2020), "FastSurfer - A fast and accurate deep learning-based neuroimaging pipeline," NeuroImage, vol. 219, p. 117012.
8. M. Liu et al. (2023), "Style transfer generative adversarial networks to harmonize multisite MRI to a single reference image to avoid overcorrection," Hum. Brain Mapp., vol. 44, no. 14, pp. 4875–4892.
9. Acknowledgements:
10. This work is supported in part by NIH grants: R01AG059874, RF1AG057892, P41EB015922, U01AG068057 and R01AG058854. This work was completed using UK Biobank Resource under application number 11559. Acknowledgments for OASIS and NACC can be found at (http://www.oasis-brains.org/#access, https://naccdata.org/publish-project/authors-checklist). Data used in the preparation of this article was obtained from the AIBL funded by the Commonwealth Scientific and Industrial Research Organization (CSIRO). AIBL researchers are listed at www.aibl.csiro.au. Data used in preparing this article were obtained from the ADNI database (adni.loni.usc.edu). As such, many investigators within the ADNI contributed to the design and implementation of ADNI and/or provided data but did not participate in analysis or writing of this report. A complete list of ADNI investigators: http://adni.loni.usc.edu/wp-content/uploads/how_to_apply/ADNI_Acknowledgement_List.pdf.

Poster No 227

Anterior insula atrophy drives progressive structural brain network alterations in FTD

Tao Chen[1], Rebekah Ahmed[1], Olivier Piguet[1], Muireann Irish[1]

[1]*The University of Sydney, Sydney, New South Wales*

Introduction: The behavioural variant of frontotemporal dementia (bvFTD) is a younger-onset dementia syndrome characterised by early atrophy of frontoinsular cortices, manifesting in profound socioemotional and behavioural disturbances (Rascovsky et al., 2011). With disease progression, atrophy gradually progresses into anterior temporal and subcortical regions (Landin-Romero et al., 2017). Converging evidence from correlational, data-driven, and computational approaches indicates large-scale network-degeneration in bvFTD. While the insula is commonly implicated, it remains unclear whether insular atrophy causally impacts progressive large-scale structural network alterations in this population.

Methods: To determine disease stage-specific grey matter atrophy in bvFTD, 82 patients were classified into very mild/mild (n=35), moderate (n=30), and severe (n=17) disease stage according to the FTLD-modified Clinical Dementia Rating (FTLD-CDR) scale (Miyagawa et al., 2020). Then, whole-brain voxel-based morphology (VBM) analysis was performed by CAT12 software to measure grey matter volume of all participants. Two-independent sample t-tests were used to compare grey matter volume between each bvFTD subgroup and corresponding healthy control groups matched for sex distribution, age, and education. These results were FDR-corrected at the voxel level ($P < 0.005$; k=300). To determine the potential causal effects of anterior insula on network-based atrophy in bvFTD, the grey matter maps of all bvFTD patients were ranked from low to high based on the FTLD-CDR sum of boxes score, supplemented by carer-rated behavioural changes on the Cambridge Behavioural Inventory. This enabled us to attribute "time-series" information to the cross-sectional structural imaging data. The left anterior insula was determined as the seed region, based on it being the most atrophied region in the overall bvFTD group (n=82) compared to controls (n=80). Using the REST software, the voxel-wise causal structural covariance network (CaSCN) was constructed to map anterior insula-driven structural network atrophy (Zhang et al., 2017). The CaSCN analysis was FDR-corrected at the voxel level ($P < 0.01$; k=300). Sex, age, education, total intracranial volume and scanning site were controlled as covariates in the above analyses. The difference between the FTLD-CDR scores across the neighbouring pseudo time points was additionally controlled for in the CaSCN analysis.

Results: Patients in the very mild/mild disease burden stage showed predominant atrophy of frontotemporal (e.g., insula, temporal pole, middle frontal gyrus), limbic (e.g., hippocampus, amygdala), and subcortical (e.g., putamen, nucleus accumbens) brain areas. The moderate disease stage patients displayed widespread atrophy, extending to the middle cingulate, paracingulate gyri, and the thalamus, while the severe disease stage patients, extending from the frontotemporal and paracingulate/thalamic atrophy to more posterior brain regions, like the fusiform gyrus and Crus I of cerebellum. Importantly, our CaSCN analysis uncovered that grey matter atrophy progressively spreads from the left anterior insula to the dorsolateral prefrontal cortex, precuneus, lingual gyrus, posterior middle temporal gyrus, fusiform.

Conclusions: Our findings suggest that atrophy of the anterior insula plays a central role in driving the progressive atrophy commonly seen in bvFTD, spreading to key regions in the executive control network and default mode network. The current study shed light into the network spread mechanism in terms of the causal influence of anterior insula atrophy on progressive brain atrophy in bvFTD.

References

1. Landin-Romero, R. (2017), "Disease-specific patterns of cortical and subcortical degeneration in a longitudinal study of Alzheimer's disease and behavioural-variant frontotemporal dementia". NeuroImage, vol. 151, pp. 72-80
2. Miyagawa, T. (2020), "Utility of the global CDR® plus NACC FTLD rating and development of scoring rules: Data from the ARTFL/LEFFTDS Consortium", Alzheimer's & dementia, vol. 16, no. 1, pp. 106-117
3. Rascovsky, K. (2011), "Sensitivity of revised diagnostic criteria for the behavioural variant of frontotemporal dementia", Brain, vol. 134, no. 9, pp. 2456-2477
4. Zhang, Z. (2017), "Hippocampus-associated causal network of structural covariance measuring structural damage progression in temporal lobe epilepsy", Human Brian Mapping, vol. 38, no. 2, pp. 753-766

Poster No 228

Quantifying Deviations and Asymmetry of Brain Structure and Function in Alzheimer's Disease

Cui Zhao[1], Yong Liu[1]

[1]*School of Artificial Intelligence, Beijing University of Posts and Telecommunications, Beijing, China*

Introduction: Altered brain structure and function have been implicated in the pathophysiology of Alzheimer's dementia (AD), mild cognitive impairment (MCI), and other neurodegenerative diseases. Identifying neurobiological differences between patients with impaired cognitions and healthy individuals has been a majority of clinical neuroscience for decades. However, recent meta-analyses have raised concerns regarding the replicability and clinical relevance of brain alternations, especially for the stage of MCI. The present study aimed to quantify the upper bounds of univariate effect sizes across neuroimaging modalities and to evaluate the predictive value of the maximum effect variables in MCI progression.

Methods: Participants from two independent datasets were included in the present study, including AD, MCI patients, and healthy controls with normal cognition (NC). Univariate statistical effect size, distribution overlapping coefficient, and classification accuracy were calculated for metrics derived from T1w structural imaging, diffusion MRI, resting-state functional MRI, and brain connectome. After determining the maximum effect variable, we further performed the Kaplan Meier analyses and Cox proportional hazards regression analyses to estimate the predictive value of this regional index and its hemispheric asymmetry in the progression of MCI.

Results: A total of 2689 participants from two independent datasets (MCADI and ADNI) were included in the present study, including 682 AD patients, 1067 MCI patients, and 940 NC adults. Using the general linear model, we found the regional gray matter volume (GMV) of the caudal hippocampus (cHipp) exhibited the highest effect size in differentiating AD, MCI, and NC participants (MCADI dataset: partial η^2 = 0.35 [95%CI: 0.32~0.39], false discovery rate [FDR]-corrected P = 1.79×10^-95; ADNI dataset: partial η^2 = 0.24 [95%CI: 0.21~0.27], FDR-corrected P = 2.69×10^-79). Based on the longitudinal follow-up of ADNI, MCI participants were divided into three gro×ups, including stable (sMCI, n = 399), reversion to NC (rMCI, n = 23), and progression to AD (pMCI, n = 164). Among three groups of MCI, significant group differences were observed in the cognitive performance at baseline (FDR-corrected Ps < 0.05). Furthermore, the probability of progression to dementia was much greater in MCI patients with hemispheric asymmetry of cortical atrophy in the cHipp (P = 0.0005). Cox proportional hazards regression analysis revealed that the lateral coefficients of cHipp had the highest Hazard Ratio (HR = 7.79, 95% CI: 1.81~33.55, P = 0.006) than the regional GMV of the bilateral cHipp.

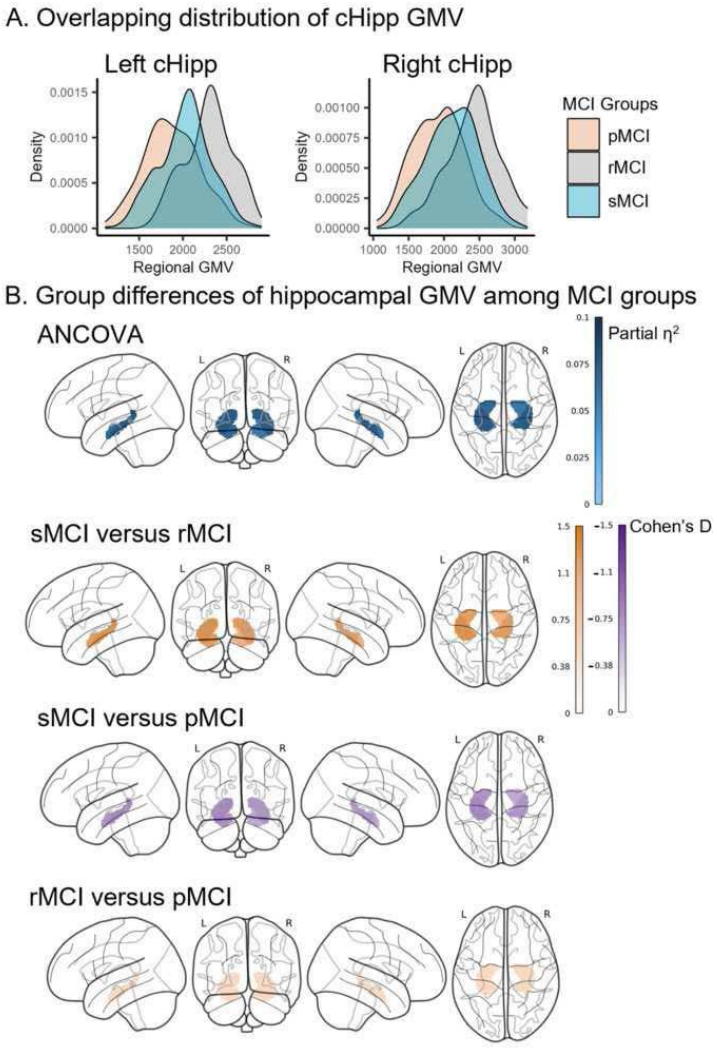

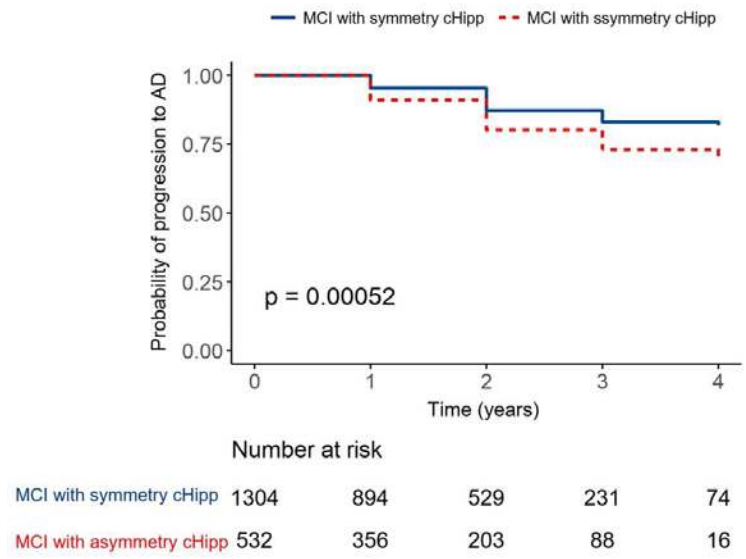

Conclusions: Results of this case-control study suggest that cortical atrophy in the hippocampus was the most significant univariable in differentiating AD, MCI patients, and cognitively healthy individuals in two dependent datasets. Hemispheric asymmetry of hippocampal atrophy exhibited a remarkably significant ability to reveal the longitudinal progression from MCI to dementia, which may serve as a valuable reference for future research on the prediction of MCI progression. Behavioral and socioemotional measures are needed to understand hemispheric asymmetry in AD.

References

1. Sven, L., et al. (2023), 'Neuroimaging in Dementia: More than Typical Alzheimer Disease', Radiology, vol. 308, no. 3, pp. e230173
2. Zhijie, L., et al. (2023), 'Hemispheric Asymmetry in Cortical Thinning Reflects Intrinsic Organization of the Neurotransmitter Systems and Homotopic Functional Connectivity', Proceedings of the National Academy of Sciences of the United States of America, vol. 120, no. 42, pp. e2306990120
3. Yao Q., et al. (2023), 'Estimating Bidirectional Transitions and Identifying Predictors of Mild Cognitive Impairment', Neurology, vol. 100, no. 2, pp. e297-e307

Poster No 229

Data Driven Staging of Genetic Frontotemporal Dementia by Neuroimaging Data

Mahdie Soltaninejad[1,2], Yasser Iturria Medina[1,2], Reza Rajabli[1,2], Gleb Bezgin[1,2], Simon Ducharme[1,2,3]

[1]McGill University, Montreal, Canada, [2]Montreal Neurological Institute, Montreal, Canada, [3]Douglas Mental Health University Institute, Montreal, Canada

Introduction: Frontotemporal dementia (FTD) is a complex disorder marked by substantial clinical, genetic, and pathological variations. Clinical presentations include behavioral changes and/or language impairment[1]. Heterogeneity poses a significant challenge for treatment development, emphasizing the need for precise biomarkers to track disease progression. Despite advancements, current biomarkers demonstrate notable variability among FTD variants, constraining their individual utility in disease staging. Our study bridges this gap by incorporating a multitude of biomarkers in progression modeling. We employ the contrastive trajectory inference (cTI) algorithm[2] to analyze multi-modal features in FTD. This approach offers a comprehensive exploration of disease staging, leveraging neuroimaging data to uncover complex patterns. Unlike previous FTD investigations that frequently oversimplify progression with a single disease trajectory assumption, our model acknowledges the potential existence of multiple disease trajectories.

Methods: Our study utilized a dataset obtained from the Genetic Frontotemporal dementia Initiative (GENFI), comprising 922 MRI scans from individuals with genetic FTD and 630 scans from healthy controls. The T1w and T2w scans of all participants were processed using the MINC toolkit in order to measure white matter hyperintensities[3]. Additionally, cortical thickness measurements were obtained through Freesurfer v7.1.1[4]. Post image processing, data harmonization was achieved through the application of the COMBAT algorithm[5], and data standardization was performed by calculating z-scores. Subsequently, we employed the cTI method which is an unsupervised machine learning algorithm for staging and subtyping high dimensional data. This process commenced with feature selection and dimension reduction facilitated by contrastive principal component

analysis. Trajectory assignment was achieved through the utilization of a minimum spanning tree, wherein subjects were categorized into distinct disease trajectories, and a corresponding disease score was calculated for each individual. Validation of our staging methodology was conducted through the comparison of disease scores with key clinical metrics. Furthermore, we employed power analysis to determine the necessary sample size for clinical trials utilizing our disease score, and we conducted a comparative analysis with commonly utilized clinical scores.

Results: Robust correlations ($p<0.001$) were observed between disease scores and critical clinical measures, including scores of MMSE ($r=-0.45$), Digit Symbol Substitution Test ($r= -0.40$), Boston Naming Test (-0.41), Verbal Fluency Task ($r=-0.30$), MiniSEA test ($r=-0.29$), and Trail Making Test ($r=0.43$). Notably, disease score exhibited a significant correlation with the estimated year of onset ($p<0.001$). Subtyping analysis identified three distinct categories: healthy controls, and two subtypes among FTD mutation carriers. Our power analysis revealed a significant reduction in required sample size when utilizing our cTI disease score as opposed to relying on clinical and neuropsychological scores.

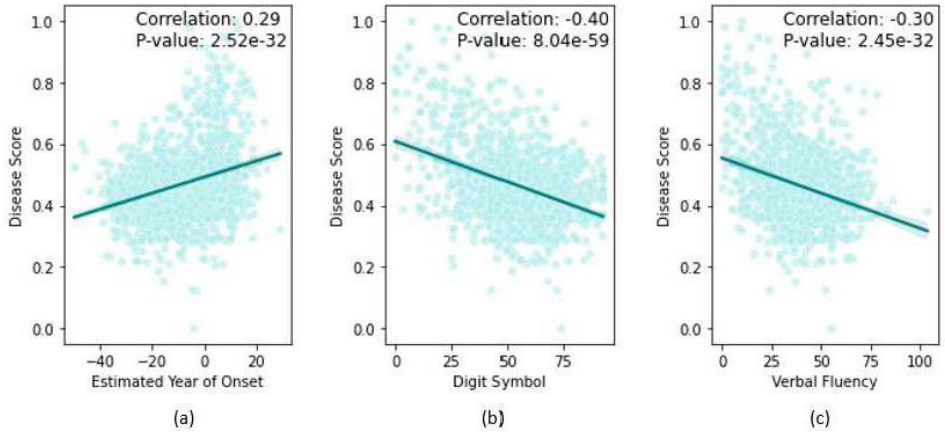

Figure 1. Correlation of cTI disease score with a) Estimated year of onset, b) Digit Symbol score, and c) Verbal Fluency score.

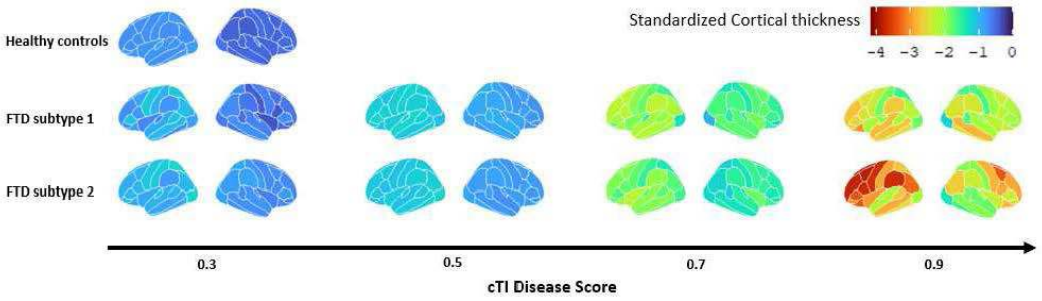

Figure 2. Cortical thinning (standardized) patterns during disease progression in two FTD subtypes identified by the cTI model.

Conclusions: Employing a data-driven method on neuroimaging data, we were able to derive individualized disease scores within a heterogenous group of individuals with FTD. Calculated disease scores exhibited correlations with a comprehensive array of clinical and neuropsychological assessments, including evaluations of behavioral symptoms, attention, memory, language, and executive functions. The encouraging indications from our findings suggest that data-driven approaches on neuroimaging features hold promise as an effective method for personalized assessment in patients and disease monitoring in clinical trials. Specifically, our cTI score demonstrated its value in guiding the planning of clinical trials for FTD. Future work will delve into the factors influencing subtypes, providing valuable insights for personalized interventions in the realm of FTD.

References

1. Greaves, C.V. (2019), 'An update on genetic frontotemporal dementia', Journal of Neurology, vol. 266, no. 8, pp. 2075–2086
2. Iturria, Y. (2020), 'Blood and Brain Gene Expression Trajectories Mirror Neuropathology and Clinical Deterioration in Neurodegeneration', Brain, vol. 143, no. 2, pp. 661-673
3. Dadar, M. (2017), 'Performance comparison of 10 different classification techniques in segmenting white matter hyperintensities in aging', NeuroImage, vol. 157, pp. 233-249
4. Fischl, B. (2012), 'FreeSurfer', NeuroImage, vol. 62, no. 2, pp. 774–781
5. Fortin, J. (2018), 'Harmonization of Cortical Thickness Measurements across Scanners and Sites', NeuroImage, vol. 167, pp. 104-120

Poster No 230

Reduced structural connectivity underlies dementia in Lewy Body disease

Naomi Hannaway[1], Angeliki Zarkali[2], Rohan Bhome[3], Ivelina Dobreva[3], Rimona Weil[4]

[1]University College London, LONDON, United Kingdom, [2]University College London, London, NA, [3]University College London, London, London, [4]University College London, London, United Kingdom

Introduction: There is continued debate over whether Dementia with Lewy Bodies (DLB) and Parkinson's Dementia (PDD) should be considered as a disease spectrum within Lewy Body Dementia (LBD) or as separate diseases. DLB and PDD have shared pathology of Lewy bodies containing alpha synuclein and shared symptoms of parkinsonism, hallucinations and fluctuations. Diffusion MRI has potential to examine differences between these groups, if present, as axonal changes are amongst the earliest changes in LBD. Diffusion weighted imaging has shown reduced fractional anisotropy in visual association, posterior temporal and posterior cingulate areas for DLB compared to PDD [Lee et al., 2010]. To date, structural connectivity has not been compared between PDD and DLB.

Methods: We performed diffusion MRI and clinical assessments in 39 PD, 14 PDD and 31 DLB patients and in 21 age-matched controls. Diffusion MRI images were pre-processed using Mrtrix3 including denoising, removal of ringing artefacts, eddy current correction, motion correction and bias-field correction. Diffusion-weighted images were upsampled to a spatial resolution of 1.3mm3 [Andersson et al., 2016]. Fibre orientation distributions for each participant were computed using multishell 3-tissue-constrained spherical deconvolution using the group-average response function for each tissue type. Anatomically constrained tractography was performed with 10 million streamlines [Smith at al., 2012] and filtered using SIFT to reduce bias. The resulting tractogram was converted into a connectivity matrix, with 232 regions of interest generated by segmenting the participant's T1 weighted imaged using the 200 cortical [Schaefer et al., 2018] and 32 subcortical regions [Tian et al., 2020]. Network-based statistics (NBS) [Zalesky et al., 2010] was used to test differences between groups: a general linear model was constructed, with PD/LBD, control/LBD and PDD/DLB as contrasts of interest. Associations with cognitive and motor scores were also tested. Permutation testing (5000 permutations) with unpaired t-tests was performed, and a test statistic calculated for each connection. Each comparison was age-corrected and thresholded at T = 3.1, PFWE <.05

Results: The ages of the PDD (mean = 73.6 (6.9), 10 male), DLB (mean = 71.5 (5.5), 28 male) and control (mean age = 73.3 (5.8), 11 male) groups did not differ significantly, but the PD group (mean = 67.9 (5.4), 16 male), were younger than the PDD and DLB groups (p=.001). The PDD and DLB groups contained more men than both the PD (p <.001) and control groups (p= .002). MoCA score did not differ between PDD (23.1) and DLB (21.3). As expected, the MoCA score was reduced for the combined LBD group compared to PD (28.6) and controls (28.8, p<.0001 for both). UPDRS-III did not differ significantly between PDD (32.9), DLB (34.4) and PD (26.2) groups. No differences in structural connectivity were observed between PDD and DLB. Using network-based statistics, a combined LBD group, consisting of PDD and DLB, showed reduced connectivity compared to PD in a network consisting of 89 nodes and 118 edges (PFWE = .009, Figure 1A). Reduced connectivity was also shown for LBD relative to controls in a network of 160 nodes and 273 edges (PFWE = .008, Figure 1B). Across all patient groups, a network of 459 nodes and 196 edges showed a significant association with MoCA score (PFWE = .02, Figure 2). There were no differences in structural connectivity associated with UPDRS-III score across patient groups.

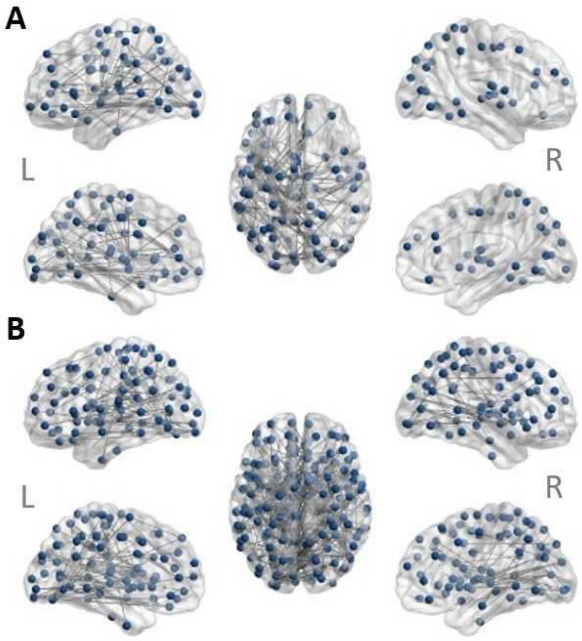

Figure 1. Network showing reduced connectivity for A) Lewy Body Dementia compared to Parkinson's disease and B) Lewy Body Dementia compared to controls. Analysis is adjusted for age. Network based statistics were thresholded at T = 3.1, FWE corrected p<.05. Nodes and edges with significant differences between LBD and controls are displayed on the ICBM152 brain.

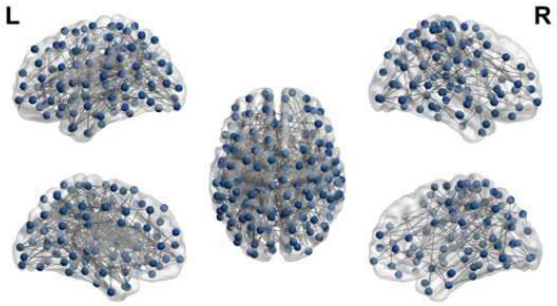

Figure 2. Network showing connectivity associated with MoCA score. Analysis is adjusted for age. Network based statistics were thresholded at T = 3.1, FWE corrected p<.05. Nodes and edges with significant association with MoCA score controls are displayed on the ICBM152 brain.

Conclusions: We report a widespread network of reduced connectivity in LBD, compared to both PD and controls. Cognitive, but not motor scores were also associated with structural connectivity changes. We found no differences between PDD and DLB groups but may have lacked power to detect these in the current analysis. In future, structural and functional connectivity could be examined in combination, to further our understanding of connectivity changes in LBD.

References

1. Andersson, J.L. (2016). An integrated approach to correction for off-resonance effects and subject movement in diffusion MR imaging. Neuroimage; 125:1063-78.

2. Lee, J. E. (2010). A. comparative analysis of cognitive profiles and white-matter alterations using voxel-based diffusion tensor imaging between patients with Parkinson's disease dementia and dementia with Lewy bodies. Journal of Neurology, Neurosurgery & Psychiatry; 81(3), 320-326.
3. Smith, R.E. (2012). Anatomically-constrained tractography: improved diffusion MRI streamlines tractography through effective use of anatomical information. Neuroimage; 62(3):1924-38.
4. Schaefer, A. (2018). Local-Global Parcellation of the Human Cerebral Cortex from Intrinsic Functional Connectivity MRI. Cerebral Cortex; 28(9):3095-114.
5. Tian, Y. (2020). Topographic organization of the human subcortex unveiled with functional connectivity gradients. Nature Neuroscience; 23(11):1421-32.
6. Zalesky, A. (2010). Network-based statistic: identifying differences in brain networks. Neuroimage; 53(4):1197-207.
7. Zarkali, A. (2020). Differences in network controllability and regional gene expression underlie hallucinations in Parkinson's disease. Brain; 143(11):3435-48.

Poster No 231

The Role of ApoE4 in The Acceleration of Tau Aggregation

Anna Steward[1], Davina Biel[1], Anna Dewenter[1], Sebastian Niclas Roemer[1], Zeyu Zhu[1], Julia Pescoller[1], Martin Dichgans[2], Michael Ewers[2,3], Amir Dehsarvi[1], Matthias Brendel[1], Nicolai Franzmeier[1,4]

[1]University Hospital LMU Munich, Munich, Bavaria, [2]Institute for Stroke and Dementia Research, Munich, Bavaria, [3]German Center for Neurodegenerative Diseases (DZNE), Munich, Germany, [4]University of Gothenburg, Gothenburg, Sweden

Introduction: Understanding the factors that affect the pathophysiological progression of Alzheimer's disease (AD) is crucial for determining the ideal timing and targets for treatment in each AD patient. One of these factors, the Apolipoprotein E ε4 allele (ApoE4), carried by 40-60% (Ward, Crean et al. 2012) of sporadic AD patients, has been associated with quicker spreading of amyloid beta (Aβ)-related tau at lower Aβ levels (Steward, Biel et al. 2023). However, the specific mechanisms driving this connection remain unclear. The major aim of this project was to understand how ApoE4 influences the pathological pathway of tau processes that lead to Aβ-related tau aggregation. Methods The influence of ApoE4 on the connection between tau hyperphosphorylation and aggregation in relation to Aβ levels was examined through the cross-sectional analysis of CSF phosphorylated tau (P-tau/Aβ40) with tau- and Aβ-PET in 284 APOE genotyped cognitively normal and mildly cognitively impaired subjects from ADNI.

Methods: The influence of ApoE4 on the connection between tau hyperphosphorylation and aggregation in relation to Aβ levels was examined through the cross-sectional analysis of CSF phosphorylated tau (P-tau/Aβ40) with tau- and Aβ-PET in 284 APOE genotyped cognitively normal and mildly cognitively impaired subjects from ADNI.

Results: Findings demonstrated that ApoE4 did not moderate the relationship between Aβ-PET and P-tau/Aβ40 (Fig2.A, β=-0.03, p=0.69) but significantly moderated the relationship between P-tau/Aβ40 and Tau-PET (Fig2.B, β=0.72, p<0.001). Furthermore, we confirm the previously observed mediation effect of P-tau/Aβ40 on Aβ-related tau aggregation (Fig2.C, ACME: B=0.28; p<0.001; ADE: B=0.206; p=0.008) and found this to be moderated by ApoE4 (B=0.21, p=0.006).

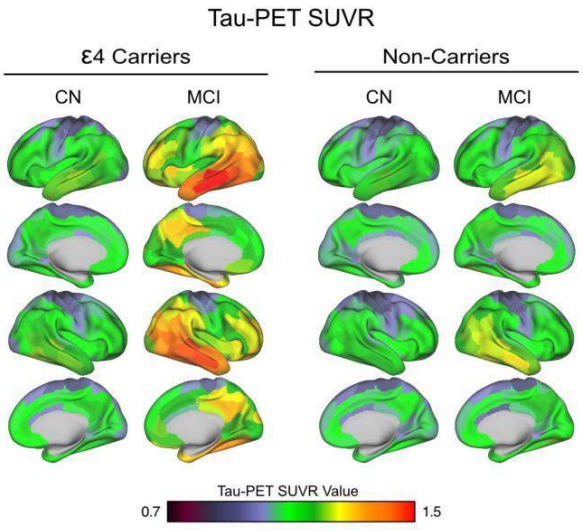

Group-average tau-PET SUVRs stratified by ApoE4 carriership and diagnostic group. Tau-PET SUVRs are showed as continuous values.

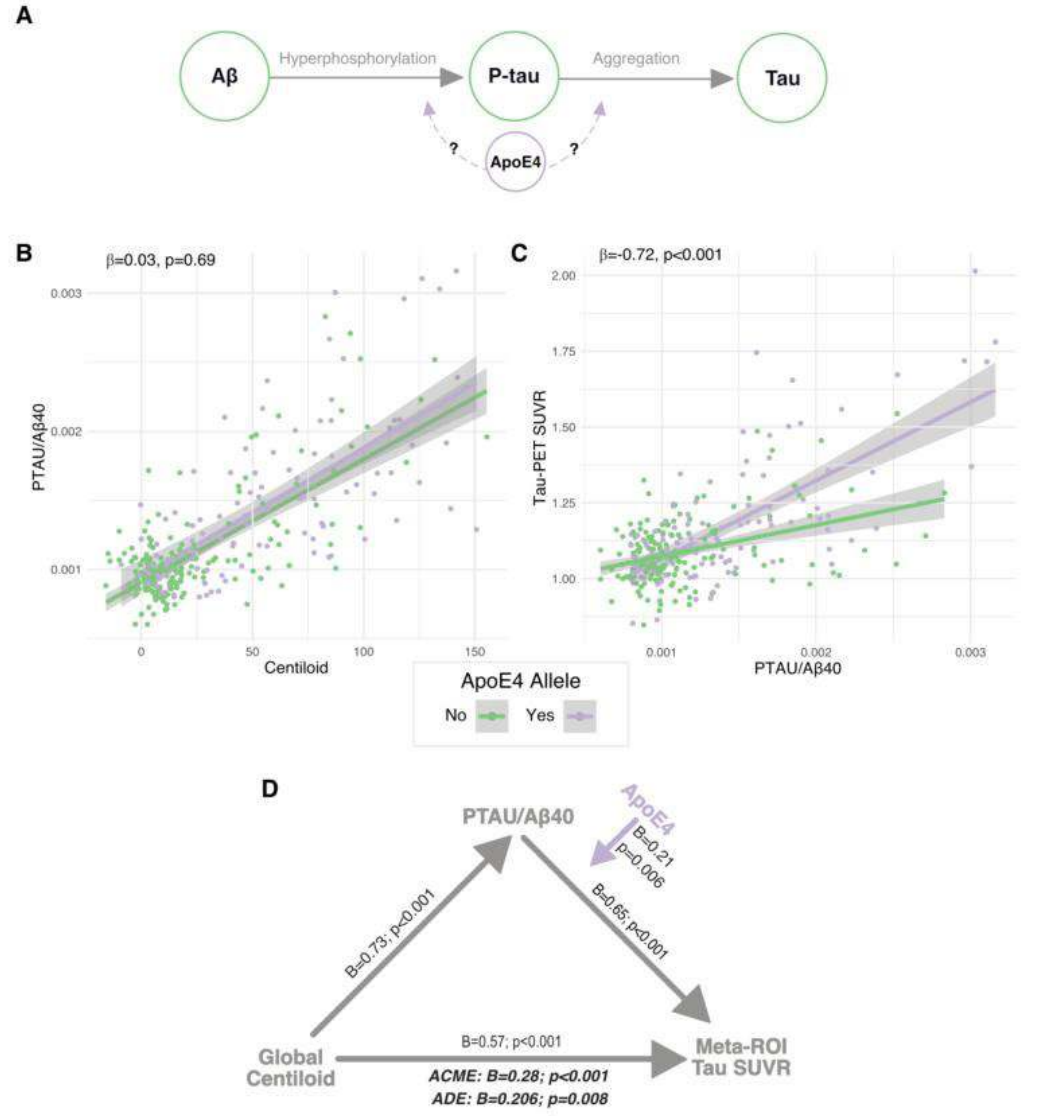

Schematic representation illustrating the interplay between Aβ, PTAU, and Tau in the presence of ApoE4, delineating the pathways of hyperphosphorylation and aggregation leading to insoluble tau pathology (A). Scatterplots illustrating the interaction effect between ApoE4 and centiloid on Ptau/Aβ40 (B) and Ptau/Aβ40 on tau-PET SUVR level in a meta-ROI (C). Moderated mediation analysis with centiloid as predictor, Ptau/Aβ40 as mediator, ApoE4 as moderator and tau SUVR in a meta-ROI as dependent variable. p-values for each path are displayed on the respective arrow. The average causal mediation effect (ACME) and the average direct effect (ADE) are displayed under each mediation triangle (D).

Conclusions: Results indicate that ApoE4 plays a role in the aggregation phase of tau but does not influence the level of Aβ-related tau phosphorylation and p-tau secretion. Furthermore, the moderated mediation analysis indicates that ApoE4 carriers experience faster tau spreading at lower Aβ levels due to ApoE4 enhancing Aβ-related aggregation of soluble tau into neurofibrillary tau tangles. These findings promote soluble tau as a potential therapeutic target in ApoE4 carriers to help prevent extensive tau aggregation across the cortex and therefore cognitive decline and dementia.

References

1. Steward, A., D. Biel, A. Dewenter, S. Roemer, F. Wagner, A. Dehsarvi, S. Rathore, D. O. Svaldi, I. Higgins and M. Brendel (2023). "ApoE4 and Connectivity-Mediated Spreading of Tau Pathology at Lower Amyloid Levels." JAMA neurology.
2. Ward, A., S. Crean, C. J. Mercaldi, J. M. Collins, D. Boyd, M. N. Cook and H. M. Arrighi (2012). "Prevalence of apolipoprotein E4 genotype and homozygotes (APOE e4/4) among patients diagnosed with Alzheimer's disease: a systematic review and meta-analysis." Neuroepidemiology 38(1): 1-17.

Poster No 232

White matter microstructure alterations in Huntington's disease: a cross-species study

Chiara Casella[1,2,3], Maxime Chamberland[1,4], Pedro Laguna[1], Brendan Kelly[5], Alvaro Murillo Bartolome[5], Bella Mills-Smith[5], Greg Parker[1], Christopher Von Ruhland[6], Syed Yasir[5], Vincent Dion[5], Anne Rosser[5,7,8], Mariah Lelos[5], Derek Jones[1], Claudia Metzler-Baddeley[1]

[1]Cardiff University Brain Research Imaging Centre (CUBRIC), Cardiff University, Cardiff, United Kingdom, [2]Centre for the Developing Brain, King's College London, London, United Kingdom, [3]Institute of Psychiatry, Psychology and Neuroscience, King's College London, London, United Kingdom, [4]Eindhoven University of Technology, Eindhoven, Netherlands, [5]School of Biosciences, Cardiff University, Cardiff, United Kingdom, [6]Electron and Light Microscopy Facility, Cardiff University, Cardiff, United Kingdom, [7]UK Dementia Research Institute, Cardiff, United Kingdom, [8]B.R.A.I.N unit, Neurosciences and Mental Health Institute, Cardiff, United Kingdom

Introduction: White matter (WM) changes have been observed in Huntington's Disease (HD) 1, but their etiology is unclear. Here, we present cross-species work aiming to better understand such changes. Firstly, we assessed WM microstructure in HD patients with ultra-strong gradients 2. We combined diffusion tensor (DT)-MRI, with the magnetization transfer ratio (MTR) as proxy measure of myelin 3, and the restricted diffusion signal fraction (FR) from the Composite Hindered and Restricted Model of Diffusion (CHARMED) 4, as proxy measure of axon density 5. Then, we assessed WM microstructure in the R6/1 HD mouse model using ex vivo MRI. We complemented DT-MRI with FR from CHARMED, and the macromolecular proton fraction (MPF) as proxy measure of myelin 3. Finally, we used light microscopy (LM) and transmission electron microscopy (TEM) in age- and sex-matched cohorts of R6/1 mice to gain insight into the neurobiological basis of imaging results.

Methods: Human Imaging: 25 premanifest patients and 25 age- and sex-matched healthy controls (HC) scanned in a 300mT/m 3T MRI scanner (MAGNETOM Skyra CONNECTOM) with multi-shell diffusion and magnetisation transfer. We computed FA, AD, RD, FR and MTR as described in 8. WM microstructure was assessed across the corpus callosum (CC). Automated CC segmentation was performed using TractSeg6 and multi-shell constrained spherical deconvolution (MSMT-CSD)7. 7 segments were delineated. Principal component analysis (PCA) was used to extract a 'magnetization transfer' and a 'axon density' component. Whole-brain microstructure was inspected with tract-based cluster analysis (TBCA)8. Rodent Imaging: 8 R6/1 and 7 wildtype (WT) mice scanned at 9.4T (Bruker Biospin) at 16 weeks of age with multi-shell diffusion and quantitative magnetization transfer. FA, AD, RD, and FR maps were computed using the same approaches as the ones used for the human data. MPF maps were obtained as described in 9. Microstructure was assessed in the CC genu, body, and splenium. MSMT-CSD7 was performed and fibres were reconstructed interactively10. Tract-based spatial statistics (TBSS) were used to examine brain-wise WM microstructure. Microscopy: LM was used to visualize neurofilament light (NF-L) and myelin basic protein (MBP) in the CC genu, body, and splenium (N=9 WT and N=9 R6/1 mice). Thickness and area fraction were quantified. For TEM, diameter and g-ratio of myelinated axons were assessed in 5 CC regions (N=3 WT and N=3 R6/1 mice).

Results: We detected lower MTR in the isthmus of patients (tractometry: $p=0.03$; TBCA: $p=0.03$) and higher in the rostrum (tractometry: $p=0.02$). MTR and CAG size in patients were positively associated in all CC segments (all $p<0.01$). Patients had higher FR in the cortico-spinal tract ($p=0.03$). FR increases ($p=0.03$) and MPF decreases ($p=0.05$) were detected in the CC of R6/1 mice. TBSS uncovered increases in FR and some decreases in MPF beyond the CC. Increased NFL and decreased MBP staining were detected in R6/1 mice. R6/1 mice had a thinner CC body ($p<0.05$) and splenium ($p<0.05$). A reduced g-ratio was detected in R6/1 mice ($p=0.05$), reflecting a thinner axonal diameter ($p<0.05$) and greater frequency of thinner axons. No difference in myelin thickness was observed.

Conclusions: We detected increased FR in both HD patients and HD mice, likely reflecting disruptions in axonal morphology (i.e., less complex, thinner axons) and organization (i.e., more densely packed axons). Our findings point to the potential of FR as cross-species MRI marker of axonal changes in HD. Our findings also suggest a link between myelin alterations and the disease mutation and show that early in disease progression WM changes are associated with a reduction in myelin proteins without alterations in myelin sheath structure.

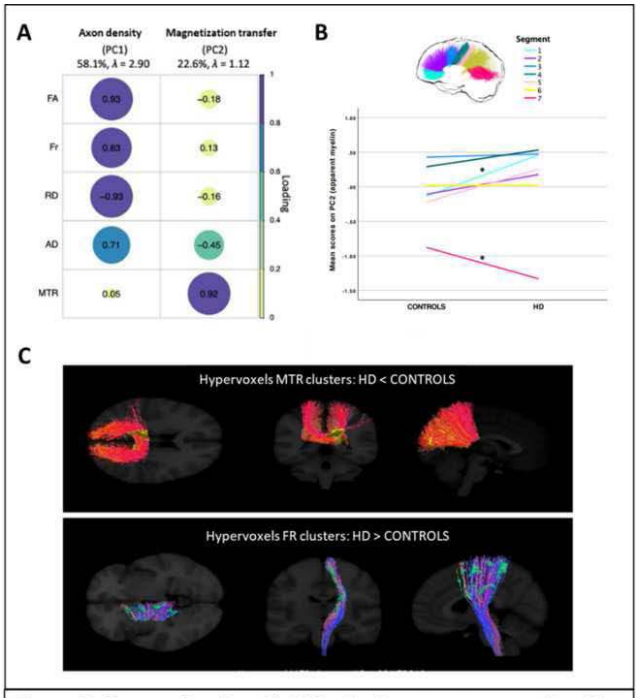

Figure 1. Human Results. A) PCA of microstructure metrics. Plot summarizing how each variable is accounted for in every principal component. The absolute correlation coefficient is plotted. Colour intensity and the size of the circles are proportional to the loading. **B) Conditional effects of group on apparent myelin for each callosal segment.** Compared to controls, apparent myelin was significantly higher in patients' segment 1 (i.e., the callosal rostrum) and significantly lower in segment 7 (i.e., the callosal genu). **C) TBCA results**. Microstructure alterations were detected in the posterior portion of the CC and the left CST.

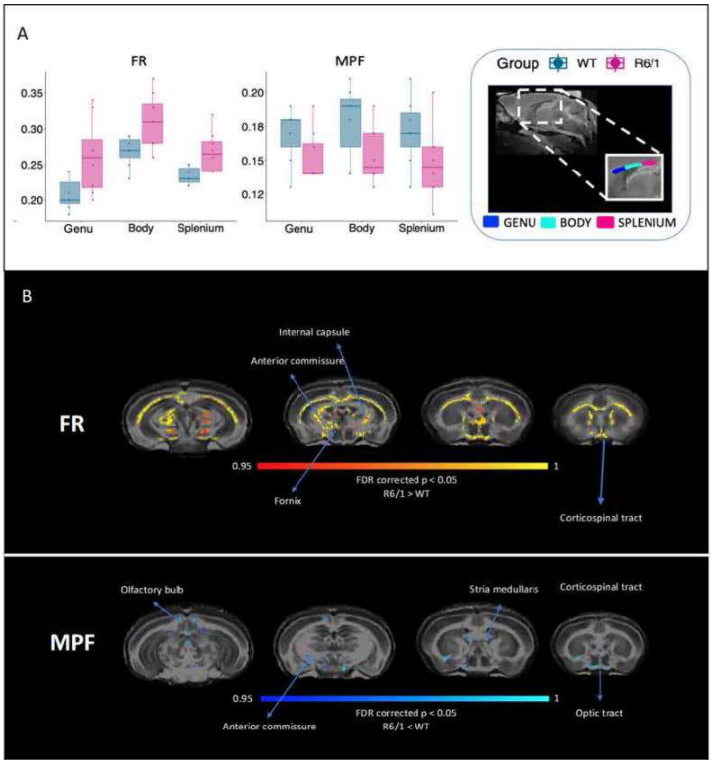

Figure 2. Animal Imaging Results. A) Tractometry analysis of the CC. FR values were significantly higher and MPF values significantly lower in the brain of R6/1 mice across the whole CC. **B) TBSS analysis results.** WM microstructural alterations were detected across the brain of R6/1 mice, revealing widespread increases in FR and some areas of decreased MPF.

References

1. Casella, C., Chamberland, M., Laguna, P.L., Parker, G.D., Rosser, A.E., Coulthard, E., Rickards, H., Berry, S.C., Jones, D.K., Metzler-Baddeley, C., 2022. Mutation-related magnetization-transfer, not axon density, drives white matter differences in premanifest Huntington disease: Evidence from in vivo ultra-strong gradient MRI. Hum. Brain Mapp. 43, 3439–3460. https://doi.org/10.1002/hbm.25859
2. Jones, D. K. et al. Microstructural imaging of the human brain with a 'super-scanner': 10 key advantages of ultra-strong gradients for diffusion MRI. Microstruct. Imaging 182, 8–38 (2018).
3. Mancini, M. et al. An interactive meta-analysis of MRI biomarkers of myelin. eLife 9, e61523 (2020).
4. Assaf, Y. & Basser, P. J. Composite hindered and restricted model of diffusion (CHARMED) MR imaging of the human brain. NeuroImage 27, 48–58 (2005).
5. De Santis, S., Drakesmith, M., Bells, S., Assaf, Y. & Jones, D. K. Why diffusion tensor MRI does well only some of the time: Variance and covariance of white matter tissue microstructure attributes in the living human brain. Neuroimage 89, 35–44 (2014).
6. Wasserthal, J., Neher, P. & Maier-Hein, K. H. TractSeg - Fast and accurate white matter tract segmentation. NeuroImage 183, 239–253 (2018).
7. Jeurissen, B., Tournier, J.-D., Dhollander, T., Connelly, A. & Sijbers, J. Multi-tissue constrained spherical deconvolution for improved analysis of multi-shell diffusion MRI data. NeuroImage 103, 411–426 (2014).
8. Luque Laguna, P. A. Neuroanatomy-based strategies for the statistical analysis of brain imaging and tractography data. (2019).
9. Ramani, A., Dalton, C., Miller, D. H., Tofts, P. S. & Barker, G. J. Precise estimate of fundamental in-vivo MT parameters in human brain in clinically feasible times. Magn. Reson. Imaging 20, 721–731 (2002).
10. Chamberland, M., Whittingstall, K., Fortin, D., Mathieu, D. & Descoteaux, M. Real-time multi-peak tractography for instantaneous connectivity display. Front. Neuroinformatics 8, (2014).

Poster No 233

Grey matter atrophy, functional connectivity and behavioral signatures of mild cognitive impairment

Damien Marie[1,2,3], Dimitra Kokkinou[2,3], Chantal Junker-Tschopp[4], Gilles Allali[5], Matthias Kliegel[3,6], Andrea Brioschi Guevara[5], Giovanni B. Frisoni[7], Clara E. James[2,3]

[1]CIBM MRI UNIGE, Geneva, Switzerland, [2]Geneva School of Health Sciences, University of Applied Sciences and Arts Western Switzerland HES-SO, Geneva, Switzerland, [3]Faculty of Psychology and Educational Sciences, University of Geneva, Geneva, Switzerland, [4]Geneva School of Social work, University of Applied Sciences and Arts Western Switzerland HES-SO, Geneva, Switzerland, [5]Leenaards Memory Center, Lausanne University Hospital and University of Lausanne, Lausanne, Switzerland, [6]Center for the Interdisciplinary Study of Gerontology and Vulnerability, University of Geneva, Geneva, Switzerland, [7]Memory Center, Geneva University Hospitals, University of Geneva, Geneva, Switzerland

Introduction: Mild Cognitive Impairment (MCI), a common pathology among older adults (10-20% of 65 years old and more[1]), represents a cognitive state between normal aging and dementia. This minor age-related loss of cognitive ability does not importantly impact daily life functioning. Cognitive impairments (memory, attention, spatial orientation, or executive functions[2]) and increased fall risk occur. While a minority of MCI patients may stay stable or recover to some extent[3], most convert to dementia[3,4]. Yet, regular cognitive training can boost or maintain cognitive and brain functions. Music or psychomotor training has been associated with cognitive benefits in MCI patients[5,6]. This study is part of a randomized controlled trial comparing the influence of those interventions on brain and behavior over 6 months in MCI patients[7]. Here, we take advantage of trial baseline data to independently evaluate behavioral, grey matter volume, and resting-state functional connectivity differences between a group of 32 MCI patients and 17 gender- and age-matched controls at baseline.

Methods: 60-80 years old participants were recruited (MCI: 71.2 ± 7.2 years old, 66% ♀; controls: 70.7 ± 4.5 years old, 71% ♀). MCI diagnosis was performed by hospital memory clinics, excluding serious physical/mental comorbidities (Mini-Mental State Examination < 24 or Montreal-Cognitive-Assessment-Test < 18, Hospital Anxiety and Depression Scale < 15). We evaluated group differences in 1 questionnaire and 7 behavioral tests, including the COGTEL[8], a global measure of cognitive function covering prospective memory, short- and long-term verbal memory, working memory, verbal fluency, and inductive reasoning. 3 T Siemens Magnetic Resonance Imaging (MRI) data acquisition included structural imaging (MP2RAGE, 1 mm isotropic voxel size) and resting-state functional MRI (2.5 mm isotropic voxel size, repetition time = 1.350 s, 440 volumes). Whole-brain voxel-based morphometry (grey matter volume maps) and seed-based functional connectivity were computed with SPM12 CAT12 and CONN toolboxes, respectively. We selected 9 seeds based on the results of a meta-analysis of MCI correlates[9]. Multiple comparison corrections were applied in all analyses.

Results: We report significant lower performances in MCI patients as compared to healthy controls for the COGTEL weighted score (Figure 1, MCI patients: 21.97 ± 7.6, controls: 32.5 ± 7.9, $F(39) = 18.31$, $p < 0.0002$), the Trail-Making Test A (MCI patients: 60.5 ± 33.5, controls: 38.4 ± 7.6, $\chi2(1) = 8.7$, $p < 0.003$) and B (MCI patients: 129.3 ± 62.7, controls: 83 ± 17.6, $\chi2(1) = 6.4$, $p < 0.02$, increased time indicates lower performance), the D2-R correct target score (MCI patients: 78.5 ± 35.2, controls: 118.9 ± 19.0, $F(39) = 17.6$, $p < 0.0002$), the binaural speech in noise perception (MCI patients: -4.3 ± 1.1, controls: -6.0 ± 1.36, $F(29) = 12.8$,

$p < 0.0002$, lower SRT indicates better performance) and the right foot unilateral balance test performance (MCI patients: 18.7 ± 15.8, controls: 56.3 ± 47.7, $F(36) = 8.2$, $p = 0.006$). The analysis of GM volume in MCI patients as compared to healthy controls (C > MCI) revealed a widespread pattern of atrophy in patients (Figure 2, $p < 0.001$, uncorrected, $k = 150$ voxels). 3 clusters centered on the left, right hippocampus, and the mid cerebellum are significant at $p < 0.05$ FWE (cluster-level). Finally, decreased functional connectivity associated with 3 seeds, corresponding to the left angular gyrus, left inferior temporal gyrus, and left putamen (Figure 2, $p < 0.05$ FDR), was detected in patients as compared to controls.

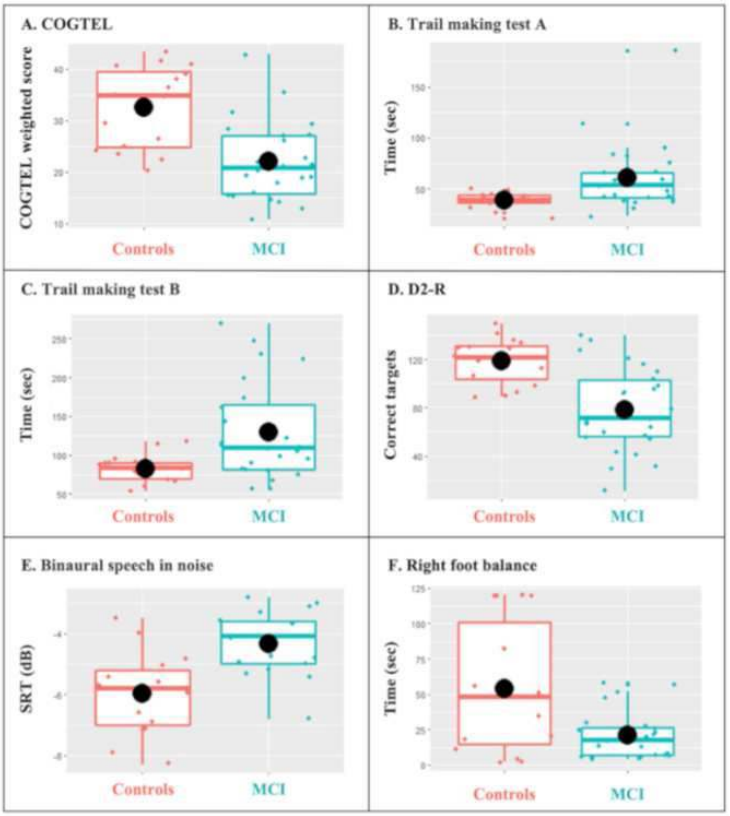

Figure 1. Significant behavioral group differences between healthy controls and mild cognitive impairment (MCI) patients. A. COGTEL weighted score. B. Trail making test A (time in seconds). C. Trail making test B (sec). D. D2-R (number of correct targets). E. Binaural speech in noise (SRT: speech reception threshold in decibels). F. Left foot balance (unilateral balance test, time in sec). Group effects are significant at a statistical threshold of $p < 0.01$. Boxplots indicate the median and data dispersion. The black dot shows the mean for each test. The group fatcor is color coded with the healthy control group in red and the MCI patient group in blue.

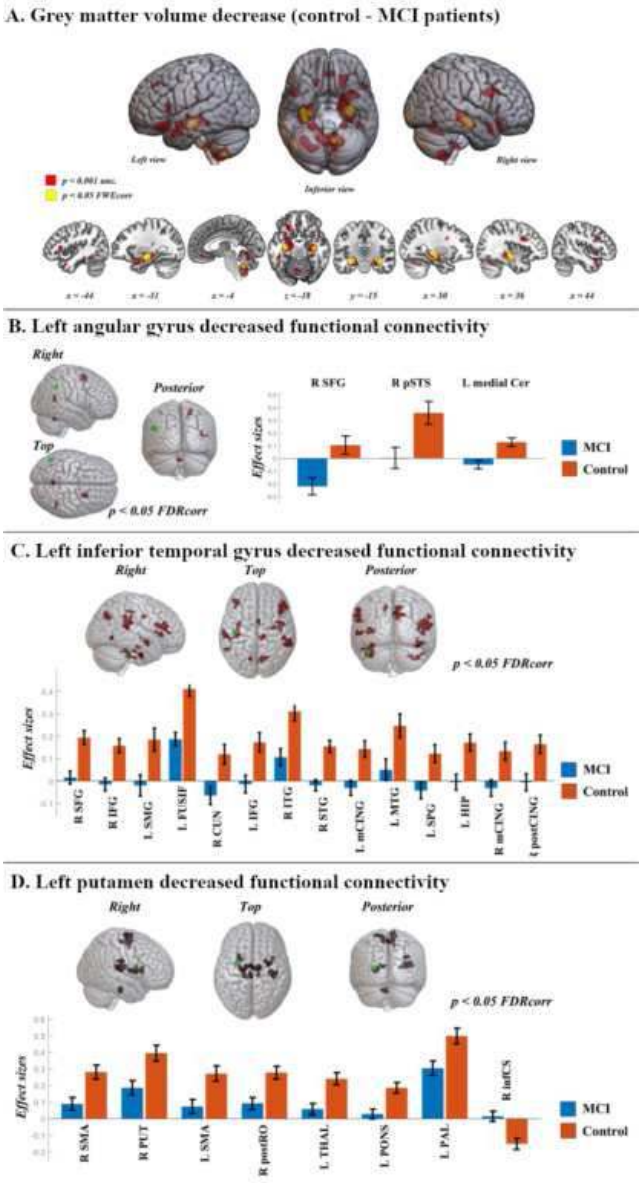

Figure 2. A. Grey matter volume decrease in MCI patients as compared to healthy older adults. B. MCI functional connectivity decrease associated with the left angular gyrus seed, C. left inferior ltemporal gyrus seed and D. left putamen seed. Effects sizes are provided (L: left, R: right, SFG: superior frontal gyrus, pSTS: superior temporal sulcus, Cer: cerebellum, IFG: inferior frontal gyrus, STG: superior temporal gyrus, IFG: inferior frontal gyrus, SMG: suprmarginal gyrus, FUSIF: fusiform gyrus, CUN: cuneus, ITG: inferior temporal gyrus, STG: superior temporal gyrus, mCING: moddle cingulate gyrus, MTG: middle temporal gyrus, SPG: superior parietal gyrus, HIP: hippocampus, postCING: posterior cingulate gyrus, SMA: supplementary motor area, PUT: putamen, postRO: posterior Rolandic operculum, THAL: thalamus, PAL: pallidum. infCS: inferior central sulcus).

Conclusions: These results enrich the anamnesis of MCI cognitive deficits and confirm the importance of the inferior temporal lobe in MCI pathology. Further evaluation of relationships between behavior, grey matter volume, and functional connectivity will be performed in the hope of refining MCI diagnosis and establishing new psychometric/neural biomarkers.

References

1. Langa, K.M. and D.A. Levine, The diagnosis and management of mild cognitive impairment: a clinical review. Jama, 2014. 312(23): p. 2551-61.
2. Petersen, R.C., et al., Mild Cognitive Impairment: Clinical Characterization and Outcome. Archives of Neurology, 1999. 56(3): p. 303-308.
3. Kaduszkiewicz, H., et al., Prognosis of mild cognitive impairment in general practice: results of the German AgeCoDe study. Ann Fam Med, 2014. 12(2): p. 158-65.
4. Busse, A., et al., Mild cognitive impairment: long-term course of four clinical subtypes. Neurology, 2006. 67(12): p. 2176-85.

5. Ito, E., et al., The Effect of Music-Based Intervention on General Cognitive and Executive Functions, and Episodic Memory in People with Mild Cognitive Impairment and Dementia: A Systematic Review and Meta-Analysis of Recent Randomized Controlled Trials. Healthcare (Basel), 2022. 10(8).
6. Pereira, C., H. Rosado, A. Cruz-Ferreira, and J. Marmeleira, Effects of a 10-week multimodal exercise program on physical and cognitive function of nursing home residents: a psychomotor intervention pilot study. Aging Clinical and Experimental Research, 2018. 30(5): p. 471-479.
7. James, C.E., et al., Musical and psychomotor interventions for cognitive, sensorimotor, and cerebral decline in patients with Mild Cognitive Impairment (COPE): a study protocol for a multicentric randomized controlled study. BMC Geriatrics, 2023. 23(1): p. 76.
8. Ihle, A., E.R. Gouveia, B.R. Gouveia, and M. Kliegel, The Cognitive Telephone Screening Instrument (COGTEL): A Brief, Reliable, and Valid Tool for Capturing Interindividual Differences in Cognitive Functioning in Epidemiological and Aging Studies. Dement Geriatr Cogn Dis Extra, 2017. 7(3): p. 339-345.
9. Eyler, L.T., et al., Resting state abnormalities of the default mode network in mild cognitive impairment: a systematic review and meta-analysis. Journal of Alzheimer's Disease, 2019. 70(1): p. 107-120.

Poster No 234

No increase in deep-brain grey matter magnetic susceptibility observed over the Parkinson's disease

George Thomas[1], Naomi Hannaway[1], Angeliki Zarkali[1], Karin Shmueli[2], Rimona Weil[1,3,4]

[1]Dementia Research Centre, UCL, London, UK, [2]Department of Medical Physics and Biomedical Engineering, UCL, London, UK, [3]Wellcome Centre for Human Neuroimaging, UCL, London, UK, [4]Movement Disorders Consortium, UCL, London, UK

Introduction: Magnetic susceptibility measured using quantitative susceptibility mapping (QSM) has previously been shown to be sensitive in detecting disease related changes in Parkinson's disease (PD). However, whether QSM can be used to track disease progression in PD is not known. Here, we present a 3-year longitudinal study of voxel-wise magnetic susceptibility in PD.

Methods: 59 PD participants within 10 years of diagnosis were recruited from October 2017 to December 2018. All subjects were seen again after an average interval of 38.5±4.4 months (mean±SD). Imaging at both timepoints comprised single echo susceptibility-weighted spoiled GRE scans and anatomical MPRAGE scans. For QSM pre-processing, phase images were unwrapped using a rapid path-based based minimum spanning tree algorithm [Dymerska et al., 2021] and brain masks calculated using BET2. Background field removal was completed with Laplacian boundary value extraction [Zhou et al., 2014] and 3D polynomial residual fitting. Susceptibility maps were estimated using Multi-Scale Dipole Inversion [Acosta-Cabronero et al., 2018]. A study-wise template was created from native space T1 images across both timepoints using a previously optimised routine [Acosta-Cabronero et al., 2017]. QSM images were transformed into this space. For voxel-wise whole brain analyses, standardised images were spatially smoothed using a 3mm Gaussian kernel, requiring the use of absolute QSM to improve statistical conditioning [Betts et al., 2016]. To investigate changes in susceptibility between visits, single-group paired t-tests in the form of permutation analyses (adjusted for age, sex, and time between scans) were performed using randomise and threshold-free cluster enhancement in FSL. Significant clusters were inferred from 10,000 permutations and reported at family-wise error (FWE)-corrected $P<0.05$. ROI analyses using both absolute and signed QSM were carried out to probe the relative contribution of diamagnetic and paramagnetic susceptibility sources to the interactions observed throughout the brain, and to further investigate regions commonly implicated in PD. The following ROIs were segmented from the anatomical template: substantia nigra pars compacta (SNpc) and pars reticulata (SNpr), dentate nucleus, red nucleus, caudate nucleus, putamen, globus pallidus, insular cortex, pars opercularis, middle temporal gyrus, precentral gyrus, and rostral middle frontal cortex. In R, linear mixed models were fitted at each ROI to investigate the effect of follow-up time on magnetic susceptibility (adjusted for age at baseline and sex). ANOVAs determined test-statistics for each model, p-values were FDR adjusted across the 12 ROIs.

Results: Voxel-wise analysis revealed increased absolute magnetic susceptibility at follow-up relative to baseline in the left precentral gyrus, left middle frontal cortex and right middle temporal gyrus in PD ($P_{FWE}<0.05$, Fig 1). Post-hoc ROI analyses investigating both signed and absolute susceptibility corroborated the pattern seen at whole brain, with no significant increases observed in the iron-rich deep brain nuclei. Moderate increases in absolute susceptibility were seen in the pars opercularis, middle temporal gyrus, precentral gyrus, and rostral middle frontal cortex ($P_{FDR}<0.05$, Fig 2). However, no such relationships were observed for signed susceptibility, suggesting these changes were not driven by gross increases in cortical iron.

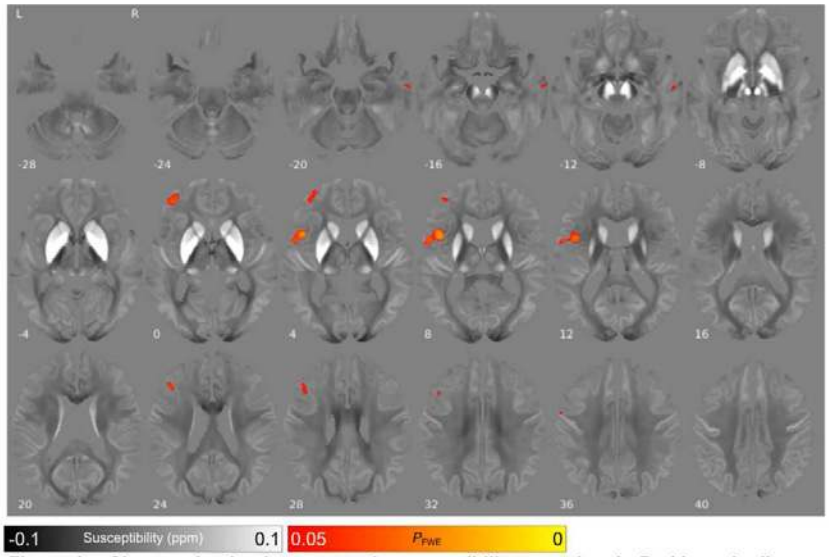

Figure 1 – Changes in absolute magnetic susceptibility over time in Parkinson's disease at whole brain. Whole brain analysis is adjusted for age at baseline, sex and time between scans. Red/yellow clusters represent voxels where absolute QSM was significantly higher at follow-up at FWE-corrected P<0.05. Results are overlaid on the study-wise QSM template in MNI152 space, and numbers represent axial slice location in MNI152 space.

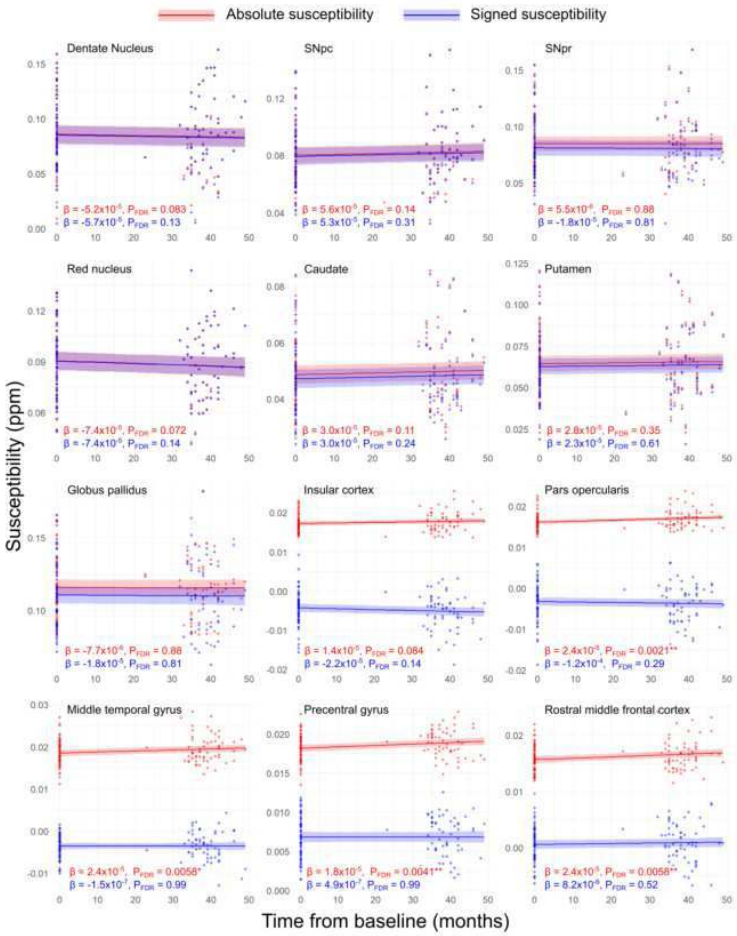

Figure 2 - Results of linear mixed modelling showing regional change in magnetic susceptibility over time in Parkinson's disease. Data and statistics relating to ROI mean absolute susceptibility are shown in red, and those relating to ROI mean signed susceptibility are shown in blue. Change in susceptibility is modelled by fixed effects for time to follow-up (months), age at baseline and sex, and a random intercept effect per subject. β is the coefficient of the fixed effect for time to follow-up on susceptibility. FDR-corrected P values indicate the significance of the effect of follow-up time on susceptibility, adjusted for age at baseline, sex and subject. SNpc/pr = substantia nigra pars compacta / pars reticulata.

Conclusions: We present the first voxel-wise longitudinal study of magnetic susceptibility in PD. We report no increases in magnetic susceptibility over a 3-year period of the iron-rich deep brain nuclei commonly associated with PD. We find sparse changes in cortical magnetic susceptibility over time that are unlikely to be driven by increases in iron. In future, sequences sensitive to other tissue measures, such as multiparameter maps, or amyloid PET-CT, could be used to enrich our interpretation of magnetic susceptibility changes in PD.

References

1. Acosta-Cabronero J, Cardenas-Blanco A, Betts MJ, Butryn M, Valdes-Herrera JP, Galazky I, Nestor PJ (2017): The whole-brain pattern of magnetic susceptibility perturbations in Parkinson's disease. Brain 140:118–131.
2. Acosta-Cabronero J, Milovic C, Mattern H, Tejos C, Speck O, Callaghan MF (2018): A robust multi-scale approach to quantitative susceptibility mapping. Neuroimage 183:7–24.
3. Betts MJ, Acosta-Cabronero J, Cardenas-Blanco A, Nestor PJ, Düzel E (2016): High-resolution characterisation of the aging brain using simultaneous quantitative susceptibility mapping (QSM) and R2* measurements at 7 T. Neuroimage 138:43–63.
4. Dymerska B, Eckstein K, Bachrata B, Siow B, Trattnig S, Shmueli K, Robinson SD (2021): Phase unwrapping with a rapid opensource minimum spanning tree algorithm (ROMEO). Magn Reson Med 85:2294–2308.
5. Thomas GEC, Leyland LA, Schrag A-E, Lees AJ, Acosta-Cabronero J, Weil RS (2020): Brain iron deposition is linked with cognitive severity in Parkinson's disease. J Neurol Neurosurg Psychiatry:jnnp-2019-322042.
6. Zhou D, Liu T, Spincemaille P, Wang Y (2014): Background field removal by solving the Laplacian boundary value problem. NMR Biomed 27:312–319.

Poster No 235

Resilience of brain networks after stroke: Impact of new events on specialization and integration

Elisabeth Dirren[1], Julian Klug[1], Cecilia Jarne[2], Emmanuel Carrera[1]

[1]University Hospital Geneva, Geneva, Switzerland, [2]Aarhus University CFIN /Universidad Nacional de Quilmes/ CONICET, Aarhus, Aarhus C

Introduction: Recurrent strokes are frequent, occurring in up to 10 % of patients within 3 months of the initial event. Whether and how the brain reorganizes to limit the consequences of a second event is largely unknown (van Assche et al, 2022). In fact, most studies investigating the physiological changes that occur after stroke have focused on the neural correlates of recovery, disregarding in turn, the processes that may increase brain resilience to further attacks. Here we used a large dataset of first-time stroke patients with resting-state connectivity assessed at three time-points within 1 year of stroke to determine how brain networks reconfigure to prevent the consequences of new lesions.

Methods: 75 first-time stroke patients and 18 healthy controls were included from a large dataset of stroke patients (Corbetta et al, 2015). Gradient echo EPI resting-state functional images and T1 structural images were obtained in healthy subjects, and at three time-points in patients: within 1-2 weeks (TP1), at three months (TP2) and at one year (TP3). After atlasing brain images using the Brainnetome atlas (Fan et al, 2016), connectivity matrices were built for each control, patient and time-point by computing Pearson correlations. We investigated resilience to recurrent strokes by evaluating changes in two graph metrics that capture network integration (global efficiency) and specialization (modularity)(Rubinov et al, 2010). Virtual lesions were applied to patients and controls' connectivity matrices by removing Brainnetome regions that had at least 50% overlap with lesion masks from 122 stroke patients taken from the present cohort and an additional in-house cohort of stroke patients (Klug et al, 2021). Global efficiency and modularity were recalculated following node deletion. We defined resilience (R) as the difference between pre- and post-virtual lesion measures. R was computed and normalized to the controls' mean R, to yield Rnorm values for each metric. Mixed linear models were built to statistically compare controls and patients at all three time-points. FDR correction was applied for multiple comparisons. Lesion and patient-specific modulators of brain resilience after virtual strokes were evaluated by building a mixed linear model with lesion size, site, side, patient age handedness, gender and acute NIHSS (a clinical stroke scale) as fixed factors and either Rnorm(global efficiency) or Rnorm(modularity) as dependent variable.

Results: We observed increased resilience in brain networks of stroke patients, with a lower impact of virtual lesions on global efficiency and modularity. Rnorm(global efficiency) was significantly higher in patients at TP1 (0.133, $p=0.04$) and TP2 (0.135, $p=0.04$) but not TP3 (0.023, $p= 0.854$), compared to controls (0.000). Similarly, Rnorm(modularity) was higher in patients at TP1 (0.661, $p<0.001$), TP2 (0.316, $p=0.073$) and TP3 (0.456, $p=0.007$), compared to controls (0.000). Lesion side, lesion site, patient age, acute NIHSS, gender and handedness modulated resilience to recurrent virtual strokes, but not lesion size.

Conclusions: Network reorganization after stroke strengthens resilience to recurrent lesions. More specifically, this reconfiguration limits the impact of recurrent virtual lesions on integration and specialization of brain networks. Both lesion and patient-specific characteristics modulated resilience. These results suggest that specific reorganization features in brain

network architecture after stroke are not only associated with clinical improvement but also with reinforcement of resilience of brain networks to future lesions.

References
1. van Assche M, Klug J, Dirren E, Richiardi J, Carrera E. Preparing for a Second Attack: A Lesion Simulation Study on Network Resilience After Stroke. Stroke 2022;53:2038-2047.
2. Corbetta M, Ramsey L, Callejas A, et al. Common behavioral clusters and subcortical anatomy in stroke. Neuron 2015;85:927-941.
3. Fan L, Li H, Zhuo J, et al. The Human Brainnetome Atlas: A New Brain Atlas Based on Connectional Architecture. Cereb Cortex 2016;26:3508-3526.
4. Rubinov M, Sporns O. Complex network measures of brain connectivity: uses and interpretations. Neuroimage 2010;52:1059-1069.
5. Klug J, Dirren E, Preti MG, et al. Integrating regional perfusion CT information to improve prediction of infarction after stroke. J Cereb Blood Flow Metab 2021;41:502-510.

Poster No 236

Distribution of amyloid Beta and Its Influence on Neuropsychiatric Symptoms in Parkinson's Disease

Eunah Yang[1], Yaeji Kim[2], Hankyu Na[3], Phil Hyu Lee[3], Yong Jeong[1]

[1]Department of Bio and Brain Engineering, Korea Advanced Institute of Science and Technology, Daejeon, Korea, Republic of, [2]Program of Brain and Cognitive Engineering, Korea Advanced Institute of Science and Technology, Daejeon, Korea, Republic of, [3]Department of Neurology, Severance Hospital, Yonsei University College of Medicine, Seoul, Korea, Republic of

Introduction: Parkinson's disease (PD) is traditionally categorized as a subcortical disorder originating from alpha-synuclein accumulation along the dopaminergic pathway, resulting in prominent motor symptoms. However, broadening this viewpoint, individuals with PD exhibit not only motor symptoms but also neuropsychiatric and cognitive symptoms. These non-motor manifestations suggest potential alterations in cortical involvement with subcortical connections. However, the correlation between the prevalence of these non-motor features and alpha-synuclein was found to be inconsistent. Consequently, this study adopts a novel approach by investigating the role of amyloid beta in the non-motor comorbidities of PD. This research aims to elucidate the amyloid burden associated with PD in relation to neuropsychiatric symptoms. Firstly, the study demonstrates the pattern of amyloid accumulation in PD patients using F-18 Florbetaben (FBB) PET imaging. This study also explores white matter microstructural changes in the amyloid-positive PD using diffusion tensor imaging (DTI).

Methods: We acquired FBB PET and T1-weighted MR images from 137 idiopathic Parkinson's disease patients, categorized into 112 amyloid beta-negative and 25 amyloid beta-positive cases. Each patient underwent FBB PET, T1-weighted MR, and diffusion tensor imaging. Additionally, they went through cognitive assessments, including the Korean Mini-Mental State Examination (K-MMSE) and Seoul Neuropsychological Screening Battery (SNSB), while behavioral and psychiatric features were evaluated with the Neuropsychiatric Inventory (NPI) and Mild Behavioral Impairment (MBI) score. Utilizing Desikan-Killiany-Tourville (DKT) cortical labeling and Freesurfer subcortical segmentation protocols, we assessed the regional standardized uptake value ratios (SUVr) across 62 cortical and 14 subcortical regions. Regions exhibiting distinct regional amyloid beta accumulation were selected based on age, sex, and disease duration-adjusted SUVr values and subsequently subjected to linear regression models with cognitive and neuropsychiatric measures. White matter deterministic tractography was conducted using MRTrix3 software. To depict differences in structural connectivity related to amyloid status, we employed threshold-free network-based statistics (TFNBS) to identify distinctive edges between the amyloid-positive and negative groups.

Results: Widespread amyloid accumulation was observed across the entire brain, including the subcortex in amyloid-positive PD. The amyloid SUVr values revealed that the most significant association with amyloid was the burden of neuropsychiatric symptoms based on amyloid status but not with cognitive performance. Specifically, the amyloid accumulation was correlated with reduced motivation and affective dysregulation. When examining structural connectivity through DTI, amyloid-positive PD showed lower connectivity involving the anterior cingulate, temporal, and subcortical structures.

Figure 1 | Amyloid deposition pattern in PD and its association with neuropsychiatric scores
(A) Demonstration of cortical amyloid deposition (B) Demonstration of subcortical amyloid deposition (C) Heatplot of linear regression models with regional SUVr values and distinct neuropsychiatric scores

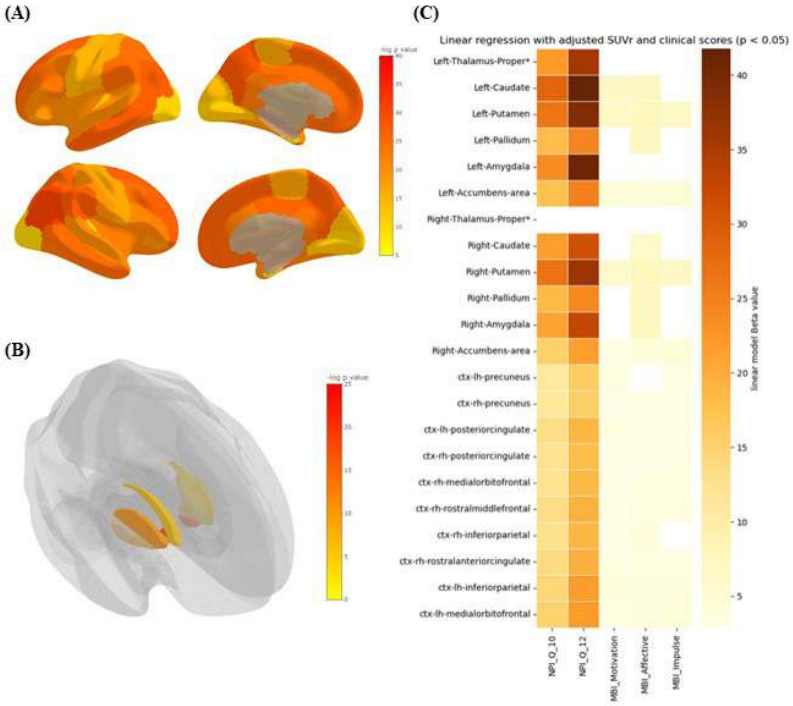

Figure 2 | Schematic representation of the structural connection altered in amyloid-positive PD
Amyloid-positive PD showed lower connectivity involving the anterior cingulate, temporal, and subcortical structures

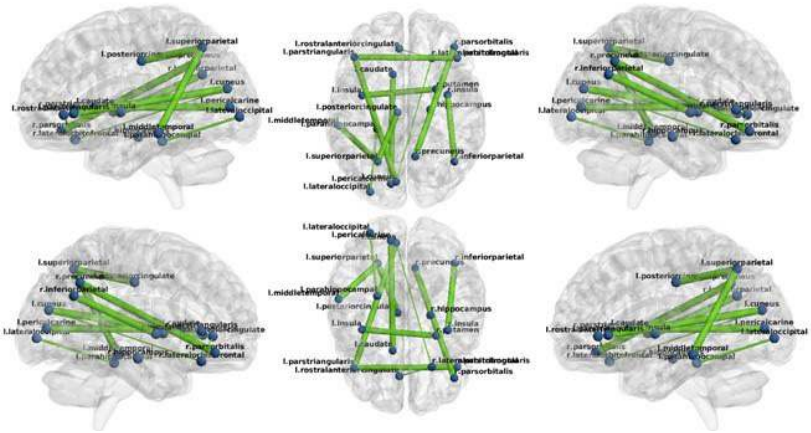

Conclusions: In summary, this study highlights the explanatory role of amyloid beta in the manifestation of decreased motivation and affective dysregulation features in PD. The widespread distribution of amyloid throughout the brain, including the subcortex, emphasizes its extensive involvement in PD pathology. Moreover, observed structural connectivity differences, particularly in the anterior cingulate and other regions, emphasizing the complex neural implications of amyloid beta. These findings focus attention on the need for targeted therapeutic strategies addressing both motor and neuropsychiatric aspects in the comprehensive management of PD.

References

1. Aarsland, Dag, et al. “Parkinson Disease-Associated Cognitive Impairment.” Nature Reviews Disease Primers, vol. 7, no. 1, 1 July 2021, www.nature.com/articles/s41572-021-00280-3, https://doi.org/10.1038/s41572-021-00280-3.
2. Chen, Yaojing, et al. “Brain Mechanisms Underlying Neuropsychiatric Symptoms in Alzheimer’s Disease: A Systematic Review of Symptom-General and –Specific Lesion Patterns.” Molecular Neurodegeneration, vol. 16, no. 1, 7 June 2021, https://doi.org/10.1186/s13024-021-00456-1.
3. Coughlin, David G., et al. “Cognitive and Pathological Influences of Tau Pathology in Lewy Body Disorders.” Annals of Neurology, 14 Dec. 2018, https://doi.org/10.1002/ana.25392.
4. Garon, Michela, et al. “Quantification of Brain β-Amyloid Load in Parkinson’s Disease with Mild Cognitive Impairment: A PET/MRI Study.” Frontiers in Neurology, vol. 12, 1 Mar. 2022, https://doi.org/10.3389/fneur.2021.760518.

5. Pagonabarraga, Javier, et al. “Apathy in Parkinson’s Disease: Clinical Features, Neural Substrates, Diagnosis, and Treatment.” The Lancet Neurology, vol. 14, no. 5, May 2015, pp. 518–531, https://doi.org/10.1016/s1474-4422(15)00019-8.
6. Petrou, Myria, et al. “Amyloid Deposition in Parkinson’s Disease and Cognitive Impairment: A Systematic Review.” Movement Disorders, vol. 30, no. 7, 16 Apr. 2015, pp. 928–935, https://doi.org/10.1002/mds.26191.
7. Wang, Linbo, et al. “Dopamine Depletion and Subcortical Dysfunction Disrupt Cortical Synchronization and Metastability Affecting Cognitive Function in Parkinson’s Disease.” Human Brain Mapping, vol. 43, no. 5, 14 Dec. 2021, pp. 1598–1610, https://doi.org/10.1002/hbm.25745.
8. Winer, Joseph R., et al. “Associations between Tau, β-Amyloid, and Cognition in Parkinson Disease.” JAMA Neurology, vol. 75, no. 2, 1 Feb. 2018, p. 227, https://doi.org/10.1001/jamaneurol.2017.3713.
9. Zetusky, W. J., et al. “The Heterogeneity of Parkinson’s Disease: Clinical and Prognostic Implications.” Neurology, vol. 35, no. 4, 1 Apr. 1985, pp. 522–522, https://doi.org/10.1212/wnl.35.4.522.
10. Zhou, Zhi, et al. “Apathy Rating Scores and β-Amyloidopathy in Patients with Parkinson Disease at Risk for Cognitive Decline.” Neurology, vol. 94, no. 4, 15 Nov. 2019, pp. e376–e383, https://doi.org/10.1212/wnl.0000000000008683. Accessed 1 Dec. 2023.

Poster No 237

Distinct Involvement of Neurotransmitter Systems in Early- And Late-Onset Alzheimer’s Disease

Ersin Ersözlü[1], Amir Dehsarvi[2], Nicolai Franzmeier[2], Boris Rauchmann[3]

[1]Department of Psychiatry and Psychotherapy, Campus Benjamin Franklin, Charité-Universitaetsmedizin, Berlin, Germany, [2]Institute for Stroke and Dementia Research, University Hospital LMU Munich, Munich, Germany, [3]Department of Radiology, University Hospital LMU Munich, Munich, Germany

Introduction: Alzheimer’s disease (AD) induces pathological changes in a heterogeneous fashion. Early onset of symptoms is associated with atypical patterns of pathology, such as increased involvement of neocortical regions, asymmetry, and non-amnestic manifestations in AD (Lu et al. 2023; Schöll et al. 2017). The role of alterations in neurotransmitter (NT) systems in heterogeneity in AD is highly unknown, while the current symptomatic treatments of mild-to-moderate AD dementia affect acetylcholine or N-methyl-D-aspartate (NMDA) receptor activities with highly variable response rates. We aimed to examine the group differences between early- and late-onset AD (EOAD and LOAD, respectively) and spatial associations between tau positron emission tomography (PET) uptake and mean neurotransmitter receptor/transporter maps in an explorative manner.

Methods: We included n=276 cognitively normal participants without abnormal Amyloid-beta (Aβ) in PET as healthy controls and n=181 patients with mild cognitive impairment or AD dementia and abnormal Aβ (n=48 EOAD, n=133 LOAD) as the patient group. We derived individual cortical [18F]AV-1451 (tau PET) uptake and used the previously published data mean NT receptor and transporter maps (Hansen et al. 2022) for cortical regions (Fig. 1) according to the Schaefer Atlas (parcellation resolution of 200). Next, we calculated tau PET abnormality in patients with AD, defined as z-scores using means and standard deviations of healthy controls in each atlas region. We then obtained the individual correlation coefficients between tau PET z-scores and mean NT maps independently for each receptor/transporter (NTxTau). We compared NTxTau between EOAD and LOAD and tested the mediation effects of NT on the relationship between tau PET uptake in temporal meta region and memory cognitive composite score.

Results: Mean differences in NTxTau revealed slightly stronger positive correlations in LOAD compared to EOAD for serotonin transporter (HTT, estimated-Δmean=0.02, p=0.03) and NMDA receptor (estimated-Δmean=0.03, p=0.002), while EOAD had slightly stronger negative correlations for vesicular acetylcholine transporter (VAChT, estimated-Δmean=0.03, p=0.046) than LOAD (Fig. 1A). The three NT with significant group differences between EOAD and LOAD were further studied in a mediation analysis. The individual correlations between tau PET uptake and HTT density mediated partially the association between tau PET uptake in meta region and memory performance that was moderated by the age at symptom onset (Index of moderated mediation: -0.033, lowest and highest bootstrap confidence intervals: -0.077 and -0.002, number of bootstrap samples: 5000). The moderation suggested that a higher regional HTT density and tau PET uptake correlation was related to a stronger association between tau PET and memory in patients with LOAD (Fig. 1B).

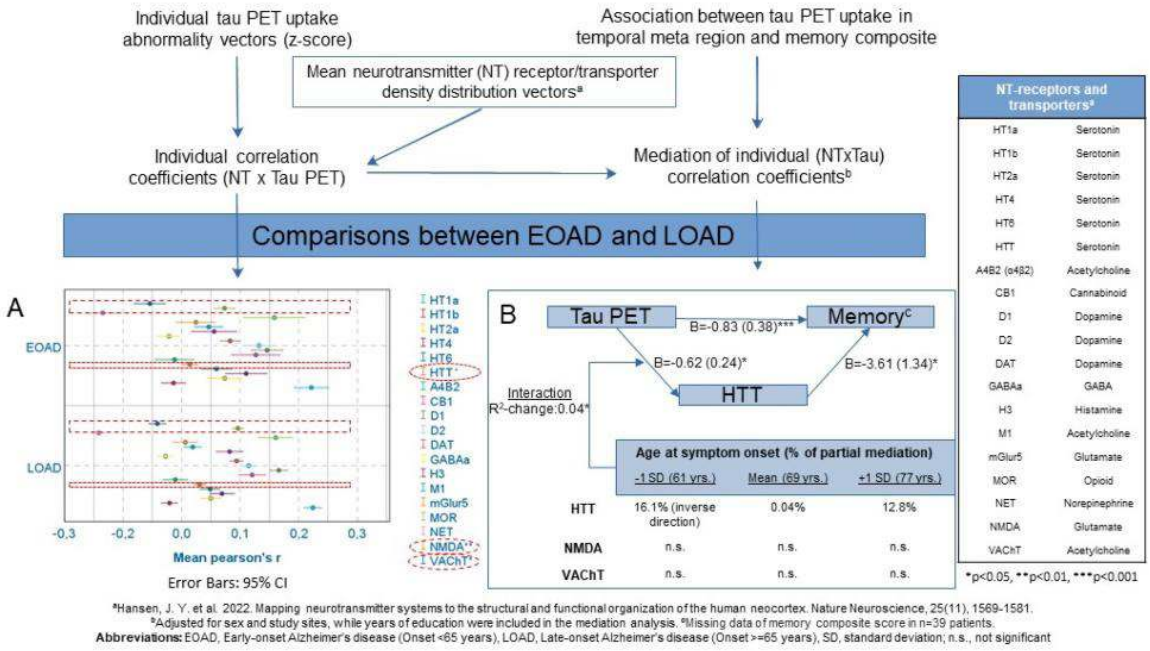

[a]Hansen, J. Y. et al. 2022. Mapping neurotransmitter systems to the structural and functional organization of the human neocortex. Nature Neuroscience, 25(11), 1569-1581.
[b]Adjusted for sex and study sites, while years of education were included in the mediation analysis. [c]Missing data of memory composite score in n=39 patients.
Abbreviations: EOAD, Early-onset Alzheimer's disease (Onset <65 years), LOAD, Late-onset Alzheimer's disease (Onset >=65 years), SD, standard deviation; n.s., not significant

Conclusions: The results of the present study suggest a distinguishable relationship, i.e., spatial correlation, between three of the nineteen NT receptors or transporters (Serotonin, Glutamat, and Acetylcholine) and neurofibrillary tau pathology. More, the mediation of HTT on the relationship between tau and memory was dependent on the age at symptom onset. Our approach can potentially be utilized in further imaging modalities, while studying the role of NT systems in neurodegenerative diseases.

References

1. Hansen JY, Shafiei G, Markello RD, Smart K, Cox SML, et al. 2022. Mapping neurotransmitter systems to the structural and functional organization of the human neocortex. Nat. Neurosci. 25(11):1569–81
2. Lu J, Zhang Z, Wu P, Liang X, Zhang H, et al. 2023. The heterogeneity of asymmetric tau distribution is associated with an early age at onset and poor prognosis in Alzheimer's disease. Neuroimage Clin. 38:103416
3. Schöll M, Ossenkoppele R, Strandberg O, Palmqvist S, Swedish BioFINDER study, et al. 2017. Distinct 18F-AV-1451 tau PET retention patterns in early- and late-onset Alzheimer's disease. Brain. 140(9):2286–94

Poster No 238

Structural equation modeling identifies differential links of pathologies and atrophy in dementia

Lena Haag[1], Elisa Lancini[1], Renat Yakupov[1], Gabriel Ziegler[1], Yeo-Jin Yi[1], Glanz Wenzel[2], Falk Lüsenbrink[1], Oliver Peters[3], Eike Spruth[4], Slawek Altenstein[3], Josef Priller[3], Luisa-Sophie Schneider[5], Xiao Wang[5], Lukas Preis[6], Frederic Brosseron[7], Nina Roy-Kluth[7], Anja Schneider[7], Klaus Fliessbach[7], Michael Wagner[8], Steffen Wolfsgruber[8], Jens Wiltfang[9], Niels Hansen[10], Ayda Rostamzadeh[11], Michael Ewers[12], Katharina Buerger[13], Robert Perneczky[13], Daniel Janowitz[14], Boris-Stephan Rauchmann[15], Stefan Teipel[16], Ingo Kilimann[17], Doreen Goerss[18], Christoph Laske[19], Matthias Munk[20], Michael Heneka[21], Peter Dechent[22], Stefan Hetzer[5], Klaus Scheffler[23], Emrah Düzel[24], Matthew Betts[25], Dorothea Hämmerer[26]

[1]Institute of Cognitive Neurology and Dementia Research (IKND), Magdeburg, Germany, [2]German Center for Neurodegenerative Diseases (DZNE), Magdeburg, Germany, [3]German Center for Neurodegenerative Diseases (DZNE), Berlin, Germany, [4]Department of Psychiatry and Psychotherapy, Charité, Berlin, Germany, [5]Charité – Universitätsmedizin Berlin, Berlin, Germany, [6]Charité – Universitätsmedizin Berlin - Institute of Psychiatry and Psychotherapy, Berlin, Germany, [7]German Centre for Neurodegenerative Diseases (DZNE), Bonn, Germany, [8]German Center for Neurodegenerative Diseases (DZNE), Bonn, Germany, [9]Department of Psychiatry and Psychotherapy, Medical University Göttingen, Göttingen, Lower Saxony, [10]University of Goettingen, Goettingen, Germany, [11]University of Cologne, Cologne, Germany, [12]Institute for Stroke and Dementia Research, Munich, Bavaria, [13]German Centre for Neurodegenerative Diseases (DZNE), Munich, Germany, [14]University Hospital, LMU Munich, Munich, Germany, [15]University Hospital, LMU Munich, München, Deutschland, [16]Rostock University Medical Center & German Center for Neurodegenerative Diseases (DZNE), Rostock, Germany, [17]German Center for Neurodegenerative Diseases (DZNE), Rostock, Germany, [18]Rostock University Medical Center, Rostock, Germany, [19]German Centre for Neurodegenerative Diseases (DZNE), Tübingen, Germany, [20]German Center for Neurodegenerative Diseases (DZNE), Tübingen, Germany, [21]University of Luxembourg, Luxembourg, Luxembourg, [22]Georg-August-University Goettingen,

Göttingen, Germany, [23]University of Tübingen, Tübingen, Germany, [24]Institute of Cognitive Neurology and Dementia Research, Magdeburg, Germany, [25]German Center for Neurodegenerative Diseases (DZNE), Magdeburg, Sachsen-Anhalt, [26]Innsbruck University, Innsbruck, Tirol

Introduction: Our main source of noradrenaline in the cortex is the locus coeruleus, a brainstem nucleus which is amongst the brain structures affected earliest by Alzheimer's disease-related tau pathology (Braak et al., 2011). Since intact noradrenergic modulation has been linked to cognitive reserve in ageing (Wilson et al., 2013), interindividual differences in the integrity of cortical noradrenaline-projection regions could be an important neural resource for cognitive reserve in ageing. The aim of this study was to determine whether volumes of brain areas known to be rich in noradrenergic receptors and transporters are relatively preserved in individuals with lower levels of Alzheimer's disease pathology.

Methods: Based on prior work on NA receptor and transporter distribution (Palomero-Gallagher et al., 2015), we distinguished between 'areas high in noradrenaline' and 'areas low in noradrenaline' and compared differential associations of atrophy in those areas with CSF amyloid-ß 42/40, CSF phosphorylated tau protein, and memory function across healthy controls (n = 122), subjects with subjective cognitive decline (n = 156) and patients with mild cognitive impairment or mild Alzheimer's disease dementia (n = 126). Analyses were carried out with structural equation modeling which allows to assess the interrelations between multiple variables while testing for group differences in these interrelations.

Results: Our analyses confirmed that regional brain volumes in 'areas high in NA' vs. 'areas low in NA' are differentially related to AD pathology markers. Only 'areas high in noradrenaline' were related to disease markers. Across all groups, atrophy in 'areas high in noradrenaline' were linked to worse memory. Moreover, groups differed in their links between atrophy in 'areas high in noradrenaline' and amyloid levels or memory capacity. In subjects with subjective cognitive decline, higher amyloid pathology predicted atrophy in 'areas high in noradrenaline' (ß = 0.343), while in patients with mild cognitive impairment and Alzheimer's disease, higher amyloid pathology was associated with memory impairment (ß = 0.295). The study also found that CSF amyloid and tau biomarkers were less correlated in the subjective cognitive decline (ß = -0.366) as compared to the mild cognitive impairment/Alzheimer's disease groups (ß = -0.424), suggesting distinguishable interrelatedness of amyloid and tau after early disease onset.

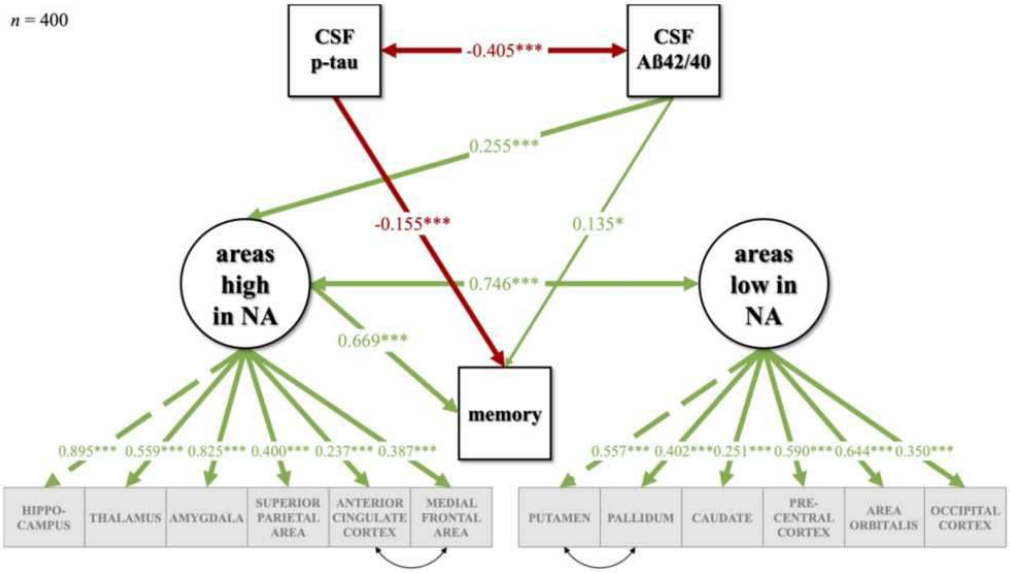

Conclusions: In summary, we showed differential links of high and low noradrenergic-projection cortical regions with Alzheimer's disease pathologies and cognitive function, indicating the relevance of considering the noradrenergic system as a protective factor in the ageing brain. Moreover, differential relationships between risk factors and their effect on areas high and low in noradrenaline in populations across the Alzheimer spectrum highlight the relevance of using analyses methods able to capture subgroup specific links between risk factors and brain atrophy in ageing.

References

1. Braak, H., Thal, D.R., Ghebremedhin, E., Del Tredici, K., 2011. Stages of the Pathologic Process in Alzheimer Disease: Age Categories From 1 to 100 Years. Journal of Neuropathology & Experimental Neurology 70, 960–969. https://doi.org/10.1097/NEN.0b013e318232a379
2. Palomero-Gallagher, N., Amunts, K., Zilles, K., 2015. Transmitter Receptor Distribution in the Human Brain, in: Brain Mapping. Elsevier, pp. 261–275. https://doi.org/10.1016/B978-0-12-397025-1.00221-9
3. Wilson, R.S., Nag, S., Boyle, P.A., Hizel, L.P., Yu, L., Buchman, A.S., Schneider, J.A., Bennett, D.A., 2013. Neural reserve, neuronal density in the locus ceruleus, and cognitive decline. Neurology 80, 1202–1208.

Poster No 239

Metabolomic-based risk score informed by neuroimaging biomarkers improves Alzheimer's disease risk

Erica Suh[1], Kwangsik Nho[2], Li Shen[1,3], Andrew Saykin[2], Dokyoon Kim[1,3]

[1]Department of Biostatistics, Epidemiology & Informatics, University of Pennsylvania, Philadelphia, PA, [2]Department of Radiology and Imaging Sciences, Indiana University School of Medicine, Indianapolis, IN, [3]Institute for Biomedical Informatics, University of Pennsylvania, Philadelphia, PA

Introduction: Early risk prediction and diagnosis of Alzheimer's disease (AD) remain challenging in the clinical setting. Polygenic risk scores (PRS), while common, fall short in specificity and sensitivity for AD risk estimation. Recent developments in neuroimaging techniques, including FDG-PET and AV45-PET, have highlighted changes in glucose metabolism, brain structure, and blood-brain barrier dysfunction, aligning with biofluid biomarker data (Sweeney et al. 2018). Metabolomic technologies, offering a more cost-effective and non-invasive approach, have identified disease-specific biomarkers, enabling the potential for metabolites to shed further light on the pathophysiological cascade of AD (Nho et al. 2021, Quintero et al. 2021). We aim to develop a novel metabolomics-based score that leverages significant correlations between lipid metabolites and PET biomarkers to enhance AD risk prediction and aid in early disease detection.

Methods: Serum-based metabolomics data containing 781 lipid species were collected from 997 fasted participants of the Alzheimer's Disease Neuroimaging Initiative (ADNI). We focused on two separate tasks: 1) cognitively normal control (CN) vs AD classification, and 2) mild cognitive impairment (MCI) conversion prediction. For each task, we measured Pearson correlation coefficients between each lipid species and the neuroimaging biomarkers, FDG- and AV45-PET. Significantly correlated lipids ($p<0.05$) were extracted to estimate a metabolomics-based risk score for each patient using a logistic regression model with an 80:20 train test split and 10-fold cross-validation. Prediction accuracy was measured using the Area Under Receiver Operating Characteristic (AUC) and Area Under the Precision-Recall Curve (AURPC). Risk-based stratification and interpretation analysis was also performed to further assess the potential clinical utility of the generated risk score. Results were compared to those of conventional PRS, as well as a baseline model which uses all lipid species as features. PRS was calculated using pruning and thresholding (PRS-pT, $p<1e-5$) with GWAS summary statistics from IGAP.

Results: The metabolomics-based score outperformed PRS and the baseline model in classifying CN vs AD, achieving an AUC of 0.797 with 187 lipid features (PRS AUC=0.605, and baseline AUC=0.678). It also showed superior performance in predicting MCI conversion, with an AUC of 0.726 using 174 lipid features (PRS AUC=0.525, baseline AUC=0.657). With the addition of covariates APOE, sex, and age, the AUC increased to 0.838 and 0.756 for each task, respectively (Figure 1). The metabolomics-based score also demonstrated lower risk in controls and, conversely, higher risk for AD patients. Stratification analysis revealed improved calibration with a smooth increase in predicted AD patients as the risk score rose. Many of the significant metabolites belonged to choline-containing phospholipids, such as lysophosphatidylcholine and phosphatidylcholine, in which pronounced increases of plasma levels have been observed in AD patients (Whiley et al. 2014, Tomioka et al., 2017).

Figure 1. Predictive performance comparison of AD risk across all risk score models. All models were evaluated using the ADNI cohort for a) CN vs AD classification and b) MCI conversion prediction. Experiments were conducted using an 80:20 train test split and 10-fold cross-validation. AUC values resulting from the test set are displayed. PRS: Polygenic risk score, LipidBaseline: baseline model using all lipid species as features, LipidPETScore: metabolomics-based risk score leveraging FDG-PET and AV45-PET biomarkers for lipid feature selection.

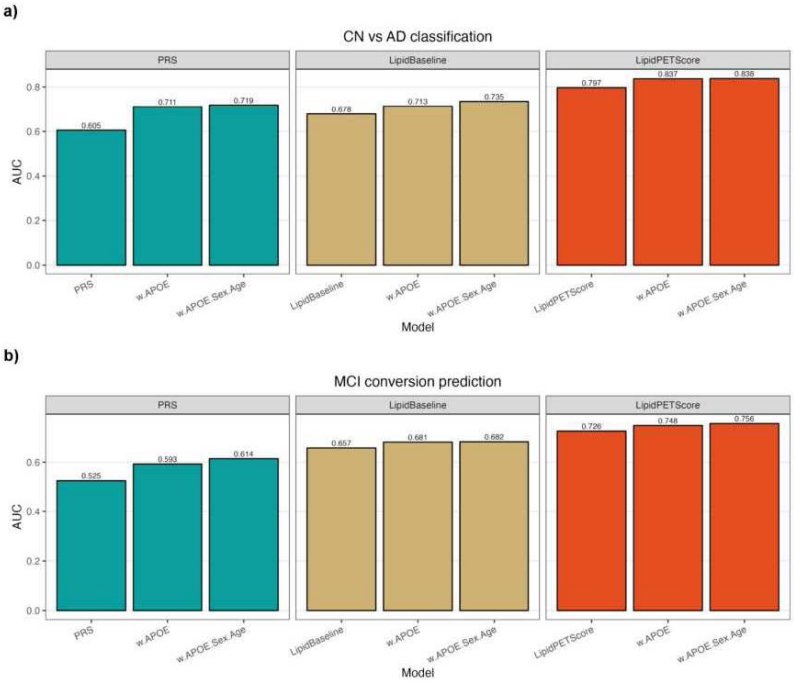

Conclusions: We developed and evaluated a novel metabolomics-based risk score which leverages PET neuroimaging biomarkers to robustly identify individuals with high or low risk of developing AD. Compared to conventional PRS, our risk score improved prediction performance and risk stratification of AD patients. Further study is required to functionally validate the selected metabolites and their roles in AD-related pathophysiology, to ultimately identify risk or progression-related biomarkers that can aid in the downstream development of therapeutic treatments for AD.

References

1. Nho, K. et al. (2021), 'Serum metabolites associated with brain amyloid beta deposition, cognition and dementia progression', Brain Communications, vol. 3, no. 3, fcab139.
2. Quintero, M.E., Pontes, J.G. de M. & Tasic, L. (2021), 'Metabolomics in degenerative brain diseases', Brain Research, vol. 1773, pp. 147704.
3. Sweeney, M.D., Sagare, A.P. & Zlokovic, B.V. (2018), 'Blood–brain barrier breakdown in Alzheimer disease and other neurodegenerative disorders', Nature Reviews Neurology, vol. 14, pp.133-150.
4. Tomioka, M. et al. (2017), 'Lysophosphatidylcholine export by human ABCA7', Biochimica et Biophysica Acta (BBA) - Molecular and Cell Biology of Lipids, vol. 1862, no. 7, pp. 658–665.
5. Whiley, L. et al. (2014), 'Evidence of altered phosphatidylcholine metabolism in Alzheimer's disease', Neurobiology of Aging, vol. 35, pp. 271–278.

Poster No 240

Interplay of plasma phosphorylated tau with GFAP, sex on hippocampal connectivity in preclinical AD

Noah Schweitzer[1], Rebecca Thurston[2], Brian Lopresti[3], William Klunk[2], Beth Snitz[4], Dana Tudorascu[2], Ann Cohen[2], M. Ilyas Kamboh[5], Edythe Eddy-Halligan[2], Thomas Karikari[2], Bistra Iordanova[1], Victor Villemagne[2], Howard Aizenstein[2], Minjie Wu[2]

[1]Department of Bioengineering, University of Pittsburgh, Pittsburgh, PA, [2]Department of Psychiatry, University of Pittsburgh, Pittsburgh, PA, [3]Department of Radiology, University of Pittsburgh, Pittsburgh, PA, [4]Department of Neurology, University of Pittsburgh, Pittsburgh, PA, [5]Department of Human Genetics, School of Public Health,University of Pittsburgh, Pittsburgh, PA

Introduction: Mounting evidence suggests that blood plasma phosphorylated tau (p-tau) may be a useful biomarker of Alzheimer's Disease (AD). Functional MRI (fMRI) studies have associated impaired memory networks with AD pathology. There have been few fMRI studies which examine the relationship between p-tau measures and the memory network. We aim to test how functional hippocampal connectivity alterations associated with p-tau measures differ based on plasma GFAP levels and sex.

Methods: This study included cognitively unimpaired (CU) elders who had their blood drawn within two years prior to their MRI scan. 23 subjects had plasma measures of Aβ42/40, GFAP and p-tau217 (n=17 female, mean age 72.4 +- 5.3 years) and 25 subjects had measures of p-tau231, p-tau181, GFAP and Aβ42/40 (n=13 female, mean age 71.7 +- 5.2 years). All subjects underwent PET imaging using [11C]PiB to assess Aβ load via PiB SUVR. A median split of GFAP was performed for each group of p-tau measures, where each subject was classified as either "high GFAP" or "low GFAP". Task fMRI was collected while participants performed a face-name associative memory task. Left and right hippocampus seeds were used to estimate functional connectivity between hippocampus and other regions in the brain. To extract regions of interest (ROI), second level analyses included two separate linear regression models testing for each p-tau measure: one model testing for the interaction between GFAP, p-tau and another model testing for the interaction between p-tau, sex. Both models controlled for age and PiB SUVR or Aβ42/40. To control for multiple comparisons, joint height and extent thresholds were determined via Monte Carlo simulations with an a priori medial temporal and frontal lobe mask (AlphaSim, AFNI).

Results: Two ROIs presented significant p-tau217 by GFAP interactions: left-right hippocampus and left-left hippocampus (between hippocampus and parahippocampus). In both ROIs, hippocampal connectivity increased with higher p-tau217 levels for high GFAP subjects, but decreased connectivity with higher p-tau217 levels for low GFAP subjects (Fig. 1A). Both ROIs were significant when controlling for PiB SUVR or Aβ42/40. For p-tau181 by sex interaction, three ROI's survived multiple comparisons when controlling for PiB SUVR but not Aβ42/40: left hippocampus-anterior cingulate cortex (Fig 1B), left hippocampus-right medial frontal gyrus (MFG), and left hippocampus-left MFG. In all three ROIs, hippocampal connectivity increased for males but not females. There were no significant ROIs observed for the interaction between p-tau181 and GFAP nor p-tau217 and sex. There were no significant ROIs observed for effects of p-tau231 on hippocampal connectivity.

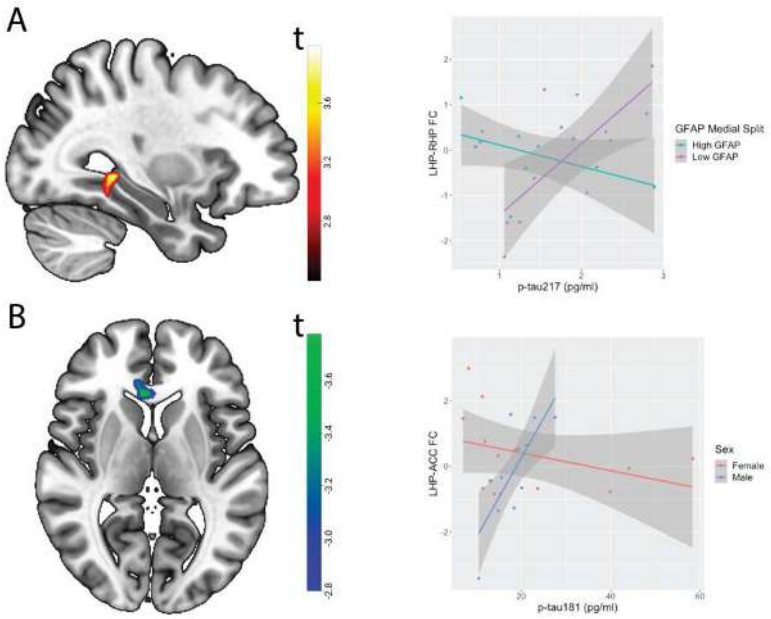

Figure 1. A.) Local hippocampal connectivity increases with higher p-tau217 levels in subjects with high GFAP. Pictured is Left-Right Hippocampus ROI ($p < 0.005$ unthresholded) with its corresponding plot of its mean beta values. B.) Hippocampal-prefrontal cortex connectivity increases with higher p-tau181 levels in males, but not females. Pictured is left hippocampus-anterior cingulate cortex ROI ($p<0.005$ unthresholded) with its corresponding plot of the mean beta values of ROI.

Conclusions: In a cohort of CU elders, we observed unique hippocampal connectivity alterations based on p-tau measures with GFAP, sex, and soluble and insoluble Aβ levels. Astrocyte reactivity has been shown to predict whether CU Aβ-positive individuals will develop tau pathology[1]. Astrocytes also play a critical role in maintaining neuronal circuit homeostasis[2]. Taken together, our observation of increased local hippocampal hyperconnectivity associated with high GFAP and increasing p-tau217 may reflect a critical point in the disease stage. P-tau217 appears earlier and has a stronger association with Aβ compared to p-tau181 in preclinical AD[3]. This may partially explain why local hippocampal hyperconnectivity is only associated with p-tau217. The ROIs observed between p-tau181, sex interaction mirrors the ROIs observed by our study examining hippocampal connectivity changes based on sex and PiB SUVR[4]. GFAP and p-tau181 have also been shown to be associated with insoluble Aβ levels measured via PET. This may partially explain why the p-tau181, sex interaction is only significant when

controlling for PiB SUVR but not Aβ42/40. In conclusion, our findings may reflect the disease progression in the hippocampus during pre-clinical AD based on different p-tau measurements.

References
1. Bellaver, B. et al. Astrocyte reactivity influences amyloid-β effects on tau pathology in preclinical Alzheimer's disease. Nature Medicine 29, 1775-1781 (2023).
2. Khakh, B.S. & Deneen, B. The Emerging Nature of Astrocyte Diversity. Annu Rev Neurosci 42, 187-207 (2019).
3. Gonzalez-Ortiz, F. et al. Plasma phospho-tau in Alzheimer's disease: towards diagnostic and therapeutic trial applications. Molecular Neurodegeneration 18, 18 (2023).
4. Wu, M. et al. Amyloid deposition is associated with different patterns of hippocampal connectivity in men versus women. Neurobiology of Aging 76, 141-150 (2019).

Poster No 241

Functional Connectivity Alterations Associated with Gray Matter Atrophy in Spinocerebellar Ataxia 10

Gustavo Padron-Rivera[1], Amanda Chirino[2], Angel Omar Romero-Molina[3], Omar Rodriguez-Mendoza[2], Diana-Laura Torres[2], Gabriel Ramirez-Garcia[2], Erick-Humberto Pasaye-Alcara[4], Juan Fernandez-Ruiz[2]

[1]Universidad Nacional Autonoma de Mexico, Mexico City, CDMX, [2]Universidad Nacional Autónoma de Mexico, Mexico City, Mexico, [3]Universidad Nacional Autónoma de Mexico, Mexico City, Mexico City, [4]Instituto de Neurobiología UNAM, Juriquilla, Queretaro

Introduction: Spinocerebellar ataxia 10 (SCA10) is a rare form of an autosomal dominant neurodegenerative disorder characterized by cerebellar ataxia and epilepsy, that is caused by an expansion of the pentanucleotide (ATTCT) repeat in ATXN10 gene on 22q13.31 [Leonardi et al.,2014;Matsuura et al.,2000]. Previous volumetric analysis showed extensive grey matter degeneration in the cerebellum, brainstem, thalamus, putamen and pallidum [Hernandez-Castillo et al.,2019;Arruda et al.,2020]. However, there is no information regarding the possible functional connectivity alterations caused by the brain degeneration in SCA10.

Methods: Twenty-six patients with SCA10 (15 female;age 50.38±9.91) and twenty-six age, and gender matched healthy subjects (HS) (15 female;age 50.65±9.28) were enrolled. All procedures were approved by the ethics committee of the UNAM in accordance with the Helsinki Declaration. Clinical assessments,including Scale for the Assessment and Rating of Ataxia (SARA) scores [Schmitz-Hübsch et al.,2006],and Montreal Cognitive Assessment (MoCA) scores [Larner,2016],were obtained for 21 patients.Functional and structural magnetic resonance imaging data were acquired at the Instituto de Neurobiologia of the UNAM,using a 3T GE MR750 Discovery with a 32-channel head coil.Voxel-based morphometry (VBM) for whole-brain volume analysis was conducted using FSL-VBM [Ashburner and Friston,2000].A two-sample t-test,with 10,000 permutations and age as a covariate, was employed to compare SCA10 patients with HS.The resulting significant clusters were identified,and their peak maxima were utilized as the center of 12-mm spheres.These spheres served as seed regions for subsequent functional analysis related to atrophy.Functional MRI were preprocessed and a voxel-wise seed-based analysis was conducted to determine Functional Connectivity (FC) between each atrophy-related seed and the bold signal of the entire brain for both groups.Finally,the functional maps obtained for each seed were compared between groups using a two-sample t-test (10,000 permutations),controlling for age.

Results: VBM analysis revealed GM decrease in SCA10 patients including right:cerebellar VIIIb,cerebellar VI, cerebellar V, cerebellar crus II, occipital fusiform gyrus and precentral gyrus.Left:precentral gyrus, occipital fusiform gyrus, temporal pole, superior frontal gyrus. Seed-based FC showed significant differences ($p < 0.05$).Seed located at the right occipital fusiform gyrus right,occipital fusiform gyrus left,and temporal pole left showed a higher FC in SCA10 patients (Fig.1-C).On the other side,seed located at the occipital fusiform gyrus right,cerebellar VI right and occipital fusiform gyrus left showed higher FC in control subjects (Fig.2-C).Finally,the analysis did not show significant correlations between the FC obtained from any seed with the SARA,or MoCA scores.

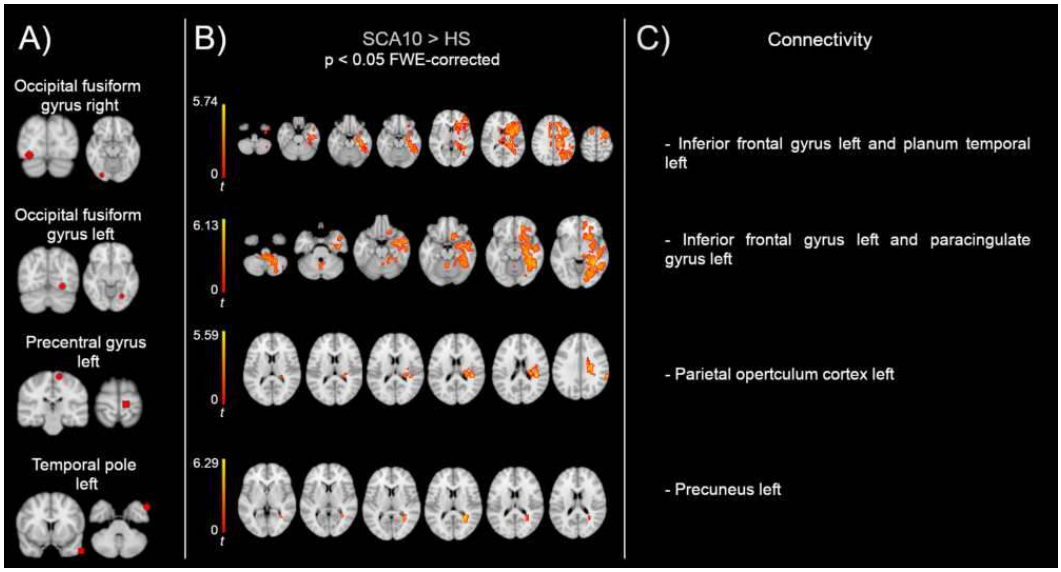

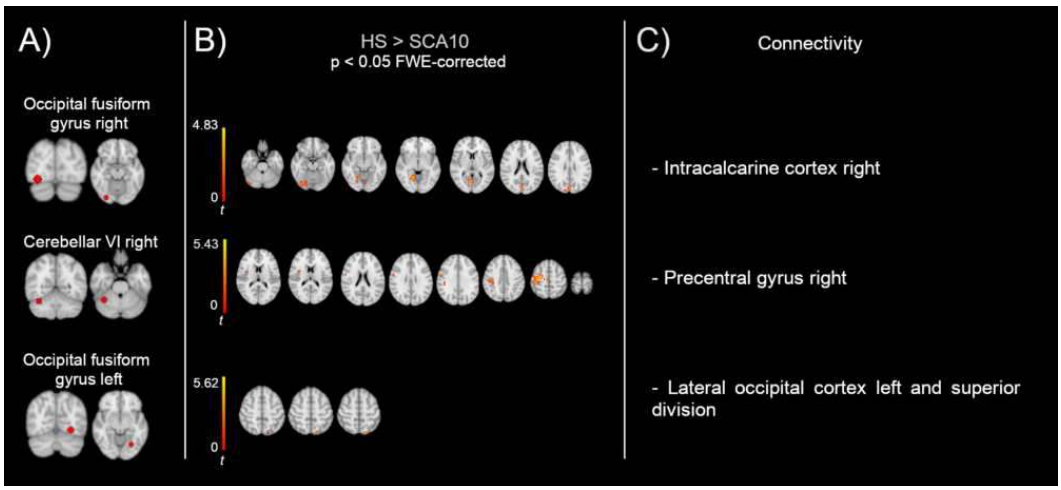

Conclusions: These results confirm the cerebellar volume decrease in SCA10,and show the significant changes in FC associated to the degeneration.The FC changes clearly show the impact of the cerebellar degeneration beyond this structure,and highlight its relationships from seed-ROIs with the rest of the brain,e.g.,seed located in cerebellar VI right showed significant FC with precentral gyrus right by HS compared to patients signifies a functional disconnection between the cerebellum and motor cortices.Notably,our results showed both increases and decreases in FC as a consequence of the neurodegeneration.Also,some FC changes were ipsilateral,and other were contralateral.Further analyses are needed to fully understand these changes and its possible consequences in the motor and cognitive performance of the patients. These findings provide valuable insights into the neural mechanisms underlying motor impairments associated with SCA10,suggesting a disrupted interplay between the cerebellum and motor-related brain regions.Support:CONAHCYT Estancias Posdoctorales por Mexico to GPR CVU 273410,PAPIIT IN220019 and CONACYT A1-S-10669 to JFR.

References

1. Arruda WO, Meira AT, Ono SE, de Carvalho Neto A, Betting LEGG, Raskin S, Camargo CHF, Teive HAG (2020): Volumetric MRI Changes in Spinocerebellar Ataxia (SCA3 and SCA10) Patients. Cerebellum 19:536–543.
2. Ashburner J, Friston KJ (2000): Voxel-Based Morphometry — The Methods 821:805–821.
3. Hernandez-Castillo CR, Diaz R, Vaca-Palomares I, Torres DL, Chirino A, Campos-Romo A,
4. Ochoa A, Rasmussen A, Fernandez-Ruiz J (2019): Extensive cerebellar and thalamic degeneration in spinocerebellar ataxia type 10. Park Relat Disord 66:182–188. https://doi.org/10.1016/j.parkreldis.2019.08.011.
5. Larner AJ (2016): Cognitive screening instruments: A practical approach. Cognitive Screening Instruments: A Practical Approach.
6. Leonardi L, Marcotulli C, McFarland KN, Tessa A, DiFabio R, Santorelli FM, Pierelli F, Ashizawa T, Casali C (2014): Spinocerebellar ataxia type 10 in Peru: the missing link in the Amerindian origin of the disease. J Neurol 261:1691–1694.
7. Matsuura T, Yamagata T, Burgess DL, Rasmussen A, Grewal RP, Watase K, Khajavi M, McCall AE, Davis CF, Zu L, Achari M, Pulst SM, Alonso E, Noebels JL, Nelson DL, Zoghbi HY, Ashizawa T (2000): Large expansion of the ATTCT pentanucleotide repeat in spinocerebellar ataxia type 10. Nat Genet 26:191–194.
8. Schmitz-Hübsch T, Du Montcel ST, Baliko L, Berciano J, Boesch S, Depondt C, Giunti P, Globas C, Infante J, Kang JS, Kremer B, Mariotti C, Melegh B, Pandolfo M, Rakowicz M, Ribai P, Rola R, Schöls L, Szymanski S, Van De Warrenburg BP, Dürr A, Klockgether T, Fancellu R (2006): Scale for the assessment and rating of ataxia: Development of a new clinical scale. Neurology 66:1717–1720.

Poster No 242

Mapping STN DBS Effects in PD: Optogenetics and fMRI Analysis of Pulse Rate-Dependent Modulation

Sung-Ho Lee[1,2,3], Yuhui Li[4], Chunxiu Yu[4,5], LiMing Hsu[1,2,3], Tzu-Wen Wang[1,2], Khoa Do[4], Hyeon-Joong Kim[1,2,3], Yen-Yu Shih[1,2,3], Warren Grill[4,6,7,8]

[1]Center for Animal MRI, University of North Carolina, Chapel Hill, NC, [2]Biomedical Research Imaging Center, University of North Carolina, Chapel Hill, NC, [3]Department of Neurology, University of North Carolina, Chapel Hill, NC, [4]Department of Biomedical Engineering, Duke University, Durham, NC, [5]Department of Biomedical Engineering, Michigan Technology University, Houghton, MI, [6]Department of Electrical and Computer Engineering, Duke University, Durham, NC, [7]Department of Neurobiology, Duke University, Durham, NC, [8]Department of Neurosurgery, Duke University School of Medicine, Durham, NC

Introduction: Deep Brain Stimulation (DBS) of the subthalamic nucleus (STN) marks a significant advancement in managing Parkinson's disease (PD), especially beneficial for patients unresponsive to dopaminergic medication or those experiencing levodopa-induced motor complications (Schuepbach et al., 2013; Hacker et al., 2018). Pioneering studies employing ChannelRhodopsin-2 (ChR2) have highlighted that STN DBS achieves therapeutic effects, in part, by antidromic activation of motor cortical neurons via the hyper-direct pathway (Gradinaru et al., 2009; Sanders et al., 2016). This has shifted the focus of DBS research towards this pathway. In our study, we utilize optogenetics and functional MRI (fMRI) to investigate the neural circuitry influenced by STN DBS, with particular attention to the differential therapeutic effects of various pulse repetition rates (PRR) (Bruet et al., 2001, Gale et al., 2013). Addressing the limitations of ChR2 observed in prior research, we examine the downstream circuits of the STN using the ultrafast opsin Chronos (Klapoetke et al., 2014). This approach builds upon our previous findings (Yu et al., 2020), which validated the efficacy of high-PRR STN-DBS in PD rat models, thereby enriching our understanding of how neural pathways contribute to high-PRR stimulation in PD treatment.

Methods: Female Sprague Dawley rats were used to model STN DBS effects via optogenetics. The process involved two stages: viral opsin expression and Parkinsonian model induction. Rats received STN injections of AAV vector viruses carrying Chronos or ChR2. After expression, a hemi-parkinsonian state was induced with 6-OHDA in the medial forebrain bundle, categorizing them into Chronos (n=5) and ChR2 (n=4) groups. Testing Circling Behavior: We investigated various STN stimulation PRRs (0, 5, 20, 75, 100, and 130 Hz) to confirm abnormal circling behavior in the PD model and assess the optogenetic intervention's efficacy in mitigating this behavior before fMRI measurements under anesthesia. fMRI Mapping: Using a BOLD-fMRI approach as described in Lee et al., 2021, we examined neural responses to optogenetic STN DBS in a Bruker 9.4T preclinical scanner. This allowed identification of network changes essential for the therapeutic efficacy of DBS. The same animals from the behavioral analysis were assessed to align behavioral responses with fMRI data across various DBS PRRs.

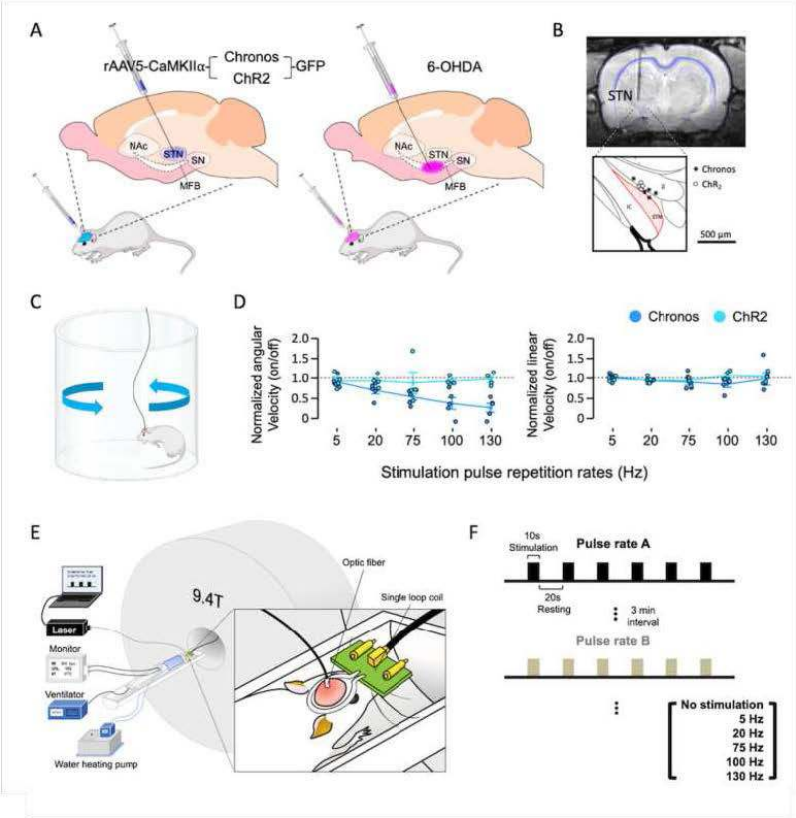

Figure 1: Optogenetic DBS, Behavioral Analysis, and fMRI Experimental Design in Rats. (A) Viral injections (rAAV5-CaMKIIα-Chronos-GFP/ChR2) and lesioning (6-OHDA) in the STN region. (B) MRI showing optical fiber placement above the STN expression site for targeted illumination. (C) Representation of counter-clockwise circling behavior indicative of the disease model. (D) Graphs of normalized angular (left) and linear (right) velocities during DBS, showing rate-dependent effects on angular velocity in Chronos rats. (E) Schematic of the MRI setup with anesthetized rat, laser, and monitoring equipment. (F) Diagram of the stimulation. paradigm for fMRI analysis.

Results: High PRR STN DBS (above 100Hz) in the Chronos group significantly reduced pathological circling behavior, a notable effect not seen in the ChR2 group. fMRI mapping using General Linear Model approaches revealed marked PRR-dependent effects in the substantia nigra (SN), globus pallidus (GP), caudate-putamen (CPu), lateral geniculate nucleus (LGN), and superior colliculus (SC). In the Chronos group, SN, GP, and CPu responses were PRR-dependent and correlated with behavioral changes. The ChR2 group showed significant responses primarily in LGN and SC, associated with visual sensory regions. The mediation analysis sought to identify brain regions mitigating pathological circling behavior, with a focus on those showing PRR-dependent responses in the Chronos group. Changes in GP and CPu activities significantly mediated the therapeutic effects of high pulse repetition rate DBS, underlining their pivotal roles in the treatment's success.

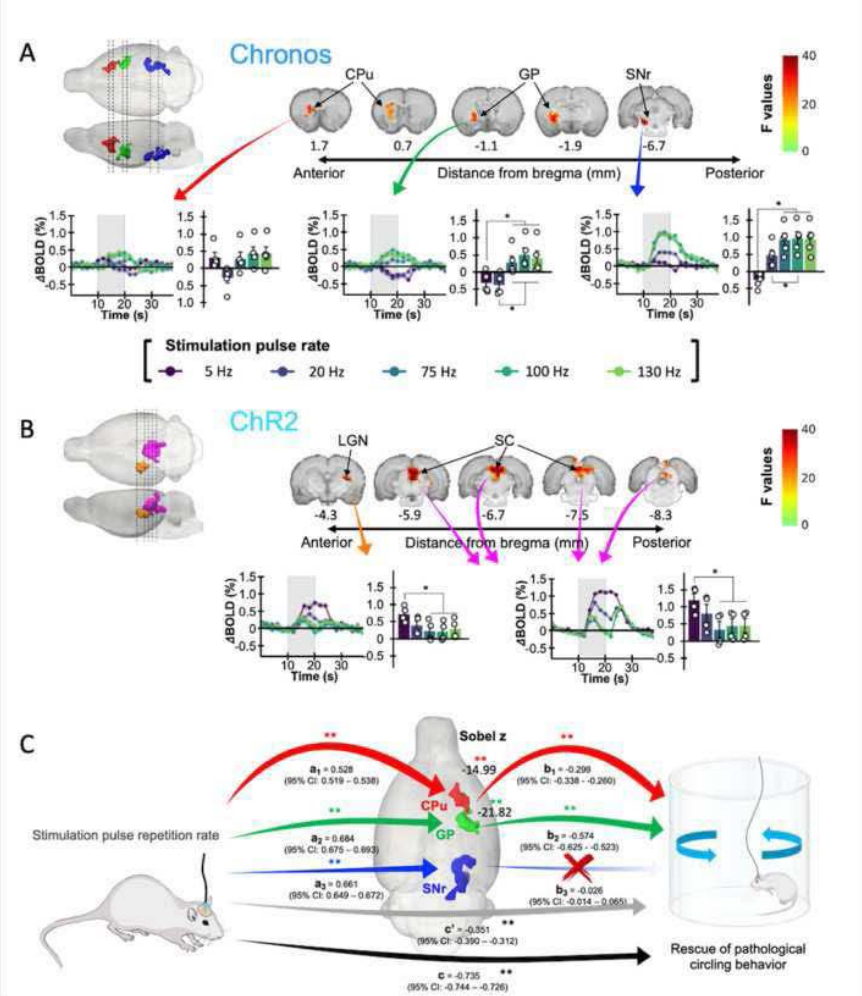

Figure 2: fMRI Response to STN Optogenetic DBS and Behavioral Mediation. (A-B) Brain-wide voxel-wise analysis demonstrates significant BOLD responses to varying STN DBS pulse rates in Chronos (A) and ChR2 (B) groups. 3D maps highlight significant clusters; cluster-specific BOLD response time-courses are depicted below, with stimulation intervals shaded in gray. Bar graphs represent peak BOLD percentage changes, with * indicating $p < 0.05$. (C) Mediation analysis reveals that CPu and GP activities mediate the amelioration of pathological circling, evidenced by Sobel test significance (Sobel z = -14.99 and -21.82 respectively, $p < 0.01$). Direct effects and mediators are quantified, illustrating their roles in behavioral rescue. Significance levels are marked as * $p < 0.05$, ** $p < 0.01$.

Conclusions: This study reevaluates the role of STN DBS in PD, focusing on the regions downstream of STN. Our findings suggest that, alongside the hyper-direct pathway, the roles of the GP and CPu are also crucial in comprehending the full spectrum of STN DBS effects.

References

1. Bruet, N. et al. (2001), 'High frequency stimulation of the subthalamic nucleus increases the extracellular contents of striatal dopamine in normal and partially dopaminergic denervated rats.', Journal of Neuropathology and Experimental Neurology, 60(1), 15-24.
2. Gale, J.T. et al. (2013), 'Electrical Stimulation-Evoked Dopamine Release in the Primate Striatum.', Stereotactic and Functional Neurosurgery, 91(6), 355-363.
3. Gradinaru, V. et al. (2009), 'Optical deconstruction of parkinsonian neural circuitry.', Science, 324(5925), 354-359.
4. Hacker, M.L. et al. (2018), 'Effects of deep brain stimulation on rest tremor progression in early stage Parkinson disease.', Neurology, 91(5), e463-e471.
5. Klapoetke, N.C. et al. (2014), 'Independent optical excitation of distinct neural populations.', Nature Methods, 11, 338-346.
6. Lee, S. et al. (2021), 'An isotropic EPI database and analytical pipelines for rat brain resting-state fMRI.', NeuroImage, 243, 118541.
7. Sanders, T.H. et al. (2016), 'Optogenetic stimulation of cortico-subthalamic projections is sufficient to ameliorate bradykinesia in 6-OHDA lesioned mice.', Neurobiology of Disease, 95, 225-237.
8. Schuepbach, W.M.M. et al. (2013), 'Neurostimulation for Parkinson's disease with early motor complications.', New England Journal of Medicine, 368(7), 610-622.
9. Yu, C. et al. (2020), 'Frequency-Specific Optogenetic Deep Brain Stimulation of Subthalamic Nucleus Improves Parkinsonian Motor Behaviors.', Journal of Neuroscience, 40(22): 4323-4334.

Poster No 243

Textural Analysis Detects Brain Regions Related to Antisocial Behavior in Patients with bvFTD

Behnaz Akbarian[1], Kilian Hett[2], Jayden Lee[2], Tony Phan[2], Ryan Darby[2]

[1]Vanderbilt University, Nashville, TN, [2]Vanderbilt University Medical Center, Nashville, TN

Introduction: Antisocial behaviors are common and problematic symptoms in patients with behavioral variant frontotemporal dementia (bvFTD). T1-weighted images are an important imaging modality for diagnosis and clinical work-up, where visual inspection of cortical brain volume is part of the diagnostic criteria for probable bvFTD. However, visual inspection as well as quantitative volumetric analysis of T1-weighted images may not find significant changes in bvFTD patients early in the disease course when antisocial behaviors are more problematic. We hypothesized that microstructural changes occurred before macrostructural changes (e.g. loss of volume) in the early stage of disease. Texture analysis can extract microstructural information from T1-weighted images based on the interrelationships between signal intensities of neighboring voxels. This study aims to determine whether microstructural differences in brain regions is related to antisocial behavior in bvFTD.

Methods: Antisocial behavior was measured using the recently validated social behavior questionnaire (SBQ), which measures the presence and severity of 26 antisocial behaviors using an informant-based questionnaire (Phan, 2023). T1-weighted scans (1X1X1 mm3) were acquired using 3T MRI (Philips Medical Systems) from 32 bvFTD patients (29 male, age: 62.5 ± 8.7 yrs.) and 33 age-matched healthy controls (21 male, age: 63.1 ± 7.9 yrs.). These scans were segmented into grey matter, white matter, and cerebrospinal fluid. AssemblyNet (Coupé, 2020) was then used to segment grey matter into 132 cortical and subcortical regions of interest (ROI) (Klein, 2012). For each ROI, textures characteristics were estimated using spatial autocorrelation, extracted using the gray-level co-occurrence method (Haralick, 1973). This method characterizes the spatial variation of intensities locally. First, linear regressions were used to measure the relationship between texture and SBQ scores within each ROI. Patients were then categorized into high and low antisocial behavior based on median SBQ scores, and an ANOVA was used to compare autocorrelation between healthy control (HC), and patients with low and high antisocial behavior. As a comparison to macrostructural abnormalities, we repeated analyses using brain structures' volumes instead of autocorrelation measure. All results are adjusted for age and gender.

Results: Autocorrelation was negatively correlated to antisocial behavior in several brain regions, including the bilateral caudate, right thalamus, right anterior cingulate, and right anterior insula (Fig. 1A-B). Group-level comparisons showed that while HC had autocorrelation values near 0 in these regions, patients with low antisocial behavior tended to have positive autocorrelations suggesting larger clusters of abnormal pixel intensities, whereas patients with higher antisocial behavior had negative autocorrelations suggesting smaller, more diffuse clusters of abnormal pixel intensities (Fig. 1C). Of these identified regions, none of them showed an association between antisocial behavior and volume (Fig. 2A-B). In the left anterior cingulate, bilateral middle and superior frontal gyrus there was a positive association between antisocial behavior and volume and atrophy was associated with lower antisocial behavior in these regions ($p<0.05$, uncorrected, not shown).

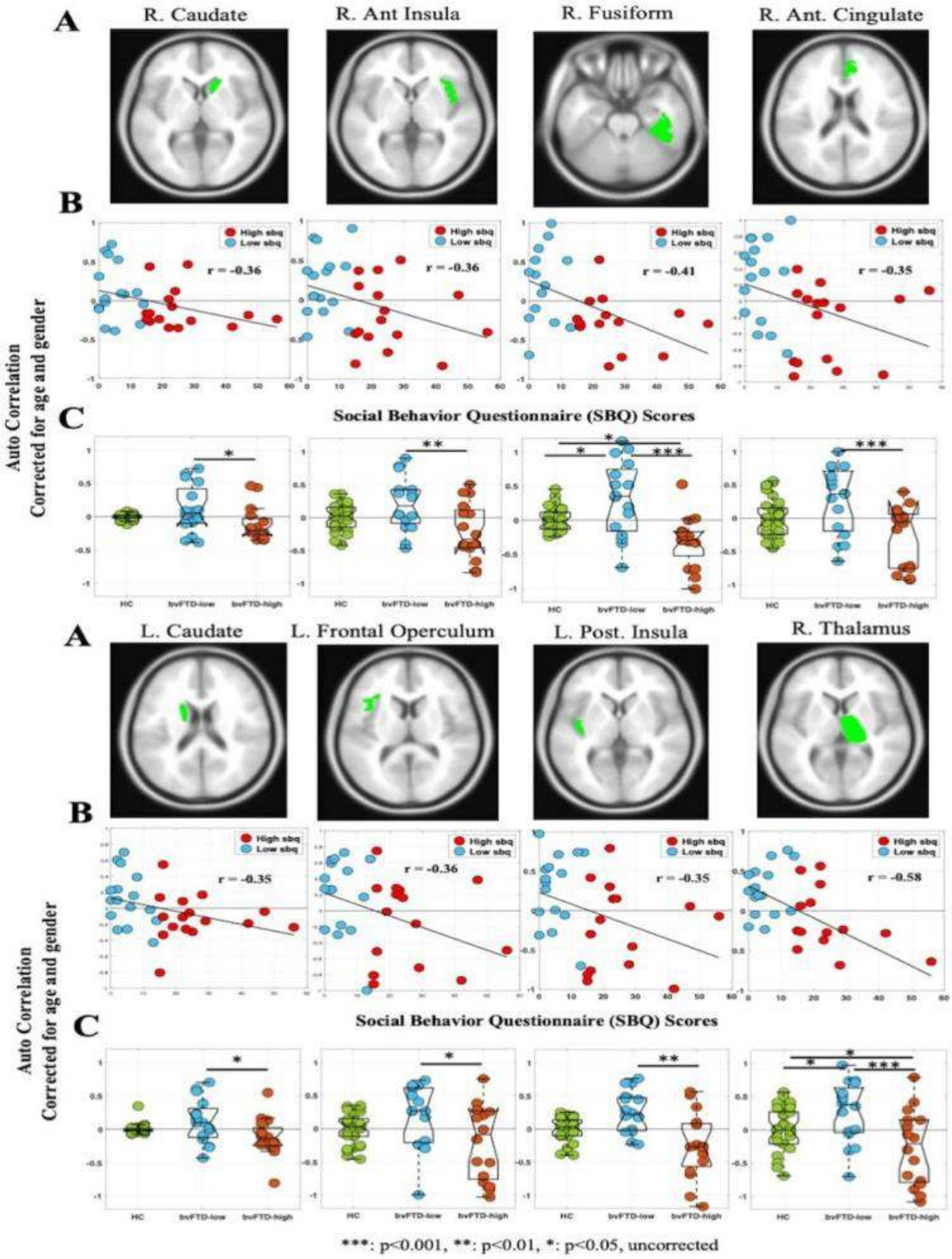
A
R. Caudate
R. Ant Insula
R. Fusiform
R. Ant. Cingulate
B
High sbq
Low sbq
r = -0.36
r = -0.36
r = -0.41
r = -0.35
Auto Correlation
Corrected for age and gender
C
Social Behavior Questionnaire (SBQ) Scores
HC
bvFTD-low
bvFTD-high
A
L. Caudate
L. Frontal Operculum
L. Post. Insula
R. Thalamus
B
r = -0.35
r = -0.36
r = -0.35
r = -0.58
Auto Correlation
Corrected for age and gender
C
Social Behavior Questionnaire (SBQ) Scores
***: p<0.001, **: p<0.01, *: p<0.05, uncorrected

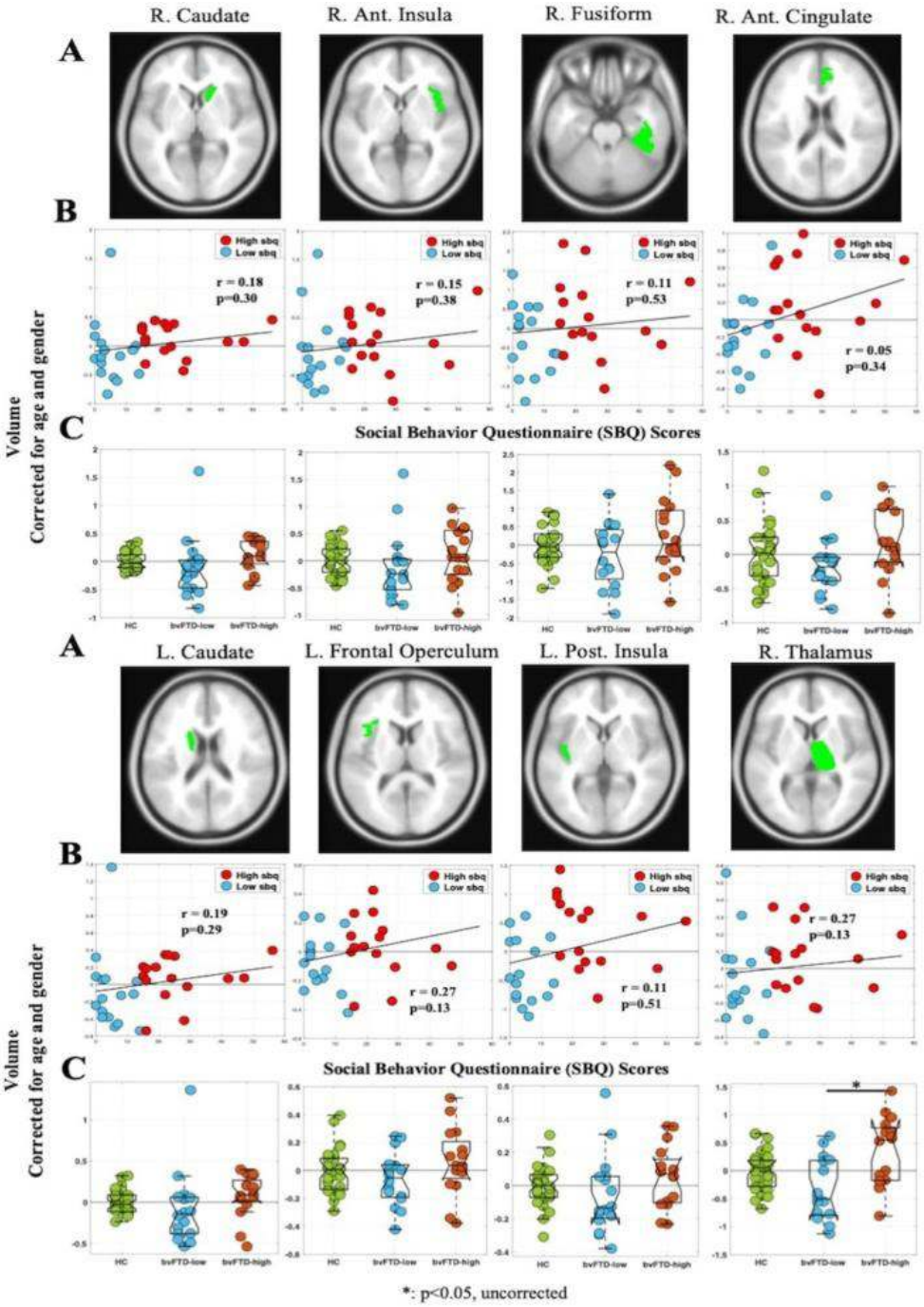

Conclusions: We found that the microstructure information is related to the severity of antisocial behaviors in bvFTD patients beyond what can be explained by macrostructural brain atrophy. Results suggest that different types of microstructural changes in bvFTD patients may help to explain the differing degrees of antisocial behavior seen across patients. At the conceptual level, our results suggest that certain problematic behaviors may be better explained by irritative micro-lesions rather than destructive macro-lesions, an approach that could lend insight into many behavioral and neuropsychiatric symptoms in neurological and psychiatric patients.

References

1. Coupé, P. (2020), 'AssemblyNet: A large ensemble of CNNs for 3D whole brain MRI segmentation', NeuroImage, vol. 219, pp.117026.
2. Haralick R.M. (1973), 'Textural features for image classification', IEEE Transactions on Systems, Man, and Cybernetics, vol. 3, no 6, pp. 610-21.
3. Klein, A. (2012), '101 labeled brain images and a consistent human cortical labeling protocol'. Frontiers in neuroscience, vol. 6, pp.171.
4. Phan, T.X. (2023), 'Measuring antisocial behaviors in behavioral variant frontotemporal dementia with a novel informant-based questionnaire', The Journal of Neuropsychiatry and Clinical Neurosciences, vol. 35, no. 4, pp.374-384.

Poster No 244

Carotid stiffness and pulsatility associated with cognitive impairment: A phase-contrast MRI study

Lirong Yan[1], Jianing Tang[1], Elizabeth Joe[2], Helena Chui[2]

[1]Northwestern University, Chicago, IL, [2]University of Southern California, Los Angeles, CA

Introduction: Arterial stiffening and increased pulsatility serve as important markers of vascular dysfunction, which lead to transmission of excessive pulse energy to downstream vasculature resulting in microvascular dysfunction. Separate MRI scans at different carotid segments are typically performed to assess carotid stiffness by measuring pulse wave velocity (PWV), which is prone to cardiac variations. Recently, a fast single-slice oblique-sagittal phase-contrast MRI (OS PC-MRI) technique has been introduced to simultaneously image multiple arterial velocity waveforms along the common carotid artery (CCA) and the internal carotid artery (ICA), which allows for multiple vascular metric measurements, including carotid PWV (cPWV), arterial pulsatility of both ICA and CCA quantified by pulsatility index (PI), and CCA-ICA damping factor (cDF). This study aims to investigate the associations of these vascular metrics with cognitive measurements in aged subjects.

Methods: Participants and clinical assessments: Forty elderly participants (22 female,73.3 ± 7.7 years) were enrolled in the study after providing written informed consent. Among them, 29 participants had Clinical Dementia Rating (CDR), 29 received Mini-Mental State Exam (MMSE), and 40 received Montreal Cognitive Assessment (MoCA). MRI experiments: The MRI experiments were conducted on a Siemens Prisma 3T MRI scanner using a 20-channel head/neck coil. A single-slice retrospectively gated 2D OS PC-MRI with a single in-plane velocity encoding (CCA to ICA) was performed on each participant to acquire blood velocity waveforms along the CCA-ICA segment simultaneously (Figures 1a & b). Imaging parameters include spatial resolution=1x1x1mm3, VENC=80cm/s, TE/TR=4.32/14.22ms, flip angle=10°, real temporal resolution=14.22ms, 70-90 phases across a cardiac cycle, scan time was 1 to 2min depending on the heart rate. Image processing and statistical analysis A reference waveform was calculated as the average of velocity waveforms obtained from all axial locations along ICA-CCA. The transit time between each waveform and the reference waveform was calculated using the time-to-foot (TTF) method. cPWV was calculated as the inverse slope of the line fitted to the transit time versus distance along the vessel (Figure 1c). PI was calculated from the average velocity waveforms along each segment i.g., CCA, ICA (Figure 1e). cDF was calculated as the ratio of the average PI values between CCA and ICA (Figure 1f). According to the normality test on the MRI and cognitive data, the correlations of carotid vascular metrics with cognitive measures were calculated across subjects using Pearson or Spearman's correlation coefficients, respectively. Age, gender, and education were considered as covariances using partial correlation.

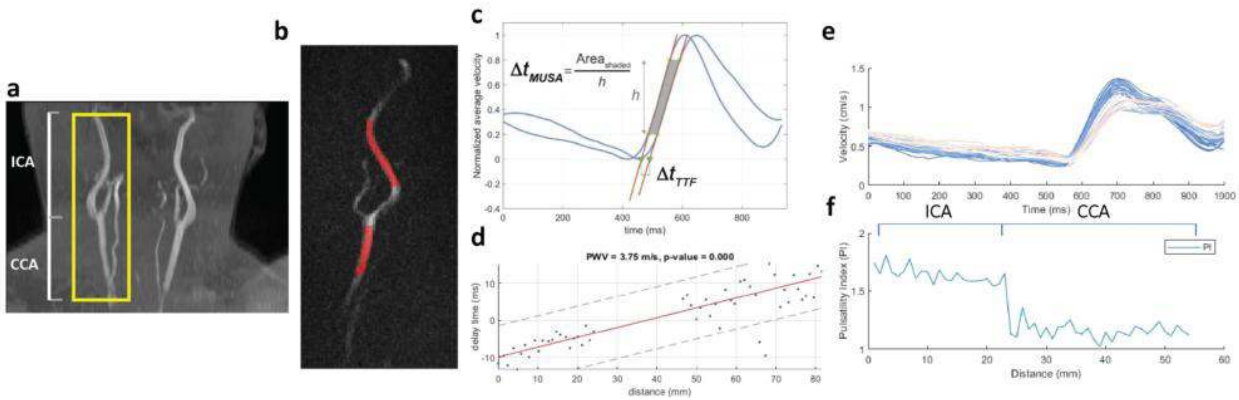

Results: cPWV showed significant negative correlations with both MoCA and MMSE (cPWV vs. MoCA: r = -0.4, p = 0.01; cPWV vs. MMSE: r = -0.57, p = 0.008;), and the correlations remained significant after controlling for age, gender, years of education (cPWV vs. MoCA: r = -0.36, p = 0.03; cPWV vs. MMSE: r = -0.53, p = 0.005;) (Figure 2). Furthermore, the participants with CDR>0 (n=19) showed higher cPWV values compared to those with CDR=0 (n=21) (p=0.0045). These results provide convergent evidence that elevated cPWV is strongly associated with cognitive decline. No significant correlations were found between the average PI values at both ICA and CCA with cognitive measures, which may be caused by the variations along vessel segments during the PI measurements. However, a significant negative correlation between cDF and MoCA was observed (p = 0.036). This finding indicates that the damping factor of arteries could be a sensitive vascular marker for cognitive impairment.

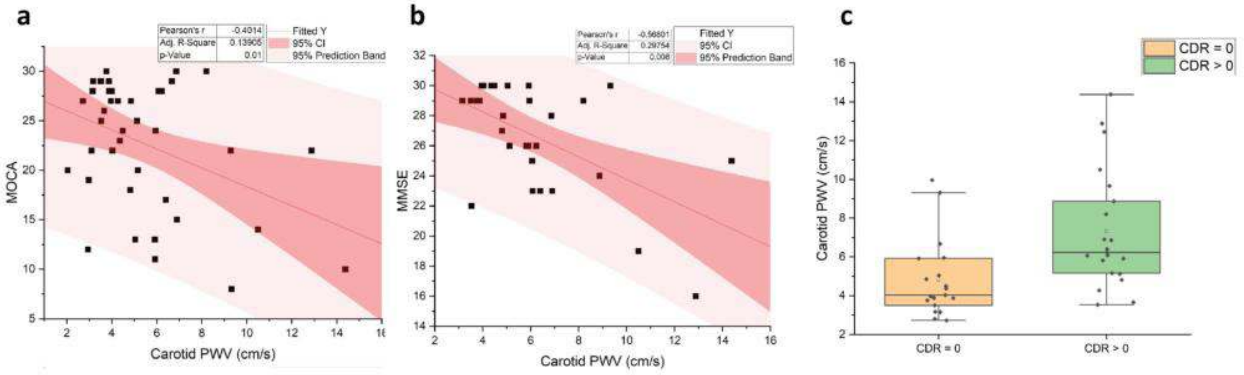

Conclusions: This study demonstrates that OS PC-MRI is a promising imaging tool to assess intracranial arterial stiffness and pulsatility, which can serve as sensitive imaging markers for cognitive impairment.

References

1. Van Sloten, Thomas T., et al. "Carotid stiffness is associated with incident stroke: a systematic review and individual participant data meta-analysis." Journal of the American College of Cardiology 66.19 (2015): 2116-2125.
2. Lau, Kui Kai, et al. "Age and sex-specific associations of carotid pulsatility with small vessel disease burden in transient ischemic attack and ischemic stroke." International Journal of Stroke 13.8 (2018): 832-839.
3. Heidari Pahlavian S, Cen SY, Bi X, Wang DJJ, Chui HC, Yan L. Assessment of carotid stiffness by measuring carotid pulse wave velocity using a single-slice oblique-sagittal phase-contrast MRI. Magn Reson Med. 2021;86(1):442-455. doi:10.1002/mrm.28677

Poster No 245

Altered amyloid-ß binding in cognitively normal middle-aged APOE-ε4 carriers: an AI-assisted study

Paolo Nucifora[1]

[1]Loyola University Chicago, Chicago, IL

Introduction: In Alzheimer's disease, amyloid deposition generally precedes the onset of objective symptoms. The duration of symptom-free amyloid deposition is unclear, but it appears to accumulate faster in APOE ε4 carriers (Gonneaud et al., 2016) and is detectable in cognitively normal elderly individuals (Li et al., 2023). In this study, the presence of amyloid-β in cognitively normal individuals under 70 years old was evaluated using PET after injection of 18F-florbetapir, a radiopharmaceutical that binds to amyloid-β. Images from APOE ε4 carriers and non-carriers were compared with an AI-assisted method of whole-brain evaluation.

Methods: Data used in preparation of this article were obtained from the Alzheimer's Disease Neuroimaging Initiative database (adni.loni.usc.edu). Baseline 18F-florbetapir images from APOE ε4 carriers and non-carriers between 60 and 70 years old were obtained for this study. These images were used to train a 3D convolutional neural network. Classification accuracy was measured with 10-fold cross-validation. By itself, the classification accuracy value is insufficient to establish a significant difference between the two groups. But as described by Golland and Fischl, the significance of an accuracy value can be determined by permutation testing, i.e. re-measuring accuracy with multiple sets of permuted data that are consistent with the null hypothesis (Golland and Fischl, 2003). If the accuracy obtained from the non-permuted dataset is significant, it is evidence against the null hypothesis and implies that the two populations are not identical. In this study, "carrier" and "non-carrier" labels were permuted 100 times, and each permutation was used to train a new 3D convolutional network. Classification accuracy of the non-permuted dataset was compared to the accuracy of all permuted datasets in order to assess the hypothesis that amyloid-beta binding is not identical in APOE ε4 carrier and non-carrier populations.

Results: The "carrier" group consisted of 33 unique individuals aged 67.0 ± 2.0 years. The "non-carrier" group consisted of 56 unique individuals aged 66.9 ± 2.2 years. The non-permuted dataset was associated with a classification accuracy of 67.4%. This was higher than the classification accuracy of all 100 permuted datasets. Therefore, "carrier" amyloid-beta binding differed from "non-carrier" amyloid-β binding at a significance level of p=0.01.

Conclusions: This study provides evidence of altered amyloid-β binding in cognitively normal APOE ε4 carriers under the age of 70, which is consistent with a recent report of altered amyloid-β binding in cognitively normal APOE ε4 carriers over 70 (Li et al., 2023). These findings support the hypothesis that amyloid-β binding is altered in APOE ε4 carriers long before they develop objective symptoms of Alzheimer's disease, and therefore suggest that early treatment of APOE ε4 carriers might be

beneficial. In addition, this study illustrates the use of AI in combination with permutation analysis for statistical hypothesis testing. Of note, useful results can be obtained even in datasets that are relatively small and unsuitable for training a high-accuracy classifier. This approach may be helpful alongside exploratory methods such as region-of-interest (ROI) analysis or voxel-based morphometry (VBM). Like VBM it may be sensitive to effects that occur at the scale of individual voxels, and may even be sensitive to complex changes that elude VBM (e.g. those that do not consistently localize to specific voxels). However, like ROI analysis it can only demonstrate whether two datasets differ, not which voxels are responsible for the difference.

References

1. Golland, P. (2003). "Permutation Tests for Classification: Towards Statistical Significance in Image-Based Studies." In C. Taylor & J. A. Noble (Eds.), Information Processing in Medical Imaging (pp. 330–341). Springer. https://doi.org/10.1007/978-3-540-45087-0_28
2. Gonneaud, J. (2016). "Relative effect of APOE ε4 on neuroimaging biomarker changes across the lifespan." Neurology, 87(16), 1696–1703. https://doi.org/10.1212/WNL.0000000000003234
3. Li, W. (2023). "Effect of APOE ε4 genotype on amyloid-β, glucose metabolism, and gray matter volume in cognitively normal individuals and amnestic mild cognitive impairment." European Journal of Neurology, 30(3), 587–596. https://doi.org/10.1111/ene.15656

Poster No 246

Identifying cognitive phenotypes and their MRI correlates with machine learning in multiple sclerosi

Elisa Colato[1], Maureen van Dam[1], Giuseppe Pontillo[2], Marcello Moccia[3], Tomas Uher[4], Manuela Vaneckova[5], Ahmed Toosy[6], Maria Amato[7], Ermelinda Meo[7], Maria Petracca[8], Matilde Inglese[9], Alessia Bianchi[10], Alex Rovira[11], Antonio Gallo[12], Einar Høgestøl[13], Gabriel Gonzalez-Escamilla[14], Guy Nagels[15], Jacqueline Palace[16], Jaume Sastre-Garriga[17], Laura Hancock[18], Maria Rocca[19], Maria Sormani[20], Massimiliano Calabrese[21], Massimo Filippi[19], Ralph Benedict[22], Sara Llufriu[23], Sarah Morrow[24], Sergiu Groppa[25], Silvia Messina[16], Tom Fuchs[22], Frederik Barkhof[26], Hanneke Hulst[27], Menno Schoonheim[1]

[1]MS Center Amsterdam, Anatomy and Neurosciences, Amsterdam Neuroscience, Amsterdam UMC location VUmc, Amsterdam, Netherlands, [2]Amsterdam University Medical Centre, Amsterdam, Netherlands, [3]University of Naples, Naples, Naples, [4]Department of Neurology and Center of Clinical Neuroscience, Charles University in Prague, Prague, Czech Republic, [5]Department of Radiology, Charles University in Prague, Prague, Czech Republic, [6]University College London, London, United Kingdom, [7]Department NEUROFARBA; Section Neurosciences, University of Florence, Florence, Italy, [8]Sapienza University of Rome, Rome, Rome, [9]University of Genoa, Genoa, Italy, [10]University of Palermo, Palermo, Italy, [11]Vall d'Hebron Univeristy Hospital, Barcelona, Spain, [12]University of Campania "Luigi Vanvitelli", Naples, Italy, [13]Department of Neurology, Oslo University Hospital, Oslo, Norway, [14]University Medical Center of the Johannes Gutenberg University Mainz, Mainz, Germany, [15]AIMS lab, Vrije Universiteit Brussel, Center for Neurosciences, Brussels, Brussels, [16]University of Oxford, Oxford, United Kingdom, [17]Vall d'Hebron University Hospital, Barcelona, Spain, [18]Neurological Institute, Cleveland Clinic, Cleveland, OH, [19]Neuroimaging Research Unit, Division of Neuroscience, IRCCS San Raffaele Scientific Institute, Milan, Italy, [20]IRCCS Ospedale Policlinico San Martino, Genoa, Italy, Genoa, Italy, [21]University of Verona, Verona, Italy, [22]University at Buffalo (UB) Jacobs School of Medicine, Buffalo, NY, [23]Hospital Clinic Barcelona, Barcelona, Spain, [24]University of Western Ontario (Western), London, Ontario, [25]Department of Clinical Neurophysiology, Turku University Hospital, Turku, Pori, [26]Amsterdam University Medical Centre, Amsterdam, Noord-Holland, [27]Leiden University, Leiden, Netherlands

Introduction: Multiple sclerosis (MS) is an inflammatory and neurodegenerative disease affecting 2.8 million young adults worldwide (Walton et al., 2020). Most people with MS (PwMS) have some degree of cognitive dysfunction, yet cognitive impairment (CI) in MS is still poorly understood. While PwMS have high heterogeneity of cognitive dysfunction, patients are dichotomously classified as cognitively preserved or impaired in most research studies. Cognitive phenotypes (CoP) have been proposed that could help to develop personalized interventions (De Meo et al., 2021). Aim. We aimed to identify cognitive phenotypes in MS using machine learning models and investigate their MRI correlates.

Methods: In this joint MAGNIMS-IMSCOGS collaborative study, we used retrospective data from 1,742 PwMS who underwent a complete cognitive assessment (BRB-N plus executive test or MACFIMS) from 15 centres from the EU and the US. MRI data were available for a subset of 421 PwMS. We adjusted raw cognitive scores for age, sex, and education according to each country's normative values, and assigned each cognitive test to the corresponding main cognitive domain. We applied an unsupervised machine learning model by means of a K-means clustering technique to identify data-driven CoPs, identifying the optimal number of phenotypes using the Elbow method. The percentage of cognitively preserved, mild CI and severe CI participants was determined for each group, and for each cognitive domain. We corrected MRI images for scanner inhomogeneities and registered T2-FLAIR images to T1w scans using the Advanced Normalization Tools (ANTs)(Tustison et al., 2010). We applied the Lesion Segmentation Toolbox (LST) for lesion segmentation (Schmidt et al., 2017). We used Freesurfer (Fischl, 2012) and SAMSEG (Cerri et al., 2021) for brain segmentation and parcellation, and normalized whole and regional

brain volumes for the total intracranial volume. We visually inspected MRI images and outcomes after each processing step. Descriptive statistics and ANOVAs determined demographic, clinical, and MRI differences across phenotypes.

Results: We identified four CoPs differing by types and number of impaired domains. CoP-1 was cognitively preserved (CP) (34% of the whole cohort). CoP-2 (22%) showed a main involvement in visuo-spatial memory. CoP-3 was multi-domain mild CI group (30%) where executive function, processing speed, and verbal memory were most frequently involved. CoP-4 was a severe multi-domain group (14%) where almost all cognitive domains were affected (Figure 1). The cognitively preserved group (CoP-1) was younger (mean and SD: 38.3(11) years) and had a shorter disease duration (7.2(7.8) years) compared to the other CoPs (P<0.001). While CoP-2 and CoP-3 did not differ in disease duration (8.7(8.4) vs .9.8(9.7) years; P>0.05), they had different educational levels (14.2(4) vs. 13.3(4) years, P<0.001). Statistically significant differences were observed among all CoPs for whole-brain grey matter, deep grey matter, thalamic volume, and cortical thickness (P<0.001) except between CoP-2 and CoP-3 (P>0.05). Lesion load did not differ between CoP-1 and CoP-2 (P>0.05).

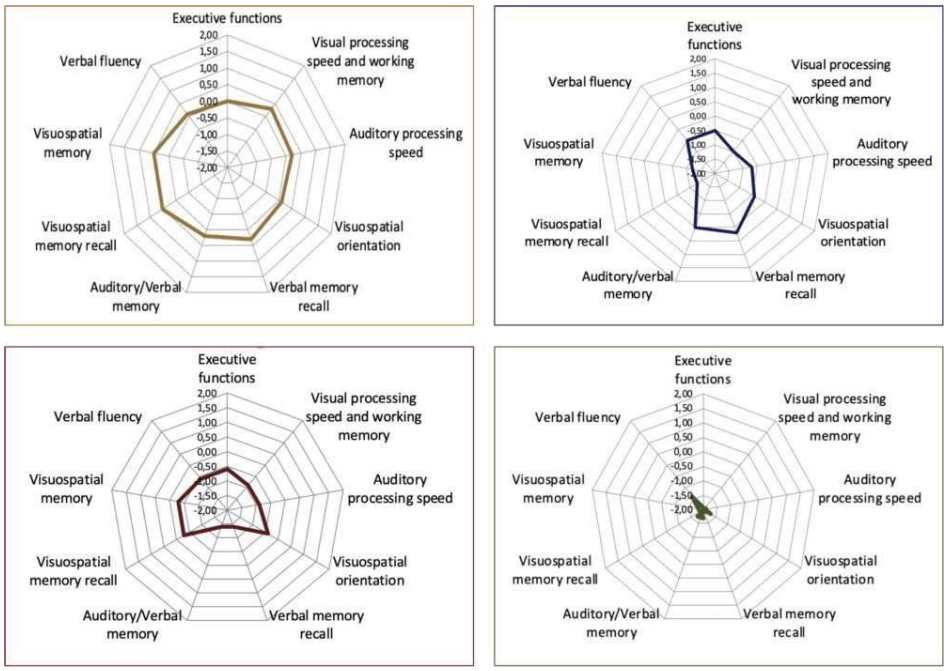

Conclusions: The degree of severity and type of cognitive functions impaired in PwMS differs, leading to different cognitive profiles. The identified CoPs differed for the content of grey matter volume and lesion load. Future studies should investigate the temporal dynamics of cognitive phenotypes in MS to determine whether they are associated to different trajectories of clinical impairment.

References

1. Cerri, S.(2021). "A contrast-adaptive method for simultaneous whole-brain and lesion segmentation in multiple sclerosis.", Neuroimage,vol. 225, p.117471
2. De Meo, E. (2021)."Identifying the distinct cognitive phenotypes in multiple sclerosis.", JAMA neurology, vol.78.4, pp.414-425
3. Fischl, B.(2012). "FreeSurfer.", Neuroimage, vol. 62.2, pp. 774-781.
4. Schmidt, P. (2017). "LST: A lesion segmentation tool for SPM." Manual/Documentation for version 2, p.15.
5. Tustison, N.J. (2010). "N4ITK: improved N3 bias correction.", IEEE transactions on medical imaging, vol. 29.6, pp.1310-1320.
6. Walton, C. (2020). "Rising prevalence of multiple sclerosis worldwide: Insights from the Atlas of MS.", Multiple Sclerosis Journal, vol.26.14, pp.1816-1821.

Poster No 247

B-amyloid indirectly affects cognition through tau and hippocampal atrophy in Alzheimer's disease

Sofia Fernandez Lozano[1], Vladimir Fonov[1], Joseph Therriault[2], Nesrine Rahmouni[2], Stijn Servaes[2], Jenna Stevenson[2], Nina Marguerita Poltronetti[2], Pedro Rosa-Neto[2], D Louis Collins[1]

[1]McConnell Brain Imaging Centre, Montreal Neurological Institute, Montreal, Quebec, [2]Translational Neuroimaging laboratory, McGill Centre for Studies in Aging, Montreal, Quebec

Introduction: Alzheimer's disease (AD) starts with gradual cerebral accumulation of β-amyloid (Aβ) decades before the onset of clinical symptoms. Recent biomarker models describe a sequence of Aβ aggregation, tau pathology, neurodegeneration,

and eventual cognitive decline (Selkoe & Hardy, 2016). Medial temporal atrophy, characterized by volume loss in the hippocampus (HC), is an early effect of neurodegeneration in AD disease progression (Rao et al., 2022). Structural equation modeling (SEM) is a statistical framework that combines factor analysis and multiple regression to examine multiple relationships among variables (Deng et al., 2018). Variables in SEM are represented as latent constructs and the relationships among them are expressed as a system of equations that examines direct and indirect pathways in a single integrated model.

Methods: We used SEM (lavaan R package (Rosseel, 2012) to explore the complex relationships between the neurobiological factors in the early stages preceding AD dementia in a longitudinal cohort of cognitively healthy (n=147) and mild cognitive impaired (n=64) participants from the TRIAD cohort (Stevenson et al., 2022). Our sample comprised 333 timepoints of neuropsychological evaluation, structural MRI, Aβ- and tau-PET. We explored the direct and indirect effects of Aβ on cognition (Montreal Cognitive assessment, MoCA) with tau pathology and HCl atrophy as potential mediators. Aβ and tau were measured with [18F]AZD4694 and [18F]MK6240 PET respectively, using the cerebellar grey matter as the reference region for [18F]AZD4694 and the inferior gray matter of cerebellum as the reference for [18F]MK6240 SUVR calculation. Aβ accumulation was quantified by the average SUVR in the neocortex. Tau accumulation was quantified as the average SUVR value for 6 Braak stage masks (Braak & Braak, 1991). Neurodegeneration was characterized by the HC-to-Ventricle ratio (HVR), a HC integrity measure that leverages the idea of ex-vacuo dilation in a single value composed of the ratio of the HC volume and the sum of the volumes of HC and the temporal horn of the lateral ventricle (Schoemaker et al., 2019). We averaged the HVR values of the left and right hemispheres and inverted the result (1–HVR) to convert the integrity biomarker into a measure of atrophy. In the SEM, we included age, sex, the number of APOE4 alleles and education as covariates. Finally, we calculated the standardized coefficients and the mediation proportion for the direct and indirect effects in our model.

Results: The demographic data of our sample is presented in Table 1. The standardized coefficients for the mediation model are represented in Fig. 1. MoCA scores were affected by tau (β=-0.64, βstd=-0.42, p<0.01), HC atrophy (β=-7.47, βstd=-0.25, p<0.01), and education (β=-0.09, βstd=-0.13, p<0.01), but not by Aβ (β=-0.3, βstd=-0.06, p=0.31), age (β=-0.03, βstd=-0.08, p=0.14) or sex (β=0.08, βstd=0.02, p=0.73) Aβ was affected by APOE4 (β=0.29, βstd=0.32, p<0.01) and age (β=0.01, βstd=0.19, p<0.01), but not by sex (β=-0.03, βstd=-0.03, p=0.54). Tau was affected by Aβ (β=1.97, βstd=0.6, p<0.01), APOE4 (β=0.53, βstd=0.18, p<0.01), and age (β=-0.02, βstd=-0.1, p=0.02), but not sex (β=-0.11, βstd=-0.03, p=0.44). HC atrophy was affected by Aβ (β=0.02, βstd=0.12, p=0.04), age (β<0.01, βstd=0.49, p<0.01), sex (β=0.04, βstd=0.20, p<0.01), and APOE4 (β=0.02, βstd=0.12, p=0.01), but not tau (β<0.01, βstd=0.08, p=0.17). The mediation proportion showed that 73.8% of the total effect of Aβ was mediated through the indirect effect of tau and 8.7% through HC atrophy.

Variable	AD, N = 32[1]	CN, N = 147[1]	MCI, N = 64[1]	p-value[2]
Sex				0.13
Female	19 (59%)	99 (67%)	34 (53%)	
Male	13 (41%)	48 (33%)	30 (47%)	
Age (years)	67 (8)	72 (6)	71 (7)	0.002
Education (years)	14.6 (3.8)	15.3 (3.7)	15.4 (3.8)	0.7
APOE4 alleles				0.001
0	14 (44%)	107 (73%)	33 (52%)	
1	14 (44%)	36 (24%)	27 (42%)	
2	4 (13%)	4 (2.7%)	4 (6.3%)	
MoCA score	15 (7)	28 (2)	25 (3)	<0.001
Number of visits				0.2
1	20 (63%)	76 (52%)	29 (45%)	
2	12 (38%)	68 (46%)	30 (47%)	
3	0 (0%)	3 (2.0%)	5 (7.8%)	
Amyloid (PET)	2.22 (0.60)	1.47 (0.36)	1.98 (0.65)	<0.001
Tau (PET)	12.32 (5.15)	5.77 (0.70)	7.21 (2.12)	<0.001
HC vol (left)	2.60 (0.38)	2.90 (0.31)	2.65 (0.35)	<0.001
HC vol (right)	2.56 (0.42)	2.95 (0.30)	2.76 (0.33)	<0.001
HVR (left)	0.56 (0.11)	0.65 (0.08)	0.60 (0.10)	<0.001
HVR (right)	0.56 (0.12)	0.67 (0.08)	0.63 (0.09)	<0.001

[1]n (%); Mean (SD)

[2]Pearson's Chi-squared test; Kruskal-Wallis rank sum test; Fisher's exact test

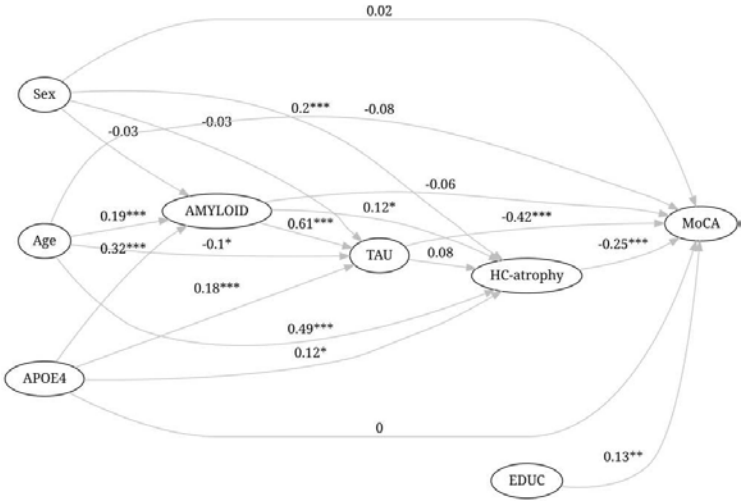

Conclusions: In our early AD cohort, we found that the direct impact of Aβ aggregation in the brain on cognitive function is not statistically significant, and rather its influence on cognition is largely explained by its mediating effects of tau pathology and, to a lesser extent, HC atrophy. Our results support Aβ aggregation as an early, upstream event in the development of dementia due to AD.

References

1. Braak, H., & Braak, E. (1991). Neuropathological stageing of Alzheimer-related changes. Acta Neuropathologica, 82(4), 239–259. https://doi.org/10.1007/BF00308809
2. Deng, L., Yang, M., & Marcoulides, K. M. (2018). Structural Equation Modeling With Many Variables: A Systematic Review of Issues and Developments. Frontiers in Psychology, 9, 580. https://doi.org/10.3389/fpsyg.2018.00580
3. Rao, Y. L., Ganaraja, B., Murlimanju, B. V., Joy, T., Krishnamurthy, A., & Agrawal, A. (2022). Hippocampus and its involvement in Alzheimer's disease: A review. 3 Biotech, 12(2), 55. https://doi.org/10.1007/s13205-022-03123-4
4. Rosseel, Y. (2012). lavaan: An R Package for Structural Equation Modeling. Journal of Statistical Software, 48, 1–36. https://doi.org/10.18637/jss.v048.i02
5. Schoemaker, D., Buss, C., Pietrantonio, S., Maunder, L., Freiesleben, S. D., Hartmann, J., Collins, D. L., Lupien, S., & Pruessner, J. C. (2019). The hippocampal-to-ventricle ratio (HVR): Presentation of a manual segmentation protocol and preliminary evidence. NeuroImage, 203, 116108. https://doi.org/10.1016/j.neuroimage.2019.116108
6. Selkoe, D. J., & Hardy, J. (2016). The amyloid hypothesis of Alzheimer's disease at 25 years. EMBO Molecular Medicine, 8(6), 595–608. https://doi.org/10.15252/emmm.201606210
7. Stevenson, J., Rahmouni, N., Chamoun, M., Benedet, A. L., Stevenson, A., Pallen, V., Therriault, J., Lussier, F. Z., Tissot, C., Bezgin, G., Pascoal, T. A., Vitali, P., Gauthier, S., & Rosa-Neto, P. (2022). TRIAD multi-dimensional biobank for biomarker discovery. Alzheimer's & Dementia, 18(S6), e067924. https://doi.org/10.1002/alz.067924

Poster No 248

Environmental complexity on spatial brain volume and behavior across the Alzheimer's spectrum

Naewoo Shin[1], Karen Rodrigue[1], May Yuan[1], Kristen Kennedy[1]

[1]*The University of Texas at Dallas, Dallas, TX*

Introduction: Spatial cognition is among the cognitive domains that exhibit decline with advanced normal aging[1]. Deficits in spatial navigation, however, are much more pronounced in Alzheimer's disease (AD) and it is considered one of the earliest signs of the disease[2,3]. While research on the role of aging on spatial navigation is growing, studies on local geospatial features in relation to AD risk are scarce. Greater opportunities for urban dwellers to utilize and strengthen cognitive maps via routinely navigating more complex spatial environments may exhibit neuroprotective properties. We recently introduced Environmental Complexity (EC), an index reflecting the frequency and density of street networks and landmark features/points of interest, computed by geo-locating participants from the National Alzheimer's Coordinating Center (NACC) for each zip-code zone across the USA. EC predicted cognitive status (cognitively normal, mild cognitive impairment (MCI), AD) with 95% classifier precision[4]. Here, we extend that work to explore the effects of EC on the maintenance of spatial navigation-related gray matter volume and spatial behavioral performance.

Methods: This study utilized a sample of 660 participants (assigned as cognitively normal [n = 378], MCI [n = 114], and AD [n = 168]) from the NACC uniform data set (45-93 years old). The sample was limited to participants who stayed in the same 3-digit zip-code over the course of their visits. The AD spectrum was contrast coded as two orthogonal contrasts: DX1 (-.66,

.33, .33) for healthy vs. non-healthy, and DX2 (0, -.5, .5) for MCI vs. AD. MRI estimation of gray matter volumes were processed following the ADNI four-tissue segmentation protocol. A priori regions of interest were selected for their association with egocentric and allocentric spatial navigation and were adjusted for ICV. We define the EC as the geometric average of diversity and abundance measures of spatial features in a 3-digit zip-code zone. Total of 20 network measures and landmark features in each 3-digit zip-code zone across the United States (154 total zones) were collected from Open Street Map and SafeGraph Core Places. EC is calculated as the square root of EntropyH* MaxRatio. EntropyH is the measure of the average diversity of all geospatial features. MaxRatio is the measure of abundance of spatial features within a 3-digit zip-code zone. Structural equation modeling was conducted to analyze the data, with EC and mean-centered age predicting latent allocentric and egocentric brain region volumes, AD spectrum status, and latent spatial behavioral performance.

Results: Results indicate that greater EC was significantly positively associated with larger brain volumes in allocentric spatial regions, but not with egocentric regions. A significant indirect effect of EC on spatial cognition was identified through allocentric regions and DX1. Greater EC, related to greater brain volume was associated with less diagnosis of MCI or AD vs being cognitively normal, and having higher spatial behavioral scores. This mediation eliminated the direct association of EC on spatial behavior. Age was negatively associated with both brain volumes, as expected. There was also no significant direct relationship between age and spatial cognition, rather this association was mediated by brain volume and cognitive diagnosis status.

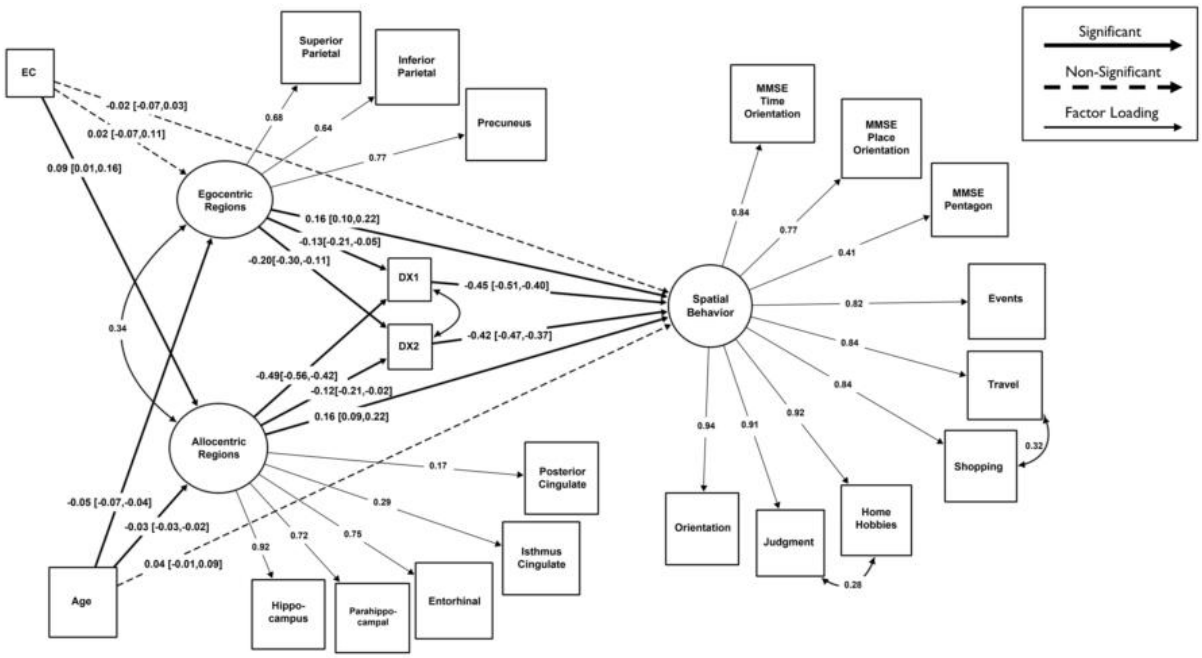

Full structural equation model with environmental complexity, age, volumetric allocentric and egocentric latent variables, diagnoses, and spatial behavioral latent variable. Solid lines represent significant paths ($p<0.05$) at 95% confidence interval, and dashed lines represent non-significant estimated paths. Standardized estimates were derived from bootstrapping 10,000 iterations. APOE, education, and sex were regressed from all latent variables. EC = environmental complexity

Conclusions: These findings suggest that residing in spatially complex environments allows for the routine usage of cognitive neural mapping across time, which may help to stave off the brain atrophy that is associated with spatial navigation difficulties seen in Alzheimer's disease, and may be a target for future interventions. In sum, prevention of AD is of paramount concern and these findings suggest that residing in and routinely navigating spatially complex environments may be one mechanism to help stave off the brain atrophy associated with spatial navigation difficulties seen in aging and Alzheimer's disease.

References

1. Klencklen, G., Després, O., & Dufour, A. (2012). What do we know about aging and spatial cognition? Reviews and perspectives. Ageing research reviews, 11(1), 123-135.
2. Lithfous, S., Dufour, A., & Després, O. (2013). Spatial navigation in normal aging and the prodromal stage of Alzheimer's disease: insights from imaging and behavioral studies. Ageing research reviews, 12(1), 201-213.
3. Possin, K. L. (2010). Visual spatial cognition in neurodegenerative disease. Neurocase, 16(6), 466-487.
4. Yuan, M., & Kennedy, K. M. (2023). Utility of Environmental Complexity as a Predictor of Alzheimer's Disease Diagnosis: A Big-Data Machine Learning Approach. The Journal of Prevention of Alzheimer's Disease, 10(2), 223-235.

Poster No 250

Cognitive Fatigue in Multiple Sclerosis Associated with Brain Iron Concentration

Bing Yao[1], Mateusz Kowalczyk[1], Hannah Ovadia[1], Sarah Wood[1]

[1]Kessler Foundation, West Orange, NJ

Introduction: Fatigue, defined as an overwhelming feeling of lack of both mental and physical energy, has been reported in over 90% of individuals with multiple sclerosis (MS)[1]. Studies have shown basal ganglia structures play a central role in fatigue[2]. Meanwhile, abnormal iron deposition has been observed in the deep gray matter structures including basal ganglia in MS[3]. In this study, we aimed to examine the correlation between brain iron concentration indicated by susceptibility contrast imaging and the severity of fatigue in MS.

Methods: Data from ten clinically definite MS patients (F/M = 8/2, age = 56.0±8.3 y/o) and ten healthy controls (F/M = 5/4, age = 37.5±12.5 y/o) were reported in this study. MRI: A 3D multi-echo gradient-echo acquisition was performed on a 3T Siemens Skyra scanner with a standard 20-ch head/neck coil. The parameters were as following: TE = 8.49/16.86/25.23/33.60/41.97 ms, TR = 49 ms, resolution = 0.9×0.9×2 mm2, flip angle= 20°, bandwidth= ±38.4 kHz. A total of 52 axial slices were acquired to cover the whole brain. A GRAPPA of 2 was used to shorten the scan time down to 5 minutes. Quantitative R2* maps were derived from exponential fitting over the 5 echo data. The Laplacian algorithm was used to unwrap the raw phase and remove the phase background. The susceptibility maps were then calculated using the LSQR algorithm based on the unwrapped phase maps and averaged over three echo data (25.23, 33.60 and 41.97 ms)[4]. Six regions of interest (ROIs) including substantia nigra (SN), red nucleus (RN), globus pallidus (GP), putamen (PU), caudate nucleus (CN), and thalamus (TH) were mapped on the magnitude images. A registered MP-RAGE image was used as an additional reference for the ROI drawing. Each ROI was drawn on multiple successive images to almost entirely cover each structure. R2*, and susceptibility values were averaged in each ROI, respectively, and then averaged across all the subjects in the group. Fatigue measures: Each individual was administrated a Fatigue Severity Scale (FSS) test and a Modified Fatigue Impact Scale (MFIS) test to measure their fatigue levels. The FSS scores and total MFIS scores with its subcategories (Physical, Cognitive, Psychosocial) subscales from each individual were correlated with R2*, Frequency shift and QSM values in all ROIs.

Results: Two representative axial slices of the MR images containing the ROI regions from one MS patient are shown in Fig. 1. The SN, RN, GP, PU, and CN are readily identifiable in the magnitude, and R2*, frequency and QSM maps. Comparing to the magnitude and R2* maps, these iron-rich structures are clearly visible and distinguishable with clear boundaries in the QSM. Fig. 2 shows A comparison of the R2* and susceptibility values between MS patients (MS) and healthy controls (HC) in different brain regions. Significant positive correlations between Frequency and FSS Total, MFIS Total, MFIS Physical subscale and MFIS Psychosocial subscale are found in CN. QSM also correlates with MFIS Total and MFIS Physical subscales significantly. Based on the data from ten subjects, no significant consistent positive correlations in the other ROIs are found. No significant correlations between R2* and all fatigue measures are observed.

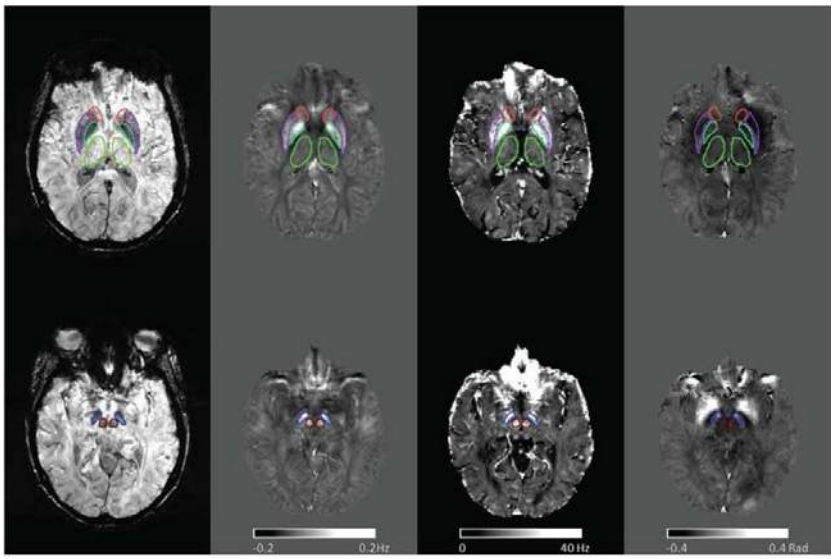

Fig 1. Illustration of two representative axial slices of the MR images containing the Regions Of Interests (ROIs) from one MS patient. The ROIs are substantia nigra (SN), red nucleus (RN), globus pallidus (GP), putamen (PU), caudate nucleus (CN), and thalamus (TH).

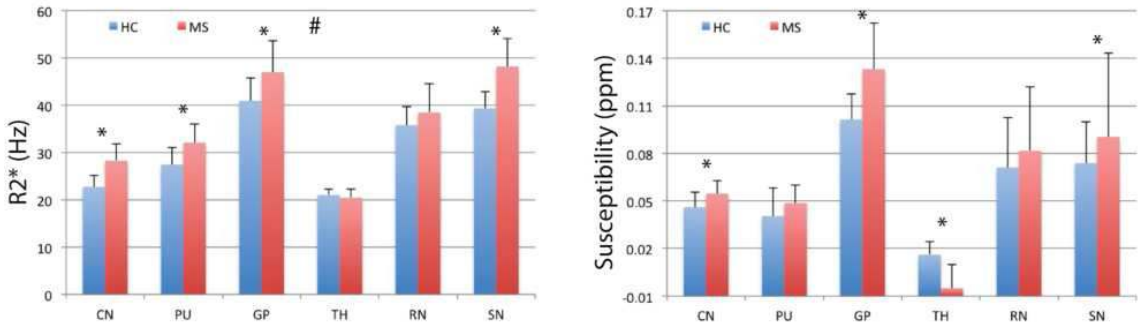

Fig. 2 A comparison of the R2* and susceptibility values between MS patients (MS) and healthy controls (HC) in different brain regions. "*" indicates a significant difference between patient and healthy groups ($p<0.05$). The error bars are standard deviations.

Conclusions: Our findings on the correlation between iron deposition measured by MR susceptibility contrast imaging and severity of fatigue is of particular interesting to understanding the fatigue mechanisms, which may lead to an effective treatment on reducing clinical symptoms in MS patients.

References

1. DeLuca J. (2008), 'Neural correlates of cognitive fatigue in multiple sclerosis using functional MRI'. Journal of the Neurological Sciences. Vol 270(1-2):28–39.
2. Chaudhuri A. (2000), 'Fatigue and basal ganglia'. Journal of the Neurological Sciences. Vol 179(1-2):34–42.
3. Yao, B. (2015), 'Detecting Iron Deposition In Multiple Sclerosis Using Susceptibility Contrast Imaging'. Proceeding of the International Society for Magnetic Resonance in Medicine vol 23.
4. Li W. (2011), 'Quantitative susceptibility mapping of human brain reflects spatial variation in tissue composition', NeuroImage. vol 15;55:1645.
5. Dobryakova E. (2013), 'Neural correlates of cognitive fatigue: cortico-striatal circuitry and effort-reward imbalance'. Journal of the International Neuropsychological Society. Vol 19(8):849–53.

Poster No 251

Evaluating Alzheimer Disease tau burden and spread in relation to cognitive domain deficits

Stephanie Doering[1], Austin McCullough[1], Brian Gordon[1], Nicole McKay[1], Pete Millar[2], Diana Hobbs[3], Rohan Agrawal[1], Andrew Aschenbrenner[1], Jason Hassenstab[2], John Morris[4], Tammie Benzinger[4]

[1]Washington University School of Medicine, Saint Louis, MO, [2]Washington University in St. Louis, St. Louis, MO, [3]Washington University in St. Louis, St Louis, MO, [4]Washington University School of Medicine, St. Louis, MO

Introduction: Alzheimer Disease (AD) tau-protein pathological progression is characterized by a distinct spatiotemporal pattern in which (1) early tau burden continues to accumulate in early-impacted brain regions as well as (2) the simultaneous tau spread to additional brain regions. Specific cognitive domain deficits are shown to correlate with the spatial distribution of tau pathology; however, summary measures of tau in neuroimaging largely focus on tau burden in early regions of interest. Recent work suggests atypical variants of AD with unique spreading patterns of tau are reflective of the type of cognitive impairments. Summary measures evaluating tau burden for typical amnestic AD are therefore insufficient in capturing inter-individual differences in tau progression. In this work, we evaluate our previously proposed metric for calculating tau spread in relation to specific cognitive domain deficits.

Methods: 469 older participants and 39 younger controls (YC) were recruited with tau positron emission tomography (PET), amyloid PET, Clinical Dementia Rating® (CDR®), and neuropsychological testing with the Uniform Data Set (UDS-3) from the Washington University in St. Louis Knight Alzheimer Disease Research Center (Knight ADRC). Older participants were split into disease stage groups according to amyloid positivity and CDR score (Older Controls [OC], Preclinical, Symptomatic). Tau burden was calculated using Tau Index (TI) (Mishra et al., 2017), a summary measure of tau sensitive to preclinical regions of interest (ROIs). Tau spread was calculated using Tau Spatial Spread (TSS) (Figure 1), the proportion of voxels with significantly abnormal tau pathology relative to YC. Cognitive domain composites previously developed (McKay et al., 2023) and the Knight ADRC Preclinical Alzheimer Cognitive Composite (Knight ADRC PACC) were calculated relative to OC. Participant baseline cognitive domain scores were evaluated across disease stage and relative to both TI and TSS with nested linear regression models evaluated with AIC and Pearson correlation. Longitudinal analyses were conducted with linear mixed effects regression to determine whether baseline TI and TSS can predict the rate of decline for each cognitive domain.

Gaussian Mixture Modeling and Estimated Marginal Means analyses were conducted for visualizations of the cognitive domain longitudinal trajectories.

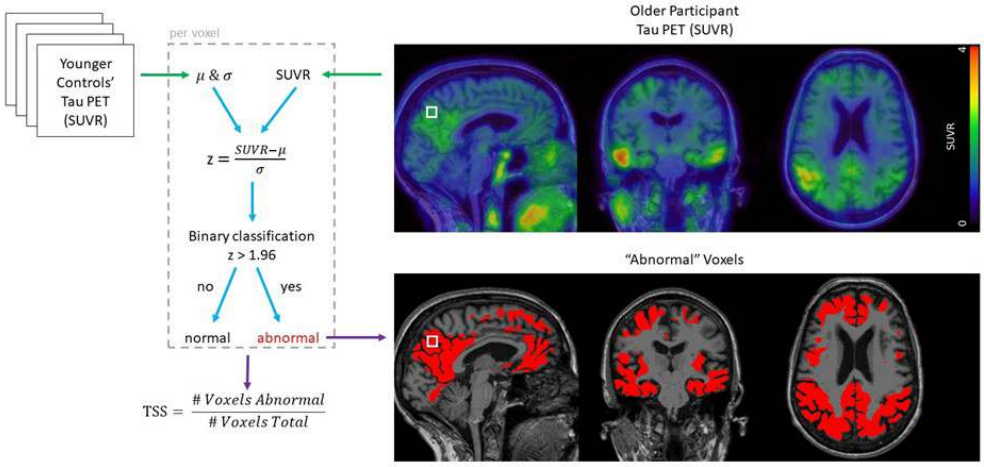

Figure 1. Calculation of Tau Spatial Spread.
Tau Spatial Spread (TSS) was calculated for older participants relative to younger controls (YC) using aligned tau PET scans with voxel-wise SUVRs. For each voxel (white square), the SUVR value is identified for the older participant. The SUVR values for the corresponding voxel are identified in all YC scans, which are then used to calculate mean and standard deviation. The older participant's voxel z-score is next calculated from participant SUVR and YC mean and standard deviation. Voxels are then classified as normal or abnormal with the threshold z>1.96. Once all voxels have been classified, TSS is calculated as the proportion of abnormal voxels. All abnormal voxels can be displayed overlaying the participant's MRI.

Results: Cognitive domain scores were significantly lower for symptomatic participants but no difference was found between OC and preclinical participants. All cognitive domains were correlated to both TI and TSS (Figure 2), however the working memory domain appears underpowered in our cohort. Baseline PACC and the Attentional domain demonstrate added benefit of modeling TSS in addition to TI according to the nested linear models. Episodic and Semantic Memory domains are inconclusive on whether there is added benefit of modeling TSS according to AIC. TI can predict the rate of decline in all domains but the effect is weak for the Working Memory domain. TSS can predict the rate of decline in the PACC, Episodic, and Semantic Memory domains, but not in the Working Memory domain or Attention domain.

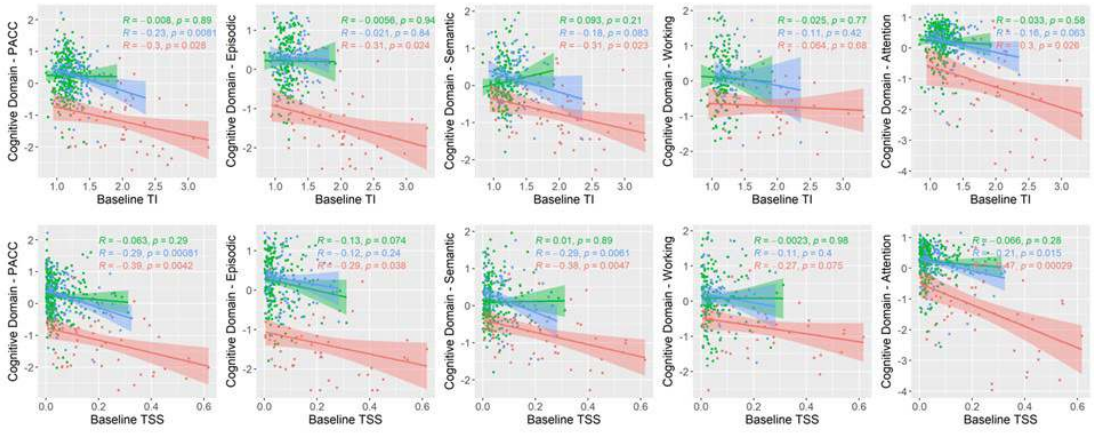

Figure 2. Tau Metrics vs Cognitive Domains.
Relationship between baseline cognitive domain score and either baseline TI or TSS. Pearson correlations and linear regressions conducted per disease stage group (green: Older Controls, blue: Preclinical, red: Symptomatic).

Conclusions: Overall, preclinical impairment in various cognitive domains is related to early tau pathology. Tau burden largely explains cognitive impairments, however tau spread captures additional impairment in the attentional domain (possibly due to the inclusion of neural correlates in later-stage regions) which may be attributed to the preclinical stage prior to episodic impairment. Tau burden can predict the trajectory of the rate of future cognitive decline across all domains, indicating it is a

strong predictive biomarker. Tau spread, however, does not predict the rate of future decline in the attentional domain despite having added benefit at baseline. This may indicate that attentional deficits appear early in AD and therefore are largely observed at baseline impairment rather than future cognitive decline.

References
1. McKay, N.S. et al. (2023) Pick a PACC: Comparing domain- specific- and general- cognitive composites in Alzheimer disease research. preprint. Open Science Framework. Available at: https://doi.org/10.31219/osf.io/kp4hr.
2. Mishra, S. et al. (2017) 'AV-1451 PET imaging of tau pathology in preclinical Alzheimer disease: Defining a summary measure', NeuroImage, 161, pp. 171–178. Available at: https://doi.org/10.1016/j.neuroimage.2017.07.050.

Poster No 252

Brain Connectivity Measured Through Spatial Covariance as a Biomarker for Neurodegeneration in AD

Débora Peretti[1], Cecilia Boccalini[1], Max Scheffler[2], Cristelle Rodriguez[2,1], Marie Montandon[2,1], Sven Haller[1,3,4,5], Panteleimon Giannakopoulos[2], Giovanni B. Frisoni[2,1], Valentina Garibotto[2,1]

[1]University of Geneva, Geneva, Switzerland, [2]Geneva University Hospitals, Geneva, Switzerland, [3]Centre d'Imagerie Médicale de Cornavin, Geneva, Switzerland, [4]Uppsala University, Uppsala, Sweden, [5]Capital Medical University, Beijing, China

Introduction: Scaled Subprofile Modelling using Principal Component Analysis (SSM/PCA) is a voxel-based technique that uses spatial covariance maps to identify disease patterns (DP) that best differentiate between two groups of subjects. This technique has been applied to 18F-fluorodeoxyglucose positron emission tomography (FDG-PET) scans to classify Alzheimer's disease (AD) patients. AD is a neurodegenerative disorder characterised by a hypometabolic pattern that affects temporal and parietal lobes, and, in advanced cases, the frontal lobe. A specific region of interest (ROI) combining angular gyrus, posterior cingulate, and temporal lobe has been shown to measure specific AD hypometabolism. Furthermore, a distinctive pattern of atrophy, observed in the temporal lobe on magnetic resonance imaging (MRI) scans, can also be used for AD identification. Atrophy and FDG-PET ROI uptake are established biomarkers of neurodegeneration in AD. The aim of this study was to compare these methods with a connectivity metric measured through SSM/PCA to assess the AD neurodegeneration pattern in a memory clinic patient cohort.

Methods: A cohort of 333 subjects from the memory clinic of the Geneva University Hospitals underwent FDG-PET, T1-MRI, and neuropsychological assessment within one year. Cognitive stage varied between cognitively unimpaired (CU), mild cognitive impairment (MCI), dementia, and psychiatric disorders (other). AD was diagnosed based on clinical assessment and available biomarkers. PET images were registered to a stereotactic space using subjects' respective MRI. Three approaches to measure neurodegeneration were used: SSM/PCA, SUVR uptake in the Landau meta-ROI, and AD cortical thickness signature. SSM/PCA was applied to a subset of 15 CU and 15 AD-dementia subjects to generate an AD-specific DP (ADDP). ADDP was validated using bootstrapping and leave-one-out cross validation. Remaining subjects were tested against the generated ADDP to retrieve pattern expression. FDG-PET images were then converted to standardised uptake value ratios (SUVR, with vermis and pons as reference) and regional uptake in the Landau meta-ROI was extracted. Finally, an AD cortical thickness signature was extracted from MRI scans using Freesurfer. For each approach, a receiver operating characteristic (ROC) curve was generated to estimate an AD-dementia threshold and calculate its performance for identifying AD-dementia patients using an independent set of CU and AD-dementia subjects. Spearman correlations between neurodegeneration methods and baseline mini-mental state examination (MMSE) score and MMSE annual rate of change were estimated in the whole group and in a subset of 165 subjects who underwent a follow-up neuropsychological assessment, respectively.

Results: Mean (SD) age of participants was 72 (7) years, and 57% of subjects were female. The threshold for AD classification for SSM/PCA scores was of -763, with an area under the curve (AUC) of 0.96, a sensitivity of 0.9, and specificity of 0.95. The meta-ROI had an SUVR threshold of 1.4 (AUC=0.9, sensitivity=0.85, specificity=0.86), and the cortical thickness threshold was 2.6 (AUC=0.89, sensitivity=0.78, specificity=0.86). All methods were significantly correlated to baseline MMSE scores (SSM/PCA=-0.43, meta-ROI=0.38, cortical thickness=0.37, $p<0.01$). Patients diagnosed with dementia (regardless of aetiology) showed a significant MMSE annual rate of change (average=-3.8±3.8 points/year) compared to other groups. SSM/PCA scores showed the highest correlation with MMSE annual rate of change (-0.52, $p<0.01$), followed by the meta-ROI (0.46, $p<0.01$), and cortical thickness (0.36, $p<0.01$).

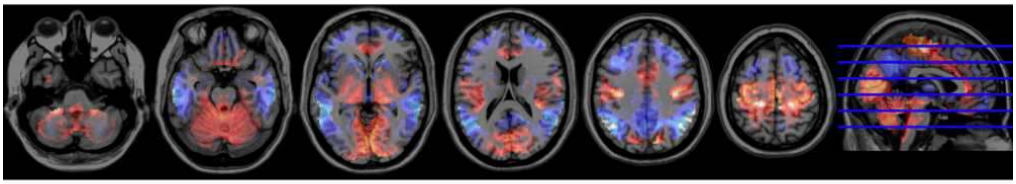

Figure 1. Characteristic ADDP map overlay on brain MRI image. Blue voxels show regions with hypometabolic changes in AD, and red voxels hypermetabolic changes.

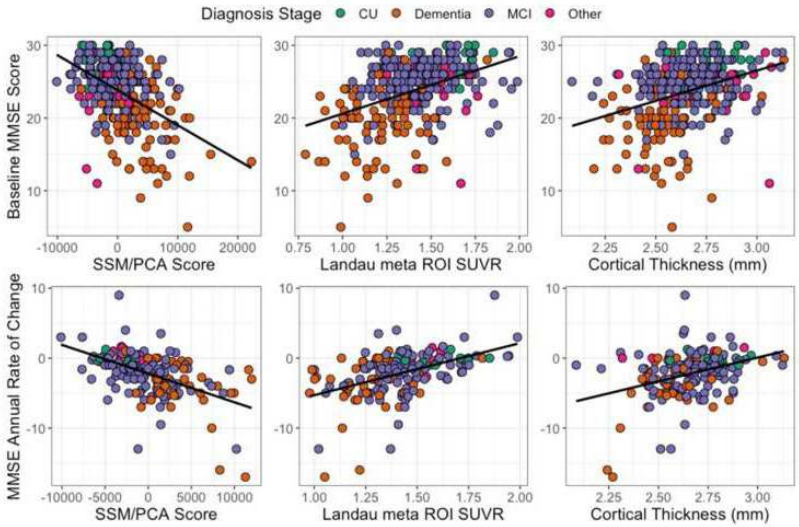

Figure 2. Correlation of baseline MMSE and MMSE annual rate of change with SSM/PCA scores, meta-ROI SUVR, and cortical thickness. The solid black lines show the linear regression estimated between measurements.

Conclusions: SSM/PCA ADDP expression provides a strong and specific marker for AD neurodegeneration, outperforming more conventional metrics. As SSM/PCA is a connectivity method that can be applied on a single-subject basis, it has a potential to be applied in clinical practice as a characterisation and prognostic biomarker.

References

1. Landau, S. M., Harvey, D., Madison, C. M., Koeppe, R. A., Reiman, E. M., Foster, N. L., Weiner, M. W., & Jagust, W. J. (2011). 'Associations between cognitive, functional, and FDG-PET measures of decline in AD and MCI'. Neurobiology of Aging, 32(7), 1207–1218.
2. Peretti, D. E., Renken, R. J., Reesink, F. E., de Jong, B. M., de Deyn, P. P., Dierckx, R. A. J. O., Doorduin, J., Boellaard, R., & Vállez García, D. (2021). 'Feasibility of pharmacokinetic parametric PET images in scaled subprofile modelling using principal component analysis'. NeuroImage: Clinical, 30, 102625.
3. Mattsson-Carlgren, N., Leuzy, A., Janelidze, S., Palmqvist, S., Stomrud, E., Strandberg, O., Smith, R., & Hansson, O. (2020). The implications of different approaches to define AT(N) in Alzheimer disease. Neurology, 94(21), e2233–e2244.
4. Meles, S. K., Pagani, M., Arnaldi, D., de Carli, F., Dessi, B., Morbelli, S., Sambuceti, G., Jonsson, C., Leenders, K. L., & Nobili, F. (2017). The Alzheimer's disease metabolic brain pattern in mild cognitive impairment. Journal of Cerebral Blood Flow and Metabolism, 37(12), 3643–3648.

Poster No 253

Diffusion Tensor Imaging as an Indicator Glymphatic Dysfunction Over Time in Patients with ALS

Rachel Sharkey[1], Filomeno Cortese[1], Bradley Goodyear[1], Lawrence Korngut[1], Keith Sharkey[1], Sanjay Kalra[2], Minh Dang Nguyen[1], Richard Frayne[1], Gerald Pfeffer[1]

[1]University of Calgary, Calgary, Alberta, [2]University of Alberta, Edmonton, Alberta

Introduction: Introduction: Amyotrophic lateral sclerosis (ALS) is a neurodegenerative disease characterized by the degeneration of upper and lower motoneurons (Yedavalli, Patil, and Shah 2018). ALS is associated with the accumulation of misfolded proteins in brain tissue. The brain's glymphatic drainage system, which consists of perivascular channels that drain fluid from the brain parenchyma through aquaporin-4 channels expressed on astrocyte endfeet, is capable of draining these proteins from the brain, thereby reducing proteinopathy. It is a relatively recent discovery and remains poorly understood in the context of neurodegeneration (Liu et al. 2023; Jessen et al. 2015). One of the major challenges in studying the human glymphatic system is the difficulty in visualizing the glymphatic flow in living tissue (Naganawa and Taoka 2022). The

perivascular spaces that make up the glymphatic system are too small to be easily viewed using conventional neuroimaging methods. The new diffusion tensor image analysis along perivascular space (DTI-ALPS) technique takes advantage of conventional diffusion analysis methods applied to the major white matter tracts, to calculate an indirect measure of glymphatic flow. DTI-ALPS can be applied to many commonly collected diffusion images sets (Taoka et al. 2017; Naganawa and Taoka 2022; Steward et al. 2021). Prior work using the DTI-ALPS index by Liu et al. has identified a reduced value in patients with early-stage ALS relative to controls at a single time point. Using DTI-ALPS, our study presents the advantage of a longitudinal analysis (three timepoints over 8 months) in a mixed cohort of patients with ALS and primary lateral sclerosis (PLS) that affects only upper motoneurons (Yedavalli, Patil, and Shah 2018).

Methods: Diffusion magnetic resonance images from the Calgary cohort of the Canadian ALS Neuroimaging Consortium (CALSNIC) (patients, n = 23; controls, n=22) were processed using custom scripts based image processing and analysis tools from FSL, SPM and MRtrix to calculate the DTI-ALPS index from voxel-wise tensor values (Taoka et al. 2017; Kalra et al. 2020). A linear mixed effects model was used to compare patients to controls across three imaging sessions over eight months, controlling for age and sex, and including an interaction with diagnosis and time. This evaluation was repeated with a second exploratory model with patients grouped by diagnosis (ALS: n = 18, PLS: n = 5). Both models were followed up with models examining diagnosis, age, sex, ALSFRS score and estimated disease progression rate, as well as their interactions with time.

Results: ALS and PLS participants had reduced DTI-ALPS index values compared to controls ($p < 0.05$). This effect was driven by ALS participants ($p < 0.01$). PLS participants do not show the same relative reduction. Data from ALS and PLS participants showed a different pattern of change over time than controls ($p < 0.05$). ALS and PLS patients have a more similar trajectory over time compared to controls, despite the difference in mean DTI-ALPS index. We did not find a significant relationship between the DTI-ALPS index with specific symptom scores or symptom progression.

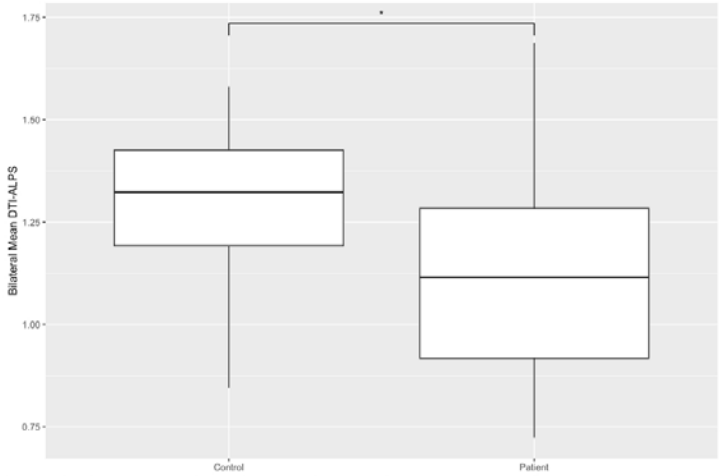

Figure 1. Differences in DTI-ALPS index between patients (amyotrophic lateral sclerosis and primary lateral sclerosis, n=23) and controls (n=22) in the CALSNIC dataset, *p < 0.05.

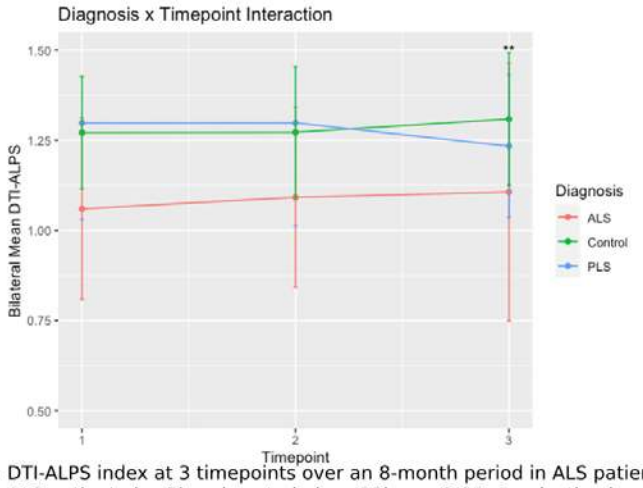

Figure 2. DTI-ALPS index at 3 timepoints over an 8-month period in ALS patients (n = 18), PLS patients (n=5) and controls (n = 22), $p < 0.05$. A reduction in DTI-ALPS in ALS patients was observed at all timepoints, and a difference in trajectory was observed between groups at the final timepoint, **$p < 0.05$.

Conclusions: We observed a reduced DTI-ALPS index in ALS patients consistent with the findings of Liu et al. but did not replicate the association they identified with ALSFRS score (Liu et al. 2023). This last finding may relate to the longer disease duration in our cohort. We also found a differing trajectory between ALS/PLS participants and controls in DTI-ALPS change over time. Patients with PLS did not show the same reduction in DTI-ALPS but did show a similar trajectory over time, suggesting that the glymphatic system plays a different role in these two motor neuron disorders given that ALS and PLS have very different clinical trajectories (Yedavalli, Patil, and Shah 2018). Future comparative studies with a larger cohort of PLS patients are warranted.

References

1. Jessen, Nadia (2015) "The Glymphatic System: A Beginner's Guide." Neurochemical Research 40 (12): 2583–99.
2. Kalra, Sanjay (2020) "A Prospective Harmonized Multicenter DTI Study of Cerebral White Matter Degeneration in ALS." Neurology 95 (8): e943–52.
3. Liu, Shuangwu (2023) "Glymphatic Dysfunction in Patients with Early-Stage Amyotrophic Lateral Sclerosis." Brain, August 16
4. Naganawa, Shinji (2022) "The Glymphatic System: A Review of the Challenges in Visualizing Its Structure and Function with MR Imaging." Magnetic Resonance in Medical Sciences 21 (1): 182–94.
5. Steward, Christopher E. (2021) "Assessment of the DTI-ALPS Parameter Along the Perivascular Space in Older Adults at Risk of Dementia." Journal of Neuroimaging 31 (3): 569–78.
6. Taoka, Toshiaki (2017) "Evaluation of Glymphatic System Activity with the Diffusion MR Technique: Diffusion Tensor Image Analysis along the Perivascular Space (DTI-ALPS) in Alzheimer's Disease Cases." Japanese Journal of Radiology 35 (4): 172–78.
7. Yedavalli, Vivek S, Abhijit Patil, and Parinda Shah. 2018. "Amyotrophic Lateral Sclerosis and Its Mimics/Variants: A Comprehensive Review." Journal of Clinical Imaging Science Dec 6: 8:53.

Poster No 254

Assessing Structural MRI Changes in Patients with Parkinson's Disease-Freezing of Gait

Alan Gardner[1], Saul Lopez[1], Zoltan Mari[2], Virendra Mishra[1]

[1]The University of Alabama at Birmingham, Birmingham, AL, [2]Cleveland Clinic Foundation, Las Vegas, NV

Introduction: Morphological studies utilizing T1-weighted (T1) magnetic resonance imaging (MRI) can provide insight into the structural brain changes such as volume, cortical thickness, cortical area, and local gyrification index (LGI) in patients with Parkinson's disease (PD) experiencing Freezing of Gait (FoG) by Utilizing FreeSurfer 7.0, the aforementioned T1-derived measures can be accurately estimated and offer insight into the pathophysiological underpinnings of FoG. We hypothesize that PD-FoG will exhibit distinctive cortical morphological differences when compared to PD patients without FoG (PD-nFOG) and healthy controls (HC). More specifically, we expect to observe differences in cortical area, volume, curvature, and thickness across the three groups, providing further insights into the structural variations associated with FoG in PD. Moreover, we expect to see a decreased LGI in the PD-FoG cohort, indicative of altered cortical folding patterns.

Methods: A total of 53 individuals were recruited at Cleveland Clinic Lou Ruvo Center for Brain Health. Among these, 16 participants were categorized as PD-FoG, 21 were PD-nFoG, and 16 were HC. The diagnosis of FoG was determined by a movement disorders specialist using direct observation of the participants. This assessment took place within the context of a tailored physical therapy task deliberately designed to elicit instances of freezing of gait. All participants utilized in this study underwent a comprehensive MRI examination and were scanned with the following T1-weighted MRI acquisition parameters on a 3T Siemens Skyra MRI scanner: resolution=1mm...3, TR/TE=2300/2.96ms. Following the guidelines outlined by Freesurfer developers, the acquired MRI data underwent the FreeSurfer 7.0 processing pipeline. Freesurfer performed an automated segmentation of brain structures and parcellation of various brain regions. Area, volume, curvature, thickness, and LGI were computed within this framework. To verify quality and reliability, the data underwent a dual quality check process that encompassed both manual and automatic methods. The manual method consisted of viewing the reconstructed T1 images of all patients and checking for any errors in their segmentation. If there were any segmentation errors, the errors were corrected manually. The automatic quality check method involved the utilization of the Computational Anatomy Toolbox (CAT). Following the quality check, we eliminated two of our participants. We then extracted the morphological values from each region identified in the Desikan-Killiany atlas from each participant. The statistical comparison and correlational analyses were executed using the Permutation Analysis of Linear Models (PALM) toolbox integrated within FSL. To account for potential confounding variables, we regressed for sex, handedness, levodopa equivalent daily dose, unified Parkinson's Disease Rating Scale scores, and intracranial volume. The results were considered significant at familywise error corrected (FWE) p... corr<0.05.

Results: The cortical volumes of the mid-posterior corpus callosum, medial orbitofrontal cortex, superior frontal cortex, and lingual cortex; cortical areas of the superior frontal, superior parietal, and medial orbitofrontal cortices; and cortical thickness

of the middle temporal cortex, right pars orbitalis, and right posterior cingulate cortex were significantly (p...corr<0.05) different between the groups (Fig.1). Regardless of the FoG status, HC showed a trend-level (p...corr<0.1) decreased LGI in the parahippocampal cortex and frontal pole. PD-FoG showed a trend-level (p...corr<0.1) higher LGI across the same regions when compared to PD-nFOG.

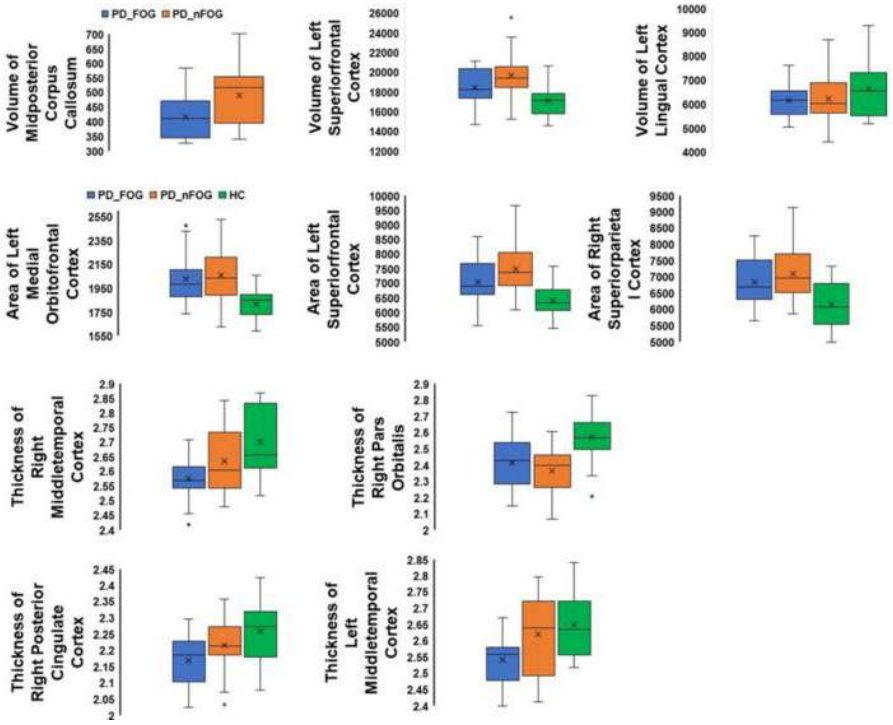

Conclusions: Our analysis suggested that significant morphological differences exist between PD-FoG, PD-nFOG, and HC. The increased LGI experienced in PD-FOG potentially contributes to the manifestation of FoG in PD.

References

1. Zhang et al (2021). J. Neurology

Poster No 255

Improved Ex-vivo Cerebral Microbleed Detection Using Simulation-Based Self-Supervised Learning

Grant Nikseresht[1], Arnold Evia[2], David Bennett[2], Julie Schneider[2], Gady Agam[1], Konstantinos Arfanakis[1]

[1]Illinois Institute of Technology, Chicago, IL, [2]Rush University Medical Center, Chicago, IL

Introduction: Cerebral microbleed (CMB) annotation on postmortem MRI scans of autopsied brains of community-based older adults is necessary for MR-pathology studies of cerebral small vessel disease (SVD) (Nikseresht 2023, Charidimou 2018). However, automation of CMB detection is challenging due to the low incidence of CMBs in community-based older adult brains and high prevalence of CMB mimics on ex-vivo MRI (Fig. 1). While data synthesis can improve model performance by increasing the amount of available training data, biases in the synthesis model can lead to poor generalization performance. Self-supervised learning (SSL) has been shown to be a powerful tool for improving representation learning in data-scarce environments such as medical imaging (Tang 2022). We propose a novel pretext task called fuzzy segmentation (FuzzSeg) that leverages the data synthesis process as a form of self-supervision. Ex-vivo CMB detection models pre-trained with FuzzSeg are shown to outperform models trained from scratch.

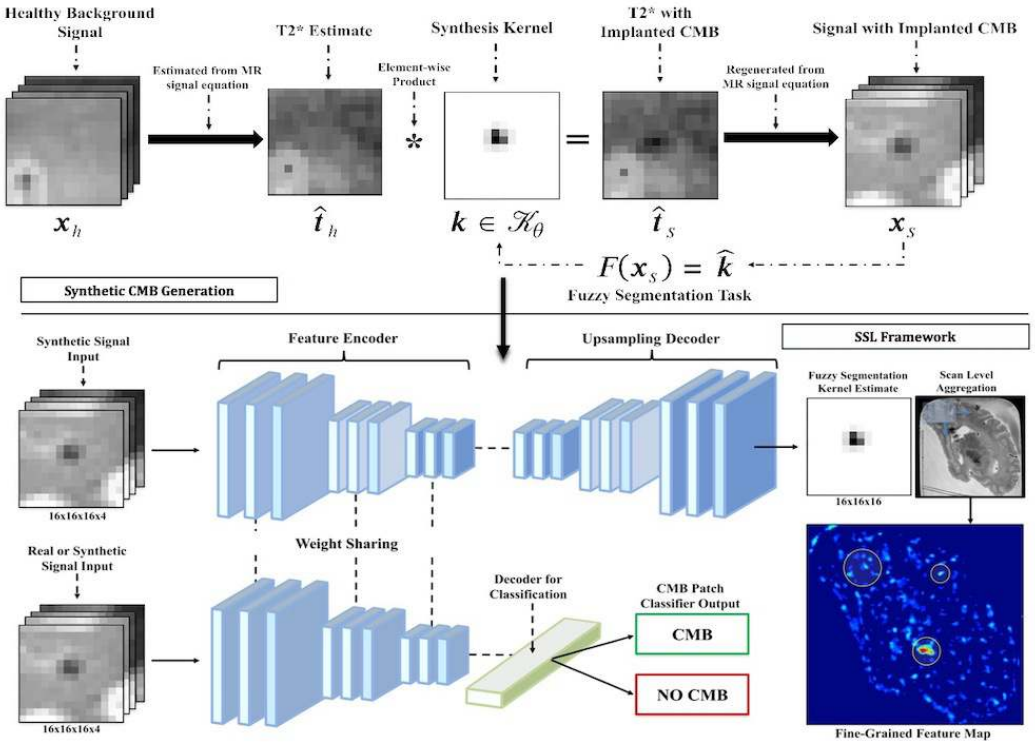

Figure 1. An overview of the data synthesis process is shown above (top). The fuzzy segmentation task involves predicting the synthesis kernel given the synthetic example as input. Knowledge is transferred from the fuzzy segmentation task to the downstream CMB detection task by replacing the decoder head with a classification layer (bottom).

Methods: 286 participants from the Rush Memory and Aging Project (Bennett 2012a) and Religious Orders Study (Bennett 2012b), two longitudinal cohort studies of aging, were included in this work. T2*-weighted gradient echo scans of autopsied brains with a voxel resolution of 1x1x1 mm3 were used after N4 bias correction. CMBs in these images were manually annotated by an experienced rater blinded to all clinical and pathological information. Given a synthetic example, the goal of fuzzy segmentation is to predict the hidden kernel used to generate it (Fig. 1). The term fuzzy segmentation refers to the fact that each kernel is interpreted as the relative scalar intensity drop in T2* at a particular voxel compared to healthy background. Fuzzy segmentation is useful for pre-training because it requires the model to learn to separate hypointense foreground from background and estimate key features of potential CMBs such as hypointensity shape and relative intensity. Two general-purpose self-supervised pretext tasks, rotation prediction and image inpainting, were also evaluated. A modified 3D ResNet20 backbone was used for feature encoding.Task-specific decoder heads were attached for pre-training. Encoder weights are learned by pre-training on the self-supervised pretext tasks and then transferred to the CMB detection task by replacing the decoder component with a classification head. An end-to-end CMB detection framework that combines data synthesis, candidate selection, false positive reduction, and full scan evaluation was used as the backbone for this work (Nikseresht 2012b). Input patches of size 16x16x16x4 were used with four signal echoes in the channel dimension. A high-sensitivity candidate selection algorithm was used to identify CMB candidates based on pre-generated image features. Training and evaluation were done using a repeated randomized 5-fold cross-validation technique, and final predictions were generated using ensembling.

Results: The CMB detection model jointly pre-trained on fuzzy segmentation and rotation prediction tasks (AP=0.3988) achieved the highest sensitivity at both 0.5 false positives per subject (36.4%) and at 16 false positives per subject (81.5%) of all models evaluated (Fig. 2). Pre-training with fuzzy segmentation alone (AP=0.3748) also led to improvements over a baseline model trained without pre-training (AP=0.3618), pre-training with rotation prediction (AP=0.3721), and pre-training with image inpainting (AP=0.3619).

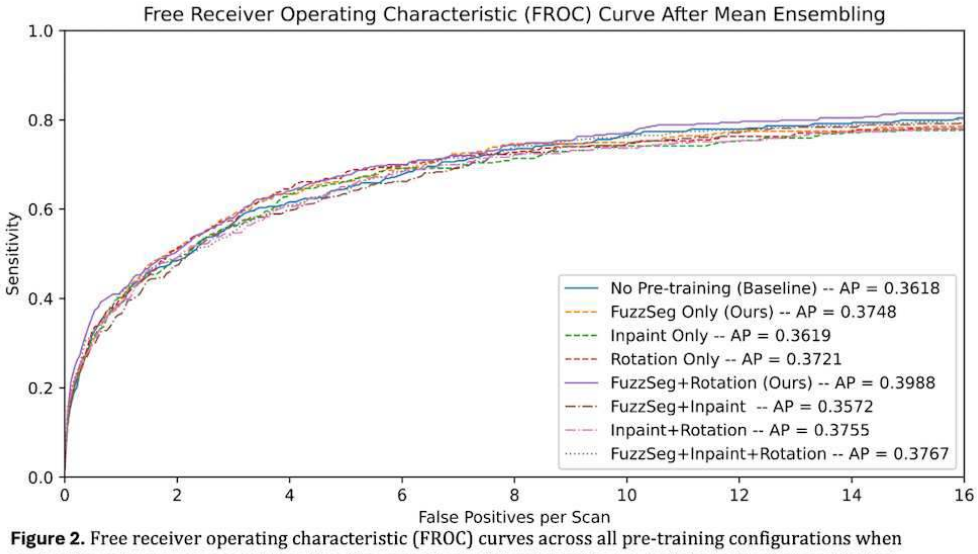

Figure 2. Free receiver operating characteristic (FROC) curves across all pre-training configurations when evaluating using mean ensembling. FuzzSeg combined with rotation for pre-training outperforms all other configurations especially at low and high false positive rates.

Conclusions: This work demonstrates that self-supervised pre-training with FuzzSeg is a data-efficient technique for improving the performance of ex-vivo CMB detection algorithms in community-based cohorts where CMB prevalence is low and mimics are abundant. This has led to reduced labeling time and increased sensitivity for partially automated CMB annotation, a critical step in the development of future MR-pathology studies examining the link between CMBs and neuropathology in community-based older adults.

References

1. Azizi, S. (2021), 'Big Self-Supervised Models Advance Medical Image Classification', Proceedings of the 2021 IEEE/CVF International Conference on Computer Vision.
2. Bennett, A. (2012), 'Overview and Findings from the Rush Memory and Aging Project', Current Alzheimer Research, vol. 9, no. 6, pp. 646-663.
3. Bennett, A. (2012), 'Overview and Findings from the Religious Orders Study', Current Alzheimer Research, vol. 9, no. 6, pp. 628-645.
4. Charidimou, A. (2018), 'Clinical significance of cerebral microbleeds on MRI: A comprehensive meta-analysis of risk of intracerebral hemorrhage, ischemic stroke, mortality, and dementia in cohort studies (v1)', International Journal of Stroke, vol. 13, no. 5, pp. 454-468.
5. Nikseresht, G. (2023), 'Neuropathologic correlates of cerebral microbleeds in community-based older adults', Neurobiology of Aging, vol. 129, pp. 89-98.
6. Nikseresht, G. (2022b), 'Microbleed detection in autopsied brains from community-based older adults using microbleed synthesis and deep learning', Poster presented at: International Society for Magnetic Resonance in Medicine; May 7-12, 2022; London, England.
7. Tang, Y. (2022), 'Self-Supervised Pre-Training of Swin Transformers for 3D Medical Image Analysis', Proceedings of the 2022 IEEE/CVF Conference on Computer Vision and Pattern Recognition.

Poster No 256

Brain Circuit Signatures of Psychosis in Alzheimer's Disease and Their Overlap with Non-AD Psychosis

Christina Young[1], Srikanth Ryali[1], Vinod Menon[1], Kaustubh Supekar[1]

[1]*Stanford University, Stanford, CA*

Introduction: Neuropsychiatric symptoms (NPS) are almost ubiquitous in individuals with Alzheimer's Disease (AD). Among these, psychotic symptoms are particularly clinically relevant, associated with rapid cognitive decline, functional impairment, increased institutionalization, and heightened mortality. Psychosis is present in nearly 41% of individuals with AD, constituting a significant public health concern. However, despite growing evidence linking psychopathology to aberrations in the functional interactions of brain circuit regions over time, the specific brain circuit signatures of AD-related psychosis remain largely unexplored. This gap in knowledge is primarily due to inconsistent findings from small-scale studies lacking the power to detect robust effects, compounded by inadequate analytical methods not well-suited for examining brain circuits. In this study, we aim to bridge the knowledge gap by using open-source data and recent artificial intelligence (AI) advances to identify brain circuit signatures unique to AD psychosis and explore their overlap with non-AD psychosis.

Methods: We examined multi-cohort clinical and task-free fMRI from 629 participants (214 with AD dementia; 40% of them had psychosis, 120 with non-AD schizophrenia, 120 with non-AD early psychosis, and 175 healthy controls), using a novel

explainable AI (XAI) based framework. The field of XAI has been revolutionized in recent years by deep neural networks (DNNs); however, no study to date has employed DNNs to identify brain circuit signatures unique to AD psychosis using functional brain imaging data. This gap is due to the many challenges associated with applying DNNs to functional brain imaging data. We addressed these challenges by developing a novel spatiotemporal DNN (stDNN) model, which takes as its input fMRI time series data from brain regions of interest and models the underlying dynamic spatiotemporal characteristics of brain activity to distinguish between groups. We trained an stDNN to distinguish AD individuals with psychosis from those without and evaluated its performance using cross-validation analysis. To determine overlap with non-AD psychosis, we trained two additional stDNNs de novo – one to distinguish non-AD individuals with schizophrenia from those without, and another to distinguish non-AD individuals with early psychosis from those without. To identify brain circuit signatures associated with AD psychosis, non-AD schizophrenia, and non-AD early psychosis, we applied an XAI method, integrated gradients, to the three trained models respectively.

Results: stDNN achieved a high cross-validation accuracy of 80.0±1.23% in distinguishing between AD individuals with psychosis and those without. Additionally, stDNN achieved high accuracies of 82.0±1.58% and 86.0±2.41% in distinguishing non-AD individuals with schizophrenia from those without, and in distinguishing between non-AD individuals with early psychosis from those without, respectively. Notably, the stDNN model trained for distinguishing non-AD individuals with early psychosis could also distinguish between AD individuals with and without psychosis. However, the model trained for distinguishing schizophrenia in non-AD individuals did not show this capability. XAI analysis revealed that brain features in the insula node of the salience network, PCC and MTL nodes of the default mode network, and DLPFC node of the frontoparietal network significantly contributed to predicting psychosis in AD as well as early psychosis in non-AD individuals.

Conclusions: Our findings reveal distinct brain circuit signatures associated with psychosis in AD, showing evidence of their overlap with early, non-AD psychosis rather than established non-AD schizophrenia within the triple-network, providing substantial empirical support for the theoretical aberrant salience-based model of psychosis. These insights advance our neurobiological understanding of psychosis in AD and inform the development of more targeted therapeutic approaches.

References

1. Ismail, Z., Creese, B., Aarsland, D. et al (2022), 'Psychosis in Alzheimer disease — mechanisms, genetics and therapeutic opportunities'. Nat Rev Neurol 18, 131–144.

Poster No 257

Understanding CBF Changes in Patients with Parkinson's Disease using 3D pCASL-MRI

Saul Lopez[1], Binu Thomas[2], Corina Catiul[1], Zoltan Mari[3], Virendra Mishra[1]

[1]The University of Alabama at Birmingham, Birmingham, AL, [2]The University of Texas at Southwestern Medical Center at Dallas, Dallas, TX, [3]Cleveland Clinic Foundation, Las Vegas, NV

Introduction: Parkinson's disease (PD) is the second most common progressive neurodegenerative disorder, characterized by the death of dopaminergic neurons in the substantia nigra leading to motor dysfunction(Kalia & Lang, 2015). Arterial Spin Labeling (ASL) MRI has been used to understand both disease severity(Pelizzari et al.) and disease progression(Joshi, Prasad, Saini, & Ingalhalikar, 2023) in PD. Due to the low spatial resolution of the acquisition of ASL-MRI, however, partial volume effects (PVE) occur. PVE bias the conclusion and the repeatability of the measures derived from ASL-MRI, such as cerebral blood flow (CBF) and arterial transit time (ATT)(Chappell et al., 2021). In this study, we investigated the effects of partial volume correction (PVC) to understand the correlations between CBF/ATT and disease severity of participants with PD.

Methods: Ten PD and 12 healthy control (HC) patients were recruited from the Cleveland Clinic Center for Brain Health, Las Vegas. 3D multi-delay pseudo-continuous ASL (pCASL) MRI were acquired with the following parameters: field of view (FOV)=224×224 mm...2, matrix=64×64, 44 axial slices, thickness=3.5 mm, TR/TE=4130/39 msec, labeling duration=1.8 seconds, multiple post-labeling delays (PLD)=[0.5, 1.0, 1.5, 2.0, 2.5] seconds. CBF and ATT maps were generated from the pCASL-MRI images and PVC was performed using the BASIL (Bayesian Inference for Arterial Spin Labeling) toolbox in FSL. The analysis procedure followed the recommendations in the ASL white paper (Alsop et al., 2015) . We statistically compared the differences in CBF and ATT between HC and PD patients in addition to performing correlations between CBF/ATT measures and PD severity (measured by Movement Disorder Society Sponsored Unified Parkinson's Disease Rating Scale (MDS-UPDRS)-III and Hoehn and Yahr (H&Y) scores), disease duration, and levodopa equivalent daily dose (LEDD) in the PD group. All statistical analyses were done using the PALM toolbox from FSL. The results were considered significant at a familywise error (FWE) corrected p-value<0.05. Sex and affected side were used as regressors. Framewise displacement (FD) (Power, Barnes, Snyder, Schlaggar, & Petersen, 2012) was computed to check for head motion.

Results: Handedness and sex were significantly different between the groups. PD patients were 70% right-handed, 20% left-handed, 10% ambidextrous and 90% male, while HC patients were 100% right-handed and 50% male. No significant difference was observed between the FD between the groups. Our analysis did not reveal any significant difference in either CBF or ATT between HC and PD. Non-PVC analysis revealed a statistically significant (p...corr<0.05) negative correlation between CBF and H&Y scores (Fig.1b and Fig.2a). The regions showing correlations encompassed predominantly frontal and temporal cortices (Fig.1b). These correlations between non-PVC and H&Y were also observed in PVC analysis (Fig.1a and Fig.2a). However, the extent and strength of the correlations were greater as compared to non-PVC analysis (Fig.1a-b and Fig. 2a). Non-PVC corrected CBF showed an unexpected positive correlation with UPDRS-III (Fig.1c and Fig.2b) which was not observed with PVC analysis. ATT measures in PD were not correlated with any clinical measures in our sample.

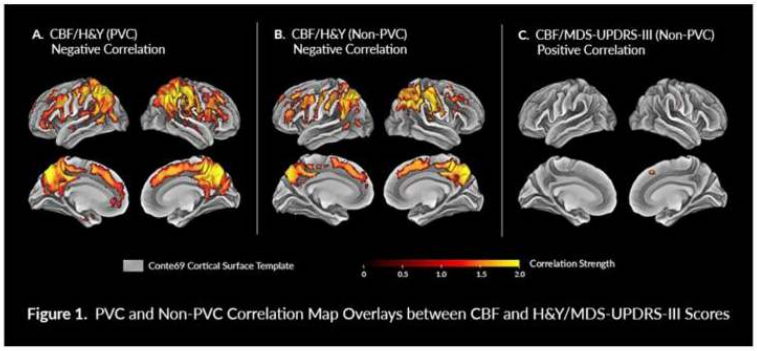

Figure 1. PVC and Non-PVC Correlation Map Overlays between CBF and H&Y/MDS-UPDRS-III Scores

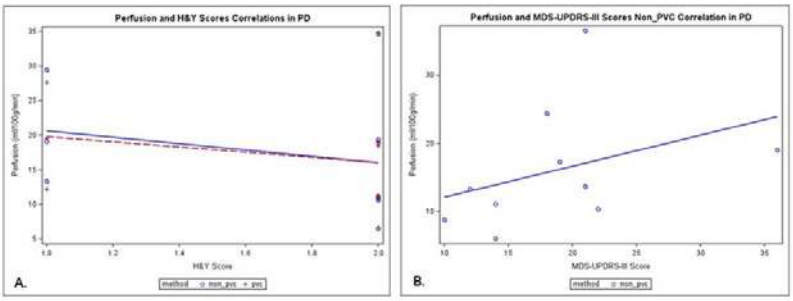

Figure 2. PVC and Non-PVC Correlations between Brain Perfusion and H&Y/MDS-UPDRS-III Scores

Conclusions: No significant differences between HC and PD in either CBF or ATT measures suggest that the pCASL-derived measures are highly variable in PD, further suggesting a larger sample to discern these differences. The seemingly false-positive correlation between non-PVC-corrected CBF and MDS-UPDRS-III was not observed in PVC-corrected data albeit a stronger correlation between PVC-corrected CBF and H&Y was observed in our sample. Overall, the results of our study suggest that 3D multi-delay pCASL can be used to measure disease severity in patients with PD but efforts should be made to jointly analyze both PVC and non-PVC CBF and ATT measures.

References

1. Alsop, D. C., Detre, J. A., Golay, X., Günther, M., Hendrikse, J., Hernandez-Garcia, L., . . . Zaharchuk, G. (2015). Recommended implementation of arterial spin-labeled perfusion MRI for clinical applications: A consensus of the ISMRM perfusion study group and the European consortium for ASL in dementia. Magnetic Resonance in Medicine, 73(1), 102-116.
2. Chappell, M. A., McConnell, F. A. K., Golay, X., Günther, M., Hernandez-Tamames, J. A., van Osch, M. J., & Asllani, I. (2021). Partial volume correction in arterial spin labeling perfusion MRI: A method to disentangle anatomy from physiology or an analysis step too far? NeuroImage, 238, 118236. doi:https://doi.org/10.1016/j.neuroimage.2021.118236
3. Joshi, D., Prasad, S., Saini, J., & Ingalhalikar, M. (2023). Role of Arterial Spin Labeling (ASL) Images in Parkinson's Disease (PD): A Systematic Review. Academic Radiology, 30(8), 1695-1708. doi:https://doi.org/10.1016/j.acra.2022.11.001
4. Kalia, L. V., & Lang, A. E. (2015). Parkinson's disease. The Lancet, 386(9996), 896-912. doi:https://doi.org/10.1016/S0140-6736(14)61393-3
5. Pelizzari, L. A.-O., Laganà, M. M., Rossetto, F., Bergsland, N., Galli, M., Baselli, G., . . . Baglio, F. A.-O. Cerebral blood flow and cerebrovascular reactivity correlate with severity of motor symptoms in Parkinson's disease. (1756-2856 (Print)).
6. Power, J. D., Barnes, K. A., Snyder, A. Z., Schlaggar, B. L., & Petersen, S. E. (2012). Spurious but systematic correlations in functional connectivity MRI networks arise from subject motion. NeuroImage, 59(3), 2142-2154.

Poster No 258

The effects of nutritional monitoring of the elderly at high risk for dementia using QEEG

Hyunna Kim[1], Ukeob Park[2], Soyoung Jung[3], Haejin Kang[3], Yejin Seo[4], Yoo Kyoung Park[5,6], Seung Wan Kang[7]

[1]iMediSync Inc., Seoul, Korea, Republic of, [2]iMediSync, Inc., Seoul, seoul, [3]Dept. of Medical Nutrition (AgeTech-Service Convergence Major), Kyung Hee University, Yongin, Korea, Republic of, [4]Dept. of Medical Nutrition(Clinical Nutrition), Kyung Hee University, Yongin, Korea, Republic of, [5]Dept of Food Innovation and Health, Graduate School of East-West Medical Nutrition, Kyung Hee Univ., Yongin, Korea, Republic of, [6]Dept. of Medical nutrition, Graduate School of East-West Medical Nutrition, Kyung Hee, Yongin, Korea, Republic of, [7]iMediSync, Seoul, Seoul

Introduction: Nutritional management has a strong correlation with dementia. There is several research indicating that nutritional therapy or intervention is effective in delaying cognitive impairment. Electroencephalography(EEG) is used to detect the electrical activity of the brain, not only for verifying the effects of various treatments and drug interventions but also for early detection and severity prediction of cognitive impairment. This project focuses on nutritional monitoring for individuals at risk of dementia. With the expectation that improving nutritional deficiencies will contribute to the management of chronic conditions, the project aims to validate the therapeutic effects of addressing nutritional deficiencies on dementia using QEEG.

Methods: A total of 112 participants from 5 institutions took part in the 10 week study. After application, two individuals did not participate, and 19 were absent in the post-measurement after the pre-measurement. Also, one participant was excluded due to age beyond the analyzable range, resulting in a total of 22 dropouts. The final dataset used for analysis comprised 90 participants with a mean age of 84 years(±8.64), and it consisted of resting-state EEG data. It was confirmed that there were no significant differences in gender and age across institutions(ANOVA p-value=0.39) This study utilized iMediSync, Inc's normative database ISB-Norm DB. The database comprises EEG data from 1,289 healthy participants(553 males,736 females) aged 4 to 80 years old. By comparing and analyzing the standard EEG database matched for age and gender, a calculated Z-score is used to eliminate variability arising from age and gender differences, allowing for a common and statistically robust analysis. At all 5 institutes, dietary intake was monitored and directions to increase the amount of food consumption was provided. EEG measurements were taken before the customized nutritional monitoring over a period of 10 weeks, and post-nutritional monitoring EEG measurements were conducted after the completion of nutritional monitoring. The resting-state EEG of eyes closed(EC) condition was measured at 19 channels of the international 10-20 system. Spectrum power, power ratio, source cortical activity, and imaginary coherence were calculated.

Results: Comparing the EEG of the group(G1) measured before nutritional monitoring with ISB-Norm DB, characteristic features of dementia were identified in G1. Figure1A illustrates an increase in slow-wave band power, a decrease in α activity, and α peak frequency slowing in G1 compared to the Norm DB. As the slow band increases, β waves increase to maintain homeostasis in healthy controls. In cases of dementia, a reduction in β power leads to a higher Theta/Beta Ratio(TBR). Figure1B indicates a significantly higher TBR in the pre-measured data compared to ISB-Norm DB. The paired T-test comparing G1 and G2(Figure2A) reveals a significant reduction of relative power δ in the overall brain region. In addition, the band powers that were decreased in G1 significantly increased in G2. However, upon examining the occipital α peak frequency(Figure2B), no substantial changes were evident in the pre/post comparison. In other words, we did not observe an improvement in the slowing of the α peak frequency. Nevertheless, Figure2C shows that the network power values in G2 are higher compared to G1, and long-distance networks are identified extending from the occipital lobe. This indicates enhancement of the brain network, accompanied by an increase in power in the α2 and β1 frequency bands.

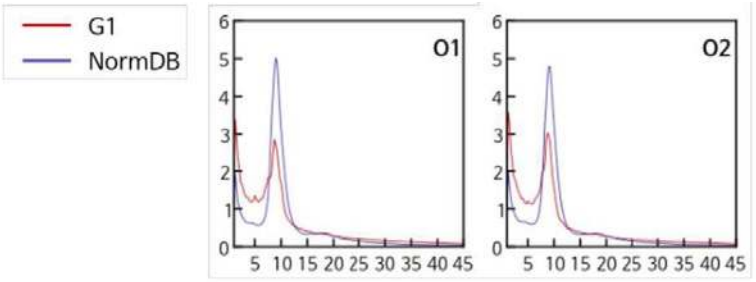

(A)

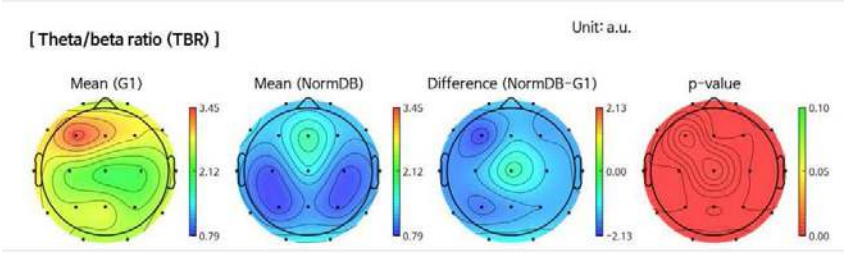

(B)

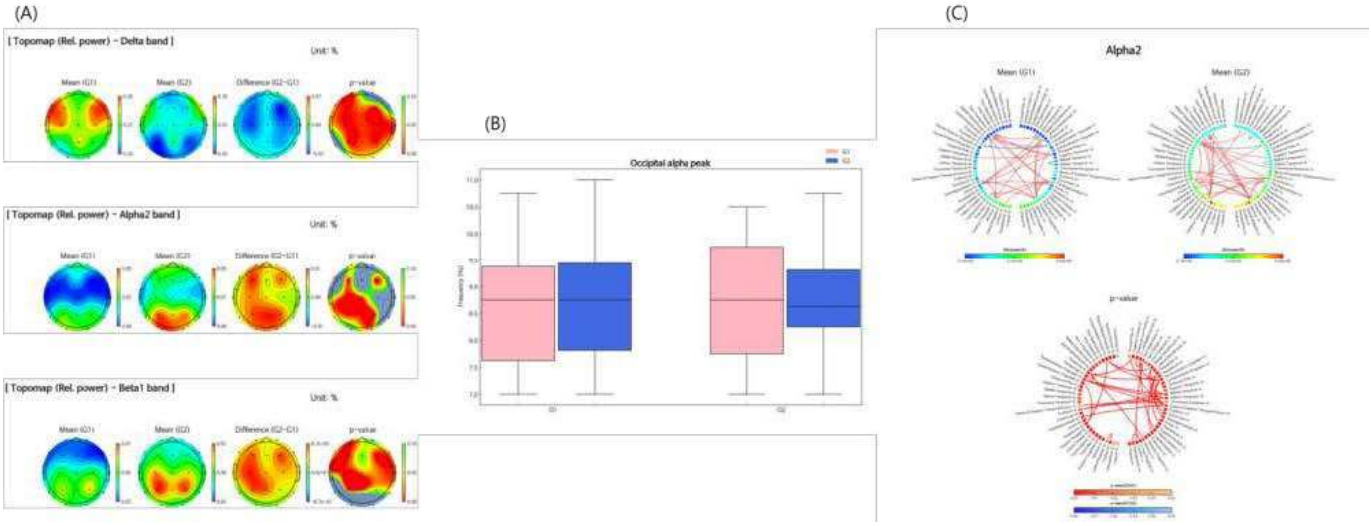

Conclusions: When conducting a paired T-test between the G1 and G2 groups, significant differences were observed in the low-frequency range. Although normalization of α peak frequency was not identified, a relative and significant increase in the previously reduced α and β power was confirmed. Therefore, it can be observed that the dementia pattern seen in the Norm DB is relatively alleviated through 10 weeks of nutritional monitoring.

References

1. Pistollato, F., Iglesias, R. C., Ruiz, R., Aparicio, S., Crespo, J., Lopez, L. D., ... & Battino, M. (2018). Nutritional patterns associated with the maintenance of neurocognitive functions and the risk of dementia and Alzheimer's disease: A focus on human studies. Pharmacological research, 131, 32-43.
2. Hickson, M. (2006). Malnutrition and ageing. Postgraduate medical journal, 82(963), 2-8.
3. Tangvik, R. J., Bruvik, F. K., Drageset, J., Kyte, K., & Hunskår, I. (2021). Effects of oral nutrition supplements in persons with dementia: A systematic review. Geriatric Nursing, 42(1), 117-123.
4. Casson, A. J., Yates, D. C., Smith, S. J., Duncan, J. S., & Rodriguez-Villegas, E. (2010). Wearable electroencephalography. IEEE engineering in medicine and biology magazine, 29(3), 44-56.
5. Ko, J., Park, U., Kim, D., & Kang, S. W. (2021). Quantitative electroencephalogram standardization: a sex-and age-differentiated normative database. Frontiers in Neuroscience, 15, 766781.
6. Popa, L. L., Dragos, H., Pantelemon, C., Rosu, O. V., & Strilciuc, S. (2020). The role of quantitative EEG in the diagnosis of neuropsychiatric disorders. Journal of medicine and life, 13(1), 8.

Poster No 259

White Matter Hyperintensity Burden is Related to White Matter Cerebrovascular Reactivity in Aging

Claire Hsu[1], Quimby Lee[2], Gregory Wheeler[1], Audrey Fan[1,2]

[1]Department of Biomedical Engineering, University of California, Davis, Davis, CA, [2]Department of Neurology, University of California, Davis, Davis, CA

Introduction: White matter hyperintensities (WMH) are regions located in the white matter (WM) of the brain that appear unexpectedly bright in fluid-attenuated inversion recovery (FLAIR) scans of magnetic resonance imaging (MRI). The pathogenesis of WMH remains unclear; however, WMH burden has been associated with both stroke risk and stroke damage, suggesting vascular contributions[1]. Cerebrovascular reactivity (CVR), or the ability for blood vessels to dilate in response to vasoactive stimuli, is an indicator of cerebrovascular health. Functional MRI (fMRI) studies have utilized the blood oxygen level dependent (BOLD) signal to measure CVR response to a vasodilation challenge, such as increased CO2 inhalation, and how it relates to cognitive decline in aging and stroke-related disorders. However, the vasodilation challenge required in traditional CVR adds to patient burden during scan acquisition. To circumvent this challenge, recent studies have proposed using relative CVR (rCVR) mapping derived solely from resting-state BOLD (rs-BOLD) signals. In this method, a frequency filtered global BOLD signal is used as a surrogate measure of the arterial CO2 timeseries to estimate cerebrovascular responses to natural CO2 fluctuations during normal breathing. With this innovation, CVR analysis can be performed on resting-state fMRI (rs-fMRI) scans without gas challenges that are more accessible to patient populations with high vascular risk. In this study, we utilize this novel rCVR mapping method to investigate the relationship between global WMH burden and tract-specific white matter CVR changes in an elderly cohort with vascular risk.

Methods: A T1-weighted structural scan, 8-minute rs-fMRI scan, and T2 FLAIR scan were acquired for 135 participants (64-97 years, 95 female) from the Alzheimer's Disease Research Center at UC Davis. Of the participants, 87 were cognitively normal, 38 were mildly impaired, and 10 were diagnosed with dementia. The T2 FLAIR scans were segmented into gray matter, white matter, cerebrospinal fluid, and WMH regions through a semi-automated procedure described in previous studies[2,3]. To calculate %WMH, the number of WMH voxels was divided by the total number of brain voxels and multiplied by 100%. %WMH was log-transformed to ensure a normal distribution. Resting-state fMRI scans were motion corrected and spatially smoothed (Gaussian kernel full-width-half-max=8mm) and CVR maps were generated using voxel-wise regression of the gray matter BOLD signal, which acted as a surrogate for the CO2 timeseries during natural breathing[4]. Maps were then normalized to global CVR to produce rCVR maps. CVR calculation was performed in native fMRI space, then transformed into T1-anatomical and MNI standard space. Finally, we calculated the average rCVR values for specific WM tracts identified by the Johns Hopkins University atlas. Relative CVR was regressed on log(%WMH), age, sex, and cognitive status for each of the 20 WM tracts.

Results: We observed a negative correlation ($p<0.05$) between %WMH and rCVR in the left and right cingulate gyrus ($m=-0.05$, $p=0.01$; $m=-0.04$, $p=0.04$), and left and right cingulum hippocampus ($m=-0.09$, $p=0.003$; $m=-0.006$, $p=0.006$). This finding aligns with our hypothesis that a greater %WMH corresponds to a lower rCVR value.

Conclusions: The identified WM tracts support the default mode network, a functional network that changes in aging and cognitive impairment, which our results associate with vascular injury (reduced rCVR)[5]. As WMH are associated with both stroke risk and damage, our research provides insight into early vascular changes that may lead to WMH and vulnerable brain structural connections which can inform stroke prevention, treatment, and rehabilitation.

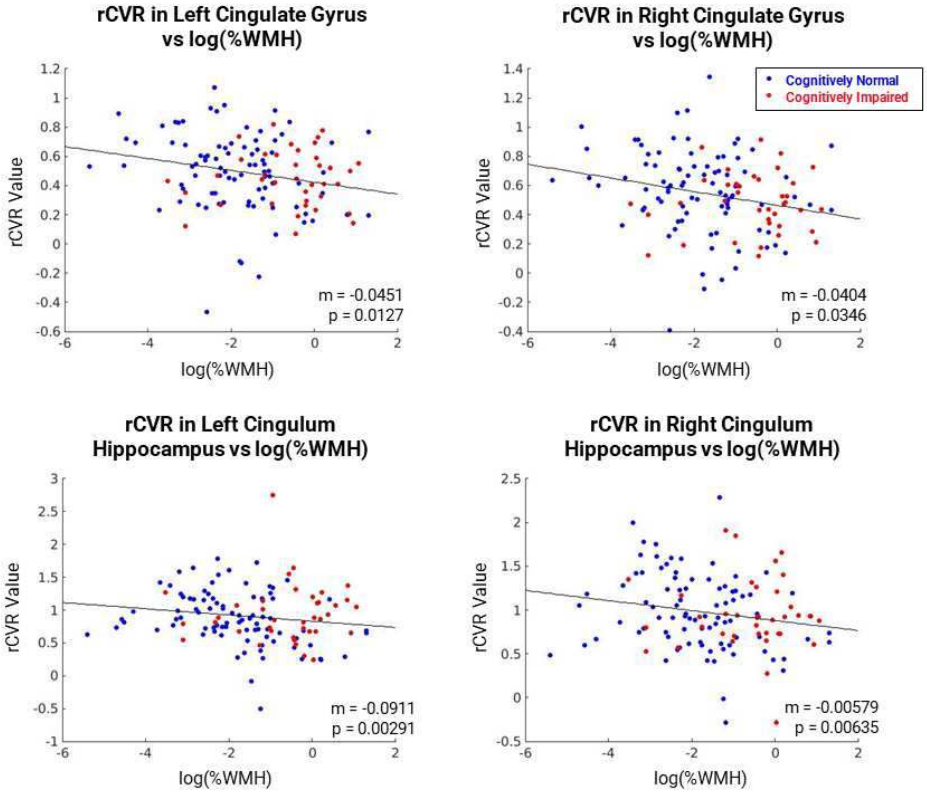

The left and right cingulate gyrus and left and right cingulum hippocampus are white matter tracts that showed a strong negative trend ($p<0.05$) between percent white matter hyperintensities (%WMH) and relative cerebrovascular reactivity (rCVR).

References

1. Ni L, et al. (2020), 'Lower Cerebrovascular Reactivity Contributed to White Matter Hyperintensity-related Cognitive Impairment: A Resting-State Functional MRI Study', Journal of Magnetic Resonance Imaging, vol. 53, iss. 3, pp. 703-11
2. DeCarli C, et al. (1992), 'Method for quantification of brain, ventricular, and subarachnoid CSF volumes from MR Images', Journal of Computer Assisted Tomography, vol.16,2, pp. 274-84
3. DeCarli C, et al. (1995), 'The effect of white matter hyperintensity volume on brain structure, cognitive performance, and cerebral metabolism of glucose in 51 healthy adults', Neurology, vol. 45,11, pp. 2077-84
4. Bhogal AA. (2021), 'Medullary vein architecture modulates the white matter bold cerebrovascular reactivity signal response to CO2: Observations from high-resolution T2* weighted imaging at 7t', NeuroImage, vol. 245
5. Seiler S, et al. (2018), 'Cerebral tract integrity relates to white matter hyperintensities, Cortex Volume, and cognition', Neurobiology of Aging. vol. 72, pp. 14-22

Poster No 261

Depression in Premanifest HD: Aberrant Effective Connectivity of Striatum and Default Mode Network

Tamrin Barta[1], Leonardo Novelli[1], Nellie Georgiou-Karistianis[1], Julie Stout[1], Samantha Loi[2], Yifat Glikmann-Johnston[1], Adeel Razi[1]

[1]Monash University, Melbourne, Australia, [2]University of Melbourne, Parkville, Australia

Introduction: Depression is one of the most common and impactful features early in Huntington's Disease (HD), in the premanifest period (pre-HD), prior to clinical diagnosis (Epping & Paulsen 2011). Depression is increasingly being conceptualised as a circuitopathy (Hannan 2018) and two large-scale networks surmised to contribute to the expression of depressive symptoms in pre-HD are the striatum and the default mode network (DMN; McColgan et al. 2017; Garcia-Gorro et al. 2019). Existing neuroimaging studies are limited and relied on functional connectivity: an inherently undirected measure of connectivity (Friston et al. 2014). Dynamic causal modelling (DCM) allows testing of neurobiologically plausible models of connectivity changes in pre-specified networks (Friston et al. 2014; Razi et al. 2015). We investigated DMN and striatal effective connectivity and depression in pre-HD, using these model-based methods.

Methods: We analysed 3T resting state fMRI data from 93 pre-HD participants (51.6% females; mean age = 42.7; Klöppel et al., 2015). Behavioural measures included history of depression, Beck Depression Inventory, 2nd Edition (BDI-II) and Hospital Anxiety and Depression Scale, depression subscale (HADS-D). An optimal cut-off score recommended for use in HD categorised clinically significant depressive symptoms (De Souza, Jones, and Rickards 2010). Regions of interest (ROIs) included medial prefrontal cortex (MPFC [3,54,-2]), posterior cingulate (PCC [0,-52,26]), hippocampus (HPC left [-29,-18,-16], right [29,-18,-16]), caudate (CAU left [-10,14,0], right [10,14,0]), and putamen (PU left [-28,2,0], right [-28,2,0]). Each ROI time series was calculated as the first principal component of the voxels' activity within an 8 mm sphere for MPFC and PCC and a 6 mm sphere for all other regions, and was further constrained within masks. Preprocessing pipeline included slice-timing correction, realignment, spatial normalisation to MNI space, and spatial smoothing by a 6 mm full-width half-maximum Gaussian kernel. Spectral DCM (Friston et al. 2014; Razi et al. 2015) was used to estimate subject level connectivity and parametric empirical bayes (Friston et al. 2016) was employed to estimate group level effective connectivity changes between participants with a history of depression and those without. We focused on connections that had a Bayesian posterior probability ≥0.99. Leave-one-out cross-validation was performed for connections that reached this criterion.

Results: The model estimation was excellent, with an average percentage variance-explained of 89.70% (SD: 4.22; range: 74.15-94.87). For pre-HD with a history of depression, we found excitatory projections from MPFC to right HPC and left PU, in line with expectations (Figure 1). The PCC had aberrant excitatory and inhibitory influence on the striatum and the hippocampus for pre-HD with a history of depression, compared to those without. Striatal connectivity patterns were notable in the more affected left cerebral hemisphere. Contrary to expectations, no aberrant connections were found from MPFC to CAU or PCC. The present study demonstrates that aberrant connectivity patterns for pre-HD with a history of depression is associated with coupling differences in depressive symptoms (Figure 2). Leave-one-out cross-validation comprised left PU, CAU and PCC self-connections, chosen as they appeared most consistently across models. Correct classification reached significance for both HADS-D, corr(91) = 0.19: p = .037, and BDI-II cut-off scores, corr(91) = 0.29, p = .002.

Figure 1

Effective Connectivity Changes Between Participants with a History of Depression and Those Without a History of Depression

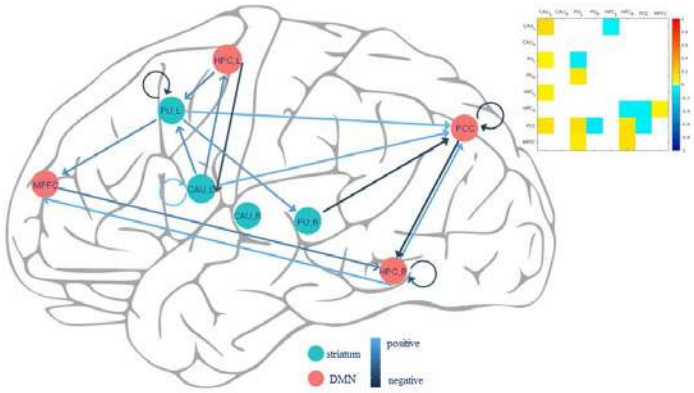

Figure 2

DMN and Striatal Effective Connectivity Changes Associated With State Depressive Symptoms

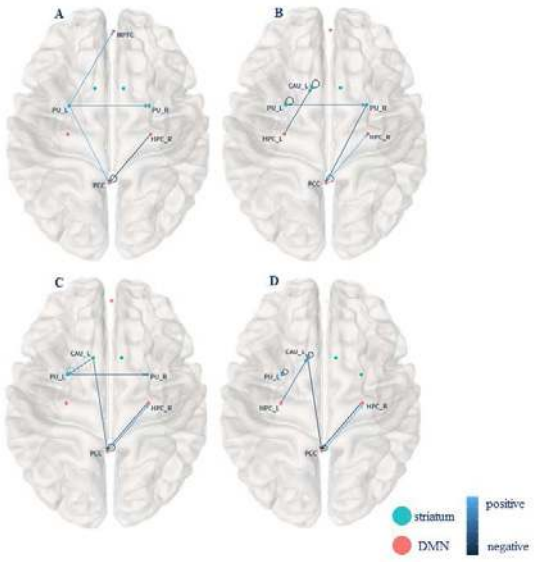

Conclusions: The present study suggests network dysconnection as a neural basis for depression in pre-HD. Aberrant effective connections were associated with trait level depression, which was differentially associated with coupling changes in state depressive symptoms. This work adds to our understanding of the pathophysiology of HD and shows that defining circuitopathies of neuropsychiatric features plays an important role in understanding the disease.

References

1. De Souza, J., et al. (2010). 'Validation of Self-Report Depression Rating Scales in Huntington's Disease'. Movement Disorders vol. 25, no. 1, pp. 91–96
2. Epping, E.A., et al. (2011). 'Depression in the Early Stages of Huntington Disease'. Neurodegenerative Disease Management, vol. 1, no. 5, pp. 407–14
3. Friston, K.J., et al., (2014). 'A DCM for Resting State fMRI'. NeuroImage, vol. 94, pp. 396–407
4. Friston, K.J., et al., (2016). 'Bayesian Model Reduction and Empirical Bayes for Group (DCM) Studies'. NeuroImage vol. 128, pp. 413–31
5. Garcia-Gorro, C., et al. (2019). 'Specific Patterns of Brain Alterations Underlie Distinct Clinical Profiles in Huntington's Disease'. NeuroImage: Clinical, vol. 23, pp. 101900
6. Hannan, A.J. (2018). 'Synaptopathy, Circuitopathy and the Computational Biology of Huntington's Disease'. BMC Biology, vol. 16, no. 1, pp. 71
7. Klöppel, S., et al. (2015). 'Compensation in Preclinical Huntington's Disease: Evidence From the Track-On HD Study'. EBioMedicine, vol. 2, no. 10, pp. 1420–29
8. McColgan, P., et al. (2017). 'Structural and Functional Brain Network Correlates of Depressive Symptoms in Premanifest Huntington's Disease'. Human Brain Mapping, vol. 38, no. 6, pp. 2819–29
9. Razi, A., et al. (2015). 'Construct Validation of a DCM for Resting State fMRI'. NeuroImage, vol. 106, pp. 1–14

Poster No 262

Distinctive Accumulation Patterns of Amyloid β in clinical progression of MCI pattern

SeonKyeong Kim[1], Yunjin Lee[1], Wonjae Sung[2], Yong Sung Kim[2], Sujin Lee[2], June Sic Kim[3], HeeJin Kim[2]

[1]Hanyang University, Seoul, Korea, Republic of, [2]Hanyang University Medical Center, Seoul, Korea, Republic of, [3]Konkuk University Medical Center, Seoul, Korea, Republic of

Introduction: Mild Cognitive Impairment (MCI) is a transitional stage between normal aging and dementia. Understanding underlying pathological background is critical to predict clinical progression and disease management. Amyloid Positron Emission Tomography (PET) imaging uses a class of radiopharmaceuticals that detect levels of amyloid in the human brain to visualize amyloid beta deposits, It has revealed brain pathology and faster clinical progression of Alzheimer's disease (AD). Previous studies primarily focused on the total amount of amyloid without conducting longitudinal studies. This study aims to explore distinct amyloid beta accumulation patterns in individuals with stable MCI compared to those progressing to dementia in definite prodromal AD patients.

Methods: Forty-five MCI patients participated. 23 of these patients were converted into AD. Amyloid β deposition was quantified using the Standardized Uptake Value Ratio(SUVR) and the Centiloid, a standardized metric for PET data. Subsequently, an one sample t-test was employed to assess the statistical significance between the two groups, which analyzes differences in amyloid deposition patterns and their respective SUVR and Centiloid values.

	MCI to MCI (n=22)	MCI to AD (n=23)
Sex (Male/Female)	12/10	15/8
Age	71.45	73
Education	10.66	11.73
CDR sum of boxes	1.28	1.95
MMSE Score	25.91	25

[Table.1] Demographics

Results: The analysis revealed a statistically significant elevation in both SUVR and Centiloid values in the right Lateral orbital gyrus (OFClat) region for the MCI to AD group compared to the MCI to MCI group. The increase in SUVR and Centiloid scores in this specific region was consistent with the hypothesis of heightened amyloid beta accumulation in individuals progressing from MCI to AD.

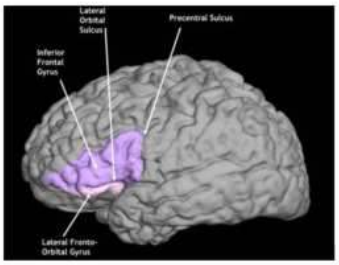

[Figure.1] Lateral orbital gyrus

	MCI to MCI	MCI to AD	p
Right OFCmed SUVR	1.367	1.476	0.177
Right OFCant SUVR	1.281	1.435	0.100
Right OFCpost SUVR	1.117	1.218	0.138
Right OFClat SUVR	1.087	1.229	0.025**
Right OFCmed Centiloid	54.809	71.477	0.177
Right OFCant Centiloid	41.650	65.208	0.100
Right OFCpost Centiloid	16.467	31.865	0.138
Right OFClat Centiloid	11.818	33.684	0.025**

[Table.2] The statistical analysis of SUVR and Centiloid values across different groups was conducted to determine their significance. OFCmed- Medial orbital gyrus, OFCant- Anterior orbital gyrus, OFCpost- Posterior orbital gyrus, OFClat- Lateral orbital gyrus

Conclusions: Our findings suggest that early amyloid beta deposition in the right Lateral orbital gyrus region may serve as a biomarker for the early detection of AD progression risk.

References

1. Edmund T. Rolls (2020), 'Automated anatomical labelling atlas 3', NeuroImage, Vol. 206, 116189.
2. 'Laboratory of Neuro Imaging Resource Innovative solutions for the investigation of imaging, genetics, behavioral, and clinical data', Keck, School of Medicine of USC, University of Southern California
3. Gary W. Van Hoesen (2000), 'Orbitofrontal Cortex Pathology in Alzheimer's Disease', Cerebral Cortex, Vol. 10, Issue 3, Pages 243–251.

Poster No 263

A Negatively Correlation Between Serum Calcium and Gray Matter Volume in Alzheimer's Disease

TAO GUO[1], Yumi Takano[1,2], Yasuko Tatewaki[1,2], Ye Zhang[1], Naoki Naoki Tomita[1,2], Michiho Muranaka[1,2], Taizen Nakase[1,2], Yasuyuki Taki[1,2,3]

[1]Department of Aging Research and Geriatric Medicine, Institute of Development, Aging and Cancer, Tohoku University, Aoba-ku, Sendai 980-8575, Japan, [2]Department of Geriatric Medicine and Neuroimaging, Tohoku University Hospital, Aoba-ku, Sendai 980-8575, Japan, [3]Smart-Aging Research Center, Tohoku University, Aoba-ku, Sendai 980-8575, Japan

Introduction: Calcium is considered involved in the pathophysiology of cognitive decline and Alzheimer's disease (AD)[1]. According to the calcium hypothesis of AD[2], the amyloidogenic pathway may function to remodel the neuronal Ca2+ signaling pathways responsible for cognition. This remodeling calcium signaling can disrupt the synaptic strength, and the increased calcium concentration can trigger apoptosis, resulting in severe cognitive decline and neuronal cell death. Previous studies have showed that serum Ca2+ can easily cross the blood-brain barrier[3]. High extracellular calcium levels may enhance calcium influx in neurons during signaling when calcium channels open, leading to calcium overload and neuronal death[4]. Current studies reported that higher serum calcium status (even if not hypercalcemia) may increase the risk of AD in elders. Serum calcium is a useful biomarker in predicting clinical progression in nondemented elders[5]. However, the potential mechanism of serum calcium as a biomarker for AD remains unclear. In our study, we aimed to investigate the relationship between serum calcium and AD by using voxel-based morphometry (VBM) based regional gray matter volume (rGMV) to visualize brain alterations associated with calcium.

Methods: The sample was derived from our memory clinic in Tohoku University Hospital, which included 76 patients (age range from 50 years to 93 years). The patients had brain MRI scans completed at the investigation. We also collected the patients' age, gender, years of education, mini-mental state examination score (MMSE), and blood test results. The exclusion criteria for all participants were: (1) other neurological disorders; and (2) severe medical conditions or terminal diseases that may influence the results of imaging studies. MRI scanner was used to acquire a 3D T1-weighted structural image. Pre-processing of structural images was performed using Statistical Parametric Mapping software (SPM12) implemented in MATLAB. We used SPM12 to conduct a whole-brain multiple regression analysis to examine the association between serum calcium level and rGMV on brain structure. The subjects' age, gender, total brain volume (TBV), years of education and MMSE score were entered as covariates of no interest in these analyses.

Results: After adjusting for age, gender, TBV, years of education and MMSE scores we found increased serum calcium level was significantly associated with decreased rGMV in the bilateral fusiform gyrus (Left: MNI coordinates at peak voxel = (-34, -38, -12); t = 5.48, pFWE = 0.002, cluster size = 1701. Right: MNI coordinates at peak voxel = (36, -38, -10); t = 4.62, pFWE = 0.008, cluster size = 1217).

Conclusions: In the present study, we found serum calcium was negatively correlated with rGMV in the bilateral fusiform gyrus after adjusting for covariates. The fusiform gyrus, a brain region that plays roles in vision for perception, object

recognition, and reading, has gained attention in epigenetic studies[6]. It has been reported that specific changes in functional connectivity of the fusiform gyrus in MCI, considered a risk factor of conversion to AD, and atrophy of the fusiform gyrus occur as a consequence of amyloid load within the hippocampus. Thus, the fusiform gyrus has been identified as a critical brain region associated with MCI, which may increase the risk of AD development[7]. In fusiform gyrus, Transmembrane O-Mannosyltransferase Targeting Cadherins 2 (TMTC2) is a novel candidate gene that is identified co-expressed in AD, and this gene is also involved in endoplasmic reticulum (ER) calcium homeostasis[7]. However, the molecular mechanism between serum calcium levels and fusiform gyrus remains to be studied. Our study suggests that a potential association between serum calcium levels and brain structural alterations, indicating that serum calcium may serve as a useful biomarker in clinical AD patients.

References

1. Bussiere R. Upregulation of the Sarco-Endoplasmic Reticulum Calcium ATPase 1 Truncated Isoform Plays a Pathogenic Role in Alzheimer's Disease. Cells. 2019 Nov 28;8(12):1539.
2. Berridge M J. Calcium hypothesis of Alzheimer's disease[J]. Pflügers Archiv-European Journal of Physiology, 2010, 459: 441-449.
3. Yarlagadda A. Blood brain barrier: the role of calcium homeostasis. Psychiatry (Edgmont). 2007 Dec;4(12):55-9.
4. Toescu EC. Ca2+ regulation and gene expression in normal brain aging Trends. Neurosci 27:614620.
5. Ma LZ. Serum Calcium Predicts Cognitive Decline and Clinical Progression of Alzheimer's Disease. Neurotox Res. 2021 Jun;39(3):609-617.
6. Srinivasan K. Alzheimer's Patient Microglia Exhibit Enhanced Aging and Unique Transcriptional Activation. Cell Rep. 2020 Jun 30;31(13):107843.
7. Ma, D. The fusiform gyrus exhibits an epigenetic signature for Alzheimer's disease. Clin Epigenet 12, 129 (2020).

Poster No 264

The impact of FreeSurfer variability on structural brain analyses in Parkinson's disease

Andrzej Sokolowski[1], Nikhil Bhagwat[2], Dimitrios Kirbizakis[1], Yohan Chatelain[1], Mathieu Dugré[1], Jean-Baptiste Poline[2], Madeleine Sharp[2], Tristan Glatard[1]

[1]Concordia University, Montreal, Quebec, [2]McGill University, Montreal, Quebec

Introduction: Software variability impacts the reproducibility of neuroimaging studies. Image processing software impacts quantification of brain measures and may impact clinical research. The goal of this study was to investigate the impact of variability between major FreeSurfer releases on the estimation of structural MRI-derived measures in patients with Parkinson's disease (PD). Clinical research questions were derived from previous studies on MRI-derived biomarkers of PD (Hanganu et al., 2014; Mak et al., 2015; Mitchell et al., 2021). We hypothesized that the software version would impact the magnitude of the group differences between healthy controls (HC) and PD patients in subcortical volume and cortical thickness (at baseline and longitudinally). We also hypothesized that software variability would impact the strength of the relationship between disease severity and subcortical volume as well as cortical thickness in patients with PD (at baseline and longitudinally).

Methods: Two hundred and nine PD patients (Mage = 62.5; SD = 9.6) and 106 HC (Mage = 60.5; SD = 10.2) were selected from Parkinson's Progression Markers Initiative database. 125 PD patients (Mage = 61.1; SD = 9.3) had two scans that were used in the longitudinal analyses. T1-weighted brain images were processed using FreeSurfer. We measured the differences in the estimation of volume, surface area, and cortical thickness between three major FreeSurfer releases (i.e., 5.3, 6.0.1, and 7.3.2). Longitudinal preprocessing stream was used to calculate the change in cortical thinning and subcortical volumes between the two study visits (Reuter et al., 2012). Unified Parkinson's disease rating scale was used to measure disease severity. We compared clinical results obtained from different software versions.

Results: The code and results are available at https://github.com/LivingPark-MRI/freesurfer-variability. We report high software variability in the estimation of all three structural measures. Estimations significantly differed between software versions in 62% to 86% regions depending on metric and FreeSurfer pair. Some regions display higher between-version than between-subject variability (Fig. 1). The variability did not differ between patients and healthy controls (ps < .05). Importantly, software variability impacted the clinical outcomes. Group differences between patients and healthy controls in subcortical volumes depended on software version; results differed between versions for the left hippocampus, right pallidum, right amygdala, and right nucleus accumbens (ps < .05) Vertex-wise analyses of group differences in cortical thickness and its correlation with disease severity showed distinct results depending on the software version (Fig. 2). More significant clusters were reported in FreeSurfer 5 than in more recent versions.

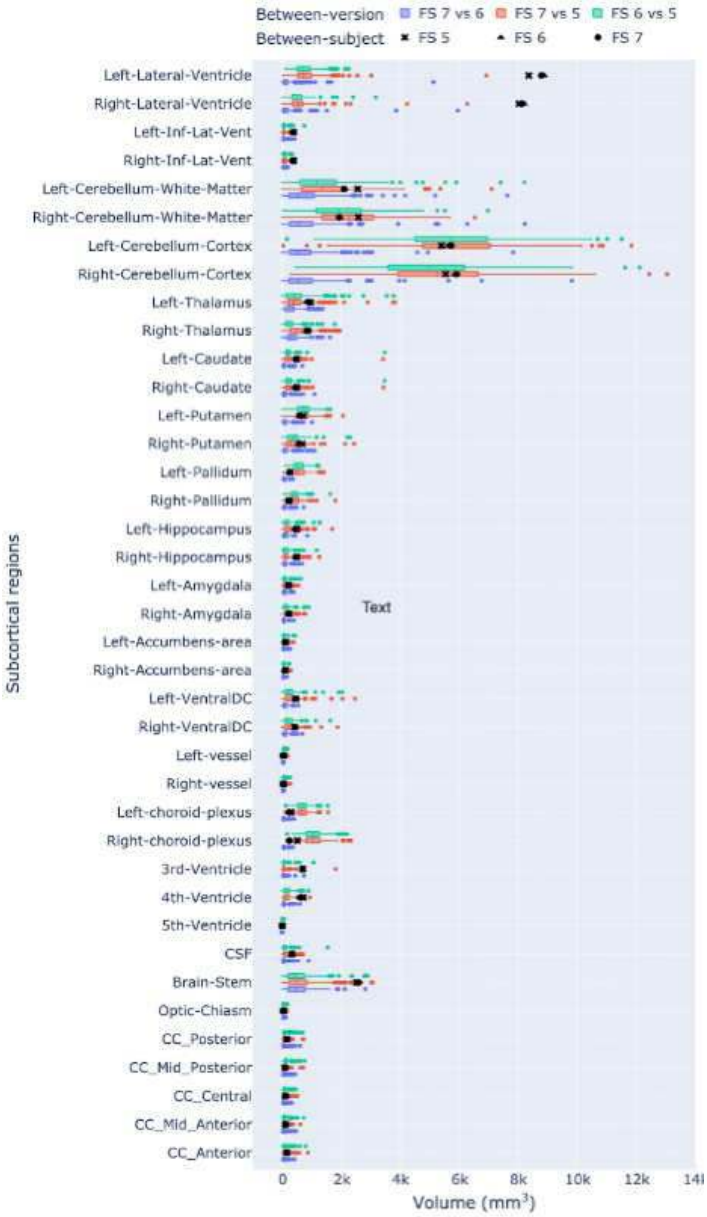

Figure 1. Between-versions and between-subject subcortical volume variability. Absolute difference between FreeSurfer versions represented as colored box plots, standard deviations represented as black markers.

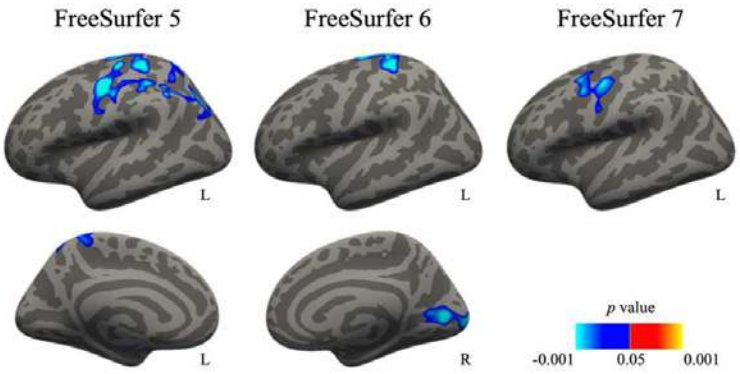

Figure 2. Vertex-wise correlation between disease severity and cortical thickness at baseline in patients with Parkinson's disease.

Conclusions: We report that software variability is not only associated with the estimation of structural measures but it also impacts the interpretation of the correlations between estimates of brain structure and clinical outcomes that are commonly used in research and in the clinic. Such variability limits the utility of MRI-derived measures of brain structure as outcomes in clinical research and poses significant challenges to their eventual integration into clinical practice. We recommend users to implement the latest available release of FreeSurfer. The most recent software versions usually have improved algorithms and fixed issues discovered in previous releases. Toolbox version should not be changed throughout the same study. Developers could track differences between versions by analyzing the same dataset with current and future releases to provide information about the degree of software variability. Providing software long-term support would be beneficial. Our study provides insight into the reproducibility of neuroimaging studies in neurodegenerative disorders.

References

1. Hanganu, A., Bedetti, C., Degroot, C., Mejia-Constain, B., Lafontaine, A. L., Soland, V., ... & Monchi, O. (2014). Mild cognitive impairment is linked with faster rate of cortical thinning in patients with Parkinson's disease longitudinally. Brain, 137(4), 1120-1129.
2. Mak, E., Su, L., Williams, G. B., Firbank, M. J., Lawson, R. A., Yarnall, A. J., ... & O'Brien, J. T. (2015). Baseline and longitudinal grey matter changes in newly diagnosed Parkinson's disease: ICICLE-PD study. Brain, 138(10), 2974-2986.
3. Mitchell, T., Lehéricy, S., Chiu, S. Y., Strafella, A. P., Stoessl, A. J., & Vaillancourt, D. E. (2021). Emerging neuroimaging biomarkers across disease stage in Parkinson disease: a review. JAMA 78(10), 1262-1272.
4. Reuter, M., Schmansky, N. J., Rosas, H. D., & Fischl, B. (2012). Within-subject template estimation for unbiased longitudinal image analysis. Neuroimage, 61(4), 1402-1418.

Poster No 265

White Matter Alterations in Major Depression Disorder with Suspected Non-Alzheimer Pathophysiology

Bo-Han Huang[1], Jing-Ru Chen[1], Chun-Hung Yeh[1], Rung-Yu Tseng[1], Ing-Tsung Hsiao[1], Kuan-Yi Wu[2]

[1]Department of Medical Imaging and Radiological Sciences, Chang Gung University, Taoyuan, Taiwan, [2]Department of Psychiatry, Chang Gung Memorial Hospital, College of Medicine, Chang Gung University, Taoyuan, Taiwan

Introduction: Depression has been identified as a factor that elevates the risk of developing Alzheimer's disease, characterized by β-amyloid pathology (Aβ)[1]. Notably, previous research has highlighted a subgroup within late-life major depressive disorder (MDD) known as Suspected non-Alzheimer Disease Pathophysiology (SNAP), where individuals exhibit Aβ negativity but display positive neurodegeneration (Aβ-/ND+)[2]. In comparison to both normal control (NC) participants and MDD individuals who tested negative for both Aβ and neurodegeneration (Aβ-/ND-), these SNAP MDD patients showed significantly reduced 18F-florbetapir levels across various cortical regions[3]. However, the extent of putative white matter alterations, whether widespread or specific to particular white fiber tracts, has remained unclear. To address this gap, this study leveraged fixel-based analysis (FBA)[4] of diffusion MRI (dMRI) data to investigate potential changes in white matter fiber tracts.

Methods: Our study enrolled 105 individuals diagnosed with late-life MDD and 21 age-matched normal controls (NC). All participants tested negative for amyloid (Aβ-) through 18F-Florberapir PET scans, and the confirmation of Aβ- status was determined using the visual rating approach[5]. Additionally, subjects were categorized as neurodegeneration-positive (ND+) if they exhibited hippocampal volume atrophy or glucose hypometabolism[6,7]. Based on these criteria, our cohort comprised 92 patients with Aβ-/ND- MDD, 13 with Aβ-/ND+ SNAP MDD, and NC exclusively consisted of Aβ-/ND- individuals. DMRI data were acquired on a 3T MRI scanner with 30 directions at b=1000 s/mm2. After data preprocessing, we followed the recommended FBA processing steps of MRtrix3[8] to compare between NC and MDD groups, based on the fixel-wise metrics of fiber density (FD), fiber-bundle cross-section (FC), and the combined metric of FD and FC (FDC)[4]. The statistical analysis of whole-brain fixel-wise metrics was conducted using the general linear model. Two-sample t-tests were performed to explore between-group differences, controlling for gender, age, education, intracranial volume, and head motion. Nonparametric permutation testing over 5000 permutations was used for multiple comparisons, with statistical significance defined at P-value <0.05 using a family-wise error control[9].

Results: NC vs MDD (Aβ-/ND-) No significant differences were found between NC and individuals with Aβ-/ND- MDD across all three fixel metrics. NC vs SNAP MDD (Aβ-/ND+) In comparison to the NC group, the SNAP MDD (Aβ-/ND+) patients exhibited the following significant differences (Fig. 1): decreased FD at the mid-body of the corpus callosum (CC) and bilateral fornix; decreased FC at the mid-body of CC and bilateral cortical-spinal tract (CST); and decreased FDC at the mid-body of CC, bilateral CST, and the right inferior fronto-occipital fasciculus (IFOF). Additionally, SNAP MDD demonstrated higher FC at the left fornix and splenium of CC as compared to NC. MDD (Aβ-/ND-) vs SNAP MDD (Aβ-/ND+) SNAP MDD showed significant reductions in FD and FDC at the right fornix and genu of CC, as compared with Aβ-/ND- MDD (Fig. 2).

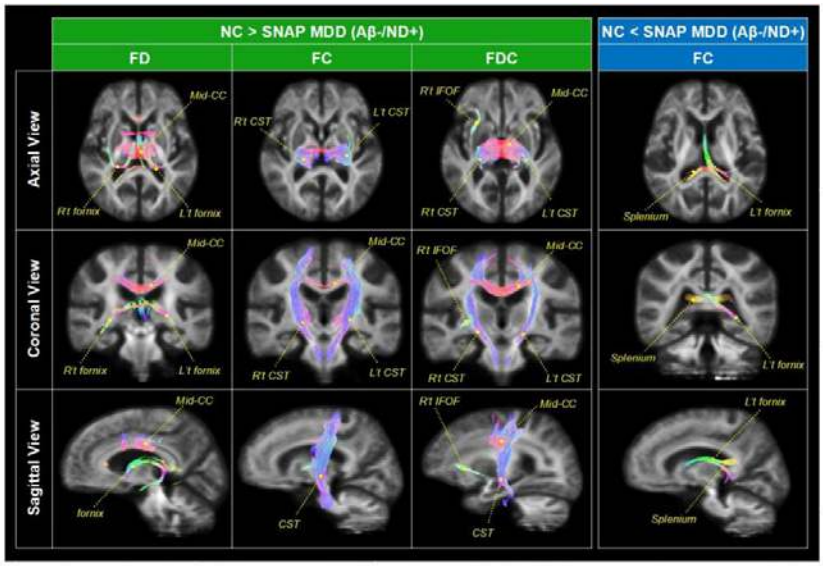

Fig. 1 Normal control (NC) versus SNAP MDD (Aβ-/ND+). White matter tract segments that have significant group differences (P<0.05) in FBA metrics are displayed and colored based on their orientations (red: left – right; green: anterior – posterior; blue: inferior – superior). All tract segments are projected onto single slices in three orthogonal views. Acronyms: CC: corpus callosum; CST: cortical-spinal tract; IFOF: inferior fronto-occipital fasciculus.

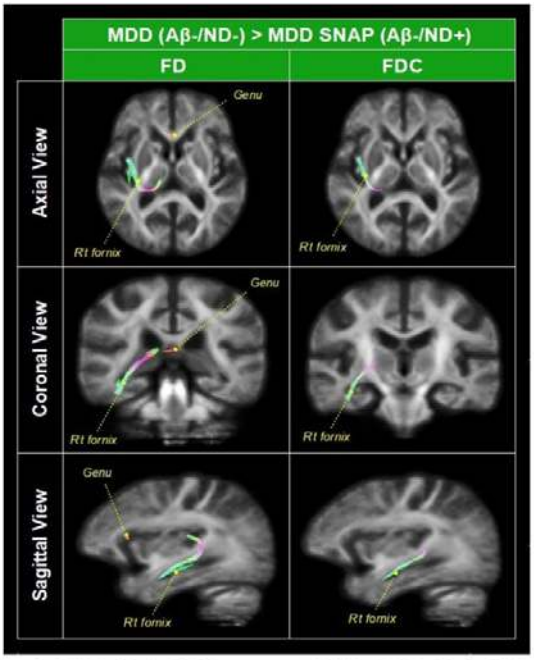

Fig. 2 MDD (A β -/ND-) versus SNAP MDD (A β -/ND+). White matter tract segments that have significant group differences (P<0.05) in FBA metrics are displayed and colored based on their orientations (red: left – right; green: anterior–posterior; blue: inferior–superior). All tract segments are projected onto single slices in three orthogonal views.

Conclusions: Our results demonstrated that patients with SNAP MDD (Aβ-/ND+) had significant white matter fiber-specific reductions, in comparison to those with MDD (Aβ-/ND-) and NC. These are consistent with lower 18F-Florbetapir uptakes in SNAP MDD than the other two groups[3]. In addition, our study suggests a potential link between white matter fiber connectivity and the pathophysiology observed in the SNAP MDD group. Such distinct patterns of white matter alterations hold implications for understanding the underlying pathogenesis of non-Alzheimer's pathology and late-life depression. Our future investigations will integrate these findings with the outcomes of cellular mechanism analysis using PET, providing insights into the relationship between cellular metabolism and white matter reductions.

References
1. Diniz, B. S., Butters, M. A., Albert, S. M., Dew, M. A., & Reynolds, C. F. (2013). Late-life depression and risk of vascular dementia and Alzheimer's disease: systematic review and meta-analysis of community-based cohort studies. The British Journal of Psychiatry, 202(5), 329-335.
2. Jack Jr, C. R., Knopman, D. S., Chételat, G., Dickson, D., Fagan, A. M., Frisoni, G. B., ... & Vos, S. J. (2016). Suspected non-Alzheimer disease pathophysiology—concept and controversy. Nature Reviews Neurology, 12(2), 117-124.
3. Wu, K. Y., Lin, K. J., Chen, C. H., Liu, C. Y., Wu, Y. M., Chen, C. S., ... & Hsiao, I. T. (2022). Decreased Cerebral Amyloid-β Depositions in Patients With a Lifetime History of Major Depression With Suspected Non-Alzheimer Pathophysiology. Frontiers in Aging Neuroscience, 14, 857940.
4. Raffelt, D. A., Tournier, J. D., Smith, R. E., Vaughan, D. N., Jackson, G., Ridgway, G. R., & Connelly, A. (2017). Investigating white matter fibre density and morphology using fixel-based analysis. Neuroimage, 144, 58-73.
5. Sabri, O., Seibyl, J., Rowe, C., & Barthel, H. (2015). Beta-amyloid imaging with florbetaben. Clinical and translational imaging, 3, 13-26.
6. Wu, K. Y., Lin, K. J., Chen, C. H., Chen, C. S., Liu, C. Y., Huang, S. Y., ... & Hsiao, I. T. (2018). Diversity of neurodegenerative pathophysiology in nondemented patients with major depressive disorder: Evidence of cerebral amyloidosis and hippocampal atrophy. Brain and Behavior, 8(7), e01016.
7. Herholz, K., Salmon, E., Perani, D., Baron, J. C., Holthoff, V., Frölich, L., ... & Heiss, W. D. (2002). Discrimination between Alzheimer dementia and controls by automated analysis of multicenter FDG PET. Neuroimage, 17(1), 302-316.
8. Tournier, J. D., Smith, R., Raffelt, D., Tabbara, R., Dhollander, T., Pietsch, M., ... & Connelly, A. (2019). MRtrix3: A fast, flexible and open software framework for medical image processing and visualisation. Neuroimage, 202, 116137.
9. Alberton, B. A., Nichols, T. E., Gamba, H. R., & Winkler, A. M. (2020). Multiple testing correction over contrasts for brain imaging. NeuroImage, 216, 116760.

Poster No 266

A Comparative Study on Diagnosing Parkinson's Disease Using Two Novel Neuromelanin MRI Sequences

Ming-Chih Kuo[1,2], Yao-Chia Shih[1], Ru-Jen Lin[3], Kai-Hsiang Chen[3], Yuh-Fen Wei[4], Yen-Chung Hsiue[4], Hui-Yu Yang[3], Xue-Zhe Lu[5], Joshua Oon Soo Goh[6,7,8,9]

[1]Graduate Institute of Medicine, Yuan Ze University, Taoyuan, Taiwan, [2]Department of Medical Imaging, National Taiwan University Cancer Center, Taipei, Taiwan, [3]Department of Neurology, National Taiwan University Hospital Hsin-Chu Branch, Hsinchu City, Taiwan, [4]Department of Medical Imaging, National Taiwan University Hospital Hsin-Chu Branch, Hsinchu City, Taiwan, [5]Siemens Healthineers Limited, Taipei, Taipei, [6]Graduate Institute of Brain and Mind Sciences, College of Medicine, National Taiwan University, Taipei, Taiwan, [7]Department of Psychology, National Taiwan University, Taipei, Taiwan, [8]Neurobiology and Cognitive Science Center, National Taiwan University, Taipei, Taiwan, [9]Center for Artificial Intelligence and Advanced Robotics, National Taiwan University, Taipei, Taiwan

Introduction: Neuronal loss in the substantia nigra pars compacta (SNpc) and/or locus coeruleus (LC) is seen in Parkinson's disease (PD) (Braak, Del Tredici et al. 2003), resulting in a visible loss of neuromelanin (NM) detected by NM-MRI (Sasaki, Shibata et al. 2006). The contrast of NM-MRI is mainly caused by magnetization transfer (MT) and T1-shortening effects. But a conventional gradient-echo-MT sequence requires longer scan time (>8min). Two novel NM-MRI sequences with shorter scan time (<6min) have shown the comparable or better contrast-to-noise ratio (CNR) of NM-MRI signals in SNpc/LC than the conventional gradient-echo-MT one, namely black-blood delay alternating with nutation for tailored excitation-prepared T1-weighted variable flip angle turbo spin echo (DANTE T1-SPACE) (Oshima, Fushimi et al. 2021) and Sandwich-NM (Ji, Choi et al. 2022). Whilst the hyperintense signals in SNpc/LC and suppressed cerebrospinal fluid and intravascular signals shown in DANTE T1-SPACE images rely on MT effect due to short rectangular pulses in wideband, Sandwich-NM adopts even number of flow saturation pulses inferior and superior to the imaging slab to enhance incidental MT effect on NM CNR without flow artifacts. However, it is underdetermined which novel NM-MRI sequence within the above two has better performance on the diagnosis of PD. Thus, we simultaneously applied both sequences to each participant within a single MRI session, and aimed to compare their SNpc/LC CNR and PD diagnostic performance.

Methods: Twenty-four patients with PD (age=64.64±8.76 years; 14 males) and 24 age- and sex-matched healthy controls (HCs, age=67.46±7.72 years, 10 males) underwent all structural brain scans on a 3T-MRI scanner (MAGNETOM Skyra, Siemens Healthineers, Erlangen, Germany) with a 20-channel head coil. The details of imaging parameters for both sequences are described in previous studies (Oshima, Fushimi et al. 2021, Ji, Choi et al. 2022). We used a MATLAB toolkit (SPM 12) to co-registered both DANTE T1-SPACE and Sandwich-NM images to a T1-weighted MPRAGE image for each subject. Two radiographers used 3D slicer software to manually draw regions of interest (ROIs) on the bilateral SNpc/LC on co-registered Sandwich-NM images. They also placed 3 circle reference ROIs on the bilateral cerebral crus (CC) and a non-SN brainstem tissue for each individual image. Both co-registered NM-MRI images thereby shared the same manually drawn ROIs that allowed us fairly calculate CNR from them. CNRSNpc in each side was calculated by the following equation: (SI_SNpc-SI_CC)/

SI_CC, whereas CNR_LC was obtained by (SI_LC-SI_non-SN)/SI_non-SN (SI: averaged signal intensity within a ROI). Finally, a receiver operating characteristic curve (ROC) analysis was performed to differentiate patients from HCs in terms of either CNR_SNpc or CNR_LC in the left, right, and bilateral sides, to compare the diagnosis performance between both NM-MRI sequences.

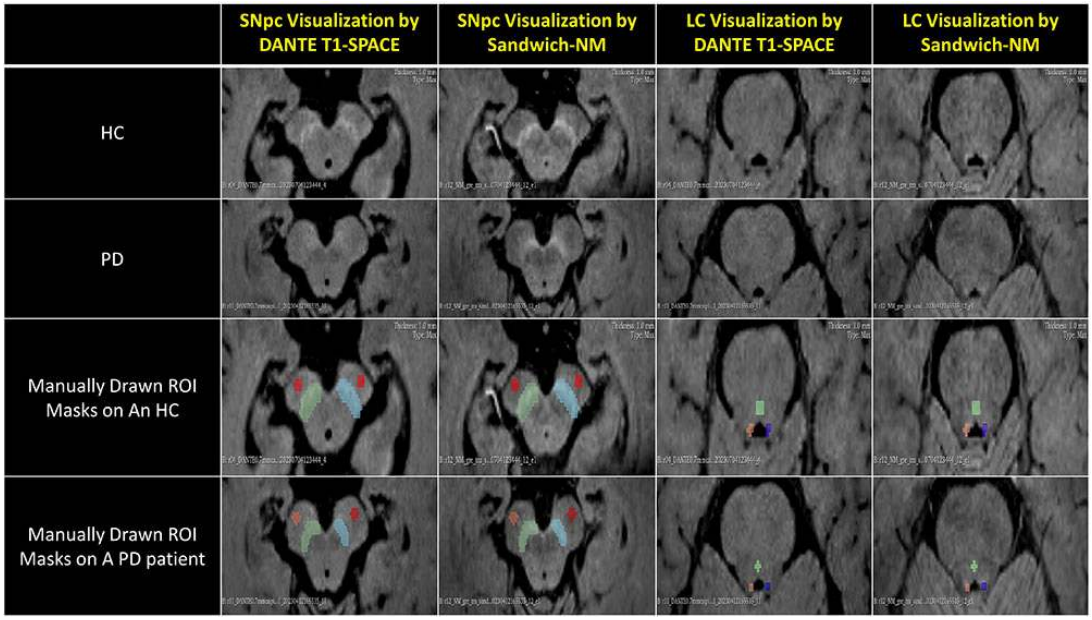

Results: Significant CNR reductions in the left, right, and bilateral SNpc in both DANTE T1-SPACE and Sandwich-NM images were found in PD compared to HC ($p<0.001$). However, CNR_LC in either of two sides disabled the differentiation between PD and HC groups. No significant differences in CNR measures between two raters. Results of ROC analysis showed that the CNR_SNpc obtained from both sides achieved great performance on discriminating PD and HC groups when using either DANTE T1-SPACE (area under the curve [AUC]=0.892) or Sandwich-NM (AUC=0.889). CNR_LC from either side failed to classify PD and HC groups (Fig. 2).

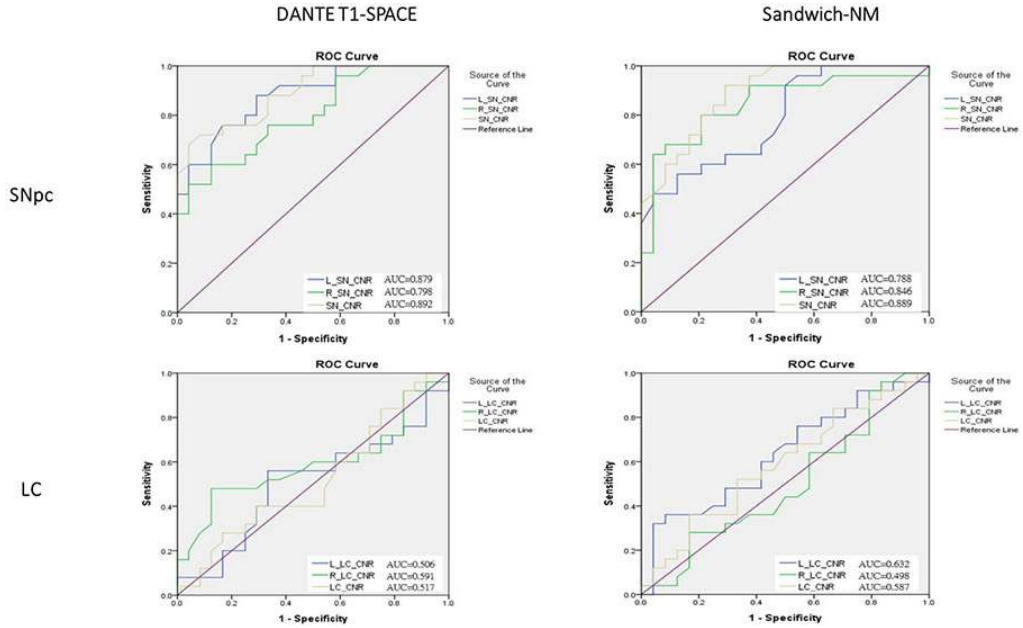

Conclusions: Our findings revealed that CNR_SNpc measures from DANTE T1-SPACE and Sandwich-NM images have comparable PD diagnostic performance, with nearly short scan time. Future works will use atlas-based ROI (Pauli, Nili et al. 2018) or deep-learning based segmentation (Le Berre, Kamagata et al. 2019) methods to improve CNR calculation, especially for potentially subjective biases due to tiny LC structure.

References

1. Braak, H., K. Del Tredici, U. Rüb, R. A. de Vos, E. N. Jansen Steur and E. Braak (2003). "Staging of brain pathology related to sporadic Parkinson's disease." Neurobiol Aging 24(2): 197-211.
2. Ji, S., E.-J. Choi, B. Sohn, K. Baik, N.-Y. Shin, W.-J. Moon, S. Park, S. Song, P. H. Lee, D. H. Shin, S.-H. Oh, E. Y. Kim and J. Lee (2022). "Sandwich spatial saturation for neuromelanin-sensitive MRI: Development and multi-center trial." NeuroImage 264: 119706.
3. Le Berre, A., K. Kamagata, Y. Otsuka, C. Andica, T. Hatano, L. Saccenti, T. Ogawa, H. Takeshige-Amano, A. Wada, M. Suzuki, A. Hagiwara, R. Irie, M. Hori, G. Oyama, Y. Shimo, A.
4. Umemura, N. Hattori and S. Aoki (2019). "Convolutional neural network-based segmentation can help in assessing the substantia nigra in neuromelanin MRI." Neuroradiology 61(12): 1387-1395.
5. Oshima, S., Y. Fushimi, T. Okada, S. Nakajima, Y. Yokota, A. Shima, J. Grinstead, S. Ahn, N. Sawamoto, R. Takahashi and Y. Nakamoto (2021). "Neuromelanin-Sensitive Magnetic Resonance Imaging Using DANTE Pulse." Mov Disord 36(4): 874-882.
6. Pauli, W. M., A. N. Nili and J. M. Tyszka (2018). "A high-resolution probabilistic in vivo atlas of human subcortical brain nuclei." Scientific Data 5(1): 180063.
7. Sasaki, M., E. Shibata, K. Tohyama, J. Takahashi, K. Otsuka, K. Tsuchiya, S. Takahashi, S. Ehara, Y. Terayama and A. Sakai (2006). "Neuromelanin magnetic resonance imaging of locus ceruleus and substantia nigra in Parkinson's disease." Neuroreport 17(11): 1215-1218.

Poster No 267

White matter hyperintensities effect on cognition in type 2 diabetes is moderated by education level

Mohamed Salah Khlif[1], Carolina Restrepo[2], Sheila Patel[3], Leonid Churilov[4], Louise Burrell[3], Amy Brodtmann[1]

[1]Cognitive Health Initiative, Central Clinical School, Monash University, Melbourne, VIC, [2]Cabrini Health, Melbourne, VIC, [3]Department of Medicine, University of Melbourne, Austin Health, Heidelberg, VIC, [4]Melbourne Medical School, University of Melbourne, Melbourne, VIC

Introduction: White matter hyperintensities (WMH) are a cerebral small vessel disease (cSVD) marker (Li et al., 2022). Factors that lead to WMH accumulation and to cSVD include increasing age, obesity, hypertension, and type 2 diabetes mellitus (T2DM). WMH burden has been linked to neurodegeneration and cognitive decline (Rizvi et al., 2018). Conversely, there is a positive association between education attainment level and cognitive ability across an adult life span (Lövdén et al., 2020). We conducted a moderation analysis in a group of people with T2DM to determine if education level attenuates the causal relationship between WMH volume and cognitive performance (see Fig. 1).

Methods: Baseline multimodal MRI was completed as part of the Diabetes and Dementia (D2) (Patel et al., 2017), an observational longitudinal case control study that followed 150 adults with T2DM. Age, obesity (BMI > 30 kg/m2), hypertension (24-hour blood pressure mean > 140/90 mmHg), and education level (0/1 based on a threshold of 12 years of education, YOE) were included as covariates. WMH volumes (predictor, mm3) were estimated using manual delineations on FLAIR images and cognitive screening (response) was done using the Montreal Cognitive Assessment (MoCA) test (Nasreddine et al., 2005). The causal effects of WMH on cognitive ability were estimated and stratified by the level of education attainment. The "WeightIt" R package was used for generating the balancing weights based on the "optweight" method (https://cran.r-project.org/web/packages/WeightIt/index.html). We used the g-computation algorithm and set 'vcov' to 'HC3' for robust estimations of causal effects and confidence intervals.

Results: We included 129 participants (age: 65.1 ± 7.2 years, men: 72): 93 participants had YOE > 12 years; 45 had current/untreated hypertension based on ambulatory BP testing, and 68 were classified as obese. The distributions of unadjusted covariates at baseline stratified by education level are shown in Fig. 1. Covariate balancing after weighting is provided in Fig. 2/A showing WMH-covariate correlations below 5%. We found a causal effect of WMH accumulation on cognitive ability ($p = 0.00154$, Fig. 2/C) only in the group of T2DM patients with lower level of education. This was also reflected in the plot of the average dose-response function (ADRF) in Fig. 2/B. Testing also showed that the education moderation effect was significant ($p = 0.00585$, Fig. 2/C).

Conclusions: In this sample of participants with T2DM, we report a significant effect of higher education attainment in attenuating the causal effects of cSVD, reflected by WMH accumulation, on cognitive abilities. These results are consistent with the concept of cognitive resilience imparted by prior educational attainment, even in the setting of increasingly cSVD.

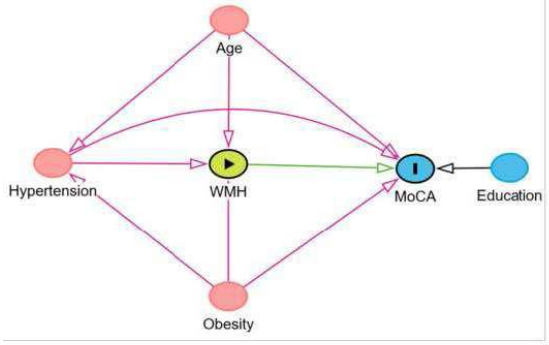

Unadjusted variables stratified by 'Education'

	0	1	SMD
N	35	93	
Age (mean (SD))	67.8 (7.4)	64.1 (6.9)	0.53
HTN (mean (SD))	0.31 (0.47)	0.37 (0.48)	0.11
Obesity (mean (SD))	0.63 (0.49)	0.48 (0.5)	0.29
WMH (mean (SD))	4328 (4325)	4635 (5659)	0.06
MoCA (mean (SD))	21.2 (3.9)	24.9 (3.2)	1.05

Figure 1: Illustration of proposed causal analysis between WMH (exposure) and outcome (MoCA) in the presence of pre-exposure confounders age, hypertension, and obesity and the moderating variable education (HTN = hypertension, MoCA = Montreal cognitive assessment, WMH = white matter hyperintensities volume, SMD = standardized mean difference).

(A)

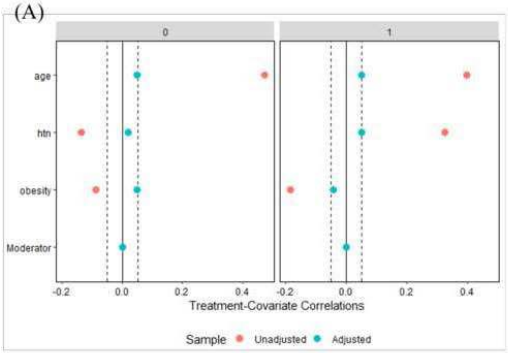

(B)

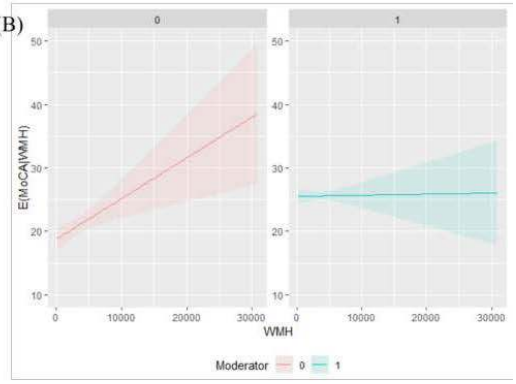

(C)

Effect of WMM burden on cognitive assessment (MoCA) stratified by moderator 'Education'

Term	Contrast	Moderator	Estimate	Std. Error	z	Pr(>|z|)	2.5 %	97.5 %
WMH mean (+1)		0	0.000644	0.000203	3.17	**0.00154**	0.000245	0.001042
WMH mean (+1)		1	0.000017	0.000154	0.11	0.91228	-0.000285	0.000319

Comparison of effects between subgroups: Testing for moderation

Term	Estimate	Std. Error	z	Pr(>|z|)	2.5 %	97.5 %
0 - 1	0.000627	0.000227	2.76	**0.00585**	0.000181	0.00107

Figure 2: A) L.O.V.E plot showing correlations between exposure WMH and confounders age, hypertension, and obesity stratified by the moderator education before and after balancing. B) Plot of the average dose-response function (ADRF) relating WMH to expected MoCA outcome shown for the two levels of education (0/1). C) Estimation of the effect of WMH on MoCA as moderated by education level and validation of moderation effect (htn = hypertension, MoCA = Montreal cognitive assessment, WMH = white matter hyperintensities volume).

References

1. Li, Y., Kalpouzos, G., Laukka, E. J., Dekhtyar, S., Bäckman, L., Fratiglioni, L., & Qiu, C. (2022). Progression of neuroimaging markers of cerebral small vessel disease in older adults: A 6-year follow-up study. Neurobiology of Aging, 112, 204-211. https://doi.org/https://doi.org/10.1016/j.neurobiolaging.2022.01.006
2. Lövdén, M., Fratiglioni, L., Glymour, M. M., Lindenberger, U., & Tucker-Drob, E. M. (2020). Education and Cognitive Functioning Across the Life Span. Psychol Sci Public Interest, 21(1), 6-41. https://doi.org/10.1177/1529100620920576
3. Nasreddine, Z. S., Phillips, N. A., Bédirian, V., Charbonneau, S., Whitehead, V., Collin, I., Cummings, J. L., & Chertkow, H. (2005). The Montreal Cognitive Assessment, MoCA: a brief screening tool for mild cognitive impairment. J Am Geriatr Soc, 53(4), 695-699. https://doi.org/10.1111/j.1532-5415.2005.53221.x
4. Patel, S. K., Restrepo, C., Werden, E., Churilov, L., Ekinci, E. I., Srivastava, P. M., Ramchand, J., Wai, B., Chambers, B., O'Callaghan, C. J., Darby, D., Hachinski, V., Cumming, T., Donnan, G., Burrell, L. M., & Brodtmann, A. (2017). Does left ventricular hypertrophy affect cognition and brain structural integrity in type 2 diabetes? Study design and rationale of the Diabetes and Dementia (D2) study. BMC Endocr Disord, 17(1), 24. https://doi.org/10.1186/s12902-017-0173-7
5. Rizvi, B., Narkhede, A., Last, B. S., Budge, M., Tosto, G., Manly, J. J., Schupf, N., Mayeux, R., & Brickman, A. M. (2018). The effect of white matter hyperintensities on cognition is mediated by cortical atrophy. Neurobiol Aging, 64, 25-32. https://doi.org/10.1016/j.neurobiolaging.2017.12.006

Poster No 268

Reduced Resting-state Inter-Hemispheric Functional Connectivity in People with Multiple Sclerosis

Costanza Iester[1], Monica Biggio[1], Laura Bonzano[1], Sabrina Brigadoi[2], Ludovico Pedullà[3], Simone Cutini[2], Giampaolo Brichetto[3], Marco Bove[4]

[1]Department of Neuroscience, DINOGMI, University of Genoa, Genoa, Italy, Genova, Italy, [2]Department of Developmental Psychology, University of Padova, Padova, Italy, Padova, Italy, [3]Italian Multiple Sclerosis Foundation, Genoa, Italy, [4]DIMES, University of Genoa, Genova, Italy

Introduction: Resting-state functional connectivity (RSFC) has predominantly been explored using functional Magnetic Resonance Imaging (fMRI)1. Existing literature highlights alterations in RSFC among specific neurodegenerative conditions, including multiple sclerosis (MS)2,3. Functional near-infrared spectroscopy (fNIRS) emerges as a potential alternative for RSFC analysis4. In contrast to fMRI, fNIRS boasts several advantages, such as portability, noiselessness, and resistance to motion artifacts. These advantages ensure unrestricted participation of all subjects, eliminating constraints associated with factors like magnetic fields and enhancing overall comfort during data acquisition. This study aims to investigate RSFC patterns using fNIRS in both healthy controls and people with multiple sclerosis (PwMS).

Methods: We enrolled 18 control participants (mean age = 55.0 ± 3.1 years) and 18 PwMS (mean age = 59.4 ± 1.7 years) for this study. The experimental protocol included a 15-minute resting-state session while recording fNIRS data. Changes in oxy-hemoglobin concentration were measured across 44 standard channel (3cm) and 8 short-separation channels (8mm). The fNIRS array covered premotor, sensorimotor, associative, parietal, and frontal areas. After signal acquisition, noisy channels were removed, and the remaining channels were converted into changes in optical density. Motion artifacts were identified, and motion-free segments were segregated5. Subsequently, motion-free segments exceeding a duration of 20 seconds were individually analysed. They were band-passed (0.009–0.08Hz)6, and the optical density data were converted into concentration changes. At the end, the short-separation channels were regressed out, and the free segments were combined. Channel signals within the same Brodmann area (BA) were averaged for each subject, resulting in 18 regions of interest (nine for each hemisphere). Subsequently, the Pearson correlation was employed to calculate the correlation matrix for each subject. Group correlation matrices were then computed by averaging individual correlation matrices within each group. Finally, to assess the statistical difference between groups, individual correlation matrices were Z-transformed and then each box of the matrix was compared between the two groups through a non-parametric test (Wilcoxon rank sum test, $p < 0.05$)7.

Results: Results revealed a robust inter-hemispheric correlation specific to homologous areas in the control group, and clusters in prefrontal, sensorimotor, and associative intra-hemispheric regions. Conversely, PwMS generally exhibited a loss or reduction in correlations compared to the control group. Specifically, PwMS demonstrated diminished connections between homologous areas (BA40, p=.001; BA7, p=.017; BA3, p= 0.0016) and, more broadly, among inter-hemispheric connections. Additionally, reductions were observed in intra-hemispheric connections related to sensorimotor and parietal areas (e.g., Left BA3-BA40, p=.014; Left BA4-BA40, p=.005; Left BA3-BA4, p=.005).

Conclusions: The decrease in functional inter-hemispheric connections could be attributed to the loss of integrity of the corpus callosum, which is typical in PwMS8. Impaired RSFC can lead to inadequate performance of daily life tasks. Therefore, exploiting the advantages of fNIRS, such as portability, quietness, and non-invasiveness, to acquire data immediately before the execution of a specific motor or cognitive task, it may be possible to investigate potential associations between the state of the brain (resting-state) and following behavioral outcomes (task).

References

1. Lowe, M. J. (2000). Correlations in low-frequency BOLD fluctuations reflect cortico-cortical connections. Neuroimage, 12(5), 582-587.
2. Van Den Heuvel, M. P. (2010). Exploring the brain network: a review on resting-state fMRI functional connectivity. European neuropsychopharmacology, 20(8), 519-534.
3. Lowe, M. J. (2008). Resting state sensorimotor functional connectivity in multiple sclerosis inversely correlates with transcallosal motor pathway transverse diffusivity. Human brain mapping, 29(7), 818-827.
4. Pinti, P. (2020). The present and future use of functional near-infrared spectroscopy (fNIRS) for cognitive neuroscience. Annals of the New York Academy of Sciences, 1464(1), 5-29.
5. Bulgarelli, C. (2020). The developmental trajectory of fronto-temporoparietal connectivity as a proxy of the default mode network: a longitudinal fNIRS investigation. Hum Brain Mapp 41, 2717–2740.
6. Mesquita, R. C. (2010). Resting state functional connectivity of the whole head with near-infrared spectroscopy. Biomed. Opt. Express 1, 324–336.
7. Iester, C. (2023). Time-of-day influences resting-state functional cortical connectivity. Frontiers in Neuroscience, 17, 1192674.
8. Evangelou, N. (2000). Regional axonal loss in the corpus callosum correlates with cerebral white matter lesion volume and distribution in multiple sclerosis. Brain, 123(9), 1845-1849.

Poster No 269

Exploring the Relationship Between Brain Structural and Antipsychotic Drug Dosage in BPSD

Bo Hong[1], Tianli Tao[2], Han Zhang[2], jianhua chen[1], Ling Yue[1]

[1]Shanghai Mental Health Center, Shanghai Jiao Tong University School of Medicine, Shanghai, Shanghai, [2]School of Biomedical Engineering, ShanghaiTech University, Shanghai, Shanghai

Introduction: Behavioral and psychological symptoms of dementia (BPSD), such as aggression, agitation, anxiety afflict over 75% of patients with Alzheimer disease (AD) (Halpern Rachel, 2019) and impose a high burden on caregivers and the patient's family (Jia J, 2018). Given that psychotropic medications are broadly prescribed among BPSD, the safety of antipsychotic drugs has always been a concern (Kuehn B.M., 2005 & Maust D.T., 2015). Furthermore, for different patients with comparative severity of BPSD, there may be significant variations in the dosages of antipsychotic drugs required. However, the objective indicators, which can be utilized for evaluating drug dosage are still lacking. Since BPSD patients may have altered brain structure, it is highly desired to investigate relationship between the brain structural alteration and the final effective antipsychotic drug dosage for BPSD patients towards precision medicine.

Methods: This study focuses on AD patients who are outpatient or hospitalized in the geriatric psychiatry department at the Shanghai Mental Health Center, China. Baseline general demographic data were collected from the patients. Their cognitive function was evaluated using the Mini Mental State Scale (MMSE) and the behavioral and psychological symptoms were evaluated by the Neuropsychiatric Inventory (NPI). 3D T1w brain structural MRI data were acquired and processed with Freesurfer 7.0, resulting in 68 cortical thickness and 16 subcortical regions of interest (ROIs) based on the Desikan-Killiany atlas (Desikan et al., 2006) and the Automatic Segmentation of Subcortical Structures (Fischl, 2002), respectively. All patients underwent standardized clinical treatment (with or without concomitant antipsychotic drugs) and were followed up until BPSD remission. Drug treatment procedures (including drug types and doses) were recorded, where the antipsychotic drugs were converted using a defined daily dose (DDD) method to obtain the final daily dose (Leucht S., 2016). We divided the patients into three groups: DDDs=0, 0<DDDs<0.3, and DDDs≥0.3, representing a non-antipsychotic group (NAP), a low-dose group (LAP), and a high-dose group (HAP). Region-wise comparisons on cortical thickness and sub-cortical volume were conducted across different groups. Finally, we investigated the relationship between the altered brain regions and the DDDs.

Results: A total of 86 AD patients who met the ICD-10 diagnostic criteria were enrolled (NAP, n=28, LAP, n=26, HAP, n= 32). Among the three groups, NAP group showed less NPI score than LAP and HAP, while no difference was observed in age, gender, education level and MMSE score (Tab. 1). ANCOVA analysis on brain region-wise cortical thickness measures, after controlling age, gender, education level, showed significant differences in the thickness at the left pars orbitalis (F=3.277, p=0.003) and the volume of left thalamus (F=4.279, p<0.001) among three groups. Post hoc analysis indicated that the HAP group had thinner cortex in the left pars orbitalis compared to the NAP group (Fig 2A). Ordinal logistic regression analysis revealed that NPI (p=0.014) and cortical thickness at the left pars orbitalis (p=0.037) were independent predictors of antipsychotic drug dosage. Further association analysis between cortical thickness of the left pars orbitalis and DDDs revealed a significant negative correlation (r=-0.229, p=0.04) even after adjusting for gender, age, education level, MMSE and NPI score (Fig 2B).

Tab. 1 Demographic and neuropsychological data for NAP, LAP, and HAP groups.

	NAP (n=28)	LAP (n=26)	HAP (n=32)	F/χ^2	*p* value	Post-hoc
age(year)	74.2±11.6	74.5±7.2	75.3±7.3	0.132	0.877	
gender(male,%)	6, 21.4%	9, 34.6%	13, 40.6%	2.578	0.296	
education level(year)	10.2±3.6	10.1±3.9	11.6±3.7	1.555	0.217	
MMSE score	15.4±6.3	12.5±7.5	11.0±6.4	1.963	0.062	
NPI score	15.8±19.7	39.1±27.6	39.5±17.0	3.140	0.004**	NAP**<LAP, HAP

Note: Continuous data presented as mean ± standard deviation. *Post hoc* group comparisons were corrected for multiple comparisons with Bonferroni correction. The analyses of MMSE and NPI score were conducted after controlling age, sex, and education level. *p < 0.05, **p < 0.01.
NAP:non-antipsychotic group, LAP:low-dose group, HAP:high-dose group, MMSE:Mini Mental State Scale, NPI:Neuropsychiatric Inventory.

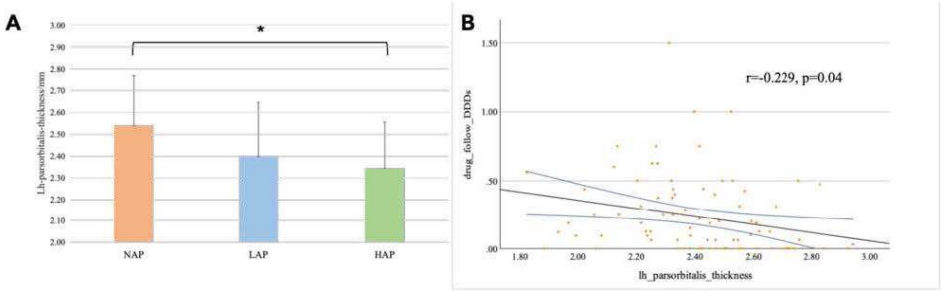

Fig. 2. The thickness of the left pars orbitalis cortex in different antipsychotic drug DDD groups (A). Significant differences in cortical thickness were found in the left pars orbitalis (F=3.277, p=0.003) after controlling age, sex, and education level. HAP individuals had thinner thickness at the left pars orbitalis cortex than NAP (p=0.015). The correlation between cortical thickness at the left pars orbitalis cortical and DDDs revealed a significant negative association (r=-0.229, p=0.04) after controlling age, sex, education level, MMSE score, and NPI score (B).

Conclusions: This study provides first-ever evidence that brain anatomical changes may serve as valuable biomarkers in prediction of antipsychotic drug dosage for patients with BPSD. The result has significant implications for optimizing clinical management strategies and offers insights into the intricate neuropathological mechanisms of BPSD.

References

1. Desikan, R. S. (2006), 'An automated labeling system for subdividing the human cerebral cortex on MRI scans into gyral based regions of interest', NeuroImage, vol. 31, no. 3, pp. 968–980.
2. Fischl, Bruce, et al. (2002), 'Whole brain segmentation: Automated labeling of neuroanatomical structures in the human brain' Neuron, vol. 33, no. 3, pp. 341–355.
3. Halpern Rachel. (2019), 'Using electronic health records to estimate the prevalence of agitation in Alzheimer disease/dementia', International Journal of Geriatric Psychiatry, vol. 34, no. 3, pp. 420-431.
4. Jia J. (2018), 'The cost of Alzheimer's disease in China and re-estimation of costs worldwide', Alzheimer's & Dementia, vol. 14, no. 4, pp. 483-491.
5. Kuehn B.M.(2005), 'FDA warns antipsychotic drugs may be risky for elderly', JAMA, vol. 293, no. 20, pp. 2462-2462.
6. Leucht S.(2016), 'Dose Equivalents for Antipsychotic Drugs: The DDD Method', Schizophrenia Bulletin, vol. 42, no. 1, pp. 90-94.
7. Maust D.T.(2015), 'Antipsychotics, Other Psychotropics, and the Risk of Death in Patients With Dementia: Number Needed to Harm', JAMA Psychiatry, vol. 72, no. 5, pp. 438-445.

Acknowledgements

This work is partially supported by the STI 2030–Major Projects (2022ZD0213100, 2022ZD0209000, and 2021ZD0200516), Shanghai Pilot Program for Basic Research–Chinese Academy of Science, Shanghai Branch (JCYJ-SHFY-2022-014), the Shanghai Science and Technology Committee (20Y11906800), and Shenzhen Science and Technology Program (No. KCXFZ20211020163408012).

Poster No 270

Investigation about Correlations Between DTI and Cognitive Domains in Mild Cognitive Impairment

Giho Jeon[1], Jake Jeong[1], Young Min Lee[2], Kwangyeol Baek[1]

[1]Pusan National University, Yangsan-Si, Gyeongsangnamdo, [2]Pusan National University Hospital, Yangsan-Si, Gyeongsangnamdo

Introduction: previous studies suggested neuropsychological tests are effective in identifying MCI and Alzheimer's disease (AD) more accurately than structural MRI measurement. Here we aimed to investigate correlations between DTI measurements and 6 cognitive domains of neuropsychological tests in MCI patients.

Methods: We acquired 3D T1-weighted and DTI images from 390 elderly MCI patients and processed them with FSL and SPM. 14 data were excluded due to preprocess quality, and 4 data were excluded due to STROOP test failure. Brain diffusion MR images were collected at Pusan National University Hospital, with b = 600 s/mm^2 diffusion weighting in 62 directions and one b = 0 image. Voxel-wise analysis of fractional anisotropy (FA) and mean diffusivity (MD) were conducted using DARTEL in SPM. SNSB(Seoul Neuropsychological Screening Battery) was used to measure patients' cognitive functions and 6 test scores were used in this study: Attention(Digit Span), Language(Korean Version Boston Naming Test; K-BNT), Visuospatial(Rey-Kim), Memory(Seoul Verbal Learning Test; SVLT), Executive function(STROOP) and Functional activity(Seoul-Instrumental Activities of Daily Living; S-IADL). In S-IADL, evaluate functional activity impairment with a cutoff score of 7.5, which is the clinical diagnostic criteria.

Results: FA values were correlated only with S-IADL scores in regions several regions including the anterior cingulate gyrus. MD values were correlated with Digit Span, ReyKim, and S-IADL scores. With MD values, Digitspan scores were correlated in

regions around mid cingulate gyrus, ReyKim scores were correlated in several regions including the parahippocampal gyrus, and S-IADL scores were correlated in white matter regions widely.

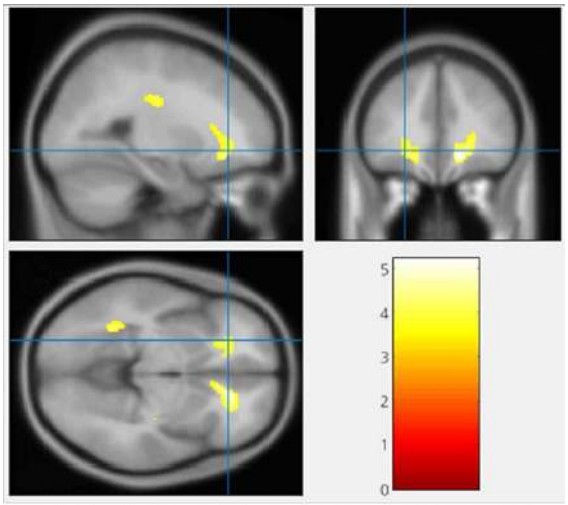

Fig 1. Significant voxels in voxel-wise correlation analysis between FA values and S-IADL. $p < 0.05$, FDR corrected.

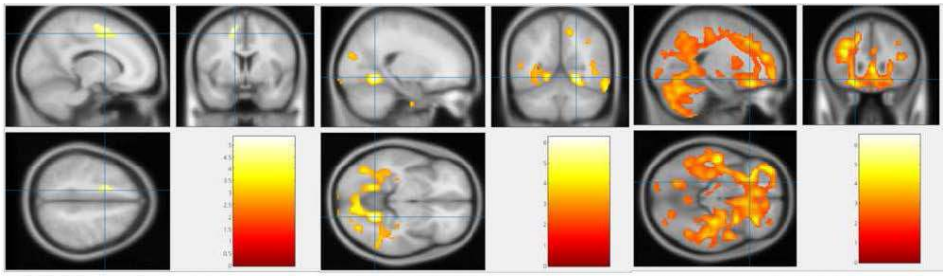

Fig 2. Significant voxels in voxel-wise correlation analysis between MD values and neuropsychological test scores. Digit span(left), Rey Kim(middle), S-IADL(right). $p < 0.05$, FDR corrected.

Conclusions: MD is more effective in detecting cognitive function decline than FA. Combining DTI data with the neuropsychological tests, we can identify microstructural changes in the brain that contribute to attention, visuospatial function, and functional activity.

References

1. Petersen, R. C. (2004), 'Mild Cognitive Impairment as a Diagnostic Entity.' Journal of Internal Medicine vol. 253, no. 3 pp. 183–94.
2. Kang, Y. (2003), 'Seoul Neuropsychological Screening Battery.' Incheon: Human brain research & consulting co.

Poster No 271

Quantitative Susceptibility Mapping in Lewy Body Dementia

Rohan Bhome[1,2], George Thomas[1], Karin Shmueli[3], James Cole[1,2], Rimona Weil[1,4,5]

[1]Dementia Research Centre, UCL, London, United Kingdom, [2]Centre for Medical Image Computing, UCL, London, United Kingdom, [3]Department of Medical Physics and Biomedical Engineering, UCL, London, United Kingdom, [4]Wellcome Centre for Human Neuroimaging, UCL, London, United Kingdom, [5]Movement Disorders Consortium, National Hospital for Neurology and Neurosurgery, London, United Kingdom

Introduction: Lewy body dementia (LBD) encompasses both Dementia with Lewy bodies (DLB) and Parkinson's disease dementia (PDD). It is common and causes significant morbidity[1]. What drives selective vulnerability of particular brain regions in LBD is poorly understood. Iron dyshomeostasis may be relevant because excessive iron interacts with α-synuclein to cause neurodegeneration in Lewy body diseases[2]. Therefore, Quantitative Susceptibility Mapping (QSM), which reflects regional differences in iron content, particularly in deep grey matter[3], may have utility in LBD. One previous study used QSM to investigate magnetic susceptibility in the substantia nigra in DLB[4]. However, it has never been used to evaluate iron deposition in other brain regions. Here, we present a whole brain QSM analysis comparing LBD with both Parkinson's disease without demenita (PD) and controls.

Methods: We included 54 participants with LBD (39 DLB; 15 PDD), 55 with PD and 34 healthy controls. We only included PD participants classed as high visual performers because this group is less likely to progress to dementia than poor visual performers[5], thereby providing an enriched PD comparator group. All participants underwent susceptibility- and T1-weighted 3T MRI scans. For QSM pre-processing, we used ROMEO[6] to unwrap phase images and brain masks were calculated from magnitude images using Brain Extraction Tool (BET2). Background field removal was performed using Laplacian boundary value extraction[7] and Multi-Scale Dipole Inversion was used to calculate susceptibility maps[8]. A study-wise template was created from all participants' T1-weighted images and QSM images were transformed into this space[9]. QSM images were spatially smoothed using a 3D Gaussian kernel (3-mm standard deviation). Voxel-wise, whole brain statistical analyses were performed using absolute QSM values as this is required for statistical conditioning. FSL Randomise was used to perform permutation analyses with threshold-free cluster enhancement. 10,000 permutations were performed to identify significant clusters which were reported at family-wise error (FWE)-corrected $P<0.05$. Regression analyses, adjusting for age and sex, were performed to compare group differences in voxel-wise magnetic susceptibility and test associations between magnetic susceptibility and clinical measures (composite cognitive score, MoCA, Hooper Visual Organisation Test, and the Movement Disorder Society Unified PD Rating Scale (UPDRS).

Results: In DLB compared to controls, there were increases in absolute susceptibility in left precentral, bilateral postcentral, left middle temporal and right supramarginal cortical regions (FWE-corrected $p<0.05$). In LBD compared to controls, there were increases in the bilateral superior and middle frontal regions, and the left superior and middle temporal regions (FWE-corrected $p<0.05$). LBD showed significant increases in absolute susceptibility in the right inferior frontal, temporal and insula regions (FWE-corrected $p<0.05$) compared to PD. The only significant association between a clinical measure and absolute susceptibility was for UPDRS in DLB where significant clusters of increased susceptibility were identified in the right middle frontal and superior temporal lobes (FWE-corrected $p<0.05$).

Conclusions: Our work is the first to investigate magnetic susceptibility throughout the brain in LBD. We found absolute susceptibility increases in several cortical regions in LBD relative to PD and controls. This could imply cortical iron dyshomeostasis in LBD and is consistent with the existing understanding of LBD being associated with cortical neuropathology[10]. Our findings highlight the relevance of QSM in LBD. Future work should utilise a region-of-interest approach to test the association between clinical measures and regional susceptibilities in LBD more precisely. This could shed further light on the potential of QSM as a clinically relevant neuroimaging measure of LBD severity.

References

1. Mueller C, Ballard C, Corbett A, Aarsland D. The prognosis of dementia with Lewy bodies. Lancet Neurol. 2017;16(5):390-8.
2. Ndayisaba A, Kaindlstorfer C, Wenning GK. Iron in Neurodegeneration - Cause or Consequence? Front Neurosci. 2019;13:180.
3. Langkammer C, Schweser F, Krebs N, Deistung A, Goessler W, Scheurer E, et al. Quantitative susceptibility mapping (QSM) as a means to measure brain iron? A post mortem validation study. Neuroimage. 2012;62(3):1593-9.
4. Chen Q, Boeve BF, Forghanian-Arani A, Senjem ML, Jack CR, Jr., Przybelski SA, et al. MRI quantitative susceptibility mapping of the substantia nigra as an early biomarker for Lewy body disease. J Neuroimaging. 2021;31(5):1020-7.
5. Zarkali A, McColgan P, Leyland LA, Lees AJ, Weil RS. Visual Dysfunction Predicts Cognitive Impairment and White Matter Degeneration in Parkinson's Disease. Mov Disord. 2021;36(5):1191-202.
6. Dymerska B, Eckstein K, Bachrata B, Siow B, Trattnig S, Shmueli K, et al. Phase unwrapping with a rapid opensource minimum spanning tree algorithm (ROMEO). Magn Reson Med. 2021;85(4):2294-308.
7. Zhou D, Liu T, Spincemaille P, Wang Y. Background field removal by solving the Laplacian boundary value problem. NMR Biomed. 2014;27(3):312-9.
8. Acosta-Cabronero J, Milovic C, Mattern H, Tejos C, Speck O, Callaghan MF. A robust multi-scale approach to quantitative susceptibility mapping. Neuroimage. 2018;183:7-24.
9. Thomas GEC, Leyland LA, Schrag AE, Lees AJ, Acosta-Cabronero J, Weil RS. Brain iron deposition is linked with cognitive severity in Parkinson's disease. J Neurol Neurosurg Psychiatry. 2020;91(4):418-25.
10. Ruffmann C, Calboli FC, Bravi I, Gveric D, Curry LK, de Smith A, et al. Cortical Lewy bodies and Abeta burden are associated with prevalence and timing of dementia in Lewy body diseases. Neuropathol Appl Neurobiol. 2016;42(5):436-50.

Poster No 272

Hypertension effects on brain volumes in presence of structural cardiac and renal function mediators

Mohamed Salah Khlif[1], Carolina Restrepo[2], Sheila Patel[3], Leonid Churilov[4], Louise Burrell[3], Amy Brodtmann[1]

[1]Cognitive Health Initiative, Central Clinical School, Monash University, Melbourne, VIC, [2]Cabrini Health, Melbourne, VIC, [3]Department of Medicine, University of Melbourne, Austin Health, Heidelberg, VIC, [4]Melbourne Medical School, University of Melbourne, Melbourne, VIC

Introduction: Hypertension and type 2 diabetes mellitus are two common, closely interlinked, comorbidities that frequently coexist in the same individual due to shared risk factors such as obesity. Hypertension causes cerebral small vessel disease

(cSVD) resulting in ischemia, accelerated brain atrophy, and higher accumulation of white matter hyperintensities (WMH) and is associated with renal and cardiac damage. These disease states are associated with increased risk of cognitive impairment and dementia (Canavan & O'Donnell, 2022). Left ventricular hypertrophy (LVH), as a marker of hypertension and an independent risk factor for cardiovascular disease, has also been associated with WMH (Nagaraja et al., 2022) and cognitive impairment (Georgakis et al., 2017). Thus, LVH may sit on a causal pathway between hypertension and pathological brain aging and cognitive impairment. We conducted causal mediation analyses (Fig. 1) to determine the extent to which the total effects of hypertension on brain global and regional atrophy and WMH accumulation may be mediated by cardiac (LVH) and renal (estimated Glomerular Filtration Rate, eGFR) metrics.

Methods: Baseline multimodal MRI was completed as part of the Diabetes and Dementia (D2) study (Patel et al., 2017). Hypertension (exposure) for 129 participants was determined on 24- hour blood pressure mean > 140/90 mmHg. All participants had eGFR > 30 mL/min/1.73m2; 36 participants were diagnosed with LVH. Total brain volume (TBV) was estimated based on FreeSurfer (v7.3.2) longitudinal segmentation of T1-weighted scans. Hippocampal and thalamic volumes were estimated using the subregion segmentation functionalities in FreeSurfer (Iglesias et al., 2015; Iglesias et al., 2018). WMH volumes were estimated using manual delineations on FLAIR scans. Age, sex, and obesity (BMI > 30 kg/m2) were included as pre-exposure confounders. Finally, the R package "mediation" (Tingley et al., 2014) was used to perform mediation and sensitivity analyses. We used bootstrap for robust effects and confidence intervals estimations.

Results: We included 129 participants (age: 65.1 ± 7.2 years, men: 72) including 97 who had a history of hypertension); 45 participants had current/untreated hypertension at baseline (64.8 ± 6.3 years, men: 26) on ambulatory BP testing. The distributions of covariates and mediators between the hypertension groups at baseline were similar (see Fig. 1). For both LVH and eGFR mediators, analyses revealed no causal mediation between current hypertension and any of the outcome measures: TBV, WMH, or hippocampal and thalamic volumes (Fig. 2). The highest mediated proportion (6.8%) of total effect was for LVH and WMH. The direct and total effects of hypertension on thalamic and WMH volumes were found to be significant (see Fig. 2). Sensitivity analyses showed that it was highly unlikely for the assumption of sequential ignorability to be violated in these cases (ρThalamus at zero effect = 0.85, ρWMH at zero effect = -0.65). Motivated by reported associations between LVH and deep WMH in acute stroke based on multivariate regression (Nagaraja et al., 2022), we completed a causal mediation analysis with deep WMH as the outcome. Again, insignificant mediation effect was found (only 7.3% of total effect).

Conclusions: In this sample of participants with T2DM, we report significant effects of hypertension on thalamic atrophy and WMH burden without mediation from the other renal and cardiac variables considered. We conclude that prior reported effects of LVH on structural brain measures may have been due to unobserved/unmeasured or imbalanced confounders.

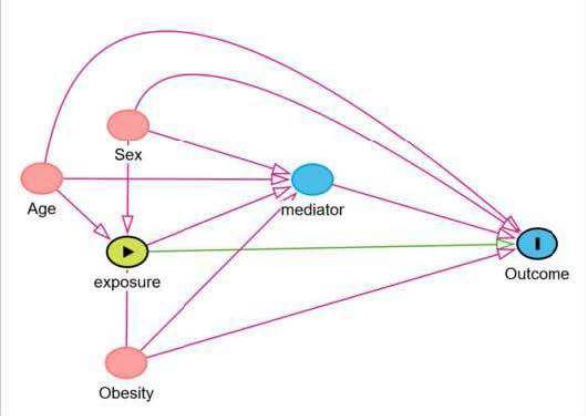

Unadjusted covariates stratified by 'Hypertension'

	0	1	SMD
N	84	45	
Age (mean (SD))	65.2 (7.7)	64.8 (6.3)	0.06
Sex (mean (SD))	0.55 (0.5)	0.58 (0.5)	0.06
Obesity (mean (SD))	0.50 (0.5)	0.58 (0.5)	0.16
LVH (mean (SD))	0.26 (0.44)	0.31 (0.47)	0.11
eGFR (mean (SD))	78.3 (15.4)	78.1 (13.1)	0.02

Figure 1: Graphical illustration of proposed causal mediation between hypertension (exposure) and outcome (TBV, HV, THV, WMH) via mediators LVH and eGFR in the presence of pre-exposure confounders age, sex, and obesity (eGFR = estimated Glomerular Filtration Rate, HV = hippocampal volume, LVH = left ventricular hypertrophy, TBV = total brain volume, THV = thalamic volume, WMH = white matter hyperintensities volume). Initial unadjusted covariates and mediators stratified by hypertension are shown on the right (SMD = standardized mean difference).

Figure 2: Causal Mediation Analysis – Exposure: hypertension
Algorithm: Nonparametric bootstrap (confidence Interval - percentile)
ACME - Average causal mediation effect, ADE - Average direct effect, Prop. Med. – Proportion mediated (%), Estimates are in mm^3

A) Mediator: Left ventricular hypertrophy (LVH)

Outcome	Estimate	95%CI Lower	CI Upper	p-value
1) Hippocampal volume				
ACME	-2.7	-20.4	14.7	0.82
ADE	-93.8	-213.2	30.4	0.12
Total Effect	-96.5	-214.2	30.8	0.12
Prop. Med.	2.8	-30.9	57	0.83
2) Thalamic volume				
ACME	-3.7	-27.1	19.4	0.86
ADE	-186.7	-359.3	-12.3	**0.036**
Total Effect	-190.4	-358	-14.4	**0.03**
Prop. Med.	1.9	-17.3	25	0.87
3) Total brain volume (x 1000)				
ACME	0.17	-2.1	2.7	0.90
ADE	-13.4	-31.7	4.9	0.15
Total Effect	-13.3	-31.4	4.8	0.15
Prop. Med.	-1.3	-42.6	41	0.89
4) White matter hyperintensities				
ACME	193.1	-288.4	614.4	0.56
ADE	2660.3	746.6	4556	**0.006**
Total Effect	2853.4	824	4738.2	**0.002**
Prop. Med.	6.8	-13.8	29	0.56

B) Mediator: estimated Glomerular Filtration Rate (eGFR)

Outcome	Estimate	95%CI Lower	CI Upper	p-value
1) Hippocampal volume				
ACME	0.5	-13.4	20.4	0.86
ADE	-95.5	-217	31	0.12
Total Effect	-95	-214	30.1	0.12
Prop. Med.	-0.5	-57.6	24	0.89
2) Thalamic volume				
ACME	0.2	-14.5	21.9	0.92
ADE	-189	-364	-12.2	**0.03**
Total Effect	-188	-360	-13.6	**0.032**
Prop. Med.	-0.12	-19.8	12	0.9
3) Total brain volume (x 1000)				
ACME	0.002	-1.3	2.67	0.83
ADE	-13.3	-31.4	5.0	0.13
Total Effect	-13.3	-31.2	4.8	0.14
Prop. Med.	-0.02	-32.2	35	0.81
4) White matter hyperintensities				
ACME	5.8	-213	239	0.95
ADE	2740	819	4619.7	**0.004**
Total Effect	2750	837	4709.1	**0.004**
Prop. Med.	0.21	-10.8	9	0.94

References

1. Canavan, M., & O'Donnell, M. J. (2022). Hypertension and Cognitive Impairment: A Review of Mechanisms and Key Concepts [Mini Review]. Frontiers in Neurology, 13. https://doi.org/10.3389/fneur.2022.821135
2. Georgakis, M. K., Synetos, A., Mihas, C., Karalexi, M. A., Tousoulis, D., Seshadri, S., & Petridou, E. T. (2017). Left ventricular hypertrophy in association with cognitive impairment: a systematic review and meta-analysis. Hypertension Research, 40(7), 696-709. https://doi.org/10.1038/hr.2017.11
3. Iglesias, J. E., Augustinack, J. C., Nguyen, K., Player, C. M., Player, A., Wright, M., Roy, N., Frosch, M. P., McKee, A. C., Wald, L. L., Fischl, B., & Van Leemput, K. (2015). A computational atlas of the hippocampal formation using ex vivo, ultra-high resolution MRI: Application to adaptive segmentation of in vivo MRI. Neuroimage, 115, 117-137. https://doi.org/10.1016/j.neuroimage.2015.04.042
4. Iglesias, J. E., Insausti, R., Lerma-Usabiaga, G., Bocchetta, M., Van Leemput, K., Greve, D. N., van der Kouwe, A., Fischl, B., Caballero-Gaudes, C., & Paz-Alonso, P. M. (2018). A probabilistic atlas of the human thalamic nuclei combining ex vivo MRI and histology. Neuroimage, 183, 314-326. https://doi.org/10.1016/j.neuroimage.2018.08.012
5. Nagaraja, N., Farooqui, A., & Albayram, M. S. (2022). Association of deep white matter hyperintensity with left ventricular hypertrophy in acute ischemic stroke. J Neuroimaging, 32(2), 268-272. https://doi.org/10.1111/jon.12950
6. Patel, S. K., Restrepo, C., Werden, E., Churilov, L., Ekinci, E. I., Srivastava, P. M., Ramchand, J., Wai, B., Chambers, B., O'Callaghan, C. J., Darby, D., Hachinski, V., Cumming, T., Donnan, G., Burrell, L. M., & Brodtmann, A. (2017). Does left ventricular hypertrophy affect cognition and brain structural integrity in type 2 diabetes? Study design and rationale of the Diabetes and Dementia (D2) study. BMC Endocr Disord, 17(1), 24. https://doi.org/10.1186/s12902-017-0173-7
7. Tingley, D., Yamamoto, T., Hirose, K., Keele, L., & Imai, K. (2014). mediation: R Package for Causal Mediation Analysis. Journal of Statistical Software, 59(5), 1 - 38. https://doi.org/10.18637/jss.v059.i05

Poster No 273

Cardiometabolic risk factors, liver fat, white matter hyperintensities, and cognition

Daniel Askeland-Gjerde[1], Sigrun Halvorsen[2], Lars Westlye[1,3], Ole Andreassen[1], Tiril Pedersen Gurholt[1]

[1]Norwegian Centre for Mental Disorders Research (NORMENT), Division of Mental Health and Addiction, Oslo, Norway, [2]Department of Cardiology, Oslo University Hospital and University of Oslo, Oslo, Norway, [3]Department of Psychology, University of Oslo, Oslo, Norway

Introduction: Cardiometabolic risk factors are associated with negative brain outcomes, including stroke and dementia (Murray et al., 2020) and non-alcoholic fatty liver disease (NAFLD) (Younossi et al., 2016). White matter hyperintensities (WMH) are indicators of small vessel disease, which causes 25% of strokes and 50% of dementia cases (Wardlaw et al., 2019). NAFLD is characterized by excessive fat accumulation in liver cells in the absence of alcohol abuse or other chronic liver disease and affects 25% of the adult population (Quek et al., 2023). While NAFLD could be related to brain health through its putative role in arterial stiffness (Rider et al., 2016), insulin resistance (Watt et al., 2019), and endothelial dysfunction (Mantovani et al., 2021), few studies have investigated the links between cardiometabolic risk factors, NAFLD, and negative brain outcomes. We used liver and brain MRI and cognitive tests in a large cohort of middle-aged and elderly participants from the UK Biobank to

assess the associations between cardiometabolic factors, liver fat, WMH volume, and cognition and whether these putative associations with WMH volume and cognition were mediated by, respectively, liver fat, and WMH volume.

Methods: We included n=32,361 UK Biobank participants with liver and brain MRI and clinical and demographic data needed for the statistical analysis. A subsample (n=20,449) had cognitive measures. We excluded participants with diseases that affect the liver or brain structure, exempting NAFLD. Liver and brain MRIs were performed at three centers with similar scanners (Miller et al., 2016). A fully automated algorithm quantified WMH volume from T1 and T2 flair MRI data (Griffanti et al., 2016). Liver fat was estimated by AMRA Medical (Linge et al., 2018). We computed a general cognitive score by principal component analysis across 11 cognitive test measures. We analyzed males and females separately, adjusting for age, age2, assessment center, time between assessments, ethnic background, educational attainment, smoking status, and alcohol consumption, and used Bonferroni correction ($p<1.7e-4$). First, we conducted multivariate linear regression analyses for individual cardiometabolic risk factors with liver fat, WMH volume, and cognition as outcomes. Second, we conducted mediation analyses with individual cardiometabolic risk factors as predictors, with liver fat as the mediator and WMH volume as the outcome, and with WMH volume as the mediator and cognition as the outcome.

Results: 4,356 males (0.28%) and 3,181 females (0.19%) had significant liver fat accumulation. Participants with significant liver fat accumulation had higher WMH volume than participants with healthy liver. Male participants were more likely to be obese, hypertensive, or diabetic. All investigated cardiometabolic risk factors were significantly associated with liver fat (|R|=0.09-0.42, Fig.1a). All investigated cardiometabolic risk factors were significantly associated with WMH volume except c-reactive protein in males (|R|=0.02-0.15, Fig.1b). Body mass index, glycated hemoglobin, and WMH volume in males, and liver fat and WMH volume in females were significantly associated with cognition (|R|=0.01-0.09, Fig.1c). Liver fat partly mediated all investigated cardiometabolic risk factors' effects on WMH volume (Proportion mediated 9% to 75%, Fig.2b). WMH volume partly mediated all investigated cardiometabolic risk factors' effects on cognition, except c-reactive protein in males and females and high-density lipoprotein cholesterol in females (Proportion mediated 12% to 76%, Fig.2d).

Figure 1: Associations between cardiometabolic risk factors and liver fat, white matter hyperintensities, and general cognition

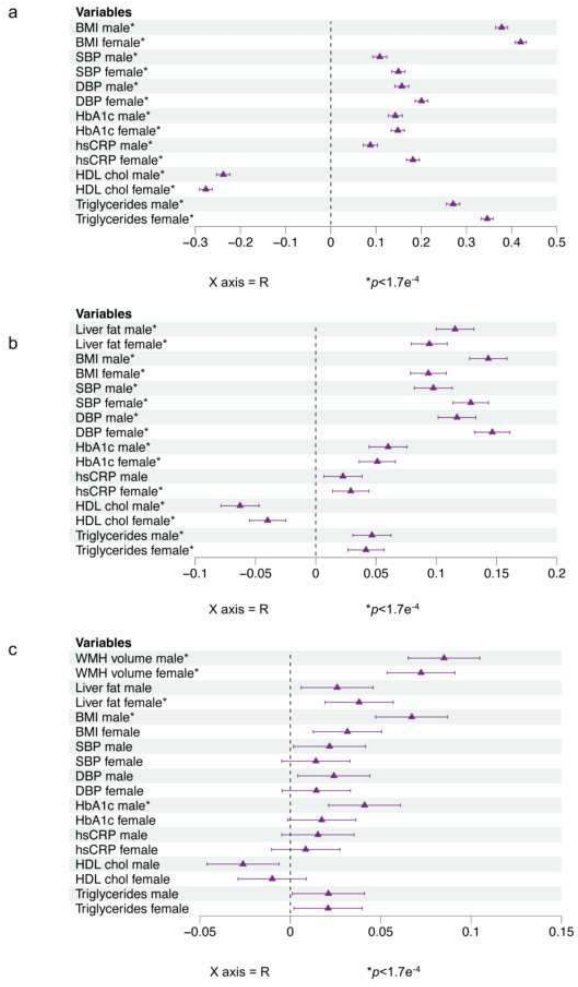

Figure 2: Liver fat mediates associations with WMH volume and WMH volume mediates associations with general cognition

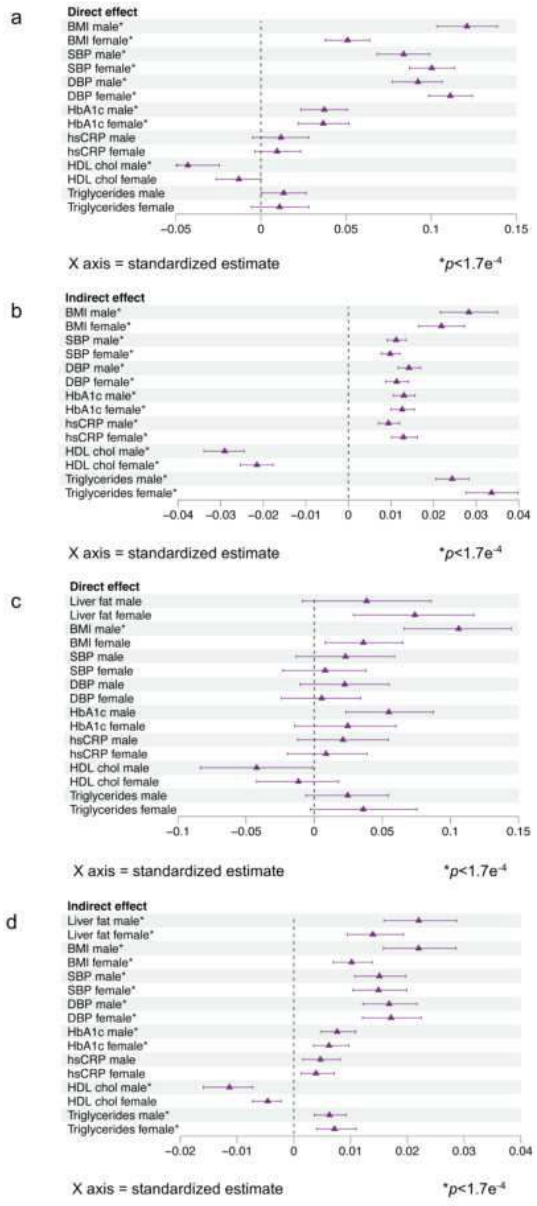

Conclusions: Our findings suggest liver fat mediates the relationship between cardiometabolic risk factors and WMH volume, which mediates the relationship between cardiometabolic risk factors and cognition. Thus, liver fat accumulation might link cardiometabolic risk factors to brain health and could be a relevant target for preventing cognitive decline and, potentially, brain diseases.

References

1. Griffanti, L. (2016). BIANCA (Brain Intensity AbNormality Classification Algorithm): A new tool for automated segmentation of white matter hyperintensities. NeuroImage, vol 141, p 191–205.
2. Linge, J. (2018). Body Composition Profiling in the UK Biobank Imaging Study. Obesity (Silver Spring, Md.), vol 26, no 11, p 1785–1795.
3. Mantovani, A. (2021). Non-alcoholic fatty liver disease and risk of fatal and non-fatal cardiovascular events: An updated systematic review and meta-analysis. The Lancet Gastroenterology & Hepatology, vol 6, no 11, p 903–913.
4. Miller, K. L. (2016). Multimodal population brain imaging in the UK Biobank prospective epidemiological study. Nature Neuroscience, vol 19, no 11, p 1523–1536.
5. Murray, C. J. L. (2020). Global burden of 87 risk factors in 204 countries and territories, 1990–2019: A systematic analysis for the Global Burden of Disease Study 2019. The Lancet, vol 396, no 10258, p 1223–1249.
6. Quek, J. (2023). Global prevalence of non-alcoholic fatty liver disease and non-alcoholic steatohepatitis in the overweight and obese population: A systematic review and meta-analysis. The Lancet Gastroenterology & Hep, vol 8, no 1, p 20-30
7. Rider, O. J. (2016). Investigating a Liver Fat Arterial Stiffening Pathway in Adult and Childhood Obesity. Arteriosclerosis, Thrombosis, and Vascular Biology, vol 36, no 1, p 198–203.

8. Wardlaw, J. M. (2019). Small vessel disease: Mechanisms and clinical implications. The Lancet Neurology, vol 18, no 7, p 684–696.
9. Watt, M. J. (2019). The Liver as an Endocrine Organ—Linking NAFLD and Insulin Resistance. Endocrine Reviews, vol 40, no 5, p 1367–1393.
10. Younossi, Z. M. (2016). Global epidemiology of nonalcoholic fatty liver disease—Meta-analytic assessment of prevalence, incidence, and outcomes. Hepatology, vol 64, no 1, p 73–84.

Poster No 274

Predicting Antipsychotic Drug Doses for BPSD: A Transfer Learning Approach Using Neuroimaging Data

Tianli Tao[1], Bo Hong[2], Siyan Han[1], Lianghu Guo[1], Ling Yue[2], Han Zhang[1]

[1]School of Biomedical Engineering, ShanghaiTech University, Shanghai, China, [2]Department of Geriatric Psychiatry, Shanghai Mental Health Center, Shanghai Jiao Tong University, Shanghai, China

Introduction: About 50-90% people with dementia would develop behavioral disturbances, namely, behavioral and psychological symptoms of dementia (BPSD) (Feast et al., 2016). Such morbidities pose challenges to both patients and caregivers. Antipsychotic medications are widely used to control severe BPSD symptoms (Ohno et al., 2019) which, however, suffers serious safety risks including death. Even for skilled doctors, determining the optimal overall dosage for BPSD patients is difficult. This gap emphasizes the need for individualized precise prediction of antipsychotic drug doses. Neuroimaging, particularly MRI, reveals brain structure associated with aging, cognitive decline, and psychiatric symptoms, making it a potential tool for predicting the drug doses. Given that available MRI data of BPSD is often limited, this study employs transfer learning to predict drug dose and offer neuroanatomical interpretation of BPSD from the perspective of deep learning. Specifically, we leveraged a Cascaded ResNet (Cas-ResNet) pretrained on a large-scale aging MRI dataset to predict drug doses for BPSD patients.

Methods: We employed a two-step process to train our model, as shown in Fig. 1. The structure of Cas-ResNet consists of three cascaded residual modules as a feature extractor and a final prediction module. Initially, a large dataset from the Chinese Brain Molecular and Functional Mapping (CBMFM) project (Gu et al., 2023) was used to pretrain the model with a brain age prediction task. After pretraining, the parameters for the feature extractor were frozen. Subsequently, the pretrained model was fine-tuned for drug dose prediction for the BPSD patients from the Alzheimer's Disease and Related Disorders Center in Shanghai Jiao Tong University (ADRDC) dataset. Finally, we utilized gradient-weighted class activation mapping to generate attention maps and conducted statistical analyses on the attention maps to identify critical brain regions for drug dose prediction. The CBMFM data were obtained at four sites using 3.0T scanners of the same model and maker (uMR790, United Imaging). We utilized T1w MRI from 646 healthy subjects (334 females and 312 males, age 18-82). The main data (i.e., drug dose prediction) was collected from ADRDC by a 3.0T scanner (Prisma, Siemens), including T1w MRI from 83 BPSD patients (27 males and 56 females, age 55-80). To determine the individual usage of different antipsychotic drugs, the concept of defined daily dose (DDD) (Lee et al., 2004) was used. The DDD, which individualized control the BPSD, was calculated, ranging from 0 to 1.5 mg/day, serving as the label for fine-tuning.

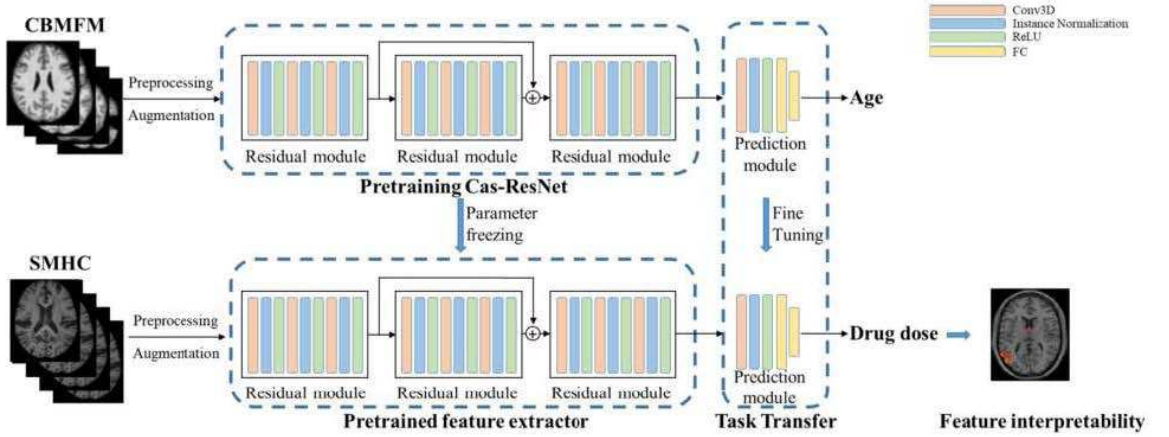

Fig 1. Schematic workflow and network architecture of our proposed method. Each residual module consists of three sequential blocks, which consist of 3D convolution layers, an instance normalization layer, and a ReLU layer. The final prediction module includes two cascaded fully connected layers, providing a predictive label. The kernel size of the 3D convolution layer is 3x3x3 with a 1x1x1 stride.

Results: The performance of our Cas-ResNet model was compared to other baseline models, including 3DCNN, VGG (Simonya et al., 2014) and DenseNet (Huang et al., 2017). The pretrained Cas-ResNet exhibited enhanced performance with fewer training epochs, achieving a competitive Pearson correlation of 0.59 between estimated and real DDD (Fig. 2a and 2c). The pretraining process enabled substantial information capture from MRI, reducing the need for extensive parameters and risk of over-fitting. Through feature interpretability analysis, we identified brain regions crucial for BPSD drug dose prediction. Five significant clusters, mainly located in the temporal lobe, including the parahippocampal area and the striatum (putamen and caudate), were identified in Fig. 2b and 2d. These findings indicate that the antipsychotic dosage to control the BPSD is linked to brain structural alterations, involving both dementia-related and emotion-regulating areas.

a)

Method	r	MAE	Epochs	Parameters
3DCNN	0.31	0.24	100	33M
VGG	0.23	0.31	100	7M
DenseNet	0.38	0.28	100	19M
Cas-ResNet w/o pretrain	0.42	0.23	100	8M
Cas-ResNet w/ pretrain	0.59	0.20	30	4M

b)

cluster	p-value	cluster center	BA	AAL
1	<0.001	-42,-20,-34	20	Temporal Inf L
2	<0.001	27, -4, -33	20	ParaHippocampal R
3	<0.001	24, 11, -7	13	Putamen R
4	<0.001	-64, -60, 12	21	Temporal Mid L
5	<0.001	-14, 20, -4	/	Caudate L

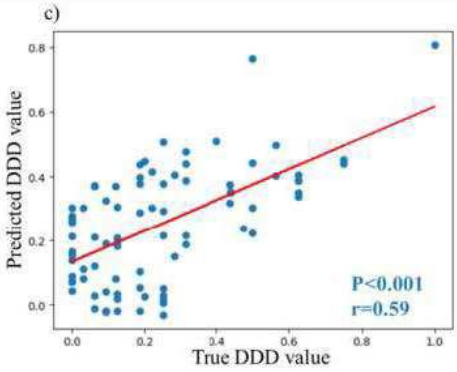

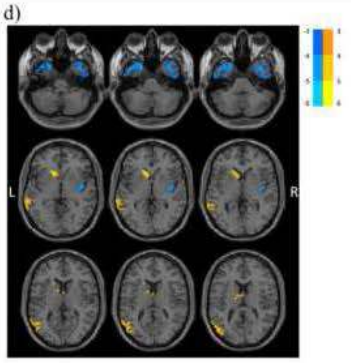

Fig 2. a) Prediction performance and the scale of different models b) Statistics and location of the activated regions c) Scatterplot of drug dose prediction (y-axis) over the ground truth (x-axis) d) The significantly contributing brain regions identified by our method for BPSD drug dose prediction.

Conclusions: For the first time, we showed a promising result of using a lightweight deep learning model to predict drug dose prescribed for controlling BPSD. Our pretrained Cas-ResNet model demonstrates efficient brain MRI representations with limited data in the clinical scenarios. The work promotes the discussion toward appropriate use of antipsychotics in patients with dementia.

References

1. Feast, Alexandra, et al. (2016), "A systematic review of the relationship between behavioral and psychological symptoms (BPSD) and caregiver well-being." International psychogeriatrics 28.11: 1761-1774.
2. Ohno, Yukihiro, et al. (2019), "Antipsychotic treatment of behavioral and psychological symptoms of dementia (BPSD): management of extrapyramidal side effects." Frontiers in pharmacology 10: 1045.
3. Lee, Philip E., et al. (2004), "Atypical antipsychotic drugs in the treatment of behavioural and psychological symptoms of dementia: systematic review." Bmj 329.7457: 75.
4. Simonyan, Karen, et al. (2014), "Very deep convolutional networks for large-scale image recognition." arXiv preprint arXiv:1409.1556.
5. Huang, Gao, et al. (2017), "Densely connected convolutional networks." Proceedings of the IEEE conference on computer vision and pattern recognition.
6. Gu, Dongdong, et al. (2023), An artificial-intelligence-based age-specific template construction framework for brain structural analysis using magnetic resonance images. Vol. 44. No. 3. Hoboken, USA: John Wiley & Sons, Inc.
7. Acknowledgement
8. This work is partially supported by the STI 2030—Major Projects (2022ZD0213100, 2022ZD0209000, and 2021ZD0200516), Shanghai Pilot Program for Basic Research—Chinese Academy of Science, Shanghai Branch (JCYJ-SHFY-2022-014), the Shanghai Science and Technology Committee (20Y11906800) and Shenzhen Science and Technology Program (No. KCXFZ20211020163408012).

Poster No 275

ENIGMA-Parkinson's Disease: A Global Consortium for Integration of Multimodal Neuroimaging

Max Laansma[1], Emile d'Angremont[2], Eva van Heese[1], Conor Owens-Walton[3], Joanna Bright[4], Rebecca Kerestes[5], Yuji Zhao[6], Sarah Al-Bachari[7], Fernando Cendes[8], Jason Druzgal[9], Hedley Emsley[10], Gaëtan Garraux[11], Rick Helmich[12], Martin Johansson[13], Samson Khachatryan[14], Johannes Klein[15], Christine Lochner[16], Corey McMillan[17], Tracy Melzer[18], Philip Mosley[19], Fabrizio Piras[20], Kathleen Poston[21], Mario Rango[22], Reinhold Schmidt[23], Duygu Tosun[24], Odile van den Heuvel[25], Chris Vriend[25], Jiunjie Wang[26], Roland Wiest[27], Ian Harding[5], Boris Gutman[6], Neda Jahanshad[28], Paul Thompson[29], Ysbrand van der Werf[30]

[1]Amsterdam UMC, Amsterdam Neuroscience, Amsterdam, Noord-Holland, [2]Amsterdam UMC, Amsterdam Neuroscience, Amsterdam, Netherlands, [3]University of Southern California, Los Angeles, CA, [4]Kings's College London, London, London, [5]Monash University, Melbourne, Australia, [6]Illinois Institute of Technology, Chicago, IL, [7]University College London, London, United Kingdom, [8]UNICAMP, Campinas, Brazil, [9]University of Virginia, Charlottesville, VA, [10]Lancaster Medical School, Lancaster, United Kingdom, [11]University of Liege, Liege, Belgium, [12]Donders Institute for Brain Cognition and Behaviour, Nijmegen, Netherlands, [13]Donders Institute for Brain, Cognition and Behaviour, Nijmegen, Netherlands, [14]National Institute of Health, Yerevan, Armenia, [15]University of Oxford, Oxford, United Kingdom, [16]SAMRC Unit on Risk & Resilience in Mental Disorders, Department of Psychiatry, Stellenbosch Universi, Stellenbosch, South Africa, [17]University of Pennsylvania, Philadelphia, PA, [18]New Zealand Brain Research Institute, Christchurch, Christchurch, [19]University of Queensland, St Lucia, Queensland, [20]IRCCS Santa Lucia Foundation, Rome, Italy, [21]Stanford University, Palo Alto, CA, [22]University of Milan, Milan, Italy, [23]Medical University of Graz, Graz, Austria, [24]University of California, San Francisco, San Francisco, CA, [25]Amsterdam UMC, Vrije Universiteit Amsterdam, Department of Psychiatry, and Department of Anatomy and, Amsterdam, Netherlands, [26]Chang Gung University, Taoyuan City, Taiwan, [27]University Hospital Bern, Bern, Switzerland, [28]Imaging Genetics Center, Keck School of Medicine of University of Southern California, Los Angeles, California, [29]Imaging Genetics Center, Keck School of Medicine of University of Southern California, Los Angeles, CA, [30]Vrije Universiteit Amsterdam, Amsterdam, Netherlands

Introduction: ENIGMA-Parkinson's Disease (PD) is a global consortium of currently 22 sites set up to identify robust PD signatures, and factors that influence them, using harmonized data processing on unprecedented large datasets. Here we present our structural MRI findings of cortical (Laansma et al. 2021), subcortical (in prep.), cerebellar (Kerestes et al. 2023), and white matter microstructure (in prep.) across PD clinical stages in ~2,800 PD participants versus ~1,300 controls. By connecting these various analyses, novel overarching interpretations can be drawn.

Methods: Regional cortical thickness (68 regions), subcortical shape (14 regions) and cerebellar volume (28 regions) were measured from T1-w MRI and microstructural metrics (e.g., fractional anisotropy, FA; 21 regions) from diffusion-weighted images. Linear mixed models compared the brain metrics at each incremental Hoehn and Yahr (HY) disease stage from 1 to 5, to an age- and sex-matched control group.

Results: Compared to the control group, stage HY1 was associated with a thinner posterior and inferior temporal cortex and smaller putamen, but focally larger thalami and anterior cerebellar lobules, as well as higher FA in the internal capsule and corona radiata. HY2 showed additional thinner posterior and temporal cortical regions, a smaller caudate nucleus and lower FA in the fornix, while the thalamus remained larger. In HY3 increasingly thinner regions towards the frontal cortex were observed with additional involvement of the amygdala and hippocampus. Lower FA was found in the fornix and sagittal stratum. Finally, HY4-5 was characterized by a widespread thinner cortex, smaller subcortical structures and posterior cerebellum, and overall lower FA. See Figure 1 for an overview of all results.

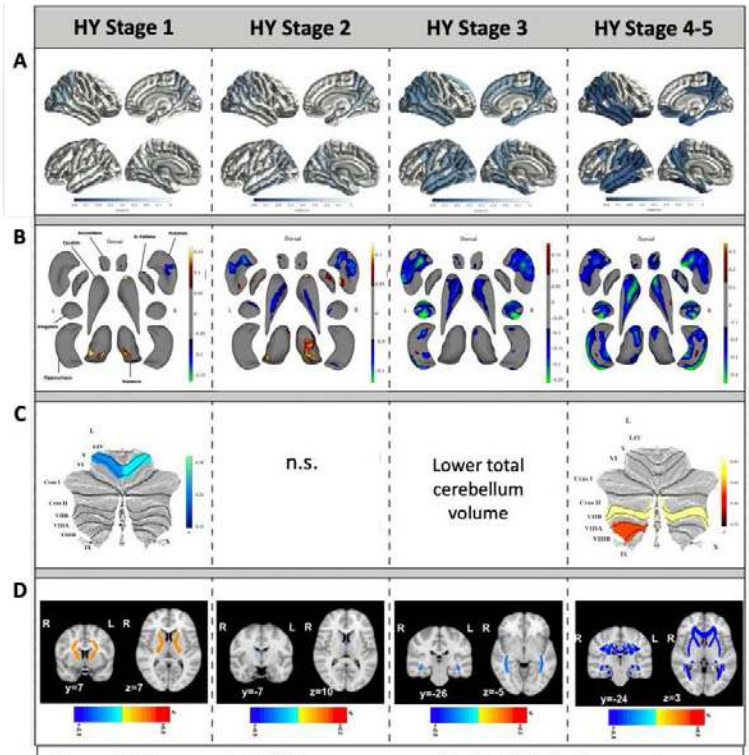

Figure 1. PD vs control differences across Hoehn & Yahr disease stages. **A** – Cortical thickness. **B** – Vertex-wise subcortical shape. **C** – Cerebellum volume. **D** – Fractional anisotropy. *HY = Hoehn & Yahr*

Conclusions: Our cross-sectional findings show a worsening and expanding pattern across disease stages that is consistent with ongoing neurodegeneration. The larger thalamic and anterior cerebellar regions in combination with suggested higher measures of microstructure of internal capsule limbs in early stage PD are striking and may indicate targeted regional compensation for neuronal/axonal loss or may reflect the consequence of hyperactive cerebellothalamic motor pathways linked to tremor.

References

1. Kerestes, Rebecca, Max A. Laansma, Conor Owens-Walton, Andrew Perry, Eva M. van Heese, Sarah Al-Bachari, Tim J. Anderson, et al. 2023. "Cerebellar Volume and Disease Staging in Parkinson's Disease: An ENIGMA-PD Study." Movement Disorders: Official Journal of the Movement Disorder Society, November. https://doi.org/10.1002/mds.29611.
2. Laansma, Max A., Joanna K. Bright, Sarah Al-Bachari, Tim J. Anderson, Tyler Ard, Francesca Assogna, Katherine A. Baquero, et al. 2021. "International Multicenter Analysis of Brain Structure Across Clinical Stages of Parkinson's Disease." Movement Disorders: Official Journal of the Movement Disorder Society 36 (11): 2583–94.

Poster No 276

Circulating NT-proBNP levels correlate with structural brain alterations in the general population

Katharina Wittfeld[1], Stefan Frenzel[1], Alexander Teumer[1], Marcus Dörr[2], Martin Bahls[2], Robin Bülow[3], Matthias Nauck[4], Henry Völzke[5], Deborah Janowitz[6], Hans Grabe[1]

[1]University Medicine Greifswald, Department of Psychiatry and Psychotherapy, Greifswald, Mecklenburg-Vorpommern, [2]University Medicine Greifswald, Department of Internal Medicine B, Greifswald, Mecklenburg-Vorpommern, [3]University Medicine Greifswald, Institute of Diagnostic Radiology and Neuroradiology, Greifswald, Mecklenburg-Vorpommern, [4]University Medicine Greifswald, Institute of Clinical Chemistry and Laboratory Medicine, Greifswald, Mecklenburg-Vorpommern, [5]University Medicine Greifswald, Institute for Community Medicine, Greifswald, Mecklenburg-Vorpommern, [6]Clinical Centre for Psychiatry und Psychotherapy, Site West, Stralsund, Stralsund, Mecklenburg-Vorpommern

Introduction: According to the World Health Organization, dementia is currently affecting over 55 million people with nearly 10 million new cases every year (WHO, 2023). Modifiable risk factors are in the focus of the scientific community to prevent dementia or postpone its onset which would reduce the personal and economic burden. During the last years, the heart-brain-axis captured increasing attention. Accumulating evidence supports the hypothesis that vascular and degenerative

structural brain changes might function as a link between cardiac disease and cognitive impairment. (Jensen, 2023; Frenzel, 2021; Veugen, 2018; Sabayan, 2015). Within these studies, cardiac diseases are accessed by blood based cardiac biomarkers: natriuretic peptides (most frequently by NT-proBNP) and cardiac troponins (e.g. hs-cTnT) which are measured in clinical routines. Besides measures for specific brain damages (e.g. white matter hyperintensities (WMH), silent brain infarcts, and cerebral microbleeds), brain atrophy is studied using global brain parameters like total brain volume, total gray matter (GM) and white matter (WM). In our work, we investigated the association of NT-proBNP and brain atrophy in a more detailed way by dividing the total GM volume into their cortical and subcortical portions and studying the different dimensions of the cortex (cortical thickness and surface area). Further, we analyzed specific brain atrophy patterns for aging and Alzheimer's Disease.

Methods: We studied 2,995 adults aged 21-90 years from two independent population-based cohorts of the Study of Health in Pomerania (SHIP-START and SHIP-TREND). (Völzke, 2022) MRI brain data were derived from structural T1- and FLAIR-sequences. (Hosten, 2021) We used FreeSurfer 7.3.2 to determine the cortical and subcortical GM, total WM, intracranial volume (ICV), hemisphere-wide cortical thickness and surface area, and local cortical thickness (Desikan-Killiany atlas; 34 regions per hemisphere). Based on the FreeSurfer data, scores were generated that summarize the atrophy patterns linked to Alzheimer's Disease (FSAD) and brain aging (FSBA). (Frenzel, 2020; Weihs, 2021) Further, we extracted the WMH with the LST toolbox. (Schmidt, 2012) Brain measures and atrophy scores were analyzed using regression models on log(NT-proBNP) with adjustment for age (non-linear), sex, cohort, ICV, and in sensitivity analyses additional for systolic and diastolic blood pressure, antihypertensive medication, diabetes, high and low density lipoprotein, BMI, smoking, alcohol intake, and education.

Results: We observed significant negative correlations of NT-proBNP with the total GM cortex volume (beta_ml=-2.82, p<1E-6) and the mean cortical thickness (beta_mm=-0.01, p<1E-6) of both hemispheres. This effect corresponds to a 0.1 ml reduced cortex volume per 10% increase in NT-proBNP. All associations remained robust in the sensitivity analyses. Subcortical GM, cerebral WM, and the WM surface area of both hemispheres did not show any significant association with NT-proBNP. Cortical thickness of over 85 % of the 68 regions defined by the Desikan-Killiany atlas reached at least nominal significance for a negative association with NT-proBNP. Additional adjustment for the mean cortical thickness of the corresponding hemisphere led to a loss in effect size and significance which points to a rather global effect on the brain than to specific local effects. Further, higher levels of NT-proBNP were significantly associated with a higher FSAD score. The association of FSBA and NT-proBNP only reached nominal significance but points to advanced brain aging with higher levels of NT-proBNP. We could not replicate the published findings concerning WMH, neither dimensional nor after dichotomization.

Conclusions: In contrast to subcortical gray matter, cortical brain measures are strongly associated with circulating NT-proBNP levels in a global way.

References

1. Frenzel, S. (2020), 'A Biomarker for Alzheimer's Disease Based on Patterns of Regional Brain Atrophy', Frontiers in Psychiatry, https://doi.org/10.3389/fpsyt.2019.00953
2. Frenzel, S. (2021), 'Cardiac Hypertrophy Is Associated With Advanced Brain Aging in the General Population', Journal of the American Heart Association, 10(17):e020994.
3. Hosten, N. (2021), 'Review - SHIP-MR and Radiology: 12 Years of Whole-Body Magnetic Resonance Imaging in a Single Center', Healthcare, 10(1): 33.
4. Jensen, M. (2023), 'Circulating cardiac biomarkers, structural brain changes, and dementia: Emerging insights and perspectives', Alzheimer's and Dementia, 19 (4):1529-1548.
5. Sabayan, B. (2015), 'N-terminal pro-brain natriuretic peptide and abnormal brain aging', Neurology, 85 (9): 813-820.
6. Schmidt, P. (2012), 'An automated tool for detection of FLAIR-hyperintense white-matter lesions in multiple sclerosis', Neuroimage, 59(4):3774–3783.
7. Veugen, M. (2018), 'Cross-sectional associations between cardiac biomarkers, cognitive performance, and structural brain changes are modified by age the Maastricht study', Arteriosclerosis, Thrombosis, and Vascular Biology, 38 (8):1948-1958.
8. Völzke, H. (2022), 'Cohort Profile Update: The Study of Health in Pomerania (SHIP)', International Journal of Epidemiology, 1-12.
9. Weihs, A. (2021), 'Associations between sleep apnea and advanced brain aging in a large-scale population study', Sleep, 44(3).
10. WHO (2023), https://www.who.int/news-room/fact-sheets/detail/dementia

Poster No 277

Synergic cholinergic and dopaminergic role in motor symptoms of sporadic Parkinson's disease

Peng Ren[1,2]

[1]Fudan University, Shanghai, Shanghai, [2]Harbin Institute of Technology, Heilongjiang, China

Introduction: Parkinson's Disease (PD) is a dominant neurodegenerative disease, characterized with various motor symptoms.[1] Despite the prevailing dopaminergic treatments for PD motor symptoms,[2] no disease-modifying drugs exist,[3] which implicates the potential involvement of non-dopaminergic neurotransmitter systems. Previous autopsy study indicated that the

α-synuclein deposition in nucleus basalis of Meynert (NbM) occurs as early as the Lewy bodies formation and dopaminergic neurons loss in substantia nigra (SN).[4] However, existing works usually explore the association between cholinergic/dopaminergic subcomponents and specific motor symptoms.[5-7] To date, there is a lack of systematic exploration for the relationship between all cholinergic/dopaminergic components and various motor symptoms. Here, using imaging data from Parkinson's Progression Markers Initiative (PPMI), we characterize the cross-sectional and longitudinal role of multimodal cholinergic/dopaminergic regional measurements in motor symptoms. By dividing the PD patients into those present stable (Any) or no/unstable (Never) non-motor symptoms, we also explore the impact of non-motor symptoms on the roles of cholinergic/dopaminergic system.

Methods: We used longitudinal T1w, T2w and DAT SPECT images from PPMI, including 151 subjects (31 control/120 PD) for voxel-based morphometric and DAT striatal binding ratios (SBR) analysis and 176 subjects (49 controls/127 PD) for T1w/T2w analysis. We calculated regional volume, SBR and T1w/T2w of cholinergic (NbM, Medial septum-diagonal band of Broca (MS/DB) and pedunculopontine nucleus (PPN)) and dopaminergic (SN, putamen, caudate, globus pallidus (GP) and ventral tegmental area (VTA)) components for each subject and time point. Baseline cross-sectional group differences were detected by appropriate tests. Linear mixed effect models were performed to examine group difference of longitudinal change, the association between longitudinal change of regional measurements and motor symptoms, as well as whether baseline regional measurements are predictors of motor symptoms progression. The baseline age, gender, education year, intracranial volume, disease duration and baseline motor severity were controlled as appropriate. Finally, in exploring the impact of non-motor symptoms on the discovered cholinergic/dopaminergic role, we repeated the above statistical analyses in the Never and Any group, separately.

Results: Cross-sectionally, we found that PD patients showed worsen global motor symptoms and subscores (bradykinesia, rigidity, gait and tremor), reduced SBR in putamen and caudate (Fig.1B). Longitudinally, PD patients showed greater decline of global motor symptom, bradykinesia, rigidity and caudate volume (Fig.1C). In addition, longitudinal increase of global motor symptom was associated with reduction of volume and SBR in putamen and caudate, T1w/T2w in NbM, PPN, SN, putamen, caudate, GP and VTA. Similar results were discovered for bradykinesia, rigidity and gait. No longitudinal associations were observed for tremor. The baseline T1w/T2w ratio of NbM predicted longitudinal increase of global motor symptom, bradykinesia and PIGD, while caudate volume, MS/DB T1w/T2w, caudate T1w/T2w and caudate SBR were additional predictors of PIGD. No significant baseline predictors were found for tremor (Fig.1D). In subgroup cross-sectional analysis, the Any group showed the least DAT SBR in putamen and caudate, followed by the Never group. Longitudinally, similar longitudinal results were only found in the Any group, but not the Never group (Fig.2).

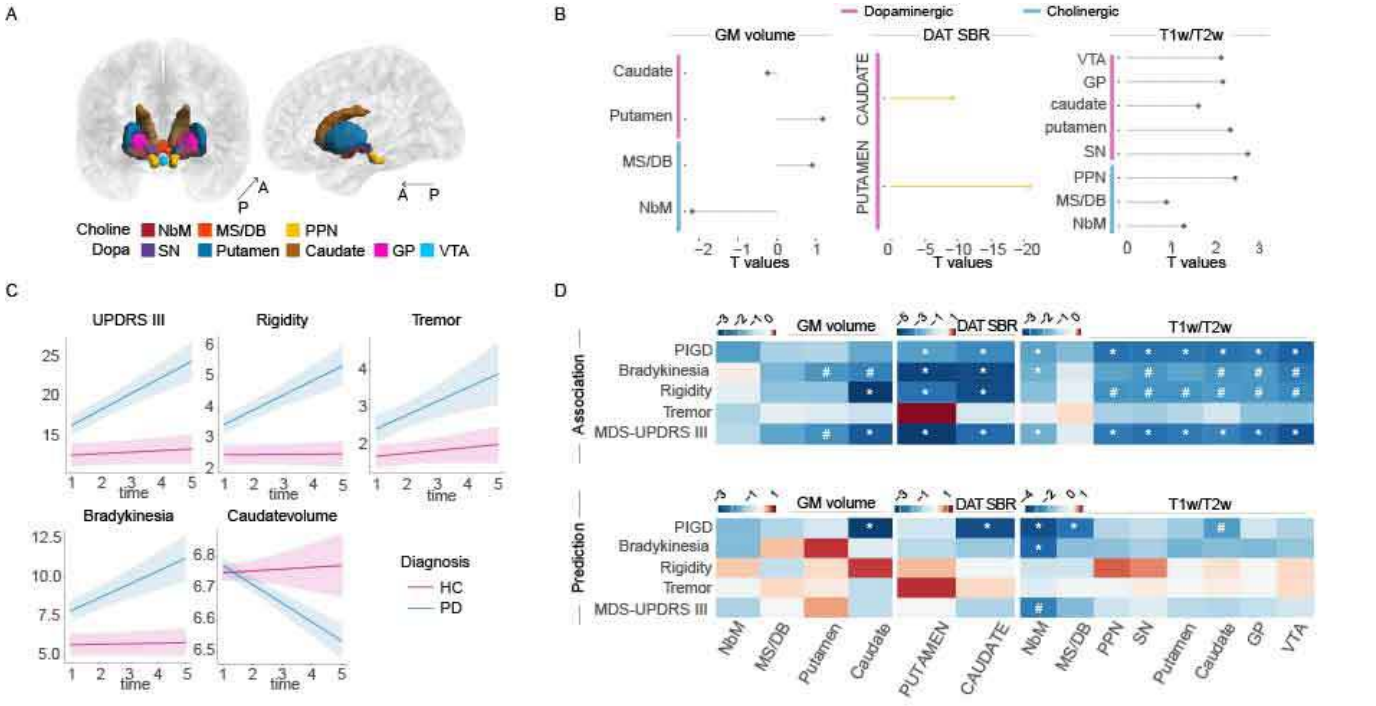

Figure 1 Cross-sectional and longitudinal role of cholinergic/dopaminergic regional measurements in PD motor symptoms. (A) Regions of interest (ROIs) for cholinergic and dopaminergic transmitter systems; **(B)** Baseline comparisons of cholinergic and dopaminergic measurements between PD and HC, significant difference shown in yellow; **(C)** The longitudinal changes of clinical characteristics and cholinergic/dopaminergic measurements that showed significant difference between HC and PD; **(D)** Longitudinal associations between regional measurements and motor symptoms, as well as prediction of motor progression with baseline regional measurements. *FDR-corrected P < 0.05, #uncorrected P < 0.05. GM, grey matter; NbM, nucleus basalis of Meynert; MS/DB, medial septum and diagonal band; PPN, pedunculopontine nucleus; SN, substantia nigra; GP, globus pallidus; VTA, ventral tegmental area; UPDRS, Unified Parkinson's Disease Rating Scale; PIGD, posture instability and gait disorder; SBR, striatal binding ratio.

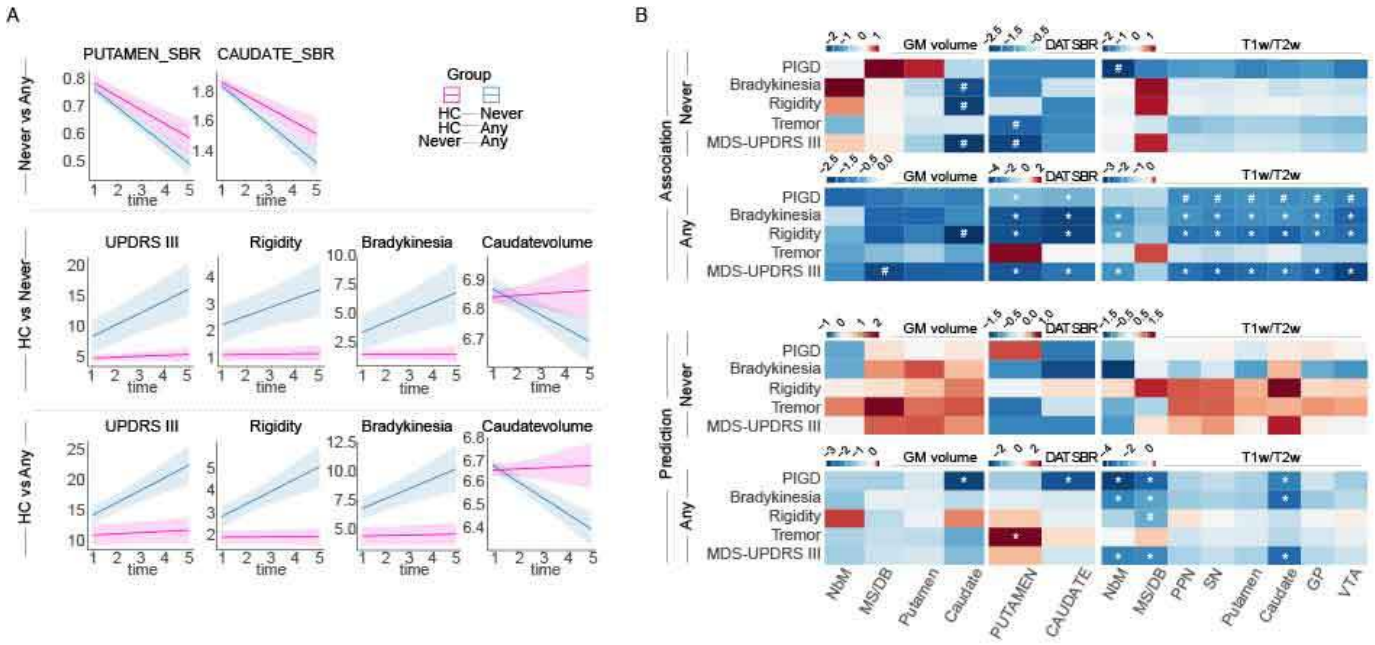

Figure 2 The cholinergic/dopaminergic role in motor symptoms of PD subgroups. (A) Longitudinal changes of clinical characteristics and cholinergic/dopaminergic neuroimaging measurements that showed significant difference between HC, Never and Any group; **(B)** Longitudinal associations between regional measurements and motor symptoms, as well as prediction of motor progression with baseline regional measurements in PD subgroups. *FDR-corrected P < 0.05, #uncorrected P < 0.05. GM, grey matter; NbM, nucleus basalis of Meynert; MS/DB, medial septum and diagonal band; PPN, pedunculopontine nucleus; SN, substantia nigra; GP, globus pallidus; VTA, ventral tegmental area; UPDRS, Unified Parkinson's Disease Rating Scale; PIGD, posture instability and gait disorder; SBR, striatal binding ratio.

Conclusions: The T1w/T2w ratio of both cholinergic and dopaminergic regions showed potential for being biomarker of PD progression and prognosis beyond regional volume and SBR. Additionally, this role is more significant with the existing of non-motor symptoms. These new findings may advance the understanding of the development of PD pathology and optimize future clinical treatment.

References

1. Moustafa, A. A., et al. (2016), 'Motor symptoms in Parkinson's disease: A unified framework', Neuroscience & Biobehavioral Reviews, vol. 68, pp. 727-740.
2. Armstrong, M. J. and M. S. Okun (2020), 'Diagnosis and Treatment of Parkinson Disease: A Review', Jama, vol. 323, no. 6, pp. 548-560.
3. Fox, S. H., et al. (2018), 'International Parkinson and movement disorder society evidence-based medicine review: Update on treatments for the motor symptoms of Parkinson's disease', Movement Disorders, vol. 33, no. 8, pp. 1248-1266.
4. Braak, H., et al. (2003), 'Staging of brain pathology related to sporadic Parkinson's disease', Neurobiology of Aging, vol. 24, no. 2, pp. 197-211.
5. Craig, C. E., et al. (2020), 'Pedunculopontine Nucleus Microstructure Predicts Postural and Gait Symptoms in Parkinson's Disease', Movement Disorders, vol. 35, no. 7, pp. 1199-1207.
6. Ray, N. J., et al. (2022), 'Free-water imaging of the cholinergic basal forebrain and pedunculopontine nucleus in Parkinson's disease', Brain.
7. Wilson, J., et al. (2020), 'Cholinergic Basal Forebrain Volumes Predict Gait Decline in Parkinson's Disease', Movement Disorders, vol. 36, no. 3, pp. 611-621.

Poster No 278

Widespread White Matter Alterations Are Associated With Neurological Severity in Wilson Disease

Ann Carolin Hausmann[1], Silja Kannenberg[1], Christian Hartmann[2], Julian Caspers[3], Christian Rubbert[3], Alfons Schnitzler[1,2]

[1]Institute of Clinical Neuroscience & Medical Psychology, Medical Faculty, Heinrich-Heine-University, Duesseldorf, Germany, [2]Department of Neurology, Medical Faculty, University Hospital Duesseldorf, Duesseldorf, Germany, [3]Department of Diagnostic & Interventional Radiology, Medical Faculty, Heinrich-Heine-University, Duesseldorf, Germany

Introduction: Wilson disease (WD) is a rare metabolic disorder, leading to pathologic copper accumulation i.a. in the brain, which may cause neurological symptoms. Diffusion tensor imaging (DTI) derived white matter (WM) alterations have been proposed as neuroimaging biomarkers in patients with WD, which correlate with neurological severity[1,2]. However, evidence is yet sparse and inconclusive, often neglecting absolute measures of diffusion[3].

Methods: 25 patients with WD (7 male; age: M=40.76±11.22 years; disease duration: M=244.56±101.04 months; on anticopper treatment) were examined with the Unified Wilson's Disease Rating Scale neurological subscale (UWDRS-N; M=7.04±9.62).

Cranial 3T multi-shell diffusion MRI was acquired according to the Lifespan Human Connectome Project in Aging protocol and preprocessed with its minimal preprocessing pipeline[4]. DTI main indices fractional anisotropy (FA) and mean diffusivity (MD) as well as the absolute measures axial diffusivity (AD) and radial diffusivity (RD) were computed with FSL v.6.0 using DTIFIT. Voxel-wise statistical analyses were carried out using general linear models and permutation testing with 5000 permutations in Tract Based Spatial Statistics (TBSS,[5]), correcting for covariate effects of age and sex. Clusters of significant correlations between DTI parameters and UWDRS-N scores were identified at a threshold of p<.05 (family-wise error corrected) and by applying Threshold-Free Cluster Enhancement (TFCE) and overlaying them to the Johns Hopkins University WM tractography atlas.

Results: TBSS analysis revealed a significant negative correlation between FA and UWDRS-N scores in the left corticospinal tract. Furthermore, significant positive correlations between MD and UWDRS-N scores were found in the following WM tracts: left corticospinal tract, bilateral genu of corpus callosum, right body of corpus callosum, bilateral anterior & superior corona radiata, bilateral anterior & posterior limb of internal capsule, right retrolenticular part of internal capsule, left external capsule, left superior longitudinal fasciculus, bilateral superior cerebellar peduncles, bilateral medial lemniscus and bilateral posterior thalamic radiation (see Fig.1). For AD, there were significant positive correlations with the neurological scores in: left anterior limb of internal capsule, left anterior & superior corona radiata as well as left superior fronto-occipital and longitudinal fasciculus. In addition, positive correlations with RD were found in: left corticospinal tract, right inferior cerebellar peduncle, bilateral medial lemniscus, left superior corona radiata, left superior longitudinal fasciculus, bilateral anterior thalamic radiation and unclassified WM tracts (see Fig.2).

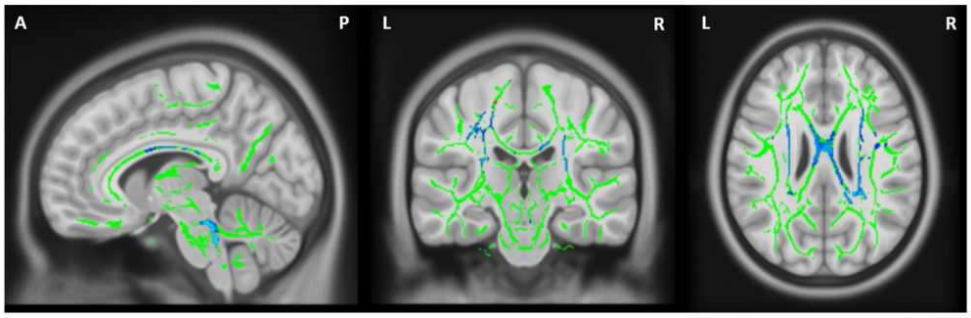

Figure 1. White matter tracts with a significant inverse association between FA and UWDRS-N (red-yellow) and those with a significant positive association between MD and UWDRS-N (blue) are overlaid onto all subjects' mean FA skeleton (green) and projected onto the MNI152-T1 template (p<.05, TFCE and FWE-corrected). A=anterior; P=posterior; L=left; R=right.

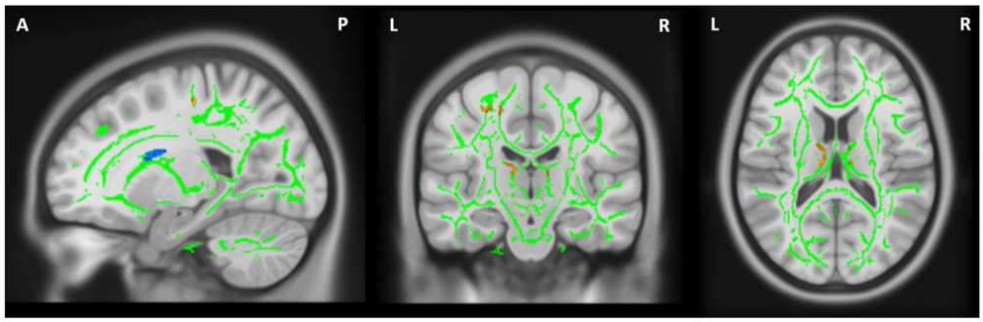

Figure 2. White matter tracts with a positive association between RD and UWDRS-N (red-yellow) and between AD and UWDRS-N (blue) are overlaid onto all subjects' mean FA skeleton (green) and projected onto the MNI152-T1 template (p<.05, TFCE and FWE-corrected). A=anterior; P=posterior; L=left; R=right.

Conclusions: Our analysis demonstrates significant correlations between alterations of all DTI indices and neurological impairment in manifold WM tracts of patients with WD, correcting for age and sex. Higher neurological severity was associated with higher MD, AD and RD in large interconnecting fibers, i.e., bilateral superior corona radiata and left superior longitudinal fasciculus, which are crucial for the transport of sensory and motor information throughout the brain. This may be supported by findings of increased diffusivities in the superior longitudinal fasciculus in WD patients relative to healthy controls[6]. Moreover, predominantly motor related WM tracts such as the left corticospinal tract, bilateral medial lemniscus and anterior limb of internal capsule were affected; for the latter, a positive association between MD and neurological scores has previously been reported in drug naive WD patients[2]. Overall, our results indicate the widespread loss of WM integrity in WD patients, presumably due to demyelination, edema and neuronal loss[7], which may contribute to observed sensory and motor

impairments. All DTI derived WM changes seem to be promising neuroimaging biomarkers for residual neurological symptom severity in treated WD.

References
1. Shribman, S. (2022). 'Neuroimaging correlates of brain injury in Wilson's disease: a multimodal, whole-brain MRI study', Brain, vol. 145, pp. 263-275
2. Jadav, R. (2013). 'Diffusion Tensor Imaging (DTI) and its clinical correlates in drug naive Wilson's disease', Metabolic Brain Disease, vol. 28, pp. 455-462
3. Karimi, A. (2022). 'Brain microstructural abnormalities in patients with Wilson's disease: A systematic review of diffusion tensor imaging studies', Brain Imaging & Behavior, vol. 16, pp. 2809-2840
4. Glasser, M. F. (2013). 'The minimal preprocessing pipelines for the Human Connectome Project', NeuroImage, vol. 80, pp. 105-124
5. Smith, S. M. (2006). 'Tract-based spatial statistics: Voxelwise analysis of multi-subject diffusion data', NeuroImage, vol. 31, pp. 1487-1505
6. Hu, S. (2021). 'Structural and functional changes are related to cognitive status in Wilson's disease', Frontiers in Human Neuroscience, vol. 15, pp. 610947
7. Wang, A. (2017). 'Study on lesion assessment of cerebello-thalamo-cortical network in Wilson's disease with diffusion tensor imaging', Neural Plasticity, vol. 2017, pp. 7323121

Poster No 279

Investigation of fibre bundle alterations in early Alzheimer's disease using fixel-based analysis

Aurélie Lebrun[1], Yann Leprince[1], Julien Lagarde[2,3,4], Pauline Olivieri[2], Marie Sarazin[2,3,4], Michel Bottlaender[1,4]

[1]UNIACT, NeuroSpin, CEA, Université Paris-Saclay, Gif-sur-Yvette, France, [2]Service de Neurologie de la Mémoire et du Langage, GHU Paris Psychiatrie et Neurosciences, Paris, France, [3]Université Paris-Cité, Paris, France, [4]BioMaps, Service Hospitalier Frédéric Joliot, CEA, Université Paris-Saclay, Inserm, Orsay, France

Introduction: Alzheimer's disease (AD) is primarily characterised by the aggregation and accumulation of specific misfolded proteins (β-amyloid and tau), which initiate focally in a subset of vulnerable neurons and consequently propagate along specific pathways throughout the brain[3,6]. In this context, studying white matter (WM) could provide crucial information. We aimed to study fibre bundle WM alterations in early AD with a fixel-based analysis (FBA) and to perform linear regressions between these alterations and (i) a clinical marker of disease severity, and (ii) the accumulation of abnormal tau protein.

Methods: This study includes 27 AD patients (14 F; mean age 70 yo; mean Mini Mental State Examination MMSE=23.4) and 19 healthy controls HC (13 F; mean age 68 yo) from the SHATAU7/IMATAU cohort[7]. All AD patients had positive AD CSF biomarkers, and amyloid and tau PET imaging when available. Participants underwent 3T MRI with a multi-shell diffusion protocol (b=200, 1700, 4200 s/mm^2, 60 directions per shell, voxel size: 1.3 mm^3 iso). We first preprocessed the data (FSL eddy[1]) then we implemented the FBA (MRtrix3[4,10]). We used a common FOD template computed with data from 32 participants of the cohort. We then extracted the FD (Fibre Density), FC (Fibre bundle Cross-section) and FDC (Fibre Density and Cross-section) metrics. We first computed a whole-brain FBA to identify WM tracts that are altered in AD with respect to HC (statistical tests on all fixels in the template using a general linear model GLM including age, sex, MMSE, and intracranial volume ICV as covariates; significance of the results assessed with CFE[9]). We then reconstructed the identified tracts on the template (Figure 1A) using beginning and ending ROIs extracted from FreeSurfer parcellation[5] on the T1-weighted images before registration on the template, and we performed tract-based analyses. To do so, we calculated the mean FD, FC and FDC for each tract by taking the average of each metric over all fixels associated with the tract, normalised by tract density. We performed statistical tests for each metric using a GLM with age, sex, MMSE, and ICV as covariates to compare AD patients and HC. For each metric, significance of the results was assessed with one-sided T-tests, and Bonferroni correction for multiple testing over the 11 tracts tested. Finally, we explored linear regressions between FDC and MMSE among the 27 AD patients only, and FDC and tau accumulation in the ipsilateral entorhinal cortex (left cortex for left temporal tracts) among 17 AD patients for whom tau ([18F]-Flortaucipir) PET images were available. To do so, we performed statistical tests for each metric using a GLM with age, sex, and ICV as covariates. For each metric, significance of the results was assessed with one-sided T-tests, and Bonferroni correction for multiple testing over the 11 or 8 tracts tested.

Results: FDC, which provides a measure sensitive to the number of fibres within the fibre bundle, was decreased in AD compared to HC in all tested tracts, which are mainly tracts of the temporal and limbic lobes (Figure 1B). Moreover, these alterations are driven more by a reduction in FC (atrophy) than in FD (fibre density loss). The temporopulvinar bundle of Arnold was particularly altered. Figure 2 further sheds light on this bundle as its alteration was significantly associated with a clinical marker of disease severity (MMSE), and with tau accumulation in the entorhinal cortex.

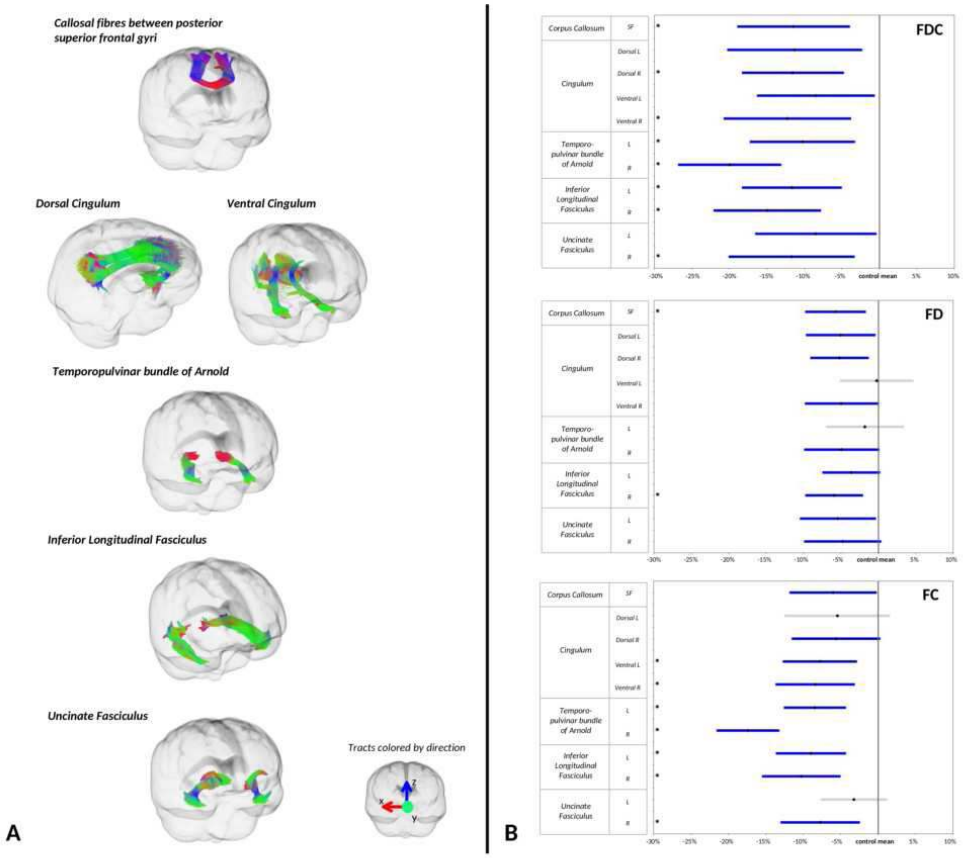

Figure 1 (A) Reconstruction on the FOD common template of the tracts identified as altered in the whole-brain fixel-based analysis, displayed through glass brains. The tracts are coloured according to fibre directions (green: anteroposterior axis, blue: inferior-superior axis, red: left-right axis).**(B) Tract-of-interest analyses: significant decrease in Fibre Density and Cross-section (FDC), Fibre Density (FD), and Fibre bundle Cross-section (FC) in Alzheimer's disease patients compared to controls in selected tracts of interest.** For each metric and each tract, the mean metric, as a percentage difference relative to controls, is represented with diamonds, and 95% confidence intervals with lines. Significant tracts ($P<0.05$) are displayed in blue, whereas non-significant tracts are in grey. For each metric, stars highlight significant tracts after Bonferroni correction over the 11 tracts tested. SF: Superior Frontal gyrus, L: Left, R: Right

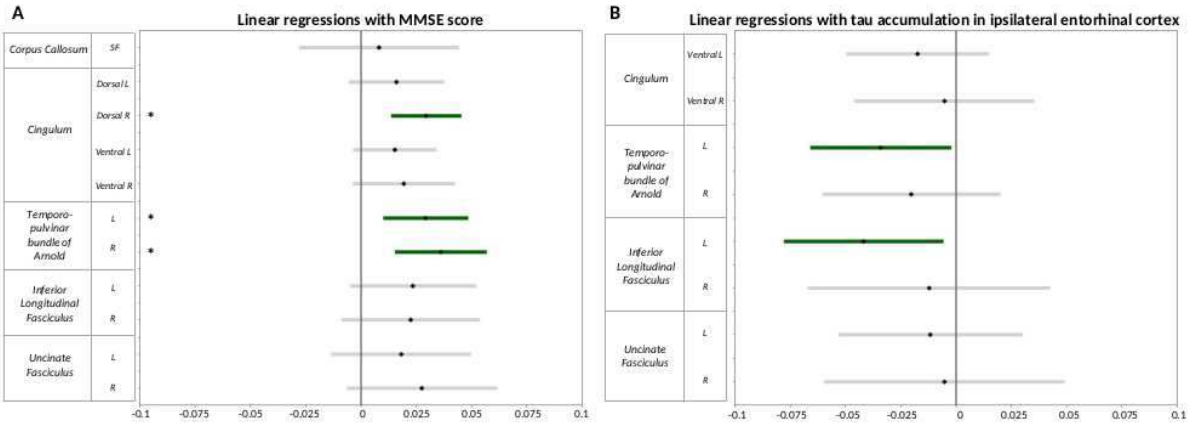

Figure 2 For each tract, linear regression among Alzheimer's disease patients only, between Fibre Density and Cross-section (FDC) and : (A) Mini Mental State Examination (MMSE), and (B) tau accumulation in ipsilateral entorhinal cortex. In both cases and for each tract, the standardized regression coefficient of the general linear model for the variable of interest (MMSE or tau accumulation) is represented with diamonds, and 95% confidence intervals with lines. Significant tracts ($P<0.05$) are displayed in green, whereas non-significant tracts are in grey. In both cases, stars highlight significant tracts after Bonferroni correction over the 11 or 8 tracts tested. Linear regressions with tau accumulation were performed among only 17 AD patients and on tracts of the temporal and limbic poles that pass near the ipsilateral entorhinal cortex. L: Left, R: Right

Conclusions: These results are consistent with previous results on WM alterations in AD and confirms that bundles of the temporal and limbic poles are the primary deteriorated bundles in AD[8]. Moreover, we highlight the alteration of the temporopulvinar bundle of Arnold, a tract that, to our knowledge, has not been described in the AD diffusion MRI literature to date. The involvement of this tract at the early stage of AD and its association with abnormal tau accumulation are congruent with neuropathological data[2].

References
1. Andersson, Jesper L. R., et al. 2016. 'An Integrated Approach to Correction for Off-Resonance Effects and Subject Movement in Diffusion MR Imaging'. NeuroImage 125:1063–78. doi: 10.1016/j.neuroimage.2015.10.019.
2. Braak, H., et al. 1991. 'Alzheimer's Disease Affects Limbic Nuclei of the Thalamus'. Acta Neuropathologica 81(3):261–68. doi: 10.1007/BF00305867.
3. Brettschneider, Johannes, et al. 2015. 'Spreading of Pathology in Neurodegenerative Diseases: A Focus on Human Studies'. Nature Reviews Neuroscience 16(2):109–20. doi: 10.1038/nrn3887.
4. Dhollander, Thijs, et al. 2021. 'Fixel-Based Analysis of Diffusion MRI: Methods, Applications, Challenges and Opportunities'. NeuroImage 241:118417. doi: 10.1016/j.neuroimage.2021.118417.
5. Fischl, Bruce, et al. 2004. 'Automatically Parcellating the Human Cerebral Cortex'. Cerebral Cortex 14(1):11–22. doi: 10.1093/cercor/bhg087.
6. Goedert, Michel. 2015. 'Alzheimer's and Parkinson's Diseases: The Prion Concept in Relation to Assembled Aβ, Tau, and α-Synuclein'. Science 349(6248):1255555. doi: 10.1126/science.1255555.
7. Lagarde, Julien, et al. 2021. 'Distinct Amyloid and Tau PET Signatures Are Associated with Diverging Clinical and Imaging Trajectories in Patients with Amnestic Syndrome of the Hippocampal Type'. Translational Psychiatry 11(1):1–10. doi: 10.1038/s41398-021-01628-9.
8. Mito, Remika, et al. 2018. 'Fibre-Specific White Matter Reductions in Alzheimer's Disease and Mild Cognitive Impairment'. Brain 141(3):888–902. doi: 10.1093/brain/awx355.
9. Raffelt, David A., et al. 2015. 'Connectivity-Based Fixel Enhancement: Whole-Brain Statistical Analysis of Diffusion MRI Measures in the Presence of Crossing Fibres'. NeuroImage 117:40–55. doi: 10.1016/j.neuroimage.2015.05.039.
10. Tournier, J.-Donald, et al. 2019. 'MRtrix3: A Fast, Flexible and Open Software Framework for Medical Image Processing and Visualisation'. NeuroImage 202:116137. doi: 10.1016/j.neuroimage.2019.116137.

Poster No 280

Word Finding Related Atrophy in ADNI's Alzheimer Disease Cohort

Grace Burt[1], Sheena Baratono[1], William Drew[2]

[1]Brigham and Women's Hospital, Boston, MA, [2]Brigham and Women's Hospital, Brookline, MA

Introduction: Word finding difficulty is common in Alzheimer's disease and considered one of the most functionally and socially debilitative symptoms of the disease (Farrel et al. 2014). Logopenic PPA (lvPPA), a subtype of Alzheimer's Disease, is characterized predominantly by deficits in language dysfunction rather than memory loss and is significantly less prevalent than typical amnestic presentation (Henry et al. 2010). Identifying the origin of word finding difficulties is challenging because it can be caused by trouble with fluency, word recall, or confrontation naming. Our goal is to determine if each of these functions maps to different anatomical regions and brain networks by comparing behavioral scores to vertex-wise cortical atrophy and atrophy connectivity in subjects with Alzheimer's disease. By better characterizing regional atrophy and the brain circuits underlying language deficits in Alzheimer's disease, we hope to identify targets for neuromodulation to improve language function in patients with Alzheimer's disease.

Methods: We used Freesurfer v7.2 to generate cortical thickness maps for participants within the Alzheimer's Disease Neuroimaging Initiative (ADNI) database. These maps were transformed using a general linear model based on controls and covarying for age and sex to generate w-maps, where each vertex is a z-score comparing each subject's cortical thickness to expected values (Tetreault et al. 2020). We compared these single subject atrophy/growth maps to their categorical fluency, Boston Naming Test and delayed verbal recall scores. To analyze this correlation, we employed a permutation analysis of linear models (PALM), identifying regions where atrophy associated with higher or lower cognitive scores. We repeated this design with network connectivity, using our weighted atrophy seeds on the Genome Superstruct Project 1000 Connectome to develop individual connectivity maps to run against behaviors using PALM. We then determined if the atrophy and atrophy-derived connectivity network associated with each symptom are differentiable and arise from a particular region through visualization and Pearson R spatial correlation.

Results: Atrophy associated with worse scores on the BNT were most prevalent in the temporal lobe, significantly in the medial temporal pole and along the ventral surface in the left hemisphere (fwe $p<.05$). Atrophy associated with the animal category fluency test showed greater similarities to the hallmark atrophy regions of Alzheimer's (Putcha et al. 2022), peaking around the IPL, precuneus, lateral and mesial temporal lobes and posterior cingulate gyrus along both hemisphere. However, the only point of significance fell within the left hemisphere insular regions (fwe $p<.05$). The 30-minute delay peaked in the mesial temporal lobe but held no significance on either hemisphere. When looking at network connectivity with each behavior, naming controlled for fluency had a correlation of $r = .69$ ($p<.05$) with delayed recall, while naming and fluency had a correlation of $r = -.33$ ($p>.05$).

Conclusions: Distinct patterns of atrophy emerge when examining the relationship between delayed recall, naming, and fluency. Specifically, we observe shared locations of atrophy in medial temporal regions for delayed recall and naming, while fluency shows a greater involvement of insular regions. These nuances are further clarified through network analyses,

revealing two specific networks: one linked to fluency, related to word generation, and the other associated with verbal delayed recall and naming, related to retrieval. These findings align with prior studies (Melrose et al. 2009), underscoring their consistency and relevance. Exploring these networks could offer valuable insights for potential transcranial magnetic stimulation (TMS) target sites, especially concerning their application in lvPPA. Future research endeavors aim to deepen our understanding of these networks, potentially unlocking novel therapeutic avenues for lvPPA.

References

1. Farrell MT, Zahodne LB, Stern Y, Dorrejo J, Yeung P, Cosentino S. Subjective word-finding difficulty reduces engagement in social leisure activities in Alzheimer's disease. J Am Geriatr Soc. 2014 Jun;62(6):1056-63. doi: 10.1111/jgs.12850. Epub 2014 Jun 2. PMID: 24890186; PMCID: PMC4238963.
2. Henry ML, Gorno-Tempini ML. The logopenic variant of primary progressive aphasia. Curr Opin Neurol. 2010 Dec;23(6):633-7. doi: 10.1097/WCO.0b013e32833fb93e. PMID: 20852419; PMCID: PMC3201824.
3. Putcha D, Eckbo R, Katsumi Y, Dickerson BC, Touroutoglou A, Collins JA. Tau and the fractionated default mode network in atypical Alzheimer's disease. Brain Commun. 2022 Mar 9;4(2):fcac055. doi: 10.1093/braincomms/fcac055. PMID: 35356035; PMCID: PMC8963312.
4. Tetreault AM, Phan T, Orlando D, Lyu I, Kang H, Landman B, Darby RR; Alzheimer's Disease Neuroimaging Initiative. Network localization of clinical, cognitive, and neuropsychiatric symptoms in Alzheimer's disease. Brain. 2020 Apr 1;143(4):1249-1260. doi: 10.1093/brain/awaa058. PMID: 32176777; PMCID: PMC7174048.

Poster No 281

The role of hippocampal subfield volumes in subjective cognitive decline

Linda MAH[1], Susan Vandermorris[2], Nicolaas Verhoeff[3], Nathan Herrmann[4]

[1]Rotman Research Institute, Baycrest, University of Toronto, Toronto, Ontario, [2]Baycrest, Toronto, Ontario, [3]Baycrest, University of Toronto, Toronto, Ontario, [4]Sunnybrook Health Sciences, University of Toronto, Toronto, Ontario

Introduction: Subjective cognitive decline (SCD), defined as perception of memory or other cognitive decline with normal test performance, is conceptualized as a possible preclinical stage of Alzheimer's disease (AD)[1]. Hippocampal volume reduction is well-established as a biomarker of AD risk[2]. The hippocampal complex includes functionally and structurally distinct subfields (cornu ammonis (CA), dentate gyrus, and subiculum) which show selective atrophy in aging and in AD[3], as well as psychiatric conditions such as major depressive disorder[4]. Previous work demonstrating patterns of subfield atrophy in Mild Cognitive Impairment (MCI), a prodrome of AD, support the utility of hippocampal subfield volumetry, over measurement of total hippocampus, to detect risk for AD[5]. Evidence of volumetric alterations in hippocampal subfields in SCD is emerging but inconsistent[6;7]. One potential reason for the discrepancy in findings is unaccounted previous diagnosis of depression in SCD participants. Depression frequently co-occurs with SCD[1] and itself is associated with hippocampal atrophy, yet the majority of studies of SCD failed to ascertain the presence of previous depression. In the current study, we measured hippocampal subfield volumes using structural magnetic resonance imaging (MRI) at 3 Tesla with the goals of identifying group differences in subfield volumes between older adults with SCD, who were free of current or past depression, and cognitively unimpaired (CU) older adults, and examining associations between hippocampal subfield volumes and subjective memory ability.

Methods: The sample included 26 SCD (13M, age 70.6 SD=5.1 years) and 25 CU (10M, age 71.4 SD=7.4 years) older adults. All participants performed within normal on a neuropsychological battery and screened negative for past or current psychiatric illnesses during psychiatric assessment. SCD was established based on affirmative responses to "Do you feel your memory is becoming worse?" "If so, are you concerned?"(1). Subjective memory ability was further quantified using the Memory Functioning Questionnaire (MFQ)(8) MR scanning was performed on a 3T Siemens Trio scanner using a 12-channel head coil. A high-resolution (voxel size 0.43 x 0.43 x 3 mm) T2-weighted scan of the medial temporal lobe was acquired in an oblique-coronal plane, perpendicular to the hippocampal long axis. The Automatic Segmentation of Hippocampal Subfields (ASHS) processing pipeline was used to extract bilateral CA1, CA2, CA3, dentate gyrus, and subiculum volumes (9). Independent t-tests were used to compare hippocampal subfields between groups. Partial correlations were performed within the total sample to examine the association between subfield volumes and MFQ Frequency of Forgetting ("How often do you...?") subscale scores, which has been linked to AD neuroimaging markers,(10) as well as long delayed recall scores on the California Verbal Learning Test (CVLT-LDR). Covariates were age, sex, and total intracranial volume. Bonferroni correction for multiple comparisons was applied.

Results: Compared to CU, left CA2 volume was reduced in SCD [t (49) = 2.00, P =.025], while right CA3 volume was greater in SCD [t (49) = -1.81, P =.038] (Figure 1), although these findings were not statistically significant following correction for multiple comparisons. Frequency of Forgetting was significantly correlated with left CA2 [r = .42, P =.003] and right subicular volume [r = .45, P =.001. In contrast, CVLT-LDR was not correlated with any hippocampal subfield volume (Figure 2).

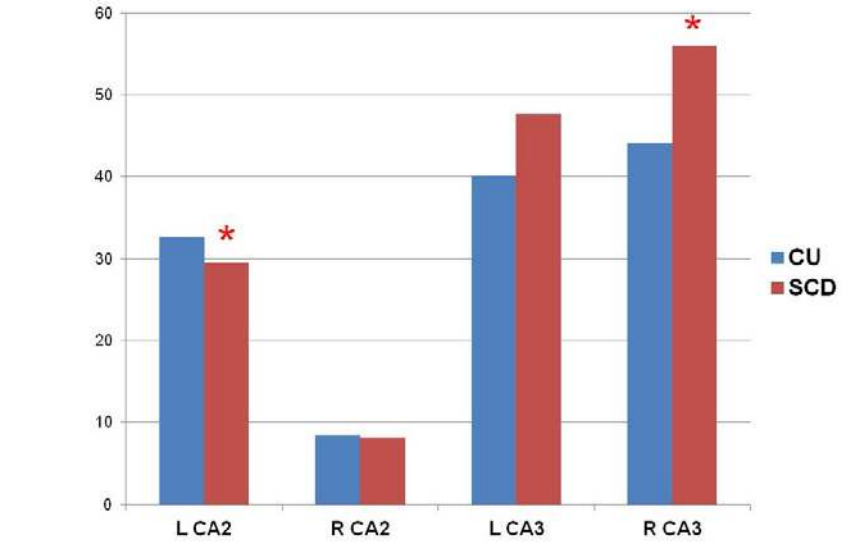

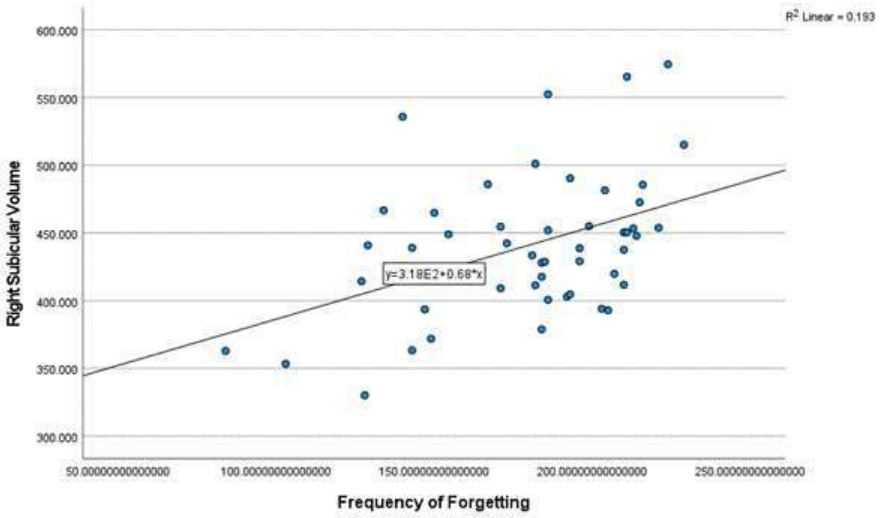

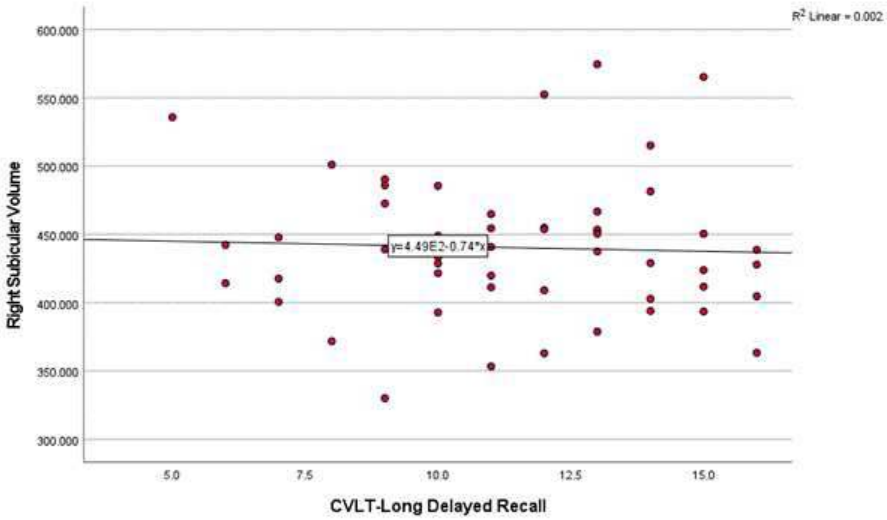

Conclusions: These findings suggest a role for CA2, a region linked to social memory in animal models, in SCD. The association between volume of subiculum, a region implicated in AD, and subjective, but not objective memory, suggests that self-awareness of change in memory in everyday life may be sensitive to subtle disease-related volumetric changes within the hippocampus in the earliest stages of the AD course.

References
1. Amariglio RE, Becker JA, Carmasin J, Wadsworth LP, Lorius N, et al. 2012. Subjective cognitive complaints and amyloid burden in cognitively normal older individuals. Neuropsychologia 50: 2880-6 (citation 10)
2. Apostolova LG, Dutton RA, Dinov ID, Hayashi KM, Toga AW, et al. 2006. Conversion of Mild Cognitive Impairment to Alzheimer Disease Predicted by Hippocampal Atrophy Maps. Archives of neurology 63: 693-99 (citation 2)
3. Hansen N, Singh A, Bartels C, Brosseron F, Buerger K, et al. 2021. Hippocampal and Hippocampal-Subfield Volumes From Early-Onset Major Depression and Bipolar Disorder to Cognitive Decline. Frontiers in Aging Neuroscience 13 (citation 4)
4. Huang Y, Huang L, Wang Y, Liu Y, Lo C-YZ, Guo Q. 2022. Differential associations of visual memory with hippocampal subfields in subjective cognitive decline and amnestic mild cognitive impairment. BMC Geriatrics 22: 153 (citation 7)
5. Jessen F, Amariglio RE, Buckley RF, van der Flier WM, Han Y, et al. 2020. The characterisation of subjective cognitive decline. The Lancet Neurology 19: 271-78 (citation 1)
6. Mueller SG, Schuff N, Yaffe K, Madison C, Miller B, Weiner MW. 2010. Hippocampal atrophy patterns in mild cognitive impairment and Alzheimer's disease. Human brain mapping 31: 1339-47 (citation 5)
7. Nadal L, Coupé P, Helmer C, Manjon JV, Amieva H, et al. 2020. Differential annualized rates of hippocampal subfields atrophy in aging and future Alzheimer's clinical syndrome. Neurobiology of aging 90: 75-83 (citation 3)
8. Perrotin A, de Flores R, Lamberton F, Poisnel G, La Joie R, et al. 2015. Hippocampal Subfield Volumetry and 3D Surface Mapping in Subjective Cognitive Decline. Journal of Alzheimer's Disease 48: S141-S50 (citation 6)
9. Yushkevich PA, Pluta JB, Wang H, Xie L, Ding SL, et al. 2015. Automated volumetry and regional thickness analysis of hippocampal subfields and medial temporal cortical structures in mild cognitive impairment. Human brain mapping 36: 258-87 (citation 9)
10. Zelinski EM, Gilewski MJ, Anthony-Bergstone CR. 1990. Memory Functioning Questionnaire: concurrent validity with memory performance and self-reported memory failures. Psychology and aging 5: 388-99 (citation 8)

Poster No 282

Functional connectivity reorganization over age and Alzheimer's disease

Jonathan Rittmo[1], Laura Wisse[2], Olof Strandberg[3], Nicola Spotorno[3], Hamid Behjat[3], Danielle van Westen[4], Sebastian Pamqvist[3], Niklas Mattsson-Carlgren[3], Shorena Janelidze[5], Erik Stomrud[3], Theodore Satterthwaite[6], Hansson Oskar[3], Jacob Vogel[7]

[1]Department of Clinical Sciences Malmö, Faculty of Medicine, SciLifeLab, Lund University, Lund, Sweden, [2]Department of Diagnostic Radiology, Clinical Sciences, Lund University, Lund, Sweden, [3]Clinical Memory Research Unit, Department of Clinical Sciences Malmö, Faculty of Medicine, Lund Univ, Lund, Sweden, [4]Department of Diagnostic Radiology, Clinical Sciences, Lund University, Lund, Sweden, Lund, Sweden, [5]Clinical Memory Research Unit, Department of Clinical Sciences Malmö, Faculty of MediLund University, Lund, Sweden, [6]Penn Lifespan Informatics and Neuroimaging Center (PennLINC), Philadelphia, PA, United States, Philadelphia, PA, [7]Lund UniversityDepartment of Clinical Sciences Malmö, Faculty of Medicine, SciLifeLab, Lund Universi, Lund, Sweden

Introduction: Cognitive aging is a phenomenon that eventually affects most elderly individuals. This process is accelerated in neurodegenerative diseases like Alzheimer's disease (AD), which involve clinical impairment and decline in functional activities of daily living. Aging is accompanied by changes in brain functional network organization, with one of the hallmarks being decrease in system segregation[1]. Similarly, nonlinear alterations to functional networks have been described in AD, posited as early neuronal responses to (and perhaps drivers of) AD pathophysiology[2]. Functional changes in aging and AD have, however, mostly been studied in isolation, and the degree to which these phenomena interrelate is not well understood. Further, little is known about how variable such changes are in the population. In this exploratory study, we investigate how the brain's functional networks are reorganized at the individual level in aging and AD independently.

Methods: The present work uses resting-state functional MRI (rsfMRI) data from the BioFINDER-2 study, encompassing 917 individuals (after quality filtering) with a baseline diagnosis of cognitively unimpaired (Normal, n=390), cognitively unimpaired with amyloid-β (Aβ) positivity (Normal+, n=95), mild cognitive impairment irrespective of Aβ (MCI, n=253) or Alzheimer's disease (AD, n=179). The rsfMRI images were acquired with a 3T scanner and preprocessed using a modified CPAC pipeline[3], including slice-timing correction, motion correction, bandpass filtering, frame censoring, and regression of physiological components, motion parameters and WM/CSF. Subjects were excluded based on mean (>0.3mm) and max (>3mm) frame-displacement. Images from the resulting dataset were smoothed (6 mm FWHM) and mean signal parcellated into 1000 regions as defined by the Schaefer atlas[4] to derive individual functional connectomes. To understand heterogeneity in functional connectivity over both age and AD, inter-subject similarity was estimated by averaging the pairwise Pearson correlation coefficients of each parcel's connectivity map between all subjects within each disease group[5]. Personalized network atlases were constructed using an iterative approach of parcel reassignment[6], with the Yeo 2011[7] atlas as prior. For each parcel, the probability of belonging to each network was estimated using logistic regression, with diagnosis, age and sex as independent variables. Network size was defined as the proportion of parcels belonging to that network for each subject and modeled

using generalized additive models with penalized thin plate splines, diagnosis and sex as grouping variables and smoothed over age.

Results: Across the majority of parcels, we observed a decrease in inter-subject similarity as both age and disease status progress, suggesting diverging patterns of age- and AD-related network fragmentation (Fig. 1A). Fig. 1B,C and Fig. 2A,D summarize migration of parcels between networks in AD and aging, while Fig. 2B,C describes changes in network size. In MCI and AD, parcels in sensory networks tended to be recruited by adjacent attention networks. Progression along the AD continuum involved consistent increase in the size of association networks; decrease in limbic network size occurred only during the MCI-AD transition. In contrast, aging was associated with substantial reorganization of the dorsal attention and limbic networks, with the former increasing in size with age and the latter decreasing sharply.

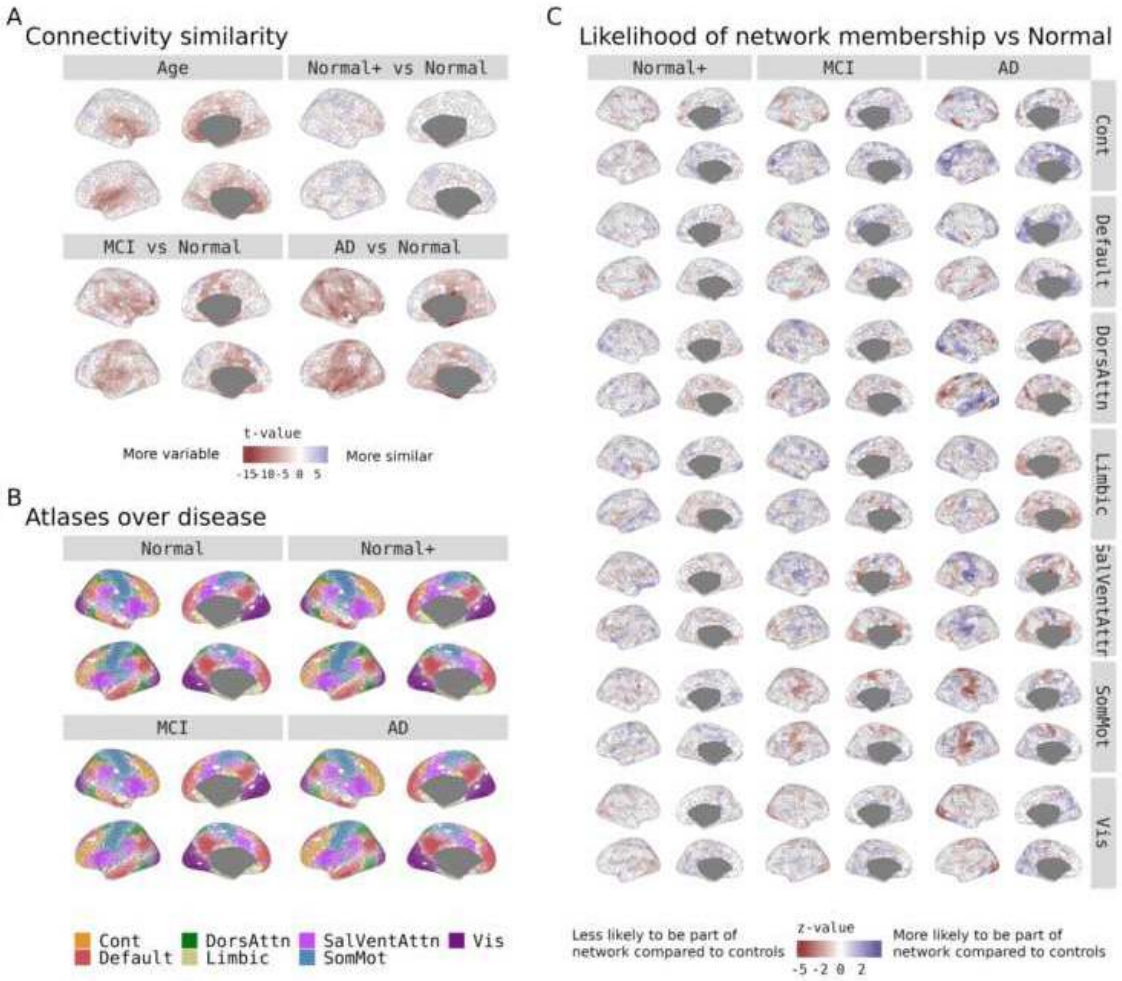

Figure 1: A) Inter-subject similarity of functional connectivity for the disease groups. This measure is based on the average correlation of connectivity patterns between all individuals and then modeled over age and disease with linear regression - for each parcel. The t-values distributed over the cortical surface represent the effects in these models for disease groups compared to normal controls and age, i.e. how similarity increases or decreases as we age. B) Representation of the "average" of the individualized atlases for each group. Parcels are colored according to the network having the highest proportion in that group, and opacity indicates the magnitude of that proportion. C) Z-values derived from logistic regression models for each parcel's likelihood of belonging to a certain network using disease, age, and sex as independent variables. Higher values indicate higher likelihood for that parcel to belong to a certain network for a certain disease group, compared to controls.

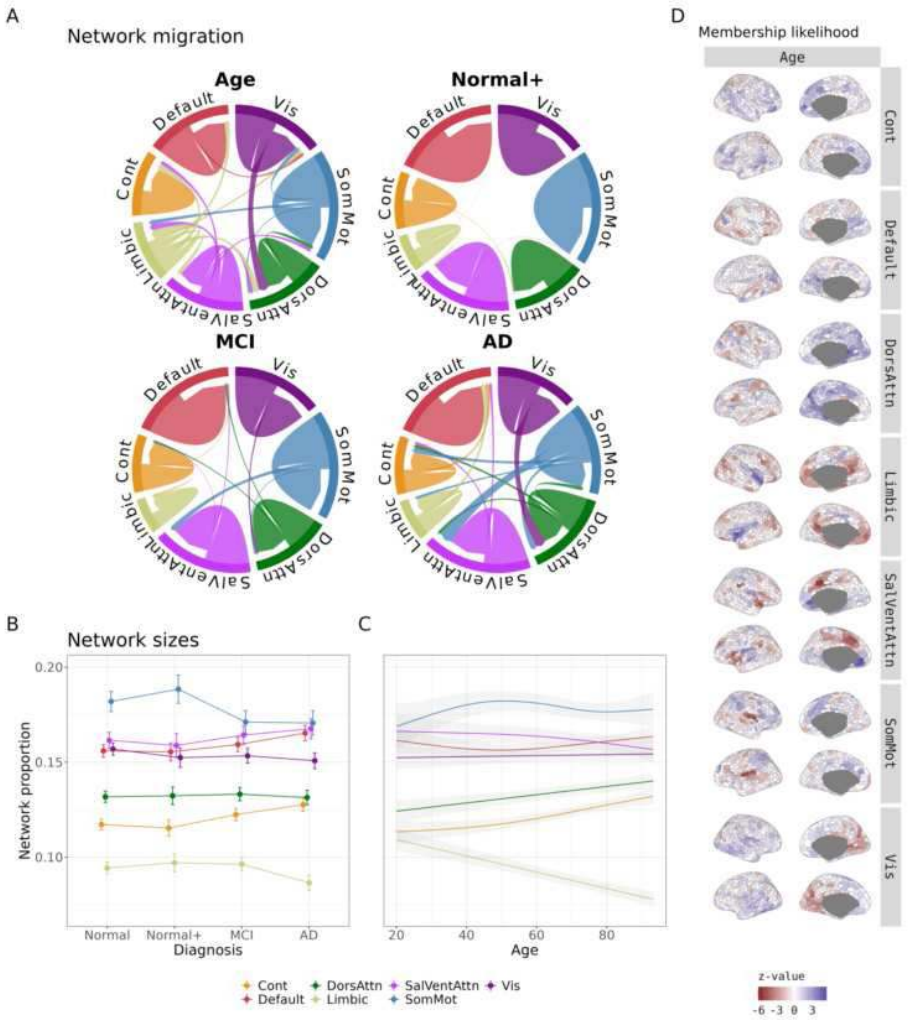

Figure 2: A) Network migration in age and across disease spectrum. Based on the logistic models for network membership, a migration was defined if a parcel had both a significant negative effect for one network and a significant positive effect for another, for age and the disease groups separately. If a parcel had more than one negative or positive effect, only the largest was considered. The diagram shows only the largest 50% of migrations. B) Network sizes (i.e. proportion of parcels) for disease groups as estimated by GAMs and adjusted for age and sex. C) Network sizes over age as estimated by GAMs and adjusted for disease group and sex. D) Z-values derived from logistic regression models for each parcel's likelihood of belonging to a certain network using disease, age and sex as independent variables. Positive values indicate that the parcel has an increased probability of belonging to the network on the facet label as age increases, negative values indicate a decreased probability of that parcel belonging to the network as age increases.

Conclusions: These preliminary findings show a complex landscape of network reorganization associated with AD and aging. The differential reorganization observed in aging and AD may highlight the brain's distinct compensatory responses to neuropathology – but such interpretation should be balanced with the possibility that the alterations might themselves be dysfunctional or pathological. Further understanding of these dynamics could open avenues for targeted (e.g., stimulation-based) interventions and therapies.

References

1. Bagarinao E, Watanabe H, Maesawa S, Mori D, Hara K, Kawabata K, et al. Reorganization of brain networks and its association with general cognitive performance over the adult lifespan. Sci Rep. 2019 Aug 6;9(1):11352.
2. Franzmeier N, Dewenter A, Frontzkowski L, Dichgans M, Rubinski A, Neitzel J, et al. Patient-centered connectivity-based prediction of tau pathology spread in Alzheimer's disease. Sci Adv. 2020 Nov 27;6(48):eabd1327.
3. Craddock C, Sikka S, Cheung B, Khanuja R, Ghosh SS, Yan C, et al. Towards automated analysis of connectomes: The configurable pipeline for the analysis of connectomes (c-pac). Front Neuroinformatics. 2013;42(10.3389).
4. Schaefer A, Kong R, Gordon EM, Laumann TO, Zuo XN, Holmes AJ, et al. Local-Global Parcellation of the Human Cerebral Cortex from Intrinsic Functional Connectivity MRI. Cereb Cortex N Y NY. 2018 Sep;28(9):3095–114.
5. Mueller S, Wang D, Fox MD, Yeo BTT, Sepulcre J, Sabuncu MR, et al. Individual Variability in Functional Connectivity Architecture of the Human Brain. Neuron. 2013 Feb;77(3):586–95.
6. Wang D, Buckner RL, Fox MD, Holt DJ, Holmes AJ, Stoecklein S, et al. Parcellating cortical functional networks in individuals. Nat Neurosci. 2015 Dec;18(12):1853–60.
7. Thomas Yeo BT, Krienen FM, Sepulcre J, Sabuncu MR, Lashkari D, Hollinshead M, et al. The organization of the human cerebral cortex estimated by intrinsic functional connectivity. J Neurophysiol. 2011 Sep;106(3):1125–65.

Poster No 283

Pattern of Thalamic Connectivity Loss Following Moderate-Severe Traumatic Brain Injury

Daniel Brennan[1], Catherine Lyons[2], Junghoon Kim[1]

[1]The City University of New York, New York, NY, [2]The Graduate Center, City University of New York, New York, NY

Introduction: Regional cortical and subcortical atrophy have been identified in the months-to-years following moderate-severe traumatic brain injury (msTBI).[1,2] Recently, we identified a pattern of cortical atrophy prior to 3 months in frontal and temporal cortices, while atrophy between 3-12 months was observed in the posterior cortical regions of the parietal and occipital lobes.[3] In this cohort, atrophy of the bilateral thalamus was observed within both of these time windows; this unique temporal pattern and the interconnected nature of the thalamus prompted us to hypothesize that thalamic white matter may show a similar spatial distribution of damage.

Methods: Thirty-nine (39) msTBI patients were evaluated at 3, 6 and 12 months post injury. Thirty-five (35) age-matched controls were evaluated once. The diffusion data were reconstructed in the MNI space using q-space diffeomorphic reconstruction[4] available in DSI studio. Voxel-wise quantitative anisotropy (QA) was extracted as the local connectome fingerprint.[5] To estimate white-matter changes in patients present at 3 months post injury, a cross-sectional connectomic analysis[6] between patients' 3-month diffusion data (N=38) and controls (N=34) was performed. A nonparametric Spearman partial correlation was used to derive the effect of group identity, and the effect of age was removed using a multiple regression model. A T-score threshold of 2.5 was assigned and tracked using a deterministic fiber tracking algorithm[7] to obtain correlational tractography. To estimate longitudinal changes, diffusion data from patients' 3-month and follow-up scan (6 or 12 months post injury; N=34) were compared using the same procedure. An FDR threshold of 0.05 was used to select tracks. To estimate the false discovery rate, a total of 4000 randomized permutations were applied to the independent variable in each analysis to obtain the null distribution of the track length.

Results: Divergent tract profiles originating from the thalamus were observed between 3 months and 3-12 months post injury. In TBI patients at 3 months post-injury, thalamic tracts with decreased QA relative to uninjured controls were identified in frontal and temporal cortices. Mean QA of these tracts was correlated with thalamic volume at 3 months within the patient group (t=3.247, p=0.00273). In contract, significant decreases in QA were observed between 3 months post injury and follow-up timepoints in tracts projecting to the temporal cortex in addition to tracts projecting dorsally to occipital, superior parietal and superior frontal cortices. Mean QA of these tracts were also significantly correlated with thalamic volume at 3 months post injury (t=2.117, p=0.0424), and approached significance at follow-up (t=1.900, p=0.0668).

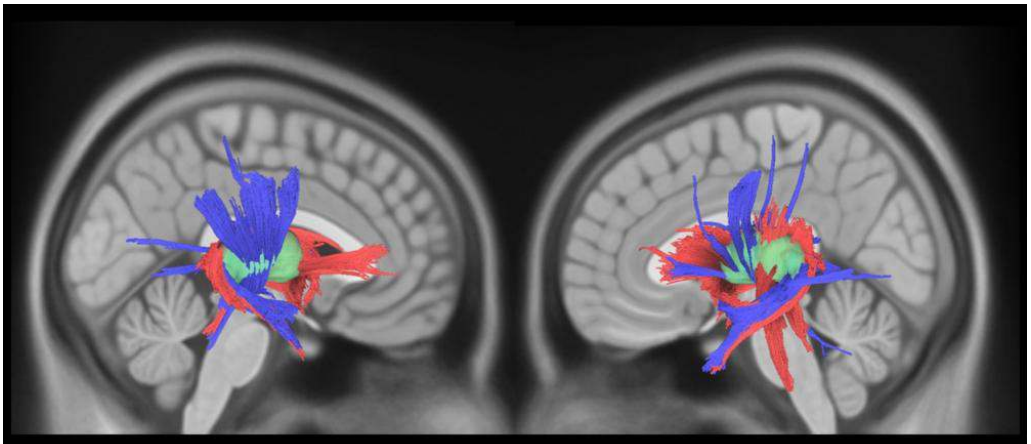

Figure 1. Significant tracts (FDR < 0.05) originating from the bilateral thalamus (green). Red: Tracts with significantly lower quantitative anisotropy (QA) in TBI-patients at 3 months post injury relative to controls. Blue: Tracts with significantly lower QA in TBI-patients at follow-up (6 or 12 months post-injury) relative to baseline (3 months post-injury).

Conclusions: White-matter microstructural integrity in thalamic fibers shows a regionally selective distribution of damage following msTBI. Qualitatively, this pattern reflects the overall spatiotemporal distribution of cortical atrophy previously observed within this cohort. The degree of microstructural integrity, measured by mean QA across all identified fibers, generally correlated with thalamic volume. These results suggest a unique spatiotemporal distribution of concomitant damage between the cortex, thalamocortical fibers, and the thalamus itself during the first year following msTBI. Future work is necessary to clarify the relationship of cortical, thalamic, or thalamocortical damage in this identified profile and the clinical implications of damage to these tracts.

References

1. Warner MA, Youn TS, Davis T, et al. Regionally Selective Atrophy After Traumatic Axonal Injury. Arch Neurol. 2010;67(11):1336–1344. doi:10.1001/archneurol.2010.149
2. Green RE, Colella B, Maller JJ, Bayley M, Glazer J, Mikulis DJ. Scale and pattern of atrophy in the chronic stages of moderate-severe TBI. Front Hum Neurosci. 2014 Mar 31;8:67. doi: 10.3389/fnhum.2014.00067. PMID: 24744712; PMCID: PMC3978360.
3. Brennan DJ, Duda J, Ware JB, Whyte J, Choi JY, Gugger J, Focht K, Walter AE, Bushnik T, Gee JC, Diaz-Arrastia R, Kim JJ. Spatiotemporal profile of atrophy in the first year following moderate-severe traumatic brain injury. Hum Brain Mapp. 2023 Sep;44(13):4692-4709. doi: 10.1002/hbm.26410. Epub 2023 Jul 3. PMID: 37399336; PMCID: PMC10400790.
4. Yeh FC, Tseng WY. NTU-90: a high angular resolution brain atlas constructed by q-space diffeomorphic reconstruction. Neuroimage. 2011 Sep 1;58(1):91-9. doi: 10.1016/j.neuroimage.2011.06.021. Epub 2011 Jun 16. PMID: 21704171.
5. Yeh F-C, Vettel JM, Singh A, Poczos B, Grafton ST, Erickson KI, et al. (2016) Quantifying Differences and Similarities in Whole-Brain White Matter Architecture Using Local Connectome Fingerprints. PLoS Comput Biol 12(11): e1005203. https://doi.org/10.1371/journal.pcbi.1005203
6. Yeh FC, Badre D, Verstynen T. Connectometry: A statistical approach harnessing the analytical potential of the local connectome. Neuroimage. 2016 Jan 15;125:162-171. doi: 10.1016/j.neuroimage.2015.10.053. Epub 2015 Oct 21. PMID: 26499808.
7. Yeh FC, Verstynen TD, Wang Y, Fernández-Miranda JC, Tseng WYI (2013) Deterministic Diffusion Fiber Tracking Improved by Quantitative Anisotropy. PLOS ONE 8(11): e80713. https://doi.org/10.1371/journal.pone.0080713

Poster No 284

Task based functional connectivity in Parkinson's Disease with increase in disease duration

Priyanka Bhat[1], S Senthil Kumaran[1], Achal K Srivastava[1], Divya M Radhakrishnan[1]

[1]All India Institue of Medical Sciences (AIIMS), New Delhi, Delhi

Introduction: Parkinson's disease (PD) is a movement disorder, progressive in nature. PD patients primarily experience bradykinesia with rigidity and tremor [Chen, 2015] along with deficits in motor planning and execution[Herz et al., 2014]. Dopamine intervention has a role in restoring the cortical activity[4], but dose requirements need to be periodically reviewed clinically. This study explores the effects of disease duration on functional cortical connectivity (cue-dependent movement execution task).

Methods: The study was approved by the institute review board. Patients with PD were recruited from the movement disorders clinics and were recruited after obtaining their informed written consent in compliance with Declaration of Helsinki. Subjects with PD as per UK Parkinson's disease Brain Bank Criteria of both gender and age above 45 years were chosen to be a part of the study. Patients with PD (n = 46) with Hoehn and Yahr (HY) ≤ 3, HAM A ≤ 14 (but not on any anxiolytics), HAM-D ≤ 7 and right sided onset of the first symptom (tremor, bradykinesia or akinesia, rigidity) were recruited. Participants with contraindications to the fMRI, history of any neuropsychiatry co-morbidities were excluded. Clinical assessments like UPDRS (Unified Parkinson's Disease Rating Scale) as well as fMRI sessions were conducted in drug ON phase. Functional MRI data was acquired on a 3 Tesla MRI scanner (Achieva 3.0T M/s. Philips Medical Systems, Netherlands) with a 32-channel head coil. A single shot echo planar imaging (EPI) sequence with 29 slices of thickness = 5 mm, Slice gap: 0 mm, orientation: transverse, Fold-over direction: RL, multi-sliced-interleaved, Reconstruction matrix: 128, Scan mode technique: fast Fourier echo (FFE), Flip angle = 90°, Field of view (FOV) = 240 mm (RL); 232 mm (AP); with TR/TE =2000/30 ms, number of dynamics 192 was acquired. The task was presented using ePrime software (version 1.0, Psychology Software Tools, USA) and an E-sys IFIS system. Task had 6 alternating rest blocks (no response by the subjects) and active blocks (response to the direction), using an MRI compatible Lumina LP 400 (Cedrus Inc., USA) response pad. During active, a set of 8 images of turns in a corridor (4 of the right turn and 4 of the left turn) were randomly presented. Subjects responded whether the turn was towards the right or left with the respective hand. Functional data were analysed using Conn (ver.21a)[Whitfield-Gabrieli and Nieto-Castanon, 2012] and demographic data with SPSS 20 (IBM Corp) [IBM Corp. Released 2013. IBM SPSS Statistics for Windows, Version 22.0. Armonk, 2013]. Pre-processing included realignment, outlier detection (using Artefact Detection Tool), co-registration (to subjects T1), normalization (to Montreal neurological institute template) and smoothing (kernel of FWHM=8mm), denoising (band-pass filter= 0.008 to 0.09 Hz). Task based connectivity (TBC) connectivity maps were computed from the active blocks of the fMRI timeseries as the Fisher-transformed bivariate correlation coefficients.

Results: The study was conducted on a total of 46 subjects and then they were categorized into 3 groups depending on the duration of disease: A= less than 5 years of disease; B= 5 to 8 years of disease; C= above 8 years. Region of Interest (ROI) to ROI connectivity (RRC) analyses and graph theory measures revealed significant differences in group C (Figures-1). No significant differences were observed in age (p=0.068), UPDRS II (p=0.270) and UPDRS III (p=0.624) across the groups (Figure-2).

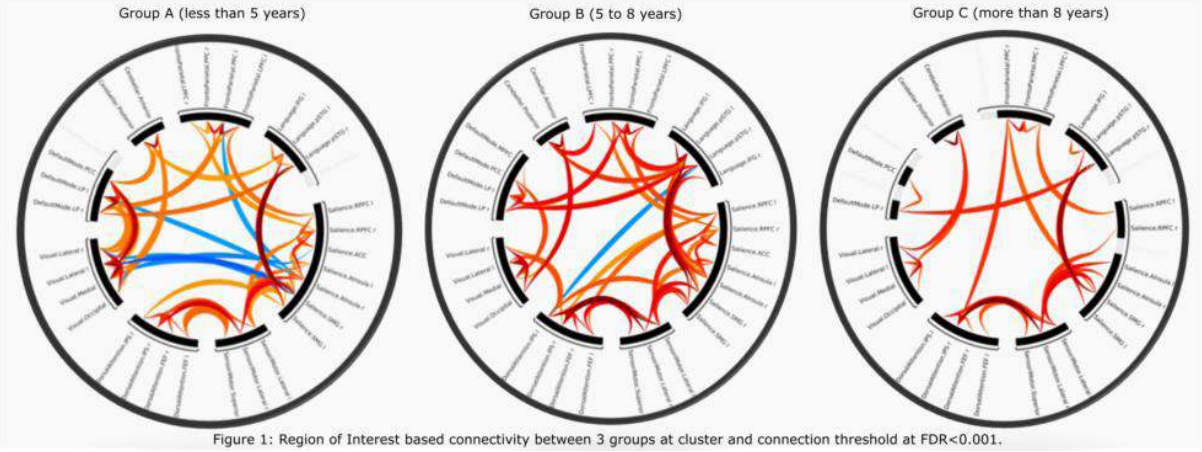

Figure 1: Region of Interest based connectivity between 3 groups at cluster and connection threshold at FDR<0.001.

Table 1- Crosstabs between Groups and Stage of HY stage of PD					
	HY stage				
	1.50	2.00	2.50	3.00	Total
A- Less than 5 years	4	12	2	0	18
B- 5 to 8 years	3	10	5	0	18
C- More than 8 years	0	6	3	1	10
Total	7	28	10	1	46

Table 2- Descriptive Statistics				
		N	Mean	Std. Deviation
Age	A-Less than 5 years	18	54.28	7.82
	B-5 to 8 years	18	60.50	8.72
	C-More than 8 years	10	59.80	8.30
Duration	A-Less than 5 years	18	3.11	0.83
	B-5 to 8 years	18	6.39	1.24
	C-More than 8 years	10	12.60	3.37
UPDRS_II	A-Less than 5 years	18	14.00	5.02
	B-5 to 8 years	18	15.39	5.25
	C-More than 8 years	10	17.20	4.24
UPDRS_III	A-Less than 5 years	18	22.06	6.24
	B-5 to 8 years	18	22.06	6.46
	C-More than 8 years	10	24.30	6.70

Table 3- Differences between 3 groups with duration of disease less than 5 years, 5 to 8 years and above 8 years.						
		Sum of Squares	df	Mean Square	F	P value
Age	Between Groups	393.94	2	196.97	2.869	0.068
	Within Groups	2951.71	43	68.64		
	Total	3345.65	45			
Duration	Between Groups	578.96	2	289.48	88.623	0.000
	Within Groups	140.46	43	3.27		
	Total	719.41	45			
UPDRS_II	Between Groups	66.49	2	33.25	1.351	0.270
	Within Groups	1057.88	43	24.60		
	Total	1124.37	45			
UPDRS_III	Between Groups	39.42	2	19.71	0.477	0.624
	Within Groups	1775.99	43	41.30		
	Total	1815.41	45			

Conclusions: With disease progression, instead of restoration of networks, a compensatory recruitment occurs between cortical and subcortical nodes in PD[Dayan and Browner, 2017; Guan et al., 2017; Kojovic et al., 2012; Little et al., 2013], as revealed by the altered functional connectivity in PD. These differences in connectivity measures are important to review specific treatments and rehabilitation strategies.

References

1. Chen N (2015): Symptoms in Parkinson Disease : 72:432–440.
2. Dayan E, Browner N (2017): Alterations in striato-thalamo-pallidal intrinsic functional connectivity as a prodrome of Parkinson's disease. 3. Neuroimage Clin 16:313–318.

3. Guan X, Zeng Q, Guo T, Wang J, Xuan M, Gu Q, Wang T, Huang P, Xu X, Zhang M (2017): Disrupted Functional Connectivity of Basal Ganglia across Tremor-Dominant and Akinetic/Rigid-Dominant Parkinson's Disease. Front Aging Neurosci 9:360.
4. Herz DM, Eickhoff SB, Løkkegaard A, Siebner HR (2014): Functional neuroimaging of motor control in parkinson's disease: A meta-analysis. Hum Brain Mapp 35:3227–3237.
5. IBM Corp. Released 2013. IBM SPSS Statistics for Windows, Version 22.0. Armonk NICorp (2013): IBM SPSS V22.
6. Kojovic M, Bologna M, Kassavetis P, Murase N, Palomar FJ, Berardelli A, Rothwell JC, Edwards MJ, Bhatia KP (2012): Functional reorganization of sensorimotor cortex in early Parkinson disease. Neurology 78:1441–1448.
7. Little S, Tan H, Anzak A, Pogosyan A, Kühn A, Brown P (2013): Bilateral functional connectivity of the basal ganglia in patients with Parkinson's disease and its modulation by dopaminergic treatment. PLoS One 8:e82762.
8. Whitfield-Gabrieli S, Nieto-Castanon A (2012): Conn : A Functional Connectivity Toolbox for Correlated and Anticorrelated Brain Networks. Brain Connect 2:125–141.

Poster No 285

Heart failure decouples the precuneus in association with social cognition and executive functions

Matthias Schroeter[1,2], Janis Godulla[3], Friederike Thiel[3], Birol Taskin[3], Frank Beutner[4], Andrej Teren[4], Julia Camilleri[5], Simon Eickhoff[6], Arno Villringer[3], Karsten Mueller[7]

[1]Max Planck Institute for Human Cognitive and Brain Sciences, Leipzig, Saxony, [2]Cognitive Neurology Clinic, University Hospital Leipzig, Leipzig, Germany, [3]Max Planck Institute for Human Cognitive and Brain Sciences, Leipzig,, [4]Heart Center Leipzig, Leipzig,, [5]Institute of Systems Neuroscience, Heinrich-Heine University, Düsseldorf, Germany, Duesseldorf, Germany, [6]Institute for Systems Neuroscience, Medical Faculty, Heinrich-Heine University Düsseldorf, Düsseldorf, North Rhine–Westphalia Land, [7]Max Planck Institute for Human Cognitive and Brain Sciences, Leipzig, Sachsen

Introduction: Aging increases the risk to develop Alzheimer's disease. Cardiovascular diseases might accelerate this process. Our study (Schroeter et al. 2023) aimed at investigating the impact of heart failure on brain connectivity using functional magnetic resonance imaging at resting state.

Methods: Brain connectivity alterations were investigated with functional magnetic resonance imaging during rest and related to heart failure and cognitive performance. Furthermore, meta-analytical data-mining approaches were conducted in the BrainMap and Neurosynth databases to extract cognitive functions associated with decoupled networks. Finally, a long-term follow-up investigation in our cohort after approximately nine years validated impairments in the long run.

Results: Here we show brain connectivity alterations related to heart failure and cognitive performance. Heart failure decreases brain connectivity in the precuneus. Precuneus disconnectivity was associated with biomarkers of heart failure, i.e., left ventricular ejection fraction and N-terminal prohormone of brain natriuretic peptide, and cognitive performance, predominantly executive function. Meta-analytical data-mining approaches as conducted in the BrainMap and Neurosynth databases revealed that social and executive cognitive functions are mainly associated with those neural networks. Remarkably, the precuneus, as identified in our study in a mid-life cohort, represents one central functional hub affected by Alzheimer's disease (Schroeter et al. 2009). A long-term follow-up investigation in our cohort after approximately nine years revealed more severe cognitive impairment in the group with heart failure than controls, where social cognition was the cognitive domain mainly affected, and not memory such as in Alzheimer's disease. Figure: Heart failure (HF) decreases brain connectivity in association with biomarker changes and cognitive decline. (A) Connectivity is decreased in heart failure (HF) in the precuneus using global correlation (GCOR) as a centrality measure (red color). Results were obtained using a two-sample t-test between patients with and without HF. The precuneus was also obtained when predicting conversion from the risk-state mild cognitive impairment to Alzheimer's dementia (green color; Schroeter et al. 2009). The overlap between the connectivity finding and the meta-analysis is shown in blue color. (B) Across all patients, a significant correlation was obtained between GCOR and HF-related biomarkers, i.e., left ventricular ejection fraction (LVEF), and N-terminal prohormone of brain natriuretic peptide (NT-proBNP) in the precuneus. Lower LVEF and higher NT-proBNP, both indicating HF, were associated with decreased GCOR. (C) Using the precuneus in a seed-based correlation analysis, decreased precuneus connectivity was found with lower cognitive performance in HF. In particular, an interaction between the factors HF and cognitive performance was obtained showing a significant group difference (HF vs. no-HF) with respect to decreased precuneus connectivity associated with lower cognitive performance in HF (red color). All analyses (A, B, C) were performed using age, sex, and body mass index as nuisance covariates. Significant results in the voxel-wise analyses were obtained with nonparametric permutation analysis using 10,000 permutations and threshold-free cluster enhancement (TFCE) with family-wise error correction ($p<0.05$). x, y, z-coordinates of the Montreal Neurological Institute (MNI) stereotactic space. L left, R right.

Conclusions: In sum, our results indicate consistently an association between heart failure and decoupling of the precuneus from other brain regions being associated with social and executive functions. Results are consistent with other studies

focusing on connectivity (Mueller et al. 2023) and structural alterations (Horstmann et al. 2010; Mueller et al. 2020) due to heart failure. Further longitudinal studies are warranted elucidating etiopathological mechanisms.

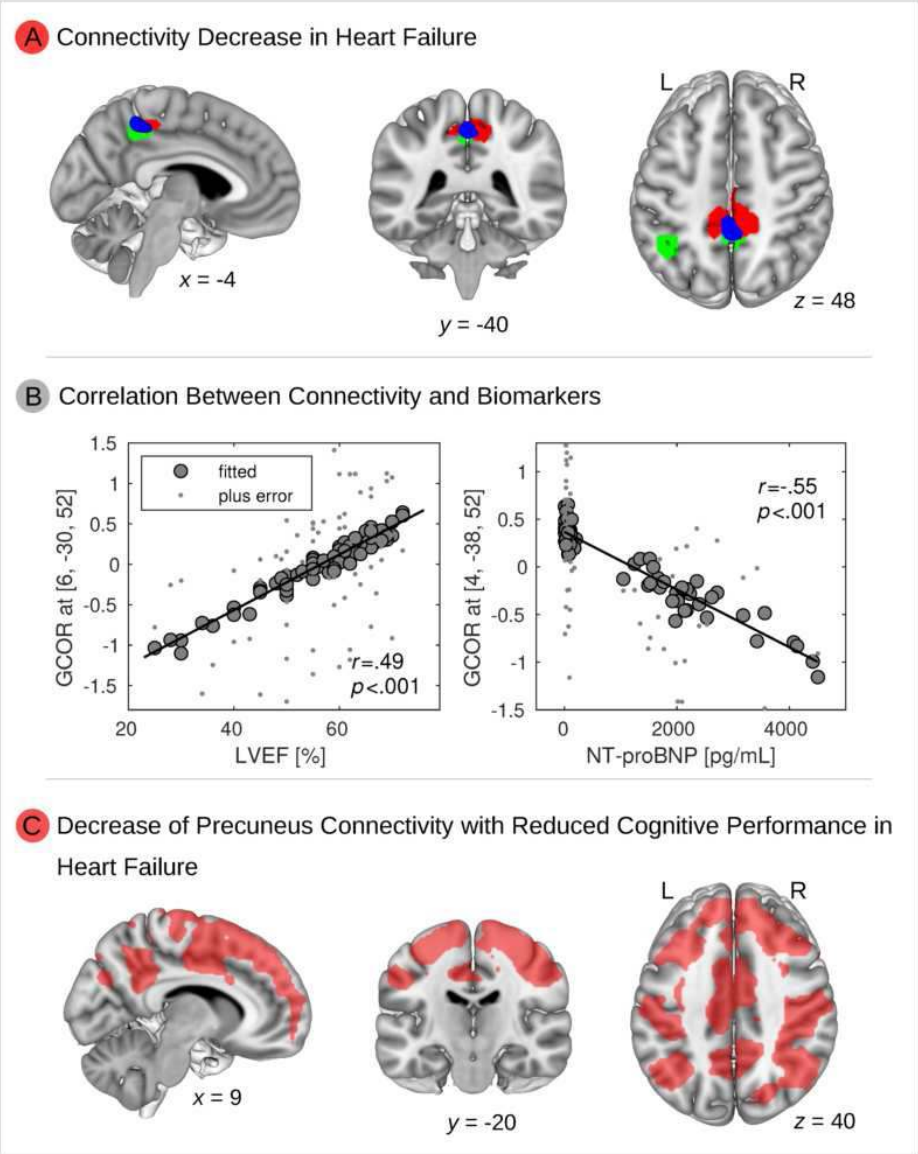

References

1. Horstmann A, Frisch S, Jentzsch RT, Müller K, Villringer A, Schroeter ML. Resuscitating the heart but losing the brain: brain atrophy in the aftermath of cardiac arrest. Neurology. 2010 Jan 26;74(4):306-12. doi: 10.1212/WNL.0b013e3181cbcd6f.
2. Mueller K, Thiel F, Beutner F, Teren A, Frisch S, Ballarini T, Möller HE, Ihle K, Thiery J, Schuler G, Villringer A, Schroeter ML. Brain Damage With Heart Failure: Cardiac Biomarker Alterations and Gray Matter Decline. Circ Res. 2020 Mar 13;126(6):750-764. doi: 10.1161/CIRCRESAHA.119.315813.
3. Mueller K, Thiel F, Taskin B, Beutner F, Teren A, Dubovoy VK, Möller HE, Villringer A, Schroeter ML. Brain dysconnectivity with heart failure. Brain Commun. 2023 Mar 30;5(2):fcad103. doi: 10.1093/braincomms/fcad103.
4. Schroeter ML, Stein T, Maslowski N, Neumann J. Neural correlates of Alzheimer's disease and mild cognitive impairment: a systematic and quantitative meta-analysis involving 1351 patients. Neuroimage. 2009 Oct 1;47(4):1196-206. doi: 10.1016/j.neuroimage.2009.05.037.
5. Schroeter ML, Godulla J, Thiel F, Taskin B, Beutner F, Dubovoy VK, Teren A, Camilleri J, Eickhoff S, Villringer A, Mueller K. Heart failure decouples the precuneus in interaction with social cognition and executive functions. Sci Rep. 2023 Jan 23;13(1):1236. doi: 10.1038/s41598-023-28338-0.

Poster No 286

Cortical thickness changes in Genetic Frontotemporal Dementia Mutation Carriers

Arabella Bouzigues[1], Matthieu Joulot[1], Nicolas Gensollen[2], Lucy Russell[3], James Rowe[4], Barbara Borroni[5], Daniela Galimberti[6], Pietro Tiraboschi[7], Mario Masellis[8], Carmela Tartaglia[9], John van Swieten[10], Harro Seelaar[11], Lize Jiskoot[12], Sandro Sorbi[13], Chris Butler[14], Caroline Graff[15], Alexander Gerhard[16], Tobias Langheinrich[16], Robert Laforce Jr[17], Raquel Sanchez-Valle[18], Alexandre de Mendonça[19], Fermin Moreno[20], Matthis Synofzik[21], Rik Vandenberghe[22], Simon Ducharme[23], Johannes Levin[24], Markus Otto[25], Florence Pasquier[26], Isabel Santana[27], Matthias Schroeter[28], Isabelle Le Ber[1], Jonathan Rohrer[3], Raffaella Lara Migliaccio[1]

[1]Paris Brain Institute, Paris, County, [2]INRIA Paris center, Paris, Other, [3]University College London, London, United Kingdom, [4]Department of Clinical Neurosciences and Cambridge University Hospitals NHS Trust, Cambridge, United Kingdom, [5]University of Brescia, Brescia, Italy, [6]University of Milan, Milan, Italy, [7]Instituto Carlo Besta, Milan, Italy, [8]Sunnybrook Research Institute, Toronto, ., [9]University of Toronto, Toronto, Ontario, [10]Erasmus Medical Center, Rotterdam, cc, [11]Erasmus Medical Center, Rotterdam, United Kingdom, [12]Erasmus Medical Center, Rotterdam, Netherlands, [13]University of Florence, Florence, Italy, [14]University of Oxford, Oxford, United Kingdom, [15]Karolinska Institutet, Stockholm, Sweden, [16]University of Manchester, Manchester, United Kingdom, [17]Université Laval, Quebec, AK, [18]University of Barcelona, Barcelona, Spain, [19]University of Lisbon, Lisbon, Portugal, [20]Hospital Universitario Donostia, San Sebastian, Spain, [21]University of Tubingen, Tubinegen, Germany, [22]UZ Leuven, Leuven, Belgium, [23]McGill University, Montreal, ., [24]Department of Neurology, LMU University Hospital, LMU Munich, Munich, Bavaria, [25]University Hospital Halle/Saale, Halle/Saale, Sachsen-Anhalt, [26]Université de Lille, Lille, France, [27]University of Coimbra, Coimbra, Portugal, [28]Max Planck Institute for Human Cognitive and Brain Sciences, Leipzig, Saxony

Introduction: Frontotemporal dementia (FTD) is a neurodegenerative syndrome with a broad range of clinical manifestations. Up to 30% of cases are familial, caused by a dominantly inherited genetic mutation. The age at which symptoms present, the phenotype and disease duration are variable, even within a family[1]. Previous work in FTD presymptomatic mutation carriers (MC) has shown grey-matter volume reductions precede clinical symptoms and diagnosis by up to 15 years[2,3]. More recently, some papers have investigated cortical thickness in presymptomatic MC which may be a more sensitive metric for detecting subtle grey-matter changes from the earliest stages of FTD[4,5,6,7]. Thus, a refined understanding of cortical thickness changes throughout the disease-course may help in early disease detection and in clarifying to what extent this measure of atrophy may be of use in future FTD preventive trials.

Methods: We assessed cortical thickness within the Genetic Frontotemporal dementia Initiative (GENFI) cohort of 301 mutation negative controls and 504 MC divided across three most common FTD genetic groups: C9orf72, MAPT and GRN. MCs were further divided into 5 stages according to their global CDR plus NACC FTLD score: 0 (asymptomatic), 0.5 (prodromal/mildly symptomatic) and 1/2/3 (varying degrees of fully symptomatic). We used a set of automated tools (Freesurfer's recon-all) to reconstruct the brain's cortical surface from T1-weighted structural MRI data and extracted cortical thickness across all vertices. We compared cortical thickness of these vertices within each of the 9 MC groups compared to controls using mixed effects regression models, including age, sex and education as covariables.

Results: We found that C9orf72 MC showed a thinner cortical layer throughout the brain compared to controls starting in the asymptomatic phase, during which clinicians see no signs of behavioural, psychiatric or language changes (Fig 1, left panel). A very different picture was found in GRN MC who showed no cortical thinning at the asymptomatic stage compared to controls. Cortical thinning started to appear at the prodromal stage within bilateral frontal lobes and left supramarginal/angular gyri before spreading to the left anterior temporal lobe and posterior cingulate cortex at the earliest symptomatic stage and finally, involving bilateral frontal, temporal and parietal lobes completely at the latest stages (Fig 1, middle panel). Finally, MAPT MC also showed a pattern of progressive cortical thinning which was very sparse in asymptomatic and prodromal stages of the disease. Cortical thinning then progressed within anterior temporal lobe, mostly on the left, remaining very focal to this region. It was only at the symptomatic phase, that cortical thinning involved bilateral anterior temporal poles and then spread to bilateral medial and superior frontal lobe and supramarginal/angular gyri (Fig 1, left panel). Next, we wish to use such cortical thickness metrics to predict symptom onset in each genetic group Finally, we will use individual MC longitudinal data to investigate to what extent their trajectory maps onto our cohort-based quasi-longitudinal models of cortical thickness progression.

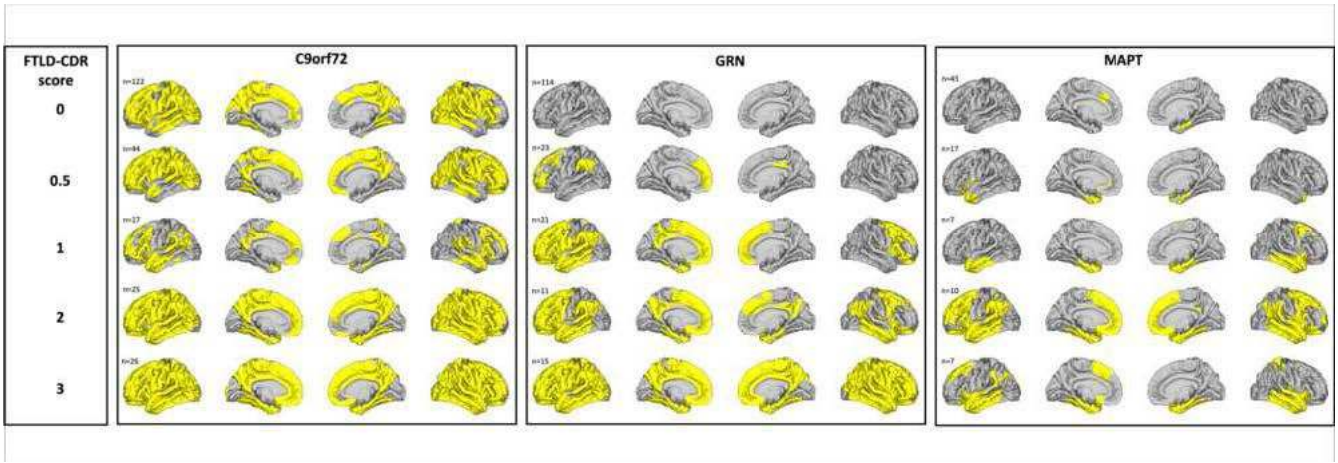

Conclusions: If FTD preventive trials are to be successful, we need to be able to identify individuals in late presymptomatic stages most likely to benefit from therapies. Our findings suggest that cortical thickness is unlikely to be useful in C9orf72 MCs as these individuals show widespread cortical thinning extremely early on at the asymptomatic stage. In line with this, previous work suggests that C9orf72 carriers have a neurodevelopmental condition[7]. Another biomarker may be better suited for this group. However, cortical thinning appears very suddenly in GRN MC and more insidiously in MAPT MC at prodromal and early symptomatic stages. Thus, cortical thinning of the regions showing the earliest changes may be of specific interest for future therapeutic trials within these FTD genetic groups.

References

1. Moore, K., Convery, R., Bocchetta, M., Neason, M., Cash, D. M., Greaves, C., ... & Genetic FTD Initiative, GENFI*. (2022). A modified Camel and Cactus Test detects presymptomatic semantic impairment in genetic frontotemporal dementia within the GENFI cohort. Applied Neuropsychology: Adult, 29(1), 112-119.
2. Rohrer, J. D., Nicholas, J. M., Cash, D. M., Swieten, J. van, Dopper, E., Jiskoot, L., Minkelen, R. van, Rombouts, S. A., Cardoso, M. J., Clegg, S., Espak, M., Mead, S., Thomas, D. L., Vita, E. D., Masellis, M., Black, S. E., Freedman, M., Keren, R., MacIntosh, B. J., ... Rossor, M. N. (2015). Presymptomatic cognitive and neuroanatomical changes in genetic frontotemporal dementia in the Genetic Frontotemporal dementia Initiative (GENFI) study: A cross-sectional analysis. The Lancet Neurology, 14(3), 253–262. https://doi.org/10.1016/S1474-4422(14)70324-2
3. Cash, D. M., Bocchetta, M., Thomas, D. L., Dick, K. M., van Swieten, J. C., Borroni, B., Galimberti, D., Masellis, M., Tartaglia, M. C., Rowe, J. B., Graff, C., Tagliavini, F., Frisoni, G. B., Laforce, R., Finger, E., de Mendonça, A., Sorbi, S., Rossor, M. N., Ourselin, S., ... Warren, J. (2018). Patterns of gray matter atrophy in genetic frontotemporal dementia: Results from the GENFI study. Neurobiology of Aging, 62, 191–196. https://doi.org/10.1016/j.neurobiolaging.2017.10.008
4. Popuri, K., Dowds, E., Beg, M. F., Balachandar, R., Bhalla, M., Jacova, C., Buller, A., Slack, P., Sengdy, P., Rademakers, R., Wittenberg, D., Feldman, H. H., Mackenzie, I. R., & Hsiung, G.-Y. R. (2018). Gray matter changes in asymptomatic C9orf72 and GRN mutation carriers. NeuroImage: Clinical, 18, 591–598. https://doi.org/10.1016/j.nicl.2018.02.017
5. Panman, J. L., Jiskoot, L. C., Bouts, M. J. R. J., Meeter, L. H. H., van der Ende, E. L., Poos, J. M., Feis, R. A., Kievit, A. J. A., van Minkelen, R., Dopper, E. G. P., Rombouts, S. A. R. B., van Swieten, J. C., & Papma, J. M. (2019). Gray and white matter changes in presymptomatic genetic frontotemporal dementia: A longitudinal MRI study. Neurobiology of Aging, 76, 115–124. https://doi.org/10.1016/j.neurobiolaging.2018.12.017
6. Le Blanc, G., Jetté Pomerleau, V., McCarthy, J., Borroni, B., van Swieten, J., Galimberti, D., Sanchez-Valle, R., LaForce Jr, R., Moreno, F., Synofzik, M., Graff, C., Masellis, M., Tartaglia, M. C., Rowe, J. B., Vandenberghe, R., Finger, E., Tagliavini, F., de Mendonça, A., Santana, I., ... Initiative (GENFI), the G. F. D. (2020). Faster Corti

Poster No 287

Dynamic analysis of resting-state EEG reveals altered brain states and functional network transition

Marjorie Metzger[1], Stefan Dukic[2], Roisin McMackin[1], Eileen Giglia[1], Matthew Mitchell[1], Emmet Costello[1], Saroj Bista[1], Colm PEELO[1], Yasmine Tadjine[1], Vladyslav Sirenko[3], Mark Heverin[1], Peter Bede[3], Muthuraman Muthuraman[4], Orla Hardiman[5], Bahman Nasseroleslami[5]

[1]Trinity College Dublin, Dublin, Dublin, [2]UMC, Utrecht, Netherlands, [3]Trinity College Dublin, Dublin, Dublin, [4]Johannes Gutenberg Hospital, Dublin, Dublin, [5]Trinity College Dublin, Dublin, Ireland

Introduction: Amyotrophic lateral sclerosis (ALS) is a progressive neurodegenerative disorder affecting motor neurons. Its multi-faceted nature encompasses a wide spectrum of symptoms, including muscle weakness and eventual paralysis, but also respiratory and cognitive symptoms. A promising approach for studying this complex condition at the level of underlying networks, involved leveraging the spectral power and functional connectivity of resting-state EEG. These measures can

discriminate the abnormal network function in individuals with ALS versus healthy controls (HC)[1–3]. Based on our recent findings in resting-state EEG microstates[4], we hypothesize that dynamic analysis of recurring patterns in resting state EEG based on source-level measures of spectral power and coherence can further elucidate the altered network function in ALS and in providing reliable domain-specific indicators of impairment in ALS. Objectives: To identify transient brain states associated with specific functional networks, using high-density resting-state EEG, as well as to characterise the spatio-spectral alterations in these brain states and their dynamics in individuals with ALS.

Methods: High-density resting-state EEG data were recorded from 99 individuals with ALS and 78 HC. To identify transient and recurrent brain states, we applied a time-delay embedded Hidden Markov Model to source-reconstructed resting-state EEG data (1-45Hz)[5]. The model was trained to convert source-reconstructed time courses into a sequence of functional networks characterised by spectral power and coherence. Subsequently, we employed non-negative matrix factorisation to break down the spectral measures for each state into four components, roughly corresponding to the frequency bands commonly used in electrophysiology (delta/theta, alpha, beta, gamma)[5]. Properties of the sequences of brain states were then analysed to determine their recurrence frequency, duration, and transition patterns. For each state, nonparametric statistical analyses, based on Area Under the Curve (AUC) [as test-statistic] and empirical Bayesian Inference (EBI)[6] [for multivariate inference], were conducted to evaluate the significance of differences in spectral measures between the ALS and HC groups. Furthermore, we explored correlations with clinical evaluations of functional, cognitive and behavioural impairments to assess how well these brain states might serve as domain-specific indicators of impairment.

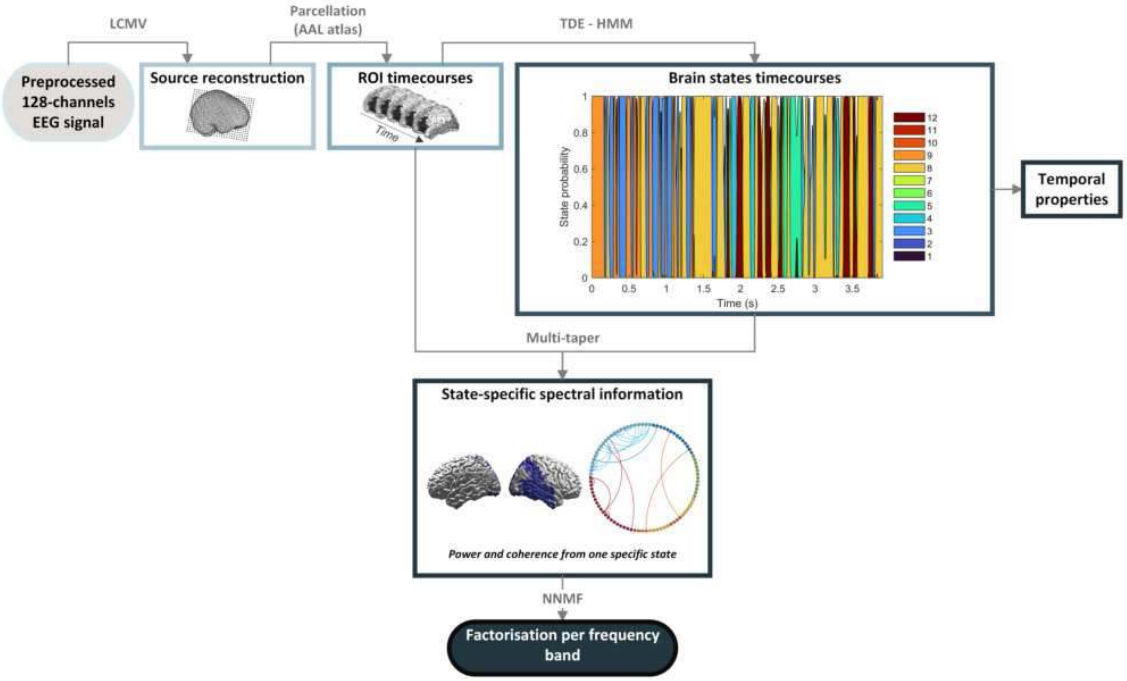

Results: Twelve brain states were identified with distinct patterns of spectral power and coherence for individuals with ALS and HC. States in HC had longer intervals, indicating a greater number of timepoints between state visits, for state 1 ($q=0.004$, AUC = 0.63, $1-\beta\_0.05=0.76$) and state 10 ($q=0.001$, AUC = 0.75, $1-\beta\_0.05=0.88$). States 1, 3, 7 and 9 showed significant association with behavioural decline (as reported using the Beaumont Behavioural Inventory[7]; $r\_s > 0.25$, $q < 0.03$, $1-\beta\_0.05 > 0.65$), while state 5 showed association with fluency decline (evaluated using the Edinburgh Cognitive and Behavioural ALS scale[8]; $r\_s = -0.3$, $q = 0.004$, $1-\beta\_0.05 = 0.83$). States 1, 7 and 10 were characterised by frontal lobe activation (spectral power higher than the average within the state), while state 3 exhibited activation in the sensorimotor network. State 5 highest spectral power was in the supplementary motor area, a region which as been linked not only with motor planning but also with speech[9].

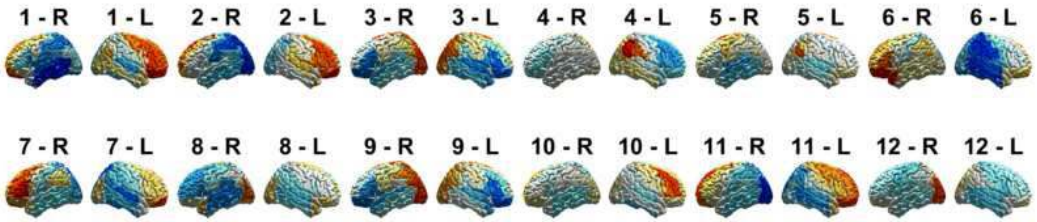

Conclusions: This study demonstrates altered dynamics of functional networks in ALS. The use of dynamical analysis of spectral brain states provides insights into transitions between functional networks. The findings confirm the potential of spectral resting-state EEG measures as potential multi-domain quantitative marker of abnormal changes in brain networks in ALS. This study also paves the way for investigating the relationship between alterations in EEG signals and specific functional domains in ALS.

References

1. B. Nasseroleslami et al., "Characteristic Increases in EEG Connectivity Correlate With Changes of Structural MRI in Amyotrophic Lateral Sclerosis," Cereb. Cortex, vol. 29, no. 1, pp. 27–41, Jan. 2019, doi: 10.1093/cercor/bhx301.
2. S. Dukic et al., "Patterned functional network disruption in amyotrophic lateral sclerosis," Hum. Brain Mapp., vol. 0, no. 0, Jul. 2019, doi: 10.1002/hbm.24740.
3. S. Dukic et al., "Resting-state EEG reveals four subphenotypes of amyotrophic lateral sclerosis," Brain, vol. 145, no. 2, pp. 621–631, Apr. 2022, doi: 10.1093/brain/awab322.
4. M. Metzger et al., "Functional network dynamics revealed by EEG microstates reflect cognitive decline in amyotrophic lateral sclerosis," Oct. 2023, doi: 10.1002/hbm.26536.
5. D. Vidaurre et al., "Spontaneous cortical activity transiently organises into frequency specific phase-coupling networks," Nat. Commun., vol. 9, no. 1, Art. no. 1, Jul. 2018, doi: 10.1038/s41467-018-05316-z.
6. B. Nasseroleslami, "An Implementation of Empirical Bayesian Inference and Non-Null Bootstrapping for Threshold Selection and Power Estimation in Multiple and Single Statistical Testing," bioRxiv, p. 342964, Jun. 2018, doi: 10.1101/342964.
7. M. Elamin et al., "Identifying behavioural changes in ALS: Validation of the Beaumont Behavioural Inventory (BBI)," Amyotroph. Lateral Scler. Front. Degener., vol. 18, no. 1–2, pp. 68–73, Jan. 2017, doi: 10.1080/21678421.2016.1248976.
8. M. Pinto-Grau et al., "Screening for cognitive dysfunction in ALS: validation of the Edinburgh Cognitive and Behavioural ALS Screen (ECAS) using age and education adjusted normative data," Amyotroph. Lateral Scler. Front. Degener., vol. 18, no. 1–2, pp. 99–106, Jan. 2017, doi: 10.1080/21678421.2016.1249887.
9. F.-X. Alario, H. Chainay, S. Lehericy, and L. Cohen, "The role of the supplementary motor area (SMA) in word production," Brain Res., vol. 1076, no. 1, pp. 129–143, Mar. 2006, doi: 10.1016/j.brainres.2005.11.104.

Poster No 288

Automated quantification of white matter lesion confluence on T2 MRI scans

Tatjana Schmidt[1], Robert Salzmann[1], Marcella Montagnese[2], Timothy Rittman[3]

[1]University of Cambridge, Cambridge, United Kingdom, [2]Cambridge University, Cambridge, United Kingdom, [3]Department of Clinical Neurosciences, University of Cambridge, Cambridge, Cambridgeshire

Introduction: White matter hyperintensities (WMH) are a histopathologically heterogeneous entity on FLAIR images and are the consequences of small vessel disease (Prins & Scheltens, 2015). They have been linked to an increased risk of stroke, dementia and death (Debette et al., 2018). The conglomeration of discrete WMHs is referred to as confluence and evidence suggests that it is a clinically useful concept since it reflects the severity of white matter disease across aetiologies (Fazezkas et al., 1993). WMH confluence is thus of great interest for neurodegenerative diseases and is of practical relevance as patients with confluent WMH are often excluded from clinical trials for AD immunotherapy due to an increased adverse effect risk (Rollin-Sillaire et al., 2013). There is currently no method to automatically quantify WMH confluence. Clinical trials rely on manual scoring with the Fazekas scale (Fazekas et al., 1987) which is time-consuming and subjective. Here we propose an algorithm to quantify the degree of confluence and express it as a value between 0 and 1. The algorithm was applied to data from "Quantitative MRI in the NHS–Memory Clinics", a real world memory clinic study, to examine the relationship between WMH confluence and clinical measures.

Methods: Participants were patients recruited from neurology-/psychiatry-led NHS memory clinics (n=350, 166 female, mean age=72) with various neurodegenerative, cognitive or psychiatric diagnoses such as Alzheimer's, vascular, or frontotemporal dementia, dementia with Lewy bodies, depression, and functional memory symptoms. Clinical data included age, diagnosis and scores from the Revised Addenbrookes Cognitive Examination (ACE-R) cognitive test. MR images were acquired on a 3T MRI system (Magnetom Prisma, Siemens Medical Systems, Germany) and included a 3D MP-RAGE and a FLAIR acquisition. WMH were automatically segmented with FSL's BIANCA toolbox (Griffanti et al., 2016) using FLAIR and T1w images and 20 training images on which WMH have been manually identified. This resulted in a probability map for each subject, indicating for each voxel its probability of belonging to a WMH. On the basis of these probability maps, the confluence algorithm was run for each subject (Fig. 1). Confluence scores subsequently entered further analysis (Fig. 2). A piecewise regression of confluence against age with a breakpoint at age 70 was calculated. A one-way ANOVA was performed to test whether there was a difference in confluence scores between diagnoses. Linear regressions of all ACE-R subtests against confluence while controlling for age were calculated in order to test whether confluence can explain cognitive performance.

Results: The piecewise regression of confluence against age showed a significant association above age 70 (β=0.0017, p=0.014), but not below. Results of the ANOVA indicated no significant difference in confluence between different diagnoses (F=2.39, p=0.069). However, visual inspection of data showed that while confluence scores of patients with mild cognitive impairment or functional memory symptoms had a compact distribution, the scores of patients with dementia (particularly Alzheimer's) showed a wider range. The regression of ACE-R subtests against confluence showed that the fluency subtest had a significant association with confluence (β=-26.2, p=0.001) after controlling for the effect of age.

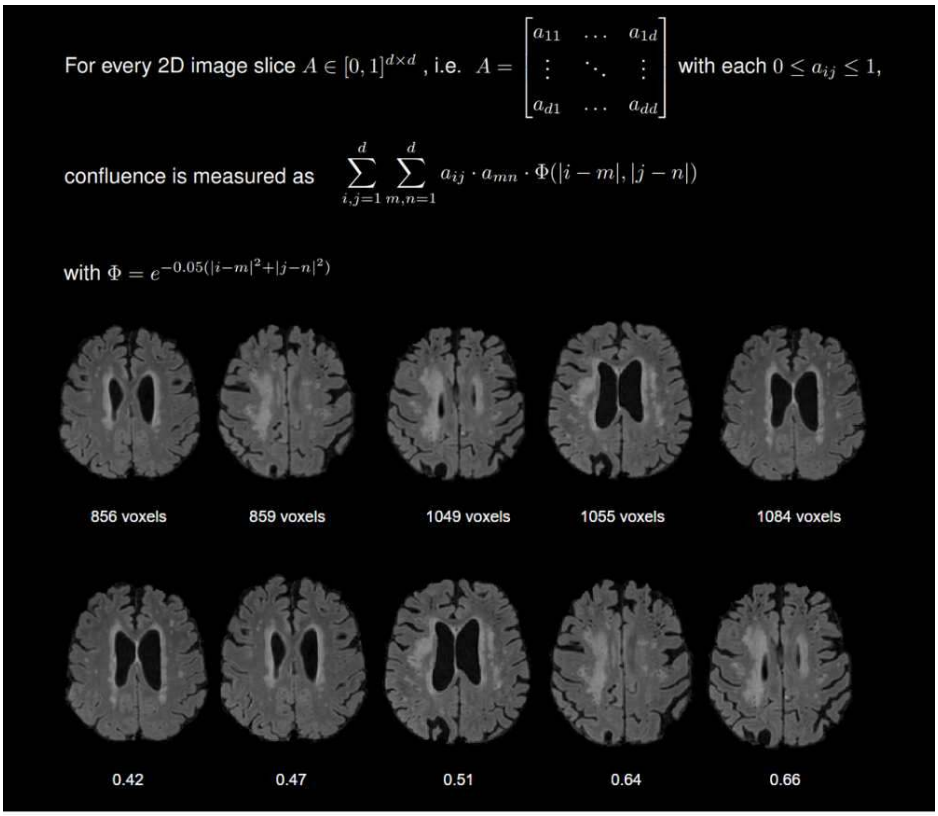

Figure 1. Top: The proposed algorithm for quantifying WMH confluence. Middle: A selection of typical FLAIR image slices with WMH patterns ranging from punctate lesions to large confluent areas of lesions, sorted by ascending WMH volume (given under each slice) which results in an implausible ranking in terms of severity. Bottom: The same selection of slices sorted by their confluence scores which results in a plausible ranking.

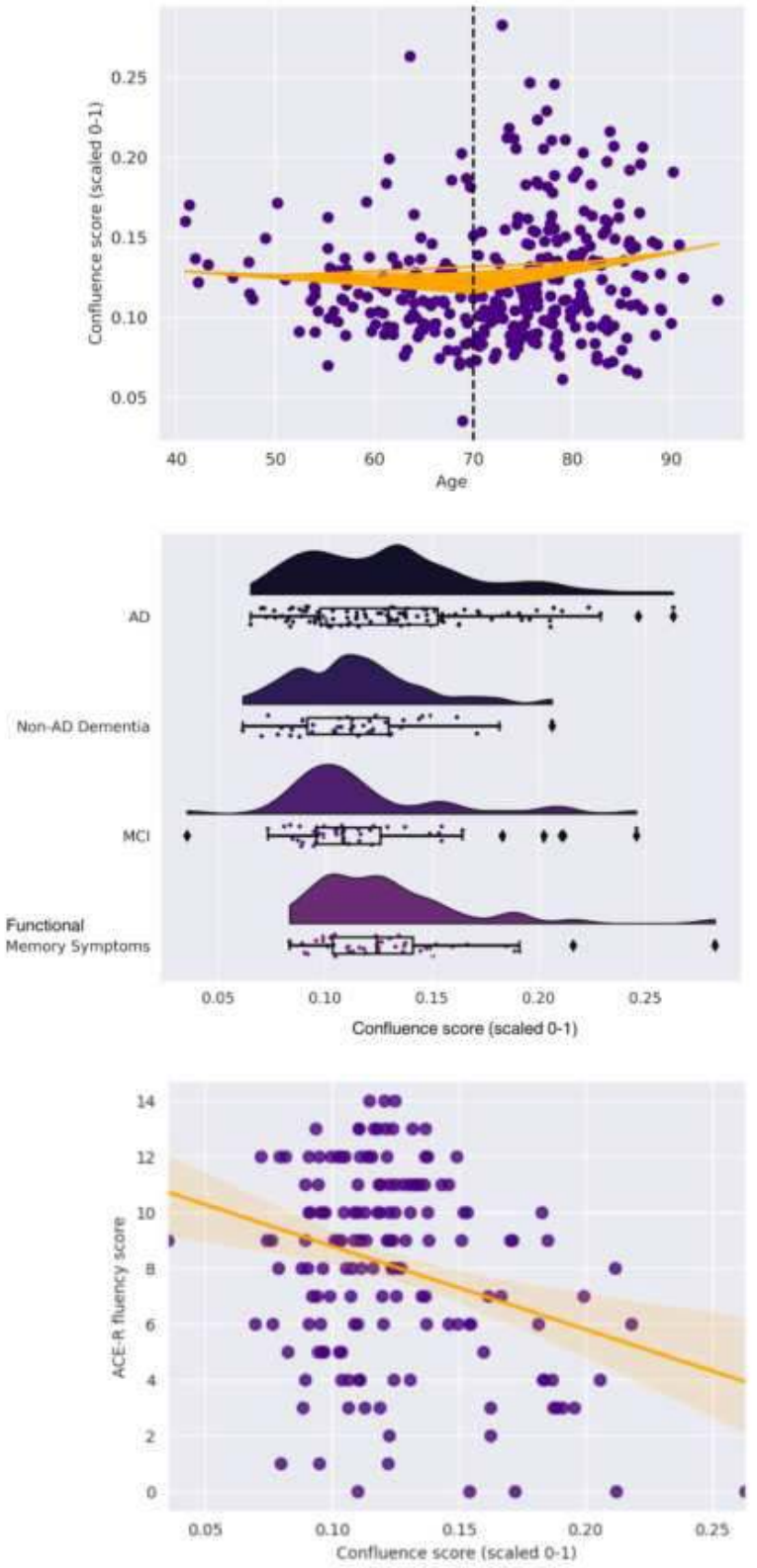

Figure 2. Top: Piecewise linear regression of WMH confluence scores against age with breakpoint at age 70. Middle: Raincloud plot of confluence scores by diagnoses (AD: Alzheimer's dementia including posterior cortical atrophy and logopenic aphasia; non-AD dementia: non-Alzheimer's dementia including behavioural variant frontotemporal dementia, non-fluent variant aphasia, semantic dementia, dementia with Lewy bodies, progressive supranuclear palsy, vascular dementia, mixed dementia, Parkinson's disease dementia; MCI: mild cognitive impairment). Bottom: Linear regression of ACE-R fluency subtest against confluence scores.

Conclusions: The proposed algorithm determining the degree of confluence of WMH successfully quantifies a concept that has previously been rated only manually. Preliminary results indicate that the confluence score increases with age, but does not differ significantly between different kinds of neurodegenerative diseases. In keeping with previous findings (Kaskikallio et al., 2021), it is selectively sensitive to changes in fluency assessed with a subtest of the ACE-R. Our new quantification of white matter lesion confluence opens up a new approach to quantifying an important aspect of cerebrovascular neuropathology.

References

1. Debette, S. (2019), 'Clinical significance of magnetic resonance imaging markers of Vascular Brain Injury', JAMA Neurology, 76(1), 81.
2. Fazekas, F. (1987), 'MR signal abnormalities at 1.5 t in Alzheimer's dementia and normal aging', American Journal of Roentgenology, 149(2), pp. 351–356.
3. Fazekas, F. (1993), 'Pathologic correlates of incidental MRI white matter signal hyperintensities', Neurology, 43(9), pp. 1683–1683.
4. Griffanti, L. (2016), 'Bianca (brain intensity abnormality classification algorithm): A new tool for automated segmentation of white matter hyperintensities', NeuroImage, 141, pp. 191–205.
5. Kaskikallio, A. (2021), 'Effects of white matter hyperintensities on verbal fluency in healthy older adults and MCI/AD', Frontiers in Aging Neuroscience, 13.
6. Prins, N. D. (2015), 'White matter hyperintensities, cognitive impairment and dementia: An update', Nature Reviews Neurology, 11(3), pp. 157–165.
7. Rollin-Sillaire, A. (2013), 'Reasons that prevent the inclusion of Alzheimer's disease patients in clinical trials', British Journal of Clinical Pharmacology, 75(4), pp. 1089–1097.

Poster No 289

Increased CSF GAP-43 leads to accelerated tau accumulation and spread in Alzheimer's disease

Nicolai Franzmeier[1], Amir Dehsarvi[1], Anna Steward[1], Davina Biel[1], Anna Dewenter[1], Sebastian Niclas Roemer[1], Fabian Wagner[1], Matthias Brendel[2], Michael Ewers[3], Kaj Blennow[4], Henrik Zetterberg[5], Michael Schöll[6]

[1]University Hospital LMU Munich, Munich, Bavaria, [2]Department of Nuclear Medicine, University Hospital, LMU Munich, Munich, Germany, Munich, Germany, [3]Institute for Stroke and Dementia Research, Munich, Bavaria, [4]Clinical Neurochemistry Laboratory, Sahlgrenska University Hospital, Gothenburg, Västergötland, [5]University College London, London, United Kingdom, [6]University of Gothenburg, Gothenburg, Sweden

Introduction: Preclinical studies found that tau spreads trans-synaptically in an activity-dependent manner, suggesting that synapses route tau spread in Alzheimer's disease (AD). Importantly, amyloid-beta (Aβ) induces aberrant synaptic activity, which may accelerate trans-synaptic tau spread. In AD patients, we found previously that tau spreads from epicenters across functionally connected regions but it is unclear whether Aβ-related synaptic changes accelerate tau spreading. The presynaptic growth-associated protein 43 (GAP-43) is implicated in synaptic plasticity and is increased in cerebrospinal fluid (CSF) in AD, suggesting that GAP-43 captures synaptic integrity deviations such as aberrant synaptic activity. We therefore tested whether higher GAP-43 is associated with faster Aβ-related tau spread.

Methods: We included longitudinal [18F]Flortaucipir tau-PET, baseline [18F]Florbetapir amyloid-PET and CSF GAP-43 from 93 subjects (controls Aβ-, n=54; cognitively normal/Mild Cognitive Impairment Aβ+, n=33/21). To model connectivity-associated tau spread, we determined a connectivity template across 200 cortical regions (i.e., Schaefer atlas) using 3T resting-state fMRI in an independent control sample. Statistical models were controlled for age, sex and diagnosis.

Results: Higher CSF GAP-43 was associated with faster Aβ-related tau-PET increase in pre-defined ROIs (centiloid x GAP-43 interaction, global/temporal-meta-ROI: b=0.0019/0.0028; p=0.009/0.007, Fig.1) as well as in the personalized Q1 ROI (b=0.0024; p=0.004) that summarizes regions most closely connected to tau epicenters with highest baseline tau-PET (Fig.2A). Importantly, the centiloid x GAP-43 interaction decreased across regions less strongly connected to tau epicenters (Q2/Q3/Q4: b=0.0017/0.0008/0.0002; p=0.009/0.080/0.344, Fig.2B-D). Further, we quantified subject-specific connectivity-associated tau spread (i.e., the regression-derived association between epicenter connectivity and tau-PET increase in remaining brain regions). Here, higher CSF GAP-43 was associated with a stronger association between Aβ and connectivity-associated tau spread (centiloid x GAP-43 interaction, b=-0.0031; p=0.037).

Conclusions: Higher CSF GAP-43 is associated with faster Aβ-related tau spread across interconnected brain regions, rendering synaptic changes a potential target to attenuate tau spreading.

Figure 1:

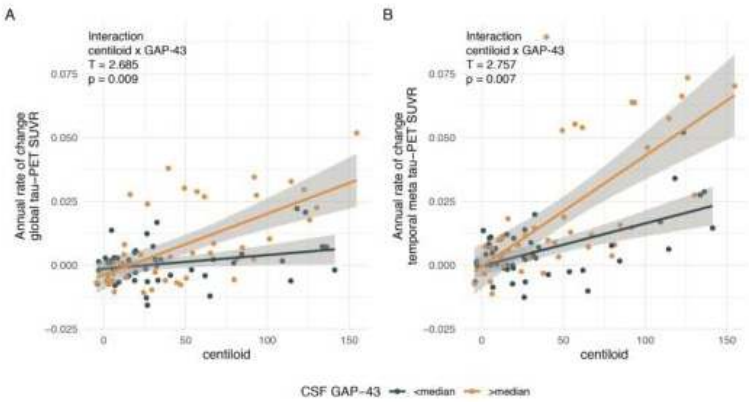

Scatterplots illustrating the interaction between amyloid-PET (i.e., centiloid) and CSF GAP-43 on tau-PET changes in a global cortical ROI (A) as well as a temporal-meta ROI (B). Regression models were controlled for age, sex and diagnosis. Note that interactions were computed using continuous GAP-43 measures, and that the median split was performed only for visualization.

Figure 2:

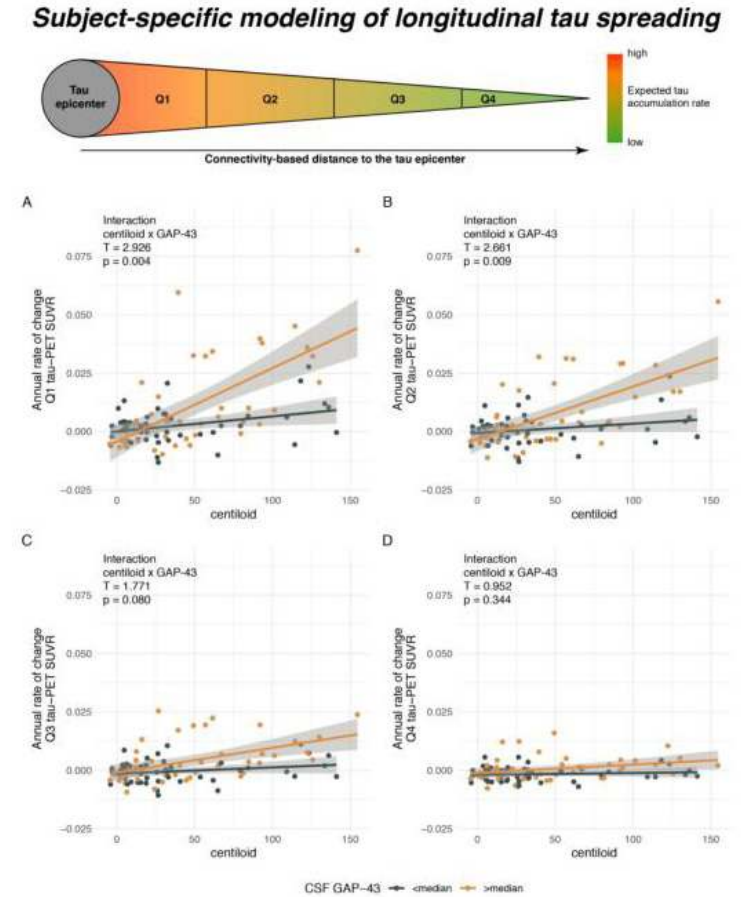

Scatterplots illustrating the interaction between amyloid-PET (i.e., centiloid) and CSF GAP-43 on tau-PET changes in connectivity-derived ROIs, ranging from regions that are closely connected to subject-specific tau epicenters (Q1, Panel A) to regions that are less strongly connected to subject-specific tau epicenters (Q2-Q4, Panels B-D). Tau epicenters were defined as 5% of brain regions with highest baseline tau-PET SUVRs. Connectivity was derived using a connectome template based on 3T multi-band resting-state fMRI data from cognitively normal Aβ- controls. Regression models were controlled for age, sex and diagnosis. Note that interactions were computed using continuous GAP-43 measures, and that the median split was performed only for visualization.

Poster No 290

Plasma neurofilament light relates to white mater and gray matter microstructure in older adults

Youjin Jung[1,2], Andrew Bender[3,4], Scott Counts[5,4], Benjamin Hampstead[6,4,7], Scott Peltier[8,4], Ana Daugherty[1,2,4], Jessica Damoiseaux[1,2,4]

[1]Department of Psychology, Wayne State University, Detroit, MI, [2]Institute of Gerontology, Wayne State University, Detroit, MI, [3]Cleveland Clinic Lou Ruvo Center for Brain Health, Las Vegas, NV, [4]Michigan Alzheimer's Disease Research Center, Ann Arbor, MI, [5]Departments of Translational Neuroscience and Family Medicine, Michigan State University, Grand Rapids, MI, [6]Research Program on Cognition & Neuromodulation Based Interventions, University of Michigan, Ann Arbor, MI, [7]VA Ann Arbor Healthcare System, Ann Arbor, MI, [8]Functional MRI Laboratory, University of Michigan, Ann Arbor, MI

Introduction: Plasma neurofilament light (pNfL) is a promising marker of neurodegeneration for Alzheimer's disease (AD), predicting gray matter (GM) atrophy and white matter (WM) microstructural changes. However, its sensitivity to microstructural characteristics of the GM and WM in early AD requires further investigation. Moreover, it remains unclear whether microstructural changes in specific WM regions exhibit stronger associations with pNfL levels. Here, we investigated how pNfL associates with different microstructural indices in different regions of the WM, and how the associations between pNfL and the neurite density of the WM and GM vary with memory functioning in older adults with and without AD-related cognitive decline.

Methods: A total of 97 older adults were included in this study – 44 with very mild to mild dementia (age: 71.3 ± 7.7; sex (m/f): 14/30; CDR (0.5/1): 39/5) and 53 cognitively unimpaired individuals (age: 70.7 ± 7.2; sex (m/f): 13/40; CDR (0/0.5): 29/24). pNfL was measured using a single-molecule array (Simoa) assay. We computed neurite orientation dispersion and density imaging (NODDI) measures from diffusion-weighted images (b = 0, 700, 2000 s/mm2), including intracellular volume fraction (VIC), orientation dispersion index (ODI), and CSF volume fraction (VISO). Our examination of the voxel-wise association between pNfL and the NODDI indices in WM employed a partial least squares correlation (PLSC) to examine the covariance between pNfL and the 3 NODDI images, VIC, ODI, and VISO. Prior to analysis, age and body mass index (BMI) were regressed out of pNfL, and age and sex were regressed out of the NODDI images. Next, to examine how the associations between pNfL and the neurite densities (VIC) of the WM and the GM vary with memory functioning, we fit a path model. The model included a memory factor score as the moderator for the link between BMI-adjusted pNfL, and the VIC of the entorhinal cortex, as well as the mean VIC of the WM clusters that reliably contributed to the covariance between pNfL and NODDI images in the first component of the PLSC analysis (Fig. 1A). The model included age and sex as covariates predicting the WM and GM VIC. The memory factor score was computed via a confirmatory factor analysis on delayed recall scores from four different memory tests.

Results: The first component of the PLSC analysis showed the association between pNfL and the NODDI indices, where higher pNfL associated with lower VIC and VISO, and higher ODI. These effects were mainly observed in the anterior temporal lobe, WM regions near the precuneus, and the inferior parietal and superior frontal WM areas. The second component showed the association between pNfL and the NODDI indices mainly in the centrum semiovale, where higher pNfL associated with lower ODI and VISO (Fig. 2). In the path analysis, the memory factor moderated the link between pNfL and the entorhinal VIC: higher pNfL levels predicted lower entorhinal VIC in older adults with lower memory function, but not in those with higher memory function. However, despite the significant main effect of pNfL on WM VIC, memory function did not moderate their relationship, indicating that higher pNfL predicted lower WM VIC regardless of memory function (Fig. 2BC).

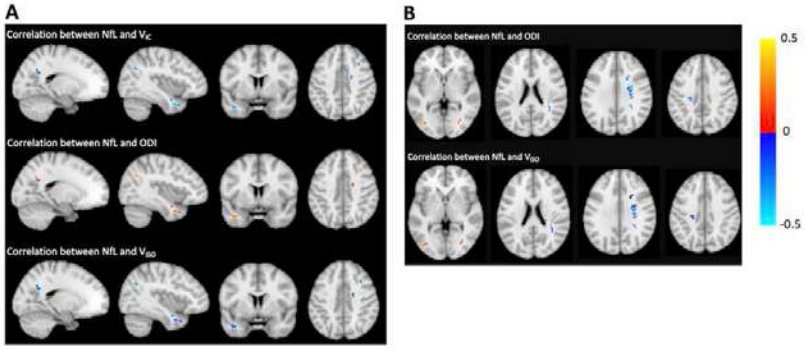

Fig. 1. Voxel-wise correlation between pNfL and NODDI metrics in the PLSC components. (A) The voxel-wise correlation between pNfL and V_{IC}, ODI, and V_{ISO} in clusters that reliably contributed to the covariance between pNfL and NODDI indices in the first PLSC component. (A) The voxel-wise correlation between NfL and ODI and V_{ISO} in clusters that reliably contributed to the covariance between pNfL and NODDI indices in the second PLSC component.

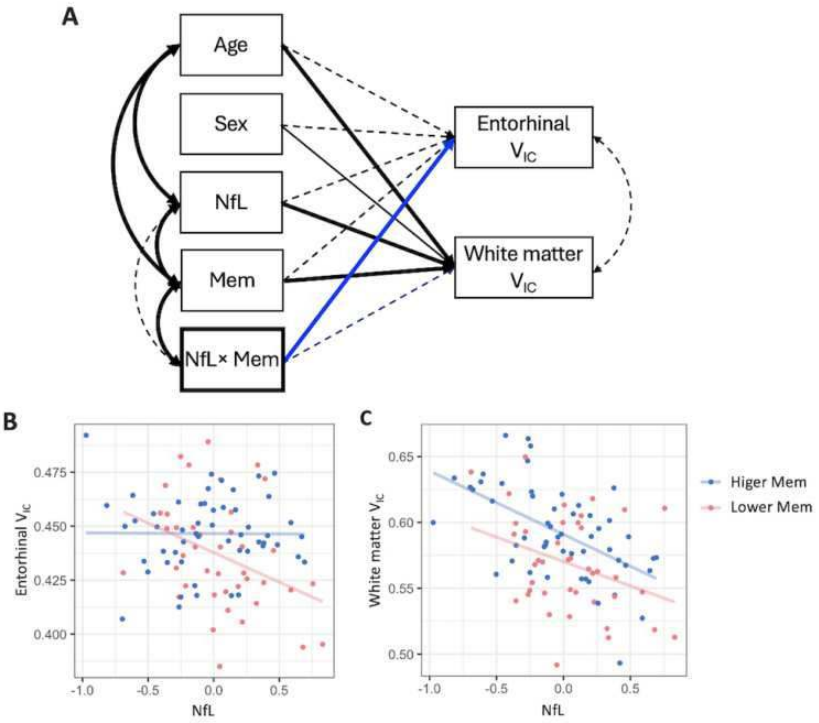

Fig. 2 The path model testing the moderating effect of memory function. (A) The diagram of the path model. The solid lines indicate significant relationships. The dashed lines indicate non-significant relationships. The blue line shows the significant moderation of memory on the link between pNfL and entorhinal V_{IC} (B) A scatter plot showing the relationship between plasma NfL and the neurite density of the entorhinal cortex by the memory factor score. (C) A scatter plot showing the relationship between plasma NfL and the V_{IC} of the white matter ROIs by the memory factor score.

The pNfL on the x-axis of the scatterplots has been log-transformed and adjusted for BMI. The V_{IC} on the y-axis has been adjusted for age and sex. The participants were split into higher and lower memory groups for illustrative purposes. The cut-off value of higher/lower memory was the value that maximized Youden's Index (sensitivity + specificity − 1) for classifying CI and CU.

Key: NfL, neurofilament light; Mem, memory factor score; V_{IC}, intracellular volume fraction

Conclusions: The PLSC analysis demonstrated that higher pNfL reflects different WM microstructural characteristics, including lower axonal density mainly in temporoparietal WM likely due to AD pathology, and lower fiber orientation variability in WM regions abundant in crossing fibers. The differing moderating effects of memory for the GM and WM VIC in the path model suggest that the pNfL concentration reflects the neurite density in both GM and WM and may be more sensitive to the WM than the GM in early AD, given the significant pNfL – WM VIC relationship irrespective of the memory score. Our findings illuminate WM microstructural changes underlying elevated pNfL and the varied sensitivity of pNfL to different neurodegenerative aspects in early AD.

References

1. Damoiseaux, J. S., Smith, S. M., Witter, M. P., Sanz-Arigita, E. J., Barkhof, F., Scheltens, P., Stam, C. J., Zarei, M., & Rombouts, S. A. R. B. (2009). White matter tract integrity in aging and alzheimer's disease. Human Brain Mapping, 30(4), 1051–1059.
2. McIntosh, A. R., & Lobaugh, N. J. (2004). Partial least squares analysis of neuroimaging data: Applications and advances. NeuroImage, 23(SUPPL. 1), 250–263.
3. Vogt, N. M., Hunt, J. F., Adluru, N., Dean, D. C., Johnson, S. C., Asthana, S., Yu, J. P. J., Alexander, A. L., & Bendlin, B. B. (2020). Cortical Microstructural Alterations in Mild Cognitive Impairment and Alzheimer's Disease Dementia. Cerebral Cortex, 30(5), 2948–2960. https://doi.org/10.1093/cercor/bhz286
4. Zhang, H., Schneider, T., Wheeler-Kingshott, C. A., & Alexander, D. C. (2012). NODDI: Practical in vivo neurite orientation dispersion and density imaging of the human brain. NeuroImage, 61(4), 1000–1016. https://doi.org/10.1016/j.neuroimage.2012.03.072

Poster No 291

Fixation Duration Effects on Microstructural Changes in Disease: Insight from Ex-vivo Diffusion MRI

Zaki Alasmar[1,2], Roqaie Moqadam[2,3], Liana Sanches[2], Yashar Zeighami[2,4], Mahsa Dadar[2,4]

[1]Integrated Program in Neuroscience, McGill University, Montreal, Quebec, Canada, [2]Cerebral Imaging Centre, Douglas Mental Health University Institute, Verdun, Montreal, Quebec, Canada, [3]Faculty of Medicine - Department of Medicine, University of Montreal, Montreal, Quebec, Canada, [4]Department of Psychiatry, McGill University, Montreal, Quebec, Canada

Introduction: Diffusion MRI (dMRI) is a common tool to assess the brain's microstructure[1]. Through dMRI, we can extract metrics assessing fibre integrity in various neurological conditions (e.g. Alzheimer's and Parkinson's Disease [AD & PD]). The Douglas-Bell Canada Brain Bank (DBCBB) is the largest Canadian repository of donated human brains from various sources including multiple neurodegenerative conditions. However, the fixation of these brains changes the tissue composition and their magnetic properties, complicating post-mortem inference of pathology and preventing ante-/post-mortem comparative mapping of the same microstructural characteristics[2]. We aimed to validate in-vivo diffusion measures when used ex-vivo by assessing the impact of sample fixation on these measures, in AD and PD, and then qualitatively compare their distribution patterns between ante- and post-mortem.

Methods: We acquired 3T structural MRI (T1w & T2w) and dMRI (32 directions, 2 phase-encoding directions, b-value = 1000 s/mm^2) of 45 donated specimens (mean age at death = 81 years, mean fixation duration =13.8 years, 20 females). We used BISON (3) to segment cortical grey and white matter and subcortical structures on the structural scans. We adapted Mrtrix3 preprocessing tools to denoise, correct eddy-currents, and bias correct (i.e., inhomogeneity correction) the dMRI[4]. From the preprocessed dMRI, we computed the tensor model and extracted its metrics (fractional anisotropy [FA], mean [MD], axial [AxD] diffusivity). We first modelled the change in dMRI microstructural metrics using linear regression models, including age at death and sex as covariates. We then qualitatively compared the microstructural patterns in a subset of participants that also had in-vivo imaging. We performed the statistical analysis in the whole sample, and in AD, PD and other neuropsychiatric conditions separately (including Amyotrophic lateral sclerosis (ALS), mood and vascular disorders, and other dementias).

Results: We found differential patterns of associations between DTI metrics and fixation time, that differed between brain regions and across diagnoses (all diagnoses: f(FA-GM)=3.73, R2=0.38, p-val=0.03, f(FA-WM)=2.94, R2=0.33, p-val=0.03; AD: f(FA-GM)=5.56, R2=0.217, p-val=0.028, PD: f(MD-subcortex)=7.7, R2=0.56, p-val<0.001, f(AxD-Total)=11.4, R2=0.65, p-val<0.001; fig.1). This effect was consistent in AD and PD specimens. Taken together, these results reflect a strongly altered microstructural environment in fixed brains, that differed between AD, PD, and other neuropsychiatric conditions, and between directional and other diffusion metrics. Based on this, we performed in-vivo and ex-vivo diffusion tensor computation in one AD subject with ante- and post-mortem scans to qualitatively test the distribution patterns of the microstructural metrics. We were able to identify several regions of the prefrontal lobe that show altered microstructure (fig.2). Overall, the associations between in-vivo and ex-vivo metrics were r(FA)=0.49, r(MD)=0.42, r(AxD)=0.43. The difference observed could be due to the localization of neuropathology that accelerated the effect of fixation on the diffusion metrics. This alteration was observed to be lower for directional FA rather than MD and RD.

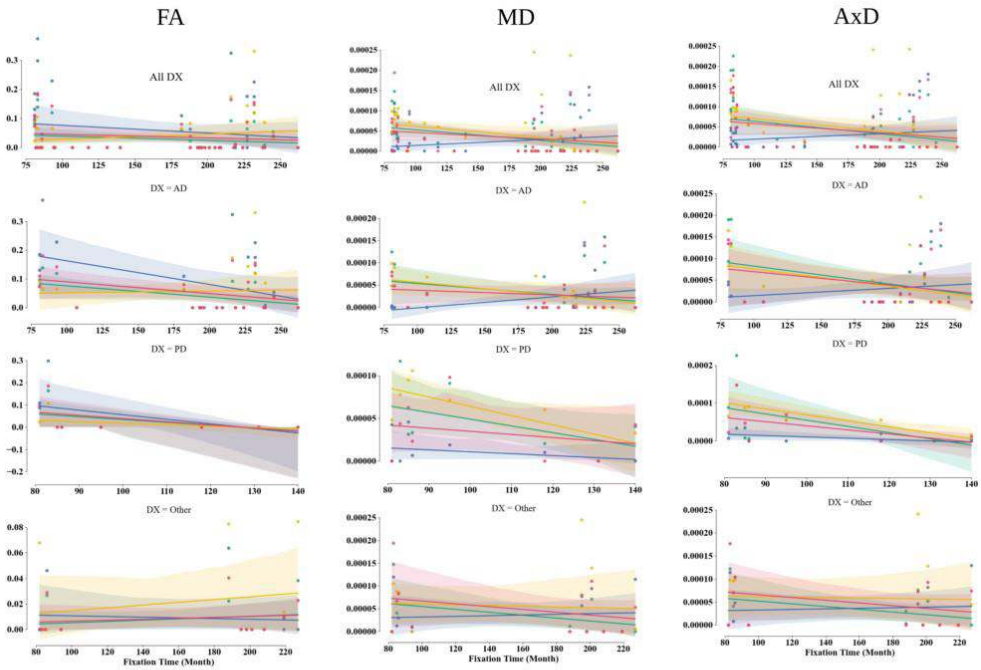

Figure 1: Association between fixation duration and median FA, MD, and AxD in grey and white matter, subcortex, and total brain, in all of our ex-vivo sample, and in AD, PD, and other neurpsychiatric conditions

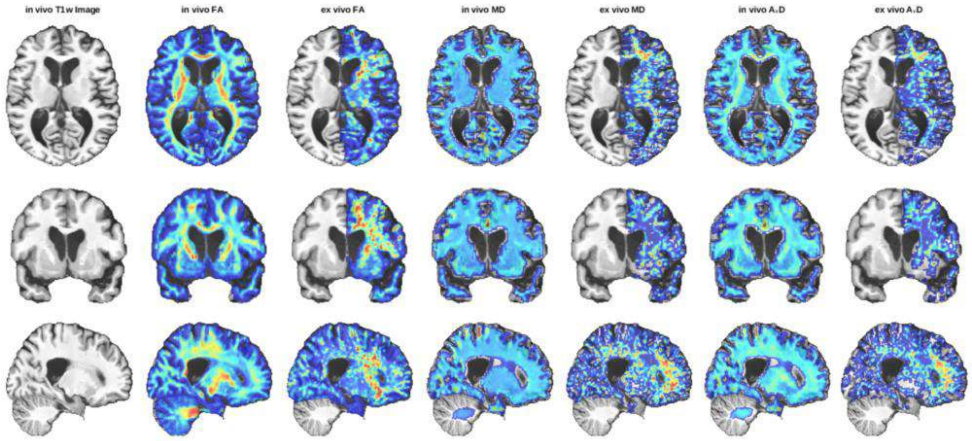

Figure 2: Comaprision between in-vivo and ex-vivo DTI metrics for the one AD subject

Conclusions: We show a strong association between brain fixation duration and the neural microstructure across several neurological diseases using directional and other diffusion measures. We demonstrated that ex-vivo diffusion scans can serve as extensions to in-vivo protocols, which could help unveil disease signature maps and neuropathology. This could enrich previous ex-vivo studies by supplementing invasive histological analyses with non-invasive neuroimaging that could then be used to compare pathological states across disease stages. Future studies should investigate these effects in other neuropsychiatric conditions such as ALS and mood disorders, and examine the effect of vasculature change in these conditions.

References

1. Dadar M. (2021), BISON: Brain tissue segmentation pipeline using T1-weighted magnetic resonance images and a random forest classifier. Magnetic Resonance in Medicine, vol. 85, no. 4. pp. 1881–1894.
2. Roebroeck A. (2019), Ex vivo diffusion MRI of the human brain: Technical challenges and recent advances. NMR in Biomedicine. vol. 32, no. 4.
3. Soares, J. (2013), A hitchhiker's guide to diffusion tensor imaging. Frontiers in Neuroscience, vol. 7.
4. Tournier J.D. (2019), MRtrix3: A fast, flexible and open software framework for medical image processing and visualisation. NeuroImage. 2019 vol. 202, pp. 116-137.

Poster No 292

Associations Between Genetics of Parkinson's Disease, Brain Structure, and Behavioral Phenotypes

Houman Azizi[1], Alexandre Pastor-Bernier[2], Christina Tremblay[3], Nooshin Abbasi[4], Peter Savadjiev[5], Eric Yu[6], Jean-Baptiste Poline[7], Ziv Gan-Or[8], Yashar Zeighami[9], Alain Dagher[10]

[1]Montreal Neurological Institute, Montreal, Quebec, [2]Montreal Neurological Institute and Hospital, McGill University, Montreal, Qc, [3]Montreal Neurological Institute and Hospital, McGill University, Verdun, Québec, [4]Montreal Neurological Institute and Hospital, McGill University, Montreal, Quebec, [5]Harvard Medical School, Cambridge, MA, [6]Department of Human Genetics, McGill University, Montreal, Quebec, [7]McGill University, Montreal, Quebec, [8]McGill University, Montreal, QC, [9]Douglas Research Centre, Montreal, Quebec, [10]Montreal Neurological Institute and Hospital, McGill University, Montreal, QC

Introduction: An important hallmark of most neurological disorders is the loss of brain tissue detectable by Magnetic Resonance Imaging (MRI). In Parkinson's disease (PD), patients show higher cortical surface area (SA) (Jubault 2011), and lower white matter fractional anisotropy (FA) (Chan 2007) and subcortical volumes (Charroud 2021). However, the local inter-relationships between these brain features as well as their associations with behavioral phenotypes are unknown. Here we test the relationship between genetic risk for PD and MRI-derived FA, cortical SA, and subcortical volume. We then study the relation between these neuroanatomical measures and behavioral phenotypes.

Methods: Demographics, behavioral, genomic and brain imaging data were obtained for 40,000 UK Biobank participants. Diffusion-weighted MRI images were analyzed using the Tractoflow pipeline to generate FA maps for each subject. White matter was then parcellated into 73 anatomical tracts using the O'Donnell's ORG atlas (O'Donnell 2007) and mean FA values of each tract were extracted. T1-weighted MRI images were analyzed using the CIVET pipeline (Zijdenbos 2002) to extract region-wise SA values for 200 cortical regions in the Schaefer atlas (Schaefer 2018). Subcortical volume measures for 14 Harvard-Oxford atlas regions (Makris 2006) were provided by the UK Biobank using the FSL's FIRST pipeline (Patenaude 2011). The relationships between PD polygenic risk score and grey and white matter morphometry were assessed by linear regression using the following set of confound variables: age, age^2, sex, age*sex interaction, center number, scanning motion, scanning bed position, genotype batch, 15 principal genetic components. Results were then corrected for multiple comparisons using False Discovery Rate (FDR) correction with p-value threshold of 0.05. Similarly, the association between each white matter tract's FA and its structurally connected cortical SA was assessed (statistical significance based on spin test). Partial least square (PLS) analysis was then used to investigate the behavioral phenotypes linked with brain features after regressing out the effect of age from all variables.

Results: Polygenic risk score of PD was positively associated with cortical SA, subcortical volume, and white matter FA across the brain (Figure 1). FA in all tracts were positively associated with SA of their structurally connected cortical regions; however, these associations remained spatially significant for only 2/73 tracts after correcting for spatial autocorrelation. The PLS analysis revealed alcohol usage, education level, household income, fluid intelligence, and height as positively associated with these brain features, and multiple deprivation index as negatively associated (Figure 2).

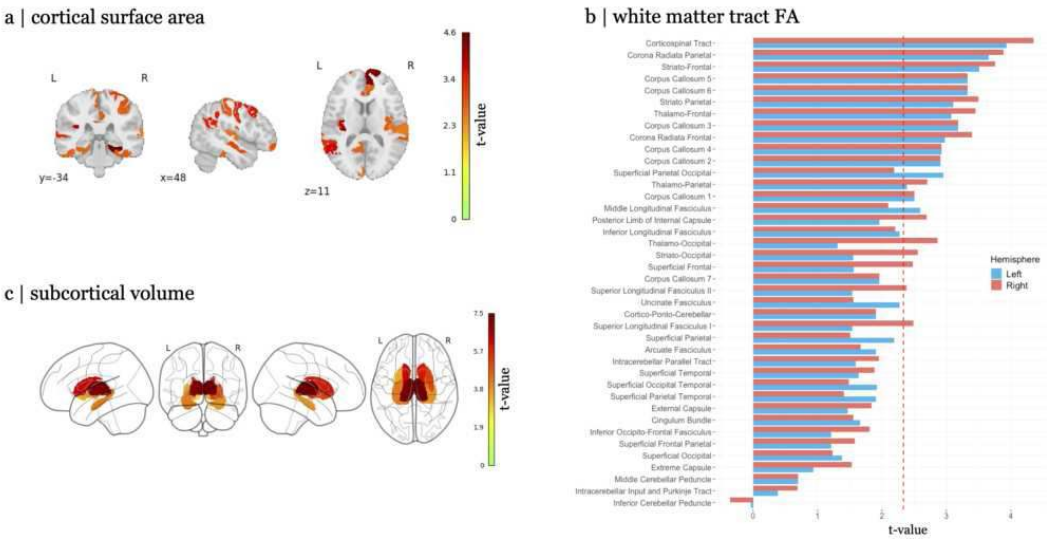

Figure 1. Association of PD-PRS with brain features. Association of PD-PRS in healthy participants of the UK Biobank with: **(a)** cortical surface area of 200 regions from the Schaefer200 atlas, **(b)** white matter fractional anisotropy (FA) of 73 tracts from the ORG atlas, and **(c)** subcortical volumes of 14 structures from the Harvard-Oxford subcortical atlas. t-values are shown after accounting for confounds and only for regions and tracts with $p_{fdr} < 0.05$ significance.

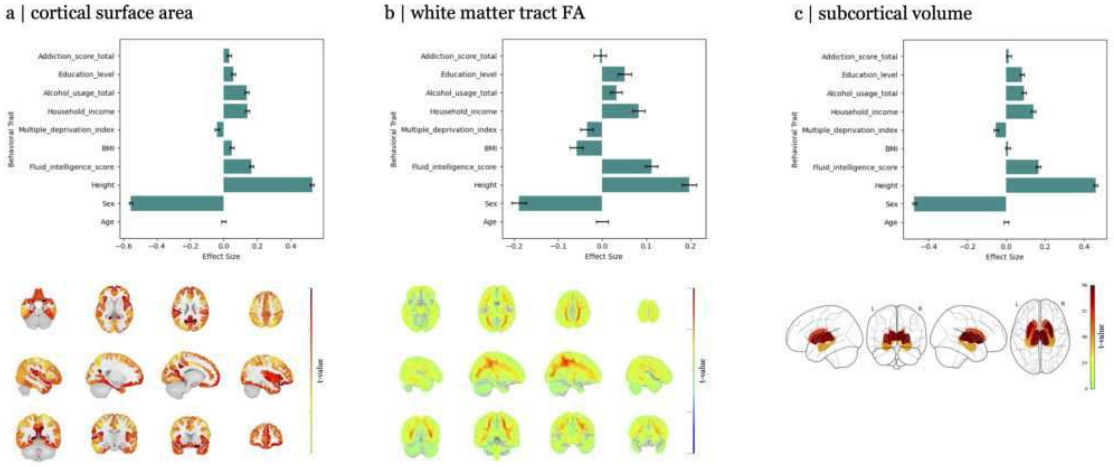

Figure 2. Association between brain features and behavioral and demographic phenotypes. Association of demographics and characteristic PD phenotypes in all participants of the UK Biobank with: **(a)** cortical surface area of 200 regions from the Schaefer200 atlas, **(b)** white matter fractional anisotropy (FA) of 73 tracts from the ORG atlas, and **(c)** subcortical volumes of 14 structures from the Harvard-Oxford subcortical atlas. Top row represents first latent variable (LV1) of each PLS analysis with $p < 0.002$ and variance explained > 86.9%. Second row represents all significant regions and tracts associations with LV1 with $p_{bootstrap} < 0.001$.

Conclusions: These results reveal a link between genetic susceptibility to PD and brain characteristics indicative of greater size of grey and higher integrity in white matter structures. This indicates that genes implicated in PD may also lead to increases in neuronal numbers and connections. These associations were not specific to pairs of spatially interconnected white matter tracts and cortical regions, suggesting a global link exists between white matter tract's FA and cortical SA rather than a spatially local one. These associations were in turn related to certain demographic and behavioral phenotypes including alcohol usage. The findings are consistent with the view that an increase in neural density may make brains vulnerable to neurodegeneration in PD.

References

1. Chan, L. L. (2007). 'Case control study of diffusion tensor imaging in Parkinson's disease', Journal of neurology, neurosurgery, and psychiatry, vol. 78(12), pp. 1383–1386
2. Charroud, C. (2021): 'Subcortical grey matter changes associated with motor symptoms evaluated by the Unified Parkinson's disease Rating Scale (part III): A longitudinal study in Parkinson's disease', NeuroImage: Clinical, vol. 31
3. Jubault, T. (2011): 'Patterns of cortical thickness and surface area in early Parkinson's disease', NeuroImage, vol. 55(2), pp. 462-467
4. Makris 2006: Makris N, Goldstein JM, Kennedy D, Hodge SM, Caviness VS, Faraone SV, Tsuang MT, Seidman LJ. Decreased volume of left and total anterior insular lobule in schizophrenia. Schizophr Res. 2006 Apr;83(2-3):155-71
5. O'Donnell, L. J. (2007). 'Automatic tractography segmentation using a high-dimensional white matter atlas', IEEE transactions on medical imaging, vol. 26(11), pp. 1562–1575
6. Patenaude 2011: Patenaude, B., Smith, S.M., Kennedy, D., and Jenkinson M. A Bayesian Model of Shape and Appearance for Subcortical Brain NeuroImage, 56(3):907-922, 2011
7. Schaefer 2018: Schaefer A, Kong R, Gordon EM, Laumann TO, Zuo XN, Holmes AJ, Eickhoff SB, Yeo BTT. Local-Global parcellation of the human cerebral cortex from intrinsic functional connectivity MRI. Cerebral Cortex, 29:3095-3114, 2018
8. Zijdenbos, A. P. (2002). 'Automatic "pipeline" analysis of 3-D MRI data for clinical trials: application to multiple sclerosis', IEEE transactions on medical imaging, vol. 21(10), pp. 1280–1291

Poster No 293

Hemispheric asymmetry in Alzheimer's Disease patients as feature for pathogenesis and prediction

Laura Broderius[1], Shammi More[2], Kaustubh Patil[1], Kathrin Reetz[3], Patrick Friedrich[4], Felix Hoffstaedter[1]

[1]Institute of Neuroscience and Medicine (INM-7: Brain and Behaviour), Research Centre Jülich, Jülich, NRW, [2]Juelich Research Center, Juelich, Germany, [3]Department of Neurology, University Hospital RWTH Aachen, Aachen, NRW, [4]Forschungszentrum Jülich, Jülich, Germany

Introduction: Hemispheric asymmetries in age-related atrophy are well documented in healthy aging and in Alzheimer's Disease (AD) with asymmetry seeming to develop differently in Alzheimer's cases than in normally aging brains (1-4). Our aim was to investigate the potential of those differences as biomarkers for the detection of AD and mild cognitive impairment (MCI).

Methods: For the asymmetry analysis, 3T structural MRI scans from the Alzheimer's Disease Neuroimaging Initiative (ADNI) (5) were analysed in five diagnostic groups: patients with AD (N=116, mean age =62,1 (SD=6,7)), early MCI (EMCI) (N=205, mean

age=60,8 (SD=5,1)), unsubdivided MCI (N=74, mean age=63,2 (SD=6,8)), late MCI (LMCI, N=105, mean age=62,9 (SD=5,3)) and cognitive normal (CN) subjects (N=198, mean age=63,4 (SD=5,43)). First, a symmetrical Shooting template was created from the IXI dataset (https://brain-development.org/ixi-dataset/) using the CAT12 Toolbox (6) in SPM12. Subsequently, the ADNI T1w images were preprocessed with default settings using the symmetrical IXI template. To investigate gray matter volume (GMV) based hemispheric asymmetry, we calculated the asymmetry index (7) and tested for univariate differences between groups using GLMs and TFCE with non-parametric FWE correction. Additionally, hemipheres were classified as left or right using the following workflow (8): 1. split images into hemispheres and alignment to the right side, 2. perform supervised RandomForest classification per group using GMV voxels as features and 3. use the Boruta algorithm to identify relevant features for hemisperic classifications6. To test those Boruta features fordetection of AD and MCI, we performed binary classifications using Julearn (9), a Python based machine learning library based on scikit-learn (10). We used a support vector machine (SVM) in a nested 5-fold-cross-validation with hyperparameter tuning (kernel = linear, c = [0.0001, 0.001, 0.01, 0.1]) with age and sex linearly modelled as confounds without data leakage.

Results: In the univariate asymmetry analysis no significant differences were found between diagnostic groups. The Boruta feature selection analysis for hemisphere classification identified thalamus, amygdala, insula, parietal operculum and putamen as biggest clusters in MCI and AD. In CN and early MCI, also thalamus and amygdala contributed relevantly to hemispheric classification, alongside the entorhinal cortex and the hippocampus. The entorhinal cortex and the motor cortex nearly disappear in the clusters of MCI, LMCI and AD, possibly becoming more symmetrical with disease progression, while the parietal operculum appears to become more asymmetrical. In general, hemisphere identifying clusters seem to become smaller and more scattered in AD. Successful classification of AD vs. CN was possible with a similar performance for the whole brain as well as only using the sparse Boruta regions with a test score > 80%. Classification of MCI vs. CN for the whole brain and Boruta regions showed a test score ~80% (Fig. 2). Of note, using the asymmetry indices as features performed considerably worse with test scores <65%.

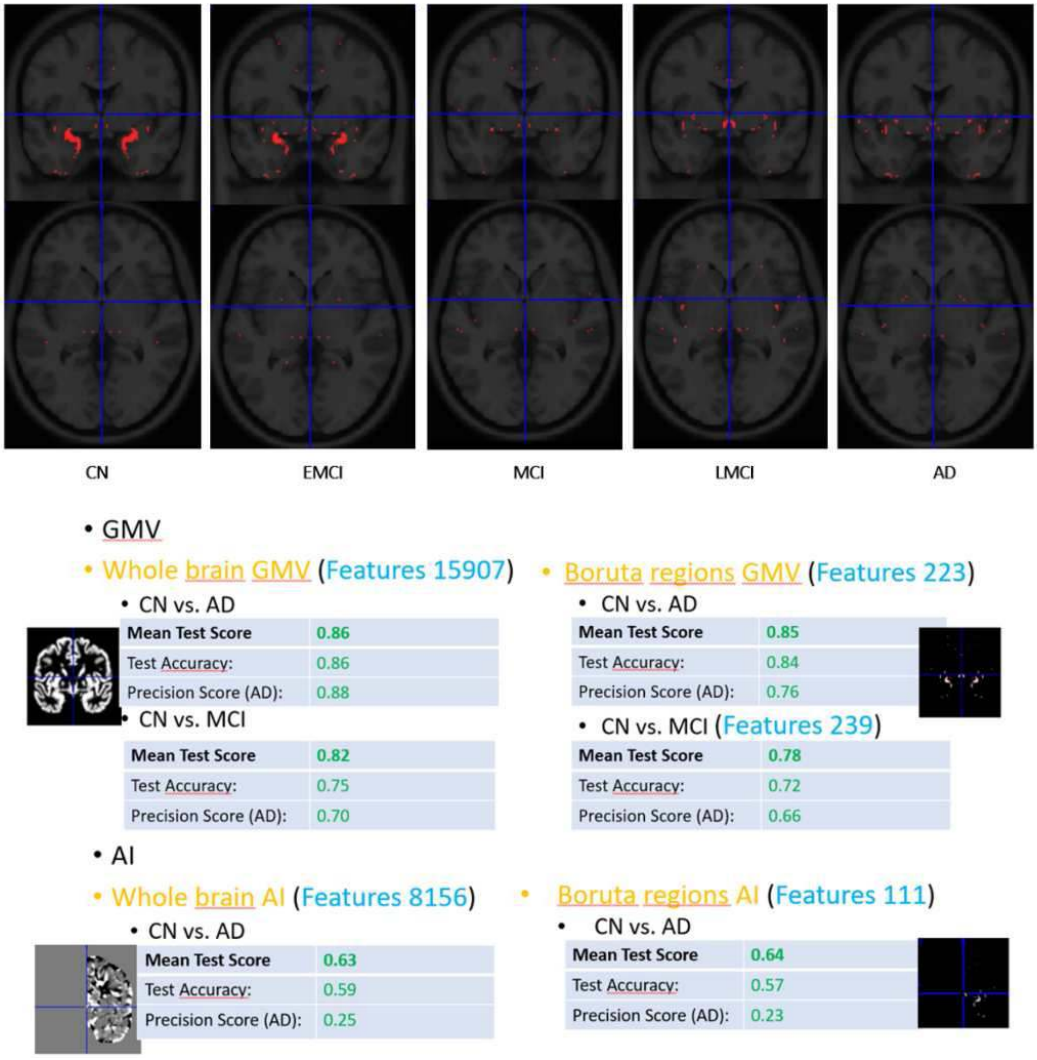

Conclusions: Hemispheric classifications using Boruta identified clusters as relevant for the decision between left vs. right and are therefore related to hemispheric asymmetry, which differs between diagnostic groups of the AD continuum. In AD Boruta regions are scattered more globally, which might be related to the decreasing structural integrity of brain tissue in AD. The performance of those regions in disease classifications was very similar to the whole brain even though they only contained <1.5% of the features relative to the whole brain. This shows strong potential for hemisphere-determining regions in the prediction of AD as well as MCI in the ADNI dataset.

References

1. Minkova L. (2017) 'Gray matter asymmetries in aging and neurodegeneration: A review and meta-analysis', Human Brain Mapping. Dec 2017;38(12):5890-5904. doi:10.1002/hbm.23772
2. Wachinger C (2016), Alzheimer's Disease Neuroimaging Initiative 'Whole-brain analysis reveals increased neuroanatomical asymmetries in dementia for hippocampus and amygdala', Brain. Dec 2016;139(Pt 12):3253-3266. doi:10.1093/brain/aww243
3. Sarica A. (2018), 'MRI Asymmetry Index of Hippocampal Subfields Increases Through the Continuum From the Mild Cognitive Impairment to the Alzheimer's Disease', Frontiers in Neuroscience 2018;12:576. doi:10.3389/fnins.2018.00576
4. Low A. (2019) 'Asymmetrical atrophy of thalamic subnuclei in Alzheimer's disease and amyloid-positive mild cognitive impairment is associated with key clinical features', Alzheimer's and dementia (Amsterdam), Dec 2019;11:690-699. doi:10.1016/j.dadm.2019.08.001
5. ADNI. https://adni.loni.usc.edu
6. CAT – A Computational Anatomy Toolbox for the Analysis of Structural MRI Data View ORCID Profile Christian Gaser, Robert Dahnke, View ORCID ProfilePaul M Thompson, Florian Kurth, Eileen Luders, Alzheimer's Disease Neuroimaging Initiative doi: https://doi.org/10.1101/2022.06.11.495736
7. Kurth F. (2015), 'A 12-step user guide for analyzing voxel-wise gray matter asymmetries in statistical parametric mapping (SPM)', Nature Protocols Feb 2015;10(2):293-304. doi:10.1038/nprot.2015.014
8. Friedrich P. (2022), 'Is it left or is it right? A classification approach for investigating hemispheric differences in low and high dimensionality', Brain Structure and Function Mar 2022;227(2):425-440. doi:10.1007/s00429-021-02418-1
9. Hamdan S. (2023), 'Julearn: an easy-to-use library for leakage-free evaluation and inspection of ML models', arXiv preprint 2023 https://doi.org/10.48550/arXiv.2310.12568
10. Pedregosa F. (2012), 'Scikit-learn: Machine Learning in Python. Journal of Machine Learning Research', 12:2825–2830, 2012. ISSN 1532-4435

Poster No 294

Functional connectivity fingerprints of hallucinations in Parkinson's Disease Dementia

Sara Stampacchia[1], Fosco Bernasconi[1], Alice Albrecht[1], Konstantin Toussas[2], John Paul Taylor[3], Alan Thomas[4], Enrico Amico[5], Olaf Blanke[6]

[1]École polytechnique fédérale de Lausanne (EPFL), Geneve, Switzerland, [2]University of Geneva, Geneve, Switzerland, [3]Newcastle University, Newcastle, United Kingdom, [4]Newcastle University, Newcastle, United Kingdom, [5]Ecole Polytechnique Federale de Lausanne, Lausanne, Switzerland, [6]EPFL, Geneva, Switzerland

Introduction: Hallucinations in Parkinson's Disease are linked to the development of dementia in Parkinson's Disease (PDD)[1]. Minor hallucinations (MH) emerge early in the disease, and previous work has shown that early-stages PD patients with and without MH are distinguishable in terms of functional connectivity (FC)[2,3]. Recently, we switched the focus from group differences to inter-subject variability, and found distinguishable FC fingerprints in PD patients with and without MH[4] The current study extends the investigation to the latest disease stages (PDD) to explore if identifiability based on FC-fingerprints persists, and whether different patterns drive inter-individual variability in patients with and without later and more structured forms of hallucinations, i.e., visual hallucinations (VH).

Methods: Forty-four patients with PDD were included (PD-VH, 27; PD-nH, N=17). The presence of VH was evaluated clinically by expert neurologists. As expected, PDD-VH had higher severity and distress of hallucinations and delusions (Neuropsychiatric Inventory – NPI: $p > .010$). There were no differences across groups for sex assigned at birth ($p=.780$) and age ($p=.144$). In line with what has been previously described in the literature, patients with PDD-VH had lower level of cognitive functioning (Cambridge Cognition Examination – CAMCOG: $p = .016$) and higher level of motor impairment (Unified Parkinson's Disease Rating Scale – UPDRS: $p<.001$) relative to PDD-nH. We estimated individual FC matrices using Pearson's correlation between the averaged BOLD signals of 278 cortical and subcortical nodes5. We estimated individual variability in FC using the following metrics introduced and estimated in healthy subjects and neurological patients 6,7. First, we calculated within (ISelf) and between (IOthers) subjects test-retest FC similarity across the first 180s and second 180s of the same scan. A second metric, IDiff, provided a group-level estimate of distance between ISelf and IOthers. Then, we explored the spatial specificity of differences across patients using edgewise intra-class correlation (ICC). ICC quantifies the within-subject similarity between test and retest for each edge (FC between 2 regions), such that the higher the ICC of an edge the more the two regions show stable patterns of functional connectivity across test and retest within-subjects, as well as variable patterns of functional connectivity between-subjects of their group.

Results: First, data showed that individual FC profiles were highly distinguishable within each group, i.e., among patients with the same diagnosis, but also specific clinical symptoms, i.e., visual hallucinations. At the whole-brain level, we found that in each group, patients were always distinguishable from other patients (ISelf>IOthers in all cases). IDiff was comparably high in both groups, there were no significant differences in ISelf across groups, and IDiff was different from null distribution at p<.001 in all groups (Fig.1A and 1B). Second, we found that FC patterns that identified patients differed between PDD-VH and PDD-nH (Fig.2A).

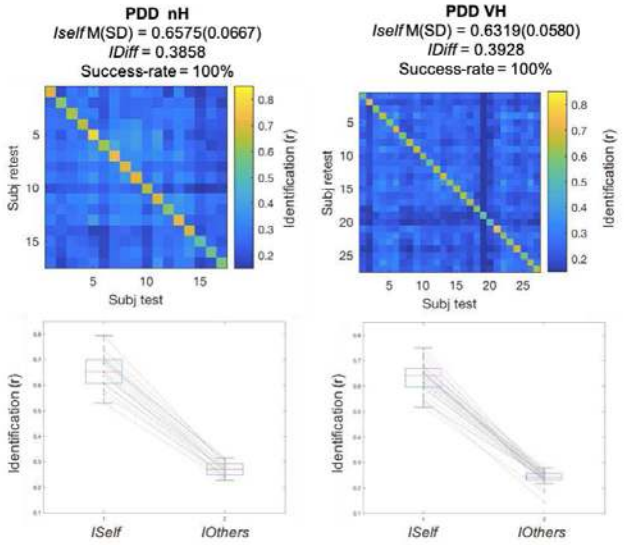

Figure 1. Within and between-subjects variability in Functional Connectivity. A) Identifiability matrices show within- (*ISelf*) and between-subjects (*IOthers*) test-retest reliability as Pearson correlation coefficient in PDD patients without hallucinations (PDD-nH) and PDD patients with visual hallucinations (PDD-VH). Individuals' *ISelf* and *IOthers* are displayed, respectively, in the diagonal and off-diagonal elements of the matrix. The average *ISelf*, *IDiff* and *Success-rate* were similar in the three groups and *IDiff* and *Success-rate* differed at $p < .001$ from random distributions. **B)** Boxplots shows that ISelf was significantly higher (paired t-test, $p < .001$) than IOthers in *all* individual cases in both PDD-nH and PDD-VH.

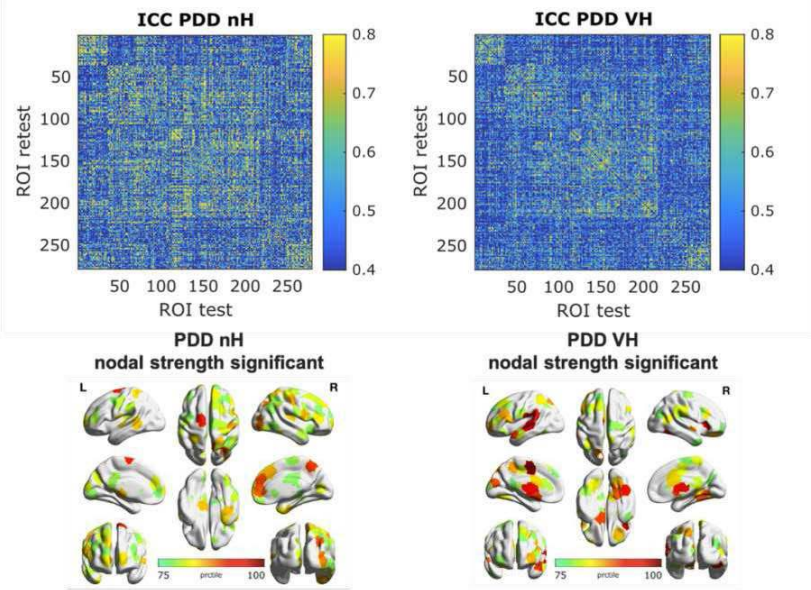

Figure 2. FC patterns making subjects identifiable differ in PDD-nH and PDD-VH. A) Edgewise intra-class correlations (ICC) matrices for Parkinson's Disease Dementia patients without hallucinations (PDD-nH) and with visual hallucinations (PDD-VH). ICC quantifies within-subjects similarity between test and retest for each edge (FC between 2 regions). Here we show that a different configuration of the edges with highest ICC in PDD-nH vs. PDD-VH. We display edges with ICC >= 0.4, which is considered good concordance for neuroimaging data [8,9]. VIS=Visual Network; SMT=Somatomotor Network; DA=Dorsal Attention Network; SA=Salience Network; L=Limbic Network; FPN=Fronto-Parietal Network; DMN=Default-Mode Network; SBC=Subcortical regions; CRB=Cerebellum. **B)** Brain renders show the significant nodes (or ROIs) in PDD-nH and in PDD-VH. Significant nodes were identified as follows: a null ICC matrix was derived by randomly shuffling subjects' group-labels across 1000 permutations; edges were considered significantly specific to the group when ICC edgewise-null was higher than edgewise-real (A) for p<.05 across the 1000 permutation runs; nodal strength was computed as average of edge weights for each ROI. We here display only the significant nodes > 75th percentiles.

Conclusions: This study extends previous work showing group-differences in FC 2,3 and in FC-fingerprints between PD patients with and without MH, by finding that the functional connections remain individual-specific also in the most advanced stages of the disease and distinguishable between patients with later forms of hallucinations7. This work confirms that the individual variability – well-known in clinical practice – is reflected by differences in FC even in the more advanced stages of the disease and during dementia (PDD). These findings help characterizing the neural basis of late hallucinations in PD (i.e., VH) and may pave the way for a personalised understanding of the altered brain mechanisms in hallucinations as well as for their early detection.

References

1. ffytche, D. H. et al. The psychosis spectrum in Parkinson disease. Nat Rev Neurol 13, 81–95 (2017).
2. Bejr-kasem, H. et al. Disruption of the default mode network and its intrinsic functional connectivity underlies minor hallucinations in Parkinson's disease. Movement Disorders 34, 78–86 (2019).
3. Bernasconi, F. et al. Robot-induced hallucinations in Parkinson's disease depend on altered sensorimotor processing in fronto-temporal network. Sci. Transl. Med. 13, eabc8362 (2021).
4. Stampacchia, S. et al. Functional connectivity fingerprints in Parkinson's disease patients with hallucinations. in (in preparation).
5. Shen, X., Tokoglu, F., Papademetris, X. & Constable, R. T. Groupwise whole-brain parcellation from resting-state fMRI data for network node identification. NeuroImage 82, 403–415 (2013).
6. Amico, E. & Goñi, J. The quest for identifiability in human functional connectomes. Sci Rep 8, 8254 (2018).
7. Stampacchia, S. et al. Fingerprinting of brain disease: Connectome identifiability in cognitive decline and neurodegeneration. 2022.02.04.479112 Preprint at https://doi.org/10.1101/2022.02.04.479112 (2022).
8. McGraw, K. O. & Wong, S. P. Forming Inferences About Some Intraclass Correlation Coefficients. Psychological Methods 17 (1996) doi:1082-989X/96/S3.00.
9. Shrout, P. E. & Fleiss, J. L. Intraclass Correlations: Uses in Assessing Rater Reliability. Psychological Bulletin 86, 420–428 (1979).

Poster No 295

Spatial pattern of brain atrophy in Alzheimer's and LATE neuropathology

Khalid Saifullah[1], Abdur Raquib Ridwan[2], David Bennett[2], Julie Schneider[2], Konstantinos Arfanakis[1,2]

[1]Illinois Institute of Technology, Chicago, IL, [2]Rush University Medical Center, Chicago, IL

Introduction: Alzheimer's disease neuropathologic change (AD-NC)1 and limbic-predominant age-related TDP-43 encephalopathy neuropathologic change (LATE-NC)2 are common in older adults and have been associated with brain atrophy, cognitive decline, and dementia3. Furthermore, AD-NC and LATE-NC are often comorbid increasing the odds for dementia4. Since AD-NC and LATE-NC are often comorbid and due to the fact that LATE-NC can only be detected at autopsy, the differential effects of the two pathologies on brain morphometry have not been systematically investigated. In this work, we combined deformation-based morphometry (DBM) on ex-vivo brain MRI and detailed neuropathological evaluation in a large number of community-based older adults (N=912) that came to autopsy to investigate the difference in brain atrophy patterns associated with AD-NC and LATE-NC.

Methods: Participants and Data Cerebral hemispheres from 912 older adults participating in four longitudinal, clinical-pathologic cohort studies of aging were included in this work: the Rush Memory and Aging Project (MAP), Religious Orders Study (ROS), Minority Aging Research Study (MARS), and the African American Clinical Core (AA Core) of the Rush Alzheimer's Disease Research Center (Rush ADRC) (Fig.1)5,6. All hemispheres were imaged ex-vivo on 3T clinical MRI scanners approximately 1-month postmortem while immersed in 4% formaldehyde solution. T2-weighted images of all hemispheres were non-linearly registered to a brain hemisphere template using ANTs. The logarithm of the Jacobian determinant (LogJ) of the deformation field was calculated in each voxel, and the resulting maps were smoothed by a Gaussian filter with FWHM=4mm. Following ex-vivo MRI, all hemispheres underwent detailed neuropathologic examination by a board-certified neuropathologist. The pathologies that were assessed were AD-NC, LATE-NC, Lewy bodies, gross infarcts, microscopic infarcts, arteriolosclerosis, atherosclerosis, and cerebral amyloid angiopathy. Participants were divided into four groups: AD-NC-neg LATE-NC-neg (n=453), AD-NC-pos LATE-NC-neg (n=108), AD-NC-neg LATE-NC-pos (n=225), and AD-NC-pos LATE-NC-pos (n=126), where AD-NC-pos was defined as moderate or severe AD-NC according to the NIA-AA criteria1, and LATE-NC-pos was defined as LATE-NC stages 2 or 3. Statistical analysis Voxel-wise linear regression was used to test the association of the deformations observed in the smoothed log Jacobian maps with the four different groups, controlling for all other neuropathologies, demographics (age, sex, years of education), postmortem intervals, and scanner. The analysis was conducted using FSL PALM7. We used 5000 permutations, and statistical significance was set at $p<0.05$ after family wise error (FWE) correction. Significant clusters were defined using threshold-free cluster enhancement (TFCE).

N	912
Age at death, years (SD)	90.6 (6.4)
Male, n (%)	256 (28)
Education, years (SD)	15.7 (3.5)
Antemortem clinical diagnosis, n (%)	
- No Cognitive Impairment	294 (32.2)
- Mild Cognitive Impairment	210 (23.0)
- Dementia	397 (43.5)
Mini-mental State Examination (MMSE), mean (SD)	19.9 (9.6)
ADNC, n (%)	
- Low AD neuropathologic change	173 (19.0)
- Intermediate AD neuropathologic change	395 (43.3)
- High AD neuropathologic change	234 (25.7)
Lewy bodies, n (%)	259 (28.4)
Gross infarcts, n (%)	370 (40.6)
Microscopic infarcts, n (%)	355 (38.9)
Atherosclerosis, n (%)	
- Mild	484 (53.1)
- Moderate	184 (20.2)
- Severe	44 (4.8)
Cerebral amyloid angiopathy, n (%)	
- Mild	387 (42.4)
- Moderate	226 (24.8)
- Severe	112 (12.3)
Arteriolosclerosis, n (%)	
- Mild	339 (37.2)
- Moderate	187 (20.5)
- Severe	62 (6.8)
LATE-NC, n (%)	
- No TDP-43 inclusions	402 (44.1)
- TDP-43 inclusions in amygdala only	159 (17.4)
- TDP-43 inclusions in amygdala and entorhinal cortex or hippocampus CA1	102 (11.2)
- TDP-43 inclusions in amygdala and entorhinal cortex or hippocampus CA1 and neocortex	249 (27.3)
Postmortem interval to fixation, hours (SD)	9.8 (7.5)
Postmortem interval to imaging, days (SD)	36.5 (16.3)
MRI Scanner, n (%)	
- 3T GE Sigma, n (%)	75 (8.2)
- 3T Siemens Trio, n (%)	82 (9.0)
- 3T Philips Achieva, n (%)	282 (30.9)
- 3T Siemens Verio, n (%)	473 (51.9)

Fig. 1. Demographic, clinical and neuropathologic characteristics of the participants used in the analysis.

Results: Both the AD-NC-pos LATE-NC-neg group (Fig.2a) as well as the AD-NC-neg LATE-NC-pos group (Fig.2b) were associated with lower tissue volume mainly in medial temporal lobe structures8. The AD-NC-pos LATE-NC-pos group (Fig.2c) showed substantially lower volume in the temporal, frontal, and parietal lobes4,9. Interestingly, the AD-NC-neg LATE-NC-pos group showed lower volume in the anterior portion of the hippocampus than the AD-NC-pos LATE-NC-neg group (Fig.2d)10.

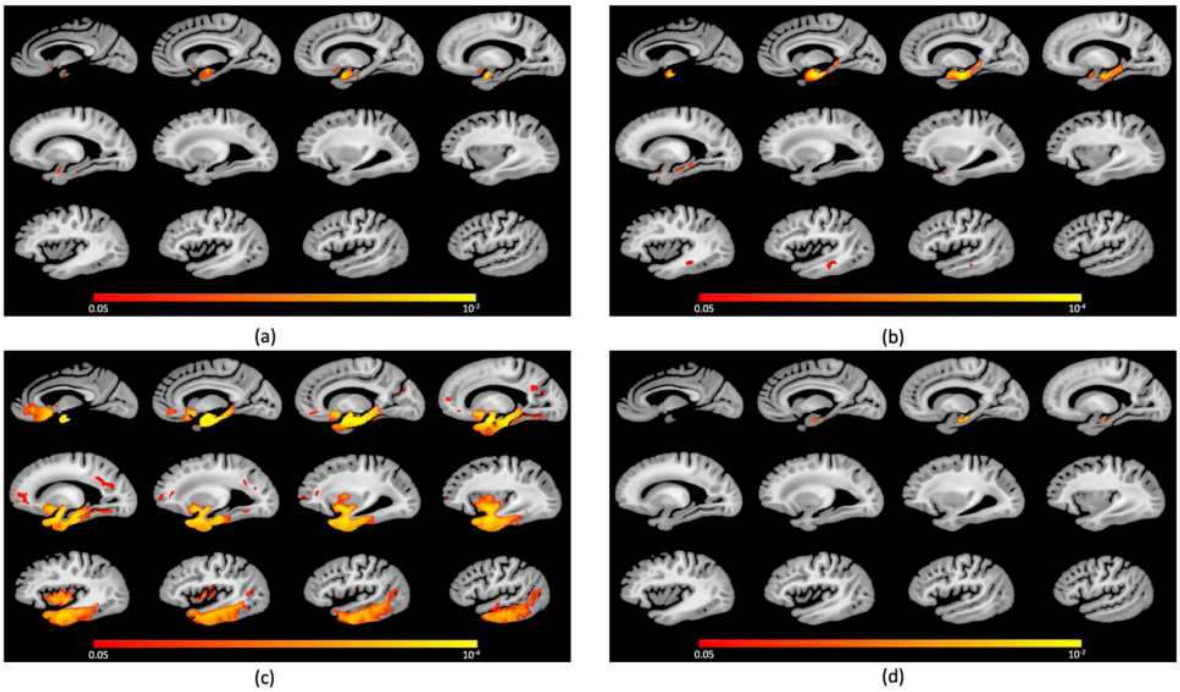

The above figure shows (a) regions with significantly lower volume in the AD-NC-pos LATE-NC-neg group, (b) regions with significantly lower volume in the AD-NC-neg LATE-NC-pos group, (c) regions with significantly lower volume in the AD-NC-pos LATE-NC-pos group, (d) regions with significantly lower volume in the AD-NC-neg LATE-NC-pos group compared to the AD-NC-pos LATE-NC-neg group controlling for other neuropathologies, demographics and covariates. The color-scale represents the FWER-corrected p-values obtained from linear regression.

Conclusions: This is the largest study combining brain morphometry and pathology in community-based older adults to date, and as such it provides strong evidence on the brain atrophy patterns associated with AD-NC and LATE-NC. Both AD-NC and LATE-NC are associated with lower volume mainly in the medial temporal lobes. Furthermore, LATE-NC stages 2 or 3 are associated with more atrophy in the anterior portion of the hippocampus compared to moderate or severe AD-NC. This finding suggests that in the presence of LATE-NC, the volume of the hippocampus cannot serve as a marker of AD-NC.

References

1. Hyman, B. T. (2012), 'National Institute on Aging-Alzheimer's Association guidelines for the neuropathologic assessment of Alzheimer's disease', Alzheimer's & dementia : the journal of the Alzheimer's Association, 8(1), 1–13.
2. Nelson, P. T. (2019), 'Limbic-predominant age-related TDP-43 encephalopathy (LATE): consensus working group report', Brain : a journal of neurology, 142(6), 1503–1527.
3. Boyle, P. A (2017), 'Varied effects of age-related neuropathologies on the trajectory of late life cognitive decline', Brain : a journal of neurology, 140(3), 804–812.
4. James, B. D. (2016), 'TDP-43 stage, mixed pathologies, and clinical Alzheimer's-type dementia', Brain : a journal of neurology, 139(11), 2983–2993.
5. Barnes, L. L. (2012), 'The Minority Aging Research Study: ongoing efforts to obtain brain donation in African Americans without dementia', Current Alzheimer research, 9(6), 734–745.
6. Bennett, D. A. (2018), 'Religious Orders Study and Rush Memory and Aging Project', Journal of Alzheimer's disease : JAD, 64(s1), S161–S189.
7. Winkler, A. M. (2015), 'Multi-level block permutation', NeuroImage, 123, 253–268.
8. Barkhof, F. (2007), 'The significance of medial temporal lobe atrophy: a postmortem MRI study in the very old', Neurology, 69(15), 1521–1527.
9. Kapasi, A. (2020), 'Limbic-predominant age-related TDP-43 encephalopathy, ADNC pathology, and cognitive decline in aging', Neurology, 95(14), e1951–e1962.
10. Yu, L. (2020), 'Contribution of TDP and hippocampal sclerosis to hippocampal volume loss in older-old persons', Neurology, 94(2), e142–e152.

Poster No 296

Oxidative stress is related to vascular brain injury in mild cognitive impairment of Alzheimer type

Flavie Detcheverry[1,2,3,4,5], Sneha Senthil[6,7,5], Winnie Motue[6,7], Chris Hosein[7,8], Rozie Arnaoutelis[9,7], David Araujo[6,7], Dumitru Fetco[6,7], Samson Antel[6,7], Douglas Arnold[6,7], Jamie Near[10], Hyman Schipper[7,8], AmanPreet Badhwar[1,2,3,4], Sridar Narayanan[7,7]

[1]Multiomics Investigation of Neurodegenerative Diseases (MIND) lab, Montreal, Quebec, Canada, [2]Department of Pharmacology and Physiology, Faculty of Medicine, University of Montreal, Montreal, Quebec, Canada, [3]Institute of Biomedical Engineering, University of Montreal, Montreal, Quebec, Canada, [4]Centre de Recherche de l'Institut Universitaire de Gériatrie de Montréal (CRIUGM), Montreal, Quebec, Canada, [5]Denotes equal contribution, Montreal, Quebec, Canada, [6]McConnell Brain Imaging Centre, Montreal Neurological Institute, Montreal, Quebec, Canada, [7]Department of Neurology and Neurosurgery, McGill University, Montreal, Quebec, Canada, [8]Lady Davis Institute, Jewish General Hospital, Montreal, Quebec, Canada, [9]McConnell Brain Imaging Centre, Montreal Neurological Institute, Montréal, Québec, Canada, [10]Sunnybrook Research Institute, Department of Medical Biophysics, University of Toronto, Toronto, Ontario, Canada

Introduction: Oxidative stress (OS), an imbalance between production and neutralization of reactive oxygen species, can damage brain cells and contribute to cognitive decline in Alzheimer disease (AD) continuum (Mandal et al., 2015). Levels of glutathione (GSH), the most prevalent endogenous brain antioxidant (Pocernich and Butterfield, 2012), can be assessed with magnetic resonance spectroscopy (MRS), and serves as a brain-OS index. Our systematic reviews (Detcheverry, et al., 2023a; Detcheverry, et al., 2023b) report that brain GSH levels decrease with age in most brain regions, with greater decreases reported in AD. Since the relationship between GSH and vascular-brain injury is not known in the dementia and the mild cognitive impairment (MCI) stages of AD, we address this gap in MCI.

Methods: MRI/MRS data from 31 MCI participants (age range: 55-86 years) were obtained using a 3T Siemens Prisma MRI scanner (Siemens, Erlangen, Germany). The MRI protocol included a whole-brain, 3D T1-weighted MP2RAGE for localization and brain volume measurements, and a 3D T2-weighted fluid attenuated inversion recovery (FLAIR) for detection of white matter hyperintensities (WMHs), a marker of small-vessel disease. Single-voxel MRS was performed using the SPin Echo full Intensity Acquired Localized (SPECIAL) technique, with one voxel positioned over the posterior cingulate cortex (PCC) and the other in frontal white matter (FWM) (Figure 1A, B). WMHs were segmented using an automated technique (Elliott et al., 2010) and manually reviewed. Hippocampi (HCP) were segmented using a locally-developed pipeline as previously described (Tremblay et al., 2018). Normalized brain volume (NBV) was computed using SIENAx (Smith et al., 2002). Vascular brain injury was assessed using WMH volume and Fazekas scores (Fazekas et al., 1987). Global and regional brain tissue preservation was assessed using NBV and HCP (whole, left, right) volumes (HCPv), respectively. Finally, cognition was assessed with the

Montreal Cognitive Assessment (MoCA). Raw MRS data was preprocessed using the FID Appliance (FID-A) (Simpson et al., 2017), before spectral fitting, and eddy current correction and spectral analysis were performed in LCModel (Provencher, 2001). Pearson correlations between (a) metabolite levels in both regions, and (b) GSH and other markers, were performed in Python (version 3.9.13).

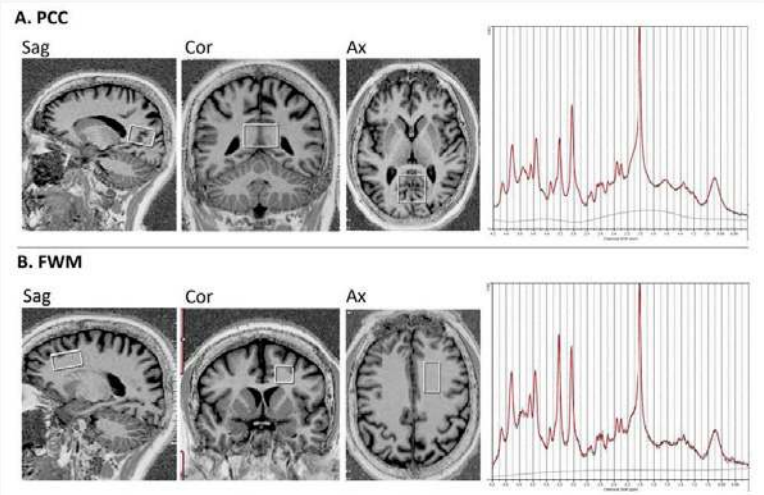

Figure 1. MRS voxels in **A.** PCC (3 x 3 x 2 (RL x AP x FH) cm^3); and **B.** FWM (1.5 x 3 x 1.5 (RL x AP x FH) cm^3). MRS spectra from the respective regions are displayed on the right panel. Abbreviations: Ax, axial; Cor, coronal; FWM, frontal white matter; MRS, magnetic resonance spectroscopy; PCC, posterior cingulate cortex; Sag, sagittal.

Results: The mean age of our MCI group was 74.41 years (Figure 2A). In general, metabolite levels were higher in PCC relative to FWM, with significant differences ($p<0.001$) in levels of tNAA, GSH/total creatine (tCr), and total N-acetylaspartate (tNAA)/tCr (Figure 2A). We found significant associations in FWM between GSH/tCr and tNAA/tCr ($r=0.38$; $p=0.04$), and between GSH and (a) WMH volume ($r=-0.37$; $p=0.04$), and (b) NBV ($r=0.38$; $p=0.04$). Linear regressions for these findings are displayed in Figure 2B. No relationship was found between GSH levels and cognition.

A.

		Mean (N=31)	Standard deviation
Age (years)		74.41	7.10
MoCA scores		24.68	2.63
Fazekas scores		0.74	0.76
GSH	PCC	1.61	0.16
	FWM	1.60	0.21
	p	0.76	
tNAA	PCC	14.54	1.18
	FWM	10.57	0.99
	p	**0.05e-20**	
GSH/tCr	PCC	0.16	0.02
	FWM	0.20	0.03
	p	**1.4e-08**	
tNAA/tCr	PCC	1.40	0.08
	FWM	1.30	0.09
	p	**1.85e-05**	
WMH volume (mm^3)		4803.00	6611.66
NBV (mm^3)		1432037.00	94238.30
HCPv (mm^3)	Whole	7345.67	1259.99
	Left	3582.50	691.33
	Right	3763.17	613.24

B.

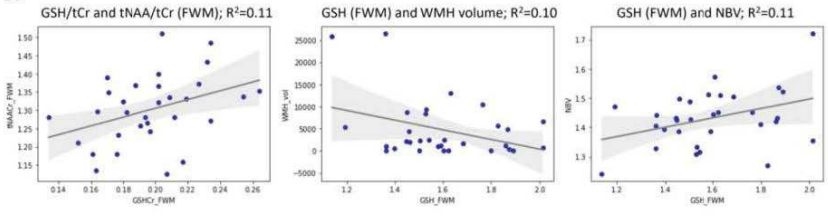

Figure 2. Demographic information and results
A. Demographics of included participants; and **B.** Linear regressions. The adjusted R^2 value is provided for every metabolite. Abbreviations: FWM, frontal white matter; GSH, glutathione; HCPv, hippocampal volume; tCr, total creatine = creatine + phosphocreatine; MoCA, Montreal Cognitive Assessment; NBV, normalized brain volume; PCC, posterior cingulate cortex; tNAA, total N-acetylaspartate = N-acetylaspartate + N-acetylaspartylglutamate; WMH, white matter hyperintensity.

Conclusions: In FWM, lower GSH was associated with (a) higher vascular brain injury, as shown with higher WMH volume, and (b) lower brain volume and axonal integrity as shown both with lower NBV and tNAA levels, respectively. Our results suggest that, in WM, OS (as indicated by elevated GSH) contributes to vascular-brain injury in MCI of the Alzheimer's type.

References

1. Detcheverry, F., et al. (2023a) 'Changes in levels of the antioxidant glutathione in brain and blood across the age span of healthy adults: A systematic review', NeuroImage: Clinical, p. 103503.
2. Detcheverry, F., et al. (2023b) 'Glutathione level variations in brain and blood in healthy aging and Alzheimer's disease continuum: A systematic review', in Alzheimer's Association International Conference. ALZ. Available at: https://alz.confex.com/alz/2023/meetingapp.cgi/Paper/78506 (Accessed: 30 September 2023).
3. Elliott, C. et al. (2010) 'Bayesian classification of multiple sclerosis lesions in longitudinal MRI using subtraction images', Medical image computing and computer-assisted intervention: MICCAI ... International Conference on Medical Image Computing and Computer-Assisted Intervention, 13(Pt 2), pp. 290–297.
4. Fazekas, F. et al. (1987) 'MR signal abnormalities at 1.5 T in Alzheimer's dementia and normal aging', AJR. American journal of roentgenology, 149(2), pp. 351–356.
5. Mandal, P.K. et al. (2015) 'Brain glutathione levels--a novel biomarker for mild cognitive impairment and Alzheimer's disease', Biological psychiatry, 78(10), pp. 702–710.
6. Pocernich, C.B. and Butterfield, D.A. (2012) 'Elevation of glutathione as a therapeutic strategy in Alzheimer disease', Biochimica et biophysica acta, 1822(5), pp. 625–630.
7. Provencher, S.W. (2001) 'Automatic quantitation of localized in vivo 1H spectra with LCModel', NMR in biomedicine, 14(4), pp. 260–264.
8. Simpson, R. et al. (2017) 'Advanced processing and simulation of MRS data using the FID appliance (FID-A)-An open source, MATLAB-based toolkit', Magnetic resonance in medicine: official journal of the Society of Magnetic Resonance in Medicine / Society of Magnetic Resonance in Medicine, 77(1), pp. 23–33.
9. Smith, S.M. et al. (2002) 'Accurate, robust, and automated longitudinal and cross-sectional brain change analysis', NeuroImage, 17(1), pp. 479–489.
10. Tremblay, A. et al. (2018) 'Thalamic and hippocampal volume associated with memory functions in multiple sclerosis', Brain and cognition, 125, pp. 61–68.

Poster No 297

Patterning of Dynamic Brain States Distinguish Parkinson's Patients with Mild Cognitive Impairments

Abigail Eubank[1], Aaron Kemp[1], James Galvin[2], Fred Prior[1], Linda Larson-Prior[1]

[1]University of Arkansas for Medical Sciences, Little Rock, AR, [2]University of Miami, Miami, FL

Introduction: Parkinson's disease (PD) is commonly associated with motor impairments, however it also causes cognitive impairments which can be classified in a range of stages from PD with normal cognition (PD-NC), PD with mild cognitive impairment (PD-MCI) (Litvan et al. 2011; 2012), to PD with dementia (Saredakis et al. 2019). Previous studies have found dynamic, time-varying measures of functional network connectivity (dFNC) derived from resting-state functional magnetic resonance imaging (rs-fMRI), may distinguish patients with PD-NC from those with PD-MCI (Díez-Cirarda et al. 2018; Jinhee Kim et al. 2017). We explored the use of a dichotomic pattern mining technique, Seq2pat (Wang et al. 2022), to determine whether sequential patterns in the ordering of dFNC states could accurately distinguish healthy control (HC) subjects from those with PD and distinguish PD-NC from PD-MCI.

Methods: Seven minutes of resting, eyes-closed fMRI data were collected on a Siemens 3T TRIO scanner from 33 individuals with PD and 22 HC subjects at the Center for Biomedical Imaging at New York University following IRB approval and informed consent. Patients with PD were categorized into PD-MCI or PD-NC subgroups, by clinical consensus. The rs-fMRI data were preprocessed using the FMRIB Software Library (FSL; Jenkinson et al, 2012), including brain extraction, B0-unwarping, slice-time and motion correction, registration to standard space (MNI 152), and Independent Component Analyses for the Automatic Removal of Motion Artifacts (ICA-AROMA; Pruim et al, 2015). Three dFNC states were derived with the Group ICA for fMRI Toolbox (GIFT; Allen et al., 2014), as determined by the elbow criterion. Sequences of letters indicating the transition across states were then used as input to a Python-based sequential pattern mining method, Seq2pat (Wang et al, 2022). One-hot encoding of sequential patterns yielded feature vectors that were then used to train Random Forrest (RF) classifiers using 80% of the data for training and 20% for testing. Separate classifiers were trained to distinguish HC from PD groups, and PD-NC from PD-MCI subgroups, and the results for each were averaged across 100 iterations.

Results: Statistical comparisons between the 3 state matrices returned from GIFT for each group (Figure 1), revealed a reduction in overall network inter-connectivity of the frontal parietal (FP) and executive control (EC) networks for both PD cohorts versus HC in State 1, while State 2 displays higher intra-connectivity within the default mode network (DMN) of the PD-MCI cohort relative to both the HC and PD-NC cohorts, and reduced intra-connectivity of the sensorimotor (SM) network in both PD-NC and PD-MCI groups relative to HC in State 3. The Seq2pat method identified 683 sequential patterns, including 227 that were unique to the HC subjects, 118 that were unique to the PD patients, and 338 that both groups displayed (Figure

2). The mean (standard deviation) values for accuracy and area under the receiver operating curve for the RF classifier trained to distinguish HC from PD was 0.71 (0.11) and 0.65 (0.12), respectively. For the RF classifier trained to distinguish PD-NC from PD-MCI, these values were 0.62 (0.15) and 0.65 (0.14), respectively. A multi-class classifier trained to distinguish all three groups yielded mean accuracy of 0.49 (0.12) and mean AUC of 0.52 (0.14).

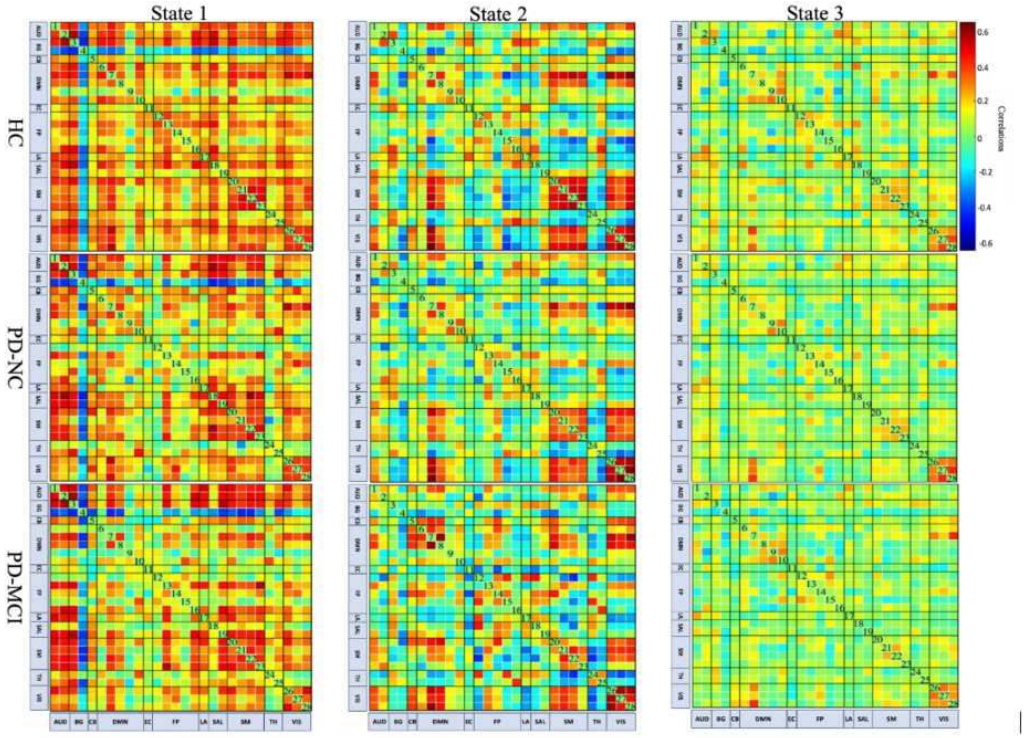

Figure 1: dFNC matrices of each group separated by state. Auditory (AUD) network, Basal Ganglia (BG) network, Cerebellar (CB) network, Default Mode (DMN) network, Executive Control (EC) network, Frontal Parietal (FP) network, Language (LAN) net network, Salience (SAL) network, Sensorimotor (SM) network, Thalamus (TH) network, Visual (VIS) network.

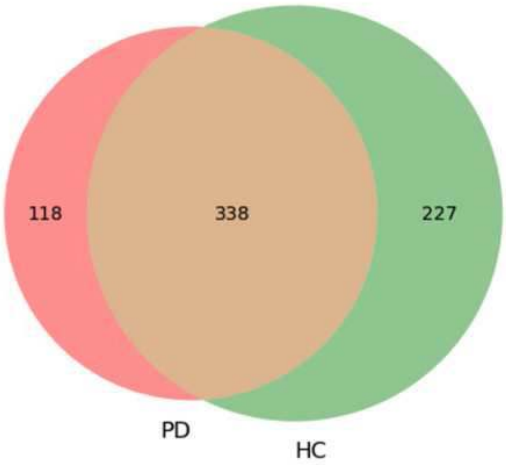

Figure 2: Seq2pat Venn diagram of Detected Sequential Patterns. PD-NC and PD-MCI combined have 118 unique patterns, HC has 227 unique patterns. There are 338 shared patterns between all participant groups.

Conclusions: We believe that this exploratory analysis highlights the potential utility of Seq2pat to detect sequential patterns in the temporal ordering of dynamic brain states, as detected using GIFT. While the results of the classifiers show only modest accuracy, the fact that they were all above chance level indicates that the sequential patterning of derived brain states warrants further investigation as possible indicators of abnormality in the dynamic, temporal organization of neural network activity among people with PD, particularly those with cognitive impairments.

References

1. Allen EA, Damaraju E, Plis SM, Erhardt EB, Eichele T, Calhoun VD. 2014. Tracking Whole-Brain Connectivity Dynamics in the Resting State. Cerebral Cortex. 24, 663–676.

2. Díez-Cirarda, María, Antonio P. Strafella, Jinhee Kim, Javier Peña, Natalia Ojeda, Alberto Cabrera-Zubizarreta, and Naroa Ibarretxe-Bilbao. 2017. 'Dynamic Functional Connectivity in Parkinson's Disease Patients with Mild Cognitive Impairment and Normal Cognition'. NeuroImage: Clinical 17: 847–55. https://doi.org/10.1016/j.nicl.2017.12.013.
3. Jinhee Kim, Marion Criaud, Sang Soo Cho, Maria Diez-Cirarda, Alexander Mihaescu, Sarah Coakeley, Christine Ghadery, et al. 2017. 'Abnormal Intrinsic Brain Functional Network in Parkinson's Disease'. Brain. Oxford University Press. https://doi.org/10.1093/brain/awx267.
4. Litvan, Irene, Dag Aarsland, Charles H. Adler, Jennifer G. Goldman, Jaime Kulisevsky, Brit Mollenhauer, Maria C. Rodriguez-Oroz, Alexander I. Tröster, and Daniel Weintraub. 2011. 'MDS Task Force on Mild Cognitive Impairment in Parkinson's Disease: Critical Review of PD-MCI'. Movement Disorders. https://doi.org/10.1002/mds.23823.
5. Litvan, Irene, Jennifer G. Goldman, Alexander I. Tröster, Ben A. Schmand, Daniel Weintraub, Ronald C. Petersen, Brit Mollenhauer, et al. 2012. 'Diagnostic Criteria for Mild Cognitive Impairment in Parkinson's Disease: Movement Disorder Society Task Force Guidelines'. Movement Disorders 27 (3): 349–56. https://doi.org/10.1002/mds.24893.
6. Saredakis, Dimitrios, Lyndsey E. Collins-Praino, Daria S. Gutteridge, Blossom C.M. Stephan, and Hannah A.D. Keage. 2019. 'Conversion to MCI and Dementia in Parkinson's Disease: A Systematic Review and Meta-Analysis'. Parkinsonism and Related Disorders. Elsevier Ltd. https://doi.org/10.1016/j.parkreldis.2019.04.020.
7. Jenkinson M, Beckmann CF, Behrens TEJ, Woolrich MW, Smith SM. 2012. FSL. Neuroimage. 62:782-790.
8. Pruim RHR, Mennes M, van Rooij D, Llera A, Buitelaar JK, Beckmann CF. 2015. ICA-AROMA: A robust ICA-based strategy for removing motion artifacts from fMRI data. Neuroimage. 2015 May 15;112:267-277.
9. Wang X, Hosseininasab A, Colunga P, Kadıoğlu S, van Hoeve WJ, 2022. Seq2pat: sequence-to-pattern generation for constraint-based sequential pattern mining. In Proceedings of the AAAI Conference on Artificial Intelligence. 2022 Jun 28 (Vol. 36, No. 11, pp. 12665-12671).

Poster No 298

Dynamic Brain Network States in Alzheimer's Disease

Tien-Tse Huang[1], Shih-Jen Tsai[2], Ching-Po Lin[3], Chiung-Chih Chang[4], Chun-Yi Zac Lo[1]

[1]Biomedical Engineering Department,Chung Yuan Christian University, Taoyuan, Taiwan, [2]Department of Psychiatry, Taipei Veterans General Hospital, Taipei,Taiwan, Taipei, Taiwan, [3]Institute of Neuroscience, National Yang Ming Chiao Tung University, Taipei, Taiwan, [4]Department of Neurology, Chang Gung Memorial Hospital-Kaohsiung Medical Center, Kaohsiung, Taiwan, Kaohsiung, Taiwan

Introduction: Alzheimer's disease is a neurodegenerative disorder, with disrupted system-level brain network organization[1]. With the development of medical imaging equipment and analysis techniques, functional Magnetic Resonance Imaging (fMRI) has increasingly become a vital tool for observing brain activity. It enables the construction of dynamic functional connectivity networks in the brain[2]. Three states of the brain's dynamic functional networks have been demonstrated which are associated with sensory, somatomotor, and internal mentation state, and highly correlated with aging[3]. In this study, we investigated the dynamic brain network states in Alzheimer's disease, and it may be as potential biomarkers in biomedical imaging.

Methods: MR data were obtained from Kaohsiung Chang Gung Memorial Hospital, including T1-weighted images (T1WI) and fMRI, with two sets of imaging acquisition protocols. Total 43 healthy volunteers (HV) and 22 AD patient MR data were acquired using a Siemens 3T skyra scanner, including 34 participants data (HV: 18 AD:16) with protocol as T1WI: voxel size: 1.0*1.0*1.0 mm^3 fMRI: TR=3660ms, TE=45ms, slice number = 50, voxel size = 3.0*3.0*3.0 mm^3, 120 volumes; and 31 participants data (HV: 25, AD: 6) T1WI: voxel size: 0.5*0.5*1.0 mm^3; fMRI: TR=2500ms, TE=27ms, slice number=43, voxel size=3.4*3.4*3.4 mm^3, 200 volumes. After preprocessing the T1-weighted and fMRI images separately[4], the fMRI data was first registered to its corresponding T1 space. Subsequently, utilizing previously computed transformation matrices, the T1 images were registered to the standard brain space (MNI152). Finally, a 6mm full-width at half-maximum Gaussian blur was applied to smooth the images. The fMRI signals were segmented into brain regions using the Automated Anatomical Labeling 2 (AAL2) atlas[5]. A sliding-window approach was used for dynamic network estimation. Employing a 20 frame time window, correlation were performed at different time window for each brain region. With that data we can derive the similarities between feature matrix of the three brain networks. Three predominant states of brain networks were estimated by feature score with the feature metrics into: sensory, somatomotor, and internal mentation[3] (Fig.1). The occurrence rates of each person in these three modes were calculated. Due to different protocols, ComBat was applied in statistical analyses[6]. Analysis of covariance (ANCOVA) was used to test the difference between groups with age, gender and education years as covariates. The presence of significant differences $P < 0.05$ was set.

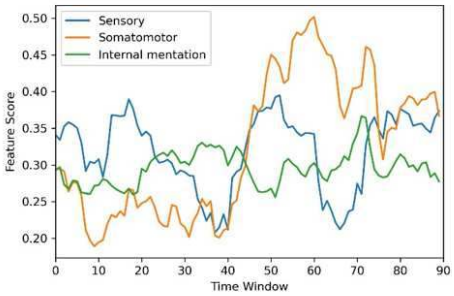

Fig1: The estimation for dynamic states by calculating feature scores (correlation) with three network states. The state for each time window was estimated by taking the corresponding state of the maximum value of the feature scores.

Results: As illustrated in Figure 2, there are significant differences in the occurrence rates of the Sensory and Somatomotor states between AD and HV group (p=0.018; p=0.014). There is no significant difference in terms of internal mentation state between groups. The occurrence rates of these two states are primarily influenced by the presence or absence of Alzheimer's disease. The findings of this study reveal that the dynamic states of the brain network in Alzheimer's disease.

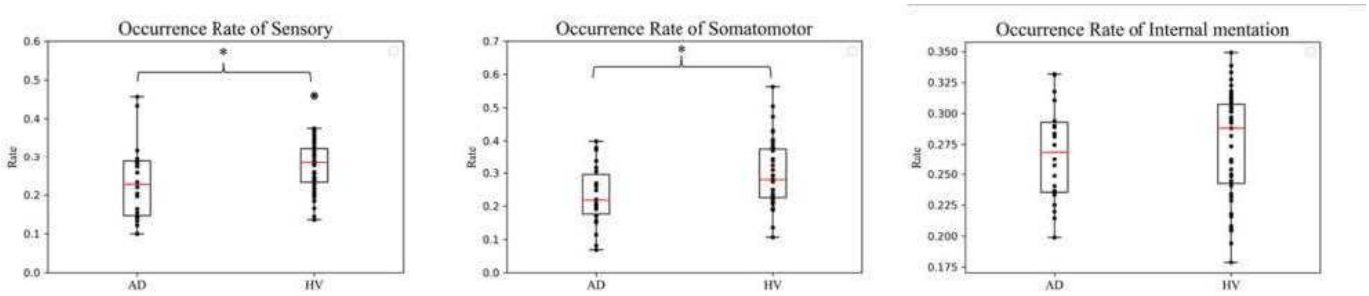

Conclusions: Alzheimer's patients showed lower occurrence rate in Sensory and Somatomotor states. Dynamic brain networks might be capable of quantifying the brain activity, serving as a reference indicator in the interpretation of Alzheimer's disease. The quantitative metrics of brain activity states assessed in this study may be as potential biomarkers in biomedical imaging.

References

1. Alzheimer's, A., 2012 Alzheimer's disease facts and figures. Alzheimers Dement, 2012. 8(2): p. 131-68.
2. Zhou, Q.J., et al., Tracking the Main States of Dynamic Functional Connectivity in Resting State. Frontiers in Neuroscience, 2019. 13.
3. Zhang, L., et al., Sensory, somatomotor and internal mentation networks emerge dynamically in the resting brain with internal mentation predominating in older age. Neuroimage, 2021. 237: p. 118188.
4. Alorf, A. and M.U.G. Khan, Multi-label classification of Alzheimer's disease stages from resting-state fMRI-based correlation connectivity data and deep learning. Comput Biol Med, 2022. 151(Pt A): p. 106240.
5. Rolls, E.T., et al., Effective Connectivity in Depression. Biological Psychiatry-Cognitive Neuroscience and Neuroimaging, 2018. 3(2): p. 187-197.
6. Johnson, W.E., C. Li, and A. Rabinovic, Adjusting batch effects in microarray expression data using empirical Bayes methods. Biostatistics, 2007. 8(1): p. 118-127.

Poster No 299

Subtype-specific patterns of tau pathology in Alzheimer's and related disorders

Diana Hobbs[1], Stephanie Doering[1], Austin McCullough[1], Pete Millar[1], Shaney Flores[1], Sarah Keefe[1], Aristeidis Sotiras[1], Tammie Benzinger[1], Gregory Day[2], Brian Gordon[1]

[1]Washington University School of Medicine, St. Louis, MO, [2]Mayo Clinic, Jacksonville, FL

Introduction: Alzheimer disease (AD) encompasses a range of neurodegenerative disorders marked by progressive cognitive decline (Hardy and Selkoe, 2002). Notably, atypical presentations like Posterior Cortical Atrophy (PCA) and Logopenic Variant Primary Progressive Aphasia (lvPPA) exhibit distinct clinical and neuroimaging profiles. PCA predominantly affects the posterior parietal and occipital lobes, leading to visuospatial deficits, while lvPPA primarily manifests as a language impairment

rooted in the temporoparietal region (Crutch et al., 2017; Gorno-Tempini et al., 2011). Unraveling the intricate biological underpinnings of these variants is crucial for understanding the heterogeneity within AD (Jack Jr. et al., 2010).

Methods: Participants diagnosed with AD dementia (n=54, female=25, Age: 75.23 ± 6.52), PCA (n = 9, female=8, Age: 62.78 ± 7.21), and lvPPA (n = 6, female=2, Age: 66.33 ± 6.38) from the Knight Alzheimer Disease Research Center (Knight ADRC) underwent 18F-AV-1451 tau-PET imaging. Standard uptake value ratios (SUVRs) highlighting tau deposition were mapped to the cortical surface (Figure 1A), along with nine other biological properties: gene expression, myelin, cortical thickness, sensorimotor association axis, evolutionary expansion, cerebral blood flow (CBF), cerebral blood volume (CBV), and cerebral metabolic rate of glucose (CMRglu) (Figure 1B). Correlation matrices and generalized linear models (GLMs) were conducted to assess the relationships between patterns of tau accumulation and biological properties.

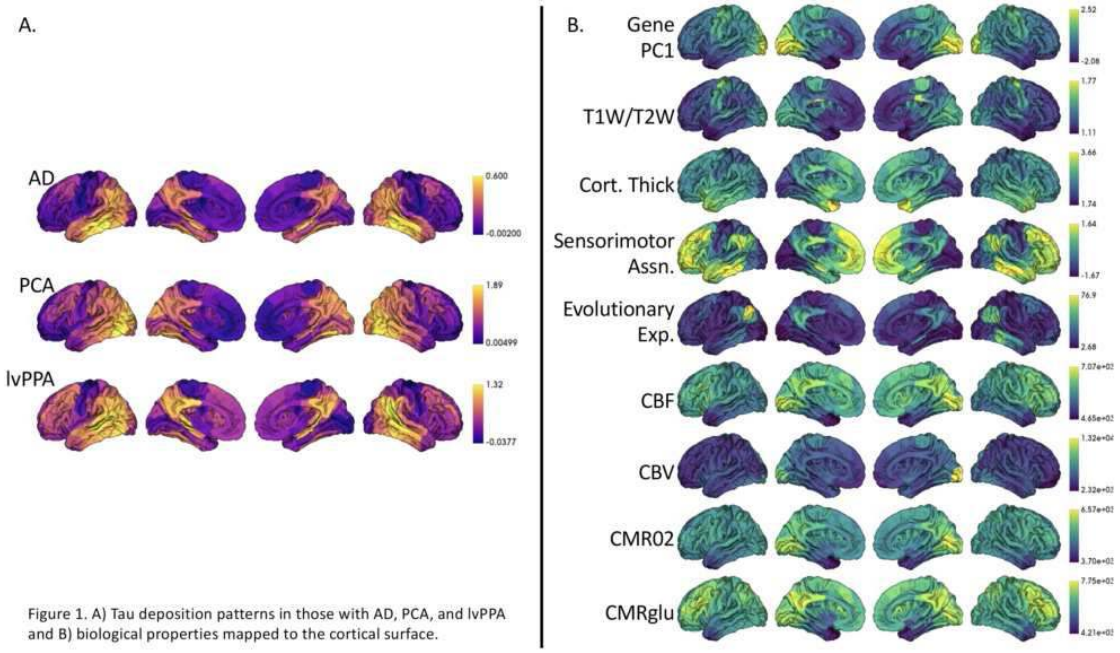

Figure 1. A) Tau deposition patterns in those with AD, PCA, and lvPPA and B) biological properties mapped to the cortical surface.

Results: A correlation matrix (Figure 2A) shows the strongest positive associations ($p<0.05$) between patterns of evolutionary expansion and tau accumulation in those with AD (r=0.53), PCA (r=0.29), and lvPPA (r= 0.56), as well as gene expression in PCA (r=0.51). Conversely, the strongest negative associations were observed in AD (r=-0.38, r=-0.15) and lvPPA (r=-0.18, r=-0.28) for CBF and myelin mapping, respectively, and in PCA (r=-0.25, -0.23) for cortical thickness and sensorimotor association axis. GLMs demonstrated significant relationships between cerebrovascular health and evolutionary expansion with measures of tau across all groups. AD (r=-0.52) and PCA (r=-0.19) exhibited negative associations with gene expression and myelin mapping, respectively, when considering all biological variables. Additionally, lvPPA (r=0.39) displayed positive association with patterns of the sensorimotor association cortex.

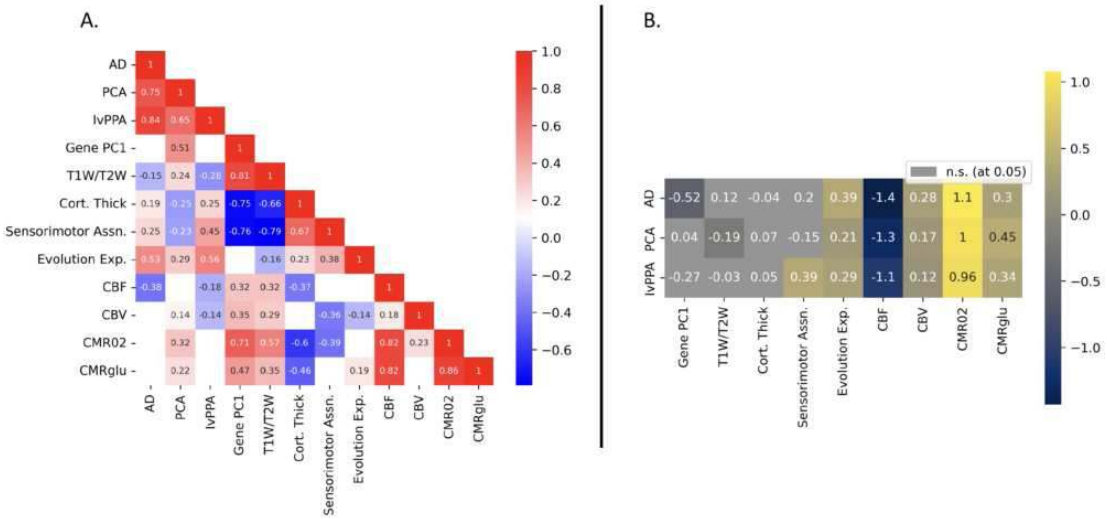

Figure 2. Associations between biological patterns and tau deposition in individuals with AD, PCA, and lvPPA depicted in an A) correlation matrix and B) generalized linear model.

Conclusions: These results elucidate distinct tau deposition patterns in AD, PCA, and lvPPA, and provide comprehensive insights into their subtype-specific pathophysiology. The correlation matrix and GLMs underscore the significance of evolutionary expansion and cerebrovascular health in influencing tau accumulation across all groups. Noteworthy associations, both positive and negative, highlight the complex interplay of gene expression, myelin mapping, and cortical thickness with tau pathology in specific variants. These findings contribute to our understanding of the heterogeneity within AD spectrum disorders and emphasize the multifaceted nature of neurodegenerative processes. Further research in this direction holds promise for refining diagnostic and therapeutic strategies tailored to the distinct neurobiological profiles observed in AD, PCA, and lvPPA.

References

1. Hardy, J. (2002), "The amyloid hypothesis of Alzheimer's disease: Progress and problems on the road to therapeutics", Science, vol. 297, no. 5580, pp. 353-356
2. Crutch, S.J. (2017), "Consensus classification of posterior cortical atrophy", Alzheimers Dementia, vol. 13, no. 8, pp. 870-884.
3. Gorno-Tempini, M.L. (2011), "Classification of primary progressive aphasia and its variants", Neurology, vol. 76, no. 11, pp. 1006-1014.
4. Jack Jr., C.R. (2010), "Hypothetical model of dynamic biomarkers of the Alzheimer's pathological cascade", Lancet Neurology, vol. 9, no. 1, pp. 119-128.

Poster No 300

Multi-scale investigation of the zona incerta subregions in Parkinson's Disease

Violet Liu[1], Ali Khan[2], Jonathan Lau[3]

[1]Western Univeristy, London, MT, [2]University of Western Ontario, London, Ontario, [3]Department of Clinical Neurological Sciences, Division of Neurosurgery, London, ON

Introduction: Parkinson's Disease (PD) is the second most prevalent neurodegenerative disorder worldwide[1]. Deep brain stimulation (DBS), a neurosurgical procedure that delivers electric pulses to specific brain regions, demonstrates long-term success in alleviating tremors in PD, especially when targeting a subcortical region named the zona incerta (ZI)[2]. However, the mechanisms behind this therapeutic effect remain elusive. Recent rodent research identifies a rostromedial ZI subregion, named the A13, that is uniquely enriched in dopaminergic neurons with connections to the nigrostriatal pathway[3,4]. Interestingly, this dopaminergic connectivity is preserved, yet undergoes re-configuration in animal PD models post-nigrostriatal degeneration[3,5]. Notably, inputs from the limbic and cortical regions are significantly downregulated, potentially contributing to the emotional processing deficit in PD[3,5]. Activation of the A13 dopaminergic neurons is also involved in nociceptive signaling, implicating this structure in PD-related chronic pain[6,7]. However, the A13 has not been identified in humans, impeding translation to clinical applications. To address this challenge, we aim to identify the A13 region using 3T and 7T MRI, and investigate the transcriptomic changes in this subregion between healthy control and PD patients. By integrating multiscale information to characterize this structure, our findings on the A13 may provide clues to the underlying mechanisms in PD, and provide future therapeutic targets for symptom control in the clinical setting.

Methods: We enrolled a cohort of healthy individuals (n=41, age 20-70) and PD patients (n = 46, age 51 - 73) for 3T and 7T MR imaging, and leveraged publicly available microarray from the Allen Human Brain Atlas (AHBA, n=68). We previously established the ability to directly visualize the ZI in vivo in humans8, and now further expand on this pipeline to identify the A13 subregion in T1-map and quantitative susceptibility mapping (QSM) MR data in MNI space. Using QSM, an established technique sensitive to tissue iron deposits, and T1-map, sensitive to progressive neuronal changes in PD patients9,10, we will identify changes in MR characteristics, such as T1-score, susceptibility score, and volumetric changes, between healthy participants and PD patients, and establish spatial correspondence between MRI with transcriptomics. The microarray from AHBA is preprocessed using the Abagen toolbox to produce a sample x gene matrix, with each sample representing an MNI coordinate. Principal component analysis (PCA) is performed followed by K-mean clustering to identify regional subclusters in Python. Optimal number of clusters was identified using WCSS and the elbow method. Gene set enrichment analyses are performed using ClusterProfile in R-studio to dissect the functional and biological relevance of clusters and examine molecular networks within the ZI.

Results: We have averaged and registered T1-map and quantitative susceptibility mapping (QSM) MR images from native to MNI space. Using the microarray data, PCA analysis (21 principal components, with a total of 81% variance explained) and K-mean clustering show 3 distinctive clusters along the rostral-caudal axis in the human ZI, corresponding to the caudal, rostral, and rostromedial regions. These clusters are enriched with significantly different cell type signatures, underscoring a unique organization within the ZI.

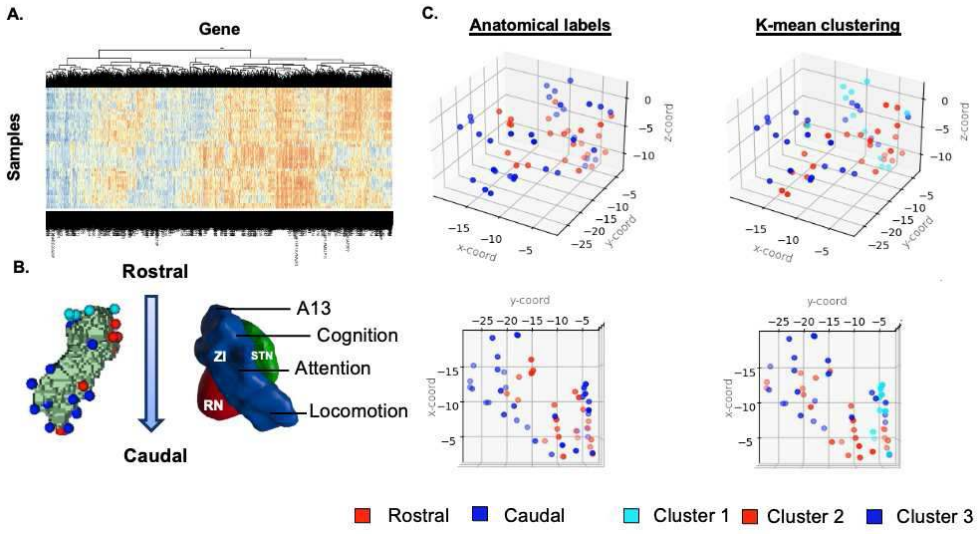

Figure 1. The human zona incerta exhibits distinctive molecular clusters. (A) Samples x gene matrix derived from the microarray dataset from the Allen Human Brain Atlas after pre-processing using Abagen (version). Each sample is correlated with a set of MRI coordinate in MNI space. (B) Area of sampling from the Allen Human Brain Atlas, compared with a schematic of the physiological functions in different ZI subregions. (C) PCA and K-mean clustering demonstrates 3 distinctive clusters based on gene expression, corresponding to the anatomical rostral, caudal, and rostromedial regions in ZI. Red nucleus, RN; Zona incerta, ZI; Subthalamic nucleus, STN.

Conclusions: Understanding the molecular and MR characteristics of ZI in healthy and diseased states represents a crucial step in unlocking its full therapeutic potential. Our findings show distinctive molecular and cellular profiles within the ZI, providing clues to identifying the A13 region in humans. A more in-depth understanding of the A13 subregion will provide opportunities to impact treatment, enhance accurate targeting in a clinical context, and ultimately improve patient outcomes.

References

1. Fujiwara, Yasuhiro, Tetsuyoshi Hirai, Tomohiro Ueda, Hiroyuki Kumazoe, and Shigeki Ito. 2021. "Quantitative T1 Mapping of the Substantia Nigra Using Phase-Sensitive Inversion Recovery Sequence at 3.0-T: A Healthy Volunteer Study." Acta Radiologica (Stockholm, Sweden: 1987) 62 (2): 243–50. https://doi.org/10.1177/0284185120920806.
2. Kim, Linda H., Taylor Chomiak, Michelle A. Tran, Stephanie Tam, Claire McPherson, Shane E. A. Eaton, Young Ou, Zelma H. T. Kiss, and Patrick J. Whelan. 2021. "Substantia Nigra Degradation Results in Widespread Changes in Medial Zona Incerta Afferent and Efferent Connectomics." bioRxiv. https://doi.org/10.1101/2021.09.01.458438.
3. Kim, Linda H., Adam Lognon, Sandeep Sharma, Michelle A. Tran, Taylor Chomiak, Stephanie Tam, Claire McPherson, Shane E. A. Eaton, Zelma H. T. Kiss, and Patrick J. Whelan. 2023. "Restoration of Locomotor Function Following Stimulation of the A13 Region in Parkinson's Mouse Models." eLife 12 (November). https://doi.org/10.7554/eLife.90832.
4. Kouli, Antonina, Kelli M. Torsney, and Wei-Li Kuan. 2018. "Parkinson's Disease: Etiology, Neuropathology, and Pathogenesis." In Parkinson's Disease: Pathogenesis and Clinical Aspects, edited by Thomas B. Stoker and Julia C. Greenland. Brisbane (AU): Codon Publications. http://www.ncbi.nlm.nih.gov/books/NBK536722/.
5. Langkammer, Christian, Lukas Pirpamer, Stephan Seiler, Andreas Deistung, Ferdinand Schweser, Sebastian Franthal, Nina Homayoon, et al. 2016. "Quantitative Susceptibility Mapping in Parkinson's Disease." PloS One 11 (9): e0162460. https://doi.org/10.1371/journal.pone.0162460.
6. Lau, Jonathan C., Yiming Xiao, Roy A. M. Haast, Greydon Gilmore, Kâmil Uludağ, Keith W. MacDougall, Ravi S. Menon, Andrew G. Parrent, Terry M. Peters, and Ali R. Khan. 2020. "Direct Visualization and Characterization of the Human Zona Incerta and Surrounding Structures." Human Brain Mapping 41 (16): 4500–4517. https://doi.org/10.1002/hbm.25137.
7. Moriya, Shunpei, and Tomoyuki Kuwaki. 2020. "A13 Dopamine Cell Group in the Zona Incerta Is a Key Neuronal Nucleus in Nociceptive Processing." Neural Regeneration Research 16 (7): 1415–16. https://doi.org/10.4103/1673-5374.300991.
8. Moriya, Shunpei, Akira Yamashita, Daiki Masukawa, Honami Setoyama, Yunsu Hwang, Akihiro Yamanaka, and Tomoyuki Kuwaki. 2020. "Involvement of A13 Dopaminergic Neurons Located in the Zona Incerta in Nociceptive Processing: A Fiber Photometry Study." Molecular Brain 13 (1): 60. https://doi.org/10.11

Poster No 301

Essential Tremor: The Relationship Between Hand Dominance and Tremor Severity by MVPA

Alma Torres-Torres[1], Jelle Dalenberg[1], A.M. Van Der Stouwe[1], Marina Tijssen[1]

[1]*University Medical Center Groningen, Groningen, Groningen*

Introduction: Essential Tremor (ET) is a prevalent movement disorder, affecting approximately 1.3% of the global population[1]. Characterized by involuntary oscillatory postural tremors of the upper limbs, ET impacts daily activities and diminishes the quality of life. Despite its prevalence, the precise etiology of ET remains unclear. This study analyses task-based functional Magnetic Resonance Imaging (task-fMRI) to explore neural activity in individuals with ET compared to healthy controls (HC). The research also delves into the intricate relationship between hand dominance and tremor severity, aiming to contribute to the understanding of the brain networks related to this heterogeneous disorder.

Methods: Eighteen ET right-handed subjects were included for this study from the Next Move in Movement Disorders (NEMO)[2]. 20 HC right-handed subjects were age-matched with the ET group. For ET the severity of each hand was assessed using the Fahn Tolosa Marin Essential Tremor Scale[3]. Participants performed a finger tapping task that alternated between left and right in a block design, as illustrated in Figure 1, this block were repeated five times. MRI data were collected on a 3T Siemens Prisma scanner at the UMCG using a Siemens 64-channel head coil. Task-based fMRI scans were acquired using a multi-band, multi-echo T2*-weighted echo-planar sequence with the following scanning parameters: TR=1.101 ms; TE=12, 36.1, 60.2 ms; voxel size=3.5 mm isotropic. The fMRI data were preprocessed using a custom pipeline, incorporating fMRIprep v22.0.2, TE-dependence analysis v0.0.12[4], and Advanced Normalization Tools v2.3.5[5]. Task-fMRI data were analyzed using searchlight multi-voxel pattern analysis (MVPA) to identify differences between ET and HC. First, BrainIAK v0.11[6] was used, classifying right hand vs. rest and left hand vs. rest for each subject using four post-stimulus time-lags. Spheres with a 5 mm radius were applied, employing radial basis function (RBF) SVM in a stratified 5-fold cross-validation from scikit-learn (v1.1.0), resulting in an accuracy map for each subject and lag. Secondly, group-level statistical analysis was performed per lag with a non-parametric permutation method, contrasting ET > HC. Age and tremor severity were added as covariates.. Statistical thresholding was set at $p < 0.001$ and FDR corrected ($\alpha=0.05$). Additionally, we investigated which brain areas correlated with tremor severity.

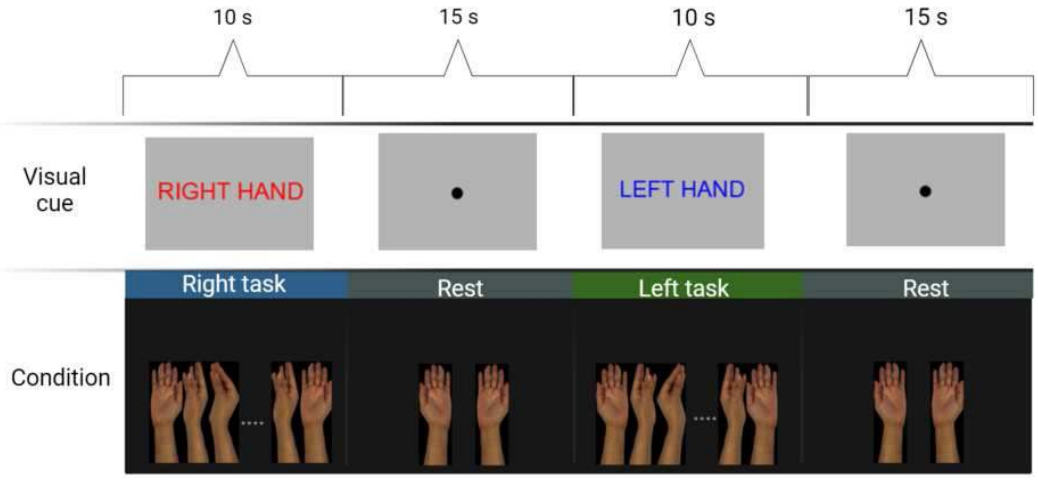

Results: In the HC, the experimental paradigm activated the expected motor networks, revealing significant differences between the dominant and non-dominant hand tasks. ET exhibited similar activation patterns within motor networks. However, ET displayed a distinctive activation pattern in the frontal lobe in both tasks, areas that were not prominent in the HC. Specifically, HC revealed lower MVPA accuracy during the non-dominant task in the cerebellum and left thalamus compared to ET. Tremor severity analysis in ET revealed a positive correlation between tremor severity and MVPA accuracy in the inferior olive region during the dominant hand task, consistent with previous reports[7]. Additionally, in the non-dominant hand task, tremor severity correlated positively with cerebellar MVPA accuracy.

Conclusions: In summary, our study aims to improve the comprehension of the brain networks in ET by leveraging this integration of MVPA analysis. Through MVPA analysis, we identified regions of interest associated with intentional movement in ET, some of which are novel and include frontal areas not previously reported in the literature. The inferior olive seems to play a modulating role ET in dominant hand, and cerebellum in the non-dominant hand. Further research on these identified regions holds promise for a deeper understanding of ET pathophysiology.

References

1. DuPre, Elizabeth, Taylor Salo, Zaki Ahmed, Peter A. Bandettini, Katherine L. Bottenhorn, César Caballero-Gaudes, Logan T. Dowdle, et al. 2021. “TE-Dependent Analysis of Multi-Echo FMRI with *tedana*.” Journal of Open Source Software 6 (66): 3669. https://doi.org/10.21105/JOSS.03669.

2. Esteban, Oscar, Christopher J. Markiewicz, Ross W. Blair, Craig A. Moodie, A. Ilkay Isik, Asier Erramuzpe, James D. Kent, et al. 2018. "FMRIPrep: A Robust Preprocessing Pipeline for Functional MRI." Nature Methods 2018 16:1 16 (1): 111–16. https://doi.org/10.1038/s41592-018-0235-4.
3. Fahn S, Tolosa E, Conceppcion M. 1993. "Clinical Rating Scale for Tremor In: Jankovic J, Tolosa E, Eds." In Parkinson's Disease and Movement Disorders., 271–280.
4. Kumar, Manoj, Michael J. Anderson, James W. Antony, Christopher Baldassano, Paula P. Brooks, Ming Bo Cai, Po-Hsuan Cameron Chen, et al. 2022. "BrainIAK: The Brain Imaging Analysis Kit." Aperture Neuro 2021 (4). https://doi.org/10.52294/31BB5B68-2184-411B-8C00-A1DACB61E1DA.
5. Louis, Elan D., and Morgan McCreary. 2021. "How Common Is Essential Tremor? Update on the Worldwide Prevalence of Essential Tremor." Tremor and Other Hyperkinetic Movements 11 (1). https://doi.org/10.5334/TOHM.632.
6. Sharifi, S., F. Luft, L. de Boer, A. W.G. Buijink, W. Mugge, A. C. Schouten, T. Heida, L. J. Bour, and A. F. van Rootselaar. 2022. "Closing the Loop: Novel Quantitative FMRI Approach for Manipulation of the Sensorimotor Loop in Tremor." NeuroImage 262 (November): 119554. https://doi.org/10.1016/J.NEUROIMAGE.2022.119554.
7. Stouwe, A.M.M. van der, I Tuitert, Ioannis Giotis, J Calon, R Gannamani, J.R. Dalenberg, S. van der Veen, M.R. Klamer, A C Telea, and M.A.J. Tijssen. 2021. "The next Move in Movement Disorders (NEMO): Developing a Computer Aided Classification Tool for Hyperkinetic Movement Disorders." BMJ Open.

Poster No 302

Impaired EEG in Amyotrophic Lateral Sclerosis correlates with distinct neurotransmitter systems

Gabriel Costa[1], Marjorie Metzger[2], Stefan Dukic[3], Orla Hardiman[4], Bahman Nasseroleslami[4]

[1]Trinity Biomedical Sciences Institute, Coimbra, Portugal, [2]Trinity College Dublin, Dublin, Dublin, [3]UMC, Utrecht, Netherlands, [4]Trinity College Dublin, Dublin, Ireland

Introduction: Amyotrophic lateral sclerosis (ALS) is a fatal neurodegenerative disease affecting primarily motor neurons, first described more than a century ago. While degeneration manifests mainly in upper and lower motor neurons there is a significant frontotemporal circuit involvement. It remains a disease with poor prognosis and no effective treatment. ALS displays clinical heterogeneity, and despite its predictable evolution the pathophysiology and triggers of the disease remain unknown. Evidence of impaired neuronal activity and network dysfunction has been identified in the spectral content of resting-state EEG in ALS when compared to healthy controls. More importantly, these EEG abnormalities have been shown to correlate with structural changes and clinical manifestations in ALS[1-3]. We have previously spatially localized this impaired neuroelectric activity, but the identity of the neuronal population and circuits affected remains unknown. Here we aim to characterize the underlying molecular and cellular features of the brain areas where these early EEG biomarkers of ALS manifest. Using source localization of high-density resting-state EEG, we have spatially correlated spectral differences between healthy controls and ALS patients with normative mappings of neurotransmitter systems.

Methods: We recorded high-density resting-state EEG from 94 individuals with ALS and 81 healthy controls. The time-series of 90 anatomically distinct brain regions (Automatic Anatomical Labelling, AAL) were obtained using LCMV beamformer for source localization in the time domain. Normalized spectral power was obtained for each region for the delta (2-4 Hz), theta (5-7 Hz), alpha (8-13 Hz), beta (14-30 Hz), low-gamma (31-47 Hz) and high-gamma (53-97 Hz) bands. Differences between controls and ALS patients were estimated as t-values which were correlated with several neurotransmitter brain mappings using a novel Python toolbox, neuromaps[4].

Results: We had previously described a significant decrease in spectral power in the alpha and beta frequency bands in ALS patients[2]. A significant correlation between alpha power differences was found for the density of 5-HT1a and 5-HT2a serotonin receptors (Spearman correlation, $\rho = 0.32$, FDR-adjusted $p < 0.05$; $\rho = 0.39$, FDR-adjusted $p < 0.01$, respectively), while beta power differences show significant correlation with 5-HT1a and with the serotonin transporter 5-HTT ($\rho = 0.50$, FDR-adjusted $p < 0.001$; $\rho = 0.46$, FDR-adjusted $p < 0.001$, respectively). These receptors correspond mainly to presynaptic serotonin receptors that exert inhibitory feedback and postsynaptic receptors that can modulate motor neuron excitation. Moreover, the strong correlation with the 5-HTT/SERT serotonin transporter suggests that the spectral differences found in the ALS EEG might arise from an impairment of the dense innervations of the serotonergic system arising from the brainstem. We have further identified that areas with reduced beta power also showed a correlation with the density of dopamine receptors D1 and D2 ($\rho = 0.38$, FDR-adjusted $p < 0.001$; $\rho = 0.44$, FDR-adjusted $p < 0.001$, respectively), suggesting that the affected areas might be involved in the interplay between serotonergic and dopaminergic systems.

Conclusions: Our study provides compelling evidence that the altered EEG signals can be a consequence of serotonergic dysfunction in ALS[5], which has been proposed as a cause of inhibitory motor control and excitotoxicity in ALS.

References
1. Dukic, S. et al (2022) Resting-state EEG reveals four subphenotypes of amyotrophic lateral sclerosis. Brain. 145(2):621-31. doi: 10.1093/brain/awab322.
2. Dukic, S. et al (2019) Patterned functional network disruption in amyotrophic lateral sclerosis. Human Brain Mapping. 40(16):4827-42. doi: 10.1002/hbm.24740.
3. Nasseroleslami, B. et al (2019) Characteristic Increases in EEG Connectivity Correlate With Changes of Structural MRI in Amyotrophic Lateral Sclerosis. Cerebral Cortex. 29(1):27-41. doi: 10.1093/cercor/bhx301.
4. Markello, R.D. et al (2022). neuromaps: structural and functional interpretation of brain maps. Nature Methods. doi: 10.1038/s41592-022-01625-w.
5. Vermeiren, Y. et al (2018) Serotonergic Dysfunction in Amyotrophic Lateral Sclerosis and Parkinson's Disease: Similar Mechanisms, Dissimilar Outcomes. Frontiers of Neuroscience. 12:185. doi: 10.3389/fnins.2018.00185.

Poster No 303

Relationship Between Cerebrospinal Fluid Flow in the Subarachnoid Space and Beta-Amyloid Deposition

Jeongchul Kim[1], Megan Lipford[1], Richard Barcus[2], Jeremy Hudson[2], Hongyu Yuan[2], Kiran Soligapram[1], Qing Lyu[1], Samuel Lockhart[1], Suzanne Craft[1], Christopher Whitlow[1]

[1]Wake Forest School of Medicine, Winston Salem, NC, [2]Wake Forest Baptist Medical Center, Winston Salem, NC

Introduction: Recent studies identified the lymphatic drainage system in the brain where cerebrospinal fluid (CSF) carries waste from brain tissue. However, it is still not well understood how CSF circulation in the brain affects waste removal. In this study, we hypothesize that CSF flow dynamics in the subarachnoid space will be correlated with beta-amyloid deposition in the brain.

Methods: Thirteen participants (7 Cognitively Normal and 2 Mild Cognitive Impairment, Age=68±7.7 yrs. M/F=5/4) who had prior amyloid PET imaging were recruited for CSF flow MRI from the Wake Forest Alzheimer's Disease Research Center. The CSF flow patterns during the cardiac cycle were measured using the phase-contrast MRI at the cerebral aqueduct, pontine cistern and cerebellomedullary cistern (Figure 1). Images were acquired for 40 cardiac cycles with a pulse oximeter and CSF flow profiles were estimated using the retrospective cardiac gating method. PET Amyloid burden in the whole gray matter (GM) was measured as the standardized update value ratio (SUVR, cerebellar gray matter as a reference region) from the prior PET imaging and corresponding MRI.

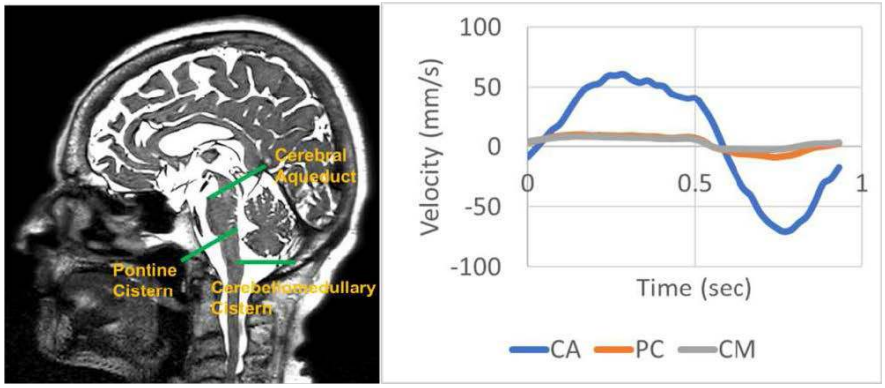

Results: CSF flow amplitude normalized by the intracranial volume (ICV) demonstrated moderate to strong correlations with beta-Amyloid SUVR in GM (Figure. 2); Pearson's correlation coefficient (rho) was -0.59 (p=0.036) and -0.84 (p=0.004) at pontine cistern and cerebellomedullary cistern, respectively. The lateral ventricle volume normalized by ICV was also moderately correlated with GM SUVR (rho=0.495).

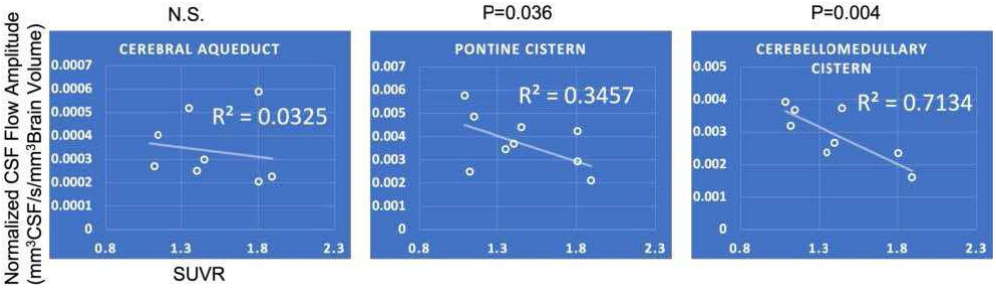

Conclusions: At an early stage of AD, the CSF circulation in the subarachnoid space could be correlated with beta-Amyloid deposition. Therefore, CSF flow in the subarachnoid space could be a useful imaging marker to predict the clearance of beta-amyloid in the brain.

References

1. Mawuenyega KG, Sigurdson W, Ovod V, Munsell L, Kasten T, Morris JC, Yarasheski KE, Bateman RJ. Decreased clearance of CNS beta-amyloid in Alzheimer's disease. Science. 2010;330(6012):1774.
2. Iliff JJ, Wang M, Liao Y, Plogg BA, Peng W, Gundersen GA, Benveniste H, Vates GE, Deane R, Goldman SA, Nagelhus EA, Nedergaard M. A paravascular pathway facilitates CSF flow through the brain parenchyma and the clearance of interstitial solutes, including amyloid beta. Sci Transl Med. 2012;4(147):147ra11.

Poster No 304

White matter abnormalities predict social gullibility in behavioral variant frontotemporal dementia

Jayden Lee[1], Derek Archer[1,2], Ryan Darby[1]

[1]Vanderbilt University Medical Center, Nashville, TN, [2]Vanderbilt Memory and Alzheimer's Center, Nashville, TN

Introduction: Risk for financial exploitation is a devastating but common problem among the elderly, amounting to an approximate loss of $30 billion each year. Older adults with behavioral variant frontotemporal dementia (bvFTD) are particularly susceptible to falling victim to financial fraud; however, only one other study has examined this social vulnerability in bvFTD (Wong 2017) and the neural substrates for this impairment are still very much unknown. Recent studies have found that measuring white matter integrity using diffusion tensor imaging (DTI) and neurite orientation dispersion and density imaging (NODDI) (Zhang 2022) may provide sensitive biomarkers for behavioral or cognitive decline even in the absence of volumetric evidence, especially in the preclinical phase. NODDI method specifically has been shown to provide higher sensitivity and greater tissue specificity compared with conventional DTI for identifying white matter abnormalities. The present study examines whether DTI and NODDI metrics for degeneration in white matter tracts are associated with increased gullible behaviors in bvFTD.

Methods: Multi-shell diffusion magnetic resonance imaging data were acquired for 39 bvFTD patients (29 male, age 63.9 ± 9.2 yrs). Diffusion images (resolution: 2mm isotropic, b-values: 0, 1000s/mm2) were collected along 32 diffusion gradient vectors and 1 B0 weighted image. Preprocessing was done using the PreQual pipeline (Cai 2021) and Synb0-DISCO (Schilling 2019) for susceptibility distortion correction. Quality assessment for all subjects' corrected images was confirmed by visual inspection. Social gullibility was measured using the informant-reported Social Vulnerability Scale, previously validated for identifying factors leading to vulnerability to exploitation (Pinsker 2011). White matter microscopic degeneration was assessed using DTI measures of fractional anisotropy, mean diffusivity (MD), and radial diffusivity (RD) and NODDI measures of intra-cellular volume fraction, i.e., neurite density index (NDI), orientation dispersion index, and isotropic volume fraction (ISOVF), i.e., extra-cellular free water within several well-established white matter tracts of interest (Archer 2019). Associations between diffusion metrics and gullibility scores were determined using multiple linear regression models controlling for age, sex, and global cognition level via MoCA (Nasreddine 2005). Statistical significance was determined at $p < 0.05$, Family Wise Error corrected.

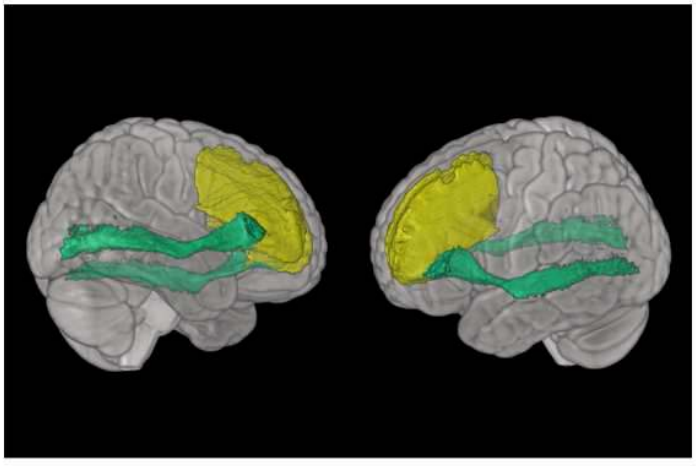

Figure 1. White matter tracts associated with gullibility in behavioral variant frontotemporal dementia (bvFTD) patients: **caudate to superior frontal** bilateral tract (in *yellow*) and **inferior fronto-occipital fasciculus** (IFOF) bilateral tract (in *green*) from tractography template (Archer 2019).

Results: DTI and NODDI analysis demonstrated significant negative associations between gullibility and loss of tissue organization in bilateral long-range association and frontostriatal tracts. Lower NDI and increased MD, RD and ISOVF in the caudate-to-superior-frontal tract and lower NDI and increased MD, RD and ISOVF in the inferior fronto-occipital fasciculus (IFOF) tract were associated with higher gullibility in bvFTD. The combination of the two patterns of disruption of decreased neurite density and increased water diffusivity (MD, RD) and increased extra-cellular free water in the same tract is an indicator of neurodegeneration (Daianu 2016) in these caudate-to-superior-frontal and IFOF tracts.

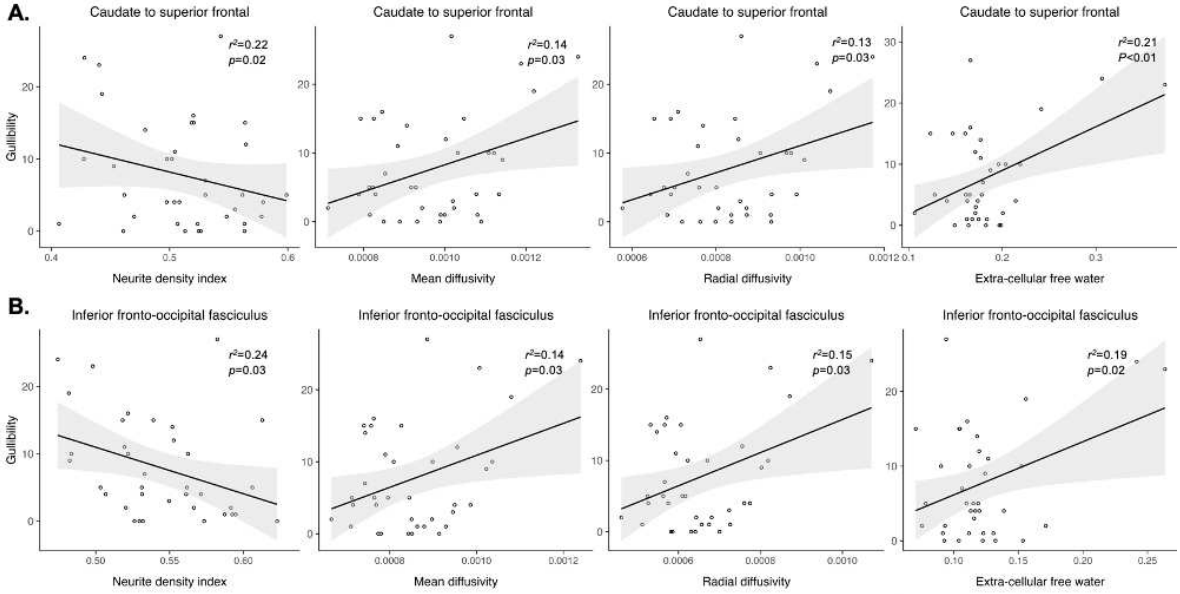

Figure 2. White matter tract degeneration, measured by decreased neurite density index and increased mean diffusivity, radial diffusivity, and extra-cellular free water in the **(A)** Caudate to superior frontal bilateral tract and the **(B)** Inferior fronto-occipital fasciculus bilateral tract are associated with increased gullibility in behavioral variant frontotemporal dementia (bvFTD) patients.

Conclusions: Our results suggest that white matter abnormalities in the caudate to superior frontal and IFOF tracts may be predictive of increased gullible behaviors in bvFTD patients, even while controlling for global cognition level. Degeneration in the IFOF and caudate frontostriatal tracts have previously been linked with interpersonal impairment and abnormal behavior (Waller 2017; Hampton 2017). The present findings relating white matter tract integrity with gullibility indicate a neural basis for this symptom in bvFTD. This is one of the first studies to use NODDI metrics in frontotemporal dementia and reveals sensitive markers for neurodegeneration, providing promise for future use of this method to studying social and behavioral impairments.

References

1. Archer DB. (2019) Development of a transcallosal tractography template and its application to dementia. NeuroImage 200:302–312.
2. Cai LY. (2021) PreQual: An automated pipeline for integrated preprocessing and quality assurance of diffusion weighted MRI images. Magnetic Resonance in Med 86(1):456–470.
3. Daianu M. (2016) An advanced white matter tract analysis in frontotemporal dementia and early-onset Alzheimer's disease. Brain Imaging and Behavior 10(4):1038–1053.
4. Hampton WH. (2017) Dissociable frontostriatal white matter connectivity underlies reward and motor impulsivity. NeuroImage 150:336–343.
5. Nasreddine ZS. (2005) The Montreal Cognitive Assessment, MoCA: A Brief Screening Tool For Mild Cognitive Impairment: MOCA: A BRIEF SCREENING TOOL FOR MCI. Journal of the American Geriatrics Society 53(4):695–699.
6. Pinsker DM. (2011) The Social Vulnerability Scale for Older Adults: An Exploratory and Confirmatory Factor Analytic Study. Journal of Elder Abuse & Neglect 23(3):246–272.
7. Schilling KG. (2019) Synthesized b0 for diffusion distortion correction (Synb0-DisCo). Magn Reson Imaging 64:62–70.
8. Waller R. (2017) White-matter tract abnormalities and antisocial behavior: A systematic review of diffusion tensor imaging studies across development. NeuroImage: Clinical 14:201–215.
9. Wong S. (2017) Should I trust you? Learning and memory of social interactions in dementia. Neuropsychologia 104:157–167.

Poster No 305

Nigrosome neuromelanin loss at 3T MRI has diagnostic value in clinical uncertain parkinsonism

Yue Xing[1,2,3], Stefan Pszczolkowski[1,2,3], Saadnah Naidu[1,2], Marta Gennaro[4,5], Andreas-Antonios Roussakis[6], Tayyib Hayat[1,2,7], Jonathan Evans[7], Antonio Martin-Bastida[4,8], Christopher Tench[1,3], Paola Piccini[4,6,9], Stefan Schwarz[1,2,10], Dorothee Auer[1,2,3]

[1]Mental Health and Clinical Neurosciences Unit, University of Nottingham, Nottingham, United Kingdom, [2]Sir Peter Mansfield Imaging Centre, School of Medicine, University of Nottingham, Nottingham, United Kingdom, [3]NIHR Nottingham Biomedical Research Centre, Queen's Medical Centre, University of Nottingham, Nottingham, United Kingdom, [4]Division of Neurology, Imperial College London, London, United Kingdom, [5]Nuclear Medicine Department, Royal Brompton & Harefield Hospitals, Guy's and St Thomas' NHS Foundation Trust, London, United Kingdom, [6]NHLI Department, Imperial College London, Hammersmith Campus, London, United Kingdom, [7]Department of Neurology, Nottingham University Hospitals, Nottingham, United Kingdom, [8]Department of Neurology and Neurosciences, Clínica Universidad de Navarra, Pamplona-Madrid, Spain, [9]Department of Brain Science, Imperial College London, London, United Kingdom, [10]Department of Radiology, Cardiff and Vale University Health Board, Cardiff, United Kingdom

Introduction: Pigmentation loss of nigrosome 1 (NS1) in the substantia nigra on neuromelanin-sensitive MRI (NM-MRI) is now well established as early sign of clinical Parkinson's (Sung, 2021). It remains unclear whether NS1 depigmentation can predict Parkinson disease (PD) even earlier when presenting with clinical uncertan parkinsonism (CUP). We aimed to address this as secondary aim of our prospective multi-centre multi-modal imaging study in CUP (Schwarz, 2017). Here we report the diagnostic value of NS1 pigmentation contrast in CUP against the diagnosis of Parkinson's or non-neurodegenerative parkinsonism at clinical follow-up. We also explored the effect of laterality and scanning site on prediction.

Methods: 110 participants (61 [34 males, 31 PD, Site1], 49 [27 males, 37 PD, Site2]) with quality-controlled NM-MRI at 3T (details in (Xing, 2023)) and clinical follow-up (FU) >1 year were included under local ethics approval (Health Research Authority East Midlands – Derby Research Ethics Committee. REC ref.: 16/EM/0229). NM-MRI was analysed using an optimised in-house pipeline (Pszczolkowski, 2023). NS1 ROIs were manually defined on normative susceptibility weighted MRI to derive averaged unilateral and bilateral NS1 pigmentation to background contrasts. Binary logistic regression was used in cohort1 [Site1] to test the effect of diagnostic status as dependent on the NS1 contrast as independent outcome variable with age and sex as covariates (first bilaterally and then unilateral-contralateral to most affected side in the subgroup with asymmetric presentation, N=60). The effect-size was calculated as adjusted t-values. The test was also repeated in the independent cohort2 [Site2] as cross-site validation.

Results: NS1 pigmentation was significantly lower in CUP with FU diagnosis of PD (0.15±0.02) compared to those with other, non-degenerative diagnoses (0.17±0.02, p=0.0005, t=-3.49, Figure1-A) in cohort1 [Site1]. The effect of future diagnosis was confirmed in cohort2 [Site2] (PD-CUP: 0.13±0.02; non-PD: 0.09±0.03, p=0.002, t=-3.1, Figure1-B), despite protocol-dependent differences in NS1 neuromelanin (NM) ratios (nonPD: 0.13±0.02; PD-CUP: 0.09±0.03, p=0.002, t=-3.1). Similar pattern of group difference is shown for unilateral NS1 in Figure2-A and Figure 2-B. Discriminative powers of bilateral and unilateral NS1 are demonstrated for both sites (Figure2-C), with highest AUC values in Site2 that exceeded the diagnostic performance considered to be clinically useful (80% sensitivity and 80% specificity-the estimated point is also shown for visual comparison). This is followed by the unilateral NS1 NM contrasts for cohort2 [Site2] and then bilateral NS1 for cohort1 [Site1], both nearly achieving the clinically useful level. The unilateral NS1 NM contrast for cohort1 [Site1] met the sensitivity but narrowly missed the specificity threshold.

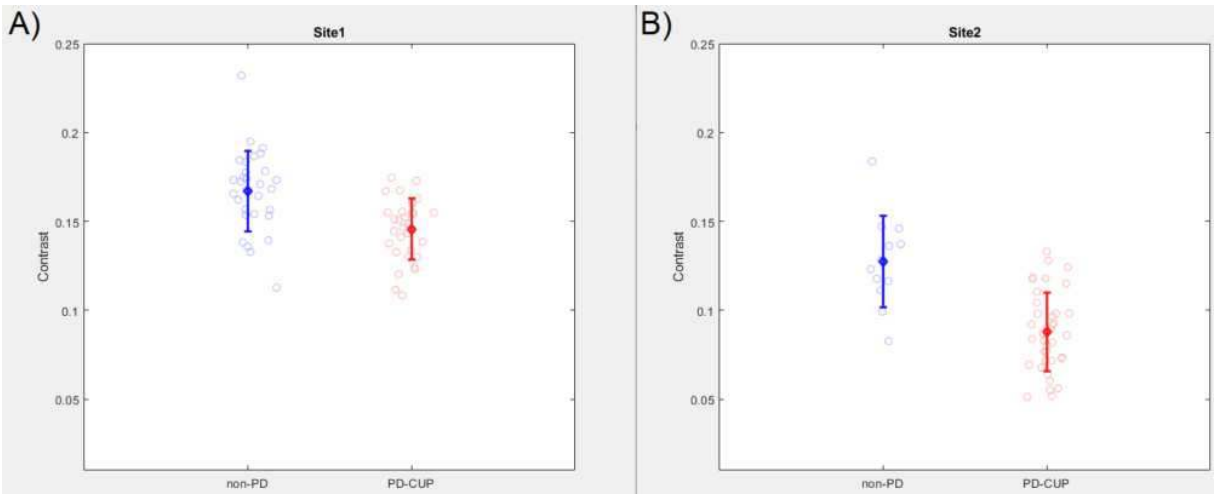

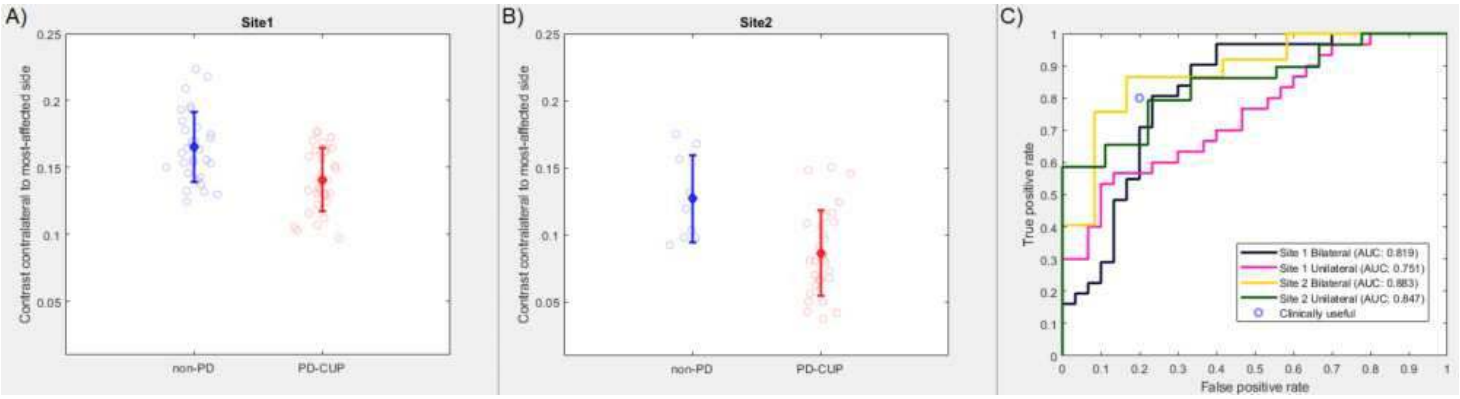

Conclusions: Our results show that MR detectable pigmentation loss of NS1 can be seen in CUP who will later be diagnosed as Parkinson's compared to other non-degenerative causes of Parkinson's. The diagnostic performance of this simple MRI test may be clinically useful with one site achieving predefined sensitivity and specificity with bilateral NS1. Further investigation is on-going to explore improved prediction models by inclusion of available baseline clinical findings including laterality and other MR modalities.

References

1. Pszczolkowski, S. (2023). SPMIC-UoN Parkinson's Processing Pipeline. GitHub. https://github.com/SPMIC-UoN/parkinsons_pipeline
2. Sung, Y. H. (2021). Early-stage Parkinson's disease: Abnormal nigrosome 1 and 2 revealed by a voxelwise analysis of neuromelanin-sensitive MRI. Human Brain Mapping, 42(9), 2823-2832.
3. Schwarz, S. T. (2017). Protocol of a single group prospective observational study on the diagnostic value of 3T susceptibility weighted MRI of nigrosome-1 in patients with parkinsonian symptoms: the N3iPD study (nigrosomal iron imaging in Parkinson's disease). BMJ open, 7(12), e016904.
4. Xing, Y. (2023). Nigrosome depigmentation as seen on neuromelanin-sensitive MRI at 3T as diagnostic marker in clinical uncertain parkinsonism: analysis plan for the secondary aims of N3iPD study. Nottingham Research Data Management Repository. https://rdmc.nottingham.ac.uk/handle/internal/10932

Poster No 306

Advancing Understanding of ALS Motor Dysfunction: 7T fMRI Explores Neural Mechanisms

Avinash Kalyani[1], Christoph Reichert[2], Alicia Northall[3], Esther Kühn[4]

[1]Otto-von-Guericke-University Magdeburg, Magdeburg, Saxony Anhalt, [2]Leibniz Institute for Neurobiology, Magdeburg, Saxony Anhalt, [3]Nuffield Department of Clinical Neurosciences, Oxford, United Kingdom, [4]German Center for Neurodegenerative Diseases (DZNE), Tübingen, Baden-Württemberg

Introduction: Amyotrophic Lateral Sclerosis (ALS) poses challenges in understanding motor learning deficits. Leveraging the heightened sensitivity of 7 T fMRI, we explored the neural substrates of motor learning in ALS. Employing Shared Response Modeling (SRM) for inter-subject normalization, we identified robust neural patterns. Partial Least Squares (PLS) analysis revealed associations between 7T fMRI data and behavioral outcomes, shedding light on the intricate neural mechanisms underlying motor dysfunction in ALS. Our study highlights the pivotal role of 7T fMRI and advanced analytical techniques in enhancing our understanding of ALS-related motor impairments which can help to develop potential therapeutic strategies.

Methods: In the study conducted between June 2018 and December 2022, 12 individuals diagnosed with Amyotrophic Lateral Sclerosis (ALS) (6 females, age: M = 60.5, SD = 12.7) were compared to an equal number of age, handedness, gender, and education-matched healthy controls (6 females, age: M = 61.1, SD = 11.9). Disease onset varied among patients, with 7 having upper limb-onset, 2 with lower limb-onset, and 3 with bulbar-onset (Alicia, 2023). Data collection utilized a 7T-MRI scanner in Magdeburg, Germany, a 1.5 mm isotropic resolution fMRI was obtained using an EPI GE-BOLD sequence. The fMRI employed a blocked-design paradigm with 12-sec movement periods (left/right foot, left/right hand, tongue) alternated with 15-sec rest intervals, with 20 trials (75 min). A GLM analysis was employed to localize the voxels specific to the body part moved. In the SRM (Chen, 2015) analysis, the data underwent reordering, and subsequently, a linear SVM was trained for both classification purposes and in the context of Partial Least Squares (PLS) analysis. The ALS Functional Rating Scale-Revised (ALSFRS-R) data served as the behavioral dataset to train and fit the PLS regression model. This approach allowed for the exploration and integration of shared neural response patterns and behavioral outcomes, providing a comprehensive understanding of the relationships between the observed brain activity and motor function in the context of ALS.

Results: The study identified significant group differences in different ROIs localized using GLM for various body part movements, evidenced by a permutation test score showing above-chance accuracy in distinguishing healthy controls from ALS patients (Figure 1, A). Tongue region classification accuracy was relatively lower, potentially due to the limited number of Bulbar onset ALS subjects. Predictability for upper limb movements in ALS was notably reduced, in line with the prevalence of upper limb onset in patients (Figure 1, B). Controls exhibited higher movement-based task stimulus classification, with mean values of 0.53 (SD = 0.16) compared to 0.45 (SD = 0.11) for ALS patients. PLS regression analysis connecting ALSFRS-R scores and fMRI data revealed higher mean squared error (MSE) for foot region and hand task behavioral scores, indicating lower predictability for hand-based measurements from foot movement-invoked fMRI data (Figure 1, C). In an exploratory analysis, scatterplots of latent variables highlighted distinct clustering for Bulbar onset ALS and other onset types, underscoring unique patterns in the association between neural and behavioral measures (Figure 1, D).

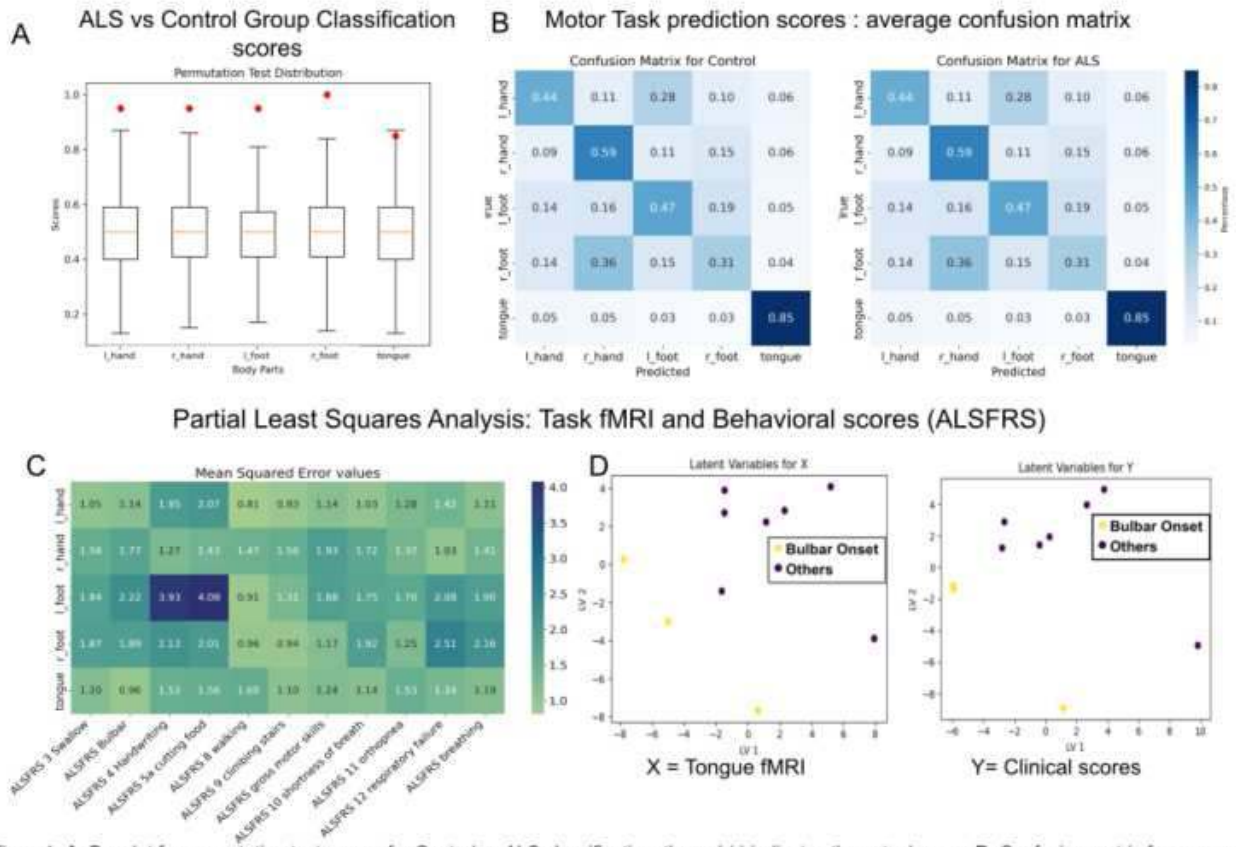

Figure1: **A.** Boxplot for permutation test scores for Control vs ALS classification, the red (.) indicates the actual score. **B.** Confusion matrix for movement prediction from the functionally aligned fMRI timeseries for control (*left*) and ALS (*right*). **C.** MSE values for different body part specific BOLD responses on the vertical axis and different ALSFRS measures on the horizontal axis. **D.** Scatterplot across the two latent variables brain and behavior data with colors indicating the ALS onset type with yellow as the Bulbar onset and purple for others.

Conclusions: In summary, our 7T fMRI study revealed group-specific differences particularly in the tongue and upper limb regions, underscored the complexity of ALS subtypes. The overall movement-based task stimulus classification favored controls, suggesting distinctive neural responses. The higher MSE for foot-related fMRI data in relation to hand-based behavioral measurements warrants careful interpretation. Additionally, our exploratory analysis highlighted separate clustering for Bulbar onset ALS, revealing potential subtype-specific patterns. These findings enhance our understanding of ALS-related motor impairments for targeted interventions.

References

1. Chen, P. H.,(2015). A reduced-dimension fMRI shared response model. Advances in Neural Information Processing Systems, 2015-Januar, 460–468.
2. Northall, Alicia, (2023). “Multimodal layer modelling reveals in vivo pathology in amyotrophic lateral sclerosis.” Brain: a journal of neurology: awad351. Doi: https://doi.org/10.1093/brain/awad35
3. Eisen, Andrew, and Markus Weber. “The motor cortex and amyotrophic lateral sclerosis.” Muscle & Nerve: Official Journal of the American Association of Electrodiagnostic Medicine 24.4 (2001): 564-573. Doi: https://doi.org/10.1002/mus.1042

Poster No 307

Characterizing levodopa-induced dyskinesias using neuroimaging, clinical and behavioural measures

Sakshi Shukla[1], Roopa Rajan[2], Sule Tinaz[3], Nivethida Thirugnanasambandam[1]

[1]Indian Institute of Technology, Mumbai, Maharashtra, [2]All India Institute of Medical Sciences, New Delhi, New Delhi, [3]Yale School of Medicine, New Haven, CT

Introduction: Levodopa-induced dyskinesia (LID) is a motor complication that arises after chronic dopaminergic therapy in over 40% of patients with Parkinson's disease (PD). Studies have shown that patients with LID show distinct changes in brain morphology and resting state functional connectivity as compared to their non-dyskinetic counterparts. However, there is lack of understanding of how task-specific cortico-subcortical networks are differentially modulated in these patient groups. In this current study, our objective is to investigate potential differential modulation in motor and executive function networks among patients with LID, and to explore its correlation with brain morphology, clinical characteristics and behavioral parameters. Employing such a multimodal approach will deepen our understanding of the pathophysiology of LID and enable identification of specific functional networks for targeted therapeutic neuromodulation.

Methods: We collected structural, resting-state and task-based functional MRI data from 17 DysPD patients, 15 nonDysPD patients, and 21 age- and sex-matched healthy subjects. Patients with mild to moderate PD (Hoehn & Yahr scale ≤ 3) and with unimpaired cognitive functioning (Montreal Cognitive Assessment score ≥ 24) were recruited. MRI was recorded on a 3T Siemens Magnetom Prisma scanner with a 64-channel head coil. The obtained structural T1-weighted data were processed using FreeSurfer v6.0.0 to extract volume, surface area and thickness measurements of subcortical and cortical regions. Region-based statistical analysis was performed using SPSS version 29.

Results: All three groups were similar in age, sex and cognitive score. Vertex-based analysis showed that DysPD patients had significantly larger cortical volume (p-corrected =0.0002) in the sensorimotor region compared nonDysPD patients. However, cortical surface area and thickness were not significantly different across subject groups at the whole-brain and region-based level. Behavioural and functional connectivity analyses are currently ongoing and will be ready for presentation at the conference.

Characteristics	Dyskinetics (D)	Non-Dyskinetics (ND)	Healthy Controls (HC)	Test Statistic	P- value
Number of subjects	17	15	21	-	-
Sex (Male/Female)	13/4	10/5	15/6	0.378[a]	0.827
Age (y)	59.18 ± 7.84	54.40 ± 11.72	53.57 ± 7.95	1.41b	0.253
H & Y	2.61 ± 1.05	1.70 ± 0.72	-	2.89c	**0.007**
Disease duration (y)	7.17 ± 4.29	4.33 ± 3.26	-	2.12c	**0.042**
UPDRS I	13.70 ± 8.13	8.06 ± 6.06	-	2.23c	**0.032**
UPDRS II	17.94 ± 8.96	10.53 ± 7.05	-	2.61c	**0.014**
UPDRS III OFF	41.17 ± 20.54	26.73 ± 16.17	-	2.22c	**0.034**
UPDRS III ON	24.43 ± 17.17	16.14 ± 9.92	-	1.64c	0.113
MoCA	26.00 ± 3.27	27.50 ± 1.01	27.04 ± 1.71	1.90b	0.159
GHQ 12	27.88 ± 5.77	24.86 ± 5.99	14.19 ± 3.04	40.56b	**3.4E-11**

Y- years, H & Y- Hoehn and Yahr scale, UPDRS- Unified Parkinson's disease rating scale, MoCA- Montreal cognitive assessment, GHQ- General health questionnaire. Values are shown in Mean ± Standard deviation.
a: Chi-square test, b: Analysis of variance, c: independent t-test. P-value < 0.05.

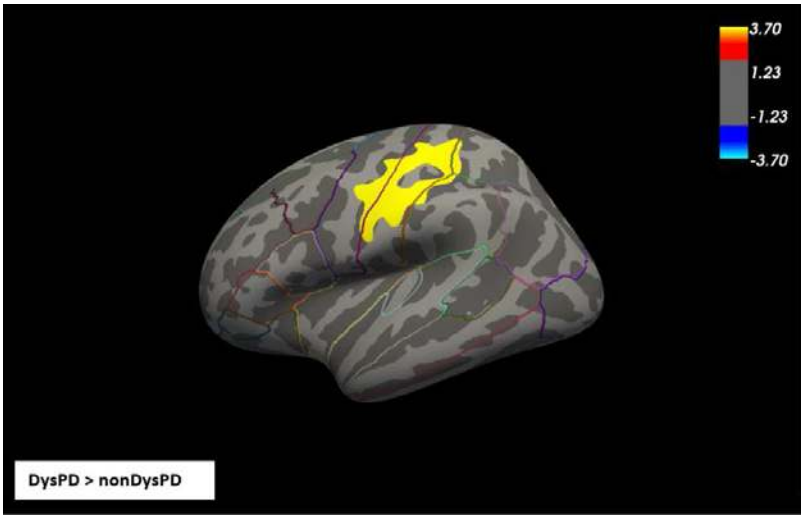

Conclusions: In this study, we found an increase in the cortical volume around the sensorimotor region of DysPD patients compared to the nonDysPD group. Such increased volume may indicate white matter inflammation with chronic dopaminergic therapy in dyskinesia. Although others have shown increased volume in the inferior frontal gyrus and supplementary motor areas, we have observed changes only in the sensorimotor region. Next steps in our ongoing analyses involve examining the relationship of these structural differences with resting-state and task-specific functional brain networks. The findings of our research will shed light on the role of distinct task-specific functional brain networks in characterizing patients with LID and their relevance to novel therapeutic strategies.

References

1. Cerasa, Antonio et al. (2012) "Prefrontal alterations in Parkinson's disease with levodopa-induced dyskinesia during fMRI motor task." Movement disorders : official journal of the Movement Disorder Society vol. 27.
2. Choi, Yera et al. (2020) "Spatiotemporal dissociation of fMRI activity in the caudate nucleus underlies human de novo motor skill learning." Proceedings of the National Academy of Sciences of the United States of America vol. 117.
3. Herz, Damian M et al. (2016), "Resting-state connectivity predicts levodopa-induced dyskinesias in Parkinson's disease." Movement disorders : official journal of the Movement Disorder Society vol. 31.
4. Li, Weihua et al. (2020), "Longitudinal functional connectivity changes related to dopaminergic decline in Parkinson's disease." NeuroImage. Clinical vol. 28.
5. Youn, Jinyoung et al. (2022), "Pallidal Structural Changes Related to Levodopa-induced Dyskinesia in Parkinson's Disease." Frontiers in aging neuroscience vol. 14.

Poster No 308

The Canadian Consortium on Neurodegeneration in Aging (CCNA) Baseline Data Sharing Initiative

Charlie Henri-Bellemare[1], Camille Beaudoin[1], Rolando Acosta[1], Milad Heshmati[1], Samir Das[2], Randi Pilon[3], Logane Gnassi[3], Turaç Aydoğan[3], Michael Borrie[4], Howard Chertkow[5], Natalie Phillips[6], Alan Evans[7]

[1]McGill University, Montreal, Quebec, [2]McGill Centre for Integrative Neuroscience, Montreal Neurological Institute, McGill University, Montreal, Quebec, [3]Lady Davis Institute, Montreal, Quebec, [4]Parkwood Institute, London, Ontario, [5]Baycrest Centre, Toronto, Ontario, [6]Department of Psychology, Concordia University, Montreal, Quebec, [7]McGill Centre for Integrative Neuroscience (MCIN), Montreal, Quebec

Introduction: In 2014, the Canadian Institutes of Health Research (CIHR) established the Canadian Consortium on Neurodegeneration in Aging (CCNA; ccna-ccnv.ca), with the aim of furthering our understanding of the neurodegenerative diseases (NDDs) that affect the Canadian population. At its core, the Comprehensive Assessment of Neurodegeneration and Dementia (COMPASS-ND) is the largest observational clinical cohort study on dementia in Canada. This national cohort required a comprehensive digital infrastructure to coordinate data collection at 32 clinical sites across the country. To ensure that data acquisition, curation, and dissemination were standardized, the LORIS system was chosen as the data management platform to support CCNA. LORIS is making all domains of imaging, clinical, biomarker, cognitive, behavioral, biospecimen, and genetic data readily available to researchers for analysis, and ultimately for open sharing within the neuroscience community. This cohort is now entering the data-sharing phase with external researchers.

Methods: LORIS is a customizable, web-based data management system. The CCNA instance of LORIS features 37 modules, each contributing to the management and monitoring of high-quality data. In the imaging domain, authorized study

coordinators can seamlessly upload patient and phantom scans as the LORIS imaging pipeline ensures organized integration into the database and filesystem. Imaging specialists can then view and/or download these scans in the Imaging Browser as they conduct quality control (QC), accompanied by detailed summaries of scan information and links to relevant data-points elsewhere in LORIS. The Imaging Quality Control module enables review of imaging files, verifying proper upload, adherence to study protocols, and successful QC checks across several scan types. The CCNA-LORIS instance supports a large scale of data through 110 instruments, featuring scoring algorithms and robust validation mechanisms custom written to ensure quality control during data entry. The Biospecimen workflow integrates a biomarker tracking infrastructure, providing information on sample transportation and analyses. This infrastructure also includes barcode scanning of matrix boxes and samples to ensure rapid and simple integration of large biomarker datasets. Key modules, such as the Study Tracker and Data Query Tool (DQT), offer coordinators and researchers efficient tools for data entry, monitoring, and retrieval. The Study Tracker provides a customized snapshot of study progression by participant, offering direct links to subsequent data entry steps, while the DQT empowers researchers to query and download data in CSV format across all modalities while implementing granular permission controls.

Results: The CCNA-LORIS instance currently serves 508 active users for COMPASS-ND. This study includes 11 different diagnostic cohorts across the dementia spectrum,with a baseline dataset of 1,173 deeply-phenotyped participants. This dataset contains brain images for 1,064 participants, and the comprehensive protocol includes 11 scan types. This exhaustive imaging dataset is supplemented with highly descriptive clinical and biomarker data for 1,108 participants, which includes 1,100 blood samples and more. Demographics and neuropsychological profiles for all participants are also available. Access to the data can be requested through the Data Access module on ccna.loris.ca.

Conclusions: The LORIS database is optimized for multi-site studies, such as COMPASS-ND, the signature clinical cohort study of CCNA. Its module-based software harmonizes and consolidates all heterogeneous data types which can then be disseminated in a user-friendly manner. This allows researchers across the world to have access to rich datasets and further the advancement of dementia research.

References

1. CCNA. (2015), COMPASS-ND Study. Retrieved December 11, 2016, from http://ccna-ccnv.ca/en/compass-nd-study/
2. Chertkow, H., Borrie, M., Whitehead, V., Black, S., Feldman, H., Gauthier, S., . . . Rylett, R. (2019). The Comprehensive Assessment of Neurodegeneration and Dementia: Canadian Cohort Study. Canadian Journal of Neurological Sciences, 46(5), 499-511. doi:10.1017/cjn.2019.27
3. Mohaddes, Z., Das, S., Blader, D., Callegaro, J., Tunteng, J., Evans, L., Campbell, T., Lo, D., Morin, P., Whitehead, V., Chertkow, H., & Evans, A. C. (2018). National Neuroinformatics Framework for Canadian Consortium on Neurodegeneration in Aging (CCNA). Frontiers in Neuroinformatics, 12, 420281. https://doi.org/10.3389/fninf.2018.00085
4. Das, S. (2012), 'LORIS: a web-based data management system for multi-center studies', Frontiers in Neuroinformatics, vol. 5, no. 37.

Poster No 309

Investigating Disruptions in Information Flow due to Sickle Cell Disease using Granger Causality

Nahom Mossazghi[1], Nadim Farhat[2], Tales Santini[3], Olubusola Oluwole[3], Enrico Novelli[3], Tamer Ibrahim[3], Sossena Wood[1]

[1]Carnegie Mellon University, Pittsburgh, PA, [2]University of Pittsburgh, Pittsburrgh, PA, [3]University of Pittsburgh, Pittsburgh, PA

Introduction: Sickle cell disease (SCD) is an inherited blood disorder characterized by a mutation in the gene encoding for the beta chain of hemoglobin[1,2]. Patients with SCD experience various complications, including a decline in executive functions. Neuroimaging studies have revealed SCD-related structural differences, yet their influence on functional connectivity remains unclear[3]. Reduced activity in the Executive Control Network (ECN) has been linked to increased pain processing, which diverts resources from the ECN in adults with SCD compared to Healthy Controls (HC)[4]. Our study applied Granger causality analysis to investigate dynamic interactions among brain regions within the ECN and other resting-state networks. Building upon previous research, we hypothesized that (1) adults with SCD would exhibit lower information flow between brain regions associated with ECNs compared to HC, and (2) SCD patients would demonstrate reduced directional influence, measured by net information flow, compared to HC.

Methods: Structural and functional MRI data were obtained from 19 adults, including steady-state patients with SCD (n=9 (8 HBSC, 1 HbSβ+thalassemia), mean age=32.3+/- 8.2 years) and matched HC (n=10, mean age=36.1+/- 8.1 years) using a 7T scanner (MAGNETOM, Siemens). The head coil consists of 16 transmit channels, and 32 receive channels and provides 5. Resting-state fMRI (rs-MRI) scans with 86 axial slices were acquired (TR/TE = 2500/20 ms, flip angle = 65°, voxel size= 1.50 mm iso, FOV = 222 × 222 mm, multiband factor = 2, slice thickness = 1.50 mm, acquisition time = 5:45 min). Preprocessing employed fMRIprep and time series extraction using the Schaefer 2018 atlas (Fig 1 (a))[6,7]. Information flow strength

between brain regions was assessed via Granger F-values, optimizing lag time via Akaike Information Criterion ($p < 0.05$ significance). We calculated average F-values for brain area pairs and employed an independent t-test to compare HC and SCD. Additionally, we computed 'net' information flow by subtracting efferent from afferent F-values for each brain area. We examined its significance using the Wilcoxon test to detect directionally influence in information flow[8].

Results: HC demonstrated stronger information exchange between pairs of ROIs, with a global mean F-value of 3.02, while patients with SCD had a global mean of 2.23 (p-value < 0.001), Fig 1(b-d). Furthermore, Fig 1(e-f) shows that inter-hemispheric information flow (between the left (L) and right (R) hemispheres) was higher in HC than in SCD patients. The mean F-values for L ➔ R were 3.32 and 2.09 for HC and SCD patients (p-value < 0.001), while the mean F-values for R ➔ L were 3.15 and 2.28 for HC and SCD patients (p-value < 0.001) respectively. The magnitude of information exchange was higher in HC than in patients with SCD, as shown in Fig 2(a, c). However, the p-value analysis in Fig 2(b, d) indicates a balanced net F-value. Nevertheless, our analysis revealed some areas exhibit directional influence, with more instances found in patients with SCD than HC. We did not observe any significant differences in other resting state networks.

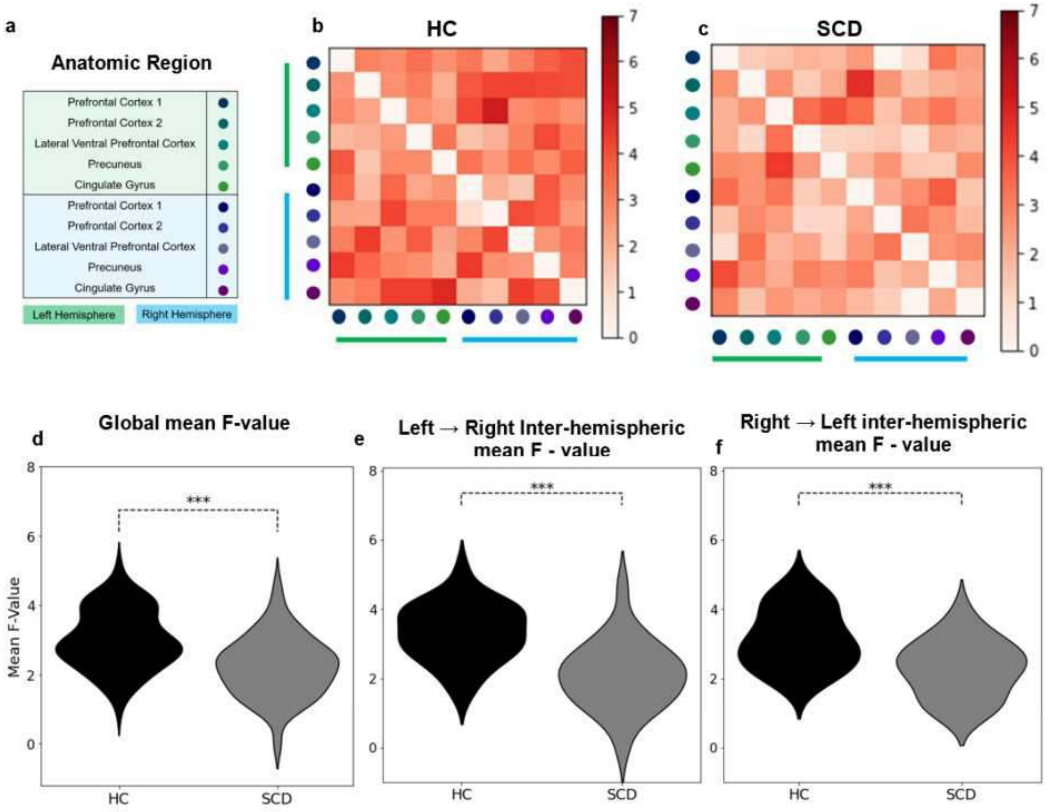

Figure 1: Average information flow within the Executive Control Network (ECN) measured by F-Value. (**a**) Brain regions identified as part of the ECN are listed according to the Schaefer atlas. Next to each region, colored dots correspond to the brain areas on the heatmap in panel (**b and c**). The colors on the table signify the hemisphere location of each brain region: green denotes the left hemisphere and blue represents the right hemisphere. (**b**) A 10 x 10 asymmetrical information flow map matrix, organized by brain region, for healthy controls, accompanied by a color bar indicating hemispheric representation. Each square represents the average F-value from 10 healthy controls. The darker the red square, the higher the information flow from brain areas on the y-axis to the brain area on the x-axis. (**c**) Mean information flow in patients with SCD. Color coding as in (**b**). (**d**) Violin plot illustrating the global mean F-value averages for HC (black) and patients with SCD (grey). An independent t-test reveals a significant difference in the global mean signal (p-value = 5.79e-09). (**e**) and (**f**). Violin plots displaying the mean interhemispheric information flow, i.e., the F-value from brain regions in the left hemisphere to the right hemisphere (L-R) and vice versa (R-L). Independent t-tests show a significant difference between healthy controls and patients with SCD for both L-R (p-value = 1.57 e-05) and R-L (p-value = 5.96e-04). Color coding adapted from (**d**).

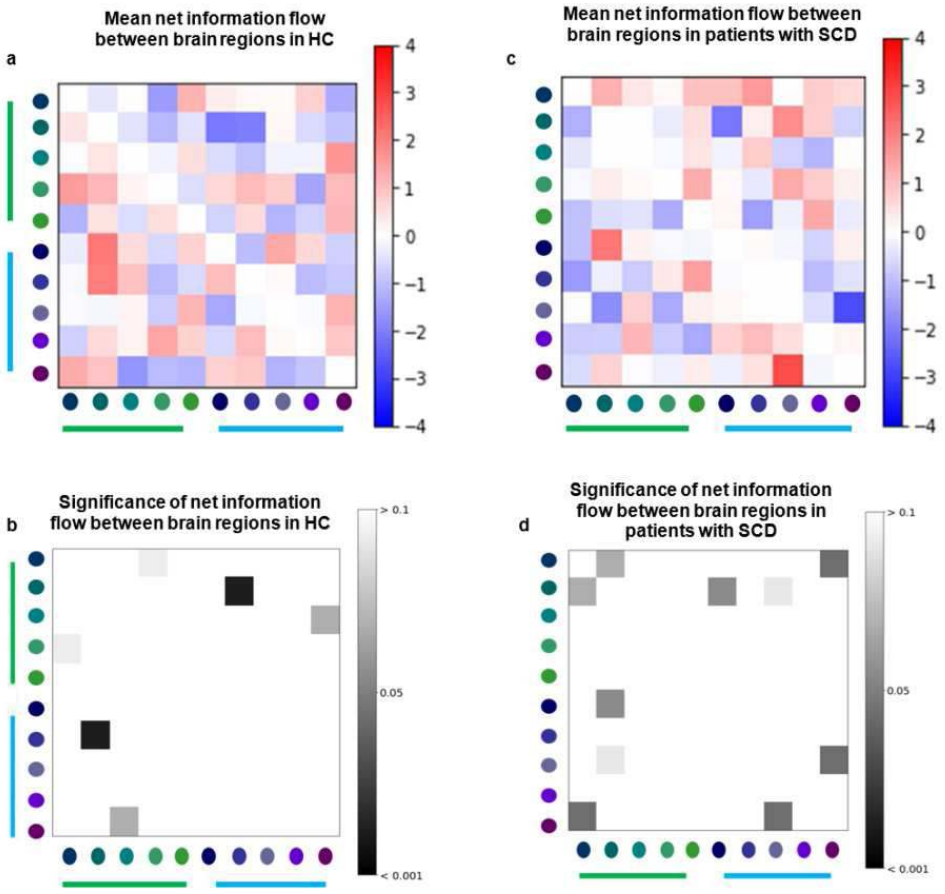

Figure 2. Net information flow map between brain areas in the ECN. **(a)** A 10 x 10 matrix showing the mean differences in information flow between brain area pairs for healthy controls. Each square corresponds to the mean net flow from the region on the y-axis (source) to the region on the x-axis (destination). Darker red squares denote higher information influx to the brain region in the y-axis, whereas darker blue squares indicate greater information outflow from the brain region in the y axis. **(b)** Corresponding p-values for the mean differences in **(a). (c)** Mean differences in net information flow between pairs of brain areas for patients with SCD. Color coding follows **(a). (d)** Corresponding p-values for the mean differences.

Conclusions: Our preliminary results further extend previous reports in SCD, which found that decreased signal in effective connectivity between brain regions within the ECN4. Similar findings have been reported in mild cognitive impairment and Alzheimer's disease studies, indicating a relationship between decreased signal and abnormalities in effective connectivity within the ECN[9,10]. Our study faced several limitations, including the small sample size we analyzed and the inherent limitations of fMRI, such as its slower neural response interpretation and the potential influence of vasculature on the BOLD signal, despite its neural basis. Future analyses will delve deeper into understanding the effects of SCD on effective connectivity through task-based DSST fMRI studies.

References

1. Sundd, P., Gladwin, M. T. & Novelli, E. M. Pathophysiology of Sickle Cell Disease. Annual Review of Pathology: Mechanisms of Disease 14, 263–292 (2019).
2. Kavanagh, P. L., Fasipe, T. A. & Wun, T. Sickle Cell Disease: A Review. JAMA vol. 328 57–68 Preprint at https://doi.org/10.1001/jama.2022.10233 (2022).
3. Santini, T. et al. Analysis of hippocampal subfields in sickle cell disease using ultrahigh field MRI. Neuroimage Clin 30, (2021).
4. Case, M. et al. Characterization of functional brain activity and connectivity using EEG and fMRI in patients with sickle cell disease. Neuroimage Clin 14, 1–17 (2017).
5. Santini, T. et al. Improved 7 Tesla transmit field homogeneity with reduced electromagnetic power deposition using coupled Tic Tac Toe antennas. Sci Rep 11, (2021).
6. Esteban, O. et al. fMRIPrep: a robust preprocessing pipeline for functional MRI. Nat Methods 16, 111–116 (2019).
7. Schaefer, A. et al. Local-Global Parcellation of the Human Cerebral Cortex from Intrinsic Functional Connectivity MRI. Cerebral Cortex 28, 3095–3114 (2018).
8. Hutchison, R. M., Womelsdorf, T., Gati, J. S., Everling, S. & Menon, R. S. Resting-state networks show dynamic functional connectivity in awake humans and anesthetized macaques. Hum Brain Mapp 34, 2154–2177 (2013).
9. Zhao, Q., Lu, H., Metmer, H., Li, W. X. Y. & Lu, J. Evaluating functional connectivity of executive control network and frontoparietal network in Alzheimer's disease. Brain Res 1678, 262–272 (2018).
10. Liu, Z. et al. Investigation of the effective connectivity of resting state networks in Alzheimer's disease: A functional MRI study combining independent components analysis and multivariate Granger causality analysis. NMR Biomed 25, 1311–1320 (2012).

Poster No 310

Neuropsychiatric symptoms in Parkinson's disease are linked to regional brain atrophy

Roqaie Moqadam[1,2], Yashar Zeighami[3], Mahsa Dadar[4], Houman Azizi[5], Alexandru Hanganu[6,7], Lucas Ronat[1,8]

[1]Faculty of Medicine, university of montreal, Montreal, Québec, [2]Douglas Mental Health University Institute, Montreal, Canada, [3]Douglas Research Centre, Montreal, Quebec, [4]McGill University, Montreal, QC, [5]Montreal Neurological Institute, Montreal, Quebec, [6]university of montreal, Montreal, Québec, [7]Faculty of Medicine, University of Montreal, Montreal, Canada, [8]Quebec Neuroimaging of Emotions Laboratory, Research Centre of University Institute of Geriatric, Montreal, Canada

Introduction: Parkinson's disease (PD) is the second most common neurodegenerative disorder after Alzheimer's disease. Detecting neurodegeneration prior to its clinical presentation is still an ongoing challenge[1]. In PD, the loss of dopamine leads to impairment of the striatal regions. Since the striatum plays a role in cognition (reinforcement learning, decision making, working memory), striatal impairment will affect the frontal cognitive regions[2]. Indeed, previous neuroimaging studies showed that in PD there are changes in the brain morphology in the temporal, dorsolateral prefrontal regions, and striatal dopaminergic circuits. These changes have been reported with respect to gray matter thickness and volumetry[3]. Recent scientific advances have shown that neuropsychiatric symptoms (NPSs) are present early in the disease and are early markers of cognitive decline. In fact, some NPSs manifest even before the clinical presentation of PD. For example, apathy is present in up to 40% of PD patients, but is also present in up to 26% of older healthy individuals. Additionally, recent studies have shown that the prevalence of depression (35%), and anxiety (31%) is higher in PD patients in comparison to older healthy individuals[4-6]. Here we assess the relationship between gray matter atrophy and NPSs in PD, to determine whether greater atrophy is associated with increased likelihood of experiencing specific NPSs and whether these relationships are regionally specific.

Methods: Imaging and clinical data were obtained from the Parkinson's Progression Markers Initiative (PPMI) study. Clinical measures included assessments such as the Unified Parkinson's Disease Rating Scale (UPDRS), cognitive evaluations, disease duration, and NPS scores. Specifically, NPS scores corresponding to the Geriatric Depression Scale (GDS), the State-Trait Anxiety Inventory total (STAI_Total), items related to motivation and mood (Apathy) within UPDRS I, and REM Sleep Behavior Disorder (RBD) assessments were included. Deformation-Based Morphometry (DBM) maps were extracted using T1w images in 350 PD patients (607 timepoints). DBM maps were calculated as the Jacobian determinant of the deformation field from the nonlinear transformation of the T1w images to the MNI-ICBM152 template, computed using ANTS[7]. Lower DBM values indicate local shrinkage of tissue; i.e. atrophy[8]. Using Schaefer and Xiao atlases average DBM values in1022 cortical and subcortical regions were measured[9,10]. A series of linear mixed effects models were used to assess the associations between NPSs and DBM, including MOCA, sex, age, handedness, and duration of disease as covariates.

Results: Figure 1 shows the t statistic maps of the significant regions for each NPS. The results showed significant associations between regional GM atrophy as measured by DBM and NPS severity in PD patients for multiple regions and scores. The list of significant subcortical regions include: a) depression: left red nucleus and left subthalamic nucleus, b) REM Sleep Behavior Disorder: right red nucleus right substantia nigra, left subthalamic nucleus, and right thalamus, c) anxiety: bilateral thalamus, d) UPDRS-I: bilateral putamen, bilateral red nucleus, bilateral pallidus interna, bilateral thalamus, left amygdala and right substantia nigra. Colder colors indicate a stronger negative association between DBM values and NPS scores. We found a decrease in average DBM in multiple networks associated with all NPSs (Figure 2) with greater effect sizes in visual network as well as ventral and dorsal attention networks.

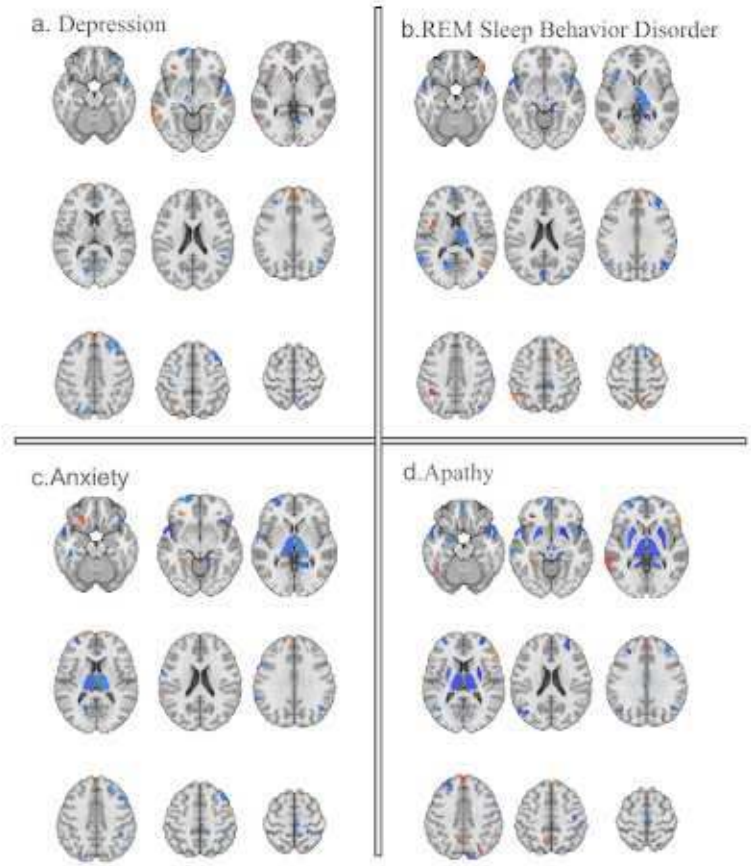

Figure 1 shows multiple regional atrophy in different subsyndromes in PD group. a. Depression, b.REM Sleep Behavior Disorder, c.Anxiety, d.Apathy

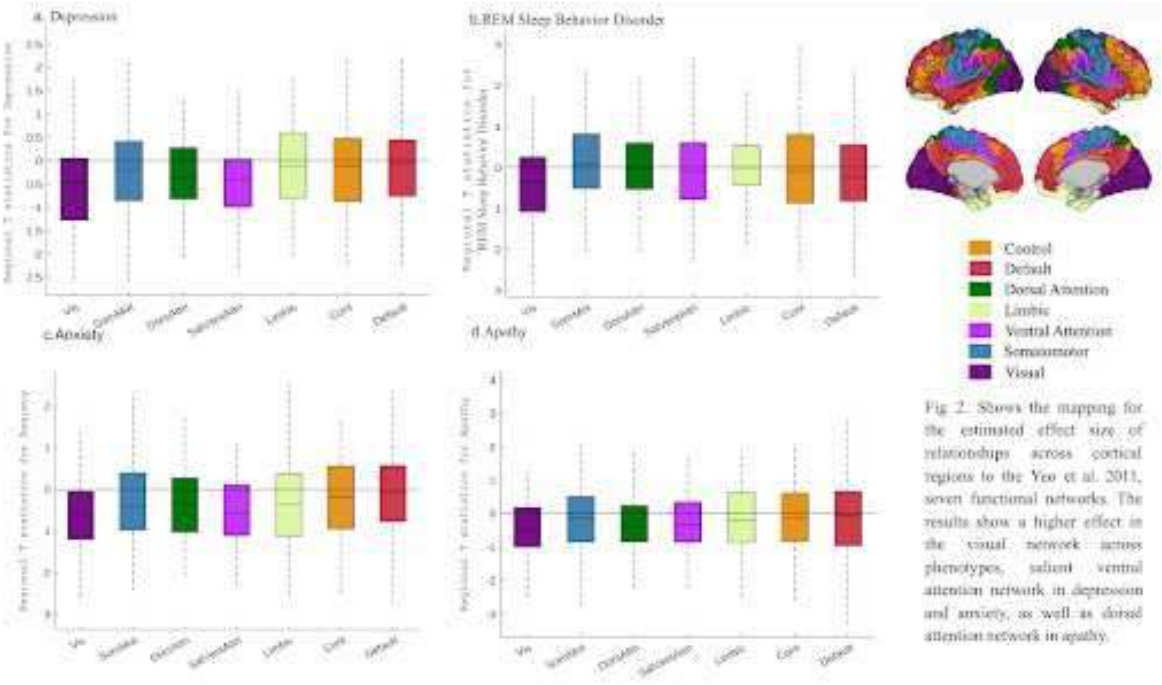

Fig 2. Shows the mapping for the estimated effect size of relationships across cortical regions to the Yeo et al. 2011, seven functional networks. The results show a higher effect in the visual network across phenotypes, salient ventral attention network in depression and anxiety, as well as dorsal attention network in apathy.

Conclusions: NPSs were associated with presence of atrophy in multiple cortical and subcortical regions. These findings suggest that the greater severity of NPSs observed in PD is associated with atrophy in regions implicated in the disease.

References

1. Chambers, Larry W., and Larry W. Chambers. Prevalence and monetary costs of dementia in `Canada. Miscellaneous Agency, 2016.

2. Provost, Jean-Sebastien, Michael Petrides, and Oury Monchi. “Dissociating the role of the caudate nucleus and dorsolateral prefrontal cortex in the monitoring of events within human working memory.” European Journal of Neuroscience 32.5 (2010): 873-880.
3. Hanganu, Alexandru, et al. “Mild cognitive impairment is linked with faster rate of cortical thinning in patients with Parkinson’s disease longitudinally.” Brain 137.4 (2014): 1120-1129.
4. Den Brok, Melina GHE, et al. “Apathy in Parkinson’s disease: a systematic review and meta-analysis.” Movement Disorders 30.6 (2015): 759-769.
5. Reijnders, Jennifer SAM, et al. “A systematic review of prevalence studies of depression in Parkinson’s disease.” Movement disorders 23.2 (2008): 183-189.
6. Broen, Martijn PG, et al. “Prevalence of anxiety in Parkinson’s disease: a systematic review and meta-analysis.” Movement Disorders 31.8 (2016): 1125-1133.
7. Avants, Brian B., Nick Tustison, and Gang Song. “Advanced normalization tools (ANTS).” Insight j 2.365 (2009): 1-35.
8. Zeighami, Yashar, et al. “Network structure of brain atrophy in de novo Parkinson’s disease.” elife 4 (2015): e08440.
9. Schaefer, Alexander, et al. “Local-global parcellation of the human cerebral cortex from intrinsic functional connectivity MRI.” Cerebral cortex 28.9 (2018): 3095-3114.
10. Yeo, BT Thomas, et al. “The organization of the human cerebral cortex estimated by intrinsic functional connectivity.” Journal of neurophysiology (2011).

Poster No 311

Dissociation of Structural and Functional Changes in Alzheimer’s Disease

Annie Dang[1], Di Wang[1], Mohamad Habes[2], Peter Fox[3]

[1]UT Health San Antonio, San Antonio, TX, [2]University of Texas Health San Antonio, San Antonio, TX, [3]The University of Texas Health Science Center at San Antonio, San Antonio, TX

Introduction: The Amyloid-Tau-Neurodegeneration (ATN) biomarker framework for Alzheimer’s disease (AD) indicates binary (positive/negative) designations for each type of pathology, without regard for anatomical distribution. Neurodegeneration is designated as positive if atrophy or hypometabolism is found on imaging[1]. However, Clifford Jack et al., 2016 noted that atrophy and hypometabolism were differently distributed and referenced each to different co-localized pathologies[2]. Thus, there exists a need to further characterize atrophy and hypometabolic changes in AD, with the goal of advancing the application of anatomically-based biomarkers in the ATN framework.

Methods: Query of the BrainMap databases of published, group-wise neuroimaging, case-control contrasts was used to identify AD and mild cognitive impairment (MCI) studies for meta-analysis. The voxel-based morphometry (VBM) and voxel-based physiology (VBP) databases were used to identify studies involving atrophy and hypometabolism respectively. 157 VBM contrasts (110 AD, 47 MCI) and 146 VBP contrasts (88 AD, 58 MCI) were identified. Activation likelihood estimation coordinate-based meta-analysis was performed separately for VBM and VBP, to identify cross-study convergence of brain alteration patterns. Mango was then used to visualize results and quantify spatial overlap between VBM and VBP.

Results: Structural (atrophy) and functional (hypophysiology) neurodegenerations in AD/MCI exhibit markedly different neuroanatomical distributions (Figure 1). Structural abnormalities chiefly involve the bilateral hippocampus and bilateral temporal lobes; functional abnormalities chiefly involve the bilateral parietal lobes and posterior cingulate. There is a small overlap (2184 mm3) between VBM and VBP, accounting for 10.1% of VBM and 7.1% of VBP.

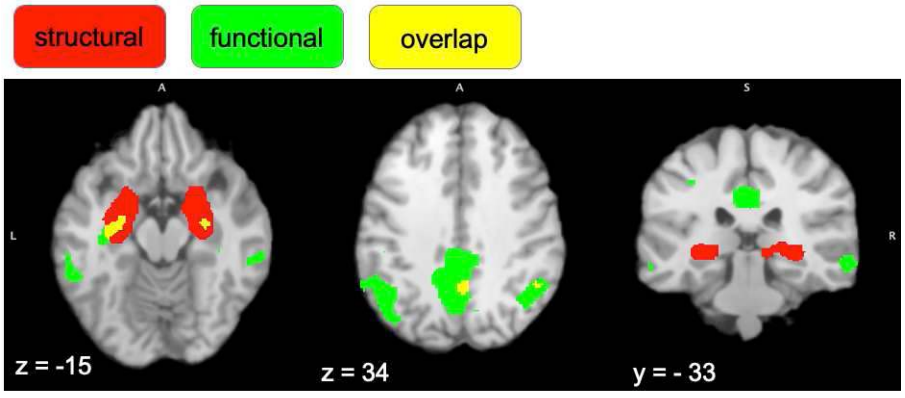

Figure 1. Dissociation of structural and functional changes in AD/MCI is shown. Structural alterations mainly involve the bilateral hippocampus and bilateral temporal lobes. Functional alterations mainly involve the bilateral parietal lobes and posterior cingulate.

Conclusions: VBM and VBP patterns of alteration appear distinct, aligning with the anterior and posterior default mode network respectively. This dissociation may reflect distinct underlying neuropathologies. We suggest that this knowledge can

be used to advance the application of anatomically-based biomarkers in the ATN framework. Network modeling of VBM and VBP data is currently ongoing.

References
1. Jack, C.R. (2018), 'NIA-AA Research Framework: Toward a biological definition of Alzheimer's disease', Alzheimer's & Dementia, vol. 14, pp. 535 - 62
2. Jack, C.R. (2016), 'A/T/N: An unbiased descriptive classification scheme for Alzheimer disease biomarkers', Neurology, vol 87, pp. 539-547

Poster No 312

Staging of tau accumulation associated with cognitive decline in AD using 18F-MK-6240 PET data

Neda Shafiee[1], Vladimir Fonov[1], Joseph Therriault[2], Nesrine Rahmouni[3], Stijn Servaes[3], Jenna Stevenson[3], Nina Marguerita Poltronetti[4], Pedro Rosa-Neto[4], D Louis Collins[1]

[1]McConnell Brain Imaging Centre, Montreal Neurological Institute, Montreal, Quebec, [2]The McGill University Research Centre for Studies in Aging, Montreal, Quebec, [3]Translational Neuroimaging laboratory, McGill Centre for Studies in Aging, Montreal, Quebec, [4]Translational Neuroimaging Laboratory, The McGill University Research Centre for Studies in Aging, Montreal, Quebec

Introduction: Alzheimer's disease is characterized by the accumulation of amyloid beta and the formation of tau neurofibrillary tangles (NFTs), leading to irreversible neurodegeneration. The formation of NFTs is believed to follow a pattern known as Braak stages. Recent studies refined Braak histopathological stages in vivo using tau tangles PET tracer 18F-MK-6240 and with manually defined regions of interest. Here we aim to analyze patterns of Tau accumulation associated with AD-related cognitive decline and build a data-driven staging system based on longitudinal data. To do so, we used an estimated latent time of disease onset based on cognitive scores to place all subjects on a common timeline disease timeline trajectory.

Methods: To evaluate an initial Tau-based staging model using the latent time of disease onset estimation, we used 18F-MK-6240 from the TRIAD dataset[2], including [n total (m unique)]: cognitively normal: 347(194), mild cognitive impairment: 163(99), Alzheimer's disease dementia: 114(77). We used the trajectory model of Kühnel et al.[3] to align patients based on their longitudinal cognitive scores along a continuous latent disease timeline. The Alzheimer's Disease Assessment Scale-cognitive subscale (ADAS-cog-13) and the Mini-Mental State Examination (MMSE) were used simultaneously to estimate time-shifts for each subject. As there were not enough longitudinal timepoints in the TRIAD dataset to directly apply this method, we first applied the method to ADNI dataset, and then used a nearest-neighbour technique to impute the disease offset for TRIAD subjects from the closest 38 subjects in the ADNI cohort. (n=38 was found to be the optimal through cross-validation within ADNI.) This supervised imputation model used baseline cognitive test scores (MMSE and CDR-SB) along with the age of participants to impute their latent disease onset.

Results: We defined 5 2-year windows on the 10-year span of the estimated latent disease offset timeline. Tau PET scans for subjects within each window were averaged, resulting in 5 average Tau templates. This staging system depicts the incremental tau accumulation along the decline in cognition. With medial temporal regions showing initial accumulation and later stages showing full brain involvement.

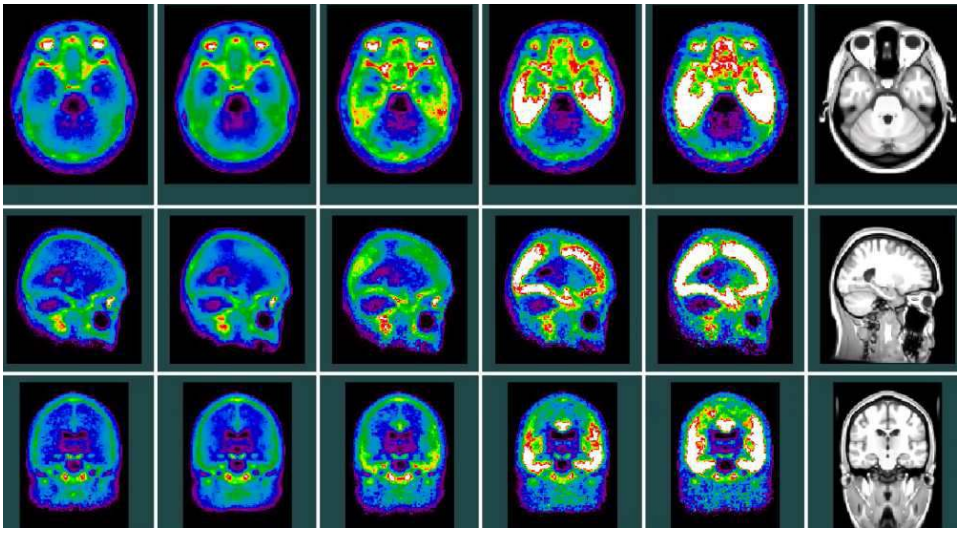

Conclusions: We were able to discern patterns of tau accumulation associated with progression of cognitive decline using a purely data-driven method. These models will help understand how Tau is associated with cognitive decline.

References
1. Kühnel, L. (2021), "Simultaneous modeling of Alzheimer's disease progression via multiple cognitive scales," Statistics in Medicine, vol. 40, no. 14, pp. 3251–3266.
2. Pascoal, T. A. (2020), "18F-MK-6240 PET for early and late detection of neurofibrillary tangles," Brain, vol. 143, no. 9, pp. 2818–2830.

Poster No 313

Long-distance neural alterations in predominant left and right anterior temporal lobe atrophy

Maria Luisa Mandelli[1], Yann Cobigo[1], Dana Leichter[1], Janhavi Pillai[1], Hulya Ulugut[1], Zoe Ezzes[1], Aaron Scheffler[2], David Baquirin[1], Rian Bogley[1], Anna Gilioli[1], Marguerite Knudtson[1], Boon Lead Tee[1], Howard Rosen[1], Bruce Miller[1], Virginia Sturm[1], Katherine Rankin[1], Jessica DeLeon[1], Zachary Miller[1], Maria Luisa Gorno-Tempini[1]

[1]Memory and Aging Center, Department of Neurology, University of California San Francisco, San Francisco, CA, [2]Department of Epidemiology and Biostatistics, University of California, San Francisco, San Francisco, CA

Introduction: Semantic dementia (SD) presents as a unique neurodegenerative disorder with focal atrophy of the anterior temporal lobes (ATLs). It is comprised of a primarily left-lateralized language syndrome[1] and a right-lateralized behavioral disorder[2]. One current challenge in this disorder is in accurately identifying distant brain regions connected to the ATLs and therefore potentially compromised. This study employs two advanced MR neuroimaging techniques-namely, fixel-based analysis and functional network analysis-to evaluate these remote areas. The first delves into white matter pathology and, unlike the tensor-derived metrics, provides fiber tract-specific measures at a within-voxel level (called fixels). The second uses BOLD signaling for a functional connectivity profile, aiding the investigation of inter-network connectivity and the broader impact of ATL atrophy on network-level architecture. By combining these modalities, we aim to enhance the understanding of neural changes in relation to the loci of atrophy and inform the development of targeted interventions that are precisely tailored to the affected neural pathways.

Methods: Participants from the Memory and Aging Center at the UCSF included individuals with left-predominant ATL atrophy (n=16), with right-predominant ATL atrophy (n=15), and demographically matched clinical normal controls (n=44). All underwent T1-weighted structural, T2*-weighted task-free functional scans, and multi-shell DWIs on a 3T Prisma MR scanner. Fixel-based analysis involved multi-tissue constraint spherical deconvolution to compute fiber orientation distribution (FODs)[3-5]. Subject-specific FOD images were registered to the template, whereafter fixels were segmented and corresponding metrics of fiber density and fiber-bundle cross-section were derived[6]. Functional connectivity was analyzed across 7 predefined networks[7] using the Brainnetome Atlas[8], with intra- and inter-network connections quantified by average correlation coefficients between regional pairs. We anticipated significant disruption in the limbic network, which includes the ATLs, and reduced connectivity with the default network, typically highly correlated with the limbic system in healthy individuals. Statistical significance among the three groups was assessed using an ANOVA, controlling for age and sex. Correction was applied using a permutation-based method with a significance threshold at $p<0.05$.

Results: Fixel based analysis revealed significant disruptions in white matter tracts extending from the compromised ATL to the angular and orbito-frontal gyrus within the same hemisphere in the patients compared to controls. Specifically, we observed significant decreases in microstructural fiber density in the inferior longitudinal and uncinate fasciculi, as well as the temporo-parietal component of the superior longitudinal fasciculus extending to the angular gyrus. Damage was predominantly in the affected hemisphere; however contralateral temporal regions and along the anterior portion of the corpus callosum was also observed (Fig 1). Functionally, there was a significant decrease in the intra-connectivity within the limbic and salience networks, and a significant decline in the inter-connectivity between the limbic system (ATL) and the default network on the affected side (encompassing the angular gyrus).

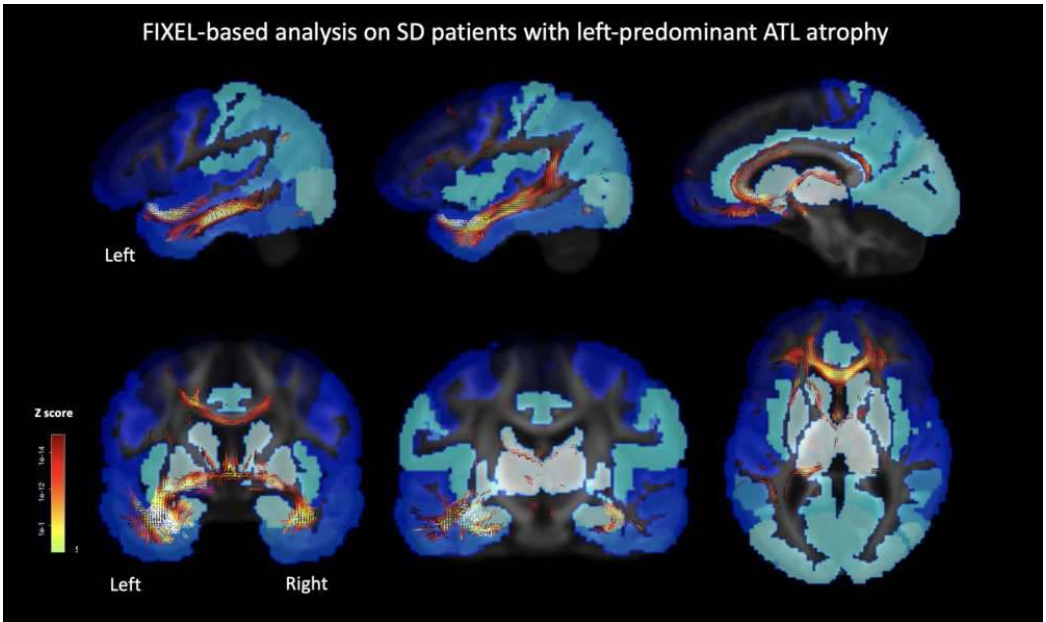

Figure 1: Fixels that are significantly decreased in SD patients with greater left ATL atrophy compared to control group. The FIXELs color code z-score between 2 to 7 sigmas within statistically significant clusters (FWEC – $p < 0.05$)

Conclusions: The convergence of findings from fixel-based and functional network analysis reveals a consistent pattern of long-range neural pathways alterations, in particular to the angular gyrus, a region within the semantic network whose relative structural preservation makes it an actionable target therapeutic strategies such as transcranial magnetic stimulation and transcranial direct current stimulation. Moreover, the precise localization and quantification of preserved structural and functional networks with these neuroimaging techniques offers a novel and potentially valuable biomarker for tracking disease progression and treatment efficacy.

References

1. Gorno-Tempini, M.L. (2011), 'Classification of primary progressive aphasia and its variants'. Neurology. vol. 76, no. 1, pp. 1006-14.
2. Younes, K. (2022), 'Right temporal degeneration and socioemotional semantics: semantic behavioural variant frontotemporal dementia'. Brain. vol. 145, no. 11, pp. 4080-4096.
3. Tournier, J.D. (2007), 'Robust determination of the fibre orientation distribution in diffusion MRI: non-negativity constrained super-resolved spherical deconvolution'. Neuroimage. Vol. 35, no. 4, pp. 1459-72.
4. Dhollander, T. (2021), 'Fixel-based Analysis of Diffusion MRI: Methods, Applications, Challenges and Opportunities'. Neuroimage. vol. 241, no. 118417
5. Jeurissen, B. (2014), 'Multi-tissue constrained spherical deconvolution for improved analysis of multi-shell diffusion MRI data'. Neuroimage. vol. 103, pp. 411-426.
6. Raffelt, D. A. (2017), 'Investigating white matter fibre density and morphology using fixel-based analysis'. Neuroimage. vol. 144, pp. 58–73.
7. Yeo, B.T. (2011), The organization of the human cerebral cortex estimated by intrinsic functional connectivity'. Journal of Neurophysiology. vol. 106, no. 3, pp. 1125-65.
8. Fan, L. (2016), 'The Human Brainnetome Atlas: A New Brain Atlas Based on Connectional Architecture'. Cerebral Cortex. vol 26, no. 8, pp. 3508-26.

Poster No 314

White Matter Cerebrovascular and Microstructure Imaging Biomarkers in Normal Cognition and MCI

Youngkyoo Jung[1], Donghoon Kim[1], Sarah Yoon[1], Timothy Hughes[2], Yu-Chien Wu[3], Danielle Harvey[1], Megan Lipford[2], Samuel Lockhart[2], Suzanne Craft[2], Laura Baker[2], Christopher Whitlow[2], Stephanie Okonmah-Obazee[2], Christina Hugenschmidt[2], Matthew Bobinski[1]

[1]University of California, Davis, CA, [2]Wake Forest School of Medicine, Winston-Salem, NC, [3]Indiana University School of Medicine, Indianapolis, IN

Introduction: Mild cognitive impairment (MCI) has been related to impairment in cerebrovascular perfusion and microstructural MRI parameters. However, the relationship between cerebrovascular perfusion and microstructure remains understudied, especially within normal-appearing white matter (NAWM). In this study, we examined whether cerebrovascular perfusion is related to NAWM microstructure in different cognitive statuses, including normal cognition (NC) and MCI.

Methods: Seventy-nine participants (Sex: 61F/28M; Age: 68.7±7.2;55NC/24MCI) underwent an MRI exam including T1-weighted, T2-FLAIR, dynamic single-PLD pseudo continuous ASL (PCASL), multi-PLD PCASL, and NODDI. The T1-weghted structural images were acquired using MPRAGE sequence with resolution of 1 x 1 x 1 mm3. T2-FLAIR images were acquired using 3D IR-SPACE with resolution of 1 x 1 x 1 mm3. Dynamic single-PLD PCASL images were obtained under a hypercapnia respiratory challenge (Kim et al. 2021) (2D EPI; TR = 4,000 ms; TE = 25 ms; resolution = 3.2 x 3.2 x 5 mm3; labeling duration = 1.8 s; PLD = 1.2 s). The dynamic single-PLD PCASL provided baseline and hypercapnic CBF. Baseline and hypercapnic CBF images were solely used to calculate CVRCBF. The baseline and hypercapnic BOLD were also acquired from dynamic single-PLD PCASL by averaging tag and control images of the dynamic single-PLD PCASL. The baseline and hypercapnic BOLD images were also used to compute CVRBOLD. The multi-PLD PCASL images were acquired with a total of 6 PLDs (0~3000 ms with increments of 600 ms) (Johnston et al. 2015). The multi-PLD PCASL provided ATT and CBF (Kim et al., 2023). Diffusion MRI for ICVF measurement (Zhang et al. 2012) was acquired with the following parameters: 2 mm isotropic resolution; 9 b0 images; 30 directions at b-value = 711 s/mm2 and 60 directions at b-value = 2855 s/mm2. White matter hyperintensity (WMH) detection in this study was achieved with a U-Net with multi-scale highlighting foregrounds (HF) (Park et al., 2021). WMH regions were excluded from all image data of each participant to investigate NAWM regions in this study. Participant demographics were compared across MCI and NC using chi-square tests and t-tests. In the global NAWM, separate multiple linear regression analyses were performed to investigate the relationship between each perfusion or microstructural metric (CBF, ATT, CVRCBF, CVRBOLD, or ICVF) and cognitive status, adjusted for covariates: age, sex, years of education, and vascular risk factors such as hypertension status, impaired glycemic status, and the presence of APOE-ε4 allele. A voxel-wise analysis was performed for each imaging parameter in the same manner.

Results: In the voxel-wise analysis, prolonged ATT was also observed in voxel clusters associated with MCI (Figure 1A). The voxel clusters were globally located in the WM. Voxel-wise analysis demonstrated no significant statistical relationships between CVRCBF and any vascular risk factors or MCI. In contrast, CVRBOLD revealed two voxel clusters that have statistically significant relationships with MCI (Figure 1B). The voxel-wise analysis identified voxel clusters with statistically significantly lower ICVF values in participants with MCI (Figure 1C). The overlapping voxels between ATT and ICVF were underwent a linear regression analysis demonstrating a significantly negative relationship between residual-adjusted ATT and ICVF with MCI. This relationship was observed exclusively among participants with MCI, as indicated by a p-value of 0.010 in Figure 2B.

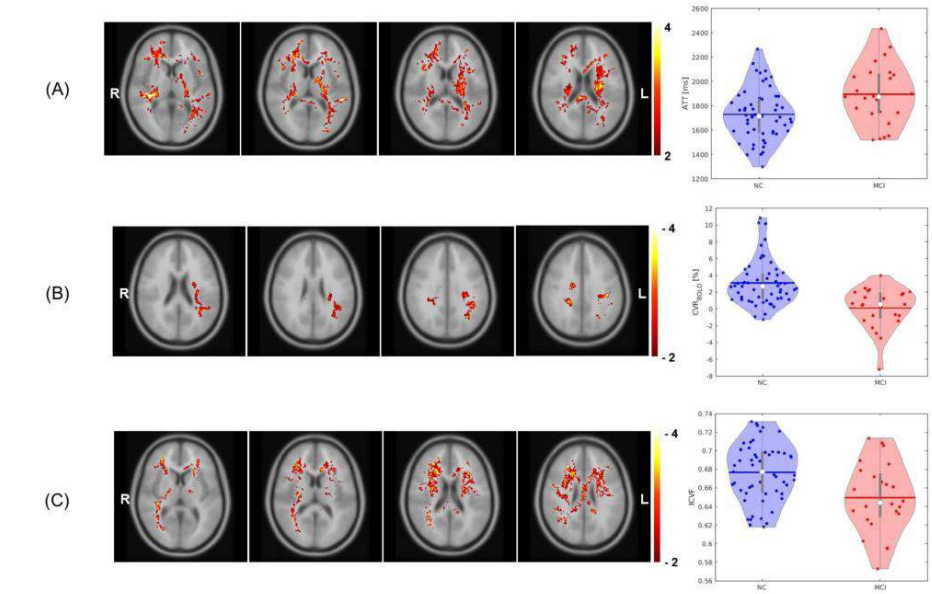

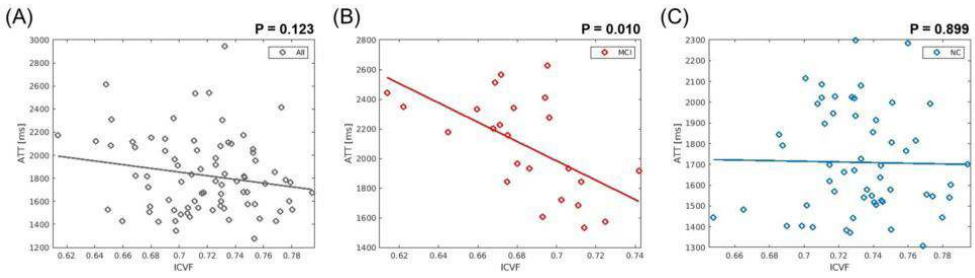

Conclusions: Impaired ATT and ICVF appeared to be closely interlinked in MCI, while CVR served as an independent imaging biomarker. These findings highlight the necessity for further research into the intrinsic link between ATT and ICVF in NAWM.

References

1. Johnston ME, Lu K, Maldjian JA, Jung Y. (2015), 'Multi-TI arterial spin labeling MRI with variable TR and bolus duration for cerebral blood flow and arterial transit time mapping', IEEE transactions on medical imaging, 34:1392-402.
2. Kim D, Hughes TM, Lipford ME, Craft S, Baker LD, Lockhart SN, et al. (2021), 'Relationship between cerebrovascular reactivity and cognition among people with risk of cognitive decline', Frontiers in Physiology, 12:645342.
3. Kim D, Lipford ME, He H, Ding Q, Ivanovic V, Lockhart SN, et al. (2023), 'Parametric cerebral blood flow and arterial transit time mapping using a 3D convolutional neural network', Magnetic Resonance in Medicine. 90(2):583-595.
4. Park G, Hong J, Duffy BA, Lee J-M, Kim H. (2021), 'White matter hyperintensities segmentation using the ensemble U-Net with multi-scale highlighting foregrounds', Neuroimage, 237:118140.
5. Zhang H, Schneider T, Wheeler-Kingshott CA, Alexander DC. (2012), 'NODDI: practical in vivo neurite orientation dispersion and density imaging of the human brain', Neuroimage, 61:1000-16.

Poster No 315

Up-sampling MRI scans can significantly increase robustness of NbM segmentation

Neda Shafiee[1], D Louis Collins[1]

[1]McConnell Brain Imaging Centre, Montreal Neurological Institute, Montreal, Quebec

Introduction: The main source of cholinergic projections to the cerebral cortex is the magnocellular neurons of the nucleus basalis of Meynert (NbM). Postmortem studies have shown high densities of Neurofibrillary tangles in NbM in early and presymptomatic stages of Alzheimer's disease. Degeneration of the cholinergic projection system has also been theorized to be an upstream event of entorhinal and neocortical degeneration, making NbM a possible biomarker early in the course of the disease. However, the precise delineation of NbM is difficult due to limited spatial resolution and contrast in MR images. The NbM also lacks strict boundaries with adjacent cell groups and different atlases used to identify NbM have reported discrepancy. To delineate this region more accurately, we propose to increase the resolution of MRI scans, before performing a deformation-based morphometry (DBM) analysis.

Methods: MRI scans of 896 subjects from ADNI dataset (219 cognitively normal amyloid negative (CN-), 117 cognitively normal amyloid positive (CN+), 131 with early mild cognitive impairment (EMCI) and 242 with late MCI (LMCI) and 187 patients with AD) were up-sampled to 0.5 mm isotropic using a method introduced by Manjón et al. This method enforces a structure-preserving constraint as opposed to imposing an arbitrary smoothness constraint: the down-sampled version of the reconstructed image should be the same as the noise-free low-resolution image for all locations. The up-sampled scans were then non-linearly registered to an ADNI-based template. The resulting deformation fields were used to compute Jacobian determinant maps. All Jacobian maps were calculated in the template space, thus normalizing for head size. Using the atlas published by Zaborszky et al. as a mask, local volume change was computed for NbM. The same analysis was repeated but without up-sampling the data and using original 1 mm isotropic scans.

Results: Comparing the results from high-resolution and original low-resolution scans shows that while both pipelines detect the general trend of NbM atrophy as the disease progresses, the high-resolution analysis finds a stronger distinction between disease stages. To quantify this distinction we used Cohen's d measurement and compared volume changes in early MCI against late MCI in both models. Upsampled scans showed a higher cohen's d and t-value, further confirming our assumption.

EMCI vs LMCI group

Region	Original low-res			Upsampled high-res		
	Cohen's d	*t-value*	*p-value*	*Cohen's d*	*t-value*	*p-value*
Right NbM	0.2	1.720	0.0568	0.4	3.601**	0.00038
Left NbM	0.31	2.149*	0.0165	0.47	4.447**	1.261e-05

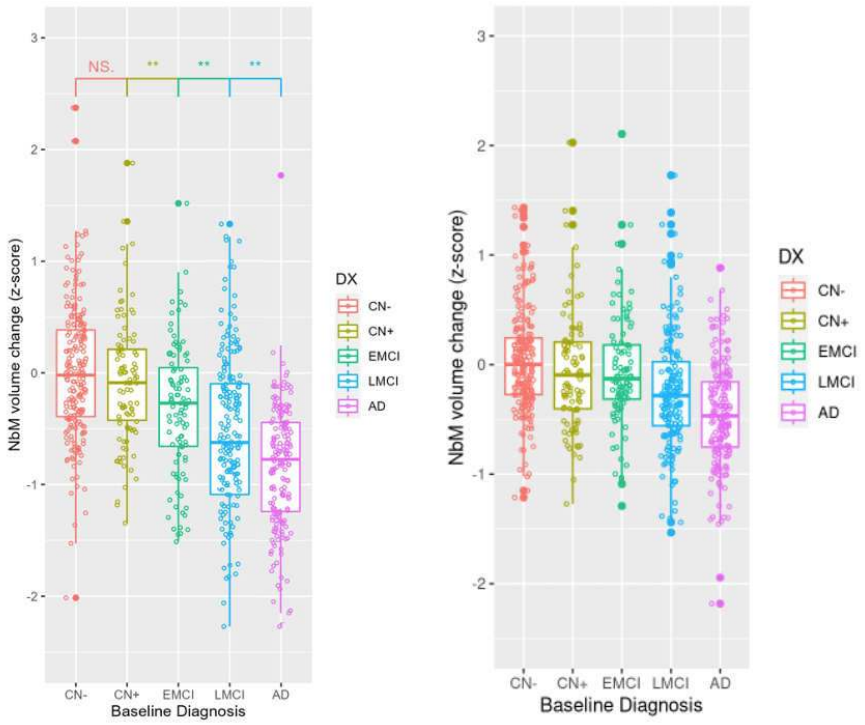

A) Up-sampled high-resolution scans B) Original low-resolution scans

Conclusions: When studying brain regions with small volumes, such as the Nucleus basalis of Meynert, enhancing the resolution would be beneficial to increase the measurement and segmentation accuracy.

References

1. Manjón, J. V. (2010), 'Non-local MRI upsampling', Medical Image Analysis, vol 14, pp. 784-792
2. Zaborszky, L. (2008), 'Stereotaxic probabilistic maps of the magnocellular cell groups in human basal forebrain', NeuroImage, vol. 42, pp. 1127-1141.

Poster No 316

The impact of connectivity estimation methods on functional connections in young and older adults

Jeremy Fleming[1], Jenna Blujus[1], Hwamee Oh[1]

[1]Brown University, Providence, RI

Introduction: Aging is associated with cognitive decline across multiple domains, underpinned by disruptions to functional connectivity within and between large-scale networks. Connectivity between brain regions is traditionally determined using a bivariate correlation approach. However, connectivity matrices resulting from bivariate correlations are afflicted with a considerable number of spurious associations, reflecting indirect connections or associations due to confounders. A recent method called combinedFC was developed to eliminate such spurious connections by sequentially applying partial and bivariate correlation methods. Through simulations and application to fMRI data in young adults, combinedFC was shown to remove spurious connections and improve causal inference. In the current study, we implemented bivariate alone and combined FC approaches in a sample of young and older adults to examine the impact of functional connectivity estimation method on resulting connections, or edges retained, in healthy young and older adults.

Methods: The sample consisted of 30 young adults (age range 18-30; M = 20.03, SD = 2.95; 20 females) and 18 older adults (age range 60-75; M = 65.33, SD = 4.37; 11 females). T1-weighted MRI and resting state fMRI (rs-fMRI) data were collected on a 3T Siemens scanner. The data were preprocessed and denoised using ENIGMA HALFpipe. Average signals from ICA noise components, white matter, and CSF were removed. The Power atlas was utilized to extract the average time series from 264 regions of interest. Functional connectivity matrices were calculated using two methods: (1) bivariate correlation alone, and (2) combinedFC. At the subject level, edges retained were determined using an alpha cutoff at 0.01. A two-way ANCOVA model was conducted using R to examine the interaction of age group (young, older) and functional connectivity method

(bivariate, combinedFC) on the proportion of edges retained in functional connectivity matrices, controlling for sex and years of education. Posthoc simple contrasts were conducted within each level of functional connectivity estimation method.

Results: As expected, there was a significant main effect of method on the proportion of edges retained ($F(1, 90)=352.83$, $p<.001$), with the bivariate approach resulting in a greater proportion of edges retained ($p<.001$). There was also a significant interaction between age group and functional connectivity estimation method on the proportion of edges retained ($F(1, 90)=6.07$, $p=.016$). Simple contrasts showed a trend that old retained a greater proportion of edges than young when the bivariate method was applied ($p=.076$), but this age difference was no longer evident when the combinedFC method was utilized ($p=.244$).

Conclusions: In line with past work, our results showed that compared to a bivariate approach, combinedFC eliminated a significant portion of potentially spurious edges, regardless of age group. We extend past findings by demonstrating that age group differences in edges retained via bivariate approaches were eradicated using the combined FC approach. The combinedFC approach may provide a complementary perspective to traditional bivariate estimates of functional connectivity and uncover alterations in direct causal connections, estimated from resting state data, which underlie age-related cognitive decline.

References

1. Sanchez-Romero, R., and Cole, M.W. (2021) "Combining multiple functional connectivity methods to improve causal inferences" Journal of Cognitive Neuroscience. https://doi.org/10.1162/jocn_a_01580
2. Jenna Blujus, Michael W. Cole, Elena Festa, Stephen Correia, Stephen Salloway, William Heindel, Hwamee Oh. Functional Redundancy of the Posterior Hippocampi, but not Anterior Hippocampi or Left Frontal Cortex, is Disrupted in Pathological Brain Aging. [preprint] bioRxiv 2022.06.18.496543; doi: https://doi.org/10.1101/2022.06.18.496543
3. Jenna Blujus & Hwamee Oh. Denoising approach affects diagnostic differences in brain connectivity across Alzheimer's continuum. [preprint] bioRxiv 2022.06.16.496466; doi: https://doi.org/10.1101/2022.06.16.496466

Poster No 317

Changes in brain structure and age in Veterans with TBI following treatment with Magnesium-Ibogaine

Andrew Geoly[1], John Coetzee[1,2], Wiebke Struckmann[1], Derrick Buchanan[1], Azeezat Azeez[1], Bora Kim[1], Kirsten Cherian[1], Nimrod Keynan[1], Maheen Adamson[2,3,4], Nolan Williams[1]

[1]Department of Psychiatry and Behavioral Sciences, Stanford School of Medicine, Stanford, CA, [2]Rehabilitation Service, VA Palo Alto Health Care System, Palo Alto, CA, [3]WRIISC-Women, VA Palo Alto Health Care System, Palo Alto, CA, [4]Department of Neurosurgery, Stanford University School of Medicine, Stanford, CA, United States

Introduction: Traumatic brain injury (TBI) is common among Veterans of recent US conflicts.[1] TBI may lead to a range of neuropsychiatric symptoms,[2] and may also be associated with accelerated brain aging,[3] increasing the risk for dementia and other neurodegenerative diseases.[4] Ibogaine, a naturally-occurring psychoactive alkaloid, has demonstrated neuroplasticity promoting properties, including increased neurogenesis and enhanced synaptic plasticity via the release of neurotrophic factors, such as brain-derived neurotrophic factor (BDNF) and GDNF (glial cell-derived neurotrophic factor).[5] This may help remodel neural circuitry and improve cognitive function, emotional regulation, and physical well-being in Veterans with TBI.

Methods: We conducted an observational study with 30 Veterans with multiple blast TBI (mbTBI) and complex clinical problems who received supervised ibogaine treatment (up to 21mg/kg) over a period of several hours, preceded and followed by multiple days of preparation and integration. At the baseline, immediate post, and 1-month time points, we performed clinical assessments and structural magnetic resonance imaging (MRI) scans. We derived cortical thickness measures for our participants with the Advanced Normalization Tools (ANTs) longitudinal cortical thickness pipeline, and evaluated thickness and volumetric statistics in cortical and subcortical gray matter and cerebellar regions of interest (ROIs), respectively. To evaluate longitudinal changes in cortical thickness and volume across the ROIs, we employed linear mixed effects (LME) models. We used the algorithm described by Cole et al. (2015)6 to determine brain age using T1s.

Results: Wald X2 test of regional LME models revealed a significant ($pFDR < 0.05$) main effect of study visit on cortical thickness in 13 ROIs. Subsequent post-hoc pairwise t-tests demonstrated significant ($pholm < 0.05$) increases in cortical thickness immediately following ibogaine therapy (~7 days) relative to the baseline visit in 11 regions. No significant changes were found between immediate-post and 1-month post visits, suggesting a likely sustained increase in cortical thickness across the study period following treatment. For subcortical volume, Wald X2 test of the subcortical LME models revealed a significant ($pFDR < 0.05$) main effect of study visit on the log-jacobian determinant in the Right Ventral Diencephalon which was sustained at the one month time point. Estimated marginal mean predicted brain age for each timepoint was as follows M(SE): baseline 39.7(1.73), immediate post 39.1(1.73), 1-month 38.1(1.74). Wald X2 test of the LME,revealed a significant change

across timepoints [X2(2) = 10.64, p = 0.0049]. Post-hoc paired sample t-tests revealed a significant (pholm < 0.05) reduction of 1.60 years in predicted brain age relative to baseline one month after ibogaine treatment (t = 3.18, p = 0.0082, d = 1.035).

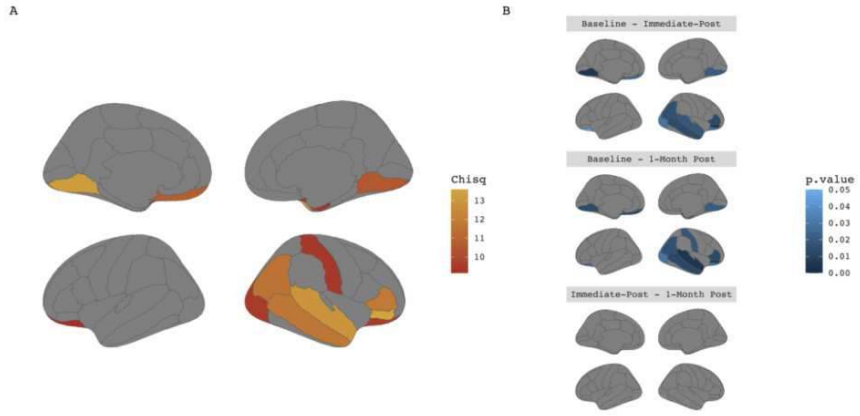

Figure 1. A) Regions with significant main effect of visit for cortical thickness (surviving FDR correction). Top row indicates medial view and bottom row corresponds to lateral view of left and right hemispheres, respectively. The red-to-orange colorbar corresponds to the X^2 Statistic for the main effect of visit on cortical thickness. Regions illustrated displayed pFDR < 0.05. **B)** Post-hoc pairwise comparisons by visit contrast for regions with significant main effects reveal significant increases in cortical thickness from baseline to immediate & 1-month post visits. P-values are holm-bonferroni corrected for 3 pairwise contrasts with surviving effects (p_{holm} < 0.05) highlighted in blue.

Conclusions: This work provides the first evidence of measurable brain morphometric changes in humans following ibogaine therapy, suggesting that ibogaine therapy may reduce signs of accelerated brain aging in Veterans with mbTBI. Given the heightened risk of dementia associated with TBI, this has important implications for the treatment of this underserved patient group. However, more research is needed to fully understand the therapeutic mechanisms by which ibogaine works and to determine the long-term impact on cortical structure.

References

1. Hayward, P. Traumatic brain injury: the signature of modern conflicts. Lancet Neurol. 7, 200–201 (2008).
2. Rickels, E. et al. The Long-Term Sequelae of Traumatic Brain Injury Over 10 Years of Follow-Up—A Matched Cohort Study Based on Routine Data of a Statutory Health Insurance Carrier. Dtsch. Arzteblatt Int. 120, 271–276 (2023).
3. Gan, S. et al. Accelerated Brain Aging in Mild Traumatic Brain Injury: Longitudinal Pattern Recognition with White Matter Integrity. J. Neurotrauma 38, 2549–2559 (2021).
4. Weiner, M. W. et al. Effects of traumatic brain injury and posttraumatic stress disorder on development of Alzheimer's disease in Vietnam Veterans using the Alzheimer's Disease Neuroimaging Initiative: Preliminary report. Alzheimers Dement. Transl. Res. Clin. Interv. 3, 177–188 (2017).
5. Marton, S. et al. Ibogaine Administration Modifies GDNF and BDNF Expression in Brain Regions Involved in Mesocorticolimbic and Nigral Dopaminergic Circuits. Front. Pharmacol. 10, 193 (2019).
6. Cole, J. H., Leech, R., Sharp, D. J. & Initiative, for the A. D. N. Prediction of brain age suggests accelerated atrophy after traumatic brain injury. Ann. Neurol. 77, 571–581 (2015).

Poster No 318

Epigenetic aging is associated with atypical neurodegenerative patterns in Alzheimer's disease

Lasya Sreepada[1], Sandhitsu Das[1], Paul Yushkevich[1], Wanding Zhou[1], David Wolk[1], Corey McMillan[1]

[1]University of Pennsylvania, Philadelphia, PA

Introduction: While Alzheimer's disease (AD) is typically considered an amnestic, multi-domain disorder, at least 15% of individuals are considered atypical presentations. Atypical presentations are associated with younger age of onset, whereas late-onset AD cases tend to present typically. Although atypical presentations tend to have younger age of onset, age is often defined chronologically, and we hypothesize that epigenetic clock measures of biological age may capture variance contributing to atypical neurodegenerative patterns. We operationalize atypicality in AD as relative neurodegeneration in cortex versus medial temporal lobe (MTL) to investigate whether epigenetic age acceleration (EAA), a robust measure of biological aging, is associated with this neurodegenerative pattern.

Methods: Subjects: 875 (55.7% female, 75.5 +/- 7.4 years) subjects from Alzheimer's Disease Neuroimaging Initiative (ADNI) with whole blood DNA methylation (DNAm) samples or T1 MRI (646 subjects with both). Using clinical diagnoses and

established PET or cerebrospinal fluid (CSF) cut-offs we defined two groups: amyloid-negative controls (N=267) and amyloid-positive MCI/AD (N=608). Subjects were further classified into chronological age groups, such that those below 65 years were labeled “early” and those older than 80 years were labeled “late”. Methylation: DNAm was assayed on Illumina EPIC arrays covering 800K+ CpG sites and beta matrices were generated using the ‘SeSAMe’ R package. Epigenetic age was computed by applying the Shireby cortical clock to the beta matrices using the ‘dnaMethyAge’ R package. EAA is defined by regressing the epigenetic clock age against chronological age and extracting the residual. Subjects were classified as biologically accelerated, neutral, or decelerated based on whether EAA was above, within, or below 1 standard deviation of the regression, respectively. Imaging: Regional cortical thickness measures were generated using FreeSurfer 5.1 and downloaded from ADNI. We applied longComBat to remove batch effects due to scanner and variation in field strength (1.5 or 3T) and adjusted for age and sex relative to healthy controls. We then computed two composite thickness z-scores in previously defined regions of interest (ROI) reflecting age-related and AD signatures of neurodegeneration (Figure 1). We define a composite thickness score in MTL as the bilateral thickness average of entorhinal cortex and parahippocampal cortex. Finally, we defined two “mismatch” scores reflecting relative MTL to age-related and AD signature thickness, respectively.

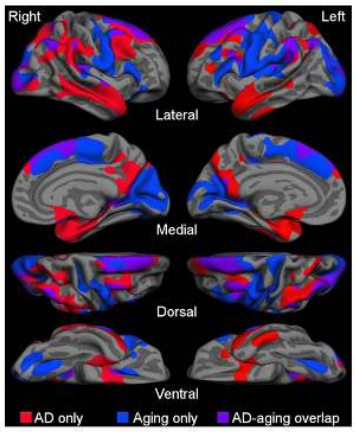

Cortical Composite Signatures using FreeSurfer ROIs	
Aging Signature (ageSig)	AD Signature (ADSig)
Pericalcarine	Inferior Temporal
Insula	Temporal Pole
Cuneus	Superior Parietal
Fusiform	Precuneus
Lateral Occipital	Supramarginal
Precentral	Superior Frontal
Inferior Frontal (Pars Opercularis, Pars Triangularis)	Middle Frontal (Rostral & Caudal)

Figure 1. Brain maps representing the cortical aging and AD signatures as defined by Bakkour et al. 2013 (left). These signatures are recreated for our analysis using thickness average measures of FreeSurfer ROIs and are only approximations of the original signatures, as the FreeSurfer ROIs may cover slightly more or less surface area than the original ROIs. The FreeSurfer ROI names used in each signature are listed in the table (right). The text color in the table corresponds to the brain maps: the 3 purple entries under the AD signature are overlapping aging and AD-related regions.

Results: Overall MCI/AD had reduced cortical thickness in both age-related and AD signatures relative to controls. As expected, mismatch scores reflecting greater cortical neurodegeneration relative to MTL, consistent with greater atypicality, were more pronounced in younger onset relative to older onset MCI/AD. Critically, the degree of cortical to MTL mismatch was greater in decelerated cases (0.13 ageSig, 0.33 ADSig) relative to accelerated cases (1.45 ageSig, 1.07 ADSig). The mismatch difference was statistically significant when using either the ageSig (p=0.003) or ADSig (p=0.01; Figure 2).

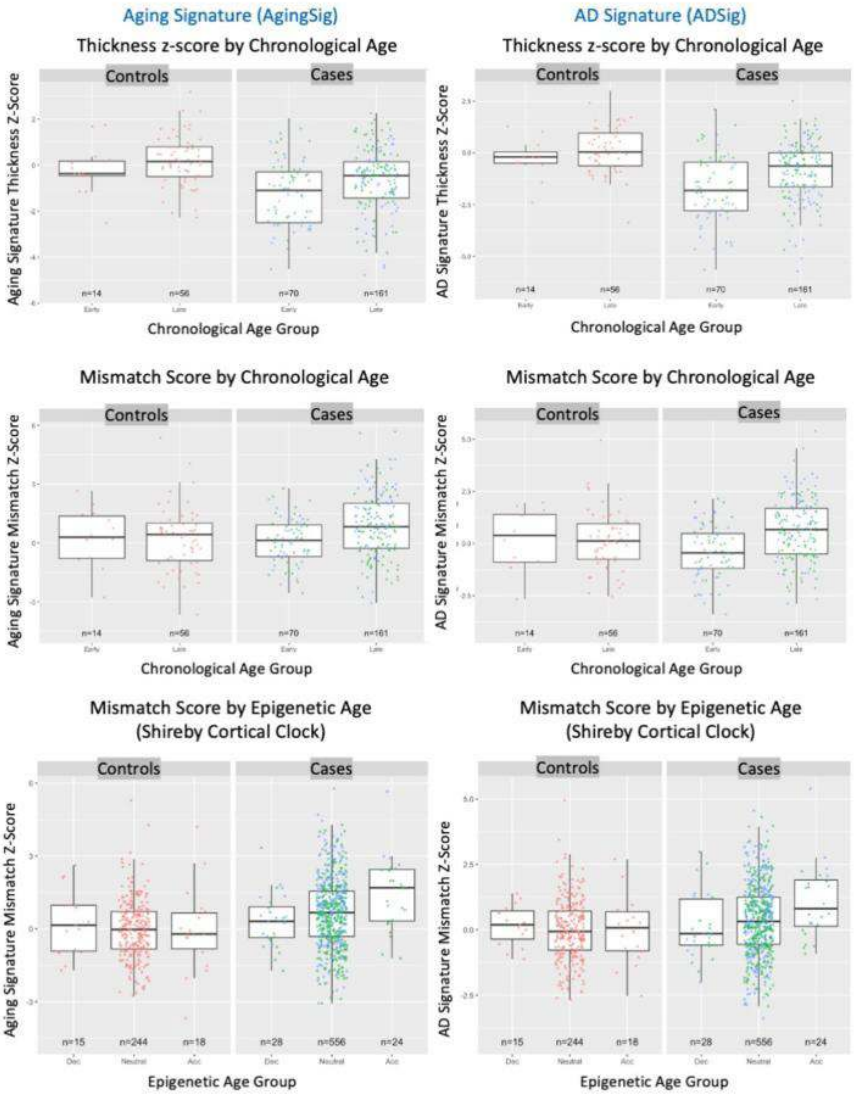

Figure 2. Comparisons of z-scores and mismatch scores across chronological age groups and/or epigenetic age groups in the Aging Signature (left) and the AD signature (right). Red dots represent controls. Within cases, blue dots represent MCI and green dots represent AD.

Conclusions: Our results demonstrate epigenetic age acceleration is significantly associated with variation in neurodegenerative patterns beyond that explained by chronological age: specifically cortical relative to MTL atrophy, a metric of atypicality. Notably, there were significant differences between decelerated and accelerated cases for both the aging and AD signatures, with decelerated cases demonstrating relatively greater cortical involvement akin to effects of younger age. This study motivates future investigation to evaluate the role of biological age specifically in heterogeneity of clinical and pathological outcomes and the enrichment of specific epigenetic markers involved in atypical disease mechanisms.

References

1. Bakkour A (2013), The effects of aging and Alzheimer's disease on cerebral cortical anatomy: specificity and differential relationships with cognition. Neuroimage, 76:332-44.
2. Beer JC (2020), Alzheimer's Disease Neuroimaging Initiative. Longitudinal ComBat: A method for harmonizing longitudinal multi-scanner imaging data. Neuroimage
3. Dickerson BC (2017), Approach to atypical Alzheimer's disease and case studies of the major subtypes. CNS Spectr, 22(6):439-449.
4. Fischl B (2012), FreeSurfer. Neuroimage, 62(2):774-81
5. Petersen RC (2010), Alzheimer's Disease Neuroimaging Initiative (ADNI): clinical characterization. Neurology, 74(3):201-9.
6. Shaw LM (2018), Derivation of cutoffs for the Elecsys® amyloid β (1-42) assay in Alzheimer's disease. Alzheimers & Dementia, 10:698-705.
7. Shireby GL (2020), Recalibrating the epigenetic clock: implications for assessing biological age in the human cortex. Brain, 143(12):3763-3775.
8. Wang HF (2016), Application of the IWG-2 Diagnostic Criteria for Alzheimer's Disease to the ADNI. J Alzheimers Dis, 51(1):227-36.
9. Wang Y (2023), Insights into ageing rates comparison across tissues from recalibrating cerebellum DNA methylation clock. Geroscience
10. Zhou W (2018), SeSAMe: reducing artifactual detection of DNA methylation by Infinium BeadChips in genomic deletions. Nucleic Acids Res, 46(20):e123

Poster No 319

The Role of Dissociable Neuromorphometric Profiles in Aduls Living with HIV

Richard Gallagher[1], Kyle Shattuck[2], David Moore[3], Ronald Ellis[3], Xiong Jiang[4]

[1]Georgetown University, Charlottesville, VA, [2]Georgetown University, Washington, DC, [3]UCSD, San Diego, CA, [4]Georgetown University Medical Center, Washington, DC

Introduction: People living with HIV (PLWH), despite having achieved viral suppression via combination antiretroviral therapy, remain at greater risk than uninfected peers for developing global cognitive deficits. Here we conducted a cross-sectional investigation of neuromorphometric changes linked to HIV-disease and HIV-associated neurocognitive disorders (HAND), respectively.

Methods: High-resolution (1mm-isometric) T1-weighted rapid-acquisition gradient echo images were acquired from 104 PLWH (40-70 years old (mean age = 56.2), 26% female at birth, 64% Black) and 46 demographically matched uninfected controls (mean age = 57.3, 33% female at birth, 52% Black) using a 3.0 Tesla Siemens Magnetom Trio scanner equipped with a 12-channel head coil (n = 88) or a 3.0 Tesla Siemens Prisma-Fit scanner and 20-channel coil (n = 62). Participants were administered a comprehensive set of neuropsychological tests for HAND diagnosis using Frascati criteria. In addition to reporting historical CD4+ T-lymphocyte counts, a proxy for disease severity, PLWH provided blood specimens to confirm viral suppression. MR data were preprocessed using fMRIPrep 20.2.6, and whole-brain voxel based morphometry analysis was performed using the CAT12 toolbox in SPM. Additional vertex-wise estimates of gray matter volume (GMv) and cortical thickness (CT) were determined via surface-based analyses in FreeSurfer v6.0. Subsequent region-of-interest (ROI) analyses were performed using general linear models in R/RStudio.

Results: Following probabilistic threshold-free cluster enhancement, whole-brain voxelwise analyses revealed significant clusters of cortical atrophy among PLWH in temporal ($pFWE\text{-}corr < .001$, $k = 397$) and right cerebellar ($pFWE\text{-}corr < .001$, $k = 720$) cortex, relative to uninfected controls. Surface-based and ROI analyses revealed additional evidence for atrophy in PLWH, relative to controls, irrespective of global cognitive impairment: At $p<.01$, lower CD4+ T lymphocyte nadir corresponded to lower GMv and CT in left caudal ACC and right temporal pole among patients, and global cognitive impairment among PLWH was strongly associated with decreased white matter volume in a right cerebellar ROI ($p<.001$). Notably, the inclusion/removal of a covariate to account for scanner type in the above models did not impact study conclusions.

Conclusions: Despite the heterogeneous nature of the studied population, there is mounting evidence for a distinguishable neuromorphometric profile linking chronic infection to cognitive decline. These findings have implications for the establishment of a noninvasive biomarker for HAND among PLWH, which could serve to identify patients at greater risk of impairment. Historically, very few studies have considered the role of cerebellum in HAND, whereas the current study demonstrated a significant association between global cognitive impairment and altered cerebellar morphometry among virally-suppressed PLWH. Future studies should further investigate the observed relationship between cerebellar atrophy and HAND diagnosis.

References

1. Antinori A, et al. (2007), 'Updated research nosology for HIV-associated neurocognitive disorders', Neurology, vol 69:1789–1799.
2. Heaton RK, et al. 92010), 'HIV-associated neurocognitive disorders persist in the era of potent antiretroviral therapy: CHARTER Study', Neurology, 75:2087–2096.
3. Israel SM et al. (2019), 'Different roles of frontal versus striatal atrophy in HIV-associated neurocognitive disorders', Hum Brain Mapp, 40(10):3010-3026.

Poster No 320

Atrophy Assessment via Freesurfer SynthSR: A Clinical Validation

Severin Schramm[1], Melissa Thalhammer[2], Benita Schmitz-Koep[1], Kirsten Jung[1], Dennis Hedderich[1]

[1]Department of Diagnostic and Interventional Neuroradiology, School of Medicine, Munich, Bavaria, [2]TUM Neuroimaging Center, Munich, Bavaria

Introduction: Structural magnetic resonance imaging (MRI) continues to inhabit an important position in research and clinical assessments of neurodegeneration, with one of its primary uses lying in the detection and monitoring of brain atrophy patterns (Knopman et al., 2016; Young et al., 2020). In clinical practice however, structural imaging protocols are often heterogeneous and subject to low spatial resolution, resulting in suboptimal image quality for brain volume assessments and limited data quality for scientific analyses (Iglesias et al., 2023). Addressing this issue, Freesurfer is a widely used open-source

software package, employed among other use-cases in volumetric and surface-based analyses of neuroimaging (Reuter, Schmansky, Rosas, & Fischl, 2012). Since the recent release of version 7.3, Freesurfer includes SynthSR, a convolutional neural network based approach able to generate 1 mm isotropic 3D T1-like synthetic imaging (T1s) from heterogeneous input sequences trained on data from 20 subjects (Iglesias et al., 2023). In previous validation approaches, the developers report strong correlations between T1s and real 3D T1 imaging (Iglesias et al., 2023). Reliable generation of T1s could improve clinical brain atrophy assessments and unlock much larger datasets of neurodegeneration-related imaging than currently available. In the present study, we attempt to further validate T1s against the gold standard of 1 mm isotropic 3D T1 imaging (GS) by investigating bilateral hippocampus volume (VHip), a notable imaging parameter in neurodegeneration assessment in patients and healthy controls (HC) (Knopman et al., 2016).

Methods: We selected a dataset of 10 representative Alzheimer's Disease (AD) cases, as well as 10 HC scanned on a 3T Siemens Biograph scanner in our local clinic. We employed Freesurfer SynthSR (Iglesias et al., 2023) to generate T1s from three different scenarios of imaging input: 1 mm 3D isotropic T2 FLAIR (Sc1), 4 mm axial T2 FLAIR (Sc2) and 4 mm coronal T2 (Sc3). The resulting T1s and GS were further segmented via CAT12 according to the LONI Probabilistic Brain Atlas (LPBA40) (Gaser et al., 2022; Shattuck et al., 2008). VHip were extracted from GS and the three sets of T1s for subsequent testing against one another via paired t-tests.

Results: After Bonferroni correction, we observed significantly higher VHip in T1s based on Sc3 compared to GS in AD (Figure 1; GS 5.867 ± 0.580 ml vs. Sc3 6.368 ± 0.604 ml, p = 0.01126). Notably, no significant differences were observed between GS and T1s of HC (GS 7.183 ± 0.644 ml; Sc1 6.979 ± 0.889 ml; Sc2 6.769 ± 0.742 ml; Sc3 7.061 ± 0.750 ml). T1s VHip overestimation was strong enough in some cases to be visually notable (Figure 2).

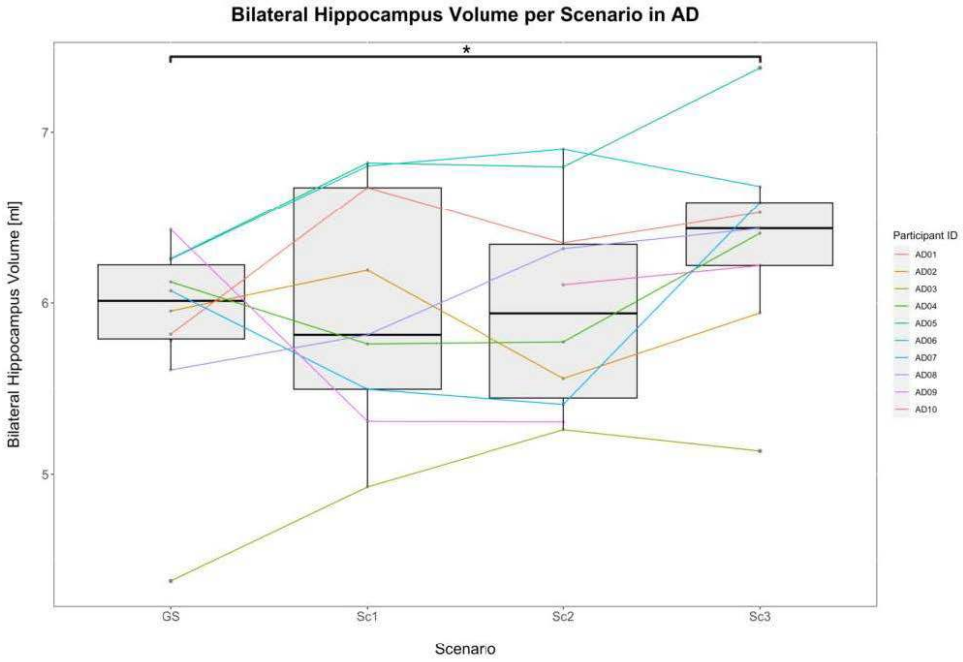

Figure 1: Bilateral Hippocampus Volume per Scenario in AD.
Figure 1 demonstrates the distribution of bilateral hippocampus volume in ml for our cohort of Alzheimer's Disease (AD) patients split according to imaging scenario. Synthetic T1 (T1s) based on Scenario 3 (Sc3; input 4 mm coronal T2) resulted in significantly higher hippocampus volumina compared to gold standard (GS; 1 mm isovoxel 3D T1). Boxes reflect middle quartiles, whiskers reflect outer quartiles, dots reflect individual measurements, line in box corresponds to median. Lines connecting dots trace volumetric measurements based on the same individual across imaging scenarios. Figure abbreviations: Gold standard (GS; 1 mm isovoxel 3D T1); Scenario 1 (Sc1; input 1 mm isovoxel 3D T2 FLAIR); Scenario 2 (Sc2; input 4 mm axial T2 FLAIR); Scenario 3 (Sc3; input 4 mm coronal T2). Figure composed with Biorender.com.

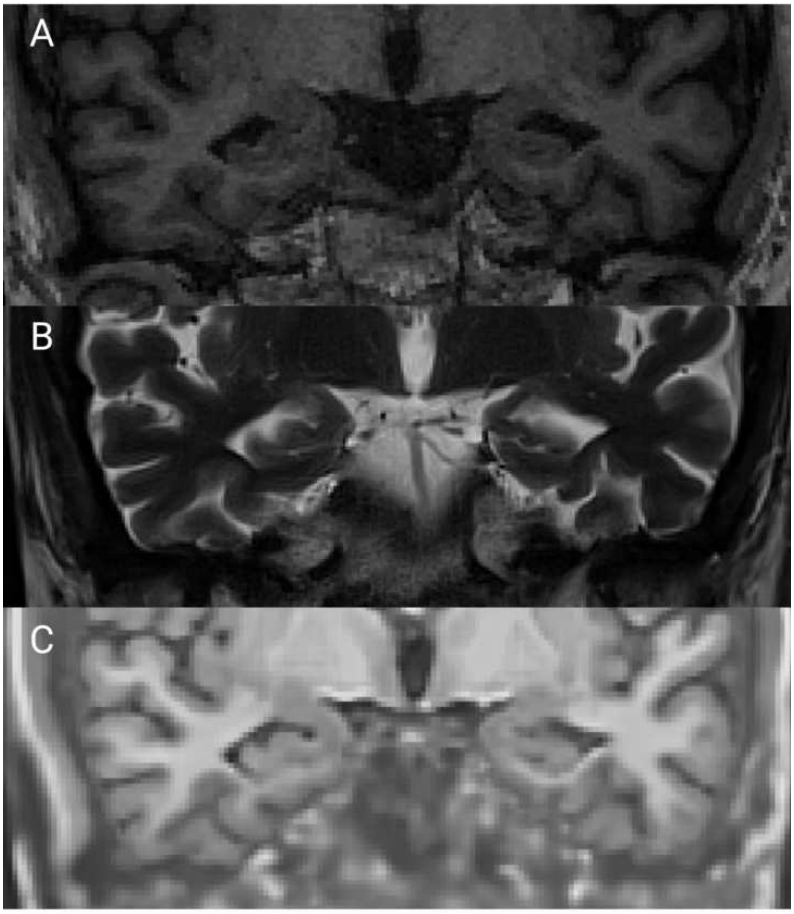

Figure 2: Exemplary Hippocampus Imaging
Figure 2 demonstrates a visual comparison of three coronal slices in an exemplary Alzheimer's Disease (AD) patient in identical position. The gold standard (GS) of 1 mm isovoxel 3D T1 (A) indicates pronounced bilateral hippocampus atrophy. In the same position within the 4 mm coronal T2 volume (B), partial volume artifact is present. Potentially consequential to this, the emerging synthetic 3D T1-like image (C) generated by SynthSR demonstrates marked overestimation of hippocampus volume compared to GS. Figure composed with Biorender.com.

Conclusions: Overall, the performance of SynthSR was not significantly different from GS for any input scenarios aside from Sc3. Regarding potential scientific and clinical use cases for T1s, these are generally encouraging results confirming high congruence with GS. Nonetheless, we observed significant overestimation of VHip in T1s synthesized from Sc3 in our limited sample of AD. One potential reason for this could lie within the training data employed in the generation of SynthSR, which despite including imaging from probable Alzheimer's cases (Iglesias et al., 2023) could introduce biases towards healthy brain volumina. This could consequently facilitate potentially faulty interpolations for e. g. partial volume effects (Figure 2). Future studies should consider validation of T1s in atypical patterns of atrophy, such as e. g. frontotemporal lobar degeneration.

References

1. Gaser, C., Dahnke, R., Thompson, P. M., Kurth, F., Luders, E., & Initiative, A. s. D. N. (2022). CAT–A computational anatomy toolbox for the analysis of structural MRI data. biorxiv, 2022.2006. 2011.495736.
2. Iglesias, J. E., Billot, B., Balbastre, Y., Magdamo, C., Arnold, S. E., Das, S., . . . Fischl, B. (2023). SynthSR: A public AI tool to turn heterogeneous clinical brain scans into high-resolution T1-weighted images for 3D morphometry. Science advances, 9(5), eadd3607.
3. Knopman, D. S., Jack, C. R., Wiste, H. J., Weigand, S. D., Vemuri, P., Lowe, V. J., . . . Mielke, M. M. (2016). Age and neurodegeneration imaging biomarkers in persons with Alzheimer disease dementia. Neurology, 87(7), 691-698.
4. Reuter, M., Schmansky, N. J., Rosas, H. D., & Fischl, B. (2012). Within-subject template estimation for unbiased longitudinal image analysis. Neuroimage, 61(4), 1402-1418.
5. Shattuck, D. W., Mirza, M., Adisetiyo, V., Hojatkashani, C., Salamon, G., Narr, K. L., . . . Toga, A. W. (2008). Construction of a 3D probabilistic atlas of human cortical structures. Neuroimage, 39(3), 1064-1080.
6. Young, P. N., Estarellas, M., Coomans, E., Srikrishna, M., Beaumont, H., Maass, A., . . . Betts, M. J. (2020). Imaging biomarkers in neurodegeneration: current and future practices. Alzheimer's Research & Therapy, 12(1), 1-17.

Poster No 321

Lumbar Spine fMRI to Quantify Efficacy of Spinal Cord Stimulation Therapy in Spinal Muscular Atrophy

Scott Ensel[1], Genis Prat-Ortega[1], Serena Donadio[1], Amy Boos[2], Luigi Borda[3], Nikhil Verma[3], Jonathan Ho[1], Daryl Fields[4], Lee Fisher[1], Doug Weber[3], Peter Gerszten[5], Robert Friedlander[4], Marco Capogrosso[1], Elvira Pirondini[1]

[1]University of Pittsburgh, Pittsburgh, PA, [2]Department of Neurology, Pittsburgh, PA, [3]Carnegie Mellon University, Pittsburgh, PA, [4]Department of Neurological Surgery, Pittsburgh, PA, [5]Department of Neurological Surgery, pittsburgh, PA

Introduction: Spinal Muscular Atrophy (SMA) is a genetic disease that causes progressive dysfunction and death of spinal motor neurons, leading to motor deficits ranging from lower limb weakness (type 4) to severe muscle weakness with respiratory failure (type 1). Recent experiments in mice indicate that SMA motor deficits are due to motor neuron death and decreased firing rates in surviving motor neurons due to a maladaptive response to a loss in the excitatory Ia sensory synapses[1]. Epidural spinal cord stimulation (SCS) can selectively activate Ia sensory fibers; thus we hypothesize that targeted stimulation of Ia afferents via epidural SCS would increase inputs to the motor neurons, resulting in increased firing ability and improved leg functions through long-term stimulation effects (Figure 1A)[2-4]. To test the efficacy of our SCS therapy we quantified long term changes in motor neuron functions by performing functional magnetic resonance imaging (fMRI) of the lumbar spinal cord during active and passive mobilization of the knee joint pre- and post- SCS therapy (Figure 1B). Spinal cord fMRI is a rapidly growing field, but the lumbar spine has largely been ignored. Therefore, we leverage recently developed cervical spinal cord fMRI techniques to create a robust lumbar spine acquisition and processing paradigm, which can be applied to any clinical population[5-7].

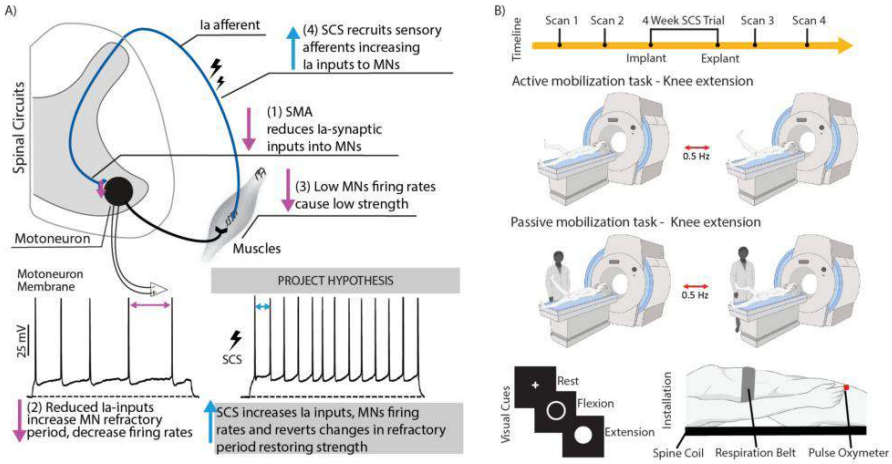

Fig. 1 | Trial and Task Design a, A diagram representing the long-term effect of SCS on the affected motor neurons in SMA. **b,** Timeline of the clinical trial with scan sessions pre and post 30-day SCS trial. During scan sessions acquisition of functional MRI from the lumbar spinal cord in for the recruitment of motor neurons in response to specific muscle recruitment. The motor neurons are recruited either by stretching the muscles in which they innervate (the limb is mobilized by a physiotherapist, aided with audio cues), or by active mobilization of the joint itself (participant aided with visual cues). Three runs are acquired for each task each session. Only the right leg muscles are tested. In addition to the functional volume series, T2 anatomical images and physiological (heart rate, respiratory) signals are acquired.

Methods: Three participants were installed in a 3T Siemens Prisma scanner in a supine position. Participants completed three runs of active and three runs of passive knee mobilization each session (Figure 1B). Functional acquisitions were performed using a gradient-echo echo-planar sequence with a ZOOMit field-of-view imaging, with repetition time (TR) = 2.5 s, echo time (TE) = 34 ms, FOV = 48x144 mm, flip angle = 80°, image resolution = 1.0 mm x 1.0 mm x 3.0 mm, 32 axial slices were acquired per volume. Physiological data (respiratory and cardiac signals) were acquired during scans. A T2-weighted high-resolution anatomical image (sequence SPACE with a resolution of 0.4 mm x 0.4 mm x 0.8 mm, TR = 1.5 s, TE = 135 ms) was also acquired for registration and normalization using the spinal cord toolbox[8]. Active block conditions were compared to baseline rest periods using a second level fixed effects analysis (subject level) by combining the three runs of each session[9].

Results: We report the Z-maps of the lumbar spinal cord fMRI during voluntary movements of the leg (Figure 2A), where we calculated both the number of activated voxels as well as the z-scores of the activations in all participants (Figure 2B). We calculated this activation in the spinal segments where the dorsal roots innervated by the quadriceps were located. In all subjects we observed an increase in the number of activated voxels as well as significantly higher z-scores indicating that after 4-weeks of SCS therapy there are long term improvement in motor neuron function. Interestingly, we observed a

statistically significant increase in the number of active voxels and z-score also during passive movements suggesting an increased synaptic drive into the motor neurons. Overall, we found an increased response in the lumbar spinal cord motor neurons post-therapy as compared to pre-therapy in all three participants.

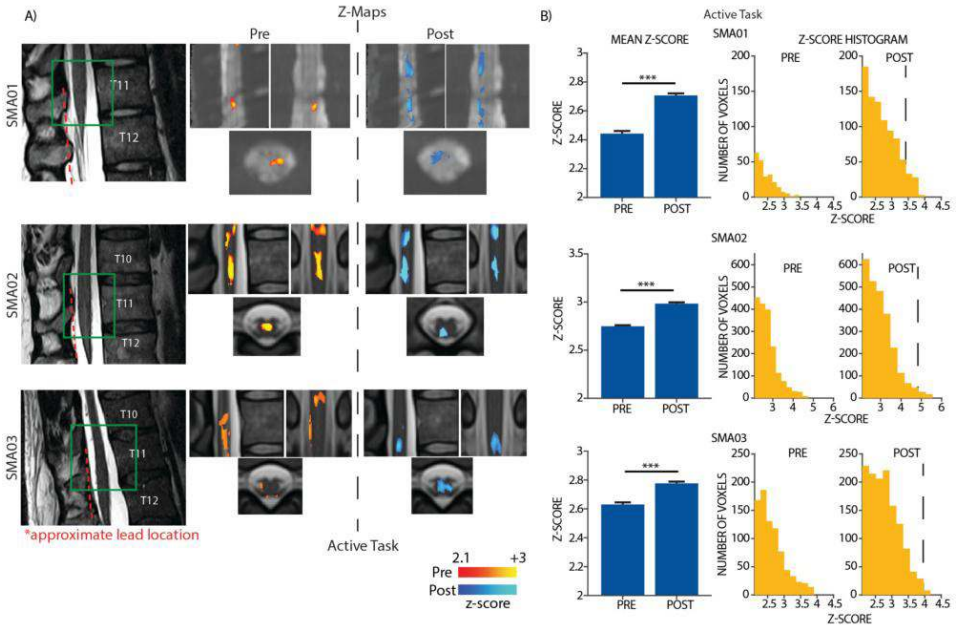

Fig. 2 | Active Task Activations a, Z-map is created from fixed effects combination of 3 runs, from a single pre-implant and post-explant session, which captures robust activations in the regions that are responsive while performing knee extension. The color bar represents the z-score values of the voxels. Z-maps are registered to the PAM50 template with either the mean functional image or the PAM50 T2 image as background. **b,** The mean z-score and a histogram of the voxels z-score for the active task in all three participants. The dashed line in the post session histograms represents the peak z-score in the pre session histogram. Asterisks represent significant differences evaluated through bootstrapping, ***, $p < 0.001$. We see there is an increased Z-score post SCS therapy compared to pre SCS therapy.

Conclusions: All participants physically improved during SCS treatments and these changes correlate with fMRI results, on both the active and passive tasks, showing an increased number of active voxels and higher voxel z-scores post SCS therapy. Our data shows that SCS is contributing to long term changes by increasing the firing rate of vulnerable motor neurons in patients with type 3 SMA resulting in improved leg motor functions and raise the possibility that SCS can provide a permanent treatment for people living with SMA. We also show that lumbar spine fMRI is viable, and this study demonstrates successful implementation of a fMRI acquisition protocol and analysis pipeline.

References

1. Fletcher, E.V., et al., Reduced sensory synaptic excitation impairs motor neuron function via Kv2.1 in spinal muscular atrophy. Nat Neurosci, 2017. 20(7): p. 905-916.
2. Formento, E., et al., Electrical spinal cord stimulation must preserve proprioception to enable locomotion in humans with spinal cord injury. Nat Neurosci, 2018. 21(12): p. 1728-1741.
3. Rowald, A., et al., Activity-dependent spinal cord neuromodulation rapidly restores trunk and leg motor functions after complete paralysis. Nat Med, 2022. 28(2): p. 260-271.
4. Wagner, F.B., et al., Targeted neurotechnology restores walking in humans with spinal cord injury. Nature, 2018. 563(7729): p. 65-71.
5. Kinany, N., et al., Functional imaging of rostrocaudal spinal activity during upper limb motor tasks. NeuroImage, 2019. 200: p. 590-600.
6. Kinany, N., et al., Dynamic Functional Connectivity of Resting-State Spinal Cord fMRI Reveals Fine-Grained Intrinsic Architecture. Neuron, 2020. 108(3): p. 424-435 e4.
7. Landelle, C., et al., Investigating the human spinal sensorimotor pathways through functional magnetic resonance imaging. Neuroimage, 2021. 245: p. 118684.
8. De Leener, B., et al., SCT: Spinal Cord Toolbox, an open-source software for processing spinal cord MRI data. Neuroimage, 2017. 145(Pt A): p. 24-43.
9. Christian, F.B., J. Mark, and M.S. Stephen, General multilevel linear modeling for group analysis in FMRI. NeuroImage, 2003. 20(2): p. 1052-1063.

Poster No 322

Early Prediction of Alzheimer's using Dynamic Functional Connectivity and Deep learning

Yuxiang Wei[1], Anees Abrol[2], Vince Calhoun[3]

[1]Georgia Institute of Technology, Atlanta, GA, [2]Georgia State University, Atlanta, GA, [3]GSU/GATech/Emory, Decatur, GA

Introduction: Alzheimer's disease (AD) is a neurodegenerative brain disorder that gradually transitions from asymptomatic pathological changes to clinical symptoms. Early diagnosis is pivotal in implementing proper treatment and potentially slowing disease progression. Functional magnetic resonance imaging (fMRI) has emerged as an non-evasive method capable of accurately capturing brain activities. In particular, the fMRI features estimated by dynamic functional connectivity approach models the dynamism of brain function, position itself as a promising biomarker for identifying AD and mild cognitive impairment symptoms. Nevertheless, studies probing asymptomatic at-risk subjects using fMRI remain relatively limited. The recent advance of deep learning enhanced the efficacy of encoding high-level information from brain dynamism, signifying a promising avenue for pre-symptom AD detection and analysis.

Methods: In this work, we introduce a transformer-convolution-based framework, building on our previous work, for predicting and analyzing subjects that are at risk for AD. We propose an innovative spatial-temporal self-attention module to learn both the spatial dependencies across brain networks and temporal contextual variations. We validate our method based on the Emory Healthy Brain Study dataset and study 303 cognitive normal and 59 high-risk subjects.

Results: Compared to other standard machine learning methods such as logistic regression that has 78.13% accuracy but 13.48% f1 score and 10.17% sensitivity on the high-risk subjects, the proposed method achieves 76.76% accuracy, 45.09% f1 and 66.10% sensitivity. To further study which brain network contributes to the final prediction, we provide interpretable analysis over the proposed framework based on the gradient-based interpretable method and present the saliency map.

Conclusions: As such, the proposed method reveals distinct relations between various brain networks and AD progression, offering a promising direction for the study of asymptomatic AD with fMRI.

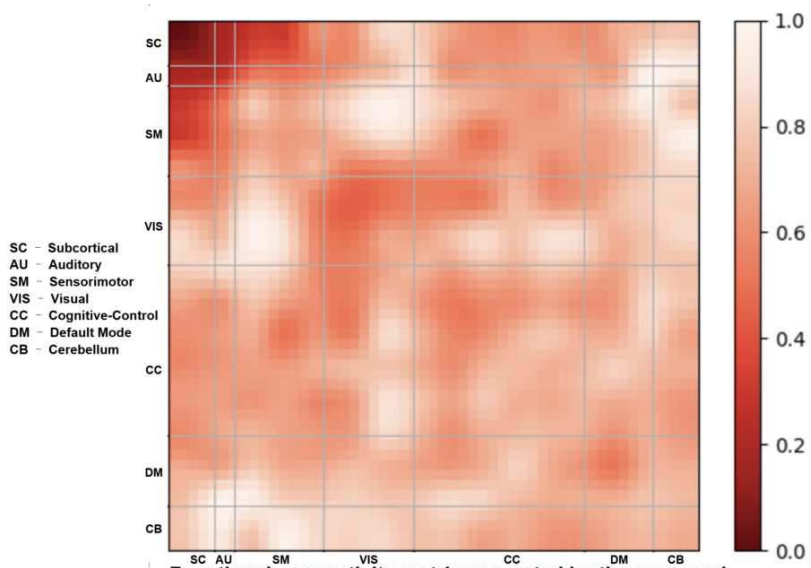

Functional connectivity matrix generated by the proposed framework for early prediction of Alzheimer's

References

1. Sperling, Reisa. (2011). 'The potential of functional MRI as a biomarker in early Alzheimer's disease'. Neurobiology of aging 32, S37-S43.
2. Wierenga, C.E., Bondi, M.W. (2007) 'Use of Functional Magnetic Resonance Imaging in the Early Identification of Alzheimer's Disease'. Neuropsychol Rev 17, pp: 127–143

Poster No 323

Lifestyle activities contribute to cognitive reserve in mid-life individuals at risk of dementia

Feng Deng[1], Sandra El-Sherbiny[1], Maria-Eleni Dounavi[2], Karen Ritchie[3], Graciela Muniz-Terrera[4], Paresh Malhotra[5], Craig Ritchie[6], Brian Lawlor[1], Lorina Naci[1]

[1]Trinity College Dublin, Dublin, Ireland, [2]University of Cambridge, Cambridge, Cambridge, [3]Institut de Neurosciences INM Inserm, Montpellier, France, [4]Ohio University, Athens, OH, [5]Imperial College London, London, London, [6]University of Edinburgh, Edinburgh, United Kingdom

Introduction: It is now acknowledged that Alzheimer's Disease (AD) processes are present decades before the onset of clinical symptoms, but it remains unknown whether lifestyle factors can protect against these early AD processes in mid-life. Intellectually, physically, and socially stimulating lifestyle activities are associated with maintenance of late-life cognitive abilities (Chan et al., 2018), and lower cognitive impairment in AD (Livingston et al., 2020). We asked whether such activities contribute to cognitive reserve (CR) from mid-life, in cognitively healthy individuals who are at risk for late-life AD.

Methods: Middle-aged individuals (aged 40–59 years, mean=52 years) from the PREVENT Dementia study (www.preventdementia.co.uk) were assessed at baseline (N=210, 62/148 male/female) and two-year follow-up (N=188, 55/133 male/female), with cognitive ability (multidomain battery) and brain health measures (total grey matter volume, functional brain network segregation). Mid-life activities were measured using the Lifetime of Experiences Questionnaire, which comprises occupational as well as intellectually, physically, and socially stimulating leisure activities. Dementia risk was assessed with the Cardiovascular Risk Factors, Aging, and Dementia (CAIDE) score.

Results: Multivariable linear regression showed that intellectual, physical, and social activities undertaken in mid-life made a unique contribution to episodic and relational memory in mid-life, independent of occupation and CAIDE at baseline (β (se) = 0.04 (0.02), p = 0.02) and follow-up (β (se) = 0.07 (0.02), p = 0.002). Furthermore, these activities moderated the relationship between cognitive ability and brain health at follow-up (β (se) = 3.47 (1.40), p = 0.01), with verbal and visuospatial functions, and short-term (conjunctive) memory of people with higher activity levels less dependent on their brain functional integrity (Figure 1), consistent with the concept of CR (Brayne et al., 2010). Such a moderation by these mid-life activities was more prominent in individuals with higher CAIDE scores (β (se) = 4.28 (1.83), p = 0.02, Figure 2).

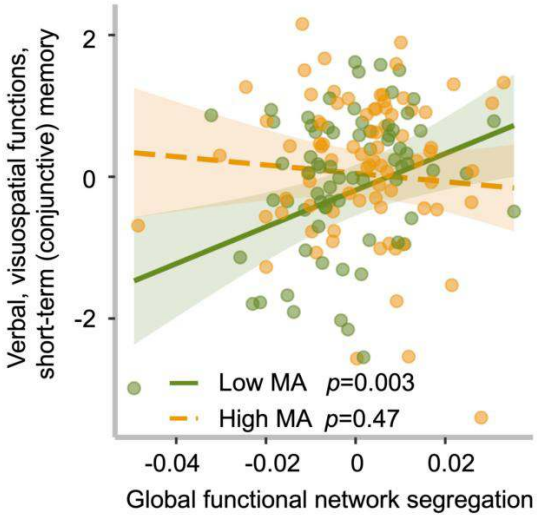

Figure 1. Physical, social and intellectual activities moderates the relationship between brain functional health (global network segregation) and cognition at follow-up. Cognitive ability of people with higher mid-life activities (MA) was less dependent on their functional brain integrity, consistent with the concept of cognitive reserve. Scatter plots show unadjusted values. Full regression statistic after controlling for occupation, education, sex and age: *β* (*se*) = 3.47 (1.40), *p* = 0.01.

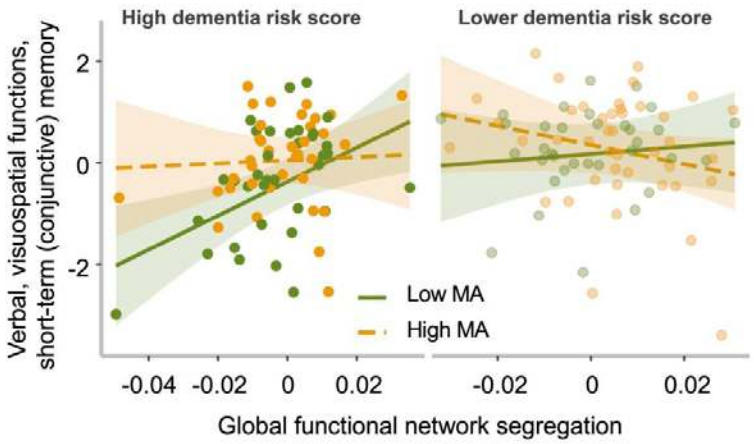

Figure 2. Physical, social and intellectual activities moderates the relationship between brain functional health (global network segregation) and cognition for individuals with high dementia risk score at follow-up. Cognitive ability of people with higher mid-life activities (MA) was less dependent on their functional brain integrity, consistent with the concept of cognitive reserve. Scatter plots show unadjusted values. Full regression statistic after controlling for occupation, education, sex and age: β *(se)* = 4.28 (1.83), p = 0.02 for individuals at high dementia risk.

Conclusions: These findings suggest that modifiable lifestyle activities contribute uniquely to CR and may offset cognitive decrements due to AD risk in mid-life. They support the targeting of modifiable lifestyle activities for the prevention of Alzheimer's disease.

References

1. Chan, D., (2018), 'Lifestyle activities in mid-life contribute to cognitive reserve in late-life, independent of education, occupation, and late-life activities', Neurobiology of aging, 70, 180–183.
2. Livingston, G., (2020), 'Dementia prevention, intervention, and care: 2020 report of the Lancet Commission', Lancet, 396(10248), 413–446.
3. Brayne, C., (2010), 'Education, the brain and dementia: neuroprotection or compensation? EClipSE Collaborative Members', Brain, 133(8), 2210-2216.

Poster No 324

Multi-Modal Approach: Classification of MCI Using Language Tasks, Eye-Tracking, fMRI and sMRI

Afrina Sallehuddin[1], Mazlyfarina Mohamad[2], Neil Mennie[3], Rogayah A Razak[4], Mohd Azmarul A Aziz[5], Mizhanim Mohamad Shahimin[1], Hazlina Mahadzir[6], Leong Yuh Yang[6], Norshuhada Sahnan[7]

[1]Universiti Kebangsaan Malaysia, Kuala Lumpur, Federal Territory Kuala Lumpur, [2]Universiti Kebangsaan Malaysia, Kuala Lumpur, Wilayah persekutuan, [3]University of Nottingham Malaysia, Semenyih, Selangor, [4]UCSI, Kuala Lumpur, Federal Territory Kuala Lumpur, [5]Universiti Sains Malaysia, Gelugor, Penang, [6]Hospital Chanselor Tunku Mukhriz, Cheras, Federal Territory Kuala Lumpur, [7]UKM Specialist Children's Hospital, Cheras, Federal Territory Kuala Lumpur

Introduction: Mild cognitive impairment (MCI) is the transitional stage of cognitive changes of normal aging, and early stages of Alzheimer's disease (AD). A decline in lexical-semantic processing is one of the earliest determinants of MCI, and language tasks are shown to be sensitive to changes in cognitive deficits. However, most neuroimaging studies identifying disruptions in language performance have only focused on a single-modality approach. -Therefore, this study aims to investigate whether combining two modalities, functional magnetic resonance imaging (fMRI), and eye-tracking (ET) data during language comprehension tasks, can provide better accuracy in classifying individuals with MCI from healthy cognitive aging (HCA) adults.

Methods: Twenty-three elderly participants (MCI = 8, HCA =15) between the age of 50-70 years old were recruited within Klang Valley, Malaysia. During both task-based fMRI and ET, participants engaged in a Semantic Battery Assessment for Malay, consisting of object and action-categorized images. Participants were instructed to select the image that best describes the word and sentence depicted. Cognitive-based Stroop Task was also performed following the completion of the battery assessment. For the result analysis, the fMRI data for brain region identification was analyzed using Statistical Parametric Mapping (SPM12), followed by Gaze Point for ET data.

Results: For HCA adults, greater activation was predominantly found in the left inferior occipital gyrus, inferior temporal gyrus, inferior frontal gyrus, and left parietal lobe regions as compared to the MCI patients. Suggesting that these areas are involved in language processing. For ET, higher saccadic regression, and irregular movements were identified in subjects who displayed weaker temporal activation whilst performing the task. Poorer behavioral performance scores were found to be consistent with the same participants across the two groups.

Conclusions: Preliminary findings suggest that the combination of fMRI and ET data during the Semantic Battery Assessment for Malay provides higher accuracy in identifying the correlation between neural activation with eye-movement behavior among Malaysian elderly adults. Predominant areas (i.e., IFG, MTG, and pFIG) associated with word comprehension were found in this study and were positively correlated with the fixation duration and accuracy response. We aim to improve further by recruiting a larger sample size, and potentially explore further with machine learning.

References

1. Burke, D. M., & Shafto, M. A. (2004). Aging and language production. Current directions in psychological science, 13(1), 21-24.
2. Poirier, G., Ohayon, A., Juranville, A., Mourey, F., & Gaveau, J. (2021). Deterioration, compensation and motor control processes in healthy aging, mild cognitive impairment, and Alzheimer's disease. Geriatrics, 6(1), 33.
3. Readman, M. R., Polden, M., Gibbs, M. C., Wareing, L., & Crawford, T. J. (2021). The potential of naturalistic eye movement tasks in the diagnosis of Alzheimer's disease: a review. Brain Sciences, 11(11), 1503.
4. Groznik, V., Možina, M., Lazar, T., Georgiev, D., & Sadikov, A. (2021, July). Gaze behaviour during reading as a predictor of mild cognitive impairment. In 2021 IEEE EMBS International Conference on Biomedical and Health Informatics (BHI) (pp. 1-4). IEEE.

Poster No 325

Structural network disruption associated with molecular pathogenesis in Alzheimer's disease spectrum

Su Rim Ham[1], Hanna Cho[2], Han-Kyeol Kim[2], Sung-Woo Kim[1], Chul Hyoung Lyoo[2], Joon-Kyung Seong[1,3]

[1]School of Biomedical Engineering, Korea University, Seoul, Korea, Republic of, [2]Gangnam Severance Hospital, Yonsei University College of Medicine, Seoul, Korea, Republic of, [3]Department of Artificial Intelligence, Korea University, Seoul, Korea, Republic of

Introduction: Alzheimer's disease involves structural and functional changes in the brain due to amyloid and tau deposition, ultimately leading to cognitive impairment[1]. While numerous medical imaging studies aim to explore the interactions among pathological markers and their relationship with connectivity disruption, a clear understanding is yet to be established[2,5]. In this study, we aim to investigate network disruption in Alzheimer's disease across early, late, and intermediate stages using multimodal imaging. Additionally, we explore the correlation between disrupted connections and pathology markers.

Methods: We constructed an FA (Fractional Anisotropy) weighted matrix based on tensors fitted using the free-water elimination (FWE) method applied to diffusion-weighted Imaging (DWI) data obtained from 147 participants at Gangnam Severance Hospital. The FWE method aims to enhance tractography by removing confounding free water from diffusion signals[4]. Amyloid and tau PET imaging were used to evaluate an individual's regional or global burden of proteins. The collected individuals were categorized into three groups based on amyloid positivity and disease state (43 amyloid-negative cognitively unimpaired (CU), 44 with mild cognitive impairment (MCI), and 60 with Alzheimer's disease (AD). Both patient groups were amyloid-positive). Comparison of connectivity between groups was conducted using network-based statistics (NBS)[6]. Additionally, cluster-based statistics (CBS) were performed to investigate significant correlations between connectivity disruption and amyloid, tau retention across the three groups[3]. The entire process of the study is shown in figure 1.

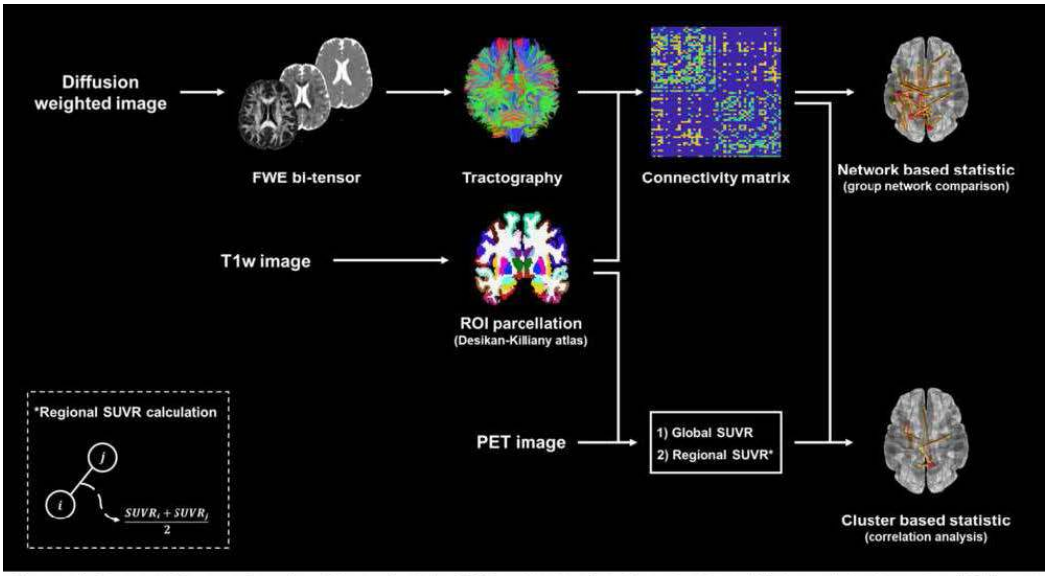

Figure 1. Research Process Overview. We applied the FWE method to fit a bi-tensor from diffusion-weighted imaging (DWI) and performed deterministic tractography. Additionally, through co-registration with T1, we utilized the parcellated Desikan-Killiany atlas to construct an FA-weighted connectivity matrix. This matrix was employed not only for group comparison (NBS) but also for correlation analyses (CBS) with global and regional standardized uptake value ratios (SUVR), calculated from amyloid, tau PET, and T1 data. As a result, subnetworks were extracted from each analysis.

Results: We observed significant disconnection through group-wise comparisons of edge strength. Subsequently, the representative region was defined as the region within the output subnetwork with the highest concentration of disrupted edges. In the comparison between CU and MCI groups, the representative region included the bilateral precuneus and right medial orbitofrontal, while in the comparison between MCI and AD groups, regions such as bilateral caudal anterior cingulate, bilateral precuneus, and cuneus. Comparing CU and AD groups to assess the overall disruption of connectivity throughout the disease, additional regions were identified, including hub nodes resulting from early or late changes (figure 2). Furthermore, we obtained subnetworks that explained the association between disruptions and accumulation of pathological markers. The precuneus, the most prominent region in CU and MCI comparison exhibited an association with global amyloid retention. In contrast, the temporal lobe, identified as the second most vulnerable in the CU and AD comparison, was confirmed to be associated with the accumulation of all protein types. On the other hand, the superior parietal region appeared to be associated with global tau. Hub regions such as bilateral caudal anterior cingulate, left paracentral, left postcentral, and bilateral cuneus either connected via edges associated with global SUVR or did not belong to the output subnetwork.

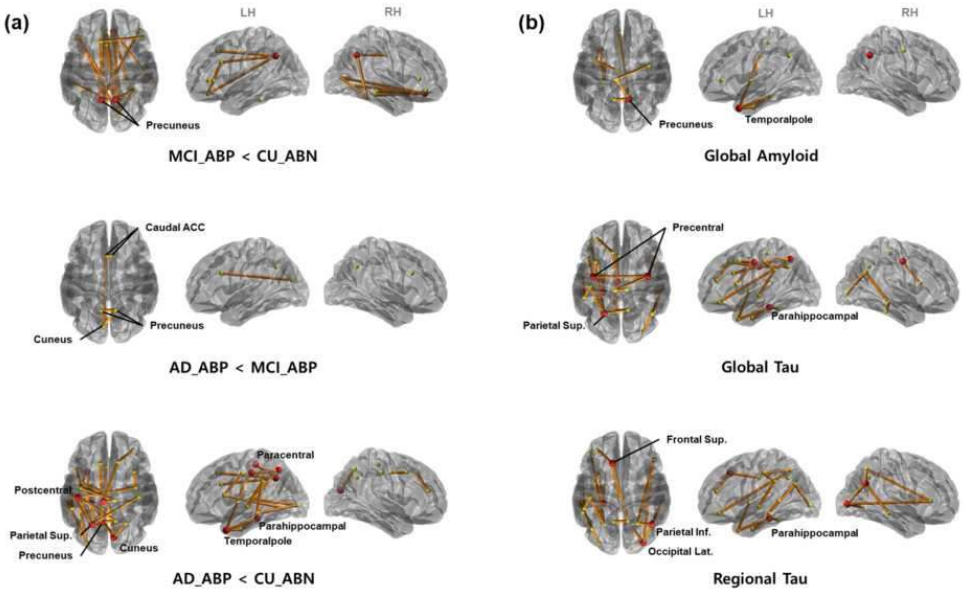

Figure 2. Subnetworks were extracted through cluster-based statistics. **(a)** Results of connectivity comparisons between each pair of groups. Each pair of groups represents early change, late change, and overall change. **(b)** Output subnetwork resulting from correlation analyses involving disrupted connections and global amyloid or tau retention. Red circles signify representative regions, defined as regions with nodal degrees exceeding the mean plus the standard deviation of overall nodal degrees within the output subnetworks.

Conclusions: We aimed to identify primary regions of disconnection and areas vulnerable to the influence of biomarkers through multimodal imaging and cluster-based statistics. In the early stages of Alzheimer's disease (AD), the bilateral precuneus and orbitofrontal cortex appeared to be the most susceptible regions to disruption, particularly influenced by amyloid. As the disease progresses, association areas, especially in the parietal and temporal lobes, appear to undergo disconnection attributed to the effects of amyloid or tau burden. Finally, the anterior cingulate cortex and unimodal cortex (including the visual cortex, primary sensory areas, and motor areas) manifest in the late stage and appear to be minimally affected or least affected by protein influence.

References

1. Blennow, K. (2006), 'Alzheimer's disease', The Lancet, 368(9533), 387-403.
2. Doré, V. (2021), 'Relationship between amyloid and tau levels and its impact on tau spreading', European journal of nuclear medicine and molecular imaging, 48, 2225-2232.
3. Han, C. E. (2013), 'Cluster-based statistics for brain connectivity in correlation with behavioral measures', PLoS one, 8(8), e72332.
4. Parker, D. (2020), 'Freewater estimatoR using iNtErpolated iniTialization (FERNET): Characterizing peritumoral edema using clinically feasible diffusion MRI data', Plos one, 15(5), e0233645.
5. Pereira, J. B. (2019), 'Amyloid and tau accumulate across distinct spatial networks and are differentially associated with brain connectivity', Elife, 8, e50830.
6. Zalesky, A. (2010), 'Network-based statistic: identifying differences in brain networks', Neuroimage, 53(4), 1197-1207.

Poster No 326

The hierarchical organization of the salience, default, and executive networks in social inferences

Yu Chen[1], Winson Yang[2], Myrthe Rijpma[1], Jesse Brown[1], Alex Lee[1], Gianina Toller[1], Howard Rosen[3], Joel Kramer[1], Bruce Miller[4], Katherine Rankin[5]

[1]University of California San Francisco, San Francisco, CA, [2]Harvard Medical School, Boston, MA, [3]UCSF, San Francisco, CA, [4]Memory and Aging Center, Department of Neurology, Weill Institute for Neurosciences, UCSF, San Francisco, CA, [5]Memory and Aging Center, Department of Neurology, University of California San Francisco, San Francisco, CA

Introduction: Dynamic interactions among salience (SN), default mode (DMN), and executive networks (EN) are implicated in the attentional capture of self-related events and the guidance of goal-directed social cognition (Menon, 2015). Socioemotional dysfunction manifests in the earliest stages of behavioral variant frontotemporal dementia (bvFTD) (Lanata et al., 2016; Piguet et al., 2011), though studies have not examined whether social cognition impairments correspond to altered directional communication between brain networks. This study aimed to determine if the resting effective connectivity among the SN, DMN, and EN networks predicts the ability to read others' intentions, in bvFTD patients and healthy adults.

Methods: Seventeen patients with bvFTD and 23 age-, sex-, and education-matched healthy controls (HC) were included in this study. The Awareness of Social Inference Test (TASIT) – Social Inference-Enriched (SIE) (McDonald et al., 2003), employing conversational videos to assess the understanding of intentions during insincere communications, was used to evaluate accuracy of social inferencing. We defined 16 bilateral regions of interest based on the Brainnetome Atlas (Fan et al., 2016): the ventral anterior insular (vAI), cingulate gyrus (CG), dorsal lateral thalamus (dlTha) for the SN; the posterior cingulate (PCC), ventral medial prefrontal cortex (vmPFC), and hippocampus for the DMN; and the middle frontal gyrus (mFG) and inferior parietal lobe (IPL) for the EN. We applied spectral dynamic causal modeling to the task-free functional MRI scans of these participants to characterize the effective connectivity patterns within and between the 3 networks separately in patients and controls. We used parametric empirical Bayes (PEB) scheme to draw subjects out of local optima using the group mean as the empirical prior that furnishes a more efficient and robust estimation of effective connectivity parameters (Friston et al., 2015). We used the second level PEB framework to specify linear models representing each group's average effective connectivity. Bayesian models were applied to account for the estimated uncertainty about the connection strengths. Finally, we performed linear regression analyses controlling for age to examine the relationship of network effective connections with individual's ability to understand social cues using the TASIT SIE "Do" Total Score.

Results: Overall, patterns of network effective connectivity for bvFTD patients differed from HCs. In HCs, 60 excitatory effective connections were identified within and between networks at a posterior probability (Pp) of 99%, with the strongest being reciprocal connections between the networks. In contrast, bvFTD patients exhibited 49 excitatory connections within and between networks, along with one inhibitory connection within the SN from the right vAI to the left dlTha. BvFTD patients performed significantly worse on the TASIT SIE than HCs, and the neural predictors of performance differed between groups. Among HCs, individuals with stronger outputs from the DMN and SN to the EN, particularly from the bilateral vmPFC to mFG and from the left CG to right PCC, were more likely to make accurate social inferences. Conversely, among bvFTDs, more accurate performance was predicted by information flow from the EN (bilateral mFG and IPL nodes) to other nodes in the EN

network, with few SN or DMN networks initiating flow to other nodes. These findings suggest that directional outputs from the SN and DMN to the EN are a preferential foundation for healthy socioemotional reasoning.

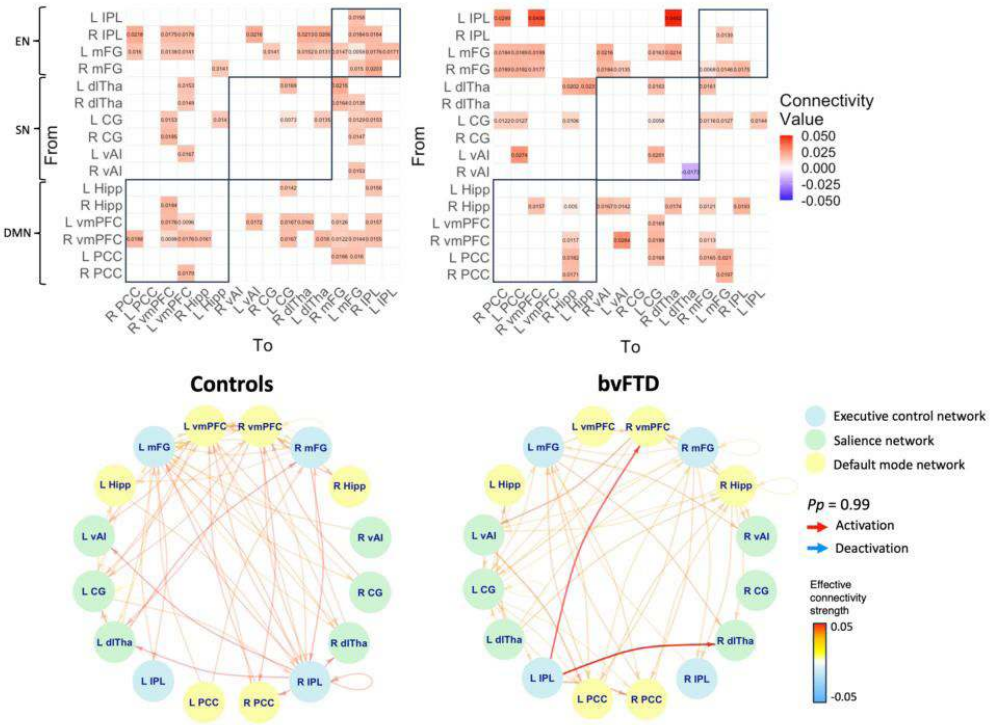

Figure 1. Matrices of mean effective connectivity of the healthy control and bvFTD group, accompanied with schematic overviews of the effective connectivity results (thickness and opacity of lines equal the effective connectivity strength between node pairs).

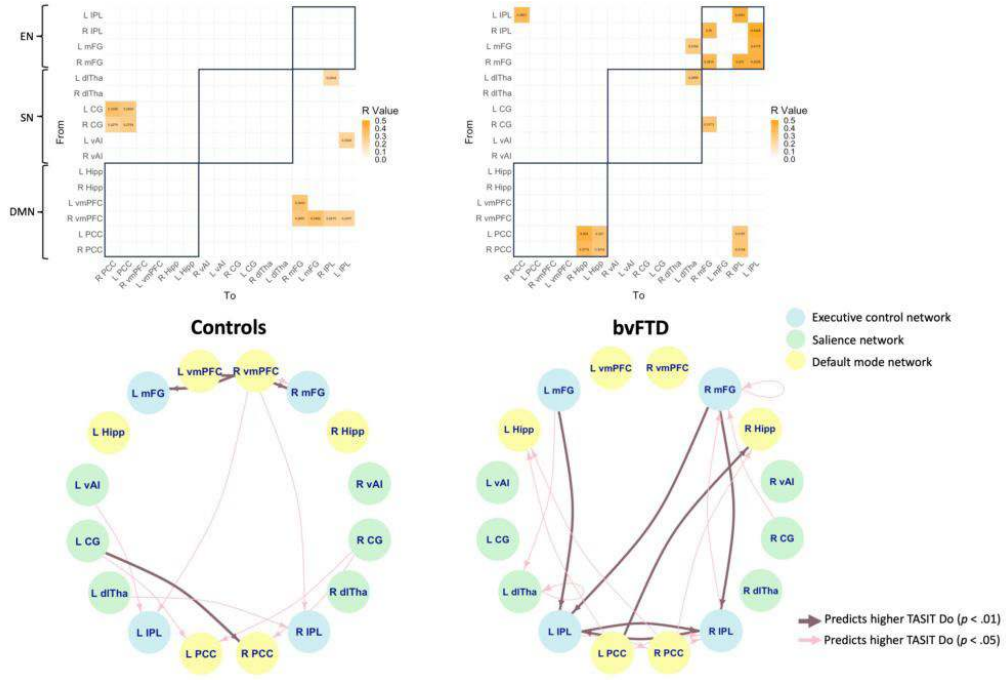

Figure 2. Matrices and schematic illustration of effective node connections that predict higher TASIT-SIE Do scores at a significance level of $p < .05$ or $p < .01$, calculated separately for healthy controls and bvFTD patients.

Conclusions: This study clarifies for the first time how directional information flow among SN, DMN, and EN networks contributes to social inferential reasoning in healthy controls and bvFTD. SN and DMN outputs to the EN are crucial for optimal social reasoning, with information flow disruption being central to bvFTD patients' deficits in making inferences about others' intentions.

References
1. Fan, L., Li, H., Zhuo, J., Zhang, Y., Wang, J., Chen, L., . . . Jiang, T. (2016). The Human Brainnetome Atlas: A New Brain Atlas Based on Connectional Architecture. Cereb Cortex, 26(8), 3508-3526. doi:10.1093/cercor/bhw157
2. Friston, K., Zeidman, P., & Litvak, V. (2015). Empirical Bayes for DCM: A Group Inversion Scheme. Front Syst Neurosci, 9, 164. doi:10.3389/fnsys.2015.00164
3. Lanata, S. C., & Miller, B. L. (2016). The behavioural variant frontotemporal dementia (bvFTD) syndrome in psychiatry. J Neurol Neurosurg Psychiatry, 87(5), 501-511. doi:10.1136/jnnp-2015-310697
4. McDonald, S., Flanagan, S., Rollins, J., & Kinch, J. (2003). TASIT: A new clinical tool for assessing social perception after traumatic brain injury. J Head Trauma Rehabil, 18(3), 219-238. doi:10.1097/00001199-200305000-00001
5. Menon, V. (2015). Large-Scale Functional Brain Organization. 449-459. doi:10.1016/b978-0-12-397025-1.00024-5
6. Piguet, O., Hornberger, M., Mioshi, E., & Hodges, J. R. (2011). Behavioural-variant frontotemporal dementia: diagnosis, clinical staging, and management. The Lancet Neurology, 10(2), 162-172. doi:10.1016/s1474-4422(10)70299-4

Poster No 327

A Resting-State fMRI Study of Suicide Ideation Correlates in Huntington's Disease

Henry Bockholt[1], Bradley Baker[2], Jordan Clemsen[1], Vince Calhoun[3], Jane Paulsen[4]

[1]GSU, Atlanta, GA, [2]TReNDs, Atlanta, GA, [3]GSU/GATech/Emory, Decatur, GA, [4]University of Wisconsin, Madison, WI

Introduction: This study aims to delineate the functional and structural brain network differences in Huntington's Disease (HD) patients with and without recent suicide ideation (SI), utilizing resting-state functional Magnetic Resonance Imaging (rs-fMRI).

Methods: The resting state functional MRI (rs-fMRI) datasets underwent a standardized preprocessing regimen, including motion correction, spatial normalization, and smoothing to reduce artifacts. We applied Spatially Constrained Independent Component Analysis (SC-ICA), following Du et al. (2020), through the GIFT toolbox to segregate functional networks from background noise. This approach enhances the detection of spatially coherent neural activity patterns. Post-ICA, K-Means clustering sorted independent components into distinct brain networks. We then computed dynamic functional network connectivity (dFNC) states using sliding-window Pearson correlation to capture the temporal variability of network interactions. This method permits the assessment of the stability and fluctuation of functional connections over time. Samples were comprised of 90 participants obtained as part of the Prevent-HD study at the University of Wisconsin-Madison. Participants with the gene mutation for Huntington's disease (HD) were separated into two groups according to findings from the Columbia Suicide Severity Rating Scale (C-SSRS), a standardized tool for evaluating the presence and severity of suicidal ideation and behavior. Suicidal ideation and behaviors are documented over a range from passive death wishes to active suicidal plans. Individuals reporting suicidal ideation (SI) within the past three months were compared with those endorsing no SI. Resting fMRI "Eyes Open" data were gathered with a 3T GE Premier (Flip Angle = 50, TE = 0.032, TR = 0.607, Slice Thickness = 2.5mm, Multiband Acceleration Factor = 8).

Results: The dynamic nature of brain connectivity was quantified, revealing patterns specific to HD participants with recent SI. Comparative analysis between groups demonstrated significant differences in the dFNC states. Specifically, reduced connectivity strength was observed in networks involving the prefrontal and limbic systems in the SI group, suggesting a potential disruption in the neural circuits related to mood regulation and executive function. Additionally, the SI group exhibited alterations in white matter integrity, indicating a possible structural basis for the observed functional discrepancies.

Conclusions: The findings illustrate the intricate relationship between functional and structural brain network disruptions and SI in persons with the gene mutation for HD. The variability in dFNC states provides a nuanced understanding of the pathophysiological mechanisms underlying SI in HD, which may inform clinical monitoring and intervention strategies. Future research should explore the longitudinal progression of these network changes and their potential as biomarkers for psychiatric comorbidities in neurodegenerative diseases.

References
1. Du, Yuhui, et al. "NeuroMark: An automated and adaptive ICA based pipeline to identify reproducible fMRI markers of brain disorders." NeuroImage: Clinical 28 (2020): 102375.
2. Rachakonda S, Egolf E, Correa N, Calhoun V. Group ICA of fMRI toolbox (GIFT) manual. Dostupnez [cit 2011-11-5]. 2007 Dec 18.
3. Sakoğlu, Ünal, et al. "A method for evaluating dynamic functional network connectivity and task-modulation: application to schizophrenia." Magnetic Resonance Materials in Physics, Biology and Medicine 23.5 (2010): 351-366.
4. Wilcoxon, Frank. "Individual comparisons by ranking methods." Breakthroughs in statistics. Springer, New York, NY, 1992. 196-202.
5. Sakoğlu, Ünal, et al. "A method for evaluating dynamic functional network connectivity and task-modulation: application to schizophrenia." Magnetic Resonance Materials in Physics, Biology and Medicine 23.5 (2010): 351-366.
6. Friston, Karl J. "Statistical parametric mapping." Neuroscience databases. Springer, Boston, MA, 2003. 237-250.
7. Posner, K., Brown, G. K., Stanley, B., Brent, D. A., Yershova, K. V., Oquendo, M. A., ... & Mann, J. J. (2011). The Columbia–Suicide Severity Rating Scale: Initial validity and internal consistency findings from three multisite studies with adolescents and adults. American Journal of Psychiatry, 168(12), 1266-1277.

8. Kachian, Z. R., Cohen-Zimerman, S., Bega, D., Gordon, B., & Grafman, J. (2019). Suicidal ideation and behavior in Huntington's disease: Systematic review and recommendations. Journal of Affective Disorders, 250, 319–329.
9. McGarry, A., McDermott, M. P., Kieburtz, K., Fung, W. L. A., McCusker, E., Peng, J., de Blieck, E. A., & Cudkowicz, M. (2019). Risk factors for suicidality in Huntington disease. Neurology, 92(14), e1643–e1651.
10. Radin, A. K., Shaw, J., Brown, S. P., Flint, H., Fouts, T., McCue, E., Skeie, A., Peña, C., Youell, J., Ratzliff, A., Powers, D. M., Biss, M., Lemon, H., Sandoval, D., Hartmann, J., Hammar, E., Doty-Jones, A., Wilson, J., Austin, G., ... Comtois, K. A. (2023). Comparative effectiveness of safety planning intervention with instrumental support calls (ISC) versus safety planning intervention with two- way text message caring contacts (CC) in adolescents and adults screening positive for suicide risk in emergency departments and primary care clinics:

Poster No 328

Neural Correlates of Finger Tapping Performance in Alzheimer's Disease

Vincent Koppelmans[1], Sarah Cote[2], Kevin Duff[3]

[1]University of Utah, Salt Lake City, UT, [2]Yeshiva University, New York, NY, [3]Oregon Health & Science University, Portland, OR

Introduction: Finger tapping performance and fine motor skill can be impaired in Mild Cognitive Impairment (MCI) and Alzheimer's Disease (AD). However, the neural mechanisms behind these impairments are largely unknown. We examined if unimanual and bimanual finger tapping performance relates to white matter microstructure using diffusion weighted imaging.

Methods: One hundred and three subjects (57 females; mean age 74.4 years; 50 cognitively intact, 29 MCI, and 24 AD) completed a computerized finger tapping test and an MRI scan. The computerized finger tapping test comprised unimanual (dominant and non-dominant hand) tapping, synchronous bimanual tapping, and alternate bimanual tapping. Outcome measures included initial reaction time, tapping speed, and variance. A T1-weighted MP2RAGE scan (1mm isotropic) and a diffusion weighted scan (one b=0 s/mm2 volume, 64 volumes with b=3000 s/mm2, 1.5mm isotropic) were collected on a 3T Siemens Prisma scanner with a 64 channel head coil. MRI data were converted to BIDS format using BIDSkit and were subsequently pre-processed with fastsurfer and qsiprep v0.19.0, which was set to perform the following steps: brainmask creation, T1 to MNI registration, diffusion denoising, intensity normalization, B1 field inhomogeneity correction, Eddy current and head motion correction, outlier replacement, and resampling to ACPC-space with 1.2mm isotropic voxels. Reconstruction was performed using MRtrix3 in the framework of qsiprep: Multi-tissue fiber response functions were estimated using the Dhollander algorithm. Fiber orientation distributions were estimated via constrained spherical deconvolution using an unsupervised multi-tissue method. A single-shell-optimized multi-tissue constrained spherical deconvolution was performed. Fiber orientation distributions were intensity-normalized. Whole brain connectivity was then tracked using the fiber orientation distribution with the fastsurfer gray-matter white-matter boundary as a constraint. Finally, ROI-to-ROI connectivity was obtained using the brainnetome atlas with 246 atlas. Because of lack of coverage of the cerebellum in our diffusion scans for the majority of subjects, cerebellar regions were excluded from analyses. Here, we analyze the connectivity between ROIs defined as the apparent Fiber density scaled by the size of the ROIs. Connectivity matrices were fed into the Network Based Statistics toolbox to a) analyze differences in the extent of network connectivity between cognitively normal, MCI and AD subjects; and b) analyze associations between structural connectivity and finger tapping performance collapse across the three experimental groups. A significant threshold of T=2.5 was set for selecting individual edges to be included in the network analysis. Analyses were adjusted for age and sex and significance of networks was adjusted for using family-wise error correction.

Results: Significant network differences were observed between cognitively intact and AD subjects ($p<.001$) and between MCI and AD subjects ($p=.015$), but no differences were observed between MCI subjects and the other two groups. These networks spanned almost the entire brain, including 95% and 88% of the ROIs in the atlas respectively. Network connectivity strength was significantly associated with finger tapping speed for all four tapping conditions ($p=.002$-$.014$), with networks spanning 79% (for the non-dominant hand) to 96% (for the dominant hand) of the ROIs. No associations with tapping variability in tapping speed or initial reaction time were found.

Conclusions: Network structural connectivity is affected in AD, but not yet in MCI. Additionally, it is related to finger tapping speed, but not variability or reaction time. These results suggest that one explanation for impaired fine motor skill in AD is global reductions in network strength due to white matter pathology. These preliminary findings deserve further investigation into the neural mechanisms of this motor impairment.

Poster No 329

Comprehensive MRI Anomaly Detection Interface for CADASIL and VCID: A Multimodal Approach

Henry Bockholt[1], Bradley Baker[2], Laura Eisenmenger[3], Michael Geschwind[4], David Liebeskind[5], Lisa Krishnamurthy[6], Jane Paulsen[3]

[1]GSU, Atlanta, GA, [2]TReNDs, Atlanta, GA, [3]University of Wisconsin, Madison, WI, [4]UCSF, San Francisco, CA, [5]UCLA, Los Angeles, CA, [6]GSU, Atalnta, GA

Introduction: To develop "NeuroVasc Imaging Interface (NVII)," a versatile MRI anomaly detection tool integrating multiple imaging modalities to enhance assessment of cerebrovascular abnormalities in conditions such as CADASIL and VCID.

Methods: NVII is designed to utilize advanced machine learning algorithms for analyzing a broad spectrum of MRI data, encompassing T1, T2, FLAIR, SWI, DTI, and ASL scans. The interface is poised to detect and visualize a wide range of neurovascular anomalies including lesions, lacunes, dilated perivascular spaces, cerebral microbleeds, and infarcts. Currently in a conceptual phase, NVII aims to employ probabilistic models for precise anomaly characterization, facilitating complex imaging pattern interpretation for clinical decision-making.

Results: This initiative addresses the pressing need for comprehensive diagnostic tools in neurovascular medicine. NVII's ability to integrate and analyze diverse MRI modalities promises to revolutionize early detection, monitoring, and management of CADASIL and VCID. Its anticipated capability to identify and categorize subtle cerebral changes has the potential to significantly improve patient care. The figure demonstrates a visualization of the NVII interface, where the user will be able to interact with each image type, each probabilistic white matter model and rate the CADA-MRIT inventory accordingly.

Conclusions: NVII, the proposed MRI anomaly detection interface, could substantially advance neuroimaging diagnostics for cerebrovascular diseases. By enabling intricate brain pathology analysis, it holds promise in enhancing treatment strategies, contributing substantially to the precision medicine paradigm. Future development will focus on integrating advanced analytics to not only diagnose but also predict disease progression in patients with CADASIL and VCID.

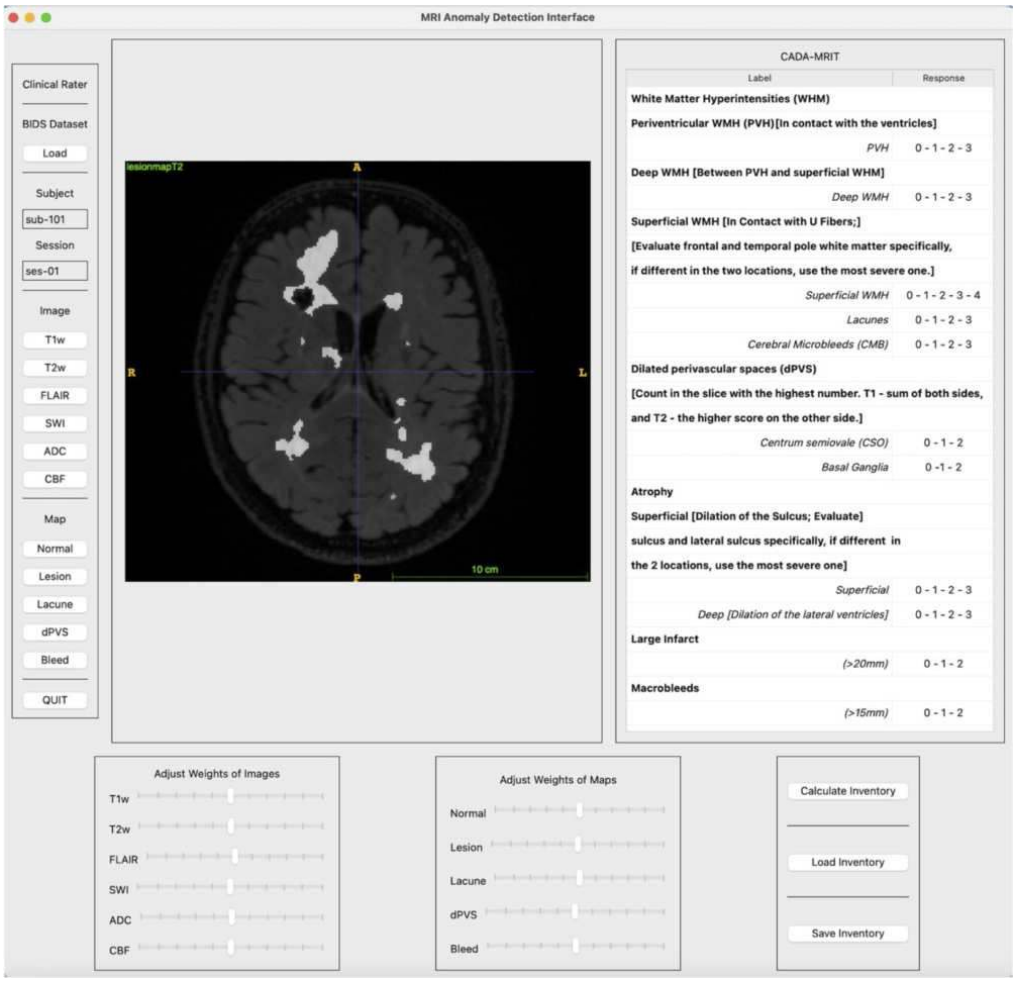

References
1. Zhang R, Chen C-H, Du Montcel ST, et al. The CADA-MRIT: an MRI Inventory Tool for evaluating cerebral lesions in CADASIL. Neurology. 2023;101(17):e1665-e77.
2. Di Donato I, Bianchi S, De Stefano N, et al. Cerebral Autosomal Dominant Arteriopathy with Subcortical Infarcts and Leukoencephalopathy (CADASIL) as a model of small vessel disease. BMC Med. 2017;15:1-12.
3. Balakrishnan R, Hernández MdCV, Farrall AJ. Automatic segmentation of white matter hyperintensities. Computerized Medical Imaging and Graphics. 2021;88:101867.
4. Wardlaw JM, Smith EE, Biessels GJ, et al. Neuroimaging standards for small vessel disease and neurodegeneration. Lancet Neurol. 2013;12(8):822-38.
5. Hobson J. The Montreal Cognitive Assessment (MoCA). Occupational Medicine. 2015;65(9):764-5.
6. Küçükdeveci AA, Kutlay Ş, Yıldızlar D, et al. Reliability and validity of the World Health Organization Disability Assessment Schedule (WHODAS-II) in stroke. Disability and Rehabilitation. 2013;35(3):214-20.
7. Yan W, Qu G, Hu W, et al. Deep learning in neuroimaging: Promises and challenges. IEEE Signal Processing Magazine. 2022;39(2):87-98.
8. Fedorov A, Johnson J, Damaraju E, et al. Learning of brain tissue segmentation from imperfect labeling. 2017 International Joint Conference on Neural Networks (IJCNN); 2017.
9. Yan W, Qu G, Hu W, et al. Deep learning in neuroimaging: Promises and challenges. IEEE Signal Processing Magazine. 2022;39(2):87-98.
10. Alsop, DC, Detre, JA, Golay, X, et al. Recommended implementation of arterial spin-labeled perfusion MRI. Magnetic Resonance in Medicine. 2015 73(1):102–116.

Poster No 330

Effects of SLC6A2 Gene on Brain Activations in Youths with Attention Deficit Hyperactivity Disorder

Chi-Yung Shang[1], Li-Ying Fan[2], Tai-Li Chou[3], Susan Shur-Fen Gau[4]

[1]National Taiwan University Hospital, Taipei, Taiwan, [2]Department of Education, National Taipei University of Education, Taipei, Taiwan, [3]Department of Psychology, National Taiwan University, Taipei, Taiwan, [4]National Taiwan University College of Medicine, Taipei, Taiwan

Introduction: Attention-deficit/hyperactivity disorder (ADHD) is a neurodevelopmental disorder with high heritability. A lot of molecular studies have explored the candidate genes for the pathogenesis of ADHD. Since the pathophysiology of ADHD involve the neurotransmitters of dopamine and norepinephrine (Xing et al., 2016), the norepinephrine transporter gene (SLC6A2) is a promising candidate gene for ADHD. For example, our previous work has shown associations of ADHD with the rs36011 (T)/rs1566652 (G) haplotype of the SLC6A2 gene (Shang et al., 2015). However, the specific neurobiological mechanism of the SLC6A2 rs36011 (T)/rs1566652 (G) haplotype for the pathogenesis ADHD still needs to be explored. Given that the neurotransmitter of norepinephrine has been found to involve in the performance on the counting Stroop task in patients with ADHD (Fan et al., 2017), the current study was to investigate the functional brain effects of the rs36011 (T)/rs1566652 (G) haplotype of the SLC6A2 gene during a counting Stroop task in ADHD children.

Methods: The present study recruited 109 drug-naïve children aged 7–16, with a clinical diagnosis of ADHD. Besides, we recruited 121 typically developing children (TDC) from similar school districts as those participants with ADHD. We employed matrix-assisted laser desorption/ionization time of flight mass spectrometry to conduct genotyping of rs36011 and rs1566652 of SLC6A2 in the blood samples of all the 230 participants. The participants were divided into four groups according to the presence of the ADHD diagnosis and the rs36011 (T)/rs1566652 (G) haplotype, including ADHD-TG, ADHD-NonTG, TDC-TG, and TDC-NonTG. The counting Stroop task was used to explore the brain activations associated with rs36011 (T)/rs1566652 (G) haplotype of SLC6A2. The experimental stimuli of the counting Stroop task were divided into three distinct conditions, including congruent, incongruent and control conditions. To explore the effects of the SLC6A2 TG haplotype and ADHD, we perform a two-way ANOVA with sex, age, and FIQ as nuisance covariates. The significant functional activations are corrected at the voxel level of family-wise error of $p < 0.05$.

Results: All the participants were classified into four groups, including ADHD-TG (n = 48), ADHD-NonTG (n = 61), TDC-TG (n = 64), and TDC-NonTG (n = 57). In group comparisons of the incongruent versus control condition, we found that the ADHD group had lower activation in the right postcentral gyrus and bilateral middle temporal gyri (MTG) than the TDC group. The rs36011 (T)/rs1566652 (G) haplotype carriers demonstrated lower activations in the left MTG, left inferior frontal gyrus (IFG), and the left anterior cingulate cortex (ACC) than those without the TG haplotype (Figure 1). Compared with the ADHD-NonTG group, the ADHD-TG group showed lower brain activations in the left paracentral lobule and bilateral precuneus. Compared with the TDC-TG group, the ADHD-TG group showed lower brain activations in the left precuneus. Besides, we found significant interactions of the rs36011 (T)/rs1566652 (G) haplotype with the diagnosis of ADHD in the left precuneus, the left MTG, and the left ACC (Figure 2).

Conclusions: The present study was the first to explore the effects of the TG haplotype on the brain activations during the counting Stroop task in drug-naïve children with ADHD. The results demonstrated that the rs36011 (T)/rs1566652 (G) haplotype

of SLC6A2 had interaction effects with the diagnosis of ADHD on functional activations in the left precuneus, the left MTG, and the left ACC. Our findings suggested that the rs36011 (T)/rs1566652 (G) haplotype of SLC6A2 could play a crucial role in the modulations of functional brain activations during the counting Stroop task in patients with ADHD. Our imaging genetic study would enhance the understanding of the gene-brain-behavior interactions associated with the pathogenesis of ADHD.

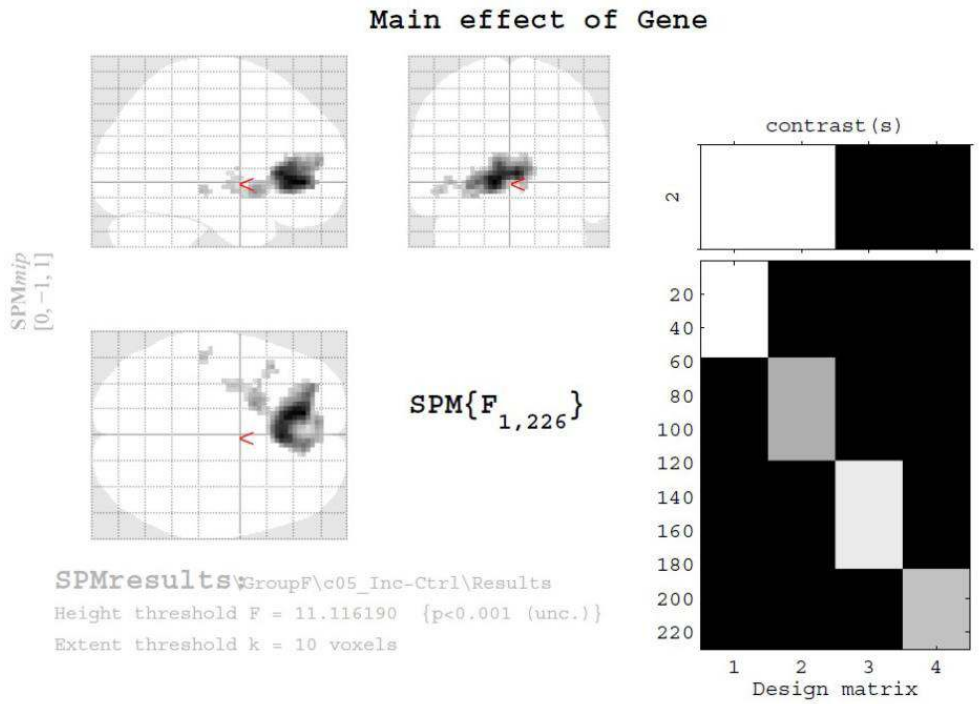

Figure 1. Main effects of the TG haplotype on brain activations for the incongruent versus control condition.

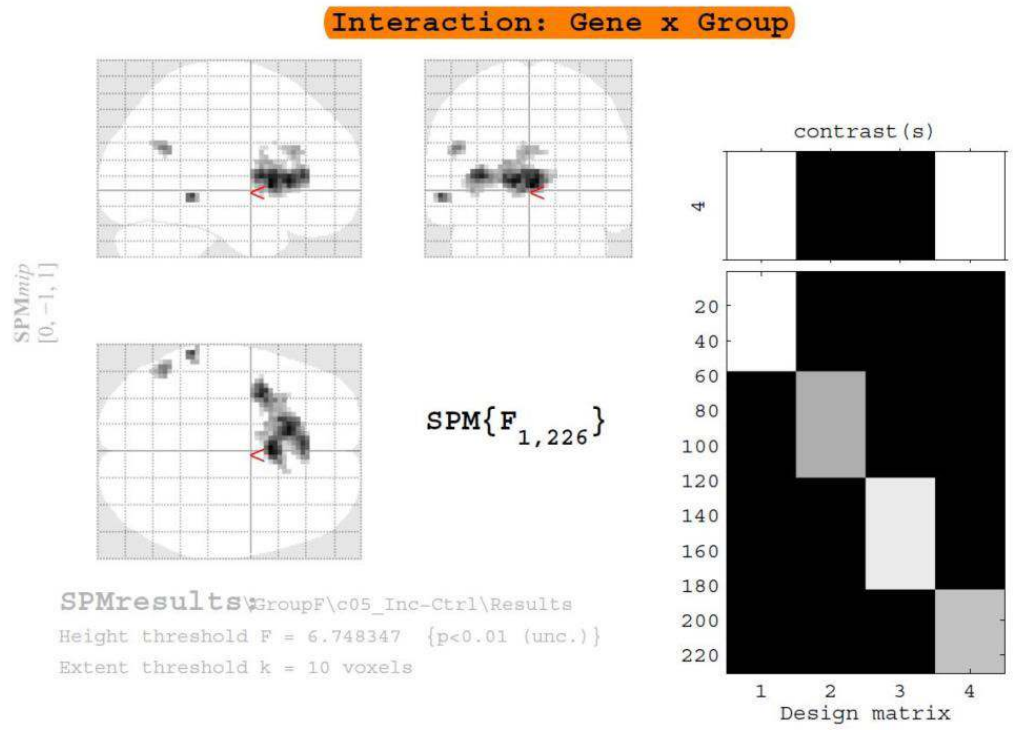

Figure 2. Effects of interaction of ADHD × TG haplotype on brain activations for the incongruent versus control condition.

References

1. Fan, L. Y. (2017). 'Neural correlates of atomoxetine improving inhibitory control and visual processing in Drug-naive adults with attention-deficit/hyperactivity disorder.' Human Brain Mapping, vol 38, pp. 4850-4864.

2. Shang, C. Y. (2015). 'A haplotype of the norepinephrine transporter gene (SLC6A2) is associated with visual memory in attention-deficit/hyperactivity disorder.' Progress in Neuro-Psychopharmacology & Biological Psychiatry, vol 58, pp. 89-96.
3. Xing, B. (2016). 'Norepinephrine versus dopamine and their interaction in modulating synaptic function in the prefrontal cortex.' Brain Research, vol. 1641, pp. 217-233.

Poster No 331

Atypical Neural Response to Hearing One's Own Name in Autistic Children

Guangfang Liu[1], Xinyue Peng[1], Li Yi[1]

[1]Peking University, Beijing, China

Introduction: Autism is a neurodevelopmental condition, characterized by atypicalities in social interaction and communication (American Psychiatric Association., 2013). A common observation is that autistic children may not be as responsive to their own names, exhibiting differences in their social behaviors compared to neurotypical children(Conine et al., 2020). However, it remains unclear the underlying neural processing of autistic children in response to their own names.This study aims to investigate the neural processing in responses to their own names in young autistic children to determine if there are deviations from typical neural processing.

Methods: Twenty-five 3- to 6-year-old autistic children and 27 age-matched neurotypical children participated in the present study. Full names of the participants (own name), familiar names (e.g., a friend's name), and unfamiliar names served as the stimuli. Each name was recorded by an AI-generated neutral voice to minimize emotional connotations. Participants were instructed to listen passively without engaging in any specific task. Their neural responses were recorded using a continuous-wave near-infrared optical imaging system (NIRSport, NIRx Medical Technologies, LLC) with 64 channels covering their bilateral dorsomedial prefrontal cortex (DMPFC), dorsolateral prefrontal cortex (DLPFC), inferior frontal gyrus (IFG), superior temporal gyrus (STG), middle temporal gyrus (MTG), and temporoparietal junction (TPJ) regions.

Results: For the own name condition, neurotypical children exhibited distinct neural activation pattern, characterized by significant decreases ($p<0.05$, FDR corrected) in mean HbO concentration in frontal regions (left DMPFC, left IFG, and bilateral DLPFC) and significant increases ($p<0.05$, FDR corrected) in mean HbO concentrationin temporal regions (bilateral STG). Conversely, autistic children did not display a similar activation pattern when hearing their own names; instead, they showed reduced activation in the right TPJ. For the other two conditions, no significant neural activation was observed in either group.

Conclusions: We found that autistic children exhibited atypical neural processing in response to their own names in the present study. This atypicality reveals differences in attention and cognitive processing in response to their own names compared to neurotypical children. The absence of neural activation in frontal and temporal regions and the presence of deactivation in TPJ in autistic children may contribute to their diminished responsiveness to social cues, potentially influencing their social interactions and communication abilities.

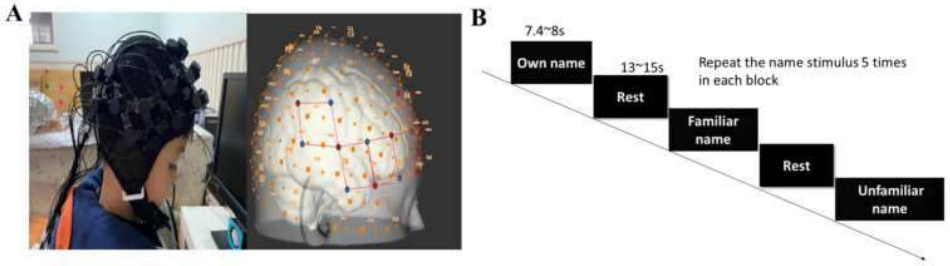

Fig.1 (A) Illustration of fNIRS data collection and arrangement of the fNIRS probe array. The red and blue dots represent the sources and detectors, respectively. Red line segments represent the positions of the measurement channels.**(B)**Experimental protocols of participants. Block stimulation was performed for 7.4~8s with an interval of 13~15s and repeated 8 times. The three stimuli were presented randomly.

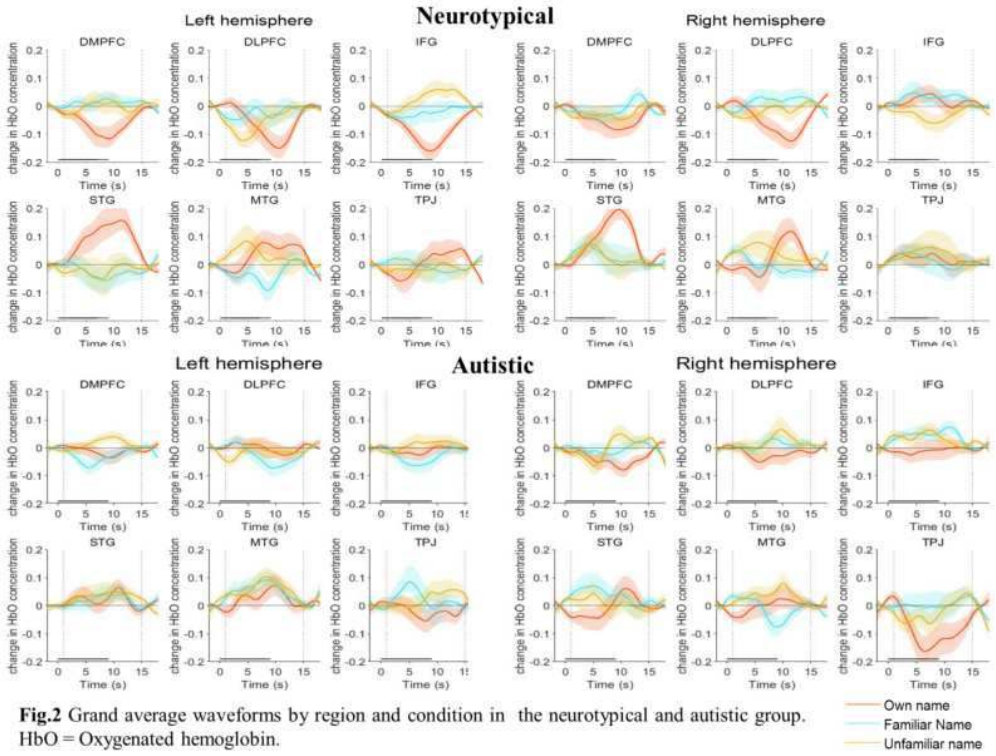

Fig.2 Grand average waveforms by region and condition in the neurotypical and autistic group. HbO = Oxygenated hemoglobin.

References

1. American Psychiatric Association. (2013). DSM-5 Diagnostic Classification. In Diagnostic and Statistical Manual of Mental Disorders. https://doi.org/10.1176/appi. books.9780890425596.x00diagnosticclassification.
2. Conine, D. E., Vollmer, T. R., Barlow, M. A., Grauerholz-Fisher, E., Dela Rosa, C. M., & Petronelli, A. K. (2020). Assessment and treatment of response to name for children with autism spectrum disorder: Toward an efficient intervention model. Journal of Applied Behavior Analysis, 53(4), 2024–2052. https://doi.org/10.1002/jaba.737

Poster No 332

ADHD Classifiers Based on GM-WM Structural Connectivity Couplings and Transcriptional Signatures

Nanfang Pan[1], Yajing Long[1], Ying Chen[1], Qiyong Gong[1]

[1]West China Hospital of Sichuan University, Chengdu, China

Introduction: Attention-Deficit/Hyperactivity Disorder (ADHD) stands as a complex neurodevelopmental disorder, drawing considerable focus in the realm of neuroimaging psychiatry. While aberrations in the neural mechanisms of both brain gray matter and white matter have been extensively pinpointed, the intricate patterns of their structural connectivity coupling and the concurrent gene expression profiles continue to elude comprehensive understanding. Herein, we established machine-

learning classifiers based on Gray-White Matter Structural Connectivity Coupling (GWSC) patterns, with a parallel exploration to unravel the underlying transcriptomes.

Methods: T1-weighted and diffusion-weighted MRI data were obtained from a cohort of children with ADHD (n = 83) and typically developing children (n = 89). Gray matter covariance networks and white matter connectivity networks were constructed using the Kullback-Leibler divergence similarity measure and probabilistic tractography respectively. We computed the strength of their regional coupling as we termed GWSC coupling. To individually classify ADHD children from typically developing controls, we established the machine-learning pipeline in pursuit of clinical applicability. Four configure learning algorithms, namely linear support vector machine (SVM), Gaussian-kernel SVM, k-nearest neighbors, and decision tree were employed to build up fitting models. Finally, we extracted gene expression data from the Allen Human Brain Atlas and performed partial least squares regression analysis to bridge the gap between abnormal GWSC coupling patterns and microarray-based transcriptomes, and gene enrichment analysis was conducted to interpret the inference of enriched gene ontology biological processes.

Results: All four classifiers we employed distinguished children with ADHD with more than 75% accuracy, wherein the Gaussian-kernel SVM enables the highest accuracy of 82.6% (95%CI: 78.4%-86.8%). Sensitivity and specificity for the discrimination were 79.5% and 85.4% respectively. In this model, the GWSC couplings in the ventromedial prefrontal cortex provided the greatest contribution to the classifier. After correcting for enrichment terms (pFDR<.05) and discarding discrete enrichment clusters, the top significant gene ontology biological process is “neuron projection development”.

Conclusions: By constructing GWSC coupling patterns in ADHD, we developed machine-learning classifiers with acceptable predictive performance, with the ventromedial prefrontal cortex severed as a central substrate. Our transcriptional findings reveal the involvement of neuron projection in the psychopathological processes of GWSC patterns in ADHD. We uncovered GWSC coupling phenotypes in ADHD and identified their transcriptional signatures, facilitating a more comprehensive understanding of ADHD.

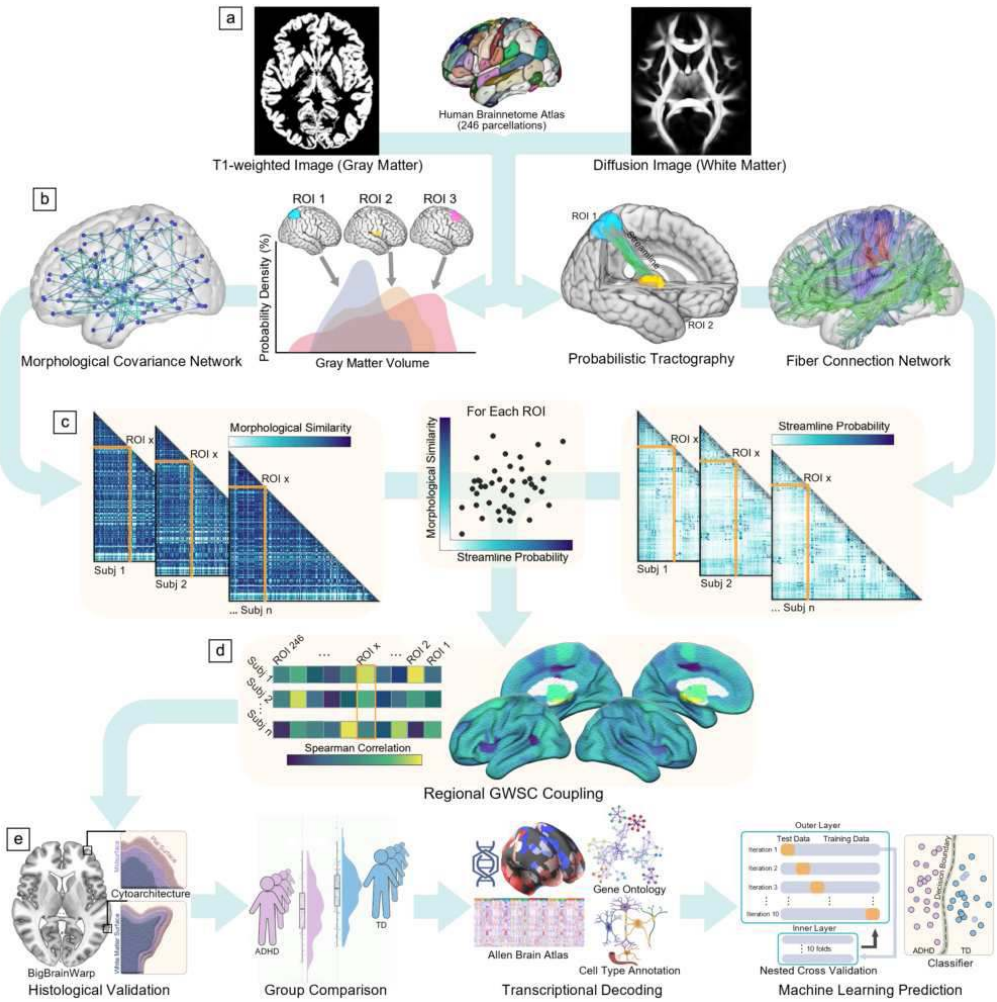

Figure 1. Schematic Overview of the Analytical Procedures for GWSC Coupling and Following Analyses.

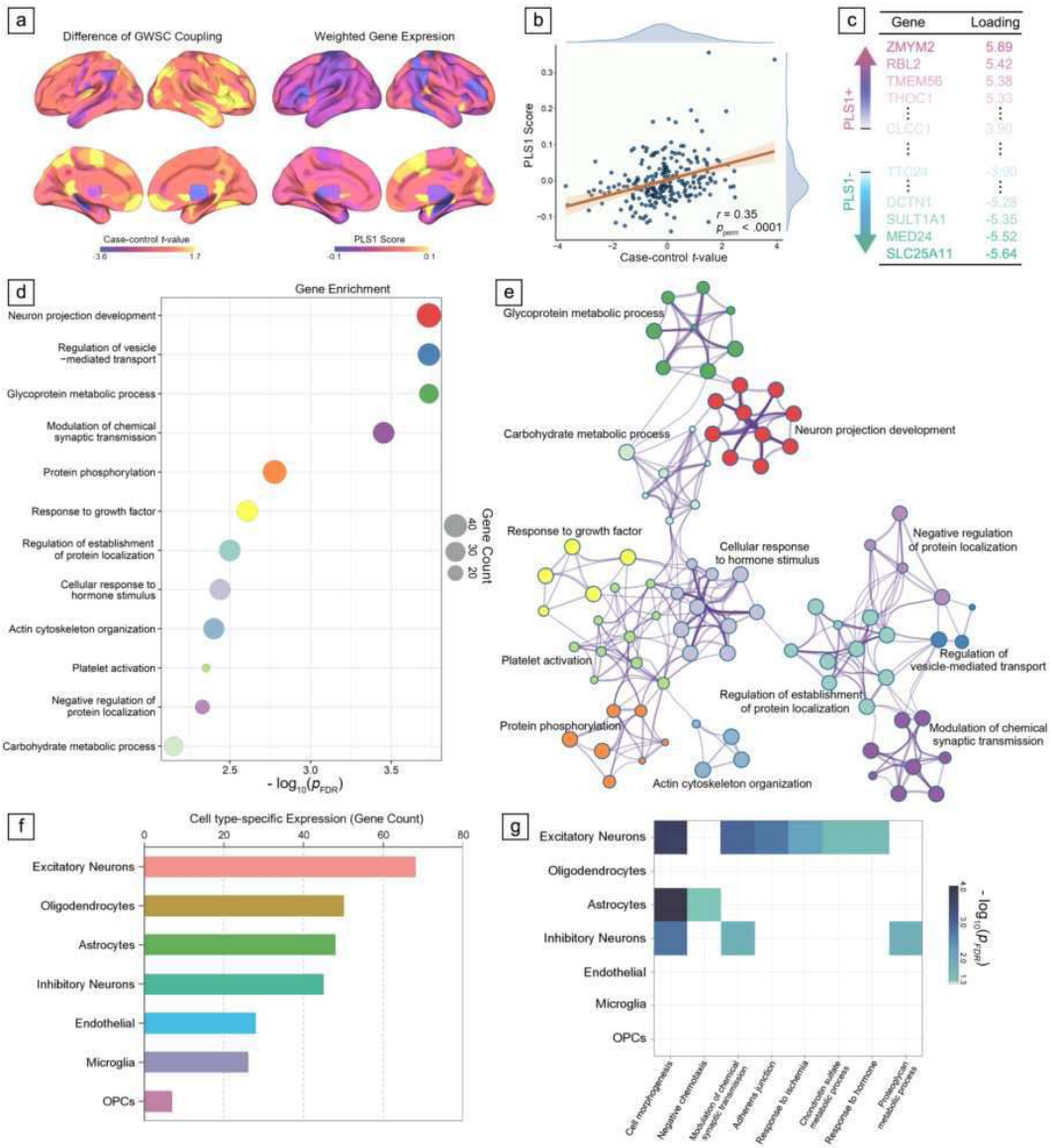

Figure 2. Transcriptional Profiles Underlying Abnormal GWSC Coupling Patterns.

References

1. Gong G, (2012). Convergence and divergence of thickness correlations with diffusion connections across the human cerebral cortex. NeuroImage. 59,2:1239-48.
2. Gu Z, (2021). Heritability and interindividual variability of regional structure-function coupling. Nat Commun. 12:1–12.
3. Baum GL, (2020). Development of structure–function coupling in human brain networks during youth. Proc Natl Acad Sci USA. 117:771–778.
4. Koutsouleris N, (2018). Prediction Models of Functional Outcomes for Individuals in the Clinical High-Risk State for Psychosis or with Recent-Onset Depression: A Multimodal, Multisite Machine Learning Analysis. JAMA Psychiatry. 75:1156–1172.
5. Li J, (2021). Cortical structural differences in major depressive disorder correlate with cell type-specific transcriptional signatures. Nat Commun. 12.

Poster No 333

Emotion dysregulation and right pars orbitalis constitute a neuropsychological pathway to ADHD

Wenjie Hou[1], Barbara Sahakian[2,3], Christelle Langley[2,3], Yuqing Yang[4], Richard Bethlehem[5], Qiang Luo[6,7,8,9,10]

[1]State Key Laboratory of Medical Neurobiology and MOE Frontiers Center for Brain Science, Institutes of Brain Science and Research Institute of Intelligent Complex Systems, Fudan University, Shang Hai, China, [2]Departments of Psychiatry, University of Cambridge, Cambridge, United Kingdom, [3]Behavioural and Clinical Neuroscience Institute, University of Cambridge, Cambridge, United Kingdom, [4]New York University Shanghai, Shang Hai, China, [5]Department of Psychology, University of Cambridge, Cambridge, United Kingdom, [6]Institute of Science and Technology for Brain-Inspired Intelligence, Fudan University, Shang Hai, China, [7]Human Phenome Institute, Fudan University, Shang Hai, China, [8]MOE Key Laboratory of Computational Neuroscience and Brain-Inspired Intelligence, Fudan University, Shang Hai, China, [9]School of Life Sciences, Fudan University, Shang Hai, China, [10]National Clinical Research Center for Aging and Medicine at Huashan Hospital, Fudan University, Shang Hai, China

Introduction: Attention-deficit/hyperactivity disorder (ADHD) affects 5.9%-7.1% of children and adolescents1 and is characterized by its clinical heterogeneity in symptoms and their trajectories2. Theoretical models, such as the dual-pathway model (i.e., the cognitive and the motivational pathways)3, have long been hypothesized to explain this heterogeneity4. However, both cognitive impairment and motivational dysfunction can be absent in about 30% of the ADHD cases5, and cannot predict the different clinical trajectories of the ADHD symptoms (e.g., the persistent or the remitting trajectories)6. Emotion dysregulation, characterized by difficulties with both awareness and regulation of emotion, has been associated with more severe and persistent ADHD symptoms and might be a key component of the self-regulation deficits in ADHD7. As yet, however, it remains unclear whether emotion dysregulation, independent of cognition and motivation, contributes to the symptom heterogeneity in ADHD as a unique pathway. Neuroimaging studies have shown that the cognitive and the motivational pathways mainly associated with the fronto-dorsal striatal and the fronto-ventral striatal circuits, respectively3. However, the neuroimaging features of these brain circuits explain only a limited proportion of the heterogeneity in ADHD symptoms (ΔR^2=0.008)4. Whereas, the emotion dysregulation has been mainly associated with the fronto-limbic circuitry8, which overlaps with many brain regions known to be associated with ADHD9. Therefore, we hypothesized that the emotion dysregulation may represent a third neuropsychological pathway to ADHD, which is separable from the cognitive and motivational pathways3,4. Advanced knowledge on the role of emotion dysregulation in ADHD may be valuable for identifying individuals at risk for persistent ADHD symptoms.

Methods: Participants: The discovery sample included 6,053 adolescents of 12 years from the Adolescent Brain Cognitive Development (ABCD) study. Emotion dysregulation, cognitive function and motivational dysfunction were assessed. The replication sample consisted of 263 patients with ADHD and 409 healthy controls. Structural brain images, genetic, transcriptomic, and blood white cell counts data were obtained. Main outcome measures: Parents were assessed for the adolescents' ADHD symptoms by Child Behavior Checklist. Design: Linear mixed-effect model and causal Bayesian network analyses were conducted to assess the associations between emotion dysregulation problems and both ADHD symptoms and structural neuroimaging features while controlling for both the cognitive and the motivational dysfunctions and medical treatment for ADHD. Longitudinal mediation analysis was used to establish the pathway from brain through emotion dysregulation to ADHD, which validated using the clinical sample. Transcriptomic analysis was performed to identify biological pathways unique to the emotion pathway.

Results: Using a large population-based cohort (n=6,053) we showed that the emotion dysregulation was associated with ADHD symptoms (partial eta2=0.21) and their persistence after controlling for the cognitive and the motivational deficits. The emotion dysregulation mediated the association between the smaller surface area of the right pars orbitalis and greater ADHD symptoms at a one-year follow-up, indicating an emotion pathway to ADHD. Notably, we found that the emotion pathway was uniquely associated with immune responses through transcriptome analysis, and that more emotion regulation problems and smaller right pars orbitalis surface area were also associated with polygenic risk score for ADHD in the ABCD European samples. Finally, we validated the emotion pathway using another clinical sample for ADHD (n=672).

Conclusions: In summary, we have shown using a large sample and a second independent sample that emotion dysregulation is a core symptom and a route to ADHD, which may not respond to the current pharmacological treatments for ADHD.

References

1. Willcutt, E. G. (2012), 'The prevalence of DSM-IV attention-deficit/hyperactivity disorder: a meta-analytic review', Neurotherapeutics, 9, 490-499.
2. Sonuga-Barke, E. J. S. (2023), 'Annual Research Review: Perspectives on progress in ADHD science – from characterization to cause', Journal of Child Psychology and Psychiatry, 64, 506-532.

3. Sonuga-Barke, E. J. (2003), 'The dual pathway model of AD/HD: an elaboration of neuro-developmental characteristics', Neuroscience and biobehavioral reviews, 27, 593-604.
4. Shen, C. (2020), 'Neural Correlates of the Dual-Pathway Model for ADHD in Adolescents', The American journal of psychiatry, 177, 844-854.
5. Stevens, M. C. (2018), 'Functional Neuroimaging Evidence for Distinct Neurobiological Pathways in Attention-Deficit/Hyperactivity Disorder', Biological Psychiatry: Cognitive Neuroscience and Neuroimaging, 3, 675-685.
6. van Lieshout, M. (2013), 'Does neurocognitive functioning predict future or persistence of ADHD? A systematic review', Clinical Psychology Review, 33, 539-560.
7. Faraone, S. V. (2019), 'Practitioner Review: Emotional dysregulation in attention-deficit/hyperactivity disorder – implications for clinical recognition and intervention', Journal of Child Psychology and Psychiatry, 60, 133-150.
8. Christiansen, H. (2019), 'Attention-Deficit/Hyperactivity Disorder (ADHD) and Emotion Regulation Over the Life Span', Current psychiatry reports, 21, 17.
9. Samea, F. (2019), 'Brain alterations in children/adolescents with ADHD revisited: A neuroimaging meta-analysis of 96 structural and functional studies', Neuroscience and biobehavioral reviews, 100, 1-8.

Poster No 334

Chronic oxytocin attenuates amygdala activity but does not improve mirror system function in autism

Kaat Alaerts[1], Ruth Op de Beeck[1], Nicky Daniels[1], Matthijs Moerkerke[1], Bart Boets[1], Jellina Prinsen[1]

[1]KU Leuven, University of Leuven, Leuven, Vlaams-Brabant

Introduction: Alterations in the action perception network or mirror system are proposed to underly social difficulties characteristic of autism spectrum disorder. Evidence to date is mixed however, with some studies demonstrating altered recruitment of the mirror system during action perception or imitation, while others demonstrated no deficit[1]. Intranasal administration of oxytocin is increasingly considered as a potential new therapeutic approach for mitigating social perception difficulties in autism, primarily through its social salience enhancing effects, facilitating attention to, and perception of social signals (e.g. from faces or bodily actions)[2]. Despite initial behavioral studies, little is known about oxytocin's role in modulating the neural correlates of mirror system functioning. Gaining a deeper understanding into the neuroplastic changes that underlie behavioral effects seems crucial, particularly upon receiving multiple-dose, chronic oxytocin administrations, as it allows delineating mechanisms of inter-individual variation in clinical treatment responses.

Methods: The aim of the current study was two-fold: (i) to investigate mirror system functioning at the neural level in children with autism (aged 8-12 years; n=56, 13 girls) compared to children without autism (n=38, 7 girls); and (ii) to explore whether chronic oxytocin administration, compared to placebo could mitigate altered mirror system function in the cohort of children with autism (n=19 oxytocin, n=25 placebo). To do so, a randomized, placebo-controlled pharmaco-neuroimaging trial was conducted, investigating the effects of chronic oxytocin administration (4 weeks, daily 24 IU) on brain activity related to action and gaze cue processing (Fig. 1). Stimuli encompassed a female model performing a simple hand movement (or static hand), while establishing direct (or averted) gaze. Mirror system function was assessed before and after the four-week oxytocin (or placebo) administration, within distinct regions-of-interests pertaining to the core fronto-parietal mirror system (inferior frontal gyrus (IFG), inferior parietal lobule (IPL), ventral premotor cortex (vPMC)) and the extended social brain network (medial prefrontal cortex (mPFC), superior temporal sulcus (STS), and amygdala).

Results: Compared to the control group, children with autism displayed a significantly reduced recruitment of the core mirror system (IFG, IPL, vPMC), particularly upon hand movement observation (pIFG= .05; pIPL= .04; pvPMC= .005) (Fig. 2A). Regions of the social brain network (amygdala and STS) displayed overall stronger activity upon processing the hand movement, compared to observing the static hand, but no significant diagnosis-related differences were apparent in recruitment of this network (all $p > .05$). Also no significant modulations depending on eye gaze were revealed, either in the mirror system or social brain network. Upon nasal spray administration, no significant modulation was revealed within any of the mirror system regions, indicating no mitigation of reduced mirror system function in autism by oxytocin. In line with prior studies[3], chronic oxytocin administration did induce an overall dampening in amygdala reactivity (pamygdala = .01; $\eta p2 = .12$) (Fig. 2B). Furthermore, this attenuation was significantly associated with improved repetitive behaviors (Repetitive Behavior Scale) (Spearman $\rho=.31$, $p=.046$) and social functioning (Social Responsiveness Scale) ($\rho=.29$, $p=.058$), as well as with higher endogenous salivary oxytocin levels ($\rho=-.34$, $p=.026$) (Fig. 2C).

Conclusions: Chronic oxytocin administration did not mitigate reduced recruitment of the fronto-parietal mirror system during action perception, indicating no overall social salience enhancing effect of oxytocin. Instead, chronic oxytocin induced an overall dampening of amygdala recruitment, likely reflecting oxytocin's anxiolytic role in facilitating stress regulation[4].

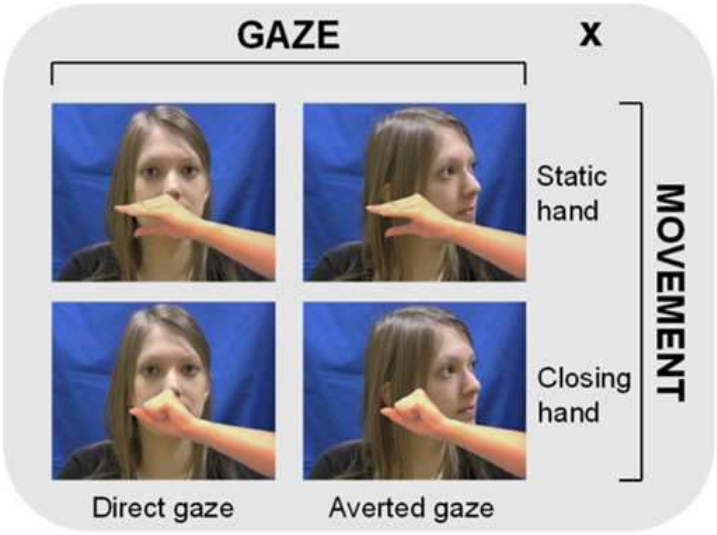

Figure 1. Task-based fMRI stimuli. Stimuli encompassed a female model performing a simple closing hand movement (or static hand), while establishing either direct (or averted gaze).

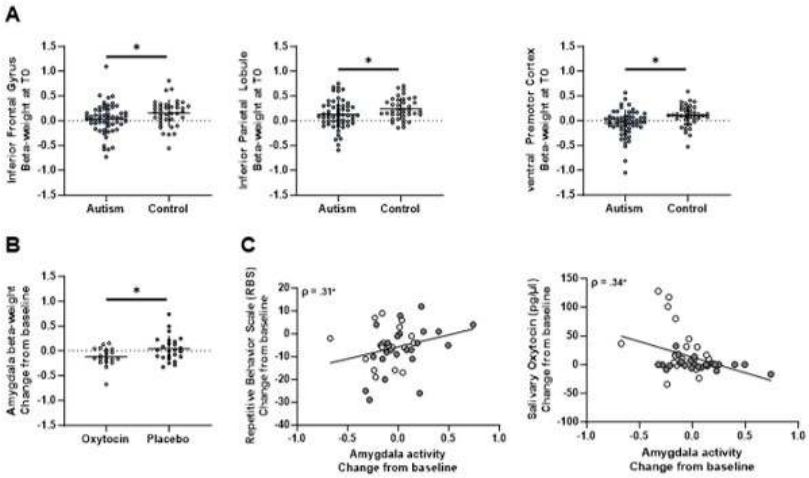

Figure 2. Task-based fMRI contrast estimates.

A. Beta-weight contrast estimates (across conditions) visualized separately for the autism and control group, and regions-of-interest pertaining to core frontoparietal mirror system (inferior frontal gyrus, inferior parietal lobule, ventral premotor cortex).

B. Change from baseline in amygdala beta-weight contrast estimate (across conditions), visualized separately for autistic children who received the oxytocin or placebo nasal spray.

C. Correlation between changes from baseline in amygdala activity (beta-weight) and repetitive behaviors or salivary oxytocin levels.

References

1. Yates, L. & Hobson, H. Continuing to look in the mirror: A review of neuroscientific evidence for the broken mirror hypothesis, EP-M model and STORM model of autism spectrum conditions. Autism 24, 1945-1959 (2020). https://doi.org:10.1177/1362361320936945
2. Shamay-Tsoory, S. G. & Abu-Akel, A. The Social Salience Hypothesis of Oxytocin. Biol. Psychiatry 79, 194-202 (2016). https://doi.org:S0006-3223(15)00639-3 [pii];10.1016/j.biopsych.2015.07.020 [doi]
3. Bernaerts, S., Boets, B., Steyaert, J., Wenderoth, N. & Alaerts, K. Oxytocin treatment attenuates amygdala activity in autism: a treatment-mechanism study with long-term follow-up. Transl Psychiatry 10, 383 (2020). https://doi.org:10.1038/s41398-020-01069-w
4. Stoop, R., Hegoburu, C. & van den Burg, E. New opportunities in vasopressin and oxytocin research: a perspective from the amygdala. Annu Rev Neurosci 38, 369-388 (2015). https://doi.org:10.1146/annurev-neuro-071714-033904

Poster No 335

Investigating the neural correlates and oscillatory dynamics of tics in Tourette Syndrome

Mairi Houlgreave[1], Aikaterini Gialopsou[1], Elena Boto[1], Matthew Brookes[1], Stephen Jackson[1]

[1]*University of Nottingham, Nottingham, England*

Introduction: In Tourette syndrome (TS), tics are commonly preceded by a premonitory urge which is thought to be a negative reinforcer of tic expression, suggesting that tics may be a voluntary response to these sensations (Capriotti et al, 2014). Voluntary movements are associated with a desynchronisation of oscillations in the 8-30 Hz range, followed by a post-movement beta (13-30 Hz) rebound (PMBR) (Jurkiewicz et al, 2006; Pfurtscheller et al, 1996). Here, we explore the oscillatory changes within the primary motor cortex during tics and voluntary movements. We also investigate the oscillatory activity within the right insula and cingulate cortex, which have been shown to be involved in urge (Jackson et al, 2011). Tic expression during neuroimaging is most often required as an overt marker of increased urge, however this can lead to a loss of large amounts of data due to head movement. Therefore, our data were collected using Optically Pumped Magnetometer (OPM) magnetoencephalography (MEG) which uses head-mounted sensors (65 triaxial), allowing participant movement throughout the scan (Boto et al, 2018).

Methods: OPM-MEG data were acquired from 16 participants with TS (7F, mean age (±SD): 34.2 ±11.1 years). Participants were asked to complete two paradigms: the first paradigm involved sixty 10 second trials involving a single index finger abduction; the second paradigm involved 4 alternating 5-minute blocks of "Rest" and "Suppress" where participants were instructed to try to suppress their tics. Video of the participants' movements was recorded, during OPM-MEG, for offline analysis of tics. Trials were defined as 4 seconds in duration and began 2 seconds prior to tic bout onset. Anatomical data (MPRAGE, 1mm isotropic) from these participants were used for linearly-constrained minimum variance beamforming (Robinson and Vrba, 1999). Timecourses were then weighted towards the central voxel for each brain region of the automated anatomical atlas, resulting in a single virtual electrode timecourse for each region. Data were standardized (Z-scored) after removal of bad channels and trials. Two datasets were excluded from both tasks due to poor data quality. Two further datasets were excluded from the voluntary movement task due to technical problems during data collection.

Results: Analyses of the spectral timecourses of mu-alpha (8-12 Hz) and beta frequencies, from the contralateral motor cortex, demonstrated significant desynchronisation during the externally cued voluntary movements (Figure 1). However, there was no significant PMBR. In contrast, there was no significant desynchronisation at tic onset across the bilateral motor cortices (Figure 2). The mid-cingulate cortex and right insula showed no significant changes in mu-alpha and beta spectral timecourses before, or at tic onset.

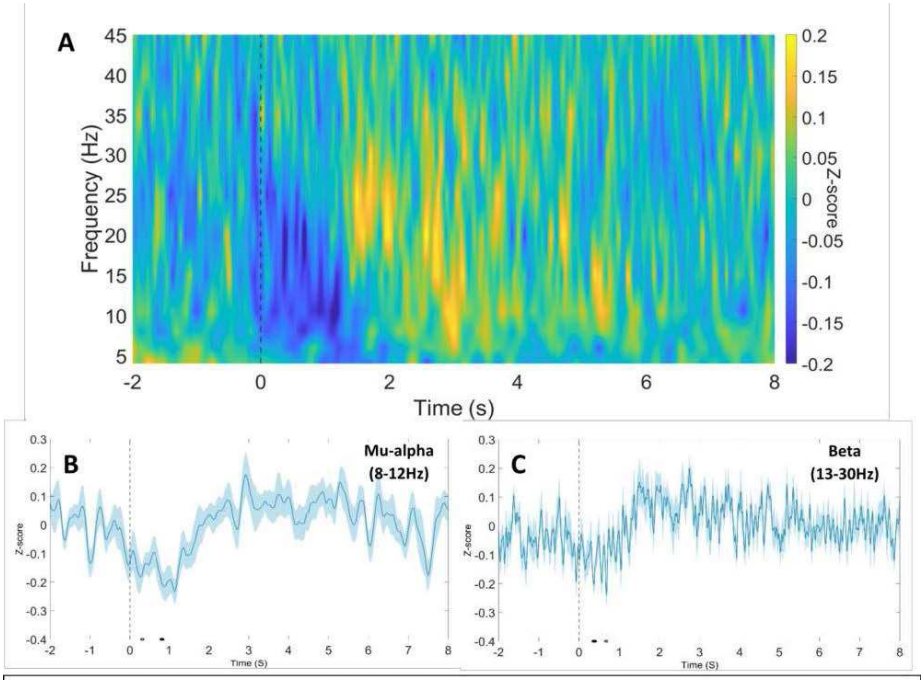

Figure 1. (A) A time frequency spectrogram of the changes in Z-scores within the contralateral motor cortex during an index finger abduction task, with movement at time 0. (B-C) Graphs showing the changes in Z-scores in the (B) mu-alpha (8-13Hz) and (C) beta (13-30Hz) frequency bands. A black line along the x-axis marks timepoints where a significant difference ($p \leq 0.05$; Wilcoxon signed rank test) from 0 is seen (false discovery rate (FDR) corrected).

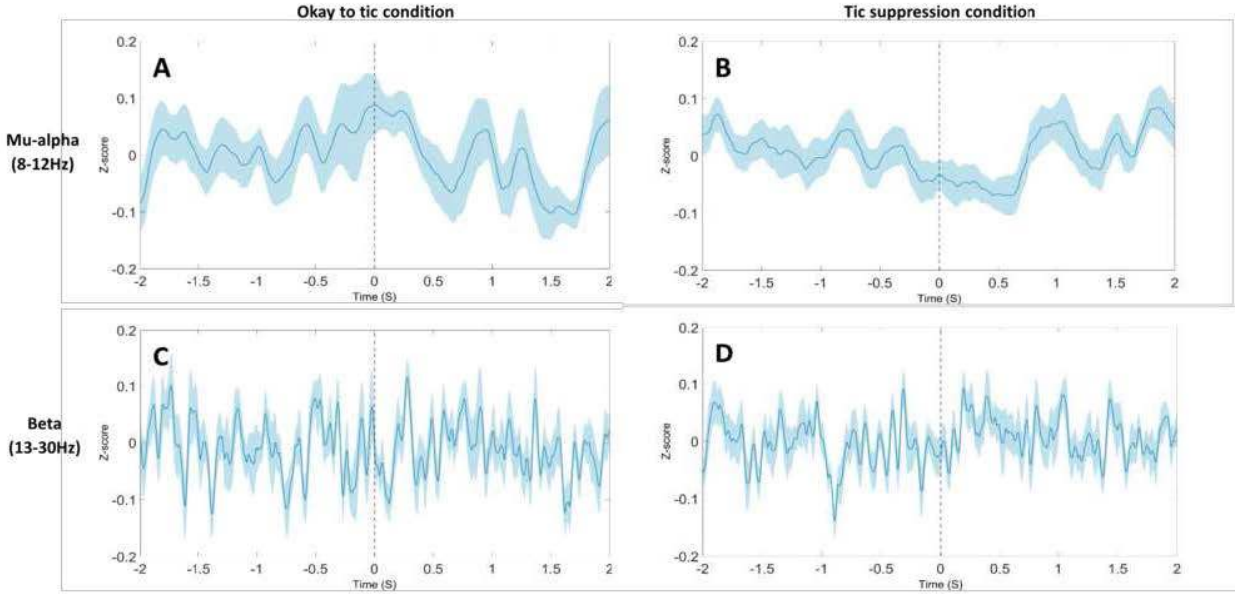

Figure 2. Graphs showing the change in Z-scores within the primary motor cortices in the (A,B) mu-alpha (8-13Hz) and (C,D) beta (13-30Hz) frequency bands during tic bouts in the (A,C) "Okay to tic" and (B,D) "Suppress" conditions. No timepoints were significantly different from 0 (p>0.05; Wilcoxon signed rank test) (FDR corrected).

Conclusions: Our finding of movement-related desynchronisation during volitional movements, but not tics, is in-line with previous research which describes desynchronisation of beta oscillations during voluntary movements using EEG, but no movement-related desynchronisation prior to tics (Morera Maiquez et al, 2022). Readiness potentials are not reliably seen before tics, despite a readiness potential being present before volitional movements (Obeso et al, 1981). Therefore, our data support the hypothesis that the oscillatory dynamics involved in tic generation differ from that of voluntary movement, suggesting that tics may be involuntary. The lack of significant changes in the 8-30 Hz range, in regions associated with urge, may be due to different regions of the insula having different roles (Kurth et al, 2010), suggesting that whole region analysis may not be ideal for identifying activity associated with urge. Regardless, OPM-MEG was shown to be capable of recording participants with TS during their tics where conventional methods such as EEG have previously shown artefacts associated with tic onset (Morera Maiquez et al, 2022).

References

1. Boto, E., Holmes, N., Leggett, J., Roberts, G., Shah, V., Meyer, S. S., Muñoz, L. D., Mullinger, K. J., Tierney, T. M., Bestmann, S., Barnes, G. R., Bowtell, R., & Brookes, M. J. (2018). Moving magnetoencephalography towards real-world applications with a wearable system. Nature, 555(7698), 657–661. https://doi.org/10.1038/nature26147
2. Capriotti, M. R., Brandt, B. C., Turkel, J. E., Lee, H. J., & Woods, D. W. (2014). Negative Reinforcement and Premonitory Urges in Youth With Tourette Syndrome: An Experimental Evaluation. Behavior Modification, 38(2), 276–296. https://doi.org/10.1177/0145445514531015
3. Jackson, S. R., Parkinson, A., Kim, S. Y., Schüermann, M., & Eickhoff, S. B. (2011). On the functional anatomy of the urge-for-action. In Cognitive Neuroscience (Vol. 2, Issues 3–4, pp. 227–243). https://doi.org/10.1080/17588928.2011.604717
4. Jurkiewicz, M. T., Gaetz, W. C., Bostan, A. C., & Cheyne, D. (2006). Post-movement beta rebound is generated in motor cortex: Evidence from neuromagnetic recordings. NeuroImage, 32(3), 1281–1289. https://doi.org/10.1016/j.neuroimage.2006.06.005
5. Kurth, F., Zilles, K., Fox, P. T., Laird, A. R., & Eickhoff, S. B. (2010). A link between the systems: functional differentiation and integration within the human insula revealed by meta-analysis. Brain Structure & Function, 214(5–6), 519–534. https://doi.org/10.1007/s00429-010-0255-z
6. Morera Maiquez, B., Jackson, G. M., & Jackson, S. R. (2022). Examining the neural antecedents of tics in Tourette syndrome using electroencephalography. Journal of Neuropsychology, 16(1), 1–20. https://doi.org/10.1111/jnp.12245
7. Obeso, J. A., Rothwell, J. C., & Marsden, C. D. (1981). Marsden CD Simple tics in Gilles de la Tourette's syndrome are not prefaced by a normal premovement EEG potential. Journal of Neurology, Neurosurgery and Psychiatry, 44, 735–738. https://doi.org/10.1136/jnnp.44.8.735
8. Pfurtscheller, G., Stancák, A., & Neuper, C. (1996). Post-movement beta synchronization. A correlate of an idling motor area? Electroencephalography and Clinical Neurophysiology, 98(4), 281–293. https://doi.org/10.1016/0013-4694(95)00258-8
9. Robinson, S., & Vrba, J. (1999). Functional neuroimaging by synthetic aperture magnetometry. In T. Yoshimoto, M. Kotani, S. Kuriki, H. Karibe, N. Nakasato, Tohoku (Eds.), Recent Advances in Biomagnetism (pp. 302-305). Univ. Press, Sendai, Japan.

Poster No 336

Automated Stratification of Cortical Network Reveals Clinically Meaningful Subgroups of ASD children

Ahmad Mheich[1], Sahar Yassine[2], Joana Maria Almeida Osório[1], Sonia Richetin[1], Vincent Junod[1], Laura Mendes[1], Katherina Gschwend[1], Victoria Aeschbach[1], Lorène Arnold[1], David Romascano[1], Paola Yu[1], Marine Jequier Gygax[1], Anne Maillard[1], Mahmoud Hassan[3,4], Nadia Chabane[1], Borja Rodríguez-Herreros[1]

[1]CHUV Lausanne, Lausanne, Vaud, [2]University of Oxford, Oxford, United Kingdom, [3]MINDIG, Rennes F-35000, Bretagne, [4]School of Science and Engineering, Reykjavik University, Reykjavik, Iceland

Introduction: Background Heterogeneity in the causes and phenotypic presentation of autism spectrum disorder (ASD) poses a major challenge to clinical and translational research. Attempts to stratify individuals with ASD have been based primarily on behavioral criteria1, but clinical subtyping is blind to the underlying neurobiological mechanisms and has limited predictive value of the forthcoming developmental path. Yet, it is still unclear whether and how atypical brain functional connectivity accounts for individual differences across ASD-related symptomatology and behaviors. Objectives The goal of the study was to identify clinically meaningful subgroups of young children with ASD based on distinctive patterns of functional brain topology, to better understand of the neural substrates underlying ASD heterogeneity.

Methods: We collected resting-state EEG data on 58 children with ASD aged 2-8 years to explore differences in functional brain network topology. We performed an unsupervised clustering analysis based on cortical network connectivity, using data-driven similarity network fusion and source-based spectral analysis2. We replicated the analysis in two independent samples of ASD participants from the NDA repository.

Results: Results We identified three subgroups of ASD children with distinct cortical network properties mainly mapped in the temporal and precentral cortices for the delta band, and in the middle frontal cortex for beta and gamma bands. These three clustered dimensions of functional connectivity and the associated ASD subgroups exhibited different clinical symptom profiles, and were reproducible in two independent samples.

Conclusions: Conclusions Our findings shed light on atypical brain network topology conferring risk for specific phenotypic manifestations of ASD, which may implicate unique underlying neurobiological mechanisms. Cross-validation stability hints at a solid stratification model to challenge ASD heterogeneity. Collectively, the stratification of well-defined neural signatures that give rise to the clinical heterogeneity of ASD has potential to provide more accurate prognosis and help to select the optimal therapeutic intervention strategy.

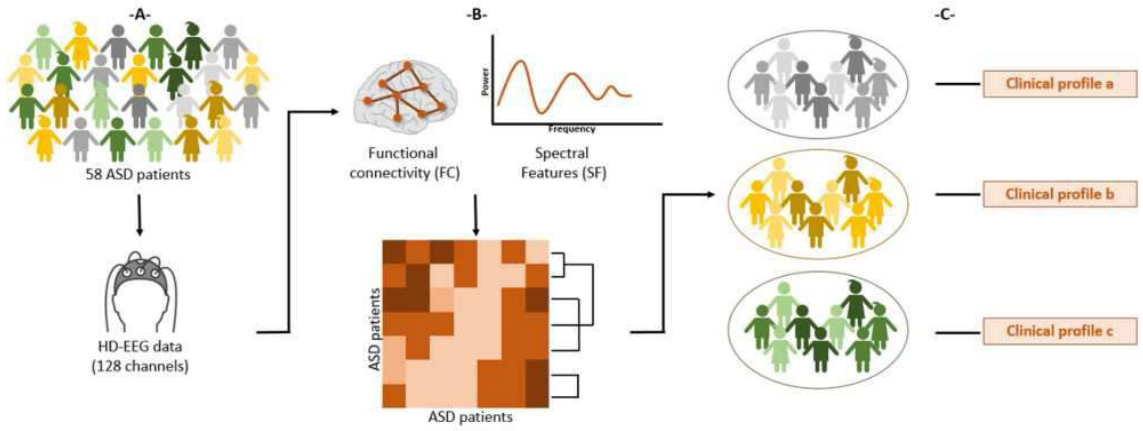

References

1. Loth, Eva, Will Spooren, Lindsay M. Ham, Maria B. Isaac, Caroline Auriche-Benichou, Tobias Banaschewski, Simon Baron-Cohen, et al. 2016. « Identification and Validation of Biomarkers for Autism Spectrum Disorders ». Nature Reviews Drug Discovery 15 (1): 70-70.
2. Wang, Bo, Aziz M. Mezlini, Feyyaz Demir, Marc Fiume, Zhuowen Tu, Michael Brudno, Benjamin Haibe-Kains, et Anna Goldenberg. 2014. « Similarity Network Fusion for Aggregating Data Types on a Genomic Scale ». Nature Methods 11 (3): 333-37. https://doi.org/10.1038/nmeth.2810.

Poster No 337

Fingerprinting individual differences in lesion impact through imaging: The FIDELITI Dashboard

Helen Carlson[1], Jordan Hassett[1], Brandon Craig[1], Alicia Hilderley[1], Keith Yeates[1], Melanie Noel[1], Jillian Miller[1], Frank MacMaster[2], Signe Bray[1], Karen Barlow[3], Brian Brooks[1], Catherine Lebel[1], Nils Forkert[1], Adam Kirton[1]

[1]University of Calgary, Calgary, Alberta, [2]Dalhousie School of Medicine, Halifax, Nova Scotia, [3]University of Queensland, Brisbane, Queensland

Introduction: Childhood and adolescence are periods of massive developmental change continuing into early adulthood. Traditionally used developmental growth charts measuring age-related trajectories for height and weight have provided insights into normal variation around reference data. Availability of very large open-source neuroimaging databases have recently afforded the creation of similar developmental trajectories in brain biomarkers. For neurodevelopmental diseases or brain injuries, deviations from typical developmental trajectories are of particular interest and may explain disabilities while predicting long-term development across the lifespan. Here we introduce the FIDELITI Dashboard (Fingerprinting Individual Differences in Lesion Impact Through Imaging), a patient-centered dashboard that visualizes multimodal brain neuroimaging biomarkers "at a glance". We present several cases illustrating clinical utility of the dashboard by capturing personalized neuroimaging profiles of children with perinatal stroke, the leading cause of hemiparetic cerebral palsy, a non-progressive but lifelong motor disability. In addition to hemiparesis, individuals may also show deficits in attention, executive function, language, and vision. Identifying areas of concern early may facilitate personalized therapeutic interventions.

Methods: The FIDELITI Dashboard was developed in Python. Reference neuroimaging biomarkers were extracted from 828 typically developing volunteers aged between 6.5-24.0 years (mean age (SD) = 14.50 (3.75) years, 47% male) from either the Human Connectome Project Development (n=609, five 3T Siemens Prisma scanners) or the Alberta Children's Hospital imaging collaboration (n=219, one 3T GE MR750w scanner). For additional clinical validation, scans of six children with perinatal stroke (mean age (SD) = 11.2 (2.4) years, 5 males, 3T GE MR750w scanner) were processed and visualized using the FIDELITI Dashboard. Cortical morphometry metrics (cortical thickness, region volumes) were extracted from T1-weighted images using CAT12. Functional connectivity between Harvard-Oxford atlas regions was extracted from resting state functional scans using CONN. White matter microstructure metrics (fractional anisotropy, mean diffusivity) were extracted for 21 major white matter bundles reconstructed using diffusion scans processed in MRtrix3. These biomarkers have previously been shown to be associated with clinical function (Craig, 2021). ComBat (Fortin, 2017) was applied to biomarkers individually to harmonize, specifying sex and age as covariates to preserve. Extensive visualization and harmonization options are provided for users to customize their dashboards. Fundamental components within the dashboard are organized into six domains based on previous literature regarding functional circuits: Sensorimotor, Language, Vision, Attention/Executive function, Memory, and Audition. Over 200 parameters across these six functional domains and four primary imaging modalities are summarized in a dashboard format providing a fully customizable, at-a-glance summary of brain imaging biomarkers.

Results: For children with stroke, deviations from the reference cohort (Figure 1) were seen for cortical thickness and volume of lesioned precentral gyrus as well as interhemispheric functional connectivity between primary motor cortices. Metrics extracted from the non-lesioned hemisphere often fell within the normal variation of the reference cohort. Additional, non-motor domains also showed deviations in some stroke participants, such as functional connectivity for language and executive function networks identifying domains that could potentially be treated with intensive cognitive therapy.

Conclusions: The FIDELITI Dashboard is patient-centered, fully customizable, and has potential applications for many other neurodevelopmental conditions or early life brain injuries. FIDELITI is available online (https://cumming.ucalgary.ca/labs/carlson-imaging/projects/fideliti-dashboard).

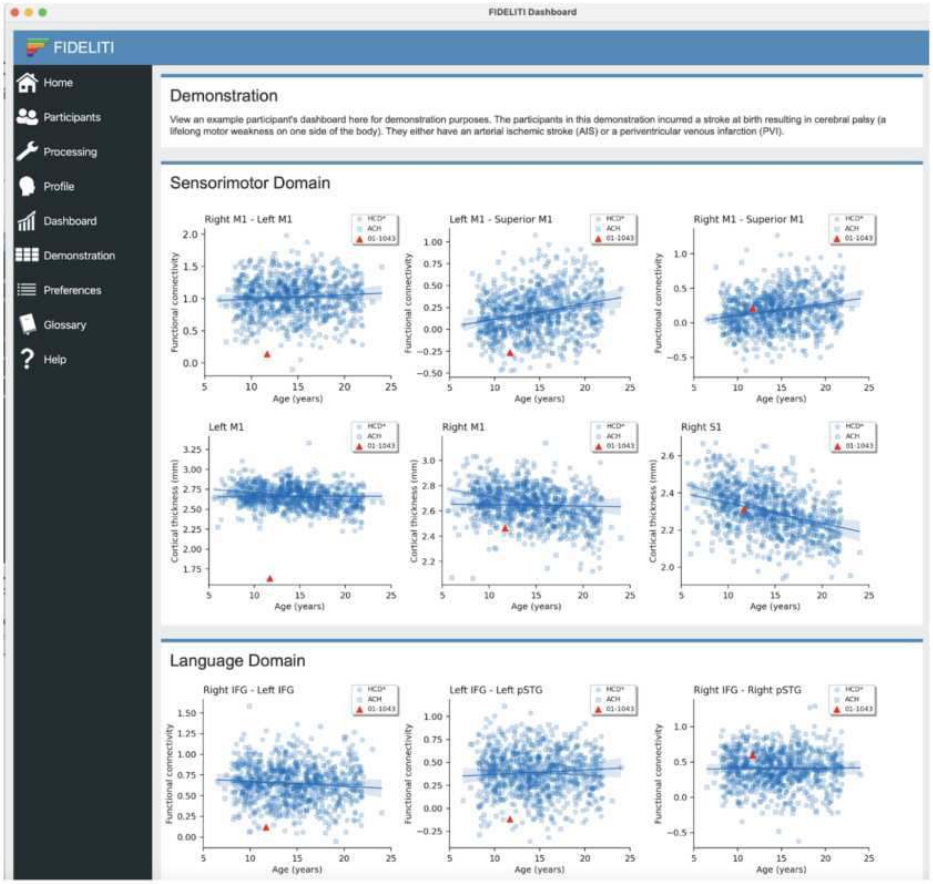

Figure 1. An illustration of neuroimaging biomarkers from an 11.7 year old male with a left hemisphere perinatal arterial ischemic stroke in relation to a large reference database using the patient-centered FIDELITI Dashboard. Biomarkers in the lesioned left hemisphere often deviate from the reference trajectory, though biomarkers from the non-lesioned right hemisphere may fall within the normal variability of the reference sample. Additional functional modalities may identify areas that could be targeted with cognitive therapy. M1 - precentral gyrus, S1 - postcentral gyrus, IFG - inferior frontal gyrus, pSTG - superior temporal gyrus (posterior), HCD - Human Connectome Project (Development), ACH - Alberta Children's Hospital collaboration.

References

1. Craig, BT (2021), Imaging Developmental and Interventional Plasticity Following Perinatal Stroke. Canadian Journal of Neurological Sciences 48, 157–171. Fortin, J.-P. (2017), Harmonization of multi-site diffusion tensor imaging data. NeuroImage 161, 149–170.

Poster No 338

Low Birthweight Associated Long-term Pubertal and Neurodevelopmental Alterations in Preterm Children

Weibin Ji[1,2], Guanya Li[1,2], Wenchao Zhang[1,2], Yang Hu[1,2], Peter Manza[3], Nora Volkow[3], Gene-Jack Wang[3], Yi Zhang[1,2]

[1]Center for Brain Imaging, School of Life Science and Technology, Xidian University, Xi'an, Shaanxi 710126, China, [2]International Joint Research Center for Advanced Medical Imaging and Intelligent Diagnosis and Treatment & Xi'an Key Laboratory of Intelligent Sensing and Regulation of trans-Scale Life Information, School of Life Science and Technology, Xidian University, Xi'an, Shaanxi 710126, China, [3]Laboratory of Neuroimaging, National Institute on Alcohol Abuse and Alcoholism, Bethesda, MD 20892, USA

Introduction: Preterm birth is often associated with low birthweight, and these infants are delivered at a critical time when brain architecture is not fully developed being at higher risk of long-term neurological and cognitive dysfunction (Ji et al., 2023; Mwaniki et al., 2012). In addition, there is also evidence that preterm birth and low birthweight could provoke adaptive changes in endocrine and metabolic processes and influence puberty, particularly early onset of adrenarche during the transition from childhood to adolescence (Charkaluk et al., 2004; Ibanez et al., 1998; Wehkalampi et al., 2011), impacting brain

health throughout development (Goddings et al., 2014; Peper et al., 2009; Peper et al., 2008). However, few studies have examined associations among birthweight, pubertal endocrine process and brain and cognitive development.

Methods: Data were selected from the Annual Curated Data Release 3.0 from the ABCD consortium (https://abcdstudy.org/index.html). The preterm group included 1706 preterm subjects (gestational age < 37 weeks) and 1865 matched full-term individuals as control group (age, gender, BMI, intracranial volume, race/ethnicity, household income, highest education and sites, P > 0.05). The indicators of onset of adrenarche integrated both perceived physical features (adrenal score) and hormone measures (salivary dehydroepiandrosterone (DHEA)) from the child aged 9-10 years (Herting et al., 2020). We tested the differences in adrenal score and salivary DHEA level between preterm and control group. A linear mined-effect model (LME) was used to test the associations of adrenal score/salivary DHEA level with cognition and brain volumes in preterm and control groups (Ji et al., 2023), all demographic characteristics were included as covariates and all statistical results were corrected for multiple comparisons using FDR correction (P < 0.05). Furthermore, a serial two-mediator analysis was implemented to assess whether adrenal score/salivary DHEA level mediated the association among birthweight, cortical volume and cognition.

Results: Compared to controls, preterm children showed lower birthweight, higher salivary DHEA level and adrenal score (Figure 1A). Salivary DHEA level was negatively associated with birthweight in both preterm and control groups, and two correlations were significantly different (Figure 1B). Adrenal score was negatively associated with birthweight in both preterm and control groups (Figure 1B); and also positively associated with salivary DHEA level in both preterm and control groups and two correlations were significantly different (Figure 1B). Adrenal score was negatively associated with multiple cortical volumes in preterm children, including lateral orbitofrontal cortex (lOFC), inferior parietal lobule, anterior cingulate cortex, middle temporal gyrus, later occipital and rostral middle frontal cortex, superior parietal lobule, inferior temporal gyrus, lingual, cuneus and precuneus (P < 0.05, FDR; Figure 2A); but not in normal children (P < 0.05, FDR). In addition, there were negative associations between adrenal score and language vocabulary knowledge, cognitive control and attention, cognitive flexibility, as well as Fluid, Cryst and Totalcomp scores in the preterm group (P < 0.05, FDR; Figure 2B), and only working memory score was negatively associated with adrenal score in controls (P < 0.05, FDR; Figure 2B). The adrenal score indirect path, cortical volume in the lOFC path, and cortical volume in the lOFC via adrenal score indirect path all significantly mediated the direct relationship between birthweight and Fluid/Totalcomp score in preterm children (Figure 2C).

Conclusions: These findings highlight the impact of low birthweight on long-term pubertal and neurodevelopmental alterations in preterm children, suggesting that preterm and low birthweight associated abnormal developmental trajectories are observable during the transition from childhood to adolescence. This understanding may help with prevention and treatment.

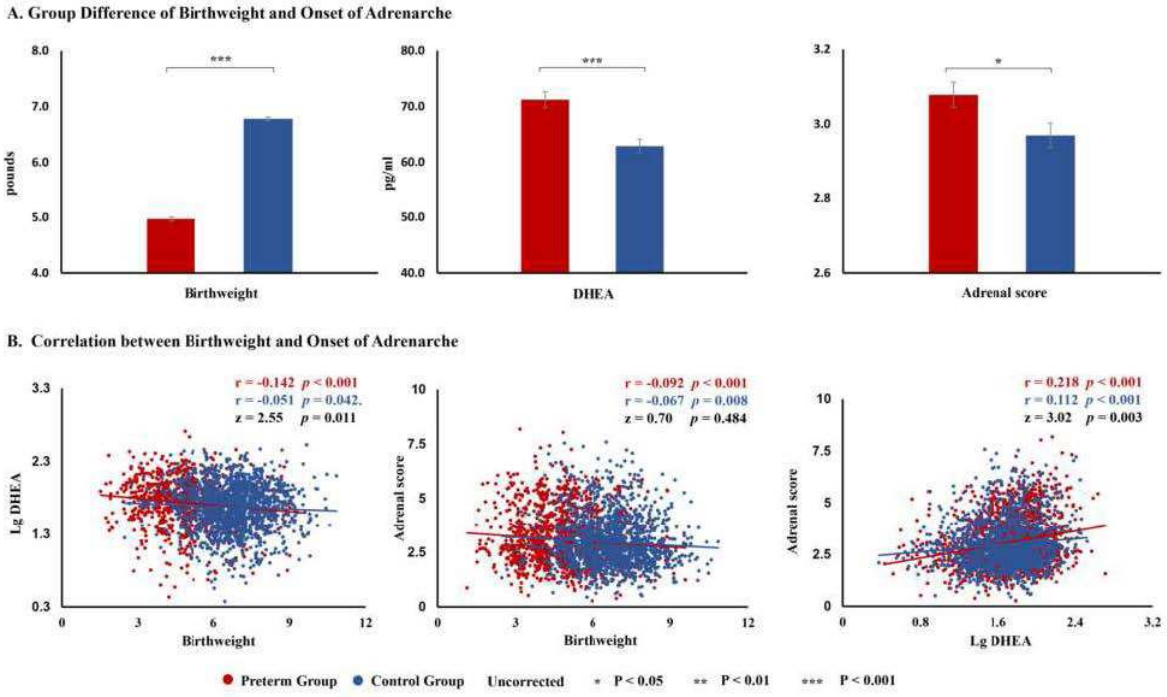

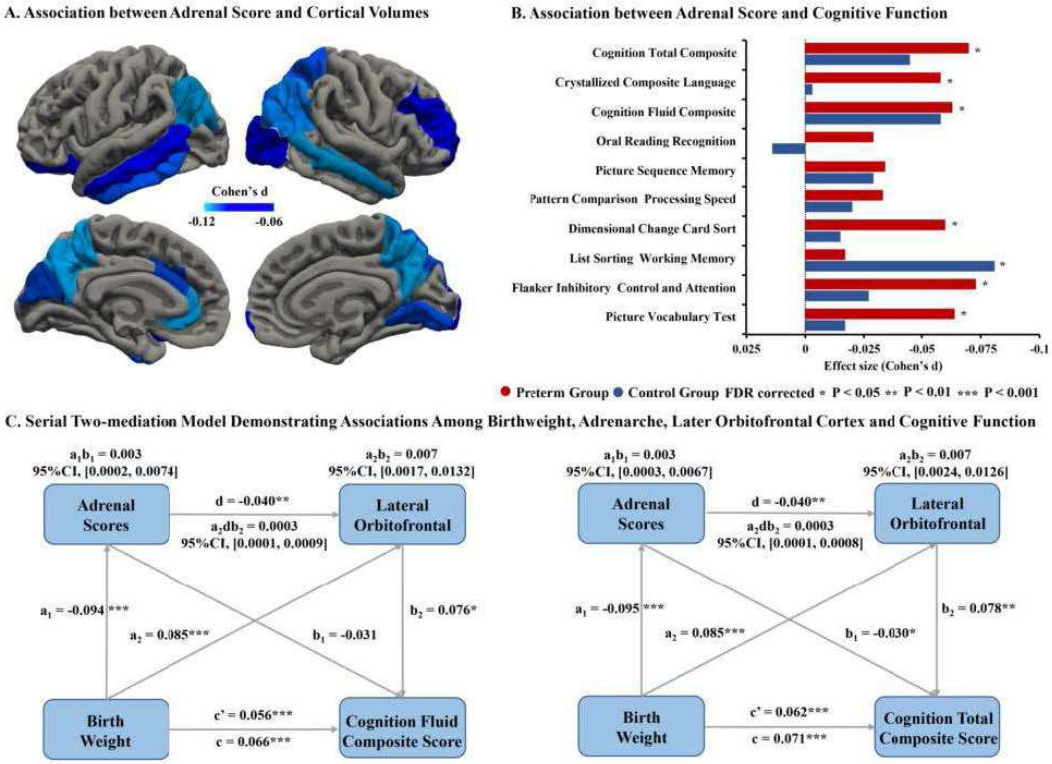

References

1. Charkaluk, M. L. (2004). Premature pubarche as an indicator of how body weight influences the onset of adrenarche. European journal of pediatrics, 163(2), 89-93.
2. Goddings, A. L. (2014). The influence of puberty on subcortical brain development. NeuroImage, 88, 242-251.
3. Ibanez, L. (1998). Precocious pubarche, hyperinsulinism, and ovarian hyperandrogenism in girls: relation to reduced fetal growth. The Journal of clinical endocrinology and metabolism, 83(10), 3558-3562.
4. Ji, W. B. (2023). Preterm birth associated alterations in brain structure, cognitive functioning and behavior in children from the ABCD dataset. Psychological Medicine.
5. Martinussen, M. (2005). Cerebral cortex thickness in 15-year-old adolescents with low birthweight measured by an automated MRI-based method. Brain, 128(Pt 11), 2588-2596.
6. Mwaniki, M. K. (2012). Long-term neurodevelopmental outcomes after intrauterine and neonatal insults: a systematic review. Lancet, 379(9814), 445-452.
7. Peper, J. S. (2009). Sex steroids and brain structure in pubertal boys and girls. Psychoneuroendocrinology, 34(3), 332-342.
8. Peper, J. S. (2008). Cerebral white matter in early puberty is associated with luteinizing hormone concentrations. Psychoneuroendocrinology, 33(7), 909-915.
9. Wehkalampi, K. (2011). Advanced pubertal growth spurt in subjects born preterm: the Helsinki study of very low birthweight adults. The Journal of clinical endocrinology and metabolism, 96(2), 525-533.

Poster No 339

Auditory Language Comprehension among Children and Adolescents with ASD: An ALE fMRI Meta-Analysis

Jun Hu[1], Hua Zihui[1], Zeng Huanke[1], Li Jiahui[1], Cao Yibo[1], Yiqun Gan[1]

[1]Peking University, Beijing, Beijing

Introduction: Autistic children and adolescents commonly manifest difficulties in auditory language comprehension. Some fMRI studies have indicated potential neural bases of such difficulties in autism. However, the findings remain mixed, and few studies have systematically examined their overall patterns. Previous relevant meta-analyses have included tasks outside the scope of auditory language comprehension (e.g., visual language processing tasks), with no studies specifically focusing on this process. Furthermore, no meta-analytic studies thus far have specifically examined this process in autistic children and adolescents, despite the crucial role played by the early stages in language development. The current study aims to complement previous work by conducting an activation likelihood estimation (ALE) meta-analysis of fMRI studies using tasks involving auditory language comprehension in autistic children and adolescents. Specifically, we aim to identify (a) commonly

activated brain regions involved in auditory language comprehension in autistic and non-autistic children and adolescents and (b) the differences in brain activation patterns during auditory language comprehension between autistic and non-autistic children and adolescents.

Methods: This study was pre-registered (PROSPERO: CRD42023413187) and conducted in accordance with the PRISMA 2020 statement. Literature search was conducted through PubMed, Web of Science, Scopus, MEDLINE, and PsycINFO. Studies using fMRI tasks that involved auditory language comprehension in autistic children and adolescents were included. A total of nine articles met inclusion criteria, with eight (participant number: 121 autistic, 131 non-autistic) included in the within-group analyses and seven (116 autistic, 124 non-autistic) included in the between-group analysis (see Figure 1 for literature search process). ALE meta-analyses were conducted to compare task versus baseline conditions in the two groups respectively, and then examined group differences in activation patterns.

Results: The within-group analyses revealed that the bilateral superior temporal gyrus (STG) was activated during auditory language comprehension in both groups, whereas the left superior frontal gyrus and dorsal medial prefrontal cortex were activated only in the non-autistic group. Furthermore, the between-group analysis showed that autistic children and adolescents, compared to non-autistic counterparts, showed reduced activation in the right superior temporal gyrus (STG), left middle temporal gyrus (MTG), and insula, whereas the autistic group did not show increased activation in any of the regions relative to the non-autistic group.

Conclusions: The overlap in activation across groups in the bilateral STG implied a shared neurobiological basis for auditory language comprehension. A less distributed pattern of brain activation during auditory language comprehension in the autistic group suggested that the development of the neural network responsible for auditory language processing might be delayed. The reduced activation in the right STG, left MTG/insula in the autistic group suggested potential difficulties in processing acoustic properties of speech and understanding prosody, as well as coordinating and integrating the substages required to reach comprehension (see Table 1 for a summary of main findings and theoretical implications). Our findings contribute to a better understanding of the potential neural mechanisms underlying difficulties in auditory language comprehension in autistic children and adolescents and provide practical implications for early screening and interventions.

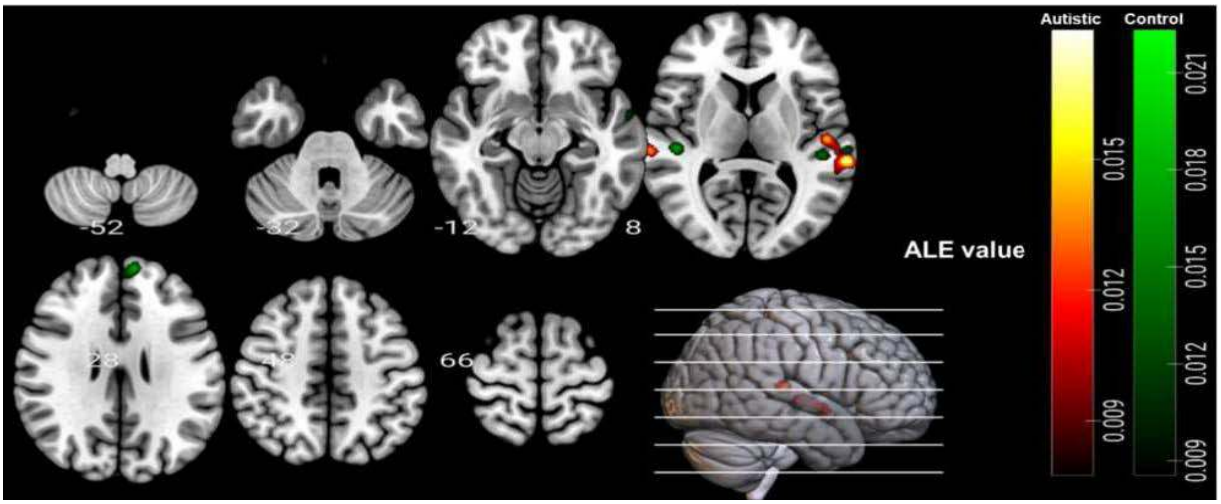

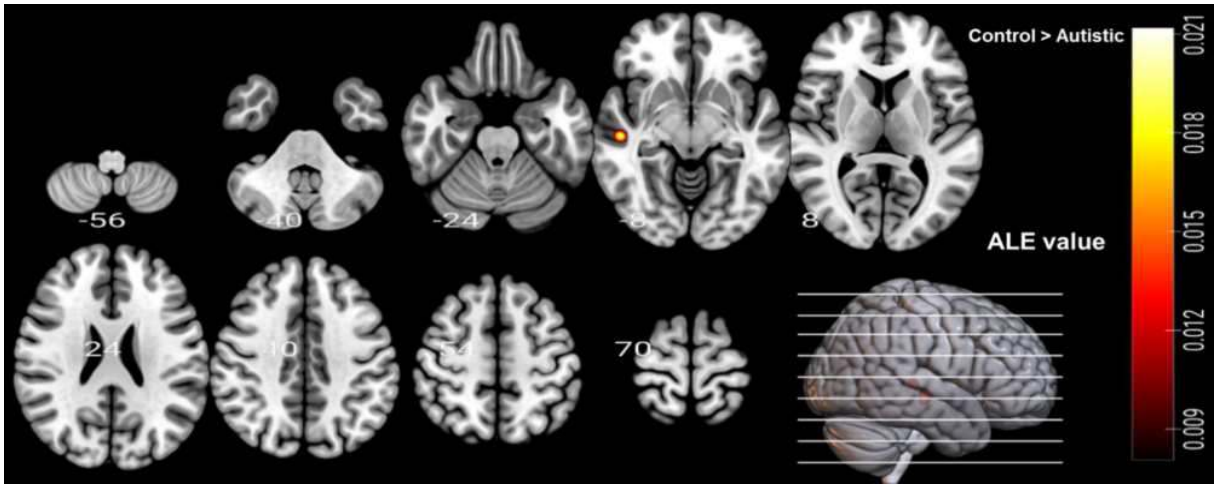

References
1. Colich, N. L., Wang, A.-T., Rudie, J. D., Hernandez, L. M., Bookheimer, S. Y., & Dapretto, M. (2012). Atypical neural processing of ironic and sincere remarks in children and adolescents with autism spectrum disorders. Metaphor and Symbol, 27(1), 70–92.
2. Green, S. A., Hernandez, L. M., Bowman, H. C., Bookheimer, S. Y., & Dapretto, M. (2018). Sensory over-responsivity and social cognition in ASD: Effects of aversive sensory stimuli and attentional modulation on neural responses to social cues. Developmental Cognitive Neuroscience, 29, 127–139.
3. Groen, W. B., Tesink, C., Petersson, K. M., van Berkum, J., van der Gaag, R. J., Hagoort, P., & Buitelaar, J. K. (2010). Semantic, factual, and social language comprehension in adolescents with autism: an FMRI study. Cerebral Cortex, 20(8), 1937–1945.
4. Herringshaw, A. J., Ammons, C. J., DeRamus, T. P., & Kana, R. K. (2016). Hemispheric differences in language processing in autism spectrum disorders: A meta-analysis of neuroimaging studies. Autism Research, 9(10), 1046–1057
5. Leipold, S., Abrams, D. A., Karraker, S., Phillips, J. M., & Menon, V. (2023). Aberrant Emotional prosody circuitry predicts social communication impairments in children with autism. Biological Psychiatry: Cognitive Neuroscience and Neuroimaging, 8(5), 531-541.
6. Lai, G., Pantazatos, S. P., Schneider, H., & Hirsch, J. (2012). Neural systems for speech and song in autism. Brain, 135(3), 961–975.
7. Leipold, S., Abrams, D. A., Karraker, S., Phillips, J. M., & Menon, V. (2022). Aberrant emotional prosody circuitry predicts social communication impairments in children with autism. Biological Psychiatry: Cognitive Neuroscience and Neuroimaging, 8(5), 531-541.
8. Philip, R. C. M., Dauvermann, M. R., Whalley, H. C., Baynham, K., Lawrie, S. M., & Stanfield, A. C. (2012). A systematic review and meta-analysis of the fMRI investigation of autism spectrum disorders. Neuroscience & Biobehavioral Reviews, 36(2), 901–942.

Poster No 340

Machine-learning-based feature selection to identify ADHD using white matter microstructure

Huey-Ling Chiang[1], Chi-Shin Wu[2], Susan Shur-Fen Gau[3]

[1]Far Eastern Memorial Hospital, New Taipei City, [Select a State], [2]National Health Research Institutes, Taipei, Taiwan, [3]National Taiwan University College of Medicine, Taipei, Taiwan

Introduction: While brain imaging has been extensively used to investigate structural and functional alterations to provide objective measurements in attention-deficit/hyperactivity disorder (ADHD), the findings have exhibited considerable variability across studies with traditional univariate approaches. Although relatively few studies have used multi-modal image-based machine-learning approaches, including diffusion imaging, all of them reported that features of diffusion imaging provided specific importance in the model to improve discriminative power for ADHD diagnosis (Chaim-Avancini et al., 2017) Here, we aimed to identify white matter features collectively distinguishing individuals with ADHD from those without ADHD. We wanted to identify neuroimaging features associated with ADHD by examining the baseline, follow-up, and yearly change rate of white matter microstructure in a longitudinal dataset (Fuelscher et al., 2023). We hypothesize that imaging features from the white matter microstructure will enhance the accurate discrimination between individuals with a childhood ADHD diagnosis and typically developing controls (TDC).

Methods: Fifty-one ADHD patients and 60 typically developing controls (TDC), underwent diffusion spectrum imaging at two time points. The generalized fractional anisotropy (GFA) was calculated for the microstructural properties of 45 white matter tracts. Machine-learning algorithms were utilized to classify ADHD and TDC. Three models were tested using machine-learning approaches. In the first model, we used baseline white matter features collected at Time 1 to classify the ADHD group from the TDC group. The second model included white matter features collected at both Time 1 and Time 2. The third model (main analysis) included a yearly change rate for each white matter tract. All analyses included age, sex, and image quality (measured by signal dropout count) as covariates. Correlation analyses were employed to depict the association between the yearly GFA values change rate and the neuropsychological performance changes for both the ADHD and TDC groups, respectively. These analyses involved selected features of ADHD in the classification model for distinguishing ADHD from TDC.

Results: The random forest algorithm demonstrated the best performance for classification. Model 1 achieved an area-under-the-curve (AUC) of 0.67. Model 3, incorporating Time 2 variables and yearly change rates, improved the performance (AUC=0.73). In addition to identifying several white matter features at two time points, we found that the yearly change rates in the superior longitudinal fasciculus, frontal aslant tract, stria terminalis, inferior fronto-occipital fasciculus, thalamic and striatal tracts, and other tracts involving sensorimotor regions are important features of ADHD (Figure 1). Correlation analyses indicated that higher yearly increasing GFA rates in certain tracts were associated with greater improvement in visual attention, spatial short-term memory, and spatial working memory after FDR corrections (Table 1).

Conclusions: Using longitudinal DSI data of white matter microstructure, this machine-learning-based analysis achieves moderate discrimination power in classifying individuals with and without childhood ADHD diagnosis. The properties of white matter white matter microstructure and its developmental change rate, which reflect deviations from typical development trajectories, serve as important biomarkers for ADHD.

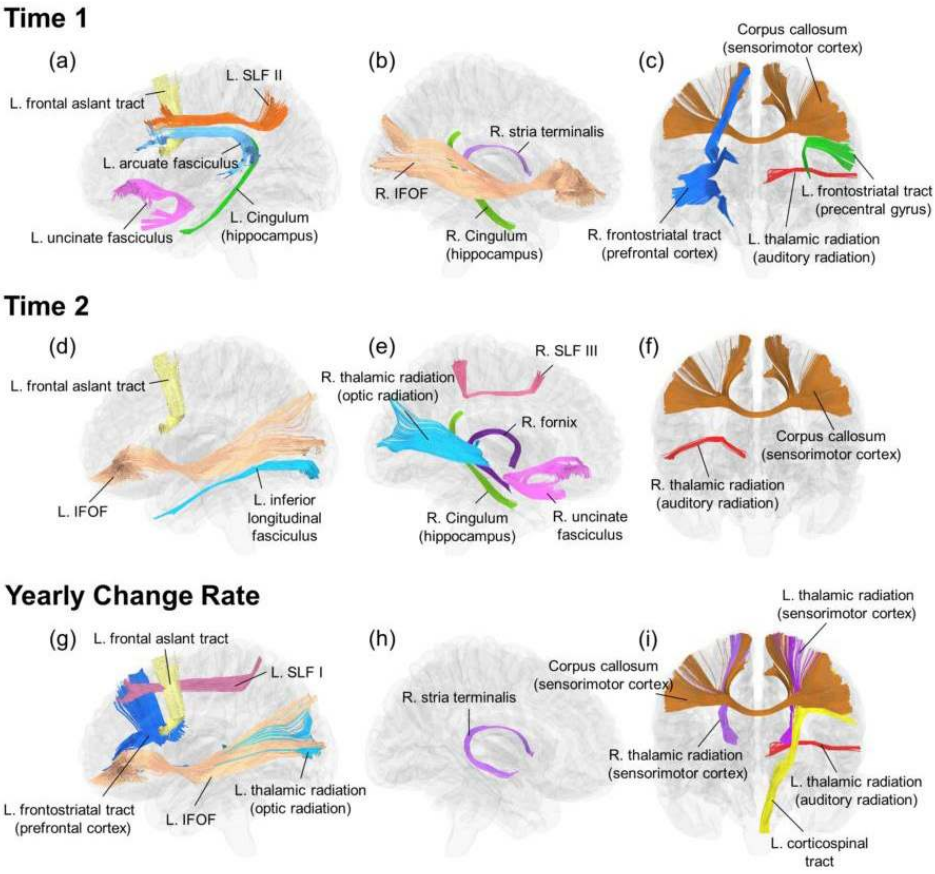

Correlation between the yearly change rate of the GFA and the development of neuropsychological function by group

	Visual attention				Spatial span				Spatial working memory			
	ADHD		Control		ADHD		Control		ADHD		Control	
	r	*p*	*r*	*p*	*r*	*p*	*r*	*p*	*r*	*p*	*r*	*p*
L. SLF I	-0.41	**0.007***	-0.20	0.153	0.42	**0.003***	-0.05	0.726	-0.09	0.566	0.01	0.953
L. frontal aslant tract	-0.31	0.046	0.08	0.594	0.19	0.216	0.22	0.127	-0.05	0.749	-0.34	**0.016***
R. stria terminalis	0.21	0.168	0.08	0.563	0.20	0.181	0.02	0.897	0.26	0.079	0.07	0.629
L. inferior fronto-occipital fasciculus	-0.40	**0.007***	-0.11	0.451	0.07	0.622	-0.08	0.595	-0.23	0.121	-0.11	0.453
L. FS (prefrontal cortex)	-0.42	**0.005***	0.02	0.897	0.28	0.063	0.13	0.359	-0.14	0.340	-0.06	0.664
L. TR (sensorimotor cortex)	-0.28	0.067	-0.17	0.230	0.32	0.030	-0.05	0.753	-0.19	0.200	-0.34	**0.017***
R. TR (sensorimotor cortex)	-0.25	0.102	0.32	0.021	0.17	0.249	0.21	0.137	-0.35	0.018	-0.42	**0.003***
L. TR (auditory radiation)	-0.33	0.029	-0.14	0.317	0.26	0.079	-0.29	0.041	-0.16	0.284	0.04	0.803
L. TR (optic radiation)	-0.14	0.381	-0.27	0.053	-0.03	0.852	-0.19	0.197	-0.14	0.351	0.09	0.533
L. corticospinal tract	-0.35	**0.022***	0.19	0.175	0.30	0.045	0.10	0.509	-0.16	0.283	-0.14	0.315
CC (sensorimotor cortex)	-0.35	**0.021***	0.02	0.909	0.20	0.193	0.09	0.546	-0.12	0.443	-0.41	**0.003***

References

1. Chaim-Avancini, T.M., Doshi, J., Zanetti, M.V., Erus, G., Silva, M.A., Duran, F.L.S., Cavallet, M., Serpa, M.H., Caetano, S.C., Louza, M.R., Davatzikos, C., Busatto, G.F., 2017. Neurobiological support to the diagnosis of ADHD in stimulant-naïve adults: pattern recognition analyses of MRI data. Acta Psychiatr Scand 136 (6), 623-636.
2. Fuelscher, I., Hyde, C., Thomson, P., Vijayakumar, N., Sciberras, E., Efron, D., Anderson, V., Hazell, P., Silk, T.J., 2023. Longitudinal Trajectories of White Matter Development in Attention-Deficit/Hyperactivity Disorder. Biol Psychiatry Cogn Neurosci Neuroimaging: S2451-9022(23)00071-X.

Poster No 341

Multimodal network dynamics underpinning executive function development in children born preterm

Abiot Derbie[1], Mekibib Altaye[2,3], Armin Allahverdy[1], Leanne Tamm[2,3], Nehal Parikh[1,3]

[1]Neurodevelopmental Disorders Prevention Center, Perinatal Institute, Cincinnati Children's Hospital, Cincinnati, OH, USA, [2]Department of Pediatrics, Cincinnati Children's Hospital Medical Center, Cincinnati, OH, USA, [3]Department of Pediatrics, University of Cincinnati College of Medicine, Cincinnati, OH, USA

Introduction: Preterm birth is closely associated with abnormal cerebral development, leading to a heightened risk of neurodevelopmental challenges including executive function (EF) impairments. Despite advancements in neonatal care, the long-term neurocognitive effects of preterm birth present enduring concerns. The research aims to delineate the development of executive functions in preterm infants, focusing on how structural and functional brain connections influence their executive development. This study aims to bridge this gap by using multimodal neuroimaging to investigate associations of magnetic resonance imaging (MRI) structural and functional brain correlates obtained in infancy (at term-equivalent age) with EF at 3 years corrected age in children born preterm (PT).

Methods: We studied a prospective cohort of PT infants born at ≤32 weeks gestational age (N = 212) from five regional NICUs. All PT infants underwent imaging procedures at Cincinnati Children's Hospital within postmenstrual age range of 39 to 44 weeks. Resting state functional MRI (rsfMRI) and structural MRI (sMRI) were performed using a single 3-tesla Philips MRI system, equipped with 32-channel receiver head coil. We used the dHCP (developing Human Connectome Project) atlas for anatomical parcellation and spatial alignment. Executive function (EF) was assessed with the nationally-normed Minnesota Executive Function Scale at 3 years corrected age (higher standard scores indicate better EF; M = 93.1, SD = 11.9). CONN Toolbox was used to extract six graph theory metrics from 82 brain regions. The graph theory metrics of both structural (SC) and functional connectivity (FC) were analyzed using non-negative matrix factorization (NMF). NMF was chosen for its ability to identify overlapping and flexible co-occurrences of network components (NC). These NCs were then used as features in a LASSO regression model, with EF scores as the outcome variable. Subsequently, variables with non-zero LASSO coefficients underwent multiple regression to isolate significant NCs. Finally, these NCs from both SC and FC informed a canonical correlation analysis, offering the interaction between SC and FC.

Results: The extracted NCs from NMF revealed the involvement of various resting state networks (RSNs) in EF, including the frontoparietal network (FPN), default mode network (DMN), and salience network (SN). The SC cost graph metric, reflecting the efficiency of network maintenance, in the anterior lateral temporal lobe, low-thalamic areas, and frontal lobe, associated to the thalamo-cortical and FPN connections and correlated with higher EF ($b = 2.03$, $t(193) = 2.03$, $p < .05$). Functionally, enhanced betweenness centrality ($b = 2.57$, $t(191) = 2.57$, $p < .05$) and local efficiency ($b = 2.22$, $t(191) = 2.22$, $p < .05$) within the SN (frontal lobe, anterior cingulate gyrus, and insula, parahippocampal gyrus) was associated with higher EF. CCA highlighted significant links between the SC of the FPN (involving regions such as the posterior cingulate gyrus (PCG) and anterior medial temporal lobe) and FC within the DMN (encompassing PCG and medial temporal areas), foundational to EF in preterm infants (Fig. 1 & 2).

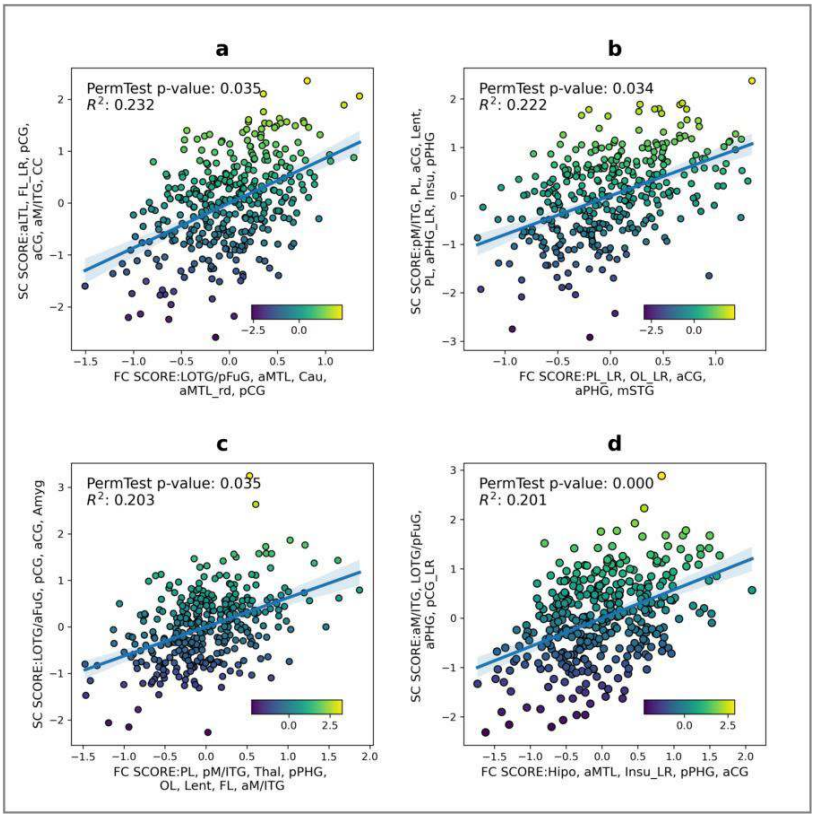

Fig. 1. Canonical plots depict the relationship between structural and functional brain connectivity. Variations in point size and color intensity illustrate the significance and strength of these correlation.

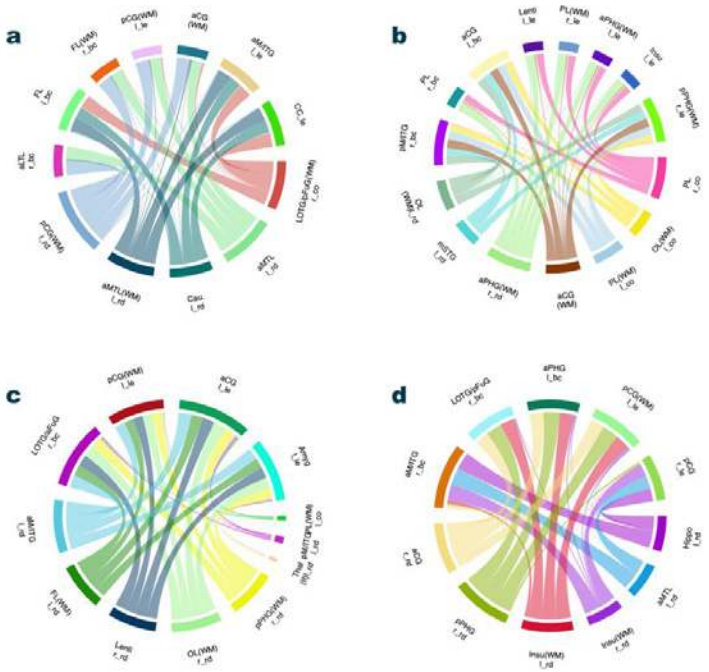

Circos plot illustrates complex connections between structural and functional brain variables, with chord thickness representing the interaction's strength within canonical pairs

Conclusions: This study provides novel insights into the developmental organization of neural substrates underpinning EF in PT infants. It reveals how large-scale structural brain connectivity fundamentally constrains and shapes the functional interactions within the DMN and SN that appear essential for EF. This study demonstrated that the frontoparietal control network structurally underpins the functional dynamics of the DMN, elucidating aspects of EF development in PT. The degree to which each contributes may vary significantly among PT children. These findings highlight the potential of multimodal neuroimaging in advancing our understanding of the connections between brain connectivity and EF in PT infants and offers promising avenues for future research on the neurodevelopmental implications of preterm birth.

References

1. Ajayi-Obe, M. (2000), 'Reduced development of cerebral cortex in extremely preterm infants', The Lancet, vol. 356, no. 9236, pp.1162-1163.
2. Caldinelli, C. (2017), 'White matter alterations to cingulum and fornix following very preterm birth and their relationship with cognitive functions', NeuroImage, vol. 150, pp. 373-382.
3. Daamen, M. (2015), 'Working memory in preterm-born adults: Load-dependent compensatory activity of the posterior default mode network', Human brain mapping, vol. 36, no. 3, pp. 1121-1137.
4. Dean, J. M. (2013), 'Prenatal cerebral ischemia disrupts MRI-defined cortical microstructure through disturbances in neuronal arborization', Science translational medicine, vol. 5, no. 168, pp. 168ra167-168ra167.
5. Honey, C. J (2009), 'Predicting human resting-state functional connectivity from structural connectivity', Proceedings of the National Academy of Sciences, vol. 106, no. 6, pp. 2035-2040.
6. Kline, J. E. (2020), 'Early cortical maturation predicts neurodevelopment in very preterm infants', Archives of Disease in Childhood - Fetal and Neonatal Edition, vol. 105, no. 5, pp. 460-465.
7. Lawrence, E. J. (2009), 'The neural basis of response inhibition and attention allocation as mediated by gestational age', Human brain mapping, vol. 30, no. 3, pp. 1038-1050.
8. Nassar, R. (2019), 'Gestational age is dimensionally associated with structural brain network abnormalities across development', Cerebral Cortex, vol. 29, no. 5, pp. 2102-2114.
9. Nosarti, C. (2007), 'Grey and white matter distribution in very preterm adolescents mediates neurodevelopmental outcome', Brain, vol. 131, no. 1, pp. 205-217.
10. Parikh, N. A. (2020), 'Objectively Diagnosed Diffuse White Matter Abnormality at Term Is an Independent Predictor of Cognitive and Language Outcomes in Infants Born Very Preterm', The Journal of pediatrics, vol. 220, pp. 56-63.
11. Parikh, N. A. (2021), 'Perinatal risk and protective factors in the development of diffuse white matter abnormality on term-equivalent age magnetic resonance imaging in infants born very preterm', The Journal of pediatrics, vol. 233, pp. 58-65. e53.

Poster No 342

Reduced brain activity for sensory and motor tasks after treatment in pediatric medulloblastoma

Jesyin Lai[1], Ping Zou Stinnett[1], Robert Ogg[1], Thomas Merchant[1], Heather Conklin[1], Amar Gajjar[1], Ranganatha Sitaram[1]

[1]St. Jude Children's Research Hospital, Memphis, TN

Introduction: Medulloblastoma is the most common malignant childhood brain tumor. Contemporary therapy consists of maximal surgical resection, craniospinal radiotherapy (RT), and chemotherapy. Current protocols stratify patients into high, average, and low risk groups by the presence or absence of metastatic or post-operative residual disease and molecular features. This has effectively improved cure rates and reduced the risk of craniospinal radiation for individuals with more favorable prognoses. However, many pediatric survivors still suffer late effects including long-term neurotoxicity, ototoxicity and endocrinopathies. Since patients in different therapeutic strata receive different RT doses and chemotherapy regimens, late effects may be disparate in these patients. As auditory, visual, and motor functions play vital roles in daily living, identifying, and tracing changes in brain activation in regions responsible for these functions provide useful information to develop interventions for cognitive rehabilitation.

Methods: Fifty-seven pediatric patients with medulloblastoma (WNT & Non-WNT/Non-SHH) were involved in this study. They were assigned to W+N1 and N2+N3 therapeutic strata based on the extent of disease and molecular classification. They received RT plus 4 (W+N1) or 7 (N2+N3) cycles of chemotherapy. To longitudinally trace their auditory, visual, and motor functions, functional magnetic resonance imaging (fMRI) data were acquired during a sensory survey task at three different time points (TP): pre-RT (TP0), post-RT/pre-chemotherapy (TP1), and post-chemotherapy (TP2: 9/12 months post-enrollment for W+N1/N2+N3). Participants aged 5-23 years (11.25 ± 4.3) at their first fMRI exams. Participants were asked to tap their right fingers actively during simultaneous auditory (dissonant ascending/descending pure tones) and visual (flashing checkboards) presentation (20s stimuli + 20s gap) in 3 blocks. Task-related brain activation patterns were analyzed using SPM software, and subsequent analysis was performed using custom Python code. To identify regions of interest (ROIs) with changes in brain activation, we used k-nearest-neighbors-based searchlight analysis to classify blood oxygenation-level dependent (BOLD) signals into TP0 vs. TP1 or TP0 vs. TP2 separately for the two strata. ROIs were identified using cut-off thresholds of 0.6-0.68

f1-score and 20 cluster-size based on the AAL atlas. Medians of BOLD signals in ROIs were computed for comparisons across TPs. Response times and frequencies (RFs = response no./stimulus duration) were calculated to assess behavior performance.

Results: Through searchlight-pattern classifications in W+N1, changes in BOLD signals across TPs were identified in the L cerebellum, L superior temporal gyrus, L thalamus, L supplementary motor area (SMA), etc. Median BOLD amplitudes were reduced across TPs in the L superior temporal gyrus, L SMA, and L thalamus. In addition, via similar analysis in N2+N3, changes in BOLD signals across TPs were identified in the R cerebellum, superior occipital gyrus, L postcentral gyrus, L calcarine cortex, etc. Decreased median BOLD amplitudes across TPs were found in the superior occipital gyri, L postcentral gyrus, and L calcarine cortex. When behavior performance was analyzed, there was a trend of RF reduction across TPs and response times were similar across TPs in W+N1. Both RFs and response times were similar across TPs in N2+N3.

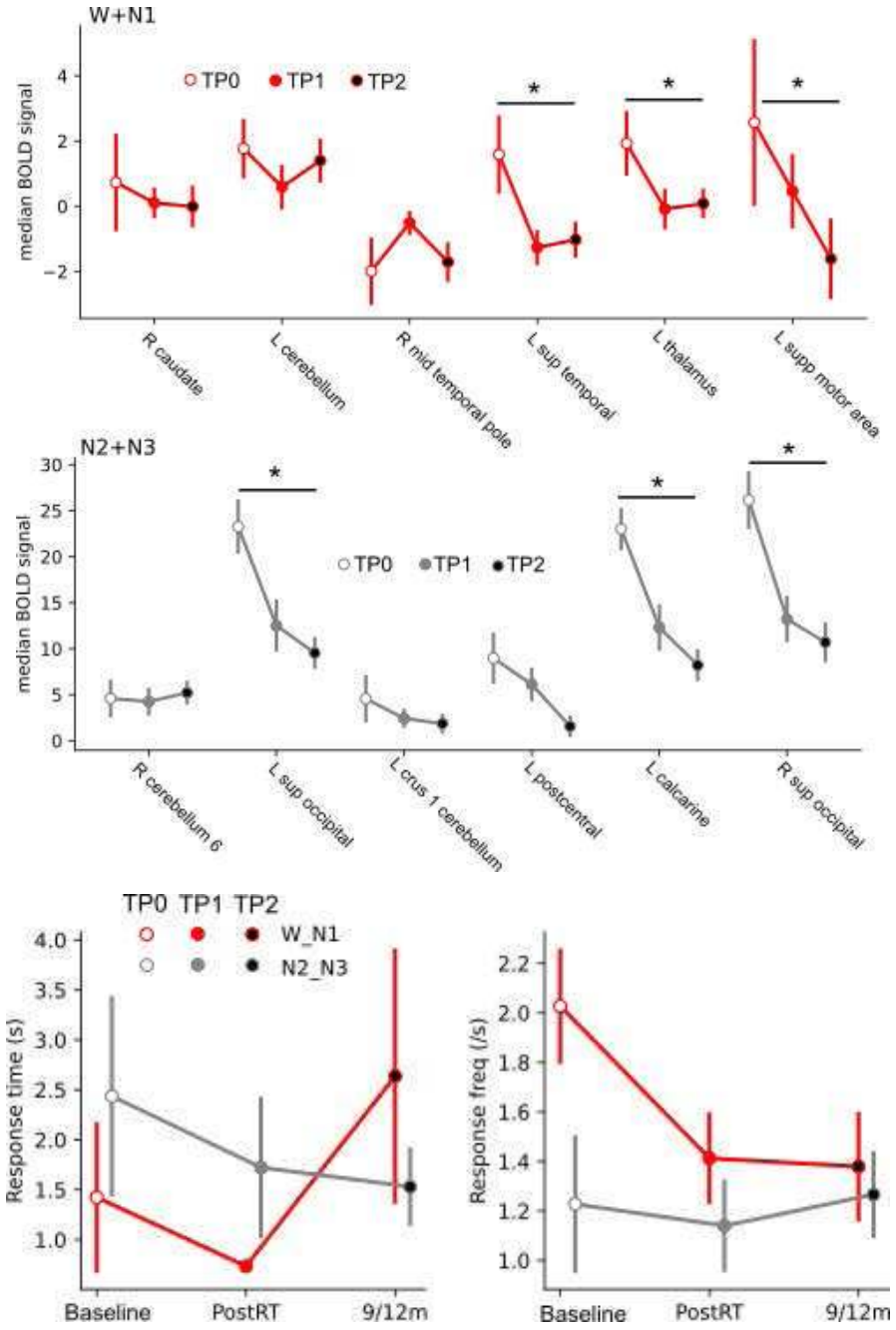

Conclusions: For W+N1, reduced BOLD signals were observed in ROIs responsible for auditory and sensory processing and movement control. For N2+N3, decreased BOLD signals were found in ROIs responsible for object recognition, sensory perception, and visuospatial processing. These observations suggest disparate deficit profiles in auditory, visual, and motor processing in the different strata, probably related to differences in disease extent and the impact of surgery, RT and chemotherapy.

References
1. Pui, C.H., et al., Challenging issues in pediatric oncology. Nat Rev Clin Oncol, 2011. 8(9): p. 540-9.
2. Packer, R.J., et al., Phase III study of craniospinal radiation therapy followed by adjuvant chemotherapy for newly diagnosed average-risk medulloblastoma. J Clin Oncol, 2006. 24(25): p. 4202-8.
3. Gajjar, A., et al., Risk-adapted craniospinal radiotherapy followed by high-dose chemotherapy and stem-cell rescue in children with newly diagnosed medulloblastoma (St Jude Medulloblastoma-96): long-term results from a prospective, multicentre trial. Lancet Oncol, 2006. 7(10): p. 813-20.
4. Rutkowski, S., et al., Survival and prognostic factors of early childhood medulloblastoma: an international meta-analysis. J Clin Oncol, 2010. 28(33): p. 4961-8.
5. Ellison, D.W., et al., beta-Catenin status predicts a favorable outcome in childhood medulloblastoma: the United Kingdom Children's Cancer Study Group Brain Tumour Committee. J Clin Oncol, 2005. 23(31): p. 7951-7.
6. Packer, R.J., et al., Treatment of children with medulloblastomas with reduced-dose craniospinal radiation therapy and adjuvant chemotherapy: A Children's Cancer Group Study. J Clin Oncol, 1999. 17(7): p. 2127-36.
7. Silber, J.H., et al., Whole-brain irradiation and decline in intelligence: the influence of dose and age on IQ score. J Clin Oncol, 1992. 10(9): p. 1390-6.
8. Mulhern, R.K., et al., Late neurocognitive sequelae in survivors of brain tumours in childhood. Lancet Oncol, 2004. 5(7): p. 399-408.
9. Hoppe-Hirsch, E., et al., Medulloblastoma in childhood: progressive intellectual deterioration. Childs Nerv Syst, 1990. 6(2): p. 60-5.

Poster No 343

Maternal perinatal depression and its impact on emotion regulation in young adulthood

Klára Marečková[1], Filip Trbusek[1], Radek Marecek[1], Lenka Andryskova[2], Jan Chladek[1]

[1]CEITEC, Masaryk University, Brno, Czech Republic, [2]RECETOX, Faculty of Science, Masaryk University, Brno, Czech Republic

Introduction: Maternal mental health during pregnancy and the first years after birth is essential for optimal brain development and mental health of the offspring. However, it is not clear whether higher levels of maternal depressive symptomatology at a specific time during the perinatal period might particularly alter the brain function and physiology during emotion regulation and lead to worse emotion regulation skills and more anxiety in young adulthood. It is also not clear whether sex of the offspring might moderate these long-term effects.

Methods: Participants included young adults from the European Longitudinal Study of Pregnancy and Childhood (ELSPAC), a prenatal birth cohort born in the Czech Republic between 1991-1992 (Piler et al., 2017), who took part in its neuroimaging follow-up at the age of 28-30 years. Maternal depressive symptoms were measured in the early 90s using the Edinburgh Postnatal Depression Scale (EPDS; Cox et al., 1987) at 4 times: mid-pregnancy, 2 weeks after birth, 6 months after birth, and 18 months after birth. Structural and functional magnetic resonance imaging (MRI) was conducted using a 3T Siemens Prisma MRI scanner. Regulation of negative affect was studied using the International Affective Picture System (IAPS) fMRI task. Participants either observed the negative and neutral images or regulated their affective response. Skin conductance response (SCR) was collected during the fMRI task and participants' anxiety trait and emotion regulation skills were assessed using Spielberger's State-Trait Anxiety Inventory (Spielberger et al., 1983) and the Emotion regulation questionnaire (Gross & John, 2003), respectively. A total of 163 participants (49% female) had perinatal maternal depression data from all 4 timepoints as well as the fMRI and behavioral data. fMRI data were processed in SPM 12 and brain response during the (1) negative observe > neutral observe and (2) regulate > negative observe contrasts was extracted. Finally, a voxelwise multiple regression tested the effect of maternal depression (4 measurements) on brain response during the two contrasts. Interactions with sex were added as a covariate. SCR data were pre-processed in LedaLab and through-to-peak (TTP) analysis was used to extract for each contrast the number of significant SCR within the response window (nSCR), response latency, and the sum of the SCR amplitudes.

Results: In women (but not men), maternal depression in mid-pregnancy predicted lower brain response during the regulate vs. negative observe contrast in left middle occipital cluster (Fig. 1A). In addition, women (but not men) exposed to maternal depression after birth had greater brain response during the regulate vs. negative observe contrast in right superior frontal cluster (Fig. 1B). Greater maternal depression after birth was also associated with higher SCR latency (AdjR2=0.10, p=0.02) and a higher sum of SCR amplitudes (AdjR2=0.05, p=0.04) during the regulate vs negative contrast in women (p>0.49). Moreover, greater SCR latency and sum of amplitudes in women during emotion regulation predicted greater brain response in the right frontal cluster. Further, greater brain response in the right frontal cluster predicted greater anxiety trait (R2=0.05, p=0.05) and greater emotion suppression R2=0.09, p=0.006) but not emotion reappraisal (p=0.220) in the young adult women. Moreover, we demonstrated that brain response in the right frontal cluster mediated the relationship between greater maternal depression after birth and greater suppression of emotions in young adulthood (ab=0.11, SE=0.05, 95% CI [0.016; 0.226]; Fig. 2).

Conclusions: These findings suggest that maternal depression after birth predisposes the female offspring to more anxiety, worse emotion regulation skills, and particularly to emotion supression in young adulthood, and that the latter relationship is mediated by greater brain response in the right frontal cluster during the emotion regulation.

1A

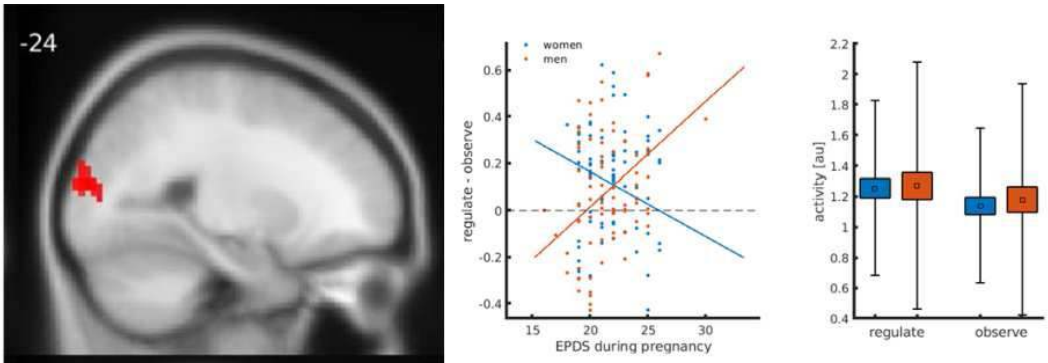

1B

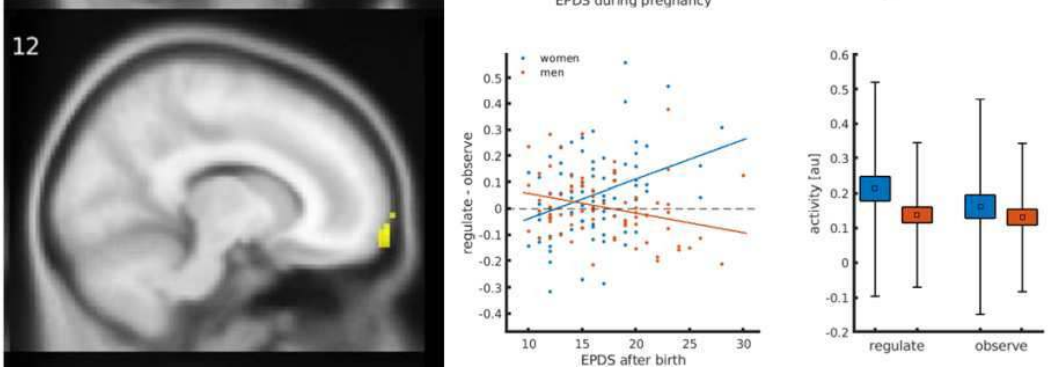

2

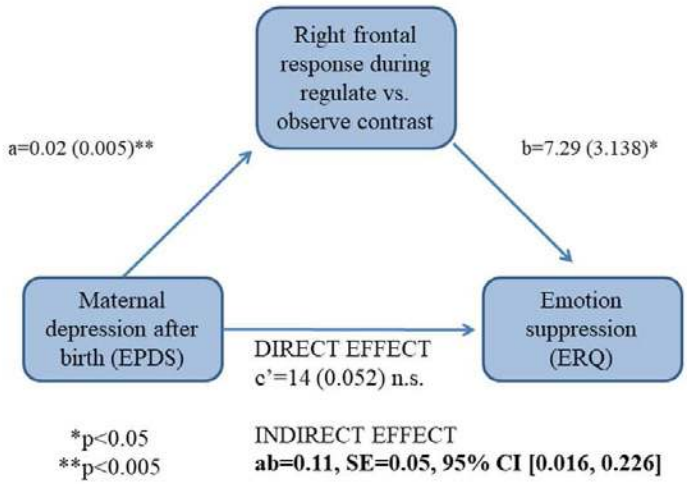

References

1. Cox, J.L. et al. (1987), 'Detection of postnatal depression. Development of the 10-item Edinburgh Postnatal Depression Scale' Br J Psychiatry, vol 150, pp. 782-786.
2. Gross, J.J. & John, O.P. (2003), 'Individual differences in two emotion regulation processes: Implications for affect, relationships, and well-being.' Journal of Personality and Social Psychology, vol 85, pp. 348-362.
3. Piler, P. et al (2017), 'Cohort Profile: The European Longitudinal Study of Pregnancy and Childhood (ELSPAC) in the Czech Republic.' Int J Epidemiol, vol 46, no. 5, pp. 1379-1379.
4. Spielberger, C.D. (1983), 'Manual for the State-Trait Anxiety Inventory (STAI Form Y), Consulting Psychologists Palo Alto. Consulting Psychologists Press, Inc.

Poster No 344

Structural brain outcomes in perinatally infected HIV toddlers with early versus late treatments

Arp-Arpa Kasemsantitham[1], Watsamon Jantarabenjakul[2,3], Montida Veeravigom[2], Weerasak Chonchaiya[2], Netsiri Dumrongpisutikul[4], Pipat Saeyap[5], Pannika Vorapaluk[5], Thanyawee Puthanakit[2,3], Jintanat Anantaworanich[6], Kathleen Malee[7], Neda Jahanshad[8], Paul Thompson[8], Chitsanu Pancharoen[2], Chaipat Chunharas[9,10]

[1]Faculty of Medicine, Chulalongkorn University, Bangkok, Thailand, [2]Department of Pediatrics, Faculty of Medicine, Chulalongkorn University, Bangkok, Thailand, [3]Center of Excellence in Pediatric Infectious Diseases and Vaccines, Faculty of Medicine, Chulalongkorn University, Bangkok, Thailand, [4]Department of Radiology, Faculty of Medicine, Chulalongkorn University, Bangkok,Thailand, [5]Department of Anesthesiology, Faculty of Medicine, Chulalongkorn University, Bangkok, Thailand, [6]SEARCH, The Thai Red Cross AIDS Research Center (TRCARC), Bangkok, Thailand, [7]Ann & Robert H. Lurie Children's Hospital of Chicago, Northwestern University, Illinois, United States, [8]Imaging Genetics Center, Keck School of Medicine of University of Southern California, California, United States, [9]Cognitive Clinical and Computational Neuroscience Lab, Chulalongkorn University, Bangkok, Thailand, [10]Chula Neuroscience Center, King Chulalongkorn Memorial Hospital, Thai Red Cross Society, Bangkok, Thailand

Introduction: Despite antiretroviral treatments (ARTs), perinatally HIV-infected children still suffer from delayed development and neurocognitive regression. Timing of treatment administration has been shown to impact neurobehavioral outcomes (Jantarabenjakul et., al., 2020); yet, rarely are they investigated on the macro and micro-structural anatomical levels (Laughton et al., 2013). In adults, HIV is known for its white matter abnormalities with sensible damage to the corpus callosum, but results are varied in the pediatric population and remain unclear in toddlers younger than age 5 (Hoare et al., 2014; Sarma et al., 2014; Andronikou et al., 2015; Hoare et al., 2018). This study aimed to investigate whether there are volumetric alterations in neuroimaging outcomes in children receiving early treatments compared to deferred ones. We hypothesize that there will be significant differences in corpus callosal volumes between the two groups. Moreover, we also hypothesize that these differences correlate with changes in neurobehavioral performances, signifying that brain connectivity and functions are overtly affected by the timing of ARTs.

Methods: Twenty children ages 2 to 5, gender- and age-matched, were initially allocated to either early ART treatments (ART initiated within 3 months of age) (ART-E; n=10) or late ART treatments (ART initiated within 3-12 months of age) (ART-L; n=10). All participants underwent MRI brain imaging on a 3T scanner and neurodevelopmental assessments at two-time points within one year apart. Overall and segmented volumes of the corpus callosum were preprocessed through Freesurfer, examined for quality, and subsequently analyzed. Domains of cognition and neurodevelopment, including motor and language, were evaluated using the Mullen Scales of Early Learning (MSEL) with global development impairment defined as Early Learning Composite (ELC).

Results: Initial analysis of the corpus callosum through 3-way ANOVA revealed a significant increase in structural volume across sessions ($F(1,18)= 13.955$, $p<0.001$); moreover, the ART-L group had marginally smaller corpus callosal volumes compared to those of the ART-E group ($F(1,18)= 4.210$, $p=0.055$; Fig. 1). When segmented into five corpus callosal regions, intergroup differences are significantly seen in the mid-anterior region known as the posterior genu ($F(1,18) = 2.457$, $p=0.024$; Fig. 2). In regards to neurodevelopment, 2-way ANOVA revealed that the ART-L group had significantly lower ELC scores compared to ART-E ($p=0.016$), with differences most pronounced in areas of fine motor ($p= 0.02$) and expressive language ($p = 0.002$). Mild correlations were found between the corpus callosum volume and neurodevelopmental scores, especially in the fine motor domain ($p=0.02$).

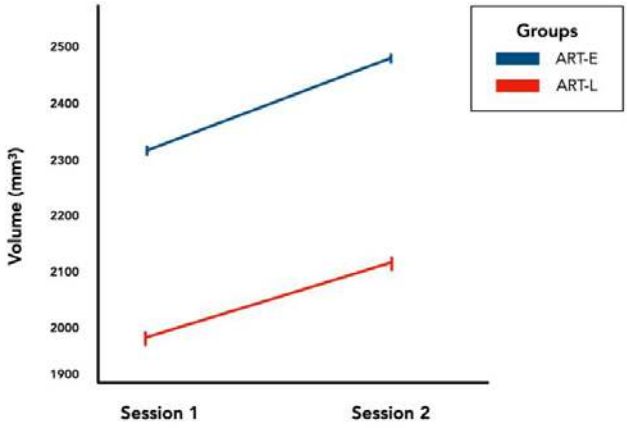

Figure 1. Changes in corpus callosal volumes between groups and across sessions. X-axis represents the number of sessions, while the y-axis represents the volume of the corpus callosum. Blue line is the ART-E group (n=10), while the red line is the ART-L group (n=10). Both groups have significantly increased corpus callosal volumes across sessions (p<0.001), while the ART-L group has marginally lower volume than the ART-E group (p=0.055). No interaction was seen.

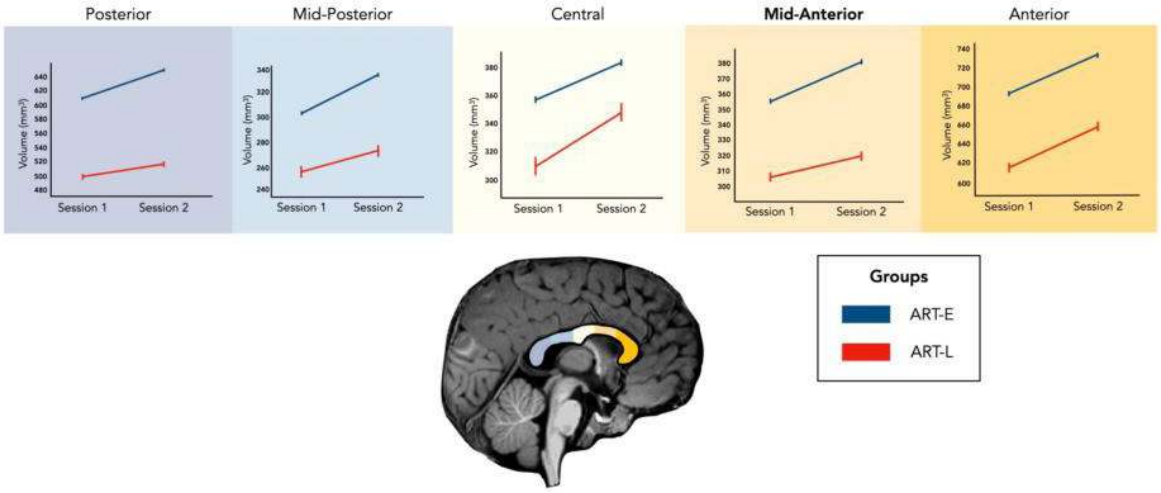

Figure 2. Changes in volumes of each segmented area of the corpus callosum, represented in different colors, between groups and across sessions. ART-L group has marginally lower volumes in all segmented areas of the corpus callosum, with a significantly lower mid-anterior corpus callosal volume (p=0.024), compared to the ART-E group. There were significant increases in volumes across sessions for all areas for both groups (p<0.001).

Conclusions: The corpus callosum volume in the ART-L group was slightly smaller than the ART-E group, particularly in the posterior genu which correlated with neurodevelopmental score. Differences in structural brain changes and neurodevelopmental outcomes can be seen with possible neuroprotective effects from early treatments for perinatally infected HIV children, revealing the likelihood for compensatory neuroplasticity in the future. We aim to explore these alterations into adulthood, as well as observe changes in other regions of the brain between the two groups.

References

1. Andronikou, S., Ackermann, C., Laughton, B., Cotton, M., Tomazos, N., Spottiswoode, B., Mauff, K., & Pettifor, J.M. (2015), 'Corpus callosum thickness on mid-sagittal MRI as a marker of brain volume: a pilot study in children with HIV-related brain disease and controls.' Pediatric Radiology, vol. 45, no. 7, pp. 1016-25.
2. Hoare, J., Ransford, G.L., Phillips, N., Amos, T., Donald, K., & Stein DJ. (2014), 'Systematic review of neuroimaging studies in vertically transmitted HIV positive children and adolescents.' Metabolic Brain Disease, vol. 29, pp. 221–229.
3. Hoare, J., Fouche, J.P., Phillips, N., Joska, J.A., Myer, L., Zar, H.J., & Stein, D.J. (2018), 'Structural brain changes in perinatally HIV infected young adolescents in South Africa.' AIDS, vol. 32, no. 18, pp. 2707-2718.
4. Jantarabenjakul, W., Chonchaiya, W., Puthanakit, T., Anugulruengkitt, S., Theerawit, T., Payapanon, J., Sophonphan, J., Veeravigrom, M., Jahanshad, N., Thompson, P.M., Ananworanich, J., Malee, K., & Pancharoen, C. (2020), 'DOET study. Behavioral problems in perinatally HIV-infected young children with early antiretroviral therapy and HIV-exposed uninfected young children: prevalence and associated factors.' AIDS Care, vol. 32, no. 4, pp. 429-437.
5. Laughton, B., Cornell, M., Boivin, M., & Van Rie, A. (2013), 'Neurodevelopment in perinatally HIV-infected children: a concern for adolescence.' Journal of International AIDS Society, vol. 16, no.1, pp. 1-11.
6. Sarma, M.K., Naharajan, R., Keller, M.A., Kumar, R., Nielsen-Saines, L., Michalik, D.E., Deville, J., Church, J.A., & Thomas, A.T. (2014), 'Regional brain gray and white matter changes in perinatally HIV-infected adolescents.' Neuroimage: Clinical, vol. 4, pp. 29-34.

Poster No 345

The individual-level, multimodal neural signature of face processing in the fusiform gyrus in autism

Dorothea Floris[1,2], Alberto Llera[2], Tzvetan Popov[1], Mariam Zabihi[3], Carolin Moessnang[4], Emily Jones[5], Luke Mason[5], Rianne Haartsen[5], Nathalie Holz[6], Ting Mei[2], Camille Elleaume[7], Bruno Hebling Vieira[1], Charlotte Pretzsch[8], Natalie Forde[9], Sarah Baumeister[6], Flavio Dell'Acqua[8], Sarah Durston[10], Tobias Banaschewski[6], Christine Ecker[11], Rosie Holt[12], Simon Baron-Cohen[13], Thomas Bourgeron[14], Tony Charman[15], Eva Loth[8], Declan Murphy[8], Jan Buitelaar[2], Christian Beckmann[2], Nicolas Langer[1], EU AIMS LEAP Group[16]

[1]Department of Psychology, University of Zurich, Zurich, Switzerland, [2]Donders Institute for Brain, Cognition, and Behavior, Radboud University Nijmegen, Nijmegen, NL, Nijmegen, Netherlands, [3]MRC Unit Lifelong Health and Aging, University College London, London, UK, London, United Kingdom, [4]Department of Psychiatry and Psychotherapy, Central Institute of Mental Health, Mannheim, Germany, Mannheim, Germany, [5]Centre for Brain and Cognitive Development, Birkbeck, University of London, London, UK, London, United Kingdom, [6]Department of Child and Adolescent Psychiatry, Central Institute of Mental Health, Mannheim, Mannheim, Germany, [7]Department of Psychology, University of Zurich, Zurich, Zurich, [8]Department of Forensic and Neurodevelopmental Sciences, IoPPN, London, United Kingdom, [9]Donders Institute for Brain, Cognition, and Behavior, Radboud University Nijmegen, Nijmegen, NL, Nijmegeb, Netherlands, [10]Department of Psychiatry, Brain Center Rudolf Magnus, University Medical Center Utrecht, Utrecht, Utrecht, Netherlands, [11]Department of Child and Adolescent Psychiatry, University Hospital, Goethe University, Frankfurt, Frankfurt, Germany, [12]Autism Research Centre, Department of Psychiatry, University of Cambridge, Cambridge, UK, Cambridge, United Kingdom, [13]University of Cambridge, Cambridge, United Kingdom, [14]Institut Pasteur, Human Genetics and Cognitive Functions Unity, Paris, France, Paris, France, [15]Clinical Child Psychology, Department of Psychology, IoPPN, London, United Kingdom, [16]Department of Forensic and Neurodevelopmental Sciences, IoPP, London, United Kingdom

Introduction: Face processing is among the most commonly reported social difficulties of autistic individuals[1,2]. While its neural underpinnings have been explored extensively across single neuroimaging modalities within key regions of the face processing network, such as the fusiform gyrus (FFG)[3,4], there is still little knowledge about how different structural and functional neurobiological markers are simultaneously implicated in face processing in autism and associated with social functioning. Extracting the joint, shared information across different modalities is essential to better elucidate complex relationships between brain structure and function leading to a more comprehensive understanding of underlying mechanisms of autism.

Methods: Here, we leveraged the large multimodal EU-AIMS Longitudinal European Autism Project dataset[5] to study the cross-modal signature of face processing within the FFG across structural magnetic resonance imaging (MRI), resting-state fMRI (rs-fMRI), task-fMRI (based on the Hariri emotional faces task) and electroencephalography (EEG) (recorded when observing facial stimuli) in a sample of 99 autistic and 105 non-autistic individuals between 6-30 years of age. After employing normative modelling[6] using the PCNtoolkit on each imaging modality to derive individual-level deviations from a normative developmental trajectory, unimodal deviation scores were merged using linked independent component (IC) analysis[7]. We next tested whether ICs significantly differed between autistic and non-autistic individuals (NAI) using a general linear model and whether multimodal ICs would outperform unimodal ICs in discriminating autistic individuals from NAI using a support vector machine under 10-fold cross-validation. To test the association between multimodal ICs and cognitive, clinical features related to either social or non-social functioning in autism, canonical correlation analysis (CCA) was employed.

Results: In total, 50 independent components were derived, among which one IC showed a significant difference between autistic and non-autistic individuals ($t=3.5$, $pFDR=0.03$) (Figure 1). This IC was mostly driven by bilateral rs-fMRI, bilateral structure, right task-fMRI, and left EEG and implicated both face-selective and retinotopic regions of the FFG (Figure 2). Furthermore, comparing areas under the curve with a permutation test, multimodal ICs performed significantly better at differentiating between autistic individuals and NAI ($p<0.001$). Finally, there was a significant multivariate canonical correlation between multimodal ICs and a set of cognitive, clinical features associated with social function ($r=0.65$, $pFDR=0.008$). This was not the case for the association with a set of non-social features.

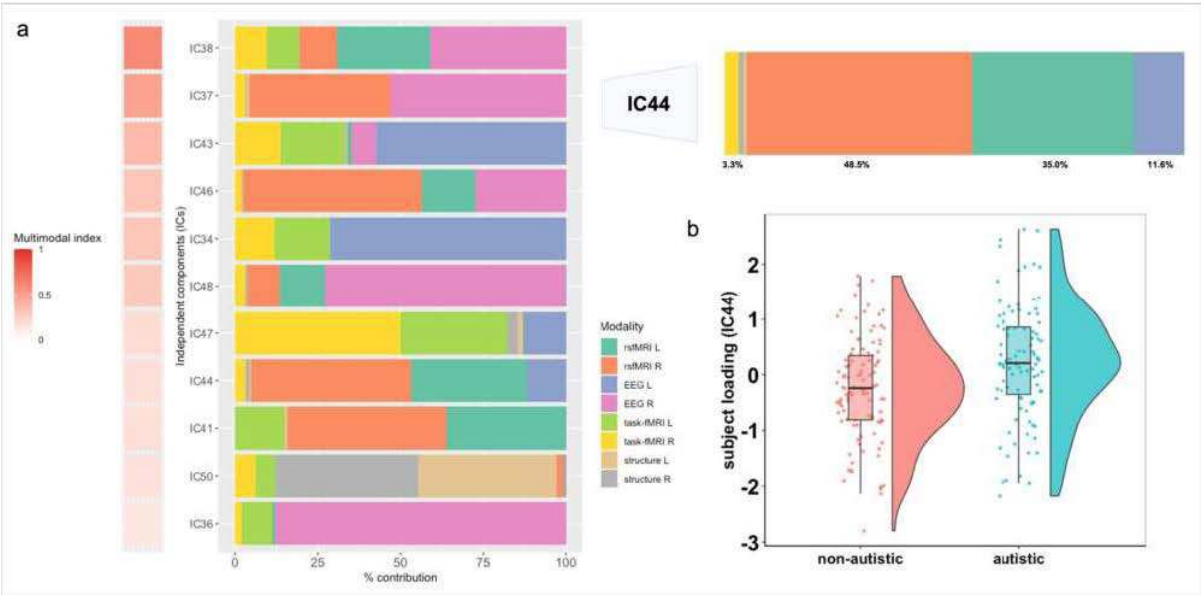

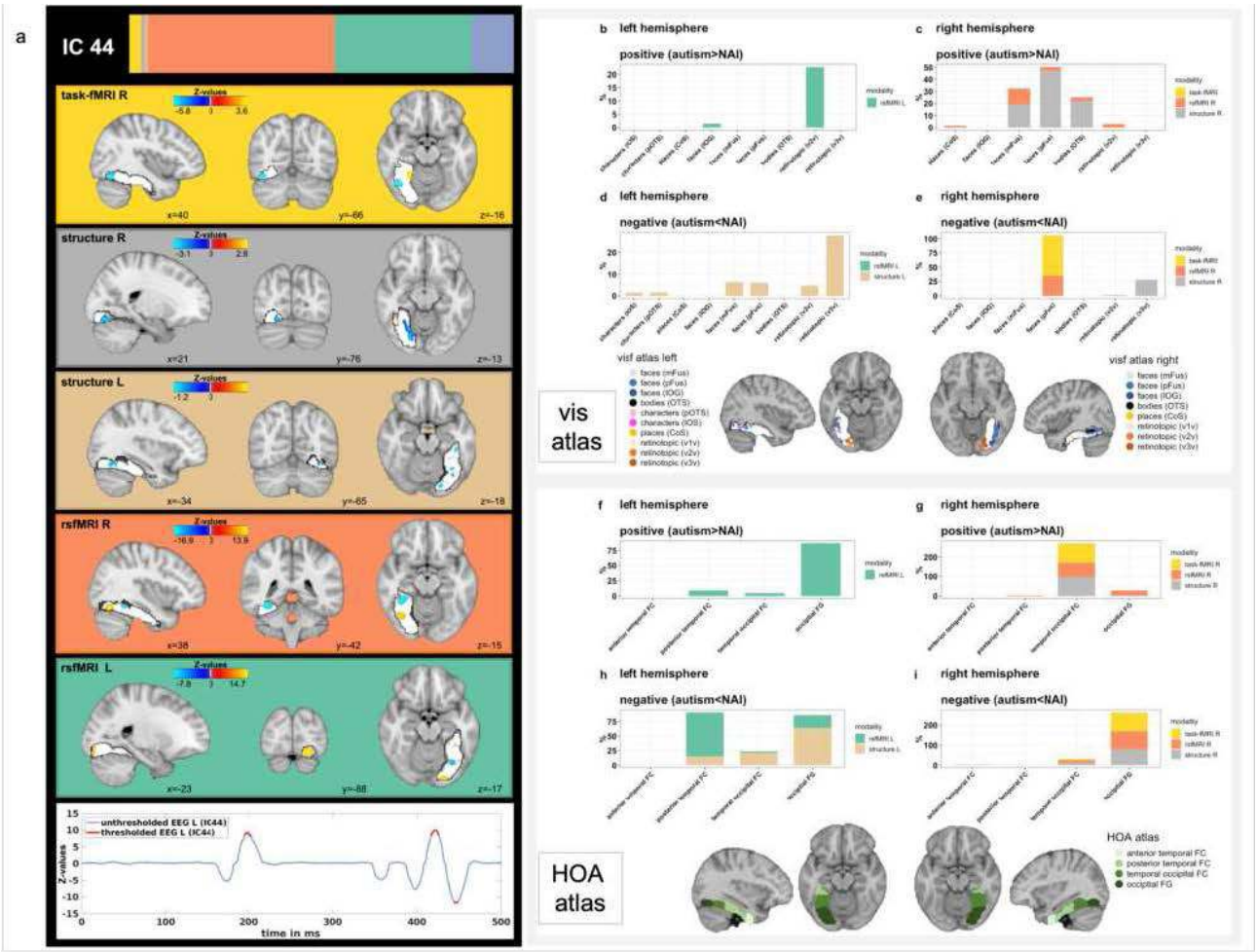

Conclusions: Results suggest that the FFG is a central region differentially implicated in autistic and non-autistic individuals across a range of imaging modalities and these can simultaneously inform mechanisms associated with core social functioning in autism. These findings further suggest that the discerning signals in this specific brain region are reliably captured through components shared across modalities, emphasizing the multidimensional nature of effects associated with autism. Elucidating a more holistic picture of neural associations of core cognitive and clinical features in autism, will pave the way for the development of more personalised support.

References
1. Meyer-Lindenberg, H. et al. Facial expression recognition is linked to clinical and neurofunctional differences in autism. Mol. Autism 13, 43 (2022).
2. Sasson, N. J. The development of face processing in autism. J. Autism Dev. Disord. 36, 381–394 (2006).
3. Engell, A. D. & McCarthy, G. Face, eye, and body selective responses in fusiform gyrus and adjacent cortex: an intracranial EEG study. Front. Hum. Neurosci. 8, (2014).
4. McCarthy, G., Puce, A., Gore, J. C. & Allison, T. Face-Specific Processing in the Human Fusiform Gyrus. J. Cogn. Neurosci. 9, 605–610 (1997).
5. Loth, E. et al. The EU-AIMS Longitudinal European Autism Project (LEAP): Design and methodologies to identify and validate stratification biomarkers for autism spectrum disorders. Mol. Autism 8, (2017).
6. Marquand, A. F., Rezek, I., Buitelaar, J. & Beckmann, C. F. Understanding Heterogeneity in Clinical Cohorts Using Normative Models: Beyond Case-Control Studies. Biol. Psychiatry 80, 552–561 (2016).
7. Groves, A. R., Beckmann, C. F., Smith, S. M. & Woolrich, M. W. Linked independent component analysis for multimodal data fusion. NeuroImage 54, 2198–2217 (2011).

Poster No 346

Atypical connectivity between the sensorimotor and salience networks for observed touch in autism

Haemy Lee Masson[1]

[1]Psychology Department, Durham University, Durham, United Kingdom

Introduction: Autistic adults experience difficulties in recognizing social and emotional cues during social interactions. In the context of social touch, brain imaging studies have shown that these challenges may be linked to atypical somatosensory responses to affective cues displayed in touch gestures (Lee Masson et al., 2019). Neurotypical adults (NT) easily interpret the meaning of touch during mere observation (Lee Masson and Op de Beeck, 2018). The neural mechanism supporting this ability involves increased communication between brain networks involved in visual, somatosensory, and social processing (Lee Masson et al., 2020). In autism, it is unclear how functional communication between these networks is modulated in response to social vs. nonsocial touch. The current study aims to determine how brain networks involved in various cognitive functions work together to process complex social touch information in autism spectrum condition (ASC).

Methods: Forty-two adults watched 39 social (e.g., hugging a person) and 36 nonsocial video clips (e.g., carrying a box) during MRI scans in our previous study (Lee Masson et al., 2019). Independent component analysis (ICA) applied to this dataset yielded 28 brain networks. Nine networks were associated with noise (e.g., networks located in the ventricles). The temporal sorting method identified ten brain networks that showed temporally coherent BOLD signal fluctuations during touch observation. These task-relevant networks include visual, social perceptual, sensorimotor, executive control, four default mode, and two salience networks (Figure 1). A generalized psychophysiological interaction (gPPI) analysis was applied to these networks to examine changes in functional connectivity during social vs. nonsocial touch observation. Finally, subject-level gPPI results were analyzed using a mixed-model repeated-measures analysis of variance (ANOVA) with one between-subjects (group: NT vs. ASC) and one within-subjects factor (touch type: social vs. nonsocial).

Results: A mixed model ANOVA on gPPI results, with multiple comparisons correction, revealed a significant group x condition interaction in the strength of functional connectivity between the sensorimotor and salience networks ($F(1, 40) = 15.1$, $P_{FDR} = 0.02$). The sensorimotor network encompasses the bilateral precentral and postcentral gyrus along with the parietal operculum. The salience network consists of bilateral insula, middle and superior temporal gyrus (MTG and STG). In NT adults, these networks demonstrated enhanced functional synchronization during the observation of social touch ($T(20) = 2.73$, $P = 0.01$), whereas enhanced functional synchronization was observed in autistic adults during nonsocial condition ($T(20) = -2.76$, $P = 0.01$). No other network pairs showed significant differences in the strength of connectivity between the two groups.

Conclusions: The postcentral gyrus and insula, which are part of the sensorimotor and salience networks respectively, have previously been implicated in vicarious affective touch (Morrison et al., 2011; Bolognini et al., 2013). Salience network 1 includes mid to anterior MTG and STG implicated in social processing. The current findings suggest that, even though autistic adults exhibit a comparable functional network architecture during touch observation, the atypical communication patterns between the sensorimotor and salience networks may be associated with the inefficient use of affective touch as a communicative tool during social interactions. Hyper-connectivity in the salience network has been linked to sensory over-responsivity in autism (Green et al., 2016). The challenges in recognizing social touch expressions in autism may be attributed to an atypical allocation of attention to nonsocial information rather than relevant social cues.

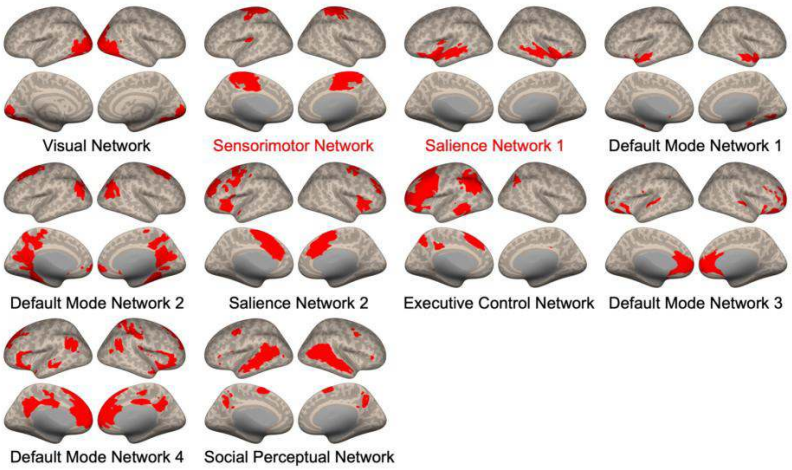

Figure 1. Ten task-relevant networks, identified by ICA, are marked in red in each brain image. Labels of each network was based on a spatial comparison, the maximum correlation between the brain template (Smith et al., 2009) and the network. The two red-labeled networks show the atypical functional communication in autism.

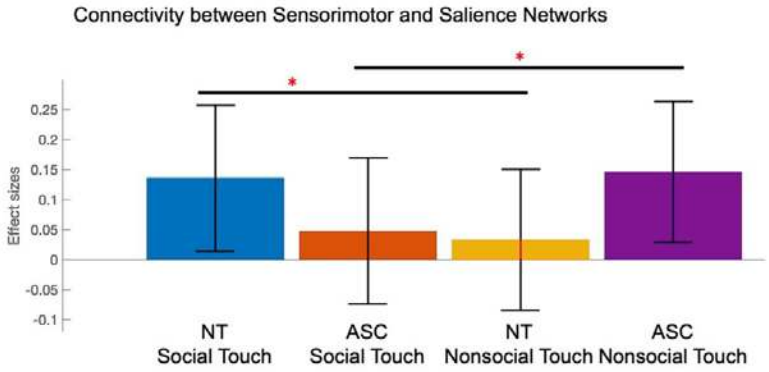

Figure 2. The results of the network pair showing a significant group x condition interaction effect on the strength of functional connectivity.

References

1. Bolognini N, Rossetti A, Convento S, Vallar G (2013) Understanding other's fellings: the role of the right primary somatosensory cortwx in encoding the affective valence of other's touch. The journal of neuroscience 33:4201–4205.
2. Green SA, Hernandez L, Bookheimer SY, Dapretto M (2016) Salience network connectivity in autism is related to brain and behavioral markers of sensory overresponsivity. Journal of the American Academy of Child & Adolescent Psychiatry 55:618–626.
3. Lee Masson H, Op de Beeck H (2018) Socio-affective touch expression database. PLOS ONE 13:e0190921.
4. Lee Masson H, Pillet I, Amelynck S, Van De Plas S, Hendriks M, Op De Beeck H, Boets B (2019) Intact neural representations of affective meaning of touch but lack of embodied resonance in autism: a multi-voxel pattern analysis study. Molecular Autism 10:39.
5. Lee Masson H, Pillet I, Boets B, Op de Beeck H (2020) Task-dependent changes in functional connectivity during the observation of social and non-social touch interaction. Cortex 125.
6. Morrison I, Bjornsdotter M, Olausson H (2011) Vicarious Responses to Social Touch in Posterior Insular Cortex Are Tuned to Pleasant Caressing Speeds. Journal of Neuroscience 31:9554–9562.
7. Smith SM, Fox PT, Miller KL, Glahn DC, Fox PM, Mackay CE, Filippini N, Watkins KE, Toro R, Laird AR, Beckmann CF (2009) Correspondence of the brain's functional architecture during activation and rest. Proceedings of the National Academy of Sciences 106:13040–13045.

Poster No 347

Thalamic Functional Connectivity Gradients in Children with Temporal Lobe Epilepsy

Xiyu Feng[1], Hua Xie[2], Rory Piper[1,3], Freya Prentice[1], Priyanka Illapani[2], Lauren Reppert[2], Seok-Jun Hong[4], Mohamad Koubeissi[5], Torsten Baldeweg[1], Leigh Sepeta[2]

[1]UCL Great Ormond Street Institute of Child Health, London, United Kingdom, [2]Children's National Hospital, Washington, D.C., USA, [3]Great Ormond Street Hospital, London, United Kingdom, [4]Sungkyunkwan University, Seoul, South Korea, [5]The George Washington University Medical Faculty Associates, Washington, D.C., USA

Introduction: The thalamus can participate in spread of epileptic activity (Wu et al., 2023) and is a target for therapeutic neuromodulation (Piper et al., 2022). Thalamic functional connectivity alterations exist in adult patients with temporal lobe epilepsy (TLE) and may affect seizure freedom after surgery (He et al., 2017). Here we used data-driven 'connectopic mapping' (Haak et al., 2018) to investigate the spatial organization (gradients) of thalamic cortical and subcortical connections in pediatric TLE. We aimed to uncover the functional gradients within the thalamus and investigate differences in thalamus to whole brain connectivity between children with TLE and healthy controls.

Methods: 64 children with TLE (5-18 years, left TLE n=51, right n=13) and 61 healthy controls (6-20 years) underwent language fMRI using a covert verb generation task at Great Ormond Street Hospital, London, UK. For children with right TLE, images were flipped so the seizure focus is the left hemisphere for all patients. fMRI data were preprocessed using fMRIprep software. 1) Connectopic mapping: We generated within-thalamus FC similarity matrices for each hemisphere and applied non-linear manifold learning to this matrix, yielding gradients for each side of the thalamus. We also created projection maps depicting changes in thalamic-to-whole brain connectivity along this gradient. 2) A SurfStat linear model (Worsley et al., 2009) assessed variations in projection maps related to disease status and duration, age and gender.

Results: The primary thalamic gradient followed an anterior-to-posterior axis (Fig. 1) for both children with TLE and controls. In the cortex, there were no differences in the projection maps between patients and controls (FDR-corrected $p>0.05$). The anterior thalamus displayed greater connectivity with prefrontal and orbitofrontal cortices, as well as the basal ganglia. The mid-thalamic gradient zone was preferentially connected to the somatosensory cortex and anterior hippocampus. The posterior thalamus was more connected with the visual cortex and posterior hippocampus. However, in the subcortex, projection maps exhibited differences between patients and controls (FDR-corrected $p<0.05$). Compared to controls, patients showed stronger connectivity of the anterior thalamus to subcortical areas (Fig. 2), including the ventral striatum, subthalamic nuclei, substantia nigra as well as amygdala and hippocampus in both ipsi- and contralesional hemispheres. Duration of epilepsy was not correlated with projection map variations in patients (FDR-corrected $p>0.05$). Age and gender did not affect the cortical or subcortical projection maps for patients or controls (FDR-corrected $p>0.05$).

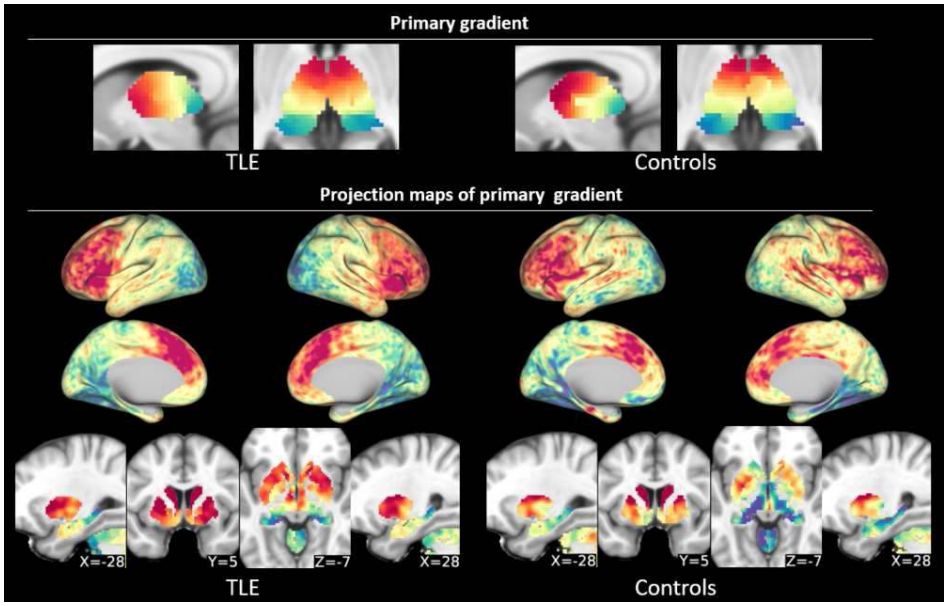

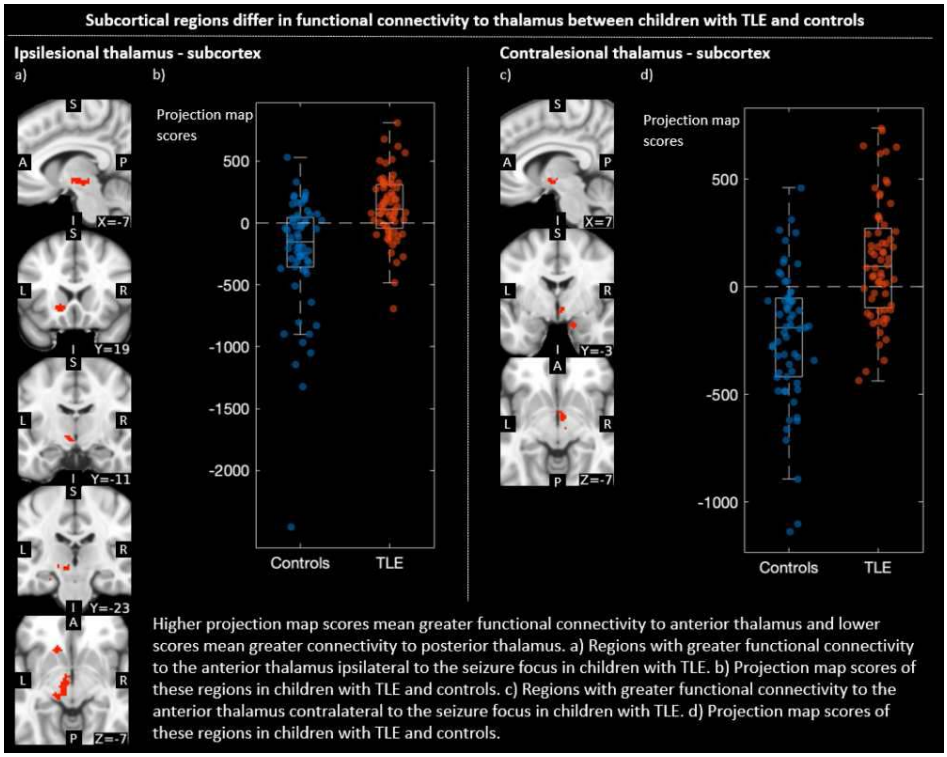

Conclusions: A primary anterior-to-posterior functional gradient was observed within the thalami in both children with TLE and their healthy peers, revealing a gradual shift of thalamic connectivity across the entire brain. While there were no group differences in connectivity between thalamus and cortical regions, there was heightened connectivity in children with TLE between the anterior thalamus and the basal ganglia, with a predominance for the ipsilesional side. It has been suggested that within the loop involving the limbic system and thalamus, the basal ganglia play a significant seizure modulating role (Bröer, 2020; He et al., 2019). Further investigations are needed to explore the clinical potential of connectopic mapping.

References

1. Bröer, S. (2020). Not Part of the Temporal Lobe, but Still of Importance? Substantia Nigra and Subthalamic Nucleus in Epilepsy. Frontiers in Systems Neuroscience, 14.
2. Haak, K. V. (2018). Connectopic mapping with resting-state fMRI. NeuroImage, 170, 83–94.
3. He, X. (2019). Disrupted basal ganglia–thalamocortical loops in focal to bilateral tonic-clonic seizures. Brain, 143(1), 175–190.
4. He, X. (2017). Presurgical thalamic “hubness” predicts surgical outcome in temporal lobe epilepsy. Neurology, 88(24), 2285–2293.
5. Piper, R. J. (2022). Towards network-guided neuromodulation for epilepsy. Brain: A Journal of Neurology, awac234.
6. Worsley, K. (2009). SurfStat: A Matlab toolbox for the statistical analysis of univariate and multivariate surface and volumetric data using linear mixed effects models and random field theory. NeuroImage, 47, S102.
7. Wu, T. Q. (2023). Multisite thalamic recordings to characterize seizure propagation in the human brain. Brain, 146(7), 2792–2802.

Poster No 348

Dynamic Mode Analysis of Autism Spectrum Disorder

Mir Jeong[1], Youngjo Song[1], Jaeseung Jeong[1]

[1]KAIST, Daejeon, Korea, Republic of

Introduction: Autism Spectrum Disorder (ASD) is a complex neurodevelopmental condition characterized by challenges in social interaction and repetitive behaviors. Despite extensive research efforts, our understanding of the functional alterations in ASD brain at a network level remains incomplete. This study introduces a novel approach to analyzing the functional aspects of ASD brain by employing Dynamic Mode (DM) decomposition of fMRI time series, where the brain activity is decomposed into synchronously evolving networks (Casorso, et al., 2019). That is, we investigated the functional variances in ASD brain networks using the DM framework to gain a deeper understanding of the unique neurofunctional dynamics in individuals with ASD.

Methods: The study utilized resting-state fMRI data preprocessed with the C-PAC pipeline and, parcellated with Craddock 200 atlas from the Autism Brain Imaging Data Exchange I (ABIDE I), which includes data from 391 individuals diagnosed with

ASD and 458 typically developing (TD) controls. The BOLD activity dynamics (measured by fMRI) are approximated as a linear dynamic system ($x(t+1)=Ax(t)+\varepsilon(t)$), where the linear operator (A), which is also referred to as connectivity matrix, describes the causal relation between successive time points (i.e., how the previous BOLD signal x(t) determines subsequent signal x(t+1)). (ε(t): noise at time t). For each individual, the linear operator (or connectivity matrix) was estimated from the BOLD signal, and DMs were identified via eigen-decomposition of this matrix. Given the temporally synchronized nature across all brain regions within each DM (Casorso, et al., 2019), we speculated that each DM is associated with a particular cognitive or operational aspect of brain functions. Thus, the primary functional involvement of each DM was decoded from its spatial characteristics using NiMARE software (Salo, et al., 2022). Then, we compared the temporal characteristics (decaying time, oscillation frequency) of each DM between the ASD and TD groups and examined their correlations with age and clinical measures. This approach enabled us to infer the distinct functional dynamics of ASD brains. For a comprehensive overview, see Figure 1.

Results: Our finding highlighted significant differences in brain dynamics between ASD and TD individuals. Notably, we found faster decay in a pair of DMs associated with autobiographical memory in the ASD group, implicating diminished episodic memory performance in ASD. Additionally, we found slower oscillations in a pair of DMs linked to visual inhibition, suggesting the potential cause of the impaired inhibition in ASD. We also discovered that the damping time of the multisensory-related DM correlated with the difficulty of communication, pointing to the importance of sensory function in developing communication abilities in ASD; meanwhile, the oscillation frequency of the social-related DM correlated with overall ASD severity. Interestingly, the two aforementioned DMs, which showed differences between ASD and TD, did not exhibit a correlation with ASD severity, highlighting the complexity of the relationship between brain functions and symptoms (e.g., non-linear transition between ASD and TD). Moreover, the age-dependent changes in DMs differed between the ASD and TD groups, suggesting different developmental trajectories in attention and pain-related functions.

Conclusions: Our novel application of DM decomposition offers a distinctive way to understand functional differences in ASD brains using just resting-state data. Remarkably, the insights gained from DM analysis align with prior research on ASD brain functions (Crane, et al., 2008; Johnston, et al., 2011). The dynamic perspective offered by DM analysis not only deepens our understanding of the neural basis behind ASD's atypical behaviors but also presents unique opportunities for evaluating intervention and therapeutic strategies in ASD, leveraging the convenience of acquiring resting-state data.

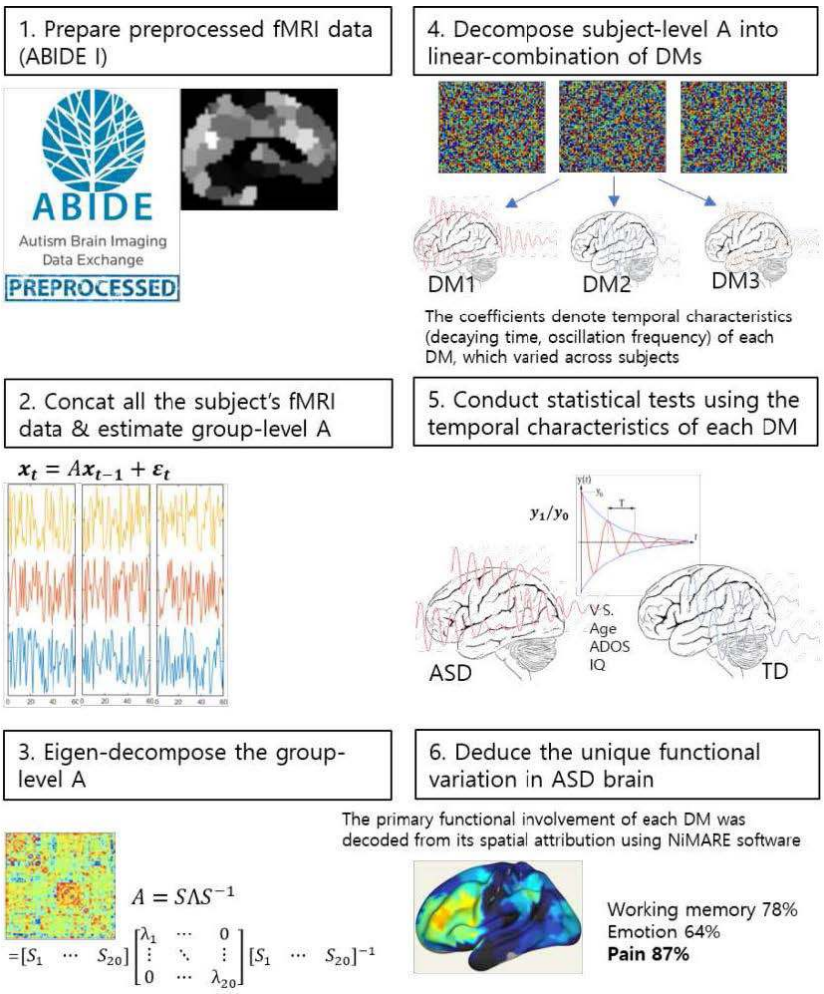

References
1. Casorso, J. (2019), 'Dynamic mode decomposition of resting-state and task fMRI', Neuroimage, vol. 194, pp. 42-54
2. Crane, L. (2008), 'Episodic and Semantic Autobiographical Memory in Adults with Autism Spectrum Disorders', Journal of Autism and Developmental Disorders, vol. 38, pp. 498-506
3. Johnston, K. (2011), 'Response Inhibition in Adults with Autism Spectrum Disorder Compared to Attention Deficit/Hyperactivity Disorder', Journal of Autism and Developmental Disorders, vol. 41, pp. 903-912
4. Salo, T. (2022), 'Developing and Validating Open Source Tools for Advanced Neuroimaging Research', FIU Electronic Theses and Dissertations. 5010.

Poster No 349

Pupillometric neuronal gain indicates the locus coeruleus to underlie predictive coding in autism

Nico Bast[1], Luke Mason[2], Emily Jones[3], Tobias Banaschewski[4], Christine Freitag[5]

[1]Goethe University Frankfurt, Frankfurt, Hessen, [2]Institute of Psychiatry, Psychology and Neuroscience, King's College, London, London, UK, London, United Kingdom, [3]Centre for Brain and Cognitive Development, Birkbeck, University of London, London, UK, London, United Kingdom, [4]Department of Child and Adolescent Psychiatry, Central Institute of Mental Health, Mannheim, Mannheim, Germany, [5]Goethe University Frankfurt, Frankfurt, Germany

Introduction: Predictive coding describes sensory processing as an updating of acquired priors to minimize costly prediction errors. Prediction errors are weighted based on an expected precision of the sensory input. Different sensory processing in autistic individuals has been suggested to include inflated prediction errors caused by increased precision weighting which (over-)emphasizes sensory input. This altered predictive coding might contribute to sensory phenomena reported by autistic individuals. The locus-coeruleus norepinephrine (LC-NE) system is a mechanism of arousal regulation that has recently been outlined to modulate neuronal gain in sensory processing.

Methods: We hypothesized that altered LC-NE functioning contributes to an increased precision weighting in autism. Matched groups of autistic (n=139) and non-autistic (n=88) individuals were assessed during an auditory oddball task (trials: k = 1400) with pupillometry and electroencephalography. The task was entirely passive and included trials of frequent standards (likelihood: 82%, tone duration: 50ms, tone pitch: 1000Hz), pitch oddballs (6%, 50ms, 1500Hz), length oddballs (5%, 100ms, 1000Hz), and pitch+length oddballs (6%, 100ms, 1500Hz). Pupillometric measure of baseline pupil size (BPS) and stimulus-evoked response (SEPR) were applied to index LC-NE tonic and phasic activity, respectively. Electroencephalography assessed amplitudes of mismatch negativity to assess an established index of prediction errors. Measures were modeled per trial to capture changes in precision weighting with task progression. A computational model assessed neuronal gain for standards. Linear mixed models were applied to investigate group differences and further confirmed by Bayesian posterior estimates.

Results: Higher LC-NE tonic activity was associated with increased mismatch-negativity-associated amplitudes (rs = -.20 - -.22). LC-NE tonic activity differed between groups. Autistic versus non-autistic individuals showed a higher initial increase (autistic: $\Delta\beta$ = 0.20 [0.17, 0.22], non-autistic: $\Delta\beta$ = 0.11 [0.08, 0.14]) and overall attenuated decrease (autistic: $\Delta\beta$ = 0.02 [-0.01, 0.06], non-autistic: $\Delta\beta$ = -0.09 [-0.13, -0.05]) with task progression (trials: 1-1400). This was supported by Bayesian posteriors (autistic: b = 0.16 [0.13, 0.18], non-autistic: b = 0.00 [0.00, 0.00]). Higher LC-NE tonic activity was further supported by a higher computational estimate of neuronal gain for standards (group difference: d = 0.41 [0.09, 0.73]). Autistic versus non-autistic individuals were further characterized by increasing LC-NE phasic activity to pitch oddballs and decreasing mismatch-negativity-associated amplitudes to standards and length oddballs with task progression.

Conclusions: We conclude that higher LC-NE tonic upregulation is a mechanism of increased precision weighting that contributes to a different updating of priors in autistic individuals. This might reflect an arousal upregulation during sensory processing. The different prior updating is characterized by increasing precision-weighted prediction errors to pitch oddballs (SEPR) and decreasing "unweighted" prediction errors to standard trials and length oddballs (MMN-amp), which reflects different sensory processing. LC-NE functioning is outlined as a neurophysiological mechanism of predictive coding that might underlie sensory phenomena in autism.

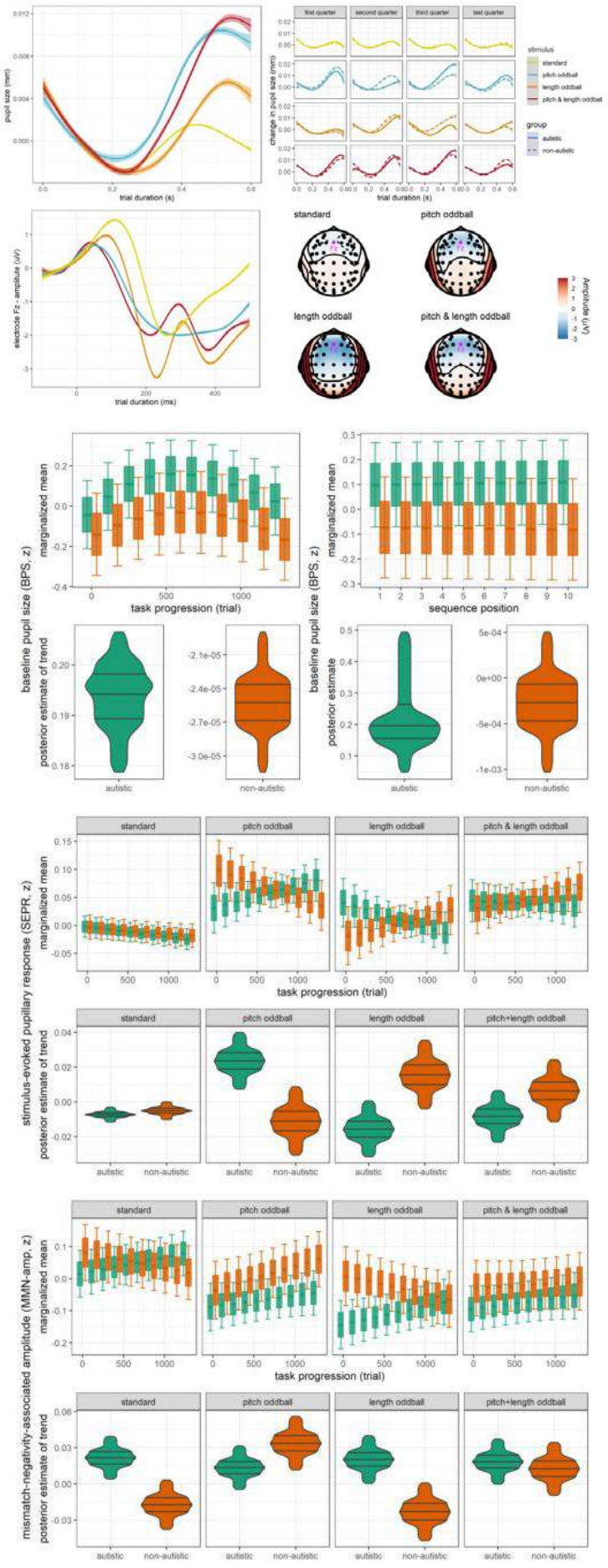
pupil size (mm)
trial duration (s)
first quarter
second quarter
third quarter
last quarter
change in pupil size (mm)
stimulus
standard
pitch oddball
length oddball
pitch & length oddball
group
autistic
non-autistic
electrode F2 - amplitude (uV)
trial duration (ms)
standard
pitch oddball
length oddball
pitch & length oddball
Amplitude (uV)
baseline pupil size (BPS, z)
marginalized mean
task progression (trial)
sequence position
posterior estimate of trend
posterior estimate
autistic
non-autistic
stimulus-evoked pupillary response (SEPR, z)
pitch+length oddball
mismatch-negativity-associated amplitude (MMN-amp, z)

References

1. Bast, N., Mason, L., Ecker, C., Baumeister, S., Banaschewski, T., . . . the, E. U. A. L. G. (2023). Sensory salience processing moderates attenuated gazes on faces in autism spectrum disorder: a case–control study. Molecular Autism, 14(1), 5. https://doi.org/10.1186/s13229-023-00537-6
2. Burlingham, C. S., Mirbagheri, S., & Heeger, D. J. (2022). A unified model of the task-evoked pupil response. Science Advances, 8(16), eabi9979. https://doi.org/doi:10.1126/sciadv.abi9979
3. Pfeffer, T., Keitel, C., Kluger, D. S., Keitel, A., Russmann, A., . . . Gross, J. (2022). Coupling of pupil- and neuronal population dynamics reveals diverse influences of arousal on cortical processing. eLife, 11, e71890. https://doi.org/10.7554/eLife.71890
4. Poe, G. R., Foote, S., Eschenko, O., Johansen, J. P., Bouret, S., . . . Sara, S. J. (2020). Locus coeruleus: a new look at the blue spot. Nat. Rev. Neurosci. https://doi.org/10.1038/s41583-020-0360-9
5. Vazey, E. M., Moorman, D. E., & Aston-Jones, G. (2018). Phasic locus coeruleus activity regulates cortical encoding of salience information. Proc. Natl. Acad. Sci. U.S.A., 115(40), E9439. https://doi.org/10.1073/pnas.1803716115

Poster No 350

Do estimates of age based on functional connectivity differ as a function of reading ability?

Oliver Lasnick[1], Jie Luo[1], Brianna Kinnie[1], Shaan Kamal[2], Spencer Low[3], Natasza Marrouch[4], Fumiko Hoeft[1]

[1]University of Connecticut, Storrs-Mansfield, CT, [2]University of Connecticut School of Medicine, Farmington, CT, [3]Boston University Chobanian & Avedisian School of Medicine, Boston, MA, [4]University of Lisbon, Lisbon, Lisbon

Introduction: Previous work has shown that brain growth charts which predict age based on properties of the brain can inform scientists about neurodevelopmental trajectories, and may be used to obtain early markers for atypical development (Dosenbach et al., 2010; Kessler et al., 2016). In this study, we extended brain-age modeling based on functional connectivity (FC) data to developmental dyslexia (reading disorder, or RD). We hypothesized that (1) models trained to predict age are biased for poor and exceptional readers compared to controls, reflecting a developmental delay for the former and acceleration for the latter; (2) a model trained with whole-brain FC data better predicts age compared to a model trained only with FC data from regions of interest (ROIs) in the brain's reading network; (3) models trained with FC data from the reading network have a greater prediction bias than the whole-brain model, i.e. they are more likely to underestimate the age of poor readers.

Methods: We used fMRI scans of N=742 participants aged 6-21 years (M=10.7, SD=3.0) from the public, de-identified CMI HBN database; IRB approval was not required. We used the Test of Word Reading Efficiency Total Word Reading Efficiency index score to classify participants as poor (PR, <=90), typical (TR, 91-109), or exceptional readers (ER, >=110). A support vector machine was trained on fMRI-FC data to predict age. An ROI correlation matrix was generated for each participant (each value is the correlation between two fMRI BOLD-signal time series). Principal component analysis (PCA) was applied to the training set of connectivity matrices to reduce the number of features. One thousand training permutations were done: for each, data was first split into the training and test sets; PCA was performed; and 5-fold cross-validation was done on the training set. A literature search for meta-analyses was performed to identify prominent brain regions associated with reading/RD. These were used to repeat the model-training procedure first using whole-brain FC data and then several more times using smaller sets of ROIs (reduced-ROI models).

Results: The ROIs present in the highest-ranked connections for the whole-brain model came from the right dorsal attention and somatosensory motor networks and bilateral visual and temporal regions (Fig 1). Interhemispheric connections were more heavily weighted than intrahemispheric ones. Of the most frequent ROIs in the top 10% of connections, 53.9% were from the right hemisphere; when top ROIs were restricted to a frequency >2 SDs above the median, 81.3% were from the right hemisphere-particularly right dorsal attention and somatosensory motor networks. The relationship between predicted age and true age was significant in all models (ps < .001). Comparing all models using Akaike's information criteria showed that the whole-brain model performed better than all others as expected. There were no main effects of Group on model predictions, however the interaction of Group x Age was significant in all models (ps < .05), indicating differences in model fit based on group (Fig 2).

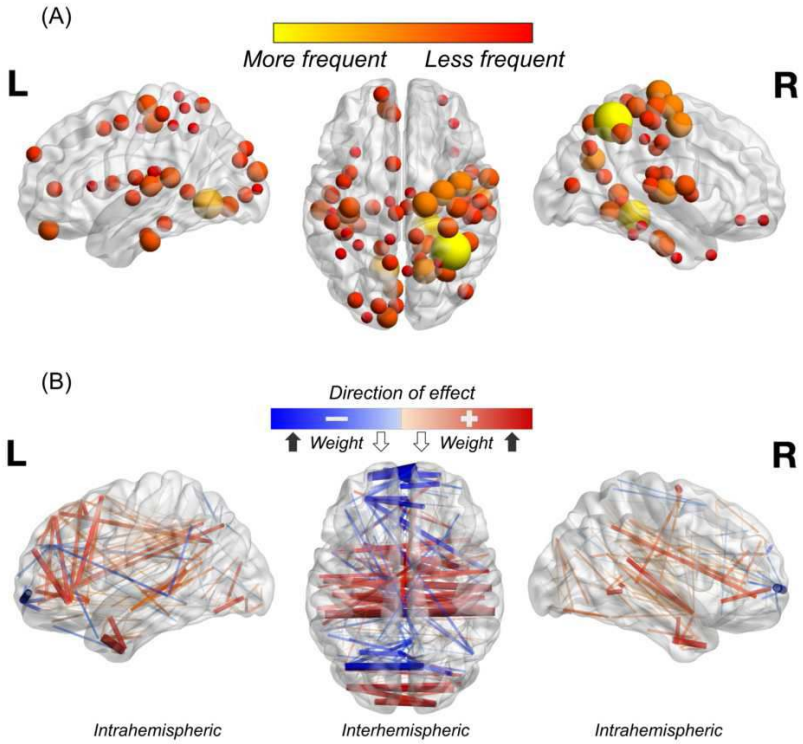

Fig 1. Top ROIs/connections in the whole-brain model. (A) ROIs are from the top 10% of connections and have a frequency >1 SD above the median. Lighter color and larger size both indicate greater frequency. (B) Top 500 connections. Direction of effect indicates the relationship to age estimates. Red: increased connectivity with age. Blue: decreased connectivity with age.

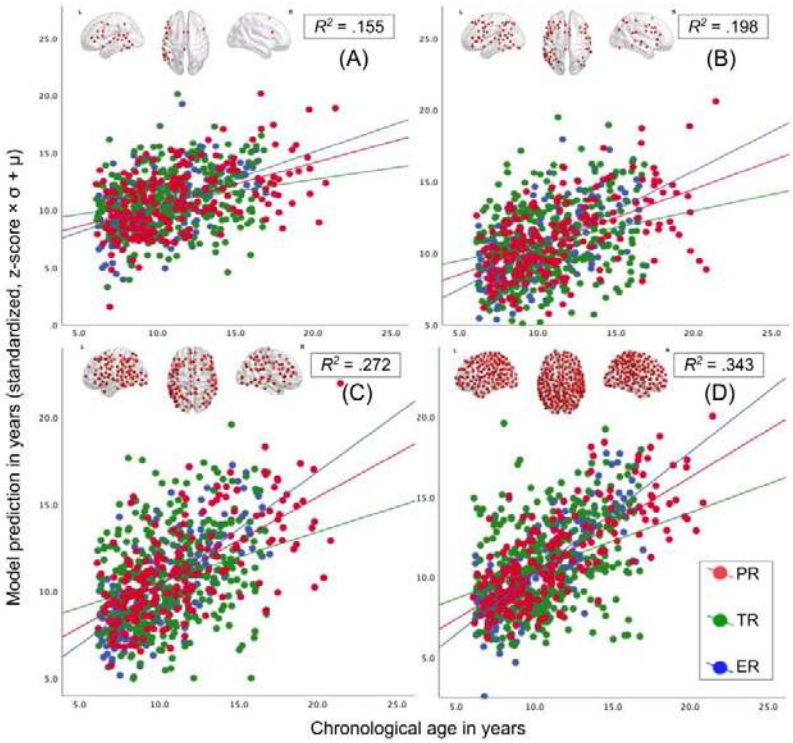

Fig 2. Relationship between true age and model age estimates based on FC data for each ROI cutoff. (A) 27 ROIs. (B) 78 ROIs. (C) 152 ROIs. (D) 400 ROIs. ROIs used to train each model are shown in the top left corner of each subplot. Line/dot color indicates reading group. R^2 values in the upper right are collapsed across groups.

Conclusions: The whole-brain model was the best predictor of age. Contrary to hypotheses, when trained with reading/language ROIs, model bias based on group did not increase. Rather, model fit varied by group, being better for the ERs/PRs compared to TRs: this effect was largest in the whole-brain model. One possibility is that variability of FC patterns is larger in TRs, hindering the ability of our model to predict age for the TRs. Finally, the difference in explained variance between

the whole-brain model (R^2 = .343) and the most-reduced model (R^2 = .155) is small relative to the difference in data used for training. While training with whole-brain data results in more accurate age estimates, accuracy is not linearly proportional to the number of ROIs/connections used to generate features. Markers of age and reading ability are present in diffuse connectivity patterns with sizable redundancy.

References
1. Dosenbach, N. U. (2010). 'Prediction of individual brain maturity using fMRI', Science, vol. 329, no. 5997, pp. 1358-1361
2. Kessler, D. (2016). 'Growth Charting of Brain Connectivity Networks and the Identification of Attention Impairment in Youth', JAMA Psychiatry, vol. 73, no. 5, pp. 481-489

Poster No 351

Neurofeedback from the anterior prefrontal cortex for obsessive compulsive disorder

Zhiying Zhao[1], Mariela Rance[2], Brian Zaboski[2], Stephen Kichuk[2], Emma Romaker[2], William Koller[2], Christopher Walsh[2], Cheyenne Harris-Starling[2], Suzanne Wasylink[2], Thomas Adams[2], Patricia Gruner[2], Christopher Pittenger[2], Michelle Hampson[2]

[1]University of Macau, Taipa, Macau, [2]Yale University School of Medicine, New Haven, CT

Introduction: Obsessive-compulsive disorder (OCD) is characterized by hyperactivity in cortico-striatal circuitry. This hyperactivity is reduced in parallel with symptom improvement after both psychotherapy and pharmacotherapy,[1] particularly in the ventral frontal cortex. Thus, we are exploring whether training this region via neurofeedback can provide therapeutic benefit. We developed a neurofeedback intervention[2] that proved promising in a subclinical population,3 and here describe it's application in an OCD clinical trial.

Methods: Participants: Individuals with OCD with primary symptom dimensions of checking or contamination (ages 18-65) were recruited through the Yale OCD Research Clinic (ocd.yale.edu). No treatment or a stable (>8 weeks) regimen of SSRIs or maintenance therapy were allowed. 36 participants were randomized (18 per group). Protocol: This randomized, double-blind trial (NCT02206945) followed methods previously described.[2,3] The Yale-Brown Obsessive Compulsive Symptom Scale[4,5] was collected before training and half a week, two weeks and one month after training. The scanning protocol involved four sessions. First, a baseline session to assess resting connectivity patterns and control over the target region during exposure to provocative images, followed by two feedback training sessions (real or yoked sham, depending on group), and a post-intervention assessment session to re-assess connectivity patterns and control over the target region after training.

Results: There were significant differences between groups in symptom change, with the neurofeedback group showing greater symptom improvement than the sham group, but the symptom changes induced by neurofeedback were too small to be clinically meaningful. Control over the brain area did not improve differentially for the two groups.

Conclusions: The improvement in symptoms in the neurofeedback relative to the sham group supports the promise of this intervention but effects must be amplified for clinical utility. Options for optimizing impact will be discussed. The measures of control over the brain area collected pre- and post-training were very noisy, possibly due to idiosyncratic levels of activation to the provocative imagery in participants. Standardized sets of provocative imagery will be replaced by personalized stimuli moving forward.

References
1. van der Straten AL, et al. Sci. Rep. 2017;7(1):17464.
2. Hampson M, et al. J Vis Exp. 2012(59).
3. Scheinost D, et al. Transl Psychiatry. 2013;3:e250.
4. Goodman WK, et al. Arch. Gen. Psychiatry. 1989;46(11):1012-1016.
5. Goodman WK, et al. Arch. Gen. Psychiatry. 1989;46(11):1006-1011.

Poster No 352

Organization of intersubject correlations parallels functional gradients during naturalistic viewing

Meaghan Smith[1], Ahmad Samara[2], Jeffrey Eilbott[3], Hallee Shearer[2], Tamara Vanderwal[4], Boris Bernhardt[5]

[1]McGill University, Montreal, Quebec, [2]University of British Columbia, Vancouver, British Columbia, [3]BC Children's Hospital Research Institute, Vancouver, British Columbia, [4]Department of Psychiatry, University of British Columbia, Vancouver, BC, [5]Montreal Neurological Institute and Hospital, Montreal, Quebec

Introduction: Many analyses have been developed to make use of the wealth of data that fMRI produces. Among these methods is gradient analysis, which uses dimensionality reduction to identify a macroscale organizational hierarchy from functional connectivity matrices[1]. In contrast, intersubject correlations (ISCs) compare BOLD signal time courses across individuals to describe how reliably a given brain region responds to the same stimulus[2]. Despite describing brain organization from different perspectives, both measures appear to capture core features of functional architecture. In particular, ISCs and gradient scores both delineate default mode regions from task-positive brain regions[1,2,3]. Here, we leverage movie-fMRI to generate robust movie gradients that have previously been shown to enhance brain-behavior associations[4]. Movie-watching also synchronizes low-level brain activity which makes higher level individual differences in functional connectivity more identifiable[5]. We then use ISC to investigate how intersubject synchronization maps onto the functional hierarchy identified via the gradient analyses. We hypothesize that there will be a significant spatial correlation between gradient scores and ISCs, revealing a parallel organization between BOLD-signal responses to complex stimuli and the hierarchical organization of functional connectivity.

Methods: Data. These analyses use minimally preprocessed movie-watching data from the Human Connectome Project (HCP) 7T data release[6,7]. From the complete dataset, 95 participants (58 females, mean age 29.5 ± 3.3) from 64 families were selected based on head motion and data availability. One hour of movie data was collected over the course of four 15-minute runs across two sessions. All analyses were first conducted in a discovery dataset of 45 subjects and replicated in the remaining 50 subjects. Gradient analysis. Gradient analyses were performed parcel-wise using the Schaefer-1000 parcellation[8]. The mean time series for each parcel was correlated with the mean time course of all other parcels in the brain to create subject-level FC matrices. Diffusion map embedding was performed at the subject level using the BrainSpace toolbox[9], and individual gradients were aligned to a group-mean template before being averaged to yield group-level gradients. Intersubject correlations. BOLD-signal timeseries data at the Schaefer-1000 level were used to compute intersubject correlations using a group mean approach. Each subjects' time course at each parcel was correlated with the group average time course at that parcel to provide a single ISC score per region. Permutation testing. Spatial autocorrelation-preserving null-models[10] were used to assess the significance of correlations between ISCs and scores along the top three gradients. Spin permutation tests were used to generate 10,000 null-models for each comparison.

Results: ISCs and movie gradients followed trends in the literature. ISCs were high in superior temporal and occipital regions. The top three gradients had poles situated in the somatosensory, visual, and auditory cortices respectively and radiated towards heteromodal association systems such as the default mode network. There was a significant spatial correlation between ISC scores and Gradient 2 scores ($r = 0.74$, $p < 0.05$), such that regions with the highest and lowest ISC scores were situated at the poles of the second gradient (i.e., visual and default networks). This relationship was reproduced in the replication dataset ($r = 0.75$, $p < 0.05$).

Conclusions: These results provide further support for a macroscale processing hierarchy within the brain that is exemplified under naturalistic conditions. These findings also suggest that when the brain is active and processing complex and ecologically valid stimulus, there is a strong correspondence between functional connectivity patterns at a whole-brain level, and BOLD signal response reliability across subjects at a parcel-level.

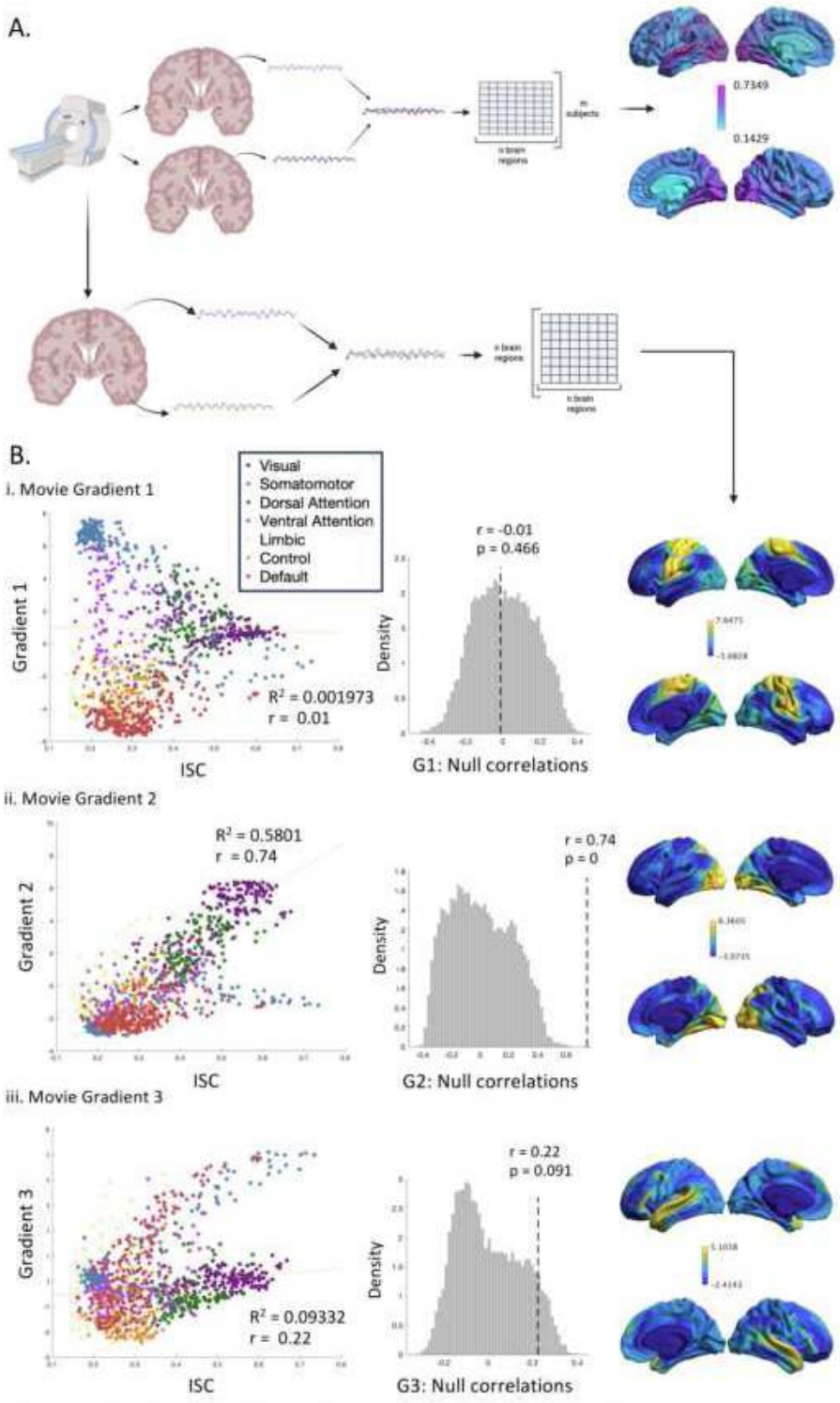

Figure 1. Spatial correlation between ISCs and gradient scores. (1A) Generation of intersubject correlation maps from pairwise timeseries correlations of BOLD signal time courses across subjects, and generation of gradient maps from pairwise correlations of BOLD signal time courses within subjects across voxels. (1B) Scatter plots of scores along the top three gradients vs. intersubject correlation coefficients, color-coded by membership in Yeo's resting-state 7-network parcellation (left). Null distributions generated from spin tests to assess the significance of the correlation between ISCs and gradient scores (middle). Scores along the top three functional movie gradients projected onto the cortical surface (right).

References

1. Margulies, D. S. (2016). Situating the default-mode network along a principal gradient of macroscale cortical organization. Proceedings of the National Academy of Sciences, 113(44), 12574–12579. https://doi.org/10.1073/pnas.1608282113
2. Hasson, U. (2004). Intersubject synchronization of cortical activity during natural vision. Science, 303(5664), 1634–1640. https://doi.org/10.1126/science.1089506
3. Golland, Y. (2006). Extrinsic and intrinsic systems in the posterior cortex of the human brain revealed during natural sensory stimulation. Cerebral Cortex, 17(4), 766–777. https://doi.org/10.1093/cercor/bhk030

4. Samara, A. (2023). Cortical gradients during naturalistic processing are hierarchical and modality-specific. NeuroImage, 271, 120023. https://doi.org/10.1016/j.neuroimage.2023.120023
5. Vanderwal, T. (2017). Individual differences in functional connectivity during naturalistic viewing conditions. NeuroImage, 157, 521–530. https://doi.org/10.1016/j.neuroimage.2017.06.027
6. Glasser, M. F. (2013). The minimal preprocessing pipelines for the Human Connectome Project. NeuroImage, 80, 105–124. https://doi.org/10.1016/j.neuroimage.2013.04.127
7. Van Essen, D. C. (2013). The Wu-minn human connectome project: An overview. NeuroImage, 80, 62–79. https://doi.org/10.1016/j.neuroimage.2013.05.041
8. Schaefer, A. (2017). Local-global parcellation of the human cerebral cortex from intrinsic functional connectivity MRI. Cerebral Cortex, 28(9), 3095–3114. https://doi.org/10.1093/cercor/bhx179
9. Vos de Wael, R. (2020). BrainSpace: A toolbox for the analysis of macroscale gradients in neuroimaging and Connectomics datasets. Communications Biology, 3(1). https://doi.org/10.1038/s42003-020-0794-7
10. Alexander-Bloch, A. F. (2018). On testing for spatial correspondence between maps of human brain structure and function. NeuroImage, 178, 540–551. https://doi.org/10.1016/j.neuroimage.2018.05.070

Poster No 353

Predictive Coding in ASD and ADHD: Modulation of P300 by Sequence Learning

Yiyuan Huang[1], Maria Gonzalez-Gadea[2], Tristan Bekinschtein[3], Agustin Ibanez[4], Zenas Chao[1]

[1]The University of Tokyo, Tokyo, Japan, [2]University of San Andres, Buenos Aires, Argentina, [3]University of Cambridge, Cambridge, United Kingdom, [4]Global Brain Health Institute, University of California, CA, United States

Introduction: Neural signatures of prediction errors elicited by unexpected stimuli have been extensively studied by mismatch negativity (MMN) and P300 responses in electroencephalography (EEG). These responses can be modulated by sequential contexts, such as attention allocation and sequence learning, and atypical modulations were found in autism spectrum disorder (ASD) and attention deficit hyperactivity disorder (ADHD). For attention allocation, the P300 response was more pronounced for unexpected tones that were attended to compared to those that were not, and the difference was observed in both healthy controls (HC) and ASD, but not in ADHD. Therefore, P300 reveals a lack of neural distinction between attended and unattended novel stimuli in ADHD, and could be an effective biomarker. For sequence learning, MMN reduced when an unexpected tone became predictable as multi-tone sequence structure is learned, but this reduction was weaker in ASD than in HC. However, it remains unclear how P300 is modulated by sequence learning and how such modulation may vary among HC, ASD, and ADHD.

Methods: In this study, we analyze EEG data from 13 HC (8 males; mean age: 11.6 ± 2.7 years old), 21 individuals with ASD (20 males; mean age: 10 ± 2 years old), and 13 individuals with ADHD (10 males; mean age: 12 ± 3 years old) during a local-global oddball paradigm. In this paradigm, two 5-tone sequences were used: xxxxy and xxxxx. The tone “y” served as a local deviant tone within the sequence which is more predictable at the global level when xxxxy was presented frequently (the highPred condition) and less predictable when xxxxy sequence was presented infrequently (the lowPred condition). To examine how P300 evoked by the local deviant tone “y” is modulated by the global sequence predictability, we compare event-related potentials (ERPs) between the two sequences (xxxxy – xxxxx) in both conditions (Figure panel A).

Results: Using a clustered-wised statistical analysis on P300, we show that HC has a positive response in the central area in the lowPred condition but a negative response in the frontal areas in the highPred condition. In ASD and ADHD, the response is positive in the parietal-occipital area in the lowPred condition but is negative in the frontal area in the highPred condition. We further evaluate the difference in P300 between the lowPred and highPred conditions. For each individual, we first identify the peak P300 amplitude in each condition from all channels and time points where P300 is significantly different from zero, and then evaluate its reduction from lowPred to highPred conditions in the three groups (Figure panel B). All three groups show a significant reduction in P300 when the sequence is predictable, and this reduction is significantly less in ASD, compared to HC and ADHD (Figure panel C).

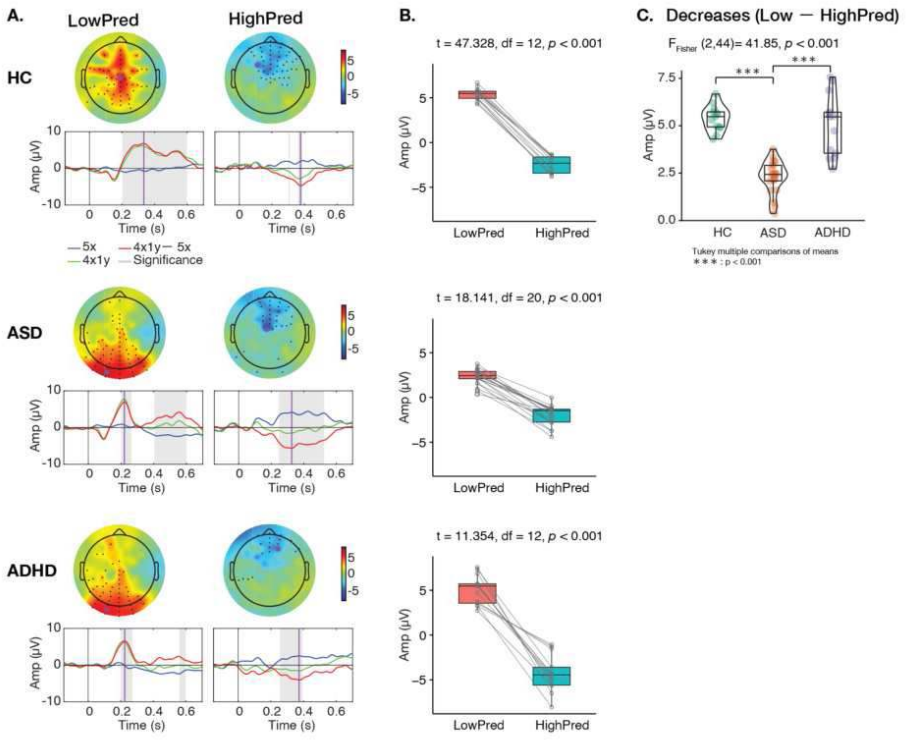

Conclusions: Our study, which builds upon prior research, demonstrates that P300 can be used to evaluate distinct predictive coding elements across disorders. Specifically, previous work showed that ADHD is associated with impairments in attention allocation, consistent with atypical prediction precision in predictive coding theory. On the other hand, the current investigation shows that ASD is linked to challenges in sequence learning, suggesting atypical prediction updates.

References

1. Bekinschtein, Tristan A., et al. (2009) "Neural signature of the conscious processing of auditory regularities." Proceedings of the National Academy of Sciences 106.5 1672-1677.
2. Gonzalez-Gadea, Maria Luz, et al. (2015) "Predictive coding in autism spectrum disorder and attention deficit hyperactivity disorder." Journal of Neurophysiology 114.5 2625-2636
3. Goris, Judith, et al. (2018) "Sensory prediction errors are less modulated by global context in autism spectrum disorder." Biological Psychiatry: Cognitive Neuroscience and Neuroimaging 3.8 667-674.

Poster No 354

The regional distribution of brain iron and its relation to behaviors in children and adolescents

Bryan Yoon[1], Lanxin Ji[2], Amyn Majbri[3], Ellyn Kennelly[4], Tanya Bhatia[3], Mark Duffy[2], Alexis Taylor[4], Moriah Thomason[5]

[1]New York University, New York, NY, [2]NYU Langone Health, New York, NY, [3]New York University Medical Center, New York, NY, [4]Wayne State University, Detroit, MI, [5]NYU Langone Medical Center, New York, NY

Introduction: Brain iron plays an essential role in human brain development by influencing neurotransmitter function, supporting myelin formation and DNA synthesis (Rouault, 2013; Ward et al., 2014) and modulating metabolic energy production (Larsen & Luna, 2015). Preadolescence represents a critical period during which non-heme iron rapidly accumulates to meet the demands of brain maturation (Treit et al., 2021). Recent studies have started to reveal close associations between adolescent basal ganglia brain iron and cognitive function (Darki et al., 2016; Hect et al., 2018), and have shown that psychiatric disorders are more prevalent in youth with iron deficiency (Cortese et al., 2011), autism (Tang et al., 2021), and first-episode psychosis (Xu et al., 2021). However, to date, no studies have addressed brain iron in the context of early adolescent brain development and its impact on internalizing, externalizing, and attention behaviors in a well-characterized, low-income, predominantly minority early adolescent sample. Assessing such behavior is particularly important as it allows for the detection of prodromal symptoms in advance, leading to early intervention and a better prognosis. We will test the hypothesis that decreased non-heme iron, indicative of delayed neurological development, will be associated with elevated behaviors in

both internalizing and externalizing domains. Furthermore, we expect specificity in which brain structures reflect different iron levels across internalizing, externalizing, and attention domains.

Methods: Imaging data were acquired from 51 adolescents and children (34 females), aged 7 to 16 (M = 12.15, SD = 2.40), who were enrolled in the ongoing Perinatal Imaging of Neural Connectivity (PINC) study. This study initially conducted fetal MRI studies in pregnant women and now follows the developmental progress of these children. Non-heme iron levels in the substructures of basal ganglia and hippocampus were measured using susceptibility-weighted imaging on a Siemens Verio 3 T scanner equipped with a 12-channel head coil. The iron content in substructures of the basal ganglia and hippocampus was estimated in vivo from an 11-echo multiple gradient-echo sequence with a voxel size of 0.5 × 0.5 × 2 mm, echo times (TE) = 5.68–31.38 ms with an inter-echo interval of 2.57 ms, repetition time = 37 ms, flip angle = 15°, bandwidth = 465 Hz/pixel, and field of view = 512 × 384. Internalizing (anxiety, depressive, and somatic symptoms), externalizing (disruptive conduct, impulsive, and addictive symptoms), and attention behaviors of children and adolescents were assessed using the Child Behavior Checklist (CBCL) (Achenbach, 1994).

Results: Lower brain iron in both the substantia nigra (Fig. 1a) and hippocampus (Fig. 1b) was correlated with poorer attention levels, as shown in Fig. 2a and Fig. 2b. Conversely, the higher brain iron content of the left red nucleus (Fig. 1c) was correlated with severe internalizing behavior, as shown in Fig. 2c.

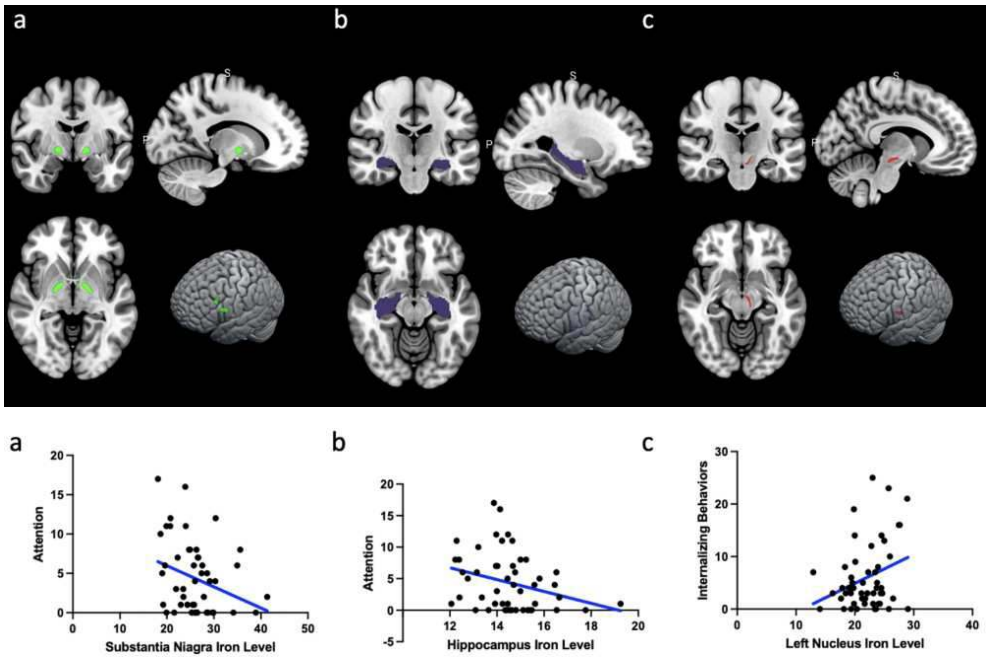

Conclusions: In this study, we present results on how different regional brain iron contents are associated with the behaviors of adolescents and children. While replicating previous studies that reported a correlation between lower brain regional iron contents and the decline in attention levels (Cortese et al., 2011), our results mark the first study to demonstrate a correlation between internalizing behavior and higher iron levels in the red nucleus. We speculate that this pattern indicates an overdevelopment of the red nucleus, responsible for managing the shift from one motor response to another. Our hypothesis is that individuals more vulnerable to anxiety, depressive, and somatic symptoms tend to undergo a process of overdeveloping the red nucleus as a compensatory mechanism. Our future work will explore whether overdevelopment is associated with heightened rumination, and whether youth with using different coping strategies show varied brain iron loading.

References

1. Achenbach, T. M. (1994). Child Behavior Checklist and related instruments. In The use of psychological testing for treatment planning and outcome assessment.
2. Cortese, S., Azoulay, R., Xavier Castellanos, F., Chalard, F., Lecendreux, M., Chechin, D., Delorme, R., Sebag, G., Sbarbati, A., Mouren, M.-C., Dalla Bernardina, B., Konofal, E., Ç Ois
3. Chalard, F., & Mouren, M.-c. (2011). The World Journal of Biological Psychiatry Brain iron levels in attention-deficit/hyperactivity disorder: A pilot MRI study Brain iron levels in attention-defi cit/hyperactivity disorder: A pilot MRI study. https://doi.org/10.3109/15622975.2011.570376
4. Darki, F., Nemmi, F., Möller, A., Sitnikov, R., & Klingberg, T. (2016). Quantitative susceptibility mapping of striatum in children and adults, and its association with working memory performance. Neuroimage, 136. https://doi.org/10.1016/j.neuroimage.2016.04.065
5. Hect, J. L., Daugherty, A. M., Hermez, K. M., & Thomason, M. E. (2018). Developmental variation in regional brain iron and its relation to cognitive functions in childhood. Dev Cogn Neurosci, 34. https://doi.org/10.1016/j.dcn.2018.05.004

6. Larsen, B., & Luna, B. (2015). In vivo evidence of neurophysiological maturation of the human adolescent striatum. Dev Cogn Neurosci, 12. https://doi.org/10.1016/j.dcn.2014.12.003
7. Rouault, T. A. (2013). Iron metabolism in the CNS: Implications for neurodegenerative diseases. In Nature Reviews Neuroscience (Vol. 14).
8. Tang, S., Xu, Y., Liu, X., Chen, Z., Zhou, Y., Nie, L., & He, L. (2021). Quantitative susceptibility mapping shows lower brain iron content in children with autism. European Radiology, 31(4). https://doi.org/10.1007/s00330-020-07267-w
9. Treit, S., Naji, N., Seres, P., Rickard, J., Stolz, E., Wilman, A. H., & Beaulieu, C. (2021). R2* and quantitative susceptibility mapping in deep gray matter of 498 healthy controls from 5 to 90 years. Hum Brain Mapp, 42(14), 4597-4610. https://doi.org/10.1002/hbm.25569
10. Ward, R. J., Zucca, F. A., Duyn, J. H., Crichton, R. R., & Zecca, L. (2014). The role of iron in brain ageing and neurodegenerative disorders. In The Lancet Neurology (Vol. 13).
11. Xu, M., Guo, Y., Cheng, J., Xue, K., Yang, M., Song, X., Feng, Y., & Cheng, J. (2021). Brain iron assessment in patients with First-episode schizophrenia using quantitative susceptibility mapping. NeuroImage: Clinical, 31, 102736-102736.

Poster No 355

Exploring Morphological Characterization of MRI-negative Child Epilepsy Based on Machine Learning

Kai Zhang[1], Jinping Xu[2], Fan Xinxin[3], Zhewei Zhang[4], Xiaodong Zhang[5]

[1]Shenzhen Institutes of Advanced Technology, Chinese Academy of Sciences, Shenzhen, GuangDong, [2]Shenzhen Institutes of Advanced Technology, Chinese Academy of Sciences, Shenzhen, Guangzhou, [3]Shenzhen Institutes of Advanced Technology, Chinese Academy of Sciences, Shenzhen, Guangdong, [4]Shenzhen Institute of Advanced Technology, Chinese Academy of Sciences, Shenzhen, Guangdong, [5]Shenzhen Institute of Advanced Technology,Chinese Academy of Sciences, Shenzhen, Guangdong

Introduction: FCD is a disease caused by abnormal proliferation and differentiation of focal cortical neurons, cortical architecture and migration, which is the most common cause of refractory secondary epilepsy in children.In epilepsy surgery, FCD accounts for about 40% to 50% of pediatric epilepsy surgery patients. Compared with adults, children's brains are still in the developmental stage, and the morphological characteristics of lesions are more subtle and difficult to distinguish. At the same time, there are few sample data for children with epilepsy, and traditional research methods based on regions or individuals are used. Therefore, for these patients, we propose a machine learning method based on brain surface vertices, which deeply utilizes the morphological characteristics of MRI-negative children with epilepsy and improves the Predictive accuracy in MRI-negative children with epilepsy and provides a theoretical basis. Provide assistance to doctors in clinical diagnosis and treatment.

Methods: A MRI-positive cohort of 72 patients from publicly available data(https://www.nature.com/articles/s41597-023-02386-7). The other one MRI-positive cohort of 11 child patients and MRI-negative cohort of 8 child patients from Shenzhen Children's Hospital following permission by the hospital ethical review board. Patients younger than 3 years of age or Prognosis is not standard (<Engel class II) were excluded. A control group of 32 participants with no history of any neurological diagnosis from publicly available data ABIDE.

All patients and controls were scanned on a 3-T MRI system. 3D structural T1w images using the following protocols [TR] = 2300 milliseconds,[TE] = 2.74 milliseconds,[FOV]= 256 × 256 mm,[FA] = 8°,voxel size=1×1×1 mm3.Cortical reconstructions were generated using FreeSurfer version 7.3(https://surfer.nmr.mgh.harvard.edu/) for all participants. Lesion masks were manually delineated for the all patients by an experienced pediatric neuroradiologist. The lesion masks were first mapped onto the individual surface reconstructions and then onto the bilaterally symmetric template(fsaverage_sym).Measures of morphological/intensity features. The following measures were calculated per vertex across the cortical surface in all participants: cortical thickness, intensity at the gray-white matter contrast, curvature, sulcal depth, intrinsic curvature and boundary sharpness coefficient(BSC).We evaluated the discrimination of BSC. All features were smoothed with a 10mm Gaussian kernel and underwent two normalization procedures: within-subject z scoring and a between-subject z scoring. And then, all features were registered to fsaverage_sym : a bilaterally symmetrical template space. The Scikit-learn toolbox was used to create a linear classifier that classifies each vertex as diseased or non-diseased. The classifier is trained using data from MRI-positive cohort. And then input features from MRI-negative cohort per-vertex and output predictions. grouped into neighbor-connected clusters of vertices. If the predicted vertex cluster hits the manually outlined ROI, it is considered a successful detection.

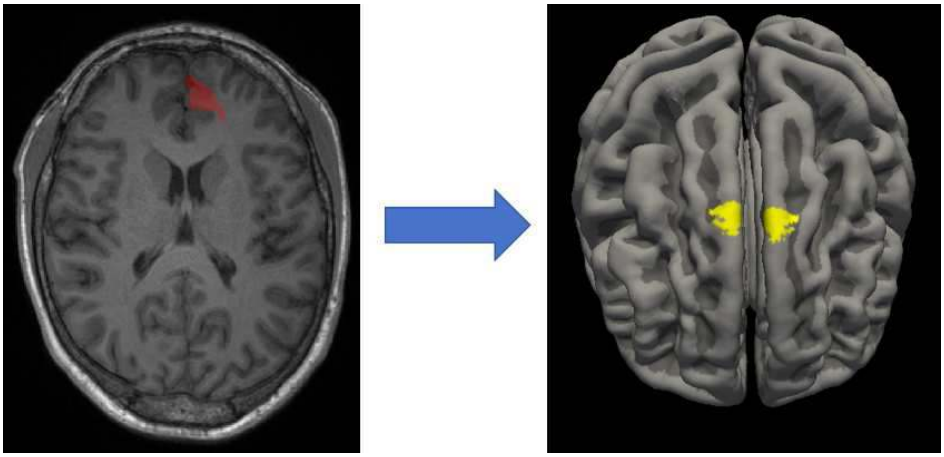

Results: The network was trained using a leave-one-out crossvalidation approach to assess the accuracy of the classifier on the MRI-positive cohort . And then trained on all 83 MRI-positive and tested on MRI-negative cohort. Of the 83 patients with visible FCD on MRI, the classifier was able to detect the lesion in 67 (sensitivity = 81%). In 5 of the 8 patients (sensitivity = 62%) with negative MRI, the predicted vertex cluster overlapped with the hand-delineated lesion mask.No clusters were detected In healthy controls(specificity = 100%).

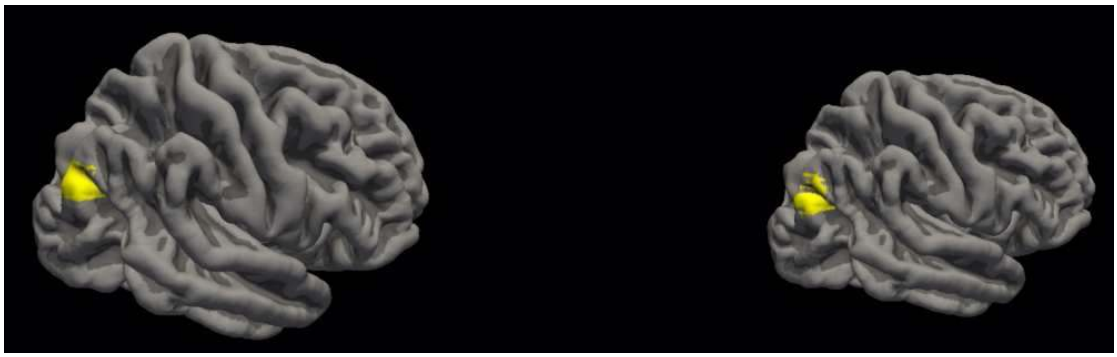

Conclusions: We propose an automatic method for detecting FCD and test the feasibility of BSC in predicting FCD lesions. After adding BSC feature, the sensitivity of vertex classification is increased by 4%. Ultimately, there was 81% sensitivity in the positive MRI cohort and 62% sensitivity in the negative MRI cohort, with a specificity of 100%.

References

1. Wyllie E. Surgical treatment of epilepsy in children. Pediatr Neurol. 1998;19:179–88.
2. McGovern RA, Knight EP, Gupta A, et al. Robot-assisted stereoelectroencephalography in children. J Neurosurg Pediatr. 2018;23:288–96.
3. Adler S, Wagstyl K, Gunny R, et al. Novel surface features for automated detection of focal cortical dysplasias in paediatric epilepsy. Neuroimage Clin. 2017;14:18–27.
4. Jin B, Krishnan B, Adler S, et al. Automated detection of focal cortical dysplasia type II with surface-based magnetic resonance imaging postprocessing and machine learning. Epilepsia. 2018;59:982–92
5. Tan, Y.-L.; Kim, H.; Lee, S.; Tihan, T.; Hoef, L.V.; Mueller, S.G.; Barkovich, A.J.; Xu, D.; Knowlton, R. Quantitative surface analysis of combined MRI and PET enhances detection of focal cortical dysplasias. NeuroImage 2018, 166, 10–18
6. Azami, M.E.; Hammers, A.; Jung, J.; Costes, N.; Bouet, R.; Lartizien, C. Detection of Lesions Underlying Intractable Epilepsy on T1-Weighted MRI as an Outlier Detection Problem. PLoS ONE 2016, 11, e0161498.
7. Lee, H.M.; Gill, R.S.; Fadaie, F.; Cho, K.H.; Guiot, M.C.; Hong, S.-J.; Bernasconi, N.; Bernasconi, A. Unsupervised machine learning reveals lesional variability in focal cortical dysplasia at mesoscopic scale. NeuroImage Clin. 2020, 28, 102438
8. Hoyos-Osorio K, Álvarez AM, Orozco ÁA, Rios JI, DazaSantacoloma G. Clustering-based undersampling to support automatic detection of focal cortical dysplasias. In: Mendoza M, Velastín S, editors Progress in Pattern Recognition, Image
9. Analysis, Computer Vision, and Applications. Cham, Switzerland: Springer; 2017:298–305.

Poster No 356

Distinct Patterns of Brain Morphology associate with Specific Dimensions of Child Psychopathology

Lei Cao[1], Stephanie Gorka[1], K. Luan Phan[1], Lei Wang[1]

[1]The Ohio State University, Columbus, OH

Introduction: To better understand the shared also unique neural substrates underlying child psychopathology, we investigated the Child Behavior Checklist (CBCL) and decomposed CBCL into one general psychopathology factor and three specific symptom factors (Conduct Problems, ADHD and Internalizing Problems). Following the guideline of National Institute of Mental Health (NIMH) Research Domain Criteria (RDoC) that explores brain function through a dimensional perspective, we examined the relationship between the psychopathology factors and brain morphology measures using all children's baseline data from Adolescent Brain Cognitive Development (ABCD) study regardless of their clinical diagnosis.

Methods: The tabulated baseline data for CBCL item scores, FreeSurfer-derived (Destrieux atlas) cortical regional brain volume, surface area, and thickness from the multisite ABCD study (release 5.0) was used in the analysis. The data included a total of 11693 subjects (9.48 ± 0.50 years old, 47.7% female). We performed factor analysis on the CBCL item scores following the methodology presented by Moore et al. (2020). Briefly, 8 items were removed due to low correlation with other items and 3 pairs of items were combined due to high correlation with each other. Exploratory factor analysis was first performed on random half of the ABCD sample, revealing 3 specific symptom factors: Conduct Problems, ADHD and Internalizing Problems. Subsequent confirmatory factor analysis was conducted on the remaining half sample defining one general psychopathology factor and 3 previously found symptom factors. All four factors were orthogonal to each other. Separate multivariate linear mixed effects models were performed on cortical regional brain volume, surface area and thickness. All above obtained factors were included in the models with additional covariate of age, sex, race/ethnicity and scanner model to examine the relationship between each of the factors and brain morphology. Family id was included as random intercept. The resulting t-value was thresholded at $p<0.05$ (FDR-corrected). Both factor analysis and multivariate linear mixed effects models take into account of the clustering of site and family by utilizing imputed raked propensity weight (Heeringa et al., 2020).

Results: A wide-spread negative association was discovered between Conduct Problems and cortical regional volume. This negative association was mostly originated from surface area. In contrast, ADHD showed a negative correlation with cortical volume stemming from a combination of decreasing in surface area and cortical thickness. Finally, Internalizing Problems showed a pattern of positive association with cortical volume reflected in increases in surface area.

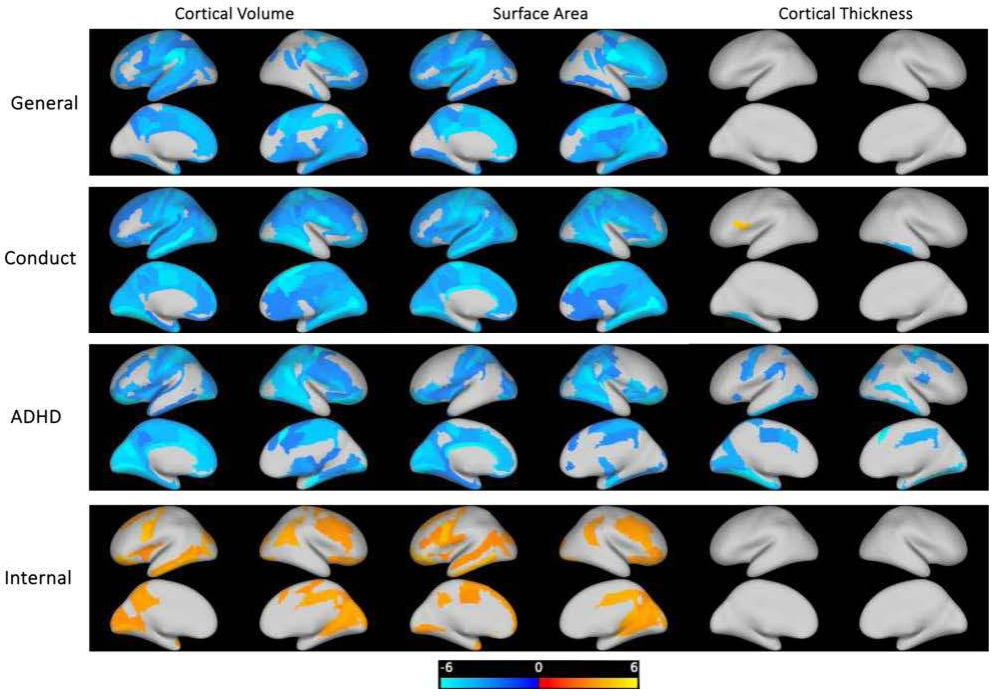

Conclusions: Our results showed distinct patterns of association between brain morphology and different symptom factors, suggesting unique neurodevelopmental brain structure profiles associate with different child psychopathology phenotypes. This unique structural abnormality may serve as potential biomarkers for predicting the emergence of psychopathology later in life.

References

1. Moore, T. M., Kaczkurkin, A. N., Durham, E. L., Jeong, H. J., McDowell, M. G., Dupont, R. M., ... & Lahey, B. B. (2020). Criterion validity and relationships between alternative hierarchical dimensional models of general and specific psychopathology. Journal of abnormal psychology, 129(7), 677.
2. Heeringa, S. G., & Berglund, P. A. (2020). A guide for population-based analysis of the Adolescent Brain Cognitive Development (ABCD) Study baseline data. BioRxiv, 2020-02.

Poster No 357

Lower Spatial Consistency on Transient States of People with Autism Spectrum Disorder

Yunge Zhang[1], Vinoo Alluri[2], Dongyue Zhou[1], Lin Lin[1], Abigail Stein[3], Shuqin Zhou[3], Huashuai Xu[4], Wei Zhao[1], Fengyu Cong[1], Huanjie Li[1], Fei Du[3]

[1]School of Biomedical Engineering, Faculty of Medicine, Dalian University of Technology, Dalian, China, [2]Cognitive Science Lab, International Institute of Information Technology, Hyderabad, India, [3]McLean Imaging center, McLean Hospital, Harvard Medical School, Boston, USA, [4]Faculty of Information Technology, University of Jyväskylä, Jyväskylä, Finland

Introduction: Social deficit is a core symptom of autism spectrum disorder (ASD). Atypical brain function of people with ASD have been widely reported on the triple network model[1], which is related to social communication and contains default mode network (DMN), executive and control network (ECN) and salience network (SN). However, it's unclear what the transient states of these networks look like in people with ASD. Co-activation pattern (CAP) is a clustering-based method to study the transient network states (TNSs)[2]. Most CAP studies focused on temporal features, the spatial stability of TNSs hasn't been well studied. In this work, we used CAP to study the spatial stability among TNSs related to triple network modal and the differences between people with ASD and healthy controls.

Methods: Data: Resting state fMRI data of 266 male subjects from 7 sites of ABIDE II dataset[3](133 ASD, 133 healthy controls (CON)) were included in this work. All subjects had full IQ higher than 80. Within a site, the age and full IQ were matched for ASD and CON groups and each group had at least 10 subjects. There were 184 subjects (92 ASD, 92 CON) with records of Social Responsiveness Scale (SRS) T scores. CAP: After normal preprocessing pipeline, a 400-node atlas[4] was used to extract time courses. The time courses of all subjects were concatenated by time and performed k-means clustering. Each frame was divided into one cluster and the cluster centers were defined as TNSs. The TNSs map were normalized by dividing the within-cluster standard deviation. After visual inspection, a threshold of 0.4 was defined as significant activation. The CAP was performed on all subjects and within each site, the TNSs of each site were matched with TNSs of all subjects based on spatial patterns. Spatial stability: The spatial stability was evaluated from three aspects: 1) Multisite spatial similarity was compared among TNSs. 2) Distance to cluster center of each frame was compared among TNSs and between ASD and CON groups using ANOVA and post hoc T tests. 3) Individual level significant activation rate (iSAR) was compared between ASD and CON groups. For one subject, the iSAR of a parcel in a TNS was defined as the n/N, n was the number of significantly activated frames with a threshold of 0.4 and N was the total number of frames in this TNS. T test was performed on iSAR of each TNS to study the group differences and canonical correlation analysis (CCA) was performed with iSAR and SRS T scores to study the relationship between them. CCA converted iSAR and SRS T scores into canonical variate (CV) pairs. The correlation between first CV pair represented relationship between iSAR and social deficits. The correlation of each raw feature and its first CV represented its contribution.

Results: We chose six as the optimized k number, which converted DMN, ECN and SN into three pairs of 'mirror' patterns. The TNSs were named according to the condition of the dominating network of it (Fig 1). The DMN TNSs showed highest spatial stability with higher multisite spatial similarity and shorter distance to center of each frame while the ECN TNSs showed lowest spatial stability. Comparing with CON, ASD group showed higher distance to center at every TNS representing the reduced spatial stability of them. Besides, ASD group showed significant lower iSAR on ECN-n and DMN-p (Fig 2A, B, E and F). The iSAR showed significant correlation with SRS T scores (Fig 2C and F). The reduced iSAR were related to severer social deficits since the iSAR values showed positive correlation while SRS T scores showed negative correlation with their first CV (Fig 2D and H).

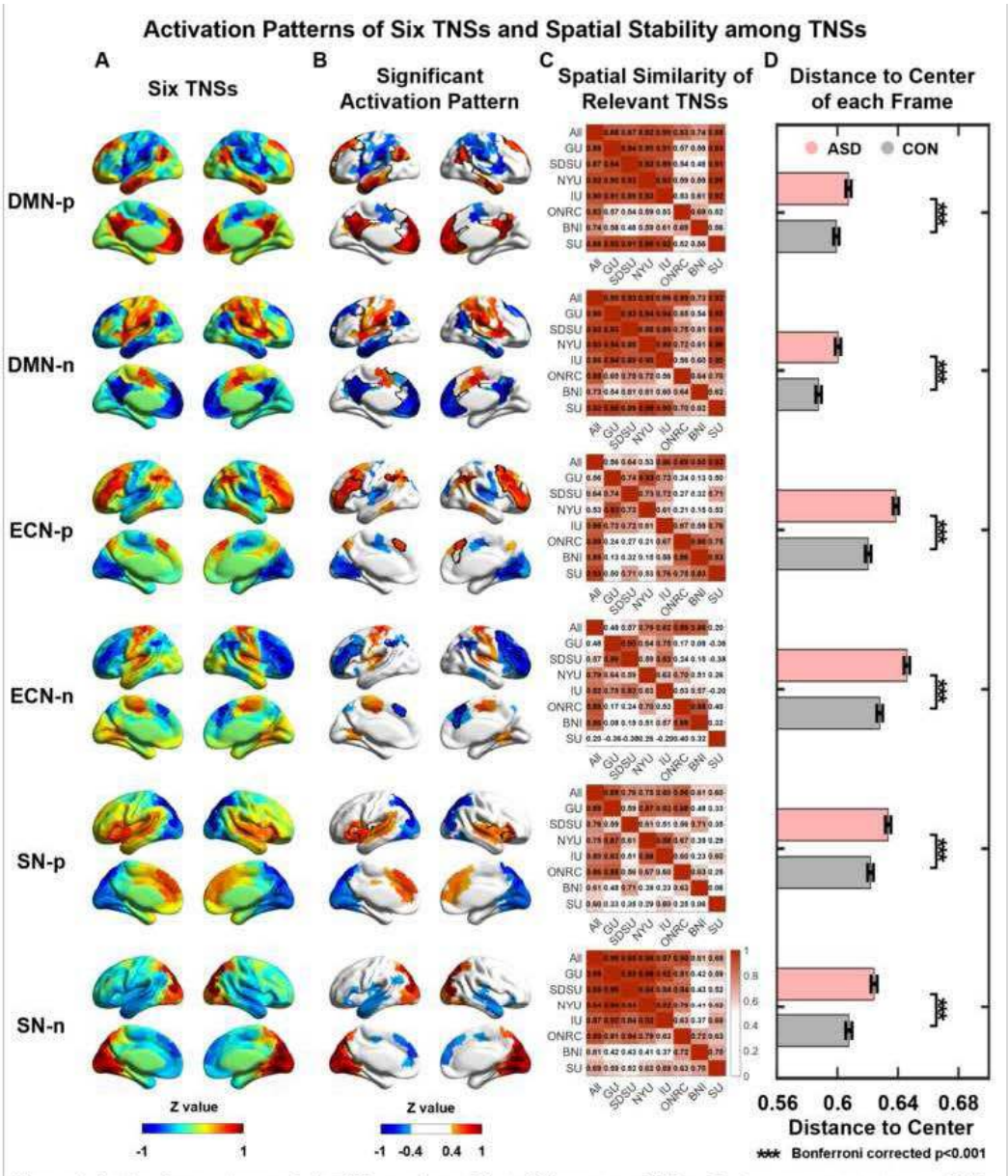

Figure 1. Activation patterns of six TNSs and spatial stability among TNSs. Each row represents one TNS. According to the spatial maps, the six TNSs are divided into three pairs, each of which represents the activation and deactivation of a network in triple network modal. (A) The normalized spatial maps. (B) The normalized spatial maps with a threshold of 0.4.The boundary of hub regions of dominating network is marked with black line. (C) The spatial similarity among relevant TNS from all subjects and each site. (D) The mean distance to center of each frame. The error-bar is standard error.

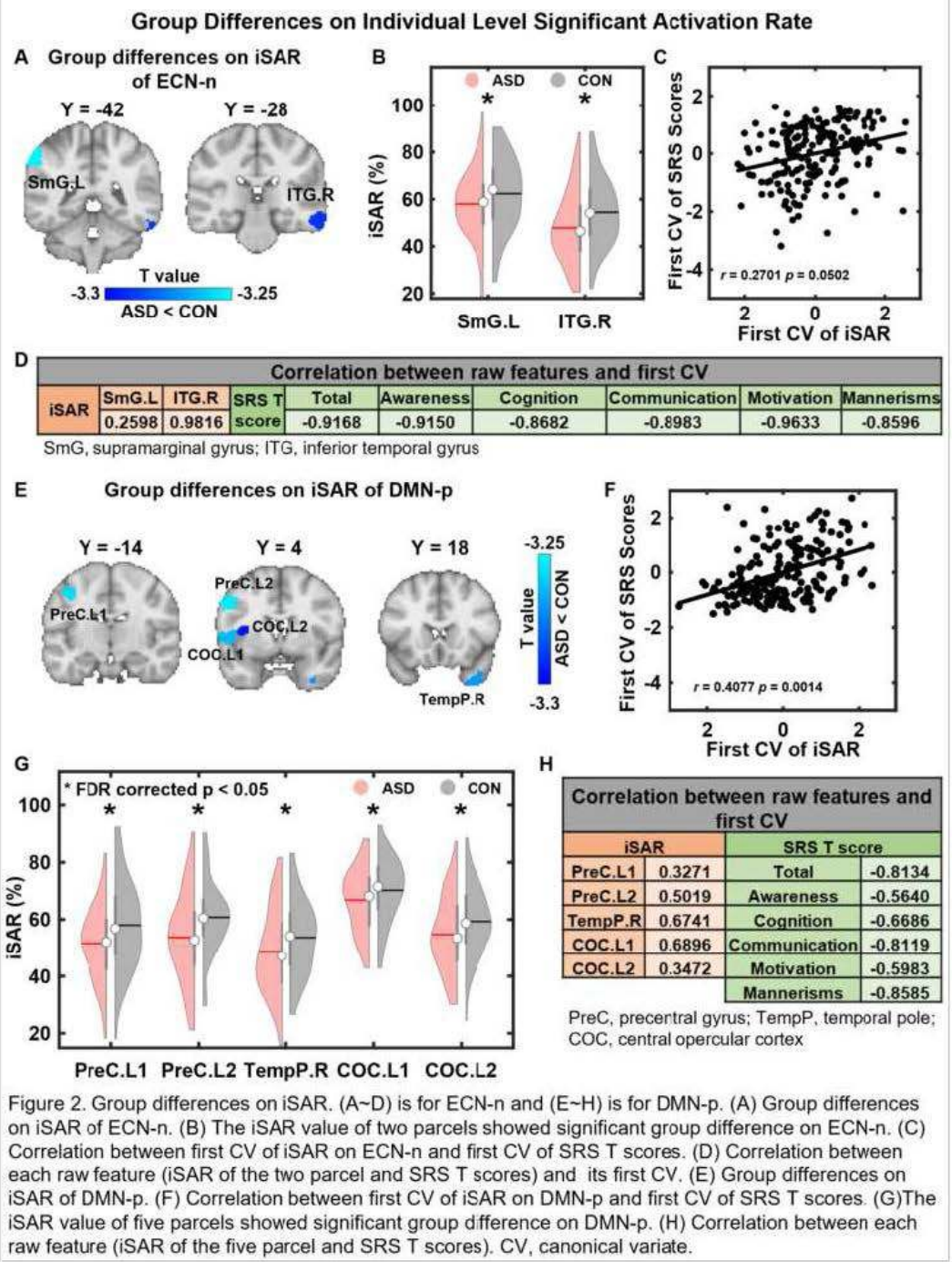

Figure 2. Group differences on iSAR. (A~D) is for ECN-n and (E~H) is for DMN-p. (A) Group differences on iSAR of ECN-n. (B) The iSAR value of two parcels showed significant group difference on ECN-n. (C) Correlation between first CV of iSAR on ECN-n and first CV of SRS T scores. (D) Correlation between each raw feature (iSAR of the two parcel and SRS T scores) and its first CV. (E) Group differences on iSAR of DMN-p. (F) Correlation between first CV of iSAR on DMN-p and first CV of SRS T scores. (G)The iSAR value of five parcels showed significant group difference on DMN-p. (H) Correlation between each raw feature (iSAR of the five parcel and SRS T scores). CV, canonical variate.

Conclusions: We defined six TNSs which yielded DMN, ECN and SN into three pairs. The DMN TNS pair had highest spatial stability while ECN TNS pair had lowest spatial stability. Besides, people with ASD had lower spatial stability on every TNS and the reduced spatial stability of ECN-n and DMN-p was related to severer social deficits.

References

1. Menon V. (2018), 'The Triple Network Model, Insight, and Large-Scale Brain Organization in Autism', Biol Psychiatry, vol. 84, no. 4, pp. 236-238
2. Liu X, et al. (2018). 'Co-activation patterns in resting-state fMRI signals', Neuroimage, vol. 180, Pt B, pp. 485-494
3. Di Martino A, et al. (2017). 'Enhancing studies of the connectome in autism using the autism brain imaging data exchange II', SCIENTIFIC DATA, vol. 4, pp. 170010
4. Schaefer A, et al. (2018). 'Local-Global Parcellation of the Human Cerebral Cortex from Intrinsic Functional Connectivity MRI', Cerebral Cortex, vol. 28, no. 9, pp. 3095-3114

Poster No 358

Synaptic-related developmental dysconnectivity in 22q11.2 deletion syndrome

Silvia Gini[1,2], Filomena Grazia Alvino[2], Antea Minetti[3], David Sastre-Yagüe[1,2], Charles Schleifer[4], Alexia Stuefer[1,2], Marco Pagani[2], Caterina Montani[2], Alberto Galbusera[2], Francesco Papaleo[5], Michael Lombardo[6], Massimo Pasqualetti[3], Carrie Bearden[4], Alessandro Gozzi[2]

[1]University of Trento, Rovereto, Italy, [2]Istituto Italiano di Tecnologia, Rovereto, Italy, [3]University of Pisa, Pisa, Italy, [4]University of California at Los Angeles, Los Angeles, CA, [5]Istituto Italiano di Tecnologia, Genova, Italy, [6]Laboratory for Autism and Neurodevelopmental Disorders, Istituto Italiano di Tecnologia, Rovereto, Italy

Introduction: 22q11.2 Deletion Syndrome (22q11DS) is a genetic syndrome characterized by an increased risk of neurodevelopmental disorders including autism and schizophrenia (Gur et al., 2017; Niklasson et al., 2009; Tang et al., 2014). 22q11DS has been consistently linked to alterations in large-scale functional connectivity (Mattiaccio et al., 2016; Scariati et al., 2016). However, the origin and biological determinants of such functional alterations remain largely unexplored. To bridge this knowledge gap, the current study leveraged a cross-species design to track the developmental trajectory of 22q11DS connectopathy and uncover its neurophysiological underpinnings.

Methods: Mouse studies We longitudinally mapped resting-state functional connectivity in wildtype (WT, n =22) and LgDel mice (n = 21), an established model of 22q11DS, at two developmental timepoints (juvenile, p33-37; adult, p105-120), using global connectivity (Cole et al., 2010). To assess the biological basis of functional connectivity alterations, we developmentally treated mice with the GSK3β inhibitor SB216763 and longitudinally mapped their functional connectivity (WT SB, n=22; LgDel SB, n=23). Spine density counting in prelimbic cortex and hippocampus was also performed in mice with and without GSK3β inhibition (Juvenile: WT n=4, WT SB n=4, LgDel n=6, LgDel SB n=7; Adult: WT n=4, WT SB n=4, LgDel n=4, LgDel SB n=4). Human studies To assess the relevance of our findings for human 22q11DS, we applied the same connectivity mapping methods to individuals with 22q11DS and healthy controls (HC) split into two age subgroups: childhood (6-11 years, 22q11DS n = 21, HC n = 31) and peri/post-puberty (12-30 years, 22q11DS n = 118, HC n = 86). Gene decoding analyses identified genes whose spatial expression matched that of significant age by genotype interaction. Gene enrichment analyses were used to test the overlap between these genes and interactors of GSK3β, or gene lists relevant for neurodevelopmental disorders. The relationship between 22q11DS dysconnectivity and Social Responsiveness Scale scores was assessed using a linear model.

Results: fMRI mapping in LgDel mice revealed patterns of age-specific fMRI dysconnectivity. Specifically, we found that widespread fMRI hyperconnectivity in juvenile mice reverted to focal hippocampal hypoconnectivity over puberty (Fig. 1a). Notably, fMRI connectivity changes were mirrored by co-occurring alterations in dendritic spine density (Fig. 1b), suggesting a synaptic origin for this phenomenon. Supporting this notion, we found that both synaptic and fMRI connectivity alterations in juvenile mice were normalized by developmental GSK3β inhibition (Fig. 1c-e). These results suggest that fMRI dysconnectivity in LgDel mice may be related to maladaptive synaptic homeostasis. In keeping with our mouse results, we identified a similar cortico-hippocampal hyper- to hypoconnectivity reconfiguration over puberty in human 22q11DS (Fig. 2a). Corroborating a synaptic origin of these changes, areas undergoing functional reconfiguration were transcriptionally enriched for synaptic proteins that interact with GSK3β (Fig. 2b, hypergeometric test: OR = 2.91, p= 0.00005). The same regions also exhibited a significant enrichment in autism-related genes (Fig. 2c), suggesting that dysconnectivity in these areas may be relevant to autism-related behavioral traits. In keeping with this notion, developmental dysconnectivity strength was strongly predictive of autism-relevant socio-behavioral symptoms (Fig. 2d).

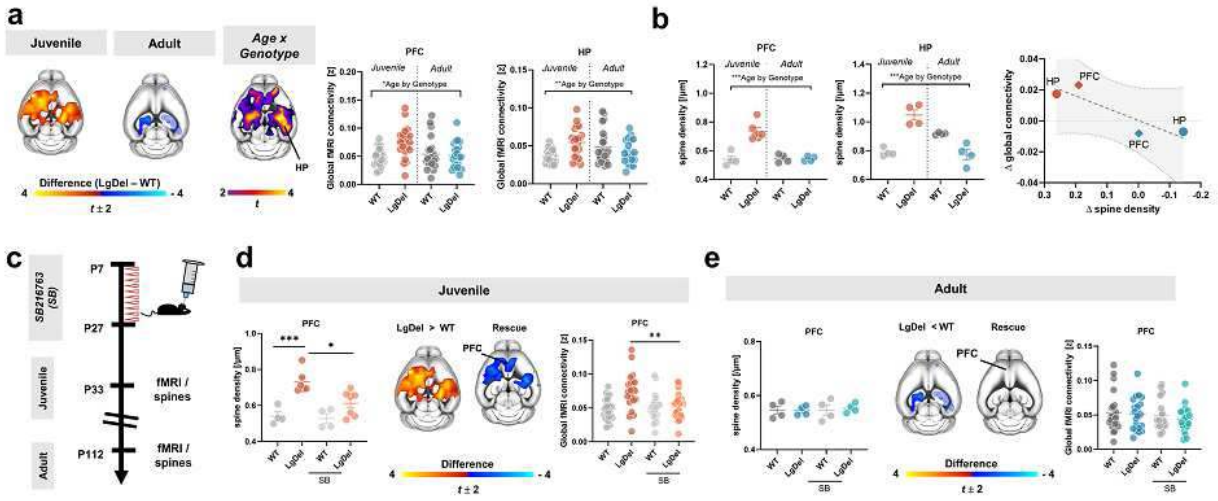

Figure 1. Functional dysconnectivity of LgDel mice undergoes developmental reconfiguration mirrored by synaptic alterations. a) Global connectivity mapping reveals cortico-hippocampal hyper-to-hypoconnectivity reconfiguration of LgDel mice's functional alterations. **b)** Dendritic spines density measurements across development in the prefrontal cortex (PFC) and hippocampus (HP) reveal a significant Age by Genotype interaction. Group differences in both global functional connectivity and spine density, calculated as delta, showed consistent trends across age (top right). **c)** Experimental timeline of the GSK3β-inhibitor (SB216763) administration. **d)** In juvenile stage, both functional connectivity and increased spine density in PFC are rescued by GSK3β inhibition. **e)** Neither functional nor synaptic alterations were observed in PFC of adult LgDel mice.

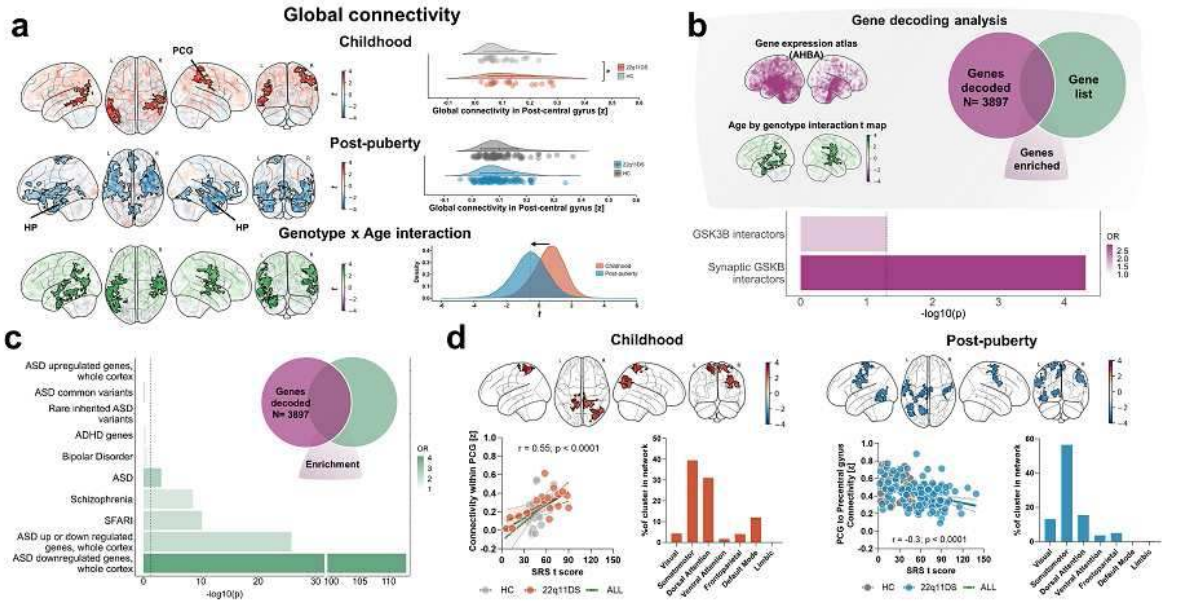

Figure 2. Developmental reconfiguration of functional connectivity in human 22q11DS is related to synaptic mechanisms and relevant for autism. a) Functional connectivity in 22q11DS undergoes the same hyper-to-hypoconnectivity reconfiguration observed in LgDel mice. **b)** Gene decoding analyses (top) suggesting a link between age-dependent dysconnectivity reconfiguration and synaptic interactors of GSK3β. **c)** Gene enrichment analyses corroborate the clinical relevance of the observed reconfiguration for autism. **d)** Correlation between functional connectivity of hubs undergoing reconfiguration and somatomotor network is correlated with autism-related traits.

Conclusions: We document a previously unreported reconfiguration of fMRI dysconnectivity in 22q11DS over puberty. Mouse and human studies converge to suggest that the observed fMRI alterations are underpinned by synaptic-dependent mechanisms, and could be predictive of socio-behavioral alterations. These results shed light on the etiopathological significance and behavioral relevance of fMRI connectivity alterations in 22q11DS.

References

1. Cole, M. W., Pathak, S., & Schneider, W. (2010). Identifying the brain's most globally connected regions. NeuroImage, 49(4), 3132-3148.
2. Gur, R., Bassett, A., McDonald-McGinn, D., Bearden, C., Chow, E., Emanuel, B., Owen, M., Swillen, A., Van den Bree, M., & Vermeesch, J. (2017). A neurogenetic model for the study of schizophrenia spectrum disorders: the International 22q11. 2 Deletion Syndrome Brain Behavior Consortium. Molecular Psychiatry, 22(12), 1664-1672.
3. Mattiaccio, L. M., Coman, I. L., Schreiner, M. J., Antshel, K. M., Fremont, W. P., Bearden, C. E., & Kates, W. R. (2016). Atypical functional connectivity in resting-state networks of individuals with 22q11. 2 deletion syndrome: associations with neurocognitive and psychiatric functioning. Journal of neurodevelopmental disorders, 8(1), 1-14.

4. Niklasson, L., Rasmussen, P., Óskarsdóttir, S., & Gillberg, C. (2009). Autism, ADHD, mental retardation and behavior problems in 100 individuals with 22q11 deletion syndrome. Research in developmental disabilities, 30(4), 763-773.
5. Scariati, E., Schaer, M., Karahanoglu, I., Schneider, M., Richiardi, J., Debbané, M., Van De Ville, D., & Eliez, S. (2016). Large-scale functional network reorganization in 22q11. 2 deletion syndrome revealed by modularity analysis. Cortex, 82, 86-99.
6. Tang, S., Yi, J., Calkins, M., Whinna, D., Kohler, C., Souders, M., McDonald-McGinn, D., Zackai, E., Emanuel, B., & Gur, R. (2014). Psychiatric disorders in 22q11. 2 deletion syndrome are prevalent but undertreated. Psychological medicine, 44(6), 1267-1277.

Poster No 359

Structural connectome differences between autism and neurotypical control groups using autoencoder

Yurim Jang[1], Hyoungshin Choi[2,3], Seulki Yoo[4], Hyunjin Park[3,5], Bo-yong Park[6,7,3]

[1]Artificial Intelligence Convergence Research Center, Inha University, Incheon, Korea, Republic of, [2]Department of Electrical and Computer Engineering, Sungkyunkwan University, Suwon, Republic of Korea, [3]Center for Neuroscience Imaging Research, Institute for Basic Science, Suwon, Korea, Republic of, [4]Convergence Research Institute, Sungkyunkwan University, Suwon, Republic of Korea, [5]School of Electronic and Electrical Engineering, Sungkyunkwan University, Suwon, Korea, Republic of, [6]Department of Data Science, Inha University, Incheon, Korea, Republic of, [7]Department of Statistics and Data Science, Inha University, Incheon, Korea, Republic of

Introduction: Autism spectrum disorder is a pervasive condition during development. Individuals with autism show deficits in sensory and social communication skills[1]. Recent neuroimaging studies based on magnetic resonance imaging (MRI) found alterations in large-scale functional brain networks using low-dimensional features[2],[3]. Here, we aimed to assess network disorganization of the brain in individuals with autism by generating low-dimensional latent features of structural connectivity using an autoencoder.

Methods: We obtained diffusion MRI of 80 individuals with autism (mean ± standard deviation (SD) age = 12.1 ± 4.9 years) and 61 neurotypical controls (13.2 ± 4.0 years) from the Autism Brain Imaging Data Exchange-II (ABIDE-II) initiative[4]. The diffusion MRI was preprocessed using MRtrix3[5], and the structural connectivity matrix was constructed based on probabilistic tractography with 200 brain regions defined using the Schaefer atlas. After controlling for age, sex, and site from the structural connectivity, we trained the autoencoder, which consisted of the encoder and decoder layers. The encoder reduces high-dimensional input data to generate low-dimensional latent features, and the decoder reconstructs the original data using the latent features. The model consisted of five encoder and decoder layers, and we used Averaged Stochastic Gradient Descent (ASGD) optimizer with a learning rate of 0.00008. The model was trained for the autism and neurotypical control groups, respectively. The performance of the model was assessed based on the linear correlations between the original and reconstructed data. We then calculated the integrated gradient values, which denote the attribution of each element of the input connectivity matrix for predicting the latent features[6]. After the z-normalization, we compared the integrated gradient values between autism and control groups using two-sample t-tests and 1,000 permutation tests. The multiple comparisons were corrected using a false discovery rate (FDR) < 0.05. We adopted canonical correlation analysis (CCA) to investigate the association between the integrated gradient values and the symptom severity of autism measured by the Autism Diagnostic Observation Schedule (ADOS). The optimal number of canonical components was determined using five-fold cross-validation, and the degrees of the associations were assessed using the explained variance.

Results: The autoencoder model revealed significant correlations between the original and reconstructed data for autism (mean ± SD; 100 bootstraps = 0.427 ± 0.165) and control groups (0.271 ± 0.133) (Fig.1A). Between-group comparison of the integrated gradient values showed the highest effects within the default-mode network and between the visual and frontoparietal/ventral networks, while the smallest effects were found within the visual network and between the somatomotor and dorsal attention networks (Fig.1B). The brain-behavior associations revealed that the three canonical components were significantly associated (1st: $r = 0.726$, $p < 0.001$; 2nd: $r = 0.732$, $p < 0.001$; 3rd: $r = 0.647$, $p < 0.001$; Fig. 2). In particular, the ADOS communication sub-score was strongly associated with the integrated gradient values within the default-mode network and between somatomotor-visual/limbic/frontoparietal networks.

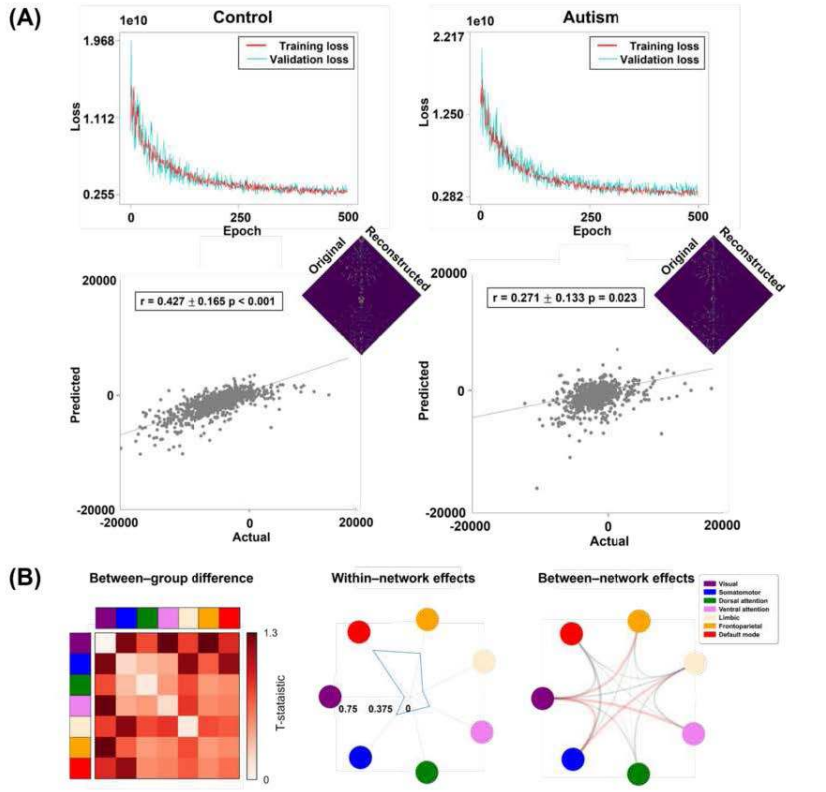

Figure 1. Feature representation learning based on the autoencoder. (A) The upper panels show the loss graphs of training and validation datasets according to epochs for autism (left) and neurotypical control groups (right). The scatter plots on the bottom represent correlations between the actual and reconstructed data. **(B)** The between-group differences in integrated gradient values within- and between-networks. The spider plot shows t-values within 7 networks, while the circos plot represents the t-values between 7 networks.

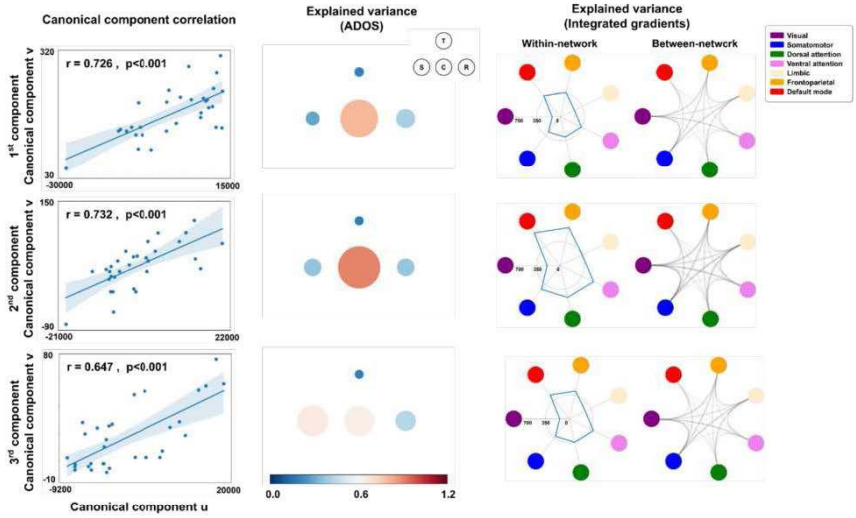

Figure 2. Canonical correlation analysis between the integrated gradient values and ADOS scores. The correlation between the canonical components *v* and *u* is plotted (left). The circle plots for each component illustrate the explained variance in symptom severity of autism, as measured by ADOS (middle). The explained variance in integrated gradient values within- and between networks (right). *Abbreviations*: ADOS, Autism Diagnostic Observation Schedule; T, total; S, social cognition; C, communication; R, repeated behavior/interest.

Conclusions: We identified structural connectivity differences between individuals with autism and neurotypical control via low-dimensional latent features of the autoencoder. In particular, sensory and transmodal regions showed significant between-group differences. Additionally, the differences were related to the communication skills in autism. Our findings may improve the understanding of autism.

References
1. D. L. Christensen et al., “Prevalence and Characteristics of Autism Spectrum Disorder Among Children Aged 8 Years — Autism and Developmental Disabilities Monitoring Network, 11 Sites, United States, 2012,” MMWR. Surveillance Summaries, vol. 65, no. 13, pp. 1–23, Nov. 2018
2. B. Park et al., “Differences in subcortico-cortical interactions identified from connectome and microcircuit models in autism,” Nat Commun, vol. 12, no. 1, Dec. 2021
3. S.-J. Hong et al., “Atypical functional connectome hierarchy in autism,” Nat Commun, vol. 10, no. 1, Dec. 2019
4. A. di Martino et al., “Enhancing studies of the connectome in autism using the autism brain imaging data exchange II,” Sci Data, vol. 4, no. 1, Dec. 2017
5. J.-D. Tournier et al., “MRtrix3: A fast, flexible and open software framework for medical image processing and visualisation,” Neuroimage, vol. 202, p. 116137, Nov. 2019
6. M. Sundararajan, A. Taly, and Q. Yan, “Axiomatic Attribution for Deep Networks,” Mar. 2017.
7. Hardoon, D. R., Szedmak, S., & Shawe-Taylor, J. (2004). Canonical Correlation Analysis: An Overview with Application to Learning Methods. Neural Computation, 16(12), 2639–2664.

Acknowledgements
Funding: NRF-2021R1F1A1052303; NRF-2022R1A5A7033499, IITP funded by (MSIT) (No. 2022-0-00448, ; No. RS-2022-00155915, (Inha University); No. 2021-0-02068, Artificial Intelligence Innovation Hub), IBS-R015-D1.

Poster No 360

Understanding the Development of Mental Disorders Through Longitudinal Neuroanatomy in Adolescents

Jiangyun Hou[1], Guido Wingen[2], Dirk Smit[2], Laurens Mortel[2], Shu Liu[2], Weijian Liu[2]

[1]Amsterdam UMC location University of Amsterdam, Amsterdam, North Holland, [2]Amsterdam UMC location University of Amsterdam, Amsterdam, Noord-Holland

Introduction: Many mental health issues are neurodevelopmental in nature with childhood and adolescence being a particularly sensitive period for onset of symptoms, which affect a significant number of adolescents[1]. Given the rising prevalence of mental health issues among adolescents in recent years, understanding the development of these conditions has become a critical public health objective. Here, we applied two separate linear models to examine between-group differences at baseline and the changes at 2 year follow up compared to baseline to identify the development of brain during the onset of mental health problems.

Methods: We selected ABCD study[2] participants with initial t-scores under 65 on the DSM-oriented CBCL scales, but who exceeded this threshold at two-year follow-up[3]. After excluding those without usable MRI data or a psychiatric history at baseline, our identified 55 individuals with ADHD, 94 with anxiety, 44 with conduct disorders, 105 with depression, 49 with oppositional defiant disorders, 144 with somatic symptoms, and 1679 controls. Our imaging data included 1876 image features from 6 modalities extracted: structural MRI, diffusion MRI, and functional MRI data (resting state MRI, task fMRI: Monetary Incentive Delay task (MID), task fMRI: stop signal task (SST), task fMRI: emotional n-back (EN-back))4. Then, we built two linear models including all controls: For baseline data: baseline data~ Group + Age +Sex +IQ + EA; For the changes from baseline to 2 year follow up: 2 year follow up data ~ Group+ baseline data + Age +Sex +IQ +EA in R for six disorders in six modalities to find if there any significant differences (p(FDR)<0.05/6) between healthy controls and patients with age, sex, IQ and educational level of parents (EA) as covariates. In addition, we also estimated correlation matrices of these six modalities based on the t values from above models to investigate the comparability of imaging effects across the disorders.

Results: We found significant development of brain from three disorders:1. the ADHD group showed higher correlation between ventral attention network (VAN) and right caudate, and a lower correlation between VAN and right putamen than HC from resting state fMRI in the changes model. 2. Individuals with conduct problems showed decreased mean beta weights for task fMRI: SST correct stop versus incorrect stop contrast in left pallidum compared to HC in the changes model. 3. Oppositional defiant group showed increased volume in left cerebral white matter from structure MRI, and increased fiber tract volume of all DTI atlas tract fiber tracts, of DTI atlas tract in the left superior longitudinal fasiculus, in the left hemisphere and left hemisphere without corpus callosum, in the left striatal inferior frontal cortex and left superior corticostriate-parietal cortex only, in the foreceps major, foreceps minor and corpus callosum, and in the left superior corticostriate. And all these features found from interaction models were not shown at baseline. However, there is no result from anxiety group, depression group and somatic group, compared to controls. From these three diseases, we can find some features close to the reading line (p=0.05/6). From the correlation matrices, the imaging data showed different correlations between different groups in both baseline and longitudinal models except for structural MRI.

Conclusions: In conclusion, we have discovered some important brain imaging indicators and brain areas in the development of ADHD, conduct, and oppositional defiant problems. At the same time, complex relationships between six diseases were found in different modalities. This will help to further understand the changes in the brain during the development of these diseases and can provide some new ideas for future intervention and treatment. Together, this has the potential to improve the treatment of children with mental health problems.

References

1. Kessler, R.C., et al. Lifetime prevalence and age-of-onset distributions of DSM-IV disorders in the National Comorbidity Survey Replication. Archives of general psychiatry 62, 593-602 (2005).
2. Jernigan, T.L., Brown, S.A. & Dowling, G.J. The adolescent brain cognitive development study. Journal of research on adolescence: the official journal of the Society for Research on Adolescence 28, 154 (2018).
3. Krol, N.P., De Bruyn, E.E., Coolen, J.C. & van Aarle, E.J. From CBCL to DSM: a comparison of two methods to screen for DSM-IV diagnoses using CBCL data. Journal of Clinical Child and Adolescent Psychology 35, 127-135 (2006).
4. Hagler Jr, D.J., et al. Image processing and analysis methods for the Adolescent Brain Cognitive Development Study. Neuroimage 202, 116091 (2019).

Poster No 361

Functional mapping of facial movements in Tourette Syndrome

Caitlin Smith[1], Mairi Houlgreave[1], Michael Asghar[2], Susan Francis[2], Stephen Jackson[1]

[1]School of Psychology, University of Nottingham, Nottingham, England, [2]Sir Peter Mansfield Imaging Centre, School of Physics and Astronomy, University of Nottingham, Nottingham, England

Introduction: Key mechanisms implicated in the mediation of cortical activity and cortical representations are surround inhibition and the inhibitory neurotransmitter γ-aminobutyric acid (GABA). For instance, animal research has shown GABA antagonist injected into the motor cortex results in the fusion of motor representations between adjacent muscles and weakens sensory map plasticity and receptive field tuning (Jacobs et al., 1991). Evidence from Focal Hand Dystonia, a movement disorder characterised by involuntary muscle contractions in the hands and arms, has supported this link with evidence of impaired sensorimotor GABAergic inhibition (Levy et al., 2002) and abnormal and disorganised cortical mapping of the hand and digits (Meunier et al., 2001). Similarly, Tourette Syndrome (TS) is a movement disorder thought to be characterised by altered inhibition (Jackson et al., 2015). TS is a neurodevelopmental, hyperkinetic movement disorder involving involuntary motor and vocal tics. However, it is unclear if functional mapping of body parts commonly involved in tics are affected in TS, as this has not yet been investigated. This study aimed to use task-fMRI to investigate the functional representations of different facial movements, a region commonly affected by tics in TS, in the motor and sensory cortices of those with TS and in healthy controls (HC).

Methods: Task-fMRI acquisition: 3T fMRI data were acquired using a 32-channel head coil (Philips, Ingenia) in 19 participants with TS or chronic tic disorder (8F, mean age: 34.7, SD: 11.2) and 13 HC participants (6F, mean age: 27.3, SD: 5.2). BOLD fMRI parameters included single-shot 2D T2*-weighted GE-EPI sequence (2.5 mm thickness, 48 slices, MB = 4, TR/TE = 1000/30 ms). Three fMRI task blocks were acquired with participants visually instructed to perform a facial movement at 1Hz (8s ON, 24s OFF; 8 cycles). Each task block consisted of a different facial movement; blinking, grimacing, and jaw clenching. These movements are very common tics experienced by those with TS (Baizabal-Carvallo et al., 2023). Video recordings were acquired during scans to obtain timings of movements. Analysis: fMRI data was distortion corrected using FSL-TOPUP and thermal noise was removed using NORDIC (Andersson et al., 2003; Vizioli et al., 2021). The resulting de-noised datasets were pre-processed and put through first-level analyses using FSL-FEAT (FMRI Expert Analysis Tool; Jenkinson et al., 2012), which included registration, high-pass temporal filtering, spatial smoothing, normalisation, and motion correction. A dataset was removed if absolute motion displacement was >2.5mm, leaving 9 TS and 12 HC datasets for the blink task, 9 TS and 10 HC datasets for the grimace task, and 10 TS and 11 HC datasets for the jaw clench task. A mixed-effects analysis was used to average responses in TS and HC groups for each block (blink, grimace, or jaw clench). Results were masked to cover bilateral supplementary motor areas (SMA) and bilateral pre- and post-central gyri as defined by the Harvard-Oxford Cortical Structural atlas, before applying cluster correction determined by a Z-threshold of 2.3 ($p = 0.05$; Worsley, 2001).

Results: Significant cluster activations were identified across the bilateral SMA and pre- and post-central gyri for blink, grimace, and jaw clench blocks in both the HC and TS groups (Figure 1; $Z=2.3$, $p<.05$). However, these clusters did not significantly differ between groups suggesting similar activations within the bilateral SMA and pre- and post-central gyri across groups.

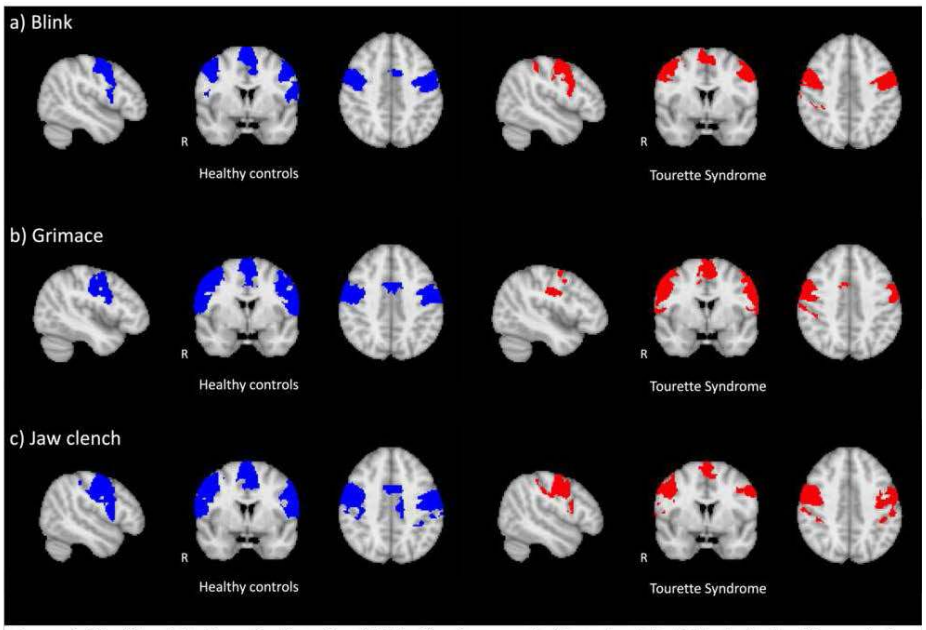

Figure 1. Significant cluster activations for a) blink, b) grimace and c) jaw clench task blocks for healthy control participants (blue) and participants with Tourette Syndrome (red). Clusters were thresholded at Z=2.3 (p<.05).

Conclusions: This data suggests that functional mapping of facial movements (blinking, grimacing and jaw clenching) are not altered in TS.

References

1. Andersson, J.L.R., et al. (2003), 'How to correct susceptibility distortions in spin-echo echo-planar images: application to diffusion tensor imaging', NeuroImage, vol. 20, no. 2, pp. 870-888.
2. Baizabal-Carvallo, J.F. et al. (2023), 'Oromandibular tics associated with Tourette syndrome', Journal of Neurology, vol. 270, pp. 2591–2596.
3. Jackson, G.M., et al. (2015), 'Inhibition, Disinhibition, and the Control of Action in Tourette Syndrome', Trends in Cognitive Science, vol. 19, no. 11, pp. 655–665.
4. Jacobs, K.M., et al. (1991), 'Reshaping the cortical motor map by unmasking latent intracortical connections', Science, vol. 251, no. 4996, pp. 944–947.
5. Jenkinson, M., et al. (2012), 'FSL', NeuroImage, vol. 62, no. 2, pp. 782–790.
6. Worsley, K.J. (2001), 'Statistical analysis of activation images', In Jezzard P., et al. (Eds.), Functional MRI: An Introduction to Methods (Ch. 14), Oxford Academic, pp. 251-270.
7. Levy, L.M., et al. (2002), 'Impaired brain GABA in focal dystonia', Annals of Neurology, vol. 51, no. 1, pp. 93–101.
8. Meunier, S., et al. (2001), 'Human brain mapping in dystonia reveals both endophenotypic traits and adaptive reorganization', Annals of Neurology, vol. 50, no. 4, pp. 521-527.
9. Vizioli, L. et al. (2021), 'Lowering the thermal noise barrier in functional brain mapping with magnetic resonance imaging', Nature Communications, vol. 12, no. 1, 5181.

Poster No 362

Sensory Symptoms May Mediate Changes of Social Symptoms and Social Brain Development in Autism

Yi-Ling Chien[1], Susan Shur-Fen Gau[1]

[1]National Taiwan University Hospital, Taipei, Taiwan

Introduction: Sensory symptoms are common in individuals with autism spectrum disorder (ASD) and are associated with social deficits in ASD. Sensory sensitivity can influence selective attention to social stimuli, decoding intentions, social reciprocity, and adherence to social norms of behavior. Whether and how sensory symptoms mediate social symptoms and social brain network during the development is unclear. This study aims to investigate how sensory symptoms mediate social deficits and the relationship between social brain network and social deficits in a longitudinal ASD sample.

Methods: This study recruited 248 individuals with ASD (mean age 10.7 years old, male 87%) and 120 typically developing controls (TDC, mean age 11.4 years, male 75%). The participants were followed for 7 years in ASD in average and 5 years in TDC. Social deficits were measured by the Social Responsiveness Scale (SRS), while sensory symptoms were evaluated by sensory items in the SRS and Short Sensory Profile. A subsample of the participants underwent head MRI at two time points. We used single and multiple mediation analysis to examine whether sensory symptoms can mediate social development. We

also examine whether sensory symptoms can mediate the prediction of the social brain structures towards social deficits at follow-up.

Results: We found that sensory symptoms were significantly correlated with social deficits at each cross-sectional time point. Besides, we found that sensory symptoms at either Time 1 or Time 2 significantly predict social deficits at Time 2, and significantly mediate social deficits from Time 1 to Time 2. In neuroimage analysis, we also found that sensory symptoms may mediate the relationship between some social brain structures at Time 1 and social deficits at Time 2, including the gray matter volume of the right posterior middle cingulate cortex, right lateral fissure (posterior part), left inferior parietal cortex (angular part and supramarginal part), left precuneus, right parieto-occipital cortex, and left superior occipital cortex.

Conclusions: Our findings suggested that sensory symptoms may mediate the changes in social deficits behaviorally and the relationship between gray matter volume of social brain structures and social deficits at follow-up. These findings suggest that clinical remediation on sensory symptoms might potentially help improvement on social functioning, that warrants further investigation.

References

1. Crasta JE, Green OJ, Gavin WJ, Davies PL. The Relationship Between Attention, Sensory Processing, and Social Responsiveness Among Adults on the Autism Spectrum. Research in Autism Spectrum Disorder. 2009; 3(4): 959–966. doi: 10.1016/j.rasd.2009.05.003

Poster No 363

Potent DWI marker to predict the improvement of core language after pediatric epilepsy surgery

Jeong-Won Jeong[1], Min-Hee Lee[1], Hiroshi Uda[1], Aimee Luat[1], Csaba Juhasz[1], Eishi Asano[1]

[1]Wayne State University, Detroit, MI

Introduction: Subsets of children with drug-resistant focal epilepsy show improvement in language skills postoperatively, which may enhance the overall quality of life for these individuals[1,2]. This study seeks to explore a preoperative imaging marker specific to children with left-hemispheric seizure focus who had a short-term postoperative language enhancement. We hypothesized that the right hemisphere of such patients would have an increase in “local efficiency of axonal connectivity” that facilitates information transfer between brain regions, especially associated with core language function.

Methods: 19 patients with drug-resistant epilepsy associated with left-hemispheric seizure focus and language dominance (11.9±4.3 years old) underwent both preoperative 3T DWI tractography scan using 55 encoding directions at b=1000 s/mm2 and pre-/postoperative neuropsychological language tests (average interval: 2.5 months, 6 patients improved core language scores after surgery). 3T DWI tractography data of 28 age-matched healthy controls were also obtained at the same scanner. Whole-brain tractography was sorted to construct two whole-brain backbone DWI connectomes (DWIC), whose elements were total tract counts of pair-wise connections weighted by average fractional anisotropy (FA) values to account for the axonal integrity inferring alterations in the axonal diameter, fiber density or myelin structure, 1) raw DWIC with a total of 1477 connections that may have false-positive tracts[3] in each connection (i.e., wiggly tract and broken tract, etc.) and 2) clean DWIC with the 1477 connections, where deep convolutional neural network (DCNN) tract classification3 removes all potential false-positive tracts in each connection. From each DWIC of two DWIC data, left and right intra-hemispheric networks were extracted. In each network, local efficiency analogue (LEA)[4] related to the average resistance distance between a given node and the remaining nodes was calculated as a metric quantifying the efficiency of local information flow from the given node. Lateralization index (i.e., LI = [right LEA–left LEA]/[right LEA+left LEA]) was extracted from individual nodes. The Kruskal-Wallis test was then used to identify key nodes showing significant difference of LI value between two groups: improvement vs. no improvement. The LI values of key nodes were fused using ranked supervised multivariate canonical correlation (SMVCCA)[5] and evaluated using a multi-layer perceptron (MLP) to predict patients with postsurgical language improvement via 3-fold cross validation.

Results: In contrast to the no improvement group, the improvement group exhibited higher LI values across multiple nodes of the intra-hemispheric network with significant group differences at $p \leq 0.05$ (Fig. 1). Notably, the LI values in the improvement group surpassed even those of healthy controls. Clean DWIC demonstrated superior accuracy in predicting three classes, with a BA of 84±9% from MLP and BA of 93±3% from MLP with ranked sMVCCA, compared to raw DWIC (68±9% and 85±2%, left plot of Fig. 2). The LI values at multiple nodes, including thalamus (THA), superior temporal gyrus (STG), precentral gyrus (preCG), superior parietal gyrus (SPG), and superior occipital gyrus (SOC), were identified as crucial markers that exhibited atypical increases of LEA values (and FA values) in the right hemisphere, contributing significantly to the prediction of short-term language improvement (right plot of Fig. 2).

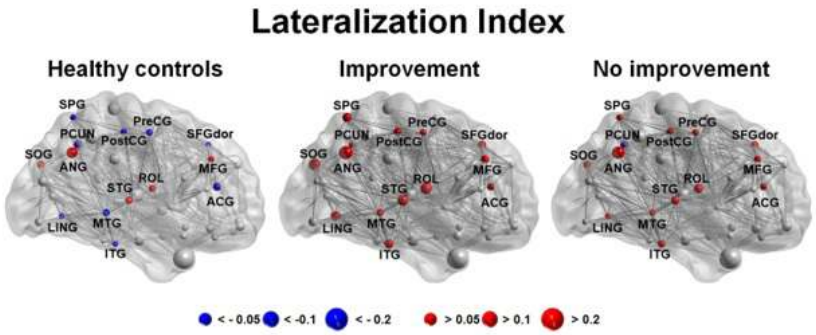

Figure 1. Lateralization index (LI) values of local efficiency analogue (LEA) obtained from individual nodes of left and right intra-hemispheric networks that were constructed from clean DWIC data of three groups: healthy control (n= 28), improvement (n= 6), and no improvement (n= 13). The size of each colored sphere indicates the magnitude of LI value averaged across subjects (i.e., red/blue for positive/negative LI representing increase of LEA in right/left hemisphere, respectively).

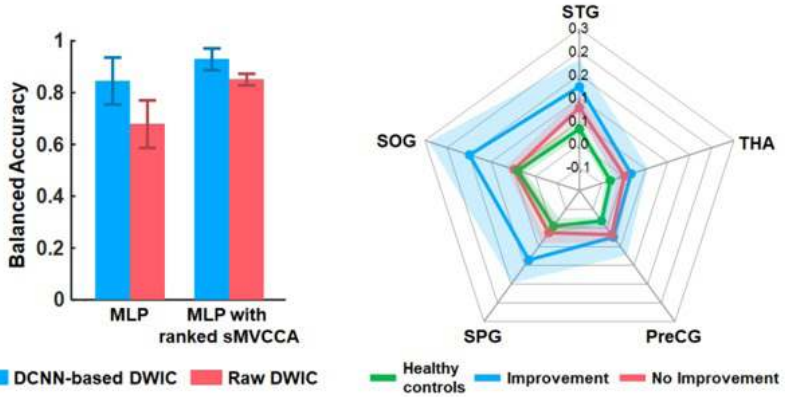

Figure 2. (left) Mean and one standard deviation of balanced accuracy (BA) obtained from 1) multi-layer perceptron (MLP) using raw LI values and 2) MLP using fused LI values as its input. (right) LI values of individual key nodes identified as the most predictive of postoperative short-term language improvement.

Conclusions: This study provided initial evidence in left-hemispheric epilepsy indicating an increase in local efficiency and axonal integrity within the contralateral motor-language-visual network that could be a specific pattern of neural plasticity influencing the favorable likelihood of postoperative language improvement. More investigation with a larger study cohort is essential to identify who is likely to benefit from early surgery.

References

1. Pestana Knight, E. M. (2015), "Increasing utilization of pediatric epilepsy surgery in the united states between 1997 and 2009", Epilepsia, vol. 56, no. 3, pp. 375–381.
2. Edwards, J. C., (2018), "Marginal decision-making in the treatment of refractory epilepsy", J. Med. Econ., vol. 21, no. 5, pp. 438–442.
3. Lee, M.-H., (2019), "Improving reproducibility of diffusion connectome analysis using deep convolutional neural network model", Proc. Int. Soc. Magn. Reson. Med., p. 3578.
4. Klein, D. J. (1993), "Resistance distance", Journal of Mathematical Chemistry, vol. 12, pp. 81–95, 1993.
5. Lee, G., (2015), "Supervised multi-view canonical correlation analysis (smvcca): Integrating histologic and proteomic features for predicting recurrent prostate cancer", IEEE Trans. Med. Imaging, vol. 34, no. 1, pp. 284–297.

Poster No 364

Identification of sex differences in autism using class imbalance mitigated functional connectivity

Jong Young Namgung[1], Jong Min Mun[2], Yeongjun Park[3], Jaeoh Kim[1,4], Bo-yong Park[1,4,5]

[1]Department of Data Science, Inha University, Incheon, Republic of Korea, [2]Marshall School of Business, University of Southern California, Los Angeles, CA, United States, [3]Department of Computer Engineering, Inha University, Incheon, Republic of Korea, [4]Department of Statistics and Data Science, Inha University, Incheon, Republic of Korea, [5]Center for Neuroscience Imaging Research, Institute for Basic Science, Suwon, Republic of Korea

Introduction: Autism spectrum disorder (ASD) is a common psychiatric condition during development, and individuals with ASD show impaired social interaction skills and restricted/repetitive behaviors (Mottron et al. 2006). The natural characteristic

of ASD is that males tend to be diagnosed more frequently than females (Werling and Geschwind 2013). Due to the sex imbalance in ASD, we lack an understanding of the differences in connectome organization of the brain between male and female individuals with ASD. In this study, we matched the sex ratio using a Gaussian mixture model-based oversampling technique and investigated the differences in functional connectivity between male and female ASDs.

Methods: We obtained T1-weighted structural MRI and resting-state functional MRI (rs-fMRI) data of 507 individuals with ASD (mean ± SD age = 17.08 ± 8.50 years; 12.22 % female) and 553 typically developing controls (mean ± SD age = 17.10 ± 7.74 years; 17.35 % female) from Autism Brain Imaging Data Exchange I initiative (ABIDE-I) (Di Martino et al. 2014), and the imaging data was preprocessed using micapipe (Cruces et al. 2022). The functional connectivity matrix was constructed by calculating linear correlations of time series between different brain regions defined using the Schaefer atlas with 300 parcels (Schaefer et al. 2018). We applied diffusion map embedding to estimate low-dimensional representations of functional connectivity (i.e., gradients) (Margulies et al. 2016; Vos de Wael et al. 2020; Coifman and Lafon 2006) and summarized it according to seven intrinsic functional networks (Thomas Yeo et al. 2011). To adjust the class imbalance problem between sexes, we estimated the gradient distribution of the female group using the Gaussian mixture model and generated synthetic samples from the estimated distributions. Then, we assessed the interaction effects of sex and group to evaluate sex-related differences in functional gradients. The significance was assessed using 1,000 permutation tests, and multiple comparisons across brain networks were corrected using a false discovery rate (FDR) < 0.05 (Benjamini and Hochberg 1995).

Results: The generated functional gradient differentiated sensory regions and default mode areas (Fig. 1a). The oversampled gradients of females with ASD and control groups showed similar spatial patterns with the actual data. When we assessed the interaction effect between sex and group, the default mode network showed a significant effect (t = -5.63, p-perm-FDR < 0.001; Fig. 1b). In addition, the visual (t = 2.22, p-perm-FDR = 0.098), somatomotor (t = 2.63, p-perm-FDR = 0.079), and dorsal attention networks (t = 2.73, p-perm-FDR = 0.079) showed moderate effects. Specifically, the gradient values decreased in females with ASD than controls in the default mode network, while those of male ASDs did not change. The gradient values of the sensory and attention networks showed opposite patterns.

Conclusions: In this study, we opted for the Gaussian mixture model-based oversampling approach to mitigate sex imbalance in the ASD dataset and observed significant sex-related differences in functional gradients in individuals with ASD. Our systematic analyses may provide insights for understanding the heterogeneity of ASD. Funding: National Research Foundation of Korea (NRF-2021R1F1A1052303; NRF-2022R1A5A7033499), Institute for Information and Communications Technology Planning and Evaluation (IITP) funded by the Korea Government (MSIT) (No. 2022-0-00448, Deep Total Recall: Continual Learning for Human-Like Recall of Artificial Neural Networks; No. RS-2022-00155915, Artificial Intelligence Convergence Innovation Human Resources Development (Inha University); No. 2021-0-02068, Artificial Intelligence Innovation Hub), Institute for Basic Science (IBS-R015-D1).

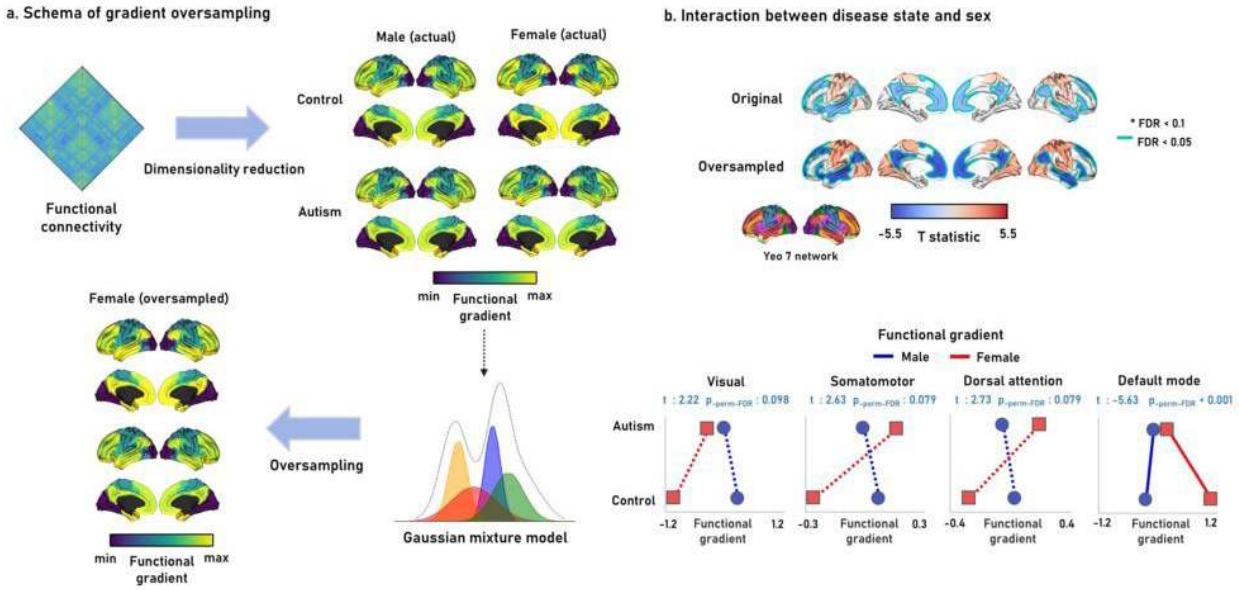

Fig. 1 | Oversampled functional gradients and sex-related differences. (a) We generated gradients from the functional connectivity data using dimensionality reduction techniques. We oversampled the gradients of female participants using a Gaussian mixture model. **(b)** T-statistics of the brain networks that showed moderate ($p_{perm\text{-}FDR} < 0.1$) and significant ($p_{perm\text{-}FDR} < 0.05$) interaction effects are shown on the brain surfaces. Significant regions are highlighted with a green border line. The interaction plots are visualized for the network that showed moderate or significant interaction effects. Solid lines indicate significant effects, and the dotted lines indicate moderate effects. *Abbreviations:* FDR, false discovery rate.

References
1. Benjamini, Yoav, and Yosef Hochberg. 1995. “Controlling the False Discovery Rate: A Practical and Powerful Approach to Multiple Testing.” Journal of the Royal Statistical Society: Series B (Methodological) 57 (1): 289–300.
2. Coifman, Ronald R., and Stéphane Lafon. 2006. “Diffusion Maps.” Applied and Computational Harmonic Analysis 21 (1): 5–30.
3. Cruces, Raúl R., Jessica Royer, Peer Herholz, Sara Larivière, Reinder Vos de Wael, Casey Paquola, Oualid Benkarim, et al. 2022. “Micapipe: A Pipeline for Multimodal Neuroimaging and Connectome Analysis.” NeuroImage 263 (November): 119612.
4. Margulies, Daniel S., Satrajit S. Ghosh, Alexandros Goulas, Marcel Falkiewicz, Julia M. Huntenburg, Georg Langs, Gleb Bezgin, et al. 2016. “Situating the Default-Mode Network along a Principal Gradient of Macroscale Cortical Organization.” Proceedings of the National Academy of Sciences of the United States of America 113 (44): 12574–79.
5. Martino, A. Di, C. G. Yan, Q. Li, E. Denio, F. X. Castellanos, K. Alaerts, J. S. Anderson, et al. 2014. “The Autism Brain Imaging Data Exchange: Towards a Large-Scale Evaluation of the Intrinsic Brain Architecture in Autism.” Molecular Psychiatry 19 (6): 659–67.
6. Mottron, Laurent, Michelle Dawson, Isabelle Soulières, Benedicte Hubert, and Jake Burack. 2006. “Enhanced Perceptual Functioning in Autism: An Update, and Eight Principles of Autistic Perception.” Journal of Autism and Developmental Disorders 36 (1): 27–43.
7. Schaefer, Alexander, Ru Kong, Evan M Gordon, Timothy O Laumann, Xi-Nian Zuo, Avram J Holmes, Simon B Eickhoff, and B T Thomas Yeo. 2018. “Local-Global Parcellation of the Human Cerebral Cortex from Intrinsic Functional Connectivity MRI.” Cerebral Cortex 28 (9): 3095–3114.
8. Thomas Yeo, B. T., Fenna M. Krienen, Jorge Sepulcre, Mert R. Sabuncu, Danial Lashkari, Marisa Hollinshead, Joshua L. Roffman, et al. 2011. “The Organization of the Human Cerebral Cortex Estimated by Intrinsic Functional Connectivity.” Journal of Neurophysiology 106 (3): 1125.
9. Vos de Wael, Reinder, Oualid Benkarim, Casey Paquola, Sara Lariviere, Jessica Royer, Shahin Tavakol, Ting Xu, et al. 2020. “BrainSpace: A Toolbox for the Analysis of Macroscale Gradients in Neuroimaging and Connectomics Datasets.” Communications Biology 2020 3:1 3 (1): 1–10.
10. Werling, Donna M., and Daniel H. Geschwind. 2013. “Sex Differences in Autism Spectrum Disorders.” Current Opinion in Neurology 26 (2): 146.

Poster No 365

In vivo mapping of cortical excitation-inhibition imbalance in temporal lobe epilepsy

Ke Xie[1], Jessica Royer[1], Raúl Rodriguez-Cruces[1], Linda Horwood[1], Alexander Ngo[1], Hans Auer[1], Ella Sahlas[1], Judy Chen[1], Yigu Zhou[1], Sofie Valk[2], Birgit Frauscher[3], Raluca Pana[1], Andrea Bernasconi[1], Neda Bernasconi[1], Boris Bernhardt[1]

[1]Montreal Neurological Institute and Hospital, Montreal, Canada, [2]Max Planck Institute for Human Cognitive and Brain Sciences, Leipzig, Germany, [3]Duke University, Durham, USA

Introduction: Excitation-inhibition (E:I) imbalance is posited as a fundamental pathophysiological mechanism in temporal lobe epilepsy (TLE).[1] However, previous evidence supporting this hypothesis has been primarily derived from experimental studies in non-human animals. This study aims to non-invasively elucidate the cortical pattern of E:I imbalance in TLE patients and explore its associations with disease severity and cognitive impairment.

Methods: We studied 40 pharmaco-resistant TLE patients (17 males; age = 35.80±11.04 years; 27/13 left/right focus) and 40 age- and sex-matched healthy controls (19 males; 34.25±3.98 years). All participants underwent multimodal MRI at 3T, as well as global cognitive testing including the Montreal Cognitive Assessment (MoCA) and EpiTrack. A subset of participants underwent follow-up MRI scans and cognitive assessment. Node-wise Hurst exponent score, reflecting scale-free properties (i.e., 1/f slop) of fMRI signal and serving as a proxy for the overall E:I ratio within a given region,[2] was estimated via the univariate maximum likelihood method and discrete wavelet transform, modeling the resting-state fMRI timeseries as multivariate fractionally integrated processes. Quantitative and surface-wide between-group differences in Hurst exponent were assessed, with P-values adjusted for false discovery rate (FDR). Subsequently, we explored the relationship between TLE-related regional changes in Hurst exponent and microcircuit parameters estimated by connectome-informed biophysically computational simulations via a parametric mean-field model.[3] Finally, we examined associations with clinical and cognitive measures at baseline, as well as prospective cognitive decline after a 2-year follow-up.

Results: In both cohorts, Hurst exponent scores exhibited a sensory-fugal distribution, being highest in the visual cortex, intermediate in the frontoparietal and default mode networks, and lowest in the paralimbic network (Fig. 1a, 1c), aligning with the sensory–fugal gradient of cytoarchitectural differentiation (healthy controls/TLE: rho = -0.41/-0.46, Pspin = 0.044/0.026). TLE patients had a significantly lower Hurst exponent score across the whole brain than healthy controls (Cohen’s d = -0.75, $P < 0.001$), indicating an overall elevated E:I ratio. Surface-based analysis further revealed marked reductions in local Hurst exponent scores in bilateral temporal lobes, dorsolateral and dorsomedial prefrontal cortices, precuneus, fusiform, and occipital cortex in TLE compared to healthy controls ($PFDR < 0.05$, Fig 1b). When stratifying the topography into functional communities, pronounced effects were observed in the transmodal association system, such as the default mode, frontoparietal, and attention networks, as well as the visual system (Fig 1c). Computational models indicated that the degree of Hurst exponent changes was closely related to atypical increases in recurrent connection strength in TLE (rho = -0.22, Pspin = 0.015; Fig 1d). Finally, lower Hurst exponent scores in TLE patients were associated with longer disease duration (whole-brain,

t = -1.91, P = 0.016; significant clusters, t = -2.02, P = 0.013) and poorer performance on both the MoCA (t = 2.33, P = 0.006; t = 2.93, P = 0.001) and EpiTrack tests (t = 2.72, P = 0.002; t = 3.06, P < 0.001). Moreover, in TLE patients, Hurst exponent scores declined significantly at the 2-year follow-up time point (Cohen's d = -0.84, P = 0.002; Cohen's d = -0.68, P = 0.006), mirroring the prospective decline in MoCA scores (t = 1.58, P = 0.035; t = 1.67, P = 0.031; Fig. 2).

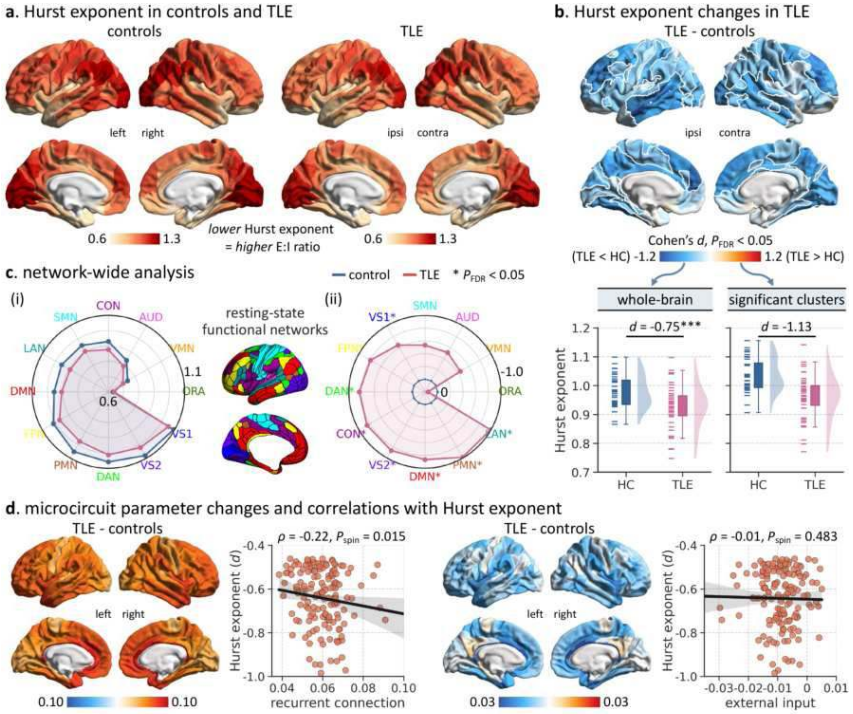

Fig. 1 | Hurst exponent reductions in TLE. **(a)** Mean regional patterns of Hurst exponent of resting-state fMRI time series in healthy control and TLE groups: the lower the Hurst exponent, the higher the excitation-inhibition ratio. **(b)** Top: statistical map of TLE-control difference in local Hurst exponent, effect size as Cohen's *d*. Significant clusters, corrected for multiple comparisons using the false discovery rate procedure ($P_{FDR} < 0.05$), were surrounded by solid white outlines. Bottom: participant-specific mean Hurst exponent scores across the whole brain and all statistically significant regions, respectively. **(c)** (i) Distribution of mean Hurst exponent scores in 12 large-scale functional networks in healthy control and TLE groups, respectively (ii) Distribution of TLE-control differences in mean Hurst exponent according to 12 large-scale functional networks ($P_{FDR} < 0.05$). **(d)** Regional differences in microcircuit parameters of recurrent connection strength (left) and subcortical inputs (right) between TLE and controls, and spatial alignments with Hurst exponent changes. *** $P < 0.001$; HC = healthy controls; TLE = temporal lobe epilepsy; ipsi = ipsilateral; contra = contralateral; VS1/VS2 = primary/secondary visual network; AUD = auditory network; SMN = somatomotor network; CON = cingulo-opercular network; DAN = dorsal attention network; LAN = language network; FPN = fronto-parietal network; DMN = default mode network; PMN/VMN = posterior/ventral multimodal network; ORA = orbito-affective network.

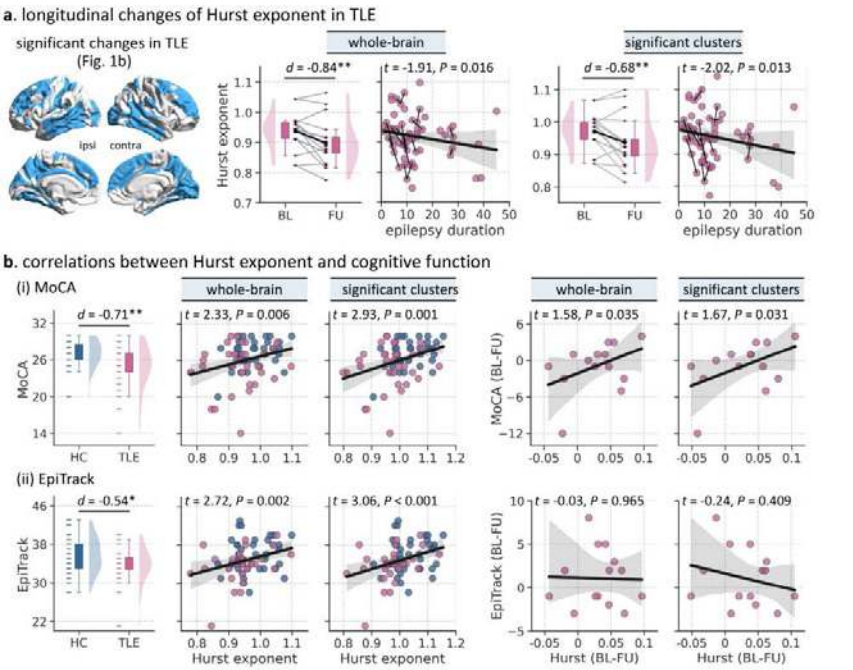

Fig. 2 | Associations of Hurst exponent scores with clinical characteristics and behavioral assessments. **(a)** Error bar plots: longitudinal changes in Hurst exponent scores for TLE patients. Spaghetti plots: associations of epilepsy duration and Hurst exponent scores across baseline and follow-up time points. **(b)** Left: MoCA and EpiTrack scores in TLE patients and healthy controls at baseline. Middle: cross-sectional associations of Hurst exponent scores with MoCA and EpiTrack scores. Right: associations between longitudinal changes in Hurst exponent, MoCA and EpiTrack scores in TLE patients. * $P < 0.05$; ** $P < 0.01$. TLE = temporal lobe epilepsy; MoCA = Montreal Cognitive Assessment; BL = baseline; FU = follow-up.

Conclusions: In TLE, our finding of reduced Hurst exponent scores likely indicates widespread cortical excitation-inhibition changes, tilting the balance towards increased cortical excitability. These changes were found to increase with ongoing disease progression and more marked cognitive impairment, highlighting the potential of the Hurst exponent as a neuroimaging biomarker for TLE-related dysfunction.

References

1. Fritschy, J. M. (2008), 'Epilepsy, E/I balance and GABA(A) receptor plasticity', Front Mol Neurosci, vol. 1, p. 5
2. Trakoshis, S. et al. (2020), 'Intrinsic excitation-inhibition imbalance affects medial prefrontal cortex differently in autistic men versus women', eLife, vol. 9, p. e55684
3. Kong, X. et al. (2021), 'Sensory-motor cortices shape functional connectivity dynamics in the human brain', Nat Commun, vol. 12, no. 1, p. 6373

Poster No 366

Diagnosis of Autism Spectrum Disorder based on Denoised Multiple Age-Specific Structural Features

Dongyue Zhou[1], Yunge Zhang[1], Wei Zhao[1], Yuxing Hao[1,2], Fengyu Cong[1], Huanjie Li[1]

[1]School of Biomedical Engineering, Faculty of Medicine, Dalian University of Technology, Dalian, Liaoning, [2]University of Jyväskylä, Jyväskylä, Finland

Introduction: Diagnosis of Autism Spectrum Disorder (ASD) based on sMRI is more objective than clinical scales due to the high heterogeneity in symptom severity. Existing studies in binary classification between ASD and control based on small sample reported remarkable classification accuracies. However, accuracies on large heterogeneous datasets were not high[1,2]. This may be due to insufficiently specific feature selection, insufficiently effective feature combination, and the presence of multi-site noise. In this paper, we applied DP-ICA method to remove the site effect, and then combined three kinds of age-specific structural features including regional, interregional features and disease vulnerability index using multiple kernel learning (MKL) for binary classification task. Results showed that our procedure reached the accuracy of 85.63% when discriminating ASD children from control.

Methods: Structural MRI data of 660 subjects from public ABIDE II dataset[3] were included in this study. We divided all people into three age groups (Age1: 340 children aged 6-12 years old; Age2: 170 adolescent aged 12-18 years old; Age3: 150 adults over the age of 18), and ensured that ASD and control group in each age stage had the same number of people and matched age (no difference between two groups). Data preprocessing was conducted by FreeSurfer. Desikan-Killiany Atlas[4] was used here for extracting three types of characteristics. (1) Morphological features (MF) included cortical thickness (CT), pial surface area (PSA), grey matter volume (GMV), folding index (FI) and curvature (CURV) were calculated in native space. (2) We constructed individual morphological brain network (MBN)[5] with each subject's grey matter maps processed by FSL-VBM. Next, DP-ICA method[6] was used for correcting site effects on MF and MBN. (3) The third type of features - regional vulnerability index (RVI)[7], which was quantified by the Pearson correlation between standardized individual brain values and the effect size from large sample meta-analysis. We performed the meta-analysis by calculating the effect size in each site separately (16 sites in our study), and then combing them (refer to[8]). After preparing these 3 features, we performed a two-step feature selection separately in 3 age stages for obtaining optimal feature subsets. Firstly, we applied two sample t-test on two high-dimensional features (MF and MBN), and features with $p>0.05$ (uncorrected) were excluded. Then, SVM-based recursive feature elimination (SVM-RFE) was conducted to evaluate the importance of these features in classification. Finally, we utilized MKL[9] with appropriate weight to combine selected and specific MF, MBN and RVI in 3 age stages. We calculated accuracy, sensitivity, specificity, area under receiver operating characteristic curve and F-score for assessment of classification performance in a five-fold cross validation. And we repeated this procedure for 100 times to evaluate the performance of MKL compared to others via a paired t-test.

Results: Fig.1 showed the superiority of MKL in combination of 3 different kinds of features, and the advantage of age-specific features in classification. It's obvious that age1-specific features performed better than that in all subjects. And RVI had the highest weight in each age stage. Fig.2 displayed the most discriminative and age-specific features in 3 age stages. We could observe the same and specific characteristics among them.

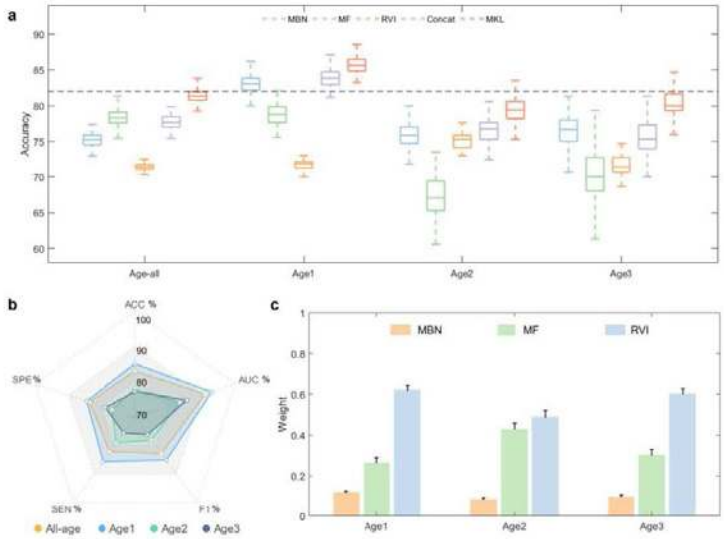

Fig.1 Classification performance based on multi-kernel learning (MKL). (a) Comparison of results from fusing three features based on MKL and single feature among different age stages. (b) Classification performance in each age stage. ACC, accuracy; SEN, sensitivity; SPE, specificity; AUC, area under receiver operating characteristic curve and F1, F-score. (c) Optimal weight of MKL in each age stage. RVI represented the highest accuracy in each age stage.

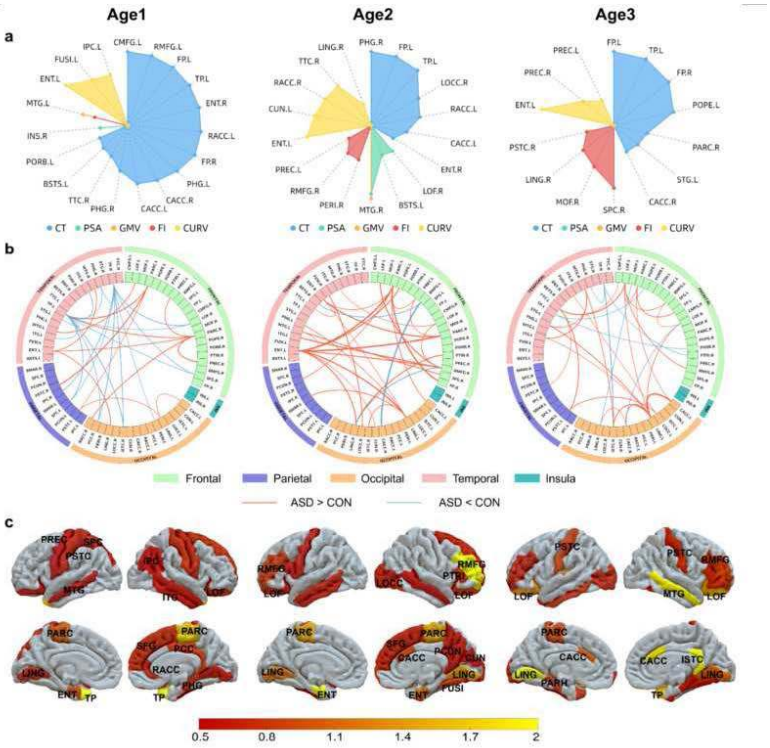

Fig.2 The most discriminative features in three age stages. (a) Top 20 discriminative MF by weight based on two-step feature selection. The center point is 0.5 and boundary is 1. (b) Top 30 MBN connection by weight. (c) Weight in brain regions that connect edges in top 30 MBN. The most connected regions among three age stages. Age1: TP, temporal pole; PARC, paracentral; ENT, entorhinal; PCC, posterior cingulate cortex; SFG, superior frontal gyrus; Age2: RMFG, rostral middle frontal gyrus; ENT; PARC; LING, lingual; FUSI, fusiform; Age3: MTG, middle temporal gyrus; LING; CACC, caudal anterior cingulate; ISTC, isthmus cingulate; TP; LOF, lateral orbitofrontal.

Conclusions: We proposed a procedure that combined three kinds of age-specific structural features in each age stage using MKL to distinguish ASD and control. Results showed that the most identifiable features differed in three age stages, thus the method sub-grouped by age was effective, especially in children group, where the accuracy was highest, indicating that abnormalities in ASD may be more easily observed in childhood.

References
1. Haar, Shlomi. (2016), 'Anatomical Abnormalities in Autism?', Cerebral Cortex, 26 (4): 1440–52.
2. Katuwal, Gajendra J. (2016), 'Divide and Conquer: Sub-Grouping of ASD Improves ASD Detection Based on Brain Morphometry.', PLOS ONE, 11 (4): e0153331.
3. Di Martino, A. (2014), 'The Autism Brain Imaging Data Exchange: Towards a Large-Scale Evaluation of the Intrinsic Brain Architecture in Autism.', Molecular Psychiatry, 19 (6): 659–67.
4. Desikan, Rahul S. (2006), 'An Automated Labeling System for Subdividing the Human Cerebral Cortex on MRI Scans into Gyral Based Regions of Interest.', NeuroImage, 31 (3): 968–80.
5. He, Changchun. (2021), 'Individual-based Morphological Brain Network Organization and Its Association with Autistic Symptoms in Young Children with Autism Spectrum Disorder.', Human Brain Mapping, 42 (10): 3282–94.
6. Hao, Yuxing. (2023), 'Site Effects Depth Denoising and Signal Enhancement Using Dual-Projection Based ICA Model.' Preprint. Neuroscience.
7. Kochunov, Peter, L. (2022), 'ENIGMA-DTI: Translating Reproducible White Matter Deficits into Personalized Vulnerability Metrics in Cross-diagnostic Psychiatric Research.', Human Brain Mapping, 43 (1): 194–206.
8. Xie, Yapei. (2022), 'Alterations in Connectome Dynamics in Autism Spectrum Disorder: A Harmonized Mega- and Meta-Analysis Study Using the Autism Brain Imaging Data Exchange Dataset.', Biological Psychiatry, 91 (11): 945–55.
9. Wee, Chong-Yaw. (2012), 'Identification of MCI Individuals Using Structural and Functional Connectivity Networks.', NeuroImage, 59 (3): 2045–56.

Poster No 368

Structural alterations associated with emotion regulation deficits in children with and without ADHD

Sikoya Ashburn[1], Nicholas Fogleman[1], Jessica Cohen[1]

[1]University of North Carolina at Chapel Hill, Chapel Hill, NC

Introduction: Emotion dysregulation (ED) is the inability to exercise any or all modulatory processes involved in emotion regulation to such a degree that it results in impaired emotional functioning (Bunford, Evans, and Wymbs 2015). ED is often associated with Attention Hyperactivity Deficit Disorder (ADHD), a neurodevelopmental disorder traditionally characterized by inattention, hyperactivity, and impulsivity (Wehmeier, Schacht, and Barkley 2010). As measured by grey matter volume (GMV), neuroimaging studies have identified altered brain structure in children with ADHD, including increased GMV in bilateral frontal regions (Wu et al. 2019) and reduced GMV in posterior cortical regions and the cerebellum (Stoodley 2014). However, studies have yet to examine the relationship between GMV, ED and ADHD. Thus, we examined: (i) behavioral measures of ED in children with ADHD relative to typically developing (TD) children; (ii) the relationship between cortical and cerebellar GMV and ED measures; and (iii) whether differences in GMV are associated with ED when comparing children with ADHD to TD children.

Methods: We included a total of 54 children (26 TD children and 28 children with ADHD) between the ages of 8 and 12 years. Parents of all children completed the Diagnostic Interview Schedule for Children Version IV (Shaffer et al. 2000) and Conners 3rd Edition (Conners 2008) to assess ADHD and the Child Behavior Checklist (CBCL; Achenbach and Rescorla 2001) and Emotion Regulation Checklist (ERC; Shields and Cicchetti 1997) to assess ED. T1-weighted images were reoriented to the anterior commissure, co-registered, and segmented (grey matter, white matter, and CSF). We then normalized our study specific DARTEL template to MNI space. CAT12 was used to calculate total intracranial volume (TIV) and to check for noise outliers. For each ED measure, we performed a one-way t-test with ED as a covariate of interest and TIV as a covariate of no interest to test the influence of ED on GMV. Next, we performed a two-sample t-test, dummy coding for group to test for effects of ED with respect to between-group differences in GMV. Lastly, we repeated these analyses on data processed through SUIT for cerebellar optimization.

Results: Children with ADHD were rated as exhibiting significantly higher ED on both the CBCL and ERC, indicating greater ED relative to TD children. Across all children, whole-brain analysis revealed that increased GMV in left inferior temporal gyrus and left subcallosal cortex, and decreased GMV in left middle frontal cortex, was associated with greater ED; these regions were consistent across both the CBCL and ERC. Additionally, greater ED, as assessed by the CBCL, was associated with increased GMV in right supramarginal gyrus and decreased GMV in left superior parietal lobule, cingulate gyrus, and right middle temporal gyrus. ED, as assessed by the ERC, was associated with decreased GMV in left postcentral and right cuneal gyri. When comparing between groups (TD > ADHD), we observed decreased GMV in children with ADHD in the left supramarginal gyrus (CBCL) and left insular cortex (ERC). Significant findings were not observed in the opposite comparison (ADHD > TD) or between cerebellar GMV and ED for either the one-way or between-group analyses.

Conclusions: Our study reinforces extant literature indicating that children with ADHD exhibit greater difficulties regulating their emotions relative to TD children, and demonstrates that cortical GMV is associated with ED in children. Additionally, several regions identified have been implicated in the emotion regulation process (Laxton et al. 2013), and are known to have

connections with cortical regions important for positive emotion regulation strategies (Scharnowski et al. 2020). In total, our study provides evidence of structural alterations associated with ED in children with ADHD and TD children.

References
1. Achenbach et al., (2001), Manual for the ASEBA School-Age Forms & Profiles: An Integrated System of Multi-Informant Assessment. Burlington, VT: ASEBA.
2. Bunford, N. et al., (2015), "ADHD and Emotion Dysregulation Among Children and Adolescents." Clinical Child and Family Psychology Review 18 (3): 185–217. https://doi.org/10.1007/s10567-015-0187-5.
3. Conners, C.K. (2008), Conners 3. North Tonawanda, NY: Multi-Health Systems, Inc.
4. Laxton, A.W. et al., (2013), "Neuronal Coding of Implicit Emotion Categories in the Subcallosal Cortex in Patients with Depression." Biological Psychiatry 74 (10): 714–19. https://doi.org/10.1016/j.biopsych.2013.03.029.
5. Scharnowski, F. et al., (2020), "The Role of the Subgenual Anterior Cingulate Cortex in Dorsomedial Prefrontal–Amygdala Neural Circuitry during Positive-social Emotion Regulation." Human Brain Mapping 41 (11): 3100–3118. https://doi.org/10.1002/hbm.25001.
6. Shaffer, D. et al., (2000), "NIMH Diagnostic Interview Schedule for Children Version IV (NIMH DISC-IV): Description, Differences From Previous Versions, and Reliability of Some Common Diagnoses." Journal of the American Academy of Child & Adolescent Psychiatry 39 (1): 28–38. https://doi.org/10.1097/00004583-200001000-00014.
7. Shields, A, and Cicchetti D, (1997), "Emotion Regulation among School-Age Children: The Development and Validation of a New Criterion Q-Sort Scale." Developmental Psychology 33 (6): 906–16. https://doi.org/10.1037/0012-1649.33.6.906.
8. Stoodley, C.J. (2014), "Distinct Regions of the Cerebellum Show Gray Matter Decreases in Autism, ADHD, and Developmental Dyslexia." Frontiers in Systems Neuroscience 8 (May). https://doi.org/10.3389/fnsys.2014.00092.
9. Wehmeier, P.M. et al., (2010), "Social and Emotional Impairment in Children and Adolescents with ADHD and the Impact on Quality of Life." Journal of Adolescent Health 46 (3): 209–17. https://doi.org/10.1016/j.jadohealth.2009.09.009.
10. Wu, Z. et al., (2019), "Linked Anatomical and Functional Brain Alterations in Children with Attention-Deficit/Hyperactivity Disorder." NeuroImage: Clinical 23: 101851. https://doi.org/10.1016/j.nicl.2019.101851.

Poster No 369

Personalized whole brain network modelling for optimizing epilepsy surgery

Huifang Wang[1], Julia Makhalova[2], Jan Paul Triebkorn[1], Fabrice Bartolomei[3], Viktor Jirsa[4]

[1]AMU, INS, INSERM U1106, Marseille, PACA, [2]APHM, Marseille, PACA, [3]AMU, INS, INSERMU1106, Marseille, PACA, [4]nstitut de Neurosciences des Systèmes, Marseille, N/A

Introduction: Personalized whole brain network modelling has been tested for estimating the epileptogenic network in 53 retrospective patients and is used in 356 prospective patients on the ongoing clinical trail (EPINOV)[1-2]. In this study, we aim to use a personalized whole brain network model to aid clinicians in planning surgical interventions for patients with drug-resistant focal epilepsy.

Methods: For each epilepsy patient, we built a patient's specific whole brain network model. The structural scaffold of the patient-specific whole-brain network model is constructed from anatomical T1 and diffusion-weighted magnetic resonance imaging. Bayesian inference methods sample and optimize key parameters of the personalized model using functional stereoelectroencephalography recordings of patients' seizures. These key parameters determine a given patient's personalized model. We performed virtual resection on this patient's personalized models based on the sampling results of Bayesian inference. We compared the results of virtual resection surgery with the outcome of the real surgery and introduced an optimization method for personalized surgical strategies. From methodologies, we compared both low-resolution of neural mass models, high-resolution neural field models and middle combination, low-resolution with high-resolution forward solutions.

Results: We give three patients examples of performing virtual surgery using different resection strategies, including clinical hypotheses and real surgery as well. We performed the virtual surgery workflow retrospectively using 40 patients with drug-resistant focal epilepsy. These 40 patients had epilepsy surgery with at least one-year follow-up outcome. The outcome predictions based on the real surgical scenario reproduced by virtual surgery, were consistent with patient's surgical results. Based on the personalized whole brain network modelling, we estimate an optimal surgery strategy. For each patient, we rank the different surgical strategies by the statistical metrics.

Conclusions: Personalized whole brain network modelling can make a prediction on the outcome of surgery and is able to suggest the surgical strategies by ranking the statistical metrics.

References
1. Wang, H. E., Woodman, M., Triebkorn, P., Lemarechal, J.-D., Jha, J., Dollomaja, B., Vattikonda, A. N., Sip, V., Medina Villalon, S., Hashemi, M., Guye, M., Makhalova, J., Bartolomei, F., & Jirsa, V. (2023). Delineating epileptogenic networks using brain imaging data and personalized modeling in drug-resistant epilepsy. Science Translational Medicine, 15(680). https://doi.org/10.1126/scitranslmed.abp8982

Poster No 370

Longitudinal behavioural and brain morphological changes before and after hemispherotomy

Ziyu Bao[1], Hao Yu[2], Yijun Chen[1], Lixin Cai[2], Gaolang Gong[1]

[1]State Key Laboratory of Cognitive Neuroscience and Learning & IDG/McGovern Institute for Brain Resea, Beijing, China, [2]Pediatric Epilepsy Center, Peking University First Hospital, Beijing, China

Introduction: Hemispherotomy is an effective surgery for treating refractory epilepsy from diffuse unihemispheric lesions[1,2]. To date, however, postsurgery neuroplastic changes following pediatric hemispherotomy remain unclear. In the present study, we aim to systematically investigate longitudinal changes in gray matter volume (GMV) before and after surgery in two groups of pediatric patients with left and right hemispherotomy.

Methods: Pediatric epilepsy patients undergoing left or right hemispherotomy at the pediatric epilepsy center and having high-quality pre- and postoperative structural MRI were included (29 left hemispherotomy patients, age of surgery: 3.5±2.5 years; 28 right hemispherotomy patients, age of surgery: 4.6±2.5 years). Longitudinal voxel-based analyses were used to determine the voxelwise GMV within the unaffected brain regions. To control for the dramatic developmental effect, age-adjusted GMV within unaffected brain regions was derived voxel by voxel using a normative modeling approach with an age-matched reference cohort of 2115 healthy children(Fig. 1).[3] For each patient, we manually outlined the mask of the cerebral hemisphere that underwent surgery on both the pre- and postoperative T1-weighted images. We then carried out VBM analyses to ensure unbiased comparisons between the two hemispheres, a symmetric T1 template in MNI space was constructed using 2115 healthy children. To evaluate how GMV changes, we performed a voxelwise linear mixed-effects model (LMEM) analysis within the GM mask of the unaffected regions, with the onset of epilepsy, age at surgery, and etiology as covariates. Multiple comparisons were corrected using the random field theory (RFT) method (uncorrected $p < .001$), and clusters with a corrected $p < .05/2$ (2 patient groups) were considered significant.

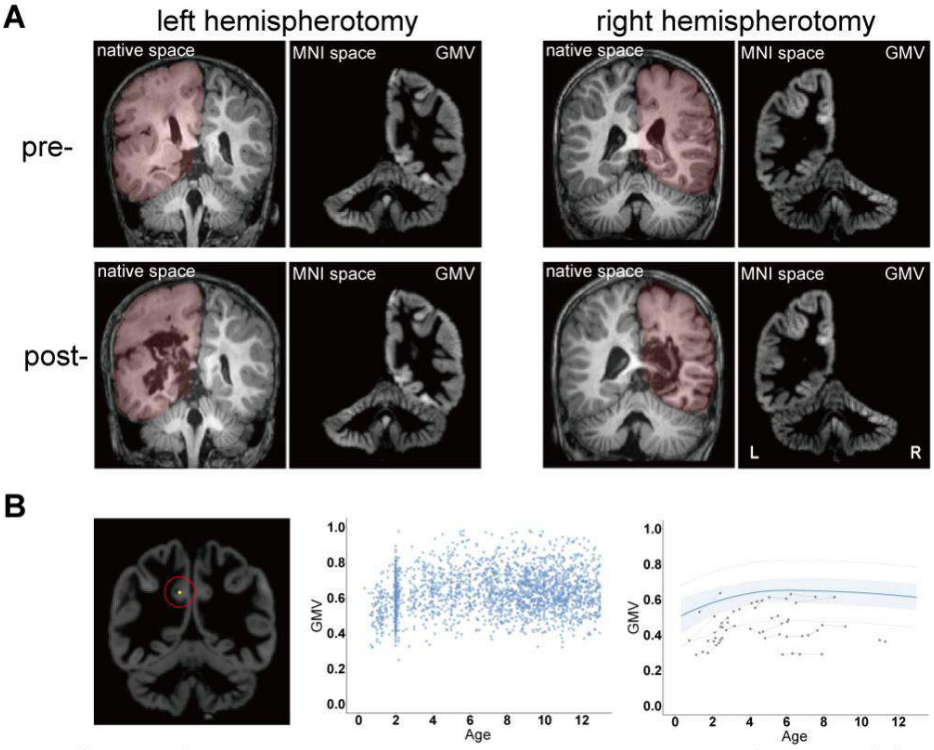

Figure 1. Schematic of MRI image processing. (A) T1-weighted (T1w) and gray matter volume (GMV) images of left and right hemispherotomy patients. The cerebral hemisphere was manually masked out (indicated by red) in the T1w native space and excluded in the GMV-based voxel-based morphometry (VBM) analyses in the MNI space. Pre: Preoperative; Post: Postoperative. **(B) Normative model of GMV, for one voxel example, as estimated by the Gaussian process regression in 2115 healthy children.** The selected voxel is indicated by yellow in the left panel. Each circle in the middle panel represents one healthy child. On the right panel, the mean of the normative model is represented by a solid blue line, while the ±1 standard deviation is indicated by dotted light blue lines. The light blue shaded area represents the 95% confidence interval. The preoperative and postoperative GMV values of each patient are indicated by two connected gray dots.

Results: The age-adjusted GMV values represent the patient's deviation from the age- and sex-matched norm: negative and positive values indicate a trend of GM shrinkage and expansion, respectively. In most patients in the two groups, both preoperative and postoperative age-adjusted GMV values were negative across the vast majority of the unaffected regions, suggesting an overall shrinking pattern and underdevelopment of GM compared with the healthy children. After

correcting for multiple comparisons, we observed 4 clusters showing significant age-adjusted GMV changes for the left hemispherotomy group (Fig. 2A) and 3 significant clusters for the right hemispherotomy group (Fig. 2B). In both groups, the largest cluster covered almost the entire contralateral cerebrum and exhibited significantly increased GMV (left hemispherotomy: $t = 6.92$, $p < 0.001$; right hemispherotomy: $t = 7.44$, $p < 0.001$). The second largest cluster was located around the entire ipsilateral cerebellum and exhibited significantly increased age-adjusted GMV (left hemispherotomy: $t = 6.95$, $p < 0.001$; right hemispherotomy: $t = 8.53$, $p < 0.001$). In contrast to the two clusters, the cluster in the contralateral cerebellum consistently showed significantly decreased age-adjusted GMV in both groups (left hemispherotomy: $t = -8.32$, $p < 0.001$; right hemispherotomy: $t = -7.73$, $p < 0.001$). Finally, there was one significantly decreased age-adjusted GMV cluster around the contralateral cingulate gyrus in the left hemispherotomy group ($t = -5.23$, $p < 0.001$) but not in the right hemispherotomy group.

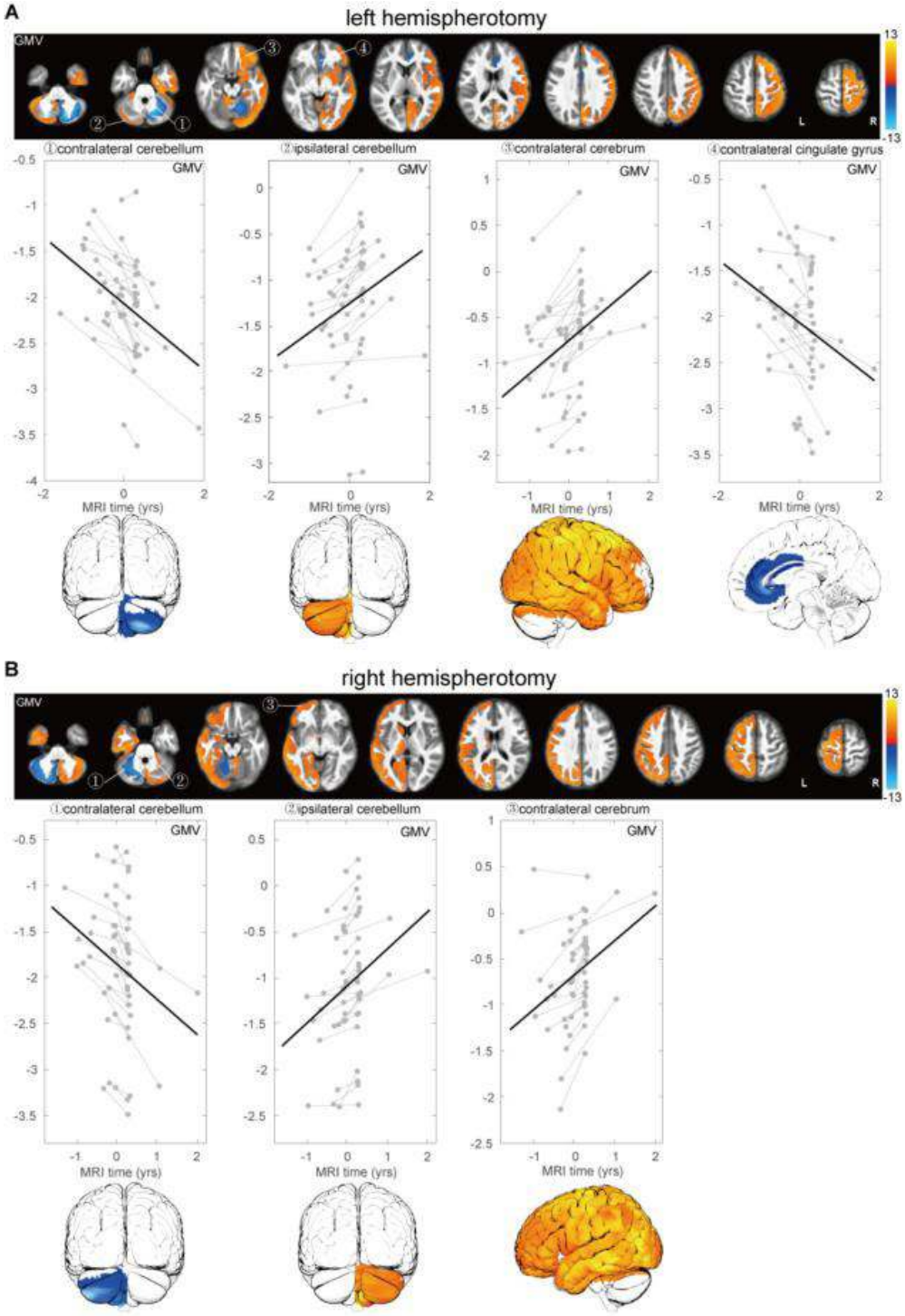

Figure 2. Longitudinal change in age-adjusted GMV before and after surgery for the two patient groups. The results for the left and right hemispherotomy are shown in figure (A) and figure (B), respectively. The first row represents the T maps of the age-adjusted GMV change from the linear mixed model for the two groups. The identified significant clusters are denoted by arrows. Within the panel of each cluster, the fitted longitudinal change in age-adjusted GMV is represented as a black thick line. The longitudinal change in each patient is indicated by a gray line.

Conclusions: Both left and right hemispherotomy patients showed widespread GMV increases in the contralateral cerebrum and ipsilateral cerebellum but GMV decreases in the contralateral cerebellum. With normative modeling, the neurodevelopment-induced and hemispherotomy-induced increases in GMV can be well differentiated. This widespread greater GM development could be considered a part of neuroplastic changes induced by the hemispherotomy.

References

1. Kossoff, E. H. et al. (2003), 'Hemispherectomy for intractable unihemispheric epilepsy Etiology vs outcome', Neurology, vol. 61, no. 7, pp. 887–890.
2. Moosa, A. N. V. et al. (2013), 'Longitudinal seizure outcome and prognostic predictors after hemispherectomy in 170 children', Neurology, vol. 80, no. 3, pp. 253–260.
3. Rutherford, S. et al. (2022), 'The normative modeling framework for computational psychiatry', Nature Protocols, vol. 17, no. 7, pp. 1711–1734.

Poster No 371

CBF and Visual, Auditory, and Motoric BOLD Responses in Pediatric Patients with Sickle Cell Anemia

Ping Zou Stinnett[1], Winfred Wang[1], Zachary Abramson[1], Jane Hankins[1], Kathleen Helton[1], Robert Ogg[1], Ranganatha Sitaram[2]

[1]St. Jude Children Research Hospital, Memphis, TN, [2]St. Jude Children's Research Hospital, Memphis, TN

Introduction: Sickle cell anemia (SCA) is characterized by rigid sickle-shaped red blood cells with low oxygen affinity. It affects all organs, including the brain. Children with SCA often suffer neurocognitive deficits[1]. Elevated cerebral blood flow (CBF) occurs in patients with SCA[2], which may be a compensatory response to their chronic anemia through cerebrovascular dilatory reserve[3]. We have found that the BOLD response to visual stimulation decreased in children with SCA[4] and speculated that their ability to increase CBF, and in turn their BOLD signal response, at the demand of neuronal activity, may be limited due to their elevated baseline CBF. Here, we report BOLD signal changes in visual, motor, and auditory cortices relative to resting CBF in pediatric patients with SCA. We also report results from a simultaneous measure of BOLD and CBF to visual stimulus in a subgroup of patients exposed to hydroxyurea[5], a treatment known to lower CBF and improve cognitive function.

Methods: Written informed consent for this IRB-approved study was obtained from each participant. 35 SCA patients (12.2 [7.8-17.8] years old) had fMRI with a 3T Siemens scanner. A pulsed ASL Q2TIPS sequence[6] (TR=2270ms, TE=23ms, TI1=700ms, TI1s=1200ms, and TI2=1400ms) was used to measure resting CBF and simultaneous BOLD and CBF responses to visual stimulation (blocked-design paradigm:22.7s stimulus in a 44.5s block for 8 blocks). A T2* weighted EPI sequence (TR=2.0s, TE=30ms) was used with a sensory survey task: finger tapping during visual and auditory stimulation. The fMRI paradigm included 4 blocks of brief task (2s task in a 30s block) and 3 blocks of long task (20s task in a 40s block). The resting CBF map was calculated from the resting ASL images. The fMRI images were pre-processed and analyzed with SPM. From the EPI images with the sensory survey task, time courses from the peak activation cluster in the primary visual, auditory, and motor cortices were retrieved for each subject. The heights of BOLD signal changes were correlated with the resting gray matter CBF in the corresponding lobes. The fMRI ASL images were analyzed for 12 patients at 2 time points: before (TP1) and after (TP2) 12 months of hydroxyurea therapy. The ASL time course of the peak-activated clusters in the primary visual cortex from BOLD activation was retrieved for each subject. The BOLD and CBF time courses were then calculated from the average of or the difference between the control and the tag signals. The BOLD and CBF changes before and after hydroxyurea were compared.

Results: From the sensory survey task in the 35 patients, activations were detected in primary visual, auditory, and motor cortices. The peak BOLD signal changes in these three cortices were less than 5% and were negatively associated with lobar gray matter CBF values in the visual (p=0.01) and auditory (p=0.01) cortices, but not in the motor cortex (Fig 1). From the fMRI ASL images in the 12 treated patients, activations in the primary visual cortex were detected. The height of CBF change was similar before and after hydroxyurea, but the base was lower at TP2. The BOLD responses were significantly higher at TP2 than at TP1 (p=0.05) (Fig 2).

Conclusions: The low BOLD signal in the SCA patients is consistent with our previous observation[3,7]. The parity in the height of CBF responses before and after hydroxyurea treatment suggests a ceiling effect for the CBF to increase in the patients. With a lowered baseline CBF, there is more room for CBF increase during neuronal activities, promoting a higher BOLD signal[7]. The negative association of the BOLD signal with gray matter CBF in the visual and auditory cortices also supports this assumption. Finally, the lack of association between BOLD and CBF in the motor cortex indicates variability in the neuro-vascular coupling adaptation across brain regions in patients with SCA.

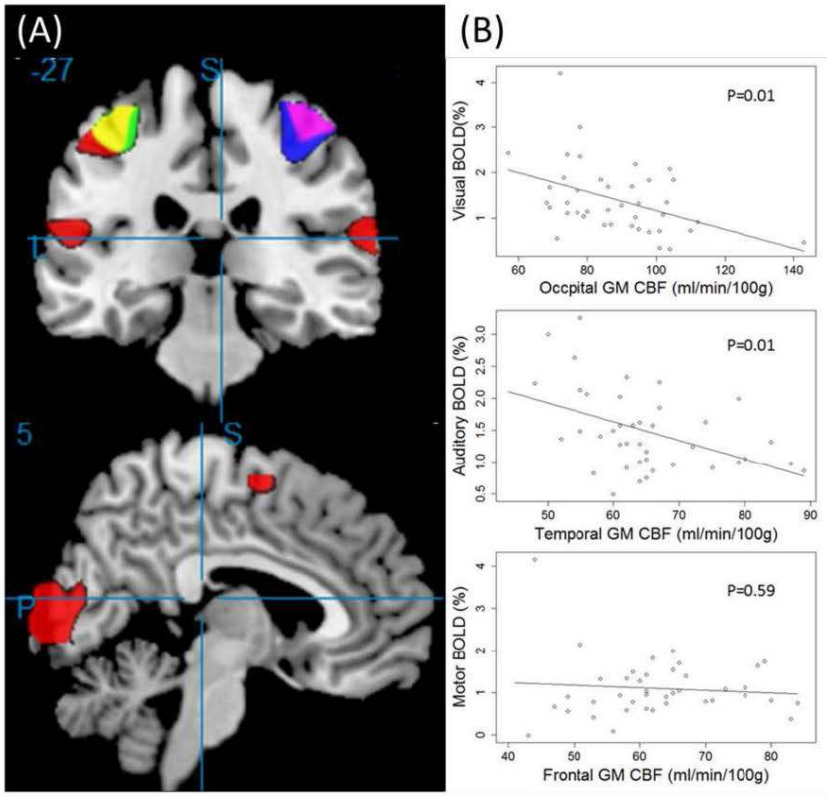

Fig 1. BOLD responses to Visual and Auditory Stimulation and Finger Tapping in SCA Patients. (A) Group Activation Map (p=0.05 FWE); (B) Peak BOLD Signal vs. Regional Gray Matter Resting CBF. BOLD signals were significantly associated with gray matter resting CBF for the visual cortex and auditory cortex but not for the motor cortex.

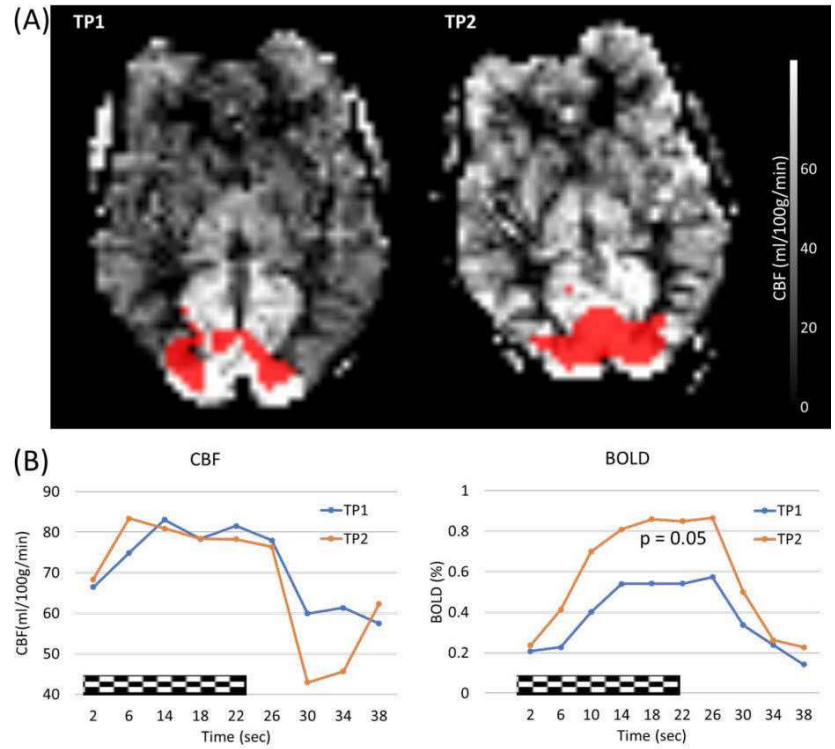

Fig 2. CBF and BOLD Responses to Visual Stimulation in SCA Patients before (TP1) and after (TP2) 12 months of Hydroxyurea Treatment. (A) BOLD activation overlaid on the CBF map for a patient; (B) Average BOLD and CBF Changes (n=12). The checkerboard shows the period for stimulus present. The BOLD signals were higher at TP2 (p = 0.05).

References

1. DeBaun MR, Kirkham FJ. (2016) Central nervous system complications and management in sickle cell disease. Blood.127(7):829-838.
2. Strouse, J. J., Cox, C. S., Melhem, E. R., Lu, H., Kraut, M. A., Razumovsky, A., et al. (2006). Inverse correlation between cerebral blood flow measured by continuous arterial spinlabeling (CASL) MRI and neurocognitive function in children with sickle cell anemia (SCA). Blood, 108, 379–381.
3. Prohovnik, I., Hurlet-Jensen, A., Adams, R., De Vivo, D. & Pavlakis, S.G. (2009) Hemodynamic etiology of elevated flow velocity and stroke in sickle-cell disease. Journal of Cerebral Blood Flow and Metabolism, 29, 803–810
4. Ping Zou, Kathleen J. Helton, Matthew Smeltzer, Chin-Shang Li, Heather M. Conklin, Amar Gajjar, Winfred C. Wang, Russell E. Ware, Robert J. Ogg (2011). Hemodynamic responses to visual stimulation in children with sickle cell anemia. Brain Imaging and Behavior, 5:295–306
5. Wang WC, Zou P, Hwang SN, Kang G, Ding J, Heitzer AM, Schreiber JE, Helton K, Hankins JS. (2021) Effects of hydroxyurea on brain function in children with sickle cell anemia. Pediatr Blood Cancer. DOI: 10.1002/pbc.29254
6. Luh WM, Wong EC, Bandettini PA, et al. QUIPSS II with thin-slice TI1 periodic saturatin: a method for improving accuracy of quantitative perfusion imaging using pulsed arterial spin labeling. Magn Reson Med 1999; 41: 1246–1254
7. Zou P, Scoggins MA, Li Y, Jones M, Helton KJ, Ogg RJ (2021). Developmental patterns of CBF and BOLD responses to visual stimulus, J Cereb Blood Flow Metab. 2021 Mar;41(3):630-640. Doi: 10.1177/0271678X20925303.

Poster No 372

Temporal Variability of Scalp EEG as a Predictor for Long-term Efficacy of rTMS Treatment in ASD

Runyang He[1], Dezhong Yao[2], Fali Li[3], Lin Jiang[1], Peng Xu[3]

[1]University of Electronic Science and Technology of China, Chengdu, Sichuan, [2]The Clinical Hospital of Chengdu Brain Science Institute, MOE Key Lab for Neuroinformation, Chengdu, China, [3]School of life Science and technology, University of Electronic Science and Technology of China, Chengdu, Sichuan

Introduction: Repetitive transcranial magnetic stimulation (rTMS) emerges as a useful therapy for autism spectrum disorder (ASD) clinically. Whereas the neural mechanisms of rTMS therapy on ASD are not fully understood, and no biomarkers until now are available to reliably predict the follow-up rTMS efficacy in clinical practice. Advancements in the analysis and processing of electroencephalogram (EEG) signals have transformed EEG into a convenient, accurate, and highly sensitive research tool for exploring the underlying mechanisms and identifying the relevant biomarkers. In the current work, we investigated the rhythmic fluctuating modes of resting-state networks over time to reveal the evidence accounting for the clinical improvement induced by rTMS for ASD patients. Afterwards, the potential relationships between the fluctuating properties and clinical scales were investigated, from which robust biomarkers were identified and models were further established to predict the longterm treatment response of rTMS intervention.

Methods: The time-resolved resting-state network within the delta (1–4 Hz), theta (4–8 Hz), alpha (8–13 Hz), and beta (13–30 Hz) bands were first constructed for both ASDs and TDs, respectively. Specifically, using a 20 s sliding-window approach with an overlapping of 98%, we constructed the time-varying networks with a 400 ms temporal resolution. Thereinto, for each segment, the phase-locking value (PLV) that can estimate the inter-regional phase synchronization was adopted to assess the synchronized strengths (Li, et al 2015). Brain temporal variability was investigated in the resting-state EEG of ASD patients, and the nonlinear complexity of related time-varying networks was accordingly evaluated by fuzzy entropy. Based on related temporal variability indexes, a stepwise multiple linear regression model was established to predict the clinical scores at the four weeks after the rTMS treatment of ASD patients.

Results: Here, Fig.1(a) presents the distinct topologies underlying network variability between pretreatment ASD patients and TDs within four concerned bands revealed by two-way repeated ANOVAs, where the green solid line presents stronger connectivity of ASDs than that of TDs. Specifically, in comparison with TDs, the stronger long-range variability connectivity spanning the distributed frontal and posterior lobes was found for pre-treatment ASDs, especially within the theta and alpha bands. Of note, in contrast to pre-treatment ASDs, after three week rTMS treatments, patients experienced reduced temporal variability in the longrange frontal-parietal and frontal-occipital linkages within the theta and alpha bands (Fig.1(b)). In short, Fig.1 demonstrated the hyper-variability in the resting-state networks of ASD patients, while three-week rTMS treatment alleviates the hyper fluctuations occurring in the frontal-parietal and frontal-occipital connectivity and further contributes to the ameliorative ASD symptoms. In addition, the changes in variability network properties are significantly correlated with clinical scores, which further serve as potential predictors to track the long-term rTMS efficacy for ASD. As proved, the predicted and actual clinical scores of ASD patients at the follow-up stage were found to be significantly correlated in Fig.2, signifying a satisfactory prediction performance.

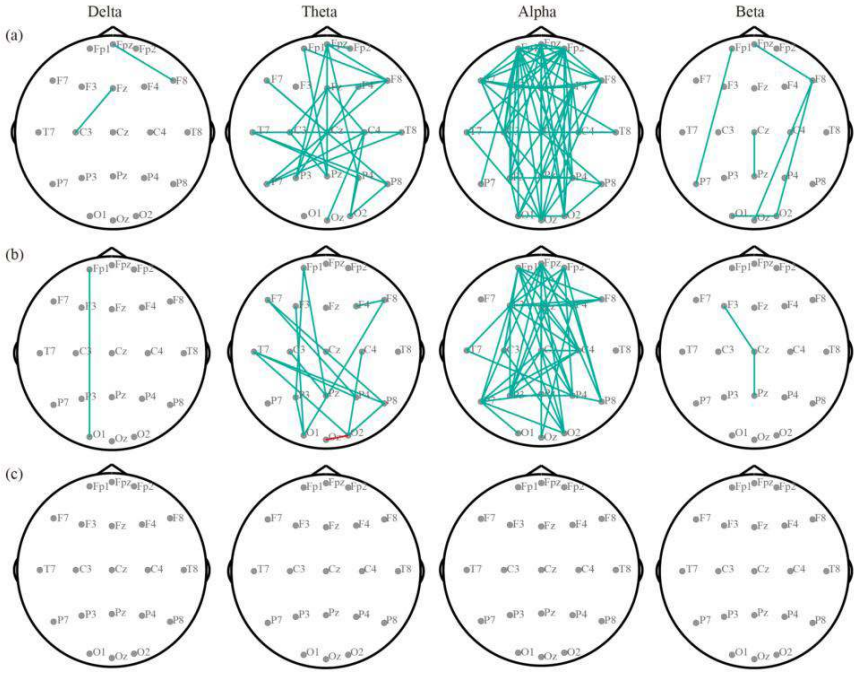

Fig 1. Differential temporal variability distributions of resting-state EEG networks in four bands. (a) Pre-treatment ASDs vs.TDs. (b) Pre- vs. post-treatment ASDs. (c) Post-treatment ASDs vs. TDs. Green-solid lines represent the stronger network variability of the ASDs than TDs, and of the pre- than post-treatment ASDs.

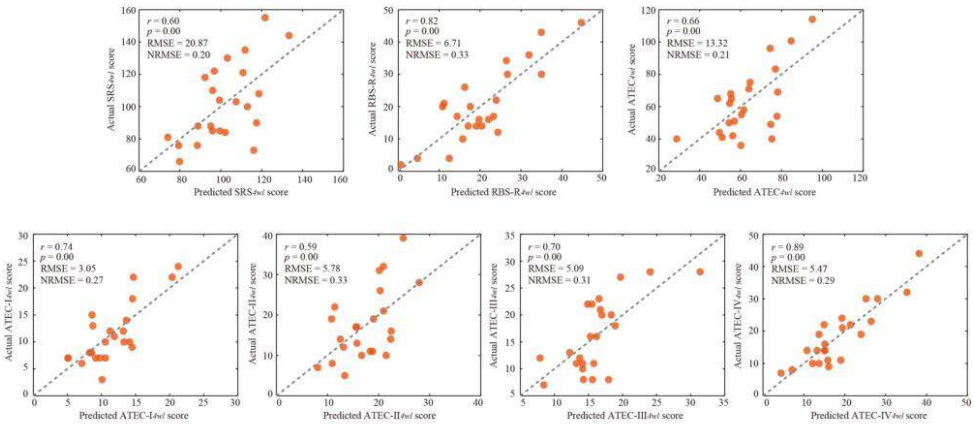

Fig 2. Prediction of the clinical scores at the 4wl-treatment stage.

Conclusions: The findings validated that the temporal variability of time-varying networks of ASD patients could be modulated by rTMS, and related variability properties also help predict follow-up rTMS efficacy, which provides the potential for formulating individualized treatment strategies for ASD.

References

1. Li F. (2015),' Relationships between the resting-state network and the P3: evidence from a scalp EEG study', Sci.Rep. 51–10

Poster No 373

Translingual neural stimulation induces brain network changes in patients with mild-to-moderate TBI

Daniel Chu[1], Jiancheng Hou[2], Veena Nair[1], Nagesh Adluru[1], Yuri Danilov[1], Kurt Kaczmarek[1], Mary Meyerand[1], Mitchell Tyler[1], Vivek Prabhakaran[1]

[1]University of Wisconsin-Madison, Madison, WI, [2]Fujian Normal University, Fuzhou, Fujian

Introduction: Traumatic brain injury (TBI) is a form of external acquired injury to the brain and is commonly associated with cognitive, emotional, social, and physical deficits (McDonald, 2013). A general deficit to the mild-to-moderate TBI (mmTBI) is balance injuries (Li et al., 2013). Translingual neural stimulation (TLNS), provided via the Portable Neuromodulation Stimulator, is a novel therapeutic intervention that combines the superficial electrical stimulation of facial and trigeminal nerves with physical therapy that focuses on reduction of balance and gait deficits (Danilov et al., 2015). A recent seed-based resting-state functional connectivity (RSFC) study demonstrated positive effects of TLNS on brain plasticity of somatosensory input, visual-vestibular interaction, and balance control in mmTBI patients (Hou et al., 2022). However, the alterations within and between whole-brain functional networks affected by TLNS on mmTBI patients are still unclear. The current study aims to examine the network FC changes and its correlations to behavioral testings of gait and balance between pre- and post-TLNS intervention in mmTBI patients.

Methods: The current study included RS-fMRI dataset collected by 3T MRI scanner with nine mmTBI patients. An experimental PoNS device (V2.5) was utilized to deliver the TLNS. All participants received both Sensory Organization Test (SOT) and Dynamic Gait Index (DGI) testing pre- and post-intervention as part of the behavioral assessment. Preprocessing for RS-fMRI data (pr- and post-intervention, respectively, for each patient) was performed using the Data Processing and Analysis of Brain Imaging (DPABI) toolbox (V6.0, http://rfmri.org/dpabi) (Yan et al., 2016), which includes slice timing, realignment, regressing out head motion parameters, normalization and smoothing. The symmetric correlation matrices for a 160 x 160 (25,600 unique pariwise) network FC was generated by the Dosenbach atlas. Paired t-test between post- vs. pre- intervention was performed to compare network FC changes. False discovery rate (FDR) corrected $p < .05$ was used for multiple comparisons correction. Moreover, the correlation analysis between SOT change (or DGI; post- minus pre-) and network FC change (post- minus pre-) was corrected at $p < .05$ with SPSS V23.

Results: Compared to pre-intervention, the post-intervention induced significantly increased: (1) behavioral scores on SOT and DGI; (2) intra-network FC in the somatosensory network (SMN), default mode network (DMN), frontoparietal network (FPN), visual network (VN) and dorsal attention network (DAN); (3) inter-network FC between the SMN and FPN (see Figures 1 and Table 1). Moreover, the behavioral SOT change had significantly negative correlation with the inter-network FC change between SMN and FPN, while the behavioral DGI change had significantly positive correlation with the intra-network FC change within SMN.

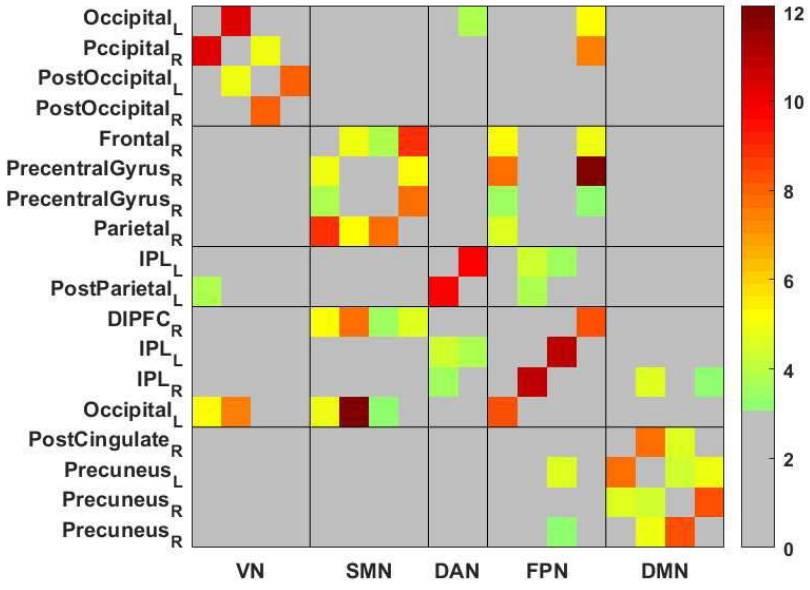

Regions		Networks		*t* value	*p* value
R frontal	R parietal	SMN	SMN	8.904	.002
R precentral	R parietal	SMN	SMN	7.817	.002
R post cingulate	L precuneus	DMN	DMN	7.762	.002
R precuneus	R precuneus	DMN	DMN	8.323	.002
L inferior parietal	R inferior parietal	FPN	FPN	10.767	.001
R dorsal prefrontal	L occipital	FPN	FPN	8.261	.002
L occipital	R occipital	VN	VN	10.247	.002
L post occipital	R post occipital	VN	VN	7.892	.002
L inferior parietal	L post parietal	DAN	DAN	9.819	.002
R precentral gyrus	L occipital	SMN	FPN	12.136	.001
R precentral gyrus	R dorsal prefrontal	SMN	FPN	7.768	.002

Note: positive *t* value means post- is greater than pre-intervention. Paired *t*-test FDR $p < .05$;
VN: visual network; SMN; somatosensory network; DAN: dorsal attention network;
DMN: default mode network; FPN: frontoparietal network; L: left; R: right.

Conclusions: The increased intra- and inter-network FC at SMN and FPN indicate that TLNS intervention is an effective in increasing somatosensory processing, vestibular-visual interaction, executive control and flexible shifting (Li et al., 2021). The increased intra-network FC at VN, DAN and DMN refers to improved visual attention, motor perception, control monitoring, goal-directed tasks, visual-guided actions and cognitive control (Yan et al., 2019). Moreover, the positive correlation between intra-SMN change and behavioral DGI change illustrates the association with increased network FC and behavioral improvement that relates to gait and stability. However, the negative correlation between inter-FPN and SMN change and behavioral SOT change indicates the association with less FC alteration but greater cognitive efficiency such as somatosensory, vision, or vestibular balance. In conclusion, the present study shows evidence that TLNS is an effective approach to improve balance and gait abilities, which also induce brain network plasticity, in mmTBI patients.

References

1. Danilov, Y. et al. (2015), 'Cranial Nerve Noninvasive Neuromodulation: New Approach to Neurorehabilitation', In Kobeissy FH, ed. Brain Neurotrauma: Molecular, Neuropsychological, and Rehabilitation Aspects. Boca Raton (FL) Press.
2. Hou, J. et al. (2022), 'Translingual neural stimulation affects resting-state functional connectivity in mild-moderate traumatic brain injury', Journal of Neuroimaging, vol. 32, no. 6, pp. 1193-1200.
3. Li, L. et al. (2021), 'Eight-week antidepressant treatment reduces functional connectivity in first-episode drug-naive patients with major depressive disorder', Human Brain Mapping, vol. 42, pp. 2593-2605.
4. Li, Y. et al. (2013), 'Individual structural differences in left inferior parietal area are associated with school childrens' arithmetic scores', Frontiers in Human Neuroscience, vol. 7, pp. 844.
5. McDonald, S. (2023), 'Impairments in social cognition following severe traumatic brain injury', Journal of International Neuropsychology, vol. 19, pp. 231-246.
6. Yan, C. et al. (2016), 'DPABI: Data Processing & Analysis for (Resting-State) Brain Imaging', Neuroinformatics, vol. 14, pp. 339-351.
7. Yan, C. et al. (2019), 'Reduced default mode network functional connectivity in patients with recurrent major depressive disorder', Proceedings of the National Academy of Sciences, vol. 116, pp. 9078-9083.

Poster No 374

Brain morphometry differences and similarities between Crohn's disease patients and healthy controls

Benjamin Yeske[1], Jiancheng Hou[2], Daniel Chu[1], Nagesh Adluru[1], Veena Nair[1], Poonam Beniwal-Patel[3], Sumona Saha[1], Vivek Prabhakaran[1]

[1]University of Wisconsin-Madison, Madison, WI, [2]Fujian Normal University, Fuzhou, Fujian, [3]Medical College of Wisconsin, Milwaukee, WI

Introduction: Crohn's disease (CD), one of the main phenotypes of inflammatory bowel disease (IBD), can affect any part of the gastrointestinal tract (Godala et al., 2022; Fiorindi et al., 2022). It can impact the function of gastrointestinal secretions, as well as increasing the intestinal permeability leading to an aberrant immunological response and subsequent intestinal inflammation (Chichlowski and Hale, 2008). Studies have reported anatomical and functional brain changes in CD patients (CDs), possibly due to increased inflammatory markers and microglial cells that play key roles in communicating between the brain, gut, and systemic immune system (Sajadinejad et al., 2012; Hou et al., 2019). To date, no studies have demonstrated similarities between functional or morphological brain changes seen in CDs and brain morphometry observed in older healthy controls.

Methods: For the present study, twelve young CDs in remission (M = 26.08 years, SD = 4.9 years, 7 male) were recruited from an IBD Clinic. Data from 12 young age-matched healthy controls (HCs) (24.5 years, SD = 3.6 years, 8 male) and 12 older HCs (59 years, SD = 8 years, 8 male), previously collected for a different study under a similar MR protocol, were analyzed as controls. T1 weighted images and structural image processing techniques were used to extract cortical thickness, fractal dimensionality, gyrification, and sulcal depth, to test our hypothesis that young CDs have different brain surface morphometry than their age-matched young HCs and furthermore, appear more similar to older HCs. The phonemic verbal fluency (VF) task (the Controlled Oral Word Association Test, COWAT) (Benton, 1976) was administered to test verbal cognitive ability and executive control.

Results: Our results demonstrated that CDs had more brain regions with differences in brain morphometry measures when compared to the young HCs (Figure 1) as compared to the old HCs (Figure 2), suggesting that CD has an effect on the brain that makes it appear more similar to old HCs. Our study did not identify any group differences for VF task performance. However, our study demonstrated that the atypical brain morphometry of CDs is associated with function on a cognitive task, with more brain regions by morphometry comparisons associated with the VF task in CDs versus the young and old HCs.

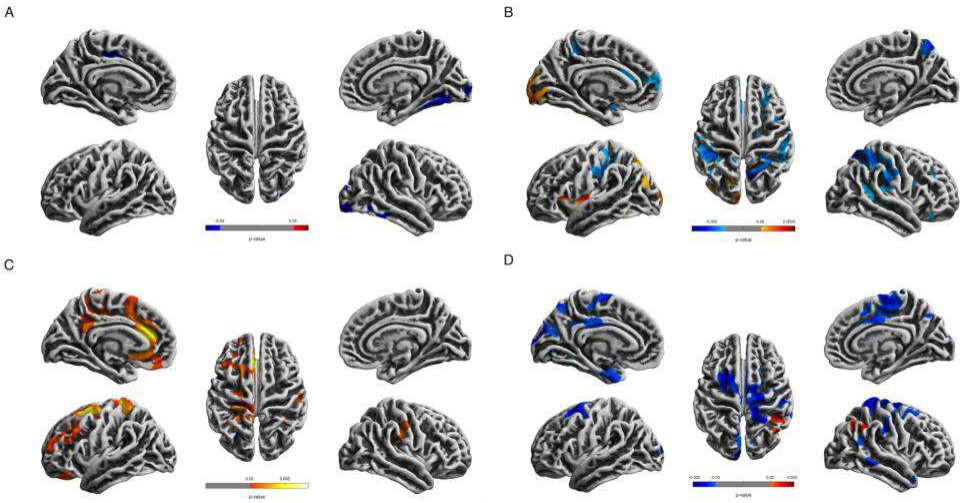

Figure 1. Surface morphometry differences between young CDs and young healthy controls

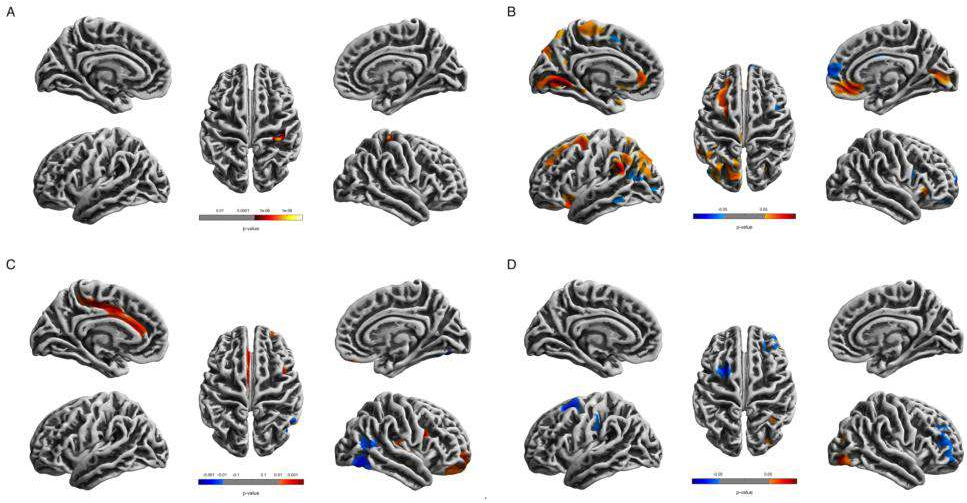

Figure 2. Surface morphometry differences between young CDs and old healthy controls

Conclusions: Our results suggest that even younger CDs may be showing some evidence of structural brain changes that demonstrate increased resemblance to older HC brains rather than their similarly aged healthy counterparts. While we didn't find evidence of VF performance differences between groups, it appears CDs recruit more brain regions in order to perform the same VF task as compared to both young and old HCs. It is possible these differences are a result of the varying medications CDs require to combat the disease process or a result of the disease process itself, but a causal relationship is not assessable within the constraints of the present study.

References

1. Benton, A. (1976), 'Multilingual aphasia examination', In Hamsher K, ed. Iowa City, IA.
2. Chichlowski, M. et al. (2008), 'Bacterial-mucosal interactions in inflammatory bowel disease: an alliance gone bad', Am J Physiol Gastrointest Liver Physiol, vol. 295, no. 6, pp. G1139-1149.
3. Fiorindi, C. et al. (2022), 'Inflammatory bowel disease and customized nutritional intervention focusing on gut microbiome balance', Nutrients, vol. 14, no. 19, pp. 126-131.
4. Godala, M. et al. (2022), 'Dietary interventions in inflammatory bowel disease', Nutrients, vol. 14, no. 20, pp. 157-168.
5. Hou, J. et al. (2019), 'Alterations in resting-state functional connectivity in patients with Crohn's disease in remission', Scientific Reports, vol. 9, no. 1, pp. 7412.
6. Sajadinejad, S. et al. (2012), 'Psychological issues in inflammatory bowel disease: An overview', Gastroenterol Res Pract, pp. 106502.

Poster No 375

Dimensional Relationships Between Conduct Problems and Brain Structure: An ENIGMA Mega-Analysis

Marlene Staginnus[1], Yidian Gao[2], Sophie Townend[1], Moji Aghajani[3,4], Eduard Klapwijk[5,6], Charlotte Cecil[7,8], Arielle Baskin-Sommers[9], Daniel Pine[10], Sophia Thomopoulos[11], Neda Jahanshad[11], Paul Thompson[11], Esther Walton[1], Stephane De Brito[2], Graeme Fairchild[1], ENIGMA Antisocial Behavior Working Group[12]

[1]Department of Psychology, University of Bath, Bath, United Kingdom, [2]Centre for Human Brain Health, School of Psychology, University of Birmingham, Birmingham, United Kingdom, [3]Institute of Education & Child Studies, Section Forensic Family & Youth Care, Leiden University, Leiden, The Netherlands, [4]Department of Psychiatry, Amsterdam University Medical Centers, VU University, Amsterdam, The Netherlands, [5]Erasmus School of Social and Behavioural Sciences, Erasmus University Rotterdam, Rotterdam, The Netherlands, [6]Brain and Development Research Center, Leiden University, Leiden, The Netherlands, [7]Department of Child and Adolescent Psychiatry/Psychology, Erasmus Medical Centre, Rotterdam, The Netherlands, [8]Department of Epidemiology, Erasmus Medical Centre, Rotterdam, The Netherlands, [9]Department of Psychology, Yale University, New Haven, CT, United States, [10]National Institute of Mental Health (NIMH), National Institutes of Health (NIH), Bethesda, MD, United States, [11]Keck School of Medicine, University of Southern California, Marina del Rey, CA, United States, [12]Universities of Birmingham and Bath, Birmingham/Bath, United Kingdom

Introduction: Conduct disorder (CD) and elevated conduct problems (CP) are associated with various negative outcomes (e.g., poor mental and physical health, delinquency) and are a substantial economic burden (Erskine et al., 2014). The first case-control analysis focusing on CD by the ENIGMA-Antisocial Behavior working group provided robust evidence of brain structural alterations in this population. Relative to controls, youth with CD showed lower surface area across most of the cortex (Gao, Staginnus et al., in preparation). However, evidence that CP occur on a continuum highlights the importance of complementary studies that investigate CP as a dimensional construct, including in non-clinical samples. Therefore, leveraging the largest-ever multi-site neuroimaging database on youth CP compiled by the ENIGMA-Antisocial Behavior working group, we aimed to evaluate associations between CP and cortical thickness, surface area, and subcortical volumes.

Methods: This pre-registered mega-analysis (doi.org/10.17605/OSF.IO/NZJ3R) combines T1-weighted MRI data of children and adolescents from 18 international case-control and community-/population-based cohorts. Data were pre-processed with FreeSurfer and quality controlled according to the standardized ENIGMA protocols. CP were assessed using the Child Behavior Checklist or the Strengths and Difficulties Questionnaire, which were transformed into a common metric using the percentage of maximum possible score method (Cohen, 1999). We used linear models to examine associations of CP with measures of regional cortical thickness, surface area (34 regions, averaged across hemispheres, respectively), and subcortical volumes (7 regions, averaged across hemispheres), controlling for age, sex, and intracranial volume. We adjusted for site effects using the modified ComBat functions (Radua et al., 2020) and applied a False Discovery Rate correction per brain metric.

Results: Preliminary analyses including 13 of the 18 cohorts and 10,576 youths (aged 7-19 years, MAge=10.35 years, 46% girls) revealed significant negative associations between CP and cortical thickness (average thickness and 7 of the 34 regions investigated), surface area (total surface area and 27 of 34 regions), subcortical volumes (3 of 7 regions, including the

amygdala), and intracranial volume (all pFDR < .05). Just one positive association between CP and caudal anterior cingulate thickness was observed (pFDR = .017). Effect sizes expressed as standardized beta estimates ranged between 0.02 and 0.10 (see Figure 1 for more details).

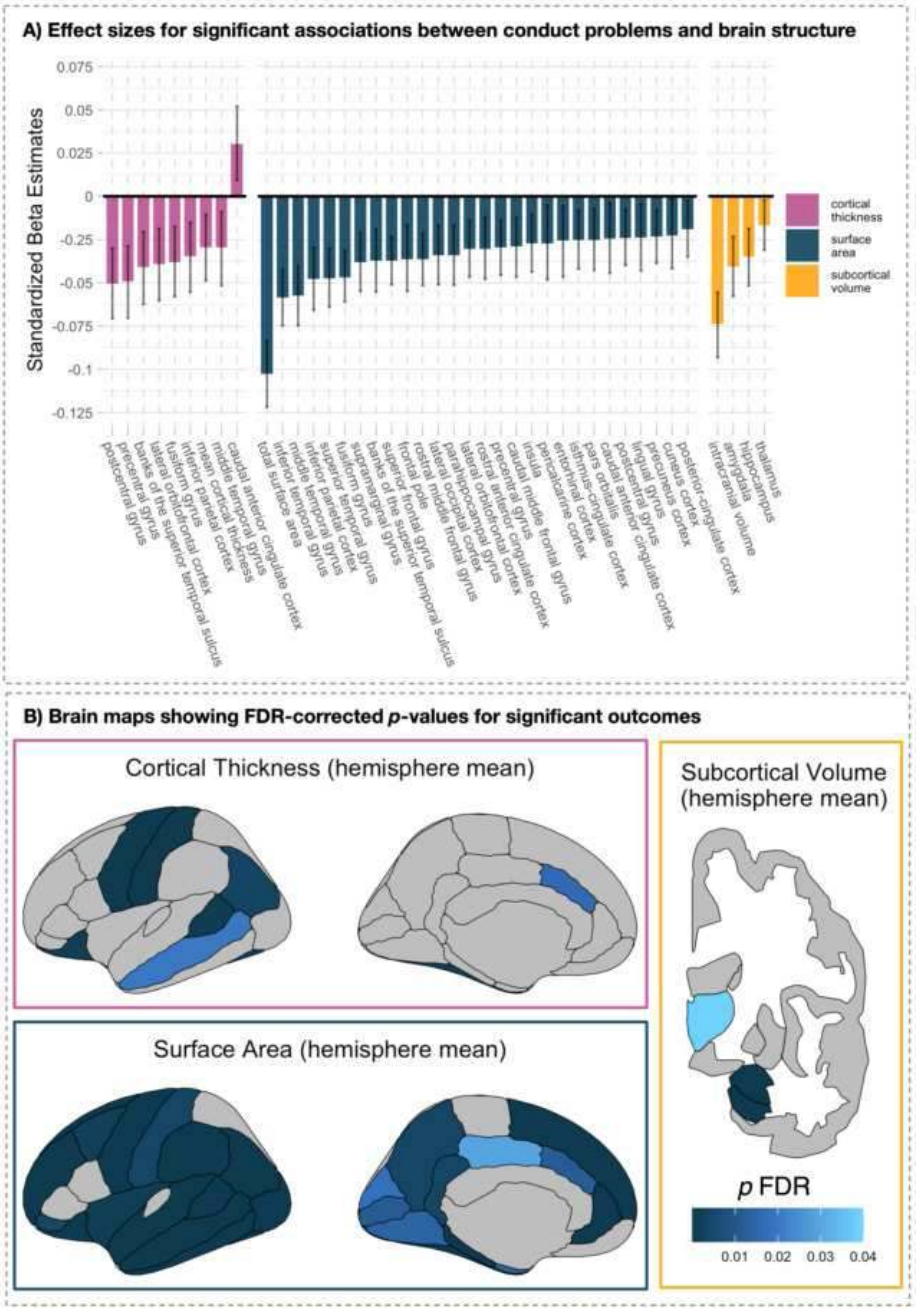

Figure 1. Significant associations between conduct problems and cortical and subcortical brain structure. Analyses were adjusted for sex, age and intracranial volume (in the case of surface area and subcortical volume). All depicted effects in panels A) and B) are significant ($p < .05$) after FDR correction for multiple comparisons. Error bars in A) represent bootstrapped (2000 resamples) 95% confidence intervals around the beta estimate. FDR = False Discovery Rate.

Conclusions: Preliminary findings indicate subtle yet widespread associations between youth CP and brain structure, especially for surface area, which largely overlap with alterations observed in the first case-control ENIGMA study of CD (Gao, Staginnus et al., in preparation; 15% participant overlap). Replicating these associations dimensionally provides robust evidence for quantitative associations between CP and brain structure across clinical and non-clinical samples. They further corroborate results from other ENIGMA disease working groups indicating that surface area is more affected than thickness in youth psychopathology (e.g., Hoogman et al., 2019; Schmaal et al., 2017). We will present findings obtained using the full sample including 18 cohorts, separate analyses of case-control and community-based samples, and interaction analyses testing whether associations between CP and brain structure differ based on age, sex, level of callous-unemotional traits, or presence of conduct disorder.

References

1. Cohen, P., Cohen, J., Aiken, L. S., West, S. G. (1999), 'The problem of units and the circumstance for POMP', Multivariate Behavioral Research, vol. 34, no. 3, pp. 315-346.
2. Erskine, H.E., Ferrari, A.J., Polanczyk, G.V., Moffitt, T.E., Murray, C.J., Vos, T., ... & Scott, J. G. (2014), 'The global burden of conduct disorder and attention-deficit/hyperactivity disorder in 2010.' Journal of Child Psychology and Psychiatry, vol. 55, no. 4, pp. 328-336.
3. Gao, Y., Staginnus, M., Aghajani, M, Klapwijk, E., Cecil, C., Baskin-Sommers, A., ... De Brito, S.A. (in preparation), 'A mega-analysis of cortical structure and subcortical volumes in conduct disorder in youth: Effects of sex, age-of-onset and callous-unemotional traits'
4. Hoogman, M., Muetzel, R., Guimaraes, J. P., Shumskaya, E., Mennes, M., Zwiers, M. P., ... Franke, B. (2019), 'Brain imaging of the cortex in ADHD: a coordinated analysis of large-scale clinical and population-based samples', American Journal of Psychiatry, vol. 176, no. 7, pp. 531-542.
5. Radua J., Vieta E., Shinohara R., Kochunov P., Quidé Y., Green M.J., ... Pineda-Zapata J. (2020), 'Increased power by harmonizing structural MRI site differences with the ComBat batch adjustment method in ENIGMA', NeuroImage, vol. 218, 116956.
6. Schmaal, L., Hibar, D. P., Sämann, P. G., Hall, G. B., Baune, B. T., Jahanshad, N., ... Veltman, D. J. (2017), 'Cortical abnormalities in adults and adolescents with major depression based on brain scans from 20 cohorts worldwide in the ENIGMA Major Depressive Disorder Working Group', Molecular Psychiatry, vol. 22, no. 6, pp. 900-909.

Poster No 376

Learning from errors: neural evidence for altered mechanisms in Autism Spectrum Disorder

Maria Camila Dias[1,2], Teresa Sousa[1,2], Susana Mouga[1,3], Miguel Castelo-Branco[1,2,4]

[1]CIBIT - Coimbra Institute for Biomedical Imaging and Translational Research, University of Coimbra, Coimbra, Portugal, [2]ICNAS - Institute for Nuclear Sciences Applied to Health, University of Coimbra, Coimbra, Portugal, [3]ICNAS PHARMA Unipessoal, Lda, Ed. ICNAS, Pólo das Ciências da Saúde, University of Coimbra, Coimbra, Portugal, [4]FMUC - Faculty of Medicine, University of Coimbra, Coimbra, Portugal

Introduction: Error monitoring involves detecting, processing, and signaling errors to prevent future mistakes. Perceiving the outcomes of our actions is vital for regulating behavior and learning (Ullsperger, Danielmeier, & Jocham, 2014). Accordingly, impaired error monitoring skills have been demonstrated in some conditions, such as Autism Spectrum Disorder (ASD) (Kim, Grammer, Benrey, Morrison, & Lord, 2018; Santesso et al., 2011). However, the alterations in the error monitoring neural circuitry in ASD remain to be fully understood. Here, we tested the hypothesis that the evolution of learning associated with error monitoring is altered in ASD.

Methods: In this study, 15 non-ASD (mean age 30.7 ± 6.1 years) and 15 ASD (mean age 29.1 ± 8.7 years) male participants performed a challenging 3T functional magnetic resonance imaging (fMRI) task based on Estiveira et al. (2022). The task had multiple concurrent cues, namely emotional facial expression and gaze cues, that signaled the appropriate action and needed to be integrated to make a correct response. To understand how neural learning processes progress in error monitoring, we conducted linear mixed-effects analyses to assess the impact of group, performance, learning, and their respective interactions on key error monitoring regions, such as the dorsal anterior cingulate cortex (dACC) and anterior insula (AI) (Dali et al., 2023; Neta et al., 2015). We also evaluated the influence of these variables on the putamen, a region linked to trial and error learning (Ashby, Turner, & Horvitz, 2010; Patterson & Knowlton, 2018). We controlled our analyses for age and Full-Scale Intelligence Quotient by including them as covariates in the linear mixed-effects models.

Results: Behaviorally, we found a significant effect of group ($F(1, 29.02) = 20.59$, $p = 9.10 \times 10\text{-}5$) and learning stage ($F(6,764.19) = 34.94$, $p = 2.05 \times 10\text{-}37$) on error rate. Both groups showed clear learning curves with decreasing error rates from the beginning to the end of the session. During the entire task, the ASD group had increased error rates compared to the non-ASD group. The fMRI results revealed that activity in the dACC and AI was modulated by the interaction between group and performance (dACC: $F(2,53.23) = 10.80$, $p = 1.16 \times 10\text{-}4$; AI: $F(2,54.21) = 25.48$, $p = 1.58 \times 10\text{-}8$), and learning and performance (dACC: $F(12,7809.34) = 5.38$, $p = 3.55 \times 10\text{-}9$; AI: $F(6,7810.24) = 7.83$, $p = 2.03 \times 10\text{-}8$). The activity in these regions was similar for correct and erroneous responses in an initial learning stage but, as learning progressed, the differences became evident. This happened due to a simultaneous decrease in activity in correct responses and an increase following errors. Although this pattern did not differ between groups, the differences between correct responses and errors were attenuated in ASD (differences being only significant in the non-ASD group). Moreover, for the ASD group, we found an inverse correlation between the difference in dACC activity between correct and erroneous responses and autistic traits ($r(11) = -0.62$, $p = 0.023$) measured by Autism Diagnostic Observation Schedule (ADOS) total scores (Lord et al., 1989). The putamen response was influenced by the interaction between group and learning ($F(6, 7808.01) = 6.84$, $p = 2.99 \times 10\text{-}7$), and learning and performance ($F(6, 7810.18) = 4.84$, $p = 6.10 \times 10\text{-}5$). In the non-ASD group, its activity increased both in correct responses and errors with learning. Nonetheless, in the ASD group, it only increased in response to errors: the activity associated with correct actions was approximately constant throughout learning.

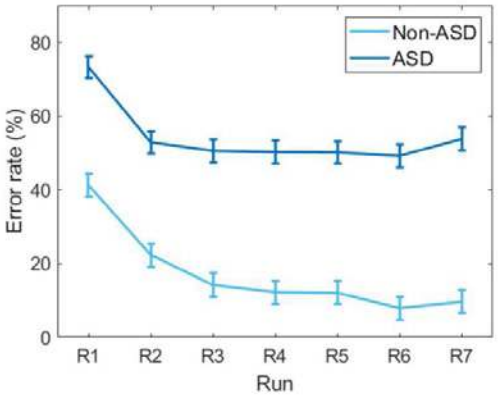

Behavioral results. Estimated marginal means of error rate along the runs for both groups. Error bars represent the SEM. A mixed-effects analysis revealed a significant impact of group and learning stage (measured by run) on error rate.

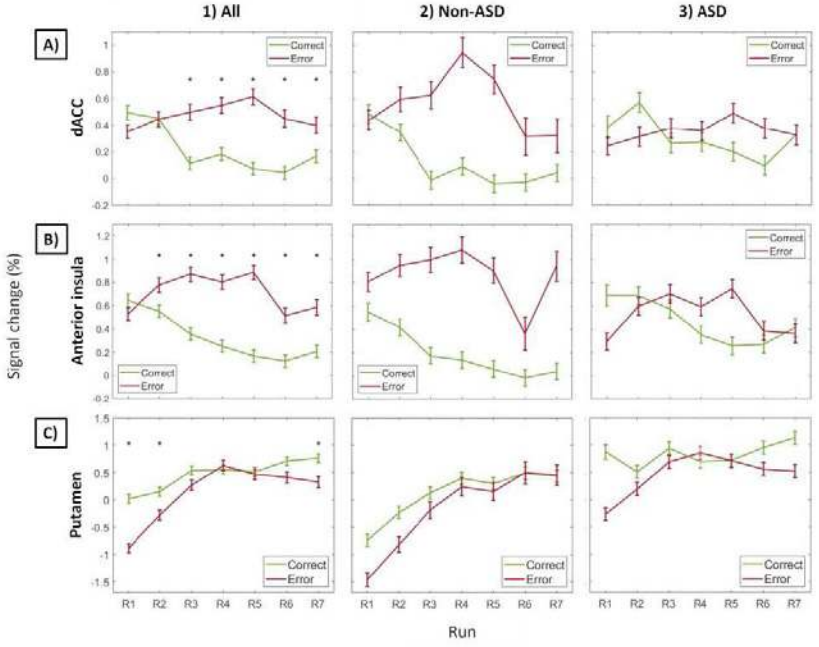

fMRI results. Estimated marginal means of A) dACC, B) bilateral anterior insula, and C) bilateral putamen percent signal change along the runs for correct and erroneous responses considering 1) all participants, 2) the non-ASD group, and 3) the ASD group. Error bars represent the SEM. Mixed-effects analyses were performed to study the effect of group, learning (measured by run), and performance on the activity of these regions. For the significant interaction between learning and performance, we analyzed each run separately to compare neural activity between correct and erroneous responses. Significant differences ($p < 0.05$) are signalized with an asterisk.

Conclusions: These findings suggest that, in ASD, error monitoring mechanisms are impaired, and the learning process is altered, possibly leading to higher error rates when integrating social cues.

References

1. Ashby, F. G., Turner, B. O., & Horvitz, J. C. (2010). Cortical and basal ganglia contributions to habit learning and automaticity. Trends in Cognitive Sciences, 14(5), 208–215. https://doi.org/10.1016/j.tics.2010.02.001
2. Dali, G., Brosnan, M., Tiego, J., Johnson, B. P., Fornito, A., Bellgrove, M. A., & Hester, R. (2023). Examining the neural correlates of error awareness in a large fMRI study. Cerebral Cortex, 33, 458–468. https://doi.org/10.1093/cercor/bhac077
3. Estiveira, J., Dias, C., Costa, D., Castelhano, J., Castelo-Branco, M., & Sousa, T. (2022). An Action-Independent Role for Midfrontal Theta Activity Prior to Error Commission. Frontiers in Human Neuroscience, 16(805080). https://doi.org/10.3389/fnhum.2022.805080
4. Kim, S. H., Grammer, J., Benrey, N., Morrison, F., & Lord, C. (2018). Stimulus processing and error monitoring in more-able kindergarteners with autism spectrum disorder: a short review and a preliminary Event-Related Potentials study. European Journal of Neuroscience, 47, 556–567. https://doi.org/10.1111/ejn.13580
5. Lord, C., Rutter, M., Goode, S., Heemsbergen, J., Jordan, H., Mawhood, L., & Schopler, E. (1989). Austism diagnostic observation schedule: A standardized observation of communicative and social behavior. Journal of Autism and Developmental Disorders, 19(2), 185–212. https://doi.org/10.1007/BF02211841

6. Neta, M., Miezin, X. M., Nelson, S. M., Dubis, J. W., Dosenbach, N. U. F., Schlaggar, B. L., & Petersen, S. E. (2015). Spatial and temporal characteristics of error-related activity in the human brain. Journal of Neuroscience, 35(1), 253–266. https://doi.org/10.1523/JNEUROSCI.1313-14.2015
7. Patterson, T. K., & Knowlton, B. J. (2018). Subregional specificity in human striatal habit learning: a meta-analytic review of the fMRI literature. Current Opinion in Behavioral Sciences, 20, 75–82. https://doi.org/10.1016/j.cobeha.2017.10.005
8. Santesso, D. L., Drmic, I. E., Jetha, M. K., Bryson, S. E., Goldberg, J. O., Hall, G. B., ... Schmidt, L. A. (2011). An event-related source localization study of response monitoring and social impairments in autism spectrum disorder. Psychophysiology, 48, 241–251. https://doi.org/10.1111/j.1469-8986.2010.01056.x
9. Ullsperger, M., Danielmeier, C., & Jocham, G. (2014). Neurophysiology of performance monitoring and adaptive behavior. Physiological Reviews, 94, 35–79. https://doi.org/10.1152/physrev.00041.2012

Poster No 377

Early Development of Brain Functional Networks

Kimhan Thung[1], WENJIAO LYU[1], Li Wang[1], Weili Lin[1], Sahar Ahmad[1], Pew-Thian Yap[1]

[1]*The University of North Carolina at Chapel Hill, Chapel Hill, NC*

Introduction: We investigated the development of baby brain functional networks from birth to 5 years old. Using over 1,200 resting state functional MRI (rs-fMRI) scans from the Baby Connectome Project (BCP), we quantified functional development during early childhood, covering sensorimotor, visual, auditory, default mode, and cerebellar networks.

Methods: We used rs-fMRI data of 280 subjects scanned in the BCP[1]. Preprocessing of rs-fMRI data[2] includes head motion correction, EPI distortion correction, fMRI to structural MRI registration guided by tissue segmentation maps, one-time resampling of fMRI data in subject native space, high-pass filtering, and ICA-AROMA denoising. We then independently performed group ICA (30 components) for each month (based on time windows defined in[4]) to obtain month-specific functional networks. For temporal consistency, we further performed group ICA (35 components) on these month-specific ICA components to obtain an overall template of functional networks, which were in turn used to compute the functional networks at each month via dual regression[3]. For each functional network, we fitted a Generalized Additive Mixed-effect Model (GAMM) to each voxel: $Y \sim s(age) + (1|RID) + (1|site)$, where s(.) is a smooth function, and (1|.) represents site and subject random effects. The developmental trajectory for each network was plotted for a high-activation point. We compared the development patterns of 5 primary function networks (i.e., 2 sensorimotor, 1 auditory, and 2 visual networks) and 5 higher order association networks (i.e., cerebellar, 2 default-mode networks, and 2 executive control networks).

Results: The development of functional networks can be observed from the spatial maps and the activation trajectory curves. Generally, all functional networks emerge since birth and stabilize after month 6. The activation increases substantially from birth to month 6 and increases gradually through month 60. The activations of association networks are in general substantially lower than the primary function networks. Fig. 1: Month-specific functional atlases for major resting state functional networks: (a) sensorimotor networks (left to right) - motor networks (SMN-lateral, SMN-medial), auditory network, and visual networks (VIS-occipital, VIS-medial); (b) association networks (left to right) - cerebellar network, default mode networks (DMN-prefrontal, DMN-Precuneus), and executive control networks (ECN-L, ECN-R). The rows correspond (top to bottom) to different months: 0, 1, 3, 9, 12, 24, and 60. Fig. 2. Developmental trajectories of functional networks. Shaded areas mark the standard errors.

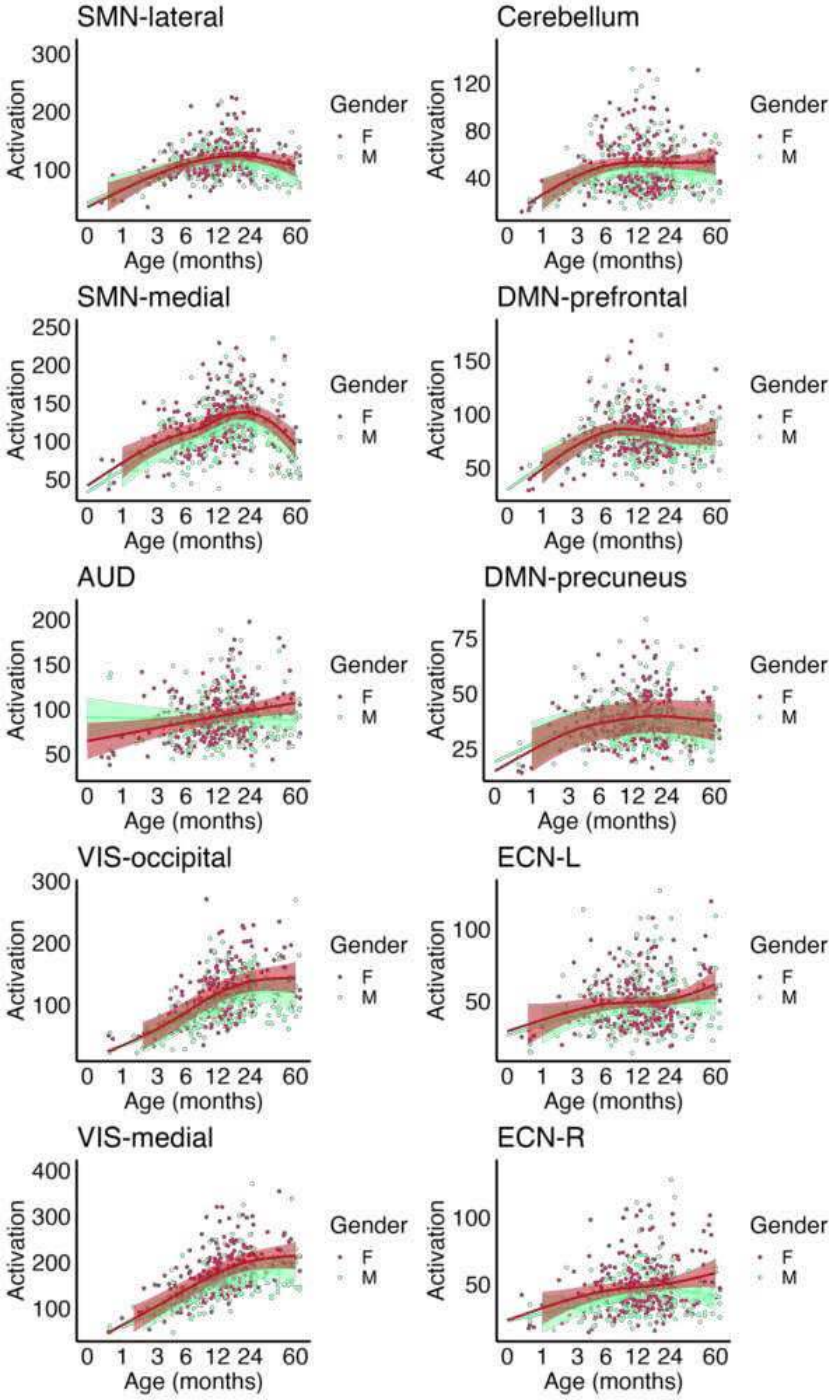

Conclusions: We constructed monthly functional atlases from birth to five years of age, capturing the spatiotemporal characteristics of early brain development.

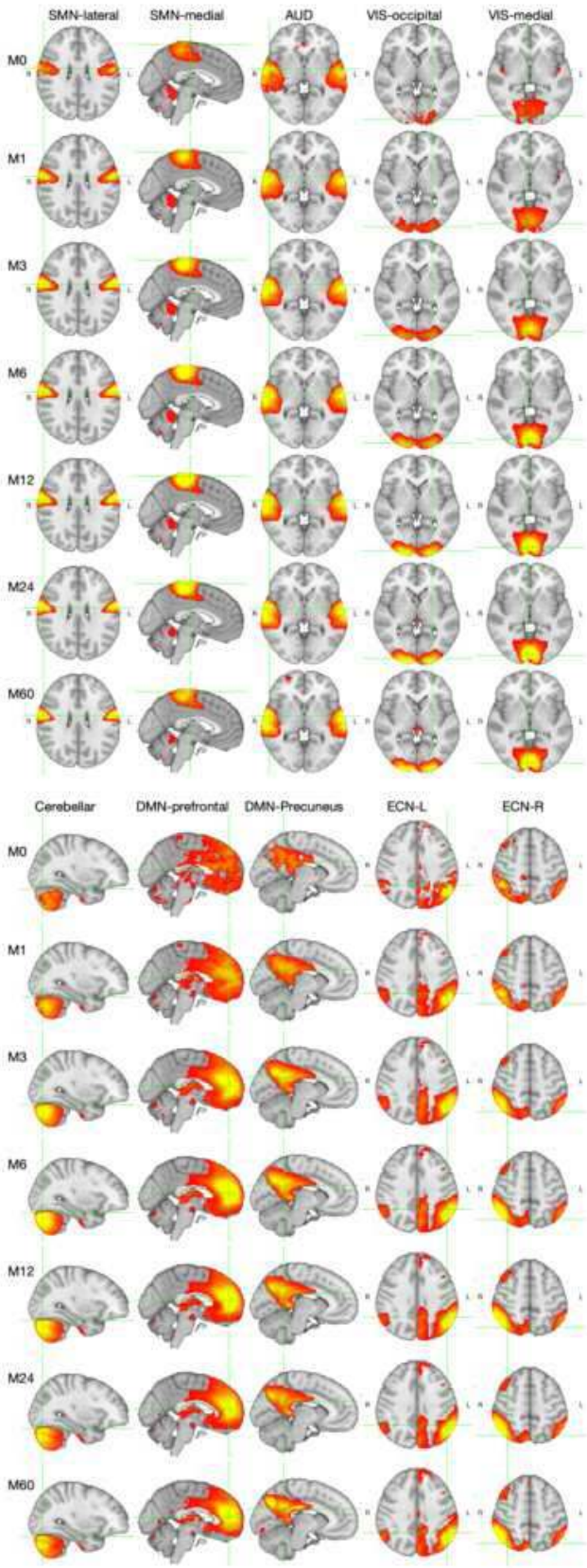

References

1. Howell et al., "The UNC/UMN Baby Connectome Project (BCP): An overview of the study design and protocol development," NeuroImage, 2019.
2. Thung et al., "Analysis of ICA-AROMA motion denoising on fMRI data in infant cohort," OHBM, 2022.
3. Beckmann et al., "Group Comparison of Resting-State FMRI Data Using Multi-Subject ICA and Dual Regression." NeuroImage, 2009.
4. Ahmad et al., "Multifaceted Atlases of the Human Brain in Its Infancy," Nature Methods, 2023.

Poster No 378

Subcortical volumes in middle-aged and older adults with and without autism spectrum disorder

Michaela Cordova[1], Stephanie Pedrahita[2], Annika Linke[3], Gioia Toro[4], Molly Wilkinson[1], Jiwandeep Kohli[5], Janice Hau[3], Inna Fishman[6], Ralph-Axel Mueller[4], Ruth Carper[4]

[1]SDSU/UC San Deigo, San Diego, CA, [2]San Diego State University, San diego, CA, [3]San Diego State University, San Diego, CA, [4]San Diego Research Foundation, San Diego, CA, [5]University of California, San Diego, San Diego, CA, [6]SDSU, San Diego, CA

Introduction: Autism spectrum disorder (ASD) is a lifelong neurodevelopmental condition with known behavioral and neurobiological correlates. In youth, those with ASD show significant differences in subcortical volumes (caudate, putamen, nucleus accumbens, and thalamus) compared to their neurotypical (NT) peers. Such volume differences have been linked to ASD-related behaviors in children and younger adults, including atypical response to reward and social challenges. In the NT population, these volumes decrease after age 40, with associated declines in memory, attention, and processing speed. Together these findings suggest that middle-aged and older autistic adults may experience an interplay between long-standing reduced subcortical volume (at least since childhood) combined with normal age-related changes after 40+ years. This may place them at risk for accelerated volume changes, with important implications for overall function. In this study, we hypothesized steeper age-associated subcortical volume decline among middle-aged and older adults with ASD, in comparison to NT peers.

Methods: Data were collected on 40–70-year-old adults with ASD and NT participants enrolled in an ongoing longitudinal study on aging in autism. ASD diagnoses were confirmed by an expert clinician using DSM-5 criteria. NT participants had no family or personal history of ASD or serious mental illness. Magnetic resonance imaging (MRI) data (T1-weighted anatomical images: TR=8.78ms, TE=3.66ms, resolution=0.8mm3) were collected on a 3T GE Discovery MR750 scanner. The Human Connectome Project (HCP) pipeline version 5.3.0 was used for preprocessing and results were visually inspected for quality assurance. An automated subcortical segmentation approach (SynthSeg, Freesurfer 7.3.1) was then used to parcellate subcortical regions. Briefly, SynthSeg employs a convolutional neural network previously trained on randomized synthetic data, to segment regions of interest (ROIs) and estimate corresponding volumes. Bilateral thalamus, caudate, putamen, nucleus accumbens and pallidum were selected for analyses. Accuracy of SynthSeg parcellations was reviewed using a 4-point scale (4=excellent, 1=unusable). Only ROIs rated 3 or 4 were included in analyses, with unusable data excluded on a per-subject, per-ROI basis. Groups were matched on age, sex, non-verbal IQ, ethnicity, and contrast-to-noise ratio. General linear models were applied to test for age-by-diagnosis interaction effects, as well as main effects of diagnostic group or age on each ROI volume, while controlling for the effects of total intracranial volume (TIV).

Results: Following SynthSeg QA, the following data were considered usable: caudate N=69, putamen N=68 (ASD=28, NT=40), nucleus accumbens N=69, thalamus N=53 (ASD=24, NT=29). The pallidum was excluded entirely due to low N (ASD=2, NT=4). There were no significant age-by-diagnosis interaction effects across all models. The ASD sample showed significantly lower volumes of the left putamen and left nucleus accumbens compared to their NT peers (Figure 1). There were significant age effects such that greater age was associated with lower subcortical volumes in the bilateral caudate and putamen (Figure 2).

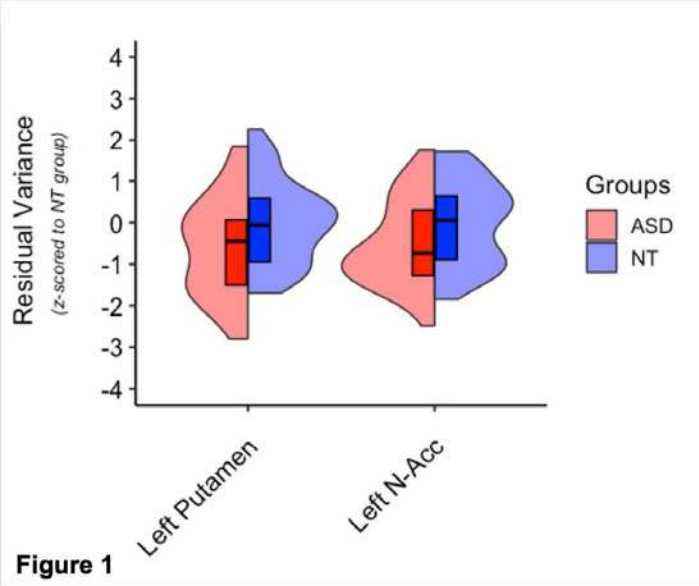

Figure 1

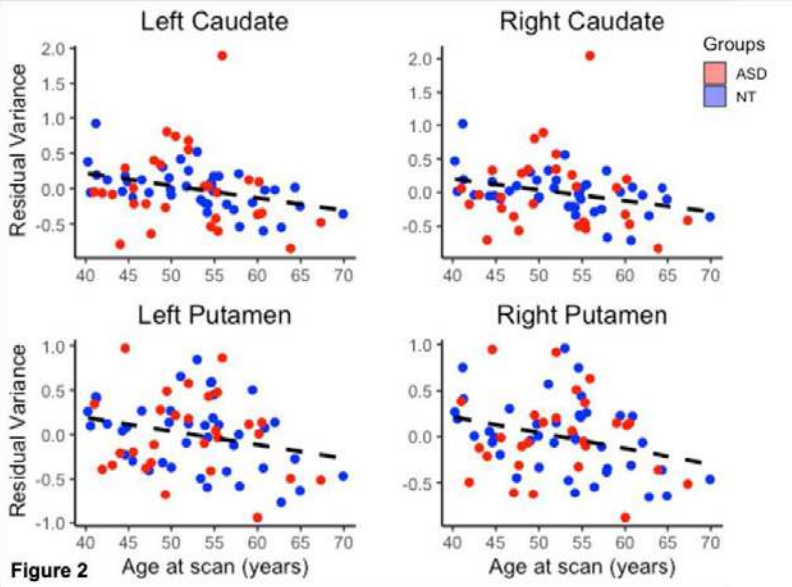

Figure 2

Conclusions: Subcortical nuclei play a role in many of the symptoms of ASD, and they are known to decrease in size during typical aging. Negative age effects found here are consistent with the previous literature. While our findings of lower subcortical volumes in the ASD than the NT group were also partially consistent with past reports, our hypothesis of accelerated volume decline was not supported. However, analysis of longitudinal measures (now being collected) and larger sample sizes will be more definitive. Neurobiological change during aging in ASD remains severely understudied but the current report, along with an increasing body of literature, has begun to make inroads.

References

1. Billot, B. et al., (2023). SynthSeg: Segmentation of brain MRI scans of any contrast and resolution without retraining. DOI: 10.1016/j.media.2023.102789
2. Cherubini, A. et al., (2009). Aging of subcortical nuclei: Microstructural, mineralization and atrophy modifications measured in vivo using MRI. DOI: 10.1016/j.neuroimage.2009.06.035
3. Dima, D. et al., (2022). Subcortical volumes across the lifespan: Data from 18,605 healthy individuals aged 3–90 years. DOI: 10.1002/hbm.25320
4. Fama, R., & Sullivan, E.V. (2015). Thalamic structures and associated cognitive functions: Relations with age and aging. DOI: 10.1016/j.neubiorev.2015.03.008
5. Hollander, E. et al., (2005). Striatal Volume on Magnetic Resonance Imaging and Repetitive Behaviors in Autism. DOI: 10.1016/j.biopsych.2005.03.040
6. Kohls, G., Yerys, B.E., & Schultz, R.T. (2014). Striatal development in autism: Repetitive behaviors and the reward circuitry. DOI: 10.1016/j.biopsych.2014.07.010
7. Langen, M. et al., (2014). Changes in the Development of Striatum Are Involved in Repetitive Behavior in Autism. DOI: 10.1016/j.biopsych.2013.08.013
8. Mason, D. et al. (2022). Older Age Autism Research: A Rapidly Growing Field, but Still a Long Way to Go. DOI: 10.1089/aut.2021.0041
9. Serbruyns, L. et al. (2015). Subcortical volumetric changes across the adult lifespan. DOI: 10.1016/j.cortex.2015.01.003
10. Tamura, R. et al. (2010). Reduced thalamic volume observed across different subgroups of autism spectrum disorders. DOI: 10.1016/j.pscychresns.2010.07.001
11. van Rooij, D. et al. (2018). Cortical and Subcortical Brain Morphometry Differences Between Patients With Autism Spectrum Disorder and Healthy Individuals Across the Lifespan. DOI: 10.1176/appi.ajp.2017.17010100
12. Walhovd, K.B. et al. (2005). Effects of age on volumes of cortex, white matter and subcortical structures. DOI: 10.1016/j.neurobiolaging.2005.05.020
13. Zuo, C. et al., (2019). Changes in the development of subcortical structures in autism spectrum disorder. DOI: 10.1097/WNR.0000000000001300

Poster No 379

Microstructural alterations of association tracts in autism localized with along-tract mapping

Gaon Kim[1], Sebastian Benavidez[1], Bramsh Chandio[1], Katherine Lawrence[1], Paul Thompson[1]

[1]Imaging Genetics Center, Keck School of Medicine of University of Southern California, Los Angeles, CA

Introduction: Autism is a heterogeneous neurodevelopmental condition characterized by subtle and widespread changes in brain morphometry and white matter microstructure of both gray and white matter as revealed by previous neuroimaging studies[1-7]. While diffusion-weighted magnetic resonance imaging (dMRI) research has uncovered microstructural alterations

associated with autism, region of interest based approaches or tract-based spatial statistics lack the precision to offer a fine-scale local mapping of microstructure[4-7]. In this pilot study, we used the advanced tractography-based approach, BUndle ANalytics (BUAN) to investigate white matter microstructure of association tracts in autism at a more refined anatomical scale.

Methods: We analyzed 3D dMRI brain scans from 172 participants (mean age: 24.3+15.2 years, 99.4% male) - 107 individuals with autism and 65 neurotypical subjects. Data was sourced from one NIMH Data Archive site and two Autism Brain Imaging Data Exchange sites and all three sites used 3T scanners (b=1000-2500s/mm^2; voxel size=2-3mm). Preprocessing steps included denoising and correction for eddy currents, head motion, bias field, and gradient distortions. Standard DTI metrics - fractional anisotropy (FA), and mean, axial, and radial diffusivity (MD, AD, RD) - were computed at each voxel. Whole-brain tractograms were generated using a constrained spherical deconvolution model and local deterministic tractography. The tracking algorithm was set to start from voxels where FA>0.3, seed count=10, step size=0.5 and stopped tracking if FA <0.2[8]. Each white matter tract was extracted using the auto-calibrated RecoBundles[9] and a standard atlas of major white matter tracts[10]. We focused on 6 separate bilateral association tracts: arcuate fasciculus (AF), extreme capsule (EMC), inferior fronto-occipital fasciculus (IFOF), inferior longitudinal fasciculus (ILF), middle longitudinal fasciculus (MdLF), uncinate fasciculus (UF). Using BUAN, each of the association tracts was divided into 100 segments per subject. Linear mixed models were used to compare microstructural metrics between the autism and neurotypical groups, adjusting for age and sex while accounting for subject and site variability. The false discovery rate was applied for multiple comparisons correction.

Results: We found significant tract segment differences for mean FA, MD, AD, and RD in association tracts (Table 1). Mean FA differences were detected in the left AF, left IFOF, left ILF, bilateral MdLF, and bilateral UF (Fig 1A-D). For mean MD, the following tracts showed significant differences between the autism and neurotypical groups: right EMC, bilateral IFOF, right ILF, left MdLF, and left UF (Fig 1E-F). Significant mean AD differences were observed in right EMC, left IFOF, left MdLF, and right UF. Finally, for mean RD the left AF, right EMC, left IFOF, right ILF, left MdLF and left UF tracts showed significant differences between groups. In sum, we found localized differences in association tracts in autism using BUAN.

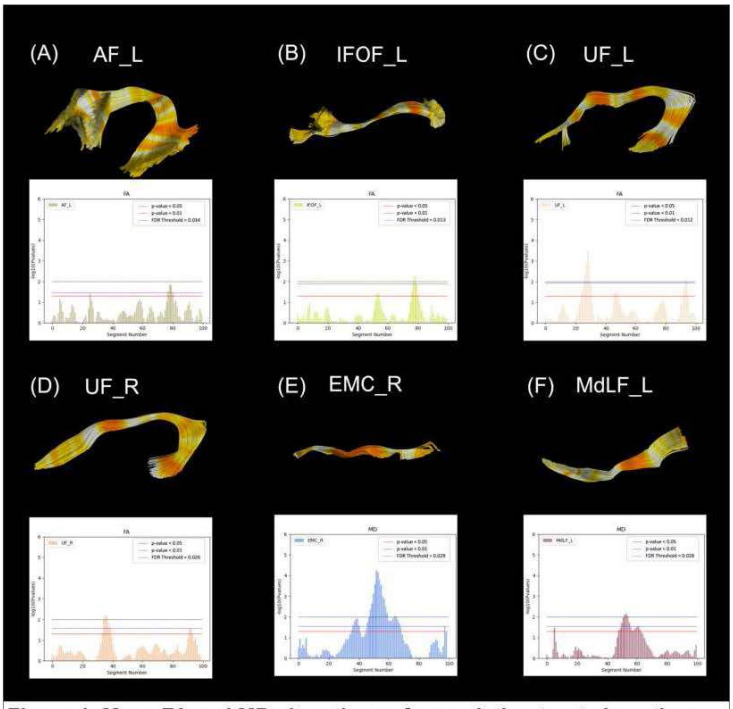

Figure 1. Mean FA and MD alterations of association tracts in autism. Compared to neurotypicals, autism was associated with localized microstructural alterations of mean FA (A-D) and mean MD (E-F) in the association tracts. FA: fractional anisotropy; MD: mean diffusivity; AF_L: arcuate fasciculus left; IFOF_L: inferior fronto-occipital fasciculus left; UF_L: uncinate fasciculus left; UF_R: uncinate fasciculus right; EMC_R: extreme capsule right; MdLF_L: middle longitudinal fasciculus left

	FA	MD	AD	RD
AF_L	*			*
AR_R				
EMC_L				
EMC_R		*	*	*
IFOF_L	*	*		*
IFOF_R		**		
ILF_L	*			
ILF_R		*		*
MdLF_L	*	*	**	*
MdLF_R	*			
UF_L	*	*		*
UF_R	*		*	

Table 1. Alterations of DTI metrics in autism. Stars indicate significant differences between neurotypicals and autism groups for each DTI metric of FA, MD, AD, and RD for each of the six bilateral association tracts. Red indicates higher mean values in neurotypicals and blue denotes higher mean values in autism. _L and _R denote the tracts in the left and right hemispheres, respectively. FA: fractional anisotropy; MD: mean diffusivity; AD: axial diffusivity; RD: radial diffusivity; AF: arcuate fasciculus left; EMC: extreme capsule left; IFOF: inferior fronto-occipital fasciculus left; ILF: inferior longitudinal fasciculus; MdLF: middle longitudinal fasciculus; UF: uncinate fasciculus

Conclusions: In this pilot study, we used BUAN - an advanced along-tract analysis method - to investigate the fine-grained microstructure of association tracts in autism. We found localized microstructural changes in the AF, EMC, IFOF, ILF, MdLF, and UF in autism compared to neurotypical controls. Microstructure was altered in localized regions, at a scale that may not be resolved with standard ROI analyses. Future work will include larger and more diverse samples, as well as associations with clinical and behavioral assessments. Whole-brain tractometry may also help to identify subgroups within autism cohorts, providing insights for interventional studies.

References

1. Lord, C. (2020) Autism spectrum disorder. Nature Reviews. Disease Primers, 6(1), 5.
2. van Rooij, D. (2018) Cortical and Subcortical Brain Morphometry Differences Between Patients With Autism Spectrum Disorder and Healthy Individuals Across the Lifespan: Results From the ENIGMA ASD Working Group. The American Journal of Psychiatry, 175(4), 359–369.
3. Postema, M. C. (2019) Altered structural brain asymmetry in autism spectrum disorder in a study of 54 datasets. Nature communications, 10(1), 4958.
4. Aoki, Y. (2013) Comparison of white matter integrity between autism spectrum disorder subjects and typically developing individuals: a meta-analysis of diffusion tensor imaging tractography studies. Molecular Autism, 4(1), 25.
5. Di, X. (2018) Disrupted focal white matter integrity in autism spectrum disorder: A voxel-based meta-analysis of diffusion tensor imaging studies. Progress in neuro-psychopharmacology & biological psychiatry, 82, 242–248.
6. Travers, B. G. (2012) Diffusion tensor imaging in autism spectrum disorder: a review. Autism research : official journal of the International Society for Autism Research, 5(5), 289–313.
7. Zhao, Y. (2022) Identify aberrant white matter microstructure in ASD, ADHD and other neurodevelopmental disorders: A meta-analysis of diffusion tensor imaging studies. Progress in Neuro-psychopharmacology & Biological Psychiatry, 113, 110477.
8. Chandio, B. Q. (2020) Bundle analytics, a computational framework for investigating the shapes and profiles of brain pathways across populations. Scientific Reports, 10(1), 17149.
9. Garyfallidis, E. (2014) Dipy, a library for the analysis of diffusion MRI data. Frontiers in neuroinformatics, 8, 8.
10. Yeh, F. C. (2018) Population-averaged atlas of the macroscale human structural connectome and its network topology. NeuroImage, 178, 57–68.

Poster No 380

Structural alterations of contralesional visual processing areas in children with perinatal stroke

Meghan Maiani[1], Helen Carlson[1], Adam Kirton[1]

[1]*University of Calgary, Calgary, Alberta*

Introduction: Perinatal stroke (PS) results in motor, cognitive and visual impairments for millions worldwide. As the leading cause of hemiparetic cerebral palsy, most PS research has focused on the motor system where the development of the contralesional hemisphere is a key determinant of outcomes. Understanding of visual development following early life stroke

remains rudimentary. Arterial ischemic stroke (AIS) is the most common PS subtype, typically damaging visual pathways and visual association areas. Diffusion weighted-imaging has shown alterations in white matter microstructure of lesioned hemisphere optic radiations of children with AIS, but structural differences in the contralesional hemisphere that may underlie developmental plasticity and visual function preservation are unexplored. Here, we compare cortical thickness and regional brain volumes in children with AIS to their typically developing peers, and correlate these with performance on perceptual testing.

Methods: Twenty-three children ages 7-18 years with AIS were recruited from a population-based cohort (the Alberta Perinatal Stroke Project) along with 23 age and sex-matched typically developing children (TDCs). Participants underwent high-resolution T1-weighted structural MRI (166 slices, 1mm isotropic voxels) and completed the Apples test, the Motor-Free Visual Perceptual Test 3rd edition (MVPT-3) and Jerry John's basic reading inventory. A custom pediatric tissue probability map (TPM) was created with Template-o-Matic based on our sample's age and sex. T1-weighted images were segmented in CAT12 using the custom TPM, and cortical thickness and region-based volumes (corrected using intracranial volume) of pre-determined visual processing areas in the contralesional hemisphere were extracted. Volumes and thicknesses were compared between groups using t-tests and associations with perceptual test results were explored using correlations.

Results: Children with AIS had greater cortical thickness of the contralesional inferior temporal lobe ($p=0.026$). Negative correlations were present between cortical thickness of the cuneus and performance on the MVPT-3 ($r=-0.227$), and between the inferior parietal lobe, pericalcarine and precuneus when compared with reading speed ($r=-0.423$, $r=-0.207$ and $r=-0.342$). Volumes of the lateral geniculate nucleus and the pulvinar showed negative correlations with the number of targets identified on the Apples test. There were no significant between group differences or correlations found in the fusiform gyrus, lingual or lateral occipital lobe.

Conclusions: Perinatal stroke may lead to developmental structural alterations in visual processing areas of the contralesional hemisphere. Thicker cortex in specific regions are associated with discrete functional deficits including decreased reading speed and perceptual function. This suggests that the visual system of the non-lesioned hemisphere may play a compensatory role after an injury in the contralateral hemisphere and reorganization may occur in the visual system. Understanding the structural differences of the visual system and associated impairments will support the advancement of diagnostic and prognostic tools, and contribute to validated therapies to reduce functional impairment.

References

1. Bickerton, W. L., Samson, D., Williamson, J., & Humphreys, G. W. (2011). Separating forms of neglect using the Apples Test: Validation and functional prediction in chronic and acute stroke. Neuropsychology, 25(5), 567–580. https://doi.org/10.1037/a0023501
2. Bieber, G., Hulac, D. M., & Schweinle, W. (2015). An Independent Evaluation of the Technical Features of the Basic Reading Inventory. Journal of Psychoeducational Assessment, 33(3), 199–209. https://doi.org/10.1177/0734282914550808
3. Craig, B. T., Hilderley, A., Kirton, A., & Carlson, H. L. (2021). Imaging Developmental and Interventional Plasticity Following Perinatal Stroke. Canadian Journal of Neurological Sciences / Journal Canadien Des Sciences Neurologiques, 48(2), 157–171. https://doi.org/10.1017/cjn.2020.166
4. Dunbar, M., & Kirton, A. (2019). Perinatal Stroke. Seminars in Pediatric Neurology, 32, 100767. https://doi.org/10.1016/j.spen.2019.08.003
5. Gaser C, Dahnke R, Kurth K, Luders E, Alzheimer"s Disease Neuroimaging Initiative. A Computational Anatomy Toolbox for the Analysis of Structural MRI Data. bioRxiv.
6. Köse, B., Karabulut, E., & Akı, E. (2021). Investigating the interchangeability and clinical utility of MVPT-3 and MVPT-4 for 7–10 year children with and without specific learning disabilities. Applied Neuropsychology: Child, 10(3), 258–265. https://doi.org/10.1080/21622965.2019.1681270

Poster No 381

Neural processing of phonological information in autistic kindergarteners as a predictor of reading

So Hyun Kim[1], Brittany Manning[2], Su Hyoung Jeong[1], Munju Kim[1]

[1]Korea University, Seoul, Seoul, [2]Northwestern University, Chicago, IL

Introduction: Phonological processing is an important foundation of reading development; however, little is known about the neural substrates of phonological processing and reading development in children with autism spectrum disorder (ASD).

Methods: We investigate early auditory event-related potentials (ERPs) in a phonological processing task and their association with reading ability. At kindergarten-entry, 29 autistic children and 27 typically developing (TD) children completed an old/new ERP paradigm with bisyllabic rhyming peudowords (/gibu/ & /bidu/), while electroencephalography (EEG) was recorded. Behavioral measures of reading ability were completed at kindergarten-entry and -exit.

Results: Results revealed a significant three-way interaction between ERP stimuli ("old" vs. "new"), diagnosis (ASD vs. TD) and reading ability. Autistic children with lower reading skills, showed greater P1 and P2 amplitude for "new" vs. "old" stimuli,

compared with TD children and those with higher reading ability. Old/new ERP difference scores significantly predicted later word decoding at kindergarten year-end, controlling for sex and nonverbal IQ.

Figure 1. Waveforms for ASD and typical groups

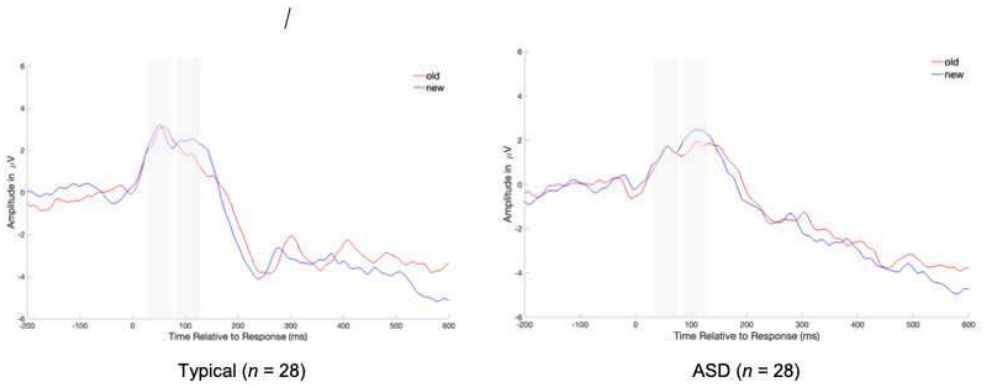

Figure 2. Waveforms for lower and higher reading groups for children with ASD

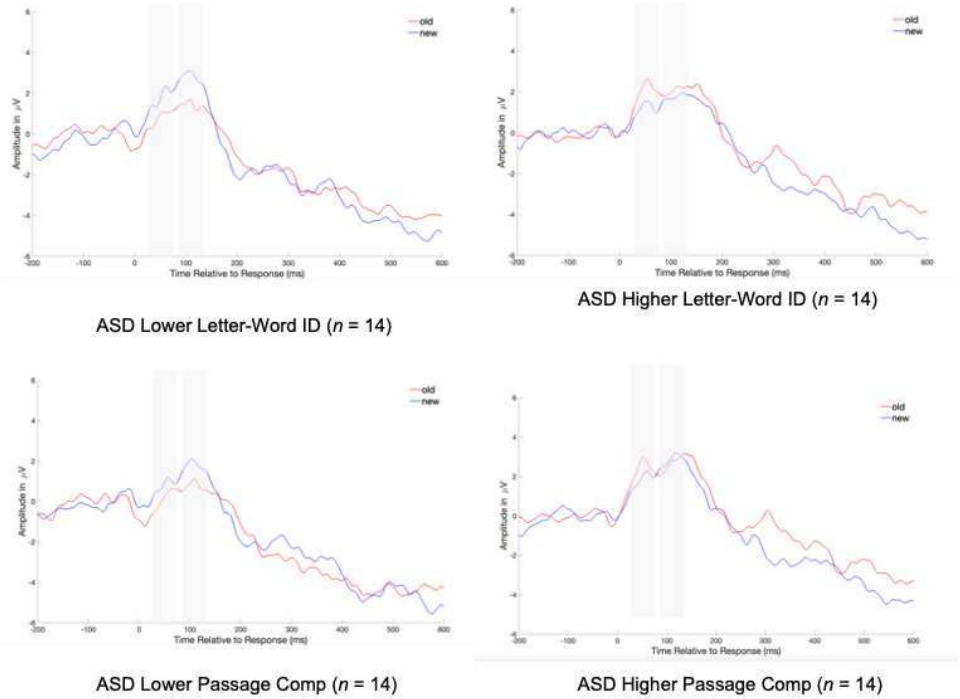

Conclusions: Autistic children with lower reading ability may require more neural resources to process "new" auditory stimuli compared to peers with greater reading ability and TD children. Better understanding the neural basis of phonological processing may inform the development of individualized intervention approaches.

References

1. Åsberg Johnels, J. (2019). Current profiles and early predictors of reading skills in school-age children with autism spectrum disorders: A longitudinal, retrospective population study. Autism, 23(6), 1449–1459.
2. Brown, H. M. (2013). A meta-analysis of the reading comprehension skills of individuals on the autism spectrum. Journal of Autism and Developmental Disorders, 43(4), 932–955.
3. Harwood, V. (2022). Event-Related Potentials to Speech Relate to Speech Sound Production and Language in Young Children. Developmental Neuropsychology, 47(2), 105–123.
4. Kim, S. H. (2018). Longitudinal follow-up of academic achievement in children with autism from age 2 to 18. Journal of Child Psychology and Psychiatry, 59(3), 258–267.

Poster No 382

White matter tracts associated with sensitivity to reward in ADHD and healthy adults

Hsin-Yu Lin[1], Hoki Fung[1,2], Su Ren Gan[1], Bhanu Gupta[3], Roger Chun-Man Ho[4], SH Annabel Chen[1]

[1]Nanyang Technological University, Singapore, Singapore, [2]Semel Institute for Neuroscience and Human Behavior, University of California, Los Angeles, CA, [3]Department of Mood and Anxiety, Institute of Mental Health, Singapore, Singapore, [4]Yong Loo Lin School of Medicine, National University of Singapore, Singapore, Singapore

Introduction: Patients with attention deficit hyperactivity disorder (ADHD) show neuropsychological impairments, including deficient executive functions and altered sensitivity to reward and punishment[1,2]. Sensitivity to reward (SR) and sensitivity to punishment (SP) vary in individuals and are believed to be regulated by the brain-behavioural systems[3,4]. White matter (WM) structure have been found to be associated with reward and punishment-related behaviour in healthy adults[5,6]. Previous studies have also suggested that alterations in WM integrity in ADHD may potentially contribute to differences in reward and punishment processing[7,8]. Hence, we aim to further investigate how the WM structure variations are associated with SR/SP in both ADHD and healthy adults. We collected diffusion images and took quantitative anisotropy (QA) to examine the WM axonal density. We hypothesize that WM structural variations in ADHD would show different correlates with SR/SP comparing to healthy controls.

Methods: SR and SP scores of 20 ADHD adults (13 Male, age M=25.77, SD=4.28) and 27 healthy adults (14 Male, age M=25.56, SD=4.69) were assessed using sensitive to punishment and sensitive to reward questionnaire (SPSRQ). All MRI scans were performed on a 3T Siemens Prisma MR scanner with a 32-channel head coil. T1w images were acquired with a magnetization-prepared 2 rapid acquisition gradient echo (MP2RAGE) sequence (TR/TE =5000/2.98, 1mm isotropic). Diffusion Spectrum Imaging (DSI) was conducted using the following parameters: 54 slices, 2.97 × 2.97× 3 mm^3, TR/TE = 4000/97.2 ms; 258 directions, max b-val = 5005 s/mm^2. The reconstruction was done using DSI Studio in the MNI space with Q-space diffeomorphic reconstruction[9] with a diffusion sampling length ratio of 1.25. Whole-brain diffusion MRI connectometry analysis was used to derive correlational tractography reflecting changes in QA correlated with SR/SP. A nonparametric Spearman partial correlation was used to derive the correlation, and the effect of age, sex, and education was removed using a multiple regression model. A T-score threshold of 2.5 and an FDR threshold of 0.05 were assigned and tracked using a deterministic fiber tracking to obtain correlational tractography. Finally, significant findings were manually segmented into bundles.

Results: A group difference was found in SR scores between control and ADHD groups (ADHD>CON, $p<.05$). There were no significant differences in age, gender, education and SP score between the groups. In the connectomery analysis, tracks with higher QA were found to be associated with lower SR in the right Corticospinal tract (CST) in the control group. In contrast, in ADHD, we observed a positive association between SR and QA in the right CST. In addition, QA negatively correlated with SR in the Corpus callosum, left and right cerebellum tracks in ADHD (Fig 1). Table 1 reported the details of each significant bundle with QA associated with SR. No significant tracks were found between QA and SP in both groups.

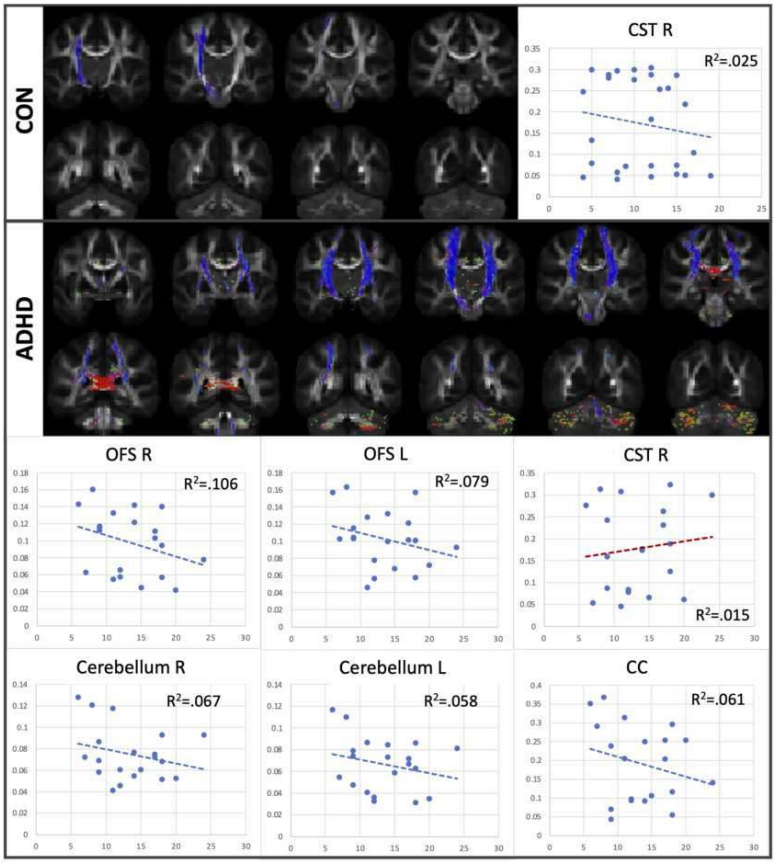

Figure 1. Tracks with QA associated with Sensitivity to Reward (FDR<0.05)
X axis: Sensitivity to Reward score; Y axis: Quantitative anisotropy (QA).

Dependent Variable	Metrics	Bundle Name		Number of tracks	Mean length (mm)	Volume (mm^3)	QA
Control		Tracts					
Reward	Decrease	Corticospinal tract (CST)	Right	63	110.34	5879.25	0.436
ADHD							
Reward	Increase	Corticospinal tract (CST)	Right	145	84.91	5690.25	0.439
	Decrease	Orbital frontostriatal (OSF)	Left	283	36.24	5052.38	0.288
			Right	1084	34.70	10013.6	0.249
		Cerebellar tracts	Left	10612	36.09	46176.8	0.183
			Right	8905	37.11	44303.6	0.203
		Corpus callosum (CC)		4972	37.7991	22190.6	0.546

Table 1. White matter bundles with QA associated with Sensitivity to Reward (FDR ≤ 0.05).

Conclusions: The finding of ADHD displaying different levels of SR compared to the control group aligns with previous studies[2,7]. The connectometry analysis further elucidated the relationship between WM integrity and SR. In ADHD, we found 6 significant WM bundles associating with SR, all known to be related to ADHD's deficits[5]. Moreover, SR in ADHD and healthy adults show opposite correlations with QA in the right CST. CST integrity has been associated with symptoms of impulsivity and inattention that were involved with certain alterations (e.g., prefer instant reward) in SR[5,10]. This suggested the potential differences in neural mechanisms underlying SR in individuals with ADHD compared to healthy adults. Our findings highlight the intricate interplay between WM integrity in specific tracts and SR, providing insight into the neural basis of reward processing in clinical populations. However, these findings warrant replications with a larger sample size.

References

1. Furukawa E. (2017) Evidence for increased behavioral control by punishment in children with attention-deficit hyperactivity disorder. J Child Psychol Psychiatry. 58(3):248-257.
2. Rapport LJ. (2001) Executive functioning in adult attention-deficit hyperactivity disorder. Clin Neuropsychol. 15(4):479-91.

3. Gray JA. (2000) The Neuropsychology of Anxiety. New York: Oxford University Press
4. Kim SH. (2015) Individual differences in sensitivity to reward and punishment and neural activity during reward and avoidance learning. Soc Cogn Affect Neurosci. 10(9): 1219–1227.
5. Parlatini, V. (2023) White matter alterations in Attention-Deficit/Hyperactivity Disorder (ADHD): a systematic review of 129 diffusion imaging studies with meta-analysis. Mol Psychiatry. https://doi.org/10.1038/s41380-023-02173-1
6. Koch K. (2014) Association between white matter fiber structure and reward-related reactivity of the ventral striatum. Hum Brain Mapp. 2014 Apr;35(4):1469-76. doi: 10.1002/hbm.22284.
7. Shaw, P. (2014). Emotion dysregulation in attention deficit hyperactivity disorder. The American Journal of Psychiatry, 171(3), 276-293.
8. Cubillo, A. (2012). A review of fronto-striatal and fronto-cortical brain abnormalities in children and adults with Attention Deficit Hyperactivity Disorder (ADHD) and new evidence for dysfunction in adults with ADHD during motivation and attention. Cortex, 48(2), 194-215.
9. Yeh FC. (2011) NTU-90: A high angular resolution brain atlas constructed by q-space diffeomorphic reconstruction. NeuroImage. 2011;58:91–99.
10. Luman M. (2010) Identifying the neurobiology of altered reinforcement sensitivity in ADHD: A review and research agenda, Neuroscience & Biobehavioral Reviews, Volume 34, Issue 5, 2010, Pages 744-754, ISSN 0149-7634, https://doi.org/10.1016/j.neubiorev.2009.11.021.

Poster No 383

Characterizing the developmental trajectory of functional hierarchy in autistic children

Sunghun Kim[1], Jong-eun Lee[2], Hyunjin Park[3]

[1]Sungkyunkwan university, Suwon-si, Gyeonggi-do, [2]Sungkyunkwan University, Suwon-si, Gyeonggi-do, [3]Center for Neuroscience Imaging Research, Institute for Basic Science, Suwon, Kyeonggi-do

Introduction: Autism Spectrum Disorder (ASD) is a complex neurodevelopmental condition characterized by a wide range of symptoms and abilities, significantly affecting socio-cognitive behaviors. Despite the high biological and clinical heterogeneity observed among individuals with ASD, considerable efforts have been made to understand this condition through neuroimaging biomarkers. Previous research has suggested that functional connectome gradients delineate the axis of connectivity variation between unimodal and transmodal networks and the phenotypical patterns in ASD are associated with a disruption in the macroscale cortical hierarchy. However, the persistent issue of heterogeneity in developing individuals remains and the maturational process of functional hierarchy is poorly understood. To address this gap, we utilized a normative modeling approach to analyze the biological trajectories in ASD, focusing on how cortical hierarchies mature across different developmental stages in children.

Methods: We constructed cortex-wide functional connectomes using the Schaefer atlas with 200 parcels and estimated the low-dimensional eigenvectors (i.e., gradients). First, a parcellation-level normative model of functional gradients was developed using generalized additive models for location scale and shape (GAMLSS), employing samples from the independent human connectome project development (HCP-D, n = 652) cross-sectional database of typically developing (TD) individuals. We used multi-parameter Sinh-Arcsinh (SHASH) distribution modeling with age and sex as regressors. Second, we estimated individual functional gradients of 503 ASD and 527 TD using the autism brain imaging data exchange (ABIDE) dataset. We then calculated the functional hierarchy score for each individual, defined by the dot-product between the normative gradients curve and the individual gradients. This score reflects the maturity of individual hierarchical organization. The functional hierarchy score was compared between two groups and was used to analyze the groups' developmental rates.

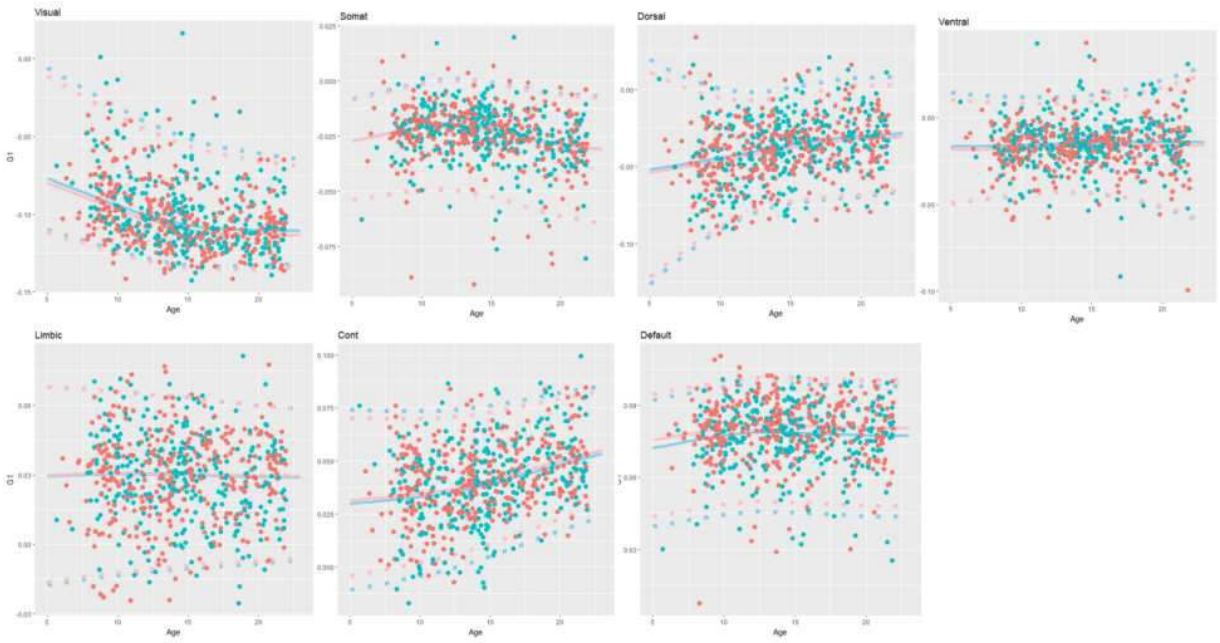

Results: Our findings reveal that with increasing age during the developmental stages, the macroscale segregation of functional hierarchy gradually became evident. Notably, the sensorimotor and association areas at both ends became increasingly distinct with age. However, individuals with ASD demonstrated a less-segregated functional hierarchy compared to TD individuals, with a significant difference (p-value < 0.001). Furthermore, we observed that the cortical hierarchy evolves in synchrony with age in both groups.

Conclusions: Developmental changes drive the hierarchical organization of the cortex. Given the high heterogeneity among individuals with ASD, the brain development of individuals with ASD may deviate from standard developmental pathways. These findings support the notion that individuals with ASD possess distinct and individualized brain development trajectories. This research was supported by the National Research Foundation (NRF-2020M3E5D2A01084892), Institute for Basic Science (IBS-R015-D1), IITP grant funded by the AI Graduate School Support Program (2019-0-00421), and ICT Creative Consilience program (IITP-2020-0-01821).

References

1. Margulies, D.S., et al., Situating the default-mode network along a principal gradient of macroscale cortical organization. Proceedings of the National Academy of Sciences, 2016. 113(44): p. 12574-12579.
2. Hong, S.-J., et al., Atypical functional connectome hierarchy in autism. Nature communications, 2019. 10(1): p. 1022.
3. Schaefer, A., et al., Local-global parcellation of the human cerebral cortex from intrinsic functional connectivity MRI. Cerebral cortex, 2018. 28(9): p. 3095-3114.
4. Rigby, R.A. and D.M. Stasinopoulos, Generalized additive models for location, scale and shape. Journal of the Royal Statistical Society Series C: Applied Statistics, 2005. 54(3): p. 507-554.
5. Somerville, L.H., et al., The Lifespan Human Connectome Project in Development: A large-scale study of brain connectivity development in 5–21 year olds. Neuroimage, 2018. 183: p. 456-468.
6. Di Martino, A., et al., The autism brain imaging data exchange: towards a large-scale evaluation of the intrinsic brain architecture in autism. Molecular psychiatry, 2014. 19(6): p. 659-667.

Poster No 384

ASD-related spatial covariance gray matter pattern revealed with a large-scale multi-center dataset

Shengzhi Ma[1], Xing-Ke Wang[2], Chen Yang[3], Wen-Qiang Dong[3], Qiu-Rong Zhang[3], Yu-Feng ZANG[4], Li-Xia Yuan[5]

[1]Hangzhou Normal University, Hangzhou, China, [2]Beijing Normal University, Beijing, Beijing, [3]Hangzhou Normal University, Hangzhou, Zhejiang Province, [4]The Affiliated Hospital of Hangzhou Normal University, Hangzhou, Zhejiang Province, [5]Zhejiang University, Hangzhou, Zhejiang Province

Introduction: Autism Spectrum Disorder (ASD) is a severe neurodevelopmental disorder, and the underlying neuroanatomy mechanism of ASD remains unclear. Many researches have used gray matter (GM) volume to investigate structural abnormalities in ASD. Until now, the majority of GM studies have applied univariate analysis approaches, including region-

of-interest-wise and voxel-wise analysis (Riddle et al., 2017; Wang et al., 2022). The scaled subprofile model of principal component analysis (SSM-PCA) is a multivariate method for exploring the disease related pattern based on the spatial covariance across different brain regions and able to identify subtle changes caused by the disease (Alexander, 1994; Yuan et al., 2018). This study aimed to obtain the ASD-related GM volume pattern with SSM-PCA to reveal the neuroanatomical mechanisms of ASD.

Methods: We utilized the Autism Brain Imaging Data Exchange (ABIDE), an open-access dataset for ASD, and performed preprocessing on the T1-weighted structural MRI images (sMRI). Anatomical segmentation was performed on sMRI from ABIDE II dataset to get the GM, and then the GM volume of each brain region defined by the automated anatomical labeling 3 (Rolls et al., 2020) template was computed by Computational Anatomy Toolbox 12. The SSM-PCA algorithm was then used for the GM volume matrix of subject-brain region to obtain the spatial covariance GM patterns (Wang et al., 2022). The sign of ASD-related GM pattern is determined by keeping higher average expression in the ASD group compared to the typically developed (TD) group. Within the 15 patterns explaining the top higher proportion of variance, two sample t-test was conducted for the expression of each GM pattern to identify those displaying significant inter-group expression differences. Then, the ASD-related GM pattern was obtained by the linear combination of these patterns. We further investigated the relationship between the ASD-related GM pattern and clinical symptoms. Next, we verified the reproducibility of the ASD-related pattern by projecting it on to ABIDE I dataset and checked the expression difference between ASD and TD and its relationship with clinical scores. In addition, we divided the cohort into three age groups, namely primary school students with [7, 12) years old, adolescents with [12, 18) years old, and adults with [18, 28) years old, to explore the influence of age on the ASD-related pattern.

Results: The expressions of the second and fourteenth pattern showed significant group difference between ASD and TD, which were linearly combined to form the ASD-related GM pattern. The pattern included thalamus, right parahippocampal gyrus, left locus coeruleus, basal ganglia, and cerebellum, which mainly concerned with cognitive functions of visual imagery, auditory, theory of mind, and Îperception. Furthermore, the expression of this patterns is correlated with scores of Social Response Scale (SRS, r = 0.18, p = 3.4×10-4) and Social Communication Questionnaire (SCQ, r = 0.17, p = 7×10-4). For reproducibility validation, the expression of the ASD-related pattern in ABIDE I revealed significantly difference in the ASD relative to the TD (Cohen's d = 0.21, p = 0.016), which is also positively correlated with the scores of SRS (r = 0.20, p = 0.0015). For age effect, the primary school group (Cohen's d = 0.37, p = 0.0013) and adult group (Cohen's d = 0.44, p = 0.038) showed significant differences, while the adolescent group illustrated no significant difference (Cohen's d = 0.21, p = 0.19) of the expression of the ASD-related pattern between the ASD and TD.

Conclusions: We captured a reproducible ASD-related GM pattern, which is related to the social deficit, and revealed its heterogeneity among different age groups. Our findings facilitate the understanding of the underlying neural mechanisms of ASD and provide therapeutic targets for individuals with ASD.

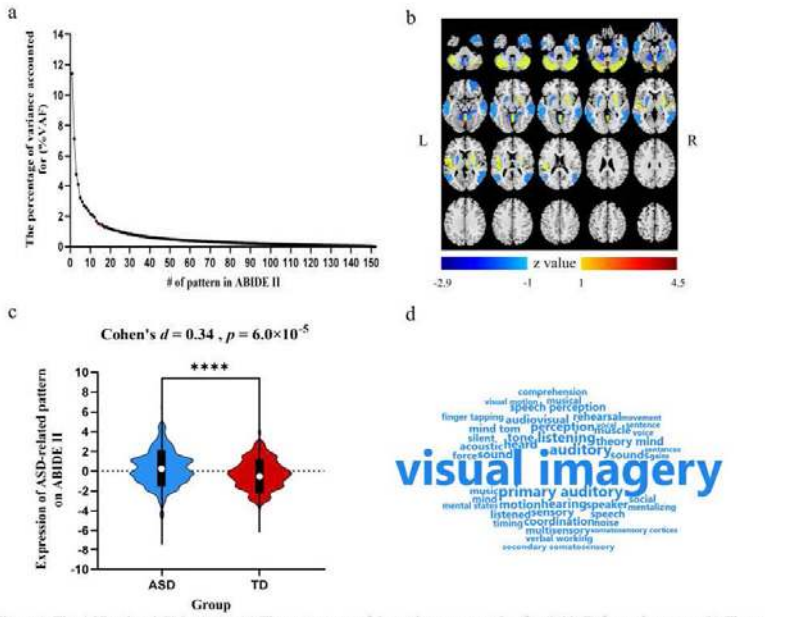

Figure 1. The ASD-related GM pattern. (a) The percentage of the variance accounting for (%VAF) for each pattern. (b) The z-transformed ASD-related GM pattern. (with |z| > 1 and the slices displayed from −40 mm to +55 mm at axis view). (c) The distribution of the pattern's expression in the ASD and TD groups. (d) Cognitive functions related to the brain regions involved in the pattern. Positive and negative z-values represented increased and reduced GM volumes in the ASD group than TD group, respectively. ****p < 0.0001. (ABIDE, Autism Brain Imaging Data Exchange; ASD, autism spectrum disorder; GM, gray matter; TD, typically developing controls.)

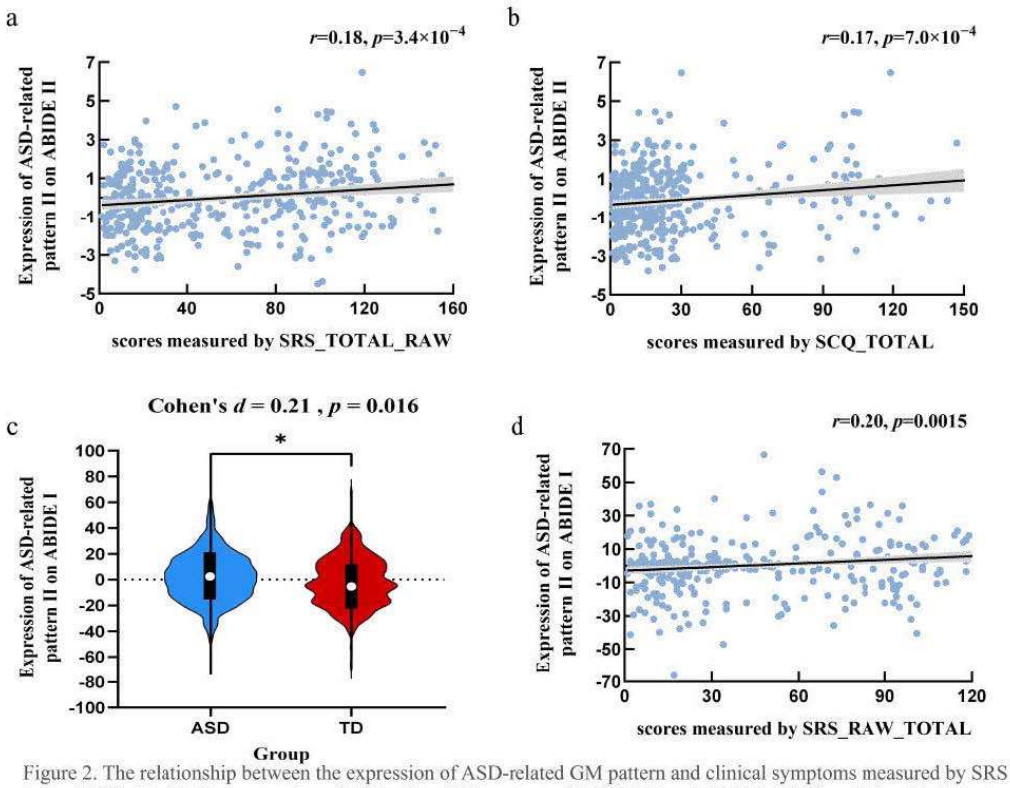

Figure 2. The relationship between the expression of ASD-related GM pattern and clinical symptoms measured by SRS (a) and SCQ (b). (c) The expression of ASD-related GM pattern of ABIDE II on ABIDE I. (d) The relationship between the expression of pattern II and clinical scores measured by SRS in ABIDE I. *p < 0.05. (ABIDE, Autism Brain Imaging Data Exchange; ASD, autism spectrum disorder; GM, gray matter; SCQ, the Social Communication Questionnaire; SRS, Social Responsiveness Scale.)

References

1. Alexander, G. E. (1994). Application of the scaled subprofile model to functional imaging in neuropsychiatric disorders: A principal component approach to modeling brain function in disease. Human Brain Mapping, 2(1–2), 79–94.
2. Riddle, K. (2017). Brain structure in autism: A voxel-based morphometry analysis of the Autism Brain Imaging Database Exchange (ABIDE). Brain Imaging and Behavior, 11(2), 541–551.
3. Rolls, E. (2020). Automated anatomical labelling atlas 3. NeuroImage, 206, 116189.
4. Wang, H. (2022). Developmental brain structural atypicalities in autism: A voxel-based morphometry analysis. Child and Adolescent Psychiatry and Mental Health, 16, 7.
5. Wang, X.-K. (2022). Gray Matter Network Associated With Attention in Children With Attention Deficit Hyperactivity Disorder. Frontiers in Psychiatry, 13, 922720.
6. Yuan, L.-X. (2018). Intra- and Inter-scanner Reliability of Scaled Subprofile Model of Principal Component Analysis on ALFF in Resting-State fMRI Under Eyes Open and Closed Conditions. Frontiers in Neuroscience, 12, 311.

Poster No 385

Exploring autism heterogeneity: fMRI and personalised saliency maps to identify autism subgroups

Ioannis Valasakis[1], Štefan Holiga[2], Juergen Dukart[3], Grainne McAlonan[1], Maria Deprez[4], Dafnis Batalle[1]

[1]Department of Forensic and Neurodevelopmental Science, King's College London, London, United Kingdom, [2]Roche Pharma Research and Early Development, Basel, Switzerland, [3]INM-7, Forschungszentrum Jülich, Jülich, North Rhine Westphalia, [4]Centre for the Developing Brain, King's College London, London, United Kingdom

Introduction: Autism is a complex neurodevelopmental condition characterised by a wide range of symptoms. Understanding atypical connectivity patterns in autistic individuals is crucial for better understanding of the underlying mechanisms and personalised support for the individuals. Prior research has highlighted the potential of functional Magnetic Resonance Imaging (fMRI) data and especially functional connectivity metrics such as the degree centrality in revealing these patterns[1]. Our research extends these efforts, aiming to refine autism subgroups through integration of functional connectivity metrics, personalised saliency maps (using Smoothgrad as a method of explainable artificial intelligence), and data-driven clustering techniques.

Methods: We conducted a comprehensive fMRI analysis on 1450 participants from the Autism Brain Imaging Data Exchange[2] (ABIDE) I and II datasets using fMRIprep[3] to ensure data consistency and quality. We focused on voxelwise weighted degree centrality, using DenseNet-121[4] for autism classification, and SmoothGrad[5] for creating personalised (per-participant) saliency activation maps (PSAMs) (Fig 1). These maps were used to identify key brain regions for classification (Fig. 2). Feature extraction was performed using Uniform Manifold Approximation and Projection (UMAP)[6] for non-linear dimensionality reduction, followed by k-means[7] clustering to identify distinct autistic subgroups within ABIDE (Fig 1d). This methodology was validated with the AIMS-2-TRIALS[8] dataset, using the same UMAP and k-means approach for direct dataset comparison (Fig 2).

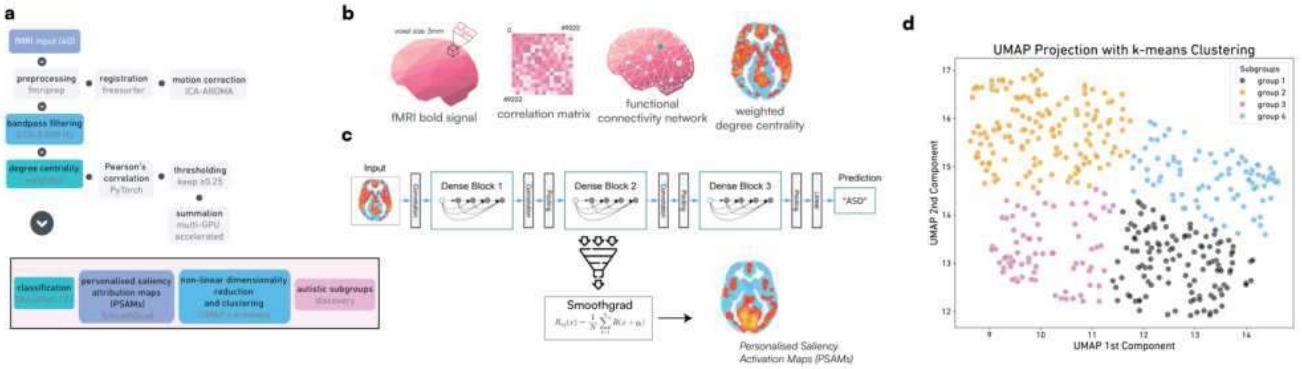

Results: Using DenseNet-121 and weighted degree centrality, our model achieved a classification accuracy of 70.16% (0.72 ROC-AUC) in the ABIDE dataset. We identified four distinct autistic subgroups, each characterised by unique functional connectivity patterns as evidenced by their PSAM maps (Fig 2c). Notably, in Group 2, we observed elevated PSAM scores predominantly in the right frontal lobe regions. This contrasts with most groups, where scores in the precentral gyrus tended to be negative, while in Group 2, they were notably positive, suggesting distinct neurobiological profiles. We found a correlation between PSAM scores and age in the groups, as depicted in Figure 2c. This correlation suggests age-related variations in neural processing within these subgroups. Further validation with the blind AIMS-2-TRIALS dataset affirmed the robustness of our approach, achieving an accuracy of 63.4%. Reprojection of this data onto the ABIDE-derived UMAP space corroborated the subgroup distinctions (Fig 2a).

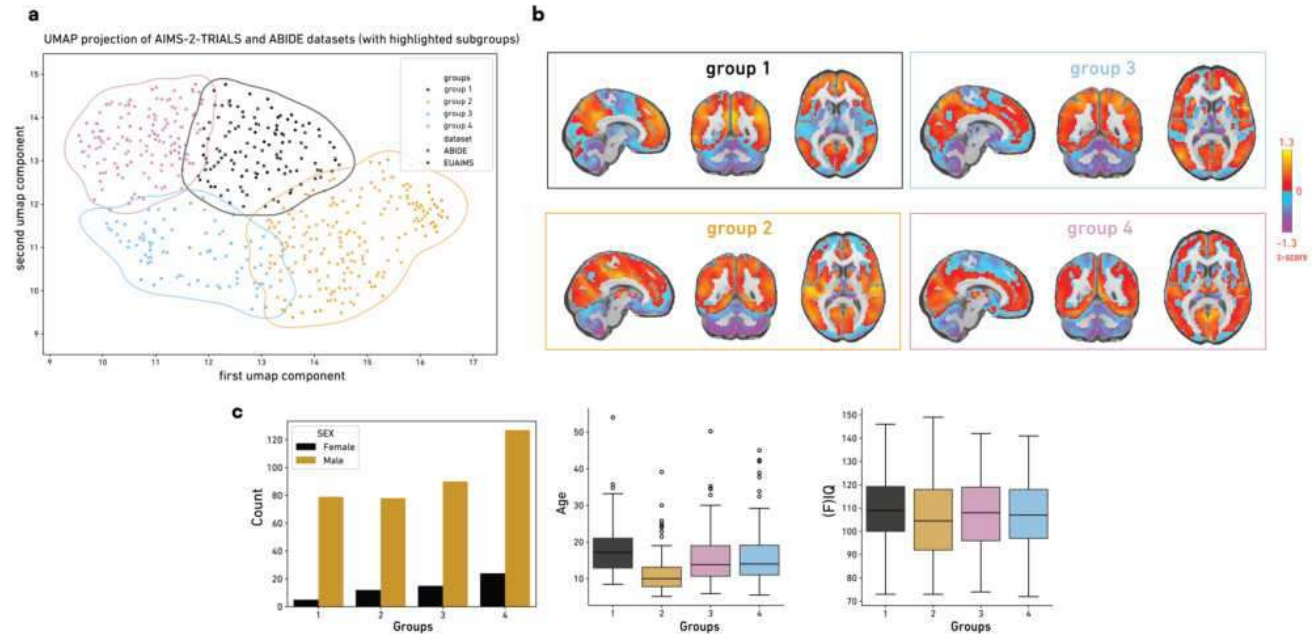

Conclusions: Our findings provide a step towards better understanding the neurobiological diversity within the autism spectrum. By integrating neuroimaging, interpretable machine learning, and ample replication strategy, we identify distinct autism subgroups. These insights foster discussions on personalised support strategies and highlight the necessity for targeted research into autism's heterogeneity. Future work will aim to enhance result interpretability, extend validation across various populations, and utilise diverse metrics to deepen the neurobiological understanding of the identified autistic subgroups.

References
1. Holiga, Š. (2019). Patients with autism spectrum disorders display reproducible functional connectivity alterations. Science Translational Medicine, 11(481). https://doi.org/10.1126/scitranslmed.aat9223
2. Di Martino, A. (2013). The autism brain imaging data exchange: towards a large-scale evaluation of the intrinsic brain architecture in autism. Molecular Psychiatry, 19(6), 659–667. https://doi.org/10.1038/mp.2013.78
3. Estéban, O. (2018). fMRIPrep: a robust preprocessing pipeline for functional MRI. Nature Methods, 16(1), 111–116. https://doi.org/10.1038/s41592-018-0235-4
4. Huang, G. (2016). Densely Connected Convolutional Networks. arXiv (Cornell University). https://doi.org/10.48550/arxiv.1608.06993
5. Smilkov, D. (2017). SmoothGrad: removing noise by adding noise. arXiv (Cornell University). https://arxiv.org/pdf/1706.03825.pdf
6. McInnes, L. (2018). UMAP: Uniform manifold Approximation and Projection. Journal of Open Source Software, 3(29), 861. https://doi.org/10.21105/joss.00861
7. Lloyd, S. (1982). Least squares quantization in PCM. IEEE Transactions on Information Theory, 28(2), 129–137. https://doi.org/10.1109/tit.1982.1056489
8. Del Bianco, T. (2023). Examining Neurodiversity and Inclusion in neuroscience research networks: A case study of the AIMS-2-TRIALS Autism Research Consortium. https://doi.org/10.22541/au.169365784.42675615/v1

Poster No 386

Prenatal Polydrug Exposure: Effects of Timing on Functional Connectivity at Birth

Janelle Liu[1], Rina Eiden[2], Karen Grewen[3], Wei Gao[4]

[1]Cedars-Sinai Medical Center, Los Angeles, CA, [2]Pennsylvania State University, University Park, PA, [3]University of North Carolina at Chapel Hill, Chapel Hill, NC, [4]Cedars Sinai Medical Center, Los Angeles, CA

Introduction: Prenatal drug exposure (PDE) impacts infant brain development with documented long-term consequences (Ross 2015). Functional magnetic resonance imaging (fMRI) studies of infants and youth with PDE reveal aberrant brain functional connectivity (Salzwedel 2020). Animal models demonstrate that PDE timing significantly impacts offspring outcome (Byrnes 2018), but most human fMRI studies use a binary categorization to assess drug exposure, limiting the ability to detect timing effects associated with PDE. Here, we use resting-state fMRI (rsfMRI) to characterize timing-related effects of PDE on the neonatal functional connectome. For the first time, we examine neural mechanisms associated with full PDE across all three trimesters (PDE-F) and partial PDE during only the first and/or second trimester (PDE-T1T2).

Methods: Subjects included drug-free controls (CTR; n=24) and neonates with PDE (n=85). The PDE group was separated into subgroups based on whether infants experienced full exposure to any drugs across all three trimesters (PDE-F; n=49) or partial exposure to any drugs during only the first and/or second trimester (PDE-T1T2; n=21). The Timeline Follow Back (TLFB; Robinson 2014) calendar/interview was conducted to assess prenatal frequency of drug use in each trimester across 9 drug categories (alcohol, nicotine, marijuana, cocaine, opioids, medication for opioid use disorder, stimulants, depressants, other). RsfMRI scans were acquired during natural sleep at 2 weeks of age. Groups were matched on sex, race, gestational age at birth, gestational age at scan, area deprivation index, and motion. Birthweight, maternal education, and maternal depression were included as covariates of no interest in all analyses to control for group differences in these variables. Functional connectivity measures were derived using a neonate functional parcellation-based atlas (Shi 2018). For each seed region of interest (ROI; n=223), the average time series was extracted and correlated with every other ROI in the brain. Next, linear regression was conducted to detect significant functional connectivity differences between the groups. Two summary measures were used: 1) the percentage of connections showing differences at $p<.05$, and 2) the percentage of connections with at least a medium effect size (bias-corrected Hedge's $g>.5$; Nakagawa 2007). These were calculated and assigned to the seed ROI. These processes were repeated for all ROIs to generate heatmaps indicating pairwise between-group differences in functional connectivity between each ROI and the whole brain.

Results: Compared to CTR, PDE infants showed differences in connectivity localized to visual, subcortical, parietal, and temporal areas. Compared with CTR, PDE-F infants showed differences mainly in parietal, subcortical, frontal, and sensorimotor regions, whereas PDE-T1T2 infants showed differences in visual frontal, temporal, and parietal areas. Direct comparison between PDE-F and PDE-T1T2 revealed widespread differences in temporal, subcortical, frontal, sensorimotor, and parietal regions. Consistent results were observed using the Hedge's g effect size as a threshold, larger differences were observed between PDE-T1T2 and CTR than between PDE-F and CTR.

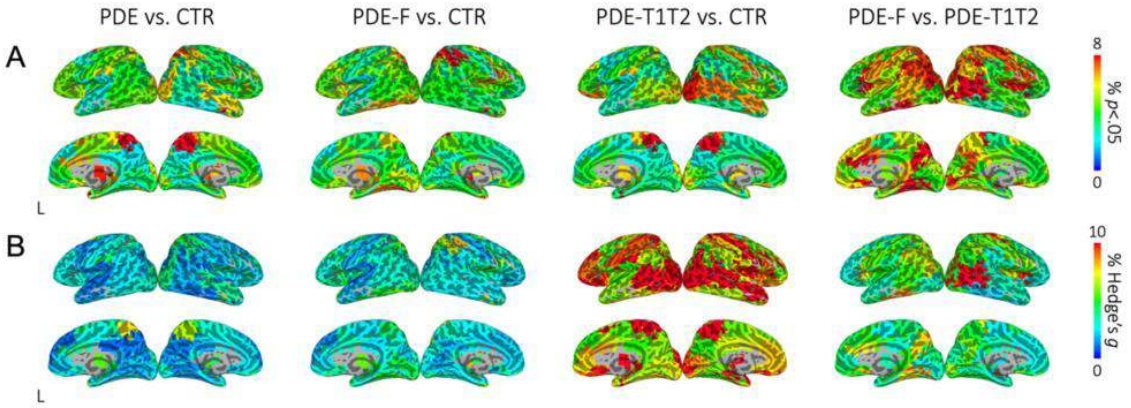

Figure 1. Heatmaps of functional connectivity alterations. A) Pairwise difference heatmaps show differences in patterns of neonatal functional connectivity between CTR and PDE groups. Widespread differences are observed between PDE-F and PDE-T1T2. The color map and the value of each ROI indicate the percentage of the connections of this particular ROI (to all other ROIs across the whole brain) showing significant differences between the two specified groups based on *p*-value thresholding ($p<.05$). B) Thresholding based on bias-corrected Hedge's *g* effect size was used to avoid sample size biases among the subgroups analyzed. This resulted in a similar topology, with the largest effect sizes observed in the difference between PDE-T1T2 and CTR. The color map and the value of each ROI indicate the percentage of the connections of this particular ROI showing differences based on bias-corrected Hedge's *g* effect size thresholding ($g \geq .5$, independent of sample size). [CTR: drug-free controls; PDE: prenatal drug exposure; PDE-F: full prenatal drug exposure across all three trimesters; PDE-T1T2: partial prenatal drug exposure across first and/or second trimester; ROI: region of interest]

Conclusions: At birth, the timing of PDE is associated with distinct effects, with PDE during the first and/or second trimester having the largest impact on early brain development. This result is surprising and may be related to the PDE-T1T2 mothers being more homogenous in their drug usage (predominantly alcohol and nicotine). By contrast, the PDE-F mothers had more heterogeneity in their drug usage, which may have resulted in smaller effects due to possible cancellation effects of different drug exposures. However, widespread functional connectivity differences between PDE-F and PDE-T1T2 point toward potential interactions between differential timing of PDE and specific neurodevelopmental processes during the prenatal period.

References

1. Byrnes, E. (2018), 'Modeling prenatal opioid exposure in animals: Current findings and future directions', Front Neuroendocrin, vol. 51, pp. 1-13.
2. Nakagawa, S. (2007), 'Effect size, confidence interval and statistical significance: A practical guide for biologists', Biol Rev, vol. 82, no. 4, pp. 591-605.
3. Robinson, S. (2014), 'Reliability of the Timeline Followback for cocaine, cannabis, and cigarette use', Psych Addic Behav, vol. 28, no. 1, pp. 154-162.
4. Ross, E. (2015), 'Developmental consequences of fetal exposure to drugs: What we know and what we still must learn', Neuropsychopharm, vol. 40, no. 1, pp. 61-87.
5. Salzwedel, A. (2020), 'Functional dissection of prenatal drug effects on baby brain and behavioral development', Hum Brain Mapp, vol. 41, pp. 4789–4715.
6. Shi, F. (2018), 'Functional brain parcellations of the infant brain and the associated developmental trends', Cereb Cortex, vol. 28, no. 4, pp. 1358-1368.

Poster No 387

EEG Microstate Analysis for Identifying Infantile Spasms

Seong-Ho Ahn[1], Han Na Jang[2], Seeun Kim[1], Min-Jee Kim[3], Mi-Sun Yum[3], Dong-Hwa Jeong[1]

[1]The Catholic University of Korea, Bucheon, Korea, Republic of, [2]Soonchunhyang University Cheonan Hospital, Cheonan, Korea, Republic of, [3]Asan Medical Center Children's Hospital, Ulsan University College of Medicine, Seoul, Korea, Republic of

Introduction: Infantile spasms (IS) is a type of epilepsy that occurs in infants. Because IS causes developmental disabilities in infants, it is important to detect it effectively (Kim, 2023). Electroencephalography (EEG) microstate analysis is one of the most effective methods for diagnosing various brain disorders. This method can reflect the temporal dynamics of brain signals and the dynamic synchronization of brain neural networks (Khanna, 2015). EEG signals of IS patients tend to be accompanied by abnormal patterns in brain signals and networks (Kim, 2023). Therefore, EEG microstate analysis can be an effective method for identifying IS.

Methods: A 19 channel interictal EEG recording was obtained from 21 normal control groups (NS) and 49 IS groups. The study was conducted according to the guidelines of the Declaration of Helsinki, and approved by the Institutional Review Board of Asan Medical Center (2020-0992). Throughout visual inspection, a clean, five-minute segment free of muscle- or eye-related artifacts was manually selected for detailed analysis. The raw EEG data, sampled at a rate of 200Hz, underwent re-referencing to a common average reference and preprocessing steps involving a 60Hz notch filter, a 2Hz–20Hz band-pass filter, and Independent Component Analysis (ICA). Each subject's EEG data was then divided into fixed-length epochs consisting of two-second windows without overlap. We obtain 5 microstate maps using modified-k-means clustering (Pascual-Marqui, 1995) from GFP of each subject. This method ignores polarity in clustering. For extracting group-level microstate maps (i.e., normal group, and IS group), we concatenate microstate maps from each subject and use modified-k-means clustering. We fit 5 microstate maps to the EEG of each subject to obtain microstate segments. We label each segment by estimating spatial correlations with group-level microstate maps. We calculate microstate features from microstate segments of each subject's EEG. We extract global explained variance (GEV), mean correlation, occurrences, time coverage, and mean time durations from 5 microstates. To demonstrate the usefulness of EEG microstate analysis, we apply statistical analysis. We use individual t-test between the normal group and the IS group to show statistical significance.

Results: The 5 microstate maps of both the normal and IS groups account for 0.8248 and 0.7669 of the Generalized Eigenvalue (GEV). In Figure 1-(a), Microstates A and B in the normal group exhibit topographic map fields characterized by diagonal axis orientations, while Microstate C displays anterior–posterior orientations and Microstate D is characterized by fronto-central extreme locations, as detailed in (Michel, 2018). Additionally, Microstate E in the normal group shares a topography resembling that observed in a previous study (Nam, S, 2023). In contrast, the IS group lacks a canonical Microstate E matching the template topographic class of the normal group. In Figure 1, Significant differences are observed in the mean correlation between the normal and IS groups for Microstates A, B, C, D, and E ($p<0.0001$; $p<0.01$; $p<0.0001$; $p<0.0001$; $p<0.01$). The GEV significantly differs between the normal and IS groups in Microstates A, C, and D ($p<0.0001$; $p<0.01$; $p<0.0001$). Noteworthy distinctions are found in the occurrence of Microstates D and E between the normal and IS groups ($p<0.01$; $p<0.01$). Additionally, the mean duration exhibits significant differences for Microstates A, B, C, and D ($p<0.05$; $p<0.05$; $p<0.01$; $p<0.05$), while time coverage differs significantly for Microstates D and E between the normal and IS groups ($p<0.05$; $p<0.05$).

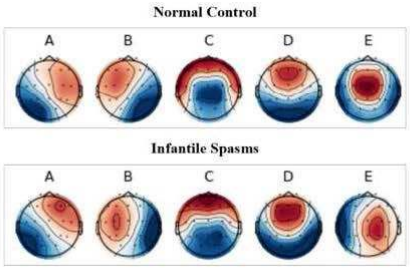

Figure 1-(a). 5 Microstate maps each group (i.e, NC, IS)

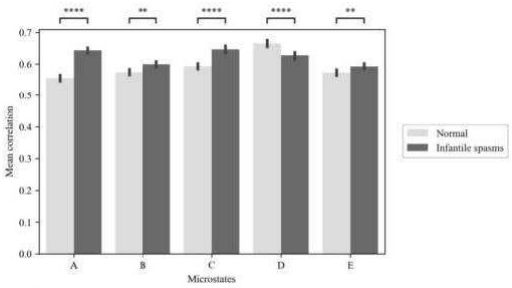

Figure 1-(b). Statistical difference of mean correlation by each group

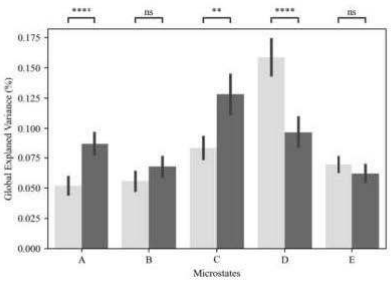

Figure 1-(c). Statistical difference of GEV by each group

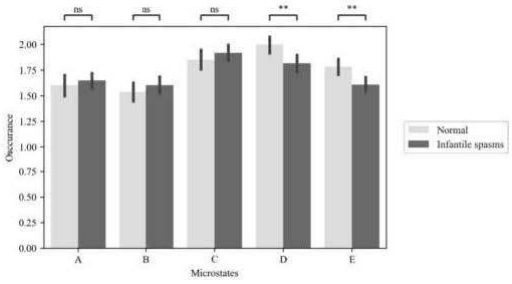

Figure 1-(d). Statistical difference of occurrence by each group

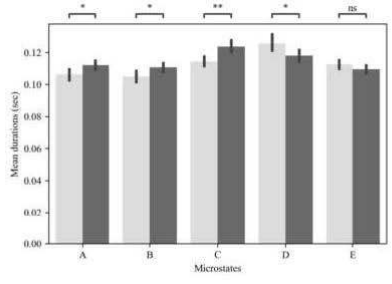

Figure 1-(e). Statistical difference of mean durations by each group

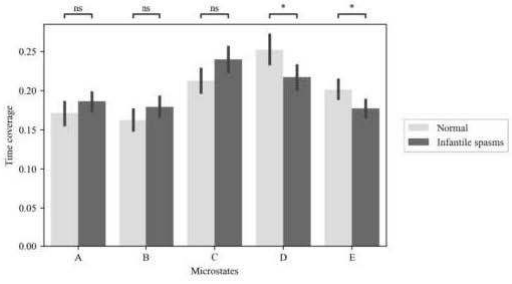

Figure 1-(f). Statistical difference of time coverage by each group

Conclusions: We find a significant difference between the normal group and the IS group through EEG microstate analysis. We show that microstate features are useful biomarkers for identifying IS. In future works, we will apply machine learning to detect IS, automatically. It can be helpful to assist clinicians by reducing efforts.

References

1. Kim, J., Kim, M. J., Kim, H. J., Yum, M. S., & Ko, T. S. (2023). Electrophysiological network predicts clinical response to vigabatrin in epileptic spasms. Frontiers in Neurology, 14.
2. Khanna, A., Pascual-Leone, A., Michel, C. M., & Farzan, F. (2015). Microstates in resting-state EEG: current status and future directions. Neuroscience & Biobehavioral Reviews, 49, 105-113.
3. Pascual-Marqui, R. D., Michel, C. M., & Lehmann, D. (1995). Segmentation of brain electrical activity into microstates: model estimation and validation. IEEE Transactions on Biomedical Engineering, 42(7), 658-665.
4. Michel, C. M., & Koenig, T. (2018). EEG microstates as a tool for studying the temporal dynamics of whole-brain neuronal networks: a review. Neuroimage, 180, 577-593.
5. Nam, S., Jang, K. M., Kwon, M., Lim, H. K., & Jeong, J. (2022). Electroencephalogram microstates and functional connectivity of cybersickness. Frontiers in Human Neuroscience, 16, 857768.

Poster No 388

Correlated Gene Expression Supports Neuromorphic Epicenter Identification in Attention-Deficit/Hyper

Pan Wang[1], Jinzhong Peng[1], Qingquan Cao[1], Yilu Li[1], Bharat Biswal[2]

[1]UESTC, Chengdu, Sichuan, [2]New Jersey Institute of Technology, Newark, NJ

Introduction: Attention-deficit/hyperactivity disorder (ADHD), a highly heritable developmental psychiatric disorder, primarily manifested the inattentive, hyperactive, and impulsive symptoms (Gallo and Posner, 2016; Lord et al., 2018; Posner et al., 2020). The neuromorphic heterogeneity and how the correlated gene expression (CGE) connectome influences morphological change in ADHD have not been investigated.

Methods: Current study employed the neuroimaging dataset from a publicly available ADHD-200 dataset (http://fcon_1000.projects.nitrc.org/indi/adhd200/), including 196 ADHD patients and 181 healthy controls (HCs). Adopting the neuroimaging subtype analysis based on W-score, we estimated the cortical thickness deviation, and further obtained the biotypes of ADHD using the density peak-based clustering analysis (Figure 1A). To construct the correlated gene expression (CGE) connectome matrix, we first obtained the regional matrix of transcriptional level (400 regions × 15,631 gene expression) in line with previous study on CGE (Arnatkeviciute et al., 2019), and then calculated the transcriptomic similarities between the distinct regional gene expressions, resulting in a symmetric CGE connectome matrix (400× 400) (Figure 1B). Partial least squares (PLS) gene list based on W-score map and WCGE-score map were put into Metascape for gene enrichment analysis (Figure 1C). Cortical epicenter regions were identified by putative epicenters if their deviation was high and their neighbors also experienced high deviation (Figure 1D).

Results: Findings from clustering analysis revealed that ADHD patients could be divided into two discriminative biotypes. The significant regions in biotype 1 primarily located in the visual peripheral network, control network and default mode network, while regions for biotype 2 mainly distributed in the salience ventral attention network. The CGE connectome exhibited modular organization with distinct robust pattern similar as previous study (Romero-Garcia et al., 2018; van den Heuvel et al., 2019). We observed that the regional W-score values were significantly positive correlations with the CGE-informed W-score for both biotypes (Biotype 1: $R = 0.4574$, $P < 0.0001$; biotype2: $R = 0.2720$, $P < 0.0001$). In addition, patterns of epicenter likelihood revealed that biotype 1 was mainly associated with the lateral prefrontal lobe and temporo-parietal junction, while biotype 2 were relating to the lateral sulcus and medial prefrontal lobe (Figure 2A and 2B). More importantly, we found 6 and 8 overlapped regions between epicenters and the top 5% regions from W-score in biotype 1 and biotype 2, respectively (Figure 2C).

Conclusions: The present study demonstrated that ADHD patients could be classified into two biotypes closely relating to CGE connectome by estimating the neighborhood cortical thickness based on regional W-score measures. Epicenter identification would promote understanding of the heterogeneity and distinct clinical manifestations in ADHD biotypes.

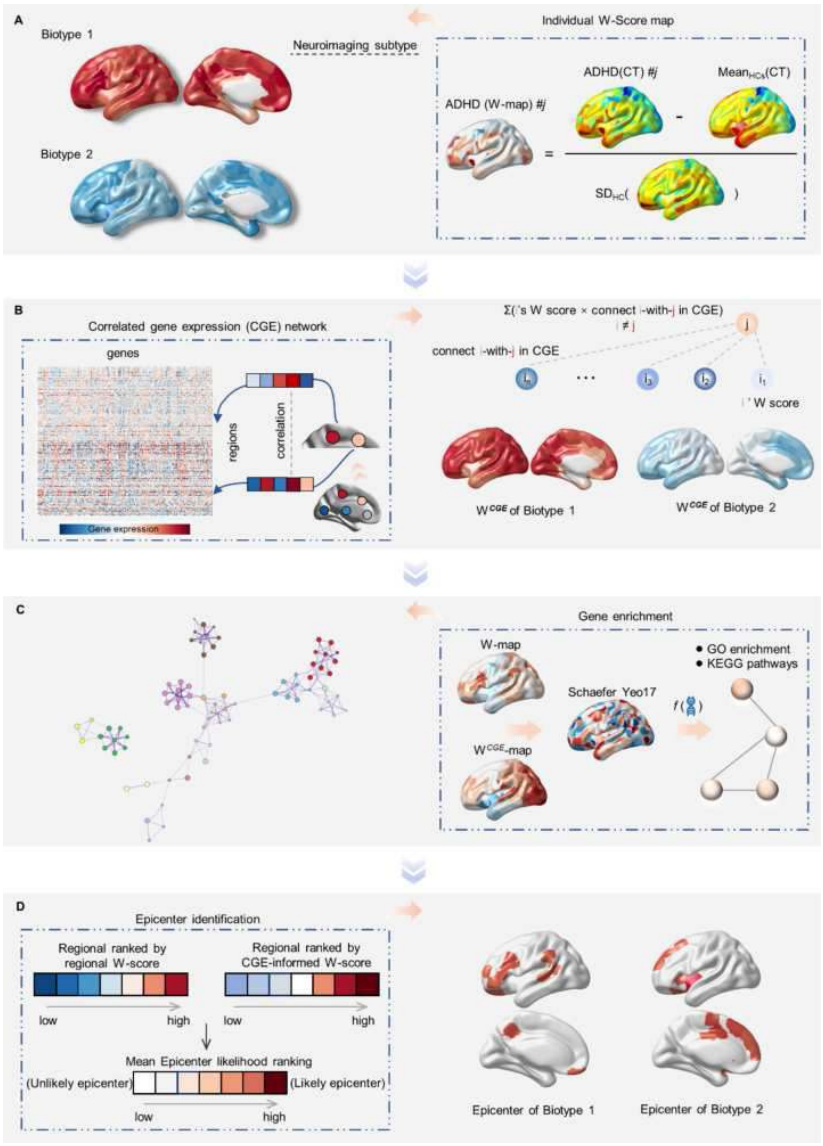
A
Biotype 1
Biotype 2
Neuroimaging subtype
Individual W-Score map
ADHD (W-map) #j
ADHD(CT) #j
Mean$_{HC}$(CT)
SD$_{HC}$( )
B
Correlated gene expression (CGE) network
genes
regions
correlation
Gene expression
Σ('s W score × connect -with-j in CGE)
i ≠ j
connect -with-j in CGE
'W score
W^{CGE} of Biotype 1
W^{CGE} of Biotype 2
C
Gene enrichment
W-map
Schaefer Yeo17
W^{CGE}-map
• GO enrichment
• KEGG pathways
D
Epicenter identification
Regional ranked by regional W-score
Regional ranked by CGE-informed W-score
low
high
Mean Epicenter likelihood ranking
(Unlikely epicenter)
(Likely epicenter)
Epicenter of Biotype 1
Epicenter of Biotype 2

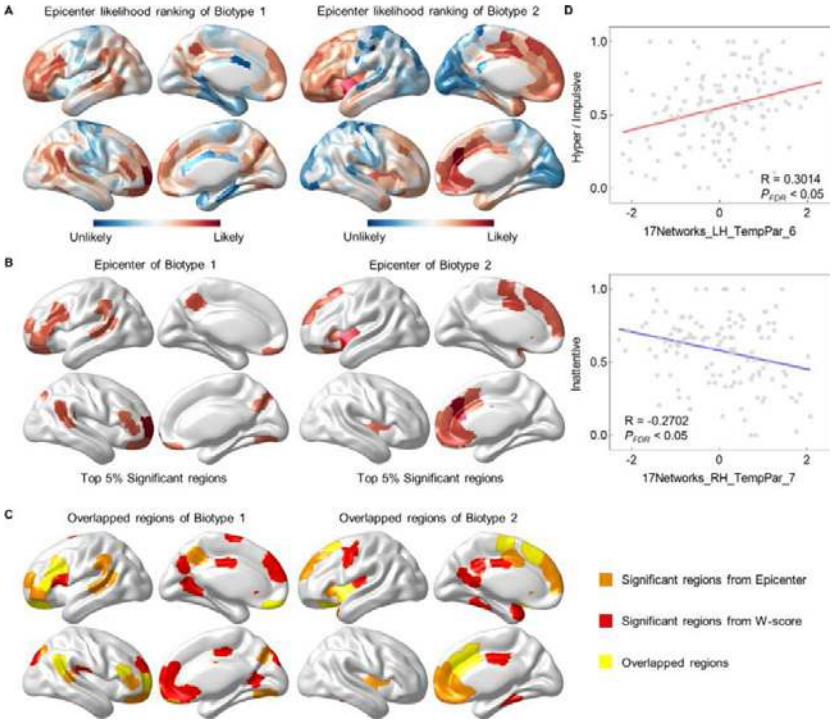
A
Epicenter likelihood ranking of Biotype 1
Epicenter likelihood ranking of Biotype 2
Unlikely
Likely
B
Epicenter of Biotype 1
Epicenter of Biotype 2
Top 5% Significant regions
C
Overlapped regions of Biotype 1
Overlapped regions of Biotype 2
D
Hyper / Impulsive
R = 0.3014
P_{FDR} < 0.05
17Networks_LH_TempPar_6
Inattentive
R = -0.2702
P_{FDR} < 0.05
17Networks_RH_TempPar_7
Significant regions from Epicenter
Significant regions from W-score
Overlapped regions

References
1. Arnatkeviciute, A., Fulcher, B.D., Fornito, A., (2019), 'A practical guide to linking brain-wide gene expression and neuroimaging data', Neuroimage, vol. 189, pp. 353-367.
2. Gallo, E.F., Posner, J., (2016), 'Moving towards causality in attention-deficit hyperactivity disorder: overview of neural and genetic mechanisms', Lancet Psychiatry, vol 3, no. 6, pp. 555-567.
3. Lord, C., Elsabbagh, M., Baird, G., Veenstra-Vanderweele, J., (2018), 'Autism spectrum disorder', Lancet, vol 392, no. 10146, pp. 508-520.
4. Posner, J., Polanczyk, G.V., Sonuga-Barke, E., (2020), 'Attention-deficit hyperactivity disorder', Lancet, vol. 395, no. 10222, pp. 450-462.
5. Romero-Garcia, R., Whitaker, K.J., Vása, F., Seidlitz, J., Shinn, M., Fonagy, P., Dolan, R.J., Jones, P.B., Goodyer, I.M., Bullmore, E.T., Vértes, P.E., Consortium, N., (2018), 'Structural covariance networks are coupled to expression of genes enriched in supragranular layers of the human cortex', Neuroimage, vol. 171, pp. 256-267.
6. Van den Heuvel, M.P., Scholtens, L.H., Kahn, R.S., (2019), 'Multiscale Neuroscience of Psychiatric Disorders', Biological Psychiatry, vol. 86, no. 7, pp. 512-522.

Poster No 389

Abnormal dynamic functional connectivity in childhood maltreatment based on the triple-network model

Haiqi Wu[1], Huiyuan Huang[1], Bingqing Jiao[1], Jiabao Lin[1], Lijun Ma[1]

[1]School of Public Health and Management, Guangzhou University of Chinese medicine, Guangzhou, Guangdong Province

Introduction: Childhood maltreatment (CM) including physical abuse, emotional abuse, sexual abuse, physical neglect, and emotional neglect, has a long-term adverse effect on children and even though throughout adults (Teicher, Gordon et al. 2021, Cay, Gonzalez-Heydrich et al. 2022). Childhood maltreatment has been confirmed as one of high-risk factors for mental illness (e.g., major depressive disorder, post-traumatic stress disorder) (Cay, Gonzalez-Heydrich et al. 2022). A meta-analysis indicated that specific brain regions might change in people with childhood maltreatment, particularly in hippocampus, amygdala, middle temporal gyrus, prefrontal cortex (PFC), anterior cingulate cortex (Heany, Groenewold et al. 2017). Moreover, previous study has implicated that most of the changes in these brain regions were associate with major depressive disorder and post-traumatic stress disorder (Cay, Gonzalez-Heydrich et al. 2022). Therefore, it is important to elucidate the neurophysiological mechanism of childhood trauma which may help for developing targeted preventive and treatment strategies. Triple network model is a core network associated with cognitive and affective dysfunction, including the default mode network (DMN), central executive network (CEN), and salience network (SN) (Menon 2011). Elton and van found differences in DMN and SN static functional connectivity between individuals with childhood trauma and healthy individuals (Elton, Tripathi et al. 2013, van der Werff, Pannekoek et al. 2013). However, as far as we know, no studies have focused on differences in interaction in the triple-network model between subjects with childhood maltreatment (CM) and without childhood maltreatment (non-CM). Moreover, most previous studies of childhood trauma have focused on static properties of the brain (He, Fan et al. 2022), but few studies consider dynamic properties. In current study, we consider the sample of young healthy adults (18-40) with CM and hypothesized that the subjects with CM and non-CM may exhibit differences in the temporal properties of dynamic functional network connectivity (dFNC) states.

Methods: The fMRI and structure data were collected from 125 right-handed healthy young adults, including 55 CM subjects and 70 non-CM controls. The severity of childhood maltreatment was assessed using the Childhood Trauma Questionnaire-Short Form (CTQ-SF) scale (Bernstein, Stein et al. 2003). The fMRI data were preprocessed using Data Processing Assistant for Resting-State fMRI (DPABI 3.0) (Yan et al. 2016). Group independent component analysis (ICA) was used to determine the spatially independent components of DMN, SN, and CEN in GIFT (version 3.0c) (Calhoun, V D et al.2001, Calhoun, V D et al.2004). We adopt the sliding window approach to construct dynamic functional network connectivity (dFNC). Finally, the dFNC states were estimated by k-means clustering and the between group difference in the temporal properties of dFNC states were evaluated using permutation test.

Results: The dFNC within the triple networks could be clustered into four states. State 1 was a more strongly and intensively interconnected state, with high positive correlation within and between DMN and CEN. While state 2 and state 3 are characterized as sparsely connected states. The RSFC pattern of State 4 resembled that of State 1 but had a reduced RSFC strength within and between DMN and CEN with moderate positive couplings. The results show that the CM spent longer mean dwell time than non-CM in state 4: MDT(CM)=16.23±14.68 > MDT (non-CM) =11.30±8.19.

Table 1. Demographic and behavior characteristics of all subjects (n = 125)

	CM group n = 55 mean (SD)	non-CM group n = 70 mean (SD)	$t/\chi 2$	p-values
Age (Years old)	26.22 (6.22)	23.76 (4.55)	2.55	0.002
Gender (Male/Female)	26/29	27/43	0.96	0.328
Educational level (Years)	14.02 (2.00)	13.91 (2.73)	0.20	0.461
Mean FD (mm)	0.059 (0.025)	0.056 (0.022)	0.80	0.228
CTQ score				
Emotional abuse	7.91 (3.16)	5.74 (0.97)	5.41	0.000
Physical abuse	6.58 (2.14)	5.33 (0.70)	4.60	0.000
Sexual abuse	5.70 (1.29)	5.00 (0.00)	4.62	0.000
Emotional neglect	13.35 (4.76)	6.74 (1.49)	10.96	0.000
Physical neglect	10.00 (2.68)	5.49 (0.67)	13.57	0.000
Total score	43.55 (8.06)	28.30 (2.58)	14.90	0.000
CTE, n (%)				
Emotional abuse	20 (36.36)			
Physical abuse	18 (32.72)			
Sexual abuse	17 (30.90)			
Emotional neglect	41 (74.55)			
Physical neglect	43 (78.18)			
Multiple Exposures	44 (80.00)			
Single Exposure	11 (20.00)			

CM, subjects with Childhood Maltreatment; non-CM, subjects without Childhood Maltreatment; FD, Framewise Displacement; CTE, Childhood Trauma Exposures; CTQ, Childhood Trauma Questionnaire; SD, Standard Deviation

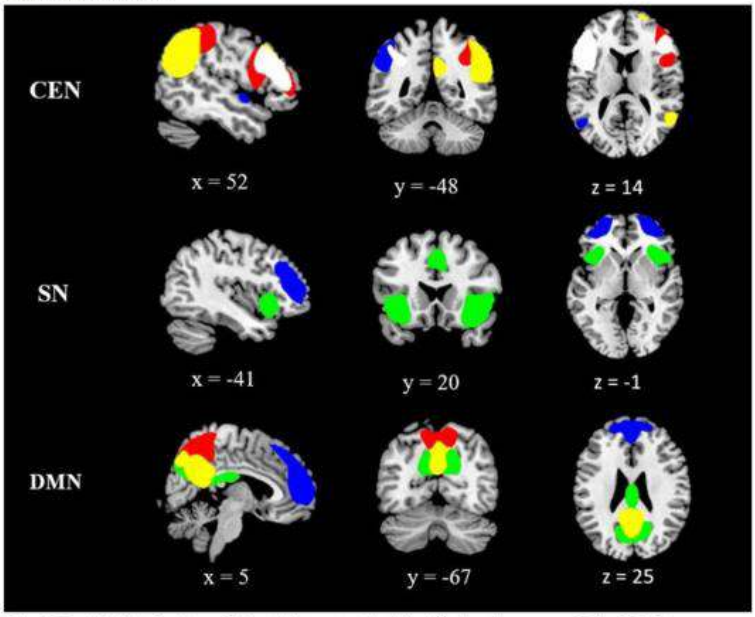

Fig. 1 Spatial distribution of the triple networks identified using group ICA. DMN, default-mode network; CEN, central executive network; SN, salience network.

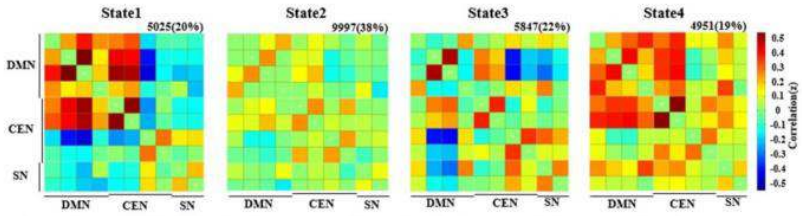

Fig. 2 Cluster centroids for the four dFNC states and its total number (percentage) of occurrence in each state. DMN, default-mode network; CEN, central executive network; SN, salience network.

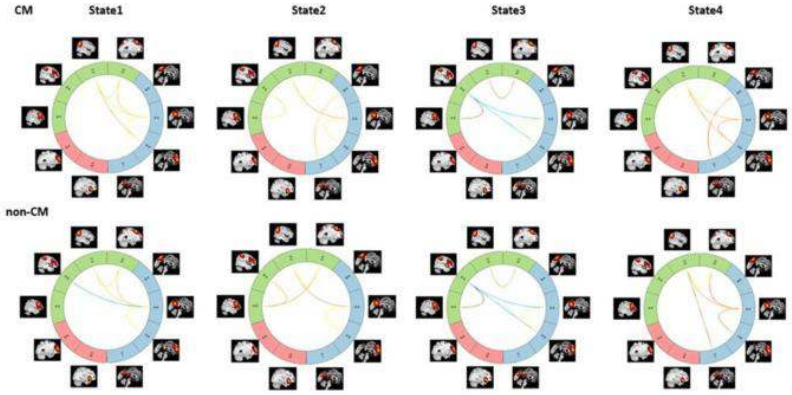

Fig. 3 Group-specific FC pattern with only top 10% of the strongest dFNC strength (i.e. the largest absolute value of correlation coefficients).

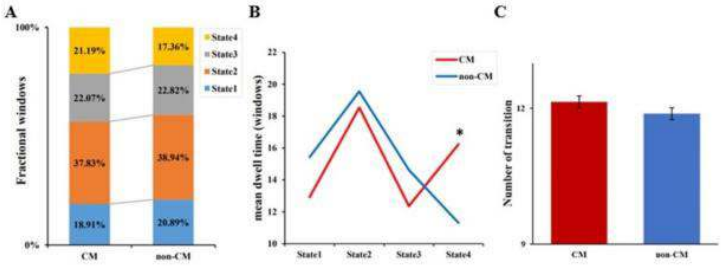

Fig. 4 Temporal properties of dFNC states. (A) Fractional windows, (B) Mean dwell time with 95% confidence interval, and (C) Number of transitions. Asterisks indicate a significant group difference ($p < 0.05$, Bonferroni correction). CM, subjects with Childhood Maltreatment; non-CM, subjects without Childhood Maltreatment.

Conclusions: Individuals with childhood trauma spent more time than non-CM in state 4 of the triple networks with dense and positive correlation within and between default-mode network and central executive network. These networks are involved in functions related to working memory, executive function, and self-cognition. These findings may help us to understand the neural mechanisms that distinguish CM from non-CM.

References

1. Bernstein, D. P., et al. (2003). 'Development and validation of a brief screening version of the Childhood Trauma Questionnaire. 'Child abuse & neglect 27(2): 169-190.
2. Cay, M., et al. (2022). 'Childhood maltreatment and its role in the development of pain and psychopathology. ' The Lancet Child & Adolescent Health 6(3): 195-206.
3. Calhoun, V D et al. (2001). 'A method for making group inferences from functional MRI data using independent component analysis. ' Human brain mapping 14(3): 140-51.
4. Calhoun, V D et al. (2004). 'Group ICA of fMRI toolbox (GIFT) . ' Available at http:// icatb.sourceforge.net.
5. Elton, A., et al. (2013). 'Childhood maltreatment is associated with a sex-dependent functional reorganization of a brain inhibitory control network. ' Human Brain Mapping 35(4): 1654-1667.
6. He, C., et al. (2022). 'Insula network connectivity mediates the association between childhood maltreatment and depressive symptoms in major depressive disorder patients. ' Translational Psychiatry 12(1).
7. Heany, S. J., et al. (2017). 'The neural correlates of Childhood Trauma Questionnaire scores in adults: A meta-analysis and review of functional magnetic resonance imaging studies. ' Development and Psychopathology 30(4): 1475-1485.
8. Menon, V. (2011). 'Large-scale brain networks and psychopathology: a unifying triple network model. ' Trends in Cognitive Sciences 15(10): 483-506.
9. Teicher, M. H., et al. (2021). 'Recognizing the importance of childhood maltreatment as a critical factor in psychiatric diagnoses, treatment, research, prevention, and education. ' Molecular Psychiatry 27(3): 1331-1338.
10. van der Werff, S. J. A., et al. (2013). 'Resilience to childhood maltreatment is associated with increased resting-state functional connectivity of the salience network with the lingual gyrus. ' Child abuse & neglect 37(11): 1021-1029.

Poster No 390

Prenatal alcohol exposure is associated with altered cortical structure and neurocognition at age 6

Chanelle Hendrikse[1], Shantanu Joshi[2], Jessica Ringshaw[1], Layla Bradford[1], Annerine Roos[1], Catherine Wedderburn[1], Nadia Hoffman[1], Tiffany Burd[1], Katherine Narr[2], Roger Woods[2], Heather Zar[1], Dan Stein[1], Kirsty Donald[1]

[1]University of Cape Town, Cape Town, South Africa, [2]University of California Los Angeles, Los Angeles, CA

Introduction: We previously reported widespread brain structural changes in 2-3-year-old children with prenatal alcohol exposure (PAE; Subramoney et al., 2022) in a South African birth cohort study, the Drakenstein Child Health Study (DCHS), which may underpin foetal alcohol spectrum disorders symptomatology. However, few studies have examined the associations between PAE-related brain structural changes and neurocognitive functions through middle childhood. We aimed to examine the potential associations between PAE and cortical and subcortical grey matter morphology and neurocognitive outcomes in 6-7-year-old children.

Methods: One hundred fifty-eight children (49 PAE, 109 controls; 46% female; mean age 76 ± 5 months) participating in a brain imaging substudy of the DCHS in Cape Town, South Africa, were included (Donald et al., 2018; Zar et al., 2015). Maternal alcohol use during pregnancy was prospectively assessed using the Alcohol, Smoking, and Substance Involvement Screening Test, with additional data on quantity and timing reported soon after birth. Using a 3T MRI scanner, high-resolution T1-weighted brain structural scans were acquired on children at 6-7 years and processed using FreeSurfer 7.1.1. In SPSS, general linear models (GLMs) were used to test the associations between PAE (categorical variable) and global and regional cortical metrics (i.e., volume [CV], surface area [CSA], thickness [CT]) and subcortical volumes. Cortical regions of interest (ROIs) spanning the frontal, parietal, temporal, and occipital lobes were assessed in a lobe-wise manner. The Benjamini-Hochberg false discovery rate (FDR) method was applied to correct for multiple comparisons. Covariates were child age, sex, maternal education, prenatal tobacco exposure, and¬-in volumetric models only-total intracranial volume. Associations between PAE and neurocognitive outcomes, as assessed using the Early Learning Outcomes Measure (ELOM; n = 119) specifically designed for South African children, were examined. The potential mediating influence of significant PAE-related brain structural effects on associations between PAE and neurocognitive outcomes was assessed using the PROCESS macro for SPSS (Hayes, 2022) while adjusting for the same covariates.

Results: PAE was associated with lower total CSA (p = 0.044), as well as regional CV and CSA reductions in frontal, parietal, and temporal lobe ROIs, and CT increases in specific parietal and occipital lobe ROIs. PAE effects on CSA in the right superior parietal and precuneus cortices survived FDR correction. A main multivariate PAE effect on regional CSA of temporal ROIs was found which survived FDR correction, eliminating the need for further FDR corrections in post hoc univariate GLMs with individual ROIs in this lobe-PAE was associated with lower CSA in the left middle temporal and right inferior temporal, fusiform and parahippocampal gyri (Figure 1). Moreover, PAE was associated with poorer ELOM total (p = 0.002) and subscale scores for the numeracy/mathematics (p < 0.001), cognition/executive functioning (p = 0.029), and language/literacy subscales (p = 0.012). CSA of the left middle temporal gyrus partially mediated the associations between PAE and ELOM total scale scores, as well as the numeracy/mathematics and cognition/executive functioning subscale scores (Figure 2).

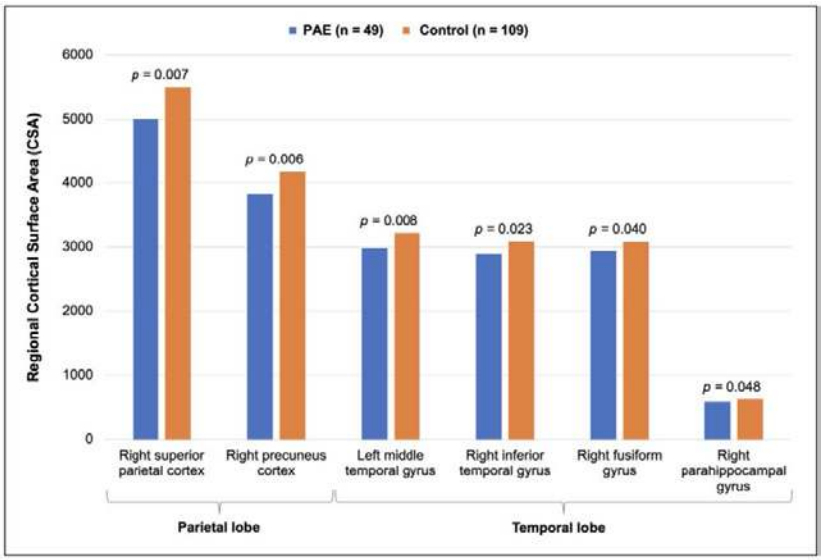

Figure 1. Regional cortical surface area means for ROIs showing significant group effects after covariate adjustment and FDR correction.

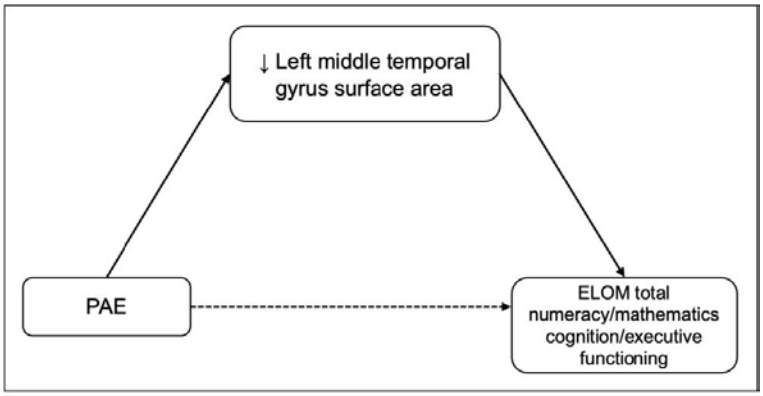

Figure 2. Illustration of mediation results.

Conclusions: We found widespread PAE effects on cortical morphology at 6-7 years, expanding our earlier findings at 2-3 years (Subramoney et al., 2022). While frontal and occipital effects were present, CSA of parietal and temporal ROIs appeared to be most affected by PAE. Smaller CSA suggests immature gyrification in these regions involved in numerous cognitive and sensorimotor functions. Increased efforts to reduce maternal drinking during pregnancy and early interventions for children with PAE are needed to enhance school readiness.

References

1. Donald, K. A., Hoogenhout, M., du Plooy, C. P., Wedderburn, C. J., Nhapi, R. T., Barnett, W., Hoffman, N., Malcolm-Smith, S., Zar, H. J., & Stein, D. J. (2018). Drakenstein Child Health Study (DCHS): investigating determinants of early child development and cognition. BMJ paediatrics open, 2(1), e000282. https://doi.org/10.1136/bmjpo-2018-000282
2. Subramoney, S., Joshi, S. H., Wedderburn, C. J., Lee, D., Roos, A., Woods, R. P., Zar, H. J., Narr, K. L., Stein, D. J., & Donald, K. A. (2022). The impact of prenatal alcohol exposure on gray matter volume and cortical surface area of 2 to 3-year-old children in a South African birth cohort. Alcoholism, clinical and experimental research, 46(7), 1233–1247. https://doi.org/10.1111/acer.14873
3. Hayes, A. F. (2022). Introduction to mediation, moderation, and conditional process analysis: A regression-based approach (3rd edition), Guilford Press, New York, NY.
4. Zar, H. J., Barnett, W., Myer, L., Stein, D. J., & Nicol, M. P. (2015). Investigating the early-life determinants of illness in Africa: the Drakenstein Child Health Study. Thorax, 70(6), 592–594. https://doi.org/10.1136/thoraxjnl-2014-206242

Poster No 391

Relationship between EEG spectral power and dysglycemia with outcomes after neonatal encephalopathy

Janie Damien[1], Phetsamone Vannasing[2], Julie Tremblay[2], Laurence Petitpas[2], Bohdana Marandyuk[2], Thameya Balasingam[2], Ramy El Jalbout[2], Natacha Paquette[2], Gianluca Donofrio[2], Anne Gallagher[3], Elana Pinchefsky[2]

[1]University of Montreal, Montreal, Québec, [2]Sainte-Justine University Hospital Centre, Montreal, Quebec, [3]Sainte-Justine University Hospital Centre, Monytreal, Quebec

Introduction: Identification of early markers of brain function is essential to aid in the prediction of neurodevelopmental outcomes following neonatal encephalopathy (NE) even with implementation of effective neuroprotective interventions like therapeutic hypothermia. Potentially modifiable risk factors such as dysglycemia are frequent in the first hours of life in neonates with encephalopathy and may contribute to impaired brain function and long-term adverse outcomes. The relationship between dysglycemia and brain function after therapeutic hypothermia and at follow-up in NE needs to be further investigated to improve prediction of outcomes. Therefore, we studied how dysglycemia and brain function on electroencephalography (EEG) following therapeutic hypothermia relate to neurodevelopmental outcomes in children with NE. We hypothesized that neonatal dysglycemia (hypo- or hyperglycemia in the first 0-48 hours of life) and EEG spectral power (measured during the post-rewarming period and the 2-month follow-up) in NE are related to neurodevelopmental outcomes at ≥18 months.

Methods: This retrospective study included 90 neonates with encephalopathy who received therapeutic hypothermia and underwent EEG monitoring according to the international 10–20 system, including electrodes Fp1\Fp2, C3\C4, T3\T4, and O1\O2. Absolute spectral power was calculated from artifact-free EEG signals during the 6-hour post-rewarming period and the 30-minute routine follow-up at 2-months, within all frequency bands (delta, theta, alpha, beta, total) and brain regions (frontal, central, temporal, occipital, and global average of all electrodes). Measures of dysglycemia (hypoglycemia, hyperglycemia, and glycemic lability) and glucose variability (mean absolute glucose change) were computed for the first 48 hours of life. Brain

magnetic resonance imaging (MRI) was also performed in neonates after the completion of therapeutic hypothermia (at 5 ± 2 days of life). Neurodevelopmental outcomes included motor, language, or global developmental delays, visual impairments, auditory deficits, cerebral palsy, mortality, and a composite measure of normal/mild or moderate/severe outcome at ≥18 months. Using logistic regression analyses with area under receiver operating characteristic (AUROC) curves, we evaluated EEG and glucose variables in separate and combined models to predict neurodevelopmental outcomes, adjusting for NE severity and MRI brain injury, and using Bonferroni correction for multiple comparisons.

Results: Global delta power during post-rewarming and dysglycemia (hyperglycemia and glycemic lability) during the first 0-48 hours of life were the variables with the highest predictive values for moderate/severe neurodevelopmental outcome (AUROC=0.8, 95%CI 0.7;0.9 for both models). The combined model including global delta power post-rewarming and neonatal dysglycemia more accurately predicted moderate/severe neurodevelopmental outcome (AUROC=0.9, 95%CI [0.8,0.9], p<.001). After adjusting for NE severity and MRI brain injury, only higher global delta power post-rewarming remained significantly associated with lower odds of moderate/severe neurodevelopmental outcome (OR=0.9, 95%CI [0.8,1.0], p=.04), gross motor delay (OR=0.9, 95%CI [0.8,1.0], p=.04), global developmental delay (OR=0.9, 95%CI [0.8,1.0], p=.04), and auditory deficits (OR=0.9, 95%CI [0.8,1.0], p=.03).

Figure 1.

ROC curves for univariable and multivariable prediction models.

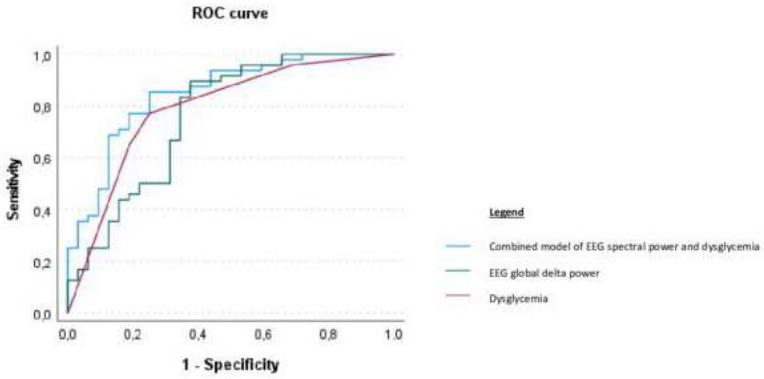

Note. The AUROC of the multivariable analysis for EEG spectral power and dysglycemia prediction models of moderate/severe neurodevelopmental outcome at ≥ 18 months. Predictive value of EEG global delta power during the post-rewarming period (all electrodes) and dysglycemia (first 48 hours of life) were graphed individually and in a combined model, with receiver operating characteristic (ROC) curves and their associated sensitivity and false positive rate (1-specificity). AUROC : Area under the receiver operating characteristic (ROC) curve.

Conclusions: This study identified quantitative EEG markers of brain function after therapeutic hypothermia that are associated with higher risks of unfavorable neurodevelopmental outcomes. Among neonates with encephalopathy, global delta power during post-rewarming and dysglycemia during the first 48 hours of life accurately predicted moderate/severe neurodevelopmental outcomes at ≥18 months, when measures were used separately, and even more so when combined. Global delta power post-rewarming predicted neurodevelopmental outcomes, even after adjusting for NE severity and MRI brain injury.

Poster No 392

Abnormality detection in white matter in utero, applied to fetuses with Congenital Heart Disease

Sian Wilson[1], Daniel Cromb[1], Vyacheslav Karolis[2], Daan Christiaens[3], Alena Uus[4], Russell Macleod[1], Anthony Price[1], Joseph Hajnal[1], A. Edwards[1], Kiho Im[5], Jonathan O'Muircheartaigh[6], Donald Tournier[1], Serena Counsell[1]

[1]King's College London, London, England, [2]King's College London, London, Not in the States, [3]KU Leuven, Leuven, Other, [4]King's College London, London, Other, [5]Division of Newborn Medicine, Boston Children's Hospital and Harvard Medical School, Boston, MA, [6]King's College London, London, London

Introduction: Impaired volumetric development of transient fetal compartments underlying white matter (WM) has been observed in fetuses with congenital heart disease (CHD), suggesting impaired WM) development in utero (Rollins et al., 2021). However, microstructural WM development in CHD has not been investigated. We present an approach to identify individual deviations from the normal trajectory of diffusion contrast change, with high spatiotemporal specificity, within specific WM fibre bundles as they emerge from transient fetal compartments. We explore whether volumetric differences in these zones are accompanied by changes at the microstructural level, using multi-shell high angular resolution diffusion imaging (HARDI), comparing healthy control fetuses to a cohort with various types of CHD.

Methods: The study population included 235 healthy controls (22 – 37 weeks gestational age (GA), 129 male) and 26 fetuses with various forms of CHD (23 – 38 weeks GA, 19 male). T2 and HARDI volumes were acquired with the Developing Human Connectome Project acquisition protocol (Price et al., 2019) on a Philips Achieva 3T system, with a 32-channel cardiac coil. HARDI data was collected with a combined spin echo and field echo (SAFE) sequence at 2 mm isotropic resolution, using a multi-shell diffusion encoding that consists of 15 volumes at b=0 s/mm2, 46 volumes at b=400 s/mm2, and 80 volumes at b=1000 s/mm2 (Christiaens et al., 2019). HARDI datasets were reconstructed to 0.8 mm, using a data driven representation of the spherical harmonics and radial decomposition (SHARD). The SHARD pipeline caters to the motion corrupted fetal data, using dynamic distortion correction and slice-to-volume motion correction framework (Cordero-Grande et al., 2019, Christiaens et al., 2021). Subsequent diffusion processing and tractography to estimate thalamocortical pathways was performed using MRtrix3 (Wilson et al., 2023, Tournier et al., 2019). 30 cross-sections were taken along the tracts (Figure 1A,B), and values of underlying diffusion metrics were sampled and averaged within each slice. We used Gaussian process regression (GPR) implemented in GPy, to predict and characterise the normative range of tissue fraction values within each cross-section (Figure 1C-F). We quantified the deviation from normal using a Z-score, computing the difference between predicted and observed values, normalised by prediction uncertainty (Marquand et al. 2016).

Results: We identified unique maturational trends within different fetal tissue types across the second to third trimester (Figure 1). We quantified different rates of change in tissue fraction maturation between deep grey matter and cortical plate compartments, and in the intermediate zone/white matter compartment, tissue fraction maturation follows a parabolic curve. We also observe fluctuations in the level of variability between individuals along the tract. When examining the z scores of fetuses with CHD, all fetuses showed a high proportion of normal z-scores along the white matter, with isolated regions deviating from the normal mean. Regions of abnormality appeared to be specific to each subject, and at this stage, we did not find consistent patterns across the cohort or for subjects with a specific diagnosis.

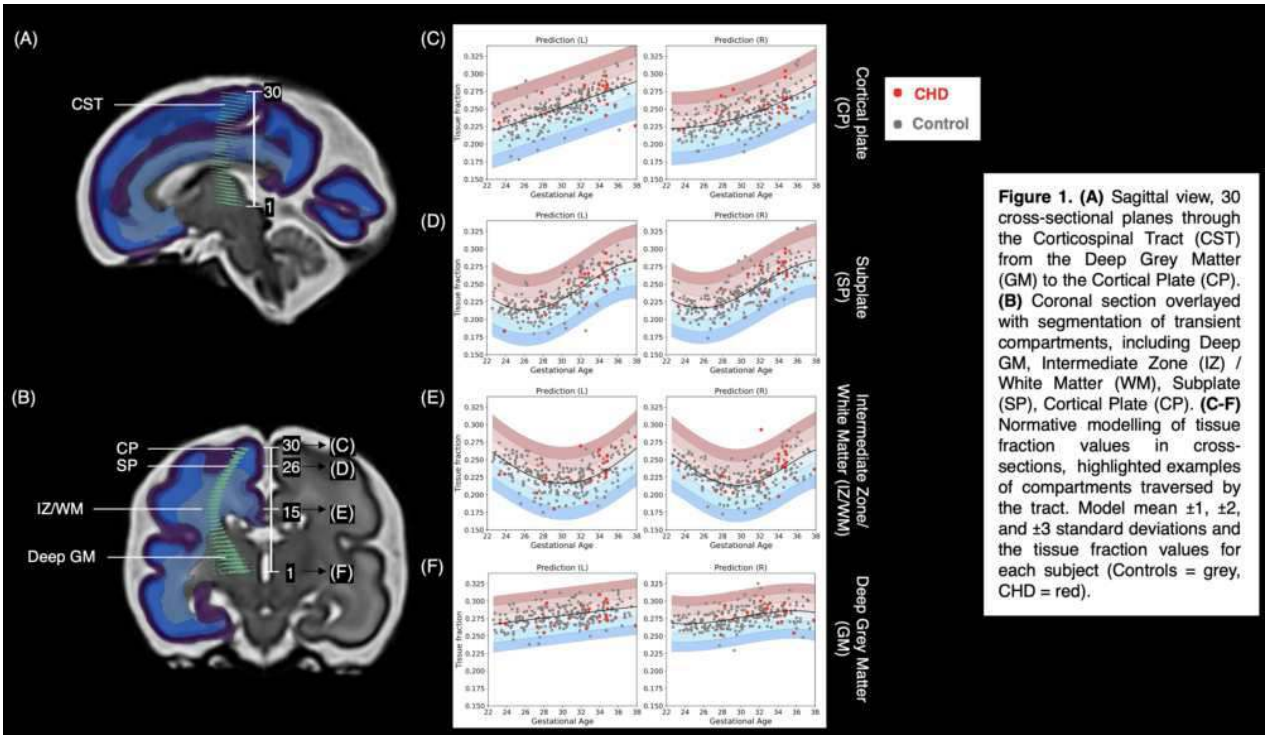

Figure 1. (A) Sagittal view, 30 cross-sectional planes through the Corticospinal Tract (CST) from the Deep Grey Matter (GM) to the Cortical Plate (CP). **(B)** Coronal section overlayed with segmentation of transient compartments, including Deep GM, Intermediate Zone (IZ) / White Matter (WM), Subplate (SP), Cortical Plate (CP). **(C-F)** Normative modelling of tissue fraction values in cross-sections, highlighted examples of compartments traversed by the tract. Model mean ±1, ±2, and ±3 standard deviations and the tissue fraction values for each subject (Controls = grey, CHD = red).

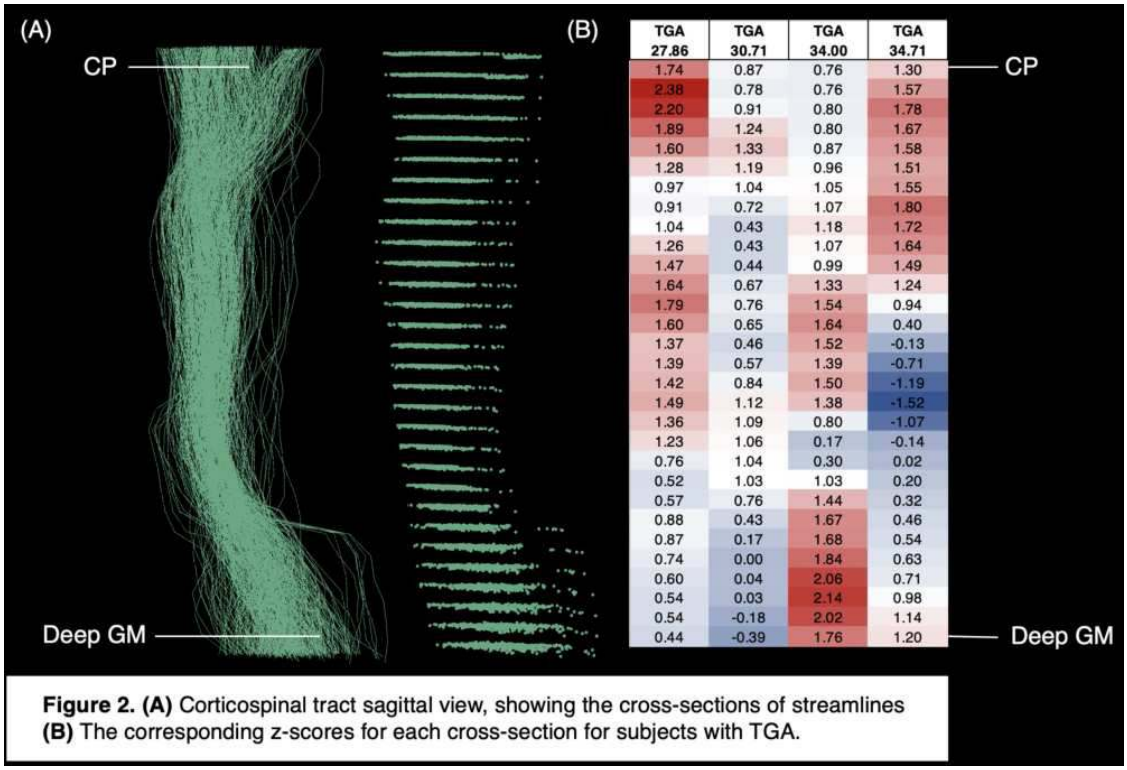

Figure 2. (A) Corticospinal tract sagittal view, showing the cross-sections of streamlines **(B)** The corresponding z-scores for each cross-section for subjects with TGA.

Conclusions: The analysis framework highlights unique maturational trends for different fetal tissue types across the second to third trimester. In fetuses with CHD we observed normal z scores along a large proportion of the WM, but identified specific regions of abnormality. Abnormal regions were unique to individuals, reflecting the highly dynamic development of the fetal brain and the heterogeneity of CHD subtypes within this cohort. Further post-hoc testing and clustering approaches will be required to investigate this further. This approach is tailored to detect differences within individuals, and we were statistically underpowered to draw conclusions about CHD at the group level.

References

1. Christiaens, D. et al. (2019) 'Fetal diffusion MRI acquisition and analysis in the developing Human Connectome Project.'
2. Christiaens, D. et al. (2021) 'Scattered slice SHARD reconstruction for motion correction in multi-shell diffusion MRI', NeuroImage, 225, p. 117437.Available at: https://doi.org/10.1016/j.neuroimage.2020.117437.
3. Cordero-Grande, L. et al. (2019) 'Complex diffusion-weighted image estimation via matrix recovery under general noise models', NeuroImage, 200,pp. 391–404. Available at: https://doi.org/10.1016/j.neuroimage.2019.06.039.
4. Cromb, D. et al. (2023) 'Total and Regional Brain Volumes in Fetuses With Congenital Heart Disease', Journal of Magnetic Resonance Imaging, p.jmri.29078. Available at: https://doi.org/10.1002/jmri.29078.
5. Limperopoulos, C. et al. (2010) 'Brain Volume and Metabolism in Fetuses With Congenital Heart Disease: Evaluation With Quantitative MagneticResonance Imaging and Spectroscopy', Circulation, 121(1), pp. 26–33. Available at: https://doi.org/10.1161/CIRCULATIONAHA.109.865568.
6. Marquand, A.F. et al. (2016) 'Understanding Heterogeneity in Clinical Cohorts Using Normative Models: Beyond Case-Control Studies', BiologicalPsychiatry, 80(7), pp. 552–561. Available at: https://doi.org/10.1016/j.biopsych.2015.12.023.
7. Price, A. et al., (2019). 'The Developing Human Connectome Project (dHCP): Fetal Acquisition Protocol. ISMRM.'Rollins, C.K. et al. (2021) 'RegionalBrain Growth Trajectories in Fetuses with Congenital Heart Disease', Annals of Neurology, 89(1), pp. 143–157. Available at:https://doi.org/10.1002/ana.25940.
8. Rollins, C.K. et al. (2021) 'Regional Brain Growth Trajectories in Fetuses with Congenital Heart Disease', Annals of Neurology, 89(1), pp. 143–157.Available at: https://doi.org/10.1002/ana.25940.
9. Tournier, J.-D. et al. (2019) 'MRtrix3: A fast, flexible and open software framework for medical image processing and visualisation', NeuroImage, 202,p. 116137. Available at: https://doi.org/10.1016/j.neuroimage.2019.116137.
10. Wilson, S. et al. (2023) 'Spatiotemporal tissue maturation of thalamocortical pathways in the human fetal brain', eLife, 12, p. e83727. Available at:https://doi.org/10.7554/eLife.83727.s Christiaens, D. et al. (2019) 'Fetal diffusion MRI acquisition and analysis in the developing Human ConnectomeProject.'

Poster No 393

A cross-etiologic study: altered network integration and modularity in newborns with severe diseases

Anna Speckert[1,2,3,4], Kelly Payette[5], Walter Knirsch[1,6,7], Michael Von Rhein[8,4], Cornelia Hagmann[9,10,6], Patrice Grehten[11,10,6,7], Nicole Ochseinbein-Kölble[11,12,1], Raimund Kottke[11,10,6,7], Giancarlo Natalucci[13,14,1], Ueli Moehrlen[1,15,11,10], Lucca Mazzone[15,11,10,6], Martin Meuli[1,11], Beth Padden[10,16,6], Spina bifida study group Zurich study group Zurich[17], Beatrice Latal[18,4,1], Andras Jakab[1,2,4,3]

[1]University of Zurich, Zurich, Switzerland, [2]Neuroscience Center Zurich, University of Zurich, Zurich, Switzerland, [3]Center for MR Research, University Children's Hospital Zurich, Zurich, Switzerland, [4]URPP Adaptive Brain Circuits in Development and Learning, University of Zurich, Zurich, Switzerland, [5]King's College London, London, UK, [6]Children's Research Center, University Children's Hospital Zurich, Zurich, Switzerland, [7]Department of Diagnostic Imaging, University Children's Hospital Zurich, Zurich, Switzerland, [8]Child Development Center, University Children's Hospital Zurich, Zurich, Switzerland, [9]Department of Neonatology, University Children's Hospital Zurich, Zurich, Switzerland, [10]Zurich Center for Spina Bifida, University Children's Hospital Zurich, Zurich, Switzerland, [11]The Zurich Center for Fetal Diagnosis and Therapy, Zurich, Switzerland, [12]Department of Obstetrics, University Hospital of Zurich, Zurich, Switzerland, [13]FLRF Center for Neurodevelopment, Growth and Nutrition of the Newborn, Zurich, Switzerland, [14]NGM Research Center, University Hospital Zurich, Zurich, Switzerland, [15]Department for Pediatric Surgery, University Children's Hospital Zurich, Zurich, Switzerland, [16]Division of Pediatric Rehabilitation, University Children's Hospital Zurich, Zurich, Switzerland, [17]Spina Bifida Study Group Zurich, Zurich, Switzerland, [18]Child Development Centre, University Children's Hospital Zurich, Zurich, Switzerland

Introduction: The human brain connectome is characterized by the duality of highly modular structure and efficient integration, supporting information processing[8]. Newborns with congenital heart disease (CHD)[5], prematurity[3], or spina bifida (SB) aperta[4] are at risk for altered brain development and developmental delay (DD), which refers to a deviation from expected developmental milestones[6]. We hypothesize that in cognitive DD, neural circuitry impairments are reflected by alterations of this connectomic organization. Our study aims to bridge this knowledge gap by using a multi-etiologic neonatal dataset to reveal potential commonalities and distinctions in the structural brain connectome and their associations with DD.

Methods: We used diffusion MRI (dMRI) on 187 neonates (42 controls, 51 CHDs, 51 preterms, 43 SB aperta). Axial dMRI data acquisition used a pulsed gradient spin-echo echo-planar imaging sequence (TR/TE 3950/90.5 ms, field of view=18 cm, matrix=128×128, slice thickness=3 mm) with 35 diffusion encoding gradient directions at a b-value of 700 s/mm2 and four b=0 images on a 3.0T MRI. The DTI sequence for preterms differed in the number of diffusion directions (21, b=1000 s/mm2). Structural connectomic analysis involved the following steps: denoising, eddy-current with slice-to-volume correction[1] and B1 bias field inhomogeneity correction. Weighted networks were constructed using constrained spherical deconvolution-based probabilistic anatomically constrained tractography from the MRtrix3 Software[7] and the Edinburgh Neonatal Atlas[2]. The assessment of connectomic structure included measures of global efficiency, modularity, and rich club coefficient. To facilitate cross-dataset comparisons by normalization, null-network models were utilized by randomizing the network edges while preserving degree-, weight- and strength- distributions[9]. The Cognitive Composite Score of the Bayley Scales of Infant and Toddler Development-III was used as outcome measure at 2 years for children born premature and with SB, and at 1 year for the control and CHD children.

Results: We revealed differences in the connectomic structure of newborns across each of the four groups after visualizing the connectomes in a two-dimensional morphospace defined by network integration and segregation (Fig. 1). Further, ANCOVA analyses, after adjustment for postmenstrual age at scan and gestational age at birth, revealed differences in global efficiency ($F(3, 182)=7.66$, $p<0.0001$), modularity ($F(3, 182)=16.97$, $p<0.0001$) and mean rich club coefficient ($F(3, 182)=3.50$, $p=0.017$) between groups. Post hoc analysis was performed with a Bonferroni adjustment (Fig. 2). The normalized mean global efficiency score was significantly greater in premature babies (-6.44+/-0.94) compared to CHDs (-10.1+/-0.50). Additionally, the mean global efficiency score was higher in SB (-7.89+/-0.38) compared to controls (-9.82+/-0.46), and CHDs, $p<0.001$. Further, the normalized mean modularity score was significantly greater in CHDs (16.5+/-0.5) compared to SB (13.4+/-0.38) and controls (15.3+/-0.46). SB newborns showed lower mean modularity than controls, $p<0.001$. Lastly, the normalized mean rich club coefficient was found to be significantly greater in SB (0.55+/-0.18) compared to controls (-0.13+/-0.21). However, in our analysis, we found no significant association between the identified neural connectivity patterns and cognitive outcome scores. This lack of association was true for both the overall study and specific for within group analysis.

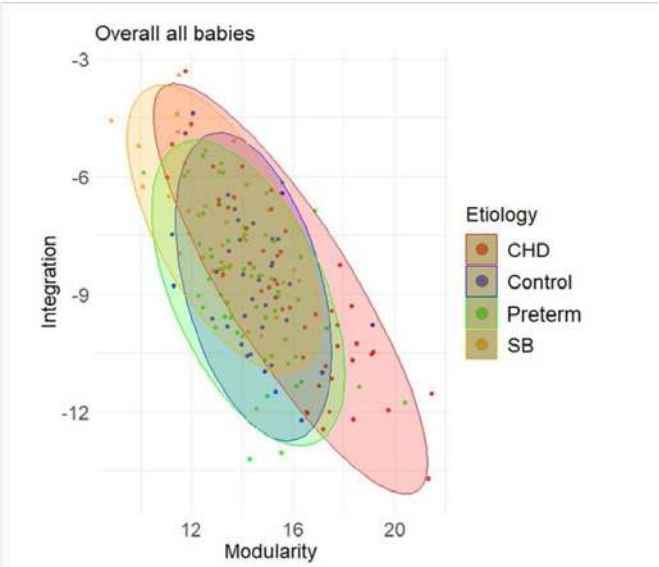

Fig. 1. Morphospace with z-normalized scores of modularity and integration (measured by global efficiency) of 42 controls, 51 CHDs, 43 SB aperta and 51 preterms.

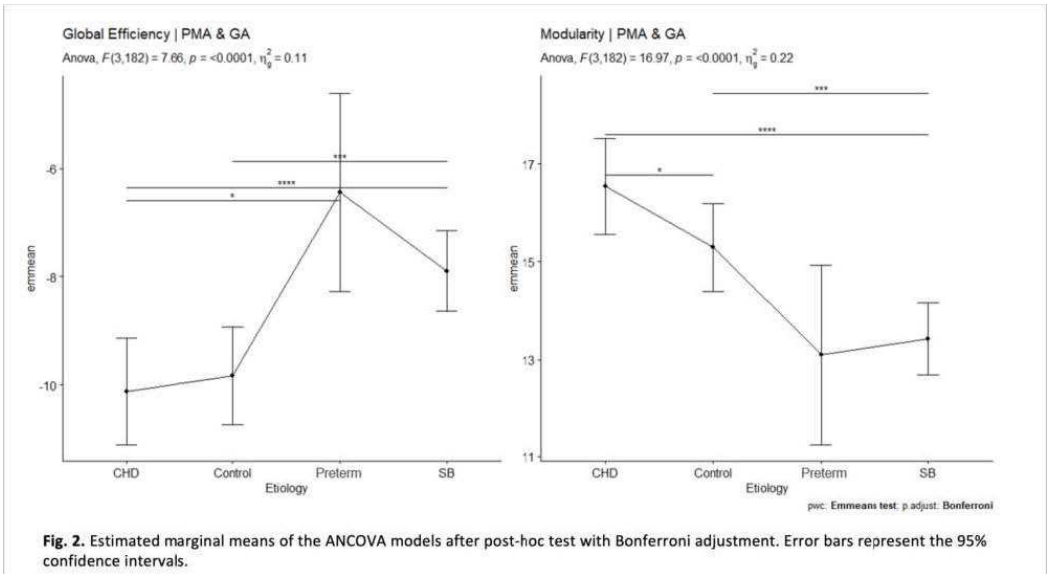

Fig. 2. Estimated marginal means of the ANCOVA models after post-hoc test with Bonferroni adjustment. Error bars represent the 95% confidence intervals.

Conclusions: In this cross-etiologic study, we identified divergent profiles of the structural brain connectome characterized by a deviation from the optimal combination of network integration and segregation. Early cognitive developmental outcomes were not yet associated with alterations in the organization of the connectome. Further work is necessary to find out if longer term cognitive outcomes are determined by such connectomic alterations.

References

1. Andersson, J. L. (2017), 'Towards a comprehensive framework for movement and distortion correction of diffusion MR images: Within volume movement', Neuroimage, vol. 152, pp. 450-466.
2. Blesa, M. (2016), 'Parcellation of the healthy neonatal brain into 107 regions using atlas propagation through intermediate time points in childhood', Frontiers in neuroscience, vol. 10, pp. 220.
3. de Almeida, J. S. (2021), 'Preterm birth leads to impaired rich-club organization and fronto-paralimbic/limbic structural connectivity in newborns', NeuroImage, vol. 225, pp. 117440.
4. Lomax-Bream, L. E. (2007), 'The impact of spina bifida on development across the first 3 years', Developmental Neuropsychology, vol. 31, no. 1, pp. 1-20.
5. Mussatto, K. A. (2014), 'Risk and prevalence of developmental delay in young children with congenital heart disease', Pediatrics, vol. 133, no. 3, pp. e570-e577.
6. Petersen, M. C. (1998), 'Classification of developmental delays. In Seminars in pediatric neurology', WB Saunders, vol. 5, no. 1, pp. 2-14.
7. Tournier J.D. (2019), 'MRtrix3: A fast, flexible and open software framework for medical image processing and visualisation', NeuroImage, vol. 202, pp. 116–37.
8. van den Heuvel, M. P. (2019), 'A cross-disorder connectome landscape of brain dysconnectivity', Nature reviews neuroscience, vol. 20, no. 7, pp. 435-446.
9. Váša, F. (2022), 'Null models in network neuroscience', Nature Reviews Neuroscience, vol. 23, no. 8, pp. 493-504.

Poster No 394

Machine-Learning-based classification of Autism Spectrum Disorder using heterogeneous factors

Yong Jeon Cheong[1], Jihyun Bae[2], Seonkyoung Lee[1], Ji Hyeong Ro[3], Hirotaka Kosaka[4], Minyoung Jung[1]

[1]Korea Brain Research Institute, Daegu, Republic of Korea, [2]Korea Brain Research Institude, Daegu, Republic of Korea, [3]Korea Brain Research Institute, Daegu, Korea, Republic of, [4]University of Fukui, Fukui,Japan

Introduction: Autism Spectrum Disorder (ASD) is characterized by a broad range of behavioral symptoms including atypical sensory responses, which reflects the etiologic heterogeneity of the disorder. There is increasing evidence on the effects of epigenetic modifications (e.g., DNA methylation; DNAm) on structure and function of the autistic human brain. Additionally, ASD is characterized by altered sensory response and altered thalamic-sensory hyperconnectivity. Integrating various features derived from epigenetic (i.e., DNAm values of oxytocin receptor (OXTR) and arginine vasopressin receptor (AVPR) genes), brain-related (i.e., volumes of cortical and subcortical regions, and values of resting-state functional connectivity (rs-FC)), and sensory behavioral factors and applying a supervised machine learning (i.e., XGBoost), this study aims to identify core features of the disorder by building three different models : 1) Full model includes the three factors, 2) Brain model has the brain-related and behavioral factors, and 3) Epigenetic model contains the epigenetic and behavioral factors.

Methods: This study includes 34 individuals with ASD (F = 12, mean [SD] age = 26.0 [4.24] years old) and 72 IQ-matched neurotypical individuals (F = 39, mean [SD] age = 32.0 [12.73] years old). We extracted DNAm values of OXTR and AVPR genes from the participants' salivary samples. Using a 3-T MR scanner, structural and functional MRI data were collected. The participants completed Adolescent/Adult Sensory profile that allows us to assess the level of abnormality of sensory behavior. Considering a small sample size with high dimensionality, we initially selected 30 baseline predictive features (i.e., 9 epigenetic, 11 brain-related, 7 behavioral and 3 demographic features) showing group difference. We split data for training (80%) and testing (20%). For each iteration, 80% of training data was used for validation. Next, we built training model while applying an ensemble feature selection procedure (i.e., feature occurrence frequency method) and an automatic hyperparameter tuning in an iterative manner. Last, the top 19 features showing the most discriminative power and best tuned hyperparameters were fed into XGBoost for testing. We estimated the area under the curve for receiver operator characteristic curves (ROC-AUCs) 1000 times for testing model, and differences in estimated accuracies were tested: 1) between Full and Brain model, 2) between Full and Epigenetic model, and 3) between Brain and Epigenetic model. To prevent the risk of overfitting and to minimize the problems derived from data imbalance, we performed our analyses using stratified 10-fold cross validation.

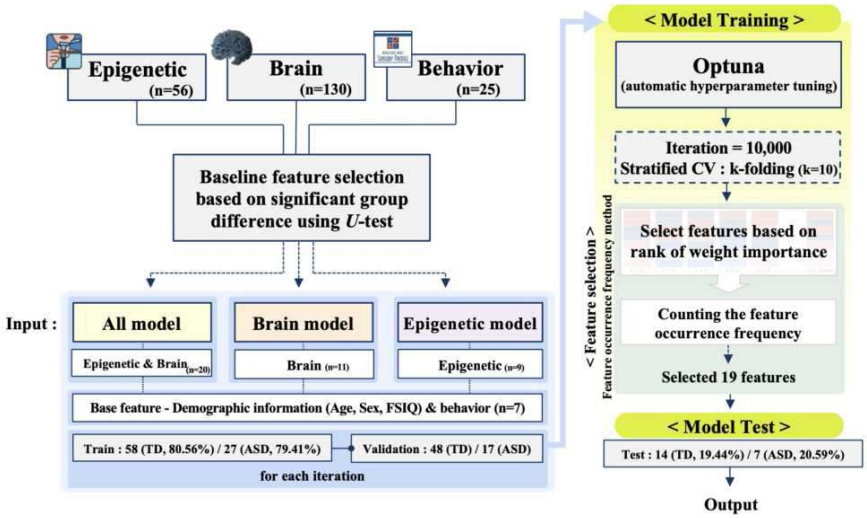

Results: We achieved average F1-score 0.832 (median = 0.83, interquartile range (IQR) = 0.88 – 0.79) and average ROC-AUC 0.8395 (median = 0.8214; IQR = 0.8929–0.7857) for Full model. Brain model had average F1-score 0.809 (median = 0.82, IQR = 0.88 – 0.77) and average ROC-AUC 0.8119 (median = 0.8214, IQR = 0.8571–0.7500). Epigenetic model showed average F1-score 0.771 (median = 0.77, IQR = 0.83 – 0.72) and average ROC-AUC 0.7689 (median = 0.7857, IQR = 0.8214–0.7143). The F1 score of Full model was significantly different than that of Brain model (U = 577147, p = 1.951x10-9) and that of Epigenetic model (U = 707230, p = 2.2 x10-16). The F1 score of Brain model was higher different from that of Epigenetic model (U = 633078, p = 2.2x10-16). The ROC-AUC of Full model was significantly different than that of Brain model (U = 596070, p = 4.989x10-14) and that of Epigenetic model (U = 739199, p = 2.2x10-16). The ROC-AUC of Brain model was higher different from that of Epigenetic model (U = 643998, p = 2.2x10-16).

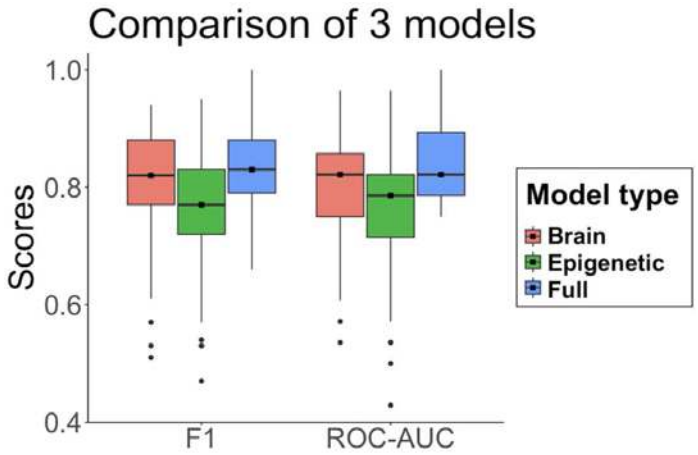

Conclusions: Full model showed higher performance in predicting ASD than Brain and Epigenetic model. Generalizable prediction of ASD can be achieved when considering interaction of epigenetic modification, brain function and structure, and sensory behaviors.

References

1. Andari, E. (2020), 'Epigenetic modification of the oxytocin receptor gene: implications for autism symptom severity and brain functional connectivity', Neuropsychopharmacology, vol. 45, no. 7, pp. 1150–1158
2. Chen, T. (2016), 'XGBoost: A scalable tree boosting system', Proceedings of the ACM SIGKDD International Conference on Knowledge Discovery and Data Mining, Association for Computing Machinery, pp. 785–794
3. Fu, Z. (2019), 'Transient increased thalamic-sensory connectivity and decreased whole-brain dynamism in autism', NeuroImage, vol. 190. pp. 191–204
4. Gregory, S. G. (2009), 'Genomic and epigenetic evidence for oxytocin receptor deficiency in autism', BMC Medicine, vol. 7, no. 82, doi:10.1186/1741-7015-7-62
5. Habata, K. (2021), 'Relationship between sensory characteristics and cortical thickness/volume in autism spectrum disorders', Translational Psychiatry, vol. 11, no. 616, doi: 10.1038/s41398-021-01743-7.
6. Hopkins, W. D. (2023), 'Vasopressin, and not oxytocin, receptor gene methylation is associated with individual differences in receptive joint attention in chimpanzees (Pan troglodytes)', Autism Research, vol. 16, no. 4, pp. 713–722
7. Insel, T. R. (2010) 'The Challenge of Translation in Social Neuroscience: A Review of Oxytocin, Vasopressin, and Affiliative Behavior', Neuron, vol. 65, no. 6. pp. 768–779
8. Ladd-Acosta, C. (2014), 'Common DNA methylation alterations in multiple brain regions in autism', Molecular Psychiatry, vol. 18, no. 9, pp. 862-871
9. Nair, A. (2013). 'Impaired thalamocortical connectivity in autism spectrum disorder: A study of functional and anatomical connectivity,' Brain, vol. 136, no. 6, pp. 1942-1955
10. Thye, M. D. (2018). 'The impact of atypical sensory processing on social impairments in autism spectrum disorder,' Developmental Cognitive Neuroscience, vol. 29. pp. 151-167

Poster No 395

Morphometry Longitudinal Study until Adolescence of Brain Growth after early lesion : Sex matters !

Pierre-Yves Postic[1], Yann Leprince[2], Soraya Brosset[1], Inès Ben Abdallah[1], Stephane Chabrier[3], Mickael Dinomais[4], Edouard Duchesnay[5], Lucie Hertz-Pannier[1]

[1]CEA Saclay NeuroSpin/UNIACT/InDEV, U1141/Inserm, Gif-sur-Yvette, Ile-de-France, [2]CEA Saclay Neurospin/UNIACT, Université Paris-Saclay, F-91191, Gif-sur-Yvette, Ile-de-France, [3]CHU Saint-Etienne, Saint-Etienne, Auvergne-Rhône-Alpes, [4]CHU Angers, Angers, Pays de la Loire, [5]CEA Saclay NeuroSpin/BAOBAB/GAIA/SIGNATURE, Université Paris-Saclay, F-91191, Gif-sur-Yvette, Ile-de-France

Introduction: While plasticity of the immature brain is deemed critical for optimized neurodevelopmental outcome, early brain lesions may result in enduring neurocognitive impairments[1], suggesting global dysfunction. However, the varied outcomes across individuals remain insufficiently elucidated. Neonatal ischemic stroke (NAIS) serves as a model for exploring the pivotal role of post-lesional plasticity in the immature brain. Among other variables, males represent 2/3 of NAIS cases, suggesting a potential sex-related effect on long-term neuroplasticity after early brain lesions. We performed a longitudinal morphometric study until adolescence of the growth dynamics of brain compartments within both ipsilesional and contralesional hemispheres in patients (P) with NAIS compared to controls (C), with a focus on sex differences.

Methods: The follow-up of the French AVCnn[2] cohort of neonates with unilateral NAIS involved clinical assessments and multimodal MRI imaging at ages 7 and 16. - P : age 7y, N = 39 (23 M, 16 F) ; age 16y, N = 29 (18 M, 11 F). No M/F significant differences of lesion severity nor side (2/3 left). - C : age 7y, N = 35 (17 M,18 F); age 16y, N = 31 (16 M, 15 F) - 22 P and 16 C assessed at both ages 3T MRI morphometry : 3DTI, 1mm and 0.9mm isotropic resolution at age 7 and 16, respectively Volumes were computed in Regions of interest (ROIs) in both ipsi- (ILH) and contra-lesional (CLH) hemispheres, and compared to C. In the ILH, ROIs were restricted to non-lesioned areas, using a combination of clinical and imaging criteria, with careful QC at each step. - Hemispheric white matter (WM), cortical grey matter (CGM) and total hemisphere (H) (CAT12, Hammers atlas[3,4]) - Lobar CGM (CerebrA atlas[5] registered from MNI to native space with ANTs[6]) - Sub-cortical GM structures (Vol2Brain[7], manually corrected) A finer investigation of the CLH involved regional CGM volumes and thickness. (CAT12, Desikan-Killiany atlas[8]). Metrics were analysed using a Generalized Linear Mixed Model (GLMM), with Age, Sex, Status (P vs. C), side and lesion severity, as co-variables. Post-hoc tests further compared P with C by age and sex.

Results: Models Factors (Fig1) showed expected developmental trajectories of most volumes in both groups: - Smaller volumes in females than in males at both ages, in P and C - CGM decreases, WM increases between 7 and 16 In patients, growth trajectories differed between ILH and CLH, according to lesion severity and sex. Lesion side had no impact on the hemisphere/lobar results, but showed varied impacts on finer assessment with the DK40 atlas (not shown here). ILH volumes were consistently 15% lower on average in patients than in controls, irrespective of age or sex (Fig2). Lesion severity impacted most ILH volumes, but not CLH ones (except caudate nucleus). In the CLH, male patients exhibited significantly lower volumes than controls, in all regions except the occipital lobe (-8 to -12%, significant). By contrast, female patients volumes were 2 to 5% larger than controls (not significant, except for the hippocampus and pallidum at age 16). These effects were similar at age 7 and 16.

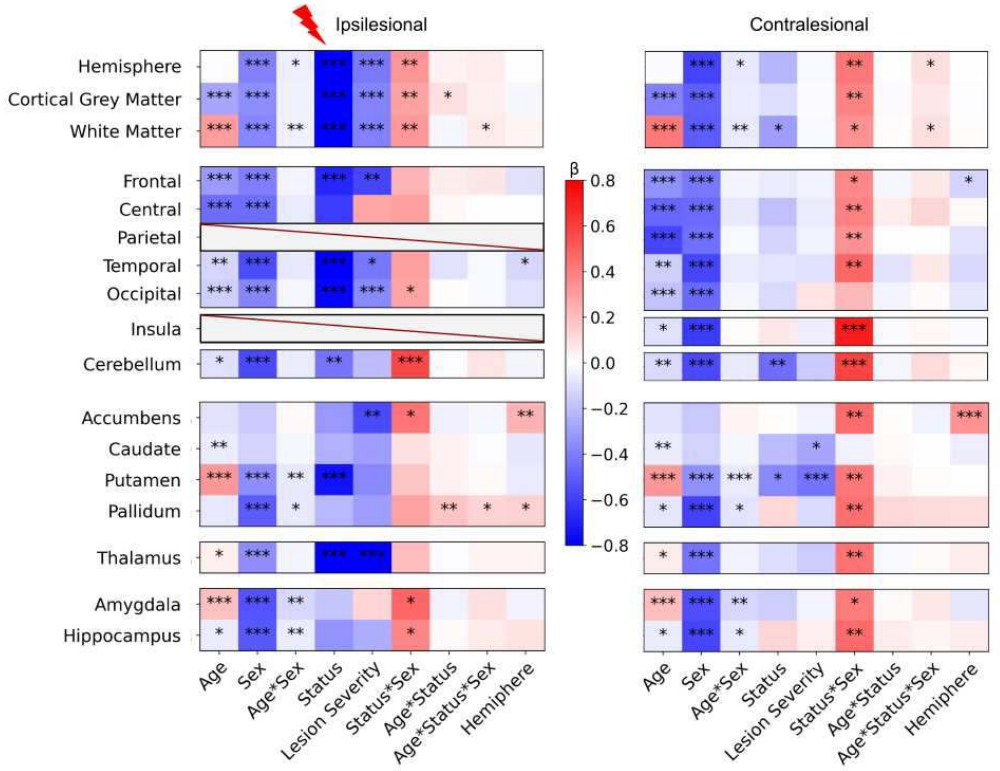

Fig1. GLMM coefficients values for each investigated subvolumes (fixed effects, main interactions and covariates).

Expressed as a proportion of the region dataset standard deviation (std) :

Reference population is control at 7 years old. Sex and Hemisphere side categorical variable are centered, with positive level for female and right hemisphere. Lesion severity is modelled by a standardized 5 level continuous covariate.

*Test if factors are significantly different from 0 : * : p<0.05, ** : p<0.01, *** : p<0.001 (uncorrected p-values)*

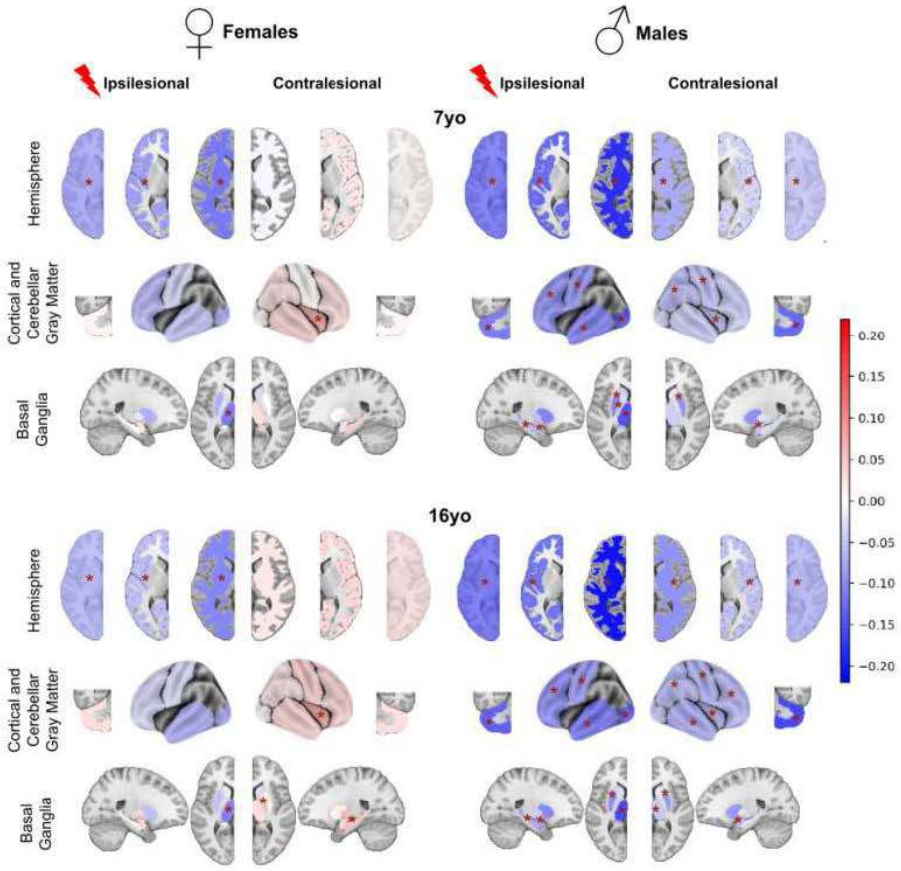

Fig2. Post hoc tests comparing patients and control for each age and sex (patient - controls).
Post-hocs tests comparing controls to patients mean volume.
Volumes differences are expressed as a percentage of mean control volume (across age and sex).
Statistic test if difference patient - control volume difference is significantly different from 0 :
** : $p < 0.05$ after False-Discovery Rate correction, with :*

- *3 tests for hemisphere-wise volumes*
- *6 tests for volumes in lobar atlas in contralesional hemisphere*
- *4 tests for volumes in lobar atlas in ipsilesional hemisphere*
- *7 tests for basal ganglia volumes*

Conclusions: Results show that the long-term impact of NAIS on ILH growth is mostly contingent on lesion severity. Conversely, the CLH is not affected by lesion severity, but shows sex-related differential effects, being more profoundly impacted in males, with females deviating minimally from the typical trajectory. This pattern is visible from childhood on, and puberty seems to exert minimal influence. Overall, these results are in line with the known perinatal vulnerability of male brains and their higher susceptibility to neurodevelopmental disorders. Preliminary clinical analyses suggest that sex-related variance of neurocognitive outcomes remains modest in comparison to other determinants, thus is often overlooked. Our results advocate for systematic differential analysis of sex effects when studying neurodevelopmental conditions.

References

1. Lehman, L. L., & Rivkin, M. J. (2014). Perinatal arterial ischemic stroke: presentation, risk factors, evaluation, and outcome. Pediatric neurology, 51(6), 760-768
2. Chabrier, S., Peyric, E., Drutel, L., Deron, J., Kossorotoff, M., Dinomais, M., ... & Vuillerot, C. (2016). Multimodal outcome at 7 years of age after neonatal arterial ischemic stroke. The Journal of pediatrics, 172, 156-161
3. Gaser, C., Dahnke, R., Thompson, P. M., Kurth, F., Luders, E., & Alzheimer's Disease Neuroimaging Initiative. (2022). CAT–A computational anatomy toolbox for the analysis of structural MRI data. biorxiv, 2022-06
4. Hammers, A., Allom, R., Koepp, M. J., Free, S. L., Myers, R., Lemieux, L., ... & Duncan, J. S. (2003). Three-dimensional maximum probability atlas of the human brain, with particular reference to the temporal lobe. Human brain mapping, 19(4), 224-247
5. Manera, A. L., Dadar, M., Fonov, V., & Collins, D. L. (2020). CerebrA, registration and manual label correction of Mindboggle-101 atlas for MNI-ICBM152 template. Scientific Data, 7(1), 237
6. Avants, B. B., Tustison, N., & Song, G. (2009). Advanced normalization tools (ANTS). Insight j, 2(365), 1-35
7. Manjón, J. V., Romero, J. E., Vivo-Hernando, R., Rubio, G., Aparici, F., de la Iglesia-Vaya, M., & Coupé, P. (2022). vol2Brain: A new online Pipeline for whole Brain MRI analysis. Frontiers in Neuroinformatics, 16, 862805
8. Desikan, R. S., Ségonne, F., Fischl, B., Quinn, B. T., Dickerson, B. C., Blacker, D., ... & Killiany, R. J. (2006). An automated labeling system for subdividing the human cerebral cortex on MRI scans into gyral based regions of interest. Neuroimage, 31(3), 968-980

Poster No 396

Braincharting autism and ADHD reveals age- and sex- specific effects

Saashi Bedford[1], Meng-Chuan Lai[2], Michael Lombardo[3], Bhismadev Chakrabarti[4], Amber Ruigrok[5], John Suckling[6], Evdokia Anagnostou[7], Jason Lerch[8], Margot Taylor[9], Rob Nicolson[10], Georgiades Stelios[11], Jennifer Crosbie[12], Russell Schachar[9], Elizabeth Kelley[13], Jessica Jones[13], Paul Arnold[14], Eric Courchesne[15], Karen Pierce[16], Lisa Eyler[17], Kathleen Campbell[16], Cynthia Carter Barnes[16], Jakob Seidlitz[18], Aaron Alexander-Bloch[18], Edward Bullmore[6], Simon Baron-Cohen[6], Richard Bethlehem[19]

[1]University of Cambridge, Cambridge, Select State/Province, [2]Centre for Addiction and Mental Health, Toronto, Ontario, [3]Laboratory for Autism and Neurodevelopmental Disorders, Istituto Italiano di Tecnologia, Rovereto, Italy, [4]University of Reading, Reading, Berkshire, [5]University of Manchester, Manchester, Lancashire, [6]University of Cambridge, Cambridge, United Kingdom, [7]University of Toronto, Toronto, Ontario, [8]Wellcome Centre for Integrative Neuroimaging, University of Oxford, Oxford, Oxford, [9]Hospital for Sick Children, Toronto, Ontario, [10]University of Western Ontario, London, Ontario, [11]McMaster University, Hamilton, Ontario, [12]The Hospital for Sick Children, Toronto, Ontario, [13]Queen's University, Kingston, Kingston, Ontario, [14]University of Calgary, Calgary, Alberta, [15]University of California San Diego, San Diego, CA, [16]University of California San Diego, San Diego, California, [17]University of California San Diego, La Jolla, CA, [18]University of Pennsylvania, Philadelphia, PA, [19]Autism Research Centre, Department of Psychiatry, University of Cambridge, Cambridge, United Kingdom

Introduction: Autism and attention-deficit/hyperactivity disorder (ADHD) are heterogeneous neurodevelopmental conditions with complex underlying neurobiology, and neuroanatomical alterations have been reported in both[1–3]. Both conditions show significant sex and age modulations on neuroanatomy[3,4], which are not yet fully understood. Normative modelling is an emerging technique that provides a unified framework for studying age- and sex-specific divergence in brain development in a common space[5]. We aimed to characterise regional cortical and global neuroanatomy in autism and ADHD, as well as sex and age differences, benchmarked against models of typical brain development based on a sample of over 75,000 individuals.

Methods: We combined T1-weighted MRIs from 49 sites across 7 datasets, for a total dataset of 4255 participants after quality control (1869 controls, 987 ADHD, 1399 autism; ages 2-64 years). Images were processed using FreeSurfer[6] 6.0.1, and regional cortical estimates extracted based on the Desikan-Killiany[7] atlas, for cortical thickness (CT), volume (CV) and surface area (SA). We also examined total grey and white matter volume, subcortical grey matter volume, ventricular volume, mean CT and total SA. We used normative reference models[8] previously generated by our group to map neuroanatomical developmental trajectories across the lifespan for global and regional neuroanatomical measures, accounting for age, sex and site/scanner. Out-of-sample normative centile scores for our study sample were generated based on these models, quantifying divergence from normative brain development in our sample. We examined diagnostic group differences in centile scores, and the interaction between diagnosis and sex, for all global volumes and regional cortical measures using multiple linear regressions. To examine age differences, we conducted a sliding-window age analysis to examine diagnostic group differences across development, in age intervals of 5 years, starting at 2 years and sliding by 1 year. We selected a random subset of 70 participants per group, bootstrapped 1000 times, and examined diagnostic group differences at each age interval, averaged across the 1000 bootstraps. This allowed us to determine change in group differences across development, and the age window with the maximum diagnostic group difference.

Results: All results were significant at 5% false discovery rate. For global measures, individuals with ADHD had significantly lower total cortical and subcortical grey and white matter volumes, and total cortical SA centile scores (d = -0.13- -0.18), but greater mean CT centiles (d = 0.09) relative to controls. Autistic individuals had significantly larger ventricular volume centiles relative to controls (d = 0.15). Individuals with ADHD showed regional CT increases (d = 0.09-0.10) but lower CV and SA centiles (d = -0.07- -0.18) across much of the cortex. Autistic individuals showed greater regional CT and CV localised to the superior temporal cortex (STG; d = 0.13-0.15). There was a significant sex-by-diagnosis interaction, and distinct diagnostic differences by sex for autism, but not for ADHD, where autistic males had greater CV and CT in the STG, but autistic females had lower SA in the fusiform gyrus, relative to controls. For autism, diagnostic group differences for the STG were strongest in the youngest age windows, across all cortical measures. For SA, and to a slightly less extent CV, this was also the case in most frontal and parietal regions. For CT, most other regions had the strongest effects in later ages, around 15-20 years. Group differences in ADHD were typically strongest at the latest age windows, starting at 14-15 years of age. Some regions showed the strongest differences in the youngest windows, including the STG for SA, and some frontal and parietal areas.

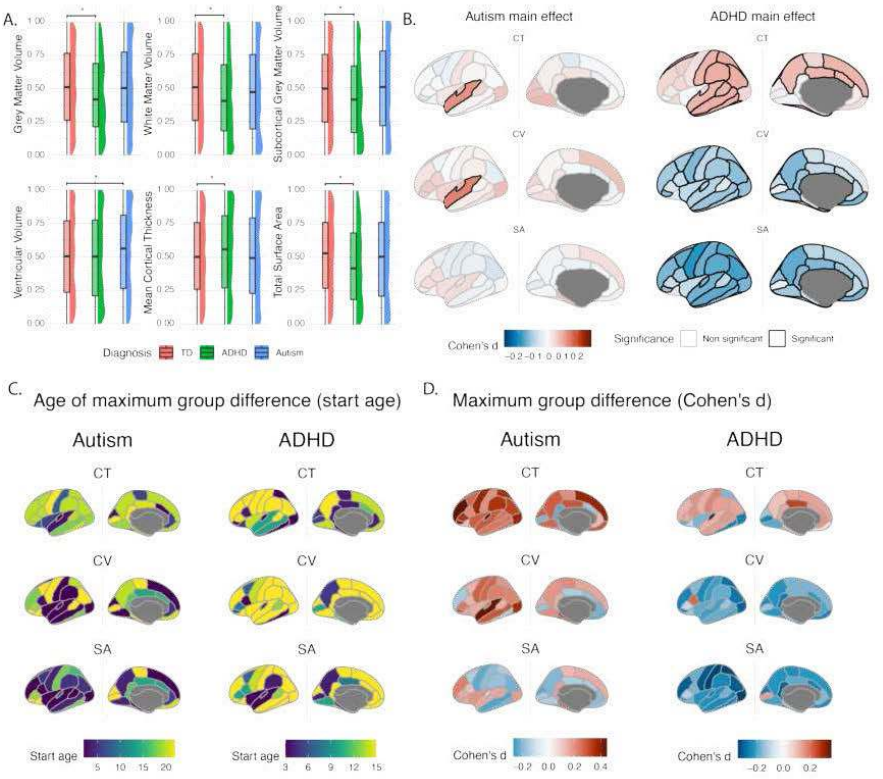

Figure 1. A. Box and raincloud plots showing the density of global neuroanatomical centiles by diagnostic group. Autistic individuals had significantly larger ventricles than non autistic individuals, but no differences were observed in any other measures. Individuals with ADHD had significantly lower cortical grey, white, and subcortical grey matter volume and total surface area centiles relative to controls, but greater mean cortical thickness centiles. B. Regional group differences. Brain maps show Cohen's D effect sizes, with significant regions (passing 5% FDR) outlined in black. Red represents positive effect sizes (autism or ADHD > controls), and blue represents negative effect sizes (autism or ADHD < controls). Autistic individuals had significantly greater CV and CT in the superior temporal gyrus. Individuals with ADHD had significant and widespread decreases in CV and SA, and increases in CT. C. Age of maximum group difference in autism and ADHD, based on largest Cohen's d effect size. Colours represent the start age of the 5-year age window. D. Maximum group difference (Cohen's d effect size) across age windows in autism and ADHD. Red represents positive effect sizes (autism or ADHD > controls), and blue represents negative effect sizes (autism or ADHD < controls).

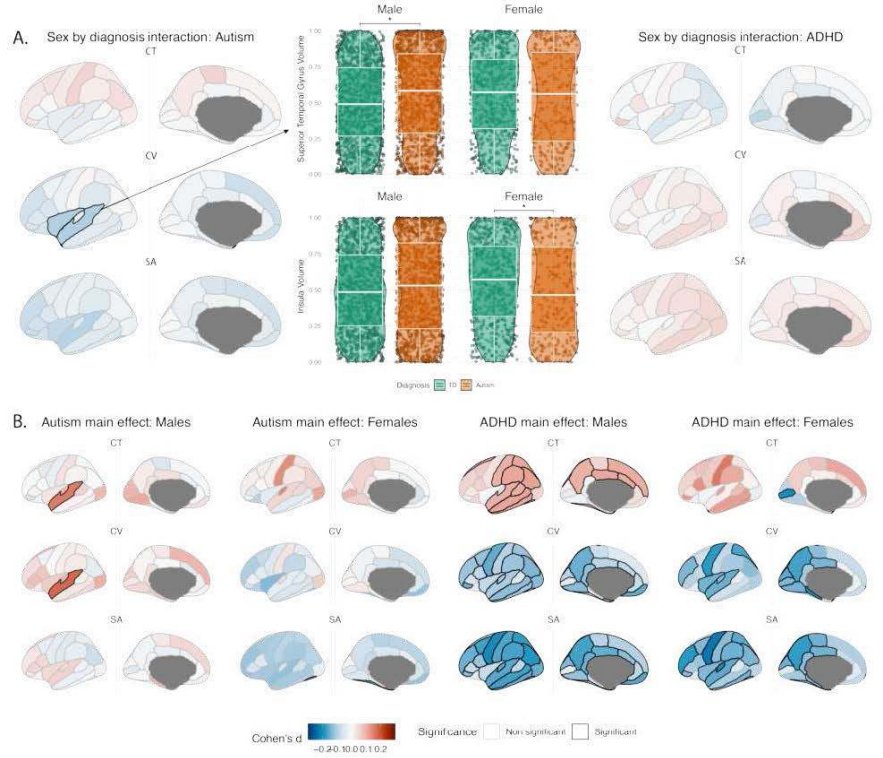

Figure 2. A. Interaction between diagnosis and sex. Brain maps showing effect sizes and significance of interaction per brain region, and box and violin plots showing comparison of values broken down by group for two significant regions. B. Sex-stratified regional association with diagnosis. All maps show Cohen's D effect sizes, with significant regions (passing 5% FDR) outlined in black. Red represents positive effect sizes (autism or ADHD > controls), and blue represents negative effect sizes (autism or ADHD < controls).

Conclusions: These results indicate distinct cortical differences in autism and ADHD that are differentially impacted by age and sex.

References
1. Luo Y, Weibman D, Halperin JM, Li X. A Review of Heterogeneity in Attention Deficit/Hyperactivity Disorder (ADHD). Front Hum Neurosci. 2019;13: 42.
2. Ecker C. The neuroanatomy of autism spectrum disorder: An overview of structural neuroimaging findings and their translatability to the clinical setting. Autism. 2017;21: 18–28.
3. Bedford SA, Park MTM, Devenyi GA, Tullo S, Germann J, Patel R, et al. Large-scale analyses of the relationship between sex, age and intelligence quotient heterogeneity and cortical morphometry in autism spectrum disorder. Mol Psychiatry. 2020;25: 614–628.
4. Mo K, Sadoway T, Bonato S, Ameis SH, Anagnostou E, Lerch JP, et al. Sex/gender differences in the human autistic brains: A systematic review of 20 years of neuroimaging research. NeuroImage Clinical. 2021;32. doi:10.1016/J.NICL.2021.102811
5. Marquand AF, Kia SM, Zabihi M, Wolfers T, Buitelaar JK, Beckmann CF. Conceptualizing mental disorders as deviations from normative functioning. Molecular Psychiatry. Nature Publishing Group; 2019. pp. 1415–1424. doi:10.1038/s41380-019-0441-1
6. Fischl B, Dale AM. Measuring the thickness of the human cerebral cortex from magnetic resonance images. Proc Natl Acad Sci U S A. 2000;97: 11050–11055.
7. Desikan RS, Ségonne F, Fischl B, Quinn BT, Dickerson BC, Blacker D, et al. An automated labeling system for subdividing the human cerebral cortex on MRI scans into gyral based regions of interest. 2006. doi:10.1016/j.neuroimage.2006.01.021
8. Bethlehem RAI, Seidlitz J, White SR, Vogel JW, Anderson KM, Adamson C, et al. Brain charts for the human lifespan. Nature. 2022;604: 525–533.

Poster No 397

Transdiagnostic mapping of corticostriatal circuit for behavior and cognition in autism and ADHD

Han Byul Cho[1], Hyunhoe An[1,2], Shinwon Park[3], Seok-Jun Hong[1,2,4,5]

[1]Center for Neuroscience Imaging Research, Institute for Basic Science, Suwon, Republic of Korea, [2]Department of Biomedical Engineering, Sungkyunkwan University, Suwon, Republic of Korea, [3]Autism Center, Child Mind Institute, New York, United States, [4]Life-inspired Neural network for Prediction and Optimization Research Group, Suwon, Republic of Korea, [5]Center for the Developing Brain, Child Mind Institute, New York, United States

Introduction: Autism spectrum disorder (ASD) and attention-deficit/hyperactivity disorder (ADHD) are the two highly comorbid developmental conditions that are characterized by heterogeneous behavioral phenotypes[1,2]. Previous studies targeting both ASD and ADHD suggested that some of their behavioral symptoms are commonly linked to the altered function of the corticostriatal circuit-a core structure for executive function[3-6]. However, those studies frequently relied on comparisons between case-control groups informed by clinically diagnosed labels, which leaves space for further exploration into the true essence of 'transdiagnostic research'. Here, we address this issue by performing a fully dimensional approach, where we pool the data of all individuals with ASD or/and ADHD and comprehensively phenotype the relationship between their behavioral spectrum and corticostriatal functional connectivity (FC), regardless of their labels.

Methods: We analyzed the male-only data of 23 ASD, 111 ADHD, 61 comorbid ASD+ADHD and 35 neurotypical (NT) individuals derived from Healthy Brain Network[7] (age: 6-21 years). The two dimensionality reduction techniques were employed: First, we performed a factor analysis to identify the bases underlying common variance of behavioral symptoms across all subjects (Fig.1A). Second, the Partial least squares (PLS) analysis investigated the correlation between resting-state FC of corticostriatal circuits and behavior symptoms (Fig.1B). We employed a permutation test (1,000 iterations) for the significance of the PLS analysis. Moreover, the composite scores from PLS (for both FC and behavioral symptoms) were sorted out into three different bins (bottom 20%, middle 60%, top 20%) to quantitatively assess the gradual changes on this brain-behavior axis (Fig.2A). After these analyses, we further performed ANOVA to identify the differences of factor scores and cognitive performance (assessed by NIH toolbox cognition battery)[8] between the diagnostic labeled groups as well as between the three binned groups based on the PLS scores above.

Results: Factor analysis identified four behavioral bases (i.e., 'social problems', 'impulsive behavior', 'emotional problems', and 'repetitive behavior'; Fig.1A), each providing a component score across all individuals. The following PLS analysis revealed a significant association between these behavioral component scores and corticostriatal FC (permutation $p = 0.05$; Fig.1B,C) across individuals, regardless of the diagnostic groups. We also checked the effect of diagnosis by extracting the PLS component scores for both corticostriatal FC and behavior symptoms and comparing them between the clinically labeled groups including NT. In this analysis, the comorbid group (ASD+ADHD) showed the most negative PLS score, suggesting their severe symptoms and corticostriatal connectivity abnormalities (Fig.1D). In the one way ANOVA with clinical diagnosis as an independent variable, each behavior score in ASD and ADHD exhibited significant impairment compared to other groups (Fig.1E). In particular, the ASD group showed a significantly lower score for cognitive flexibility, corroborating previous

findings[9] (Fig.1F). The same analysis based on the PLS-score based three binned groups revealed significant differences for the behavior scores (Fig.2B). In the assessment of cognitive performance, however, the score showed only a trend of positive correlation, except for the working memory (Fig.2C).

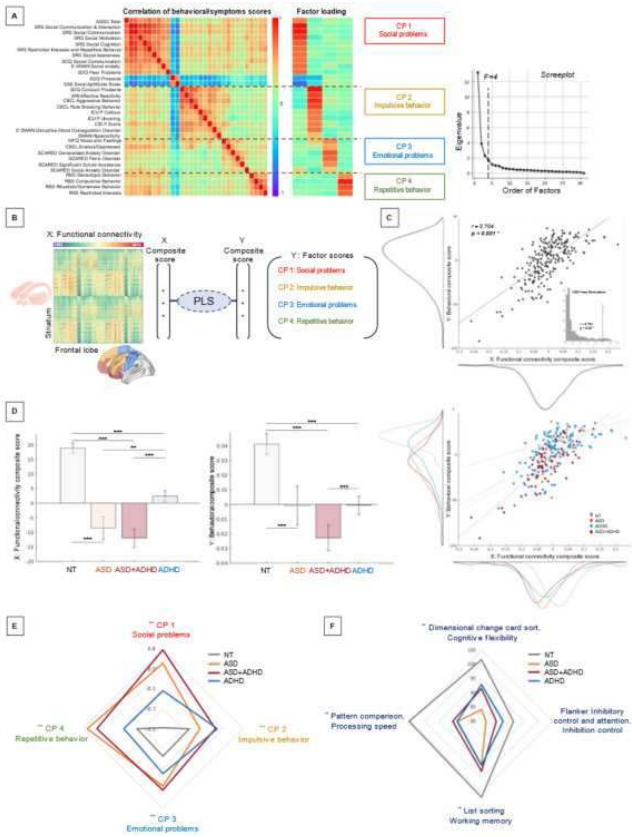

Figure 1.
(A) Factor analysis for the assessments of behavioral symptoms. Four behavior components were determined based on the scree plot of eigenvalue. The extracted components were labeled as 'social problems', 'impulsive behaviors', 'emotional problems', and 'repetitive behavior'.
(B) Correlations between corticostriatal functional connectivity and behavior component scores were quantified using PLS.
(C) A scatter plot with histograms illustrates the relationship between functional connectivity and behavioral composite scores derived from PLS. Significance testing between the functional connectivity composite score and the behavioral symptoms composite score ($r = 0.704$, $p < 0.001$) was performed using a permutation test (1,000 iterations; $p < 0.05$).
(D) Significance in differences among clinical diagnostic groups was assessed for both functional connectivity composite scores (left bar graph) and behavioral symptoms composite scores (middle bar graph). The scatter plot with histograms in (C) (on the right) displays the overlapped distribution of clinical diagnostic groups. PLS composite scores effectively explained the impaired corticostriatal functional connectivity observed in diagnosed neurodevelopmental disorders. Within the ASD, ADHD and comorbid ASD+ADHD, the functional connectivity composite score accurately distinguished the presence of ASD. Meanwhile, the behavioral composite score effectively differentiated the presence of comorbidity compared to the pure diagnosis group.
(E) A radar plot illustrating the average and differences of each extracted behavioral component score among clinical diagnosis groups. For all components, the clinical diagnosis group exhibited significantly higher behavioral symptoms severity component scores compared to the NT, excluding CP 2 Impulsive behavior score. Within the ASD, ADHD, and comorbid ASD+ADHD, CP 1 Social problems score and CP 4 Repetitive behavior score were significantly higher in the ASD and comorbid ASD+ADHD compared to the ADHD. The CP 3 Emotional problems score was significantly higher in the comorbid ASD+ADHD compared to the ADHD and NT. CP 2 Impulsive behavior score showed no significant difference between the NT and ASD, while those diagnosed with ADHD exhibited significantly higher scores.
(F) A radar plot depicting the average and differences in each cognition test score by NIHTB-CB among clinical diagnosis groups. The dimensional change card sort test exhibited a significantly lower score in the ASD-diagnosed group compared to the NT. The list sorting working memory test and pattern comparison test showed lower scores in the clinical diagnosis group than the NT. The flanker inhibitory control and attention test revealed no significant differences between the groups.

$^{*}p < 0.05$, $^{**}p < 0.01$, $^{***}p < 0.001$
Abbreviations. CP, Component; PLS, Partial least squares analysis; NT, Neurotypical control; ASD, Autism spectrum disorder; ADHD, Attention deficit hyperactivity disorder; ASD+ADHD, Comorbid ASD and ADHD; NIHTB-CB, NIH toolbox cognition battery.

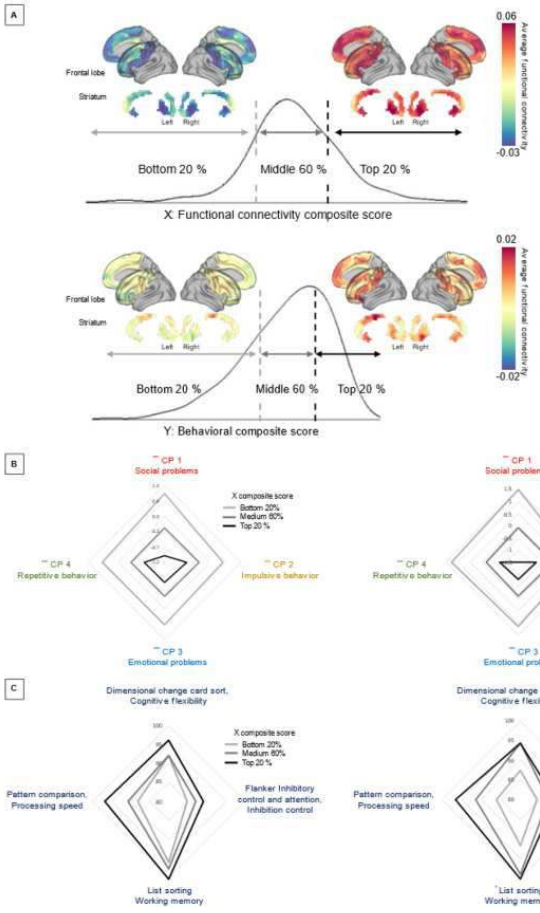

Figure 2.
(A) The histograms representing the distribution of quantified corticostriatal functional connectivity composite scores and behavioral symptoms composite scores obtained from PLS. Each composite score was sorted out in three different bins: bottom 20%, middle 60%, top 20%. Maps of functional connectivity in corticostriatal circuits illustrate the average functional connectivity at the bottom 20% and top 20% stages in each functional connectivity composite score and behavioral composite score.
(B) Radar plots illustrating the average and differences of composite scores segmented into three stages for each extracted behavioral component score. All component scores showed significant differences between the segmented stages of both composite scores.
(C) Radar plots depicting the average composite scores segmented into three stages for each cognition test score. Although each cognition test score displayed trends of positive association to the corresponding composite score calculated by PLS, there were no statistically significant differences among the stages, except for list sorting working memory in the behavioral composite score ($F = 4.49$, $p < 0.05$).

$^{*}p < 0.05$, $^{**}p < 0.01$, $^{***}p < 0.001$
Abbreviations. CP, Component; PLS, Partial least squares analysis; NT, Neurotypical control; ASD, Autism spectrum disorder; ADHD, Attention deficit hyperactivity disorder; ASD+ADHD, Comorbid ASD and ADHD; NIHTB-CB, NIH toolbox cognition battery.

Conclusions: In this study, we found compelling evidence of a common biological axis that transgresses the boundaries of clinically diagnosed ASD, ADHD and their comorbid groups. This axis revealed the spectrum of transdiagnostic pathogenicity on brain-behavior relationships as well as on cognitive performance, potentially indicating their shared developmental etiology and manifestation. Our findings can provide a novel insight to a neuroimaging-based disease modeling in the future RDoC research10.

References

1. Sinzig J et al (2009) 'Attention deficit/hyperactivity disorder in children and adolescents with autism spectrum disorder' Journal of Attention Disorders 13(2):117-2
2. Simonoff E. et al., (2008) 'Psychiatric disorders in children with autism spectrum disorders: prevalence, comorbidity, and associated factors in a population-derived sample' Journal of the American Academy of Child and Adolescent Psychiatry 47, 921–929.
3. Di Martino A et al (2011) 'Aberrant striatal functional connectivity in children with autism' Biological Psychiatry 69(9): 847–56.
4. Tomasi D et al., (2012) 'Abnormal functional connectivity in children with Attention-Deficit/Hyperactivity Disorder' Biological Psychiatry 71 (5): 443–50.
5. Uddin LQ, (2021) 'Cognitive and behavioural flexibility: neural mechanisms and clinical considerations' Nature Reviews Neuroscience 22(3): 167–79.
6. Westbrook A et al.,(2021) 'A mosaic of cost-benefit control over cortico-striatal circuitry' Trends in Cognitive Sciences 25(8): 710–21.
7. Alexander LM et al., (2017) 'An open resource for transdiagnostic research in pediatric mental health and learning disorders' Scientific data 4, 170181
8. www.nihtoolbox.org
9. Cho HB et al., Transdiagnostic mapping of striatal connectivity and behavior-circuit modeling in autism and ADHD. Canada. 2023.07.22-26. OHBM 2023.
10. RDoC Matrix. https://www.nimh.nih.gov/research/research-funded-by-nimh/rdoc/constructs/rdoc-matrix

Poster No 398

Transdiagnostic interindividual differences in brain coactivation dynamics in autism and ADHD

Phoebe Thomson[1], Patricia Segura[1], Shinwon Park[1], Michael Milham[1], Ting Xu[1], Adriana Di Martino[1]

[1]Child Mind Institute, New York, NY

Introduction: Collectively, 10% of children worldwide are affected by autism spectrum disorder (ASD) or attention-deficit/hyperactivity disorder (ADHD), and they often co-occur[1–3]. Current evidence points towards altered intrinsic brain functional connectivity with convergence on atypicalities in the default mode network (DMN) in both conditions. However, findings within and across diagnoses have been inconsistent[4–5]. Most prior work has focused on static connectivity and case-control comparisons that may obscure meaningful sources of heterogeneity. As such, dynamic connectivity and dimensional approaches are increasingly used to understand these neurodevelopmental conditions. Prior studies have revealed that greater time spent in a DMN dominant state is associated with fewer ASD symptoms[6] and greater ADHD symptoms[7]. However, these studies have been conducted in ASD and ADHD youth separately, and have not accounted for co-occurring symptoms in a single transdiagnostic sample. This study uses coactivation pattern (CAP) analysis to examine interindividual differences in the associations between dynamic connectivity and symptom severity of ASD and/or ADHD in a transdiagnostic youth sample.

Methods: Data from 166 children (6–12 years old) with ASD and/or ADHD (75% male) completed T1w structural and 6-minute resting state functional MRI (fMRI) scans on a 3T Prisma Siemens MRI scanner (fMRI: TR=800ms, TE=30ms, voxel size=2.4x2.4x2.4mm). Data with median framewise displacement (FD)<0.2 mm were preprocessed using the Configurable Pipeline for the Analysis of Connectomes (CPAC) version 1.7.2. CAP analysis was then run on fMRI timeseries (using the method from[8]) to derive 8 CAPs across the sample, and dwell times, occurrence rates, and incidence rates for each CAP and person. Pearson partial correlations tested for dimensional associations between CAP properties and ASD/ADHD symptom severity, covarying for age, sex and FD. Symptoms were measured using rigorous clinical measures, Autism Diagnostic Observation Schedule-2 (ADOS-2) total, Social Affect (SA), Restricted and Repetitive Behaviors (RRB) scores for ASD[9], and Kiddie Schedule for Affective Disorders and Schizophrenia (KSADS) total, hyperactivity/impulsivity (HI) and inattention (IN) scores for ADHD[10]. A priori analyses focused on CAPs showing coactivation in the DMN; further analyses explored behavior associations with properties of other identified CAPs.

Results: Two CAP pairs were identified with strong coactivation in the DMN (states 1/2 and 5/6; see Figure 1). Dwell time of CAP 6 positively correlated with ADOS-2 total scores (r=.18, p=.019; Figure 2A) and negatively correlated with KSADS ADHD totals (r=-.20, p=.011; Figure 2D). When separated by symptom subdomain, these correlations were specific to ADOS SA (r=.16, p=.039; Figure 2B) and KSADS HI (r=-.21, p=.008; Figure 2E) symptoms. There were no other correlations between properties of DMN-related states and ASD/ADHD symptoms. Exploratory analysis of visual and dorsal attention dominant CAP properties

revealed that lower incidence rate of the visually dominant CAP (state 3) was associated with higher ADOS-2 total severity (r=-.26, pFDR=.019) and SA (r=-.25, pFDR=.019) scores.

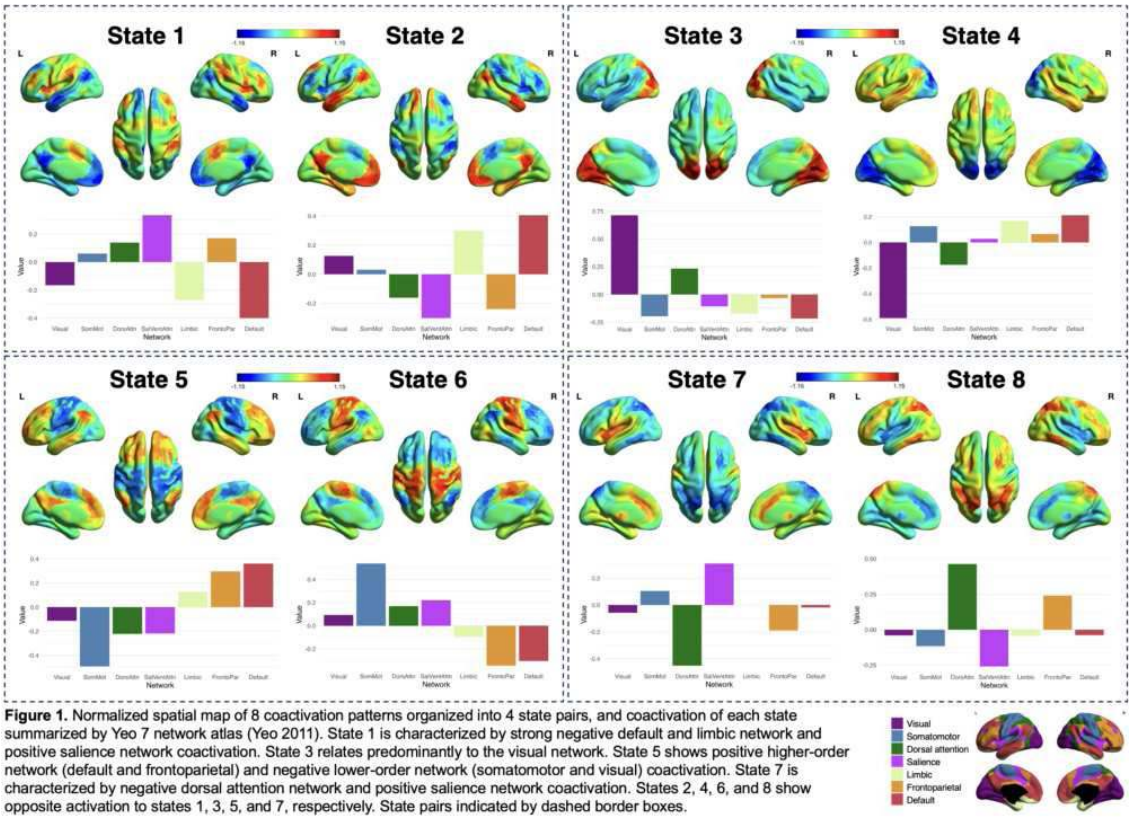

Figure 1. Normalized spatial map of 8 coactivation patterns organized into 4 state pairs, and coactivation of each state summarized by Yeo 7 network atlas (Yeo 2011). State 1 is characterized by strong negative default and limbic network and positive salience network coactivation. State 3 relates predominantly to the visual network. State 5 shows positive higher-order network (default and frontoparietal) and negative lower-order network (somatomotor and visual) coactivation. State 7 is characterized by negative dorsal attention network and positive salience network coactivation. States 2, 4, 6, and 8 show opposite activation to states 1, 3, 5, and 7, respectively. State pairs indicated by dashed border boxes.

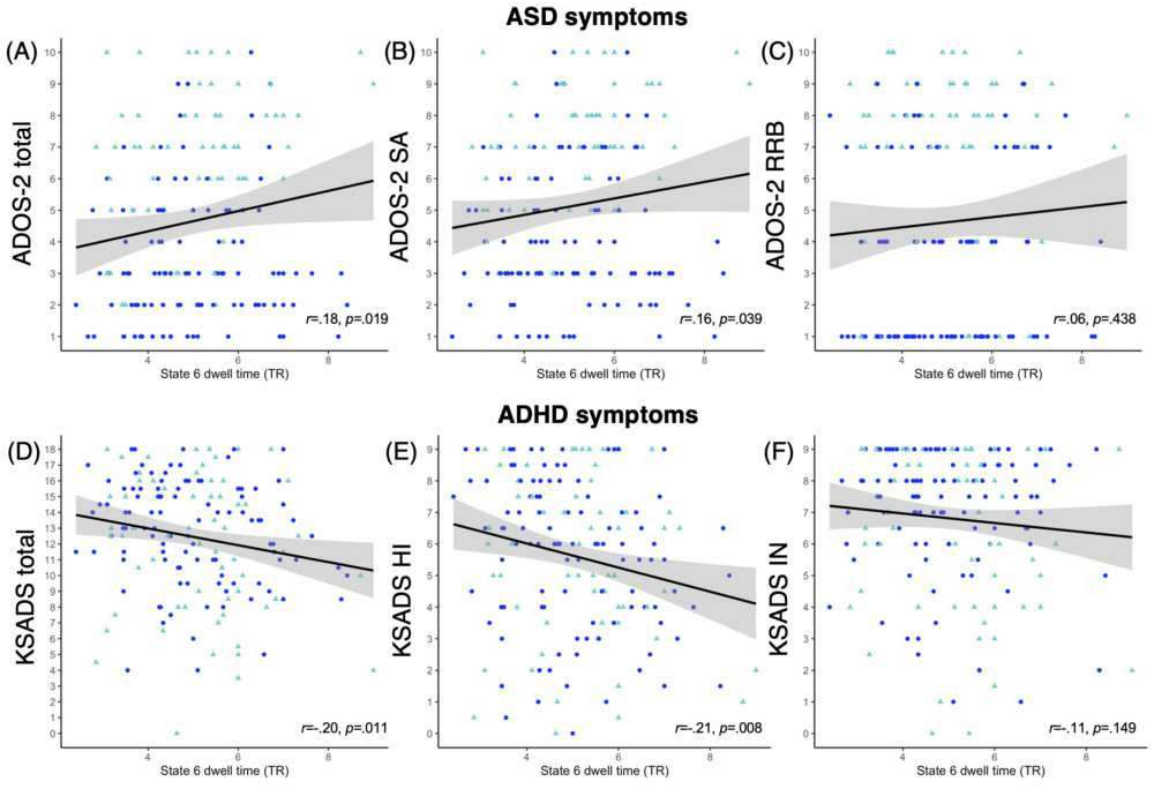

Figure 2. Scatterplot of dwell time of CAP 6 and ASD (**A–C**) or ADHD (**D–F**) total and subtotal severity scores. ASD symptoms are indexed by Autism Diagnostic Observation Schedule-2 (ADOS-2) total, Social Affect (SA), Restricted and Repetitive Behaviors (RRB) calibrated severity scores [9]. ADHD symptoms are indexed by the Kiddie Schedule for Affective Disorders and Schizophrenia (KSADS) total, hyperactivity/impulsivity (HI) and inattention (IN) scores [10]. Partial correlation covarying for age, sex and framewise displacement are displayed in the lower right corner for each plot. Primary diagnostic classification is indicated by data point style (blue circle=ADHD group, turquoise triangle=ASD group). Results show that more time in CAP 6 was associated with higher total ASD and lower total ADHD symptoms. When separated by symptom domain, these correlations were specific to ADOS-2 SA and KSADS HI symptoms, with no significant correlations for ADOS-2 RRB and KSADS IN.

Conclusions: Our findings show a double dissociation by diagnostic symptom domain involving the brain state characterized by simultaneous deactivation of DMN and frontoparietal network and activation of the somatomotor network. Children with higher ASD symptoms, particularly in the social affective domain, spent more time in this brain state, whereas shorter dwell time occurred in children with higher ADHD symptoms, particularly in the hyperactivity/impulsivity subdomain. Results clarify the role of the DMN in ASD and ADHD symptoms in a transdiagnostic and comorbid sample.

References

1. Kogan, et al. (2018). The prevalence of parent-reported autism spectrum disorder among US children. Pediatrics,142(6).
2. Polanczyk, et al. (2014). ADHD prevalence estimates across three decades: an updated systematic review and meta-regression analysis. International Journal of Epidemiology, 43(2), 434-442.
3. Leitner, Y. (2014). The co-occurrence of autism and attention deficit hyperactivity disorder in children–what do we know?. Frontiers in human neuroscience, 8, 268.
4. Di Martino, et al. (2013). Shared and distinct intrinsic functional network centrality in autism and attention-deficit/hyperactivity disorder. Biological psychiatry, 74(8), 623-632.
5. Harikumar, et al. (2021). A review of the default mode network in autism spectrum disorders and attention deficit hyperactivity disorder. Brain connectivity, 11(4), 253-263.
6. Kupis, et al. (2020). Evoked and intrinsic brain network dynamics in children with autism spectrum disorder. Neuroimage: Clinical, 28, 102396.
7. Agoalikum, et al. (2021). Differences in disrupted dynamic functional network connectivity among children, adolescents, and adults with attention deficit/hyperactivity disorder: a resting-state fMRI study. Frontiers in Human Neuroscience, 15, 697696.
8. Gutierrez-Barragan, et al. (2023). Evolutionarily conserved fMRI network dynamics in the mouse, macaque, and human brain. bioRxiv, 2023-07.
9. Lord, et al. (2012). Autism diagnostic observation schedule, second edition (ADOS-2). Torrance, CA: Western Psychological Services.
10. Kaufman, et al. (1997). Schedule for affective disorders and schizophrenia for school-age children-present and lifetime version (K-SADS-PL): initial reliability and validity data. Journal of the American Academy of Child & Adolescent Psychiatry, 36(7), 980-988.

Poster No 399

The neurogenetics of functional connectivity changes in Autism: Insights from subtyping 657 patients

Javier Rasero[1], Antonio Jimenez-Marin[2], Ibai Diez[3], Roberto Toro[4], Mazahir Hasan[5], Jesus Cortes[2]

[1]University of Virginia, Charlottesville, VA, United States of America, [2]Biobizkaia Health Research Institute, Barakaldo, Bizkaia, Spain, [3]Massachusetts General Hospital and Harvard Medical School, Boston, MA, United States of America, [4]Institut Pasteur, Paris, France, [5]Achucarro Basque Center for Neuroscience, Leioa, Bizkaia, Spain

Introduction: Autism Spectrum Disorder (ASD) is a diverse condition with social and behavioral variations, and whose origin involves complex interactions of genetic, cellular, and environmental factors, potentially linked to developmental excitation/inhibition imbalances. Neurobiologically, ASD exhibits a great deal of heterogeneity in brain morphology and network patterns. Subtyping efforts may offer a solution to overcome such multiscale heterogeneity, which is the most significant challenge in the development of effective therapies. This study, combining functional connectivity profiles, consensus clustering and transcriptomics, aims to further understand ASD heterogeneity.

Methods: A subtyping approach based on consensus clustering of multi-study harmonized functional brain connectivity patterns was applied to a population of 657 ASD individuals with quality-assured neuroimaging data from the ABIDE consortium. Subsequently, by means of a Multivariate Distance Matrix Regression analysis, functional architecture alterations of each subtype relative to the typically developing control (TDC) group (884 subjects) were estimated. The resulting brain maps were associated with high-resolution gene transcriptomics while controlling for spatial autocorrelations. The subset of genes showing a significant spatial similarity in these associations were then submitted to an enrichment analysis and a protein interaction analysis to characterize the molecular mechanism behind each subtype.

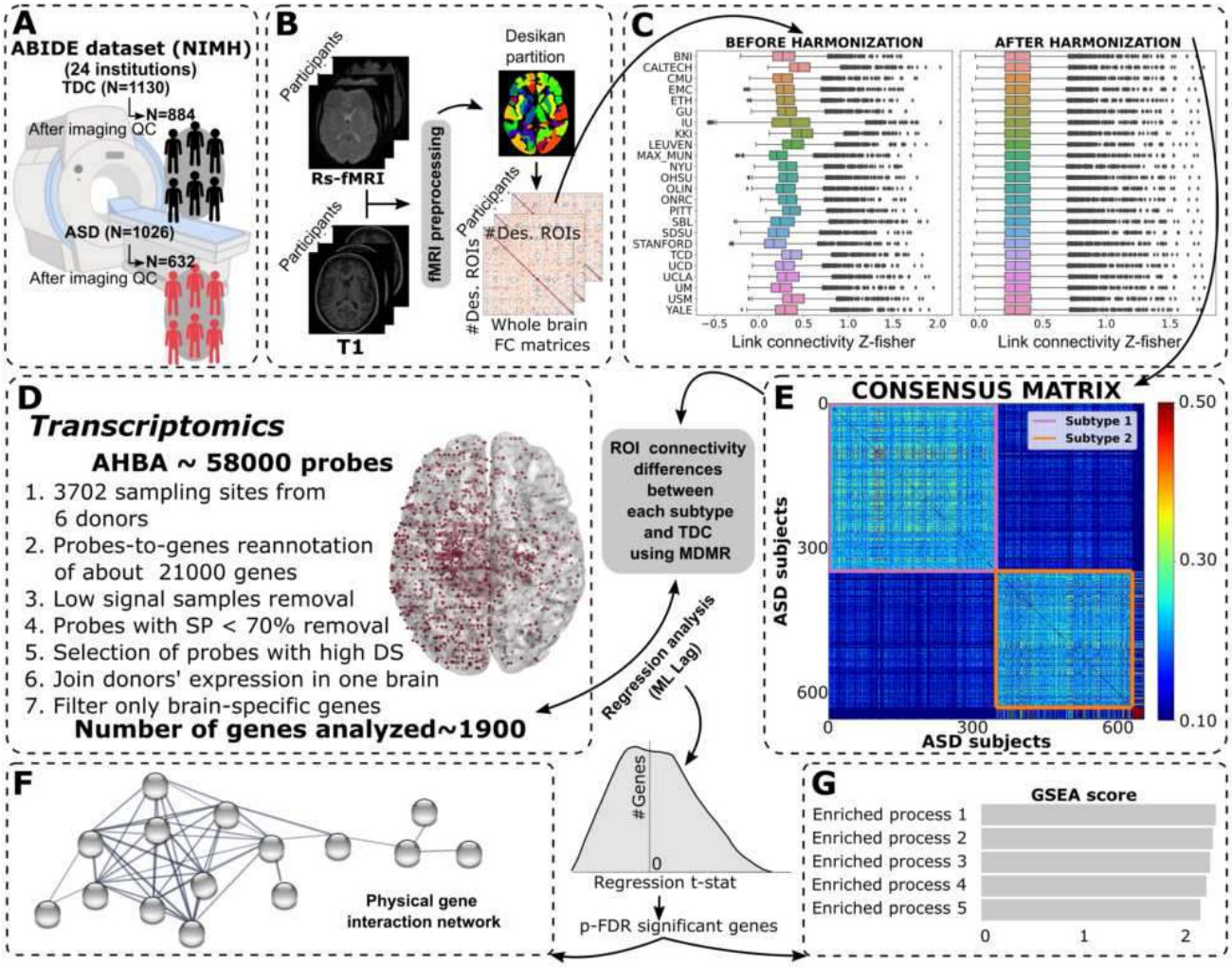

Results: Two major stable subtypes were found (panel A): subtype 1, comprising about 53% of ASD subjects and exhibiting hypoconnectivity (less average connectivity than TDC participants); and subtype 2, involving about 43% of ASD subjects and showing hyperconnectivity. Both subtypes did not differ statistically in structural imaging metrics in any of the regions (68 cortical and 14 subcortical) or in any of the behavioral scores (IQ, Autism Diagnostic Interview, and Autism Diagnostic Observation Schedule) analyzed. Functional network alterations of subtype 1 relative to TDC mainly involved the superior temporal gyrus, posterior cingulate cortex, and the insula. For subtype 2, higher differences were found in the thalamus, putamen, and precentral gyrus. Thus, alterations affecting the default mode network were common to both subtypes, but one (subtype 1) also showed specific disruptions involving the salience network and the other (subtype 2) in the somatomotor network (panel B). Subsequently, an association analysis of such alterations with transcriptomic data found 195 significant negative-associated (NEG) genes and 364 positive-associated (POS) genes for subtype 1. Significant NEG genes, also present in the SFARI gene human database with a relevance score of 1, were GFAP, CHD7, SKI, SHANK3, ANK3, and CACNA1E, while POS genes were ASXL3, MAP1A, STXBP1, DPYSL2, KNCB1, SCN8A, RIMS1, and CDKL5. Similarly, for subtype 2, we found 142 NEG genes, of which GRIA2, RFX3, SHANK2, GRIN2B, DLG4, LRRC4C, ARX, and GABRB3 were also present in the SFARI list, and 180 POS genes, including MAGEL2 and IQSEC2. Finally, a gene enrichment analysis showed (panel C) significant enrichments after multiple testing corrections only for subtype 2 (not even using instead the whole ASD group), and included GO biological processes and Reactome pathways related to glutamate signaling (affecting both AMPA and NMDA receptors) and synapse organization in relation to the E/I imbalance occurring during the development of brain circuits. Likewise, NEG genes participated in each biological process and pathway, mostly prominent by genes DLG4, GRIN2B, GRIA2, and SHANK2.

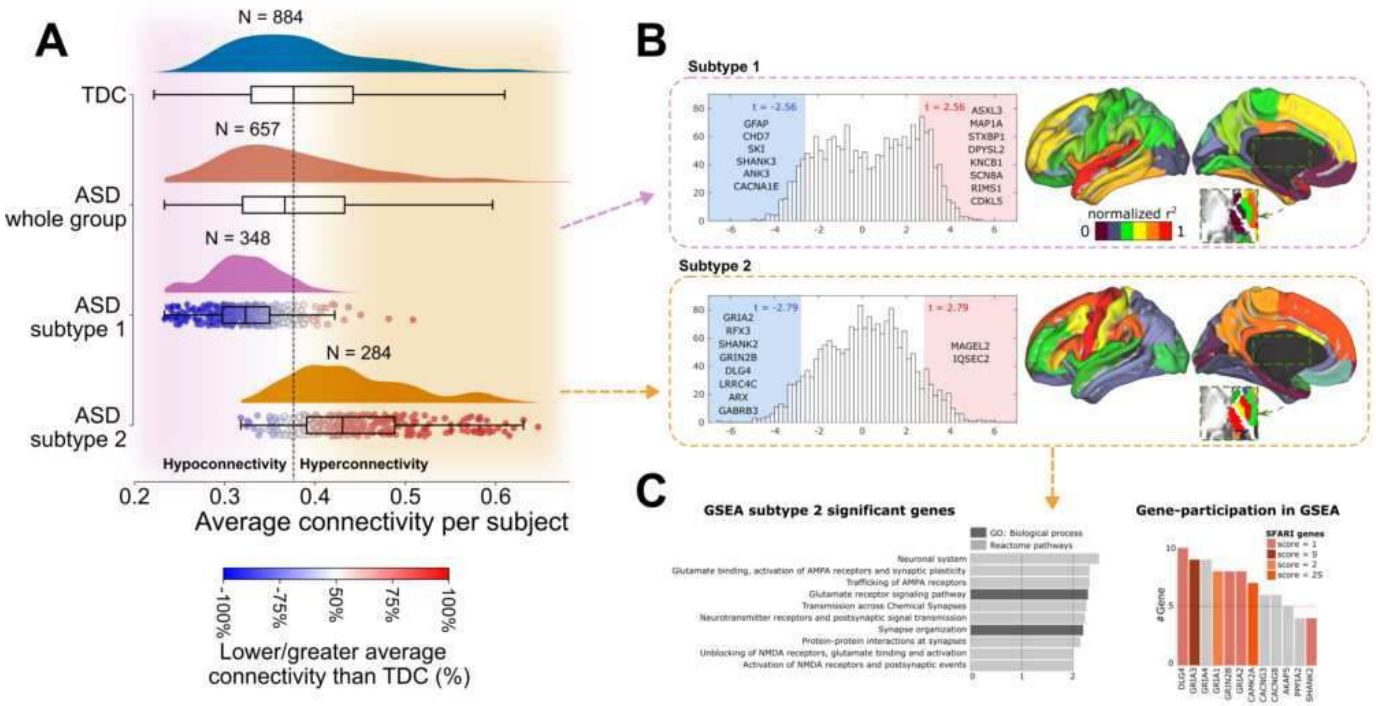

Conclusions: Our results support a link between excitation/inhibition imbalance, a leading well-known primary mechanism in the pathophysiology of ASD, and functional connectivity alterations. This, however, affects only one subpart of ASD, overall characterized by brain hyperconnectivity and major alterations in somatomotor and default mode networks.

References

1. Rasero, J. (2023). 'The Neurogenetics of Functional Connectivity Alterations in Autism: Insights From Subtyping in 657 Individuals', Biological Psychiatry, vol. 94, no. 10, pp. 804-813.
2. Hawrylycz, M. (2023), 'Linking Neurogenetics and Functional Connectivity in Autism', Biological Psychiatry, vol. 94, no 10, pp 765-766.

Poster No 400

Altered brain network organization in adults with Asperger's syndrome

Fabian-Alexande Tietze[1], Nooshin Javaheripour[2], Gerd Wagner[2], Feliberto De La Cruz[3], Martin Walter[2], Gregor Szycik[4]

[1]Charité Universitätsmedizin Berlin, Berlin, Berlin, [2]Department of Psychiatry and Psychotherapy, Jena University Hospital, Jena, Thuringia, [3]Department of Psychosomatic Medicine and Psychotherapy, Jena University Hospital, Jena, Thuringia, [4]Medizinische Hochschule Hannover, Hannover, Lower Saxony

Introduction: Autism spectrum disorder (ASD) is a neurodevelopmental disorder that persists into adulthood with both social and cognitive disturbances. Asperger's syndrome (AS) was a distinguished subcategory of autism in the DSM-IV-TR defined by specific symptoms including difficulties in social interactions, inflexible thinking patterns, and repetitive behaviour without any delay in language or cognitive development. Studying the functional brain organization of individuals with these specific symptoms may help to better understand Autism spectrum symptoms.

Methods: The aim of this study is therefore to investigate functional connectivity as well as functional network organization characteristics using graph-theory measures of the whole brain in male adults with AS compared to healthy controls (HC) (AS: n = 15, age range 21-55 (mean ± sd: 39.5 ± 11.6), HC: n = 15, age range 22-57 [mean ± sd: 33.5 ± 8.5]).

Results: No significant differences were found when comparing the region-by-region connectivity at the whole-brain level between the AS group and HC. However, measures of "transitivity," which reflect local information processing and functional segregation, and "assortativity," indicating network resilience, were reduced in the AS group compared to HC. On the other hand, global efficiency, which represents the overall effectiveness and speed of information transfer across the entire brain network, was increased in the AS group.

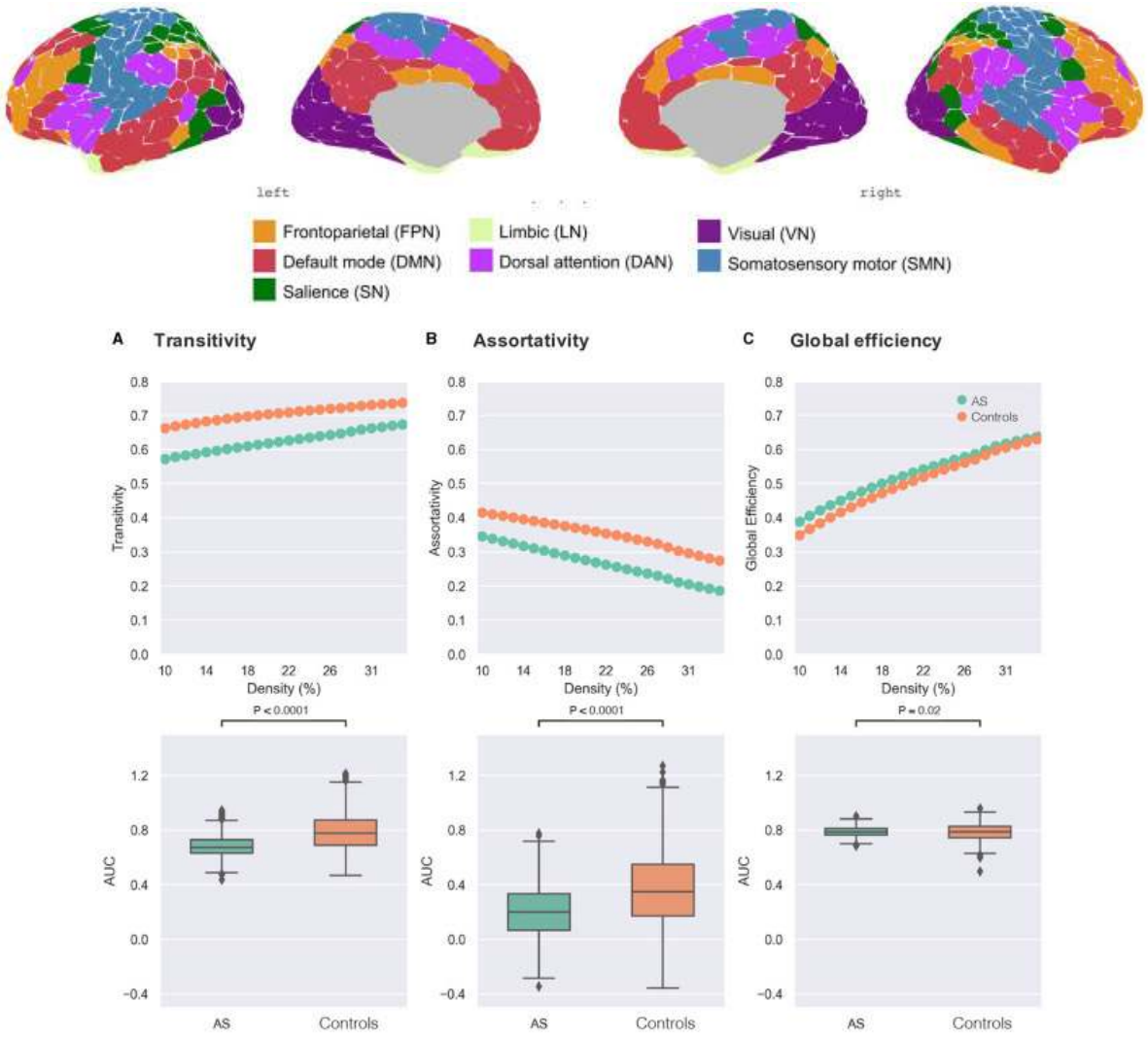

Conclusions: Our findings suggest that individuals with AS may have alterations in the organization and functioning of brain networks, which could contribute to the distinctive cognitive and behavioural features associated with this condition. We suggest further research to explore the association between these altered functional patterns in brain networks and specific behavioral traits observed in individuals with AS, which could provide valuable insights into the underlying mechanisms of its symptomatology.

References

1. Javaheripour N, Wagner G, de la Cruz F, Walter M, Szycik GR, Tietze FA. Altered brain network organization in adults with Asperger's syndrome: decreased connectome transitivity and assortativity with increased global efficiency. Front Psychiatry. 2023 Aug 17;14:1223147. doi: 10.3389/fpsyt.2023.1223147. PMID: 37701094; PMCID: PMC10494541.

Poster No 401

Whole Brain Mapping of Disturbed Semantic Representation in Autism Spectrum Disorder

Jong-eun Lee[1], Kyoungseob Byeon[2], Boris Bernhardt[3], Michael Milham[2], Hyunjin Park[4], Seok-Jun Hong[5]

[1]Sungkyunkwan University, Suwon-si, Gyeonggi-do, [2]Child Mind Institute, New York, NY, [3]Montreal Neurological Institute and Hospital, Montreal, Quebec, [4]Center for Neuroscience Imaging Research, Institute for Basic Science, Suwon, Kyeonggi-do, [5]Sungkyunkwan University, Gyeonggi-do, Suwon-si

Introduction: It is widely accepted that the children with autism spectrum disorder (ASD) differently perceive the external world1. The two leading theories, namely Weak Central Coherence2 and Enhanced Perceptual Functioning3 theories, may provide a possible account for this phenomenon, given that both commonly indicate the detail-oriented sensory processing in ASD. Notably, this atypical cognitive style has been also associated with the failure of prototype-based categorical learning in

ASD4. However, how all these cognitive symptoms are mechanistically related and how the atypical perception is represented on the functional brain in ASD remain largely unknown. To address these questions, we implemented a novel analytical framework to probe whole-brain semantic representation based on movie-watching fMRI. By estimating low-dimensional bases and dimensionality of this semantic representation, we sought to reveal the underlying mechanism of atypical perceptual process and the neural correlates for altered categorical learning in ASD.

Methods: We analyzed movie-watching fMRI from 123 individuals with ASD and 79 with the typically developing brain (movie clip: 'Despicable Me' [600 secs; TR: 0.8s])5. We manually annotated the temporal events of entities and actions that appear in movie frames (Fig 1a) and used them as regressors for semantic representation. Notably, gaze patterns, decoded from fMRI signals of the eyeball6., were used to model the effect of visual attention, providing a continuous weight for each regressor (Fig 1b). All these regressors were then linearly modeled with whole-brain fMRI signals to derive a semantic coefficient matrix (Fig 1c). To test the generalizability, we split the movie-fMRI into training and test datasets using 3-fold cross-validation and checked the correlation between actual and predicted fMRI signals (Fig 1d). Finally, the coefficient matrix underwent dimensionality reduction (i.e., PCA), which resulted in multiple principal components (=PCs) summarizing the semantic representation (Fig 1e).

Results: Fig 1i shows the semantic axis of PC1, which strongly differentiates between social-vs.-non-social categories, which is validated by independent semantic ratings7 (Fig 1j). By projecting the coefficient matrix onto this axis, the extent to which each brain region reflects the social-vs.-non-social axis was measured. The TPOJ, MT+ complex, and PCC are the brain regions that prominently align with one end of axis, while the early visual, superior parietal, and somatosensory areas are closely associated with the opposite end of axis (Fig 1k,l). Next, the group comparison analysis showed that ASD has significant alterations in PC1 scores mostly in DMN areas (Fig 1m-o). To identify a possible account for this group differences, we further estimated the representational dimensionality (=RD) of a semantic coefficient matrix at each brain area8 (Fig 2a). The whole-brain mean RD for each group is shown in Fig 2b. The RD of ASD showed an increased pattern (i.e., a lack of generalizability) in widespread brain areas, with notable effects primarily emerging from DMN (Fig 2c,d). While both groups showed higher RD in unimodal regions compared to transmodal regions, the RD in the ASD group was consistently higher in both modality systems (Fig 2e-g). Finally, the posthoc analysis revealed that the RD significantly mediates the autistic social behavior through altered PC1, suggesting the existence of their potential mechanistic links for the symptom manifestation (Fig 2h).

Conclusions: This study sheds light on how the unique perception of ASD affects their semantic processing, particularly along the social-vs.-nonsocial axis. Our experimental evidence supporting atypical neurocognitive pathway for social impairment in ASD may offer a potential hint to improve the strategy of future behavioral treatments in this prevailing developmental condition.

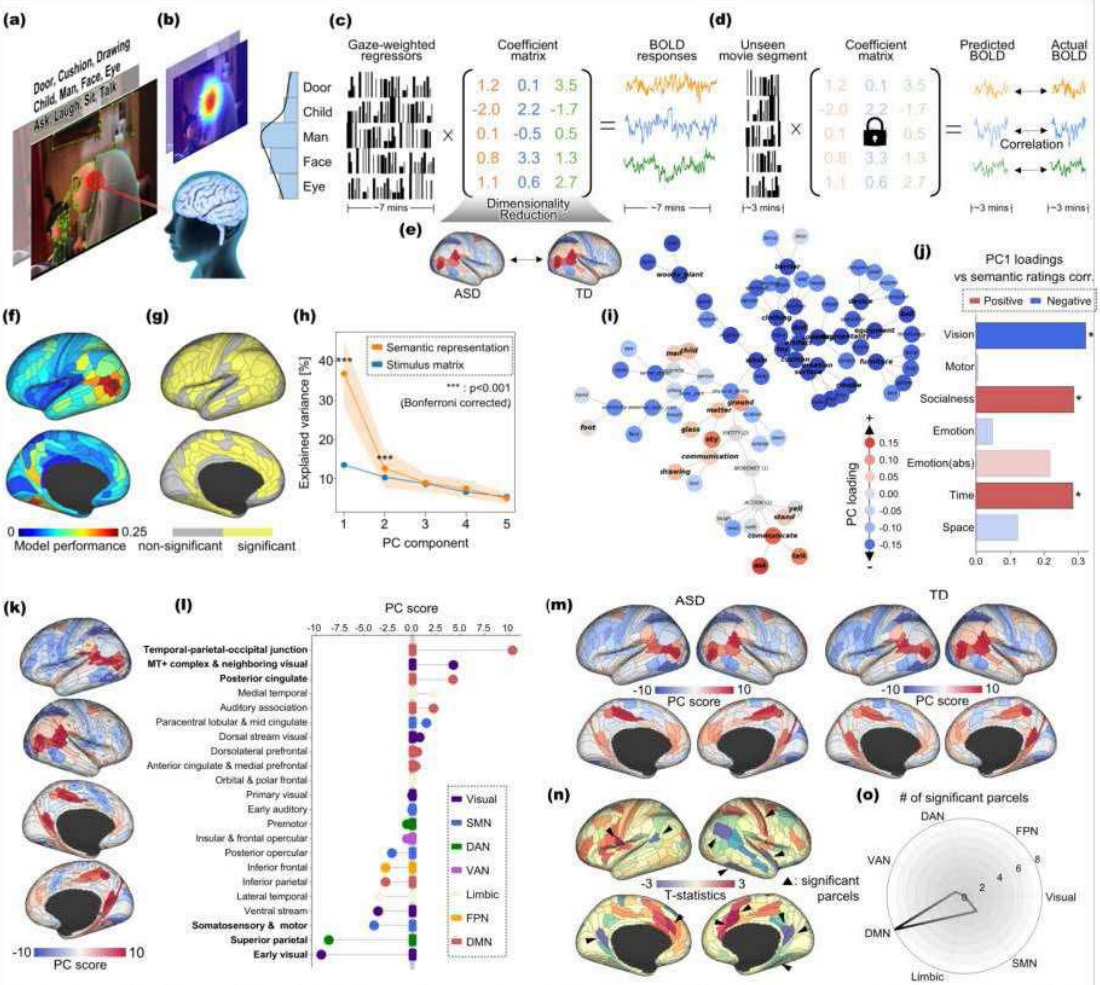

Figure 1. Schematic of semantic mapping analysis and group comparison results. a) Temporal events of entities and actions in a movie clip. b) Gaze pattern decoded from eyeball fMRI signals. c) A regression model was estimated for fMRI signal of each brain parcel with gaze-weighted regressors. d) Model is evaluated by correlating between the actual and predicted fMRI signals from unseen movie segment. e) Principal components (=PCs) are estimated from coefficient matrix and compared between groups. f) Average model performance across all subjects. g) Brain parcels that showed significant prediction by the model. h) Amount of explained variance by PCs of coefficient matrix and regressors. i) Semantic axis represented by PC1, organized according the WordNet hierarchy. j) Correlation between PC1 loadings of semantic axis and semantic ratings. k) Projection of coefficient onto PC1 axis (i.e., PC score). l) Distribution of PC scores by brain network. m) Average PC1 score for each group. n) Statistical comparison between groups, with increases/decreases in ASD shown in red/violet. o) Radar chart showing the number of significant parcels across different brain networks.

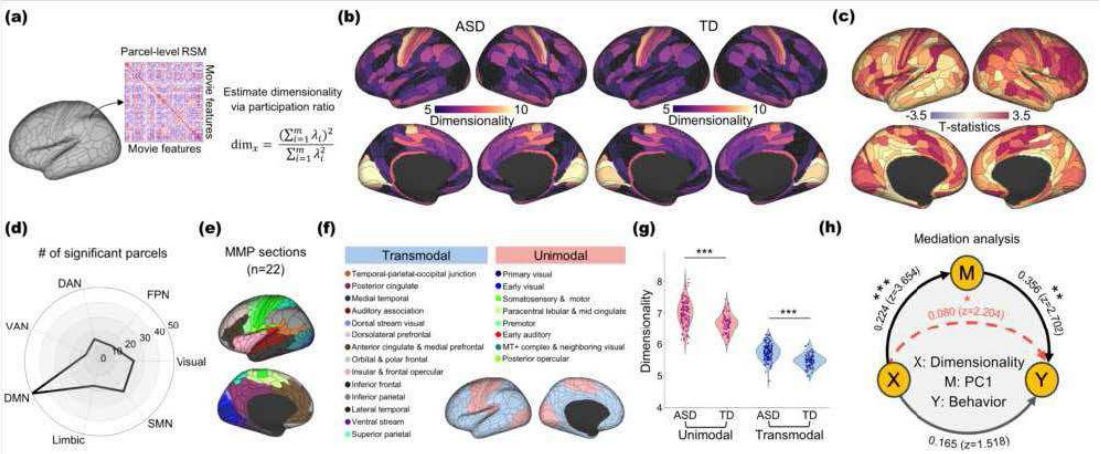

Figure 2. a) We estimated the representational dimensionality (RD) from participation ratio of parcel-level representational similarity matrix (RSM) which implies that the parcels with low RD exhibit uniform responses common to many categories (i.e., high generalizability). B) Average RD map for each group. c) Statistical comparison between groups, with increases/decreases in ASD shown in red/violet. d) Radar chart showing the number of significant parcels across different brain networks. e) Depiction of the 22 sections of the multimodal parcellation (MMP) of the brain. (f) MMP sections categorized by their function into unimodal and transmodal networks. g) Violin plots comparing dimensionality between ASD and TD groups in unimodal and transmodal regions. h) Mediation analysis model illustrating the effect of representational dimensionality (X) on social behavior (Y) with PC1 (M) as the mediator, showing a significant indirect effect through mediator but not a direct effect on behavior.

References
1. Robertson, C. E. (2017). Sensory perception in autism. Nature Reviews Neuroscience, 18(11), 671-684.
2. Happé, F. (2006). The weak coherence account: detail-focused cognitive style in autism spectrum disorders. Journal of autism and developmental disorders, 36(1), 5-25.
3. Mottron, L. (2006). Enhanced perceptual functioning in autism: An update, and eight principles of autistic perception. Journal of autism and developmental disorders, 36, 27-43.
4. Vanpaemel, W. (2021). Prototype-based category learning in autism: A review. Neuroscience & Biobehavioral Reviews, 127, 607-618.
5. Alexander, L. M. (2017). An open resource for transdiagnostic research in pediatric mental health and learning disorders. Scientific data, 4(1), 1-26.
6. Frey, M. (2021). Magnetic resonance-based eye tracking using deep neural networks. Nature neuroscience, 24(12), 1772-1779.
7. Wang, S. (2023). A large dataset of semantic ratings and its computational extension. Scientific Data, 10(1), 106.
8. Ito, T. (2023). Multitask representations in the human cortex transform along a sensory-to-motor hierarchy. Nature Neuroscience, 26(2), 306-315.

Poster No 402

Virtual epileptic patient cohort: generation and evaluation

Borana Dollomaja[1], Huifang Wang[2], Maxime Guye[3], Fabrice Bartolomei[4], Viktor Jirsa[5]

[1]Institut de Neurosciences des Systemes UMR1106, Marseille, Marseille, [2]AMU, INS, INSERM U1106, Marseille, PACA, [3]Aix Marseille Université, Marseille, PACA, [4]AMU, INS, INSERMU1106, Marseille, PACA, [5]nstitut de Neurosciences des Systèmes, Marseille, N/A

Introduction: Epilepsy is one of the most common brain diseases, affecting 1% of the world's population. Drug-resistant epilepsy (DRE) in particular affects 1 in 3 epileptic people. Recurrent seizures which characterize the disorder, occur due to sudden abnormal activity in the brain. This activity is generated in the so-called epileptogenic zone (EZ) network. A precise detection of the epileptogenic zone is crucial to treat DRE. Seizure recordings are used by clinicians to estimate the EZ network. In addition, brain stimulation is used to induce seizures (George 2020). By varying stimulation parameters via trial and error, clinicians aim to pinpoint regions responsible for seizure activity. In this work, we built a virtual epileptic patient cohort and evaluated this modeling framework for capturing empirical SEEG data.

Methods: In our study, we collected brain imaging data from 30 DRE patients, consisting of T1-MRI, diffusion-weighted MRI (DW-MRI) and recordings from implanted stereoelectroencephalography (SEEG) electrodes. The SEEG recordings consist of spontaneous seizures, stimulated seizures and interictal spikes. For each patient, we built virtual brain copies based on personalized whole-brain models (Wang 2023). We combined T1-MRI and DW-MRI to build brain network models. Brain regions are parcellated according to a brain atlas and represented as nodes in the network. The white matter fiber connections are represented as edges in the network. Brain region activity is simulated using a model which captures spatiotemporal seizure dynamics (Jirsa 2014). This model is placed in each node of the brain network model. In particular, the model's parameter x0 determines the node's epileptogenicity. We set epileptogenic nodes based on the EZ clinical hypothesis. Epileptogenic nodes generate seizure dynamics autonomously which propagate following edge connections from white matter tracts. Simulations are performed on the whole-brain level. Implanted SEEG electrodes are reconstructed in 3D from the post-implantation CT scan. Using euclidean distances between brain network nodes and electrode contact locations, we map the simulated brain activity onto the SEEG electrodes.

Results: Based on this workflow, we built the virtual epileptic patient cohort in BIDS format (Appelhoff et al. 2019). We set up metrics to compare patient-specific empirical and simulated SEEG seizures, such as binary overlap and correlation of the spatio-temporal time series. We built a control cohort where the EZ hypothesis was chosen randomly and show that patient-specific EZ hypothesis captures empirical SEEG data features significantly better than a randomly chosen one. For stimulated seizures, we also interrogated the stimulation parameters used to generate seizures. We built control cohorts where the same virtual model is used and only stimulation parameters vary, such as stimulation amplitude and stimulation location. We showed that as we get further away from the empirical stimulation amplitude or location, the simulated SEEG time series fail to capture the empirical SEEG seizure dynamics. Finally, we compared interictal spike time series by measuring spike rate for each SEEG channel. We showed that patient-specific EZ hypothesis captures spike rate better than a randomly chosen one, however not to the same extent as seizure dynamics are captured. This result confirms previous works (Bartolomei 2016, Luders 2006), where the interictal spike network is not identical to the EZ network, but overlaps with it.

Conclusions: In conclusion, we provided a virtual epileptic cohort and demonstrated the capacity of personalized whole brain models in capturing empirical brain activity of drug-resistant epilepsy patients. In particular, our personalized modeling framework captures stimulated seizure dynamics, where patient-specific stimulation parameters reproduce the observed

seizures. This approach can be useful in estimating optimal stimulation parameters that induce habitual seizures to diagnose epilepsy.

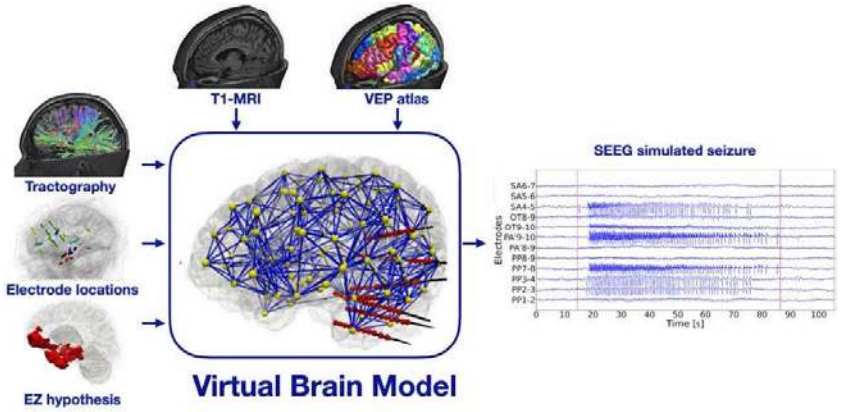

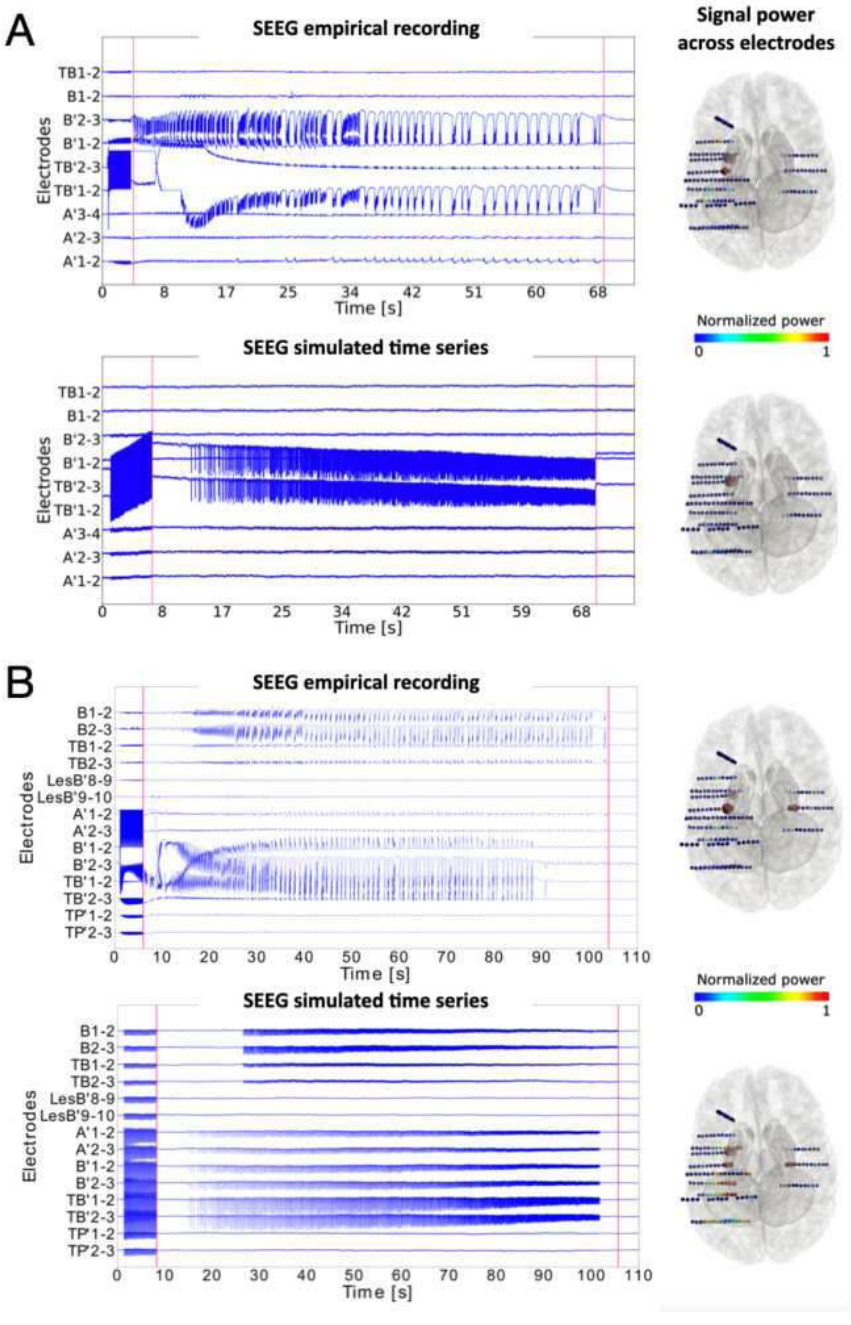

References

1. Appelhoff, S. et al. (2019). MNE-BIDS: Organizing electrophysiological data into the BIDS format and facilitating their analysis. Journal of Open Source Software, 4(44).
2. Bartolomei, F. et al. (2016), 'What is the concordance between the seizure onset zone and the irritative zone? A SEEG quantified study.' Clinical Neurophysiology, 127(2), 1157-1162.
3. George, D. D. et al. (2020). Stimulation mapping using stereoelectroencephalography: current and future directions. Frontiers in Neurology, 11, 320.
4. Jirsa, V. K. et al. (2014), 'On the nature of seizure dynamics', Brain : a journal of neurology, 137(Pt 8), 2210–2230.
5. Lüders, H. O. et al. (2006), 'The epileptogenic zone: general principles', Epileptic disorders, 8, S1-S9.
6. Wang, H. E. et al. (2023), Delineating epileptogenic networks using brain imaging data and personalized modeling in drug-resistant epilepsy. Science Translational Medicine, 15(680), eabp8982.

Poster No 403

Lower neonatal brain volumes following prenatal exposure to maternal COVID

Julie Sigurdardottir[1], Dafnis Batalle[1], Ayesha Javed[1], Molly Eddison[1], Mary Rutherford[1], Deena Gibbons[1], Katie Doores[1], Lucilla Poston[1], A. Edwards[1], Grainne McAlonan[1]

[1]King's College London, London, United Kingdom

Introduction: Epidemiological and animals studies indicate that maternal immune activation (MIA) during pregnancy may alter fetal brain development and increase the likelihood of psychiatric and neurodevelopmental difficulties in the offspring. The advent of COVID provided an opportunity and responsibility to directly examine the potential effect of prenatal exposure to maternal COVID infection on fetal brain development. In this preliminary prospective study, we examined brain regions previously implicated in psychiatric and neurodevelopmental conditions in neonates likely and unlikely to have been exposed in utero.

Methods: A UK sample of n=145 neonates (75 males) from the Brain Imaging in Babies Study born at mean(sd) 39.4(1.7) postmenstrual weeks of age and with no known family history of neuropsychiatric conditions, were scanned on a 3T MRI scan at mean(sd) 41.4 (2.1) weeks. Of those, 88 developed in utero during the COVID pandemic. From T2-weighted brain imaging data, volumes were calculated using the automated segmentation pipeline of the developing Human Connectome Project for the bilateral amygdala, hippocampus, caudate, insula, thalami, lentiform, cerebellum and for frontal lobe and anterior temporal lobe grey and white-matter [GM,WM] and total brain volume (TBV). Blood samples from mother and child were obtained at scan from the pandemic cohort. Prenatal exposure to maternal SARS-CoV-2 was defined as: positive Nucleocapsid-antibody response (>4 fold change above background) in either individual and/or a positive spike-antibody response if sampled prior to the vaccination roll-out. Multivariate multiple regressions were used to assess the effect of exposure on brain volumes, adjusted for sex and age at scan and age at birth.

Results: Likely COVID-MIA exposure was determined in 33 of the 145 neonates (37.5% of the pandemic cohort). Exposure was associated with lower TBV, total cortical GM, right anterior temporal GM, left amygdala and left thalamus (p-uncorrected <0.05). Excluding neonates born preterm <37 weeks attenuated the effect on the left thalamus only.

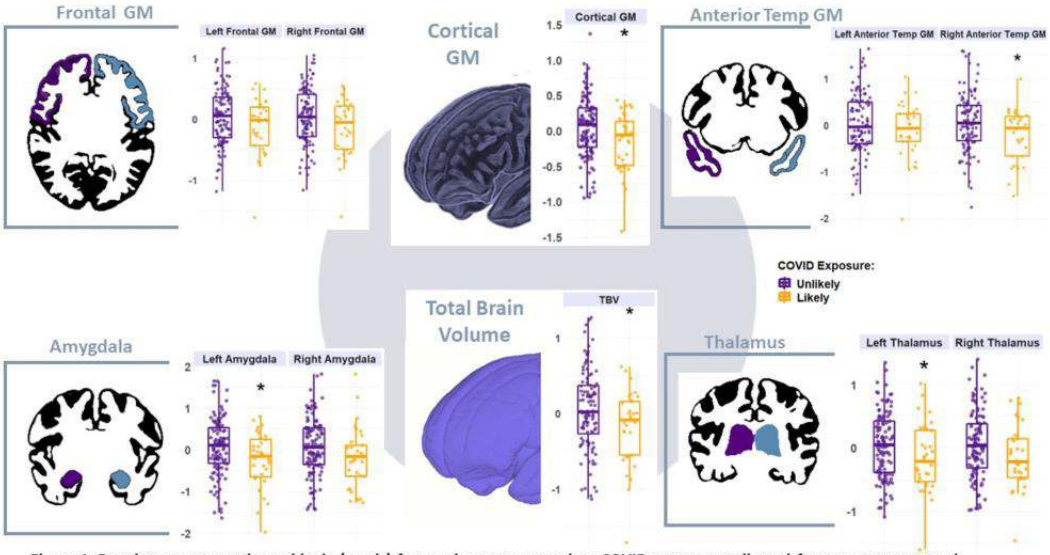

Figure 1. Boxplots represent the residuals (y-axis) from volumes regressed on COVID exposure, adjusted for sex, postmenstrual age at scan and age at birth. * represents a significant effect of exposure on volume. GM: Grey matter, TBV: Total brain volume.

Conclusions: Fetal brain development was altered in children exposed to COVID-MIA, specifically volumes in areas involved in neurodevelopmental psychiatric conditions and cortical GM were lower in those likely exposed. However, we emphasize that we cannot entirely exclude the effect of other important maternal and environmental factors (including antenatal stress). We also do not yet know if these brain alterations are functionally and clinically relevant and this is the focus of on-going study.

References

1. Al-Haddad, B. J., Oler, E., Armistead, B., Elsayed, N. A., Weinberger, D. R., Bernier, R., ... & Waldorf, K. M. A. (2019). The fetal origins of mental illness. American journal of obstetrics and gynecology, 221(6), 549-562.
2. Edwards, A. D., Rueckert, D., Smith, S. M., Abo Seada, S., Alansary, A., Almalbis, J., ... & Hajnal, J. V. (2022). The developing human connectome project neonatal data release. Frontiers in neuroscience, 16, 886772.
3. Knuesel, I., Chicha, L., Britschgi, M., Schobel, S. A., Bodmer, M., Hellings, J. A., et al. (2014). Maternal immune activation and abnormal brain development across CNS disorders. 10, 643–660.
4. Lombardo, M. V., Moon, H. M., Su, J., Palmer, T. D., Courchesne, E., & Pramparo, T. (2018). Maternal immune activation dysregulation of the fetal brain transcriptome and relevance to the pathophysiology of autism spectrum disorder. Molecular psychiatry, 23(4), 1001-1013.
5. Makropoulos, A., Gousias, I. S., Ledig, C., Aljabar, P., Serag, A., Hajnal, J. V., ... & Rueckert, D. (2014). Automatic whole brain MRI segmentation of the developing neonatal brain. IEEE transactions on medical imaging, 33(9), 1818-1831.
6. Shook, L. L., Sullivan, E. L., Lo, J. O., Perlis, R. H., & Edlow, A. G. (2022). COVID-19 in pregnancy: implications for fetal brain development. Trends in molecular medicine, 28(4), 319-330

Poster No 404

Microstructural Grey-Matter Covariance and Functional Connectivity in Preterm and Full-term Infants

Andrea Gondova[1,2], Sara Neumane[1,2], Tomoki Arichi[3,4], Jessica Dubois[1,2]

[1]Université Paris Cité, Inserm, NeuroDiderot, F-75019, Paris, France, [2]UNIACT, NeuroSpin, CEA, Université Paris-Saclay, F-91191, Gif-sur-Yvette, France, [3]Centre for the Developing Brain, School of Biomedical Engineering and Imaging Sciences, King's Co, London, United Kingdom, [4]Paediatric Neurosciences, Evelina London Children's Hospital, Guy's and St Thomas' NHS Foundation Trust, London, United Kingdom

Introduction: The third trimester of pregnancy is characterized by complex neurodevelopmental processes which shape the brain's structural and functional networks[1]. In grey matter (GM) regions, micro-structural changes observed with diffusion MRI show distinct spatiotemporal profiles during this period[2]. While GM microstructural synchrony across regions belonging to the same developing functional networks is expected[3], the grey matter microstructural covariance (MC) and its relationship to functional connectivity (FC) assessed with resting-state functional MRI (rs-fMRI) remains underexplored. Our study aimed to examine the developmental changes in these two modalities and the MC-FC relationships in the last pre-term weeks and their potential alterations in the context of prematurity.

Methods: We analysed anatomical, diffusion, and resting-state functional MRI data from the developing Human Connectome Project (dHCP) database[4]: 45 preterm (PT) infants without overt brain lesions (26 males, gestational age at birth – GA at birth – median 32.3 weeks, range [25.6w–36.0w]) scanned close to birth at median postmenstrual age – PMA at scan – 34.9 weeks, range [28.3w–36.9w](PT:ses1) and near term equivalent age (TEA) (median PMA at scan 41.3 weeks, range [38.4w–44.9w]) (PT:ses2) and a control group of 45 full-term (FT) infants matched to preterms on sex and PMA at TEA scan (Figure1a). Median cortical microstructure for cortical and subcortical regions (ROIs) was evaluated with diffusion tensor imaging (DTI)[5] and neurite orientation dispersion and density imaging (NODDI)6 models before computing a MC for each pair of ROI within each group (Figure1b,c). Average FC for each group between the same set of ROIs was derived as a Pearson's correlation. Connectivity matrices were compared for different conditions (PT:ses 1 vs ses2; PT:ses2 vs FT, within or between MC and FC modalities) using Wilcoxon signed-rank test and correlation analyses with FDR correction. Overlap of the MC and FC in terms of network structure described with hierarchical clustering over all possible cluster sizes was evaluated with average mutual information.

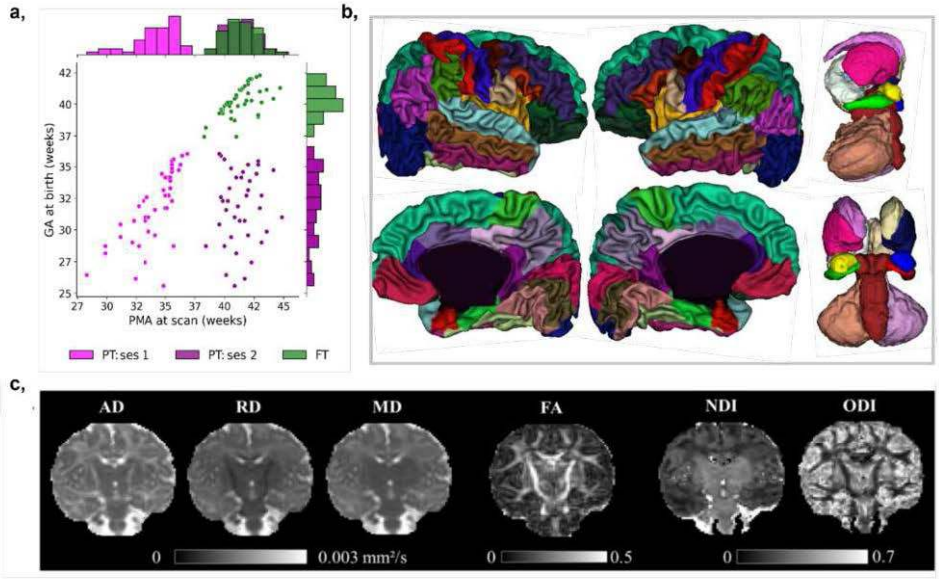

Figure 1a, Joined distribution of PMA at scan and GA at birth for the 3 infant groups. ***b,*** Visualisation of regions of interest used in the study. 31 bilateral cortical regions were parcellated using the infant-specific M-CRIB-S tool[7]. Subcortical regions were derived from volumetric segmentations provided in the dHCP[4]. ***c,*** Descriptor maps used to evaluate grey matter regional microstructural covariation resulting from DTI (AD, RD, MD, and FA) and NODDI (NDI, ODI) models for a representative full-term infant (GA at birth 40.4w, PMA at MRI 44.1w).

Results: Both MC and FC showed a global strengthening of regional connectivity between birth and TEA in preterms. Initially weaker and widespread at birth (PT:ses1), MC covariance selectively strengthened, particularly between lobes, with development (PT:ses2, FT). Differences in FC between preterm sessions indicated concurrent functional development. Additionally, both MC and FC showed significant differences between PT infants at TEA and FT, implying substantial microstructural and functional alterations in prematurity (MC – PT:ses2 > FT, $p<0.001$; FC – PT:ses2 < FT, $p<0.001$). Despite these differences, both MC and FC remained highly correlated between these two groups, indicating that while prematurity impacted regional covariance strengths, overall connectivity profiles were not drastically modified (Figure 2a). Direct comparisons between MC and FC revealed a significant relationship that decreased during development ($Z=17.39$, $p<0.001$) (Figure 2b). On the network level, analyses revealed an initially low but increasing overlap between MC and FC-derived networks, suggesting the emergence of a shared underlying network architecture between grey matter microstructural covariance and functional connectivity (Figure 2c).

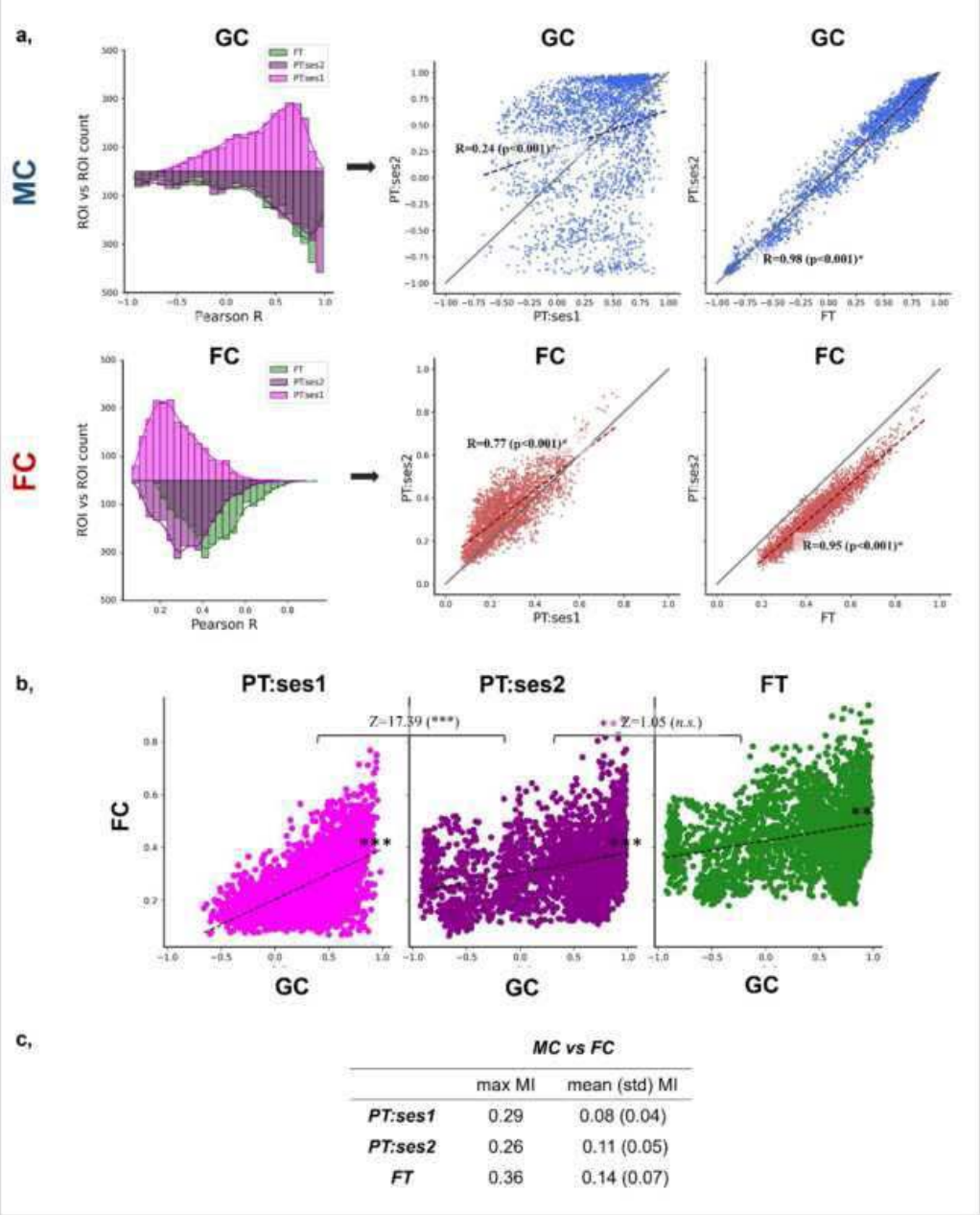

	max MI	mean (std) MI
PT:ses1	0.29	0.08 (0.04)
PT:ses2	0.26	0.11 (0.05)
FT	0.36	0.14 (0.07)

Figure 2a, Distribution of ROI pair correlations (Pearson coefficient R) across infant groups (right) and scatter plots showing relationships between the ROI pair similarity between PT:ses1 vs PT:ses2 (middle) and FT vs PT:ses2 (left) for MC (top row) and FC (bottom row). The dotted line in scatter plots shows the group correlation (with R: Pearson's coefficient), while the solid line represents the identity relationship. (NB: points show connectivity strength between ROI pairs from upper triangle of symmetric connectivity matrices in all plots.) ***b,*** Relationship between MC and FC connectivity per ROI pair ($p < 0.001$ ***, $p < 0.001$ **, $p > 0.05$ n.s.). Z: Z-score comparing the slopes of linear regression. ***c,*** Summary of distribution of mutual information (MI) comparing networks derived from hierarchical clustering of MC and FC for each infant group.

Conclusions: Our results bring new insights into the early development of grey matter microstructural covariance and functional connectivity in the context of prematurity. This study emphasizes the value of integrating descriptors of MC in addition to more commonly used white matter structural connectivity to better understand early structure-function relationships. In the future, it will be crucial to investigate potential alterations of the MC-FC relationships within individual subjects8 and their ability to serve as neuroimaging markers for the diagnosis and prognosis of neurodevelopmental disorders frequently observed in preterm-born children.

References

1. Gilmore, J.H., Knickmeyer, R.C., Gao, W., (2018). Imaging structural and functional brain development in early childhood. Nat. Rev. Neurosci. 19, 123–137. https://doi.org/10.1038/nrn.2018.1
2. Ouyang, M., Jeon, T., Sotiras, A., Peng, Q., Mishra, V., Halovanic, C., Chen, M., Chalak, L., Rollins, N., Roberts, T. P. L., Davatzikos, C., & Huang, H. (2019). Differential cortical microstructural maturation in the preterm human brain with diffusion kurtosis and tensor imaging. Proceedings of the National Academy of Sciences, 116(10), 4681–4688. https://doi.org/10.1073/pnas.1812156116
3. Alexander-Bloch, A., Giedd, J. N., & Bullmore, E. (2013). Imaging structural co-variance between human brain regions. Nature Reviews Neuroscience, 14(5), 322–336.https://doi.org/10.1038/nrn3465
4. Edwards, A.D., Rueckert, D., Smith, S.M., Abo Seada, S., ..., Hajnal, J.V. (2022). The Developing Human Connectome Project Neonatal Data Release. Front Neurosci. May 23;16:886772. doi: 10.3389/fnins.2022.886772
5. Basser, P. J., Mattiello, J., & Lebihan, D. (1994). Estimation of the Effective Self-Diffusion Tensor from the NMR Spin Echo. Journal of Magnetic Resonance, Series B, 103(3), 247–254. https://doi.org/10.1006/jmrb.1994.1037
6. Zhang, H., Schneider, T., Wheeler-Kingshott, C.A., Alexander, D.C., (2012). NODDI: practical in vivo neurite orientation dispersion and density imaging of the human brain. NeuroImage 61, 1000–1016. https://doi.org/10.1016/j.neuroimage.2012.03.072
7. Adamson, C. L., Alexander, B., Ball, G., Beare, R., Cheong, J., Spittle, A. J., Doyle, L. W., Anderson, P. J., Seal, M. L., & Thompson, D. K. (2020). Parcellation of the neonatal cortex using Surface-based Melbourne Children's Regional Infant Brain atlases (M-CRIB-S). Scientific Reports, 10(1),4359. https://doi.org/10.1038/s41598-020-61326-2
8. Fenchel, D., Dimitrova, R., Seidlitz, J., Robinson, E. C., Batalle, D., Hutter, J., Christiaens, D., Pietsch, M., Brandon, J., Hughes, E. J., Allsop, J., O'Keeffe, C., Price, A. N., Cordero-Grande, L., Schuh, A., Makropoulos, A., Passerat-Palmbach, J., Bozek, J., Rueckert, D., ... O'Muircheartaigh, J. (2020). Fench et Development of Microstructural and Morphological Cortical Profiles in the Neonatal Brain. Cerebral Cortex, 30(11), 5767–5779. https://doi.org/10.1093/cercor/bhaa150

Poster No 405

Interactive Effects of Prenatal Drug Exposure and Socioeconomic Status on Early Brain Connectivity

Gabriella Vavala[1], Janelle Liu[1], Rina Eiden[2], Karen Grewen[3], Wei Gao[1]

[1]Biomedical Imaging Research Institute (BIRI), Cedars-Sinai Medical Center, Los Angeles, CA, [2]Pennsylvania State University, University Park, PA, [3]University of North Carolina at Chapel Hill, Chapel Hill, NC

Introduction: Prenatal drug exposure (PDE) and socioeconomic status (SES) are known to independently affect newborn brain functional network development (Gao 2015, Salzwedel 2015, Liu 2022). Resting-state functional magnetic resonance imaging (rsfMRI) studies in infants and children with PDE show connectivity disruptions in limbic regions involved in reward processing and emotion regulation (Morie 2019, Ross 2015, Salzwedel 2015, Liu 2022). SES has also been linked with infant functional connectivity development in the default-mode network (Gao 2015). However, little is known about the combined effect of PDE and SES on early neurodevelopment. In this study, we used rsfMRI to examine both the unique and potentially interactive effects of PDE and SES (i.e., indexed by maternal education (MEdu)) on functional connectivity at birth.

Methods: Participants were enrolled as part of two projects examining the impact of PDE on early brain development. Subjects in both datasets included drug-free control neonates (CTR; Dataset 1: n=54; Dataset 2: n=28) and neonates with PDE (Dataset 1: n=61; Dataset 2: n=81), including: alcohol, nicotine, marijuana, cocaine, and opioids. Data from 100 drug-free control neonates from the University of North Carolina Early Brain Development Study (reference dataset; Gao 2017; Gilmore 2018) were also used. For all datasets, rsfMRI scans were acquired during natural sleep at 2 weeks of age. Participants were matched on sex, race, age at birth, age at scan, and motion. Birthweight and maternal depression were included as covariates of no interest in all analyses. Functional connectivity measures were derived using a neonate functional parcellation-based atlas (Shi 2018). For each seed region of interest (ROI; n=223), the average time series was extracted and correlated with every other ROI in the brain to compute a correlation matrix for each subject. Linear regression was used to identify main effects (PDE, MEdu) as well as interactive effects (PDExMEdu) on each neonate functional connection. A p-value thresholding strategy ($p<.05$) was used to generate heatmaps revealing main effects of PDE, main effects of MEdu, and interactive effects between PDE and MEdu on functional connectivity between each ROI and the whole brain.

Results: In Dataset 1, main effects of PDE and MEdu were concentrated in similar regions, including temporal, frontal, and occipital areas. Additionally, there was a main effect of PDE, but not MEdu, in the left mid-cingulate gyrus. Significant interaction effects were observed in frontal, temporal, occipital, and mid-cingulate regions. A different distribution of effects was observed in Dataset 2. Main effects of PDE were observed in the left mid-cingulate gyrus, right anterior cingulate gyrus, orbitofrontal cortex, and fusiform gyrus. Widespread effects were observed for MEdu, concentrated in the anterior cingulate gyrus as well as frontal, parietal, and occipital areas. Significant interaction effects were observed in Dataset 2, driven by PDE. Across both datasets, the main effect of PDE on mid-cingulate gyrus was highly consistent.

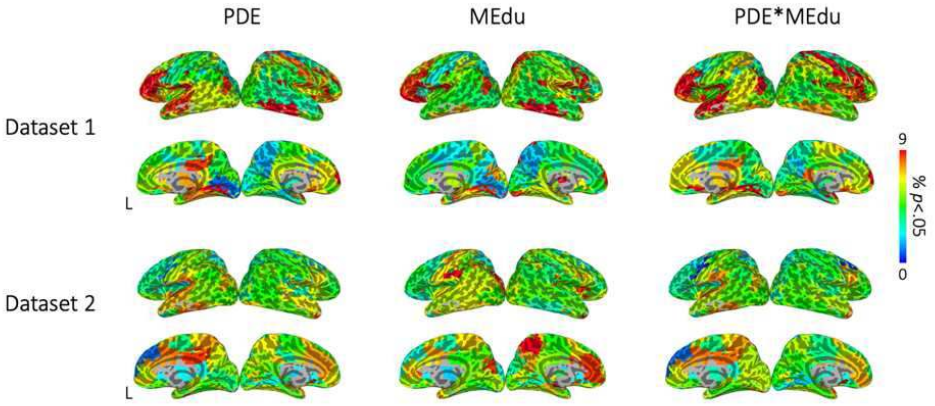

Figure 1. Heatmaps of functional connectivity alterations. Pairwise difference heatmaps show main effects of prenatal drug exposure (PDE), main effects of maternal education (MEdu), and interactive effects between PDE and MEdu on neonatal functional connectivity. The color map and the value of each ROI indicate the percentage of the connections of this particular ROI (to all other ROIs across the whole brain) showing significant effects based on *p*-value thresholding ($p<.05$), where a summary measure defined as the percentage of connections showing differences at $p<.05$ was calculated and assigned to each seed ROI. [PDE: prenatal drug exposure; MEdu: maternal education; ROI: region of interest]

Conclusions: At birth, distinct effects on functional connectivity are observed for both PDE and MEdu. In line with prior studies in children and youth with PDE demonstrating altered structure and function of the cingulate cortex (Morie 2019, Ross 2015), we observed a significant effect of PDE on mid-cingulate functional connectivity across both datasets. Importantly, widespread interactive effects were also observed, indicating that the two risk factors may combine and interact with each other to have differential impacts on pre-/perinatal functional connectivity development depending on the situation. Between the two datasets, we observed markedly different distributions of the effects of PDE and MEdu as well as the interactive effects between PDE and MEdu, which may be due to the heterogeneous polydrug profiles in this population.

References

1. Gao, W. (2015). 'Functional Network Development During the First Year: Relative Sequence
2. and Socioeconomic Correlations.' Cereb Cortex, vol. 25, pp. 2919-2928.
3. Gao, W., (2017). 'Functional Connectivity of the Infant Human Brain: Plastic and Modifiable.'
4. Neuroscientist, vol. 23, pp. 169-184.
5. Gilmore, J. H., (2018). 'Imaging structural and functional brain development in early childhood.' Nat Rev Neurosci, vol. 19, pp. 123-137.
6. Liu, J., (2022). 'Evidence for the Normalization Effects of Medication for Opioid Use Disorder on Functional Connectivity in Neonates with Prenatal Opioid Exposure.' The Journal of Neuroscience, vol. 42, pp. 4555-4566.
7. Morie, K. P., (2019). 'Prenatal drug exposure from infancy through emerging adulthood: Results from neuroimaging.' Drug Alcohol Depend, vol. 198, pp. 39-53.
8. Ross, E. J., (2015). 'Developmental consequences of fetal exposure to drugs: what we know
9. and what we still must learn.' Neuropsychopharmacology, vol. 40, pp. 61-87.
10. Salzwedel, A. P., (2015). 'Prenatal drug exposure affects neonatal brain functional connectivity.' J Neurosci, vol. 35, pp. 5860-5869.
11. Shi, F., (2018). 'Functional Brain Parcellations of the Infant Brain and the Associated
12. Developmental Trends.' Cereb Cortex, vol. 28, pp. 1358-1368.

Poster No 406

Cortical atrophy before and after surgery map to distinct brain networks in temporal lobe epilepsy

Sara Larivière[1], Ke Xie[2], Frederic Schaper[1], Jessica Royer[3], William Drew[4], Sheena Baratono[5], Yifei Weng[6], Zhengge Wang[6], Zhiqiang Zhang[7], Boris Bernhardt[8], Michael Fox[1]

[1]Brigham and Women's Hospital, Harvard Medical School, Boston, MA, [2]McGill University, Montreal, Quebec, [3]Montreal Neurological Institute and Hospital, Montreal, QC, [4]Brigham and Women's Hospital, Brookline, MA, [5]Brigham and Women's Hospital, Boston, MA, [6]Nanjing University, Nanjing, Nanjing, [7]Jinling Hospital, the First School of Clinical Medicine, Southern Medical University, Nanjing, Jiangsu, [8]Montreal Neurological Institute and Hospital, Montreal, Quebec

Introduction: Surgery is the most effective treatment to control seizures in pharmaco-resistant temporal lobe epilepsy (TLE)[1-3]. Although this approach focuses on the hippocampus and nearby temporal lobe structures, most patients also show widespread cortical atrophy beyond this disease epicenter. How these alterations elsewhere in the brain are affected by a

surgical lesion, however, remains a debate. Here, we assessed whether functional connectivity from surgical lesion locations map to brain networks that are associated with cortical atrophy before and after surgery.

Methods: We studied adults with pharmaco-resistant TLE (n=37) who underwent anterior temporal lobectomy as a treatment of their seizures. All patients underwent longitudinal MRI before and after surgery. We segmented patient-specific surgical lesions using the postoperative T1-weighted MRIs (Figure 1A). Using an atlas of normative connectivity (n=1000), we identified the brain networks that were functionally connected to each patient's surgical lesion (Figure 1B)[4,5]. We then tested whether these brain networks could differentiate cortical regions that are atrophied before surgery, after surgery, or at both time points.

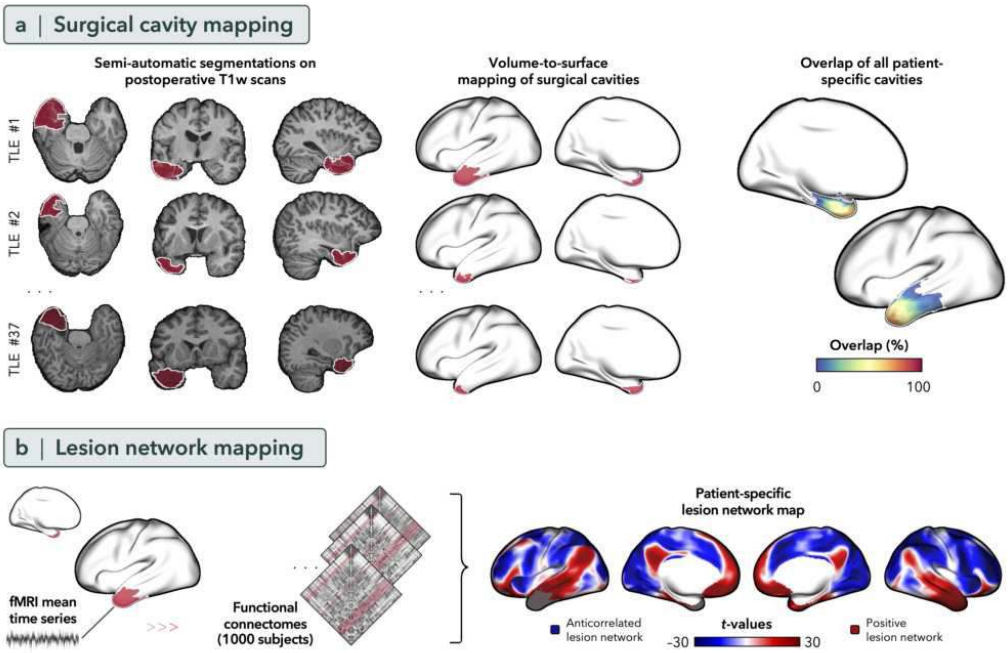

Figure 1. Lesion network mapping approach. (**a**) Surgical cavities were segmented from postoperative T1w MRIs. Cavity masks were excluded in all analyses. (**b**) Example lesion network map (*i.e.*, regions functionally correlated to the surgical lesion). The resulting patient-specific lesion network map shows negative connectivity (or anticorrelation) to fronto-parietal regions (blue regions) and positive connectivity to the temporo-limbic, medial prefrontal, precuneus, and inferior parietal cortices (red regions).

Results: Surgical lesions in all patients were negatively correlated to fronto-parietal regions (henceforth, "anticorrelated lesion network") and positively correlated to the temporo-limbic, medial prefrontal, precuneus, and inferior parietal cortices (henceforth, "positive lesion network"; Figure 1B). Individualized pre- and postoperative cortical atrophy maps were then obtained by comparing cortical thickness in each patient with TLE versus a group of age- and sex-matched healthy controls (n=31). Preoperative cortical atrophy across individual patients peaked in bilateral fronto-central regions (maximum overlap of 51.3%), whereas postoperative atrophy peaked in ipsilateral temporo-insular regions (maximum overlap of 100%; Figure 2A). Testing for morphological associations with the anticorrelated and positive lesion networks revealed significantly more preoperative cortical atrophy in the anticorrelated, relative to the positive, network ($t=-4.16$, $p=1.90\times10-4$). In contrast, more postoperative cortical atrophy was observed in the positive, relative to anticorrelated, network ($t=10.10$, $p=4.79\times10-12$; Figure 2B). Cortical atrophy that was observed in the same regions before and after surgery showed no network preference ($t=1.95$, $p=0.059$).

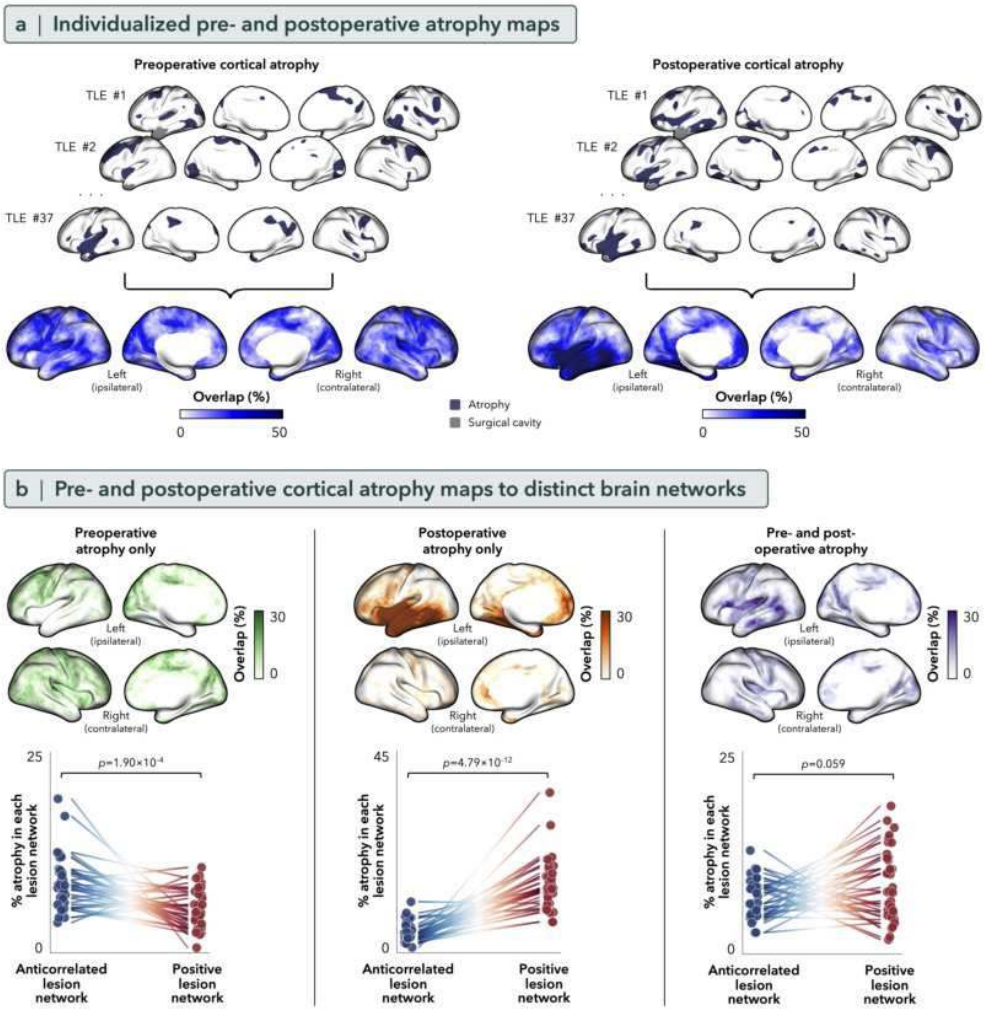

Figure 2. Pre- and postoperative atrophy maps to distinct brain networks. (**a**) *Top*: Example pre- (*left*) and postoperative (*right*) cortical atrophy maps in three individuals with temporal lobe epilepsy (TLE). *Bottom*: Overlap showing percentage of patients with cortical atrophy in the same vertices. (**b**) *Top*: Cortical atrophy before surgery only (*left*), cortical atrophy after surgery only (*middle*), and cortical atrophy before and after surgery (*right*). *Bottom*: Patient-specific percentages of atrophied cortical vertices at each time point in each lesion network, controlling for network size, showing (*left*) greater preoperative atrophy in the anticorrelated (blue), relative to positive (red), lesion network, (*middle*) greater postoperative atrophy in the positive, relative to the anticorrelated, network, and (*right*) no network differences in atrophy that was common before and after surgery.

Conclusions: Brain networks functionally connected to surgical lesions in TLE differentiate pre- from postoperative cortical atrophy patterns. Our findings suggest that atrophy before and after surgery may serve different functions (e.g., compensation vs. disconnection).

References

1. Chen, Z. (2018), 'Treatment Outcomes in Patients With Newly Diagnosed Epilepsy Treated With Established and New Antiepileptic Drugs: A 30-Year Longitudinal Cohort Study', Journal of the American Medical Association Neurology, vol. 75, no. 3, pp. 279-286.
2. Engel, J. (2012), 'Early surgical therapy for drug-resistant temporal lobe epilepsy: a randomized trial', Journal of the American Medical Association, vol. 307, no. 9, pp. 922-930.
3. Wiebe, S. (2001), 'A randomized, controlled trial of surgery for temporal-lobe epilepsy', New England Journal of Medicine, vol. 345, no. 5, pp. 311-318.
4. Holmes, A.J. (2015), 'Brain Genomics Superstruct Project initial data release with structural, functional, and behavioral measures'. Scientific Data, vol. 2, no. 1, pp. 150031.
5. Fox, M.D. (2018), 'Mapping symptoms to brain networks with the human connectome', New England Journal of Medicine, vol. 379, no. 23, pp. 2237-2245.

Poster No 407

Decreased BOLD signal variability in middle-aged and older adults with autism

Stephanie Pedrahita[1], Annika Linke[2], Michaela Cordova[2], Molly Wilkinson[2], Janice Hau[2], Gioia Toro[2], Kalekirstos Alemu[2], Jiwandeep Kohli[2], Ralph-Axel Mueller[2], Ruth Carper[2]

[1]San Diego State University, San diego, CA, [2]Brain Development Imaging Labs, Department of Psychology, San Diego State University, San Diego, CA

Introduction: Autism spectrum disorder (ASD) is a lifelong neurodevelopmental disorder. Preliminary evidence suggests an increased risk for accelerated or early-onset cognitive and neurological decline[5,8,9]. While it is well established that brain development in children, adolescents and young adults with ASD diverges from neurotypical (NT) peers, it is unknown how brain function is impacted in older adults with ASD and what consequences this may have for cognition and behavioral abilities. Better understanding of age-related changes of brain function in ASD is crucial to establish best practices for cognitive and health screenings in adults with ASD and develop preventions that might reduce the risk of accelerated decline. Decreases in blood-oxygenation-level-dependent (BOLD) signal variability in typical aging have been shown across multiple studies[2,3,10], likely reflecting declining Gamma-Aminobutyric Acid (GABA) activity[4,7], and are associated with poorer cognitive performance[1,3]. We hypothesized that adults with ASD would show reduced BOLD signal variability compared to the NT group with steeper negative age associations in the ASD than NT group, potentially reflecting accelerated aging in this cross-sectional sample.

Methods: This study assessed BOLD signal variability in a cohort of adults (40-70 years), 26 with ASD and 37 age-matched typical controls, who participated in a multimodal longitudinal study of aging in ASD. All participants completed two eyes-open 6-minute resting-state fMRI scans acquired on a 3T GE MRI using a fast multiband EPI sequence (TR=0.8s, 2mm iso. voxel size). There were no significant differences between the ASD and NT groups on age, gender, non-verbal IQ, body mass index, co-occurring hypertension, or head motion (RMSD) during the scan. fMRI data underwent standard pre-processing using SPM12 and the CONN toolbox, including rigid-body realignment, normalization to the MNI template, bandpass filtering, and nuisance regression to remove physiological and motion confounds. Average BOLD signal time series were extracted from the Harvard-Oxford anatomical parcellation and BOLD signal variability calculated as the standard deviation of the timeseries for each region of interest (ROI). ROIs were those identified by Lalwani et al.4 to show significant age-related reductions in BOLD signal variability and included frontal, temporal, parietal, occipital and insular cortical areas. General linear models tested for main effects of diagnostic group (ASD, NT), age and group-by-age interactions (controlling for RMSD) in each region. Multiple-comparison corrected statistical significance was defined as Benjamini-Hochberg FDR-adjusted $p<0.1$.

Results: For all ROIs, BOLD signal variability decreased with age across groups (Figure 1A) with right insular cortex and bilateral IFG showing significant age effects when adjusted for multiple comparisons. Significant group-by-age interactions were observed for right insular, left temporal occipital fusiform and right inferior lateral occipital cortex (Figure 1B) with BOLD signal variability showing strong negative associations with age in the ASD but not NT group (Figure 1C).

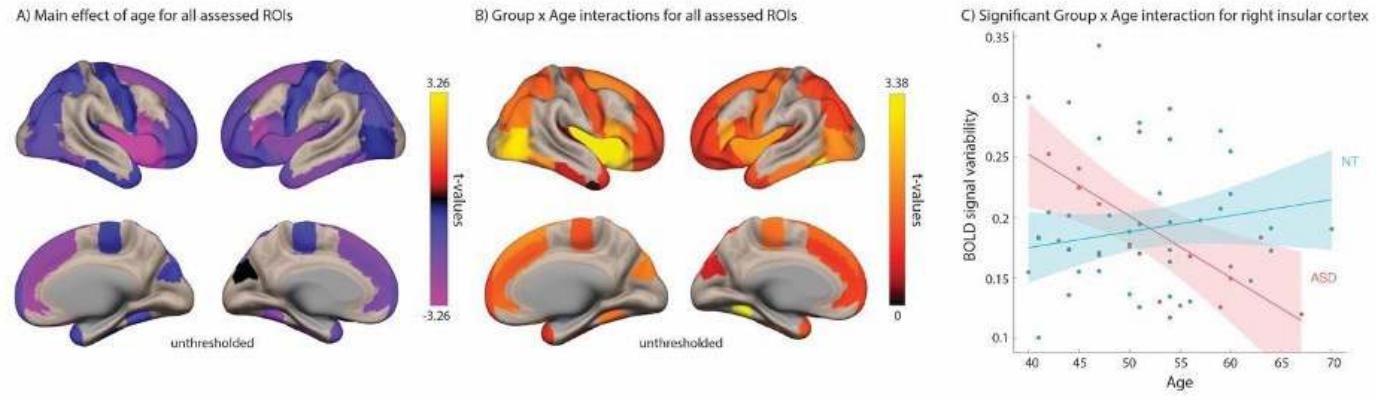

Conclusions: The only previous study assessing BOLD signal variability in ASD was conducted in children and adolescents and found no significant group differences6. When examining older adults with ASD we found cross-sectional age-related changes in BOLD signal variability. Together, these two findings may indicate that decreased BOLD signal variability arises only later in adulthood in ASD, potentially as a result of accelerated aging. However, given limited prior research and evidence from postmortem and animal studies as well as MRI spectroscopy of altered GABA activity across the lifespan in ASD,

additional longitudinal analyses will be necessary to determine if the results presented truly reflect accelerated aging or arise from lifelong persistent differences in brain function.

References

1. Burzynska, A. Z., Wong, C. N., Voss, M. W., Cooke, G. E., McAuley, E., & Kramer, A. F. (2015). White matter integrity supports BOLD signal variability and cognitive performance in the aging human brain. PloS one, 10(4), e0120315.
2. Garrett, D. D., Kovacevic, N., McIntosh, A. R., & Grady, C. L. (2011). The importance of being variable. The Journal of neuroscience : the official journal of the Society for Neuroscience, 31(12), 4496–4503.
3. Grady, C. L., & Garrett, D. D. (2018). Brain signal variability is modulated as a function of internal and external demand in younger and older adults. NeuroImage, 169, 510–523.
4. Lalwani, P., Garrett, D. D., & Polk, T. A. (2021). Dynamic Recovery: GABA Agonism Restores Neural Variability in Older, Poorer Performing Adults. The Journal of neuroscience : the official journal of the Society for Neuroscience, 41(45), 9350–9360.
5. Mason, D., Ronald, A., Ambler, A., Caspi, A., Houts, R., Poulton, R., Ramrakha, S., Wertz, J., Moffitt, T. E., & Happé, F. (2021). Autistic traits are associated with faster pace of aging: Evidence from the Dunedin study at age 45. Autism Research, 14(8), 1684–1694.
6. Nomi, J. S., Bolt, T. S., Ezie, C. E. C., Uddin, L. Q., & Heller, A. S. (2017). Moment-to-Moment BOLD Signal Variability Reflects Regional Changes in Neural Flexibility across the Lifespan. The Journal of neuroscience : the official journal of the Society for Neuroscience, 37(22), 5539–5548.
7. Shew, W. L., Yang, H., Yu, S., Roy, R., & Plenz, D. (2011). Information capacity and transmission are maximized in balanced cortical networks with neuronal avalanches. The Journal of neuroscience : the official journal of the Society for Neuroscience, 31(1), 55–63.
8. Torres, E. B., Caballero, C., & Mistry, S. (2020). Aging with Autism Departs Greatly from Typical Aging. Sensors, 20(2), 572. MDPI AG.
9. Walsh, M. J., Ofori, E., Pagni, B. A., Chen, K., Sullivan, G., & Braden, B. B. (2022). Preliminary findings of accelerated visual memory decline and baseline brain correlates in middle-age and older adults with autism: The case for hippocampal free-water. Frontiers in Aging Neuroscience, 14, 1029166.
10. Waschke, L., Kloosterman, N. A., Obleser, J., & Garrett, D. D. (2021). Behavior needs neural variability. Neuron, 109(5), 751–766.

Poster No 408

Atypical Development of Functional Brain Networks in Neonates with Congenital Heart Disease

Jung-Hoon Kim[1], Josepheen De Asis-Cruz[1], Nickie Andescavage[1], Adre du Plessis[1], Catherine Limperopoulos[1]

[1]Children's National Hospital, Washington, DC

Introduction: A major risk factor for newborns with congenital heart disease (CHD) is delayed brain development, enduring long-term neuromotor and neurocognitive deficits[1,2]. Previous studies have suggested neurobehavioral dysfunction in CHD is already evident in the neonatal period[3,4]. Our previous work has suggested that newborns with CHD showed aberrant brain circuitry[5]. Up to now, however, it remains unknown which large-scale brain networks corresponding to different neurocognitive functions, e.g., visual, somatosensory, auditory, or attention, are vulnerable in CHD. In this work, by leveraging two population-scale datasets acquired from independent sites, we investigated atypical development of brain networks in high-risk CHD prior to open heart surgery compared to healthy controls.

Methods: We analyzed two resting-state functional MRI (rsfMRI) datasets; one public dataset (dHCP dataset) from developing Human Connectome Project consisting of 167 good quality rsfMRI scans of healthy neonates (postmenstrual age, PMA≥41wks; PMA=42.46±1.10wks)[6] and another dataset, acquired at our institute, consisting of 137 healthy neonates (PMA=41.71±1.78wks) and 74 neonates with CHD (PMA=39.96±1.83wks). The dHCP dataset was utilized to define the normative set of functional brain networks (FBNs) with melodic ICA[7]. The number of FBNs was set to 15 heuristically while consistency over varying # of FBNs (=10, 20, and 30) was observed. Our dataset was used for investigating the difference in FBNs between healthy control and CHD. The reconstruction degree was measured by averaging squared correlation between original- and reconstructed cortical patterns using entire or individual FBN(s) over whole timepoints. The occurrence frequency of each FBN per scan was calculated by assigning volume to one of 15 FBNs given minimal cosign distance and dividing by the total volumes. Finally, the group-specific FBN maps were derived by using dual regression.

Results: Fifteen FBNs defined from the healthy newborn population represented various brain networks spanning sensory-related regions (Figure 1A, sensorimotor: FBN1, 2, 3, and 5; visual: 9 and 13, auditory: 7 and 10). Some FBNs covered trans-modal regions, e.g., 6, 7, 8, 11, 12, 14, and 15. We observed the reconstruction degree increased over aging in healthy controls (Figure 1B; r=0.47, p<10-7), but this was not observed in the CHD (r=0.18, p=0.12). CHD showed worse reconstruction level than control when considering age as a covariate (top row, Figure 1C). Interestingly, the association of reconstruction level to age and CHD was distinct across different FBNs (Figure 1D). For example, FBN1 covering sensorimotor regions varied significantly by CHD but not by age. Conversely, the reconstruction degree of FBN7 spanning auditory-associated regions was associated with age but not with CHD. Next, we further investigated group-wise difference in FBN1 (CHD vs. age-matched control; n=45, PMA<41wks). We found that the occurrence of FBN1 was greater in controls than CHD group (Figure 2B, control; 11.55±3.36%

vs. CHD; 8.03±5.21%, p<10-4) while both groups shared similar patterns compared to the normative FBN pattern (Figure 2A; pattern similarity in CHD, r=0.83 vs. in control, r=0.84).

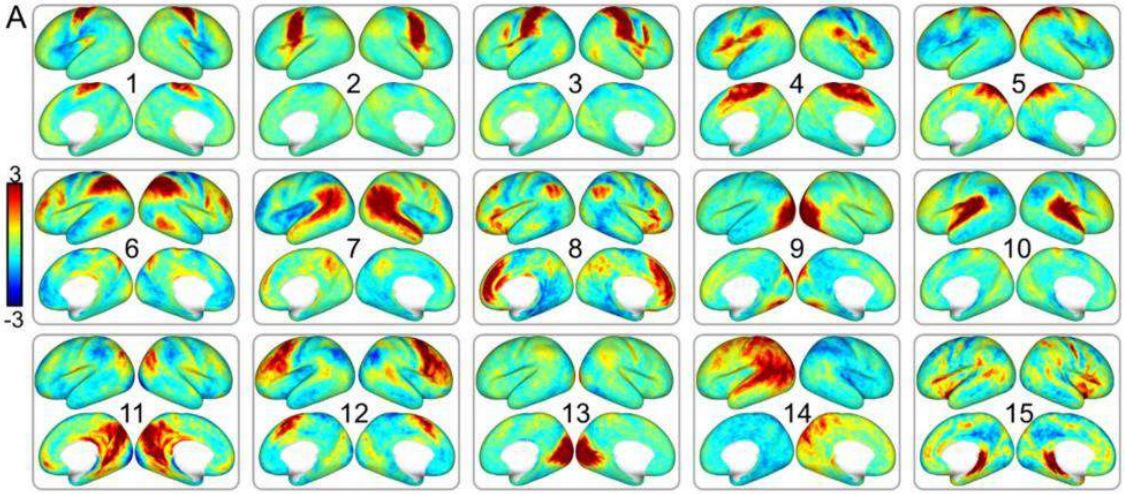

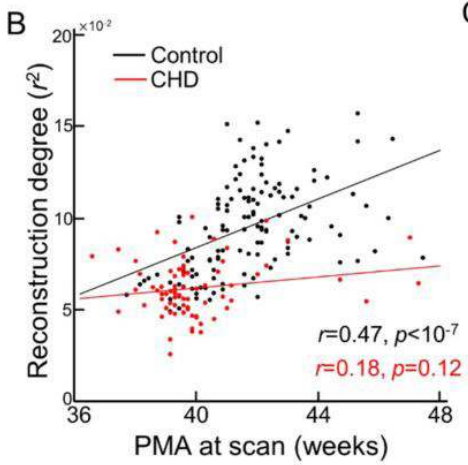

C General Linear Model: Reconstruction degree ~ PMA at scan + Condition

FBN	PMA at scan		Condition (Control vs. Case)	
	T-value	P-value	T-value	P-value
Full FBN	5.92	<10-7	7.72	<10-12
FBN1	1.95	0.05	7.12	<10-10
FBN2	2.73	0.006	5.28	<10-6
FBN3	3.37	0.0009	4.98	<10-5
FBN4	2.56	0.01	4.49	<10-4
FBN5	3.90	0.0001	3.45	0.0007
FBN6	3.46	0.0006	4.56	<10-5
FBN7	3.2	0.001	1.86	0.06
FBN8	3.78	0.0002	4.05	<10-4
FBN9	5.01	<10-5	3.99	<10-4
FBN10	0.94	0.35	4.78	<10-5
FBN11	3.92	0.0001	4.27	<10-4
FBN12	4.84	<10-5	3.15	0.002
FBN13	3.44	0.0007	3.68	0.0003
FBN14	3.43	0.0007	3.18	0.002
FBN15	1.72	0.09	1.32	0.19

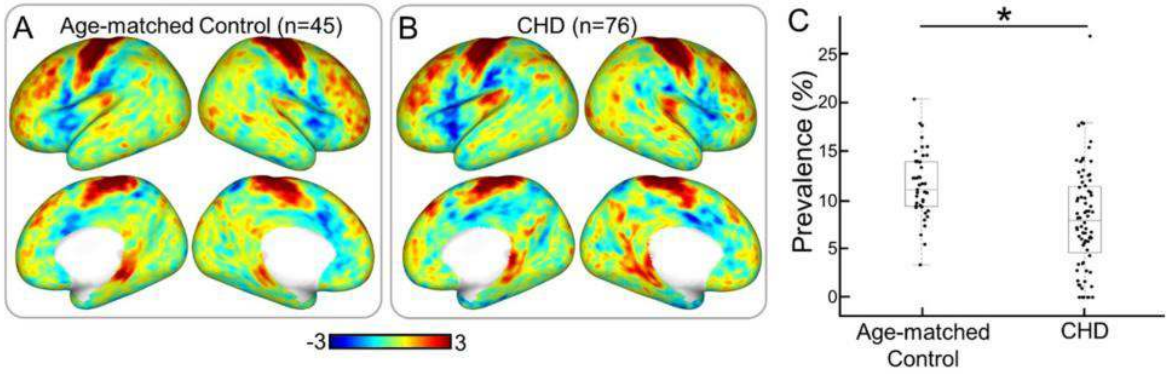

Conclusions: We report that newborns with CHD exhibit atypical brain activity patterns compared to healthy newborns prior to open heart surgery. Notably, unimodal brain networks, specifically related to sensorimotor system, were less represented in the CHD group. Interestingly, while both CHD and healthy controls share similar patterns of sensorimotor network, the occurrence of this network was less frequent in CHD. Our findings provide novel insights into the adverse effect of CHD on functional brain networks. In future works, we plan 1) to investigate the diversity of FBNs across subtypes of CHD and 2) to relate the variations of FBNs in CHD with neurodevelopmental outcomes.

References

1. McQuillen, P.S., Barkovich, A.J., Hamrick, S.E.G., Perez, M., Ward, P., Glidden, D.V., Azakie, A., Karl, T., Miller, S.P., 2007. Temporal and anatomic risk profile of brain injury with neonatal repair of congenital heart defects. Stroke 38, 736–741. http://dx.doi.org/10.1161/01.STR.0000247941.41234.90.
2. Donofrio, M.T., Massaro, A.N., 2010. Impact of congenital heart disease on brain development and neurodevelopmental outcome. Int. J. Pediatr. 2010, 1–13. http://dx.doi.org/10.1155/2010/359390.

3. Clouchoux, C., du Plessis, A.J., Bouyssi-Kobar, M., Tworetzky, W., McElhinney, D.B., Brown, D.W., Gholipour, A., Kudelski, D., Warfield, S.K., McCarter, R.J., Robertson, R.L., Evans, A.C., Newburger, J.W., Limperopoulos, C., 2013. Delayed cortical development in fetuses with complex congenital heart disease. Cereb. Cortex 23, 2932–2943. http://dx.doi.org/10.1093/cercor/bhs281.
4. Limperopoulos, C., Tworetzky, W., McElhinney, D.B., Newburger, J.W., Brown, D.W., Robertson, R.L., Guizard, N., McGrath, E., Geva, J., Annese, D., Dunbar-Masterson, C., Trainor, B., Laussen, P.C., du Plessis, A.j., 2010. Brain volume and metabolism in fetuses with congenital heart disease: evaluation with quantitative magnetic resonance imaging and spectroscopy. Circulation 121, 26–33. http://dx.doi.org/10.1161/CIRCULATIONAHA.109.865568.
5. Miller, S.P., McQuillen, P.S., Hamrick, S., Xu, D., Glidden, D.V., Charlton, N., Karl, T., Azakie, A., Ferriero, D.M., Barkovich, A.J., Vigneron, D.B., 2007. Abnormal brain development in newborns with congenital heart disease. N. Engl. J. Med. 357, 1928–1938. http://dx.doi.org/10.1056/NEJMoa067393.
6. De Asis-Cruz J., Donofrio M. T., Vezina G., Limperopulous C., 2018. Aberrant brain functional connectivity in newborns with congenital heart disease before cardiac surgery. NeuroImage:Clinical, 17 (2018) 31-42, http://dx.doi.org/10.1016/j.nicl.2017.09.020.
7. Fitzgibbon, S.P., Harrison, S.J., Jenkinson, M., Baxter, L., Robinson, E.C., Bastiani, M., Bozek, J., Karolis, V., Grande, L.C., Price, A.N. and Hughes, E., 2020. The developing Human Connectome Project (dHCP) automated resting-state functional processing framework for newborn infants. Neuroimage, 223, p.117303.
8. Jenkinson, M., Beckmann, C.F., Behrens, T.E., Woolrich, M.W. and Smith, S.M., 2012. Fsl. Neuroimage, 62(2), pp.782-790.

Poster No 409

Widespread Associations between Behavioral Metrics and Brain Microstructure in ASD

Benjamin Newman[1], Haylee Ressa[1], Zachary Jacokes[1], Jason Druzgal[1], Kevin Pelphrey[1], John Van Horn[1]

[1]University of Virginia, Charlottesville, VA

Introduction: Autism spectrum disorder (ASD) is a complex, multifaceted condition involving a number of behavioral and cognitive components and diagnosed via behavioral and cognitive tests administered by a trained clinician[1,2]. A recent paper[3] demonstrated that changes in two diffusion MRI cellular microstructural metrics of neuronal capacity, termed aggregate g-ratio and aggregate conduction velocity, are significantly different in autistic individuals compared to non-autistic individuals. If differences in these metrics are representative of genuine neurological differences contributing to ASD, then similar relationships should be observed in validated behavioral tests used to evaluate ASD.

Methods: Participants: 273 subjects (mean age = 154.3 months ±35.21 S.D., 133 female [49%]) were included in this study. 148 were diagnosed with ASD (mean age = 150.8 months ±34.31 S.D., 70 female [47%]) and 124 non-autistic participants (mean age = 154.3 months ±35.21 S.D., 62 female [50%]). Behavioral and Cognitive Metrics: All subjects were evaluated using several widely utilized neuropsychiatric metrics: Clinical Evaluation of language Fundamentals (CLEF-4), Behavior Rating Inventory of Executive Function (BRIEF), Repetitive Behavior Scale (RBS-R), Child Behavior Checklist (CBCL), Adolescent/Adult Sensory Profile, Differential Ability Scales (DAS-School Age), Vineland adaptive behavior scales, and individuals with ASD were further evaluated using the Autism Diagnostic Observation Schedule (ADOS-2), age at language acquisition, and the Autism Diagnostic Interview-Revised for a total of 94 different metrics when subscales from each evaluation were included. Image Acquisition: Diffusion, T1-weighted, and T2-weighted images were acquired from each subject. Diffusion images were acquired with an isotropic voxel size of 2×2×2mm, 64 non-colinear gradient directions at b=1000 s/mm2, and 1 b=0. T1-weighted MPRAGE images with a FOV of 176×256×256mm and an isotropic voxel size of 1×1×1mm, TE=3.3; T2-weighted images were acquired with a FOV of 128×128×34 with a voxel size of 1.5×1.5×4mm, TE=35. Image Processing: As described in more detail in previous work3 images were preprocessed with MRtrix34, FSL5, and Freesurfer6 to calculate voxel-wise aggregate g-ratio and aggregate conduction velocity. The mean value of these metrics was measured within each of the 164 regions of the Destrieux Cortical Atlas and 48 regions of the JHU WM Atlas. Linear models tested the association between the score on each component of each behavioral test and the mean microstructural value in each ROI while controlling for age, sex, scanning site, total brain volume, and IQ with a Benjamini and Hochberg multiple comparison correction.

Results: When examined using data from all subjects, conduction velocity was associated with 47 different subscales in at least 1 ROI (Fig. 1a). The BRIEF, RBS-R, CELF-4, CBCL, SRS-2 and Vineland-II were significantly associated with conduction velocity measured across a wide variety of cortical ROIs but particularly in the superior and frontal cortex, and subcortical gray matter (Fig. 2a). G-ratio was not as widely nor strongly associated across ROIs with the behavioral metrics, with the largest associations found in the deep WM in the BRIEF and DAS. However this pattern was reversed when the associations were considered exclusively within the autistic participants (Fig. 1b). G-ratio was more strongly associated with metrics across a number of ROIs, particularly the CBCL, than conduction velocity. G-ratio relationships were largely located in the motor cortex and WM (Fig. 2b).

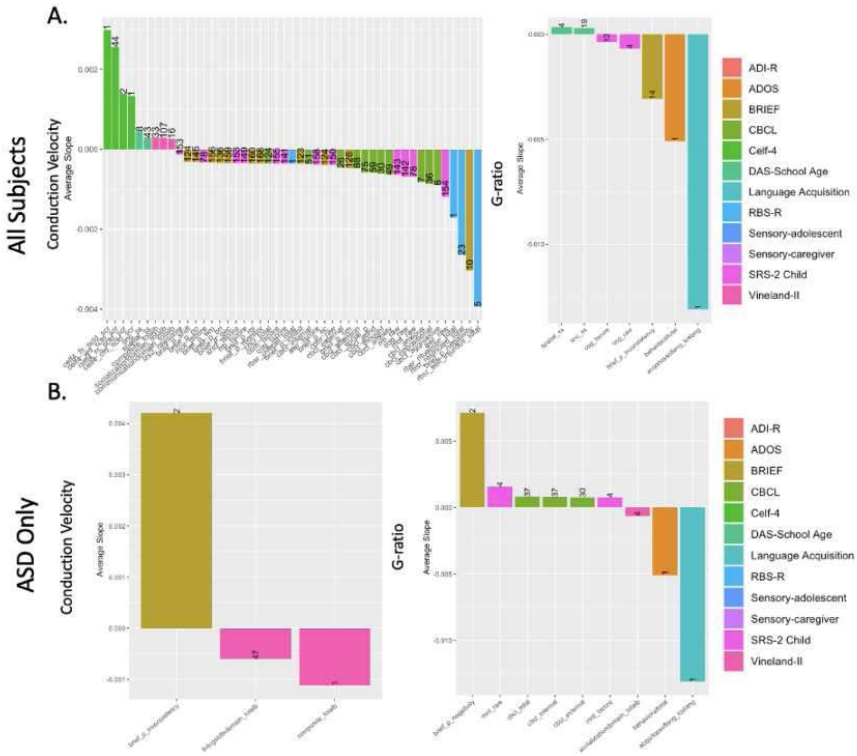

Figure 1: Bar charts showing the mean slope of ROIs significantly associated with each subscale metric, colored by parent metric, and separated by either conduction velocity or g-ratio. Number on bar specifies the number of ROIs that were significantly associated with each metric after multiple comparison correction. Charts show relationships between brain cellular microstructure from a sample that includes all autistic and non-autistic subjects (A) or exclusively subjects diagnosed with ASD (B).

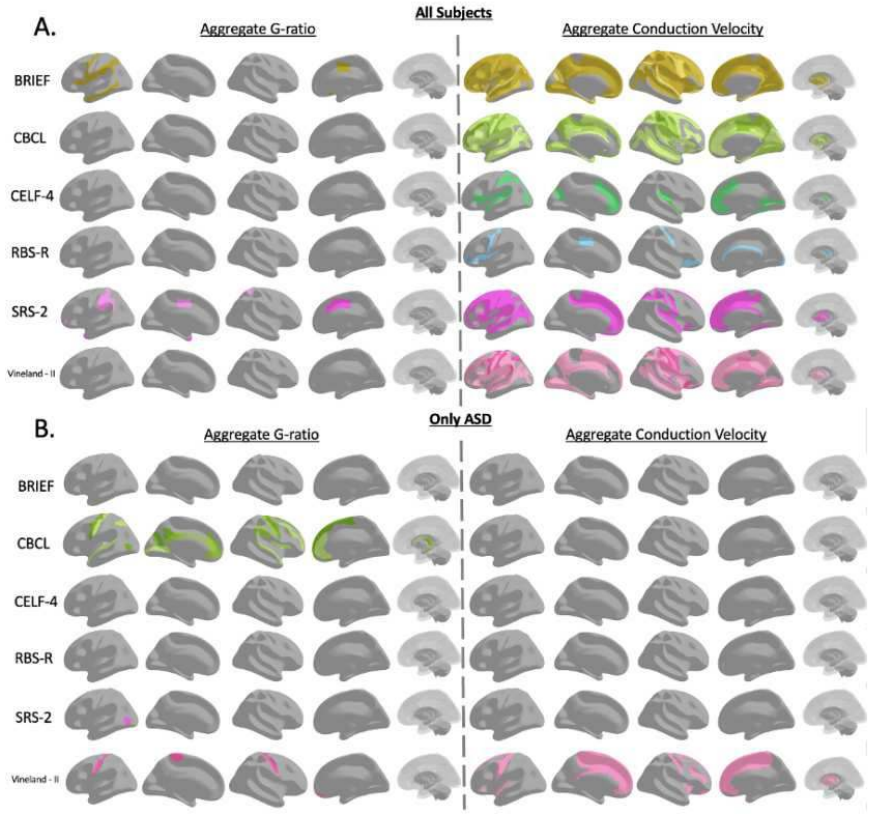

Figure 2: Illustrations showing the location of ROIs significantly associated with each major parent evaluation. Color is consistent with the bar charts in Fig. 1 and is darker if the region is associated with more subscales within the parent evaluation. Illustrations show relationships between brain cellular microstructure from a sample that includes all autistic and non-autistic subjects (A) or exclusively subjects diagnosed with ASD (B).

Conclusions: Despite differences in evaluations there was a great deal of overlap in brain regions associated with the various metrics, particularly when non-autistic subjects are included. However the switch to more significant g-ratio measurements when evaluating exclusively autistic subjects suggests that behavioral severity in autism may not follow the same neurological mechanism as diagnosis.

References

1. Berument, S. K., Rutter, M., Lord, C., Pickles, A., & Bailey, A. (1999). Autism screening questionnaire: Diagnostic validity. The British Journal of Psychiatry, 175(5), 444–451.
2. Constantino, J. N., & Charman, T. (2016). Diagnosis of autism spectrum disorder: Reconciling the syndrome, its diverse origins, and variation in expression. The Lancet Neurology, 15(3), 279–291.
3. Fischl, B. (2012). FreeSurfer. Neuroimage, 62(2), 774–781.
4. Jenkinson, M., Beckmann, C. F., Behrens, T. E., Woolrich, M. W., & Smith, S. M. (2012). Fsl. Neuroimage, 62(2), 782–790.
5. Newman, B. T., Jacokes, Z., Venkadesh, S. T., Webb, S. J., Kleinhans, N. M., McPartland, J. C., Druzgal, T. J., Pelphrey, K. A., Van Horn, J. D., & Consortium, G. R. (2023). Conduction Velocity, G-ratio, and Extracellular Water as Microstructural Characteristics of Autism Spectrum Disorder. bioRxiv, 2023.07. 23.550166.
6. Tournier, J.-D., Smith, R., Raffelt, D., Tabbara, R., Dhollander, T., Pietsch, M., Christiaens, D., Jeurissen, B., Yeh, C.-H., & Connelly, A. (2019). MRtrix3: A fast, flexible and open software framework for medical image processing and visualisation. NeuroImage, 202, 116137.

Poster No 410

Tourette and Chronic Tic disorders: Results from multimodal Brain Imaging Studies in Korea

Jae Hyun Yoo[1], In-Hyang Kim[2], Soo-Min Jang[3], Woo-Seok Choi[4], Yu-Bin Lim[4], Bung-Nyun Kim[4]

[1]The Catholic University of Korea, Seoul St. Mary's Hospital, Seoul, Korea, Republic of, [2]Hanyang University Medical Center, Seoul, Not required for this country, [3]SMG-SNU Boramae Medical Center, Seoul, Not required for this country, [4]Seoul National University Hospital, Seoul, Not required for this country

Introduction: Tic and tourette disorders are neurodevelopmental disorders that develop in early childhood. Literature suggested tic symptoms are associated with widespread structural changes including cortico–striatal–thalamocortical pathway and ascending cortical inputs. Still, methods and sample size have varied widely across imaging studies, findings from stuructural imaging have not been converged yet in tic disorder. In the current study, we aimed to find neural correlates of tic disorder by exploring subcortical morphologic changes and associated anatomical connectivity findings.

Methods: Current study recruited 62 subjects with chronic tic disorder and 62 age-matched controls. To reveal collective alterations alongside subcortical structures and white matter, we sequentially analyzed multimodal imaging data. Using FIRST of FSL, comparison of morphologic alteration has been conducted using high-resolution T1-weighted images. Hence, regions with significant change inputted as seed mask for diffusion tractography by mrtrix3.

Results: The shape ofsubcortical structure among participant with tic disorder showed significant shrinkage in posterodorsal facet of right amygdala (p=0.017), ventromedial facet of right putamen (corrected p=0.029), posterior and lateral facet right pallidum (corrected p=0.041), inferior and lateral facet of right thalamus (corrected p=0.030) and posterodorsal facet of left thalamus (corrected p =0.029). Seed based tractography revealed that tic group showed reduced connectivity between right thalamus-right inferior insula (p=0.001), right thalamus-right posterior lateral fissure (p=0.043), and right putamen-right inferior insula (p=0.037). In contrast, connectivity between right putamen-right orbital area (p=0.028), and right pallidum-right caudate (p=0.013) was stronger in tic group than that of control group.

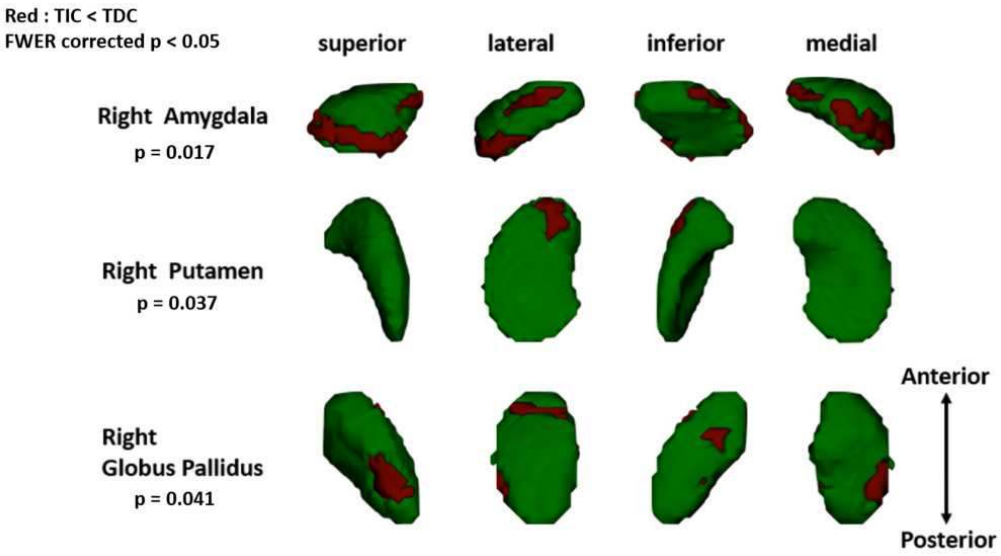

Comparison of the subcortical shape differences between patients with Tourette's and chronic tic disorders and typically developing children.

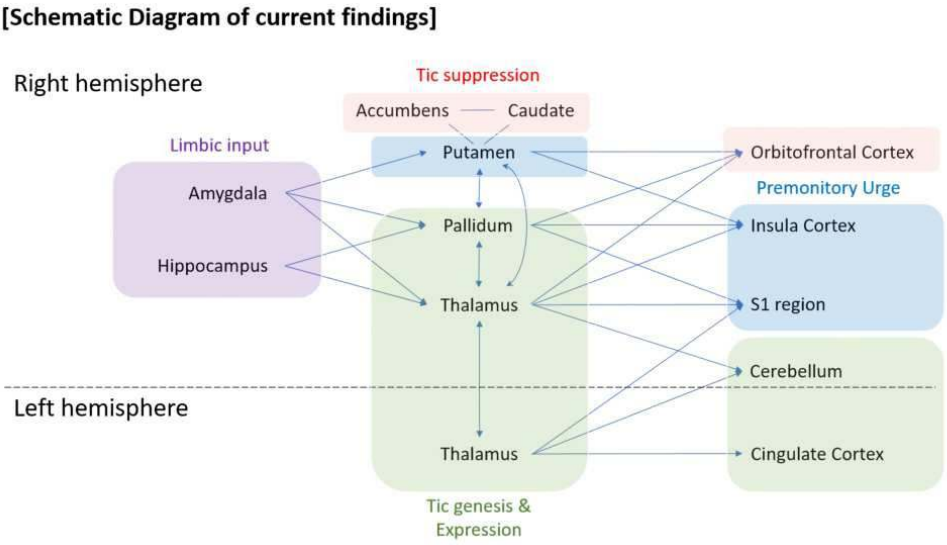

Subcortical-to-cortical network connectivity alterations in patients with Tourette's and chronic tic disorders estimated from current fiber tractography findings.

Conclusions: Current study highlighted that children with chronic tic disorder had morphological changes across several subcortical regions including thalamus, putamen, pallidum and amygdala. In addition, cortical connectivity network from such regions are also well corresponded to neural correlates of genesis, premonitory urge, and suppression of tic.

References

1. Rae, C. L., Critchley, H. D., & Seth, A. K. (2019). A Bayesian Account of the Sensory-Motor Interactions Underlying Symptoms of Tourette Syndrome. Frontiers in Psychiatry, 10, 29. doi: 10.3389/fpsyt.2019.00029. PMID: 30890965; PMCID: PMC6412155.
2. McCairn, K. W., Nagai, Y., Hori, Y., Ninomiya, T., Kikuchi, E., Lee, J. Y., Suhara, T., Iriki, A., Minamimoto, T., Takada, M., Isoda, M., & Matsumoto, M. (2016). A Primary Role for Nucleus Accumbens and Related Limbic Network in Vocal Tics. Neuron, 89(2), 300-307. doi: 10.1016/j.neuron.2015.12.025. PMID: 26796690.
3. Hashemiyoon, R., Kuhn, J., & Visser-Vandewalle, V. (2017). Putting the Pieces Together in Gilles de la Tourette Syndrome: Exploring the Link Between Clinical Observations and the Biological Basis of Dysfunction. Brain Topography, 30(1), 3-29. doi: 10.1007/s10548-016-0525-z. Epub 2016 Oct 25. PMID: 27783238; PMCID: PMC5219042.

Poster No 411

Machine Learning Analysis of Infant Brain Odor Responses in an fMRI Study

Dahyeon Kang[1], Sarah Reeser[1], Allegra Johnson[1], Stephen Dager[1], Mary Larimer[1], Natalia Kleinhans[1]

[1]University of Washington, Seattle, WA

Introduction: With the legalization of cannabis, pregnant women have increasingly turned to cannabis products to alleviate symptoms such as nausea, anxiety, and pain during pregnancy.[1] Yet, there remains a significant gap in research regarding the impact of prenatal cannabis exposure on infant brain development. Infant brains pose unique challenges for study due to their rapid developmental trajectories.[2] While functional Magnetic Resonance Imaging (fMRI) has provided a means to study infant brain development, traditional fMRI statistical methods (e.g., general linear models) encounter limitations in precisely identifying task-dependent brain activation. This is due to the heterochronicity in the maturation process across brain regions, potentially influencing the hemodynamic response function. Therefore, integrating models capable of handling multiple variables, i.e., machine learning, becomes crucial in understanding these complexities. Our study, using fMRI data from infants aged 6 to 9 months with prenatal cannabis exposure (PCE) and a control group (CON), aims to uncover nuanced insights into how such exposure might affect neural processing and responses to olfactory stimuli during this early developmental period.

Methods: Twenty-eight infants (14 PCE, 14 CON) provided valid fMRI data (57.1% male) under natural sleep. Olfactometer tubes were positioned toward the infant's nose to present phenylethyl alcohol, a rose-like odorant which was presented in a block-design, with 'odor+air' for 9s and 'air only' for 18s, repeated 4 times. Olfactometer equipment setup was as previously described.[3] Quiet BOLD fMRI scans were obtained on a Philips Ingenia Elition 3T with a 32-channel head coil (TR/TE=1500/30ms, 2.5 mm^3 isotropic, MB 3, SENSE factor=2, 72 dynamics). Preprocessing was performed using FMRIB's Software Library and included motion correction, brain extraction, detrending, band pass filtering, and registration to the 7.5 month infant template.[2] The regions of interest (ROIs) included in the analyses covered both primary and secondary olfactory cortex (Fig. 1).[4] Python with Scikit-Learn was used for data analysis. A Random Forest Regression was chosen for its capability in handling high-dimensional data and managing multicollinearity among features. SHAP (SHapley Additive exPlanations) values were computed for interpreting feature importance within the defined ROIs.

Results: The Random Forest model demonstrated strong performance in distinguishing between odor and air sensory processing, accounting for 43% of the observed response variance, R^2=0.43, MSE=0.125. SHAP analysis highlighted specific ROIs, such as the pars orbitalis, entorhinal, pallidum, and insula, among others, showing substantial influence in predicting hemodynamic responses to odor (Fig. 1). Further, using multi-level modeling, group- and individual-level differences in time to peak activation and SHAP-values were examined. A significant main effect of Group (b=-0.004, t=-2.131, p=0.03) and an interaction between time-to-peak-activation and Group (b=0.002, t=5.685, p<0.01) were found in the medial orbitofrontal cortex (Med OFC). Specifically, PCE infants exhibited lower SHAP values and longer time-to-peak-activation (10.5s vs. 6s post-stimulus in CON) in the Med OFC (Fig. 3). Lastly, among PCE infants, significant associations were discovered between tetrahydrocannabinol (THC) exposure levels and SHAP values in the left pallidum (b=0.0001, t=2.334, p=.04), such that higher levels of THC correlated with lower SHAP values.

Conclusions: This study offers initial evidence supporting the potential of machine learning in delineating precise neural responses to sensory stimuli in infant brains. By revealing key contributors and their temporal dynamics, it highlights the intricate interplay within the developing brain during sensory processing tasks, thereby opening avenues to develop more precise models of the hemodynamic response that will allow for deeper investigations into early neurodevelopmental processes.

Figure 1. (a) Regions of Interest and (b) Feature Importance Analysis

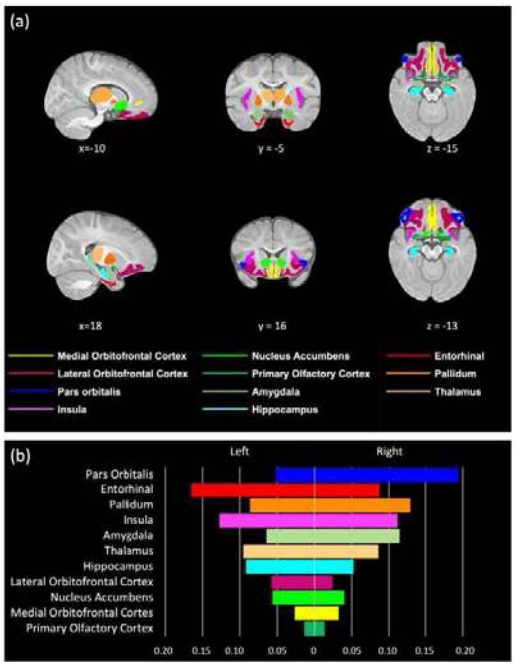

* Primary Olfactory Cortex consisted of a combination of the anterior olfactory nucleus, olfactory tubercle, and frontal and temporal piriform cortices. [4]

Figure 2. Mean |SHAP value| across time at medial orbitofrontal cortex

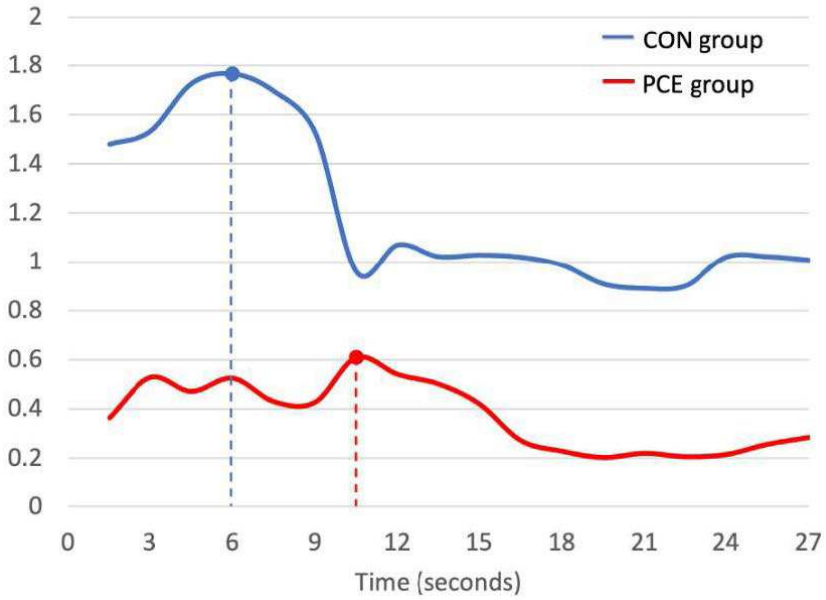

References

1. (Young-Wolff et al., 2019) Young-Wolff, K. C., et al. Trends in marijuana use among pregnant women with and without nausea and vomiting in pregnancy, 2009–2016. Drug Alcohol Depend. 196, 66–70.
2. (Sanchez et al., 2012) Sanchez, C. E., Richards, J. E., & Almli, C. R. Neurodevelopmental MRI brain templates for children from 2 weeks to 4 years of age. Dev. Psychobiol. 54, 77–91.
3. (Kleinhans et al., 2019) Kleinhans, N. M., et al. FMRI correlates of olfactory processing in typically-developing school-aged children. Psychiatry Res. Neuroimaging 283, 67–76.
4. (Zhou et al., 2019) Zhou, G., Lane, G., Cooper, S. L., Kahnt, T., & Zelano, C. Characterizing functional pathways of the human olfactory system. eLife 8, e47177.

Poster No 412

Abnormal imaging neuroanatomy in childhood autism spectrum disorder and schizophrenia

Bin Lu[1], Chaogan Yan[2]

[1]Institute of Psychology, Beijing, Beijing, [2]Chinese Academy of Sciences, Beijing, China

Introduction: Autism spectrum disorder (ASD) and schizophrenia (SCZ) are neurodevelopmental disorders with high morbidity. They share some genetic risks, clinical symptoms and neuroanatomical architectures but also show divergence in these aspects. In the current study, we aim to disclose the consistent and inconsistent atypical imaging-based neuroanatomy of pediatric and adolescent ASD and SCZ patients. The former morphological studies on SCZ consistently reported comprehensively decreased cortical grey matter. For ASD, a study based on large-scale data exchange project - ABIDE - announced lower cortical thickness in a wide-range age group of ASD participants (Haar et al., 2016), but the conflicted results are also frequently reported (see (Baribeau and Anagnostou, 2013) for review). In addition to structural neuroanatomy, resting-state fMRI can illustrate the in vivo functional organization of the brain using connection-based methods including connectome, functional gradient (Margulies et al., 2016), and graph-theoretical indices (Bullmore and Sporns, 2009), which are collectively termed as connectomic anatomy. However, a direct comparison of imaging-based neuroanatomy between pediatric ASD and SCZ was lacking.

Methods: For our multi-center dataset, 229 high-functioning autism individuals, 186 schizophrenia individuals in acute phase under 18 years old, meeting DSM-IV criteria and 128 typical development participants were enrolled through the outpatient clinic and accepted T1-weighted and R-fMRI scans at 5 scanning sites. The procedure was approved by the Ethics Committee of Peking University Sixth Hospital. The MR images were preprocessed and quality controlled using DPABISurf (Yan et al., 2021). After that, surface-based metrics including cortical thickness, subcortical volume, connectome, functional gradient and graph-theoretical indices to depict the abnormal structural and connectomic neuroanatomy of ASD and SCZ.

Results: In general, noteworthy differences exist in the direction and extent of the abnormal structural and connectomic neuroanatomy in ASD and SCZ. For structural neuroanatomy, both ASD and SCZ showed decreased cortical thickness and subcortical volume. However, compared to ASD, SCZ has a thinner bilateral intra-parietal sulcus, right temporo-parieto-occipital junction, and smaller hippocampal volume. For connectomic neuroanatomy, only ASD exhibits a decrease at the network-level in connectome and efficiency, which SCZ does not. Importantly, the decrease in brain network efficiency in ASD may be related to its gradient compression (e.g. decreased gradient range). Almost all (92.3%) brain regions with decreased nodal efficiency show a decline in the primary-to-transmodal gradient or the sensorimotor-to-visual gradient, and all (100%) nodes that decline on both gradients show a significant decrease in efficiency.

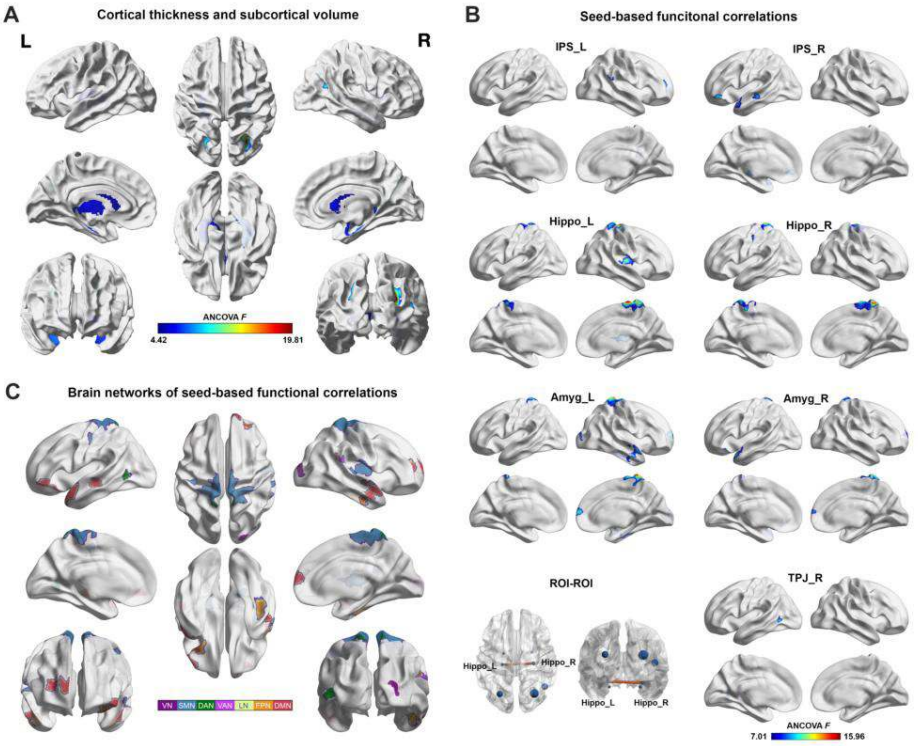

Figure 1. The brain areas showing significant difference in cortical thickness, subcortical volume and anatomical-seed-based functional connection among ASD, SCZ and HC individuals. (A) The brain areas showing significant difference in cortical thickness and subcortical volume among three groups. (B) The brain areas showing significant difference in seed-based functional connections among three groups. The seeds of the functional connections were the brain areas showed atypical anatomy. (C) The overlay map showed the involved brain areas in functional connection distraction.

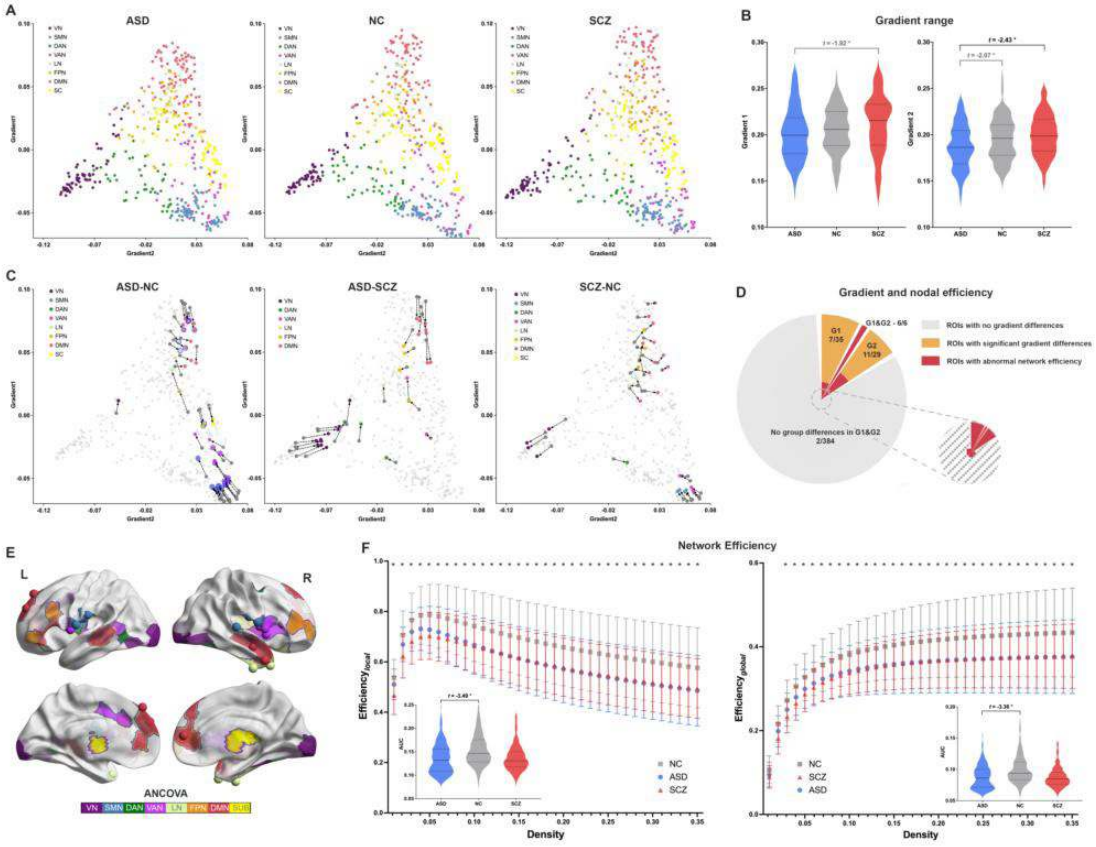

Figure 2. The abnormal functional gradient and network efficiency among ASD, SCZ and HC individuals. (A) The first and second functional gradient profiles of three groups. The color of different node indicated the different brain functional networks. (B) The gradient range of ASD, SCZ and HC individuals. (C)The network nodes showed gradient difference in ASD-HC, ASD-SCZ, and SCZ-HC. The nodes showed no significant difference were marked in grey and the nodes showed significant difference were marked by difference color according to the networks they belong to. The direction of gradient change was marked as arrow line.(D) Overlap of nodes with abnormal nodal efficiency and gradient anomalies. (E) Distribution of nodes with gradient or nodal efficiency abnormalities in the brain. Brain areas with gradient abnormalities are projected onto the brain surface, and nodes with efficiency abnormalities are displayed as colored spheres. (F) The overall differences in local and global network efficiency among the three groups.

Conclusions: In sum, SCZ has greater structural variations, while ASD has more pronounced functional abnormalities. The structural and connectomic neuroanatomical profile of ASD and SCZ showed both shared and distinct brain characteristics.

References

1. Baribeau, D.A., Anagnostou, E., 2013. A Comparison of Neuroimaging Findings in Childhood Onset Schizophrenia and Autism Spectrum Disorder: A Review of the Literature. Front. Psychiatry 4. https://doi.org/10.3389/fpsyt.2013.00175
2. Bullmore, E., Sporns, O., 2009. Complex brain networks: graph theoretical analysis of structural and functional systems. Nat Rev Neurosci 10, 186–198. https://doi.org/10.1038/nrn2575
3. Haar, S., Berman, S., Behrmann, M., Dinstein, I., 2016. Anatomical Abnormalities in Autism? Cereb. Cortex 26, 1440–1452. https://doi.org/10.1093/cercor/bhu242
4. Margulies, D.S., Ghosh, S.S., Goulas, A., Falkiewicz, M., Huntenburg, J.M., Langs, G., Bezgin, G., Eickhoff, S.B., Castellanos, F.X., Petrides, M., Jefferies, E., Smallwood, J., 2016. Situating the default-mode network along a principal gradient of macroscale cortical organization. Proc. Natl. Acad. Sci. U.S.A. 113, 12574–12579. https://doi.org/10.1073/pnas.1608282113
5. Yan, C.-G., Wang, X.-D., Lu, B., 2021. DPABISurf: data processing & analysis for brain imaging on surface. Science Bulletin 66, 2453–2455. https://doi.org/10.1016/j.scib.2021.09.016

Poster No 413

EEG Microstates Reveal Altered Default-mode Network Dynamics Related to Attention in Narcolepsy

Xiao Han[1], Feiyan Chen[1]

[1]Bio-X Laboratory, School of Physics, Zhejiang University, Hangzhou, China

Introduction: Narcolepsy is a chronic neurological disorder characterized by the dysfunction of hypocretin system. In addition to cataplexy and excessive daytime sleepiness, patients always exhibit cognitive disturbances, such as difficulty in attention sustaining and decision making, accompanied by depression, anxiety(Bassetti et al., 2019). Previous neuroimaging studies in narcolepsy have reported the functional abnormalities of default-mode network (DMN) in resting-state functional magnetic resonance imaging (fMRI) (Fulong et al., 2020). In this study, we aim to investigate abnormalities of DMN by the electroencephalographic microstates. Moreover, we seek to explore the relationship between the anomalous DMN and the sustaining attention disturbances, neuropsychological assessment, clinical data in narcolepsy.

Methods: Narcolepsy type 1 patients (NT1, n=40) and control group (Control, n=40) were recruited to collect their resting-state EEG data before and after their participations in Sustained Attention to Response Task (SART) (each lasting three minutes). Before EEG recordings, neuropsychological assessment was applied. We used resting-state EEG data before the task for data analysis, and the data after the task as the validation set. EEG data was filtered with a 0.5-30 Hz band-pass for further microstates analysis. EEG microstates were analyzed by the k-means clustering, which yielded seven prototypes for group comparisons (Figure 1.A). Four of the prototypes correspond to the classic microstate prototypes used in other brain disease studies (da Cruz et al., 2020; Lei et al., 2022). Previous studies suggested that microstate C and microstate F mainly contributed to the posterior cingulate cortex (PCC) and the dorsal anterior cingulate cortex (ACC) which belong to DMN. Microstate E also involves DMN and Microstate G might be associated with the sensorimotor network (Custo et al., 2017). the relationship between microstates properties and the sustaining attention disturbances, neuropsychological assessment, clinical data was analyzed with correlation analyses.

Results: At the group level, the NT1 exhibits a significant decrease in microstate C properties, including time coverage and occurrence (Figure 1). It is also accompanied by an increase in microstates E and F properties significantly, indicating that the disrupted temporal dynamics of DMN. In correlation analyses, the occurrence of MS C in the NT1 was negatively correlated with the reaction time variability in the SART task ($r = 0.65$, $p < 0.001$). It revealed that the decline of PCC activity in DMN might impair the stability of sustained attention. The coverage and duration of MS F in the NT1 was positively associated with Patient Health Questionnaire-9 (PHQ-9) ($r = 0.42$, $p = 0.010$) and Barratt Impulsiveness Scale Version 11 (BIS11) ($r = 0.49$, $p = 0.002$). This result suggested the abnormal activity in the ACC, which might result in patients more prone to impulsivity and emotional dysregulation. Furthermore, the occurrences of microstates E and G showed significantly positive correlations with N3 sleep latency ($r = 0.45$, =0.011) and REM latency ($r = 0.56$, $p < 0.001$) respectively. These results encouraged future study to pay more attention to the relationship between microstates and sleep indicators for clinical treatment in the narcolepsy.

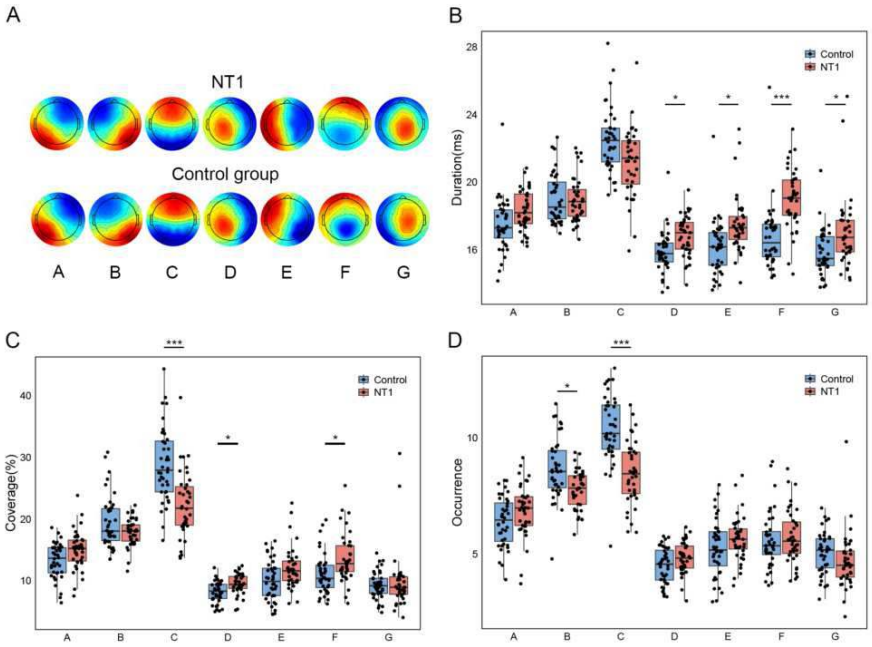

Figure 1: Measures of electroencephalographic microstate (MS) in Narcolepsy type 1 vs. control group. (A) the seven electroencephalographic MSs for the two conditions: NT1, Control group. (B) Mean Duration of each MS. (C) Time coverage of each MS. (D) Occurrence of each MS. Bonferroni corrected for 21comparisons. ***$p < 0.001$, *$p < 0.05$.

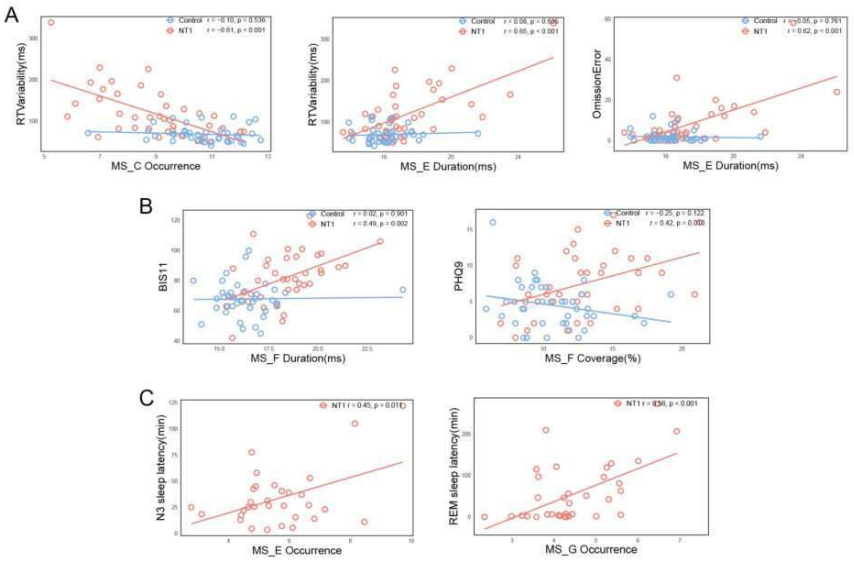

Figure 2.Brain-behavior associations(A), brain-neuropsychology associations(B), brain-clinic associations(C)

Conclusions: Our study utilized the property of EEG MS as a biomarker for narcolepsy. We demonstrated that narcolepsy presented anomalous temporal dynamics of DMN. Further, the differential characteristics of microstates suggest that distinct regions of DMN exhibit divergent abnormalities, implying a complex pathological landscape within DMN in NT1. Additionally, the DMN may play an essential role in the sustained attention, emotional regulation, sleep rhythms. It suggests that abnormalities in DMN may cause patients poorer sustained attention ability and more prone to impulsivity and depression, along with abnormalities of sleep.

References

1. Bassetti, C. L. A., Adamantidis, A., Burdakov, D., Han, F., Gay, S., Kallweit, U., Khatami, R., Koning, F., Kornum, B. R., Lammers, G. J., Liblau, R. S., Luppi, P. H., Mayer, G., Pollmächer, T., Sakurai, T., Sallusto, F., Scammell, T. E., Tafti, M., & Dauvilliers, Y. (2019). Narcolepsy—Clinical spectrum, aetiopathophysiology, diagnosis and treatment. Nature Reviews Neurology, 15(9), 519–539. https://doi.org/10.1038/s41582-019-0226-9
2. Custo, A., Van De Ville, D., Wells, W. M., Tomescu, M. I., Brunet, D., & Michel, C. M. (2017). Electroencephalographic Resting-State Networks: Source Localization of Microstates. Brain Connectivity, 7(10), 671–682. https://doi.org/10.1089/brain.2016.0476
3. da Cruz, J. R., Favrod, O., Roinishvili, M., Chkonia, E., Brand, A., Mohr, C., Figueiredo, P., & Herzog, M. H. (2020). EEG microstates are a candidate endophenotype for schizophrenia. Nature Communications, 11(1), Article 1. https://doi.org/10.1038/s41467-020-16914-1
4. Fulong, X., Spruyt, K., Chao, L., Dianjiang, Z., Jun, Z., & Fang, H. (2020). Resting-state brain network topological properties and the correlation with neuropsychological assessment in adolescent narcolepsy. Sleep, 43(8), zsaa018. https://doi.org/10.1093/sleep/zsaa018
5. Lei, L., Liu, Z., Zhang, Y., Guo, M., Liu, P., Hu, X., Yang, C., Zhang, A., Sun, N., Wang, Y., & Zhang, K. (2022). EEG microstates as markers of major depressive disorder and predictors of response to SSRIs therapy. Progress in Neuro-Psychopharmacology and Biological Psychiatry, 116, 110514. https://doi.org/10.1016/j.pnpbp.2022.110514

Poster No 414

Characterizing neuroinflammation in human patients with temporal lobe epilepsy using [18F]FEPPA PET

Theodore Imhoff-Smith[1], Alan McMillan[1], Mariel Aparicio[1], Brinda Sevak[1], Rosario Ciliento[1], Veena Nair[1], Vivek Prabhakaran[1], Nagesh Adluru[1], Aaron Struck[1]

[1]University of Wisconsin-Madison, Madison, WI

Introduction: Drug resistance in epilepsy is associated with increased mortality, poor quality of life, and cognitive, affective, and social disabilities. Epilepsy is also characterized by widespread neuroinflammation, a potential causative factor and consequence of seizures. Pathology from temporal lobe epilepsy (TLE) patients and mouse models of epilepsy have found elevated levels of interleukins, toll-like receptors, microglial/monocyte activation, and Tumor Necrosis Factors (TNFs), underscoring the inflammatory nature of the condition. Translocator Protein (TSPO) serves as a biomarker for neuroinflammation in humans and animals, predominantly reflecting microglial activation. [18F]FEPPA, a third generation TSPO radioligand, has demonstrated success in human positron emission tomography (PET) studies, offering favorable binding kinetics for effective imaging of neuroinflammation in humans. Despite its potential, application of FEPPA for understanding brain inflammation in humans, particularly in epilepsy, is in its early stages. This study employs [18F]FEPPA PET/MR to characterize neuroinflammation in TLE patients to better understand the interplay between seizures and neuroinflammation in humans.

Methods: Clinical data, T1-weighted MR and FEPPA PET images were acquired from 15 patients (age=35+/-12.4, 10 male) and 12 controls (age=39.5+/-12.0, 6 male) on a GE HealthCare Signa simultaneous 3T PET/MR system. T1-weighted MR images were processed using FreeSurfer (v7) to skull-strip, register and derive anatomical parcellations of reconstructed PET images using the Destrieux atlas for region of interest (ROI) analysis of the PET data. Participants were classified as high, low, or mixed-affinity binders based on TSPO polymorphism (rs6971). Preliminary analysis excluded participants with a low allele and those missing clinical or imaging data, resulting in 10 patients (age=38.7+/-12.9, 6 high allele, 6 males) and 7 controls (age=33.3+/-8.3; 5 high allele, 5 males). FEPPA binding was quantified with standard uptake values (SUVs) for motion-corrected PET images reconstructed between 50-70 minutes post injection. Mean SUV was computed for each ROI and group differences were tested for significance using linear modeling via the lm package in R by regressing mean SUV on group for each allele type. ROI analyses were corrected for false discovery rate (FDR) using the Benjamini-Hochberg procedure.

Results: As shown in Fig. 1, FEPPA uptake is greater in TLE patients compared to controls when grouped over both alleles ($t(15)=2.45$, $p=.027$) and within the high allele group ($t(9)=2.75$, $p=.023$). Group differences in the mixed allele group were not significant ($t(4)=0.58$, $p=.595$). Increased FEPPA SUV ($p<.05$, FDR corrected) was observed in TLE patients compared to controls across at least 25% of brain regions within all lobes of participants with the high allele (Fig. 2).

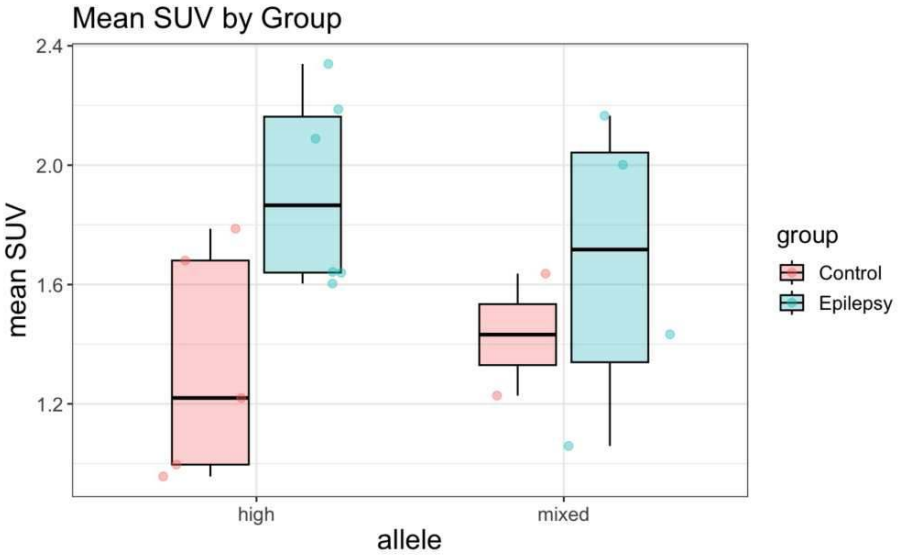

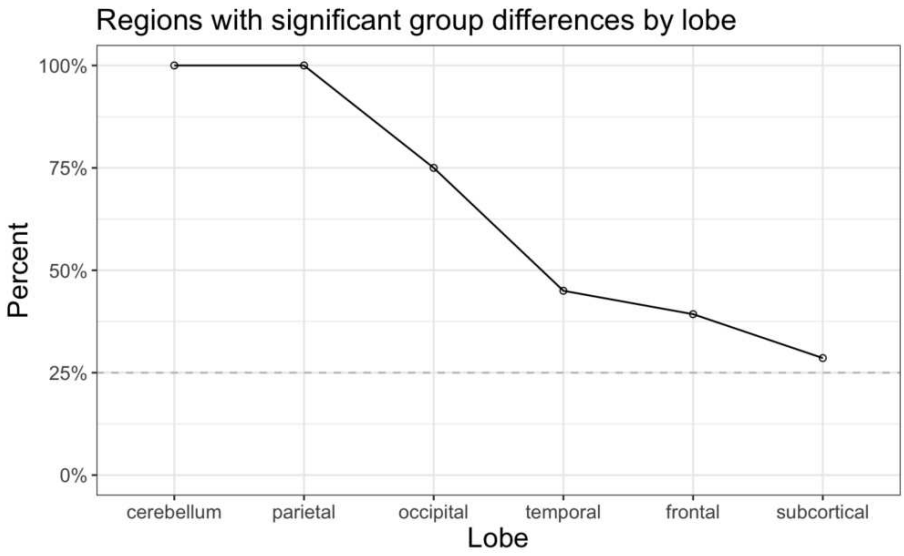

Conclusions: This study provides promising preliminary insights into neuroinflammation in human patients with epilepsy. Elevated FEPPA uptake across brain regions in humans with TLE aligns with the established link between epilepsy and heightened levels of interleukins, toll-like receptors, and microglial/monocyte activation in animal models and underscores the pervasive nature of neuroinflammation in the disorder. These results show promise for future analysis investigating relationships between FEPPA uptake, seizure occurrence, and other clinical variables, highlight the importance of targeting inflammation as a potential avenue for therapeutic interventions, and the potential of FEPPA as a sensitive neuroinflammatory biomarker for monitoring disease progression and treatment responses in humans with epilepsy.

References

1. Chen MK, et al. (2008), 'Translocator protein 18 kDa (TSPO): molecular sensor of brain injury and repair', Pharmacology & Therapeutics, 118(1), 1-17.
2. Löscher, W., et al. (2020), 'Drug Resistance in Epilepsy: Clinical Impact, Potential Mechanisms, and New Innovative Treatment Options', Pharmacological Reviews, 72(3), 606-638.
3. Maroso, M., et al. (2010), 'Toll-like receptor 4 and high-mobility group box-1 are involved in ictogenesis and can be targeted to reduce seizures', Nature Medicine, 16(4), p. 413-9.
4. Rusjan PM, et al. (2011), 'Quantitation of translocator protein binding in human brain with the novel radioligand [18F]-FEPPA and positron emission tomography', Journal of Cerebral Blood Flow & Metabolism, 31(8), 1807-1816.
5. Vezzani, A., et al. (2011), 'The role of inflammation in epilepsy', Nature Reviews Neurology, 7(1), p. 31-40.

Acknowledgements

We thank Heather Floerke for her contribution processing the blood samples.

Poster No 415

Functional Imaging Derived ADHD Biotypes Based on Deep Clustering May Guide Personalized Medication

Aichen Feng[1], Dongmei Zhi[2], Yuan Feng[3], Rongtao Jiang[4], Zening Fu[5], Ming Xu[6], Shan Yu[7], Michael Stevens[8], Li Sun[3], Vince Calhoun[9], Jing Sui[10]

[1]Institute of Automation, Chinese Academy of Sciences, Beijing, China, Beijing, China, [2]Beijing Normal University, Beijing, Select a State, [3]Peking University Sixth Hospital/Institute of Mental Health, National Clinical Research Center for M, Beijing, China, Beijing, China, [4]Yale School of Medicine, New Haven, CT, [5]Tri-institutional Center for Translational Research in Neuroimaging and Data Science (TReNDS) Georgi, Atlanta, GA, [6]Institute of Automation, Chinese Academy of Sciences, Beijing, Select a State, [7]Brainnetome Center and National Laboratory of Pattern Recognition, Institute of Automation, Chinese, Beijing, Beijing, [8]Department of Psychiatry, Yale University School of Medicine, New Haven, CT, United States., New Haven, CT, United States., New Haven, CT, United States., [9]GSU/GATech/Emory, Decatur, GA, [10]Beijing Normal University, Beijing, China

Introduction: Attention deficit hyperactivity disorder (ADHD) is one prevalent neurodevelopmental disorder with childhood onset, however, there is no clear correspondence established between clinical ADHD subtypes and primary medications. Identifying objective and reliable neuroimaging markers for categorizing ADHD biotypes may lead to more individualized, biotype-guided treatment.

Methods: A population graph was first constructed based on functional network connectivity (Fig. 1a) and phenotypic information (age, gender) to build individual mappings; where FNCs serve as the feature of the nodes and the similarities between two subjects, which were abstracted from gender and age serve as edges. Then we applied GCN-BSD to learn embeddings that are both group-discriminative between ADHD and controls, as well as adapted to the clustering constraint through K-Means loss (Fig. 1b). We selected 1069 ADHD patients from the ABCD study as the discovery dataset, identified K=2 for biotype division via the cluster sum of square (CSS) using the elbow method31, and evaluated the clustering performance of 4 popular algorithms, including (1) agglomerative clustering, (2) conventional K-Means, (3) DNN with deep K-Means, and (4) autoencoder GCN with K-Means with GCN-BSD based on Davies-Bouldin Index (DBI) and Calinski-Harabasz Index (CHI)32 (Fig. 1c). As a result, two ADHD biotypes were identified, manifesting with different FNC patterns and distinguishing cognitive abilities. Then we used 130 ADHD and 105 controls collected from Peking University Sixth Hospital as validation dataset to test the generalizability and potential clinical use of the identified biotypes. Interestingly, we found that ADHD biotypes identified in ABCD and PKU showed high similarity and replicability in FNC patterns(Fig. 1d). The most contributing FNCs and clinical records were compared dedicatedly between two biotypes. Specifically, biotype 1 presented milder symptoms while biotype 2 manifested more severe hyperactivity/impulsivity symptoms and worse cognitive levels. Finally, we compared the symptom relief and treatment outcome of two biotypes from 44 out of 130 ADHD patients either treated by MPH or ATX at PKU6 according to our division (Fig. 1e).

Results: Biotype 1 contained more patients, presented milder symptoms, and overrepresented several wildly recognized brain aberrations including frontal gyrus and cerebellum. In contrast, biotype 2 included fewer patients, presented more severe symptoms especially hyperactive/impulsive, and showed greater degrees in regions from DM to SM, as well as the connectivity between the cerebellum and fusiform gyrus. Interestingly, in addition to differences in cognitive performance and hyperactivity/impulsivity symptoms, biotype 1 treated with methylphenidate demonstrated significantly better recovery than biotype 2 treated with atomoxetine ($p<0.05$, FDR corrected).

Conclusions: Collectively, in this study, we proposed a novel framework, GCN-BSD, that can jointly characterize brain imaging data and phenotypic association and further use this knowledge to guide disease biotype detection. Importantly, the identified two ADHD biotypes exhibit significant group differences in functional networks and multiple cognitive abilities and symptoms, especially in fluid intelligence and hyperactive/impulsive. All the above findings indicate the validation of the frontoparietal circuits to serve as a key signature to ADHD and provide the first evidence for the connection from the cerebellum to the fusiform gyrus to be used as a biomarker in the uncommon subgroup. This study helps move forward from a conventional biotype detection approach to the use of a more flexible deep learning-based analysis.

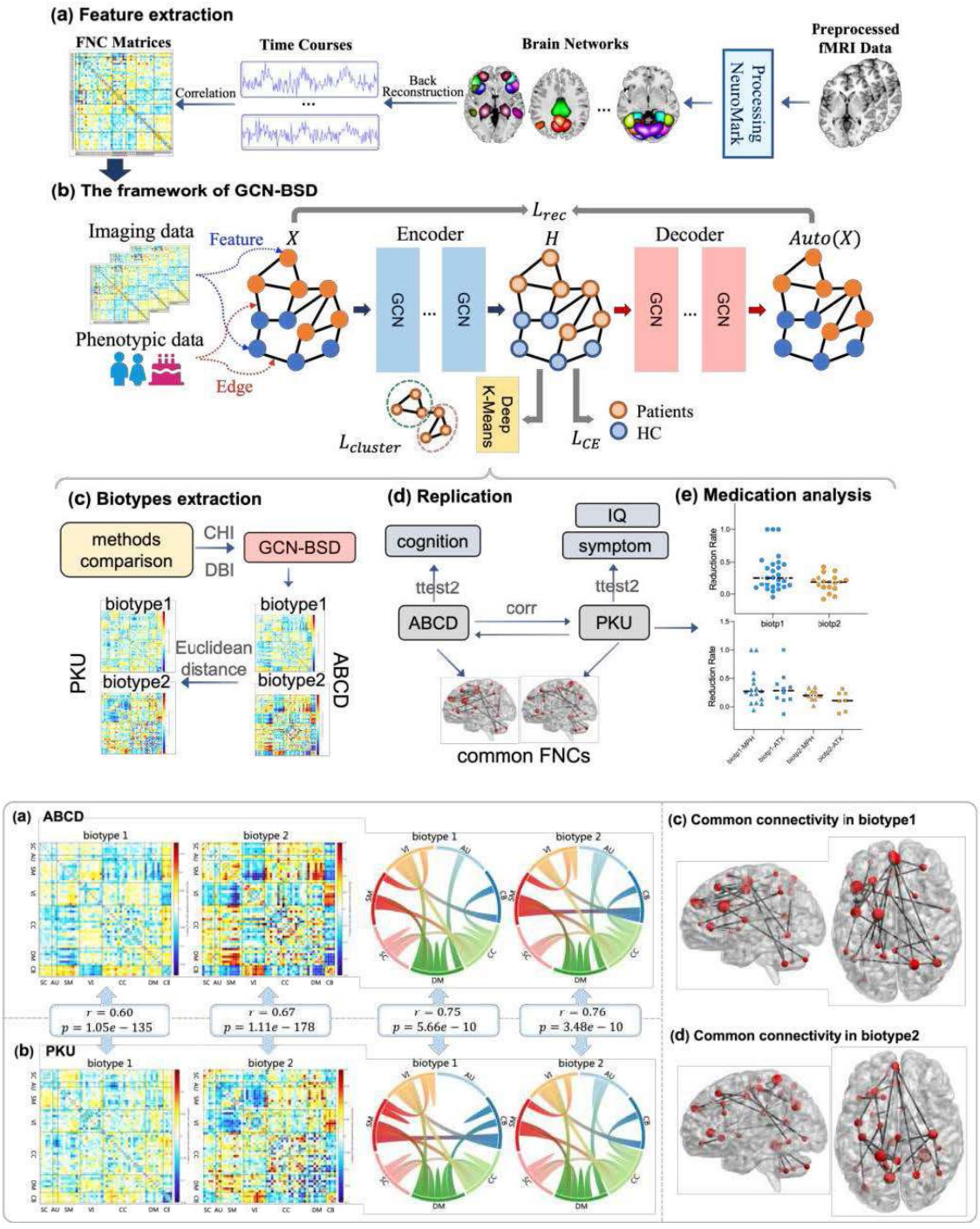

References

1. Association, A.P. Diagnostic and Statistical Manual of Mental Disorders, Fifth Edition - Coding Update. (2014).
2. Sobanski, E., et al. Subtype differences in adults with attention-deficit/hyperactivity disorder (ADHD) with regard to ADHD-symptoms, psychiatric comorbidity and psychosocial adjustment. European Psychiatry 23, 142-149 (2008).
3. Mentales, M. Kaplan & Sadock's synopsis of psychiatry. (2007).
4. Gorman, E.B., Klorman, R., Thatcher, J.E. & Borgstedt, A.D. Effects of methylphenidate on subtypes of attention-deficit/hyperactivity disorder. Journal of the American Academy of Child & Adolescent Psychiatry 45, 808-816 (2006).
5. Blondeau, C. & Dellu-Hagedorn, F. Dimensional analysis of ADHD subtypes in rats. Biological psychiatry 61, 1340-1350 (2007).
6. Grizenko, N., Paci, M. & Joober, R. Is the inattentive subtype of ADHD different from the combined/hyperactive subtype? Journal of attention disorders 13, 649-657 (2010).
7. Li, T., et al. Characterizing neuroanatomic heterogeneity in people with and without ADHD based on subcortical brain volumes. Journal of child psychology and psychiatry 62, 1140-1149 (2021).
8. Karalunas, S.L., et al. Subtyping attention-deficit/hyperactivity disorder using temperament dimensions: toward biologically based nosologic criteria. JAMA psychiatry 71, 1015-1024 (2014).
9. Kofler, M.J., et al. Executive functioning heterogeneity in pediatric ADHD. Journal of abnormal child psychology 47, 273-286 (2019).

Poster No 416

Differentiating Autism Spectrum Disorder from Schizophrenia Based on Grey Matter Alteration

Wei-ting Ko[1], Chih-Min Liu[1], Susan Shur-Fen Gau[1]

[1]Department of Psychiatry, National Taiwan University Hospital, Taipei, Taiwan

Introduction: Autism spectrum disorder (ASD) and schizophrenia spectrum disorder (SCZ) were heritable and polygenetic neuropsychiatric disorders. Shared genetic factors between ASD and SCZ modulated grey matter volume. Previous studies reported that adults with ASD have greater regional gray matter volume (rGMV) in the middle and superior temporal gyrus, postcentral gyrus, and parahippocampal gyrus and reduced rGMV in the anterior cingulate cortex and cerebellum oppositely. In SCZ, rGMV loss in left insula, amygdala, and parahippocampus happened at the beginning oThe aim of our study was to compare rGMV between SCZ, ASD, and HC in a single MRI and analyzed the correlation between rGMV and symptomatology.

Methods: SCZ, ASD, and HC were aged 18-28. SCZ group included schizophrenia, schizophreniform disorder, and first-episode psychosis according Statistical Manual of Mental Disorders, Fourth Edition (DSM-IV). The inclusive criteria of ASD based on the DSM-IV and DSM-5 diagnostic criteria for ASD. We used the Positive and Negative Syndrome Scale to measure the symptoms of SCZ and the Social Responsiveness Scale to assess the social deficit and autistic traits of ASD. We applied a three-dimensional magnetization-prepared rapid gradient-echo sequence in a 3T MRI system (Trio, Siemens, Erlangen, Germany) to acquire high-resolution T1-weighted image. Cat12 toolbox (http://dbm.neuro.uni-jena.de/cat/) implemented in SPM12 (http://www.fil.ion.ucl.ac.uk/spm/software/spm12/) were used to extract individual's regional rGMV according to neuromorphometrics atlas (https://www.neuromorphometrics.com/). One-way analysis of covariance (covariate variables were age, sex, and total intracranial volume) performed on the SAS 9.4 software (SAS Institute Inc., Cary, NC). We also applied post-hoc pairwise comparison and multiple-comparison correction. We calculated the Pearson's correlation coefficient between rGMVs and symptomology.

Results: We finally included 64 SCZ (57 males), 75 ASD (64 males), and 107 HC (92 males). The mean age (SD) of SCZ was 22.85 (2.57), ASD was 21.22 (2.33) and HC was 22.31 (2.86). SCZ has extensive rGMV loss apart from bilateral pallidum, which was larger than ASD and HC. The direction of post-hoc analyses were (1) ASD> SCZ: right (R) precuneus gyrus, R parahippocampal gyrus (PHG), and left (L) parahippocampal gyrus. (2) HC, ASD >SSD: R Amygdala, bilateral hippocampus, R ventral diencephalon, bilateral anterior cingulate gyrus (ACG), bilateral anterior insula (AIN), R angular gyrus, L central operculum (CO), bilateral frontal operculum (FO), bilateral fusiform gyrus (FG), R inferior occipital gyrus, L inferior temporal gyrus, R lingual gyrus, bilateral middle cingulate gyrus, R superior frontal gyrus (SFG) medial segment, bilateral middle temporal gyrus, bilateral occipital fusiform gyrus, R posterior cingulate gyrus, bilateral posterior insula, L parietal operculum, R superior frontal gyrus, R supplementary motor cortex, bilateral supramarginal gyrus (SPMG), and bilateral superior temporal gyrus (STG). (3) HC>SSD: L amygdala, L middle frontal gyrus, and R temporal pole. SCZ's rGMVs were statistically significant low to moderate negative correlations with psychiatric symptoms (disorganization symptoms: bilateral AIN and FO; positive symptoms: bilateral FG, R SFG, L SPMG, R STG, and R PHG; excitement symptoms: bilateral pallidum; emotional distress: L posterior insula). ASD's rGMV were statistically significant low negative correlations with autistic symptoms (social emotions: R STG, R amygdala, R precuneus; social awareness: R ACG and L CO; social communication deficits: R SPMG).

Conclusions: First, we found that SCZ has diffuse grey matter reduction in multiple brain regions comparing with healthy controls and ASD. Second, the rGMVs between ASD and HC were not significantly different. Third, the rGMVs in ASD and SSD have associations with their symptomology, respectively.

References

1. Chow, E.W. (2011), 'Association of schizophrenia in 22q11.2 deletion syndrome and gray matter volumetric deficits in the superior temporal gyrus', American Journal of Psychiatry, vol.168, no. 6, pp. 522-529
2. Gudbrandsen, M. (2020), 'Neuroanatomical underpinnings of autism symptomatology in carriers and non-carriers of the 22q11.2 microdeletion', Molecular Autism, vol. 11,no. 1, pp. 46
3. Gupta, C.N. (2015), 'Patterns of Gray Matter Abnormalities in Schizophrenia Based on an International Mega-analysis', Schizophrenia Bulletin, vol. 41, no. 5, pp. 1133-1142
4. Liloia, D. (2021), 'Updating and characterizing neuroanatomical markers in high-risk subjects, recently diagnosed and chronic patients with schizophrenia: A revised coordinate-based meta-analysis.', Neuroscience & Biobehavioral Reviews, vol. 123, pp. 83-103
5. Lin, H.Y. (2017), 'Shared atypical brain anatomy and intrinsic functional architecture in male youth with autism spectrum disorder and their unaffected brothers', Psychological Medicine, vol. 47, no. 4, pp. 639-654
6. Padula, M.C. (2018), 'Cortical morphology development in patients with 22q11.2 deletion syndrome at ultra-high risk of psychosis', Psychological Medicine, vol. 48, no. 14, pp. 2375-2383

Poster No 417

Accessing Brain Network in ADHD Using Relative Phase Analysis

Younghwa Cha[1,2], Joon-Young Moon[1,2]

[1]Center for Neuroscience Imaging Research, Institute for Basic Science, Suwon, Republic of Korea, [2]Sungkyunkwan University, Suwon, Republic of Korea

Introduction: Attention-deficit hyperactivity disorder (ADHD) is a psychological disorder that produces difficulties in focusing and controlling attention and behavior in a daily life of the affected individuals. To address the challenges caused by ADHD, it is crucial to receive an accurate diagnosis and appropriate treatment at their respective stages. However, despite many studies on the disorder, developing accessible and accurate quantitative diagnostic methods presents significant challenges[1]. Furthermore, the underlying causes of the disorder remain relatively unknown. As an attempt to develop effective diagnostic tools and understand the mechanism of the disorder, we analyzed the relative phase patterns of brain waves across the whole brain network to examine the unique properties of the ADHD groups against the control group using their electroencephalography (EEG) data.

Methods: To effectively capture the differences in brain information processing between the ADHD group and the control group, we focused on the phase relationship. In a system, the phase of each signal refers to the specific timing or position of the signal within a periodic waveform. We hypothesized that differences in the phase directionality during resting states between the two groups can assist in diagnosing ADHD and uncovering its characteristics. To examine phase directionality, we calculated the relative phase by subtracting the global mean phase from each electrode's phase within the whole brain area. Relative phase demonstrates the phase-lead and -lag relationships of EEG signals at each time point, thus revealing temporal dynamics in the brain[2,3]. We applied relative phase analysis to eyes closed and eyes open resting state EEG data from the Healthy Brain Network Biobank from the Child Mind Institute, constituting a total of 44 ADHD inattentive patients and 66 control individuals aged 11 and above[4].

Results: we observe a robust switching pattern in the brain networks of both groups between top-down mode (where the higher-order hub regions phase-lead the peripheral sensory regions) and bottom-up mode (where the peripheral regions phase-lead hub regions). To compare the switching patterns between the two groups, we conducted k-means clustering. Based on our analysis, we found significant differences between the ADHD and the control group in mode 4 (the higher-order hub regions phase-lead), both in the eyes closed and eyes open states, at the p-value level of 0.001 from the student-t test (see Fig 1). In the ADHD group, the ratio of mode 4 is 7.98% higher and the dwelling time of mode 4 is 24.30% longer during the eyes closed state compared to the control group. To examine the transition frequency of each mode, we created a transition matrix illustrating the average transition frequency (Hz) between modes (see Fig 2). In both the eyes-open and eyes-closed states, the ADHD group exhibited 57.92% and 32.05% more transitions from mode 4 to mode 4 (staying at mode 4), respectively, compared to the control group. Furthermore, the ADHD group showed fewer instances of staying in mode 2 and mode 3, which serve as pathways connecting mode 1 (the peripheral regions phase-leading) and mode 4 (the higher-order hub regions phase-leading). Our findings suggest that inattentive characteristics of the group may arise from the slower information processing represented by lower switching frequency between the modes.

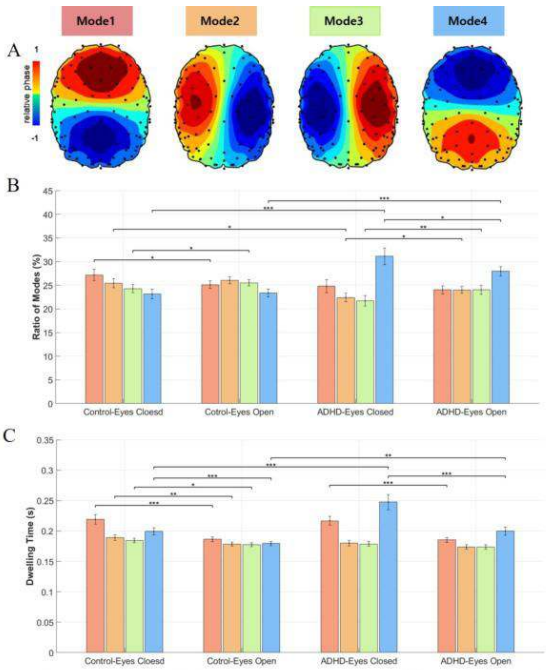

Fig. 1. Ratio of Modes and Dwell Time. Asterisks (*) indicate the results of pairwise t-tests between eyes closed and eyes open states, and of two-sample t-tests between the two groups (statistical significance levels, * = p<0.05, ** = p<0.01, *** = p<0.001). **(A)** Topographic plots of 4-means clustering centroids for the control group during the eyes closed state. Red means phase-leading and Blue means phase-lagging. **(B)** The distribution and t-test results for the ratio of modes based on 4-means clustering indices. The result shows significant differences in the ratio between the ADHD and control groups during mode 4 in the eyes closed and open states. **(C)** The distribution and t-test results for the dwelling time of modes based on 4-means clustering indices. In mode 4, dwelling times are significantly different between the two groups during the eyes closed and open states.

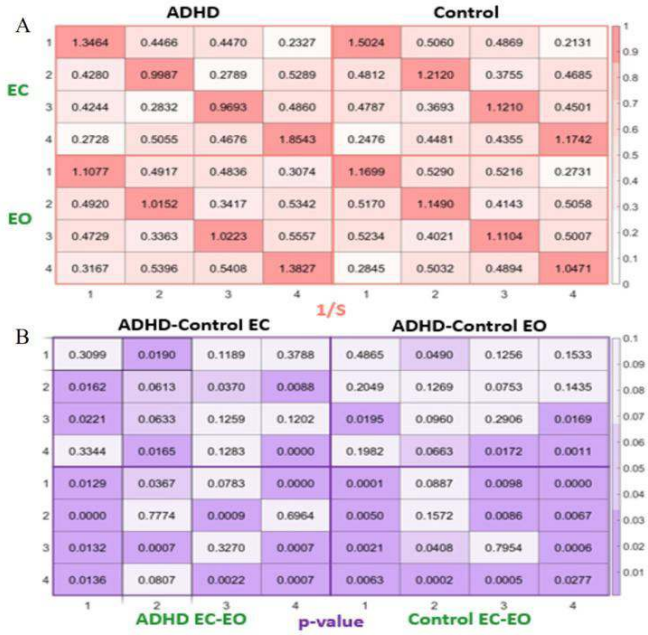

Fig. 2. Transition Matrix. (A) The average transition frequency (Hz) between 4-means clustering modes. The upper and lower rectangles represent transitions during the eyes closed and eyes open. The left and the right side present the transition frequency for the ADHD group, and the control group. Transition frequency from mode 4 to itself showed most significant differences between the ADHD and control groups. **(B)** The p-value matrix showing the results of Student's t-test. The top-left and the top-right rectangles show p-values of two-sample t-tests between the two groups. The lower-left and lower-right contain the results of pair-wise t-tests between the eyes closed and open states.

Conclusions: When considering the differences in ratio, dwelling time, and transition frequency between the two groups in mode 4, we can identify the potential utility of relative phase analysis as a physiological diagnostic tool for the ADHD inattentive subtype. In addition, it can be postulated that the prolonged stay at mode 4 is linked with the underlying mechanisms of ADHD-inattentive type. For future studies, the phase-lead/lag relationship across different brain areas for children under 10 years old and different ADHD subtypes will be completed.

References

1. Brandeis, D., Loo, S. K., McLoughlin, G., Heinrich, H., & Banaschewski, T. (2018). Neurophysiology. Oxford textbook of attention deficit hyperactivity disorder, 82-93.
2. Moon, J. Y., Lee, U., Blain-Moraes, S., & Mashour, G. A. (2015). 'General relationship of global topology, local dynamics, and directionality in large-scale brain networks'. PLoS computational biology, 11(4), e1004225.
3. Moon, J. Y., Kim, J., Ko, T. W., Kim, M., Iturria-Medina, Y., Choi, J. H., ... & Lee, U. (2017). Structure shapes dynamics and directionality in diverse brain networks: mathematical principles and empirical confirmation in three species. Scientific reports, 7(1), 46606.
4. Alexander, L. M., Escalera, J., Ai, L., Andreotti, C., Febre, K., Mangone, A., ... & Milham, M. P. (2017). An open resource for transdiagnostic research in pediatric mental health and learning disorders. Scientific data, 4(1), 1-26.

Poster No 418

Oxygen-carrying Capacity Impacts Gross Motor in Congenital Heart Disease by Altering Brain Structure

Pengcheng Xue[1], Meijiao Zhu[2], Siyu Ma[2], Yuting Liu[2], Peng Liu[2], Bin Jing[3], Daoqiang Zhang[1], Ming Yang[4], Xuming Mo[2], Xuyun Wen[1]

[1]Nanjing University of Aeronautics and Astronautics, Nanjing, Jiangsu, [2]Children's Hospital of Nanjing Medical University, Nanjing, Jiangsu, [3]Beijing Key Laboratory of Fundamental Research on Biomechanics in Clinical Application, Beijing, Beijing, [4]Children's Hospital of Nanjing Medical University, Nanjing, China

Introduction: Congenital Heart Disease (CHD), as the most prevalent congenital anomaly, profoundly affects numerous newborns[1]. While advanced medical interventions have substantially enhanced the survival rates of infants with CHD, a significant proportion of these patients, especially those with complex conditions, experience persistent neurodevelopmental disorders[2]. These disorders detrimentally affect both their physical and mental health. Recent research efforts have thus been focused on elucidating the neurological underpinnings of these disorders, aiming to improve early intervention and treatment strategies. Prior studies in the realm of CHD neurodevelopment have identified a correlation between cortical structural anomalies and adverse neurodevelopmental outcomes[3]. Additionally, many studies has underscored the critical role of abnormal oxygen supply in contributing to brain injuries in CHD patients[45]. Nevertheless, the association between oxygen supply capacity and neurodevelopmental levels remains inadequately investigated. This study, therefore, seeks to integrate multimodal data, including clinical biology, neuroimaging, and neurodevelopmental evaluations, to investigate the relationship between blood oxygen-carrying capacity and gross motor skills in CHD infants.

Methods: In this study, 83 infants with complex CHD and 86 age-matched healthy controls (HCs), aged 1 to 2 years, were enrolled from the Children's Hospital of Nanjing Medical University. We assessed the HB and HCT scores as surrogate markers of blood oxygen-carrying capacity for each participant. Additionally, T1-weighted imaging data were acquired to evaluate cortical developmental levels, and the Gesell Scale was utilized for gross motor performance assessment. Initially, a linear regression model was applied to ascertain the direct correlation between blood oxygen-carrying capacity and gross motor performance. Thereafter, a mediation analysis was conducted to examine the potential indirect relationship between these two variables with the cortical surface area of abnormal brain regions in CHDs serving as the mediator. Specifically, T1-weighted data underwent preprocessing using a specialized infant pipeline[6]. The cerebral cortex was then parcellated into 68 regions using the Desikan-Killiany atlas[7], and cortical surface area of each region was calculated. Abnormal brain regions were identified through group-level two-sample t-tests and Gaussian Process Regression (GPR), as depicted in Fig. 1. The GPR model employed a multi-kernel, multi-output strategy to enhance its effectiveness, trained on 60% of the HCs and tested on the remaining 40% to identify abnormal developmental brain regions in CHDs.

Results: The linear regression analysis revealed no significant correlation between gross motor skills and either HB or HCT scores (HB: normalized $\beta = 0.068$, $p = 0.568$; HCT: normalized $\beta = 0.042$, $p = 0.725$). This suggests the absence of a direct relationship between blood oxygen-carrying capacity and gross motor performance. The results of the mediation analysis were depicted in Fig. 2, underwent bootstrapping validation for each pathway. We discovered multiple significant indirect relationships between gross motor performance and both HB and HCT, mediated by cortical surface area. The patterns of mediation effects for HB and HCT were similar, predominantly observed in the temporal, inferior parietal, orbitofrontal,

and primary motor regions. Notably, the left middle temporal area, left inferior temporal area, and left precentral area demonstrated the strongest mediation effects among these regions.

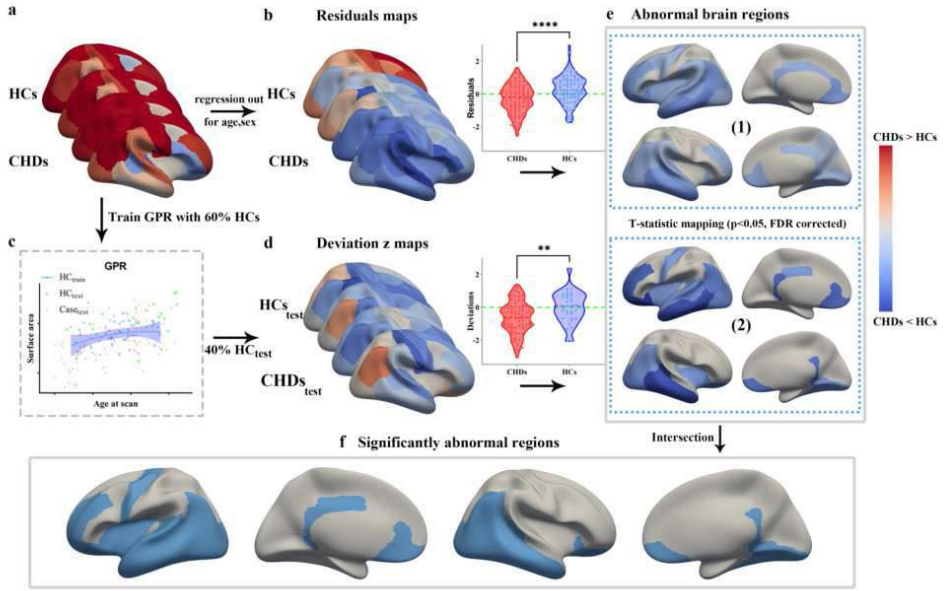

*Fig. 1 Illustrations of detecting brain developmental abnormalities in CHDs by using the group-level comparison (Figs. a,b, and e1) and brain development regression model (Figs. a,c, d, and e2). HCs represent the cohort of healthy controls, and CHDs represent the patients with complex CHD. ** means <0.01, and **** means <0.0001*

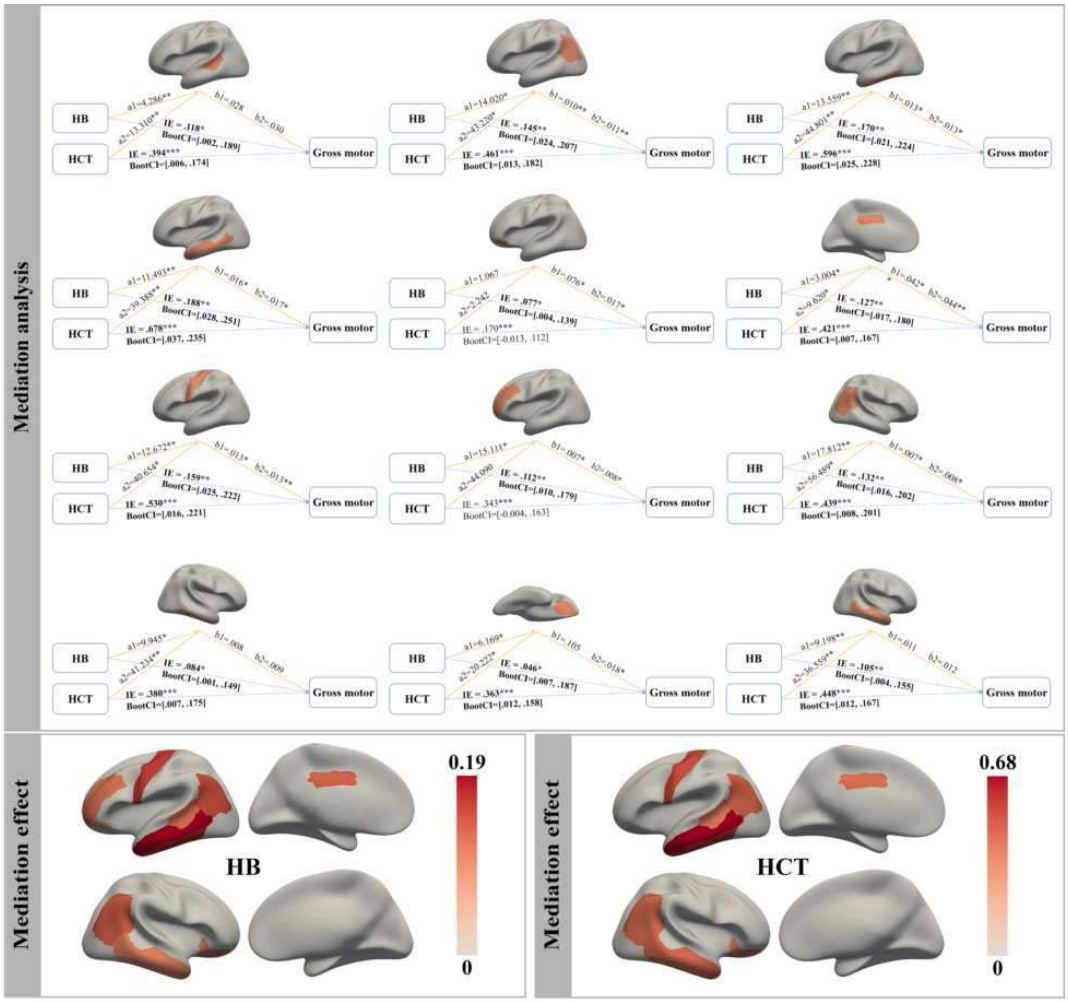

*Fig. 2 Results of mediation analysis between HB (HCT) and gross motor with regional surface area as mediators. IE and BootCI represent the indirect effect and bootstrap confidence interval of the pathway, respectively. Pathways with significant mediating effects were bolded. * means p<0.05. ** means p<0.01. *** means p<0.001.*

Conclusions: This study reveals an indirect association, mediated by cortical surface area, between blood oxygen-carrying capacity and gross motor abilities in infants with complex CHD. This discovery is crucial in deciphering the complex neurodevelopmental disorders associated with CHD.

References

1. Bellinger D C, Jonas R A, Rappaport L A, et al. Developmental and neurologic status of children after heart surgery with hypothermic circulatory arrest or low-flow cardiopulmonary bypass[J]. New England Journal of Medicine, 1995, 332(9): 549-555.
2. Bonthrone A F, Dimitrova R, Chew A, et al. Individualized brain development and cognitive outcome in infants with congenital heart disease[J]. Brain communications, 2021, 3(2): fcab046.
3. Sadhwani A, Wypij D, Rofeberg V, et al. Fetal brain volume predicts neurodevelopment in congenital heart disease[J]. Circulation, 2022, 145(15): 1108-1119.
4. Kelly C J, Makropoulos A, Cordero-Grande L, et al. Impaired development of the cerebral cortex in infants with congenital heart disease is correlated to reduced cerebral oxygen delivery[J]. Scientific reports, 2017, 7(1): 15088.
5. Nagaraj U D, Evangelou I E, Donofrio M T, et al. Impaired global and regional cerebral perfusion in newborns with complex congenital heart disease[J]. The Journal of pediatrics, 2015, 167(5): 1018-1024.
6. Zöllei L, Iglesias J E, Ou Y, et al. Infant FreeSurfer: An automated segmentation and surface extraction pipeline for T1-weighted neuroimaging data of infants 0–2 years[J]. Neuroimage, 2020, 218: 116946.
7. Desikan R S, Ségonne F, Fischl B, et al. An automated labeling system for subdividing the human cerebral cortex on MRI scans into gyral based regions of interest[J]. Neuroimage, 2006, 31(3): 968-980.

Poster No 419

The causal roles of glutamate and GABA genes on brain and behavior in autism

Viola Hollestein[1], Tom Claassen[2], Jan Buitelaar[3], Nicolaas Puts[4]

[1]Donders Institute, Nijmegen, N/A, [2]Donders Institute, Nijmegen, Gelderland, [3]Donders Institute for Brain, Cognition, and Behavior, Radboud University Nijmegen, Nijmegen, NL, Nijmegen, Netherlands, [4]Institute of Psychiatry, London, N/A

Introduction: One of the most influential theories of the underlying mechanisms of autism suggests that an imbalance between excitation and inhibition (E/I) in the brain causes behavioral differences in autism. However, how these E/I differences arise, and how these relationships link to brain function and differ across behavioral characteristics is not well understood. Understanding these relationships is important for developing more targeted support options. Using large multimodal datasets we aimed to infer probable causal relationships between the genetic underpinnings of glutamate (excitation) and GABA (inhibition) communication pathways in the brain, functional activity during inhibitory control, and several behavioral measures of autism. We further examined whether these links were mediated by other variables.

Methods: We used two samples. First, the discovery sample was the Longitudinal European Autism Project (LEAP) cohort, part of the AIMS-2-TRIALS clinical research programme (https://www.aims-2-trials.eu/)[1] consisting of 638 participants (autistic = 359, non-autistic = 279), aged 6-30 years old. Second, the replication sample was the TACTICS cohort (www.tactics-project.eu), including 164 participants (autistic = 60, non-autistic = 104), aged 8-13 years old. We selected gene-sets of glutamate and GABA communication pathways in the brain using Ingenuity Pathway Analysis software (http://www.ingenuity.com/). With these, we calculated individual's polygenic score for autism based on the glutamate and GABA gene-sets, using PRSet in PRSice[2]. In both cohorts, functional MRI during inhibitory control was measured, and successful and failed inhibitory control contrasts created. In TACTICS, MR Spectroscopy measures of glutamate concentrations in striatum and ACC were also available. We used the placement of the MRS voxels in ACC and striatum to extract beta values of the successful and failed inhibitory control contrasts in these specific regions of interest using MarsBar[3]. We included behavioral measures capturing what is typically called 'core characteristics' of autism; repetitive behaviors, social behaviors and sensory processing, which were measured through questionnaires[4-6]. In the autistic participants the diagnostic interviews ADI-R[7] and ADOS-2[8] were also included as measures of autistic traits. Additionally, to account for potential influence of the most common co-occurring conditions (ADHD, anxiety, depression), questionnaire measures of these were included. To investigate direct and indirect causal relationships between all these observational measures we used Bayesian Constraint-based Causal Discovery (BCCD) algorithms[9]. This method combines the strengths of constraint-based methods giving clear causal relationships, and of score-based methods estimating confidence measures of the inferred causal relationships. The output is a graphically presented model of the causal structure, reporting on estimated reliability of inferred causal relationships.

Results: In our discovery sample we found likely, direct, causal interactions with Bayesian statistical reliability of at least 80% probability between glutamate polygenic scores and ADI-R (see Figure 1), which was subsequently replicated in the TACTICS replication sample. The fMRI derived beta contrasts were causally linked to each other, but not to other behavioral or genetic measures.

Conclusions: Our results suggest a direct link between glutamate communication pathways in the brain and autistic characteristics measured in the ADI-R. This was replicated in an independent cohort, further strengthening the confidence of these results. This gives strong evidence for differences in the balance between excitation and inhibition in the brain causing autism characteristics. This is one of the first in vivo human studies suggesting causal links between the genetics of E/I (glutamate and GABA) to differentially underlie autism phenotypes.

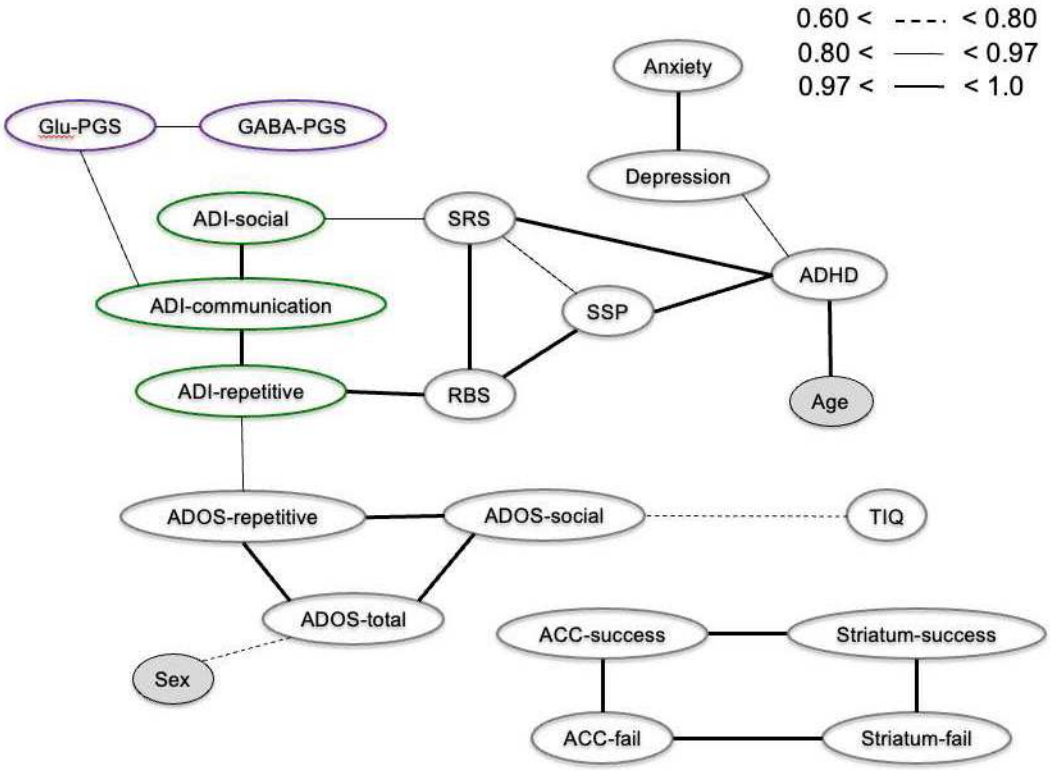

Figure 1: Graph of causal relationships in the autistic participants in the LEAP sample, between all variables. The estimated reliability of these causal relationships are indicated by the thickness of the line between variables. The causal relationship of main interest is the one from the "Glu-PGS" indicating the polygenic store for autism in the glutamate gene-set, with the ADI-communication subscale. This relationship was additionally replicated in the TACTICS sample of autistic participants.

References

1. Loth, E., Charman, T., Mason, L., Tillmann, J., Jones, E. J., Wooldridge, C., ... & Buitelaar, J. K. (2017). The EU-AIMS Longitudinal European Autism Project (LEAP): design and methodologies to identify and validate stratification biomarkers for autism spectrum disorders. Molecular autism, 8(1), 1-19.
2. Shing Wan Choi, Paul F O'Reilly (2009). PRSice-2: Polygenic Risk Score software for biobank-scale data, GigaScience, 8(7).
3. Brett, M., Anton, J.-L., Valabregue, R., Poline, J.-B., 2002. Region of interest analysis using an SPM toolbox. NeuroImage 2002 (16), 497.
4. Bodfish JW, Symons FJ, Parker DE, Lewis MH. Varieties of repetitive behavior in autism: comparisons to mental retardation. J Autism Dev Disord. 2000. https:// doi.org/10.1007/978-1-4419-1698-3_894
5. Constantino J, Gruber C. Social responsiveness scale 2nd ed. Los Angeles: Western Psychological Services; 2002.
6. Tomchek SD, Dunn W. Sensory processing in children with and without Autism: a comparative study using the short sensory profile. Am J Occup Ther. 2007; 61:190–200.
7. Rutter M, Le Couteur A, Lord C. Autism diagnostic interview-revised. West Psychol Serv. 2003. https://doi.org/10.1007/978-1-4419-1698-3_894
8. Lord C, Risi S, Lambrecht L, Cook EH, Leventhal BL, DiLavore PC, et al. The Autism diagnostic observation schedule–generic: a standard measure of social and communication deficits associated with the spectrum of autism. J Autism Dev Disord. 2000;19:205–23.
9. Sokolova, E., Groot, P., Claassen, T., & Heskes, T. (2014). Causal discovery from databases with discrete and continuous variables. In European Workshop on Probabilistic Graphical Models (442-457). Springer, Cham.

Poster No 420

Automated detection of lesions from MRI in children with focal epilepsy: a pilot study

Mathilde Ripart[1], Maria Eriksson[1,2], Rory Piper[1,2], Chris Clark[1], Felice D'Arco[2], Kshitij Mankad[2], Torsten Baldeweg[1], Sophie Adler[1], Konrad Wagstyl[3]

[1]UCL GOSH Institute of Child Health, London, United Kingdom, [2]Great Ormond Street Hospital, London, United Kingdom, [3]UCL Wellcome Centre for Human Neuroimaging, London, United Kingdom

Introduction: Drug-resistant focal epilepsy can be caused by a broad range of structural brain abnormalities, from large tumours to subtle cortical malformations (Eriksson et al. 2023). It can be cured with resective epilepsy surgery provided that the abnormality is detected on MRI scans. AI models have recently been developed to aid the detection of specific epilepsy pathologies, such as focal cortical dysplasia (FCD) (Spitzer, Ripart et al. 2022). However, FCD represents less than half of the subtle epilepsy pathologies that can be missed on clinical review of MRI scans and there is an urgent clinical need to develop models capable of detecting a broader range of epilepsy pathologies. In this study, we investigate whether a single classifier can segment multiple pathological causes of focal epilepsy.

Methods: This study was performed on 111 paediatric patients with a histologically confirmed cause of focal epilepsy and 90 paediatric healthy controls acquired for research purposes, from Great Ormond Street Hospital in London, UK. Patients' histopathologies included FCD, hippocampal sclerosis (HS), low-grade epilepsy-associated tumours (LEAT) – including dysembryoplastic neuroepithelial tumours (DNET), ganglioglioma – and other pathologies such as ganglioglioma, hypothalamic hamartoma, cavernoma non-diagnostic histopathologies. All participants had a 3D T1w scan acquired on a 1.5T or 3T MRI scanner, which was acquired preoperatively in patients and used to draw manual lesion masks by one of two expert radiologists. The cohort was split into training/validation (89 patients, 71 controls) and test datasets (22 patients, 19 controls) (Table 1). We used nnU-Net (Isensee et al. 2021), an open-source deep learning model specialised for robust performance in biomedical image segmentation, to segment focal epilepsy abnormalities from the T1w MRI scans using the manual lesion mask as ground truth. The nnU-Net was trained on the training/validation dataset for 1000 epochs with the '3d_lowres' configuration. It was evaluated on the test dataset for its sensitivity in detecting lesions (i.e. overlap between the prediction and the manual lesion mask) and specificity in controls (i.e. no prediction).

		Training/validation dataset	Test dataset
Healthy controls (n)		**71**	**19**
Age at scan, years (median [IQR])		13.4 [10.2-17.1]	13.6 [11.0-15.9]
Sex (m:f)		20:51	5:14
Patients (n)		**89**	**22**
Age at scan, years (median [IQR])		7.7 [5.8-14.1]	8.96 [4.3-15.0]
Sex (m:f)		47:42	10:12
Age of epilepsy onset, years (median [IQR])		2.5 [0.8-6.0]	1.6 [1.0-3.0]
Histopathology (n)	FCD	33	9
	HS	16	4
	LEAT	25	5
	Other	15	4
Ever reported MRI-negative (n)		7	4

***Table 1:* Demographic and clinical information of the training/validation and test datasets.** *(FCD: focal cortical dysplasia, DNET: dysembryoplastic neuroepithelial tumours, HS: hippocampal sclerosis, IQR: interquartile range, LEAT: low-grade epilepsy associated tumours)*

Results: The model detected 14 out of the 22 focal epilepsy abnormalities in patients (64% sensitivity). It accurately detected 67% of FCD (n=6/9), 75% of HS (n=3/4), 80% of LEAT (n=4/5) and 25% of the other pathologies (n=1/4). Notably, the model accurately detected two out of the four abnormalities previously reported MRI-negative (one FCD and one LEAT). Patients had no more than one false-positive clustered prediction, and the model accurately predicted no putative lesions in 18 out of 19 healthy controls (95% specificity). Figure 1 depicts examples of three accurate predictions in patients with different pathologies: FCD 2B, HS and DNET. The radiological characteristics visibly differ between the three pathologies (Panel A). Nonetheless, the model was able to segment these three pathologies with a good overlap with the manual lesion masks (Panel B).

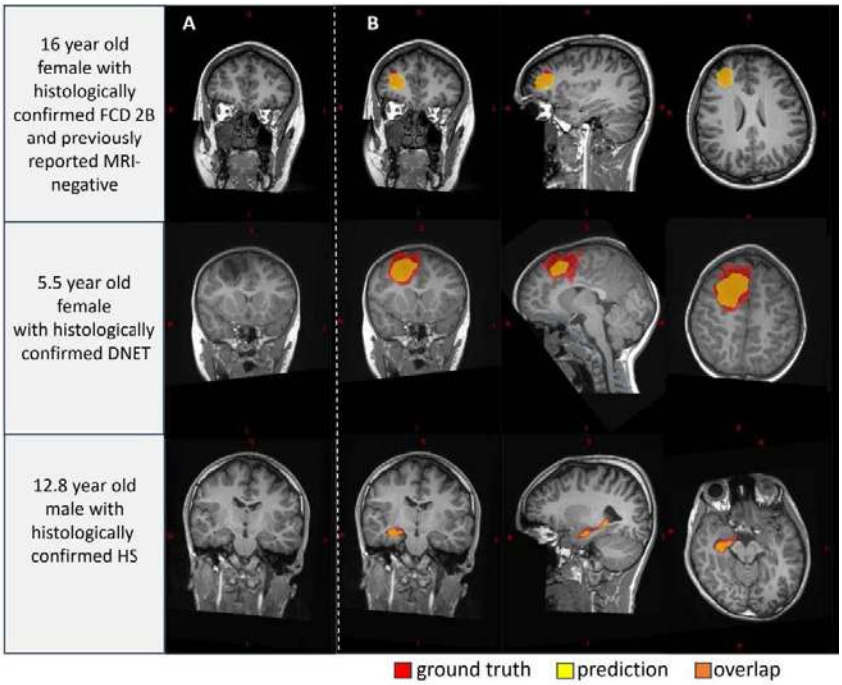

***Figure 1:* Examples of segmentation of multiple focal epilepsy pathologies.** *A) Coronal view of patient T1w scan. B) Coronal, sagittal, and axial views of the patient T1w scan with manual lesion mask (red), model prediction (yellow), and their overlap (orange) overlayed.*

Conclusions: We demonstrate that a single deep-learning model can segment multiple focal epilepsy pathologies on T1w MRI scans using a modest cohort of paediatric patients for training. This work paves the way for a larger, multi-centre study, aiming to develop a robust automated lesion segmentation tool that could help in the presurgical planning of patients with focal epilepsy.

References

1. Eriksson et al. 2023. "Pediatric Epilepsy Surgery from 2000 to 2018: Changes in Referral and Surgical Volumes, Patient Characteristics, Genetic Testing, and Postsurgical Outcomes." Epilepsia, June.
2. Isensee et al. 2021. "nnU-Net: A Self-Configuring Method for Deep Learning-Based Biomedical Image Segmentation." Nature Methods 18 (2): 203–11.
3. Spitzer, Ripart et al. 2022. "Interpretable Surface-Based Detection of Focal Cortical Dysplasias: A Multi-Centre Epilepsy Lesion Detection Study." Brain: A Journal of Neurology, August.

Poster No 421

Longitudinal Associations of Autistic Traits with Brain Structure during Adolescence

Zhixi Chen[1], Norihide Maikusa[2], Yinghan Zhu[2], Atsushi Nishida[3], Shuntaro Ando[2], Naohiro Okada[4], Kiyoto Kasai[2], Yuko Nakamura[2], Shinsuke Koike[2]

[1]Center for Evolutionary Cognitive Sciences, Graduate School of Arts and Sciences, The University of, Tokyo, Tokyo, [2]The University of Tokyo, Tokyo, Tokyo, [3]Tokyo Metropolitan Institute of Medical Science, Tokyo, Tokyo, [4]University of Tokyo Institutes for Advanced Study, Tokyo, Tokyo

Introduction: Autism spectrum disorder (ASD) is a pervasive neurodevelopmental disorder which is characterized as impairment in reciprocal social interaction and communication, as well as restricted, repetitive, and stereotyped patterns of behavior, interests, and activities (American Psychiatric Association, 2013). In addition, the characteristics in ASD have been extended to a continuum of autistic traits in the general population (Baron-Cohen S, J Autism Dev Disord 2001), since some typically developing individuals would also display autistic traits. MRI studies have revealed morphometric brain differences in patients with ASD. Longitudinal and cross-sectional studies have also demonstrated early brain overgrowth during infancy in ASD, followed by a plateau and an accelerated rate of decline, introduced as "pseudo-normalization", or decrease into adulthood (Brandan et al., Brian 2014). Therefore, adolescence appears to be a key period of brain maturation in ASD, but whether this longitudinal trajectory would extend into the general population is still unclear. Our present study aims to

highlight adolescent brain structure trajectories and investigate autistic trait-related morphometric differences and changes in the general population.

Methods: The study includes 479 participants, who took part in the population neuroscience Tokyo Teen Cohort (pnTTC) study (Okada et al., Psychiatry Clin. Neurosci 2019) every two years. Autistic traits were measured using Autism Spectrum Quotient (AQ) (Baron-Cohen S, J Autism Dev Disord 2001) in two waves (age-11 and age-17) from their main caregivers. Freesurfer image analysis software (Fischl, NeuroImage 2012) was used to parcellate and extract the cortical thickness and cortical surface area in 34 regions of interest per hemisphere and 7 subcortical volumes. Then, a general additive mixed model (GAMM) (Wood, Generalized Additive Models 2017) was used to evaluate adolescent non-linear brain trajectory patterns and explored the relationships between brain features and autistic traits. Multiple testing was corrected using a false discovery rate (FDR) method.

Results: Autistic traits showed good intraindividual stability and exhibited no significant changes with age. Cross-sectionally, we did not observe strong evidence supporting an association between autistic traits and brain structures in this adolescent sample. However, longitudinal findings revealed that different domains of autistic traits had diverse effects on the trends of brain regions, particularly between males and females. For example, high scores on autistic traits in males were associated with age-related increases in the nucleus accumbens (NAc), whereas males with low autistic trait scores and females exhibited an on-going decrease in NAcc volumes. These results were replicated in the social (SC) domain. Conversely, females with high scores in the Restricted and Repetitive Behaviors (RRB) domain displayed an acceleration of normative thickness decrease in frontotemporal cortical thickness and surface area.

Conclusions: The results suggest unique non-linear brain structural changes during adolescence, which were partly explained by autistic traits, supporting the neurobiology of autistic traits should be extended into the general population. It also revealed that the SC and RRB domains of autistic traits may be fractionable, underpinned by different brain structures.

References

1. American Psychiatric Association. (2013). Diagnostic and Statistical Manual of Mental Disorders (DSM-5). American Psychiatric Journal.
2. Baron-Cohen, S., Wheelwright, S., Skinner, R., Martin, J., & Clubley, E. (2001). The autism-spectrum quotient (AQ): Evidence from Asperger syndrome/high-functioning autism, males and females, scientists, and mathematicians. Journal of Autism and Developmental Disorders, 31(1), 5-17.
3. Zielinski, B. A., Prigge, M. B. D., Nielsen, J. A., et al. (2014). Longitudinal changes in cortical thickness in autism and typical development. Brain, 137(6), 1799-1812.
4. M, Bundo M, Iwamoto K, Tanaka SC, Kasai K. (2019). Population-neuroscience study of the Tokyo TEEN Cohort (pn-TTC): Cohort longitudinal study to explore the neurobiological substrates of adolescent psychological and behavioral development. Psychiatry Clin Neurosci, 73(5), 231-242. doi: 10.1111/pcn.12814.
5. Fischl, B. (2012). FreeSurfer. NeuroImage, 62(2), 774–781.
6. Wood, S. N. (2017). Generalized Additive Models: An Introduction with R, Second Edition (2nd ed.). Chapman and Hall/CRC. https://doi.org/10.1201/9781315370279

Poster No 422

Working Memory Related Functional Connectivity in Adults with ADHD and Associated Training Effects

Tuija Tolonen[1], Sami Leppämäki[2], Kimmo Alho[1], Pekka Tani[3], Anniina Koski[3], Matti Laine[4], Juha Salmi[5]

[1]University of Helsinki, Helsinki, Finland, [2]Terveystalo Healthcare, Helsinki, Finland, [3]Helsinki University Hospital, Helsinki, Finland, [4]Åbo Akademi University, Turku, Finland, [5]Aalto University, Espoo, Finland

Introduction: Working memory (WM) deficits are amongst the most prominent cognitive impairments in attention deficit hyperactivity disorder (ADHD; Alderson et al. 2013). While functional connectivity is a prevailing approach in brain imaging of ADHD, the network level alterations in synchronized activation between brain areas and their malleability by cognitive training are not well known. Here, we studied WM related differences in whole brain functional connectivity between adults with and without ADHD. In addition, we conducted a randomized controlled trial examining the effects of WM training on functional connectivity patterns in a trained and an untrained task in adults with ADHD. This study extends our previous findings with the same sample, showing reduced structural connectivity (Tolonen et al. 2023) and a training-related restoration of regional brain activity (Salmi et al. 2020) in adults with ADHD.

Methods: 41 adults with ADHD and 36 neurotypical (NT) controls matched in age, gender, handedness, and education level performed visuospatial and digit n-back WM tasks (levels from 0-back to 3-back) during functional magnetic resonance imaging (fMRI). The adults with ADHD continued to a 5-week randomized controlled WM training trial with 20 participants practicing a dual n-back task and 18 adults performing an active control task, after which the fMRI measurement was repeated. Functional connectivity of the whole brain was measured by calculating pairwise correlations of mean brain activity in 164 pre-

defined parcels (Destrieux et al. 2010; Patenaude et al. 2011). Subnetworks indicating group differences and training effects (on a trained visuospatial task and an untrained digit task) on functional connectivity were identified with Network-Based Statistic (Zalesky et al. 2010), a data-driven method for clustering single connected components. A post-hoc analysis further examined whether the subnetworks differentiating adults with and without ADHD respond to training.

Results: Adults with ADHD had decreased functional connectivity in wide-spread networks compared with the NT controls during both visuospatial and digit n-back tasks ($p = .03$ and $p < .01$, respectively, FWE-corrected; Figure 1). The networks encompassed prefrontal, temporal, parietal and occipital cortices, the insula, the cingulate cortex, the cerebellum, and subcortical structures such as the thalamus and the striatum, areas consistently associated with WM (Yaple et al. 2019). The network related to digit (verbal) n-back task was overall larger and especially included areas related to language processing. We found no group × time interaction effects of WM training surviving correction for multiple comparisons.

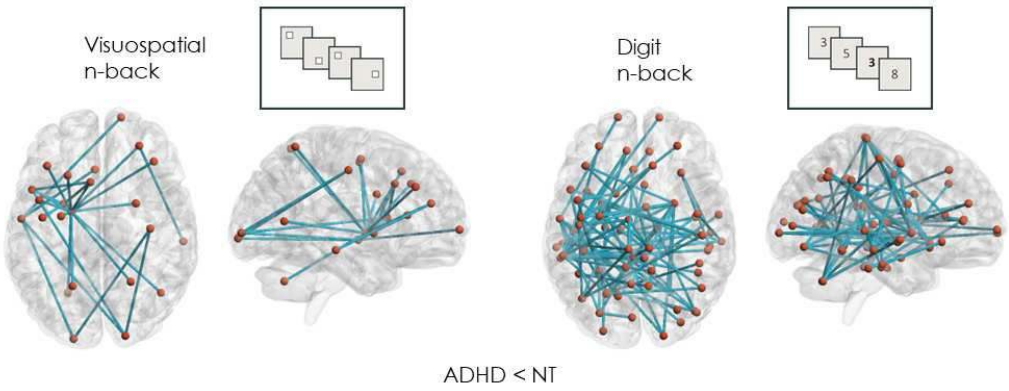

Figure 1. Adults with ADHD had decreased functional connectivity in wide-spread networks compared with the neurotypical (NT) controls during both visuospatial (left) and digit (right) n-back tasks ($p = .03$ and $p < .01$, respectively, FWE-corrected).

Conclusions: Our results indicate that large-scale abnormalities in functional networks underlie deficits in verbal and visuospatial WM commonly faced in ADHD. However, their plasticity by WM training may be restricted to regional level.

References

1. Alderson, R.M. (2013), 'Attention-deficit/hyperactivity disorder (ADHD) and working memory in adults: A meta-analytic review', Neuropsychology, vol. 27, no. 3, pp. 287–302.
2. Destrieux, C. (2010), 'Automatic parcellation of human cortical gyri and sulci using standard anatomical nomenclature', NeuroImage, vol. 53, no. 1, pp. 1–15.
3. Patenaude, B. (2011), 'A Bayesian model of shape and appearance for subcortical brain segmentation', NeuroImage, vol. 56, no. 3, pp. 907–922.
4. Salmi, J. (2020), 'Working memory training restores aberrant brain activity in adult attention-deficit hyperactivity disorder', Human Brain Mapping, vol. 41, no. 17, pp. 4876–4891.
5. Tolonen, T. (2023), 'Abnormal wiring of the structural connectome in adults with ADHD', Network Neuroscience, vol. 7, no. 4, pp. 1302–1325.
6. Yaple, Z.A. (2019), 'Meta-analyses of the n-back working memory task: fMRI evidence of age-related changes in prefrontal cortex involvement across the adult lifespan', NeuroImage, vol. 196, pp. 16–31.
7. Zalesky, A. (2010), 'Network-based statistic: Identifying differences in brain networks', NeuroImage, vol. 53, no. 4, pp. 1197–1207.

Poster No 423

Age-related effects on the association between alcohol use severity and resting-state fMRI

Karis Colyer-Patel[1], Maik Derksen[2], Gabry Mies[3], Steven Scholte[3], Ingo Willuhn[2], Heidi Lesscher[4], Janna Cousijn[1]

[1]Department of Psychology, Education & Child Studies, Erasmus University Rotterdam, Rotterdam, Netherlands, [2]Department of Psychiatry, Amsterdam University Medical Centers, University of Amsterdam, Amsterdam, Netherlands, [3]Department of Psychology, University of Amsterdam, Amsterdam, Netherlands, [4]Department of Population Health Sciences, Unit Animals in Science and Society, Utrecht University, Utrecht, Netherlands

Introduction: Adolescence marks a period of neurodevelopmental and cognitive change, encompassing normative increases in reward sensitivity and risk-taking behaviour, alongside challenges in behavioural control. This is suggested to increase the risk of the initiation of alcohol use as well as later dependence[1,2]. One explanation for this increased risk, is suggested to be due to the impact of alcohol on neurodevelopment, particularly on the maturation of brain networks during this timeframe.

There is currently limited evidence directly testing the differential impact of alcohol use during adolescence versus adulthood, as well as exploring the effects of low versus heavy alcohol consumption. The purpose of the present study was to investigate age-related differences on the association between resting-state functional connectivity (RSFC) and alcohol use severity in a sample of rodents that initiated low or heavy alcohol use during adolescence or adulthood.

Methods: Lister hooded rats were allowed to consume alcohol according to an intermittent alcohol access schedule across a two-month period starting from postnatal day 42 (adolescent-onset) or postnatal day 77 (adult-onset). In total 42 rats were selected: adolescent-onset low (N = 12) and high drinking (N= 7) rats, and adult-onset low (N = 11) and high drinking (N = 12) rats. Rats were anaesthetized with 2.0-3.0% isoflurane induction and isoflurane was continuously delivered. Once positioned, a bolus injection of 0.020 mg/kg dexmedetomidine was administered, followed with a maintenance dose of 0.040 mg/kg/h. Importantly, this allowed the rats to remain conscious during the MRI scans. Resting-state fMRI was measured at a resolution of 6002 × 20 slices with a FOV of 32.4, slice thickness of 1.0mm, and voxel size of 3 x 10 x 3mm. The preprocessing of fMRI images was conducted using RABIES software[3] which included highpass filtering (0.01Hz), and spatial Gaussian smoothing filtering (0.3mm FWHM). As part of the RABIES pipeline, the timeseries of all scans were concatenated to compute a group-ICA decomposition. Dual regression was performed using FSL to model the individualised connectivity of brain networks first identified through group-ICA. Permutation tests (N =5000) using FSL randomise were conducted with threshold-free cluster enhancement and family-wise error correction (=.05), to test for main effects of age of onset of alcohol use, severity of use, and interactive effects.

Results: There was significantly higher RSFC in regions of the sensorimotor network (SMN), namely the globus pallidus, in high alcohol drinking rats compared to low alcohol drinking rats. Additionally, there was higher RSFC in the caudoputamen and motor area of the SMN, as well as the salience network (SN), of low alcohol drinking rats compared to high alcohol drinking rats. No significant differences in RSFC were found between adolescent and adult-onset rats. There were significant interactions effects; adult-onset high drinking rats compared to adolescent-onset high drinking rats showed higher RSFC in the SMN. Whereas adolescent-onset high drinking rats compared to adult-onset high drinking rats showed higher RSFC in the SN. No differences were found when comparing adolescent-onset low drinking to adult-onset low drinking rats and vice versa.

Conclusions: As expected, heavy alcohol use was found to be associated with higher RSFC in the SMN, a network associated with habitual formation. However, contrary to expectations, higher RSFC was found in the SN of low alcohol drinking rats. The higher RSFC in the SN of adolescent-onset high drinking rats likely reflects heightened reward sensitivity in adolescents compared to adults. And the higher RSFC in the SMN of high drinking adult rats likely reflects the shift to habitual responding in adults compared to adolescents. These findings highlight the importance of considering age when investigating processes associated with the development and maintenance of Alcohol Use Disorder.

References

1. Conrod, P. (2016) Annual research review: on the developmental neuropsychology of substance use disorders. Journal of Child Psychology and Psychiatry, 57, 371–394.
2. Cousijn, J. (2018) Adolescent resilience to addiction: a social plasticity hypothesis. The Lancet Child & Adolescent Health, 2, 69–78.
3. Desrosiers-Gregoire, G. (2022). Rodent Automated Bold Improvement of EPI Sequences (RABIES): A standardized image processing and data quality platform for rodent fMRI. bioRxiv.

Poster No 424

Predicting 2-year neurodevelopmental outcomes in preterm infants using MRI and machine learning

Hyun Ju Lee[1], Yong Hun Jang[1], Hyun-A Kim[1], Joo Young Lee[1], Gangi Lee[1]

[1]Hanyang University Hospital, Seoul, Republic of Korea

Introduction: There are ongoing reports of developmental disorders, school failure, and psychiatric problems in extremely preterm infants (EP; < 28 weeks' gestation) and very-to-late preterm infants (V-LP; 28 ≥ and < 37 weeks' gestation) without brain injuries[1]. Despite advances in artificial intelligence improving the predictive power of later neurodevelopmental outcomes in preterm children, there are limitations in ignoring potential associations between perinatal variables and failing to account for non-linear relationships or interactions between variables[2]. We aim to develop a model for predicting 2-year neurodevelopmental scores that combines perinatal clinical characteristics and brain white matter predictors to provide quantitative and qualitative information about preterm infants in need of early intervention.

Methods: This study used a retrospective database of 62 extremely preterm and 131 very-to-late preterm infants recruited between 2017-2021. We performed volumetric segmentation on T2-weighted images using MANTiS protocol. Brain white matter fibers were reconstructed using probabilistic tractography on diffusion tensor images, and global and local connectivity

metrics were calculated based on graph theory. We used graphical network analysis (GNA) to identify local connectivity predictors that were significantly associated with each subset of Bayley Scales of Infant and Toddler Development Third Edition (BSID-III) after accounting for postmenstrual age and other local connectivity variables. We tested the training and performance of predicting developmental scores with linear (ElasticNet) and nonlinear (Random Forest; XGBoost) regression models across preterm, very early, and late preterm birth groups, and compared performance across models and modalities using root mean square error and r-squared. Finally, we identified the most contributing predictors of the best performing model.

Results: Neonatal and maternal data, clinical information derived during follow-up, and BSID-III subscale results are presented in Table 1. In the GNA, various local connectivity features showed significant net correlations with the BSID-III subscale across the whole brain ($p<.05$ with 95% confidence interval). Language prediction results for all groups showed improved performance for models including local connectivity predictors. For cognition, local connectivity predictors performed high in the overall preterm group, and for motor, they performed high in preterm and V-LP group. Cortical regions with feature importance frequencies of 5 or 4 were found in left middle frontal gyrus, left precuneus, right calcarine cortex, and right hippocampus, and white matter regions included left cingulate gyrus and uncinate fasciculus, which connect to the frontal lobe (Figure 1).

Table 1. Preterm and maternal characteristics

	Preterm (n = 193)	EP (n = 62)	V-LP (n = 131)	*p-value (EP vs. V-LP)*
Demographics and maternal characteristics				
Gestational age, mean (SD)	29.87 (3.55)	25.65 (1.4)	31.23 (2.74)	< 0.001
Postmenstrual age, mean (SD)	37.8 (2.16)	38.34 (2)	37.56 (2.38)	< 0.027
Birth weight (g), mean (SD)	1355 (594)	872 (195)	1583 (583)	< 0.001
Small for gestational age, n (%)	28 (15)	9 (15)	19 (14)	1
Male sex, n (%)	85 (44)	28 (45)	57 (44)	0.952
Maternal age, mean (SD)	33.69 (4.13)	33.75 (4.81)	33.66 (3.77)	< 0.896
Maternal education, n (%)				
6 years <	2 (1)	1 (1.6)	1 (1)	
12 years <	37 (19)	13 (21)	24 (18)	
16 years <	123 (64)	45 (73)	78 (60)	
16 years >	8 (4)	1 (1.6)	7 (5.3)	
Unknown or not reported	23 (12)	2 (3.2)	21 (16)	
Clinical characteristics				
5 Apgar, mean (SD)	5.1 (1.81)	6.79 (1.63)	6.23 (1.62)	< 0.001
IVH, n (%)	52 (27)	21 (34)	31 (24)	0.187
IVH grade I, n (%)	45 (87)	17 (81)	28 (82)	
IVH grade II, n (%)	7 (13)	4 (19)	3 (18)	
BPD, n (%)	106 (55)	59 (95)	47 (36)	< 0.001
BPD grade I, n (%)	96 (91)	51 (86)	45 (96)	
BPD grade II, n (%)	10 (9)	8 (14)	2 (4)	
> 7 days Dexamethasone, n (%)	34 (18)	25 (40)	9 (6.9)	< 0.001
Infants who received oral iron, n (%)	193 (100)	62 (100)	131 (100)	1
Follow-up characteristics				
Mean (SD) BSID-III Scores				
Cognitive	99.77 (14.43)	93.92 (13.91)	102.53 (13.83)	< 0.001
Language	93.35 (13.08)	86.82 (13.08)	94.96 (12.23)	< 0.001
Motor	100.6 (15.51)	95 (13.64)	103.25 (15.63)	< 0.001

Data are presented as the mean ± SD or number (%). Abbreviations: EP, extremely preterm; V-LP, very-to-late preterm; SD, standard deviation; IVH, interventricular hemorrhage; BPD, bronchopulmonary dysplasia; BSID-III, Bayley Scales of Infant and Toddler Development, Third Edition.

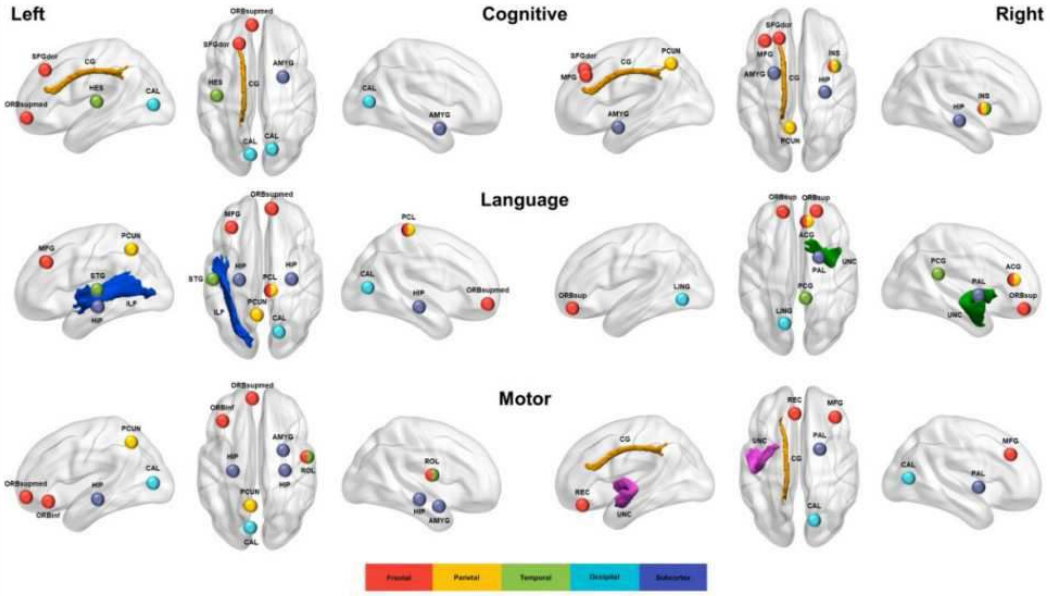

Conclusions: A machine learning method to predict BSID-III score using multi-modal white matter features could provide practical guidance for infants who benefit from early intervention.

References
1. Latal B. (2009). Prediction of neurodevelopmental outcome after preterm birth. Pediatric neurology, 40(6), 413–419.
2. Baker, S., & Kandasamy, Y. (2023). Machine learning for understanding and predicting neurodevelopmental outcomes in premature infants: a systematic review. Pediatric research, 93(2), 293–299.

Poster No 425

Predicting brain age using functional connectivity in attention-deficit/hyperactivity disorder

Yingxue Gao[1], Zilin Zhou[1], Weijie Bao[1], Xinyue Hu[1], Hailong Li[1], Lianqing Zhang[1], Xiaoqi Huang[1]

[1]Huaxi MR Research Center (HMRRC), Department of Radiology, West China Hospital of Sichuan University, Chengdu, China

Introduction: Attention-deficit/hyperactivity disorder (ADHD) is a neurodevelopmental disorder with apparent roots in atypical brain development. The concept of 'brain age' derived from neuroimaging data holds the potential for a quantitative biomarker, reflecting the level of brain maturation along with neural development. Previous studies of brain age prediction all used structural MRI measures and found either older (Kaufmann et al., 2019) or younger appearing brains in individuals with ADHD (Kurth et al., 2022). But functional connectivity patterns are also crucial in characterizing brain maturity (Dosenbach et al., 2010) and exhibit abnormalities in ADHD (Gao et al., 2019). Therefore, in this study, we quantified the brain age using functional connectivity of brain resting-state networks (RSN) and a well-validated machine learning algorithm to enhance our understanding in abnormal developmental mechanism of ADHD.

Methods: We recruited 360 male participants aged 7 to 18 years old [187 patients with ADHD and 173 typically developing controls (TDC)] from three sites. Resting-state fMRI and T1-weighted images were obtained on 3T MRI scanner and were preprocessed using the standardized pipeline in DPARSF. We used the Power atlas with 231 spherical ROIs that assigned to 11 large-scale RSN to construct functional connectivity matrices. The connectivity matrices were harmonized using Block-ComBat (Chen et al., 2022). Then, the within- and between-network connectivity were estimated for each subject. The brain age prediction model was constructed using the linear support vector regression (SVR) based on obtained network connectivity features (Figure 1). The model was trained on TDC using a nested cross-validation (leave-one-out cross-validation for outer loop and 10-fold cross-validation for inner loop). Data from ADHD patients were used for testing using the model trained in all TDC subjects. We used the mean squared error (MSE), mean absolute error (MAE) and Pearson correlation coefficient (r) between the predicted and actual age to assess the prediction performance. We calculated the brain age gap to represent the difference between the predicted age and the chronological age for each subject. A covariance analysis was applied to compare the difference in brain age gap between ADHD patients and TDC with chronological age as covariates.

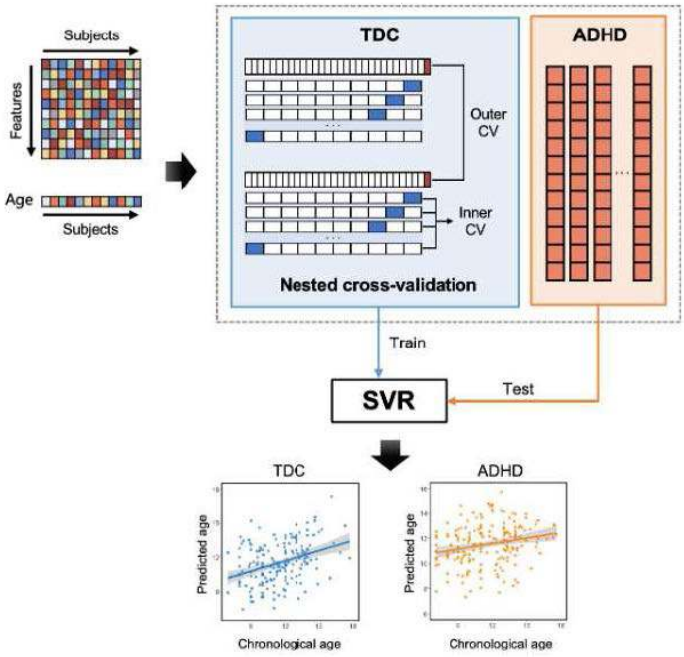

Figure 1. The flowchart of brain age estimation using linear SVR.

Results: The mean brain age gap for the TDC was 0.04 years (MSE = 5.14 years, MSE = 1.77 years, r = 0.370, p < 0.0001). Application of the brain age model to the patients with ADHD yielded a mean brain age gap of -0.06 years (MSE = 7.03 years, MSE = 2.23 years, r = 0.228, p = 0.0017). The top 10 features contributing the most to the brain age prediction model were shown in Figure 2B. There was no significant difference in the brain age gap between patients with ADHD and TDC (p = 0.869). However, when we divided the participants into child and adolescent groups, we found that the brain age gap of adolescents with ADHD (-2.06 years) was significantly lower than that of healthy adolescents (-1.24 years) (p = 0.021), but it did not significantly differ in children (p = 0.084, Figure 2D).

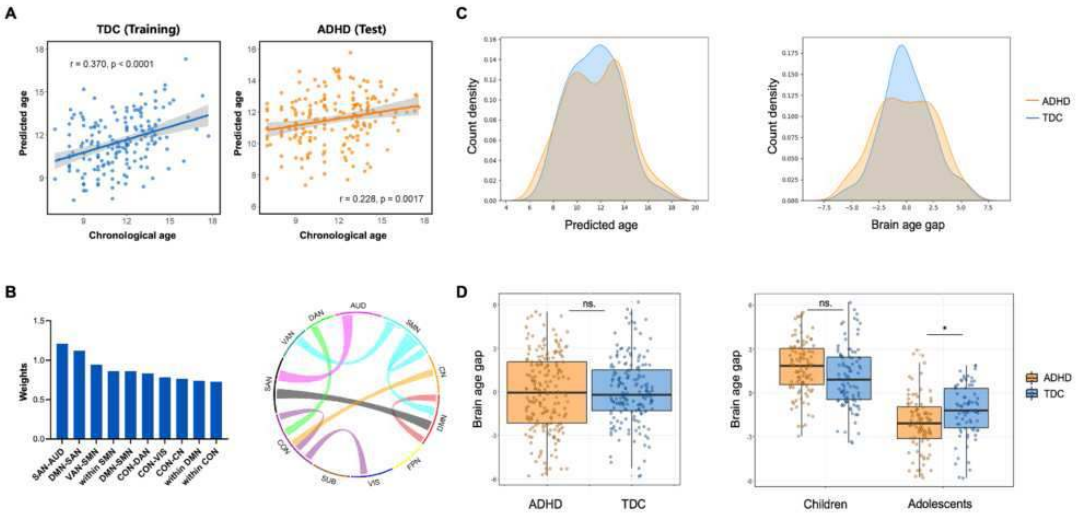

Figure 2. A: Correlation between the predicted age and chronological age in TDC and ADHD groups. **B:** The top 10 features that contribute the most to the brain age prediction model. **C:** Distribution of the predicted age and brain age gap in the two groups. **D:** Group differences of the brain age gap in whole subjects (left), children and adolescents (right). *: $p < 0.05$.

Conclusions: This study represents the first attempt to predict brain age in patients with ADHD using functional network connectivity. We found that the brain age was significantly lower than chronological age in adolescents with ADHD, while no significant difference was observed in brain age gap between children with ADHD and TDC. This suggests that apparent developmental delays in brain functional networks of ADHD boys may not manifest until adolescence, providing new insights into the neurodevelopment mechanisms of ADHD.

References
1. Chen AA, Srinivasan D, Pomponio R, et al. Harmonizing functional connectivity reduces scanner effects in community detection. Neuroimage. 2022;256:119198.
2. Dosenbach NU, Nardos B, Cohen AL, et al. Prediction of individual brain maturity using fMRI [published correction appears in Science. 2010 Nov 5;330(6005):756]. Science. 2010;329(5997):1358-1361.
3. Gao Y, Shuai D, Bu X, et al. Impairments of large-scale functional networks in attention-deficit/hyperactivity disorder: a meta-analysis of resting-state functional connectivity. Psychol Med. 2019;49(15):2475-2485.
4. Kaufmann T, van der Meer D, Doan NT, et al. Common brain disorders are associated with heritable patterns of apparent aging of the brain [published correction appears in Nat Neurosci. 2020 Feb;23(2):295]. Nat Neurosci. 2019;22(10):1617-1623.
5. Kurth F, Levitt JG, Gaser C, et al. Preliminary evidence for a lower brain age in children with attention-deficit/hyperactivity disorder. Front Psychiatry. 2022;13:1019546.

Poster No 426

Thalamic connectivity gradients analysis reveal atypical thalamic-insula interactions in autism

Shinwon Park[1], Phoebe Thomson[1], Han Byul Cho[2], Sofie Valk[3], Boris Bernhardt[4], Michael Milham[1,5], Seok Jun Hong[6,7], Adriana Di Martino[1]

[1]Child Mind Institute, New York, NY, [2]Center for Neuroscience Imaging Research, Institute for Basic Science, Suwon-si, Gyeonggi-do, [3]Max Planck Institute for Human Cognitive and Brain Sciences, Leipzig, Germany, [4]Montreal Neurological Institute and Hospital, Montreal, Quebec, [5]Nathan S. Kline Institute for Psychiatric Research, Orangeburg, NY, [6]Center for Neuroscience Imaging Research, Institute for Basic Science, Suwon, Gyeonggi-do, [7]Department of Biomedical Engineering, Sungkyunkwan University, Suwon, Korea, Republic of

Introduction: Thalamocortical connectivity is crucial for sensory information processing and cognitive integration. Evidence from our work and others indicate that thalamocortical connections with the salience network plays a pivotal role in distinguishing between internally and externally oriented functional networks.[1,2] Extending this framework, we hypothesized that atypical thalamocortical connectivity may underlie the atypical sensory processing and social communication often observed in autism spectrum disorder (ASD). The aim of this study is to examine thalamocortical functional connectivity maps (CMAP) and their neocortical projections (NEOMAP) in ASD compared to age- and sex-matched neurotypicals (NT) and analyze their association with clinical symptoms.

Methods: Utilizing the Autism Brain Imaging Data Exchange-I (ABIDE-I)[3] dataset from 3 different sites (i.e., NYU, PITT, USM), our study involved 107 ASD and 113 NT individuals, all male, aged 6.4 – 50 years. We used the Brainspace toolbox[4] to derive the CMAPs using diffusion map embedding with a normalized angle kernel, and Procrustes alignment for aligning individual CMAPs to the group mean average of all participants. Next, the NEOMAPs were extracted by multiplying the CMAPs (thalamus voxels x n maps) to the thalamus-cortex correlation matrix (thalamus voxels x cortex vertices). Thus, NEOMAPs can be interpreted as the projections of the CMAPs onto the neocortical surface. CMAPs and NEOMAPs were statistically tested for significant group difference effects, controlling for age and head motion (mean framewise displacement) using surface-based linear models implemented in a MATLAB toolbox, SurfStat.[5] Potential site effects were controlled using ComBat harmonization.[6] To interpret these maps, we profiled them using theYeo-Krienan 7 network parcellation.[7] Finally, we examined associations with the calibrated severity total scores of the Autism Diagnostic Observation Schedule (ADOS CSS).[8]

Results: Across groups, CMAP patterns resulting from our analyses were consistent with those observed in our prior study of neurotypical thalamocortical connectivity. Group comparisons revealed significant differences between ASD and NT groups in the first CMAP (pFDR<0.05, Figure 1A, 1B). These differences were localized to specific thalamic nuclei: the pulvinar associated with visual processing, the ventral lateral posterior nucleus linked to somatosensory functions, the medial geniculate nucleus integral to auditory processing, and the centromedian nucleus, known for its role in 'gate control' of salient features. The second CMAP did not show significant group differences (Figure 1C). Based on these results, follow up analyses focusing on the first NEOMAP, ranging from salience/somatosensory to default mode networks showed a more compressed gradient in ASD compared to NT (Figure 2A, 2B). A vertexwise analysis revealed significant differences in regions of the right insula, superior temporal, and visual cortices (PRFT-Cluster<0.05; Figure 2C), where ASD showed lower values compared to NT. Network profiling of these regions based on Yeo-Krienan 7 networks,[7] revealed that these differences were most pronounced in the visual, somatosensory, salience, and default mode networks (Figure 2D). Notably, among the regions showing significant group differences (ASD<NT), the right insula, within the salience and somatomotor networks, showed a significant negative correlation with autism symptom severity (r = -0.30, p = 0.002; Figure 2E).

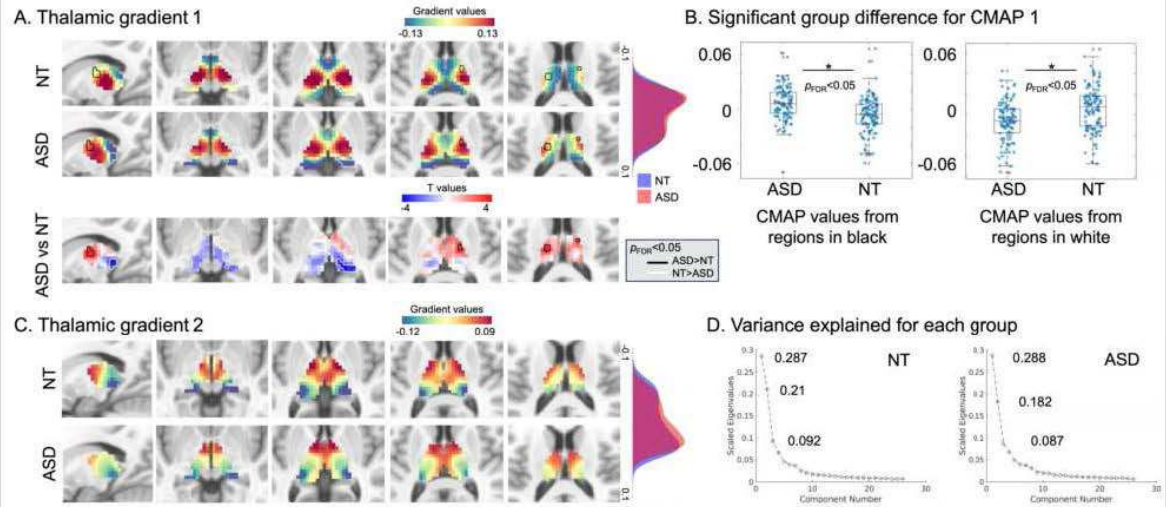

Figure 1. Comparison of thalamocortical functional connectivity maps (CMAP) in neurotypical (NT) and autism spectrum disorder (ASD) groups. **(A)** The first CMAP for both groups are presented along with a t-value map showing regions of statistically significant group difference. Significance was determined using P_{FDR} <0.05. The highlighted regions in black indicates areas where gradient values are higher in the ASD group compared to NT, while those outlined in white have higher values for the NT group. **(B)** Box plots indicate the significant differences (left: ASD>NT; right: NT>ASD) in the gradient values between the ASD and NT groups for the first CMAP. **(C)** The second CMAP is shown for both groups. There were no statistically significant group differences. **(D)** The line graphs represent the variance explained by each CMAP for NT (left) and ASD (right) groups. The Y-axis shows the scaled eigenvalues, indicating the amount of variance each component accounts for, while the X-axis represents the component number.

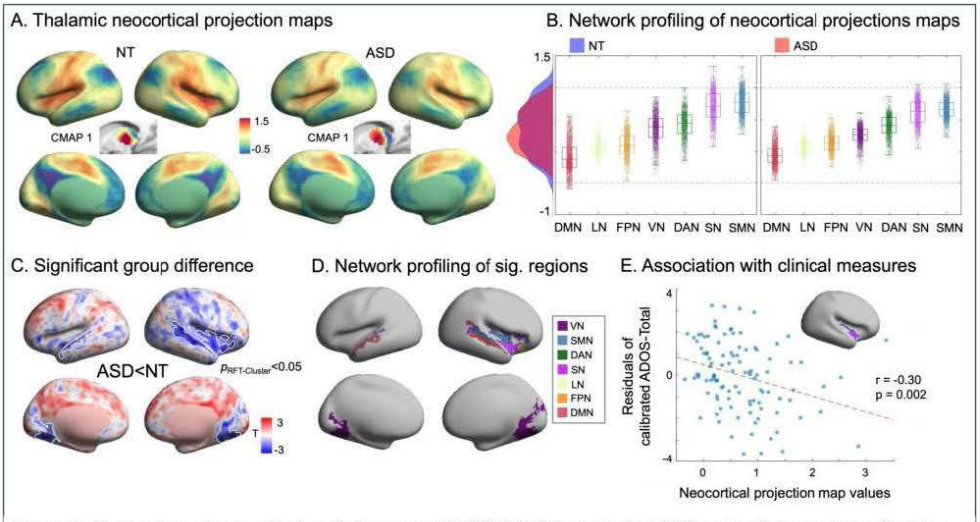

Figure 2. Comparison of neocortical projection maps (NEOMAP) in neurotypical (NT) and autism spectrum disorder (ASD) groups and their association with autism symptoms. **(A)** The average NEOMAPs are displayed for both NT and ASD groups. Matching colors indicate a connection between the regions on the surface with the same color in the CMAP. **(B)** Box plots show the distribution of NEOMAP values based on the Yeo-Krienan 7 network atlas. The NEOMAPs largely spread from the salience/somatosensory network to the default mode network. **(C)** The t-value map indicates regions where significant differences in the NEOMAP are observed between ASD and NT groups. Blue shades indicate regions where ASD is lower than NT, and red shades where ASD is higher than NT. Among the blue shaded regions, those delineated in white contour lines indicate a significant group difference (ASD<NT), where significance is denoted by $p_{RFT\text{-}Cluster} < 0.05$. **(D)** The significant regions were masked using the Yeo-Krienan 7 network atlas to profile the characteristics of these regions showing group difference. **(E)** A vertexwise analysis using SurfStat identified regions showing significant correlation with calibrated Autism Diagnostic Observation Schedule (ADOS) total calibrated scores. This region is mostly concentrated in the salience and somatomotor networks within the insula, as highlighted in the inset brain map. The scatter plot shows significant negative correlation between NEOMAP values and the residuals of the ADOS-Total calibrated score after controlling for the effects of age and head motion.

Abbreviations: CMAP (thalamocortical functional connectivity maps), VN (visual network), SMN (somatosensory network), DAN (dorsal attention network), SN (salience network), LN (limbic network), FPN (frontoparietal network), DMN (default mode network), RFT (random field theory).

Conclusions: Our study demonstrates that atypical thalamocortical connectivity, particularly involving the insula, a key node of the salience network, may underlie ASD symptom severity. Further research, however, is necessary to understand the impact of these atypical thalamo-insular connections in ASD, particularly in terms of how they influence the interaction between regions processing internally and externally oriented information.

References

1. Park, S. et al. A shifting role of thalamocortical connectivity in the emergence of large-scale functional brain organization across lifespan development. in.

2. Alves, P. N. et al. An improved neuroanatomical model of the default-mode network reconciles previous neuroimaging and neuropathological findings. Commun Biol 2, 370 (2019).
3. Di Martino, A. et al. The autism brain imaging data exchange: towards a large-scale evaluation of the intrinsic brain architecture in autism. Mol. Psychiatry 19, 659–667 (2014).
4. Vos de Wael, R. et al. BrainSpace: a toolbox for the analysis of macroscale gradients in neuroimaging and connectomics datasets. Commun Biol 3, 103 (2020).
5. Worsley, K. J. et al. A Matlab toolbox for the statistical analysis of univariate and multivariate surface and volumetric data using linear mixed effects models and random field theory. in NeuroImage Organisation for Human Brain Mapping 2009 Annual Meeting vol. 47 S102 (math.mcgill.ca, 2009).
6. Fortin, J.-P. et al. Harmonization of multi-site diffusion tensor imaging data. Neuroimage 161, 149–170 (2017).
7. Yeo, B. T. T. et al. The organization of the human cerebral cortex estimated by intrinsic functional connectivity. J. Neurophysiol. 106, 1125–1165 (2011).
8. Gotham, K., Pickles, A. & Lord, C. Standardizing ADOS scores for a measure of severity in autism spectrum disorders. J. Autism Dev. Disord. 39, 693–705 (2009).

Poster No 427

Brain Activity Dynamics in Children with and without Attention-Deficit Hyperactivity Disorder (ADHD)

Marie Hédo[1], Louisa Schilling[2], Parker Singleton[3], Keith Jamison[2], Amy Kuceyeski[2]

[1]Weill Cornell Medicine, Ithaca, NY, [2]Weill Cornell Medicine, New York City, NY, [3]Weill Cornell Medicine, New York, NY

Introduction: Attention-deficit/Hyperactivity Disorder (ADHD) is one of the most common neurodevelopmental conditions, however achieving conclusive evidence on neural correlates of ADHD has proven challenging. Additionally, the disorder disproportionally affects boys compared to girls, and there exist sex differences in their symptom profile, behavioral expression, and risk of comorbidities. However, it is unclear whether sex-specific neural correlates underlie sex differences in the disorder presentation. Here, the associations between functional brain activity dynamics and energy landscapes and ADHD symptoms across boys and girls were assessed in a population-based sample of children using network control theory (NCT) tools and multimodal imaging data. Finally, we studied whether comorbid internalizing and/or externalizing symptoms alter the energy landscape.

Methods: We used data from a subset of individuals (N = 2226, 1200 girls, age = 10-11 years) from the Adolescent Brain Cognitive Development (ABCD) study. Pre-processed resting-state fMRI time-series were parcellated into 86 regions by combining the Desikan-Killiany gyral atlas (68 regions; Desikan et al., 2006) and 18 subcortical structures (Fischl et al., 2002). K-means clustering was applied to identify four distinct recurring patterns of brain activity in the time series (called brain states). An average 86-region structural connectome was reconstructed based on diffusion-weighted imaging through probabilistic tractography. We used NCT to calculate the minimum transition energy (TE) required to transition between the four states as described previously (Cornblath et al. (2020) and Singleton et al. (2022)). Average TEs across all state transitions were computed at regional and functional network (Yeo et al., 2011) levels. Network TEs were computed by averaging the regional TEs of all the regions assigned to that network. We used scores on the attention-deficit/ hyperactivity problems DSM-oriented scale from the child behavior checklist completed by parents or guardians to assess ADHD symptoms. The associations between TEs, ADHD symptoms, and sex were analyzed by general linear models (GLMs) with sex, ADHD scores, and their interaction as outcome predictors and age, stimulant use, handedness, family socioeconomic status, scanner type, and frame-wise displacement as covariates. False discovery rate correction was applied to all p-values. We grouped the participants into high and low ADHD (cutoff score of 5) and conducted a principal component analysis (PCA) on all six DSM-oriented problem scales to assess comorbid symptomology profiles and their effect on energy demands. Associations between the principal component (PC) scores of behavior and TE were analyzed by additional GLMs.

Results: The GLM for network-level TE revealed that girls had higher TEs in the dorsal attention, ventral attention, and limbic network. ADHD was not associated with differences in TEs in any of the networks. However, a positive association with ADHD was found in the left banks of the superior temporal sulcus in the regional TE analysis. The PCA of behavioral scores resulted in three components, summarized as both high externalizing and internalizing symptoms (PC1), high externalizing symptoms (PC2), and high internalizing symptoms (PC3). PC3 was positively associated with TE in default mode network (DMN) regions. No associations between PC1 and PC2 and network, or regional TE were observed.

Figure 1

Conceptual Idea and Results of Network Control Theory

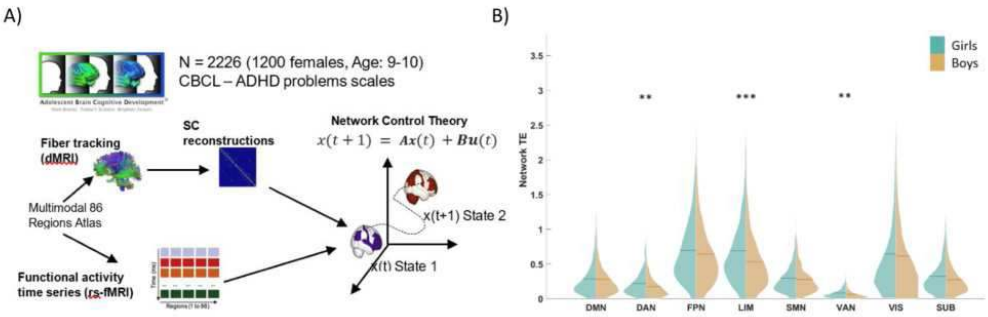

Note. **A)** Data were derived from the Adolescent Brain Cognitive Development (ABCD) study, and the participants' (N = 2226) ADHD symptoms were assessed by the DSM-oriented ADHD problem scale of the child behavior checklist (CBCL). Multimodal data were used and parcellated into 86 regions. The structural connectome (SC) was reconstructed based on diffusion magnetic resonance imaging (dMRI) data, and the functional time-series were derived from resting-state functional MRI (rs-fMRI). Network control theory (NCT) was used to calculate the minimum transition energy (TE) required to transition from one state x(t) to the next x(t+1). Here, states are defined as recurrent functional brain activity patterns derived from k-means clustering. A is the structural connectome, B is the control vector matrix, and u(t) is the time-dependent TE vector. **B)** The network-levels TEs are shown in the violin plots for girls (green) and boys (orange). The network TEs are the mean TEs of the regions assigned to each of the seven Yeo-resting state networks and one subcortical one. The horizontal bars indicate the means for girls or boys, respectively and differences between girls and boys were assessed. Abbreviations: DMN = default mode network, DAN = dorsal attention network, FPN = frontoparietal network, LIM = limbic network, SMN = somatomotor network, VAN = ventral attention network, VIS = visual network, SUB = subcortical network.
* $p < .05$. ** $p < .01$. *** $p < .001$. All p-values are corrected for multiple comparisons.

Figure 2

Principle Component Analysis

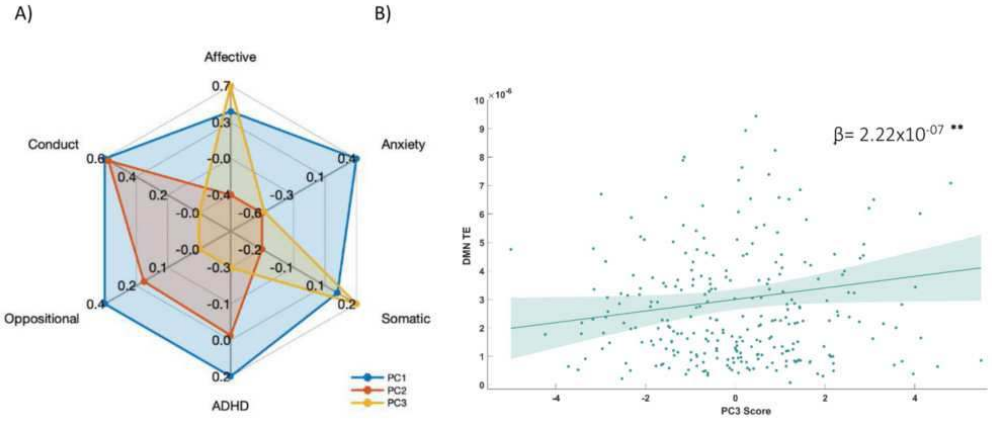

Note. The results of the PCA analysis on the six DSM-oriented scales led to a three-component solution. **A)** Shows the loadings on each scale for every component. The first component had high loadings on both externalizing and internalizing scales (blue) and is termed high ADHD-EI. The second component had high loadings on externalizing scales (red), termed high ADHD-E. Lastly, the third component had high loadings on internalizing scales except for the anxiety problems scale, termed ADHD-I. **B)** The scatterplot shows the association between scores on the third component and default mode network (DMN) TEs.
Abbreviations: ADHD = Attention Deficit/ Hyperactivity problems, DMN = Default Mode Network, TE = Transition Energy, PC3 = Principle Component 3
** $p < .01$. All p-values are corrected for multiple comparisons.

Conclusions: The control energy required to move through the brain's state space differs at a network level between girls and boys and highlights the importance of sex-specific analysis. Additionally, ADHD symptomatology is associated with region-specific increases in control energy. Only the internalizing symptoms in children with high ADHD scores were associated with an increase in TE in the DMN, indicating that the general psychopathology symptom profile has some implications in brain dynamics and energetic needs.

References
1. Cornblath, E. J. (2020),'Temporal sequences of brain activity at rest are constrained by white matter structure and modulated by cognitive demands', Communications Biology, 3(1).
2. Desikan, R. S. (2006), 'An automated labeling system for subdividing the human cerebral cortex on MRI scans into gyral based regions of interest', NeuroImage, 31(3), 968–980.
3. Salerno, L. (2020), 'Neuromodulation in Attention- Deficit/Hyperactivity Disorder: Toward a Precision Psychiatry approach', In Springer eBooks (pp. 107–122).
4. Fischl, B. (2002), 'Whole brain segmentation: Automated Labeling of Neuroanatomical Structures in the Human Brain', Neuron, 33(3), 341–355.
5. Murphy, A. B. (2017), 'A network neuroscience of neurofeedback for clinical translation', Current Opinion in Biomedical Engineering, 1, 63–70.
6. Singleton, S. (2022), 'Receptor-informed network control theory links LSD and psilocybin to a flattening of the brain's control energy landscape', Nature Communications, 13(1).
7. Yeo, B. T. (2011), 'The organization of the human cerebral cortex estimated by intrinsic functional connectivity', Journal of Neurophysiology, 106(3), 1125–1165.

Poster No 428

Investigating reward processing in autism: a replication study in the EU-AIMS Longitudinal Europea

Pan Zhou[1], Marianne Oldehinkel[2], Sarah Baumeister[3], Jan Buitelaar[4]

[1]Donders Institute for Brain, Cognition and Behaviour, Nijmegen, Gelderland Province, [2]Radboud University Medical Centre, Donders Institute for Brain, Cognition and Behaviour, Nijmegen, Gelderland, [3]Department of Child and Adolescent Psychiatry, Central Institute of Mental Health, Mannheim, Mannheim, Germany, [4]Donders Institute for Brain, Cognition, and Behavior, Radboud University Nijmegen, Nijmegen, NL, Nijmegen, Netherlands

Introduction: Social motivational theories (SMT) suggest a lack of interest in attending to and processing of social stimuli as a basic problem in Autism Spectrum Disorder (ASD)[1-2] . The SMT can be tested by examining how the brain reward circuitry is processing social and non-social reward stimuli, and whether this differs between ASD and non-ASD participants[2]. The monetary and social incentive delay task (MID and SID) consisting of a reward anticipation and a reward delivery phase, are common tasks that can be used for this purpose[3-4]. The EU-AIMS Longitudinal European Autism Project (LEAP) aimed at identifying biomarkers for ASD and includes the MID and SID tasks. The analysis of the MID/SID task data in the baseline assessment of LEAP (LEAP-1) showed lower activation in the ventral striatum (VS) in ASD compared to the typical developing control (TD) group during the anticipation of both monetary and social reward, but not during reward delivery[5], hereby not providing evidence for SMT but suggesting a general reward deficit in ASD. The main aim of this study was to repeat and extend the analyses of the MID and SID in the 2-year follow-up assessment of LEAP (LEAP-2) in a replication effort.

Methods: We included 150 ASD and 123 TD participants who completed the SID and MID tasks (see Figure 1) in both LEAP-1 and LEAP-2. We employed identical methods for preprocessing, quality control, whole-brain analysis, and region of interest (ROI) analysis across the two timepoints. After quality control and preprocessing, the SID and MID tasks were combined as two sessions in a general linear model (GLM) at the first level. To quantify differential reward-specific responses between tasks, we generated a contrast image for the interaction between condition (win, neutral) and task (SID, MID), for both the anticipation and delivery of reward. Contrast images were subjected to second-level GLMs with group (ASD vs TD) as between-subject factor and covariates for age, (biological) sex, and scan site. We additionally performed region of interest (ROI) analyses (repeated measures ANOVAs) to increase sensitivity for putative diagnostic differences within a-priori defined ROIs including the VS (comprising the caudate head and Nucleus Accumbens (NAcc)), insula, and putamen.

Results: Whole-brain analysis In line with previous work, we observed a widespread increase in activation during the anticipation of reward vs neutral cues across both ASD and TD (Figure 2A). Similarly we observed a main effect of condition during delivery (Figure 2D; $F(1,269)=36.18$, $pFWE<.001$, $k=19$). Furthermore, we observed lower activation in ASD compared to TD in the striatum during anticipation of both monetary and social rewards ($F(1,271)=56.31$, $pFWE<.001$, $k=132$; Figure 2B), hereby replicating the results from LEAP-1. Additionally, we found lower activation in the thalamus, ACC, precentral gyrus, postcentral gyrus and cerebellum in ASD during reward anticipation. There was no diagnosis-by-task interaction effect. During reward delivery, the ASD group also showed significant lower activation in the striatum ($F(1,269)=34.03$, $pFWE<.001$, $k=29$) compared to TD group, which is in line with findings in LEAP-1. ROI analysis We observed a significant effect of diagnosis during reward anticipation (ASD < TD) for all investigated ROIs, see figure 2G (left VS: $F(1,271)=5.375$, $p=.021$; right VS: $F(1,271)=6.172$, $p=.014$; left insula: $F(1,271)=8.942$, $p=.003$; right insula: $F(1,271)=6.915$, $p=.009$; left putamen: $F(1,271)=6.324$, $p=.012$; right putamen $F(1,271)=5.650$, $p=.018$). There was no interaction effect of reward type by diagnosis. For reward delivery, no significant effects were observed at all.

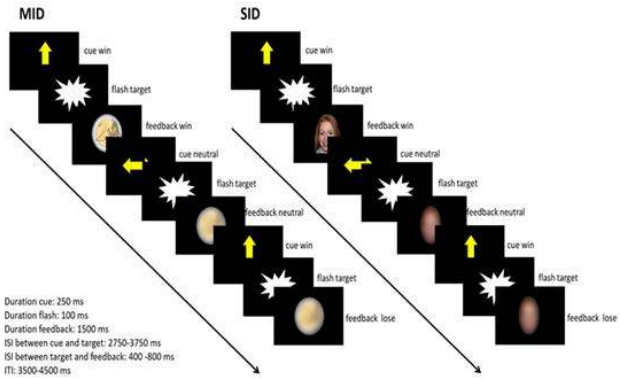

Figure 1. Task paradigm. During the SID task participants can 'win' a social reward (happy face) whereas during the MID task participants can win a monetary reward (2€ or £2). They were asked to respond (button press) on a win trial or a neutral trial based on the direction of the arrow (win: ↑; neutral: →). If participants responded fast enough for win trials a 2€/2£ coin would be presented in the MID and a smiling female face in the SID. A blurred coin or smiling face was presented in neutral trials and as feedback following slow responses in win trials. The presentation of a cue is defined as the anticipation phase, the presentation of a cue is defined as the anticipation phase.

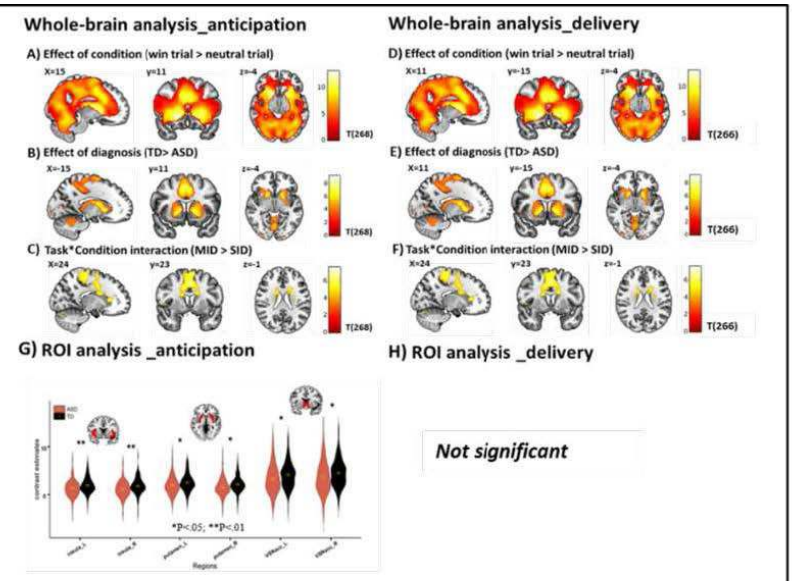

Figure 2. Brain activation during the anticipation and receipt of reward. Whole brain FWE-corrected effects of A,D) condition (win > neutral), B,E) diagnosis (TD>ASD) and C,F) interaction of task by condition (MID>SID) during reward anticipation (A,B,C) and reward receipt (D,E,F). G) Distribution plots of the contrast estimates for the ASD and TD group for the six investigated ROIs (left and right ventral striatum, insula and putamen) during reward anticipation. H) No significant effects of reward receipt were observed in the ROI analysis. Abbreviations: FWE=Family-Wise Error; MID=Monetary Incentive Delay; SID=Social Incentive Delay; ROI=Region of Interest, NAcc=Nucleus Accumbens.

Conclusions: We replicate the results from LEAP-1 and demonstrate that the lower activation during reward anticipation observed in the ASD group, is not specific to social reward. Our findings do thus not support the SMT, but suggest a general reward-processing deficit in ASD.

References

1. Levy SE, Mandell DS, Schultz RT. 2009. Autism. Lancet, 1627-1638.
2. Chevallier C, Kohls G, Troiani V, et al. (2012). The social motivation theory of autism. Trends in Cognitive Sciences, 16(4):231-239.
3. Knutson, B., Westdorp, A., Kaiser, E., & Hommer, D. (2000). FMRI visualization of brain activity during a monetary incentive delay task. Neuroimage, 12(1), 20-27.
4. Spreckelmeyer, K. N., Krach, S., Kohls, G., Rademacher, L., Irmak, A., Konrad, K., ... & Gründer, G. (2009). Anticipation of monetary and social reward differently activates mesolimbic brain structures in men and women. Social cognitive and affective neuroscience, 4(2), 158-165.
5. Baumeister, S., Moessnang, C., Bast, N., Hohmann, S., Aggensteiner, P., Kaiser, A., ... & Brandeis, D. (2023). Processing of social and monetary rewards in autism spectrum disorders. The British Journal of Psychiatry, 222(3), 100-111.
6. Clements, CC., Zoltowski, A. R., Yankowitz, L. D., Yerys, B. E., Schultz, R. T., & Herrington, J. D. (2018). Evaluation of the social motivation hypothesis of autism: a systematic review and meta-analysis. Jama Psychiatry.

Poster No 429

Disruptions of Fractional Amplitude of Low-Frequency Fluctuations in Autism Spectrum Disorder

Samuel Joseph[1], Sheeba Anteraper[2]

[1]Austin Preparatory School, Reading, MA, [2]UT Southwestern Medical Center, Dallas, TX

Introduction: Whole-brain connectome-wide data-driven studies have reported disruptions in cerebrocerebellar intrinsic functional connectivity (FC) in young adults with high-functioning autism spectrum disorder (ASD)[1]. Detecting the fractional amplitude of low-frequency fluctuations (fALFF)[2] of the BOLD signal in the frequency window of interest can provide insights complementary to FC measures. To test this, we examined fALFF in a highly sampled (temporal resolution < 0.5s) resting-state fMRI dataset obtained from the Autism Brain Imaging Data Exchange (ABIDE II).

Methods: Data Acquisition: We used the public dataset on ABIDE II (n=51; 16 ASD, 35 healthy controls) contributed by Michal Assaf, MD (Olin Neuropsychiatry Research Center), collected on 3T Siemens Skyra. Functional data (3mm voxels) had TR/TE/flip angle of 475ms/30ms/60°, multi-band factor 8, and 947 time-points. Anatomical data (0.8 mm voxels) had TR/TE/TI/flip angle of 2200ms/2.88ms/794ms/13°. Data Analyses: CONN 22.a[3] and SPM12[4]. Preprocessing: A flexible pipeline[5] was used for realignment with correction of susceptibility distortion interactions, outlier detection, direct segmentation and MNI-space normalization, and smoothing (5 mm Gaussian kernel). Outlier scans were identified using ART[6] as acquisitions with framewise displacement above 0.5 mm or global BOLD signal changes above 3 standard deviations[7]. Functional and anatomical data were normalized into standard MNI space, segmented into grey matter, white matter, and CSF tissue classes, and resampled to 2 mm isotropic voxels following a direct normalization procedure using SPM unified segmentation and normalization[8] with the default IXI-549 tissue probability map template. Denoising: This pipeline includes the regression of potential confounding effects characterized by white matter and CSF timeseries, motion parameters and their first order derivatives, outlier scans, session effects and their first order derivatives, and linear trends within each functional run, followed by bandpass filtering (0.008-0.09 Hz) of the BOLD timeseries. CompCor[9] noise components within white matter and CSF were estimated by computing the average BOLD signal as well as the largest principal components orthogonal to the BOLD average, motion parameters, and outlier scans within each subject's eroded segmentation masks. First-level analysis: fALFF maps characterizing low-frequency BOLD signal variability at each voxel were estimated as the ratio between the root mean square of the BOLD signal after denoising and band-pass filtering, divided by the same measure computed before band-pass filtering[2]. Group-level analyses: For each individual voxel a separate General Linear Model was estimated, with first-level connectivity measures at this voxel as dependent variables (one independent sample per subject), and groups as independent variables. Voxel-level hypotheses were evaluated using multivariate parametric statistics with random-effects across subjects and sample covariance estimation across multiple measurements. Results for the between group analyses (ASD vs. healthy controls) were thresholded using a cluster-forming $p < 0.005$ (two-sided) voxel-level threshold, and a false discovery rate corrected $p < 0.05$ cluster-size threshold.

Results: Results from fALFF analyses in ASD vs. healthy controls are shown in Fig. 1/Table 1. The two cerebellar clusters (bilateral Crus I and II), visualized on a flat map, and the cerebral cluster (left frontal pole) overlaid on a surface representation, overlap with the regions attributed to social cognition. There was no statistically significant difference in head-motion between the two groups.

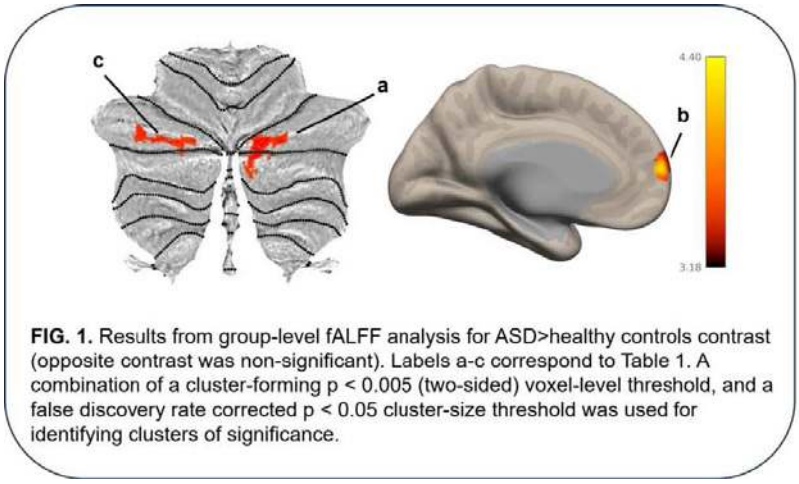

FIG. 1. Results from group-level fALFF analysis for ASD>healthy controls contrast (opposite contrast was non-significant). Labels a-c correspond to Table 1. A combination of a cluster-forming $p < 0.005$ (two-sided) voxel-level threshold, and a false discovery rate corrected $p < 0.05$ cluster-size threshold was used for identifying clusters of significance.

Table 1. Results from group-level fALFF analysis for ASD>healthy controls contrast (opposite contrast was non-significant).

Brain Region	MNI Coordinates	Cluster Size
a. Cerebellum CrusI/II Right	+20 -82 -26	98
b. Frontal Pole Left	-10 +62 +10	93
c. Cerebellum CrusI/II Left	-36 -80 -32	85

Conclusions: By leveraging a high-temporal resolution public dataset, and by using fALFF, a metric complementary to FC measures, we add to the growing body of evidence highlighting the role of cerebellum in autism[10]. Overall, our findings support the role of cerebrocebellar circuitry in brain function and dysfunction.

References

1. Arnold Anteraper, S., Guell, X., D'Mello, A., Joshi, N., Whitfield-Gabrieli, S., & Joshi, G. (2019). Disrupted Cerebrocerebellar Intrinsic Functional Connectivity in Young Adults with High-Functioning Autism Spectrum Disorder: A Data-Driven, Whole-Brain, High-Temporal Resolution Functional Magnetic Resonance Imaging Study. Brain connectivity, 9(1), 48–59.
2. Zou, Q. H., Zhu, C. Z., Yang, Y., Zuo, X. N., Long, X. Y., Cao, Q. J., ... & Zang, Y. F. (2008). An improved approach to detection of amplitude of low-frequency fluctuation (ALFF) for resting-state fMRI: fractional ALFF. Journal of neuroscience methods, 172(1), 137-141.
3. Nieto-Castanon, A. & Whitfield-Gabrieli, S. (2022). CONN functional connectivity toolbox: RRID SCR_009550, release 22. doi:10.56441/hilbertpress.2246.5840.
4. Penny, W. D., Friston, K. J., Ashburner, J. T., Kiebel, S. J., & Nichols, T. E. (Eds.). (2011). Statistical parametric mapping: the analysis of functional brain images. Elsevier.
5. Nieto-Castanon, A. (2020). FMRI minimal preprocessing pipeline. In Handbook of functional connectivity Magnetic Resonance Imaging methods in CONN (pp. 3–16). Hilbert Press.
6. Whitfield-Gabrieli, S., Nieto-Castanon, A., & Ghosh, S. (2011). Artifact detection tools (ART). Cambridge, MA. Release Version, 7(19), 11.
7. Power, J. D., Mitra, A., Laumann, T. O., Snyder, A. Z., Schlaggar, B. L., & Petersen, S. E. (2014). Methods to detect, characterize, and remove motion artifact in resting state fMRI. Neuroimage, 84, 320-341.
8. Ashburner, J. (2007). A fast diffeomorphic image registration algorithm. Neuroimage, 38(1), 95-113.
9. Behzadi, Y., Restom, K., Liau, J., & Liu, T. T. (2007). A component based noise correction method (CompCor) for BOLD and perfusion based fMRI. Neuroimage, 37(1), 90-101.
10. Anteraper, S. A., Guell, X., Taylor, H. P., D'Mello, A., Whitfield-Gabrieli, S., & Joshi, G. (2019). Intrinsic Functional Connectivity of Dentate Nuclei in Autism Spectrum Disorder. Brain connectivity, 9(9), 692–702.

Poster No 430

New Insights into Atypical Corticospinal Tract Microstructure in Children with Cerebral Palsy

Alexandra Hruby[1], Divya Joshi[1], Julius Dewald[1], Carson Ingo[1]

[1]Northwestern University, Chicago, IL

Introduction: Unilateral brain injuries in early childhood can result in hemiplegic cerebral palsy (CP), characterized by deficits such as weakness in the hand[1,2] and loss of independent motor control between hands, known as mirroring[3,4]. Since previous studies in CP have not focused on quantitative measurement of these hand impairments, the objective of this diffusion MRI (dMRI) study is to investigate the relationships between atypical development in each hemisphere and quantitative measures of hand impairment severities of weakness and mirroring.

Methods: Structural scans were acquired using an MPRAGE sequence (TR=2.3s, TE=2.94ms, TI=900ms, FOV 256x256mm2 with a voxel resolution of 1 mm3) and used to identify anatomical regions of interest (ROIs) using a standardized atlas[5-7]. Five cortical areas with typical or potential corticospinal tract connectivity -- precentral gyrus, postcentral gyrus, superior frontal gyrus, middle frontal gyrus, and superior parietal gyrus -- were masked with the CST (Fig. 1) to determine the overlap volume, which was then normalized by the total volume of the ROI. dMRI data were acquired using a spin-echo EPI sequence (TR=5s, TE=85ms, matrix size=150x150, FOV=225x225mm, slice thickness = 1.5mm, interslice gap = 0.1 mm, number of slices = 90) with diffusion weighting at b=1000 s/mm2 in 60 different directions and 8 scans without diffusion weighting (b=0 s/mm2). dMRI data were pre-processed as previously described to estimate diffusion metrics (FA, MD, RD, AD)[8,9]. Anatomical landmarks were used to guide probabilistic tractography of the corticospinal tract (CST) to calculate the mean and standard deviation

of diffusivity metrics. Hand grip strength and mirroring were measured using simultaneous recording of two handheld digital dynamometers in the non-affected and affected hands (Fig. 2)[10]. Spearman correlation analyses were performed between diffusivity metrics and hand impairment measures with age and sex as covariates. A Mann-Whitney U test was performed to determine if there was a significant difference in tract termination ratios between participants with early-onset hemiplegic CP and controls. Statistical significance was set at $p<0.05$.

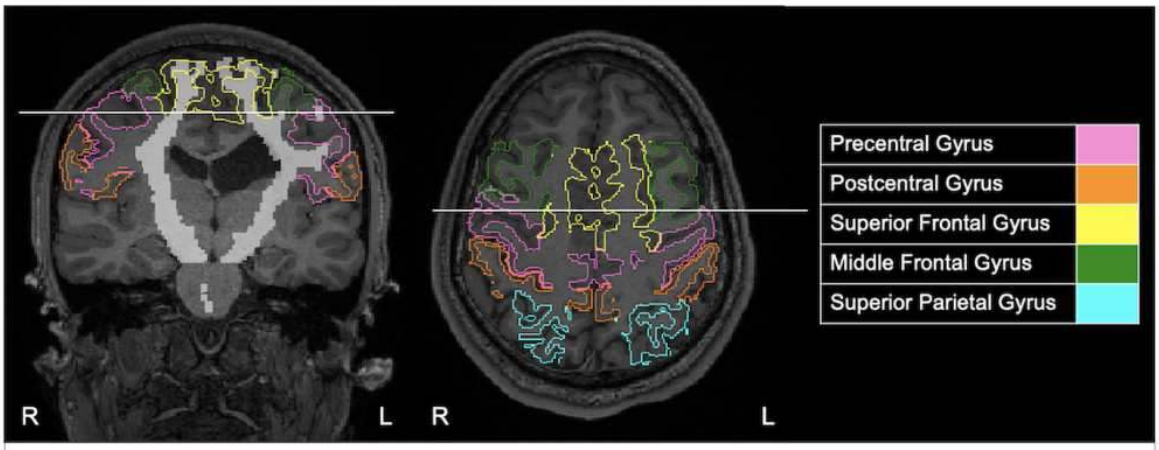

Figure 1. Structural T1 images with outlined regions of interest from pediatric atlas-based parcellation and shaded corticospinal tract.

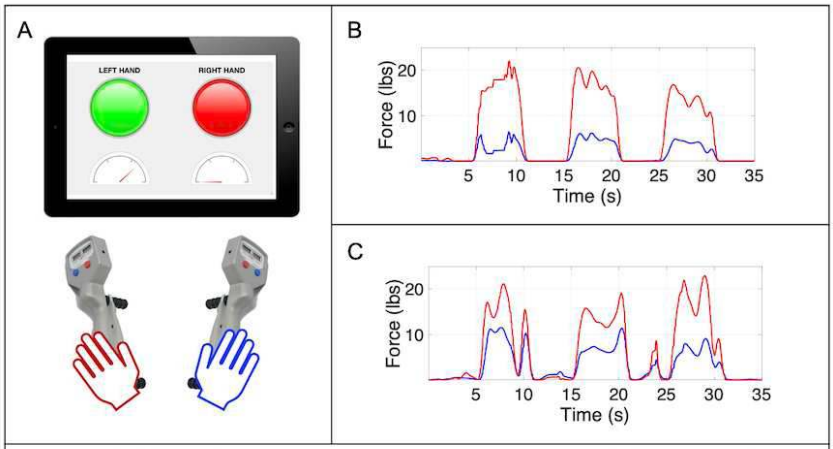

Figure 2. (A) Setup for bilateral grip strength assessment. (B) Example force measurement trace exhibiting mirroring from trial with left hand cued. (C) Example force measurement trace exhibiting grasp weakness from trial with both hands cued.

Results: Preliminary results include 9 children with early-onset hemiplegic CP (5M, 13.6±6.8y) and 8 controls (2M, 13.4±5.5y). There was a significant negative correlation between FA in the ipsilesional CST and grasp weakness severity (rho=-0.60, p=0.017) that was primarily driven by a significant positive correlation between RD in the ipsilesional CST and grasp weakness severity (rho=0.60, p=0.017). There was also a significant negative correlation between FA in the contralesional CST and hand mirroring severity (rho=-0.52, p= 0.049) that was primarily driven by a significant positive correlation between RD in the contralesional CST and hand mirroring severity (rho=0.56, p=0.030). There were no significant group differences in tract termination ratios for the cortical ROIs in the affected hemisphere. In the unaffected hemisphere, there was a significant decreased density of tract termination in the precentral gyrus for early-onset hemiplegic CP participants in comparison to controls (p=0.035). Conversely, there was an increased density of tract termination in the unaffected superior parietal gyrus for early-onset hemiplegic CP participants in comparison to controls (p=0.048).

Conclusions: Here, we show that there is a significant relationship between supraspinal neural microstructure and impairments in normal hand function in individuals with early-onset hemiplegic CP. Hemiplegic CP presents with unilateral motor deficits; however, these results show an injury early in development can have detrimental effects on the unaffected hemisphere, specifically the motor pathways and association areas, and involvement of the unaffected hand. Characterization of the changes in the unaffected hemisphere may reveal a basis for new therapy and treatment approaches for hand motor impairments.

References
1. Friel, K. M. (2013), 'Pathophysiological mechanisms of impaired limb use and repair strategies for motor systems after unilateral injury of the developing brain', Developmental Medicine & Child Neurology, vol. 55, no. 4, pp. 27-31. doi:10.1111/dmcn.12303
2. Holmstrom, L. (2010), 'Hand function in relation to brain lesions and corticomotor-projection pattern in children with unilateral cerebral palsy', Developmental Medicine & Child Neurology, vol. 52, no. 2, pp. 145-152. doi:10.1111/j.1469-8749.2009.03496.x
3. Woods, B. T. (1978), 'Mirror movements after childhood hemiparesis', Neurology, vol. 28, no. 11, pp. 1152-1157. doi:10.1212/wnl.28.11.1152
4. Martin, J. H. (2005), 'The corticospinal system: from development to motor control', Neuroscientist, vol. 11, no. 2, pp. 161-173. doi:10.1177/1073858404270843
5. Mori, S. (2016), .MRICloud: Delivering High-Throughput MRI Neuroinformatics as Cloud-Based Software as a Service. Computing in Science & Engineering', vol. 18, no. 5, pp. 21-35. doi:10.1109/mcse.2016.93
6. Rapallo, F. (2013), 'Bayesian Parameter Estimation and Segmentation in the Multi-Atlas Random Orbit Model', PLoS One, vol. 8, no. 6. doi:10.1371/journal.pone.0065591
7. Wang, H. (2013), 'Multi-atlas segmentation with robust label transfer and label fusion', Information Processing in Medical Imaging, vol. 23, pp. 548-559. doi:10.1007/978-3-642-38868-2_46
8. Smith, S. M. (2004), 'Advances in functional and structural MR image analysis and implementation as FSL', Neuroimage, vol. 23, suppl. 1, pp. S208-219. doi:10.1016/j.neuroimage.2004.07.051
9. Owen, M. (2017), 'Upper Extremity Motor Impairments and Microstructural Changes in Bulbospinal Pathways in Chronic Hemiparetic Stroke', Frontiers in Neurology, vol. 8. doi:10.3389/fneur.2017.00257
10. Hill, N. M. (2021), 'Between Limb Muscle Co-activation Patterns in the Paretic Arm During Non-paretic Arm Tasks in Hemiparetic Cerebral Palsy', Frontiers in Neuroscience, vol. 15, suppl. 666697. doi:10.3389/fnins.2021.666697

Poster No 431

Decoding differences between neural responses to sustained and transient auditory sounds in dyslexia

Josiane Mukahirwa[1], Qianli Meng[1], Keith Schneider[1]

[1]University of Delaware, Newark, DE

Introduction: The magnocellular system theory of developmental dyslexia suggests a pervasive dysfunction of the magnocellular system, specialized for temporal processing, throughout the brain (Stein, 2019). However, this has only been extensively investigated in the visual system (Livingston et al.,1991). Here, we measure the contributions of the magnocellular system in the auditory cortex in people with dyslexia compared to normal readers.

Methods: Using fMRI at 3T, we imaged whole-brain responses in 10 subjects with dyslexia and 11 normal readers as they passively listened to sustained and transient non-linguistic sounds in a block of ~8 s during 8– 40 functional ~5 min runs. Trial-wise estimates for individual subjects were used to perform multi-voxel pattern analyses (MVPA) to discriminate between the sustained and transient responses in localized regions (searchlight) in the whole brain. The results were compared to contrasts between the stimuli obtained with a general linear model (FSL FEAT).

Results: MVPA group results showed that in the normal readers, regions surrounding Heschl's gyrus (primary auditory cortex) were able to consistently (FWE, $p < .05$, TFCE) discriminate between the sustained and transient stimuli. In contrast, the subjects with dyslexia exhibited no regions that discriminated above the threshold, although there was consistent subthreshold discriminability in the auditory cortex. However, there were no significant differences between the groups. The GLM contrasts did not exhibit any significant differences between the sustained and transient stimuli or between groups, but there were large areas in the auditory cortex with subthreshold activity within groups.

Conclusions: Our findings indicate that in normal readers, MVPA but not GLM analyses revealed significant discrimination in the auditory cortex between transient and sustained auditory stimuli, whereas no discrimination exceeded the statistical threshold in the dyslexia group. However, the discrimination differences between groups were not reliable in our small sample.

References
1. J. Stein (2019), "The current status of the magnocellular theory of developmental dyslexia," Neuropsychologia, vol. 130, no. September 2017, pp. 66–77, doi: 10.1016/j.neuropsychologia.2018.03.022.
2. M. S. Livingstone, G. D. Rosen, F. W. Drislane, and A. M. Galaburda (1991), "Physiological and anatomical evidence for a magnocellular defect in developmental dyslexia," Proceedings of the National Academy of Sciences., vol. 88, no. 18, pp.7943–7947, doi: 10.1073/pnas.88.18.7943.

Poster No 432

Altered brain connectivity in Autistic-Like behaviors of SHANK3 mutant beagle dogs

Xueru Liu[1], Rui Tian[2], Hui Zhao[2], Yong Q. Zhang[2], Yan Zhuo[1], Zhentao Zuo[1,3]

[1]State Key Laboratory of Brain and Cognitive Science, Institute of Biophysics, CAS, Beijing, China, [2]Institute of Genetics and Developmental Biology, CAS, Beijing, China, [3]University of Chinese Academy of Sciences, Beijing, China

Introduction: Autism spectrum disorder (ASD) is a childhood-onset neurodevelopmental psychiatric disorder characterized by profound deficits in social interaction and communication, as well as repetitive stereotyped behaviors or restricted interests[1]. Previous MRI studies showed varied structural and functional brain abnormalities in ASD patients, but there is still no definitive conclusion[2,3]. Several studies have identified the genetic defects that cause ASD, and with advances in gene-editing technology, it has become feasible to establish non-human primate models in ASD[4]. Given that dogs show stronger social bonds with humans through reading human social communicative cues[5,6], our team developed and characterized multiple lines of Beagle SHANK3 (bShank3) mutants[7]. We performed neuroimaging analysis on the mutants to explore whether there are abnormalities in brain functional connectivity between generations of mutant dogs.

Methods: All animals (wild types, WT: 2.40 ± 0.18 years, N=17; F0 mutants, F0: 1.40 ± 0.07 years, N=4; F1 mutants, F1: 0.90 ± 0.01 years, N=10)7 were scanned at a Siemens Prisma 3.0T MR scanner with the same protocol of anesthesia and MRI parameters following we previously described8. Resting-state functional MRI data were acquired using a T2-weighted gradient echo echo-planar imaging sequence (TR/TE = 2.2 s/29 ms, flip angle = 90°, 1.8 × 1.8 mm in plane resolution and slice thickness of 1.8 mm), with contiguous and interleaved 240 volumes. fMRI data were motion-corrected, realigned, normalized to structural scans of the Beagle brain template[8] and spatially smoothed with a 4-mm full-width at half maximum Gaussian kernel. An unbiased data-driven approach was applied for resting-state global (between a seed voxel and all other voxels in the brain) and local (between a seed voxel and its neighboring voxels within 15 mm radius) functional connectivity analysis by CONN toolbox in Matlab[9].

Results: These abnormalities include hyper-connectivity in two loci of ESR 1 and 2 within the temporal cortex of F0 mutants (Figure 1). We also found reduced global- and local-range functional connectivity in the two loci of gPC (loci 2 & 4), and local hypo-connectivity in the gPCC (locus 7) of F0 mutants. Loci gPC and gPCC are located in the anterior and posterior gyrus of the central sulcus, respectively, and are homologous to the sensorimotor cortex in the human brain[10]. We further revealed global hypo-connectivity in the gCR (locus 3), a homologous region to the dorsolateral PFC in humans[10]; and local hyper-connectivity in the SSR (locus 6), a region involved in auditory processing in F0 mutants In F1 mutants, altered connectivity patterns were observed in four of the seven brain regions identified in F0 mutants with abnormal connectivity pattern (loci 2 and 4–6). We found no correlation between connection abnormalities with the elevated shuttle in mutants (Figure 2A). However, a significant negative correlation was observed between stress tails and local connectivity in the ESR2 (locus 5; Figure 2B), between withdrawal and global connectivity in the gPC (locus 2; Figure 2C), and between social approach and local connectivity in the SSR (locus 6; Figure 2D). The coordinates and full names of the various loci were listed in Figure 2E.

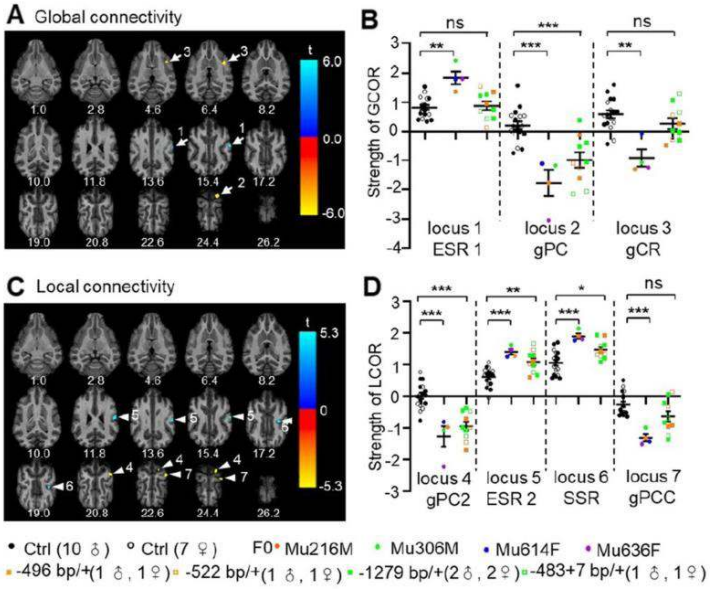

Figure 1. Altered global and local connectivity in the cortex of the left-brain hemisphere of F0 and F1 Shank3 mutants. Two-tailed two sample t test was used for fMRI analysis of whole brain with uncorrected $P < 0.001$ (with a cluster-forming threshold of $k > 20$) and Two-tailed Mann–Whitney U-test was used for comparison of the seven loci (ROI analysis) . (A/C) Multi-axial views of differential global and local connectivity between control and mutant groups. Brain regions with robust alteration of global connectivity are highlighted by an arrow and numbered. Numbers below the images in A and C indicate Z coordinates (mm). The t values are calculated by comparison between Shank3 mutants and WT groups. (B) Normalized strength of global correlation (GCOR) showed increased strength for locus 1 but reduced strength for loci 2 and 3. (D) Normalized strength of local correlation (LCOR) showed reduced strength for loci 4 and 7, but increased strength for loci 5 and 6. *p<0.05, **p<0.01, ***p<0.001, ns, no significant.

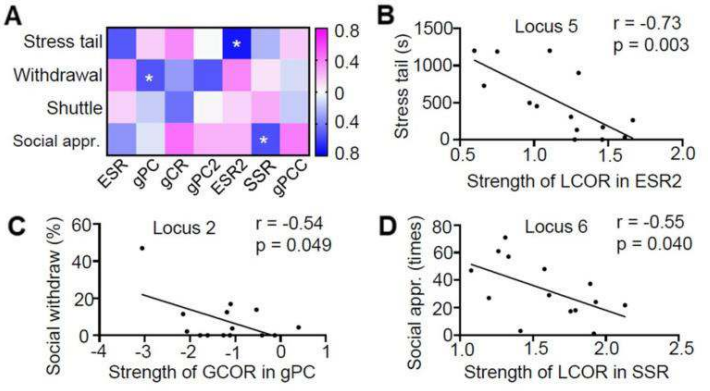

E

Locus	Name	Short name	Coordinates (mm) in BBT x	y	z	Cluster Size (voxels)
1	ectosylvius rostralis	ESR	-21	-7	14	20
2	gyrus precruciatus	gPC	-7	8	24	29
3	gyrus compositus rostralis	gCR	-15	1	6	33
4	gyrus precruciatus 2	gPC2	-7	7	23	26
5	ectosylvius rostralis 2	ESR2	-20	-9	13	39
6	suprasylvius rostralis	SSR	-12	-10	18	22
7	gyrus postcruciatus cortex	gPCC	-11	0	25	32

Figure 2. Pearson correlation analysis between behaviors and GOCR/LOCR of the seven loci of four F0 and ten F1 mutants. (A) Pearson correlation analysis between behaviors and GOCR/LOCR of the seven loci of four F0 and ten F1 mutants. The significant correlation was indicted with a white asterisk. Negative correlation between the strength of LCOR in ESR2 and the duration of stress tails (B), between the strength of GCOR in gPC and social withdrawals (C), and between the strength of LCOR in SSR and social approaches (D). (E). The coordinates of seven loci with altered global/local connections in the cortex of the left-brain hemisphere of *Shank3* mutants. Loci 1, 5 and 6 were in the temporal cortex. Loci 2, 4, and 7 were located in the sensorimotor cortex, while locus 3 was in the dorsolateral PFC.

Conclusions: In the present study, we found mutants revealed altered connectivity in the cortex of the left-brain hemisphere through voxel-based analysis of global and local functional connectivity. The aberrant patterns in both global and local functional connectivity in the mutant dogs were not only present in the F0 generation but were also inherited in the F1 generation. Our findings demonstrate the validity and unique value of genetically modified dogs to model ASD and possibly other psychiatric diseases. Acknowledgement: This work was supported by 2019YFA0707103, 2020AAA010560, CAS-2021091, and YSBR-068.

References

1. Levy SE, Mandell DS, Schultz RT (2009) Autism. Lancet 374:1627–1638.
2. Postema MC, van Rooij D, Anagnostou E, et al (2019) Altered structural brain asymmetry in autism spectrum disorder in a study of 54 datasets. Nat Commun 10:1–12.
3. Cardinale RC, Shih P, Fishman I, et al (2013) Pervasive Rightward Asymmetry Shifts of Functional Networks in Autism Spectrum Disorder. JAMA psychiatry 70:975.
4. Zhou Y, Sharma J, Ke Q, et al (2019) Atypical behaviour and connectivity in SHANK3-mutant macaques. Nat 2019 5707761 570:326–331.
5. Hare B, Brown M, Williamson C, Tomasello M (2002) The domestication of social cognition in dogs. Science 298:1634–1636.
6. Bunford N, Andics A, Kis A, et al (2017) Canis familiaris As a Model for Non-Invasive Comparative Neuroscience. Trends Neurosci 40:438–452.
7. Tian R, Li Y, Zhao H, et al (2023) Modeling SHANK3-associated autism spectrum disorder in Beagle dogs via CRISPR/Cas9 gene editing. Mol Psychiatry.
8. Liu X, Tian R, Zuo Z, et al (2020) A high-resolution MRI brain template for adult Beagle. Magn Reson Imaging 68:148–157.
9. Whitfield-Gabrieli S, Nieto-Castanon A (2012) Conn: a functional connectivity toolbox for correlated and anticorrelated brain networks. Brain Connect 2:125–141.
10. Szabó D, Czeibert K, Kettinger Á, et al (2019) Resting-state fMRI data of awake dogs (Canis familiaris) via group-level independent component analysis reveal multiple, spatially distributed resting-state networks. Sci Rep 9:1–25.

Poster No 433

Characterising structural similarity networks in the marmoset using Morphometric Inverse Divergence

Ed Hutchings[1], Stephen Sawiak[1], Richard Bethlehem[2], Angela Roberts[1], Edward Bullmore[3]

[1]University of Cambridge, Cambridge, Cambridgeshire, [2]Autism Research Centre, Department of Psychiatry, University of Cambridge, Cambridge, United Kingdom, [3]University of Cambridge, Cambridge, United Kingdom

Introduction: Many psychiatric disorders are in part neurodevelopmental, motivating the need to characterise healthy brain development. MRI provides a non-invasive, non-ionising, and high detail way to track brain development. MRI has been used with network approaches, such as graph theory, which models regions as nodes and connections as edges[1]. Graph theoretic properties, such as hubs and modules, are thought to play specific roles in information processing and have been implicated in various mental disorders[1]. Structural similarity has increasingly been used to generate networks from structural MRI images, in which edges reflect genetic similarity as well as axonal connectivity[2]. Regions with high structural covariance (a type of similarity) tend to develop together as coordinated units, and disturbances in this coordination may play a role in the aetiology of psychiatric disorders[3]. This technique generates group level networks, and later approaches have aimed to generate networks within individuals. One such approach is Morphometric Inverse Divergence (MIND), which has been biologically validated in humans and macaques[4]. Understanding how structural similarity in early life relates to brain morphology and behaviour across development of individuals requires longitudinal imaging. We turned to the common marmoset as an animal model due to their short life history yet cortical and behavioural complexity[5]. As a preliminary analysis, we generated MIND networks from a mean MTsat image (a measure of myelin[6]) to assess biological validity and characterise network properties.

Methods: N=119 marmosets were scanned longitudinally (Fig 1A) using a 9.4T system. Three 3D multi-gradient echo sequences (PDw/MTw/T1w) were acquired. Estimation of MTsat parameter maps followed previously published methods[6]. Preprocessing was performed using SPM12 in Matlab. The SPMMouse toolbox[7] was used with DARTEL to generate population templates. These were warped to create a mean MTsat map across all animals, and a cortical parcellation consisting of 232 regions was applied[8]. MIND networks were generated using code from[4].

Results: Building and validating the network Highest edge weights were found between homotypic interhemispheric regions (Fig. 1B, D). To assess the extent to which similarity was driven by distance between regions, we correlated the raw MIND matrix with a matrix formed from Euclidian distance between region centroids (Fig. 1C). There was a small negative correlation ($r = -0.16$, $p = 1.022e-5$), indicating a slight decay in similarity with distance. Network analysis Node strength distribution of the raw matrix was negatively skewed (Fig 2A). Hubs of the network (top 20 node strengths) concentrated in frontal and paracentral areas (Fig 2B). Lowest node strengths were found in the occipital lobe, with a decreasing gradient from V3 to V1. We clustered the network to see if we could identify modules with distinct myeloarchitecture. Optimal Louvain clustering

found two modules (modularity = 0.0603), containing mainly superior temporal cortex (Fig. 2C). Hierarchical clustering found a smaller cluster, containing only visual and auditory parabelt regions (Fig. 2D). We performed a principal component analysis on edge weights. The first principal component explained 40% of the total variation in edge weights (Fig. 2E) separating auditory and visual regions from frontal and temporo-parietal association areas.

Figure 1

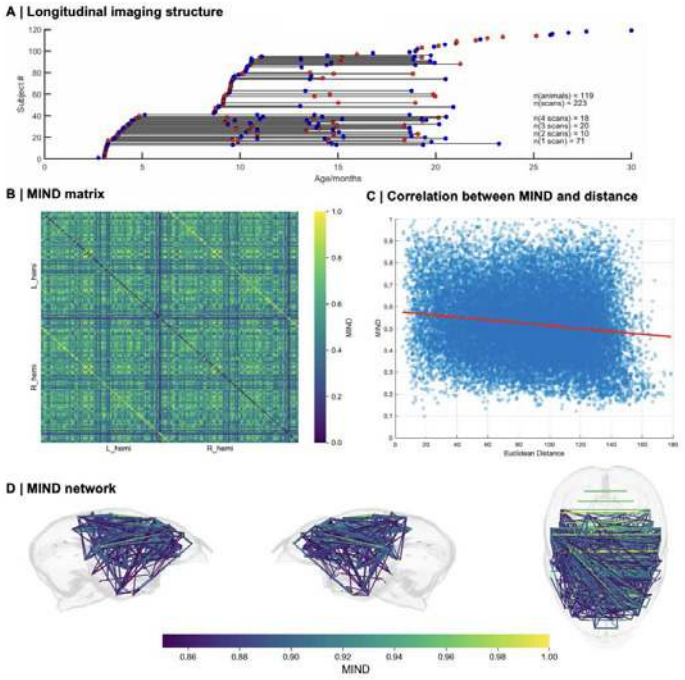

Figure 2

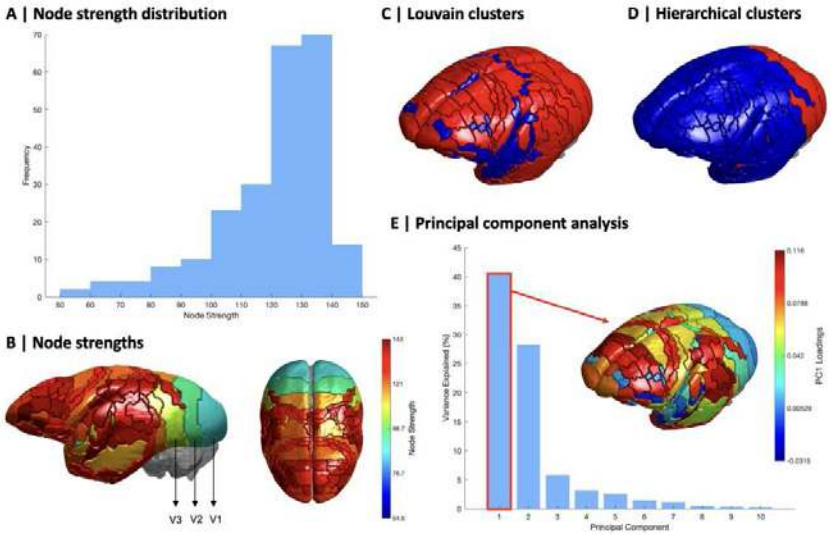

Conclusions: MTsat MIND networks show strong interhemispheric similarity and decay with distance, suggesting they are biologically valid[4]. Principal component analysis identified a primary sensory to association gradient anchored in visual and auditory cortex at one end and fronto-temporal cortex at the other, accounting for 40% of variance in edge weights. This finding echoes the sensory-association gradient of myeloarchitecture found in human[9] and may suggest conserved organisational principals between species.

References

1. Bullmore, Ed, and Olaf Sporns. 2009. 'Complex Brain Networks: Graph Theoretical Analysis of Structural and Functional Systems'. Nature Reviews Neuroscience 10 (3): 186–98
2. Evans, Alan C. 2013. 'Networks of Anatomical Covariance'. NeuroImage 80 (October): 489–504
3. Alexander-Bloch, Aaron, Jay N. Giedd, and Ed Bullmore. 2013. 'Imaging Structural Co-Variance between Human Brain Regions'. Nature Reviews Neuroscience 14 (5): 322–36

4. Sebenius, Isaac, Jakob Seidlitz, Varun Warrier, Richard A. I. Bethlehem, Aaron Alexander-Bloch, Travis T. Mallard, Rafael Romero Garcia, Edward T. Bullmore, and Sarah E. Morgan. 2023. 'Robust Estimation of Cortical Similarity Networks from Brain MRI'. Nature Neuroscience 26 (8): 1461–71
5. Okano, Hideyuki, Keigo Hikishima, Atsushi Iriki, and Erika Sasaki. 2012. 'The Common Marmoset as a Novel Animal Model System for Biomedical and Neuroscience Research Applications'. Seminars in Fetal and Neonatal Medicine 17 (6): 336–40
6. Sawiak, Stephen J., Nigel I. Wood, Guy B. Williams, A. Jennifer Morton, and T. Adrian Carpenter. 2013. 'Voxel-Based Morphometry with Templates and Validation in a Mouse Model of Huntington's Disease'. Magnetic Resonance Imaging 31 (9): 1522–31
7. Weiskopf, Nikolaus, John Suckling, Guy Williams, Marta M. Correia, Becky Inkster, Roger Tait, Cinly Ooi, Edward T. Bullmore, and Antoine Lutti. 2013. 'Quantitative Multi-Parameter Mapping of R1, PD*, MT, and R2* at 3T: A Multi-Center Validation'. Frontiers in Neuroscience 7
8. Paxinos, George and Watson, Charles and Petrides, Michael and Rosa, Marcello and Tokuno, Hironobu. 2012. The Marmoset Brain in Stereotaxic Coordinates. San Diego: Elsevier Academic Press.
9. Huntenburg, Julia M., Pierre-Louis Bazin, and Daniel S. Margulies. 2018. 'Large-Scale Gradients in Human Cortical Organization'. Trends in Cognitive Sciences 22 (1): 21–31

Poster No 434

Thalamic connectivity and sleep-onset problems in infants at high likelihood for autism

Emily Chiem[1], Lauren Wagner[1], Kate de Guillenchmidt[1], Mirella Dapretto[1]

[1]UCLA, Los Angeles, CA

Introduction: Sleep disruption is pervasive in autism spectrum disorder (ASD)[1] and one of the first concerns raised by parents before diagnosis[2]. While proper sleep is critical for neurodevelopment, it is unclear how sleep problems may impact brain development in infancy and later developmental outcomes. Studying infant siblings of autistic children can offer insights into the relationship between sleep and neurodevelopment because 20% of infant siblings will receive a diagnosis[3]. Thalamocortical connectivity plays an important role in mediating sleep states[4] and is altered in infants with a family history of ASD[5-6] as well as in older autistic individuals where it has been associated with both sleep[7] and sensory sensitivities[8]. In this study, we examined how early thalamocortical connectivity might relate to sleep-onset problems in 6-month-old infants at high familial likelihood for ASD.

Methods: Data were collected as part of the Infant Brain Imaging Study (R01HD055741). Infants with an older sibling with ASD were deemed high likelihood (HL), while those with no first or second-degree relatives with ASD were deemed typical likelihood (TL). Resting-state fMRI scans were collected during natural sleep at 6 months of age (N=60). Scans were preprocessed and analyzed using FSL, including linear registration to an infant brain template (10), spatial smoothing, motion correction using ICA-AROMA, bandpass filtering, and CSF, white matter, and global signal regression. Five items from the Infant Behavior Questionnaire were used to create an Infant Sleep-Onset Problems (ISOP) score. Between-group comparisons were conducted using left and right thalamus seeds, masked by joint group-level functional connectivity maps. Similar connectivity patterns were observed from both seeds; thus, the bilateral thalamus was used in subsequent analyses ($Z > 2.3$, cluster-corrected at $P < 0.05$). Due to limited variability in ISOP scores in TL infants, parameter estimates of global thalamic connectivity were correlated with ISOP scores only for HL infants. A region-of-interest (ROI) analysis in HL infants correlated ISOP scores with connectivity between thalamus and bilateral somatosensory cortices.

Results: HL infants had weaker thalamic connectivity with the right orbitofrontal cortex and left cerebellum compared to TL infants. Additionally, in HL infants, stronger thalamic connectivity with both cortical and subcortical regions related to higher ISOP scores ($P=0.05$). Subsequent ROI analysis showed that thalamic connectivity with bilateral somatosensory cortex was positively correlated with ISOP scores in HL infants ($P=0.03$).

Conclusions: Our finding that HL infants displayed thalamic hypoconnectivity with right orbitofrontal cortex is consistent with prior reports of weaker thalamic connectivity with right prefrontal cortex in 1.5-month-old HL infants[5], indicating a stable pattern of thalamic-prefrontal underconnectivity in HL infants across the first 6 months of life. Similarly, our finding of weaker thalamic-cerebellar connectivity in HL infants shows that the underconnectivity between thalamus and cerebellum previously observed in 9-month-old HL infants[10] is already present at 6 months of age. We also found that worse sleep-onset problems in HL infants were associated with heightened thalamic connectivity with both cortical and subcortical regions, suggesting a link between global thalamic overconnectivity and longer sleep latencies. Our result that stronger thalamic connectivity with somatosensory cortices is associated with worse sleep-onset problems in HL infants is line with previous evidence that thalamic hyperconnectivity with the somatosensory cortex is also associated with sensory over-responsivity[6]. Altogether, these results revealed consistent atypicalities in thalamic connectivity in HL infants in the first 9 months of life and indicated a relationship between altered thalamocortical connectivity and sleep-onset problems in HL infants.

References

1. Maenner, M. J. (2021), 'Prevalence and Characteristics of Autism Spectrum Disorder Among Children Aged 8 Years—Autism and Developmental Disabilities Monitoring Network, 11 Sites, United States, 2018', Morbidity and Mortality Weekly Report. Surveillance Summaries, 70(11), 1–16.
2. Guinchat, V. (2012), 'Very early signs of autism reported by parents include many concerns not specific to autism criteria', Research in Autism Spectrum Disorders, 6(2), 589–601.
3. Ozonoff, S. (2011), 'Recurrence Risk for Autism Spectrum Disorders: A Baby Siblings Research Consortium Study' Pediatrics, 128(3), e488–e495.
4. Picchioni, D. (2014), 'Decreased Connectivity between the Thalamus and the Neocortex during Human Nonrapid Eye Movement Sleep', Sleep, 37(2), 387–397.
5. Nair, A. (2021), 'Altered Thalamocortical Connectivity in 6-Week-Old Infants at High Familial Risk for Autism Spectrum Disorder' Cerebral Cortex, 31(9), 4191–4205.
6. Wagner, L. (2023), 'Associations between thalamocortical functional connectivity and sensory over-responsivity in infants at high likelihood for ASD', Cerebral cortex, 33(12), 8075–8086.
7. Linke, A. C. (2021), 'Sleep Problems in Preschoolers With Autism Spectrum Disorder Are Associated With Sensory Sensitivities and Thalamocortical Overconnectivity. Biological Psychiatry',Cognitive Neuroscience and Neuroimaging, S2451-9022(21)00202-0
8. Green, S. A. (2017). 'Reduced modulation of thalamocortical connectivity during exposure to sensory stimuli in ASD', Autism research: official journal of the International Society for Autism Research, 10(5), 801–809.
9. Chen, L. (2022), 'A 4D infant brain volumetric atlas based on the UNC/UMN baby connectome project (BCP) cohort', NeuroImage, 253, 119097.
10. Okada, N. J. (2022), 'Atypical cerebellar functional connectivity at 9 months of age predicts delayed socio-communicative profiles in infants at high and low risk for autism', Journal of child psychology and psychiatry, and allied disciplines, 63(9), 1002–1016.

Poster No 435

Altered brain state dynamics in children with a family history of substance use disorder vary by sex

Louisa Schilling[1], Parker Singleton[2], Ceren Tozlu[3], Keith Jamison[1], Amy Kuceyeski[1]

[1]Weill Cornell Medicine, New York City, NY, [2]Weill Cornell Medicine, New York, NY, [3]Weill Cornell Medicine, NYC, NY

Introduction: Identifying factors that elevate an individual's risk of substance use disorder (SUD) is vital to public health. An individual's risk of SUD is shaped by a complex interplay of biosocial factors, with genetics being a particularly potent factor. As such, family history of SUD is a strong predictor of an individual's susceptibility (Bogdan et al., 2023). Current developmental models describe individual vulnerability to SUD as being due to an aberrant reward system, reduced inhibitory control, or a combination of these (Heitzeg et al., 2015). Yet, few studies have explored how family history affects brain function and structure prior to substance use. Herein, we used a network control theory approach (NCT) to quantify sex-specific differences in brain state dynamics in youth with (FHP) and without (FHN) a family history of SUD.

Methods: We analyzed a subset of 1244 youth (675 females, aged 9-11) from the baseline visit of the Adolescent Brain Cognitive Development (ABCD) study who were scanned on a Siemens MRI (Casey et al., 2018). Parent-reported family history of SUD was used to categorize subjects as FHP (1+ parent and/or 2+ grandparents with SUD) or FHN (no parental nor grandparental SUD). We analyzed pre-processed rsfMRI and structural connectivity data – as described in Chen et al. (2022) – parcellated into a FreeSurfer-based atlas of 86 cortical and subcortical regions. Following previous work (Singleton et al., 2022 & Cornblath et al., 2020), we performed k-means clustering (k=4) of brain activity into recurring brain states. For all transitions between states, we calculated the transition probability (TP; i.e., likelihood of transition) and the NCT-derived transition energy (TE) required to drive the brain towards a given transition (Gu et al., 2015). All p-values were Benjamini–Hochberg (BH) corrected.

Results: For each state (k=4), we calculated the cosine similarity of its high and low-amplitude activity to a priori resting-state networks (Figs 1A-B; Yeo et al., 2011). States were identified as 2 pairs of anti-correlated states: default mode (DMN+/-) and visual (VIS+/-). First, to assess whole-brain energetics, we averaged across all pairwise TEs to calculate a global TE for each subject. Two-sample t-tests revealed lower global TE in FHP males (M-FHP) compared to M-FHN (pFDR= 0.049; Fig 1C). In contrast, FHP females (F-FHP) exhibited a trend towards higher global TE compared to F-FHN, although not statistically significant (pFDR= 0.14). An ANOVA conducted on global TE, controlling for variables including sex, age, family history of SUD, motion (mean framewise displacement), study site, and sex*family history of SUD, revealed significant effects for sex (pFDR < 0.0001), motion (pFDR=0.04), study site (pFDR < 0.0001), and sex*family history of SUD (pFDR=0.013). For pairwise transitions, M-FHP individuals had significantly decreased TE for all transitions to DMN+/- (Fig 2A & F), lower TP from DMN- to DMN+, and increased TP from VIS+ to DMN+ (Fig 2C) compared to M-FHN. F-FHP youth had significantly increased TE when persisting in VIS+/-states (Figs 2B & E) but no significant differences in TP (Fig 2D) compared to F-FHN.

Conclusions: The effect of family history of SUD on brain function and structure is modulated by biological sex. M-FHP youth exhibit lower TE, particularly when transitioning to or persisting in DMN. This suggests, given that transitions from VIS to

DMN reflect bottom-up processing, there is a decreased energy barrier for bottom-up transitions in M-FHP. Indeed, M-FHP youth exhibit an increased probability of transitioning from VIS+ to DMN+. F-FHP, on the other hand, exhibit increased TE when persisting in VIS. This may reflect a higher energy barrier to persist in the VIS state and thus a tendency to shift bottom-up. Together, these results indicate a sex-specific mechanism by which FHP individuals may be biased towards bottom-up transitions and therefore more prone to heightened reward sensitivity and reduced inhibitory control.

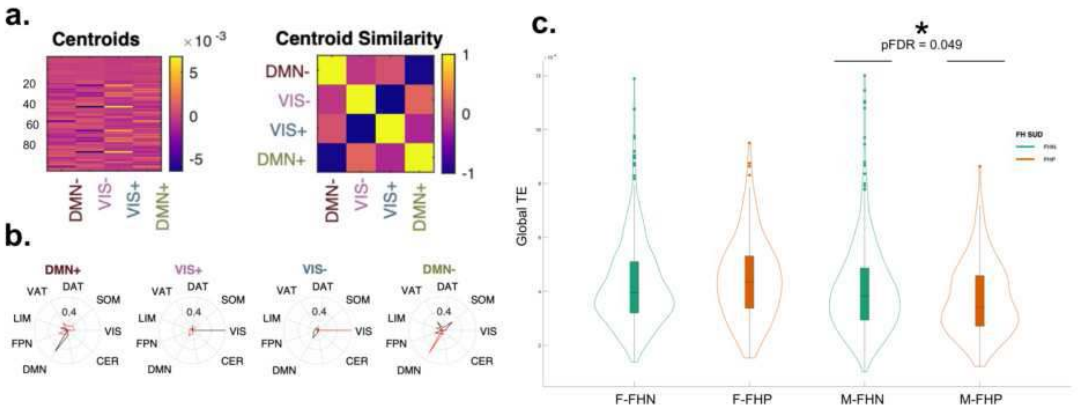

Figure 1. (**A**) Left: Cluster centroids calculated as the mean of all fMRI time points assigned to a given cluster. Color represents regional fMRI signal values. Right: Pearson correlation values between each cluster centroid. (**B**) Radial plots of similarity measures for each (k=4) state for which we calculated the cosine similarity of its high-amplitude (black) and low-amplitude (red) activity to a priori resting-state networks8. (**C**) Violin plots of global TE (i.e., the mean TE across pairwise state transitions) by sex and family history of SUD. Abbreviations: Default Mode Network (DMN); Visual Network (VIS); Limbic Network (LIM); Frontoparietal Network (FPN); Somatomotor Network (SOM); Dorsal Attention Network (DAT); Ventral Attention Network (VAT); Transition Energy (TE); Female family history positive (F-FHP); Female family history negative (F-FHN); Male family history positive (M-FHP); Male family history negative (M-FHN).

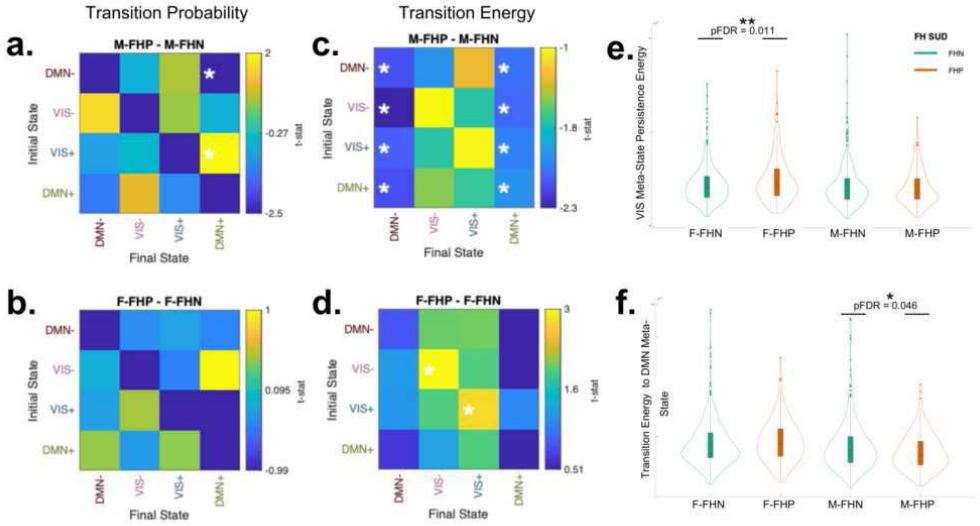

Figure 2. (**A**) T-statistic from two-sample t-tests comparing M-FHP and M-FHN empirically observed TPs from a given state to each other state. (**B**) Same as (A) comparing F-FHP and F-FHN. (**C**) T-statistics from two-sample t-tests comparing M-FHP and M-FHN TE for each pairwise state transition. (**D**) Same as (C) comparing F-FHP and F-FHN. (**E**) Violin plots of TE required to persist in VIS meta-state (average of TEs for VIS+ to VIS+ and VIS- to VIS-) by sex and family history of SUD. (**F**) Violin plots of energy required to transition to the DMN meta-state from any other state (averaged across TEs of all transitions to DMN+ and DMN-) by sex and family history of SUD. Abbreviations: Transition Energy (TE); Transition Probability (TP); Default Mode Network (DMN); Visual Network (VIS); Female family history positive (F-FHP); Female family history negative (F-FHN); Male family history positive (M-FHP); Male family history negative (M-FHN).

References

1. Bogdan, R., Hatoum, A. S., Johnson, E. C., & Agrawal, A. (2023). The Genetically Informed Neurobiology of Addiction (GINA) model. Nature Reviews Neuroscience, 24(1), 40-57.
2. Heitzeg, M. M., Cope, L. M., Martz, M. E. & Hardee, J. E. Neuroimaging Risk Markers for Substance Abuse: Recent Findings on Inhibitory Control and Reward System Functioning. Curr. Addict. Rep. 2, 91–103 (2015).
3. Casey, B. J., Cannonier, T., Conley, M. I., Cohen, A. O., Barch, D. M., Heitzeg, M. M., ... & Dale, A. M. (2018). The adolescent brain cognitive development (ABCD) study: imaging acquisition across 21 sites. Developmental cognitive neuroscience, 32, 43-54.
4. Chen, J., Tam, A., Kebets, V., Orban, C., Ooi, L. Q. R., Asplund, C. L., ... & Yeo, B. T. (2022). Shared and unique brain network features predict cognitive, personality, and mental health scores in the ABCD study. Nature communications, 13(1), 2217.

5. Singleton, S. P., Luppi, A. I., Carhart-Harris, R. L., Cruzat, J., Roseman, L., Nutt, D. J., ... & Kuceyeski, A. (2022). Receptor-informed network control theory links LSD and psilocybin to a flattening of the brain's control energy landscape. Nature communications, 13(1), 5812.
6. Cornblath, E. J., Ashourvan, A., Kim, J. Z., Betzel, R. F., Ciric, R., Adebimpe, A., ... & Bassett, D. S. (2020). Temporal sequences of brain activity at rest are constrained by white matter structure and modulated by cognitive demands. Communications biology, 3(1), 261.
7. Gu, S., Pasqualetti, F., Cieslak, M., Telesford, Q. K., Yu, A. B., Kahn, A. E., ... & Bassett, D. S. (2015). Controllability of structural brain networks. Nature communications, 6(1), 8414.
8. Yeo, BT Thomas, et al. (2011). "The organization of the human cerebral cortex estimated by intrinsic functional connectivity." Journal of neurophysiology.

Poster No 436

Metabolite-Autism Symptom Associations Mediated by Amygdala-Frontal Resting State Connectivity

Sofronia Ringold[1,2], Aditya Jayashankar[1,2], Jennifer Labus[3,4,5], Emily Kilroy[1,2], Christiana Butera[1,2], Swapna Mahurkar-Joshi[3,4,5], Skylar Tanartkit[3,4,5], Arpana Gupta[3,4,5], Emeran Mayer[3,4,5], Lisa Aziz-Zadeh[1,2]

[1]Chan Division of Occupational Science and Occupational Therapy, University of Southern California, Los Angeles, CA, [2]Brain and Creativity Institute, University of Southern California, Los Angeles, CA, [3]Oppenheimer Center for the Neurobiology of Stress and Resilience, David Geffen School of Medicine, Los Angeles, CA, [4]Vatche and Tamar Manoukian Division of Digestive Diseases, David Geffen School of Medicine, Los Angeles, CA, [5]Goodman-Luskin Microbiome Center, David Geffen School of Medicine, University of California Los Angeles, Los Angeles, CA

Introduction: The gut microbiome modulates sensory processing, socio-emotional behavior, and cognition through a bidirectional relationship with the brain, known as the brain-gut-microbiome (BGM) system (Zhu et al., 2017). As cognitive, sensory, social, and gastrointestinal issues are highly prevalent in Autism Spectrum Disorder (ASD), attention has been paid to the role of the BGM system in ASD symptomatology, with many studies reporting abnormal gut profiles compared to healthy controls (Kang et al., 2018; Needham et al., 2021). Preclinical studies have shown that gut metabolites in the tryptophan pathway are associated with sensory, socio-emotional, and cognitive differences characteristic of ASD thus the BGM system, may be related to outcomes in autistic children, such as school performance (Chen et al., 2022; Chernikova et al., 2021; Needham et al., 2022). As sensory processing has a greater impact on academic performance in autistic children than level of intelligence, we posit that gut metabolites are influencing neural activity, subsequently impacting school performance (Butera et al., 2020). Here we focus on resting state functional magnetic resonance imaging (rs-fMRI) in typically developing (TD) and autistic children as established connectivity differences between the groups has been linked to ASD symptom severity which may be linked to school performance (Christian et al., 2022; Khandan Khadem-Reza et al., 2023).

Methods: Data Collection: 37 TD (M age=12.02 years, 18 males) and 29 autistic children (M age=12.4 years, 22 male) collected a stool sample at home within 24 hours prior to completing a rs-fMRI. Parents completed the Child Behavior Checklist/6-18 to assess school performance (Achenbach & Edelbrock, 1991). Data Analysis: Resting state connectivity between brain regions based on the Detstrieux, Harvard Oxford subcortical and Harvard Ascending Arousal Network Atlases was computed using the functional connectivity toolbox. Untargeted metabolomic profiling on the stool samples were performed by Metabolon Inc. General linear models (GLM) were used to determine if the groups differences and associations between school performance and med-adjusted tryptophan metabolites and functional connectivity, tryptophan metabolite levels, age, sex, body mass index and IQ scores. The R library, mediation, was applied to test whether neural activity mediated the association between metabolite levels and school performance in ASD with age as a covariate.

Results: There was a significant difference between the groups on school performance (ASD<TD, $q<0.01$, 5% FDR). GLMs demonstrated a significant difference in functional connectivity between the right orbital sulcus and the left amygdala (ASD<TD, $q<0.001$) that was associated with abundance of the tryptophan metabolite, oxindolylalanine ($q<0.05$). In ASD, connectivity in the right orbital sulcus and the left amygdala was negatively correlated with school performance ($q<0.05$). The right orbital sulcus-the left amygdala connectivity significantly mediated the relationship between oxindolylalanine and school performance (B=1.11, 95% CI:0.10-2.54).

Figure 1: Directed acyclic graph representing the mediation model with the beta values and 95% confidence intervals for each effect. *= p<0.05

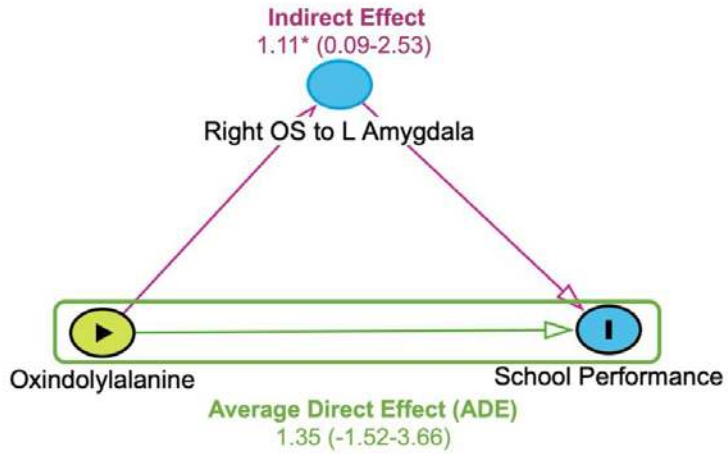

Conclusions: Previous rs-fMRI research in ASD suggests that decreased connectivity between the amygdala and frontal lobe regions may underlie emotion regulation and sensory sensitivities (Khandan Khadem-Reza et al., 2023). Here we show that this decreased connectivity is also related to lower gut levels of oxindolylalanine and lower school performance. Specifically, our data support the hypothesis that the metabolites in the tryptophan pathway modulate the brain, which in turn affects behavior in ASD. This is the first study to explore the complex interplay between gut metabolites, resting state functional connectivity, and behavioral outcomes in autistic children.

References

1. Achenbach, T. M.(1991). Child behavior checklist. Burlington (Vt), 7, 371-392.
2. Butera, C. (2020). Impact of Sensory Processing on School Performance Outcomes in High Functioning Individuals with Autism Spectrum Disorder. Mind Brain Educ, 14(3), 243-254. https://doi.org/10.1111/mbe.12242
3. Chen, Y.-C. (2022). Altered gut microbiota correlates with behavioral problems but not gastrointestinal symptoms in individuals with autism. Brain, behavior, and immunity, 106, 161-178. https://doi.org/10.1016/j.bbi.2022.08.015
4. Chernikova, M. A. (2021). The brain-gut-microbiome system: Pathways and implications for autism spectrum disorder. Nutrients, 13(12), 4497. https://doi.org/10.3390/nu13124497
5. Christian, I. R.(2022). Context-dependent amygdala-prefrontal connectivity in youths with autism spectrum disorder. Research in autism spectrum disorders, 91, 101913. https://doi.org/10.1016/j.rasd.2021.101913
6. Kang, D.-W.(2018). Differences in fecal microbial metabolites and microbiota of children with autism spectrum disorders. Anaerobe, 49(C), 121-131. https://doi.org/10.1016/j.anaerobe.2017.12.007
7. Khandan Khadem-Reza, Z. (2023). Altered resting-state functional connectivity of the brain in children with autism spectrum disorder. Radiological physics and technology, 16(2), 284-291. https://doi.org/10.1007/s12194-023-00717-2
8. Needham, B. D.(2021). Plasma and Fecal Metabolite Profiles in Autism Spectrum Disorder. Biological psychiatry (1969), 89(5), 451-462. https://doi.org/10.1016/j.biopsych.2020.09.025
9. Needham, B. D. (2022). A gut-derived metabolite alters brain activity and anxiety behaviour in mice. Nature (London), 602(7898), 647-653. https://doi.org/10.1038/s41586-022-04396-8
10. Zhu, X., (2017). Microbiota-gut-brain axis and the central nervous system. Oncotarget, 8(32), 53829-53838. https://doi.org/10.18632/oncotarget.17754

Poster No 437

Atypical cortical responses to changes in sound source location in ASD

Sergio Osorio[1,2], Jasmine Tan[1,2], Grace Levine[1,2], Seppo Ahlfors[3,2], Steven Graham[1], Fahimeh Mamashli[1,2,3], Sheraz Khan[3,2], Robert Joseph[4], Ainsley Losh[1], Stephanie Pawlyszyn[1], Nicole McGuiggan[1], Matti Hämäläinen[3,2,5], Hari Bharadwaj[6], Tal Kenet[7]

[1]Department of Neurology, Harvard Medical School, Massachusetts General Hospital, Boston, MA, [2]Athinoula A. Martinos Center for Biomedical Imaging, Massachusetts General Hospital, Boston, MA, [3]Department of Radiology, Harvard Medical School, Massachusetts General Hospital, Boston, MA, [4]Department of Anatomy and Neurobiology, Boston University School of Medicine, Boston, MA, [5]Department of Neuroscience and Biomedical Engineering, School of Science, Aalto University, Espoo, Finland, [6]Department of Communication Science and Disorders, University of Pittsburgh, Pittsburg, PA, [7]Massachusetts General Hospital, Boston, MA

Introduction: Abnormal cortical auditory processing has been documented across a wide range of stimuli in individuals with autism spectrum disorder (ASD) (Emre et al., 2018; O'Connor et al.,2012). However, spatial auditory processing(Shinn-

Cunningham et al, 2017; Soskey et al., 2017; ElMoazen et al., 2020), i.e., our ability to perceive and track changes in sound source location, which is critical for social interactions, remains understudied despite evidence of malformed binaural brainstem structures in ASD (Kulesza et al., 2011).

Methods: To study spatial auditory processing in ASD, we collected magnetoencephalography (MEG) data from 22 ASD (mean age = 13.56, SD = 2.69) and 31 TD (mean age = 13.07, SD = 3.42) individuals as they listened to 1000ms-long auditory stimuli where at 550ms after the onset, 400 microsecond discontinuities in opposite directions were introduced between the ears creating an interaural time delay (ITD)-change and a percept of a spatial jump (jump condition). Responses were also collected for control stimuli where the 400 microsecond discontinuities were introduced in the same direction in each ear, leaving the ITD unchanged and the percept stationary (stay condition). Structural T1 MRI images were used to obtain individual cortical surfaces and to compute BEM head models. sLORETA-MNE source modeling was then used to extract responses from subject-specific labels (see figure 1b inset for examples) within temporal regions corresponding to the peak activation to jump events in left (TD mean latency = 744ms, SD = 0.045ms; ASD mean latency = 731ms, SD = 0.040ms) and right (TD mean latency = 729ms, SD = 0.059ms; ASD mean latency = 734ms, SD = 0.061ms) hemispheres.

Results: Results showed cortical responses time locked to the onset of jump events in both ASD and TD groups (figure 1a). Subject-specific peak latency windows were visually identified for each subject in response to jump events, and the area under the curve was obtained for both jump (TD: mean AUC left = 377.24, SD = 268.26; mean AUC right = 412.03, SD = 271.41; ASD: mean AUC left = 236.18, SD = 154.35, mean AUC right = 271.27, SD = 142.23) and stay (TD left = 109.57, SD = 54.21; TD right = 137.76, SD = 95.80; ASD left = 105.21, SD = 71.13, ASD right = 126.27, SD = 60.11) conditions. A linear mixed effect model for the interaction of group, condition and hemisphere as fixed effects and random intercepts for subject outperformed a null model ($X^2(9) = 121.02$, $p = 2.2e\text{-}16$). Adding a random slope for group significantly increased model fit ($X^2(2) = 19.44$, $p = 6.0e\text{-}05$). The best fitting model (R^2 conditional = 0.55, R^2 marginal = 0.33) showed a statistically significant effect of group (TD: $\beta = 144.40$, SE = 44.24, $p = 0.001$) and condition (stay: $\beta = -130.97$, SE = 45.51, $p = 0.002$), and for the interaction between condition and group. No effect for hemisphere was observed. A post-hoc pairwise test showed that the ASD diagnosis significantly predicts decreased AUC values for jump events compared to TD individuals ($\beta = -143.9$, SE = 34.5, $p = 0.0001$, figure 1c).

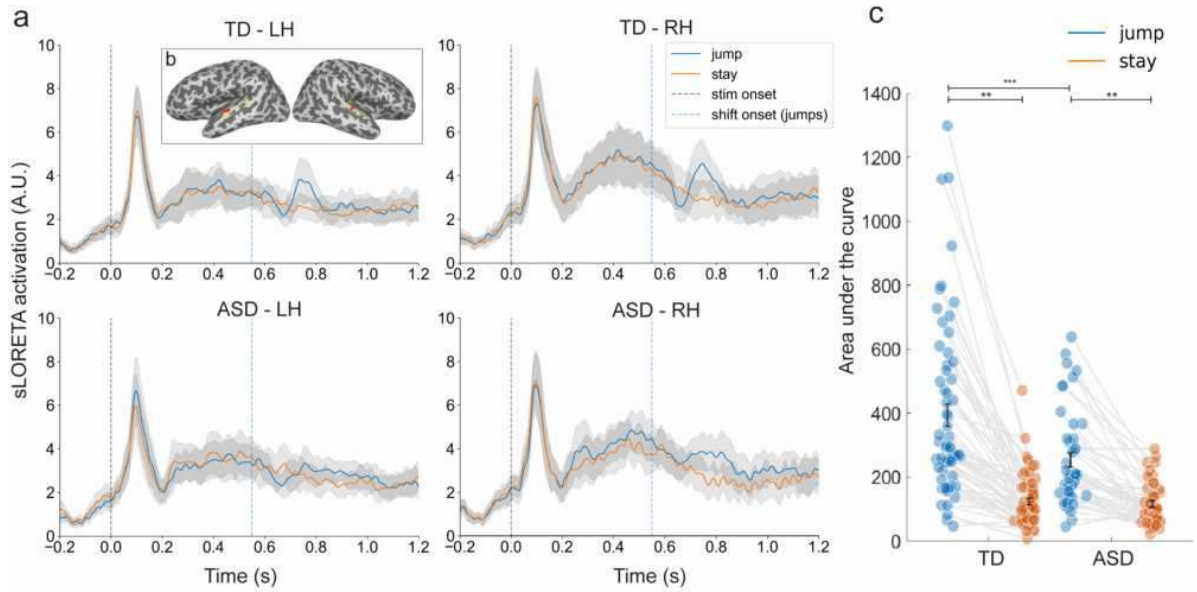

Figure 1. a. Top left: Grand-average of source space activation in response to jump and stay events in the left hemisphere of TD participant, with representative example of auditory labels from one participant presented in inset Top right: Same for the right hemisphere. **b.** Same as (a), but for ASD participants. **c.** Main effect of condition and condition-by-group interaction. Whiskers show the mean and Standard Error of the Mean (SEM). ** $p < 0.01$, *** $p > 0.001$.

Conclusions: These results support the hypothesis that spatial auditory processing is altered in ASD. Our findings highlight the need to further investigate whether and how such atypical sensory processes may impact goal-directed and social behaviors among ASD individuals.

References

1. ElMoazen, D., Sobhy, O., Abdou, R., & AbdelMotaleb, H. (2020). Binaural interaction component of the auditory brainstem response in children with autism spectrum disorder. International journal of pediatric otorhinolaryngology, 131, 109850.
2. Emre, O. C. A. K., Eshraghi, R. S., Danesh, A., Mittal, R., & Eshraghi, A. A. (2018). Central auditory processing disorders in individuals with autism spectrum disorders. Balkan medical journal, 35(5), 367-372.

3. Kulesza Jr, R. J., Lukose, R., & Stevens, L. V. (2011). Malformation of the human superior olive in autistic spectrum disorders. Brain research, 1367, 360-371.
4. O'Connor, K. (2012). Auditory processing in autism spectrum disorder: a review. Neuroscience & Biobehavioral Reviews, 36(2), 836-854.
5. Shinn-Cunningham B., Best V., Lee A. K. (Middlebrooks J. C., Simon J. Z., Popper A. N., Fay R.R. (Eds.), Auditory object formation and selection. In The Auditory System at the Cocktail Party (pp. (2017). Springer.7–40).
6. Soskey, L. N., Allen, P. D., & Bennetto, L. (2017). Auditory spatial attention to speech and complex non-speech sounds in children with autism spectrum disorder. Autism Research, 10(8), 1405-1416.

Poster No 438

Altered Cortical Microstructure and Morphology Within and Beyond Resected Epileptic Foci

Ella Sahlas[1], Alexander Ngo[1], Raúl Rodriguez-Cruces[1], Thaera Arafat[1], Jessica Royer[1], Ke Xie[1], Hans Auer[1], Judy Chen[1], Raluca Pana[1], Birgit Frauscher[2], Neda Bernasconi[1], Andrea Bernasconi[1], Boris Bernhardt[1]

[1]Montreal Neurological Institute and Hospital, Montreal, QC, [2]Duke University, Durham, NC

Introduction: The advent of high-resolution neuroimaging has revolutionized how epilepsy is understood, diagnosed, and treated[1]. In particular, magnetic resonance imaging (MRI) methods have enabled previously unparalleled precision in localizing tissue responsible for epileptic seizures and assessing seizure etiology[2]. Localizing epileptogenic tissue is especially critical to delivering care to patients with pharmaco-resistant seizures, for whom resective surgery is often the most effective treatment[3-5]. Research has also revealed global changes in the properties of the cortex in epilepsy patients relative to controls[6]. However, there is a clear need to advance precise and non-invasive methods of localizing the origin of seizure activity and uncovering alterations beyond the seizure focus. This will ultimately allow more pharmaco-resistant patients to benefit from targeted resection that maximally spares surrounding tissue, with fewer risks than invasive pre-surgical investigations[7-9].

Methods: Patients were a consecutive cohort of 22 adults (17F, mean±SD age = 34.55±11.44 years) with pharmaco-resistant focal epilepsy who underwent pre-operative MRI at the Montreal Neurological Institute and Hospital, a resective neurosurgical procedure (14 temporal, 4 parietal, 2 occipital, and 2 frontal), and post-operative MRI. Of the 21 Engel outcomes available, 12 were IA, 4 were IB, 1 was IIA, 1 was IIIa, and 3 were IVC. The healthy control cohort comprised 100 adults (46F, mean±SD age = 31.62± 9.30 years) who underwent the same MRI protocol as patients did pre-surgery. This high-resolution 3T MRI protocol included diffusion-weighted imaging (DWI, 1.6mm isovoxels), T1-weighted scans (T1w, 0.8mm isovoxels), quantitative T1 relaxometry (0.8mm isovoxels), and resting-state functional MRI (rsfMRI, 3mm isovoxels). We preprocessed this data using micapipe[10]. Maps of mean diffusivity (MD) and fractional anisotropy (FA) were derived from DWI, maps of cortical thickness (CT) were derived from T1w scans, and maps of quantitative T1 relaxation time (qT1) were derived from quantitative T1 relaxometry; we normalized these features vertex-wise in each patient relative to controls (Fig. 1A). For each patient, we generated a functional connectivity matrix from rsfMRI, a structural connectivity matrix from DWI, and a geodesic distance matrix from T1w imaging. We segmented the resection site semi-automatically in each patient's post-operative T1w scan, co-registered with pre-operative T1w scans. We mapped the resection site to the surface and determined the 0-5%, 5-10%, 10-15%, 15-20%, 20-25%, 25-30%, 30-35%, 35-40%, 40-45%, and 45-50% of vertices most functionally coupled, structurally connected, and geodesically close to this site (Fig. 1B). We quantified relative alterations in MD, FA, CT, and qT1 in the surgical target and as a function of functional, structural, and geodesic distance from the target.

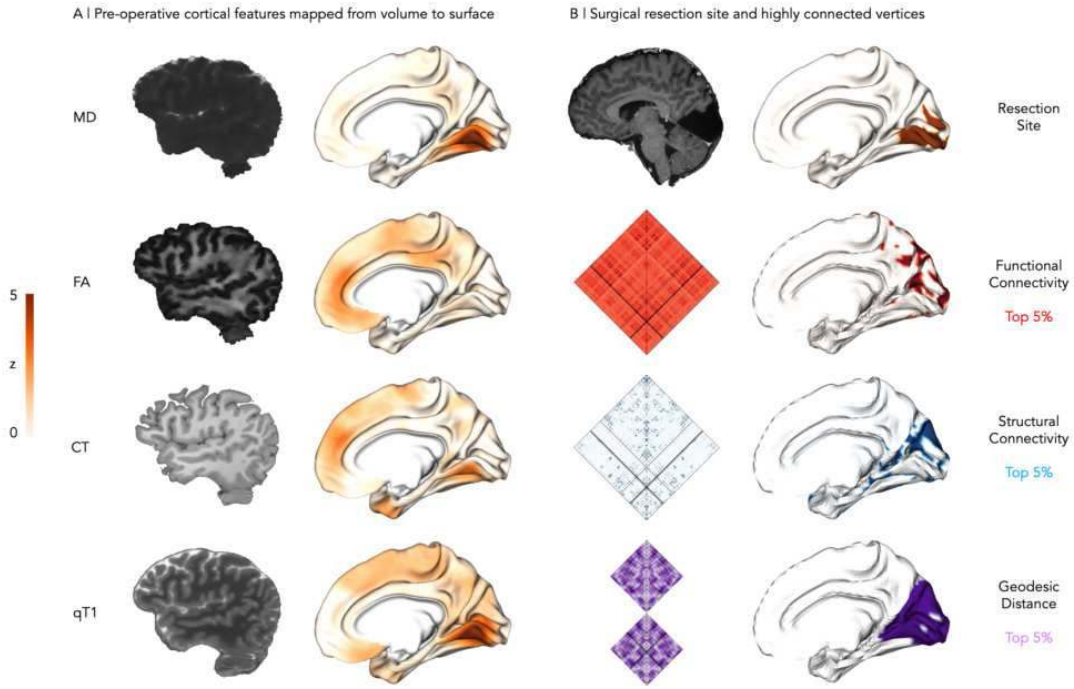

Figure 1. Mapping cortical microstructure and morphology and the epileptic surgical resection site. A | Pre-operative cortical feature maps derived from the 3T MRI of a patient with refractory focal epilepsy. Left, from top to bottom: volumetric MD, FA, T1w, and qT1 maps. Right: cortical features normalized to 100 healthy control participants (maps display absolute z-scores) and mapped to the fs-LR 32k-vertex surface template. B | Top row: post-operative T1w MRI of the same patient; surgical resection site mapped to the fs-LR 32k-vertex template after semi-automatic segmentation and co-registration to the pre-operative T1w MRI. Bottom rows: Patient-specific functional connectivity matrix, structural connectivity matrix, and geodesic distance matrix, with resection site vertices in black; 5% of vertices most functionally coupled, structurally connected, and geodesically close to the surgical resection site.

Results: Alterations were significantly increased within the surgical target relative to the rest of the brain for MD in 19/22 patients (86.36%), FA in 19/22 patients (86.36%), CT in 18/22 patients (82.82%), and qT1 in 18/22 patients (82.82%), z-tests, FDR-adjusted $p < 0.01$. Group mean MD, FA, CT, and qT1 alterations decreased with increasing functional connectivity distance from the target (Fig. 2A), as well as with structural connectivity distance (Fig. 2B) and geodesic distance (Fig. 2C). For each cortical feature and across all three distance metrics, alterations were significantly higher in the surgical target than in vertices at the fifth nearest level of distance to the target, paired t-tests, $p < 0.01$.

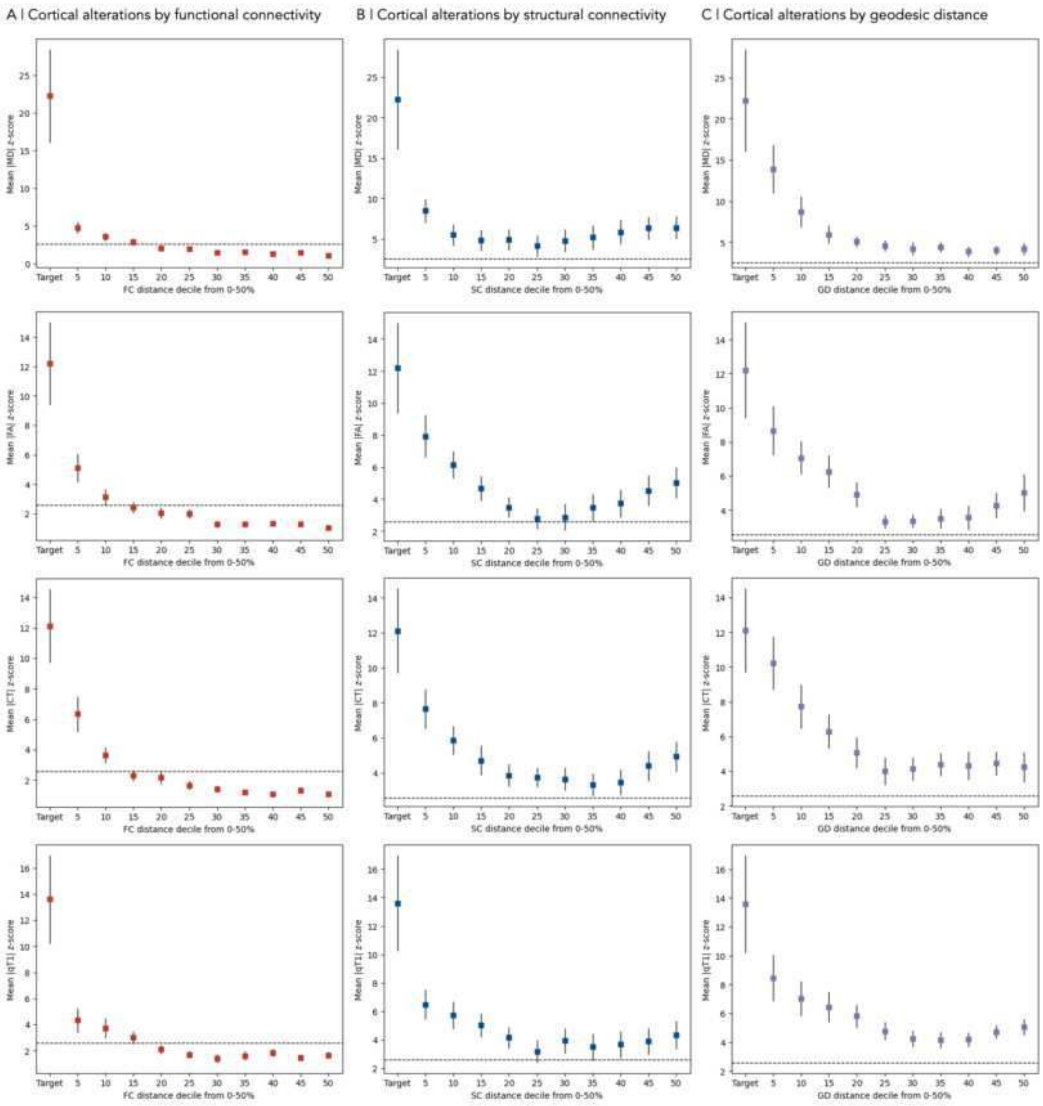

Figure 2. Alterations in cortical microstructural and morphology with increasing distance from the surgical resection site. A | MD, FA, CT, and qT1 alterations (z-scored) in vertices at increasing functional connectivity distance from the resection site relative to the rest of the brain. B | MD, FA, CT, and qT1 alterations (z-scored) in vertices at increasing structural connectivity distance from the resection site relative to the rest of the brain. C | MD, FA, CT, and qT1 alterations (z-scored) in vertices at increasing geodesic distance from the resection site relative to the rest of the brain. Each panel displays absolute z-scores averaged across all 22 consecutive patients. Dashed line: significance threshold (99% CI).

Conclusions: Mapping the epicenter of alterations in cortical microstructure and morphology in individual patients carries potential to assist in localizing the surgical target non-invasively. Functional, structural, and geodesic relationships to the epileptic focus may impact the magnitude of microstructural and morphological changes in cortical regions beyond the focus of seizures.

References

1. Shorvon, S.D. (2009), 'A history of neuroimaging in epilepsy 1909-2009', Epilepsia, vol. 50, suppl. 3, pp. 39-49
2. Bernasconi, A. (2022), 'The role of MRI in the treatment of drug-resistant focal epilepsy', European Neurology, vol. 85, no. 5, pp. 333-341
3. Thijs, R.D. (2019), 'Epilepsy in adults', Lancet, vol. 393, no. 10172, pp. 689-701
4. Sheng, J. (2018), 'Drug-resistant epilepsy and surgery', Current Neuropharmacology, vol. 16, no. 1, pp. 17-28
5. Pittau, F. (2014), 'The role of functional neuroimaging in pre-surgical epilepsy evaluation', Frontiers in Neurology, vol. 5, p. 31
6. Hatton, S.N. (2020), 'White matter abnormalities across different epilepsy syndromes in adults: an ENIGMA-Epilepsy study', Brain, vol. 143, no. 8, pp. 2454-2473
7. Andrzejak, R.G. (2015), 'Localization of epileptogenic zone on pre-surgical intracranial EEG recordings: Toward a validation of quantitative signal analysis approaches', Brain Topography, vol. 28, no. 6, pp. 832-837
8. Schmidt, R.F. (2016), 'Complications of subdural and depth electrodes in 269 patients undergoing 317 procedures for invasive monitoring in epilepsy', Epilepsia, vol. 57, no. 10, pp. 1697-1708
9. Arya, R. (2013), 'Adverse events related to extraoperative invasive EEG monitoring with subdural grid electrodes: a systematic review and meta-analysis', Epilepsia, vol. 54, no. 5, pp. 828-839
10. Cruces, R.R. (2022), 'Micapipe: A pipeline for multimodal neuroimaging and connectome analysis', Neuroimage, vol. 263, p. 119612

Poster No 439

Beta Frontal Lobe Entropy and Infant Sadness Associated with Attention Deficit in Toddlerhood

Madison Monroe-Mohajerin[1], Meghan Puglia[1]

[1]*University of Virginia, Charlottesville, VA*

Introduction: Attention-deficit/hyperactivity disorder (ADHD) is a common childhood disorder characterized by impairments in attention, working memory, and inhibitory control. In infants, differences in temperament (a baby's behavioral style in regards to situational reactivity, emotion regulation and expression), are associated with ADHD in later childhood[1]. Attentional differences in ADHD are also linked to an increase in neural variability – moment-to-moment electrical fluctuations intrinsic within neuronal networks[4]. This project aims to identify associations between infant temperament, neural variability, and ADHD symptoms in early childhood to characterize early markers of attention deficit.

Methods: 122 infants (F = 57, M = 66) initially underwent EEG and parent reported behavioral ratings at 4, 8, and 12 months of age. Participants were re-invited as toddlers at 3-5 years-of-age (M = 38, F = 27), to assess ADHD symptomology. Infant temperament was assessed via the Infant Behavioral Questionnaire (IBQ-R), and ADHD symptomatology was assessed using the ADHD Rating Scale IV. The EEG paradigm consisted of four conditions, resulting in a 2 × 2 design of social or non-social, visual or auditory stimuli. This project utilizes the social visual condition, which consisted of women turning their heads and smiling. Several studies have reported greater reactivity to visual stimuli in children with ADHD, including larger initial reactions and a lack of habituation[6,9]. Neural noise was computed via multiscale entropy, a measure of temperodynamic neural variability, using the automated preprocessing pipe-line for the estimation of scale-wise entropy from EEG data (APPLESEED) at a scaling rate of 250 Hz[8]. Entropy measures irregularity by determining the frequency of a pattern m repeating relative to a pattern of m+1 using the formula [m+1: ln(m/m+1)]. Low entropy designates higher regularity, and high entropy values designate higher irregularity in signal[8]. The ROI is the frontal lobe, as infant EEG attention studies have shown sources of brain activity in attentional tasks are scattered in the prefrontal cortex[10].

Results: Exploratory Graph Analysis (EGA) was used to reduce data dimensionality before performing regression analyses. EGA utilizes the Triangulated Maximally Filtered Graph (TMFG) method which builds a triangulation maximizing a score function associated with the amount of information retained by the network and nodes with the highest sum of correlations[7]. It arranges data into a meaningful network structure that can be used for clustering, community detection, and modeling. The Walktrap algorithm utilizes distance metrics based on the strength of the association between nodes, and organizes the nodes into communities[3]. Together, TMFG and the Walktrap algorithm identifies latent clusters of variables. EGA identified infant sadness and 13-29 Hz frequency band (beta) as the variables of interest for multivariable regression (Figure 1). Multivariable regression revealed a significant relationship between infant sadness (β = 1.6477, p < .01), beta frontal lobe entropy (β = -1.7892, p < .05), and ADHD symptomology (F(2, 50) = 7.02, p = 0.002, adjusted R2 = 0.19). An interaction effect emerged between the variables suggesting infant sadness could act a moderator in the relationship between entropy in infancy and ADHD symptomatology (Figure 2b).

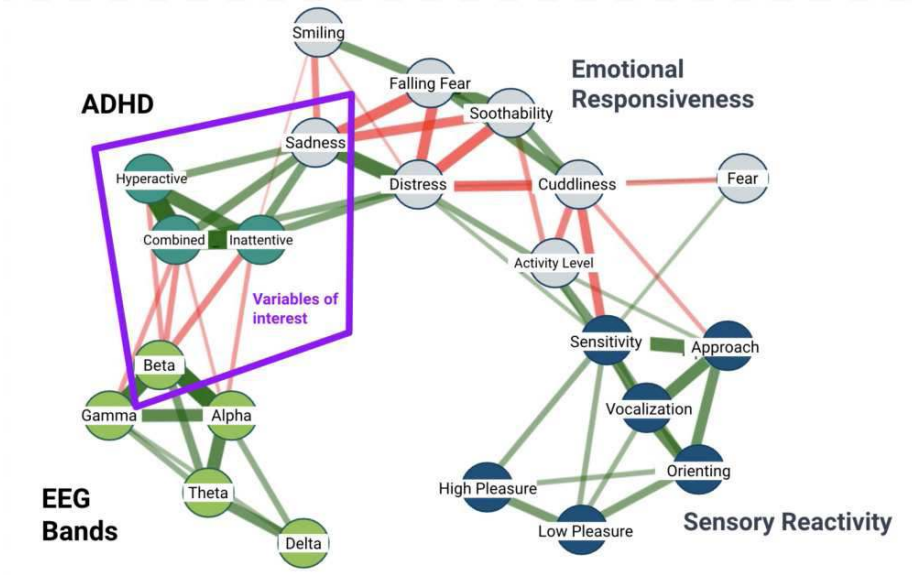

Figure 1: The Exploratory Graph Analysis package, EGAnet, displays the strength of the relationship between variables by thickness of the lines in between each variable, with a thicker, more opaque line indicating a stronger relationship. It displays the general correlational relationship between them with color, with green indicating a positive relationship, and red indicating a negative one. Frontal Lobe Entropy in the Beta band and Infant Sadness were the closest in proximity to the ADHD cluster, formed associations with all 3 ADHD scores, and are the variables to be further investigated.

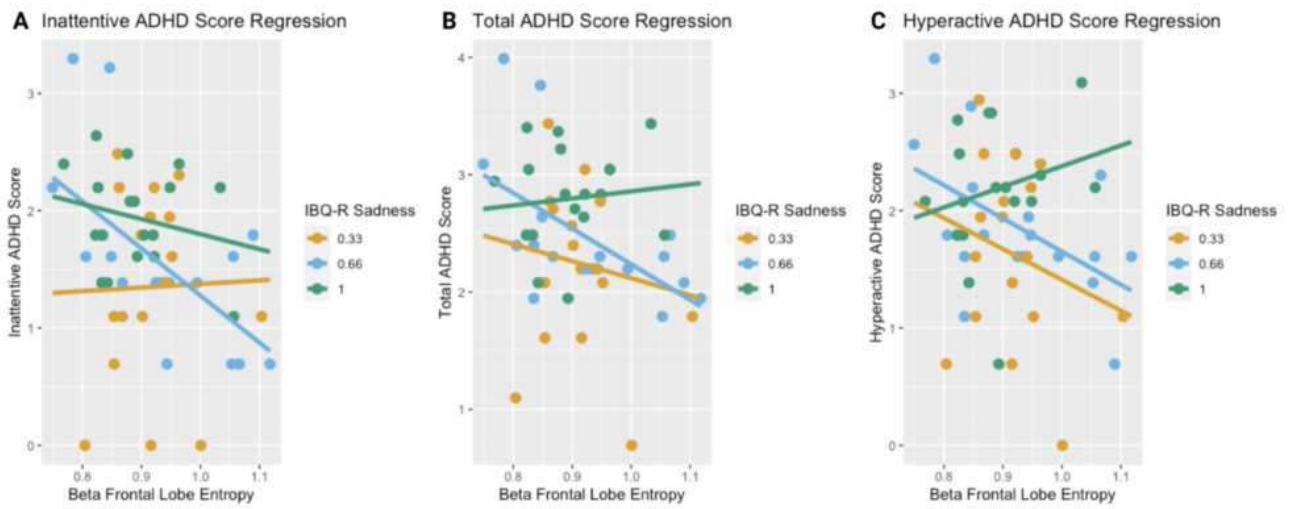

Figure 2: Multivariable Regression Analysis at 4 Months. Results from the multivariable linear regression with inattentive ADHD score as the response variable (a), hyperactive ADHD score as the response variable (c), and total ADHD score (b). Beta frontal lobe entropy was plotted on the X axis and IBQ sadness scores were separated into tertiles, with the linear models between each of the tertiles and ADHD scores graphed.

Conclusions: Results revealed a significant relationship between Beta Frontal Lobe Entropy, IBQ Sadness, and ADHD symptoms. Newer research implicates higher amounts neural variability as a typical feature of social development in infancy, and a necessary component of neural development[2]. The results also corroborated the findings in a 2021 paper that infant sadness was the earliest behavioral predictor of ADHD at 3 months of age[5]. Overall this work can help provide insight into the infant's developing brain and identify signatures reflective of different developmental trajectories.

References

1. Bilgin, A., et al. (2020), 'Early crying, sleeping, and feeding problems and trajectories of attention problems from childhood to adulthood', Child development, vol. 91, no. 1, pp. e77-e91
2. Garrett, D. (2011), 'The importance of being variable', Journal of Neuroscience, vol. 31, no. 12, pp. 4496-4503.
3. Golino, H. (2019), 'EGAnet: Exploratory Graph Analysis: A framework for Estimating the Number of Dimensions in Multivariate Data Using Network Psychometrics, Version 0.4; 2019'.
4. Gonen-Yaacovi, G. (2016), 'Increased ongoing neural variability in ADHD', Cortex, vol. 81, pp. 50-63.
5. Gustafsson, H.C. (2021), 'Early development of negative and positive affect: Implications for ADHD symptomatology across three birth cohorts', Development and psychopathology, vol. 33, no. 5, pp. 1837-1848.
6. Mangeot, S.D. (2001), 'Sensory modulation dysfunction in children with attention-deficit-hyperactivity disorder', Developmental Medicine & Child Neurology, vol. 43, no. 6, pp. 399-406.
7. Massara, G.P. (2016), 'Network filtering for big data: Triangulated maximally filtered graph', Journal of complex Networks, vol. 5, no. 2, pp. 161-178.
8. Puglia, M.H. (2022), 'The Automated Preprocessing Pipe-Line for the Estimation of Scale-wise Entropy from EEG Data (APPLESEED): Development and validation for use in pediatric populations', Developmental Cognitive Neuroscience, vol. 58, 101163.
9. Reynolds, S. (2008), 'Diagnostic validity of sensory over-responsivity: A review of the literature and case reports', Journal of autism and developmental disorders, vol. 38, pp. 516-529.
10. Richards, J.E. (2010), 'The neural bases of infant attention', Current Directions in Psychological Science, vol. 19, no. 1, pp. 41-46.

Poster No 440

Derailed functional connectivity in infants later diagnosed with autism spectrum disorder

Zening Fu[1], Sarah Shultz[2], Vince Calhoun[3]

[1]Tri-Institutional Center for Translational Research in Neuroimaging and Data Science (TReNDS), Atlanta, GA, [2]Emory University School of Medicine, Atlanta, GA, [3]GSU/GATech/Emory, Decatur, GA

Introduction: Mechanisms of social adaptive action are disrupted during the first postnatal months in infants later diagnosed with autism spectrum disorder (ASD) (Sarrett and Rommelfanger, 2015), suggesting that alterations in brain development may already be present during early infancy (Kanner, 1968). Characterizing the trajectory of functional connectivity (FC) to examine brain changes from birth might offer new insight into sensitive periods during which interventions are likely to have the greatest impact on infant brain growth (Johnson and Karmiloff-Smith, 2008). In this study, we implemented a data-driven group independent component analysis (ICA) on longitudinal resting-state fMRI data collected from typically developing

infants and infants later diagnosed with ASD from birth to 8 months. We hypothesize that ASD infants show different longitudinal trajectories in FC from birth, with between-group differences becoming more pronounced over time.

Methods: Participants were infants with a low likelihood of ASD (LL; no family history of ASD) or elevated likelihood of ASD. All infants were enrolled at birth, and the diagnostic outcome was confirmed at 2 years old using the standard assessment for ASD. We applied a group ICA (Fu et al., 2018) to all high-quality infant data, identifying reliable functional brain networks that are active during infancy. Further analysis was performed on the ASD group (includes 40 scans from 21 infants later diagnosed with ASD) and healthy control (HC) group (includes 112 scans from 45 LL infants), including the trajectory analysis and group comparison. Correlation was calculated between time courses of brain networks to measure the static functional network connectivity (sFNC). A linear mixed-effect model (Cheng et al., 2021) was implemented to estimate the associations between sFNC and age. Finally, we performed a group comparison on sFNC between HC and ASD infants at different phases of infancy to explore when between-group differences are present and which sFNC are disrupted.

Results: Fig. 1 shows the flowchart to explore FC abnormalities in infancy ASD. Group ICA identified 71 ICNs that were arranged into 9 domains according to their prior functional information (Allen et al., 2014). Fig. 2 displays the correlations between sFNC and age from birth to the 8th month for each group. Despite many similar sFNC trajectories shared by both groups, infants with ASD show markedly different trajectories, especially for sFNC involved in the sensory domains (Fig. 2A). HC infants show significantly positive correlations between age and the sFNC within the auditory (AUD) and visual (VS) domains. Instead of showing widespread positive correlations between age and the sFNC within the VS domain, ASD infants show stronger positive correlations between age and the sFNC within the AUD domain (Fig. 2B). For the group comparison, we separated the data into early (birth~4th month) and the later (5th~8th month) infancy. In early infancy, sFNC between the right superior temporal gyrus (STG) and left temporal pole, and sFNC between the right STG and middle temporal gyrus is significantly lower in infants with ASD ($p < 0.05$. FDR corrected, Fig. 2C). In later infancy, sFNC between the AUD and VS domains is significantly lower in ASD infants, suggesting continuous incoordination between sensory cortices (Fig. 2D).

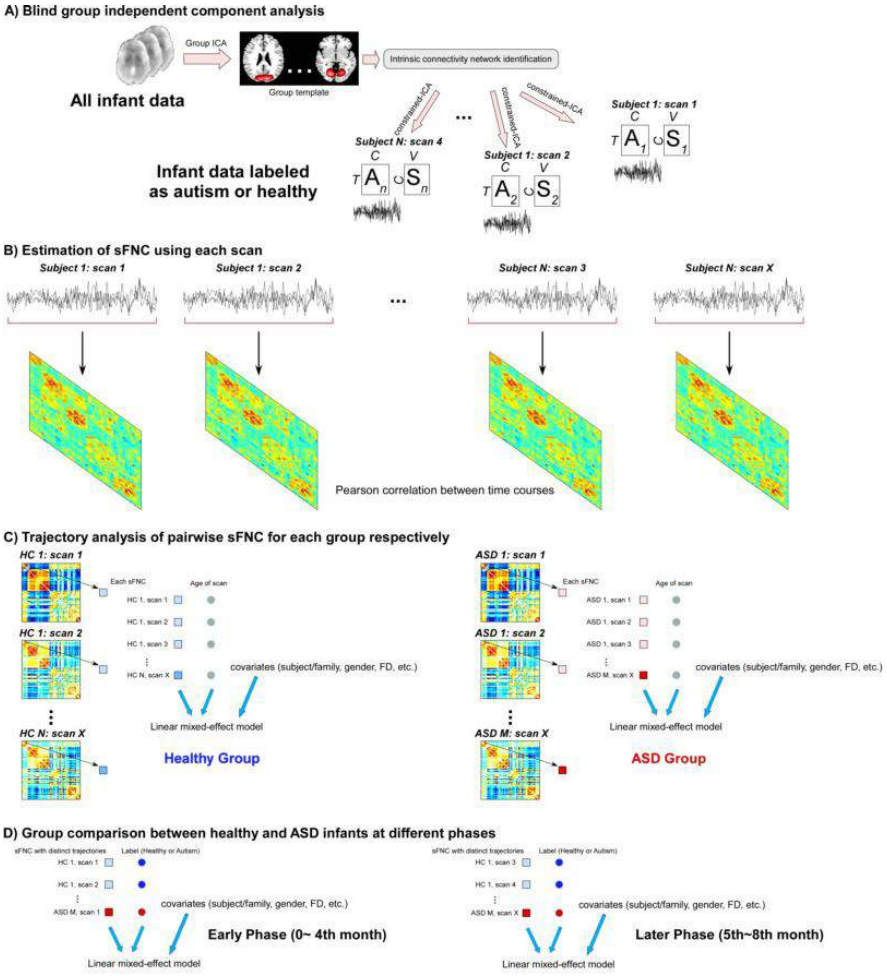

Figure 1. The flowchart of the sFNC analysis investigates brain connectivity abnormalities during the early infancy. A) Group ICA framework extracts robust functional components for the infant data. B) sFNC is estimated using the TCs of components from each scan. C) Trajectory analysis is performed via linear mixed-effect model (LMM) to characterize the correlation relationships between age and sFNC in each group. D) Group comparison between healthy and ASD infants is performed on the early phase of data (birth~4th month) and the later phase of data (5th~8th month) respectively.

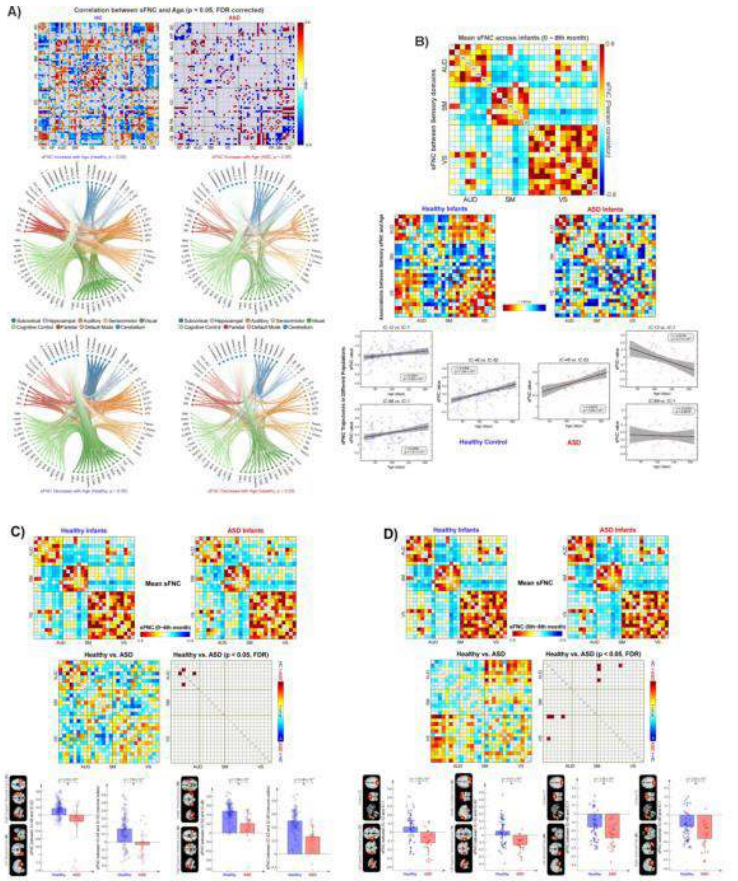

Figure 2. A) Associations between sFNC and age over the first 8 months of life. Analysis is performed for each population respectively. Correlations with p values smaller than 0.05, FDR corrected for the multiple comparison correction were displayed at the top row. Circular plots show the positive and negative correlations with p values smaller than 0.05, uncorrected. B) sFNC between sensory domains over the first 8 months and their correlation relationships with age in the healthy and ASD populations. Mean sFNC between auditory, sensorimotor, and visual domains across all infant scans. B) correlations between sensory involved sFNC and age for healthy and ASD group respectively. Example sFNC showing similar and different trajectories between healthy and ASD infants are displayed. C) Abnormal sFNC between sensory domains in early phase (birth~4th month) of infancy. D) Abnormal sFNC between sensory domains in later phase (5th~8th months) of infancy. T values of group comparison between healthy infants and ASD infants are provided. All t values and t values after FDR correction are displayed. Bar plots show the comparison between groups ($p < 0.05$, FDR corrected for the multiple comparison correction).

Conclusions: This study investigated the developmental trajectories of infants during the first 8 postnatal months to identify early differences in ASD using resting-state sFNC, the network analog of FC. Preliminary findings reveal alterations in sFNC trajectories in infants with ASD relative to their HC counterparts, providing compelling evidence that tracking sFNC across resting-state networks can enhance our understanding of ASD traits in early infancy. Altered FC trajectories in infants later diagnosed with ASD are potential brain markers of the developmental unfolding of ASD, signs of the unraveling of typical mechanisms of social adaptive action.

References

1. Allen, E. A. et al. (2014) 'Tracking whole-brain connectivity dynamics in the resting state', Cerebral Cortex, 24(3), pp. 663–676. doi: 10.1093/cercor/bhs352.
2. Cheng, W. et al. (2021) 'Sleep duration, brain structure, and psychiatric and cognitive problems in children', Molecular Psychiatry, 26(8), pp. 3992–4003. doi: 10.1038/s41380-020-0663-2.
3. Fu, Z. et al. (2018) 'Characterizing dynamic amplitude of low-frequency fluctuation and its relationship with dynamic functional connectivity: An application to schizophrenia', NeuroImage, 180. doi: 10.1016/j.neuroimage.2017.09.035.
4. Johnson, M. H. and Karmiloff-Smith, A. (2008) 'Neuroscience Perspectives on Infant Development', Theories of Infant Development, pp. 121–141. doi: 10.1002/9780470752180.ch5.
5. Kanner, L. (1968) 'Autistic disturbances of affective contact.', Acta Paedopsychiatrica, 35(4), pp. 100–136. Available at: http://www.th-hoffmann.eu/archiv/kanner/kanner.1943.pdf (Accessed: 30 November 2023).
6. Sarrett, J. C. and Rommelfanger, K. S. (2015) 'Commentary: Attention to Eyes Is Present but in Decline in 2–6-Month-Old Infants Later Diagnosed with Autism', Frontiers in Public Health, 3. doi: 10.3389/fpubh.2015.00272.

Poster No 441

Brain dynamics in toddlers with and without autism spectrum disorder

Lauren Kupis[1], Ashley Kim[2], Eric Courchesne[3], Jason Nomi[4], Lucina Uddin[5]

[1]UCLA, Los Angeles, CA, [2]UCLA, Los Angeles, CA, [3]UCSD, San Diego, CA, [4]University of California, Los Angeles, Los Angeles, CA, [5]Department of Psychiatry and Biobehavioral Sciences, University of California, Los Angeles, Los Angeles, CA

Introduction: Autism spectrum disorder (ASD) affects one in 36 children.[1] Early diagnosis is critical for optimizing outcomes, yet children are not typically diagnosed until 4 years of age.[2] In concert with early behavioral signs, early neural markers could identify toddlers at risk of developing ASD to aid earlier diagnosis and targeted interventions. Neuroimaging studies have primarily examined structural brain alterations in toddlers at high risk of developing ASD.[3] While innovative dynamic functional magnetic resonance imaging (fMRI) methods reveal candidate brain networks of dysfunction in older children with ASD (7-12 years of age),[4–6] little work has been done to examine brain network dynamics in toddlers with ASD. The goal of this project is to identify early functional brain biomarkers of ASD.

Methods: Participants were enrolled through community referrals and a screening approach in collaboration with pediatricians. All toddlers underwent clinical assessments, including the Autism Diagnostic Observation Schedule (ADOS), and received an official diagnosis at 36 months. The clinical testing took place at the University of California, San Diego Autism Center of Excellence. Clinical scores and fMRI scans were collected from 9 ASD and 9 TD toddlers (age-matched (ASD =27.9 mos; TD = 23.2 mols; p>.05). The small sample size is due to the difficulty of collecting sleep fMRI scans, inclusion criteria (a full rest fMRI scan, a diagnosis of ASD or TD at 36 months of age, a MRI scan prior to their official diagnosis, head motion < .5 mean FD). More participants are planned to be included in the completed study. All toddlers underwent a 10-minute sleep fMRI scan. The fMRI data underwent preprocessing using the multi-echo independent component analysis pipeline 'meica. py' implemented in AFNI and Python. Motion correction parameters were determined based on the first TE images (TE 15 ms) using a rigid-body alignment procedure. Both principal and independent component analyses were used to denoise the data. Data were subsequently smoothed with an 6 mm full-width at half-maximum Gaussian kernel. Head motion was assessed using framewise displacement (FD). There were no significant differences in head motion between the ASD and TD groups (p =.37). Next a group ICA was conducted to identify large-scale brain networks in the sample and the network affiliation of each component was determined based on the brain region. Finally, a dynamic functional connectivity (dFC) analysis was performed using only non-noise ICA components (Figure 1). DFC steps included using a window size of 20 TRs and L1 regularization. Next, an elbow criterion was determined for all participants followed by k means clustering. Lastly, dynamic metrics were computed including transitions, dwell time, and frequency of the states for each participant. This was followed by group comparisons (t-tests) for each dynamic metric and between the groups (ASD, TD).

A) Participant Information

	ASD (N = 9) Mean	TD (N = 9) Mean	*p*-value
Age	27.88 mos	23.22 mos	.07
Mean FD	.07	.09	.37
Dwell Time State 1	0 TRs	24.5 TRs	.33
Frequency of Occurrence State 1	0	.1	.33
Dwell Time State 2	217 TRs	151 TRs	.17
Frequency of Occurrence State 2	.89	.66	.11
Dwell Time State 3	27.2 TRs	30.6 TRs	.92
Frequency of Occurrence State 3	.11	.21	.98
Transitions	0	.78	.03

B) Elbow Criterion

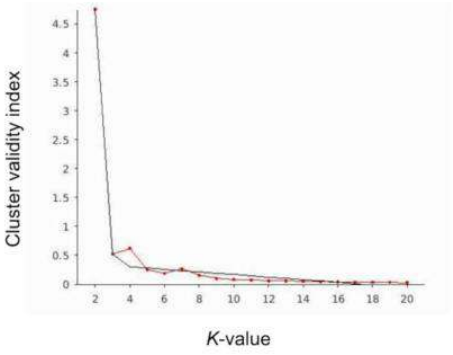

Figure 1A. Participant information for both groups. Figure 2B. Elbow analysis to determine the optimal *k* or brain states across all participants.

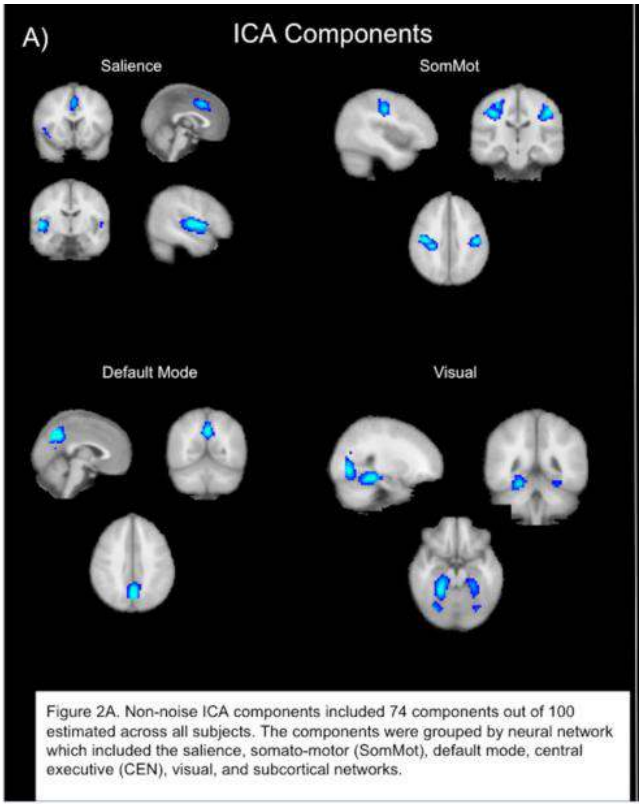

Figure 2A. Non-noise ICA components included 74 components out of 100 estimated across all subjects. The components were grouped by neural network which included the salience, somato-motor (SomMot), default mode, central executive (CEN), visual, and subcortical networks.

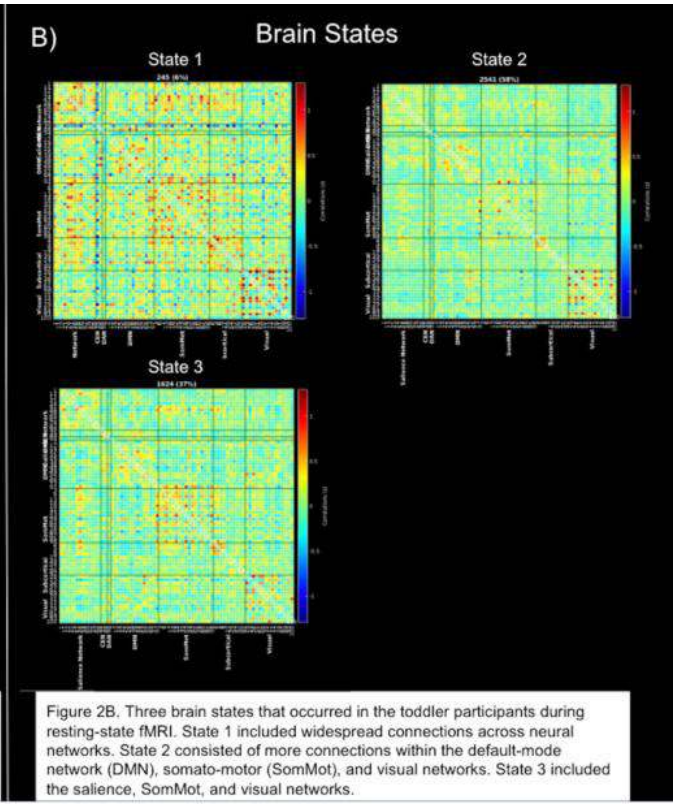

Figure 2B. Three brain states that occurred in the toddler participants during resting-state fMRI. State 1 included widespread connections across neural networks. State 2 consisted of more connections within the default-mode network (DMN), somato-motor (SomMot), and visual networks. State 3 included the salience, SomMot, and visual networks.

Results: The elbow criterion indicated 3 states were optimal for the groups included in the study. The networks involved in each state are depicted in Figure 1. There were no significant differences between the groups for dwell time and frequency of occurrence of brain states (p's > .05). However, TD toddlers exhibited more transitions between states compared with ASD toddlers (TD = .6 transitions; ASD = 0 transitions on average; p<.05). Thus, ASD toddlers stayed in one state (either 2 or 3) throughout the scan, whereas TD toddlers transitioned between two of the three states throughout the scan. Across all groups, toddlers spent significantly more time in state 2 compared with states 1 and 3. State 2 also occurred more frequently in all participants (See Figure 2).

Conclusions: This is one of the first studies to assess brain network dynamics in toddlers later diagnosed with and without ASD and provides a better understanding of early brain network development in this increasingly prevalent neurodevelopmental disorder.

References

1. Maenner, M. J. Prevalence and Characteristics of Autism Spectrum Disorder Among Children Aged 8 Years — Autism and Developmental Disabilities Monitoring Network, 11 Sites, United States, 2020. MMWR Surveill. Summ. 72, (2023).
2. Dawson, G. Early behavioral intervention, brain plasticity, and the prevention of autism spectrum disorder. Dev. Psychopathol. 20, 775–803 (2008).
3. Molnar-Szakacs, I., Kupis, L. & Uddin, L. Q. Neuroimaging Markers of Risk and Pathways to Resilience in Autism Spectrum Disorder. Biol Psychiatry Cogn Neurosci Neuroimaging 6, 200–210 (2021).
4. Kupis, L. et al. Evoked and intrinsic brain network dynamics in children with autism spectrum disorder. Neuroimage Clin 28, 102396 (2020).
5. Watanabe, T. & Rees, G. Brain network dynamics in high-functioning individuals with autism. Nat. Commun. 8, 16048 (2017).
6. Uddin, L. Q. & Karlsgodt, K. H. Future Directions for Examination of Brain Networks in Neurodevelopmental Disorders. J. Clin. Child Adolesc. Psychol. 47, 483–497 (2018).

Poster No 442

Connectome-based predictive modeling analysis of infant cue impacts from early childhood trauma

Nolan Brady[1], Alexander Dufford[2], Shannon Powers[3], Genevieve Patterson[3], Jenna Chin[3], Seungwook Lee[4], Tom Yeh[4], Pilyoung Kim[3]

[1]University of Colorado Boulder, Boulder, CO, [2]Oregon Health & Science University, Portland, OR, [3]University of Denver, Denver, CO, [4]University of Colorado - Boulder, Boulder, CO

Introduction: Trauma exposure across the lifespan is associated with an increased risk for post-traumatic stress disorder (PTSD) and mood disorders. During the transition to parenthood, exposure to trauma was also associated with altered brain responses to infant cues, which can lead to suboptimal parenting. However, how trauma-related brain adaptations affect functional connectivity (FC) associated with infant cues remains largely unknown. In this study, we aimed to assess the impact of trauma during childhood on maternal functional brain connectivity in response to infant crying sounds. Using connectome-based predictive modeling (CPM), we identified brain network connectivity patterns associated with trauma (Shen et al., 2017). Analyzing traumatic events in distinct childhood intervals and adulthood enhances our understanding of which developmental periods are more susceptible to lasting functional brain changes related to infant cry responses. Past research suggests that heightened plasticity in early childhood makes individuals more prone to long-term neurological alterations due to various types of events, including trauma (Kim, 2021). Our hypothesis posited that early childhood trauma would have a more robust association with task-related connectivity.

Methods: Birthing parents (N=80) had early postpartum fMRI scans (M = 1.33 months, SD = 1.01) for an infant cry task involving their own infant crying, another infant's cry, or pattern-matched white noise (Olsavsky et al., 2021). Trauma was assessed by combining Life Events Checklist (LEC) and Adverse Childhood Experiences (ACEs) scores in early and middle childhood, adolescence, and adulthood. The LEC and ACEs data were combined for a more comprehensive evaluation of the subject's past trauma. fMRI data underwent preprocessing with fMRIPrep and XCPD (Esteban et al., 2019, Mehta et al., 2023), followed by calculating functional connectivity matrices (268x268) using the Shen atlas (Shen et al., 2013). These matrices informed a Connectome-based Predictive model examining brain-wide task-related FC and combined LEC/ACEs scores via leave-one-out cross-validation with a feature selection threshold of $p < 0.01$ (Shen et al., 2017).

Results: The CPM analysis suggests that only early childhood (defined as 0-5 years of age) traumatic events were significantly associated with the infant cry task functional connectivity ($p = 0.007$, $r = 0.2983$, MSE = 31.86). The combined LEC/ACEs scores measured in our sample had a mean (M) of 3.44 and a standard deviation (SD) of 5.84. The data represent the number of traumatic experiences (scored 0-30) that occurred at each developmental period. The significant edges for the model indicated that FC between the salience and frontoparietal network was positively associated with more frequent early childhood trauma. Conversely, the default mode network (DMN) FC was negatively associated with increased early childhood trauma. The FC results indicate that with increased traumatic events in early childhood, there is more functional connectivity between the salience and frontoparietal networks and less functional connectivity between the DMN and the motor, visual association, and subcortical networks. Reduced FC within the DMN was also indicative of a higher number of traumatic events in early childhood.

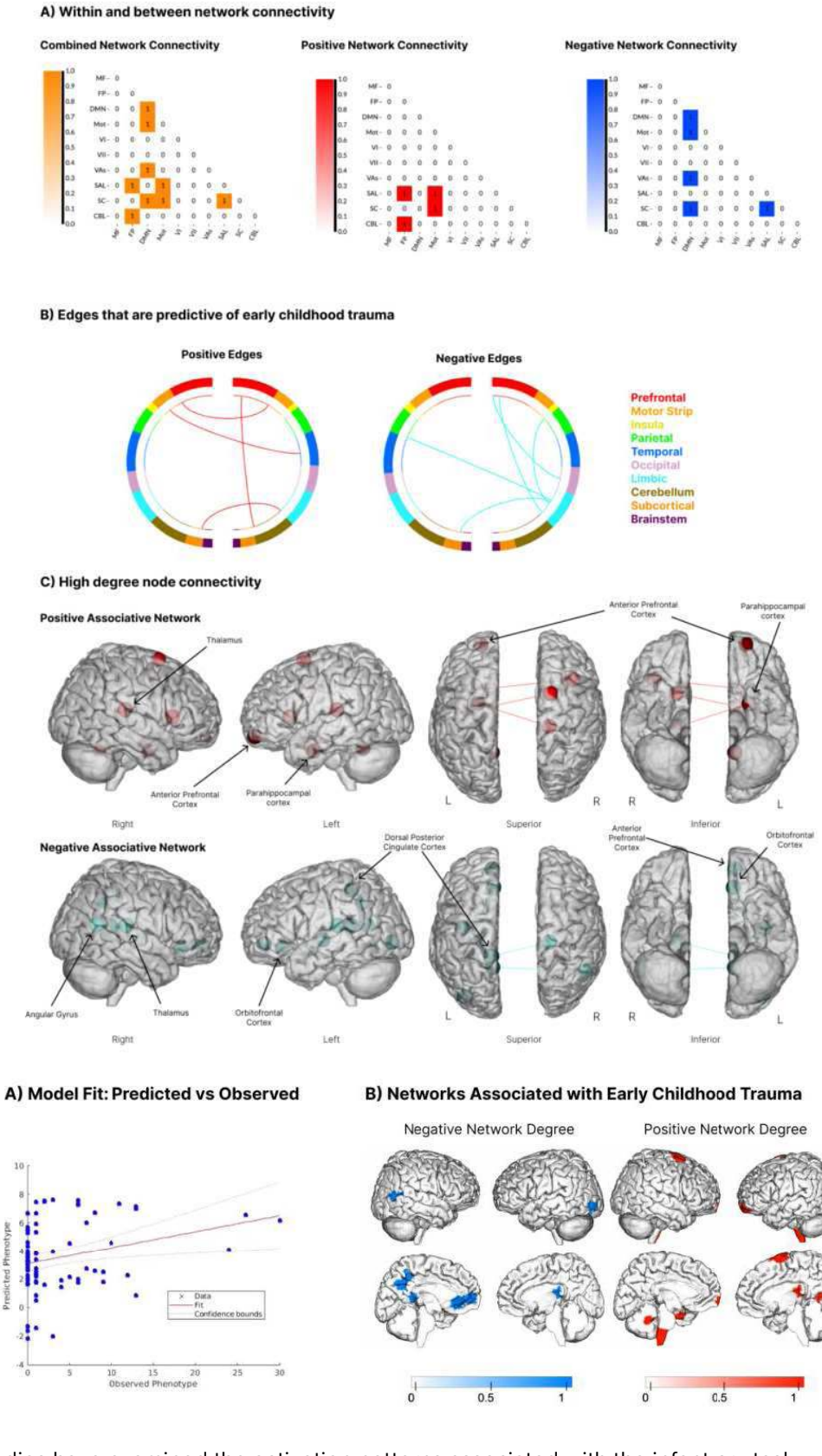

Conclusions: While studies have examined the activation patterns associated with the infant cry task, we examined how task-related functional connectivity during the task was associated with traumatic events in childhood. Greater traumatic events were associated with reductions in DMN connectivity and decreased insula-to-limbic network connectivity. Elucidating the brain-wide functional connectivity patterns associated with childhood trauma is a critical step forward in understanding potential neural mechanisms underlying the intergenerational transmission of childhood trauma.

References

1. Cisler JM. Childhood Trauma and Functional Connectivity between Amygdala and Medial Prefrontal Cortex: A Dynamic Functional Connectivity and Large-Scale Network Perspective. Frontiers in Systems Neuroscience. 2017;11. Link
2. Esteban O, Markiewicz CJ, Blair RW, et al. fMRIPrep: a robust preprocessing pipeline for functional MRI. Nat Methods. 2019;16(1):111-116. Link
3. Kim P. How stress can influence brain adaptations to motherhood. Frontiers in Neuroendocrinology. 2021;60(Complete). Link
4. Mehta K, Salo T, Madison T, et al. XCP-D: A Robust Pipeline for the post-processing of fMRI data. Published online November 21, 2023:2023.11.20.567926. Link
5. Olsavsky AK, Stoddard J, Erhart A, Tribble R, Kim P. Reported maternal childhood maltreatment experiences, amygdala activation and functional connectivity to infant cry. Social Cognitive and Affective Neuroscience. 2021;16(4):418-427. Link
6. Pang Y, Zhao S, Li Z, et al. Enduring effect of abuse: Childhood maltreatment links to altered theory of mind network among adults. Human Brain Mapping. 2022;43(7):2276-2288. doi:10.1002/hbm.25787
7. Shen X, Finn ES, Scheinost D, et al. Using connectome-based predictive modeling to predict individual behavior from brain connectivity. Nat Protoc. 2017;12(3):506-518. Link
8. Shen X, Tokoglu F, Papademetris X, Constable RT. Groupwise whole-brain parcellation from resting-state fMRI data for network node identification. Neuroimage. 2013;82:403-415. doi:10.1016/j.neuroimage.2013.05.081
9. Zhang J, Zhao T, Zhang J, et al. Prediction of childhood maltreatment and subtypes with personalized functional connectome of large-scale brain networks. Hum Brain Mapp. 2022;43(15):4710-4721. doi:10.

Poster No 443

Reward anticipation predicts psychotic-like experiences in youth exposed to cannabis prenatally

Carolyn Amir[1,2], Dara Ghahremani[3,4], Sarah Chang[3,2], Hoki Fung[3,2], Ziva Cooper[5,6], Carrie Bearden[3,7]

[1]Department of Psychiatry and Biobehavioral Sciences, Semel Institute for Neuroscience and Human Beha, Los Angeles, CA, [2]Neuroscience Interdepartmental Program, University of California, Los Angeles, Los Angeles, CA, [3]Semel Institute for Neuroscience and Human Behavior, Los Angeles, CA, [4]Center for Cannabis and Cannabinoids University of California, Los Angeles, Los Angeles, CA, [5]Semel Institute for Neuroscience and Human Behavior, Los Angeles, CA, [6]Center for Cannabis and Cannabinoids University of California, Los Angeles, Los Angeles, CA, [7]Department of Psychology, University of California, Los Angeles, Los Angeles, CA

Introduction: Recently, prenatal cannabis exposure (PCE) has been linked to psychotic-like experiences (PLEs) in early childhood along with growing evidence for associations between early cannabis use and elevated psychosis risk. However, underlying neural mechanisms and the relationship between PCE and PLEs in early adolescent development are not well understood. The neurocognitive and neurochemical substrates involved in reward processing may be implicated in this association. Prenatal cannabis exposure may modify reward circuitry implicated in psychosis risk (Fig.1). Task-based functional neuroimaging during a reward incentive task provides an informative way to study these neurobiological relationships.

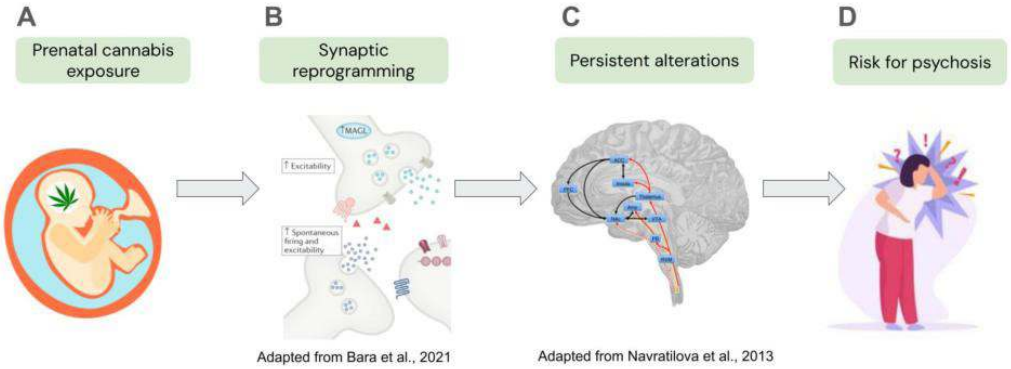

Figure 1: Proposed model of increased risk for psychotic-like experiences following prenatal cannabis exposure. PCE leads to synaptic changes in reward-related regions during fetal development, leading to persistent cannabis-related neurobiological alterations. B) PCE is associated with synaptic-level perturbations including increased excitability and sensitization of dopaminergic and glutamatergic pathways. C) This may lead to persistent neurobiological changes involved in reward-driven behavior, such as persistent dopaminergic hyperactivity in mesocorticolimbic reward pathways. D) These persistent alterations may increase the risk for subsequent psychosis onset.

Methods: We analyzed functional magnetic resonance imaging (fMRI) and behavioral data collected during performance of the Monetary Incentive Delay (MID) Task from 11,876 participants in the Adolescent Brain and Cognitive Development (ABCD) study (exposed youth N=655 at baseline, and unexposed N=11,221 at baseline). We examined three waves of data: baseline (Mage=9.91±0.63 years, 47.61% females), two-year follow-up (N=11,862), and four-year follow-up (N =3,062). We tested cross-

sectional relationships between activation in reward-related brain regions during reward anticipation and PLEs (total score and distress) at baseline assessed by the Prodromal Questionnaire – Brief Child Version (PQ-BC). Group (unexposed vs. exposed)-by-region interactions were tested on each region of interest, including the striatum and ventromedial prefrontal cortex (vmPFC). Covariates included site, family membership, age, sex, and socioeconomic status. False discovery rate correction was applied. Behavioral performance measures on the MID task (response accuracy and reaction time) were analyzed across the three waves of data with mixed-level analyses of variance. Factors included trial type (6 levels: -$5, -$.20, +$0, +$.20, +$5; within-subjects) and group (2 levels: exposed to cannabis prenatally; between-subject).

Results: PCE was positively associated with PLE scores (std. β =1.350, q<.001) and distress (std. β =1.340, q <.001), longitudinally across three waves of data. Across groups, PLEs were inversely associated with reward anticipation-related activation in the striatum (std. β = -.030, q< .001), and vmPFC (std. β =-.026, q=.010) at baseline. Significant group-by-ROI interactions indicated that activation was more blunted in both striatum (q<.001) and vmPFC (q<.001) in PCE youth (see Table 1 for full results). PCE youth displayed faster reaction time in the MID task, regardless of trial type, compared to unexposed youth (main effect of group on RTs: p<.001). Despite faster reaction times, PCE youth were less accurate when responding to large loss, neutral, and small reward trials (p's<.001) in comparison to unexposed youth; however, there were no statistically significant group differences in accuracy for small loss or large reward trials. Greater PLEs were associated with higher accuracy for large reward trials (std. β = .194, q=.023) in the PCE group. Greater PLEs were also associated with slower reaction times across trial types in the PCE group (std. β = .004, q<.001).

		A) Prenatal cannabis exposure (longitudinal)	B) Striatal activation (baseline)	C) vmPFC activation (baseline)	D) Striatal activation by prenatal cannabis exposure interaction (baseline)	E) vmPFC activation by prenatal cannabis exposure interaction (baseline)
Psychotic-like Experiences (distress)	**β**	1.350	-.030	-.026	-.047	-.002
	q	<.001	<.001	.010	<.001	<.001

Table 1. Associations between psychotic-like experiences, prenatal cannabis exposure (A; across 3 waves of data), and activation in reward-related brain regions during reward anticipation (B,C; at baseline). Group-by-ROI interactions are also reported at baseline (D, E).

Conclusions: Our findings indicate that the association between prenatal cannabis exposure and psychotic-like experiences persists into early adolescence. Neurobehavioral response to reward anticipation is altered in youth exposed to cannabis prenatally and is associated with the severity of psychotic-like symptoms. PLEs are associated with blunted neural responses to reward-related cues, with stronger effects for those exposed to cannabis prenatally. This dampened activation in reward-related regions may represent a biomarker of disrupted reward processing during development. Faster reaction times across trials and trial-type accuracy differences in youth exposed to cannabis may reflect heightened reward-related motivation.

References

1. Bara, A. et al. (2021). Cannabis and synaptic reprogramming of the developing brain. Nature Reviews Neuroscience 22, 423-438.
2. Fine, J. D. et al. (2019). Association of Prenatal Cannabis Exposure With Psychosis Proneness Among Children in the Adolescent Brain Cognitive Development (ABCD) Study. JAMA Psychiatry 76, 762-764.
3. Gunasekera, B. et al. (2022). Cannabinoids, reward processing, and psychosis. Psychopharmacology 239, 1157-1177.
4. Karcher, N. R. et al., (2015). Examining Associations between Psychosis Risk, Social Anhedonia, and Performance of Striatum-Related Behavioral Tasks. Journal of Abnormal Psychol 124, 507-518.
5. Khokhar, J. Y. et al (2018). The link between schizophrenia and substance use disorder: A unifying hypothesis. Schizophrenia Research 194, 78-85.
6. Kwarteng, A. E. et al. (2021). Child reward neurocircuitry and parental substance use history: Findings from the Adolescent Brain Cognitive Development Study. Addictive Behaviors
7. Poulia, N. et al (2021). Detrimental effects of adolescent escalating low-dose Œî9-tetrahydrocannabinol leads to a specific bio-behavioural profile in adult male rats. British Journal of Pharmacology 178, 1722-1736 .
8. Yanes, J. A. et al. (2018). Neuroimaging meta-analysis of cannabis use studies reveals convergent functional alterations in brain regions supporting cognitive control and reward processing. Journal of Psychopharmacology 32, 283-295.

Poster No 444

Developmental trajectories in functional brain network properties of preterm and at-term neonates

Nelsiyamid López Guerrero[1], Sarael Alcauter[1]

[1]*Instituto de Neurobiología, Universidad Nacional Autónoma de México, Querétaro, México*

Introduction: The human brain undergoes rapid growth during the first years of life. Premature infants, born before 37 weeks of gestation can have consequences on development, even when no anatomical lesions are evident (Rogers et al.,2018). Resting state functional (MRI) naturally sleeping babies allows the characterization of the brain functional connectome, showing decreased long range connectivity (Smyser et al., 2010). Preterm infants have shown alterations in connectivity measures globally and in specific networks (Gozdas et al., 2018). In this work, we characterize the developmental trajectories in the functional brain network in preterm and term neonates.

Methods: We included 454 preprocessed structural-functional datasets from the developing Human Connectome Project (Hughes et al., 2017), acquired between 26 -44 weeks of postmenstrual age (PMA) and with no radiological signs of white matter lesions. For each subject, we estimated the connectivity matrix as the correlation of the BOLD time series between all possible pairs of the 90 regions within the neonate AAL atlas (Shi et al., 2011). Subsequently, these matrices were thresholded to keep only the ten percent of the highest connections. From these thresholded matrices, we computed graph theory measures as clustering coefficient, node strength, global efficiency and shortest path length, using the Brain Connectivity Toolbox. To characterize the developmental trajectories of the graph theory properties here explored, linear, quadratic, and log-linear mixed models were constructed with gestational age at scan as an independent fixed-effect variable. Random effects were added for the intercept and subject ID. Significance was defined as $p < 0.05$, and the model with the lowest Akaike Information Criterion (AIC) was selected as the best model to describe the data.

Results: The best-fitting models showed non-linear trajectories for all the properties in preterm neonates and two of them in at-term neonates (Figure 1 and Figure 2). When compared by sex, at-term infants showed no significant differences between males and females; females preterm showed increased connectivity in clustering coefficient ($p < 0.02$), node strength ($p < 0.01$) and global efficiency ($p < 0.01$).

Preterm neonates

I.

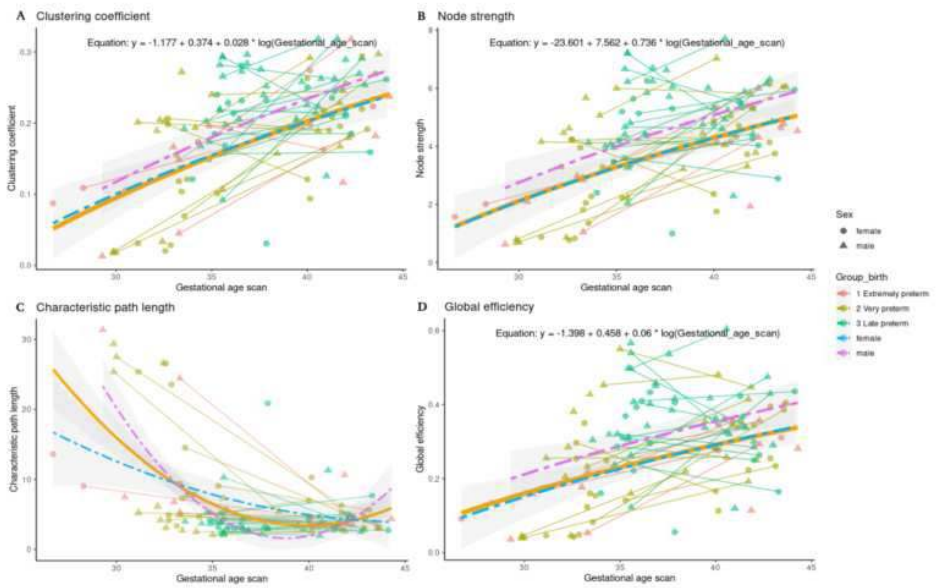

II.

	Clustering coefficient			Node strength			Characteristic path length			Global efficiency		
	F value	Pr(>F)	AIC	F value	Pr(>F)	AIC	F value	Pr(>F)	AIC	F value	Pr(>F)	AIC
Lineal model	57.19	8.92×10^{-11}	-283.7938	46.14	2.67×10^{-09}	430.4784	35.72	1.15×10^{-07}	747.1826	25.99	2.68×10^{-06}	-141.1299
Quadratic model	11.54	9.65×10^{-04}	-275.5133	13.82	3.26×10^{-04}	430.5893	23.74	4.34×10^{-06}	**735.6559**	15.49	1.52×10^{-04}	-138.0371
Logarithmic model	60.23	2.89×10^{-11}	**-293.1881**	49.06	9.08×10^{-10}	**421.0729**	39.52	2.97×10^{-08}	737.1098	28.28	1.07×10^{-06}	**-150.2163**

Figure 1. Preterm neonates. I. Best fitting models for the network properties in preterm infants. A) Clustering coefficient. B) Node strength. C) Characteristic path length. D) Global efficiency. Clustering coefficient, node strength and global efficiency increase as gestational age scan increases. II. The table compares the linear, quadratic, and logarithmic fit models for each graph theory measure in preterm. The lower the AIC value indicates the best fitting model; it is highlighted in bold.

At-term neonates

I.

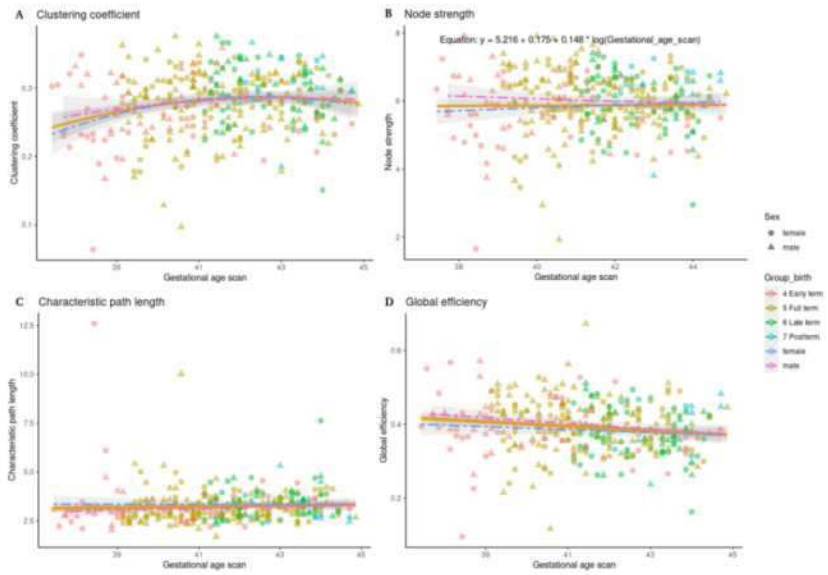

II.

	Clustering coefficient			Node strength			Characteristic path length			Global efficiency		
	F value	Pr(>F)	AIC	F value	Pr(>F)	AIC	F value	Pr(>F)	AIC	F value	Pr(>F)	AIC
Lineal model	7.94	5.14×10^{-03}	-1117.0615	0.0002	9.88×10^{-01}	887.5415	0.76	3.84×10^{-01}	**902.8121**	7.03	8.42×10^{-03}	**-825.5566**
Quadratic model	8.01	4.92×10^{-03}	**-1119.3961**	0.0002	9.99×10^{-01}	887.8418	0.76	3.84×10^{-01}	904.0926	7.00	8.52×10^{-03}	-823.5578
Logarithmic model	8.20	4.45×10^{-03}	-1117.3221	0.002	9.62×10^{-01}	**887.5338**	0.72	3.97×10^{-01}	902.8408	6.99	8.58×10^{-03}	-825.5487

Figure 2. At-term neonates. I. Best fitting models in at-term infants. A) Clustering coefficient. B) Node strength. C) Characteristic path length. D) Global efficiency. Clustering coefficient, nod global efficiency increase as gestational age scan increases. II. The table compares the linear, quadratic, and logarithmic models for each graph theory measure in at-term neonates. The lower the AIC value indicates the best fitting model, highlighted in bold for each case.

Conclusions: Overall, our results confirm that the functional connectivity, integration and segregation properties of the preterm brain follow nonlinear trajectories with a clear sexual dimorphism for these brain network properties.

References

1. Gozdas, E. et al. (2018) 'Altered functional network connectivity in preterm infants: antecedents of cognitive and motor impairments?', Brain structure & function, 223(8), pp. 3665–3680.
2. Hughes, E. J. et al. (2017) 'A dedicated neonatal brain imaging system', Magnetic resonance in medicine: official journal of the Society of Magnetic Resonance in Medicine / Society of Magnetic Resonance in Medicine, 78(2), pp. 794–804.
3. Rogers, C. E., Lean, R. E., Wheelock, M. D., & Smyser, C. D. (2018). Aberrant structural and functional connectivity and neurodevelopmental impairment in preterm children. Journal of neurodevelopmental disorders, 10(1), 38.
4. Shi, F. et al. (2011) 'Infant brain atlases from neonates to 1- and 2-year-olds', PloS one, 6(4), p. e18746.

Poster No 445

Brain Mapping of Coherent and Scrambled Biological Motion Processing in Autistic School-Age Children

Dalin Yang[1], Alexandra Svoboda[1], Tessa George[2], Muriah Wheelock[2], Mariel Schroeder[1], Sean Rafferty[2], Arefeh Sherafati[1], Joseph Culver[2], Adam Eggebrecht[2]

[1]Washington University School of Medicine, Saint louis, MO, [2]Washington University School of Medicine, St. Louis, MO

Introduction: Autism Spectrum Disorder (ASD) is characterized by deficits in social communication and enhanced presentation of restricted interests and repetitive behaviors. The perception of biological motion (BM) plays a crucial role in recognizing emotions and intentions, representing a deeply ingrained and early developing mechanism. Investigating disruptions in the neural systems responsible for BM perception in autistic children may enhance early diagnosis and the creation of targeted interventions. However, mapping brain function in young children with ASD has proven challenging using traditional neuroimaging modalities, i.e., functional magnetic resonance imaging (fMRI)that requires participants to recline and maintain

still within a noisy and confined environment. To overcome these challenges while maintaining fMRI-comparable data, we use high-density diffuse optical tomography (HD-DOT), a wearable and minimally constraining neuroimaging modality that can map brain function in an open, silent, naturalistic environment more amenable to studies on children with ASD[1-3]. Herein, we aimed to establish the feasibility of HD-DOT in school-age children with ASD using a passive paradigm of BM perception, previously shown with fMRI to reveal differences in brain activity in autistic children as compared to non-autistic controls (NAC)[4].

Methods: We recruited 95 school-age children (Fig. 1A), age 9 to 17 years, including 46 autistic individuals and 49 NAC children. Informed consent was obtained from legal guardians for all participants and the research was approved by the Human Research Protection Office at Washington University. Each participant was assessed with HD-DOT while watching 6 blocks of alternating 24-second-long movies of coherent and scrambled point-light animations of biological motion (Fig. 1B) 4. The HD-DOT instrument contains a dense array of 96 sources and 92 detectors that provides a smooth sensitivity profile on the cortical surface (Fig. 1C). The Social Responsiveness Scale (SRS), a parent report measure of social reciprocity, was collected in all participants. Data were processed in MATLAB using the NeuroDOT toolbox (https://www.nitrc.org/projects/neurodot), with motion artifact quantified using the global variance of the temporal derivative (GVTD)5, and registered to the MNI atlas for group analyses. Standard GLM analyses were used with an HD-DOT-derived adult hemodynamic response function2 and contrast maps were assessed within and across groups. Cluster-extent based thresholding was performed in SPM12.

Results: No statistically significant differences in head motion were observed between the two groups ($p = 0.32$, $t = 0.48$), indicating both ASD and NAC groups tolerated the HD-DOT scan. In response to the biological motion perception task, the NAC group exhibited greater activity during coherent than scrambled BM in bilateral frontal gyrus (IFG), right middle occipital gyrus (MOG), left inferior occipital gyrus (IOG), right superior temporal sulcus, and right precentral gyrus (PCG) (Fig. 1E). In contrast, the ASD group exhibited stronger activity in the right hemisphere, including middle frontal gyrus, MOG, PCG, and middle temporal gyrus. Furthermore, the NAC exhibited a significantly greater activity than with the ASD group in bilateral IFG, left IOG, left fusiform gyrus, left TMG, left PCG, right IOG, and right PCG.

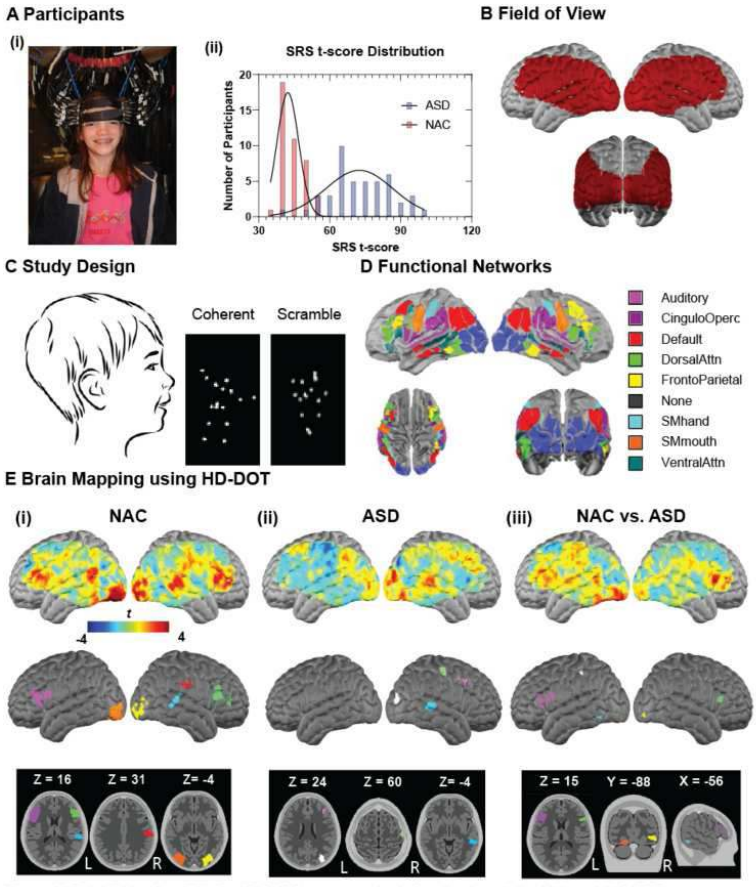

Figure 1 | Establishing feasibility for HD-DOT to measure brain function in autistic children. A HD-DOT array on a school age participant and (ii) distribution of the Social Responsiveness Scale-2 t-scores. B The study design: alternating 24 second movies of coherent and scrambled point light animations of motion. C The field of view of the HD-DOT system reaches up to ~2.0 cm below the scalp surface and D includes multiple functional networks as shown with the Gordon parcellation. E Within- (NAC or ASD) and between- group (NAC vs. ASD) random effect unthresholded t-maps, cluster correction regions of biological motion show strong contrasts (coherent > scrambled). Cluster corrected maps are thresholded at voxel-wise $p < 0.0075$ and FDR-corrected at a cluster significance of $p < 0.00125$.

Conclusions: This study validates the feasibility of using HD-DOT to map brain function in both school-age ASD and NAC children. Ongoing investigations are exploring the association between variations in brain function and behavioral metrics (i.e., sex, age, IQ, and motion). Also, we are leveraging the open scanning environment of HD-DOT to investigate simultaneous eye gaze and brain function during naturalistic motor imitation.

References

1. Eggebrecht, A. T., et al. (2014). "Mapping distributed brain function and networks with diffuse optical tomography." Nature photonics, vol. 8, pp. 448-454.
2. Hassanpour, M. S., et al. (2014). "Statistical analysis of high density diffuses optical tomography", NeuroImage, vol. 85, pp. 104-116.
3. Ferradal, S. L., et al., (2016). "Functional imaging of the developing brain at the bedside using diffuse optical tomography", Cerebral cortex, vol. 26, no. 4, pp.1558–1568.
4. Kaiser, M. et al. (2010) "Neural signatures of autism." Proceedings of the National Academy of Sciences, vol. 107, no. 49, pp. 21223-21228.
5. Sherafati, A. et al. (2020). "Global motion detection and censoring in high-density diffuse optical tomography. Hum. Brain Mapp. vol. 41, pp. 4093–4112.

Poster No 446

Large scale brain network level excitation and inhibition imbalance in patients with epilepsy

Hui Chen[1], Min Wang[1], Yin Wang[1], Zhoukang Wu[1], Liangjiecheng Huang[1], Mengyuan Liu[1], Zhiqiang Zhang[2], Xiaosong He[1]

[1]University of Science and Technology of China, Hefei, Anhui, [2]Jinling Hospital, the First School of Clinical Medicine, Southern Medical University, Nanjing, Jiangsu

Introduction: Epilepsy is a neurological disorder characterized by an enduring predisposition to generate epileptic seizures, which are abnormal neural discharges arising from disrupted excitation and inhibition (E:I) balance of the brain. Evidence from both surface and intracranial EEG support the notion that epilepsy is associated with E:I imbalance in epileptogenic regions[1]. Nonetheless, due to the known limits of both EEG techniques, whether and how large scale brain network level E:I balance are disrupted in patients with epilepsy remains largely unknown. A previous study has provided evidence that the E:I ratio can also be effectively evaluated through the resting-state BOLD signals, as the inverse of the time series' Hurst exponent (H)[2]. Such measure of E:I ratio is also associated with myelination and shapes the structure-function coupling of the brain, supporting its biological relevance[3]. Accordingly, here we employ resting-state fMRI (rsfMRI) to evaluate the E:I ratio of large scale brain networks among different types of epilepsy, encompassing both focal epilepsy such as temporal lobe epilepsy (TLE) and idiopathic generalized epilepsy (IGE).

Methods: We enrolled 209 patients with epilepsy and 100 demographically matched healthy controls (HC) in this study. Prior to any surgery, all subjects underwent rsfMRI and T1 scans using a 3T MRI scanner. The patient group was subsequently devided into 3 subgroups: (1) patients with TLE with left-sided hippocampal sclerosis (LHS, 80 in total); (2) patients with TLE with right sided HS (RHS, 80 in total); and (3) patients wtih IGE (49 in total). RsfMRI data were preprocessed using fMRIPrep[4] and XCP-D[5], including slice-timing correction, head-motion correction, segmentation, coregistration, normalization, despiking, nuisance regression, interpolation, temporal filtering (0.01-0.08 Hz), and smoothing. We used the 200 parcel version of 7 network Schaefer atlas[6] and the 32 parcel version of the Melbourne subcortex atlas[7] to extract BOLD time-series for each subject. Each time series was modeled as multivariate fractionally integrated processes, and the corresponding Hurst exponent was estimated via the univariate maximum likelihood method and a discrete wavelet transform[2]. We then summarized the Hurst exponent by each functional network by hemisphere. We also summarized the subcortical regions into a subcortical network for each hemisphere, except for amygdala and hippocampus which were grouped into the limbic network[8]. Statistical inferences were made with permutation-based independent t-tests with FWE correction for multiple comparisions[9]. We applied 1000000 permutations for each test.

Results: We found significant but yet selective differences between patients with epilepsy and HC. In specific, patients with LHS presented bilateral reduction of Hurst exponent in the limbic network (left: t=-3.15, p=0.022; right: t=-3.65, p=0.004) (Fig 1A, Fig 2A), while patients with RHS exhibits unilateral reduction of Hurst exponent in the right limbic network (t=-3.47, p=0.008), right control network (t=-3.25, p=0.017), and right default mode network (t=-4.04, p=0.001) (Fig 1B, Fig 2B). Interestingly, after correction for multiple comparison, we did not observe any significant difference between patients with IGE and HC ($|t|<1.62$, $p>0.661$).

Conclusions: At large scale brain network level, we found significant E:I imbalance in patients with focal epilepsy, but not in patients with generalized epilepsy. Such difference may be attributed to the more prominent structural abnormalites (i.e.,

HS) in the former cohort. Regardless, the revealed E:I imbalance largerly overlaps with known epileptogenic networks. There results may further our understanding of the neural mechanisms underlying the diagnosis and prognosis of epilepsy.

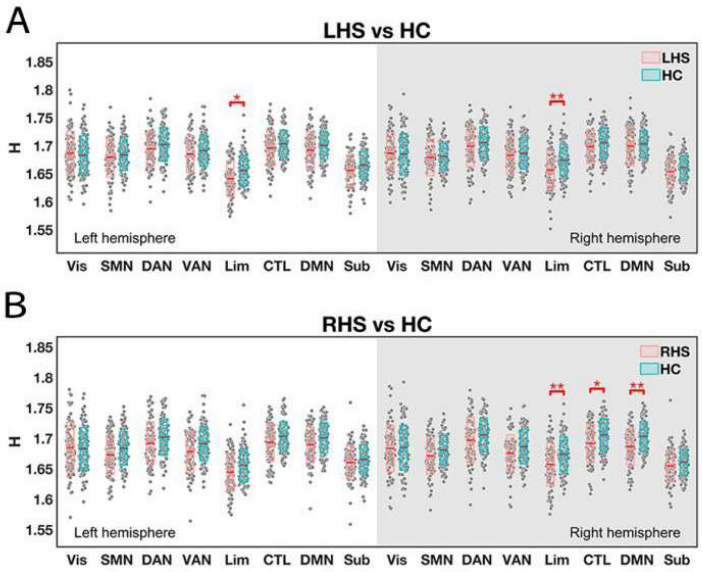

Figure 2. Boxplot of Hurst exponent (H) in patients with epilepsy and healthy controls (HC). (A) Comparisons between pateints with left hippocampus sclerosis (LHS) and HC showed significant differences in the bilateral limbic networks; (B) Comparisons between pateints with right hippocampus sclerosis (RHS) and HC showed significant differences in the right limbic, control and default mode networks. Note that due to the lack of group difference, map for patients with idiopathic generalized epilepsy is hence omitted. *, $p < 0.05$; **, $p < 0.01$; all corrected for multiple comparisons.

References

1. Burrows, D. (2021), 'Single-Cell Networks Reorganise to Facilitate Whole-Brain Supercritical Dynamics During Epileptic Seizures', preprint, Neuroscience.
2. Trakoshis, S. (2020), 'Intrinsic Excitation-Inhibition Imbalance Affects Medial Prefrontal Cortex Differently in Autistic Men versus Women', eLife, 9, e55684.
3. Fotiadis, P. (2023), 'Myelination and Excitation-Inhibition Balance Synergistically Shape Structure-Function Coupling across the Human Cortex', Nature Communications, 14 (1), 6115.
4. Esteban, O. (2019), 'fMRIPrep: A Robust Preprocessing Pipeline for Functional MRI', Nature Methods, 16 (1), 111–116.
5. Mehta, K. (2023), 'T. D. XCP-D: A Robust Pipeline for the Post-Processing of fMRI Data', preprint; Neuroscience.
6. Schaefer, A. (2018), 'Local-Global Parcellation of the Human Cerebral Cortex from Intrinsic Functional Connectivity MRI', Cerebral Cortex, 28 (9), 3095–3114.
7. Tian, Y. (2020), 'Topographic Organization of the Human Subcortex Unveiled with Functional Connectivity Gradients', Nature Neuroscience, 23 (11), 1421–1432.
8. He, X. (2022), 'D. S. Uncovering the Biological Basis of Control Energy: Structural and Metabolic Correlates of Energy Inefficiency in Temporal Lobe Epilepsy', Science Advances, 8 (45), eabn2293.
9. He, X. (2020), 'Disrupted Basal Ganglia–Thalamocortical Loops in Focal to Bilateral Tonic-Clonic Seizures', Brain, 143 (1), 175–190.

Poster No 447

Investigating neuronal noise as a mechanism of tic generation

Aikaterini Gialopsou[1], Caitlin Smith[1], Mairi Houlgreave[1], Isabel Farr[1], Stephen Jackson[1]

[1]University of Nottingham, Nottingham, England

Introduction: Tourette syndrome (TS) is a neurodevelopmental disorder characterised by chronic involuntary motor and vocal tics. TS is linked to sensory hypersensitivity (Isaacs & Riordan, 2020) which could reflect the reduced sensorimotor gating and the altered perceptual processing. Moreover, prior research has suggested that tics could reflect motor noise, resulting in uncertainty of the voluntary movement and the occurrence of tics. This enhanced neuronal noise may reflect the imprecise forward model of action planning, inherent in TS (Münchau et al., 2021; Albin & Mink, 2006). Experimental data has confirmed

increased 1/f or pink noise in the TS population during a sensorimotor task (Adelhöfer et al., 2021). Hence in this study, we aimed to quantify the difference in the neuronal noise between TS participants and age and gender-matched controls (HC). We defined neuronal noise as the variability of the cortical oscillations during median nerve stimulation (MNS).

Methods: Data were collected from a group of 19 right-handed participants, who were diagnosed with TS or other tic disorders (10F, mean age (± SD): 30.8 ±10.9). Additionally, 19 right-handed HC participants with no prior neuropsychological diagnosis were included (10 F, mean age (± SD): 28.3, ± 6.7). Cortical measurements were conducted utilizing a 64-channel system to record Somatosensory Evoked Potentials (SEPs) elicited by a single pulse of MNS. MNS electrodes were placed on the dominant hand over the median nerve with the anode proximal to the hand. A total of 75 single pulses were delivered, interspersed with an inter-trial interval of 11 s (±2 s). The MNS motor threshold (MT) was individually determined for each participant as the minimum intensity necessary to evoke a visible thumb twitch. We focused our analysis on small time windows around the well-defined SEP component; N20 (20ms ±10), N60 (60 ms±20), P100(100ms ±20) and P260 (260ms ±50). We assessed the variability in the latency and amplitude of SEPs across and between the two groups.

Results: The component analysis revealed enhanced variability in SEPs within the TS group compared to the HC. Specifically, Figure 1 Illustrates the grand average TS and HC SEPs, revealing increased amplitude in the former across all onset components. Significant differences in RMS of SEP amplitude were observed between the two groups (N20: TS 2.13 HP:2.27, N60: TS 3.9 HP 4.7, P100: TS: 9.06 HP: 5.6, P260: TS 10.28 HC 9.5). Similarly, figure 2 shows the average time onset of each SEP component between the two groups. The temporal RMS was significantly different between the TS (blue) and the HC (red) groups for the N20, N60, and P100 components but not for the P260 (N20: TS 20 HP:19.06, N60: TS 60.8 HP 60.1 P100: TS: 100.55 HP: 99.17).

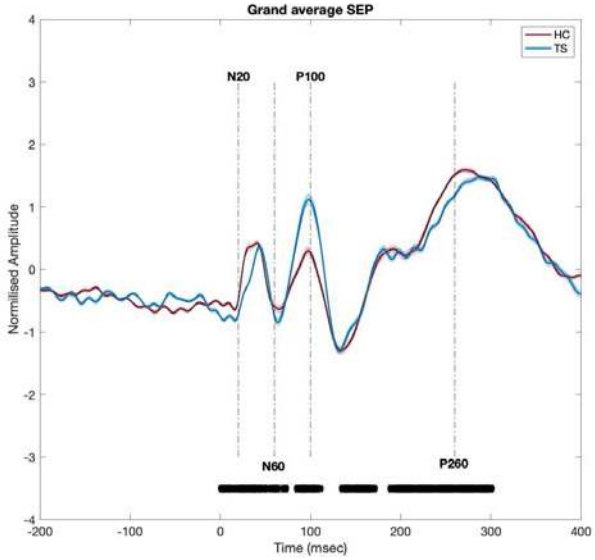

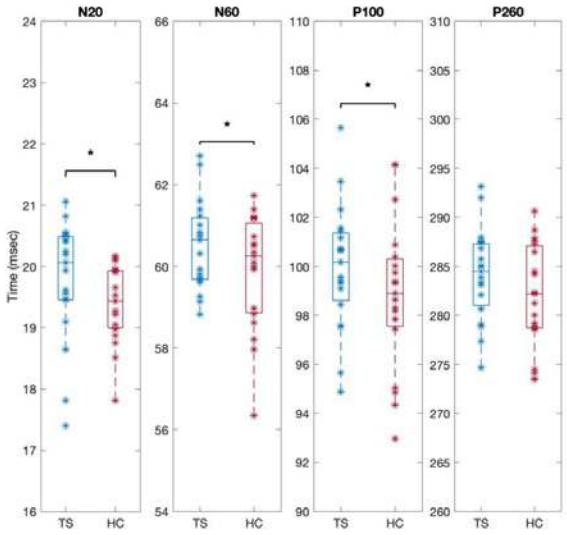

Conclusions: The significantly enhanced variability in TS amplitude and latency could reflect the increased asynchronous neuronal activity, i.e. neuronal noise. These findings contribute to our comprehension of the mechanisms underlying tic generation in Tourette Syndrome. Innovative interventions seeking to synchronize specific neuronal oscillations may mitigate neuronal noise, offering therapeutic benefits.

References

1. Münchau, A. et al. (2021) 'A neural noise account of Gilles de la Tourette syndrome', NeuroImage: Clinical, 30, p. 102654. doi:10.1016/j.nicl.2021.102654.
2. Albin, R.L. and Mink, J.W. (2006) 'Recent advances in Tourette Syndrome Research', Trends in Neurosciences, 29(3), pp. 175–182. doi:10.1016/j.tins.2006.01.001.
3. Isaacs, D. and Riordan, H. (2020) 'Sensory hypersensitivity in Tourette Syndrome: A Review', Brain and Development, 42(9), pp. 627–638. doi:10.1016/j.braindev.2020.06.003.
4. Adelhöfer N, Paulus T, Mückschel M, Bäumer T, Bluschke A, Takacs A, et al. Increased scale-free and aperiodic neural activity during sensorimotor integration—a novel facet in tourette syndrome. Brain Communications. 2021;3(4).

Poster No 448

Multimodal Patterns Associated with Social Interaction Through Gray and White Matter in Autism

Long Wei[1], Xin Xu[1], Suyu Zhong[2]

[1]Shandong Jianzhu University, Jinan, Shandong, [2]Beijing University of Posts and Telecommunications, Beijing, Beijing

Introduction: Autism spectrum disorder (ASD) patients are characterized by deficits in various aspects of social interaction. Based magnetic resonance imaging (MRI) data, multimodal fusion methods[1,2] are widely applied to explore brain regions related to social impairment in ASD but the role of white matter in brain function has always been underestimated. Using gray and white matter data can help to understand how ASD patients differ from healthy control (HC) in information processing and transmission. So, we have improved the data preparation step to extract purer gray and white matter information and explore multimodal neuroimaging patterns associated with social impairment.

Methods: 699 male participants (ASD/HC: 343/356) from Autism Brain Imaging Data Exchange(ABIDE)I&II were included, who have total social responsiveness scale (SRS) scores, T1-weighted structural-MRI (sMRI) and resting-state functional MRI (rs-fMRI). sMRI and rs-fMRI data were preprocessed by pipeline tools CAT12[3] and DPARSF[4] respectively. More specifically, white matter signals were not regressed out and controlled maximum head motion less than 5mm or 5° during the rs-fMRI preprocessing stage. All participants calculated gray matter volume (GMV) map from sMRI and fractional amplitude of low-frequency fluctuations retaining white matter signals (WM-fALFF) map from rs-fMRI. Then, overlaid the white matter mask file onto all processed WM-fALFF maps to save the white matter tissue data only. Finally, we converted all kinds of maps into Z-score maps and obtained two matrices by reshaping each subject's map into a row of vectors and stacked sequentially for each modality. Meanwhile, we concatenated total SRS scores into one-dimensional vectors according to the same sequence. After data preparation, a supervisory data-driven analysis method called "multi-site canonical correlation analysis with reference + joint independent component analysis" (MCCAR +jICA)[5] was used, which can identify joint multimodal component more relevanted to the social interactions by setting total SRS scores as reference data based on two modal matrices (Figure 1).

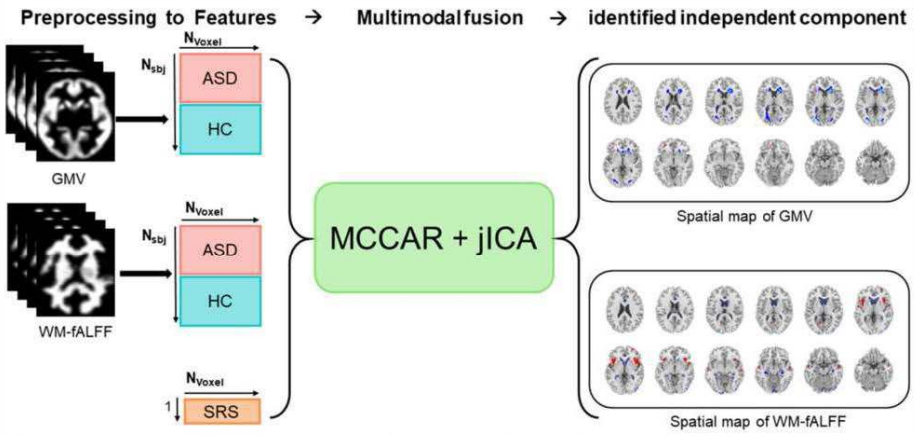

Figure 1.Flowchart of the study design.Firstly, assembled the preprocessed GMV images and WM-fALFF images into feature matrix, and then used the "MCCAR+jICA" method to identify significant independent components for each modality.SRS,social responsiveness scale.

Results: Figure 2A showed the spatial maps of identified independent component(ICs)for two modality. For GMV, the identified brain regions mainly located in bilateral insula, bilateral caudate and bilateral hippocampus, accompanied with WM-fALFF mainly located in bilateral corpus callosum, right internal capsule, left inferior longitudinal fasciculus and fornix. Figure 2B indicated that ICs were significantly($p < 0.0005$) positive correlations with total SRS scores on all modalities (GMV: $r = 0.127$, $p = 7.33x10\text{-}6$; WM-fALFF: $r = 0.164$, $p = 1.32x10\text{-}5$). The higher loadings, the worse social function. We conducted two sample t-test on IC loadings between ASD and HC to explore the group difference (as shown in Figure 2C). The ICs differs significantly across all modalities, and ASD had higher means (GMV: $t= 3.52$,$p = 0.0005$; WM-fALFF $t= 4.60$,$p = 4.92x10\text{-}6$).

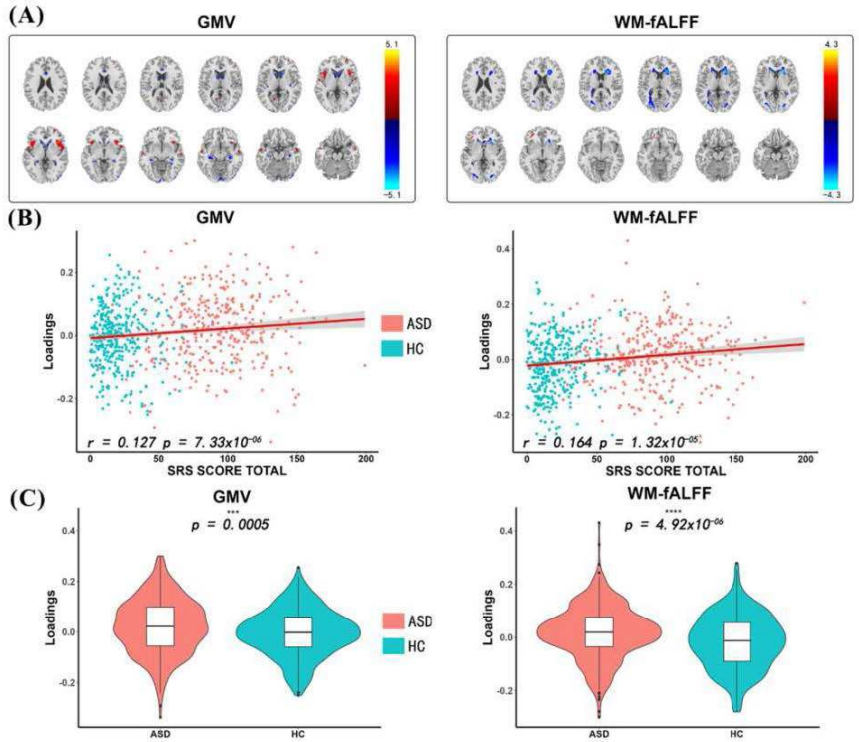

Figure 2. The identified joint component. (A) The spatial maps are visualized at $|Z| > 2$ thresholds, where the red regions mean positive GMV or WM-fALFF, and the blue regions mean negative GMV or WM-fALFF. (B)The results of correlation between loadings of IC and total SRS scores.(C) The results of two sample t-test on the loadings.SRS,social responsiveness scale.

Conclusions: Our study found a significant gray and white matter function pattern associated with social impairment in ASD, whose brain regions related to information integration, emotional control, language expression, physical movement and external stimuli response. These foundings might provide potential insights to study the causes of social behavior disorders in ASD patients.

References

1. Sui, Jing et al.(2018), 'Multimodal neuromarkers in schizophrenia via cognition-guided MRI fusion', Nature communications, vol. 9, no.1, pp. 3028.
2. Qi, Shile et al.(2020), 'Common and unique multimodal covarying patterns in autism spectrum disorder subtypes', Molecular autism, vol. 11, no.1, pp. 90.
3. Gaser C et al.(2022), 'A Computational Anatomy Toolbox for the Analysis of Structural MRI Data', bioRxiv.
4. Yan, C.G et al.(2016), 'DPABI: Data Processing & Analysis for (Resting-State) Brain Imaging', Neuroinformatics, vol. 14, no. 3, pp. 339-351.
5. Li T et al.(2019), 'Multimodal neuroimaging patterns associated with social responsiveness impairment in autism: A replication study', 2019 IEEE 16th International Symposium on Biomedical Imaging (ISBI 2019), pp. 409-413.

Poster No 449

Structural brain alterations in autism: A large-scale voxel-based morphometry mega-analysis

Emily Laltoo[1], Katherine Lawrence[2], Sebastian Benavidez[3], Emma Gleave[1], James McCracken[4], Paul Thompson[5], Priya Rajagopalan[1]

[1]University of Southern California, Los Angeles, CA, [2]Imaging Genetics Center, Mark and Mary Stevens Neuroimaging & Informatics Institute, USC, Marina del Rey, CA, [3]Mark and Mary Stevens Neuroimaging & Informatics Institute, University of Southern California, Marina del Rey, CA, [4]Department of Psychiatry, University of California San Francisco, San Francisco, CA, [5]Imaging Genetics Center, Keck School of Medicine of University of Southern California, Los Angeles, CA

Introduction: Autism spectrum disorder (ASD) is a neurodevelopmental condition characterized by alterations in social communication and by repetitive behaviors. ASD is three to four times more prevalent in boys compared to girls and has a widespread impact on individuals, including diminished overall quality of life. A recent large-scale study examined gross cortical morphometry and subcortical structures in ASD (Van Rooij, 2018). Here we examined whole-brain voxel-wise volumetric differences in ASD versus neurotypical controls in an unbiased manner as a knowledge of the specific brain structural changes associated with ASD may aid in diagnosis and therapy for ASD. We investigated voxel-wise brain correlates of ASD, including subgroups stratified by sex. We used a mega-analysis approach based on voxel-based morphometry (VBM) across multiple independent publicly available databases.

Methods: We analyzed 3D T1-weighted structural brain MRI data from 3,407 participants (1,730 with autism, 1,677 neurotypical controls; 76% male; age: 4-64 years) across 47 publicly available datasets from the Autism Brain Imaging Data Exchange (ABIDE), NIMH Data Archive (NDA) and Healthy Brain Network (HBN). Regional gray and white matter morphometry was quantified voxelwise using the CAT12 segmentation and analysis toolbox. A regression analysis was carried out at each voxel across the brain, to assess gray and white matter volume differences between the ASD and neurotypical groups, using the multiple regression equation: $y=\beta 0+\beta dxdx+ \beta ageage+\beta agesquaredagesquared+\beta sexsex+\beta ICVICV+\beta SiteSite+\varepsilon$ Here the dependent variable 'y' is a vector representing voxel-wise gray and white matter volumes, dx denotes diagnosis of ASD, agesquared is the squared variable for de-meaned age as recommended in prior studies, ICV denotes intracranial volume and S denotes site. The error term ε accounts for unobserved factors and measurement error.

Results: Relative to neurotypical controls, the ASD group showed significantly lower gray matter volumes in the frontal lobes, bilateral putamen, amygdala, thalami and cerebellum. White matter volumes were also lower in the forceps minor, forceps major, genu and splenium of corpus callosum, and the brain stem in the ASD group. Within the stratified group of females (smaller in number than the males), we detected no significant differences in gray matter between ASD and controls. However, we found minimally lower white matter volume (standard-FDR critical P-value=0.001; q=0.05) in the brainstem. Within the larger male cohort, significantly smaller gray matter volumes in frontal lobes, amygdala, thalami and cerebellum were noted in ASD compared to neurotypicals (standard-FDR critical P-value=0.004; q=0.05). Males with ASD also exhibited significantly smaller white matter volumes than neurotypical males (standard-FDR critical P-value=0.02; q=0.05) in the forceps minor, forceps major, genu and splenium of the corpus callosum, and the brain stem.

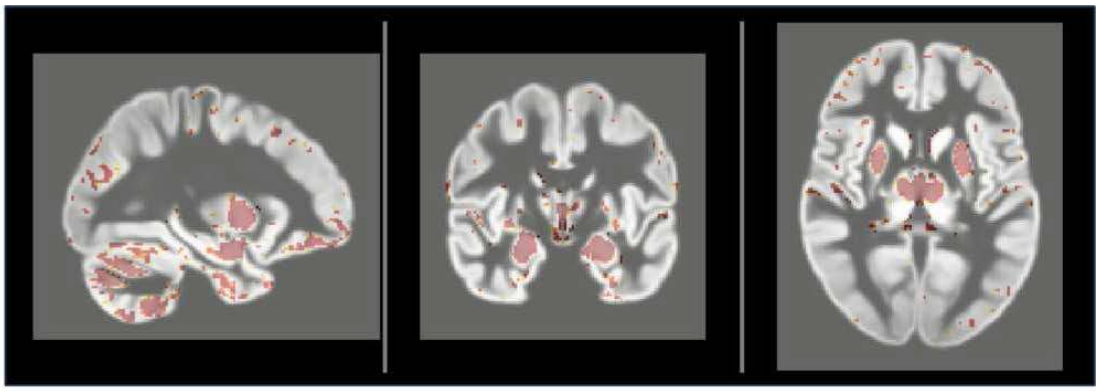

Figure 1. Alterations of gray matter regions in ASD compared to NT .

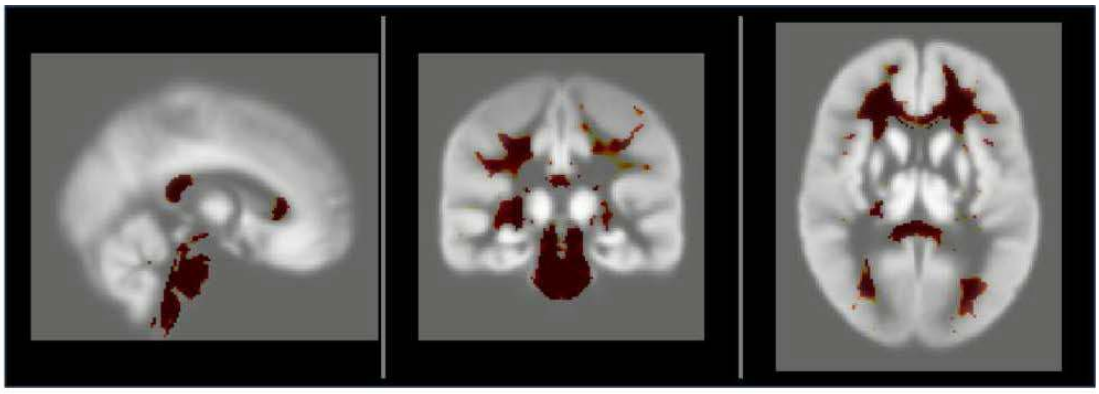

Figure 2. Alterations of white matter regions in ASD compared to NT.

Conclusions: Our big-data mega-analysis demonstrates voxel-wise brain structural associations of ASD. The smaller sample size likely contributed to less significant associations within the female cohort. Lower gray matter volumes include key regions previously implicated in ASD, including the amygdala (Van Rooij, 2018), cerebellum (Wang et al., 2016) and white matter alterations within the corpus callosum (Loomba et al., 2021) and brainstem (Hanaie et al., 2016), align with findings in the ASD literature. Although limited by a cross-sectional design, our findings offer insight into regional brain differences in ASD. Our study underscores the need to recruit more female participants and evaluation of sex-specific neurobiological characteristics in ASD.

References

1. Hanaie R., et al., (2016), "White matter volume in the brainstem and inferior parietal lobule is related to motor performance in children with autism spectrum disorder: A voxel-based morphometry study," Autism Research, vol. 9, no. 9, pp. 981–992.
2. Loomba, N., et al., (2021), 'Corpus callosum size and homotopic connectivity in Autism spectrum disorder,' Psychiatry Research: Neuroimaging, vol. 313, p. 111301.
3. Van Rooij, D., et al. (2018), 'Cortical and Subcortical Brain Morphometry Differences Between Patients With Autism Spectrum Disorder and Healthy Individuals Across the Lifespan: Results from the ENIGMA ASD Working Group,' AJP, vol. 175, no. 4, pp. 359–369.
4. Wang, S.S., et al., (2016), 'The cerebellum, sensitive periods, and autism,' Neuron, vol. 83, no. 3, pp. 518-532.

Poster No 450

Development of microstructural correlations of white matter in ASD between 6-24 months

Sooyeon Sung[1], Jed Elison[1], Brittany Howell[2]

[1]University of Minnesota, Minneapolis, MN, [2]Virginia Tech, Roanoke, VA

Introduction: Neuroimaging studies suggest that autism spectrum disorder (ASD) is associated with altered white matter microstructure. Evidence from prospective studies demonstrated that infants later diagnosed with ASD had higher fractional anisotropy (FA) values at 6 months, but lower FA values at 24 months compared to infants not diagnosed with ASD. Most studies, however, focus on group differences in the mean values of DTI parameters rather than inter-tract correlations. Some previous studies have shown that the network inefficiency and less coherent white matter microstructure linkage pattern are observed in ASD participants. This study examined the development of white matter correlations in infants diagnosed with ASD later (ASD+) compared to infants not diagnosed with ASD (ASD-) based on FA as quantified using diffusion MRI (dMRI).

Methods: The data was collected as part of the Infant Behavior Imaging Study (IBIS), an ongoing longitudinal study investigating brain and behavioral development in infants at high and low familial likelihood for developing ASD. The total sample included 324 (276 ASD-, 48 ASD+), 340 (296 ASD-, 44 ASD+) and 311 (261 ASD-, 50 ASD+) participants at 6, 12, and 24 months, respectively. Diagnostic classification of ASD was determined at 24 months using DSM-IV-TR criteria. Diffusion MRI was collected at four US sites using Siemens 3T TIM Trio MR scanners using a 12-channel head coil. The dMRI sequence was acquired as an ep2d_diff pulse sequence (TR=12,800–13,300ms, TE=102ms, b=0 - 1,000 s/mm2, 25 gradient directions, 2mm res). Tracts were traced as previously described. Tracts are shown in Figure 1. First, the mean FA value of each tract was compared between the ASD- and ASD+ groups at each time point using pair-wise t-test. Second, correlation coefficient between each tract and every other tract was calculated for the ASD- and ASD+ groups and the equality of two correlation matrices were tested by Jennrich's test at each time point. Lastly, each correlation coefficient was transformed to z-score using Fisher's r-to-z transformation and the differences of the pairwise inter-tract correlations between the ASD- and ASD+ groups were tested using z-test at each time point.

Results: The mean FA value of each tract did not significantly differ between the ASD- and ASD+ groups at any time point (the lowest $p = 0.18$ FDR corrected). The examination of correlation coefficient matrices showed overall significant differences in the inter-tract correlation matrices between the ASD- and ASD+ groups at all time points ($ps < .000$). (Figure 2) Compared to the ASD- group, the ASD+ group had stronger inter-tract correlations at 6 months but had weaker inter-tract correlations at 24 months. Finally, the examination of discrete entries of the correlation matrices using z-test showed differences between the ASD- and ASD+ groups at 24 months. The inter-tract relatedness of left cingulum to bilateral arcuate and uncinate was decreased in the ASD+ group at 24 months ($ps < .05$ uncorrected). The inter-tract relatedness of the body of the corpus callosum to bilateral CST, ALIC, and ATR was also decreased in the ASD+ group at 24 months ($ps < .05$ uncorrected). (Figure 2)

Conclusions: The results support the importance of investigating inter-tract relatedness given that the differences in white matter development between the ASD- and ASD+ group were observed in the inter-tract correlations rather than in the mean values of the DTI parameter. The decreased in inter-tract correlations in the ASD+ group at 24 months is consistent with previous findings that showed decreased network efficiency in ASD group. The decreased correlations observed in the cingulum, arcuate, and uncinate and the corpus callosum, CST, ALIC, and ATR are particularly interesting because those

tracts have been related to the symptom of ASD. In future studies, the relation of the decreased correlations to ASD symptom severity can be examined.

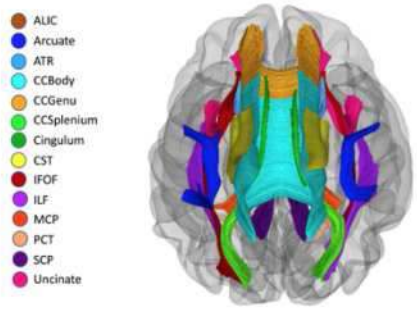

Figure 1: White matter fiber bundles.
All white matter bundles tracted and included in the current study. Key: ALIC - anterior limb of the internal capsule; Arcuate – arcuate fasciculus; ATR – anterior thalamic radiation; CCBody – body of the corpus callosum; CCGenu – genu of the corpus callosum; CCSplenium – splenium of the corpus callosum; Cingulum – cingulum bundle; CST – corticospinal tract; IFOF – inferior fronto-occipital fasciculus; ILF – inferior longitudinal fasciculus; MCP – middle cerebellar peduncle; PCT – pontine crossing tract; SCP – superior longitudinal fasciculus; Uncinate – uncinate fasciculus.

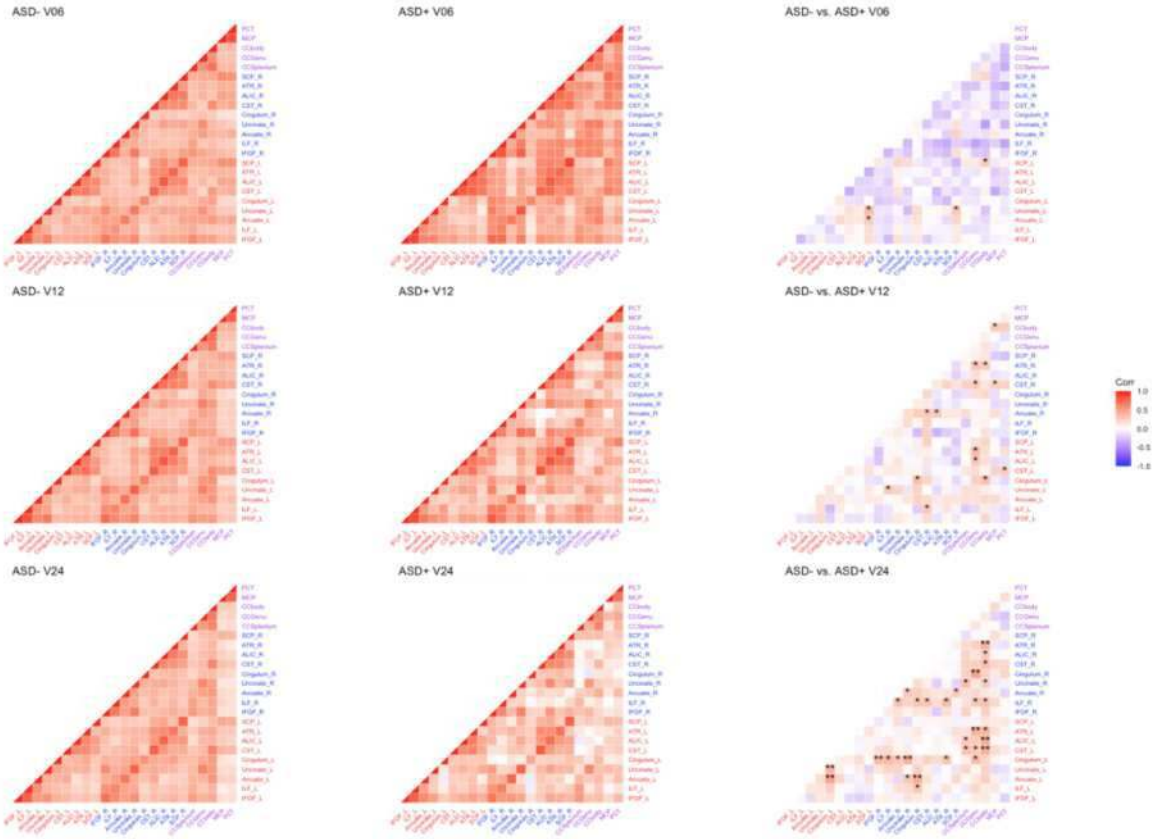

Figure 2. Inter-tract correlation matrices and between-group difference matrices. The z values from between-group difference test were inverse transformed to r in this figure. Asterisk in the between-group difference matrices represent significant differences. * < .05, ** <.001 (FDR uncorrected)

References

1. Wolff, J. J., Gu, H., Gerig, G., Elison, J. T., Styner, M., Gouttard, S., ... & Evans, A. C. (2012). Differences in white matter fiber tract development present from 6 to 24 months in infants with autism. American Journal of Psychiatry, 169(6), 589-600.
2. Lewis, J. D., Evans, A. C., Pruett, J. R., Botteron, K., Zwaigenbaum, L., Estes, A., ... & Dager, S. (2014). Network inefficiencies in autism spectrum disorder at 24 months. Translational psychiatry, 4(5), e388.
3. Dean III, D. C., Travers, B. G., Adluru, N., Tromp, D. P., Destiche, D. J., Samsin, D., ...Lainhart, J.E., & Alexander, A.L. (2016). Investigating the microstructural correlation of white matter in autism spectrum disorder. Brain connectivity, 6(5), 415-433.
4. Zhao, Y., Yang, L., Gong, G., Cao, Q., & Liu, J. (2022). Identify aberrant white matter microstructure in ASD, ADHD and other neurodevelopmental disorders: A meta-analysis of diffusion tensor imaging studies. Progress in Neuro-Psychopharmacology and Biological Psychiatry, 113, 110477.

Organization for
Human Brain Mapping

Advancing Understanding of the Human Brain

ORGANIZATION FOR HUMAN BRAIN MAPPING

www.humanbrainmapping.org

1935 County Road B2 W, Ste 165
Roseville, MN 55113
info@humanbrainmapping.org
952-641-2294